IMDC-IST 2021

Proceedings of 2nd International Multi-Disciplinary Conference
Theme: Integrated Sciences and Technologies

Sakarya, Turkey
7-9 September 2021

EDITORS

Abd-Alhameed Raed
A. Al-Hussaibi Walid
Rana Zubo

CORE

EAI
RESEARCH MEETS INNOVATION

Proceedings of the 2nd International Multi-Disciplinary Conference: "Integrated Sciences and Technologies"

7-9 September 2021, Sakarya, Turkey

IMDC-IST 2021

General Chairs

Prof. Raed A. Abd-Alhameed, University of Bradford, UK
Prof. Rabee H. Alabbasi, Southern Technical University, Iraq

Technical Programme Chair

Prof. Alaa F. Abdulahad, Southern Technical University, Iraq
Prof. Walid A. Al-Hussaibi, Southern Technical University, Iraq
Dr. Rana Zubo, University of Bradford, UK, and NTU, Iraq

Preface

We are delighted to introduce the proceedings of the second edition of the International Multi-Disciplinary Conference Theme: "Integrated Sciences and Technologies" (IMDC-IST-2021). This conference has brought researchers, developers and practitioners around the world who are leveraging and developing the rise of Big Data, Artificial Intelligence powered applications, Cognitive Communications, Green Energy, Adaptive Control and Mobile Robotics towards advance future technologies. In addition of digital health, well-being, home care, and patient-centred era for the benefit of patients and healthcare providers.

The technical program of IMDC-IST-2021consisted of 158 full papers. The conference tracks were: Track 1 - Engineering Technologies; Track 2 - Health and Medical Sciences; Track 3 - Agricultural and Water Sciences; Track 4 - Computational and Informational Sciences; Track 5 - Energy and Climate Change; Track 6 - Finance and Business Technologies; Track 7 - Green Industrial Technology; Track 8 - Natural Sciences and Technology; and Track 9 - Virtual Education, e-Learning Techniques, and Social Sciences. Aside from the high-quality technical paper presentations, the technical program also featured eight keynote speeches, five invited talk and three technical workshops. The five keynote speakers were Prof. Hakan S. Soyhan (Sakarya University, Turkey); Dr. Mansour Al Qubeissi (Coventry University, UK); Prof. Walid A. Al-Hussaibi (Southern Technical University, Iraq); Prof. Nadir A G Ahmed (Idvac Ltd, Ex-Visiting Professor at Salford University); Dr. Luis Sanabria-Russo (Centre Tecnològic de Telecomunicacions de Catalunya – CTTC, Spain).

The three workshops organized were

1. the EERT 2021 – 6th International Workshop on Energy Efficient and Reconfigurable Transceivers (EERT): Towards a Green Internet of Things. The Committee Chair: Prof. Raed Abd-Alhameed, University of Bradford, UK.
2. Importance of eLearning & Blended Learning in Institutes of Higher Education (eLBL-IHE 2021). The Chair: Dr. Rami Hikmat Al-Hadeethi, Vice President of International Relations, University of Victoria, UK.
3. Plasma Technology for Surface Engineering and Medical applications The Chair: Prof. Nadir A G Ahmed. Idvac Ltd, Ex-Visiting Professor at Salford University.

Coordination with the steering chairs, Prof. Raed A. Abd-Alhameed and Prof. Rabee H. Alabbasi, was essential for the success of the conference. We sincerely appreciate their constant support and guidance. It was also a great pleasure to work with such an excellent organizing committee team for their hard work in organizing and supporting the conference. In particular, the Technical Program Committee, led by our TPC Chairs, Prof. Alaa F. Abdulahad, Prof. Walid A. Al-Hussaibi and Dr. Rana Zubo who have completed the peer-review process of technical papers and made a high-quality technical program.

We strongly believe that IMDC-IST-2021 conference provides a good forum for all researcher, developers and practitioners to discuss all science and technology aspects. We also expect that the future IMDC-IST conference will be as successful and stimulating, as indicated by the contributions presented in this volume.

Prof. Raed A. Abd-Alhameed, Prof. Walid A. Al-Hussaibi and Dr. Rana Zubo

Conference Organization

Steering Committee

Prof.Dr. Yuliandri, SH, MH	Universitas Andalas, Indonesia
Dr.-Ing. Ir. Uyung Gatot Syafrawi Dinata, M.T	Universitas Andalas, Indonesia
Prof. Emy Susanti, MA	Asosiasi Studi Wanita, Gender dan Anak Indonesia
Dr. Jendrius, M.Si	Universitas Andalas, Indonesia

Organizing Committee

Chair Person

Dr. Ike Revita, M.Humi	Universitas Andalas, Indonesia

Vice Chairperson

Rozidateno Putra Hanida, S.IP, MA	Universitas Andalas, Indonesia

Vice Chairperson

Dr. Yuerlita	Universitas Andalas, Indonesia

Treasurer

Dra. Yunarti	Universitas Andalas, Indonesia

Secretary

Andri Rusta, S.IP, M.PP	Universitas Andalas, Indonesia

Secretariat

Desmaisi, S.Sos, M.Si	Universitas Andalas, Indonesia
Adek Albusra	Universitas Andalas, Indonesia
Silvia yanasti, S.Sos, M.Si	Universitas Andalas, Indonesia
Alqadrifal Permana	Universitas Andalas, Indonesia

Program Chair

Vonny Indah Mutiara, Ph.D	Universitas Andalas, Indonesia

Conference Programmer

Putiviola Elian Nasir, S.S., MA	Universitas Andalas, Indonesia
Dr.dr. Dien Gusta Anggraini Nursal, MKM	Universitas Andalas, Indonesia
Yantri Maputra, Ph.D	Universitas Andalas, Indonesia
Seswita, SS, M.Hum	Universitas Andalas, Indonesia
Dr. Rima Devi, S.S, M.Hum	Universitas Andalas, Indonesia

Publication Chair

Dr. Sri Setiawati, M.A	Universitas Andalas, Indonesia

Publication and Proceeding

Maryam Jamilah, S.IP, M.Si	Universitas Andalas, Indonesia

Logistic and Venue Chair

Dr. Yessy Markalinda, S.Si, M.Repro	Universitas Andalas, Indonesia

Logitic and Venue

Melisa yenti, SKM, MKM	Universitas Andalas, Indonesia
Anggela Pradiva Putri, SKM, MKM	Universitas Andalas, Indonesia

Suci Maisyarah Nasution, S.ST, MKM	Universitas Andalas, Indonesia

Scientific Board

Prof. Dr. Siti Kusujiarti	Warren Wilson College, Unites States
Dr. Adis Duderija	Griffith University, Australia
Prof. Dr. Emy Susanti, M.A	Universitas Airlangga, Indonesia
Prof. Dr. Ir. Keppi Sukesi, MS	Universitas Brawijaya, Indonesia
Dr. Ir. Arianti Ina Restiani Hunga, M.Si	Universitas Kristen Satyawacana, Indonesia
Prof. Evelyn Blackwood	Purdue University, United States
Prof. Dr. Ir. Rudi Febriamansyah, M.Si	Universitas Andalas, Indonesia
Prof. Dr. Afrizal, M.A	Universitas Andalas, Indonesia
Prof. Alimatul Qibtiyah, M.A, Ph.D	UIN Sunan Kalidjaga, Indonesia
Prof. Dr. Ir. Yonariza, M,Si	Universitas Andalas, Indonesia
Dr. Jendrius, M.Si	Universitas Andalas, Indonesia

Contents

1-Engineering Technologies

Protection of Copper Alloy Condenser Tubes by Coating 1
Wasan Alkaron, Qais A. Reshack

Application of Drucker-Prager Plasticity Model for Concrete Confined with Fiber Reinforced Cementitious Mortar (FRCM) 17
Ali Hadi Adheem, Majid M.A. Kadhim, Akram Jawdhari, Mohammed J. Altaee

Optimal Operation of Energy Hub with high penetration of renewable energy sources 26
Patrick Sunday Onen, Geev Mokryani, Rana H.A. Zubo

Shunt Active Power Filter Implementation Using PQ Theory With LabView 37
Faisal Falah Aiwa, Mahmood T. Alkhayyat, Mohammed Y. Suliman

Using Treated Recycled Demolition Aggregate in Concrete 49
Safana Qahtan Ragab, Hasan Jasim Mohammed

Using Geographic Information System (GIS) as a Supporting Tool in Public Facilities Planning: A Case Study on the City of Nasiriyah 55
Ahmed Salman Hasan, Khaldoon T. Falih

Wi_Fi Positioning Utilizing Triangulation Strategies and AoA In Indoor Environments 64
Zahraa Abbas, Mahmood F Mosleh, Faeza A. Abed

Novel Technical Design Of An Early Protection System For An Electronic Fuel Injection System 76
Abdullah J. H. Al Gizi, Saadi faisal radhi, Yaerobe Mohammed Mthbob

Implementations of Smart Cities in USA, Europe, and the Far East Countries 85
Fatima AlQaoud, Andrew Carruthers, Mumtaz Kamala

Analysis of Load flow and Transient stability of 10-bus multi-machine system with PV penetration 97
Sarah Alasady, Rasheed Almansory, Haider Alrudainy

Hierarchical Feature Mining for Image Classification and Segmentation 108
Hayder Yousif, Zahraa Al-Milaji

Energy Saving by Reinforcement Learning for Multi-Chillers of HVAC Systems 118
Lubna A. Hussein, Adnan A. Ateeq, Raad Z. Homod

The Impact of the Vane Angle on the Hydraulic Behaviour Around the Cylinder 140
Tahseen Ali Jabbar, Rafi M. Qasim, Bassam A. Mohammed

Design And Analysis of New Compound Journal Bearing 150
Nadhim N., Mahmood R

Particle Swarm Optimization for Maximum Power Point Tracking Under Varying Atmospheric Conditions 162
Ali Nasser Hussain, Alaa Mokdad Talib

Thermal cooling analysis of single Li-ion battery cell with elliptic heat sink with perforation 172
Karim Egab, Mushtaq Talib Hamzah, Hayder Hasan, Ali Lateef Tarish

UWB Radar Technology 183
Imran Ahmad, Raed Abd-Alhameed

New Trends in Location-Based Services Technology 196
Imran Ahmad, Raed Abd-Alhameed

Radar Recognition Using Pulse Repetition Interval Technology 206
Imran Ahmad, Raed Abd-Alhameed

A Planar Multi-Antenna Design Supporting 3.4-4.2 GHz for 5G Smartphone Applications 215
Naser Ojaroudi Parchin, Raed Abd-Alhameed

F-Shape Dual-Band MIMO Antenna System for Next-Generation Smartphone Applications 226
Atta Ullah Atta Ullah, Raed Abd-Alhameed

Infrared Imagery and Border Control Systems 236
George Kumi Kyeremeh, Raed A Abd-Alhameed

The Impacts of Depth Camera and Multi-Sensors for Face and Fingerprint Recognition in 2D and 3D - A Case Study 249
Mohamed Abdul-Al, George Kumi Kyeremeh, Raed A Abd-Alhameed

Design of Optimum Microstrip to Substrate Integrated Waveguide Transition 262
Nassir Guellil, I T.E Elfergani, Raed A Abd-Alhameed

UHF Radio Channel Measurements and Prediction for Maritime Communications 271
F. Salazar Quiñonez, M. Abdulaziz, Raed Abd-Alhameed

Beam Steering of Wearable Antenna with Metamaterial Structures for Patient Monitoring 281
Parisa Shirvani, Farzad Khajeh Khalili, Raed A Abd-Alhameed

A GaAs pHEMT MMIC Doherty Power Amplifier for 5G Mobile Handset 291
Maryam Sajedin, Issa Elfergani, Jonathan Rodriguez, Raed Abd-Alhameed

Planar Monopole UWB Antenna for Microwave Medical Image System 300
Adel Y.I. Ashyap, Z. Z. Abidin, S. H. Dahlan

Wear Resistance of Gray Cast Iron Under High-Temperature Conditions 308
Ali A. G. Alkhafaji

Deep Learning for Self-Driving Vehicles 322
Safa Jameel Dawood Al-Kamil, Mohammed Salah Al-Radhi

Design a High Transmission FSS Structure for THz Applications 329
Muaad Hussein, Haider Alrudainy

Design and simulation of Hybrid Renewable Energy System for on-grid applications 339
Ali S. Saleh, Rakan Khalil ANTAR, Ahmed J. Ali

Smart energy management of Wind/PV/Battery renewable energy sources based on IoT 355
Ahmed Abdul Nasser, Emad Ahmed Mohammed, Ahmed Jadaan Ali

Dynamic Voltage Restorer Using (PQ) Theory with LabView 372
Mohammed Y. Suliman, Mahmood T. Alkhayyat, Ibrahim F. Fakhraldeen

Crime Prediction Using Big Data Analysis 383
Hussam Hashim Hussein, Ahmed Talib Abdulameer

Autonomous Control of Multi-Speed Split Unit Air Conditioning for Space Load Response 393
Wasan Asaad Jwad, Ali Lateef Tarish

Performance enhancement of Dicode Pulse Position Modulation System by means of LDPC code 404
Yasmeen M. Hussein, Basman M. Al-Nedawe, Ammar Hussein Mutlag

Numerical Study of flow-through the perforations for angle perforation 180° and 90° in horizontal wellbore 413
Mohammed A. Mustafa, Qais A. Rishak, Mohammed A. Abdulwahid

Dual-layer Antifouling Membrane of Electrospun PAN: PMMA Nonwoven Nanofibers for Oily Wastewater Treatment 428
Sura M. Alkarbouly, Basma I. Waisi

An Integrated GIS and Satellite Image-based Model using a Reduced Simple Ratio Index for Evaluating the Efficacy of the Hammer Marsh Restoration Plan 439
Mahmoud S. Al-Khafaji, Imzahim A. Alwan, Bayda A. Dhaidan

Performance and Analysis of the Altitude for Optical Channel Drones 447
Abdullah Jameel Mahdi, Wamidh Jalil Mazher, Osman Nuri Ucan

Practical Performance Investigation of the Solar (PV) Panel System of the Electronic and Control Engineering Department – Kirkuk 456
Montassar Aidi Sharif, Mahmoud Shakir Wahhab, Kaesar Sabah Khalaf

Building Geo-Database for Geotechnical Properties of Thi-Qar Governorate Area Using Modern Digital Techniques 464
Kasim A.Abed Al-Abas, Sophia R. Al-timimy, Kamil Y. Husain

Intelligent Controller Design of the Vehicle Sonar Tracking Checker Fault and Repair of High Voltage Transmission Line 476
Saja Raad Abdulbari Hani, Abdullah Al Gizi

Evaluation of the Iraqi Road Safety System in Light of Crash Severity Indicators 490
Ali A. Aldhalemi, Fadhil A. Abidi

Solving Suggested Problems using Grey Wolf Optimization 502
Nawras A. Issa, Zaid Alaa, Issa Ahmed Abed

Numerical Analysis by Computational Fluid Dynamic Simulation of Fluid Flow in A T- Junction 516
Marwa S. Luaibi, Mohammed A. Abdulwahid

Seismic Analysis of the Steel Frame with Rubber-Sleeved Bolt in the Column-Base Connections 533
Teeba A. Jassim, Amer M. Ibrahim, Bozhou Zhuang, Ibrahim A. Ali

Design of class-E Power Amplifier (PA) with minimum harmonious termination for Cellular phones 548
Zahraa Mohammed younis saed, Khalid Khaleel

Computational Fluid Dynamic Analysis of the Flow though T-junction and Venturi Meter 555
Enas Salman Taha, Mohammed A. Abdulwahid, Akeel M. Ali Morad

Performance Analysis of Various SDN Controllers with Different Network Size in SDWN 563
Fidha Ezzaldin Aslan, Mohammed Basheer Al-Somaidai

A New Version of Modified Camel Algorithm for Engineering Applications 574
Ramzy S. Ali, Jawad R. Mahmood, Hussein M. Badr

Comparison and Assessment of Two Load Flow Methods for Optimum Under Voltage load Shedding in Distribution Power System 590
Waleed Khalid Shakir Al-Jubori, Ali Nasser Hussain

Doppler Shift Effect with Non-Orthogonal Multiple Access Technology for 5G System 605
Roaa Ali Hussein, Saad Ahmed Ayoob

A literature Survey on Well-known Algorithms of Optimum Power Flow 620
Baqer Atiyah Allamey, Falah Jaber Kshash, Warid Warid Warid

Characterization of Iraqi crude oil using Aspen Hysys 638
Fatimah Azer Naji, Adnan A. Ateeq, Mohammed A. Al-Mayyahi

Experimental Study of the Wet Cooling Tower using Different Packing Materials 645
Alaa H. Hussein, Safaa H. Faisal, Bassam A. Mohammed

Numerical Study of the Effect of Orientation Angles on Combined Convection in a Cavity Contain Rotation Cylinder 656
Sana M Shrama, Falah Assi Abood, Sana J. Yaseen, Amani J. Majeed

5G Uplink Performance of Symbol-Based Schedulers with Network Slicing 669
Omar Ghanim Al Taee, Ali Othman Al Janaby, Younis M. Abbosh

Energy Management Optimization of Generators Using Modified Firefly Algorithm 680
Wafeeqa Abdulrazak Hasan, Issa Ahmed Abed, Diyah Kammel Shary

A Survey on Monitoring Water Quality by Aid of IoT 691
Ali Hadi Abdulwahid, Muwaffaq Jameel Salih

Design and implementation of control Cabinet Based Siemens S7-300 Programmable Logic Controller PLC 698
Basim Mohsin Abdulwahid Al-Najari

A Comparison Study of Velocity Controller of Indirect Field Oriented Control of Linear Induction Motor Drive Using Model Predictive Controller 718
Fatimah F. Jaber, Diyah K. Shary, Haider Alrudainy Alrudainy

Comparative Performance of mmWave 5G System for many Beamforming Methods 729
Shaymaa A. Ahmed, Saad A. Ayoob, Ali Othman Al Janaby

PC/PLC Based Simultaneous Running of More than One Laboratory Experiments Using WxPython and Pymodbus 738
Jawad Radhi Mahmood, Ramzy Salim Ali

Simulation of Indirect Field Oriented Control on 5-Phase Synchronous Reluctance Motor 752
Namariq Abdulameer Ameen, Ali Kadhim Abdulabbas, Habeeb Jaber Nekad Jaber Nekad

Network Utility Maximization for Information Frequency Adaptation in Vehicular Networks 772
Hayder M Amer, Hawraa H. Al Mohammed, Lyudmila Mihaylova

The effect of the electrode tool material type on the surface roughness and tool wear in EDM 784
Abbas Fadhil Ibrahim

Optimum Design Parameters with the Lowest Cost of Basra Refinery Kettle Reboiler 792
Husam J. Alsaemre, Adnan A. Ateeq, Ali N. Kalaf

Lightweight Authentication Protocol For Smart Healthcare 807
Saja A. Hussein, Issa Ahmed Abed, Zaid Alaa Hussien

Short Circuit and Stability Analysis of a Multi-Machine System with Wind Turbine Using the ETAP Program 819
Sara Ismail Abd-Al Huseen, Rushed Almansory

The Effect of Baffle Inclination on a Heat Recovery Ventilator Performance 833
Hawraa Imad Abdulhafedh, Saadoon Fahad Dakhil, Raed Sabri Hameed

Allocation and Sizing of the Distributed Generation for Power System Instability Prevention 847
Dhafer Mayoof Dahis

The Effect of Fins on the Performance of the Plate Heat Recovery Ventilator 859
Braihan Abdulwadood Salman, Sadoun Fahad, Raed Sabri

Position Control of the Surface Motor Based on Artificial Neural Network 871
Abdulhasan F. Abdulhasan, Rabee H. Thejel, Diyah K. Shary

Thermal Enhancement for Solar Water Heating System by Using Phase change Materials 880
Zahraa A. Abdalaali, Saadoon F. Dakhil, Tahsien A. Jabbar

Three-Stage Charging of Lead Acid Batteries by Artificial Intelligence Fuzzy Logic Controller 895
Abdullah J. H. Al Gizi, Wadullah Hatem

A PV generation system based on P&O MPPT algorithm and SVPWM inverter for standalone applications 906
Duha Khalf, Kadhim H. Hassan, Diyah K. Shary

Design of a Hexagonal Printed Monopole Antenna with Circular Slot for UWB Breast Cancer Imaging Applications 923
Salamatu Abubakar Ibrahim, Isah Musa Danjuma, Mohamed Abdul-Al, Raed Abd-Alhameed

Low profile Substrate Integrated Waveguide (SIW) wideband antenna for Ku-band Applications 930
Faris Mohammed Ali

Seismic Performance Assessment and Upgrading of Al-Karamah Teaching Hospital Building under 2017 Halabjah Earthquake 939
Haider A. Abass, Husain K. Jarallah

Effect of Imperfection Factors on Simulation of the Slender RC Columns Strengthened by SFR Using ABAQUS 956
Wameedh I. Braidi, Mohammed S. Al-Helfi

Flexural Behaviour of Recycled Demolition Waste Reinforced Concrete Beams 969
Husham Mohammed Rashid, Hasan Jasim Mohammed

Risk Factors of Glycaemia Control among Children and Adolescents with Type 1 Diabetes in Basra City/Iraq 977
Shukur Abdulkareem Mahmood, Majid A. Maatook, Dhaigham E. Aatwan

Implementation of LTE in Mosul city: problems and solution 985
Mahmood Samir Sadoon, Saad Ahmed Ayoob

Wireless Sensor Networks Applications, Challenges, and Security Requirements 996
Ali Hadi Abdulwahid, Muwaffaq Jameel Salih

Look-up Table Reduction for Subcarrier Activation in OFDM with Index Modulation Systems 1007
Abdulrahman Ikram Siddiq, Hussein Nadhem Fadhel

A review of Effect the Zinc Oxide deposition on Crystalline Silicon Solar Cells 1016
Ali Kadhim Naser, Dhafer Manea Hachim, Qahtan A Abed

Enhancing Battery Recharge Performance through an Intelligent MPPT for Photovoltaic Solar Panels 1031
Baqer Turki Atiyah, Naeib Faisal, Ali Idham Alzaidi

Speed Control of Permanent Magnet Synchronous Motor Using SVPWM Vector Control 1038
Doaa AL-Mansory, Issa Ahmed Abed, Diyah AL-Thammer

Improved Path Planning of Mobile Robot using Atom Search Optimization Algorithm 1051
Shahad M. Majeed, Issa Ahmed Abed, Alaa A. Al-Saffar

Multi-level Chaos-Shift-Keying for Non-Orthogonal Multiple Access with Physical Layer Security 1063
Walid A. Al-Hussaibi, Israa M. Al-Musawi, Falah H. Ali

The Prevalence of Cryptosporidium in rivers water in Basra Province 1073
Mahmoud S. Thamer, Maitham H. Shanoot, Wathiq A. Al-Rmadhan

Detection of Cryptosporidium spp. in Animals' Zoo of Basra City 1078
Mahmoud S. Thamer, Wathiq A. Al-Rmadhan, Maitham H. Shanoot

Ameliorating effect of Alteplase in bleomycin-induced pulmonary fibrosis in adult rats 1082
Mahdi M. Thuwaini

Assess the Extent to Which Nursing Staff Adhere to Safety and Prevention Measures Against the Corona Virus at Basra General Hospital / Iraq 1090
Farzdq Fakhir Gatae Al-husseinawi

Estimate some immunoglobulin's and complement cascade in pregnant women suffering from urinary tract infection 1100
Fidan Fikrat Ahmed

Virulence Characteristics and Antibiotic Resistance of Klebsiella pneumoniae Isolated from Clinical Sources 1106
Mohammed Hussein Amer, Hasan Abd Ali Khudhair, Khwam R Hussein

Assessment of Hepatitis C virus (HCV) associated with hemodialysis patients in Thi-Qar province, Iraq 1118
Ali Abdulhussein Khalaf, Khwam R Hussein

Evaluation the Diagnostic Values of Direct and Indirect Non-invasive Biochemical Markers of Liver Fibrosis in Patients with Chronic Hepatitis B Virus 1128
Dawood Salman Mahdi

Investigating the Gene Expression Profiles of Immune Checkpoints in Breast Cancer Microenvironment and Peripheral Blood: A Comparative Study 1135
Howraa J Bakal, Khairallah A.S Mohammed, Naael H. Ali

Evaluation of Some Biomarkers in the Diagnosis and Severity Identification of Patients with COVID-19 1143
Haider Nasser Jabber, Mahdi Murshid Thuwaini, Hamed Jaddoa Abbas

Assessment of Physical and Chemical hazards Among Health Care Workers in Wasit Governorate 1150
Nassa Sattar Yaqoob Al-mayahi, Shrouk Abdulrazk Hassan Alibraheem, Alaa Kadhim Jasim

Development of a wireless power transfer system for electric vehicle charging using an E-Class power amplifier 1166
Ali Nasser Hussain, Sadik Kamel Gharghan, Rasha Majid Abd Al-nabe

Isolation and Identification of Dermatophytesis and Fungal Factors Samples from Infected Patients in Basra – Iraq 1178
Ahmed Hamid Dawood Alatbee, Entiha abdulzahra abdulkareem, Shafeeqa Abdusayed Obaid

Assessment of Preventive Measures Among Health Care Workers Regarding Nosocomial Infections in Kut City Hospitals 1184
Qasim Abbas Khyoosh Al.Eqabi, Shrouk Abdulrazak Hassan Al.Ibraheem, Tareq Mahdi AL.Qassab

Molecular Characterization of Staphylococcus Haemolyticus Isolated from Vaginitis and Some of Their Virulence Factors 1192
Enas R. Alwaily, Ruaa M. Khazaal, Mohammed H. Flaih, Khwam R. Hussein

Detection of Mutations in the 81 Bp RRDR of Rpob Gene in Mycobacterium Tuberculosis Clinical Isolates Using Xpert®MTB/RIF in Basra/Iraq 1201
Ghorob S Khudhair, Khairallah A.S Mohammed

Effect of Parvovirus B19 in Diabetes Mellitus Type 1 1207
Ahmed Hasan Mohammed, Alzahraa Albatool Ibrahim saber

Assessment of Existing Bond-Slip Models of Adhesively Bonded CFRP-Steel Joints 1213
Mohammed J. Altaee, Majid M.A. Kadhim, Sarmed A.S. Altayee, Akram Jawdhari

Effect of Ginger on Oxidative Stress Induced by Hydrogen Peroxide in Male Quail 1224
Abdullah F. Abdul-Majeed, Saeb Y. Abdul-Rahman

Screening of extracellular polymeric substance producing bacteria isolated from environmental sources and testing their ability to seal fractures zones of oil reservoir rocks 1233
Asaad Faraj Hamzah, Wijdan Hussein Al-Tamimi

Study the Extent of The Relationship Among Hormonal Disturbance, Vitamin D Deficiency and Age in Women with Polycystic Ovary Thi-Qar City, Southern Iraq 1243
Shalan H. Al-Saedy, Ali E. Al-Snafi

Investigation of the Effect of Diabetes on Lower Limb Muscles with Surface Electromyography (EMG) 1252
Mahmoud I. Al-Kadi

Clinical Significance of Some Tumour Biomarkers in the Diagnosis of Breast Cancer in Comparison with Histopathological Biopsy 1261
Adil Nadhim Radhi, Mahdi Murshd Thuwaini, Hamed Jaddoa Abbas

Determination of Y-aminobutyric acid (GABA) in Ziziphus Tuffahi fruit & Earmotiun 1267
Firas Jameel Jabbar

Paediatric Germ Cell Tumours: Case Study Oncology Centre of Basra Between 2004-2015 1275
Nayef J. Farhan Al-Khafaji, Wasan H. Saud Al-Ibadi, Aqila A. Sahi Kadhim

Evolution the Correlation Between the Severity of Cytomegalovirus Infection among Aborted Women with Vitamin D and Oxidative Stress Biomarkers 1282
Batool A. Hussein A. Hussein

Investigation of Vertical Ground Reaction Force during Walking with the Exoskeleton for Patient with Unilateral Lower Limb Weakness 1289
Niaam Kh. Al-Hayali, Jumaa S. Chiad, Somer M. Nacy

Time Trends of Noncommunicable Diseases Mortality in Basra province During 2010-2019 1296
Sadiq A. Rahmah, Shrouk Abdulrazak Hassan Alibraheem, Rajaa A. Mahmoud

Influence of Genetic polymorphism of IL-2 and IL-6 on susceptibility to Helicobacter pylori infection and prognosis of Gastroduodenal Diseases 1302
Khairallah A.S Mohammed, Methaq M. Neamah AL-Hilfi, Naael H. Ali

Comparison of toxic effects of some nonsteroidal anti-inflammatory medications on the kidney and lung tissues of rats 1313
Manal N. Al-Hayder N. Al-Hayder, Tamadir H. W. Aledani, Rafid A. Doulab A. Doulab

Agricultural and Water Sciences

Response of Apricot Trees to Ground Fertilization and Foliar Spraying 1322
Raad Taha Mohammed Ali, Akram Abdul-Kadhim Hadi, Mawahib Midhat Hussein

Computational and Informational Sciences

Flow Field Simulation between Angle Vane and Cylinder 1334
Rafi M. Qasim, Tahseen A. Jabbar, Ihsan A. Abdulhussein

NoSQL: Will it be an alternative to a relational database? MySQL vs MongoDB comparison 1353
Basit alyasiri, Bushra Sahi, Nassir AL-Khafaji

Evaluating The Effect of Intent Factors on the Student's Intention to Register for External Exams via The Internet: Directorate of Education in Dhi-Qar as A Case Study 1368
Mohammed Jaber Farhan, Bushra Sahi Chassab, Nassir Jabir Al-Khafaji

Precipitation Forecast for Thi-Qar Province of Iraq Utilizing Machine Learning Approaches 1378
Anwar Alnawas Alnawas, Nassir Jabir Al-Khafaji, Hayder Hussein Azeez

Smart Energy Metering Based on Arduino, GSM, and Raspberry pi3 as Server 1387
Doaa S. Al-sehail, Osama Y.K Al-Atbee, Ali Marhoon

Estimation of the Parameters by Using non-Bayesian in Modified Weibull Extension Distribution 1399
Shaima,a B. Yass, Iden H. Al Kanani

A Theoretical Study of the Supercontinuum Generation for the Photonic Crystal Fibre 1414
Mohammed Salim Jasim, Nadia Al-Aboody

A Survey on Physical Layer Security for FSO Communication Systems 1424
Wafaa Mohammed Ridha Shakir, Ruwaida A. Abdulkareem

A Recent update of phase change materials (PCM's) in cooling application 1435
Ahmed H. N. Al-Mudhafar, Ali Lateef Tarish

Fuel Cell 3D Contour Simulation of Serpentine Flow Field Inside Cubic Channels 1447
Akeel M. Ali Morad, Hala E. Obeed, Fatima A. Khalaf

Experimental and Theoretical study to improve the spark ignition engine performance 1458
Ali R. Badr, Saadoon F. Dakhil, Tahseen A. Jabbar

Accounting Education and Its Role in Light of Contemporary Trends in The Accounting Profession - An Applied Study 1468
Jenan Abd AL-Abbas Al Dulamy, Ade Ghani Hamadi

The effect of using fair value accounting in activating the Iraqi stock market (A field study on companies registered in the Iraqi market for financial markets) 1485
Nahla Ghalib Abdul Rahma, Abdulhussain Tofeeq Shibli, Jalil Ibrahim Salih

The Active Role of Servant Leadership to Improve Performance of employees 1504
Manal Abdul majeed Abdul Majeed, Haider jare Mahsen

Using Time Driven-Activity Based Costing TD-ABC approach for controlling 1521
Jaber H. Ali

Visual Management and its Impact on Reducing Wastage (3M) According to the Perspective of the Agile 7S Methodology: An Applied Study in Al-Rayan Company 1536
Hasshim Nayef Hashim, Hussam Abdulameer Mohammed Alsalman

A Comparison Between the International Standards PRINCE2 and PMBOK in Project Management 1549
Sana`a Hassan Zubon, Maher Kadhim Taher

Analytical Procedures and Their Impact on Reducing Audit Risks in the Auditor's Report 1561
Sawsan Fadel jassim, Alaa Fareed Abdulahad

The Role of Internal Control in Reducing Administrative and Financial Corruption Applied Research at the Technical Institute / Nasiriya 1576
Hamida Athab Khudair, Ali Khalaf Gatea

The Role of the Ethical Responsibility of Management in Promoting Financial Disclosure 1589
Ali Khalaf Gatea, Zina Hamza Gali, Amal Essa Abdullah

Box-Jenkins Modelling and Forecasting of WTI Crude Oil Price 1598
Maitham A. Rodhan, Adnan H. Jaaz

Bankruptcy Prediction: Evidence-based Experiences in the Banks 1611
Sanaa Hasan Hilo, Khelood A. Mkalaf

An Integrated Approach to Improving Strategic Performance Management in Higher Education: University of Kufa is a model from developing countries 1621
Ahmed Maher Mohammed Ali, Yasir Sahib Malik, Hassnain Kadhem Ojah

Sensitivity analysis of air-intake temperature on the performance of a gasoline engine of Daewoo prince (1800 cc) 1627
Hayder Mnati, Asaad Almayyahi, Mudhar Al-Obaidi

The Effect of Adopting Technology in Intellectual Capital 1636
Mustafa Abdullah Mohammed, Abbas Ali Muhammad, Alhamzah Alnoor, Marwa Al-Maatoq

The influence of financial critical success factors on project success: Evidence from several electric power projects in Iraq 1646
Aymen Raheem Abdulaali, Alhamzah Alnoor, Hadi Al-Abrrow, Hasan Oudah Abdullah, Sammar Abbas

Green Industrial Technology

Design, Simulation and Implementation High DC-DC Converter with 1-Phase Inverter Feeding Load from a Single Photovoltaic Panel 1658
Khalid Badr Yas

Examining Mechanical Properties of Recycled Aggregate Concrete 1670
Ali Alsalman Alsalman, Jamal Khudair, Rahman S. Kareem, Lateef Assi, Canh N Dang, Martí Vargas

Natural Sciences and Technology

Design for Sustainability & Product Differentiation An Empirical Study at SALSAL factory for Purified Water 1690
Abdul Salam Ibrahim Obeyed, Hamid Shakir Mahmoud

Synthesis and Study the Mechanical Properties for New Interpenetrating Polymer Network Based on HBPU/ECA 1708
Firas Jameel Jabbar

The physical properties of the addition of reinforcement metals of Aluminum and silica microparticles with unsaturated composite materials 1719
Najah Rustum Mohsin, Ahmed Sahib Mahdi, Ayad Abdul ameer Abdul ameer, Mohammad Sukri Mustapa

Virtual Education, e-Learning Techniques, and Social Sciences

The effect of electronic collective scientific conversations on developing creative thinking and the ability of discussion among technical university students 1729
Ethar Abdul muhsin Qasim Al- Mayyahi, Mowaffaq Abdulaziz Al-Hisnawi

An International Comparison of Responses to the Covid-19 Pandemic by Universities and Schools 1739
Fatima Al-Qaoud Al-Qaoud, Andrew Carruthers

Legalization of Cannabis Cultivation a Comparative Study 1759
Samer Hameed Safer

Visual Materials and their Impact on Students' Achievement during Virtual Learning 1767
Baan Jafar Sadiq

Protection of Copper Alloy Condenser Tubes by Coating

Wasan Alkaron[1], Qais A. Reshack[2]
{w.alkaron@stu.edu.iq[1], qais.rashck@uobasrah.edu.iq[2]}

Technical Institute of Basra, Southern Technical Unversity[1]
College of Engineering, University of Basrah[2]

Abstract. The protective coating acts as a layer against erosion, corrosion, and fouling associated with scale deposits. In this study, two laboratory test rigs were installed one for the corrosion rate estimation and another for evaluation of the heat transfer resistance. Three different types of epoxy resin were employed for coating tube surface interiors using different ratios of resin to solvent to produce different coat thicknesses. The results obtained from the corrosion rate and heat transfer resistance measurements showed that the epoxy coating type (a) (ratio of 2: 1 epoxy: solvent) is efficient in reducing the corrosion rate to $21.1x10^{-2}$ mpy; for example, the efficiency of 92.2% and the heat transfer resistance increased from $12.88x10^{-4}$ to $18.37x10^{-4}$ m^2K/W compared to other types of coating.

Keywords: condenser tube, copper alloy, corrosion rate, epoxy coating, heat resistance.

1 Introduction

The coating technique has been widely used in recent years to form a protective film by some resins. Internal tubes coated with thin-film thickness can improve the heat transfer rate and the overall performance of condenser tubes. The coating tends to inhibit the passage of oxygen through the coating which is inert to chemical or biological attack and protected from scaling and corrosion [1,2]. Tube coating offers an obvious advantage to re-tubing. The most advantages of coating are:

1. Tubes coating eliminated any further corrosive influence of the water upon the copper alloy tube surfaces. Therefore, tubes having up to 80% loss of metal can be successfully coated, re-condition, and returned to service.
2. The addition of thin-film produces no significant effect deterioration in heat transfer efficiency.
3. Depending on the application and fluid parameters, the polymer coating has a service life of 10-12 years.
4. The polymer will reduce the surface tension; this inhibits the attachment of foreign debris and microbiological growth to the tube wall.
5. Return plugged, leaking tubes to the service. Plugging can cause side effects such as heart rate efficiency reduction, flow pattern changes, and increased velocity.
6. Produce a very economical alternative to retubing. Retubing of condenser tubes requires a long time, and it is very expensive, costing millions of dollars in large condenser units [3], [4].

IMDC-IST 2021, September 07-09, Sakarya, Turkey
Copyright © 2022 EAI
DOI 10.4108/eai.7-9-2021.2315501

2 Experimental Work

2.1 Specimens Preparation

A condenser tube segment each of 1.25 mm thickness and 25.40 mm outer diameter were taken from the Hartha power station. Tube samples used in the present experimental work were admiralty brass (AB)(C 44300) having the chemical composition shown in Table 1. The tubes are cut using an electric cutter into 21 pieces each 10 cm in length. These pieces are used to test the corrosion rate in the presence and absence of an epoxy coat. Seven samples of 1m are used 1m length were used for coating inner tubes with different epoxy resins to test the heat transfer resistance.

Table 1. The chemical composition of the used admiralty brass sample was taken from the Hartha power station condenser.

%Cu	%Zn	%Sn	%Fe	%Pb	%As
70.3	28.3	1.1	0.2	0.05	0.05

2.2 Specimens Coating Procedure

Before surface coating, the surface of tubes samples was subjected to the following procedure:

a) Washing and drying at room temperature.
b) Preparing coating material by blending epoxy resin, hardener, and thinner, using variable ratios of resin to solvent as 2:1 and 4:1, with a constant adding of hardener in each case in a ratio of 0.5 to facilitate curing of the epoxy. The tube samples were closed from one end and filled with a coating material. Then, the coating material was drained by rotating the tube samples which were left to dry for 24 hours at room temperature. Fig 1 shows the application of different coating materials on admiralty brass samples.

3 Corrosion Rate

Using the following equation, corrosion rates were calculated using weight loss methods under various parametric environmental circumstances of exposure duration and fluid velocity [5].

$$CR= (K*w)/ (T*A*D) . \quad (1)$$

Where CR is the corrosion rate (mpy), K is a constant ($3.45*10^6$), T is the time of exposure (hr), w is weight loss (g), A is surface area (cm^2) and D is the density of specimen (g/cm^3). The protection efficiency conferred by coat can be calculated from the following formula [5].

$$\% \text{ Efficiency} = (CR_o-CR_i)/ (CR_o)*100 . \quad (2)$$

Where CR_o and CR_i are the corrosion rates of the metal in the presence and absence of the coat. The corrosion rate of uncoated and coated samples with different thicknesses of epoxy resins

was estimated using the treatment test rig shown in Fig 2. All samples were connected using flexible tubes. The outer surfaces of tube samples were insulated by Teflon to eliminate oxidation due to exposure to atmospheric conditions. The corrosion rates were determined under various conditions of the exposure time and fluid velocity [6], [7].

Fig 1. Application of different coating materials on admiralty brass (a) Epoxy resin type (a), (b) Epoxy resin type (b), and (c) Epoxy resin type (c).

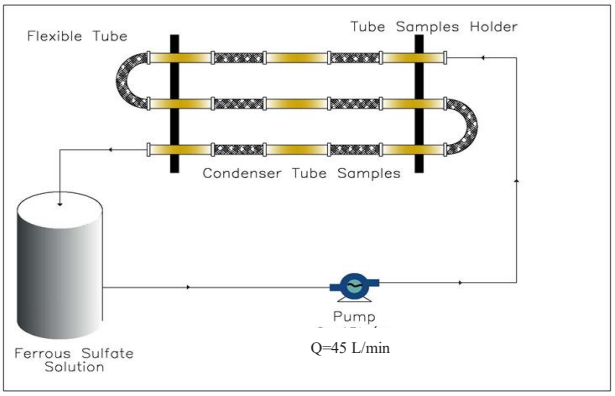

Fig 2. Schematic diagram of test rig used to estimate the corrosion rate.

3.1 Effect of exposure time

The samples' corrosion rates were calculated as a function of exposure time. The water velocity in the recirculation system was increased to 1.6 m/s. After a 7-day extension of the test period, the samples were removed from the rig and scales were removed with emery paper and cotton cloth. The corrosion rate was calculated using the weight loss determined. The experiment was then repeated for a total of seven days. All of the tests were carried out at a temperature of 25±2 °C degrees Celsius..

3.2 Effect of fluid velocity

The effect of velocity on the corrosion rate was studied at four different velocities (0.8, 1.2, 1.6, and 1.8 m/s), Fluid velocity was calculated as follow:

$$Q_t = V_m/t \, . \tag{3}$$

Where Q_t is the volumetric flow rate (m^3/s), V_m volume of a vessel (m^3), and t is the time(s).

$$u = Q_t / a \, . \tag{4}$$

The velocity (m/s) is given by u, while the cross-section area is given by a. (m2). To modify the specified velocity required in each situation, the flow rate was varied using a controlled valve. Each test velocity was performed for seven days at a pace of five hours each day. The corrosion rate was determined using the weight loss data. At a temperature of 27±2°C, the experiment was carried out.

4 Heat Transfer Resistance

A heat transfer resistance (HTR) test rig assembled in at college of engineering, Basra university shown in Fig 3 consisted of the following parts:

1. **Heating Element:** The coil resistance is placed within an electric insulator and wounded at a distance of 12 cm on the external surface of each test tube. To produce varied levels of heat power, three types of coil resistance were used. The heating

element is sealed off from the outside world, allowing all of the heat to pass through the tube wall and into a stream of running water from a reservoir.

2. **Thermocouples:** Three thermocouples were inserted under the heating element to measure the temperature of the heated surface (Ts), while the other two thermocouples were placed in the test tube's intake and outflow to measure the temperature of the bulk water (T_b).
3. **Cooling System:** It's a closed-loop system that includes a cooling water reservoir, two tiny centrifugal pumps, and a cooler. A bypass return to the related reservoir is used to manually control the flow to the test section. The water runs through the cooler after passing past the test portion. This cooler was used to keep the cooling water at the desired temperature before returning it to the reservoir.

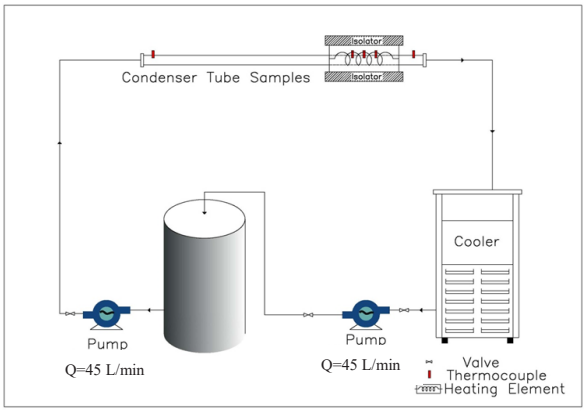

Fig. 3. The schematic diagram for the test rig was used to determine the heat transfer resistance.

The requirements of the thermal procedure can be detailed as:

1. Surface Finish: To remove tarnish coatings and provide a smooth, clean surface finish, all of the tested tube parts are abraded with emery paper grad 400. This was done to ensure that the HTR measurement was related to the inner diameter surfaces, rather than being confounded by tarnish layers on the outer diameter..
2. Temperature Readings: The average temperature readings of three thermocouples placed under the heating element were used to calculate the temperature of the heated surface (Ts). The average temperature readings of the entrance and outflow were used to determine the bulk water temperature (Tb)..
3. Heat Flux: The heating element applied a heat flux of 880, 726, 628 W via the external surface of the tube under test. Coil resistance was measured with a digital multimeter with an accuracy of (0.001m), and current was measured using a digital clamp metre with an accuracy of (0.001 A). The heating element's power input is equal to

Input Power = V*I. (5)

Or

$= I^2*R.$ (6)

4. Adjusted Velocity: Water was recirculated at a known velocity from the reservoir through the tested tube portion.

The following equation [8] was used to determine the heat transfer resistance HTR for each run:

$$HTR= (A (T_s-T_b))/Q \quad (7)$$

Ts is the temperature of the heated surface (K), Tb is the temperature of bulk water (K), and Q is the applied heat flux, where A is the area of the heated surface (m), Ts is the temperature of the heated surface (K), Tb is the temperature of bulk water (K), and Q is the applied heat flux (W). The HTR values for each tube were calculated using data from four separate test runs at four distinct velocities (0.8, 1.2, 1.6, and 1.8) m/s. The steady-state was reached in about 2 hours for each test run.

5 Determination of the Coating Thickness

It was aimed to determine the thickness of the applied epoxy resin coat on the inner tube surface. Therefore, tube thickness before and after coat application was measured to determine the thickness deference which refers to the thickness of the coat. The coated tube was longitudinally cut and the thickness was measured by Micrometer in different positions.

6 Results and Discussion

6.1 Corrosion Rate Measurement Results

Under dynamic test conditions, the exposure time and velocity were found to alter the corrosion rate results. Both of these factors are studied at specified working ambient conditions.

A) Effect of Exposure Time based on Corrosion Rate

The results of corrosion rate of admiralty brass (AB) tube samples coated with different types of epoxy resins (Case 1) type (a, b, and c) in which epoxy coating material having a ratio of 2:1 epoxy: solvent is shown in Fig 4. Although the coating material covered the whole surface, the surface still shows a very small value of corrosion rates. This can be attributed to the barrier properties and low permeability of the epoxy coating layer [8]. The corrosion rates at a test period of 35 days are (27.0, 18.8, and 14.8)*10^{-2} mpy, for epoxy (a, b, and c) respectively. Thus, it was found that the efficiency of each type of epoxy coating in reduction of the corrosion rate was 90.4 %, 93.3%, and 94.7% at 35 days maximum exposure time of for epoxy (a, b, and c) respectively, as compared with untreated samples. Therefore, type (c) epoxy resin showed a greater reduction in corrosion rate than types a and b.

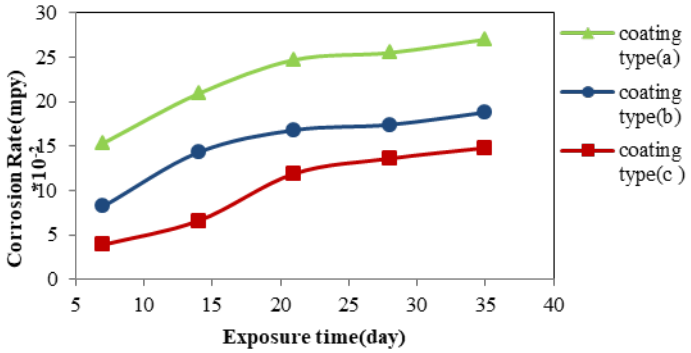

Fig. 4. Corrosion rate as a function of time for epoxy coated (Case1) types a, b and c, at velocity 1.6 m/s of filtered water, pH 7.6, at 25°C.

The comparison between the corrosion rate value of the three types of epoxy resins (Case2) types (a, b, and c) in which epoxy coating material having a ratio of 4:1 epoxy: solvent is shown in Fig 5.

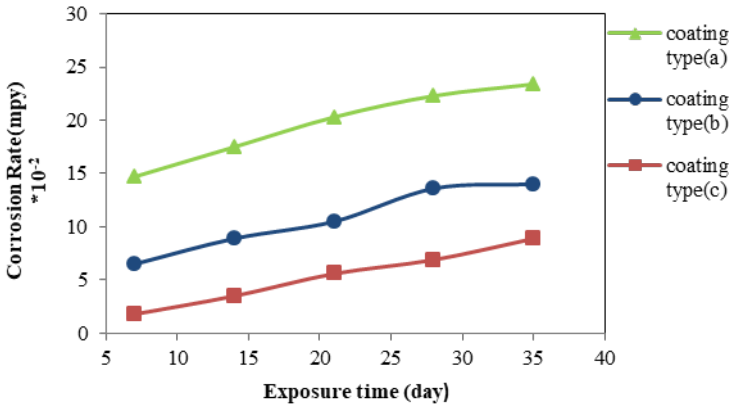

Fig. 5. Corrosion rate as a function of time for epoxy coated (Case2) types a, b and c at velocity 1.6m/s of filtered water, pH 7.6, at 25°C.

The results indicated that the corrosion rate was slightly increased with increasing exposure time, the coating materials tend to inhibit the passage of oxygen through the coating layer and reduced further corrosive influence of the environment [1,2]. The 35 days corrosion rates are (23.4, 14.0, and 8.9)x10^{-2} mpy for epoxy types (a, b, and c) respectively. The efficiency of each type of epoxy coating in reduction of corrosion rate was 91.7 %, 95.2%, 96.8% at a maximum exposure time of 35 days for epoxy types (a, b, and c)respectively, as compared with untreated samples. Thus, type (c) epoxy resin showed higher reduction efficiency the corrosion rate than types (a) and (b) i.e. it can be regarded as an excellent protective coating.

B) Effect of velocity on corrosion rate

The corrosion rates of the three types of epoxy resins (Case1) type (a, b, and c) are shown in Fig 6. The corrosion rates at a velocity of 1.8m/s are (21.1, 13.2, 7.8)x10^{-2} mpy for epoxy type (a, b, and c) respectively. The efficiency of each type of epoxy coating in reduction of corrosion rate was 92.2%, 95.1%, 97.1%, for epoxy types (a, b, and c) respectively, as compared with untreated samples. Thus type (c) epoxy resin showed a better reduction of corrosion rate than types (a and b). Comparison between corrosion rate of the three types of epoxy resins (Case 2) type (a, b, and c) are shown in Fig 7. The corrosion rates at maximum velocity used of 1.8m/s are (17.6, 10.2, 6.2)x10^{-2} mpy for epoxy type (a, b, and c) respectively, and it was found that the efficiency of the epoxy coating in minimizing the corrosion rate was found 93.5%, 96.2%, 97.7% for epoxy type (a, b, and c) respectively. Thus, type (c) epoxy resin exhibits a lesser corrosion rate and higher efficiency than types (a and b).

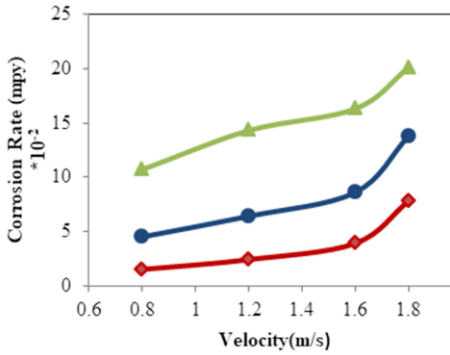

Fig. 6. Corrosion rate as a function of velocity for epoxy coating (Case1) types a, b and c, in filtered water for 7 days, pH 7.6, at 27°C.

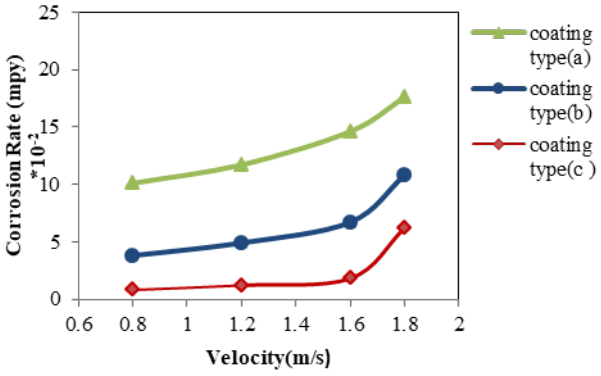

Fig. 7. Corrosion rate as a function of velocity for epoxy coating (Case 2) types a, b and c, in filtered water for 7 days, pH 7.6, at 27°C.

C) Comparisons of the Corrosion Rates

A comparison is made between the results of the corrosion rates of uncoated and coated samples, to select the best type of coating that reduces the corrosion rate to the minimum value.

i. By comparison of the corrosion rates values as a function of time for uncoated and coated samples, Figs 8 and 9 showed that epoxy coating (Case 2) type (c) is the best coat for reduction of corrosion rate of AB.

ii. By comparison the corrosion rate values as a function of velocity for uncoated and coated samples. Figs 10 and 11 showed that epoxy coating (Case 2) type (c) is the best coat for the reduction of corrosion rate of AB. This can be attributed to the high adhesive force against the turbulent flow, excellent corrosion resistance to flowing water, and excellent adhesion properties [10]. On other hand, it was showed that the corrosion rates of epoxy coating (Case 2) are lower than the corrosion rate of epoxy coating (Case 1), as the ratio of epoxy: solvent increased, the thickness of the coating film increased which result in a reduction of the corrosion rate. Since the heat transfer in condenser tubes is a very important factor, so select the best type of protective coating did not rely only on the reduction of the corrosion rate, but also depending on the loss of heat transfer rate imposed by the presence of coat layer, this will be discussed in the following section.

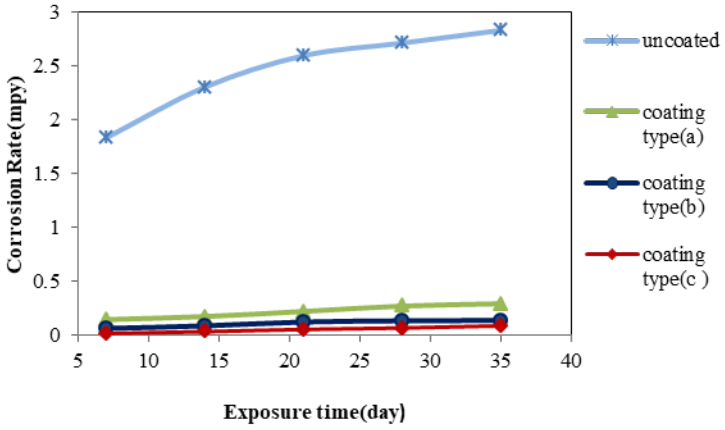

Fig. 8. Comparison of the corrosion rate with time for uncoated, coated admiralty brass with epoxy coating (Case 1) types a, b and c.

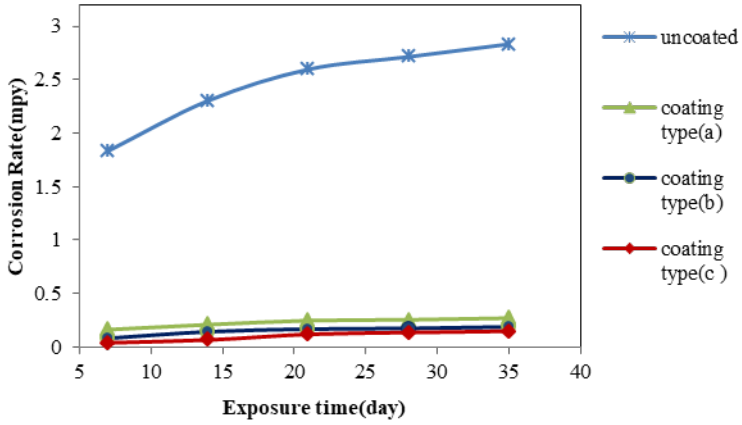

Fig. 9. Comparison of the corrosion rate with time for uncoated, coated admiralty brass with epoxy coating (Case 2) types a, b and c.

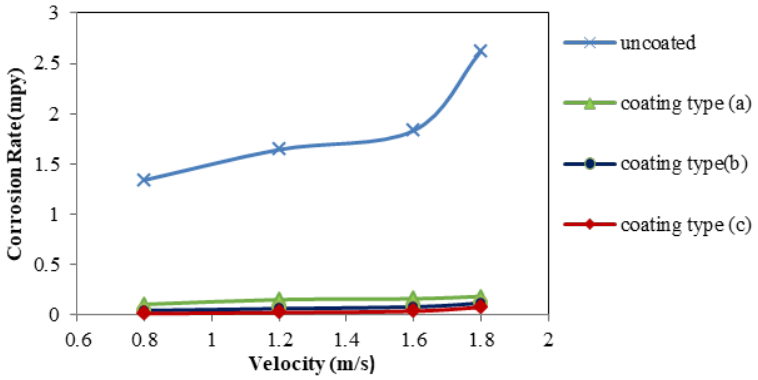

Fig. 10. Comparison of the corrosion rate with velocity for uncoated, coated admiralty brass with epoxy coating (Case 1) types a, b and c

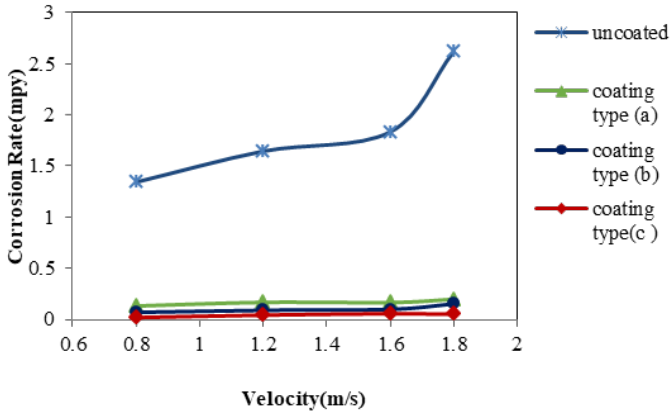

Fig. 11. Comparison of the corrosion rate with velocity for uncoated, coated admiralty brass with epoxy coating (Case 2) types a, b and c.

6.2 Resistance of Heat Transfer

Heat transfer resistance with a velocity of uncoated and coated AB tube samples with epoxy resins are shown in Fig 12 to Fig 18. In general, increasing water velocity led to a reduction of the heat transfer resistance, the amount of heat which able to flow through the wall tubes depended upon the temperature difference which exists between the heated surface and cooling water temperature. If the heat flux remains constant, the increased water velocity led to a reduction of temperature difference [11]. However, the temperature difference is a function of heat transfer rate, so lesser temperature difference led to higher heat transfer rate and lesser HTR [8]. The obtained results were found agreed well with that reported by Phull [8]. It was observed that increasing applied heat will led to reduction of heat transfer resistance in each type of (uncoated and coated) tube samples. This can be attributed to that the increase of the heat flux led to increase the amount of the heat transfer rate through the wall tubes, so that the heat transfer resistance values will be reduced [12].

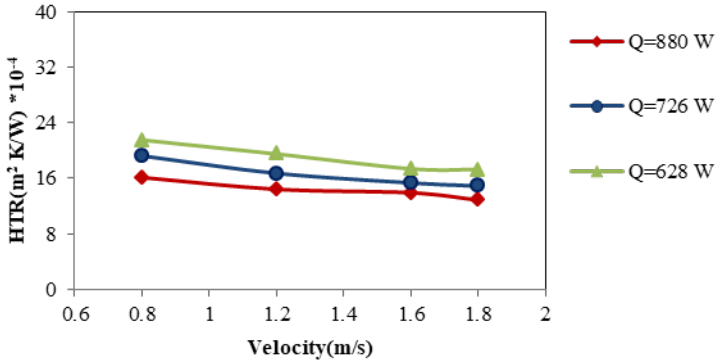

Fig. 12. Heat transfer resistance with velocity for uncoated admiralty brass tubes at different applied heat, at 30°C.

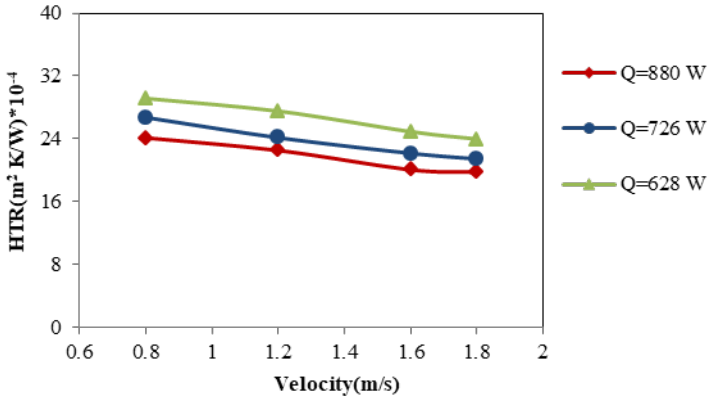

Fig. 13. Heat transfer resistance with velocity for epoxy coating (Case 1) type (a) at different applied heat, at 30°C.

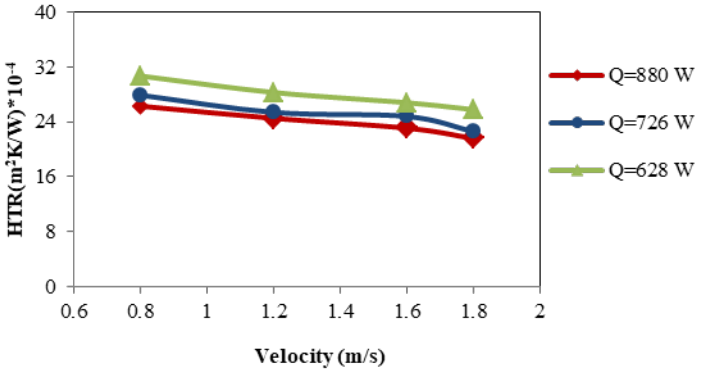

Fig. 14. Heat transfer resistance with velocity for epoxy coating (Case 2) type (a) at different applied heat, at 30°C.

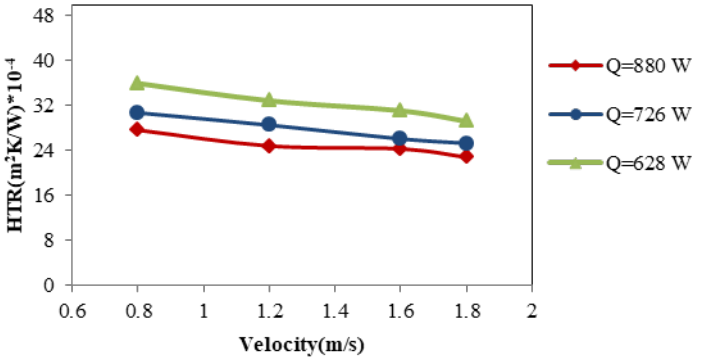

Fig. 15. Heat transfer resistance with velocity for epoxy coating (Case 1) type (b) at different applied heat, at 30°C.

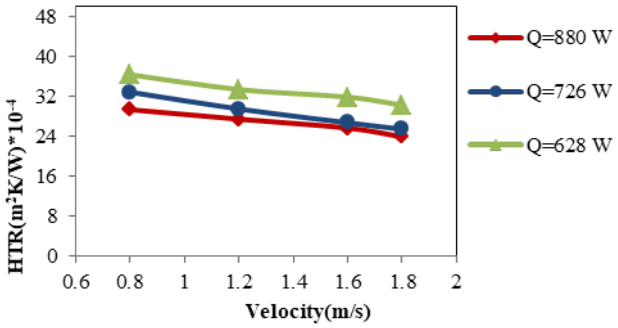

Fig. 16. Heat transfer resistance with velocity for epoxy coating (Case 2) type (b) at different applied heat, at 30°C.

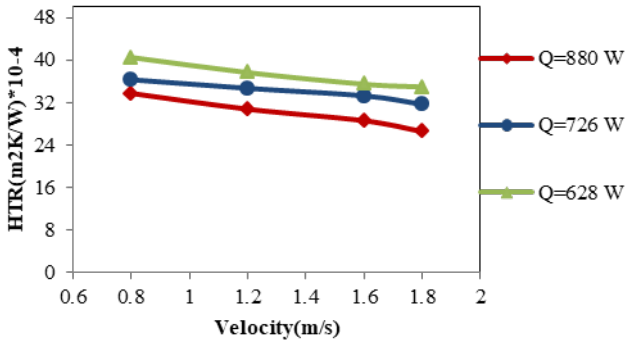

Fig. 17. Heat transfer resistance with velocity for epoxy coating (Case 1) type (c) at different applied heat, at 30°C.

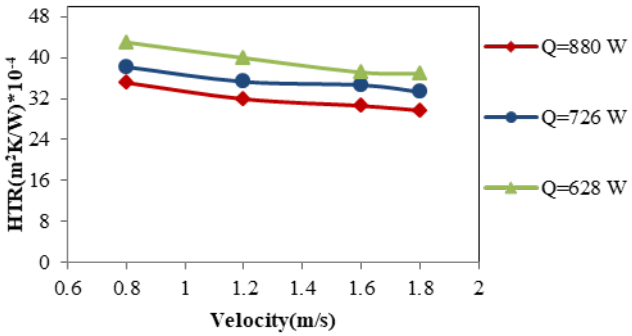

Fig. 18. Heat transfer resistance with velocity for epoxy coating (Case 2) type (c) at different applied heat, at 30°C

6.3 Comparison of HTR Results

Comparison of HTR results between uncoated and coated AB tubes is carried out to show the best type of protective coating that has less amount of HTR value. Figures 19 and 20 show the HTR findings for uncoated and coated AB tubes at different heat applications (880, 726, and 628) W. The figures reveal that increasing applied heat reduced HTR; for example, the greater applied heat of 880W during the experiment had the lowest HTR when compared to the HTR at 726 and 628 W, respectively. Fig 19 indicates that the HTR at 880W and 1.8m/s are (12.88, 18.37, 22.88, 26.51, 21.67, 23.95, and 29.98)*10^{-4} m^2.K/W for uncoated, coated, epoxy (Case 1) types (a, b, c) and epoxy (Case 2) types (a, b, c) respectively. It is clear from Fig 19 that epoxy coating (Case 1) type (a) showed a lesser HTR value than other types of epoxy coating. HTR through the wall tubes depended on tube thickness [8], higher coating thickness led to an increase in the temperature difference between heated surface and bulk water temperature that reduced the heat transfer rate and increased heat transfer resistance. These results showed good approximation with the study of Nagata and Sato [10].

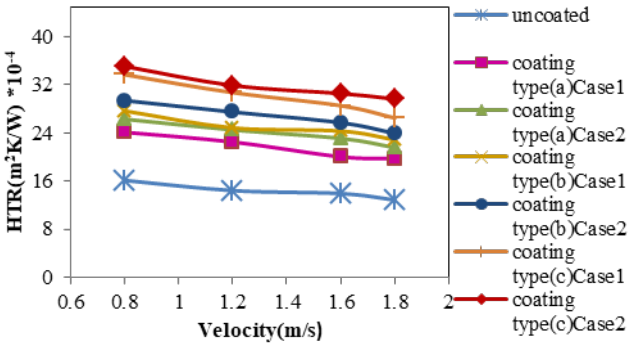

Fig. 19. Comparison of the effect of velocity on heat transfer resistance of uncoated and epoxy-coated samples at applied heat of 880W.

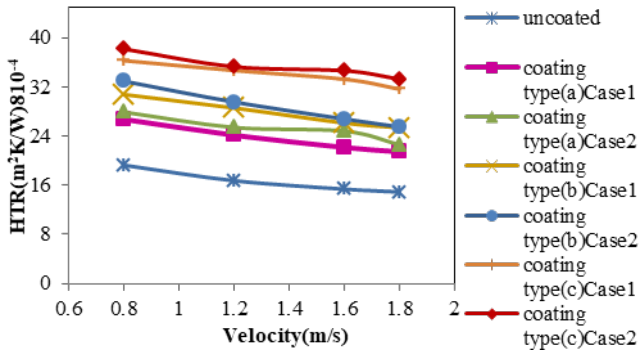

Fig. 20. Comparison of the effect of velocity on heat transfer resistance of uncoated and epoxy-coated samples at applied heat of 726W.

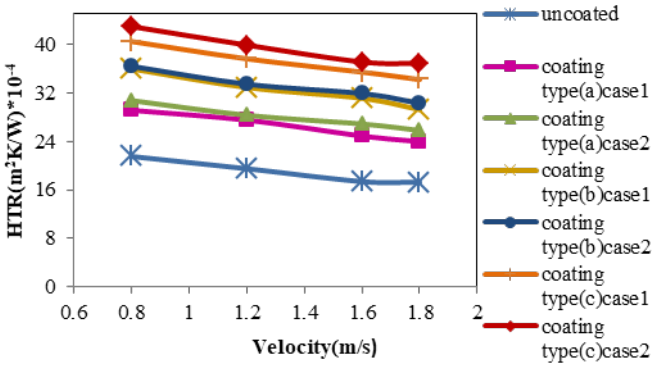

Fig. 21. Comparison of the effect of velocity on heat transfer resistance of uncoated and epoxy-coated samples at applied heat of 628 W.

7 Results of Coating Thickness Measurement

The results of thickness measurements of the three types of epoxy resins (Case 1 and 2) are shown in Table 2 and Table 3. The results indicated that the range of thickness is 0.02-0.07 mm, 0.04-0.12 mm, and 0.08-0.18 mm for epoxy resin (Case1) type (a, b, c) respectively, while the range of thickness for epoxy resin(Case 2) is 0.20-0.30 mm, 0.27-0.39 mm and 0.37-0.50 mm for epoxy resin type (a, b, c) respectively. The coating thickness relies on adhesion properties and the density of resin. The high density and excellent adhesion led to a high value of coating thickness. By comparison between epoxy coating (Case1 and 2), it appeared that epoxy resin (Case 1) (ratio of 2:1 epoxy: solvent) showed minimum thickness than (Case 2) (ratio of 4:1 epoxy: solvent).

Table 2. The thickness of epoxy resin (Case1) type (a, b, c) (all in mm)

(a)		(b)		(c)	
Thickness after coat	**Thickness of coat**	**Thickness after coat**	**Thickness of coat**	**Thickness after coat**	**Thickness of coat**
1.27	0.02	1.29	0.04	1.33	0.08
1.28	0.03	1.31	0.06	1.35	0.10
1.30	0.05	1.32	0.07	1.37	0.12

1.30	0.05	1.34	0.09	1.38	0.13
1.32	0.07	1.37	0.12	1.43	0.18

Table 3. The thickness of epoxy resin (Case 2) type (a, b, c).

(a)		(b)		(c)	
Thickness after coat (mm)	**Thickness of coat (mm)**	**Thickness after coat (mm)**	**Thickness of coat (mm)**	**Thickness after coat (mm)**	**Thickness of coat (mm)**
1.45	0.20	1.52	0.27	1.62	0.37
1.49	0.24	1.54	0.29	1.64	0.39
1.49	0.24	1.58	0.33	1.68	0.43
1.53	0.28	1.60	0.35	1.69	0.44
1.55	0.30	1.64	0.39	1.75	0.50

The results indicated that decreasing ratio of resin: solvent led to reduction of the coating thickness. Minimum coating thickness was useful for reduction of the heat transfer resistance, epoxy resin (Case1) type (a) with a film thickness of 0.02-0.07 mm showed lesser heat transfer resistance than other types of epoxy resins.

8 Conclusions

We can conclude the folowing:

1) It is found that increasing epoxy resin to solvent ratio increases coating thickness, which improved corrosion resistance of AB, but increased heat transfer resistance.

2) It is found that epoxy resin type (a) (ratio of 2:1 epoxy: solvent) is efficient in reducing the corrosion rate to $21.1*10^{-2}$ mpy such as the efficiency of 92.2% and the heat transfer resistance increased from $12.88x10^{-4}$ to $18.37x10^{-4}$ $m^2.K/W$ i.e. epoxy coating resistance of $5x10^{-4}$ $m^2.K/W$ compared to other types of coating that showed more increase in heat transfer resistance due to increase in film thickness.

References

[1] B. Yu, Y. Liu, L. Wei, X. Zhang, Y. Du, Y. Wang, S. Ye, "A Mechanism of Anti-Oxidation Coating Design Based on Inhibition Effect of Interface Layer on Ions Diffusion within Oxide Scale", Coatings, 2021; vol. 11, no. 454.

[2] H. Rein, M.Rourke, G. John, “The Antifouling Effects of Copper-Oxide Filler Incorporated Into Paint-Based Protective Films Applied to Steam Surface Condenser Tubes”, Journal of Thermal Science and Engineering Applications, February, 2018.

[3] Tube Coating With Teflon An Outstanding Alternative to Condenser and Chiller tube Replacement, Technical Bulletin, 2002.

[4] D. Chugunkovl, G. Seyfelmlyukova1, A. Skurikhina1, "Method and device for applying protective coatings to heat exchange tubes of system heaters", IOP Publishing Ltd, Journal of Physics; vol. 1370, 2nd International Conference on Fusion Energy and Plasma Technologies ; 7–9 October 2019; Moscow, Russian Federation.

[5] S. Gowda, "Multi Scale Effect of Corrosion on Steel Structures", Doctoral dissertation, University of Akron, 2016.

[6] S. Sato, T. Nosetani, "Allowable Water Velocity and Cleanliness Factor of Aluminum Brass Condenser Tube With Ferrous Addition Into Sea Water", Sumitomo Light Metal Industries ,Technical Reports, 1996, pp.11, No.4.

[7] H. Hack, T. Lee, "The Effect of Ferrous Sulfate on Sulfide-Induced Corrosion of Copper-Base Condenser Alloys in Aerated Seawater", Report, Naval Ship Research and Development Center, Maryland, January, 1990.

[8] B. Phull, "The Laque Center for Corrosion Technology Heat Transfer Evaluations of Condenser Tubes", EPRI, Florida Power Corporation, 2004.

[9] L. Fedrizzi, F. Andreatta, F. Paussa, L., Deflorian,F. Maschio, "Heat Exchangers Corrosion Protection by Using Organic Coatings", Progress in Organic Coatings, Italy 2008; vol. 63, pp. 299–306.

[10] K. Nagata, S. Sato, "Experiences of APF Condenser Tubes" Sumitomo Light Metal Industries, 1985, pp.18-20.

[11] M. Lakovic, S. Mitrovic, M. Jovic, "The choice of surface condenser in function of energy efficiency of thermal power plant", International conference Power Plants, Zlatibor; October 2014; Serbia.

[12] S. Sato, "Condenser Biofoling Control ", Symposium, The State of The Art, EPRI, 1990.

Application of Drucker-Prager Plasticity Model for Concrete Confined with Fiber Reinforced Cementitious Mortar (FRCM)

Ali Hadi Adheem[1], Majid M.A. Kadhim[2]*, Akram Jawdhari[3] , Mohammed J. Altaee[4]
{inkr.ali@atu.edu.iq[1], majid.mohammed@uobabylon.edu.iq[2], akram.hassan@uky.edu[3], mohammed.altaee@uobabylon.edu.iq[4]}

Kerbala Technical Institute, Al-Furat Al-Awsat Technical University, 56001 Kerbala, Iraq[1], College of Engineering, University of Babylon, Hilla, Iraq[2] , Department of Construction and Projects, University of Babylon, Hilla, Iraq[3],Environmental Research and Studies Centre, University of Babylon, Hilla, Iraq[4].

Abstract Wrapping concrete columns with fiber reinforced polymer (FRP) jackets can result in a significant increase of compressive strength and ductility, and can mitigate deterioration due to aging, chemical attacks, overloading, and seismic activity. Cementitious mortar has recently been used as a binder for FRP reinforcement, leading to a sustainable and environmental friendly construction, in lieu of synthetic binders (e.g. epoxy) which suffer from a number of drawbacks. The system is termed fiber reinforced cementitious mortar (FRCM) and can be used to repair concrete in shear and flexure, or in columns confinement. In this study, a comprehensive three-dimensional (3D) finite element (FE) model was developed to study the behavior of concrete confined with FRCM jackets. The model incorporated a Drucker-Prager (DP) plasticity law to simulate effects of confinement on concrete core, a composite damage mechanics (CDM) criteria to predict rupture of FRP mesh, and a concrete plasticity model to simulate cracking of the cementitious mortar. The model predictions were compared with test results of 11 FRCM-confined concrete cylinders comprising various dimensions, FRCM layers, and concrete strengths. The model was able to accurately predict the peak compressive strength of confined concrete (f_{cc}), peak axial strain (ε_{cc}), and entire stress-strain curve in addition to the failure mode of each analyzed specimen. Calibrated model will enable examination of several geometric and material parameters, and assist in establishing an accurate confinement model for FRCM-confined concrete.

Keywords: FRCM, confinement, columns, finite element, drucker prager, plasticity.

1 Introduction

Fiber-reinforced polymer (FRP) systems have become widely used in concrete construction with applications ranging from reinforcement of new members to repair and strengthening of old ones. Laboratory tests showed that confining of reinforced concrete (RC) columns with FRP sheets and plates can increase compressive strength and ductility, as well as the ability to carry more vertical and lateral loads [1-4]. Although offering many outcomes ex. high strength, lightweight, ease and speed of application, and resistance to corrosion, FRPs still have some limitations particularly those related to the use of synthetic adhesives (e.g. epoxy), including degradation of bond and stiffness under elevated temperature, difficulty in application on

IMDC-IST 2021, September 07-09, Sakarya, Turkey
Copyright © 2022 EAI
DOI 10.4108/eai.7-9-2021.2315489

wet surfaces, poor performance under fire, low compatibility with the substrate, and moisture impermeability [5, 6].

In response to these drawbacks, inorganic binders, such as from cement or geopolymer mortars, have been implemented to provide a sustainable and environmentally-friendly adhesive. The new system is known in literature as textile reinforced mortar (TRM) or fiber reinforced cementitious mortar (FRCM), and it consists of orthogonal FRP fabric meshes or grids, embedded in the mortar [5-10]. FRCM technique has been successfully used in strengthening RC beams in flexure, shear and torsional loading cases [7, 11, 12]. It was also investigated for the case of strengthening RC columns [6, 8, 9] and plain stub columns [5, 10].

Application of FRCM technique for stub columns demonstrated potential enhancement to concrete strength as a result of confinement. Several studies have confirmed that the use of FRCM on concrete compression members can significantly improve stiffness, strength and ductility [5]. Recently, Trapko [10] conducted an experimental study on concrete cylinders confined by either FRCM jackets or conventional FRP sheets, considering the effects of two parameters; temperature and number of transverse reinforcement layers. The FRCM jacket consisted of a polyparaphenylene benzobisoxazole (PBO) fiber mesh embedded in cement-based mortar. Both systems were able to increase the compressive strength and modulus of elasticity, but FRCM showed a superior performance under elevated temperature. The strength and stiffness increased proportionally with number of CFRP or PBO mesh layers.

Ombres [5] conducted research on concrete cylinders reinforced with multi-layers of PBO fibres embedded in an inorganic matrix to evaluate the efficiency of the FRCM system. The effect of fibre reinforcement ratio and fibre orientation was investigated. The results showed that this technology has a strong potential to raise the restricted concrete's peak strength and axial strain. Excessive dilatation caused concrete to bulge, which was followed by cracking in the mortar and debonding at the fabric and mortar interface.

The confinement of low-strength concrete with FRCM composites was also investigated by Gonzalez-Libreros, et al. [13], considering several parameters including: types of fibers, using carbon or glass; cross-section shape, using circular, square and rectangular; specimen size for cylinders with a constant slenderness ratio (h/d) of 2, where h is height and d is diameter; and effects of a pre-existing damage. The experimental results showed that the strength and ductility gains depend on composite type; cross-section geometry and specimen dimensions. In addition, it was found that the damaged specimens can achieve full strength recovery when carbon-FRCM system was applied.

With FRCM system proving to be a viable option for concrete confinement, the technical database needs to be expanded beyond the few available experimental and analytical studies, in order to bridge the gap in knowledge, examine the effects of more parameters, and finally establish an accurate confinement model similar to that used in conventional FRP sheets. Although multiple studies implemented finite element (FE) modeling technique in studying the effects of FRCM system in enhancing shear, flexure, and torsion behavior of concrete, very few focused on confined axial members. This study goal to establish a robust 3D FE model for FRCM-confined concrete. The calibrated model is intended to be used in a large parametric analysis on effects of several variables such as fiber properties and orientation, number of layers, thickness of fiber mesh, cross-section type, slenderness ratio, corner radius of square sections, and concrete compressive strength. The main objective is to provide a larger population of investigated parameters in order to enable an accurate stress-strain confinement scheme for this new system.

2 Experimental Summary

The model results were compared with those from experimental tests on standard concrete cylinders confined with FRCM jackets. Eleven specimens, 3 from a study by Trapko [10] and 8 from a study by Ombres [5], were selected as a validation data and were chosen because they represented a wide range for geometric and material variables and contained all inputs needed for modeling, such as the stress-strain curve. The cylinders from Trapko [10] were 300 mm in height (H) and 113 mm in diameter (D); while those from Ombres [5] had an H of 290-295 mm, and D of 152-153 mm. Different number of FRCM layers, ranging from 1 to 4, were used, resulting in multiple confinement ratios. The FRCM system was applied by dampening the cylinder's surface and applying an initial coat of mortar, followed by wrapping with the fiber mesh, and then covering with a final coat of mortar. The average total thickness of the mortar ranges from 3 to 5 mm, per one FRCM layer. In all specimens, the fiber mesh within FRCM system was applied by orienting the main fibers parallel to the hoop direction. Compressive strength of unconfined concrete (fco) ranged from 15.4 to 29.3 MPa. Table. 1 lists the geometrical and material properties of the cylinder tests, along with key results and comparisons between test and FE model. The mechanical properties of PBO-fiber mesh and the mortar are listed in in Table, 2, as reported in Trapko [10] and Ombres [5].

Table 1. Key experimental and FE results for FRCM-constrained cylinders.

Label	D	H	n	t_f	f_{co}	f_{cc} (MPa)		Exp.	ε_{cc}		Exp./
	mm	mm		(mm)	MPa)	Exp.	FE	/FE	Exp.	FE	FE
M1-1	113	300	1	0.0455	22.60	32.66	33.39	0.98	0.0070	0.0068	1.03
M2-1	113	300	2	0.0455	22.60	42.48	44.50	0.95	0.0121	0.0131	0.92
M3-1	113	300	3	0.0455	22.60	55.80	57.78	0.97	0.0171	0.0211	0.81
CRP1-I	152	290	1	0.0455	15.40	24.69	22.73	1.09	0.0115	0.0134	0.86
CRP2-I	152	290	2	0.0455	15.40	35.00	34.11	1.03	0.0200	0.0253	0.79
CRP3-I	152	290	3	0.0455	15.40	41.45	41.04	1.01	0.0290	0.0274	1.06
CRP4-I	152	290	4	0.0455	15.40	49.24	48.01	1.03	0.0264	0.0289	0.91
CRP1-II	153	294	1	0.0455	29.26	43.55	39.14	1.11	0.0080	0.0147	0.54
CRP2-II	153	292	2	0.0455	29.26	47.00	44.83	1.05	0.0148	0.0168	0.88
CRP3-II	153	292	3	0.0455	29.26	56.60	53.27	1.06	0.0193	0.0215	0.90
CRP4-II	153	295	4	0.0455	29.26	56.23	55.88	1.01	0.0216	0.0217	1.00

Note: D= diameter; H= height; t_f = equivalent fiber thickness in one FRCM layer; n= number of fabric meshes; f_{co}= compressive strength of unconfined specimens; f_{cc}= peak compressive strength of confined concrete; ε_{cc}= peak axial strain of confined concrete.

3 Finite Element Analysis

The FE models for FRCM-confined concrete cylinders were prepared in general purpose software ANSYS v 17.2 [14], using a nonlinear three-dimensional (3D) modeling approach. The concrete core is represented by an 8-node brick element SOLID185 (Fig. 1), having three translational degrees of freedom (DOFs) in x, y, and z orthogonal Cartesian directions. This

element can be used to develop non-linear model ex. plasticity, stress stiffening, large deformation, and large strain [14]. Two cylindrical steel plates (Fig. 1), each is 10 mm thick, were added at the top and bottom surfaces of the cylinder to minimize stress concentration within the concrete, and were also modeled by SOLID185.

Table 2. Mechanical and geometrical properties of FRCM strengthening system.

No.	Reference	E_f (GPa)	f_{fu} (MPa)	ε_{fu}	E_m (GPa)	f_{cm} (MPa)
1	Trapko [10]	270	5270	2.15	6.0	29.0
2	Ombres [5]	270	5800	2.00	6.1	30.4

Note: E_f = elastic modulus of PBO mesh; f_{fu} = ultimate tensile strength of PBO mesh; ε_{fu} = failure strain of PBO mesh; E_m = elastic modulus of mortar; f_{cm} = compressive strength of mortar.

The mortar layer was modelled as a distinct solid portion with a thickness (tm) as reported from the tests in order to replicate mortar cracking, which was a frequently found failure mode in FRCM-confined concrete columns. In addition, the mortar is believed to aid confinement, especially prior to breaking. The mortar was modelled using SOLID65, an 8-node brick element with 3 translational DOFs. Because of its unique capacity to portray concrete and the incorporation of cracking and crushing algorithms [14]. the element was chosen. Shell element SHELL181 was used to simulate the fibre mesh in the FRCM system (Fig. 1). The element has 4 nodes with six DOFs (three translational and three rotational), and is able to resist both membrane and bending forces [14]. In order to simplify the modeling process, the fiber mesh in FRCM system which is an open grid of orthogonal fiber strips, was replaced by a continuous fabric with thicknesses in the orthogonal directions determined from equating the axial stiffness of the grid to that of the fabric [11,12]. The fibre mesh and mortar were assumed to have a full bond, which was numerically idealised by establishing a same mesh size for both portions and then merging the duplicate nodes. Multiple FRCM layers were replaced with one central fabric layer embedded in one mortar layer if more than one FRCM layer was used. The idealised fabric (ta) and mortar (tm) thicknesses are simply multiplied by the number of layers in the multi-layer confinimeent system.

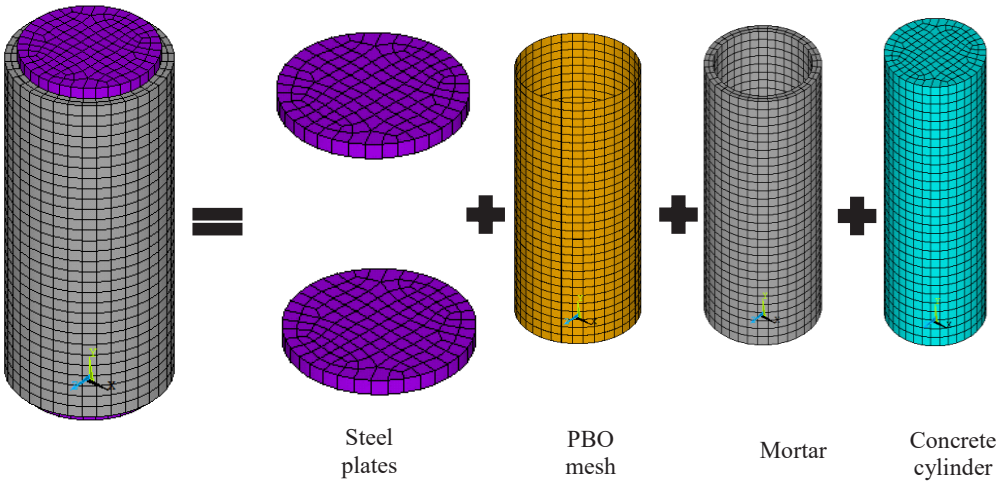

Figure 1. Modelling of concrete cylinder confined with FRCM system.

4 Material modelling

The DP concrete model [15, 16], which is a plasticity model based on the premise of elastic-perfectly plastic response, has been widely used in modelling concrete confined with FRP sheets and jackets. The model accounts for concrete dilatation under axial compression and has produced positive results in several numerical studies (Ghanem, 2016). Traditional DP models, on the other hand, ignore the substantial difference in concrete's compressive and tensile strengths, and are unable to account for softening after cracking or crushing [14].

A modified Drucker-Prager (DP) concrete model is included in ANSYS version 17.2, which includes a separate failure criterion for tension and compression, nonlinear stress-strain response in compression, and several hardening/softening mechanisms including linear, exponential, piece-wise linear, and fracture energy [14]. The modified DP model was used to simulate the confined concrete cylinders investigated in this study. The DP model is not readily available in ANSYS library of materials and can't be inputted from the typical graphical user interface (GUI). Therefore, a command subroutine was used to implement the model within ANSYS environment. The elastic modulus of concrete (Ec) and Poisson's ratio are also required in the DP model (v). Ec was determined from ACI-318-14 [17] equation, while v was assumed to be 0.2 [18].

The mortar was simulated by a nonlinear model suggested by [19] , and widely used in research for grout and concrete materials [18]. The model utilizes a five-parameter failure criteria proposed by [20], and considers cracking and crushing failures. Material properties required to develop the model were taken from Trapko (2014b) [10] and (Ombres 2014) [5] and were reported in Table. 2. Both the open and closed shear fracture parameters were set to 0.3, with v set to 0.2. The steel plates that were added were modelled as a linear elastic material with a s modulus of elasticity (Es) of 200 GPa and a Poisson's ratio (v) of 0.3.

Until it failed, the fabric was modelled as an orthotropic elastic material. As described in the experimental experiments, Table 2 summarises some of the mechanical qualities required for the model. Other material parameters, such as transverse elastic moduli, shear moduli, and

Poisson's ratios, were not provided in the tests and were instead derived from [18]. In this investigation, a composite damage mechanics (CDM) model available in ANSYS was used to explicitly simulate fabric rupture. The rupture failure initiated when the stress exceeds the tensile strength, f fu specified in Table. 2. After failure initiation, the stiffness drops to a small value representing the brittle nature of fiber mesh failure. More information on the CDM are detailed in [18][21].

5 Validation of FE model

The findings of the numerical model were compared with the known practical results to verify the accuracy of the FE model [5, 10]. The axial stress-strain curve, maximum stress, and failure pattern were all compared. Various mesh sizes were investigated in order to find one that strikes a reasonable balance between computational effort and accuracy. When compared to smaller meshes, a mesh with an element side length of 10 mm for all parts (concrete, cloth, and mortar) was determined to be sufficient and produced a maximum stress divergence of less than 1%.

5.1 Peak strength and axial strain

The maximum value of stress throughout the test is represented by the peak compressive strength of confined concrete (fcc). Table 1 shows the peak compressive strength values and their related peak strain values. The amount of PBO mesh layers has a significant impact on peak strength values, as can be shown in this table. This pattern holds true for both experimental and FE results.. It can also be concluded from this table that the maximum divergence between the results obtained from the experimental and FE was less than 11%. With regard to peak axial strain (ε cc), the FE model can also predict the experimental values of peak strain in good agreement apart from specimen CRP1-II. The numerical divergence for this specimen is because it experienced an early peaking in stress in the experiment, which was significantly different from the rest of specimens.

5.2 Stress strain response

Figures 2 and 3 show the degree of convergence between test and computed results. It indicated that the FE model has the ability to simulate laboratory tests with a high degree of accuracy. It can also be seen that the overall response in terms of stress-strain curves obtained experimentally are well predicted by the FE model. The stress-strain curves for most specimens are similar in shape for both experimental and FE data, indicating a bilinear hardening trend. The slope of the second line (E2) represents confinement effects and is controlled by a variety of factors such as the jacket material, thickness, and number of layers, among others. E2 grows proportionally with the number of applied FRCM layers, as shown in the figures. This tendency can be seen in both experimental and FE findings, indicating that the FE model can accurately predict the behaviour of concrete jacketed with FRCM systems.

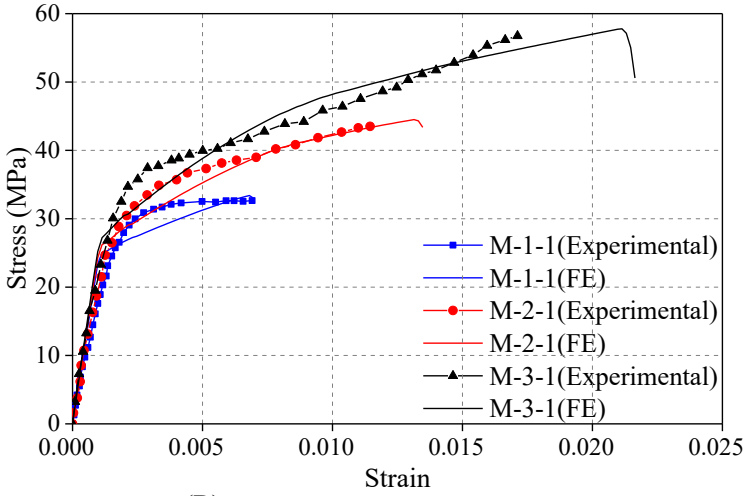

Figure 2. Comparison between stress-strain curves of FE results and concrete cylinders [10].

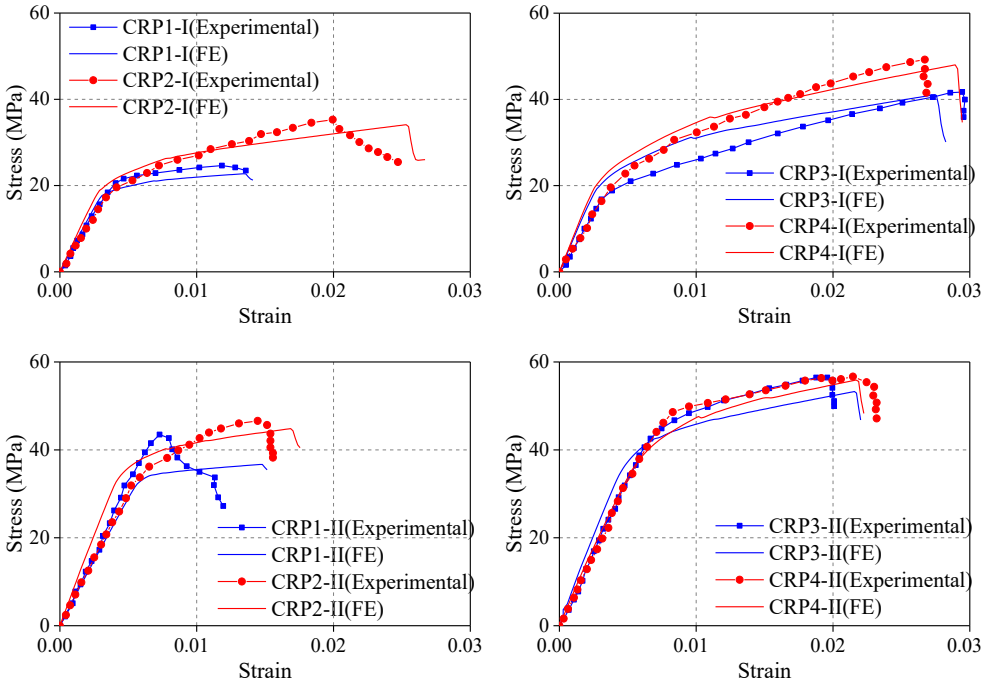

Figure 3. Comparison of experimental [5] and FE results on stress-strain curves of constrained concrete cylinders.

5.4 Failure modes

The FRCM jacket burst in the hoop direction, which was the most common failure mode of FRCM-jacketed concrete cylinders that preceded by extensive cracking in the mortar layer (Fig. 4). In the FE model, the failure criteria for PBO mesh was inputted to ensure that accurate results

can be obtained from this model. Figure 4 shows the failure modes obtained from the FE model and the practical tests of both sets of experiments [5, 9]. The failure mode was reasonably captured by the FE model, as shown in this diagram (PBO mesh rupture). Based on the foregoing explanation, it can be inferred that the FE model is capable of capturing the full behaviour of the FRCM-reinforced concrete cylinders. This result was reached based on a high level of agreement between the FE model and the matching experimental data.

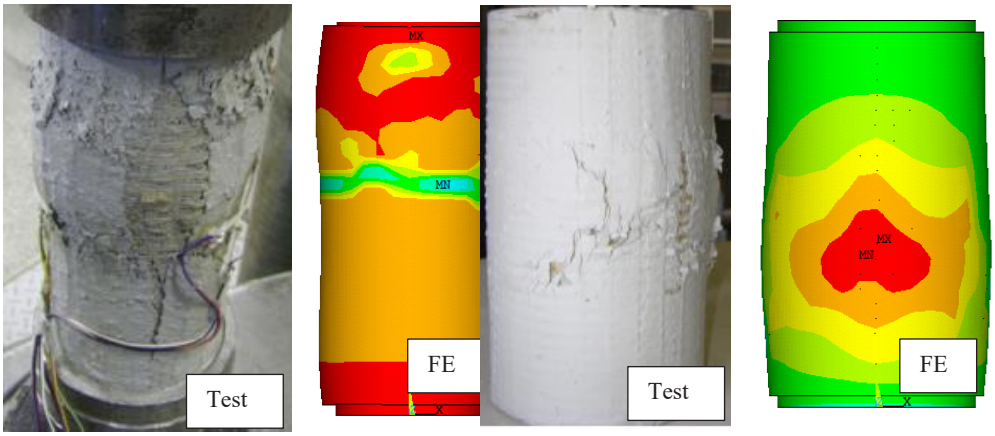

(a) (b)

Figure 4. Comparison of failure modes for FE results and experimental obtained from (a) Trapko [10] and (b) Ombres [5].

Conclusions

The stress-strain behaviour of concrete axial members constrained by a fiber-reinforced cementitious mortar (FRCM) system was investigated using a thorough three-dimensional finite element (FE) model created in this study. The concrete core was modelled using a modified Druker Prager (DP) model, which included a separate failure criterion for tension and compression, nonlinear stress-strain response in compression, and multiple hardening/softening parameters. Mortar cracking and fiber mesh rupture failures were explicitly simulated, using proper element and material models.

The results of 11 tests on FRCM-confined concrete cylinders, featuring varying material and geometric properties as well as different confinement layers. Comparisons in terms of the axial stress-strain curve, maximum stress (f cc) of confined concrete, and failure pattern, showed the model's ability to reproduce the behavior of tested specimens. The model's divergence for (f cc) was less than 11%. More importantly, the model was capable of capturing the effects of different confinement levels obtained from using various numbers of FRCM jackets. Following validation, the model will be utilised to do a broad parametric analysis on the effects of various critical parameters, as well as to create an accurate analytical stress-strain confinement model for concrete wrapped with the FRCM system.

References

[1] Nanni, A.Bradford, N.M., FRP jacketed concrete under uniaxial compression. Construction and Building Materials, 1995. 9(2): p. 115-124.

[2] Berthet, J., Ferrier, E. and Hamelin, P., Compressive behavior of concrete externally confined by composite jackets. Part A: experimental study. Construction and Building Materials, 2005. 19(3): p. 223-232.

[3] Kadhim, M.M.A., Nonlinear FE analysis of reinforced HS concrete continuous beam strengthened with CFRP sheet. International Journal on Advanced Science, Engineering and Information Technology, 2011. 1(6): p. 597-601.

[4] Realfonzo, R.Napoli, A., Concrete confined by FRP systems: confinement efficiency and design strength models. Composites Part B: Engineering, 2011. 42(4): p. 736-755.

[5] Ombres, L., Concrete confinement with a cement based high strength composite material. Composite Structures, 2014. 109: p. 294-304.

[6] Ombres, L.Verre, S., Structural behaviour of fabric reinforced cementitious matrix (FRCM) strengthened concrete columns under eccentric loading. Composites Part B: Engineering, 2015. 75: p. 235-249.

[7] D'Ambrisi, A., Feo, L. and Focacci, F., Experimental analysis on bond between PBO-FRCM strengthening materials and concrete. Composites Part B: Engineering, 2013. 44(1): p. 524-532.

[8] Kadhim, M.M., Altaee, M.J., Adheem, A.H. and Jawdhari, A.R. A robust 3D finite element model for concrete columns confined by FRCM system. in MATEC Web of Conferences. 2019. EDP Sciences.

[9] Trapko, T., Effect of eccentric compression loading on the strains of FRCM confined concrete columns. Construction and Building Materials, 2014. 61: p. 97-105.

[10] Trapko, T., Confined concrete elements with PBO-FRCM composites. Construction and Building Materials, 2014. 73: p. 332-338.

[11] Kadhim, M., Adheem, A.H. and Altaee, M.J., Shear Strengthening of RC Beams with FRCM Technique. Int. J. Eng. Technol., 2019: p. 169-176.

[12] Alabdulhady, M.Y., Sneed, L.H. and Carloni, C., Torsional behavior of RC beams strengthened with PBO-FRCM composite–an experimental study. Engineering Structures, 2017. 136: p. 393-405.

[13] Gonzalez-Libreros, J., Zanini, M.A., Faleschini, F. and Pellegrino, C., Confinement of low-strength concrete with fiber reinforced cementitious matrix (FRCM) composites. Composites Part B: Engineering, 2019. 177: p. 107407.

[14] ANSYS, Release 17.2 Documentation for ANSYS. Version 17.2, ANSYS Inc., Canonsburg, PA, USA, 2016.

[15] Ghanem, S.Y., Circular RC columns partially confined with FRP. 2016.

[16] Mirmiran, A., Zagers, K. and Yuan, W., Nonlinear finite element modeling of concrete confined by fiber composites. Finite Elements in Analysis and Design, 2000. 35(1): p. 79-96.

[17] ACI-318-14, Building code requirements for reinforced concrete. American Concrete Institute, 2014.

[18] Jawdhari, A.Harik, I., Finite element analysis of RC beams strengthened in flexure with CFRP rod panels. Construction and Building Materials, 2018. 163: p. 751-766.

[19] Kent, D.C.Park, R., Flexural members with confined concrete. Journal of the Structural Division, 1971.

[20] William, K.Warnke, E., Constitutive model for the triaxial behavior of concrete international association for bridge and structure engineering proceedings, 1975, Bergamo.

[21] Altaee MJ., Kadhim M., Altayee S., Adheem A., Employment of damage plasticity constitutive model for concrete members subjected to high strain-rate. IMDC-SDSP EAI. 2020.

Optimal Operation of Energy Hub with high penetration of renewable energy sources

Patrick Sunday Onen [1], Geev Mokryani[2], and Rana H.A. Zubo[3]
{ p.s.onen@bradford.ac.uk , g.mokryani@bradford.ac.uk, r.h.a.zubo@ntu.edu.iq }

University of Bradford, Uk[1,2] ,Northern Technical University, Iraq[3]

Abstract. Integration of electricity and gas networks increases system flexibility while also increasing energy efficiency. In such a connected infrastructure, the energy hub (EH) plays a critical role in energy production, conversion, and storage. This research provides a new method to EH operation that takes into account renewable energy sources (RESs) and battery energy storage systems (BESS). The suggested model's goal is to reduce total energy costs by optimising total energy prices based on hourly power and heat demand while taking into account hub restrictions. The impact of energy prices, load demands, RESs, and BESS on the EH model's performance has also been explored. Three operational case studies based on distinct EH structures were used to investigate the optimization problem. The CPLEX solver in the general algebraic modelling system (GAMS) software is used to solve a Mixed integer linear programming (MILP) formulation for the optimization problem. The simulation findings demonstrate a decrease in the cost of market-purchased energy.

Keywords: Energy hub, optimal operation, Renewable energy source, Battery energy storage system, Energy costs.

1. Introduction

A. Background and Motivation

Growing worldwide energy consumption and the environmental implications of fossil fuels in traditionally operated power plants have heightened the clamour for a shift to more environmentally benign and economically viable renewable energy sources. [1, 2]. Furthermore, electricity is not the only energy consumed by consumers for their daily activities, heating is also required by the consumers too. However, the electricity, gas, and heating energy infrastructure have traditionally operated separately which has led to lower efficiency of the system and a higher operational cost with greater emission to the environment. Hence, Multi-vector energy system integration can solve the issue by combining different sources of energy together in order to complement each other to enhance the system reliability, flexibility, sustainability and reduce energy costs [3, 4].

IMDC-IST 2021, September 07-09, Sakarya, Turkey
Copyright © 2022 EAI
DOI 10.4108/eai.7-9-2021.2315488

In addition, when compared to a typical power plant, the integration of combined heat and power (CHP) with the electricity network has grown tremendously to meet the consumer's electrical and heat demands concurrently from a single gas source with minimal emissions and energy expenditures. The EH idea, in which numerous energy carriers are converted, conditioned, and stored to meet the end user's demand, can be used to efficiently implement the coupling of different energy infrastructure. As a result, the economy of energy systems will be boosted by enhancing energy efficiency, lowering fuel consumption, and improving system flexibility, all of which are essential factors in the integration of renewable energy sources. Furthermore, the high shares of RESs generation into the EH systems, will reduce the amount of energy that will be purchased from the market. Hence, reduced the total energy costs.

Literature review

EH is a relatively new concept in energy system integration, and a promising approach to implementing future energy system integration. Recent studies on the optimal operation of EH have taken a variety of approaches, each with its own set of goals and constraints. During a 'Future energy network vision' project at ETH Zurich in 2007, Ref [5] was the first to explain the meaning and the EH idea. The authors of [6, 7] look at the challenge of determining the best power flow for multi-energy carriers using a variety of renewable energy sources. Ref [5] investigated a general model for power flow as well as an optimization technique for EHs with multiple energy carriers, such as district heating, natural gas, and electrical networks. [8] looked at deterministic and stochastic situations, as well as the best way to operate an EH with a wind turbine (WT), energy storage, and demand response. The operation of EH in the face of responsive loads and stochastic wind generation was investigated in ref [9]. [10] proposed an economic dispatch model of eleven interconnected EH to investigate the impact of wind energy uncertainty. Past studies on the EH operations have been implemented based on different consumer’s need such as residential [11], commercial [16], industrial [19], and agricultural consumers [6]. From the above analysis, this paper mainly solves the optimal operation problem of the EH model in relation to energy costs, considering different hourly electricity prices and load demand. Precisely, the proposed EH model can provide electricity and heat loads simultaneously using RESs generation from WT and PV, CHP, GB, and energy purchased from the market. The model can connect and interchange multiple types of energy to get the best energy flow with the lowest running expenses. Finally, the model in this research employs BESS to improve system efficiency. BESS is a critical component of increasing power supply dependability and flexibility. Indeed, the BESS has been extensively employed in operations and planning to minimise investment costs and the cost of acquiring power from the system, as well as to accommodate significant shares of renewable energy output at peak production capacity, all with the purpose of enhancing economic efficiency.

B. Aim and objectives

This work aims to “perform and analyze optimal operations of EH with high penetration of renewable energy resources.

This work is based on the following objectives:

- Mathematically modelling of optimal operation of EH to optimize total energy costs based on hourly demand of electricity and heat using the MILP model to mitigate the computational burden in the optimal operation problem.
- Examine the impact of load demand and energy prices on the EH model's performance.
- Investigate the impact of high penetration of RESs and BESS on the performance of the EH model.

C. Paper organization

The approach and problem solving in this paper are organized in the following manner. Section 2 represents the basic concept of the EH, the EH model and the description of the proposed EH structure. Section 3 delves into the mathematical model, including objective functions (OFs) and mathematical limitations such as the EH model's input and output power balance, equipment conversion limits, and system power capacity limits. Section 4 depicts the optimal operation problem answered in simulation results and comments using the GAMS programming languages. Section 5 concludes with findings and future research directions.

2. Basic concept of EH

The EH idea is a compelling representation of how numerous energy carriers are converted, conditioned, and stored to improve the system's energy efficiency and resource use. In a multi vector energy system, an EH is an input-output dual-port model that describes energy supply, load demand, network switching, and coupling interactions [11]. The coupling matrix is widely used in multi vector energy system planning and operation analysis to synergies various energy carriers, non-hierarchical structure, and integrated management of different energy infrastructures that have traditionally operated independently in the past, and it is widely used in multi vector energy system planning and operation analysis to synergies various energy carriers, non-hierarchical structure, and integrated management of different energy infrastructures that have traditionally operated independently in the past. The EH coupling matrix, which describes the input energy and output load port, can be used to represent various coupling relationships such as conversion, storage, and transmission between various forms of energy such as electricity, heat, and gas, and can be useful in the planning and operation of EH [12].

- ***Energy Hub Model***

A generic model of EH applies a coupling matrix C, which consist of various coupling factors as shown in Fig. 1 below [13, 14]

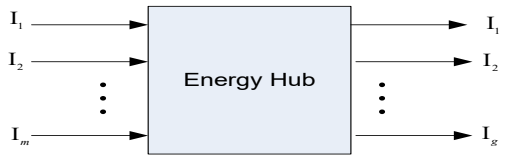

Fig.1 Energy carriers Transformation through an EH [14].

The coupling matrix can be expressed in Eq. (1):

$$\begin{bmatrix} I_1 \\ I_2 \\ \vdots \\ I_m \end{bmatrix} \begin{bmatrix} C_{11} & C_{12} & \cdots & C_{1n} \\ C_{21} & C_{22} & \cdots & C_{2n} \\ \vdots & \vdots & \ddots & \vdots \\ C_{m1} & C_{m2} & \cdots & C_{mn} \end{bmatrix} = \begin{bmatrix} L_1 \\ L_2 \\ \vdots \\ L_n \end{bmatrix} \quad (1)$$

where C_{mn} denotes the coupling coefficients between input carrier I and output carrier L, and m and n denote the input and output carrier numbers, respectively [15].

- ***Proposed Energy Hub***

To begin, the proposed EH model is based on energy and heating load demand. At the input ports connected to the energy infrastructures, various sources of energy are received, and the energy is delivered at the output ports. Converter technologies such as TR, CHP, GB, and BESS are used to convert and condition various sources of energy. The energy vectors at the input

ports of the EH are purchased from the market and renewable energies (WT and PV). The diagram in figure 2 illustrate the proposed EH to enhance operational flexibility and achieve effectiveness of energy supply. The input forms of energy are converted through the converter technologies to supply the load demands. The electrical load demand is supplied electricity via TR, RESs and the CHP. While the CHP and GB supplies the heating load demand. Lastly, the BESS is used in this model to improve efficiency.

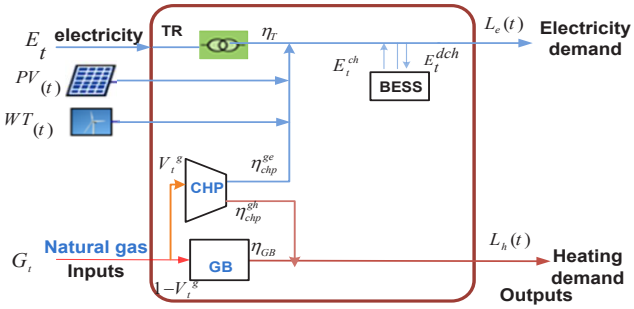

Fig.2 Proposed Energy hub structure.

3. Mathematical Model

A. Object function

The problem's purpose is to reduce EH's total energy costs. As a result, Eq. (2) is the minimum objective function of the cost of buying energy from the market each day, with Et and Gt indicating the amount of electricity and natural gas purchased from their respective networks at each hour of the day.

$$\text{Min OF} \sum_{t=1}^{Nh} \lambda_t^e E_t + \lambda_t^g G_t \tag{2}$$

where λ_t^e is the price of electricity per hour t and λ_t^g is the constant natural gas price per hour t; and the Nh is the total number of hours a day (24h).

B. The constraints

The mathematical model should include the following restrictions to ensure the smooth functioning and power of the equipment in the proposed EH model.

- **Energy balance constraints of the EH**

Based on the operating principles of the EH, the relationship between the energy demands L_e (t), L_h(t) and energy purchased from the network E_t and G_t at time t is expressed in (3) & (4):

$$\eta_{ee}^T E_t + \eta_g^{Chp} G_t + Pw(t) + PV(t) + E_t^{dch} - E_t^{ch} = L_e(t) \tag{3}$$

$$\eta_{gh}^{Chp} G_t + \eta_{gh}^{GB} G_t = L_h(t) \tag{4}$$

where E_t^{ch} and E_t^{dch} are the charge and discharge power of the BESS at hour t, respectively; PV(t) and PW(t) are the electrical power produced from RESs at hour t. The L_e (t) and L_h(t) are the output load demand of electricity and heat. The $\eta_{ge}^{Chp} G_t$ and $\eta_{gh}^{Chp} G_t$ are the gas to electricity and heat conversion efficiency of the CHP. While the η_{gh}^{GB} is the conversion efficiency of the GB and the η_{ee}^T is the efficiency of the TR.

- **Battery Storage system (BESS) constraint**

Within a 24-hour cycle, the features of the electricity price and renewable energy generation change. During peak hours, the price of electricity is higher, and vice versa. As a result, as demonstrated in Eq. 1, the total energy stored and sent back to the EH system must be balanced (5). Eqs. (6) and (7) took into account the BESS limits, which are the battery's lowest to maximum charging and discharging power capacities, respectively (i.e., the entire storage capacity of BESS must be smaller than the maximum capacity of BESS) [16]. Depending on the model operation, the BESS can work in charge or discharge mode and can be charged from the system. To prevent charge and discharge at the same time, the binary variables of charge and discharge are used in (8).

$$\sum_{t=1}^{Nh} \eta_{BESS} . I_{BESS}^{ch}(\mathrm{t}) . E_{BESS}^{ch}(\mathrm{t}) = \sum_{t=1}^{Nh} I_{BESS}^{dch}(\mathrm{t}) . E_{BESS}^{dch}(\mathrm{t}) \tag{5}$$

$$E_{\min}^{ch} I_t^{ch} \le E_t^{ch} \le E_{\max}^{ch} I_t^{ch} \tag{6}$$

$$E_{\min}^{dch} I_t^{dch} \le E_t^{dch} \le E_{\max}^{dch} I_t^{dch} \quad (7) \qquad I_t^{ch} + I_t^{dch} \le 1 \qquad I_t^{ch}, I_t^{ch} \in \{0,1\} \tag{8}$$

Similarly, the BESS must be less than the max. capacity of BESS, E_{BESS}^{max}, with constraints as expressed in (9) and (10) below:

$$0 \le E_{BESS}(t) \le E_{BESS}^{\max} \tag{9}$$

$$E_{BESS}(t) = E_{BESS(t-1)}^{ch} + E_{BESS}^{ch}(t) - E_{BESS}^{dch}(t) \qquad \forall t \in Nh \tag{10}$$

- **The constraints of power flow**

The optimal operation of the EH model is to control the power flow of the TR, CHP, BESS, and GB devices. Therefore, the conversion limits of the mentioned devices at time t are expressed below:

$$0 \le \eta CHP(t) \le 1 \tag{11}$$

$$0 \le \eta TR(t) \le 1 \tag{12}$$

$$0 \le \eta GB(t) \le 1 \tag{13}$$

- **The constraints of power purchased from the market.**

The capacity and energy stored in the system limit the system's supply capacity. Consequently, the constraint utilized are represented in Eq. (14) and (15):

$$E(t) \le E^{\max} \tag{14}$$

$$G(t) \le G^{\max} \tag{15}$$

where E^{max} and G^{max} are the max. allowable electrical energy and natural gas, respectively. The purchased energy within a day to the proposed EH is limited by the energy that can be supplied from the electricity and gas network mentioned above are expressed in Eq. (16) and (17) respectively.

$$\sum_{t=1}^{Nh} E(t) \le E_{\max}^{e} \tag{16}$$

$$\sum_{t=1}^{Nh} G(t) \le E_{\max}^{g} \tag{17}$$

where E_{max}^{e} and E_{max}^{g} are the supplied power from the electricity and natural gas network.

Wind speed constraints

The O/P of WT a day is.

$$P_{wind}^{e}(w(t)) = \begin{cases} P_{out}^{w} \\ \dfrac{\omega(t) - \omega_i^{cut}}{\omega_r^{w} - \omega_i^{cut}} (P_{out}^{w}) \omega_i^{cut} \le \omega(t) \le \omega_r^{w} \\ 0 \end{cases} \tag{18}$$

$$\omega_r^w \le \omega(t) \le \omega_o^{cut},\ \omega(t) \le \omega_i^{cut} \text{ or } \omega(t) \ge \omega_o^{cut}$$

Eq. 1 shows the limits imposed by this dependency (18).
The output power of the WT is computed at time t using the equation. When considering varied levels of wind speed, this output power can occur in a variety of ranges. ω_i^{cut}, ω_o^{cut}, ω_r^W, ω(t) and (P_{out}^W) represent cut in and cut out speed state of WT, rate of speed of WT, hourly wind speed at time t and power output, respectively

PV constraint
The PV panels' output power is determined by the sun irradiation at different times of the day. Eq. (19) shows the output power constraints from the PV panels.

$$P_{PV}^e(S(t) = PV_{array} df^{PV} \left(\frac{Si(t)}{Si,STC}\right)[1+\alpha\rho(T_c - T_{cSTC})] \quad (19)$$

The PV_{array} (kW) represent the PV rated capacity of array. Where df^{PV},αρ, *Si,STC, Tc,STC, Tc* represent derating factor, temperature coefficient, solar irradiance and temperature of PV cell at standard test condition, and temperature of PV cell respectively. WT and PV panels create power based on random variables such as wind speed and solar irradiation.

4. Reults and discussion

The optimization of input power and energy expenses of the EH for each day is computed to highlight the advantages of the proposed EH with the mathematical model described in section 3. Additionally, the effect and role of high penetration of RES and BESS on the operation of the EH are also compared in three model cases, as presented in Table 1.

Table 1. Calculated Cased study of the EH structure

Case	Input	Converter	BESS	RES	Output
1	E, G	CHP, TR, GB	–	–	E, H
2	E, G	CHP, TR, GB	–	PW, PV	E, H
3	E, G	CHP, TR, GB	BESS	PW, PV	E, H

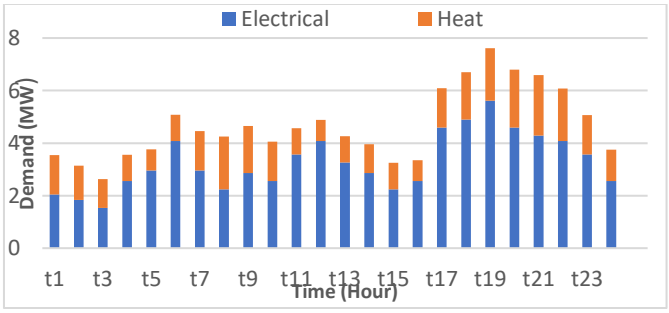

Fig.3 The hourly electrical and heating output load of the EH

Assumptions and database analysis

Electrical and heating demand
During day-to-day operations, the planned EH's energy load need fluctuates dramatically. As a result, in this research, the typical daily electrical and heating load characteristics are depicted

in Fig (3). Where the greatest load output power is at 7 p.m. with a 5.5 MW capacity and the minimum load power is at 3 a.m. with a 1.5 MW capacity, equal to a 26 percent percentage while achieving the maximum. With a power capacity of 2.38MW, the heating load is rather small.

Gas and Electrical energy prices

Currently, gas prices have fluctuated slightly in the near term, so it is roughly 5.5$/KWh on a regular day. Electricity rates fluctuate a lot over time and are determined by the market. Figure 1 depicts the highest electricity price per hour in this article. In figure (4), electricity price reaches its highest price at 7PM which is the higher assumed peak time in this paper. It is assumed that at 7PM most of consumers are back home from their daily activities and the demand of electricity has gone up due to many customers using different appliances at the same time. Therefore, it is logical to state that when the demand is high the price will also be high as it can be seen from both figure (3) and (4) respectively. Furthermore, it can be seen from both figure (3) and (4), that at 3AM in the early hours of the day, when most of the consumers, are assumed to be sleeping, the loads demand is at its lowest state, here the price of electricity at that period is also at its lowest price. Demand response could be incorporated in future studies to help shift consumers load demand from 7PM (peak time and highest electricity price) to 3AM (lowest demand time and less electricity price).

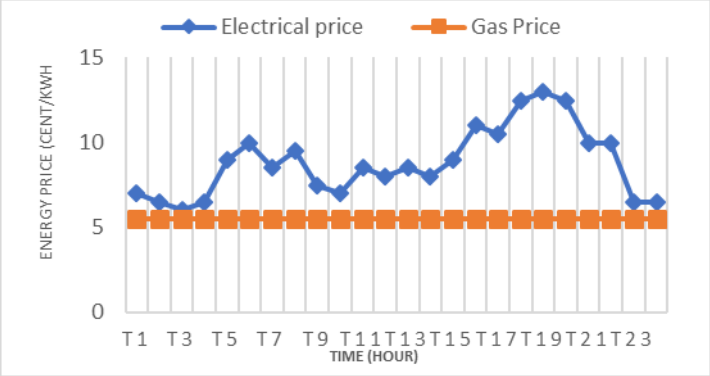

Fig.4 Electricity and gas price

Table 2 shows that energy conversion equipment has a high efficiency. CHP has a total conversion efficiency of 0.85, with 40% of the energy converted to electricity and 50% converted to heat. The efficiency of the GB is 0.9 and the efficiency of the BESS is 0.9. The TR has the highest efficiency of 95%.

Table 2. Efficiency data of equipment

η_T	η_{cHP}^{ge}	η_{CHP}^{gh}	η_{GB}	η_{BESS}
0.95	0.4	0.45	0.9	0.9

Table 3 shows the equipment's power restrictions, as well as the capacity of the BESS and the system, to ensure the equipment's correct operation and ability to supply the system. Finally, take into account the previously stated assumptions. The CPLEX solver of GAMS software was used to solve the proposed MILP problem in this paper, which is one of the most powerful solvers of MILP problems. The proposed optimization problem takes around 62 seconds to solve.

Table 3 Capacity data of equipment and the system

Parameters	**Value**	**Parameters**	**Value**
E_{max}^{e} (MWh)	100	G^{max} (MW)	5
E_{max}^{g} (MWh)	50	E_{BESS}^{max} (MW)	0.15

E^{max} (MW)	10	$E_{min}^{ch/dch}$	0

Results Analysis and Discussion

The model computed with the assumed hypothetical parameters. The results determine the energy flow in the devices in all the operations throughout the hours of the day. The minimum load of energy flow is during 3AM in the early hours of the day (the electricity load is at 1.5MW, the heat load is at 1.13MW), and the maximum load is at 7PM which is the 19th hour of the day (the electricity load reaches 5.5MW, the heat load is at 2.38MW) as shown in Figure 3.
Case 1: At peak load times (between 5 a.m., 7 a.m., 9 a.m., and 5 p.m., 10 p.m.), CHP was chosen to offer additional load with a high capacity of 4.0 MW, because the electricity price was 13 cents per kWh and the gas price was just 5.5 cents per kWh. Hence, it is cheaper to buy natural gas which enable the CHP to simultaneously meet the EH electrical and heat demand. 1.0 MW was obtained by the transmission capacity through. Although, the CHP even at its maximum capacity was not able to meet the assumed high peak load demand of 5.5MW electrical demand. Hence, the remaining 1.5MW electrical load demand was purchased from the electricity network to complement with the 4.0MW electrical load supplied by the CHP. Unfortunately, due to cost of electricity from the market, the total energy cost will increase in this case as seen in Figure 9.

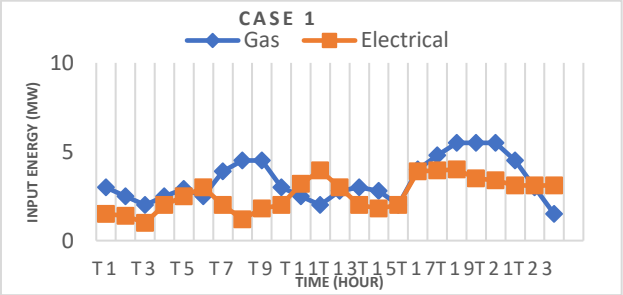

Fig. 5 Total energy input of case 1 in each hour.

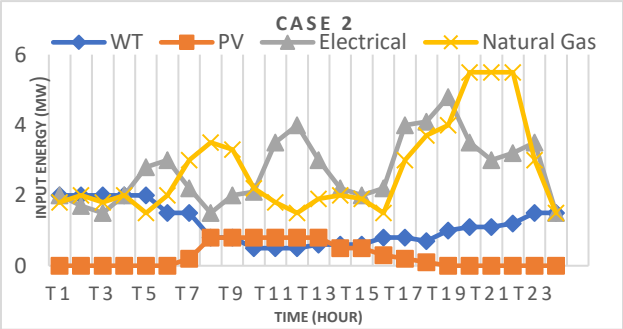

Fig. 6 Input energy of case 2.

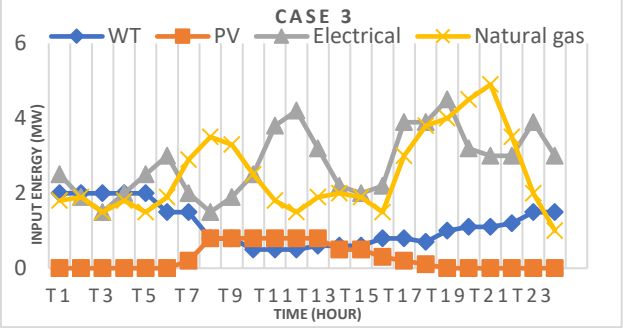

Fig. 7 Input energy of case 3.

When the load is the smallest, the optimal energy flow was chosen in case 2 (i.e., between 1am to 3am and 8am to 11am) as seen in figure (3). The CHP was operating at 1.5MW capacity, and the power capacity of GB is 0.42MW. Additionally, the RESs were introduced to the system in this case to generate extra local electrical power for the EH system. The wind turbine (WT) and the photovoltaic (PV) maximum generation capacity are between 1am to 5am and 8am to 13pm, respectively. Hence, it is assumed that both the WT and PV are generating at their maximum capacity in this case. The WT was operating at 2.0MW, while the PV was operating at 0.8MW. Also, at lower load demand, the electricity price from the market is always cheaper, hence, the EH operator, takes the advantage of lower price to buy more electricity (1.5MW) from the market. From figure (3) the average load demand between 1am to 3am and 8am to 11am was between 1.5MW to 3.5MW. This is because it is assumed that the most consumers are either sleeping or have gone to work. Hence, there is low load demand. In this case, with the utilization of locally clean generated electricity from the WT and PV there is a total of 2.8MW load from the RESs to the EH. Hence, the total sum of CHP electrical load (0.6MW), the purchased electricity from the network (1.5MW), and the 2.8MW load from the RESs was equal to 4.9MW as against the average load demand of between 1.5MW to 3.5MW. From the Calculation, the EH operator in this case is left with about 1.4MW of load that was not consumed. The introduction of RESs have helped the EH operator to purchase less electricity from the market, thereby reducing the EH energy cost. However, the used of RESs in this case have led to the production of high electrical load that is beyond the maximum operating capacity of the EH within the assumed period. This have disrupted the EH operation reliability due to high electricity generation that is beyond the EH demand capacity. To solve this challenge, BESS will be introduced in case 3 to solve the above mention challenges.

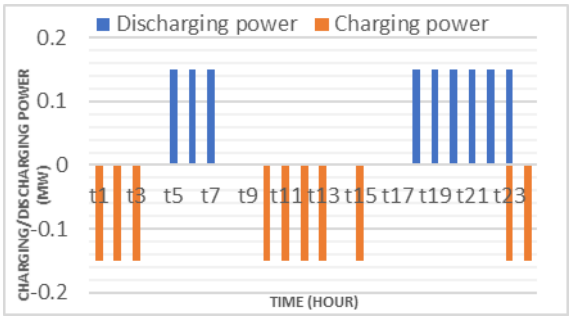

Fig. 8 BESS's charging/discharging power

In case 3, the effect of utilizing BESS locally generated clean renewable energies from WT and PV is analysed on the optimum performance of the EH system. In this case, the BESS was able to store the 1.4MW excess electrical load that was not utilised in case 2. And discharge the load during the EH higher peak demand (between 5AM, 7 AM, 9 AM and from 5 PM to 10 PM) and the RESs are not at their maximum production capacity due to its variability. This will enable the EH operator to purchase less electrical load from the market as compared to case 1 and 2. With this action, the BESS have not only assisted the EH operator to reduce its energy cost but have also created reliability in the EH system by storing the excess 1.4MW load that have caused disruption to the optimum operation of the EH in case 2. BESS also charges with a maximum power of 0.15 MW, which corresponds to the maximum capacity, during the lower electricity pricing hours (from 1AM to 3AM, from 10AM to 1PM, 3PM, and 11PM, 12PM) (8). BESS discharges 0.15 MW back to the EH system during high electricity pricing hours and high peak hours (at 5 a.m., 7 a.m., 9 a.m., and from 5 p.m. to 10 p.m.). In comparison to cases 1 and 2, total energy expenses decreased by 21.5 percent. As a result, the EH's total energy expenses in this example are merely $5572.6 per 24 hour calculation cycle. Furthermore, by incorporating BESS into the efficient operating of EH and optimising the energy flow between CHP and BESS, the total energy purchased by EH is reduced. The calculation result of overall EH

operating costs presented in Fig. 9 reveals that BESS has a significant impact on the EH system's performance. In all three scenarios, the EH optimises the energy flow and kinds. Cases 1 and 2 had operational costs of $10492.6 and $7348.2, respectively. In case 3, the total cost of energy purchased dropped dramatically to $5572.6 or 21.5% when compared to case 2.

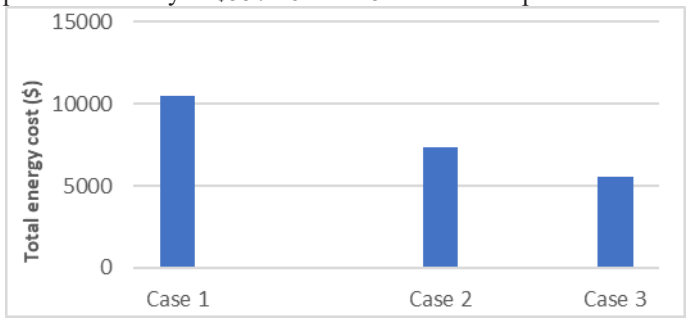

Fig. 9 Total energy cost in the three studied cases

5. Conclusions

The following important concerns are addressed in this study:
1. An EH model with numerous loads that is more profitable is proposed. The BESS is taken into account in the model to boost operational flexibility and efficiency. As a result, the EH's economic and technical elements have also improved.
2. Under high shares of RESs and BESS, the EH's ideal operation schedules are computed with the goal of lowering the energy cost purchased from the system. Three case studies with varied architectures have been provided to compare the different EH models that include RESs and BESS. The optimization results demonstrate that by combining an EH with RES generation and a BESS, the overall cost of energy purchased from the market could be reduced by 21.5 percent while completely satisfying demand.. The EH's BESS minimises the amount of electrical energy purchased from the system and lowers the EH's operating costs. As a result, the calculations in this study may be applicable to real-world challenges. Finally, the EH model in this work primarily solves the EH model's optimal operating problem in terms of energy costs. The uncertainties of loads (electricity and heating), electricity prices, and RESs of WT and PV generators, as well as the device investment cost, are not taken into account. In future work, all of the aforementioned topics should be researched further in order to optimise the planning and operation of EH problems.

References

[1] S. Shokrzadeh and E. Bibeau, "Sustainable integration of intermittent renewable energy and electrified light-duty transportation through repurposing batteries of plug-in electric vehicles," *Energy,* vol. 106, pp. 701-711, 2016.

[2] H. H. Larsen and L. S. Petersen, "DTU International Energy Report 2015: Energy systems integration for the transition to non-fossil energy systems," 2015.

[3] M. F. Tahir, C. Haoyong, K. Mehmood, N. Ali, and J. A. Bhutto, "Integrated energy system modeling of China for 2020 by incorporating demand response, heat pump and thermal storage," *IEEE Access,* vol. 7, pp. 40095-40108, 2019.

[4] J. Reynolds, M. W. Ahmad, and Y. Rezgui, "Holistic modelling techniques for the operational optimisation of multi-vector energy systems," *Energy and Buildings,* vol. 169, pp. 397-416, 2018.

[5] M. Geidl and G. Andersson, "A modeling and optimization approach for multiple energy carrier power flow," in *2005 IEEE Russia Power Tech*, 2005: IEEE, pp. 1-7.

[6] M. Schulze, L. Friedrich, and M. Gautschi, "Modeling and optimization of renewables: applying the energy hub approach," in *2008 IEEE International Conference on Sustainable Energy Technologies*, 2008: IEEE, pp. 83-88.

[7] S. M. Ezzati, F. Faghihi, H. M. Shourkaei, S. B. Mozafari, and S. Soleymani, "Optimum operation of multi-energy carriers in the context of an energy hub considering a wind generator based on linear programming," *Journal of Renewable and Sustainable Energy,* vol. 10, no. 1, p. 014702, 2018.

[8] S. Pazouki, M.-R. Haghifam, and A. Moser, "Uncertainty modeling in optimal operation of energy hub in presence of wind, storage and demand response," *International Journal of Electrical Power & Energy Systems,* vol. 61, pp. 335-345, 2014.

[9] S. Pazouki and M. Haghifam, "Market based short term scheduling in energy hub in presence of responsive loads and renewable resources," 2013.

[10] M. Moeini-Aghtaie, A. Abbaspour, M. Fotuhi-Firuzabad, and P. Dehghanian, "Optimized probabilistic PHEVs demand management in the context of energy hubs," *IEEE Transactions on Power Delivery,* vol. 30, no. 2, pp. 996-1006, 2014.

[11] A. Vian, F. Bignucolo, and M. De Carli, "Modelling and Optimization Approach of Residential Energy Hub: The GHOTEM Project," in *2019 1st International Conference on Energy Transition in the Mediterranean Area (SyNERGY MED)*, 2019: IEEE, pp. 1-6.

[12] M. Salimi, H. Ghasemi, M. Adelpour, and S. Vaez-ZAdeh, "Optimal planning of energy hubs in interconnected energy systems: a case study for natural gas and electricity," *IET Generation, Transmission & Distribution,* vol. 9, no. 8, pp. 695-707, 2015.

[13] A. Y. Abdelaziz, A. M. El-Zonkoly, and A. M. Eladl, "Energy hub optimization using modified firefly algorithm," in *2017 8th International Renewable Energy Congress (IREC)*, 2017: IEEE, pp. 1-6.

[14] M. Geidl, G. Koeppel, P. Favre-Perrod, B. Klockl, G. Andersson, and K. Frohlich, "Energy hubs for the future," *IEEE power and energy magazine,* vol. 5, no. 1, pp. 24-30, 2006.

[15] L. Ni *et al.*, "Optimal operation of electricity, natural gas and heat systems considering integrated demand responses and diversified storage devices," *Journal of Modern Power Systems and Clean Energy,* vol. 6, no. 3, pp. 423-437, 2018.

[16] A. Soroudi, *Power system optimization modeling in GAMS*. Springer, 2017.

Shunt Active Power Filter Implementation Using PQ Theory With LabView

Faisal Falah Aiwa[1], Mahmood T. Alkhayyat[2], Mohammed Y. Suliman[3]
{faisal.aiwa@ntu.edu.iq[1], m.t.alkhayyat@ntu.edu.iq[2], mohammed.yahya@ntu.edu.iq[3]}
Department of Electrical Power Techniques Engineering, Technical Engineering College, Northern Technical University, Mosul, Iraq[1,2,3]

Abstract. A shunt active power filter (SAPF) is a suitable harmonics suppression solution in power systems. Traditional SAPF researchers have generally used the Matlab/Simulink platform in the design and implementation. Which is allows validation of the SAPF algorithm and theoretically simulates the compensation effect. However, such SAPF cannot apply in practical cases. LabView is a popular application for data collection and instrument control. With external equipment such as a Data Acquisition Card (DAQ), LabView can monitor and control the system in real-time. The main goal of the work presented in this paper is to use the LabView platform with NI USB - 6009 DAQ in the design and implementation of a shunt active power filter. With the aid of LabView intelligent control software, the harmonic components of the source current are extracted using the Instantaneous Active-Reactive Power Theory (PQ) theory. The performance of a shunt active power filter has been demonstrated in simulation and experimental setup.

Keywords: shunt active power filter(SAPF), LabView, Data acquisition system (DAQ), total harmonic distortion (THD), power quality, PQ theory.

1 Introduction

Energy users have become more conscious and sensitive to power quality variations as sensitive electronic equipment has become more common. Harmonics [1] are the primary cause of power quality degradation. A harmonic is the sine component of a periodic wave whose frequency is an integer multiple of the fundamental frequency. The total harmonic distortion (THD) equation [2] is used to calculate harmonic distortion in an electrical power system.

Harmonic distortion in electrical power systems is mostly caused by non-linear loads. Bridge rectifiers, both uncontrolled and controlled, speed-controlled motor drives, televisions, led bulbs, personal computers, and uninterruptible power supply (UPSs) [3] are examples.

Reduced power factor, decreased efficiency, power system voltage fluctuations, communications interference, circuit breaker dysfunction, equipment heating, and breakdown and injury are some of the effects of harmonics. Harmonics can thus be thought of as a pollutant that affects the entire power system [4]. Passive filters have traditionally been used to minimise harmonics, however they have issues and drawbacks such as huge size and weight, greater cost, fixed compensation, and resonance issues with loads. As a result, a focus on a power electronic solution, such as shunt active power filters (SAPF), has become necessary in the electrical power system [5]. Because of its modest physical size and versatility, SAPF is an excellent solution for power quality issues. In addition, it has a lower cost and operating loss.

Shunt active power filters (SAPF) based on voltage source inverters, as shown in Figure 1, are appropriate solutions for reducing current harmonics and improving power quality. SAPF's core concept is to use power electronics to provide current compensation components that

IMDC-IST 2021, September 07-09, Sakarya, Turkey
Copyright © 2022 EAI
DOI 10.4108/eai.7-9-2021.2315487

eliminate harmonic current components that develop as a result of non-linear loads [7].

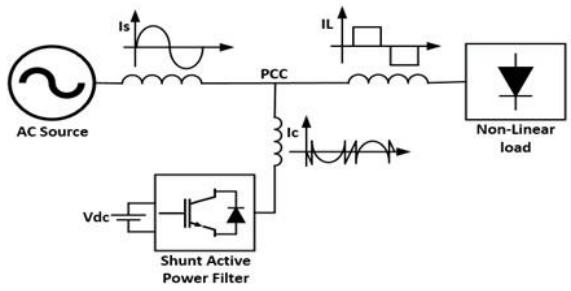

Fig. 1. Principal of SAPF.

Many researchers were worked to improve Power quality based on the harmonic current detection methods and compensation current control strategies in the literature. The authors in [8] presented four controls algorithm to control the shunt active filter. The theory (PQ), an adaptive phase locked loop (PLL), Instantaneous active and reactive current method (DQ), and Synchronous detection method (SD) are designed in Matlab Simulink to generate the reference current of SAPF for mitigation of source current harmonics. The authors in [9] have proposed a DQ-PQ technique for compensating unbalanced nonlinear loads and different in line currents. As well as, eliminating the negative and zero sequence components of the line currents using SAPF. Matlab simulation was used in the design and implementation. The research in [10] have presented the SAPF simulation based on the (PQ) theory in Matlab and LabView software and compare the results.

In this study, the SAPF control circuit based on (PQ) theory was implemented in real-time using Laboratory Virtual Instrument Engineering Workbench (LabView) and NI USB - 6009 DAQ to mitigate source current harmonics caused by non-linear loads and improve power quality by lowering THD.

2 Shunt Active Power Filters (SAPF)

In 1976, Gyugyi and Strycula proposed the notion of shunt active filtering for the first time. It's the most popular type of active filter. SAPF converter could be a voltage source inverter or a current source inverter, and it can be single-phase or three-phase. This filter works as a current source, injecting the load's harmonic components but with a 180° phase shift [11]. Its controller calculates the compensating current reference in real time and compels a power electronic converter to correctly synthesize it. This method allows for selective and adaptive active filtering. In other words, a SAPF can correct for a nonlinear load's harmonic current and periodically track changes in its harmonic content [12].

3 Instantaneous Active-Reactive Power Theory (PQ)

In (PQ), the reference current signal calculation is based on measuring the three-phase voltages and currents to the power system, then transforming them into (α-β) coordinates by an algebraic transformation (Clarke Transformation) [12], [13]. **Figure 2.** depicts a simple schematic of PQ.

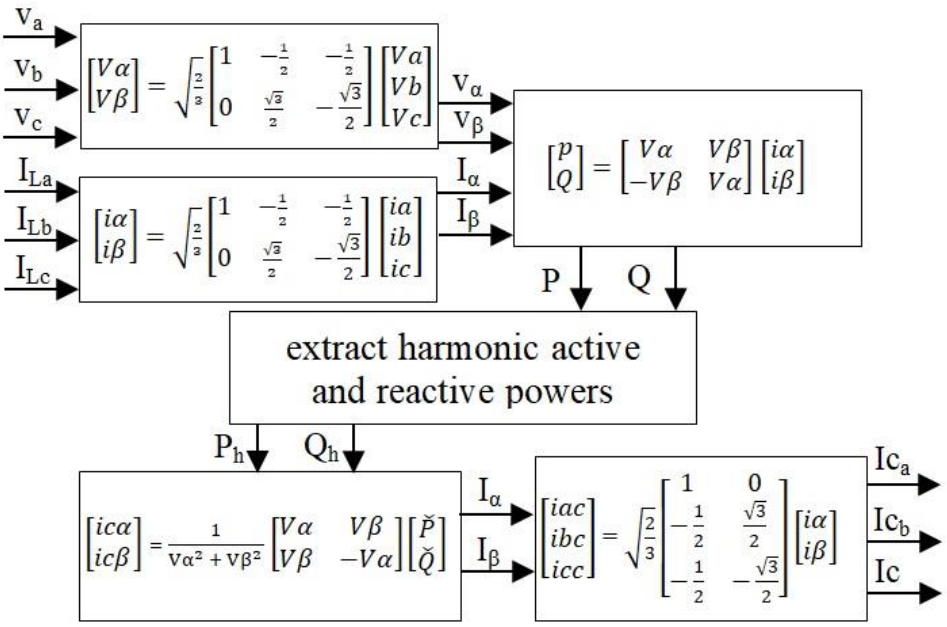

Fig. 2. Simple schematic representation of (PQ) theory.

The Clarke transformations are used to convert the three-phase voltages and load current in the α-β coordinates as follow:

$$\begin{bmatrix} V\alpha \\ V\beta \end{bmatrix} = \sqrt{\frac{2}{3}} \begin{bmatrix} 1 & -\frac{1}{2} & -\frac{1}{2} \\ 0 & \frac{\sqrt{3}}{2} & -\frac{\sqrt{3}}{2} \end{bmatrix} \begin{bmatrix} Va \\ Vb \\ Vc \end{bmatrix} \tag{1}$$

$$\begin{bmatrix} i\alpha \\ i\beta \end{bmatrix} = \sqrt{\frac{2}{3}} \begin{bmatrix} 1 & -\frac{1}{2} & -\frac{1}{2} \\ 0 & \frac{\sqrt{3}}{2} & -\frac{\sqrt{3}}{2} \end{bmatrix} \begin{bmatrix} ia \\ ib \\ ic \end{bmatrix} \tag{2}$$

Then, for the three-phase system, calculate the value of instantaneous active and reactive power as follows:

$$\begin{bmatrix} p \\ Q \end{bmatrix} = \begin{bmatrix} V\alpha & V\beta \\ -V\beta & V\alpha \end{bmatrix} \begin{bmatrix} i\alpha \\ i\beta \end{bmatrix} \quad (3)$$

Where:
p: real power.
Q: reactive power.

Observing the equation (3) the P and Q can be put them in the following form:

$$P = \bar{P} + \check{P} \quad (4)$$

$$Q = \bar{Q} + \check{Q} \quad (5)$$

Where:
$\bar{P}$: is the average component of P and is linked to conventional fundamental active current.
$\check{P}$: is the oscillating part of P and linked with harmonics caused by the oscillating component of instantaneous real power.
$\bar{Q}$: is the average part of Q and is linked with reactive power due to the fundamental component of currents and voltages.
$\check{Q}$: is the oscillating part of Q and is linked with harmonic currents from the oscillating components of instantaneous reactive power.

A low pass filter is used to extract the fluctuating sections of the real and reactive power. In α-β coordinates, compensating currents are calculated as follows:

$$\begin{bmatrix} ic\alpha \\ ic\beta \end{bmatrix} = \frac{1}{V\alpha^2 + V\beta^2} \begin{bmatrix} V\alpha & V\beta \\ V\beta & -V\alpha \end{bmatrix} \begin{bmatrix} \check{P} \\ \check{Q} \end{bmatrix} \quad (6)$$

Finally, the currents in α-β coordinates are converted to a-b-c coordinates as follows:

$$\begin{bmatrix} ica \\ icb \\ icc \end{bmatrix} = \sqrt{\frac{2}{3}} \begin{bmatrix} 1 & 0 \\ -\frac{1}{2} & \frac{\sqrt{3}}{2} \\ -\frac{1}{2} & -\frac{\sqrt{3}}{2} \end{bmatrix} \begin{bmatrix} ic\alpha \\ ic\beta \end{bmatrix} \quad (7)$$

After that, the shunt active filter controller uses the three-phase compensation current as a reference signal.

4 Simulation in LabView

The performance of the SAPF was tested by using the LabView program by designing the PQ theory and simulated the source voltage and distorted load current using a signal generator block. **Figure 3.** shows the PQ theory designed in LabView.

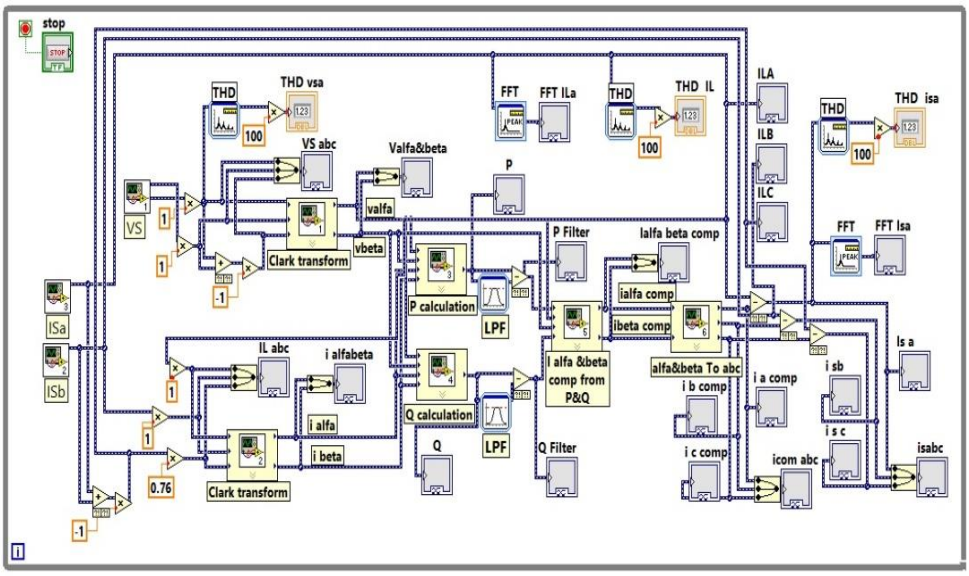

Fig. 3. PQ theory in LabView.

Figure 4. shows the waveform of three-phase source voltage. Which it is found that there is no distortion.

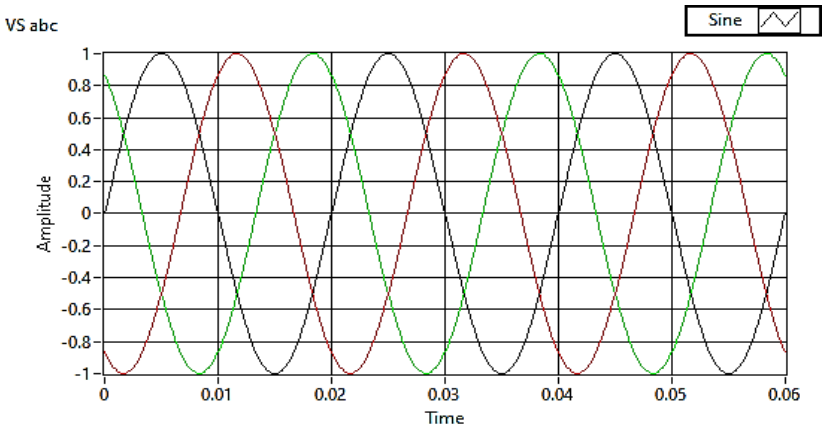

Fig. 4. Source voltage without and with SAPF.

The waveform of phase (a) current of the load, SAPF compensation currents, and current of the source is showing in **Figure 5.** The SAPF mitigates the THD of source current from 22.36% to 1.86%.

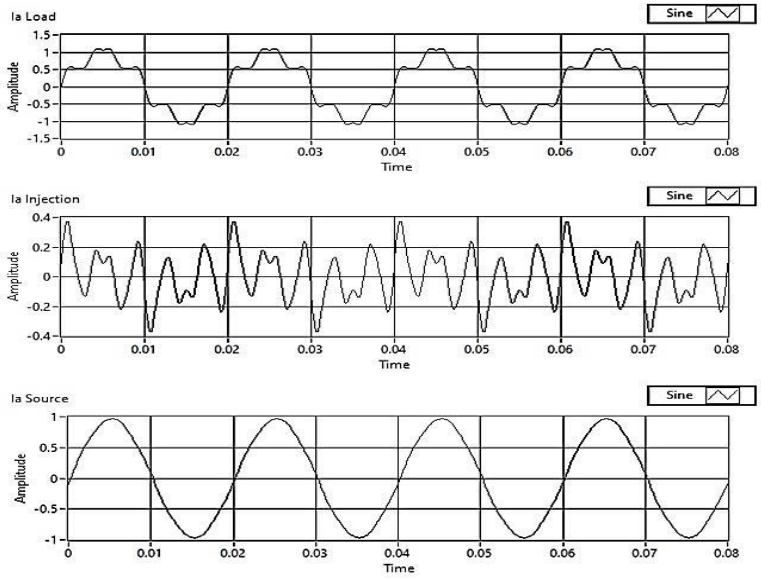

Fig. 5. load, injection, and source current with SAPF.

The F.F.T of source current without and with SAPF is shown in **Figure 6.** The SAPF mitigated the 5th, 7th, and 11th harmonics orders, which were causes the source current distortion.

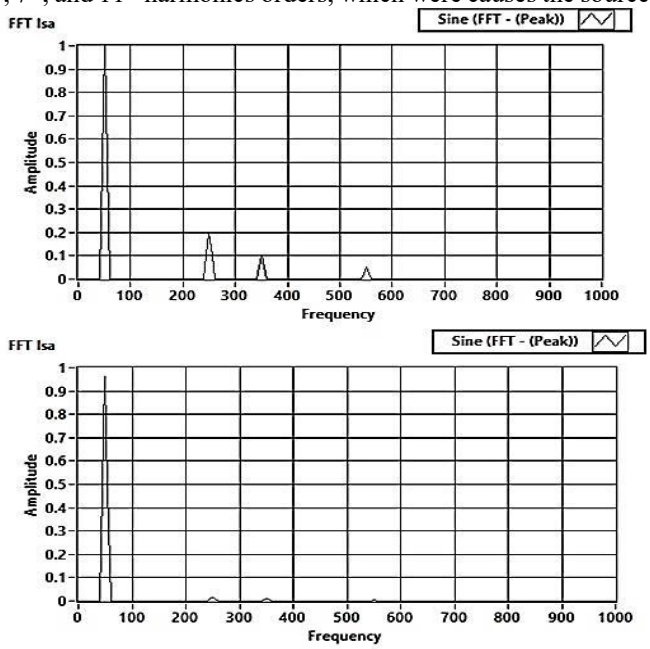

Fig. 6. F.F.T analysis for source current without and with SAPF.

5 Experimental Work and Results

The experimental block diagram is shown in **Figure 7.**

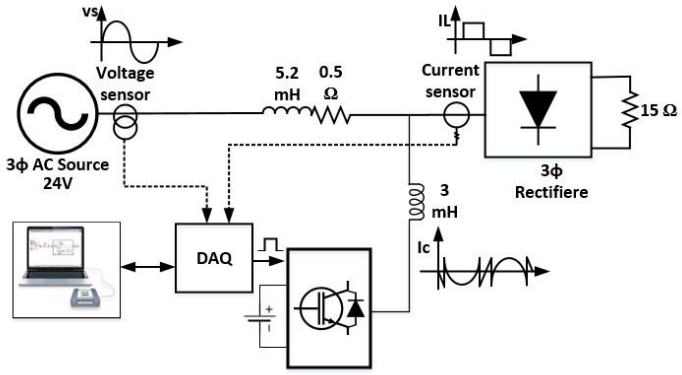

Fig. 7. Experimental block diagram.

The sensors that have been used in the practical circuit are the current transformer (ZMCT103C-ETC) [14] and voltage sensors (170640) [15] as shown in **Figure 8.**

Fig. 8. Voltage sensor and current transformer.

The DataAcquisition (NI USB - 6009) [16] that has been used is shown in **Figure 9.**

Fig. 9. NI USB – 6009 DAQ.

The complete experimental setup of the SAPF based on PQ theory with the DAQ USB-6009 control is shown in **Figure 10.**

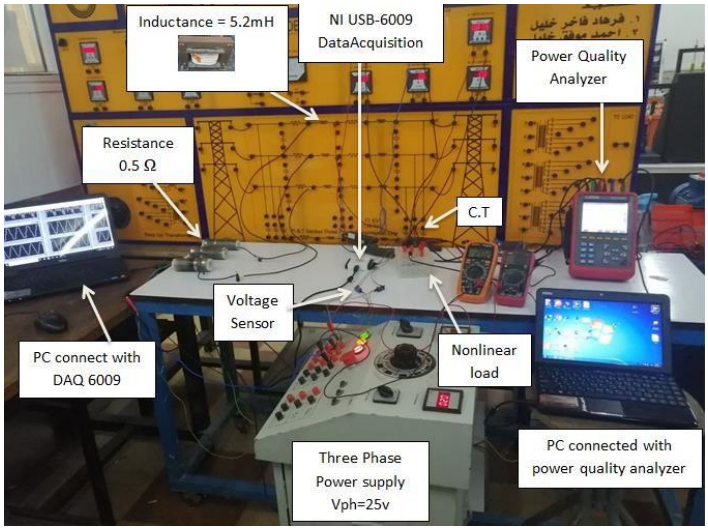

Fig. 10. Experimental setup.

Figure 11. shows the LabView control circuit based on PQ theory SAPF. The input signal coming from the voltage and current signal was input by using the DAQ assistant block.

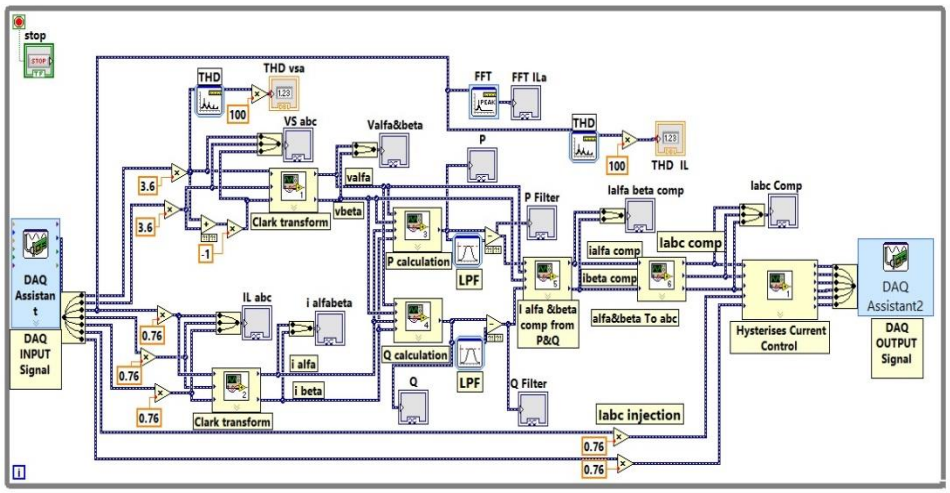

Fig. 11. LabView control circuit.

Figure 12. Three-phase sinusoidal system using a power quality analyzer (HZCR5000) [17].

Fig. 12. Three-phase source voltage with THD.

Figure 13. shows the source current waveform without SAPF, and it is THD about 21.5%, and F.F.T analysis is shown in **Figure 14.**

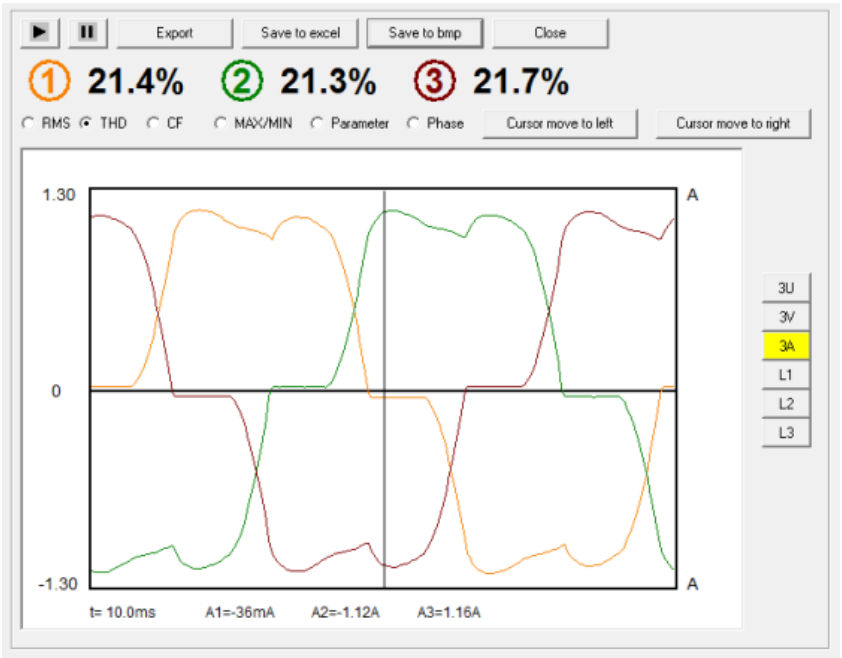

Fig. 13. THD without SAPF Source current.

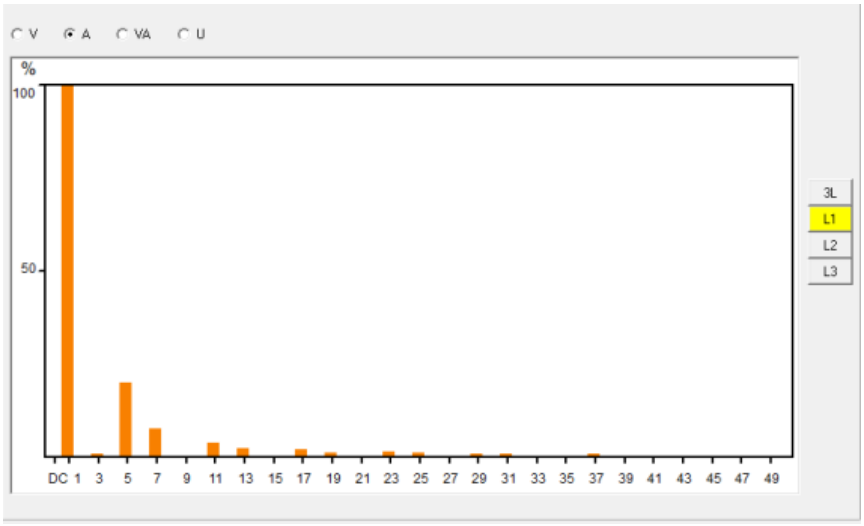

Fig. 14. F.F.T analysis of source current phase without SAPF.

Figure 15. shows the load, SAPF injection, and source current phase (a) with SAPF.

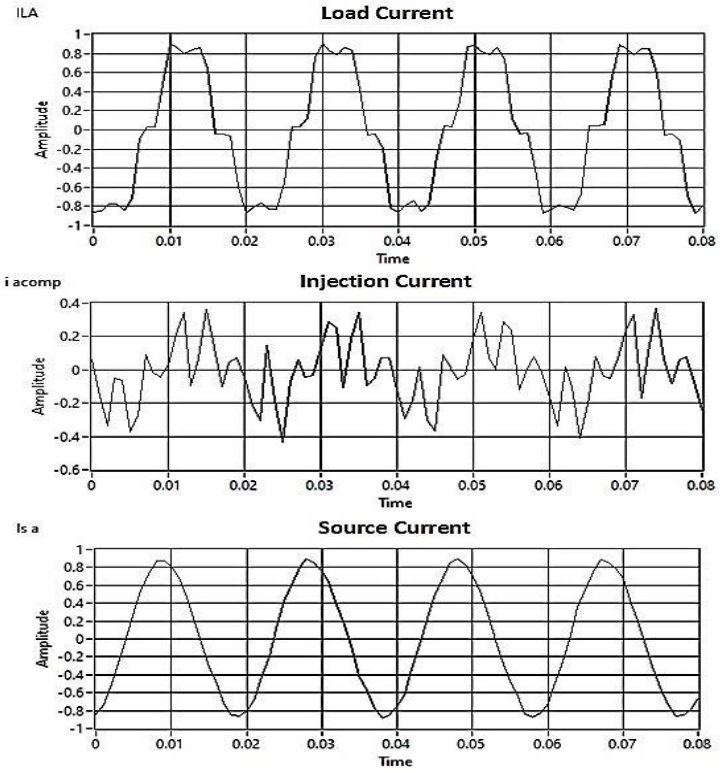

Fig. 15. load, injection, and phase of the source current.

The THD of source current with SAPF was reduced to 3.47%. The F.F.T of source current with SAPF is shown in **Figure 16.**

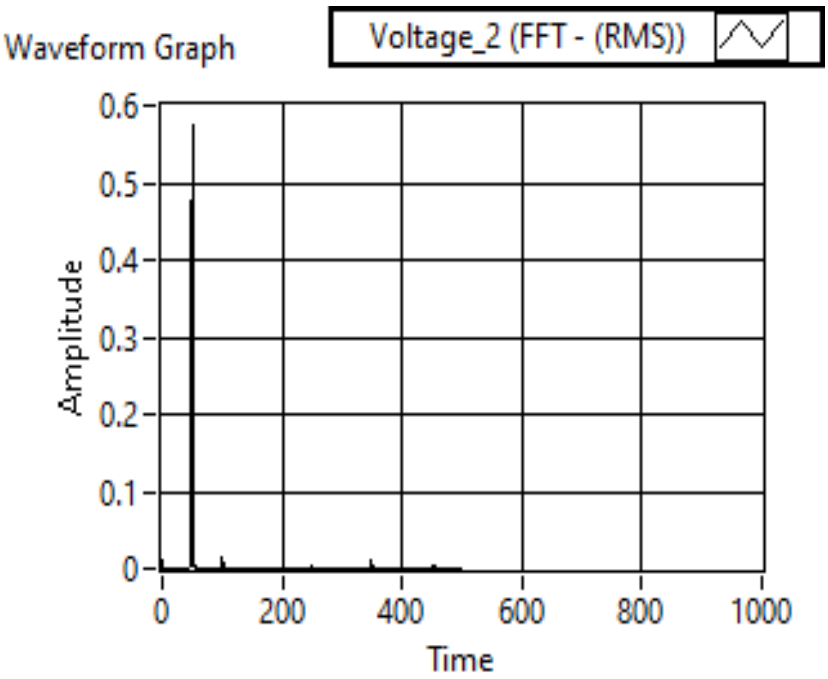

Fig. 16. F.F.T of source current.

6 Conclusion

The proposed study demonstrates an effective monitoring and regulating mechanism for a shunt active power filter, allowing SAPF for harmonic mitigation to be implemented in practise. Because it is versatile, easy, flexible, and reliable, the LabView platform performs well for creating and implementing power quality monitoring systems and harmonic reduction. For the simulation of the SAPF control circuit, LabView was initially employed. Current and voltage sensors provide analogue signals, which are fed into the PC through the NI USB-6009 DAQ card. LabView is then used to process and analyse the raw data. It's a sophisticated application that can swiftly acquire, analyse, and show any electrical signal. It aids in the research, measurement, analysis, and control of power system harmonics. Simulations are used to verify the effectiveness of the (PQ) control method, which is then confirmed by findings from an experimental setup. The results show that the SAPF controller based on the LabView package performs well, decreases source current distortion, and improves power quality..

References

[1] Asia'u Talatu Belgore, Bara'u Gafai Najashi. Control Techniques for Shunt Active Power Filters. International Journal of Engineering Research & Technology (IJERT). 2020. vol. 9 (no. 09). pp. 1054–1059.
[2] D. M. Soomro, M. A. Omran, and S. K. Alswed. Design of a shunt active power filter to mitigate the harmonics caused by nonlinear loads. ARPN J. Eng. Appl. Sci. 2015. vol. 10 (no. 19). pp. 8774–8782.
[3] Z. Salam, P. C. Tan, and A. Jusoh. Harmonics mitigation using active power filter: a technological review," Elektrika. 2006. vol. 8 (no. 2). pp. 17–26.
[4] C. Rejil and A. K. R. Design and Simulation of Three Phase Shunt Active Power Filter Using SRF Theory. Adv. Electron. Electr. Eng. 2013. vol. 3 (no. 6). pp. 651–660.
[5] N. Booma and S. R. Reddy. Design And Simulation Of Hybrid Active Power Filter For Power Quality Improvement. i-manager's J. Electr. Eng. 2012. vol. 6 (no. 2). pp. 16–21.
[6] Almaita, Eyad KH. Adaptive Radial Basis Function Neural Networks-Based Real Time Harmonics Estimation and PWM Control for Active Power Filters. Western Michigan University. 2012. Dissertations. 9.
[7] M. Halawa, B. Abou-zalam, and A. Sobaih. Power Quality Improvement Using a Shunt Active Power Filter Based on the Hysteresis Current Controller. Int. Electr. Eng. J. 2016. vol. 7 (no. 5). pp. 2266–2278.
[8] B. Abd El-Rahman, E. G. Shehata, A.-H. El-Sayed, and Y. S.Mohamad. Performance Analysis of Active Power Filter Controllers for Harmonics Mitigation in Power Systems. J. Adv. Eng. Trends. 2020. vol. 39 (no. 1). pp. 77–88.
[9] M. T. Mahmood Alkhayyat and S. M. Bashi. Mitigation Unbalance Nonlinear Loads and Dissimilar Line Currents Using Shunt Active Power Filter SAPF. Int. J. Adv. Eng. Manag. Sci. Infogain Publ. 2016. vol. 2 (no. 10). pp. 2454–1311.
[10] Z. Zhang, H. L. Jiang, H. J. Zhang, and J. P. Wang. Active power filter design and simulation by combining LabVIEW and Simulink. International Conference on Advanced Power System Automation and Protection. 2011. vol. 2. pp. 1104–1109.
[11] Ali Emadi, Abdolhosein Nasiri and Stoyan B. Bekiarov. UNINTERRUPTIBLE POWER SUPPLIES AND ACTIVE FILTERS. Muhammad H. Rashid. United States of America. CRC Press LLC. 2005. no. 11–12.
[12] M. A. HIROFUMI AKAGI, EDSON HIROKAZUWATANABE. INSTANTANEOUS POWER THEORYAND APPLICATIONS TO POWER CONDITIONING. Tariq Samad. Inc. Hoboken, New Jersey. John Wiley & Sons . 2017. 30-45
[13] M. Chakravarthy, S. N. Saxena, and S. Ram. Control of Shunt Active Power Filter Using LabVIEW. International Journal of Engineering and Innovative Technology (IJEIT). 2012. Volume 2 (no.3). pp. 2277-3754
[14] ["ZMCT103C.5A Range AC Current Transformer Current Sensor Module General."
[15] S. G. Technology, "Model : Voltage Sensor / 170640 Reference Code :," no. 1000. p. 170640, 2015.
[16] National Instrument Team, "User Guide Ni Usb-6008/6009.". 2015. pp. 1–26
[17] "HZCR5000-Power-Quality-Analyzer.pdf." .

Using Treated Recycled Demolition Aggregate in Concrete

Safana Qahtan Ragab[1], Hasan Jasim Mohammed[2]
{engsafana2020@gmail.com[1], dr.hassanjassim@tu.edu.iq[2]}

Department of Civil Engineering, Faculty of Engineering, Tikrit University, P.O. Box (42) Tikrit, Iraq[1,2]

Abstract. The investigation focuses on the mechanical properties of treated recycled demolition aggregate, which was treated in two ways: one by immersing recycled demolition aggregate in NaOH solution for 24 hours and the other soaking in cement neat. The mixes were produced by substituting treated recycled demolition aggregate for 0%, 20%, 40%, and 60% of the coarse aggregate weight in both methods. The weight of the cement is replaced by 10% silica fume. Compressive strength, splitting tensile strength, modulus of rupture, and density tests were done. The compressive strength and modulus of rupture of treated recycled demolition aggregate concrete rose by 61% and 27%, respectively, as the treated recycled demolition aggregate ratio increased. Treated recycled demolition aggregate concrete has a 17 percent lower tensile strength and 12.5 percent lower density than conventional concrete. Recycled demolition aggregate that has been treated is suitable for use in concrete and meets all requirements.

Keywords: Treated recycled demolition aggregate, coarse aggregate, NaOH, Cement neat, Mechanical properties.

1 Introduction

Concrete is often made with natural elements such as coarse aggregate, fine aggregate, and cement. When pressured, compression has the strength of concrete, but it is brittle. High elasticity, twisting resistance, low creep, and porosity are only a few of the benefits of concrete [1].

Extensive studies have been carried out to assess the use of recycled demolition aggregate (RDA) in concrete. This topic is also important because of the expected increase in noticeable coarse aggregate usage [2]. Demolition is frequently regarded as a waste product as represented in Fig 1. To reduce the negative environmental consequences of waste, a recycling method is required. Demolition trash produces when ancient structures are destroyed by explosion or demolition. Using a way of recycled demolition waste of the buildings would help to enhance the environment. Recycled demolition aggregate (RDA) is a type of demolition waste-derived aggregate [1], [3]. The problem with demolition aggregate is that the dust and other materials in the aggregate cause less bonding between the RDA and the cement

IMDC-IST 2021, September 07-09, Sakarya, Turkey
Copyright © 2022 EAI
DOI 10.4108/eai.7-9-2021.2315486

paste. As a result, it is critical to address this issue by treating the RDA to reduce the effect of these materials [3].
The study aims are to address the mechanical properties of concrete that contains treated recycled demolition aggregate (TRDA). TRDA was treated in two methods: one by immersing RDA in NaOH solution for 24 hours and the other soaking in cement neat. TRDA components are used in various ratios as a partial replacement for coarse aggregate weight in concrete mixes, with varying amounts of (0 %, 20 %, 40 %, and 60 %), for two methods. 10% silica fume is used to replace the cement weight (SF). The mechanical parameters of TRDA concrete are investigated, including compressive strength, tensile strength, density, and modulus of rupture.

Fig 1. Demolition waste.

2 Materials and Testbed

The Portland cement type I was utilized. Cement was tested the chemical and physical features according to reference [4]. The sand was used as the fine aggregate. Its tests were performed according to reference [5] sieve grading, chemical, and physical property testing criteria. The normal coarse aggregate (gravel) size was 12.5 mm. Gravel was tested following requirements as in [6].
RDA was gathered from building demolition and used to substitute natural coarse aggregate weight at four different weight ratios: 0%, 20%, 40%, and 60%. As depicted in Figure 2, RDA was created out of brick, ceramic, tile, and concrete elements. RDA was treated in two ways: first, it was immersed in NaOH solution for 24 hours, and then thoroughly rinsed with running water before being left on sheets in the sun to achieve the condition of saturated surface dry SSD. Second, it was immersed in cement neat for two hours before use, as shown in Fig 2. RDA sieve analysis shows that it corresponds to coarse aggregate grading according to reference [6], as shown in Table 1.

Table 1. Sieving of RDA test

Size of sieve	Passing Cumulative (%)	Specifications [6]
20 mm	100	100
14 mm	97	90 – 100
10 mm	71	50 – 85
5 mm	7	0 – 15
2.36 mm	2	0 – 5

a) Demolition collected.

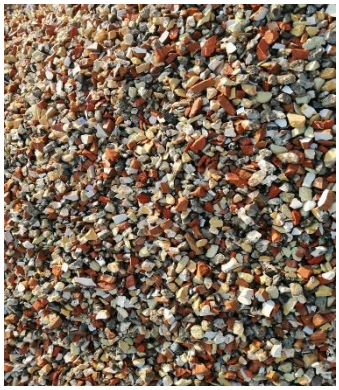

b) Recycled demolition aggregate.

c) RDA treated using cement neat.

b) RDA treated using NaOH

Fig 2. RDA collected and treated.

SF is used in place of the equivalent cement (10 % by weight). SF strengthens the bond between the cement paste and the TRDA, as in previous references [2], [3]. The used mixture is illustrated in Table 2. TRDA is used to replace 0%, 20%, 40%, and 60% of the weight of coarse aggregate in the mixes (two methods of treatment). The normal concrete uses similar mix concrete technique as designated by the ACI code requirements [7].

Standard test specimens were used to test the various parameters. A slump test was performed on all types of combinations in accordance with reference [8]. Reference [9] employed six cylinders with a diameter of 150 mm and a height of 300 mm to determine compressive strength after 28 days of cure. It can be used to determine the splitting tensile strength (ASTM C496 / C496M-17) [10] and the density of concrete (ASTM C29 / C29M-17a) [11]. Prism specimens ranging in size from 100 x 100 x 500 mm were cast to calculate the modulus of rupture, as presented in Figure (3). The test was carried out by reference [12].

Table 2. Materials amounts in mixes.

Mixes	Cement (kg/m^3)	SF (kg/m^3)	Sand (kg/m^3)	Coarse Aggregate (kg/m^3)	Water (kg/m^3)	Treated DA (kg/m^3)		% Replaced
						NaOH	Cement mortar	
NC	490	0	680	960	191	0	0	0
TN20	441	49	680	768	153	192	0	20
TN40	441	49	680	576	153	384	0	40
TN60	441	49	680	384	153	576	0	60
TC20	441	49	680	768	153	0	192	20
TC40	441	49	680	576	153	0	384	40
TC60	441	49	680	384	153	0	576	60

SP : 4.9 kg/m^3

Fig. 3. Modulus of rupture test (sample failure).

3 Results and Discussion

Table 3 shows the outcomes of several concrete compositions. In this investigation, a typical concrete mixture was used as a comparison guide. A major variable was employed in the other mixes to replace the regular coarse aggregates with a TRDA material. In addition, silica fume was used to increase compressive strength. In addition, a super-plasticizer was employed to increase TRDA concrete's workability. An increase in the ratio of TRDA substitution leads to an increase in the slump's results. Because of the super-plasticizer effect,

this happened. When the ratio of TRDA in the mixes was increased, the compressive strength increased (TN20, TN40, TN60, TC20, TC40, and TC60). This is due to the use of the SF and SP. SF aids in the strengthening of the bond between the TRDA and the cementitious materials. Furthermore, the SF is stronger than ordinary cement.
TRDA concrete compressive strength and modulus of rupture increased by 61% and 27%, respectively, as the TRDA ratio increased. The use of SF helps in the building on solid bond among the cementitious materials and the TRDA. The role of SF as in previous references [1], [2]. Tensile strength is reduced by 17% when compared to normal concrete. It also show the density of concrete-TRDA is approximately 12.5 % lower than that of normal concrete. The compressive strength of TRDA concrete treated with cement neat is greater than that of NaOH solution. This happened because cement neat bonded better than NaOH solution between concrete components. TRDA is suitable for use in concrete and meets all criteria due to the strength in the limits of the requirements.

Table 3. Concrete mixes results.

Mixes	Slump (mm)	Fresh density (kg/m^3)	Tensile stress (MPa)	Compressive strength (MPa)	Modulus of rupture (MPa)
NC	40	2360	3.89	39.3	10.3
TN20	55	2250	3.79	54.6	13.1
TN40	59	2123	3.65	58.0	12.5
TN60	68	2065	3.39	53.0	12.0
TC20	62	2310	3.68	60.1	12.7
TC40	67	2189	3.43	63.4	12.5
TC60	75	2102	3.22	56.6	11.9

4 Conclusions

A test of the concrete mechanical characteristics including TRDA was provided for the current experimental effort. This is part of a recent trend of studies involving the substitution of rubbish and trash for existing concrete gravel. The following conclusions were reached: The slump's outcomes improve as the ratio of TRDA substitution is increased. The super-plasticizer effect was to blame. By reducing the amount of coarse aggregate used and replacing it with lighter recycled TRDA, a concrete density reduction of up to 12.5 percent of the typical mixed density can be achieved. The recycled TRDA content in the concrete mix, while just a partial substitution for gravel, boosts the compressive strength by roughly 61 percent when compared to standard concrete. Finally, recycled TRDA material has a substantial impact on concrete splitting tensile strength, resulting in a drop of roughly 17 percent, while the modulus of rupture is raised by up to 27 percent in the maximum substitution ratio with recycled TRDA.

Acknowledgments

Tikrit University has provided support for this study. The authors would like to convey their gratitude to the academic experts who helped them with this research.

References

[1] Bai G., Zhu C., Liu C., and Liu B., An evaluation of the recycled aggregate characteristics and the recycled aggregate concrete mechanical properties. Construction and Building Materials. 2020; 240: 117978.
[2] Shirani Bidabadi M., Akbari M., and Panahi O., Optimum mix design of recycled concrete based on the fresh and hardened properties of concrete. Journal of Building Engineering. 2020; 32: 101483.
[3] Kazemian F., Rooholamini H., and Hassani A., Mechanical and fracture properties of concrete containing treated and untreated recycled concrete aggregates. Construction and Building Materials. 2019; 209: 690-700.
[4] ASTM, C150M-19a C. Standard specification for Portland cement; 2019.
[5] ASTM, C778-17. Specification for standard (sand) fine aggregate; 2017.
[6] ASTM, C33M-18 C. Specification for standard concrete aggregates; 2018.
[7] ACI, 211 C. Standard Practice for Selecting Proportions for Normal, Heavyweight, and Mass Concrete; 1991.
[8] ASTM, C143M-15a C. Standard test method for slump of hydraulic-cement concrete; 2015.
[9] ASTM, C39/C39M-18. Standard test method for compressive strength of cylindrical concrete specimens; 2018.
[10] ASTM, C496M-17 C. Standard test method for splitting tensile strength of cylindrical concrete specimens; 2017.
[11] ASTM, C29M-17a C.. Standard test method for bulk density (“unit weight”) and voids in aggregate; 2017.
[12] ASTM, C78–02.. Standard test method for flexural strength of concrete (using simple beam with third-point loading); 2002.

Using Geographic Information System (GIS) as a Supporting Tool in Public Facilities Planning: A Case Study on the City of Nasiriyah

Ahmed Salman Hasan[1], Khaldoon T. Falih[2]
[ahmed.hassan@stu.edu.iq[1], khaldoon@alayen.edu.iq[2]]

Nasiriyah Technical Institute, Southern Technical University, Iraq[1]
Petroleum Engineering College, Al-Ayen University, Dhi-Qar, Iraq[2]

Abstract. The accessibility and development of new park facilities is an important aspect of city planning. Nasiriyah (Iraq) is a city that is in dire need of park facilities. Thus, this study aims to examine the availability of the land and select the optimum locations for public parks in the city. To achieve this, first, the existing public parks are investigated using carried out within the framework of the Analytic Hierarchy Process (AHP) by integrating with Geographic Information System (GIS). Then, a Euclidean-allocation model was used to provide a useful tool for the allocation of public facilities and to measure the accessibility for the best locations of parks. Using a decision support system software with weighting three attributes of land availability, land value, and population density. The final results identified 6 potential sites which represent only 2.1% of the total area as the most suitable land for parks.

Keywords: Geographic Information System, Park Facilities Planning, City Planning.

1 Introduction

Public facilities planning involves the application of planning standards. For example, how much space and area is required for planning of public parks for the welfare of people in a city. Since planning standards specified the area needed where the public facilities should be provided to the people, therefore, green spaces are an important element in bringing life into urban cities on a both social and ecological scale [1]. Green spaces reduce the rising the temperature in urban areas and make the environment very healthy and favourable [2]. Open spaces generally provide a low level of intervention and continuous functioning of the ecosystems and survival of a better environment in urban areas. The functions of open spaces are manifold but they can be categorized into two such as; the provision of recreation and the provision of better services to the people living in the society in the specified area of the city [3].

One of the important aspects of urban life is the provision of green spaces, which creates a positive contrast to the concrete structures in the city. However, there is a higher focus on other social issues such as employment, education, and safety since they have a higher effect on the general populace. As the cities begin to grow and evolve, the building of parks and green spaces in becoming an issue that can affect the city in a positive way. Thus, it is slowly becoming more important, as the city grows both financially and culturally and environmental factors start to gain more traction among the general population [4].

IMDC-IST 2021, September 07-09, Sakarya, Turkey
Copyright © 2022 EAI
DOI 10.4108/eai.7-9-2021.2315484

There are several studies performed in the last decade that focus on the importance of the well-being of the inhabitants of the society [5]. Most of these researches attributes the problems faced in urban environments due to an overflow of population and increasing density in urban areas. The existence of green environments in forms of parks and other forms of green elements in the city contribute towards its environmental sustainability [6].

There are also deeper ramification than simple sustainability, such as psychological relief particularly due to the COVID-19 pandemic [7]. The pandemic itself had created an environment of isolation that psychologically affected the people living in the city. The existence of parks creates the perfect starting point for people to reintegrate into society as the counties and cities open up.

One of the tools used in order to aid in the urban planning of a city, is the, the Geographic Information System (GIS) [8]. This application supports and involves all these factors in resolving the facility location problems of urban and regional planning [9]. Since planning itself contains a wide range of infrastructures such as transportation planning; infrastructure planning and public facility planning.

However, GIS can be used as an intelligent tool to find the location for public facilities and make information accessible. A facility location model used in GIS can help to minimize the travel cost and also find the closest facility location or service areas of the facility [10]. It is a viable tool used by planners in the decision-making process. This model may cover optimization solutions, which can be vital in urban planning and site planning [11]. However, it helps to find the best sites for public and private facilities in an efficient way. It is also a useful application in regional planning to predict the optimal sites for facilities within the regions by using GIS.

Furthermore, land suitability is a first phase and an effective way to decide suitable land parcels for public facilities planning. It is associated with public facility planning for example, which comprises the integration of GIS and location-allocation models [12]. GIS helps in the finding of optimal locations for public facilities and solves facilities problems, such as locating open spaces, public parks, public health facilities, and optimal location for solid waste management and the location of landfill sites [13]. It addresses the issue of the proper distribution of land use evaluation of Cities to see the public facilities of public parks, is the main single feature of the existence of urban public parks, for citizens' accessibility. It seems to be difficult for Iraq as a country to evaluate the need for public facilities using the application of GIS.

Nasiriyah is among the most populated cities in Iraq and the population is only growing. Thus, the need for sustainable public facilities is rising every year [14]. However, since Nasiriyah is located in the south of Iraq, it is prone to hot and dry weather, which can be mitigated by the inclusion of green spaces [15]. Thus, the issue of accessibility of parks as well as their abundance existence becomes even more critical in southern cities that experience above average temperature.

In this study, the issue of accessibility of parks in Nasiriyah city is addressed using land suitability analysis and facility location-allocation models through spatial analysis method of GIS. An optimal site for future public park development is based on the availability of the suitable land to be allocated, as well as other metrics that play an important role in the existence of the parks and greenspaces.

2 Methodology

In this section the methodology used to conduct the research as well the location of the study are illustrated and explained. The main goal of this study is to use existing supporting tools in order to plan for the allocation of parks and green spaces in Nasiriyah. In order to do this, there first needs to be a study on Nasiriyah itself as a city and its various geographical and social aspects. Secondly, the related tools that are used to analyse the obtained data need to be examined and explained further. Finally, the methods used in order to combine the data and turning it into a readable database needs to be elaborated further.

2.1 Study Location

This study covers the locations of public parks for city of Nasiriyah. This city is considered to be among the top most important states and settlements in Iraq. It is centrally located on 32º 30´-north latitudes and 47º 12´-east longitudes. Nasiriyah experienced an increase in population growth of about 3.0% to 3.5% from the years 1937 to 2017. Assuming the same growth rate, the population of Nasiriyah will increase from 285,707 in 1937 to 219,3253 in 2017 and 235,8075 in 2020 Nasiriyah [16]. The location map of Nasiriyah city is shown in Figure 1.

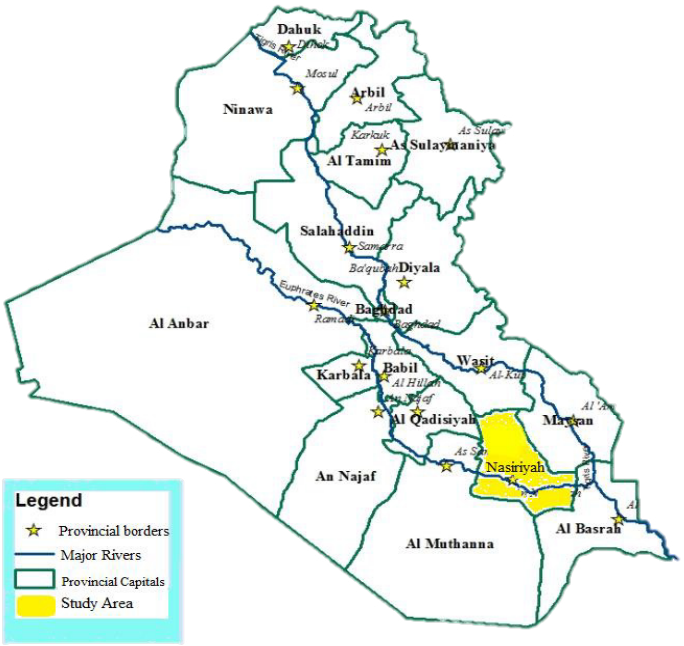

Fig. 1. Map of Iraq highlighting the location of Nasiriyah

2.2 Data Source

The data sources for this study are based on several sources such as official government documents, published reports, books and journals, literature studies and architectural sources. The base map was obtained the city planning department in form of a spatial map. The land value was obtained via a market survey. The report published by the city under the title of "The development plan of Nasiriyah (2000 – 2020)" provided both the population density as well as the income level [16]. Everything else included in this research was obtained via official sources.

2.3 Methods

The land Suitability Analysis and Analytic Hierarchy Process (AHP) manages the several criteria/factors of a problem into a hierarchy related to a tree form arrangement, it is mandatory to build up a Hierarchical Structure Model (HSM) for Land Suitability Analysis (LSA) based on experts discussions to define the goal, criteria, and parameters to solve and set the problem [17]. The HSM is the major component of this study. It is divided into three main levels; goal, criteria, and sub-criteria. The goal level is the uppermost level, which defines the problem. The second level is the level of criteria comprising three aspects. The third level consists of various sub-criteria. This hierarchical model is illustrated in Figure 2.

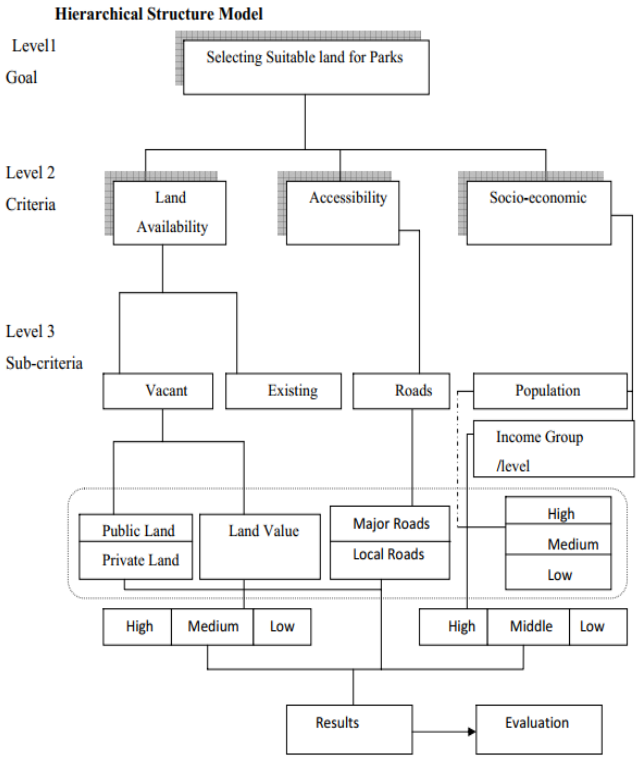

Fig. 2. Hierarchical Structure Model of selecting suitable Land for Parks

2.4 Database Development

Using the HST illustrated in Figure 2, the GIS database is developed using the level 2 and level 3 criteria. ArcGIS 9.2 is used in order to convert the scanned map of Nasiriyah into digitized data layers based on the mapped out earth coordinates previously geo referenced. The development purpose of the database was to generate data layers for this project including land-use (polygons) and roads (Line). The other data layers created land value, population density, and income group level. In addition, data layers were applied to evaluate existing parks, land suitability analysis to find out suitable land for public parks planning and to determine optimal locations for public parks planning [18].

A Multiple Criteria Decision Making (MCDM) is used in order to interlink the criteria via the system. MCDM operates by using a set of alternatives that are evaluated based on differing and incommensurate criteria. With the use of an Expert Choice (EC) software, the composite weights are calculated using a pairwise comparison system. Using this form of sorting helps in identifying the perfect priorities in relation to the attributes and their relative weight to one another. Once the composite weights is calculate or each of the parameters, a suitability analysis is performed using the special analysis function of GIS. This function helps to produce composite scenario maps for park development.

A suitability analysis is performed in order to create three scenarios by using spatial analysis in geographic information system (GIS). Each of these scenarios correspond to the attributes calculated using the expert system based on the hierarchical structure model in Figure 2. In this case, the three chosen scenarios are based on land availability, land value and population density. These attributes have shown to narrow down the suitability analysis in a more accurate method based on each scenario.

The results of the multiplication of weights were added to get the total. Factors and parameters were determined based on scenarios, for land suitability. The results of composite weights were used in GIS spatial analysis to generate scenario maps finding suitable land for park development.

2.5 Data Reclassification and Projection

The reclassification of values from old values to new values was accomplished with the support of spatial analyst ArcGIS 9.2. Then the raster dataset is transformed from one projection to another. The obtained land suitability scenario maps were projected after using the Weighted Sum function [19]. The coordinate system enabled the map to be represented in two dimensions, as x, y coordinates. Then the function of times is to multiply the values of two rasters on a cell-by-cell basis. This function is applied to produce the suitability map [20]. The results of suitability analysis are several suitability maps that represent areas from most suitable to least suitable. The final map of suitability was created into non-developable (excluded) and most suitable (or developable). Scenarios were assessed by using number of grid cells for the degree of land suitability analysis such as most suitable, moderately suitable, and least suitable. Euclidean allocation model was applied to determine the accessibility by using GIS spatial analysis for suitable land of parks.

3 Results

Suitability analysis was done through the combination of GIS and AHP methods. All three scenarios are calculated using the AHP method. To produce all three scenarios in ArcGIS (9.2), a land-use map was converted into raster format by using Spatial Analyst to classify sub-criteria (parameters). Several steps were taken in order to create land availability scenario. First, the sub-criteria (parameters) were reclassified in order to produce excluding maps. Then, all classified maps were added on a composite weight (Wi). All the maps were projected, and summed together. Finally, the summed up maps were projected to get the land availability scenario. Figure 3 illustrates the maps for each of the three scenarios.

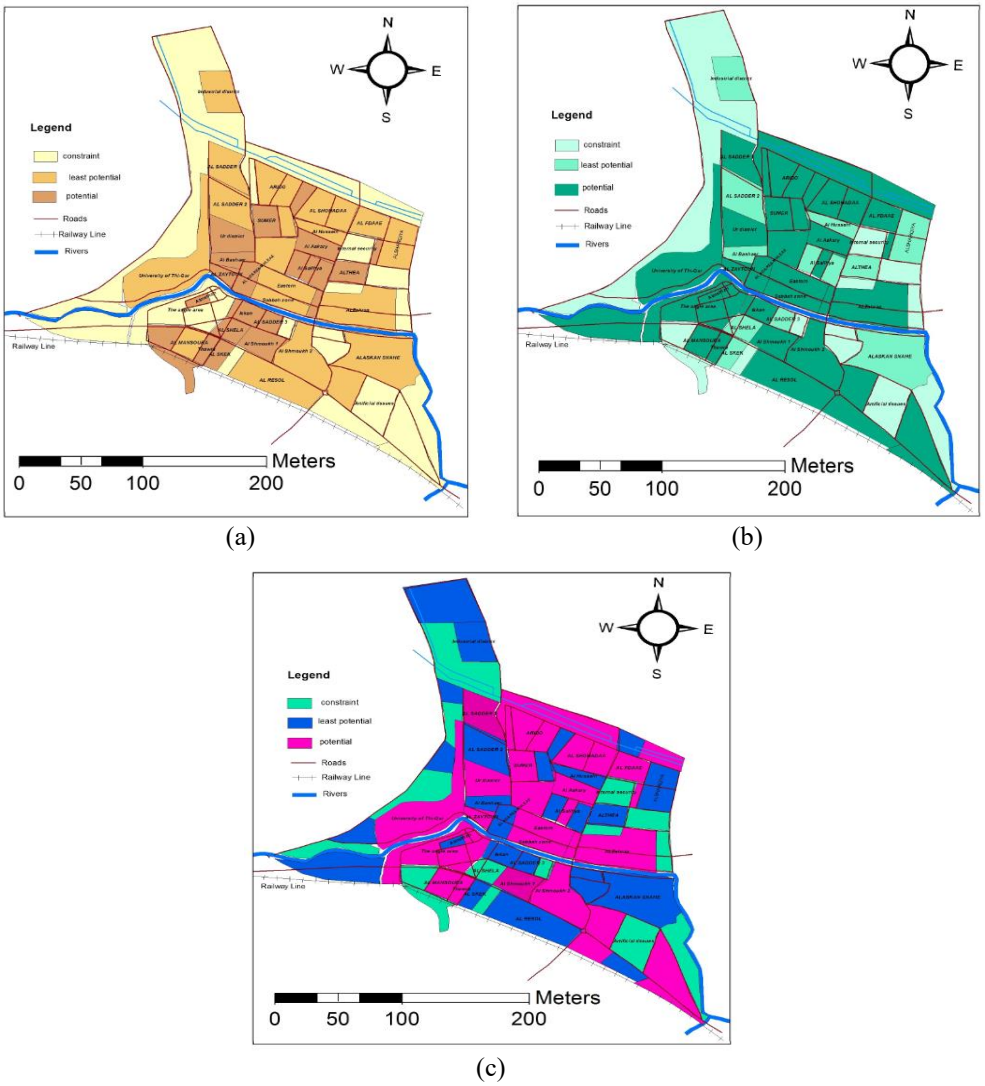

Fig. 3. Maps for (a) scenario 1 – Land Availability, (b) scenario 2 – Land Value, (c) scenario 3 – Population Density

The maps illustrated are a total of 510,880 grid cells in total for Nasiriyah. Performing the AHP and GIS methods for public parks suitability analysis resulted in three categories of potential, least potential and constraint land. For the first scenario based on land availability resulted in only 15% of the land being marked as potential (73,400 grid cells), while 60% and 25% are least potential and constraint land respectively with 288,240 and 149,240 grid cells. For the second scenario, the focus is land value in which roughly 63% is considered potential land (296,120 grid cells), while the remaining 14% and 23% are least potential and constraint land respectively. For the final and third scenario, the focus is on population density and the potential land is considered 69%, which translates to 326,080 grid cells. The remaining 25% and 6% are leas potential and constraint land.

4 Discussion

The results indicate that from 510880 total grids, an estimated 316080 grids (66% or 790.2 hectares) are potential land, 84120 grids (15% or 210.3hectares) are the least potential land and 110600 grids (19% or 276.5 hectares) are a constraint for parks development. All scenarios reclassified in model builder as added through Weighted Sum to produce potential land. While the potential land map was projected to get the correct suitability map for park locations in Nasiriyah city. Figure 4 illustrates the suitability map for park allocation in Nasiriyah with potential spots marked in red, less potential marked with dark green and constraint areas marked with bright green.

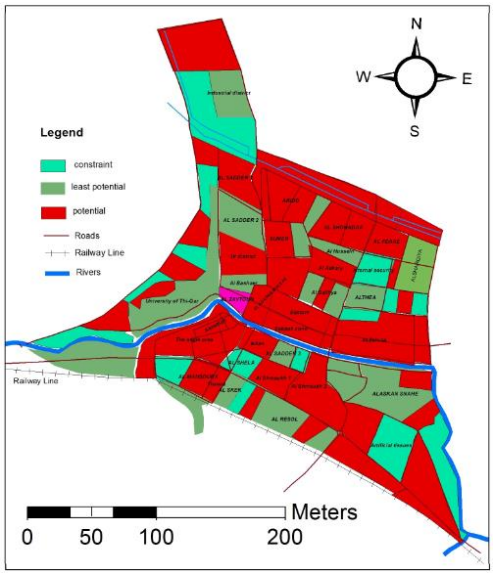

Fig. 4. Suitability map for park allocation in Nasiriyah

5 Conclusion

The main objective of this study was to determine the best location for parks in Nasiriyah city (Iraq). In order to accomplish this, an Analytic Hierarchical Process (AHP) based on GIS integrated approach was used. This research provided a framework based on MCDA that was applied on park planning in a GIS spatial map network. Using this context, a hierarchical structure model was used for selecting the suitable land based on a set of criteria and sub criteria. Using the parameters, the problem of locating facility planning for parks ultimately lead to identification of several potential park locations with a degree of success.

Using the GIS combined with AHP, the results indicated that based on each parameter and scenario, the land availability was identified to be as follows. For the first scenario, of land availability, the potential land for parks was identified to be at only 10%, and the second scenario of land value the availability was set at 64%. Finally, for the third scenario, the population density, the potential land was identified to be at 69%. This data is then combined into a single map that can mark the most potential locations for maps.

This research can be further improved by the use of more accurate data. This is mainly because the data was not readily available from the various governmental institutes. The more data applied to the decision making system, the more accurate the results will be. Ultimately, this research is very useful for further studies that plan a similar objective on a different location. Other researchers can use the framework provided in this research in order to identify the suitability of parks in different location and cities.

References

[1] Wolf, K.: 'The health benefits of small parks and green spaces', Parks & Recreation. 52 (4): 28-29., 2017, 52, (4), pp. 28-29

[2] Barbosa, O., Tratalos, J.A., Armsworth, P.R., Davies, R.G., Fuller, R.A., Johnson, P., and Gaston, K.J.: 'Who benefits from access to green space? A case study from Sheffield, UK', Landscape and Urban planning, 2007, 83, (2-3), pp. 187-195

[3] Maruani, T., and Amit-Cohen, I.: 'Open space planning models: A review of approaches and methods', Landscape and urban planning, 2007, 81, (1-2), pp. 1-13

[4] Van Herzele, A., and Wiedemann, T.: 'A monitoring tool for the provision of accessible and attractive urban green spaces', Landscape and urban planning, 2003, 63, (2), pp. 109-126

[5] Bahriny, F., and Bell, S.: 'Patterns of urban park use and their relationship to factors of quality: a case study of Tehran, Iran', Sustainability, 2020, 12, (4), pp. 1560

[6] Li, Z., Wei, H., Wu, Y., Su, S., Wang, W., and Qu, C.: 'Impact of community deprivation on urban park access over time: Understanding the relative role of contributors for urban planning', Habitat International, 2019, 92, pp. 102031

[7] Geng, D.C., Innes, J., Wu, W., and Wang, G.: 'Impacts of COVID-19 pandemic on urban park visitation: a global analysis', Journal of forestry research, 2021, 32, (2), pp. 553-567

[8] Ergen, M.: 'Using geographical information systems to measure accessibility of green areas in the urban center of Nevşehir, Turkey', Urban Forestry & Urban Greening, 2021, 62, pp. 127160

[9] Church, R.L.: 'Geographical information systems and location science', Computers & Operations Research, 2002, 29, (6), pp. 541-562

[10] Miller, H.J., and Shaw, S.-L.: 'Geographic information systems for transportation: principles and applications' (Oxford University Press on Demand, 2001. 2001)

[11] Zhou, J., Wu, Y., Wu, C., He, F., Zhang, B., and Liu, F.: 'A geographical information system based multi-criteria decision-making approach for location analysis and evaluation of urban photovoltaic charging station: A case study in Beijing', Energy Conversion and Management, 2020, 205, pp. 112340
[12] Rahman, M., Chen, N., Islam, M.M., Dewan, A., Pourghasemi, H.R., Washakh, R.M.A., Nepal, N., Tian, S., Faiz, H., and Alam, M.: 'Location-allocation modeling for emergency evacuation planning with GIS and remote sensing: A case study of Northeast Bangladesh', Geoscience Frontiers, 2021, 12, (3), pp. 101095
[13] Chiesura, A.: 'The role of urban parks for the sustainable city', Landscape and urban planning, 2004, 68, (1), pp. 129-138
[14] Satchet, M.M.S., and Aodah, M.H.H.: 'Transit GIS Applications For parking in Nasiriyah City, Iraq', Journal of university of Thi-Qar scientific Vol, 2010, 5, (1), pp. 12
[15] Vieira, J., Matos, P., Mexia, T., Silva, P., Lopes, N., Freitas, C., Correia, O., Santos-Reis, M., Branquinho, C., and Pinho, P.: 'Green spaces are not all the same for the provision of air purification and climate regulation services: The case of urban parks', Environmental Research, 2018, 160, pp. 306-313
[16] Falih, K.T.: 'Spatial Analysis of Educational Services Using GIS in Nasiriyah City', Turkish Journal of Computer and Mathematics Education (TURCOMAT), 2021, 12, (5), pp. 1974-1984
[17] Yariyan, P., Zabihi, H., Wolf, I.D., Karami, M., and Amiriyan, S.: 'Earthquake risk assessment using an integrated Fuzzy Analytic Hierarchy Process with Artificial Neural Networks based on GIS: A case study of Sanandaj in Iran', International Journal of Disaster Risk Reduction, 2020, 50, pp. 101705
[18] Stewart Fotheringham, A., and Rogerson, P.A.: 'GIS and spatial analytical problems', International Journal of Geographical Information Science, 1993, 7, (1), pp. 3-19
[19] Wong, N.H., and Jusuf, S.K.: 'GIS-based greenery evaluation on campus master plan', Landscape and urban planning, 2008, 84, (2), pp. 166-182
[20] Mendoza, G.A.: 'GIS-based multicriteria approaches to land use suitability assessment and allocation', United States Department Of Agriculture Forest Service General Technical Report NC, 2000, pp. 89-94

Wi_Fi Positioning Utilizing Triangulation Strategies and AoA In Indoor Environments

Zahraa A. Hamza [1] , Mahmood F Mosleh [1], Faeza A. Abed [2]
{ Zahraaabbasct9@gmail.com[1],drmahmoodfarhan@gmail.com[2],
dr.faeza.khafaji@gmail.com[3]}

Middle Technical University, Electrical Engineering Technical College, Baghdad, Iraq [1],
Middle Technical University- Institute of Technology- Baghdad [2]

Abstract. Implementing a limiting framework for an indoor climate has been complicated by multipath and blockage difficulties. The Angle of Arrival (AoA) is the most commonly used method for such situations in the area, and it should be strengthened, especially for additional obstructions due to massive multipath issues. A contextual investigation of a chosen fabricating is chosen in this paper to use the offered approach of this analysis. This concept is based on the triangulation approach. The Wireless Insite Software (WIS) was used to reconstruct the contextual analysis territory, with 30 Receivers (RXs) and 2 Transmitters (TXs) placed in appropriate locations. Following the estimation of AoA and saving them into the database, the coordinates of RXs are determined using MATLAB programming. The findings show that the estimated locations are reasonably near to the genuine locations, with an average error of (0.24) metre for the X-coordinate and (0.205857) metre for the Y-coordinate. As a result, we find that under the Triangulation method, the AoA approach is more effective in evaluating indoor localisation.

Keywords: WIS, AoA, Triangulation.

1 Introduction

As the popularity of mobile devices such as smartphones, smart watches, laptops, and some connected devices has grown, so has the number of Location-Based Services (LBS) available to assist us in areas such as emergency services, navigation, childcare, geophone, social networking, entertainment/gaming, asset monitoring, and so on **[1]**. Clients with smartphones, for example, can easily plan their trips using Google Maps and hail a nearby cab. The Global Positioning System (GPS) essentially determines the exact area (GPS). However, the GPS signal is too severely degraded to be obtained in inside situations. To meet the growing need for indoor LBS applications, a variety of solutions have been developed **[2]**. In contrast to Line-of-Sight (LoS) limitation in outdoor environments, where worldwide route satellite frameworks are for all intents and purposes, the default arrangement presents advances for indoor environments in Non-Line-of-Sight (NLoS) conditions have not united to a universally perceived arrangement **[3]**. Consequently, this subject draws in broad exploration interest **[4]**. The primary objective in NLoS conditions is to utilize the all-around sent earthbound innovations and concentrate data from the got radio signs, like Received Signal Strength (RSS) **[5]**, Time of Arrival (ToA) **[6]**, AoA **[7]**, Time Difference of Arrival (TDoA) **[8]**, Phase Difference of Arrival (PDoA) **[9]** or a hybrid of them **[10]**. As usual, indoor conditions are convoluted, so some difficulties and impediments impact the exactness of gadgets. In the instance of NLoS, this impact happens when articles recognize senders and collectors **[11]**. The example of transmission assumes a

IMDC-IST 2021, September 07-09, Sakarya, Turkey
Copyright © 2022 EAI
DOI 10.4108/eai.7-9-2021.2315379

huge part in the estimate. The got signal at that point enters the beneficiary from dividers or different articles, hence the regard of the ToA from the association with another. The other consequence weakens as recipients respond to a weak signal, making it difficult to determine the proper area based on this signal [12]. To overcome these challenges, the analysts suggested a variety of solutions for increasing gadget productivity by limiting the effects of NLoS and other constraints. NLoS identification [13], or the unique mark technique advocated in a few studies, such as [14], to the estimated specific RSS esteem, is one of these options. The fact that triangulation is proposed for assessing localizability in this study. Following that, by iteratively applying Triangulation to a network, it is possible to find localizable hubs. Triangulation is widely used in practise [15] since it is adaptable, simple to execute, and effective in terms of correspondence and computation [16]. The following is a breakdown of the content of this document. The indoor localization theory is presented in the second section. The details of the case study building are detailed in section three. The proposed approach's results and analysis are reported in section four. Finally, in part five, the conclusion is presented.

2 Indoor localization theory

There are various strategies for tending to data with respect to the space of the position. A rudimentary sort of spatial portrayal is a mathematical depiction. A graphical diagram depicts the space with its mathematical structure and a collection of coordination focuses under a Cartesian arrange reference plot. The space model has a strong representation that is commonly used with directions to communicate a theoretical space, such as (X, Y, Z). Truly, a room describes by various mathematical structures. A mathematical structure surely is a crude structure 2D or 3D. Specifically, executions, the type of development can be applied to more perplexing structures. Directions are picked and requested for each space in an unmistakable construction regarding the mathematical type of room. The meaning of directions is carefully associated with the mathematical type of room. Utilizing the crucial ideas of the convergence of different lines and the privileged mathematical detailing to rough the heading of a hub, the specific point in the situating area strategies can be resolved. The position directions of the hubs are determined from numerous points of view, like AoA, ToA, TDoA, and RSS. To gauge the course places of a hub utilizing lines and points, these methods depended on mathematical standards. Instances of these ideas are Triangulation, trilateration, and exaggerated **[17]**.

2.1 Triangulation technique

The Triangulation situating the area method utilizes the mathematical properties of triangles to assess a hub situating. This standard comprises three focuses, two reference focuses (Z_1 and Z_2), and an objective point (T). At the crossing point of the line from Z_1 to T and from Z_2 to T, we get the two points Θ_1 and Θ_2 as demonstrated in **Figure 1**, and geometrical capacities are utilized to compute the objective position **[18]**.

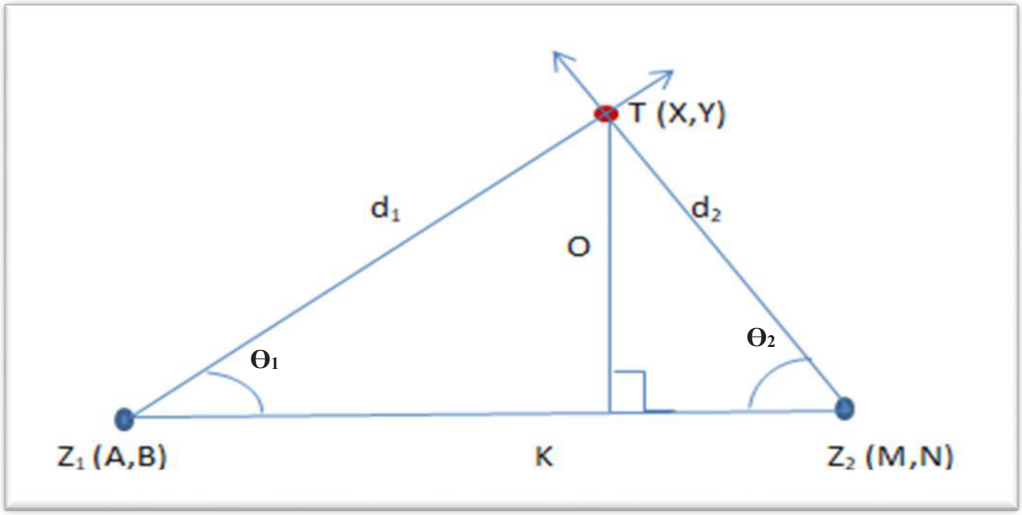

Fig. 1. Triangulation guideline.

$$K = \frac{O}{\tan\Theta_1} + \frac{O}{\tan\Theta_2} \quad (1)$$

$$O = \frac{K.\sin\Theta_1 .\sin\Theta_2}{\sin(\Theta_1+\Theta_2)} \quad (2)$$

$$\Theta_1 = tan^{-1}(\frac{B-Y}{A-X}) \quad (3)$$

$$\Theta_2 = tan^{-1}(\frac{N-Y}{M-X}) \quad (4)$$

Where K is the line that connects the reference focuses Z1 and Z2, and O is the line that connects target T and line K. d1 is the line that connects a target point T to a reference point Z1, and d2 is the line that connects a target point T to a reference point Z2.. Z_2, Θ_1 is the point between line d1 and line K, Θ_2 is the point between line d_2 and line *K*, (*A, B*) are the directions of the reference point Z_1 and (*M, N*) are the directions of the reference point Z_2, (*X, Y*) are the directions of the target T.

The directions of the objective (*X, Y*) can be determined as referenced beneath:

$$X = \frac{N-B-M\tan\Theta_2+A\ \tan\Theta_1}{\tan\Theta_1-\tan\Theta_2} \quad (5)$$

$$Y = N - M\tan\Theta_2 + X\tan\Theta_2 \quad (6)$$

To discover the distances between focuses Z_1, Z_2, and the target point T, we utilize the following conditions **[19]**.

$$d_1 = \sqrt{((A-X)\text{^}2 + (B-Y)\text{^}2)} \quad (7)$$

$$d_2 = \sqrt{((M - X)\text{^}2 + (N - Y)\text{^}2\ )} \quad (8)$$

2.2 Triangulation technique based on AoA method

AoA is an organization-based situating area strategy that actions the time take by radio signs to show up at a few focuses. AoA technique utilizes a receiving wire containing a different component cluster in which the specific area of each AoA component is known definitely. Every component is little and fit for getting a different sign. By estimating signal strength, the season of appearance, and the stage at every cluster component, it is feasible to figure the view way from the transmitter to the recipient. Putting another collector with a similar radio wire design in an alternate area permits rehashing the cycle. The convergence point of the two view ways addresses the area of the sending hub. The AoA technique requires at least two reference stations with directional radio wires with thin bar widths. This strategy is not difficult to carry out and is utilized in specific applications like reviewing, finding the wellspring of an unlawful transmitter, and following objective hubs. The AoA strategy utilizes the basic triangulation rule to figure the area of an objective hub and depends on vector running. The technique needs, at any rate, two reference stations to quantify the course of the got radio signs. The objective hub addresses the place of the crossing point of lines attracted from reference stations to the objective hub. A couple of vectors structure a solitary point in a moment that they cross with one another. The point of appearance figuring and other important data can be utilized to ascertain the situation of an objective hub. Handset stations with reference to arranging should be utilized as a reference to get exact figurings of the necessary data in this strategy. The data about AoA can be estimated in three different ways. The main sort dependent on estimating the got signal stage contrasts between the reception apparatus exhibit components. The second is to quantify a pillar shaping or ghostly thickness across the radio wire cluster of the recipient. The third method of assessing the situation of an objective gadget; to discover AoA is by utilizing sectored multi-pillar reception apparatuses. This technique utilized in cell networks that were at that point received cell-sectoring in the organization to accomplish more solid interchanges **[20]**.
Allow us to assume we have a communicated signal from the target hub, organized (X, Y) to i^{th} handset station, which coordinates(X_i, Y_i). The line among the transmitter and the reference point converge with X-pivot makes a point Θ_i as demonstrated in **Figure 2**, this point will be the point of appearance which is characterized as:

$$\tan \Theta_i = \frac{Y - Y_i}{X - X_i} \quad (9)$$

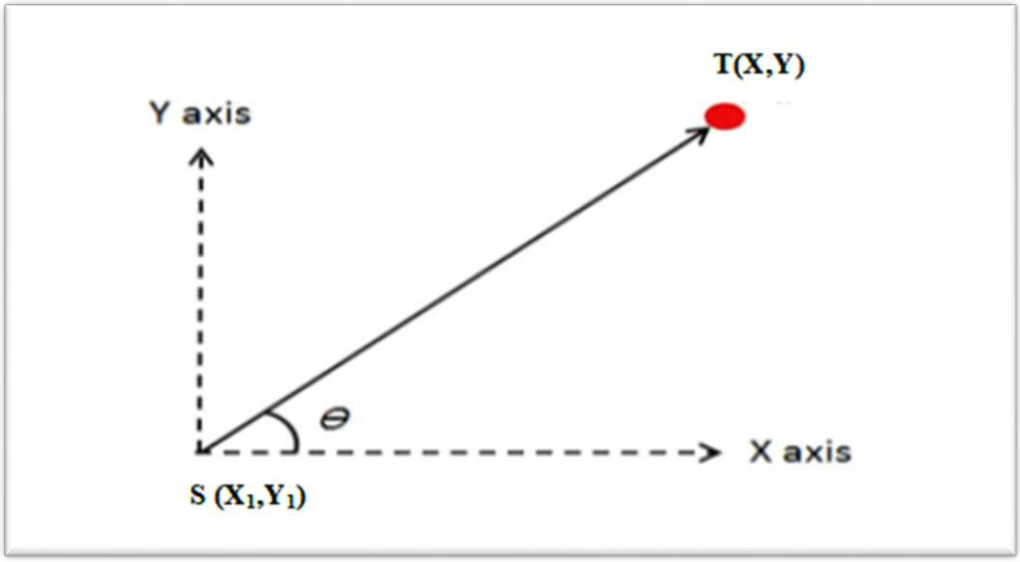

Fig. 2. The AoA theory.

To decide the directions of the target hub T, we can utilize the accompanying conditions **[21]**:

$$X = \frac{K \tan(\theta_2)}{\tan(\theta_2) - \tan(\theta_1)} \tag{10}$$

$$Y = \frac{K \tan(\theta_2) \tan(\theta_1)}{\tan(\theta_2) - \tan(\theta_1)} \tag{11}$$

Where K is the distance between the reference stations Z_1 and Z_2, Θ_1 is the point of landing in the reference hub Z_1, Θ_2 is the point of landing in the reference hub Z_2, (X, Y) are the directions of the target hub T. **Figure 3** shows the AoA technique.

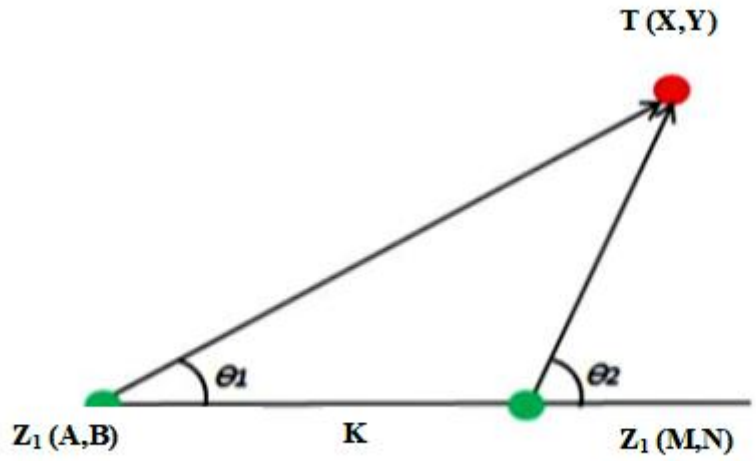

Fig. 3. AoA technique.

3 Design case study building

The EE Technical Building Campus decided to use the indoor localization metyhoology. A framework like this was created in simulation and experimental settings; the model was based on WIS. In the side half of the simulation, such a programme can calculate relevant parameters. The experimental data gathered using the WIS programme will represent the characteristics of AoA measurement and utilising the MATLAB programme to determine the coordinates of RXs in the experimental side section.

3.1 Simulation Process

WIS-based architecture in three dimensions (3D), conisdfering true model. In addition to the two places for TXs, thirty positions were chosen for RX deployment to measure AoA, which were separated into 10 groups as shown in Figure 4.

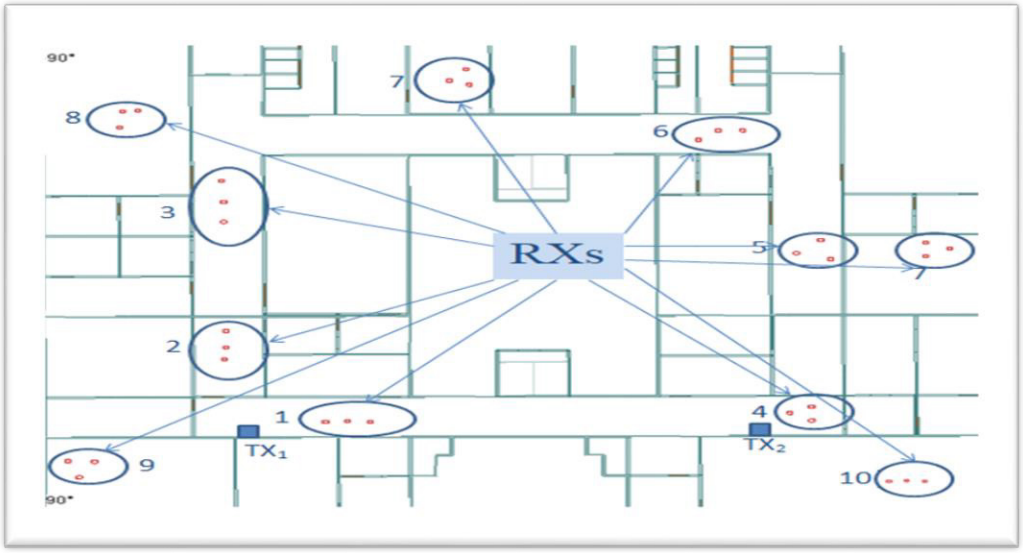

Fig. 4. Model of case study.

The transmitter and receiver parameters in WIS can be changed to fit the experimental devices, allowing the TXs and RXs mentioned in Table 1 to be assigned. All TXs and RXs are Omni-Directional to one experimental antenna, and the operational frequency is 2.4 GHz.

Table 1. The antennas properties

Properties of antennas	**TX**	**RX**
Antennas type	Omni.D.	Omni.D.
Input Power (dBm)	12.5	-
Gain (dBi)	7.5	2.2
E-Plane HPBW	13˚	94˚
Waveform	Sinusoid	Sinusoid
Temp. (k)	296	296
Polarizations	V	V
Received Threshold (dBm)	-150	-150

The configuration of all materials' Permittivity and Conductivity to deal with actual ones is one of the key features of WIS. There are constant parameters to apply, as seen in table 2 and table 3. Based on such factors, conductivity and permittivity are calculated for each material. According to (), the conductivity denoted by () can be calculated as follows **[22]**:

$$\sigma = c \times f^{d} \tag{12}$$

Table 2 illustrates the constants c and d. The Permittivity () is calculated in the following way:

$$\eta = a \times \mathrm{f}^{\mathrm{b}} \tag{13}$$

The constant *a* and *b* are related to each material used to construct the chosen building, which is listed in Table 3.

Table 2. The constant (*c* and *d*) is used in (12).

Material type	***c***	***d***
Concrete	0.0326	0.8095
Brick	0.038	0
Wood	0.0047	1.0718
Glass	0.0043	1.1925

Table 3. The constant (*a* and *b*) is used in (13).

Material type	***a***	***b***
Concrete	5.31	0
Brick	3.75	0
Wood	1.99	0
Glass	6.27	0

As previously indicated, the 2.4GHz frequency employed based on equns (12) and (13). (13). The Permittivity and Conductivity are shown in Table 4 for reference frequency. The values in Table 4 will be set out in the WIS for materials used in building construction.

Table 4. Materials at 2.4GHZ.

Material type	**σ**	**ε**
Concrete	0.0926	5.31
Brick	0.1079	3.75
Wood	0.0134	1.99
Glass	0.0122	6.27

3.2 Side of experiment

On the side of experimentation, Figure 5 shows the coordinates of the RXs extracted using WIS data for AoA in the MATLAB algorithm.
The effectiveness of measures to deal with practical measurements in the complete building improves in diverse contexts by taking various places in the case study building. In the case study context, two points were employed to empirically measure AoA with 30 samples each. The measured data are included in the database alongside the other measurements from the other two sites.
Finally, using the triangulation approach, the MATLAB programme supplied to convert the best data was recorded in the database to distance lead to RX coordinates.

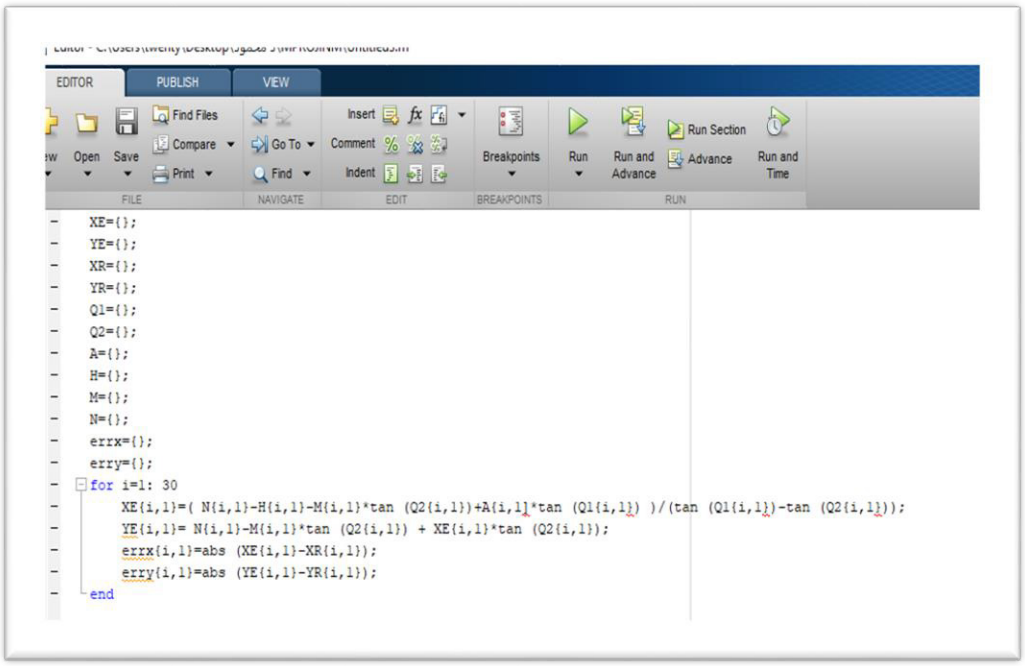

Fig. 5. Sample of MATLAB code.

4 Results and analysis

The approximate distance was calculated using AoA measurements; therefore, accurate AoA measurements would result in accurate distance calculation. The AoA method's error ratio between the real and estimated coordinates is shown in Figure 6, where the X-maximum ratio error is 0.9 metre and the Y-error ratio is 0.700262 metre. The error ratio for the X-lowest coordinate is 0.02 metre, while the Y-coordinates are 0.001643 metre. These findings are matched to those of [23]. The results obtained in such a reference said that ToA is superior to RSS and that inaccuracies (0.48-1.52) metres have been detected. Furthermore, the researcher [24] used min/max positioning based on static ToA and RSS readings. When compared to our results, which show an average error of (0.24) metre for X-coordinate and (0.205857) metre for

Y-coordinate based on AoA, the biconical antennas were installed with a frequency range of 3-11 GHz in order to apply the trilateration technique, which gives better results than the min/max method with a range of errors between (0.21-2.09) metre.

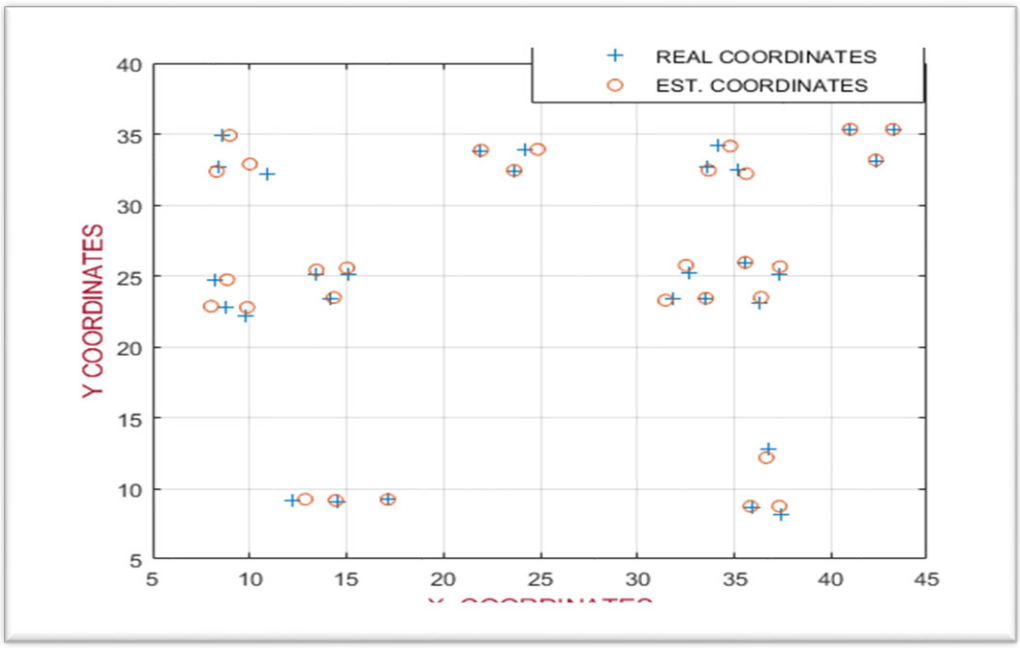

Fig. 6. AoA coordinates.

5 Conclusions

In this paper, with AoA methods, a proposed Triangulation strategy is completed to discover target areas in 10 positions conveyed in a choice building. These structures have been built to ascertain AoA dependent on WIS. In an appropriate area inside the contextual investigation building, two 2.4 GHz-based TXs were conveyed. On the trial line, WIS was used to measure AoA in two TXs circumstances, each with 30 RXs cases. The outcomes reveal that a significant reduction in blunder (determined as the contrasts between the dramatic and recreated AoA). The average error for AoA (0.24,0.205857) metre coordinates is shown as a result of our investigation. As a result of the the AoA strategy is effective than other techniques in computing indoor localisation.

References

[1] Roba Abbas, Katina Michael, MG Michael. The regulatory considerations and ethical dilemmas of location-based services (LBS): A literature review. Information Technology \& People. 2014; 27 (1): 2-20.

[2] Gautam M. Borker, A. R. Mahajan. A review on propagation of secure data, prevention of attacks and routing in mobile ad-hoc networks (MANETs). International Journal of Data Science. 2018; 3(4): 353-389.

[3] Robert F. Keefe, Ann M. Wempe, Ryer M. Becker, Eloise G. Zimbelman, Emily S. Nagler, Sophie L. Gilbert, Christopher C. Caudill. Positioning Methods and the Use of Location and Activity Data in Forests. Forests. 2019; 10(5): 458.

[4] M. M. Abdulwahid, O. A. Shareef Al-Ani, M. F. Mosleh, R. A. Abd-Alhmeed. A Comparison between Different C-band and mmWave band Frequencies for Indoor Communication. Journal of Communications. 2019; 41(10): 892-899.

[5] Yogita Chapre, Prasant Mohapatra, Sanjay Jha, Aruna Seneviratne. Received signal strength indicator and its analysis in a typical WLAN system. 38th Annual IEEE Conference on Local Computer Networks; 2013; Sydney, NSW, Australia. IEEE; 2013. P. 304-307.

[6] Ismail Guvenc, Chia-Chin Chong. A Survey on TOA Based Wireless Localization and NLOS Mitigation Techniques. IEEE Communications Surveys \& Tutorials. 2009; 11(3): 107-124.

[7] Igor Dotlic, Andrew Connell, Hang Ma, Jeff Clancy, Michael McLaughlin. Angle of arrival estimation using decawave DW1000 integrated circuits. 2017 14th Workshop on Positioning, Navigation and Communications (WPNC); 2017; Bremen, Germany. IEEE; 2017. P. 1-6.

[8] Venkata B. M., R. K. Jeyachitra. Low Complexity Indoor Positioning System with TDOA Algorithm Using Hilbert Transform Method. Advances in Electrical and Computer Technologies; Singapore; Springer, 2020. p. 667-679.

[9] Yongtao Ma, Bobo Wang, Shuyang Pei, Yunlei Zhang, Shuai Zhang, Jiexiao Yu. An Indoor Localization Method Based on AOA and PDOA Using Virtual Stations in Multipath and NLOS Environments for Passive UHF RFID. IEEE Access. 2018; 6(1): 31772—31782.

[10] Sheng Zhang, Pengfei Du, Chen Chen, Wen-De Zhong, Arokiaswami Alphones. Robust 3D Indoor VLP System Based on ANN Using Hybrid RSS/PDOA. IEEE Access. 2019; 7(1): 47769-47780.

[11] Feng Lyu, Nan Cheng, Hongzi Zhu, Haibo Zhou, Wenchao Xu, Minglu Li, Xuemin Sherman Shen. Intelligent context-aware communication paradigm design for IoVs based on data analytics. IEEE Network. 2018; 32(6): 74—82.

[12] Sun Ji-Ping, LI Chen-Xin. TOA underground coal mine target positioning method based on WiFi and timing error suppression. Journal of China Coal Society. 2014; 39(1): 192-197.

[13] Chen Huang, Andreas F. Molisch, Ruisi He, Rui Wang, Pan Tang, Bo Ai, Zhangdui Zhong. Machine learning-enabled LOS/NLOS identification for MIMO systems in dynamic environments. IEEE Transactions on Wireless Communications. 2020; 19(6): 3643-3657.

[14] Chavalit Koweerawong, Komwut Wipusitwarakun, Kamol Kaemarungsi. Indoor localization improvement via adaptive RSS fingerprinting database. The International Conference on Information Networking 2013 (ICOIN); 2013; Bangkok, Thailand. IEEE; 2013. P. 412-416.

[15] Wiegert, Roy F. Magnetic anomaly surveillance system using spherical trilateration. United States: Google Patents; 2013. 1-18.

[16] Khelifi, Fekher, et al. A survey of localization systems in the internet of things. Mobile Networks and Applications. 2019; 24(3): 761-785.

[17] Burrough, Peter A ,McDonnell, Rachael , McDonnell, Rachael A , Lloyd, Christopher D. Principles of geographical information systems.3rd Edition. United Kingdom. Oxford university press: 2015. 1-315.

[18] Luka Batistić, Mladen Tomic. Overview of indoor positioning system technologies. 2018 41st International Convention on Information and Communication Technology, Electronics and Microelectronics (MIPRO); 2018; Opatija, Croatia. IEEE; 2018. P. 0473-0478.

[19] Hui Liu, Houshang Darabi, Pat Banerjee, Jing Liu. Survey of Wireless Indoor Positioning Techniques and Systems. IEEE Transactions on Systems, Man, and Cybernetics. 2007; 37(6): 1067-1080.

[20] Khalel, Ayad MH. Position location techniques in wireless communication systems. Digitala Vetenskapliga Arkivet. 2010; 1(1): 53.

[21] Bensky, Alan. Wireless positioning technologies and applications. 2nd Edition. London: Artech House; 2016. 1-393.

[22] P. Series. Effects of building materials and structures on radiowave propagation above about 100 MHz. Recommendation ITU-R. 2015; 1(1) :2040-1.

[23] Aditep Chaisang, Sathaporn Promwong. Indoor localization distance error analysis with UWB wireless propagation model using positioning method. 2018 International Conference on Digital Arts, Media and Technology (ICDAMT); 2018; Phayao, Thailand. IEEE; 2018. P. 254-257.
[24] Suppachai Monta, Sathaporn Promwong, Vongkeo Kingsakda. Evaluation of ultra wideband indoor localization with trilateration and min-max techniques. 2016 13th International Conference on Electrical Engineering/Electronics, Computer, Telecommunications and Information Technology (ECTI-CON); 2016; Chiang Mai, Thailand. IEEE; 2016. P. 1-4.

Novel Technical Design Of An Early Protection System For An Electronic Fuel Injection System

1st Dr. Abdullah J. H. Al Gizi[1], 2nd Msc . Saadi faisal radhi[2] and 3rd Msc. Yaerobe Mohammed Mthbob[3]
{abdullal.algizi@stu.edu.iq ,ss2014ra@gmail.com, Yaareb.m.m@stu.edu.iq}
Thi-Qar technical collage Electromechanical Engineering ,Southern Technical University, Iraq[1], Shatrah Insitutes, Agrculter Mechine Southern Technical University, Iraq[2] , Electrical Networks Engineering Department, Southern Technical University, Iraq[3]

Abstract. The system of sensors was designed and controlled for early warning that the fuel sprayer will stop working and be controlled. When the fuel sprayer stops working, the electronic-control-unit (ECU) or computer gets electrical signals from (current, voltage) various sensors, but there are no sensors, which may result in fuel waste and engine combustion, posing a risk to passengers. Electric motors drive the fuel injection pump, the pressure control valve is set to 100 bars, and the standardising fluid is injected through the nozzle in the computing cylinder. This proposed system consists of sensors and signal processor that control, giving an early warning about the state of the sprinkler through a screen and after that turning off the engine when it does not respond to the warning and treatment. This technique was utilised to examine a 40[MP]capable conventional Gide inwardly-opening multi-hole fuel inoculation scheme using new fuel system mechanisms, injector dynamics, spray characteristics, and a single cylinder engine burning evaluation.. It also appears that the system provides a significant savings in fuel consumption and reduced material losses that result from engine damage and biography and maintain the vehicle users 'modesty and improve the quality of the protection and warning system and intelligent treatment of vehicles. The achieved system is demonstrated to be efficient and robust in improving fuel sprayer control system and capacity.

Keywords: ECU,Early Warning, Sprayer,Sensors,Protection.

1 Introduction

The Electronic-Fuel-Injection scheme can be separated into three: elementary sub-system. These are the the electronic control system and fuel delivery system, air induction system,.

This implies the progress of optical sensors with suitable organization software for online discernment.The conservative example for vehicle security has been an ***self-governing*** method to include a large amount of sensors in each automobile so that adequate attention can be providing to classify adjacent objects that could cause chances and keep the passengers and vehicle driver safety.

To this end, a spray boom postponement must be intended to absorb tractor of the most new horizontal strips of pixels from the optical sensor delivers information J.De Baerdemaeker [1]. J.De Baerdemaeker [1]A practical review on steering schemes of agrarian independent off-road vehicles.[2] Proposed the Investigational data were verified with essential sensors (encoders ultrasonic sensors, etc.). [3] examines the processes of a 40 [MPA] accomplished conservative GDI inwardly-opening multi-hole fuel inoculation method, as well as injector nuances, spray features, and a single cylinder engine burning investigation. Change

IMDC-IST 2021, September 07-09, Sakarya, Turkey
Copyright © 2022 EAI
DOI 10.4108/eai.7-9-2021.2315366

of a piezoelectric energy garnering scheme for applying wireless devices on the tires.[4] Proposed the Demonstrating and imitation of rain for the examination of automotive sensor schemes. Advance of a sensor-based precision herbicide appeal system [5]. Application and description of a keen space system founded on 3-axis magnetic devices are proposed by [6]. Proposed by[7] Railroad bridge nursing using wireless smart sensors. Smart Self-governing Movement Light Changing by Movement Density Amount finished Sensors[8]. [9] Devices and actuators are used, often schmoozed in a dispersed regulator scheme, in a number of uses changing from manufacturing automation to ecological condition nursing regulator, to brainy transportation schemes or to fatherland defense. Low cost unmanned aerial automobile intensive care using smart phone skill[10]. The effects of straight water inoculation (WI) on burning and release physiognomies for a hydrogen (H2)-fueled stimulus explosion (SI) engine were investigated experimentally in this paper[11]. With experimental fuel split inoculation, dual-fuel combustion using diesel and high-octane quantity (ON) biofuel of n-butanol blends to ignite battered normal gas (CNG) was investigated[12]. A novel combustion mode, intelligent charge compression ignition (ICCI), was developed in the future to be predictable for ultra-high competence and low emissions at the same time [13]. The burning physiognomies for n-butanol and petrol were investigated in this work on a four-cylinder spark explosion petrol engine with self-governing port fuel inoculation and straight inoculation systems in various operating conditions[14]. Spread Generation (DG)[15] is a unique idea in electric power schemes, primarily in delivery systems, as a result of this miracle. The goal of this study is to look at a problem that comes from the cumulative spread of distributed energy capitals in control schemes: the design and testing of defensive devices with more complex topologies and power flow patterns[16]. The effects of adding PODE3-4 to diesel on macroscopic spray physiognomies were studied in a continuous volume spray chamber with varying injection pressures[17]. Straight hydrogen fuel cell electric automobiles (FCEVs) produce just water as a byproduct, eliminating tailpipe carbon and standard air pollutant emissions associated with internal combustion engines (ICEVs)[18]. Fuel cells (FCs) are well-organized energy conversion devices that can be employed for both energy conversion and storage[19]. 3-phase four-wire delivery methods are utilised to house single- and three-phase customer loads as well as renewable energy sources (RES) in numerous housing and profitable low voltage (LV) networks[20].. Characteristically, fuel Cell Hybrid Electric Vehicle (FCHEV) contains of fuel cell, cordless and/or ultracapacitor (UC) as the power sources[21]. An automatically activated fuel inoculation valve and a example electronic control system are industrialized [22]. [23] discusses the future of the automative electronic schemes. A regulatory model for the cooling scheme of an train was industrialized in order to decrease fuel ingesting and engine releases through the use of manageable engine cooling mechanisms counting an electrical water pump, an electrical fan, and a heated regulator[24]. [25] increases the amount of energy consumed in the gasoline manufacturing process, raises the cost of fuel, and produces undesired by-products. The main weakness of such an style is the in height cost of the scheme as a consequence of the large amount of sensors .Current advances of communiqué and interrelating skills have allowable a new obliging model for vehicle safety schemes, in which, via conventional vehicle-to-vehicle communiqué links, vehicles not only share info everywhere their . The electronic controller unit (ECU) or the computer accepts electrical signals (current ,voltage) from different sensors, but there are no sensors when the fuel sprayer stops working, which may cause waste of fuel and the burning of the engine and thus a risk to passengers, This paper presents system consists of sensors and signal processor that control giving early warning about the state of the sprinkler through a screen and after that turning off the engine when it does not respond to the warning and treatment.

2 System of Early Warning of the Fuel Sprayer

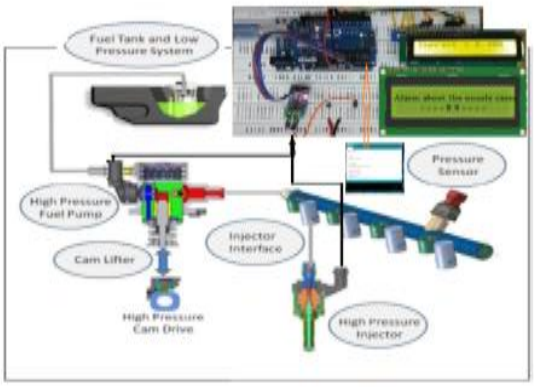

Fig. 1. GDi (Gross domestic income) Fuel System and Components

Make connections as shown above in Fig.1.The Major advantage of utilizing the Acs712 hall effect sensor interfacing with Arduino is that helpful to the cheap. This technique recovers overall accuracy, efficiency, and real-time alarm sign competence. Each gadget has the ability to detect current density and process the information using a microprocessor. Each sensor is placed in the line at various calculated nozzle and fuel-pump locations. These sensors are connected to the microcontroller via electrical connections.
A magnetic field is created when AC or DC current passes over a copper transmission route. The room effect sensor interacts with this electro-magnetic field. Depending on the input current variety, the room effect circuit converts this electro-magnetic field into relative voltage, either AC or DC. With the help of Arduino or any other microcontroller, this output voltage is measured..

2.1 Basic Block Diagram

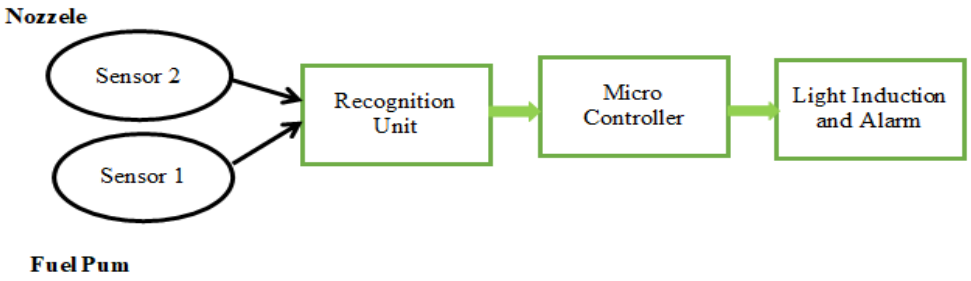

Fig. 2. Block Diagram Of early warning of the fuel sprayer

The block plan shown in Fig.2 contains of numerous sub-systems like recognition unit, micro-controller and indicated light unit. Discovery unit has a number of ACS- 712 current-sensors for fuel pump and nozzele associated. A low power micro-controller is devoted to the Light Indication scheme and alarm. Each scheme applied in the fuel sprayer scheme has the

same sub-systems of Fig. 2..

3 Recognition And Early Warning Of The Fuel Sprayer System

3.1 Detection Unit

Fig. 3. Hall sensor (ACS- 712) for fuel pump

The discovery unit has acs712 sensors on each lane, as illustrated in Fig.3, that detect the current AC or DC of the nozzle and fuel pump on that lane and provides the data to the microcontroller for processing. Every line is equipped with a number of sensors that are dependent on the current on a certain cct. These sensors are placed at a specific current level to detect precise nozzle and fuel pump current consumers. The current cumulative or decreasing gives as the induction, which causes problems nozzle or a fuel pump and challenges in most cars of modern models . The implementation of this system overcomes the events that lead to accidents of cars burn engine and overall the car with the user.

3.2 Working of ACS712 current sensor

A lined room result circuit and a copper transmission pathway are included in the ACS712 sensor. The copper transmission path wraps around the die's surface. A magnetic field is created when ac or dc electricity passes over a copper transmission route. This electro-magnetic field interacts with the sensor that detects the room effect. The room effect circuit converts this electro-magnetic field into relative voltage, depending on whether the input current is ac or dc. With the help of an arduino or any other microcontroller, the output voltage is measured. After you've calculated this voltage, you'll need to convert it to current using sensitivity equations, which I'll explain below. When the current flowing through the sensor is zero, the output voltage is calculated as Vcc / 2. If the voltage supply to the ACS712 is 5 volts, the current sensor's Vout will be 2.5 volts and the current ACS712=0 will pass through the sensor. The sensor's offset voltage, also known as the base voltage, is 2.5 volts and must be deducted from the measured value. When current becomes transitory across the sensor, Vout decreases. As a result, using the procedures below, you can determine I dc: Voltage = (adcvalue / 1024.0) * 5000; Adcvalue = analogRead(A0);
The amount of current by the preceding three lines of Arduino code is current = ((Voltage – voltage offset) / mVperAmp). In the first line, the Arduino analogue Read function is used to calculate the output voltage of the hall effect present sensor. 'The calculated digital value is saved in the mutable 'Adcvalue' variable. In the second line, convert the digital value of voltage back to equivalent voltage in mili ampere by raising it with the resolving factor and dividing it by 1000. Slow voltage is subtracted from offset voltage and alienated by the compassion factor

to obtain current from slow voltage in the third line. I hope that this explanation clarifies how this code works and how you may calculate dc current using the acs712 hall result current sensor.

4 Experimental Setup

One goal of Gdi (gross domestic income) schemes is to recoup the low cost of gasoline for gasoline-powered cars. The entire fuel system, from the gasoline tank to the injector, must be thoroughly examined and optimised. The fuel pump transports fuel from the fuel tank to the GDi high-weight pump's inlet. The fuel enters the high-pressure pump by the damper body, goes through the input metering valve, gets hassled by the plunger, and finally exits the high-weight side of the fuel scheme via the outlet check valve. A fuel line connects the pump opening to the high-pressure (common) rail, which distributes the fuel to the individual injectors. The fuel pressure sensor is usually installed on the fuel rail to allow for exact dimensioning and regulation. The ECU is in charge of the actuator that injects the fuel into the engine (electronic control unit). Fig. 4 showed the experimental set up the proposed system. Our systems consist of fuel pump electrical control unit with current sensor acs712 with Arduino Uno The Arduino Uno, a DC power supply (UNI-T UTP3315TFL 0-30V/ 0-5A), a digital oscilloscope (GDS-3252 GW INSTEK,Oscilloscope), and a nozzle were all used.

Fig. 4. The Components OF experimental testing Fuel System

5 Results and Discussion

In many cases, the nozzle is damaged or undergoes from a leak in the fuel extrusion or open and it is not possible to control the fuel extrusion, as the fuel continues to flow in the cabin, which leads to the leak of fuel outside the engine, which causes the vehicle to burn at any spark and at the same time it causes Consuming large quantities of fuel, and since there is no early warning about a nozzle malfunction, this proposed off spring will give an early warning of a nozzle malfunction, i.e. if this malfunction, whether it is a leak, a blockage, or the flow of fuel will pass through the nozzle inspection system that consists of an electrical control unit and sensors Current and voltages .

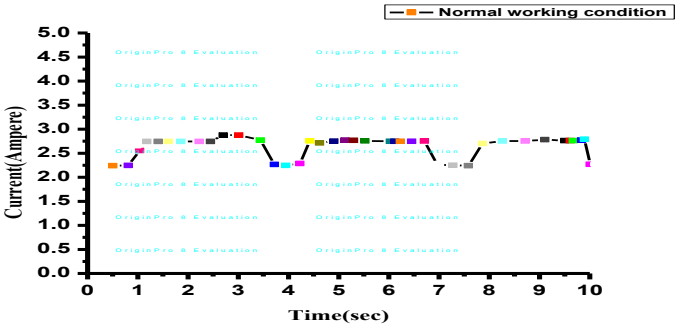

Fig. 5. The nozzle open and close induction depends on the current of the fuel pump under the normal operation condition

The cases of study state operation of the nozzles when the nozzle currents is in the range dependents on the types cares and the model , the new models of cares the system of control and units of ECU developed by the early alarm for nozzle defected needed more interesting for protection the cares and the user. In normal operation condition, the nozzle the current consumed by the fuel pump, is 2.24 amps to open and 2.78 amps to close. The working condition, periodic (2.245 A and 2.78 A) of the nozzle open and close induction depends on the current of the fuel pump under the normal operation condition as shown in Fig.5.

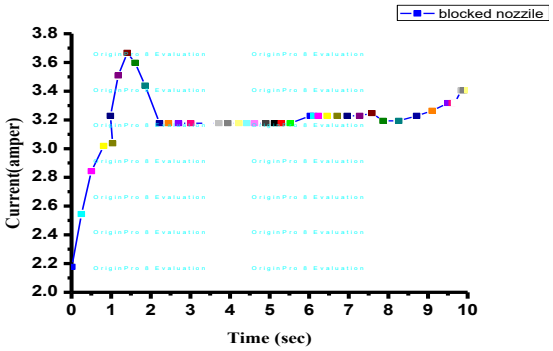

Fig. 6. The nozzle is blocked periodic

Our technique is dependents up on the electrical control unit and the currents that needs to nozzle operation .Where the current is induction for the operation conduction open and close of the nozzles depends on the current of the fuel pump. On the other hand in case the nozzle is blocked periodic as shown in Fig.6 the current consumed by the fuel pump is increasing from 2.80 A until 3.67 A. The clogging of nozzle lead to the increasing pressures for fuel pump and also increasing the current of fuel pump may damage the coil that control of nozzle fuel gate. The leakage state in the fuel, leads to decreasing the nozzle current from 3.5A to 2.6 A and decreasing pressure on the fuel pump so that have two types of leakage the fuel the fuel leakage from piping system as shown in Fig.7 and the current of nozzle pump between (2.54A and 2.8A) and the nozzle as in Fig.8

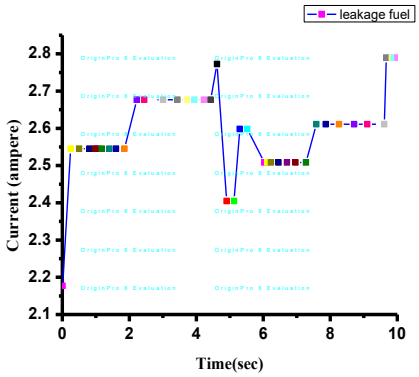

Fig. 7. Leakage the fuel the fuel leakage from piping system that between the pump and nozzle

The leakages fuel from the nozzle because of the damage the nozzle gates that lead to the continuous the flow of fuel without control, in this case the current of nozzle pump between (2.54A and 3.28A) as shown in Fig.8. Continuous the flow of fuel without control leaded to full the combustion chamber and flow outside it. That may be causes of burning the internal combustion and the overall the car.

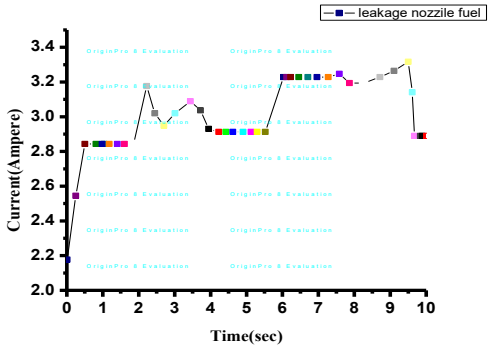

Fig. 8. The leakages fuel from the nozzle because of the damage the nozzle

Based on the findings of this research, control and alarm indication based on the present sensor's result appears to be the most promising option due to its simplicity and flexibility in including new factors into the control. However, based on the findings presented in the literature to far, it is possible to determine which method is the best to use as an early warning for nozzle pump work. Thus, the proposed technique procedure is efficient under dissimilar values the presentation of the proposed methods when compared with all cases established.

6 Conclusions

The proposed technique following system is projected and applied to improve the achievement of control system. This research described a low-cost real-time recognition and early warning system for the fuel sprayer system that uses sensors to prevent a collision between a burning car engine and the body. Also save the lives of drivers and passengers

to reducing the losses economic and human. The prototype was simply used to confirm the design, with the trials demonstrating an increased ability for control and warning indication based on the results obtained from the current sensor. With enough financing, this idea can be developed on a wide scale to produce an even better Early Warning Of The Fuel Sprayer System to compete with the existing ones on the market. The Early Warning Of The Fuel Sprayer System is tested and measured using a current sensor, which is then relayed to a microcontroller for automatic control. The system can able to save the lives of drivers and passengers to reducing the economic and human losses and preventing these accidents in vehicles. The achievement system is demonstrated to be efficient and robust in improving the fuel sprayer control system and capacity. Experimental results demonstrated the improvement in attaining to the desired control system using the proposed technique of control to provide good control performance in difference operating conditions.

References

[1] J. De Baerdemaeker, A. Munack, H. Ramon, and H. Speckmann, "Mechatronic systems, communication, and control in precision agriculture," *IEEE Control Systems Magazine,* vol. 21, no. 5, pp. 48-70, 2001.

[2] P. Gonzalez-de-Santos *et al.*, "Fleets of robots for environmentally-safe pest control in agriculture," *Precision Agriculture,* vol. 18, no. 4, pp. 574-614, 2017.

[3] G. Hoffmann, B. Befrui, A. Berndorfer, W. F. Piock, and D. L. Varble, "Fuel system pressure increase for enhanced performance of GDi multi-hole injection systems," *SAE International Journal of Engines,* vol. 7, no. 1, pp. 519-527, 2014.

[4] S. Hasirlioglu, I. Doric, C. Lauerer, and T. Brandmeier, "Modeling and simulation of rain for the test of automotive sensor systems," in *2016 IEEE Intelligent Vehicles Symposium (IV)*, 2016, pp. 286-291: IEEE.

[5] L. Tian, "Development of a sensor-based precision herbicide application system," *Computers and electronics in agriculture,* vol. 36, no. 2-3, pp. 133-149, 2002.

[6] C. Trigona *et al.*, "Implementation and characterization of a smart parking system based on 3-axis magnetic sensors," in *2016 IEEE International Instrumentation and Measurement Technology Conference Proceedings*, 2016, pp. 1-6: IEEE.

[7] F. Moreu, R. E. Kim, and B. Spencer Jr, "Railroad bridge monitoring using wireless smart sensors," *Structural Control and Health Monitoring,* vol. 24, no. 2, p. e1863, 2017.

[8] Y. Jagadeesh, G. M. Suba, S. Karthik, and K. Yokesh, "Smart autonomous traffic light switching by traffic density measurement through sensors," in *2015 International Conference on Computers, Communications, and Systems (ICCCS)*, 2015, pp. 123-126: IEEE.

[9] S. Saponara, E. Petri, L. Fanucci, and P. Terreni, "Smart transducer interface in embedded systems for networked sensors based on the emerging IEEE 1451 standard: H2 detection case study," in *2009 Seventh Workshop on Intelligent solutions in Embedded Systems*, 2009, pp. 49-55: IEEE.

[10] P. Wong, D. Nguyen, A. Abukmail, R. Brown, R. Ryan, and M. Pagnutti, "Low cost unmanned aerial vehicle monitoring using smart phone technology," in *2015 12th International Conference on Information Technology-New Generations*, 2015, pp. 286-291: IEEE.

[11] P. Xu *et al.*, "Effects of direct water injection on engine performance in a hydrogen (H2)-fueled engine at varied amounts of injected water and water injection timing," *International Journal of Hydrogen Energy,* vol. 45, no. 24, pp. 13523-13534, 2020/05/05/ 2020.

[12] X. Meng, J. Wang, Y. Zhou, H. Tian, W. Long, and M. Bi, "Study of using diesel/high-ON biofuel blends as the pilot fuel with large proportion and split injection in the dual-fuel combustion," *Fuel,* vol. 268, p. 117345, 2020/05/15/ 2020.

[13] Z. Li *et al.*, "Dual fuel intelligent charge compression ignition (ICCI) combustion: Efficient and clean combustion technology for compression ignition engines," *Fuel,* vol. 279, p. 118565, 2020/11/01/ 2020.

[14] B.-Q. He, X. Chen, C.-L. Lin, and H. Zhao, "Combustion characteristics of a gasoline engine with independent intake port injection and direct injection systems for n-butanol and gasoline," *Energy Conversion and Management,* vol. 124, pp. 556-565, 2016/09/15/ 2016.

[15] S.-E. Razavi *et al.*, "Impact of distributed generation on protection and voltage regulation of distribution systems: A review," *Renewable and Sustainable Energy Reviews,* vol. 105, pp. 157-167, 2019/05/01/ 2019.

[16] J. Snodgrass and L. Xie, "Overvoltage analysis and protection of lightning arresters in distribution systems with distributed generation," *International Journal of Electrical Power and Energy Systems,* 123, p. 106209, 2020. .

[17] H. Huang, W. Teng, Z. Li, Q. Liu, Q. Wang, and M. Pan, "Improvement of emission characteristics and maximum pressure rise rate of diesel engines fueled with n-butanol/PODE3-/4diesel blends at high injection pressure," *Energy Conversion and Management,* vol. 152, pp. 45-56, 2017/11/15/ 2017.

[18] S. T. Thompson *et al.*, "Direct hydrogen fuel cell electric vehicle cost analysis: System and high-volume manufacturing description ,validation, and outlook," *Journal of Power Sources,* vol. 399, pp. 304-313, 2018/09/30/ 2018.

[19] M. A. Abdelkareem, K. Elsaid, T. Wilberforce, M. Kamil, E. T. Sayed, and A. Olabi, "Environmental aspects of fuel cells: A review," *Science of The Total Environment,* p. 141803, 2020/08/20/ 2020.

[20] F. H. M. Rafi, M. J. Hossain, M. S. Rahman, and S. Taghizadeh, "An overview of unbalance compensation techniques using power electronic converters for active distribution systems with renewable generation," *Renewable and Sustainable Energy Reviews,* vol. 125, p. 109812, 2020/06/01/ 2020.

[21] H. S. Das, C. W. Tan, and A. H. M. Yatim, "Fuel cell hybrid electric vehicles: A review on power conditioning units and topologies," *Renewable and Sustainable Energy Reviews* ,vol. 76, pp. 268-291, 2017/09/01/ 2017.

[22] C. A. MacCarley and W. D. Van Vorst, "Electronic fuel injection techniques for hydrogen powered i.c. engines," *International Journal of Hydrogen Energy,* vol. 5, no. 2, pp. 179-203, 1980/01/01/ 1980.

[23] - 11"Future Automotive Electronic Systems," in *Understanding Automotive Electronics (Sixth Edition)*, W. B. Ribbens, N. P. Mansour, G. Luecke, C. W. Battle, E. C. Jones, and L. E. Mansir, Eds. Burlington: Newnes, 2003, pp. 401-442.

[24] A. K. Haghighat, S. Roumi, N. Madani, D. Bahmanpour, and M. G. Olsen, "An intelligent cooling system and control model for improved engine thermal management," *Applied Thermal Engineering,* vol. 128, pp. 253-263, 2018/01/05/ 2018.

[25] V. Lawlor and A. G. Olabi, "Review of scientific research regarding PPO, tallow and RVO as diesel engine fuel," *Fuel,* vol. 145, pp. 25-38, 2015/04/01/ 2015.

Implementations of Smart Cities in USA, Europe, and the Far East Countries

Fatima AlQaoud[1], Andrew Carruthers[2], Mumtaz Kamala[3], and Raed Abd-Alhameed[4]
{fnhalqao@bradford.ac.uk[1], A.Carruthers@bradford.ac.uk[2], m.a.kamala@bradford.ac.uk[3]}

Kuwait University, Block 4, Al-khaldiya, Kuwait[1]
Faculty of engineering and informatics, University of Bradford, Bradford, BD7 1DP, UK[2,3]
Information and Comms Eng. Dept., Basrah University College of Science and Technology, Basrah 24001, Iraq[4]

Abstract. This paper presents definitions of the 'Smart City' that have been discussed academically and examines different implementations of the smart city in the United States and some European countries such as the United Kingdom, Germany, and Far East countries such as Japan, South Korea, and Singapore. With the emergence of many global problems such as climate change, transportations, high populations, limited resources of food and medicine, all developed countries must amalgamate their efforts and cooperate to find an ultimate smart city, considering the most appropriate standards for constructing such a city. This paper also presents a comparison of different implementations of the smart city and various initiatives which have been undertaken by different countries to solve worldwide problems.

Keywords: Smart City, virtual environment, Online learning, online environment, smart environment, online system, ICT, technology, educational system, Society 5.0, U-City, sensor deserts, sustainability.

1 Introduction

Engaging with the technology era has required all government departments and private sectors to share the same database and compatible systems to use the same information to operate it in a way that enables them to process, proceed, and manage operations related to citizens or clients. Researchers have been conducting investigations into the recent technological developments and they describe the city or the country that implements the most advanced technology as the 'Smart City' to indicate the progress of the country economically, socially, and academically.

To be classified as a smart city, several projects must be accomplished; thus, it is important to shed light on the definition, concept, and principles of the 'Smart City' from the perspective of academic research[1]. The size of the city can determine certain characteristics that shape an ideal smart civilized city because it is dependent on its accessibility to other cities and accessibility to service centres; thus, governments should consider inhabitants, size, and proper functions to construct a smart city [2]. Thus, smart citizens, smart thriftiness, smart management systems, and smart environment are characteristics of smart city construction [3].

Previous studies such as that by Caragliu [4], have proposed that similar schemes and solutions have been defined using several terms but with close similarities with one another. For example,

IMDC-IST 2021, September 07-09, Sakarya, Turkey
Copyright © 2022 EAI
DOI 10.4108/eai.7-9-2021.2315364

intelligent city, wired city, and digital city have a similar meaning; however, similarities and variations were not yet determined in these terms. On the other hand, Chen [5] insists that technology is the main constituent for the smart city and in particular ICT, which enables links to be made to different agents in the civilized arena and to provide technical services. The most significant agents are universities, research institutions, and companies with high technology [6, 7]. Dameri [1] introduced the definition of a smart city relying on three characteristics which are: terminology; components and boundaries and scope. Similarly, 'Smart Cities' are considered as ecosystems that are defined as interacted organisms in communities and their environment and described as complex shaped networks through interdependent resources [8]. Ecosystems consist of agents, organizations, material infrastructures, and symbolic resources that are independently collected into a social system [9].
Hollands (2020) [10] summarised three difficulties to established definitions of a smart city, such that the term 'smart city' appeared to be based on assumptions by an academic which became conflated with another one. The second difficulty is filtering the promotion and use of such terms for marketing reasons [11-13] as disagreeing to referring to the current infrastructural change or proof of practical and effective IT legislations. The third problem is that those terms imply a positive and uncritical viewpoint regarding urban progress.
This work highlights several Smart Cities that have been implemented by different countries, in the United States, Europe, and the Far East to draw comparisons between them.

2 Smart City in the United States and Europe

It is noticed that ideological representation of crisis usually related to smartness emerged before 2008 from the emphasis on sustainability and climate change to post-financial crisis combat with entrepreneurship and phantomization. Recently, the United States and Europe have adopted deviating paths towards having control over big technology companies in local and international markets [14]. However, the relationship between the expected media vision of smartness and their change must be considered since it started as a space in which expectations and calculations of societal futures are created at present [15-17].

2.1 United States

Generally, technological industries have relied on algorithms, artificial intelligence, and machine learning to become well-known in the market. However, recently those industries have been focusing on climate change which is the new direction to form a new vision of the smart city. For instance, in the early 2000s, energy scarcity and sustainability were the main challenges to both Cisco and IBM's initial propositions about smart cities. Cisco was asked to act towards alleviating climate change and specifically to launch the Connected Urban Development (CUD) program to increase the efficiency of traffic flow through new technologies, thereby decreasing carbon emissions. Several cities took advantage of such a project including San Francisco, Seoul, Amsterdam, Madrid, and Hamburg. To form cities to be a model of infrastructural efficiency; Cisco stated that 'Our fundamental belief is that today's flow of people, goods, energy, information, media, and services in cities can be as efficient as the traffic of digital products on the internal'[18]. Likewise, IBM's president and CEO Samuel Palmisano declared their vision of a 'Smart Planet' in 2008 in a speech to the Council on Foreign Relations., announcing that cities that share similar crisis ideological representations facing several

difficulties and threats to their long-life existence across all their central systems that they need to outline holistically, IBM's program recommended that technology must be used by a smart city to shift its central systems and optimize the return from largely limit resources[19].

2.2 United Kingdom

By 2020, cities are expecting to spend US$ 20 billion on sensor technologies [20]. Smart city agendas have appeared during the post-2008 era following an economic recession crisis and raising worldwide and regional injustice. Most cities are now more unevenly divided between rich elites and those in poverty than during the past decade, despite the level of wealth generation that has not been seen before [21]. New sensor technologies contact social procedures and they can present well-documented social and environmental inequalities [22]. 'Sensor deserts' is a term that refers to a situation that arises when attempting to produce new data and knowledge about cities, where gaps appear in understanding the exact urban population. However, networks cannot cover all areas, despite their tendency to give signals of ubiquity regarding an urban environment. Therefore, sensor deserts are a smart-specific term for inequalities, focused on areas that have a scarcity of coverage as well as a poor investment, conceptual, and legality related to smart cities[23].
'Sensor deserts' are deserts in sensor coverage where it is difficult to collect data; these become obvious in physical sensor infrastructure and the data they yield. They can be attached to lampposts or fixed on kerbsides. Their function is to indicate investment priorities and therefore, that people and places are recognised as important by smart city efforts. Changing the place of sensor infrastructure from the gaps and following biases in collected data. Significantly, sensors cannot cover all areas and are selective in terms of positioning. Consequently, Robinson [23] conceptualised and analysed sensor deserts through two case studies: Newcastle's Urban Observatory (UK) and Chicago's Array of Things (USA); despite the limitations these studies faced, the results demonstrated best practice in the design of fair sensor networks [23].

2.3 Germany

The primarily top-down smart city strategies adopted in Germany have led to considering raising bottom-top activism to retrieve the urban commons [24-27]. This requires keeping the capitalist sense for more democratic, community-based dominant away from governance practices, legislations, and infrastructure[28]. Constructing a smart city is not only limited to ICT and digital enhancement fixed market-economic sense [29, 30], but also have been prepared to satisfy urban sustainability, approaches, and strategies which concentrated on the 'enhance efficient skills, the individual and household behaviour, and settlement of consumer culture' [31].
Smart City Cologne (SCC) emerged in 2011 aiming to protect the environment by creating a sustainable and resilient city[32]. To that purpose, the local energy provider "RheinEnergie" (RE) and the city of Cologne entered a partnership. The implementation of SCC has influenced both austerity-inclined financial policies and the federal government's Energiewende (Energy Transition) policy. German municipalities have experienced a continuous rise in debts and a decline in leverage to enforce taxes on commerce and land, because of the high competition among cities to gain more business and private capital [33]. In the 1980s, when Germany attempted to implement de-industrialisation, the city of Cologne concentrated on economic development and setting up strong occupation markets, through a partnership of public and private sectors and cost efficiency considerations in planning [34].

Citizens' engagement was regarded as the overriding feature of SCC (Smart City Cologne Website), and the website of SCC encouraged all people to participate and the approach was "bottom-up" in its aim, therefore, in this development, re-politicisation of smart city strategies and social innovation is seen to be independent on each other[28].

2.4 Spain

To design and build a successful smart city, vendors of applications and software system developers must understand all needs and requirements of a smart city. Therefore, it is important to know which software systems that international organizations are offering (open or close), those software systems to which smart city axes are related, to which communication technologies that the smart city system is compatible with, and what the software solutions have been designed for [35].
Urban planners and policymakers need to make the best decisions when choosing software systems to implement and construct smart cities. Giffinger et al.[36] presented a guide as a standard to lead platform providers to determine the domains of work as shown in Fig 1. [36]. The figure shows that smart cities fall into six different axes: Smart economy- that is related to economic competencies; Smart environment- that can be described by natural conditions such as climate, green space, in addition to the management of pollution and resource management; Smart governance- that comprises aspects of political engagement and citizen services; Smart living- this consists of different aspects of life quality, health, safety, and housing; Smart mobility- which concerns the transport systems and communication technology; and eventually, Smart people- that represents social interactions and human life.

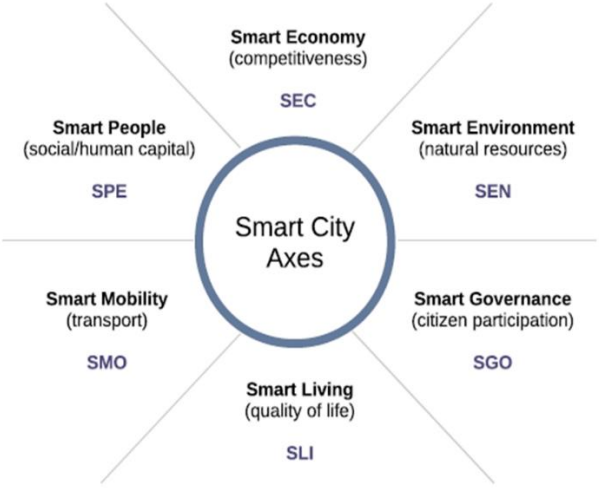

Fig 1. Six axes of a Smart City (Adopted from Giffinger (2007)[36]).

Saborido [35] states that two main obstacles impede the implementation of a powerful smart city solution. First, the utilization of ICT, which had relied on traditional systems that are not interoperable and now need to be upgraded as they are not mobile across cities, are not able to expand nor are they cost-effective. The second obstacle relates to some of the architectural design achievements which are currently in the process but have not yet combined, and this

issue raises some concerns for stakeholders. However, the researcher offers a solution in terms of the contributions of international standards organizations, professional organizations, and international communities which will minimize the impacts of such obstacles. Saborido [35] demonstrates how such organizations can cooperate to form Smart City Standardizations as shown in Fig 2. [35] below.

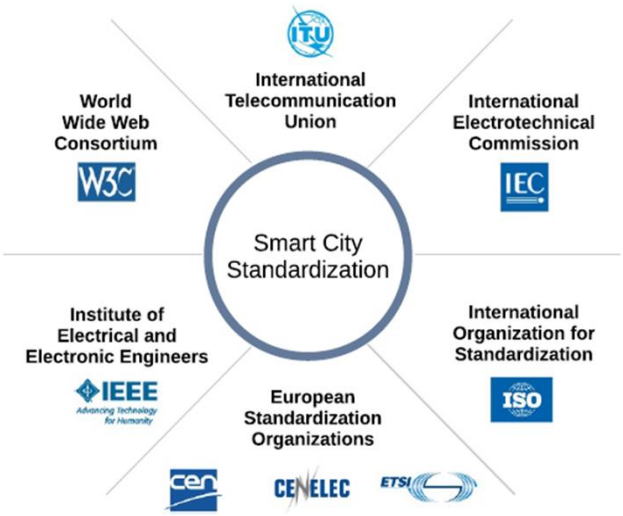

Fig 2. International standards of organizations to build up the smart city (Adopted from[35]).

The lack of interoperability among platforms causes confusion and differences of standards and prevents the timely evolution of low-level IoT Technologies which slows down services to be delivered by smart cities [37]. Several recent smart cities have relied on closed systems, in which the interior design and architecture were anonymous. This is the opposite of the open systems that are based on components that are compliant with manufacturing standards. Therefore, it is recommended that policy-makers and urban planners use software systems that present public Application Programming Interface(APIs) because this signifies that the vendors are authorized to use software functions and features compatible with the requirements of smart cities [35].

3 Smart City in the Far East

With the emergence of smartphones, people have practiced a new way of shopping, new ways of performing their jobs, and new ways of exporting and importing services. This development has involved a significant change that has been witnessed over the past 30 years due to digital technology, which has contributed to transforming societies from an industrial society based on fabrication into an information-based society [38]. According to the International Electrical Commission [39], it is expected that 66% of the global population will live in urban regions by 2050. Therefore, basic needs such as energy, clean water, sufficient food must be supplied in ways that are compliant with the need for economic, social, and environmental sustainability [40].

3.1 Japan

Information Communication Technologies (ICT) enable initiatives related to smart cities to be taken. ICT is viewed as a fundamental factor to help cities to enhance transformative solutions to detect the problems of global change and build up sustainable and resilient communities. Such solutions are essential to enhance urban sustainability, integrating intelligent basic rules with sustainability measure tools [41].

Due to current situations related to the growth of cities and demand for services, the realization of 'super-smart city' was given top priority for developed countries and considered as the first pillar in the 5th Science and Technology Basic Plan [42], and "Society 5.0" is considered one of the most popular initiatives towards this realization [43]. ICT is being used as a digital infrastructure regarding catastrophe countermeasures in Japan specifically this includes the use of social media such as 'twitter' and Geographic Information Systems (GIS) that played a key role in catastrophe countermeasures. Since the real world and virtual spaces have close relationships and have become integrated into super-smart city societies such as in Japan, this has led to the sharing of information in virtual space which helps to support activities in the real world. Therefore, if a disaster in the real world happened, the reception of disaster-related information would be readily available and broadcast in virtual space through different information communication channels simultaneously [43].

It is important to highlight an exceptional experience of Japanese technology; Deguchi [38] presented a vision of a future society called 'Society 5.0', which is guided by scientific and technological innovation in Japan such that; according to this concept as shown in Fig 3. [38]: "The first step of combining the physical space as 'the real world' with the cyberspace by supporting ICT to its fullest, suggesting an optimal form of Japanese future society, which can be described as a 'super-smart society' which will make people wealthier. The series of such innovations are being now more deepened and intensively advertised as 'Society 5.0'". According to Deguchi [38], Society 5.0 is a model used to connect the government's vision of a future society to manufacturing and the general public. Therefore, it is important to understand the basic ideas to obtain a complete picture of 'Society 5.0', as well as cyberspace and physical space to satisfy the concept of 'Society 5.0'.

3.2 South Korea

South Korea has the necessary experience required to build smart cities as national basic industries to grow the economy. Despite the challenges faced by the government such as a declining economy, and inability to achieve smart functionality to the U-City, the government has implemented policies and legislations for smart cities such as 1) promoting and implementing solutions for South Korean smart cities 2) implementation of developed technology and governmental action which had been suggested by majority public opinion 3) requirements of a wide scope approach and strategic plan which integrates software applications with developed technologies; 4) engagement of private and public sectors through investments to achieve social progress [44].

In the early 2000s, South Korea established the U-City before the smart city term appeared. The U-City "Ubiquitous City Act" was constructed to manage the transportation, environmental, and energy-related problems of cities. According to[45], the expression 'Smart City' has replaced the term 'U-City' after Apple released the iPhone in 2007. The smart city is the most popular concept that concerns building a low-cost, high-efficiency space to set up social capital since

the U-City was created as an integrated system for effective use of information through the construction of ICT-based solutions [46].
Recent smart city policies of each ministry in South Korea concentrate on technology enhancement and the configuration of integrated systems, as well as consumer-oriented services since policies of smart city, have been developed to promote the smart city and to be extended to serve international markets [47]. Different projects have been used under different names such as U-City and e-city by several ministries in South Korea causing conflicts in objectives, directions, strategies, and weak cooperation among them; therefore, using the big data-based approach indicates the general tendency of the smart city in South Korea. Smart cities appeared as a solution to different future urban challenges such as global warming, energy problems, and high population [44].

	Society 1.0	Society 2.0	Society 3.0	Society 4.0	Society 5.0
Society	Hunter-gatherer	Agrarian	Industrial	Information	Super smart
Productive approach	Capture/Gather	Manufacture	Mechanization	ICT	Merging of cyberspace and physical space
Material	Stone・Soil	Metal	Plastic	Semiconductor	Material 5.0*
Transport	Foot	Ox, horse	Motor car, boat, plane	Multimobility	Autonomous driving
Form of settlement	Nomadic, small settlement	Fortified city	Linear (industrial) city	Network city	Autonomous decentralized city
City ideals	Viability	Defensiveness	Functionality	Profitability	Humanity

Fig 3. Contextualizing Society 5.0. Categories created by the authors. Source: Produced by authors.
∗Research conducted by the University of Tokyo's Material Innovation Research Centre-According to Deguchi [38]

3.3 Singapore

Singapore has achieved a highly context-sensitive sustainable city through focusing on farming and conceiving smart urban initiatives and schemes. Constructing a smart city in Singapore required reshaping an urban environment that had relied on shifting from a 'Smart in a box' product version to a 'Smart in the city's approach. The most common feature of the urban condition is coping with large-scale growth to transfer to megacities through continuous urbanization which handles the issues of high energy consumption, crowded vehicles, greater consumption of natural resources, and rapid population growth [48]. According to [49, 50], the most prevalent highly ranked smart cities are Singapore, Barcelona, New York, Amsterdam, and London, which share similar advanced infrastructure of towns such as Songdo (South Korea) or Masdar (Abu Dhabi-UAE). These developments are provided as models for building smart cities. Despite differences among these cities, they all share the same characteristics such as successful growing cities, handling problems of high population, and the effective management of mobility. Therefore, to shift from 'Smart in a box' to 'Smart in the City, people and citizens who live in them must be engaged to be the main component of the smart city rather than technology. This has been pointed out by Hollands [51] who stated that the smart city can

become more economically, socially, and culturally polarized and divided by raising divisions between received knowledge and creative workers, and the non-competent and IT ignorant people [52, 53].
In the same manner, to achieve smart city goals; communication, interaction, involvement, and contributions of basic components must be considered. This should include collecting and accessing usage-based data and feedback from end-users that can be used to enhance existing services. This can be accomplished by taking advantage of smartphones, the Internet of Things (IoT), and cloud computing technology. Participation of government agencies such as profit organizations (for example, Startups, major tech firms, and legacy businesses) as well as non-profit organizations in the ecosystem through addressing solutions and developing pilots will lead to the appropriate mechanisms to align incentives [54].

4 Result and Discussion

All countries around the world are facing the same ecosystem problems such as climate change, high emission of carbon from industries, trains, airplanes, and cars, as well as high population growth with limited resources of food and medicines. Consequently, most developed countries have changed their direction from manufacturing and producing with more advanced recognition to the creation of smart cities, which will achieve a sustainable environment for all people around the world to live longer and healthier.

Countries in the West such as the USA and Europe, for example, The United Kingdom, Germany, and Spain as well as countries in The Far East e.g.: Japan, South Korea, and Singapore; have taken actions towards resolving global issues as shown in Table 1. As we can see, the United States, like Germany, is working to find solutions for climate change. The USA has engaged Cisco to release the Connected Urban Development (CUD) program to increase the efficiency of traffic flow through new technologies, thereby decreasing carbon emissions. Germany implemented the Smart City Cologne (SCC) as a sustainable and resilient city to protect the climate and to minimise rising debts due to the decline in leverages to enforce taxes on commerce and land, through the partnership between the local energy provider “RheinEnergie” (RE) and SCC. Additionally, citizens have been engaged as a basic structure of SCC.
On the other hand, The United Kingdom spent efforts to build up a network as ‘sensor deserts’ that can cover all areas and are selective in terms of positioning to gather precise data and information. Similarly, Japan has dedicated its efforts to building the Society series and now has released ‘Society 5.0’ which can be used to combine the real world with virtual spaces for effective sharing of information. This helps to support activities in the real world and by effectively dealing with catastrophic events. Both the UK and Japan are seeking for accuracy of the information, while South Korea has its own experience with different systems that have been used by different ministries. Therefore, the smart city concept has appeared as a unified solution to be used among all ministries to solve different future urban challenges such as global warming, energy problems, and high population. Likewise, Singapore started ‘smart in a box’ and transformed to ‘smart in a city’ to handle the issues of high energy consumption, crowded vehicles, increased consumption of natural resources, and rapid population growth. In agreeing with Germany’s policy, citizens who live in them must be engaged to be the main component of the smart city rather than technology, as well as encouraging profit and non-profit organizations to participate in building up the smart city [54].

Table 1. Initiatives used to implement smart cities in the USA, Europe, and the Far East.

Country	Initiative	Purpose	Smart City
USA	Connected Urban Development (CUD) program	to increase the efficiency of traffic flow through new technologies, thereby decreasing carbon emissions	San Francisco, Seoul, Amsterdam, Madrid, and Hamburg
UK	Sensor deserts network	to indicate investment priorities, therefore, people and places are recognised by smart city efforts	Newcastle, Chicago
Germany	Smart City Cologne (SCC)	to protect the climate to be a key sustainable and resilient city, and to achieve a stable raise in debts and a decline in leverage to enforce taxes on commerce and land	Cologne
Japan	Society 5.0	catastrophe countermeasures	Japan
South Korea	U-city "Ubiquitous City Act" / e-city	to manage the transportation, environment, and energy-related problems of cities, and to find a solution to different future urban challenges such as global warming, energy problems, and high population	Several ministries
Singapore	Smart in a box / Smart in the city	to transfer to megacities through continuous urbanization which handle the issues of high energy consumption, crowded vehicles, more consumption of natural resources, and the quick growth of population.	Singapore

5 Conclusion

Developed countries are competing to construct the ultimate smart city as a sustainable environment to solve many worldwide problems such as climate change, transportation, traffic flow, and energy-related problems of cities. However, no single solution has emerged, despite different efforts that have been made to construct a smart city. Since no standardisation of the main components of a smart city, each city has released its initiative for similar purposes.
Urban planners and policy-makers need to make the best decisions when choosing software systems to implement and construct smart cities. Spain calls for contributions of international standards organizations, professional organizations, and international communities to set up

unified standards that all developed countries can utilize when setting up smart cities. Specifically, Giffinger et al. [36] presented a guide as a standard to lead platform providers to determine the domains of work, to construct a smart city. Additionally, governmental parties, citizens, profit and non-profit organizations need to be participants in setting up a smart city.

References

[1] R. P. Dameri, "Searching for smart city definition: a comprehensive proposal," *International Journal of computers & technology,* vol. 11, no. 5, pp. 2544-2551, 2013.

[2] R. Katoshevski-Cavari, T. A. Arentze, and H. J. P. Timmermans, "Sustainable city-plan based on planning algorithm, planners' heuristics and transportation aspects," *Procedia-Social and Behavioral Sciences,* vol. 20, pp. 131-139, 2011.

[3] A. Kirimtat, O. Krejcar, A. Kertesz, and M. F. Tasgetiren, "Future trends and current state of smart city concepts: A survey," *IEEE Access,* vol. 8, pp. 86448-86467, 2020.

[4] A. Caragliu, C. D. Bo, and P. Nijkamp, "Smart Cities in Europe «3rd Central European Conference in Regional Science–CERS," *A13 L,* vol. 90, p. O18, 2009.

[5] Y.-T. Chen, "Sketch industry promotion framework for smart living services by leveraging living lab harmonization cube," *International Journal of Electronic Business Management,* vol. 10, no. 2, p. 149, 2012.

[6] E. Cosgrave and T. Tryfonas, "Exploring the relationship between smart city policy and implementation," 2012, pp. 79-82.

[7] R. P. Dameri, "Defining an evaluation framework for digital cities implementation," 2012: IEEE, pp. 466-470.

[8] U. Gretzel, H. Werthner, C. Koo, and C. Lamsfus, "Conceptual foundations for understanding smart tourism ecosystems," *Computers in Human Behavior,* vol. 50, pp. 558-563, 2015.

[9] D. Maheshwari and M. Janssen, "Reconceptualizing measuring, benchmarking for improving interoperability in smart ecosystems: The effect of ubiquitous data and crowdsourcing," *Government Information Quarterly,* vol. 31, pp. S84-S92, 2014.

[10] R. G. Hollands, "Will the real smart city please stand up?: Intelligent, progressive or entrepreneurial?," in *The Routledge Companion to Smart Cities*: Routledge, 2020, pp. 179-199.

[11] I. Begg, *Urban competitiveness: policies for dynamic cities*. Policy Press, 2002.

[12] D. Harvey and F. D. Harvey, *Spaces of hope*. Univ of California Press, 2000.

[13] J. R. Short, C. Breitbach, S. Buckman, and J. Essex, "From world cities to gateway cities: Extending the boundaries of globalization theory," *City,* vol. 4, no. 3, pp. 317-340, 2000.

[14] B. Baykurt and C. Raetzsch, "What smartness does in the smart city: From visions to policy," *Convergence,* vol. 26, no. 4, pp. 775-789, 2020.

[15] V. Albino, U. Berardi, and R. M. Dangelico, "Smart cities: Definitions, dimensions, performance, and initiatives," *Journal of urban technology,* vol. 22, no. 1, pp. 3-21, 2015.

[16] A. Cocchia and R. P. Dameri, "Exploring smart city vision by university, industry and government," in *Blurring the boundaries through digital innovation*: Springer, 2016, pp. 259-270.

[17] O. Halpern, R. Mitchell, and B. D. Geoghegan, "The smartness mandate: Notes toward a critique," *Grey Room,* pp. 106-129, 2017.

[18] N. Villa and S. Mitchell, "Connecting cities achieving sustainability through innovation," 2010.

[19] S. Dirks and M. Keeling, "A vision of smarter cities: How cities can lead the way into a prosperous and sustainable future," *IBM Institute for business Value,* vol. 8, 2009.

[20] SmartCitiesWorld. "Smart city technology market to grow by $263 billion by 2028." (accessed June, 6 2021, 2021).

[21] UN-Habital. "World Cities Report 2016: Urbanization and Development." (accessed June 1 2021, 2021).

[22] S. Safransky, "Geographies of algorithmic violence: redlining the smart city," *International Journal of Urban and Regional Research,* vol. 44, no. 2, pp. 200-218, 2020.
[23] C. Robinson and R. S. Franklin, "The sensor desert quandary: What does it mean (not) to count in the smart city?," *Transactions of the Institute of British Geographers,* 2020.
[24] A. Baier, T. Hansing, C. Müller, and K. Werner, *Die welt reparieren: open source und selbermachen als postkapitalistische praxis*. transcript Verlag, 2016.
[25] A. Follmann and V. Viehoff, "A green garden on red clay: creating a new urban common as a form of political gardening in Cologne, Germany," *Local Environment,* vol. 20, no. 10, pp. 1148-1174, 2015.
[26] L. Hatzelhoffer, *Smart City konkret: Eine Zukunftswerkstatt in Deutschland zwischen Idee und Praxis; Evaluation der T-City Friedrichshafen*. Jovis, 2012.
[27] J. Stollmann *et al.*, *Beware of smart people! Redefining the smart city paradigm towards inclusive urbanism: Proceedings of the 2015 "Beware of Smart People!" symposium*. Universitätsverlag der TU Berlin, 2016.
[28] S. Leitheiser and A. Follmann, "The social innovation–(re) politicisation nexus: Unlocking the political in actually existing smart city campaigns? The case of SmartCity Cologne, Germany," *Urban Studies,* vol. 57, no. 4, pp. 894-915, 2020.
[29] N. Taylor Buck and A. While, "Competitive urbanism and the limits to smart city innovation: The UK Future Cities initiative," *Urban studies,* vol. 54, no. 2, pp. 501-519, 2017.
[30] J. M. White, "Anticipatory logics of the smart city's global imaginary," *Urban Geography,* vol. 37, no. 4, pp. 572-589, 2016.
[31] C. J. Martin, J. Evans, and A. Karvonen, "Smart and sustainable? Five tensions in the visions and practices of the smart-sustainable city in Europe and North America," *Technological Forecasting and Social Change,* vol. 133, pp. 269-278, 2018.
[32] B. Möhlendick, "Köln auf dem Weg zur Smart City," *Informationen zur Raumentwicklung,* vol. 1, no. 2017, pp. 24-33, 2017.
[33] B. Keller, "The continuation of early austerity measures: the special case of Germany," *Transfer: European review of labour and research,* vol. 20, no. 3, pp. 387-402, 2014.
[34] A. Mattissek, "Die neoliberale Stadt," ed: transcript-Verl., 2008.
[35] R. Saborido and E. Alba, "Software systems from smart city vendors," *Cities,* vol. 101, p. 102690, 2020.
[36] R. Giffinger, C. Fertner, H. Kramar, and E. Meijers, "City-ranking of European medium-sized cities," *Cent. Reg. Sci. Vienna UT,* pp. 1-12, 2007.
[37] W3C. "White Paper for the Web of Things." (accessed June 1 2021, 2021).
[38] A. Deguchi, "From Smart City to Society 5.0," *Hitachi-UTokyo Laboratory (H-UTokyo Lab.),* p. 43, 2020.
[39] S. City. "International Electrotechnical Commission." (accessed 28 May 2021, 2021).
[40] C. S. Lai *et al.*, "A review of technical standards for smart cities," *Clean Technologies,* vol. 2, no. 3, pp. 290-310, 2020.
[41] A. Sharifi, S. Kawakubo, and A. Milovidova, "Urban sustainability assessment tools: toward integrating smart city indicators," in *Urban Systems Design*: Elsevier, 2020, pp. 345-372.
[42] (2016). *5th*

Science and Technology Basic Plan.
[43] K. Yamamoto, "Utilization of ICT as a digital infrastructure concerning disaster countermeasures in Japan," *Information,* vol. 11, no. 9, p. 434, 2020.
[44] C. Choi, J. Choi, C. Kim, and D. Lee, "The smart city evolution in South Korea: Findings from big data analytics," *The Journal of Asian Finance, Economics, and Business,* vol. 7, no. 1, pp. 301-311, 2020.
[45] C. Choi and C.-I. Kim, "The 4th industrial revolution, smart cities, and sustainable urban regeneration: A perspective study," *환경정책,* vol. 25, no. 특별호, pp. 61-91, 2017.
[46] W. J. Shin, D. N. Kim, Y. T. Cho, and S. W. Park, "Comparative Analysis Research on the Difference Between U-City and Smart City for the Establishment of International

Competitiveness of U-City-By a Comparative Analysis of Smart Cities Index Indicators and U-City Plans Established by the Local Governments in Korea," *Journal of the Urban Design Institute of Korea Urban Design,* vol. 16, no. 5, pp. 5-16, 2015.

[47] (2017). *Smart city policies and future directions*.

[48] A. Aurigi and N. Odendaal, "From “Smart in the Box” to “Smart in the City”: rethinking the socially sustainable smart city in context," *Journal of Urban Technology,* vol. 28, no. 1-2, pp. 55-70, 2021.

[49] Chaturvedi. "Did You Know Which Are the Top 3 Smart Cities in the World?" Geospatial World. (accessed February 5, 2019., 2019).

[50] Ierek. "“List of Top 5 Smart Cities in the World,”." Ierek: Research, Knowledge, Enrichment. (accessed February 6, 2019., 2019).

[51] R. G. Hollands, "Will the real smart city please stand up? City: Analysis of Urban Trend, Culture, Theory," *Policy, Action,* vol. 12, no. 3, pp. 303-320, 2008.

[52] J. Peck, "Struggling with the creative class," *International journal of urban and regional research,* vol. 29, no. 4, pp. 740-770, 2005.

[53] D. J. Smith, "Today's control systems evolved from early pioneers' dreams," *Power Engineering,* vol. 100, no. 4, pp. 17-21, 1996.

[54] S. Hasija, Z.-J. M. Shen, and C.-P. Teo, "Smart city operations: Modeling challenges and opportunities," *Manufacturing & Service Operations Management,* vol. 22, no. 1, pp. 203-213, 2020.

Analysis of Load flow and Transient stability of 10-bus multi-machine system with PV penetration

Sarah Alasady[1], Rasheed Almansory[2], and Haider Alrudainy[3]
{yaramn8@gamil.com[1], r.s.almansory@stu.edu.iq[2], and h.m.a.alrudainy@ stu.edu.iq[3]}

Southern Technical University, Technical Engineering College, Iraq, Basra[1,2,3]

Abstract. The increasing importance of solar energy to support and stabilize electrical power networks and reduce dependence on fossil fuels has recently received remarkable attention. This research deals with the analysis of the load flow and transient state stability of a network consists of 10-bus with solar cells using the ETAP software toolbox. Further, Transient stability analysis is presented in this paper for the design of the proposed power system with grid-connected photovoltaic (PV) systems under large perturbations (middle of transmission line fault), Integrating PV generations at bad locations can cause serious degradation to system Transient stability, Selecting the location of solar energy in the network and its size has a beneficial effect on the stability of the network, the analysis demonstrates that photovoltaic (PV) power system facilitated sustain stability and drastically enhance the reliability of the examined system, thus having an advantageous influence on the electric power system.

Keywords: Photovoltaic, power grid, transient stability analysis, load flow analysis, three-phase fault, IEEE 10 bus system, ETAP.

1 Introduction

In recent years, owing to their ecological operations and considerably fluctuated prices of fossil fuels, sustainable energy sources worldwide have gained remarkable attention. The photovoltaic (PV) system produces electricity from naturally available sunlight and is becoming one of the most common (Renewable Energy Sources) RES systems. Two modes of use, standalone and grid-connected, are more convenient in the literature as this reduces the costs of building power storage than the first. Furthermore, there are initiatives motivating governments of some countries to integrate network-connected photovoltaic (PV) systems. Accordingly, these have led in recent years to the emergence of more PV systems on the rooftop [1][2].

The implementation of PV generators however affects electricity systems' efficiency. PV penetration degrades power systems' reliability, for instance, because PV generators have no synchronizing time torque; for example, an internal torque to maintain generator synchronization. A lot of studies have been carried out to date to solve this issue. A PV model for the interaction of PV generators with power systems was designed, for example. The effects of photovoltaic (PV) penetration on the voltage properties and transient stability of the electric power systems have been studied by other researchers. The controller architecture has also been implemented for photovoltaic (PV) systems linked to the power network [3].

Another paper,[4] addressed the influence of a grid-connected photovoltaic (PV) system on the stability of dynamic and static voltage. This work shows that the PV system impacts the reliability of the distribution and transmission systems rely on factors such as temperature,

IMDC-IST 2021, September 07-09, Sakarya, Turkey
Copyright © 2022 EAI
DOI 10.4108/eai.7-9-2021.2315308

shading effect, photovoltaic latitude, and the form of photovoltaic plant integration at different degrees of penetration. Moreover, work in [5] has addressed minor signal disorders in a stand-alone environment that is not incorporated into the electrical power grid for the transient reliability of a PV-diesel hybrid system. In [6] the impact of PV systems has been shown on short-term voltage stability and the findings of the study suggest that short-term voltage stability was severely affected when voltage sage and the PV system were disconnected.

The integration of solar photovoltaic power in a 10-bus electricity grid was simulated and investigated to explore the effect stability of solar cells on the network. Our model was established by using Electrical Transient Analyses (ETAP) simulation tool which is an extensive framework for the study of generation, transmission, delivery, industry, and industrial energy systems for the architecture, simulation, operation, controls, automation, and optimization.

2 Load Flow and System Stability

2.1 Power System Stability

The stability of the electric power system is interpreted as follows based on the description in the well-known report [7]. Power system stability (PSS) can be defined as the capability of an electric power system, for a particular initial working condition, to retrieve the equilibrium condition after being exposed to a physical disturbance, with major system variables reduced to allow the whole system to remain practically unchanged. The categorization of power system stability can be seen as illustrated in Fig. 1.

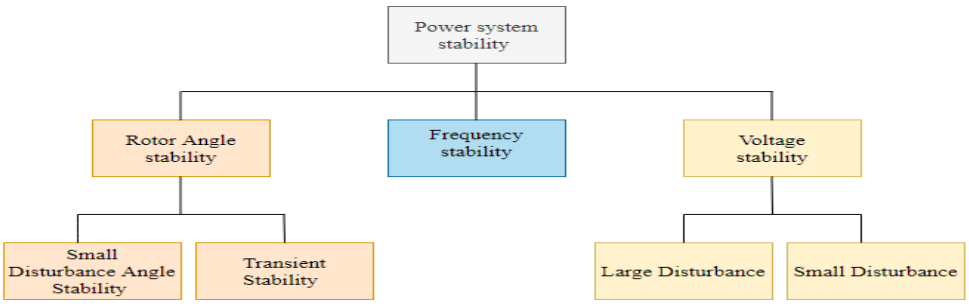

Fig. 1. Shows the types of power system stability.

Transient Stability: Transient stability can be explained as the capability of the electric power system to preserve synchronism throughout large disturbances [7]. Such disruptions might include a failure of a bus or the transmission line, equipment, loss of a large load, and generation. The study discussed in this section aims to analyze whether such great system turbulence has an effect on the system with PV penetration, a technique known as the Equal-area criterion can be adopted. This approach has relied on the graphical representation of the energy contained in the spinning mass to help to regulate if the machine is stable after a perturbation. This approach applies only to a one-machine system that is connected to an endless bus or two-machine system.

Consider the swing equation:

$$M\frac{d^2\delta_m}{dt^2} = P_m - P_e \quad (1)$$

Where M is inertia constant. It is considered not constant when the rotor velocity drifts from the synchronous speed.

p_m= Shaft power input.
p_e=electical power output.
δ_m=mechanical power angle

$$\frac{d^2\delta}{dt^2} = \frac{1}{M}(P_m - P_e) = \frac{P_a}{M}. \quad (2)$$

Where p_a is the acceleration power

$$M = \frac{H}{\pi f} \text{ in pu system.} \quad (3)$$

$$\frac{d^2\delta}{dt^2} = \frac{\pi f}{H}(P_m - P_e) \quad (4)$$

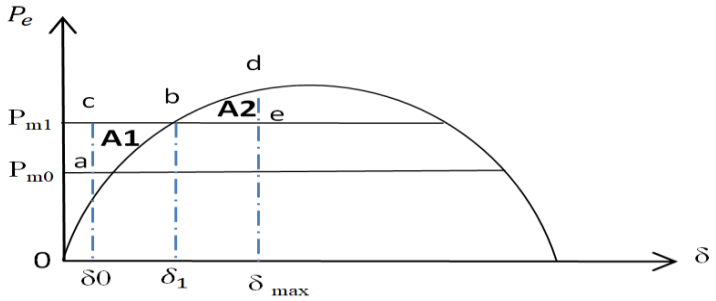

Fig. 2. Demonstrates the equal-area criterion.

Consider the machine working at the equilibrium point δ0, which is the mechanical input power $P_{m0} = P_{e0}$ as shown in fig.2. Take into consideration a sudden rise in the input power of horizontal line P_{m1}. Since $P_{m1} > P_{e0}$, the rotor is accelerating positively, increasing the power angle δ. The amount of excess energy saved at first acceleration in the rotor is:

$$\int_{\delta_0}^{\delta_1} (P_{m1} - P_e)d\delta = \text{ area } abc = \text{area } A_1. \text{ (Accelerating Area)} \quad (5)$$

The rotor shall swing past point b until the rotating masses give up the same amount of energy. The energy the rotor gives when it slows down to synchronous speed is,

$$\int_{\delta_1}^{\delta_{max}} (Pe - P_{m1})d\delta = \text{ area } bde$$

$$= \text{area } A_2 \text{ . (Decelarating Area)} \quad (6)$$

For stability, the area under the graph must be zero against δ; i.e. the graph's positive (accelerating) area must be equal to the negative (decelerating) area. This criterion is thus well-known as the equal-area principle for stability. This can be illustrated in Fig.2.
As a consequence, the rotor swings to b and δ_{max} at which point.

$$|\text{the area } A_1| = |\text{ area } A_2| . \quad (7)$$

This is well-known as the equal-area principle. Then at its normal frequency, the rotor angle can oscillate back and forth betweenδ_0 and δ_{max}. The damping in the system would result in the subsidizing of these oscillations and the new steady-state operating point would be settled at point b[8].

2.2 Load Flow Analysis

Studies of power flow, usually called load flow, constitute an essential part of the study of energy systems. They are needed for the preparation, financial planning, control, and potential expansion of existing systems. The problem is to estimate the voltages and phase angle of each bus and active and reactive power flows for each line. The device is assumed to work in balanced conditions in solving a power flow problem and is applied with one-step models. Each bus is linked to four amounts including phase angle, voltage magnitude, reactive power, and a real power. In general, systems buses are divided into three types:- slack buses, load buses, Regulated buses [9].

i) Flow Calculation Methods

Four methods of load flow calculations: Newton-Raphson, Adaptive Newton-Raphson, Accelerated Gauss-Seidel, and Fast-Decoupled. All four diverse ways of measuring load flow have various convergence requirements that each should be. to produce optimal results and fewer errors in a given situation. Any of these methods can be chosen depending on the topology of the structure, type of generation, loading status, and the initial value of the bus voltages.

ii) Accelerated Gauss-Seidel Method

We can write the system nodal voltage equation as:

$$[I] = [Y_{BUS}][V]. \quad (8)$$

The Gauss-Seidel accelerated technique adopts the load flow equation and iterations to produce the following results:

$$[\boldsymbol{P} + \boldsymbol{jQ}] = [\boldsymbol{V^T}][\boldsymbol{Y^*_{BUS}}][\boldsymbol{V^*}] . \quad (9)$$

where P and Q are the true and reactive bus power vectors, Y_{BUS} is the electrical system's entry matrix, and V is the bus voltage vector. V* and Y^*_{BUS} are the V conjugates and Y_{BUS} respectively. V^T is the transposed V matrix that is the bus stress.

3 Analysis of Case Studies

3.1 Power System Model with PV Penetration

In this section, a simple test system is introduced. This test system is used to present fundamental concepts and principles of power system stability, specifically Transient stability, considering a penetration level of PV generation. The stability of the test system is studied in response to large disturbances; for example, severe system faults. The considered test system is based on an adapted for the specific needs to study Transient stability.

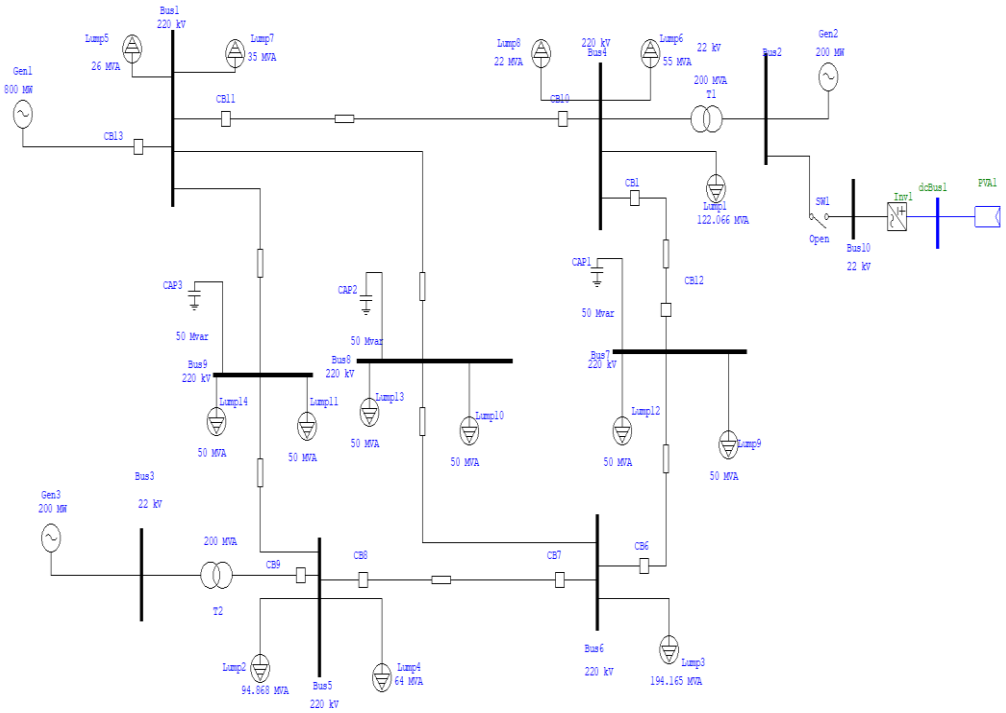

Fig. 3. Indicates the single-line illustration of the IEEE10-Bus system with the photovoltaic array.

Table 1. Shows the generator data of the IEEE10 Bus system.

	Model		Value		Model		Value2	Value3
Generator1	Operation mode	Swing	--------	Generator2,3	Oper. mode	Voltage control	-----	---------
	Rating	MVA	941.176		Rating	MVA	235.29	235.29
		KV	220			KV	22	22
	Imp/model	x_d "	12		Imp/model	xd "	12	12
	Inertia	RPM	1500		Inertia	RPM	1500	1500
		WR^2	1524975			WR^2	76249	56043
		H	20			H	4	2.10

Table 2. Data of PV Array.

PV array	Rated power (kW)	240
	No.of modules	2800
	The voltage at max. power (Vmp)	17.93
	Current at max. power (Imp)	4.78
	Open circuit voltage (Voc)	22.04
	Short circuit current (Ioc)	5.18
	Total number of cells in series (Ns)	100
	Total number of cells in parallel (Np)	28
	PV cell type	Multi-crystalline
Inverter	Number of units	1
	Rated capacity	240 kW
	Input DC Volt	22V
	Output voltage	22V
	Frequency	50HZ

The single-line diagram of the 10-bus test system is depicted in Fig.3 For this study the original test system a slightly modified IEEE-6 bus system is considered[10]. in this paper, a typical 10-bus system comprises three generators connected to a network of three different busses. Generator1 is known as the swing bus, Generator 2 and Generator 3 are considered to be the form of the voltage control, bus It has 14 loading points, also, a generator PV has been added on bus No. 2. Penetration PV injects a great deal of energy through the system that affects all existing buses' active and reactive capacity. Results included in this work are estimated by using ETAP (power system analysis software). The main part of this paper is to study the impact of the PV plants on the performance of the grid. The validated model has been used to study and analyze the impact of the planned PV power plants on the transient stability of the power system. Moreover, the combination with PV solar to improve the overall stability of the system will be considered in the research plane.

3.2 Load Flow Results

Results of the load flow obtained from the IEEE 10-bus power grid with the photovoltaic (PV) systems are used in load-flow analysis to guarantee that electrical power transfer from generators to consumers through the network is reliable and stable, Due to its active power generation and voltage control. There may be several load flow cases to be studied relying on the kind of plant. The aim is to determine the worst and best working conditions. Various load flow solution algorithms are utilized in the industry such as Newton-Raphson, Gauss-Seidel, and current injection. Thus, The basic load flow results for an IEEE 10 bus system without and with the photovoltaic (PV) power system are illustrated (in Table.3 and Table.4), The Standard Newton-Raphson Method.

Table 3. Load-flow results of the IEEE 10 bus network without an PV system.

Bus	Voltage	Generation	Load	Load flow

ID	KV	%Mag.	Ang.	MW	Mvar	MW	Mvar	ID	MW	Wvar	Amp
Bus1	220	106	0.0	568.636	181.889	51.850	32.134	Bus4	155.492	34.864	394.5
								Bus9	213.274	34.600	534.9
								Bus8	148.020	80.291	416.9
Bus2	22	104	-16.8	150	220.887	0	0	Bus4	150.000	220.887	6737.5
Bus3	22	103	-17.8	100	177.351	0	0	Bus5	100.000	177.351	5187.5
Bus4	220	98.667	-18.8		0	165.450	110	Bus1	-147.574	15.355	394.6
								Bus7	131.732	78.496	407.9
								Bus2	-149.608	-204.414	673.8
Bus5	220	98.675	-19.2	0	0	144.400	63.714	Bus6	69.753	77.835	278.0
								Bus9	-114.349	26.036	311.9
								Bus3	-99.805	-167.584	518.8
Bus6	220	83.643	-26.2	0	0	160.000	110.000	Bus5	-66.830	-58.438	278.5
								Bus7	-41.786	-46.583	196.3
								Bus8	-51.385	-4.979	162.0
Bus7	220	92.105	-23.3	0	0	85.000	10.262	Bus4	-128.348	-63.551	408.1
								Bus6	43.348	53.289	195.7
Bus8	220	88.290	-17.8	0	0	85.000	13.703	Bus1	-137.908	-26.459	417.4
								Bus6	52.908	12.757	161.8
Bus9	220	99.609	-11.8	0	0	85.000	3.069	Bus1	-202.883	8.565	535.0
								Bus5	117.883	-11.634	312.1

Table 4. Load-flow results of the IEEE 10 bus network with an PV system.

Bus		Voltage		Generation		Load		Load flow			
ID	KV	%Mag.	Ang.	MW	Mvar	MW	Mvar	ID	MW	Wvar	Amp
Bus1	220	106	0.0	570.61	207.54	51.850	32.133	Bus4	153.428	51.650	400.8
								Bus9	215.918	36.487	542.1
								Blus8	149.049	87.277	427.6
Bus2	22	100	-16.8	150	197.68	0	0	Bus4	150.000	197.686	6512.3
								Bus10	-0.238	2.437	5571.9
Bus3	22	103	-18.1	100	188.81	0	0	Bus5	100.000	188.815	5443.8

Bus4	220	95.03	-18.9		0	165.4	110	Bus1	-145.253	0.249	401.1
								Bus7	129.436	71.485	408.3
								Bus2	-149.634	-182.295	651.2
Bus5	220	98.39	-19.5	0	0	144.40	63.71	Bus6	71.941	88.164	303.5
								Bus9	-116.556	26.182	318.6
								Bus3	-99.785	-178.060	544.4
Bus6	220	81.46	-26.9	0	0	159.99	109.99	Bus5	-68.456	-64.984	304.1
								Bus7	-39.779	-37.792	176.8
								Bus8	-51.763	-7.224	168.4
Bus7	220	88.74	-23.8	0	0	85	13.30	Bus4	-126.046	-56.496	408.5
								Bus6	41.046	43.192	176.2
Bus8	220	86.88	-18.1	0	0	85	14.93	Bus1	-138.409	-30.605	428.1
								Bus6	53.408	15.675	168.1
Bus9	220	99.41	-11.9	0	0	85	3.267	Bus1	-205.244	7.866	542.2
								Bus5	120.244	-11.133	318.8
Bus10	22	100	-16.8	0.238	2.437	0	0	Bus2	0.238	2.437	5571.9

Table 3 without a PV system shows the load flow effects under normal operating conditions. Under these conditions, the generator connected to a slack bus requires a considerable amount of reactive power, which is much more than the reactive power taken from the device loads (343.44 MVAR). Table 4 shows the outcomes and effects of the PV system, Under these conditions, the output of reactive power is decreased. In the network, the PV bus draws (2.437 MVAR) reactive capacity. Increased PV capacity penetration replaces the peak load value by load demand throughout the day. The contribution of photovoltaic to the highest load reduction is therefore excessive and necessities to be adjusted to the changed situation of demand with a new increase in PV power.

4 Simulation Results of Transient Stability

For designing, simulating, automating of generation, distribution of industrial power systems, and ETAP comprehensive toolbox analysis platform has been used. The IEEE 10-bus system has been investigated and the photovoltaic grid is connected to the power supply as indicated in Fig.3. A comprehensive simulation analysis was performed to estimate the impact of the PV on the transient stability of a power system, based on observing the electrical grid terminal voltage, generator velocity, rotor angle, and power production. A power system disruption is abrupt variations in one or more elements of the power system or a series of changes. The presence of a fault on line 1 in the IEEE 10 bus network is a major disturbance. The key problem was the dissemination of active power of the photovoltaic power system to the network to compensate for the rapid shift in the electrical power grid. Some of these case studies are investigated as can be seen below.

4.1 Simulation Results in the Case Without PV Implemented

The influence of PV on the IEEE-10 bus system was examined on two criteria: the first was without PV connection and the second was PV connection; Concerning transient stability, major disruptions like a three-phase fault occur, The impact on the power system transient

performance owning to line fault taking place in it without photovoltaic (PV) set up has been investigated. A fault has been placed at line1 at "9.00 second", and it is then cleared at "9.12 second". The electrical power, bus voltages, terminal current of the generator have been noted and plotted for a "100second" period, as indicated in Fig. 4. The voltages at bus 1 and bus 5 are plotted. In this study, both voltages have been investigated as bus 1 is close to a fault and bus 5 is a little far away from the fault. The oscillations after the fault for the base case are minute and converging to a stable value. The oscillations case was relative with higher amplitude, and it was maintaining irregular value. The voltage dips are very high. But it was maintaining stabilized value after a while, The results of the simulation show that the system is stable, and the generator is synchronized with the network.

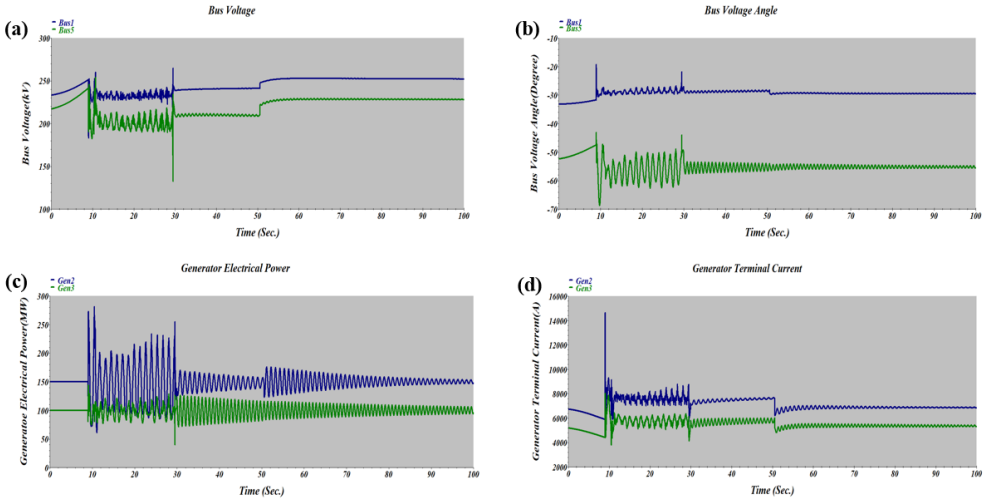

Fig. 4. IEEE 10 bus network simulation results without the photovoltaic power system: (a) voltage of the bus; (b) angle of voltage; (c)electrical power; (d) current terminal.

4.2 Simulation Results In The Case With PV Implemented

Most PVs are designed so that immediately after a major disruption the system is disconnected, particularly when a system fault happens in or near the photovoltaic power plant. Solar PV plant has been integrated into bus 2 of the IEEE 10-bus system, as described in the previous section. The same system that was used previously for steady-state analysis has been considered for transient analysis too. The "Transient Stability Analysis" module of the ETAP has been used for the simulation and analysis. The results show that the power system is much more stable with a PV system, to investigate the ideal position of the solar generator and maximum safe instantaneous penetration in the event of large disturbances, considering the stability of the system and its safety limits. Furthermore, the PV penetration increases and this contribution is more essential. These plants can contribute to the system control and stability similarly to traditional producing units if a certain level of active power reserve or storage is given, as shown in Fig. 5.

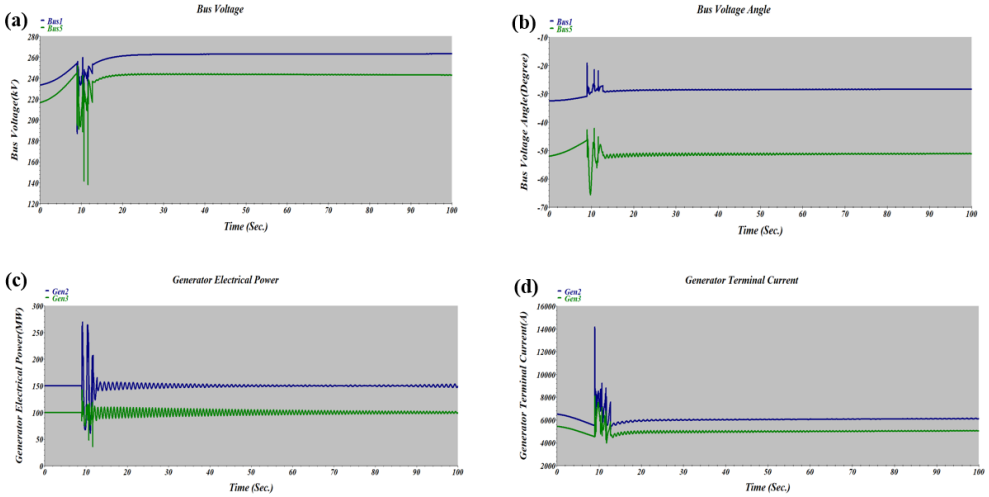

Fig. 5. IEEE 10 bus network simulation results with the photovoltaic plant : (a) voltage of the bus; (b) angle of voltage; (c) electrical power; (d) current terminal.

5 Conclusion

This paper provides a case study evaluating the effect of PV power permeation on steady-state and transient power system stability on the grid. Considering the Original IEEE 10 bus and the photovoltaic system of the electric power system, simulation analyzes were carried out. Results of the simulation study show the reliability and stability of test systems are maintained by the PV system penetration. By improving the voltage stability of the power grid under a short circuit middle of line1 (between bus 1 and bus 4) with the PV system, reactive power compensation is increased via a PV system. The location of the fault and fault clearing time affect the stability of the voltage and Voltage instability is reasoned as one of the major threats to the secure operation of electric power systems around the globe. Thus, the PV panel connected to the grid impacts the stability of the power system.

References

[1] M. R. Mahmud, A. F. Abdou, and H. Pota, “Stability analysis of grid-connected photovoltaic systems with dynamic phasor model,” *Electron.*, vol. 8, no. 7, 2019, doi: 10.3390/electronics8070747.

[2] M. Luomi, *The International Relations of the Green Economy in the Gulf: Lessons from the UAE’s State-led Energy Transition*, no. May. 2015.

[3] S. Izumi, Y. Karakawa, and X. Xin, “Analysis of small-signal stability of power systems with photovoltaic generators,” *Electr. Eng.*, vol. 101, no. 2, pp. 321–331, 2019, doi: 10.1007/s00202-019-00778-w.

[4] Z. A. Kamaruzzaman, A. Mohamed, and H. Shareef, “Effect of grid-connected photovoltaic systems on static and dynamic voltage stability with analysis techniques—A review,” *Univ. Kebangs. Malaysia*, vol. 2015, no. 1, pp. 1–8, 2015.

[5] P. Kumar and D. K. Palwalia, “Decentralized Autonomous Hybrid Renewable Power

Generation," *J. Renew. Energy*, vol. 2015, pp. 1–18, 2015, doi: 10.1155/2015/856075.

[6] H. M. Sultan, A. A. Zaki Diab, O. N. Kuznetsov, Z. M. Ali, and O. Abdalla, "Evaluation of the impact of high penetration levels of PV power plants on the capacity, frequency and voltage stability of Egypt's unified grid," *Energies*, vol. 12, no. 3, pp. 1–22, 2019, doi: 10.3390/en12030552.

[7] C. Andersson, J. E. Solem, and B. Eliasson, "Classification of power system stability using support vector machines," *2005 IEEE Power Eng. Soc. Gen. Meet.*, vol. 1, no. 2, pp. 650–655, 2005, doi: 10.1109/pes.2005.1489266.

[8] Nagrath Kothari , "Power System Engineering Second Edition",2008.

[9] P. Venkatesh, B. V. Manikandan, S. C. Raja, and A. Srinivasan, *Electrical Power Systems: Analysis, Security and Deregulation*. 2012.

[10] A. Jaiswal, M. Kumar, A. Kumar, and R. Kumar, *LOAD FLOW AND STABILITY ANALYSIS OF MULTI-MACHINE : 2019.*

Hierarchical Feature Mining for Image Classification and Segmentation

Hayder Yousif[1] and Zahraa Al-Milaji[2]
{hayder.yaqoob@stu.edu.iq[1], zahraa.a.nejim@stu.edu.iq[2]}

Basra Engineering Technical College, Southern Technical University, Iraq[1,2]

Abstract. To identify and segment two different types of images, supervised and unsupervised learning are utilised. First, we design a fast and accurate feature extraction strategy using our deep learning classification model. We create a DCNN model that is 18 times faster than the current state-of-the-art AlexNet model while sacrificing only a little amount of accuracy. Second, several classifiers have been trained on the characteristics retrieved from the deep convolutional neural networks' fully connected layer (DCNN). Finally, we perform K-means graph-cut segmentation and compare the results to those of supervised segmentation. Natural scenes and biomedical image processing were used to investigate image-level and region-level classification. On a biomedical picture dataset, our experimental results show that the suggested strategy outperforms existing methods..

Keywords: DCNN, supervised learning, unsupervised learning, K-means, graph-cut

1 Introduction

In intelligent image analysis, classifying and segmenting items from an image is a crucial and enabling step. DCNN [1, 2] has recently made significant contributions to a variety of computer vision challenges, including object detection and semantic segmentation. By creating a graph and computing the smallest cut, graph cut methods tackle energy reduction challenges. The minimal cut challenge aims to locate a cut with a capacity equal to the graph's fewest overall cuts [3]. The minimum is found by calculating the sum of all cuts that divide the graph into two nonempty pieces [4]. Subspace segmentation can be done as a data grouping issue by first learning an affinity matrix from the input data, and then using spectral clustering methods like Normalized Cuts (NCut) to get the final segmentation results [5, 6]. The vast number of social networks dedicated to the sharing of photographs of cats and dogs [7] suggests that people care deeply about their domestic animals. Object category recognition and segmentation have been integrated in various ways in the past. However, segmentation of the entire image has been a common goal of various approaches [8].

Recent studies have worked on epithelium and stroma on the TMAs samples. Epi-stroma dataset [9] contains two annotated image classes in which each the image corresponds to the presence of either epithelium or stroma collected from

IMDC-IST 2021, September 07-09, Sakarya, Turkey
Copyright © 2022 EAI
DOI 10.4108/eai.7-9-2021.2315306

643 patients tissue samples with colorectal cancer. [10] extracted morphological features from super pixels of breast cancer tissue samples. Bianconi et al [11] used perceptual feature space to classify image blocks into tumour epithelium and stroma classes. Linder et al. [9] have performed texture analysis for images divided into rectangular regular blocks in digitized tumour tissue microarrays (TMAs). AiPing et al [12] have extracted pixel-level colour and texture features to identify epithelial carcinoma tissue from stromal tissue.
In this paper, two image analysis tasks have been studied. In the first task, DCNN model which is an application of deep learning was used for automated feature extraction. Then, different classifiers are evaluated using different metrics. In the second task, graph-cut is used to separate the image regions based on their spatial connectivity.

2 Datasets

We employed two datasets in this study, each with its own set of image gathering settings. The Oxford-IIIT Pet dataset, for example, contains 7,349 photos of cats and dogs of 37 different breeds, 25 of which are dogs and 12 of which are cats. This dataset is separated into two parts: a training set with 3680 photos, and a testing set with 3669 images. Figure 1 depicts samples from this collection.

Fig. 1. Oxford-IIIT Pet dataset samples.

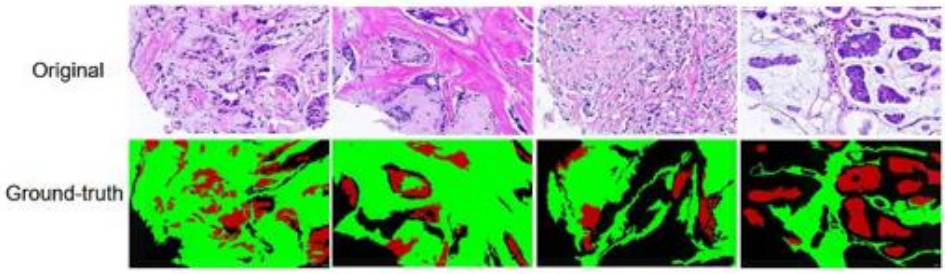

Fig. 2. Samples from the VGH dataset.

The epi-stroma dataset from the Vancouver General Hospital (VGH) is the second dataset. Pathologists manually annotated epithelial and stromal areas in this dataset. Only 36 images are used for training and 15 images are used for testing in this example. Figure 2 shows samples from the VGH dataset. Green represents the stromal regions, whereas red represents the epithelial regions. The pathologists have not classified the dark areas.

3 Region Extraction and Pre-processing for the VGH Images

For the VGH dataset, we divide the image into 96 × 96 overlapped regions in both training and testing steps. At this point, we need to extract a pure single class region for more accurate training without overfitting. We propose to purify the mixed class regions and replace the non-classified by a pathologist (black ground truth regions) by white pixel. The white pixels region has no texture information that may cause information corruption. Fig. 3 shows some refined regions.

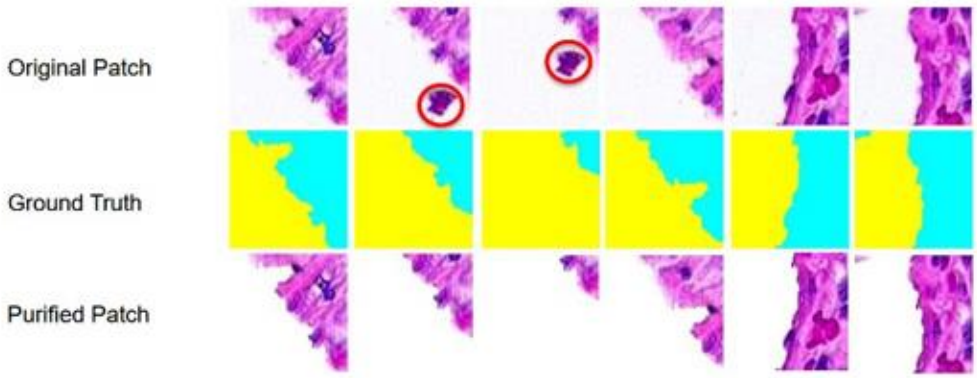

Fig. 3. Mixed class region purifying in the VGH dataset.

4 DCNN for Feature Extraction

In the DCNN, we investigate the complexity-accuracy trade-off. The DCNN, as we all know, is a computationally expensive algorithm. As a result, there is a pressing need to accelerate the DCNN while retaining its classification accuracy. The input size, number of layers, and number of filters are three important parameters that can be used to efficiently regulate the computational complexity of DCNN. The 14 levels of our developed DCNN architecture are shown in Table 1. Rectified Linear Unit ReLU layer follows each convolutional layer, while normalisation and pooling layers follow the ReLU layer.

Table 1. Our CNN networks architecture.

Layer	Type	K size	Filter #	Stride	Pad
1	Conv1	6	128	2	0
4	Pool1	3	2	0	
5	Conv2	5	128	1	2
8	Pool2	5	2	0	
9	Conv3	5	128	1	1
11	FC4	7	2048	1	0

Using FC5, we create a 2048-dimensional feature vector from each region proposal. We use the linear SVM, SoftMax, KNN, and Random-Forest trained for that class to score the extracted feature vector for each class. Table 2 shows the resource needs and testing speed related with various DCNN systems. We can see that constructing smaller input images (9696 pixels) with fewer layers reduces complexity by 18 times while sacrificing classification accuracy.

Table 2. DCNN Training Memory allocation and patch testing time comparison.

DCNN	Memory(MB)	(patch/ms)
AlexNet [1]	217	336.1
VGG-F [13]	316	395.6
VGG-S [13]	393	304.7
ours	50	17.9

5 Classifiers

Here, we briefly describe the functionality of the used classifiers.

5.1 SoftMax

SoftMax regression (also known as multinomial logistic regression) is a multiclass expansion of logistic regression. The labels in logistic regression are considered to be binary: $y^{(i)} \in \{0, 1\}$. Remember that in logistic regression, we had a training set of m labelled samples (x(1), y(1)),..., (x(m), y(m)), where the input features were $x^{(i)} \in \Re^n$. In the binary classification context of logistic regression, the labels were y(i) 0 and 1. The hypothesis was as follows:

$$h_\theta(x) = \frac{1}{1 + \exp(-\theta^\top x)}, \tag{1}$$

$$J(\theta) = -\left[\sum_{i=1}^{m} y^{(i)} \log h_\theta(x^{(i)}) + (1 - y^{(i)}) \log(1 - h_\theta(x^{(i)}))\right] \tag{2}$$

6 SVM

SVM has grown in popularity as a method for handling classification, regression, and novelty detection problems. The determination of the model parameters corresponds to a convex optimization problem, therefore any local solution is also a global optimum, which is an important property of support vector machines.

The decision boundary in support vector machines is chosen to be the one for which the margin is maximized. SVM is a kernel-based algorithm that has sparse solutions so that predictions for new inputs depend only on the kernel function evaluated at a subset of the training data points. Our goal is now to maximize the margin between classes while softly penalizing points that lie on the incorrect side of the margin boundary.

6.1 Random-Forest

Random forest picks a subset of features at random to build a fully developed decision tree on the n data points, using the sub-feature set as a replacement sample. Then repeat these two processes to make a random forest with many trees. Apply the decision to test data for each tree in the forest, then use the majority vote of all trees to make the final prediction.

6.2 K-Nearest Neighborhood

KNN is one of the nonparametric approaches that place very mild assumptions on the data distribution and provides good models for complex data [13]. For example, inserting a cell about x and letting it grow until it captures kn samples, where kn is some predetermined function of n, can be used to estimate p(x) given n training samples. These are x [14's kn nearest-neighbors samples. The distribution of all its class data points determines the distance measurement type and number of neighbours for a given data point. We used cosine distance for both datasets. SNPHEp-2 and Epistomes were chosen by a majority vote among 7 and 3 local points, respectively.

7 Graph cut for Unsupervised Image Segmentation

G = V, E > is a directed weighted graph with a set of nodes V and directed edges E connecting them.

$$D_{xyk} = \| I_{xyk} - C_{xyk} \|^2 \quad (3)$$

Pixels, voxels, and other features are usually represented by nodes. Classes are additional special nodes seen in some graphs [15]. The edges of all graphs are given a weight or cost. N-links and T-links are the two types of graph edges. N-links join adjacent pixels or voxels together. As a result, in the image, they represent a neighbourhood system.

The cost of N-links is a penalty for pixels that are not connected. The pixel interaction term Vx,y in energy is used to calculate these expenses. Pixels with class are connected by T-links. A penalty for assigning the corresponding class to a pixel relates to the cost of a T-link connecting a pixel and a class. The connectedness of each pixel value to the class prototype is measured using Euclidean distance.:

We used a square matrix M with K rows and columns to represent the cost. When the matrix size is increased, the neighbourhood constraints are strengthened even more and the segments become larger. To produce the final segmentation result, graph cut is done to the distance D with the cost M.

8 Experimental Results

8.1 Quantitative Results

To compute the classification outputs, we use the following performance metrics:

$$Recall = \frac{TP}{TP + FN}, \tag{4}$$

$$Precision = \frac{TP}{TP + FP}, \tag{5}$$

$$F - measure = \frac{2 \times Recall \times Precision}{Recall + Precision}. \tag{6}$$

The total number of true positives, false positives, and false negatives are represented by the letters TP, FP, and FN, respectively. Note that the F-measure needs to be as high as possible, to minimize the classification errors. In Table 3, we evaluate the classification accurateness of various classifiers on Oxford-III pet dataset. Because the required square input image needs to be fed to the DCNN, we rescale the different aspect ratio input images to fit with the required size. This corrupts the spatial information of the cats and dog effect the discrimination decision. The division of the VGH dataset into overlapping blocks cannot generate perfect epithelial-stromal regions but it is still a reliable solution even with non-smooth blocky output. Our pre-processing of the training patches (regular blocks extracted from an image) helps to improve the classification accuracy to outperform the most recent work [16] on the VGH images.

Table 3. Performance comparison on Oxford-III Pet dataset using different classifiers.

Classifier	Accuracy %	Precision %	Recall %	F-measure %
SoftMax	81.11	64.67	73.56	68.83
SVM	81.08	62.89	74.47	68.19
Random-Forest	80.81	64.16	73.05	68.32
KNN	78.36	39.31	86.95	53.94

Table 4. Performance comparison on Oxford-III Pet dataset using different classifiers.

Classifier	Accuracy %	Precision %	Recall %	F-measure %
SoftMax	88.99	88.89	97.48	92.98
SVM	88.92	88.81	97.43	92.92
Random-Forest	88.11	87.6	97.88	92.46
KNN	84.96	83.77	98.97	90.74
Xu et. al [16]	88.34			

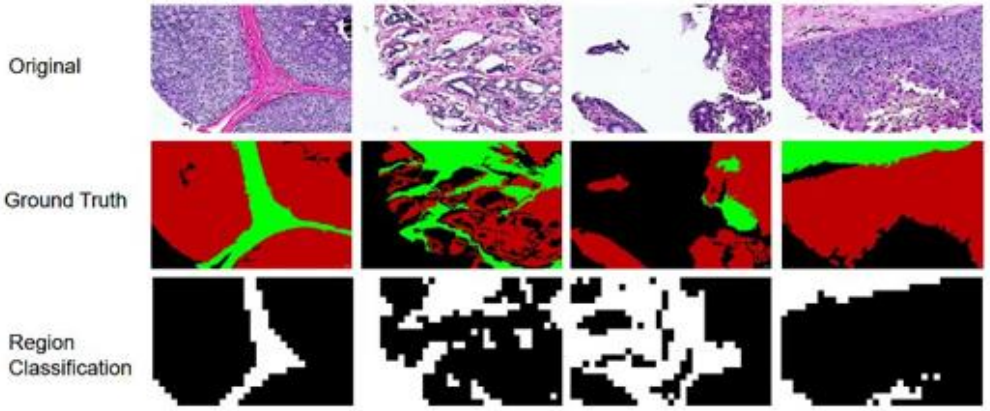

Fig. 4. VGH dataset classification results.

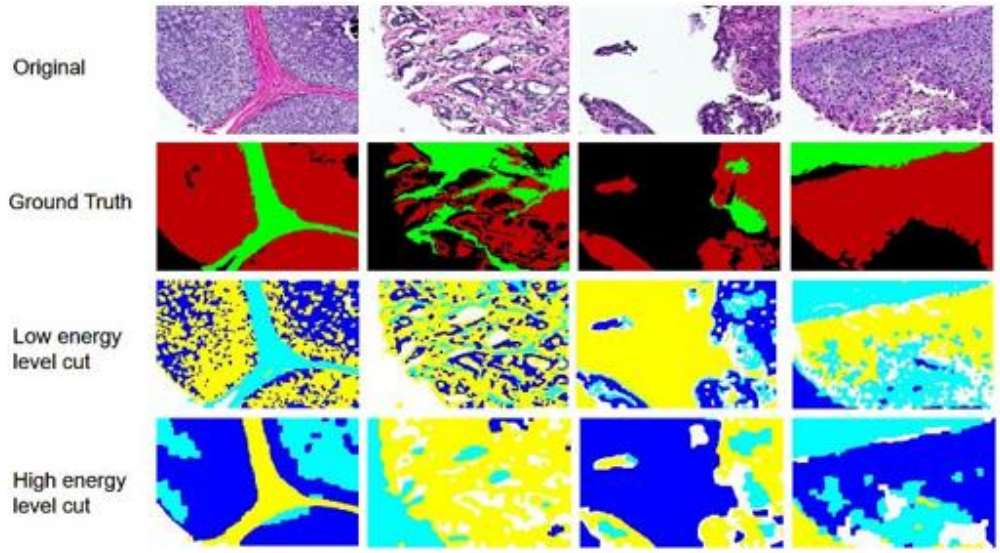

Fig. 5. VGH dataset graph-cut segmentation results.

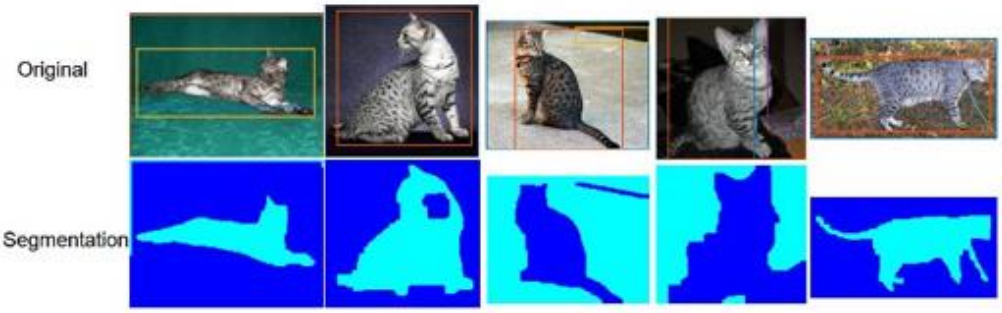

Fig. 6. Oxford-III pet dataset graph-cut segmentation results.

8.2 Qualitative Results

Fig. 4 shows the qualitative results after concatenating the classification labels of the SoftMax to fit with their locations in the original image. Stromal regions are in white colour on the classification output are corresponding to green regions in the ground truth image. Epithelial regions are in black on the classification output is corresponding to red regions in the ground truth image.
We also tried to segment the VGH images using an unsupervised method called graph cut. From Fig. 5, we can see the smooth regions produced by this method as compared with the supervised method used in Fig. 4. However, in the un-supervised learning the class label is not known for the regions. It has been tried two levels of energy minimization to illustrate its effect on the region size and smoothness. We used the graph cut to separate a pet from the background to avoid training the classifier on noisy features. Fig. 6 shows some samples of the segmentation output. Again, we can see only two regions in the output but no label for that region to tell the difference between foreground and backdrop regions.

9 Conclusion

We used the DCNN as an automated method for feature extraction instead of using handcrafted features like HOG and LBP. Our experiments show that SoftMax outperforms the other classifiers. Mixed class purifying increases the classification accuracy to outperform VGH data. For pet data, rescaling different aspect ratio images to fit with square input image for DCNN decreases the classification accuracy. We also tried to segment the image by applying constraints to the K-means using graph-cut. Changing the level of energy controls the shape and the size of the segmentation regions. Fusion of the supervised and unsupervised method may increase the detection/segmentation performance.

References

[1] Krizhevsky A, Sutskever I, Hinton GE. Imagenet classification with deep convolutional neural networks. In: Advances in neural information processing systems; 2012. p. 1097-105.

[2] LeCun Y, Bottou L, Bengio Y, Haffner P. Gradient-based learning applied to document recognition. Proceedings of the IEEE. 1998;86(11):2278-324.

[3] Tao W, Tai XC. Multiple piecewise constant with geodesic active contours (MPC-GAC) framework for interactive image segmentation using graph cut optimization. Image and Vision Computing. 2011;29(8):499-508.

[4] Wu Z, Leahy R. An optimal graph theoretic approach to data clustering: Theory and its application to image segmentation. IEEE transactions on pattern analysis and machine intelligence. 1993;15(11):1101-13.

[5] Shi J, Malik J. Normalized cuts and image segmentation. IEEE Transactions on pattern analysis and machine intelligence. 2000;22(8):888-905.

[6] Liu G, Lin Z, Yan S, Sun J, Yu Y, Ma Y. Robust recovery of subspace structures by low-rank representation. IEEE Transactions on Pattern Analysis and Machine Intelligence. 2013;35(1):171-84.

[7] Parkhi OM, Vedaldi A, Zisserman A, Jawahar C. Cats and dogs. In: Computer Vision and Pattern Recognition (CVPR), 2012 IEEE Conference on. IEEE; 2012. p. 3498-505.

[8] Parkhi OM, Vedaldi A, Jawahar C, Zisserman A. The truth about cats and dogs. In: Computer Vision (ICCV), 2011 IEEE International Conference on. IEEE; 2011. p. 1427-34.

[9] Linder N, Konsti J, Turkki R, Rahtu E, Lundin M, Nordling S, et al. Identification of tumor epithelium and stroma in tissue microarrays using texture analysis. Diagn Pathol. 012;7(22):1596-7.

[10] Beck AH, Sangoi AR, Leung S, Marinelli RJ, Nielsen TO, van de Vijver MJ, et al. Systematic analysis of breast cancer morphology uncovers stromal features associated with survival. Science translational medicine. 2011;3(108):108ra113-3.

[11] Bianconi F, Álvarez-Larrán A, Fernández A. Discrimination between tumour epithelium and stroma via perception-based features. Neurocomputing. 2015;154:119-26.

[12] Qu A, Chen J, Wang L, Yuan J, Yang F, Xiang Q, et al. Two-step segmentation of Hematoxylin-Eosin stained histopathological images for prognosis of breast cancer. In: IEEE International Conference on Bioinformatics and Biomedicine (BIBM); 2014. p. 218-23.

[13] Vedaldi A, Lenc K. Matconvnet: Convolutional neural networks for matlab. In: Proceedings of the 23rd ACM international conference on Multimedia. ACM; 2015. p. 689-92.

[14] Duda H, Hart P, et al.. Stork, Pattern Classification. John Wiley & Sons; 2001.

[15] Boykov Y, Veksler O, Zabih R. Fast approximate energy minimization via graph cuts. IEEE Transactions on pattern analysis and machine intelligence. 2001;23(11):1222-39.

[16] Xu J, Luo X, Wang G, Gilmore H, Madabhushi A. A deep convolutional neural network for segmenting and classifying epithelial and stromal regions in histopathological images. Neurocomputing. 2016;191:214-23.

Energy Saving by Reinforcement Learning for Multi-Chillers of HVAC Systems

Lubna A. Hussein[1], Adnan A. Ateeq[2], Raad Z. Homod[3]
{lubna.ali15783@gmail.com[1], adnan_ateeq@stu.edu.iq[2], raadahmood@yahoo.com[3]}

Engineering Technical College of Basra, Southern Technical University, Iraq[1,2]
Oil and Gas Engineering Department, Basra University for Oil and Gas, Iraq[3]

Abstract. This paper presents a method for controlling and operating a multi-chillers system: (1) Model-based control approach was used by MATLAB/SIMULINK to model a building containing two non-identical chillers depending on thermal loads. (2) ON/OFF all chillers alternately using the model reinforcement learning controller (RL-control) to select the appropriate chiller for the building conditioning process. The results were in terms of energy efficiency and performance of the enhanced learning control for the chiller, and a control unit signal (PID) was applied to make a comparison with the signals of energy, power, and temperatures. After comparison, it was found that the energy saving through the proposed controller is 45% of the traditional (PID) strategy, where can the proposed strategy control for the chiller appropriate for the building's conditioning process.

Keywords: Multi-chillers system, Reinforcement Learning, Model-based control, Chilled water system.

1 Introduction

The Heating, Ventilating, and Air Conditioning (HVAC) system is a vast field. In general, the categories of building service and (HVAC) systems make up the main sources of energy use in buildings, and it is estimated that HVAC is responsible for 50% of the building's total energy consumption. Buildings are responsible for a considerable amount of energy use as the global building strip currently consumes about 40% of the overall energy produced [1][2][3]. In the HVAC system same, the most energy-consumption portion is the chiller unit system, that made up of chillers, pumps, cooling towers, and some other equipment. The chiller which is widely used to provide the cooling load is one of the main energy-consuming equipment, the energy consumption reduction of the multi-chillers system is of great importance in the HVAC system [4]. Reinforcement learning (RL) was initially demonstrated as a practical approach to control HVAC systems [5]. System selection depends on the building configuration, the environmental conditions, which HVAC design should consider different agents such as load variations, operating precision, Energy preservation, and total cost, and flexibility, etc. while selecting the equipment, and considered some standards that can be such as environment alteration (e.g., temperature, humidity, and pressure). All water systems are suitable for low-cost centralized HVAC systems in high-rise commercial applications, and it is the ideal solution to replace all air systems in high-rise buildings and is more suitable in buildings requiring individual control [6][7].
Liu and Henze (2006) have been proposed Simulated RL, a hybrid control planner that combines aspects of model-based optimum control with model-free learning control — is used

IMDC-IST 2021, September 07-09, Sakarya, Turkey
Copyright © 2022 EAI
DOI 10.4108/eai.7-9-2021.2315301

to control the building. The feasibility performance testing demonstrated that employing both active and negative thermal storage inventories, the hybrid control strategy can supply reliable control. Using the measured data, the hybrid control technique realized an 8.3 % cost provides during the basis state [8]. Dalamagkidis et al. (2007) the RL controller is created and simulated in the MATLAB/SIMULINK environment [9]. Fan et al. (2011) proposed an optimal control strategy for a multi-chiller system based on the probability density distribution of cooling load ratio,. At the same time, unnecessary chillers switch on/off behaviour can be prevented [10]. Huang et al. (2015) suggested chiller scheduling based on cooling demands Their goal was to control the on/off the multi-chiller systems to reduce the total energy consumption when compared with two existent sequence control methods—the optimal load distribution technique and the critical points reset strategy based on cooling capacity [11]. Azuatalam et al. (2020) proposed a new RL architecture for the control HVAC system with leveraging its demand response possible, design an active RL controller for a whole building model in compared to a handcrafted baseline controller, simulation results show that using RL for plain HVAC process will result in maximum weekly energy decreasing of up to 22% [12]. Yao et al. (2004) a mathematical model of optimal running for the refrigeration system are developed, the results showed that by applying the optimal model to the refrigeration system, energy savings of up to 10% are possible [13]. Qiu et al. (2020) this approach is based on Q-learning, a classic RL method, and it proposes a model-free optimal chiller loading method for optimizing chiller operating by altering the set points of the chilled water exit temperature. According to the simulation results, the proposed method can save 4.36 % of chiller energy during the first refrigerating season when compared to the baseline control [14]. Qiu et al. (2020) a model-free optimal control method depends on RL is proposed to control building refrigerating water, [15]. Homod et al. (2021) the HVAC system established was adopted as the system performance model; it provided dynamic system modelling, simulation, and monitoring cooling system performance. The test results show that significant energy saving through reducing the system operation cost and that by improving the four variables: the cooling water supply temperature (Tcws) from the chillers, the chilled water supply temperature (Tchws) from the chillers, (Tchw) from the heat exchangers, and the supply air temperature of the air handling units (AHU) [16]. The main objectives were to study the operating strategies of chillers alternately as follows:

1. A model-based control approach was used by MATLAB/Simulink to model a building containing two non-identical chillers depending on thermal loads.
2. ON/OFF for all chillers alternately using the model reinforcement learning controller (RL-control) to select the appropriate chiller for the building conditioning process.

HVAC system modelling is necessary to study and organize energy-consuming and kind of internal environment [17]. In general, three types of modelling are used for HVAC systems:

a) The black box models: The black-box model concept is an appropriate transport function model to the input/output real model data to produce polynomials coefficient, and relevance between the input and output variables is identified using mathematical techniques. Use of the black-box model is at times preferred because it is simple to construct and there is no requirement to know the system's internal structure [18][19]. Black-box models are simple to build and computationally efficient [20].
b) The white box models: The system models are created utilizing the governing laws and extensive understanding of the underlying process in this type of approach,

which is known as a physics-based method. Mathematical models are commonly used to represent the processing signal in the realm of HVAC system modelling. This signal, however, is formed using conservation rules such as components, mass, momentum, and energy balance [18][19][20].

c) The Gray box models: Compared to black-box models and white-box models, these models have good precision and better generalization capabilities, but they are also the hardest to build. For some (HVAC) subsystems, the underlying physical phenomenon may be difficult to represent [17][18][19].

2 Chillers

Chillers are important commercial components as they expand the cooling capabilities of (HVAC) systems. When choosing a chiller, you must correspond to the requirements for the cooling temperature and how efficient they are. For large complexes of buildings used large chiller or multiple chillers to produce chilled water that can be provided to meet the air-conditioning demands of the different buildings [21][22]. And to meet different load requirements, air-conditioned buildings contain several centralized refrigeration systems for multi chillers. Different types of chillers are used in (HVAC) systems, the chiller may be the best choice for one application, but it may be too expensive or inconvenient for another [22] [23].

Air-cooled chillers (Direct chillers): These chillers remove heat from the refrigerant by using fans that push air through tubes to condense the hot refrigerant. Air is a poor conductor of heat as compared to water, so air-cooled chillers are larger and less effective. Air-cooled devices have a higher compressor ratio, which means they use less energy to cool per watt [24][25].

Water-cooled chillers (Indirect chillers): This type of chiller removes heat utilizing pumps that send water through the condenser to recycle the water from the cooling tower to condense the refrigerant. They work well in medium and large commercial HVAC installations because they aren't affected by the ambient temperature. These chillers are more efficient because of water's high heat capacity but cost more to install and maintain [25].

In HVAC plants of medium-high refrigeration capacity, multiple chiller systems (MCSs) are often adopted, these systems consistency of multiple chillers, as the arrangement of chillers are differentiated through performance. The series arrangement is better because it can transfer heat, but it is not with a better efficiency than Parallel. Every chiller can be operated at various capacities to meet various refrigeration demands [26][27].

One of the most important problems with MCSs is to save more energy by reducing the total electrical energy consumption of the chillers, since the electrical consumption of MCSs increases significantly when the chillers are poorly handled; improving the efficiency of MCSs may result in substantial energy savings. The amount of energy saved by converting from a single chiller to a multi-chiller cooling plant varies depending on the type of building and environment [28].

The use of multiple chillers compared to a single chiller provides some advantages such as operational flexibility, standby capacity, maintenance is less disruptive, as well as using more than one chiller is better economical and reducing energy cost in the case of partial loading. Also, the coefficient of performance (COP) is better and will give high efficiency, as if we use one chiller and with high capacity, its cost will be high as well, and because these systems

depend on many factors including (capacity, partial load efficiency of each chiller, selection of refrigeration unit, refrigeration circuit design, type and number of compressors), etc [21].

3 Reinforcement Learning (RL)

Reinforcement learning (RL) is a branch of machine learning that studies how software agents should behave in each environment to maximize the concept of cumulative reward. Along with supervised and unsupervised learning, the RL is one of three fundamental machine learning paradigms. In the RL domain, we will only provide our algorithms with a (reward function), which refers to a learning factor when it is performing well, and when it is performing poorly, the learning algorithm's task is to know how to choose actions over time to obtain big rewards. The goal of "RL" is to guide the agent to determine what action to take that maximizes (or minimizes) the sum of all RL signals (the numerical reward) or punishment, it receives over time, called the total expected reward [29].

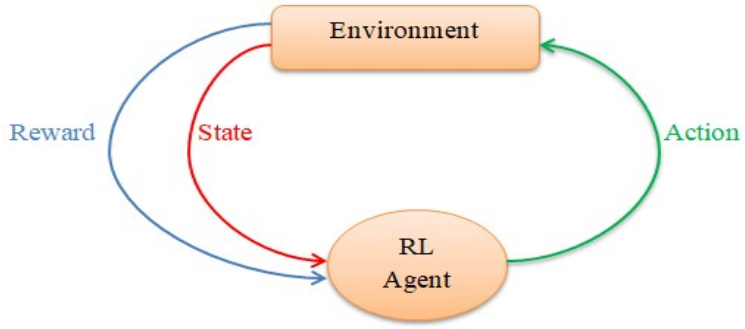

Fig. 1. RL Agent-Environment Interaction.

According to Fig. 1. If the agent performs one of many possible acts on the environment, it arrives in one of many possible states and is rewarded or punished for that specific action. This reward is intended to provide feedback to the agent about how well it is performing at each decision time step [12].

Markov Decision Processes (MDPs) are a fundamental formalism for reinforcement learning (RL). The method of sequential agent-environment interactions including state, actions, and rewards in the RL trouble can be expressed as an MDP since it includes sequential decision making, the problem consists of sequential decisions that an action (A) must be taken in each state (S) that is by the agent [30][31].

The major components for the RL system are agent, state, action, policy, reward signal, value function, and model. Agent: In RL, an agent learns to accomplish an objective by reacting with the environment repeatedly. State (s): (RL) concentrated on learning how good it is for the agent to be in each state in the long run. State indicates the current position returned by the environment. Action (a): actions are the Agent's method for reacting to and varying its environment, and thus transporting between states. Any action the Agent takes results in a reward from the environment [30][32]. Policy (π): a policy is the learning agent's way of behaviour at a specific time. Simply the policy maps something that perceived states of the environment to actions to be taken when in those states. The policy is the essence of the "RL" agent in the mean that it is a strategy that applies by the agent to determine the next action

based on the current state. Finding the optimal policy is the basic object of the (RL) process [31]. Reward signal (R): the reward signal (R) refers to how good or poor an occurrence is, and it determines the problem's target, which is for the agent to increase the total reward obtained. The better action is chosen by values of states or actions because the higher value gets about the biggest amount of reward in the long run. The learning agent will then be able to optimize the total reward it gets. Depending on the action taken, the agent receives a positive or negative reward [30][31]. Value function (V): The value function is an expectation of the future overall rewards, specifies which is good in the long run. The state-value function V^{π} (s) is the predicted return when beginning from a state "***s***" [31].
Model-based methods, such as dynamic programming, require a model of the environment, whereas model-free methods are learning without one. Model-based methods study the transmission and reward models from reaction to the environment and then utilize the learned model to compute the optimal policy through value iteration.. Model-free methods optimize the value function instantly from the observed experiment and do not depend on the transition and reward models, value functions are learned by trial and error [30].

4 Description of the Building

The Basra International Airport building model was chosen to study the operating strategies of chillers alternately. This building includes 2-chillers "York" and the type of gas used is R-134a. Fig. 2, photo of the real system (chiller 1) in Basra International Airport. The basic information about the building and chiller system is listed in Table 1:

Table 1. Building and Chillers System Data.

Building location	Basra, Iraq
Cooling system	Water-cooled
Pump system	The primary pump, the secondary pump
Chillers	2 units
Setpoint of temperature	5.6°C
Compressor	Centrifugal Chiller
Capacity	1900 ton
Cooling towers	6 units

Fig. 2. Photo of the Real System (Chiller 1) in Basra International Airport.

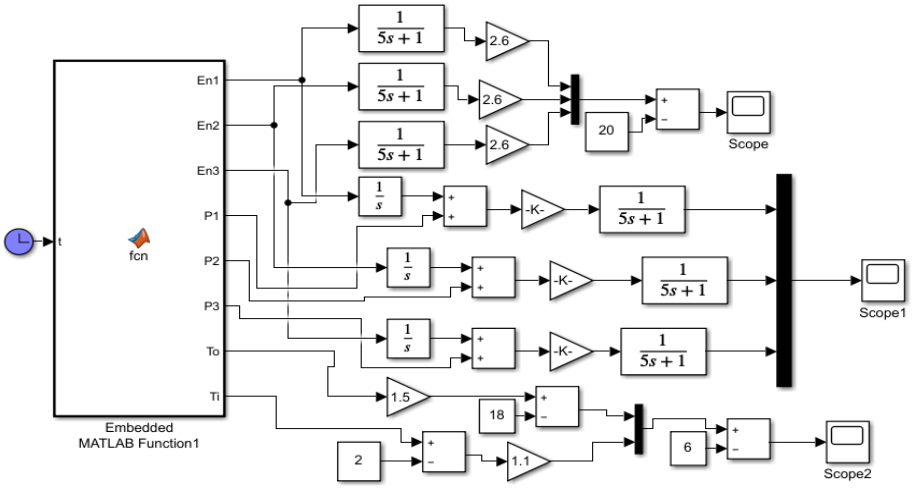

Fig. 3. Simulation of the Cooling System.

4.1. Building structure, simulation of cooling system

The proposed model was built to determine the suitable chiller for a building adaptation process using a model-based control approach. The major advantage of choosing model-based learning. As shown in Fig. 3, the model of the cooling system for an airport building by using MATLAB / SIMULINK. This model represents the products of the solutions (white box), the mathematical model. First, the thermal loads of the airport building are calculated. By calculating these loads, we find the signals of energy, power, and temperatures. The method recommended is for a chilled water system with non-identical units (i.e., non-identical chillers). The chilled water system should also be disconnected (constant primary chilled

water flow rate and variable secondary chilled water flow rate). This study depended on the computation of heating and cooling loads for opaque surfaces [33].

4.1.1. Opaque surfaces

The rate of energy stored can be calculated by applying the basic theory of energy conservation to the HVAC process [33]:

$$\frac{dE_s}{dt} = \sum_i \dot{E}_{in} - \sum_i \dot{E}_{out} \quad (1)$$

Where denotes the rate of change in the system's total stored energy, and , denotes the rate of net energy transfer. The left-hand side of Eq. 2 represents the cumulative rate of energy of opaque surfaces, through the control volume from inside to outside [33].

$$M_{wl} cp_{wl} \frac{dT_{wl,t}}{dt} = \sum_i \dot{Q}_{opq_{in}} - \sum_i \dot{Q}_{opq_{out}} \quad (2)$$

is the heat capacitance (J/K), and and are the heat gains. The surface area , and the surface cooling factor determine how much heat enters) through the control volume across opaque surfaces. Thus, it is possible to write it mathematically as follows [34]:

$$\dot{Q}_{opq_{in}} = A_{w_j} \times CF_{opq_j} \quad (3)$$

$$CF_{opq} = U(OF_t \Delta t + OF_b + OF_r DR) \quad (4)$$

Where represents the building -factor, W/(m2.K), represents the cooling design temperature differential (◦C), , , and represent the opaque surface cooling factors, and represents the cooling daily range (K) [33].

$$\dot{Q}_{opq_{in}} = \sum_j A_{w_j} U_j \ OF_t \left(T_{wl_{ou}} - T_{Wl_{in}}\right) + \sum_j A_{w_j} U_j \ OF_b + \sum_j A_{w_j} U_j \ OF_r DR \quad (5)$$

The heat transfer due to convection into the conditioned area is represented by the second part in Eq. 2. For convection heat transmission, Newton's law of cooling is as follows [35]:

$$\dot{Q}_{opq_{out}} = \sum_j A_{w_j} h_{i_j} \ \left(T_{Wl_{in}} - \ T_r\right) \quad (6)$$

As a result, using Eq. 2, apply the RL approach to the entire building. The time-dependent thermal balance equation can be explained using the empirical formula [36]:

$$M_{wl} cp_{wl} \frac{T_{wl_{ou},t} - T_{Wl_{in},t}}{\Delta t} = \sum_j A_{w_j} U_j \ OF_t \left(T_{wl_{ou},t} - T_{Wl_{in},t}\right) + \sum_j A_{w_j} U_j \ OF_b + \sum_j A_{w_j} U_j \ OF_r DR -$$

$$\sum_j A_{w_j} h_{i_j} \ \left(T_{Wl_{in},t} - \ T_{r,t}\right) \quad (7)$$

The empirical formula given in Eq. 7, the temperature varies for the opaque surfaces of the building, given by a linear combination of and . This method works well for thin, homogenous building materials, but for thick, heavy materials, the equation shows a variance in mistakes, and the only way to eliminate these errors is to offer a larger number of nodes in

the equation, such as , , , …, , the temperature curve must be expressed as a linear set of functions to be approximated to , , , …, , [33].

$$M_{wl}cp_{wl}\frac{dT_{Wl_{in},t}}{dt} = \sum A_{w_j}U_j\ OF_t\left(T_{wl_{ou},t} - T_{Wl_{in},t}\right) + \sum_j A_{w_j}U_j\ OF_b + \sum_j A_{w_j}U_j\ OF_r DR - \sum_j A_{w_j}h_{i_j}\ \left(T_{Wl_{in},t} - T_{r,t}\right) \quad (8)$$

We take the Laplace transformation for both sides of Eq. 8 and assume initial conditions are zero, and to simplify the expression further it is possible to use the transfer function in the spatial domain (s-domain) [33].

$$G_{1,11} = k_1/(\tau_5 s + 1),\ T_{Wl_{in}}(s) = [G_{1,11} \quad G_{1,12} \quad G_{1,13}]\begin{bmatrix} T_o(s) \\ k_2 \\ T_r(s) \end{bmatrix} \quad (9)$$

Where, $G_{1,12} = 1/(\tau_5 s + 1)$, $G_{1,13} = k_3/(\tau_5 s + 1)$, $\tau_5 = M_{wl}cp_{wl}/(\sum_j A_{w_j}U_j\ OF_t + \sum_j A_{w_j}h_{i_j})$,

$k_1 = \sum_j A_{w_j}U_j\ OF_t/(\sum_j A_{w_j}U_j\ OF_t + \sum_j A_{w_j}h_{i_j})$,

$k_2 = (\sum_j A_{w_j}U_j\ OF_b + \sum_j A_{w_j}U_j\ OF_r DR)/(\sum_j A_{w_j}U_j\ OF_t + \sum_j A_{w_j}h_{i_j})$,

$k_3 = \sum_j A_{w_j}h_{i_j}/(\sum_j A_{w_j}U_j\ OF_t + \sum_j A_{w_j}h_{i_j})$

In Eq. 9, Outdoor temperature (), thermal resistance and solar radiation incident (), and room temperature () are the inputs for the opaque internal temperature surface (), () is the function of thermal resistance and external temperature (◦C), and () is the function of thermal resistance [33].

4.1.2. Transparent Fenestration Surfaces

This area's heat transport differs from that of opaque surfaces. We can utilize it in Eq. 2. To calculate the heat gain, the following factors are used: area and surface cooling factor [35].

$$\dot{Q}_{fen} = \sum_j A_{fen_j}\ CF_{fen_j} \quad (10)$$

Where is a given by $CF_{fen} = u_{NFRC}(\Delta t - 0.46DR) + PXI \times \text{SHGC} \times IAC \times FF_s$ is the fenestration cooling load (W), is fenestration area (m^2), is the surface refrigeration factor (W/m^2), is the fenestration NFRC heat U-factor ($W/(m^2.K)$), NFRC is the National Fenestration Rating Council, and is the refrigeration design difference in temperature (K), DR stands for cooling daily range (K), PXI stands for peak exterior irradiance (W/m^2), SHGC stands for fenestration rated, IAC stands for internal shading attenuation coefficient, and [34]. The following formula is used to calculate PXI:

$$PXI = T_x E_t \quad \text{(Unshaded fenestration)} \quad (11)$$

$$PXI = T_X[E_d + (1 - F_{shd})ED] \quad \text{(Shaded fenestration)} \quad (12)$$

Where PXI is the peak exterior irradiance (W/m2), , , and are the peak total, diffuse, and direct irradiance (W/m2), is the transmission of exterior attachment, and is the fraction [33].
The values,, and are based on two surface conditions: horizontal surfaces and vertical surfaces.
For horizontal surfaces [33]:

$$E_t = 952 + 6.49L - 0.166L^2,\ E_d = min(E_t, 170), \text{ and } ED = E_t - E_d \quad (13)$$

$$\phi = \left|\frac{\psi}{180}\right| \text{ (normalized exposure, } 0 - 1)$$

For vertical surfaces [33]:

$$E_t = 453.4 + 1341\phi - 5279\phi^3 + 3260\phi^4 - 34.09\phi L + 0.2643\phi L^2 - 12.83L - 0.8425L^2 + \left[\frac{0.9835L^2}{\phi+1}\right]$$

(14)

$$E_d = min\left(E_t, 357 - 86.98\phi^2 + 1.764\phi L - \frac{108.4\sqrt[4]{L}}{\phi+1}\right) \quad (15)$$

Where L is the site latitude, and °N is the exposure.

For any fenestration shadowed by nearby for peak hours, the fraction can be taken as 1. An estimated equation provides simple overhang shading [33]:

$$F_{shd} = min\left[1, max\left(0, \frac{SLF \times D_{oh} - X_{oh}}{h}\right)\right] \quad (16)$$

Where is the shade line factor, is the depth of overhang (from the plane of fenestration) (m), is the vertical distance from the top of the fenestration to the overhang (m), and is the height of the fenestration (m).

The following is how values are calculated [33]:

$$IAC = 1 + F_{cl}(IAC_{cl} - 1) \quad (17)$$

Where the interior attenuation coefficient, is the shade fraction, and is the interior attenuation coeff. [33].

The heat gain through a fenestration is given as [34].

$$\dot{Q}_{fen} = \sum_j A_{fen_j}\, u_{NFRC_j}(T_o - T_{g_{in}}) - \sum_j A_{fen_j}\, u_{NFRC_j} \times 0.46DR + \sum_j A_{fen_j}\, PXI_j \times \mathrm{SHGC_j} \times IAC_j \times FF_{s_j}$$

(18)

The transfer function can be determined using the same approach as the opaque surfaces after obtaining the heat transmitted into the control volume. The outcome is the glass's internal temperature , which is defined as [33]:

$$T_{g_{in}}(s) = [G_{1,14} \quad G_{1,15} \quad G_{1,16}]\begin{bmatrix} T_o(s) \\ T_r(s) \\ f_{DR} \end{bmatrix} \quad (19)$$

Outdoor temperature , indoor temperature , and conditioned place location are used as inputs, and the result is inside glass temperature .

$G_{1,14} = R_g f_1/(f_1 R_g + 1)(\tau_g S + 1)$.

$G_{1,15} = 1/(f_1 R_g + 1)(\tau_g S + 1)$,

$G_{1,16} = -R_g/(f_1 R_g + 1)(\tau_g S + 1)$, $\tau_g = Cag\, R_g/(f_1 R_g + 1)$

$f_{DR} = \sum_j A_{fen_j}\, u_{NFRC_j} \times 0.46DR$

$R_g = (1/\sum_j A_{fen_j}\, h_{i_j})$, $f_1 = \sum_j A_{fen_j}\, u_{NFRC_j}$ (W/k) [33].

4.1.3. Slab floors

The slab floor is a significant thermal capacitance storage capacity. It is the greatest and also most complex to calculate the building's several components. Eq. 2, energy conservation law can be rewritten like this [35]:

$$M_{slab} cp_{slab} \frac{dT_{slab,t}}{dt} = \sum_i \dot{Q}_{slab_{in}} - \sum_i \dot{Q}_{slab_{out}}$$

(20)

Where and are the heat gain and lossof the slab, respectively (*W*) and is the heat capacitance of slab (*J/K*).
According to [37] heat gain is largely through the perimeter, rather than the floor and earth [38].
Overall heat loss/gain is more almost related to the length of the perimeter than to the area of the floor, and it may be computed by the following equation for both unheated and heated slab floors [33].

$$\dot{Q}_{slab_{in}} = f_t P(T_{slab_{in}} - T_o) \quad (21)$$

Where is the heat gain through slab floors (W), is the heat loss of the perimeter, *W*/ (*m.K*), is the perimeter or exposed edge of the floor (m), is the inside slab floor temperature, and is the outdoor temp. [33].
The ASHRAE organization calculated the heat loss from a concrete slab floor using the same procedures as for opaque and fenestration surfaces [39]. As a result, the heat production of the control volume is as shown in Eq. 22.

$$\dot{Q}_{slab_{out}} = \sum_j A_{slab_j} Cf_{slab_j} \quad (22)$$

Where is the area of the slab (m2), $(Cf_{slab_i} = 1.9 - 1.4h_{srf})$ is cooling factor (W/m2), given by

$$h_{srf} = 1/(R_{cvr} + 0.12)$$

Where is the effective surface conductivity, which includes slab covering substance resistance , like carpet (Representative values can be found in [40].
Eqs. 21 and 22 are substituted into Eq. 20 to produce the slab floor transfer function, and then after simplifying the expression, Laplace transformation is used on both sides of the resultant equation [34].
As illustrated below, the slab floors insides are slabbed floors area () and outside temperature , while the slab floors outcomes are internal slab floors temperature [33].

$$T_{slab_{in}}(S) = [G_{1,17} \quad G_{1,18}] \begin{bmatrix} A_{slab} \\ T_o \end{bmatrix} \quad (23)$$

Where $G_{1,17} = (1.9 - 1.4h_{srf})/(\tau_{slab}S + 1)$, $G_{1,18} = f_t P/(\tau_{slab}S + 1)$, $\tau_{slab} = C_{slab}/f_t P$,

$C_{slab} = \sum_i M_{slab_i} cp_{slab_i}$, is the heat capacitance of slab floors (J/k) [33].

4.2. Building System Control of the Reinforcement Learning (RL) Process

Reinforcement Learning (RL) is a framework in which an agent interacts with its environment and learns the best set of behaviours to achieve a goal, which is represented by a policy. RL focuses on the learning agent that adjusts its behaviours in response to the environment's reward to achieve a specified objective, such as getting the maximum amount of reward [41]. Instead of a priori knowledge, the agent's actions are based on his or her own experience gained during the game. Research has been done in the field of building control to apply RL to model-based control [15].
In this research, the environment is the model for the airport building described previously. The agent's learning goal is expressed through a reward, which is a scalar feedback value that

quantifies how the agent is acting about the learning objective. A MDP is characterized by a tuple (S, A, R, P, γ), is used to formalize the agent-environment interaction. [41] stated S is the set of states, A is the set of actions, r: S × A → R is the reward function, P is a state transition probability matrix; the transition function specifies the probability of transition from the state (s) to state on acting (a) and γ is a discount factor, $\gamma \in [0, 1]$ [41].
The state-value function is the predicted discounted return when beginning from a state "s" [41].

(24)

Where "Rt" represents the total rewards received during the period "t", "rt+k" represents the signal of an instant return, and (γ) represents the discount rate, calculated inside the inqulaity to check that (Rt) is limited [12].

(25)

(26)

The (RL) agent uses an optimal strategy to discover the ideal state-value function. It may be written as the sum of all state-values in Eqs. 27, 28, and 29. A set of equations known as the "Bellman Optimality Equations" can resolve into instant return and discounted future values [12].

(27)

(28)

(29)

The agent optimizes its policy π: S → P(A), which describes its behaviour in the environment, where P(A) is a probability distribution among the global set of actions, over a discrete sequence of time steps. The goal of the policy improvement technique of optimal policy ($\pi*$) for better action that maximizes the projected discounted return [42].
In our problem, (energy, temperature) are state components, and the agent chooses an action from a finite set of feasible actions that represent the chillers' capacity at each time step (0, 25, 40, and 65). As a result, the state of the environment is changed to st+1, and the agent receives a reward. These incentives have a real-world value and can be good or negative, but they must be constrained. The agent can detect all conceivable states of the environment. According to the Markov transition model, the likelihood of transitioning from state (s) to state (s') after acting an A is solely determined by the current state, not by the history of previous states. Based on specific needs represented by the reinforcement function, a policy for an agent of the building management system to work on the HVAC system is obtained in these trials. Each episode is divided into numerous time steps t, with the building management system deciding on an action to adjust the temperature inside the building based on its policy at each step [43].
The goal of applying the RL algorithm to the HVAC management system is to conserve energy while maintaining comfort, the reward function's learning aim must account for a trade-off between the two components of comfort and main energy consumed.

4.3. Chiller Operation

The HVAC system considers for more than 50% of a building's total energy usage, chilled water chillers represent 30-40% of the energy used for this system. As a result, chillers must be run properly to increase energy efficiency. The chiller operates based on the refrigeration load for the building (i.e., appropriately switching chillers ON/OFF) [44]. Furthermore, most chillers' operation strategies necessitate reliable real-time monitored cooling water system data. Chiller operation techniques are occasionally designed to improve chiller COP to reduce energy consumption and improve chiller efficiency. It is possible to clarify the following chiller operation strategies:

1. Chilled water is turned ON/OFF based on measured cooling load data.
2. The cooling limit of the chiller exceeds the refrigeration load by a large quantity, and based on the building cooling load, the chillers are turned ON/OFF.

The flowchart in Fig. 4, is based on the case presented that consists of a large chiller with a capacity of (4.0 Mw) and a small chiller with a capacity of (2.5 Mw), with the chiller capacity dictated by the system load. In other cases, the chiller's ON/OFF alternately is to increases the partial load and improves energy efficiency. The structure with two non-identical chillers is depicted in the diagram. When one or more chillers are in use, another chiller should not be turned ON/OFF unless load exceeds the system's cooling load.

a) If the cooling load of the building is lower than the limit of the chillers, all chillers are switched off.
b) The small chiller is operated with a capacity (2.5MW) if the load exceeds the capacity of this chiller.
c) If the load exceeds the limit of the small chiller, it will be off and the large radiator with a capacity (4.0MW) is turned on.
d) If the load exceeds the limit of the large chiller, all chillers will be operated when the building load is at its peak.

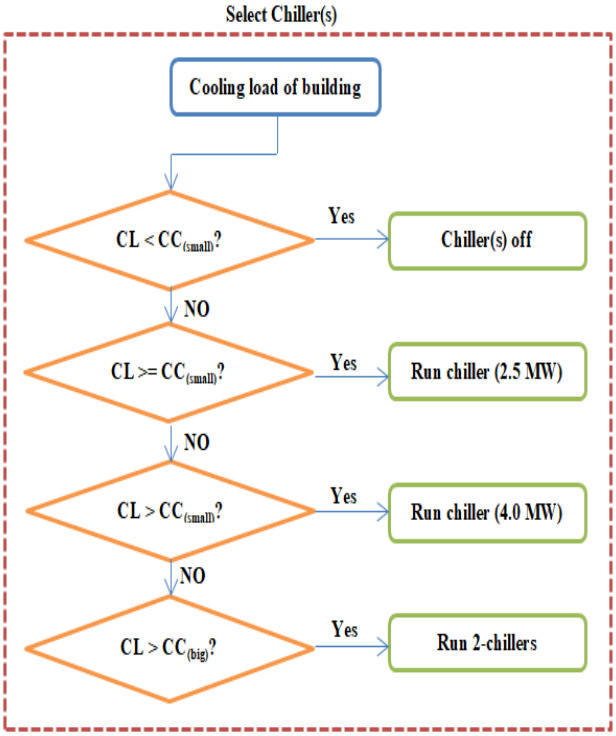

Fig. 4. Workflow of the proposed method.

4.4. Chiller sequencing control

The goal of chiller sequencing control is to save enough cooling to maintain building indoor thermal comfort while maintaining chiller plant high energy efficiency.
Fig. 5, depicts the chiller sequencing control principle, with the x-axis representing the building's cooling load (CL), given by:

(30)

Where is the calculated cooling load (kW), is the specific thermal capacity of water (J/kg.°C), is the measured chilled water flow rate (kg/s), , are the chilled water return and supply temperatures (°C) respectively.

Each chiller's ON/OFF status should be regulated at the start of each time step. To identify suitable ON/OFF signals, the following rules are used:

a) If the system cooling load is less than 1 chiller's rated cooling capability, the entire central chilled water system is shut off.
b) The cooling load on the system determines the number of chillers necessary; when the cooling load on the system exceeds the current cooling capacity, an extra chiller is activated.

c) The ON/OFF case of the main chilled water pump is synchronized with the condition of the chillers. When the chiller is turned ON/OFF, the principal chilled water pump is also turned ON/OFF.

The first phase entails selecting the chiller(s) based on the chillers' cooling capacity (CC) and cooling load. In this method, the chiller partial load rate (PLR) is maximized; the COP of centrifugal chillers is also tuned because the PLR of centrifugal chillers increases with the COP.

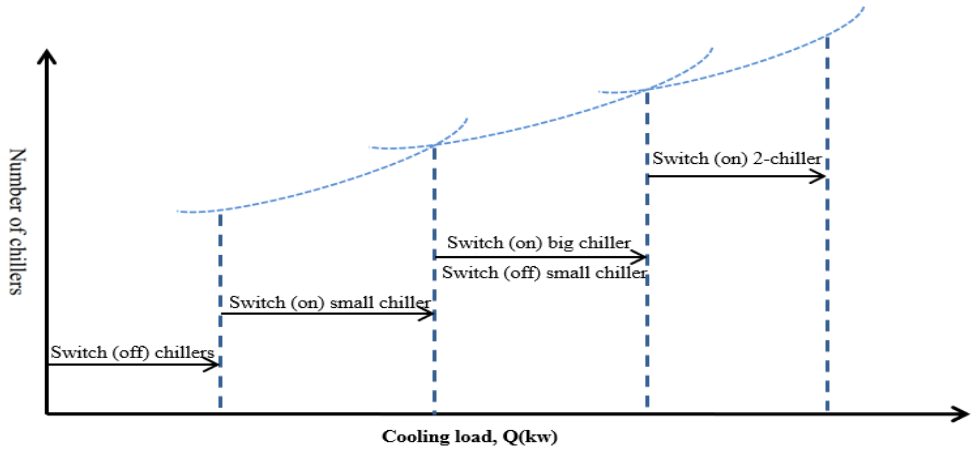

.**Fig. 5**. The basic principle of chiller sequencing control

The buildings inside temperature setpoints from 20 °C to 24 °C in the second step [44]. After we built the control model-based for the airport building, which is the product of the equations of the mathematical model, we found the thermal load signal for a whole day (24 hours) for the multiple chillers. We take the signal for this load and build an RL-control on, it as it learns the ON/OFF process for each chiller, the energy and temperature indication will be (state), and the action represents the capacity of the two chillers (2.5 MW, 4.0 MW) respectively. If the building load exceeds the capacity of the first chiller (2.5 MW), then RL-control will operate the second chiller (4.0 MW) instead of the first chiller, and when the building's load exceeds the capacity of the second chiller at the peak, RL-control will operate the two chillers together and thus the capacity of the two chillers is (6.5 MW). The reason for our use of more than one chiller is to conserve the largest amount of energy possible and reduce the energy consumed, while when operating a single chiller and with a high capacity while the building load is low, it will be exposed to faults or damage.

5 Results and Discussion

The HVAC system is simulated under the supervision of a mathematical model, and the performance of the RL-controller and the PID controller is compared by turning the mismatched chillers ON/OFF every 30 minutes for 24 hours.

In Fig. 3, a full-day Airport system operation is simulated every half-hour for various chillers under the management of model-based control. The model results were discussed in terms of

energy consumption, the controller's learning process, control actions, and system water temperature, as well as the load equations for opaque, transparent surfaces, and slab floors, which were used to computr the building cooling load for 24 hours using model-based control. These calculated cooling load results were to know the temperatures, power, and energy inside the building.

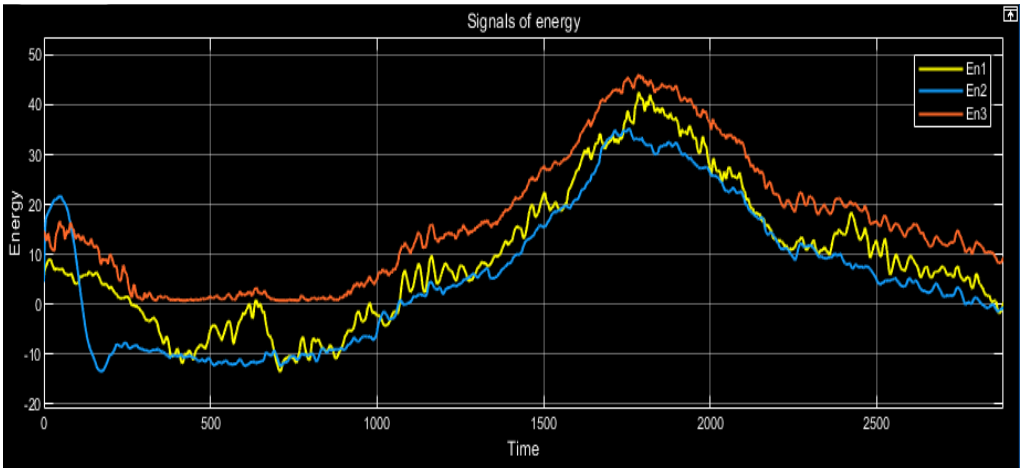

Fig. 6. Signals of Energy.

Figs. 6, 7, and 8 represent the signals (energy, power, indoor and outdoor temperatures) coming out of the Simulink, changing with time, for the model of chillers with capacities (2.5 MW, 4.0 MW, and 6.5MW) respectively.

Where Fig. 6, represents the energy signals and it is dependent on the cooling coil, which is the thermal loads of the airport building, where we see these loads and how they work with temperature and time and will be within 24 hours. As Fig. 7, it represents the power signals of the HVAC system, which is the electrical power that the system dissipates over time. Fig. 8, represents the temperatures of the building, where we note that the indoor temp. is less than the outdoor temperature, and in this case, the HVAC system will not work and the difference in temperatures depends on the insulation of the building, walls, and others.

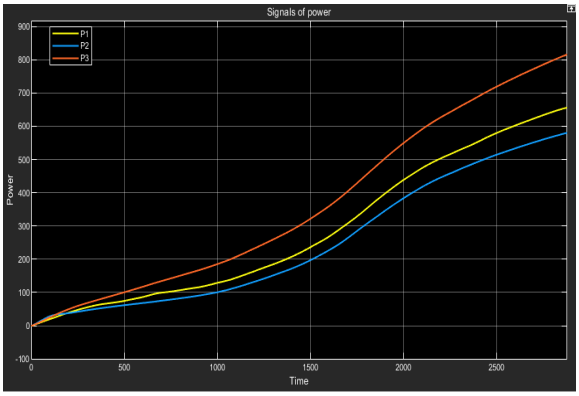

Fig. 7. Signals of Power.

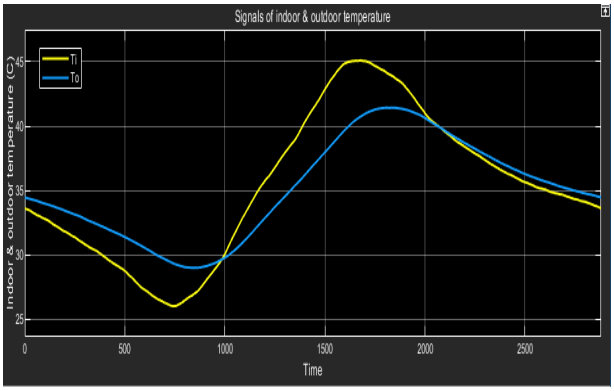

Fig. 8. Signals of Indoor & Outdoor Temperature.

Fig. 9, illustrates the cases of reinforcement learning for indoor and outdoor temperatures (°C) with time (hours). The black line represents the temperature outside the building and the red line is the temperature inside the building, which is within the limits of thermal comfort, which is between 20 °C to 24 °C. The chiller plant must remove the cooling load accumulated throughout the night as well as the potential heat of the air conditioning system at the start of the day, resulting in a tremendous load met by chillers. The chillers should be turned on/off at the maximum energy-efficient point, which is usually less than 100 percent, according to the chiller sequencing control. When the cooling load is plainly changing, this is fair for chiller energy efficiency. In comparison with Fig. 10, where the reinforcement learning of the building's internal temperature using multiple HVAC systems, the traditional building control proportional integral derivative (PID) was used for the HVAC system and it was within the comfort limits of the building, but it was not stable compared with the reinforcement learning when the ON/OFF control.

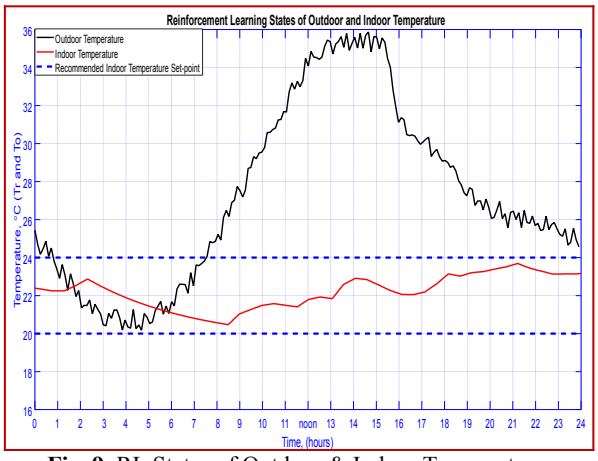

Fig. 9. RL States of Outdoor & Indoor Temperature.

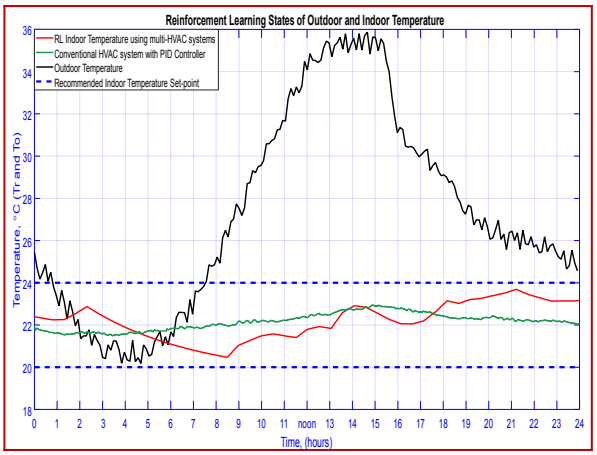

Fig. 10. RL States of Outdoor & Indoor Temperature with PID Controller

As shown in Fig. 11, the performance comparison between the three control strategies for the response step, is the reinforcement learning for the energy-based multi-HVAC system, the traditional HVAC system with the controller (PID) in addition to the real or calculated response to the building strength. After comparing the performance, we found that saving energy through the proposed controller is (45%) from the traditional strategy.

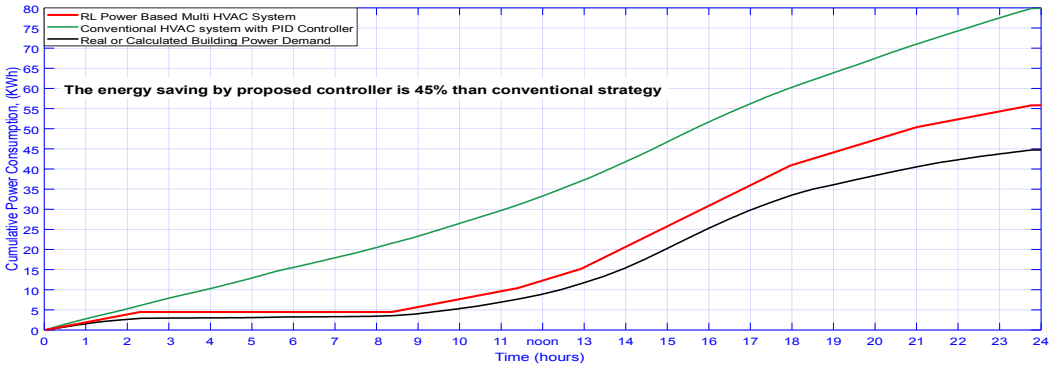

Fig. 11. Performance Comparison between Three Controllers' Strategies for the Step Response

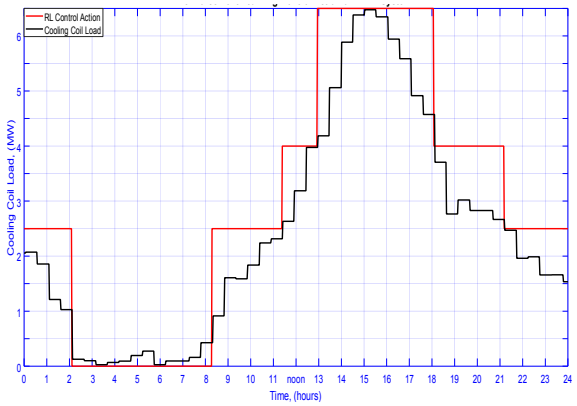

Fig. 12. Reinforcement Learning Control Action of the HVAC system.

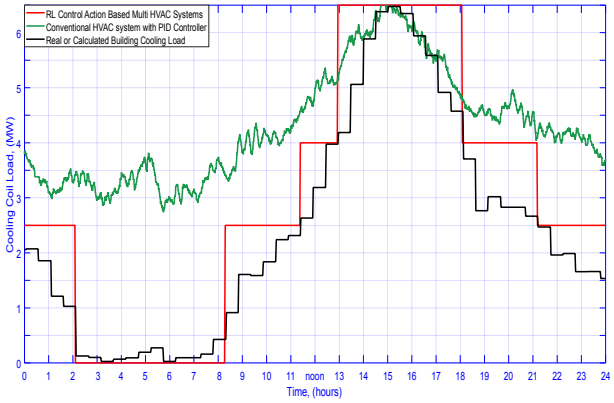

Fig. 13. Reinforcement Learning Control Action of Multi HVAC System.

In Fig. 12, illustrating the HVAC system reinforcement learning (RL) control action for the cooling load profile (MW) and time (hours), use the reinforcement learning to perform the control with the building cooling load. This action features temperature control by adjusting the flow rate of the cooling coil water related to indoor/ outdoor temperature indication. The law of control is also based on the "ON/OFF" algorithm. While in Fig. 13, represents a control based RL for multiple HVAC systems with a conventional "PID" control strategy for a real or computed building cooling load. HVAC systems varies the cooling profile (energy consumption) and the reinforcement learning of the control procedure is calculated utilizing iterative techniques in the "MATLAB code". During the day, energy consumption increases, this indicates an increase in the number of chillers by 100%, especially at peak to improving energy efficiency.

Fig. 14, shows the value function for energy saving in the case of multi-chillers system operation. The RL control algorithm was trained using iterators in the MATLAB code for states and actions to the maximum value using the reward function to build the value function by applying the Bellman Eq. 30. After optimizing the value function, we chose the best value to guarantee the control policy. In addition, when agent rewarded after taking action for each time step of control depends on the energy and temperature, if a low outdoor temp. is maintained and to avoid punishing the agent for taking heavy action, there is no need to turn

on the chiller because it is considered energy consumption. For Fig. 15, consider the existing analysis which represents the best function of the control policy for actions (0, 2.5, 4.0, and 6.5) to find the best suitable chiller for the building conditioning process and the best possible efficiency. The best action applied to operate the chiller suitable for the building cooling load is the best policy than calculating the maximum value function from the Bellman equation. Therefore, the optimum energy efficiency for cooling the building is obtained when both small and large chillers are operated.

In conclusion, the reinforcement learning control technique suggested in this work has the potential to conserve more energy. Furthermore, the proposed strategy's energy-saving effectiveness can be increased while maintaining internal thermal comfort. As a result, the proposed technique can slightly shorten the operating duration of the tiny chiller by removing certain superfluous starting activities.

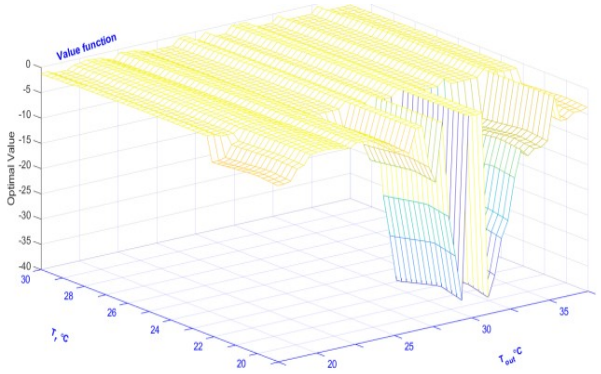

Fig. 14. Optimal value function.

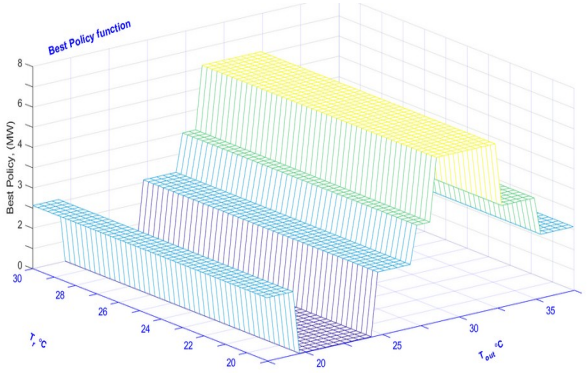

Fig. 15. Best policy function.

6 Conclusion

This study demonstrated a modelling technique for HVAC systems using the MATLAB/Simulink platform, as well as the use of the RL-controller strategy to rise the energy efficiency of cooling load. To control the multi-chillers system, an ideal model-based control strategy has been developed. In this method, energy and temperature are the states, chillers capacities are the actions, and the reward is energy savings, chilled water pumps, and chillers. A model-based simulation is performed under the supervision of a white box (mathematical model). The simulation results for 24 hours indicate that the proposed energy and power controller (RL-Controller) can save 45% of the energy compared to the traditional PID controller. This limited application in an airport terminal model cooling plant using non-identical chillers; it takes a whole day to simulate the operation of the whole system which is controlled every half hour by the proposed reinforcement learning control strategy. Where the reinforcement learning control (RL-control) system for multiple chillers can improve system stability and energy efficiency. Hence, it is concluded the method can lower the energy consumption of the building, which is acceptable for engineering applications.

Acknowledgment

I would like to express my thanks and appreciation to the Basra International Airport, which supported the research and assisted me in obtaining the required information.

References

[1] Homod, R.Z., Gaeid, K.S., Dawood, S.M., Hatami, A. and Sahari, K.S., 2020. Evaluation of energy-saving potential for optimal time response of HVAC control system in smart buildings. Applied Energy, 271, p.115255.

[2] Homod, R. Z., Almusaed, A., Almssad, A., Jaafar, M. K., Goodarzi, M., & Sahari, K. S. M. (2020). Effect of different building envelope materials on thermal comfort and air-conditioning energy savings: A case study in Basra city, Iraq. Journal of Energy Storage, 101975.

[3] Homod, R.Z., Togun, H., Abd, H.J. and Sahari, K.S., 2020. A novel hybrid modelling structure fabricated by using Takagi-Sugeno fuzzy to forecast HVAC systems energy demand in real-time for Basra city. Sustainable Cities and Society, 56, p.102091.

[4] Dong He, Qingyu Xiong, Xuyang Zhang, Yunchuang Dai and Ziyan Jiang, A Decentralized, Flat-Structured Control System for Chiller Plants (2019).

[5] Bingqing Chen, Zicheng Cai and Mario Bergés, Gnu-RL: A Precocial Reinforcement Learning Solution for Building HVAC Control Using a Differentiable MPC Policy, Nov. (2019).

[6] Homod, R.Z., 2018. Analysis and optimization of HVAC control systems based on energy and performance considerations for smart buildings. Renewable Energy, 126, pp.49-64.

[7] Poe, W. A., & Mokhatab, S. (2017). Process Control. Modeling, Control, and Optimization of Natural Gas Processing Plants, 97–172.

[8] Liu, S., & Henze, G. P. (2006). Experimental analysis of simulated reinforcement learning control for active and passive building thermal storage inventory. Energy and Buildings, 38(2), 148-161.

[9] Dalamagkidis, K., Kolokotsa, D., Kalaitzakis, K., & Stavrakakis, G. S. (2007). Reinforcement learning for energy conservation and comfort in buildings. Building and Environment, 42(7), 2686–2698.

[10] Fan, B., Jin, X., & Du, Z. (2011). Optimal control strategies for multi-chiller system based on probability density distribution of cooling load ratio. Energy and Buildings, 43(10), 2813–2821.

[11] Sen Huang, Wangda Zuo, Michael D. Sohn (2015). A NEW METHOD FOR THE OPTIMAL CHILLER SEQUENCING CONTROL, 14th Conference of International Building Performance Simulation Association, Hyderabad, India, Dec. 7-9, 2015, 316-323.

[12] Azuatalam, D., Lee, W.-L., de Nijs, F., & Liebman, A. (2020). Reinforcement learning for whole-building HVAC control and demand response. Energy and AI, 2, 100020.

[13] Yao, Y., Lian, Z., Hou, Z., & Zhou, X. (2004). Optimal operation of a large cooling system based on an empirical model. Applied Thermal Engineering, 24(16), 2303–2321.
[14] Qiu, S., Li, Z., Li, Z., & Zhang, X. (2020). Model-free optimal chiller loading method based on Q-learning. Science and Technology for the Built Environment, 1–22.
[15] Qiu, S., Li, Z., Li, Z., Li, J., Long, S., & Li, X. (2020). Model-free control method based on reinforcement learning for building cooling water systems: Validation by measured data-based simulation. Energy and Buildings, 218, 110055.
[16] Homod, R.Z., Almusaed, A., Almssad, A., Jaafar, M.K., Goodarzi, M. and Sahari, K.S., 2021. Effect of different building envelope materials on thermal comfort and air-conditioning energy savings: A case study in Basra city, Iraq. Journal of Energy Storage, 34, p.101975.
[17] Afroz, Z., Shafiullah, G., Urmee, T., & Higgins, G. (2018). Modeling techniques used in building HVAC control systems: A review. Renewable and Sustainable Energy Reviews, 83, 64–84.
[18] Afram, A., & Janabi-Sharifi, F. (2014). Review of modeling methods for HVAC systems. Applied Thermal Engineering, 67(1-2), 507–519.
[19] Homod, R. Z. (2013). Review on the HVAC System Modeling Types and the Shortcomings of Their Application. Journal of Energy, 2013, 1–10.
[20] Homod, R.Z., Sahari, K.S.M., Almurib, H.A. and Nagi, F.H., 2012. RLF and TS fuzzy model identification of indoor thermal comfort based on PMV/PPD. Building and Environment, 49, pp.141-153.
[21] Poe, W. A., & Mokhatab, S. (2017). Process Control. Modeling, Control, and Optimization of Natural Gas Processing Plants, 97–172.
[22] Krarti, M., 2011. Energy Audit for Building Systems: An Engineering Approach, 2nd ed. CRC Press, Francis, and Taylor, Roca Baton, FL, 600 pp.
[23] Rao, R. V. (2015). Optimization of Multiple Chiller Systems Using TLBO Algorithm. Teaching Learning Based Optimization Algorithm, 115–128.
[24] A. Bhatia (2012). HVAC Equipments and Systems, PDHonline Course M322 (7 PDH).
[25] Carrier Corporation (2005). Commercial HVAC Chiller Equipment.
[26] Beghi, A., Cecchinato, L., Cosi, G., & Rampazzo, M. (2010). Two-layer control of multi-chiller systems. 2010 IEEE International Conference on Control Applications.
[27] Ardakani, A. J., Ardakani, F. F., & Hosseinian, S. H. (2008). A novel approach for optimal chiller loading using particle swarm optimization. Energy and Buildings, 40(12), 2177–2187.
[28] Askarzadeh, A., & Coelho, L. dos S. (2015). Using two improved particle swarm optimization variants for optimization of daily electrical power consumption in multi-chiller systems. Applied Thermal Engineering, 89, 640–646.
[29] Diniz, A. A. R., Pires, P. R. M., de Melo, J. D., Neto, A. D. D., Filho, A. J. J. L., & Kanazava, S. M. (2010). Reinforcement Learning for Controlling a Coupled Tank System Based on the Scheduling of Different Controllers. 2010 Eleventh Brazilian Symposium on Neural Networks.
[30] Miyoung Han (2018). Reinforcement Learning Approaches in Dynamic Environments.
[31] Ahmad Hammoudeh (2018). A Concise Introduction to Reinforcement Learning.
[32] B. Abdulhai, R. Pringle, and G.J. Karakoulas (2001). Reinforcement Learning for ITS: Introduction and a Case Study on Adaptive Traffic Signal Control.
[33] Homod, R.Z., Sahari, K.S.M., Almurib, H.A. and Nagi, F.H., 2011. Double cooling coil model for non-linear HVAC system using RLF method. Energy and buildings, 43(9), pp.2043-2054.
[34] Homod, R.Z. and Sahari, K.S.M., 2013. Energy savings by smart utilization of mechanical and natural ventilation for hybrid residential building model in passive climate. Energy and Buildings, 60, pp.310-329.
[35] Homod, R.Z., Sahari, K.S.M. and Almurib, H.A., 2014. Energy saving by integrated control of natural ventilation and HVAC systems using model guide for comparison. Renewable Energy, 71, pp.639-650.
[36] Homod, R.Z., Sahari, K.S.M., Almurib, H.A. and Nagi, F.H., 2012. Gradient auto-tuned Takagi–Sugeno fuzzy forward control of a HVAC system using predicted mean vote index. Energy and Buildings, 49, pp.254-267.

[37] F.S. Wang, Mathematical modeling and computer simulation of insulation systems in below grade applications, in: ASHRAE/DOE Conference on Thermal Performance of the Exterior Envelopes of Buildings, Orlando, FL, 1979.
[38] T.P. Bligh, P. Shipp, G. Meixel, Energy comparisons and where to insulate earth sheltered buildings and basements, Earth covered settlements, U.S. Department of Energy Conference, Fort Worth, TX, 1978, K. Elissa, Title of paper if known, unpublished.
[39] ASHRAE, Residential cooling and heating load calculations, handbook— fundamentals, chp. 17, in: J. Clerk Maxwell (Ed.), American Society of Heating, Refrigerating, and Air-Conditioning Engineers, A Treatise on Electricity and Magnetism, vol. 2, 3rd ed., Clarendon, Oxford, 2009[1892], pp. 68–73.
[40] ASHRAE, HVAC Systems and Equipment' Handbook—Fundamentals, American Society of Heating, Refrigerating, and Air-Conditioning Engineers, 2008 (Chp. 6).
[41] Sutton, R. S. and A. G. Barto (1998). Introduction to Reinforcement Learning, Volume 135. MIT press Cambridge.
[42] Mastropietro, A., Castiglione, F., Ballesio, S., Enrico Fabrizio, E. (2019). Reinforcement Learning Control Algorithm for HVAC Retrofitting: Application to a Supermarket Building Model by Dynamic Simulation. Conference: Building Simulation 2019.
[43] Fazenda, P., V., Veeramachaneni, K., Lima, P., O'Reilly, U. (2014). Using Reinforcement Learning to Optimize Occupant Comfort and Energy Usage in HVAC Systems. Journal of Ambient Intelligence and Smart Environments · January 2014.
[44] Qiu, S., Feng, F., Zhang, W., Li, Z., & Li, Z. (2019). Stochastic optimized chiller operation strategy based on multi-objective optimization considering measurement uncertainty. Energy and Buildings, 195, 149–160.

The Impact of the Vane Angle on the Hydraulic Behaviour Around the Cylinder

Tahseen Ali Jabbar[1], Rafi M.Qasim[2], Bassam A. Mohammed[3]
{tahseen.ali@stu.edu.iq[1], rafi.mohammed@stu.edu.iq[2], bassam.moh@stu.edu.iq[3]}

1,2 Department of Fuel and Energy, Southern Technical University, Basra, Iraq.

3 Department of thermal mechanical, Southern Technical University, Basra, Iraq

Abstract. The flow around an obstacle represents a challenge in fluid mechanics problems and practice. So, it is significant to investigate the hydraulic behaviour around the obstacle and the response of the obstacle which encounters the flow suddenly. The target of the present paper deal with the investigation numerically the effect of changing the vane angle on the hydraulic field around the cylinder and the response of the cylinder to the angle change. The vane has an angle shape with different angles ranging from 20 degrees to 90 degrees, the dimension of the angle is adopted as a function of the cylinder diameter. The study concentrates on the average flow velocity, strain rate, shear stress, static pressure, dynamic pressure, pressure coefficient, skin friction coefficient, drag coefficient, and lift coefficient. The obtained result shows a noticeable variation in the response of the hydraulic field around the cylinder especially in average flow velocity, static pressure, dynamic pressure, strain rate, and shear stress. The negative lift coefficient and negative drag coefficient appear in the numerical investigation. Also, a negative pressure coefficient is found. Many reasons will lead to the negative response like pressure difference from section to section, changing inflow velocity owing to the existence of the vane in addition to the cylinder, flow separation zone expansion, flow velocity dissipation owing to the existence of the vane, momentum transfer from section to section and turbulence level.

Keywords: Cylinder, flow field, turbulent flow, vane angle.

1 Introduction

A turbulent hydraulic flow field around a circular body like piers, piles, and pipes is considered as a significant and noticeable problem in fluid mechanics and hydraulic structure design consideration, especially in the subject of the, scour around bridge pier and pile, therefore, many papers deal with this subject from the previous time to present to find a suitable solution and avoid any hydraulic problem which reflects on the flow field – structure interaction. Catalano et al. (2003) [1] studied the turbulent flow around a circular in the supercritical regime at high Reynolds numbers. The large eddy simulation is adopted in the study and compared with the Reynolds- average Navier-Stokes Solution. Based on the obtained result the large eddy simulation was significantly more accurate as compared with Reynolds-average Navier-Stokes. Rajani et al. (2009) [2] dealt with the three-and two-dimensional flow which passes a cylinder with a circular section in various regimes of laminar flow. The analysis concentrated on the

IMDC-IST 2021, September 07-09, Sakarya, Turkey
Copyright © 2022 EAI
DOI 10.4108/eai.7-9-2021.2315298

verification between the measured data and the computational result. Singha et al. (2010) [3] investigated numerically the flow around a cylinder with a circular section placed centrally inside a channel. The blockage ratio is studied by change the distance between the walls of the channel. The investigation concentrated on vortex shedding, wake pattern, drag coefficient, lift coefficient, and strouhal number. Ashtiani et al. (2013) [4] made a comparison between flow field around a single pier and tandem piers set up on a laboratory flume with a moderately flat rough bed. The flow velocities were measured by an Acoustic Doppler Velocimeter. The contours of the turbulent intensity, turbulent kinetic energy, velocity components, and Reynold shear stress are studied. Vectors and streamlines are adopted to study the flow features. Yagmur et al. (2015) [5] investigated numerically and experimentally the flow pattern in the wake region of various bluff bodies like a triangle, square and circular cross-section of cylinders placed horizontally and perpendicularly to the flow. The experimental work is carried out in an open channel at water Reynolds numbers 10000 and 5000. While the numerical analysis is performed by ANSYS Fluent software. Elbatran (2016) [6] made a three-dimensional numerical study to reveal the turbulent flow characteristics around a cylinder which has a circular section. A detached eddy simulation model with a Reynolds number equal to 43000 is adopted in the numerical study. The obtained numerical result was compared with experiments and theoretical results found by the other researchers. Khassaf and Obied (2018) [7] carried out an experimental study to investigate the impact of the guide panels on local scour which happens around the bridge pier. They found from the experiments as the panel height decrease, the scour depth has been decreased. Abdulhussein et al (2019) [8] performed an experimental study to reveal the impact of the strip guide flow panel on local scour which occurs around the pier. They obtained from the experiments; the use of the strip guide reduces the scour depth. Here the guide is mounted upstream of the pier. Marelius and Sinha (1998) [9] investigated numerically and experimentally the flow velocity profile around the submerged vanes. The paper's purpose concentrates on the impact of vane angle influence on the altered hydraulic flow pattern around a cylinder. Here, the vane is installed upstream of the cylinder. The numerical study includes the investigation of the following average flow velocity, strain rate, shear stress, drag coefficient, lift coefficient, skin friction coefficient, pressure coefficient, static pressure, and dynamic pressure.

2 Numerical Modelling

The problem is considered in two dimensions. Here, the water flow passes the vane and then passes the cylinder at Reynolds number 18094.8. The problem is modelled and simulated by ANSYS Fluent software. Fig 1 illustrates the dimension of the water domain which includes the vane and the cylinder. Here, the vane is placed upstream of the cylinder, while Fig 2 illustrates the fine mesh with numbers of the element (42000 elements). The water is the flow material and is considered an incompressible material with a density of $998.2\,Kg/m^3$ and viscosity $0.001003\ Kg/m.s$. The boundary condition of the hydraulic system is given in table (1). The bed of the channel is considered horizontal, fixed, and flat. The vane angle adopted in the study has a range between 30^o and 90^o with an angle interval equal to 5^o. The time which is used to achieve the numerical analysis is 8 seconds.

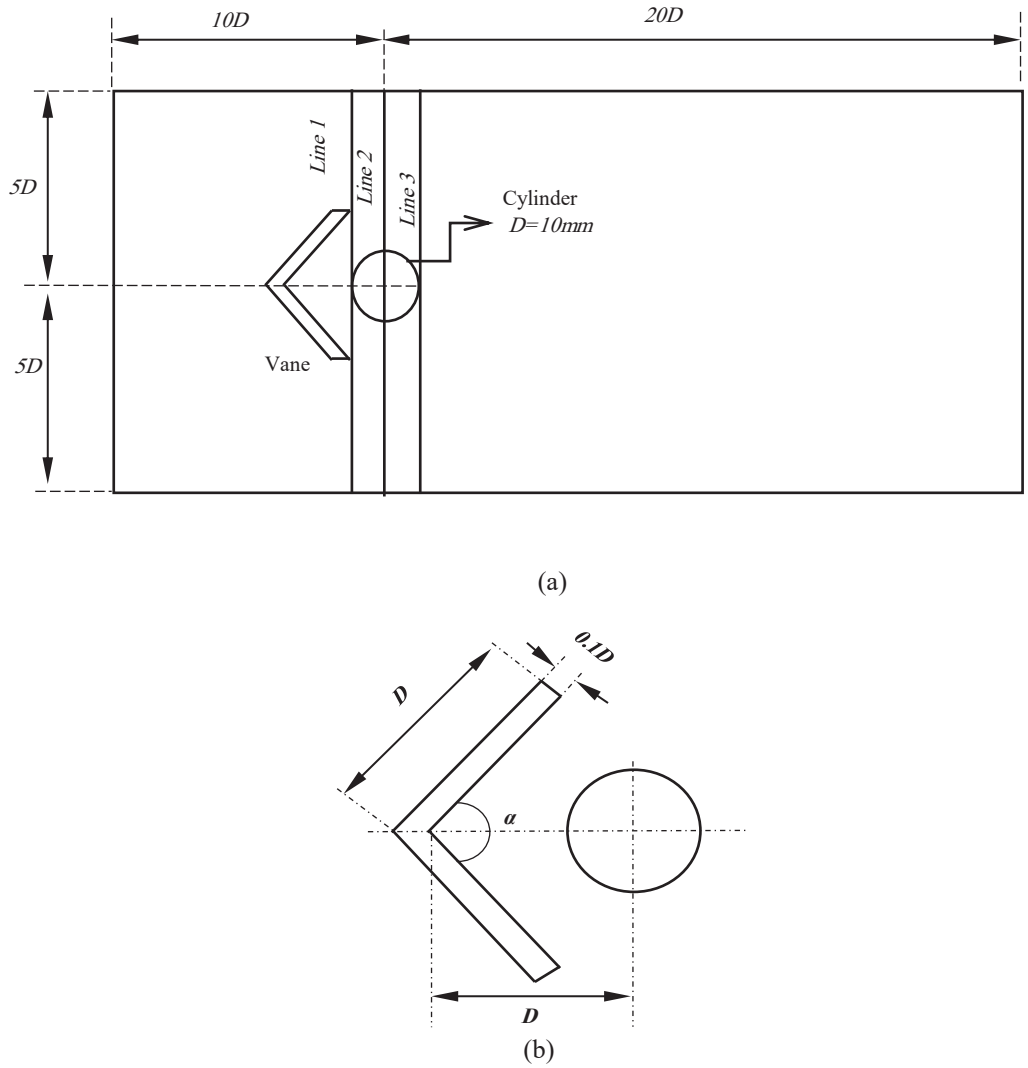

Fig. 1. Shows the hydraulic system components with hydraulic domain (a) full domain (b) the vane and cylinder.

Table 1. Boundary condition of the hydraulic system.

Inlet	Velocity at inlet
Outlet	Pressure at outlet
Cylinder	No slip-Wall
Vane	No slip-Wall
Channel bed	No slip-Wall

Channel sides	No slip-Wall
Top surface of flow	Atmospheric Pressure

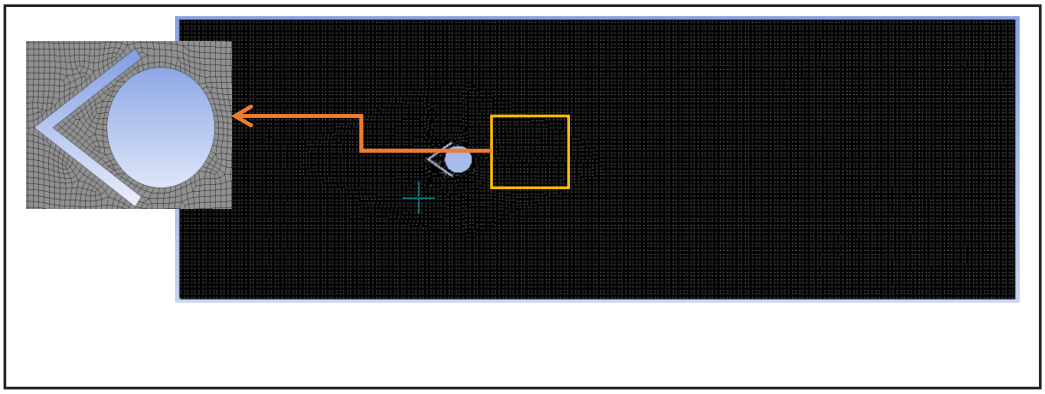

Fig. 2. The mash of the model (42000 elements).

The CFD governing equations that will be used for the simulation are the conservation of momentum equation and incompressible fluid continuity equation are shown in equations (1) to (4), respectively.

$$u\frac{\partial u}{\partial x}+v\frac{\partial u}{\partial y}+w\frac{\partial u}{\partial z}=-\frac{1}{\rho}\frac{\partial P}{\partial x}+\frac{\mu}{\rho}\left(\frac{d^2u}{dx^2}+\frac{d^2u}{dy^2}+\frac{d^2u}{dz^2}\right) \quad (1)$$

$$u\frac{\partial v}{\partial x}+v\frac{\partial v}{\partial y}+w\frac{\partial v}{\partial z}=-\frac{1}{\rho}\frac{\partial P}{\partial y}+\frac{\mu}{\rho}\left(\frac{d^2v}{dx^2}+\frac{d^2v}{dy^2}+\frac{d^2v}{dz^2}\right) \quad (2)$$

$$u\frac{\partial w}{\partial x}+v\frac{\partial w}{\partial y}+w\frac{\partial w}{\partial z}=-\frac{1}{\rho}\frac{\partial P}{\partial z}+\frac{\mu}{\rho}\left(\frac{d^2w}{dx^2}+\frac{d^2w}{dy^2}+\frac{d^2w}{dz^2}\right) \quad (3)$$

$$\frac{\partial(\rho u)}{\partial x}+\frac{\partial(\rho v)}{\partial y}+\frac{\partial(\rho w)}{\partial z}=0 \quad (4)$$

2.1 Fluent verification

It is important to verify the software before using it, to analyse the present problem, therefore, the fluent software is used to implement the case study in reference [10] and the obtained results have been compared with results that have been obtained in the reference (10). Reference (10) dealt with the analysis of the flow pattern around a pier which has a square cross-section in three dimensions. Table (2) review the detail of case study in reference [10] while table (3) review the comparison between the drag coefficient value which obtained from the present analysis and the drag coefficient value which given in reference [10].

Table 2. reference [10] case study details.

D (m)	V (m/s)	H (m)	$\rho\ (kg/cu.m)$	Re (no unit)
1	0.292	2	1.225	20000

Table 3. comparison between present and previous study respectively.

Reference studies	Reynolds Number	Setup	C_d
Zaid et al. (10)	20000	Numerical	2.1951
Present study	20000	Numerical	2.15

2.2 Mesh Independent

The velocity of the fluid has a great influence on the properties of the flow, so the mesh independence was adopted on the average velocity at three different Lines. Fig 3 shows that the average velocity value of these Lines remains constant when the number of elements is greater than 30000.

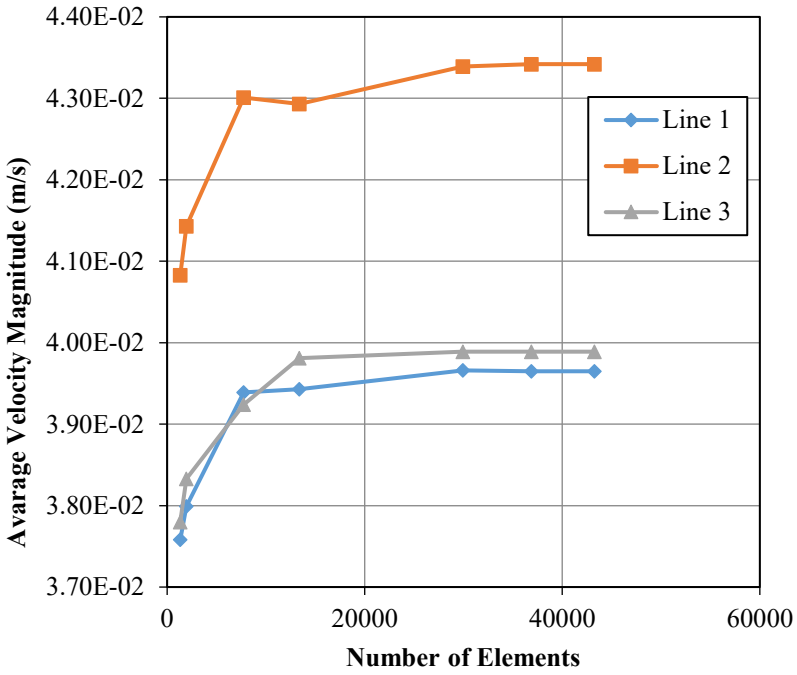

Fig. 3. Show the mesh independently.

3 Result and discussion

The numerical investigation is done by ANSYS software and concentrated on some hydraulic variables which are discussed below. The variation of the average flow velocity with a variation of the vane angle is shown in Fig 4. The variation is drawn at three lateral lines where the line (2) pass at the centre of the cylinder while the lines (1) and (3) passes at the edge of the cylinder. The variation of the average flow velocity at the centre of the cylinder (line2) is higher as compared with the variation at the edge of the cylinder (lines 1 and 3). It is clear from the Fig the variation at line 1 and line 3 is approximately identical. Fig reveal when the vane angle increase, this led to an increase in average flow velocity variation especially at line2 with a noticeable fluctuation at line1 and line3 and it is observed clearly at angle 60 degrees. Fluctuation depends on the flow separation zone, change in turbulence level, and water flow confinement at the vane. Here all these hydraulic variables dominate the magnitude of the flow velocity variation. Also, the vane shares inflow velocity dissipation.

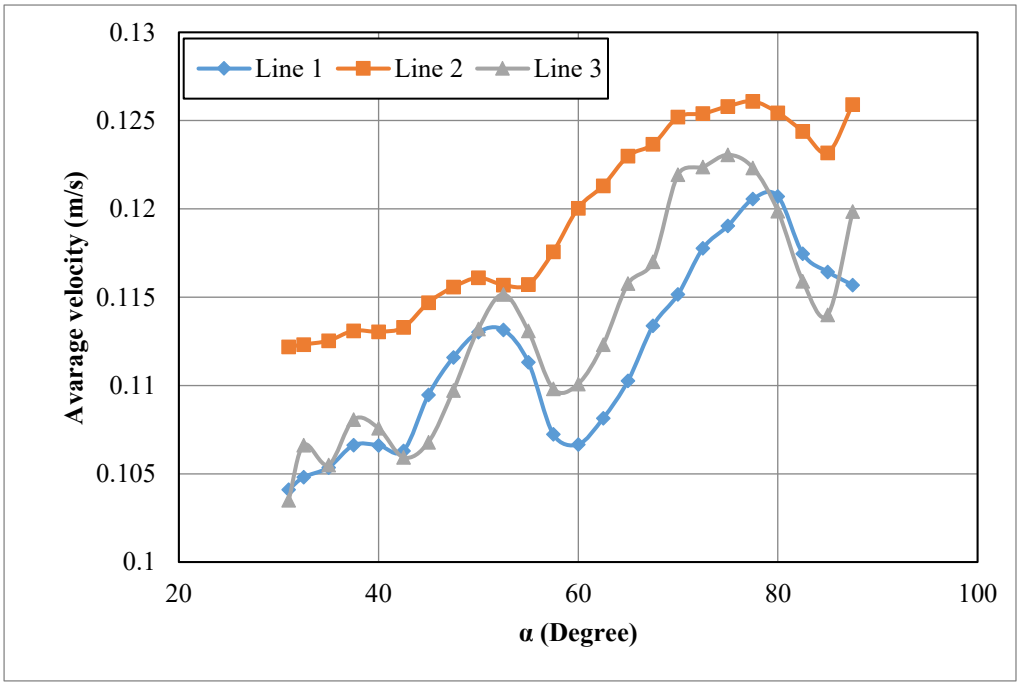

Fig. 4. variation of the average velocity with vane angle.

Fig 5 consists of two parts, the first one shows the relationship between drag coefficient and vane angle while the second shows the relationship between the lift coefficient and vane angle. it is very strange to shows the values of lift and drag coefficient respectively have a negative sign but at the same time there is no law or principle encourage to avoid the negative sign. It is observed from the figure a dramatically altered in values of drag and lifts coefficient respectively with the altered in the vane angle. expansion of flow separation zone, boundary layer growth, and development, the difference in pressure field around the vane and the cylinder, the interaction between the flow velocity field around the vane and the cylinder and the change

in momentum transfer between the vane and the cylinder, all these variables will create and encourage to develop the negative lift and drag coefficient respectively.

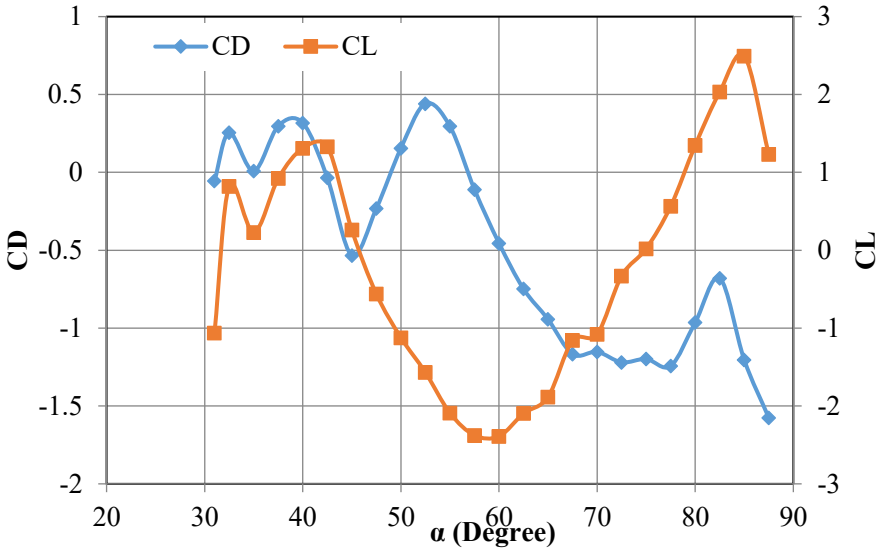

Fig. 5. variation of the drag coefficient and lift coefficient with the vane angle.

Fig 6 shows the variation of the static pressure and the dynamic pressure with the vane angle. It is obvious from the figure, the static pressure decreases with an increase in the vane angle, while the dynamic pressure increases with an increase in the vane angle. For both cases, pressure is more affected by the flow separation zone, stagnation points where the pressure is zero, the turbulence level, and the flow confinement by the vane, especially in static pressure.

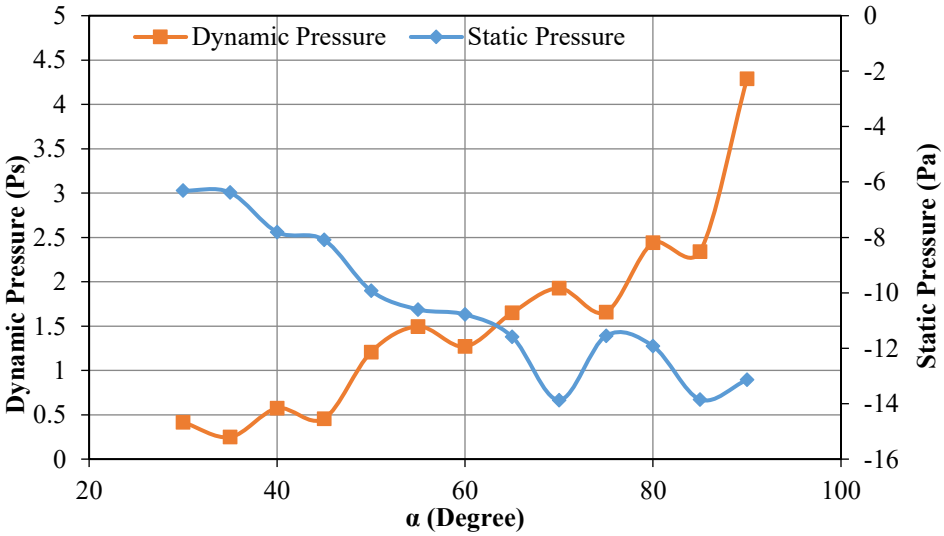

Fig. 6. Variation of the static pressure and the dynamic pressure with the vane angle.

Fig 7 illustrates the relationship between the skin friction coefficient with the vane angle. It is clear from the figure; the skin friction coefficient increases with the increase in the vane angle values. Skin friction refers to the drag between the water flow and surface area. In general, the presence of the vane leads to reduce the water flow velocity, and as the flow velocity decreases the skin friction coefficient which grows at the cylinder surface will be increased. In addition to the shear stress which grows around the cylinder will reduce the flow velocity and increase the skin friction coefficient.

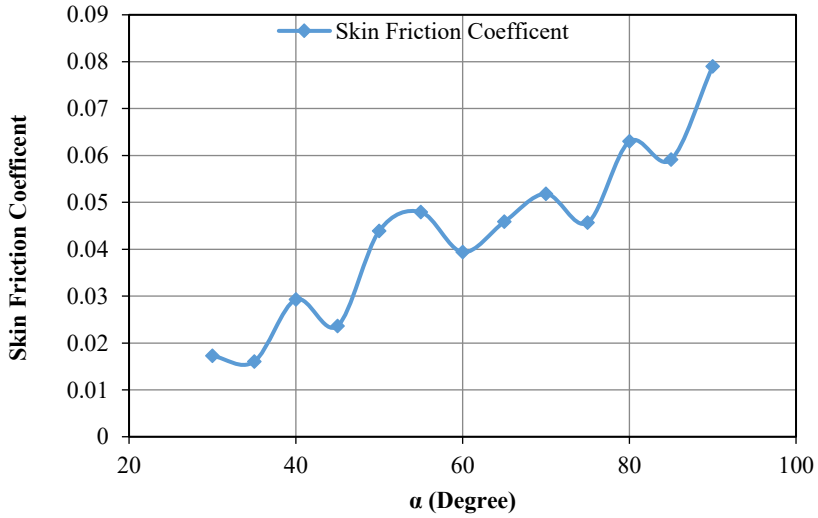

Fig. 7. Variation of the skin friction coefficient with the vane angle.

Fig 8 consists of two parts, the first one shows the relationship between strain rate and vane angle while the second shows the relationship between the shear stress and vane angle. It is obvious from the figure that both variables increase with increasing the vane angle. The flow velocity gradient and the flow momentum exchange between the downstream of the vane and the upstream of the cylinder will be reflected on the trend of the relationship. Also, the flow separation by the vane, the flow dissipation by the vane, and the turbulence level will be reflected on the relationship directly.

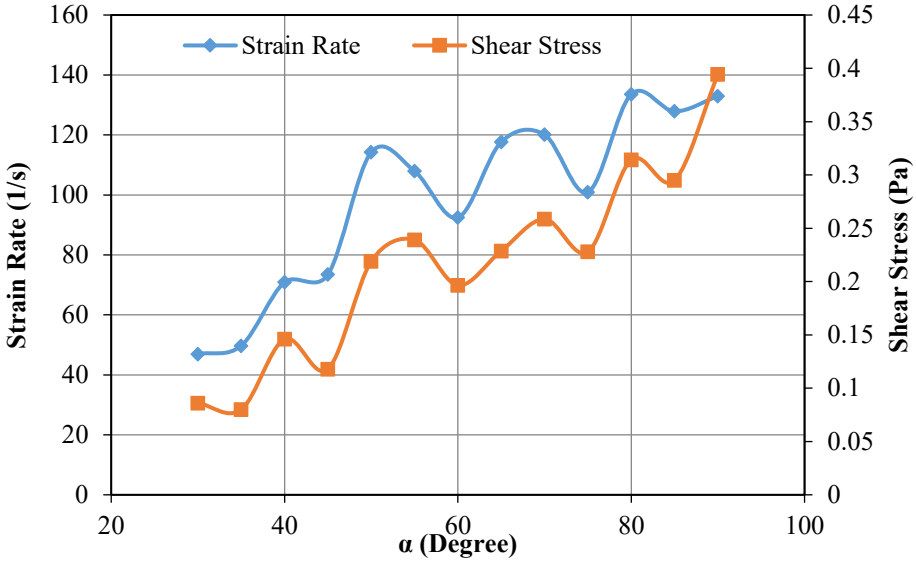

Fig. 8. Show the variation in strain rate and shear stress respectively with the vane angle.

Fig 9 illustrates the relationship between the pressure coefficient and the vane angle. The figure refers to the negation pressure coefficient. It is clear from the figure; the pressure coefficient decreases with an increase in the vane angle values. The change in vain angle leads to the change in the pressure around the cylinder or in other words leads to the difference between the upstream pressure and downstream pressure around the cylinder. So, this difference will lead to a negative pressure coefficient. Also, the pressure coefficient will be influenced by flow separation, flow velocity, and turbulence level.

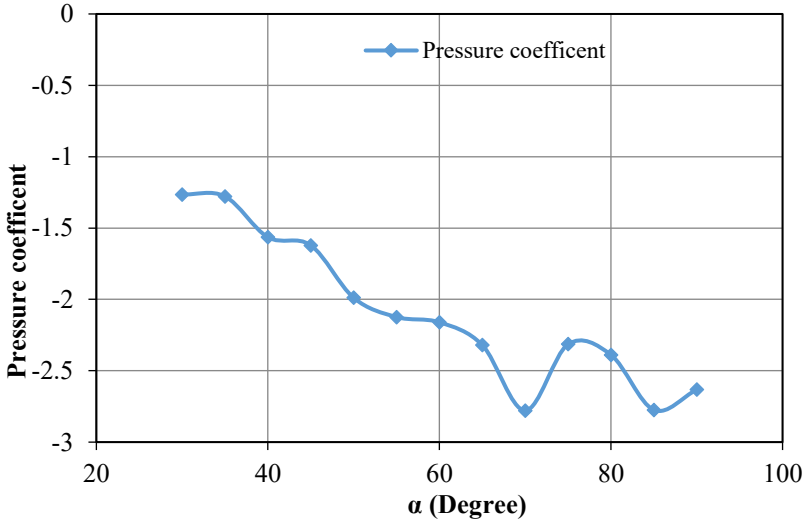

Fig. 9. Shows the variation in pressure coefficient with the vane angle.

4 Conclusion

The following noticeable point can be considered from the current numerical study.

1. The vane angle controls the hydraulic interaction between the flow field around the cylinder and the flow field around the vane.
2. The negative lift coefficient and negative drag coefficient appear owing to change in pressure, momentum transfer, flow separation, and level of turbulence.
3. Skin friction is affected by the flow velocity in the region between the vane and the cylinder.
4. The velocity gradient has a direct effect on the strain rate and shear stress.
5. The difference in pressure between the upstream of the cylinder and the downstream of the cylinder has a major effect on the pressure coefficient.
6. Turbulence level, pressure difference, flow separation has a major effect on the static and dynamic pressure respectively.
7. The vane angle has a major role in control the variation of the average flow velocity at different functions.

References

[1] Catalano, P., Wang, M., Iaccarino G., Moin, P "Nmerical simulation of the flow around a circular cylinder at high Reynolds numbers" International Journal of Heat and Fluid Flow 24 (2003) 463-469.

[2] Rajani, B., N., Kandasamy, A., Majumdar, S." Numerical simulation of laminar flow past a circular cylinder" Applied Mathematical Modelling 33 (2009) 1228-1247.

[3] Singha, S., Sinhamahapatra, K., P." Flow past a circular cylinder between parallel walls at low Reynolds numbers" Ocean Engineering 37 (2010) 757-769.

[4] Ashtiani, B., A., Kordkandi, A., A., "Flow field around single and tandem piers" Flow Turbulence Combust (2013) 90: 471-490.

[5] Yagmur, S., Dogan, S., Aksoy, M., H., Canli, E., Ozgoren, M." Experimental and numerical investigation of flow structures around cylindrical bluff bodies" EPJ Web of Conferences 92, 02113 (2015).

[6] Elbatran, A., H." DES of the turbulent flow around a circular cylinder of finite height" Journal of Naval Architecture and Marine Engineering. 13(2016) 179-188.

[7] Khassaf, S., I., Obied, N., A." Experimental study: bridge pier protection against local scour using guide panels" IOP Conf. Series: Materials Science and Engineering 433 (2018) 012006 doi:10.1088/1757-899X/433/1/012006.

[8] Abdulhussein IA, Al-Asadi K, Qasim RM "Pier scouring reduction using a Strip Guide Flow Panel device" RUDN Journal of Engineering Researches. 2019;20(3):229–235.

[9] Marelius, F., and Sinha, S., K. "Experimental investigation of flow past submerged vanes" J. Hyd. Eng., ASCE, 1998, 124(5): 542-545.

[10] Zaid M., Yazdanfar Z., Chowdhury H., Alam F., "Numerical modeling of flow around a pier mounted in a flat and fixed bed" Energy Procedia, 160: 51-59, 2019.

Design And Analysis of New Compound Journal Bearing

Nadhim. N[1], Mahmood. R[2]
{Nadhim.naseer@mtu.edu.iq[1], Mahmech2001@yahoo.com[2]}

Al-Nahrain University, College of Engineering, Mechanical Engineering Department, Iraq [1]
Al-Nahrain University, College of Engineering, Prosthetics [2]

Abstract. One of the main challenges that are widely faced is the maintenance of the journal bearing requires extra time and effort. Therefore, in this work a new design of journal bearings system was developed with low friction which would help with: A) relatively higher load as it would create duplicated pressure and B) Due to the use of the Nano Lubrication as one of the new system's components, it will support an enhanced and persistent oil viscosity of the mechanical system which would support a mechanical system of a consistent temperature. To accomplish all the above, a mathematical model for the new journal bearing design was developed, the mathematical model was additionally resolved using Reynold's equation and using the finite difference method. A MATLAB code was also developed to solve the governing partial differential equation to find journal-bearing parameters. The preliminary results of this work indicated an increase of pressure value of 50% as compared with the traditional bearing. Furthermore, the new design indicated a consistent oil viscosity/temperature when adding the Nanoparticles to the system and improve all bearing parameters.

Keywords: Hydrodynamic journal bearing, Nano lubricants, Viscosity, Pressure distribution, Load carrying capacity.

1 Introduction

Journal bearings are a common engineering component that can be found in practically any machine. To achieve great efficiency and dependability, combustion engines and turbines rely almost entirely on journal bearings [1]. A journal bearing is made up of a revolving shaft (journal) and a stationary bush. The hydrodynamic film that supports the load is created between the shaft's moving surfaces and the bush's moving surfaces. Because the operating surfaces of such bearings are completely separated by a lubricating film, the friction coefficient is kept low, around 0.005, and bearing failure is rare, occurring only after incorrect operation. The mechanism of lubrication is explained by Reynolds' hypothesis, which involves the formation of a viscous liquid film between the moving surfaces. The prerequisite is that the surfaces must move with enough velocity relative to each other to create such a film [1]. All hydrodynamic lubrication can be mathematically represented using an equation devised by Reynolds. Normal journal bearings have some drawbacks in many applications, such as cavity pressure, power loss, instability, and so on. To boost capacity and efficiency, a variety of designs have been proposed, including offset and preload bearings, multi-lobe bearings, and step bearings [2]. The effect of lubricant and improving its performance is studied by many researchers. In this regard is K. G. Binu et al. [3] employed TiO2 nanoparticles to manufacture nano lubrication as a lubricant additive with a particle concentration of 0.02 to investigate the static performance

IMDC-IST 2021, September 07-09, Sakarya, Turkey
Copyright © 2022 EAI
DOI 10.4108/eai.7-9-2021.2315287

properties of Journal bearings in low shear states. For TiO2 nanolubricants, static characteristics such as pressure, load capacity, and friction force were simulated in this study. When comparing mild shear to high shear, the results show an increase in pressure and load-carrying capacity. Han et al. [4] produced a CFD result. For the parallel sliding surface with spherical dimples, it was demonstrated that the lubricant's load-carrying capacity improves while its friction coefficient drops.

2 Theory

In the present design, the traditional journal bearing is modified as a compound bearing with is consisted of; inner and outer journal bearing and as follows; the shaft is bored, and an inner bush is pressed to perform the inner journal while the shaft outer surface makes the outer journal with both housings as shown in Fig 1. To allow for oiling of the inner bush the housing support is supplied with oil entry consisted of two perpendicular holes. The journal geometry is a hollow cylinder in which the two-journal bearing is introduced [3]. The first is the inner between the inner bush and the central support study. The second is the outer between the outer surface and the bush at the support. In other words, two parallel journals bearing are introduced. It is to be noted that the inner. In this case, the inner journal operates in a reverse manner as compared with the outer where the bush is rotated and the journal is fixed, the outer journal is working as usual. However, since there exists a relative motion, the hydrodynamic principle can be applied. The main difference here is that at the static position the contact at the inner bearing occurs at the upper point while the outer journal bearing occurs at the lower point as shown in Fig 1.

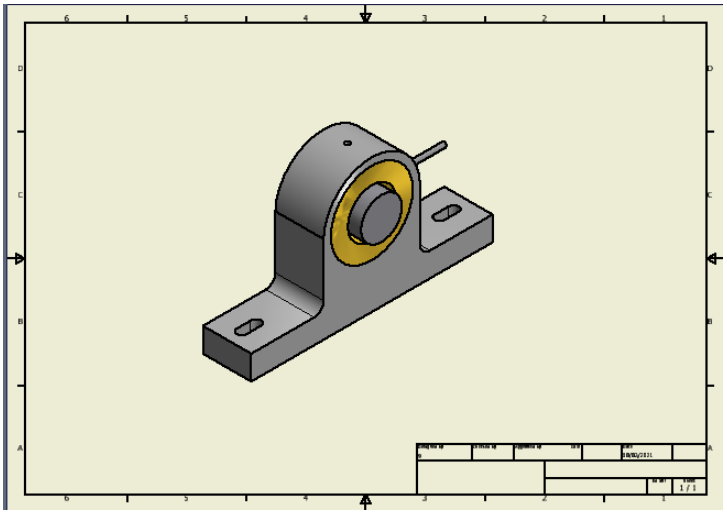

Fig. 1. Solid work drawing of compound journal bearing.

The schematics representation of the compound journal is shown in Fig 2. As it is clear from the figure two pressure profiles are generated due to the hydrodynamic effect for the two film thicknesses of the inner and outer bearing parts. Mathematically the two distinct parts of the compound journal can be treated separately.

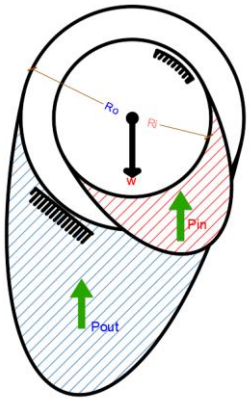

Fig. 2. Pressure profiles of compound journal bearing.

2.1 Numerical Analysis

The hydrodynamic Reynolds equation of journal bearing with constant viscosity Newtonian lubricant can be expressed as [1].

$$\frac{\partial}{\partial x}\left(h^3\frac{\partial p}{\partial x}\right)+\frac{\partial}{\partial y}\left(h^3\frac{\partial p}{\partial y}\right)=6U\eta\frac{dh}{dx} \tag{1}$$

Where:
C, R, L and **U** are bearing radial clearance, radius, axial length and entraining velocity respectively.
H, P and η: hydrodynamic film thickness, pressure and dynamic viscosity of the bearing respectively.
Whereas **x**, y are coordinates of hydrodynamic film.

Due to the complexity of the analytical solution of the differential equation for real-sized journals unless in some cases such as for short or very long cases [5]. The main aim of the numerical analysis is to evaluate the main journal parameters such as maximum pressure, load capacity, friction force. In its non-dimensional form, the Reynolds equation is [6]:

$$\frac{\partial}{\partial x^*}\left(h^{*3}\frac{\partial p^*}{\partial x^*}\right)+\left(\frac{R}{L}\right)^2\frac{\partial}{\partial y^*}\left(h^{*3}\frac{\partial p^*}{\partial y^*}\right)=\frac{\partial h^*}{\partial x^*} \tag{2}$$

Where;

$$h^*=\frac{h}{c}\ .x^*=\frac{x}{R}\ ,\ y^*=\frac{y}{L},\ p^*=\frac{pc2}{6U\eta R}$$

The Vogelpohl parameter was invented in the 1930s by Vogelpohl [1] to increase the accuracy of numerical solutions of the Reynolds equation. Mv is the Vogelpohl parameter, and its definition is as follows:

$Mv = p*h*^{1.5}$ (3)

Substituting into eq.2 one gets

$$\frac{\partial^2 M_v}{\partial \chi^2} + \left(\frac{R}{L}\right)^2 \frac{\partial^2 M_v}{\partial \gamma^2} = FM_v + G \quad (4)$$

Where;

$$F = \frac{0.75\left[\left(\frac{\partial \lambda}{\partial \chi}\right)^2 + \left(\frac{R}{L}\right)^2 \left(\frac{\partial \zeta}{\partial \gamma}\right)^2\right]}{\zeta^2} \quad (5)$$

$$G = \frac{\left(\frac{\partial \lambda}{\partial \chi}\right)}{\zeta^{1.5}} \quad (6)$$

'Finite difference' approaches are typically used to solve journal and pad bearing difficulties, while 'Finite element' methods have also been used [9]. The finite difference approach works by calculating the difference between function values at two or more consecutive nodes to approximate a differential quantity. By subtracting the formula for ∂Mv/∂x* at the i-0.5 nodal location from the i+0.5 nodal position and dividing by δx*, the second differential ∂2Mv/∂x*2 is found:

$$\left(\frac{\partial^2 \mu_v}{\partial \chi^{*2}}\right)_i = \frac{\mu_{v,i+1} + \mu_{v,i-1} - 2\mu_{v,i}}{(\Delta \chi)^2} \quad (9)$$

Substitute into eq.4 to get.

$$\mu_{v,i,j} = \frac{\left(\frac{1}{(\Delta \chi)^2}\right)(\mu_{v,i+1,j} + \mu_{v,i-1,j}) + \left(\frac{R}{L}\right)^2 \left(\frac{1}{(\Delta \gamma)^2}\right)(\mu_{v,i+1,j} + \mu_{v,i-1,j}) - G_{i,j}}{2\frac{1}{(\Delta \chi)^2} + 2\frac{1}{(\Delta \gamma)^2} + F_{i,j}} \quad (10)$$

The finite difference approach for solving the Reynolds equation is based on this expression. Its solution yields the necessary Mv nodal values [7].
MATLAB software is introduced to solve eq 10 and evaluating the journal bearing parameters.

2.2 Bearing Parameters

The main parameter to be investigated are as follows:

2.2.1 Pressure Distribution

The numerical solution of the Reynolds equation can give the pressure distribution at the nodes [8]. The resulting pressure in dimensionless the actual pressure can be found from the following equation.

$p = p*(6U\eta R)/C^2$ (11)

2.2.2 Load Capacity

Integrating the pressure surrounding the bearing yields the total load that the bearing can support. The Half-Sommerfeld condition was utilised in the early literature for load estimates, which meant that the negative pressures in one-half of the bearing were discounted. The load is frequently divided into two parts, one acting parallel to the shaft and bush centres and the other acting perpendicular to the first [12].

$$W = W^* \left(\frac{6R^2 LU\eta}{c^2}\right) \quad (12)$$

2.2.3 Friction Force

By integrating the shear stress 'τ' throughout the bearing area, the friction force may be determined [19]:

$$F = \int_0^L \int_0^{2\pi R} \tau \, dxdy \quad (13)$$

where the shear stress 'τ' is given by:

$$\tau = \frac{\eta U}{h} + \frac{h}{2}\frac{dp}{dh} \quad (14)$$

$$\tau = \frac{1}{h^*} + 3h^* \frac{dp^*}{dx^*} \quad (15)$$

and equation (11) can be reduced to:

$$F = F^* \left(\frac{RL\eta U}{c}\right) \quad (16)$$

2.2.4 Coefficient of Friction

The coefficient of friction of a bearing is calculated once the load and friction forces are Known [16]:

$$\mu = \frac{F}{W} = \frac{F^* \left(\frac{RL\eta U}{c}\right)}{W^* \left(\frac{6R^2 LU\eta}{c^2}\right)} = \left(\frac{C}{6R}\right)\left(\frac{F^*}{W^*}\right) \quad (17)$$

2.2.5 Bearing Geometry

Journal bearings are analysed using the same method as the linear and converging-diverging wedges previously discussed. After defining the film shape, the Reynolds equation is used to calculate the pressure field and load capacity [18].

$$h = c(1 + \varepsilon \cos\theta) \quad (18)$$

3 Experimental Work

3.1 Compound Journal Bearing Manufacturing

The new design of the journal bearing was manufacturing in Middle Technical University (MTU) By using CNC Machen as shown in figure 3. The new design of journal bearing was design to meet the need of the machine with high load capacity, The double journal bearing can be expected to bear more load with less wearing.

Fig. 3. manufacturing process of new design prototype of compound journal bearing using high accuracy cutting tools machine.

3.2 Testing Rig

The testing rig of the double journal bearing is designed to meet the experiments recommend, Fig 4 shown the testing rig. The testing rig has a three-phase motor with a speed reach of 4000 rpm. One side has been fixing with normal journal bearing and the other side compound journal.

The displacement has been measured with an eddy current sensor with a sensitive reach of 1 micrometre. Fig 5 shows the eddy current sensor. The sensor is attached to amplifier the signal.

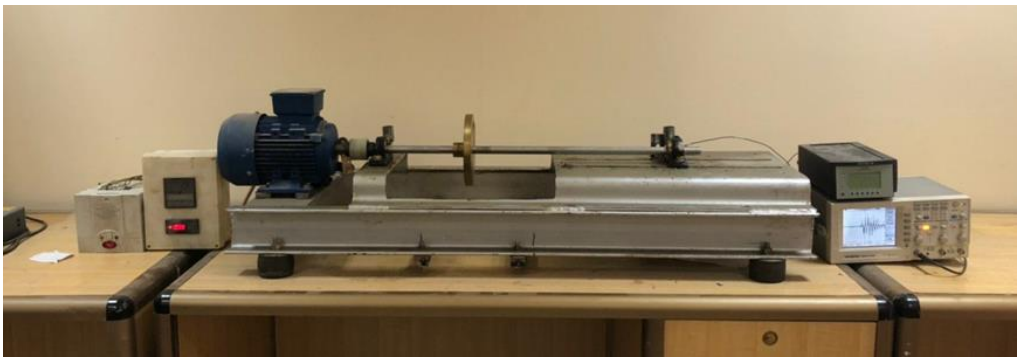

Fig 4. Testing rig.

Fig. 5. Eddy's current sensor.

The amplifier is attached to the oscilloscope; as shown in Fig.. 5. The signal of the oscilloscope is transferred to the computer for analysis. The signal is shown in Fig. 6.

Fig. 6. Collecting the data.

3.3 Shaft Alignment

Shaft alignment is required to ensure that the rotational centres of the driver and drive shafts are aligned when the machines are in regular operation. As indicated in Fig 8, misalignment has two components: offset (or parallel) and angular (or face). The distance between the shaft centres of rotation measured in the plane of power transmission from the driving unit to the driven unit is the offset misalignment. The coupling centre is usually where this is measured. The angular misalignment, on the other hand, is the difference in the slope of one shaft (the moveable part) compared to the slope of the other machine's shaft (the stationary part). As already indicated.

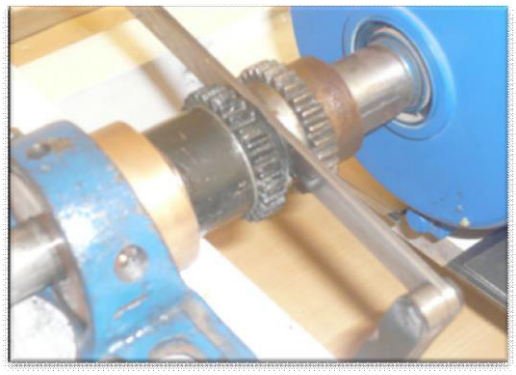

Fig 7. Face measurement by using failure gauge.

3.4 Experimental Procedures

The following steps are made for testing and measuring the journal bearing.

1- Selecting the motor speed by adjusting the speed control.
2- Checking the system alignment to avoid any vibration and noise.
3- Reading the output of the proximate sensor probe.
4- Transferring the real-time data l to oscilloscope and computer to analysis the signal. and find the associated pressure

5- Repeating the procedures for many points and different rotating speeds.

4 Results and Discussion

To compare the improvement of the new design journal bearing the pressure distribution for the normal and compound bearing are solved and plotted in Figs 8 and 9. These figures show that the pressure profile and the maximum pressure increased to about 50% for the compound bearing.

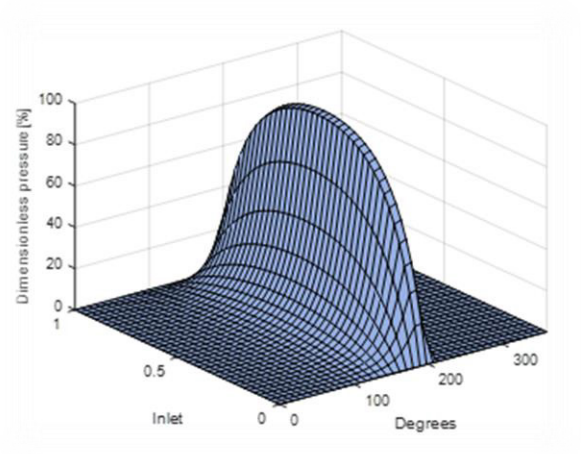

Fig 8. Pressure distribution of normal journal bearing.

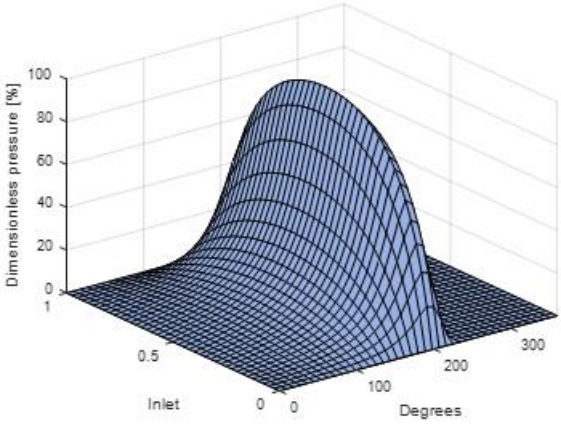

Fig 9. pressure distribution of compound journal bearing.

The effects of change of eccentricity ratio from 0.5 to 0.9 with L/D =1 is studied and presented in Table 1. it is clear the load capacity and maximum pressure are increased as the eccentricity ratio increases while both attitude angle and coefficient of friction are decreased.

Table 1. Effect of change of eccentricity ratio of compound bearing.

Case	e	W(kg)	P(N/m)	β	μ
1	**0.5**	**0.2962**	**0.33034**	**58.758°**	**43.199**
2	**0.6**	**0.43644**	**0.52964**	**52.099°**	**40.43**
3	**0.7**	**0.67912**	**0.92012**	**44.856°**	**27.175**
4	**0.8**	**1.1894**	**1.8762**	**36.714°**	**11.317**
5	**0.9**	**2.8044**	**5.4389**	**26.888°**	**5.397**

The effect of L/D ratio for the bearing is studied when the ratio is decreased from 1.6 to 0.6 with constant eccentricity ratio = 0.8 as presented in Table 2. The outcomes show a proportional relation between this ratio and load capacity, maximum pressure, and attitude angle while the coefficient of friction is inversely proportional.

Table 2. Effect of change of L/D ratio of compound bearing.

Case	L/D	**W(kg)**	**P(N/m)**	**β**	**μ**
1	**1.6**	**1.6078**	**2.2636**	**40.592°**	**7.0293**
2	**1.4**	**1.4902**	**2.1712**	**39.567°**	**7.4233**
3	**1.2**	**1.3572**	**2.0529**	**38.145°**	**7.9469**
4	**1**	**1.1894**	**1.8762**	**36.714**	**11.317**
5	**0.8**	**0.97757**	**1.6165**	**35.384°**	**23.8**
6	**0.6**	**0.72555**	**1.265**	**33.664°**	**69.237**

4 Conclusion

The following conclusions can be drawn from the discussion of the findings:

1- The suggested compound journal bearing increase the pressure profile and the maximum pressure increased about 50%
2- Raising the eccentricity raises the pressure and load capacity while lowering the friction coefficient.
3- Increasing the L/D ratio lowers pressure and increases load capacity while lowering friction coefficient.
4- The performance of the compound bearing can be modified by proper design for eccentricity and L/D ratio.

References

[1] Gwidon W. Stachowiak. Engineering Tribology. United Kingdom. Butterworth-heinemann Vol. 14 pp.26-31 ,2017.
[2] F.M. Meng . L. Zhang . Y. Liu . Effect of compound dimple on tribological performances of journal bearing. TribolLett Vol 12, pp. 55-61, 2015.
[3] Etsion I, Halperin G,BrizmerV,KligermanY. Experimental investigation of laser surface textured parallel thrust bearings. Vol.9 pp.295–300, 2004
[4] Lu XB, Khonsari MM .An experimental investigation of dimple effect on the stribeck curve of journal bearings. Vol. 71 pp.80-94, 2016
[5]. A. Birket and J.K. Lancaster, Counterface Effects on the Wear of a Composite Dry-Bearing Liner, Proc. JSLE
Int.Tokyo, Japan, Elsevier, pp. 465-470, Vol.157 , 2019
[6] Ling DT, Li ZP, Xiong SW, Grzina D, Cao J, Wang JQ, et al. Surface texturing of drill bits for adhesion reduction and tool life enhancement, Vol. 67, pp.43-51, 2011.
[7] Wng JD, Han ZL, Chen HS, Chen DR. Drag reduction by dimples on surfaces in plane – plane contact lubrication, Vol.10, pp.189-194, 2015.
[8] Kngo S, Sharma RK, Pandey RK. Comparative analysis of textured and grooved hydrodynamic journal bearing. Proc IMechE, Vol. 64, pp.547-552, 2019.
[9] Shen C, Khonsai MM. Effect of dimple's internal structure on hydrodynamic lubrication, Vol.67, pp.104-110, 2014.
[10] Arghir M, Rocou N, Helene M, Frene J. Theoretical analysis of the incom- pressible laminar flow in a macro-roughness cell, Vol.10, pp.241-251, 2013.
[11] Sahin F, Glavatskih SB, Almqvist T, Larsson R. Two-dimensional CFD-analysis of micro-patterned surfaces in hydrodynamic lubrication.
[12] ANSYS Help manual, release 14.5, Inc., Pittsburgh, Pennsylvania of USA; 2012.
[13] Cupillrd S, Glavatskih S, Cervantes MJ. Computational fluid dynamics analysis of a journal bearing with surface texturing. Proc Inst IMechE J.
[14] Go GY, Yin ZW, Jiang D, Zhang XL. Numerical analysis of plain journal bearing under hydrodynamic lubrication by water.
[15] Baun D, Greiner C, Schneider J, Gumbsch P. Efficiency of laser surface texturing in the reduction of friction under mixed lubrication.
[16] Etion I, Halperin G, Brizmer V, Kligerman Y. Experimental investigation of laser surface textured parallel thrust bearings.

[17] Lu XB, Khnsari MM. An experimental investigation of dimple effect on the stribeck curve of journal bearings.
[18] Meg FM, Yang T. Preliminary study on mechanism of cavitation in lubricant of textured sliding bearing. Proc Inst Mech Eng J: J Eng Tribol 2013;227 (7):695–708.
[19] K. G. Binu, B. S. Shenoy, D. S. Rao, and R. Pai, A Variable Viscosity Approach for the Evaluation of Load Carrying Capacity of Oil Lubricated Journal Bearing with TiO2 Nanoparticles as Lubricant Additives, Procedia Mater. Sci., vol. 6, no. Icmpc, pp. 1051–1067, 2014.

Particle Swarm Optimization for Maximum Power Point Tracking Under Varying Atmospheric Conditions

Ali Nasser Hussain[1], Alaa Mokdad Talib[2]
{alinasser1974@yahoo.com[1], alaamokdad.t96@yahoo.com[2]}

Electrical Engineering Techniques College, Middle Technical University, Baghdad, Iraq[1,2]

Abstract. Based on research into Photovoltaic (PV) systems under diverse conditions, and a new maximum power-point tracking approach was developed. Due to the presence of variable circumstances, PV curves have several peaks, decreasing the efficiency of the conventional techniques. As a result, the suggested algorithm, based on the technique of particulate swarm (PSO) optimization, enhances the output power of photovoltaic (PV) systems under such abnormal conditions and outperforms existing methods. The suggested method is evaluated using MATLAB under numerous scenarios involving non-uniform irradiation and varying temperature levels, and to investigate its performance sufficiently, the outputs of the method suggested are compared for the P&O technique This study aims to explain the design and simulation of a particle swarm optimization (PSO) technique with a boost converter for determining the maximum permissible power of solar photovoltaic panels under changing climatic conditions. The simulations showed that the tracker ability of the PSO algorithm is highly effective, much quicker, and has a shorter settling time and overshoot than conventional techniques.

Keywords: Photovoltaic (PV) Systems, DC-DC Converters, Maximum Power Point Tracking (MPPT), Particle Swarm Optimization (PSO).

1 Introduction

Photovoltaics (PV) has become increasingly popular because of its many advantages, including lower operating costs and less pollution. The amount of electricity generated by a photovoltaic module is mostly determined by the circumstances of the surrounding environment, such as temperature and radiation. This is a big drawback because the efficiency of each solar cell is just approximately 20%, which is a significant reduction inefficiency. As a result, determining the peak point of a photovoltaic system is crucial to maximize efficiency and extract the greatest value from solar energy. To provide the maximum load power, the photovoltaic system has only one operating peak that can be reached. The Maximum Power Point (MPP) is the highest point reached during the test. [1]. Maximum power point tracking techniques are categorized into three broad groups. The first group is referred to as the traditional group, which includes the Perturb and Observe (P&O) and Incremental Conductance methods (INC). Because of its unsteady operating point, the P&O-based maximum power point tracking algorithm is successful, but it is unsuited for PV array form [2]. Because of the disruption in the system, this algorithm modifies the power of the module [3], which is necessary for it to work. As a result of this disorder, the power will be amplified, and the disturbance will

IMDC-IST 2021, September 07-09, Sakarya, Turkey
Copyright © 2022 EAI
DOI 10.4108/eai.7-9-2021.2315285

continue in this manner. In any other case, the disturbance is reversible. This is the process by which MPP is obtained. The power continues to oscillate near the MPP and is unable to obtain the proper MPP. To accommodate quick variations in irradiance, this method must be modified. Among the several techniques, the perturb observe algorithm is the most straightforward and cost-effective [4]. Incremental Conductance (INC) is a more advanced version of the (P&O) method to address all of the algorithm's shortcomings. To produce the best output possible, the previous output is continuously compared to the current output. Although the incremental conductance (INC) technique is highly efficient, it is rarely employed due to its complexity in comparison to the Perturb and Observe (P&O) technique [5]. The disadvantages of this category are laziness in monitoring, stable fluctuation at (MPP), and low efficiency. Soft computing solutions are being developed to solve these drawbacks. The second group of techniques includes Evolution Algorithmic (EA), Fuzzy Logic Controllers (FLC), and Artificial Neural Networks (ANN). Additionally, these groups have significant weaknesses because of various complexity, such as the requirement for periodic practice and the utilization of additional memory, in bio-inspired behaviours, it is challenging to apply these features. Implementing a bio-inspired style is difficult. [6]. The third group is the algorithms that are involved under the type of Evolutionary computing, Ant colony optimization (ACO) Particle swarm optimization (PSO), Genetic Algorithm (GA), and Ant colony optimization (ACO) [7]. This paper presents the method for tracking the Maximum PowerPoint for photovoltaic modelling using Particle Swarm Optimization (PSO) at varying temperatures and irradiation. This technique is a swarm intelligence-based algorithm that is used to obtain the global optimal power allowable for a load. The performance of this method is tested by simulation using MATLAB/Simulink and can be divided into three main parts. first, the source of the PV array (DSP210D panel) is mainly dependent on atmospheric conditions like irradiation and temperature. Secondly, the DC-DC step-up boost converter gives higher efficiency and low cost. lastly, the PSO algorithm is used to achieve MPPT from the PV array. The simulation result shows improvement in efficiency compared with the conventional method, also achieved the maximum permissible power produced by solar cells.

This paper explains the process for using Particle Swarm Optimization (PSO) to track the Maximum Power Point (MPP) for photovoltaic modelling at varying temperatures and irradiation to achieve the maximum permissible power for a solar photovoltaic panel and therefore increasing the efficiency of photovoltaic systems (PV).

The following is how the paper is structured: Section 2 introduces the output characteristics of PV arrays, as well as the mathematical model of the PV module and the tracking of the Maximum PowerPoint. Section 3 contains an overview and implementation of the PSO algorithm. Section 4 discusses the outcomes of the simulations as well as their practical application. Section 5 presents the work's conclusion, which is the final section.

2 Photovoltaic Modelling

2.1 The Equivalent Circuit of PV Cell Model

In this paper, the equivalent circuit for a single diode model of PV cell consists of a photocurrent I_{ph}, diode, parallel resistance R_{sh} denoting the leakage current, and a series resistor R_s representing the internal resistance to current in the circuit [8]. As shown in Fig 1.

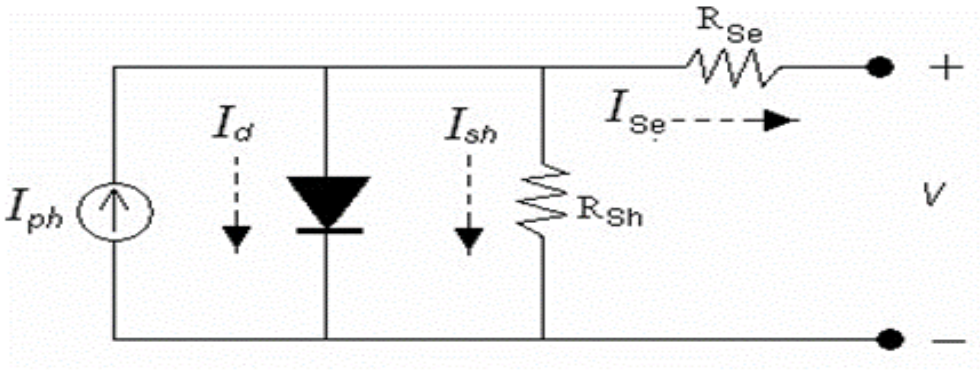

Fig. 1. single diode model of PV cell.

It has relatively good approximate accuracy and maybe the most suitable model for diagnosing the photovoltaic arrays because it provides a good compromise between the approximate accuracy and simplicity [9,10].

2.1 Mathematical Model

A mathematical model describes the terminal voltage and current properties of the solar cell. It is deduced from the physical principles of the PN junction, which generally represents the distinctive behaviour of a photovoltaic cell, that the exponential equation of the single model for a photovoltaic cell may be obtained. The photovoltaic cell that was investigated may be theoretically modelled using the equations that follow. [11]:

$$I = I_{ph} - I_{se} * \left[exp\left\{q\frac{(v+R_sI)}{AkT}\right\} - 1\right] \quad (1)$$

$$I = N_pI_{ph} - N_pI_s * \left[exp\left\{q\frac{(v+R_sI)}{N_sAkT}\right\} - 1\right] \quad (2)$$

$$I_{ph} = I_{ph}(T_{ref})\left[1 + a(T - T_{ref})\right] \quad (3)$$

$$I_{ph}(T_{ref}) = I_{sc}(T_{ref}) * \frac{E}{E_0} \quad (4)$$

$$a = \frac{I_{sc}(T_2) - I_s(T_1)}{I_s(T_1)} * \frac{1}{T_2 - T_1} \quad (5)$$

$$I_d = I_s * \left[exp\left\{q\frac{(v+R_sI)}{AkT}\right\} - 1\right] \quad (6)$$

$$I_s = I_{so} * \left(\frac{T}{T_{ref}}\right)^{\frac{3}{A}} * exp\left[\left(-\frac{Eg}{Ak}\right) * \left(\frac{1}{T} - \frac{1}{T_{ref}}\right)\right] \quad (7)$$

$$I_{so} = \frac{I_{sc}(T_{ref})}{\left(exp\left(q\frac{voc(T_{ref})}{AkT_{ref}}\right) - 1\right)} \quad (8)$$

Where:

V The voltage produced by a PV cell. (Volt).

I The current flowing from a PV cell's output. (Ampere).

Ns The number of series-connected modules.

N_p The number of parallel-connected modules.

I_{ph} In a photovoltaic cell, light produces current. (Ampere).

I_s Saturation current of photovoltaic cells(Ampere).

R_s A photovoltaic cell's series resistance(Ohm).

A Ideality factor (Unit less).

K Boltzmann constant (Joule per kelvin).

T Cell temperature (Kelvin).

q Electron charge (coulomb).

T_{ref} Reference temperature (Kelvin).

I_{sc} Short-circuit current of a photovoltaic cell under normal conditions circuit at 25°C and 1000 (Watt per square meter).

a Short-circuit current temperature coefficient at I_{sc}(Ampere).

R_{sh} A photovoltaic cell's shunt resistance(Ohm).

E Illumination of photovoltaic cells (Watt per square meter).

I_{s0} Saturation current at T_{ref} (Ampere).

E_g The bandgap for silicon (Electron volt).

2.2 Maximum Power Point Tracking

When solar panels work at the voltage which the global maximum for the photovoltaic characteristic curve is found, the maximum power (MP) is obtained so that the maximum output power of the solar module can be obtained, especially for an operating point. A photovoltaic function is known as Maximum PowerPoint (MPP). This point is often at the knee of the solar panels. To summarize, the I-V curve of a solar module has a point called the Maximum Power Point (MPP) that always occurs at the knee of this curve and is where photovoltaic power generation is maximum**.** Fig 2 shows the MPP located on the knee of the I-V curve and defined by a black dot. The MPP position is changed continuously when the temperature and irradiation values are changed. The temperature and irradiation have a dynamic nature, so the MPP tracking algorithm can work primarily in real-time by continually updating the duty cycle and thus keeping tracking accuracy and speed [12]. The Simulink model is composed of two major components, the tracking algorithm used to track the MPP, and the DC-DC boost converter to convert the producing voltage for the required load level [13]

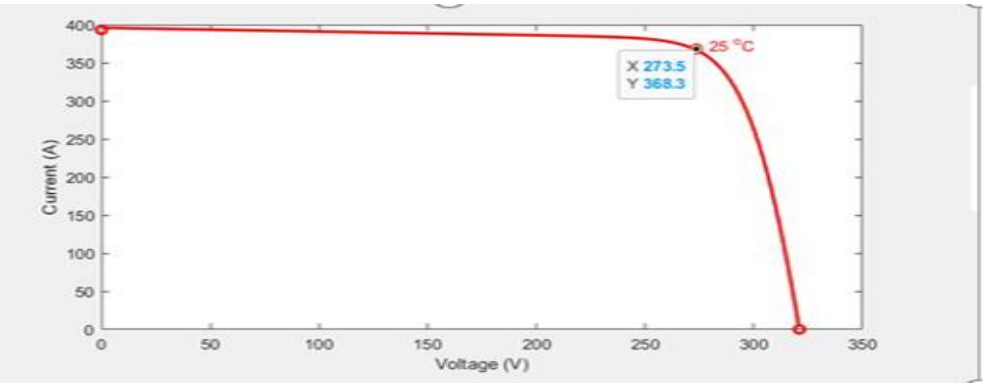

Fig 2. I-V characteristic curve.

3 PSO Algorithm

3.1 Overview of the PSO Algorithm

A simple and effective meta-heuristic method, which applies to a multivariable optimization function with numerous local optimal points, is known as the particle swarm optimization method. It is inspired by fish schooling, bird flocking, and others. PSO operates on the pair of main teachings; one is to get from the past data and the other to carry current information among the swarm agents [14].
PSO algorithm contains many particles. Each particle will replace the data obtained during the research process and provided the solution to find the best choice. According to the simple mathematical relationships, these particles move in the search field and the velocity and position of the particles are updated according to Eqs. (1) and (2) [15].
In this study, the particles of the PSO algorithm are taken to search for the optimal duty cycle space and the fitness function is the output power of the PV system. By the following equations, this particle positions di is updated [16].

$$d_i^{k+1} = d_i^k + v_i^{k+1} \tag{1}$$

Where:
v_i is the step size at the iteration $k+1$
d_i^k is the position of the particle

$$v_i^{k+1} = wv_i^k + c_1 r_1 \left(P_{best} - d_i^k\right) + c_2 r_2 (G_{best} - d_i^k) \tag{2}$$

Where:
r_1 and r_2 are random values from [0,1]; w is the inertial weight; c_1 and c_2 are the acceleration coefficient; G_{best} is the best position in the whole population; P_{best} is the best position of particle i .

3.2 Implementation for PSO Algorithm

The first step is to determine the number of particles to be used and the search parameters to be used, as well as the velocity and position limits. Initialize the velocity and position of each particle using a random number generator in Step two. The fitness value of each particle is calculated in Step three. Step four. The G_{best} particle is the particle with the highest fitness score (Global Best). Update the velocity and position of each particle concerning the G_{best} .
Repeat Steps three and four as many times as necessary until the ideal solution has been found. The optimal value is obtained by performing Step seven G_{best} at the end of the final iteration.
Step eight, calculate the Duty-cycle using the given equation $D = \frac{1}{1+\sqrt{\frac{R_{in}}{R_{out}}}}$.

4 Simulation Result

In the MATLAB program, the Simulink model as shown in Fig 3 consists of a PV array (DSP210D) panel, a step-up DC-DC boost converter, and PSO MPP tracker that simulated to study and verify the performance and accuracy of this method. The used solar panel contains 6 parallel strings and 2 series cells per string. The cell temperature is assumed to be constant at 25℃ and 1000 W/m^2 irradiation.

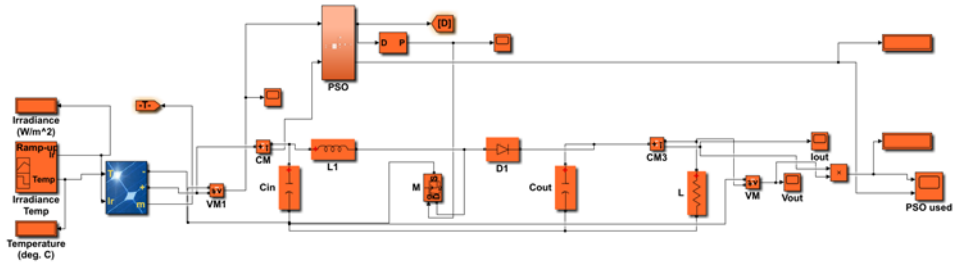

Fig.3. The Simulink model for system configuration.

Fig 4 depicts the results of a simulation of a PV system using the PSO and P&O algorithms, respectively. This figure illustrates the results gained by employing PSO with P&O MPPT techniques, where the maximum output power is obtained for varied temperature and irradiation conditions. It has also been observed that the PSO method is more efficient and increases its effectiveness. Thus, the cost is lower. Additionally, this algorithm has a shorter settling time, which results in less oscillation and overshoot. These properties result in high steady-state output power with high accuracy and stability when compared to conventional algorithms. As a result, we can track the real MPP under a variety of conditions.

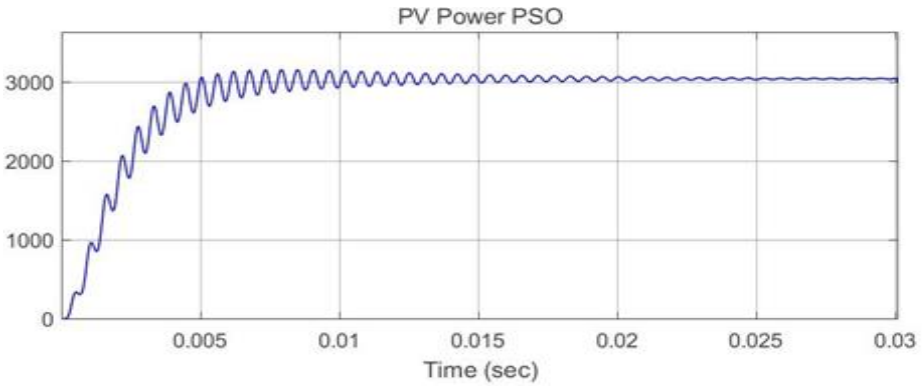

(a) The PSO model's output power curve at constant isolation **1000** $\boldsymbol{w/m^2}$and temperature $\mathbf{25^0}$

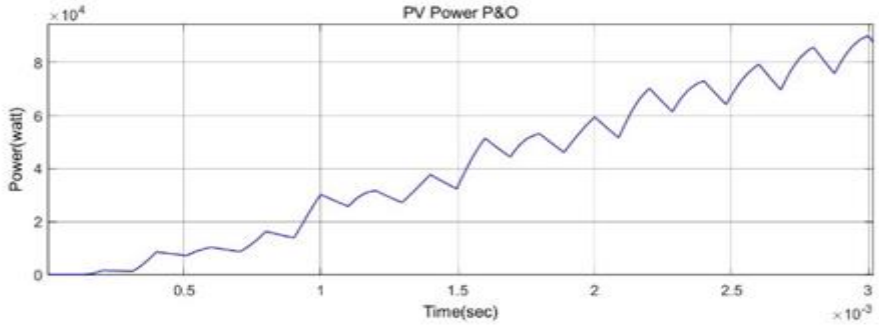

(b) The P&O model's output power curve at constant isolation **1000** $\boldsymbol{w/m^2}$and temperature $\mathbf{25^0}$

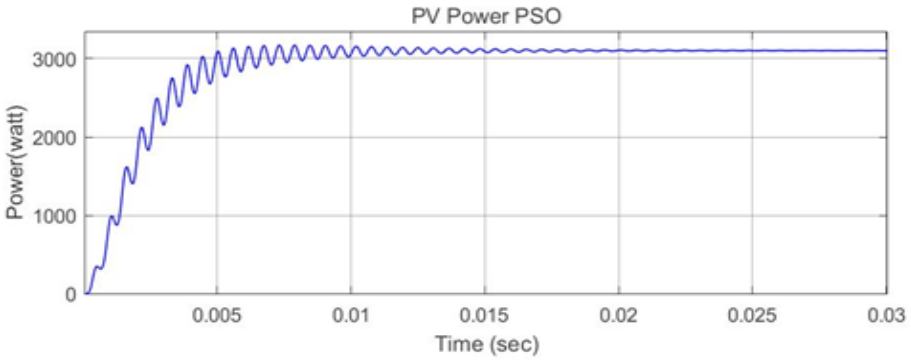

(c) The PSO model's output power curve at constant isolation 1000 $\boldsymbol{w/m^2}$and temperature $\mathbf{45\ C^0}$

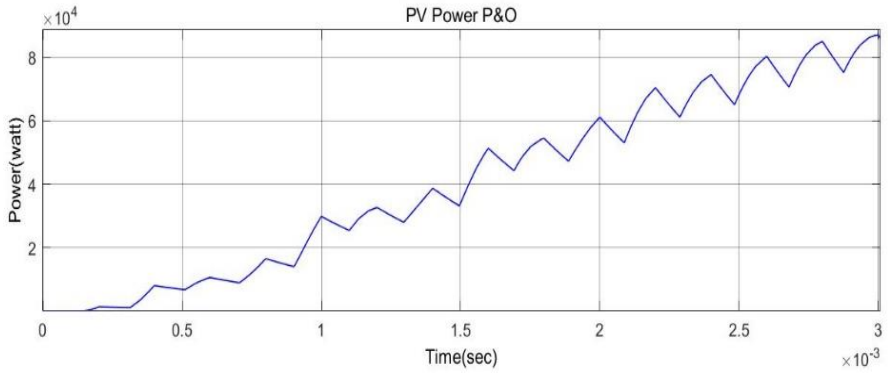

(d) The P&O model's output power curve at constant isolation $\mathbf{1000\ w/m^2}$and temperature $\mathbf{45^0C}$

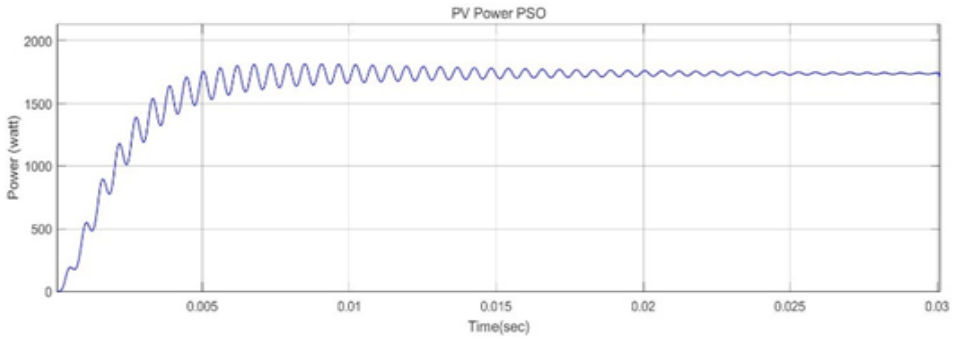

(e) PSO model output power curve at various isolation at to $\mathbf{750\ w/m^2}$ and temperature $\mathbf{25^0C}$

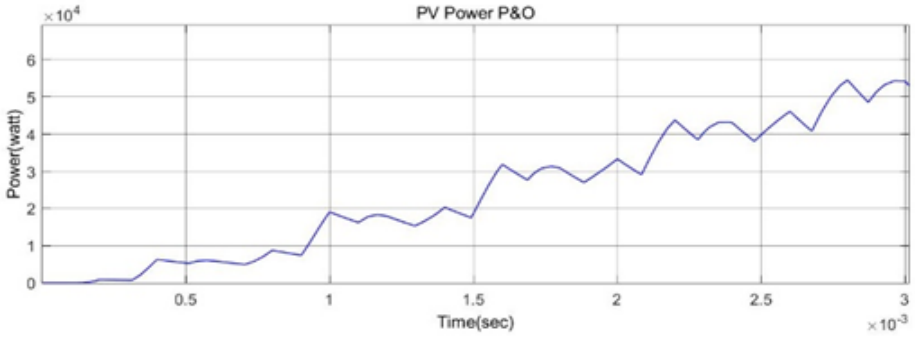

(f) P&O model output power curve at various isolation at $\mathbf{750\ w/m^2}$ and temperature $\mathbf{25^0C}$

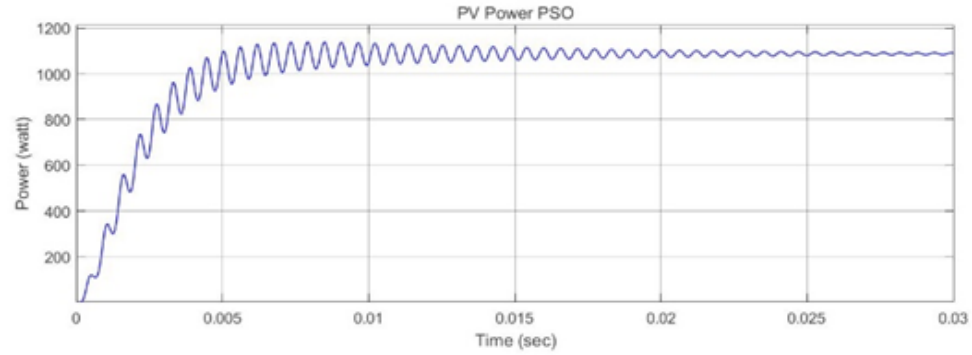

(g) Step isolation output power curve for the PSO model **(600-1000)** $\boldsymbol{w/m^2}$ and temperature $\mathbf{25^0C}$

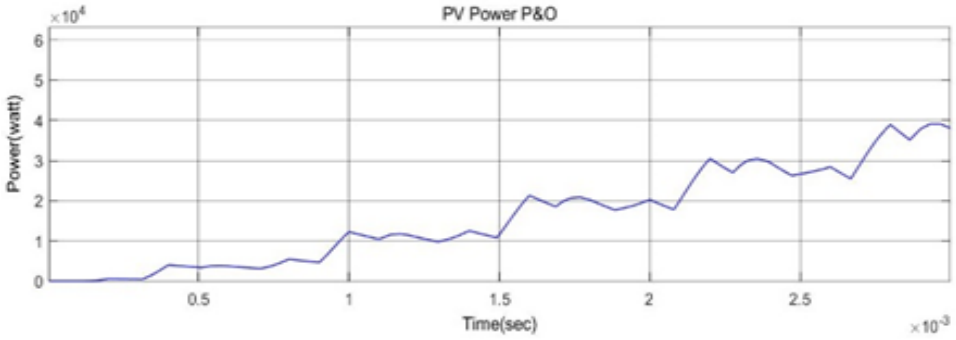

(h) Step isolation output power curve for the P&O model **(600-1000)** $\boldsymbol{w/m^2}$ and temperature $\mathbf{25^0C}$

Fig.4. The output power of PSO and P&O algorithm

5 Conclusion

The purpose of this research is to simulate and execute Maximum Power Point tracking using a particle swarm optimization algorithm to obtain the maximum permissible power for photovoltaic panels. So, the PSO is used under varying atmospheric conditions to achieve the best results in various circumstances. The simulation results showed the PSO algorithm gives more efficiency than conventional algorithms. In addition, the output response of this technique is faster, with less overshoot and low oscillation than classical techniques. In the future, we want to connect Multi-Level Inverter with DC-DC boost converter with PSO technique to achieving pure AC output waveform with less overshoot and Total Harmonic Distortion Thus, we increased the efficiency by using the photovoltaic source.

References

[1] M. Balamurugan, S. Narendiran, S. K. Sahoo, R. Das, and A. K. Sahoo, "Application of particle swarm optimization for maximum power point tracking in a PV system," 2016 3rd Int. Conf. Electr. Energy Syst. ICEES 2016, no. March, pp. 35–38, 2016.

[2] K. L. Lian, J. H. Jhang, and I. S. Tian, "A Maximum Power Point Tracking Method Based on Perturb-and-Observe Combined With Particle Swarm Optimization," pp. 626–633, 2014.

[3] Richa Verma, B. Bhargav, and P. Srinivasa Varma, "Comparison of different MPPT algorithms for a PV system," Int. J. Eng. Technol., vol. 7, pp. 158–163, 2018.

[4] R. Suryavanshi, D. R. Joshi, and S. H. Jangamshetti, "PSO and P & O based MPPT Technique for SPV Panel under Varying Atmospheric Conditions," vol. 1, no. 3, pp. 110–115, 2012.

[5] A. DOLARA, R. FARANDA, and S. LEVA, "Energy Comparison of Seven MPPT Techniques for PV Systems," J. Electromagn. Anal. Appl., vol. 01, no. 03, pp. 152–162, 2009, DOI: 10.4236/jemaa.2009.13024.

[6] C. Kamalakannan, L. Padma Suresh, S. S. Dash, and B. K. Panigrahi, "Power Electronics and Renewable Energy Systems: Proceedings of ICPERES 2014," Lect. Notes Electr. Eng., vol. 326, pp. 1339–1348, 2014.

[7] L. P. Suresh, S. S. Dash, and B. K. Panigrahi, "Artificial Intelligence and Evolutionary Algorithms in Engineering Systems: Proceedings of ICAEES 2014, Volume 1," Adv. Intell. Syst. Comput., vol. 324, 2015.

[8] S. Mishra and M. Gupta, "Modeling & Simulation of a Photovoltaic Energy System," Int. J. Electr. Electron. Eng. Res., vol. 3, no. 1, pp. 61–66, 2013

[9] S. B. Ch, "Modeling and Simulation of PV Array and its Performance Enhancement Using MPPT (P&O) Technique," no. January 2015.

[10] S. Sholapur, K. R. Mohan, and T. R. Narsimhegowda, "Boost Converter Topology for PV System with Perturb And Observe MPPT Algorithm," IOSR J. Electron. Electron. Eng., vol. 9, no. 4, pp. 50–56, 2014, DOI: 10.9790/1676-09425056.

[11] H. Bounechba, K. Nebti, A. Bouzid, and H. Benalla, "Modeling and Simulation of Perturb and Observe MPPT Algorithm for PV systems," no. December 2013.

[12] H. S. Saad, M. S. M. Elksas, S. F. Saraya, and M. M. Abdelsalam, "An Improved Particle Swarm Optimization Algorithm for Maximum Power Point Tracking Of Photovoltaic Cells in Normal and Under Partial Shading Conditions," vol. 46, no. 1, pp. 10–21, 2021.

[13] R. Suganya, M. V. Rajkumar, and P. Pushparani, "Simulation and Analysis of Boost Converter with MPPT for PV System using Chaos PSO Algorithm," vol. 5, no. 11, pp. 97–105, 2017.

[14] P. S. Gavhane, S. Krishnamurthy, R. Dixit, J. P. Ram, and N. Rajasekar, "EL-PSO based MPPT for Solar PV under Partial Shaded Condition," Energy Procedia, vol. 117, pp. 1047–1053, 2017, DOI: 10.1016/j.egypro.2017.05.227.

[15] M. GREEN et al., "Solar cell efficiency tables (version 40)," Ieee Trans Fuzzy Syst, vol. 20, no. 6, pp. 1114–1129, 2012.

[16] H. Rezk, A. Fathy, and A. Y. Abdelaziz, "A comparison of different global MPPT techniques based on meta-heuristic algorithms for a photovoltaic system subjected to partial shading conditions," Renew. Sustain. Energy Rev., vol. 74, no. December 2016, pp. 377–386, 2017

Thermal cooling analysis of single Li-ion battery cell with elliptic heat sink with perforation

Karim Egab[1], Mushtaq Talib Hamzah[2], Hayder Hasan[1] and Ali Lateef Tarish[2]

k.egab@stu.edu.iq[1], mushtaq.hamza@stu.edu.iq[2] , hayder.mohammad@stu.edu.iq[1], aliali@stu.edu.iq[2]

[1]Electromechanical System Engineering Department, Thi-Qar Technical College, Southern Technical University, Iraq
[2]Thermal Mechanics Engineering. Dept., Eng. Technical College-Basra, Southern Technical University, Iraq

Abstract. The performance of Li-ion batteries is highly dependent on the conditions and temperature distribution inside the battery units. Most of the batteries suffer from high heat dissipation and temperature which influence the battery unit life and efficiency. Therefore, a thermal cooling system is important to regulate the battery unit temperature and reduce the high heat dissipation effect. This study aims to examine the thermal cooling efficiency of a single Li-ion battery unit with a modified heat sink. The study was performed in a laminar flow regime with Reynolds numbers ranging from 20 to 120. The operating fluid is air and the heat sink is aluminum. The Li-ion battery units' heat sink was adjusted with elliptic holes as perforation located inside the walls of each fin. The elliptic holes are spaced evenly along with the fins with constant size and gap between them. The thermal performance in the battery unit is calculated using the MSMD function which is solved using the Ansys 18.1 software. The results indicate that the maximum battery unit temperature measured in the case is 343.1 K without a cooling system. The battery unit temperature decreased by 13% when only air cooling was applied. The use of a heat sink with elliptic perforation plays an important role in lowering the battery unit temperature. The temperature decreased by 21% compared to the case of without cooling. Furtheremore, analysis of velocity, pressure drop and firiction losses losses were optimized of the heat sink.

Keywords: Battery unit, Heat Sink, Perforation, Heat Transfer, Temperature.

Nomenclature

L	The battery unit length (mm)	*Greek symbols*	
W	The battery unit width (mm)	Δ	Difference
L_t	The two tabs Length (mm)	ρ	Air density (kg/m^3)
W_t	The two tabs width (mm)	μ	Air dynamic viscosity (Pa s)
s	The distance between two tabs (mm)		
L_f	The fin's hiegtht (mm)	*Subscripts*	
W_f	The fin's width (mm)	f	fluid
v	Air velocity (m/s)	in	inlet
$C_{p,f}$	Air specific heat (KJ/kg.K)	s	solid
k_f	Fluid thermal conductivity of the (W/m.K)	(BC)	Battery unit
Nu	Nusselt number	(BC-A)	Battery unit with air cooling
T_f	Fluid temperature (K)	(BC-AH)	Battery unit with air heat sink
k_s	Solid thermal conductivity (W/m.K)	(BC-AHP)	Battery unit with air heat sink and perforation
T_s	Solid surface temperature (K)	g	The distance between elliptic perforation
P	Air pressure (pa)	a	Major length of an ellipse
Re	Reynold number	b	Minor length of an ellipse
D_h	Hydraulic diameter	PCM	Phase change material

IMDC-IST 2021, September 07-09, Sakarya, Turkey
Copyright © 2022 EAI
DOI 10.4108/eai.7-9-2021.2315179

U	Total velocity (m/s)
q_{eff}	Effective heat transfer rate (W)

1 Introduction

Li-ion battery units provide clean energy used in electrical generation, transportations, and our life needs due to high energy density. High cell temperature reduces cell performance and is long-lasting. Therefore, a cooling system is important to regulate the cell temperature and prevent the high-temperature effects. The cooling performance of electronic devices, thermal energy, and battery units that generate high heat removal are investigated using air forced convection [1]–[3]. The spacing among the cell is considered to increase the convection heat transfer. The temperature of the cell is decreased by 8 C with an increase in the air velocity. The cooling system using mini-channel and nanofluid is modeled to regulate the battery unit temperature in electric vehicles [4]. The cell temperature with the use of the nanofluid was reduced by 28.65 % in comparison with the battery unit without a cooling system. Cooling of electric battery unit system using PCM with metal foam to obtain acceptable temperature ranges is investigated [5]. Phase change material delay reaching the critical temperature and the metal foam helps distributes the thermal energy in PCM which increase the long life of battery unit. Thermal management cooling using heat pipe in 8-battery unit as a pack delivered 400 watts as energy is investigated [6]. The cooling system can dissipate 50W as heat in each cell with maintaining the pack at safe temperature limits. Mini-channel like tree heat sink designs applied to cool Li-ion battery unit at 4 C discharge rate in electric vehicles is investigated [7]. The like tree mini channel better cooling thermal management system than the straight mini channel. The battery unit temperature reduces significantly with an increase in the pressure drop penalty. A comparison of different cooling methods to maintain the temperature at 15°C to 35°C for a lithium-ion battery unit is achieved [8]. The findings demonstrate that a system of air-cooling requires between 2 and 3 times more energy than other systems, in order to maintain the same temperature in the range of time; an indirect liquid cooling has the highest peak increase of the temperature. The thermal behaviors of Li-ion cells and modules were studied under a range of electrical charges and cooling conditions [9]. Results from the simulation show that the 3D electro-thermal model used for this analysis adequately characterizes the electro-thermal comparability of Li-ion battery units. Heat transfer with phase change materials (PCMs) where the PCM is combined with a Li-ion cell was proposed [10]. The findings show that when PCM can be used, the maximum temperature and temperature escapade in the cell is decreased. The temperature is reduced by 3.0 K that used a PCM with a thickness of 12 mm. A computational fluid dynamic (CFD) study is proposed to analyze the air cooling mechanism for a 38,120 cell battery unit pack [11]. When the battery unit pack is wide and complete transient simulation is not feasible, the CFD offers a convenient way to measure the battery unit's thermal efficiency. Three-dimensional thermal simulation of a single Li-ion battery unit was discussed [12]. The cell temperature rapidly approaches 40 °C with low cooling system velocity, and temperature non-uniformity approaches the maximum value of 5 °C during the 5C self-discharge condition; but under external short-selling status, temperature increases significantly and reaching nearly the 80 °C levels, which can cause a temperature increase. The heat sink with diffrernt diffrernt designs has a significant influent on Li-ion battery unit temperature [13]. The heat sink reduced the battery unit temperature while the dimples cause a slightl influence on battery unit temperature. A liquid-cooled rectangular battery unit module concept and experimental constructions are analyzed [14]. At a coolant flow rate of 0.001 Kg/s, the system's thermal resistance was calculated to be less than 0.2 K/W. The experimental liquid-cooled unit proved to be a feasible alternative for keeping cylindrical Li-ion cells close to their ideal operating temperature. Direct cooling efficiency specifications of Li-ion batteries using dielectric fluid submerged cooling were studied. [15]. The results indicate that a Li-ion pouch cell submerged in the liquid coolant with tab cooling performed better than normal convection at a 3C discharge rate, with a 46.8% decrease in the maximum temperature at the critical point.

In this work, an analysis of thermal performance and heat transfer in a single battery unit with a heat sink is investigated. The heat sink was modified using ellipse perforation located in the sidewall of each

channel. The ellipse perforation has the same size and the gap between them is constant. The study was conducted at different ranges of Reynolds from (20-120) of laminar flow regime. Air is used as a working fluid and heat sink made from aluminum. The determinations of the influence of the heat sink in battery unit temperature, Nusselt number, and friction losses are conducted.

2 Methodology

2.1 Physical Model

The battery unit schematic design is illustrated in **Figure 1**. The unit of 60 mm length and 40 mm width was considered. The positive and negative tab lengths and widths (L_t*W_t) are (12.5*10) mm and the gap length between them is 10 mm. The cell and tabs have the same thickness of 2 mm. The cell is made from Lithium and the battery unit tabs are made from Nickel. The battery unit generates heat to the atmosphere as heat flux of 100 W through all battery unit directions during its operation. The heat transfer through the cell is conduction while the heat transfer by convection in the case of the cooling system. The heat sink size is H × W = 100 mm × 100 mm. The fins' height and width are (3*2) mm which are located along with the battery unit. The heat sink is made from pure aluminum that is assumed to have constant thermal properties. The working fluid is air, which the thermal properties of air are calculated at an average temperature. The heat sink is placed at the two large sides of the battery unit to dissipate more heat through discharging. The heat sink with perforation is conducted using elliptic holes through the sidewalls of the heat sink. The elliptic holes are distributed horizontally along with the fins with a constant gap among them. The case of the only battery unit is named BC, the case of battery unit with cooling called BC-A, the case of using battery unit with heat sink is (BC-AH), and the last case of using battery unit with heat sink with perforation which called BC-AHP. For more details, the modified heat sink with perforation of battery unit with cooling case (BC-AHP) is shown in **Figure 2**.

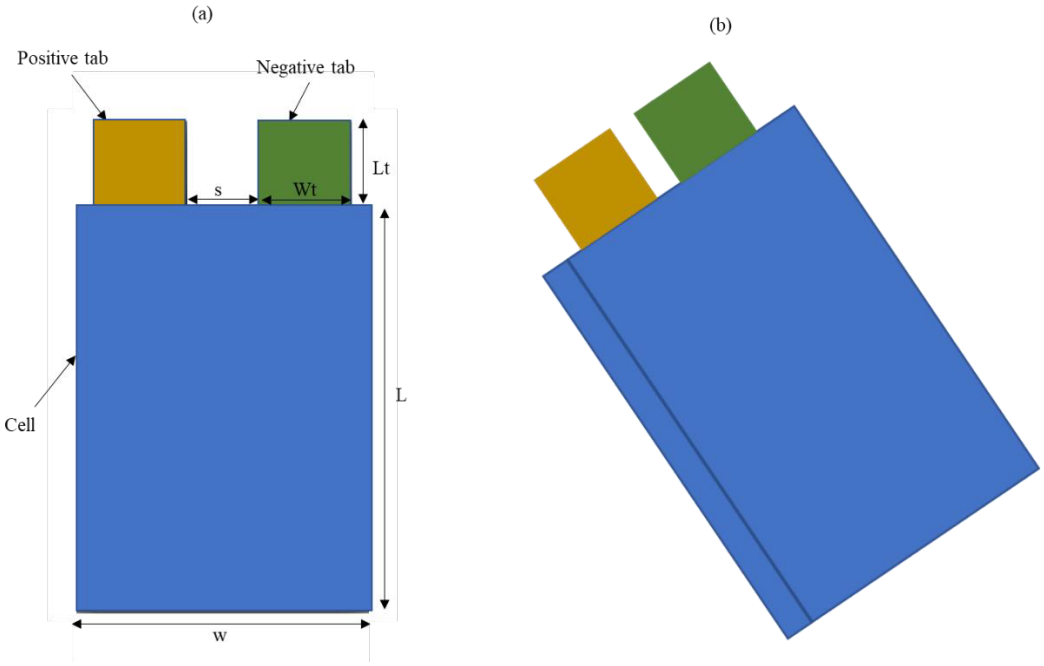

Fig. 1 (a) The the battery unit schematic design (b) The 3-D view of battery unit.

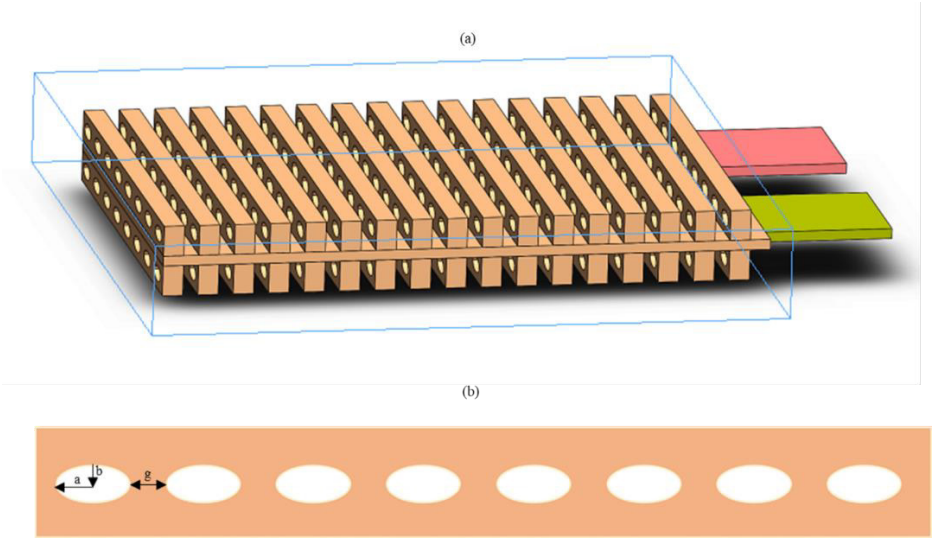

Fig. 2 The modified heat sink with perforation of (a) Cooling system of battery unit in case of (BC-AHP) (b) perforated elliptic heat sink design.

2.2 Governing Equations and Boundary Conditions

To evaluate the heat transfer and fluid flow in heat sink bounded the battery unit, solution of the governing equations of continuity, momentum, and energy equations should be performed as:

Continuity equation:

$$\frac{\partial u}{\partial x}+\frac{\partial v}{\partial y}+\frac{\partial w}{\partial z}=0 \tag{1}$$

Momentum equation:

$$\rho_f\left(\vec{U}.\nabla\vec{U}\right)=-\nabla P+\nabla.(\mu_f\nabla\vec{U}) \tag{2}$$

Energy equation:

$$\rho_f C_{p,f}\left(\vec{U}.\nabla T_f\right)=\nabla.(k_f\nabla T_f) \tag{3}$$

Where $\vec{U}$, P, T_f, ρ, C_p, μ and k are velocity, pressure, temperature, specific heat, viscosity, and thermal conductivity. The subscripts f and s refer to fluid and solid respectively. The calculations of thermal load in battery unit heat sink were found numerically but the parameters like Reynold and Nusselt number were obtained from the below correlations. The hydraulic diameter of the channel is defined as:

$$D_h=\frac{4(W_l*H_f)}{2(W_l+H_f)} \tag{4}$$

The Reynolds number can be defined as:

$$R_e=\frac{\rho_f u_i D_h}{\mu_f} \tag{5}$$

The overall heat transfer coefficient is [16] as:

$$h=\frac{Q''_{ef}}{(T_w-T_f)} \tag{6}$$

The Nusselt number is:

$$N_u = \frac{hD_h}{k_f} \tag{7}$$

The friction loss is:

$$f = \frac{2\Delta P D_h}{\rho_f L u_m^2} \tag{8}$$

Uniform boundary conditions are asumed in the battery unit and heat sink and constant temperature. The boundary conditions in the battery unit heat sink are explained in **Table 1**. Air was used as working fluid while the heat sink was made from aluminum. The flow was laminar and variable air velocity ranging (10.-0.5) mm were applied. The constant thermal conductivity and dynamic viscosity are considered. **Table 2** shows the of properties of Li-ion battery unit.

Table 1 The boundary conditions.

Zone	Boundary conditions	Expression
Inlet	Velocity-inlet	y = 0, u = u_{in}, u_{in} = (0.1-0.5) m/s, T_{in} = 300 K
Outlet	Pressure outlet	y= L, $P_f = P_{out}$ = 0 (gauge pressure)
Top and Bottom walls	Constant heat flux	x = 0, $-k_s \frac{\partial T_s}{\partial y} = q = 100$ W
Left and right walls	Symmetry	$\frac{\partial T_s}{\partial y} = 0$
Inner walls	No slip	$u = v = w = 0$,
Other walls	Adiabatic	$\frac{\partial T_s}{\partial y} = 0 = \frac{\partial T_f}{\partial y}$

Table 2 The battery unit, aluminum, and air properties.

Material	ρ	c_p	k	μ
Aluminum	2719	871	202.4	-
Air	1.242	4181	0.0242	0.00000176
Positive tab	2100	800	1	-
Negative tab	1400	800	1.48	-
cell	1299	1978	18.1	-

2.3 Numerical Solution

The generated heat in the battery unit is obtained using the MSMD function which is solved using finite volume method Ansys software. The physical properties of the battery unit and tabs are assumed to be constant. The governing equations of continuity, momentum, and energy were solved. The battery unit geometry and heat sink were modeled using Solidwork 2013. In this work, the SIMPLEC algorithm was used for calculations of velocity, temperature, and pressure drop, and a second upwind scheme was applied. The residual results for continuity, momentum, and energy equations are set to be less than 10^{-6}, 10^{-6}, 10^{-9} respectively to get a suitable converging for Navier-stokes equations.

2.4 Mesh Independence Study

The importance of obtaining reliable solution results depends mainly on the study of mesh independence. To perform a mesh independence study, the finer mesh was applied to all systems with considering the mesh of elliptic perforation in this study. The perforation is modeled using finer mesh than fined heat sink and battery unit. The battery unit temperature with finned heat sink case (Li-AH) for various mesh sizes at a constant air velocity of 0.1 m/s is considered. The mesh sizes of (1104531, 1150345, 1240387, 1289301and1357123) are tested to optimize the best mesh size that does not affect the solution results. The mesh size of 1357123 provides fair temperature results which can be carried out in the present study. **Figure 3** shows the mesh of the battery unit with the cooling system of the heat sink and elliptic perforation case (BC-AH).

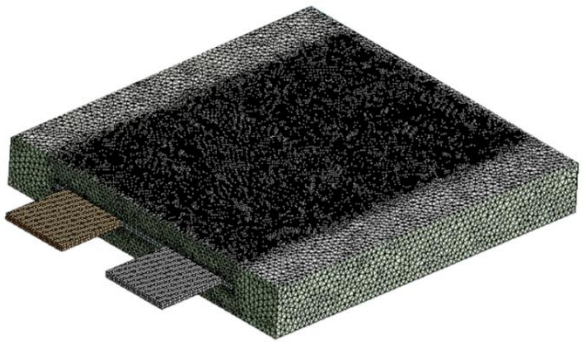

Fig. 3 Mesh of cooling system in the battery unit including the heat sink and elliptic perforation case (BC-AH).

3 Model Validation

To validate the model results, geometry, boundary conditions, and different discharge rate of single battery units are similar to the study in [17]. The influence of discharge rates on battery unit temperature is shown in **Figure 4**. Increase the discharge rate increases the heat dissipation which increases the battery unit temperature. A good agreement between the model results and the results of [17] with a 2% error. Therefore, the numerical model is accurate and can perform investigations of the effect of cooling systems on battery unit temperature distributions.

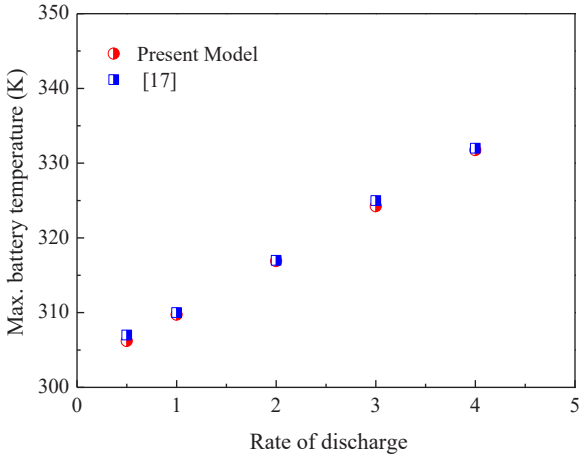

Fig. 4 The influence of discharge rates on battery unit temperature.

4 Results and Discussions

The heat sink and elliptic perforated design cooling performance were evaluated with regards to battery unit heat generation, temperature, and thermal performance criteria. This analysis was conducted by study the influence of the cooling system on battery unit temperature distributions and characteristics of velocity, pressure drop, and friction losses. The optimization to find the best thermal performance criteria is achieved.

4.1 Characteristics of Thermal Distributions

To evaluate the influence of applying heat sink and perforation for the battery unit cooling, four configurations of the only battery unit (BC), battery unit with air cooling (BC-A), battery unit with air heat sink (BC-AH), and battery unit with an elliptic air heat sink and perforation (BC-AHP) were performed. The perforation was applied at the sidewalls of fins with constant areas of the ellipse. The gap between the perforation is kept constant. The battery unit generates the same heat flux in all cases

and the same boundary conditions in the heat sink applied to other case studies. The study was considered at ranges of Reynolds number of (200-1200) to ensure laminar flow. The temperature distributions in the battery unit with different cooling configurations are shown in **Figure 5** at Reynolds number 30. The maximum battery unit temperature is 343.1 K in a single battery unit without a cooling case (BC). With applying air cooling case (BC-A), the battery unit temperature reduced by 13% which shows how significant the air cooling affects maximum battery unit temperature. The heat sink plays an important role in reducing the battery unit temperature as in the case (BC-AH) where the battery unit temperature decreased by 21% compared to only battery units without cooling. The perforation increases the convection heat transfer area and causes a change in airflow behavior through the channels. The battery unit temperature using a perforation heat sink case (BC-AHP) was reduced by 28%. The battery unit temperature reduced with an increase in the Reynolds number values. **Figure 6** shows the battery unit temperature at different Reynolds numbers. The heat dissipation increases with increase the values of Re which leads decrease battery unit temperatures. In the perforation heat sink, the lowest battery unit temperature is noticed because of the flow disturbance and circulation inside the perforated areas. The Nusselt number calculation in all cases is shown in **Figure 7** at various Reynolds number values. The Nusselt number increases with the increase in the value of the Reynolds number. The Nusselt number in case (BC-AHP) is the best because of the highest momentum forces due to increasing air velocity. The Nusselt number is 30% and 20% higher compared to case (BC-A) and (BC-AH) respectively. It is noticed that how perforation enhances the heat transfer in the heat sink which reduced the battery unit temperature.

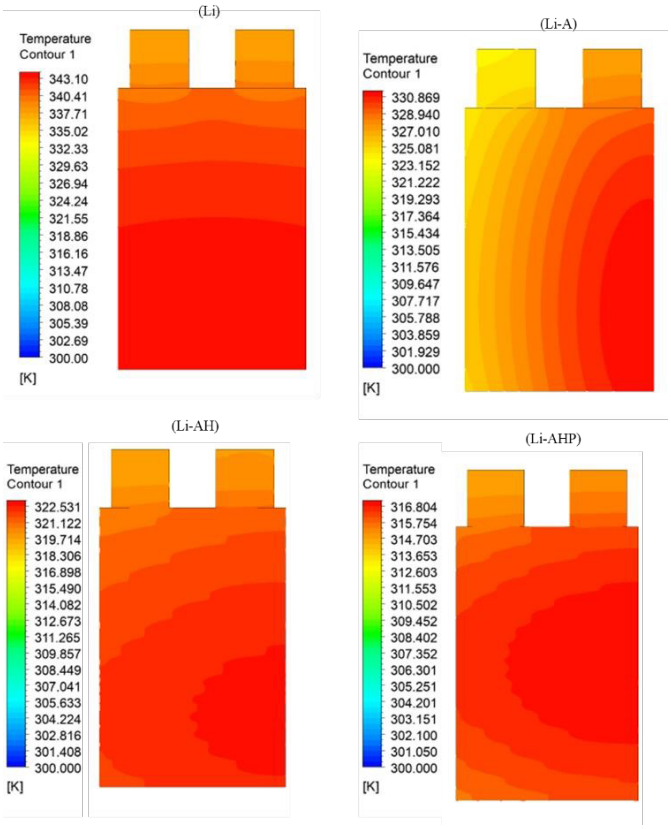

Fig. 5 The temperature distributions in the battery unit with different cooling configurations.

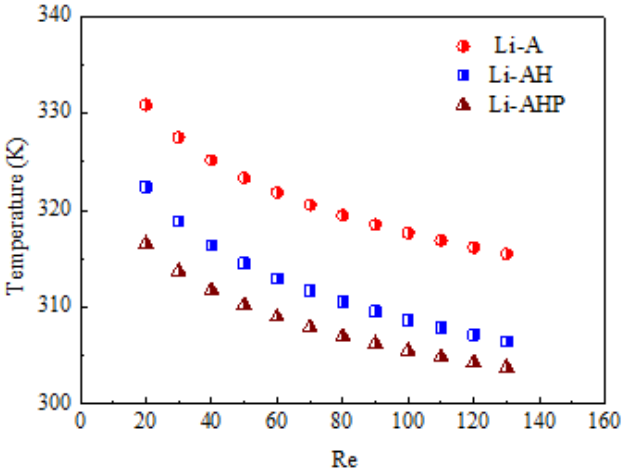

Fig. 6 The battery unit temperature at different Reynolds numbers.

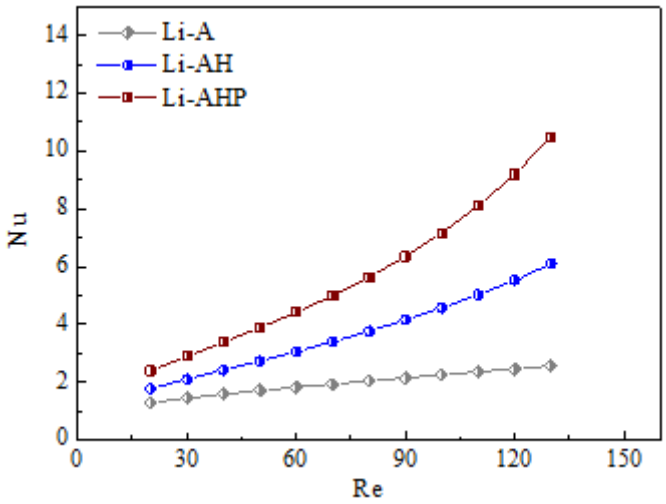

Fig. 7 Nusselt number value in all cases.

4.2 Characteristics of Velocity, Pressure, and Friction Losses

The hydrodynamic characteristics in heat sink battery units are investigated due to the importance of fluid flow behavior's effect on thermal performance. Therefore, the velocity distribution of the cooling system in the battery unit is investigated in the case of (BC-A), (BC-AH), and (BC-AHP). The contour of velocity distributions is shown in **Figure 8** at Reynolds number is 20 and z = 2.5 mm. The perforations in the case of (BC-AHP) have a significant influence on flow velocity since they cause small mixing and disturbance compared to the flow in the case of (BC-AH). The high velocity reduces the effect of thermal boundary layers and enhances the heat transfer performance. However, high-pressure penalty and friction losses increase in the case of (BC-AHP) compared to other cases. **Figure 9** shows the pressure penalty in cases of (BC-A), (BC-AH), and (BC-AHP) in the x-y plane at z=2.5 mm and Reynold number of 20. Linear reduce in pressure losses in case of battery unit with air (BC-A) along the channel. However, further increase in pressure losses in perforation with heat sink due to the inducing flow circulation and interruption at the locations of perforation existing. The pressure drops in the case of (BC-AHP) increased by 3 times compared to (BC-AH). Therefore, the heat sink with perforation enhances the thermal performance, but it increases the pressure losses.

Figure 10 shows the friction losses in the battery unit heat sink cases at ranges of Reynolds number (20-120). The heat sink with perforation (BC-AHP) has the highest friction losses compared to other cases at all ranges of RE. The friction losses in case (BC-AHP) are 3 times higher than in case (BC-AH) which

means the viscous forces become dominant in the heat sink with perforation. In the case of (BC-AH) and (BC-A), the friction losses reduce slowly at different ranges of Re but the friction losses decrease becomes faster in the case of (BC-AHP).

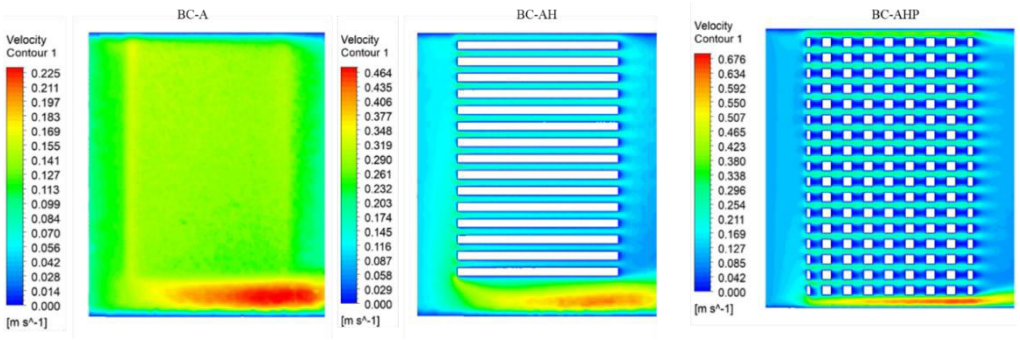

Fig. 8 Contour of velocity distributions in cases of (BC-A), (BC-AH), and (BC-AHP) in the x-y plane at z=2.5 mm and Reynold number of 20.

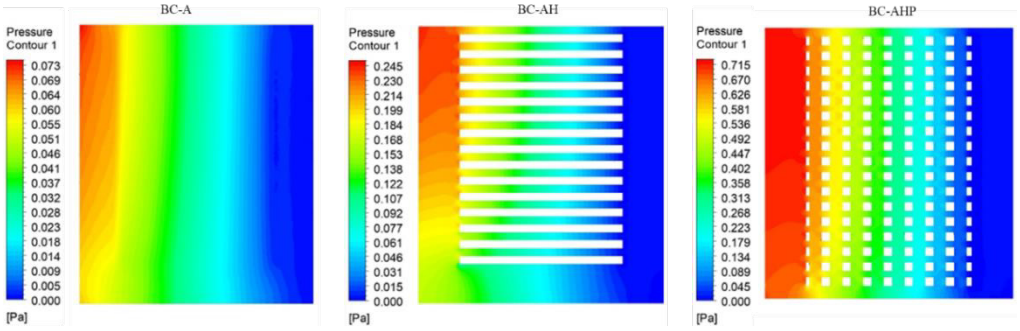

Fig. 9 The pressure penalty in cases of (BC-A), (BC-AH), and (BC-AHP) in the x-y plane at z=2.5 mm and Reynold number of 20.

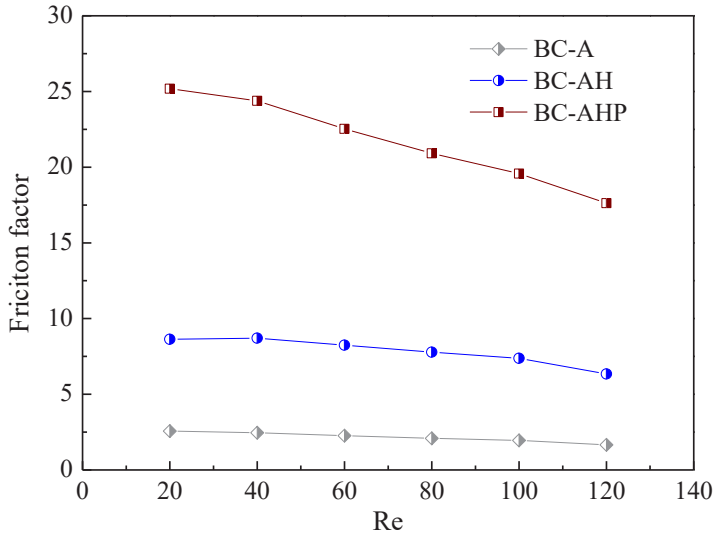

Fig. 10 The friction losses in the battery unit heat sink cases at Re ranges (20-120).

5 Conclusions

Thermal cooling analysis with use of elliptic heat sink and perforation is performed on a single Li-ion battery unit. The key aim of using the single Li-ion battery unit for cooling with an elliptical perforated thermal sink minimizes heat and keeps the temperature steady. The induced heat in the battery unit is calculated with the MSMD variable, which is solved with the Ansys software using the finite volume procedure. The battery unit's and tabs' physical properties are considered to be unchanged. In both cases, the battery unit produces the same heat flux and the heat sink has the same boundary conditions as in the other case studies. To ensure laminar flow, the analysis was conducted at Reynolds number ranges of (200-1200). In the case of a power outage, the maximum battery unit temperature is 343.1 K. (BC). The battery unit temperature dropped by 13% when the case (BC-A) was used, demonstrating how important air cooling is for optimum battery unit temperature. The perforation enhances the diffusion distance for convection heat transfer and alters the airflow behavior across the channels. The temperature of the battery unit with the case (BC-AHP) was decreased by 28%. In both cases, the battery unit temperatures decreased as the Reynolds number increased, due to increased air velocity, which improved heat removal. Because of the highest momentum forces due to increased air velocity, the Nusselt number in case (BC-AHP) is the best. In comparison to cases (BC-A) and (BC-AH), the Nusselt number is 30% and 20% higher, respectively. In the case of (BC-AHP), however, the high-pressure penalty and friction losses are greater than in other cases. In the case of (BC-AHP), the pressure reduction was three times higher than in the case of (BC-AHP) (BC-AH). As a result, although the heat sink with perforation improves thermal efficiency, it also increases pressure losses.

References

[1] R. D. Jilte and R. Kumar, “Numerical investigation on cooling performance of Li-ion battery unit thermal management system at high galvanostatic discharge,” *Eng. Sci. Technol. an Int. J.*, vol. 21, no. 5, pp. 957–969, 2018.

[2] S. K. Oudah, R. Fang, A. Tikadar, K. Egab, C. Li, and J. A. Khan, “The effects of hybrid sandblasting patterns on the heat transfer performance in a single-phase microchannel heat sink,” in *ASME International Mechanical Engineering Congress and Exposition, Proceedings (IMECE)*, 2017, vol. 8.

[3] K. Egab, A. Okab, H. S. Dywan, and S. K. Oudah, “Enhancing a solar panel cooling system using an air heat sink with different fin configurations,” in *IOP Conference Series: Materials Science and Engineering*, 2020, vol. 671, no. 1.

[4] S. Wiriyasart, C. Hommalee, S. Sirikasemsuk, R. Prurapark, and P. Naphon, “Thermal management system with nanofluids for electric vehicle battery unit cooling modules,” *Case Stud. Therm. Eng.*, vol. 18, no. December 2019, p. 100583, 2020.

[5] B. Buonomo, “Thermal cooling behaviors of lithium-ion batteries by metal foam with phase change materials,” *Energy Procedia*, vol. 148, pp. 1175–1182, 2018.

[6] J. Smith, R. Singh, M. Hinterberger, and M. Mochizuki, “thermal management system for electric vehicle using heat pipes,” *Int. J. Therm. Sci.*, vol. 134, no. June 2017, pp. 517–529, 2018.

[7] H. ling Liu, H. bo Shi, H. Shen, and G. Xie, “The performance management of a Li-ion battery unit by using tree-like mini-channel heat sinks: Experimental and numerical optimization,” *Energy*, vol. 189, p. 116150, 2019.

[8] D. Chen, J. Jiang, G. H. Kim, C. Yang, and A. Pesaran, “Comparison of different cooling methods for lithium ion battery units,” *Appl. Therm. Eng.*, vol. 94, pp. 846–854, 2016.

[9] K. Yeow, H. Teng, M. Thelliez, and E. Tan, “3D Thermal Analysis of Li-ion Battery units with Various Geometries and Cooling Conditions Using Abaqus,” *Imechanica.Org*, no. Figure 1, pp. 1–17, 2012.

[10] N. Javani, I. Dincer, G. F. Naterer, and B. S. Yilbas, “Heat transfer and thermal management with PCMs in a Li-ion battery unit for electric vehicles,” *International Journal of Heat and Mass Transfer*, vol. 72, pp. 690–703, 2014.

[11] L. H. Saw, Y. Ye, A. A. O. Tay, W. T. Chong, S. H. Kuan, and M. C. Yew, “Computational fluid dynamic and thermal analysis of Lithium-ion battery unit pack with air cooling,” *Appl. Energy*, vol. 177, pp. 783–792, 2016.

[12] Y. Li, Z. Zhou, and W. T. Wu, “Three-dimensional thermal modeling of Li-ion battery unit and 50 V Li-ion battery unit pack cooled by mini-channel cold plate,” *Appl. Therm. Eng.*, vol. 147, pp. 829–840, 2019.

[13] K. Egab and S. K. Oudah, “Thermal management analysis of li-ion battery unit-based on

cooling system using dimples with air fins and perforated fins," *Int. J. Therm. Sci.*, vol. 171, no. July 2021, p. 107200, 2022.

[14] D. M. Arun, D. Hamilton, M. N. Krishna, and M. Minakshi, "Design , Development and Thermal Analysis of and Stationary Applications," *energies*, vol. 13, 2020.

[15] M. Suresh Patil, J. H. Seo, and M. Y. Lee, "A novel dielectric fluid immersion cooling technology for Li-ion battery unit thermal management," *Energy Convers. Manag.*, vol. 229, no. September 2020, p. 113715, 2021.

[16] M. I. Hasan, "Investigation of flow and heat transfer characteristics in micro pin fin heat sink with nanofluid," *Appl. Therm. Eng.*, vol. 63, no. 2, pp. 598–607, 2014.

[17] Y. S. Ranjbaran, M. H. Shojaeefard, and G. R. Molaeimanesh, "Thermal behavior of a commercial prismatic Lithium-ion battery unit applied in electric vehicles," *Int. J. Automot. Eng. Veh.*, vol. 8, no. 2, pp. 2700–2708, 2018.

UWB Radar Technology

Imran Ahmad[1], A.S. Hussaini[1,2,3], I.T.E. Elfergani[3], Ahmed S.I. Amar[1,4], J. Rodriguez[3,5], R.A. Abd-Alhameed[2]
{iahmad3@bradford.ac.uk[1], ash.hussaini@aun.edu.ng[2], i.t.e.elfergani@av.it.pt, a.a.s.ismail@bradford.ac.uk, jonathan@av.it.pt r.a.a.abd@bradford.ac.uk[2]}

[1]Bradford-Renduchintala Centre for Space AI, Faculty of Eng. & informatics, Univ. of Bradford, BD7 1DP, UK.
[2]School of Engineering, American University of Nigeria, Yola
[3]Instituto de Telecomunicações – Aveiro, Portugal i.t.e.elfergani, ash, jonathan}@av.it.pt
[4]Faculty of Engineering, Ain Shams University, Cairo, Egypt
[5]University of South Wales, Pontypridd CF37 1DL, UK

Abstract. The purpose of this study is to describe how Ultra Wideband (UWB) radars differ from regular narrow band radars. The aspects described in the paper are the creation, radiation, and processing of Ultra Wideband radar signals elicited by changes in the signal waveform during the localization operation, as well as the appearance of mutual dependency between the signal waveform and antenna directivity. The receipt of the target radio image has been depicted. The major advantages of UWB radar that have been discussed in this paper are large bandwidth, carrier less signal and ultra-short width of the pulse.

Keywords: UWB Radar Technology, UWB, Ultra Wideband Radars, Features of Ultra Wideband Radars, Advantages of UWB, Disadvantages of UWB, Target Selection in UWB Radar of RFID, Detection of Target in UWB Radar.

1. Introduction

For transmitting information, the vast majority of existing radio systems use a restricted frequency array and moving waveforms that use harmonic (sinusoidal) or related quasi-harmonic signals. The explanation for this is simple: the RLC vibration scheme, which is a simple electrical vibratory system, generates sinusoidal vibrations [1]. Ultra-Wideband radar depends upon a short pulse duration methodology and is utilized for transmitting the signal at high bandwidth frequency that is, ranging from 3.1 to 10.6 GHz. Thus, the power of this radar is very low per MHz, that is; $-41.3\,\frac{dBm}{MHz}$

The significant properties of the current radio system consent to pick signals relying on their densities. Thus, the density array of the majority of the radio manufacturing systems is very less as compared to the broadcasted density they utilize. Both the assumption and rehearse of the current radio systems takes this offbeat attribute into contemplation. At the same time, the contracted density array of the signal diminishes the explanatory power of the radio scheme. It is for that reason, it is necessary to increase the density array for boosting the data space [2]. The only alternate is enlarging the communication time. This complexity is particularly vital for radar, when the disclosure time is continually severely incomplete [3].

The general radars with the occurrence array having not more than 10% of the shipping occurrence have almost worn out their informational aptitude. As a result, radar deception in

IMDC-IST 2021, September 07-09, Sakarya, Turkey
Copyright © 2022 EAI
DOI 10.4108/eai.7-9-2021.2314985

service of signals with regularity arrays up to 1 GHz (the duration of the radiated pulses approximately 1 ns) has increased [4]. Due to the range devaluation of the pulse dimensions of radar, the informational content in the UWB position grows. As a result, when a sounding pulse's dimension changes from 1s to 1ns, the pulse's power decreases from 300 m to 30 cm [5].

It can be assumed that the appliance that examines the liberty, becomes extra fine and delicate. It permits the attainment of the radio image of the object.

The bandwidth of Ultra-Wideband radar is extremely high approximately possessing a 500MHz range, fractional bandwidth (BW) higher than 20% of the center frequency(f_c). Large Absolute Bandwidth (BW) is a range of frequency on either side to the central frequency. The power of each side of the band is 10dB. The upper-frequency band is depicted by f_H and the lower frequency band is depicted by f_L and bandwidth is represented below:

$$BW = f_H - f_L$$

The formula for central frequency is given below:

$$f_c = \frac{1}{2}(f_H + f_L)$$

The formula of the fractional bandwidth [6] is as follows:

$$B_f = \frac{BW}{f_c} = \frac{f_H - f_L}{\frac{1}{2}(f_H + f_L)} = \frac{2(f_H - f_L)}{(f_H + f_L)} \times 100\%$$

Downrange resolution refers to detection on the vertical direction, referee ΔR has a direct (directly proportional) relationship with the speed wave v (m/s) and it has an inverse relationship with the bandwidth wave B (Hz) which is measured in meters (m). It is given below:

$$\Delta \mathrm{R} = \frac{v}{2B}$$

It can differentiate and make the detection of an object in the horizontal direction by utilization of the Cross-range resolutionΔCR. It relies on the beam width of an antenna and is determined by the antenna aperture size, which is given below:

$$\Delta CR = \theta R$$

Ultra Wideband (UWB) RADAR systems discharge signals over a broad range of frequency which is amid 3GHz to 10GHz as compared to the conventional RADAR systems and remain extremely difficult to be detected. The transmitted signal is vital to a very low power spectrum. The most common and best solution to generate Ultra Wideband (UWB) transmitted signal is to generate pulses with a very short time duration, generally known as PRF which are usually less than a Nano-second. Ultra-wideband radar systems utilize the transmitter antenna for transmitting the input signal possessing a very low duration of pulse mostly in nanoseconds. This input signal coming from the input transmitter antenna travels at the speed of light to be received at the receiver side. At the receiver signal, the signal is scattered in all directions. To calculate the range of the signal propagation time algorithm is used as the UWB signal travels at the speed of light [7]. Based on this range calculation, there are two kinds of Ultra Wideband radar system which are long-range and short-range Ultra Wideband radar system. The implementation of short-range radar is at the industrial level as it has the capability of detecting the signal of centimeters up to meters and provides high regulation with maximum precision

[8]. Whereas, long-range Ultra Wideband radar systems are used for surveillance purposes frequently in the Synthetic Aperture Radar.

2. Major Possibilities of Ultra Wideband (UWB) Radars

The decline of the gesture extent in the Ultra Wideband (UWB) radar permits for the following major possibilities:

2.1 Advanced Detected Object Array Dimension

One of the major possibilities of the decline of the gesture extent in the Ultra Wideband (UWB) radar is the advanced detected object array dimension efficiency [9]. This result is an increase in radar resolution for all coordinates, although target motion by one coordinate does not need target settling by other coordinates.

2.2 Recognition of Object Class and Sort

Another important potential is object class and sort identification, because the received gesture contains information not only about the item as a whole, but also about its divide aspect [10].

2.3 Reduction in the Radar Possessions of Reflexive Obstruction

Another major possibility is the decrease in the radar possessions of reflexive obstruction from rain, mist, aerosols, metalized strips, etc. [11]. This is because the diffusion cross-section of obstruction source within a small pulse level is compact close to the object scattering the cross-section.

2.4 Improved Cohesion Observing Point

A main possibility of the decrease of the gesture extent in the Ultra Wideband radar is the enhanced cohesion observing point at low ascent edge at the liability of excluding the intrusion gaps in the wire arrangement [12]. This is because the main signal and any landscape return gesture appear at the wire at specific times, which facilitates their choice.

2.5 Development of the Feasibility of Object Detection

Another major possibility is the advancement of the feasibility of object detection and enhanced balance observing, a point at the liability of lobe format rejection, the trivial radiation mould of irradiated targets because oscillations reflected from the entity parts of the goal do not hinder and abandon, providing a more identical radar cross segment [13].

2.6 Exemption of the Radar to the Outside Narrowband

The development of the radar's exemption from outside narrowband electromagnetic emission possessions and commotion is another key option for reducing the gesture range in the UWB radar [14].

2.7 Amplifying the Furtiveness of Radar

Another major possibility is the amplification of the furtiveness of the radar by a gesture, which will be tough to identify. The above-mentioned rewards are possibly achievable [15]. Their functioning requires an abstract pedestal permitting for the estimation of the characteristics of

UWB radars. The motive has to do with the important distinctions of the procedure of especially wideband annotations from the related procedure when ordinary narrow-band signals are used.

3. Major Characteristics of UWB Radars

The main characteristics of Ultra Wideband (UWB) Radars are the change in signal waveform during detection and range, as well as the antenna pattern's dependence on the signal duration and waveform. These are described in detail below:

3.1 Alteration in the Signal Waveform in the Procedure of Detection and Ranging

Signals in the narrow band – sinusoidal and quasi-sinusoidal – have unique properties. The shape (waveform) of sinusoidal and quasi-sinusoidal signals remains unchanged while using common gesture conversions like addition, subtraction, isolation, and combination; the signals have the same shape as the creative role and can only change in amplitude and time move [16]. The shape is defined as the law of variation of a signal in time from here on out. It changes not only the parameters but also the shape on the divergence, at the ultra-wideband gesture at certain conversions.

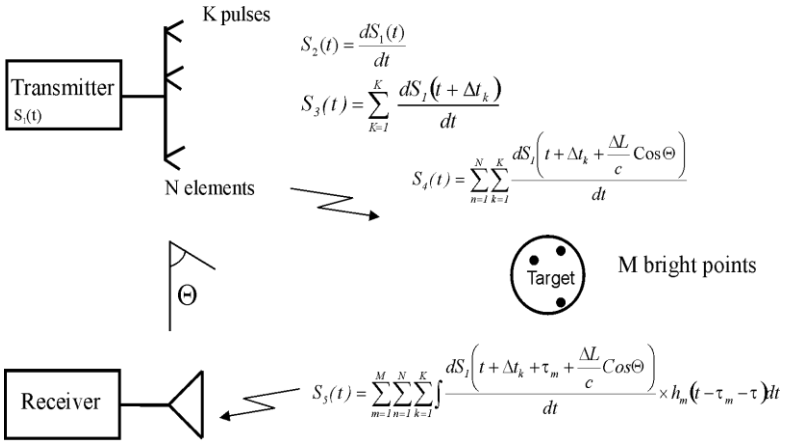

Fig. 1: The signal process.

The Ultra Wideband (UWB) signal S1 (Fig.1) is thought to be created and sent to the aerial as a current pulse. The linear size of the warmer L is less than the pulse period in space c (c is light speed, and is pulse period in time domain). Because the strength of radiated electromagnetic ground increases proportionally with the imitative (first or higher) of the aerial current, the first modification of the Ultra Wideband (UWB) signal shape (S2 in Figure 1) occurs during pulse emission.

When the aerial is agitated in one spot and modern pulses progress along the warmer [17], the contour transforms next. In this situation, the aerial rudiments with a span of ΔL=c will emit a series of electromagnetic gesture pulses. As a result, a single pulse becomes a series of K pulses separated by time intervals Δt. (S3 in Figure 1). The length of the apparent warmer varies

depending on the angle between the ordinary and the aerial range, as well as the orientation towards the point of acceptance. As a result, inter-pulse intervals differ depending on the angle:

$$\text{Inter Pulse} == \Delta t \sin(\Theta)$$

The third change in the figure is caused by the obstruction of fields in space, which are radiated by N rudiments of the aerial. When compared to the pulse radiated by the adjacent antenna element, the pulse radiated by one aerial aspect at the angle Θ is delayed by the time (d/c) cos Θ. In comparison to the pulse emitted by the closest aerial aspect, the pooled pulse will have a variety of shapes and sizes at various angles Θin the far ground (S4 in Fig. 1).

The goal disperses this UWB gesture. As a result, it changes shape for the fourth time (S5 in Figure 1). M local dispersal rudiments ("bright points") are put alongside the line Lt. for the UWB signal c <<Lt. The pulse progression is formed by a UWB gesture that reflects separate target rudiments. The number of pulses, the time delay hm, and the power are all affected by the object form and aspect pulse response hm.

"Target image" is the name given to this pulse sequence. The entire image depicts the time allocation of sprinkled energy, which is achieved by using a time distance of toto=2Lt/c. As a result, the target RCS becomes a time-dependent magnitude (the theory of immediate RSC was introduced). The image varies as the screening angle changes. The inferior outline of the target is non-stationary and varies in this scenario. Dotted signals do not last and do not produce "nulls" in the derived outline. This ensures a steady view of the object. The frequency spectrum of some target rudiments may be outside of the UWB signal continuum. Regularity filters are examples of such rudiments, which alter the shape even more.

At the answer, the shape changes for the fifth time. The reason for this is the same as for emission: temporal differences between current pulses caused by the electromagnetic ground in aerial rudiments at varied distances from the objective. Because of variable signal attenuation in different incidence bands, the 6th transform happens through signal broadcast from side to side in the ambient.

Figure 2 shows an actual illustration of a UWB signal reflected off the target.

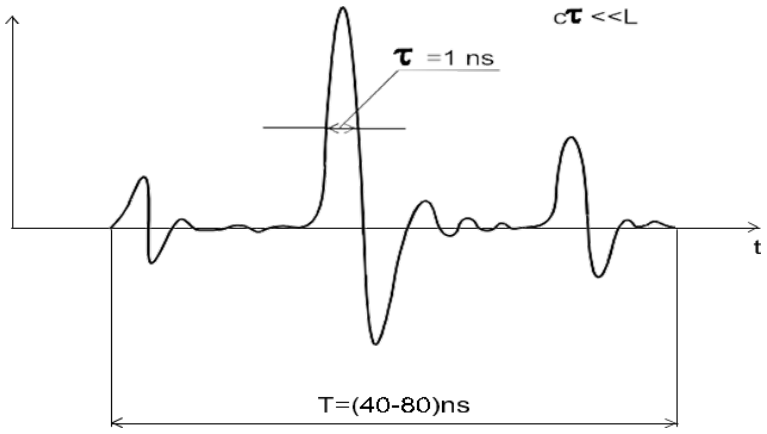

Fig. 2: Target reflected signal

3.2 Signal Length and Waveform Differences Due to Antenna Pattern

When the circumstance L Cos $\Theta > c\tau$ is satisfied, the signal waveform begins to vary depending on the direction of radiation (reception), i.e. the space coordinates. In this scenario, there is no specific relationship between the signal amplitude and its power natural in narrow-band oscillations. The construction of a typical aerial pattern based on the ground is hampered by this situation.

As a result, the aerial pattern production for UWB signals is established based on the power (Figure 3). These aerial patterns differ from the parallel aerial patterns of aerial's beam melodic and quasi-harmonic signals in important ways. There is no lobe environment in them. In order to control such an IPC mechanism, the following situation must be met.

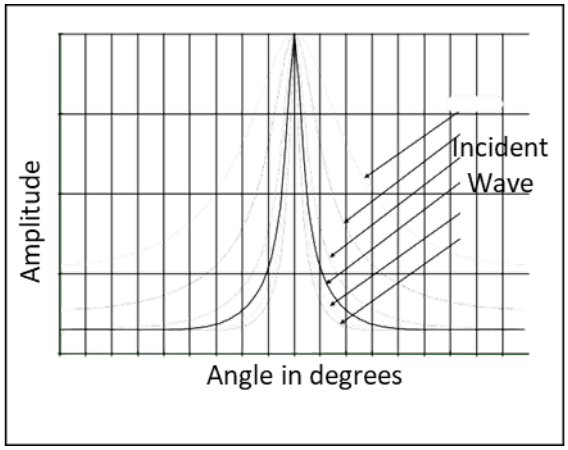

Fig. 3: Aerial Pattern Production based on the Power in UWB signals

Another difference is that adjusting the ratio between c and the radiator spacing d of an aerial array can change the measurement of the central lobe of an assortment's aerial pattern. The aerial pattern width for both the UWB signal and the narrow-band gesture is decreasing as d is reduced or amplified. In contrast to the latter, however, its development does not become multi-lobe due to the lack of interference from entity radiator oscillations. This technology may theoretically be used to make the aerial pattern of a UWB signal emitting aerial as small as desired.

As a result, the aerial pattern for the UWB gesture is determined not only by gaunt coordinates, but also by the time-dependent waveform S. As a result, the jargon for the UWB gesture aerial pattern will take the following shape:

$$P(\Theta, \varphi, S, t) \text{ and } W(\Theta,, \varphi, S, t)$$

The directivity aspect G (Θ, S, t), the expand feature K (Θ, S, t), and the efficient cross-section A (,, S, t) of an aerial become relying on the gesture parameters because the aerial pattern of an aerial radiating or receiving the UWB gesture gets reliant on the signal waveform and period.

4. Moving Target Selection in the UWB Radar

When used under static jamming conditions, the UWB radar has an extra feature that distinguishes it from narrow-band radars [18]. Without employing the Doppler result, impacting targets can be separated with a small pulse amount. If a goal schedules a reserve beyond a sort aspect (30 cm at | = 1ns) above the repetition period T, the gesture of this item will be split up and the signals of immobile or low-mobility targets will be hidden when interleaved episodic exclusion is functional.$c\tau < 2V_R T$

Where VR refers to an object's radial speed. This method of variety does not use "blind" velocities or impose specific desires on the lucidity of radiated signals. The object rate is always clearly determined. By changing the array to an object, the object radial rate VR may be resolved in the variety method. The minimum quantity that may be determined about an object's speed is:$V_{Rmin} = c</ 2T$

The pulse reappearance period as described above; however, the amount of conflict in flowing into and out of a small pulse number may be similar to the magnitude of interferences present at this level. This could lead to a significant de-correlation of blockage and a deterioration in the exchange-phase allowance equipment's competence. Thus, when the pulse length decreases and the radar pulse level decreases, two distinct tendencies emerge: a reduction in intrusion power and an increase in their obstruct de-correlation. Figure 4 depicts the reliance on the pulse span τ for the gesture-to-intrusion ratio Q/Q0. The notations on this diagram are as follows:ω_d-Doppler frequency of interference

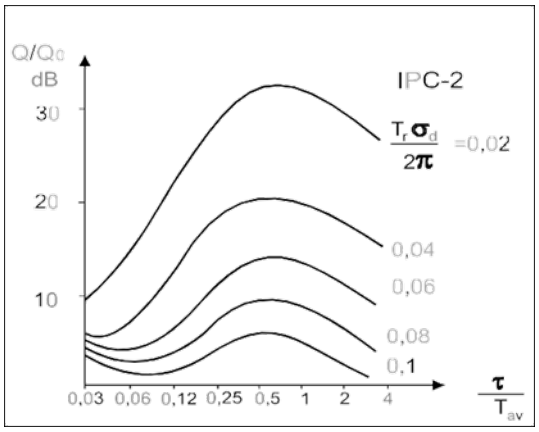

Fig. 4: Gesture-to-Intrusion Ratio

Q - signal-to-interference ratio at the alternate-period compensation output;
Q_0- signal-to-interference ratio at τ=1 and ω_d /**T**=0.1.

The percentage of the normal Doppler occurrence to the pulse recurrence density d /T is the parameter of the family of curves. The con claims that the hint-to-interference ratio rises initially due to the pulse capacity devaluation and subsequently falls due to the amplifying in the inter

period de-correlation of noise as the pulse length contracts. The swap-period incentive system stops working completely for very small pulse spaces, and the increase in the signal-to-interference proportion is accounted for by reducing the amount of incursion inside the pulse size. Due to a stronger sensitivity of this swap-period intrusion compensation to the association features of blockage, the stipulated regularities are more clear for the more competent double swap-period wage of intrusion. As a result, in short-range, the usage of the affected target hint is appropriate for adequately slender-band interferences (e.g. local items) and a satisfactorily soaring repetition frequency.

5. Detection of Target in the UWB Radar

Counting the gear of signal dispersal from object intense locations, the UWB pointer alters its outline many times during the object placement method. As a result, the evolution of pulses with opening parameters is warped into a returning gesture. Because it conveys knowledge of not only object occurrence and object positions, but also object arrangement, this gesture is frequently referred to as "target image" [19]. The ability to recognise an object and generate a radio image of it is made possible by proper picture distribution. It is necessary to identify the object at an early stage of location before appreciating it. Because the arrangement of the UWB returned indicator is completely unknown, standard approaches such as finest signal dispensation by coordinated filtering or correlation with the suggestion signal are not recommended for UWB signal recognition.

It is possible to find a nameless multiunit target using normal methods. If the number of independent resolution intervals, P, organised along a target exceeds the number of intervals, Q, including radiant points, all combinations of P intervals taken Q bright points at a time must be accounted for in order to produce the best detector. However, this algorithm's comprehension lacks a large number of processing channels. Approaches for dispensing such messages in a quasi-optimal manner are well-known. However, when compared to optimum detectors, all quasi-optimal detectors suffer significant damage [20]. As a result, extending an optimal detector for UWB signals disseminated by a structured aim is critical.

The only known parameter of such signals is the replication period T. This constraint could be used to create the best detector for UWB signals. It employs an inward signal as the mentioned gesture in the bordering repetition era, and it is deferred at the time spell T. As a result, the accepted signal is compared to the precise imitation signal rather than the specified signal as in a common correlation. In this situation, the external noise in two repetition durations that are close together is unrelated. As a result, the signal slice becomes the framework for resolving the correlation radar's ability (Figure 5).

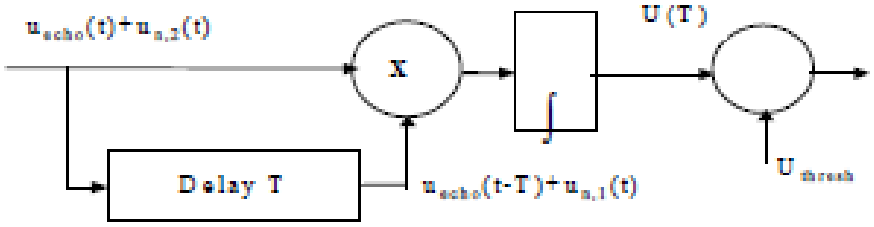

Fig. 5: Interleaved Periodic Correlation Processing (IPCP)

Interleaved periodic correlation processing is the name given to this type of signal processing (IPCP).
a) The acknowledge signal is compared to a signal dispersed by a target, rather than a radiated signal.
b) Explosion stimulates the correlator inputs on both sides. There is a distribution activity for the output of typically distributed explosions at the Correlator outlet. c) the time of assimilation The inspection lay off, that is, the scattered signal span, deceives Ti, not the diffuse signal extent (if a physical object range is Lt, the integration time is equal to Ti=(2Lt/c)- τ, where is the lifetime of a radiated signal). Cogent phrases for disposal service for the device of ordinarily dispersed sounds at the IPCP outlet are really important. The graphing of the disclosure quality is done using mathematical modelling.
Figures 6a and 6b demonstrate the IPCP disclosure quality for a signal dispersed by a stagnant target at two false alarm rates of 10^{-2} and 10^{-4} (D – probability of detection, q – signal-to-noise ratio).

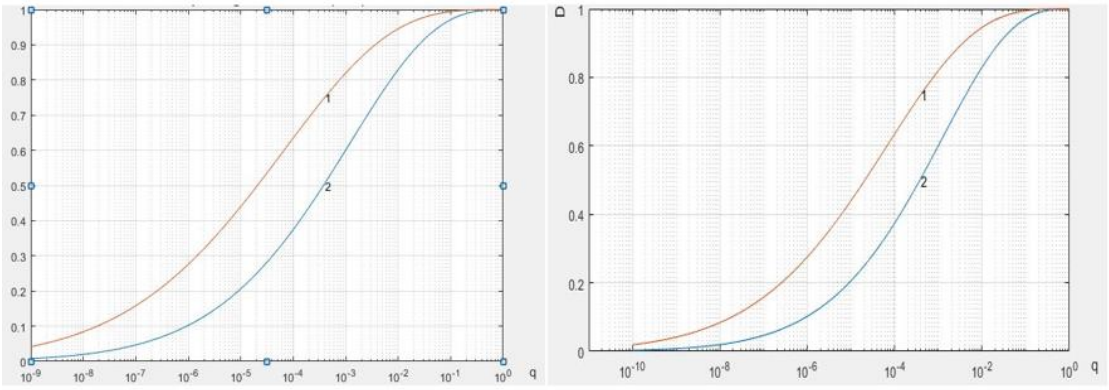

Fig. 6: Disclosure Quality of IPCP

The disclosure quality of an ordinary correlation for completely known gestures is also shown in these figures. The span of a received gesture is identical to the span of a light up gesture in order to make the comparison accurate (one point target). The results reveal that the IPCP espial personality approach, which includes the conventional correlate disclosure personality, is responsible for significant false alarm rates (10^{-2}). The difference in these people's situations when it comes to lowering the number of false alarms (10^{-4}). This can be explained by the extended "tails" of the disposal activities for the regularly assigned explosive product. Setting the verge level higher in IPCP than in the standard correlator allows the given level of incorrect alarm count to be maintained. At the same time, the IPCP's revealing personality is far superior to the strength radar's.The confidence of the disclosure personality on the integration time Ti is depicted in Fig. 7. (found by a target length). For modelling, the distorted alarm rate10-4 and integration times Ti of 2, 10, and 20 were used. This illustration also depicts the espial that distinguishes an ordinary correlator. The graphic shows that as the target length increases, the IPCP espial distinct for a static purpose approaches the standard correlator feature more and more when it exposes the entire known signal [21]. The explanation behind this is that the

circulation purpose for the ordinarily shared explosion access the regular circulation while including the fragment.

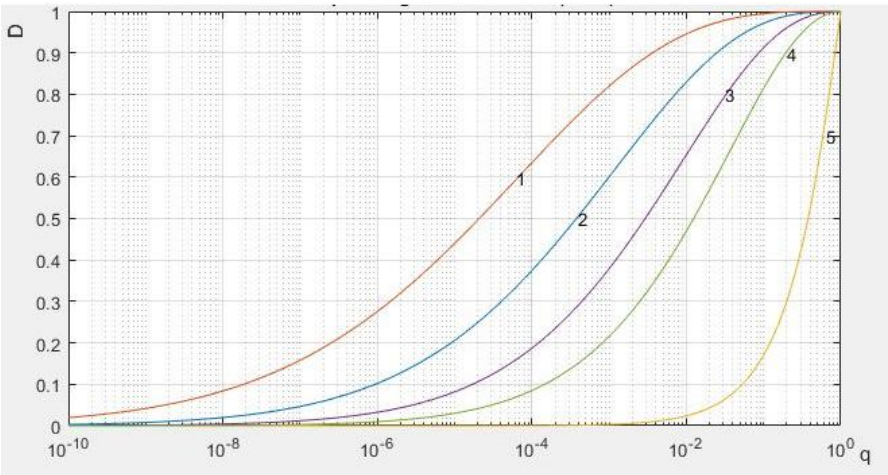

Fig. 7: Confidence of Disclosure Personality on the Integration Time

6. Detecting the Target in Motion

In this paper, the researcher has dealt with the detection quality in the case of an inactive object. In case, if an object is in motion, the complication arises when it passes from one resulting cell to another cell during the appearance of the pulse repetition stage [22]. This problem can be overcome by using a multi-channel device that is connected to a Doppler filtration system that organises the best revelation of moving objects. When recognising objects with varied physical lengths L, the corresponding multichannel design can be used to choose the best integration time T. The losses resulting from the design's multichannel structure can be measured by employing the same multi-channel digital Doppler systems' general processes.

7. Advantages of Ultra Wideband (UWB) Radar

The major advantages of UWB radar are large bandwidth, carrier less signal and ultra-short width of the pulse. These are explained below:

7.1 Large Bandwidth

The bandwidth of the UWB signal is very large so it covers a large range. This feature is good for image processing such as for high resolution of image and high rate of data transmission. High rate assists in getting the same signal through the walls and in getting images related to biomedical. The range of frequency for UWB is from 3.1 to 10.6 GHz which assists the UWB radars in increasing the resolution of the image [23].

7.2 Ultra-short Pulse Width

This feature also provides a high resolution of the signal and also increases the data rate of the signal being transmitted. The signal transmitted from UWB has low power due to an ultra-short pulse. This feature helps in increasing the localizing accuracy and also reduces the effect of

interference. Hence, these features increase the resolution of the signal [24]. This feature is mostly utilized for indoor localization.

7.3 Carrier less Signal

The advantage of UWB is that there is no need for a carrier signal to module the signal in case of UWB radar systems. It can modulate the signal over the high bandwidth without utilizing the carrier signal [25]. The signal is transmitted in the form of pulse which is a digital transmission, so due to this reason, the UWB radar system has a simple hardware structure. Due to its low power feature, it operates on the low range of power.

8. Conclusion

The main possibilities of UWB radars include advanced detected object array dimension efficiency, identification of object class and sort, reduction in the radar possessions of reflexive obstruction, enhanced cohesion observing point at low ascent edge, development of the feasibility of object detection and enhanced balance observing, slender aerial mould by changing the radiated signal quality, development of the radar's exemption to outside narrowband electromagnetic emission possessions and commotion, reduction in the radar "dead zone" and amplification of the radar's furtiveness by a gesture. The main characteristics of UWB radars are the variations in signal waveform during detection and ranging, as well as the antenna pattern's dependence on the signal duration and waveform. When used under static jamming conditions, the UWB radar has an extra feature that distinguishes it from narrow-band radars. In order to detect a target in the UWB Radar, correct picture dispensation is required, which allows for the distinction of an object and the generation of a radio image of that object. A moving object can be detected by means of a multi-channel device-related Doppler filtration system. The major advantages of UWB radar are large bandwidth, carrier less signal and ultra-short width of the pulse.

Acknowledgments

The European Union's Horizon 2020 research and innovation programme under grant agreement H2020-MSCA-ITN-2016 SECRET-722424 and the UK's Research Council (EPSRC) under grant EP/E022936 partially sponsored this work.

Reference:

1. Neekoogar, F., *Ultra-Wideband Communications*, NJ, 2005: Englewood Cliffs, Prentice Hall.
2. Arslan, H., Chen, Z. N., and Benedetto, M. G. D., *Ultra Wideband Wireless Communication*, 2006: New York, Wiley.
3. Nikookar, H., and Prasad, R., *Introduction to Ultra Wideband for Wireless Communications*, 2008: New York, Springer-Verlag.
4. Immoreev, I., *Use of Ultra-Wideband Location in Air Defense: Questions of Special Radio Electronics*, Radiolocation Engineering Series, 1991. **22**: p. 76-83.
5. Immoreev, I., *Ultrawideband (UWB) Radar Observation: Signal Generation, Radiation and Processing*, European Conference on Synthetic Aperture Radar (EUSAR'96), Konigswinter, Germany, 1996.

6. Skolnik, M. I., *Introduction to Radar*, 1962: Radar Handbook, vol. 2.
7. Richards, M. A., Scheer, J. A., and Holm, W. A., *Principles of Modern Radar*, 2010: Citeseer.
8. Kang, Y., Kim, K., and Scott, W. R., *Modification of Sinuous Antenna Arms for UWB Radar Applications*, IEEE Transactions on Antennas and Propagation, 2015. 63: p. 5229-5234.
9. Z. Ruan, Li, C., and Peng, L., *Design and Analysis of Planar Antenna with Dual WLAN Band-Notched for Integrated Bluetooth and UWB applications*, Journal of Electromagnetic Waves and Applications, 2010, 24: p.1817-1828,.
10. Bond, E. J., Xu, L., Hagness, S. C., and Veen, B. D. V., *Microwave Imaging Via Space-Time Beamforming for Early Detection of Breast Cancer*, IEEE Transactions on Antennas and Propagation, 2003, 51:p. 1690-1705,.
11. Muqaibel, A., Safaai-Jazi, A., Bayram, A., Attiya, A., and Riad, S., *Ultrawideband Through-the-Wall Propagation*, IEE Proceedings-Microwaves, Antennas and Propagation, 2005, 152: p. 581-588.
12. Sharkawy, M., Demir, V., and Elsherbeni, A. Z., *Plane-wave Scattering from Three-Dimensional Multiple Objects Using the Iterative Multi-region Technique Based on the FDFD Method*, IEEE transactions on antennas and propagation, 2006, 54: p. 666-673,.
13. Allen, B., Dohler, M., Okon, E., and Malik, W., Brown, A., and Edwards, D., *Ultra-wideband Antennas and Propagation for Communications*, Radar and Imaging, 2006, John Wiley & Sons.
14. Zhang, G.X., Jin, W.D. and Hu, L.Z., *Radar Emitter Signal Recognition Based on Complexity Features*, Journal of Southwest Jiaotong University, 2004. **12**(2):p.116-122.
15. Kawalec, A. and Owczarek, R., Radar Emitter Recognition Using Intrapulse Data. In 15th International Conference on Microwaves, Radar and Wireless Communications, IEEE Cat. No. 04EX824), 2004, **2**: p. 435-438.
16. Immoreev, I., *Ultrawideband Location: Main Features and Differences from Common Radiolocation*, Electromagnetic Waves and Electronic Systems, 1997. **2**(1): p. 81-88.
17. Immoreev, I., *Signal Processing in Ultra Wide Band (UWB) Radars*, Fifth International Conference on Radar Systems (RADAR'99), France, Brest, 1999.
18. Immoreev, I., and Taylor, J. D., *Selective Target Detecting Short Pulse Ultra-wideband Radar System,* Euro Electromagnetic (EUROEM2000), Scotland, Edinburgh, 2000.
19. Immoreev, I., Main Features Ultra-Wideband (UWB) Radars and Differences from Common Narrowband Radars, *Ultrawide Band Radar Technology*, 2000: Boca Raton, London, New Work, Washington, CRC Press.
20. Immoreev, I. Features of Signals Detecting in the UWB Radars, *Ultrawide Band Radar Technology*, 2000: Boca Raton, London, New Work, Washington, CRC Press.
21. Immoreev, I., and Shunjun, W., *Use Ultra Wideband Radar Systems for Increased Information About Target*, 2001 CIE International Conference on Radar, RADAR 2001, Beijing, China, October 15- 18, 2001.
22. Batra, A., Lingam, S., and Balakrishnan, J. *Multi-band OFDM: A Cognitive Radio for UWB*, Proceedings of 2006 IEEE International Symposium, 2006: p. 4097.

23. Venkatasubramanian, V., and Leung, H., *A Novel Chaos-Based High-Resolution Imaging Technique and its Application to Through-the-Wall Imaging*, IEEE Signal Processing Letters, 2005. **12:** p. 528-531.
24. Immoreev, I. I., and Fedotov, P. D. V., Ultra-Wideband Radar Systems: Advantages and Disadvantages, Ultra Wideband Systems and Technologies, 2002: p. 201-205.
25. Palmer, J., Longstaff, I., Martorella, M., and Littleton, B., *ISAR Imaging Using an Emulated Multi-Static Radar System*, IEEE Transactions on Aerospace and Electronic Systems, 2005. **41**: p. 1464-1472, 2005.

New Trends in Location-Based Services Technology

Imran Ahmad[1], Mohammed S BinMelha[1,2], Mohammed J. Ngala[3], Raed Abd-Alhameed[2,4]
I.ahmad3@bradford.ac.uk, abofaras@yahoo.com, mjngala@heatoned.co.uk, R.A.A.Abd@bradford.ac.uk

[1]Faculty of engineering and informatics, University of Bradford, Bradford, BD7 1DP, UK.
[2]System Maintenance Controller, Saudi Air Navigation Sevices, Saudia
[3]Heaton Education Bradford UK
[4]Information and Communication Eng. Department, Basrah University College of Science and Technology, Basrah 24001, Iraq

Abstract. Because of technological advancements, location-based services are always evolving with the passage of time. The current study discussed significant developments in the field of location-based services technology. LBS Indoor Systems, LBS Satellite Systems, LBS GPS System, and Outdoor Systems employing Terrestrial BSs are all part of the localization infrastructure. The report also discusses the benefits and drawbacks of various outdoor systems that employ Terrestrial Base Stations, such as the Global System for Mobile Communications. WCDMA (with IPDL, TA-IPDL, and OTDOA-PE), Smart Antenna Systems, and Distributed Antenna Systems, GSM (with E-OTD), GSM (with CELL-ID), CDMA/GPRS (with A-GPS), CDMA/GPRS (with A-GPS), CDMA/GPRS (with A-GPS), CDMA/GPRS (with A-GPS), CDMA/GPRS (with A-GP (with A-GPS) - AFLT+AGPS, Wireless Assisted GPS and AFLT: GPS One A Hybrid Solution, WCDMA (with IP), WCDMA (with IP), WCDMA (with IP), WCDMA (with IP), WCDMA (with IP), WCDMA (with IP), WCDMA (DAS). Some of the techniques discussed in this paper are localization by Cell-ID, localization by Prediction, localization by Angle of Arrival (AOA), localization by Time of Arrival (TOA) and Observed Time Difference of Arrival (TDOA), localization by Finger Printing, and Hybrid Localization AOA-TOA Based. Low-power wide-area networks (LPWANs), cellular 5G-based positioning technologies, ZigBee (Mesh Protocols), and WiFi6 have all been studied in relation to the Internet of Things (IOT). This document also covers NLBS (which includes Bluetooth Low Energy technology, WLAN, and Infrared), UWB, and Vehicle to Vehicle Communications.

Keywords: Location-Based Services, LBS, GSM and RFID Systems, GPS, LBS, applications of LBS, AOA, TDOA, UWB

1. Introduction

LBSs are a hybrid of commercial and consumer services that rely on the users' placement. Position Level, Tracking Level, and Planning Level are three different degrees of location-based services. The user's current position is required by the Position Level. The Tracking Level requires the user's current and previous positions, whereas the Planning Level requires the user's current, past, and future positions [1]. Itinerant (services provided to a moving user), Distributed (offering the same services to any place within the network), and Ubiquitous (providing the same services to any location inside the network) are further characteristics that define and characterise LBS technology.

2. Categorization of LBS

Radio-based systems, ultrasonic-based systems, active infrared-based systems, camera-based systems, and Smart Floor systems are all used in LBS. The disadvantage of radio-based systems is that the objects to be located require particular hardware. Kemper and hybrid systems, such as Active Badge, use ultrasonic-based technologies. The Active Badge System is based on Active Infrared [2]. Camera-based systems have the advantage of being hardware-independent. The Easy-Living-Tracker is an example of this. Wireless networks, user devices, location technologies, geographical data servers, and application servers are all used in LBS [3]. The use of a distributed architecture in LBS can help to reduce network congestion.

There are several methods for determining the positions of items in Location-Based Services, including Terminal-Based Approaches and Network-Based Approaches. Based techniques include the Global Positioning System (GPS), Assisted Global Positioning System (A-GPS), and Enhanced Observed Time Distance (E-OTD). Cell Global Identity (CGI) and Time of Arrival are two examples of

IMDC-IST 2021, September 07-09, Sakarya, Turkey
Copyright © 2022 EAI
DOI 10.4108/eai.7-9-2021.2314984

network-based approaches (TOA). In Location-Based Services, there are various positioning systems for mobile terminals that differ in terms of dependability, precision, and computations. Satellite positioning systems, network-based positioning systems, and local positioning systems are examples of these systems [4]. The reliability, efficiency, and performance of Location Based Services are all influenced by positioning technologies. Indoor, outdoor, or hybrid positioning systems are available. Indoor localization necessitates high precision and signal strength. Flora, Ficco, Russo, and Vecchio (2005) suggested a software architecture that combined interior and outdoor location sensing. The client-side mechanism and zoning location sensing approach were used to create this architecture. It complies with JSR-179 requirements [5].

LBS Indoor Systems, LBS Satellite Systems, and LBS Outdoor Systems Using Terrestrial BSs are all part of the localization infrastructure. Localization accuracy, availability, and consistency, applicability, power consumption, hardware size, software size, processing load, supported positioning modes, network-dependent and signalling load, cost, standardisation, and delay are all quality criteria for localization technologies. The advantages, disadvantages, and applications of different Outdoor System Localization are discussed below:

2.1 Radio Frequency Identification (RFID)

The RFID beacons are small and light. It works by sending out little radio packets at short wavelengths. RFID employs biometrics, voice recognition, smart cards, optical character recognition, bar codes, and other forms of automatic identification. It collects data about a specific item via electromagnetic waves or inductive coupling [6]. RFID advancements have resulted in various benefits, including resource optimization, increased corporate transaction efficiency, and improved health-care systems. RFID is utilised in manufacturing for resource management, quality control management, inventory management, and tracking management [7]. RFID is utilised for shipping management, picking management, and receiving management in warehousing [8]. In the transportation industry, it's utilised to control safety, distribution, and material processing. The truck drivers, trucks, and the company to which the trucks belong are all verified using RF tags on the trucks. The Commercial Driver's License with the tags validates that they are visiting the terminals for business. The contents of the containers on the trucks can also be determined using this system [9]. For checkout management, shelf-stock management, and inventory management in the retail industry. RFID inventory management enhances merchandise on-shelf availability and delivers applications like smart fitting rooms, smart checkout, and product location tools [10]. It can be used for crop identification, animal tracking, and animal diagnostics in agriculture. This technology is employed throughout the seed quality management process, including seed cultivation, storage, and transportation to the supervision department, seed quality confirmation, and seed distribution to farmers [11]. It can be utilised for public transportation tickets, automatic vehicle locating, toll collection, and smart car keys in ticketing and traffic control. It is utilised in pre-paid access cards with an incorporated microchip for toll payment. An Automated Parking Management System employs RFID technology. The Integrated Recognition and Identification System (IRIS) [12] connects Automatic Number Plate Recognition (ANPR) technology with RFID technology in this system. RFID can be employed in a variety of applications, including aged care, pharmaceutics, hospital equipment and personnel management, implants, prosthesis, and patient medical history tracing. To combat the problem of counterfeit medications in the United States, the Food and Drug Administration (FDA) has mandated the use of RFID pedigrees on all wholesale prescription drug shipments [13]. In Finance, it can be used in smart cars and currency identification. The American Express launched a credit card in 2005, which provided the facility to the customers to purchase items without swiping their cards [14]. It can be used for digital identification, electronic passports, facility access, and punishment system management. The rate of crime can be minimised by adopting RFID technology for human identification management because there will be less risks of fraud or theft.

In sports and games management, it can be used for gaming chips, sports event timing and tracking golf balls [15]. The Washington Major League Football team has made the football game more interesting by employing RFID technology in tickets, purchasing of food and drinks at refresher stands. This system has also been introduced at Nationals' Park. Fortress GB, which is a British sports and entertainment technology is deploying RFID enabled card for ticketing systems [16]. In clothing, it can be used for laundry ID and cleaning control system management. RFID tags are also useful for the garment business. RFID tags provide enough space for data storage for a wide range of information and applications. Miniature RFID tags are utilised in teaching and research. For example, in 2009, Bristol

University researchers used RFID transponders to analyse ant behaviour [17]. As a result, RFID technology is very beneficial for studying animal and bird life patterns, habitats, and habits.

2.2 Global Positioning Systems (GPS)

The GPS is a functioning system that includes an earth-orbiting satellite-based routing system [18]. The Global Positioning System is used by military units, sailors, utility companies, evaluators, pilots, and hikers with small hand-held receivers. GPS satellites have feeble transmissions that cannot pass the walls of buildings, therefore it does not perform well in an inside environment. GPS technology is employed in a wide range of applications. The following sections go over some of the applications:

Satellite navigation in ships, aircraft, and cars is the most common use of GPS. It allows a GPS receiver to pinpoint their location or speed with pinpoint accuracy. It not only gives cars with a path to follow, but it also delivers traffic alerts. In emergency scenarios, GPS can be quite useful. It aids hikers in staying on track and arriving at their intended destination [19].

GPS is inexpensive and so accessible to the general public. It provides unrestricted access all over the world [20]. GPS delivers high-resolution data for mapping and surveying. When compared to other mapping and surveying approaches, the data collection is far too fast - less than a single day. The data collected from GPS can be displayed on maps that can be stored or manipulated. One of the most important applications of GPS regarding surveying is that it is not restricted to the sight visibility between survey stations [21]. In global financial systems, millions of money transfers and transactions whether local or international takes place every day. GPS can provide accurate dates and times for electronic funds transfer, ultimately serving a critical purpose for financial systems worldwide. GPS is used in engineering applications such as construction, mining and guiding heavy vehicles. It allows the driver to follow a surveyors' preprogrammed site plans to reach for the nearest accuracy and efficiency in work [22].

Glimpse is a mobile location sharing programme that allows users to broadcast their position via text messaging and social media. This app also provides route information, traffic alerts, and alternate routes. By employing their cell phone's application, GPS track pro may simply locate anyone [23]. The jamming properties of GPS have a considerable application in military navigation. The positioning of forces is critical in military processes and operations. It assists in the tracking and monitoring of possible targets [24]. Other techniques, such as photo-reconnaissance, can be used in these tracking procedures to improve awareness and information about bombing missions. Unmanned Aerial Vehicles (UAVs) are used in military operations all over the world in the current day. GPS Jammer Location (JLOC) [25] is one of the military applications. It's made to keep track of GPS interference threats and send out alerts if any are identified in the region.

Assisted GPS is ubiquitous in today's GPS systems, yet few people are aware of it. The satellite system and an external server are used by A-GPS [26]. The most significant benefit of A-GPS is that the signals are always whole and contain no fragments. Second, it is speedier because it makes advantage of the nearby cell towers, which provide a clear picture of the location. A subscription is necessary to utilise A-GPS, which is pricey. Because most A-GPS devices are reliant on an external server, they may not function effectively without it [27].

2.3 Outdoor system using Terrestrial BSs

The Outdoor system employing Terrestrial includes GSM (with E-OTD), GSM (with CELL-ID), CDMA/GPRS (with A-GPS), CDMA/GPRS (with A-GPS) - AFLT+AGPS, Wireless Assisted GPS and AFLT: GPS One A Hybrid Solution, WCDMA (with IPDL, TA-IPDL, and OTDOA-PE), Systems with Smart Antennas, and Distributed Antenna (DAS). The advantages and disadvantages of these systems are discussed below:

2.3.1 Global System for Mobile Communication (GSM)

The modern cellular technology used to transmit voice and data around the world is known as the GSMC. Users of GSM phones can travel to more than 218 countries with the same number. Different algorithms can be used by GSM users to obtain location fixes [28]. GSM has a number of drawbacks, including bandwidth slowness and a proclivity to interact with certain electronic devices. Its pulse transmission method can interfere with a pacemaker or airport radio communications.

2.3.2 GSM (with E-OTD)

GSM mobile operators employ E-OTD as a multi-lateration positioning approach to find its users [29]. It's similar to the TDA technique, except that algorithm and all other calculations are done in the user's device or handset instead of the base station or server. A lot of data is needed to make the equations easier to understand, including different time measurements, which are referred to as Location Measurement Units (LMU) [30]. Installing Location measurement equipment throughout the coverage area, as well as equipping the user's handset with appropriate software, is both costly.

2.3.3 GSM (with Cell- ID)

Network providers is assigned base transceiver stations to ensure full coverage. The regions were then further separated, with each receiving a Cell ID and BS to to connect with users. As a fix to the Cell ID would limit the position to some amount, GSM providers might now utilise multiple localization techniques to place a user [31].

2.3.4 CDMA/GPRS (with A-GPS)

The GSM GPRS tracker is one of popular location trackers on the market. The CDMA GPS trackers differ from the GPRS GPS trackers in that they use a GPS-One chipset, which is less accurate. Assisted GPS is used by the CDMA tracker. To locate an object, A-GPS uses fragmented data stored on a network server [32]. The CDMA tracker is substantially expensive to GPRS since it requires additional server storage.

2.3.5 CDMA/GPRS (with A-GPS) - AFLT+AGPS

When it comes to outdoor positioning, the Hybrid GPS and AFL Trilateration is the best and most accurate. Even when a GPS-only solution is unavailable, our hybrid approach gives the most precise position. There is a tiny drawback in acknowledging that if a GPS-only solution is not accessible, and a direct LoS of trilateration requires three BSs and there is a danger of inaccuracy or ambiguous placement [33].

2.3.6 Wireless Hybrid Assisted GPS and AFLT

Mixture localization (hybrid solution) combines the best of both worlds. The cellular network and GPS are used by GPS-One. It improves GPS receiver sensitivity and delivers accurate localizations even when less than four satellites are visible [34]. The only drawback is that it comes with its own hardware and software, as well as the need for an installed chipset.

2.3.7 Systems with Smart Antenna

Adaptive array antennas are used in Smart Antennas to improve the efficiency of wireless communications networks. Signal processing algorithms can be used for tracking user with new arrangement of array antennas [35]. Using smart antennas provides a variety of advantages, including the ability to cater to a considerably many users at the same time. Furthermore, because of their directionality, they provide greater security and less interference than traditional Omni-directional antennas.

2.3.8 Distributed Antenna Systems (DAS)

A DAS is a system that uses coaxial wire, fibre optic cable, and antennas to boost cellular, public safety, and other communications inside a building [36]. The DAS system is crucial in radar applications, such as vehicle-mounted surveillance radars and radar system such as anti-missile with restricted energy sources [37]. DAS improves wireless coverage, data speed, and call clarity in these circumstances by eliminating poor wireless reception. In a Neutral Host DAS concept, the expense of providing services based on sharing the number of carriers, allowing low and high data rate venues to become economically viable [38].

3. Techniques for the Existing Localization

Some of the existing localization approaches are Cell-ID, Prediction (Dead-Reckoning Method), Localization by Angle of Arrival (AOA), Localization by Time of Arrival (TOA) and Observed Time Difference of Arrival (OTD), Hybrid Localization AOA-TOA Based, and Localization by Finger Printing. The advantages and disadvantages of these technologies are discussed below:

3.1.1 Localization by Cell-ID

To locate a mobile user, position of Cell ID needs the existing cellular network address. Covering multiple cells and smaller regions the base transceiver station communicates ware responsible to provide that bases. The BTS connects with the user's device via a distinct signal transmitter and Cell ID for each cell. The network examines the user Cell ID who has requested localisation while positioning.

3.1.2 Localization by Dead -Reckoning

While navigating, Dead Reckoning is a mechanism for calculating position of user from previously calculated positions and forwarding it based on predicted motion. Advanced satellite systems have sealed the market for dead reckoning in the world of navigation; [40] however, inertial navigation systems that give precise information about direction, use Dead Reckoning efficiently and are very widely applied.

3.1.3 Localization by AOA

After determining the angle at which signals are received at numerous receivers on a base station, localization by Angle of Arrival is performed by computing node locations using fundamental geometry formulae. Angle of Arrival (AOA) approaches, in general, produce more accurate localization results than Received Signal Strength Indicator (RSSI)-based techniques, however the hardware cost of this technology is relatively high. Localization by AoA is particularly inaccurate and time-consuming for a rapidly moving item since the many receivers at the BS do not account for the time gap [41].

3.1.4 Localization by TOA and Observed TDOA

Localization by TOA is an approach for calculating a mobile user's location [42]. When user in LoS this technique is quite accurate. However, there is a problem that the wave progression in air varies depending on environmental variables such as temperature and humidity. This causes error in distance estimation-based localisation [43].
Localization by Observed TDoA, is a multi-iteration technique. In this technique, the system localizes a user by using time-synchronized receivers. Localization is done by multiple nodes of known locations that report the relative time measurements of receiving a signal, rather than the absolute time.

3.1.5 Hybrid Localization AOA-TOA

Hybrid reference are a combination of several single localization approaches that solve the problems, such as TOA, AOA, and TDoA, have when used alone. LoS between the receiving beacon and the mobile source is resolved using a hybrid of Time of Arrival and Angle of Arrival. Because Angle of Arrival can't tell the difference between direct and reflected signals, the system uses a variety of efficient techniques to get around issue. The advantages are clarity, accuracy, and dependability. One of the drawbacks of the Hybrid system is the increased computational cost, as more calculations are at hand now. To speed up the localisation, new and far more complicated algorithms are applied [44]. Furthermore, specialised hardware may be more durable and costly [45]. Both ends should be time-synchronized for TOA-AOA to work.

3.1.6 Localization by Finger Printing

The term "fingerprinting" refers to a method of recognising a certain location based on the data that represents it. Fingerprinting approaches are particularly successful at identifying a mobile user in an indoor setting, as well as in complex problem the traditional localization techniques based on ToA or triangulation are promoted but with major inaccuracies, such as canyons and tunnels [46]. The fingerprinting database must be sized big to obtain more accuracy. Furthermore, the database must be updated every time the environment changes. Fingerprinting is very precise and accurate but very expensive to run and maintain in the outdoors.

4. Internet of Things (IOT)

It comprises of a system of interconnected computing devices, mechanical as well as digital machines, animals, objects, or humans that are supplied with unique identifiers and the capability of communicating without needing human-to-human interaction or human to computer interaction [47]. Examples of Internet of Things include sensors for monitoring traffic conditions, heart sensors for cardiac patients, security and home management, moisture sensors for directing irrigation, location sensors for cattle, sensors for monitoring hazardous material in industries, sensors for managing employees' working conditions, automated inventory control, etc. The Internet of Things comprises of leading technologies such as Low Power Wise Area Network (LPWANs), Cellular 5G based positioning methods, ZigBee (Mesh Protocols) and WiFi6.

4.1 Low Power Wise Area Network (LPWANs)

It is the novel technology in Internet of Things that supports large-scale Internet of Things networks ranging over wide industrial and commercial sites [48]. Low Power Wise Area Networks can link all kinds of Internet of Things sensors, such as assisting several applications from asset tracking, monitoring of environment, facility management, consumables monitoring, occupancy detection, etc. The drawback of LPWANs is that it can only transmit small blocks of data at a low rate, and hence is appropriate for cases that do not need high bandwidth and are not time-bound.

4.3 ZigBee (Mesh Protocols)

Zigbee is a low-power, short-range, wireless standard (IEEE 802.15.4) that is usually implemented in mesh topology for extending coverage by transmitting sensor data over numerous sensor nodes. In comparison to Low Power Wise Area Network, Zigbee gives high data rates, but simultaneously, less power efficiency due to mesh configuration [50]. ZigBee are appropriate for medium-range Internet of Things applications with a uniform allocation of nodes in adjacent propinquity. Generally, Zigbee is an ideal addition to Wi-Fi for different home automation usages such as HVAC controls, security management, energy management, smart lighting, etc.

4.4 WiFi6

WiFi 6 is the novel Wi-Fi generation that comprises of improved network bandwidth (that is; <9.6 Gbps) for enhancing data per user in over-crowded places [51]. The use of WiFi 6 can raise public Wi-Fi infrastructure and transforms the experience of the consumers with novel digital mobile services, such as, retail and entertainment segments. Moreover, it can be used in car networks for the purpose of infotainment and On-board Diagnostics (Vehicles' self-diagnostic reporting).

5. Near Location Based Services (NLBS)

NLBS are a collection of wireless technologies [52]. This programme allows users to get information based on their current location. It's especially well-suited to use in confined places, small spaces, or restricted areas. Usual ranges for other technologies are included.

5.1 Bluetooth Low Energy (BLE) Technology

BLE has been initiated to handle small-scale consumer applications related to the Internet of Things, it enabled devices are mainly utilized in combination with electronic devices, usually the smart phones that act as a hub for transmitting data to the cloud network [53]. In the modern era, Bluetooth Low Energy is extensively incorporated in fitness as well as medical wearable (such as glucose meters, smart watches and pulse oximeters) and Smart Home devices (for instance, door locks).

5.2 Wireless Local Area Network (WLAN)

WLAN is a network that allows devices to connect and communicate wirelessly [54]. The Dynamic Host Configuration Protocol is commonly used to add and configure new devices (DHCP). They can communicate with other devices on the network in the same way that a wired network would. It enables homeowners and businesses to set up local networks without the need for Ethernet wiring.

5.3 Infrared

Infrared (IR) technology, often known as infrared light, is a type of Electromagnetic Radiation (EMR) with visible light wavelengths. Infrared wavelengths are typically defined as spanning from 700 nm (f=430 THz) to 1 mm (f =300 GHz) in the visible spectrum [55]. Nearly all infrared wavelengths are released by black radiation that are near to room temperature. Infrared broadcasts energy and momentum and has the attributes of both a wave and a particle, the photon, as a type of electromagnetic radiation. When molecules change their vibrational rotational motion, they absorb or emit infrared radiation [56]. It induces vibrational modes in a molecule by changing the dipole moment for studying the energy levels. Infrared spectroscopy studies the absorption and emission of photons in the infrared region. Humans or animals can be viewed without revealing the observer using night vision systems that use active near-infrared illumination [57]. Sensor-equipped telescopes are used in infrared astronomy to penetrate dusty parts of space, and flow of blood within the skin.

6. Ultra Wideband (UWB)

UWB is a radio technology that can communicate over a large area of the radio spectrum while using low energy. In non-cooperative radar imaging, Ultra Wideband has a traditional implementation [58]. The current applications are focused on collected data by sensors, localised precision, and tracking. UWB [59] is a method for broadcasting information over a large BW>500 MHz. Because of its use in Synthetic Aperture Radar (SAR) technology, Ultra Wideband has received a lot of interest [60]. UWB Pulse-Doppler radars are also utilized for the monitoring of significant signs inside the body of humans, for instance, heart rate, baby monitoring, human gait analysis, respiration signals, fall detection, etc.

7. Vehicle to Vehicle (V2V)

V2V communication facilitates vehicles to wirelessly exchange information relevant to their location, speed and direction. The technology that is used in V2V communication permits the vehicles up to 10 times/sec messages thus establishing a 360 degree "awareness" of the other vehicles in propinquity [61]. Vehicles that have appropriate software (or safety applications) can utilize the messages from surrounding vehicles for determining the possible crash threats that they can face [62]. The V2V communication messages possess a range of above 300 meters and have the ability of detecting the dangers that have been concealed by weather, terrain, or traffic [63]. V2V communication extends and improves the current accessible crash avoidance systems that utilize radars and cameras for the detection of collision threats. V2V communication system can enhance the performance of vehicle safety systems and can assist in saving lives. The linked vehicle technologies can provide drivers with the tools they require for anticipating possible crashes and considerably reducing the number of lives that are lost yearly.

8. Conclusion

Location-Based Services' indoor and outdoor localization strategies have a number of advantages and disadvantages. RFID advancements have resulted in resource optimization, higher corporate transaction efficiency, improved health-care systems, and improved customer service. The disadvantage is that programming RFID for individual applications takes a long time. In comparison to other navigation systems, the GPS system is particularly cost-effective, and the receiver is unaffected by weather or climatic changes. The disadvantage is that it does not perform well in an indoor environment because GPS satellites have feeble signals that cannot penetrate building walls. GSM technology enables global communication and coverage, although there is a BW latency. Smart Antennas have the benefit of simultaneously connecting a higher number of users, re-usable frequencies, various pathways, increased BW, and cost-effective; nevertheless, managing their vast size and position necessitates a lot of planning. DAS minimises shadowing and penetration data losses, but it comes with a significant infrastructure cost and is difficult to maintain. Cell-ID localization is low-power, however it does not cover a large area. Path integration is used in the Dead Reckoning technique of localization, although it has the drawback of error accumulation because the location is predicated on the previously determined position. AOA approaches provide more exact localization results, but they come at a considerable expense in terms of technology.

TOA might use a variety of signals, including RF, infrared, ultrasonic, and so on, but it has the downside of requiring the user to be in LoS of the received signal beacons. Observed TDOA uses time-synchronized receivers to locate a user. This technology is less expensive and quicker, but it requires LoS. Localization Hybrid is a fusion of several single localization approaches of AOA and TOA. Its disadvantage is that it has a higher computational cost. Fingerprinting-based location is particularly effective for indoor and complex environments. It is precise and accurate, but the database must be updated every time the environment changes, which is time consuming and expensive. In the modern era, new technologies have been introduced such as the Internet of Things (IOT) which involves Power Wise Area Network (LPWANs), Cellular 5G based positioning methods, ZigBee (Mesh Protocols) and WiFi6. Moreover, NLBS (involving Bluetooth Low Energy technology, WLAN and Infrared), UWB and Vehicle to Vehicle Communications have improved the localization techniques. Researchers have offered a number of methods for improving the technology and services that are now available for LBSs. LBSs have a bright future into our smart communities.

Acknowledgments

The European Union's Horizon 2020 research and innovation programme under grant agreement H2020-MSCA-ITN-2016 SECRET-722424 and the UK's Research Council (EPSRC) under grant EP/E022936 partially sponsored this work.

Reference:

1. Abulleif, T. and Al-Dossary, A., *Location Based Services (LBS)*, Surveying Services Division, Saudi Aramco, Dhahran, Saudi Arabia, 2008.
2. Want, R., Hopper, A., Falcao, V., and Gibbons, J., *The Active Badge Location System, Olivetti Research Ltd. (ORL*), Tech. Rep., 1992.
3. Adusei, I. K., and Kyamakys, F. E. *Location Based Services: Advances and Challenges*, Master's Dissertation, Institute of Communication Engineering, 2005, University of Hannover.
4. Tsalgatidou, A., et al., *Mobile E-Commerce and Location-Based Services: Technology and Requirements*, 2003, The University of Athens.
5. Flora, C., Ficco, M., Russo, S., and Vecchio, V., *Indoor and Outdoor Location Based Services for Portable Wireless Devices*, Proc. 25th International Conference on Distributed Computing Systems Workshop (ICDCSW'05), 2005.
6. S.A. Weis, *RFID (Radio Frequency Identification): Principles and Applications*, Master's Dissertation, CSAIL, 2007.
7. Ilie-Zudor, E., Kemen, Z., Egr, P., and Monostori, L., *The RFID Technology and its Current Applications*, Proc. The Modern Information Technology in the Innovation Processes of the Industrial Enterprises- MITIP, 2006: p. 29-36.
8. Shutzberg, L., *Radio Frequency Identification (RFID) In the Consumer Goods Supply Chain*, Rock-Tenn Company.
9. Nguyen, T. *Port trucks get RFID*, Fleet Owner, 2006.
10. ZIH Corp. Zebra, *Traceability in Retail: Reducing RFID Media Costs for Best Value*, 2013.
11. Li, H. *Application of RFID in Agricultural Seed Quality Tracking System*, Proc. 8th World Congress on Intelligent Control and Automation (WCICA), IEEE, Jinan, China, 2010: p. 3073-3077.
12. Gifford, J., *RFID Application in Transportation Operations*, George Mason University, San Diego, 2006.
13. United States Department of Health and Human Services, *Combating Counterfeit Drugs*, Food and Drug Administration, Technical Report, 2004.
14. Swedberg, C., *MEX Adds RFID to Blue Credit Cards*, RFID Journal, 2005.
15. Smith, A., Balakrishnan, H., Goraczko, M., and Priyantha, N., *Tracking Moving Devices with the Cricket Location System*, Proc. 2nd International Conference on Mobile Systems, Applications and Services (Mobisys 2004), ACM, Boston, MA, USA, June 2004: p. 190-202.
16. Swedberg, C., *RFID is the Ticket at Washington Nationals' Park*, RFID Journal, 2012.
17. TFOT, *Hitachi Develops World's Smallest RFID Chips*, 2007.
18. Jechlitschek, C. *A Survey Paper on Radio Frequency Identification (RFID) Trends*, 2006.
19. Ergen, et al., *Application of GPS to Mobile IP and Routing in Wireless Networks*, University of California Berkeley, 2002.
20. MiTAC International Corporation, Applications Of GPS, Available on: www.mio.com/technology-applications-of-gps.htm
21. Griffin, R. T., *Top Benefits Of Using A Handheld, Walking, Or Hiking GPS*, Ezine Articles, 2011.
22. Aughey, R. J., *Applications Of GPS Technologies To Field Sports,* International Journal Of Sports Physiology And Performance, 2011: p. 295-310.
23. Maddison, R. and Clion, N.M. *Global Positioning System: A New Opportunity In Physical Activity Measurement*, International Journal of Behavioral Nutrition and Physical Activity, 2009.
24. National Coordination Office for Spaced-Based Positioning, *GPS: Surveying and Mapping Applications* , Navigation and Timing, 2016.
25. Locata Corporation Private Limited, *Civilian Applications Of GPS*, Australia, 2016.
26. Patil, B., Patil, R., and Pittet, A. *Energy Saving Techniques for GPS Based Tracking Applications,* Proc. Integrated Communications, Navigation and Surveillance Conference (ICNS), 2011: p. 8-10.
27. Yongwei, M. *A Study of Localization Methods on Mobile Platform and WIFI-Based User Movement Detection*, University of Delaware. UMI. ProQuest LLC, 2015.
28. Walia, V., and Kaur, S. *Survey of Different Localization Techniques of Wireless Sensor Networks*, IJEEE, 2014.

29. Oscar, R., Martin, E. I., and Francisco, A., *A Field Study on Satellite and Cellular Signals as Sources for Location*, Proc. 2nd International Conference on Computer Engineering and Applications, Bali Island, Indonesia, 2010: p. 474-478.
30. Charitanetra, S. and Noppanakeepong, S. *Mobile Positioning Location using E-OTD Method for GSM Network*, Proc. Student Conf. Research and Development, 2003: p. 319 -324.
31. Nazarpour, F. A., *New Method for Cell Id Assignment for Distance Based Location Management in Cellular Communication Systems*, Proc. 3rd International Conference on Information and Communication Technologies: From Theory to Applications (ICTTA), 2008: p. 1–5.
32. Patil, B., Patil, R., and Pittet, A., *Energy Saving Techniques for GPS Based Tracking Applications*, Proc. Integrated Communications, Navigation and Surveillance Conference (ICNS), 2011.
33. Chia-Yenand, S., and Marron, P. J, *COLA: Complexity-Reduced Trilateration Approach for 3D Localization in Wireless Sensor Networks*, Proc. 4th International Conference on Sensor Technologies and Applications (SENSORCOMM), 2010: p. 24-32.
34. Soliman, S., et al., *GPSOne: A Hybrid Position Location System*, Proc. 6th International Symposium on Spread Specturm Techniques and Applications (ISSSTA), IEEE, 2000: p. 1.
35. Zhu, X., Wang, Y., and Zhu, H., *A Precise 2-D Wireless Localization Technique Using Smart Antenna*, Proc. International Conference on Cyber-Enabled Distributed Computing and Knowledge Discovery, CyberC, 2010: p. 59-63
36. Hoglund, D. H. *Distributed Antenna Systems for Healthcare*, IT horizons. Inc., 2010.
37. Godrich, H., Petropulu, H. and Poor, H. V., *Resource Allocation Schemes for Target Localization in Distributed Multiple Radar Architectures*, Procs. 18th European Signal Processing Conference, 2010.
38. Dahrouj, H., and Yu, W., *Coordinated Beamforming for the Multicell Muti-Antenna Wireless System*, IEEE Transactions on Wireless Communications, 2010. **9**(5): p. 1784-1759.
39. Trevisani, E. and Vitaletti, A. *Cell-id Location Technique, Limits and Benefits: An Experimental Study*, Proc. 6th International Workshop on Mobile Computing Systems and Applications (WMCSA), IEEE, Dec 2004: p. 51–60.
40. Samuel, H., et al., *Indoor localization Using Pedestrian Dead Reckoning Updated with RFID-based Fiducials*, Proc. 333rd Annual International Conference on Engineering in Medicine and Biology Society, IEEE, 2011: p. 7598–7601.
41. Mesmoudi, A., Feham, M., and Labraoui, N., *Wireless Sensor Networks Localization Algorithms: A Comprehensive Survey*, International Journal of Computer Networks and Communications (IJCNC), 2013.
42. Zhang, D., Xia, F., Yang, Z., Yao L., and Zhao, W., *Localization Technologies for Indoor Human Tracking*, Proc. 5th International Conference on Future Information Technology (FutureTech 10), May 2010.
43. Walia, V., and Kaur, S., *Survey of Different Localization Techniques of Wireless Sensor Networks*, IJEEE, 2014.
44. Khan, M. W., Salman, N., and Kemp, A. H., *Enhanced Hybrid Positioning in Wireless Networks 1: AoA-ToA*, Proc. International Conference on Telecommunications and Multimedia, TEMU, 2014.
45. Gantea, A. D., and Sillera, M., *A Survey of Hybrid Schemes for Location Estimation in Wireless Sensor Networks*, Proc. Iberoamerican Conference on Electronics Engineering and Computer Science. Procedia Technology, 2013: p. 377 – 383.
46. Yu, L., Laaraiedh, M., Avrillon, S., and Uguen, B., *Fingerprinting Localization Based on Neural Networks and Ultra-Wideband Signals,* Proc. International Symposium on Signal Processing and Information Technology (ISSPIT), IEEE, Bilbao, Spain, 2011: p. 184 -189.
47. Mattern, F., and Floerkemeier, C., (2010). *From the Internet of Computer to the Internet of Things,* Informatik-Spektrum. 2010. p. 107–121.
48. Beser, N. B., *Operating Cable Modems in a Low Power Mode*, U.S. Patent No. 7,2008: p.389,528.
49. Rappaport, T. S., et al., *Millimeter Wave Mobile Communications for 5G Cellular: It Will Work*, IEEE Access, 2013. p. 335–349.
50. Bellido-Outeirino, F. J., *Building Lighting Automation through the Integration of DALI with Wireless Sensor Networks*, IEEE Transactions on Consumer Electronics, 2012. **58** (1): p. 47–52.
51. Khorov, E., Kiryanov, A., Lyakhov, A., and Bianchi, G., *A Tutorial on IEEE 802.11ax High Efficiency WLANs.* IEEE Communications Surveys & Tutorials. IEEE. 2019. p. 197–216.
52. Martin, E.., Vinyals, O., Friedland, G., and Bajcsy, R., *Precise Indoor Localization Using Smart Phones*, ACM Multimedia*,* 2010: p. 787–790.
53. Honkanen, M., Lappetelainen, A., and Kivekas, K., *Low end extension for Bluetooth*. 2004 IEEE Radio and Wireless Conference 19–22 September 2004. IEEE. 2004: p. 199–202.
54. Al Shourbaji, I., An Overview of Wireless Local Area Networks, Computer Networks Department, Jazan University. Jazan, Saudi Arabia, 2005.

55. Rowan-Robinson, M., *Night Vision: Exploring the Infrared Universe*, 2013: Cambridge University Press, p. 23.
56. Haynes, William M., (2011). *CRC Handbook of Chemistry and Physics* (92nd ed.), 2011: CRC Press, p. 10.233.
57. Lynch, David K.; Livingston, William Charles (2001). *Color and Light in Nature* (2nd ed.), 2001: Cambridge, UK: Cambridge University Press, p. 231.
58. Zhou, Y., Law, C. L., Xia, J. (2012). *Ultra low-power UWB-RFID System for Precise Location Aware Applications*, IEEE Wireless Communications and Networking Conference Workshops (WCNCW*)*, 2012: p. 154–158.
59. Kshetrimayum, R., *An Introduction to UWB communication Systems*, IEEE Potentials, 2009. p. 9–13.
60. Ren, L., Wang, H., Naishadham, K., Kilic, O., and Fathy, A., *Phase-Based Methods for Heart Rate Detection Using UWB Impulse Doppler Radar,* IEEE Transactions on Microwave Theory and Techniques, 2016. p. 3319–3331.
61. Boehmlaender, D., et. al., *Advantages in Crash Severity Prediction Using Vehicle to Vehicle Communication*, 2015 IEEE International Conference on Dependable Systems and Networks Workshops. IEEE, 2015: p. 112–117.
62. Harding, J., *Vehicle to Vehicle Communications: Readiness of V2V Technology for Application*, 2014: U.S Department of Transportation, NHTSA.
63. Zorkany, M., Yasser, A., and Galal, A. I., *Vehicle To Vehicle "V2V" Communication: Scope, Importance, Challenges, Research Directions and Future*, The Open Transportation Journal, 2021. 14(1): p. 86-98.

Radar Recognition Using Pulse Repetition Interval Technology

Imran Ahmad[1], Mohammed S BinMelha[1,2], Ahmed S.I. Amar[1,3], Mohammed J. Ngala[4], Raed Abd-Alhameed[2,5]
I.ahmad3@bradford.ac.uk, abofaras@yahoo.com, a.a.s.ismail@bradford.ac.uk, mjngala@heatoned.co.uk, r.a.a.abd@bradford.ac.uk

[1]Faculty of engineering and informatics, University of Bradford, Bradford, BD7 1DP, UK.
[2]System Maintenance Controller, Saudi Air Navigation Services, KSA
[3]Faculty of Engineering, Ain Shams University, Cairo, Egypt
[4]Heaton Education Bradford UK
[4]Information and Communication Eng. Department, Basrah University College of Science and Technology, Basrah 24001, Iraq

Abstract. Recognition of pulse repetition interval modulation (PRI) of a radar signal is important. It helps in identifying the radar's functional purpose and assists in emitter identification. This paper discusses two methods, the gate time pulse method and feature extraction, used for PRI modulation recognition. These features are based on both sequential and statistical information of the pulse intervals. The extracted features can be used for emitter recognition by feeding the information in a neural network.

Keywords: RPI modulation, PRF, Radar Recognition, Variable PRI emitters, Fixed PRI emitter Location Based Services, LBS, Smart City, Emitter recognition, Radar recognition, Pulse Repetition Interval, Signals Intelligence, PRF.

1. Introduction

Advances in the radar technology result in the usage of complicated radar waveforms. The radar signal uses various pulse repetition frequencies (PRF) and is altered either intentionally or unintentionally. Measurement of the pulse repetition frequency provides information about the purpose of the radar. This forms an important step in electronic support (ES) receivers. The obtained information is further processed for emitter identification in radar intercept receivers. Modern radars are employed in secret operations during crisis and in electronic warfare. This increases the need for emitter identification having no prior knowledge of the transmitted waveform, to understand the radar's purpose. Emitter identification helps in identifying possible threats from enemy and thus forms a necessary first step to counter the enemy threat emitters [2]. Previous methods for emitter recognition include passing the sorted pulse train and a delayed version through a coincident circuit. Another method uses the time of arrival of the incoming pulses while another method using autocorrelation function is discussed in [8]. All these methods are computationally very complex and result in overloading of the processor. Blanking is used in emitter recognition in a dense environment where pulses related to a particular emitter are blanked once that emitter has been recognized. Most of the radar waveforms can be classified in 6 major modulations types either fully or piece by piece fashion namely constant, staggered, jittered, sliding, dwell and switch and periodic PRI [1]. These different PRIs can be described using the function

$$F(n) = t_{n+1} - t_n = x_n, \quad for\ n = 1,2, \dots N-1$$

Where, $t_{n+1} - t_n$ defined the time of arrival and x_n is the pulse repetition interval. Fig. 1 illustrates the same for all the six types of modulation PRIs. Jittered PRI here describes the random intentional variation of the PRI, and is different from unintentional PRI variation due to radar transmitters and receivers.

IMDC-IST 2021, September 07-09, Sakarya, Turkey
Copyright © 2022 EAI
DOI 10.4108/eai.7-9-2021.2314983

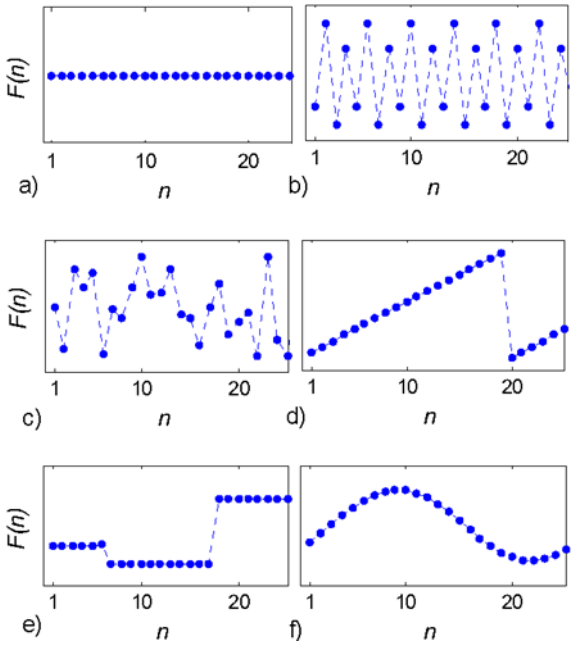

Figure 1a) Constant, b) Stagger, c) Jittered, d) Sliding, e) Dwell and Switch, and f) Periodic PRI.

PRI recognition is done by using statistical properties like a histogram. This method however requires a high number of pulses and also loses the sequential properties of the waveform. Another difficulty faced with histogram-based PRI recognition is with choosing the right detection threshold and bin width. Also, histogram-based methods can identify constant, staggered and jittered PRI. Waveform recognition based on the sequence of the PRI is also done in [3] using a neural network classifier.

This study aims to recognize all the mentioned PRI waveforms with arbitrary modulation parameters automatically. Here, 5 different features are chosen based on either statistical properties or the sequential properties of the waveform and a multi-layer perceptron (MLP) classifier is used. A pulse sorter is used along with time of arrival method and simulations are performed considering the noisy signal environment [6].

However, in practical radars, the PRI is often varied to overcome blind speed in moving target indicator (MTI) and for anti-jamming techniques. The discussed method deems unfit for use in case of variable PRI methods and in dense environments [2]. Thus, for emitter recognition, gate time interval method is discussed which works well for variable PRI as well as in dense environments. Also, the computational complexity for this method is less than the feature selection method using neural network.

2. Feature Selection

Feature selection refers to selecting a unique quantifier to differential the waveforms amongst themselves. These features should provide good separation capability for waveforms of different class while maintaining invariability with parameter variation within the same category. Also, the computation required to calculate the selected features should be less so as to maintain real-time emitter identification. 5 features are selected based on statistical and sequential information of the pulses and scaled between 0-1.

2.1 Features based on statistical properties

Histogram-based PRI modulation recognition works well for constant, staggered and dwell and switch PRI but is complicated for periodic, jittered and sliding PRI as the histogram is based on the bin widths. The peak detection used in the histogram is very sensitive.

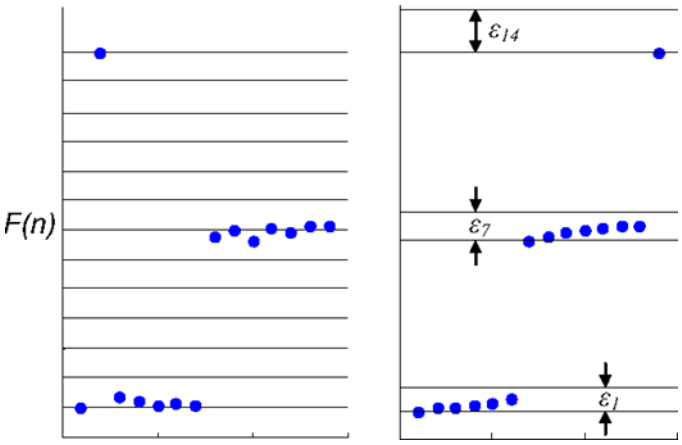

Figure 2: Removing the effect of unintentional jitter

The unintentional jitter causes the pulse peak to leak into adjacent bin widths. Thus, the new technique is used in which the histogram bins are defined to include the unintentional jitter given by:

$$p_n = 2.p.x_n$$

Where, p represents the maximum expected unintentional jitter and x_n is the bin width. In this method, the pulses are sorted in ascending order and pulses belonging to the respective bins including the tolerances are collected. Fig. 2 shows the traditional histogram and the updated histogram for dwell and switch PRI. Unintentional jitter is seen in fig. 2a. An outliner is also seen which is due to a missing pulse. While in fig. 2b, the pulses are sorted and leaked pulses are also collected based on the maximum expected unintentional jitter.

Feature 1: Single histogram peak

Single histogram peak is the ratio of second highest peak and the highest peak in the modified histogram. It defines the amount of constant PRI present and is given by:

$$f_1 = \frac{n_{max-1}}{n_{max}}$$

Where, n_{max} is the highest peak and n_{max-1} is the second highest peak. The single histogram peak value for constant PRI is small. This is because the constant PRI consists of single strong peak in the histogram thus making n_{max}value very high and low n_{max-1}. Thus, this feature is used to distinguish constant PRI waveform from other waveforms.

Feature 2: Stable sum

Stable sum uses the sequential difference histogram (SDIF) to calculate higher order histograms [7]. In a k^{th}level histogram, where k is the difference level, consisting of N pulses, the number of intervals is given by

$$M^k = N - k - 1$$

In this, the value of k is varied and highest peak of these histograms are recorded. A high value of single peak as compared to others indicated presence of periodic pulse train. Thus, for this feature, the ratio of the highest peak to the total pulse intervals is calculated. This is given by:

$$f_2 = \max(N_{max}^k / M^k) \qquad k = 2,3 \ldots k_{max}$$

Where, k_{max} is the highest difference level and N_{max}^k is the highest histogram value for given k. Stable sum is used to differentiate periodic waveforms from non-periodic waveforms. As seen from fig. [1] That staggered waveform is periodic while PRI in jittered waveform is random, hence, stable sum is used to differential between them.

A. Features based on sequential information

Histogram-based features lead to ambiguity while separating all the discussed PRI waveforms. Therefore, new features are discussed. These features are based on the sequential information of the pulses. Eq. 1 is differentiated resulting in second difference time of arrival (TOA) [5]

$$z_n = x_{n+1} - x_n, \qquad n = 1,2, \ldots . N-2$$

As the information required is the ordering of the pulses, therefore, above equation is transformed to a signum function as

$$s = sgn(z)$$

Where,

$$sgn(z_n) = \begin{cases} -1 & for\ z_n < -\epsilon_n \\ 0 & for\ |z_n| \leq -\epsilon_n \\ +1 & for\ z_n > \epsilon_n \end{cases}$$

Where, ϵ_n is the tolerance level for different bin widths

Feature 3: Pulse interval changes

Pulse interval changes is used to distinguish the stable pulse interval waveforms from those having continuous changes in pulse intervals. The feature is defined as the ratio of the amount of pulse interval changes with the number of pulses.

$$f_3 = \sum_{k=1}^{N-2} \frac{|s_k|}{N-2}$$

Where, s_k is the $k-th$ element in vector s

Feature 4: Directional pulse interval change

To distinguish the pulses in which the pulse interval change either increases or decreases, i.e., changes in one direction only, this feature is used. It is given by:

$$f_4 = {|\sum_{k=1}^{N-2} S_k|}/{N-2}$$

As seen from fig. 1, siding pulse waveform has pulse interval change in one direction only, increasing here, this feature is used to distinguish this waveform from others and has a high value for sliding PRI type waveform.

Feature 5: Local extrema of pulse intervals

In case, the pulse waveform has many local maxima and minima, this feature can be used. In this feature, the signum function is differentiated as:

$$h_k = s_{k+1} - s_k, \qquad k = 1,2, \ldots \ldots N-3$$

And the feature is given by:

$$f_5 = {\sum_{k=1}^{N-3} |sgn(h_k)|}/{N-3}$$

Pulses with many local maxima and minima will have a higher value of this feature as compared to other pulses which do not have many local maxima and minima. As seen in fig. 1, staggered and jittered pulse waveform has many local maxima and minima, hence, is used to distinguish them from other waveform types.

3. Limitations and Classification Capability

It is assumed that the environment is constant during the observation period. Dwell and switch PRI type cannot be distinguished from constant PRI if less than one stage is simulated. Therefore, in case of Dwell and switch, two stages of stable pulse interval are simulated. Also, periodic PRIs having observation time less than one modulation period are not simulated.

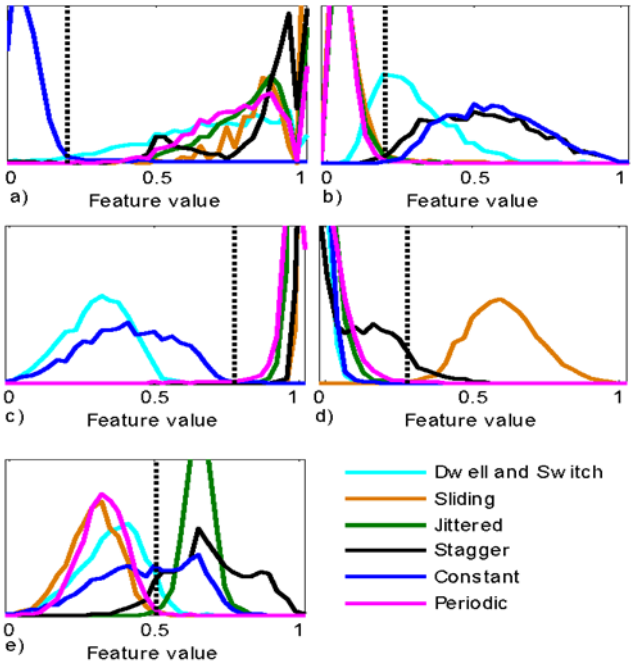

Figure 3: Features and their values for different

Fig. 3 shows the probability distribution for different features discussed above for all the mentioned waveforms. The features which do not overlap are able to distinguish the modulation type without any ambiguity.

	Feature				
	1	2	3	4	5
Constant	0	1	0	0	X
Stagger	1	1	1	X	X
Jittered	1	0	1	0	1
Sliding	1	0	1	1	0
Dwell and switch	1	X	0	0	X
Periodic	1	0	1	0	0

Figure 4: Separation capability of the features

Table in figure 4 shows the performance of the features for different types of modulation PRI. The values given are 0,1 and X. The features with value 0 provide good separation from features with value 0. And X essentially means it doesn't provide good feature separation. For eg, feature 1 has value 1 for all waveform type but constant PRI. Thus, this feature can be used to distinguish constant PRI type waveform [6]. Thus, it can be said that the selected features either individually or collectively can be used to identify the PRI modulation type and ultimately for emitter recognition.

I. GATE TIME METHOD

In this method, the waveform data is first collected for the given observation period, T, which is then divided into gate intervals, τ. The number of pulses occurring in the given gate pulse is recorded. After this, the relative frequency of the pulses in the gate interval is calculated as shown:

$$x_t = n_t - n_{min}$$

Where, n_t is the number of pulses in gate interval t and n_{min} is the minimum number of pulses recorded in any gate interval during the observation period. This recorded relative pulse gives information about the waveform type. Also, in the case of the dense environment, i.e. in the case of multiple emitters, the recorded pulses are found to be of the order of the number of emitters.

The discussed method is a probabilistic method where the probability of occurrence of states are found and compared. The computational complexity offered using this method is less compared to the TOA method [4]. Here, it is assumed that the environment is kept constant during the observation period and the pulses are unsynchronized to consider a realistic scenario. A case of fixed PRI and variable will be discussed in detail below.

II. EMITTERS WITH FIXED PRI

In case of fixed PRI, the gate time, τ, is selected as:

$$Wz < \tau < (W+1)z$$

Where, z is the PRI and W represents a non negative integer. Let us assume the time from gate pulse to pulse starting time be θ_t. Now, consider a case where PRI is given by 1.2 and gate pulse as shown. In this case, the values are given in table

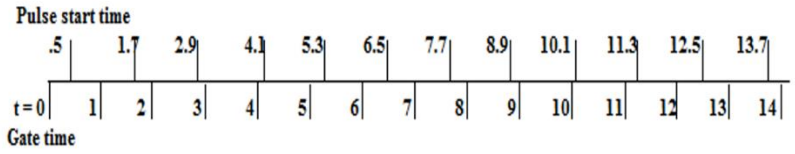

Figure 5: Gate time and pulse start time for fixed PRI

Thus, it can be seen that $x_t = 0$ if $0 < \theta_t < \tau - wz$ and $x_t = 1$ if $\tau - wz < \theta_t \leq z$

Gate interval	θ_t	x_t
0-1	.5	1
1-2	.7	1
2-3	.9	1
3-4	1.1	0
4-5	.1	1
5-6	.3	1
6-7	.5	1
7-8	.7	1
8-9	.9	1
9-10	1.1	0
10-11	.1	1
11-12	.3	1
12-13	.5	1
13-14	.7	1

In this case, the states for x_t is 0 and 1 with probabilities,

$$p_0 = \frac{(w+1)z - \tau}{z} \; and \; p_1 = \frac{\tau - Wz}{z}$$

Dense environment

Considering K fixed PRI emitters, the state value is given by $x_t = \{0,1,2 \ldots . k\}$ where $k = N_{max} - N_{min}$. In this case, the probabilities of the states p_j^k, where j is the state value and k is the number of emitters is given in terms of p_0^k as:

$$P_{j,K} = \sum_{i_1,i_2,\ldots,i_j=1}^{K} (1 - p_{i_1})(1 - p_{i_2})\ldots(1 - p_{i_j})\, p_{i_j+1}\, p_{i_j+2} \cdots p_{i_K}$$

$$i_1 < i_2 < \ldots < i_j$$

$$\{i_j + 1, i_j + 2, \ldots, i_K\} = \{1, 2, \ldots, K\} - \{i_1, i_2, \ldots, i_j\}$$

$$, j = 1, 2, \ldots, K.$$

Thus, for fixed PRI, in case of dense environment, each possible state will have a fixed probability and thus can be identified using maximum likelihood by observing the sequence of x_t

4. Emitters with Variable PRI

In case of single emitter, the number of states can be more than 2 depending on the gate time and type of emitter. Using the similar approach as of fig. [4], The probabilities of different states for 2 stagger waveforms having PRI, z_1 *and* z_2 is found shown in fig. [5]. The gate time is considered to be less than both PRI and $z_1 < z_2$

Case	Gate time (τ) limits W = 0,1,2...	Possible number of pulses	States of model	Model state probabilities
A	$W(z_1+z_2)$,	2W	0	$p_0 = \frac{(2W+1)(z_1+z_2) - 2\tau}{z_1+z_2}$
	$W(z_1+z_2) + z_1$	2W+1	1	$p_1 = \frac{2\tau - 2W(z_1+z_2)}{z_1+z_2}$
B	$W(z_1+z_2) + z_1$,	2W	0	$p_0 = \frac{W(z_1+z_2) + z_2 - \tau}{z_1+z_2}$
		2W+1	1	$p_1 = \frac{2z_1}{z_1+z_2}$
	$W(z_1+z_2) + z_2$	2W+2	2	$p_2 = \frac{\tau - z_1 - W(z_1+z_2)}{z_1+z_2}$
C	$W(z_1+z_2) + z_2$,	2W+1	0	$p_0 = \frac{(2W+2)(z_1+z_2) - 2\tau}{z_1+z_2}$
	$(W+1)(z_1+z_2)$	2W+2	1	$p_1 = \frac{2\tau - (2W+1)(z_1+z_2)}{z_1+z_2}$

Figure 6: Probability of state for variable PRI

Similar results can be found for 3 stagger waveform and above and are discussed in [3]. The results of state probability for fixed PRI and 2 stagger variable PRI can be used to find the state probability for different PRI for different gate time intervals. And using the appropriate probability density function, the state probability of any PRI can be found.

Type of PRI variation	$\tau < a$	$\tau = \tau_1 = (a+b)/2$	$\tau = 2\tau_1 = a+b$
Fixed PRI	$p_0 = (z-\tau)/z$ $p_2 = 0$	$p_0 = 0$ $p_2 = 0$	$p_0 = 0$ $p_2 = 0$
Two position stagger	$p_0 = \frac{z_1+z_2-2\tau}{z_1+z_2}$ $p_2 = 0$	$p_0 = \frac{z_2-z_1}{2(z_1+z_2)}$ $p_2 = p_0$	$p_0 = 0$ $p_2 = 0$
Uniform	$p_0 = \frac{a+b-2\tau}{a+b}$ $p_2 = 0$	$p_0 = \frac{b-a}{4(a+b)}$ $p_2 = p_0$	$p_0 = \frac{b-a}{3(a+b)}$ $p_2 = p_0$
Sinusoidal	$p_0 = \frac{a+b-2\tau}{a+b}$ $p_2 = 0$	$p_0 = \frac{b-a}{\pi(a+b)}$ $p_2 = p_0$	$p_0 = \frac{4(b-a)}{\pi^2(a+b)}$ $p_2 = p_0$

Figure 7: Probabilities for PRI recognition and parameter identification

In the case of a dense environment, i.e. when many emitters are present, the estimation is similar as discussed above. The probabilities of different states are estimated, the polynomial coefficient can be estimated, which in turn helps in finding the number of emitters and emitter parameters like τ, z, a, b

5. PRI Type Recognition and Parameters Estimation

Another important step in emitter identification is PRI recognition and estimation of parameters(τ, z). In this, the state probabilities are calculated considering:

$$\tau < a, \tau = \frac{a+b}{2} \; and \; \tau = a + b.$$

The calculated probabilities are compared with standard results shown in fig. [7] for PRI estimation. Once the type of PRI is estimated, which is then furthered into parameter estimation using maximum likelihood. It first checks for fixed PRI, then 2 position stagger and finally uniform PRI. It faces difficulty in estimating uniform and sinusoidal PRI variations.

6. Adaptive Identification and Pulse Identification

In identifying when any new emitter starts transmitting, it is assumed that the emitter starts or stops transmitting one by one. In this case, the polynomial before the change in emitter behavior is considered known and the polynomial after emitter state change is calculated. Then comparing both the polynomial, before emitter state change and after state change, the emitter type is recognized. In this way, the computational burden in greatly reduced.

Another important step is the detection of any new overlapping pulses. In this case, the IF signal is calculated and is seen that whenever a new pulse starts or stops, there is a sharp change in IF signal amplitude and phase. However, a detector to detect this change is very costly. Therefore, a combination of band pass filters and logic gate switch pulse detector is used. In this, if there are two overlapping pulses, it will be seen as two pulses at the pulse counter detector.

7. Limitation and Detection Capability

In emitter recognition using probabilistic method, for accurate estimates made from maximum likelihood, the zeroes of the polynomial should be real. Also, it is seen that correct estimates are made for a longer observation period. It is also seen that the value of τ for which the maximum value of discriminant of a polynomial is obtained, provides the best result for emitter recognition. However, it is seen that instead of finding the roots of the polynomial, the adaptive approach works better for PRI identification and estimating other parameters.

8. Conclusion

Waveform recognition or emitter recognition forms a challenging problem especially if time domain agility is present. Automatic recognition of waveform is essential to take timely measures. Here, recognition is done based on PRI modulation. 5 features are discussed based on statistical and sequential properties of the signal. A multi-layer perceptron neural network was formed for validating the separation performance of the features. It is seen that the selected features can distinguish very well between constant, dwell and switch, jittered, staggered, periodic, sliding-type PRIs. Hence, the selected features along with the application of neural networks work fine for emitter recognition. The discussed approach however doesn't work for variable PRI and in a dense environment.

The gate time method discussed above is an adaptive method and adapts itself with changes in the environment. Also, this method doesn't involve any searches for features and this provides a lower computational burden. Thus, this method allows emitter with time agility to be recognized with high accuracy even in a dense environment at a reasonable cost.

Acknowledgments

This work was supported partially by Research Council (EPSRC) in the UK under grant EP/E022936 and the European Union's Horizon 2020 research and innovation programme under grant agreement H2020-MSCA-ITN-2016 SECRET-722424.

Reference:

[1] Kauppi, J. P., & Martikainen, K. S. (2007). An efficient set of features for pulse repetition interval modulation.

[2] Hawkes, R. M. (1980). Radar emitter recognition using pulse repetition interval. ELECTRONICS RESEARCH LAB ADELAIDE (AUSTRALIA).

[3] Noone, G. P. (1999, February). A neural approach to automatic pulse repetition interval modulation recognition. In 1999 Information, Decision and Control. Data and Information Fusion Symposium, Signal Processing and Communications Symposium and Decision and Control Symposium. Proceedings (Cat. No. 99EX251) (pp. 213-218). IEEE.

[4] Hawkes, R. M. (1980). Radar emitter recognition using pulse repetition interval. ELECTRONICS RESEARCH LAB ADELAIDE (AUSTRALIA).

[5] Zade, A. A. T., & Pezeshk, A. M. (2016, November). Pulse repetition interval detection using statistical modeling. In Proceedings of the 8th International Conference on Signal Processing Systems (pp. 100-104).

[6] Norgren, E. (2019). Pulse repetition interval modulation classification using machine learning.

[7] Milojević, D. J., & Popović, B. M. (1992, February). Improved algorithm for the deinterleaving of radar pulses. In IEE Proceedings F (Radar and Signal Processing) (Vol. 139, No. 1, pp. 98-104). IET Digital Library.

[8] Ahmadi, M., & Mohamedpour, K. (2012). PRI modulation type recognition using level clustering and autocorrelation. American Journal of Signal Processing, 2(5), 83-91.

A Planar Multi-Antenna Design Supporting 3.4-4.2 GHz for 5G Smartphone Applications

Naser Ojaroudi Parchin*[1], Haleh Jahanbakhsh Basherlou[2], Yasir I. A. Al-Yasir[3], Yim F. Hu[4], and Raed A. Abd-Alhameed[5,6]
{N.OjaroudiParchin@Bradford.ac.uk[1*]}

Faculty of Engineering and Informatics, University of Bradford, Bradford BD7 1DP, UK[1,3,4,5]
Bradford College, Bradford, West Yorkshire, BD7 1AY, UK[2]
Information and Communication Engineering Department, Basrah University College of Science and Technology, Iraq[6]

Abstract. A MIMO antenna array with suitable features for 5G mobile phone applications is presented in this study. With 75×150×0.8 mm^3 FR-4 dielectric, two rows of tiny monopole antenna arrays are mounted on the right and left sides of the mainboard. A modified T-shaped resonator with discontinuous feeding and a protruded L-shaped strip make up the monopole element's schematic. The design parts have all been etched into the same layer of the ground. The proposed array is extremely compact and takes up very little space on the PCB plane. The presented MIMO smartphone antenna is designed to support the sub 6 GHz 5G network and provides a 3.4-4.2 GHz operation band. Also, due to the arrangement of the elements, it could operate as two sets of 1×4 phased arrays with high-gain and beam steerable radiation patterns. The MIMO performance, user-hand effect, and critical properties of the introduced monopole antenna array design are studied.

Keywords: 5G, MIMO system, mobile-phone antenna, a monopole antenna, wireless communications.

1 Introduction

Multiple-input-multiple-output (MIMO) with multiple radiation elements has been gaining a lot of interest for next-generation (5G) communication networks to meet the rising demand for transmission rate and throughput for various applications [1-5]. The 5G communication system also requires an array antenna with an enhanced number of antenna elements and dual-polarization capability in the case of massive MIMO [6-10]. MIMO antennas have been seen in a variety of smart and portable devices, including smartphones, laptops, and tablets. Many problems must be overcome in order to achieve an efficient MIMO operation for user equipment [11-18].
Monopole resonators, among the numerous forms of MIMO antennas, are more ideal due to their appealing properties. Recently, various MIMO antennas with narrow bandwidth and large sizes are represented for sub 6 GHz mobile-phone applications [19-25]. We introduce here a MIMO monopole antenna array with eight elements and a wide operation band of 3.4-4.2 GHz. The employed monopole antenna elements have low profiles, and their configuration

IMDC-IST 2021, September 07-09, Sakarya, Turkey
Copyright © 2022 EAI
DOI 10.4108/eai.7-9-2021.2314981

contains a modified T-shaped resonator with discrete feeding and a protruded L-shaped strip. The experiment was conducted using the EM simulation CST programme [26].
The scattering parameters, patterns, efficiency, and gain of the planned array have all been evaluated and achieved for best performance. Furthermore, the suggested 5G antenna performs well in the proximity of the user-hand phantom. Based on the research work discussed in the following, sufficient characteristics are achieved with straightforward structure and novel. Section 2 presents the schematic and design details. Its fundamental characteristics and the MIMO antenna performance are illustrated in section 3. Section 4 investigates the antenna radiation behaviour with a double-hand phantom. The last section of the paper will conclude this research study.

2 Configuration and Geometrical Details

The introduced phased array is depicted schematically in Fig 1. It includes eight monopole antennas that are arrayed in two sets of 14 linear array on both sides of the PCB plane, as seen. The antenna was mounted on the same layer of the ground. Table 1 lists the antenna parameters and their values.

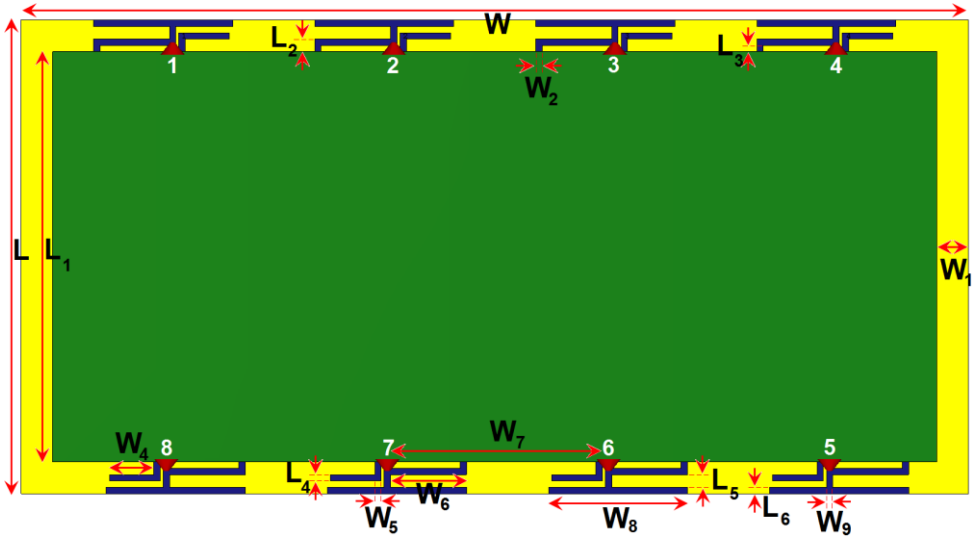

Fig 1. Antenna elements handset.

Table 1. Dimension of the antenna structure all in mm.

W	L	W1	L1	W_2	L2	W_3	L_3
150	75	5	65	0.5	2	0.5	1
W4	L4	W5	L5	W6	L6	W7	W8
7	1	0.5	2	12	1	35	22

3 Characteristics of the MIMO Array

Figs 2 (a) and (b) illustrate S_{nn} (scattering parameters) and S_{mn} (transmission coefficient) properties of the designed MIMO monopole array, respectively. As seen from Fig 2 (a), a wide operating frequency band of 800 MHz for $S_{nn} \leq$- 10 and 1400 MHz for $S_{nn} \leq$ -6 dB is obtained. In addition, sufficient mutual couplings have been obtained as illustrated in Fig 2 (b).

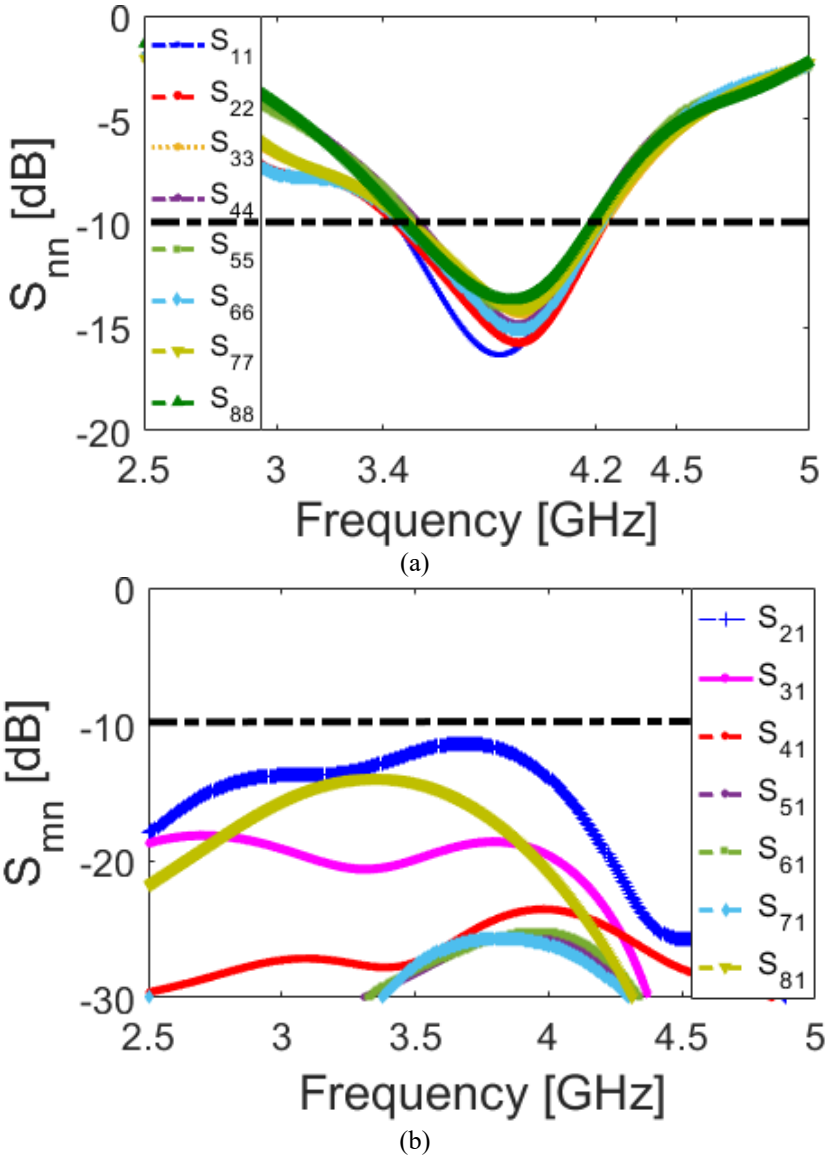

Fig 2. Scattering parameters, (a) S_{nn} and (b) S_{mn}.

Figures 3 (a) and 3 (b) illustrate the efficiencies of the proposed antenna elements. At 3.4-4.2 GHz, it has been observed that sufficient and high-efficiency results have been produced. A higher than 80% radiation efficiency characteristic is attained for 3.4 4 GHz, as illustrated in Fig 3 (a). Furthermore, as shown in Figure 3 (b), more than 65 percent of total efficiencies have been achieved [27-30].

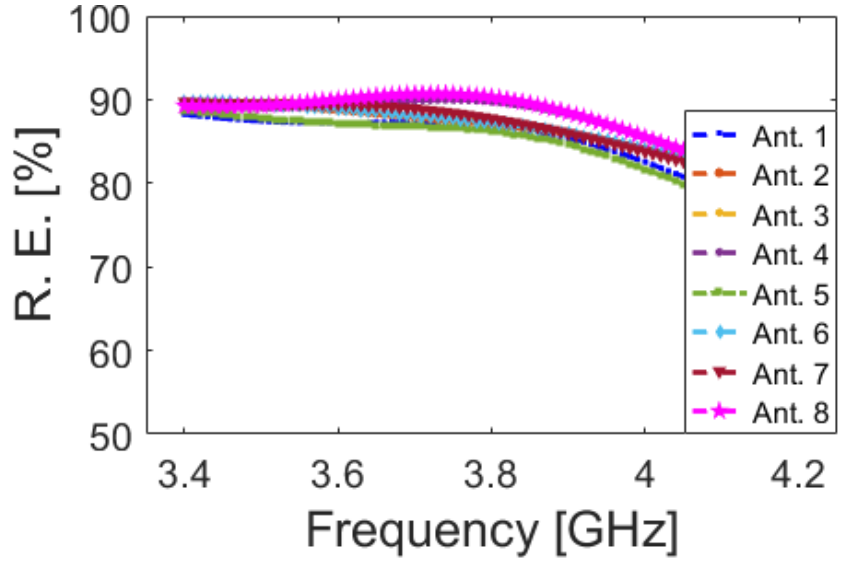

(a)

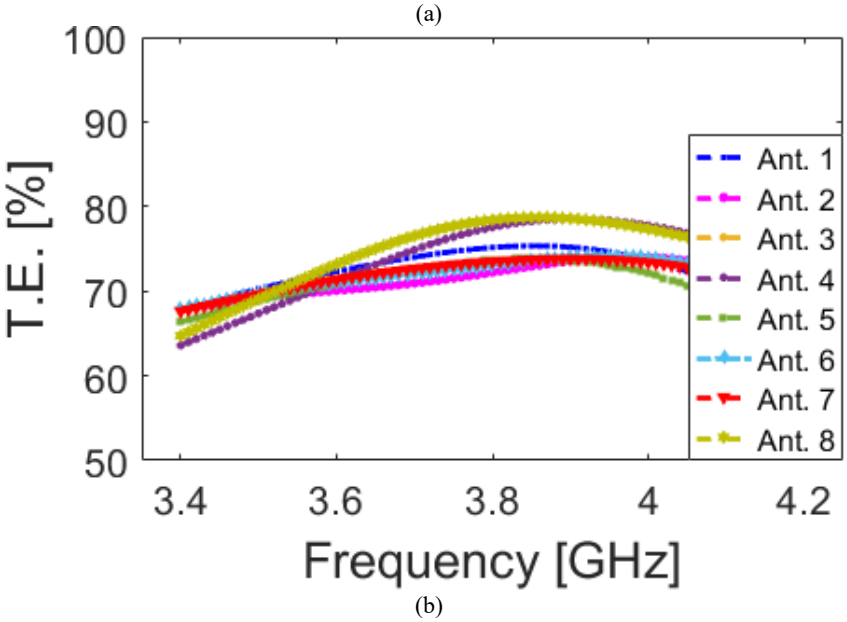

(b)

Fig 3. (a) Radiation efficiency and (b) total efficiency results.

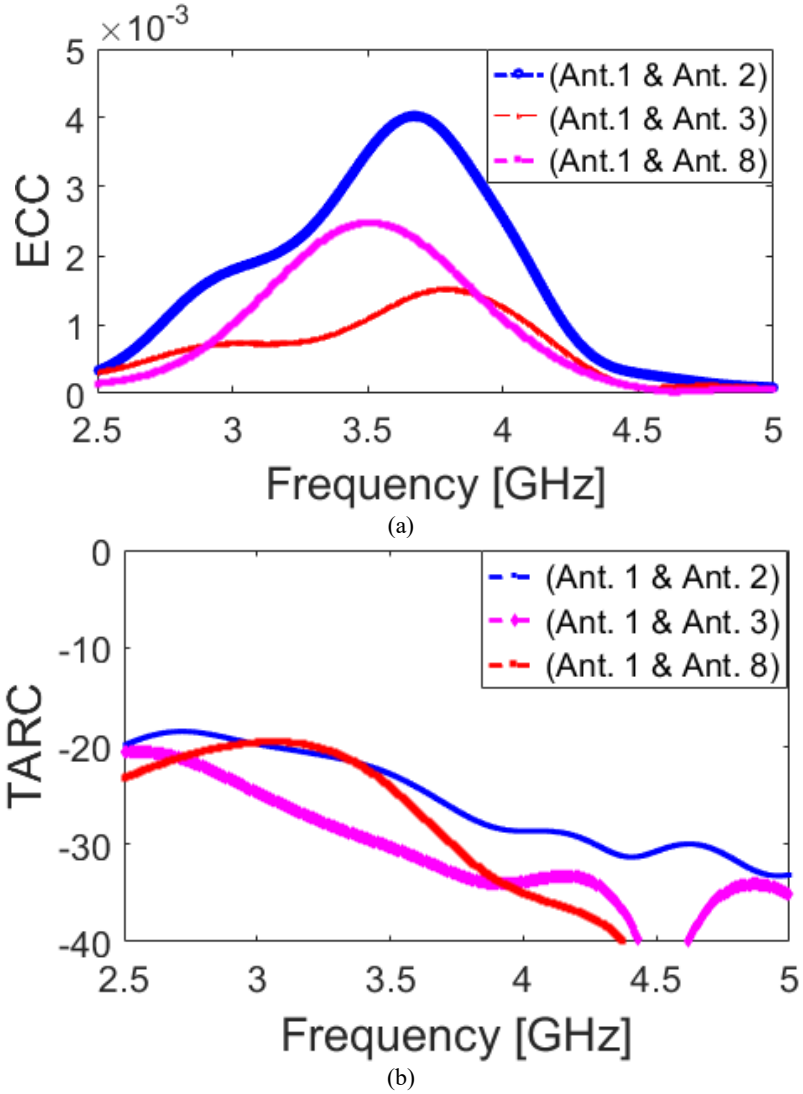

Fig 4. a) ECC, b) TARC properties.

ECC and TARC requirements are critical in MIMO systems and should be kept as small as possible [31-32]. The variations of these parameters for a closely spaced element are shown in Figures 4 (a) and (b). Within the operation band, these values are quite low. At the intermediate frequency (3.8 GHz), the 3D fluctuation of the radiated field for the antenna elements is investigated and depicted in Fig. 5. This diagram illustrates the field shape and how the elements of the MIMO antenna may support different sides of the handset while also improving the design's performance [33-36]. In addition, good gain values are achieved for each antenna resonator. As mentioned earlier, the set of antennas could operate as two sets of 1×4 phased arrays with high-gain and beam-steerable radiation patterns. Fig 6 investigates the radiation performance of the sub-arrays at the resonance frequency (3.8 GHz) and different

scanning angles. According to obtained results, it is found that each set of 1×4 sub-array could provide high gain radiation beams with a wide beam-steering. Figure 7 plots and compares the main characteristics of the element and the main sub-array antenna over 3.4 to 4.2 GHz. As see, the element can provide 2-4.5 dBi maximum gain while the sub-array exhibits a high maximum gain characteristic (6-8.5 dBi) over the antenna operation band [37-42].

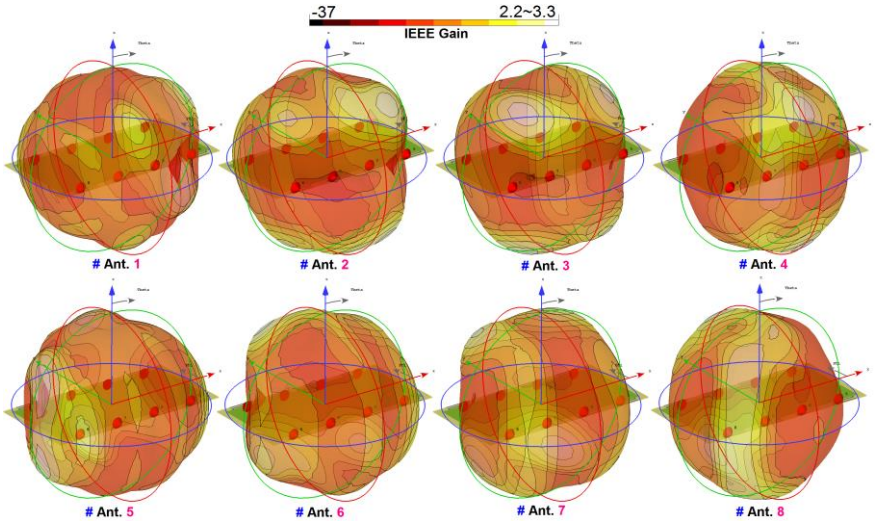

Fig. 5. 3D Radiations of each antenna element at 3.8 GHz.

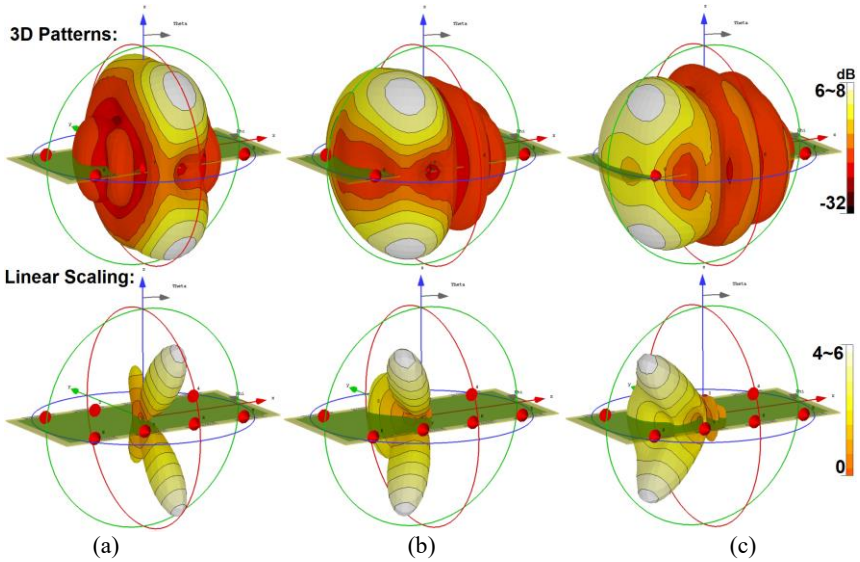

Fig 6. Beam patterns of the sub-arrays (1×4 linear array) at (a) 0, (b) 30, and (c) 60 degrees.

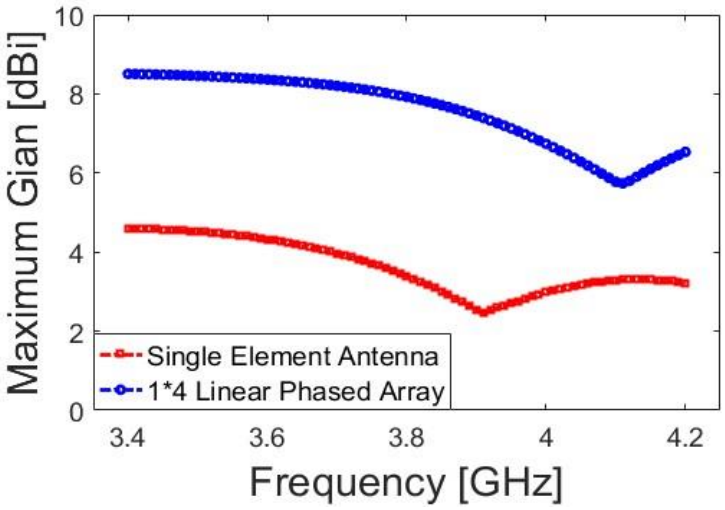

Fig 7. Max gains of a single element and the sub-array antennas.

4 User-Hands Impact

It is possible to lower the antenna performance with the user hand. This is also dependent on the antenna component's distance and positioning [43-45]. The features of the inserted antenna elements in the presence of the double-hands model are illustrated in the following section.. The placement and S_{nn} results in the double-hand scenario are depicted in Figs. 8 and 9, respectively. As depicted, the introduced mobile antenna design exhibits sufficient S_{nn} results supporting the target frequency band.

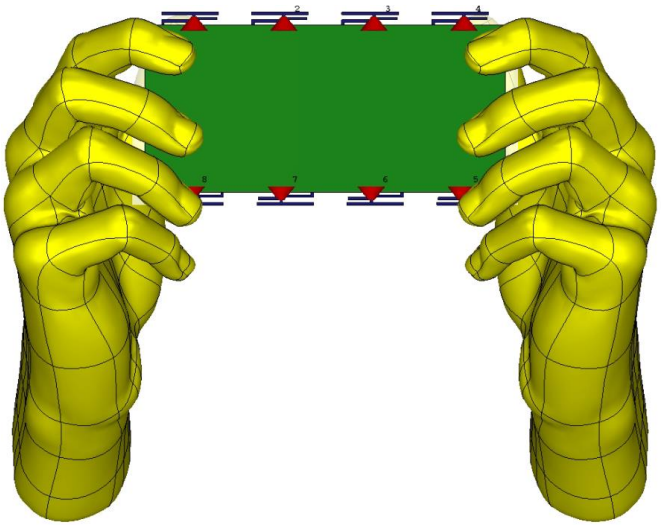

Fig 8. In double-hand mode, the antenna is positioned.

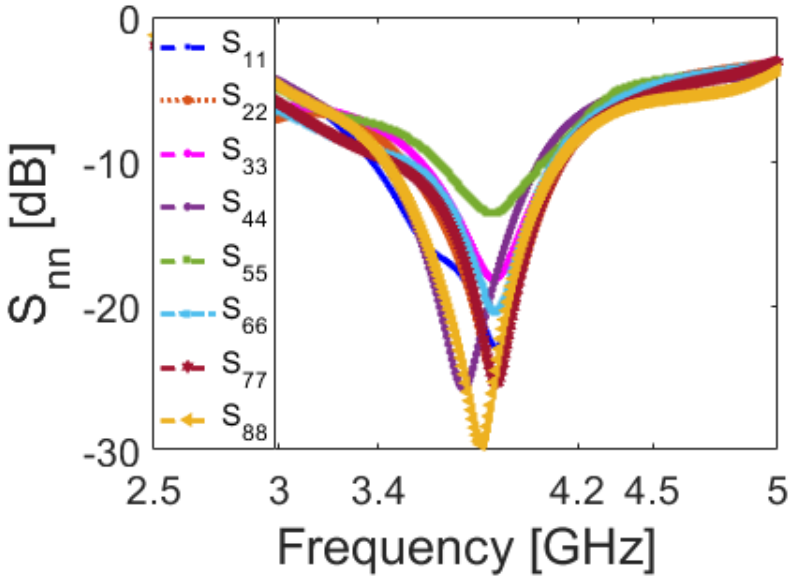

Fig 9. The variations of S_{nn} with user's hand.

Furthermore, the suggested mobile-phone antenna has high efficiency (30 percent -60 percent). The antennas' efficiency levels are reduced, but not dramatically, as seen in Fig. 10. This could be owing to the used element's tiny and compact sizes, which are not covered by the user's hand. It's worth mentioning that the resonators partially encompassed by the phantom show the greatest decreases in performance [46].

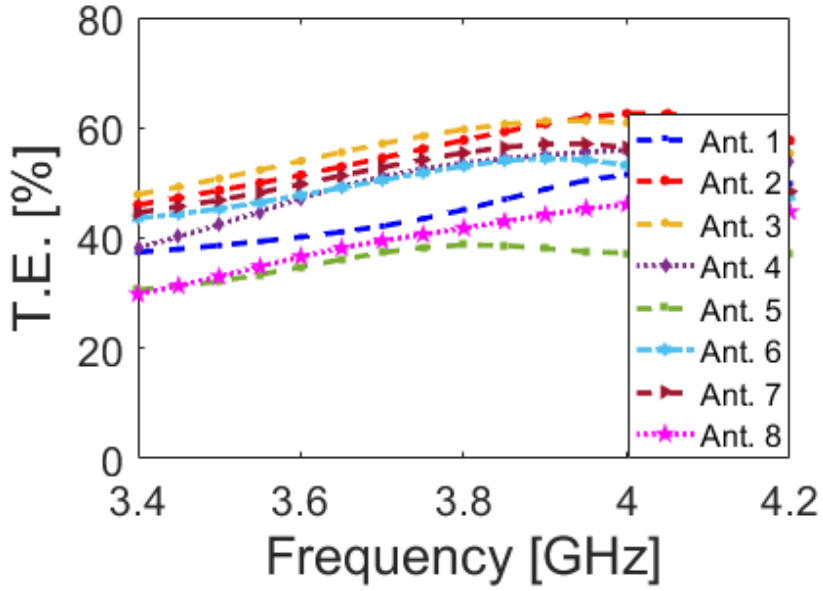

Fig. 10. Antenna total efficiencies with user's hand.

5 Conclusion

For 5G mobile phone applications, an antenna array with compact resonators and large impedance bandwidth has been introduced. At both sides of mobile phone mainboard, eight small monopole antenna arrays are designed to function in the 3.4-4.2 GHz sub-6 GHz 5G band. A modified T-shaped resonator with discrete feeding and a protruded L-shaped strip are included in each monopole antenna element. It also takes up a minimal amount of space on the PCB plane and has sufficient properties. The most important parameters of the designed handset were explored.

Acknowledgment

The European Union's Horizon 2020 innovation programme under grant agreement H2020-MSCA-ITN-2016 SECRET-722424 and the UK Engineering and Physical Sciences Research Council (EPSRC) under grant EP/E022936/1 supported this research.

References

[1] Osseiran A, et al. Scenarios for 5G mobile and wireless communications: the vision of the METIS project. IEEE Commun. Mag. 2014, 52:26-35.
[2] Parchin, N. O. et al.: Microwave/RF components for 5G front-end systems. Avid Science. 2019, 1-200.
[3] Parchin, N. O. et al.: Wide-scan phased array antenna fed by coax-to-microstriplines for 5G cell phones. 2016 21st International Conference on Microwave, Radar and Wireless Communications. MIKON 2019, Krakow, Poland.
[4] Al-Yasir, Y. et al.: New radiation pattern-reconfigurable 60-GHz antenna for 5G communications. Modern Printed Circuit Antennas, IntechOpen. 2019.
[5] Ullah, A. et al.: Coplanar waveguide antenna with defected ground structure for 5G millimeter wave communications. IEEE MENACOMM'19, 2019, Bahrain.
[6] Yang HH, Quel YQS. Massive MIMO meet small cell. SpringerBriefs in Electrical and Computer Engineering. 2017. DOI 10.1007/978-3-319-43715-6_2.
[7] Parchin, N. O. et al.: Dual-polarized MIMO antenna array design using miniaturized self-complementary structures for 5G smartphone applications. EuCAP 2019, Krakow, Poland.
[8] Mazloum, J. et al.: Compact triple-band S-shaped monopole diversity antenna for MIMO applications. ACES Journal, 2015, 28:975-980.
[9] Parchin, N. O. and Abd-Alhameed: A compact Vivaldi antenna array for 5G channel sounding applications. EuCAP 2018, London, UK.
[10] Parchin, N. O. et al.: Mobile-phone antenna array with diamond-ring slot elements for 5G massive MIMO systems. Electronics. 2019, 8:521.
[11] Zhang Z, Antenna Design for Mobile Devices. Wiley-IEEE Press. 2011, NJ, USA.
[12] Ojaroudi, N. and Ghadimi, N.: Dual-band CPW-fed slot antenna for LTE and WiBro applications. Microw. Opt. Technol. Lett. 2014, 56:1013–1015.
[13] Musavand, J. et al.: A Compact UWB Slot Antenna with Reconfigurable Band-Notched Function for Multimode Applications. ACES Journal, 2016, 31:14-18.
[14] Ojaroudiparchin, N. et al.: 8×8 planar phased array antenna with high efficiency and insensitivity properties for 5G mobile base stations. EuCAP 2016, Switzerland.
[15] Parchin, N. O. et al.: Frequency reconfigurable antenna array with compact end-fire radiators for 4G/5G mobile handsets. IEEE 2nd 5G World Forum. 5GWF 2019, Dresden, Germany.
[16] Ojaroudiparchin, N. et al.: Low-cost planar mm-Wave phased array antenna for use in mobile satellite (MSAT) platforms. Telecommunications Forum, TELFOR 2015, Belgrade, Serbia.

[17] Ojaroudi, N.: A novel design of microstrip antenna with reconfigurable band rejection for cognitive radio applications. Microw. Opt. Technol. Lett. 2014, 56:2998–3003.
[18] Jensen M, Wallace J. A review of antennas and propagation for MIMO wireless communications. IEEE Trans. Antennas Propag. 2004, 52: 2810–2824.
[19] Abdullah M, et al. Eight-element antenna array at 3.5GHz for MIMO wireless application. PIER C. 2017, 78: 209-217.
[20] Parchin NO, et al. Dual-polarized MIMO antenna array design using miniaturized self-complementary structures for 5G smartphone applications. EuCAP 2019, Krakow, Poland.
[21] Li Y, et al. High-isolation 3.5-GHz 8-antenna MIMO array using balanced open slot antenna element for 5G smartphones. IEEE Trans. Antennas Propag. 2019, 67: 3820-3830.
[22] Wang L, et al. Compact UWB MIMO antenna With high isolation using fence-type decoupling structure. IEEE Antennas and Wireless Propagation Letters. 2019, 8:1641-1645,.
[23] Basherlou, H. J. et al.: MIMO monopole antenna design with improved isolation for 5G WiFi applications. International Journal of Electrical and Electronic Science. 2019, 7:1-5.
[24] Parchin, N. O. et al.: Multi-mode smartphone antenna array for 5G massive MIMO applications. EuCAP 2020, Copenhagen, Denmark.
[25] Chen WS, Lai YC, and Sim CYD, MIMO dongle antenna design for next generation mobile communication system. ICCEM. 2017, 320–322.
[26] CST Microwave Studio, ver. 2017, CST. 2017, Framingham, MA, USA.
[27] Parchin, N. O. et al.: Beam-steerable microstrip-fed bow-tie antenna array for fifth generation cellular communications. EuCAP 2016, Switzerland.
[28] Ullah. A, et al:. A Modified Design of Phased Array Antenna for UWB-5G Cellular Communications. 2020 IMDC-SDSP 8-10 April 2020, Antalya- Turkey
[29] Parchin, N. O. et al.: Dual-Polarized Array Antenna with Quasi-End-Fire Radiation for 28 GHz 5G Mobile terminals. 2020 IMDC-SDSP 8-10 April Antalya- Turkey
[30] Al-Yasir, Y. et al.: New pattern reconfigurable circular disk antenna using two PIN diodes for WiMax/WiFi (IEEE 802.11a) applications. IEEE SMACD 2019, Lausanne, Switzerland.
[31] Sharawi MS, Advancements in MIMO antenna systems. Developments in antenna analysis and synthesis. 2018, Chapter-4. IET.
[32] Musavand A, et al. A compact UWB slot antenna with reconfigurable band-notched function for multimode applications. Appl Comp Electromagn Soc J. 2016, 31:14-18.
[33] Sharawi MS, Printed multi-band MIMO antenna systems and their performance metrics [wireless corner]. IEEE Antennas Propag. Mag. 2013, 55: 218–232.
[34] Parchin NO, Low-profile air-filled antenna for next generation wireless systems. Wirelss Personal Communications. 2017, 97: 3293– 3300.
[35] Chen Q, et al. Design considerations for millimeter wave antennas within a chip package. IEEE International Workshop on Anticounterfeiting, Security, Identification. 2007, Xiamen, China.
[36] Abdollahi, M. M. et al.: Octave-band monopole antenna with a horseshoe ground plane. ACES Journal, 2015, 30:773-778.
[37] Zolghadr, J. et al.: UWB slot antenna with band-notched property with time domain modeling based on genetic algorithm optimization. ACES Journal, 2016, 31:926-932.
[38] Syrytsin I, et al.: Performance investigation of a mobile terminal phased array with user effects at 3.5 GHz for LTE advanced. IEEE Antennas and Wireless Propagation Letters. 2017, 1847-1850.
[39] Kamalvand, A. et al.: Omni-directional/multi-resonance CPW-fed small slot antenna for UWB applications. ACES Journal. 2013, 28:829-835.
[40] Ojaroudi, N.: Microstrip monopole antenna with dual band-stop function for ultrawideband applications. Microw. Opt. Technol. Lett. 2014, 56: 818–822.
[41] Valizade, A. et al.: Band-notch slot antenna with enhanced bandwidth by using Ω-shaped strips protruded inside rectangular slots for UWB applications. ACES Journal, 2012, 27: 816–822.

[42] Siahkal-Mahalle, B. H. et al.: A new design of small square monopole antenna with enhanced bandwidth by using cross-shaped slot and conductor-backed plane. Microwave Opt Technol Lett. 2012, 54:2656–2659.

[43] Khan R, et al. User influence on mobile terminal antennas: A review of challenges and potential solution for 5G antennas. IEEE Access. 2018, 6:77695–77715.

[44] Yasir I. A. Al-Yasir et.al., Trisection Open-Loop Varacter-Based Tunable Filter for 5G Wireless Communications, Proceedings of the 1st International Multi-Disciplinary Conference Theme: Sustainable Development and Smart Planning, 28-30 June 2020, Cyberspace, pp. 315-322.

[45] Atta Ullah and et.al., Dual-Band MIMO Antenna System for Next Generation Smartphone Applications, Proceedings of the 1st International Multi-Disciplinary Conference Theme: Sustainable Development and Smart Planning, 28-30 June 2020, Cyberspace, pp. 331-338.

[46] Ilvonen J, et al. Mobile terminal antenna performance with the user's hand. IEEE Antenna and Wireless Propagation Letters. 2000, 10:772775.

F-Shape Dual-Band MIMO Antenna System for Next-Generation Smartphone Applications

Atta Ullah[1], Naser Ojaroudi Parchin[2], Waqas Manan[3], Yasir I. A. Al-Yasir[4], Raed A. Abd-Alhameed[5,6]

{A.Ullah5@Bradford.ac.uk[1], N.OjaroudiParchin@Bradford.ac.uk[2], R.A.A.Abd@Bradford.ac.uk[5,6]}

Faculty of Engineering and Informatics, University of Bradford, Bradford BD7 1DP, UK[1,2,3,4,5]
Information and Communication Engineering Department, Basrah University College of Science and Technology, Iraq[6]

Abstract. This work presents a 6-element dual-band multiple-input multiple-output (MIMO) antenna in an F-shape for smartphone mobile communication.. It has six antenna elements covering dual-frequency bands that cover the sub-6 GHz spectrum at 3.42-3.77 GHz and the sub-6 GHz spectrum at 5.30-5.63 GHz. The fundamentals are served by F-shaped microstrip feeding positions while the ground is cut in L shape with every antenna element. The proposed scheme's essential elements are examined. It is concerned with respectable S-parameters, adequate isolation, adequate radiation analysis, and efficiency. As proposed by the double-band frequency of 5G smartphones, Ant 3 has a maximum return loss of -35dB at 3.6 GHz and Ant 5 and Ant 6 have a maximum return loss of -38dB at 5.4 GHz.

Keywords: 5G communication, dual-band antenna, smartphone compacted antenna array.

1 Introduction

Following the release of the 5G New Radio (NR) in June 2018, fifth-generation (5G) telecommunications technology is once again anticipating exponential growth, necessitating the development of a 5G antenna design [1-2]. As mobile and communication technology becomes more widely adopted, the use of wireless technology and its applications has grown at a rapid pace. Artificial intelligence (AI), the internet of things (IoT), and mobile video streaming have all contributed to this significant advancement in wireless communication [3-4]. Fifth-generation mobile networks (or 5G) offer the latest solution for advancing wireless communication technology and achieving the mounting need for cell phone communictaions throughout the subsequent phase pending 6G arrives [5-8]. 5G is the definitive answer for wireless communication technology to achieve improved data rates and low latency [9-10].
Presently, the 5th generation of cellular phone communication of the band is recognized as dual regularity bands in 3.42 – 3.77 GHz and 5.30 – 5.63 GHz. The aggregate of 700 MHz bandwidth can be achieved1[11-13]. Then in communication structures, multiple-input multiple-output (MIMO) practises can substantially enhance series operation and channel capability without increasing transmit power and increasing extra transmission bandwidth.

IMDC-IST 2021, September 07-09, Sakarya, Turkey
Copyright © 2022 EAI
DOI 10.4108/eai.7-9-2021.2314980

Nevertheless, as the reduction and probability of wireless gadgets turn out to be the typical mainstream, the accessible spaces for the antenna are further inadequate [14-16]. Hence, it is extremely crucial to project an efficient MIMO antenna. To adopt the frequently utilized wireless machines, publishing MIMO antenna is additional alternatives. Though, there is powerful mutual coupling when the space amongst MIMO antenna components is very close together. It is perverse to the aspiration for sharper isolation and lowers envelop correlation coefficients. Therefore, it is crucial to diminish the mutual coupling among the antenna components [17-18].

However, as the shrinking and compactness of developed wireless systems mainstream, the obtainable planetary for antennas is more restricted. Consequently, it is very compulsory to project a compressed MIMO antenna. To adapt to the usually used wireless systems, printing MIMO antennas is a basic choice [19]. However, there is solid mutual coupling when the detachment between MIMO antenna basics is very adjacent. It is conflicting to the aspiration for higher isolation and lower envelope correlation coefficients. It is crucial to decrease the mutual coupling among the antenna fundamentals [20].

5.30–5.63 GHz is accessible in the suggested architecture to facilitate Sub 6GHz 5G mobile communications. The modernization of the decoupling proposal proposed in this editorial not only efficiently increases separations, but also creates a new booming theme in an alternative frequency band, which covers 5.30 – 5.63 GHz to achieve dual-band working performance, allowing space use in mobile devices to be efficiently developed [21-23]. It describes the S-parameter, maximum gain, user effects, radiation, and efficiency results of the given MIMO compact antenna array.

2 Design and Configuration

With the aid of CST Microwave Studio electromagnetic simulation software an F-shaped 6 Fatal antenna array is designed for this compact mobile MIMO system [24]. FR4 was used with a dielectric loss δ=0.019 and ε_r=4.3 in the proposed project. The dimension of the central substrate is 140×70 mm^2 shown in Figs. 1 and 2 show the Front Side and BackSide respectively. Table 1 demonstrate the comprehensive scopes of the antenna parameters.

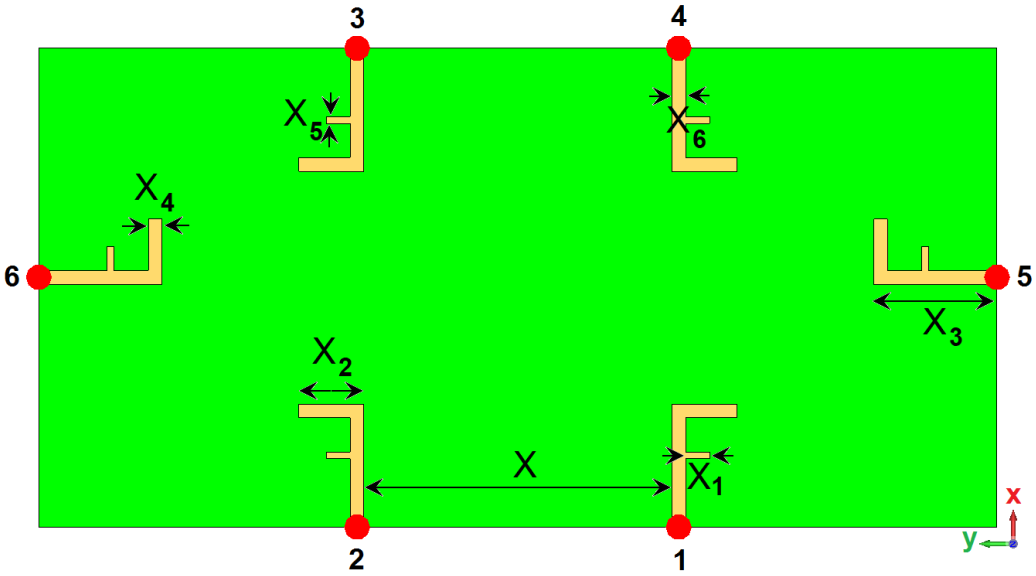

Fig 1. Front View of Schematic structure of the planned MIMO smartphone antenna.

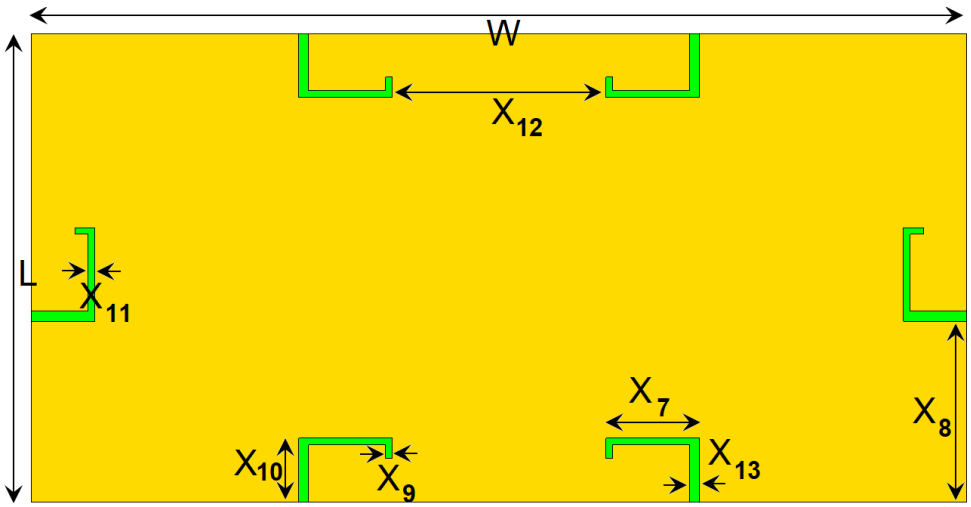

Figure 2. Bottom View of Schematic arrangement of the planned handset.

Table 1. Concluding magnitudes of the antenna parameters.

	W	L	h_{sub}	X	X_1	X_2	X_3	X_4	X_5
Value (mm)	140	70	0.8	48	4	8	18	2	1
Parameter	X_6	X_7	X_8	X_9	X_{10}	X_{11}	X_{12}	X_{13}	
Value (mm)	2	11.5	41.5	1	9.5	1	32	1.5	

3 Results and Discussions

Figure. The characteristics and performance of the suggested six-element MIMO antenna arrays are analysed using CST software in this proposed study [28]. The antenna was developed to achieve the specified divergence return loss, radiation pattern, resonance frequency, and gain, and it uses a 50-ohm SMA connector to produce the required S-parameters. All of these limitations are explained in this article.

In order to support Sub 6GHz of 5G mobile communications, a 6-fundamentals MIMO array offers dual-band radio frequencies from 3.42 to 3.77 GHz and from 5.30 to 5.63 GHz. Figure 3 shows the planned antenna's Snn. The proposed antenna's Smn (m not equal n) is shown in Figure 3. The computer-generated S55 and S66 are both less than -20dB at 3.6 GHz, whereas the simulated S11, S22, S33, and S55 are all less than -20dB at 5.45 GHz. However, at 3.6 GHz, the Snn results for antenna fundamentals 1, 2, 3, and 4 are less than -35 dB, whereas the Snn results for antenna fundamentals 5 and 6 are greater than -35 dB. The results are less than -40dB. The frequency is 5.45GHz. This is primarily owing to the antenna basics' positioning [29-33]. At dual working bands, the antenna fundamentals show good mutual coupling results better than -15 dB and -12 dB, as shown in Fig. 4.

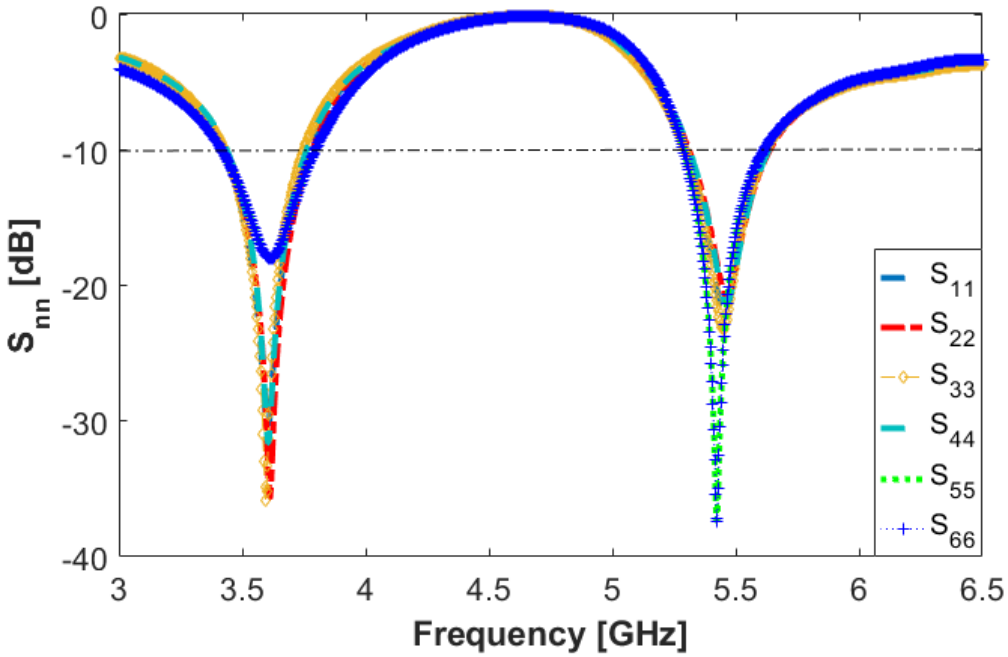

Figure 3. S_{nn} of the array elements.

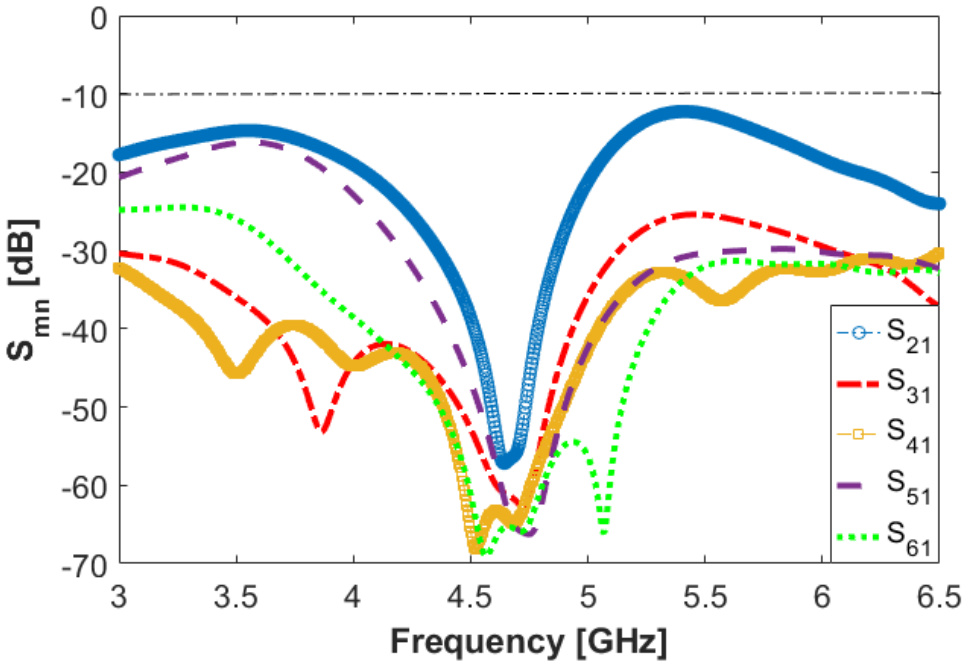

Figure 4. Computed S_{mn} of the array antenna.

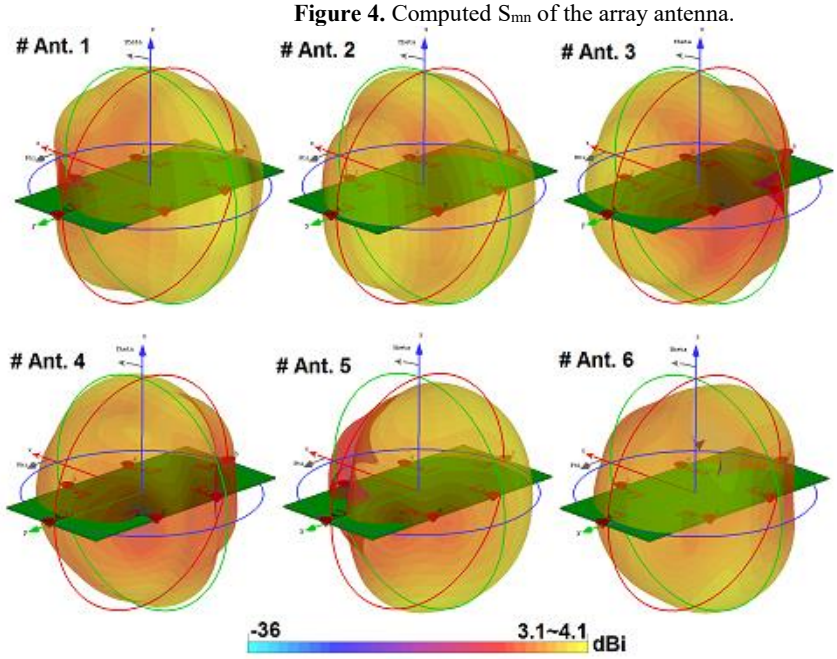

Figure 5. 3D antenna patterns at 3.6 GHz.

Figures 5 and 6 show the 3-D radiation patterns for the six fundamental components of the primary design at both frequencies. This approved 6-part MIMO antenna is capable of providing sufficient radiation analysis for individual radiators [34-37]. Based on the illustrated results, this varies from 3.1-3.11 dB. However, at 5.45 GHz, the fundamentals exhibit a constant gain of 5.8 dB.

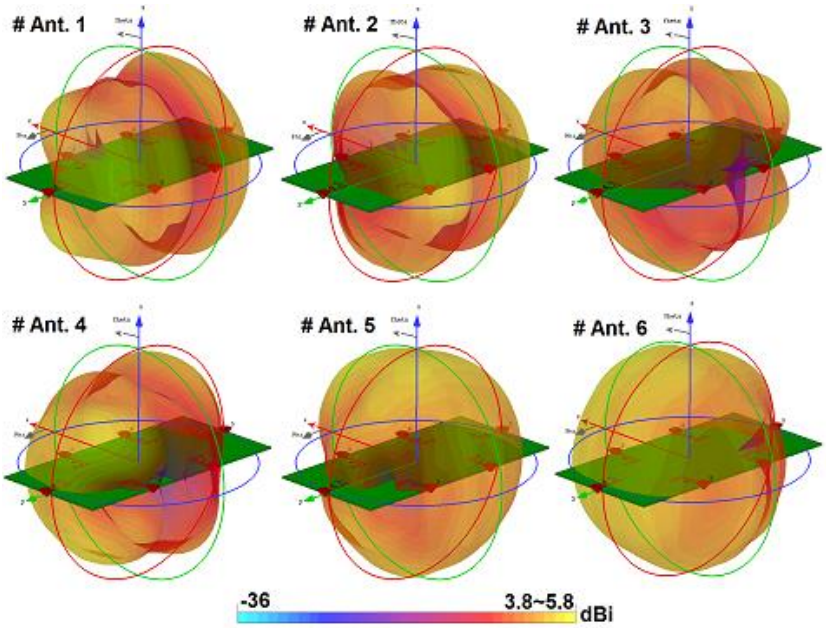

Figure 6. 3D radiation patterns at 5.45 GHz.

In Figures 7 and 8, we also show the antenna efficiencies. Inside the operating bands, extraordinary efficiencies with minor variations can be attained [38-44]. Figure. At the primary and additional working bands, radiation efficiencies exceed 95% and 90%, respectively, for the fundamentals of the proposed MIMO project. Furthermore, as shown in Figure 8, the antenna principles provide overall efficiencies of between 75 and 80 percent.

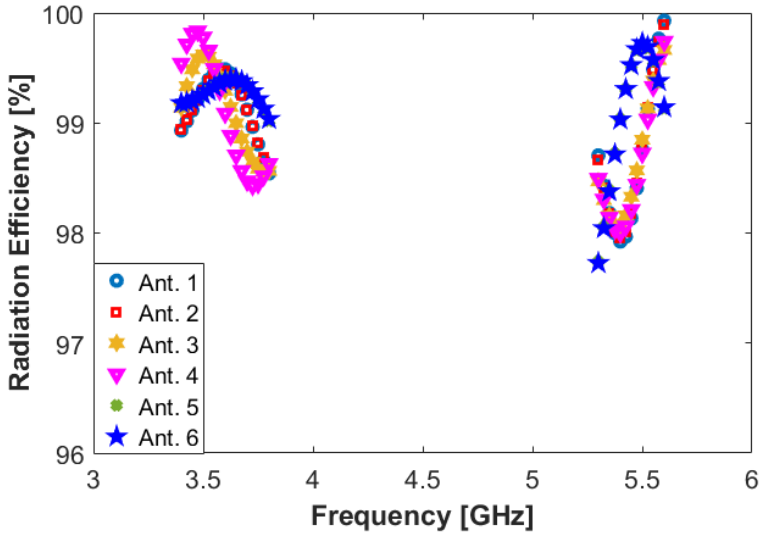

Figure 7. Variations of radiation efficiency versus frequency.

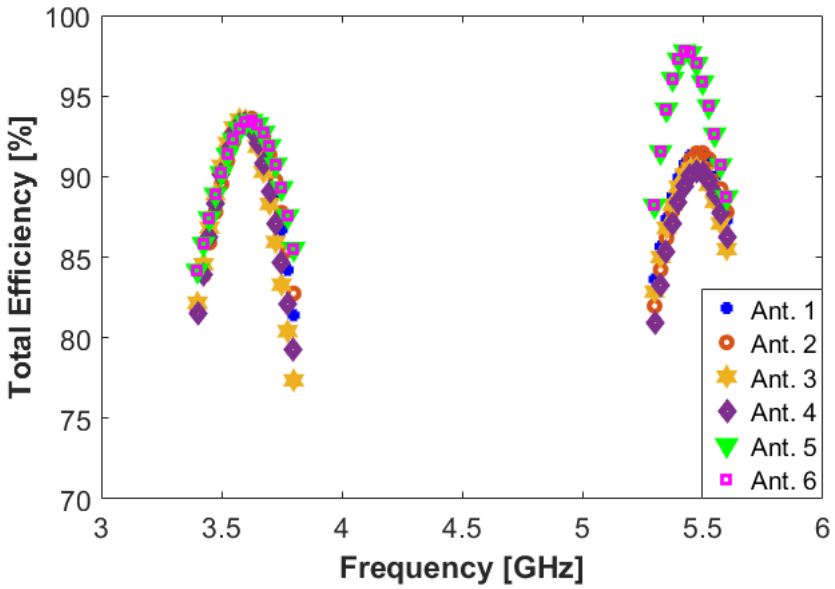

Figure 8. Variations of total efficiency against frequency.

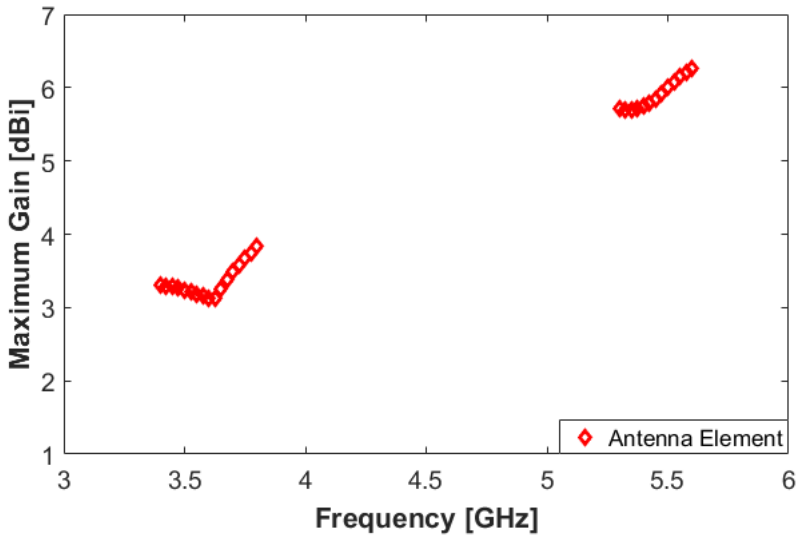

Figure 9. Power gain distribution.

At various frequencies, all antenna essentials display superior gains of greater than 3 dBi up to 6.5 dBi. As can be seen, unlike the first operation band with a centre frequency of 3.6 GHz, the antenna's maximum gains at the second resonance are nearly constant at 6 dBi.

4 Conclusion

An F-shape double-band 6-port 5G MIMO handset has been presented in this article. By exploiting some of the copper's radiation properties, the antenne array should suitably operate in a metal-framed smartphone. It is confirmed that 3.42 - 3.77 GHz and 5.30 - 5.63 GHz covered the required bandwidth. The antenna achieved 80% and 90% radiation and total efficiencies. Aveged over the bandwisth.

References

[1] Lun Cui ,N et al: " An 8-Element Dual-Band MIMO Antenna with Decoupling Stub for 5G Smartphone Applications" IEEE ANTENNAS AND WIRELESS PROPAGATION LETTERS, VOL. 18, NO. 10, OCTOBER 2019.

[2] 3GPP, "Rel-15 success spans 3GPP groups," 2018. [Online]. Avaliable: http://www.3gpp.org/news-events/3gpp-news/1965-rel-15_news

[3] Parchin, N. O. et al.: Microwave/RF components for 5G front-end systems, Avid Science (2019)

[4] Atta Ullah, N. et al: "Dual-Band MIMO Antenna System for Next Generation Smartphone Applications" 2020 IMDC-SDSP 8-10 April 2020, Antalya- Turkey

[5] Agiwal, M. Roy, A. and Saxena, N.: Next generation 5G wireless networks: A comprehensive survey. IEEE Commun. Surveys Tuts. Vol. 18, pp. 1617–1655 (2016)

[6] Ullah. A, N. Et al: "A Modified Design of Phased Array Antenna for UWB-5G Cellular Communications" 2020 IMDC-SDSP 8-10 April 2020, Antalya- Turkey

[7] Li, S. Q.: 5G: Intelligent mobile communication 1.0.ZTE Technol. Vol.5, pp. 47–48 (2016)

[8] Naser Ojaroudi Parchin, N. et al: Dual-Polarized Array Antenna with Quasi-End-Fire Radiation for 28 GHz 5G Mobile terminals" 2020 IMDC-SDSP 8-10 April Antalya- Turkey

[9] Ojaroudiparchin, N. et al.: Design of Vivaldi antenna array with end-fire beam steering function for 5G mobile terminals. TELFOR 2015, Belgrade, Serbia, pp. 587–590 (2015)

[10] Parchin, N. O. et al.: Eight-element dual-polarized MIMO slot antenna system for 5G smartphone applications. IEEE Access. Vol. 9, pp. 15612-15622 (2019)

[11] Andrews J. G. et al.: What will 5G be?," IEEE J. Sel. Areas Commun. Vol. 32, 1065–1082 (2014)

[12] Ojaroudi Parchin. N, et al: "Small-Clearance Phased Array Antenna Design with Miniaturized Elements for 5G Communications" 2020 IMDC-SDSP 8-10 April Antalya- Turkey.

[13] Jensen, M., Wallace, J.: A review of antennas and propagation for MIMO wireless communications. IEEE Trans. Antennas Propag. Vol. 52, pp. 2810–2824 (2004)

[14] Zhang, Z.: Antenna Design for Mobile Devices. Hoboken, NJ, USA: Wiley-IEEE Press (2011)

[15] Li, Y. et al.: High-isolation 3.5-GHz 8-antenna MIMO array using balanced open slot antenna element for 5G smartphones. IEEE Trans. Ant. Propag.(2019) doi:10.1109/TAP.2019.2902751.

[16] Parchin, N. O. et al.: Mobile-phone antenna array with diamond-ring slot elements for 5G massive MIMO systems. Electronics. Vol. 8, 521 (2019)

[17] Wang, L. et al.: Compact UWB MIMO antenna With high isolation using fence-type decoupling structure. IEEE Antennas and Wireless Propagation Letters. Vol. 8, pp. 1641-1645 (2019)

[18] Parchin, N. O. et al.: Dual-polarized MIMO antenna array design using miniaturized self-complementary structures for 5G smartphone applications. EuCAP Conference (2019)

[19] Mazloum, J. et al.: Compact triple-band S-shaped monopole diversity antenna for MIMO applications. ACES Journal, Vol. 28, pp. 975-980 (2015)

[20] Ojaroudi, N. and Ghadimi, N.: Design of CPW-fed slot antenna for MIMO system applications. Microw. Opt. Technol. Lett. Vol. 56, pp. 1278–1281 (2014)

[21] Al-Yasir, Y. et al.: New radiation pattern-reconfigurable 60-GHz antenna for 5G communications. Modern Printed Circuit Antennas, IntechOpen (2019)

[22] Y.Al-Yasir, et al.: A new polarization-reconfigurable antenna for 5G wireless communications. BroadNets'2018, Faro, Portugal (2018)

[23] Parchin, N. O. et al.: Frequency reconfigurable antenna array with compact end-fire radiators for 4G/5G mobile handsets. IEEE 2nd 5G World Forum (5GWF), Dresden, German (2019)

[24] Ojaroudi, N.: Design of microstrip antenna for 2.4/5.8 GHz RFID applications. German Microwave Conference. GeMic 2014, RWTH Aachen University, Germany, March 10-12 (2014)

[25] Valizade, A. et al.: Band-notch slot antenna with enhanced bandwidth by using Ω-shaped strips protruded inside rectangular slots for UWB applications. ACES Journal, Vol. 27, pp. 816–822 (2012)

[26] Ojaroudi, N.: Circular microstrip antenna with dual band-stop performance for ultra-wideband systems. Microw. Opt. Technol. Lett. Vol. 56, pp. 2095-2098 (2014)

[27] Kamalvand, A. et al.: Omni-directional/multi-resonance CPW-fed small slot antenna for UWB applications. ACES Journal. Vol. 28, pp. 829-835 (2013)

[28] CST Microwave Studio; ver. 2018; CST: Framingham, MA, USA (2018)

[29] Al-Yasir, Y. et al.: A new polarization-reconfigurable antenna for 5G applications. Electronics, Vol. 7, pp. 1-11 (2018)
[30] Ojaroudiparchin, N. et al.: 8×8 planar phased array antenna with high efficiency and insensitivity properties for 5G mobile base stations. EuCAP 2016, Switzerland (2016)
[31] Ojaroudiparchin, N. et al.: Low-cost planar mm-Wave phased array antenna for use in mobile satellite (MSAT) platforms. Telecommunications Forum, Serbia, pp. 528-531 (2015)
[32] Al-Yasir, Y. et al.: New pattern reconfigurable circular disk antenna using two PIN diodes for WiMax/WiFi (IEEE 802.11a) applications. IEEE Proceeding of International Conference on Synthesis, Modeling, Analysis and Simulation Methods and Applications to Circuit Design (SMACD) 2019, Lausanne, Switzerland (2019)
[33] Parchin, N. O. et al.: Multi-band MIMO antenna design with user-impact investigation for 4G and 5G mobile terminals. Sensors. Vol. 19, pp. 1-16 (2019)
[34] Ojaroudi, N. et al.: Design of triple-band monopole antenna with meander line structure for MIMO application**.** Microw. Opt. Technol. Lett. Vol. 54, pp. 2168–2172 (2012)
[35] Basherlou, H. J. et al.: MIMO monopole antenna design with improved isolation for 5G WiFi applications. International Journal of Electrical and Electronic Science. Vol. 7, pp. 1-5 (2019)
[36] Parchin, N. O. et al.: Multi-mode smartphone antenna array for 5G massive MIMO applications. EuCAP 2020, Copenhagen, Denmark (2020)
[37] Abdollahi, M. M. et al.: Octave-band monopole antenna with a horseshoe ground plane. ACES Journal, Vol. 30, pp. 773-778 (2015)
[38] Zolghadr, J. et al.: UWB slot antenna with band-notched property with time domain modeling based on genetic algorithm optimization. ACES Journal, Vol. 31, pp. 926-932 (2016)
[39] Siahkal-Mahalle, B. H. et al.: A new design of small square monopole antenna with enhanced bandwidth by using cross-shaped slot and conductor-backed plane. Microwave Opt Technol Lett. Vol. 54, pp. 2656–2659 (2012)
[40] Mazloum, J. et al.: Compact oscillator feedback active integrated antenna by using interdigital coupling strip for WiMAX applications. ACES Journal. Vol. 28, pp. 844-850 (2013)
[41] Ojaroudi, N.: Circular microstrip antenna with dual band-stop performance for ultra-wideband systems. Microw. Opt. Technol. Lett. Vol. 56, pp. 2095-2098 (2014)
[42] Ojaroudi, N.: A novel design of microstrip antenna with reconfigurable band rejection for cognitive radio applications. Microw. Opt. Technol. Lett. Vol. 56, pp. 2998–3003 (2014)
[43] Ullah, A. et al.: Coplanar waveguide antenna with defected ground structure for 5G millimeter wave communications. IEEE MENACOMM'19, Bahrain (2019)
[44] Naser Ojaroudi Parchin and et.al., Small-Clearance Phased Array Antenna Design with Miniaturized Elements for 5G Communications, Proceedings of the 1st International Multi-Disciplinary Conference Theme: Sustainable Development and Smart Planning, 28-30 June 2020, Cyberspace, pp. 139-149.

Infrared Imagery and Border Control Systems

George Kumi Kyeremeh[1], Mohamed Abdul-Al[2], Rami Qahwaji[3] and Raed Abd-Alhameed[4]
{g.k.kyeremeh@bradford.ac.uk[1], m.abdul.al@bradford.ac.uk[2], r.s.r.qahwaji@bradford.ac.uk[3]; r.a.a.abd@bradford.ac.uk[4]}

Faculty of Engineering and Informatics, University of Bradford[1], Bradford, BD7 1DP, UK[1,2,3,4]

Abstract. The growing need for passenger authorization at international border crossing points (BCPs) is prompted research into more effective methods. Automated border control (ABC) is gaining attention in its ability to improve traveller ease, BCP throughput, and national security. Individuals are automatically recognized using a feature vector generated from their behavioural and/or physiological characteristics in biometric recognition. Biometric identification systems have been able to offer reliable personal recognition methods useful to validate or identify an individual. Visible spectrum images have some porosity and the effort to deal with it resulted in the introduction of Infrared imaging. This article is looked at verification and identification as the major components of a biometric system and the need for a multimodal system over a unimodal system of identification. It explained how infrared imaging support identification and verification and addresses some shortcomings of the visible spectrum with a comparison of the advantages and disadvantages of both media. Some limitations of Infrared imaging were also identified with multi-modal combining algorithms. The ethical issue to be observed in biometric identification are also discussed and the whole work concluded.

Keywords: Automated border control (ABC), Biometrics, Borders, e-Gate, electronic machine-readable travel document (e-MRTD), unimodal and multimodal, Infrared (IR), Visible spectrum.

1 Introduction

Biometric is derived from Greek words bios (life) and metrikos (measurement). Traditional recognition methods rely on what a person knows, such as a password, biometric recognition systems depend on who a person is, what they do, or how they respond to certain external stimuli. Biometrics offers several inherent advantages over conventional methodologies, biometric technology has developed as an enabling solution to automatically recognize people at a faster rate [1].

Border management broadly covers the concept of security and functionality. The security concept comes to play as borders are the primary line of defence for a sovereign country or nation. Border management implies a balance between these two concepts. The close borders will harm the economy and safety of any country while open borders will create security insufficiency. Establishing a sense of balance between enabling the flow of goods and persons across borders and delivering security procedures triggers the need for a Border Management Model. [2], [3]. A biometric system is a recognition system that identifies an individual based on an element vector derived through a characteristic of the behaviour or physiology. It can also

IMDC-IST 2021, September 07-09, Sakarya, Turkey
Copyright © 2022 EAI
DOI 10.4108/eai.7-9-2021.2314979

be simply referred to as a pattern of recognition technology that works by collecting biometric data from a person, extracting a feature set from that data, and comparing that feature set to the system's registered template set. A biometric system can function in either verification or identification mode, depending on the application environment After useful data being extracted, the feature vector is usually saved in a database or on a smart device for the person. It may be easier to incorporate these data into a specific application, a biometric system dependent on physiological parameters is often more dependable than one based on behavioural variables [4], [5]. Passive sensors collect the infrared radiations generated by Thermal Imaging systems for any objects with temperatures above absolute zero. This technique of detection was originally developed for military surveillance and night vision devices, but it is now more economically viable, allowing for a wider range of applications than ever before.[6]. Most biometric systems rely on ordinary video cameras to record facial images in the visual spectrum. However, there is a growing need for infrared cameras due to an increased desire for a better security system and better monitoring in dark and poorly illuminated regions. The heat generated by the surveillance subject is captured by the thermal infrared camera, which creates a thermogram image utilising infrared radiation. These pictures are utilised in surveillance systems for object detection, identification, and the capacity to characterise observed things in detail. Because the camera can record faces from a distance, it is a non-intrusive method of identifying a person. People's identification or verification based just on thermal information may not be adequate for identification, but it might help a lot. [7], [8]. Biometrics has helped solve questions asked on daily basis such as:

1. Is this the right person to be allowed access to?
2. Does this person belong to this country?
3. Is this the authorized person for such action?

2 Biometric Systems

Four fundamental components make up a typical biometric system:

1. The biometric data is collected via a sensor module.
2. Feature vectors are extracted by processing the collected data in the feature extraction module.
3. Feature vectors are matched to the template in the matching module.
4. The user's identification is established and approved or denied in this decision-making module [5].

Biometric systems work in two different methods: verification and identification. The obtained biometric data is compared to templates corresponding to the claimed identity in verification, whereas the collected biometric data is compared to templates belonging to all users in the database in identification. As a result, identification and verification are two independent tasks that should be addressed individually as indicated in Fig. 1.

Verification: The system verifies the identity of a person in the verification mode by comparing recorded biometric data to the biometric template stored in the system database. The goal of identity verification is to prevent several persons from utilizing the same identity [9].

Identification: With identification, the system looks for a match in all the users' templates in the database to identify the individual. As a result, the system does a comparison of one too many to determine an individual's identification without requiring the subject to claim an identity; for example, "Whose biometric data is this?"). Negative recognition applications rely on identification to determine whether the person is who she claims to be (implicitly or explicitly). Negative recognition's goal is to stop a single individual from assuming many identities. For the sake of convenience, identification can also be employed in positive recognition. While traditional means of personal identification such as PINs and passwords, may work for identification, biometric is the sole way to establish negative identification [9].

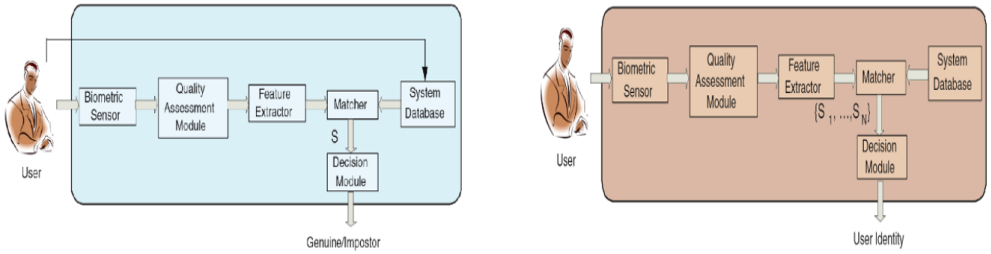

Fig 1. A block diagram of the tasks for verification and identification.[10].

2.1 Unimodal Biometric Systems

The limits of biometric systems that operate on a single biometric feature are as follows:

1. **Presence of noise in sensed data:** Data collected might be noisy or inaccurate. Defective or poorly maintained sensors or unfavourable ambient circumstances such as low lighting in a face recognition system can also cause noisy data. Biometric data that is noisy may be mismatched with database templates, resulting in an erroneous rejection of a user.
2. **Intra-class variations:** The authentication of an individual biometric data obtained may differ significantly from the data used to build the template during enrolment, causing the matching process to fail. During the verification phase, this variance is generally produced by a user who interacts with the sensor inappropriately or when sensor properties are changed.
3. **Distinctiveness:** Biometric characteristic is anticipated to vary considerably among people with the feature sets employed to describe these qualities may have a considerable inter-class similarity. The biometric trait's discriminability is limited because of these restrictions and as a result, every biometric characteristic has a theoretical upper constraint on its capacity to discriminate.
4. **Nonuniversality:** While every user is supposed to have the biometric feature that is being obtained, it is possible that a subset of users will not have that biometric. Due to the low quality of the ridges, a fingerprint biometric might unable to extract

characteristics from the fingerprints of specific individuals. As a result, utilizing a single biometric characteristic is associated with a failure to enrol (FTE) rate. According to estimates, up to 4% of the population may have low-quality fingerprint ridges that resulting in FTE mistakes.

5. **Spoofing attack:** To circumvent the system, an imposter could try to impersonate a valid registered user's biometric characteristic. When behavioural features like signature and voice are employed, spoofing attacks becomes much more significant whiles physical characteristics, on the other hand, are vulnerable to spoofing as well when used in a unimodal biometric system [11], [12, 13],[4].

2.2 Multimodal Biometric Systems

The use of many biometric modalities helps to overcome some of the limitations of unimodal biometric systems. These systems, known as multimodal biometric systems, are thought to be more trustworthy due to the availability of several, independent pieces of evidence. [10]. Multimodal biometric systems use more than one physiological or behavioural feature for enrolment, verification, or identification. Because the amount of data accessible for recognition has increased, these systems may be able to perform more reliable identity verifications. [14]. Face-based identity verification may not be effective in combatting identity theft unless multimodality is implemented. Improved matching performance would also result in a better user experience and an increase in passenger flow efficiency. The multimodal approach to identity verification is gaining traction in ABC systems, as seen by the growing number of deployments that have begun to use this technology [15]. Multimodal systems, on the other hand, have higher costs, acquisition times, and computational durations than typical monomodal systems and users may perceive a greater invasion of their privacy [16]. The multimodal biometric systems can be used under five conditions which as indicated in Fig. 2 is as follows:

1. Multiple sensors: information collected from multiple sensors for the same biometric is merged. Sensors based on optical and ultrasonic, for example, are available to obtain fingerprints.
2. Multiple biometrics: multiple biometric features are integrated, such as fingerprints and faces. These systems will very certainly have many sensors, each of which will detect a distinct biometric feature. Multiple biometrics are generally employed in a verification system to increase system accuracy, but a suitable combination scheme may also improve matching speed in an identity system.
3. Multiple units of the same biometric: Two or more fingerprints of a person's fingers may be combined, or one image from each of a person's two irises may be merged.
4. Multiple snapshots of the same biometric: for enrolment and/or recognition, more than one instance of the same biometric is utilised. Numerous imprints of the same finger, multiple voice samples, or multiple pictures of the face, for example, maybe merged.
5. Multiple matching and representations algorithms for the same biometric entails integrating diverse techniques and matching of the biometric trait after the feature has been extracted. There are two scenarios in which this may be useful. To begin, such a combination method can be used to create a recognition choice by a verification or identification. Second, such a combination technique for indexing may be used by an identifying system [11].

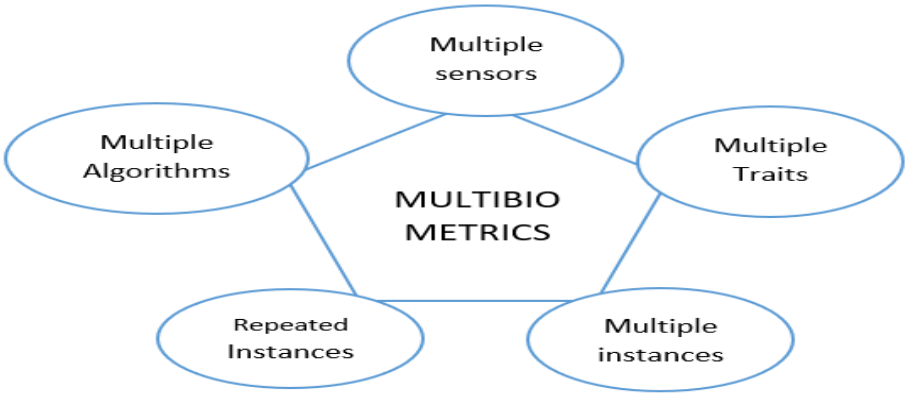

Fig 2. Five conditions under which multimodal biometric systems can be used [11].

3 Infrared (IR) System

Infrared radiation is the electromagnetic radiation that is released corresponding to the amount of heat created or reflected by an object, hence infrared imaging is also known as thermal imaging. The imaging wavelengths of visible light are shorter than infrared and renders invisible to the human eye. Infrared thermal sensors capture objects based on infrared light reflection or emitted infrared radiation [17]. The human face possesses a biometric characteristic that may be used to identify or authenticate people in security systems. Face recognition systems' major problem is properly matching the input face with a face image of the same person previously recorded in the system database. Face thermograms are used in the case of thermal face identification. The detection of a face in a picture is a related job and a requirement for facial recognition. A thermal face image should possess biometrics features that emphasize thermal face characteristics and are compact and straightforward to use for classification for thermal face identification [8]. It is important to identify characteristics that might be utilized in thermal biometrics since thermal face photographs give different information than visible spectrum images.

The study by [18],[19] considered face recognition under different environments intra-spectral and cross-spectral problems. They executed a test on different infrared bans against visible face images to evaluate the performance. They also verified under different environmental conditions and distances the different bands of infrared. An accuracy of 100 percent was obtained with visible image versus the (SWIR) of the IR band. This was done under a controlled environmental condition with a 30-meter distance.

Data collected with infrared cameras offer significant benefits than data collected with visible-spectrum cameras for face identification [20]. Thermal infrared images of the face may be produced in any lighting situation, even full darkness, and there is some indication that thermal infrared is more resistant to changes in facial expression [21]. Thermal infrared radiation is also less influenced by smoke or dust dispersion and absorption than visible light. In contrast to visible spectrum, infrared may extract not only external but also vital internal anatomical data, such as a face's vascular system [22], [23].

3.1. Limitations to Infrared Imaging

Using infrared images for automated facial identification comes with its own set of difficulties. In healthy persons, the human facial temperature is uniform and varies between 35.5°C and 37.5°C, producing a constant unique thermal signature to everyone.

1. The main disadvantage of thermal sub-band images in automatic face recognition is that several influencing factors affect the pattern of heat emitted the face is emitting, including postprandial metabolism, airflow, exercise, and ambient temperature. Regarding images by MWIR and LWIR, there is an aspect of sensitivity to external temperature, the subject's emotional, alcohol use, physical, as well as health state [24], [25].
2. The opaqueness of eyeglasses to most of the IR spectrum might be a concern (LWIR, MWIR, and SWIR). This implies that if a subject wears eyeglass, a substantial section of the face may be blocked, resulting in the loss of critical discriminative information [26], [27].
3. Another point of interest is the effect of sunshine on recognition if it is done outside and throughout the day. Although infrared sub-bands in the NIR and SWIR is unaffected by changes in visible light illumination, the appearance of infrared in the NIR and SWIR sub-bands is influenced by sunshine, which contains large spectral components [28], [26].
4. A survey by [62] exposed a series of shortcomings with which inhibited the further exploitation of infrared imaging, and they included the significant costs for thermal sensors, low resolution and excessive noise levels in pictures, the absence of publicly accessible infrared image data sets with the few available ones indicated in Table 1.

The mentioned shortcomings have predictably, led to and encouraged a new direction of study. Research by [29] suggested combining information from IR and visible ways to resolve the difficulty caused by opaque lenses. In combination with optical recording in infrared thermal imaging to alleviate the influence of emotional and health conditions on thermal images. Comparative thermal and optical images were analysed and able to record both optical and thermal images using charged coupled device (CCD) and low wave infrared (LWIR) microbolometer.

Table 1. Show a summary of main facial databases acquired in the infrared spectrum (Ghiass et al., 2014). The existence of variability data is signified by (●), limitation of variability signified by (ɵ), and very little to no variability by ○().

NAME	Primary Source	Used In	Subjects	Variability			
				Illumination	Pose	Expression	Time-Lapse
Equinox	[30]	[31],[32], [33], [34],[35], [36],[37], [38], [39], [39], e.t.c	90	●	○	●	○

IRIS thermal/Infrared	[40]	[41], [42],[43], [44]	32	●	●	●	○
IRIS-M3	[45]	[46], [45], [47], [48]	82	●	○	○	
University of Notre Dame	[49]	[50], [51],	241	ɵ	○	ɵ	●
University of Houston	[52]	[22],[53], [52],[54], [55]	138	○	●	●	○
Surveillance Camera Face Database	[56]		130	●	●	ɵ	ɵ
Florida State University	[57]	[57], [33]	10	○	●	●	○
UC Irvine hyperspectral	[58]	[58], [59], [60]	200	○	●	ɵ	●
West Virginia University Multispectral	[61]	[61], [62], [63]	50	○	●	○	ɵ
The Hong Kong Polytechnic University	[64]	[65]	335	○	ɵ	●	○
Laval University	[66]		200	○	●	●	●

Table 2. Recognition technique comparison for Thermal and Visual Imaging. (Kong et al., 2005)

Imaging methods	Advantages	Disadvantages
Visual Imaging	❖ Well-developed algorithms for recognition. ❖ The extraction and location of facial features are easier. ❖ Performs great when illumination conditions are controlled. ❖ Equipment (cameras) are less costly	❖ Facial expressions and illumination variation will lead to poor performance. ❖ In a cluttered scene, segmenting the face is difficult. ❖ Not useful under low lighting conditions. ❖ Difficult to detect disguise.
Thermal imaging	❖ Easy to segmentation, locate and detect faces. ❖ Smaller interclass variation. ❖ Not affected by illumination and facial expression. ❖ Great at detecting disguise.	❖ Thermal images are obstructed by the glass. ❖ Not suitable for objects/persons moving under speed. ❖ Thermal images have low image resolutions. ❖ Thermal equipment is expensive. ❖ Calibration will be required as environmental temperatures and activities can change the calibration.

Visual/Thermal Imaging	❖ Recognition accuracy is highly improved. ❖ Very broad areas of application ❖ Combined benefits of both cameras/sensors ❖ Detailed information of the anatomical and facial information of the face for better identification.	❖ Computational requirements are high. ❖ The complicated process of image setup. ❖ Thermal and Visual images require co-registration for data fusion

4 Ethical, Societal, And Legal Issues

Biometrics technology is widely recognized to pose significant ethical, societal, and legal issues. Ethical challenges are conditions in which a person must choose between two options that must be mediated as ethical or unethical. Social difficulties are issues that arise from regular social activities and have the potential to affect a significant number of people in a community. Legal challenges are official inquiries into the legality of the action and whether it is being carried out in conformity with the law.

Table 3. Values and the related vulnerabilities, risks, and mitigation measures [2].

VALUE	VULNERABILITY	RISK	POTENTIAL MITIGATION MEASURE
Right to no discrimination	Existing systems may be classified based on sex, race, ethnicity, or socioeconomic background, genetic characteristics, religion or belief, political stance, handicap, age, or sexual orientation, among other factors.	Individual sorting, social inclusion or exclusion, intolerance, and social inclusion or exclusion.	Biometrics for border control following human rights legislation must guarantee a non-discrimination policy.
Right to no information tracking	Current methods lack notifications and information regarding individual tracking.	Individuals and/or family members are subjected to monitoring because of violations of personal rights and legitimate purpose requirements.	Surveillance should be permitted and compliant with EU and national legislation if it serves a legitimate purpose.
Right to personal data protection	Personal data may slip into the wrong hands or be transferred between businesses under current methods.	Right to security principles such as confidentiality, integrity, and availability are violated.	Border control biometrics must provide Security by Design in order to preserve the continued confidentiality, availability, resilience, and integrity of processing systems and services.
Right to privacy and confidentiality	Modern systems may compromise the confidentiality, giving unauthorized access to sensitive data.	Violation of personal privacy.	Biometrics for border control must ensure the use of confidentiality enhanced technology to

			secure data in compliance with the law.
Concerning human dignity	Current solutions do not let individuals decide on the biometrics to enrol or utilize.	Right to human dignity, as well as cultural-religious practices, are violated	Unless choice is inapplicable, biometrics ay border control should give data explaining why biometrics are employed, as well as al-low choice rules and procedures.

5 Conclusion

Biometrics technology used in border control in two different perspectives has been presented. The primary objective of biometrics technology is to enhance management at border controls and increase the flow of people while considering ethical, legal, and social considerations have been considered. It was observed that Multimodal biometric systems are expected to have a lot of potential for future enhancement since they resolve issues posed by the unimodal biometric systems of recognition. Multimodal biometric systems may combine data at several levels, with fusion at the matching score level being the most common. They also solve the issues of non-universality and spoofing as well as increasing matching performance. Infrared imaging with IR thermal sensors can extend the life of lighting changes and work in low-light conditions. Additional physiological and anatomical face-related data, such as blood vessel structure and the thermal facial signature, may be collected via IR images and used by individuals as unique biometrics. Thermal face accuracy is fairly good, but there is still room for improvement. High accuracy is critical for security systems, since even the tiniest error might compromise national security and access control. The use of multi-modal combining methods by comparing thermal and optical pictures has emerged as a viable solution to curb any irregularities in the IR imaging system, and has been improved by employing a single charged coupled device (CCD) and low wave infrared (LWIR) microbolometer simultaneously.

Acknowledgments

This project has received funding from the European Union's Horizon-MSCA-RISE-2019-2023, Marie Skłodowska-Curie, Research and Innovation Staff Exchange (RISE), titled: Secure and Wireless Multimodal Biometric Scanning Device for Passenger Verification Targeting Land and Sea Border Control.

References

[1] A. K. Jain, A. A. Ross, and K. Nandakumar, *Introduction to biometrics*. Springer Science & Business Media, 2011.

[2] M. Abomhara, S. Y. Yayilgan, A. H. Nymoen, M. Shalaginova, Z. Székely, and O. Elezaj, "How to do it right: a framework for biometrics supported border control," in *International Conference on e-Democracy*, 2019: Springer, pp. 94-109.

[3] L. R. Carlos-Roca, I. H. Torres, and C. F. Tena, "Facial recognition application for border control," in *2018 International Joint Conference on Neural Networks (IJCNN)*, 2018: IEEE, pp. 1-7.

[4] S. Prabhakar, S. Pankanti, and A. K. Jain, "Biometric recognition: Security and privacy concerns," *IEEE security & privacy,* vol. 1, no. 2, pp. 33-42, 2003.

[5] K. Delac and M. Grgic, "A survey of biometric recognition methods," in *Proceedings. Elmar-2004. 46th International Symposium on Electronics in Marine*, 2004: IEEE, pp. 184-193.

[6] M. Rai, T. Maity, and R. Yadav, "Thermal imaging system and its real time applications: a survey," *Journal of Engineering Technology,* vol. 6, no. 2, pp. 290-303, 2017.

[7] D. O. Gorodnichy, E. Granger, and P. Radtke, "Survey of commercial technologies for face recognition in video," 2014.

[8] M. Kristo and M. Ivasic-Kos, "An overview of thermal face recognition methods," in *2018 41st International Convention on Information and Communication Technology, Electronics and Microelectronics (MIPRO)*, 2018-05-01 2018: IEEE, doi: 10.23919/mipro.2018.8400200.

[9] J. L. Wayman, "Fundamentals of biometric authentication technologies," *International Journal of Image and Graphics,* vol. 1, no. 01, pp. 93-113, 2001.

[10] A. K. Jain, "Biometric recognition: overview and recent advances," in *Iberoamerican Congress on Pattern Recognition*, 2007: Springer, pp. 13-19.

[11] A. K. Jain, A. Ross, and S. Prabhakar, "An introduction to biometric recognition," *IEEE Transactions on circuits and systems for video technology,* vol. 14, no. 1, pp. 4-20, 2004.

[12] T. Matsumoto, H. Matsumoto, K. Yamada, and S. Hoshino, "Impact of artificial" gummy" fingers on fingerprint systems," in *Optical Security and Counterfeit Deterrence Techniques IV*, 2002, vol. 4677: International Society for Optics and Photonics, pp. 275-289.

[13] A. Eriksson and P. Wretling, "How flexible is the human voice?-a case study of mimicry," in *Fifth European Conference on Speech Communication and Technology*, 1997.

[14] A. K. Jain and A. Ross, "Multibiometric systems," *Communications of the ACM,* vol. 47, no. 1, pp. 34-40, 2004.

[15] M. Kosmerlj, T. Fladsrud, E. Hjelmås, and E. Snekkenes, "Face recognition issues in a border control environment," in *International Conference on Biometrics*, 2006: Springer, pp. 33-39.

[16] A. Ross, K. Nandakumar, and A. Jain, "Handbook of Multibiometrics, ser. Int. Series on Biometrics. Secaucus," ed: NJ: Springer-Verlag, 2006.

[17] C. Solomon and T. Breckon, *Fundamentals of Digital Image Processing: A practical approach with examples in Matlab*. John Wiley & Sons, 2011.

[18] K. R. Kakkirala, S. R. Chalamala, and S. K. Jami, "Thermal infrared face recognition: A review," in *2017 UKSim-AMSS 19th International Conference on Computer Modelling & Simulation (UKSim)*, 2017: IEEE, pp. 55-60.

[19] T. Bourlai and B. Cukic, "Multi-spectral face recognition: Identification of people in difficult environments," in *2012 IEEE International Conference on Intelligence and Security Informatics*, 2012: IEEE, pp. 196-201.

[20] G. Friedrich and Y. Yeshurun, "Seeing people in the dark: Face recognition in infrared images," in *International Workshop on Biologically Motivated Computer Vision*, 2002: Springer, pp. 348-359.

[21] F. Nicolo and N. A. Schmid, "A method for robust multispectral face recognition," in *International Conference Image Analysis and Recognition*, 2011: Springer, pp. 180-190.

[22] P. Buddharaju, I. T. Pavlidis, and P. Tsiamyrtzis, "Physiology-based face recognition," in *IEEE Conference on Advanced Video and Signal Based Surveillance, 2005.*, 2005: IEEE, pp. 354-359.

[23] I. Pavlidis and P. Symosek, "The imaging issue in an automatic face/disguise detection system," in *Proceedings IEEE Workshop on Computer Vision Beyond the Visible Spectrum: Methods and Applications (Cat. No. PR00640)*, 2000: IEEE, pp. 15-24.

[24] A. Matthews, "Ophthalmic antimicrobial therapy in the horse," *Equine Veterinary Education,* vol. 21, no. 5, pp. 271-280, 2009.

[25] F. J. Prokoski and R. B. Riedel, "Infrared identification of faces and body parts," in *Biometrics*: Springer, 1996, pp. 191-212.

[26] S. Z. Li, R. Chu, S. Liao, and L. Zhang, "Illumination invariant face recognition using near-infrared images," *IEEE Transactions on pattern analysis and machine intelligence,* vol. 29, no. 4, pp. 627-639, 2007.

[27] S.-Q. Wu *et al.*, "Infrared face recognition by using blood perfusion data," in *International Conference on Audio-and Video-Based Biometric Person Authentication*, 2005: Springer, pp. 320-328.

[28] S.-Q. Wu, L.-Z. Wei, Z.-J. Fang, R.-W. Li, and X.-Q. Ye, "Infrared face recognition based on blood perfusion and sub-block DCT in wavelet domain," in *2007 International Conference on Wavelet Analysis and Pattern Recognition*, 2007, vol. 3: IEEE, pp. 1252-1256.

[29] S. G. Kong, J. Heo, B. R. Abidi, J. Paik, and M. A. Abidi, "Recent advances in visual and infrared face recognition—a review," *Computer Vision and Image Understanding,* vol. 97, no. 1, pp. 103-135, 2005.

[30] D. Socolinsky, "Human Identification at a Distance Database," *Equinox Corp., USA*.

[31] D. A. Socolinsky and A. Selinger, "A comparative analysis of face recognition performance with visible and thermal infrared imagery," in *Object recognition supported by user interaction for service robots*, 2002, vol. 4: IEEE, pp. 217-222.

[32] D. A. Socolinsky, A. Selinger, and J. D. Neuheisel, "Face recognition with visible and thermal infrared imagery," *Computer vision and image understanding,* vol. 91, no. 1-2, pp. 72-114, 2003.

[33] A. Srivastava and X. Liu, "Statistical hypothesis pruning for identifying faces from infrared images," *Image and Vision Computing,* vol. 21, no. 7, pp. 651-661, 2003.

[34] A. Gyaourova, G. Bebis, and I. Pavlidis, "Fusion of infrared and visible images for face recognition," in *European Conference on Computer Vision*, 2004: Springer, pp. 456-468.

[35] J. Heo, S. G. Kong, B. R. Abidi, and M. A. Abidi, "Fusion of visual and thermal signatures with eyeglass removal for robust face recognition," in *2004 Conference on Computer Vision and Pattern Recognition Workshop*, 2004: IEEE, pp. 122-122.

[36] B. Abidi, S. Huq, and M. Abidi, "Fusion of visual, thermal, and range as a solution to illumination and pose restrictions in face recognition," in *38th Annual 2004 International Carnahan Conference on Security Technology, 2004.*, 2004: IEEE, pp. 325-330.

[37] P. Buddharaju, I. Pavlidis, and I. Kakadiaris, "Face recognition in the thermal infrared spectrum," in *2004 Conference on Computer Vision and Pattern Recognition Workshop*, 2004: IEEE, pp. 133-133.

[38] S. Singh, A. Gyaourova, G. Bebis, and I. Pavlidis, "Infrared and visible image fusion for face recognition," in *Biometric technology for human identification*, 2004, vol. 5404: International Society for Optics and Photonics, pp. 585-596.

[39] J. Heo, M. Savvides, and B. Vijayakumar, "Advanced correlation filters for face recognition using low-resolution visual and thermal imagery," in *International Conference Image Analysis and Recognition*, 2005: Springer, pp. 1089-1097.

[40] Y. M. Elbarawy, N. I. Ghali, and R. S. El-Sayed, "Facial expressions recognition in thermal images based on deep learning techniques," *International Journal of Image, Graphics and Signal Processing (IJIGSP),* vol. 11, no. 10, pp. 1-7, 2019.

[41] O.-K. Kwon and S. G. Kong, "Multiscale fusion of visual and thermal images for robust face recognition," in *CIHSPS 2005. Proceedings of the 2005 IEEE International Conference on Computational Intelligence for Homeland Security and Personal Safety, 2005.*, 2005: IEEE, pp. 112-116.

[42] M. K. Bhowmik, D. Bhattacharjee, M. Nasipuri, D. K. Basu, and M. Kundu, "Classification of polar-thermal eigenfaces using multilayer perceptron for human face recognition," in *2008 IEEE Region 10 and the Third international Conference on Industrial and Information Systems*, 2008: IEEE, pp. 1-6.

[43] M. K. Bhowmik, D. Bhattacharjee, M. Nasipuri, D. K. Basu, and M. Kundu, "Optimum fusion of visual and thermal face images for recognition," in *2010 Sixth International Conference on Information Assurance and Security*, 2010: IEEE, pp. 311-316.

[44] O. Arandjelović, R. Hammoud, and R. Cipolla, "Thermal and reflectance based personal identification methodology under variable illumination," *Pattern Recognition,* vol. 43, no. 5, pp. 1801-1813, 2010.

[45] H. Chang, H. Harishwaran, M. Yi, A. Koschan, B. Abidi, and M. Abidi, "An indoor and outdoor, multimodal, multispectral and multi-illuminant database for face recognition," in *2006 Conference on Computer Vision and Pattern Recognition Workshop (CVPRW'06)*, 2006: IEEE, pp. 54-54.

[46] H. Chang, A. Koschan, B. Abidi, and M. Abidi, "Physics-based fusion of multispectral data for improved face recognition," in *18th International Conference on Pattern Recognition (ICPR'06)*, 2006, vol. 3: IEEE, pp. 1083-1086.

[47] H. Chang, Y. Yao, A. Koschan, B. Abidi, and M. Abidi, "Spectral range selection for face recognition under various illuminations," in *2008 15th IEEE International Conference on Image Processing*, 2008: IEEE, pp. 2756-2759.

[48] H. Chang, Y. Yao, A. Koschan, B. Abidi, and M. Abidi, "Improving face recognition via narrowband spectral range selection using Jeffrey divergence," *IEEE Transactions on Information Forensics and Security,* vol. 4, no. 1, pp. 111-122, 2009.

[49] J. Doyle and K. Bowyer, "Notre Dame Image Database for Contact Lens Detection in Iris Recognition—2013," ed, 2014.

[50] X. Chen, P. J. Flynn, and K. W. Bowyer, "IR and visible light face recognition," *Computer Vision and Image Understanding,* vol. 99, no. 3, pp. 332-358, 2005.

[51] X. Chen, P. J. Flynn, and K. W. Bowyer, "PCA-based face recognition in infrared imagery: Baseline and comparative studies," in *2003 IEEE International SOI Conference. Proceedings (Cat. No. 03CH37443)*, 2003: IEEE, pp. 127-134.

[52] P. Buddharaju, I. T. Pavlidis, P. Tsiamyrtzis, and M. Bazakos, "Physiology-based face recognition in the thermal infrared spectrum," *IEEE transactions on pattern analysis and machine intelligence,* vol. 29, no. 4, pp. 613-626, 2007.

[53] P. Buddharaju, I. T. Pavlidis, and P. Tsiamyrtzis, "Pose-invariant physiological face recognition in the thermal infrared spectrum," in *2006 Conference on Computer Vision and Pattern Recognition Workshop (CVPRW'06)*, 2006: IEEE, pp. 53-53.

[54] P. Buddharaju and I. Pavlidis, "Physiological face recognition is coming of age," in *2009 IEEE Conference on Computer Vision and Pattern Recognition*, 2009: IEEE, pp. 128-135.

[55] S.-Y. Cho, L. Wang, and W. J. Ong, "Thermal imprint feature analysis for face recognition," in *2009 IEEE International Symposium on Industrial Electronics*, 2009: IEEE, pp. 1875-1880.

[56] M. Grgic, K. Delac, and S. Grgic, "SCface–surveillance cameras face database," *Multimedia tools and applications,* vol. 51, no. 3, pp. 863-879, 2011.

[57] A. Srivastava, X. Liu, B. Thomasson, and C. Hesher, "Spectral probability models for infrared images and their applications to ir face recognition," in *º Proc. Workshop Computer Vision Beyond Visual Spectrum*, 2001.

[58] Z. Pan, G. Healey, M. Prasad, and B. Tromberg, "Face recognition in hyperspectral images," *IEEE Transactions on Pattern Analysis and Machine Intelligence,* vol. 25, no. 12, pp. 1552-1560, 2003.

[59] Z. Pan, G. E. Healey, M. Prasad, and B. J. Tromberg, "Hyperspectral face recognition under variable outdoor illumination," in *Algorithms and Technologies for Multispectral, Hyperspectral, and Ultraspectral Imagery X*, 2004, vol. 5425: International Society for Optics and Photonics, pp. 520-529.

[60] Z. Pan, G. E. Healey, and B. Tromberg, "Multiband and spectral eigenfaces for face recognition in hyperspectral images," in *Biometric Technology for Human Identification II*, 2005, vol. 5779: International Society for Optics and Photonics, pp. 144-151.

[61] T. Bourlai, N. Kalka, A. Ross, B. Cukic, and L. Hornak, "Cross-spectral face verification in the short wave infrared (SWIR) band," in *2010 20th International Conference on Pattern Recognition*, 2010: IEEE, pp. 1343-1347.

[62] T. Bourlai and Z. Jafri, "Eye detection in the middle-wave infrared spectrum: towards recognition in the dark," in *2011 IEEE International Workshop on Information Forensics and Security*, 2011: IEEE, pp. 1-6.

[63] N. D. Kalka, T. Bourlai, B. Cukic, and L. Hornak, "Cross-spectral face recognition in heterogeneous environments: A case study on matching visible to short-wave infrared imagery," in *2011 International Joint Conference on Biometrics (IJCB)*, 2011: IEEE, pp. 1-8.

[64] B. Zhang, L. Zhang, D. Zhang, and L. Shen, "Directional binary code with application to PolyU near-infrared face database," *Pattern Recognition Letters,* vol. 31, no. 14, pp. 2337-2344, 2010.

[65] L. Shen, J. He, S. Wu, and S. Zheng, "Face recognition from visible and near-infrared images using boosted directional binary code," in *International Conference on Intelligent Computing*, 2011: Springer, pp. 404-411.

[66] R. S. Ghiass, O. Arandjelović, H. Bendada, and X. Maldague, "Illumination-invariant face recognition from a single image across extreme pose using a dual dimension AAM ensemble in the thermal infrared spectrum," in *The 2013 International Joint Conference on Neural Networks (IJCNN)*, 2013: IEEE, pp. 1-10.

The Impacts of Depth Camera and Multi-Sensors for Face and Fingerprint Recognition in 2D and 3D - A Case Study

Mohamed Abdul-Al*[1], George Kumi Kyeremeh[2], Rami Qahwaji[3] and Raed Abd-Alhameed[4]
{m.abdul.al@bradford.ac.uk*[1], g.k.kyeremeh@bradford.ac.uk[2], r.s.r.qahwaji@bradford.ac.uk[3], r.a.a.abd@bradford.ac.uk[4]}

Faculty of Engineering and Informatics, University of Bradford[1], Bradford, BD7 1DP, UK[1,2,3,4]

Abstract. This paper reviews the multi-modern sensors for multimodal (Face ad Fingerprint) of a biometric system by using a depth camera. The use of face authentication in biometric data allows this innovation to expand and be used in a variety of fields. Recently, attendance monitoring systems depending on biometric identification for higher education are underutilization, presenting an excellent chance to do fascinating experiments. The installation of biometric attendance systems necessitates the use of both hardware and software components. The first deep CNN (Convolutional Neural Network) method for light source-oriented Face Recognition (FR) takes advantage of the more detailed data given in a lens let display technology picture and that has been used in different borders such as airports, seaports, and land ports. In addition, the use of 3D camera technology for measuring medical outcomes in the healthcare marketplace is growing. The Intel® RealSense TM is one of the top 3D thermal imaging cameras systems on the market today, and it is well-suited for usage in a variety of areas such as medical systems, automation, and medical. Advances in in-depth sensor cameras technology have led to a considerable rise in the incorporation of these innovations into moveable systems, implying the great future potential for widespread in clinic and sector medical screening systems. Furthermore, initially, the use of dispersion maps in conjunction with depth maps and Two-Dimensional Red Green Blue (2D-RGB) pictures has been examined in terms of a fusion strategy to increase FR performance. The suggested approach employs the 2D-RGB crucial radiations emitted viewpoint, and depth maps and dispersion derived from the whole collection of radiations emitted pictures connected with a lens let light source. Following that, feature separation was carried out with the use of a VGG- deep sighs description for texturing and individually well their representations for depth maps and dispersion. The collected characteristics are then combined and supplied into a classification model.

Keywords: Face Recognition (FR), Fingerprint, Sensor, Intel RealSense Camera, 2D-RGB, 3D-RGB, Feature Extraction, Depth maps, VGG-Face, and Facial Tracking.

1 Introduction

One most popular accepted, collectible, and ubiquitous biometric modalities are Face Detection or Face Recognition (FD/FR), attracting considerable interest from both the research

IMDC-IST 2021, September 07-09, Sakarya, Turkey
Copyright © 2022 EAI
DOI 10.4108/eai.7-9-2021.2314977

world and the industry [1] [2]. Significant gains in FR systems have been achieved in recent decades due to the advent of deep learning technologies and the accessibility before training of deep learning systems [3]. Unsurprisingly, deep CNN (Convolutional Neural Network) approaches lead to the presence of modern technology in FR/FD. Face photos are known to pose hurdles for precise recognition including for individuals, particularly in unsupervised scenarios with substantial variability in age, mood, stance, light, occlusion, and so on [4], and hence even deep learning systems might fail when faced with this obstacles. Concurrent with advancements in feature representation and classification for face identification, great strides have been made in the creation of richer image sensors, such as lens let light field cameras, stereo, depth, NIR (Near Infrared), and thermal. Industrial lens let light field cameras, including Lytro [5], have lately brought light intensity imaging technology to the forefront. These camera sensors not just the brightness of light on a single 2D (Two-Dimensional) level point, as well as the brightness of visible light originating from other directions [6] [7]. Furthermore, lens let light field cameras are gaining popularity in the forensic and biometric fields for facial identification and verification [8] [9] [10] [11] [12] [13].

In the current marketplace, there are a rising number of 3D (Three-Dimensional) camera sensors technologies, resulting in an extensive region of technical uses in a variety of industries. Identifying a one-of-a-kind solution in healthcare research, 3D gaming, scanning, motion capture, wellness applications, and clinical is thus becoming increasingly challenging. One among the most popular notable 3D depth-sensing camera is the Intel RealSense, particularly with the recent revelation that production of the Microsoft Kinect Sensor V2/2.0 has already ended, likely signalling the end of Microsoft's engagement in this equipment field [14]. While Kinect assistance for the dynamic responses will keep going in the meantime, the restricted availability of this innovation for purchasing decisions will most likely herald a shift in the acceptance and usage of this specific objective device for innovation projects.

The depth sensor generates pictures in the same way as a standard camera does. Rather than colour, the brightness of every image pixel shows the range to the associated point. This is where these devices truly shine in areas such as computer vision technology. Therefore, depth sensors are often referred to as 3D cameras at times. PrimeSense [15] owns the patent for the depth detecting system used in the Kinect sensor system. Depth sensors are used in a multitude of scenarios other than gaming, such as reconstructing the forms of observed things [16] [17], indication language interpretation systems [18] [19], touching systems [20] [21], rehabilitation and ergonomics [16] [17] and interacting with Google Earth [16] [22]. According to M. Andersen et al. [23] investigated many features of the Kinect sensor that are significant in the development of real-world FR systems.

2 Biometric Sensor

To capture an individual's biometric characteristics, biometric sensors are used. The sensors serve two functions in the biometric presence monitoring system. Detectors are employed first to collect biometric information that will be used in models. Following that, each framework is labelled with a named person or roll number. These models, including the participants' data, are then saved in a server as a guide for future contrast by newly gathered biometric information. This stage is just completed once at the beginning of each school semester. Whenever a lecture is held, the sensors' next goal is to collect a fresh set of biometric information from every learner. The identity of each learner must always be memorized to identify the class's involvement. The

newly gathered biometric information can be compared to the models to track the proper time, name, and date of the pupils participating in the lecture. The next subtypes will cover the different sensors, as well as the circumstance or situation required to record failure biometric information, also to examining the role and relevance of detectors in the biometric-based presence scheme.

2.1 Fingerprint (FP) Sensor

The fingerprint image is captured using various types of sensors. Essentially, there are different categories of FP image sensors [24]:

a) State of matter
b) Visual
c) Ultrasound

Optical sensors may be used in a range of methods to acquire fingerprint images. The first and most extensively utilized biosensors are dependent on the flawed proposed design of total interior contemplation (FTIR). An optical system dependent on FTIR includes CMOS (Complementary Metal-Oxide-Semiconductor) camera, a CCD (Charge-Coupled Device) or a light source, a glass/plastic prism, and a lens. As the viewer contacted the prism's highest place, the CCD or mirrored illumination from the lenses was caught by the CMOS camera via the concentrating lens. An FP classifies diverse patterns of the valley and ridge characteristics [25]. There are numerous benefits when utilizing an optic detector. Because the device only identifies the finger with a 3D (Three-Dimensional) form, replicated FP magic cannot readily fool it. Furthermore, it can capture multiple pictures resolutions and generate top-notch photos. Although these benefits, the sensor module dependent on FTIR is vulnerable to a wet or dry and warm or cold finger, resulting in a bad impression or a saturated [26]. Furthermore, it cannot be built and tested because of the lack of flexibility of lowering the optical length, which might produce optical error in a picture.

Semiconductor device detectors often described as silicon detectors, are intended to utilise small detectors that constitute pixels of the array. Semiconductor device detectors are classified into 4 categories: i) piezoelectric, ii) capacitive, iii) thermal and iv) electric field [24]. Perhaps the most prevalent is the capacitive kind. A capacitive detector is made up of 2 panels. The first panel is made up of a 2D (Two-Dimensional) array of capacitors positioned under the finger photoactive layer, while another panel is the epithelium of the finger. Semiconductor devises detectors can alleviate issues involved with sensing devices, including a smaller footprint and tuneable electrical parameters, when resolving a wet or dry and warm or cold FP picture. Moreover, because a 3D finger layer is detected based on distance calculation, these detectors cannot be readily replicated by a copy or fraudulent FP picture. While their advantages, Semiconductor devices detectors are susceptible to ESD (Electro-Static Discharges). Furthermore, after several applications of the detector [27], white blobs are apparent in the FP image. Additionally, clean-up is essential to create a nice and clear FP image.

Ultrasound devices are utilized to distinguish between valleys and the sound reflection depths of hills [26]. The detector is made up of a transmitter that creates an audio signal and a receiver that receives the associated revealed or resonance signal from the FP layer. Ultrasound detectors can seizure a high-quality picture deprived of existence influenced by oil, soil, or new impurities on the finger [24]. These detectors, on the other hand, are large, costly, and need an extra period to acquire FP images [25].

When selecting an FP reader, consider the collection area, resulting in picture quality, and structural accuracy [24]. The optimal FP detection region is 1 x 1 inch2 (25 4 x 25 4 mm^2). Nevertheless, the bulk of industrial readers are shorter to decrease cost and size. Furthermore, the lowest photo quality is roughly 500 dpi (pixels per inch). The structural deformation caused by the FP reader is used to determine the correctness of the geometry. Other characteristics to choose include the supporting OS (Operating System) version, I/O connection, FPS (Frames Per Second), automated finger identification, and encryption.

2.2 Sensor Face

FR capabilities provided or detectors are cameras utilized to record video frames or capture photos. Face information obtained can be 2D intensity picture shape, 3D brightness, and depth data displays, or IR (Infrared) [1]. A camera's crucial elements are lenses and image sensors [28]. Typically, the camera module converts light into electrical ions via the lens of the camera and then to a digital signal. The electrical signal in an input photo is equal to the intensity of the bright, with brighter pictures having more charges than dull ones. CCD and CMOS image sensors are classified as one of two categories. The cumulative energy is equal to the illumination that reaches every pixel, which is the basis for these detectors. For voltage conversion in a CCD detector, the voltage by 1 pixel is transmitted successively to the next pixel till a constant voltage receives. Furthermore, the CCD sensor has an analogy signal. Every pixel in a CMOS sensor converts ions to energy immediately [29].
The photodetector is connected with several attributes including pixel sensitivity, frame rate, and spatial resolution [1]. The film was mainly composed of photos taken in sequential order, commonly defined as frames. As a result, the edge level is described as the number of pictures taken every moment [30]. The sharpness of a picture is similarly proportional to its quality. A video picture's resolution is clear as the whole quantity of pixels in the picture, or by the number of lines and pixels in the vertical and horizontal aspects [31]. Furthermore, pixel sensitivity denotes the sensor's visual disturbances. A back-illuminated detector was created to improve depth perception by utilizing the contralateral silicon layer for a more efficient visible region [28].

3 Face Identification with Modern Image Sensors

New image detectors, including stereo cameras, depth, NIR, and thermal, have been typically adopted for diverse facial biometric purposes [32] [33] [34]. The richer descriptions gained from the environment, as well as their resilience versus specific fluctuations in facial features, inspired the decision to utilise current image detectors. Depth pictures, for instance, could be more resistant to illumination changes [35], but several views of pictures are less susceptible to alterations [36]. Fig 1 summarises a variety of current, comprehensive, and acceptable FR systems dependent on developing image detectors, organised by release date. Fig 1 contains data on the photodetector utilised, the kind of technique for extracting characteristics, a categorizer, and the level of fusion if needed. FR solutions that integrate, it is not uncommon to have many characteristics derived from different image sensors or extracting characteristics algorithms [37]. Learning algorithms control the modern technology in FR based on novel detectors, as shown in Fig 1. In the case of fusion FR solutions, fusion is generally conducted at the different scales since it contains more rich FR data.

Year	Sensor for Imaging	A Categorizer	Technique for Extracting Characteristics	Level of Fusion	References
2014	Kinect and 2D-RGB	NNC	DLBP	Characteristic	(Aissaoui et al. 2014)
2014	Kinect, 2D-RGB and Thermal	WNNC	HAAR, HOG and LBP	Characteristic	(Nikisins et al. 2014)
2015	3D Stereo	SURF	SF, HGORP and AHE	Choice	(Nigam et al. 2015)
2016	Kinect and 2D-RGB	Soft-max, SVM and WNCC	CNN, HOG, HOGOM, LBP and HAAR	Choice and Characteristic	(Simón et al. 2016)
2016	Kinect and 2D-RGB	SVM	CNN	Characteristic	(Lee et al. 2016)
2016	NIR, Kinect and 2D-RGB	Logistic Regression	3D-LBP, LBP, VGG-Face Descriptor, FHOG and PHOW	Characteristic	(Freitas et al. 2016)
2016	Kinect and 2D-RGB	Soft-max	NN	N/A	(Chowdhury et al. 2016)
2016	Thermodynamic	SRC	DSF, WLD, LBP and Gabor jet	Characteristic	(Bi et al. 2016)
2016	NIR and 2D-RGB	DTL	O-CNN	Characteristic	(Liu et al. 2016)
2016	NIR	Soft-max	CNN	N/A	(Reale et al. 2016)
2017	NIR	NNC	Personality in Patches	Characteristic	(Joardar et al. 2017)
2017	Thermodynamic	NNC	SURF, WLD, Gabor, LBP and SIFT	N/A	(Hermosilla et al. 2017)
2017	NIR and 2D-RGB	NNC	CNN	Characteristic	(He et al. 2017)
2017	NIR and 2D-RGB	Soft-max	CNN	Characteristic	(Lezama et al. 2017)
2018	RGB, Depth, Skeleton, Hybrid	RGB-D	CNN, RNN	N/A	(Wang et al. 2018)
2019	RGB, Depth	N/A	Action Representation, Ineraction Recognition	N/A	(Zhang et al. 2019)
2019	RGB, Depth	SVM	CNN, RNN	Characteristic	(Liu et al. 2019)
2019	Mobile, Wearable Sensors, Video	SVM	KNN, ANN, LDC, MKL, GK, NB, DT, HMM	Characteristic	(Nweke et al. 2019)
2020	Video	SVM, SURF	Tb, GM, DM, KNN, RNN, CNN	Characteristic	(Jegham et al. 2020)

Fig 1. A look at some of the developing – anti-field detectors that are being used for FR. The following abbreviations have been utilized in this Figure: AHE stands for (Adaptive Histogram Equalization). DLBP stands for (Depth Local Binary Patterns); DNM stands for (Discriminant Normal Maps); DSF stands for (Down Sampling Feature); FHOG stands for (Felzenszwalb's HOG); HAOG stands for (Histogram of Averaged Oriented Gradients); HOGOM stands for (Histograms of Gabor Ordinal Measures). HPOG stands for (Histograms of Principal Oriented Gradients); HGORP stands for (Horizontal Gradient Ordinal Relationship Pattern); LDA stands for (Linear Discriminant Analysis); LDP stands for (Local Derivative Pattern); O-CNN stands for (Ordinal Convolutional Neural Network); PCA stands for (Principal Component Analysis); PSIFT stands for (Pyramid Scale Invariant Feature Transform). RS-LDA stands for (Random Subspace Linear Discriminant Analysis); SRC is for (Sparse Representation Classifier); SURF is for (Speeded Up Robust Features), and SF stands for (Steerable Filter); WNNC stands for (Weighted Nearest Neighbour Classifier); N/A stands for (Not Applicable).

The suggested method leverages the additional data present in the display technology picture by combining characteristics generated from the 2D-RGB sector directly aspect, and even the depth maps and contrast, and is projected to outperform 2D-RGB+depth and 2D-RGB FR methods. The recommended FR solution necessitates the necessary stages:

a) **Before-processing:** The programme Light Area Toolkit v0.4 [38] has been utilized to generate the sub-hinge several views vector. The facial section is then cut throughout all sub-hinge photos dependent on the features in the dataset, and the cut sub-hinge pictures are shrunk to (24 × 24) pixels**.**

b) **Disproportion map removal:** A dispersion map is recovered from the trimmed sub-hinge array of several views, collecting the geometric data accessible in the display technology picture. The display technology dispersion map was recovered utilizing the approach provided in [39] and [40], which generates the discrepancy map as slopes of unipolar plane images.

c) **Extraction of depth maps:** A feature vector is recovered from the clipped several views of the sub-hinge array, giving feature vectors on the placement and form of the

face elements. The feature vector was retrieved utilising the approach provided in [41], which predicts several views audio correlations and then improves them utilizing the analysis to identify.

d) **VGG-Face characteristics removal:** Before training the VGG deep markers, which were originally formed for 2D FR, are well-adjusted individually for depth map and mismatch. The depth characteristics, texture, and disparity are extracted from the 2D-RGB core image, and also the depth maps and disparity, utilizing three deep learning solutions depending on the VGG-Face classifier [42].

e) **Level of Fusion Characteristics:** For every input, the collected characteristics are concatenated into a single category using Fusion of Different Scales.

f) **SVM classification:** The synthesized extracted features are given to the SVM classifier (developed with [43]), which returns the participants' privacy. In this research, the accuracy of a soft-max classifier was also tested, with SVM operating slightly better than soft-max, explaining SVM's selection as the last classifier.

4 Extraction of VGG-Face Features

VGG-Very-Deep-16 has been one of the best CNN designs for numerous image processing applications [44]. Around 2.6 million face photos were trained to create such a before training the VGG-Face model for FR, which includes rich changes in lighting, voice, posture, and occlusion. Since the VGG-deep model is the first training with 2D pictures, it cannot be adequate for FR to specify dispersion and depth data. This research has before trained the VGG-Face model using the VGG-Very-Deep-16 CNN levels, taking depth maps and dispersion into account at the entry and away from the gradient descent impacts. Despite some researcher gathers and space limits, the fine-tuning for both depths maps and dispersion was conducted utilising a total of 30 epochs, LR (Learning Rate = 0.005) and a BS (Batch Size) of 32. The VGG-deep character produced by executing the VGG-Very-Deep-Face CNN deprived of the final 2 attached layers, as established in [42], is utilised to remove characteristics from the 2D-RGB centre representation and also depth maps and dispersion. The outcome is a VGG-Face specification with an entire number of 4,096 characteristics to every entry, described as completely integrated level 6 characteristics. Before training the VGG-Face model was utilised for 2D-RGB pictures, while fine-tuned models were employed for depth maps and dispersion.

5 Tracking of the Face

The Intel RealSense camera series could be utilized to detect and observe face emotions and actions either with or without hairstyle and spectacles. It can identify approximately 78 face features points in 3D, which could aid in the creation of facial animation, avatars, and emotion identification [45]. Intel RealSense could also identify head position across 3D coordinates for roll, yaw, and pitch. Based on the camera used, tracking up to 4 people with indicated squares for face boundaries is possible. This is especially important in platforms when the environment cannot be handled since it allows the person to be recognized and observed solely. In comparison to several of the recent industry frontrunners, such as the Microsoft Kinect 2.0.0, the Intel RealSense camera series will offer high-quality and sampling rates. The higher the pixel density and sample rate, while monitoring fine or fast movement, the better.

5.1 Intel RealSense Camera F200, R200 and SR300

The Intel RealSense SR300 is a simple, transmitted light 3D camera sensor that has one of the lowest 3D depths and 2D digital cameras presently commercially available. The Intel RealSense SR300 provides customers the option to engage with active sense by integrating depth detection with a 1080p RGB sensor. Hand movement recognition, background segmentation, 3D scanning, and facial recognition are all examples of techniques that can be used. The Intel RealSense SR300 camera is appropriate for reality and wearable technology applications like hand and finger tracking, face tracking and detection, checking and localization, and scene segmentation. This is accomplished by the simultaneous employment of an IR projector and a Light detector with coded emission spectra [46].

A globe USB 3.0 thermal imager that can provide video feeds in IR is the Intel RealSense Camera R200, colour, and depth and may be utilized with a variety of compatible devices including Ultrabook's TM, 2-in-1, All-in-One, or portable systems (Intel 2016). The R200 has an IR depth detecting capability and a full HD colour camera. Its 3 cameras, which comprise RGB and stereoscopic IR, are used to produce depth. The VGG-Face description produced by executing the VGG-Deep-Face CNN omitting the previous two convolution levels, as proved to be successful in [47], is utilized to detect edges from the 2D-RGB centre perspective and also depth maps and dispersion. The outcome is a VGG-Face specification with a maximum number of 4096 characteristics for every entry, described as completely integrated level 6 characteristics. Utilizing ultrasounds, the developer may generate 3D printable things and sections, such as the capacity to create and edit bespoke avatars, by computationally recording individuals or stuff in a 3D space. The formation of 3D avatars or things yields things that might be integrated into real-life fields and applications to aid with visualization [45]. Avatars have also been utilized in rehabilitation programmers where people do not wish to view themselves afterward distress permanently or temporarily bodily damaged.

The Intel RealSense spectrum has continuously advanced in current decades, notably in terms of performance capture accuracy, camera capacity, and area of vision lengths. Fig 2 depicts a comparative evaluation of the F200, R200, and SR300 systems' key characteristics.

The Intel RealSense SDK, SDK elements, and deepness camera operators for the F200, R200, and SR300 models are no further getting upgraded leading to the release of the latest software of the visual range [46], as indicated below. Fig 3 provides an in-depth evaluation of the SDK application's running regions and applications.

The Intel RealSense SDK has 3D human tracking include certain critical qualities that aid in the development of strong and productive apps. This means the capability to offer accurate results in the influence of environmental aberrations like piercings or spectacles over a wide variety of colours. Facial hair could be another factor that can significantly affect object tracking; nevertheless, the Intel RealSense SDK will mitigate this effect. Obstacles could also critically degrade the object pursuing of many camera detection systems; common actions like yawning, wiping the face, and so on can affect detection and information collecting. This is something that the Intel RealSense camera spectrum can consider and decide to pursue properly.

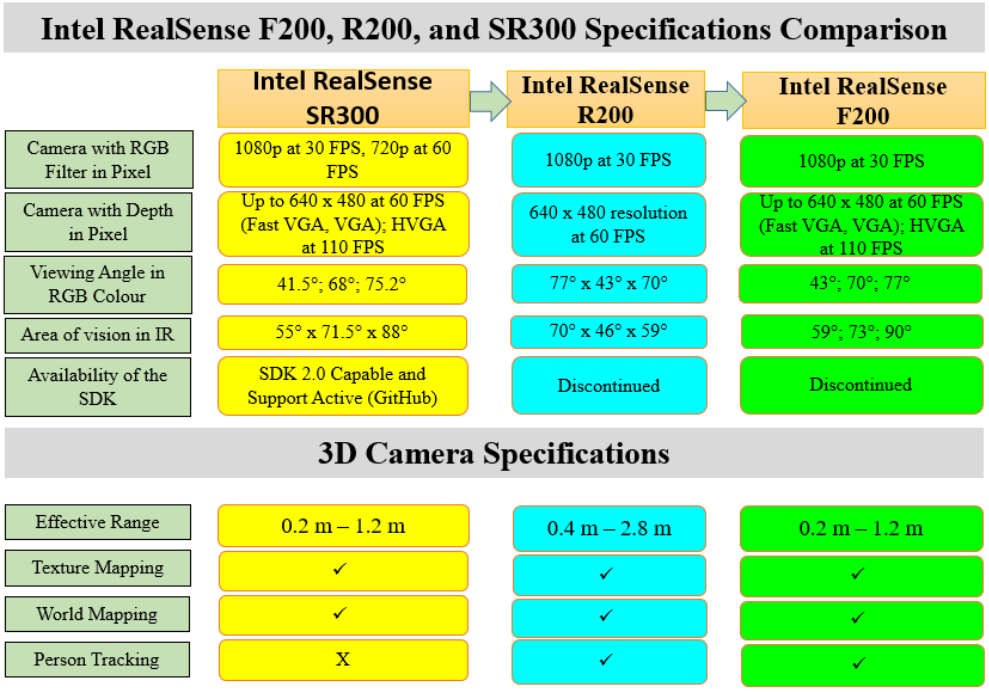

Fig 2. Intel RealSense F200, R200, and SR300 Characteristically Analysis [46].

The constancy of the monitoring can be harmed by changing light sources, and previously, it has been observed that the detection of feature vectors has been substantially harmed; this was especially apparent in the development of Microsoft Kinect [48]. Vision-based detection systems frequently function best in controlled situations with few changes including shape, skin tone and clothing colour, illumination level, and position level. In addition, peripheral clutter is kept to a minimum. Utilizing this technology in the house for health assessment could be challenging for distant individuals because the temperature will not be appropriate [48]. On the other hand, the Intel RealSense works well during poor-light circumstances, when the other technologies strain and are also troublesome due to large variations in illumination.

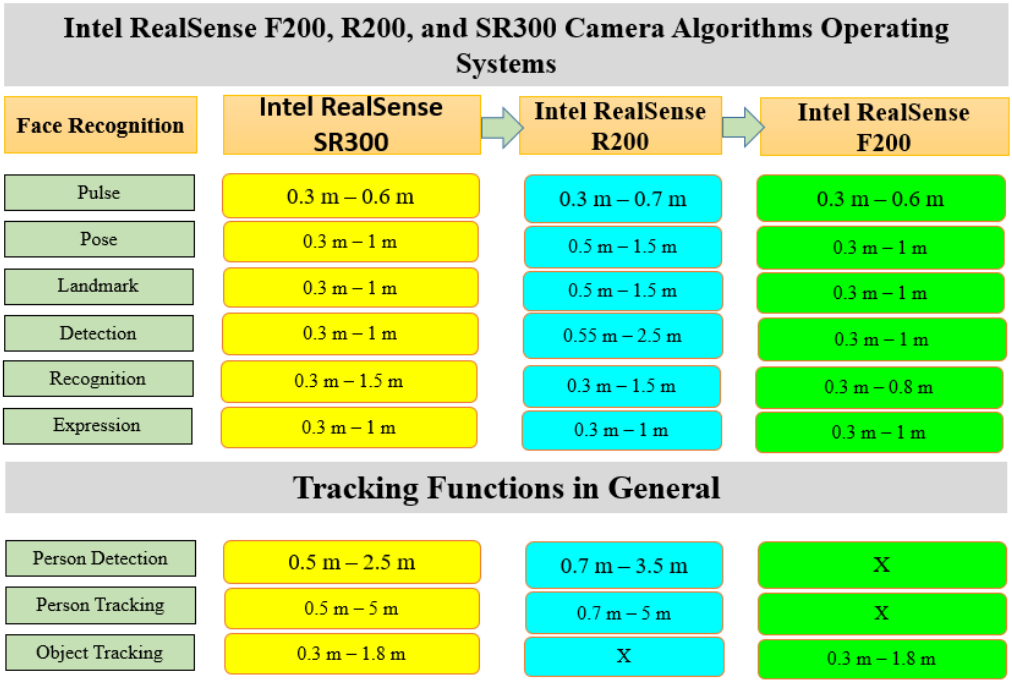

Fig 3. Intel RealSense F200, R200, and SR300 Systems Required to operate Environment [46].

5.2 Intel RealSense Camera ZR300, D415 & D435

As the marketplace for the manufacturing of Intel Real-Sense and SDK has grown, so has the requirement for both long - short-term thermal imaging cameras, leading to the creation of the D435, ZR300, and D415 Intel Real-Sense Camera systems.

The ZR300 has a high-quality depth camera with an incorporated powerful motion detection mechanism. The ZR300 offers a wide range of uses because of its high-quality deepness detecting, extremely durable monitoring, long-term assistance, outdoor and indoor usage, and low energy consumption. The camera has an inside variety of around 3.5 m and an outside length capable of capturing far thousands of miles. The recommended option, on the other hand, changes based on the lighting and situation [45]. The Intel RealSense Peripheral Device ZR300 is viewed as an appropriate option for educational videos, mechanical development, and systems engineering, among several other proposed options. The ZR300 can provide 3D spatial awareness by utilizing object tracking, spatial awareness, and region training. Most significantly, the ZR300 provides a full edge level, that allows 3D perusing systems and prompts mechanical actions to measure activity in a variety of environments [45].

Intel just launched a new D400 system set with the most sophisticated information fusion performance to time. The D415 and D435 deepness identifying cameras would cover the newest Intel RealSense vision system and component. Besides that, to the dynamic picture flash and normal angle of vision, the Intel RealSense Deepness Camera D415 provides a critical option with straightforward deepness channel information collection. The D435, on the other hand, can record and transmit depth data from object detection, as well as a global picture shutter and a broader range of vision, resulting in great depth perception accuracy in movement [46]. The

optimum situation for the D400 sequence has been significantly enhanced over earlier incarnations of the Intel RealSense Camera line, with information gathering achievable at intervals close to and beyond 600 seconds in both inside and outside scenarios [46].

6 Conclusion

It is still difficult to select appropriate kinds of computers for designing a biometric attendance monitoring system. The two often used biometrics qualities of the present scheme are the face and fingerprint because of their simplicity and high acceptance ratio. For FP or facial picture capture, an optical system is necessary. CMOS is the most common sensor in virtually most cameras. FR attendance systems save time by eliminating the requirement for individuals to wait and make eye contact with the detector. To communicate attendance records, the communication network is critical. Wi-Fi is an excellent choice since it can carry large volumes of information in a little period of interval. This is beneficial for tracking presence in real-time. Moreover, with the growing usage of smartphones in the IoT (Internet of Things) age, biometric attendance systems are being pushed toward the next level. Currently, new smartphones have built-in hardware and software including a fingerprint sensor, facial recognition, camera, and iris scanner.

The Intel RealSense family is still in its development, but it is rapidly developing thanks to an ever-improving camera and an ever-growing SDK. Because of its 3D scanning, FR, and FP identification features, the Intel RealSense system is regarded as a competitive, if not improved, a competitor to the Microsoft Kinect, and thus seen as a viable tool for research & innovation in the healthcare industry.

As a result, for future study, there is an option to collect attendance simply utilizing cell phones rather than putting up a program with different system components. Utilizing a wireless router on the smartphone, the biometric features may be captured and transferred to the cloud server for verification. Future studies will examine a reorganized photo as additional light field input data to raise the efficiency of an unfocused range of values for different factors located at varying spaces; it may be highly valuable for several faces' identification challenges.

Acknowledgments

This project has received funding from the European Union's Horizon-MSCA-RISE-2019-2023, Marie Skłodowska-Curie, Research, and Innovation Staff Exchange (RISE), titled: Secure and Wireless Multimodal Biometric Scanning Device for Passenger Verification Targeting Land and Sea Border Control.

References

[1] A. K. Jain, K. Nandakumar, and A. Ross, "50 years of biometric research: Accomplishments, challenges, and opportunities," *Pattern recognition letters,* vol. 79, pp. 80-105, 2016.

[2] M. Günther, L. El Shafey, and S. Marcel, "2D face recognition: An experimental and reproducible research survey," Idiap, 2017.

[3] G. Hu *et al.*, "When face recognition meets with deep learning: an evaluation of convolutional neural networks for face recognition," 2015, pp. 142-150.

[4] L. Best-Rowden, H. Han, C. Otto, B. F. Klare, and A. K. Jain, "Unconstrained face recognition: Identifying a person of interest from a media collection," *IEEE Transactions on Information Forensics and Security,* vol. 9, no. 12, pp. 2144-2157, 2014.

[5] M. Rerabek, L. Yuan, L. A. Authier, and T. Ebrahimi, "[iso/iec jtc 1/sc 29/wg1 contribution] epfl light-field image dataset," ISO/IEC JTC 1/SC 29/WG1, 2015.

[6] R. Ng, M. Levoy, M. Brédif, G. Duval, M. Horowitz, and P. Hanrahan, "Light field photography with a hand-held plenoptic camera," 2005.

[7] M. Levoy and P. Hanrahan, "Light field rendering," 1996, pp. 31-42.

[8] R. Raghavendra, K. B. Raja, and C. Busch, "Exploring the usefulness of light field cameras for biometrics: An empirical study on face and iris recognition," *IEEE Transactions on Information Forensics and Security,* vol. 11, no. 5, pp. 922-936, 2015.

[9] R. Raghavendra, B. Yang, K. B. Raja, and C. Busch, "A new perspective—Face recognition with light-field camera," in *2013 International Conference on Biometrics (ICB)*, 2013: IEEE, pp. 1-8.

[10] R. Raghavendra, K. B. Raja, B. Yang, and C. Busch, "Multi-face recognition at a distance using light-field camera," in *2013 Ninth International Conference on Intelligent Information Hiding and Multimedia Signal Processing*, 2013: IEEE, pp. 346-349.

[11] R. Raghavendra, K. B. Raja, B. Yang, and C. Busch, "Comparative evaluation of super-resolution techniques for multi-face recognition using light-field camera," in *2013 18th International Conference on Digital Signal Processing (DSP)*, 2013: IEEE, pp. 1-6.

[12] A. Sepas-Moghaddam, P. L. Correia, and F. Pereira, "Light field local binary patterns description for face recognition," in *2017 IEEE International Conference on Image Processing (ICIP)*, 2017: IEEE, pp. 3815-3819.

[13] A. Sepas-Moghaddam, F. Pereira, and P. L. Correia, "Ear recognition in a light field imaging framework: a new perspective," *IET Biometrics,* vol. 7, no. 3, pp. 224-231, 2018.

[14] O. S. Good, "Kinect is officially dead. Really. Officially. It's dead," *Polygon. https://www. polygon. com/2017/10/25/16543192/kinect-discontinued-microsoft-announcement. Accessed,* vol. 20, 2017.

[15] K. Khoshelham, "Accuracy analysis of kinect depth data," in *ISPRS workshop laser scanning*, 2011, vol. 38, no. 1.

[16] M. Zollhöfer, M. Martinek, G. Greiner, M. Stamminger, and J. Süßmuth, "Automatic reconstruction of personalized avatars from 3D face scans," *Computer Animation and Virtual Worlds,* vol. 22, no. 2-3, pp. 195-202, 2011.

[17] Y. Cui and D. Stricker, "3d shape scanning with a kinect," in *ACM SIGGRAPH 2011 Posters*, 2011, pp. 1-1.

[18] K. F. Li, K. Lothrop, E. Gill, and S. Lau, "A web-based sign language translator using 3d video processing," in *2011 14th International Conference on Network-Based Information Systems*, 2011: IEEE, pp. 356-361.

[19] A. D. Wilson, "Using a depth camera as a touch sensor," in *ACM international conference on interactive tabletops and surfaces*, 2010, pp. 69-72.

[20] H. Haggag, M. Hossny, S. Nahavandi, and D. Creighton, "Real time ergonomic assessment for assembly operations using kinect," in *2013 UKSim 15th International Conference on Computer Modelling and Simulation*, 2013: IEEE, pp. 495-500.

[21] M. N. K. Boulos, B. J. Blanchard, C. Walker, J. Montero, A. Tripathy, and R. Gutierrez-Osuna, "Web GIS in practice X: a Microsoft Kinect natural user interface for Google Earth navigation," ed: BioMed Central, 2011.

[22] S. Izadi *et al.*, "KinectFusion: real-time 3D reconstruction and interaction using a moving depth camera," in *Proceedings of the 24th annual ACM symposium on User interface software and technology*, 2011, pp. 559-568.

[23] M. R. Andersen *et al.*, "Kinect depth sensor evaluation for computer vision applications," *Aarhus University,* pp. 1-37, 2012.

[24] D. Maltoni, D. Maio, A. K. Jain, and S. Prabhakar, *Handbook of fingerprint recognition*. Springer Science & Business Media, 2009.

[25] D. Maltoni, "A tutorial on fingerprint recognition," in *Advanced Studies in Biometrics*: Springer, 2005, pp. 43-68.

[26] N. K. Ratha, A. Senior, and R. M. Bolle, "Automated biometrics," in *International Conference on Advances in Pattern Recognition*, 2001: Springer, pp. 447-455.

[27] A. Ross and A. Jain, "Biometric sensor interoperability: A case study in fingerprints," 2004: Springer, pp. 134-145.

[28] S. C. Hoo and H. Ibrahim, "Biometric-Based Attendance Tracking System for Education Sectors: A Literature Survey on Hardware Requirements," *Journal of Sensors,* vol. 2019, 2019.

[29] D. Litwiller, "CCD vs. CMOS: Facts and Fiction. Phothonics Spectra," ed: Laurin Publishing Co. Inc, 2001.

[30] I. D. Aronson, *DV filmmaking: from start to finish*. " O'Reilly Media, Inc.", 2006.

[31] H. Zettl, *Television production handbook*. Nelson Education, 2014.

[32] S. Ouyang, T. Hospedales, Y.-Z. Song, X. Li, C. C. Loy, and X. Wang, "A survey on heterogeneous face recognition: Sketch, infra-red, 3D and low-resolution," *Image and Vision Computing,* vol. 56, pp. 28-48, 2016.

[33] T. D. S. Freitas, "3D face recognition under unconstrained settings using low-cost sensors," 2016.

[34] Z. Cai, "Feature learning for RGB-D data," University of Sheffield, 2017.

[35] B. Y. Li, M. Xue, A. Mian, W. Liu, and A. Krishna, "Robust RGB-D face recognition using Kinect sensor," *Neurocomputing,* vol. 214, pp. 93-108, 2016.

[36] M. Du, A. C. Sankaranarayanan, and R. Chellappa, "Robust face recognition from multi-view videos," *IEEE transactions on image processing,* vol. 23, no. 3, pp. 1105-1117, 2014.

[37] A. Ross and A. Jain, "Information fusion in biometrics," *Pattern recognition letters,* vol. 24, no. 13, pp. 2115-2125, 2003.

[38] D. Dansereau, "Light field toolbox v0. 4," *MathWorks R File Exhange. MathWorks R,* 2015.

[39] S. G. Marto, N. B. Monteiro, J. P. Barreto, and J. A. Gaspar, "Structure from plenoptic imaging," in *2017 Joint IEEE International Conference on Development and Learning and Epigenetic Robotics (ICDL-EpiRob)*, 2017: IEEE, pp. 338-343.

[40] N. B. Monteiro, S. Marto, J. P. Barreto, and J. Gaspar, "Depth range accuracy for plenoptic cameras," *Computer Vision and Image Understanding,* vol. 168, pp. 104-117, 2018.

[41] H.-G. Jeon *et al.*, "Accurate depth map estimation from a lenslet light field camera," in *Proceedings of the IEEE conference on computer vision and pattern recognition*, 2015, pp. 1547-1555.

[42] O. M. Parkhi, A. Vedaldi, and A. Zisserman, "Deep face recognition," 2015.

[43] C.-C. Chang and C.-J. Lin, "LIBSVM: A library for support vector machines," *ACM transactions on intelligent systems and technology (TIST),* vol. 2, no. 3, pp. 1-27, 2011.

[44] K. Simonyan and A. Zisserman, "Very deep convolutional networks for large-scale image recognition," *arXiv preprint arXiv:1409.1556,* 2014.

[45] Intel. "Introducing the Intel® RealSense™ R200 Camera (world facing)." https://software.intel.com/en-us/articles/realsenser200-camera (accessed 30 November 2020.

[46] Intel. "A Comparison of Intel® RealSense™ Front-Facing Camera SR300 and F200." https://software.intel.com/en-us/articles/a-comparison-of-intel-realsensetm-front-facing-camera-sr300-andf200. (accessed 30 November 2020.

[47] L. Luna-Oliva *et al.*, "Kinect Xbox 360 as a therapeutic modality for children with cerebral palsy in a school environment: a preliminary study," *NeuroRehabilitation,* vol. 33, no. 4, pp. 513-521, 2013.

[48] L. Shires, S. Battersby, J. Lewis, D. Brown, N. Sherkat, and P. Standen, "Enhancing the tracking capabilities of the Microsoft Kinect for stroke rehabilitation," in *2013 IEEE 2nd International Conference on Serious Games and Applications for Health (SeGAH)*, 2013: IEEE, pp. 1-8.

Design of Optimum Microstrip to Substrate Integrated Waveguide Transition

Nassir Guellil[1], Chemseddine Zebiri[2,3], Djamel Sayad[5] ,I.T.E. Elfergani[3,4], Farid Djahli[1], Abdalfettah Asharaa[3], Jonathan Rodriguez[4], and Raed Abd-Alhameed[3]

{ i.t.e.elfergani@av.it.pt*}

[1]LIS laboratory, Department of Electronics, Ferhat Abbas University of Sétif 1, Sétif, Algeria, guellilnassir@yahoo.fr, fdjahli@yahoo.fr
[2]Department of Electronics, University of Ferhat Abbas, Sétif -1-, 19000 Sétif, Algeria; czebiri@univ-setif.dz
[3]Bradford-Renduchintala Centre for Space AI, University of Bradford, BD71DP, UK
[4]Instituto de Telecomunicações, Campus Universitário de Santiago, Aveiro, Portugal i.t.e.elfergani@av.it.pt
[5]Department of Electrical Engineering, University of 20 Aout 1955-Skikda, 21000 Skikda, Algeria

Abstract. The excitation of a Substrate Integrated Waveguide (SIW) makes use of costly and complex structures. In this paper, two simple structures have been presented to validate our computing results. This is a step discontinuity added to the microstrip line to produce an impedance matching between the SIW line and the line. Based on a small approximation of reflection, design equations are deduced, which allowed an optimal dimensioning of the step discontinuity (L×W). This design strategy was tested by simulating several waveguides, and a good agreement between the optimal geometric parameters and the calculated values was obtained.

Keywords: SIW, transition, small reflection approximation.

1 Introduction

Substrate Integrated Waveguide is a new form of the waveguide. It is a mixed technology between the waveguide and printed circuits that benefit from the advantages and high performances of both technologies [1]. This new structure consists of a substrate metalized on up and down sides with two parallel rows of metallic vias inserted in the substrate. If the diameter of the metallic vias and the distance between them are chosen properly, the energy leaking between consecutive vias is negligible, hence, the structure behaves like a classical rectangular waveguide [2]. Because of the advantages of this technology most microwave components in a classical waveguide, such as filters, couplers, antenna and beam former, were modeled in SIW technology [3- 7].

To interface a signal between microstrip technology and SIW structure a transition is used. Figure (1) presents the transition structure used in this work to connect a 50 Ω microstrip line to the planar SIW. The integral design is realized on the same substrate. The purpose of the transition is to transform the quasi-TEM mode in the microstrip line to the dominant TE10 mode

IMDC-IST 2021, September 07-09, Sakarya, Turkey
Copyright © 2022 EAI
DOI 10.4108/eai.7-9-2021.2314976

in the SIW. Since there is an impedance matching between the microstrip line and the SIW structure, return loss will be minimum, for this reason, the length and width of the transition structure has to be optimized.

This paper presents design equations for geometrical parameters (width and length) of the structure. These equations allow, in almost all cases, a direct calculation of the optimum width and length of the transition without a full-wave simulator. This method has been tested by applying it to microstrip to SIW transition with three examples using different substrates at different frequencies.

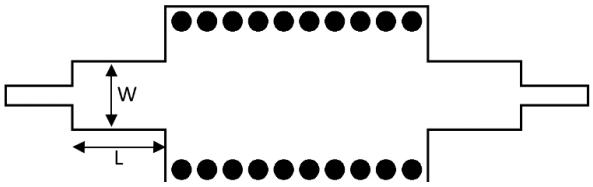

Fig. 1.Microstrip line to substrate integrated waveguide transition.

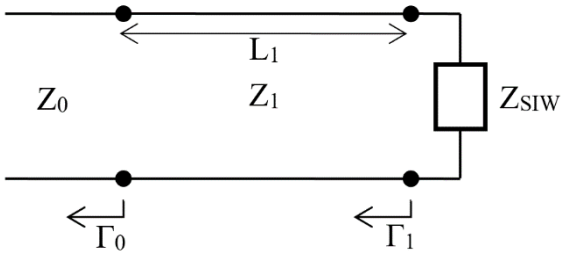

Fig. 2. Equivalent electric circuit.

2 Design Procedure

First, based on our previous work [7], a new formula for calculating the optimum width of a SIW, corresponding to the dominant mode, is used in this paper, by applying the Finite Difference Frequency Domain (FDFD) method. Secondly, the transition is a step discontinuity on a microstrip line as it is shown in Figure 1, where a microstrip line with a characteristics impedance Z0=50 Ohm, connected to another microstrip line of impedance Z1 and length L1. The transition is responsible to realize the impedance matching between the impedance of the feeding line and the SIW impedance. So, to make a good compromise between impedances, the geometrical parameters W2 and L2 must be suitably chosen to get a lower return loss. Figure 2 shows a schematic of impedance matching considered in this work [8].

By using small reflection approximation, we can compute the total reflection Gamma seen by the feed line (Equation 1). We note that we ignore the mismatch at the end of the microstrip line where the quasi-TEM mode in the microstrip couples to theTE10 of the SIW [9].

$$\Gamma = \Gamma_0 + \Gamma_1 e^{-2j\theta} \qquad (1)$$

where;$\Gamma_0 = \frac{Z_1 - Z_0}{Z_1 + Z_0}$, $\Gamma_1 = \frac{Z_{siw} - Z_1}{Z_{siw} + Z_1}$, $\theta = \frac{2\pi}{\lambda_g} L_1$

In the TE_{10} propagation mode frequency region of interest, the SIW is equivalent to a conventional rectangular waveguide filled by a dielectric, hence, for the TE_{10} mode, the cross section impedance can be written as follows

$$Z_{siw} = \frac{2h}{W_{eff}} \frac{\eta_0}{\sqrt{\varepsilon_r}} \left[1 - \left(\frac{f_c}{f}\right)^2\right]^{-\frac{1}{2}} \qquad (2)$$

We know that maximum power transfer from the input matching network to the waveguide structure will occur when:

$$\frac{\partial^2 \Gamma(Z_1, L_1)}{\partial Z_1 \partial L_1} = 0 \qquad (3)$$

Solutions of (3) are:

$$\begin{cases} L_1 = (k+1)\frac{\lambda_g}{2} \\ \quad and \\ Z_1 = \frac{Z_{siw}\sqrt{Z_o} - Z_o\sqrt{Z_{siw}}}{\sqrt{Z_{siw}} - \sqrt{Z_o}} \end{cases} \qquad (4)$$

The design of the presented transition is split into two steps; in A band width of nearly 2.5 GHz is achieved the first step, an empty substrate integrated waveguide is designed, its impedance is calculated using the closed Equation (2). A 50 Ω microstrip line width is also calculated in this step. In the second step, Equation (4) allows to calculate Z_1, then the width W_2 is determined [9]. Later, Equation 2-b gives the length L which corresponds to the minimum return loss. An additional step (if necessary), is to use a full-wave simulator as HFSS in order to refine the values of Z_1 and L_1.

$$Z_1 = \frac{120\pi}{\sqrt{\varepsilon_{eff}}\left(\left(\frac{w_1}{h}\right) + 1.393 + 0.667 \ln\left(\frac{w_1}{h} + 1.444\right)\right)} \qquad (5)$$

3 Simulation Results

Table 1 recapitulates values of three SIW structures versus frequency, geometrical parameters are calculated using the presented procedure and compared with values obtained using HFSS software. We can see that this method gives a quick solution and, at least an initial optimum point for sizing the transition. These obtained calculations of dimensions (L×W) can be taken into account as a first optimization. Simulation software can quickly obtain better optimization.

TABLE I. GEOMETRICAL PARAMETER VALUES IN MILLIMITER.

Parameters	**Optimum value using HFSS**		**Calculated parameters**		**Relative error %**	
	W1	***L1***	***W1***	***L1***	***W1***	***L1***
f_0=10 GHz, εr=4.4	1.8121	3.9105	1.98510	3.5730	8.7149	8.6306
f_0=14.5 GHz, εr=2.2	2.4152	3.8221	2.2214	3.3368	8.0242	12.6972
f_0=21 GHz, εr=3.55	1.3945	2.1572	1.2204	1.8082	12.4848	16.1784

The presented design procedure has been used in order to design transition for a substrate integrated waveguide working at 10 GHz with FR4-epoxy substrate, ε_r=4.4. The impedance of the transition is Z_1=36.2307 Ω, which corresponds to a width of 1.9810 mm.

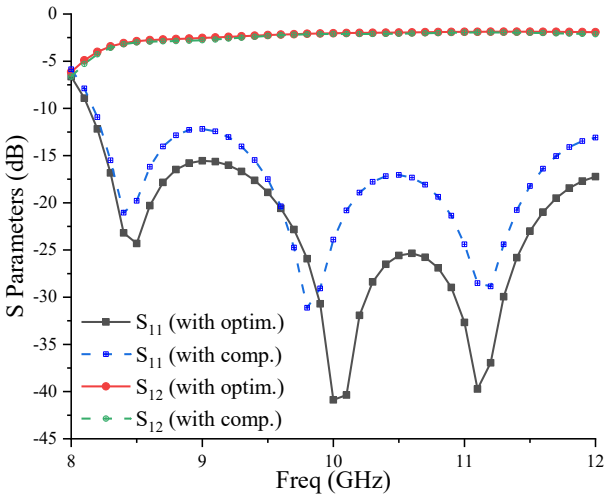

Fig. 3.Scattering parameters of SIW with deduced and HFSS optimized (L×W) transition dimension for f=10GHz.

Comparisons between the S parameters of the first structure for our calculated values (L×W) and those optimized by HFSS of the 3 different frequency values are presented in Figs. 3, 4 and 5, we can note:

1- A bandwidth of around 2.5 GHz is reached for the first range of frequency (Fig.3).

2- A good agreement is obtained between the calculated and optimized (L×W) of S parameters.

3- For high-frequency values our optimal values of (L×W) give a better result of S parameter than that given by the optimal values obtained with HFSS (Figs.5 and 6).

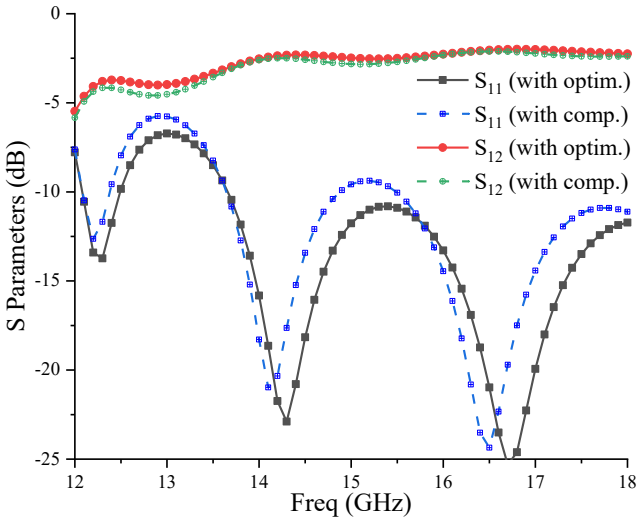

Fig. 4.Scattering parameters of SIW with deduced and HFSS optimized (L×W) transition dimension for f=14.5GHz.

Now we turn our attention to the directional coupler, where the design method presented below is used to set, this time, a microstrip-to-directional coupler transition. The directional coupler is a cruciform H-plane 3dB/90^0 hybrid coupler that consists of a rectangular cavity connected to four input/output ports. Metallic vias are inserted within the crossing area in order to produce the desired directional properties [10-13], Figure 6 shows the structure of the considered coupler.

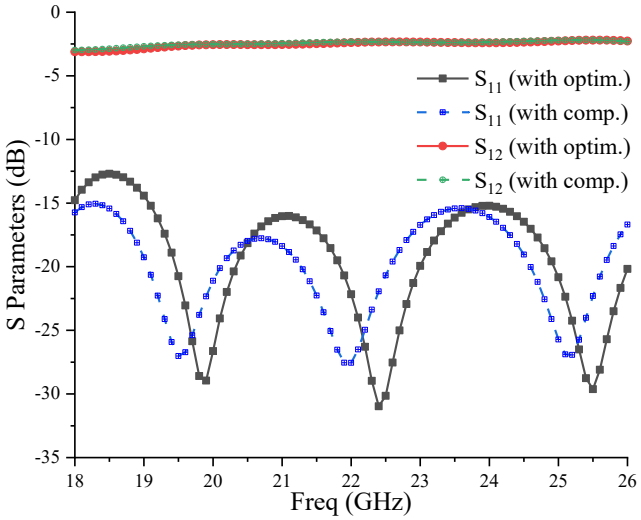

Fig. 5.Scattering parameters of SIW with deduced and HFSS optimized (L×W) transition dimension for f=21GHz.

In this section, we won't present the coupler design method, but we only focus on the design of transition using the method presented below. A directional coupler is a network of four impedances that can be used as a power divider or power combiner by using an even-odd mode analysis technique and symmetric across the mid-plane characteristic. The coupler can be decomposed to a simple circuit as presented in Figure 7. The input impedance at any port of the coupler can be expressed by Equation 5. In this case $Z_{siw} = Z_o$ [9].

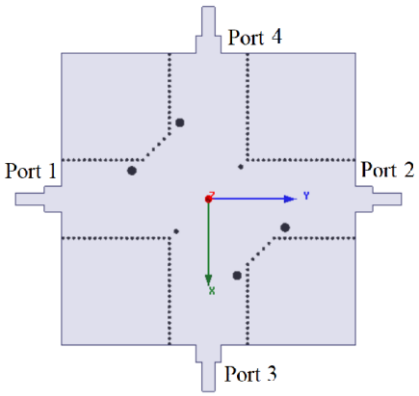

Fig. 6.Cruciform H-plane 3dB/90° hybrid coupler

The design strategy is divided into two parts; the first part consists in optimizing the coupler without transition, where the geometrical parameters of the metallic via give the desired S parameters. In the second part; the transition will be added where the dimensions of this one

will be calculated by the method presented below. Note that the impedance of the load is the impedance of the equivalent waveguide.

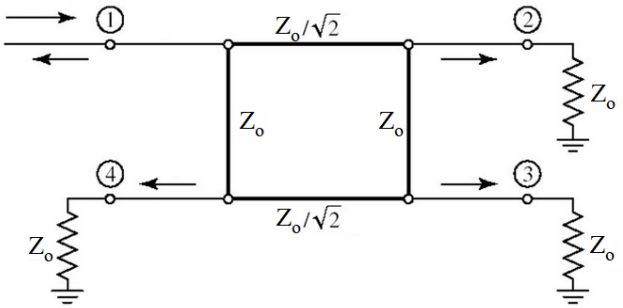

Fig. 7.Circuit of the branch-line hybrid coupler.

A 3dB coupler operating on the X-band is designed. The substrate is Duroid 5870 with ε_r = 2.33 and h = 0.787 mm. the transition dimensions are optimized using HFSS simulator and using the proposed method. The optimized length and width are 6.63 mm and 4.76 mm, respectively. The calculated length and width are 5.2 mm and 4.2 mm, respectively. It can be seen that the calculated dimensions are close to the optimized dimensions. It should be noted that it is impossible to determine the correct dimensions using the presented method but it can be used to determine start values for optimization.
Figures 8 and 9 show the coupler S-parameters, we have a return loss lower than -35dB at the operating frequency.

According to Figure 8, a simple shift in the bandwidth is noticed, even the optimization of the HFSS is similar to our case for S_{11} and S_{13}, whereas for s_{12} and s_{14}, they are almost identical (Fig.9).

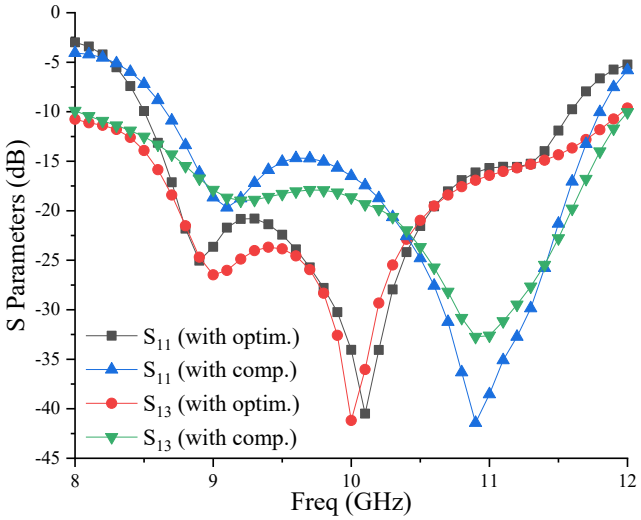

Fig. 8.Simulated S_{11} and S_{13} parameters of cruciform coupler with optimized and our computed (L×W).

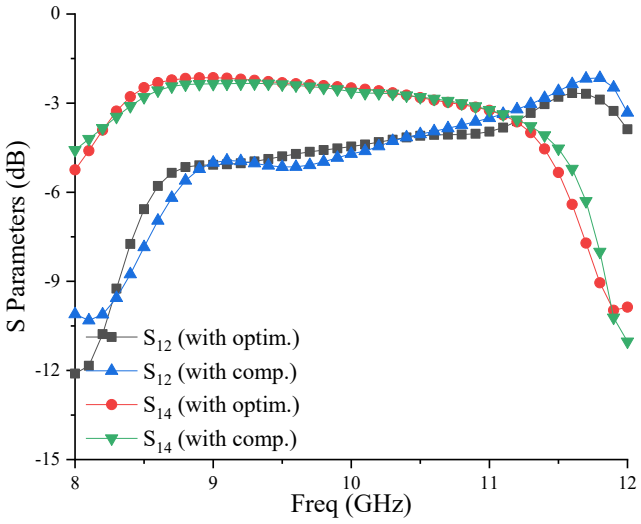

Fig. 9.Simulated S_{11} and S_{13} parameters of cruciform coupler with optimized and our computed (L×W).

4 Conclusion

In this work, analytical equations for the design of a discontinuity step transition are presented. The low reflection approximation method is used in order to find the relationship between all impedances and reflection factors. The proposed equations have been applied to

design several transitions at different frequencies. In all cases, a good return loss has been obtained. The design procedure was applied for a microstrip-to-directional coupler transition. It allows finding a good starting point for optimization.

Acknowledgments. This work is funded by FCT/MCTES through national funds under the project UIDB/50008/2020-UIDP/50008/2020. This work is part of the POSITION-II project funded by the ECSEL joint Undertaking under grant number Ecsel- 345 7831132-Postitio-II-2017-IA.

References

[1] M. Ando, J. Hirokawa and Al, “Novel single-layer waveguides for high-efficiency millimeter wave arrays”, IEEE millimeter waves conference proceedings, pp.177-180, 1997.

[2] D. Deslandes and K. Wu, "Accurate modeling, wave mechanism, and design consideration of a substrate integrated waveguide," IEEE Trans. Microwave Theory & Tech., vol. 54, no. 6,pp. 2516-2526, Jun. 2006.

[3] Th. R. Jones and M. Daneshmand, “Miniaturized Slotted Bandpass Filter Design Using a Ridged Half-Mode Substrate Integrated Waveguide ”, IEEE Microwave and Wireless Components Letters, Vol. 26, no. 5, pp 343-346, MAY 2016

[4] L. Jie, Q. Cui and F. Lin, ‘’Reconfigurable HMSIW Quadrature Coupler ’’, IEEE Microwave and Wireless Components Letters, Vol.29 , no: 10 , pp. 648-651 Oct. 2019.

[5] A. E. I. Lamminen, A. R. Vimpari, and J. Säily, “UC-EBG on LTCC for 60-GHz Frequency Band Antenna Applications ”, IEEE Transactions on antennas and propagation, vol. 57, no. 10, pp. 2904-2912, october. 2009.

[6] K. Tekkouk, M. Ettorre and R. Sauleau, ‘’ Multibeam Pillbox Antenna Integrating Amplitude Comparison Monopulse Technique in the 24 GHz Band for Tracking Applications’’, IEEE Transactions on Antennas and Propagation, Vol.66 , no. 5 , pp. 2616 – 2621, May 2018.

[7] N. Guellil, F. Djahli, and C. Zebiri, “A new formula for the optimum width of Substrate Integrated Waveguide”. Advanced Electromagnetics, 8(4), 39-43, 2019.

[8] E. Miralles, H. Esteban, C. Bachiller, A. Belenguer and Vicente E. Boria, “Improvement for the design equations for tapered Microstrip-to-Substrate Integrated Waveguide transitions”, International Conference on Electromagnetics in Advanced Applications, Oct. 2011.

[9] D. M. Pozar, “Microwave Engineering”, John Wiley & Sons, Inc, 4th ed. USA, 2012.

[10] T. Djerafi and K. Wu, “Super-compact substrate integrated waveguide cruciform directional coupler,” IEEE Microw.Wireless Compon. Lett., vol. 17, no.11, pp. 757-759, Nov. 2007.

[11] T. Djerafi, J. Gauthier, and K. Wu, “Quasi-optical cruciform substrate integrated waveguide (SIW) coupler for millimeter-wave systems,” International Microwave Symposium Digest (MTT), pp 1-4, 2010.

[12] Elfergani, I.T.E.; Hussaini, A.S.; Rodriguez, J.; Abd-Alhameed, R. Antenna Fundamentals for Legacy Mobile Applications and Beyond; Springer: Cham, Switzerland, 2017; pp. 1–659.

[13] Issa Elfergani, Amjad Iqbal, Chemseddine Zebiri, Abdul Basir, Jonathan Rodriguez, Maryam Sajedin, Artur De Oliveira Pereira, Widad Mshwat, Raed Abd-Alhameed, Sadiq Ullah. Low-Profile and Closely Spaced Four-Element MIMO Antenna for Wireless Body Area Networks. Electronics. 2020; 9 (2):258.

UHF Radio Channel Measurements and Prediction for Maritime Communications

F.Salazar-Quiñonez[1], M. Abdulaziz[2], A. Hussaini[3], R.A. Abd-Alhameed[4], A.Cowley[5], D. Bladen[6]
{fsalazar@dragonsystemsltd.co.uk[1], maiwadaabdulaziz@yahoo.com[2], ash.hussaini@aun.edu.ng[3], r.a.a.abd@bradford.ac.uk[4], andy@cowley.eu[5], derek.bladen@commercial-radio.co.uk[6]}

Dragon Systems LTD, Milford Haven, SA73 2ND, United Kingdom[1]
Mobile and Satellite Faculty of Engineering and Informatics, University of Bradford, Bradford, BD7 1DP, United Kingdom[2,3,4],
Home Sensor LTD, Milford Haven, SA73 2QN, United Kingdom[5]
Commercial Radio Systems, Cardiff, CF11 8BA, United Kingdom[6]

Abstract. Radio Service Coverage Area of UHF Repeater systems is one of the most important performance elements for a ship to shore radio communications within industries around the world. Each implemented system is designed to fulfill their specific demands, which in this case is balancing coverage limitations and transmission power restrictions due to petrochemical industry regulations. This paper presents the performance of an Analogue UHF Repeater Extender characterized by a 3D Shoot and Bounce Ray Tracing Propagation Model combining efforts of field strength distribution, time of arrival, and propagation-channel environment. The work is focused on the extender's field measurements results in comparison to a Wireless InSite 3D SBR simulation model.

Keywords: UHF Repeater Extender, Marine Communications, Ship to Shore, 3D SBR, Shoot, and Bounce Ray Tracing Technique, ATEX Radios, LNG Cargo.

1 Introduction

Reliable Maritime Radio Communications for any Military, Industrial or Private Cargo Vessel and the port ashore it's crucial for safe coordination of manoeuvres and operations such as docking, sailing, loading, unloading, as well as handling emergencies. Depending on each situation the communication quality amongst the crew members, coordinators, and the control room is paramount to perform risk-free tasks [1]. Each cargo vessel holds goods and/or materials that could be in nature hazardous such as petrochemicals or could represent a hazard if not handled correctly, for example, military equipment, heavy cargo containers. In this case, significant degradation of the signal is experienced when radio communications try to penetrate from the shore control room using UHF radio repeaters to handheld UHF radios inside the control room from the ship.

In a petrochemical cargo tanker, this degradation of the signal is present due to a mixture of factors such as the complexity of the metallic structure of the vessel as well as the transmit

IMDC-IST 2021, September 07-09, Sakarya, Turkey
Copyright © 2022 EAI
DOI 10.4108/eai.7-9-2021.2314956

power limitation due to ATEX regulations for communications within hazardous explosive atmospheres that applies to the vessel as well shore equipment [2].

1.1 Studies on Measurements

Several studies have been developed over many years to evaluate the radio wave propagation from maritime vessels communicating with the shore for different applications. [3-6]. Some literature has experimented on theoretical analysis against measurement campaigns for a line of sight (LOS) and non-line of sight (NLOS) Scenarios [4-6] implementing antenna diversity or MIMO antennas network to extend the coverage of the communications within the ship [7] as well as ad-hoc network system for multiple vessels [8] for security and positioning purposes [9-10].

1.2 Studies on Simulation

The use of radio propagation simulation software on large scenarios facilitates a relatively fast estimation of the channel characteristics, such as the power delay profile, signal field distribution, time of arrival, among others [11-18]. The following studies have simulated radio repeater propagation environments [11], using 3D Simulation software to evaluate the radio frequency propagation on outdoor to indoor scenarios for high-speed communications [12-13] as well as a vessel to harbour communications using a Shoot and bounce ray-tracing technique [14] with different vessel location LOS and NLOS. Using techniques have a better resolution importing computer-aided design CAD models for the complex structure of the ship [15].

1.3 Studies on Simulation vs Measurements

A combination of Measurements Campaigns and Simulation models have been applied to some studies to corroborate results in oversea radio propagation [16-18] using radio channels in frequencies above the 5GHz [17-18] to investigate the Line-of-Sight propagation and Non-Line of Sight standoff distances for different size of vessels measuring power delay profile (PDP) and comparing it with 3D propagation models. In the same way, the paper [18] analyses channel characteristics of the UHF band (225 -450 MHz) onboard a merchant ship providing a good representation for the shape of the impulse response for a cluttered environment. Investigations such as [19] demonstrate that the Wireless InSite 3D simulation tool provides a good estimation of the measurement results.

2 Repeater Extender System

The idea presented in this paper to overcome the lack of signal without affecting the system's transmission power will be achieved by implementing an innovative design of an extender repeater radio system array. This system will be located at the top of the jetty or berth building, closer to the vessel, and will interact with the existing repeater system. The new system will relay the signal from within the main system's range creating a new and stronger radio transmission able to find a path to reach inside the ship as well as to be close enough to receive the transmissions from the vessel's handhelds.

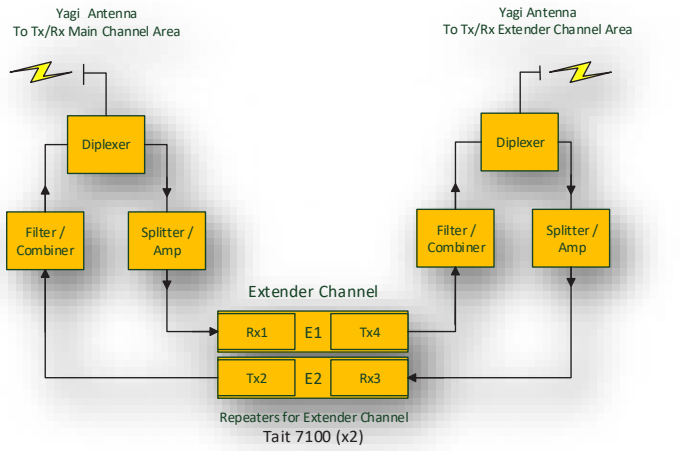

Fig. 1. Extender Array.

The extender array consists of two radio repeaters TAIT 7100 (for this case study), Rx1/Tx2 working together to emulate a normal portable radio, and Rx3/Tx4 working as a normal repeater. Radio Repeater "E1" receives the transmission signal on frequency 1 (Rx1) from the Main Channel and re-transmits on Tx4 into the Extender Channel to communicate to handheld radios on this channel. "E2" receives the signal Rx3 from the handheld radios on the Extender Channel and retransmits to Tx2 to the main repeater as represented in Fig 1. Once the re-transmission from the Extender Repeater reaches the Main repeater, it is then broadcasted on Tx1 to the handheld radios on the Main Channel as well as a return of transmission to "E1". This system allows handheld radios to intercommunicate on two different channels at different coverage areas as shown in Fig 2. Four Element Yagi antennas were located at the top of a jetty port control building (10m height) on a 3m pole and connected to the diplexer using cable RG 213/U. A bird thru line wattmeter tester was utilised to verify that 2W was the power transmitted at the antenna level, as per ATEX regulations [2]. In the same way, the handheld radios' maximum transmission power is 1W by design.

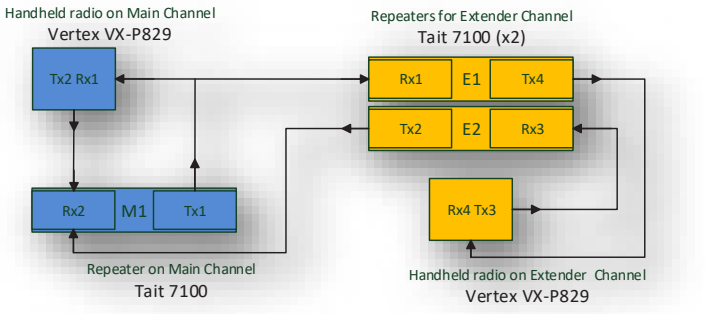

Fig. 2. Extender Transmission System.

3 Measurement Setup

The measurements were accomplished using a Field Strength Analyser Protek 3290N to simulate a handheld radio, this has been calibrated to analyse narrowband signals at 12.5 kHz Channel Bandwidth and specifically for frequencies 1 and 4 (Rx1, Rx4). The sensitivity range was set from 0-120 dB and localised at 1.5m from the floor on each test location. Due to weather factors that may affect the received signal, this campaign was done on a clear and dry day. Date and time were also recorded to evaluate the tide level and relative position to locate the height of the ship about the shore side, for modelling references [20].

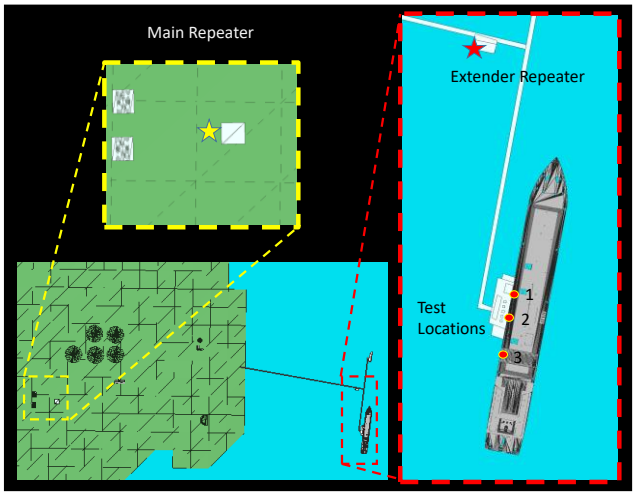

Fig. 3. Scenario Layout

In Fig 3, the yellow star represents the Main Repeater Antenna, and the red star the Extender Repeater antenna. The Field Strength Analyser was tested along with three different locations on the ship. Test locations “1” and “2” are located outside the cargo, where unload operations require reliable communications, and test location “3” is located inside the control room from the ship. The received signal strength index (RSSI) was measured at these three locations on transmissions from the Main repeater system as well as the Extender Repeater system.

4 Simulation Model

A simulation 3D model was created to estimate and co-validate the performance of the proposed Extender system. The model was created using Wireless InSite software working on a Study Area of 2157.43m x 4339.97m x 146m. The terrain profile from the land was uploaded from Google Earth using Google Sketchup 7.0 with the application of the Geo-Location tool as shown in Fig 4 [21].

Fig. 4. Terrain profile.

The rest of the buildings, the jetty trestle, the fort (in red), the tank farm, and the ship were also created on Sketchup 7.0, converted into objects, and imported into the Wireless InSite model as shown in Fig 5. The size of each of the objects was also corroborated with their correspondent structural drawings to match each of the features and sizes to the real-world scenario. The ship and the Tank farm designs were designed available from a 3D warehouse and modified to fit the study purposes [22].

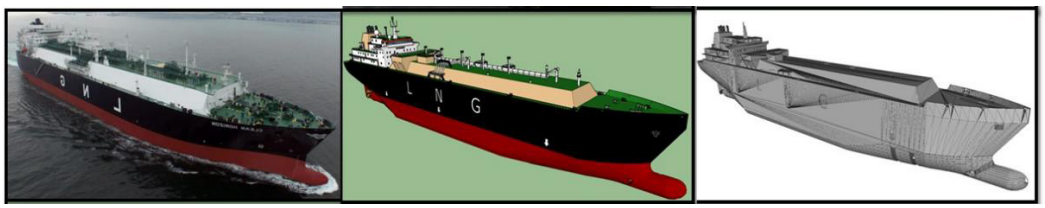

Fig. 5. Image of Ship [23], Model on Sketchup 7.0 [22] and Wireless InSite.

4.1 Materials

As the integrity of all the elements is crucial in the investigation, therefore the material specifications were taken from the Remcom database library [24]. Terrain profile is set up as wet earth, buildings as concrete, and the fort of brick material. The Ship and the tank farm will be considered as perfect electric conductors (PEC).

Table 1. Materials [24].

Material	Permittivity	Conductivity (s/m)	Thickness (m)
Concrete	15	0.015	0.3
Wet Earth	25	0.02	0
Brick	4.44	0.001	0.125
Sea Water	81	20	0

4.2 Ship

To have an accurate location of the vessel in the model, there are a couple of important factors to consider. One is the tide level and the second is the relative position of the ship against the berth. The tide level at the time of measurements was 4.48 mts to locate the ocean level

regarding the height of the Jetty and the berth. In the same way, the relative position of the ship regarding the shore was -5.1 mts. This was done measuring from the vessel's upper deck level to the upper platform from the shore side. This is important to consider because a ship unloading material loses weight from the cargo, therefore it increases its floating capabilities meaning that rises gradually from the water.

4.3 Antennas and Locations

The transmit antennas in the main channel consist of a Half-wave dipole antenna transmitting at 33dBm to represent a four-element stacked array dipole antenna mounted on a 22m height mast. In extender system will transmit at 33dBm using a Directional dipole antenna to simulate a 4 element Yagi antenna mounted on a 3m pole on top of the Jetty Building.
The receive antennas that will simulate handheld radios will be represented by short dipole antennas at different test locations. These antennas will have the same sensitivity range as the real test measurements of 0-120 dBm. Test location scenarios for the receivers 1, 2 (both outside) and 3 (inside) on the measurement campaign will be represented by Rx Out 1, Rx Out 2, and Rx IN in the simulation, respectively as shown in Fig 6.

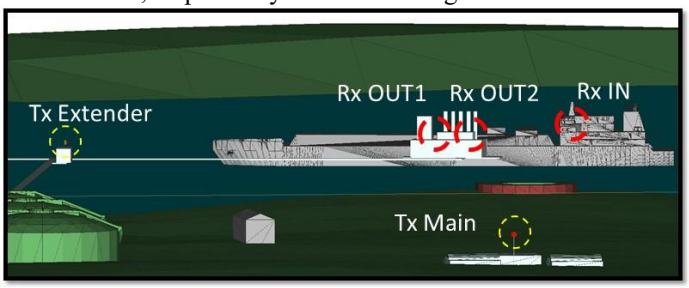

Fig.6. Antenna Positioning.

Additional losses were introduced into the study due to cable type, length, connectors, and couplers for the Main and the Extender antennas connection.

Table 2. Antenna Losses.

Main Antenna		Extender Antenna	
LDF - 550	Loss	RG213/U	Loss
50 mts	1.5 dB	30 mts	5 dB
Connector (x2)	2 dB	Connector (x2)	3 dB
Coupler	1.5 dB	Coupler	2 dB

From Table 2 it was deduced that the Main antenna cable loss calculation is approximately 5 dB, and the Extender antenna cable loss is calculated to be at least 10 db.

4.4 Study Area

The model calculations on Wireless InSite were performed using the Full 3D model. This model is based upon the shoot and bounces ray-tracing technique in a 3D model using 0.25° ray spacing, 6 reflections, 4 transmissions, and 1 diffraction. This allowed the calculation of the path loss through the interaction of the transmitted rays with the basic multipath mechanisms

(transmission, reflection, diffraction, and scattering) and evaluating the rays that reached the receiver.[25]

5 Results

The measurement campaign was performed using a Signal Strength Analyser to simulate a handheld radio and capture the Received Signal Strength Indicator (RSSI) from the Main Transmitter as well as the Extender Transmitter. These measurements were evaluated at 3 locations, two outside the ship and one inside the ship, each at 1.5m from the floor. The readings at each location were averaged for simpler analysis. The 3D simulation model was created using Wireless InSite and performed accurate calculations using the shoot and bounce ray-tracing technique. The 3D SBR ray-tracing technique applies an image method approach to capture a large scenario precisely. The calculation time of the simulation time was done in 4hrs and 35 mins using PC intel core duo @ 4GB of RAM. Transmissions from Main and Extender created multipath that reached the receivers located outside and inside the ship. There was not any Line-of-Sight transmission able to reach the receiver inside the ship as represented in Figs 7 and 8.

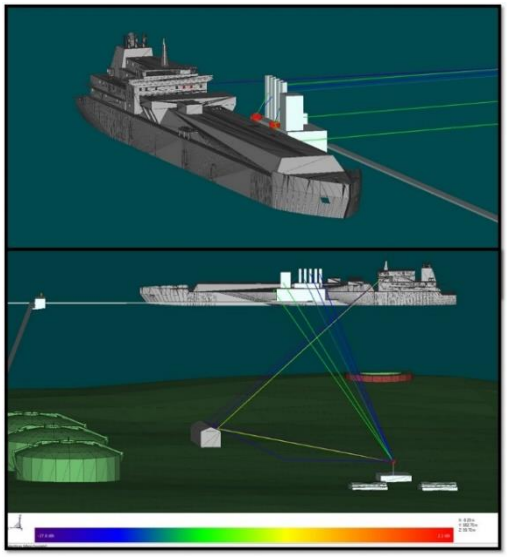

Fig. 7. Main Tx to Ship Rx.

Fig 7 shows the few transmission paths from the Main Transmitter that reached the receivers on the Ship. Structural buildings interact as obstructions or multipath features for the ray trajectory. The signal received on the ship from this calculation fluctuates from -79 dBm to -86 dBm (averaged values) which represents the low numbers of rays received, therefore the lack of strong or reliable communications.

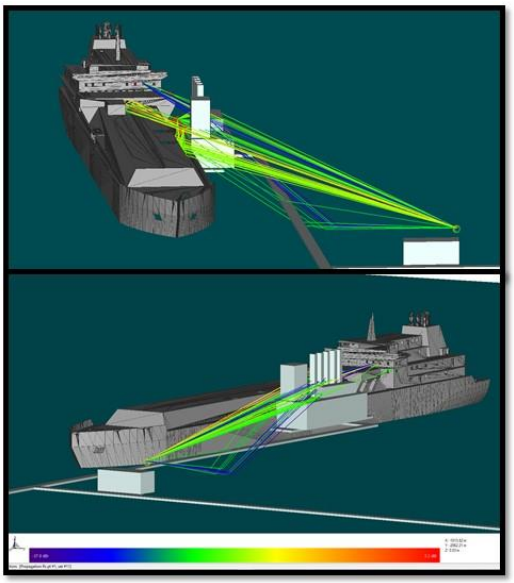

Fig. 8. Extender Tx to Ship Rx.

With the implementation of the Extender system closer to the ship, the results showed an increased number of rays reaching the Ship's receivers as shown in Fig 8 despite the location of the control tower, loading arms, high-pressure pumps, and pipework that could be obstructing the signal's path. As well as the higher quantity of paths reaching the receivers a stronger signal is received inside the ship, improving with this the quality and reliability of communications. The range of the signal received is from -58 dBm to -66 dBm (mean values).

Table 3. Mean Measurements vs Mean Simulation Results.

Tx/Rx	Rx OUT 1		Rx OUT 2		Rx IN	
	Simulation	RSSI	Simulation	RSSI	Simulation	RSSI
Tx Main (dB)	-79.2763	-80	-84.9540	-86	-86.3110	-85
Tx Extender (dB)	-58.9581	-58	-59.3064	-61	-66.2826	-64
Improvement (dB)	20.3182	22	25.6476	25	20.0284	21

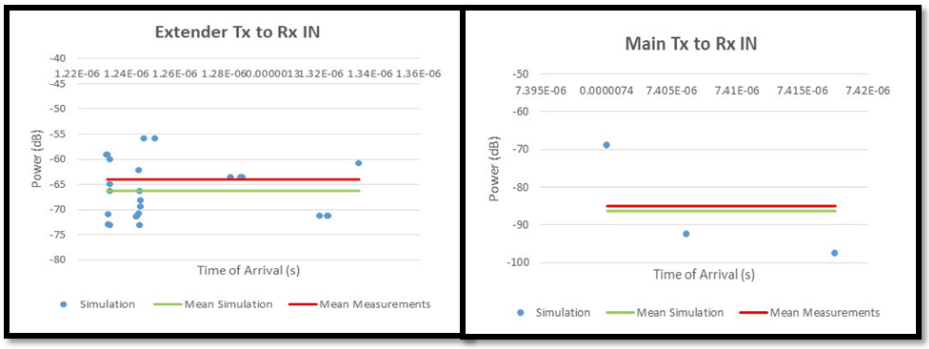

Fig. 9. Power vs ToA to Rx IN.

Table 3 shows the compilation of the RSSI from the measurements and the simulation at each of the locations. This table compares the simulation against the measurement and shows an improvement of a minimum of 20dB from the Extender system against the Main System.
Fig 9 demonstrate visually the proximity of the mean RSSI values from the measurements and the mean signal strength received inside the ship on the simulation including the intensity of rays at each system.

6 Conclusion

The implementation of the UHF Extender Repeater System had a strong impact on the communications with the ship, making more reliable transmissions and increasing the coverage area. Once compared with the RSSI from the UHF Main Repeater system the measurements of the field strength distribution showed that the Extender system provided a minimum of 20dB improvement on RSSI inside the control room in the ship. The implementation of the 3D SBR simulation model using Wireless InSite software provided a good estimation of the channel propagation without exhausting computational effort. The comparison between the results obtained from the simulation data and the measurements had a high correlation of 99.25%. Despite the high accuracy of the model, the complexity of the plant design limits the possibility of it being used in the future. Further improvements could be made to the extender system in the future to reduce losses from cable and connectors.

7 References

[1] H. Karahalios, “The Severity of Shipboard Communication Failures in Maritime Emergencies: A Risk Management Approach,” International Journal of Disaster Risk Reduction, 2018.

[2] T. Jespen “ATEX—Ignition Sources. In: ATEX—Explosive Atmospheres,” Springer Series in Reliability Engineering. Springer, Cham. 2016

[3] Y. M. Le Roux, J. Ménard, C. Toquin, J. P. Jolivet and F. Nicolas, "Experimental measurements of propagation characteristics for maritime radio links," 2009 9th International Conference on Intelligent Transport Systems Telecommunications, (ITST), Lille, 2009, pp. 364-369.

[4] J. Yu, W. Chen, K. Yang, C. Li, F. Li, and Y. Shui, “Path Loss Channel Model for Inland River Radio Propagation at 1.4 GHz,” International Journal of Antennas and Propagation, vol. 2017, Article ID 5853724, 15 pages, 2017.

[5] K. Yang, T. Roste, F. Bekkadal, K. Husby and O. Trandem, “Long-Distance Propagation Measurements of Mobile Radio Channel over Sea at 2 GHz," 2011 IEEE Vehicular Technology Conference (VTC Fall), San Francisco, CA, 2011, pp. 1-5.

[6] K. Yang, T. Roste, F. Bekkadal and T. Ekman, Land-to-Ship Radio Channel Measurements over Sea at 2 GHz," 2010 6th International Conference on Wireless Communications Networking and Mobile Computing (WiCOM), Chengdu, 2010, pp. 1-4.

[7] V. J. Dwivedi, & N. A. Kotak, “Simulation and Performance Analysis of Blast Structure in MIMO Environment,” International Journal of Research in Engineering and Technology. April 2014.

[8] X. Su, B. Hui, K. Chang & S. Kim. “Improvement of the Link Reliability for Ship Ad-Hoc Network by Employing Multiple Antennas,” The Journal of Korea Information and Communications Society, 2012.

[9] H. Luo, K. Wu, Z. Guo, L. Gu and L. M. Ni, "Ship Detection with Wireless Sensor Networks," in IEEE Transactions on Parallel and Distributed Systems, vol. 23, no. 7, pp. 1336-1343, July 2012.

[10] B. Hui, K. Jeon, K. Chang, S. Kim, J. Park and Y. Lim, "Design of radio transmission technologies for VHF band ship ad-hoc network," ICTC 2011, Seoul, 2011, pp. 626-629.

[11] A. Hastings, "Modeling of RF propagation in a radio repeater environment," 2016 IEEE/ACES International Conference on Wireless Information Technology and Systems (ICWITS) and Applied Computational Electromagnetics (ACES), Honolulu, HI, 2016, pp. 1-2.
[12] E. Semaan, F. Harrysson, A. Furuskär and H. Asplund, "Outdoor-to-indoor coverage in high frequency bands," 2014 IEEE Globecom Workshops (GC Wkshps), Austin, TX, 2014, pp. 393-398.
[13] W. Manan, H. Obeidat, A. Al-Abdullah, R. Abd-Alhameed and F. Hu "Indoor to Indoor And Indoor To Outdoor Millimeter Wave Propagation Channel Simulations At 26 Ghz, 28 Ghz And 60 Ghz For 5G Mobile Networks" The International Journal of Engineering and Science (IJES), Volume 7, Issue 3, Ver. II, Pages PP 08-18, 2018
[14] J.K. Infantolino, K. L. Labowski, "Complex 3D Modeling of Sea to Land Scenario" 29th Annual Review of Progress in Applied Computational Electromagnetics, ACES, 2013/3/24.
[15] L.E. Rodriguez-Gallo "Propagation Modeling od Wireless Systems on Shipboard External decks," MSc Thesis Naval Postgraduate School, Monterey, California. USA. 2006.
[16] Y. H. Lee, F. Dong, Y. S. Meng. "Stand-off distances for non-line-of-sight maritime mobile applications in 5GHZ band". Progress In Electromagnetics Research, 2013, pp 321-336.
[17] F. Dong and Y. H. Lee, "Non-line-of-sight communication links over sea surface at 5.5GHz," Asia-Pacific Microwave Conference 2011, Melbourne, VIC, 2011, pp. 1682-1685.
[18] X. H. Mao and Y. H. Lee, "UHF Propagation Along a Cargo Hold on Board a Merchant Ship," in IEEE Transactions on Wireless Communications, vol. 12, no. 1, pp. 22-30, January 2013.
[19] Y. Dama, R. Abd-Alhameed, F. Salazar-Quiñonez, D. Zhou, S. Jones and S. Gao, "MIMO indoor propagation prediction using 3D shoot-and-bounce ray (SBR) tracing technique for 2.4 GHz and 5 GHz," Proceedings of the 5th European Conference on Antennas and Propagation (EUCAP), Rome, 2011, pp. 1655-1658.
[20] S. Balkees P A, K. Sasidhar and S. Rao, "A survey-based analysis of propagation models over the sea," 2015 International Conference on Advances in Computing, Communications and Informatics (ICACCI), Kochi, 2015, pp. 69-75.
[21] T. S. Rappaport, J. N. Murdock, D. G. Michelson and R. Shapiro, "An Open-Source Archiving System," in IEEE Vehicular Technology Magazine, vol. 6, no. 2, pp. 24-32, June 2011.
[22] https://3dwarehouse.sketchup.com/model/u3c83a3e6-67504410-80a7-af656dc0298b/LNG-carrier, Fabio D.
[23] www.dynagas.com
[24] Remcom, The Wireless Insite User's Manual Release 3.1.0.1. Pennsylvania, USA: Remcom Inc. , 2017.
[25] P. Pajusco, "Propagation channel models for mobile communication," Comptes Rendus Physique, vol. 7, pp. 703-714, 2006.

Beam Steering of Wearable Antenna with Metamaterial Structures for Patient Monitoring

Parisa Shirvani, Farzad Khajeh-Khalili and Raed A. Abd-Alhameed
{shirvaniiiparisaaa@gmail.com[1], khalili.farzad@gmail.com[2], r.a.a.abd@bradford.ac.uk[3]}

Electrical and Biomedical Department, Sepahan Institute of Science and Technology of Higher Education, Isfahan, Iran[1]
Electrical Department, Kian Institute of Higher Education, Shahin Shahr, Isfahan, Iran[2]
Bradford-Renduchintala Centre for Space AI, Faculty of Engineering and Informatics, University of Bradford, Bradford BD7 1DP, UK[3]

Abstract. At 5.2 GHz, in the industrial, scientific, and medical (ISM) sub-channels, a unique metamaterial (MTM) structure is used to tilt the beam and boost the directivity of a wearable antenna. The antenna substrate in this design is made of a typical jean cloth, which is a wearable and flexible material. The dielectric constant of normal denim fabric is 2.17, the thickness is 3.175 mm, and the tan (δ) value is 0.002. The antenna's radiation beam is steered in the right direction for healthcare purposes utilising this architecture. The radiation beam is slanted by 9^o in the E-plane, according to the simulation results. At 5.2 GHz, the gain was found to be 6.35 dB. Additionally, the specific absorption rate (SAR) is ideal for medicinal applications. The results show that the proposed antenna is a viable biomedical technology option.

Keywords: Wearable; Metamaterial; Patient monitoring; Beam tilting.

1 Introduction

Recently, there has been an increase in the development of wearable smart systems that are utilised for patient monitoring, tracking, physical training, and rescue system geo-positioning. It is obvious that the constant development of wearable systems features radically improves the performance of telecommunication systems in the health care area. One of the vital components of medical/telecommunication systems is wearable antennas which faced many challenges such as low profile, high gain, and high sensitivity. In addition to telecommunication discussions about antennas, wearable antennas that are used as part of clothing should meet medical standards such as high flexibility, make the patient comfortable, and be resistant to patient movements. To achieve these aims, some researchers have focused on choosing the best material as a substrate of the wearable antenna [1, 2]. Some characteristics such as low-cost, high flexibility, widely available, and small loss tangent are assessed to choose the best material for the substrate of wearable antenna. Reducing the specific absorption rate (SAR) by the body is another arguable issue about the wearable antenna. The SAR parameter indicates the rate of absorbed energy per unit mass by the human body when it is exposed to electromagnetic waves. The SAR value is defined by The United States (US) and European Union (EU) regulatory authorities to maintain safety restrictions [3]. Different methods to gain enhancement and bandwidth improvement of a wearable antenna are presented in [4, 5]. Reconfiguring the

IMDC-IST 2021, September 07-09, Sakarya, Turkey
Copyright © 2022 EAI
DOI 10.4108/eai.7-9-2021.2314955

radiation pattern is a key factor to enhance the performance of the antenna which leads to interference reduction and system security increment. Some artificial periodic structures such as metamaterial (MTM) [6,7], artificial magnetic conductor (AMC) [8], electromagnetic bandgap (EBG) [9], and frequency selective surface (FSS) [10] had been employed for providing the beam tilting. Metamaterial structures are artificial compounds with remarkable electric and magnetic properties which employed to a revolution in the performance of antennas such as gain enhancement, radiation patterns improvement and widening bandwidth, the smaller size of the antenna, beam tilting, etc [11,12]. In [6], a metamaterial structure with four switches is used to tilting the radiation beam at 28 GHz. This structure can tilt the radiation beam at angles in the E-plane. In addition, the gain enhancement is 24.8% and 22.4% for ± tilting angles, respectively. In [13], a stairway-shaped resonator (SSR) as a novel metamaterial for beam tilting at 28 GHz has been designed. Two-pin diodes are used in the gaps of the structure to create four states with different refractive indexes. In [14], a negative refractive index metamaterial structure is designed to beam tilting of a double-feed dielectric resonator antenna. The main beam of the antenna can be tilted from over the frequency range of 5-5.5 GHz.
The body of this paper is as follows: Section 2 introduces the recommended design and its performances. In Section 3, the simulation results of the proposed antenna characteristics will be accessible. Then the significant advantages of the proposed wearable antenna will be expressed. Finally, in Section 4, a conclusion will be presented.

2 Proposed Design

In this section, the model features of a wearable antenna with the metamaterial unit-cells for use in medical/telecommunication systems are accessible. A novel MTM structure is employed to beam tilt optimization of a wearable antenna in health care networks. The aim is to control the inclination of the tilt angle of the antenna to optimize a set of network performance indicators such as reducing unwanted interfaces and increasing healthcare network security. As a result, the health care network works better, and more people trust telemedicine applications.

2.1 Antenna Design

A modified wearable antenna at 5.2 GHz is shown in Fig 1. The suggested antenna is a very thin conductive material connected to a feedline as an upper layer at which the signal is to be transmitted. The wearable and flexible standard denim fabric is utilized as a middle layer with dielectric constant $\varepsilon_r = 2.17$, $\tan \delta = 0.002$, and thickness 3.175 mm. The most significant feature of this dielectric is its high flexibility, low cost, and availability. The ground plane is also the last thin conductive layer. Table 1 introduces the antenna structure elements. The simulations were done with CST software.

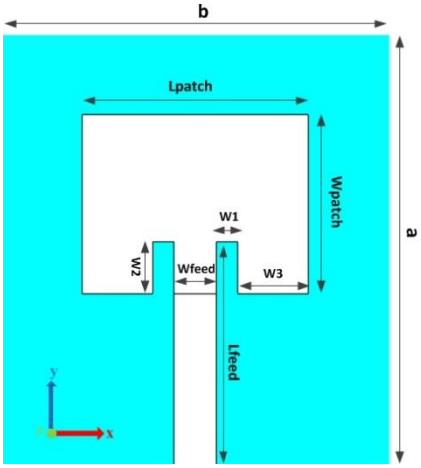

Fig. 1. Configuration of the proposed wearable antenna

Table 1. The dimension of the patch antenna

Parameters	Dimensions (mm)
a	120.47
b	92
Lpatch	52.63
Wpatch	41.72
W1	4.934
W2	12.109
W3	16.447
Wfeed	9.868
Feed	52.48

In Fig 2a, the reflection at the input port is informed. According to this figure and assuming S_{11} < -10 dB, the frequency range of 5.16-5.4 GHz is covered. In Fig. 2 (b), the reported surface current at frequency 5.2 GHz indicates good radiation.

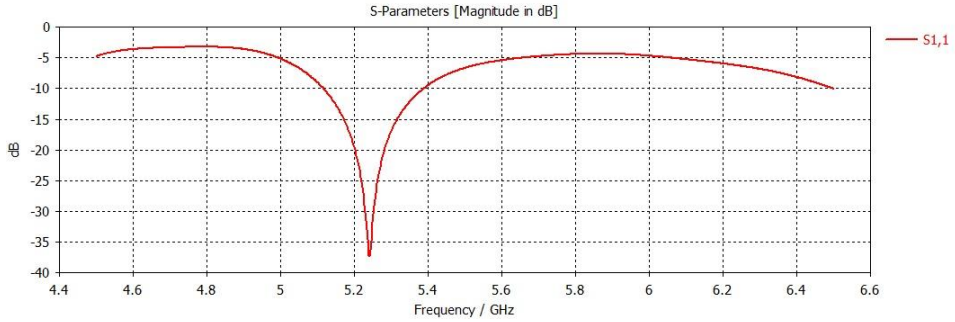

(a)

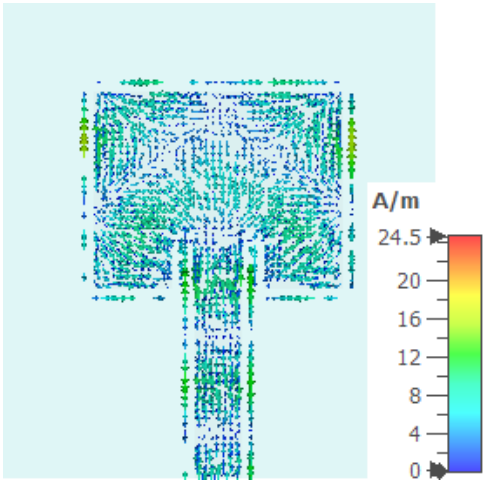

(b)

Fig. 2. The antenna results, (a) S_{11}, (b) surface current distribution.

2.2 Metamaterial Design

The geometric of the MTM cell is illustrated in Fig. 3, where a square ring with some cross-diagonal bars are notified. For full-wave analysis, along the *z*-axis, two waveguide ports are located, and in the *XY* and *YZ* planes, perfect magnetic and electric conductors (PMC and PEC) boundaries are located respectively. The dimensions of the proposed MTM unit cell are stated in Table (2).

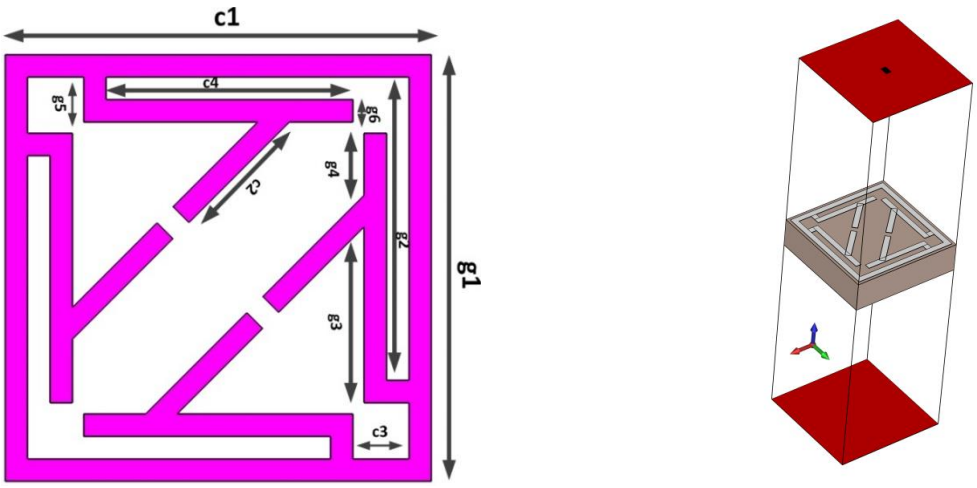

(a) (b)

Fig. 3. The proposed metamaterial cell; (a) front view, (b) side view.

Table 2. The dimension of MTM cell

Parameters	c1	c2	c3	c4	g1	g2	g3	g4	g5	g6
Dimensions (mm)	5.7	1.9	0.75	3.3	5.7	4.05	2.35	0.83	0.6	0.3

The S21 parameter and permeability of the recommended MTM structure are revealed in Fig 4. It displays the results of the S_{21} from scattering parameters (S-parameters) as well as the permeability coefficient. According to Fig 3a. and assuming S_{21} < -10 dB, the bandwidth of this stopband is about 1 GHz (5-6 GHz). Also, according to Fig 3b., within 3.2 to 5.7 GHz, the permeability is less than zero. The negativity of the permeability attests that this structure is a metamaterial unit-cell that can have a dramatic effect on improving the wearable antenna.

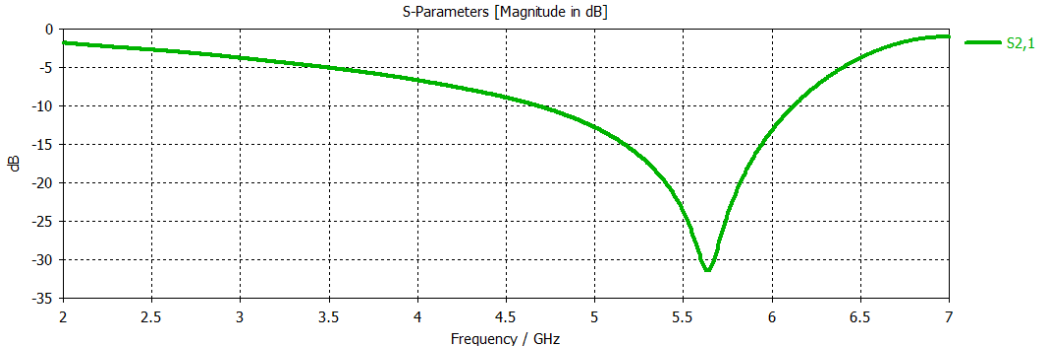

(a)

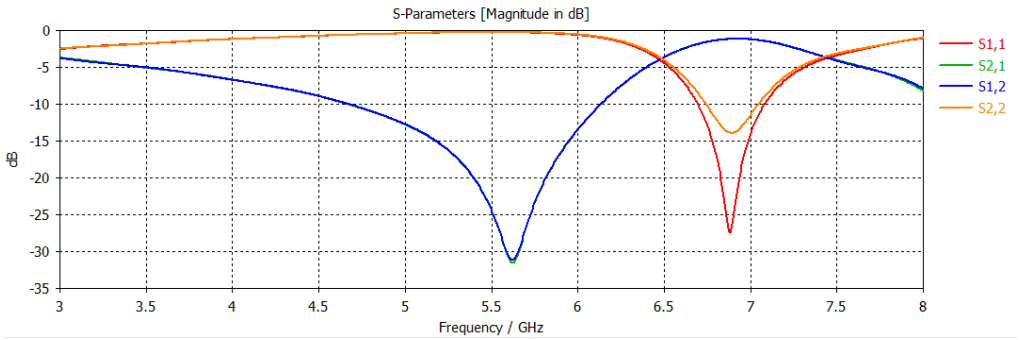

(b)

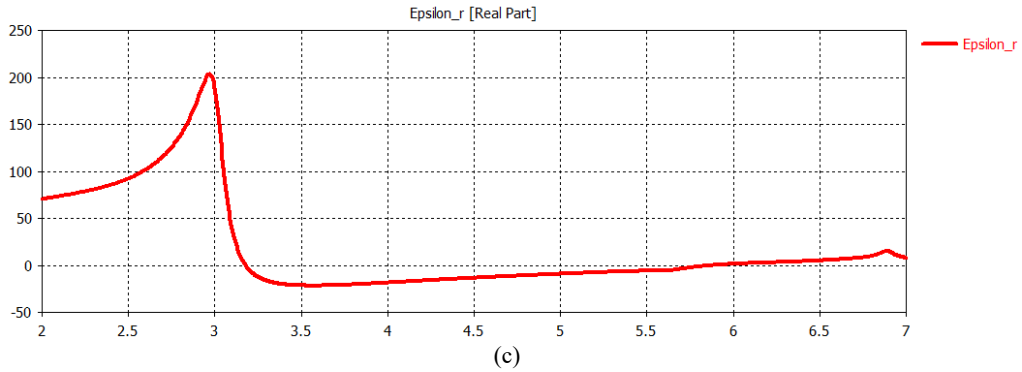

(c)

Fig. 4. (a) S21 parameter, (b) S-pars, (c) permeability of the present metamaterial cell.

To better justify the proposed MTM unit-cell behaviour, a report on the changes at the dimensions and the expression of its result in the performance of the structure is presented. The slot size effect on the S_{21} parameter is shown in Fig 5. According to this figure, with increasing gap size, the transmission-zero has changed to lower frequency values. Note that this feature proves the "tunability" of the proposed structure. In [15], this issue has been thoroughly investigated in the same way.

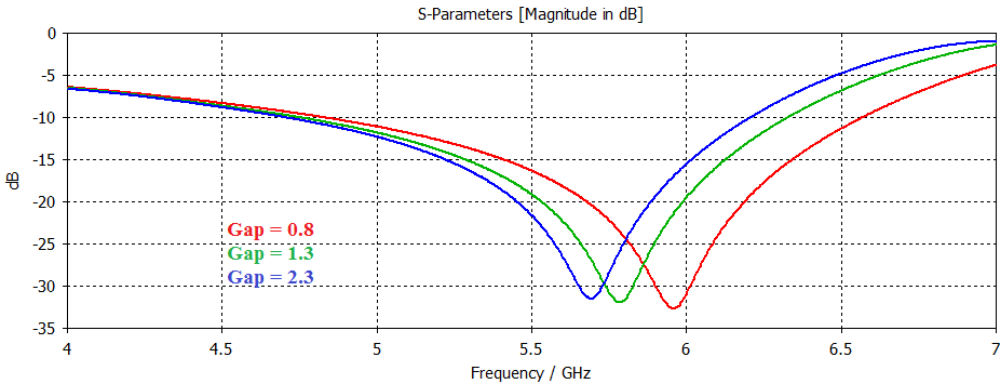

Fig. 5: S_{21} parameter with different gap sizes

The slot size effect on the permeability parameter is shown in Figure 6.

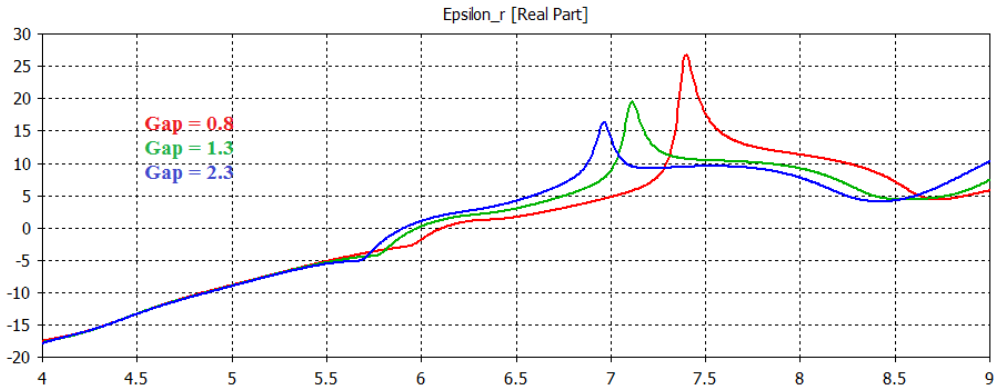

Fig 6: permeability parameter with different gap sizes

3 Final Design and Results

The effect of using different numbers of the metamaterial unit cells in the main beam rotation is available in Table 3.

Table 3. The effect of different numbers of unit cells

Different Designs	Number Unit Cell (Row×Column)	Beam Rotation
1	1×5	3°
2	2×5	5°
3	3×5	7°
4	2×3	4°
5	3×3	6°
6	3×10	4°
Final Design	6×5	9°

The final design is obtained by placing six rows of five of the MTM unit cells at 3 mm of the antenna shown in Fig 7. The results show that the best location for the metamaterial structure is 3 mm from the antenna to achieve a change within the main beam angle. The distance between the rows is equal to 2 mm.

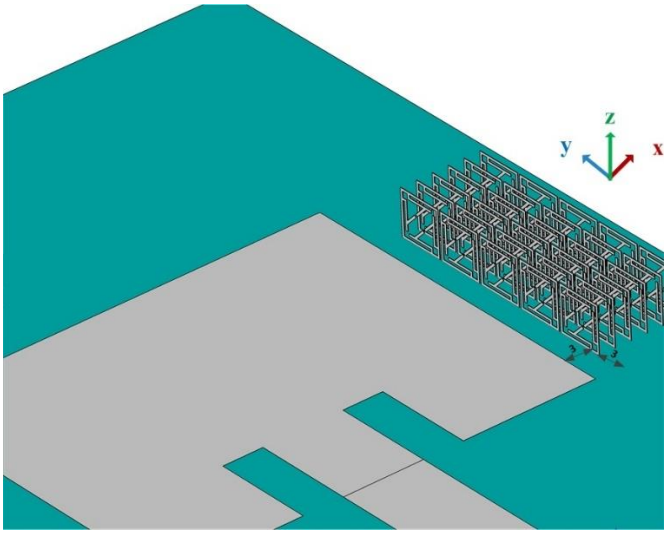

Fig. 7. Arrangement of wearable antenna.

The radiation beam of the suggested antenna loaded by MTM construction is slanted by 9° in the E-plane, according to the simulation findings. Furthermore, the directivity is improved by 1.56. It is obvious from the results the antenna proposed is a suitable candidate for wearable application. In cases where the patient is in a fixed place, the direction of the beam can be controlled using the proposed wearable antenna. According to [3], SAR parameter should be lower than 1.6 for 1g of tissues. The SAR value of the proposed structure is equal to 0.17 which is acceptable based on IEEE standards. The beam steering of the suggested antenna is presented in Fig. 8.

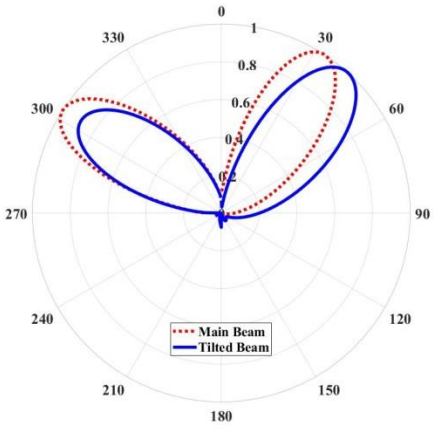

(a)

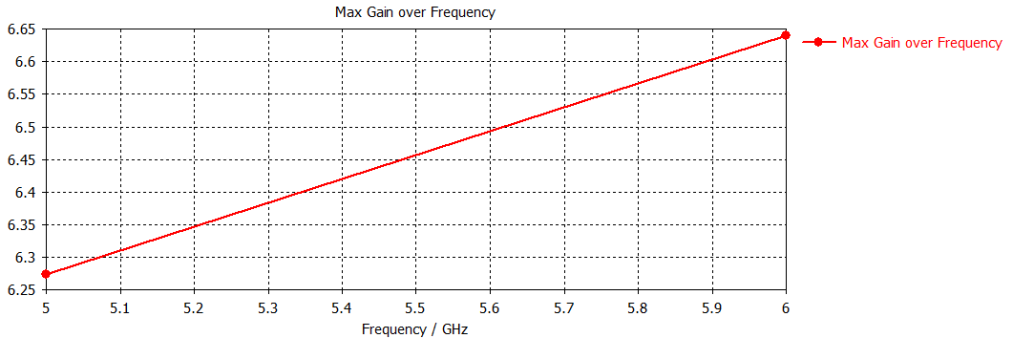

(b)

Fig 8. (a) Radiation pattern and tilted radiation pattern (b) simulation performances of the proposed antenna.

4 Conclusion

A new metamaterial assembly next to a wearable antenna is presented for medical applications at 5.2 GHz. This flexible antenna is located on a denim fabric as a dielectric substrate which is lightweight, widely available, and low cast. According to the wearable antennas that have been provided so far, this antenna can change the beam angle. This feature makes it possible to reduce unwanted interfaces and increase the security of the medical/telemedicine network. It also provides better network access for patients who are in a fixed place by adjusting the beam angle. This proposed structure steers the beam of the offered antenna at the angle of 9° in *E*-plane. Also, the directivity is enhanced by 1.56 dB. The simulated results of the suggested structure create it a worthy selection for medical applications.

References

[1] Z. Hamouda, J. L. Wojkiewicz, A. A. Pud, L. Koné, S. Bergheul, and T. Lasri. Magnetodielectric nanocomposite polymer-based dual-band flexible antenna for wearable applications. IEEE Transactions on Antennas and Propagation, 2018; 66(7): 3271-3277.

[2] R. B. V. B. Simorangkir, A. Kiourti, and K. P. Esselle. UWB wearable antenna with a full ground plane based on PDMS-embedded conductive fabric. IEEE Antennas and Wireless Propagation Letters. 2018; 17(3): 493-496.

[3] F. Faisal, M. Zada, A. Ejaz, Y. Amin, S. Ullah, and H. Yoo. A miniaturized dual-band implantable antenna system for medical applications. IEEE Transactions on Antennas and Propagation. 2020; 68(2): 1161- 1165.

[4] F. Khajeh-Khalili, A. Shahriari, and F. Haghshenas. A simple method to simultaneously increase the gain and bandwidth of wearable antennas for application in medical/communications systems. International Journal of Microwave and Wireless Technologies. 2020; 3(4): 374-380.

[5] P. Shirvani, F. Khajeh-Khalili, and Mohammad H. Neshati. Design investigation of a dual-band wearable antenna for tele-monitoring applications. AEU-International Journal of Electronics and Communications, 2021; 138.

[6] B. A. F. Esmail, H. A. Majid, S. H. Dahlan, and Z. Z. abiding. Reconfigurable metamaterial structure for 5G beam tilting antenna applications. Waves in Random and Complex Media, latest articles. 2020; 1-14.

[7] Elfergani, I.T.E.; Hussaini, A.S.; Rodriguez, J.; Abd-Alhameed, R. Antenna Fundamentals for Legacy Mobile Applications and Beyond; Springer: Cham, Switzerland, 2017; pp. 1–659.

[8] M. Mantash, A. Kesavan, and T. A. Denidni. Millimetre-wave antenna with tilted beam for future base station applications. IET Microwave, Antennas & Propagation. 2019; 13(2): 223-230.

[9] M. K. Abdulhameed, Z. Zakaria, I. M. Ibrahim, and et al. Radiation control of microstrip patch antenna by using electromagnetic band gap. AEU-International Journal of Electronics and Communications. 2019; 110: 1-11.

[10] M. B. Kakhki, M. Mantash, A. Kesavan, M. M. Tahseen, and et al. Millimeter-wave beam-tilting Vivaldi antenna with gain enhancement using multilayer FSS. IEEE Antennas and Wireless Propagation Letters. 2018; 17(12): 2279-2283.

[11] H. Jiang, L. M. Si, and W. Hu. A symmetrical dual-beam Bowtie antenna with gain enhancement using metamaterial for 5G MIMO applications. IEEE Photonics Journal. 2019; 11(1): 1–9.

[12] B. A. Esmail, H. B. Majid, and S. H. Dahlan. Planar antenna beam deflection using low-loss metamaterial for future 5G applications. International Journal of RF and Microwave Computer-Aided Engineering. 2019; 29(10).

[13] B. Esmail, H. A. Majid, Z. Z. abiding, and S. H. Dahlan. New metamaterial structure with reconfigurable refractive index at 5G candidate band. JOAM - Journal of Optoelectronics and Advanced Materials. 2019; 21(1): 101-107.

[14] J. Li, Q. Zeng, R. Liu, and T. A. Denidni. Beam-tilting antenna with negative refractive index metamaterial loading. IEEE Antennas and Wireless Propagation Letters. 2017; 16: 2030-2033.

[15] F. Khajeh-Khalili, M. A. Honarvar, M. Naser-Moghadasi, and M. Dolatshahi. Gain enhancement and mutual coupling reduction of multiple-input multiple-output antenna for millimeter-wave applications using two types of novel metamaterial structures. International Journal of RF and Microwave Computer-Aided Engineering. 2020; 30: 1-9.

A GaAs pHEMT MMIC Doherty Power Amplifier for 5G Mobile Handset

Maryam Sajedin[1], Issa Elfergani[1,2], Jonathan Rodriguez[1]
Manuel Violas[1], Raed Abd-Alhameed [2], Monica Fernandez-Barciela[3]
Ahmed M.Abdulkhaleq[4], Chemseddine Zebiri[5]
{Maryam.sajedin*, i.t.e.elfergani, jonathan, manuelv@av.it.pt [1]
R.A.A.Abd@bradford.ac.uk [2], monica.barciela@uvigo.es [3], a.abd@sarastech.co.uk[4]}

Instituto de Telecomunicações, Aveiro, Portugal [1], Faculty of Engineering and Informatics, Bradford University, Bradford BD7 1DP, UK [2], AtlanTTic Research Center, Universidade de Vigo 36310, Spain,[3], SARAS Technology Limited, Leeds LS12 4NQ, UK[4]. Electronics Department, Faculty of Technology. University of Ferhat ABBAS SETIF[5]

Abstract. The design approach for a developed Doherty power amplifier (DPA) based on the WIN Semiconductors foundry's 0.1 m AlGaAs–InGaAs pHEMT technology is presented in this work. It is shown that altering a driver stage improves the DPA's gain performance. The wideband post-matching approach used here can minimise chip area while increasing average efficiency. The simulation results show that at 4V operation voltage, the monolithic drive load modulation PA produces a maximum output power of 29dBm at 1dB compression point. Over the frequency range of 25-27 GHz, the suggested DPA can give a 15dB power gain, as well as 35 percent PAE at peak power and 29 percent PAE at the 6dB OBO. The MMIC load modulation technique was created for 5G mobile handsets and takes up 4 mm2 of space.

Keywords: Doherty Power Amplifier, MMIC, mm-waves

1 Introduction

The unparalleled 5G evolution reshapes the wireless networks by optimizing the transceiver architectures, protocols and operations. For enhanced user experience and ultra-high speed services, the massive multiple-input multiple output (mMIMO) antennas at mm-wave spectrum are deployed that rely on the integrated RF front-end modules, including the power amplifier, filters, switches, phase shifter and various passives [1]. Moreover, advances in semiconductor technologies have resulted in promoting a cost-effective system. As a result of integration of several functions on a single chip, the space occupied by RF-Front-end is reduced attaining a compact transceiver system. Therefore, test and mounting costs have reduced and system reliability has improved. This degree of flexibility reflects the need for energy-aware power amplifier units.

Besides, as a result of employing phase-array MIMO antennas for spectrum efficiency improvement, the number of power amplifiers will be increased that place more stringent low power design requirements of a unit Power Amplifier (PA) at the emergence of a new radio frequency front-ends.

IMDC-IST 2021, September 07-09, Sakarya, Turkey
Copyright © 2022 EAI
DOI 10.4108/eai.7-9-2021.2314954

On the other hand, anticipating wireless data traffic volume will require a spectrum bandwidth for connectivity [2]. Hence, wireless networks have already started deploying commercial 5G cellular network to accommodate the enormous expansion of data traffic by employing new frequency bands of mm-waves and the sub-6GHz spectrum. High-frequency spectrum is utilized in synergy with the multi-cellular topology for achieving improved wireless communication systems. This requirement propels the PA design towards wideband operating in contrast to 4G systems.

In battery-operated wireless communication systems such as mobile handset devices, the power saving is critical for longer battery lifetime. Since the PAs consume the largest portion of the current consumption budget, and the power and heat dissipation for the entire TX are determined by its power added efficiency (PAE) [3]. The PA's high power consumption is mostly attributable to two factors: the PA's limited attainable efficiency and the dynamic range within which it may achieve linear amplification. It is become an important enabler for energy-aware transmitter when deploying in a large amount of small and low power radios. The main research attention in 5G and beyond communication to overcome the daily re-charging issues of equipment has focused on low power consumption and elongated battery charge life duration. Among existing efficiency enhancement techniques, the dynamic load modulation Doherty PA (DPA) has become one of the most widely used Base-Stations (BSs) PAs market to maintain the modulated signals with high peak to average power ratio [4,5]. Based on good efficiency at deep power back-offs whilst enabling wideband operational capacity, DPA has been extensively explored to meet the 5G multimode applications.

This work develops a post matching DPA taking advantages of the MMIC technology, at mm-wave frequencies. Section 2 presents an optimized design procedure of a DPA based on the AlGaAs–InGaAs (pHEMT) process with high-yield 0.25-μm gate length on a 100-μm thick substrate. The circuit is designed using WIN process design kit. The large-signal simulation results of the two-stage DPA with a small supply voltage are presented in Section 2 as well. Some conclusion is discussed in Section 3.

2 Design Procedure of an Asymmetrical MMIC Doherty PA

2.1 Stability of the Device

It is paramount important to assure that no oscillation phenomena arise. In this work, an RC network can increase the input impedance of the device at the lower spectrum and provide a flat gain. The equivalent impedance of the stability at higher spectrum will be reduced by a shunt capacitor. Here, the compensation network consists of a TRF resistor and a MIM capacitor that can compensate the gain roll-off of the transistors in a wide frequency band. The K, Δ stability derived load and source factors [6,7] are shown in **Figure 1. (a,b)**.

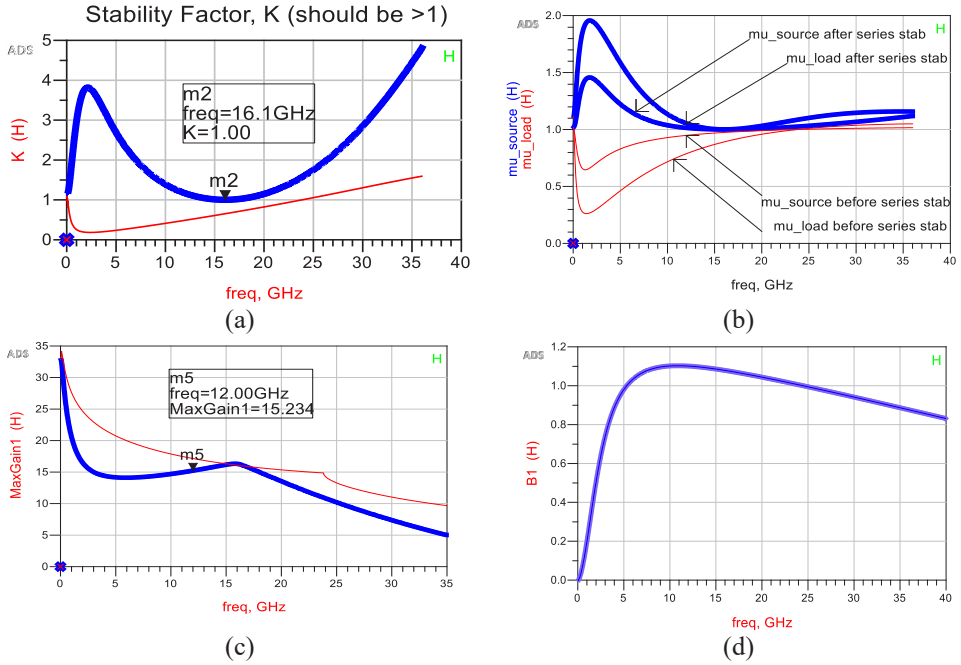

Fig. 1. Stability before (red) and after (blue) of the active cell, (a) K factor, (b) Mu factors. (c) MAG before (red) and after (blue) stabilizing (d) $|\Delta|$ factor.

Figure 1. (c plots the reduction of maximum available gain at the expense of preventing oscillations. **Figure 1. (d),** indicates that the stability is ensured by $|\Delta| > 0$ at all frequencies.

2.2 Matching Networks Design Flow

Figure 2 depicts the post-matching DPA technique that matches the load to lower impedance (Z_{sum}) towards the optimum impedances of main and peaking PAs. It is considered that main and peaking PAs are ideal current generators. In the symmetrical DPA the power ratio ($\beta = \frac{P_{sat\,peak}}{P_{sat\,main}}$) must be equal to one that delivers the maximum 6dB BO efficiency as the BO= $20\log(\beta + 1) = 6dB$. Since the PAPR of a modulated signal is typically up to 8.5dB, an asymmetrical Doherty ($\beta > 1$) with larger back-off efficiency is more desired. The output current of the main and peaking PAs (i_p and i_m), have the similar power at ($i_p = \beta i_m$) saturation region, since the voltage is constant, therefore, the add up impedance can be given by :

$$Z_{sum} = \frac{Z_m \cdot Z_p}{Z_m + Z_P} = \frac{\beta Z_p^2}{(\beta+1)Z_p} = \frac{\beta}{\beta+1} Z_p \qquad (1)$$

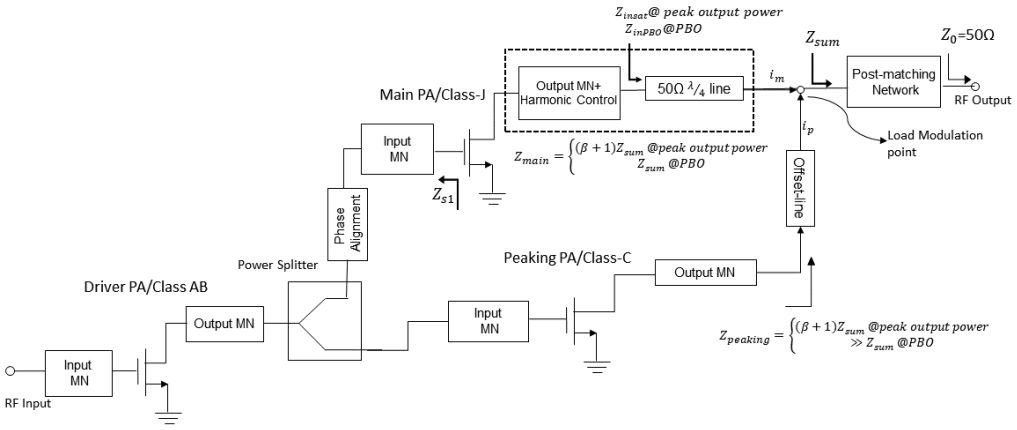

Fig. 2. The complete schematic of the proposed DPA.

Where the Z_p and Z_m are the optimum impedance of main and peaking PAs at the Doherty region. The Z_p , Z_m and the input impedance (Z_{insat}) of the impedance inverter can be obtained by,

$$Z_p = \frac{\beta+1}{\beta} Z_{sum} \tag{2}$$

$$Z_m = (\beta+1) Z_{sum} \tag{3}$$

$$Z_{insat} = \frac{(\beta+1)^2 {Z_{sum}}^2}{(\beta+1) Z_{sum}} = (\beta+1) Z_{sum} \tag{4}$$

The maximum output power of the main PA and the total output one ($P_{out,T}$) are obtained by,

$$P_{out,m} = \frac{1}{2} Z_m |i_m|^2 = \frac{\beta+1}{2} Z_{sum} |i_m|^2 \tag{5}$$

$$P_{out,T} = (\beta+1) P_{max,m} = \frac{(\beta+1)^2}{2} Z_{sum} |i_m|^2 \tag{6}$$

At the back-off the $Z_p = \infty$ and $i_p = 0$ therefore, the main PA impedance is $Z_{mod} = Z_{sum}$ and Z_{inBO} can be expressed as,

$$Z_{inBO} = \frac{(\beta+1)^2 {Z_{sum}}^2}{Z_{sum}} = (\beta+1)^2 Z_{sum} \tag{7}$$

The ratio between the load main PA impedance at the back-off (Z_{mod}) and at the peak (Z_m) where $Z_{inBO} = Z_{mod}$ and $Z_{insat} = Z_m$ are expressed by,

$$\Gamma = \frac{Z_{mod} - Z_m}{Z_{mod} + Z_m} = \frac{\big((\beta+1)^2 - (\beta+1)\big) Z_{sum}}{((\beta+1)^2 + (\beta+1)) Z_{sum}} = \frac{(\beta+1)\beta}{(\beta+1)(\beta+2)} = \frac{\beta}{\beta+2} \tag{8}$$

$$SWR = \frac{1+|\Gamma|}{1-|\Gamma|} = \frac{1+\frac{\beta}{\beta+2}}{1-\frac{\beta}{\beta+2}} = \frac{2\beta+2}{2} = \beta + 1 \tag{9}$$

Therefore, the ratio of BO output power and saturated output power is given by (12):

$$i_{mBO} = \frac{i_m}{\beta+1} \tag{10}$$

$$P_{out,BO} = \frac{1}{2}(\beta+1)^2 Z_{sum} \cdot \left|\frac{i_m}{\beta+1}\right|^2 \tag{11}$$

$$\frac{P_{out,BO}}{P_{out,m}} = \frac{1}{(\beta+1)^2} \tag{12}$$

For maximum efficiency the load impedance when the device is compressed can be extracted using load-pull simulation. The load-pull simulation in **Figure 3. (a)** indicates that the best impedance at Z_m =7.8+j*4 Ω at 27dBm for the main PA output power. The main PA is biased at Class-B biasing condition of (-0.9V). Having obtained the efficiency and output power contours, the load-pull simulation is conducted at average output power of 24dBm, which is 6dB lower than the max o/p of 1W DPA. When the peaking PA is off, the load impedance of the main PA is determined by drawing VSWR $= \beta + 1$ circle [8]. The green circle of VSWR $=$ 2 in **Figure 3. (b)** is centered by Z_m helps to determine the Z_{mod}. The optimum impedance at the edge of VSWR circle and counters delivers the best compromise between gain and efficiency thus, the selected Z_{mod} is 6.6+j9 Ω.

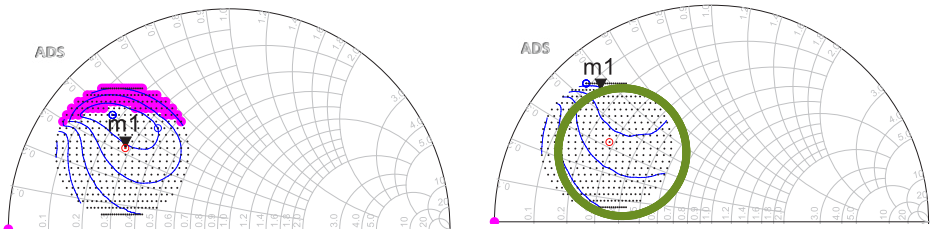

(a) (b)

Fig. 3. Load-pull dataset of the main PA (a) at saturation (b) at the Back-off.

At the main path the output matching network (OMN) transfers the $2Z_{sum}$ to Z_m if β =1 in equation (3) and simultaneously it matches Z_{mod} to Z_{sum}. Here, $2Z_{sum}$ is selected to be 25-j*20 and the post-matching network matches this impedance to 50Ω load termination. The peaking PA only handels the signals at peak, therefore it requires an OMN to transfer the $2Z_{sum}$ to Z_p =3.4+j*3.7 at the saturation. The $2Z_{sum}$ impedance is identical for both devices and the Z_p is extracted by the load-pull simulation of the stabilized transistor for the peaking PA with the gate periphery of (8*100μm). The peaking PA is biased as Class-C (-1.6 V) conduction angle, so it starts to turn on at 6dB BO.

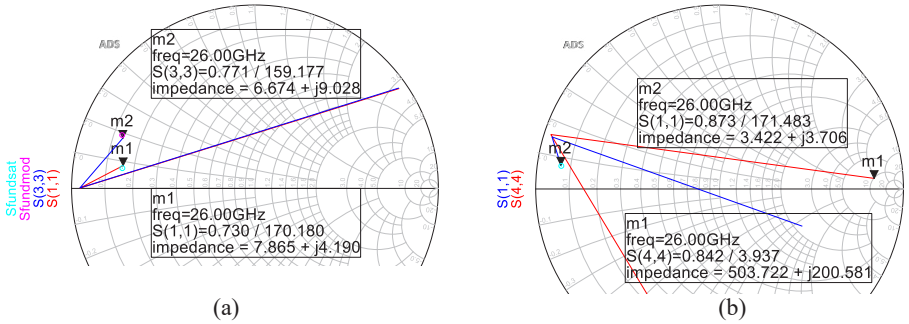

Fig. 4. S-pars of the OMNs (a)Main and (b) Peaking PAs.

The Peaking PA is off at the lower power operation therefore, $Z_p$must be a very high impedance to prevent RF leakage, thus a delay line is embedded with the OMN of peaking PA. **Figure 4. (a, b)** respectively indicate the s-parameters results of designed OMN for Main PA and Peaking PA where the offset line is tuned for a high impedance of 500+j*200 Ω at BO. It should be noted that the phase delay imposed in peaking PA is necessary to compensate at the main PA to get the DPA output in-phase at the summing node. Hence, an offset line is placed at the main PA input path to align the phase. The main transistor input matching is computed to provide the conjugate match of the input impedance of Z_{in} = 2.4+j*19Ω and the IMN of peaking PA also transfers the conjugate of Z_{in}= 2.8+j*25Ω to the 50 Ω. Finally, asymmetrical Wilkinson power divider provides an in-phase flow of signal to both main and peaking PAs without loss.

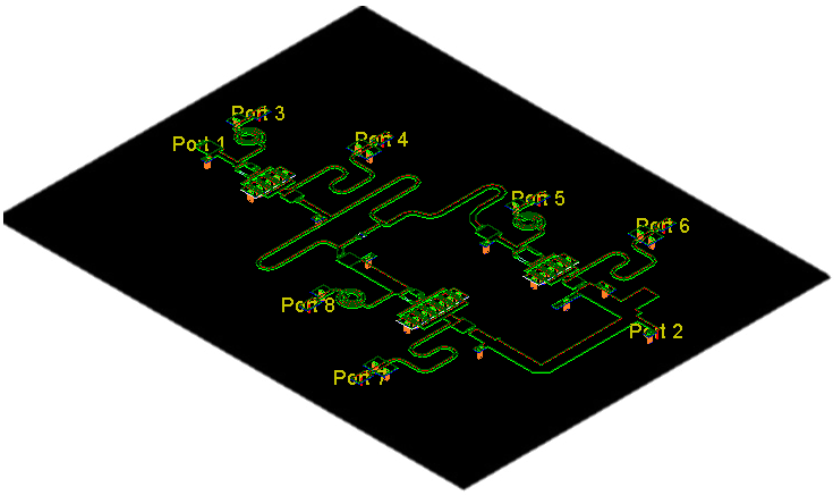

Fig. 5. The 3D review of complete MMIC DPA layout with die area size of $4mm^2$.

Figure 5 illustrates the complete layout of designed PA including a driver stage. The transistors include backvias to minimize the reduced channel temperature.

2.4 Simulation Results

In **Figure 6. (a)** a maximum PAE of 34% at the output power of 29dBm and 29% at 6dB OBO are achieved. **Figure 6. (b)** shows the DPA can deliver 14dB power gain at 26GHz. Under large-signal conditions, the gain is gradually reduced with increasing the output power. The $P_{out,1dB}$ is 29dBm. The driver stage incorporates the device size of 4×100 µm gate to achieve gain flatness. **Figure 6. (c)** shows that the DPA exhibits a gain flatness of above 15dB over the frequency range of 25.5-27.5GHz, While the Main PA provides 7dB power gain. The DPA maintains a power gain variation when peaking PA active that requires higher voltage for conducting current. **Figure 6. (d)** indicates that at the lower power levels the peaking device consumes no power and once it turns ON, its voltage increases based on C biasing condition at the Doherty region, and at the peak power, both main and peaking PAs provide the same voltage. The outcomes of the proposed DPA is related with recently reported ones in Table 1. The results confirm that the presented MMIC DPA offers an reasonable operation based on gain, back-off efficiency and output power for 5G mobile handset application.

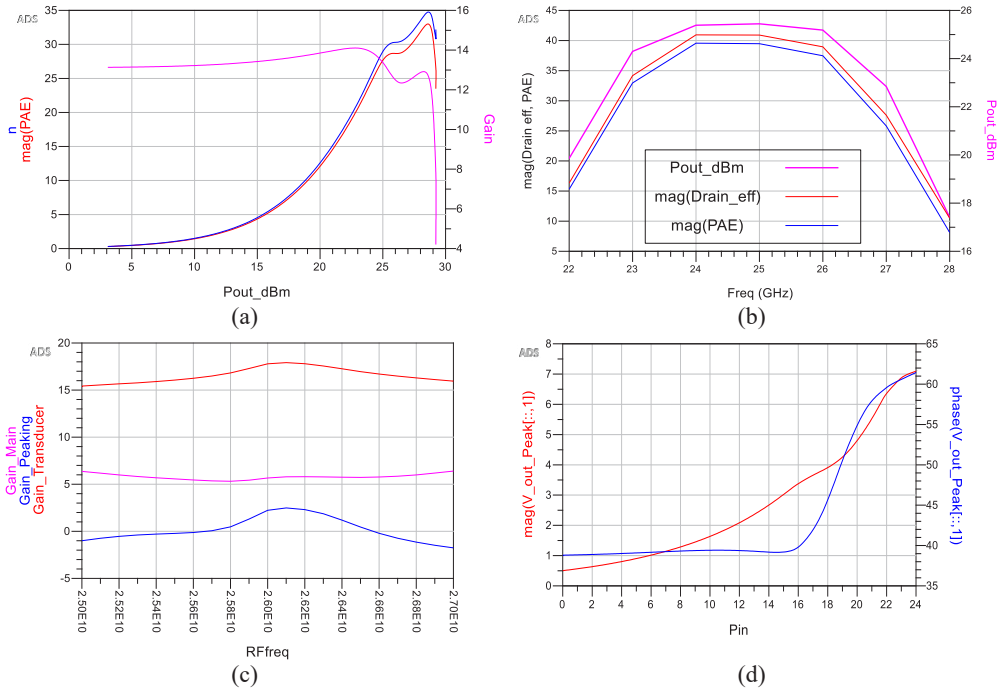

Fig. 6. (a) Modelled PAE, drain efficiency and power gain (b) frequency responses of the PAE, Darain efficiency and output power, (c) transducer power gain, gain of Main PA (pink line) and peaking PA (blue line) over the band frequency. (d) Voltage behavior of the main (blue) and peaking (red) PAs.

Table 1. The mm-waves Doherty power amplifiers

Ref.	Technology	Freq. (GHz)	Gain (dB)	Pout (dBm)	PAE% at BO	Area (mm^2)
[9]	SiGe BiCMOS	28	18.2	16.8	19.5	1.76
[10]	0.15-µm GaAs	28	12	26	29	2.85
[11]	COMS	34	19.8	20.7	13.1	0.45
[12]	0.15-µm GaAs	23	12.5	30	28	4.29

This work	0.1-µm GaAs	25-27	15	29	29	4

3 Conclusion

In summary, the design methodology of a developed mm-wave MMIC Doherty PA is described. The DPA is designed based on a 0.1-μm gate GaAs pHEMT on a 50- μm substrate thickness occupying an area size of $4\ mm^2$. Wideband impedance matching based on L-type topology is employed exploiting the foundry design kit. The output power of DPA at the 1-dB compression point corresponds to the 800 mW/mm power density based on the output power of the two devices.

Acknowledgments

FCT/MCTES is funding this study with national money and, when applicable, EU funds through the project UIDB/50008/2020-UIDP/50008/2020. This research is part of the POSITION-II project, which is supported by the ECSEL Joint Undertaking under grant number Ecsel-345 7831132-Postitio-II-2017-IA. The authors would like to express their gratitude to WIN Semiconductors for supplying the MMIC GaAs pHEMT PDK used in this study as well as technical assistance.

References

[1] Rodriguez, J. *et al*., Secure Virtual Mobile Small Cells: A Stepping Stone Towards 6G. IEEE Communications Standards Magazine. 2019, doi: 10.1109/MCOMSTD.001.2000019.

[2] Sajedin, M., A survey on RF and Microwave Doherty Power Amplifier for Mobile Handset Application, Electronics. Vol. 8, pp. 1-31

[3] Sajedin, M., *et al*., Design of a Wideband Harmonically Tuned Class-J Power Amplifier, Proceedings of the 1st International Multi-Disciplinary Conference Theme: Sustainable Development and Smart Planning, 28-30 June 2020, Cyberspace, pp. 219-229. ISBN: 978-1-63190-261-1, ISSN: 2593-7642, http://eudl.eu/series/CORE | www.eai.eu

[4] Elfergani, I., *et al*., Antenna Fundamentals for Legacy Mobile Applications and Beyond, Springer, Sept., 2017, pp. 1-659, ISBN: 978-3-319-63966-6 Online ISBN 978-3-319-63967-3

[5] Sajedin, M., A new high-efficiency power amplifier for modulated waves, Springer International Publishing, AG 2018.

[6] Quaglia, V. et al., K-Band GaAs MMIC Doherty power amplifier for microwave radio with optimized driver, IEEE Trans. Microw. Theory Techn, 2014., vol. 62, no. 11, pp. 2518–2525. doi: 10.1109/TMTT.2014.2360395.

[7] Nguyen, D.P, A compact 29% PAE at 6 dB power back-off E-mode GaAs pHEMT MMIC Doherty power amplifier at Ka-band, IEEE MTT-S Int. Microwave Symp. (IMS), 2017, pp.1683–1686. doi: 10.1109/MWSYM.2017.8058964.

[8] Chen, W., Lv, X., Liu, D., Wang, F., Doherty PAs for 5G Massive MIMO. IEEE Microwave Magazine, 2020, vol. 21, no. 5, pp. 78-93, doi: 10.1109/MMM.2020.2971183.

[9] Hu, S. Wang, F and Wang, H., A 28, 37, 39 GHz Linear Doherty Power Amplifier in Silicon for 5G Applications, IEEE Journal of Solid-State Circuits, 2019, vol. 54, no. 6, pp. 1586-1599, doi: 10.1109/JSSC.2019.2902307.

[10] Cho, Y. Kang, D. Moon, K. Jeong, Kand Kim, B.: A Handy Dandy Doherty PA: A Linear Doherty Power Amplifier for Mobile Handset Application, IEEE Microwave Magazine, 2017, vol. 18, no. 6, pp. 110-124, doi: 10.1109/MMM.2017.2712040,

[11] Chen, Y. Lin, Y. Lin, J and Wang, H., A Ka-Band Transformer-Based Doherty Power Amplifier for Multi-Gb/s Application in 90-nm CMOS, IEEE Microwave and Wireless Components Letters 2018, vol. 28, no. 12, pp. 1134-1136, doi: 10.1109/LMWC.2018.2878133.

[12] Lv, G. Chen, W. Chen, X. Ghannouchi, M. and Feng, Z., A Compact Ka/Q Dual-Band GaAs MMIC Doherty Power Amplifier with Simplified Offset Lines for 5G Applications,2019, IEEE Transactions on Microwave Theory and Techniques, vol. 67, no. 7, pp. 3110-3121, doi: 10.1109/TMTT.2019.2908103.

Planar Monopole UWB Antenna for Microwave Medical Image System

1st Adel Y.I. Ashyap[1], 2nd Z. Z. Abidin[2],3rd S. H. Dahlan[3], 4th H. A. Majid[4], 5th N. A.M.Alduais[5], 6th S. Alamri [6] ,7th Raed A. Abd-Alhameed[7]
{ashyap2007@gmail.com[1], zuhairia@uthm.edu.my[2] samsulh@uthm.edu.my[3]}

Center for Applied Electromagnetic (EMCenter) , Universiti Tun Hussein Onn Malaysia, Batu Pahat 86400, Malaysia[1,3,4],
Research Center of Wireless and Radio Science (WARAS), Faculty of Electrical and Electronic Engineering, Universiti Tun Hussein Onn Malaysia, Batu Pahat 86400, Malaysia[2],
Faculty of Computer Science and Information Technology (FSKTM), Universiti Tun Hussein Onn Malaysia, (UTHM) Batu Pahat 86400, Malaysia[5],
Faculty of Engineering, Al Baha University, Al Baha, KSA[6],
Faculty of Engineering and Informatics, University of Bradford, Bradford, BD7 1DP, UK[7],

Abstract. A planar monopole UWB antenna for microwave medical imaging systems is presented, and its operating frequency range from 3.09 GHz to 10.65 GHz. The overall size of the design is 30×20×1.6 mm^3. Two phantom models were developed to represent the arm and breast models to evaluate the design performance in terms of reflection coefficient, SAR, directivity and efficiency. The results showed that even with the phantom models, UWB bandwidth is still maintained. The directivity and efficiency of the design with and without the phantom models were studied, and its good performance was proved. The specific absorption rate (SAR) was also investigated, and it showed a value far below the safety limit. Therefore, the planar monopole UWB antenna is very suitable for microwave medical imaging systems.

Keywords: UWB, microwave medical imaging systems, SAR, microwave imaging.

1 Introduction

Microwave imaging systems are a method that employs an electromagnetic signal to penetrate the internal structure of tissues. It identifies and locates cancer tumours based on the high dielectric properties in contrast to normal tissues. Microwave imaging systems have several appealing features in medical applications, such as low interference, robustness to multipath fading, low cost, low complexity, precision, low power density, high-speed data rate; therefore, it has aroused a lot of research interest in the field. The current medical equipment's ability to detect tumours is not enough to meet the needs of society. The need to create a new and more reliable inspection system becomes essential. According to reports in the literature, cancer tissues exhibit different dielectric properties than normal tissues at microwave frequencies [1].

Since the researchers began using microwaves for medical purposes, the quest for an appropriate antenna has attracted a great deal of interest. Ultra-Wide Band antennas (UWB) are usually required in microwave imaging systems, especially for those who work in radar principles. It has extensive applications in high-speed and short-range wireless systems, including but not limited to personal entertainment systems, smartphones, personal health care

IMDC-IST 2021, September 07-09, Sakarya, Turkey
Copyright © 2022 EAI
DOI 10.4108/eai.7-9-2021.2314952

systems, breast cancer detection, ground penetrating radars, identification system, medical imaging system, and military[2].

UWB planar antenna for a variety of applications has been developed. Planar antennas play a significant role among several other kinds of antennas because of their many features, such as easy incorporation with another device, high flexibility, ease of design, and small size. In the past few years, several academisation around the world have developed planar antennas to obtain wide bandwidth. Among all the introduced antenna structures, monopole UWB antennas are very common. The monopole UWB antenna has a simple structure, a low profile, a large bandwidth, and a high radiation efficiency. These types of antennas are easy to work in imaging systems. Therefore, a monopole UWB-based microwave imaging system that uses microwave radiation of a spectrum in the range of 3.1 to 10.6 GHz is becoming one of the most feasible technologies for detecting human cancer cells [1-3].

Various designs of UWB antennas had been proposed to use microwave imaging systems to image breast tissue [4-15], such as microstrip patch antenna for the ultra-wideband (UWB) [4-6], UWB MIMO [7], circular modified UWB [8], tapered slot Vivaldi UWB[9], Conformal Polymeric wideband antenna [10], Egg-shaped UWB [11], Ultra-Wideband Microwave Antenna [12],[13], wideband magneto-electric dipole antenna [14], EBG ultra-wideband (UWB) [15]. The above-listed design [4-15] was also utilized for different microwave imaging systems, but their bandwidth, SAR, efficiency, and directivity do not reach the predicted standard.

In this paper, a very simple planar monopole UWB antenna is presented in the range of 3.09 GHz- 10.65 GHz. The design was investigated on two types of human model tissues that mimic the arm and breast. CST Microwave Studio was used to design and optimized the monopole UWB antenna.

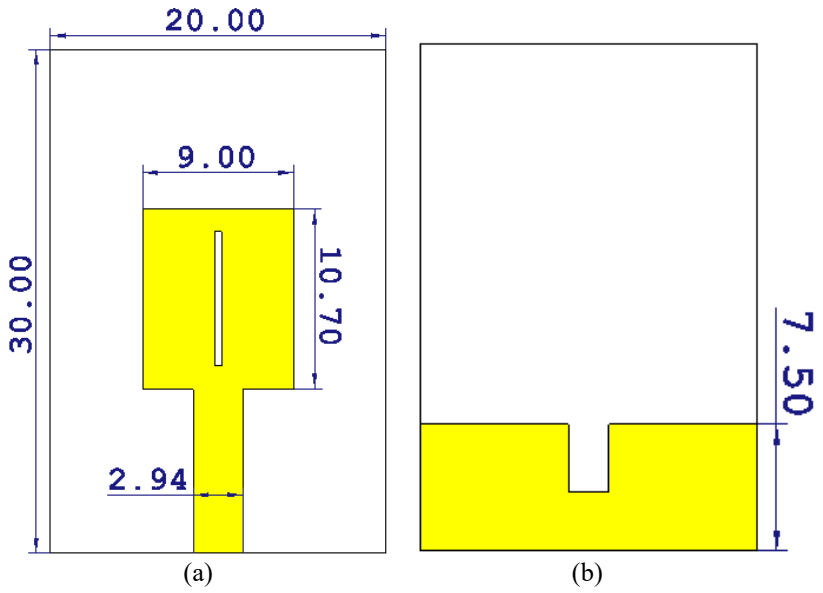

Fig. 1. Configuration of the planar monopole UWB antenna(a) Front view, and (b) Back view.

2 Planar Monopole UWB Antenna Design

Figure.1 illustrates the structure of the planar monopole UWB antenna. The antenna was designed on an FR-4 substrate with a dielectric constant of 4.4, a thickness of 1.6 mm, and a loss tangent of 0.025. The radiating elements are made of copper with a thickness of 0.035. The antenna is fed by a 50-ohm microstrip-fed line with a width of 2.94 mm. The design initially started with a conventional microstrip patch shape then optimized to achieve the desired band covering 3.09 GHz to 10.65 GHz. Three steps were taken to achieve the UWB range. The first step is to modify the ground from full to partial. The second step introduces a rectangular slot on the patch with a length of 8 mm and a width of 0.4 mm as seen in **Figure 1(a)**. Lastly, the third step introduces a slot on the ground with a length of 4 mm and a width of 2.4 mm as seen in **Figure 1(b)**. The final antenna has an overall dimension of $30\times20\times1.6$ mm^3.

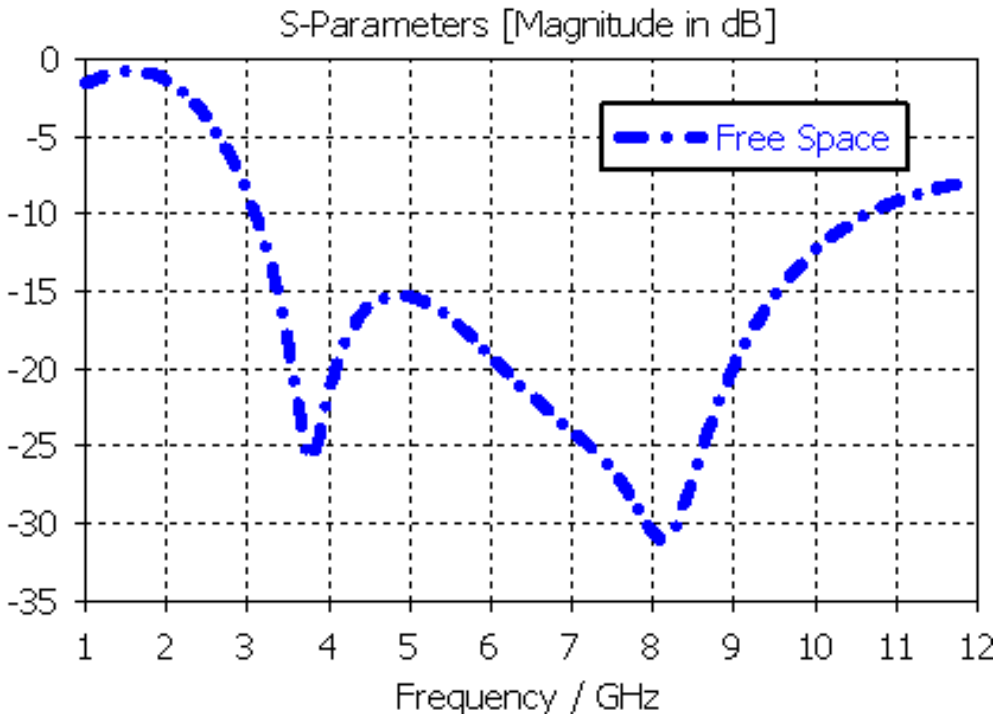

Fig. 2. Reflection coefficient of the planar monopole UWB antenna.

The reflection coefficient of the presented planar monopole UWB antenna is depicted in **Figure 2**. The result shows that the antenna operates from 3.09 GHz to 3.65 GHz, which is suitable for microwave imaging systems applications. The antenna demonstrates minimum directivity of 3.03 dBi at a lower frequency (3.5GHz) and a maximum directivity of 4 dBi at a higher frequency (9.5 GHz). The presented design has an efficiency of 69.9% at a lower frequency (3.5GHz) and 81.4% at a higher frequency(9.5 GHz).

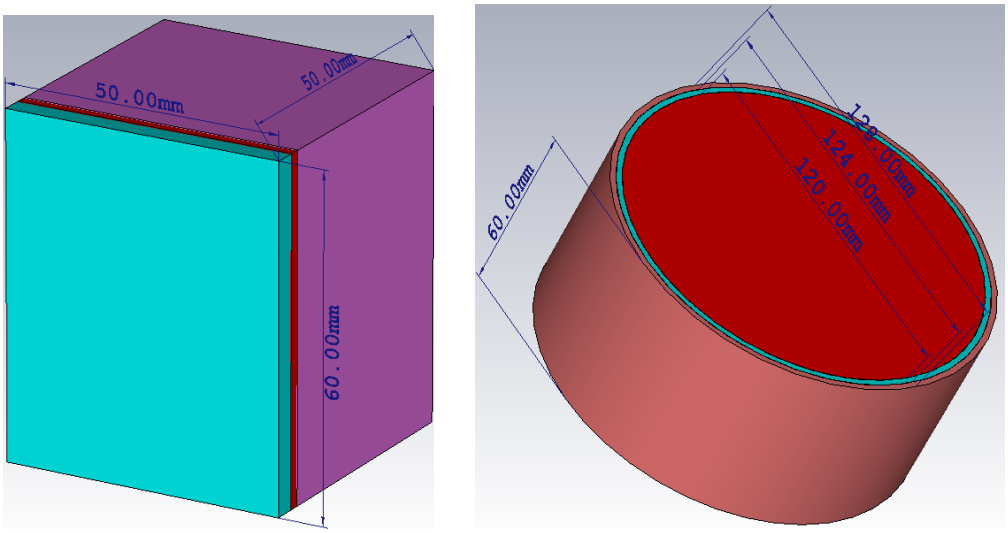

(a) (b)

Fig. 3. Phantom models(a) Chest,and (b) Breast

3 Performance of the UWB Antenna on Body

To better understand the planar's monopole UWB antenna's performance near human tissues, two Phantom models were developed for this research, which consists of three layers. The first model is a rectangular shape imitating an arm model, and the second model is a cylindrical shape imitating a breast tissue model. The arm model consists of muscle ($\sigma = 1.74$, thickness = 34, $\varepsilon r = 52.73$), fat ($\sigma = 0.1$, thickness = 2, $\varepsilon r = 5.28$), and skin ($\sigma = 1.59$, thickness = 4, $\varepsilon r = 45.85$). These values are evaluated at 3.1 GHz [16]. The breast model uses the same layers as the arm model, except the muscle layer was changed with a plastic cover with permittivity of 1.7.

As illustrated in **Figure 3(a)**, the dimension of the rectangular arm is 60×50×50 mm^3, whereas **Figure 3(b)** depicts the breast tissue model with a diameter of 128 mm and length 60 mm. **Figure 4** shows the planar monopole UWB antenna's reflection coefficient placed in free space, on the arm model, and the breast model. The result shows that the desired UWB band is achieved from 3.1 GHz to 10.6 GHz in all cases.

The planar monopole UWB antenna's performance in terms of directivity and efficiency while operating on the arm and breast model was carried out. The results are presented in Table 1. It is realized that when the design is placed on the phantom models, the directivity is increased compared to the case of free space. This is due to the interaction between the antenna ground plane and the phantom models as the phantom models act as an additional dielectric that directs the front's directivity. It also realized that the efficiency drop compared to free space. This is due to the high conductivity of phantom models.

Table 1. Directivity and efficiency of planar monopole UWB antenna on arm, breast, and free space at 3.5 GHz and 9.5 GHz.

Phantom Models	Directivity (dBi)		Efficiency(%)	
	3.5 (GHz)	9.5(GHz)	3.5 (GHz)	9.5 (GHz)
Arm Model	6.32	9.87	57.7	73.3
Breast Model	5.91	7.07	58.25	70.1
Free space	3.03	4	69.9	81.4

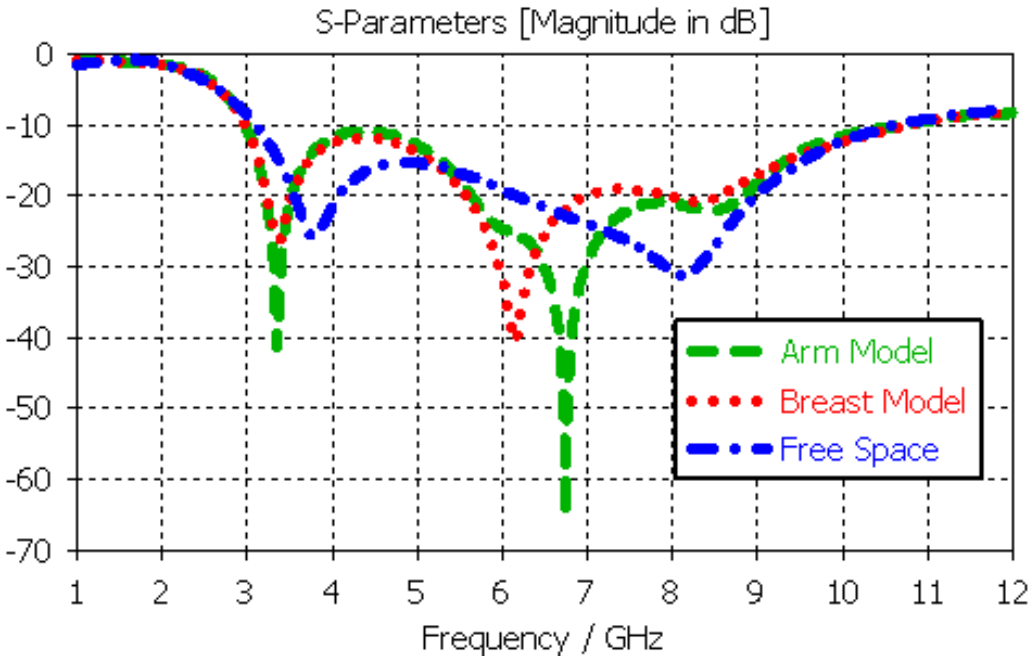

Fig. 4. Reflection coefficient of the planer monopole UWB antenna on arm, breast models.

The specific absorption rate (SAR) of the planar monopole UWB antenna over a human body was carried out to find the total power that the planar monopole UWB antenna can transmit within the safety restrictions. The assessment is conducted in accordance with the standards established by FCC. The safety limit should not be greater than 1.6 W/kg over 1 g of tissue. The SAR values were taken at 3.5 GHz and 9.5 GHz based on IEEE C95.1 with an input power of 100 mW [17-20]. The results are depicted in **Figure 5 and Figure 6**. The SAR values of the arm and breast models were 0.369 w/kg and 0.254 w/kg at 3.5 GHz, and 0.4 w/kg and 0.364 w/kg at 9.5 GHz, respectively. It is revealed that the design meets the standard with values far below the safety limits, which will not affect the body.

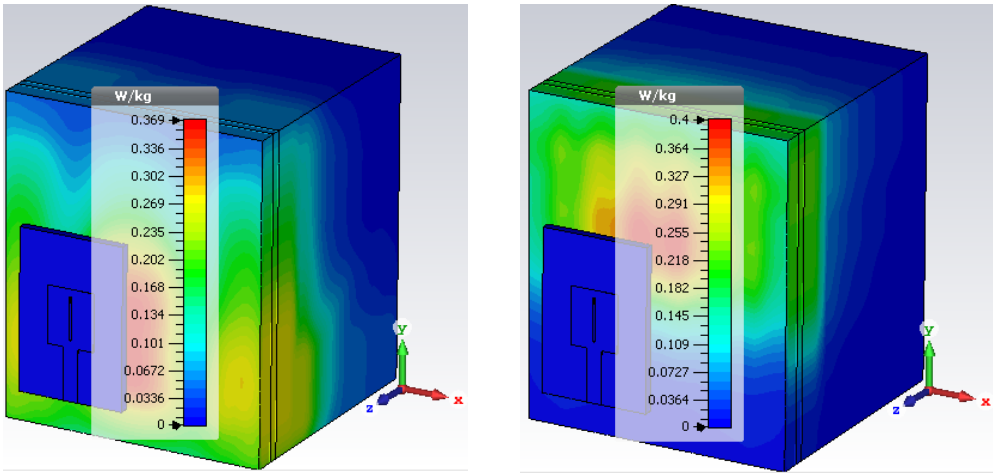

(a) (b)

Fig. 5. 3D SAR results of the planar monopole UWB antenna on the arm at frequencies of (a) 3.5 GHz and (b) 9.5 GHz.

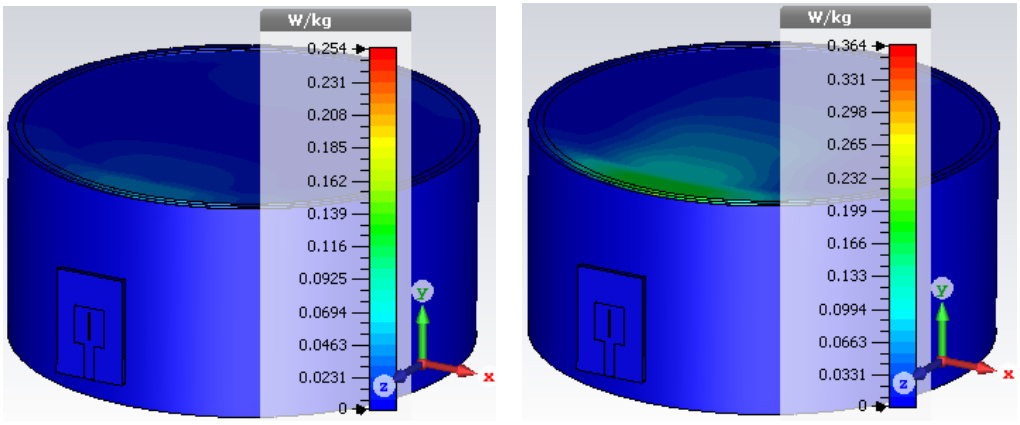

(a) (b)

Fig. 6. 3D SAR results of the planar monopole UWB antenna on the breast at frequencies of (a) 3.5 GHz and (b) 9.5 GHz.

4 Conclusion

A planar monopole UWB antenna for microwave medical imaging systems is introduced. The operating frequency covers the UWB bandwidth from 3.09 GHz to 10.65 GHz with an overall dimension of 30 × 20 × 1.6 mm^2. Two phantom models were developed, a rectangular

shape mimics the arm, and a cylindrical shape mimics the breast. The design revealed a good reflection coefficient with and without the presence of the phantom models covering the UWB bandwidth from 3.09 GHz to 10.65 GHz. The design also shows a directivity of 4 dBi (free space), 9.87dBi (arm model), and 7.07 dBi (breast mode), while an efficiency of 81.4%, (free space), 73.3% (arm model), and 70.1% (breast mode) at a frequency of 9.5 GHz. The SAR was investigated based on the arm and breast models, and the results demonstrated that the SAR values were 0.4 w/kg and 0.364 w/kg, respectively, at a frequency of 9.5 GHz.

References

[1] Mahmud, M. Z., Islam, M. T. & Samsuzzaman, M. A high performance UWB antenna design for microwave imaging system. *Microw. Opt. Technol. Lett.* 58, 1824–1831 (2016).

[2] Mahmud, M., Islam, M., Misran, N., Almutairi, A. & Cho, M. Ultra-Wideband (UWB) Antenna Sensor Based Microwave Breast Imaging: A Review. *Sensors* 18, 2951 (2018).

[3] Seman, F. C. *et al.* performance evaluation of a star-shaped patch antenna on polyimide film under various bending conditions. *prog. electromagn. Res. Lett.* **85**, 125–130 (2019).

[4] Hammouch, N. & Ammor, H. A confocal microwave imaging implementation for breast cancer detection. *Indones. J. Electr. Eng. Informatics* 7, 263–270 (2019).

[5] Sheela, J. J. J. *et al.* Novel Directional Antennas for Microwave Breast Imaging Applications. in *2020 International Conference on Smart Electronics and Communication (ICOSEC)* 00, 599–603 (IEEE, 2020).

[6] Karli, R., Ammor, H. & El Aoufi, J. Miniaturized UWB microstrip antenna for microwave imaging. *WSEAS Trans. Inf. Sci. Appl.* 11, 122–129 (2014).

[7] Ziani, D., Meriah, S. M. & Merad, L. UWB MIMO array design for medical applications. in *2016 International Conference on Electrical Sciences and Technologies in Maghreb (CISTEM)* 1–3 (IEEE, 2016).

[8] Widyatama, P. Z., Nugroho, B. S. & Nur, L. O. Design of Circular Modified UWB Antenna Microstrip for Brain Cancer Detection. in *2019 IEEE Asia Pacific Conference on Wireless and Mobile (APWiMob)* 33–36 (IEEE, 2019). doi:10.1109/APWiMob48441.2019.8964123

[9] Akazzim, Y., Kanjaa, M., Mrabet, O. EL, Jofre, L. & Essaaidi, M. An UWB Tapered Slot Vivaldi Antenna (TSA) with Improved Characterestics. in *2019 IEEE 19th Mediterranean Microwave Symposium (MMS)* 2019-Octob, 1–4 (IEEE, 2019).

[10] Limbah, M. H., Lago, H., Soh, P. J. & Teo, K. T. K. Wideband Conformal Polymeric Based Antenna for Microwave Medical Imaging System. in *2020 IEEE 2nd International Conference on Artificial Intelligence in Engineering and Technology (IICAIET)* 1–4 (IEEE, 2020).

[11] Cherian, P., Anjit, T. A. & Mythili, P. A compact egg-shaped UWB antenna for breast dielectric profile imaging. *Int. J. Sci. Technol. Res.* 9, 4672–4681 (2020).

[12] Aminudin Jamlos, M. *et al.* High Gain of Directional Ultra-Wideband Array Antenna Using Flat Reflector Structure for Microwave Imaging. *IOP Conf. Ser. Mater. Sci. Eng.* 557, 012018 (2019).

[13] Ahmed, S. S., Mahdi, J. F. & Kadhim, M. A. Design of Ultra-Wideband Microwave Antenna Array for Detection Breast Cancer Tumours. *IOP Conf. Ser. Mater. Sci. Eng.* 881, 012112 (2020).

[14] Chen, L. *et al.* Design of a UWB Antenna for Microwave Imaging. *ISAP 2018 - 2018 Int. Symp. Antennas Propag.* 825–826 (2019).

[15] Shanwar, A. R. & Othman, N. S. UWB printed antenna for medical applications. in *TENCON 2017 - 2017 IEEE Region 10 Conference* 2017-Decem, 2931–2936 (IEEE, 2017).

[16] Danjuma, I. M., Akinsolu, M. O., See, C. H., Abd-Alhameed, R. A. & Liu, B. Design and Optimization of a Slotted Monopole Antenna for Ultra-Wide Band Body Centric Imaging Applications. *IEEE J. Electromagn. RF Microwaves Med. Biol.* 4, 140–147 (2020).

[17] Ashyap, A. Y. I. *et al.* Robust and efficient integrated antenna with EBG-DGS enabled wide bandwidth for wearable medical device applications. *IEEE Access* 8, 56346–56358 (2020).

[18] Ashyap, A. Y. I., Abidin, Z. Z., Dahlan, S. H., Majid, H. A. & Seman, F. C. A compact wearable antenna using EBG for smart-watch applications. *Asia-Pacific Microw. Conf. Proceedings, APMC* 2018-November, 1477–1479 (2019).

[19] I. Ashyap, A. Y. *et al.* A wearable antenna based on fabric materials with circular polarization for Body-centric wireless communications. *Indones. J. Electr. Eng. Comput. Sci.* 18, 335 (2020).

[20] Ashyap, A. Y. I. *et al.* An Overview of Electromagnetic Band-Gap Integrated Wearable Antennas. *IEEE Access* 8, 7641–7658 (2020).

Wear Resistance of Gray Cast Iron Under High-Temperature Conditions

Ali A. G. Alkhafaji[1]
{alkhafaji.ali@stu.edu.iq[1]}

Al-Nasiriyah Technical Institute/ Southern Technical University, Iraq[1]

Abstract. Three different matrices Gray cast irons were produced with different carbon content and alloying elements and tested for this research purpose. A new wear test rig is designed, manufactured, and developed especially for this research. It uses to examine test materials by exposing them to a sequence of heating to (600, 850 ºC) by friction with automobile brake pads in suitable condition and then air-cooled to (400 ºC). Comparisons were made between test materials in terms of weight loss after a certain number of thermal cycles, in addition to hardness number before the test as well as before and after the heat treatment. Fine grains – fully ferritic iron structure demonstrates high as-cast hardness as well as after stress relief annealing. Moreover, such material showed the best wear resistance among the test materials at (600, 850 ºC). At low temperatures up to 600 ºC, some Gray irons have good wear resistance, but this is lost in the (to transformation) range. Hardness isn't the only criterion for high-temperature wear resistance.

Keywords: Cast iron, wear test, high temperature, wear resistance, test rig.

1 Introduction

Glass blow moulds, for example, must have tight dimensional tolerances and must be resistant to thermal shock, thermal conductivity, dimension stability, and wear. These moulds usually receive molten glass at around 1000oC, which is subsequently cooled to around 500-600oC before being discharged. Mold materials such as cast nickel, cast iron, and tool steel are commonly used.

In high-temperature applications, grey cast iron is a popular choice. Glass blow-moulds, for example, are subjected to extremely harsh circumstances and must contain a specific set of qualities in order to be successful: Wear resistance; growth and oxidation resistance; good surface finish; surface heat checking and significant cracking (thermal shock) resistance; high thermal conductivity; and machinability [1].

Peter Elliott [2] tried answering the question: how to select alloys for high temperatures, stresses, and the presence of elements such as oxygen or sulphur. There are no significant problems up to (400 ºC), few up to (750 ºC), but the choice of successful alloys becomes somewhat limited above (800 ºC). Some alloys¸ have high nickel content and high nickel–beryllium alloys, for example, have excellent properties but the cost is the main barrier to use these alloys in glass container blow moulds [3]. Matteis P, et al [4] concluded that the major

IMDC-IST 2021, September 07-09, Sakarya, Turkey
Copyright © 2022 EAI
DOI 10.4108/eai.7-9-2021.2314950

damage mechanisms of cast iron are the oxidation at more than 750°C and thermo-mechanical fatigue of their test material which is usually used as an exhaust manifold of heavy tracks. Cast iron has a high resistance to oxidation, growth, and scaling, as well as a low inclination for deformation [7]. Scheidhauer N, et al [5] and Xiang S [6] focused on ferritic Simo cast iron which intend to use for heavy-duty engine components. They believed that aluminium and silicon increase the (α to γ transformation) temperature, 860°C as they mentioned. Such ferritic SiMoAl cast iron reveals excellent oxidation resistance and mechanical properties at high temperatures. High–carbon cast iron has a high heat conductivity and a low modulus of elasticity, making it resistant to thermal shock. However, it might have a coarse, open-grained surface with a poor initial finish, a predisposition to deep oxidation, and poor wear resistance as a result. Close-grained surfaces, on the other hand, can overcome these drawbacks [1].

S. Y. Buni, et al. [8] studied the effect of graphite morphology and matrix structure on the unconstrained cast iron specimens exposed to low-frequency thermal cycling. The specimens were heated inside a tubular furnace to the desired temperatures (300ºC, 500ºC, 600ºC, and 700ºC). The results show that au tempered ductile iron has the highest thermal cycling resistance in the above temperature range, followed by pearlitic ductile iron and compacted graphite iron, with Gray cast iron having the lowest resistance. Thermal cycling induces matrix disintegration and grain growth in all iron castings, resulting in a loss in hardness.

Wear is mechanically induced surface damage or changed surface topography because of progressive removal of material. Sometimes, wear is too big, the naked eye can see it, but with others, measuring instruments or microscopes are used to observe it. Wear as a term used in the mechanical industry indicates huge money losses due to its effect on the production facilities and products.

Junichiro Yamabe and colleagues [9] devised a new approach for evaluating thermal fatigue by replicating a high–speed braking test with a real disc brake rotor made of Gray cast iron. The quantity of graphite atoms in the microstructure increases thermal fatigue strength, according to the findings.

Cueva, et al. [10] compared the wear resistance of three different types of Gray cast iron used in car brake disc rotors (exposed to heating and cooling) to that of compacted graphite iron.

Wear, growth, thermal fatigue, and other factors can cause damage to grey cast irons in a high-temperature environment. A wear test at high temperature is required to recognise the performance of Gray cast iron used as a glass blow mould in order to acquire actual practical and dependable results. Because most commercial tribotester machines do the test at ambient temperature, the findings will be far from accurate.

Standard testing procedures will not satisfy everyone's need for wear data. Some types of wear tests have been standardised by organisations such as the American Society for Testing and Materials (ASTM), the International Organization for Standardization (ISO), and the Society of Automotive Engineers (SAE). For all types of wear, standard test procedures do not exist. Some existing standards are tailored to specific purposes, while others are more generic and based on simple geometries.

2 Test Materials

2.1 Gray Cast Iron Production

Gray iron castings' attributes are determined by their chemical composition as well as the cooling rate of the casting, which is influenced by the casting's section thickness and shape. The size, quantity, and distribution of graphite flakes, as well as the structure of the metal matrix, determine the properties of Gray irons. These, in turn, are determined by the iron's chemical composition, particularly its carbon and silicon content; as well as on manufacturing variables such as melting method, inoculation strategy, and casting cooling rate. Total carbon, silicon, and phosphorus are the three cast iron elements that have the greatest impact on strength and hardness. The Carbon Equivalent Value (CEV) is an index that incorporates the effects of these factors. In the binary Fe–C system, the Gray iron eutectic occurs at a carbon concentration of 4.3 percent. The carbon content of the eutectic is reduced when silicon and phosphorus are present. The statement describes the influence of Si and P levels on carbon content. Hypoeutectic irons are cast irons with carbon equivalent values less than 4.3 percent, while hypereutectic irons have carbon equivalent values greater than 4.3 percent [9].
Three groups of Gray iron materials were manufactured with a different chemical composition that containing different levels of CEV, Equation (1). The results are shown in Table (1).

$$Carbon\ Equivalent\ Value\ (CEV) = T.C\ \% + \frac{Si\ \% + P\ \%}{3} \quad (1)$$

To produce a certain weight (Q kg) of a destination alloy, material No.1 for example, it needs to know the furnace charge components and their weight exactly. A set of instantaneous linear equations was built and solved for this purpose. The amount of destination alloy is:

Q * (Chemical composition of material No.1)

Q * (3.61%C + 2.03%Si + 0.74%Mn)

Table 1. Chemical composition of test materials.

Materials		Material No. 1	Material No. 2	Material No. 3
Chemical Composition %	Carbon	3.61	3.15	2.98
	Silicon	2.03	2.25	5.117
	Manganese	0.74	0.671	0.355
	Phosphorus	0.09	0.108	0.11
	Sulphur	0.067	0.062	0.057
	Molybdenum	0.0052	0.006	0.0057
	Chromium	0.021	0.021	0.022
	Nickel	0.063	0.069	0.071
	Vanadium	0.0041	0.0052	0.0034
	Copper	-	-	1.329
	Ferrous	Balance	Balance	Balance
Carbon Equivalent Value		4.317	3.936	4.722

The furnace charge is:

(S kg of Scrap + X kg of Ferrosilicon + Y kg of Ferromanganese + Z kg of Graphite)
Referring to Tables (1), (2) and (3), and;

For Carbon is: 0.02503S + 0X + 0.065Y + 0.985Z = 0.0361Q …… (i)

For Silicon: 0.01426S + 0.75X + 1.2Y + 0Z = 0.0203Q …… (ii)

For Manganese: 0.00257S + 0X + 0.75Y + 0 Z = 0.0074Q …… (iii)

For Ferrous: 0.9554S + 0.2478X + 0.1726Y + 0Z = 0.9337Q …… (iv)

To produce the test alloys from previously prepared materials and correct alloys, a computer program was designed based upon the Gauss elimination method. The weight losses during melting and casting of each element should be added. Scrap castings were weighed by using a (100 kg) balance. Other raw materials were weighed by using Sartorius GM612 electronic balance with an accuracy of (0.01 gr).

Table 2. Chemical composition of alloying elements.

Alloy	Ferrosilicon	Ferromanganese	Graphite
Carbon %	-	6 – 7	98 – 99
Silicon %	75	1.2	-
Manganese %	-	75	-
Phosphorus %	-	Max 0.02	-
Sulfur %	-	Max 0.02	0.35 max
Ferrous %	24.78	17.26	-

Table 3. Scrap chemical composition before and after treated with limestone.

Alloy	Untreated	Treated
Carbon %	2.614	2.503
Silicon %	1.568	1.426
Manganese %	0.243	0.257
Phosphorus %	0.526	0.113
Sulphur %	0.103	0.0691
Molybdenum %	0.0063	0.0062
Chromium %	0.0195	0.02
Nickel %	0.076	0.069
Ferrous %	Balance	Balance

2.2 Heat Treatments

The microstructure of material No. 1 and material No. 2 revealed graphite flakes embedded in ferrite and pearlite matrix. The inclusion of pearlite in the construction could cause material degradation, especially if it's employed at high temperatures. The breakdown of coupled carbon (cementite Fe_3C) in pearlite causes growth. Theoretically, graphitisation of mixed carbon (1%) should result in an increase in the volume of (2.04 percent). The actual rate of increase is always higher [1]. When casting with a pearlite structure is used at high temperatures, particularly in the (α to γ) transition temperature range, thermal cracks can form and propagate. The application of ferritic irons can prevent growth caused by pearlite breakdown. By annealing grey irons, ferritic structures can be achieved.

Deep oxidation can be accelerated by annealing above the critical temperature at which transformation occurs; however, pack annealing with graphite can impede this. The critical temperature for each test material is obtained in Table 4 using the formula below [1]:

$$Critical\ Temp. = 730 + 28(\%Si) - 25(\%Mn) \quad (2)$$

The graphite was packed into the specimens in a sealed steel box.

No. 3 Material: The as-cast microstructure was flakes of graphite in the ferritic matrix due to the high silicon content (5.117 percent Si) and carbon content (2.98 percent C). This structure is ordinary ferritic, and there is no room for expansion in the absence of coupled carbon.

3 Wear Test Rig at High-Temp

Wear is the most common cause of cast iron deterioration when used at high temperatures. As in a glass blow mould, it alters the mould feature and fine curves on the cavity surface. Wear teste rigs at room temperature are commonly used to investigate material wear resistance.
When two substances rub against each other with a high relative velocity and axial pressure, they become heated. When steel - steel specimens rub against one other, for example – the temperature can reach (1300 ºC) under ideal conditions, while nonferrous materials can reach (100 ºC) before melting. The friction welding process [12] and [13] make use of this phenomena. Based on the foregoing occurrence, a new pin–on–disc wear test rig is constructed in this study. The Gray cast iron specimens are examined with this equipment. Friction between a tested material and an automobile brake pad with acceptable qualities to attain the specified temperature causes high temperature.

3.1 Basic Theory

The test is based on the principle that heat is generated owing to friction force when a controlled contact pressure is applied perpendicular to the contact surface of two specimens with a relative sliding velocity between them. The generated heat is felt by the contacting substance as warmth. As a result, the temperature of the two specimens rises. Its size is determined by a number of factors, including:

1. relative sliding velocity.
2. The difference in axial pressure between the two specimens
3. Roughness of the surface.
4. Material characteristics (surface hardness, thermal conductivity, etc.).
5. The coefficient of friction.
6. The duration of the film.

A digital thermocouple or an infrared thermocouple can be used to measure and record temperature.

3.2 The Test Rig Description

In the absence of conventional equipment, a custom rig was devised and built specifically for these tests to match the criteria. Figure 1 depicts the unit's schematic diagram. The pad is rotated at the desired velocity through the gearbox by a 1450 rpm, 7.5 kW, three-phase electric motor. To secure the pad carrier, a lathe chuck is attached on the gearbox output shaft. A drill chuck installed in the tailstock held the test specimen in place. Through the system gearbox, a speed selector can be used to select the appropriate relative sliding velocity.

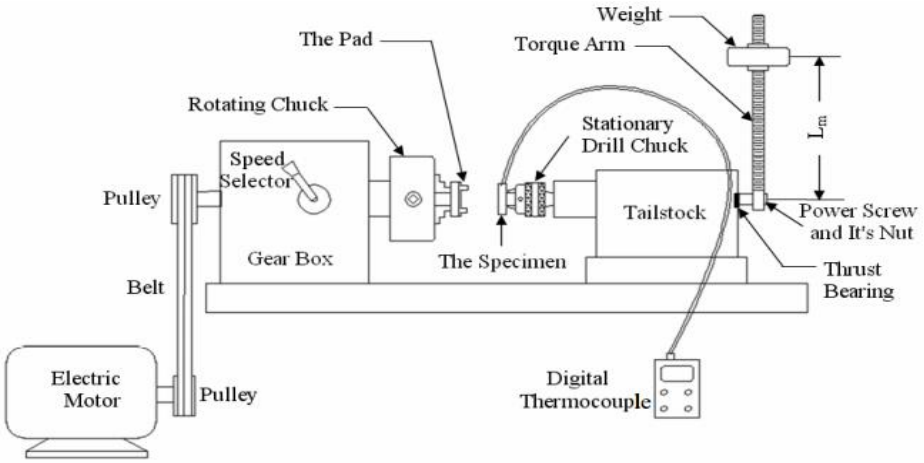

Fig 1. Schematic diagram of the high temperature wears test rig.

An axial load on a tailstock power screw can generate contact friction pressure. This pressure must be maintained in order to achieve the desired temperature. A suspended (1kg) weight on a completely threaded bar is used to rotate the screw. The required torque is determined by adjusting the torque arm's distance from the spinning centre. Wear occurs in various amounts in both the specimen and the pad during the test, resulting in a loss of thickness. The pressure value is lost or reduced as a result of this. The pressure remains constant during the free fall of the hanging load. A digital thermocouple is positioned near the friction surface to monitor temperature.

3.3 Test Specimen Preparation

Each material's test specimen was cut from the as-cast end and machined to the dimensions (in centimetres) illustrated in Fig 2. Machining parameters were chosen to avoid specimen temperature rise. The friction surface was within (5 mm) from the quenched end. Annealed specimens had the same dimensions that in Fig 2 and the friction surface was (5 mm) from the heat-treated surface. By adjusting the torque arm length, one specimen from each material was utilised to weld a thermocouple tip and estimate the needed temperature (to set the contact pressure). At that temperature, this will remain constant for that material. Following a standard procedure, the friction face was machined, polished, and then etched for microscopic analysis. The specimen was cleaned again right before the test to remove oil, grime, fingerprints, and any other foreign substance after it was fastened into the rig's tailstock chuck. To rub the test specimen, a brake pad from a car was employed as friction material.

3.4 Estimating the Test Temperature

First and foremost, the rig must be free of grease, oil, dust, and any other foreign matter. The specimen and pad, on the other hand, should be clean, dry, and well-tightened before beginning the test. The motor is started up and the chuck is allowed to rotate to reach the required speed (1000 or 1400 r.p.m. to reach 600°C or 850°C respectively) for a while before making contact slightly to avoid any shock. The specimen is warm due to friction because of the relative velocity and appropriate contact pressure. A digital thermocouple was used to track temperature changes,

as well as the time it took to achieve the cycle's maximum temperature. Increased contact pressure and temperature arise from increasing the torque arm of the free-full hanging load. The pressure is released when the required temperature (600 or 850ºC) is attained, and the time required to reach the lowest temperature in the thermal cycle is calculated. The test is repeated several times in order to examine all parameters. The hanging weight is mounted in its position using a fully threaded torque arm and a couple of check nuts to achieve the necessary effect and hence the requisite temperature.

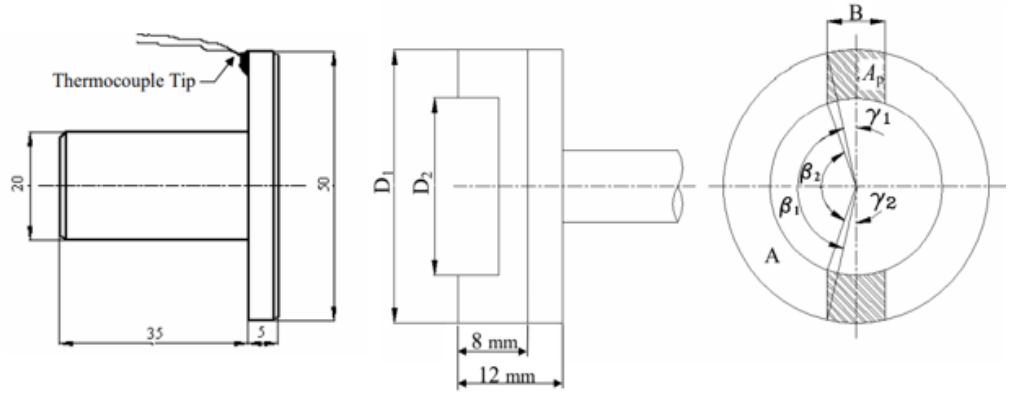

Fig 2. Wear test specimen and friction pad.

4 Calculations

A power screw with the following specification mounted in the tailstock is used to produce the contact pressure, Figure (3). A suspended weight (W = 10 Newton) is mounted at a distance (L_m mm) on a uniform fully screwed rod. The rod's moment around the power screw axis is (M_r = 620 N.mm) and the moment of the weight is (M_w). If the unit runs at (N r.p.m.), the temperature of the specimen will rise to be (T_{max} ºC) within (t_{he} sec.). When the load is released and stops contacting, the specimen is air-cooled and takes (t_c sec) to reach (T_{min} ºC).

$$Total\ torque\ acting\ on\ the\ power\ screw\ is\ (T_u) = M_w + M_r M_w = W.L_m \quad (3)$$

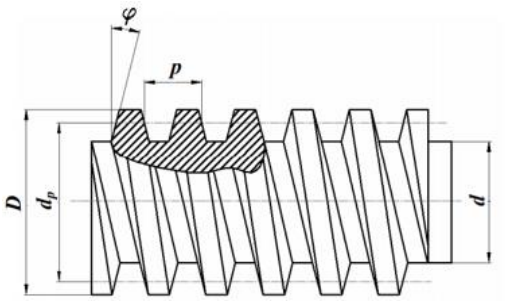

Fig 3. Single Start of Acme Thread of Power Screw.

To apply the required load to have a contact pressure between the specimen and the pad, a single–start Acme thread power screw with the following specification is used:

- Major diameter D = 26mm
- Minor diameter d = 21mm
- Pitch p = 5mm
- Lead L = p for single start screw
- Pitch diameter d p = 23.5 mm
- Acme teeth angle φ = 14.5º
- The material of the screw and nut is hard steel then the coefficient of friction μ is 0.15 for a static lubricated situation [14].

The relative motion between the screw and nut is too slow and can be assumed as a static case. The coefficient of friction for thrust ball bearing light series DIN 711 (Aug. 1942) symbol (51206) is 0.02 [15].

$$T_u = T_{su} + T_b = \frac{F \cdot d_p}{2} \cdot \frac{(\mu \cdot \pi \cdot d_p + L \cdot \cos\varphi)}{(\pi \cdot d_p \cdot \cos\varphi - \mu \cdot L)} + \mu_b \cdot F \cdot \frac{d_p}{2} \quad (5)$$

The second term of Equation (5) can be eliminated by using a sufficient load added to the torque arm weight allowing the screw to rotate freely, then Equation (5) becomes:

$$T_u = T_{su} = \frac{F \cdot d_p}{2} \cdot \frac{(\mu \cdot \pi \cdot d_p + L \cdot \cos\varphi)}{(\pi \cdot d_p \cdot \cos\varphi - \mu \cdot L)} \quad (6)$$

The contact pressure area A_p can be calculated by referring to Figure (2) which has the following data: D1 = 46 mm, D2 = 30 mm, and B =15 mm

$$A_p = \frac{\pi}{4}(D_1^2 - D_2^2) - 2A \quad (7)$$

$$Area\ of\ segment\ of\ circle = \frac{r^2}{2}(\hat{\beta} - \sin\beta) \quad (8)\ [16]$$

Then;

$$A = \frac{D_1^2}{8}(\hat{\beta}_1 - \sin\beta_2) - \frac{D_2^2}{8}(\hat{\beta}_2 - \sin\beta_2) \quad (9)$$

$$(\hat{\beta} = \beta\ in\ circular\ measure)$$

Then;

$$\hat{\beta}_1 = \frac{\pi}{180^\circ} \cdot \beta_1 \quad \& \quad \hat{\beta}_2 = \frac{\pi}{180^\circ} \cdot \beta_2 \quad (10)\ [16]$$

From Fig 2

$$\beta_1 = 180 - 2\gamma_1 \quad \& \quad \beta_2 = 180 - 2\gamma_2 \quad (11)$$

And

$$\gamma_1 = \sin^{-1}\left(\frac{B}{D_1}\right) \quad \& \quad \gamma_2 = \sin^{-1}\left(\frac{B}{D_2}\right) \quad (12)$$

Then; $A_p = 247.078\ mm^2$

Friction mean linear velocity υ [mm/sec] is;

$$\upsilon = \frac{\pi \cdot D_m \cdot N}{60} \quad (13)$$

$$D_m \frac{D_1+D_2}{2} \quad (14)$$

4.1 Furnace Charge

The furnace charge needed to produce the test materials shown in Table 1 from the alloying elements shown in Table 2 and pre-treated scrap with the chemical composition shown in Table 3. A computer program was built to determine the quantities. Table 5 shows the output of the program.

4.2 Heat Treatment

Stress relief annealing was carried out on the test materials. Brinell hardness test was carried out before and after annealing. The results as the average of five hardness numbers for each tested material are shown in Table 5.

Table 5. Furnace charge to produce 10 kg and Brinell hardness number of each single material

Materials	1	2	3
Scrap (kg)	9.788	9.855	9.525
Ferrosilicon (kg)	0.09196	0.1229	0.55104
Ferromanganese (kg)	0.07474	0.06962	0.01837
Graphite (kg)	0.12982	0.07491	0.06791
Copper (kg)	-	-	0.13424
Brinell hardness number			
Before annealing	260	240	319
After annealing	145	141	328

The matrix structures of No. 1 and No. 2 are pearlitic and ferritic, respectively, as shown in Fig 4. Pearlite has a higher hardness than ferrite. After annealing, the microstructure changes from pearlite and ferrite to totally ferritic, resulting in a significant reduction in hardness (Fig 4).
Among the test materials in this study, Material No. 3 had the greatest as-cast hardness number. The presence of copper (1.329 percent Cu) and a high silicon content (5.117 percent Si) cause hardness to increase, as indicated in Table 5. They make ferrite stronger and give it a fine grain size [1]. Because there is a lot of fine-grained structure, there is a lot of thermal conductivity. The structure becomes totally ferritic with a high amount of graphite flakes when the silicon content is high, which reduces crack propagation and boosts heat conductivity [9]. Because of its ferritic as-cast structure, Material No. 3 offers outstanding growth resistance. High silicon content combined with copper presence will limit deep oxidation growth [1]. Because the silicon will be resolved and distributed in ferrite, the hardness value of stress relief casting will be larger than before, resulting in an increase in hardness by reinforcing the mechanism.

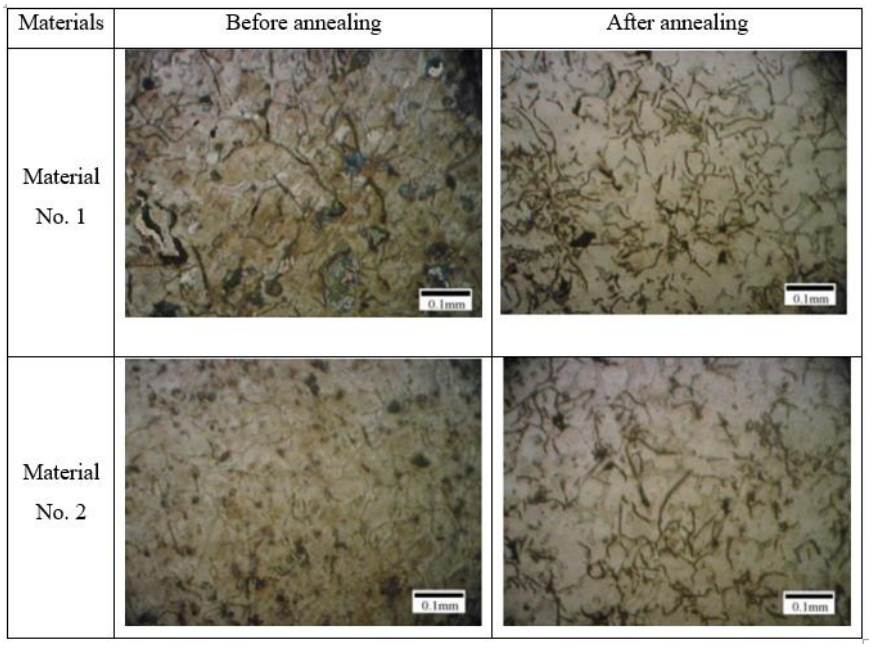

Fig 4. Microstructure of material No. 1 and No. 2 before and after annealing.

5 High-Temperature Wear Test

5.1 Wear Test at 600ºC

Table 6 shows the residual characteristics from the first wear test, which was conducted at (T_{max} = 600 ºC) and (T_{min} = 400 ºC). Three specimens of each test material were tested to ensure that the results were repeatable.

Table 6. Wear test parameters at 600 ºC.

T_{max} (ºC)	600
T_{min} (ºC)	400
T_h (sec)	50
Soaking time (sec)	10
t_c (sec)	85
N (r.p.m.)	1000
L_m (mm)	176
T_u (N.mm)	2346.56
P (MPa)	3.592
υ (m/sec)	1.9897

As a consequence of the test, the wear in specimens was assessed as a cumulative mass loss after each (25 thermal cycles). Figure 5 shows the average results for each test material area.

Material No. 3 has the highest hardness number among the test materials, as shown in Table 5, and it has the lowest weight loss due to its chemical composition and microstructure; for example, a high amount of graphite flakes with silicon - strengthen ferrite as shown in Fig 6.

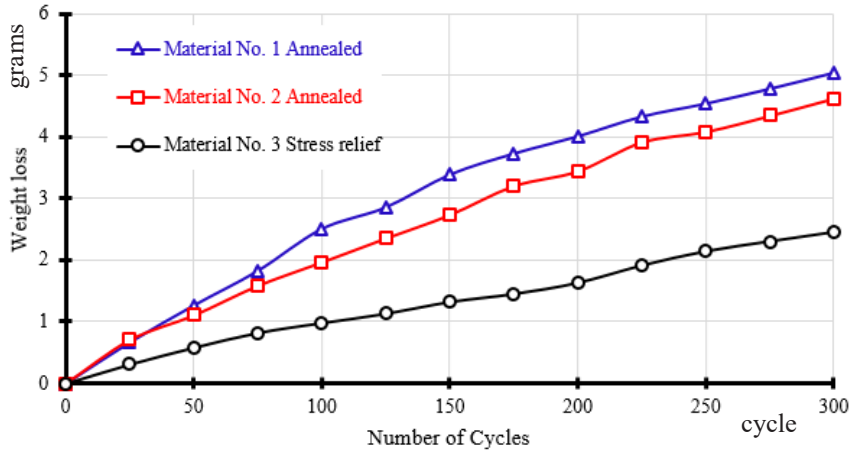

Fig 5. Weight losses as a function of several thermal cycles at 600 °C.

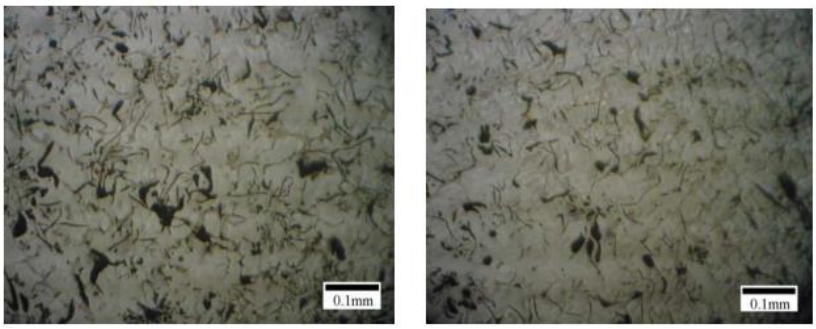

Fig 6. Microstructure of material No. 3.

5.2 Wear Test at 850ºC

A second set of testing was performed at temperatures of (Tmax= 850 ºC) and (Tmin= 400 ºC), with the remaining test parameters indicated in Table 7. Three specimens of each test material were tested to ensure that the results were consistent. The cumulative mass loss after each test was used to determine how worn the specimens were (10 cycles). Figure 6 shows the average of the results for each test item. As indicated in Table 5, Material No. 3 has the greatest hardness number among the test materials and gives the least weight loss up to 850°C. Figure 7 demonstrates that of the test materials, substance No.2 has the greatest weight reduction, followed by material No.1. Meanwhile, for its chemical composition and microstructure, material No. 3 has the lowest weight loss each cycle of all test materials; for example, a high quantity of graphite flakes with silicon - reinforce ferrite as shown in Fig 6. Material No.1 and

material No.2 were evaluated in the (to transition temperature range), which resulted in both pearlites break down and matrix oxidation, as indicated in Table 8. Growth will produce rapid fracture initiation and propagation, and graphite flakes will dislocate small sections of the surface.

Table 8 shows that Material No.3 was tested at a temperature below its critical temperature. The microstructure of material No.3 is ferritic, as seen in Fig 6. There is no growth in the absence of cementite and pearlite, implying that combined carbon is broken down. As a result of the high silicon and copper content, matrix oxidation and growth are inhibited.

Table 7. Wear test parameters at 850 °C.

T_{max} (°C)	850
T_{min} (°C)	400
T_h (sec)	110
Soaking time (sec)	10
t_c (sec)	175
N (r.p.m.)	1400
L_m (mm)	185
T_u (N.mm)	2434.85
P (MPa)	3.727
υ (m/sec)	2.7855

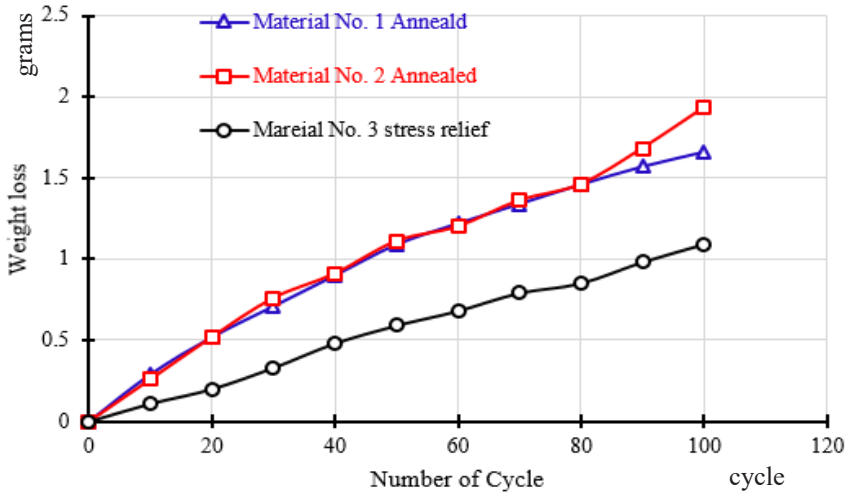

Fig 7. Weight losses as a function of the number of thermal cycles at 850 °C.

Table 8. Critical Temperature for the test materials.

Materials	Critical Temperature °C
Material No. 1	765.35
Material No. 2	776.225
Material No.3	864.401
Critical Temperature =730 + 28(%Si) - 25(%Mn) [1]	

6 Conclusions

The following are the key results reached as a result of this research:

1. The wear tests reveal that hardness is not the essential criterion for abrasive wear resistance, particularly at high temperatures.
2. For the same chemical composition, pearlitic structure material has higher hardness at room temperature than ferritic, and it has superior wear resistance than ferritic at high temperatures prior to transformation; for example, up to roughly 600 oC as well as at room temperature.
3. Ferritic Gray cast iron has a stronger wear resistance than pearlitic Gray cast iron in the (to transformation) temperature range due to its resistance to pearlite growth, free cementite break down, and deep oxidation.
4. Some grey cast iron, such as pearlite structure, mottled structure, and white cast iron, has great wear resistance at low temperatures, but it is weak at higher temperatures, particularly in the (α to γ transformation) temperature range. As a result, if Gray cast iron is meant to be utilised near the critical temperature, a wear test at ambient temperature will never give a good indication of material wear resistance.

Acknowledgments

The author wishes to acknowledge Al-Nasiriyah Technical Institute - Southern Technical University, Iraq as the test rig was fabricated and the practical tests were accomplished at its workshops.

References

[1] H. T. Angus. Cast Iron: Physical and Engineering properties. Second edition. Butterworths; reprinted, 1978.
[2] CORROSION/2000 (NACE International 55th Annual Conference and Exhibition: Peter Elliott. Choose Materials for High – Temperature Environments, Based on a paper presented at CORROSION/2000 (NACE International 55th Annual Conference and Exhibition), Mar. 26 – 31, 2000, Orlando, FL, USA.
[3] OMCO. Mould data sheet. I – 12 (September 1975).
[4] Journal article: Matteis P, Scavino G, Castello A, Firrao D. High temperature fatigue properties of a Si-Mo ductile cast iron. Procedia Materials Science. 2014 Jan 1;3:2154-9.
[5] OMCO. Mould data sheet. I – 6 (June 1975).
[6] Scheidhauer N, Dommaschk C, Wolf G. Oxidation Resistant Cast Iron for High Temperature Application. In Materials Science Forum 2018 (Vol. 925, pp. 393-399). Trans Tech Publications Ltd.
[7] Xiang S. High-temperature corrosion-fatigue of cast alloys for exhaust manifolds (Doctoral dissertation, KTH Royal Institute of Technology).
[8] OMCO. Mould data sheet. I – 6 (June 1975).
[9] S. Y. Buni, N. Raman and S. Seshan. The Role of Graphite Morphology and Matrix Structure on Low Frequency Thermal Cycling of Cast Irons. Sadhana, India. February 2004; Vol. 29; Part 1: 117 – 127.
[10] Junichiro Yamabe, Masami Takagi and Toshiharu Matsui. Development of Disc Brake Rotors for Heavy – and Medium – Duty Trucks with High Thermal Fatigue Strength. 2003; Technical papers; Technical Review; No. 15.
[11] G. Cueva, A. Sinatora, W. L. Guesser and A. P. Tschiptschin. Case Study, Wear Resistance of Cast Irons Used in Brake Disc Rotors, Wear; 255(2003): 1256 – 1260.
[12] John R. Brown. Foseco Ferrous Foundryman's Handbook. Oxford: Butterworth-Heinemann, Foseco International Ltd;2000.
[13] R. F. Tylecote. Friction Welding, The solid phase welding of metals. 1968; pp. 226-257, 1968.

[14] F. D. Duffin and A. S. Bahrani. The mechanics of friction welding mild steel. Metal Construction. 1976; Vol. 8: No. 6.
[15] Robert L. Norton. Machine Design an Integrated Approach. Prentice-Hall. Inc.; 1998. pp. 894 – 906
[16] Gustav Niemann. Machine Elements Design and calculation in mechanical engineering. Berlin: Springer – Verlag; 1978. Vol. 1.
[17] Kurt Gieck. Engineering Formulas. Fifth American edition. USA: McGraw-Hill, Inc. 1986.

Deep Learning for Self-Driving Vehicles

Safa Jameel Dawood Al-Kamil[1], Mohammed Salah Al-Radhi[2]
{safa.alkamil@stu.edu.iq[1], malradhi@tmit.bme.hu[2]}

Southern Technical University, Basra, Iraq[1]
Budapest University of Technology and Economics, Budapest, Hungary[2]

Abstract. Self-driving vehicles (SDV) and advanced safety features offering the greatest challenges and opportunities for Artificial Intelligence. The understanding of human intention is a very difficult task. As a result, predicting other drivers' future behaviour is critical for perceiving their past motion, analysing their interactions with other agents, and processing the data available from the scene. Automated driving systems (ADSs) promise to make driving safer, more comfortable, and more efficient. The Deep Structured Self-Driving Network (DSDNet) is proposed in this work that uses a single neural network to conduct object identification, motion prediction, and motion planning. The deep structured energy-based model, on the other hand, is improved. DSDNet also takes advantage of the expected forthcoming predicted actors to prepare a safe manoeuvre. Experiments The results reveal that it considerably increases detection, prediction, and planning performance.

Keywords: Self-driving vehicles, DSDNet, Deep learning, Prediction, and planning.

1 Introduction

Many discoveries in computer vision [1], robotics [2], and natural language processing (NLP) [3] were made possible by deep learning (DL) and artificial intelligence (AI). These methods have excellent control features on the future current autonomous driving in academics and industry. A self-driving vehicle (SDV) must monitor and predict surrounding actors' future behaviours, as well as plan safe manoeuvres. To be able to drive safely on the road. The success of DL, the prediction problem remains difficult due to the difficulties. Furthermore, motion planners must be improved in order to account for the uncertainty of forecasts. Parametric distributions have been used in the past to model multimodality in motion prediction. Because of their close-form inference, a combination of Gaussians [1, 2] is a natural approach. Nonetheless, deciding on the number of modes ahead of time is challenging. Furthermore, through training, these techniques suffer from mode collapse [3, 2, 4]. An alternative is to use neural networks to predict the data distribution through a series of training data. The multi – sensor operations carried out by CVAE [8], showed that the latent variables can be used to represent actor interactions, as shown in [5, 6, 7].
In this study, DSD- Net is suggested as a single neural network that leverages raw sensor data to jointly detect actors in the scene, forecast a multimodal distribution across their future behaviours, and build safe SDV plans. Typically, planning is framed as a problem of cost

IMDC-IST 2021, September 07-09, Sakarya, Turkey
Copyright © 2022 EAI
DOI 10.4108/eai.7-9-2021.2314949

minimization over trajectories. The fitness function can be manually constructed to ensure specific properties [16, 17,18, 19], or it can be trained from data via imitation learning or inverse reinforcement learning [20, 21]. These planners, however, believe that detection and prediction are exact and certain, which is not the case in fact. As a result, take into account the uncertainty of other players' actions and define collision avoidance in a probabilistic manner. Uncertainty-aware motion planning is explicitly applied to model the interactions between the SDV and the other dynamic agents, to achieve safer planning. Furthermore, our planning cost functions explicitly account for safety.

With a sample-based paradigm, this paper focuses on the costly probabilistic inference. Deep structured models, which use DNNs to provide the energy terms of probabilistic graphical models, have recently exploded in popularity as a way to encode prior knowledge (PGMs). DS models have been effectively used to several computer vision problems, such as semantic segmentation anomaly detection, and contour segmentation [22], by combining the powerful learning capability of DNNs with the task-specific structure imposed by PGMs. Inference for continuous random variables, on the other hand, is extremely difficult. We build a deep structured model called sample-based belief propagation (BP) that can learn complicated human behaviours from vast data processing based on past knowledge, which is influenced by this research. We also use a physically valid sampling approach to get over the issue of continuous variable inference.

2 Methods and experiments

In this study, we propose a new design technique (DSDNet) that discovers and predicts a generally regular multimodal allocation after temporal activities, as well as providing safe self-driving car movement plans.

The middle feature maps are evaluated using a backbone network before being developed further. Subsequently recognising performers using a detection header and taking into account their reactions, a deep organised probabilistic deduction module generates future trajectories, which indicates that allocations of actors will occur. Finally, the projected track takes into account the information stored in the feature maps, In addition, the model's likely futures. Our proposed strategy is depicted in Fig 1 as a high-level overview.

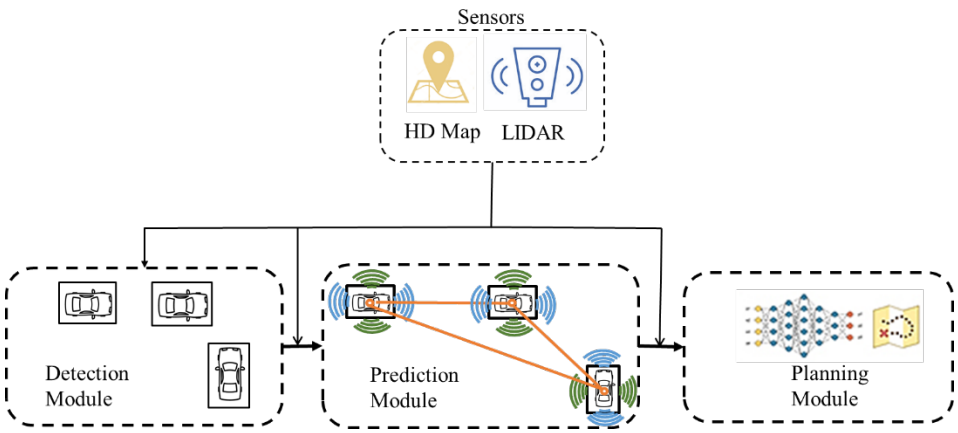

Fig 1. The multimodal trajectory prediction module is described in detail.

The following is a breakdown of the paper's structure: SDV's Methods and Experiments are explained in Section 2. The Experimental Evaluation is discussed in Section 3. And finally conclusions was addressed in section 4.

2.1 Object Detection and the Backbone Network

We vowelized the most recent 8 LiDAR sweeps to create a 3D tensor. LiDAR is a vital signal that can be sparse and utilised to detect and forecast the movement of performers. We utilise HD maps because they give us a good idea of what's going on. Besides the lanes are predicted by the traffic signal and like turning or straight into multiple pathways and let 3D LiDAR tensor to manage the control presentation. After that, we use a deep convolutional network backbone to process this 3D tensor and construct a backbone feature map, which must be followed by using a specific header pointer to the map the boundary squares in the scene. 2D convolution layers is applied, in which, one for organising location is taken by an performer and the other for retracting each actor's place offset, dimensions, direction, and velocity. The prediction and planning modules in this paper will choose the suitable prediction map for entry to provide both demeanors and safe planning.

2.2 Probabilistic Multimodal Trajectory Prediction

We used a path plan represented by a series of 2D intermediate sampled at T discrete timestamps on a birds-eye view (BEV). We calculate the movement prediction allocation and a movement of each sensor occurs, and time sample T.

2.3 Output Parameterization

We propose a solution from a limited number of samples to develop the required continuous space distribution. A few K samples to predict the future trajectory from random distribution for each actor, is illustrated in Fig. 2. Then limit each actor's conceivable future state to one of those K samples. The Neural Motion Planner (NMP) [9] is used. To maintain the whole diverse and reasonable distribution, a mix of circle, square, and colthood arcs are used.

2.4 Inference of Message Passing

Our motion planner demands us to examine all conceivable actor futures for safety reasons. As a result, motion forecasting that deduces the likelihood of each performer following a specific future path. As a result, we do marginal inference on the joint distribution. We also employ the crossing between the sum and product of data to assess the peripheral distribution of each fitness element, that considers the marginalisation impacts of the other elements under considerations.

2.5 Safe Motion Planning

Our last goal is to arrive our target and side-stepping collisions and following traffic laws in the motion planning module. To do this, we create fitness formula that reduce the complicity and to achieve excellent route compared to less safe other routes. The development idea was completed by determining the most cost-effective trajectory. We use a multi-task loss to train

the entire model (backbone, detection, prediction, and planning) in collaboration with a multi-class cost, which maintain the best supervision and the reliable training. We use a common detection methodology, that is a combination of classification and regression loss. We use cross-entropy between our discrete distribution and the genuine goal based on samples collected for the performers conduct. The main goal to achieve minimum Euclidian distances for the trajectory samples for the best predicable future trajectory.
This work established wide safety margins for potentially harmful behaviours such as collision paths. As a result, our approach can punish risky behaviours more severely.

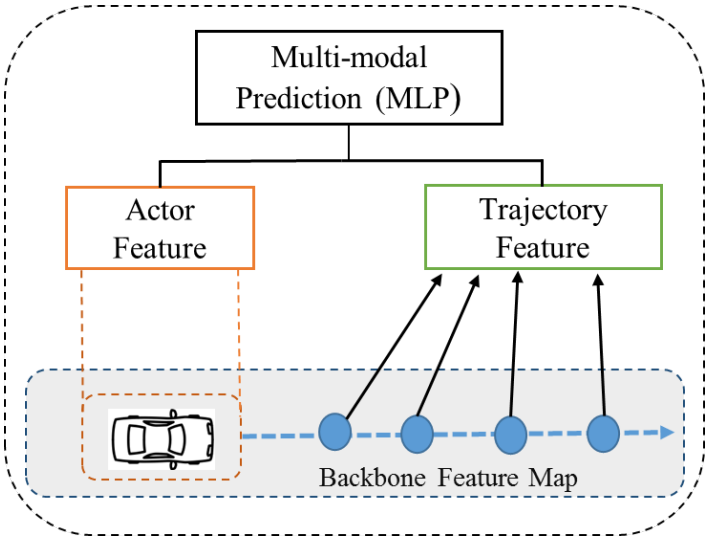

Fig 2. The neural header for evaluating Trajectory.

3 Experimental Evaluation

In this article, the model is tested for all three tasks: detection, prediction, and planning. On two large-scale real-world self-driving datasets, it outperforms the state-of-the-art on public benchmarks: scenes, as well as our own data ATG4D. In addition to the CARLA simulation dataset prediction module is tested. The benefits of explicitly modelling actor interactions are demonstrated in this work. When compared to rival systems, this article planning module produces the safest planning outcomes and reduces the rate of collisions and lane violations significantly. The proposed model continues the detection even over a single backbone with implication. In the supplementary material, we detail the dataset as well as the implementation.

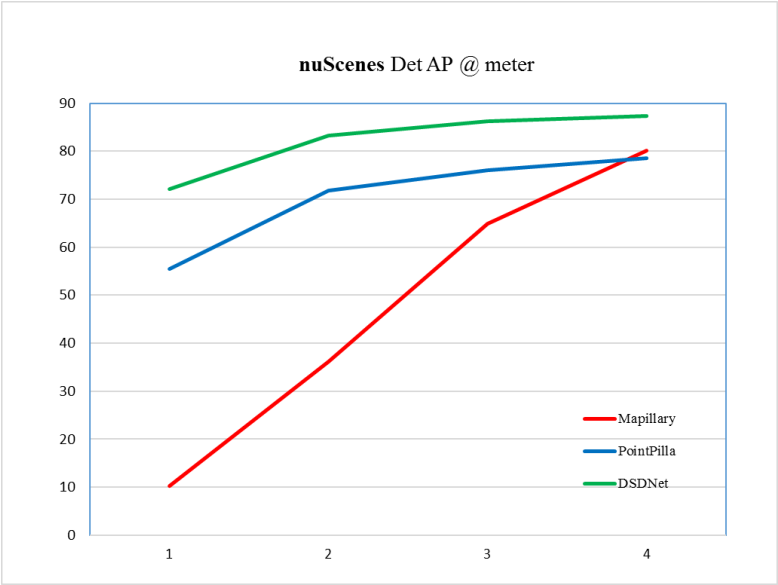

Fig 3. Detection performance of scenes.

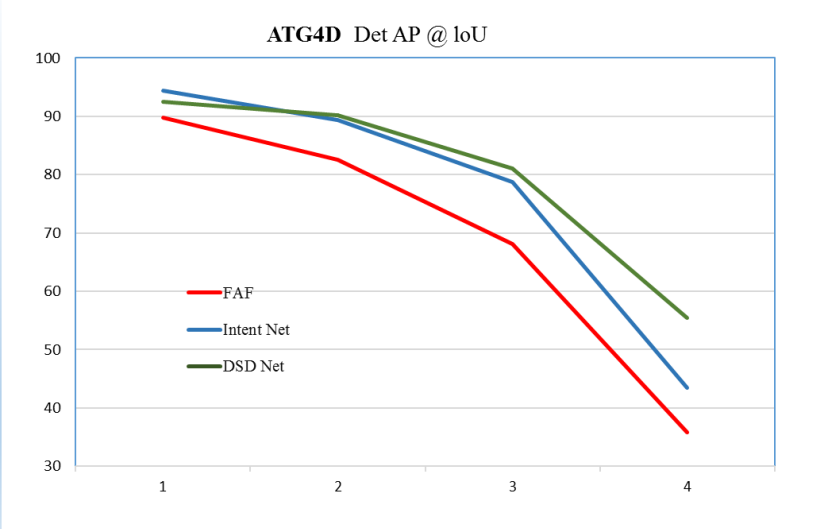

Fig 4. The results of ATG4D's detection performance.

On both datasets, as demonstrated in Figs 3 and 4, our technique produces the best results. This is significant because conventional baselines employ L2 as a training target and are thus directly favoured by the L2 error metric, whereas our techniques learn correct distributions and capture multi-modality via cross-entropy loss. Multimodal approaches are regarded to have the lowest score in this metric. We show that modelling multi-modality while attaining lower L2 error is

attainable due to the adaptable performers' behaviour. The method lowers collisions between the anticipated trajectories of the actors, demonstrating the value of our multi-agent interaction modelling. This evaluation is carried out on CARLA, which has been used in all prior techniques. As seen in Fig 4, our strategy exceeds prior best findings by a wide margin. Our detections, forecasts, the expected uncertainties that are all visualised. We use different colours for various future timestamps to denote high-probability performers' future positions estimated via our prediction module. The predictions are certain when vehicles drive along the lanes (left), but when vehicles approach a junction, multi-modal predictions are seen (middle, right).

4 Conclusion

Self-driving vehicles (SDV) and how the safety feature offering the highest challenge for Artificial Intelligence has been presented. Our planning modules produce the safest planning results, with significant reductions in the rate of collisions and lane violations. In this paper, we have suggested DSDNet, to serve under a unified framework. Perception, prediction, and planning.

Experiments Results on a self-driving dataset show that our model improves the performance of detection, prediction, and planning remarkably. We want to understand more about structured energies and how to build excellent reward functions for autonomous agents, as well as how to incorporate safety into decision-making reinforcement learning systems.

References

[1] Chai Y., Sapp B., Bansal M., Anguelov D. Multipath: Multiple probabilistic anchor trajectory hypotheses for behavior prediction. arXiv preprint arXiv:1910.05449 (2019).

[2] Hong J., Sapp B., Philbin J. Rules of the road: Predicting driving behavior with a convolutional model of semantic interactions. In: Proceedings of the IEEE Conference on Computer Vision and Pattern Recognition. pp. 8454-8462 (2019).

[3] Jain A., Casas S., Liao R., Xiong Y., Feng S., Segal S., Urtasun R. Discrete residual flow for probabilistic pedestrian behavior prediction. arXiv preprint arXiv:1910.08041 (2019).

[4] Rhinehart N., Kitani K.M., Vernaza P. R2p2: A reparameterized pushforward policy for diverse, precise generative path forecasting. In: European Conference on Computer Vision. pp. 794-811. Springer, Cham (2018).

[5] Rhinehart N., McAllister R., Kitani K., Levine S. Precog: Prediction conditioned on goals in visual multi-agent settings. arXiv preprint arXiv:1905.01296 (2019).

[6] Lee N., Choi W., Vernaza P., Choy C.B., Torr P.H., Chandraker M. Desire: Distant future prediction in dynamic scenes with interacting agents. In: Proceedings of the IEEE Conference on Computer Vision and Pattern Recognition. pp. 336{345 (2017).

[7] Tang Y.C., Salakhutdinov R. Multiple futures prediction. arXiv preprint arXiv:1911.00997 (2019).

[8] Sohn K., Lee H., Yan X. Learning structured output representation using deep conditional generative models. In: Advances in neural information processing systems. pp. 3483-3491 (2015).

[9] Zeng W., Luo W., Suo S., Sadat A., Yang B., Casas S., Urtasun R. End-toend interpretable neural motion planner. In: Proceedings of the IEEE Conference on Computer Vision and Pattern Recognition. pp. 8660{8669 (2019).

[10] Liang M., Yang B., Zeng W., Chen Y., Hu R., Casas S., Urtasun R. Pnpnet: End-to-end perception and prediction with tracking in the loop. In: Proceedings of the IEEE/CVF Conference on Computer Vision and Pattern Recognition. pp. 11553-11562 (2020).

[11] Wang T.H., Manivasagam S., Liang M., Yang B., Zeng W., Raquel U. V2vnet: Vehicle-to-vehicle communication for joint perception and prediction. In: Proceedings of the European Conference on Computer Vision (ECCV) (2020).
[12] Luo W., Yang B., Urtasun R. Fast and furious: Real time end-to-end 3d detection, tracking and motion forecasting with a single convolutional net (2015).
[13] Casas S., Luo W., Urtasun R. Intentnet: Learning to predict intention from raw sensor data. In: Billard, A., Dragan, A., Peters, J., Morimoto, J. (eds.) Proceedings of The 2nd Conference on Robot Learning. Proceedings of Machine Learning Research, vol. 87, pp. 947-956. PMLR (29{31 Oct 2018).
[14] Casas S., Gulino C., Suo S., Luo K., Liao R., Urtasun R. Implicit latent variable model for scene-consistent motion forecasting. In: Proceedings of the European Conference on Computer Vision (ECCV) (2020).
[15] Casas S., Gulino C., Suo S., Urtasun R. The importance of prior knowledge in precise multimodal prediction. In: IROS (2020).
[16] Buehler M., Iagnemma K., Singh S. The DARPA urban challenge: autonomous vehicles in city traffi c, vol. 56. springer (2009).
[17] Fan H., Zhu F., Liu C., Zhang L., Zhuang L., Li D., Zhu W., Hu J., Li H., Kong Q. Baidu apollo em motion planner. arXiv preprint arXiv:1807.08048(2018).
[18] Montemerlo M., Becker J., Bhat S., Dahlkamp H., Dolgov D., Ettinger S., Haehnel D., Hilden T., Homann G., Huhnke B., et al. Junior: The Stanford entry in the urban challenge. Journal of eld Robotics 25(9), 569{597 (2008).
[19] Ziegler J., Bender P., Dang T., Stiller C. Trajectory planning for bertha|a local, continuous method. In: Intelligent Vehicles Symposium Proceedings, 2014 IEEE. pp. 450-457. IEEE (2014).
[20] Sadat A., Ren M., Pokrovsky A., Lin Y.C., Yumer E., Urtasun R. Jointly learnable behavior and trajectory planning for self-driving vehicles. arXiv preprint arXiv:1910.04586 (2019).
[21] Wulfmeier M., Ondruska P., Posner I. Maximum entropy deep inverse reinforcement learning. arXiv preprint arXiv:1507.04888 (2015).
[22] Marcos D., Tuia D., Kellenberger B., Zhang L., Bai M., Liao R., Urtasun R. Learning deep structured active contours end-to-end. In: Proceedings of the IEEE Conference on Computer Vision and Pattern Recognition (2018).

Design a High Transmission FSS Structure for THz Applications

Muaad Hussein[1], Haider Alrudainy[2]
{muaad.hussein@stu.edu.iq[1], h.m.a.alrudainy@stu.edu.iq[2]}

Electrical Power Techniques Engineering, Southern Technical University, Basra, Iraq[1,2]

Abstract. A unique frequency selective surface (FSS) structure was proposed as a terahertz bandpass filter in this study. The proposed structure is simple to make, has a high transmission of up to 96 percent, a wide bandwidth, and excellent band-edge transitions at THz frequencies. Based on an investigation of the FSS structure geometry configuration and the distribution of the electric field in it, a theoretical equivalent circuit model is presented to characterise the structure. It has been demonstrated that the comparable circuit model's outputs are in good agreement with numerical simulation tools. The filter is simulated using CST Microwave Studio's frequency selective surface (FSS). To simulate the equivalent circuit, Advanced Design Systems (ADS) is used..

Keywords: THz, mesh, FSS, filter, equivalent circuit.

1 Introduction

Terahertz (THz) is a frequency range that falls between microwave and optical frequencies. In open space, the emitted signal at 1 THz has a wavelength of 300 m. THz systems have been introduced as a brilliant wireless interface approach in recent years. THz systems are used for medical imaging, THz spectroscopy, security scanning, high-speed wireless communication, and remote sensing [1-2]. THz bandpass filter could be realized as a combination of frequency-selective surfaces (FSS) comprising arrays of metal print on the front side or both sides a dielectric.

Metal mesh and related structures are suitable elements for the construction of THz filters. The fundamental frequency selective surfaces are classified into the bands top patch type and the bandpass mesh type, as shown in Fig 1. The representation of the THz properties of the grids by an equivalent circuit is very useful to apply the well-developed transmission line theory to calculate THz filters consisting of two or more grids [3-6]. The equivalent circuits for a band stop FSS type and bandpass FSS type are shown in Fig 2. The grids consist of a thin layer of metal and are supported by a dielectric film. A cross dipole is the most common bandpass grid shape and unit cell, as depicted in Fig 3. (a). Periodicity P, cross member length d, and cross-member width W define the geometry. The frequency response of the filter is determined by the slot dimensions. If P is substantially less than the wavelength, linearly scaling the dimensions P, d, and W can alter the filter profile [7-8].

IMDC-IST 2021, September 07-09, Sakarya, Turkey
Copyright © 2022 EAI
DOI 10.4108/eai.7-9-2021.2314948

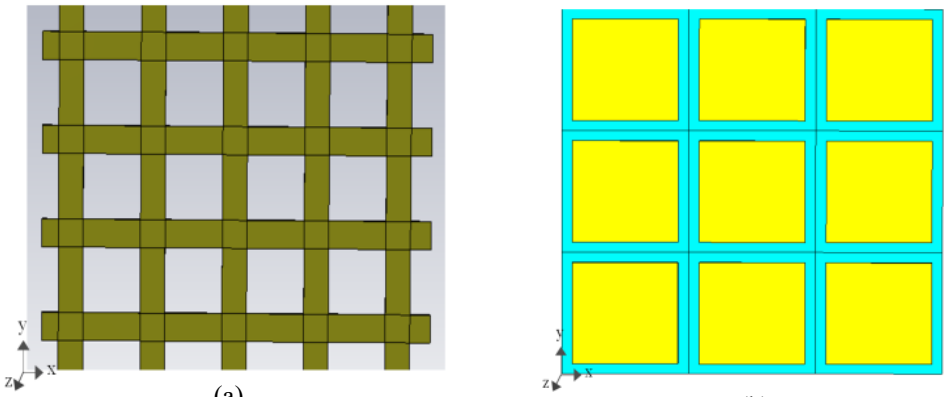

(a) (b)

Fig 1. (a) Bandpass mesh frequency selective surface (Inductive grid) and (b) Band stop patch frequency-selective Surface (capacitive grid)

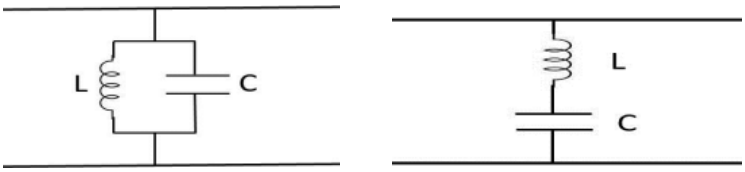

(a) (b)

Fig 2. (a) Equivalent circuit for mesh-type bandpass FSS and (b) Equivalent circuit for patch-type bandstop FSS

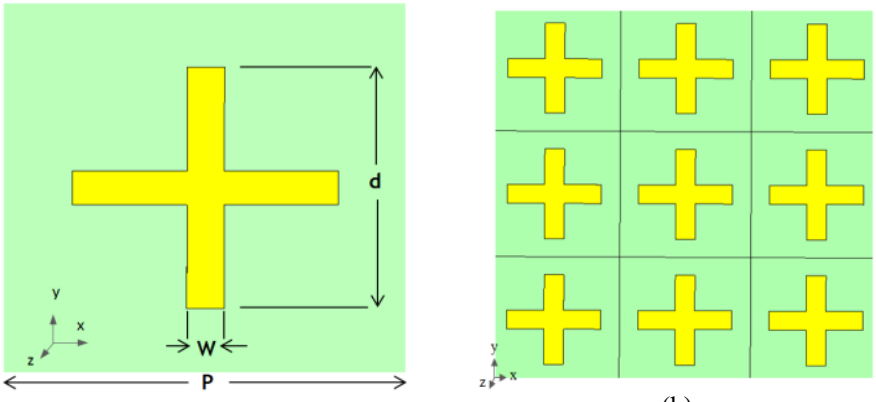

(a) (b)

Fig 3. (a) Cross-shaped filter design parameters lattice constant (P), a width of the cross (W) length of the cross (d), and (b) 3×3-unit cells of the cross-shaped filter.

Different frequency responses of a filter can be achieved by different FSS element shapes, the conductivity of FSS metal, dielectric constant of the substrate, and incident angle of the signal.

Figure 3 depicts the cross dipole's 3×3-unit cells (b). Dual-band and high transmission bandpass filters with up to 90% transmission have been achieved using dielectric-metal-dielectric [9]. The meta-material-based bandpass filter could have an extremely narrow transmission bandwidth [10-11]. The passband's 3 dB fractional bandwidth is less than 25% in both cases when utilising two layers of the cross-slot structure and four layers of the wire-plate structure. The transmission amplitude is greater than 80% [12]. The bandwidth of the filter can be increased by reducing the capacitance effects of the FSS structure [3]. A ring with two splits and two roadways inside the ring is the proposed unit cell structure.
The value of resonant frequency and bandwidth can be adjusted by changing parameters dimensions such as the widths of the ring and the roads, and gap distances as well as road-to-road separation. The advantages of the proposed filter are a high transmission up to 96%, sharp band edge, and a fractional bandwidth of 37% can be achieved by simulation of the structure. Due to the FSS structure constructs by a metal-dielectric and the smallest dimension at 1.2 THz is 10 μm, the structure is easy to fabricate. Traditionally, a single metal-dielectric-metal or multi-layer structure is needed to achieve comparable performance.

2 Filter design and simulation

The filters are designed to pass 0.4 THz with the least amount of loss. The proposed resonator is constructed by printing a metal structure on one side of a dielectric substrate. The structure was created with the goal of achieving the lowest possible mutual capacitance between unit cells. Copper is the metal, and it has a thickness of 0.15 μm. The substrate is 20 μm thick Mylar with a permittivity of 2.89. The ring diameter is 100 μm. The width of the road is 10 μm, the gap of each split is 10 μm and the gap of the centre of ring G_c is 10 μm as shown in Fig. 4. The periodic constant P is 60 μm. The grid of unit cells of the proposed filter is shown in Fig. 5. The simulated result of the terahertz bandpass filter is shown in Fig. 6. The centre frequency is 1.268 THz, and the S_{11} parameter has reached –28 dB. The filter exhibits high performances, characterized by the high transmission of the THz wave with a 3 dB bandwidth of up to 465 GHz and good band edge transition. According to the incident angle of the electric field and electric current distribution, as shown in Fig. 7, the corresponding equivalent circuit model is found as shown in Fig. 8. This simple RLC circuit can represent the frequency response of an inductive frequency selective surface. L/2 represents the parallel of two inductances, 2C is the gap of ring centre capacitance, and R/2 represents the losses. The response obtained by the equivalent circuit model is in good agreement with the numerical simulation of the distribution structure. The transmitted power for this equivalent circuit can be obtained using Eq. 1 [4].

$$T = \frac{R^2 + {Z_0}^2 / \left(\frac{w}{w_0} - \frac{w}{w_0}\right)}{(1+R)^2 + Z_0^2 / \left(\frac{w}{w_0} - \frac{w}{w_0}\right)} \quad (1)$$

where Z_0 is the characteristic impedance of the transmission line, and w_0 is the resonant frequency. The lumped elements value to achieve this response is capacitance 15.1fF and inductance 1.03 pH and resistances as shown in Fig. 9. The splits in the circumference of the ring can decrease the capacitive effect between unit cells and neighbours. The incident angle of an electric field cannot induce capacitive effects in the circumference splits of the ring as shown in Fig. 7. The main capacitive effect is achieved by the centre gap G_c. This can give full

control of the resonant frequency by changing the centre gap (G_c). The resonant frequency is tuned from 1.268 THz to 1.18 THz with 0.370 fraction bandwidth by decreasing the centre gap G_c from 14 µm to 10 µm.

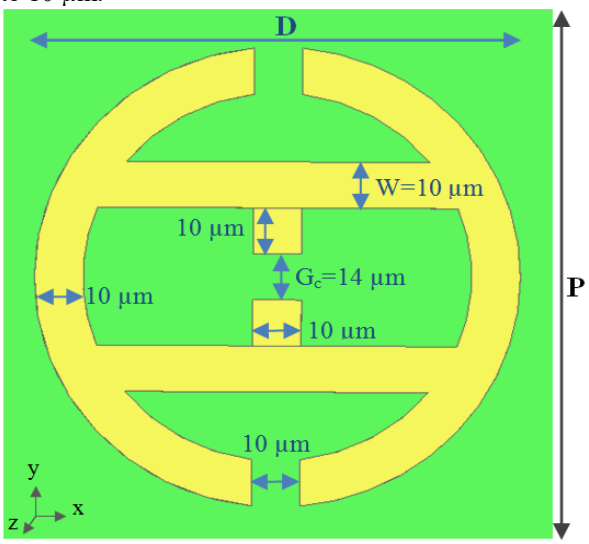

Fig 4. New shaped filter design parameters lattice constant (P), the gap (g), the diameter of the ring (D), and roads width (W).

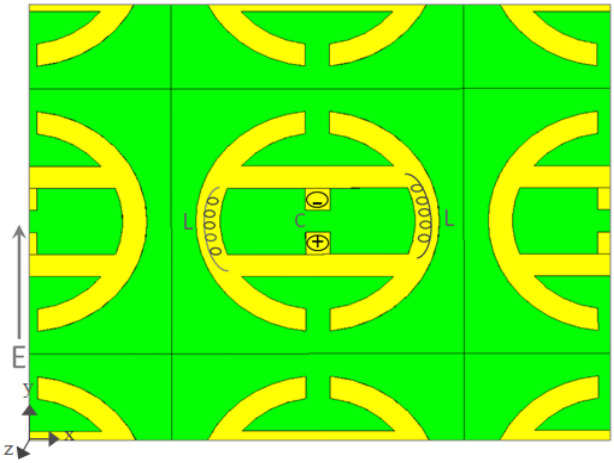

Fig 5. Grid of unit cells of the proposed filter.

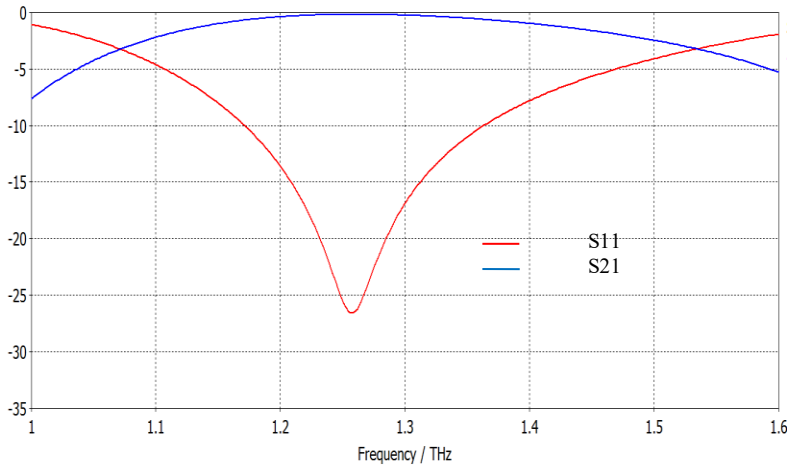

Fig 6. S11 and S21 of proposed bandpass filter by simulated distribution structure in CST.

While the resonant frequency shifted to 1.31 THz when the G_c became 18 µm with 0.385 fraction bandwidth. Fig 10 explains the effect of changing G_c on the resonant frequency. The transmitted power for all cases of changing the Gc is 96%. These responses obtained by tuning the value of capacitance (c) in the equivalent circuit to 17.1 fF and 14.3 fF, respectively. Changing the wave incident angle can Increase the fraction bandwidth, but at the same time cause a decrease in the transmitted power. Moreover, it can shift resonant frequency towards the lower band as shown in Fig 11.

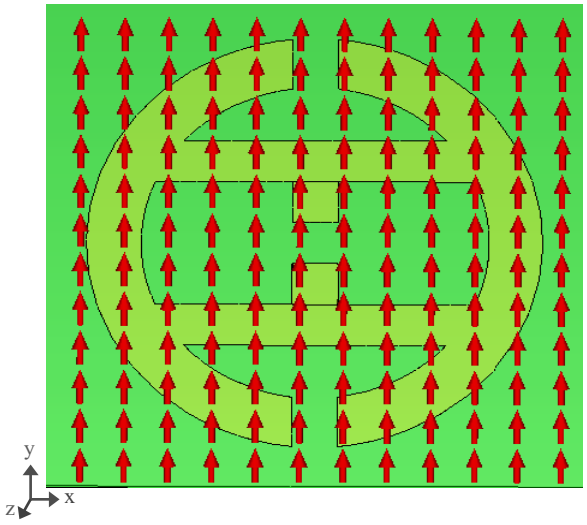

Fig 7. The incident angle of the electric field on the structure is 0 degree.

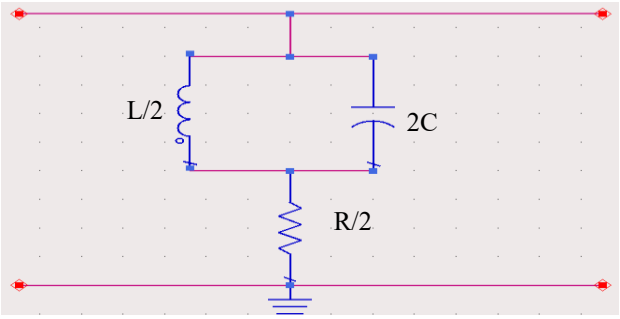

Fig 8. The proposed circuit model.

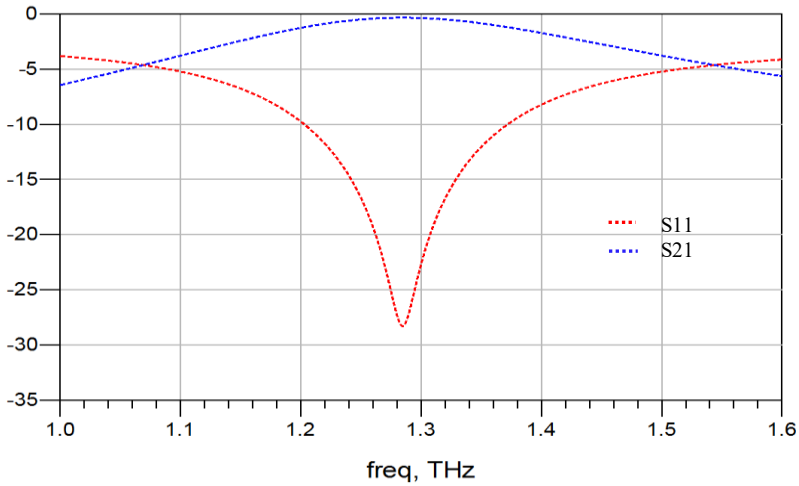

Fig 9. S11 and S21 of proposed bandpass filter by the simulated equivalent circuit in ADS.

For instance, changing of wave incident angle to 15° can shift the resonant frequency to 1.22 THz and enhance the fraction bandwidth to 40%, while the transmitted power is decreased by 23%. At an incident angle of 40°, the fraction bandwidth is enhanced to be 45% with an 85% reduction in transmitted power. After the 45° angle of the incident wave, the fraction bandwidth starts to decrease, and the transmitted power continues to decrease. It is worth mentioning with changing the incident angle that the resonant frequency is shifting towards the lower frequency. It can use Snell's law to prove that the transmitted power is influenced by changing the incident angle of the wave plane [13]. Thus, a smaller bandwidth is achieved when the Q factors are higher at the resonant frequency with greater amplitudes. Increasing the permittivity can decrease the bandwidth and resonance frequency of the filter. Reducing the thickness of the substrate can increase the resonance frequency and bandwidth. Table 1 exhibits the metal mesh bandpass filter of different authors [7].

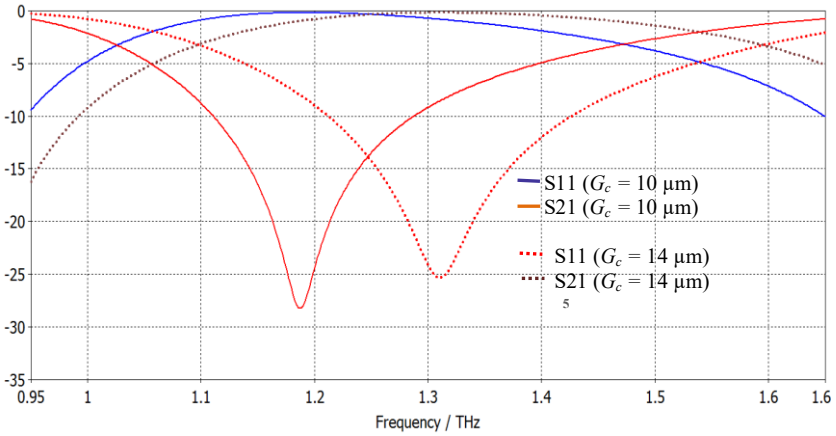

Fig 10. Transmission and reflection of a proposed bandpass filter with G_c = 12 µm & 14 µm (simulate distribution structure in CST).

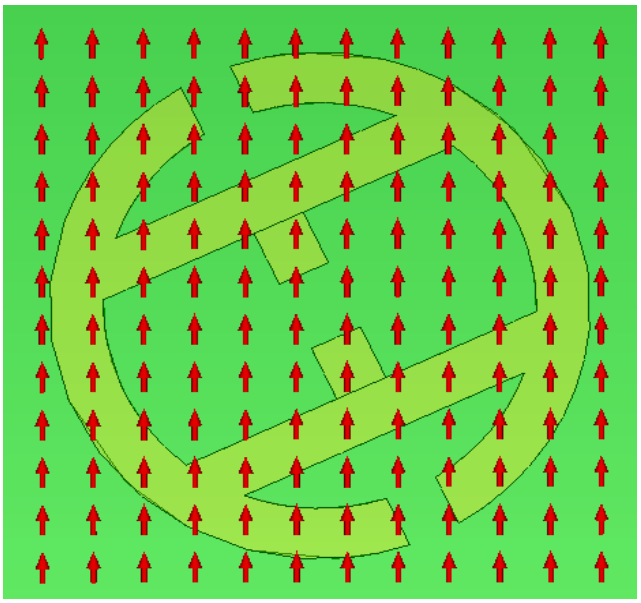

Fig 11. The incident angle of the electric field distribution from 0 degree.

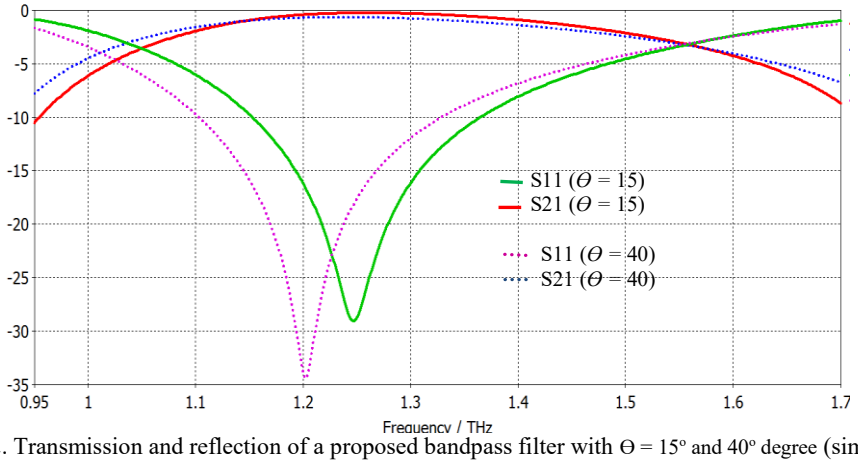

Fig 12. Transmission and reflection of a proposed bandpass filter with Θ = 15° and 40° degree (simulate distribution structure in CST).

Table 1. Bandpass metal mesh filters from published work.

Reference	Frequency (THz)	Transmission (%)	Bandpass width (%)
[14]	0.510	78	33
[15]	1.195	100	16.9
[16]	1.5	51	40
[15]	1.523	97	18.6
[17]	3.75	59	30
Proposed FSS	1.268	96	37

3 Conclusion

For the construction of THz filters, a unique structure is proposed. Due to its simple structure, which consists of a single metal layer and a dielectric layer, the suggested filter is relatively straightforward to manufacture. The proposed shape has been proved to have a 3 dB

bandwidth of up to 45 percent and efficient band edge transition. As a single band FSS, this construction can be used. The counterpart of a clumped-LC-network is found. ADS was used to model the similar circuit. The response generated by the comparable circuit model is very similar to the FSS structure's response. The tuning of frequency resonators with constant fractional bandwidth can be achieved by changing the gap in the centre of the ring G_c. The study shows that the increase of the centre gap G_c from 10 µm to 14 µm and 18 µm can shift the resonant frequency from 1.18 THz to 1.268 THz and 1.31 THz with gradually increasing in bandwidth. It is shown that the bandwidth can be increased when the incident angle is more than 0^o until 45 degrees, but at the same time the transmitted power continues to decrease for angle incident wave more than 0^o. A comparison of the proposed structure result with bandpass metal mesh of different authors has been done.

References

[1] T. K. Nguyen, H. Han, I. Park "Highly Efficiency Resonant Antennas for Terahertz Photomixers", iWAT, 2012

[2] B. S. Rawat, A. Bhat, J. Pistora, "THz Band Nanoantennas for Future Mobile Communication", NY 89557-0260, U.S.A. 2013

[3] F. Costa, A. Monorchio, G. Manara, "Efficient Analysis of Frequency-Selective Surfaces by a Simple Equivalent-Circuit Model", IEEE Antennas and Propagation Magazine, vol. 54, no. 4, 2012

[4] Lioubtchenko, A. V. Räisänen, and S. A. Tretyakov, "Simple and Accurate Analytical Model of Planar Grids and High-Impedance Surfaces Comprising Metal Strips or Patches," IEEE Transactions on Antennas and Propagation, AP-56, 6, 2008, pp. 1624-1632.

[5] R. Ulrich, "Far-Infrared Properties of Metallic Mesh and its Complementary Structure," Infrared Physics, **7**, 1967, pp. 37-55

[6] L. Whitbourn, R. Compton, "Equivalent-circuit formulas for metal grid reflectors at a dielectric boundary", APPLIED OPTICS, Vol. 24, No. 2, 1985

[7] A. Melo, A. Gobbi, M. Piazzetta, A. da Silva, "Historical Review and Results Cross-Shaped Terahertz Metal Mesh Filters" Advances in Optical Technologies, Volume 2012

[8] Y. J. Chiang, T. J. Yen, "A high-transmission dualband terahertz bandpass filter by exciting multiresonance of metamaterials" , Taiwan 2010

[9] N. Jin, J. Li, "Terahertz Wave Bandpass Filter Based on Metamaterials", Microwave and Optical Technology Letters, 2010

[10] L. Si, Y. Yuan, H. Sun, X. Lv, "Characterization and Application of Planar Terahertz Narrow bandpass Filter with Metamaterial Resonators", International Workshop on Metamaterials, 2008, China, 2008

[11] I. Al-Naib, Ch. Jansen, M. Koch, "Very Compact Bandpass Filter Based on Spiral Metamaterial Resonators", 34th International Conference on Infrared, Millimeter, and Terahertz Waves, 2009. IRMMW-THz 2009

[12] O. Paul, R. Beigang, M. Rahm,"Highly Selective Terahertz Bandpass Filters Based on Trapped Mode Excitation", OPTICS EXPRESS, 2009

[13] Y. Lee, "Principles of terahertz science and technology", 1st ed. New York, NY: Springer, 2008

[14] L. A. Page, E. S. Cheng, B. Golubovic, J. Gundersen, and S. S.Meyer, "Millimeter-submillimeter wavelength filter system," Applied Optics, vol. 33, no. 1, pp. 11–23, 1994.

[15] D. W. Porterfield, J. L.Hesler, R. Densing, E. R. Mueller, T. W. Crowe, and R. M. Weikle II, "Resonant metal-mesh bandpass filters for the far infrared," Applied Optics, vol. 33, no. 25, pp.6046–6052, 1994.

[16] Kuznetsov, V. V. Kubarev, P. V. Kalinin et al., “Development and their application in high-power experiments at Novosibirsk of metal mesh based quasi-optical selective components S. A. terahertz FEL,” in Proceedings of the FEL, 2007.

[17] Y. Ma, A. Khalid, T. D. Drysdale, and D. R. S. Cumming, “Direct fabrication of terahertz optical devices on low-absorption polymer substrates,” Optics Letters, vol. 34, no. 10, pp. 1555–1557, 2009.

Design and simulation of Hybrid Renewable Energy System for on-grid applications

Ali S. Saleh[1], Rakan Khalil ANTAR[2], Ahmed J. Ali[3]
{ali.alhafidh@ntu.edu.iq[1], rakan.antar@ntu.edu.iq[2], ahmed.j.ali@ntu.edu.iq[3]}

Northern Technical University Technical Engineering College/Mosul, Iraq[1,2,3]

Abstract. A hybrid renewable energy system (HRES) refers to a system that uses a combination of RESs such as wind and PV solar energies to improve and increase energy production and system efficiency. Since one energy source is used to provide electricity, the other one may be available or unavailable. This study is dealt with the design and analysis of a grid connected HRES conversion based on PV solar and wind turbine energy sources that use a DC converter and a permanent magnet synchronous generator. The goal of this work is to suggest a better dc bus voltage regulation approach for PV/Wind power generation systems that are grid-connected. To get a maximum amount of power generation, a maximum power point tracking controller based on Perturb and Observation algorithm is used. This approach improves efficiency and reduces harmonic content problems. The THD value of the output voltage was 0.94%. The HRES is built and modelled by the MATLAB program.

Keywords: hybrid renewable energy system, solar cell, wind turbine, MPPT, Boost Converter, H-bridge inverter.

1 Introduction

The most pressing challenge in recent decades has been the efficient utilization of renewable energy sources. As a result of increased energy demand and limited fossil fuel resources, pollutants and save on fuel expenses have been reduced. Renewable Energy Systems (RESs) are getting popular and becoming more economically effective than traditional energy generation systems for supplying dependable energy in areas where conventional power grids are not available [1],[2]. RESs are inherently changeable and fluctuate, and often provide little power as compared to traditional power generation. As a result, to supply more dependable and sustainable energy, a way of combining varied sources is required [3]. A hybrid RES (HRES) is formed by the combination of multiple RESs, which provides continuous electricity to customers as opposed to a system that is based on a single source [4],[5]. Power converters are used in HRES to allow flexible and effective connectivity of RESs and to utilize in either grid-connected or standalone mode. Nonetheless, the HRES cannot deliver adequate and consistent electricity to fulfil the demand power due to the random and unpredictable nature of PV and wind systems [6]. To assure the HRES's dynamics, certain reliable power sources such a fuel cells (FC) [7], batteries, diesel generators, or super capacitors[8], must be included in the HRES particularly in "standalone" mode and in the utility in "grid-connected" mode. Various hybrid

IMDC-IST 2021, September 07-09, Sakarya, Turkey
Copyright © 2022 EAI
DOI 10.4108/eai.7-9-2021.2314947

grid-connected circuit topologies illustrated in Figure (1) depict the Wind/PV energy system [9]. Figure 1(a) illustrates a grid-connected hybrid Wind/PV generation system with two separate converters dc/dc/ac that is ac-shunted. Each of them can deliver the maximum amount of energy generated by the PV solar or wind turbine (WT). However, because solar and wind power are complementary, the circuit architecture depicts in Fig 1(a) may be simplified to another type as illustrated in Fig.1(b). The two dc-dc converters are relocated and linked in parallel. The overall power ratings of the two separate dc-ac inverters are larger than the output power of the dc-ac inverter for the dc-shunted grid-connected power system[10]. It has the potential to shrink the size and expense of the power system. However, the circuit architecture illustrated in Fig. 1(b) may be reduced even further, as illustrated in Fig. 1(c) where the two separate converters are replaced with a multi-input (MI) dc-dc converter.

The following survey gives an idea about some studies that deal with wind and solar units. In 2015 [11], a hybrid distributed generator topology based on solar and wind-powered PMSG was presented. Only one single boost converter and inverter are used to connect the sources to the grid. A model of the suggested strategy is created in the d-q axes reference frame. For the new hybrid scheme, two low-cost controllers are proposed to individually activate the converter DC-DC and the inverter. The generator's voltage and current THD meet IEEE's recommended power quality standards. In 2016[12], a hybrid power monitoring and management laboratory-scale system for micro-grids dependent on wind, solar, and batteries was suggested. The system is intended to regulate the operation of PV solar panels using MPPT. The wind energy conversion system (WECS) is managed by a feedback control rule for speed following. In 2017 [13], a hybrid renewable energy system was presented. Power converters are used to connect the wind turbine, solar panel, supercapacitor, and battery storage to a DC connection. To accomplish operating PowerPoint taking instead of MPPT, wind and solar sources are coupled to corresponding converters with a boost. In 2019 [14], two micro-grid-linked PMSG wind turbine systems were examined. In the first concept, a rectifier circuit with a filter-boost converter and a common DC bus is linked to the PV solar, WT, and batteries banks. In the second path, an inverter circuit is used to connect both the PV array and the storage batteries. The WT is connected to the three-phase AC directly via a back-to-back conversion and a step-down transformer. The first model, according to simulation findings, provides higher power quality and reduced voltage harmonics. The second model can provide more residential supply due to the performance of the advanced transformer and inverter. In 2020 [15], a solar-wind hybrid system was designed and analysed. The alternating energy of the wind generator is transformed to a constant DC value that may be utilized to charge the batteries or subsequently converted to AC voltage to operate AC loads using an AC-DC inverter. A boost converter based on the MPPT system is designed to extract the most power feasible. This method gives greater harmonic reduction. As mentioned in the previous study, a HERS shown in Fig. 2 is suggested and adopted in this study.

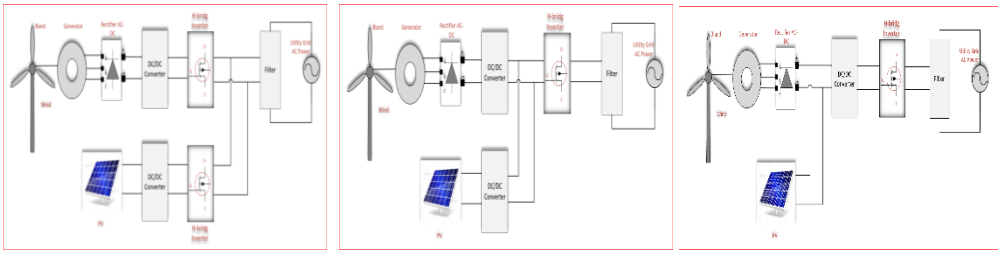

(a) (b) (c)

Fig 1. Circuit Topologies available For ON-Grid Utility Hybrid PV/Wind Power Plant generation system with (a) ac-shunting and (b) with dc-shunting. (c) MI grid-connected system.

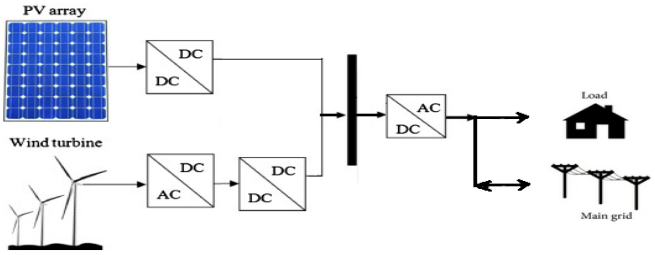

Fig 2. Suggested circuit of the wind- PV Hybrid System.

2 Design of Hybrid Wind/PV Power generation System

The planned HRES is divided into solar energy conversion, wind energy conversion system with PMSG, DC-DC converter based on MPPT algorithm, and full-bridge inverter with SPWM control. The suggested system's block diagram is represented in Fig. (3). The HRE with solar and wind systems is designed with two synchronous boost converters running in parallel. The two units are modelled and simulated by MATLAB software to generate an output voltage with low distortion. The implemented model has a low cost and a simpler design. The controller is configured to balance the H-bridge inverter input voltage by controlling the inputs of both the PV solar panel and the wind turbine through the boost converter by using the P&O MPPT algorithm. The following is a description of the complete system modelling.

2.1 Modelling of PV Cell

PV cells are basically like a large area p-n junction of the diode. The equivalent circuit of the PV cell is depicted in Fig(4). The PV cell mathematical model may be established using MATLAB/Simulink. The characteristics of the Solar PV (P-V and I-V curve) depicted in Fig.(5) is characterized according to the PV current equation below [16],[17].

$$I = I_{pv} - I_o\left[exp\left(\frac{q(V+I)}{N_{ser}\times K\times T\times a}\right) - 1\right] - \frac{V+I\times R_s}{R_{sh}} \quad (1)$$

where I_{pv} , V_t , I_o , a, R_{sh} , R_s, k, T, and q are PV current, array thermal voltage, saturation current, the ideality element of diode's, series and parallel resistance of the array, Boltzmann's constant, temperature, and the charge of electron respectively. The PV rating voltage can be increased through connects extra cells in series (U_{ser}), whereas the current rating can be improved by producing more parallel connections (N_p). Since R_s is low and R_{sh} is high, the panel's short circuit current is exactly equivalent to the PV panel current. Irradiation and temperature factors affect the current provided by PV, which is expressed as [18]:

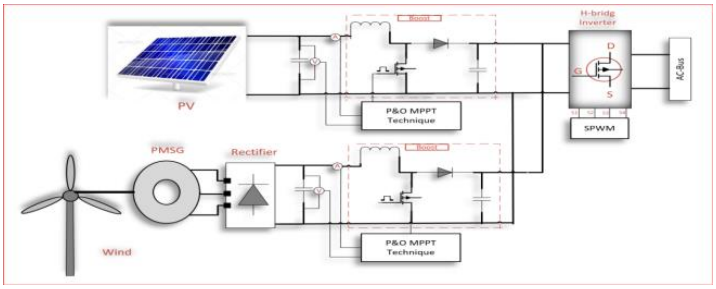

Fig 3. Suggested the system's block diagram for HRE.

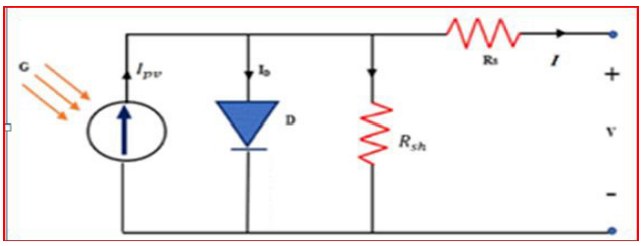

Fig 4. A photovoltaic cell's equivalent circuit

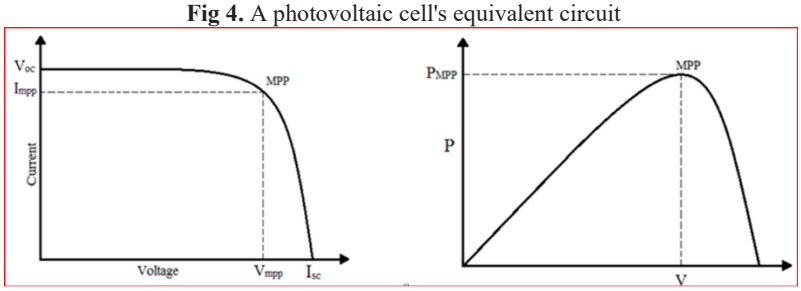

(a) (b)

Fig 5. (a) I-V, (b) P-V features of the PV cell

$$I_{pv} = \left(I_{pv,st} + K \times \Delta T\right) \frac{G}{G_{st}} \tag{2}$$

where $I_{pv,st}$, ΔT , G_{st} and G denote the induced current at normal temperature and irradiance of PV, temperature variation concerning typical one, standard irradiation, and irradiance.

$$I_o = I_{o,st} \left(\frac{T_{st}}{T}\right)^3 exp\left[\frac{q \times E_g}{n \times K}\left(\frac{1}{T_{st}} - \frac{1}{T}\right)\right] \tag{3}$$

where E_g, $I_{o,st}$, T and T_{st}, represent semiconductor bandgap energy, standard temperature, saturation current under standard conditions, and actual temperature, respectively [19]. Furthermore, $I_{o,n}$ can be written as:

$$I_{o,n} = \frac{I_{sc,n}}{exp\left(\frac{V_{oc,n}}{n \times V_{t,n}}\right) - 1} \tag{4}$$

2.2 Modelling of PMSG

The PMSG is created by projecting its equations onto a reference coordinate system that rotates in time with the magnet flux. A phase-locked loop (PLL) is utilized to synchronize the d-q rotating reference frame with the ABC three-phase frame [20]. After that, the following is a dynamic model of the surface-mounted PMSG [21].

$$V_{ds} = R_s.i_{ds} + L_s\frac{di_{ds}}{dt} - \omega.\Psi_{qs} \quad (5)$$

$$V_{qs} = R_s.i_{qs} + L_s\frac{di_{qs}}{dt} + \omega.\Psi_{ds} \quad (6)$$

Where L_s, R_s, w, Ψ_{ds}s and Ψ_{qs} are the generator inductance and resistance, electrical generator speed, and the d-q axis magnet flux, which are represented as follows:

$$\Psi_{ds} = L_s.i_{ds} + \varphi \quad (7)$$

$$\Psi_{qs} = L_s.i_{qs} \quad (8)$$

Where φ is the flux of the magnet. In the synchronous reference frame, the electrical model of PMSG may be represented as follows:

$$\frac{di_{ds}}{dt} = \frac{1}{L_s}\left(-R_s.i_{ds} + \omega \times L_s.i_{qs} + V_{ds}\right) \quad (9)$$

$$\frac{di_{qs}}{dt} = \frac{1}{L_s}\left(-R_s.i_{qs} - \omega.L_s.i_{ds} - \omega.\varphi + V_{qs}\right) \quad (10)$$

The electromagnetic torque of PMSG's non-salient poles is expressed as:

$$T_{em} = \frac{3}{2}.p.\varphi.i_{qs} \quad (11)$$

Where p is the number of pole pairs in the generator. Eq.(10) demonstrates that the q_{axis} current in the stator may be used to adjust the generator torque directly. The following statement may be used to define the mechanical dynamics model of the specified wind turbine system:

$$j_T.\frac{d\omega_r}{dt} + \mathrm{f}.\varphi_r = T_T - T_{em} \quad (12)$$

where T_T, j_T, f, $and\ \omega_r$ denoted as mechanical torque, a moment of inertia, coefficient of friction, and mechanical speed, which is connected to electrical rotating ω as follows:

$$\omega = \mathrm{p}.\omega_r \quad (13)$$

The WT dynamic model with PMSG is built using MATLAB/Simulink. The system has been implemented to make sure the model and the proposed control techniques. The input of the WT is wind, and the output is mechanical power that moves the generator rotor. The following formulae for a variable speed wind turbine provide the output mechanical power and torque generated by a wind WT turbine [22].

$$P_{mec} = \frac{1}{2}.\rho.\pi.R^2.C_p(\lambda,\beta).v_w^3 \quad (14)$$

$$T_{mec} = \frac{P_{mec}}{w_{mec}} \quad (15)$$

The power coefficient (C_p) for the WT is also a function of the tip speed ratio (λ), blade pitch angle (β) (in degree) which is defined by [23]:

$$C_p(\lambda,\beta) = 0.5\left(\frac{116}{\lambda_i} - 0.4 * \beta - 5\right) e^{-\frac{21}{\lambda_i}} \quad (16)$$

Where λ is defined to be the ratio between the turbine speed (w) and the wind speed (v_w) and is given by.

$$\lambda = \frac{R*\omega_m}{v_w} \quad (17)$$

Consequently, equation (17) can be used to calculate the mechanical angular speed of a turbine, which represents the relationship between mechanical and electrical torque, incorporating the generator and turbine masses:

$$J * {dw_{mec}}/{dt} = T_{elc} - T_{mec} - B_{mec}.* w_{mec} \quad (18)$$

Fig 6 shows the whole Simulink wind turbine model for wind turbines may be created using the equations descript from (13) to (15). This figure shows that for a certain wind velocity (v_w), the generated power by turbines (P_{mec}) is affected by the value of C_p, air density (ρ), and parameters of the turbine. The density of the air and the characteristics of the turbine (which are defined by the design) are constant [24]. As a result, in a turbine with a fixed blade pitch angle, the output power has been mostly depending on the value of C_p, which is determined by the wind turbine's rotor speed. As a result, when C_p is in the great value, the output power of the wind turbine is maximum. This ideal value of C_p occurs with various values of λ as shown in equation (16). For a given wind speed, there will be only one ideal rotor speed where the C_p is at maximum value. The factor C_{p_max} is obtained at optimal value of (λ_{opt}) to maximize the extracted power. Fig 7 shows C_p at its maximum value (C_{p_max}) and λ at its optimum value (λ_{opt}).

The amplitude and frequency of the voltage output from a PMSG vary for a variable speed wind turbine when the wind speed changes from time to time, while in this circumstance the generator power output should be stabilized. Therefore, PMSG with wind turbine in this configuration is linked to the DC bus through a three-phase rectifier, as illustrated in Fig 2. The WECS is connected to a rectifier followed by a filtered-DC boost converter circuit based on the MPPT algorithm and P&O method. The parameters of the wind turbine system with a PMSG, used in the simulation, are presented in Table 1. A PMSG WT is modelled in a Simulink environment as seen in Fig 8. The mechanical torque T_m is generated by feeding the wind and rotor speeds into the control block.

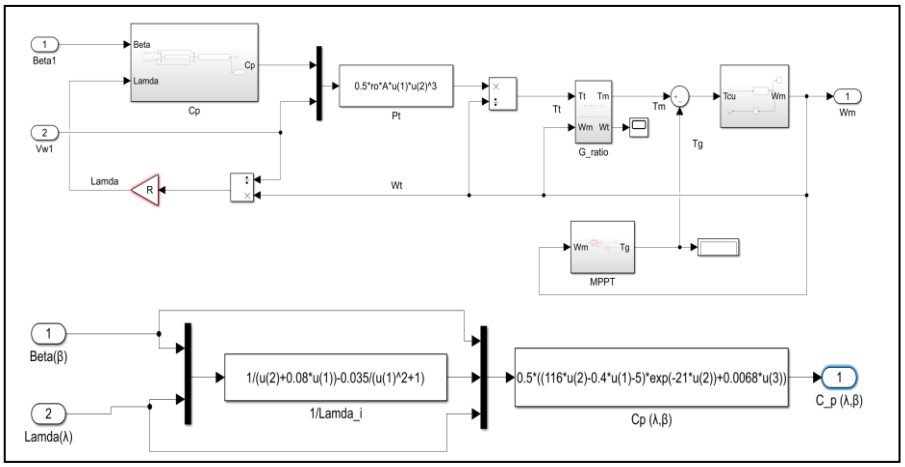

Fig 6. MATLAB Block Diagram of a Wind Turbine.

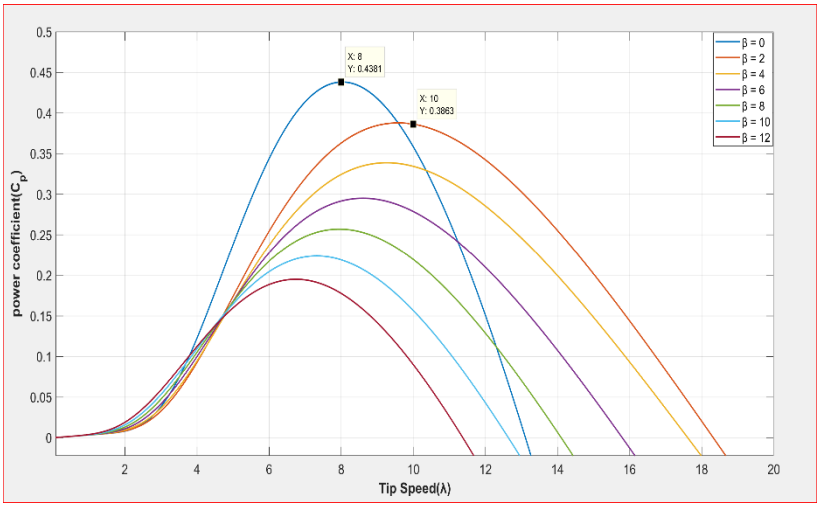

Fig 7. The maximum value of (C_p) and the optimum value of (λ).

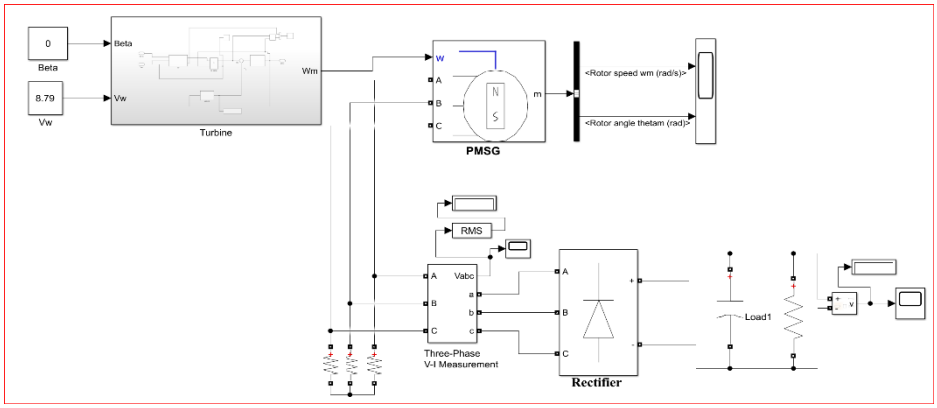

Fig 8. Modeling of the Turbine System using MATLAB.

Table 1. Simulation Parameters of the PMSM

Value	Parameters
1000 (w)	Rated power
1500 (rpm)	Rated speed
240 (V)	Output voltage
3	Number of phases
10	Number of poles
15	Number of coils
1.2 Ω	stator phase resistance,
0.000835H	Inductance
7[mm]	Thickness of PM
1000 (w)	Rated power

2.3 DC-DC Boost Converters

The boost converter circuit is often used as an interface device between load and PV panel, where the PV output is combined with the load to obtain maximum power. It converts the magnitude of the input DC voltages to variable DC voltages. The power circuit of the boost converter used in this study is shown in Fig (9). The duty ratio is used to regulate the output voltage provided by the boost converter circuit.

$$V_o = \frac{V_{in}}{1-D} \tag{19}$$

where D, V_{in} and V_o are duty ratio, input, and output DC voltage. The following calculations are used to quantify and choose the inductor and capacitor values of a boost converter [25].

$$L = \frac{V_{in}}{f_{sw} \times (\Delta I_l) D} \tag{20}$$

$$C = \frac{I_o}{f_{sw} \times (\Delta V_o) D} \tag{21}$$

Where ΔI_l , f_{sw} and ΔV_o are the ripple of input current, switching frequency, and output voltage ripple respectively. To increase utilization of the PV panel, A MPPT method is employed. As the power provided by these panels varies constantly with environmental conditions like temperature and irradiance, this technique is critical for ensuring the transition of the maximum power from PV to load. Many different techniques such as constant voltage, open voltage, P&O, neural network, fuzzy logic control, and incremental conductance have been developed to optimize the generation of solar energy [26]. These strategies vary in terms of difficulty, expense, level of effectiveness and tracking speed, popularity, hardware, and so on. An accurate cost analysis of this MPPT algorithm can be prepared by understanding the method (analogy or digital) used in the control system, the number of used sensors, and any additional power components, while keeping all additional costs (power components, electronic components, boards...) constant overall systems[27]. In this paper, the P&O technique is used because of its

simplicity and required only one sensor. The algorithm is formed by perturbing a small increment in voltage of PV and observing the power change. Figure (10) illustrates a flowchart of the P&O method [28].

2.4 Power Inverter

The inverter is an electrical circuit that enables a voltage to be applied in both directions along with a load. The H-Bridge is created by combining four solid-state switches and controlled based on the pulse width modulation (SPWM) method. A sinusoidal with a triangle waveform is compared to creating this sort of signal.

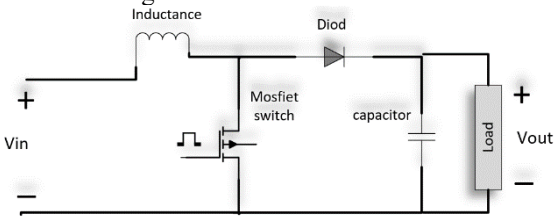

Fig. 9. Boost converter circuit.

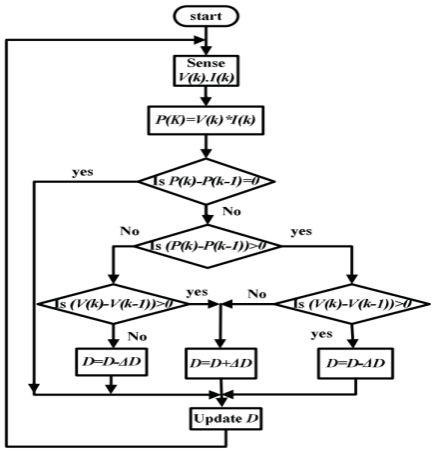

Fig 10. Flowchart of the PO algorithm[28].

3 Modelling and Simulation of Grid-Connected HREs

A circuit diagram of a dc/dc boost converter, filters for the dc bus, inverter (full bridge), and an abased controller is shown in Fig (11). The input dc-dc boost converter may transmit the electricity generated by the PV array and WT to the dc bus separately or simultaneously. If one of the energy sources fails, the other dc/dc boost converter can still transmit the required power to the dc bus from the other energy source. The MPPT functionality is available for both the PV array and the WT. The inverter creates a sinusoidal AC and injects it into the grid or load or both. A grid-connected hybrid may simultaneously supply energy to both the load and the utility grid at the same time. When it is linked to the grid, suitable power electronic controllers are necessary to manage voltage, frequency, and harmonic regulations, as well as load sharing. In

the proposed model, a grid is added with the model so that unused power can be supplied to the grid. The MPPT controllers are suggested for operating wind and PV generators at maximum power, which improves the amount of energy captured from wind speed and solar radiation. To optimize the output power of the PV and wind generator, an MPPT controller is P&O included in the system. The PWM inverter is used to maintain the inverter's output voltage at the rated voltage regardless of the output load. A voltage control strategy is proposed for this single-phase inverter to regulate the DC bus voltage to a constant value of 311V. The control loop is depicted in Fig (12). To fix the magnitude inverter voltage and synchronized with the grid, a comparison between the inverter output voltage and the grid voltage is made where the angle between the inverter's AC output voltage (Vinv) and the grid's AC voltage (Vgrid) is regulated by a single-phase lock loop to adjust inverter frequency with grid frequency. To modify the required output voltage, the reference grid side voltage can be established in the controller.

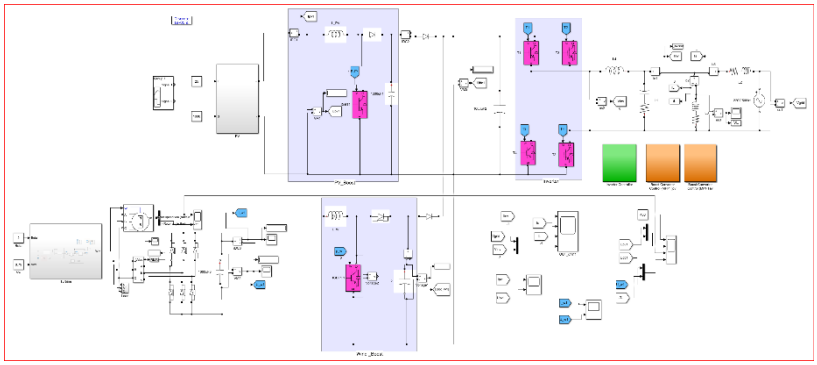

Fig 11. The architecture of a typical wireless sensor node.

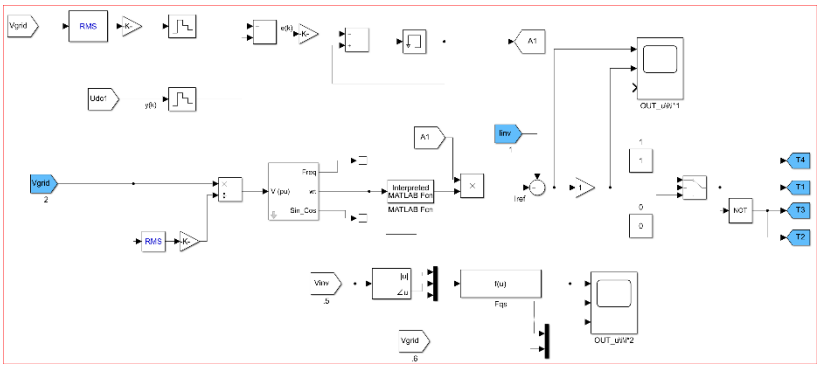

Fig 12. Control of Gating Signals for on-Grid Inverters.

4 Results of the Simulation

The HRES is simulated using MATLAB/Simulink software, where the work is divided into several stages, according to the load source fitted at standard test weather conditions, changing weather conditions, and the disturbance in the load (increase or decrease). In the first stage, the system is tested under standard weather conditions (1000W/m^2 insolation and 25℃ temperature), wind speed of 8 m/sec, and load value of 150 ohms. Figure 13 depicts the boost

converter's output voltage as well as the input voltage responses (PV and wind HREs). The graph demonstrates that the output voltage is relatively steady and equal to 311V. Fig 14 depicts the waveform of a centralized inverter of HREs supplies electric power to both the load and the utility grid. therefore, the phase difference between the inverter current and the grid current is 180 degrees. The output waveform of the inverter (V_{inv}) is synchronized with the grid voltage. The total inverter current is 10A, where the load is consumed 2A, and 8A is sent to the grid when the load is 150 ohms. Under the same conditions, the system is tested when a disturbance occurs on the load (decreasing resistance to 70 ohms). Fig 15 shows the waveform of the load current that consume 4.4A and the grid that draws 5.6A

Finally, it is assumed a natural fluctuation occurs on the renewable energy sources which cause a reduction in the generated power of wind/ PV sources. The decrease in renewable power is achieved due to fluctuations in weather conditions (irradiation, temperature, and wind speed). HREs and grid currents are used to supply the load in this scenario. The system is simulated under the weather conditions (400W/m^2 insolation and 25C temperature) and wind speed (3m/sec – 21.5 rad/sec). This leads to the load current is greater than the inviter current. The boost converter output and the input voltage responses (PV and wind HREs) at 70ohm are illustrated in Fig 16. This figure illustrates that the output voltage is constant and equal to 311v, while the inverter current of HREs and grid current are sharing between them to supply the load with the required power. The waveform of the output voltage for the inverter (V_{inv}) is synchronized with the grid voltage as shown in Fig 17a. The total load current, inverter current, and grid current at a load of 70 ohms are 4.4A, 2.8A, and 1.6A, respectively. Figure (17b) shows the FFT analyser for voltage and current of the output inverter.

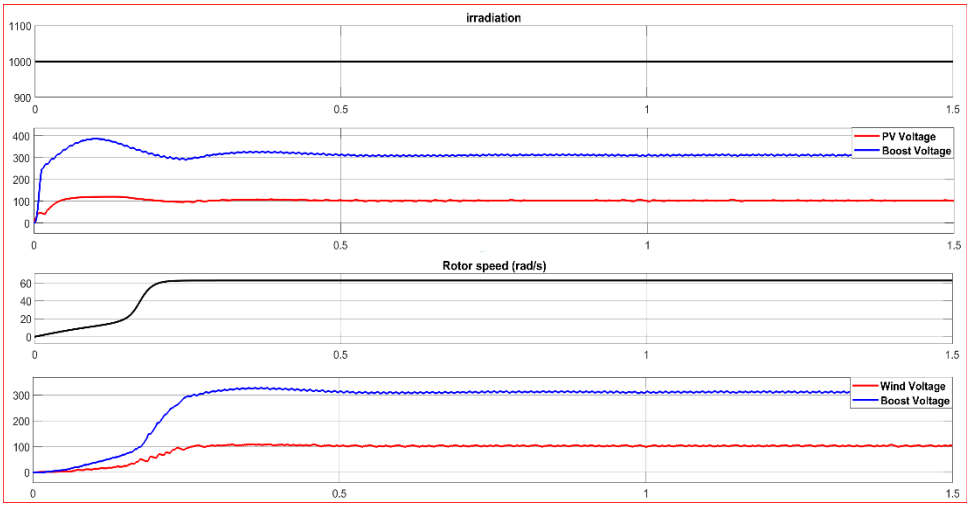

Fig 13. Input and Output Voltage Response of the Boost Converter Based on PV and Wind HRES.

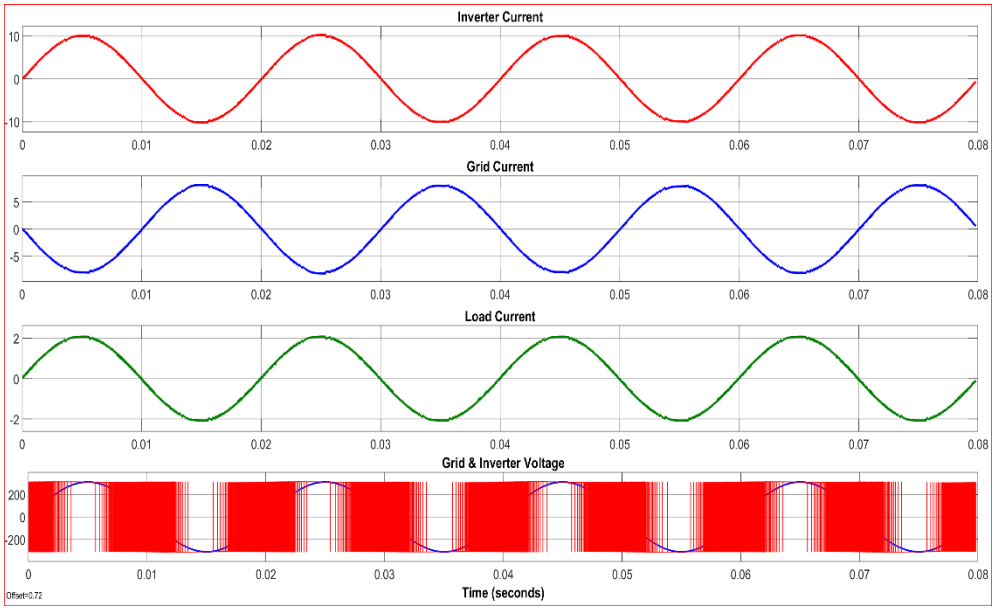

Fig 14. HREs Currents that Supplies Load and Grid with Voltage Centralized with an inverter at 150ohm.

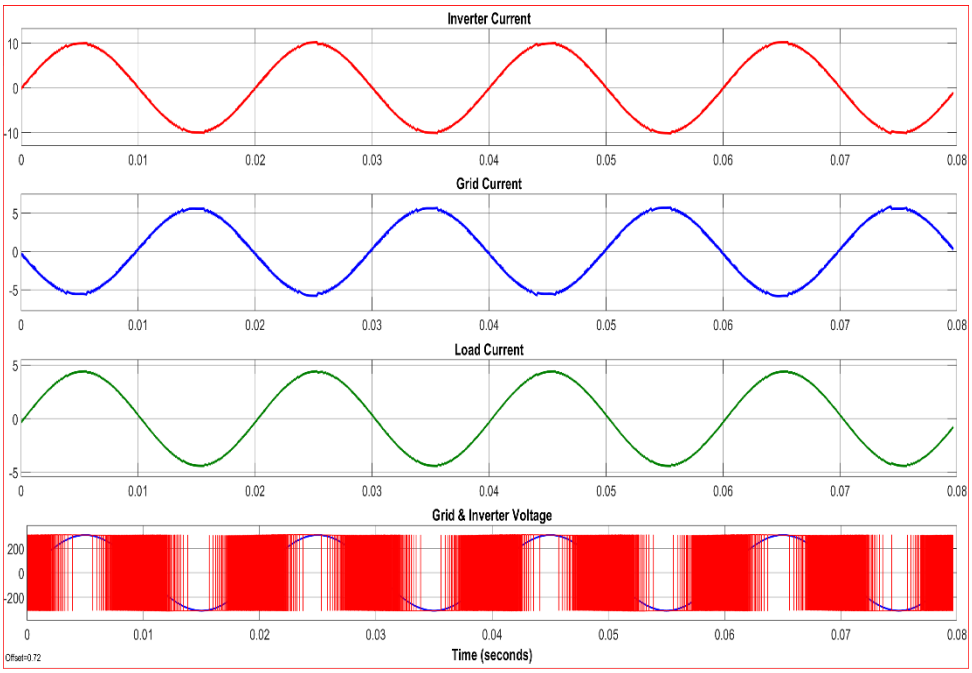

Fig 15. HREs Currents that Supplies Load and Grid with Voltage Centralized with an inverter at 70 ohms.

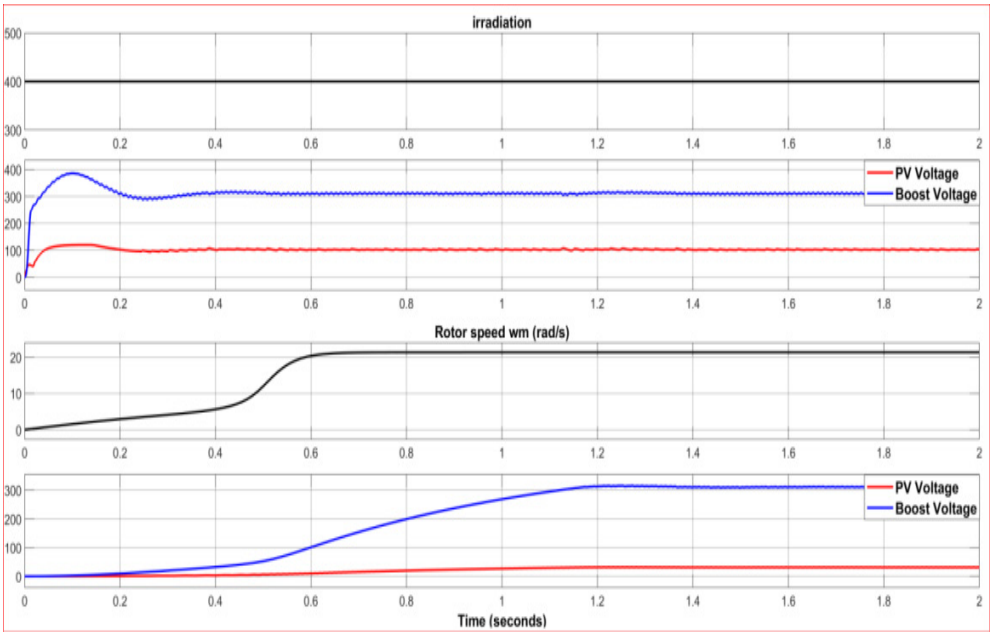

Fig 16. Input and Output Voltage of the Boost Converter.

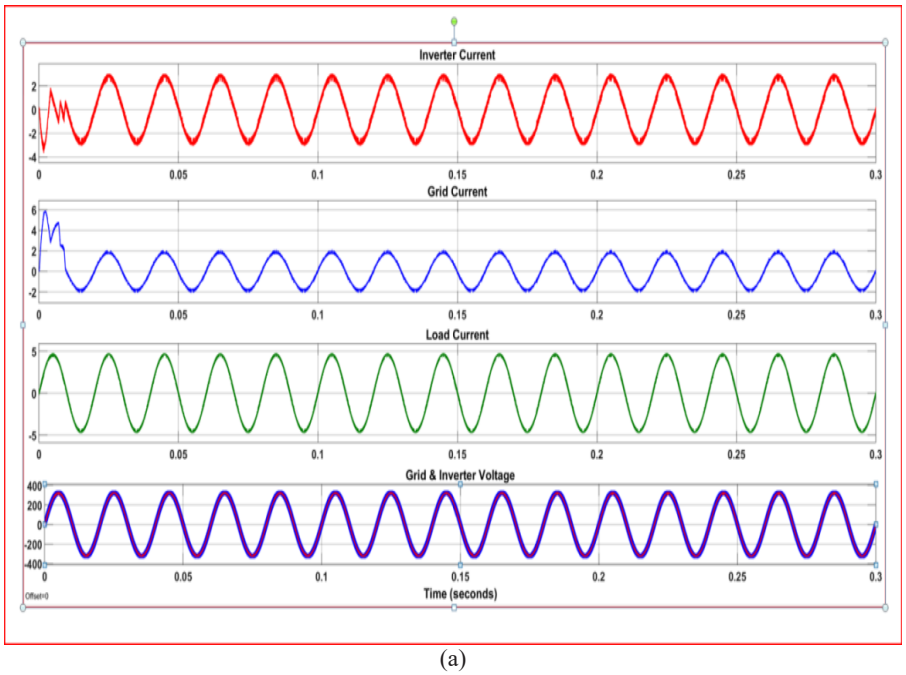

(a)

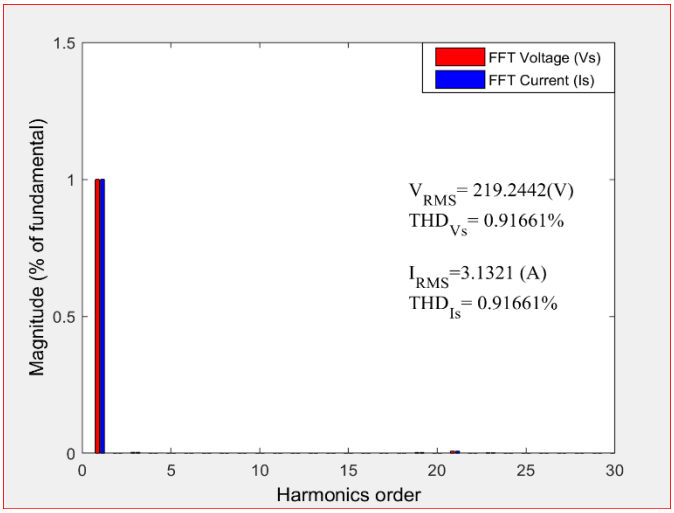

(b)

Fig 17. (a) HREs and grid currents sharing to supply load, (b) FFT analyser of inverter output voltage and current.

5 Conclusion

In current work, an HRES which is consists of two types of RESs (PV module and a wind turbine connected by PMSG) has been designing and simulated to compensate for the deficit that occurs, as well as to reduce the cost of preparing the electric power generated by the traditional electric power system. Also. It is used to improve the quality and quantity of the generated power. The generated power of the PV module is connected to the load via a common DC bus that links through a DC-DC boost converter. While the WT PMSG is connected directly to the DC bus side through a separate DC-DC boost converter after converting the AC output of the PMSG to DC by using a three-phase rectifier. In addition, two separate MPPT algorithms are used to maximize the generated power from the two RES. The output power of the two boost converters is connected to the common DC bus to supply a single phase SPWM inverter that is used to feed a generated power to the load. The hybrid system is modelled using MATLAB/Simulink. To check the ability of the suggested HRES to supply the shortage in the required power, different operating conditions are considered. Three PV modules are selected and connected in series to get an input voltage of 110V. To adjust the output voltages of both PV and wind turbine generators, the MPPT algorithm based on the P&O technique has been used. In addition, an SPWM technique has been used to produce the gate signals of the single-phase inverter. The system is tested with varying input parameters of solar radiation, wind speed, and temperature. The obtained results show that the simulated model has acceptable performance, and it is having the ability to fill the shortage in the supply of electricity. Moreover, the THD values of the simulated systems are lay within standards limits.

References

[1] Ali, A. J., Suliman, M. Y., Khalaf, L. A., Sultan, N. S., "Performance investigation of stand-alone induction generator based on STATCOM for wind power application", International Journal of

Electrical & Computer Engineering, (2088-8708), 10(6), 2020.

[2] A. Ghafoor and A. Munir, “Design and economics analysis of an off-grid PV system for household electrification,” Renew. Sustain. Energy Rev., vol. 42, pp. 496–502, 2015.

[3] B. L. Yong, D. B. Chia, R. K. Rajkumar, V. K. Ramachandaramurthy, and J. Pasupuleti, “Operation and management of an islanded mode hybrid power system e a Malaysian perspective,” 2010.

[4] R. K. Rajkumar, V. K. Ramachandaramurthy, B. L. Yong, and D. B. Chia, “Techno-economical optimization of hybrid pv/wind/battery system using Neuro-Fuzzy,” Energy, vol. 36, no. 8, pp. 5148–5153, 2011.

[5] P. Thounthong, S. Sikkabut, P. Sethakul, and B. Davat, “Control algorithm of renewable energy power plant supplied by fuel cell/solar cell/supercapacitor power source,” in The 2010 International Power Electronics Conference-ECCE ASIA-, 2010, pp. 1155–1162.

[6] A. N. Hussain, A. J. Ali, F. S. Ahmed,"Power quality improvement based on hybrid coordinated design of renewable energy sources for DC link channel DSTATCOM", International Journal of Electrical & Computer Engineering, (2088-8708) 10.5 (2020).

[7] Rakan Khalil Antar, Nashwan S. Sultan, Ahmed J. Ali, "Speed Control of Three-Phase Induction Motor Fed by Renewable Energy Source", 2nd International Conference on Electrical, Communication, Computer, Power and Control Engineering (ICECCPCE), Mosul, Iraq, IEEE 2019, pp.7–12, doi:10.1109/ICECCPCE46549.2019.203739.

[8] G. Tian, X. Ding, and J. Liu, “Study of control strategy for hybrid energy storage in wind-photovoltaic hybrid streetlight system,” in 2011 IEEE international workshop on open-source software for scientific computation, 2011, pp. 77–81.

[9] Y.-M. Chen, C.-S. Cheng, and H.-C. Wu, “Grid-connected hybrid PV/wind power generation system with improved DC bus voltage regulation strategy,” in Twenty-First Annual IEEE Applied Power Electronics Conference and Exposition, 2006. APEC’06., 2006, pp. 7-pp.

[10] Rakan Khalil Antar, Basil M. Saied, Rafid A. Khalil, “Using seven-level cascade H-bridge inverter with HVDC system to improve power quality”, First National Conference for Engineering Sciences (FNCES), Baghdad, Iraq, IEEE, pp. 1-7, 2012, doi:10.1109/NCES.2012.6740457.

[11] M. M. R. Singaravel and S. A. Daniel, “IEEE TRANSACTIONS ON INDUSTRIAL ELECTRONICS MPPT with Single DC-DC Converter and Inverter for Grid Connected Hybrid Wind-Driven PMSG-PV System,” vol. 0046, no. c, 2015, doi: 10.1109/TIE.2015.2399277.

[12] A. Merabet, K. T. Ahmed, H. Ibrahim, R. Beguenane, and A. M. Y. M. Ghias, “Energy management and control system for laboratory scale microgrid based wind-PV-battery,” IEEE Trans. Sustain. energy, vol. 8, no. 1, pp. 145–154, 2016.

[13] R. Sharma and S. Suhag, “Novel control strategy for hybrid renewable energy-based standalone system,” Turkish J. Electr. Eng. Comput. Sci., vol. 25, no. 3, pp. 2261–2277.

[14] K. Tazi, M. F. Abbou, and F. Abdi, “Performance analysis of micro-grid designs with local PMSG wind turbines,” Energy Syst., pp. 1–33, 2019.

[15] G. M. S. U. Al-Mamun, M. R. Hasan, M. I. Hossain, A. A. Atik, S. M. D’ Al Jubair Hossain, and A. R. A. S. M. Costa, “Design and Analysis of a Solar-Wind Hybrid System.”

[16] A. S. Saleh, R. K. Antar, and A. J. Ali, “Design and Implementation of Single-Phase PV Power System,” Ann. Rom. Soc. Cell Biol., vol. 25, no. 6, pp. 12078–12087, 2021.

[17] H. M. Ridha, C. Gomes, H. Hizam, M. Ahmadipour, D. H. Muhsen, and S. Ethaib, “Optimum design of a standalone solar photovoltaic system based on novel integration of iterative-PESA-II and AHP-VIKOR Methods,” Processes, vol. 8, no. 3, 2020, doi: 10.3390/PR8030367.

[18] A. M. T. IbraheemAlnaib, “Simulation and Characteristics Study of Solar Photovoltaic Array using Matlab/Simulink,” J. Tech., vol. 29, no. 1, 2016.

[19] M. T. Chughtai, “Temperature compensated bias supply circuit for photodiodes,” Przegląd Elektrotechniczny, vol. 94, no. 10, pp. 207–209, 2018.

[20] S.-K. Chung, “Phase-locked loop for grid-connected three-phase power conversion systems,” IEE Proceedings-Electric Power Appl., vol. 147, no. 3, pp. 213–219, 2000.

[21] F. Khater and A. Omar, “A review of direct driven PMSG for wind energy systems,” J. Energy

Power Eng., vol. 7, no. 8, 2013.
[22] H. I. Karim Belmokhtar and M. L. Doumbi, “A Maximum Power Point Tracking Control Algorithms for a PMSG-based WECS for Isolated Applications: Critical Review,” Wind Turbines Des. Control Appl., p. 199, 2016.
[23] S. H. Chichester and J. Hindmarsh, “Grid integration of wind energy conversion systems,” Wiley, 385p, 1999.
[24] Z. M. Abdullah, A. M. T. I. Alnaib, and O. T. Mahmood, “Design of Wind Turbine Energy System Based on Matlab/Simulink,” Eng. Tech. J., vol. 32, 2014.
[25] E. Mattos, A. M. S. S. Andrade, G. V. Hollweg, J. R. Pinheiro, and M. L. da Silva Martins, “A review of boost converter analysis and design in aerospace applications,” IEEE Lat. Am. Trans., vol. 16, no. 2, pp. 305–313, 2018.
[26] T. C. C. Saibabu and J. S. Kumari, “Modeling and simulation of pv array and its performance enhancement using MPPT (P&O) technique,” IJCSCN, vol. 1, pp. 9–16, 2011.
[27] J. Chauhan, P. Chauhan, T. Maniar, and A. Joshi, “Converters Based Photovoltaic Systems,” pp. 476–481, 2013.
[28] B. Sah and G. V. E. S. Kumar, “A comparative study of different MPPT techniques using different dc-dc converters in a standalone PV system,” in 2016 IEEE Region 10 Conference (TENCON), 2016, pp. 1690–1695.

Smart energy management of Wind/PV/Battery renewable energy sources based on IoT

Ahmed Abdul Nasser[1], Emad Ahmed Mohammed[2], Ahmed Jadaan Ali[3]
{ahmednaser@ntu.edu.iq[1], e.a.mohammed@ntu.edu.iq[2], ahmed.j.ali@ntu.edu.iq[3]}

Northern Technical University /Technical Engineering College/Computer Engineering Technology, Mosul, Iraq[1,2]

Northern Technical University /Technical Engineering College/ Electrical Power Technology Engineering Mosul, Iraq[3]

Abstract. The smart grid allows consumers and utility grids to communicate, allowing for the most efficient use of generated energy based on environmental, price, and system technical factors. One of the primary advantages of this system is energy management, which is carried out in conjunction with the internet of things (IoT), with real-time monitoring of devices and control data processing. The purpose of the Internet of Things in this project is to build a smart control system to manage generated electricity among several Nano grids by remotely monitoring generated and used power. A set of multi-function sensors is used to wirelessly sense real-time data and convert it into the necessary format, as well as to help move the sensed data over the network cloud via the 'Internet Connection'. Several slave nodes are present in a microgrid (SN). Every SN serves as its own grid (Nano grid), with two or three independent renewable energy sources connected to the master node of the central control unit (MN). To assure a satisfactory outcome, a prototype was built using solar cells and wind turbines as power sources, with an ARDUINO microcontroller managing and controlling power transfer between slave nodes. The practical results showed a good match between the simulated and practical results.

Keywords: IoT, Photovoltaic, Wind turbine, hybrid energy, energy management

1 Introduction

The growth in building in addition to increase the in population leads to an increase in the demand for electric power to fill the request. This means that CO2 emissions from fossil fuels will increase, resulting in more pollution and harm to the environment. However, fossil fuels such as oil, coal, and natural gas are only available in finite quantities. Because it is necessary to keep extracting them, fossil fuels will eventually run out. Although fossil fuels are produced by natural processes, they do not replenish as quickly as they are consumed by humans. As a result, creating energy from these resources has a significant negative impact on our ecosystem, contaminating our air, land, and water. Renewable energy has grown at a higher rate than all other energy sources since 2011. Renewable energy enjoyed again another record-breaking year in 2019 [1], with installed power capacity increasing by more than 200 Gigawatts (GW), the

greatest increase in history. Renewable energy comes from natural resources that renew in less than a human lifetime without diminishing the planet's resources. Sunlight, wind, rain, tides, waves, biomass, and thermal energy stored in the earth's crust are all resources that are available in some form or another almost everywhere. They're practically indestructible. What's more, they have little impact on the climate or the ecosystem. There have been international campaigns to promote self-sufficient renewable energy systems. This approach has resulted in the development of renewable power generation systems that can generate self-sufficient power using multiple renewable energy sources [2-3]. The most often employed hybrid renewable energy sources are solar and wind energy [4-5]. Because both of these sources of energy are intermittent, an energy storage system (ESS) is required in off-grid applications [6-7]. To ensure an effective transfer of generated power, multiple control mechanisms are used to govern the functioning of hybrid renewable energy systems. The type of energy conversion system and the type of converters utilised at various points in the system determine the system design [8-10]. The microgrid in DC. DC loads and resources make up the majority of a DC microgrid. [11,12]. Pumps, heating, ventilation, and air conditioning (HVAC) systems, fans, elevators, mills, and traction systems all employ DC power in Variable Speed Drives (VSD)[13]. AC Microgrids is the second. Due to the ease with which voltage levels may be changed using low-frequency transformers and the ease with which faults and protection can be handled, this system has dominated the DC system for many years. Furthermore, AC electricity is simple to transport, and most industrial gadgets require AC power. In recent years, AC RESs like as wind turbines, tidal, biogas, and wave turbines have been combined with AC Microgrids [14]. [15]. Hybrid-AC/DC-Microgrid is the third type. This structure combines the advantages of AC and DC microgrids, making it easier to connect AC and DC loads to their respective sources[16].These Microgrids need to be managed monitor and controlled by the central unit to regulate resources and chose appropriate one or combine two sources to meet the demand of the microgrid this operation can be done by using IoT protocol. The Internet of Things (IoT) is concerned with the management of data among devices on a network frame that is available. The Internet of Things (IoT) is a new technology that allows devices to connect with one another via the cloud. IoT embedded devices can provide enhanced functionality while avoiding the complexities of traditional computer-based systems. These systems communicate with the real environment using sensors, and actuators [17][18], kinds are given in Fig 1. IoT devices are used in both hardware and software components, such as Arduino and Raspberry Pi. Over the last few years, the Internet of Things (IoT) has been increasingly popular. The technology itself allows the user the flexibility to a free or paid term for the use of the internet cloud memory. The Internet of Things (IoT) refers to physical objects that are linked to wired and wireless networks [19] via an application programming interface (API). IoT is employed in a variety of industries besides consumer electronics and appliances, including smart cities, healthcare, smart homes, smart cars, smart grid systems, and a variety of other industrial applications [20]. The IoT protocol and microcontroller can be applied to monitor and control the power generation source and connect the sensed parameters like voltage, current and power signals to an application. In [21] IoT is used to produce a cheap solar monitoring system, where this example gives an idea about how to deal with other types of power sources. In [22], the authors proposed an Intelligent Smart Energy Management Systems (ISEMS) architecture for demand-side energy management that takes renewable energy into account. PV-generated data is collected for prediction models in the proposed structural design, which also includes a smart energy management system for load scheduling and an IoT environment enabling the user to access energy details and control. This setup will demonstrate the use of a microcontroller and the Internet of Things protocol to control and monitor several nodes. The authors of the [23] study concentrated their efforts on leveraging

IoT to control hybrid energy systems. There are different structures for connecting hybrid renewable energy sources that are all alternatives to one another, such as solar energy, wind energy, biofuel, fuel cell, and so on. When hybrid energy sources are deployed for household or commercial use, they must be controlled. As a result of this, the Internet of Things plays a significant role in regulating power flow in the electric system. The issue in demand-side energy management, according to [24], is to maximise the use of renewable energy while reducing power usage. In a smart grid setting with high renewable penetration, an Intelligent Smart Energy Management System (ISEMS) is proposed to address energy demand. The suggested approach compares a number of prediction models for precise energy forecasts with hourly and daily planning. In terms of performance accuracy, the PSO-based SVM regression model outperforms various other prediction models. Finally, using the projected data, the ISEMS experimental set-up is demonstrated and assessed with several settings that include user comfort and priority aspects. Integration of the IoT ecosystem is also being developed for user monitoring. In This paper we use inexpensive board and sensors to reduces the cost of the system instead of using expensive and large component for the same purpose. System parts are Arduino UNO board, NODMCU, voltage sensor ,current sensor and ESP8266 Wi-Fi Module that helps to process and transfer the sensed data to the Thing speak Cloud. The control unit computes the value loads of all SNs, then it sends a control orders to manage the power among the nodes that had a shortage in its generated power.

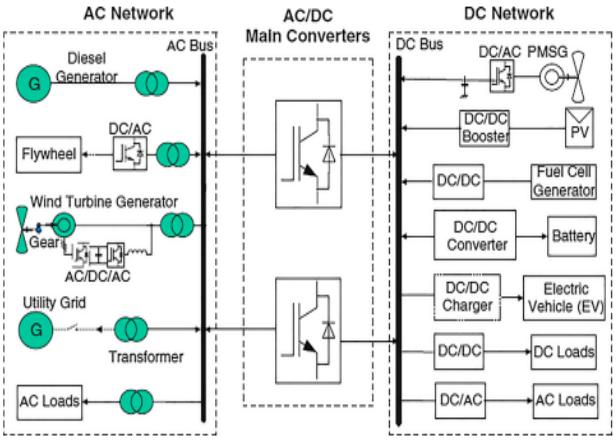

Fig 1. types of microgrid [12]

2 Structure of Energy Management System

In the current work, a stand-alone power system has a Microgrid, which is considered as a master node (MN) with three slave nodes (Nano grids), is considered as a base unit for the energy management system. A PV module is connected to the load via a DC-DC boost converter and common DC-bus system. While the wind turbine generator is connected to the load through an AC-DC converter and common DC-bus. In the following paragraphs a brief description of each component of a microgrid.

2.1 Photovoltaic

The photovoltaic module consists of photovoltaic cells that are connected in parallel and series [25]. These cells are p-n junctions that are fabricated in thin-film semiconductors such as silicon that enables to converts the light energy into electricity [26]. As the cell exposed to light energy, the photon that hits the cells will be absorbed by semiconducting material as the electron will be flow and creating electricity [27]. An ideal PV cell is modelled as a single diode circuit as shown in Fig 2. The current I_{PH} represents the photocurrent of the cell [28]. I_O represents the PV saturation current and while R_{sh} and R_s both are intrinsic shut and series resistances of the cell respectively. Both value of R_{sh} and R_s are always neglected to simplify the analysis due to the value of R_{sh} is very large and R_s is very small [29]. To have a high value of voltage and current, PV cells are connected to form a module that is usually covered by a cover of glass and mounted together. Then, when the modules are connected parallel and series configurations, they form a PV array. Equus (1 -8) below shows the mathematical model of the PV panel [30-31]

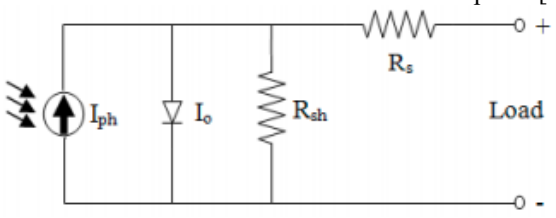

Fig 2. DC equivalent model of solar cell [32].

Thermal Voltage Equation

$$V_T = V_B T_{OPT} / q \quad (1)$$

Diode Current Equation

$$I_D = N_p I_S [e^{\left({}^{V}/_{N_s} \right) + \left({}^{IR_S}/_{N_s} \right) N V_T C} - 1] \quad (2)$$

Load Current Equation

$$I_L = I_{ph}\, N_p - I_D - I_{SH} \quad (3)$$

Photocurrent Equation

$$I_{ph} = [K_i \ (T_{OPT} - T_{REF}) + I_{SC}\ ]\ I_{RR} \quad (4)$$

Shunt Current Equation

$$I_{SH} = (IR_S + V)/ R_{SH} \quad (5)$$

Reverse Saturation Current

$$I_S = [I_{RS} \ (T_{OPT}/T_{REF})^3 * q^2 \text{ Eg } /\text{N} K_B * e^{(1/T_{OPT} - \ 1/T_{REF})} \quad (6)$$

Reverse Current Equation

$$I_{RS} = I_{SC} / [e^{\left(\frac{qV_{oc}}{KCT_{OPT}}\right)} - 1] \quad (7)$$

Output Power

$$P=VI \tag{8}$$

The MATLAB Simulink software is used to construct the design of a Photovoltaic based on (1-8) equations explained in Fig 3. Where: V I stands for Thermal Voltage, while V stands for Operating Voltage. Junction Voltage (V-J). Open Circuit Voltage (V-OC). I PH: Irradiation and junction temperature photocurrent function. I S : Diode Reverse Saturation Current. Short Circuit Current (ISC)). CELL OUTPUT CURRENT (I) T (RFE): Cell's Reference Operating Temperature. T (option): Cell Operating Temperature (°C). Shunt Resistance of Cell (R sh). R (S): Cell Series Resistance. For instance, consider the Energy Band Gap. N is the Optimal Factor. Boltzmann constant (1.38 10^{-23} J/K): K (B). Current proportionality constant (2.2*10^{-3}), K (i). K (V) = Constant of Voltage Proportionality (73*10-23).
q is the charge of an electron (1.602 x 10^{-19} C). N (S) is the number of cells in a series. N (P): Number of parallel cells.
Irradiance (1000W/m^2). G: Irradiance (1000W/m^2). C is the number of cells in a module.

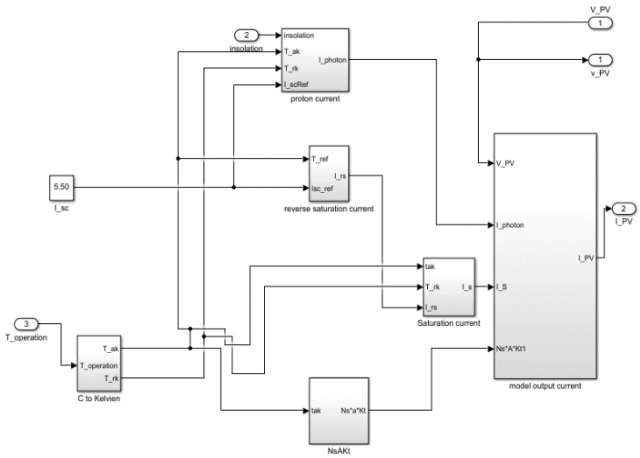

Fig 3. Solar panel construction using MATLAB Simulink.

2.2 Wind Turbine Generator

Wind energy is converted into electricity using a wind turbine generator. The rotor, which includes the blades and is connected to the generator through a shaft to convert wind energy to low-speed rotational energy, is one of the three basic components of a wind turbine system. The second component is the generator, which consists of the electrical generator, which includes all control circuits as well as a gearbox that converts the rotating low speed into electric power, and finally, the tower and nacelle, which houses all of the previous components. The axis on which a wind turbine revolves can be classified into two groups. There are two types of axes: horizontal and vertical. The horizontal axis is more familiar and frequent than the vertical axis because it can capture the most amount of wind energy for the time of day and alter its blade pitch angle to avoid high windstorms. (32-33). A wind turbine turns the energy contained in moving air into

electricity. As indicated in Eqs. (9-11), air density, power coefficient, air density, and turbine swept area are all factors that affect the captured energy,

$$P_m = 0.5 \times \rho \times C_P \times V_m \times A \quad (9)$$

A wind turbine's tip speed ratio (TSR) is defined as:

$$\lambda = (w_m \times R) / V_m \quad (10)$$

The rotor power coefficient, represented by Cp, is calculated using the TSR and blade pitch angle β. The rotor power coefficient can be determined using the following formula:

$$C_P = P_{\text{rotor}} / Pwind \quad (11)$$

Where P = Mechanical power in the moving air (Watt). ρ = Air density (kg/m³). A = Area swept by the rotor blades (m²). V = Velocity of the air (m/s). C_P = Power coefficient. P_{rotor} =Extracted power.
$Pwind$ =Power in wind

2.3 Permanent Magnet Synchronous Generator (PMSG) Model

The dynamic model of PMSG can be represented in the Park's (d, q) system using the following equations (12-14):

$$\begin{bmatrix} v_d \\ v_q \end{bmatrix} = -\begin{bmatrix} R_s & 0 \\ 0 & Rs \end{bmatrix} \begin{bmatrix} I_d \\ I_q \end{bmatrix} - \begin{bmatrix} L_s & 0 \\ 0 & Ls \end{bmatrix} \frac{d}{dt} \begin{bmatrix} I_d \\ I_q \end{bmatrix} - w_e \begin{bmatrix} 0 & -L_q \\ L_d & 0 \end{bmatrix} \begin{bmatrix} I_d \\ I_q \end{bmatrix} + w_e \begin{bmatrix} 0 \\ \Psi_m \end{bmatrix} \quad (12)$$

Where
R_s is the stator resistance (Ω)Ld and Lq are the inductances (H) of the generator on the d and q axis respectively Ψ_m is the permanent magnetic flux (Wb) and We is the electrical rotating speed (rad/s) of the generator, defined by:

$$w_e = P \times Wm \quad (13)$$

The number of generating pole pairs is denoted by P. The electromagnetic torque equation is calculated as follows:

$$C_{em} = \frac{3}{2} \; p\,[(L_d - L_q)\, I_d\, I_q - \Psi_m\, I_q] \quad (14)$$

design of the construction Wind Turbine Generator is shown in Fig 4.

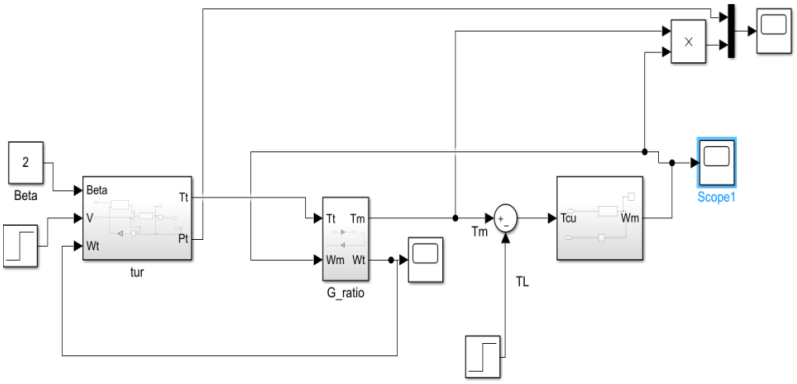

Fig 4. Wind Turbine Generator construction using MATLAB /Simulink

3 Methodology

Figure 5 depicts the planned smart energy management system for the smart grid. Two different units make up the generation system: a PV modular unit and a tiny wind turbine direct-drive PMSG unit. On the other hand, the load side has a number of DC units with varying power ratings. To provide a constant supply of power to the load, the two units (supply-demand) are connected via a direct DC line system. However, a hybrid energy system (HES) with multiple types of renewable energy sources should be established to provide a continuous supply of power when renewable energy sources are unavailable. One of the primary issues that the HES faces is the capacity to meet load demand even when the generated electricity from renewable energy sources varies dramatically owing to weather conditions. Another issue that these HES have to deal with is keeping the voltage and frequency ratings within acceptable levels. The Smart grid is made up of several Microgrids, each of which is made up of multiple Nano grids. There are two types of control in a Nano grid structure: supply-side management (SSM) and demand-side management (DSM) (DSM). Photovoltaic modules, small-scale wind turbines, batteries, the utility grid, and other power sources are examples of supply for the Nano grid. The demand is the amount of energy consumed by household loads such as refrigerators, televisions, and heaters. Both supply and demand are extremely volatile, typically fluctuating between maximum and minimum consumption/production in a single day.

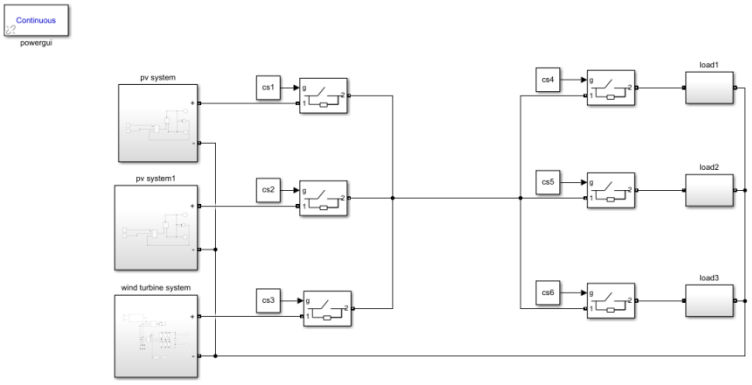

Fig 5. smart energy management system.

Unfortunately, in an unregulated Nano grid system, high consumption and production times rarely coincide. As a result, supply/demand management is an important component of Nano grid control. Supply-side management is used to improve the behaviour of the Nano grid's power sources in order to best match power production to the consumption curve and to maximise the utilisation of renewable energy sources. Demand-side management is used to match the power output of the Nano grid's sources to the consumption curve of the Nano grid's loads. It is feasible to develop and promote new energy services to address national society's challenges, such as the continual rise in energy demand, avoiding power peaks, and dealing with future trends. This can be accomplished by creating energy IoT-based energy management services, distributed energy paradigm development, and energy grid-based energy trading services[34]. To enable smart grid interoperability and other extra services, it is important to design a web connectivity service implementation environment. Master nodes serve as a centralised controller and manager for Microgrids, collecting data from all Nano grids (slave nodes) on the system's power output and consumption. All control decisions are made from a master node. If any Nano grids (slave nodes) are in short supply and require additional power, the master node will look for a suitable slave node to fill the gap. The master node reads parameters in real time, allowing the system to respond quickly to commands. And a slave node that represents homes, buildings, and other structures that have renewable energy sources by using sensors to measure voltage, current, power consumption, and power production, and a parameter called needed power if the node can't meet the demand and the load is above its maximum capacity. The slave node, on the other hand, receives signals from a master node in the event that another slave node requires power, and then uploads the requisite order to the internet's cloud. The master node can then read it and act in accordance with the reads, since IoT is a wide-ranging system of everyday detailed things connected to the internet that are capable of identifying themselves and informing data to objects on an internet network. When the slave node is connected to the internet, it begins to read sensor values, voltage, and current, as well as calculate power, extra power, which represents the power of the node that is not in use and can be shared with the node that is, and needed power, which represents the power required to meet the node's needs due to a power shortage. It can be calculated by subtracting consumed power from System capacity, which is the maximum power the system can generate, and needed power, which represents the power required to. After computing these numbers, it uploads them to the cloud through the internet. The slave node continuously checks for a signal from the master node indicating that their node requires power, as shown in Fig. 6.

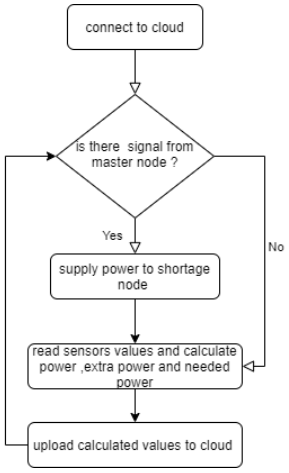

Fig. 6. Flow-chart of slave operation

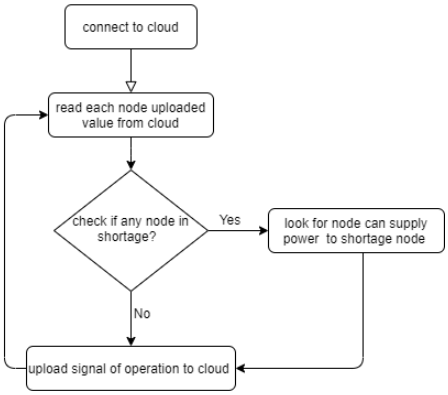

Fig 7. Flow diagram master node operation.

After being connected to the internet, the master node functions as a management, control, and balance system. It begins by reading the voltage, current, power, extra power, and needed power values of each node from the cloud. The most crucial values are needed power and extra power, which indicate whether the node is in low supply and whether it can supply power to neighbouring nodes. The Master node will first check each node's required power value; if any node's required power value is more than zero, the node is in need of power. The second step is to select a suitable node that can deliver the required power to the node by comparing the additional power values of each node to the required power of the shortage node. It will update the operation signal that determines which node will provide electricity. Every time the slave nodes update their values to the cloud, they verify this signal. Figure 7 depicts the flow diagram for a master node.

4 Thing speak of IoT Web Service

Things talk is a web-based open API IoT source information platform that stores sensor data from various 'IoT apps' and conspires the detected data output in graphical form at the web level. Thing speak communicates with the help of an internet connection that acts as a 'data packet' carrier between the connected 'things' and the Thing speak cloud, retrieving, saving/storing, analysing, observing, and working on the sensed data from the connected sensor to the host microcontroller such as an Arduino, TI CC3200 module, Raspberry-pi, and so on. The Thing Speak aids in the formation of enthralling sensor-based logging applications, location/place tracing applications, and a'social network' of objects/things with updated status, and we can also have control over 'Home automation' products that are connected to the public domain network (via the Internet) from the location of existing and potential customers. The word 'Channel,' which has a field for data, a field for location, and a field for status for various sensed data, is the most important component of Thing Talk functionality. Once the channels have been constructed in 'Thing talk,' the data can be implemented_ or the data may be processed and visualised using MATLAB, and the data can be responded to with tweets and other forms of notifications [35]. Thing talk also has a function that allows you to construct a public-based channel that you can use to analyse and evaluate it. To engage the 'Things/objects' in sensing the respective data and transmitting across the Internet, one must go beyond simply connecting data from a PC, objects to collect (sensors), and to do so, data must be network uploaded that are in the form of servers (that run applications), and such types are referred to as Cloud. The 'Cloud' employs graphical visualisation operations and is available in the form of a virtual server for users. Objects communicate with the cloud via possible 'wireless internet connections' available to users, with the majority of objects relying on sensors/actuators to provide information about our environmental analogy data. The Internet of Things (IoT) helps to connect everything and allows us to communicate with our own devices, as well as allowing objects/things to interact with each other. [36-37].

5 Results

Based on MATLAB/Simulink software, a model of the smart energy management system has been constructing t for each master and slave node with all connected power supply and loads as shown in Fig 9. The system has been tested for all-day intervals and under different load variation conditions as explained in Fig 10. From the results shown in previous figures, it’s clear that the suggested smart system has a high ability to monitor, compute and control the generated power from PV and wind generator to supply the load connected at the terminal of the DC bus. and measurements values each node will have its renewable source PV or wind turbine and microcontroller to measure the voltage using a voltage divider to measure the voltage of the source and current sensor for measure current across the load of the node and calculate the power consumption of the node. The extra power and needed power are calculated since each node has a max power value. It can say if the power consumption of the node is greater than max power the node is in shortage and need power and if the power consumption of the node is less than max power the node has the extra power to shear in case other nodes need.

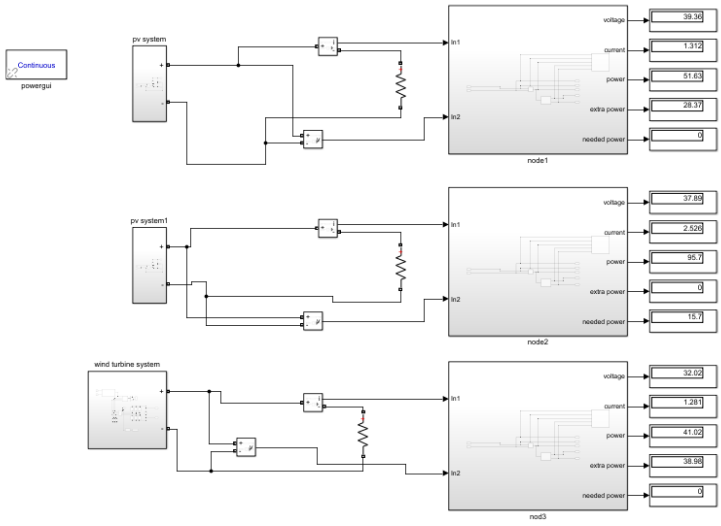

Fig 9. MATLAB/Simulink of nodes and reading

Once the node has switched on and connected to Thing Speak it starts to upload variation in the generated and consumed power to its channel as in Fig 11. The status channel is the master node updated after reading all nodes values if any node needs power. In this case, the master node will look for a suitable node to provide needed power and update the status channel both the needed node and provider node will change to 1 in which, each slave node continuous read its status from corresponding flew in the status channel.

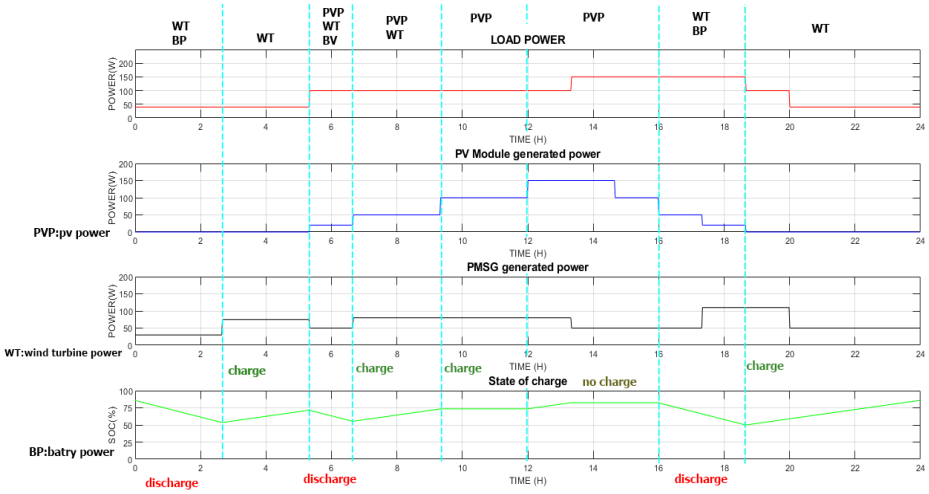

Fig 10. Variations of load with generated power.

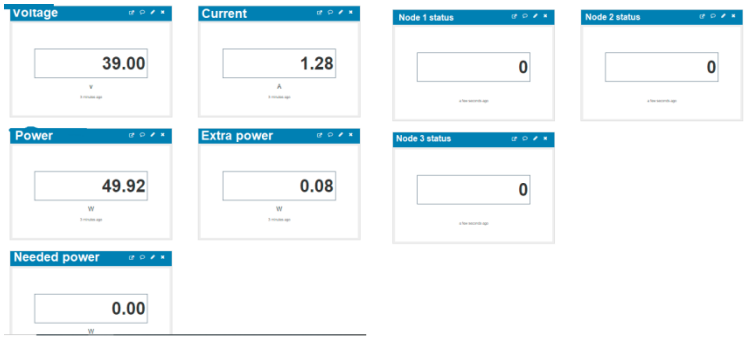

Fig 11. Node1 channel and status channel.

Fig 12. shows master node reading all nodes values from the cloud, by accessing to node's channel and read the uploaded values, by checking the extra power and needed power values for each node and check if any node had needed power value more than zero if so this node has shortage in power the master node immediately check other nodes extra power values and Comparing with needed power of node which needs power if it was bigger than the needed power this node will supply power to the node else it will check another node, after selecting shortage node and provider node operation signal will upload to status channel, as shown in Fig 12 there is no node need for power the status channel and its fields will remain 0. The master node will check if there is any node that had extra power to transmitted to node3 node2 can supply the needed power. Below is the table with parameters from each node channel and status channel.

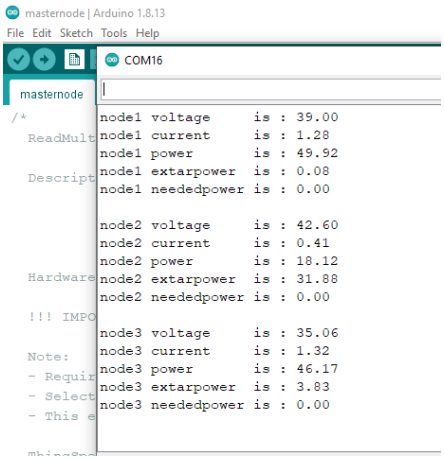

Fig 12. Master node reading all node values.

Table 1. Master node reading along with status signal

Node Number	Voltage	Current	Power	Extra Power	Needed Power	Status	Time	Measure No.
Node1	39	1.28	49.92	0.08	0	0	12:04:35	1
Node2	42.6	0.41	18.12	31.88	0	0	12:04:35	
Node3	35.06	1.32	46.17	3.83	0	0	12:04:36	
Node1	39	1.28	49.92	0.08	0	0	12:04:40	2
Node2	42.6	0.41	18.12	31.88	0	1	12:04:41	
Node3	31.86	2.46	78.47	-28.47	28.47	1	12:04:40	
Node1	39	1.28	49.92	0.08	0	0	12:04:45	3
Node2	34.92	1.3	45.4	4.6	0	1	12:04:46	
Node3	35.2	1.42	49.88	0.12	0	1	12:04:45	
Node1	37.32	0.37	13.925	36.07	0	1	12:04:51	4
Node2	46.05	0.51	23.485	26.5145	0	0	12:04:51	
Node3	33.341	1.9035	63.467	-13.4672	13.46724	1	12:04:52	
Node1	35.21	0.9254	32.58	17.41	0	1	12:05:03	5
Node2	46.05	0.51	23.485	26.5145	0	0	12:05:00	
Node3	35.0586	1.3169	46.1716	3.82833	0	1	12:05:01	
Node1	37.3210	0.3731	13.9251	36.0749	0	0	12:05:13	6
Node2	45.72	0.46	21.0312	28.9688	0	0	12:05:10	
Node3	36.0767	1.0628	38.3436	11.65638	0	0	12:05:16	

6 Practical implementation of Smart Energy System

To validate the simulated model, a complete system is shown in Fig. 13 is constructed. The following components make up the hardware system. A relay is a switch that is controlled by electricity. It has a set of input terminals for one or more control signals, as well as a set of working contact terminals. When the node needed power the master node sends an upload operation signal to the cloud the node reads this signal and if there is a node that can provide the power relay is open and allow the power flow to the load and supply to the required power. A voltage divider is a type of passive linear circuit that generates an output voltage (Vout) that is a fraction of the input voltage (Vin). The outcome of dividing the input voltage among the divider's components called voltage division. Two resistors are linked in series to form a voltage divider, with the input voltage applied across the resistor pair and the output voltage emerging from the connection between them. Voltage dividers made of resistors are frequently used to lower the magnitude of a voltage so that it may be measured. The current sensor from ACS712 works on the Hall Effect to measure electric current. This sensor can detect both direct current (DC) and alternating current (AC). The microcontroller is an important part of the system, each node has its microcontroller which is used to Measures different parameter in the system. This work we use Arduino Uno which is microcontroller has analog and digital pins to read or write from/to and each system has pre-defined maximum system capacity(MSC) .all slave nodes should

Measures voltage, current, power and then calculate extra power and needed power and continuously check operation signal from status channel, using voltage divider which is Circuit use to Measure more than 5v, then measuring the current using current sensor .calculate power, extra power(EP) and needed power(NP) using the following eq. (15-17)

$$P = V \cdot I \tag{15}$$

$$EP = MSC - P \tag{16}$$

If EP was a negative value this indicates that node needs the power to calculate how much power the system want

$$NP = P - MSC \tag{17}$$

These values need to be uploaded to the cloud to be read by the master node the Arduino connects to the internet using esp8266 Wi-Fi that connects Arduino to the cloud to uploaded calculated values and read operation signal from the status channel and check to wither to open relay or not. Fig 14. shows slave node components. For the master node, the node MCU microcontroller is used as shown in Fig 15., since the master node has no measure operation it's only a software operation. the node MCU connects to the internet and accessing to slave node values starts to save these values in the node MCU . after complete read operation next step is to check if there any node needs power, the master node check if the NP is more than zero this means the node need power and look of suitable node has enough power to supply by checking EP if it more than the needed power NP, for example, if node1 has shortage in power the NODE1.NP will be more than zero so the master node will make a Comparison between NODE1.NP and NODE2.EP
IF NODE1.NP < NODE2.EP then node 2 will provide power to node 1
IF NODE1.NP < NODE3.EP then node 3 will provide power to node 1
The final step is to updating status channel values to send a signal to the node to open or Close really to supply or Receive Power.

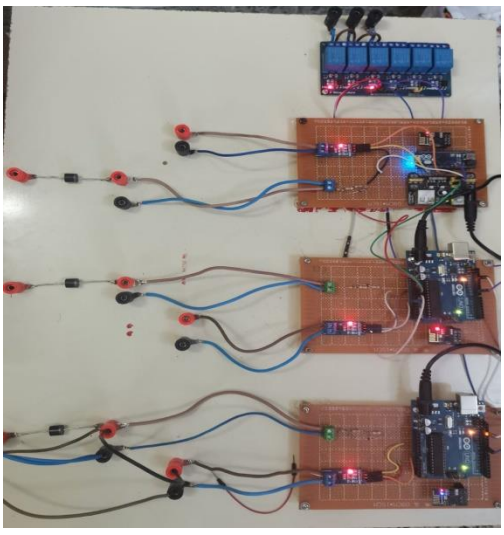

Fig 13. Energy management control unit based on Arduino.

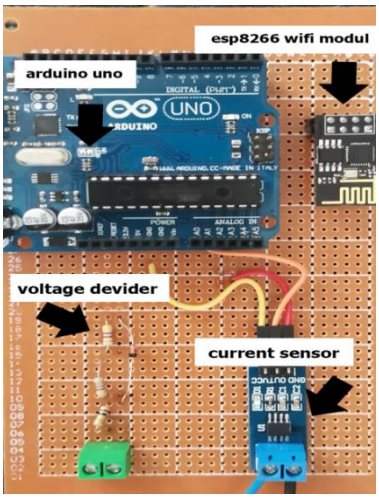

Fig 14. slave node component

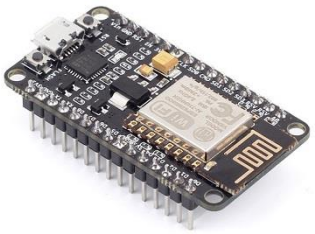

Fig 15. Nodmcu Master Node

7 Conclusion

This paper presents smart energy management for wind-solar hybrid systems for microgrids using IoT. A hybrid system helps in augmenting the level of renewable generation from the available level of resources. Integration of renewable energy resources can be helpful in commercial areas where there is a large electricity demand. Since renewable energy resources are incorporated there are no negative impacts on nature. The invariability in the output that is obtained while operating as a single source is also reduced to a large extent. When an IoT energy management system is incorporated it will increase the efficiency of energy available. The extent up to which the efficiency is improved depends on the renewable energy source used. Also increases the reliability and economics of energy supply. This system also promises quicker energy restoration after power disturbances. Using Microcontroller Arduino and 'Thing Speak' cloud to allow nodes to send and receive parameters and signals, slave node sends upload their parameter to 'Thing Speak' cloud channel and the master node will read this parameter and determine whether node need power or not and if so master node look for a suitable node to supply power from by sending a signal to both nodes. the system has been tested in Simulink using MATLAB and expectantly the result was a match, and the object of the system has been achieved, power-sharing and balancing between nodes help decrease demand power from the utility grid and decrease the cost of electrical power.

References

[1] Photovoltaic and Wind Turbine Generation System for Constant Power Supply with IoT-based Monitoring and Control,2018

[2] Atika Qazi et al., "Towards Sustainable Energy: A Systematic Review of Renewable Energy Sources, Technologies, and Public Opinions", IEEE Access, vol. 7, pp. 63837 – 63851, May 2019.

[3] Trieu Mai et al., “Renewable Electricity Futures for the United States” IEEE Trans. on Sustainable Energy, vol. 5, no. 2, pp. 372-378, Apr. 2014.
[4] M. H. Nehrir et al., “A Review of Hybrid Renewable/Alternative Energy Systems for Electric Power Generation: Configurations, Control, and Applications” IEEE Trans. on Sustainable Energy, vol. 2, no. 4, pp. 392-403, Oct. 2011.
[5] Pranav M.S et al., “Hybrid Renewable Energy Sources (HRES) - A Review” International Conference on Intelligent Computing, Instrumentation and Control Technologies (ICICICT) 2017, pp.162- 165.
[6] Xiaotong Song et al., “Reliability Varying Characteristics of PV-ESSBased Standalone Microgrid”, IEEE Access, vol. 7, pp. 120872– 120883.
[7] A.A. Jamali et al., “Energy storage systems and their sizing techniques in power system- A review” IEEE Conference on Energy Conversion (CENCON), 2015, pp.215-220.
[8] Caisheng Wang et al., “From hybrid energy systems to microgrids: Hybridization techniques, configuration, and control”, IEEE PES General Meeting, USA, pp. 1-4, Jul. 2010.
[9] Saroja Kanti Sahoo et al., “Control Techniques in AC, DC, and Hybrid AC–DC Microgrid: A Review”, IEEE Journal of Emerging and Selected Topics in Power Electronics, vol. 6, iss. 2, pp. 738–759, Jun. 2018.
[10] Venkata Yaramasu et al., “High-power wind energy conversion systems: State-of-the-art and emerging technologies”, Proceedings of the IEEE, vol. 103, iss. 5, pp. 740–788, May, 2015.
[11] M. Ryu, H. Kim, J. Kim, J. Baek, J. Jung, Test bed implementation of 380V DC distribution system using isolated bidirectional power converters, in: IEEE Energy Conversion Congress and Exposition (ECCE), 2013, pp. 2948–2954.
[12] B.A. Thomas, Edison revisited: impact of DC distribution on the cost of LED lighting and distribution generation, in: 27th Annual IEEE Applied Power Electronics Conference and Exposition (APEC), 2010, pp. 588–593.
[13] W. Yu, J.-S. Lai, H. Ma, C. Zheng, High-efficiency DC–DC converter with twin bus for dimmable LED lighting, IEEE Trans. Power Electron. 26 (2011) 2095–2100.
[14] A. Al-Diab, C. Sourkounis, Integration of flywheel energy storage system in production lines for voltage drop compensation, in: IEEE 37th Annual Conference Industrial Electronics (IECON), 2011, pp. 3882–3887.
[15] B.H. Kenny, R. Jansen, P. Kascak, T. Dever, W. Santiago, Integrated power and attitude control with two flywheels, IEEE Trans. Aerosp. Electron. Syst. 41 (2005) 1431–1449
[16] Ren21, Renewables. “Global statusreport.” Renewable energy policy network for the 21st century. http://www.ren21.net [accessed June 1, 2018].
[17] Elsayed Ahmed T, Mohamed Ahmed A, Mohammed OA. DC microgrids and distribution systems: an overview. Electr Power Syst Res 2015;119:407–17
[18] Planas E, Andreu J, Gárate JI, Martínez De Alegría I, Ibarra E. AC and DC technology in microgrids: a review. Renew Sustain Energy Rev 2015;43:726–49.
[19] Microgrid Opportunity: What Stands in the Way for 2017? – Renewable Energy World http://www.renewableenergyworld.com/articl es/2017/01/microgridopportunity-whatstands-in-the-way-for-2017.html [accessed October 29, 2016].
[20] P. Pawar, M. TarunKumar, P. Vittal K, An IoT based Intelligent Smart Energy Management System with Accurate Forecasting and Load Strategy for Renewable Generation, Measurement (2019), doi: https:// doi.org/10.1016/j.measurement.2019.107187
[21] Ranhotigamage, Chagitha, and Subhas Chandra Mukhopadhyay."Field trials and performance monitoring of distributed solar panels using a low-cost wireless sensor network for domesticapplications." IEEE Sensors Journal11.10 (2011): 2583-2590.
[22] Constantin, Suciu, et al. "GPRS based system for atmosphericpollution monitoring and warning." Automation, Quality andTesting, Robotics, 2006 IEEE International Conference on. Vol.2.IEEE, 2006.
[23] Reddy, S. R. N. "Design of remote monitoring and control systemwith automatic irrigation
[24] Prakhar Srivastava, Mohit Bajaj, Ankur Singh Rana.” IOT Based Controlling of Hybrid Energy System using ESP8266” 2019.
[25] P. Pawar, M. TarunKumar, P. Vittal K, An IoT based Intelligent Smart Energy Management System with AccurateForecasting and Load Strategy for Renewable Generation, Measurement (2019).

[26] S. Lyden, M. E. Haque, A. Gargoom, M. Negnevitsky, and P. I. Muoka, “Modelling and Parameter Estimation of Photovoltaic Cell,” in Universities Power Engineering Conference (AUPEC), 2012 22nd Australasian, 2012, pp. 1–6.
[27] N. Pandiarajan and R. Muthu, “Mathematical modeling of photovoltaic module with Simulink,” in 2011 1st International Conference on Electrical Energy Systems, ICEES 2011, 2011, no. Icees, pp. 258–263.
[28] M. Edouard and D. Njomo, “Mathematical Modeling and Digital Simulation of PV Solar Panel using MATLAB Software,” vol. 3, no. 9, pp. 24–32, 2013.
[29] H. Mahamudul, M. Saad, and I. Henk, “A Modified Simulation Method of Photovoltaic Module in Simulink Environment,” no. 1, pp. 607–610, 2012.
[30] T. Marnoto, K. Sopian, W. A. N. Ramli, and W. A. N. Daud, “Mathematical model for determining the performance characteristics of multi-crystalline photovoltaic modules,” International Conference on Mathematical and Computational Methods in Science and Engineering , pp. 79–84, 2007.
[31] Dr.P.Sangameswar Raju, Mr. G. Venkateswarlu, “Simscape Model Of Photovoltaic cell”, International Journal of Advanced Research in Electrical, Electronics and Instrumentation Engineering, Vol. 2, Issue 5, May 2013.
[32] M. Vyas, M. Singh, and S. Santoso,, "Handbook Of Wind Power System", Springer, 2011.
[33] Thomas Ackerman, "Wind Power In Power Systems", Royal Institute of Technology Stockholm, Sweden, Edition: John Wiley and sons, Ltd, 2005.
[34] T. Burton, D. Shape, N. Jenkins, E. Bossany, "Wind Energy Handbook", J. Wiley & Sons, Ltd. 2001.
[35] ThingSpeak – an API and Web Service for the Internet of Things, a published paper
[36] ThingSpeak: Open Source Platform for Connected Products and Services(PR Newswire)
[37] The open data platform for the Internet of Things.https://thingspeak.com (2015)

Dynamic Voltage Restorer Using (PQ) Theory with LabView

Mahmood T. Alkhayyat[1] , Mohammed Y. Suliman[2,] Ibrahim F. Fakhraldeen[3]
{ m.t.alkhayyat@ntu.edu.iq[1], mohammed.yahya@ntu.edu.iq[1] ,ibrahim.furat@ntu.edu.iq[3]}

Department of Electrical Power Techniques Engineering, Technical Engineering College, Northern Technical University, Mosul, Iraq[1,2,3]

Abstract. Power quality became very important for utilities as well as users. The cause of the power quality problem is instability (voltage, current, and frequency). Voltage sag and voltage swell are common voltage disruptions. They are caused by faults, disturbances arising in the transmission system, etc. This paper deals with the voltage instability compensation of linear sensitive loads by dynamic voltage restorer (DVR) using instantaneous power theory. The practical experiment results were obtained using the data acquisition card (DAQ) and LabView real-time software. The new design can compensate the voltage for ±15% of the nominal value for the two conditions sag/swell. Also, the designed controller enhanced the response of less than 110% overshot at stalling time of less than 0.2 sec.

Keywords: Data acquisition (DAQ), Dynamic voltage restorer (DVR), Instantaneous power theory, (Sag and Swell), PI controller, Power Quality.

1 Introduction

Modern power systems are complex power networks where transmission or distribution networks interconnect hundreds of generating loads and thousands of loads [1]. Providing reliable and quality power supply is the main concern for the customer, but the production of the power supply is reasonably stable while the power quality can be poor in developed countries. The perfect power supply system provides its consumer with a steady sinusoidal voltage at the contracted voltage magnitude and frequency with continuous energy flow [2]. The problem power quality appears by (voltage sage/swell, voltage unbalance, flickers, harmonics, problems, and interruption). As a result of load switching, motor starting, faults, non-linear loads, lightning, etc., voltage sag/swell occurs. It has an essential impact both on loads based on microprocessors and sensitive loads [3]. Voltage sags decrease in the normal-voltage level between 10% and 90% nominal voltage (RMS) at the control frequency, for a period of 0.5 cycles to 1 minute. The increase in RMS voltage at the power frequency for durations from 0.5 cycles to 1 minute defines the voltage swell; typical magnitudes are between 1.1 and 1.8 p.u [4]. Different types of custom power devices are used to improve the voltage sag and swell on the loads, such as transformer with tap changer, constant voltage (Ferro-resonant) transformer, servo-controlled voltage stabilizer, connect a large-load to points of common-coupling, etc.[5]. Some of the disadvantages of these methods are the static transfer switch and one possible form of voltage sag mitigation. These instruments will move the load from the usual supply feeder to the alternate supply feeder within half a cycle upon identification of voltage sag [6]. In addition

IMDC-IST 2021, September 07-09, Sakarya, Turkey
Copyright © 2022 EAI
DOI 10.4108/eai.7-9-2021.2314944

to that, there are other compensation techniques, such as (STATCOM, TCSC, SVC, and UPFC) [7]. A dynamic voltage restorer (DVR) is a FACTS (Flexible Alternating Current Transmission Systems) system that compensates for voltage sag and voltage swell that happens on transmission lines. The (DVR) is used for critical load safety (digital machines, advanced medical equipment, the web of financial transfers, elevators, etc.) From voltage-based problems with power quality [8]. DVR is a circuit made up of diodes and thyristors, which are power electronic devices. Because of its small size and effective service, it is widely used. Maintaining the voltage level in the transmission line within the specified limits is critical; Since it is overloaded conditions will cause all components connected to it to shut down. The Dynamic Voltage Regulator (DVR) is the SSSC's equivalent. While both are used to compensate for series voltage sag, their operating concepts are different. A balanced voltage is injected in series with the transmission line by the static synchronous series compensator. The DVR, on the other hand, compensates for unbalanced supply voltage between phases [9]. The load voltage is lower than the nominal value during sag. To ensure a steady voltage on the load, DVR injects the appropriate voltage into the circuit (the direction of the injected voltage is the same as the direction of the load voltage) [10]. The load voltage is higher than the nominal value during swelling. DVR injects needed voltage into the system (the direction of the injected voltages is opposite the direction of the source voltage) to sustain a steady voltage through the load [11]. The compensation techniques in dynamic voltage restorer depend mainly on the factors specified, such as DVR power ratings, different load conditions, type of voltage sag, and swell. Some loads are non-linear against the 1 hop step angle, some are susceptible to magnitude changes. Therefore, the control strategies primarily rely on the form of characteristics of the load [12]. There are three types of methods of DVR :

a- Pre_sag compensation method.
b- In _ Phase compensation method.
c- Minimum energy compensation method.

Fig 1 shows the phasor diagram of three methods. This paper will design based on the second method illustrated in Fig 1b. In this compensation procedure, the voltage injection is in phase with the utility voltage. The magnitude of the injection voltage in the in-phase correction for the specified voltage sag state is minimum as compared to the other current compensation methods. The dc-link voltage level is also lower if the form of compensation is in phase [13]. In Fig 2, the DVR configuration is shown.

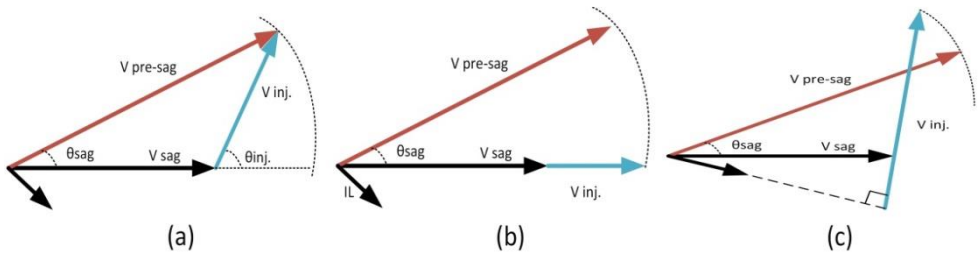

Fig 1. Phasor diagram of (a) Pre-sag compensation (b) In-phase compensation (c) Minimum energy compensation.

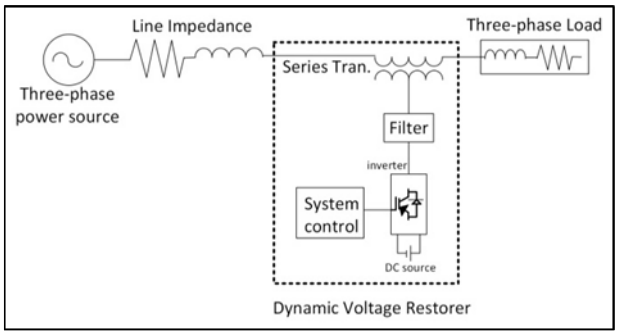

Fig 2. Schematic diagram of DVR.

Dynamic voltage restorer consists of [14] : (1-Inverter. 2-Series transformer/injection transformer. 3-Filters. 4-Control system.5- And energy storage device). Based on the voltage sag in the literature, several studies have been suggested to increase power quality. In [15], the DVR control system using adaptive neuro-fuzzy logic has been used. Takagi-Sugeno fuzzy rules are trained using an off-line neuro-fuzzy system in this controller. In [16], a DQ theory in DVR was used to detect the (sag/swell) with sinusoidal pulse width modulation (SPWM) and voltage supply inverter (VSI). The authors in [17] presented DVR using three-dimensional space vector modulation (3DSVM) and validated it by simulations in PSCAD-EMTDC software. While the authors in [18] used a proportional-integral (PI) controller for (DVR) to improve suppress voltage sag. In [19] used as a STATCOM to enhance the profile of the voltage. This paper proposed a dynamic voltage restorer (DVR) based on instantaneous power theory, with enhanced PI limiting to improve the voltage sag/swell condition that happens in the system.

2 DVR Based (PQ) Theory

The load voltages are calculated in this methodology based on active and reactive power components [20]. The Phase-Locked Loop (PLL) is often used to obtain the phase angle (θ) and source voltage frequency [21]. Using the Clark transformations [22], the three-phase device voltages and three-phase load voltage in the a-b-c coordinates are translated to the (α-β) coordinates as follows:

$$\begin{bmatrix} v\alpha \\ v\beta \end{bmatrix} = \sqrt{\frac{2}{3}} \times \begin{bmatrix} 1 & -1/2 & -1/2 \\ 0 & \sqrt{3}/2 & -\sqrt{3}/2 \end{bmatrix} \times \begin{bmatrix} vla \\ vlb \\ vlc \end{bmatrix} \quad (1)$$

$$\mathrm{V}\sum = \sqrt{v\alpha^2 + v\beta^2} \quad (2)$$

Where (V∑) is the (RMS) aggregate voltage. The aggregate voltage is compared with the desired voltage to generate error signals (ΔV). This signal is processed in the PI controller [23]:

$$\mathrm{U} = \mathrm{Kp} + \mathrm{Ki} \int edt \quad (3)$$

$$\mathrm{E}_{\Delta v} = (V_{ref.} - V_{\sum})(Kp + \frac{Ki}{s}) \quad (4)$$

Where, EΔv (voltage to generate error signal), Vref (reference voltage), Kp (proportional gain), Ki (integral gain).
Fig 4 Show the (PQ) theory of Dynamic voltage restorer (DVR).

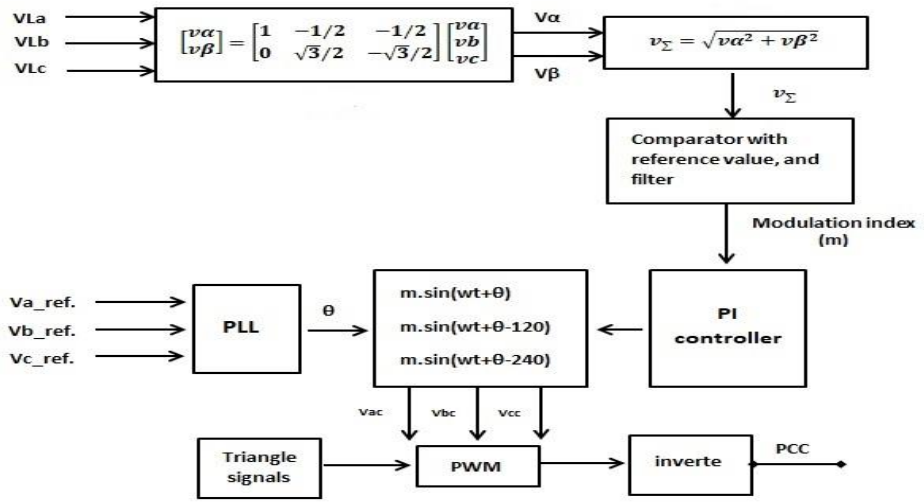

Fig 4. Dynamic voltage restorer-based PQ theory

3 Prototype and Experiment Results

DVR is designed in the laboratory to compensate for the (Sag / Swell) problems. The design was considered to verify the DVR based on (PQ) theory. The model is shown in Fig 5.

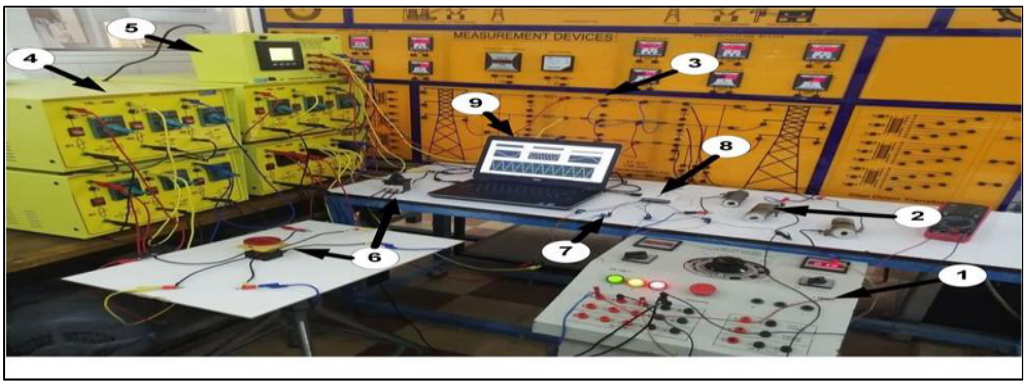

Fig 5. DVR prototype.

The DVR model is comprised of: (1- Three-phase source: It is a device that equips a working circuit with a three-phase voltage balanced by a fixed phase difference between the phases of 120 degrees. 2- Resistances in the transmission line. 3- Inductive in the transmission line. 4- Three-phase loads. 5- Three-phase electric meter. 6- Three-phase switches: for add /remove loads on the sensitive loads. 7-Voltage sensors. 8-Data Acquisition card. 9-Laptop).
The proposed model was verified by applying (PQ) theory using LabView software [24]. The results were acquired in real-time by the control card (DAQ). Block diagram of (PQ) theory for Dynamic voltage restorer (DVR) in LabView is shown in Fig 6.

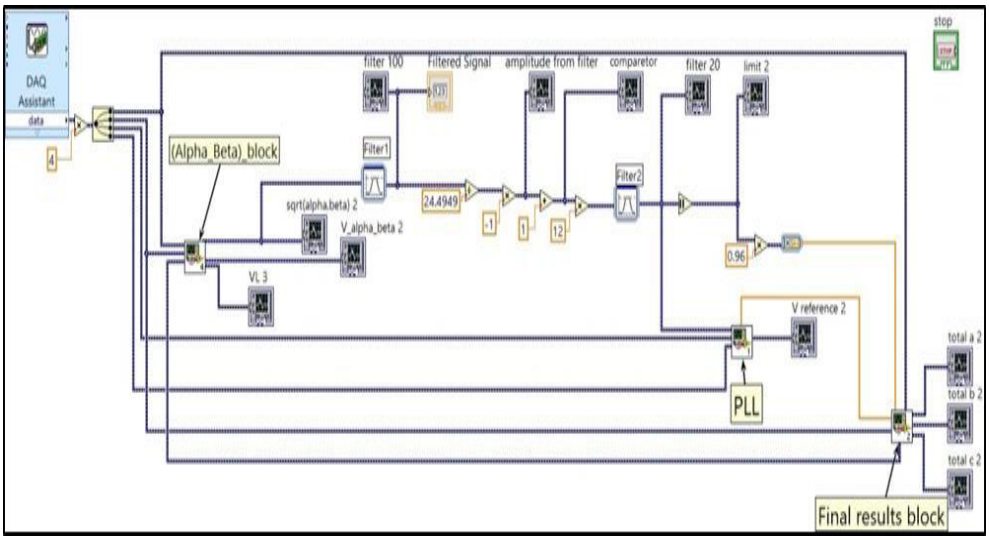

Fig 6. Schematic block diagram of (DVR) based (PQ) theory.

Fig 7a Shows a block diagram of the Clark transformation. It's the first part of the PQ theory using LabView. The phase-locked loop (PLL) design by LabView to synchronize the injected voltage with the system is shown the Fig 7b. The block diagram of the output of PQ theory (modulation index) multiplying with (wt) from (PLL) is shown in Fig 7c to show the results.

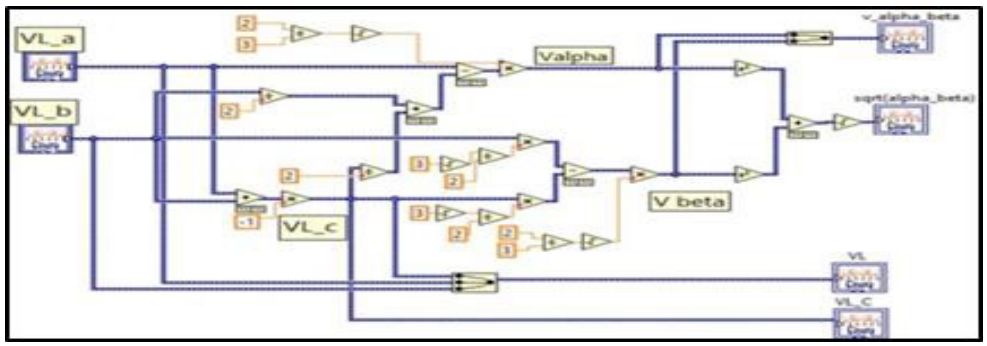

(a)

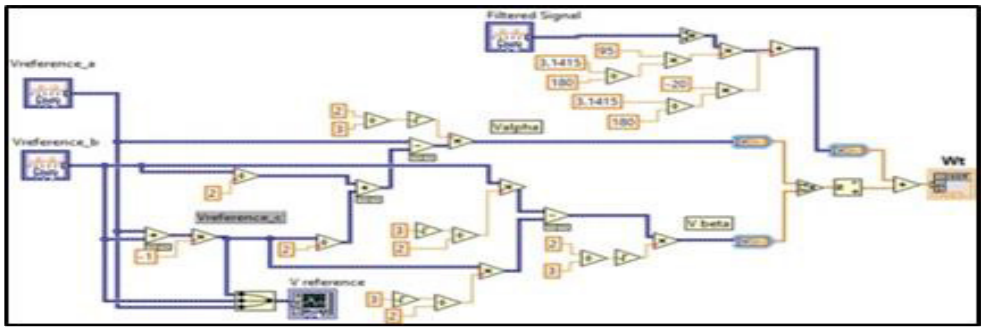

(b)

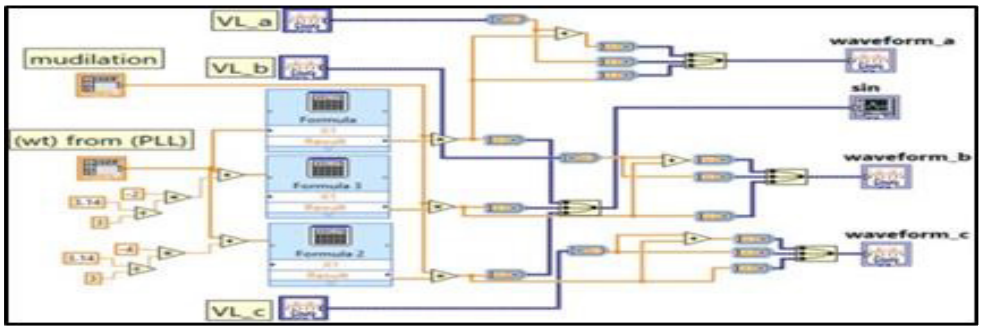

(c)

Fig 7. (a) Clark transformation structure. (b) structure of phased-locked loop (PLL). (c) Block diagram of results.

The data acquisition card (DAQ) is utilized to collect data from (voltage sensors) and then use this data as feedback for the control circuit. The data acquisition used in this paper is (Ni USB-6009) [25]. Fig 8 shows the signal description of DAQ and illustrates the inputs signals used from voltage sensors

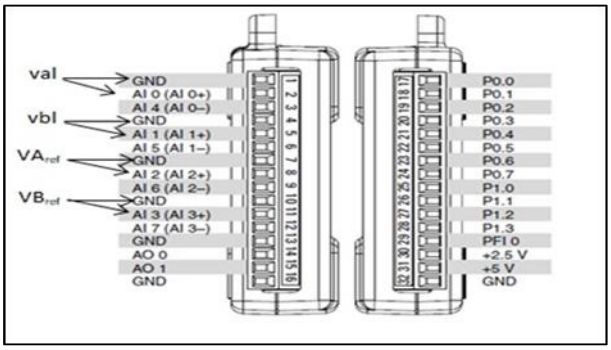

Fig 8. Signal description of DAQ.

The procedure of prototyping the laboratory model is shown in Fig 5. starting with the nominal operating condition. At this condition, the load is only a sensitive load, represented by (RL1 and RL2). At the Nominal value condition in system voltage, the switch (SW1) is open, and the switch (SW2) is closed as shown in Fig 9a. The value of the output controller at nominal condition, a value resulted from a comparison between the reference voltage with aggregate voltage, is close to zero, as shown in Fig 9b. When SW1 is closed, the loads (RL3, RL4) are added in parallel with the sensitive loads. In this case, the nominal value is decreased by a certain percentage to make sag condition. In this case, the output control unit value increases from the zero value to achieve the value of the injected voltages it acts as compensation for the lower voltage value on the loads. When (sw1) and (sw2) are open, the load is only RL1. The nominal value is increasing by a certain percentage to make the swell voltage condition. The value of the output controller in this condition decreasing from zero to achieve the value of opposite injected voltages that act as compensation for the value of the swell voltage on the load.

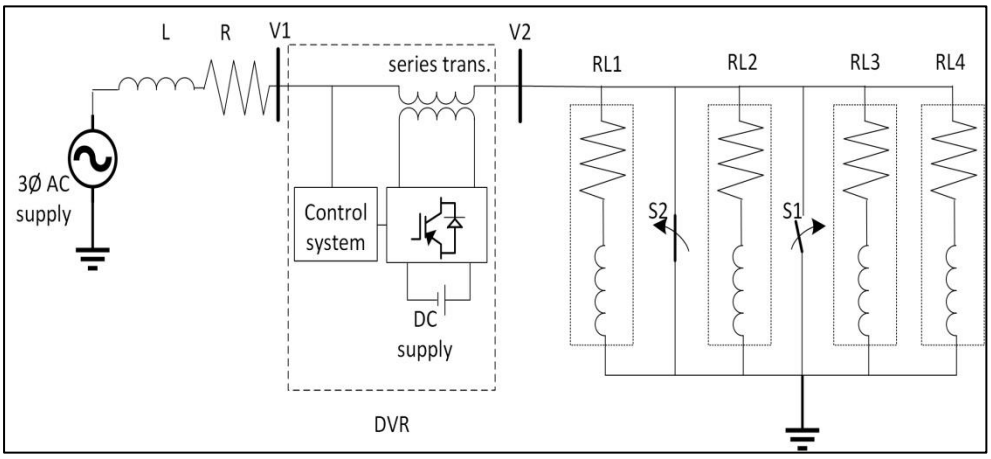

(a)

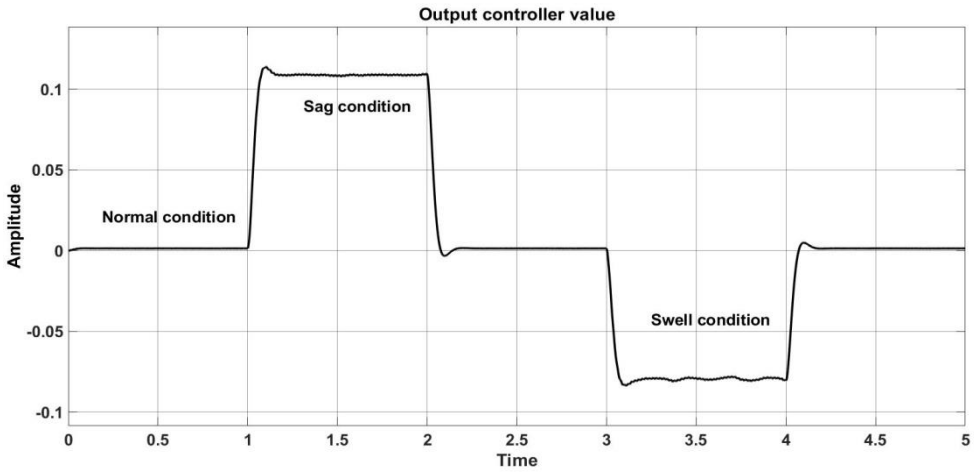

(b)

Fig 9. (a)) Experimental setup for DVR. (b) The value of output controller.

The proposed work is carried out by several cases:

Case1 (Normal condition): The circuit is equipped with a three-phase power supply with a voltage of 20V as shown in Fig 10. the injection wave represented by the green line is equal to zero, meaning there is no injection.
Case2 (Sag condition): In this case, during the Normal operation, sudden loads are added to the sensitive loads (RL3, RL4). Decrease of 12.5% in the voltage at the ends of the load to 17.5V. During this instantaneous dwindling, a compensating voltage will be injected from the inverter is shown in Fig 11. The sine wave represented in the red line is the Sag wave. Also, the sine wave represented in the green line is the injection magnitude wave whose value is 2V. Finally, the sine wave represented in black is the sum of the Sag wave and the injection wave.
Case3 (Swell condition): In this case, it is a sudden departure from sensitive loads (the only load is RL1). An increase of 10% in the voltage at the end of this load to 22V. As shown in Fig 12, the sine wave represented in red is the L wave. The sine wave represented in green is the injection wave, which is opposite to the increasing wave. The sine wave represented in black is the product of the sum of the previous two waves.

The response of injected voltage in (Sag and Swell) cases (with/without) PI controller obtained in Fig 13.

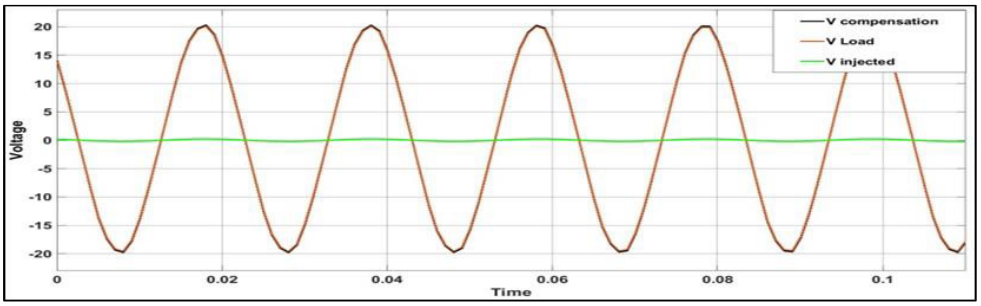

Fig 10. The waveform at Normal condition.

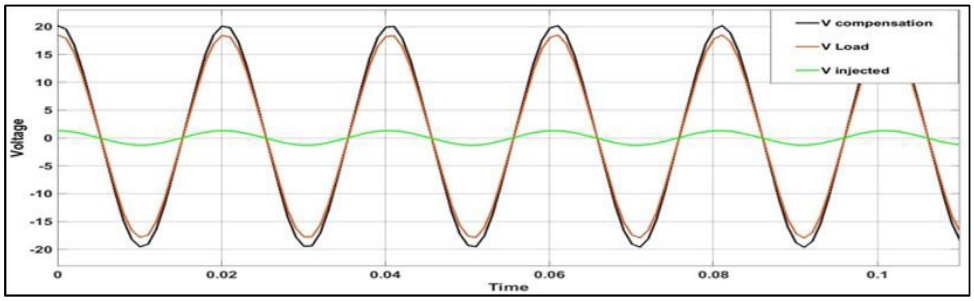

Fig 11. The waveform at Sag condition

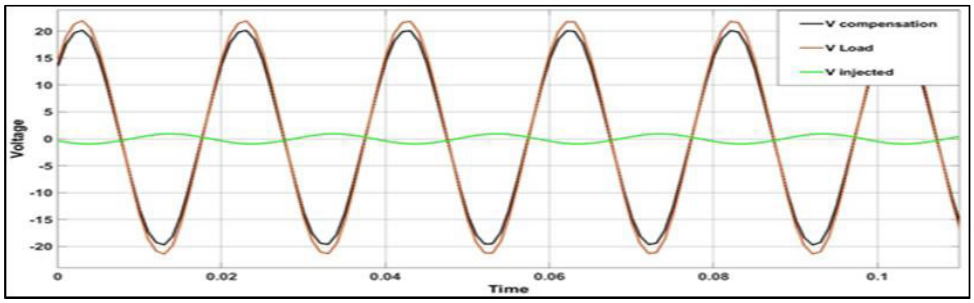

Fig 12. The waveform at Swell condition

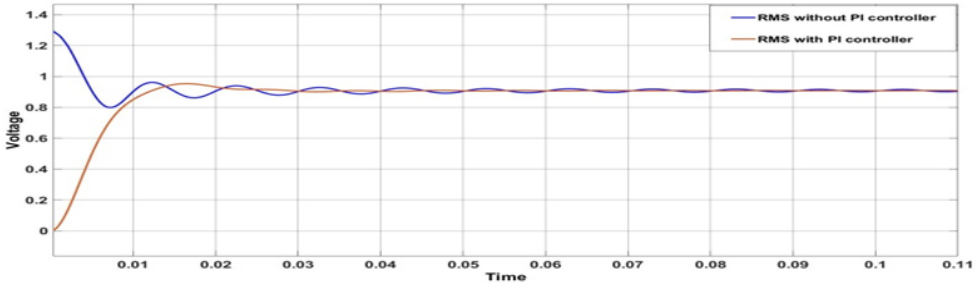

Fig 13. RMS value (with/without) PI controller.

4 Conclusion

In this paper, dynamic voltage restorer (DVR) performance is presented to instantaneously reduce sag and swell in voltages, which is one of the power quality problems on sensitive loads. PQ theory is used to control the amount of injected and compensated voltages. Compensation of 10% of the total value of sag (12.5%) obtained in the system. The swelling compensation rate is 8% of the total value of swelling (10%) in the system. The future work is now preparing to obtain compensated voltage for dip voltage conditions and upgrade the controller to utilize adaptive controller like adaptive Neuro-Fuzzy system.

5 Appendix

In prototype model:

a- All loads used in the prototype have equal values R=140Ω,L=471mH.

b- Voltage Detection Sensor Module 25v [26].

Acknowledgments

We would like to express our appreciation to the staff of the power system and machines laboratory, in the Technical Engineering College/Mosul, for their help and support to make the required tests and measurements.

References

[1] M.T .Alkhayyat Mahmood, and Sinan M. Bashi. "Mitigation Unbalance Nonlinear Loads and Dissimilar Line Currents Using Shunt Active Power Filter SAPF." International Journal of Advanced Engineering, Management and Science 2.10: 239666.

[2] N. L. Ismail, H. D. M. Hidzir, S. Thanakodi, N. S. M. Nazar, P. Ibrahim, and C. K. M. S. C. K. Ali, "Modeling voltage sag mitigation using dynamic voltage restorer and analyzing power quality issue," AIP Conf. Proc., vol. 1930, no. February, 2018, doi: 10.1063/1.5022921.

[3] Van Minh, N., Khanh, B. Q., and Phuong, P. V. (2017, July). Comparative simulation results of DVR and D-STATCOM to improve voltage quality in distributed power system. In 2017 International Conference on System Science and Engineering (ICSSE) (pp. 196-199). IEEE.

[4] Abas, N., Dilshad, S., Khalid, A., Saleem, M. S., and Khan, N. , " Power Quality Improvement Using Dynamic Voltage Restorer". IEEE Access, vol .8,pp.164325-164339, doi:10.1109/access.2020.3022477,(2020).

[5] Edomah, Norbert. " Effects of voltage sags, swell and other disturbances on electrical equipment and their economic implications" , IEEE Proc. of 20th International Conference on Electricity Distribution, p. 1-4, doi: 10.1049/cp.2009.0502 ,2009.

[6] DASGUPTA, Anindya; SENSARMA, Parthasarathi. "Voltage Sag Mitigation", Springer Singapore, pp. 91-106,doi: 10.1007/978-981-10-3831 ,2017.

[7] Mohammed Y. Suliman and Mahmood T. Al-Khayyat. "Power flow control in parallel transmission lines based on UPFC." Bulletin of Electrical Engineering and Informatics 9.5 (2020), pp.1755-1765.

[8] Pradhan, M., and Mishra, M. K. (2018). Dual P-Q Theory based Energy Optimized Dynamic Voltage Restorer for Power Quality Improvement in Distribution System. IEEE Transactions on Industrial Electronics, 1–1. doi:10.1109/tie.2018.2850009

[9] Ital, A. V., and Borakhade, S. A.," Compensation of voltage sags and swells by using Dynamic Voltage Restorer (DVR)",2016 International Conference on Electrical, Electronics, and Optimization Techniques (ICEEOT), doi:10.1109/iceeot.2016.7754936,(2016).

[10] Singh, S. K., and Srivastava, S. K. "Enhancement in power quality using dynamic voltage restorer (DVR) in distribution network", 2017 International Conference on Innovations in Information, Embedded and Communication Systems (ICIIECS) , doi: 10.1109/ICIIECS.2017.8275918,pp. 1-5, (2017, March).

[11] Shraddha, B., R, S., Pillai, S. J.and Modi, S. ,"Simulation and Analysis of Dynamic Voltage Restorer", 2018 3rd IEEE International Conference on Recent Trends in Electronics, Information & Communication Technology (RTEICT). doi:10.1109/rteict42901.2018.9012532 , (2018).

[12] Rahman, S. A., et al. "A Novel DVR Topology to Compensate Voltage Swell, Sag, and Single-Phase Outage." Iranian Journal of Electrical and Electronic Engineering 17.4 (2021) , pp. 2036-2036.

[13] Venugopal, S. and Agarwal, V. A," novel control strategy for an ultra-capacitor based dynamic voltage restorer with controllable dc-link voltage", 2015 IEEE 6th International Symposium on Power Electronics for Distributed Generation Systems (PEDG) , pp. 1-7, IEEE, (2015, June).

[14] El Sayed, N. G., El-Saady, G., Ibrahim, E. N. A. and Mohamed, M. A.," Dynamic Voltage Restorer for Enhancing Distribution Systems Power Quality", 2019 7th International Japan-Africa Conference on Electronics, Communications, and Computations,(JAC-ECC),pp. 210-215, IEEE, (2019, December).

[15] Mohammed Y.Suliman and Sameer Sadoon Al-Juboori ,"Design of Fast Real Time Controller for the Dynamic Voltage Restorer Based on Instantaneous Power Theory." International Journal of Energy and Power Engineering 5.2-1 , doi: 10.11648/j.ijepe.s.2016050201.11 ,pp. 1-6 , 2016.

[16] S. S. Sananse and M. Alkathakur, “Dynamic Voltage Restorer (DVR) Through MATLAB Simulation,” pp. 184–190, 2015.
[17] Tashackori, A., Hosseini, S. H., Sabahi, M. and Nouri T. A ,"Three-phase four-leg DVR using three dimensional space vector modulation", In 2013 21st Iranian conference on electrical engineering (ICEE) , pp. 1-5 , doi: 10.1109/IranianCEE.2013.6599761 , 2013, May.
[18] Kakar, F., bin Mohd Zin, A. A. and Bin Habibuddin, M. H. ,"Performance of PI Controller Based Dynamic Voltage Restorer for Power Quality Improvement.", In Applied Mechanics and Materials ,Vol. 818, pp. 52-57 , Trans Tech Publications Ltd. (2016).
[19] M. Y. Suliman, “Voltage profile enhancement in distribution network using static synchronous compensator STATCOM,” International Journal of Electrical and Computer Engineering (IJECE) , 2020, vol. 10, no. 4, pp. 3367-3374.
[20] Akagi, H., Watanabe, E. H. and Aredes M. ,"Instantaneous power theory and applications to power conditioning". John Wiley & Sons.,(2017).
[21] Katole, D. N., Daigavane, M. B., Gawande, S. P. And Daigavane, P. M." Vector based analysis for design of single phase SRF controller in Dynamic Voltage Restorer". IEEE International Conference on Power Electronics, Drives and Energy Systems (PEDES). 2018,doi:10.1109/pedes.2018.8707774.
[22] M. Y. Suliman,. and Bashi S. M. "Fast response SSSC based on instantaneous power theory." In 2013 International Conference on Electrical Communication, Computer, Power, and Control Engineering (ICECCPCE) , pp. 174-178, IEEE. (2013, December).
[23] A. Mohamed Eltamaly, Y. Sayed Mohamed, A. H. Mustafa El-Sayed, and A. N. Abd Elghaffar, “Enhancement of Power System Quality Using PI Control Technique with DVR for Mitigation Voltage Sag,” 2018 20th Int. Middle East Power Syst. Conf. MEPCON 2018 - Proc., pp. 116–121, 2019, doi: 10.1109/MEPCON.2018.8635221.
[24] National-Instruments, “LabVIEW User Manual - Getting Started with LabVIEW,” no. June, p. 349, 2013, .
[25] National Instrument Team, “User Guide Ni Usb-6008/6009.” pp.1–26,2015,: pdf/manuals/371303n.pdf.
[26] S. G. Technology, “Model : Voltage Sensor / 170640 Reference Code :,” no. 1000. p. 170640, 2015.

Crime Prediction Using Big Data Analysis

Hussam Hashim Hussein[1], Ahmed Talib Abdulameer[2]
{dac0019@mtu.edu.iq[1], Dr.ahmed.talib@mtu.edu.iq[2]}

Information Technology dept., Technical College of Management-Baghdad, Middle Technical University, Baghdad, Iraq[1,2]

Abstract. Crime is one of the most dangerous phenomena around the world. It is impossible to find a country or society free of crime, where criminals use all modern techniques and advanced technological methods in committing crimes, for example, cybercrime. In recent years, the generation of raw big crime data has been increased, therefore big data analysis become mandatory. Deep Learning is employed by using (LSTM) which is one of the Recurrent Neural Network (RNN) types. 'Criminal data in Chicago' is used as a dataset. An intelligent model is proposed for type, time, and place crime prediction to address the problem of high crime rates and reaching to help (police agencies - law enforcement institutions) to predict crime, reduce the spread of crime, as well as to make the best usage of security sources of (police elements - resources).

Keywords: Crime, Big Data Analysis, Deep Learning, Machine Learning, Recurrent neural network (RNN)/Long Short-Term Memory (LSTM).

1 Introduction

Crime is one of the most dangerous phenomena for any country. It is impossible to find a country or society free of Crime because Crime goes beyond the limits of harm or threatening the safety of others but rather affects the government and society in economic, cultural, and other terms. Crime prediction is an attempt to identify and limit future crime; crime prediction uses past data. After analysing the data, we notice that previous data related to criminal activities help expect crime Also, crime is one of the main problems in any society or country in this era. Even criminals are using all modern technologies and advanced technological methods to commit crimes, for example, cybercrime. Therefore, crime has become the focus of a challenge for both the police department and law enforcement agencies to reduce the spread of crime and use modern techniques to predict and reduce the spread of crime.

Many police departments use artificial intelligence algorithms and use big data tools to help them to predict where crimes are occurring. For example, police departments in places like Seattle, Los Angeles, and Atlanta have experimented with predictive police programs which try to identify the geographic area where crime is likely to occur in the future. At the same time, the Chicago Police Station used an algorithm based on a heat list that tries to identify people as criminals for violent crimes or repeated abuse.

To reduce the spread of crime, new technologies can deal with the vast amount of data, where traditional analysis techniques cannot analyse the data; therefore, artificial techniques and algorithms use big data to analyse crime data.

IMDC-IST 2021, September 07-09, Sakarya, Turkey
Copyright © 2022 EAI
DOI 10.4108/eai.7-9-2021.2314943

2 Related Works

Big data analytics (BDA) has been extensively applied and studied in data science. Londhe and Rao [1] presented various software frameworks available for BDA and discussed some widely used data mining algorithms. Grady et al. [2] illustrated the implications of an agile process for the cleansing, transformation, and analytics of data in BDA. Liu et al. [3] exemplified the utilization of BDA in the tourism domain in terms of the datasets, data capture techniques, analytical tools, and analysis results to provide insights for Destination Management. Fisher et al. [4] explained the conception of big data in BDA, its analytics, and the associated challenges when interacting among them. In [5] is to explores a methodology for reliably predicting the location, time, or likelihood of future residential burglaries. First, suitable data structure designs stored spatial/temporal information and aggregated counts of crime-related events categorized by the city's police department. Second, an ensemble of data mining classification algorithms is applied to perform residential burglary forecasting. In addition, it explores whether the crime rate will emerge or increase at specific locations (called' heating up'). Finally, in [6], a multivariate time series clustering technique based on dynamic time wrapping (DTW) and parametric Minkowski model is proposed to discover similar trends in crime data and subsequently use this information for future crime trends prediction. The algorithm has been tested on real-world datasets (provided by the Indian National Crime Records Bureau), performing separate analyses for various crimes such as murder, kidnapping, and so on.

3 Big Data

Data is everywhere and affects almost all aspects of life. Recently, many private institutions and national governments such as the United States have paid great attention to Big Data where these institutions and governments have become interested in the high potential of Big Data. For example, in July 2012, the United Nations released the Additional Data for Development Report, explicitly examining how governments have used additional data [7].
Many government agencies have announced master plans to accelerate Big Data research and its applications, such as research initiatives and projects. For example, the US National Science Foundation (NSF), as part of the Big Data Initiative launched by the Obama administration, announced BIG DATA in March 2012. The initiative resulted in several winning projects to investigate the foundations of Big Data Management (led by Washington University), analytical approaches for computing Big Data, and machine learning technologies. These projects seek to develop methods, algorithms, frameworks, infrastructure, and research that allows for analyzing this Big Data and explore data and extract information or knowledge to take advantage of them in the future, as well as to reduce this large amount of data to a manageable range and its interpretation by the human[8]. As for private, non-governmental organizations, over the past few years, almost all major companies, including Oracle, IBM, Microsoft, Google, Amazon, Facebook [8]. However, people who work in the Big Data field still have different opinions about defining Big Data:

1. Big Data: originally the volume of data that cannot be processed (efficiently) by traditional methods and database methods and tools [9].
2. Big Data: it refers to data sets that are both large and high in variety and speed, making them difficult to handle by using traditional tools [10].

3. Big Data: it is the amount of data that exceeds the ability of technology to store, manage and process efficiently [11].

4 Recurrent Neural Network

It is a type of deep learning network used for the first time in the 1980s and 1980s. It is used to solve deep learning network problems. It contains recurrent loops within the network, which gives it memory effect operations by using a state-based structure that uses previous information to estimate the next value. This network is beneficial in recognizing the sequence dependence of specific data (predicting the next value from the chain). It retains some essential features of the sequential data and forecasts future data.

4.1 Long Short-Term Memory(LSTM)

Long-term memory networks, commonly called "LSTM", are a particular type of repetitive neural network, introduced by Hochreiter & Schmidhuber 1997, which works or can learn long-term by using the Cell State where it maintains the state of the cell and passes it to the next cell to link previous data to current data to ensure that data is not lost .on the other hand, the LSTM is explicitly designed to solve the problem of addressing the problem of gradient fading when updating the weights with the best expectations which are reached of the model in the recurring network model . LSTM (Long Range Memory) is an advanced RNN that aims to solve the fading gradient problem and achieve excellent results on longer sequences. The memory determines the most information to pass in each step of the time. Each cell in LSTM contains:

1. RNN Cell
2. Cell State= long term memory (Ci)
3. Forget gate (ft)
4. Input gate (it)
5. Output gate (Ot)

5 Problem Definition and Goal

Crime has always been among the phenomena that have attracted the attention of scholars due to its connection with the social structure of society. The research problem can be summarized in the high crime rates in addition to the existence of huge raw crime data for the Chicago-US research community for the period (2001-2017) [12]. Our goal is to build an intelligent model developed to help the competent authorities (police agencies - law enforcement institutions) for predicting the type, time, and place of crime.

5.1 The Proposed Developed Intelligent Model

To understand how the proposed developed intelligent crime prediction model works using big data analysis, it is necessary to start with the proposed model architecture, as in Fig 1, to understand the model clearly. The proposed intelligent model design to predict different types of predictions, such as predicting the rate of a specific crime type, as well as predicting a crime rate in a particular district in Chicago city, additionally predicting the rate of crime at times.

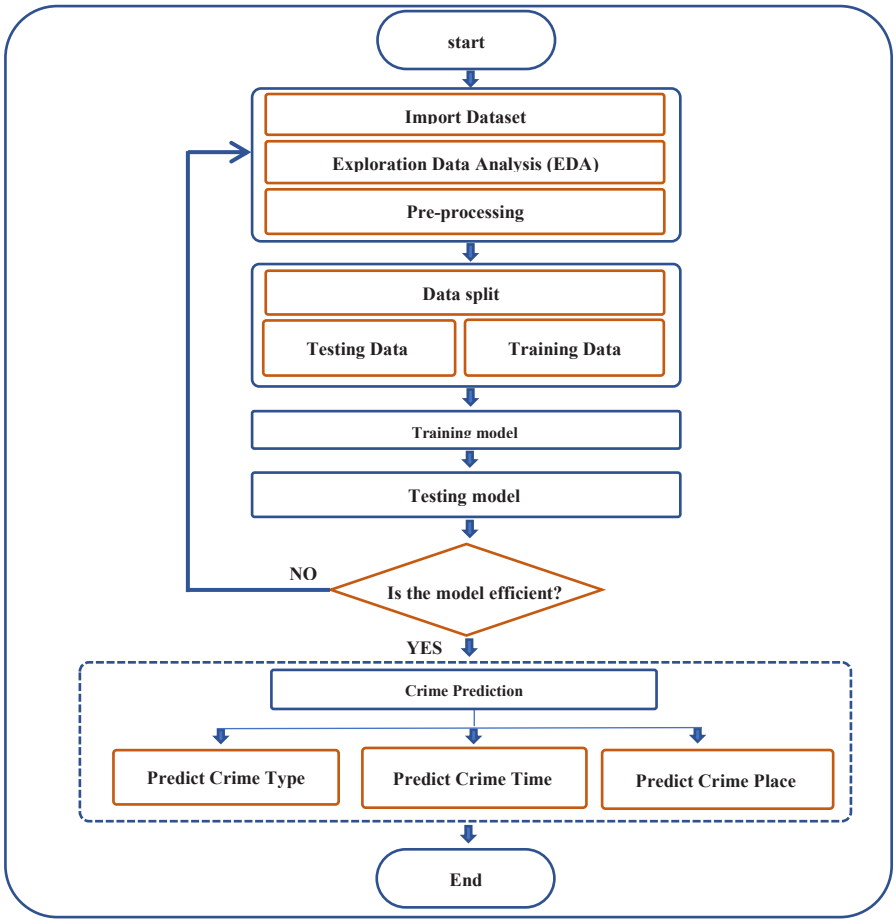

Fig 1. The architecture of the proposed developed intelligent model.

5.2 Data Description

The crime dataset used in this model was gathered from a publicly available dataset of the United States as mentioned in [12]. Each crime describes by 23 features (i.e., type of crime, location district, date, x-longitude, y-latitude, and others). The dataset contains (7,951,232) records of crime, the snapshot of the original dataset is depicted in Fig 2.

	Unnamed: 0	ID	Case Number	Date	Block	IUCR	Primary Type	Description	Location Description	Arrest	...	Ward	Community Area	FBI Code	X Coordinate	C
0	879	4786321	HM399414	01/01/2004 12:01:00 AM	082XX S COLES AVE	0840	THEFT	FINANCIAL ID THEFT: OVER $300	RESIDENCE	False	...	7.0	46.0	06	NaN	
1	2544	4676906	HM278933	03/01/2003 12:00:00 AM	004XX W 42ND PL	2825	OTHER OFFENSE	HARASSMENT BY TELEPHONE	RESIDENCE	False	...	11.0	61.0	26	1173974.0	1.!
2	2919	4789749	HM402220	06/20/2004 11:00:00 AM	025XX N KIMBALL AVE	1752	OFFENSE INVOLVING CHILDREN	AGG CRIM SEX ABUSE FAM MEMBER	RESIDENCE	False	...	35.0	22.0	20	NaN	
3	2927	4789765	HM402058	12/30/2004 08:00:00 PM	045XX W MONTANA ST	0840	THEFT	FINANCIAL ID THEFT: OVER $300	OTHER	False	...	31.0	20.0	06	NaN	
4	3302	4677901	HM275615	05/01/2003 01:00:00 AM	111XX S NORMAL AVE	0841	THEFT	FINANCIAL ID THEFT:$300 &UNDER	RESIDENCE	False	...	34.0	49.0	06	1174948.0	1.!

5 rows × 23 columns

Fig 2. Snapshot of Chicago dataset.

5.3 Data Pre-Processing

Data pre-processing is a technique that involves converting raw data into an understandable format. Unfortunately, real-world data is often incomplete or inconsistent, and it will likely contain many errors. Therefore, the pre-processing of crime data is an essential step before starting to train the model on this data; a sequence of pre-processing steps is performed for data as follows:

1. Features Selection: select an important feature from a dataset.
2. Missing value: checking and handling missing values.
3. Data scaling: normalized data.
4. Reshape Input Data: to be adequate with LSTM network.

5.4 Exploratory Data Analysis (EDA)

Through this exploration, the researcher can know the valuable data that lead the model to predict the crime (the goal of the proposed model). We found the types of recorded crimes have (35) different types of crimes as in Fig 3, for example, the crime of theft, extortion, kidnapping, theft of private property, and others. In addition, it finds that the most common type of crime that occurred is a theft crime.

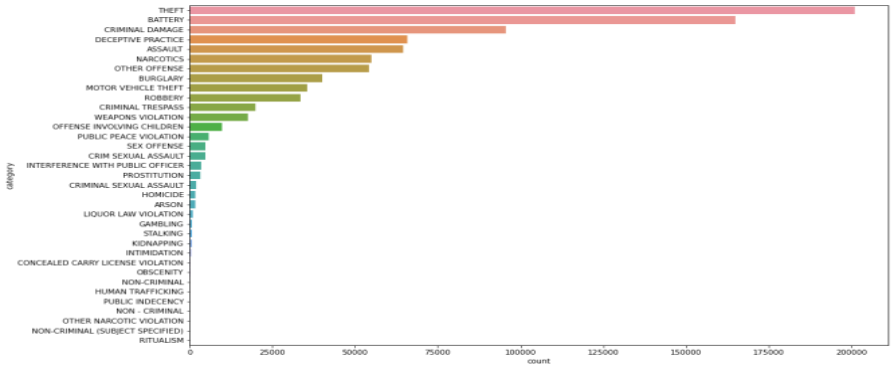

Fig 3. The types of crimes in the dataset.

Additionally, to know which days are the most dangerous (there are more crimes in it than on other days), we found through the graphical chart in Fig 4 that the crimes occurred on all days, and this is a clear indication that there is a high rate of crimes on all days of the week and for most types of crimes.

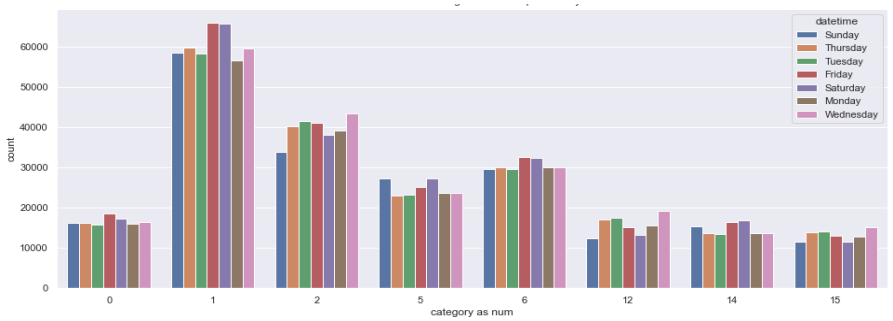

Fig 4. The number of crimes by days of the week.

During the exploration of the data, we found that the crime rate for each province is different from one to the other. The crimes that occur in District No. (11) are more incidence than in the rest of the provinces. District No. (20) recorded the lowest crime rate compared with other provinces.

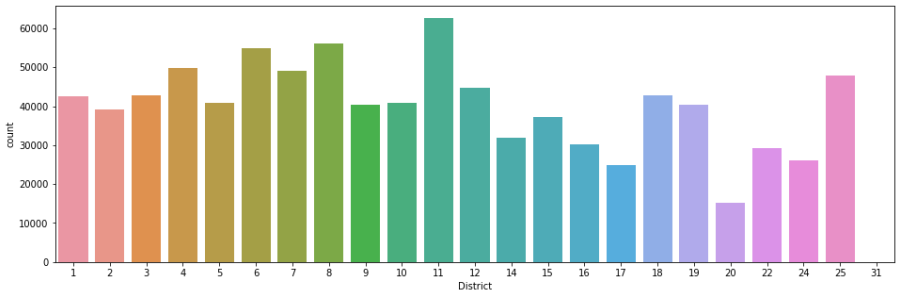

Fig 5. The number of crimes by District No.

5.4 Experiments Results

This section deals with the results of the proposed model. Experiments' results and trained model settings are shown in Table 1 and Table 2 respectively.

Table 1. Root Mean Square Error (RMSE) results for the Proposed Model

Prediction Model	RMSE
Crime Type prediction model	51.546612
Crime Time prediction model	11.25940
Crime Place prediction model	0.65185

Table 2. Hyper-parameters for the Proposed Model.

HYBER PARAMETER	VALUE
NODES OF LSTM 1st LAYER	50
NODES OF LSTM 2nd LAYER	50
NODES OF DENCE LAYER	1
LEARNING RATE	0.001
OPTIMIZER	Adam
ACTIVATION FUNCTION	Relu

Crime Type Prediction: The researcher tested the proposed model by (80%) of training data, from the original data. The original data are collected by month of each year from 2001 to 2017. The researcher reached RMSE (51.546612) to predict the type of crime.
Crime Time Prediction: The researcher tested the proposed model by (80%) of training data, from the original data. To predict a specific time (10:00 PM) for 'theft' crime, the researcher reached RMSE (11.25940).
Crime Place Prediction: The researcher tested the proposed model by (80%) of training data, from the original data. to select a specific place (a district in Chicago city) to predict 'ARSON ' crime, the researcher reached RMSE (0.65185).

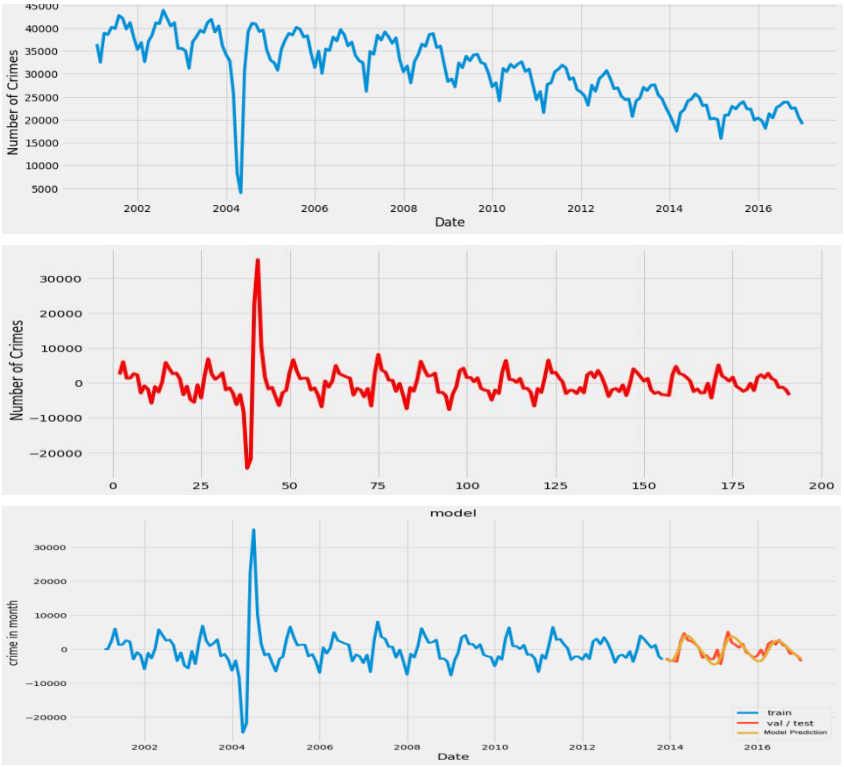

Fig 6. Crime Type Prediction by the proposed model.

Fig 7. Time Crime Prediction by the proposed model.

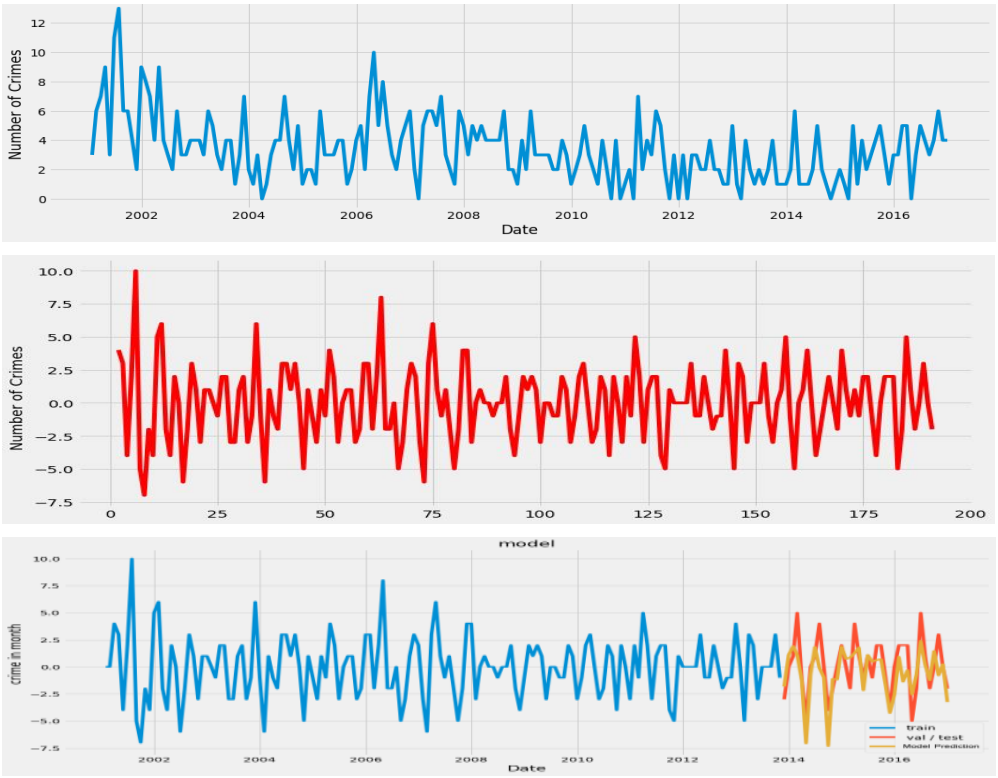

Fig 8. Crime Place Prediction by the proposed model.

From the results of the root mean square error (RMSE) and experiments' results, the researcher showed the results of different types of prediction, as well as it is considered that the model works on crime data in a way that can predict the crime efficiently.

6 Conclusion

Crime is one of the most dangerous phenomena for any country. To reduce and non-proliferation of crime, it requires new techniques that can deal with the vast amount of data, where the data cannot be analysed with traditional analysis techniques. Therefore, Deep Learning algorithms techniques were employed through using repeated neural network (RNN) and the employment of one of its types (LSTM). Our contribution is to build an intelligent crime prediction model, where the model predicts different types: crime type, time of the crime, the place of crime). In addition, many deep learning techniques have been employed such as dropout and early stopping for addressing the problem of high crime rates and helping the competent authorities (police agencies - law enforcement institutions) to predict crime, reduce the spread of crime as well as make the best use of security sources of (police elements - resources), and employ them properly.

References

[1] Londhe A, Rao PP, editors. Platforms for big data analytics: Trend towards hybrid era. 2017 International Conference on Energy, Communication, Data Analytics and Soft Computing (ICECDS); 2017: IEEE.
[2] Grady NW, Payne JA, Parker H, editors. Agile big data analytics: Analytics Ops for data science. 2017 IEEE international conference on big data (big data); 2017: IEEE.
[3] Liu Y-Y, Tseng F-M, Tseng Y-H. Big Data analytics for forecasting tourism destination arrivals with the applied Vector Autoregression model. Technological Forecasting and Social Change. 2018;130:123-34.
[4] Fisher D, DeLine R, Czerwinski M, Drucker S. Interactions with big data analytics. interactions. 2012;19(3):50-9.
[5] Yu C-H, Ward MW, Morabito M, Ding W, editors. Crime forecasting using data mining techniques. 2011 IEEE 11th international conference on data mining workshops; 2011: IEEE.
[6] Chandra B, Gupta M, Gupta M, editors. A multivariate time series clustering approach for crime trends prediction. 2008 IEEE International Conference on Systems, Man and Cybernetics; 2008: IEEE.
[7] Janssen M, van der Voort H, Wahyudi A. Factors influencing big data decision-making quality. Journal of business research. 2017;70:338-45.
[8] Kaisler S, Armour F, Espinosa JA, Money W, editors. Big data: Issues and challenges moving forward. 2013 46th Hawaii international conference on system sciences; 2013: IEEE.
[9] Chen CP, Zhang C-Y. Data-intensive applications, challenges, techniques and technologies: A survey on Big Data. Information sciences. 2014;275:314-47.
[10] Hashem IAT, Yaqoob I, Anuar NB, Mokhtar S, Gani A, Khan SU. The rise of “big data” on cloud computing: Review and open research issues. Information systems. 2015;47:98-115.
[11] Williams ML, Burnap P, Sloan L. Crime sensing with big data: The affordances and limitations of using open-source communications to estimate crime patterns. The British Journal of Criminology. 2017 Mar 1;57(2):320-40.
[12] Feng M, Zheng J, Ren J, Hussain A, Li X, Xi Y, Liu Q. Big data analytics and mining for effective visualization and trends forecasting of crime data. IEEE Access. 2019 Jul 22; 7:106111-23.

Autonomous Control of Multi Speed Split Unit Air Conditioning for Space Load Response

Wasan Asaad Jwad[1] , Ali Lateef Tarish[2]
{E-mail addresses wasan.alansary@stu.edu.iq[1], alialali@stu.edu.iq [2]}

Control and Automation Eng. Dept., Eng.Technical College-Basra, Southern Technical University, Basra, Iraq[1]
Thermal Mechanics Eng. Dept., Eng.Technical College-Basra, Southern Technical University, Basra, Iraq[2]

Abstract. Succeeding comfort conditions in hot climates region with minimum power consumption is the important requisite in designing the air conditioning system such as split unit air conditioning (SUAC). Under Iraqi conditions, the current study compared the energy consumption of SUAC in two classrooms at Southern Technical University/Engineering Technical College-Basra (STU/TCB). Additionally, this paper developed an autonomous cooperative controller for sensing changes in dynamic space load and auto response of a variable speed compressor over a 12-hour period. The first classroom has a single-speed SUAC compressor, while the second classroom has a variable-speed SUAC compressor with a total capacity of 6 Ton. The results show that in June, the largest amount of energy saved was 51.5 % at 7 AM, while the least amount of energy saved was 10.9 % at 14 PM. SUAC with autonomous controller was discovered to be the highest control unit with less energy utilized than other SUACs, achieving a value of 24.8 % energy savings. The split unit control (SUC) could result in a significant reduction in SUAC compressor power in class 2 at seasonal energy efficiency rating (SEER) levels 8 or 20, resulting in a 75% reduction in operating costs throughout the year.

Keywords: Air conditioning application; Split unit; multi speed compressor; autonomous control; energy saving.

1 Introduction

In Iraqi cities, split unit air conditioners (SUAC) are commonly used in both residential and commercial buildings. The SUAC working with conventional vapor compression refrigeration cycle [1]. The air conditioning appliance accounts for 70% of the energy consumed in the building. The significant replenishing demand on the electricity systems in Iraq during the summer contributes mainly to peak loads, due to the warm weather in Iraq [2]. Moreover, the costs of power generation are raised because of a high renewal load, but overall network efficiency is also lowered [3]. In recent years, SUAC single speed compressors in home and industrial buildings worldwide have been replaced by SUAC variable speed compressors that have lower electricity consumption. The SUAC variable speed compressor operates under varying frequencies and includes a variety of refrigeration capabilities to more rapidly and efficiently satisfying altering comfort requirements. Two ways are existed to control compressor

IMDC-IST 2021, September 07-09, Sakarya, Turkey
Copyright © 2022 EAI
DOI 10.4108/eai.7-9-2021.2314936

speed in SUAC variable speed compressors. The first have been controlled manually, but the other one senses the required temperature of the condition space and change speed dependently. Inside design condition cannot be achieved using these ways due to the outdoor design condition in Iraq reach to 50 C [2]. Under this viewpoint, a need for a more responsible control system is raised. A multi-Agent system (MAS) is one of more suitable proposed control strategy for such systems, due to its properties such as intelligence, autonomous, modularity and social ability [4]. MAS consists of a society of entities inhabiting an environment, interacting with their environment and cooperating with each other in a distributed fashion to achieve whole delegated task [5].

The previous studies has looked at the usage of a multi-speed compressor SUAC, building energy demand, and HVAC control methods for the purpose of minimize high energy demand in residential and commercial buildings. The electrical expansion valve controllers with variable speed compactors were suggested by Alaa and Ahmed [6]. The results revealed that the use of the right control technique can have a substantial impact instead of the kind of controller on the performance coefficient (COP) and system stability. Moaomao & et al.[7] were using the probability relation test technique to investigate variable speed SUAC in order to get the most acceptable energy performance model. Test results show that COP and capacity estimates for the conventional multi speed SUAC can be efficiently selected with moderate complexity and satisfactory exactness using the model evaluation technique. Jaehun Lim et al. [8] experimentally evaluated the saving energy of the inverter SUAC to assess the constant-speed SUAC in a Korean environment with four various climates and a warm temperatures in Saudi Arabia during the year. The inverter air conditioner's energy savings were primarily determined by variations in temperature and cooling demand over the course of a day or season. The machine learning technique was utilized for variable speed SUAC, according to Zhijie Chen et al.[9]. To create simulation data under diverse settings of distinct situations, a machine learning augmented inverse modeling approach is given. The clustering technique is used to categorize the training data while keeping the weights of different conditions suitably balanced. Amr and Kayed [10] studied the thermal performance of an SUAC with a variable speed compressor in the environment. According to the results, increasing the condenser input air temperature by 7 ^{o}c raised power consumption by 18% while lowering the COP by 15%. The multi agent and other control systems were investigated by the researchers in determining the most effective control and energy savings for the air conditioning system [11-14].

According to previous research, the SUAC single speed compressors switch on or off when the thermostat indicates that the condition space temperature is higher or lower than the required set temperature. It is important to note that the SUAC single-speed compressors in Iraq city will be running 24 hours a day for the next three months (June, July and August). Furthermore, the compressor power and electric demand are both high due to the controlled SUAC identification is limited. Up to author’s knowledge, investigating the relationship between space load and multi-speed SUAC has not been yet achieved under Iraqi conditions.

In this work, multi-speed compressor SUAC is operated with a control autonomous reactive agent to optimize compressor speed with space load. Over the day, there is a significant gap between space load demand and SUAC capacity, where space load fluctuating throughout the day but SUAC capacity remaining constant, resulting in energy customer fixed during the day. In addition, the SUAC variable speed compressor operates at a set speed without consideration to the space load in the condition space. This study intends to propose an autonomous competent control model for multi speed SUAC that can work depending on a wide variety of space load and is appropriate for using in STU/TCB during the 12hr. This allows the SUAC to obtain the best comfort temperature while using minimal energy. As a result, a new

autonomous cooperative controller for sensing changes in dynamic space load and auto response of a variable speed compressor has been developed. A comparison of energy savings between a single-speed SUAC compressor and a multi-speed SUAC compressor is presented. The SEER was used to evaluate energy input to compressor based on the examined SUAC to provide assessment of SUAC efficiency and electric cost.

2. Multi Speed SUAC Description

Figure 1 depicts the SUAC schematic diagram. The SUAC is in the process of completing a vapor compression refrigeration cycle. The heat from the conditioned space in the classroom is absorbed by the evaporator. The multi-speed compressor is then used to increase the refrigerant pressure from evaporator to condenser pressure, with heat being rejected to the environment in the condenser and pressure being reduced from condenser to evaporator temperature in the expansion device. Multi-speed compressors use an inverter to alter the motor's working speed by speeding up or slowing it down. The compressor is powered with a set voltage by the inverter, which saves energy.

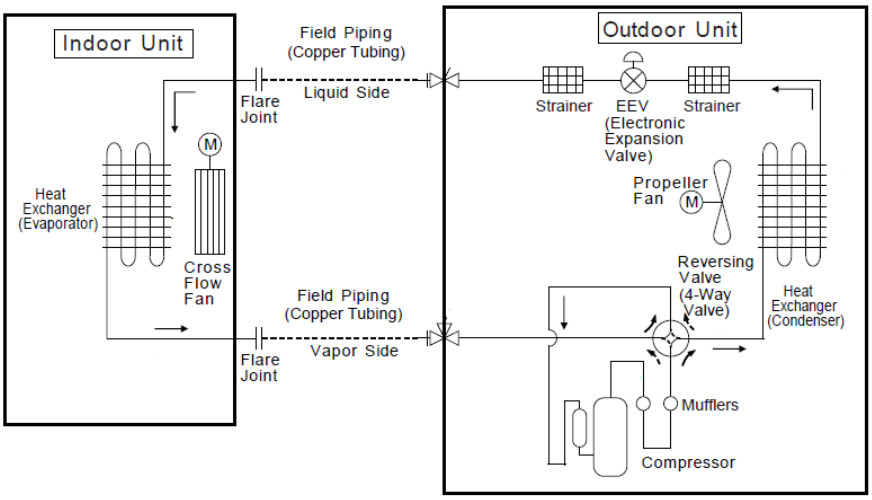

Fig. 1. SUAC diagram.

3. Methodology

The autonomous cooperative controller's purpose is to identify changes in dynamic space load across a large working range (three month). To achieve the auto response of a variable speed compressor SUAC, the SUAC is operated while the compressor speed and cooling load are varied in this study. The space load is altered every hour, with the hypothesis that the space load will not change significantly in that time. During a 12-hour period, the space load for two classrooms (lecture theatre) is determined (8 AM to 8 PM). A single-speed SUAC compressor with a total capacity of 6 Ton is in the first classroom, while a variable-speed SUAC compressor with a total cooling capacity of 6 Ton is in the second. The dynamic space load is input into two SUACs and the suitable speed compressor is determined by negotiation between them. The method and procedures for the current work will be described in the following sections.

3.1. Space Load Estimation

Solar radiation, conduction load, ventilation/infiltration load, and interior load are the four components that make up the classroom space load. The overall space load is estimated by calculating all of these loads separately and summing all together. The CLTD technique is used to calculate the cooling load for the classroom in the TCB. Figure 2(a) shows the case study TCB ground building, whereas Figure 2(b) depicts two classrooms with SUAC. The SUAC with constant capacity is used in the first class, whereas the SUAC with SUC is used in the second class. The heat transmission during wall, roof, floor, door and glass as the following [15]:

$$Q = UA\ CLTD_C \tag{1}$$

$$CLTD_C = [\ (CLTD + LM)k + (25.5 - T_r) + (T_o - 29.4)\ ]f \tag{2}$$

Solar heat gain:

$$Q_s = A.SC.SH.CLF \tag{3}$$

The equipment load in the classroom:

$$Q_e = P.CLF \tag{4}$$

The sensible and latent heat of student [16]:

$$Q_{so} = N.G_s.\ CLF_s \tag{5}$$

$$Q_{lo} = N.G_l \tag{6}$$

The ventilation and infestation [16]:

$$Q_v = N.(\text{liters/ sec per person}) \tag{7}$$

$$Q_i = V.ACH/3600 \tag{8}$$

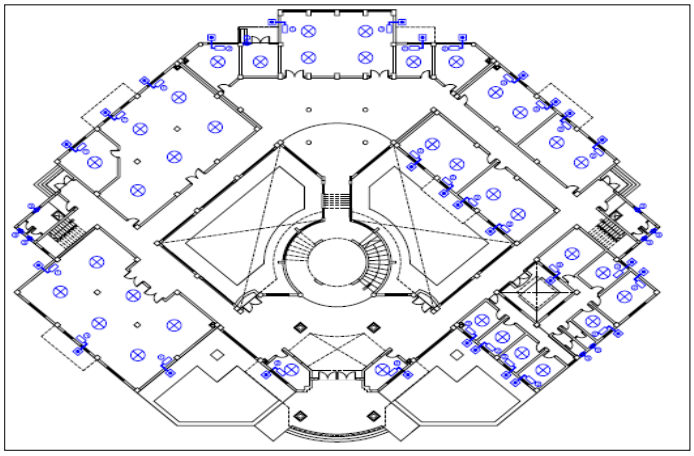

Fig. 2 (a). TCB ground building.

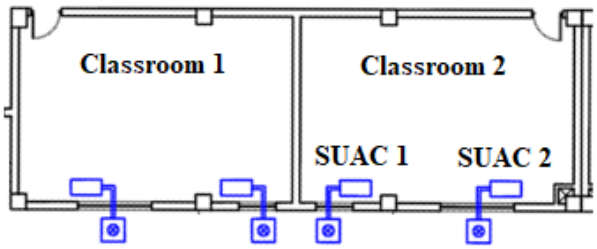

Fig. 2 (b). Case study classrooms.

3.2. SUAC Control Behavior

Aggregating the split unit's sub-activities should yield the overall behavior of an SUAC system. Each unit inhabited in environment and has the ability to interact with it. Singular one adheres to a general strategy that explains how to solve the problem at hand. The proposed work's strategy incorporates reactive response. The system has the ability to solve problems autonomously, which implies it can govern its internal states and make decisions on how to operate in its surroundings without the need for human intervention. Making decision will be as a reactive action that described as a request/reply wave of interactions among system units to take an action that affect environment and solve the current state.

3.3. Unit Control Architecture

Split unit control (SUC) is the given name to the proposed system controllers. The SUC architecture shows how a structure can be divided into a series of modules to handle certain tasks, as well as how these components interact, and how information and control travel between modules to determine what actions should be taken [17-19]. The general structure of the SUC is modular, comprises of seven modules activated separately at moment to perform the dedicated duty at the time. These modules connected together and centered around an essential centralized one called the Decision-Making module which responsible for taking decision depending on related rules and databases. The SUC modules comprises three essential modules which are: Input module for entering the information from environment.

The second module is the Decision-Making Module, the key module where all decision-making processes are based on the overall strategy for completing the targeted tasks. The third critical module is the Action module, which carries out the decisions made by the decision making module and transmitted as reactions to the environment. In addition, there are other supported modules like the Data Base Update (DB Update) module is in capable of updating data in the database. Reactive Knowledge Base (Reactive KB) module which hosts all rules needed to make decision. Strategy selection module which has two paths to select. And finally, the Negotiation Module that is triggered when there is a need to interact with other SUC to solve problem (see figure 3).

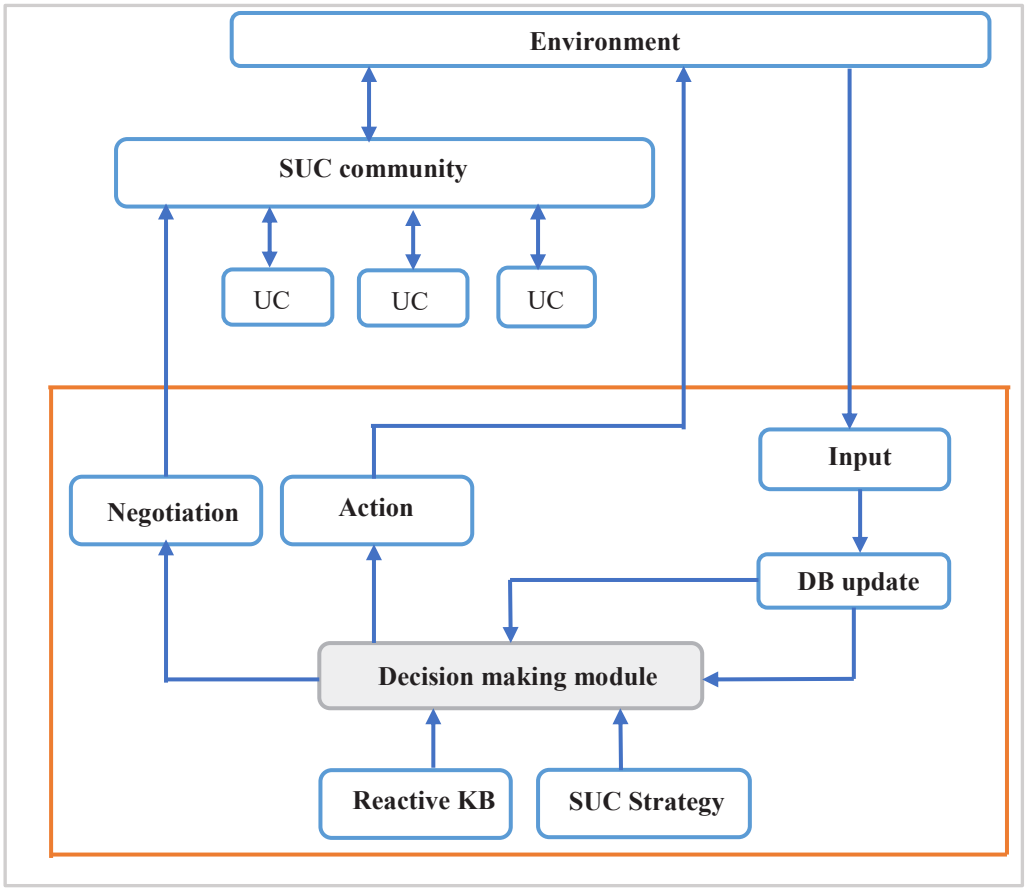

Fig. 3. SUC architecture.

4. Results and Discussion

The purpose of design a proposed system is to manage the compressor speed of SUAC in classroom, where this speed is suitable with space load. There are two SUAC in classroom, each one has SUC to manage its speed per hour. The main task that dedicated to controller is to reduce compressor speed in hour therefor the investigating of energy saving could be achieved. The total space load that set as the input parameter of the model has been considered by decision making module which in turn attempts to take a decision as an action about compressor speed. Decision making module determines the strategy path according to the entered load, where there are two paths: reactive reaction means determining the suitable speed in the limited range as speed1, speed2, or speed3. While the other strategy path is urged when the total input load is over the limited range in SUC, so there is a need to negotiate with a fellow SUC to solve the problem and accomplish the delegated task. The other important module is the reactive knowledge base module who stores the rules that is relied by decision making module to change compressor speed under conditions.

For example, if the total space load in the range of speed1 or 2 the compressor speed will be work in speed1 or 2, otherwise if the range in speed3 then the SUC1 will take half of load as input and test in which range of speed it is, then send the remaining load to other partner SUC who in turn tries to take it role to solve problem in the same strategy of SUC1.

4.1. Space load

During three months, the space load calculation for two classrooms is changed every hour from 10.2 kW to 19.5 kW. Due to solar heat gain, heat transformation, and student activity, the space load varies from 8 AM to 8 PM. Figure 4 depicts the space load on the first day from the mouth in June, July, and August. The space loads show a significant variation in hour 13 (see Figure 4) attributed to the reason that the classroom is empty at this time which lead to reduce the internal loads.

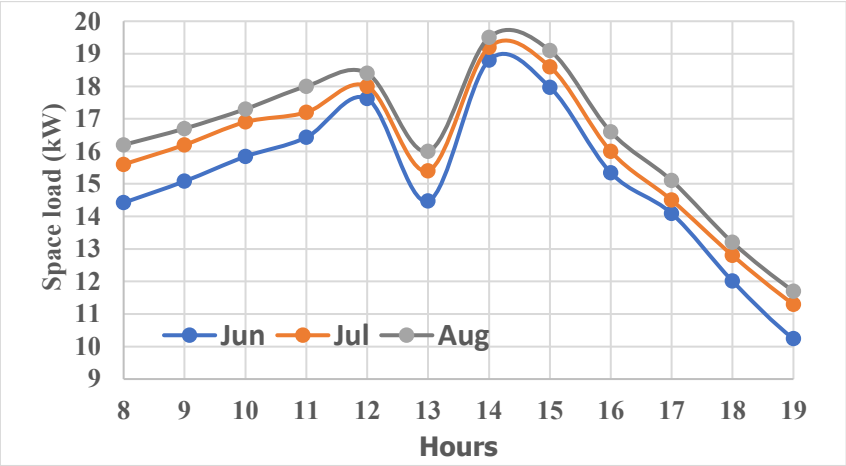

Fig. 4. Space load variation over a 12-hour period.

4.2. Negotiation of SUC

Two split units in studying room in TCB are utilized to challenge the SUAC ability to manage such compressor speed. This is fortified with calculated total loads starting from 8 AM until 8 PM as show in the Table 1. Other input parameter is the total capacity which is calculated by summation the SUC1 and SUC2' capacities, in case study it equals 6 Ton (21.096 kW). The decision making module utilizes the input information to take decision depending on rules stored in Reactive KB module. To do so, in hour 7 PM in June month, the space load is 14.42 kW, SUC1 is triggered to start work, the capacity of SUC1 in speed1 or 2 cannot cover this value, so the independent strategy is by dividing load and trying to change speed into speed1 or 2 ranges autonomously. Then send packet with the remaining load to fellow SUC in classroom to start negotiation with him. SUC2 receives a packet requesting to do a task from SUC1 to solve the problem. SUC2 is working with a half of load in same strategy of SUC1. Check if speed1, 2 or 3 can cover the remaining load then send reply packet to SUC1 with the result of achievement job. In hour 8 AM, SUC1 changes speed to speed2, and SUC2 works in speed2

too, so both SUCs do not work in full power and save 31% of energy in this hour (see Figure 5). Table 1 shows the behavior of SUCs in 12 hours in three days in June, July and August, where selected speeds each hour and the percentage of saved energy with the proposed system. The maximum value of save energy in June is 51.5% in hour 7 AM, because solar energy decreased. While the minimum value is 10.9% in hour 14 due to full load caused by maximum solar energy in Basrah city, and other space load. As shown in Table 1 in hour 15 the space load in June day is 17.97 kW, in July is 18.6 kW, and in August is 19 kW. In June and July, both SUCs work with speed 2 and cooperate to reduce lost energy. However, in August SUC1 work with speed2 while SUC2 work with speed3 to cover the load and save energy as possible.

Table 1. Compressor speed response for space load for three months.

						01-Jun						
Hours	8	9	10	11	12	13	14	15	16	17	18	19
Space Load (kW)	14.42	15.08	15.84	16.43	17.62	14.47	18.8	17.97	15.34	14.09	12.01	10.24
Comp_Speed SUC1	2	2	2	2	2	2	2	2	2	2	2	1
Comp_Speed SUC2	2	2	2	2	2	2	2	2	2	2	2	1
Save_Energy %	31.65	28.52	24.91	22.12	16.48	31.41	10.88	14.82	27.28	33.21	43.07	51.46
						01-Jul						
Hours	8	9	10	11	12	13	14	15	16	17	18	19
Space Load (kW)	15.6	16.2	16.9	17.2	18	15.4	19.2	18.6	16	14.5	12.08	11.03
Comp_Speed SUC1	2	2	2	2	2	2	2	2	2	2	2	1
Comp_Speed SUC2	2	2	2	2	2	2	3	2	2	2	2	2
Save_Energy %	26.10	23.20	19.90	18.50	14.70	27	9	11.80	24.20	31.30	42.70	47.70
						01-Aug						
Hours	8	9	10	11	12	13	14	15	16	17	18	19
Space Load (kW)	16.2	16.7	17.3	18	18.4	16	19.5	19.1	16.6	15.1	13.2	11.7
Comp_Speed SUC1	2	2	2	2	2	2	2	2	2	2	2	1
Comp_Speed SUC2	2	2	2	2	2	2	3	3	2	2	2	2
Save_Energy %	23.20	20.80	18	14.70	12.80	24.20	7.60	9.50	21.30	28.40	37.40	44.50

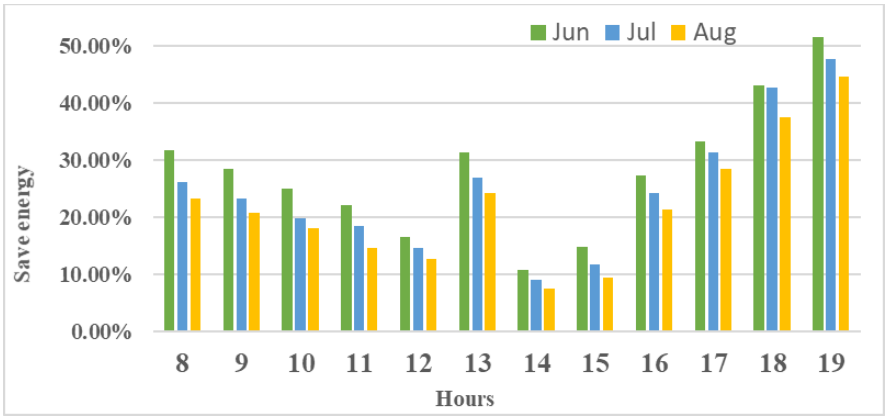

Fig. 5. Save energy for SUAC.

4.3. SUAC Efficiency

The Seasonal Energy Efficiency Rating (SEER) evaluates SUAC efficiency, which is computed by dividing the refrigeration capacity for a standard cold period by the total electrical power input over the same time period [20]. For example, if your SUAC has a SEER rating of 20, that is its maximum efficiency. The energy input to SUAC equal to capacity for year divide SEER. The results indicate that SUC could lead to significant reductions in SUAC compressor power in classroom 2 at constant SEER values (see Table2), resulting in reduced operating expenses throughout the year. This explains the observed decrease in energy input to compressor with constant capacity during the year.

Table 2. The SEER and annual running costs.

SEER	Capacity SUAC 1 (BTU/hr)	Capacity SUAC 2 (BTU/hr)	Total capacity (BTU/hr)	Operating time 12hr/day	Operating time 200day/year	Capacity for year BTU/year	Energy input kW.hr/year	Cost $ kW.hr	Cost $/year	Cost IQD/year
					Lecture theatre 1					
8	36000	36000	72000	12	200	172800000	21600	0.1	2160	3240000
					Lecture theatre 2					
8	36000	36000	72000	12	200	172800000	7200	0.1	540	810000
					Lecture theatre 1					
20	36000	36000	72000	12	200	172800000	8640000	0.1	864	1296000
					Lecture theatre 2					
20	36000	36000	72000	12	200	172800000	8640000	0.1	216	324000

5. Conclusions

The proposed SUC's architecture is developed to control the SUAC's compressor speed in the classroom when that speed is adequate for loading space. The proposed system is self-contained and requires no human interaction. The classroom space load is estimated for three months in Iraqi climates. The maximum space load is 17.97 kW in June, 18.6 kW in July, and 19 kW in August. In June the maximum saving power in hour 7 AM was 51.5% due to a low in solar energy. The minimum amount of save energy is 10.9 % at an hour 14 due to full solar heat loads. Both SUCs work with speed 2 in June and July and cooperate in reducing energy loss. SUC1 works with speed2 however in August, whereas SUC2 works with speed3 to cover the load and reduce energy. The multi speed SUAC with SUC was discovered to be the higher control unit with less energy used than other SUACs, in which the 24.8 % energy saving value is achieved. The SUC could lead to a large decrease of the SUAC compressor power in class 2 at SEER levels 8 or 20, with the result that the operating cost could be decreased by 75 percent throughout the year. The results indicated that the SUC architecture may be regarded a successful and efficient solution for multi-speed SUAC verification, and that it can be used in classroom applications at Southern Technical University/Engineering Technical College-Basra without requiring human interaction.

Nomenclature

Symbol	Definition
A	Area (m^2)
ACH	Air change per hour
CLF	Cooling load factor [-]
CLFs	Cooling load factor for occupants [-]
CLTD	Cooling load temperature difference (°C)
$CLTD_c$	Cooling load temperature difference correction (°C)
f	Attic fan factor [-]
G_l	Activity of occupants (latent) (W)
G_s	Activity of occupants (sensible) (W)
k	Colour factor [-]
LM	Latitude month correction
N	Number of occupants
Q	Heat transmission (kW)
P	Power of equipment (W)
Q_e	Equipment load (kW)
Q_i	Infiltration load (m^3/sec)
Q_{lo}	Latent occupant load (kW)
Q_s	Solar heat gain (kW)
Q_{so}	Sensible occupant load (kW)
Qv	Ventilation load (liter/sec)
SC	Shading coefficient [-]
SH	Solar heat (W/m^2)
T_o	Outside room temperature (°C)
T_r	Inside room temperature (°C)

References

[1] Tarish, A. L., et al. "Exergy and performance analyses of impact subcooling for vapor compression refrigeration system utilizing eco-friendly refrigerants." IOP Conference Series: Materials Science and Engineering. Vol. 997. No. 1. IOP Publishing, 2020. https://doi.org/10.1088/1757-899X/997/1/012158

[2] Tarish, Ali Lateef, Mushtaq Talib Hamzah, and Wasan Assad Jwad. "Thermal and exergy analysis of optimal performance and refrigerant for an air conditioner split unit under different Iraq climatic conditions." Thermal Science and Engineering Progress 19 (2020): 100595. https://doi.org/10.1016/j.tsep.2020.100595

[3] Yoon, Ji Hoon, Ross Bladick, and Atila Novoselac. "Demand response for residential buildings based on dynamic price of electricity." Energy and Buildings 80 (2014): 531-541.

[4] Russell, Stuart, and Peter Norvig. "Artificial intelligence: a modern approach." (2002).

[5] Wooldridge, Michael. An introduction to multiagent systems. John wiley & sons, 2009.

[6] Al-Badri, Alaa R., and Ahmed H. Al-Hassani. "A control method using adaptive setting of electronic expansion valve for water chiller systems equipped with variable speed compressors." International Journal of Refrigeration 119 (2020): 102-109.

[7] Hu, Maomao, Fu Xiao, and Howard Cheung. "Identification of simplified energy performance models of variable-speed air conditioners using likelihood ratio test method." Science and Technology for the Built Environment 26.1 (2020): 75-88.

[8] Lim, Jaehun, et al. "Feasibility study on variable-speed air conditioner under hot climate based on real-scale experiment and energy simulation." Energies 12.8 (2019): 1489.

[9] Chen, Zhijie, et al. "Machine learning enhanced inverse modeling method for variable speed air conditioning systems." International Journal of Refrigeration 118 (2020): 311-324.
[10] Elsayed, Amr Owes, and T. S. Kayed. "Dynamic performance analysis of inverter-driven split air conditioner." International Journal of Refrigeration 118 (2020): 443-452.
[11] Wang, Beibei, et al. "Consensus control strategy of an inverter air conditioning group for renewable energy integration based on the demand response." IET Renewable Power Generation 12.14 (2018): 1633-1639.
[12] Windham, Andrew Winsome. "A multi-agent decision process for controlling heating, ventilation, and air-conditioning systems." (2014).
[13] Lee, Dasheng, and Fu-Po Tsai. "Air conditioning energy saving from cloud-based artificial intelligence: Case study of a split-type air conditioner." Energies 13.8 (2020): 2001.
[14] Lork, Clement, et al. "An uncertainty-aware deep reinforcement learning framework for residential air conditioning energy management." Applied Energy 276 (2020): 115426.
[15] Nielsen, Peter Vilhelm, et al. "Indoor Environmental Modelling: Chapter 34 in ASHRAE Handbook, Fundamentals." ASERAE Handbook, Fundamentals. American Society of Heating, Refrigerating and Air-Conditioning Engineers, Inc., 2005.
[16] McQuiston, Faye C., Jerald D. Parker, and Jeffrey D. Spitler. Heating, ventilating, and air conditioning: analysis and design. John Wiley & Sons, 2004.
[17] McArthur, Stephen DJ, and Euan M. Davidson. "Concepts and approaches in multi-agent systems for power applications." Proceedings of the 13th International Conference on, Intelligent Systems Application to Power Systems. IEEE, 2005.
[18] Sycara, Katia P. "Multiagent systems." AI magazine 19.2 (1998): 79-79.
[19] Wasan A.Jwad and gasim “A Probabilistic Finite State Machine based Residential Environment for Obligation Agent Development” The Third Southern University International Conference. Vol.6. P.164.
[20] Kim, Woohyun, and James E. Braun. "Evaluation of the impacts of refrigerant charge on air conditioner and heat pump performance." International journal of refrigeration 35.7 (2012): 1805-1814.

Performance enhancement of Dicode Pulse Position Modulation System by means of LDPC code

Yasmeen M. Hussein[1], Basman M. Al-Nedawe[2], Ammar Hussein Mutlag[3]
{bbc0030@mtu.edu.iq[1] , b.al-nedawe@mtu.edu.iq[2], ammar_alqiesy@yahoo.com[3]}

Middle Technical University, Electrical Engineering Technical College, Baghdad, Iraq[1,2,3]
Middle Technical University, Technical Institute of Baquba, Diyala, Iraq[2]

Abstract. Several types of Pulse Position Modulation (PPM) formats were proposed as coding schemes for optical communication such as Differential Pulse Position Modulation (DPPM) and Multiple Pulse Position Modulation (MPPM). However, these coding schemes result in a large bandwidth expansion factor that deduces an excessively high final data rate. On the other hand, Dicode Pulse Position Modulation (DiPPM) is an unconventional coding scheme that has superior characteristics beyond the PPMs proposed. More specifically, DiPPM has been developed to resolve the bandwidth consumption issue of PPM formats. For the first time, this study intends to overcome the DiPPM errors issue via the implication of forwarding Error Correction (FEC). In this regard, low-density parity-check (LDPC) is used in conjunction with multi-level coding, multi-stage encoding, and trellis-based signal shaping to create a bandwidth-efficient modulation format. The optimum code rates for different fibre normalised bandwidths of maximum transmission efficacy will be investigated.

Keywords: Dicode pulse position modulation (DiPPM); forward error correction (FEC) code; Low-density parity-check (LDPC); log-likelihood ratio (LLR); Bandwidth consumption issue**.**

1 Introduction

The communication device transmits data from the source to the receiver by a channel or transmitted media such as wired or wireless. The change and specifically the external noise of the channel are the main parameters controlling the reliability of obtained data. The noise is the main reason for signal interference and errors in transmitted data [1]. Channel coding is a smart way to increase interface performance in low-turbulence situations. In this regard, various types of PPM formats were presented in the literature as coding schemes for optical communication. For instance, MPPM and DPPM [2]. PPM is widely used in deep-space optical communication due to its high energy consumption, good anti-interference efficiency, and high detection frequency. However, one of the most drawbacks of PPMs is the production of an extremely high final data rate due to a large bandwidth expansion factor [3]. In other words, the final line rate may be extremely high, restricting its usefulness. Therefore, these coding schemes are appropriately used to synthesize directed lines of sight networks of glass optical fibre cables where bandwidth is not essential. In this aspect, optical fibre connections are widely used in low-bandwidth magnetic recording networks due to their inexpensive characteristics [4]. Thus, to resolve the challenge of bandwidth, DiPPM has been developed by Sibley (2003a) as an unconventional coding scheme that has superior characteristics beyond the PPMs proposed. More specifically, the DiPPM was developed to eliminate the main concern of bandwidth dissipation via the PPM.

LDPC codes are extensively used as efficient codes compared to other adaptable codes due to their applications with competent and reliable information transfer over bandwidth links in the existence of corrupting noise. Therefore, LDPC codes can operate in a wide range of channels. However, the reliability and accuracy of these codes and techniques deteriorate as the block length gets smaller. Only data transformations are sent in this signalling format, and no signal is sent with fixed data [5].

IMDC-IST 2021, September 07-09, Sakarya, Turkey
Copyright © 2022 EAI
DOI 10.4108/eai.7-9-2021.2314935

LDPC and PPM iterative demodulation systems are popular in deep space algorithms due to their output is close to the Shannon limit. The Shannon limit of a communication channel denotes the extreme rate of error-free data which can be transferred over the channel if the link is subjected to random data transmission errors, for a specific noise level. Reed Solomon code (RS) was also invented by Reed and Gustave Solomon in 1960 (Reed and Solomon, 1960) to control DiPPM error sources. Reed and Solomon (1960) confirmed the superiority of DiPPM to efficiently check the errors despite the packet error rate performance can be enhanced using the RS algorithm at the time of error detection. Additionally, the DiPPM errors acquired during the transmission can be eliminated using the MLSD error corrector [6].

Up to the authors' knowledge, the examination of DiPPM and LDPC code decoding techniques have not been yet applied to mitigate the issues of bandwidth expansion in PPM. Thus, this paper intends to resolve this challenge via incorporating the DiPPM and LDPC code to eliminate the errors and investigating the optimum parameters of LDPC.

2 Dicode Pulse Position Modulation (DiPPM)

To address the issue of bandwidth expansion in PPM, DiPPM was suggested [7]. DiPPMs have a similar trend to the PPMs formats. DiPPM has four-time slots, which was employed in the pulse code modulation (PCM) of a single time interval amplification. PCM approach helps to digitally signify sampled analogy signals. Specifically, the amplitude of the analogy signal is tested frequently at identical intervals for a PCM stream, and each sample is estimated to the nearest value within a range of digital steps.

A SET (S) pulse is sent to the 1st slot, while a SET (S) pulse is sent to the 2nd slot. The 2nd slot is used for a RESET (R) pulse, and the 3rd and 4th fourth slots are used as guard slots to prevent inter-symbol interference (ISI). Due to a PCM data inversion from 0 to 1, the S pulse is coded, whereas the R pulse is produced at a one-to-zero inversion. This is schematically presented in Fig. 1. Fig. 1 demonstrates the translation of PCM data from the top trace into a middle trace of dicode and bottom trace of DiPPM. The alphabet of DiPPM symbols is depicted in Table 1.

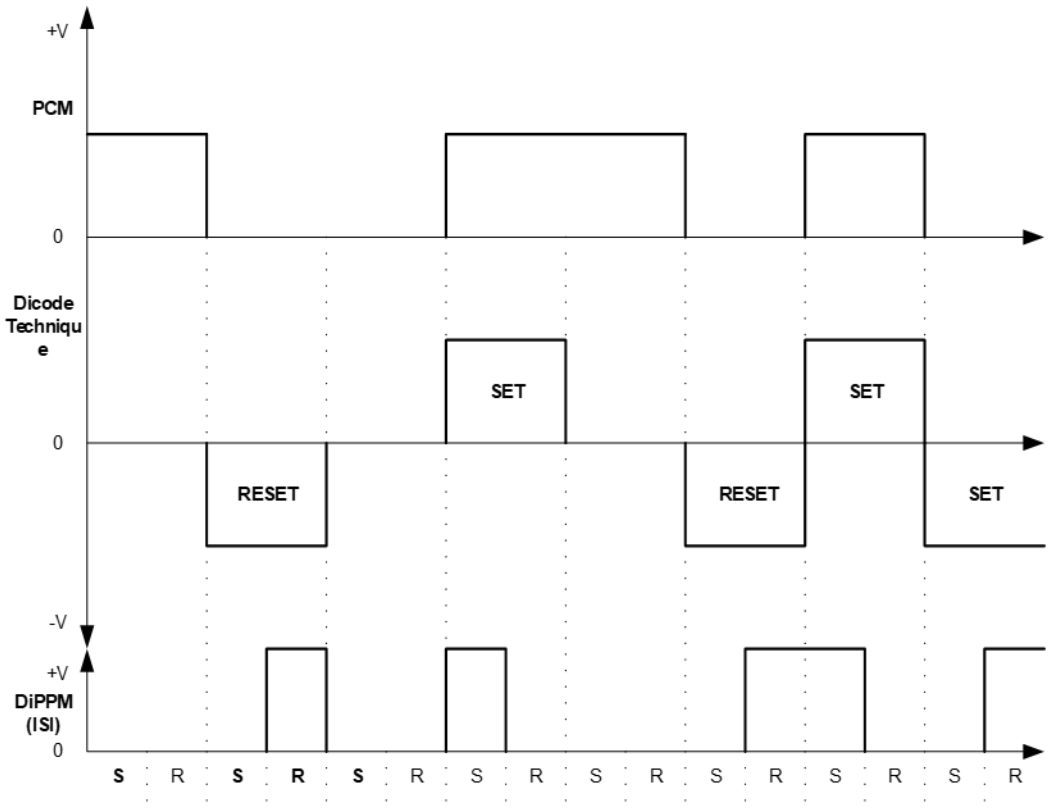

Fig 1. Translation of top trace (PCM data) into middle trace (Dicode) and bottom trace (DiPPM).

Table 1. DiPPM symbol alphabet

PCM	DiPPM	Symbol
00	**No pulse**	N
01	**SET**	S
11	**RESET**	R
011	**NO Pulse**	N

Although the PCM data remains unchanged, no pulse is transmitted. However, the inter-symbol interference was minimised due to the implication of central decision detection to substitute the slope detection technique. In other words, the central decision detection technique has reduced the difficulty of the DiPPM decoder via deploying a simple 1st order preamplifier in cascade and a 3rd order Butterworth filter [8]. More specifically, the DiPPM's line rate was reduced to twice the real data because of the lack of guard bits. Thus, it is fair to confirm the viability of the DiPPM format to compete with other PPM formats implemented in optical fibre systems because of its high efficacy and simplicity.

3 DiPPM ERROR

Three types of detection errors can be found in DiPPM format including wrong-slot, erasure, and false alarm [9]. The next sections highlight the description and probabilities of these errors in detail.

3.1 Wrong-Slot Errors

Wrong-slot errors occur when noise on the rising edge of a detected pulse causes the pulse to be presented in contiguous time slots. Therefore, the pulse must be identified to reduce these errors in the middle of the Ts-width time slot. Also, a new pattern is formed when the edge transfers by [Ts/2].

3.2. Erasure Errors

Erasure errors of a pulse occur when the peak signal voltage falls under the threshold level. Specifically, this happens at a high level of noise.

3.3. False-Alarm Errors

False-alarm errors occur if the noise crosses a threshold limit in any unused data slot.

4 Low-Density Parity Check (LDPC) Code

The Low-Density Parity Check (LDPC) code has been proposed with a matrix of the parity search that has N columns and M rows and is represented as H = [HMxN]. LDPC code contains several 0s and a restricted amount of the 1s. In other words, systematic LDPC codes have been deliberated with special characteristics. The characteristics specify that each column has a fixed "1" number such as weight of the column and each row has a fixed "1" number (i.e. weight of the row). However, there is no consistency between the weight of the column and the line weight. The LDPC code has been specified by the code of the LDPC (N,y, k). N signifies the recurrent, use a different code-word term length, and j, k is the LDPC code’s column and row

weight, respectively. 1-y / k = 1-M / N is the LDPC code rate. The 8-bit code length normal parity-check matrix is identified as [10]

$$v_1 v_2 \cdots \cdots \cdots \cdots v_x$$

$$H = \begin{bmatrix} 0\,1\,0\,1\,1\,0\,0\,1 \\ 1\,1\,1\,0\,0\,1\,0\,0 \\ 0\,0\,1\,0\,0\,1\,1\,1 \\ 1\,0\,0\,1\,1\,0\,1\,0 \end{bmatrix} \begin{matrix} c_1 \\ c_2 \\ \vdots \\ c_y \end{matrix} \quad , \text{x = 1, 2, … N and y = 1, 2, ….., M}$$

Fig. 2 depicts another configuration of the H matrix where the Tanner graph contained check nodes sets and variable nodes that corroborate each matrix row and column, respectively.

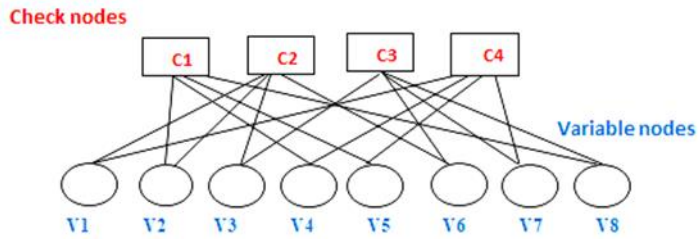

Fig. 2. A graphical representation of LDPC codes

5 System Model

The optimal parameters of LDPC code with DiPPM format have been investigated using slope detection and central detection techniques. However, it is vital to building an accurate system model to carry out a successful simulation. A system model describes the relationships between the inlet and outlet parameters. Fig. 3 represents a block diagram of the receiver system that signifies the FEC communication system, which is reliant on the LDPC error-control code.

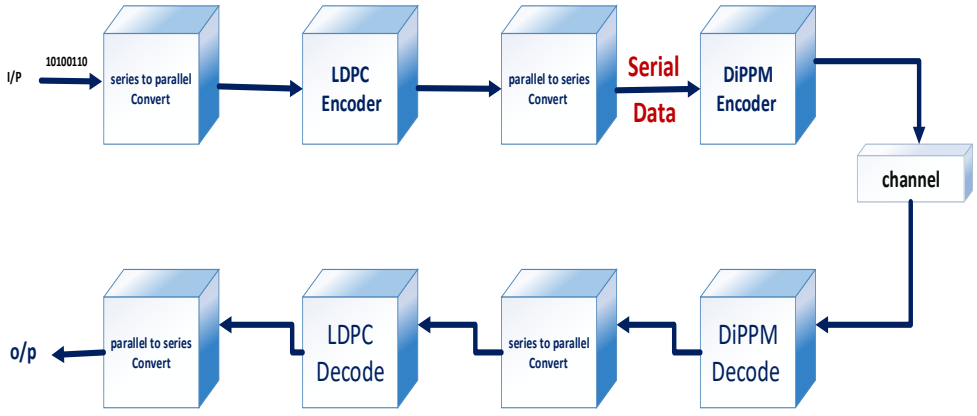

Fig. 3. System model.

This system characterizes by using a new device variable denotes as v (Eq. 1) that signifies the division of the decision voltage to the peak signal voltage. Therefore, the system has capsulated both the peak voltage of the signal (v_{pk}) and threshold crossing voltage (v_d) as illustrated below

$$v = \frac{v_d}{v_{pk}} \tag{1}$$

The effectiveness of transmission (ρ) for both uncoded and coded DiPPM (when the LDPC code is used) can be calculated using Eqs. 2 and 3, respectively, based on the number of photons per pulse (b). It is important to note that using an LDPC code would reduce the system's transmission efficacy based on the code rate (r), as depicted in Eq. 3. Thus, it is important to reduce b and utilize the optimal code rate in the deployment of an LDPC code to guarantee an accepted transmission efficacy [11].

$$\rho = \frac{\ln 2}{b} \tag{2}$$

$$\rho = \frac{r \ln 2}{b} \tag{3}$$

Eq. 4 is used to compute the bandwidth expansion for coded DiPPM

$$BWE_{coded\ DiPPM} = \frac{n}{k} \times BW_{DiPPM} \tag{4}$$

The simulation has considered a white-noise spectrum at the output of an optical receiver with restricted bandwidth as depicted in Fig. 3. Specifically, the pre-detection filter was used as a feasible matched filter due to having a receiver of a white-noise spectrum. The signal obtainable to the threshold detector was considered for transmission of dicode PPM via graded-index POF. Accordingly, the time variation of the device variable ($v_o(t)$) is mathematically represented as

$$v_o(t) = b\eta q R_T \, \frac{\omega_c}{2} \exp(\alpha^2 \omega^2) \times \exp(-\omega_c t) erfc[\alpha\omega_c - (\tfrac{t}{2\alpha})] \tag{5}$$

η is the detector's quantum efficiency, q is the electronic charge, R_T is the receiver's mid-band trans-impedance, and ω is the change of the Gaussian pulse obtained. α is the fibre bandwidth that can be estimated from Eq. 6

$$\alpha = \frac{0.1874 T_b}{f_n} \tag{6}$$

T_b is the bit-time of PCM and f_n is the fibre bandwidth normalised to the PCM data rate. (n_o) signifies the noise performing on the signal as given in the context of Eq. 7

$$\left\langle n_o^2 \right\rangle = S_o \, \frac{\omega_c}{2} R_T^2 \exp(\alpha^2 \omega_c^2) erfc(\alpha\omega_c) \tag{7}$$

S_o is the equivalent double-sided input-noise current spectral density of the preamplifier. The distribution of the channel log-likelihood ratio (LLR) is used to analyse LDPC codes. The channel LLR L is frequently measured by supposing the code words are all zeros. (x = +1) was conveyed and therefore L is clearly expressed as

$$L = \log \frac{p(x=+1|y)}{p(x=-1|y)} \tag{8}$$

LLRs have asymmetric Gaussian distribution for the BIAWGN(σ) with mean μ = 2/σ2 and variance 4/σ2. A detection error exists with negative values of LLR. This study uses N samples of this distribution in each realization of the channel compared to a pure Gaussian LLR distribution. Thus, there is no consistency between pure Gaussian distribution and LLR distribution with a considerable diverge. However, the LLR distribution and the channel parameter remain constant. It is worth noting that a single parameter would not be able to completely describe this deviation.

The probability distribution of average bit error for the finite-length case is computed by considering the N samples from the symmetric Gaussian LLR distribution. In this regard, each sample orbit is incorrect within negative LLR. Accordingly, the likelihood of error of each sample (Fpobs) is mathematically defined on x in the following equation (Eq. 9). In this regard, the summation of all corresponding errors divided by N would signify the whole probability of errors.

$$Fp_{obs}(x) = \binom{N}{Nx} p_o^{Nx} (1 - p_0)^{N-Nx} \tag{9}$$

N x is an integer, and $0 \leq N\ x \leq N$. However, The Fpobs is approximated defined by a Gaussian pdf N(p0, p0(1p0)/N) with insignificant values for x outside [0, 1] for large N.

6 Results and Discussion

The intension of this section is to focus on discussing the influence of the number of photons per pulse (b) in the DiPPM coded format using slope and central detection systems at different code speeds. The number of photons is measured using a 2M code word length, besides considering M values between 3 to 7. It is important to realize that b increases as the LDPC code rate raises. This is due to the consistent correlation between the LDPC code rates and the number of data symbols. Also, b is proportionate to the normalised bandwidth when using the slope detection process. This is also due to the reliance on the slope detection approach to the form of established signal. Fig. 4 demonstrates the variation of b for DiPPM system using LDPC against LDPC code rate at different normalised bandwidths. The minimum numbers of photons can be determined at different LDPC code rates and different normalised bandwidths. It is worth noting that the system kept the number of errors to an absolute minimum. More importantly, b is inversely proportionate to the number of normalised bandwidths as depicted in Fig. 4. Specifically, the lowest b is confirmed for the highest normalised bandwidth. Also, there is an exponential increase of b against the increase of the LDPC code rate. In this regard, it is vital to perceive the importance of mitigating b to accordingly generate the optimal code rate in the application of an LDPC code and to accelerate the highest performance of the device.

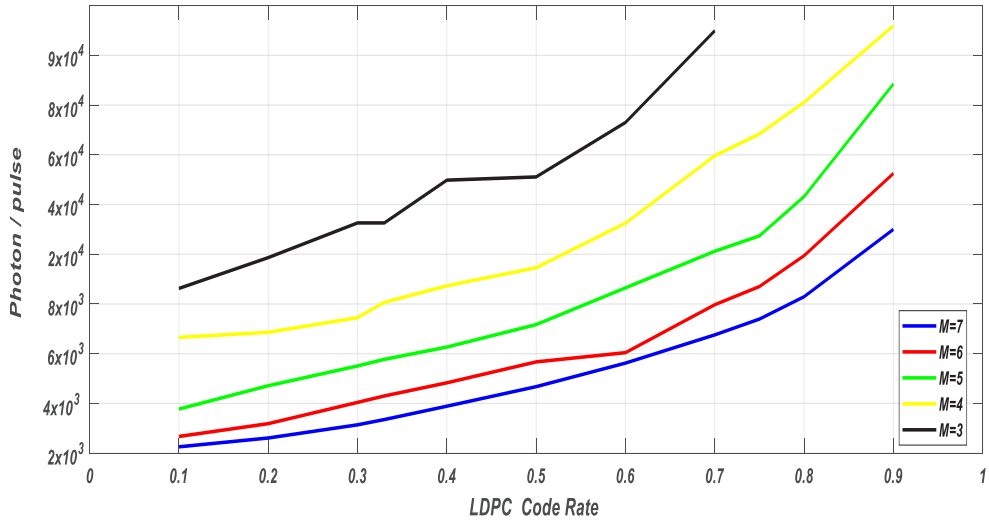

Fig. 4. Number of photons against LDPC code rate at different normalised bandwidths

Fig. 5 depicts the coded DiPPM system's transmission efficacy against LDPC code rates for several fibre normalised bandwidths. Fig. 5 confirms an optimum transmission efficacy at approximately 0.6 of LDPC code rate for the highest normalised bandwidths. However, the optimum transmission efficacy exists within higher LDPC code rates of approximately 0.7 for the lower normalised bandwidths. It is important to perceive the existence of an exponential relationship between the transmission efficacy and the code rate as the efficacy is reduced after gaining the optimal code rate. In other words, the uncoded symbol errors have increased even further due to an increase in code rate. Thus, the transmission of corrected symbols and the system's efficacy is reduced. In this regard, the redundancy, and the redundancy rate increase beyond the optimum code rate. However, higher fibre normalised bandwidths are successfully empowered the transmission efficacy.

Figs. 4 and 5 can also affirm the necessity of reducing *b* with LDPC codes to applicably improve the transmission efficacy of the DiPPM.

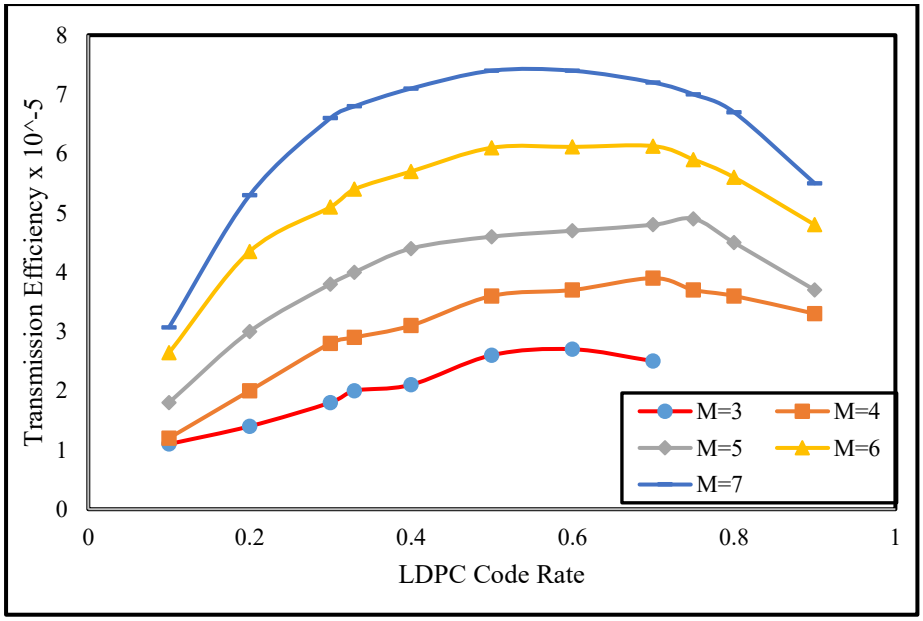

Fig. 5. The transmission efficacy of coded DiPPM system against LDPC code rates within different normalised bandwidths**.**

Fig. 6 demonstrates the variation of the number of photons per pulse for the coded PCM system against LDPC Code Rate for several normalised fibre bandwidths (f_n). It can be stated that there is a direct positive relationship between the number of photons per pulse and the LDPC Code Rate for any selected normalised bandwidth. Specifically, the number of photons increases as the Code Rate increases for a particular bandwidth.

Fig. 7 clarifies the relationship between the transmission efficiency of PCM employing LDPC code system against the LDPC Code Rate for various fibre bandwidths (f_n) normalised to the PCM data rate. It can be concluded that employing an optimum value of 0.7 of the Code rates would maximise the overall efficiency. The coded DiPPM using the LDPC code realizes the highest transmission efficiency for the low dispersive channel. This can be attributed to the bandwidth's extension which would consume more energy by adding the redundancy symbols. The calculation of transmission efficiency for the PCM using LDPC code system is carried out using the relationship of Sibley (2005) as follows

$$\alpha = \frac{0.1874T_b}{f_n} \tag{10}$$

T_b is the PCM bit-time. The noise acting on this signal is elucidated in the following equation

$$\rho = \frac{r \ln 4}{b} \tag{11}$$

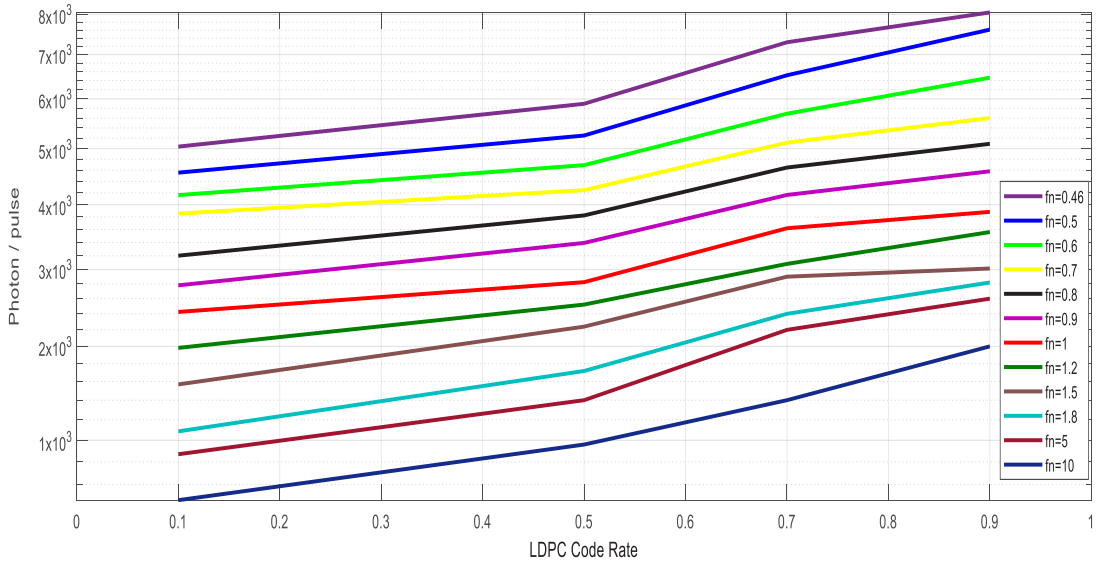

Fig. 6. Variation of photons' number against LDPC code rate at different normalised bandwidth.

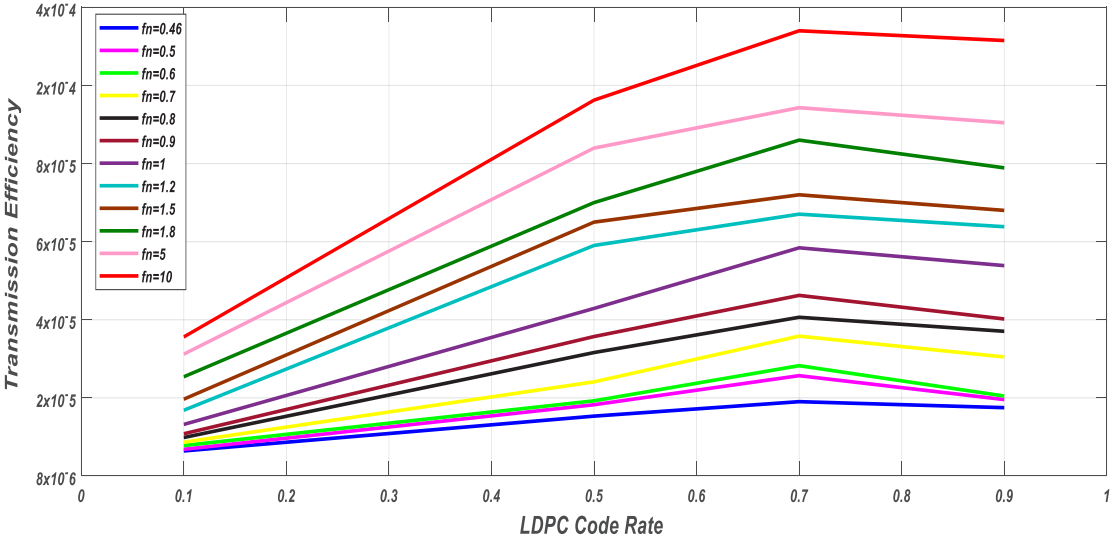

Fig. 7. Transmission efficiency versus LDPC code rate at different normalised bandwidth

7 Conclusions

LDPC codes with DiPPM were investigated in this paper for improving the transmission efficacy, bandwidth expansion, and several photons necessitated per pulse. The DiPPM coded system outperforms the uncoded system. To manage the main aim of this study, the obtained signal was detected using two improved techniques of the slope detection and central detection. It can be stated that reducing the number of photons with LDPC codes would significantly enhance the DiPPM's transmission efficacy. Furthermore, the machine efficiency can be improved by increasing the LDPC codeword. More importantly, the study delivered the optimum LDPC code rates for high and low fibre normalised bandwidths that entailed the maximum transmission efficacy.

References

[1] Al-Nedawe, B. M., Buhafa, A.M., Sibley, M.J., and Mather, P.J., 2013. Improving error performance of dicode pulse position modulation system using forward error correction codes. In 2013 21st Telecommunications Forum Telfor (TELFOR) (pp. 331-334). IEEE.

[2] Charitopoulos, R. and Sibley, M.J., 2009. Experimental coder/decoder of dicode pulse position modulation. University of Huddersfield.

[3] Ghassemlooy, Z., Hayes, A.R. and Wilson, B., 2003. Reducing the effects of intersymbol interference in diffuse DPIM optical wireless communications. IEE Proceedings-Optoelectronics, 150(5), pp.445-452.
[4] Li, E., Declercq, D., and Gunnam, K., 2013. Trellis-based extended min-sum algorithm for non-binary LDPC cod es and its hardware structure. IEEE Transactions on Communications, 61(7), 2600-2611.
[5] Li, H., Liu, H., and Vafi, S., 2014. Bipolar chaotic pulse position modulation communication system based on cyclic LDPC. EURASIP Journal on Wireless Communications and Networking, 2014(1), 1-9.
[6] Reed, I.S. and Solomon, G., 1960. Polynomial codes over certain finite fields. Journal of the society for industrial and applied mathematics, 8(2), pp.300-304.
[7] Sibley, M.J., 2003a. Analysis of dicode pulse position modulation using a PINFET receiver and a slightly/highly dispersive optical channel. IEE Proceedings-Optoelectronics, 150(3), 205-209.
[8] Sibley, M.J., 2003b. Dicode pulse-position modulation: a novel coding scheme for optical-fibre communications. IEE Proceedings-Optoelectronics, 150(2), 125-131. [
9] Sibley, M., 2005. Performance analysis of a dicode PPM system, operating over plastic optical fibre, using maximum likelihood sequence detection. IEE Proceedings-Optoelectronics, 152(6), 337-343.
[10] Wang, H., Su, Y., Zhang, G., and Zhang, T. (2007). Performance analysis for LDPC-coded optical PPM communication system in weak turbulence. In Second International Conference on Space Information Technology (Vol. 6795, p. 67956V). International Society for Optics and Photonics.
[11] Yazdani, R., and Ardakani, M., 2007. An efficient analysis of finite-length LDPC codes. In 2007 IEEE International Conference on Communications (pp. 677-682). IEEE.
[12] Hussein, Y. M., Mutlag, A. H., & Al-Nedawe, B. M. (2021, June). Comparisons of Soft Decision Decoding Algorithms Based LDPC Wireless Communication System. In IOP Conference Series: Materials Science and Engineering (Vol. 1105, No. 1, p. 012039). IOP Publishing.

Numerical Study of flow-through the perforations for angle perforation 180° and 90° in horizontal wellbore

Mohammed A. Mustafa[1], Qais A. Rishak[2], Mohammed A. Abdulwahid [3]
{Pgs2338@uobasrah.edu.iq[1], qais.rashck@uobasrah.edu.iq[2], mohw2016@stu.edu.iq [3]}

The University of Basrah. Mechanical Engineering Department [1]
The University of Basrah. Materials Engineering Department[2]
Southern Technical University, Basrah. Thermal Mechanical Engineering Department [3]

Abstract. A numerical study is carried out on the perforation pipes with phase angles of 180° and 90° in a horizontal wellbore. To understand the effect of the above two-phase angles on the flow inside the wellbore, the CFD simulation of computational fluid dynamics is used. ANSYS FLUENT's simulation of the flow in the well has been used to calculate the pressure drop, friction factor, wall shear stress, productivity index, etc. The standard $(k-\varepsilon)$ model has been used to predict the turbulent behavior of radial flow. The conclusion showed that the overall pressure drop increase as the flow rate ratio increase which leads to an increase in the radial flow through the perforations, thereby keeping the axial flow through the pipe constant. Therefore, the percentage error of the total pressure drops for the phasing of the 180° and 90° perforations in test 5 is about 5.4 %. In addition, the main flow increases when the flow through the perforation increases, and this leads to an increase in the average of wall shear stress.

Keywords: CFD, Perforation, Horizontal Well, Pressure Drop, Productivity Index

1 Introduction

Horizontal wells have become commonplace in the petroleum business. Due to the pressure drop in the well, the productivity of horizontal wells will be limited. During flow from the horizontal end (toe) to the end (heel) horizontal, the pressure drop in the well is imminent. Therefore, the pressure drop in the well is important to compare to the storage tank, pulling the tank along the length of the good changes, therefore production along the good length will also change. Locke [1] proposed a new theoretical model to predict horizontal good productivity, by building a very right simulation model, precise limit element methods were used to simulate operations. These analyses confirmed previous results that the angle of the perforations 90 degrees is better than the test angles 0, 120, and 180 degrees, but it produces greater amounts of inflow through the perforations. Subsequently, others [2-5] continued their research, and they proposed different coupling models of well flow and perforation into the reservoir. However, in some case studies, only the friction component is observed to study the pressure drops across the wellbore.The most probable case: acceleration was considered when studying pressure drop, and other effects such as flow, mixing, etc. were ignored.

The first study of fluid mixing between internal and main flow was raised flow provided by Su and Gudmundsson [6] studied the effect of the overall pressure drop in a perforated horizontal wellbore with fluid flow through the perforation where two fluids are mixed at junctions. Using the experimental parameters on a perforated pipe has an inner diameter of 22.2 mm, length of 2 m, and a Perforation diameter of 3 mm, a perforation density of 12 spf, and a 60° phasing. The results explain that the friction wall drop of pressure is about 80%, the flow mixing pressure drop (including perforation roughness) is about 15% and the acceleration pressure drop is about 5% of the overall pressure drop. Novy [7] studied the effect of friction losses on the pressure drop inside the horizontal wellbore, flow throughout the system is single phase and steady. The results showed that the decrease in pressure is important for shrinkage (the pressure difference

IMDC-IST 2021, September 07-09, Sakarya, Turkey
Copyright © 2022 EAI
DOI 10.4108/eai.7-9-2021.2314933

between the reservoir and the wellbore), so the pressure can approximately equal the pressure in the reservoir. Asheim et al. [8] suggested a model for fluid resistance for a theoretically horizontal perforated well. This model has one or two perforations with a diameter of 12.7 mm and length are 200 mm and it is made from the experimental group of test section pipe (50, 100, and 150 mm). The results showed that the proposed fluid flow resistance model gives excellent compatibility compared to the experimental results. Campos et al. [9] a mathematical model is developed based on conservation equations for mass and momentum. The experimental results showed excellent compatibility with the proposed fluid flow resistance model. From this work, the determined the effects of an acceleration and friction pressure drop on the total oil well productivity index. Fayal and Lakhdar [10] proposed a research model for the established pressure drop caused by friction and acceleration in a horizontal well with constant and single-phase flow. ANSYS FLUENT and disordered (k-ε) models were used to determine the entrance length. The result showed that the pressure drop due to acceleration was significant and equal to 30% of the total pressure and friction pressure drop due to perforation was neglected.
Abdulwahid et al. [11] provided a numerical simulation model of a pipeline flow with two perforations, one on the upper and one on the lower surface. Using ANSYS to analyse the overall pressure drops, the static pressure, and the average wall shear stress distribution of a horizontal well with a diameter of 22 mm and a length of 1 m. There are two perforations with perforation diameters of 0.006 m and 0.003 m. It is used the RNG (k-ε) model in the plane of symmetry model. Their results showed that the total pressure drop increases as increasing the axial velocity and vice versa.

The main objective of this paper is to analyse numerically the effect of pressure drop in perforation of a horizontal wellbore. Which is including the wall friction, mixing, and acceleration, that contribute to the total pressure drop in a perforated pipe. As well as study the effect of the friction factor, productivity index, and the effect of the change in the quantities of flow through the perforations and the axial flow in perforation a horizontal well of the angle of 180°, and 90°. It is noticed that the productivity index of the angle perforation 90° is higher than the perforation angle of 180°. As a result of increasing the amount of flow through the perforations for an angle of 90° greater than the angle of 180°.

2 Numerical Simulations

The rapid advancement of computer technologies and software enables the solution of theoretical simulations for complex applications. This paper investigates a Numerical analysis of a single-phase flow through a horizontal wellbore. The mathematical simulation with a 3D model with turbulent flow in the horizontal wellbore is performed. Using CFD ANSYS FLUENT. The horizontal wellbore simulation is carried out using the conservation law (mass, momentum) in conjunction with the perturbation (k-ε) model.

The numerical analysis of the fluid flow field is solved using ANSYS FLUENT. The ANSYS FLUENT is used to solve the numerical analysis of the fluid flow field. The cell-vertex finite volume method is used by ANSYS FLUENT solvers. A fixed number of the control volumes are created from the fluid region.

3 Description of the Models

In the current study, the numerical analysis is made with ANSYS FLUENT. It is used the stander k-ε model. The physical models are developed in the two PVC pipes with a perforations surface roughness of 0.03mm. The first pipe is 18 perforations divided into two lines with 180^{o} perforation phasing. Each line has 9 perforations. The second pipe has 20 perforations divided into four lines with perforation phasing 90^{o} each line has 4 perforations. The length of the pipe that drawing in ANSYS is 2 m, 44 mm inner diameter, and 4 mm perforation diameter. The pipe is divided into three sections. The first section in length 0.250 m is blank, and the second

is part of the pipe of 1 m of the perforation phasing 180 ° and 90°. The third section in length 0.75 m is blank, As shown in Fig.1 the model of the perforation pipe.

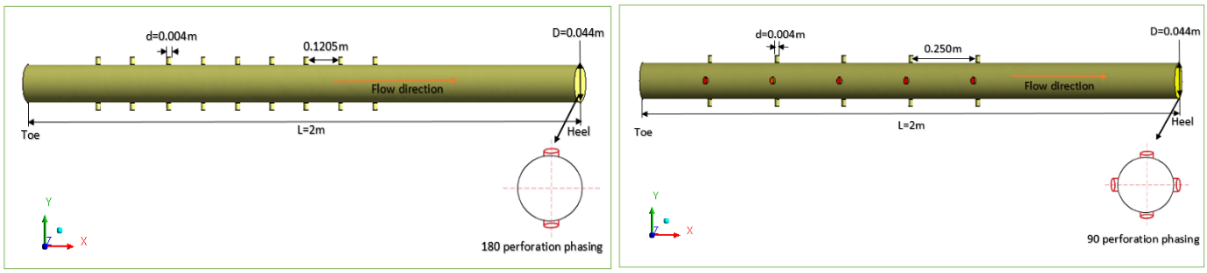

Fig.1. The physical model for 180° and 90° perforation phasing.

4 Assumptions and Simulation Parameters

The water density of 1000 kg/m^3, the dynamic viscosity of 0.00103 kg/ms, and water at 25° of the water (isothermal) are applied in our work. It is analysed the pressure, friction, and productivity index.

The present work is based on single-phase, turbulent flow, steady-state flow, Newtonian fluid, incompressible flow, and no heat transfer related the system to surroundings.

4.1 Boundary Condition

The solving of the management equations system of a CFD can only be used if the solution meets certain boundary constraints. As a result, we must supply boundary conditions to a CFD solver. Boundary inputs can be utilized to convert a CFD model counterpart to a real situation in a variety of ways. In ANSYS fluent, there are numerous techniques for describing fluid limitations.

Inlet B.C

The inlet boundary condition is used where the flow is directed mainly to the domain, the normal velocity is specified directly at the inlet. This process occurs during the Fluent-Solver process.Axial flow through the main horizontal wellbore

$$Q = U_1 * A \tag{1}$$

Q = axial flow rate of the main pipe m^3 /s

Radial flow through a perforation in the pipe

$$q = \mathrm{n}\frac{\pi}{4}\mathrm{d}^2\ \mathrm{U}_2 \tag{2}$$

q =inflow through perforation flow rate m^3/s

Tests are performed at different flow rates of the axial flow through the main pipe and radial flow through the perforations in all these tests are shown in Table 1. In the case of turbulent flow, the flow rates are selected based on the values of Reynolds number, which is greater than 4000.

Table 1. Details of the flow.

Flow Test	Axial flow (lit/min)	Radial flow rate (lit/min)
Test 1	40	**0 – 80**
Test 2	60	**0 – 80**
Test 3	80	**0 – 80**
Test 4	120	**0 – 80**
Test 5	160	**0 – 80**

Outlet B.C

The outlet boundary condition can be used where the flow is known to be out of the domain. In the present cases, the present relative static pressure (Ps) at the output is zero. The inlet pressure required to sustain the specified flow will be determined using ANSYS fluent.

$$P=Ps=0 \tag{3}$$

4.2 Governing Equations

Pressure variations owing to friction losses in the horizontal pipe and perforations, perforation roughness, mixing effect, acceleration, and changes in the volume of flow between the perforations and the main pipe all affect fluid flow in a horizontal perforated wellbore. Therefore, the two main equations for fluid flow (the equations for mass and momentum) are required to properly describe these physical changes [12].

Conservation of mass

The equation for conservation of mass is described as follows:

$$\rho \frac{\partial}{\partial x_i}(u_i) = 0 \tag{4}$$

Conservation of Momentum

In Cartesian coordinates, the momentum conservation equation is represented as follows:

$$\frac{\partial}{\partial t}(\rho u_i) + u_j \frac{\partial(\rho u_i)}{\partial x_j} = -\frac{\partial P}{\partial x_i} + \frac{\partial}{\partial x_j}(\tau_{ji}) + F_i \tag{5}$$

The strain rate tensor can be used to rewrite the viscous stress tensor.

$$\tau_{ji} = \mu\left(\frac{\partial u_j}{\partial x_i} + \frac{\partial u_i}{\partial x_j}\right) = 2\mu S_{ji} \tag{6}$$

Substitute Eq. (5) into Eq. (4), This produces;

$$\rho \frac{\partial}{\partial x_j}(u_i u_j) = -\frac{\partial P}{\partial x_i} + \frac{\partial}{\partial x_j}(2\mu S_{ji}) + F_i \tag{7}$$

In turbulent flow, the instantaneous quantities can be broken up into mean and fluctuating components.

$$u_i = \bar{u}_i + u_i' \ . \ u_j = \bar{u}_j + u_j' \ . P = \bar{P} + P'$$
$$S_{ji} = \overline{S_n} + S_{ji}' \tag{8}$$

Substituting Eq. (7) into Eq. (6) and taking the time-averaged, called Reynolds-averaged Navier-Stokes.

$$\rho\overline{u_j}\frac{\partial}{\partial x_j}(\overline{u_i}) = -\frac{\partial \bar{P}}{\partial x_i} + \frac{\partial}{\partial x_j}\left(2\mu\overline{S_{ji}} - \rho\overline{u_i' u_j'}\right) + \mathrm{F_i} \tag{9}$$

To calculate the Reynolds stresses, we employ the well-known Boussinesq relationship.

$$\rho\overline{u_i' u_j'} = \frac{2}{3}\mathrm{k}\delta_{ij} - \mu_t\left(\frac{\partial\overline{u_j}}{\partial x_i} + \frac{\partial\overline{u_i}}{\partial x_j}\right) \tag{10}$$

Where:
the Kronecker delta, $\delta_{ij} = 1$ if i = j and $\delta_{ij} = 0$
if $i \neq j$

4.3 Turbulence models (Stander $k-\epsilon$ model)

The standard $(k-\epsilon)$ model is a type of two-equation model that deals with two different transport equations. The following transport equations of k are used in the regular k-model.
the following transport equations are used for k;

$$\rho u_j\frac{\partial \mathrm{k}}{\partial x_j} = \frac{\partial \mathrm{k}}{\partial x_j}\left((\mu + \frac{\mu_t}{\sigma_k})\frac{\partial \mathrm{k}}{\partial x_j}\right) + 2\mu_t S_{ij}.S_{ij} - \rho\epsilon \tag{11}$$

and ϵ;

$$\rho u_j\frac{\partial \epsilon}{\partial x_j} = \frac{\partial \epsilon}{\partial x_j}\left((\mu + \frac{\mu_t}{\sigma_\epsilon})\frac{\partial \epsilon}{\partial x_j}\right) + C_{1\epsilon}\frac{\epsilon}{k}\mu_t S_{ij}.S_{ij} - C_{2\epsilon}\rho\frac{\epsilon^2}{\mathrm{k}} \tag{12}$$

The values for these constants were determined by fitting extensive data to the standard $k-\epsilon$ model. The values are [13]:

C_μ	σ_k	σ_ϵ	$C_{1\epsilon}$	$C_{2\epsilon}$
0.09	1.00	1.30	1.44	1.92

5 Theoretical Model

The total pressure drop of the perforated pipe can be calculated from.

$$\Delta P_T = \Delta P_f + \Delta P_{per} + \Delta P_{mix} + \Delta P_{acc.} \tag{13}$$

5.1 Friction Pressure Drop

This is caused by wall friction resulting from the sum of (wall friction pressure drop and perforations roughness). According to most researchers [3, 6, 8, 14]. For all types of fully developed flows in wellbore internal flows (laminar and turbulent flow) and rough or smooth surfaces, the pressure drop due to pipe wall friction is calculated using the Darcy Weisbach 1986 equation for all types of fully developed flows in wellbore internal flows (laminar and turbulent flow).

$$\Delta P_f = f_t \frac{L}{D} \frac{\rho u^2}{2} \quad (14)$$

f_t: represents the total friction factor for pipe (dimensionless).
L: total length of the pipe, D inner diameter of the pipe

The total friction factor quantifies the force produced by the fluid on the wall in a turbulent flow. The equation can be used to compute the friction factor.

$$f_t = f_o + \mathrm{f_p} \quad (15)$$

The friction factor in turbulent pipe flow is Haaland (1983) equation [15].

$$\frac{1}{\sqrt{f_0}} = -1.8 \log\left(\frac{6.91}{Re} + \left(\frac{\epsilon}{3.7D}\right)^{1.11}\right) \quad (16)$$

A mathematical model to calculate the friction factor is presented in [9], in which this gives

$$f_p = 4D\ \frac{q}{Q} + 2\frac{D}{n}(\frac{q}{Q})^2 \quad (17)$$

5.2 Acceleration Pressure Drop

The acceleration pressure drop is caused by axial velocity change (momentum change). It depends on the density of the liquid and the average velocity at the end of the outlet pipe.

$$\Delta P_{acc.} = \rho(u_{out}^2 - u_{in}^2) \quad (18)$$

Where u_{in} , u_{out} the average velocity of the fluid at inlet and outlet of the pipe, respectively.

5.3 Mixing Pressure Drop

Pressure drops owing to passage through perforations causing mixing. It is caused by the complicated interplay of perforation and wellbore flow, which causes disruptions in the boundary layer and hence impacts the pressure drop. When liquid fluid enters the wellbore through a perforation, it mixes with the mainstream and adds to the well's bulk. Su and Gudmundsson [16] created formulae that can be used to determine the mixing pressure drop when the flow rate is larger than 0.0025, this equation is applied.

$$\Delta P_{\mathrm{mix}} = 760\left(\frac{q}{Q}\right) \quad (19)$$

$\frac{q}{Q}$: The total flow rate ratio (q) is the total perforation flow rate divided by the total flow rate at the pipe outlet.

5.4 Productivity Index (PI)

The productivity index is defined based on the mathematical equation resulting from dividing the outflow from the main pipe on the total pressure drop.

$$PI = \frac{Q_3}{\Delta P_T} \quad (20)$$

5.5 Average wall shear stress

The distribution of wall shear stress is altered by changes in the velocity gradient at the wall. The velocity gradient at the wall and the local effective viscosity, which is the sum of molecular and turbulent viscosity, determine wall shear stress in turbulent flow [17].

$$\tau_W = (\mu + \mu t)\frac{du}{dy} \quad (21)$$

6 Grid Independence Test

To verify the results of the numerical solution using the ANSYS FLUENT program. The maximum mesh size is determined to obtain the correct values in the first phase of the numerical simulation. In this study, the mesh is constructed using a CFD tetrahedron with different maximum mesh sizes. The maximum mesh changing is used to show the best mesh properties that can be used for a simulation for all cases in this simulation. Three boundary layers are used on the wall of the pipe, representing the type of mesh methods in Fig.2, and represent the mesh properties in Table 2.

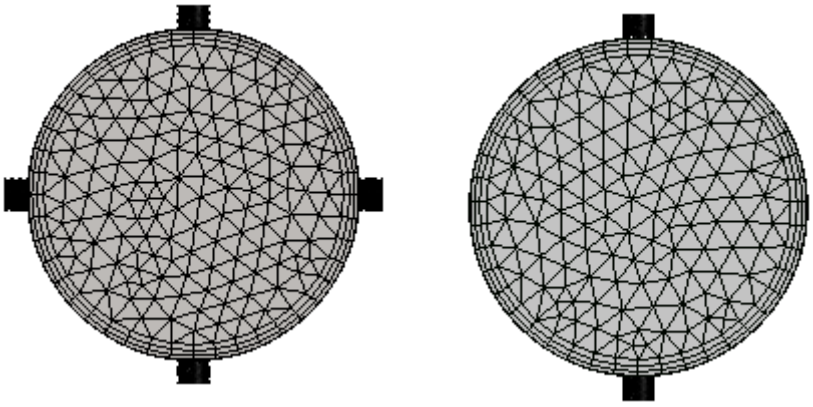

Fig. 2. Cross geometry of the test pipe in the 180° and 90° perforation phasing.

Table 2. Mesh properties.

Number of perforation	perforation Phasing	nodes	element	Mesh metric
19	180°	254372	974705	**Skewness**
20	90°	275394	1063960	**Skewness**

7 Model Validation

The numerical models for the validity of the solution must be validated by comparing the results acquired by other researchers. The validation is carried out by comparing the CFD FLUENT findings to the experimental results of Ref [7]. A partially perforated 3-D horizontal pipe length of 1300 mm and 22mm inner dim, perforation phasing of 60°, and a perforation density of 12 SPF. This validation's boundary conditions are as follows in Table 3.

Table 3. Details of the flow in Ref [7].

Test	Axial Flow (lit/hr)	Radial Flow (lit/hr)
Test 1	5618- 5157	**0 - 854**
Test 2	3836- 3361	**0- 841**

Fig. 3 shows the pressure drop of the present work and [7]. The figure explains that the maximum error is 14.2% for the first flow test at zero flow rate ratio and decrease to 4.4% at total flow rate ratio equal to 0.13391, for flow test 2 the maximum error is 14.8% at total flow rate ratio equal to zero and decrease to 4.5 % at total flow rate ratio equal to 0.1865. It also demonstrates that there is a difference across all tests. This is due to a different range of Reynolds number values and higher than experimental experiments. As well as the difference between the experimental values calculated from the device and the values calculated from the Ansys program.

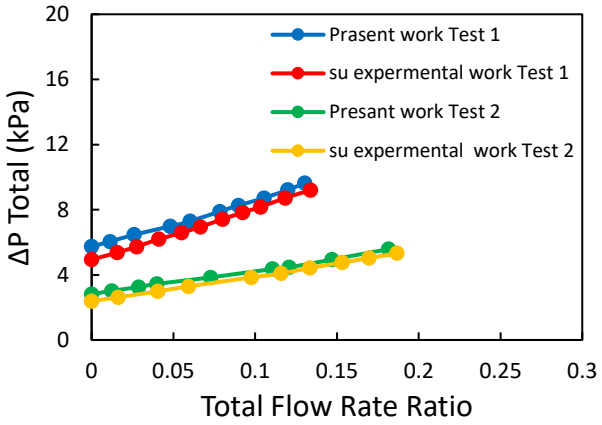

Fig. 3. Comparison of the present work with Ref [7].

8 Results and Discussion

A numerical study by using ANSYS Fluent and equations conducted on the perforated pipe at an angle of 180° and 90° to calculate pressure drop, friction, acceleration, and mixing. As well as, the study of the apparent friction factor, productivity index, velocity profile, and wall shear stress. The study is conducted for several flow rates as illustrated in Table 1.

8.1 Total Pressure Drop

Figs 4 and 5 represent the variations of pressure and flow rate ratio. It is shown that the total pressure drop increase as the flow rate ratio increase (an increase in radial flow for keeping the axial flow through the pipe constant). It is noticed this increase in the overall pressure drop is due to an increase in acceleration pressure drop. The tests line for the axial flow is 40, 60, 80,120, and 160 lit/min and constant radial flow from 0 - 80 lit/min. The Percentage error between 180° and 90° degrees for the five tests are 4.5%,3.2%,2.4%,4.2%, and 5.4%, respectively.

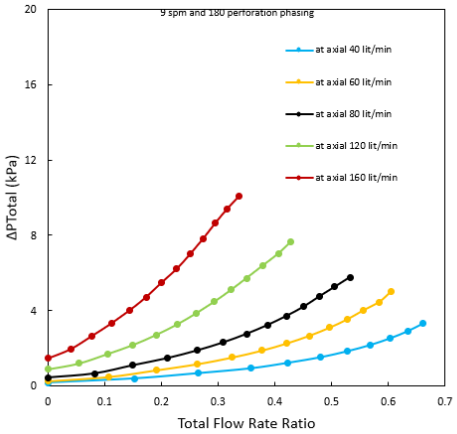

Fig.4. Total pressure drop in 180° perforation phasing

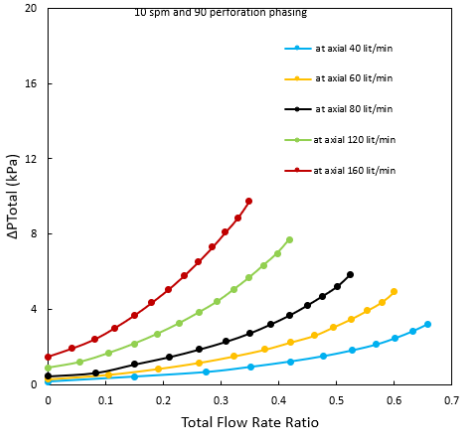

Fig. 5. Total pressure drop in 90° perforation phasing

8.2 Pressure Drop in Perforation Pipe

Figs 6 and 7 represent the variations of pressure drop and the total flow rate ratio. It is found that the total pressure drops increases with increasing the total flow rate ratio. This effect was caused by a larger decrease in wall frictional pressure as flow velocity increased. The proportion of the flow rate increases as the rate of the flow-through perforations increases, and increased the pressure drop. The main reason is that the perforations results in a greater decrease in the acceleration pressure caused by the flow through the perforations, thus increasing the mixing effect. It is observed that the acceleration values are lower in the wellbore pressure drop than the frictional pressure drops in resulting (wall friction and perforation roughness). For the results in the 180° perforations angle, the wall friction pressure reduced to 65.9% of the whole pressure rate, along with 31.6% acceleration pressure and 2.5% of mixing pressure. While for results in the 90° perforations phasing, the friction pressure drop is about 68.7%, and 28.5% acceleration pressure drop, and 2.8% drop of mixing pressure. The percentage error between 180° and 90° of test 5 is 5.4%.

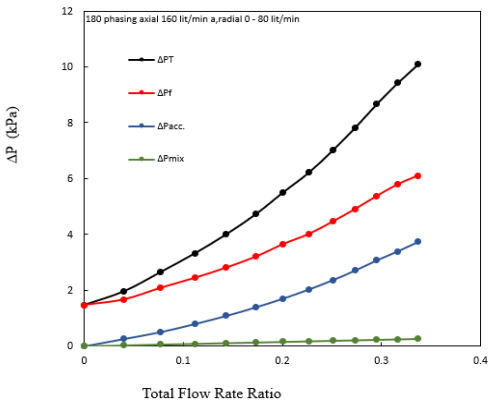

Fig. 6. Pressure Drop in 9 spm and 180° phasing

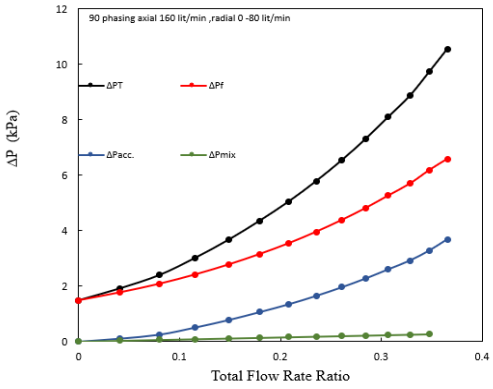

Fig. 7. Pressure Drop in 10 spm and 90° phasing

8.3 Static Pressure Drop

Figs.8 and 9 represent distribution pressure contour for the perforated pipe at 160 lit/min axial flow and 80 lit/min of radial flow. It is noticed from the results of the pressure decreases gradually, because of higher density and viscosity in this area. The maximum percentage error of pressure contour between 180° and 90° perforation phasing is 3.94%.

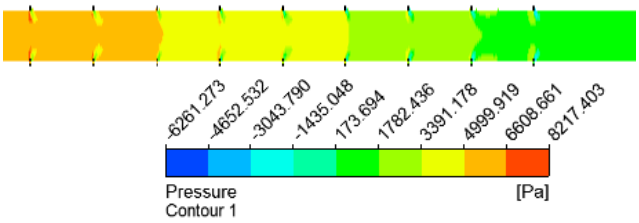

Fig. 8. Pressure at the perforated pipe in the 180° perforation phasing

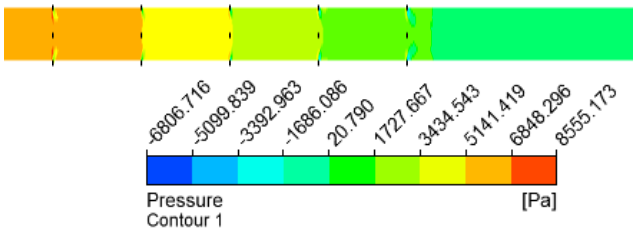

Fig 9. Pressure at the perforated pipe in the 90° perforation phasing.

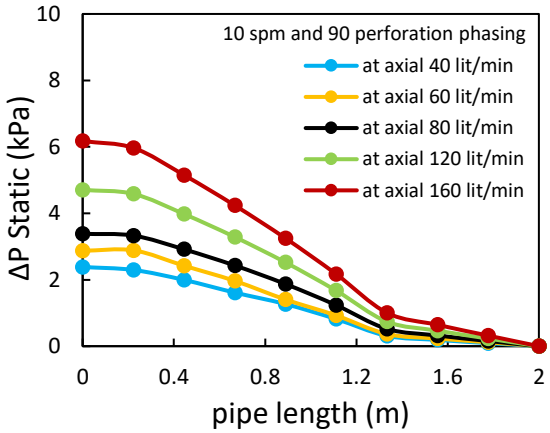

Fig. 10. Static pressure drops along the pipe length.

Figs10 and 11 represent the pressure drop along the centreline of the horizontal wellbore at various flow rates. The gradient has arrived at a fixed value as the pressure drop increased at the pipe's entry because entrance approximately 0.2 m downstream, and a sharp dropping of pressure at the horizontal pipe flow equalize the radial perforations flow. The static pressure at the pipe exit is going to be constant. When the axial-flow are 40,60,80,120,160 lit/min and the constant radial flow is 80 lit/min.

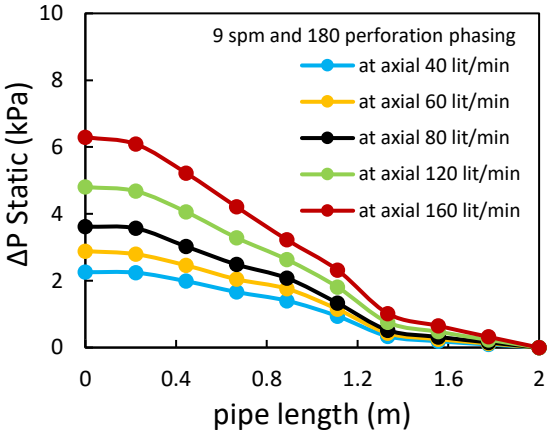

Fig 11. Static pressure drops along pipe length in the 180° perforation phasing in the 90° perforation phasing.

8.4 Friction Factor

Figs12 and 13 represent the relation between the total Friction factor and the total flow rate ratio. This is increased with increasing flow ratio rate, due to the change in the velocity field resulting from the flow through the perforations. The axial and radial flow rates were selected from Table 1.

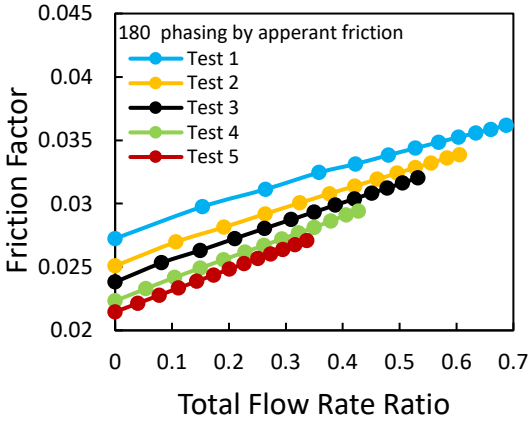

Fig.12. Total friction factor in the 180° phasing phasing

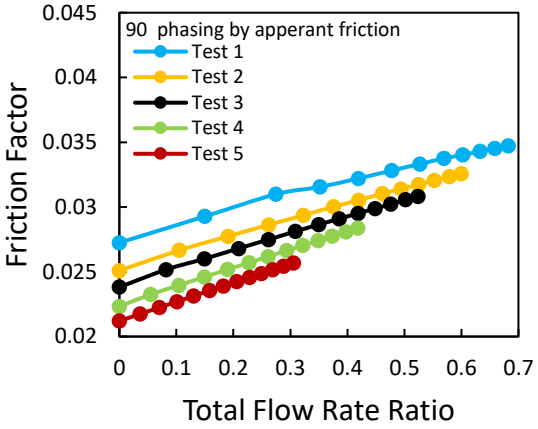

Fig.13. Total friction factor in the 90°

8.5 Productivity Index

Fig.14 and Fig. 15 represent the relationship of the productivity index with the total flow rate ratio. It is observed that the productivity index lowered with increasing the flow rate ratio, the reason for the decrease in the productivity index is due to the increases in the total pressure drop along the pipe. Also, the increase of the overall pressure drop is greater than the flow rate of the main pipe through the perforations, which leads to decreases in the productivity index. The axial and radial flow rates were selected from Table 1.

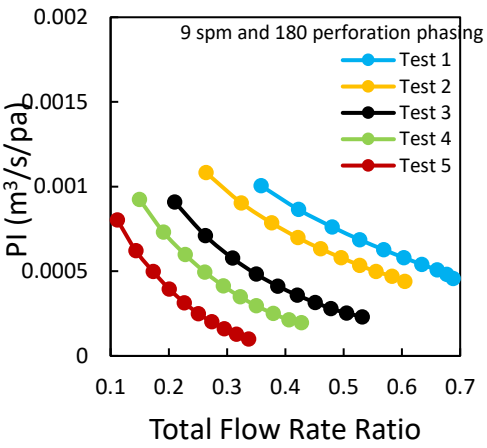

Fig. 14. Productivity index in the 180° phasing

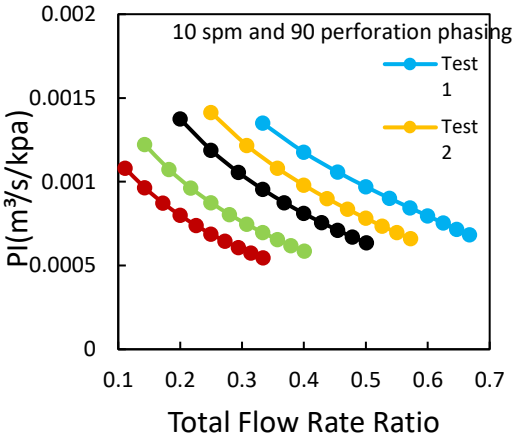

Fig. 15. Productivity index in the 90° phasing

8.6 Average velocity in the centre-line of perforation pipe

Figs16 and 17 represent the variations of velocity of planes along the pipe length. It is observed the flow in the perforation disrupts the axial flow in the pipe. and this increases the velocity in the wellbore pierced due to the radial flow entering through the perforation. Also, because of the reduction in the velocity of fluid flow near the wall. The test line for the flow of constant of radial flow 80 lit/min, and change of axial flow from range 40, 60,80,120,160 lit/min. It is noted from the figure that the distribution of the perforations has an angle of 90° better than 180°, and this leads to that the velocity out main of the pipe 90° is more stable than 180°.

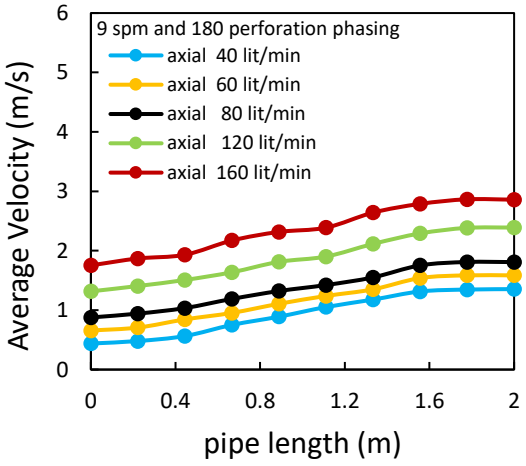

Fig 16. Average velocity along pipe length in the 180° perforation phasing

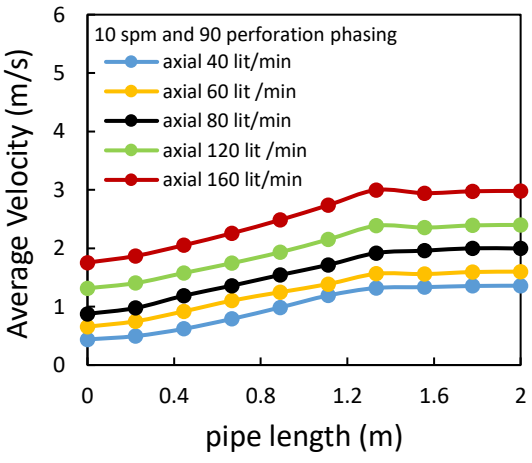

Fig 17. Average velocity along the pipe length in the 90° perforation phasing

Figs 18 and 19 represent the velocity distribution contour for the test pipe along the good pipe with flow 160 lit/min, and radial 80 lit/min. It is noticed that the axial/radial flow at the junction causes the flow velocity to increase in the perforation section of the pipe. It is observed that there is a pressure drop and rises the perforated rate.

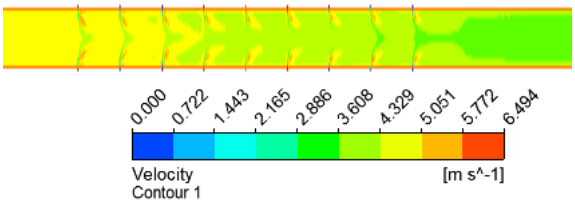

Fig.18. velocity contour in the 180° phasing

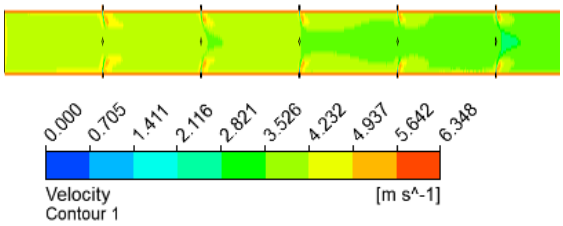

Fig 19. Velocity contour in the 90° phasing.

8.7 Velocity Profile

Figs 20 and 21 represent the velocity profiles in the direction of changing cross-section in exit perforation section for plane x=1.35 m for a perforated phasing 180° and 90° with at change the axial flow 40,60,80.120.160 lit/min and constant radial flow through the perforations of 80 lit/min. It is noted that axial flow rate increases with constant perforations, the change in velocity become higher with the direction of the change of cross-section.

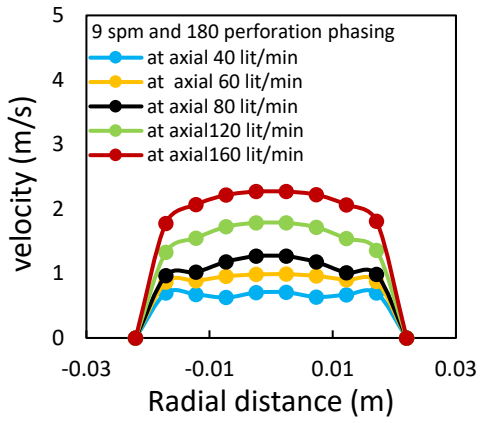

Fig 20. Distribution of velocity profile at the exit perforation section in the 90° perforation phasing

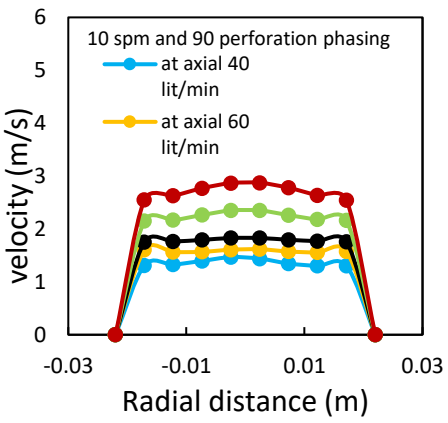

Fig 21. Distribution of velocity profile at the exit perforation section in the 180° perforation phasing

8.8 Average wall shear stress

The link between the average wall shear stress and the overall flow rate ratio is depicted in Figures 22 and 23. Because of the interplay between the axial flow and the inflow through the perforation, the average wall shear stress increases as the total flow rate ratio rises. As a result, inflow elevates and expands the turbulent boundary layer, increasing axial velocity beyond the layer while lowering velocity within it, as the mass conservation equation dictates.. The

maximum percentage error of average wall shear between 180° and 90° perforation phasing of test 5 is 10%.

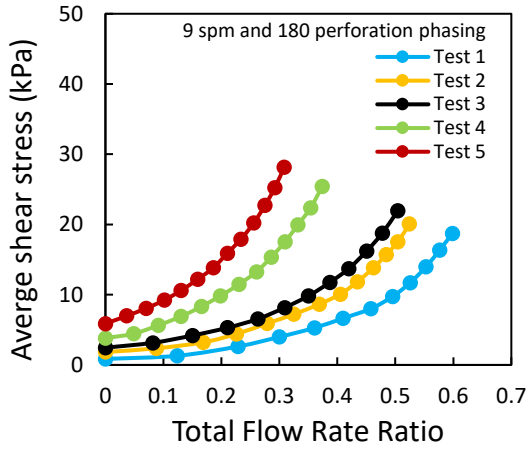

Fig. 22. Average well shear stress in the 180° perforation phasing

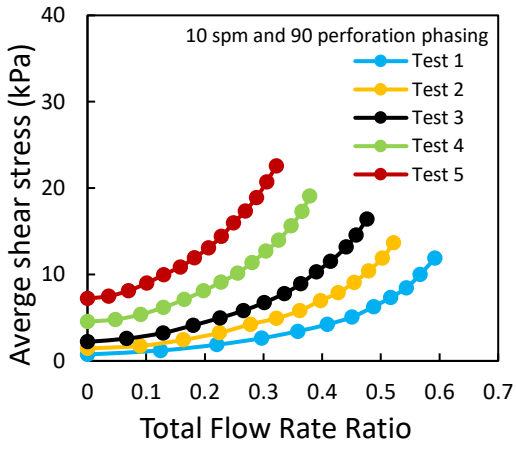

Fig. 23. Average well shear stress in the 90° perforation phasing

9 Conclusions

Numerical simulations of pipe flow, a numerical study has been conducted on the perforated pipe in 180°and 90° perforation angle of the flow horizontally wellbore. Simulation conducted using the ANSYS and stander $k-\varepsilon$ model. The study shows the following conclusions:

1- The total pressure reduced linearly with increasing the total flow rate ratio. The total pressure drop has the angle of the perforations 90° greater than the angle of the perforations 180° because the distribution of the perforations at the angle 90° is better than 180°

2-It is noticed that the greater the flow through perforations increase pressure drop and vice versa.

3- Field velocity at the entrance is completed as the flow increases up to the perforations. Axial direction collides with each other with radial flows, the fluid velocity in the downstream wellbore wall is less than the velocity from the inlet pipe wall to the upstream, but the velocity behaviour throughout the centre from the whole pipe does not change.

4- It is concluded that the flow rate increased, which leads total pressure drop and lower the productivity index. The productivity index of the angle perforation 90° is more productive than the perforation angle of 180°. Flow-through wellbore with an angle of 90 ° greater than 180 ° increases.

5- Increasing the flow rate through the perforations increases the wall shear stress.

References

[1] Stanley Locks., "An Advanced Method for Predicting the Productivity Ratio of a Perforated Well," Society of Petroleum Engineers of AIMf, (1981) ; SPE-8804-PA- 23: 2481-2488.

[2] Islam, M.R. and Chakma., "A Comprehensive Physical and numerical Modeling of a Horizontal Well," Annual Technical Conference and Exhibition of the SPE ; New Orleans, LA, September 23-26, (1990) ; SPE 20627.

[3] Folefac, J.S. Archer, and Issa. Chakma.," Effect of Pressure Drop Along Horizontal Wellbores on Well Performance," Offshore Europe Conference, held in Aberdeen , September 3-6- (1991); SPE 23094.

[4] Knut Seines, Ivar Aavatsmark, and S.C. Lien.," Considering Wellbore Friction Effects in Planning Horizontal Wells," Society of Petroleum Engineers of AIMf, October 1993; SPE-21124-PA.

[5] Cem Sarica, U. of Tulsa, Erdal Ozkan ,and Mustafa Haciislamoglu.," Influence of Wellbore Hydraulics on Pressure Behavior and Productivity of Horizontal Wells," Annual Technical Conference and Exhibition of the SPE; New Orleans, LA, September 25-28, (1994) ; SPE 28486 .

[6] Su, Z. and Gudmundsson, J.S., " Pressure Drop in Perforated Pipes," Asia Pacific oil & gas Conference held in Meibourna of the SPE; Australia, November 7-10- 1994 ; SPE 28800.

[7] Harald Asheim ,Johnny Kolnes ,and Piet Oudeman., "A Flow Resistance Correlation for Completed Wellbore," J. Petrol. Sci. Eng, February 10, (1992) ; pp. 97-104 .

[8] Novy, R.A., " Pressure Drops in Horizontal Wells: When Can They be Ignored," Society of Petroleum Engineers, February (1995) ; SPE-24941-PA .

[9] Wellington Campos, Rogério Campos,and Divonsir Lopes., " Frictional and Accelerating Pressure Drops Effects on Horizontal Oil Well Productivity Index," 18th International Congress of Mechanical Engineering, November 6-11, (2005).

[10] Zeboudj Faycal Fayal and Bahi Lakhdar., " Horizontal Well Performance Flow Simulation CFD-Application," pSPE Production and Operations Conference and Exhibition; Tunis, June (2010) ; SPE 133269.

[11] Mohammed Abdulwahid, Niranjan Injeti and Sadoun Dakhil.," Numerical Simulation of Flow through Wellbore for Horizontal Wells," Proceedings of the International Conference on Applied Mathematics and Computational Methods in Engineering., (2013) ; pp. 40-48.

[12] Thomas Vyzikas., " Application of numerical models and codes," MERiFIC University of Plymouth. Numerical Modelling. February (2014) ; pp. 57 – 83.

[13] Versteeg HK, Malalasekera W.," An Introduction to Computational Fluid Dynamics," Turbulence and its modelling. Prentice Hall, (2007) ; pp. 66 -78.

[14] Hua L, Yan L, Xiaodong P, Xindong L, Laichao .," Pressure Drop Calculation Models of Wellbore Fluid in Perforated Completion Horizontal Wells," IJHT, Vol. 34, No. 1, March, (2016); pp. 65-72

[15] Haaland S.E.," Simple and Explicit Formulas for the Friction Factor in Turbulent Pipe Flow," Journal of Fluids Engineering 10, Mar (1983) ; pp. 589-590.

[16] Su, Z. and Gudmundsson, J.S.," Perforation Inflow Reduces Frictional Pressure Loss in Horizontal Wellbores," J. Petrol. Sci. Eng. March (1998) ; pp. 223-232.

[17] White, F.M., " Viscous Fluid Flow," Second Edition, McGraw-Hill, Inc. 1991: pp. 104 - 212.

Dual-layer Antifouling Membrane of Electrospun PAN: PMMA Nonwoven Nanofibers for Oily Wastewater Treatment

Sura M. Alkarbouly[1] and Basma I. Waisi[2*]
{Sora.moath@gmail.com, Basmawaisi@coeng.uobaghdad.edu.iq}

Department of Chemical Engineering, College of Engineering, University of Baghdad[1,2]

Abstract. Antifouling membranes have gained considerable interest in water filtration applications. A dual layer of nonwoven nanofibers membranes was fabricated via the electrospinning method using hydrophilic and hydrophobic polymers. The first (base) layer was hydrophilic polyacrylonitrile (PAN) based electro spun nanofibers. In contrast, the second (top) layer was hydrophobic polymethyl methacrylate (PMMA) based electro spun nanofibers. A series of dual-layer nonwoven nanofiber membranes with various PAN: PMMA amount percentages were fabricated and characterized regarding their morphology and chemical composition using Scanning electron microscopy (SEM) and X-ray diffraction (XRD). The chemical functional groups on the membrane surface were detected using the Fourier transform infrared (FTIR). Also, the roughness and wettability of the membrane surface were measured using the atomic force microscopy (AFM) and the contact angle, respectively. The prepared nanofiber membranes efficiency was examined in emulsified oil/water separation using a crossflow filtration system. The results showed that the fouling resistance and permeate flux were significantly improved by spinning the hydrophobic (PMMA) nanofibers on the surface of the hydrophilic (PAN) nanofibers membrane.

Keywords: Electro spun nanofibers, emulsified oil, polyacrylonitrile, polymethyl methacrylate, filtration.

1 Introduction

Membrane technology, with its high efficiency and integrity, plays a key role in delivering sustainable water and energy resources [1,2]. Microfiltration (MF) is a membrane-based technique for pre-treating feed for reverse osmosis desalination units or removing colloids, bacteria, and oil from recovered wastewater [3,4]. In general, oil contaminates water in different forms, including emulsified oil which is not easy to remove because of its aqueous phase stability [5]. Emulsions pose particular challenges because of the deformability of the droplets, coalescence in bulk and on the membrane surface, membrane wetting by droplets and films, pore blockage, and oil intrusion [6]. In oil filtration membranes, the structural characteristics and surface qualities are crucial, including the permeable structure and wettability (the ability to separate oil from water) [7–9]. Recently, the membranes' hydrophilicity and hydrophobicity development offer an alternative direction for oil/water separation [9–11]. Polymeric fibres are amongst the most acceptable alternatives for functional materials with regulated porosity and selected wettability [12,13]. Electro spun polymeric nanofiber membranes have gotten much attention in recent years because of their unique properties such as the high surface-to-volume ratio, high permeability, the ability to manufacture various materials by chemical alteration, and the ability to create coaxial structures [14,15] [16]. The nanofiber membrane is made using the electrospinning technique, which involves charging a jet of fluid that travels through a

IMDC-IST 2021, September 07-09, Sakarya, Turkey
Copyright © 2022 EAI
DOI 10.4108/eai.7-9-2021.2314932

capillary tube with a high-voltage power source [17]. Because of their great mechanical and chemical resilience, polysulfide (PSU), polyether sulfone (PES), polyvinylidene fluoride (PVDF), and polyacrylonitrile (PAN) are commonly utilised to make nonwoven nanofiber membranes [15,18].
On the other hand, fouling is a common problem for oil-removing membranes, causing a significant reduction in initial membrane hydraulic permeability and durability (19)(20). Membrane fouling formed due to the reversible and irreversible deposition of particles, colloids, macromolecules, salts, and other components. Fouling mitigation approaches can be made in various ways, including membrane surface modification and backwashing. Fouling mitigation on membranes has been suggested using surface functionalization and the application of blending additives to promote surface hydrophilicity or pore architecture [6,21][22]. Incorporating high porosity nanofiber layers also can reduce the contact time between the fouling and filtrating layers [23]. A polymeric mixture of polyethylene terephthalate and polyacrylonitrile has been electro spun to make a nanofibrous composite that serves as a support layer for thin active coatings to increase the membrane fouling resistance and water permeability (24)(25). Also, the electro spun polymeric membrane has been utilized as a porous layer with reduced porosity in thin-film composite nanofiltration membranes to enhance permeability [26].
This project aims to make dual-layer antifouling membranes by electrospinning a top layer of polymethyl methacrylate (PMMA) nonwoven nanofiber on a layer of polyacrylonitrile (PAN) nonwoven nanofiber producing a dual-layer PAN: PMMA nonwoven nanofiber membrane. The fabricated nanofibers membranes were characterized using scanning electron microscopy (SEM), X-ray diffraction (XRD), Atomic force microscopy (AFM), Fourier Transform Infrared (FTIR), water contact angle (WCA), and Porosity. The dual-layer nanofiber membranes efficiency was applied in a crossflow filtration system using the emulsified Kerosene in water as a model of organic pollutant.

2 Materials and Methods

2.1 Materials

Polyacrylonitrile (PAN) (Mwt. of 150,000 g/mole) and polymethyl methacrylate (PMMA) (Mwt. of 350,000 g/mole) were supplied by Aldrich. N, N-Dimethylformamide (DMF) (density of 0.948 g/cm3) was supplied from Alfa Aesar and used as a solvent to dissolve PAN. Acetone (ACE) (density of 0.7845 g/cm3) was ordered from Sigma-Aldrich to be used with DMF in dissolving the PMMA. Kerosene (from midland Iraqi refineries company) was used to prepare the synthetic emulsion solution.

2.2 Methods

To prepare 11 wt.% PAN solutions, a specific amount of PAN was dissolved in DMF and stirred continuously for 4 hr at 60 °C. Also, to prepare a homogeneous precursor solution of 6 wt.% PMMA solution, a certain amount of PMMA was dissolved in a binary solvent of DMF/ACE (weight ratio of 4:6) using a magnetic stirrer for 6 hr in room temperature. Although DMF is a good solvent to dissolve PMMA, ACE should be added with the DMF to achieve a spun-able precursor solution of PMMA [27]. The DMF solvent demonstrated a low degree of macromolecule chains overlap and aggregation in solutions, leading to lower solution viscosity and formation beads. The ACE, on the other hand, presents a larger degree of macromolecule chain overlap and aggregation in solutions, which stops polymer chains from flowing, favouring increased solution viscosity and continually inhibiting beads formation in manufactured PMMA nanofibers [28].
All the nonwoven nanofibers membranes in this work were fabricated using the electrospinning technique, a pulling motion of polymer droplets to solve the surface tension in a high-voltage

electrostatic field. The main fabricated nanofiber membranes were a pure 11 wt.% PAN/DMF and a pure 6 wt.% PMMA (DMF: ACE). The other fabricated nanofiber membranes were dual layers of different amounts percentages of the two polymers PAN: PMMA (75:25, 50:50, and 25:75). Firstly, the base layer of nonwoven PAN-based nanofibers membranes was fabricated by spinning a certain amount of 11 wt.% PAN/DMF solution using a voltage of 21 kV. Then, a top layer of nonwoven nanofibers was fabricated by spinning a certain amount of 6 wt.% PMMA/(DMF: ACE) precursor solution using a voltage of 18 kV.
For all fabricated membranes, the electrospinning parameters were unchanged: flow rate of 1 ml/hr, the distance between the needle and collector of 15 cm, collector rotating speed of 70 rpm, and the relative humidity (10% -20%) at room temperature [29–31].

2.3 Characterization of membranes

The surfaces' structure and morphologies of the pure PAN and the pure PMMA nonwoven nanofiber membranes and the dual-layers of PAN: PMMA nonwoven nanofibers before and after oil removal were visualized. The samples were coated with a thin layer of gold by sputtering for 80 seconds to acquire a clear surface picture of the membrane surface by field emission scanning electron microscopy (FE-SEM, mara-3, TESCAN). The average fibre size of the PAN and PMMA nonwoven nanofibers was calculated using Image J software from SEM images [30]. The Fourier Transform Infrared (FTIR) and energy-dispersive X-ray spectroscopy (EDX) were also utilised to identify the chemical components of the membranes. The atomic force microscope (AFM) was used to evaluate the surface roughness of the nonwoven fibre membrane samples. The contact angles of the nonwoven nanofiber membrane samples were measured at room temperature using a CAM (CAG-20, Jikan). The values were taken as an average of five points after 10 seconds with 5 ± 0.5 μL water droplet volume. The membrane's porosities were measured using the following method. Each nanofibers membrane sample was weighed and recorded as dry weight. Next, the nanofibers membranes were immersed in distilled water for 1 hr. Then, the membrane sample was weighted after 30 minutes from removing them from the distilled water. Then porosity by the nanofibers membranes was calculated using equation 1 (32):

$$\text{Porosity } (\varepsilon_m) = \frac{(W_1 - W_2)}{A * t * \rho} \quad (1)$$

Where the porosity of the membrane is (ε), W_1 is the weight of the wet membrane, W_2 is the weight of the dry membrane. A, t, and ρ are the effective membrane area, membrane thickness, and water density at room temperature, respectively.

2.5 Emulsion Separation Performance

To prepare a stable emulsion solution of 250 mg/l concentration (the feed solution), Kerosene was mixed with distilled water using Hielscher ultrasonic processor (Hielscher UP400s, Teltow, Germany) at 10,000 rpm for 10 minutes at room temperature (25–30) °C. The feed emulsion was pumped to the crossflow filtration module cell using a pump. The effective filtration membrane area was 20 cm^2. The permeate flow containing the passing components flew through the membrane. The Permeate flux and its oil content concentration were measured over experiment time 2 hr in each trial using a UV–vis spectroscopy based on the absorbance at a wavelength of 196 nm. The permeation flux (J) and rejection rate (R) were calculated according to the following formulas 1 and 2 [33]:

$$J = \frac{V}{A * t} \quad (2)$$

$$R\% = \left(1 - \left(\frac{C_p}{C_f}\right)\right) * 100 \quad (3)$$

where J, A, and t are the volume of permeated water, membrane effective area, measurement time, respectively. And R is the oil rejection and C_f and C_p are the oil concentrations in feed and permeate solutions, respectively.

3 Results and Discussion

3.1 Membranes characterizations

Adding to the surface membrane SEM images of the fabricated pure 11 wt.% PAN/DMF and pure 6 wt.% PMMA/(DMF: ACE) based nonwoven nanofibers membranes, the images of surface morphologies of the various amounts of the prepared dual-layers (PAN: PMMA) nonwoven nanofibers membranes are shown in Figure1. The images indicated that both 11 wt.% PAN/DMF and 6 wt.% PMMA/(DMF: ACE) membranes were successfully fabricated and composed of long, free of beads, homogeneous and continuous nanofibers with average fibre diameters of 200 and 800 nm, respectively.
The various dual-layers (PAN: PMMA) nonwoven nanofibers membranes ((75:25), (50:50), and (25:75)) showed a mixture of fibre sizes confirming the existence of a layer of PAN and a layer of PMMA in the membrane sample. PAN-based fibbers' small size appeared in the bottom layer of the membrane, where the larger size of PMMA based fibres formed a continuous top layer above the PAN layer. Increasing the ratio of the PMMA in the dual-layer membrane increases the number of the large fibres in the dual-layer membrane.

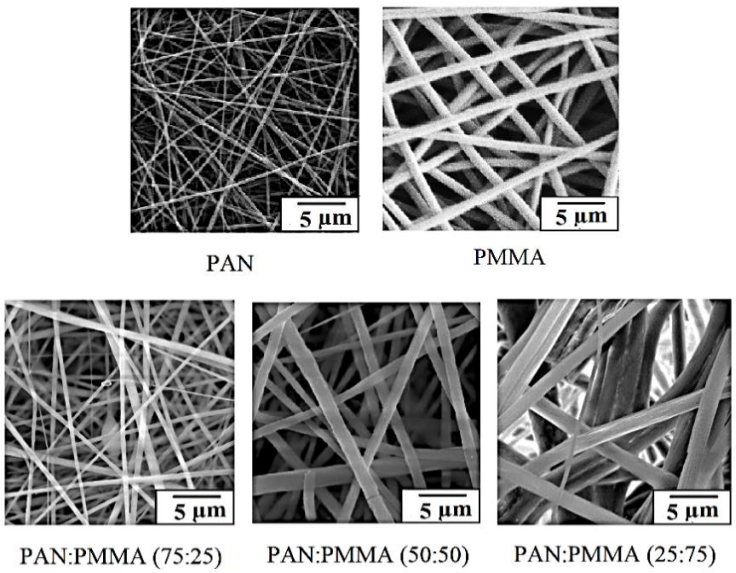

Fig 1. The surface SEM images of the various fabricated nanofibers membranes.

Table 1. The EDX analysis results of the various fabricated nanofibers membranes.

Element	PAN	75:25 PAN:PMMA	50:50 PAN:PMMA	25:75 PAN:PMMA	PMMA
C	77.03	78.12	76.10	74.15	94.50
N	19.63	0.00	0.00	0.00	0.00

O	3.34	21.88	23.90	23.90	5.15
		Total:	100		

Adding to the surface morphology, the roughness also influences the membrane fouling, which can be characterized using atomic force microscopy (AFM) analyser and showed in Table 2. The average roughness of the fabricated nonwoven nanofiber membrane based on pure PAN recorded a larger value than that of the PMMA base membrane. As a result, in the fabricated dual-layer nanofiber membrane, increasing the amount of PMMA based nanofiber (the top layer) led to a decrease in the surface membrane roughness. In other words, the existing several PAN-based nanofibers in the membrane structure resulted in increasing the roughness of the membrane.

The measured water contact angles also were summarized in Table 2. The PAN-based nanofiber membrane recorded the lowest value because of its high hydrophilicity. In contrast, the PMMA based nanofiber membrane showed the highest contact angle due to its high hydrophobicity (34). As a result, spinning a top layer of the high hydrophobic PMMA based nanofibers (110 º) on the layer of high hydrophilic PAN-based nanofibers (33 º) caused a hydrophobic dual-layer nanofiber membrane (around 88 º). Existing hydrophilic and hydrophobic nanofibers in the same membrane resulted in trapping the water in the micro and rough nanoscale structure due to the hydrophilicity and catching the oil droplets inside the hydrophobic fibres instead of clogging the membrane pores.

The other important characterization is the membrane porosity measured depending on water uptake for all fabricated membranes and showed in Table 2 too. The PAN and PMMA based nanofibers showed the highest and lowest porosities, respectively, which can be attributed to the big difference in their hydrophilicity. Existing the hydrophilic PAN-based nanofibers in the dual-layers nanofibers membranes resulted in high porosities. The porosity increases as the PAN content increases, which could be attributed to the nonwoven nanofibers membranes' decreasing average fibre diameter [35].

Table 2. The measured values of average roughness (Ra), porosity, and contact angle of the fabricated nanofiber membranes

Samples name	**Roughness (Ra) nm**	**Porosity (-)**	**Contact angle (º)**
PAN	108.4	94	33
(75:25) PAN:PMMA	59.28	94	83
(50:50) PAN:PMMA	60.15	95	88
(25:75) PAN:PMMA	60.88	96	95
PMMA	40	79	110

FTIR spectrum study of pure PAN and pure PMMA based nanofiber membranes defining functional groups is shown in Fig 2. The apparent sharp, intense peak at 1732.08 cm-1 in the analysis of PMMA based nanofibers is due to ester carbonyl group stretching vibration. The C-O (ester bond) stretching vibration is responsible for the broad peak extending from 1250-1149.57cm-1. The broadband from 990 to 420 cm-1 is also due to C-H bending. Stretching vibration is responsible for the broad peak ranging from 3523-2950 cm-1[36].

Due to the CN stretching band stretching of the acrylonitrile unit in the polymer chain, the most recognisable peak in the displayed FTIR analysis of PAN-based nanofibers in Fig 2 was seen at 2245.14 cm1 [37]. C=O stretching and CH stretching aliphatic CH groups are allocated to the other peaks at 1666.5 and 1373.32 cm1, respectively [38]. The stretching frequencies of the (C–O) groups, which are coupled to the carbon atoms of the 1, 2, 3-propanetriol and the succinimide ester (C–O), are associated with the peaks at 1097.50 and 1066.67 cm1. C–N

stretch peaks, CH2 bending, C=O stretching, CH band, and the stretching vibrations of the -OH bond emerged from absorbed water at 1236.3 7, 1452.40, 1737.86, 2926.31, and 3441.01 cm-1, respectively [37,39,40].

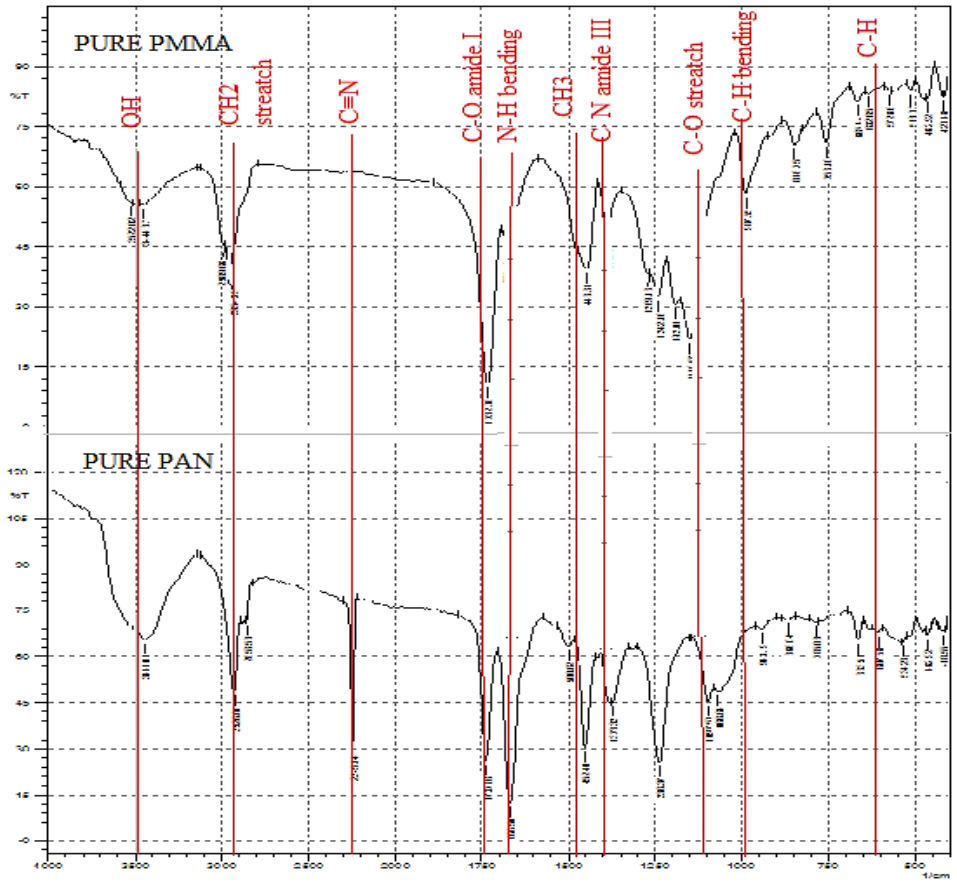

Fig. 2 The Fourier Transform Infrared (FTIR) for pure PAN and PMMA nanofiber membranes.

3. 2 Filtration performance

The fabricated membrane's efficiency in removing the emulsified oil from water according to the permeate flux and oil rejection percentage is shown in Fig 3 a and b, respectively. The pure PAN-based nanofiber membrane showed a low permeate flux (900 LMH) and high oil rejection percentage (96%) due to the accumulated oil droplets on the membrane surface, and clogged membrane pores permeate flux passage, as shown in Fig 4. However, the pure PMMA based nanofiber membrane revealed a much higher permeate flux which can be attributed to the large pore's sizes due to the large size of the PMMA based fibres. Also, the high hydrophobicity surface of PMMA based nanofiber implies a high oil affinity and avoids the formation of an oil fouling layer on the top surface of the membrane.

According to Figs 3 and 4, the dual-layer PAN: PMMA nanofiber membranes also showed a high permeate flux and low fouling participation due to the high hydrophobicity of the membrane surface that wicked the oil droplets into the fibre matrix and decreased the fouling layer on the surface [20]. Incorporating the electro spun PMMA based nanofiber layer did not offer significant additional hydraulic resistance, and hence the electro spun material did not restrict the pores of the PAN-based nanofiber layer. The high permeability obtained using hydrophilic and hydrophobic nanofiber membranes resulted in hydrophilic pores interacting with the water molecules and facilitating water flux. At the same time, the hydrophobic pores

interact with the oil droplets and decrease the organic layer accumulation on the membrane surface [41][42].

The oil rejection results of the various fabricated nanofibers membranes ranged from 80 ± 0.7 % for pure PMMA to 95.5 ± 0.6 % for pure PAN membranes. The dual-layers nanofibers membranes showed a reasonable oil rejection (> 87%) with a slight difference between the various dual-layers membrane. Consequently, incorporating the electro spun layer of PMMA affects the membrane efficiency as expected, considering the PMMA membrane hydrophobicity and pore sizes. The extracted oil droplets were attracted to the hydrophobic surface of the top layer in the dual-layer membrane instead of accumulating on the surface, resulting in an almost free fouling layer, as shown in Fig 4.

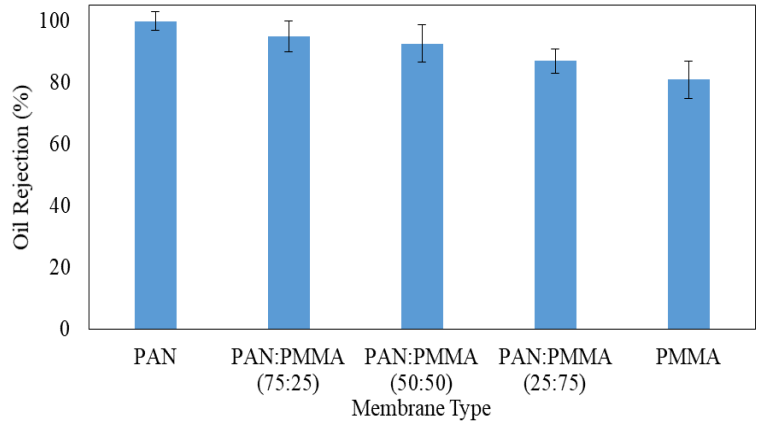

(a)

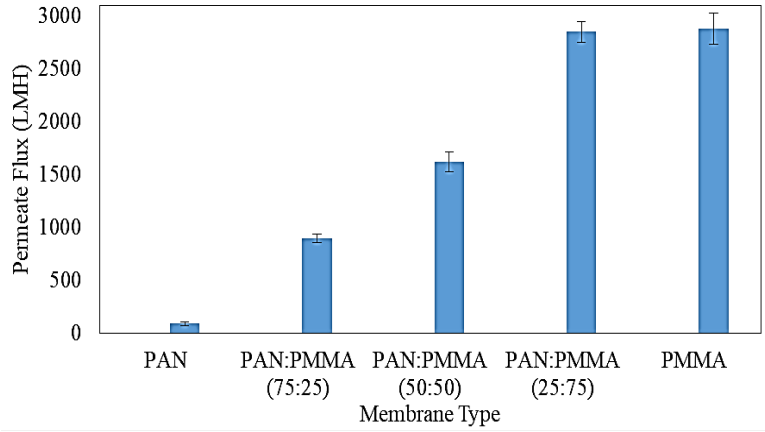

(b)

Fig. 3 Oil/water filtration efficiency using the various fabricated nanofibers membranes (a) permeate flux and (b) oil rejection percentage.

Adding to the hydrophobicity of the nanofiber's surface effect on the fouling formation, the roughness plays an important role. The collection of oil at the valley of the rough surface increases the fouling tendency as the roughness increases [43]. The influence of surface roughness on membrane fouling appears to be reliant on the size of oil droplets in relation to the roughness's characteristic length. The fouling tendency decreases if the oil droplets are much larger than this characteristic length. On the other hand, if the oil droplets are small in comparison to the roughness, they may become caught in the rough surface's valley, resulting in oil collection and membrane fouling [44].

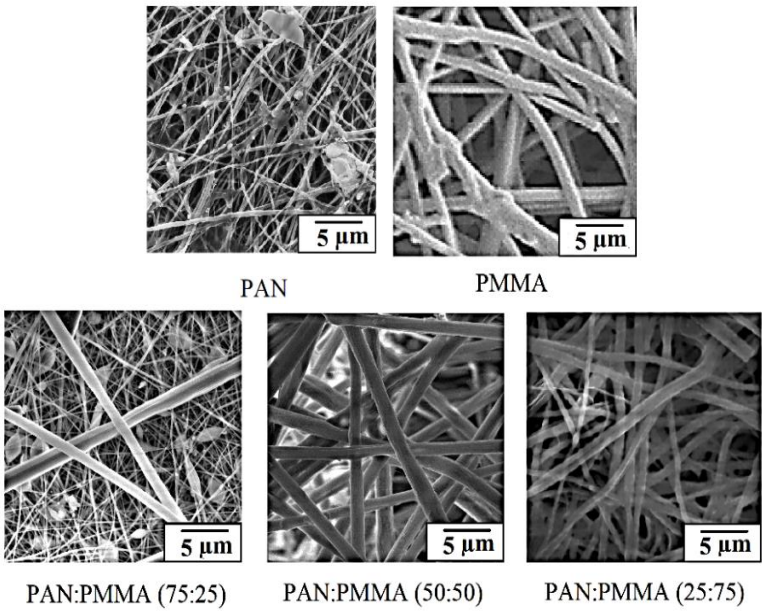

Fig. 4 various SEM images fabricated nano-membranes following oil filtration process.

4 Conclusion

In this work, dual-layer nanofiber membranes with high organic fouling resistance were successfully fabricated via the electrospinning technique. The fabricated membrane consisted of a top layer of the hydrophobic PMMA nanofibers that spun on the hydrophilic PAN nanofibers membrane base layer. The characterization analysis of the fabricated membranes showed the high effect of the spinning nanofiber layer of PMMA on the base layer of PAN, including the fibre size, porosity, wettability, and roughness. The various prepared membranes were tested in emulsified oil removal using a crossflow filtration system. The dual-layer nanofibers membranes showed a significant improvement in the permeate flux and fouling resistance. Spinning hydrophobic nanofibers of PMMA upon the hydrophilic PAN membrane surface resulted in increasing the permeate flux, which can be argued to the large fibre size (800 nm) of the top layer helped the water droplets to flow through easier and cross to the small fibres (200 nm) of the hydrophilic layer. At the same time, the high hydrophobicity of PMMA nanofibers surface interacts with the oil droplets inside the fibres leading to an almost free fouling membrane.

Reference

1. Elimelech M, Phillip WA. The Future of Seawater Desalination: Energy, Technology, and the Environment. Science (80-). 2011;333:712–7.

2. Rajasulochana P, Preethy V. Comparison on efficiency of various techniques in treatment of waste and sewage water–A comprehensive review. Resour Technol. 2016;2(4):175–84.

3. Chakrabarty B, Ghoshal AK, Purkait MK. Ultrafiltration of stable oil-in-water emulsion by polysulfone membrane. J ofMembrane Sci. 2008;325:427–37.

4. Waisi BIH, Karim UF a., Augustijn DCM, Al-Furaiji MHO, Hulscher SJMH. A study on the quantities and potential use of produced water in southern Iraq. Water Sci Technol Water Supply. 2015;15(2):370.

5. Ibrahim S, Wang S, Ang HM. Removal of emulsified oil from oily wastewater using agricultural waste barley straw. Biochem Eng J. 2010;49(1):78–83.

6. Tummons E, Han Q, Tanudjaja HJ, Hejase CA, Chew JW, Tarabara V V. Membrane fouling by emulsified oil: A review. Sep Purif Technol. 2020;248:116919.

7. Ma W, Zhang Q, Hua D, Xiong R, Zhao J, Rao W, et al. Electrospun fibers for oil-water separation. Vol. 6, RSC Advances. Royal Society of Chemistry; 2016. p. 12868–84.

8. Ying Q, Lili Z, Haixiang S, Li Peng. PAN / PS elctrospun fibers for oil spill cleanup PAN / PS elctrospun fibers for oil spill cleanup. IOP Conf Ser Mater Sci Eng. 2014;62:7.

9. Jeyakumar N, Jeyakumar N, Program M, Seering W. Signature redacted _ Signature redacted ___ Signat-ure redacted. 2017;(2000).

10. Zeiger C, Kumberg J, Vüllers F, Worgull M, Hölscher H, Kavalenka MN. Selective filtration of oil/water mixtures with bioinspired porous membranes. RSC Adv. 2017;7(52):32806–11.

11. Salahi A, Noshadi I, Badrnezhad R, Kanjilal B, Mohammadi T. Nano-porous membrane process for oily wastewater treatment: Optimization using response surface methodology. J Environ Chem Eng. 2013;1(3):218–25.

12. Rajkiewicz M. CHEMICAL AND APPLIED ENGINEERING MATERIALS Interdisciplinary Research and Methodologies www.EngineeringBooksLibrary.c. Canada: Apple Academic Press, Inc; 2015. 362 p.

13. Zoka L. Effect of Surface Modification With Electrospun Nanofibers on The Performance of The Ultrafiltration Membrane. 2018.

14. Li D, Xia Y. Electrospinning of nanofibers: Reinventing the wheel? Adv Mater. 2004;16(14):1151–70.

15. Suja PS, Reshmi CR, Sagitha P, Sujith A. Electrospun Nanofibrous Membranes for Water Purification. Polym Rev. 2017;57(3):467–504.

16. Toriello M, Afsari M, Shon HK, Tijing LD. Progress on the fabrication and application of electrospun nanofiber composites. Membranes (Basel). 2020;10(9):1–35.

17. Alghoraibi I, Alomari S. Different methods for nanofibers design and fabrication. Handb Prop Text Tech Fibres. 2019;(February 2018):47.

18. Al-furaiji M, Arena JT, Ren J, Benes N, Nijmeijer A. Triple-Layer Nanofiber Membranes for Treating High Salinity Brines Using Direct Contact Membrane Distillation. Membranes (Basel). 2019;9(60):2–10.

19. Shu W, Liangyin CHU, Wenmei C. Fouling-resistant Composite Membranes for Separation of Oil-in-water Microemulsions. Chinese J ChemEng. 2006;14(1):37–45.

20. Waisi B, Arena JT, Benes NE, Nijmeijer A, McCutcheon JR. Activated Carbon Nanofiber Nonwoven for Removal of Emulsified Oil from Water. Microporous Mesoporous Mater. 2020;296:109966.

21. Abdelrasoul A, Doan H. Ultrasound for membrane fouling control in wastewater treatment and protein purification downstream processing applications. In: Advances in Membrane Technologies. IntechOpen; 2020.

22. Gao H, Sun X, Gao C. Antifouling polysulfone ultrafiltration membranes with sulfobetaine polyimides as novel additive for the enhancement of both water flux and protein rejection. J Memb Sci. 2017;542:81–90.

23. Karbownik I, Rac-Rumijowska O, Fiedot-Toboła M, Rybicki T, Teterycz H. The preparation and characterization of polyacrylonitrile-polyaniline (PAN/PANI) fibers. Materials (Basel). 2019;12(4):20.

24. Yoon K, Kim K, Wang X, Fang D, Hsiao BS, Chu B. High flux ultrafiltration membranes based on electrospun nanofibrous PAN scaffolds and chitosan coating. Polymer (Guildf). 2006;47(7):2434–41.

25. Hoover LA, Schiffman JD, Elimelech M. Nanofibers in thin-film composite membrane support

layers: Enabling expanded application of forward and pressure retarded osmosis. Desalination. 2013;308:73–81.

26. Lu T-D, Chen B-Z, Wang J, Jia T-Z, Cao X-L, Wang Y, et al. Electrospun nanofiber substrates that enhance polar solvent separation from organic compounds in thin-film composites. J Mater Chem A. 2018;6(31):15047–56.

27. Ahmad B, Ameer Hamza, Ahmed S, Najam Z, Ishtiaq A. Synthesis and Characterization of PMMA Nanofibers for Filtration of Drinking Water. J Mech Contin Math Sci. 2019;14(4):102–16.

28. Gohari RJ, Lau WJ, Matsuura T, Ismail AF. Effect of surface pattern formation on membrane fouling and its control in phase inversion process. J Memb Sci. 2013;446:326–31.

29. Wang R, Liu Y, Li B, Hsiao BS, Chu B. Electrospun nanofibrous membranes for high flux microfiltration. J Memb Sci. 2012;392–393:167–74.

30. Waisi BI, Manickam SS, Benes NE, Nijmeijer A, McCutcheon JR. Activated Carbon Nanofiber Nonwovens: Improving Strength and Surface Area by Tuning the Fabrication Procedure. Ind Eng Chem Res. 2019;58:4084–9.

31. Guo JW, Wang CF, Chen SH, Lai JY, Lu CH, Chen JK. Highly efficient self-cleaning of heavy polyelectrolyte coated electrospun polyacrylonitrile nanofibrous membrane for separation of oil/water emulsions with intermittent pressure. Sep Purif Technol. 2020;234(July 2019):116106.

32. Abdel-aty AAR, Aziz YSA, Ahmed RMG, Elsherbiny IMA, Panglisch S, Ulbricht M, et al. High Performance Isotropic Polyethersulfone Membranes for Heavy Oil-in-Water. J Pre-proofs. 2020;117467.

33. Wang J-J, Yang H-C, Wu M-B, Xi Zhang and Zhi-Kang Xu. Nanofiltration Membranes with Cellulose Nanocrystals as an Interlayer for Unprecedented Performance. Mater Chem A. 2017;7.

34. Liu Z, Zhao JH, Liu P, He JH. Tunable surface morphology of electrospun PMMA fiber using binary solvent. Appl Surf Sci. 2016;364:516–21.

35. Yanılmaz M, Zhang X. Polymethylmethacrylate/Polyacrylonitrile Membranes via Centrifugal Spinning as Separator in Li-Ion Batteries. Polymers (Basel). 2015 Apr;7:629–43.

36. Vijayakumari G, Selvakumar N, Jeyasubramanian K, Mala R. Investigation on the electrical properties of polymer metal nanocomposites for physiological sensing applications. Phys Procedia. 2013;49(December):67–78.

37. Shuker H. Antibacterial Activity of Chitosan/PAN Blend Prepared at Different Ratios. AIP Conf Proc. 2019 Dec;2190.

38. Nithya, S., Selvasekarapandian, S., Premalatha, M. Synthesis and characterization of proton-conducting polymer electrolyte based on polyacrylonitrile (PAN). Ionics (Kiel). 2017;23(10):2767–74.

39. Abdouss M, Shoushtari A, Haji A, Moshref B. Fabrication of chelating diethylenetriaminated PAN micro-and nano-fibers for heavy metal removal. Chem Ind Chem Eng Q. 2012 Jan;18:27–34.

40. Ulianas A, Heng LY, Ahmad M. A biosensor for urea from succinimide-modified acrylic microspheres based on reflectance transduction. Sensors. 2011;11(9):8323–38.

41. Habimana O, Semião AJC, Casey E. The role of cell-surface interactions in bacterial initial adhesion and consequent biofilm formation on nanofiltration/reverse osmosis membranes. J Memb Sci. 2014;454:82–96.

42. Yu W, Brown M, Graham NJD. Prevention of PVDF ultrafiltration membrane fouling by coating MnO 2 nanoparticles with ozonation. Sci Rep. 2016;6(1):1–12.

43. Jayalakshmi A, Kim IC, Kwon YN. Cellulose acetate graft-(glycidylmethacrylate-g-PEG) for modification of AMC ultrafiltration membranes to mitigate organic fouling. RSC Adv. 2015;5(60):48290–300.

44. Huang S, Ras RHA, Tian X. Antifouling membranes for oily wastewater treatment: Interplay between wetting and membrane fouling. Curr Opin Colloid Interface Sci. 2018;36:90–109.

An Integrated GIS and Satellite Image-based Model using a Reduced Simple Ratio Index for Evaluating the Efficacy of the Hammer Marsh Restoration Plan

Mahmoud S. Al-Khafaji[1] , Imzahim A. Alwan[2], Bayda A.Dhaidan[3]
{mahmoud.s.alkhafaji@uotechnology.edu.iq[1], 40164@uotechnology.edu.iq[2],
bayda.bh1@gmail.com[3]}

University of Technology- Civil Engineering Department, Baghdad, Iraq[1,2,3]

Abstract: Iraqi Marshes in Mesopotamia are considered one of the major wetland ecosystems in the world. These marshes were subjected to a deliberate drought several times. This paper aims to conduct a spatiotemporal assessment for the reality and compliance of the land cover in the Western part of the Hammer Marsh versus the inundation processes. The OLI Landsat satellite images and GIS were integrally used to implement a land cover wetness evaluation model using the reduced simple ratio index (RSR). This model was applied to assess the marsh land cover wetness level and to study the impact of inundation processes in the marsh for the period from 2013 to 2020. The results indicated a positive relationship between the RSR index values and inflow discharges, where the RSR index classes (1.5-3), which represent the moderate wetness class, increased to 23.69% and 23.21% of the marsh area in 2019 and 2020 while decreased to 19.13% and 16.23% in 2015 and 2018 in conjunction with the increase and decrease in the inflow discharge. In general, there is no noticeable improvement in the inundation of the study area, except a slight and temporary improvement in 2019 and 2020 based on the increase and continuity of inflow discharges. Fluctuation of the inflow discharges reduces the efficacy of the restoration process. However, to achieve the aim of the restoration plan, a continuous and stable supply of the specified discharges in the restoration plan must be maintained without a considerable fluctuation. The developed RSR model with the aid of integral use of GIS and satellite images can be sufficiently applied to monitor and evaluate the spatiotemporal change of the wetness level of the marsh land cover.

Keywords: RSR, Hammer Marsh, GIS, Satellite-based Model.

1 Introduction

Wetlands are among the most productive ecosystems on Earth [1]. Wetlands play critical roles in providing habitats, improving water quality, reducing erosion, and mitigating flood severity [2]. Even with their significance in preserving biodiversity and providing ecosystem requirements, wetland loss has been widespread worldwide [3]. Salinization, pesticide and heavy metal pollution, loss of fringing vegetation, and altered hydrological regimes caused by urbanization and agricultural practices are all obvious and direct causes of wetland degradation [4]. Drought is regarded as one of the most serious effects of climate change, affecting the worldwide ecosystem, particularly in Africa and Asia. Drought caused deterioration of nature and life, as well as depleted vital water resources. Therefore, protecting ecological systems and confronting threats resulting from drought and desertification has become a very serious and vital issue. The Iraqi marshes have been suffered from intentional drying and drought in several periods. After the year 2003, the Iraqi Ministry of Water Resources (IMoWR) seriously attempted to restore these marshlands. However, these marshes have markedly been affected by Overexploitation of water from upstream countries that caused high shortage in water supply and the extensive intentional drying activities over the 1980s to 1990s. However, the Integrating Remotely Sensed (RS) data with Geographical Information System (GIS) techniques by building a model based on satellite images is a unique opportunity to conduct the spatiotemporal assessment of the wetlands. In monitoring and assessment of the wetlands ecology, the spectral vegetation indices (SVIs) are commonly used efficient tools for evaluating the land cover of these wetlands. In [5], the leaf area index (LAI), the normalized difference vegetation index (NDVI), the simple ratio (SR), and the

IMDC-IST 2021, September 07-09, Sakarya, Turkey
Copyright © 2022 EAI
DOI 10.4108/eai.7-9-2021.2314926

reduced simple ratio (RSR) were computed from Landsat ETM for two sites in Finland. For all the computed SVIs, a fair positive correlation is indicated with LAI. However, a more dynamic response is indicated for the RSR to LAI than these of SR or NDVI. Using the RSR, the maps of computed LAI are highly agreed with these of measured LAI [5]. Results from [6], regarding a study about relationships among LAI, SR, and RSR by relationships between LAI comprising data from the major boreal tree species in Canada, showed that, for both coniferous and deciduous stands, RSR correlated better with LAI compared to SR. This paper aims to detect and assess the response and compliance of the land cover in the Western part of the Hammer Marsh to the inundation plan and applied processes. To this end, the GIS and satellite images were integrally used to implement a satellite image-based model using the RSR.

2 Materials and Methods

The method used to achieve the research objective relied on using a model based on Landsat 8 satellite imagery using the RED and SWIR bands to apply the Low Simple Ratio Index (RSR). After downloading the images that cover the study area and implementing the necessary pre-processing such as radiometric calibration, layer stack, mosaicked, and image subset, the result of RSR was categorized into four categories by the soil moisture level and vegetation cover to describe the soil class and vegetation cover within the marsh. Then, the area of each class is calculated and compared to the inflow discharge of the same period to obtain the required evaluation.

2.1 RSR

The Reduced Simple Ratio Index (RSR) is sensitive to soil and vegetation wetness and can skyrocket immediately after rainfall or irrigation, making it only appropriate for forests in LAI retrieval algorithms. The RSR Index is defined as bellow:

$$RSR = \frac{NIR}{RED}\left[1 - \frac{SWIR - SWIR_{min}}{SWIR_{max} - SWIR_{min}}\right] \quad (1)$$

Where NIR is the near-infrared, RED is the visible wavelength and SWIR is the shortwave-infrared [6]. RSR is more significantly correlated with the Leaf Area Index (LAI) for different jungle lands because it is very sensitive to the variation in LAI. Therefore, RSR is particularly useful for mixed cover types; The middle-infrared (MIR) reflectance is very sensitive to the land cover greenness because of the high absorption of MIR by understorey moss, and grass. Therefore, the impact of the background optical properties is very small on RSR. [5] [6].

2.2 Study Area

Hammer Marsh is the largest water body in the southern part of Iraq. It is located to the right side of the Euphrates River between latitudes ($30^{\circ}\ 33' - 30^{\circ}\ 58'N$) and longitudes ($46^{\circ}\ 24' - 47^{\circ}39'E$). It extends from near Al-Nasiriyah City to the suburbs of Basra City in the east. To the south, it is adjacent to the southern desert and saline lakes. Historically, this marsh has an area of around 2800 km^2, expanding to approximately 4500 km^2 during the flood years. The marsh length and width were approximately 120 km and 25 km, respectively with a maximum water depth of 3 m [7].

Hammer Marsh is separated into two parts by the Hammer dike. The western part of the Hammer Marsh, which is in Thi-Qar province with an area of 1326 km^2 shown in Fig 1, extends from near Al-Nasiriyah to the northwest of Al-Basra Province in southern Iraq and it is fed by many rivers, while the east part within Al-Basra City which is fed by the tidal phenomenon through the Shatt Al-Arab River. Euphrates River and Main Outfall Drain (MOD) are the main water sources of the western part of the Hammer Marsh. The marsh is fed by the AlKurmashia, UmNakhal, and Al-Hamedy rivers. Moreover, the marsh is fed by sub-rivers, which are the BC3, BC3 opining, BC4, BC4 opining, Central opening, which sometimes work as feeders and other times as outlets, conveying the water from Euphrates River to the marsh body and sometimes from the marsh to Euphrates River depending about

water levels in the marsh and these rivers. Al-Khamissiya works as a feeder to convey the water from the MOD to the marsh. However, the west part of the marsh is reconnected with the MOD at the southern east by several pipes to be the main outlet, as shown in Fig 1.

2.3 Western Part of the Hammer Marsh Inflow Discharge

The average annual discharges inflow into the Western part of the Hammer Marsh from Euphrates River and Main Outfall Drain (MOD) were as shown in Fig 2. (CRIMW, 2020 unpublished data). These discharges were ranged between 0 to 143 m^3/sec.

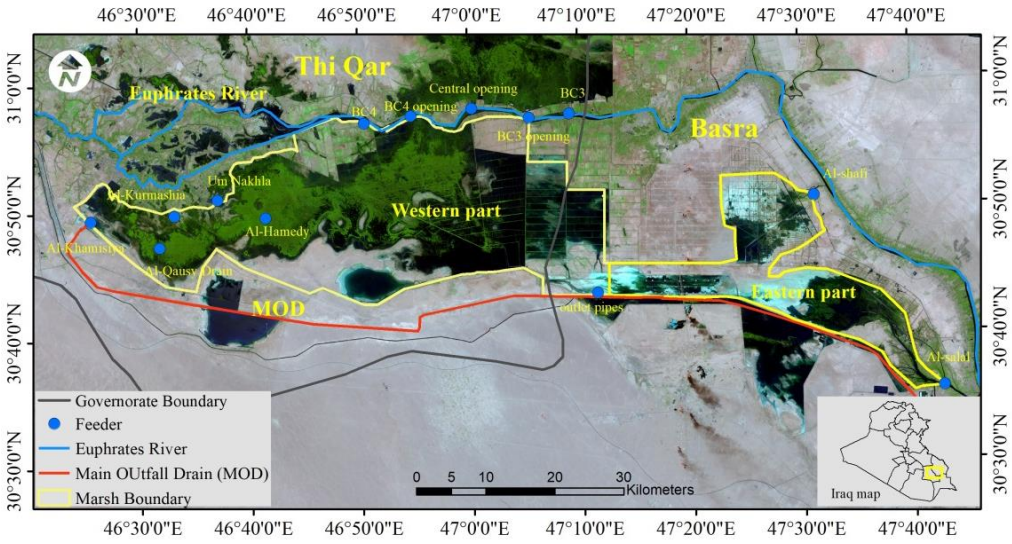

Fig. 1. Location of the study area with feeders and outlets.

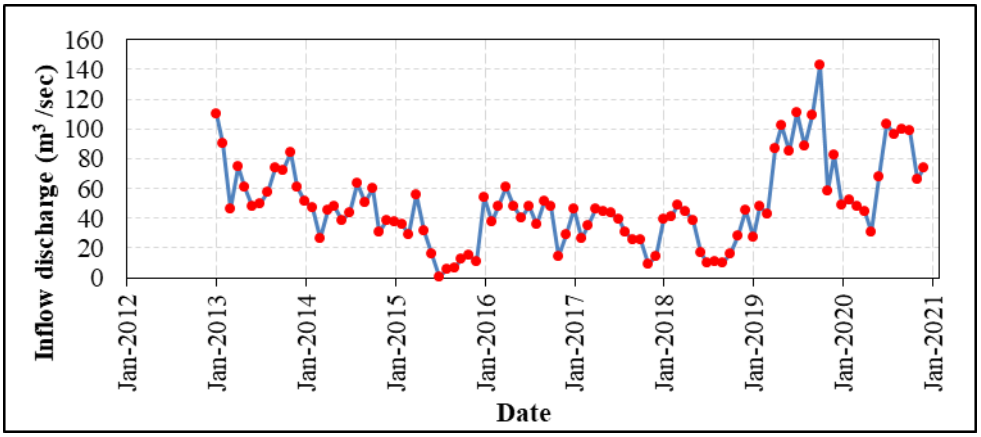

Fig. 2. Monthly inflow discharge into the western part of the Hammer Marsh in m^3 /sec recorded by (Based on CRIMW, 2020 unpublished data).

2.4 Remote Sensing Data

Landsat data are widely used for land cover classifications due to the reliability of their spatial resolution (30 m), revisit period (16 days), and spatial coverage (185×185 km). A series of Landsat 8 satellite images for the summer season was chosen to cover the study area from 2013 to 2020, as listed in Table 1. These images were downloaded from the United States Geological Survey (USGS) with a free cloud cover. During this time of the year, there is no rainfall, and the water sources are completely dependent on the water inflow that is provided to the marshes from the main outlets listed in the study area description.

The Landsat 8 images were successfully mosaicked after converting them to top-of-atmosphere spectral reflectance values to account for the radiometric contrast using ENVI 5.3.

Table 1. The available Landsat data for the Western part of Al-Hammer Marsh.

Satellite	Date of acquisition	Path/Row	Date of acquisition	Path/Row
Landsat 8	12/07/2013	166/39	03/07/2013	167/39
	15/07/2014	166/39	06/07/2014	167/39
	18/07/2015	166/39	09/07/2015	167/39
	05/08/2016	166/39	27/07/2016	167/39
	23/07/2017	166/39	30/07/2017	167/39
	27/08/2018	166/39	17/07/2018	167/39
	27/06/2019	166/39	04/07/2019	167/39
	29/06/2020	166/39	06/07/2020	167/39

3 Results

3.1 RSR Computation Model

The GIS model builder was used to implement a satellite based RSR index computation model by adopting Eq. (1), where the spectral bands 4, 5, and 6 of the Landsat 8 represent RED, NIR, and SWIR, respectively. The max is the maximum reflectance of SWIR and, the min is the minimum reflectance of SWIR in Landsat 8. The developed model is shown in Figs 3 and 4.

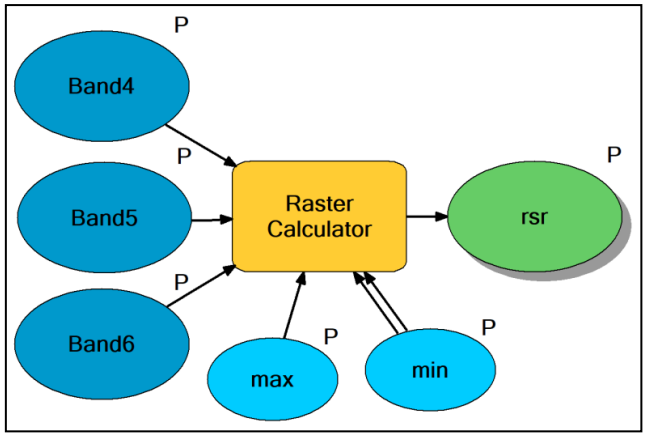

Fig. 3. Prepared RSR model in the environment of Arc GIS model builder.

.

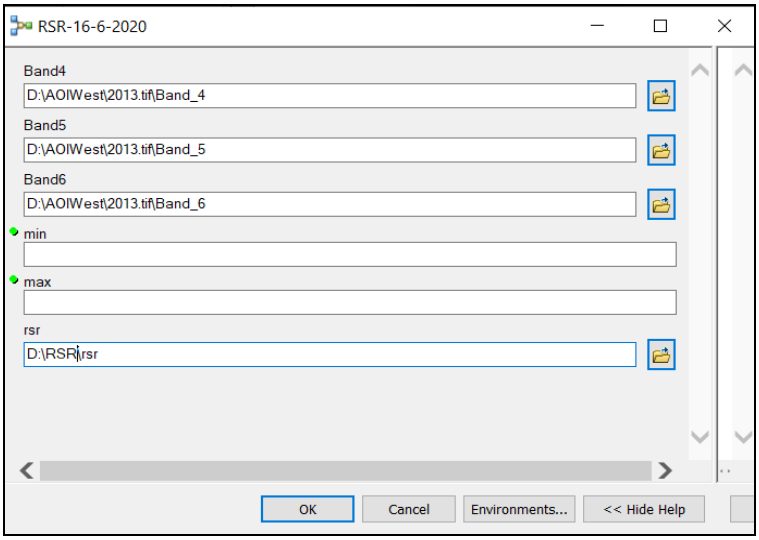

Fig. 4. Input and output menu for the RSR model.

3.2 Spatiotemporal Distribution of the RSR Index

The spatial distribution of the RSR index is shown in Fig 5. The values of the RSR index were classified into four classes according to the wetness level of the soil and vegetation. The (0.0-1.5), (1.5-3.0), (3.0-4.5), and (4.5-6.0) classes of RSR index represent the Low, Moderate, High, and Very high wetness levels, respectively of the soil and vegetation cover within the marsh.

The considerable moderate to high values of the RSR index is concentrated in the middle zone of the marsh and near the main feeders, where it represented the wetting area and vegetation cover. While the low values of the RSR index, which represented the dry areas, were distributed within the near-border areas of the marshes. These results are consistent with the topography of the region, where the near-border areas have high levels, while the levels are low in the middle, and the distribution of inundation areas and the vegetation cover are mainly distributed within these low-level zones and along with the marsh's feeders and outlets.

As shown in Fig 6, the low wetness class of the RSR (0.0-1.5) was the dominant class within the marsh with 71% and 73 % from the total marsh area in 2013 and 2014, respectively, then it increased in 2015 and 2018 to be 81% and 83%, respectively. While it decreased in 2016 and 2017 to 70% and 66%, respectively. Then, it decreased in 2019 and 2020 to 72% and 66%, respectively. It clearly shows an increase in the percentage of low-wetness lands during the considered period, especially in the years 2015 and 2018, which was accompanied by severe outflow decreases.

However, the moderate wetness class, RSR (1.5-3.0), was 29% and 27% in 2013 and 2014, respectively. Then, it decreased to 19% in 2015. While it increased in 2016 and 2017 to 27% and 34%, respectively. In 2018, it decreased to 16% and increased again to 24% and 23% in 2019 and 2020, respectively. This indicates an increase in the moderate wetness class with the increase in inflow discharges in 2017, 2019, and 2020.

The high wetness class of RSR (3.0-4.5) was the lowest and the less apparent class during the studied period with 3%, 4%, and 0.1% in 2016, 2019, and 2020, respectively, while it was closer to zero percent in the remaining study periods. Moreover, the very high wetness class of RSR index (4.5-6.0) rarely appears during the study period with a very small area, and it only appeared within a very small area (around zero percent) in 2019 and 2020 while it did not exist in other years.

In general, the relationship is positive between the results of the RSR index and the inflow discharge, where the RSR value increased in conjunction with an increase in the inflow discharge. The fluctuation in the quantities and times of water releases makes the inundation process useful and there is no noticeable improvement in the inundated areas, as the results showed fluctuation in the areas of inundation between an increase and decrease in conjunction with inflow discharges.

4 Conclusions

Implementation of plans to restore the Iraqi marshes after subjecting these marshes to deliberate drought several times in conjunction with the shortage in water sources necessitates the development of methods and techniques for monitoring the spatiotemporal change of the land cover response and assessing the restoration plans. The integration between remote sensing techniques and GIS is an efficient tool in monitoring the enhancement and/or deterioration of marsh's land cover, which gives more effective results, continuous, spatiotemporal, and low-cost monitoring of the large wetland area, especially when using a time series of appropriate periods that allows continuous monitoring of the changes that occur in the study area. It also assists in studying the changes, which gives clear results about the reality of the marsh and the response to the implemented inundation plans. From the results of the RSR index, there is no noticeable improvement in the inundation areas, as the results showed fluctuation in the inundation areas between an increase and decrease in a way that coincides with the increase and decrease of inflow discharge, as the areas of dry land increased in the category (0-1.5) of the RSR index for the years 2015 and 2018 with a severe decrease in the amount of water entering the marsh. The fluctuation in the inundation areas in conjunction with the fluctuation with the inflow discharge between an increase and a decrease shows that the conducted inundation does not serve the restoration plants in the region, as the inundation areas recede due to the lack of water releases and the water does not remain for a period to restore life to the plants. The relationship is positive between the inflow discharge and the improvement of the vegetation cover, but the improvement in a temporary manner depends on the increase and continuity of inflow discharge, and since the inflow discharges are irregular and there is considerable fluctuation in the quantities and timings of inflow discharge, the restoration process became insufficient and useless.

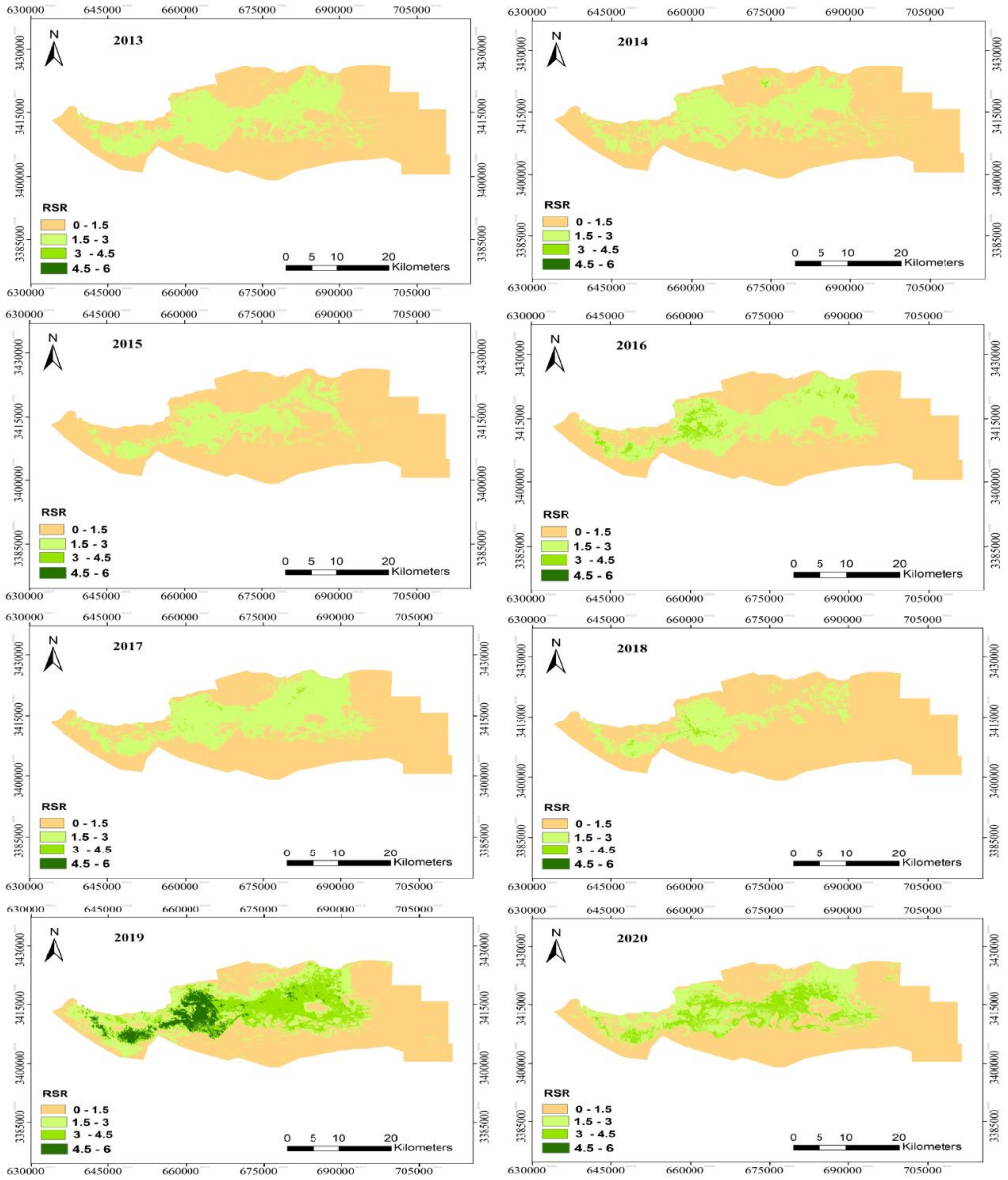

Fig. 5. Spatial distribution of RSR index.

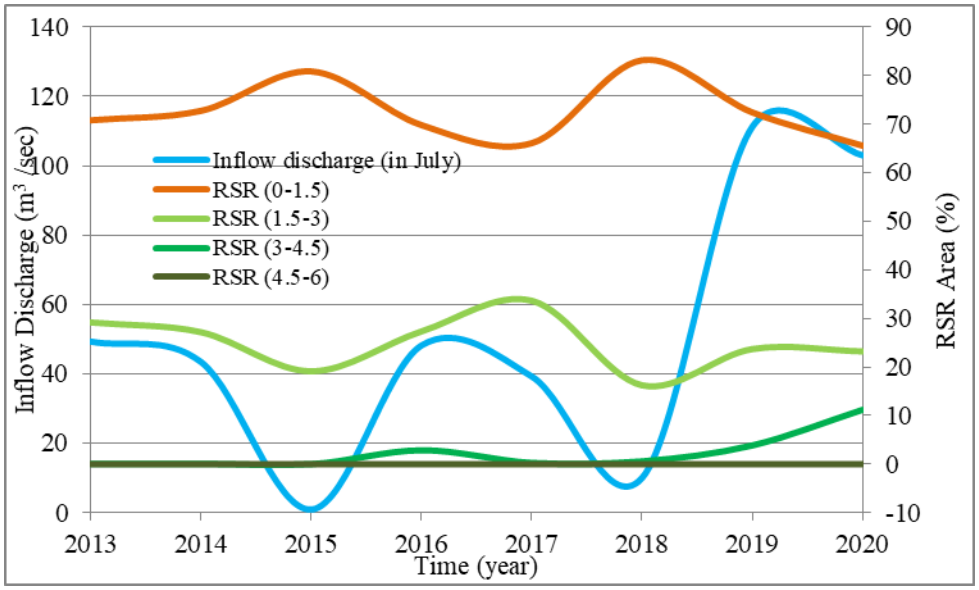

Fig. 6. Variation of RSR class area.

References

[1] A. Ghermandi, J. C. J. M. van den Bergh, L. M. Brander, H. L. F. de Groot, and P. A. L. D. Nunes, "The economic value of wetland conservation and creation: A meta-analysis," 2008.

[2] C. R. Lane, H. Liu, B. C. Autrey, O. A. Anenkhonov, V. V. Chepinoga, and Q. Wu, "Improved wetland classification using eight-band high resolution satellite imagery and a hybrid approach," *Remote Sens.*, vol. 6, no. 12, pp. 12187–12216, 2014, doi: 10.3390/rs61212187.

[3] R. D. Robarts, A. V Zhulidov, and D. F. Pavlov, *The state of knowledge about wetlands and their future under aspects of global climate change: The situation in Russia*, vol. 75, no. 1. Springer, 2013.

[4] J. A. Davis and R. Froend, "Loss and degradation of wetlands in southwestern Australia: underlying causes, consequences and solutions," *Wetl. Ecol. Manag.*, vol. 7, no. 1, pp. 13–23, 1999.

[5] P. Stenberg, M. Rautiainen, T. Manninen, P. Voipio, and H. Smolander, "Reduced simple ratio better than NDVI for estimating LAI in Finnish pine and spruce stands," *Silva Fenn.*, vol. 38, no. 1, pp. 3–14, 2004, doi: 10.14214/sf.431.

[6] L. Brown, J. M. Chen, S. G. Leblanc, and J. Cihlar, "A shortwave infrared modification to the simple ratio for LAI retrieval in boreal forests: An image and model analysis," *Remote Sens. Environ.*, vol. 71, no. 1, pp. 16–25, 2000, doi: 10.1016/S0034-4257(99)00035-8.

[7] Z. A. Abdulraheem, "Allocating the best representative water quality monitoring station dadity," p. M.Sc. Thesis, 2015.

Performance and Analysis of the Altitude for Optical Channel Drones

Abdullah Jameel Mahdi[1], Wamidh Jalil Mazher[2], and Osman Nuri Ucan[3]
{abdullahas396@gmail.com[1], wamidh.mazher@stu.edu.iq[2], Osman.Ucan@altinbas.edu.tr[3]}

Collage of Engineering, Electromech Engineering Department, University of Samarra, Samarra [1],
Thi Qar Technical College, Electrical Technical Department, Southern Technical University, Al-shatraa[2]
Electrical, and Computer Engineering, Altinbas University, Istanbul[3]

Abstract. A drone is a vehicle with no human pilot, staff, or passengers aboard recently used in various civil and military applications. Drones are controlled remotely by a human operator and flown. The technical advantages of free-space optical (FSO) technology motivated the researchers to continue investigating to use it in the communication between drones. Nevertheless, every technology face limiting factors that degrade performance. In this paper, the channel gain H effect was taken into consideration. The purpose is to compare the performance among different topologies that the system consists of, determine the effect of increase the drone's number on the system impacts, and extract the highest altitude *h* the system can reach. The system was modelled using MATLAB 2020, and the results showed that as the number of drones increased, the Signal-to-Noise ratio (SNR) increased. The maximum link distance *Z* between any two parts and the maximum altitude *h* the system reached was 7800 m.

Keywords: Drone, Free space optical, Signal-to-Noise ratio, Channel gain, Altitude, Link distance.

1 Introduction

The drone is applying in low-altitude and short-length applications. The drone is one type of unmanned aerial vehicle (UAV), and the latter is part of an unmanned aircraft system (UAS), which needs a ground-based controller [1]. The UAV is classified according to its size and configuration, total take-off weight, operational altitude, ownership, launch system [2]. As control technologies advanced and costs decreased, their utilization expanded quickly and applied in several applications [3] in which some of the drone services available. The FSO technology links the drone and the controller or between the drones themselves. FSO uses the laser to propagate in free space to transmit data wirelessly. Many merits encourage using FSO technology as an alternative to RF technology, such as licensed free, high bit rates, long-range operation, immunity to electromagnetic interference, high security [4], and so on.
On the other hand, many limiting factors existing in both the atmospheric layer and in laser. The atmospheric layer liming factors are fog, rain, pollution, aligned stability in the wind [5], [6]. At the same time, the limiting factors in a laser beam are narrow beamwidth that complicates the alignment between two transceivers, the choice of laser wavelength that is subject to minimal

IMDC-IST 2021, September 07-09, Sakarya, Turkey
Copyright © 2022 EAI
DOI 10.4108/eai.7-9-2021.2314924

losses, etc. As a result of these factors, the receiver signal gets attenuated and limits the valuable distance, resulting in a higher bit error ratio (BER).
In addition to the mentioned limiting factors, the channels connected between drones were classified as a non-stationary link. One significant problem arising from such a link is the pointing error (misalignment) between Tx and Rx. Many studies on systems-based FSO terrestrial links took into account the weather conditions and beamed pointing errors such as [7], [8], and [9]. In contrast, the studies on drone based FSO links are recent and rare, especially in pointing error limiting factors. The study [10] looked at how to improve the UAV system by using relay-assisted to reduce the effects of various atmospheric variables on the FSO signal quality. The research in [11] looked at how the Ground-UAV and UAV-UAV scenarios performed in the presence of air turbulence. As illustrated in [12], the BER goal was met by selecting the optimal beamwidth to reduce transmitted power. The survey [13] focused on the continual movement and changing relative speeds of participating UAV members, making it challenging to establish a line-of-sight (LOS) FSO link in a swarm scenario. The performance of a non-static and tilted link between the stationary station on the ground and the UAV was measured in the study [14]. The study [15] counted the number of drones that may be used to identify and make important decisions for area surveillance (e.g., oil pipeline leak). By describing source-to-relay and relay-to-destination channel models, the study's goal [16] is to calculate the ideal three-dimensional coordinates of the UAV relay and optimal beam pattern to reduce outage probability.
This paper aims to compare the performance among different topologies that the system consists of, determine the effect of increasing the drone number on system performance, and extract the highest altitude h the flying system can reach.

2 The system configuration

Drones networking is no longer restricted to point-to-point communication between drones or between drones and remote controllers. Many network configurations can the drone's shape as mentioned in [17] and [18]. In addition, numerous channel kinds, such as Single Input-Single Output (SISO) link, Multiple Input-Single Output (MISO) link, Single Input-Multiple Output (SIMO) link, and Multiple Input-Multiple Output (MIMO) link, can be linked between drones in the network [15], [19] [15], [19]. In this research, the drone swarm's system configuration is the V-shape arrangement, as depicted in Fig 1. Many multi-rotor drones with SISO and MISO channels make up the configuration. The SISO channel is the link between the drones in an arm as well as the channel between the Ground Station (GS) Controller and the Main Drone (DM). The DM is the MISO channel, and it connected the last drones in both arms (D11 and D21). In [15], this V-shape design was used. At the transmitter end, the SISO topology has one transmitting aperture and one receiving aperture. The optical signals can be sent from the MISO's many transmitting antennas. The optical signals from many transmitting antennas are received by just one receiving antenna, implying that different sources are available but only one destination is available [20].
The drones in this study move at a constant speed and alter their altitude h at the same time. The drones will be on one side, while the GS will be on the other. As shown in Table 1, the system parameters differ for each channel in the system.

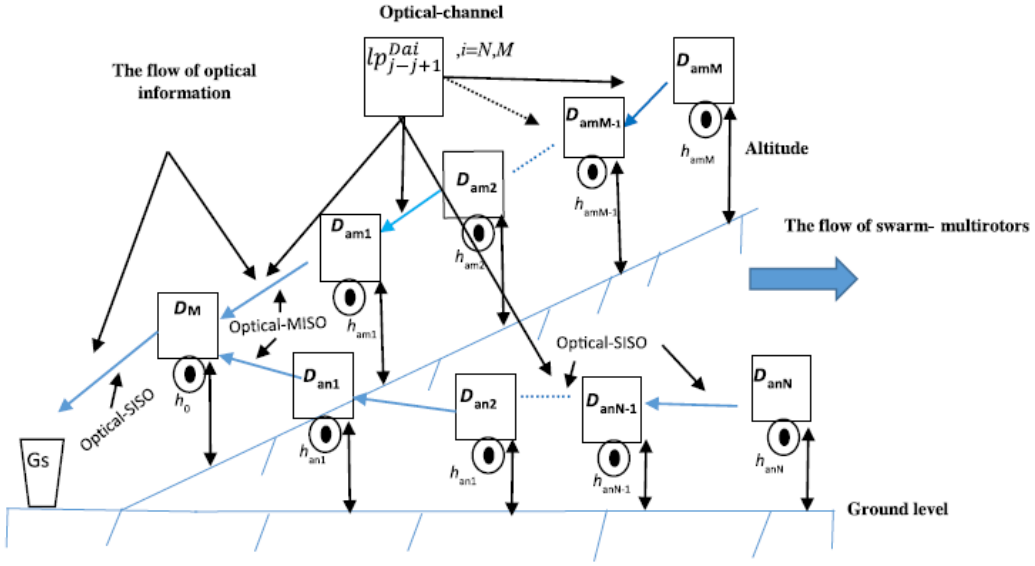

Fig. 1. V-shape swarm FSO-drones perspective illustration [15].

Table 1. The system parameters.

Parameter	Symbol	Set to
Rate of Transmission	Rate	1 Gbps
OTP	P_t	40 mW (16 dBm)
Responsivity	R	1
Separated distance	Z	Varying
Altitude	h	Varying
Wavelength	λ	1550 nm
Receiver Diameter	D_R	1 cm
Pointing Error Angle	θ_r	1×10^{-5} rad
Beam Waist at z=0	w_0	5×10^{-2} cm

The width w_o of the transmitted optical beam from the transmitter Tx is measured by the beam waist wo. The D_R value of the receiver aperture is 1 cm. It depends on the drone design and weight tolerance; the operating wavelength λ is 1550 nm because it has a smaller attenuation transmission window. The distance Z between two drones or between D_M and GS was assumed to vary. The altitude of the drones was assumed to vary also.

3 The Channel mathematical model

The channel gain H is made up of three factors: atmospheric attenuation Ha, atmospheric turbulence H_f, and pointing error factor H_p. Each of these factors represents an impairment that faces the FSO system. H_a and H_f have modelled the weather condition and the atmosphere's turbulence, and H_P has modelled the optical beam pointing with channel gain H:

$$H = \prod_{m=1}^{M} H_{a_m} H_{f_m} H_{p_m}, \qquad m=1,2,3,...M \tag{1}$$

where M is the topology's channel count (for SISO, M=1, and MISO=2).
The Beer-Lambert law, represented as [21], has been used to simulate the atmospheric attenuation H_{am}:

$$\mathrm{H_{a_m}} = exp(-Z_m \sigma) \tag{2}$$

where Z_m is the link distance of the mth channel and σ is the attenuation coefficient, which is a function of visibility [22]. The channel fading of atmospheric turbulence H_{fm} can be expressed as:

$$H_{f_m} = \frac{2P_{r_m}}{\pi W_m} \tag{3}$$

Where P_{rm} and W_m are the received optical power and the beam spot radius of the mth channel at the receiver. The pointing error H_{pm} of the optical beam between the transmitter and receiver given as:

$$H_{p_m} = A_{0_m} \exp\left(\frac{-2r_m^2}{W_{Zeq_m}^2}\right) \tag{4}$$

where optical beam radial displacement is $r_m = Z.\theta_r^m$, pointing error angle is θ_{r_m} of the m^{th} channel with $\leq 10^{-4}$ [23], $A_{0_m} = [erf(v_m)]^2$ is the fraction of collected power at the radial displacement r= 0 [24], and beam radius $\mathrm{W_{Zeq_m}}$ in the m^{th} channel that can given as [24]:

$$W_{Zeq_m} = \mathrm{w}_{Z_m}^2 \frac{\sqrt{\pi}\mathrm{erf}(v_m)}{2\mathrm{v}\exp(-v_m^2)} \tag{5}$$

where beam radius is w_{z_m} at e^{-2} of the axial Z_m distance and beam width w_0 at Z_m=0 as $w_{z_m} \approx w_0[1 + \varepsilon_m(\lambda Z_m/\pi w_0^2)^2]^{\frac{1}{2}}$, where $\varepsilon_m = (1 + 2\mathrm{w}_0^2/\rho_0^2(Z_m))$, and the coherence length $\rho_0(Z_m) = (0.55C_n^2(h)K^2Z)^{-3/5}$, and $v_m = \left(\sqrt{\pi}\, a\right)/\left(\sqrt{2}\ \mathrm{w}_{z_m}\right)$, where receiver radius is a [25]. The received optical signal [26] is:

$$y = xR\sum_{m=1}^{M} H_m + v_n, \qquad m=1,2,3,....M \tag{6}$$

Where x denotes the transmitted signal, R the photodetector responsivity, v_n the additive white Gaussian noise (AWGN) with variance _σ_n=N_0/2.0, and H_m the mth channel gain. The parameters of the two MISO topology channels are assumed to be equal for Simplicity, as are the parameters of the two arms SISO channel.

4 Measuring performance

The performance was measured based on Average (mean) BER (ABER) and can be computed using the results from [27] and expressed as:

$$ABER = \int_0^{\infty} BER_{sim}\,(H) \times f_H\,(H)dH \tag{7}$$

where $BER_{sim}\,(H)$ is the conditional simulated BER. The $f_H(H)$ is the channel gain H Probability Distributed Function (PDF). In weak turbulence, the log-normal distribution is applied. For the SISO channel, the PDF of the channel gain H is as mentioned in [25], while the PDF of the MISO and SISO channels are similar except dividing the variance σ_x by number of transmitting elements [28]. The ABER is counted independently and thus whole variation can be calculated as:

$$TABER = 1 - \prod_{i=1}^{N}(1 - ABER_i) \qquad i=1,2,\ldots\ldots\ldots N \tag{8}$$

i represents the ith drone, N represents the number of drones equal to the number of channels in the proposed system, and ABERi represents the average bit error rate for each channel..

5 Results and discussion

When setting the distance between the two drones in the same arm 60 m, the distance between the GS and D_M 1000 m, and the altitude can vary from 1 m to 1000 m, the performance of each subsystem against the system BER shown in Fig. 2, which demonstrate the operation of subsystems and whole system with ABER $\approx 10^{-8}$.

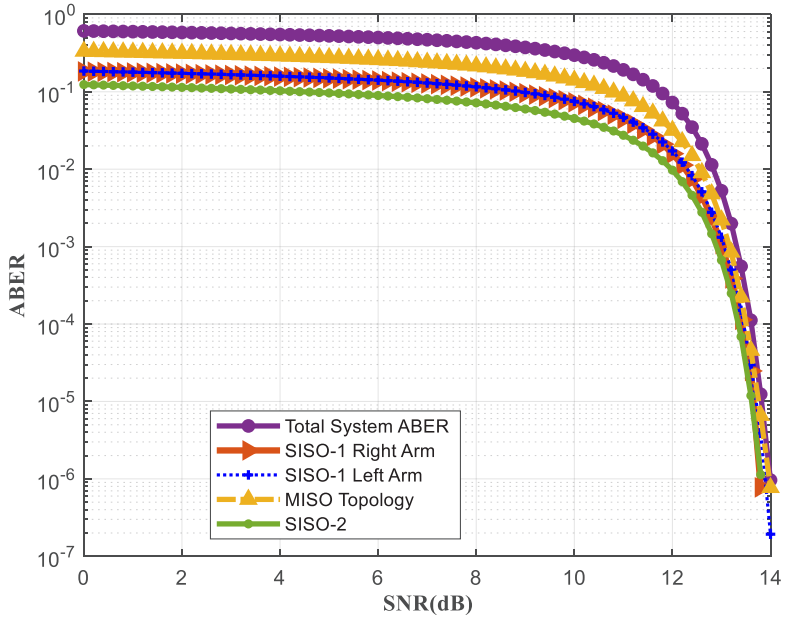

Fig. 2. Subsystems compared to whole system operation.

To see the SNR differences between the subsystems and the overall system, setting the ABER=10^{-4} as a reference value, the difference in SNR for each part that is shown in Fig. 3.

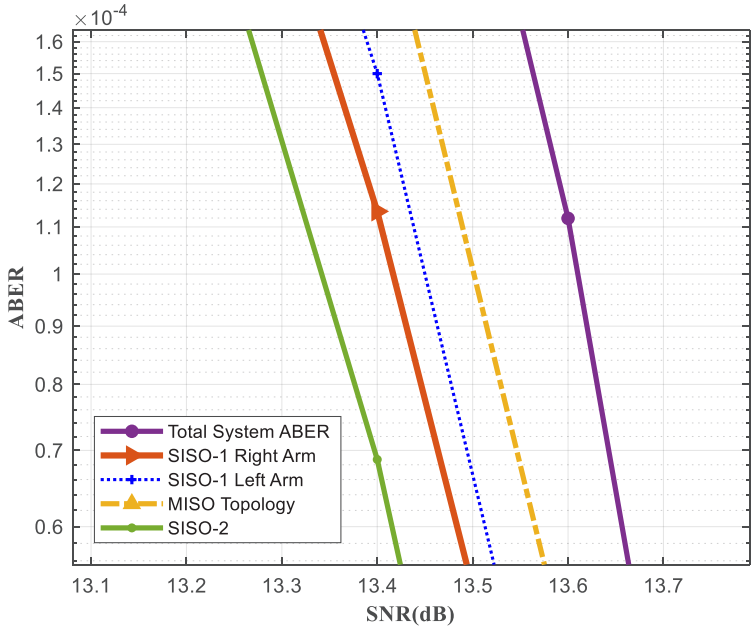

Fig. 3. The SNR differences between the subsystem and the overall system.

Fig 3 clarified that as the number of drones increased in the system, the ABER increased; therefore, the SNR values increased to get high performance. For example, if the system has only one drone, the SNR is 13.349 dB, whereas when the system has five drones, the SNR is 13.62 dB; this increases in SNR is to compensate for the increase in the bit errors of the five drones and have the same performance as for one drone. Table 2 summarized the SNR differences in numbers for each part of the flying system and the whole system is shown in Table 2.

Table 2. Differences in SNR for the whole system and the subsystems.

System Part	Number of Drones	SNR(dB)
The whole system	5	13.62
MISO topology	3	13.50
SISO-1 left arm	2	13.45
SISO-1 right arm	2	13.425
SISO-2	1	13.349

The subsequent test examined the system performance as the link distance Z increased more than 1000 m. For example, link distances Z = 2000, 6000, and 8500 m as samples. In this case, the flying drones are considered a single system connected optically to the GS; therefore, we

take the whole system's total average BER (TABER). The flying system becomes perpendicular to the GS when the altitude h equals the link distance Z value; therefore, this test can be generalized to the Z *and* h respectively distance and altitude h. Fig 4 showed that at SNR< 10 dB, all the distances (or altitude h) showed the worst performance. After SNR $\geq$ 10 dB, there was an enhancement in the performance until TABER $\approx 10^{-7}$ for distances Z or h= 2000 m and 6000 m. When Z or h increases, the system performance decreases, and vice versa. Table 3 summarized the SNR differences when setting TABER= 10^{-4}.

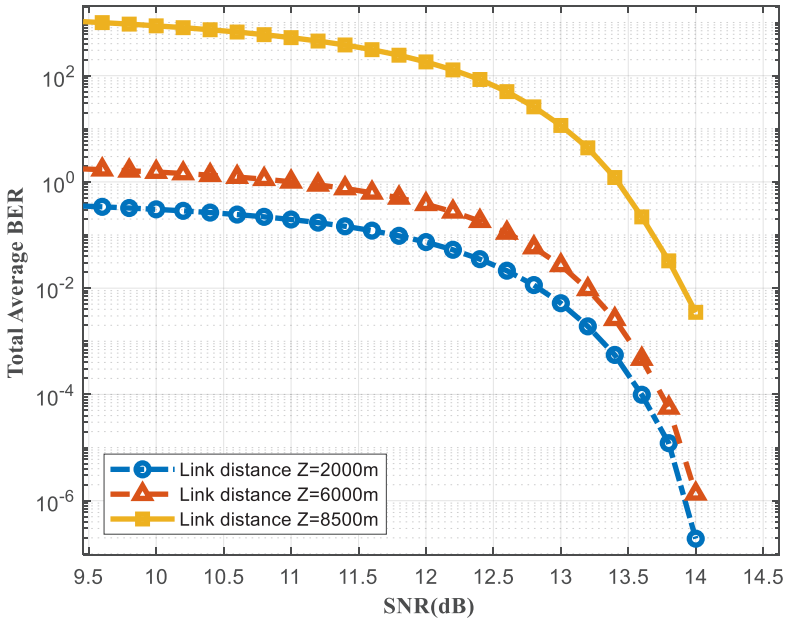

Fig. 4. System performance at various Z - distances.

Table 3. Outcomes when the distance Z or the altitude h increases.

The link distance Z or the altitude h (m)	SNR (dB)
2000	13.601
6000	13.75
8500	-

At Z = 8500 m, the system showed the highest BER; therefore, Z must be < 8500 m; more specifically, Z = 7800 m got high performance for the values given parameter. The later distance can be applied between two drones and not just between the flying and GS. Also, the flying system can reach the highest altitude h at 7800 m, and the performance keeps high.

6 Conclusions

The ABER for each subsystem was determined, followed by the total ABER for the entire system. Each subsystem can be considered an independent system; then, the subsystems built the flying system. The results showed that as the number of drones increased, the SNR increased also. At SNR < 10 dB, all of the results revealed that the ABER improves marginally. There are considerable increases in system performance after SNR ≥ 10 dB. The maximum distance *Z* and altitude *h* could the flying system reach and got high performance was 7800 m. Increases in the link distance Z are used to determine the maximum distance that the drones can travel for the characteristics listed in Table 1. The beam becomes wider as the connecting distance Z increases. A portion of the incident light is captured by the receiver. When the performance of the link degrades, the controller can change the link distance Z. For future study, critical factors affecting system performance, such as transmission power P_T and receiver aperture diameter D_R, can be tuned to achieve ideal values.

References

[1] J. Hu and A. Lanzon, "An innovative tri-rotor drone and associated distributed aerial drone swarm control," *Rob. Auton. Syst.*, vol. 103, pp. 162–174, 2018.

[2] C. Yan, L. Fu, J. Zhang, and J. Wang, "A Comprehensive Survey on UAV Communication Channel Modeling," *IEEE Access*, vol. 7, pp. 107769–107792, 2019.

[3] C. Koparan, A. B. Koc, C. V. Privette, C. B. Sawyer, and J. L. Sharp, "Evaluation of a UAV-assisted autonomous water sampling," *Water (Switzerland)*, vol. 10, no. 5, 2018.

[4] M. A. Khalighi and M. Uysal, "Survey on free space optical communication: A communication theory perspective," *IEEE Commun. Surv. Tutorials*, vol. 16, no. 4, pp. 2231–2258, 2014.

[5] S. Bloom, E. Korevaar, and J. Schuster, "Understanding the performance of free-space optics [Invited]," vol. 2, no. 6, pp. 178–200, 2003.

[6] H. Kaushal and G. Kaddoum, "Optical Communication in Space: Challenges and Mitigation Techniques," *IEEE Commun. Surv. Tutorials*, vol. 19, no. 1, pp. 57–96, 2017.

[7] I. S. Ansari, F. Yilmaz, and M. S. Alouini, "Impact of pointing errors on the performance of mixed RF/FSO dual-hop transmission systems," *IEEE Wirel. Commun. Lett.*, vol. 2, no. 3, pp. 351–354, 2013.

[8] M. Sharma, D. Chadha, and V. Chandra, "Performance Analysis of Multihop Free Space Optical Communication System with Pointing Errors," *J. Opt. Commun.*, vol. 36, no. 1, pp. 24–27, 2015.

[9] G. Immadi, M. Venkata Narayana, A. Sree Madhuri, and V. L. Tejaswani Sabbasani, "Simulation of free space optical communication under different weather conditions," *Int. J. Pure Appl. Math.*, vol. 117, no. 18 Special Issue, pp. 143–148, 2017.

[10] W. Fawaz, C. Abou-rjeily, and C. Assi, "UAV-Aided Cooperation for FSO Communication Systems," *IEEE Communications Magazine*, no. January, pp. 70–75, 2018.

[11] E. Leitgeb, K. Zettl, S. S. Muhammad, N. Schmitt, and W. Rehm, "Investigation in free space optical communication links between unmanned aerial vehicles (UAVs)," *Proc. 2007 9th Int. Conf. Transparent Opt. Networks, Ict. 2007*, vol. 3, no. 1, pp. 152–155, 2007.

[12] J.-B. Wang, M. Sheng, X. Song, Y. Jiao, and M. Chen, "Comments on `BER Performance of FSO Links over Strong Atmospheric Turbulence Channels with Pointing Errors'," *IEEE Commun. Lett.*, vol. 16, no. 1, pp. 22–23, Jan. 2012.

[13] S. Sheikh Muhammad *et al.*, "Challenges in establishing free space optical communications between flying vehicles," in *Proceedings of the 6th International Symposium Communication Systems, Networks and Digital Signal Processing, CSNDSP 08*, 2008, pp. 82–86, 2008.

[14] A. Hatziefremidis, K. E. Zarganis, H. C. Leligou, and N. Pleros, "Bit error rate analysis along a slanted path link between UAVs and Ground Stations," *15th International Conference on Transparent Optical Networks (ICTON)*, pp. 1–4, 2013.

[15] W. J. Mazher, H. T. Ibrahim, O. N. Ucan, and O. Bayat, "Drone swarm with free-space optical communication to detect and make deep decisions about physical problems for area surveillance,"

Optical Engineering, vol. 57, no. 3, March 2018.

[16] M. T. Dabiri and S. M. S. Sadough, "Optimal Placement of UAV-Assisted Free-Space Optical Communication Systems With DF Relaying," *IEEE Commun. Lett.*, vol. 24, no. 1, pp. 155–158, Jan. 2020.

[17] C. Chlestil *et al.*, "Optical Wireless on Swarm UAVs for High Bit Rate Applications," *IEEE CSNDSP*, 2006, no. July 2015, pp. 634–638, 2015.

[18] S. S. Muhammad *et al.*, "Challenges in establishing free space optical communications between flying vehicles," *6th International Symposium on Communication Systems, Networks and Digital Signal Processing*, pp. 82–86, 2008.

[19] A. A. Khuwaja *et al.*, "A Survey of Channel Modeling for UAV Communications," *IEEE Commun. Surv. Tutorials*, vol. 20, no. 4, pp. 2804–2821, 2018.

[20] C. R. Shah, "Performance and Comparative Analysis of SISO ,SIMO,MISO, MIMO," *Int. J. Wirel. Commun. Simul.*, vol. 9, no. 1, pp. 1–14, 2017.

[21] N. a Mohammed, A. S. El-wakeel, and M. H. Aly, "Pointing Error in FSO Link under Different Weather Conditions," *Int. J. Video Image Process. Netw. Secur.*, vol. 12, no. 1, pp. 6–9, 2012.

[22] M. T. Dabiri, S. Mohammad, S. Sadough, and M. A. Khalighi, "Channel Modeling and Parameter Optimization for Hovering UAV-Based Free Space Optical Links," *IEEE J. Sel. Areas Commun.*, vol. 36, no. 9, pp. 2104–2113, 2018.

[23] T. Song, Q. Wang, M.-W. Wu, T. Ohtsuki, M. Gurusamy, and P.-Y. Kam, "Impact of Pointing Errors on the Error Performance of Intersatellite Laser Communications," *J. Light. Technol.*, vol. 35, no. 14, pp. 3082–3091, Jul. 2017.

[24] M. T. Rahman, S. Iqbal, and M. M. Islam, "Modeling and performance analysis of free space optical communication system," *International Conference on Informatics, Electronics and Vision, ICIEV 2012*, no. April 2019, pp. 211–218.

[25] A. A. Farid and S. Hranilovic, "Outage capacity optimization for free-space optical links with pointing errors," *J. Light. Technol.*, vol. 25, no. 7, pp. 1702–1710, 2007.

[26] K. Prabu, D. S. Kumar, and R. Malekian, "BER analysis of BPSK-SIM-based SISO and MIMO FSO systems in strong turbulence with pointing errors," *Optik (Stuttg).*, vol. 125, no. 21, pp. 6413–6417, Nov. 2014.

[27] J. B. Wang, M. Sheng, X. Song, Y. Jiao, and M. Chen, "Comments on 'BER performance of FSO links over strong atmospheric turbulence channels with pointing errors,'" *IEEE Commun. Lett.*, vol. 16, no. 1, pp. 22–23, 2012.

[28] M. Abaza *et al.*, "MIMO Techniques for High Data rate Free Space Optical Communication System in Log-Normal Channe," *The International Conference on Technological Advances in Electrical, Electronics and Computer Engineering, TAEECE 2013*, pp. 1-5, 2013.

Practical Performance Investigation of the Solar (PV) Panel System of the Electronic and Control Engineering Department - Kirkuk

Montassar Aidi Sharif [1,2], Mahmoud Shakir Wahhab[1], Kaesar Sabah Khalaf[1]
{ msharif@ntu.edu.iq, mahmoud.eng777@ntu.edu.iq, kaesarsabah@ntu.edu.iq}

[1] Electronics and Control Engineering Department, Technical Engineering College- Kirkuk, Northern Technical University, Kirkuk, Iraq
[2] Computer Engineering Department, Technical Engineering College- Kirkuk, Northern Technical University, Kirkuk, Iraq

Abstract. Scientific research and development in solar cell systems is often focused on studies that include radiation availability, some effective operating strategies, and re-engineering of these systems. In Iraq in particular, the experience of using solar energy systems is almost new to be used to provide clean energy. Therefore, it was necessary when installing solar energy systems in Kirkuk governorate in Iraq, especially in the Department of Electronics and Control Engineering in the Kirkuk Engineering Technical College, that the performance of these cells or systems should be examined and measured, especially that the department made full use of solar energy. The electrical performance of photovoltaic panels has been experimentally studied for the effect of dust particles deposited, as well as when there is fog and when there is bright sun and for a number of consecutive days. The energy efficiency and energy output of the photovoltaic system are calculated based on experimental data. The conclusion is that dust significantly reduces the efficiency of photovoltaic solar panels.

Keywords: Solar Panels, Renewable Energy, Performance of Solar Cells, Photovoltaic.

1 Introduction

These days, elements of strength have come to be very fundamental. It includes, for example, rational and low cost makes use of of resources, in addition to environmental affects related to emissions, pollution and intake of non-renewable resources [1]. For those reasons, there may be a developing and accelerating hobby global in sustainable strength manufacturing and strength savings [1,2]. Among the technology that would play a position in sustainable and big-scale strength era, thrilling answers are photovoltaic (PV) cells, wind generators, biomass flora and gasoline cells. In particular, photovoltaic structures may be taken into consideration as one of the maximum famous answers with big margins of development even as making sure electricity era with low environmental impact [2].

Solar panels are utilized to capture the energy of sunlight to convert it into electrical energy [3]. When multiple systems are combined, the photovoltaic units are installed as an integrated system, pointing to a single surface, called the power panel [1,3]. Photovoltaic is a new technology field with relatively new applications in solar power generation, but it is still often used exclusively for generating electricity from sunlight [2,3]. Photovoltaic cells are used to

IMDC-IST 2021, September 07-09, Sakarya, Turkey
Copyright © 2022 EAI
DOI 10.4108/eai.7-9-2021.2314918

detect light or other electromagnetic radiation near the visible light matrix, such as detecting infrared radiation or measuring light intensity [3].

Photovoltaic cells through which sunlight is directly converted into electricity, by using semiconductors such as silicon, which is extracted from pure sand [2,3]. Generally, the materials of these blocks are coarse-crystalline materials such as crystalline silicon or fine amorphous materials such as amorphous silicon aSi and cadmium or other materials. Their energy is considered a clean and renewable energy because it does not cause waste, pollutants, radiation, noise, or even no fuel [4]. But compared with other energy sources, the acquisition cost is higher. Solar cells continue to produce direct electricity (such as traditional dry batteries and liquid batteries) [5, 6]. The current intensity depends on the duration of the sun and the intensity of solar radiation, as well as the efficiency of the photovoltaic cell itself in converting solar energy into electrical energy. When connected in series, these solar cells can provide hundreds of volts of direct current (DC) [7].The resulting energy can also be stored in lead-acid or nickel-cadmium-acid batteries [8]. DC current can be converted into AC current by inverters for use and management of ordinary household and industrial electrical appliances [9, 10]. Its advantage is that it has no moving parts subject to failure [11]. For this reason, it operates over satellites with high efficiency, especially since it does not require maintenance, repairs, or fuel, as it operates in silence, but the dirt of the photovoltaic cells as a result of pollution or dust leads to a reduction in their efficiency, which calls for cleaning them at intervals [6, 11,12,13].

Few research analyzed this impact and the resultant performance degradation. Current studies on PV device overall performance and the results of the deposition of dirt is confined because of the reality that powder is a complicated phenomenon this is encouraged with the aid of using distinctive environmental and climate conditions [12,14]. A quick experimental illustration of the elements that determines the setup of the PV panels is proven in setup of experiment. A targeted evaluation of the impact of the PV modules overall performance is proposed on this paper. Based on most of these statistics the results of the PV panels electric performances were highlighted. During the examine of the overall performance of sun pv panel with and without, then the subsequent elements considered:

2 Experimental Methodology

The test is performed through the use of the three 360 w solar panel installed on a stand. The electric parameters like voltage & current were measured to examine the impact of environmental numerous impact. The internet impact of fog, dirt, and direct solar at the energy discount turned into evaluated & analyzed. The impact of dirt may be quantified through evaluating the performance of panel uncovered to dirt & with out dirt. In this work, the machine of measurements is includes a silicon sun panel of vicinity 2 m*m, MUST inverter turned into used for size of producing the the voltage, current, and the temperature and something associated with the solar panel. The experimental examine turned into carried out withinside the Kirkuk city, Technical Engineering College - Kirkuk, Electronics and Control Department. The ambient temperature fluctuates withinside the variety of 15 to 33ºC in the course of the measurements. The sun photovoltaic panel turned into examined and the parameters like Voc, Isc, solar irradiance, and ambient temperature ,etc, wished for the assessment of the structures have been measured at interval of 1 hour and a half between 10.30 AM and 12.00 PM. The ambient temperature and the incident solar radiation depth turned into measured the use of the inverter.

Table 1. Specifications of the PV module

Parameter	Value
Model	Tata BP 184459
Maximum power	360 W
Open circuit voltage	12V
Short circuit current	2A
Number of cells	60
Dimensions	2*1*0.1 m^3
Wieght	25 kg

3 Experimental Setup

In this part of the research, an integrated solar energy system was established on the Department of Electronics and Control Engineering Technique with a capacity of 5 kilowatts, 30 solar Panels and 8 batteries of 200 amp/hour, but the experiment was done on 3 panels only 360 watts (all information is in Table 1) A smart MTS invertor was used to take measurements and data. Figure 1 represents the practical part and its details that were already explained. It is noted that the solar panels are divided, and this is what can be made good to collect the most possible energy, and even if there is shadow or dust on part of the panels and the cells, the rest of the panel will not be affected as a result of the panel division into two parts, meaning that the first part does not affect the second part and vice versa. The readings were taken as shown in Figure 2, where a laptop was used, and a program was installed to take the readings directly from the inverter that was connected between the batteries and the solar panels.

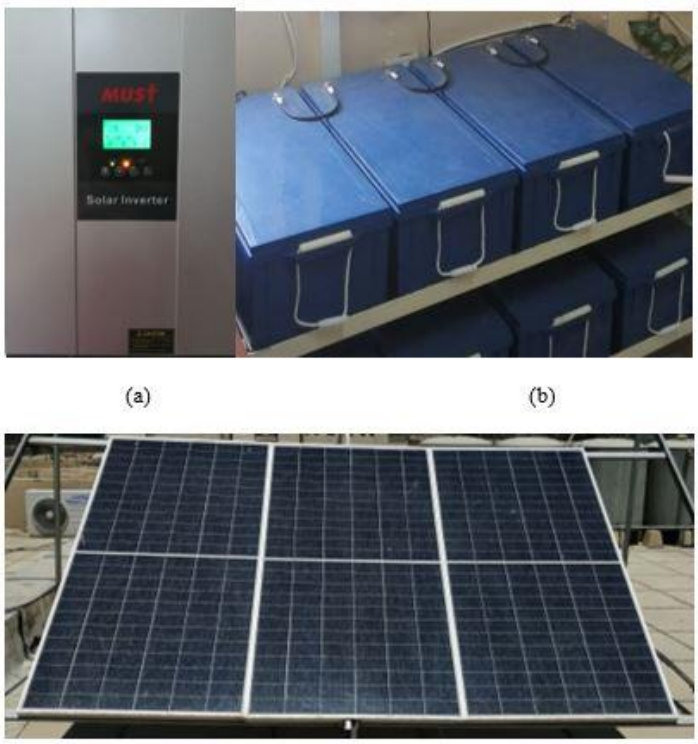

Fig. 1. The parts of the system: (a) Inverter (MUST); (b) Recharchabel battery (200 A/h); (c) Solar panel (360 w)

Fig. 2. Collecting data process from the system

4 Results and Discussion

The experiments were carried out in different weather conditions. The first test took place on the first day, as the weather on the first day was mostly dusty, which was very suitable for doing the first test. The data recording process took place from ten thirty in the morning until twelve o'clock in the afternoon, and it represents a full 8 hours. As for the date of today's test, the first day was 8th of April, 2021. As for the second day, it was 3 days after the first day, when the weather was partly cloudy. On the third and fourth day, the weather was clear and the maximum temperature was 33 degrees Celsius as well as we tested one dusty day.

The results of the temperature of the solar panels as well as the power were recorded in all the conditions mentioned above. It is noticeable in Figure 3, that the temperature of the solar panels increases as the time approaches noon, and this is actually expected, especially in the month of April in Iraq, regardless of the weather.

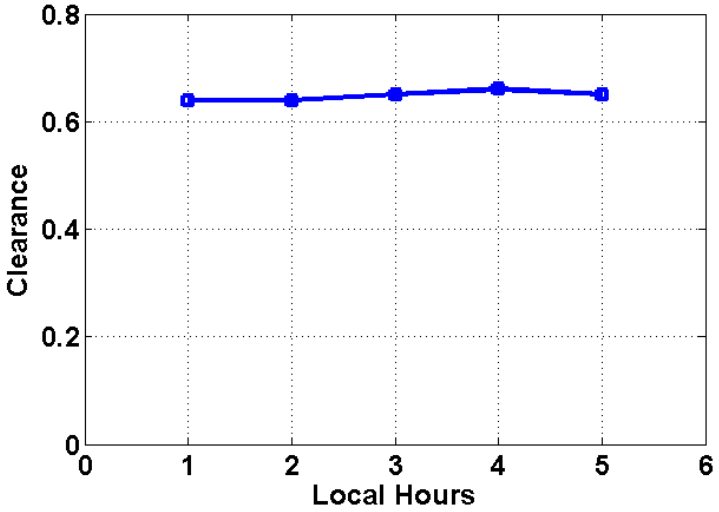

Fig. 4. The recorded clearance of the weather for five continuing days

As for the energy obtained, it is volatile in most circumstances, but it is noted in Figure 4 that the power obtained on a day when the weather is clear, the power is high compared to other days, especially if the weather is cloudy or dusty.

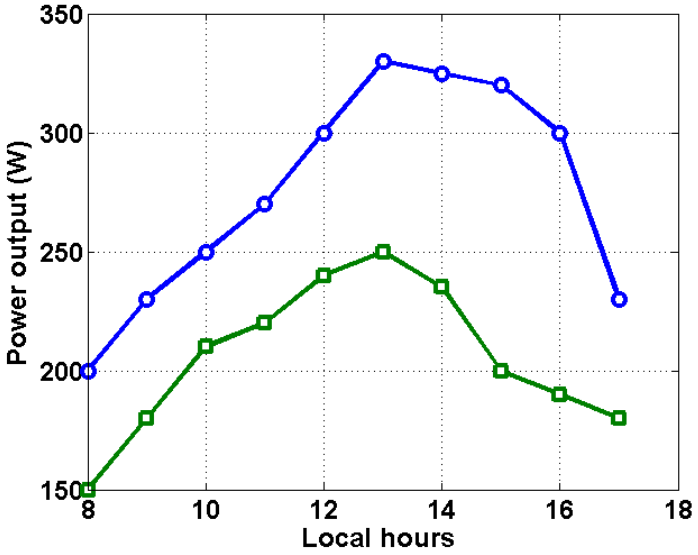

Fig. 4. Power of the panel of two days clear day (blue) and cloudy day (grean) versus local hour

Figure 5 shows the power taken for three days one clear day and cloudy day and the last day is the dusty day.

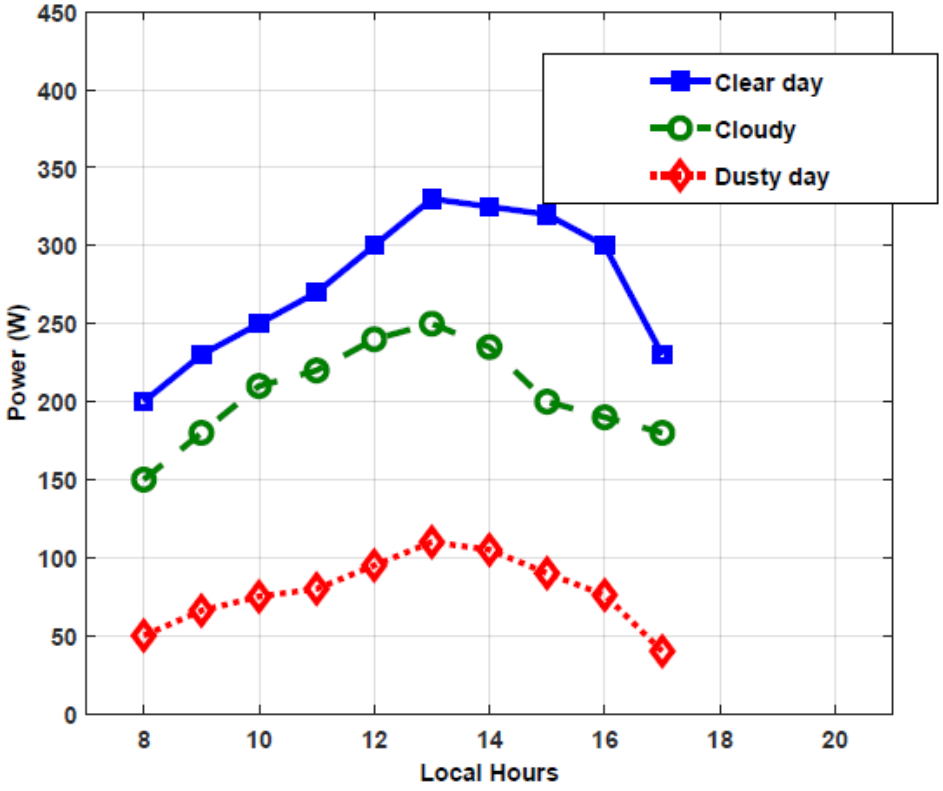

Fig. 5. Power versus local hours for three different days

References

[1] Paranthaman, M. Parans, Winnie Wong-Ng, and Raghu N. Bhattacharya, eds. Semiconductor materials for solar photovoltaic cells. Vol. 218. Switzerland: Springer International Publishing, 2016.

[2] Chenni, R., et al. "A detailed modeling method for photovoltaic cells." Energy 32.9 (2007): 1724-1730.

[3] Sargunanathan, S., A. Elango, and S. Tharves Mohideen. "Performance enhancement of solar photovoltaic cells using effective cooling methods: A review." Renewable and Sustainable Energy Reviews 64 (2016): 382-393.

[4] Masson, Valéry, et al. "Solar panels reduce both global warming and urban heat island." Frontiers in Environmental Science 2 (2014): 14.

[5] Rosa-Clot, Marco, et al. "Submerged photovoltaic solar panel: SP2." Renewable Energy 35.8 (2010): 1862-1865.

[6] Rajput, Dayal Singh, and K. Sudhakar. "Effect of dust on the performance of solar PV panel." International Journal of ChemTech Research 5.2 (2013): 1083-1086.

[7] Zaini, N. H., et al. "The effect of temperature on a mono-crystalline solar PV panel." 2015 IEEE Conference on Energy Conversion (CENCON). IEEE, 2015.

[8] Ike, C. U. "The effect of temperature on the performance of a photovoltaic solar system in Eastern Nigeria." Research Inventy: International Journal Of Engineering And Science 3.12 (2013): 10-14.

[9] Amelia, A. R., et al. "Investigation of the effect temperature on photovoltaic (PV) panel output performance." International Journal on Advanced Science Engineering Information Technology 6.5 (2016): 682-688.
[10] Bhol, Rajeshwari, et al. "Environmental effect assessment on performance of solar PV panel." 2015 International Conference on Circuits, Power and Computing Technologies [ICCPCT-2015]. IEEE, 2015.
[11] Sathyanarayana, P., et al. "Effect of shading on the performance of solar PV panel." Energy and Power 5.1A (2015): 1-4.
[12] Hachicha, Ahmed Amine, Israa Al-Sawafta, and Zafar Said. "Impact of dust on the performance of solar photovoltaic (PV) systems under United Arab Emirates weather conditions." Renewable Energy 141 (2019): 287-297.
[13] Khan, TM Yunus, et al. "Optimum location and influence of tilt angle on performance of solar PV panels." Journal of Thermal Analysis and Calorimetry 141.1 (2020): 511-532.
[14] Sharif, M. A. (2021). Numerical Simulation of a Ground-Supported Solar Panel PV Array Subjected to Periodic Flow. NTU Journal of Renewable Energy, 1(1), 50-55.

Building Geo-Database for Geotechnical Properties of Thi-Qar Governorate Area Using Modern Digital Techniques

Kasim A.Abed Al-Abas[1], Sophia R. Al-timimy[2], Kamil Y. Husain[3], Saleem Ethaib[4] ,Hasan Swadi Njeban[5], Falah H. Rahil[6], Abdul-Razzak T. Ziboon[7]
{ksmabd@stu.edu.iq[1] , sophia.razaq@stu.edu.iq[2], kamil.hussain@stu.edu.iq[3]}

Al-Shatrah Technical Institute, Southern technical university[1,2,3]
The University of Thi-Qar[4,5]
The University of Technology[6,7]

Abstract. The construction field is developed together with other economic activities around the world. But the construction still is an expensive field because of proper investigation under the surface laboratory test, as well as it is important but needs a lot of time and cost for the complex subsurface layer. So, this work aims to investigate soil properties using geotechnical techniques via remote sensing and GIS with multiprogram. to prepare the comprehension geodatabase including GPS, land cover, land use, to a large area. So, it will be a contribution by building a model too large area with a geotechnical model that will be reducing time, cost from a laboratory test, as well as a reference, can use instead of Certified laboratory investigate, as a first model for the governorate of Thi-Qar and can be used to other governorates.

Keywords: GIS-Rock work, Geotechnical map, Bearing capacity.

1 Introduction

A complex subsoil stratum below the ground surface, especially in Thi-Qar Governorate the case study of research. That led to, economical and safe design is important for construction projects. That makes Geotechnical investigation of geological materials most important. But facing geological surprises and adverse geological events leads to cost overruns and many times compromising the integrity of structures [1].In this sense, proper subsurface investigations play a crucial role in an economical and safe construction project. It is well known that the main objective of the sub-soil investigation of civil engineering is to determine the geotechnical properties of the soil underlying the site. Anyhow, identifying the subsoil stratum below the ground surface is a complicated process in large areas. For instance, the traditional methods of soil investigation include several processes including boring (or) drilling works, test pits, plate load tests, dynamic soil tests, and the laboratory chemical analysis of soil. By the same token, these processes are expensive and take a long time[2]. These reasons led to the aim of our research to use new approaches to overcome the defects of traditional soil investigations methods dependent on: Firstly, geographical information system (GIS) is one of the promising techniques that is widely applied for different purposes. GIS has the capability for acquiring, storing, manipulating, analysing, and displaying spatially referenced data. So GIS provides manage, analyse, effectively display and disseminate spatial information.[3] The spatially

IMDC-IST 2021, September 07-09, Sakarya, Turkey
Copyright © 2022 EAI
DOI 10.4108/eai.7-9-2021.2314917

referenced data is defined according to its geographic location. Spatial or geographic data can be obtained from a variety of sources such as existing maps, satellite imagery, and the Global poisoning system (GPS). Secondly, GPS includes a network of satellites that continuously transmit coded information to precisely identify the location on earth by measuring the distance from the satellites [4]. The basic method for positioning with GPS can be done through the use of course acquisition C/A code on the carrier wave. By multiplying this travel time of the speed of transmission of the signal, the distance from the satellite to the receiver is obtained. In theory, it would be possible to determine the three-dimensional coordinates of the receiver from observations to three satellites [5]. Finally, the Rock Works Application as one of the important software programs utilized to produce maps sections, models, depended on soil properties such as (classification, borehole lithology, stratification, water level, concentrations of some of the soil materials). In that way, RockPlot3D can display three-dimensional surfaces that are based on grid models. These might result from drawdown surface (Hydrology/ Drawdown Surface) or from modelling stratigraphic surfaces in the Borehole Manager (Stratigraphy/ Structural Elevations) [6]. This technique can be applied to the investigation of soil and the geotechnical process by using GIS and rock work programs to protect geodatabase to land cover, land use, change detection over a large area. When cooperation with Previous studies as Al-Baghdadi research investigates the different soil contributions from (1.5 to 15m)to An-Najaf City by using contour map depend on the (SURFER 11)program. [7] But in al Basra city by investigation of the soil by 39 boreholes into a depth of 30 m, the research tries to prove topographic of the case study are located within a flat plain called Mesopotamian Plain with a semi-arid climate. [8] In that case, we will use multi programs to protect the geotechnical model to the Thi-Qar governorate then do verification of it to build geodatabase use in projects with a new idea that can use to another governorate.

2 Methodology

In this research multi programs to produce a lithology model of soil to Thi-Qar governorate were used. Several applications were employed including Global Mapper v.12 and Surfer v. 9 to survey the elevation of the study area. Erdas v. 9.1 of Arc-map GIS 9.3 was used to build geodatabase and draw the 2D map of the study area. Rock Works v.15 was applied to make a longitude section with Integrate Arc-map GIS v. 9.3 and Rock Works v.15. Then the verification of research results was carried out to improve via civil works.

2.1 Study Area

Iraq is one of the most populous Arab countries with a population exceeding 40 million. Iraq is administratively divided into eighteen governorates as can be seen in Fig 1. The Thi-Qar governorate (alternatively spelled Dhi-Qar) is one of the 18th Iraqi governorates and is in the south. Al-Nassriya city is the capital of Thi-Qar governorate lies on the Euphrates River about 370 km southeast of Baghdad, near the ruins of the ancient Ur city [6]. This governorate lies to the north of Al-Basra with an area of about (13751.6) km2, between latitude (30°40′-32°00′)N and longitude (45°40′-47°10) E as can be seen Fig 1. Thi-Qar governorate is a part of the Mesopotamian plain and a small sector of the southern desert plateau. The Mesopotamian plain can be physio graphically separated into two areas: the active flood plain area on both sides of the Euphrates and the Al-Graf rivers. The abandoned flood plain between the above-mentioned

rivers the exposed geological formations range in age from Middle Eocene, represented by the Dammam Formation up to lower [9]. Most of the sediments with exposure in the study area are from the sediment of modern rivers, Tigris and Euphrates, Shatt al-Arab, it includes deposits of the bottom of the river, their banks, and sediment of the flood, which is added to the sediment chemical gypsum, carbonates, and fossils, though most of these sediments are sand, silt, and clay origin. [10] This formation extends along the edges of southern and south-western AL-Hammar marsh and Euphrates River within the slopes of low-lying. It consists of the formation of limestone cretaceous white, especially in the southwest of Al-Nasiriyah city. [11].

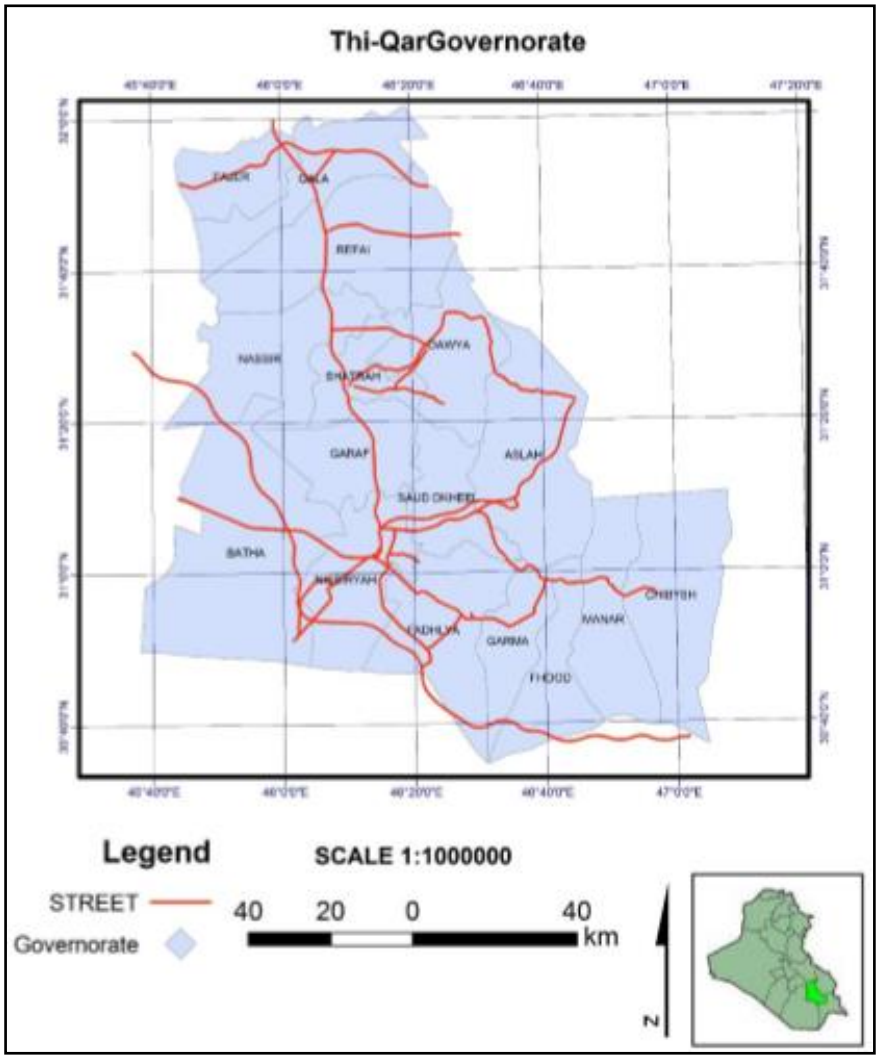

Fig. 1. The study area, **source:** researcher by Arc-map GIS v.9.3.

2.2 Data Collection

To gridding and interpolation of well log data for building lithological model, the reports of soil investigation were collected from many possible sources (such as AETL, NCCLR, Al-Mawal, Al-Mustanserya University, Basra University, and (some other private sector laboratory). The reports included the results of standard laboratory tests regarding the physical properties such as γ dry unit weight, initial void ratio, and grain size analysis of engineering properties of soil such as standard penetration test (S.P.T), unconfined compressive strength (qu), compression index (cc), chemical soil properties such as sulphate ions (%SO3) and (Water Table Level (W.T.L). The water table level at the time of testing was recorded, and the elevation of the surface at the borehole location was noticed. Some properties were calculated from interpolation between other properties of the study area busied on computerized techniques. The position of each borehole was determined approximately from many methods such as coordinate available in the report itself by GPS instrument which was used much and database map. All data used to build geodatabase in Arc-Map GIS 9.3 as Fig 2. The number of the borehole is (205) because of many constraints in the field they become (76) boreholes as Fig 3.

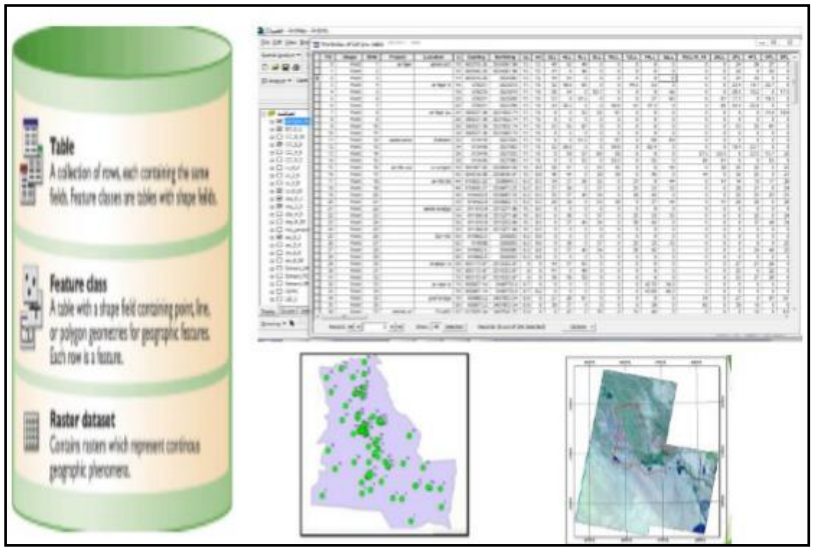

Fig.2. Geodatabase elements in GIS software.

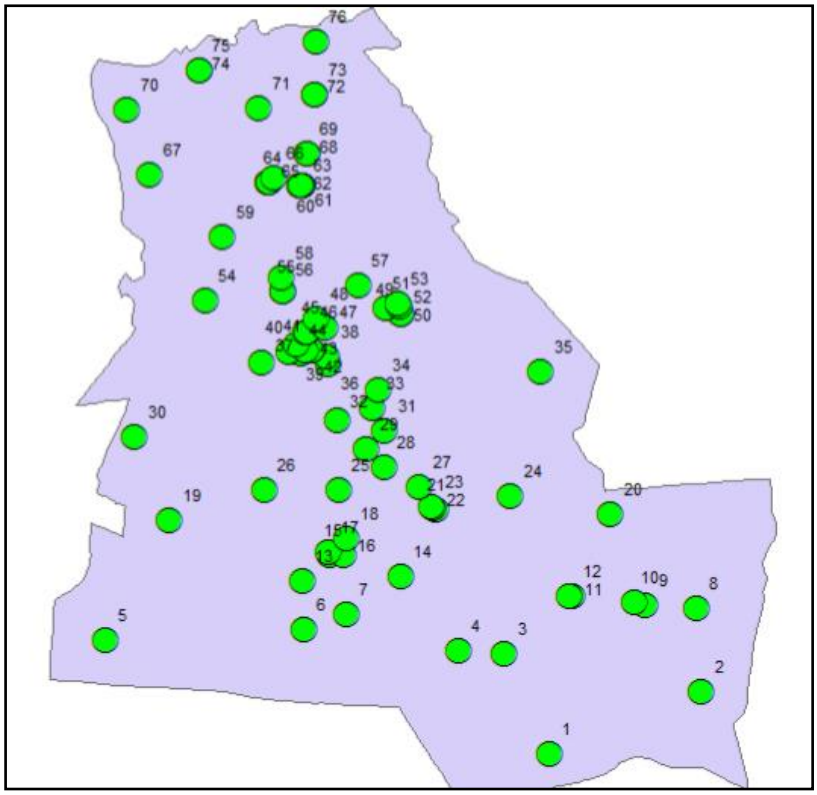

Fig. 3. Distribution of borehole location, **Source:** researcher by-map GIS v.9.3 depend on laboratory investigate from(AETL, NCCLR, Al-Mawal, Al-Mustanserya University, and Al-Basra University (besides private sector laboratory).

Besides the borehole there was a Topography section as in Fig 4. that represented the elevation between points set by its location as in Fig 5.

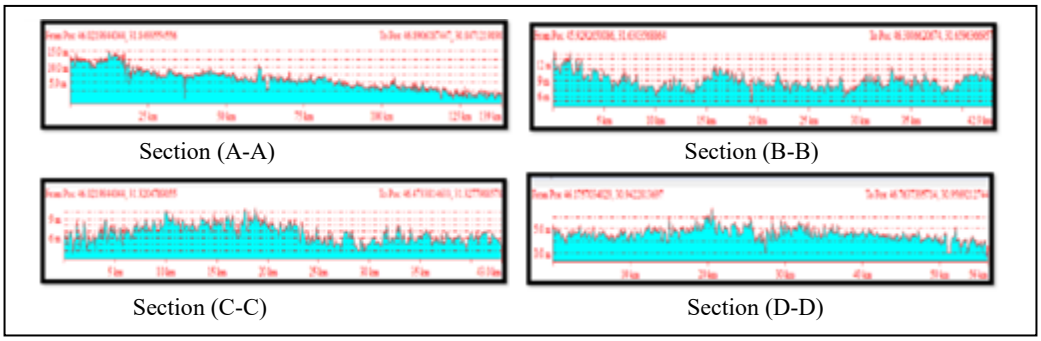

Fig. 4 borehole Sections by the global mapper.

Fig. 5 Topography section, **Source:** researcher by Arc-map GIS v.9.3.

Wherever spectral reflectance characteristics of features on the earth's surface can be quantified by the proportion of energy reflected by the feature at different wavelengths. So, characteristics of several surfaces can illustrate the spectral which may be of interest in civil engineering [12]. Such as in Fig 6 to classification the surface as a 2D plan.

Rock Works Modelling Techniques by using (Rock Work v.15). The study depends on using well log data such as Bearing capacity (t/m2) shows in Figure 10, and the techniques of lithological model available in rock works.

This software package is used for this study due to its friendly user interface, capabilities in managing borehole and well log data. The complex geological sitting forms the background of the lithological model that aims to develop a voxel-based 3D model from the available borehole data.

So, in Fig 7 the Longitudinal section between two points (AA) that show in Fig 5 from the study area, same as in Fig 8 shows the Longitudinal section between two points (CC).

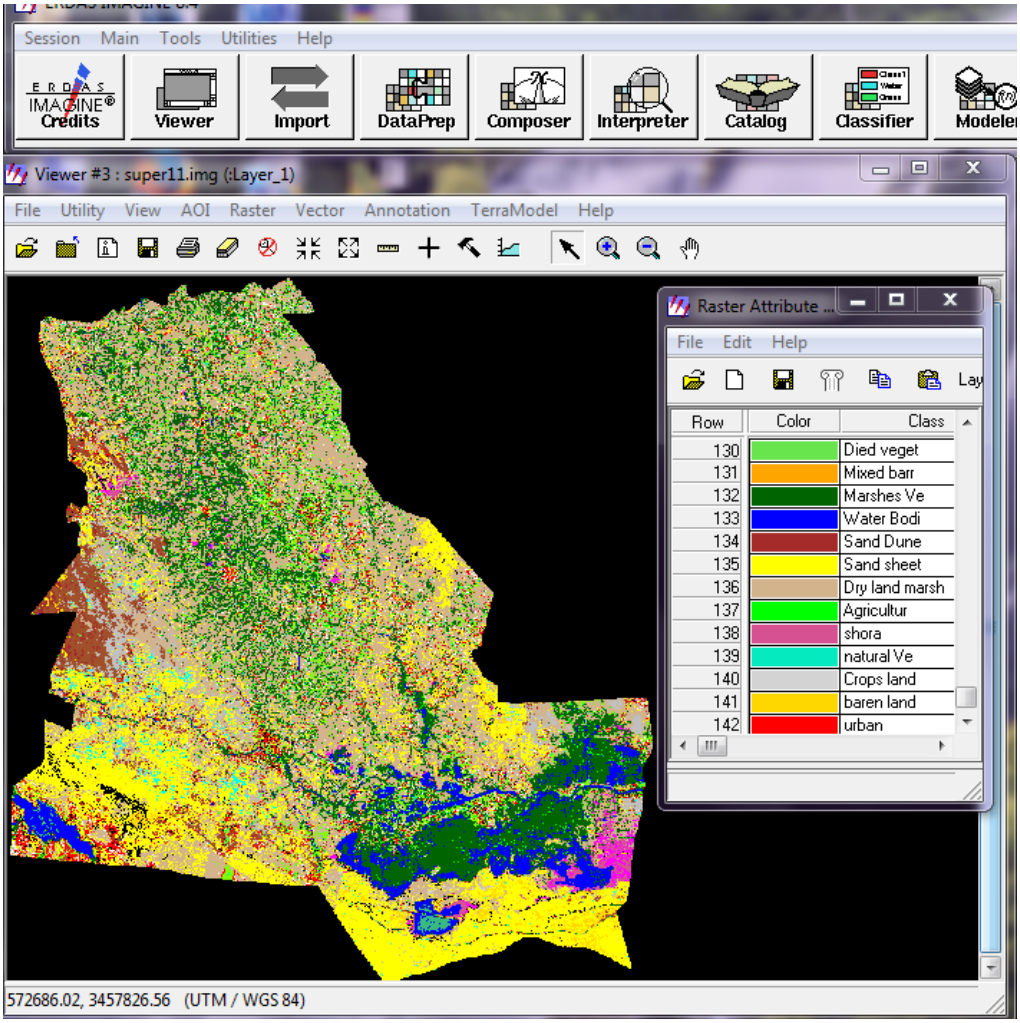

Fig .6. Classification Map of Thi-Qar governate By Erdas 8.4 from Landsat-7 ETM 2011.

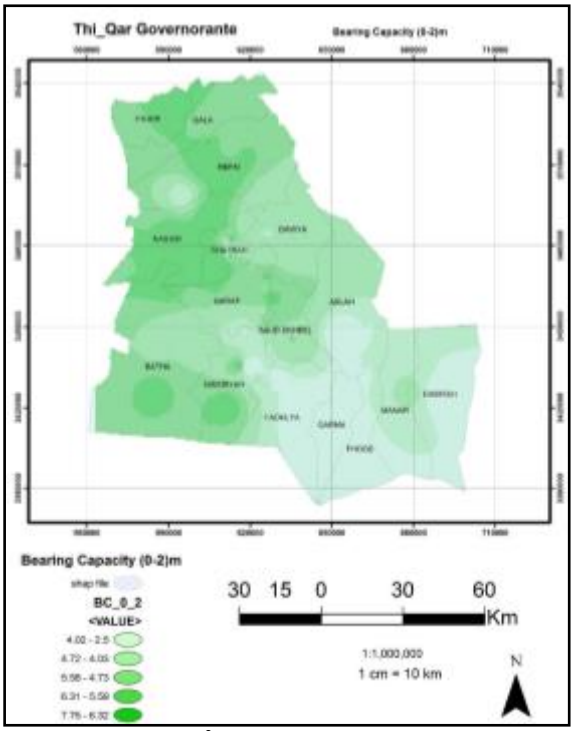

Fig.7. Bearing capacity (t/m^2) ,**source:** researcher by Arc-map GIS v.9.3.

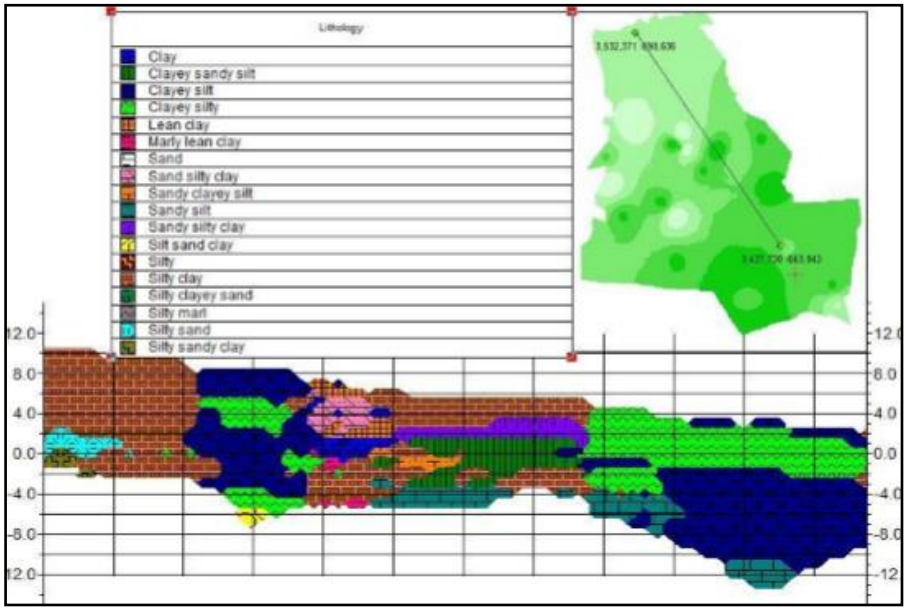

Fig.8. Longitudinal section from Al-Fajer to Al-Chibish distract **source:** integration between Arc-map GIS v.9.3 and Rockwork v.15 programs.

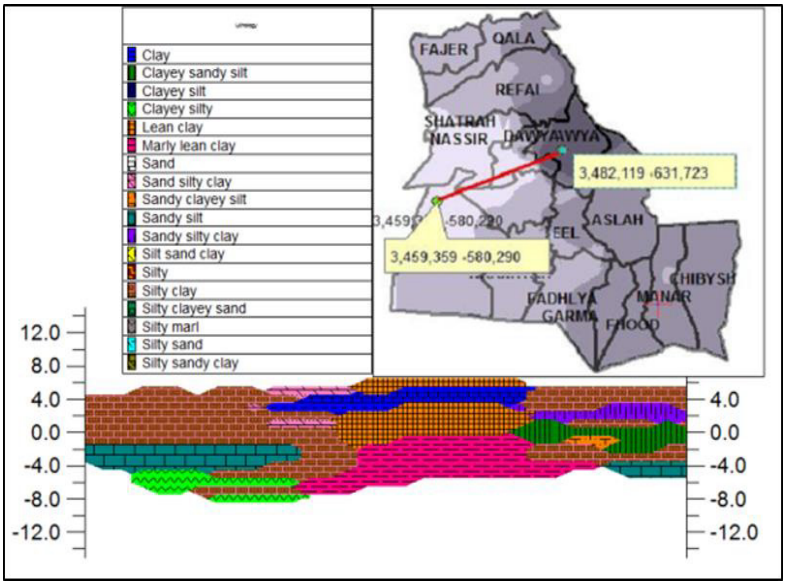

Fig.9. Longitudinal section from Al-Bat-ha to Al-Dawya district, **source:** integration between Arc-map GIS v.9.3 and Rockwork v.15 programs.

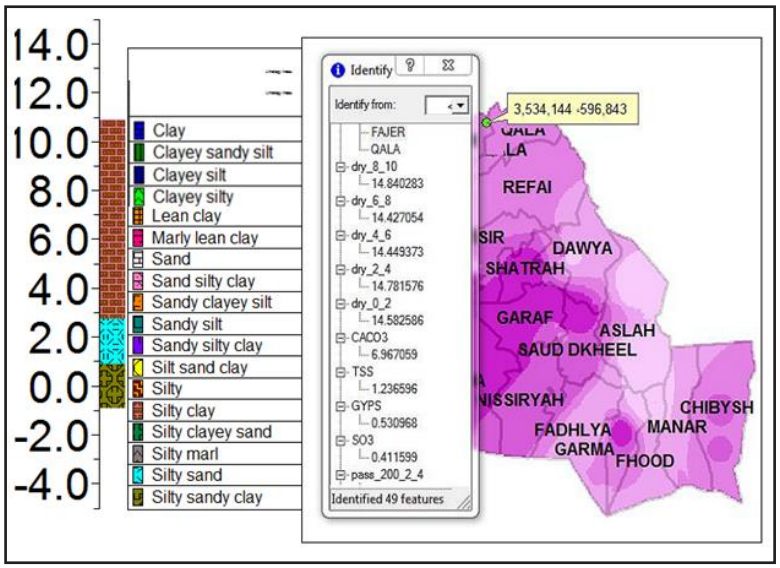

Fig. 10. Borehole (3) section with soil properties, **source:** integration between Arc-map GIS v.9.3 and Rockwork v.15 programs.

3 Results and discussions

By integrating between Arc-map GIS 9.3 and Rockwork 15 and result of all programs the 3D model product as in Fig. 15. The results show that the difference of ground level from north to south is 10m, the soil is silty clay with a bearing capacity range (2-7) t/m2. An empirical

correlation is obtained by relating the overburden pressure with depth this relation has (R2=0.8842) and SPT with depth which has (R2=0.6845).
The results of this research showed that the soil in the study area is clay silt with a small amount of sand in some regions in different depths and the water table is between (0.1-1.9)m below the natural ground surface (N.G.S). The results also showed that number values (N) of the standard penetration test (SPT) is between (4-63) blows. The moisture content (M.C) is between (16.2%-32.4%) of the sample's weight. Plasticity index (P.I) is (4%-53%), Liquid limit (L.L) of soil is between (29%-63%), the plastic limit (P.L) is (3%-43%) and the evaluation bearing capacity of soil at shallow (0-2) m between (2.5-7.75) t/m2, the soil classified to salty-clay with loos – medium-very dense which is a wide range. The results of chemical tests of soil showed that the sulphate contact of soil is between (0.23-0.71) %, total soluble salts (T.S.S.) between (0.02-2.9) %, and gypsum content between (0.16-0.62) percent. The investigation and lab test showed that soil needs engineering treatments before constructing any building on it. Table 1.

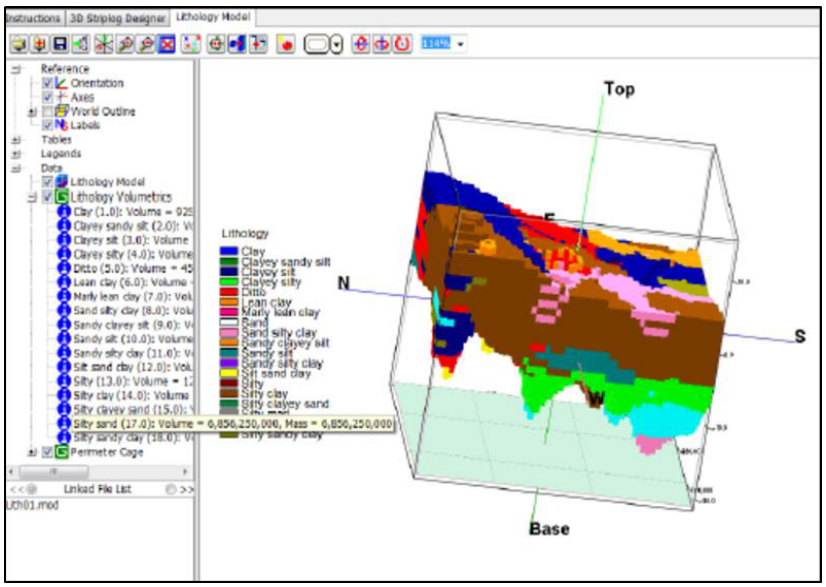

Fig. 11. Lithology model of the study area by Rock work v.15.

Table 1. results of the geotechnical map.

D m	B.C T/M^2	LL%	PI%	Dry Density KN/M^3	Specific Gravity	CU kap	eo	cc	cr	Sieve Analysis% Passing No.200	Gyp.%	TSSP PM	SPT
0-2	5.5-6.5	45	24	15	2.68	105	0.67	0.2	0.04	94	0.46	2.18	5
2-4	6.5-7.5	50	27	16		123	0.64	0.21	0.04	89			7
4-6		52	27	15		119	0.62	0.23	0.03	83			10

All data collection completed on 1/1/2014 and product programs results as a model and geotechnical map as well as Table (1) Fig 12. After that on 27/3/2014 at the location (611603E-

3477068N) in the study area laboratory test was taken as a result in Table 2. Then the researcher compared two cases that give accuracy of geotechnical map was more than 80%.

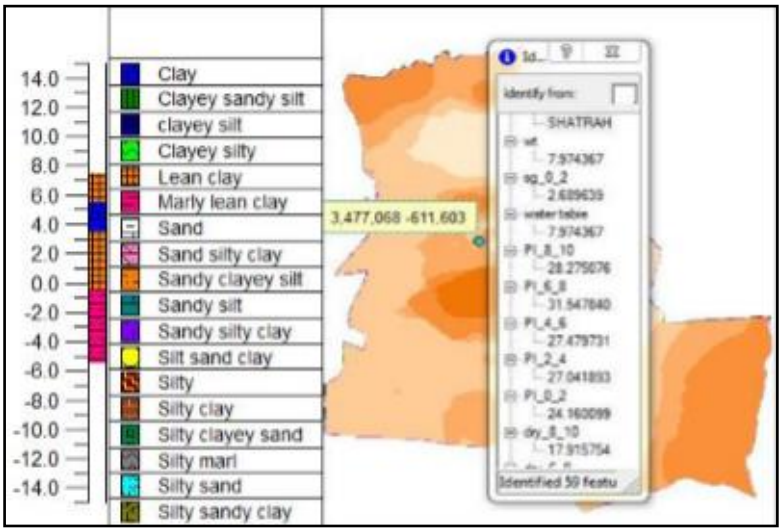

Fig. 12. lithology and soil properties from the soil report, **source:** integration between Arc-map GIS v.9.3 and Rockwork v.15 programs.

Table 2. results of the soil report.

D m	B.C T/M^2	LL%	PI%	Dry Density KN/M^3	Specific Gravity	CU kap	eo	cc	cr	Sieve Analysis% Passing No.200	Gyp.%	TSSP PM	SPT
0-2	5.5-6.5	47	32	15	2.7	61	0.58	0.21	0.03	96	2.75	8.1	
2-4	7.5-8.0	50	32	15		195	0.69	0.2	0.03	91			11
4-6	8.0-9.0	52	20	15		158	0.68	0.22	0.03	83			12

4 Conclusions

A laboratory test and geotechnical model from programs were carried out to characterize and discuss the various formations constituting the soil of Thi-Qar governorate province. Accordingly, the following conclusions are obtained:

1. Al-Nasiriya soil stratification is erratic and, depositions conditions.
2. Due to the integration between Rock Works & Arc-Map GIS to produce 3D visual digital geotechnical maps to the study area, which employed the geotechnical techniques are representative many characteristics such as easy used, saved time, and cost, as well as represented ground in the 3D geotechnical model in real vision a simple manner.

3. The geotechnical model lithology gives an accuracy of more than 80%. That depending on the distance between boreholes, and their number, as well as distribution in the study area.
4. The thematic map of supervised classification (12classes used) gives a good representation of some classes and merges the others

References

[1] Stalin, V. K., and Muttharam, M.Geotechnical Characterisation and Geoenvironmental Engineering: IGC 2016. Springer; 2018.p.37.0

[2] Wood, D. M., (2003). Geotechnical modelling (Vol. 1).CRC press, pp: 311–318.

[3] Mohammed, I. H., Accuracy Assessment of 2D and 3D Geometric Correction Models for Different Topographic Regions in Iraq .M.Sc. Thesis, Baghdad, Iraq: University of Technology,2011.

[4] Strom, Steven R. Charting a course toward global navigation. The Aerospace Corporation: Crosslink 2002.

[5] Ethaib, Saleem. Solid waste situation in Thi-Qar governorate. In IOP Conference Series: Materials Science and Engineering, IOP Publishing, 2019; 584(1): p. 012023.

[6] Al-Baghdadi, N. H. Geotechnical mapping of An-Najaf City, Iraq. J. University of Babylon, 2016; 24(4):pp. 962-22.

[7] Al-Taie, A. J. (2015). Profiles and geotechnical properties for some Basra soils. Al-Khwarizmi Engineering Journal, 11(2), 74-85.

[8] Ayman A. Ahmed. Using lithological modelling techniques for aquifer characterization and groundwater flow modelling of the Sohag area, Egypt,Faculty of Science, Sohag University, Geology Department, 2009.

[9] Jassim, Saad Z., Jeremy C. Goff. Geology of Iraq. London: DOLIN, sro, distributed by Geological Society of London, 2006. p.341.

[10] Albadran., B.N.,Sedimentology and mineralogy of the Al-Hammar Marsh /Southern Iraq, Marsh Bulletion, 2006. p.33.

[11] Jassim, S. Z., Karim. S. A., Basi. M., Al-Mubarak. M. A. and Munir. J. Final Report on the Regional Geological Survey of Iraq. VOL. 3 Stratigraphy. Manuscript report. Geological Survey of Iraq.1984.

[12] Behdinian, B. Generating Orthoimage from IKONOS Data, Asian Conference on Remote Sensing (ACRS), Taiwan. 2002.

Intelligent Controller Design of the Vehicle Sonar Tracking Checker Fault and Repair of High Voltage Transmission Line

Saja Raad Abdulbari Hani[1], Dr. Abdullah Al Gizi[2]
{saja.alhilfi@gmail.com[1], abdullah.algizi@stu.edu.iq[2]}

Engineering Technical College /Basra, Southern Technical University

Abstract. Inspection of high-voltage transmission lines is a dangerous and time-consuming activity that requires specially trained technicians to work tens of meters above the ground and near-live lines carrying thousands of volts. This paper presents the development of a teleoperated Intelligent Controller Vehicle Sonar Tracking Checker designed by use UAV in the collection of data power lines for preventive maintenance of high-voltage lines. The Vehicle Sonar Tracking Checker was designed with mobility in mind, so those cable spacers, suspension clamps, and other obstacles, which so far have prevented the inspection of high-voltage lines, will not be prevented the inspection of the lines. The safe operation of the transmission line and its components, on the other hand, necessitates periodical inspections to detect corrosion and other climatic and mechanical problems and flaws. The necessity for rapid and robust algorithms for the interpretation of photos or video obtained by drones during inspections has increased as the usage of unmanned autonomous vehicles (UAVs) for ecological observation grows. use UAV in the collection of power lines data and for analysis defects, various algorithms are used from image processing with MATLAB and python.

Keywords: overhead power line, open-source computer vision, image processing, UAV

1 Introduction

Creating modern shrewd cities requires to coordinate a few savvy arrangements different areas together and putting all these solutions into home in a perfect way" most perfect way. As portion of this global scene, numerous things about were distributed within the final few long time presenting the modern term ‘‘smart grids” into our life. This unused era of control frameworks ought to be able to keep an ideal execution for all stages of the control era counting the final organize of control utilization and the exchange stages. This exceedingly wanted execution requires a part of imaginative thoughts. As a result, new clever self-maintenance scenarios can provide a robust mending execution while reducing the associated time and expenses when compared to traditional upkeep tactics. Foot watch or helicopter-based exams are the most well-known methods of inspecting control lattice hardware[1]. Luis f. Luque-vega, Bernardino Castillo-toledo, and alexander loukianov cinvestav-ipn unidad guadalajara in [2] present an aerial robotic system for power line inspection implemented from scratch, including the flight control system, the payload for inspection system makes use of a colour camera and IR (infrared) camera to inspect the devices and components in power line corridors. The most common method is modest and generally ineffective. Helicopter-assisted assessments are faster, but because they are unable to wander more than a short distance from the control frameworks, their visual frameworks or any other sensor will be unable to provide reliable estimates

IMDC-IST 2021, September 07-09, Sakarya, Turkey
Copyright © 2022 EAI
DOI 10.4108/eai.7-9-2021.2314898

following that, an unmanned ethereal vehicle-based robot plan is proposed here to investigate and implement a few critical upkeep techniques for various control framework components. The paper [3] shows the defect detection result of an electrical insulator with simulated crack. It gives the edge detection of original ceramic electrical insulators without crack and defects ceramic electrical insulators with crack. W. Jiang, f. Wenkai, and l. Qianru in [4] describes a UAV with a multi-path ground coordinating system based on 2d plane lase radar. Both finals ponder were enthralled by the encirclement of the exchange lines, but they were unconcerned about the condition of the lines themselves. A new algorithmic approach for bunch drops is in[5]. Fault detection and location determination are based both on spatial morphological glass and ceramic insulators. Features proposed. Features proposed. The solution given can be applied to recognize UAV captured aerial photos with complicated background spatial-based glass and ceramic insulators features. The target area can then be morphologically determined developed to emphasize the position of the fault. In consequence, the fault insulators can be located based on the identity and features of the space. M. Pech, j. Vrchota, and j. Bednář [6] used the kalman channel and the Hough change to monitor the control lines based on a video arrangement stream. A climbing robot has been proposed by a few thinkers, as shown in, this robot can walk along cables to induce a close examination of the state of electrical components and to achieve the needed results. The study is organized as follows: within another section, we examine the many types of sensors and actuators that are required to conduct a few specific electrical lines support methods. The paper points to audit the current writing concerning prescient upkeep and shrewdly sensors in savvy factories. The projection is analysed utilizing the facilitates and distinguishing proof focuses for recognizing the object[7]. Siddiqui, Zahid Ali park, unsung in [8] proposed method to detect the fault of splits and puncture in polymer insulator by using ellipse detection algorithm and then apply the splits algorithm on individual caps, also proposed method to detect the broken or missing ceramic disk by colour clustering and morphological operations. In their research paper [9] they developed and implemented powerful algorithms for artificial vision, distance calculation, and hot spot detection[9].this paper[10] talks about the utilize of multi-agent frameworks as a reasonable arrangement to address this challenge by analysing their benefits when applying them to the field of savvy lattices and looking over existing works and activities. The foremost important specialized details of this robot are delineated within the third segment. Within the fourth section, a few fundamental computer vision algorithms are used to need a few estimations and readings from the flying robot's environment. Within the fifth segment, a modern locale proposition method that depends on a discrete wavelet change (dwt)[11]. Also, this work uses a flying robot named the butterfly to repair damaged or weakened exchange or dispersion control links, especially in inaccessible areas or high mountains. This robot is also required to continuously inspect all components of a control system using various types of visual and thermal sensors to rapidly identify any issues that may jeopardize its functionality. There are many difficulties you encounter when using drone such as the sales are expected 6 million and specific drones can used more one sensors[12].this article, we used a vehicle, as shown in fig. 1, to scan a power transmission line and distinguish between the line conductor and insulator in order to repair damaged or debilitated exchange or dispersion control lines, particularly in difficult places or high mountains. The subject of high-power lines fault detection using drones is an interesting and important subject to be considered due to risk, cost time consuming and difficulties associated with geographical areas of line towers.

Fig.1. A view of the vehicle robot from the front[11].

2 Methodology of The Proposed System

The drone will be equipped with a thermal camera reader, which will take warm images that will be useful for inspecting cables, electrical connections, switches, and circuit breakers across the area. The HD cameras worked depends on takes pictures are valuable to check cables. Our transmission line examination system is consisting of a thermal camera, an HD camera, and a drone. This system is examining all parts of the transmission line and taking close-up pictures in which the status of each transmission line part are examined, for example, towers, insulators, transmission poles, insulators, borselen beacon, sag adjusters, and the external appearance of the outer surface of the conveyor line (the skin layer) and checked for fracture, smash and corrosion with the external perimeter of the transmission line and store these images until the external processors are images MATLAB or python. The main aim of using this system is to reduce monitoring time and costs without declining quality, to enhance employee safety during the inspection. Fig.1 showing a view of the vehicle robot from the front that is crucial for the secure transfer of power between a network station and a local distribution station. These components can withstand extreme weather (direct sunlight, strong winds, snow, rain, and so on) as well as severe mechanical tension and high temperature due to high voltage. The proposed techniques are a combination of image MATLAB processing and python techniques.

2.1 Thermal camera

The Stefan–Boltzmann law, which quantifies the power emitted from an object as an item of the Stefan–Boltzmann consistent, and the thermodynamic temperature of that question within the power of 4, is the foundation of thermal imaging. The most common idea is to create a picture using infrared radiations emitted by a question that is proportional to its temperature. Warm cameras differentiate radiations in the long wave of range extend (8–14 lm) or the mid-wave of range extend (3–5 lm) for the most part. Warm images are useful for inspecting cables, electrical connections, switches, and circuit breakers, and identifying a variety of control system flaws such as voltage switch oxidation, overheated or incorrectly secured connections, and the effects of collapsed protection. Insulator heating is not due to corona activity but there may be heating if leakage currents are flowing either on the surface insulator or through the heart. Heating inside

the heart may indicate a damaged core during leakage current activity on the insulator surface may indicate damage to sheds and insulating sheath or perhaps associated with small partial brackets (dry tape brackets) on surface appearance[13]. As a rule, when the control framework changes any half-value of available vitality into extraneous calamities (warm), its capability decreases. To find the defect component of the overhead power line from IR image using the mean of the temperatures in each hot spot is obtained for comparison. If the temperature obtained from the thermal map hot spot is the same, then there is no fault and the temperature of all component's same degree. If there is a difference in hot spot temperature for the same component, then there is a fault that must be repaired or replaced. We used a method for analysing thermal images including convert colour images to grey images and apply k-means clustering unsupervised machine learning algorithm with k=18 to segment different parts of an image using OpenCV in python, with otsu-threshold and dilation operation mask (8,8) to highlight the hot spot region[14]. Fig 2 shows the algorithm steps where we can see two insulators in the infrared image, one defective and the other normal. The faulty insulator appears as the highlight and hotspot extraction region, while the normal insulator disappears in the hotspot region. the main aim is to reduce monitoring time and costs without declining quality, to enhance employee safety during the inspection. Transmission power lines, transmission shafts, insulators, balance beacons, and sag adjusters are important components of an electric transmission system. These components can withstand extreme weather (direct sunlight, strong wind, snow, rain, etc.) As well as high mechanical stress and temperature extremes due to high voltage. Traditional inspection methods include sending a skilled inspector up a power pole to look for electrical problems or managing the electrical health of goods by time-consuming, expensive, and dangerous experimental operations[1].

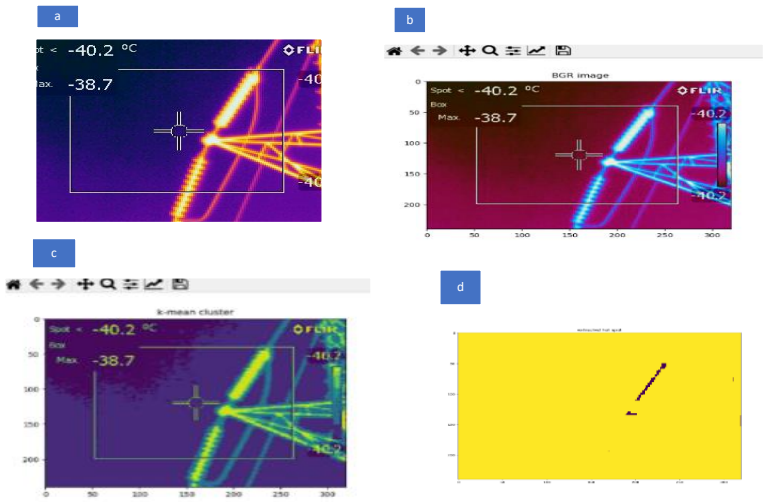

Fig.2. a) The thermal image shows two insulators, one defective and the other normal, b) Thermal image processing in BGR space, c) Thermal image after segmentation is applied, d) The result of the algorithm used to process the thermal image shows the hot spot of a defective high-temperature insulator.

2.2. Overhead Power Line HD IMAGES

Many elements, such as attitudes of employees, terrain structure, and climate, can affect the traditional method of human inspection. The drone inspection can therefore increase overall efficiency and quality and guarantee the safe functioning and operation of the transmission line with faulty automatic insulator detection algorithm[15].because it can take a few aerial pictures from short distances for suspected or harmed control components, and because it can stay floating within the discussion about the same component as shown in fig.3.the quadcopter becomes a capable instrument to precisely look at any control electrical framework by using progressive pictures taken from various points (principal component analysis), as well as the proposal techniques are a combination between the image MATLAB processing and python techniques. This proposed method is based on the use of the drone in examining the network of high-voltage transmission lines by taking high-resolution images with the HD camera. These images are processed in two ways, either by using MATLAB through the image processor, analysing and comparing them with the standard to determine the quality of this conductor or insulator. The third way is to examine the line or network with the naked eye through filming a video in which all parts of the line are examined, including insulators, lines, connectors, and suspension tools from fracture, shattering, corrosion, and oxidation. For example, the algorithm for broken insulators disk defect in MATLAB is done by converting an RGB image to Gray image, apply canny edge detection, show and compare defect region and the normal region as shown in figs.7,8,9.

Fig.3. Overhead power line visible image.

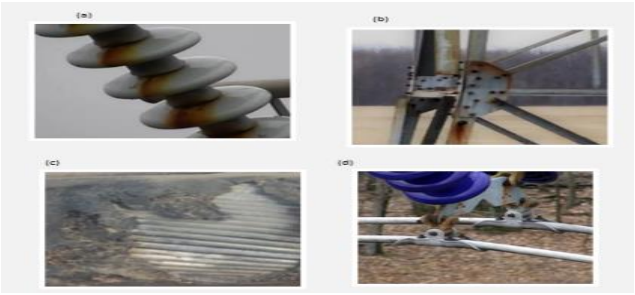

Fig. 5. Types Of Transmission Line Components Faults (A) Insulator Flashover (B) Transmission Tower Corrosion (C) Broken Power Line (D) Sag Adjusters Corrosion.

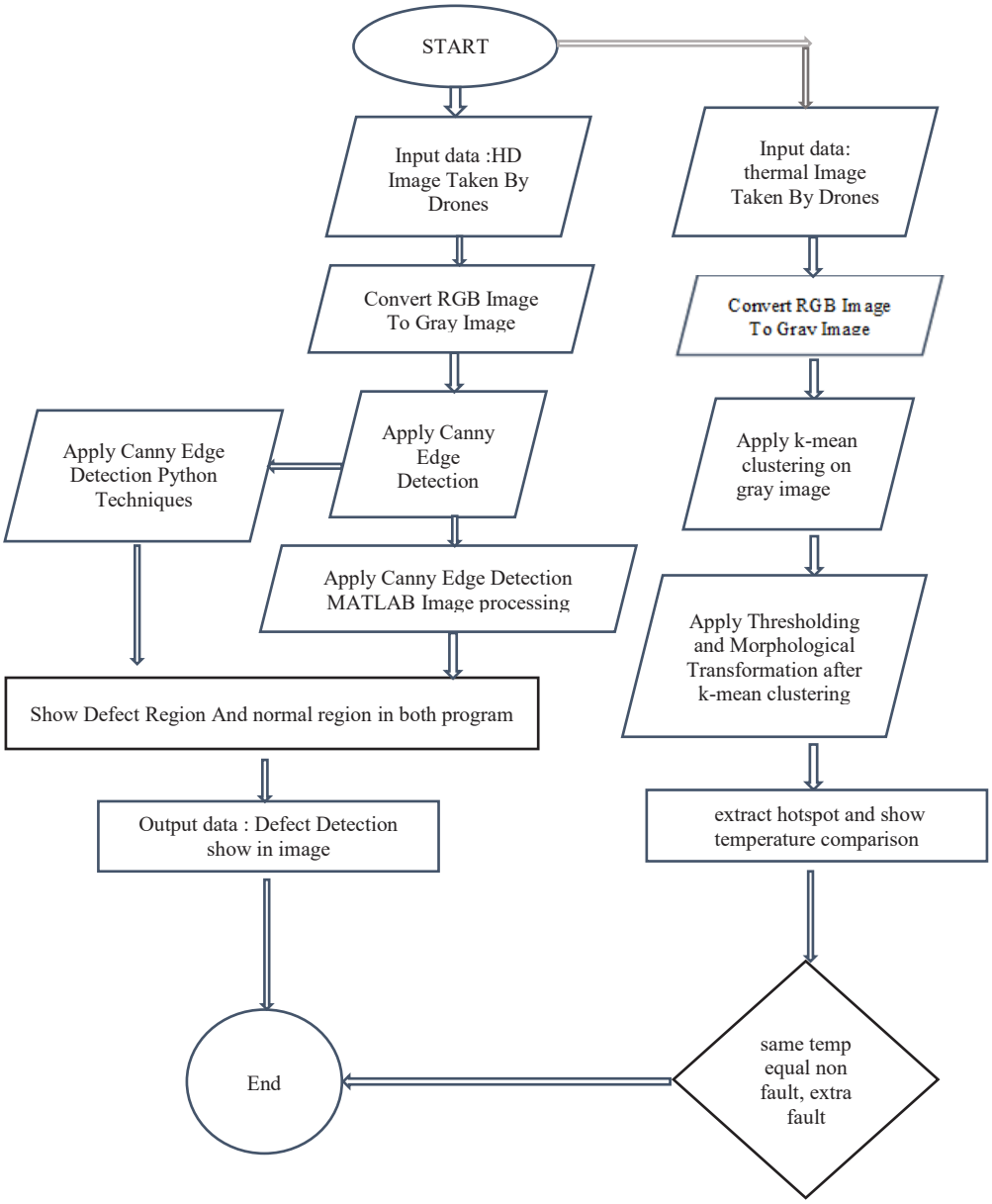

Fig.4 Methodology of The Proposed System.

2.3 Insulator Defect Detection

2.3.1 Defect A Broken Insulators Disk

Broken insulators defect begins with small cracks on the ceramic disk Surface, because of thermal stress. Due to high winds and mechanical stress, these cracks grow over time, which completely breaks single disks apart. As shown in Fig. 6.

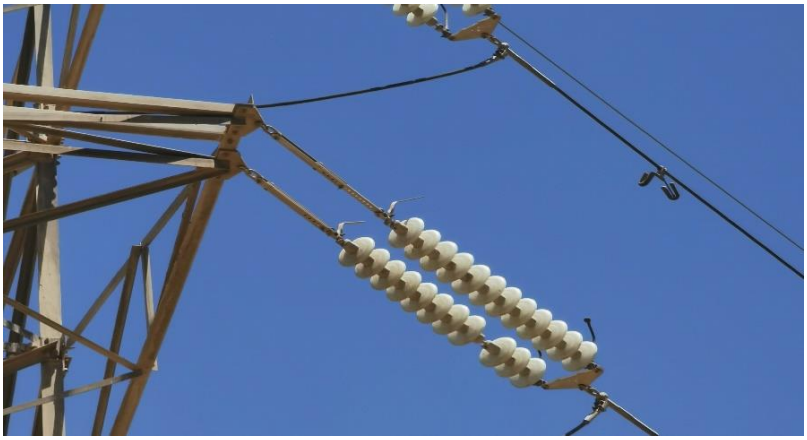

Fig. 6. Insulators broken shed.

2.3.1.1 MATLAB Technique

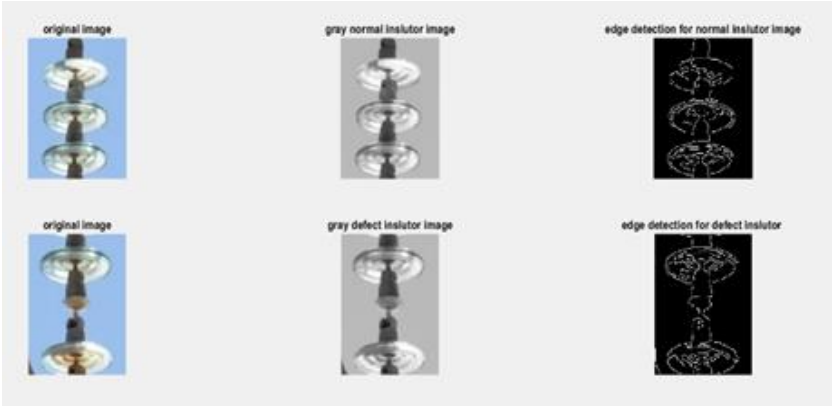

Fig. 7.image processing for normal and defect glass insulators

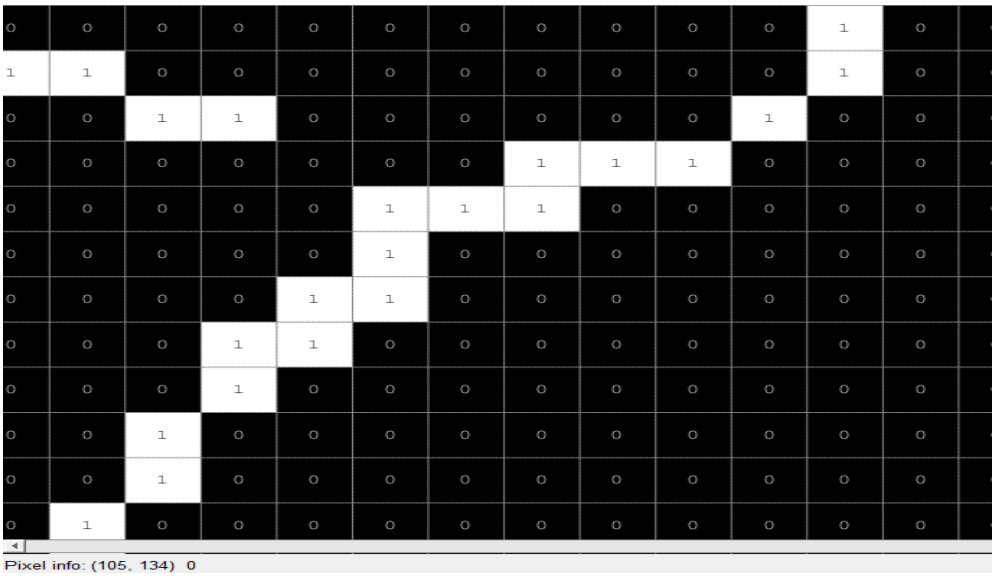

Fig. 8. Pixel region (105,134) for normal glass insulator region**.**

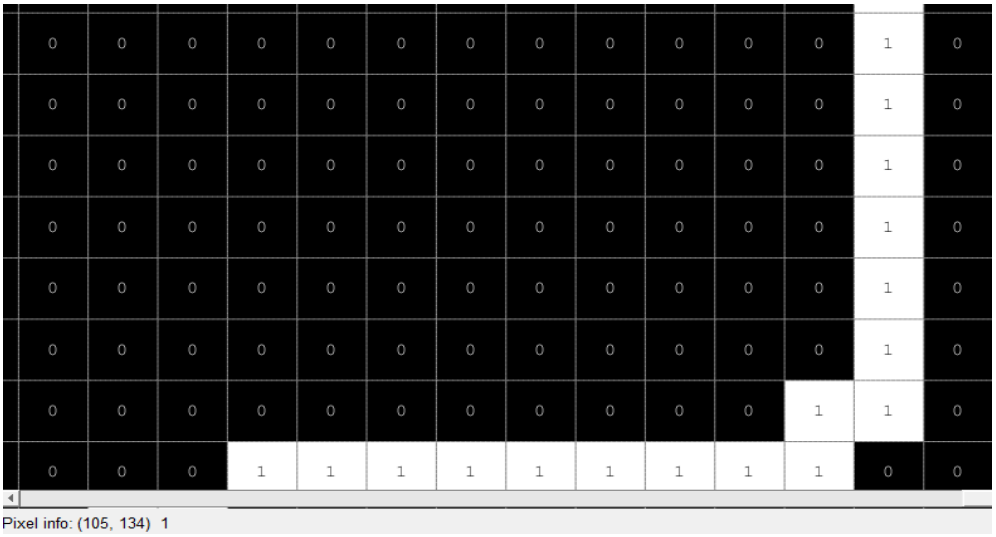

Fig. 9. Pixel region (105,134) for defect glass insulator region.

2.3.1.2 Python Technique

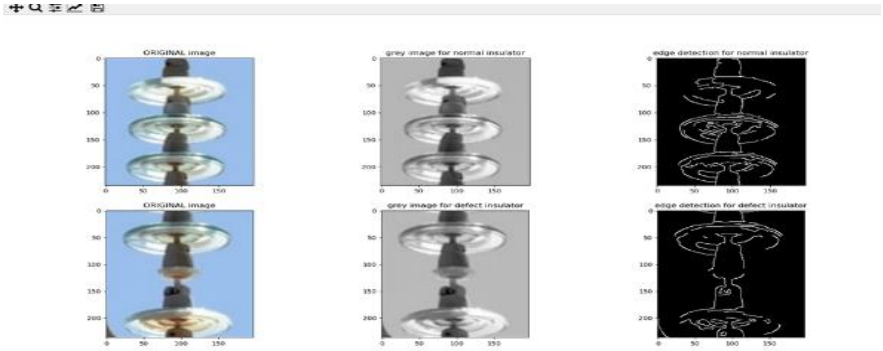

Fig.10. image processing for normal and defect glass insulators.

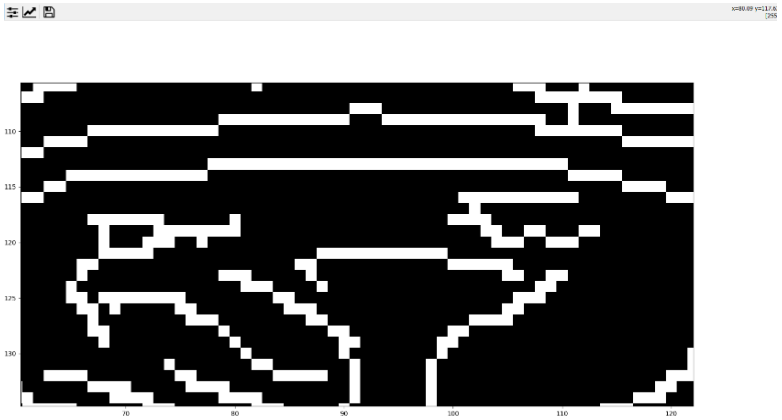

Fig. 11. Pixel region(80.09,117.62) for normal glass insulator region.

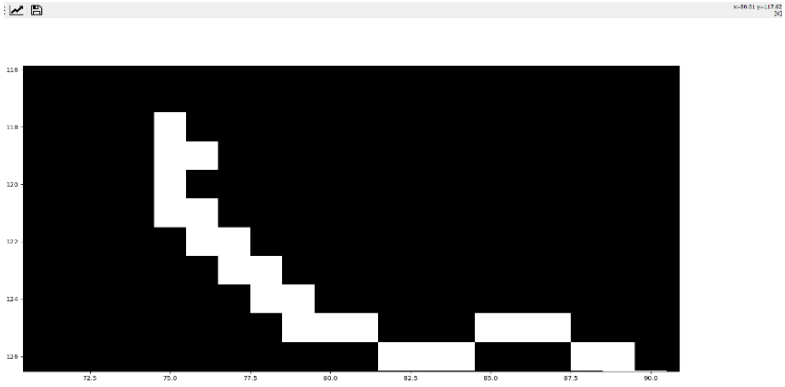

Fig. 12. Pixel region(80.09,117.62) for defect glass insulator region.

2.3.2 Defect A Flashover Insulators

In a flashover case, pollution like the lightning, the bird, icing, and Desert is the most important factor. One of the most serious high voltage energy transmission matters is the flashover of polluted high voltage insulators.

2.3.2.1 MATLAB Technique

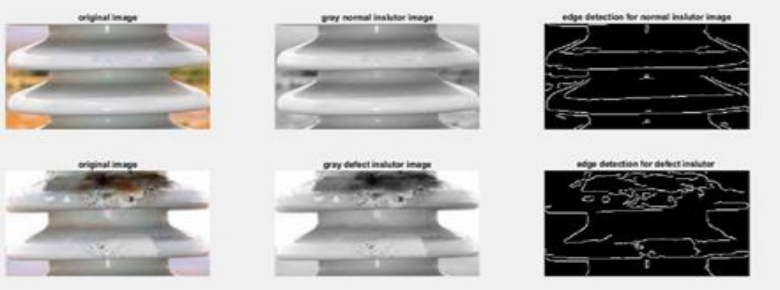

Fig.13. image processing for normal and defect porcelain insulators

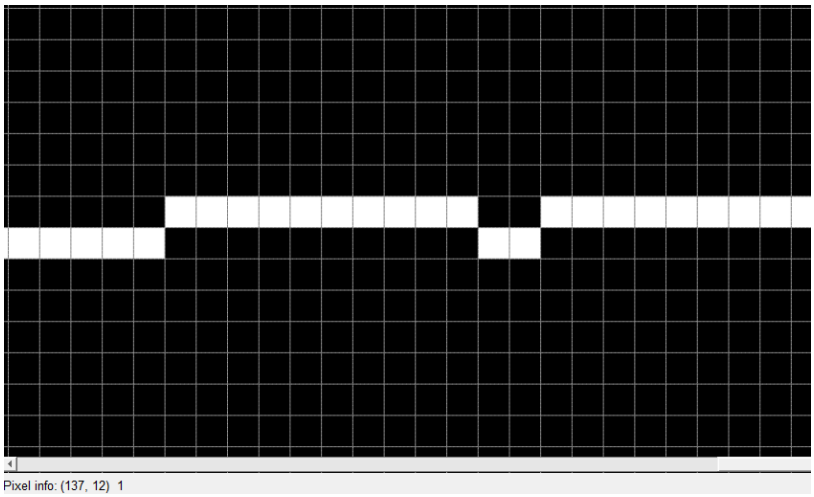

Fig.14. Pixel region(137,12) for normal porcelain insulator region.

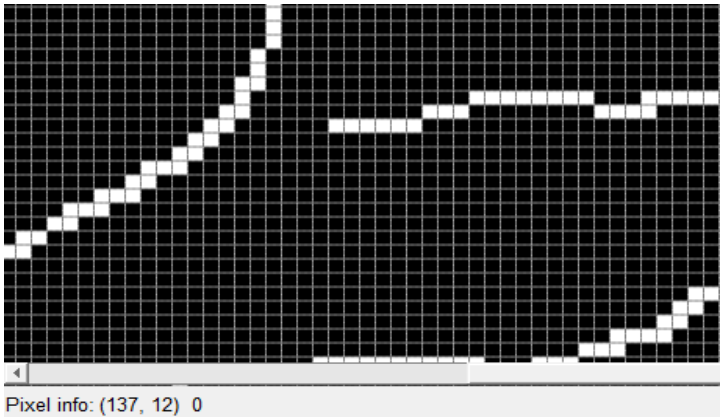

Fig.15. Pixel region (137,12) for defect porcelain insulator region

2.3.2.2 Python Technique

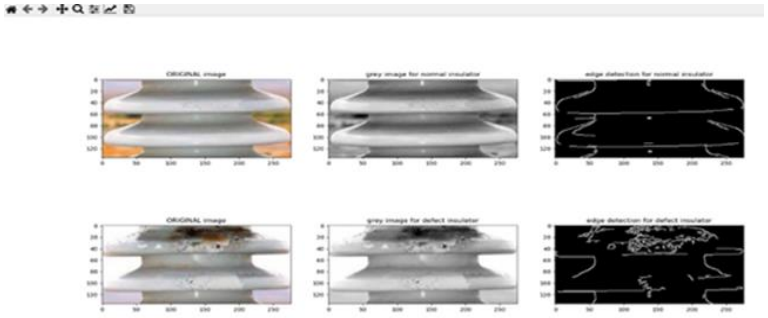

Fig.16. image processing for normal and defect porcelain insulators

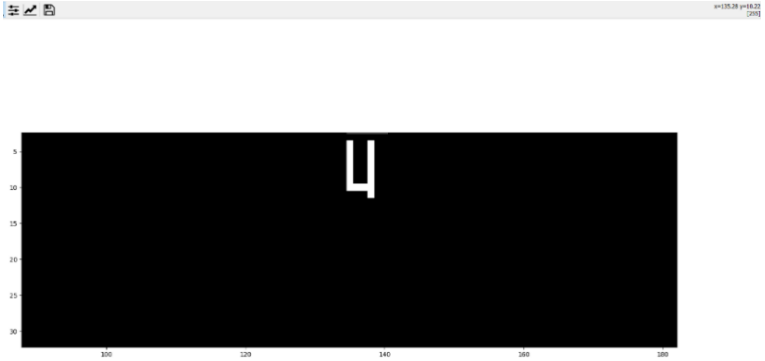

Fig. 17. Pixel region(135.03,10.09) for normal porcelain insulator region.

Fig.18. Pixel region (135.03,10.09) for defect porcelain insulator region

2.4 Discuss the Results

In this paper, the algorithm is designed to process HD images of power line components captured by drones. That should be filtered by canny edge detection. Defect insulators were used by canny edge detection to diagnose the finding of rough and soft areas in python and MATLAB and discuss the results in both programs to find the best results. Canny edge detection is a multi-stage algorithm that includes the first step is denoising the image with a gaussian filter then the smooth image is filtered with a Sobel kernel and then a full image scan is done to remove any unwanted pixels which may not be from the edge. The final step hysteresis thresholding this stage decides which edges are true edges and which are not. Cranny's method is not easily disturbed by noise and true weak edges can be revealed. The advantage is that two different thresholds are used to detect the strong edge and the weak edge respectively. When the weak edge and the strong edge are connected, the weak edge is included in the output image. Therefore, it is easy to specify the upper and lower threshold values to display changes in the image such as select original object editors, delete edges of noise effect, and adjust the lighting intensity. the result is more accurate in python, although it allows setting a factor a threshold of less than 1 in MATLAB. Matplotlib library in python for display pixel areas is more accurate than using MATLAB's image tools.

3. Conclusion

This paper focuses on texture features that can detect the external structure of an image. Although the ordinary insulator and the defect insulator have different values for the property

of the fabric. Edge detection algorithm used in matplotlib plot order in python and image order tool in MATLAB to manually select important pixels in images. The pixels estimate the x-axis and y-axis in MATLAB as follows (105,34) is equal to zero indicating that the region has no defect or equal to one which indicates a defective region as shown in fig. 7.8. The pixel area in python (80.09117.62) applied the same rule as shown in fig. 11,12. The value of the area of the ceramic insulator in MATLAB (137,12) was found to be 0 for normal insulators and one for defect, as shown in fig. 14.15. While it is found in python (138.06, 24.97) as shown in fig. 17.18. These pixel areas appear in black and white based on the edges that can be found in the image. White indicates the large number of raised edges represented by 1 or 255, while black indicates the smooth area represented by 0. In this method, an insulator representing the normal sample and the defect sample must be used for the comparison value to explain the difference between them. Also, in this less expensive method is used to treat the thermal image by obtaining a hot spot from a faulty insulator or another compound from the power line. As a result, such a defect in the insulator may lead to breakdown due to a malfunction in the power line network and will be the cause of stopping the power supply to the consumer.

References

[1] X. Xie, Z. Liu, C. Xu, and Y. Zhang, "A multiple sensors platform method for power line inspection based on a large unmanned helicopter," *Sensors (Switzerland)*, vol. 17, no. 6, pp. 1–17, 2017, DOI: 10.3390/s17061222.

[2] L. F. Luque-Vega, B. Castillo-Toledo, A. Loukianov, and L. E. Gonzalez-Jimenez, "Power line inspection via an unmanned aerial system based on the quadrotor helicopter," in *MELECON 2014-2014 17th IEEE Mediterranean electrotechnical conference*, 2014, pp. 393–397.

[3] L. Guo, Y. Liao, H. Yao, J. Chen, and M. Wang, "An Electrical Insulator Defects Detection Method Combined Human Receptive Field Model," *J. Control Sci. Eng.*, vol. 2018, 2018, doi: 10.1155/2018/2371825.

[4] J. Wu, W. Fei, and Q. Li, "An integrated measure and location method based on airborne 2d laser scanning sensor for UAV's power line inspection," *Proc. - 2013 5th Conf. Meas. Technol. Mechatronics Autom. ICMTMA 2013*, pp. 213–217, 2013, doi: 10.1109/ICMTMA.2013.58.

[5] Y. Zhai, R. Chen, Q. Yang, X. Li, and Z. Zhao, "Insulator fault detection based on spatial morphological features of aerial images," *IEEE Access*, vol. 6, pp. 35316–35326, 2018, doi: 10.1109/ACCESS.2018.2846293.

[6] M. Pech, J. Vrchota, and J. Bednář, "Predictive maintenance and intelligent sensors in smart factory: Review," *Sensors*, vol. 21, no. 4, pp. 1–39, 2021, doi: 10.3390/s21041470.

[7] P. S. F. Sheron, K. P. Sridhar, S. Baskar, and P. M. Shakeel, "Projection-dependent input processing for 3D object recognition in human robot interaction systems," *Image Vis. Comput.*, vol. 106, p. 104089, 2021, doi: 10.1016/j.imavis.2020.104089.

[8] Z. A. Siddiqui and U. Park, "A Drone Based Transmission Line Components Inspection System with Deep Learning Technique," *Energies*, vol. 13, no. 13, 2020, doi: 10.3390/en13133348.

[9] J. I. Larrauri, G. Sorrosal, and M. Gonzalez, "Automatic system for overhead power line inspection using an Unmanned Aerial Vehicle - RELIFO project," *2013 International Conference on Unmanned Aircraft Systems, ICUAS 2013 - Conference Proceedings*. pp. 244–252, 2013, doi: 10.1109/ICUAS.2013.6564696.

[10] P. Leitao, P. Vrba, and T. Strasser, "Multi-agent systems as automation platform for intelligent energy systems," *IECON Proc. (Industrial Electron. Conf.*, pp. 66–71, 2013, doi: 10.1109/IECON.2013.6699113.

[11] A. Baba, "A new design of a flying robot, with advanced computer vision techniques to perform self-maintenance of smart grids," *J. King Saud Univ. - Comput. Inf. Sci.*, no. xxxx, 2020, doi: 10.1016/j.jksuci.2020.07.009.

[12] M. Korki, N. D. Shankar, R. N. Shah, S. M. Waseem, and S. Hodges, "Automatic Fault Detection

of Power Lines using Unmanned Aerial Vehicle (UAV)," *2019 1st International Conference on Unmanned Vehicle Systems-Oman, UVS 2019*. 2019, doi: 10.1109/UVS.2019.8658283.

[13] "infrared-and-ultraviolet-2002 (2).pdf." .

[14] B. Jalil, G. R. Leone, M. Martinelli, D. Moroni, M. A. Pascali, and A. Berton, "Fault detection in power equipment via an unmanned aerial system using multi modal data," *Sensors*, vol. 19, no. 13, p. 3014, 2019.

[15] F. Gao *et al.*, "Recognition of insulator explosion based on deep learning," *2016 13th International Computer Conference on Wavelet Active Media Technology and Information Processing, ICCWAMTIP 2017*, vol. 2018-February. pp. 79–82, 2017, doi: 10.1109/ICCWAMTIP.2017.8301453.

Evaluation of the Iraqi Road Safety System in Light of Crash Severity Indicators

Ali A. Aldhalemi[1], Fadhil A. Abidi[2]
{alialdhalemi@atu.edu.iq[1], abidy_fadhil@atu.edu.iq[2]}

Engineering and Management Technical College/Najaf, Al-Furat Al-Awsat Technical University[1,2]

Abstract. The deaths due to road traffic crashes (RTCs) represent the 8th cause of death in Iraq in 2017 and the 7th cause in 2019. The present work aims to investigate the Iraqi RTCs reports during the years (2006-2019) to evaluate the road safety status and its relationship with the government commitment to reducing fatalities by the year 2020. The research also presents a quantitative analysis to study the ratios and rates concerning the severity indicators of the crashes and comparing them with some other countries. The results showed that in 2019, each of the crashes, mortalities, and morbidities increased by 21%, 5%, and 30% respectively compared with 2010 and so the governmental commitment appears far-fetched. On the other hand, most of the severity indicators revealed mitigation in the burden of population and motorization during the studied period. The authors concluded that the security situation had a strong impact on road safety and the year 2012 (which came between two waves of terrorist actions) witnessed peak values of crashes, mortalities, and morbidities. Compared with the population and vehicles, the Gross Domestic Product per Capita showed the highest Pearson Correlation Coefficients with each of the crashes, mortalities, and morbidities. Enhancing the road safety system in Iraq is urgently recommended to reduce the numbers of RTCs' casualties in line with the global trend where many countries had reduced the fatalities and now, they are working toward ((Vision Zero)) projects.

Keywords: Road safety; Severity indicators; Mortalities; Morbidities, Correlation Coefficient.

1 Introduction

The road traffic crash (RTC) is not an ((accident)), and it is completely preventable. So, huge efforts and investments are planned and implemented worldwide to control this human-made epidemic. According to (The Global Status Report on Road Safety, 2018) issued by the World Health Organization (WHO) [1], there were significant reductions in numbers and rates of RTCs' casualties in Europe and North America but there were no similar results in the rest regions of the world. The report classified Iraq as a middle-income country with an estimated rate of mortalities of 20.7 per 100,000 population based on data of 2016. Because of many sources of data and different definitions of periods of death after crashes, as well as inaccurate vital registration systems, the WHO report applied an adjustment factor to the number of mortalities reported by the local agencies in each country. Iraq was classified in the fourth group: countries without eligible death registration [2]. According to (The Iraqi Ministry of Health (MoH), Annual Statistical Reports 2017,2019) [3][4], road traffic deaths represent the 8th cause of death in Iraq with a ratio of (3.47%) in 2017 and the 7th cause (4.9%) in 2019. The Iraqi government (in May 2011) had launched "The Decade of Action for Road Safety 2011-2020" and pledged to reduce the level of road traffic casualties by 2020 [5].

The present work aims to investigate the Iraqi RTCs reports during (2006-2019) to evaluate the results of the countermeasures implemented to meet the Iraqi government commitment. The research also presents a descriptive analysis to study the severity indicators of the crashes and comparing them with some other countries. Besides, the study aims to evaluate the road safety system during the studied period. The present work represents a scientific guide for all central and local authorities, engineers, social activities, and all practitioners who are interested in mitigating road safety problems in Iraq. Statistical Package for Social Sciences (SPSS-V23) was used to compute the correlation between each of the number of crashes, mortalities, and

IMDC-IST 2021, September 07-09, Sakarya, Turkey
Copyright © 2022 EAI
DOI 10.4108/eai.7-9-2021.2314895

morbidities and each of the vehicles, population, and Gross Domestic Product (GDP) Per Capita. Because of the unstable security situation in Iraq after the war of 2003, the Ministry of Planning/Central Statistical Organization (CSO) published ((estimations)) of RTCs data for the years 2002,2003,2004, and 2005 depending on the report of 2001 (CSO Estimates of Traffic Accidents 2004-2005) [6]. However, the CSO report of RTCs 2006 (Statistics of Registered Traffic Accidents 2006) [7] was based on actual records in all governorates of Iraq (except the three governorates of the Kurdistan Iraq Region) and this report seems like a suitable starting point. The RTCs report 2020 issued by the CSO [8] showed a decrease in each crash, mortalities, and morbidity. The year 2020 was an exceptional year due to the full and partial lockdowns that were imposed after the spread of the COVID-19 pandemic, which led to a significant reduction in movement within cities and between governorates. Accordingly, data for the year 2020 were excluded.

2 Literature review

The World Health Organization (WHO) in 2013,2015, and 2018 released three comprehensive and detailed reports to describe the global status of road safety. These reports aimed to evaluate the results of the measures implemented in all countries towards achieving the targets of the global Plan for the Decade of Action for Road Safety 2011-2020 and the UN Sustainable Development Goal (SDG) 3.6 to halve the number of casualties by 2020. The Eastern Mediterranean Region (EMR), where Iraq is classified geographically, reported a rate of 18 deaths per 100000 population [1]. The report concluded that except for the EMR, the rate of road traffic mortalities per 100000 population generally decreases as income increases.

To overcome the lack of experts in highway safety and to reduce Road Traffic Crashes (RTCs) in Iraq, Al-Jameel (2016) [9] developed an expert computer system to suit the present status of highway safety. The first phase of the system was the diagnostic phase which identifies the problem and determines probable causes. The second phase was the remedy phase which provides the user with suitable solutions for each probable cause. The author considered the procedure of reporting the RTCs as one of the main problems of the road safety system in Iraq.

Leidman et al. (2016) [10] studied the road traffic fatalities in 8 selected governorates in Iraq for the period (2010-2013) depending on data from the Iraqi MoH. The authors concluded that the rates of mortalities ranged from 8.6 to 10.7 per 100,000 population, 80% of them were males, and nearly half of them were pedestrians. They believed that mortalities decreased in 2013 because of increased insurgency.

Diah et al. (2017) [11] investigated RTCs mortalities in Babil Governorate (middle of Iraq) for the period 2010-2014. They concluded that the peak number of deaths occurred in 2012 and the ratio of males to females was 3.25:1. They reported that 72% of the crashes occurred on the main roads.

Asad (2017) [12] shed light about road safety in Iraq by reviewing the available evidence-based literature concerning traffic crashes during the decade (2005-2015). He surveyed 26 published academic types of research and classified them according to their objectives, data sources, research design, analysis methods, and findings. The retrieved studies had reported that drivers and motorcyclists had low knowledge about traffic signs, not wearing seat belts/or helmets, and driving without licenses.

Mohammed et al. (2018) [13] analyzed data of RTCs in Iraq during (2005-2011) based on the CSO reports of 15 governorates. Among other results, they reported that extreme weather resulted in a higher number of crashes. The authors concluded that Baghdad and Babil governorates witnessed a higher number of collision type crashes while higher ratios of overturning type were recorded in Al- Qadissiya, Baghdad, Babil, and Basrah governorates because of the wetted roads indicating the absence of enough precautions during rainy days.

Albayati and Lateif (2018) [14] conducted a descriptive analysis of the road traffic data in Iraq (2003-2015). Based on their results, the run-over crashes accounted for 46% of the total crashes and collisions accounted for 43%, and males' deaths were four times as often as females. The authors concluded that in each one accident the mortality rate was 0.27 while the morbidity rate was 0.97. They also reported that statistically there was no ascending or descending trend in the development of the number of crashes for the period (2003-2015).

Al-Jameel et al. (2019) [15] conducted a study about the traffic safety level in Al-Najaf city in the middle of Iraq. They designed a questionnaire form to collect opinions of engineers and engineering students about the causes and solutions of the traffic crashes problem in the city.

The authors analyzed the responses and concluded that the main causes of crashes in the city refer to the unlicensed drivers on the roads without accounting by the traffic police, vehicles with low safety standards, and poor traffic regulations.
Mohammed et al. (2019) [16] reported that road crashes were relatively high in extreme weather months (August -September, October-November, and December). The authors concluded that the human factor was responsible for 80% of crashes while each of the roads and the vehicles were responsible for 10%. The researchers recommended that road safety standards in Iraq should include four main factors: exposure, behavioral factors, road environment, and vehicles.
Albayati and Lateef (2019) [17] studied RTCs in Baghdad city for the period (2006-2016). They concluded that the run-over crash represented 53% of all the crashes while the collision and overturning represented 39% and 7% respectively. They reported that 27% of RTCs were associated with people aged 24–29 years, followed by people in the 30–35 age group (22%), and the 19–23 age group (20%). The authors concluded that 22% of RTCs were associated with fatalities, 67% were associated with only injuries, 6% included fatal and injury and 4% included property damage only.
Joni et al. (2020) [18] collected datasets of RTCs in Iraq for the period (2003-2017). They arranged the data of RTCs numbers, mortalities, and morbidities in spreadsheets based on monthly records. The authors observed that the highest monthly rates of crashes, mortalities and morbidities occurred during 2014, 2015, 2016, and 2017 consecutively. They reported that the highest monthly rate during the studied period was 9% for crashes number, 12% for morbidities, and 21% for mortalities. They attributed the increase in the rates during the years (2014-2017) to the bad security condition and absence of safety precaution countermeasures. However, the data used in this research may need more accurate revision.

3 Data Analysis and Results

Table 1 summarizes the main data concerning the RTCs in Iraq during the period (2006 – 2019). Data of population and GDP per Capita were drawn from the website of the World Bank (World Bank Data) [19] while the other data were drawn from the annual reports of The Iraqi Central Statistical Organization (CSO). It can be seen that between 2006 and 2018, the year 2012 witnessed the peak number in each of the crashes, mortalities, and morbidities. In 2019 there were new two peaks in the crashes and morbidities which were slightly higher than the records of 2012. There were continuous annual increases in each of the number of vehicles and population while a peak of (7077) US$ was noticed in GDP per Capita in 2013.

Table 1. Main data of RTCs in Iraq during the period (2006 – 2019).

Year	Crashes	mortalities	morbidities	Vehicles	Population	GDP per Capita (US$)
2006	3389	1151	3303	2386612	27448124	2373
2007	3135	1210	3252	2471461	27911248	3183
2008	5502	1863	5499	2491711	28385746	4637
2009	7452	2151	7955	2527335	28973162	3854
2010	**8861**	**2508**	**8996**	**2662946**	**29741976**	**4657**
2011	10082	2703	10198	2763667	30725300	6046
2012	**10709**	**3132**	**11009**	3043975	31890011	6836
2013	9725	2951	10694	3527534	33157050	**7077**
2014	8814	2769	9210	4239818	34411951	6819
2015	8836	2514	9429	4458780	35572261	4990

2016	8763	2531	9016	4987925	36610632	4777
2017	8824	2621	9388	5225794	37552781	5205
2018	9852	2767	10439	5359792	38433600	5834
2019	**10753**	**2636**	**11651**	**5547385**	**39309783**	**5955**

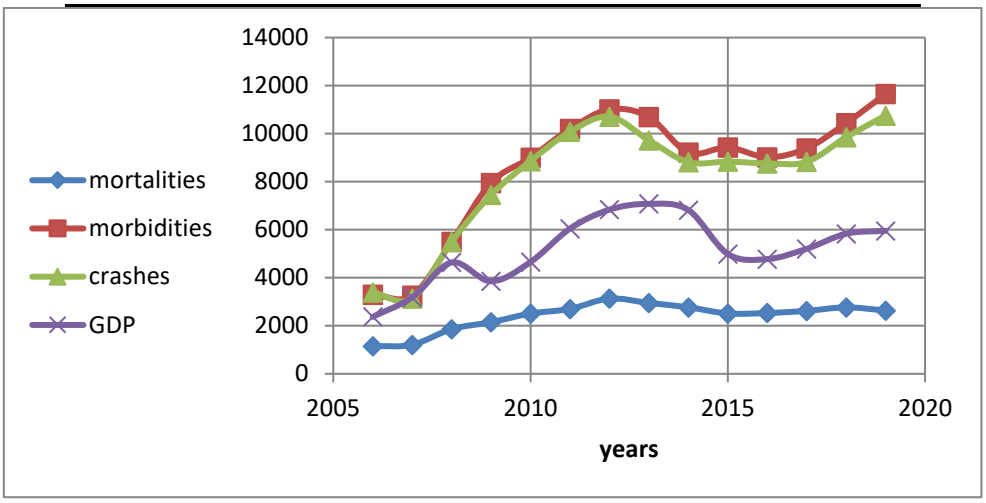

Fig. 1. Annual distribution of crashes, mortalities, morbidities, and GDP per Capita in Iraq (2006-2019).

Table 2. SPSS output of Pearson Correlation Coefficients (PCCs)

		Crashes	Mortalities	Morbidities	Vehicles	Population	GDP
Crashes	Pearson Correlation	1	.968**	.996**	.564*	.685**	.850**
	Sig. (2-tailed)		.000	.000	.036	.007	.000
	N	14	14	14	14	14	14
Mortalities	Pearson Correlation	.968**	1	.963**	.514	.634*	.915**
	Sig. (2-tailed)	.000		.000	.060	.015	.000
	N	14	14	14	14	14	14
Morbidities	Pearson Correlation	.996**	.963**	1	.597*	.715**	.852**
	Sig. (2-tailed)	.000	.000		.024	.004	.000
	N	14	14	14	14	14	14
Vehicles	Pearson Correlation	.564*	.514	.597*	1	.987**	.426
	Sig. (2-tailed)	.036	.060	.024		.000	.129
	N	14	14	14	14	14	14
Population	Pearson Correlation	.685**	.634*	.715**	.987**	1	.543*
	Sig. (2-tailed)	.007	.015	.004	.000		.045
	N	14	14	14	14	14	14

GDP	Pearson Correlation	.850**	.915**	.852**	.426	.543*	1
	Sig. (2-tailed)	.000	.000	.000	.129	.045	
	N	14	14	14	14	14	14

**. Correlation is significant at the 0.01 level (2-tailed).

*. Correlation is significant at the 0.05 level (2-tailed).

3.1. Trend of development

Fig 1 shows that there are similar trends of development for each of the crashes, mortalities, morbidities, and GDP across the studied period. The T-test statistical technique (Ott, 1989) [20]and (SPSS-V23) computer software was used to determine the type of the development trend for these four variables. The null hypothesis (H_o) assumed that there is no descending or ascending trend.

This hypothesis was rejected because the results of the T-test showed 0.000 (2-tailed) significance values for all the four variables which were less than the significance level (α = 0.05). So, it can be concluded that each of the crashes, mortalities, morbidities, and GDP per Capita had an ascending trend of development as shown graphically in Fig 1.

Fig 1 also shows a sharp increase in the number of crashes between (2006- 2012) followed by a continuous decrease. This decrease may be attributed to the increased insurgency in 2013 followed by occupying of 3 governorates (Anbar, Salahaldeen, and Nineveh) by ISIS terrorist groups in 2014. Another increase in the number of crashes occurred in 2017 associated with the beginning of liberating the occupied governorates from ISIS groups and a maximum number (10753) was noted in 2019. GDP per Capita showed nearly a similar trend of change during the same periods. GDP per capita increased from 2373 US$ in 2006 to 7077 US$ in 2013 and then descended to 4777 US$ in 2016. GDP per Capita again increased in 2017 and ascended to 5955 US$ in 2019. On the other hand, the number of vehicles (as well as the population) witnessed a different trend of development than crashes. Table 1 declares that the number of registered vehicles gradually and continuously increased in an ascending trend from 2386612 in 2006 to 5547385 in 2019 and so the motorization level (the number of vehicles per 1000 population) increased from 87 in 2006 to 95 in 2012 and 141 in 2019. The vehicle ownership (persons per vehicle) has decreased from 12 in 2006 to 10 in 2012 and 7 in 2019.

Table 2 displays the output of the SPSS-V23 computer software used to compute the Pearson Correlation Coefficient (PCC) between each of the number of crashes, mortalities, and morbidities, and each of the number of vehicles, population, and GDP per Capita. It can be concluded that the number of crashes has the highest PCC with GDP per Capita (0.850) followed by the population (0.685) and the vehicles (0.564). Table 2 also shows that the mortalities have the highest PCC with GDP per Capita (0.915) followed by the population (0.634) and the vehicles (0.514). The same table shows that the morbidities also have the highest PCC with GDP per Capita (0.852) followed by the population (0.715) and the vehicles (0.597).

Table 3. Severity indicators of RTCs in Iraq (2006-2019).

Year	The ratio of fatal crashes per 100 crashes	Rate of crashes per 1000000 population	Rate of crashes per 10000 vehicles.	The ratio of mortalities to total casualties	Rate of mortalities per 100 crashes	Rate of mortalities per 10000 vehicles.	Rate of mortalities per 100000 population
2006	28	123	14.2	26%	34	4.8	4.2
2007	**30**	112	12.7	**27%**	**39**	4.9	4.3

2008	30	194	22.1	25%	34	7.5	6.6
2009	26	257	29.5	21%	29	8.5	7.4
2010	**25**	**298**	**33.3**	**22%**	**28**	**9.4**	**8.4**
2011	24	328	**36.5**	21%	27	9.8	8.8
2012	27	**336**	35.2	22%	29	**10.3**	**9.8**
2013	27	293	27.6	22%	30	8.4	8.9
2014	29	256	20.8	23%	31	6.5	8.0
2015	25	248	19.8	21%	28	5.6	7.1
2016	25	239	17.6	22%	29	5.1	6.9
2017	27	235	16.9	22%	30	5.0	7.0
2018	25	256	18.4	21%	28	5.2	7.2
2019	**24**	**274**	**19.4**	**18%**	**25**	**4.8**	**6.7**
Average	27	246	23.1	22%	30	6.8	7.2

3.2. Severity indicators

Table 3 has been prepared to compute the severity indicators expressed as ratios and rates during the period (2006-2019).

3.2.1. Ratio of fatal crashes per 100 total crashes

The values of this ratio ranged from 24 (2011) to 30 (2006) with an average of 27. The ratio in 2019 (24) was very close to the ratio in 2010 (25) and there is a (4%) reduction.

3.2.2. Rate of crashes per 1000000 population:

This rate represents the registered number of crashes for each 1000000-population providing us with a fair indicator for the burden of the population. This rate ranged from (112) in 2007 to a maximum (336) in 2012 and then decreased to (274) in 2019. Despite the continuous increase in population from 2006 to 2019, the change in this rate seems like the change in the number of crashes, the number of mortalities, and the number of morbidities when 2012 corresponded to a peak value in each of them. There was a slight reduction (8%) in this rate between 2010 (298) and 2019 (274).

3.2.3. Rate of crashes per 10000 vehicles:

This rate reveals the burden of vehicles on the number of crashes that occurred annually. The values of this rate ranged from (12.7) in 2007 to (36,5) in 2011 with an average of (23.1). It can be noticed that the peak rate occurred in the year 2011and there was a reduction of (42%) between 2010 (33.3) and 2019 (19.4) which means a lower impact of motorization on the number of crashes.

3.2.4. Ratio of mortalities to total casualties:

It is the ratio between the number of mortalities to the total number of human casualties (mortalities and morbidities) which is considered as an important pointer of the severity of crashes. This ratio ranged from 18% in 2019 to 27% in 2007 with an average of 22%. Since 2009 the ratio didn't exceed 23% indicating a slight decrease in severity which may be attributed to better first aids and post-crash care. There was a reduction of (18%) in this ratio in 2019 compared with 2010.

3.2.5. Rate of mortalities per 100 crashes:

This rate ranged from 25 (2019) to 39 (2007) with an average of 30 for the period (2006-2019). It means that among every 100 crashes in 2019 there were 25 deaths, and this is a very high rate. If all crashes were recorded, including property damage and light injury crashes as in many other countries, the annual number of crashes will be increased and so this rate will be much lower. However, there was a reduction of (11%) in this rate in 2019 compared with 2010.

3.2.6. Rate of Mortalities per 10000 vehicles:

This rate ranged from 4.8 (2006, 2019) to 10.3 (2012) with an average of 6.8. Despite the rapid and continuous increase in vehicles and motorization levels during the studied period, there was a peak in 2012 and then the rate decreased to 4.8 in 2019. It can be concluded that there was a reduction of (49%) in this rate in 2019 compared with 2010.

3.2.7. Rate of Mortalities (per 100000 population):

Death is the worst impact of any crash, so this rate is widely used globally to compare the severity of traffic crashes between different countries taking into consideration their population. The rate of mortalities per 100000 population from 2006 to 2019 according to the CSO's annual reports were 4.2,4.3,6.6,7.4,8.4,8.8,9.8,8.9,8.0,7.1,6.9,7.0,7.2, and 6.7 respectively. The rate increased from 4.2 in 2006 to a maximum of 9.8 in 2012 then begun to decline and reached 6.7 in 2019. Similar rates were reported by other researchers [9,13], but a much higher rate for Al-Diwaniya city (33) was reported by Al-Obaedi (2015) [20]. Table 3 shows a reduction of (20%) in 2019 compared with 2010.

Table 4. Rates of morbidities during the period (2006-2019)

Year	Morbidities to total casualties	Morbidities per 100 crash	Morbidities per 10000 vehicles	Morbidities per 100000 population
2006	74%	97	14	12
2007	73%	104	13	12
2008	75%	100	22	19
2009	79%	107	31	27
2010	**78%**	**102**	**34**	**30**
2011	79%	101	37	33
2012	78%	103	36	35
2013	78%	110	30	32
2014	77%	104	22	27
2015	79%	107	21	27
2016	78%	103	18	25
2017	78%	106	18	25
2018	79%	106	19	27
2019	**82%**	**108**	**21**	**30**
average	78%	104	24	26

3.2.8. Rates of morbidities:

Table 4 summarizes the rates of morbidities in Iraq for the period (2006-2019). The rate of morbidities per 100 crashes ranges from 97 in 2007 to 110 in 2013 with an average of 104. It can be concluded that there is no reduction in this rate between 2010 and 2019 but there was an increase (6%) from 102 to 108. Table 4 also shows that the rate of morbidities per 10000

vehicles ranged from 13 in 2007 to 37 in 2011. There was a reduction of (38%) in the rate of morbidities per 10000 vehicles in 2019 compared to 2010. The rate of morbidities per 100000 population ranged from 12 in 2006 and 2007 to a maximum of 35 in 2012 with an average of 26. During the years between 2010 and 2019, there was a fluctuation in the rate of morbidities per 100000 population, but the value (30) was the same in each of 2010 and 2019.

4 Discussion

4.1. Underreporting of Data

Table 1 shows a total of (114697) crashes occurred in Iraq during the period (2006–2019) with an annual average of (8193). However, the actual numbers are expected to be higher than those recorded by the CSO reports because of underreporting. Reporting a crash in a police station is frequently conducted only when a person is killed, or somebody seriously injured [8]. Even in some of these cases, the relatives of the driver and the victim resort to understanding and agreement, and no lawsuits are registered in the police stations. As for cases of crashes involving light wounds or damage to personal property only, they are usually not recorded in police stations except when the two parties do not agree on a settlement and financial compensation. The police usually record any traffic crash that results in damage to state property to get a fine from the perpetrator and repair the damage. Al-Obaedi (2015) [21] reported that 21% of traffic crashes are not recorded by the police in Al-Diwaniya city. Underreporting is not limited to the number of crashes only, data reported by the Iraqi MoH always differ from those published by the CSO which is based on police agencies. For example, in 2019 the Iraqi MoH recorded 4232 deaths because of RTCs [4] while the CSO (as in Table 1) reported 2636 mortalities which were recorded at the scene of the crash (not after 30 days) by the traffic police. For the same year, MoH reported 101709 morbidities while the CSO recorded 11651 only. There is no coordination between the MoH and the CSO concerning unifying traffic casualties' data according to international standards. However, underreporting was experienced in many developed and developing countries because of the differences between the hospitals' data and the police records [22,23,24,25].

4.2. Impact of the Security Status

The results show that during the period 2006 to 2018, the year 2012 witnessed the peak number of crashes (10709), the peak number of mortalities (3132), and the peak number of morbidities (11009). But 2019 witnessed increases in the number of crashes (10753) and the number of morbidities (11651) compared with 2012. Because of a lack of data concerning total vehicle kilometers traveled each year, no exposure-based interpretation could be presented. However, it can be said that the year (2012) came between two periods of fragile security status after 2003. The first one was between (2003-2007) when terrorist explosions covered most of the Iraqi cities, and the second one was between (2013-2016) when the insurgency increased again, and ISIS terrorist groups occupied three governorates. During the period of a safe security situation (2008-2012), Iraqi people have begun to move and travel making more trips for work, education, entertainment, and internal tourism and there was clear prosperity covering all Iraqi cities associated with high GDP Per Capita. Despite the continuous increase in each of the population and motorization level after 2012, there was a reduction in each of the crashes, mortalities, and morbidities. This reduction may be a result of the second round of terrorism (2013-2016) which affected activities of people day and night resulting in a lower number of trips and less exposure to crashing. We can notice an increase in each of the crashes, mortalities, and morbidities associated with an increase in GDP per Capita during the years (2017- 2019) after the liberation of the three governorates occupied by ISIS terrorists and stability of the security situation. Accordingly, it can be concluded that the security status had a strong impact on the development of RTCs and their casualties in Iraq after 2003.

4.3. Comparison with Other Countries

The results show that the lowest ratio of fatalities to total casualties during the studied period was 18% in 2019. This ratio is considered very high compared with 1% in each of Sweden, Austria, and Belgium and 5% in France, and Denmark (United Nations Economic Commission

of Europe (UNECE), 2017) [26]. However, 2019 witnessed (18%) reduction in this ratio compared with 2010 and if this reduction continued during the coming years, it will be serious mitigation of the impact of RTCs in Iraq.
As mentioned earlier, WHO adopted a special equation to estimate fatalities based on the data mostly provided by the health agencies rather than police agencies in each country. In Jordan, for example, the official police statistics (The Annual Report of Traffic Accidents in Jordan 2018**)** [27] reported a rate of mortalities per 100000 population (6.75) for the year 2016 while the rate estimated by WHO was (24.4). When comparing the rate of mortalities per 100000 population of Iraq with the neighboring countries based on WHO Global Report 2018 [1], it can be concluded that the rate of Iraq (20.7) was higher than the global rate (18.2), Turkey (14.5), Kuwait (17.6), and Iran (20.5). On the other hand, it was lower than the rate of Jordan (24.5), Syria (26.5), and Saudi Arabia (28.8). Besides, the average rate of mortalities per 100000 population in the 28 European Union member states (2018) was 4.9 with a reduction of 21% compared to 2010 (European Commission-Fact Sheet, 2019) [28].
The rate of morbidities per 10000 vehicles in Iraq in 2018 was (19) while the corresponding rates in Jordan, Kuwait, and Saudi Arabia (as computed by the authors) were (99,50, and 44) respectively [27,29,30]. In 2018 not only morbidities in Iraq (10439) were lower than those in Jordan (16203) but also several vehicles in Iraq (5359792) were much higher than that in Jordan (1637981). So, it can be concluded that the burden of motorization on traffic morbidities in Iraq is less than that in Jordan.

4.4. The Governmental Commitment

According to the previous results, it can be concluded that the commitment launched by the Iraqi government in 2011 to improve road safety and reduce the number of casualties, unfortunately, appears far-fetched. There was no reduction in the number of crashes, mortalities, and morbidities during the period 2010-2019. On the contrary, in 2019, crashes, mortalities, and morbidities were increased by 21%, 5%, and 30% respectively when compared with 2010. On the other hand, there was a reduction in the burden of motorization on each of the crashes (42%), mortalities (49%), and morbidities (38%). Also, there was a reduction in the burden of population on each of the crashes (8%), and mortalities (20%). The rate of morbidities per 100000 population witnessed the same value (30) in each of 2010 and 2019. Besides, there was a reduction (11%) in the rate of mortalities per 100 crashes and (6%) in the rate of morbidities per 100 crashes.

4.5. Evaluation of the Road Safety System

4.5.1. Legislation

The traffic law which was applied in Iraq since 2004 (Coalition Provisional Authority, 2004) [31] was not sufficient to achieve the goal of reducing the number of victims because it did not impose fines commensurate with the seriousness of the offense committed, nor did it impose adequate safety measures on drivers or vehicles [12]. Law No. 86/2004 did not specify sufficient conditions for safety when registering vehicles and did not require seat belts, airbags, or anti-lock braking system (ABS) as well as it did not require the wearing of a helmet for a motorcyclist. The law imposed a prison sentence for anyone who drives a vehicle without a license and increased the penalty for anyone who causes harm to others because of recklessness or because of driving under the influence of alcohol or drugs. In 2019, a new traffic law (No.8) was issued by the Iraqi Parliament [32]. The new law imposed high fines for violators and the wearing of a helmet was imposed on motorcyclists. In this law, fines were imposed for using a mobile phone while driving, and children under the age of 8 years were prohibited from sitting in the front seats of the vehicle next to the driver. On the other hand, there was an indulgence in the ages specified for granting driving licenses. The law reduced the penalty for driving without a license, recklessness, or driving under the influence of alcohol or drugs. Many of the severe punishments in this law can be canceled upon the occurrence of concession or compromise between the two quarreling parties. Both Traffic Laws (86/2004 and 8/2019) did not specify the allowable level of alcohol in the driver's blood. (Jindi and Piramis Omar, 2020) [33] have indicated that there is a deficiency and an imbalance in both laws regarding punishments for the crimes of killing and wrongdoing resulting from the traffic crashes.

4.5.2. Enforcement

Despite the existence of the traffic law, researchers [12,16] have noticed that many of its important articles did not find actual application in the street after 2003. The WHO Global Report 2018 recorded low scores for Iraq when assessing its road safety status, especially for the enforcement element. Violations are carried out before the eyes of the traffic policemen without exposure to accountability. The reason may be attributed to the weakness of the security situation and the spread of financial and administrative corruption in the country. So, the people resort to resolve their various disputes (including traffic crashes) away from the judiciary relying on tribal solutions through agreeing on financial compensation apart from the traffic law. The poor performance of the granting license online system resulted in the weak implementation of the law and led to the spread of teenage and even adult drivers without licenses. Drivers generally not followed the instructions of the traffic police such as wearing seat belts, concern for the safety of the vehicle, not exceeding the prescribed speed, avoiding using a mobile phone, children sitting in the vehicle, avoiding driving under the influence of alcohol or drugs, and wearing helmets for motorcycles drivers, and so on. This risky driver behavior may be due to the psychological culture of the society. Many researchers have described the relation between the behavior and socio-cognitive factors like habits, social norms, attitudes, intention, perceived behavior control, and risk perception [34,35,36].

4.5.3. Reporting and Technology

A poor safety system begins with poor paper recording forms lacking necessary information like accurate crash details and precise location [12,16]. The traffic safety system also suffers from the lack of adopting of modern technologies for monitoring and control like using the Geographic Information System (GIS), the inefficiency of the existing cameras system inside the cities, in addition to the absence of red-light cameras at the intersections or speed cameras (mobile or fixed, hidden or visible) on the roads linking the main cities. The use of speed cameras in Kuwait, for example, has reduced deaths by 15% (Aljassar et al., 2004) [37]. Boos (2009) [38] reviewed the important role of speed cameras in improving traffic safety, reducing speed, and reducing deaths and injuries in many regions of the world. Besides, traffic police agency, as well as drivers, have little knowledge about Internet and Communication Technology and their applications for better road safety and effective communication with society.

4.5.4. Infrastructure

During the studied period there were no effective measures to improve road infrastructures to serve the increasing numbers of vehicles and population. Road's lengths increased from 40755.5 Km in 2006 to 45519 Km in 2018 (Annual Statistical Abstract, 2019) [39] which was not proportional to the increasing number of vehicles and population during this period. There were few additional bridges and grade-separated intersections (or interchanges), no special priorities for public transport, no suitable regulations for trucks, bicycles, motorcycles, and three wheels vehicles. As a general assessment for the road safety status in Iraq, The Global Road Safety Facility (GRSF) hosted by the World Bank reported [40]: "Iraq has a lead agency present, which isn't funded in the national budget. Iraq has a road safety strategy that is also not funded. The functions of the agency include coordination, legislation, and monitoring and evaluation of road safety strategies. The country has no known road safety target." As mentioned previously in the Introduction, the road safety target of Iraq is known but unfortunately, and according to the present results cannot be reached.

5 Conclusions

According to the results of the research, the following conclusions could be drawn:

1. There were no reductions in several crashes, mortalities, and morbidities during the decade (2010-2019) despite the mitigation in the burden of each motorization and population.

2. During the period 2006 to 2018, the security status had a strong impact on RTCs, and the year 2012 witnessed the peak values in each of the crashes, mortalities, and morbidities.
3. There were similar trends of development for each of the crashes, mortalities, morbidities, and GDP per Capita during the studied period and the general trend was statistically ascending. The GDP per Capita showed the highest Pearson Correlation Coefficients with each of the crashes, mortalities, and morbidities while the population and vehicles showed lower corresponding correlation values.
4. The road safety system needs measures to address the lack in each of legislation, enforcement, reporting, technology, and infrastructure. More effective work is urgently required to reduce numbers of RTCs' casualties in line with the global trend where many countries, after their success in reducing these numbers, are now working toward ((Vision Zero)) projects.

References:

[1] Global status report on road safety 2018. Geneva: World Health Organization. (2018). https://www.who.int/publications-detail/global-status-report-on-road-safety-2018

[2] Iaych, Dr Kacem, (2017). WHO road safety data collection experience. SafeFITS Round Table, Geneva. http://www.who.int/violence_injury_prevention/en/

[3] Annual Statistical Report 2017, Ministry of Health, Iraq. http://www.moh-planning.com/pdf/2017.pdf

[4] Annual Statistical Report 2019, Ministry of Health, Iraq. https://moh.gov.iq/upload/upfile/ar/1349.pdf

[5] WHO Regional Office for the Eastern Mediterranean, 2011.(accessed on 15-9-2020) http://www.emro.who.int/violence-injuries-disabilities/countries/iraq-roadsafety.html

[6] Statistics of Estimated Traffic Accidents 2004-2005, Ministry of Planning, The Central Statistical Organization, Iraq, 2006.

[7] Statistics of Registered Traffic Accidents 2006, Ministry of Planning, The Central Statistical Organization, Iraq, 2007.

[8] Statistics of Registered Traffic Accidents 2020, Ministry of Planning, The Central Statistical Organization, Iraq, 2021.

[9] Al-Jameel HA. Reducing the number of accidents in Iraq by using expert system. Journal of University of Babylon.2016; 24(4):1099-1112. https://www.iasj.net/iasj/article/116537

[10] Leidman E, Maliniak M, Sultan ASS, Hassan A, Hussain SJ, Bilukha OO. Road traffic fatalities in selected governorates of Iraq from 2010 to 2013: Prospective Surveillance. Conflict and Health.2016; 10(1):2-10. DOI 10.1186/s13031-016-0070-0

[11] Diah B, Baiee HA, AlShalah M. Epidemiological features of road traffic accident deaths in Babylon province during the period 2010-2014. Journal of Babylon University/Pure and Applied Sciences.2017 3(25):1129-1138. https://www.iasj.net/iasj/article/128765

[12] Asad FHA. Road traffic accidents in Iraq: A review of evidence-based literature. International Journal for Traffic and Transport Engineering.2017; 7(2): 256 – 275. DOI: http://dx.doi.org/10.7708/ijtte.2017.7(2).09.

[13] Mohammed AA, Ambak K, Mosa AM, Syamsunur D. Traffic accidents in Iraq: An analytical study. Journal of Advanced Research in Civil and Environmental Engineering.2018; 5(1&2):10-22. https://adrjournalshouse.com/index.php/civil-environment-engineering/article/view/169.

[14] Albayati AH, Lateif RH). Statistical analysis of mortality and morbidity due to traffic accidents in Iraq. Journal of Engineering.2018; 1(24): 20-40. https://iasj.net/iasj/download/d4cd89d88f06c63a.

[15] Al-Jameel HA, Abdullah MM, Almosawi BKA. Studying the traffic safety level in Al-Najaf city. Global Journal of Engineering Science and Research Management.2019; 6(2):1-7.

[16] Mohammed AA, Ambak K, Mosa AM, Syamsunur D. A review of traffic accidents and related practices worldwide. The Open Transportation Journal.2019; 13:65-83. DOI: 10.2174/1874447801913010065

[17] Albayati AH, Lateef IM. Characteristics of traffic accidents in Baghdad. Civil Engineering Journal.2019; 5(4): 940-949. https://civilejournal.org/index.php/cej/article/view/1421.

[18] Joni HH, Mohammed AA, Shakir AA. Classification of traffic accidents datasets between 2003-2017 in Iraq. Data in Brief.2020; 28:1-9. https://www.sciencedirect.com/science/article/pii/S2352340919312570.

[19] World Bank Data https://data.worldbank.org/country/iraq (accessed on 20-10-2020).

[20] Ott, L. An introduction to statistical methods and data analysis, 3rd Edition, Boston Mass, USA, PWS-KENT Press.1989.

[21] Al-Obaedi JTS. Evaluation of traffic accidents rates in Al-Diwaniya city. Journal of Babylon University/Engineering Sciences.2015; 3(23): 571-578. https://www.iasj.net/iasj/download/d137b1296b0a550f.

[22] Singh P, Lakshmi P, Prinja S, Khanduja P. Under-reporting of road traffic accidents in traffic police records- A cross sectional study from North India. International Journal of Community Medicine and Public Health.2018; 5(2):1-6. DOI:10.18203/2394-6040.ijcmph20180232.

[23] Watson A, Watson B, Vallmuur K. Estimating under-reporting of road crash injuries to police using multiple linked data collections. Accident Analysis and Prevention.2015; 83:18-25. https://www.sciencedirect.com/science/article/abs/pii/S0001457515300063.
[24] Samuel J C, Sankhulani E, Qureshi JS, Baloyi P, Thupi C, Lee CN, Miller W C, Cairns B A, Charles AG. Under-Reporting of road traffic mortality in developing countries: Application of a capture-recapture statistical model to refine mortality estimates. PLoS ONE.2012; 7(2), e31091. https://doi.org/10.1371/journal.pone.0031091
[25] Reurings MC, Stipdonk HL. Estimating the number of serious road injuries in the Netherlands. Ann Epidemiol.2019; 21(9):648-653. doi:10.1016/j.annepidem.2011.05.007. PMID: 21820630.
[26] United Nations Economic Commission for Europe. Statistics of road traffic accidents in Europe and North America, Volume LIV.2017. https://www.unece.org/fileadmin/DAM/trans/main/wp6/publications/RAS-2017.pdf.
[27] The Annual Report of Traffic Accidents in Jordan in 2018. The Public Security Department, Ministry of Interior, Jordan.2019. https://www.psd.gov.jo/images/jti/2018.pdf.
[28] European Commission - Fact Sheet.(2019). Road safety statistics: what is behind the figures?. Brussels. 2018. https://ec.europa.eu/commission/presscorner/detail/en/MEMO_19_1990.
[29] State of Kuwait. Central Statistical Bureau. Statistics of Transportation 2018.https://www.csb.gov.kw/Pages/Statistics?ID=41&ParentCatID=70
[30] Kingdom of Saudi Arabia. The General Authority for Statistics. Annual Yearbook 2018. https://www.stats.gov.sa/sites/default/files/2018_0.rar.
[31] Coalition Provisional Authority Order Number 86. May 2004.https://govinfo.library.unt.edu/cpa-iraq/regulations/20040520_CPAORD86_Traffic_Code_with_Annex_A.pdf
[32] The Iraqi Waqai'a. The Official Newspaper of Republic of Iraq. No. 4550.Year 61. 5/8/2019.
[33] Jindi KY, Piramis Omar DA. Legislative treatment of the crime of killing and wrongdoing resulting from traffic accidents. Academic Journal of Nawroz University.2020; 9(3): 290-304. https://doi.org/10.25007/ajnu.v9n3a796.
[34] Meesmann U, Torfs K, Cools M (2020). Socio-cognitive factors in road safety monitoring – cross-national comparison of driving under the influence of Alcohol, drugs or medication. IATSS Research.2020; 44(3):180-187. https://doi.org/10.1016/j.iatssr.2020.09.004.
[35] Chen HYW, Donmez B. What drives technology-based distractions? A structural equation model on social-psychological factors of technology-based driver distraction engagement. Accident Analysis and Prevention.2016; 91:166–174. https://doi.org/10.1016/j.aap.2015.08.015.
[36] Nordfjaern T, Rundmo T, Jørgensen S. A cross-cultural comparison of road traffic risk perceptions, attitudes towards traffic safety and driver behavior. Journal of Risk Research.2011; 14(6): 657–684. doi:10.1080/13669877.2010.547259.
[37] Aljassar AH, Ali MA, Al-Anzi MS). An investigation on the effect of traffic cameras on road safety in Kuwait. 2nd Gulf Road Conference. Paper No. E5.2004. Abu Dhabi. UAE.
[38] Boos MA. Speed cameras as a tool to reduce road fatalities. Virginia Department of Transportation Research Library, Research Synthesis Bibliography No. 23:1-30.2009. https://safety.fhwa.dot.gov/speedmgt/ref_mats/fhwasa1304/resources2/17%20-%20Speed%20Cameras%20as%20a%20Tool%20to%20Reduce%20Road%20Fatalities.pdf.
[39] Annual Statistical Abstract (2018-2019) Part 6: Transportation and communications. Ministry of Planning. The central statistical organization. Iraq.2019. http://cosit.gov.iq/ar
[40] The Global Road Safety Facility (GRSF) https://www.roadsafetyfacility.org/country/iraq (accessed on 3-8-2021)

Solving Suggested Problems using Grey Wolf Optimization

Nawras A. Issa[1], Zaid Alaa[2,] and Issa Ahmed Abed[3]
{nwrsb372@gmail.com[1], zaid.alaa@stu.edu.iq[2], issaahmedabed@stu.edu.iq[3]}

Basrah Engineering Technical College, Southern Technical University, Iraq[1]
Management Technical College – Basra, Southern Technical University, Iraq[2,3]

Abstract: In this research, the Grey Wolf Optimizer (GWO) algorithm was applied, which is a type of metaheuristic optimization algorithms that is important for identifying problems and finding ways to improve them. In 2014, Seyedali Mirjalili came up with this algorithm. Its social hierarchy is modeled after that of grey wolves in nature. These wolves live in groups consisting of(5 – 12) individuals. Wolves are divided into four levels, alpha represents the first level it is accountable for the manufacture of important resolutions for the peak like hunting, bedtime, wake up, etc. As for the second level in the hierarchy, it represents the beta wolf and is the advisor of the alpha. Beta can be the leader after the death of one of the alpha wolves. The third level represents delta, which follows the commands of alpha and beta. it is the dominant omega. omega represents the last level, which obeys all other wolves. Furthermore, the chief algorithm stages such as chasing, searching the prey, encircle and attack the prey were applied. GWO algorithm was tested on three benchmarks test functions using MATLAB R2014a. the results were confirmed by comparing GWO through another intelligent swarm algorithm like Particle Swarm Optimization (PSO) algorithm. results showed the superiority GWO in achieving better results and high convergence speed.

Keywords: Metaheuristic Algorithm, Grey Wolfe Optimizer.

1. Introduction

optimization is getting the best result under certain conditions like minimum costs, maximize efficiency or maximize revenues. Some optimization strategies have been created that are conceptually different from traditional techniques. Modern optimization approaches are based on biological, molecular, insect swarm, and neurobiological systems features and behavior[1]. With the advancement of information technology, a large number of optimization problems develop in a variety of disciplines like Internet routing, economics, and engineering design, which can be solved using a variety of ways such as, Fuzzy Logic[2],[3]. Sine Cosine Algorithm(SCA)[4]. ant colony optimization (ACO)[5], PSO algorithm [6], and so on.
Meta-heuristic algorithms are more reliable and usable by researchers in different fields rather than traditional optimization algorithms. Because these algorithms are population-based stochastic algorithms, their solution quality is far superior to that of traditional optimization techniques because of fewer parameters, high convergence speed, simplicity implementation [7]. It can be divided into three categories: i) Evolutionary Algorithms (EA), like Genetic Algorithm (GA)[8], A Differential Evolution Algorithm (DE)[9]. ii) physics-based algorithms, like gravitational search algorithm (GSA)[10],Harmony Search Algorithm[11] and Simulated Annealing[12].iii) Swarm intelligence (SI)-based algorithm, like Particle Swarm (PSO)[13],

IMDC-IST 2021, September 07-09, Sakarya, Turkey
Copyright © 2022 EAI
DOI 10.4108/eai.7-9-2021.2314893

Ant Colony Optimization(ACO)[14], Artificial Bee Colony[15], Fish Swarm Optimization(FSA)[16], Cuckoo Search algorithm (CS)[17], Bat Algorithm(BA)[18], Firefly Algorithm(FA)[19],[20]. and grey wolf optimization (GWO)[21]. GWO is inspired by grey wolves in nature, who are always looking for the best approach to catch their prey. In nature, the GWO algorithm uses the same process to organize the various functions in the wolf pack, which follows the pack hierarchy [22]. Pack's members are divided into four levels. alpha, beta, delta, and last level omega. it is best among the intelligent swarm algorithms because of simple, straightforward to use, and scalable, with a unique capacity to find the correct equilibrium between exploration (searching) and exploitation (attacking) in the search [23],[24]. GWO uses a small number of parameters to solve non-deterministic polynomial (NP)-hard problems over several rounds [25]. As a result, it was used in a variety of applications see figure 1.
(GWO) was used in different optimization processes such as the hybrid power generation system's optimal design to the less total cost.[26].to determine the best operating strategy for economic load dispatch (ELD) [27]. to solve the challenge of robot path planning to find the shortest path [28]. In WSNs, used for cluster head selection [29]. to achieve a stable network and have high energy-efficient [30]. In the industrial world, optimizing fuel use is the most significant concern. Several causes have played a role in the recent rise in relevance. Increasing energy consumption and dwindling fossil fuel supplies are two of these factors. Instead of fossil fuels, nuclear energy can be used in most power-producing systems. Because nuclear fuel production is such a complicated process, it's critical to think about how it's used. based on neutronic and thermal-hydraulic parameters, to establish the optimal pattern for the core of the Bushehr nuclear power station [31]. The optimal parameters of a PID controller for load frequency regulation in a multi-source single area power system were estimated using the GWO algorithm, which is based on evolutionary intelligence. The power grid is made up of thermal, gas, and hydroelectric power facilities with mechanical hydraulic governors [32]. To minimize load bus voltage variations and system power losses, the grey wolf optimizer (GWO) was used to determine the appropriate placement of STATCOM devices on the power system grid. [33]. Controlling electrical machinery with the DTC method is common. To match the speed to the specified reference, the parameters of the conventional Proportional Integral (PI) speed controller are manually changed. The grey wolf algorithm(GWO) is used to modify the PI speed controller parameters to improved Direct Torque Control (DTC) and to improve the performance of the Induction Motor (IM)[34]. The GWO algorithm is implemented. The main goals of this report are i) study the GWO algorithm to identify problems and find the best solutions. ii) comparison of the GWO with PSO algorithm. iii) simulation of the algorithm using MATLA environment. The results proved the efficiency of GWO in finding the optimal solution, high convergence speed, and avoiding local optimization.

2 Grey Wolf Optimization (GWO)

GWO is population-based swarm intelligence. That imitates grey wolf dominance. Mirjalili had proposed it in 2014. Grey wolves are social animals that live in packs of 5 to 12 individuals. for each iteration, the three best probable solutions are known to the alpha wolf, beta wolf, and delta wolf they lead to wide areas of the search. The dominant hierarchy in the group is divided into four levels [25],[26] as shown in Figure 2. this algorithm has been employed by several academics due to its simplicity and ease of use. The grey wolf optimization (GWO) uses a few numbers of parameters to solve non-deterministic polynomial (NP)-hard problems over several iterations.

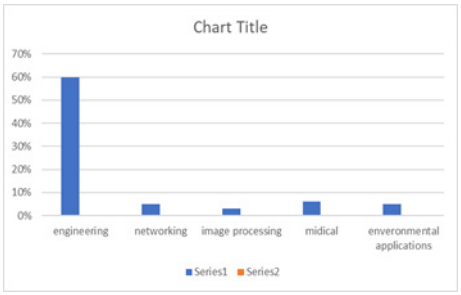

Fig 1. GWO application.

Fig 2. Grey wolf social hierarchy.

2.1 Social Hierarchy

Alpha wolf (α), who can be male or female, is the group's leader. It is the pack's highest-ranking member, in charge of hunting, sleeping arrangements, and walking schedules. Beta (β)The second type of wolves in the pack, which help the alpha in their decisions about days activities. the third level in the dominant social hierarchy is called delta wolf (δ) and submits to alpha and beta members. Omega wolf (ω) has the last hierarchical rank in the group and submits to all the other wolves, but it plays a critical role in balancing hierarchy [35].

2.2.1. Encircling Process

Grey wolves surround their victim as part of the hunting phase, see figure 3. the following equations are used to quantitatively model encircling behavior mathematically as shown below [36].

$$|\vec{D} = |\vec{C} \cdot \vec{X}_p(t) - \vec{X}(t)\ | \tag{1}$$

$$\vec{X}(t+1) = \vec{X}_p(t) - \vec{A} \cdot \vec{D} \tag{2}$$

when (t) refers to the current iteration, (A $\vec{}$) and (C $\vec{}$) represents the coefficient vectors see equations (3) and (4). (Xp) $\vec{}$ indicates the location vector of the prey, and (X $\vec{}$) refers to the location vector of a grey wolf [36].

$$\vec{A} = 2\vec{a} \cdot \vec{r}_1 - \vec{a} \tag{3}$$

$$\vec{C} = 2 \cdot \vec{r}_2 \tag{4}$$

When (r_1) $\vec{}$and (r_2) $\vec{}$ represented to random vectors in the range [0,1] so the component of a $\vec{}$ is reduced linearly from (2 - 0) across repeated iterations. the grey wolves update positions for (2D) and (3D) are shown in Figure 4. (a and b).

Fig 3. Grey wolf hunting behavior: (A) chasing, impending, and following victim(B–D) troublesome, and surrounding (E)attack and fixed state.

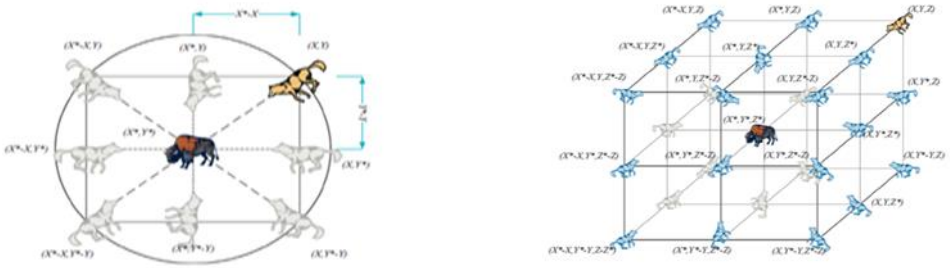

(a) (b)

Fig 4. (a) 2 dimensions position vectors, (b)3 dimintions position vectors.

2.2.2 Hunting Process

The leader (alpha) guides the other wolves (beta)and (delta) through the procedure for hunting. in the mathematical model, the alpha represents the overall best solutions, while beta (β) and delta(δ) refer to the second and third best candidate solutions respectively in the population. All solutions are updated their positions according to the location of the best first three solutions (alpha(α), beta(β), and delta(δ) successively)[37]. The formula of the mathematical equation of the hunting process is shown below.

$$\begin{aligned} \vec{D}_\alpha &= \left|\vec{C}_1 \cdot \vec{X}_\alpha - \vec{X}\right| \\ \vec{D}_\beta &= \left|\vec{C}_2 \cdot \vec{X}_\beta - \vec{X}\right| \\ \vec{D}_\delta &= \left|\vec{C}_3 \cdot \vec{X}_\delta - \vec{X}\right| \end{aligned} \tag{5}$$

$$\vec{X}_1 = \vec{X}_\alpha - \vec{A}_1 \cdot \left(\vec{D}_\alpha\right)$$

$$\vec{X}_2 = \vec{X}_\beta - \vec{A}_2 \cdot (\vec{D}_\beta) \quad (6)$$
$$\vec{X}_3 = \vec{X}_\delta - \vec{A}_3 \cdot (\vec{D}_\delta)$$

$$\vec{X}(t+1) = \frac{\vec{X}_1 + \vec{X}_2 + \vec{X}_3}{3} \quad (7)$$

When ($X^{\rightarrow}$_1), ($X^{\rightarrow}$_2), and ($X^{\rightarrow}$_3) refer to the first three solutions in the population. Figure 5. A search agent's position is updated based on alpha, beta, and delta coordinates. In the context of a two-dimensional search space.

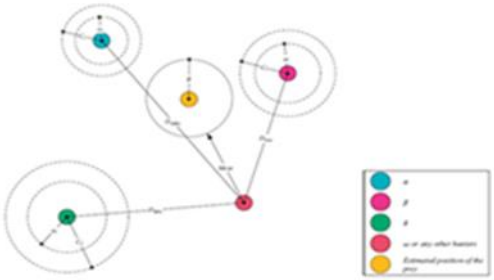

Fig 5. Position updating to grey wolves.

2.2.3. Attacking Process (Exploitation)

The hunt is completed when the prey is attacked. When the vector(A)is a random number in the interval [-2a, 2a] and a decreased liberty from (2 to 0) throughout iterations, the wolves progress towards the prey. figure 6(a) demonstrates that |A| < 1 makes the wolves attack prey. [36],[37].

2.2.4. Search Process for Prey (Exploration)

Each wolf modifies its location dependent on alpha and data's positions to hunt for prey. Diversification or exploration is the term for this procedure. When |A|> 1, the wolves (solutions) are driven to leave the prey in search of more suitable prey. Figure 6 (b) indicates that when |A| > 1 grey wolves are forced to diverge from their prey in the hopes of finding a fitter prey. C is an additional component that aids the algorithm in finding new solutions. when C >1 emphasize or C< 1 deemphasize random weights for the prey [36],[37].

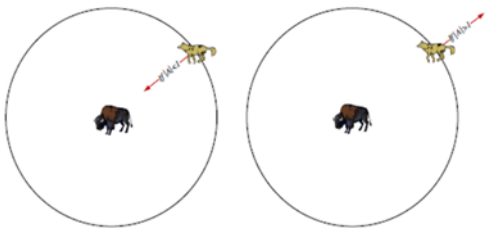

Fig 6. (a) Attacking prey,(b) searching for prey.

2.2. Optimization Processing and Pseudo-Code to GWO Algorithim

The GWO optimization method begins with a randomly generated grey wolf population (candidate solutions). Throughout the iterations, the wolves' alpha, beta, and delta assess the prey's likely location (optimum solution). The distance between grey wolves and their prey determines how they position themselves. Parameter a should be reduced from 2 to 0 to emphasize the exploration process and exploitation process during the search phase [38]. The pseudo-code is represented in Fig 7.

Algorithm 1 GWO pseudo-code

Initialize the grey wolf population $X_i (i = 1, 2, \ldots, n)$;
Initialize a, A, and C;
Calculate the fitness value for each grey wolf;
$\vec{X}_{\alpha}^{0}$ = the initial position of the leader wolf;
$\vec{X}_{\beta}^{0}$ = the initial position of the second-best wolf;
$\vec{X}_{\delta}^{0}$ = the initial position of the third-best wolf;
Calculate the initial position of prey ($\vec{X}_P^0$) according to Equation (5);
While (t < Max number of iterations)
For each grey wolf
Update the position of current grey wolf by Equation (1);
end For
Update a, A, and C;
Calculate the fitness value for each grey wolf;
Update $\vec{X}_{\alpha}^{t}$, $\vec{X}_{\beta}^{t}$, and $\vec{X}_{\delta}^{t}$;
Calculate the position of prey ($\vec{X}_P^t$) according to Equation (5);
$t = t + 1$;
End while
return $\vec{X}_{\alpha}^{t}$.

Fig 7. Pseudo-code of GWO algorithm[39].

3. Simulation Results and Comparison

The GWO was implemented in MATLAB R2014a.Laptop specifications , device name DESKTOP-14BPU59,Processor Intel(R) Core(TM) i7-8565U CPU @ 1.80GHz 1.99 GHz,Installed RAM 8.00 GB (7.88 GB usable), System type 64-bit operating system. Windows 10 Pro.

We employ three benchmark test functions[36],[40] to compare the proposed GWO algorithm against other population-based approaches to assess its performance. Table 1 shows these test functions. the GWO method was compared to the PSO algorithm. with the same setting of the parameters, that is, dimension (numbers of variables) is set to 4, the size of the population is set 30, and numbers of maximum iterations (30, 90, 150) for all test functions. we tested each function 10 times. each algorithm was performed ten times to find the best solution, average value and standard deviation of extracted results were evaluated. Table 2 shows the first case (max.iter.=30), GWO gives the better results (best, mean) for all functions f1, f2, f3.also the standard deviation of GWO is less than the PSO algorithm. when the standard deviation is less, the GWO is stable. Table 3 shows the second case (max.iter.=90) when the iteration process is

increased, GWO gives better results compared to the first case for all functions. Table 4 shows the third case (max.iter.=150). when iteration increases the advantages of GWO to find the best solution, the mean increases too, compared to PSO. the best value is close to the optimal value and the standard deviation is as little as possible, which makes the GWO more stable in optimization operations. Figure 8(a,b,c) , Figure 9(a,b,c) and Figure 10(a,b,c) illustrate the convergence curves of fitness values with deference to the number of maximum iterations for the 3 functions to test respectively. The GWO algorithm is more effective than the PSO algorithm in reaching the optimal solution for all test functions under the same conditions as iteration increases.

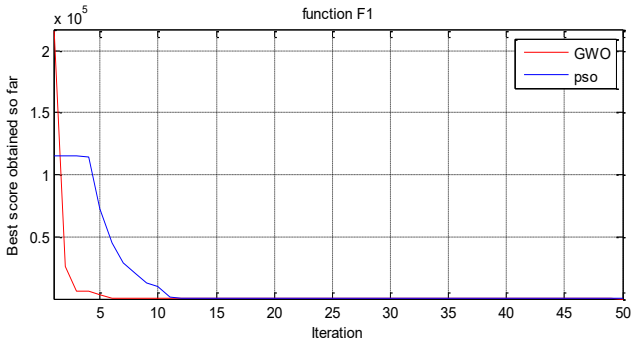

(a)

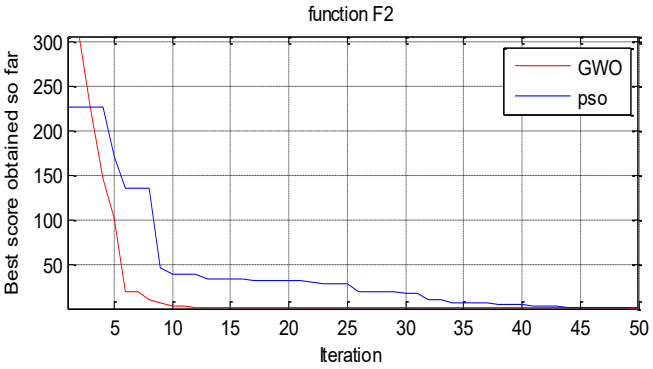

(b)

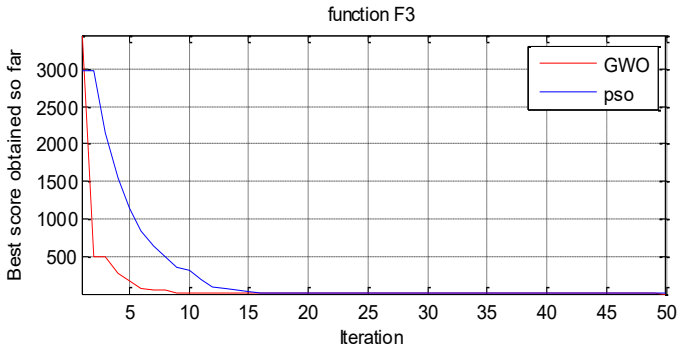

(c)

Fig 8. (a,b,c). convergence curve of GWO ana PSO with maximum iteration 50 for 3 test functions f1,f2, and f3.

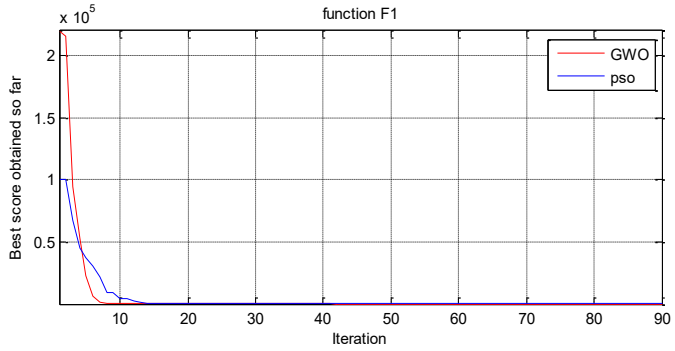

(a)

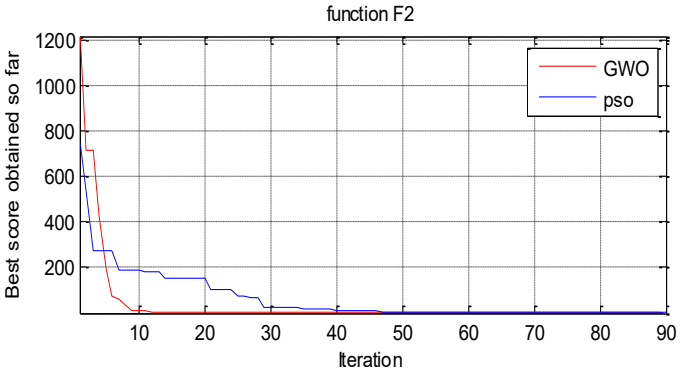

(b)

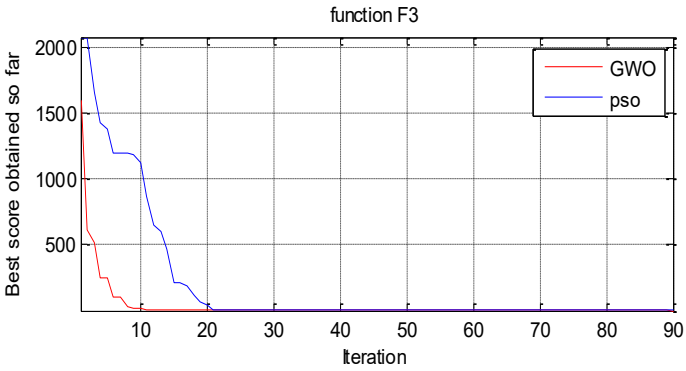

(c)

Fig 9. (a,b,c). convergence curve of GWO ana PSO with maximum iteration 90 for 3 test functions f1,f2, and f3.

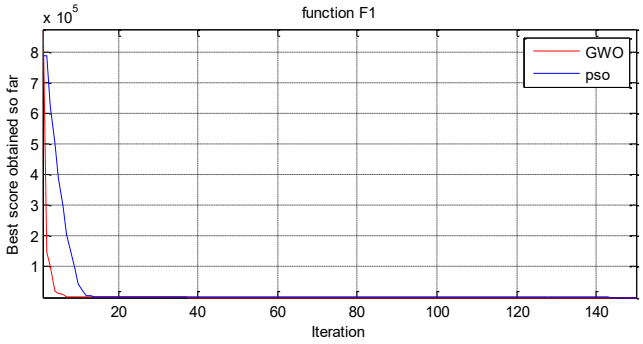

(a)

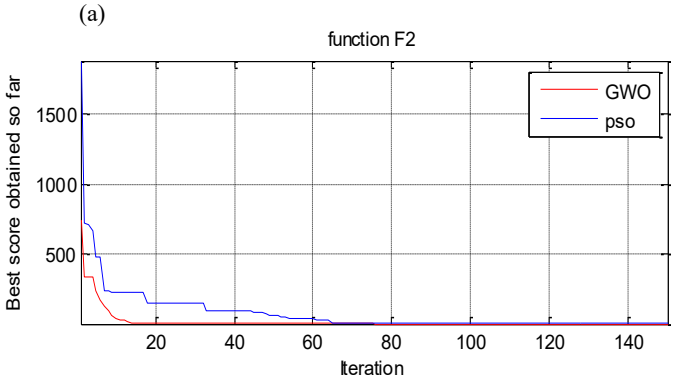

(b)

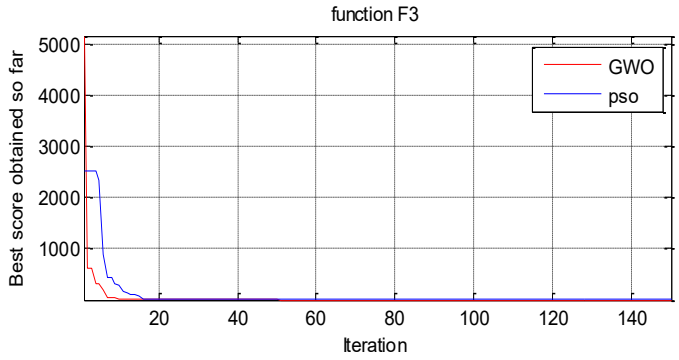

(c)

Figure 10. Convergence curve of GWO ana PSO with maximum iteration 150 for 3 test functions f1,f2, and f3.

Table 1. Unimodel benchmark test functions (standard optimization functions).

Function	Pop. zize	max.Iter.	Dim.	Rang	min
$f_1(x) = \sum_{i=1}^{n} x_i^2$	30	(30, 90, 150)	4	[-100,100]	0
$f_2(x) = \sum_{i=1}^{n} \lvert x_i \rvert + \prod_{i=1}^{n} \lvert x_i \rvert$	30	(30, 90, 150)	4	[-10,10]	0
$f_3(x) = \sum_{i=1}^{n} \left(\sum_{j-1}^{i} x_j\right)^2$	30	(30, 90, 150)	4	[-100,100]	0

Table 2. Experimental results comparison of GWO and PSO with max.Iteration 30 and run10 for 3 test functions.

Function	Algorithm	Best values	Mean values	St.dev.
F1	GWO	1.84E-06	1.08E-03	0.002935557
	PSO	1.81E-02	2.63E-01	0.273849719
F2	GWO	0.0013555	0.01357527	0.014878658
	PSO	0.8733	2.09849	1.309364767
F3	GWO	0.0015572	0.06622358	0.113190574
	PSO	0.0085606	0.06569306	0.067863718

Table 3. Experimental results comparison of GWO and PSO with max.Iteration 90 and run10 for 3 test functions.

Function	Algorithm	Best values	Mean values	St.dev.
F1	GWO	1.45E-23	1.80E-16	3.99084E-16
	PSO	1.71E-08	1.21E-07	1.08387E-07
F2	GWO	2.60E-10	7.51E-10	4.37614E-10
	PSO	7.82E-04	3.17E-03	0.002436537
F3	GWO	4.03E-13	3.63E-09	8.3739E-09
	PSO	1.65E-07	2.49E-06	1.63563E-06

Table 4. Experimental results comparison of GWO and PSO with max.Iteration 150 and run10 for 3 test functions.

Function	Algorithm	Best values	Mean values	St.dev.
F1	GWO	7.09E-37	5.26E-29	1.56403E-28
	PSO	6.84E-16	3.15E-13	6.00861E-13
F2	GWO	4.15E-19	2.65E-16	6.24844E-16
	PSO	1.26E-06	7.58E-06	5.41036E-06
F3	GWO	4.18E-21	1.37E-17	2.88086E-17
	PSO	2.01E-12	7.84E-10	1.39874E-09

4 Conclusions

This paper defined the grey wolf optimizer (GWO) algorithm, which is a meta-heuristic algorithm that is quite recent. as it depends on population diversity to discover the optimum solution and achieving a balance between the exploration and exploitation process. GWO algorithm is inspired by the hunting behavior of the grey wolves in nature(hunting mechanisms and social hierarchy). As well, this research included mathematical models for encircling, tracking, and hunting. to verify the results of the GWO algorithm, three test benchmark functions were used to compare with another algorithm like PSO with the same conditions. the simulation results obtained using MATLAB R2014a environment proved the ability of GWO to achieve faster and better results access the optimal global solution and escaping local solutions.

References

[1] K. Suresh, G. V. Kumar, and K. N. Raju, “Cost optimization for intelligent enterprises using modified GWO,” Proc. 3rd Int. Conf. Smart Syst. Inven. Technol. ICSSIT 2020, no. Icssit, pp. 87–91, 2020, doi: 10.1109/ICSSIT48917.2020.9214166.

[2] Y. Tao, J. Zhang, and L. Yang, “An unequal clustering algorithm for wireless sensor networks based on interval type-2 tsk fuzzy logic theory,” IEEE Access, vol. 8, pp. 197173–197183, 2020, doi: 10.1109/ACCESS.2020.3034607.

[3] M. Mirsadeghi, A. Mahani, and M. Shojaee, “A Novel Distributed Clustering Protocol Using Fuzzy Logic,” Procedia Technol., vol. 17, pp. 742–748, 2014, doi: 10.1016/j.protcy.2014.10.193.

[4] S. Mirjalili, “SCA: A Sine Cosine Algorithm for solving optimization problems,” Knowledge-Based Syst., vol. 96, pp. 120–133, 2016, doi: 10.1016/j.knosys.2015.12.022.

[5] C. Shin and M. Lee, “Swarm-intelligence-centric routing algorithm for wireless sensor networks,” Sensors (Switzerland), vol. 20, no. 18, pp. 1–13, 2020, doi: 10.3390/s20185164.

[6] M. Ren, X. Huang, X. Zhu, and L. Shao, “Optimized PSO algorithm based on the simplicial algorithm of fixed point theory,” Appl. Intell., vol. 50, no. 7, pp. 2009–2024, 2020, doi: 10.1007/s10489-020-01630-6.

[7] M. Abdel-Basset, L. Abdel-Fatah, and A. K. Sangaiah, Metaheuristic algorithms: A comprehensive review. Elsevier Inc., 2018.

[8] S. Chen, T. R. Newman, J. B. Evans, and A. M. Wyglinski, “Genetic algorithm-based optimization for cognitive radio networks,” 33rd IEEE Sarnoff Symp. 2010, Conf. Proc., 2010, doi: 10.1109/SARNOF.2010.5469780.

[9] R. Knobloch, “A differential evolution algorithm in the optimization task with a Lipschitz continuous cost function,” AIP Conf. Proc., vol. 2048, no. December, 2018, doi: 10.1063/1.5082064.

[10] H. A. Kherabadi, S. E. Mood, and M. M. Javidi, “Mutation: A new operator in gravitational search algorithm using fuzzy controller,” Cybern. Inf. Technol., vol. 17, no. 1, pp. 72–86, 2017, doi: 10.1515/cait-2017-0006.

[11] A. Askarzadeh and E. Rashedi, Harmony search algorithm: Basic concepts and engineering applications, no. April. 2017.

[12] J. Zeng, Z. Huang, Y. Chen, W. Liu, and S. Chu, “A simulated annealing approach for optimizing composite structures blended with multiple stacking sequence tables,” Struct. Multidiscip. Optim., vol. 60, no. 2, pp. 537–563, 2019, doi: 10.1007/s00158-019-02223-9.

[13] D. Wang, D. Tan, and L. Liu, “Particle swarm optimization algorithm: an overview,” Soft Comput., vol. 22, no. 2, pp. 387–408, 2018, doi: 10.1007/s00500-016-2474-6.

[14] A. S. Pontes et al., “Ant colony optimization for variable selection in discriminant linear analysis,” J. Chemom., vol. 34, no. 12, pp. 1–12, 2020, doi: 10.1002/cem.3292.

[15] B. Crawford, R. Soto, R. Cuesta, and F. Paredes, “Application of the artificial bee colony algorithm for solving the set covering problem,” Sci. World J., vol. 2014, 2014, doi: 10.1155/2014/189164.

[16] C. Zhang, F. M. Zhang, F. Li, and H. S. Wu, “Improved artificial fish swarm algorithm,” Proc. 2014 9th IEEE Conf. Ind. Electron. Appl. ICIEA 2014, vol. 11, pp. 748–753, 2014, doi: 10.1109/ICIEA.2014.6931262.

[17] A. S. Joshi, O. Kulkarni, G. M. Kakandikar, and V. M. Nandedkar, “Cuckoo Search Optimization- A Review,” Mater. Today Proc., vol. 4, no. 8, pp. 7262–7269, 2017, doi: 10.1016/j.matpr.2017.07.055.

[18] M. A. Al-Betar and M. A. Awadallah, “Island bat algorithm for optimization,” Expert Syst. Appl., vol. 107, pp. 126–145, 2018, doi: 10.1016/j.eswa.2018.04.024.

[19] N. Farahlina Johari, A. Mohd Zain, N. Haszlinna Mustaffa, and A. Udin, “Machining Parameters Optimization using Hybrid Firefly Algorithm and Particle Swarm Optimization,” J. Phys. Conf. Ser., vol. 892, no. 1, pp. 0–11, 2017, doi: 10.1088/1742-6596/892/1/012005.

[20] W. A. Hasan, I. A. Abed, and D. K. Shary, “Management of Microgrid System Based on Optimization Algorithm,” *Journal of Physics: Conference Series*, vol. 1773, no. 1. 2021, doi: 10.1088/1742-6596/1773/1/012006.

[21] S. Saremi, S. Z. Mirjalili, and S. M. Mirjalili, “Evolutionary population dynamics and grey wolf optimizer,” Neural Comput. Appl., vol. 26, no. 5, pp. 1257–1263, 2015, doi: 10.1007/s00521-014-1806-7.

[22] N. Jayakumar, S. Subramanian, S. Ganesan, and E. B. Elanchezhian, “Grey wolf optimization for combined heat and power dispatch with cogeneration systems,” Int. J. Electr. Power Energy Syst., vol. 74, pp. 252–264, 2016, doi: 10.1016/j.ijepes.2015.07.031.

[23] A. Al-Moalmi, J. Luo, A. Salah, and K. Li, "Optimal virtual machine placement based on grey wolf optimization," Electron., vol. 8, no. 3, pp. 1–22, 2019, doi: 10.3390/electronics8030283.

[24] S. Y. Li, S. M. Wang, P. F. Wang, X. L. Su, X. S. Zhang, and Z. H. Dong, "An improved grey wolf optimizer algorithm for the inversion of geoelectrical data," Acta Geophys., vol. 66, no. 4, pp. 607–621, 2018, doi: 10.1007/s11600-018-0148-8.

[25] A. Farshin and S. Sharifian, "A chaotic grey wolf controller allocator for Software Defined Mobile Network (SDMN) for 5th generation of cloud-based cellular systems (5G)," Comput. Commun., vol. 108, pp. 94–109, 2017, doi: 10.1016/j.comcom.2017.05.003.

[26] A. Yahiaoui, F. Fodhil, K. Benmansour, M. Tadjine, and N. Cheggaga, "Grey wolf optimizer for optimal design of hybrid renewable energy system PV-Diesel Generator-Battery: Application to the case of Djanet city of Algeria," Sol. Energy, vol. 158, no. August, pp. 941–951, 2017, doi: 10.1016/j.solener.2017.10.040.

[27] M. Pradhan, P. K. Roy, and T. Pal, "Grey wolf optimization applied to economic load dispatch problems," Int. J. Electr. Power Energy Syst., vol. 83, pp. 325–334, 2016, doi: 10.1016/j.ijepes.2016.04.034.

[28] T. F. Abaas and A. H. Shabeeb, "Safe and optimum navigation of wheeled mobile robot using grey wolf optimization algorithm," IOP Conf. Ser. Mater. Sci. Eng., vol. 928, no. 2, 2020, doi: 10.1088/1757-899X/928/2/022006.

[29] D. Agrawal et al., "GWO-C: Grey wolf optimizer-based clustering scheme for WSNs," Int. J. Commun. Syst., vol. 33, no. 8, pp. 1–15, 2020, doi: 10.1002/dac.4344.

[30] A. Kaushik, S. Indu, and D. Gupta, "A Grey Wolf Optimization Approach for Improving the Performance of Wireless Sensor Networks," Wirel. Pers. Commun., no. 0123456789, 2019, doi: 10.1007/s11277-019-06223-2.

[31] A. Naserbegi, M. Aghaie, and A. Zolfaghari, "Implementation of Grey Wolf Optimization (GWO) algorithm to multi-objective loading pattern optimization of a PWR reactor," *Ann. Nucl. Energy*, vol. 148, no. xxxx, p. 107703, 2020, doi: 10.1016/j.anucene.2020.107703.

[32] N. Paliwal, L. Srivastava, and M. Pandit, "Application of grey wolf optimization algorithm for load frequency control in multi-source single area power system," *Evol. Intell.*, no. 0123456789, 2020, doi: 10.1007/s12065-020-00530-5.

[33] A. A. M. El-Gaafary, Y. S. Mohamed, A. M. Hemeida, and A.-A. A. Mohamed, "Grey Wolf Optimization for Multi Input Multi Output System," *Univers. J. Commun. Netw.*, vol. 3, no. 1, pp. 1–6, 2015, doi: 10.13189/ujcn.2015.030101.

[34] G. M. Fadhil, I. A. Abed, and R. S. Jasim, "Controlling of Induction Motor Using Grey Wolf Optimization Algorithm," *J. Phys. Conf. Ser.*, vol. 1773, no. 1, 2021, doi: 10.1088/1742-6596/1773/1/012007.

[35] J. Too, A. R. Abdullah, N. M. Saad, N. M. Ali, and W. Tee, "A new competitive binary grey wolf optimizer to solve the feature selection problem in EMG signals classification," Computers, vol. 7, no. 4, 2018, doi: 10.3390/computers7040058.

[36] S. Mirjalili, S. M. Mirjalili, and A. Lewis, "Grey Wolf Optimizer," Adv. Eng. Softw., vol. 69, pp. 46–61, 2014, doi: 10.1016/j.advengsoft.2013.12.007.

[37] H. Joshi and S. Arora, "Enhanced grey Wolf optimization algorithm for global optimization," Fundam. Informaticae, vol. 153, no. 3, pp. 235–264, 2017, doi: 10.3233/FI-2017-1539.

[38] Z. Wang, H. Xie, Z. Hu, D. Li, J. Wang, and W. Liang, "Node coverage optimization algorithm for wireless sensor networks based on improved grey wolf optimizer," J. Algorithms Comput. Technol., vol. 13, 2019, doi: 10.1177/1748302619889498.

[39] X. Zhao, S. Ren, H. Quan, and Q. Gao, "Routing protocol for heterogeneous wireless sensor networks based on a modified grey wolf optimizer," Sensors (Switzerland), vol. 20, no. 3, pp. 1–18, 2020, doi: 10.3390/s20030820.

[40] Abed, I. A., S. P. Koh, K. S. M. Sahari, S. K. Tiong, M. M. Ali, and AA Abdul Kadhim. "A New Proposed Pendulum-Like with Attraction-Repulsion mechanism Algorithm

for Solving Optimization Problems." In *IOP Conference Series: Materials Science and Engineering*, vol. 881, no. 1, p. 012132. IOP Publishing, 2020.

Numerical Analysis by Computational Fluid Dynamic Simulation of Fluid Flow in A T- Junction

Marwa S. Luaibi[1], Mohammed A. Abdulwahid[2]
{Marwa.salman1988@gmail.com[1]/ Marwa.salman@stu.edu.iq[1] , mohw2016@stu.edu.iq[2]}

Engineering Technical College, Southern Technical University, Iraq[1,2]

Abstract. The flow in a T-junction is very important in industrial and equipment. Prediction of the loss coefficient and velocity profile of fluid with the turbulent incompressible flow in T-junction pipe for non-symmetrical dividing and non-symmetrical combining helps to understand this type of fitting. The angle of the tee is 90º, sharp edge, the area ratio is equal to one and Three-dimensional the specification of geometry at steady state. The model of turbulent uses the stander k-ε and solving the Navies- Stocks equation by finite volume method in the SIMPLE algorithm in ANSYS FLUENT R1 2020. Comparison of the numerical results with previous work to study the effect of the flow rate ratio with different Reynolds numbers in the range (3000-30000). The results show the loss coefficient is independent of Re numbers. The non-symmetrical dividing the maximum flow move in the straight pipe when the change flow rate ratio to (0.8) forced the fluid to move in the branch and formation high vortex and recirculation. The non-symmetrical combining the high velocity in outlet branch with small eddies especially increased at a flow rate ratio (0.8).

Keywords: T-junction, non-symmetrical, turbulent flow, loss coefficient, flow rate ratio.

1 Introduction

The networks and industrial contain several pipes and T-junction. The T- junction consider is the most common complex section of networks pipe that is mainly employed for the transportation and supply of gases and liquids. The T-junction is utilization to merge (combining) flows from branch pipes to the main pipe. Separate (dividing) the flow from the main pipe to several branching pipes. as shown in Fig 1.

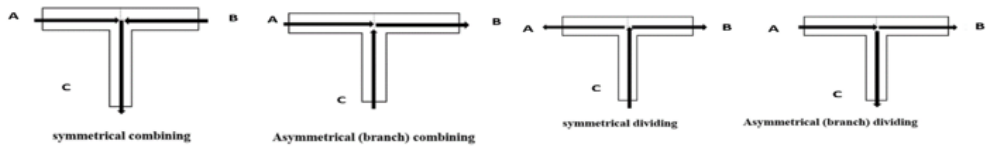

Fig 1. Various possibilities of fluid in the junction.

IMDC-IST 2021, September 07-09, Sakarya, Turkey
Copyright © 2022 EAI
DOI 10.4108/eai.7-9-2021.2314888

The numerical simulations can provide a lot of insight into this area and given the scientific, academic, and industrial relevance of the understanding of this type of flow. The loss coefficient and energy losses at junctions have been studied for several years. Therefore a more developing description of the T-junction had to be arrived at by Miller [1] cases that the cause of pressure loss coefficient and major energy loss and pressure for T and Y junctions is due to the converge and diverge of flows with different areas ratios, flow rate ratio, and angle. In A. Marc Serre et al [2] Although a considerable quantity of theoretical research exists on pressure loss coefficients for tee and pressure drop (head losses). Sierra Espinosa et al. [3] scrutinized round-edge tees and compared a limited set of measurements with simulations by the standard Reynolds stress (RSM) turbulence model, standard k- ε model, and (RNG) k- ε models. These models were able to predict the mean flow for numerical Fluent and comparison with experimental. G. Gan et al. [4] the pressure loss coefficient determines the use of fluent CFD for division and combination for duct junction with a square cross-section. Another author's prompt description of the T- junction is provided by Oka [5] to determine the pressure loss coefficient and power losses coefficient for combining and dividing, and comparison with the experimental result for area ratio 11.44. N. Crawford [6] the total coefficients, total pressure, equivalent length evaluated by the experiment and the CFD ANSYS FLUENT computation for air working fluid for T, Y junction, and elbow. Pérez [7] predicted the loss coefficient has been related to the extrapolated Mach number with different flow rate ratios for symmetrical combining and symmetrical dividing by experimental and numerical in FLUENT. N. P. Costa [8] The flow arrangement is that of a combining flow in a 90° T-junction with sharp and around corners by numerical and experimental methods, explained the optimize of fluid flow in T-Junction. P. R. Vasava [9] did fundamental work in the field of major head loss and minor losses effort during fluid flow through a T-junction and angles of T-junctions. He calculated the values obtained by simulations in ANSYS FLUENT and compared them with the classical formulas of Vazsonyi and Gardel. Researchers [10-13] Studied the 3D T-Junction for steady-state and turbulent flow by the numerical method in ANSYS and predicted the loss coefficient, pressure drop, and velocity profile in T-junction. Other researchers [14 and 15] Worked by numerical in ANSYS FLUENT and experimental (PIV) measurements to compare velocity profiles and streamline between them. M. D. Bassett et al. [10] developed simple expressions are provided that allow all of the pressure loss coefficients for a three pipe T-junction, with any side branch angle or area ratio, to be calculated. N. A. Ferede [11] Studied The head losses, pressure loss, velocity profile, and drag coefficient in T-junction where the working fluid used the mercury in CFX. The goal of this paper is to calculate the pressure loss coefficient with different flow rate ratios, area ratios equal to one. present the numerical results of turbulent flow. The flow is steady state, the cases of T-junction for non-symmetrical combining and non-symmetrical dividing. The Reynolds number in the range from 3000 to 30000 falls within a range in the real application. The result was extracted from ANSYS FLUENT R1 2020. It is expected thus that the results of this investigation may be of help to engineers dealing with similar Reynolds numbers and flow configurations. chooses the flow rate ratio from (0.1-0.8) to show the effect of the different flow rates on the loss coefficient and velocity profile.

2 Numerical Description

2.1 Geometry

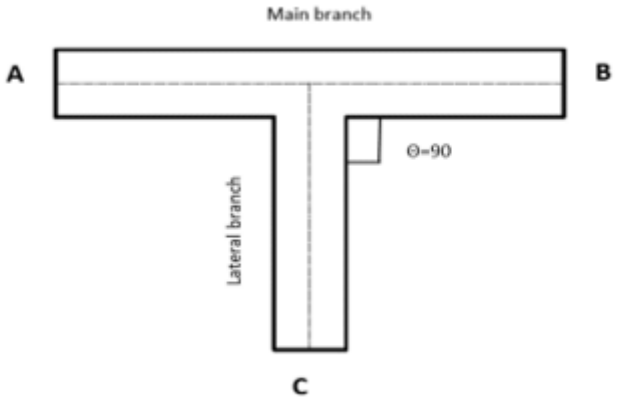

Fig 2. Schematic representation of the T-junction.

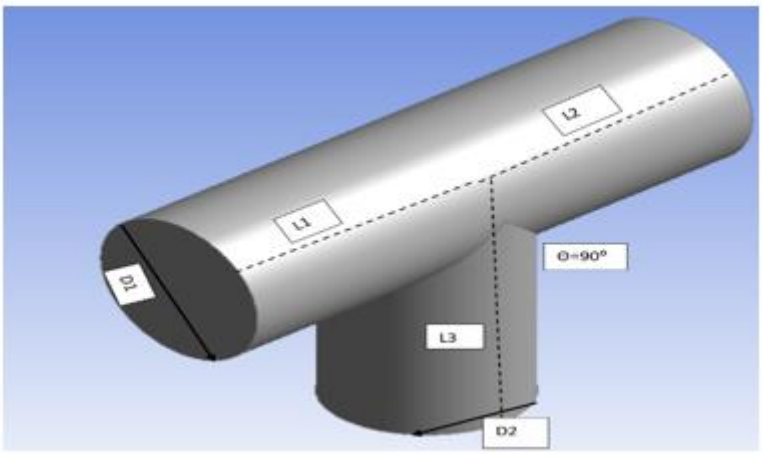

Fig 3. 3D Geometry of T- junction.

The geometry of the fluid domain of the T-junction is created on ANSYS R1 2020 FLUENT to study the fluid flow phenomenon occurring on the fluid in two cases: case1, the fluid flow enters a T junction from branch A and outlet from branch C and B (non-symmetrical dividing). In case 2, the fluid flow enters from the A and C branches and outlet from B (non-symmetrical combining) as shown in Fig 2. The inner diameters D1of the main inlet branch pipe is 0.0254m, also the same value as the inner diameter D2 of the lateral branch pipe. the length of each branch, $L_1=L_2=L_3=$ 0. 04m. The flow arrangement is that of combining and dividing flow in a 90˚T-junction with sharp corners. as shown in Fig 3.

2.2 CFD Mesh Model

To establish the CFD mesh model, the flow zone is divided into several subdomains for meshing. The tetrahedron elements are finer and the number of elements is determined by checking computations. The number of elements is (488747) and the number of nodes is (121790) for non-symmetrical dividing and non-symmetrical combining. The element size is (1mm) with five boundary layers. Calculations are carried out with commercial finite volume code ANSYS R1 2020 Fluent as shown in Fig 4. To checking the mesh by using mesh independence as shown in Fig 5. Reynold's number is calculated at the same place in T-junction for three planes at velocity 0.04 m/s without changing another parameter just element size. Choose this meshing to save time and good accuracy.

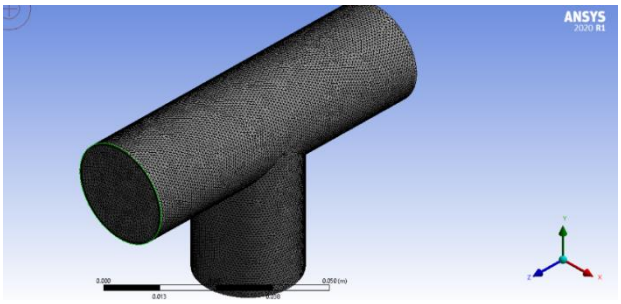

Fig 4. the T-junction meshing.

element size	node	element	skwence	Re1	Re2	Re3
6mm	2010	4393	0.8639	851.8836	977.0119	183.1929
3mm	8384	22922	0.8804	830.9025	959.8225	156.2713
2 mm	21788	69312	0.84866	843.2889	951.9862	135.7705
1.5 mm	43643	154055	0.78561	845.8168	949.4584	135.1133
1.3mm	62470	231223	0.77186	851.8836	945.9194	136.3267
1.2	76470	289938	0.78136	866.2923	952.239	135.6694
1.1mm	95681	373059	0.75457	868.8201	957.5475	138.9556
1mm	121790	488747	0.7971	856.1809	953.7557	136.3772
0.8mm	218718	932770	0.82834	866.7979	963.8671	136.3772
0.7mm	309021	1368403	0.83272	872.8647	959.8225	135.6189

Fig 5. Mesh independent.

2.3 Boundary Condition and Simulation Parameters

The water is employed in the simulations with a constant density of 998.2 kg/m^3 and dynamic viscosity of 0.001003 kg/ms. The fluid is supposed an incompressible flow and constant temperature at 20℃. It is assumed that no slip boundary condition at all the walls. The boundary condition is velocity inlet (upstream), the velocity is uniform, and the boundary condition at the outlet is pressure outlet (downstream) zero-gauge pressure. The second-order upwind scheme is used for the discretization of transport equations for momentum, k, and ε. The pressure values at the faces were interpolated using the standard scheme and the transport equations are solved using the SIMPLE algorithm.

2.4 Governing Equations

The Naiver-Stokes equations are solved for an incompressible flow, the conservation of mass Equation (1), and momentum Equation (2).

$$\frac{\partial u_i}{\partial xi} = 0 \tag{1}$$

$$\frac{\partial \rho u_i}{\partial t} + \frac{\partial \rho u_j u_i}{\partial x_j} = -\frac{\partial \bar{P}}{\partial x_i} + \frac{\partial}{\partial x_j}[\mu\left(\frac{\partial u_i}{\partial x_j} + \frac{\partial u_j}{\partial x_i}\right) - \rho\overline{u_i u_j}] \tag{2}$$

Many researchers have an effort to solve these equations. Naiver-Stokes equations can be solved numerically by using the finite volume method equation (1-2), but the solutions are obtained after making some assumptions and some of them are not stable at high Reynolds number. The k-ε model is one of the most used turbulence models. It includes two transport equations to represent the turbulent properties of the flow. The first transported variable is turbulent kinetic energy k, and the second transported variable is the turbulent dissipation ε. These variables determine the scale of the turbulence and the energy in the turbulence. $\rho\overline{u_i u_j}$ represent the last term of equation (2) as a time average eddy shear stress in the momentum equation, where the molecular diffusion shear stress $\mu\frac{\partial \bar{u}}{\partial x_i}$. The Transport equations of k$-\varepsilon$ model for k.

$$\frac{\partial}{\partial t}(\rho k) + \frac{\partial}{\partial x_i}(\rho k u_i) = \frac{\partial}{\partial x_j}[(\mu + \frac{\mu_t}{\sigma_k})\frac{\partial k}{\partial x_i}] + p_k - p_b \ - \rho\varepsilon - Y_k + S_k \tag{3}$$

And for ε

$$\frac{\partial}{\partial t}(\rho\varepsilon) + \frac{\partial}{\partial x_i}(\rho\varepsilon u_i) = \frac{\partial}{\partial x_j}[(\mu + \frac{\mu_t}{\sigma_\varepsilon})\frac{\partial \varepsilon}{\partial x_i}] + C_{1\varepsilon}\frac{\varepsilon}{K}(p_k + C_{3\varepsilon}p_b\ ) - C_{2\varepsilon}\rho\frac{\varepsilon^2}{k} + S_\varepsilon \tag{4}$$

The turbulent viscosity is modelled as:

$$\mu_t = \rho C_\mu \frac{K^2}{\varepsilon} \tag{5}$$

Production of k

$$P_k = -\rho\overline{\acute{U}_i \acute{U}_j}\frac{\partial U_j}{\partial x_i} \tag{6}$$

$$P_k = \mu_t S^2 \tag{7}$$

S is the modulus of the mean rate-of-strain tensor

$$S = \sqrt{2S_{ij}Sij} \tag{8}$$

k-ε model is only useful in regions with turbulent, high Reynolds number flows. The k- ε model is most used to describe the behavior of the turbulent flow equation from(3-8). The equations contain five adjustable constants in Table1. The standard k -ε model uses values for the constants that are arrived at by comprehensive data fitting for a wide range of turbulent flows:

Table 1. Numerical values of some parameters.

σ_k	σ_ε	$C_{1\varepsilon}$	$C2_\varepsilon$	C_μ
1.00	1.30	1.44	1.92	0.09

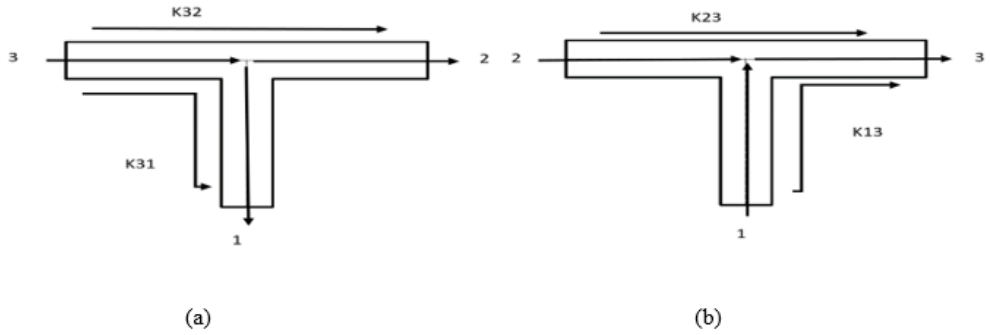

Fig 6. Configurations of flow arrows indicate the direction of flow.

The arrangement of flow through a tee-junction with a straight main pipe is shown in Fig 6. The common branch is 3 (inlet flow) in non-symmetrical dividing, 1 and 2 are outlet branches. Also, the common branch is 3 (outlet flow), 1 and 2 are inlet branches for non-symmetrical combining flow type. The energy equation for the division flow is given by:

$$\mathrm{P_3} + 0.5\rho\mathrm{U_3^2} = \mathrm{Pi} + 0.5\mathrm{U_i^2} + \mathrm{f_i}\,\frac{\mathrm{l_i}}{\mathrm{D_i}}\,0.5\rho\mathrm{U_i^2} + \mathrm{f_3}\,\frac{\mathrm{l_3}}{\mathrm{D_3}}\,0.5\,\rho\mathrm{U_3^2} + \Delta\mathrm{p_{3i}} \tag{9}$$

Also, the energy equation for the combined flow is given by:

$$\mathrm{Pi} + 0.5\rho\mathrm{U_i^2} = \mathrm{P_3} + 0.5\mathrm{U_3^2} + \mathrm{f_i}\,\frac{\mathrm{l_i}}{\mathrm{D_i}}\,0.5\rho\mathrm{U_i^2} + \mathrm{f_3}\,\frac{\mathrm{l_3}}{\mathrm{D_3}}\,0.5\,\rho\mathrm{U_3^2} + \Delta\mathrm{p_{i3}} \tag{10}$$

In which ΔP_{3i} is the energy loss (pressure drop) due to the dividing of flow.

Where $\Delta P_{3i} = (P_3 + 0.5\,\rho U_3^2) - (P_i + 0.5\,\rho U_i^2)$ (11)

in which ΔP_{i3} is the energy loss (pressure drop) due to the combination of flow.

Where $\Delta P_{i3} = (P_i + 0.5\,\rho U_i^2) - (P_3 + 0.5\,\rho U_3^2)$ (12)

The loss coefficient of dividing flow is defined by:

$$(K_d)_{31} = \frac{\Delta P_{31}}{0.5\,\rho U_3^2} \quad (13)$$

The flow rate ratio for

$$(K_d)_{31} = \frac{Q_1}{Q_3} \quad (14)$$

$$(K_d)_{32} = \frac{\Delta P_{32}}{0.5\,\rho U_3^2} \quad (15)$$

The flow rate ratio for

$$(K_d)_{32} = \frac{Q_2}{Q_3} \quad (16)$$

Similarly, the loss coefficient of combining flow is defined by:

$$(K_c)_{13} = \frac{\Delta P_{13}}{0.5\,\rho U_3^2} \quad (17)$$

The flow rate ratio for

$$(K_c)_{13} = \frac{Q_1}{Q_3} \quad (18)$$

$$(K_c)_{23} = \frac{\Delta P_{23}}{0.5\,\rho U_3^2} \quad (19)$$

The flow rate ratio for $(K_d)_{23} = \frac{Q_2}{Q_3}$ (20)

3 CFD Simulation and Result

The losses coefficient is calculated from equations (13), (15), (17), and (19). the pressure drop is calculated from equations (11) and (12). Also, The velocity profile with ansys fluent for combination and division flow type.

3.1 For Non-Symmetrical Dividing

3.1.1 Loss Coefficients Effect of Flow Rate Ratio and Re

Figs. 7 and 8 show the variation of the loss coefficient K_{31}, K_{32} at different inlet Re numbers and flow rate ratios. It is important to note the inlet Reynolds number measured at low to high for turbulent flow. In contrast, compares the loss coefficient with literature at high Re 30000. The loss coefficient is already independent of the Re number. Figs .7a and 8a, show the loss coefficient for dividing flow with flow rate ratio at different Re numbers and comparing with previous work. The K_{31} decreases with an increased flow rate ratio for the present work, G. Can [4] and Costa[8] the same behaviour but the Miller[1]and Crawford [6] are different because of the variations in geometry, the material used, working fluid, and difference in the inlet boundary condition. It shows when the flow rate ratio decreased at 0.8 at non fully develop flow and recirculation occurs near the T-junction. The higher value of flow rate causing a pressure drop. The K_{32} decreased with an increased flow rate ratio for the present work and Crawford [6] opposite that the Miller [1] and G.Can [4]. The difference between the numerical result (present work) and others is because of the different variations in geometry and inlet flow conditions. Figs. 7b and 8b, have shown the variation of loss coefficients with a flow rate ratio at Re 30000. The coefficient minimum value of flow rate of K31 nearly 0.6, k_{32} nearly 0.6 equal 0.998 to 0.274, respectively. Figs. 7c and 8c, depict the loss coefficients with different Re numbers at a flow rate ratio of 0.1. The loss coefficient is decreasing, when increasing in Re because of the increase in the velocity inlet. the circulation of the T- junction and disturbing the coming flow, therefore, the pressure drop is taking place.

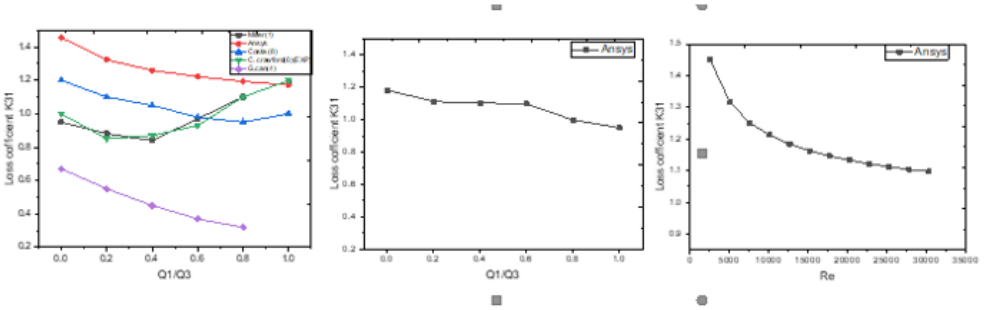

Fig 7. Variation of loss coefficient K_{31} comparison with literature(a) effect flow rate ratio at different Re (b) effect flow rate ratio at Re 30000 (c) effect of different Re at flow rate 0.1.

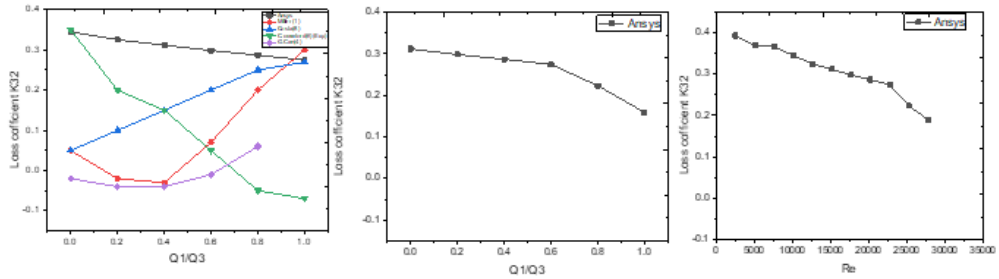

Fig 8. variation of loss coefficient K_{32} and comparison with literature (a) effect flow rate ratio at different Re (b) effect flow rate ratio at Re 30000 (c) effect of different Re at a flow rate ratio 0.1.

3.1.2 Head Losses (Energy Losses)

The minor losses in-branch dividing noticed the pressure drop increased with increased velocity inlet in Figs.9(a), (b) show the pressure drop with inlet velocity due to friction in the pipe and turbulence losses at the junction. The head loss in branches 3-1 reached nearly (800 Pa) at a velocity of 1.2 m/s. Also, the pressure loss in branches 2-3 reached nearly (200 Pa) at the same velocity. The reason for the difference is dependent on the flow rate ratio where Q_1/Q_3 is equal to 0.1, and the pressure drop is normalized by the square of the velocity.

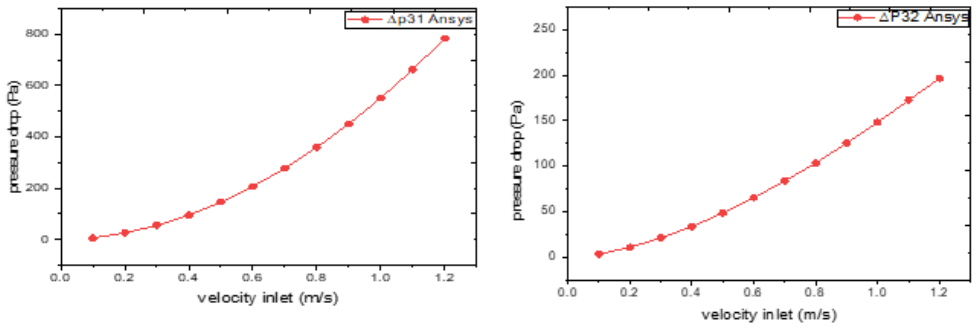

(a) (b)

Fig 9. Head losses(a) the branch 3-1 (b) the branch 3-2.

3.1.3 Velocity Profile

Figs 10 and 11 show the velocity profile and streamline where the velocity inlet is 1.2 m/s and Reynolds number is (30000) for variation of flow rate ratio 0.1, 0.5, and 0.8. In Figs 10a, b, and c noticed that the velocity profile for the value of velocity in branch 3-2 (1.07 m/s) and branch 3-1 (0.142 m/s) at a flow rate ratio 0.1. Whereas the velocity in branch 3-2 (0.6 m/s) and branch 3-1 (0.7 m/s) at flow rate ratio 0.5. Finally, inflow rate ratio 0.8 the velocity in the branch 3-2 (0.321 m/s) and branch 3-1 (0.948 m/s). It is clear the formation of vortex and recirculation in the lateral branch near the junction at a flow rate ratio of 0.5 and increased 0.8, especially in branches 3-1. Small eddies arise in branches 3-1 when increase the flow rate ratio at 0.8 increased the size of eddies.

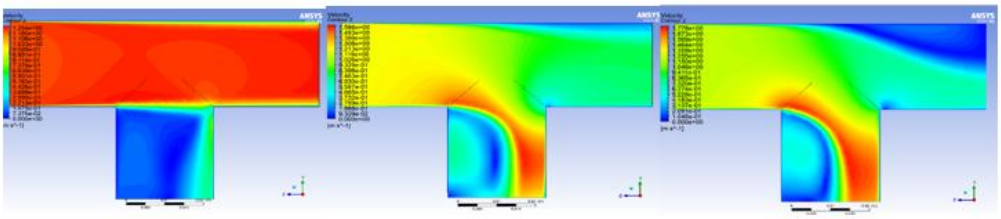

(a) (b) (c)

Fig 10. Velocity profile at different flow rate ratio (a) 0.1(b) 0.5(c) 0.8.

In contrast, in Fig 11(a), (b), and (c) shows the streamline of the same velocity is (1.2 m/s) with different flow rate ratio (0.1, 0.5, and 0.8). The streamline helped to visualize all different possible flow patterns in tee junction. The non-symmetrical dividing shows very little fluid tends to branch 3-1 and maximum fluid moving in the straight pipe branch 3-2 at flow rate 0.1. Also,

the change of flow rate ratio to 0.5 noticed the same mount fluid in the two-leg of the tee causing circulation of the branch 3-1. Lastly, when changing the flow rate ratio to 0.8 the fluid is forced to move to branches 3-1 which causing the small eddies in two branches.

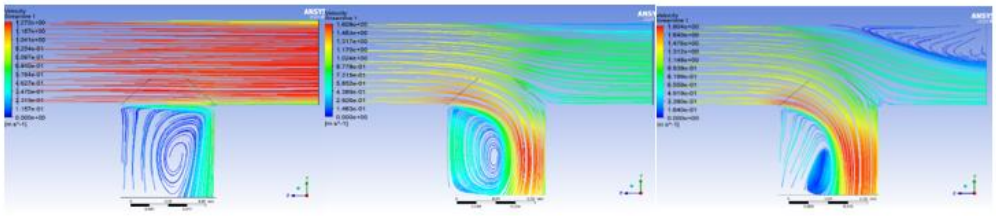

(a) (b) (c)

Fig 11. Streamline at different flow rate ratio (a) 0.1 (b) 0.5 and (c) 0.8.

Fig 12 a, b, and c shows the velocity profile at the different cross-sections of the tee junction pipe at inlet velocity (1.2 m/s), Re (30000), and flow rate ratio 0.5. Fig 12a shows the velocities at various distances of the main pipe. The stable value of velocities at z=0.039,0.03 and 0.02m and the same behaviour to hence non reached to fully developed flow. The maximum value of the velocity at z=0.01 m and centreline midpoint of tee because the separation of fluid affected of developing flow. The profile velocities at the cross-section depict non-fully developed flow because the length of the downstream is not sufficient to reach the fully developed flow. Fig 12b shows the velocity at the different lines in branch 3-1 of the outlet at line y=-0.01m the velocities increased due to the separation of fluid flow in two branches. The velocities at other lines behave the same in maximum value at z= -0.005m but decrease at z=0.0 m due to the circulation in the branch. Fig12c shows the velocity at the different lines in branches 3-2 observed the same behaviour at the line z=-0.01,-0.02,-0.03.-0,039. The higher value of the velocity at y= 0.005 m and returned to a low value due to the small eddies.

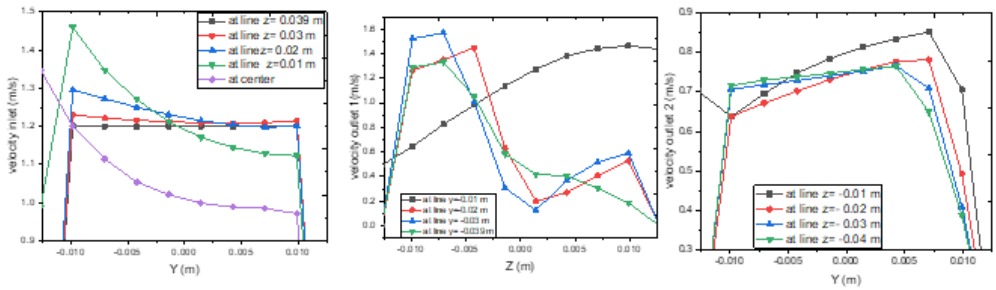

(a) (b) (c)

Fig 12. comparison of the velocity profile at V3=1.2 m/s (a) the inlet branch (b) the outlet branch 3-1 (c) the outlet 2 branches 3-2.

3.2 For Non-Symmetrical Combining

3.2.1 Loss Coefficient Effect of Flow Rate Ratio and Re

Figs. 13 and 14 provided the variation of the loss coefficient K_{13}, K_{23} at different inlet Re numbers and flow rate ratios. In important, when compares the loss coefficient with literature at high Re 30000. Figs.13a and 14a, showing the loss coefficient with flow rate ratio at different Re numbers and comparison with the previous work. The loss coefficient K_{13}, K_{23} decreased with an increased flow rate ratio but in Miller increased. The difference between the loss coefficient when comparing the present work with literature for many reasons is the variations in geometry, the material used, working fluid, and difference inlet boundary conditions. Figs. 13b and 14b, have shown the variation of loss coefficients with flow rate ratio at Re 30000 decreased when flow rate ratio increased. The K_{13}, K_{23} at a flow rate ratio of 0.8 decreases reached at 0.333 and 0.47 respectively. Figs. 13c and 14c, depict the loss coefficient for different Re numbers at a flow rate ratio of 0.5. The K_{13}, K_{23} decrease with an increased flow rate ratio. The generation of eddies and swirl on the outlet causes therefore rotational kinetic energy and increased pressure drop.

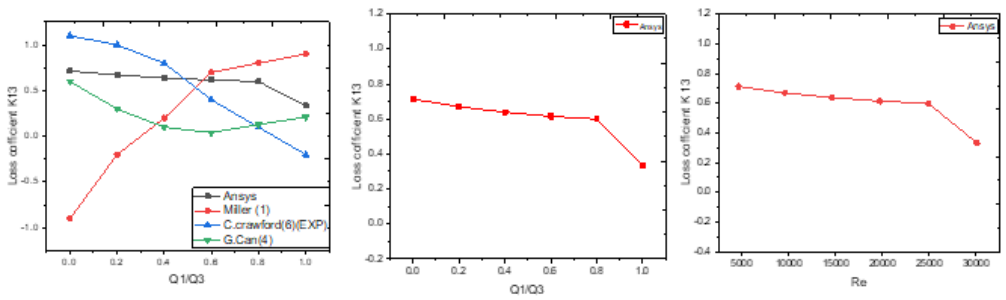

Fig 13. Variation of loss coefficient K_{13} and comparison with literature (a) effect flow rate ratio at different Re (b) effect flow rate ratio at Re 30000 (c) effect of different Re at a flow rate ratio 0.5.

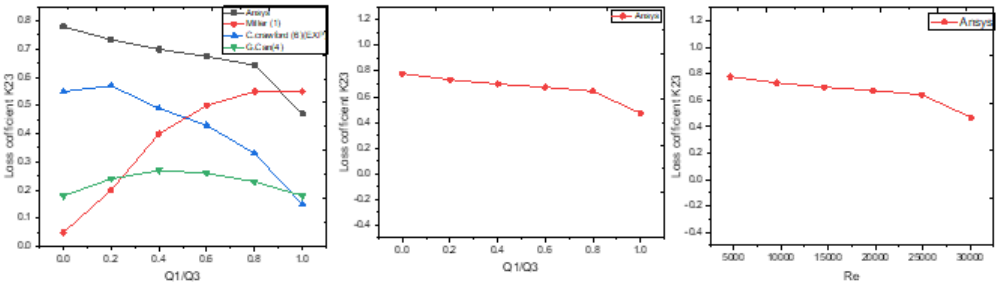

(a) (b) (c)

Fig 14. variation of loss coefficient K_{23} and comparison with literature (a) effect flow rate ratio at different Re, (b) effect flow rate ratio at Re 30000 (c) effect of different Re at a flow rate ratio 0.5.

3.2.2 Head Loss (Energy Losses)

Figs.15 shows the pressure drop (the minor losses) for non-symmetrical combing with inlet velocity observed the pressure drop increases with increased velocity inlet. Also, the pressure drops in branches 1-3 reached nearly (526 Pa) ANSYS at a velocity inlet of 0.6 m/s for two branches. However, the pressure drops in branches 2-3 reached nearly (576 Pa) in ANSYS at the same velocity for two inlets. The reason for the difference is dependent on the flow rate ratio where Q1/Q3 equals 0.5. the higher value of pressure drops at increased velocity towards the outlet.

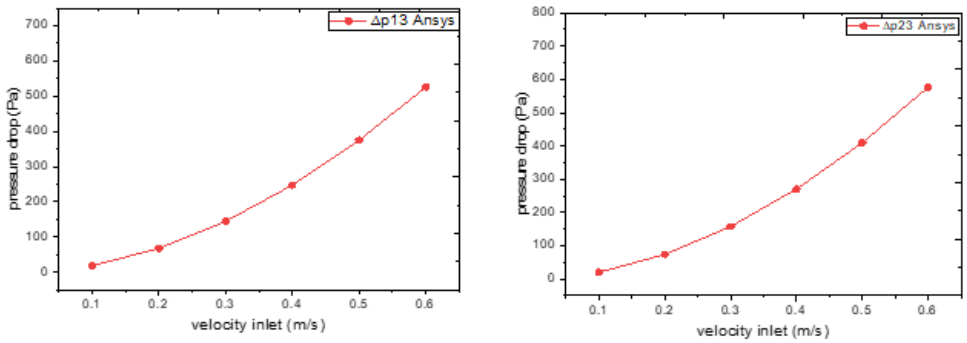

(a) (b)

Fig 15. Head losses(a) the branch 1-3 (b) the branch 2-3.

3.2.3 Velocity Profile

Figs 16a, b, and c show the velocity profile at Re (30000) for variation of flow rate ratio 0.1,0.5,0.8. Noticed that the value of velocity inlet in branch 2-3 (0.9 m/s) and branch 1-3 (0.3m/s) in flow rate ratio 0.1. Whereas the velocity inlet in branch 2-3 (0.6 m/s) and branch 1-3 (0.6 m/s) at flow rate 0.5. Finally, the flow rate ratio 0.8 the velocity in the branch 2-3 (0.2 m/s) and branch 3-1 (1 m/s). It is cleared that the generation of vortex and circulation at a flow rate of 0.5 and increased 0.8, especially in the outlet branch. no separation of flow is observed at a flow rate ratio of 0.1. When the flow rate ratio is high, the flow separation is present in the junction, but the degree of separation is little at a flow rate of 0.8.

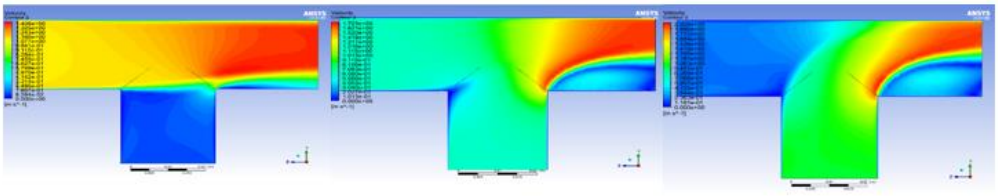

(a) (b) (c)

Fig 16. Velocity profile with different flow rate ratio (a) 0.1 (b) 0.5 (c) 0.8.

On the other hand, in Figs 17a, b, and c manifest the streamline of the same Re (30000) and the outlet velocity (1.2 m/s) with different flow rates (0.1, 0.5, and 0.8). The non-symmetrical combing shows the high-velocity zone observed in the outlet branch of the T-junction. Fig17b illustrates the streamlines change the direction and create a recirculation near the tee junction zone. the velocity is the same for the two branches there is less circulation which there is less pressure loss towards the outlet. Fig 17c at flow rates ratio 0.8 the velocity inlet2 is great than the velocity inlet1 the result in decreasing the pressure towards the outlet.

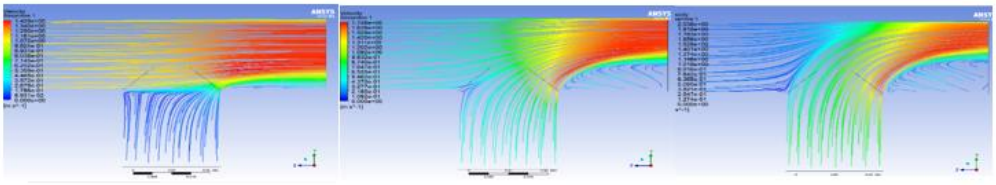

(a) (b) (c)

Fig 17. Streamline with different flow rate ratio (a) 0.1 (b) 0.5 (c) 0.8.

Figs 18 illustrate the velocity profile at different line cross-sections of Tee at Re (30000) and velocity value equal 0.6 for two inlets flow rate ratio 0.5. Fig 18a shows the velocities stable at line z= 0.039, 0.03, and 0.02 m non reached to fully develop flow but increased at line z= 0.01 and centerline because of reached to T-junction. The velocity at the centreline is higher when merged with velocity from inlet 2. Fig 18b shows the velocities at the different lines at inlet 2. the velocities stable at line y= -0.039, -0.03, and -0.02 m the same with inlet 1. Fig 18c represents the velocities of the outlet at the different lines it clears the raised velocity at line z= -0.02, -0.03, and-0.039 m due to merge the two inlets. Line z= -0.01 The profile velocities at

the cross-section depict non-fully developed flow because the length of the downstream is not sufficient to reach the fully developed flow.

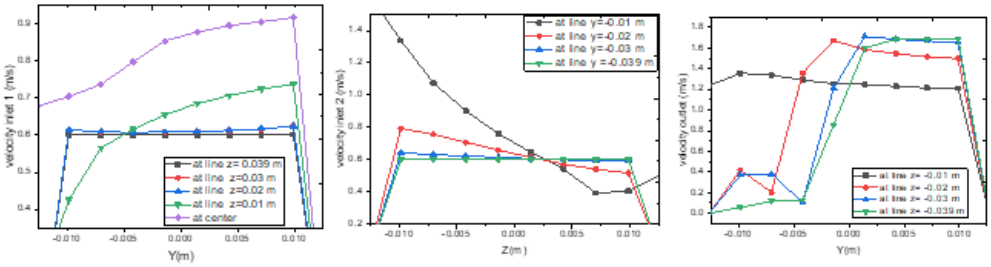

(a) (b) (c)

Fig 18. Comparison of the velocity profile at V_3=1.2 m/s (a) the inlet 1 branch (b) the inlet 2 branch (c) the outlet branch.

4 Conclusion

The predicted the pressure loss coefficient, and pressure drop, velocity profile in T-junction with the turbulent flow with a sharp edge. Studied two cases the non-symmetrical dividing and non-symmetrical combing for different flow rate ratios and Reynold number with area ratio equal one. The comparison of numerical results with literature work. The pressure drops increases with an increase in the velocity inlet for two cases of flow. The loss coefficient was dependent on the flow rate ratio. In the non-symmetrical combing, the velocity in the outlet branch is high with formation recirculation. The non-symmetrical dividing the small eddies and recirculation with increased flow rate to 0.8 in branch 1-3. Due to recirculation of flow from a branch pipe, the value of the pressure loss coefficient K_{23} for branch pipe was higher than K_{13} for straight pipe.

Nomenclature

L1, L2, L3 (m)	length of pipe 1, 2 and 3	A(m^2)	cross-section area
D1 (m)	diameter of the main pipe	D2 (m)	diameter of branch pipe
$C_1\varepsilon$,$C_2\varepsilon$, C_k (-)	stander K- epsilon model constants	K (m^2/s^2)	turbulent kinetic energy
Q (m^3/s)	flow rate	t (s)	time
Re (-)	Reynolds number	P_k (-)	production of K
S (-)	modulus of the mean rate of the strain tensor	P (Pa)	pressure

K_d (-) pressure loss coefficient for dividing (3-2), (3-1)	K_c(-) pressure loss coefficient for combing (2-3), (1-3)
P_b (-) effect of buoyancy	u_i (m/s) mean velocity ith component
u (m/s) velocity (mean x-component)	v (m/s) velocity (mean y-component)
U (m/s) bulk velocity	$\bar{u}_i$ (m/s) velocity (fluct.ith component)
Δp (Pa) different pressure	ρ (kg/m^3) density
μ (kg/ms) dynamic viscosity	μ_t (kg/ms) turbulent viscosity
α (-) energy shape factor	ε (m^2 /s^2) turbulent dissipation rate
σ_k (-) turbulent prandtl of K	$\sigma\varepsilon$ (-) turbulent prandtl of ε

References

[1] D. Miller, *Internal Flow Systems by Donald Stuart Miller (z-lib.org)1984.pdf*.

[2] A. Marc Serre, ~ A. Jacob Odgaard, z Member, ASCE, and Rex A. Eider, 3 Fellow, "ENERGY LOSS AT COMBINING PIPE JUNCTION," vol. 120, no. 7, pp. 808–830, 1994.

[3] F. Z. Sierra-Espinosa, C. J. Bates, and T. O'Doherty, "Turbulent flow in a 90°pipe junction. Part 2: Reverse flow at the branch exit," *Comput. Fluids*, vol. 29, no. 2, pp. 215–233, 1998, doi: 10.1016/S0045-7930(99)00005-5.

[4] G. Gan and S. B. Riffat, "Numerical determination of energy losses at duct junctions," *Appl. Energy*, vol. 67, no. 3, pp. 331–340, 2000, doi: 10.1016/S0306-2619(00)00026-X.

[5] K. Oka, "Energy Losses at Tees With Large.pdf," *J. Fluids Eng.*, 2005.

[6] N. Crawford, "Pressure Losses at Bends and Junctions .pdf," 2005.

[7] J. Pérez-García, E. Sanmiguel-Rojas, J. Hernández-Grau, and A. Viedma, "Numerical and experimental investigations on internal compressible flow at T-type junctions," *Exp. Therm. Fluid Sci.*, vol. 31, no. 1, pp. 61–74, 2006, doi: 110.1016/j.expthermflusci.2006.02.001.

[8] N. P. Costa, R. Maia, M. F. Proença, and F. T. Pinho, "Edge effects on the flow characteristics in a 90 deg tee junction," *Journal of Fluids Engineering, Transactions of the ASME*, vol. 128, no. 6. pp. 1204–1217, 2006, doi: 10.1115/1.2354524.

[9] P. R. Vasava, "Fluid Flow in T-Junction of Pipes," 2007.

[10] Mohammed .A. Abdulwahida, Prof. Niranjan .K. Injetib,Ass. Prof. Sadoun. F. Dakhil, "Numerical prediction of pressure loss of fluid in a T-junction," *Int. J. Energy Environ.*, vol. 4, no. 2, pp. 253–264, 2013.

[11] Mohammed .A.Abdulwahida, Prof. Niranjan .K. Injetib, Ass. Prof. Sadoun Fahad Dakhil, "CFD Simulations and Flow Analysis Through a T-Junction Pipe," *Int. J. Eng. Sci. Technol.*, vol. 4, no. 7, pp. 3392–3407, 2012.

[12] G. Paál and F. T. Pinho, "Numerical predictions of turbulent flow in a 90° tee junction," no. May 2014, 2003.

[13] C. S. M. Gajbhiye1, A.K. Chaturvedi2, S.S. Sawant1, S.N. Gosavi1, H.A. Kulkarni1, "CFD SIMULATIONS OF FLOW AND PRESSURE DROP IN T-JUNCTION.pdf," 2015.

[14] Y. B. Lukiyanto, I. N. G. Wardana, W. Wijayanti, and M. A. Chiron, "Flow visualization pattern on sharp edge T-junction through dividing flow channel," *Appl. Mech. Mater.*, vol. 493, pp. 62–67, 2014, DOI: 10.4028/www.scientific.net/AMM.493.62.

[15] J. Ŝtigler, R. Klas, M. Kotek, and V. Kopecký, "The fluid flow in the t-junction. The comparison

of the numerical modeling and PIV measurement," *Procedia Eng.*, vol. 39, no. December, pp. 19–27, 2012, doi: 10.1016/j.proeng.2012.07.003.

[16] M. D. Bassett, D. E. Winterborne, and R. J. Pearson, "Calculation of steady flow pressure loss coefficients," vol. 215, pp. 861–881, 2016.

[17] N. A. Ferede, "Numerical analysis and CFD simulation of fluid flow in T- Junction pipe By using ANSYS CFX," vol. 10, no. 10, pp. 504–513, 2019.

Seismic Analysis of the Steel Frame with Rubber-Sleeved Bolt in the Column-Base Connections

Teeba A. Jassim[1], Amer M. Ibrahim[2], Bozhou Zhuang[3], and Ibrahim A. Ali[4]
{teebalii94@gmail.com[1], amereng76@yahoo.com[2], zbz@tongji.edu.cn[3],
ibrahimabbas790@gmial.com[4]}

Department of Civil Engineering, College of Engineering, University of Diyala, Iraq[1,2,4]
Department of Bridge Engineering, Tongji University, Shanghai 200092, China[3]

Abstract. When earthquakes occur, catastrophic damage occurs, and hundreds of people are killed. It became necessary to find an effective method to reduce the seismic effect on the Structure. This is done by using rubber-sleeved bolts in the connection of the steel frame. This study is a numerical study that contains four models that were analysed in the ABAQUS program. The difference between these models is the presence of rubber at the base of the model only and the presence of rubber at the base of the model and in the connection between the column and the beam. The results showed that the residual displacement, cumulative energy, drift ratio, and ductility index of the model containing rubber in the base connection and the beam-column connection increases by (2.536,46.029, 155.613, and 155.626) % respectively, compared to the model that contains rubber in the base connection only.

Keywords: Steel Frame, Earthquake, Rubber, Damping, Connection.

1 Introduction

When an earthquake occurs, it results in a ground movement that travels in the form of a wave in the earth's crust, then this wave movement is transmitted to the base of the structure, where this wave movement is in two directions, a horizontal direction, and a vertical direction [1]. Earthquake is also defined as a geophysical phenomenon, formed in the form of waves, and these waves result in movement in the earth's crust up and down, as this movement resulting from the seismic wave moves to the foundation of the structure, then this movement resulting from the seismic wave works on violation of the vertical movement of the structure and this results in a failure in the foundation of the structure [2]. Therefore, it became necessary to study the effect of the seismic wave on the buildings and how to reduce the effect of the seismic wave on the buildings. For any building or structure to be earthquake-proof, its foundation must be resistant to sideways loads. The load will be lesser if the building is light. To reduce the load of the building, you need to focus on the top as the maximum weight is on the roof. However possible, the roof should be made of extremely lightweight material. There are several methods to reduce the risk of earthquakes on buildings among the most prominent of these methods are shear wall and steel bracing.

IMDC-IST 2021, September 07-09, Sakarya, Turkey
Copyright © 2022 EAI
DOI 10.4108/eai.7-9-2021.2314884

Fadhil, H. et al. (2018) studied the use of steel corrugated shear walls in seismic impact resistance. Models for this study were tested under seismic load to note their effect on the performance of the shear wall under the seismic influence [3].
Shamivand, Abbas et al. (2019) studied an aside strengthening system that is in the form of a loop and is called Shami lateral bracing system (SLBs)). This system provides a new component that has a good ability to dissipate energy in addition to giving sufficient flexibility to the system [4]. However, these methods require a large amount of time and cost, in addition to the fact that these methods result in a high weight based on the structure [5].
This study suggests the use of rubber-sleeved bolts that is affordable in addition to being easy and quick to install compared to other energy dissipation methods. This study is a numerical study, which includes the use of rubber-sleeved bolts in the shear-tap that connects between the beam and the column in the steel frame and using the rubber-sleeved bolts in the base connection of the steel frame. This study aims to develop the connection of the steel frame using the rubber-sleeved bolts, as the rubber-sleeved bolts absorb the energy resulting from the seismic effect, increases the bearing load of the steel frame, and increases the amount of displacement.

2 FEM and Validation

2. 1 Validation of the Experimental Models

Relying on the researcher's experimental models [6] (suhab-2020), the finite element models were analysed, using the (ABAQUS-2017) [7] program to verify the validity of these results. This part includes the analysis of two experimental models tested under inclined quasi-static cyclic load. The design of the models was based on (AISC-14Th) [8]. Each model consists of one beam (IEP160) with a depth of 1000 mm. And two columns HW125×125 with a depth of 1500 mm. The beam is connected to the column on each side using a shear tap, with dimensions of 110 x 90 x 8 mm. The shear tap is connected to the beam by a one-line of bolts and each column by a line of the weld. The right column support of the model is pin-support, and the left column support is fixed-support, whereby the right column is strengthened by 4 stiffeners that in turn strengthen the column to prevent failure and focus the failure position on the bolts of the connection between the column and the beam.
The diameter of the bolt used is 7 mm, the diameter of the bolt holes in the beam and the shear-tap is 8.5 mm for the first model, which is the reference model, and the diameter of the bolt holes in the second model in which the connection bolts between the beam and the column are rubber-sleeved is 17. 5 mm.
Where the symbol for the first experimental model is the reference model (I.0.STD.1), as this model does not contain rubber-sleeved bolts in the beam-column connection. The second model is a symbol (I.150.LSL.2), which contains rubber-sleeved bolts in the beam-column connection by 150% of the bolt diameter, where the diameter of the rubber-sleeved bolt becomes 17.5 mm, and the thickness of the rubber is 5.25 mm on each side of the rubber-sleeved bolt. The shape of the numerical model, the experimental model, and the shape of the rubber-sleeved bolts are shown in Fig 1.

B: FEM model A: experimental model C: Details of the rubber-sleeved bolts.

Fig. 1. The FE Model and Experimental model.

The effect of each material and geometrical proprieties is considered. The first important geometric condition is the selection of element shapes. During this study, different orders and types of the element were tested in the FEM models until arriving at the element order and that type gives results that are close to the results of the researcher's [6] (suhab-2020) experimental analysis. The solid type sections are used because the thickness of the section, compared to other dimensions, is not small. In addition, first-order reduced integration C3D8R was selected for all the frame modelling.

2. 2 The Material properties

For the Poisson ratio, young's modulus, and density, hardening-isotropic material were used in the elastic zone. The ABAQUS program required input data such as elastic modulus, density, and Poisson's ratio as illustrated in Table 1 for the rubber and the steel components of the model.

Table 1. The Mechanical properties for Components Model [6].

The Sections	Density	Elastic Modulus MPa	Elongation Ratio
Steel-Beam	7.83 e -09	1.95 e +05	0.3
Steel-Column	7.83 e -09	1.87 e +05	0.3
Shear-Tap	7.83 e -09	2.11 e +05	0.3
Steel-Bolt	7.83 e -09	2.75 e +05	0.3
Steel-Washer	7.83 e -09	2.75 e +05	0.3
Rubber	1.52 e -09	91.120	0.5

In simulation programs (the ABAQUS program), the values of the engineering strain and stress data are not used, but they are converted to true values by using the following equations [6].

$$\sigma_{True} = \sigma_{Engineering} * (1 + \varepsilon_{Engineering}) \quad (1)$$

$$\varepsilon_{True} = \ln(1 + \varepsilon_{Engineering}) \quad (2)$$

$$\varepsilon_{Plastic} = \ln(1 + \varepsilon_{Engineering}) - \left(\frac{\sigma_{True}}{E_{Modulus}}\right) \quad (3)$$

The true strain and stress values that were converted through the above equations and based on the engineering strain and stress values that were used to define materials in the ABAQUS program are shown in Table 2.

Table 2. The True Value of the Properties [6].

Steel Section	Yield-stress MPa	Plastic-Strain mm/mm
Steel Beam	250.4375	0
	400.7	0.301135883
Steel Column	250.4375	0
	400.7	0.283362250
Shear Tap	312.546	0
	422.7385	0.283242381
Steel Bolt	588.6	0
	648	0.073721041

2. 3 Boundary condition and mesh design

At the beginning of the meshwork, the sections must be first divided into pieces for these to be uncomplicated sections. In other words, the program does not understand the non-divided sections because their mesh is complex and thus does not give correct results.

The First order-hexahedral cubic elements were used for regularly shaped regions of model mashing. The mash size for columns, beam, stiffeners, shear tap, nut, bolt, rubbers, and washers are (100,50, 100, 25, 10, 10, 10, and 10) mm respectively.

The type of load used in this study is an inclined cyclic load that was applied depending on the protocol like the loading protocol in the experimental program. In all models, the load is placed on the top and side edges of the right and left columns, also, boundary conditions consisted of a pin and fix, as shown in Fig 2.

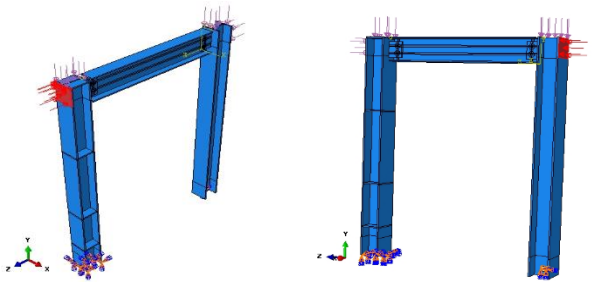

Fig. 2. Load Case and boundary conditions in the ABAQUS Program.

2. 4 The Validation Results

Through the numerical representation of the model and then comparing the form of failure and the results of the numerical analysis with the experimental test, it was found that there is a great convergence in the form of failure between the experimental and numerical models.
Whereas in the experimental model, the failure is concentrated on one area, where is the connection between the column and the beam, a fracture occurs in the bolts for most models which is induced a fracture of the rubber covering the bolt. To clarify the form of convergence, the shape of failure in the experimental and numerical test models is presented in Figure 3.

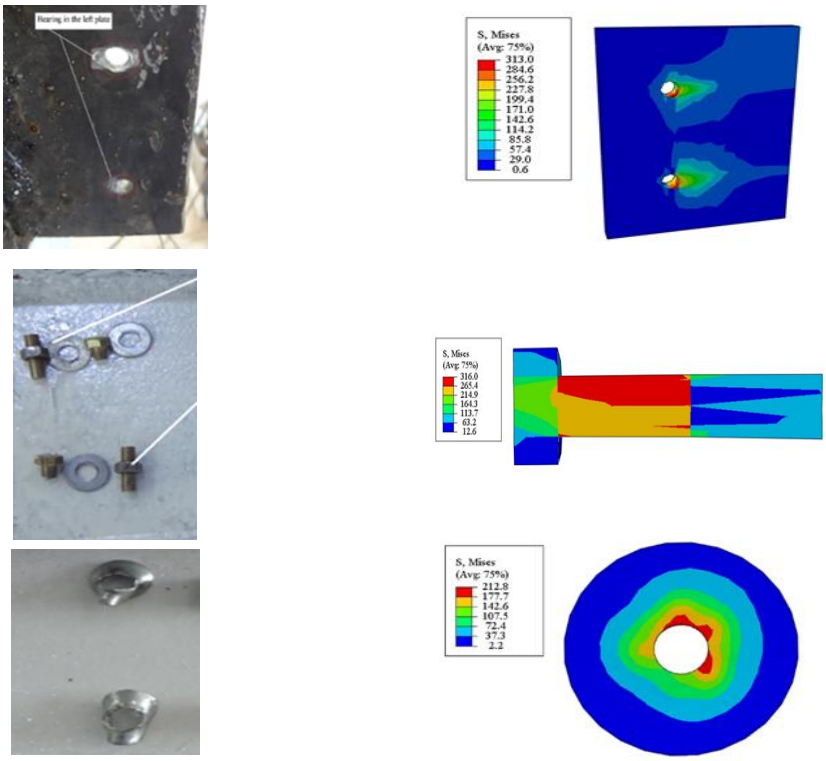

Fig. 3. Failure Shap of Experimental and Numerical Models.

When comparing the results obtained from the numerical program with those obtained from the experimental results, the envelope curve is shown in Figs 4 and 5.

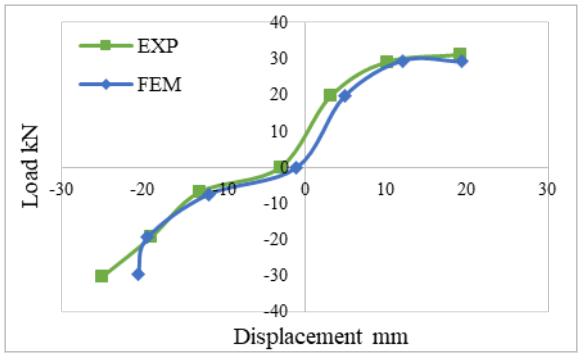

Fig 4. Envelope Curve for Experimental and Numerical Analysis of the I.0.STD.1 Model.

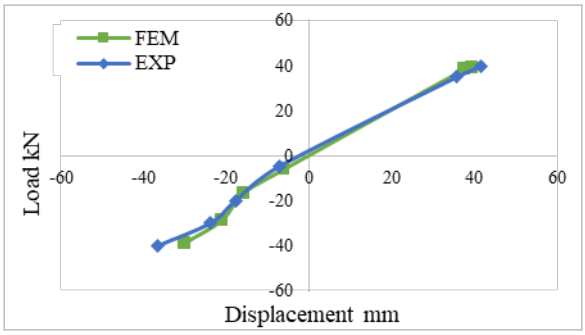

Fig 5. Envelope curve for Experimental and Numerical Analysis of the I.150.LSL.2 Model.

From these figures, we can prove that the result convergence very largely. In addition, this convergence, which is shown in Table 3, includes the results of the experimental and numerical models in terms of displacement and loading.

Table 3. Displacement and Load Result for Experimental and Numerical Analysis.

Model name	Load kN		The ratio of convergence of load (FEM/EXP)	Displacement mm		Ratio of convergence of displacement (FEM/EXP)
	FEM	EXP		FEM	EXP	
I.0.STD.1	29.187	31.053	0.939	19.347	19.265	1.00
I.150.LSL.2	39.087	39.927	0.978	39.478	41.468	0.952

3 The Case Study

In this study, two models were tested, each model contains 2-bolts in the beam-column connection and 8-anchors bolts in the base connection. The first model contains rubber around all base connection bolts at 50% of the bolt diameter. The second model contains rubber around the connection bolts between the column and the base at 50% of the diameter of the bolt and contains rubber at 150% of the diameter of the bolt connection between the beam and the column. The models of this group were tested under inclined cyclic loads. The effects of residual displacement, cumulative energy, equivalent viscose damping, drift, and ductility index are discussed. Models with rubber in the connection between the beam-column and the base connection, the role of the rubber was evident by increasing the displacement and load value of the models. The sections are designed to depend on the AISC Manual. The reason for the use of the inclined cyclic load, when the structure is exposed to seismic effect, the beam-column connection is subjected to shear force, moment, and axial forces. Based on what the researcher [9] mentioned, who says that these forces lead to a rotation in the connection, and to represent this rotation and this effect, the inclined cyclic load was used, in which one of its components is the vertical component that results in a moment in the beam-column connection resulting from the drift that it gets between the bolt line and the welded. The load applied in this type of loading is at an angle of 10 degrees. The load is shed on the upper side end of both columns, which represents the horizontal component, while the vertical component is shed on the upper end of both columns of the model. The shape of the model that is tested in the ABAQUS / CAS (2017) program is shown in Fig 6. Section (A) shows the shape of the rubber at the base of the model, where this rubber works as the damper which is used in the bases of models to dampen seismic intensity.

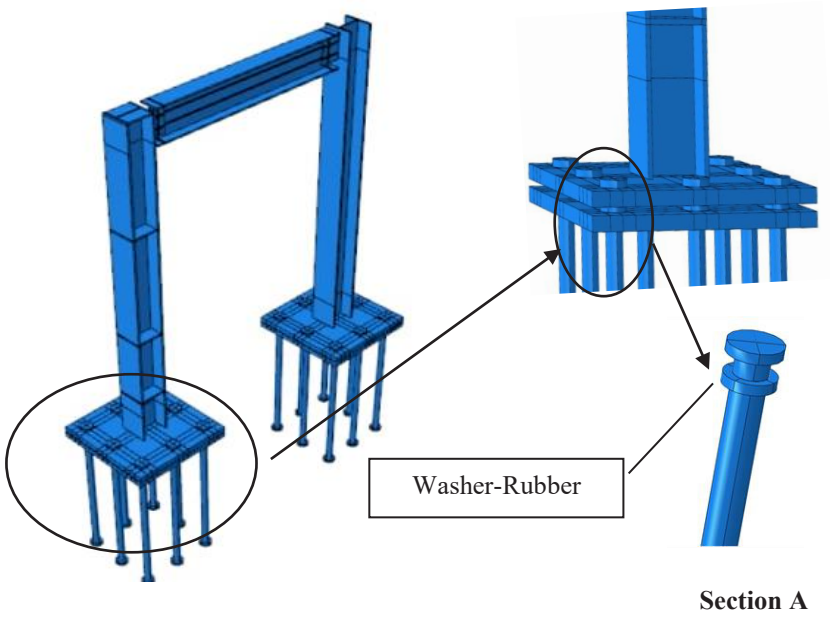

Fig. 6. The Washer-Rubber in the Base of the Model.

The symbolize of all models that study in this paper is listed in Table 4.

Table 4. The Symbolize of all models that study in this paper.

No.	Name of the Models	Type of load	Number of Bolts		Rubber ratio%		Location of Rubber
			Shear Tap	Base Plate	Shear Tap	Base Plate	
1	RF.I.2B.50A.	Inclined-cyclic-load	Two bolts	Eight anchor bolts	0%	50%	Rubber around 8 anchor bolts in the base plate only.
2	F.I.2B.50A.150B.				150%	50%	Rubber around 8 anchor bolts and 2 bolts in the shear tap connection

4 The Numerical Results

4. 1 The Residual displacement

These curves are represented by special equations where the equation for the x-axis represents the ratio of the highest displacement value in each cycle of the hysteresis curve divided by the yield displacement value, which is the value from which the model shifts from the elastic stage to the inelastic stage, where this ratio is called the displacement ductility, as the text of the equation is explained below:

$$\text{Displacement Ductility} = |dm/dy| \quad (4)$$

Where: d_m: Maximum displacement in each cycle of the hysteresis curve.
dy: Yield displacement[10].

While the y-axis represents a ratio of the residual displacement index represented by the value of the intersection of the curve of each cycle of the hysteresis curve with the x-axis divided by the yield displacement value, where this ratio is called the residual displacement index, as the text of the equation is explained below, [10]:

$$\text{Residual displacement ratio} = |dr/dy| \quad (5)$$

Where: dr:- Residual displacement.
dy:- Yield displacement.

Through the above equations, comparison curves were made.

In this section, the model that contains the rubber at the base connection is compared with the model that contains the rubber at the base connection and in the beam-column connection. The residual displacement of the two models of this study compared with experimental models is shown in Fig 7.

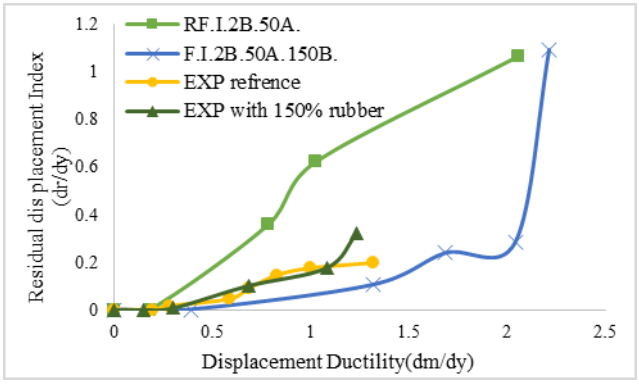

Fig.7. Displacement Ductility versus Residual Displacement Index.

The presence of rubber only at the base connection increased the residual displacement by 447.692% compared to the reference experimental model that does not contain the rubber and increased the residual displacement by 233.75% compared to the experimental model that contains the rubber in beam-column connection.

The residual displacement of the model containing rubber in the base connection and the beam-column connection increases by 2.536% compared to the model that contains rubber in the base connection only, increase by 242.438% compared to the experimental model that contains rubber in beam-column connection only, and increases by 462.051% compared to the reference experimental model that does not contain the rubber.

The presence of rubber in the two most influential regions, the beam-column connection and the base connection of the model increased the flexibility of the model due to them that the displacement value after the elastic stage is large, then this means that the model will be exposed to plastic deformations, and these plastic deformations will continue to the stage after the end of the seismic effect.

These plastic deformations occur in the places of greatest damage, which are in the beam-column connection because of these areas it is made up of more than one material, such as bolts, plate, beam, net, washer, and so on from the materials in the connection, so each connection material has a different behaviour than the other material in the same area, so the level of potential damage in these dangerous areas cannot be assessed. We work to reduce future damage and give rise to sudden failure.

4. 2 The Cumulative Energy

A relationship between displacement ductility and cumulative energy is drawn to see how much energy the model would dissipate if the rubber were used in the base connection and beam-column connection. The energy for the model is counted by calculating the area under the envelop curve according to the researcher [10]. Displacement ductility represents the maximum displacement value at each hysteresis curve divided by yield displacement [11]. The cumulative energy of the two models of this study is compared with experimental models and is shown in Fig 8.

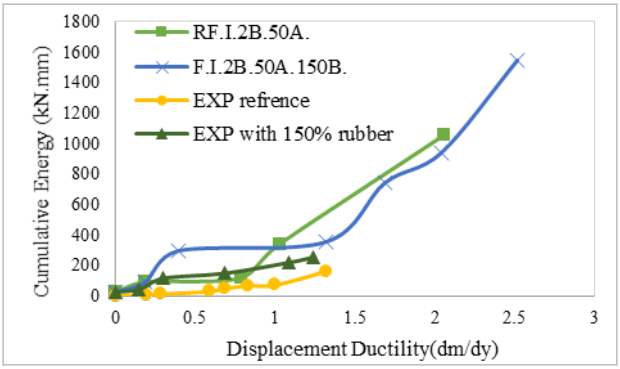

Fig.8. Displacement Ductility versus Cumulative Energy.

All models behave the same at a displacement ductility value of about 0.25. After this value 5 of displacement ductility, the variation in the behaviour of the models begins to appear. The rate of cumulative energy of the model containing the rubber in the base connection is 564.839% higher compared to the reference experimental model and 313.140% higher as compared to the experimental model containing the rubber in the beam-column connection.
The cumulative energy of the model containing the rubber in the base connection and the beam-column connection is 46.029% higher compared to the model containing the rubber in the base connection, 503.306% higher as compared to the experimental model containing the rubber in the beam-column connection, and 870.860% higher compared to the reference experimental model. The reason that the model that contains rubber in the base connection and the beam-column connection has a higher cumulative energy is that this model gives a load of 64.704 kN and a displacement of 222.455 mm, and the model that contains rubber in the base only gives a load of 29.423 kN and a displacement of 86.841 mm, since it depends the cumulative energy depends on the value of the maximum load and the displacement of the model, so the model that contains the rubber at the base connection and the beam-column connection has higher cumulative energy. The presence of rubber at the base connection and the beam-column connection gives a high displacement of the model because the presence of rubber dissipates energy and stress and makes it spread over a larger area and that the presence of rubber at the base of the model increases the flexibility and reduces the stiffness, so when the flexibility increases, it increases the ability of the model move more to the right and left.

4. 3 The Equivalent Viscous Damping

Damping is defined as the amount of loss in system energy, and that this loss results from the energy that may be internal or external, such as friction energy. A relationship between displacement ductility and equivalent viscous damping is drawn to see damping properties. Equivalent viscous damping was calculated using the following relationship [11]:

)(6 $$\xi_{eq.} = \frac{1}{4\pi} * \frac{\mathbf{E_{cumulative}}}{\mathbf{E_{elastic}}}$$

Where:
Cumulative energy.$\mathbf{E_{cumulative}}$
$\mathbf{E_{elastic}}$: Elastic energy.

The equivalent viscous damping of the two models of this study compared with experimental models is shown in Fig 9.

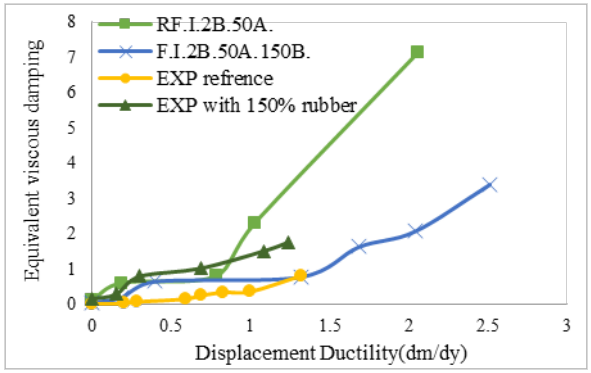

Fig. 9. Displacement Ductility versus Equivalent Viscous Damping.

The equivalent viscous damping is about 1 during the elastic response of all models and then increased to approximately 7.126 in the model that containing rubber in the base connection. The equivalent viscous damping is 807.771% higher in the model that containing rubber in the base connection than the reference experimental model. Also, the equivalent viscous damping is 308.133% higher in the model that containing rubber in the base connection than the experimental model that contains rubber in the beam-column connection only. Also, the equivalent viscous damping is 110.704% less in the model that containing rubber in the base connection and beam-column connection than the model containing rubber in the base connection only. Also, the equivalent viscous damping is 93.699% higher in the model that containing rubber in the base connection and beam-column connection than the experimental model that contains rubber in the beam-column connection only, and 330.828% higher in the model that containing rubber in the base connection and beam-column connection than the reference experimental model. The equivalent viscous damping of the model that contains rubber in the base connection is higher than the model that contains rubber in the base connection and beam-column connection because the cumulative energy in the elastic phase of the model that contains rubber at the base connection is 223.171% less than the cumulative energy in the elastic phase of the model that contains rubber in the base connection and beam-column connection.

4. 4 The Drift ratio

The ratio of the difference between the displacement values of two stories and the division of these two displacements by the height of this story is called the drift ratio. For the multi-story buildings, the difference between the displacements of the two-story is divided this different on the height of the story. As for one-story buildings, which areas in our study, we divide the greatest displacement of the model by the height of the whole model, which is the height of the column.

In Table 5, the drift values are calculated for two models of this study tested under inclined cyclic load and compare with the drift ratios of experimental models.

Table 5. The Drift of the Models that Contains Rubber in Base Connection and Connection that Tested under Inclined Cyclic Load.

Model name	($\delta_y$mm)	Yield drift ($\delta_y/1500$)	($\delta_u$mm)	Ultimate Drift ($\delta_u/1500$)
EXP. reference	18.98	0.012	19.2647	0.0128
RF.I.2B.50B.	42.218	0.0282	86.841	0.0579
Exp. With 150% rubber	32.29	0.021	41.468	0.0277
F.I.2B.50A.150B.	100.419	0.0669	222.455	0.148

δ_y: Yield displacement at yield load,δ_u: Ultimate displacement

By observing the results, the drift of the model containing the rubber in the base connection is 352.343% higher compared to the reference experimental model and 109.025% higher as compared to the experimental model containing the rubber in the beam-column connection. The drift of the model containing the rubber in the base connection and the beam-column connection is 155.613% higher compared to the model containing the rubber in the base connection and 434.296 % higher as compared to the experimental model containing the rubber in the beam-column connection. The drift value of the model that contains the rubber in the base connection and the beam-column connection is higher than the drift value of the model that contains the rubber at the base connection only because the model that contains the rubber in the base connection and the beam-column connection give high displacement than the model containing the rubber in the base connection only the drift of the model that containing the rubber in the base connection and the beam-column connection give high drift.

4. 5 The Ductility Index

It is defined as the ability of a material to have a plastic deformation without failure in this structure. Mathematically, it is defined as the ratio of drift at the highest load to a ratio of yielding drift of the reference model. Whereas the reference model for this group is the model that contains rubber in the base connection only. A material with high ductility will be deformed without fail, and this material is called the ductile material, while a material that is of little ductility is referred to as a brittle structure and early failure occurs in this structure before the deformation becomes of high value compared to the ductile material. In Table 6, the ductility index is calculated for two models of this study tested under inclined cyclic load and compare with the ductility index of experimental models.

Table 6. The Ductility Index of the Models that Contains Rubber in Base and Connection that Tested under Inclined Cyclic Load.

Models name	Yield drift Δ_y	ultimate drift Δ_u	Ductilityindex Δ_u/Δ_{yr}
EXP. reference	0.012	0.0128	1.0667
RF.I.2B.50B.	0.0282	0.0579	2.053

EXP. With150% rubber	0.021	0.0277	2.308
F.I.2B.50A.150B.	0.0669	0.148	5.248

Δ_{yr}: Yield drift of the reference model, Δ_u: Ultimate drift.

The presence of rubber has a great effect on increasing the ductility index, the ductile index of the model containing the rubber in the base connection is 92.463% higher compared to the reference experimental model and 12.421% less as compared to the experimental model containing the rubber in the beam-column connection only. The ductile index of the model containing the rubber in the base connection and the beam-column connection is 155.626% higher compared to the model containing the rubber in the base connection and 127.383% higher as compared to the experimental model containing the rubber in the beam-column connection only. The presence of rubber at the base connection and in the beam-column connection increased the ductility of the model because the value of ductility depends mainly on the drift value of the model, and the model that contains the rubber in the base connection and the beam-column connection gives a drift of 46.064% higher than the model that contains the rubber in the base connection only, so the ductility of the model that contains the rubber in the base connection and the beam-column connection is high due to the presence of rubber in the connection, which led to an increase in the portability of the model in movement and the distribution of stresses in the connection over larger areas.

5 Conclusions

By testing the models under inclined cyclic load, the following was concluded:

1. The presence of rubber in the two most influential regions, the beam-column connection and the base connection of the model increased the flexibility of the model and then increase the residual displacement of the model.
2. The presence of rubber in the beam-column connection and the base connection of the model makes the displacement value after the elastic stage is large, then means that the model will be exposed to plastic deformations, and these plastic deformations will continue to the stage after the end of the seismic effect.
3. The presence of rubber in the beam-column connection and the base connection of the model increases the flexibility and reduces the stiffness, so when the flexibility increases, it increases the ability of the model to move more to the right and left.
4. The presence of rubber in the connection, which led to an increase in the portability of the model in movement and the distribution of stresses in the connection over larger areas.
5. The equivalent viscous damping of the model that contains rubber in the base connection is higher than the model that contains rubber in the base connection and beam-column connection.
6. The drift and ductility index of the model that contains the rubber in the base connection and the beam-column connection is higher than the drift and ductility index of the model that contains the rubber at the base connection only.
7. Finally, the presence of rubber at the base connection of the model and in the beam-column connection increases the flexibility of the connections, which leads to a delay in the failure time of the model and thus improves the performance of the model.

References

[1] Earthquake Resistant Steel Structures. ArcelorMittal Europe - Long Products Sections and Merchant Bars. Patented.

[2] Engineering and Technology Journal .Ali, Suhaib J., Amer M. Ibrahim, and Sarmad Shafeeq. "Experimental Study and Numerical Simulation of Plane Steel Frame with Rubberized Connecting Technology Subjected to Seismic Effect." 39.3A (2021): 415-425.

[3] Civil Engineering Journal. Fadhil, H., Ibrahim, A., & Mahmood, M. (2018). Effect of Corrugation Angle and Direction on the Performance of Corrugated Steel Plate Shear Walls. 4(11), 2667-2679.

[4] International Journal of Steel Structures .Shamivand, Abbas, and Jalal Akbari. "Ring-shaped lateral bracing system for steel structures." (2019): 1-11

[5] Materials Science and Engineering .Ali, Suhaib J., Amer M. Ibrahim, and Sarmad Shafeeq. "Innovative Steel Connections with Composites Steel Bolts/Rubber Subjected to Horizontal/Inclined Cyclic Loads." IOP Conference Series: Vol. 745. No. 1. IOP Publishing, 2020

[6] Amer M. Ibrahim, Sarmad Shafeeq, Suhaib Jamal Ali. Structural Behavior of Plane Steel Frame Under Inclined Cyclic Loading with Smart Connection.(Doctoral dissertation)

[7] ABAQUS Theory Manual (2017), Dassault Systemes Simulia Corp., Providence, RI, USA Abaqus, 2017. Abaqus 2017

[8] AISC, 2011 .AISC Manual of Steel Construction, 14th Edition. Am. Inst. Steel Constr. Chicago, AISC, no. February

[9] Astaneh, A. (2005). Design of shear tab connections for gravity and seismic loads. Retrieved September 2, 2015.

[10] Wood and Fiber Science Seaders. P., Gupta, R., & Miller, T. H. (2009). Monotonic and cyclic load testing of partially and fully anchored wood-frame shear walls., 41(2), 145-156

[11] ACI Structural Journal. Oudah, F., & El-Hacha, R. (2018). Innovative Self-Centering Concrete Beam-Column Connection Reinforced Using Shape Memory Alloy. 115(3)

[12] In IOP Conference Series: Materials Science and Engineering .Ali, S. J., Ibrahim, A. M., & Shafeeq, S. (2020, February). Development of steel structure connections for seismic resistance using composite steel bolts/rubber. (Vol. 737, No. 1, p. 012014). IOP Publishing.

[13] In IOP Conference Series: Materials Science and Engineering. Jassim, T. A., Zhuang, B., Ibrahim, A. M., & Ali, I. A. (2021, February). Using Wasted Rubber Material for Reducing Loads and Energy Dispersal in Building Industries: State of the Art. (Vol. 1076, No. 1, p. 012114). IOP Publishing.

[14] Diyala Journal of Engineering Sciences .Salman, W. D. (2013). Finite element analysis of reinforced concrete slabs with spherical voids, 6(4), 15-37.

Design of class-E Power Amplifier (PA) with minimum harmonious termination for Cellular phones

Zahraa Mohammed younis saed[1], Dr. Khalid Khaleel[2]
{Zahraaalslam530@gmail.com[1], khalid.khaleel@uoninevah.edu.iq[2]}

Mosul University, Electrical Engineering Department[1]
Nineveh University[2]

Abstract. Power efficiency is a critical element in the design of RF power amplifiers for contemporary wireless applications. Improved power efficiency results in longer battery life, less heat dissipation needs, a more compact design, and increased dependability. A high-efficiency Amplifier with class-E power is described in this article, which is based on a GaAs transistor and is optimized for operation in the 1.8 GHz LTE band. It is possible to improve the efficiency and output power of a transmission line-based output network by decreasing the harmonic powers of the transmission lines. It is found that all harmonic level values down than -90 dBc were suppressed by the proposed class-E amplifier. With a 7-dB increase in output power, the peak power-added efficiency (PAE) is 82 percent at 30 dBm output power, resulting in a power gain of 82 percent.

Keywords: Gallium Arsenide (GaAs), Amplifier of class-E power (PA), Harmonic suppression, power-added efficiency (PAE).

1 Introduction

Radiofrequency (RF) amplifiers are essential components in a wide range of communication systems, including satellite communications. All the application in point-to-point communication or wireless communication usually uses the advantages modern power amplifier, which is critical components. The working frequency of the amplifiers is determined by the application, and it may range from extremely low to microwave frequencies in the frequency range. In situations when a signal must be amplified to a known value at any application frequency, RF power amplifiers are used to achieve the desired results (PAs). The power outputs of the amplifiers may likewise range from milliwatts to megawatts in output. The most popular RF amplifiers are usually classified into the A, B, AB, C, D, E, F, and S classes. In this section, we will show the amplification of a linear or nonlinear signal using several topologies. Nonlinear amplification is achieved by utilizing amplifiers with Class A, B, or AB amplifiers topologies; linear amplification is achieved by employing amplifiers with Class C, D, E, F, and S amplifiers topologies. The amplifier classes D, E, F, and S have been classified as switch-mode amplifiers because it performs the role of a switch during amplifier operation. The following is an explanation of the relationship between the RF signal forms amplifiers input and output:

IMDC-IST 2021, September 07-09, Sakarya, Turkey
Copyright © 2022 EAI
DOI 10.4108/eai.7-9-2021.2314881

$$v_o(t) = \beta vi(t) \quad (1)$$

Nonlinear operation of the amplifier results in the signals at the input and output being represented as a power series, as shown in Equation 2:

$$v_o(t) = \alpha_o + \alpha_1 vi(t) + \alpha_2 vi^2(t) + \alpha_3 vi^3(t) + \ldots.. \quad (2)$$

Equation 2 illustrates the amplifier response's modest nonlinearities. When there is just minor distortion [1].

2 Class-E (PA)

Sokal and Sokal [2] were the first to develop a class-E power amplifier (PA), which was introduced in 1975. According to the theory, the Class-E amplifier may achieve high efficiency because it prevents the simultaneous presence of nonzero switching voltage and current [3]-[6]. Amplifiers of class-E power and variants have been extensively employed in wireless communications. Amplifiers of class-E power PAs have theoretical efficiencies approaching 100%[7]. Its circuit comprises a switching transistor, a load network, and a load impedance. A shunt capacitor and a series resonant circuit comprise the load network [8]. Due to its great efficiency, a class-E power amplifier achieves very high dc to ac conversion efficiency at high frequencies, owing to the substantial decrease in switching losses. The switching power amplifier technology's fundamental concept is that the transistor enters a saturated state and switches on and off the voltage or current, depending on the kind of amplifier [4].

3 Design and Simulation OF Class-E PA

The design starts with the single-ended class-E PA selects GaAs MESFET transistor, GaAs MESFET makes the amplifiers at microwave frequencies. It is common for the bias voltage Vgs of a class-E transistor to be equal to the threshold voltage of the transistor to ensure that the transistor functions in the switch state. Construction of the basic circuit for a class-E power amplifier is then shown in Fig 1 There are three parts to this circuit: a direct current source VDD, an RF choke Lf, and a load network that is composed of a series resonant L_oC_o the resonance frequency of L_oC_o will be the same as input frequency which means that the two frequency is tuned together, and a shunt capacitor Cs.

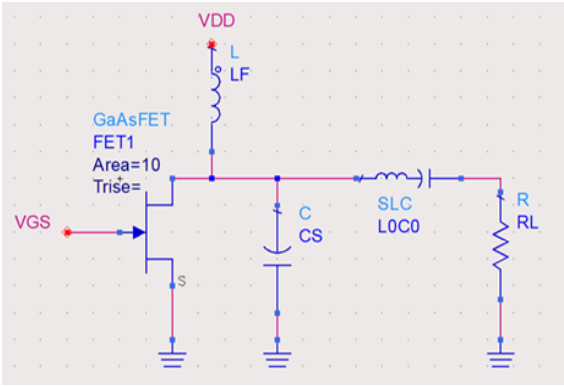

Fig.1. The basic circuit of a class-E PA.

Then designed output and input matching circuit, if we can control an unlimited number of harmonics in the amplifier output through an LnCn series resonator tuned to the nth harmonic, the amplifier's efficiency will approach 100%. Significant control is feasible only for certain harmonics and only a few output harmonics will dominate. Using a series of tank LC circuit to generate resonance at a certain harmonic in the output spectrum and a load resistance R is an efficient method to do this. The values of the components in the circuit shown in Figure (1) (a parallel capacitance Cs, a series resonant L_oC_o circuit) are calculated at output power Pout = 32 dBm, operating frequency f_o = 1.8 GHz, loaded quality factor Q_l = 10 and VDD= 4 V using the following equations [5] and theoretical value of this parameter shown in Table 1.

$$R = \frac{8VDD^2}{\pi^2+4P_o} \approx 0.5768\ \frac{VDD^2}{P_o} \tag{3}$$

$$XC_s = \frac{1}{\omega C_s} = \frac{\pi(\pi^2+4)R}{8} \approx 5.4466R \tag{4}$$

Where $\omega=2\pi f_o$

$$XL_o = \omega L_o = Q_l R \tag{5}$$

$$XC_o = \frac{1}{\omega C_0} = \left[Q_l - \frac{\pi(\pi^2-4)}{16}\right] R \approx (Q_l - 1.1525)R \tag{6}$$

Then, a matching circuit was built. After determining ZL and Zs via load-pull and source pull simulations and designing output and input matching circuits in ADS using the Smith chart tool, the Q-factor of inductor utilized to calculate matching circuit is equal to 10 in this case. It is the matching of outputs that is the core of class-E PA technology. Stability, gain, and other characteristics are significantly influenced by the input circuit. The output circuit, on the other hand, may modify the waveform and therefore increase the output power and efficiency. Then, for harmonic termination, an LnCn series resonator tuned to frequencies 2 f_o, 3 f_o, 4 f_o, and 5 f_o was developed. All harmonic components should have an open circuit in the harmonic

termination network. Because the output matching network does not open to all harmonics, in an ideal class-E architecture, the nonideal series resonant filter results in undesirable harmonics at the output, degrading the amplifier's performance. As a result, harmonic powers are suppressed, and losses are minimized. For class-B operation at 1.8 GHz, a class-E PA was constructed using GaAs with a P_o = 30dBm, a gain of 7dB, and power-added efficiency (PAE) of 82 percent at 4V. The class-E PA is designed using the following formulae (3)–(6) to determine the value of each load network component. Table (1) contains the values for the elements.

Table1.shows the element values of the load network.

Parameter	Value	Unit
operating frequency f_o	1.8	GHz
R	5.8	Ω
L_o	5.5	nH
C_o	1.723	pF
Cs	*2.798*	pF

It should be noted that the values of the designed circuit elements have undergone a tuning software process in ADS to obtain the best results , and then design input and output matching circuit and harmonious termination circuit, the input matching elements of L4 and C5 were 0.5nH and 1.5pF, respectively. And C6, L5 was 3.9 pF and 1.5159 nH respectively represent output matching circuit, and four-stage LnCn series resonator represents harmonious termination circuit, after implementation the power amplifier circuit we convert all the amplifier components to micro- strips line, because at high frequencies, the effect of stray capacitors and inductors is noticeably visible, as well as the poor performance of capacitors and inductors that are used in amplification circuits. Micro strips are one of the types of transmission lines that are used to transfer power from one point to another with high efficiency. The design is based on an ideal schematic of a microstrip circuit, and we must convert it into a real microstrip circuit to use it effectively. Because the dielectric constant is 4.3, the dielectric substratum is used in this study as the dielectric substratum. The thickness of the substrate is h=1.6 mm. ADS is an acronym that stands for Automated Data Collection. The electric length E and characteristic impedance Z_o converted into actual length L and width W of the micro-strip line by Linecalc module was called were Z_o equal 50Ω.

4 Simulation Results

The proposed power amplifier circuit Fig 2 has been modelled with the help of the ADS software package's harmonic balancing simulator with P_o=30dBm with 7dB and 82 percent power-added efficiency (PAE) gains at 1.8 GHz.

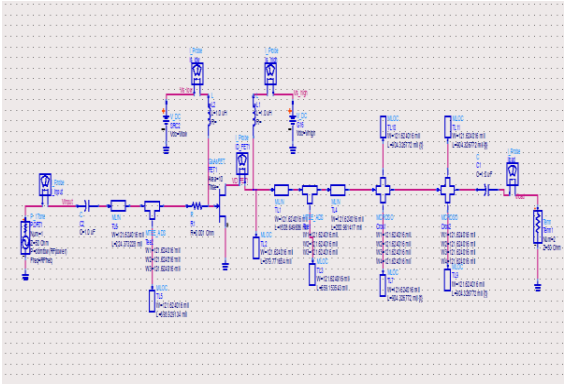

Fig.2. a complete micro-strip line circuit for a class-E power amplifier.

Fig 3 depicts the drain voltage and current waveforms of a GaAs transistor operating at 1.8GHz. It is approximate approximation of half-wave sinusoidal pulses that are used in the simulation of drain voltage and current waveforms. As illustrated in figure [3], the drain current waveform should be out of phase with the drain voltage waveform with the least amount of overlap. This non-overlapping behaviour minimizes power dissipation in the GaAs transistor's drain, thus increasing the power amplifier's efficiency.

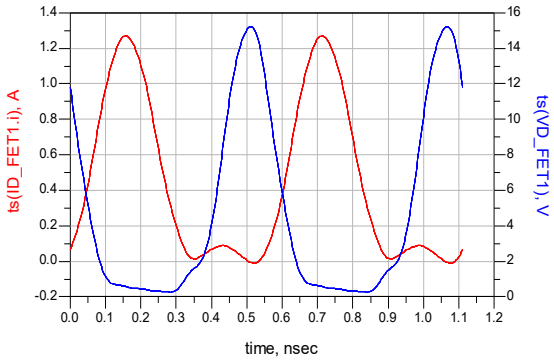

Fig.3. Waveforms of drain voltage and drain current.

The output voltage waveform of the power amplifier circuit is shown in Fig 4. The sinusoidal shape of this waveform is due to the output matching network's low pass filtering effect, which reduces the amplitudes of the harmonic components.

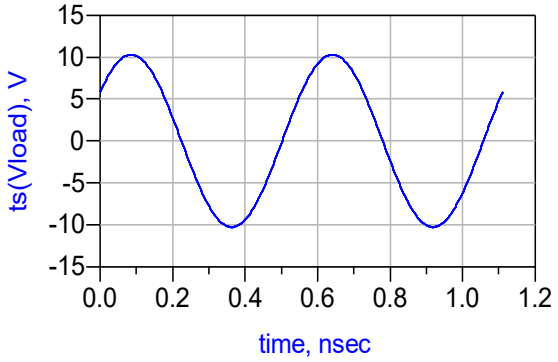

Fig.4. output voltage waveform.

The output spectrum waveform of the power amplifier circuit is sketched in Fig [5] for fundamental harmonics, it can be shown that the second and third harmonics are well suppressed to -70dBm compared to the fundamental harmonic which mean that the out of band noise is reduced to a minimum value.

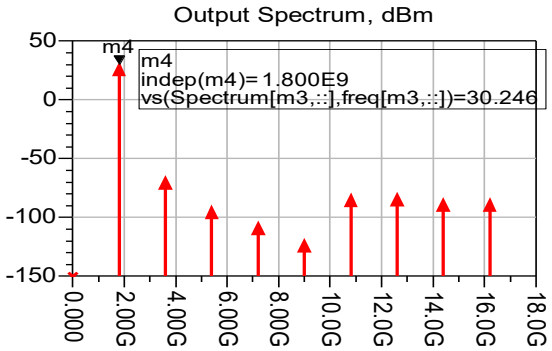

Fig.5. The output spectrum of the power amplifier circuit.

Result optimised can be is comfortable with another research and this same to be very good in the value of power added efficiency-optimised and suppressing second and third harmonic powers and with minimum overlap between current and voltage drain.

5 Conclusion

A high-efficiency class-E PA circuit based on a GaAs MOSFET was developed and constructed in this work to enhance the overall performance and increase the efficiency by suppressing second and third harmonic powers as much as feasible. The harmonic power levels of the power amplifier circuit utilized for a single tone were kept below -90 dBc throughout the output power range of 24 to 30 dBm using the single tone circuit. It was possible to achieve a peak PAE of 82 percent with a power gain of 7 dB for an output power of 30 dBm while operating at 1.8 GHz and therefore achieve a power gain of 7 dB for the output power.

References

[1] EROGLU, Abdullah. Introduction to RF power amplifier design and simulation . CRC press, 2018.Chapter one, Radio Frequency Amplifier Basics; p. [1].

[2] N. O. Sokal and A. D. Sokal. “Class E-A new class of high-efficiency tuned single-ended switching power amplifiers”, IEEE Journal of SolidState Circuits, SC-10, pp. 168-176, June 1975.

[3] LENG, Yongqing, et al. An extended topology of parallel-circuit Amplifier of class-E power using transmission-line compensation . IEEE transactions on microwave theory and techniques, 2013, 61.4: 1628-1638.

[4] YUSMARNITA, Y., et al. Design and analysis of 1MHz Amplifier of class-E power. WSEAS Journal, 2015, 14.

[5] Kazimierczuk, M. K. (2008). RF power amplifiers . (Vol. 1). New York:: Wiley.Chapter five, Class E Zero-Voltage Switching RF Power Amplifiers ;p.[255].

[6] LIU, Chang; CHENG, Qian-Fu. Analysis and design of high-efficiency parallel-circuit class-E/F power amplifier. IEEE Transactions on Microwave Theory and Techniques, 2019, 67.6: 2382-2392.

[7] WANG, Jingyuan; YU, Hongxi; YANG, Fei. Design of GaN HEMT class-E power amplifier for satellite communication. In: 2018 International Conference on Microwave and Millimeter Wave Technology (ICMMT). IEEE, 2018. p. 1-3.

[8] RAAB, Frederick. Idealized operation of the class E tuned power amplifier. IEEE transactions on Circuits and Systems, 1977, 24.12: 725-735.

Computational Fluid Dynamic Analysis of the Flow though T-junction and Venturi Meter

Enas Salman Taha[1], Mohammed A. Abdulwahid[2], Akeel M. Ali Morad[3]
, Qusay A Maatooq[4]
{umabody.1979@gmail.com[1], mohw2016@stu.edu.iq[2], akeel@stu.edu.iq[3]}

Southern Technical University, Basra Eng. Technical College, Thermal Mechanical Engineering and Fuel Energy Deartmentt[1,2,3,4]

Abstract. This study investigates the influence of turbulent parameters on the characteristic centreline of a fluid flow through a T-junction connected to a Vinturi tube through a pipe. Continuity equation, Momentum equation, and Energy equation of water are modelled and solved by using the ANSYS FLUENT 2020R1 Software free Demo. While the turbulent model with standard (k-ε) type is used to compute the turbulent parameters such as turbulent kinetic energy and turbulent dissipation rate for a pipe inner diameter of (D =25 mm) with a length from the T-junction centre line and at the outlet of the Venturi meter is (350 mm). The Reynolds number variation ranged from ($1x10^4$ to $3x10^4$) at the step of (5000). The water flowing is considered in an x-direction flow to show the effects of the above parameters. The model is obtained on the velocity distribution, pressure drop distribution, turbulent kinetic energy, and turbulent dissipation rate. The results showed a discrepancy in the values of the effect of the T-junction on theVenturi meter concerning the velocity distribution and pressure drop, while they showed similar behaviour for the turbulence parameters.

Keywords: CFD, Turbulent Flow, Characteristics centreline, T-junction, Venturi meter.

1 Introduction

When flowing in pipes and ducts, it encounters resistance to its flow. In pipes, this resistanceis represented by the roughness of the pipe surface and friction losses, and there are other losses due to the presence of gate valves, ball valves, sudden expansions, or connections such as T-junction, and all these factors affect the values of velocity, pressures, and other parameters of the flow.

There are two basic types of flow in pipes, depending on the nature of the different components outlined above that affect the flow. The first form is laminar flow, which is defined by fluid passing across smooth layers of laminae. This form of fluid motion is known as streamline flow because all of the fluid particles travel in parallel lines.

When the flow velocity reaches a particular point, the flow becomes turbulent rather than laminar. A particle's mobility becomes random in a turbulent flow and fluctuates up and down in a perpendicular and parallel to the mean flow direction. The Reynolds numbers (Re) are important in assessing whether the flow pattern in a pipe is laminar or turbulent [1]. Pipe networks depend on T-junction, a common component of water and industrial systems. Divide (diverge) the flow from the main pipe to multiple branch streams and gather (converge) flows from two pipes. The energy losses produced by the combining and division of flow at tees

IMDC-IST 2021, September 07-09, Sakarya, Turkey
Copyright © 2022 EAI
DOI 10.4108/eai.7-9-2021.2314880

should be considered when planning and analysing piping systems. Line sizing necessitates a precise estimate of energy losses at junctions, which can have a major impact on hydraulic calculations and, in some situations, pump selection [2]. The Venturi will need to be calibrated in a laboratory using the identical installation setup as it will be in the field to reliably measure flow. Depending on the Venturi size and piping layout, this calibration may or may not be possible [3]. Around 1791, Giovanni B. Venturi discovered the Venturi tube. When a Venturi tube is used for flow metering, a pressure differential is created dependent on the rate of flow, which is known as a Venturi metre. Venturi meters measure the flow rate by measuring the increase in flow velocity and corresponding pressure drop due to the converging section of the pipe. Water supply companies have been using them for many years. Analysed the effect of a tee junction on the measurement of the flow rate of a Venturi flow meter constructed downstream of the branch. Results suggest that the measuring of flow rate was less influenced when all flow wasentering the tee branch and more affected when less flow entered to its. The difference between experimental and numerical results increases as the flow split entering the Venturi decreases [4]. It is dependent on the Venturi installation experimental and analytical study about the pressure loss of a fluid with turbulent incompressible flow through a 90° tee junction. The study found at various Reynolds numbers, the effect of the flow rate ratio q (ratio between the flow rate in the branch and outlet pipes) on pressure drop and velocity profile was expected. It is also the pressure and total energy losses arise as the flow rate ratio is increased. A study by [5] was conducted to measurements of pressure variation, mean, and turbulent velocities were forthe flow of water in two 90° tee junctions with sharp and rounded edges. It was found the losscoefficient of the branched flow was greater than that of the straight flow. A study conducted by [6] resulted in the flow rate ratio has a significant effect on the pressure loss and then the outlet flow rate, also it was found the pressure loss coefficient km depends upon the flow rateratio q, but not upon the Reynolds. [7] A steady, incompressible fluid flow was examined with CFD through a T-junction. Water velocity is strongly affected by the 90-degree angles ofthe T-junction of the pipe, water velocity increases significantly with decreasing diameter of the test section, and energy loss can be reduced by reducing the angle of the T-junction of thepipe. In a study by [8], computational parametric analysis of turbulent flow in90 T-junctions with sharp and curved corners was performed. In the main pipe (K32), the loss coefficient is the same in both instances, but it is considerably lower in the branch pipe (K31). To determine the effect of pipe size and beta values on discharge coefficients, various models of the flow meters were studied. For typical Reynolds numbers, the Venturi, V-cone, and wedge flow meters all have relatively constant discharge coefficients. Studying the influences of geometricparameters such as convergent cone angle, divergent cone angle, beta ratio, and throat length on pressure drop, [9] found that beta ratio was the most significant parameter. [10] Have studied CFD and laboratory data to determine the relationship between the classical Venturi meter design's recovery cone angle and associated head loss. As a result, the beta ratio and Reynolds number determine the best recovery cone angle for minimising head loss. The purpose of [11] was to assess the performance of Venturi Meters positioned downstream of the bend. They discover that the length of straight pipe required is determined by the meter's upstream fitting type and the ratio of the throat to inlet diameter. The accuracy of a Venturi metre is dependent on the length of straight pipe upstream of the metre.

The above-mentioned kinds of literature have done studies on the Tee Junction or the Venturi meter separately. But in this study, the objective was to determine the effects of different turbulent Reynolds numbers entering the T-junction on the performance of the Venturi meter based on the method of CFD.

2 Description of the Venturi Meter

A typical Venturi tube made from a transparent material (Epoxy) calibrated in water with diameter ratio β = 0.6 was derived from [12]; the convergent and the divergent angles were set at 10.5 and 3.5, respectively. The length of the inlet cylinder is equal to the internal diameter of the branch pipe D = 25mm, the length of the throat section is equal to the internal diameterof throat d = 15mm, the divergent section length is 82mm. Venturi meter length is 150 mm, upstream pipe length is 8 D.

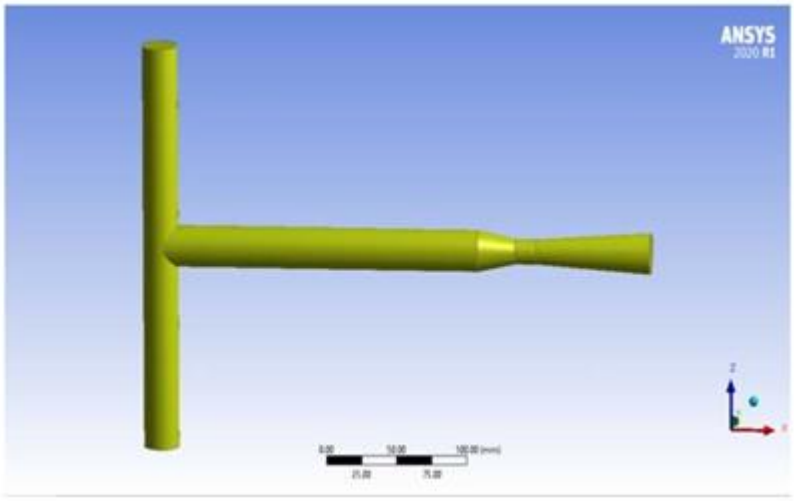

Fig 1. The geometry of the T-junction & Venturi meter.

3 Mathematical Model

The water flowing through the T-junction and Venturi metre can be thought of as an incompressible, steady flow, which is in accordance with mass and momentum conservation laws. Therefore, the continuity and the Navier-Stokes equations are included in the basic equations [13]:

$$\frac{\partial u}{\partial x} + \frac{\partial v}{\partial y} + \frac{\partial w}{\partial z} = 0 \tag{1}$$

Where u, υ, ω is the velocity components in x, y, z-direction, respectively.

$$\frac{\partial(\rho u)}{\partial t} + \nabla(\rho u U) = -\frac{\partial P}{\partial x} + \mu\nabla^2 u + F_x$$
$$\frac{\partial(\rho v)}{\partial t} + \nabla(\rho v U) = -\frac{\partial P}{\partial y} + \mu\nabla^2 v + F_y$$
$$\frac{\partial(\rho w)}{\partial t} + \nabla(\rho w U) = -\frac{\partial P}{\partial z} + \mu\nabla^2 w + F_z \tag{2), (3), (4)}$$

Where t is time, U is velocity vector, ρ is the water density, p is the pressure of the fluid, μ is the dynamic viscosity of water, Fx, Fy, Fz respectively. When the mass force is only the gravity and Z-axis is vertical, then comes Fx = 0, Fy = 0, and Fz = −ρg.
Both turbulent kinetic energy and turbulent dissipation rate can calculate [14].

$$k = (\mu + \mu_T)(V_u + (V_u)^1) - \frac{4}{3}(\mu + \mu_T)(V_u) - \frac{4}{3}\rho K_T \quad (5)$$

Where K is turbulent kinetic energy, ϵ is turbulent dissipation rate.
Reynolds number ranged (from $1x10^4$ to $3x10^4$) and the flow section changed. For numerical simulation, the standard (k- ε) type of turbulent model is used. In the (k-ε) turbulence model, turbulent kinetic energy is k, dissipation ratio is ε.

4 Flow Parameters

4.1 Flow Geometry

The T-junction and Venturi meter are drawn using the Cartesian coordinate system presentedin Fig 1. The diameter of the pipe used (D = 0.025 m), the origin of the coordinate system is located at the beginning of the throat section therefore the length of the throat section is from (0 – 0.015 m), the convergent section is from (0 _ -0.025 m), the entrance section from (- 0.025 – - 0.05 m). The upstream of Venturi meter is 8D from (- 0.05 _ - 0.25 m) on characteristic centreline of X-axis as in Fig 3.

4.2 Simulation Paramters

The fluid used in the simulation is water with a constant density of 998 kg/m^3 and 0.001 kg/ms dynamic viscosity. The fluid flow is assumed incompressible. The boundary conditionsare set as a velocity at the inlet and zero initial gauge pressure. The velocity of the inlet pipe isfully developed. Assumed that all the walls have no-slip boundary conditions. The simulation analysis is carried out using the CFD software ANSYS FLUENT2020 R1. Using the finite volume method and a first-order upwind difference scheme in this software, differential equations might be reduced to algebraic equations. The discrete equations' pressure-velocity rate is calculated using the coupling procedure. The unstructured computational grid (tetrahedron) shown in Figure (2) is made up of 767487 nodes and 2431372 elements, with five boundary layer cells and an element size of 0.75mm**.**

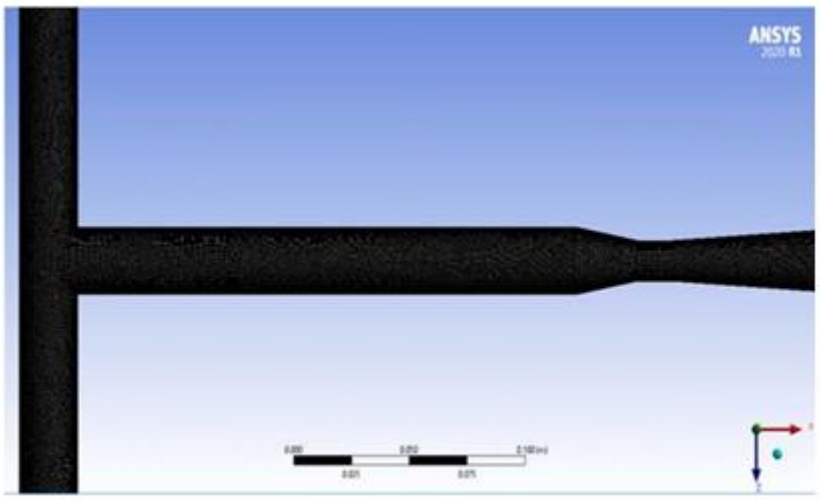

Fig 2. The unstructured mesh for T-junction &Venturi meter.

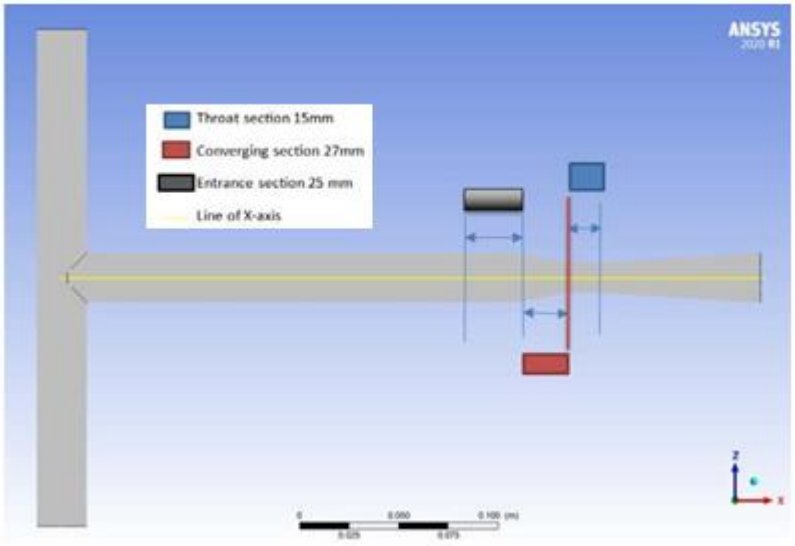

Fig 3. The geometry plotted of characteristics centreline.

5 Results and Discussion

A characteristic line is plotted from the centre of the T-junction extended to the end of the Venturi meter to describe the effects of the T-junction on the water flow through the Venturi. The length of this line is (350 mm) as shown in Figure 3. The CFD analysis for turbulent flow with the (k-ε) standard method is used to show the effects of the velocity distribution, pressure distribution, turbulent kinetic energy and dissipation rate for Reynolds numbers of ranges (from $1x10^4$ to $3x10^4$) with an average of 5,000 steps. The velocity distribution is shown in Fig 4 when flow enters the pipe after the T- junction, the velocity suddenly drops and remains almost constant along the length of the pipeuntil entering the Venturi section. We notice a gradual change in velocity, especially in the throat section, due to the reduction in the area, so the velocity increases.

Fig 5 illustrates the behaviour of the pressure distribution of the characteristic line as a result of friction through the T-junction and beyond. As the Reynolds number increases, the pressure drop in the connected pipe increases until it reaches its lowest value (-45 pa) at the point (1.5 D) of the pipe, then the drop decreases until it reaches (15Pa) at the point (8D) at the entrance to the venturi tube, at the throat, it reaches (0Pa) and then begins to drop to reach (-15Pa) at the end of the throat section for (Re =30000).

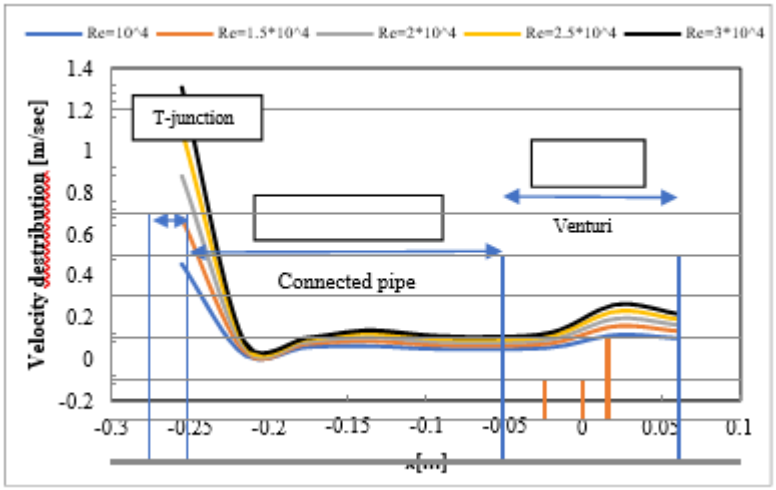

Fig 4. Velocity distribution of the characteristic line at five Reynolds numbers.

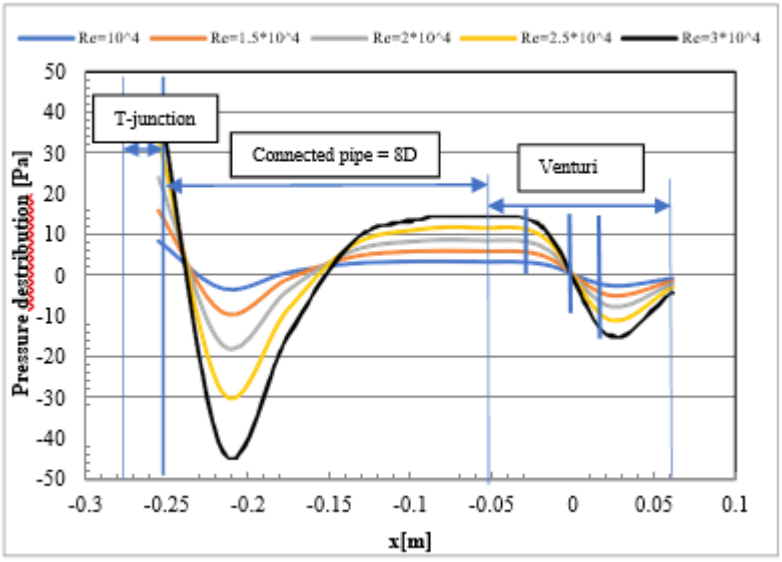

Fig 5. Pressure drops distribution of the characteristic line at five Reynolds numbers.

Under turbulent flow conditions inside the conduct's channels such as pipes, fittings, and so on. There are two important parameters notified to predict the power reflected in the fluid flow. Turbulent kinetic energy describes the amount and behaviour of the transformed energy to the fluid inside the conducted channels, while the turbulent dissipation rate is given the amount of energy deformed into the flow stream.

Figs 6 and 7 explained the turbulent kinetic energy and the dissipation rate respectively. Same behaviour of the two parameters along the characteristic line of the flow, thetwo figures show a very slight chance of the turbulence parameters through the Venture tube, while a very clear change in the values appears along the connected pipe, as the higher the Reynolds number, increase the effect on the values through the connected pipe.

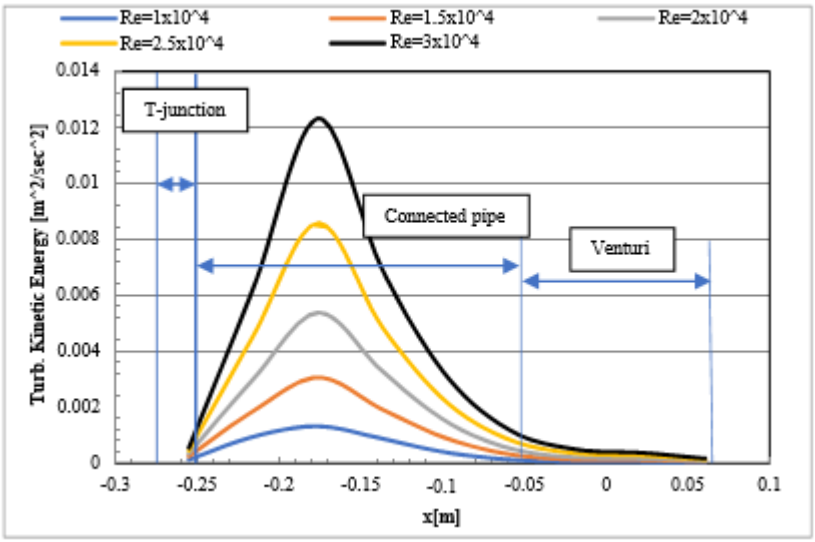

Fig 6. The turbulent kinetic energy of the characteristic line at five Reynolds numbers.

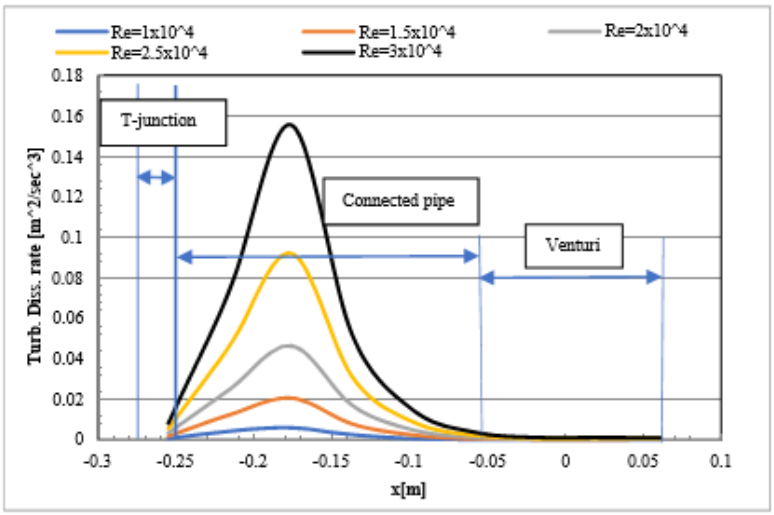

Fig 7. Turbulent dissipation rate of the characteristic line at five Reynolds Number.

6 Conclusion

Five turbulent Reynolds numbers are used to investigate the behaviour of the water flowing from the centreline of the T-junction to the outlet of the Venturi. This line is called the characteristic centreline of water flowing, through this line all changes of parameters related to turbulent flow can be discovered. It was concluded by changing the Reynolds number for various values which lead to show the behaviour of each of the velocity distribution, pressure drop distribution, turbulent flow parameters, turbulent kinetic energy, and dissipationrate. So, the conclusions can be explained as follows:

1. For the velocity distribution, the velocity is nearly uniform along the connecting pipe,

but it suffers from a significant decrease at the T-junction and a relative change through the Venturi tube due to the change in the cross-sectional area through it.

2. As for the pressure distribution, there is a significant fluctuation in the pressure drop along the characteristic line, which becomes more apparent as the Reynolds number increases.
3. Turbulent kinetic energy and dissipation rate are two important characteristics of turbulent flow. These variables changed the turbulent conditions, allowing researchers to find out how much the water's flow power changed. The results show the same behaviour for an increase in the Reynolds number, which is associated with the changes in these parameters.

References

[1] R. Gürbüz, "Measuring local losses in pipe flows utilising data acquisition cards and acomputer," vol. 2, no. 3, pp. 461–464, 2003.

[2] C. T. Michalos, "A Review of Available Minor Loss Coefficients for Combining and Dividing Flow Tees," pp. 1116–1123, 2011.

[3] Benjamin G. Sandberg, "VENTURI FLOWMETER PERFORMANCE INSTALLED DOWNSTREAM OF THE BRANCH OF A TEE JUNCTION," 2020.

[4] S. F. D. Mohammed Abdulwahhab, Niranjan Kumar Injeti, "Numerical prediction of pressureloss of fluid in a T-junction," Int. J. Energy Environ., vol. 4, no. 2, pp. 253–264, 2013.

[5] M. F. P. N. P. Costa, R. Maia, F. T. Pinho, "EDGE EFFECTS ON THE FLOW CHARACTERISTICS IN A 90° TEE JUNCTION," pp. 1–44, 2006.

[6] G. B. Nimadge and S. V Chopade, "CFD ANALYSIS OF FLOW-THROUGH T-JUNCTIONOF PIPE," no. 2, 2017.

[7] G. Paál, F. Pinho, and R. Maia, "THE EFFECT OF CORNER RADIUS ON THE ENERGYLOSS IN 90 ° T - JUNCTION TURBULENT FLOWS," 2006.

[8] C. L. Hollingshead, M. C. Johnson, S. L. Barfuss, and R. E. Spall, "Discharge coefficient performance of Venturi, standard concentric orifice plate, V-cone and wedge flow meters at low Reynolds numbers," J. Pet. Sci. Eng., vol. 78, no. 3–4, pp. 559–566, 2011, DOI: 10.1016/j.petrol.2011.08.008.

[9] C. Sanghani and D. Jayani, "Optimization of Venturimeter Geometry for Minimum PressureDrop using CFD Analysis," vol. 3, no. 2, pp. 31–35, 2016.

[10] Z. B. Sharp, M. Asce, M. C. Johnson, M. Asce, S. L. Barfuss, and M. Asce, "Optimizing the ASME Venturi Recovery Cone Angle to Minimize Head Loss," vol. 144, no. 1, pp. 1–9, 2018, DOI: 10.1061/(ASCE)HY.1943-7900.0001387.

[11] M. C. Johnson and J. G. Gilbert, "Performance of Venturi Meters," no. April, pp. 156–164, 2006, DOI: 10.1002/j.1551-8833.2006.tb07643.x.

[12] R. L. Wakeland, "A study of venturi tubes," Int. Conf. Nucl. Eng. Proceedings, ICONE, vol. 4,no. 1, pp. 885–892, 2012, DOI: 10.1115/ICONE20-POWER2012-55212.

[13] H. Reza and M. Reza, "Optimizing Different Angles of Venturi in Biodiesel Production UsingCFD Analysis," vol. 38, no. 6, pp. 285–295, 2019.

[14] Akeel M. Ali Morad, Rafi M. Qasim, Amjed Ahmed Ali (2020). STUDY OF THE BEHAVIOURS OF SINGLE-PHASE TURBULENT FLOW AT LOW TO MODERATE REYNOLDS NUMBERS THROUGH A VERTICAL PIPE. PART I: 2D COUNTERS ANALYSIS. (2020), «EUREKA: Physics and Engineering» Number 6. PP.108-122. DOI: 10.21303/2461-4262.2020.001538.

Performance Analysis of Various SDN Controllers with Different Network Size in SDWN

Fidha Ezzaldin Aslan[1], Mohammed Basheer Al-Somaidai[2]
{fidha.enp18@student.uomosul.edu.iq[1], MohammedBasheerAbdullah@uomosul.edu.iq[2]}

Department of Electrical Engineering, Mosul University, Mosul, Iraq[1,2]

Abstract. Software-defined Wireless Networking (SDWN) is the next generation of wireless networks. It performs the same Software Defined Networking (SDN) operation by decoupling the control plane from the data plane on the network device and transfers it to the controller, to provide easy control and centralized management to the network. Since the controller represents the most important part of the software-defined network architecture. In this paper, we examine the performance of four SDN controllers: POX, RYU, Open Daylight (ODL), and Open Network Operating System (ONOS) in different sizes of the emulated wireless network in terms of the network parameters such as throughput, delay, jitter and packet loss using the Mininet WIFI platform. Tests of this experiment help to choose the appropriate controller according to various parameters and states of the wireless network.

Keywords: Controller performance, Mininet-Wi-Fi, OpenFlow, ODL, ONOS, POX, RYU, SDWN.

1 Introduction

Because of the continuous development in networks and the rapid growth of data traffic resulting from the increase in the number of connected devices and the requirements of speed performance, the traditional network architecture is not catching up with these increasing demands, Which Requires a new network architecture. This new network architecture is known as a software-defined network that addresses problems in the traditional network and provides easy control and centralized management of the network and being cost-effective.

SDN is a new network model that separates the network control plane from the Data forwarding plane in devices and transfers it to a central server called the controller, to make the network more controllable and less complicated [1]. As a result, the SDN reduces the role of the devices to only data forwarding and implementing control orders issued by the controller. The controller has a global view of the network and it is responsible for all control decisions and communicates with the forwarding elements distributed at the network level via standard interfaces [2].

SDWN, a subset of SDN, is recently launched to meet the increasing demand for wireless networking. SDWN performs the same SDN operation by switching the control plane from the data plane of the network beyond the access points to an external software control plane [3]. The access points manage the stations connected to them, according to the flow rules arranged by the controller, Having access to all information that is reported by the network devices [4], this new software-defined approach presents a cost-effective alternative for high-speed network services [5]. it enables administrators to define network behaviour in a logically central and

IMDC-IST 2021, September 07-09, Sakarya, Turkey
Copyright © 2022 EAI
DOI 10.4108/eai.7-9-2021.2314875

higher-level way through APIs provided by the controller platform that implements southbound interfaces (i.e OpenFlow protocol) to the forwarding devices to connect and set up these devices, there are several southbound interfaces but OpenFlow is the most popular one [6]. Since the controller represents the most important part of the software-defined wireless network architecture. It is necessary to evaluate the performance of different types of controllers, study their features and the extent of each effect on the network's performance to choose the appropriate controller by the network operators in line with the requirements of the service they want to provide in the network. Although there are many studies on comparing the performance of different types of controllers in wired networks, there are not enough studies on comparing their performance in wireless networks [9]. In this paper, we have studied the effect of increasing the size of the wireless network on the performance of different types of controllers POX, RYU, ODL, and ONOS and evaluated their performance based on network parameters that include delay, throughput, jitter, and packet loss. We have used the Mininet WIFI platform as an environment to emulate the SDWN and conduct the experimental tests, as well as a qualitative-evaluation has been done.
The remainder of this paper is structured as follows: Section 2 presents related works. Section3 discusses SDN platforms and OpenFlow, section 4 describes SDN Controllers, section 5 Methodology describes the steps of our experiments, section 6 analysis the simulation results and section 7 conclude the paper**.**

2 Related Works

Due to the importance of the controller in the SDN Architecture, which is attracting the attention of many researchers for being a revolutionary technology in the world of networks, many studies were conducted on the types of controllers and a comparison between their performance in wired and wireless networks. In addition to studies on the performance of wireless networks based on SDN.
The performance of two SDN controllers has been compared in [7], Open Daylight and Floodlight in terms of latency and loss in various network topologies and loads implemented in Mininet, wired network emulators. The authors evaluated the performance of controllers to choose the best in these topologies at different loads. They showed through the results using the confidence interval 95% that there are cases in which the ODL outperforms Floodlight in terms of delay in tree networks with light and medium loads, while floodlight showed better performance in terms of packet loss in tree networks with a heavy load, also in terms of delay in linear networks. In addition, there were cases in which the two controllers did not show any difference in performance.
I. T. Haque and N. Abu-Ghazaleh [8] presented a survey paper about the use of Software Defined Networking (SDN) in wireless networks. They evaluated four different types of wireless networks: cellular, sensor, mesh, and home networks. Moreover, a brief overview of SDN's implementations in other types of wireless networks.
The performance of the software-defined wireless network was analysed in [5], by constructing single and linear topologies using the Mininet WIFI platform with OpenFlow controller. Throughput performance decreased with the increase in the number of stations and access points and as a solution to this problem, load balancing between APs has been proposed to move stations from heavily loaded AP to other AP using the handover process.

In The paper [9], the Authors made a comparison between four SDN controllers, Ryu, Floodlight, ONOS, and ODL based on their features, in addition to evaluating their performance by measuring the delay and throughput using the bench tool with increase the load on the network. From the comparison of features, ODL was one of many features in terms of vendor support for interfaces, while from the performance evaluation comparison, ONOS showed the best throughput performance, and ryu showed the least delay performance.
S. Islam et al. [10] evaluated the performance of four SDN controllers Ryu, ONOS, Pox, and Floodlight in a wireless network (linear topology) which is simulated using Mininet WIFI in terms of network parameters such as throughput, delay, and jitter measured by iperf and tcpdump tools, to determine which one is most suitable for the wireless network. The controllers showed different performances in terms of delay and jitter, while the performance was similar in terms of throughput. These research focused on evaluating the performance of controllers in wired networks. In addition to studying the effect of increasing the network size on the throughput performance of SDWN using the default program controller, as well as evaluating the performance of the controllers in the (linear,3) topology of SDWN. The effect of increasing the network size on the performance of the different controllers in the wireless network has not been studied, which is what was focused on in our research

3 SDN Platforms and OpenFlow

3.1 Mininet

Mininet is a virtual network simulation platform that supports the rapid evolution of SDN (SDN emulator) using OpenFlow protocol. Bob Lantz and Brandon Heller developed Mininet 1.0, which was based on the original Mininet model provided by Bob Lantz. Mininet creates a virtual network using the Linux kernel with Python scripts from hosts, OpenFlow switches, and controllers in any network structure that the researcher uses on a single machine [11]. Where the network can be simulated, connected, and switched on the same computer, which helps to develop, test, and clarify the network structures related to the SDN. The software in the basic system of this virtual operation can also be transferred to a real environment.

3.2 Mininet-Wi-Fi

Minnie-Wi-Fi is an open-source software-defined wireless network emulator that was expanded from Mininet by adding virtual wireless stations and access points [12], In addition, to use Mininet nodes such as hosts, switches, and OpenFlow controllers and retaining the original SDN features [13].

3.3 OpenFlow

Network devices communicate with the controller via a southbound interface using the OpenFlow protocol, the most used protocol for the southbound interface of the SDN, which separates the data plane from the control plane. OpenFlow was initially proposed (firstly suggested) by Stanford University 2009 [14] and it was developed by the Open Networking Foundation (ONF), An organization dedicated to supporting and implementing Software

Defined Networking (SDN) and managing the OpenFlow standard. OpenFlow first appeared in the year 2009 according to OpenFlow v1.0, and updates continued until it reached the current version of OpenFlow v1.5 [15].

4 SDN Controllers

The central component of any SDN infrastructure is an SDN Controller, which has a network overview that includes all data plane devices. The controller interfaces these resources to the application plane and performs flow control actions through data plane devices based on application policies [16]. This section introduces four SDN controllers: POX, RYU, ODL, and ONOS.

4.1 POX

POX is a Python-based SDN platform. It began as an OpenFlow controller, but it can now also act as an OpenFlow switch, making it useful for networking software development in general. It currently supports OpenFlow 1.0 and the Open vSwitch/Nicira extensions. POX must be run under Linux, Mac OS X, and Windows. On some platforms, some features are not accessible. the most feature-rich operating system is Linux. [17]. POX has no official graphical user interface. Since it is written in Python; it has a weak performance comparable to that of other programming languages such as Java or C++. Furthermore, POX only supports OpenFlow version 1.0 and does not function in a distributed way, and does not support multi-threading [18].

4.2 Ryu

Ryu [19] is a multi-threaded SDN controller written in Python and based on the line went event wrapper. It supports all OpenFlow versions (1.0, 1.2, 1.3, 1.4, 1.5, and Nicira Extensions), Netconf, OF-config, and other Southbound APIs. [20] multi-threading helps Ryu to perform much better with heavy loads. However, it is still considered as a poor performance compared to newer controllers by many criteria. Ryu comes with a very simple web-based GUI which displays topology and flow details [16].

4.3 Open Daylight [21]

The Linux Foundation Sponsored In 2013 Open Daylight Project with the contribution of several companies with the project such as HP, Cisco, NEC, and IBM. The project aims to enhance the software-defined network (SDN) by offering a community-led and industry-supported system for the Open Daylight Controller, which has been called the Open Daylight Platform. It is an open-source controller and the base for many proprietary controllers, such as Ericsson's SDN Controller and Fujitsu's Virtuora, written in Java and supports many southbound protocols, including OpenFlow, Border Gateway Protocol (BGP), Open vSwitch Database Management Protocol (OVSDB), Simple Network Management Protocol (SNMP), NETCONF and Path Computation Element Communication Protocol (PCEP). ODL Supports multi-threading and distributed controllers and comes with rich documentation but these documents

are somewhat old in some features, such as The DLUX GUI and the L2switch module are still mentioned in documentation even though they were both retired [22- 23].

4.4 ONOS

Open Network Operating System (ONOS) was developed in 2014 and is a Java-based open-source SDN controller. It is part of The Linux Foundation's collaboration project, such as ODL. This controller has the properties of high performance, availability, and scalability [15]. and is the base for many controllers, such as Huawei. ONOS is one of the controllers with a broader range of SBI coverage due to its extensive SBI support for OpenFlow, P4, NETCONF, TL1, SNMP, BGP, RESTCONF, and PCEP protocols. It comes with excellent documentation and is simple to implement in the market [23]. ONOS can run in both distributed and multi-threaded mode and be created with the primary purpose of assisting in the management of large-scale, fast networks, with a focus on the ISP market segment**.** ONOS has a very useful web-based GUI [24].

5 Methodology

The performance of software-defined wireless networks is greatly affected by the number of end stations and access points that configure the network. In this section, we have created a linear topology with different numbers of access points and end stations on a Mininet WIFI environment as shown in Fig 1. Each end station in linear topology is connected with one access point which is in turn connected linearly and each access point is connected to the remote controller, four SDN controllers were used in our experimental evaluation, (ONOS, ODL, Ryu, Pox) as a remote controller We have changed the topology size every time as illustrated in Table 1, then we measured the network parameters (Throughput, Delay, Jitter, and Packet loss) for each case To evaluate the performance of the SDN controllers in the network

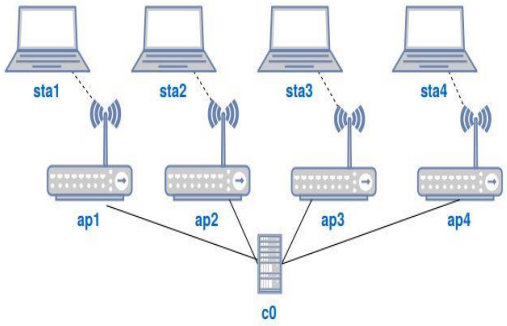

Fig. 1. Linear topology.

Table 1. Several access points and end stations of the linear topology.

No. of access points	No. of end stations
25	25
50	50
75	75
100	100

Mininet-Wi-Fi and controllers were installed and run on a Laptop with Intel core ™ i5-3320M CPU@2.60GHzx4, 8GB memory, and Ubuntu 18.04 LTS-64-bits, which is one of the more famous Linux kernel distributions as an operating system. Throughput is an actual measure of the amount of data that is successfully transferred from source to destination. Throughput has been measured using iperf (internet performance), benchmarking tool that has the functionality of client and server and it can create TCP (Transmission Control Protocol) traffic or UDP (User Datagram Protocol) traffic to calculate throughput in one or both directions between the two ends in the network. In addition, we have used Wireshark, a network performance monitoring tool to capture and analyse the traffic generated by iperf in TCP mode between the two farthest stations in the network to measure throughput and packet loss. The following equation is used to find the throughput. Throughput (b/sec) = Number of received packets × packet size / Elapsed time. (1) Delay has also been measured between the two farthest stations in the network as RTT (Round Trip Time) using the ping command for testing the connectivity between two stations (hosts) in the network. Ping sends one or more ICMP (Internet Control Message Protocol) Echo Request packets to the certain network destination IP and waits for a response**,** when the packet arrives at its destination; it sends an ICMP echo reply. Jitter has measured using the iperf command in UDP mode, between the first and the last station in the network. Jitter is the variation in delay of packet flow between two ends over time. This is often happening because of the Congestion on the network as well as path shifts. The effect of jitter is not seen in services that do not need actual time for delivery, such as data transfer, while its effect is significant in real-time services such as video and audio services.

6 Simulation Results and Analysis

This section describes the carried-out tests with iperf tool, ping command, and Wireshark tool, It can be seen that the parameters (Throughput, Delay, Packet loss, and Jitter) are directly related to increased network size as shown in the summarized results below:

6.1 Throughput

The throughput of each network is found using iperf tool at the TCP mode, considering the last station as a server and the first station as the client where through this tool the network traffic is generated and the performance of the iperf tool was analysed using Wireshark. The number of transmitted packets was about 35,320 packets, with a transmission time of 30 seconds for each

measurement. The results obtained in Fig 2, where the X-axis represents the number of stations and the Y-axis represents throughput in Mbits/sec, shows the effect of increasing the network size on the throughput of the network for all controllers used in this research

1. Linear25: there is no significant difference between the controller's performance, as the ODL controller shows the best performance (10.3 Mbits / sec), followed by the ONOS controller (9.9 Mbits / sec), then the RYU (9.2 Mbits / sec) and Pox (about 8.9 Mbits / sec)
2. Linear50: the performance of ONOS controller and ODL controller is close (9.6 Mbits / sec) and (9.3 Mbits / sec), respectively, then RYU (8.9 Mbits / sec) and Pox (8.1 Mbits / sec).
3. With the increase in network size to linear 75, the ONOS controller outperforms the rest controllers (9.2 Mbits / sec), followed by Ryu (7.1 Mbits / sec), Pox (6.3 Mbits /sec), while ODL is the least performing (5.8 Mbits / sec.)
4. Linear100, ONOS is the best performance in throughput (7.3 Mbits / sec), while ODL is the lowest (3.8 Mbits / sec) and the rest shows a comparable performance (5.2 Mbits / sec) for ryu and (5 Mbits / sec) for pox.

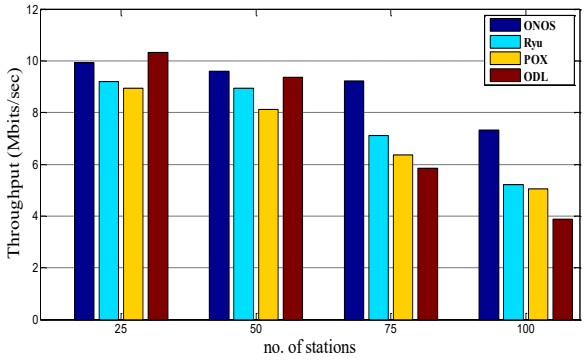

Fig. 2. Throughput comparison

6.2 Delay

As indicated in the previous part, RTT delay was calculated by creating a connection via ping command for 10 packets between the first station and the last station in the network. In Fig 3, the X-axis shows the number of stations in the network and the y-axis represents the RTT delay in msec
In all of the different network sizes, RYU and ODL are the least delayed and outperform POX and ONOS.

1. Linear25: ODL is least delayed (1.1 msec) then RYU (1.2 msec), pox (msec7.4), and ONOS (8.9 msec).
2. Linear50: ODL (3.5 msec), RYU (3.7 msec), pox (62.5 msec), onos (71.4 msec)
3. Linear75: With increased network size, RYU is the least delayed (6.1 msec), as ODL performance decreases (12.8 msec), pox (7.4 msec), ONOS (8.9 msec).

4. Linear100: RYU (17.5 msec), ODL (23.1 msec), pox (164.2 msec), ONOS (300.6 msec).

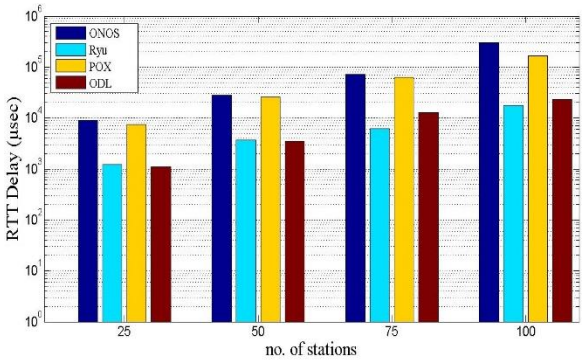

Fig. 3. RTT Delay comparison

6.3 packet loss

Fig 4 represents the relationship between the increase in the network size and the loss of the packets within 30 seconds of sending and receiving the packets and capturing them with the Wireshark tool (about 35,000 packets) where the X-axis represents the number of stations, and the Y-axis represents the number of lost packets for each controller.

1. Linear25: at linear25 ONOS controller is like RYU in packet loss, about (16) packets and (15) packets respectively. ODL and Pox also shows similar packet loss results,(21) packets and (20) packets respectively
2. Linear50: the four controllers show almost the same performance of packet loss, ONOS (53) packets, RYU (49) packets, POX (50) packets, ODL (55) packets.
3. Linear75: ODL shows worse in terms of packet loss (220) packets while Ryu shows less packet loss (81) packets, POX and ONOS show almost similar performance (122) packets and (114) packets respectively.
4. Linear100: ODL shows the worst performance of packet loss (321) packets, while RYU shows the best packet loss performance among them (124) packets. ONOS controller shows about (177) packets and pox (140) packet lost.

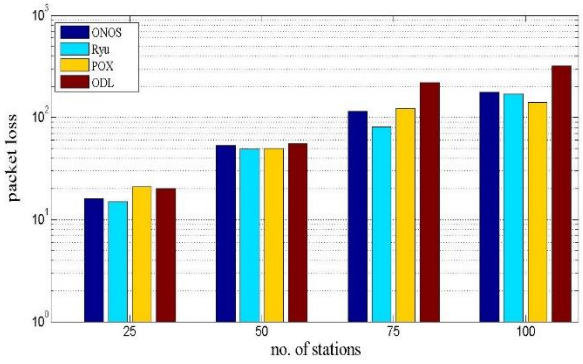

Fig. 4. Packet loss comparison

6.4 Jitter

In Fig 5, the X-axis represents the number of stations, and the Y-axis represents the average jitter in msec. The jitter was measured for 30 seconds, and the average value has been taken. We noticed the following:

1. Linear25: the four controllers show a converging performance, ODL is the least jitter (0.035 msec), ONOS (0.047 msec), POX (0.048 msec), and RYU (0.05 msec)
2. Linear50: the worst performer is RYU (4.575 msec) followed by POX (4.395 msec) and ODL (4.214 msec) and the best performance is ONOS (4.199 msec)
3. Linear75: onos performs worse compared to other controllers (5.716 msec), followed by RYU (5.479 msec), pox (5.301 msec), then ODL (5.254 msec)
4. Linear100: the performance of ONOS is the worst (7.03 msec), then RYU (6.724 msec), pox (6.695 msec), and ODL (6.348 msec).

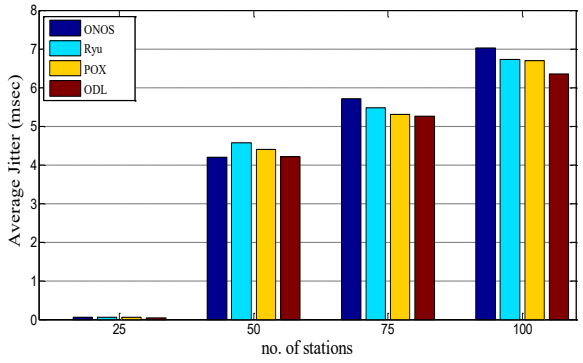

Fig. 5. Average jitter comparison

7 Conclusion and Future work

SDWN is a new structure for wireless networks by separating the control plane from the data plane and centralizing the network control through the controller to overcome the complexity in the traditional network architecture due to the rapid growth in data traffic because of the increasing demand for a fast-performing and low-cost network. In this paper, a performance evaluation of four SDN controllers has been done. The performance evaluation results showed that ONOS performs well with the increase in the network sizes in terms of throughput and packet loss. In terms of delay, ODL and Ryu showed the best delay results under different network sizes. Jitter results showed that ODL is the least Jitter results. The future work will focus on evaluating the performance of different SDN controllers in a custom wireless network topology using mobile devices with a handover mechanism between access points when one of the access points is overloaded.

References

[1] Agarwal S, Kodialam M, Lakshman TV. Traffic engineering in software defined networks. In2013 Proceedings IEEE INFOCOM; 2013 Apr 14; Turin, Italy. (pp. 2211-2219). IEEE.

[2] Kim H, Feamster N. Improving network management with software defined networking. IEEE Communications Magazine. 2013 Feb 14;51(2):114-9.

[3] Jany MH, Islam N, Khondoker R, Habib MA. Performance analysis of OpenFlow based software defined wired and wireless network. In:2017 20th International Conference of Computer and Information Technology (ICCIT); 2017 Dec 22; Dhaka, Bangladesh. (pp. 1-6). IEEE.

[4] Yang M, Li Y, Jin D, Zeng L, Wu X, Vasilakos AV. Software-defined and virtualized future mobile and wireless networks: A survey. Mobile Networks and Applications. 2015 Feb;20(1):4-18.

[5] Assegie S, Nair P. Performance analysis of emulated software defined wireless network. Indonesian Journal of Electrical Engineering and Computer Science (IJEECS). 2019 Oct;16(1):311-8.

[6] Fontes RD, Mahfoudi M, Dabbous W, Turletti T, Rothenberg C. How far can we go? towards realistic software-defined wireless networking experiments. The Computer Journal. 2017 Oct 1;60(10):1458-71.

[7] Rowshanrad S, Abdi V, Keshtgari M. Performance evaluation of SDN controllers: Floodlight and OpenDaylight. IIUM Engineering Journal. 2016 Nov 30;17(2):47-57

[8] Haque IT, Abu-Ghazaleh N. Wireless software defined networking: A survey and taxonomy. IEEE Communications Surveys & Tutorials. 2016 May 19;18(4):2713-37.

[9] Mamushiane L, Lysko A, Dlamini S. A comparative evaluation of the performance of popular SDN controllers. In:2018 Wireless Days (WD); 2018 Apr 3; Dubai, United Arab Emirates. (pp. 54-59) . IEEE.

[10] Islam S, Khan MA, Shorno ST, Sarker S, Siddik MA. Performance Evaluation of SDN Controllers in Wireless Network. In:2019 1st International Conference on Advances in Science, Engineering and Robotics Technology (ICASERT); 2019 May 3; Dhaka, Bangladesh. (pp. 1-5). IEEE.

[11] Al-Somaidai MB, Yahya EB. Survey of software components to emulate OpenFlow protocol as an SDN implementation. American Journal of Software Engineering and Applications. 2014 Dec 16;3(6):74-82.

[12] Fontes RR, Afzal S, Brito SH, Santos MA, Rothenberg CE. Mininet-WiFi: Emulating software-defined wireless networks. In:2015 11th International Conference on Network and Service Management (CNSM); 2015 Nov 9; Barcelona, Spain. (pp. 384-389). IEEE.

[13] Fontes RR, Rothenberg C. Wireless Network Emulation with Wireless Network Emulation with Mininet-WiFi. Columbia (USA): Christian Esteve Rothenberg; 2019. p. 14

[14] Braun W, Menth M. Software-defined networking using OpenFlow: Protocols, applications and architectural design choices. Future Internet. 2014 Jun;6(2):302-36.

[15] "Open Networking Foundation." https://opennetworking.org/ (accessed Mar. 11, 2021).

[16] Zopellaro Soares AA, Lucas Vieira J, Quincozes SE, Ferreira VC, Uchôa LM, Lopes Y, Passos D, Fernandes NC, Monteiro Moraes I, Muchaluat-Saade D, Albuquerque C. SDN-based teleprotection and control power systems: A study of available controllers and their suitability. International Journal of Network Management. 2021 May;31(3):e2112.
[17] "Installing POX — POX Manual Current documentation." https://noxrepo.github.io/pox-doc/html/ (accessed Mar. 11, 2021).
[18] Stancu AL, Halunga S, Vulpe A, Suciu G, Fratu O, Popovici EC. A comparison between several Software Defined Networking controllers. In2015 12th international conference on telecommunication in modern satellite, cable and broadcasting services (TELSIKS); 2015 Oct 14; Nis, Serbia. (pp. 223-226). IEEE.
[19] "GitHub - faucetsdn/ryu: Ryu component-based software defined networking framework." https://github.com/faucetsdn/ryu (accessed Mar. 11, 2021).
[20] Ahmad S, Mir AH. Scalability, Consistency, Reliability and Security in SDN Controllers: A Survey of Diverse SDN Controllers. Journal of Network and Systems Management. 2021 Jan;29(1):1-59.
[21] "Home - OpenDaylight." https://www.opendaylight.org/ (accessed Mar. 11, 2021).
[22] Eftimie A, Borcoci E. SDN controller implementation using OpenDayLight: experiments. In2020 13th International Conference on Communications (COMM) 2020 Jun 18; Bucharest, Romania. (pp. 477-481). IEEE.
[23] Neto FJ, Miguel CJ, de Jesus AC, Sampaio PN. SDN Controllers-A Comparative approach to Market Trends. In9th International Workshop on ADVANCEs in ICT Infrastructures and Services (ADVANCE 2021) 2021 Feb 2.
[24] "ONOS - ONOS - Wiki." https://wiki.onosproject.org/display/ONOS/ONOS (accessed Mar. 11, 2021).

Acknowledgments. The authors wish to acknowledge mosul university for providing the facilities needed for this paper.

A New Version of Modified Camel Algorithm for Engineering Applications

Ramzy S. Ali [1], Jawad R. Mahmood[2], Hussein M. Badr[3]
{ramzy.ali@uobasrah.edu.iq[1] , Jawad.mahmood@uobasrah.edu.iq[2],
cse.61104@uotechnology.edu.iq[3]}

Electrical Engineering Department, College of Engineering, University of Basrah, Iraq[1,2]
Training and Energy Research Office, Ministry of Electricity, Iraq, Baghdad[3]

Abstract. The new modified camel algorithm (NMCA) is presented as a novel optimization method for tackling optimization problems in this research. The modified camel algorithm (MCA) and other metaheuristic algorithms are not the same as NMCA. Where it offers a fresh perspective on global optimization. The suggested method is validated using power distribution system challenges (engineering problems) that are frequently encountered in the optimization field. The IEEE 69- and 33-bus systems were used in the simulations. The NMCA algorithm was able to find the best answers in a variety of test circumstances. The findings of the NMCA are compared to those of the MCA and other well-known optimization techniques. The findings suggest that the NMCA is capable of addressing optimization problems effectively.

Keywords: New modified camel algorithm; distributed generation; solar photovoltaic; congestion problem; power loss; voltage profile.

1 Introduction

The use of metaheuristic algorithms expands considerably as the spatial and temporal complexity of power resource management problems grows. To tackle various challenges in power resources and engineering difficulties in general, many algorithms are presented and utilised. Solar photovoltaic (PV) power is one of the most important power sources. In distribution grids, the photovoltaic distribution generator (PVDG) is one of the most promising renewable power sources. PVDG generation capacity has expanded significantly in recent years [1-2] because to its flexibility in scale application and pollution-free nature.

According to the literature review, optimization methods are commonly employed to solve complicated power system challenges (optimization problems). In comparison to traditional methods based on mathematical programming, metaheuristic algorithms are generally more powerful [3]. The researcher in [4] investigates the topic of network reconfiguration in the presence of distributed generation (DG) by employing a Harmony Search Algorithm (HS) to concurrently reconfigure and find the best places for DG unit installation in a distribution grid. Amin [5] presented a hybrid configuration of particle swarm optimization (PSO) with ant colony optimization (ACO) algorithm called hybrid PSO–ACO algorithm to solve the distribution network minimizing power losses problem and improving the voltage profile problem. The major points in the modified camel traveling algorithm are the diversification and intensification

IMDC-IST 2021, September 07-09, Sakarya, Turkey
Copyright © 2022 EAI
DOI 10.4108/eai.7-9-2021.2314874

[6-7]. The diversification phase ensures that the MCA efficiently traverses the search space, while the intensification phase sorts through the current best solutions and chooses the best candidates. MCA was created in order to solve engineering problems more quickly and with more reliable solutions [6]. For global optimization, a new modified camel algorithm (NMCA) is introduced in this study. Congestion difficulties and distribution network losses are used to test the NMCA's performance and efficiency. The results show that NMCA may be used to solve distribution network optimization problems. In addition, the NMCA can outperform existing optimization methods..
The following is a breakdown of the paper's structure: Section 2 introduces the MCA and NMCA, as well as the suggested NMCA's properties and algorithm formulation. Section 3 contains the problem formulation and constraint. The NMCA algorithm's usefulness for congestion, voltage profile power losses, and other problems is discussed in Section 4. The suggested algorithm's performance is evaluated in section 5 using congestion problems, voltage profiles, and power losses in distribution networks. The suggested NMCA algorithm's convergence mobility is discussed in Section 6. Finally, in Section 7, there are concluding observations and recommendations for future research.

2 The Camel Travelling Algorithm

The Camel Travelling Algorithm (CA) is a swarm intelligence-based technique proposed by Ramzy and Mohammed in 2016 [8]. CA is inspired by the traveling behaviour of camels during foraging. The CA algorithm has a complex structure that negatively affects the execution speed and memory size, where the CA consists of multi-loop nesting and several parameters selection. In 2019 Ramzy introduce the modified Camel traveling algorithm (MCA) with a simple structure, which significantly improve its convergence and computation speed [6]. The MCA is presented to solve engineering optimization problems. In this section, a new version of the MCA algorithm (New-MCA) is presented. The NMCA uses to find the optimum configuration (size, position, and number) of the PV units in the distribution grid to solve the congestion problem, improve voltage profile and reduce power losses. NMCA works in the same manner as MCA, with the following modification:

1. Modification of the mutation step.
2. Modification of the location equation.
3. Addition of the velocity equation.
4. Addition of the velocity limits.
5. Addition of the location limits.

Simulation of camel visibility in the MCA algorithm is employed in the same manner as the mutation simulation in other algorithms like the GA algorithm. There are two situations for updating each camel's location in the MCA algorithm. The update function is a switch from the main location equation to the second location equation when the camel visibility v exceeds a certain visibility threshold. The goal of modified mutation in NMCAs is to add variety to the camel sites. Mutation operators are employed to avoid local minima by avoiding camel sites from getting too identical to one another, which slows or even stops convergence to the global optimum.

The visibility of the camel and the simple location equation in MCA, inefficient for solving congestion problems and other distribution problems due to the following reasons:

1. The mutation step in the food searching equation must not take place in a position taken close to the food source because this affects the solution convergence.
2. The updated locations of camels might not generate a feasible solution and rounding off the new food source becomes essential.
3. MCA algorithm does not have limits applied on location equation where this affects the solution.

In NMCA, the modified mutation process was included to keep a certain level of heuristic knowledge. In the original MCA, the camels will look for a new food source in their recollection of a nearby site. In NMCA, the camels will look for a new food supply in a nearby place that they remember, and they will retain certain knowledge from the stored favourable results. The optimization algorithm will quickly converge as a result of this method. A camel develops a candidate food position by probabilistically modifying the camel location in her memory for finding a new food source. It is assumed that there are N camels (Camel Caravan) going through a (D) dimensional camel environment for the implementation of the new modified camel algorithm. Where $x^{i,itr}$ denotes the location of the camel I at the time of iteration (itr):

$$x^{i,itr} = \left\{x_1^{i,itr}, \quad x_2^{i,itr}, \quad \dots., \quad x_D^{i,itr}\right\} \tag{1}$$

and
$i = 1,2, \dots., N.$
itr: Iteration, $\quad itr = 1,2, \dots., itr_{max}.$

At the beginning ($itr = 0$), where the camels are spread in the desert and looking randomly for the water supply and food as demonstrated in the formula below:

$$\gamma = (x_{max} - x_{min}) \tag{2}$$

$$x_d^{itr} = \gamma\, R + x_{min} \tag{3}$$

Where

$R \in [0,1]$
$d = 1,2, \dots., D.$
x_d^{itr} : Location of a camel.
x_{min}: Minimum location of a camel.
x_{max} : Maximum location of a camel.
γ: Rang of camel location
The temperature (T) and effect of the temperature on the camel endurance (E) of camel i at the time iteration as shown below:

$$T_d^{itr} = (T_{max} - T_{min})Rand + T_{min} \tag{4}$$

$$E_d^{itr} = \frac{\left(T_d^{itr} - T_{min}\right)}{(T_{max} - T_{min})} \tag{5}$$

Where

T_{min}: Min amount of temperature
T_{max}: Max amount of temperature
T_d^{itr}: Temperature
E_d^{itr}: Endurance
The camel velocity and velocity limits terms can be mathematically expressed by:

$$v_{max} = 0.25\,\gamma \tag{6}$$

$$v_{min} = -v_{max} \tag{7}$$

$$v_d^{itr} = \Theta\, v_d^{itr-1} + \left(x_d^{best} - x_d^{i,itr-1}\right) E_d^{i,itr} * c \tag{8}$$

Where

v_{min}: Minimum velocity of a camel.
v_{max} : Maximum velocity of a camel.
v_d^{itr}: Velocity of a camel.
Note: $c \in [1,3]$ and $\Theta \in [0,1]$ are constants.
Finally, the main location equation is:

$$x_d^{itr} = x_d^{itr-1} + v_d^{itr} \tag{9}$$

Algorithm: New Modified CA

Begin

Step 1: Initialization: Set the temperature range and the location range Tmin and Tmax; set the camel caravan size and the dimensions; set the visibility threshold; set std. threshold; set c and Θ values; initialize the location of each camel from Eq. (3).

Step 2: Subject the locations to a certain fitness function; determine the current best location; randomly assign visibility (v) for each camel.

Step 3: While ($\boldsymbol{itr < itr_{max}}$) do
for i=1: Camel Caravan size
Compute the temperature T from Eq. (4)
Compute the endurance E from Eq. (5)
Compute the Std. of Best Costs.
Update the camel velocity from Eq. (8)
Apply velocity limits
If v <visibility threshold and Std. <Std. threshold
then
Update the camel location from Eq. (3)
else
Update the camel location from Eq. (9)
end If

```
                    Apply location limits
                        end for
          Subject the new locations to the fitness function
            If  the new best location is better than the older one
                    the new best is the global best
                  end If
                  Update the Std. counter for best costs
                  Assign new visibility for each camel
Step 4: End While
Step 5: Output the best solution
End
```

3 Problem Formulation

In today's modern power systems with large loads and renewable sources, including solar power, network security limits, such as thermal, angular stability, or voltage stability are violated. When renewable energy penetration is high, it can have a negative impact on power flow in the system and cause congestion in transmission and distribution systems. In electricity systems, a congestion problem occurs when demand for transmission capacity exceeds transmission grid capabilities. While congestion reduction will become increasingly crucial for this reason [9]. This research focuses on the network's congestion problem at the distribution level.

3.1 Objective Function

Total active power losses are one of the four key components of the multi-objective function; the L∞ to handle the voltage profile, congestion lines in the distribution network, and PVDG which are installed at the distribution level.

3.1.1 Total Active Power Loss

In the optimal operation of a working power system, total active power loss (TPL) can be considered, the major factor of economic performance, where this issue is the main objective in the optimal power system. The mathematical expression of total active power loss is given equation (10) [2, 9]:

$$T_1 = TPL = \sum_{n=1}^{N_{br}} I_n^2 \; R_n. \tag{10}$$

N_{br}: several branches in the system.

I_n: the current magnitude of the n^{th} branch.

R_n: The resistance of the n^{th} branch.

The TPL will be from zero to 10^{th} of MW.

3.1.2 The Congestion Lines in the Distribution System

One of the factors that prevent the integration of PVDG power in a distribution system is the congestion of a distribution grid due to the limited availability of distribution grid capacity. Therefore, the selection of the maximum congestion line in the distribution grid is the major factor in the objective function to solve the congestion problem in this study. The selection of the maximum congestion line is performed by employing the contingency ranking. The performance index is the main factor used for ranking the system. The circuit current-based index is used to represent the line overloads as in equation (11):

$$J_C = \sum_j W_j \left(\frac{I_j}{I_{N,j}}\right)^{2n} \quad (11)$$

$j = 1,2, \ldots . , mj$.

Where,

j : number of lines.

W_j : weighting factor, $0 < W_j < 1$.

$I_{N,j}$: thermal limit of the current line.

I_j : actual current through circuit j.
n : the exponent factor.

The term of maximum congestion line in objective function depends on the relation between the magnitude of actual current through the circuit and current-based thermal limit of the line as in equation (12) [10]:

$$T_2 = max \left(\frac{I_j}{I_{N,j}}\right) * 100 \quad (12)$$

3.1.3 PVDG Injected Power

The PVDG is available in sizes from several kilowatts to tens of megawatts and is connected to the power system at the substation or distribution levels. To find optimal PVDG with minimum total power injected in distribution level, equation (13) is used in multi-objective function as[11]:

$$T_3 = \sum_{i=1}^{N_P} P_P, i \quad (13)$$

Where,

N_P : The number of the PVDG in the Distribution system.

P_P : The power of the gth PVDG.

3.1.4 The L_∞ Technique

The injection of PVDG in the radial distribution system has many benefits to the system. But it represents an influencing factor on the voltage rise in the system. The voltage rise is the bottleneck of PVDG in the radial distribution system. Therefore, many previous studies attempted to address the question of how much PVDG can be penetrated in a distribution grid without risking overvoltage. In this study, the L_∞ the technique is proposed to improve the voltage profile, with an optimal algorithm to select the optimal size and placement of PVDG.
The ∞-norm: As $p \to \infty$, the L_p norm tends to the so-called ∞-norm, or L_∞ norm, which defines the L_∞ norm as the supremum (least upper bound) of the absolute value as in equation (14) [12]:

$$\|x\|_\infty = sup_{\ t}\ |x(t)| \tag{14}$$

For the vector $V = \{v(1), \ \dots, \ v(N_{bus})\}^T$, with, $i = 1,2,\dots,N_{bus}.$, where the N_{bus} is the number of buses in the distribution system. V is the measured voltage of the distribution system and, $v(i)$, is the measured voltage at the bus (i) in the distribution system. To find the supremum of the vector V:

$$\|V\|_\infty = sup_{\ i}\ |v(i)| \tag{15}$$

$$v_p(i) = (v(i) - 1) * 100 \tag{16}$$

$$V_P = \{v_p(1), \ \dots, \ v_p(N_{bus})\}^T \tag{17}$$

Now, the L_∞ norm will be applied to V_p to find the supremum of the vector V_p, where the V_p vector can represent the values of voltage change at each bus in the distribution system

$$T_4 = \|V_p\|_\infty = sup_{\ i}\ |v_p(i)| \tag{18}$$

The multi-objective function of the PVDG in the grid is considered as follows:

$$T = (K_1T_1) + (K_2T_2) + (K_3T_3) + (K_4T_4) \tag{19}$$

Here, T is the fitness function which is required to be minimized to reduce congestion and get minimum losses with K_1, K_2, K_3 and K_4 are represent the penalty factors.

3.2 Constraints

The objective function in equation (19) is subjected to a set of constraints, as shown below:

3.2.1 Balance Constraints of the Applied Power

The flow of current via impedances of electrified conductors causes power losses, which can be computed using equation (10). The power balance restriction is expressed as [2]:

$$\sum_{i=1}^{N_l} P_l, i \; - \; P_{Grid} \; - \sum_{i=1}^{N_P} P_P, i \; + \sum_{n=1}^{N_{br}} P_{loss}, n \; = 0 \tag{20}$$

3.2.2 The Voltage and Current Limits

The distribution grid is modelled as buses connected by a set of transmission lines with PVDGs connect to the grid. Bus 1 is the slack bus and has a constant voltage magnitude and phase, and the buses (i = 2,, $Nbus$) have variable voltages within allowable limits to ensure the required quality of service of the system. The lower and upper bounds for the voltage are 0.95 to 1.05 pu in distribution systems [13].

$$V_{min} \leq |V_i| \leq V_{max} \tag{21}$$

V_i : magnitude of the variable voltage.
V_{min}: min voltage limits.
V_{max}: max voltage limits.

The line current limitation in the transmission line between buses (i and j) is imposed as in equation (22) [2, 13]:

$$I_{ij} \leq \; I_{i\,j}^{max} \tag{22}$$

3.2.3 The PVDG Units' Capacity Limits

The acceptable voltage limits in the distribution network will be violated due to the further addition of PVDGs, which cause an increase in network losses due to the reverse power flow. Thus, the hosting capacity of PVDG of the distribution network is limited by overvoltage. The power of each PVDG unit is select within a specific range:

$$P_P^{min} \leq P_P \leq P_P^{max} \tag{23}$$

Also, the sum of the capacity of all PVDG units should not be exceeded the load demand in the distribution grid as represented in equation (24):

$$\sum_{i=1}^{N_P} P_P, i \leq \sum_{i=1}^{N_l} P_l, i \tag{24}$$

4 NMCA Optimization Algorithm for PVDG Units

PVDG planning is one of the most essential concerns with considerable economic and technical implications. With the rapid development in the number of PVDG units connected to the power grid, multiple methods for solving optimization issues with various objective functions and constraints have been developed. An extra power source can be introduced to the grid by strategically placing and sizing PVDGs. This will help to improve the system and alleviate congestion. In this section, NMCA has been used to determine the appropriate location and size of PVDG units in order to alleviate congestion and reduce overall power loss. The following is a detailed description of the entire process of applying the NMCA algorithm for optimal PVDG unit allocation in a radial distribution power system:

Step 1: Initialization:

Set the temperature range T_{min} and $T_{min}$and the location range set the camel caravan size and the dimensions, set the Visibility threshold, set Std. threshold set c and Θ values, initialize the location of each camel.

Upload system data, that includes bus and line data of the radial distribution system.

Define the constraints of the problem.

Step 2: Subject the locations to a certain fitness function, determine the current best location, and randomly assign visibility (v) for each camel.

To calculate the fitness function:

Subject the solution (PV location and size) to the Distribution system.

Run power flow to obtain all variables.

Run contingency analysis.

Calculate L_∞ .

Calculate total power loss, then calculate fitness function (multi-objective function) by using Equation (19).

For r=1: Run

Step 3:

While (iter < itermax) do

For i=1: Camel Caravan size

Compute the temperature T.

Compute the endurance E.

Compute the Std. of Best Costs.

Update the camel velocity.

Apply Velocity Limits

If v < visibility threshold and Std. < Std. threshold then

Update the camel location from Eq. (3)

Else

Update the camel location from Eq. (9)

End If

Apply location limits

End for

Subject the new locations to the fitness function

Calculate the fitness function

If the new best location is better than the older one

The new best is the global best

End If

Update the Std. counter for best costs

Assign new visibility for each camel

Step 4: End While

Step 5: If the problem limits are satisfied then

Output the best solution

Else

Rule out the solution

End If

Step 6: If the new best solution is better than the older one.

Then the new best is the global best

End If

End for

End

5 The Radial Distribution System as a Testbed for the Proposed Algorithm

The in this section, different case studies are conducted to evaluate the overall performance of the proposed strategy. Two IEEE test systems are considered here:

1. Scenario 1: normal load-case of 33-bus with PVDG.
2. Scenario 2: heavy load case of 33-bus with PVDG.
3. Scenario 3: normal load-case of 69-bus with PVDG.
4. Scenario 4: heavy load case of 69-bus with PVDG.

5.1 Case Study (1)

The proposed strategy is applied to IEEE 33 bus structure system. Here, the problem is to find an optimal configuration (the number, locations, and sizes) of PVDGs. This system has been modified such that the current load is 3.7 MW active power and 3.53 MVAR reactive power, whereas the original system with 3.7 MW active power and 2.3 MVAR reactive power [14]. the modification's purpose is to create a suitable environment for congestion problems and voltage droop problems. The power calculation has been done assuming Sbase = 100 MVA and Vbase =12.66 kV. Figs 1 and 2 reflect the system behaviour with and without PVDGs for normal loading conditions. Figures (1) show the system busses current with the presence and absence of PVDGs in addition with line limits. From the figure one can conclude the flowing points:

1- Reduction of lines current. Such that all the current droop below limits values.
2- Reduction of current has a significant effect on reduced power loss and relief the congestion in the system.

Fig 2 shows the voltage profile of the system under consideration with and without PVDGs installation. From the obtained result's one can see when there are no PVDGs the voltage profile suffers from noticeable voltage droop special in buses (16-17-18), where voltage droop to (0.8658 pu). but on the application of PVDGs, the system profile improved efficiently, and the voltage profile tolerated between (1 and 0.9901) pu.

5.2 Case Study (2)

In this case, the system has been tested for heavy loading represented by 5.1401MW active power and 4.942MVAR reactive power. also, the power calculation has been done assuming Sbase = 100 MVA and Vbase =12.66 Kv. From Fig 3 the following points are clear:

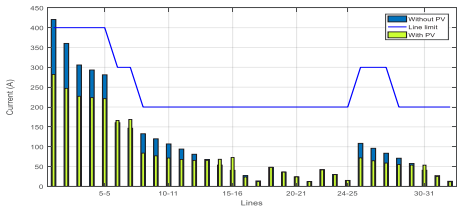

Fig. 1. Lines current without and with PVDG 33-bus system with a normal load

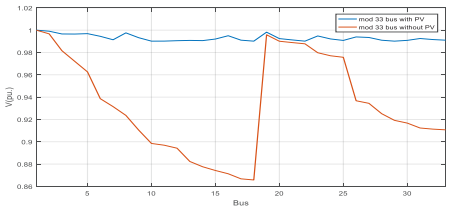

Fig. 2. Volt profile without and with PVDG units for the same bus of Fig. 1

1. When there is no PVDGs power the system loading for lines (1-2,2-3, 3-4, 4-5, and 5-6) exceding their thermal limits and the system cannot deal with such loading specific in these buses.
2. On the application of PVDGs the bus's current droop below their thermal limits and there (inline (1-2) the current before installing PVDGs is (611A) and after installed PVDGs is (399A).

From Fig 4 the following points are clear:

1. When there are no PVDGs the system suffers from a high deviation in voltage profile where it reaches (0.8003 pu) and the accepted limit in distribution grid is (1.05 to 0.95) pu.
2. The PVDGs Improve the voltage profile when installed, where the deviation in the voltage profile reduces from (0.8003 pu) to (0.9861 pu).

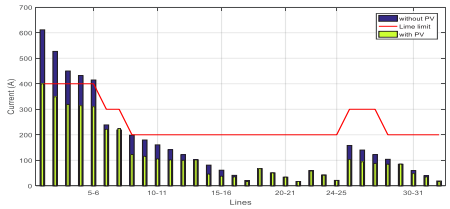

Fig. 3. Lines current with and without PVDG units, for a 33-bus system with a heavy load.

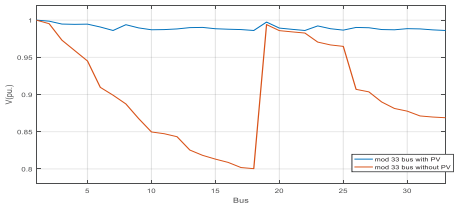

Fig. 4. Volt profile with and without PVDG units For the same bus of Fig. 3

5.3 Case Study (3)

The proposed strategy has been applied to IEEE 69 bus structure system. In this case, the system has been tested for normal loading represented by 3.8 MW active power and 2.7 MVAR reactive power [15]. also, the power calculation has been done assuming Sbase = 100 MVA and Vbase =12.66 Kv Figure(5) and figure (6) demonstrate the results for applied PVDGs in IEEE 69 system. From figure (5), the following points are clear:

1. On the application of PVDGs the buses current droop below their thermal limits and there (inline (1-2) the current before installing PVDGs is (387.18 A) and after installed PVDGs is (216.1A)
2. The result of the reduction of current is power loss reduction and relief of the congestion in the system.

From the figures (6) the following points are clear:

1. When there are no PVDGs the system suffers from a high deviation in voltage profile where it reaches (0.9092 pu).
2. The voltage profile Improved when PVDGs has installed, where the deviation in the voltage profile reduces from (0.9092 pu) to (0.9966 pu).

5.4 Case Study (4)

In this case, the system has been tested for heavy loading (1.6 from normal) represented by 6.082224MW active power and 4.30976 MVAR reactive power. also, the power calculation has been done assuming Vbase =12.66 K, and Sbase = 100 MVA. Fig. 7 and Fig. 8 demonstrate the results for applied PVDGs in IEEE 69 system. From Figure 7, the following points are clear:

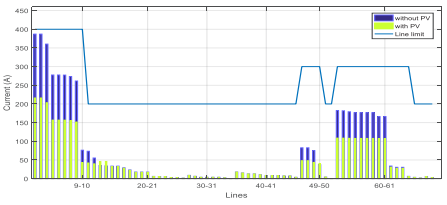

Fig. 5. Lines current without and with PVDG for 9-bus system with a normal load

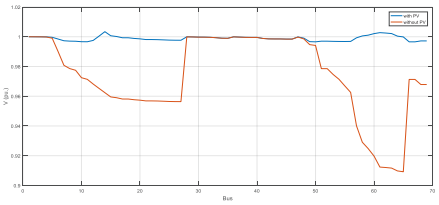

Fig. 6. Volt profile with and without PVDG units for the same bus of Figure 5.

1- When there is no PVDGs power the system loading for lines (1-2 , 2-3, 3-4, 4-5, 5-6, 6-7, 7-8, 8-9, 51-52, 9-53, 53-54, 54-55, 55-56, 56-57, 57-58 and 58-59) exceeding there thermal limits.
2- On the application of PVDGs the buses current droop below their thermal limits and there (inline (1-2) the current before installing PVDGs is (644.3694 A) and after installed PVDGs is (348.5021 A).

From the Fig 8 the following points are clear:

1. When there are no PVDGs the system suffers from a high deviation in voltage profile where it reaches (0.8445 pu).
2. The PVDGs Improve the voltage profile when installed, where the deviation in the voltage profile reduces from (0.8445 pu) to (0.9947 pu).

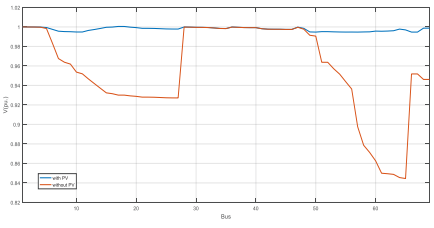

Fig. 7. Lines current with and without PVDG for a 69-bus system with a heavy load

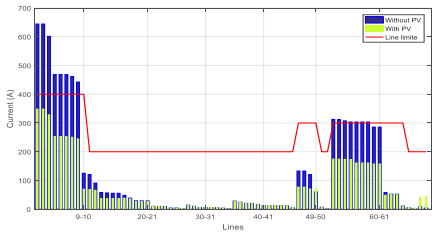

Fig. 8. Volt profile with and without PVDG units for the same Bus of Figure 7.

For verifying the performance of NMCA, eight other methods (Firefly algorithm (FA), Grey Wolf Optimizer (GWO), particle swarm optimization (PSO), Improved invasive weed optimization algorithm (IWO), Artificial Bee Colony (ABC) Optimization, Harmony Search (HS), modified Camel Algorithm MCA and Salp Swarm Algorithm (SSA)) are applied on the IEEE 33 and IEEE 69 systems (in case of normal and heavy load). For each algorithm in case (1) has been 20 trials, and the other cases have been 30 trials (in MATLAB program), and for

each run, 400 iterations with 400 particles. The results of these cases are shown in tables (1) to table (4). From Tables (1-4). The following points can be concluded:

1. Minimum cost and minimum mean cost (in all cases) find by The NMCA algorithm.
2. The performance of NMCA is significantly better than that of MCA, in all cases, wherein case (4) for mean cost improved (14.72%).
3. The numerical results have verified the effectiveness of NMCA on the eight other methods.

Table 1. Eight methods outcomes for the IEEE 33-bus system (normal load).

optimization Algorithms	Min cost	Max cost	Mean cost
ABC	3.297414	3.337504	3.317941
MCA	3.292848	3.394979	3.324087
FA	3.282356	3.406839	3.323749
GWO	3.282579	3.634918	3.323069
HS	3.297804	3.347978	3.321397
IWO	3.293783	3.382496	3.31921
PSO	3.290107	3.345048	3.31598
SSA	3.287941	3.634899	3.362063
NMCA	3.282302	3.316998	3.300953

Table 2. Eight methods outcomes for IEEE 33-bus system (heavy load).

optimization Algorithms	Min cost	Max cost	Mean cost
ABC	19.75975	21.8354	20.40861
MCA	19.70274	23.54049	21.05797
FA	19.52142	19.77067	19.58841
GWO	19.51542	19.72042	19.56593
HS	19.51121	19.64605	19.58954
IWO	19.52976	22.9247	20.25597
PSO	19.51977	19.80548	19.62532
SSA	19.51679	20.11197	19.71944
NMCA	19.5	19.683	19.56436

Table 3. Eight methods outcomes for the IEEE 69-bus system (normal load).

optimization Algorithms	Min cost	Max cost	Mean cost
ABC	2.868379	3.033751	2.943347
MCA	2.851789	3.251348	2.965185
FA	2.851863	4.125542	3.129453
GWO	2.851981	3.312213	2.97743
HS	2.87181	3.143175	3.039544
IWO	2.851788	3.376668	3.084053
PSO	2.908849	3.275703	3.030924
SSA	2.85179	3.402151	3.106977
NMCA	2.851787	3.054887	2.858705

Table 4. Eight methods outcomes for IEEE 69-bus system (heavy load).

optimization Algorithms	Min cost	Max cost	Mean cost
ABC	11.93381	12.26654	12.14651
MCA	12.09206	16.05889	13.79611
FA	11.74758	13.41285	12.25348

GWO	11.74021	12.12139	11.9055
HS	11.88661	12.12976	11.99741
IWO	11.73223	15.15766	12.56227
PSO	11.73144	12.59769	11.80033
SSA	11.74168	12.86283	12.22365
NMCA	11.70647	12.09886	11.76586

The minimum cost and minimum mean cost in two cases normal and heavy load for 69-bus system reached by NMCA algorithms. Implement the NMCA algorithm to discover the best PVDG unit allocation to reduce traffic congestion, reduce power loss, and keep all bus voltages within an acceptable range. The NMCA algorithm is run on two study systems: an IEEE 33-bus system and an IEEE 69-bus system.

6 Discussion on NMCA convergence

The convergence rate (CR) value is determined for all the investigated situations to test the convergence speed to further examine the performance of the proposed NMCA to handle the primary problems in the distribution grid (power losses, congestion, and voltage profile) as follows [15]:

$$CR = \left(1 - \frac{NFE^R}{NFE^{max}}\right) \times 100\ \% \tag{25}$$

NFE : evaluations number.
NFE^{max} : the max of NFE.
The worst and best convergence profiles of the considered method are indicated by CR ∈ [0, 1], and the values of CR equal to zero and unity, respectively. [15] is the adopted technique for determining the value of CR for any number of optimization methods:

1. Run all the optimization methods up to NFE^{max}.
2. The value of interest is determined as the defined minimum objective value (in the case of the minimization issue).
3. Determine which NFE each algorithm has reached this value and mark it as NFER in that NFE.
4. Calculate the CR for each algorithm using the formula indicated in equation (25).

The best-obtained convergence profiles of the observed test cases are used to calculate the CR value. Table 5 shows that the suggested NMCA algorithm has the greatest average CR value, indicating that it converges to the optimum solution in a less number of NFFEs than any of the other approaches considered. Figures 9 and 10 show comparative graphs of the fitness function for all of the optimization approaches investigated. In most circumstances, NMCA finds the lowest fitness value with a faster convergence profile. In this investigation, it outperforms the other examined algorithms.

Table 5. The values of CR running over many methods.

Algorithms	CR%	
	IEEE 33 bus	IEEE 69 bus

	Case1	Case2	Case3	Case4
ABC	51.5	22.5	10.5	6
MCA	46.5	54	46.5	1
FA	84	84	81	67.5
GWO	7	11	20	0.5
HS	17	31.5	2.5	4.5
IWO	45	23	66	17.5
PSO	2.5	12.5	35	19.5
SSA	29.5	34	35.5	23.5
NMCA	86	89	83	69.5

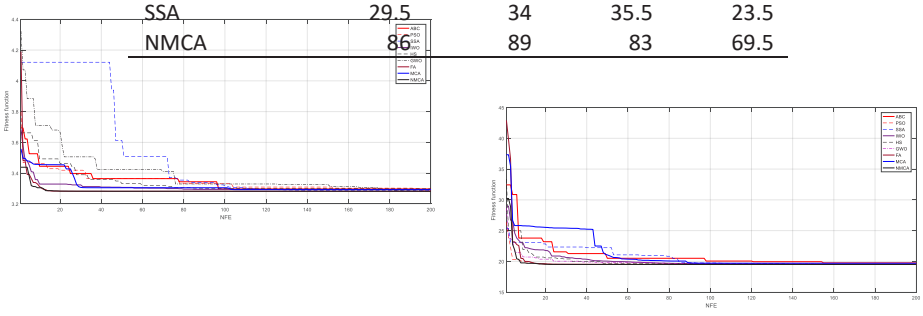

Case 1 Case 2

Fig. 9. Fitness function convergence over various algorithms over IEEE 33-bus: Case 1 and Case2

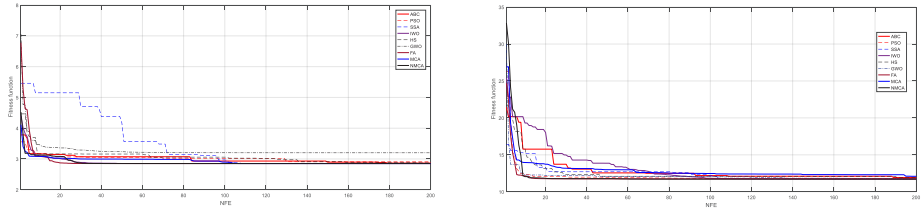

Case 3 Case 4

Fig. 10. Fitness function convergence over various algorithms about IEEE 69-bus: Case 3 and Case 4

7 Conclusion

An optimal configuration of PVDGs to relieve congestion problems in the power system has been adopted in this work. This was accomplished using a unique NMCA algorithm. The NMCA was inspired by camels' behaviour in searching for food and water in the desert. The suggested approach is fairly basic, and it only needs a few parameters to modify, therefore it can be used to a broader class of optimization issues than just engineering problems. The validity of the NMCA is tested utilising power system issues. The overloaded lines, voltage profile, and power losses in the distribution system are all taken into account. On IEEE 33-bus and IEEE 69-bus test power systems, the suggested NMCA approach has been effectively implemented. The present method can outperform the well-known algorithms (like ABC, MCA, FA, GWO, HS, IWO, PSO, and SSA) and the convergence of the algorithm is evaluated here using convergence rate and convergence plots. The suggested technique is also very effective for limited engineering situations, according to the results. Because NMCA is so effective, it's possible to make enhancements in design, such as for multi-objective and high-dimensional

optimization problems. Future researchers will find NMCA to be an effective optimization technique for dealing with multi-objective large-scale power system challenges.

References

[1] Pillai, D.S.; Rajasekar, N. A comprehensive review on protection challenges and fault diagnosis in PV systems. *Renewable & sustainable energy reviews* 2018, *91*, 18-40.

[2] Duong, M.Q.; Pham, T.D.; Nguyen, T.T.; Doan, A.T.; Tran, H.V. Determination of Optimal Location and Sizing of Solar Photovoltaic Distribution Generation Units in Radial Distribution Systems. *Energies* 2019, *12*, 174.

[3] Sahab, M.G.; Toropov, V.V.; Gandomi, A.H. 2 - A Review on Traditional and Modern Structural Optimization: Problems and Techniques. In *Metaheuristic Applications in Structures and Infrastructures*, Gandomi, A.H., Yang, X.-S., Talatahari, S., Alavi, A.H., Eds.; Elsevier: Oxford, 2013; pp. 25-47.

[4] Rao, R.S.; Ravindra, K.; Satish, K.; Narasimham, S.V.L. Power Loss Minimization in Distribution System Using Network Reconfiguration in the Presence of Distributed Generation. *IEEE Transactions on Power Systems* 2013, *28*, 317-325, doi:10.1109/TPWRS.2012.2197227.

[5] Heidari, M.A. Optimal network reconfiguration in distribution system for loss reduction and voltage-profile improvement using hybrid algorithm of PSO and ACO. *CIRED - Open Access Proceedings Journal* 2017, *2017*, 2458-2461.

[6] Ali, R.S.; Alnahwi, F.M.; Abdullah, A.S. A modified camel travelling behaviour algorithm for engineering applications. *Australian Journal of Electrical and Electronics Engineering* 2019, *16*, 176-186, doi:10.1080/1448837X.2019.1640010.

[7] Yang, X.-S. *Nature-Inspired Optimization Algorithms: Second Edition*; 2020.

[8] Mohammed Khalid, I.; Ramzy Salim, A. Novel Optimization Algorithm Inspired by Camel Traveling Behavior. *Iraqi Journal for Electrical And Electronic Engineering* 2016, *12*, 167-177.

[9] Abdul Kadir, A.F.; Mohamed, A.; Shareef, H.; Wanik, M.Z.C.; Ibrahim, A.A. Optimal sizing and placement of distributed generation in distribution system considering losses and THDv using gravitational search algorithm. *Prz. Elektrotech. Przeglad Elektrotechniczny* 2013, *89*, 132-136.

[10] Stefopoulos, G.K.; Fang, Y.; Cokkinides, G.J.; Meliopoulos, A.P.S.; Proceedings. 37th North American Power, S. Advanced contingency selection methodology. 2005, 67-73.

[11] Mukherjee, V.; Verma, S. Optimal real power rescheduling of generators for congestion management using a novel ant lion optimizer. *IET Generation, Transmission & Distribution* 2016, *10*, doi:10.1049/iet-gtd.2015.1555.

[12] Doyle, J.C. Feedback Control Theory. 2013.

[13] Wazir, A.; Arbab, N. Analysis and Optimization of IEEE 33 Bus Radial Distributed System Using Optimization Algorithm. 2016.

[14] Gonzalez, G.; Barragan, L.; Rivas, E. Locating distributed generation units in radial systems. *Contemporary Engineering Sciences* 2017, *10*, 1035-1046, doi:10.12988/ces.2017.79112.

[15] Aman, M.M.; Jasmon, G.B.; Bakar, A.H.A.; Mokhlis, H. A new approach for optimum simultaneous multi-DG distributed generation Units placement and sizing based on maximization of system loadability using HPSO (hybrid particle swarm optimization) algorithm. *Energy* 2014, *66*, 202-215, doi:https://doi.org/10.1016/j.energy.2013.12.037.

[16] Gandomi, A.H. Interior search algorithm (ISA): A novel approach for global optimization. *ISA Transactions* 2014, *53*, 1168-1183, doi:https://doi.org/10.1016/j.isatra.2014.03.018.

Comparison and Assessment of Two Load Flow Methods for Optimum Under Voltage load Shedding in Distribution Power System

Waleed Khalid Shakir Al-Jubori[1], Ali Nasser Hussain[2]
{waled_k@atu.edu.iq /wjubori@gmail.com[1], alinasser1974@yahoo.com[2]}

Technical College of Al-Mussaib, Al-Furat Al-Awsat Technical University, Babil, Iraq[1]
Electrical Engineering Technical College, Middle Technical University, Baghdad, Iraq[2]

Abstract. Under voltage load shedding is considered to avoid voltage collapse. Usually, the loads are modelled as constant power types, while different load models are used in load flow studies. A study of optimal load shedding is presented in this research, along with a comparison and evaluation of two load flow methods taking into account various load models. The algorithm is used optimised Dolphin method to oachieve the voltage values of buses while also reducing losses. Under the health and fault cases of the system, a comprehensive comparison and assessment of the optimization performances for four different load shedding models constant power, constant current, constant impedance, and composite ZIP models were performed to determine which model provides the most improvement in the voltage profile and loss reduction using the MATLAB programme.

Keywords: Voltage stability, Under voltage load shedding, Backward-Forward load flow, Dolphin optimization algorithm.

1 Introduction

The electrical power system is often operated with its stability boundaries. The in equipoise of active and reactive power can lead to simultaneous voltage instability and if the imbalance between the reactive and active power increased the system will be collapse eventually [1]. The under-voltage scheme is designed as it represents the ultimate line of protection against voltage instabilities based on the determination of distribution for load shedding using the voltage magnitude datum. A methodology of Under Voltage Load Shedding (UVLS) is proposed and solved utilizing Particle Swarm Optimization (PSO) [2].

An efficient load shedding using a genetic algorithm to improve the voltage stability is given in reference [3]. The taking apart (outage) of a considerable generating unit or failure of a highly loaded transmission line can cause the system (collapse). Under such a situation, load shedding is undertaken to avoid the voltage failure situation after exhausting all other countermeasures. An advanced method of UVLS is submitted which deals in the emergency condition without manipulated the constraints [4]. It uses the P-V curves and a UVLS logic relay design in the MAT LAB Simulink.

The UVLS scheme based on voltage stability index (VSI) for distribution network is proposed in [5]. A distribution network energized by two DGs has been implemented in PSCAD software to test the UVLS scheme. In [6], a UVLS scheme is proposed. The optimal pattern of load shedding subject to technical constraints is determined using the proposed scheme. The

IMDC-IST 2021, September 07-09, Sakarya, Turkey
Copyright © 2022 EAI
DOI 10.4108/eai.7-9-2021.2314872

predefined voltage stability margin is determined using the minimum load shedding pattern results for the proposed algorithm while meeting the operational constraints.
A new technique of load shedding by using hybrid optimization is proposed in reference [7]. In addition to weak buses identification by its capability of identifying critical areas in a large power system using the Quick Voltage Stability Index (QVSI), determining the voltage failure point, the highest allowable load, and an interlinked scheme of the most important line. A modern adaptive and centralized of (UVLS) to reduce the short-term voltage instability while analysing the UVLS core challenges is produced in reference [8]. The load shedding is estimated and dependent on the local measurements needed for the proposed method. The (UVLS) scheme using Ant Lion Optimizer (ALO) is presented in reference [9]. The position of the load bus to be shed is selected based on the (VSI).

2 Optimal Load Shedding for Distribution System

UVLS assesses itself as to be such a technique for voltage instability and collapse prohibition as it is very frugal and simple to implement [10]. The voltage on the most sensitive buses decreases when the system heavily loads which results in a shortage of reactive power backup and also this can happen due to poorly organized reactive power service. The UVLS is defined as a correction factor after some control actions failed to react with the critical operating mode which results in the power flow can be unresolved [11]. Because of economic reasons, the use of optimal load shedding can decrease financial losses and enhance the voltage profile. The optimal load shedding with a suitable optimization algorithm provides the following advantages:

1. The accurate and optimum calculation for load shedding.
2. Reliable and powerful performance.
3. The ability to implement in modern and complex systems.

3 Methodology of Load Flow

Traditional load flow strategies example Newton Raphson Method (NRM) are insufficient and can differ due to radial and high ratio of R/X ratio electrical distribution systems [12]. As a result, other methodologies, such as the Direct Backward – Forward Sweep Method, are more advanced (DBFSM). Under-voltage load shedding is used, and a comparison of the methodologies is used to demonstrate the effectiveness of DBFSM load flow. [13] describes the main phases of the load (power) flow mechanism.

4 Types and Load Modeling

The findings of study into stability and load flow have highlighted choices that are necessary to improve the overall effectiveness of the power system. As a result, all component models must be combined into a single mathematical model to describe the overall power system. The load simulation can affect the outcome of this study. The static and dynamic load models are the two types of load representation models, and this study focuses on the static load

model. Two variants of the static load model: exponential and polynomial models, which are most generally used for load flow solutions. [14].

4.1 Exponential Load Model

Active and reactive powers are derived from this model as a function of the bus bar given (voltage & frequency). An exponential voltage (V) of static load is given by:

$$P_d = P_0(\mathrm{V}/V_0)^{np} \tag{11}$$

$$Q_d = Q_0(\mathrm{V}/V_0)^{nq} \tag{12}$$

Where: (P_d, Q_d) are represent the desired of active and reactive power, (P_0, Q_0) are represent the consumption of active and reactive load power, (n_p, n_q) indicatethe exponent of active and reactive power and (V, V_0) are supply and rated voltage. The magnitudes of np and nq are stated in [15].

4.2 Model of Polynomial Load

In electrical power systems, many types of loads are employed, and each node has a specific fraction of these loads, which fluctuate over time. ZIP model is the most widely used model that incorporated with (P-model), (I-model), and (Z-model). This model is evident as [16]:

$$P = \alpha P_0 V^2 + \beta\, P_0\, V + \gamma\, P_0 \tag{13}$$

$$Q = \alpha Q_0 V^2 + \beta\, Q_0\, V + \gamma\, Q_0 \tag{14}$$

$$\alpha + \beta + \gamma = 1 \tag{15}$$

The percentage contribution of constant (Z), constant (I), and constant (P) in each node is expressed by α, β, and γ. Active power and reactive power are only studied based on the alterations in voltage, but the disparity in power dependent on alterations is not investigated. In this study, α =0.6, β=0.2, and γ=0.2 are selected to provide the best outcomes for reducing the system losses and improving the voltage level.

5 Application of Dolphin for Load Shedding Problem

Initially, Dolphins explore all areas in the seeking area around it to expose the prey. The Dolphin narrows the search process at the moment the Dolphin hits the target and increases the swill clicks to focus on the position of the prey. This technique imitates the control of pursuing the echolocation of the Dolphin about the mileage from the bait [17]. The seeking space should be arranged based on the organizing form tabulated in [18]. The detailed steps of DOA are explained in the reference [19]. The optimal DOA parameters are recorded in Table 1.

Table 1. Optimum DOA parameters

Parameter Type	Rate (Value)
Population	30

Probability	0.1
No. of Iteration = Max (N. R)	30
No. of Iteration = Max (B − F)	90

6 Objective Functions

Minimize Ploss within multi-objective functions is profitable including the boost of voltage values for system buses (voltages profile).

6.1 Reduction of ($\mathbf{P_{loss}}$) (objective function. 1)

$$(ob.fun.1) = P_{loss} \tag{15}$$

$$P_{loss} = \sum_{l=1}^{N_{br}} P_{lossl} \text{ kW} \tag{16}$$

$$P_{lossl} = {I_l}^2 * R_l \text{ kW} \tag{17}$$

Where: P_{loss} : is the overall losses, N_{br}: is the branches, R_l : is the resistance of branch l , I_l : is the flowing current in the branch l.

6.2 Voltage Profile Enhancement (ob. fun. 2)

Appropriate voltages range should be applied:

$$(ob.fun.2) = V_C * Re_v + C_C * Re_i \tag{18}$$

Where Vc denotes the bus voltage limitations, Cc denotes the branch current limits, and Rev: Bus voltage retaliation variable. Branch currents' vengeance element, according to Rei. If the branch current fails to reach the thermal limit, this parameter is set to zero.
After implementing the load shedding process, optimizing problem savings depends on the cost of base power losses, taking into account the cost coefficient equal to (0.06 $/KWH [20].To brew the compound final objective function ($ob.fun.f$), the two objective functions of lowering (P_{loss}) ($ob.fun.1$) and improving the voltage profile ($ob.fun.2$) are combined

$$ob.fun.f = ob.fun.1 + ob.fun.2 \tag{19}$$

7 General Constraints

7.1 The Technical Constraints

The constraints have stated the limits required into of the following groups:

i. Limitations(constraints) of bus voltage

The voltage value for each of the system buses can be stated as:

$$|V_{jmin.}| \leq |V_j| \leq |V_{jmax.}| \qquad j \in N_{bus}, \tag{20}$$

Where: (N_{bus}) is the number of buses on the network.
The voltage buses are $(0.95 - 1.05)\ p.u$[21].

ii. Limitations (Constraints) of branch current

On the one hand, the branch current must not exceed a predetermined maximum amount while still assuring load power transmission continuity [22].

$$|I_l| \leq |I_{lmax.}| \qquad l \in N_{br.} \tag{21}$$

Where: $(N_{br.})$ is the number of branches of the system.

7.2 Operational Limitations (Constraints)

These kinds of constraints are known as boundaries of equality and are divided into two sorts:

i. Radial (constraints) for whole system loads

The radial system configuration condition is verified by looking at the determinant of the [A], which has rows = branches and columns = number of buses, as shown below [23]:

$$[A] = \begin{cases} 1 \ \ If\ the\ \ branch\ \ i\ is\ out\ \ from\ bus\ j \\ -1\ if\ the\ branch\ i\ is\ \ inside\ into\ bus\ j \\ 0\ if\ \ the\ branch\ i\ is\ \ not\ linked\ \ to\ bus\ j \end{cases} \tag{22}$$

ii. Constraint) of balancing real power

$$P_{Sup} = P_{Dem} + P_{loss} \tag{23}$$

Where (P_{sub}) is the sum of real power that supplied to the power system, (P_{Dem}) is the overall demand of real power from the load.

8 Simulated Results

The DOA optimization procedure was designed and implemented in a computer programme using the MATLAB program. It is applied to reduce the searching space for the IEEE Radial Distribution System (RDS), which is used to choose shaded bus locations and shading amounts. Figure 1 depicts the RDS single-line diagram case study.

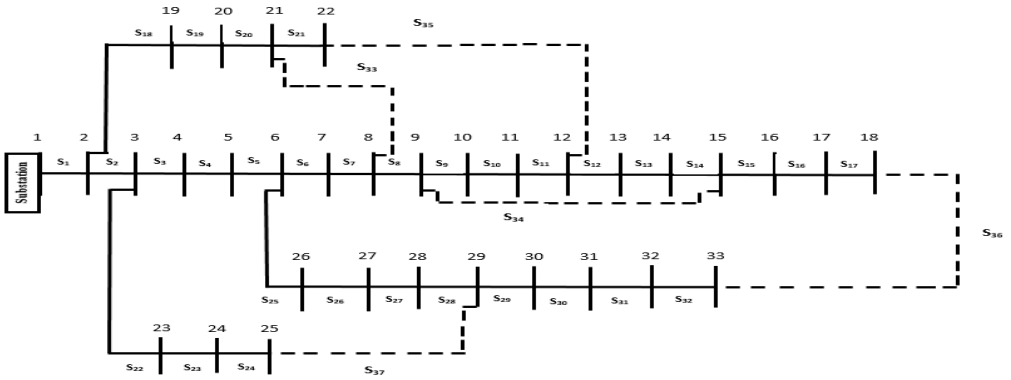

Fig 1. The RDS single line diagram of standard IEEE- 33 bus.

It includes (1 primary, 3 lateral) feeders, 37 branches, 5 opened and 32 closed switches. The system data with tie switches are given in [24]. The steps for UVLS are carried out by the selection of 3- buses. The network is studied for healthy and faulty cases when one of the lines is isolated and the network reconnected using an alternative tie-line.

8.1 Standard IEEE 33 bus for healthy case

Table 2 shows the results and comparisons between several load models with UVLS towards the optimal path of 3 buses using DOA and a healthy network for the optimal option of three buses using DOA and a healthy network.

Table 2. Results without and with UVLS by using (N.R) method at the healthy case.

Item	Normal (Const.P) model		Const. (I) model		Const. (Z) model		ZIP model	
	W.O	W.	W.O	W.	W.O	W.	W.O	W.
P. loss (kW)	202.23	158.04	175.99	137.09	162.92	125.97	157.55	120.2
Q.loss (kVAr)	134.47	95.11	116.95	85.57	108.24	80.56	104.65	78.04
Location	-	6, 28,13	-	6, 8, 13	-	6, 8,13	-	6, 28,13
Proportional Shed Amount	-	0.191,0.24, 0.19	-	0.19,0.23, 0.189	-	0.189,0.23, 0.188	-	0.116,0.16, 0.115
Shed Percentage	-	20.7%	-	20.67%	-	20.59%	-	13.2%
Losses Reduction%	-	21.85%	-	22.1%	-	22.67%	-	23.65%
Vol.min.	0.911	0.95	0.918	0.95	0.9226	0.95	0.924	0.95
Vol. max.	1.00	1.00	1.00	1.00	1.00	1.00	1.00	1.00

(W.O. = Without, W = With)

When comparing various UVLS models using the N.R approach, the results reveal that the best model is the ZIP type. The implementation of a backward-forward technique based on the optimal selection of buses by DOA, as shown in Table 3, improves these findings.

Table 3. Results without and with UVLS by using (B-F) method at the healthy case.

Item	Normal (Const.P) model		Const. (I) model		Const. (Z) model		ZIP model	
	W.O	W.	W.O	W.	W.O	W.	W.O	W.
P.loss (kW)	202.677	158.18	176.627	137.55	156.87	120.61	151.14	113.92
Q.loss kVAr)	577.99	91.85	117.51	83.87	104.17	77.16	100.47	74.72
Location	-	6, 28, 13	-	6, 28, 13	-	6, 28, 13	-	6, 28, 13
Proportional Shed Amount	-	0.214,0.167, 0.185	-	0.201,0.154, 0.172	-	0.177,0.13, 0.148	-	0.15,0.103, 0.121
Shed.Percent.	-	18.87%	-	17.58%	-	15.18%	-	12.46%
Losses Reduction%	-	21.95%	-	22.12%	-	23.11%	-	24.62%
Vol.min.	0.913	0.95	0.919	0.95	0.924	0.95	0.9256	0.95
Vol..max.	1.00	1.00	1.00	1.00	1.00	1.00	1.00	1.00

Table 3 demonstrates how the ZIP model with the B-F approach improved the voltage values of system buses while lowering the values of real losses. In addition, each bus's shed quantity is lowered. With two power flow methods, Figs 2-9 illustrate the voltage values of system buses (voltage profile) and the values of power losses for each system branch in the healthy condition.

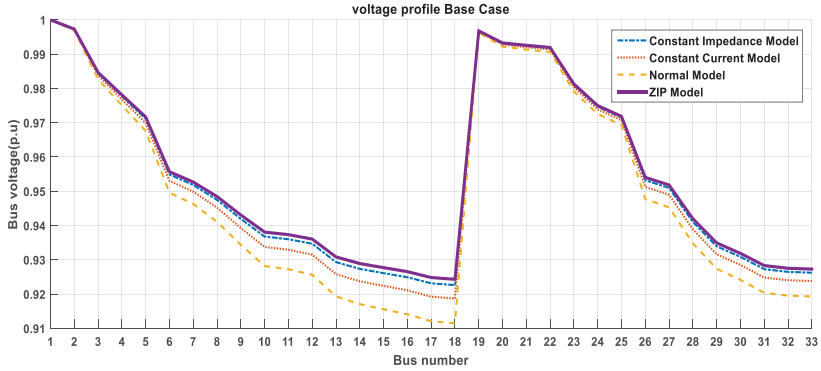

Fig 2. Voltage profile without UVLS at healthy case by using (N.R.).

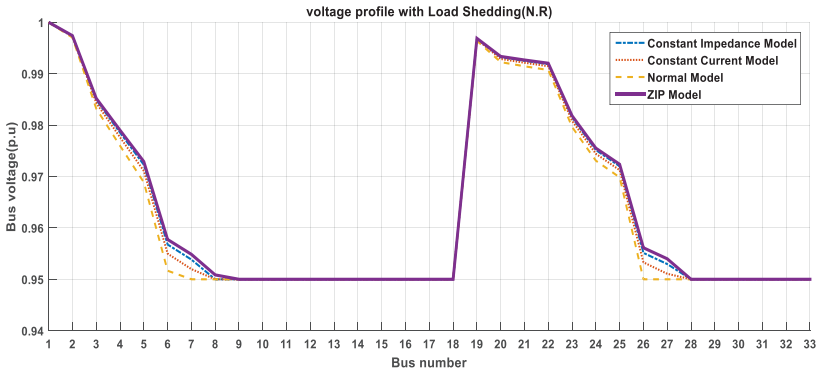

Fig 3. Voltage with UVLS at healthy case by using (N.R.).

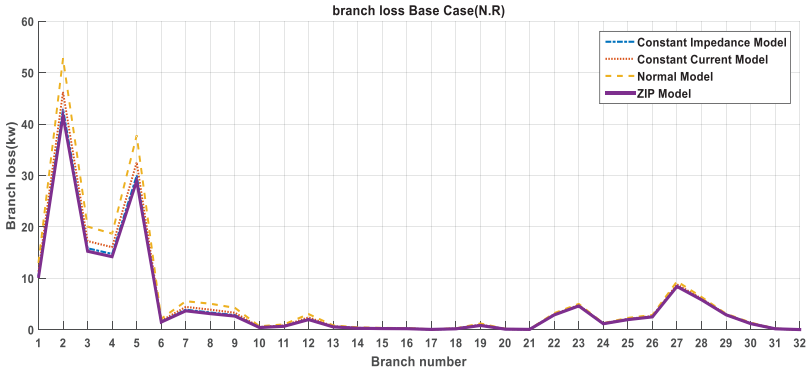

Fig. 4. Branch loss without UVLS at healthy case by using (N.R.).

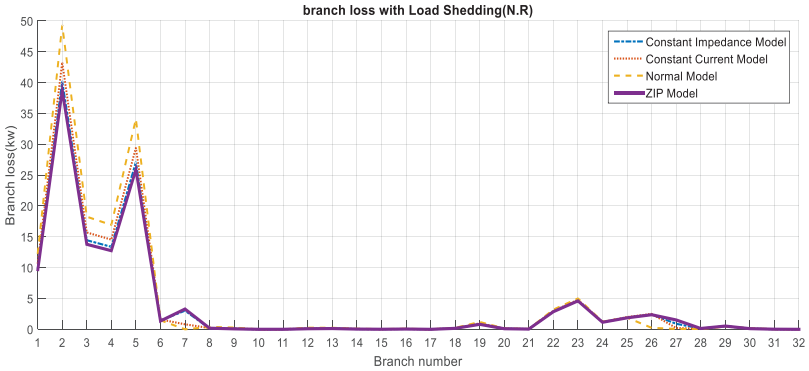

Fig. 5. Branch with UVLS at healthy case by using (N.R.).

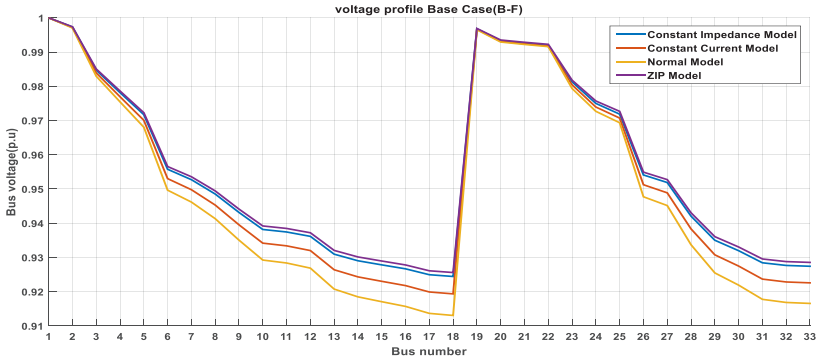

Fig. 6. Voltage profile of standard 33 bus network without UVLS at healthy case by using (B-F).

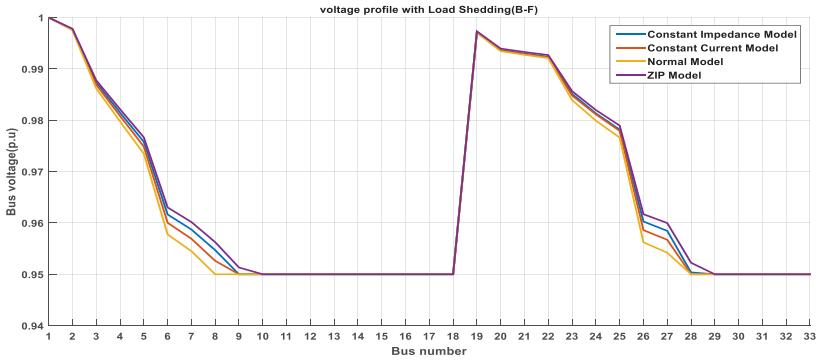

Fig.7. Voltage profile with UVLS at healthy case by using (B-F).

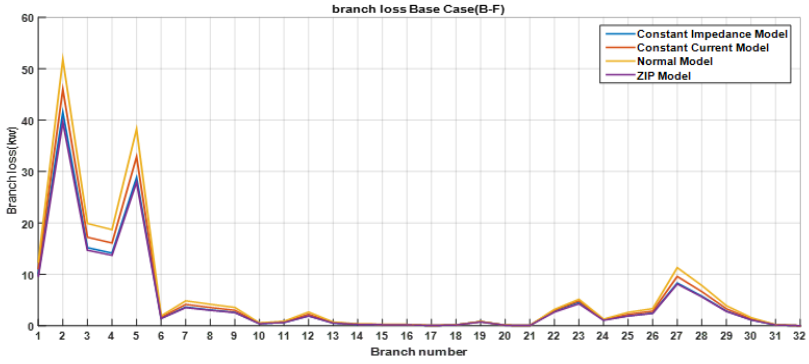

Fig. 8. Branch loss without UVLS at healthy case by using (B-F).

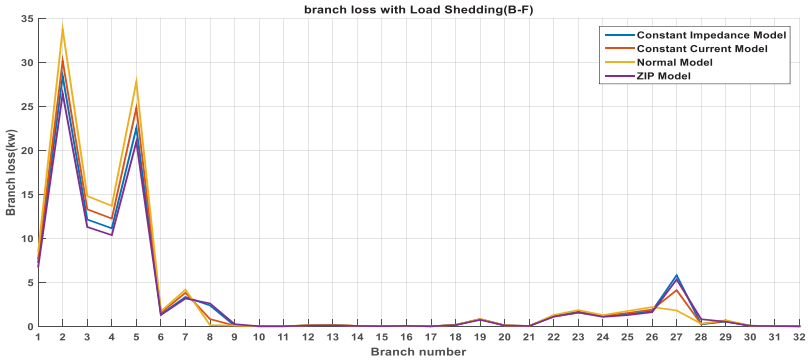

Fig. 9. Branch loss with UVLS at healthy case by using (B-F).

8.2 Standard IEEE 33 Bus for Faulty Case

The acquired results and rapprochement for the optimal option of three buses utilising DOA and defective network using various load models based on the power flow of Newton-Raphson technique without and with UVLS. The network is rejoined using tie-line (25-29), where there are five tie switches in the network, after line (28-29) is isolated.
The results reveal that the ZIP model type outperforms all other models when it comes to UVLS utilising the N.R approach. The B-F technique, which is based on DOA's optimal selection of shaded buses, improves these findings (see Table 4).
The results show that the ZIP model type is the best load model among the other models for UVLS utilising the N.R approach.

Table 4. Results of standard 33 bus without and with UVLS by using (N.R) method at the faulty case.

Item	Normal (Const. P) model		Const. (I) model		Const. (Z) model		ZIP model	
	W.O	W.	W.O	W.	W.O	W.	W.O	W.
P.loss (kW)	236.02	168.46	207.13	146.51	192.66	134.21	186.69	127.84
Q. loss kVAr)	159.46	92.44	140.02	90.82	130.28	86.07	126.27	84.89
Location	-	6, 28, 13	-	6, 28, 13	-	6, 28, 13	-	6, 28, 13
Proportional Shed Amount	-	0.26,0.15, 0.148	-	0.19,0.17, 0.17	-	0.16,0.15, 0.145	-	0.13,0.12, 0.132
Shed Percentage	-	18.96%		17.85%	-	15.18%	-	12.76%
Losses Reduction%	-	28.62%		29.26%	-	30.33%	-	31.52%
Vol.min.	0.906	0.95	0.911	0.95	0.913	0.95	0.915	0.95
Vol.max.	1.00	1.00	1.00	1.00	1.00	1.00	1.00	1.00

The B-F technique, which is based on DOA's optimal selection of shaded buses as shown in Table 5, improves these findings.

Table 5. Results of standard 33 bus without and with UVLS by using (B-F) at the faulty case.

Item	Normal (Const. P) model		Const. (I) model		Const. (Z) model		ZIP model	
	W.O	W.	W.O	W.	W.O	W.	W.O	W.
P. loss (kW)	190.74	134.37	170.08	119.64	153.59	106.63	146.63	100.2
Q. loss (kVAr)	125.2	81.74	111.57	75.54	100.69	69.48	96.16	65.37
Location	-	24, 25, 6	-	24,25,6	-	24,25,6	-	24,25,6
Proportional Shed Amount	-	0.17,0.143, 0.222	-	0.188,0.117, 0.222	-	0.106,0.105, 0.222	-	0.106,0.105, 0.153
Shed Percentage	-	17.86%	-	17.56%	-	14.44%	-	12.16%
Losses Reduction%	-	29.55%	-	29.65%	-	30.59%	-	31.6%
Vol.min.	0.928	0.95	0.932	0.95	0.936	0.95	0.937	0.95
Vol. max.	1.00	1.00	1.00	1.00	1.00	1.00	1.00	1.00

Additionally, utilising UVLS and the ZIP load model with the B-F approach, the findings obtained show an improvement in the voltage values of system buses (voltage profile) as well as loss reduction. In addition, each bus's shed quantity is lowered. Figures 10-17 depict the voltage values of system buses (voltage profile) and the values of power losses for each system branch in the defective situation using two power flow techniques, indicating that the ZIP model with B-F load flow method is superior to other models.

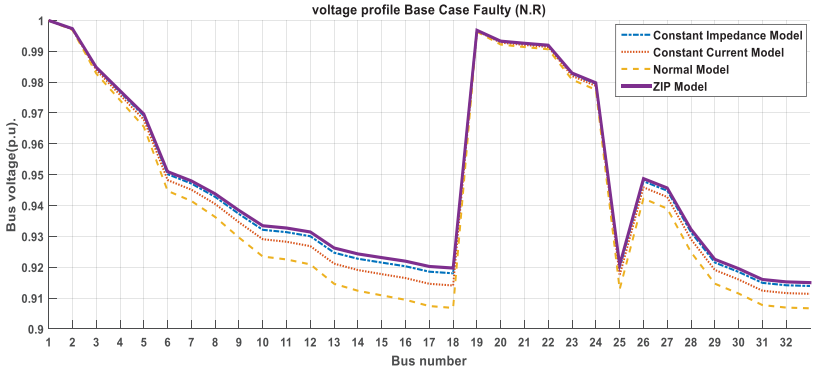

Fig. 10. Voltage profile without UVLS at faulty case by using (N.R.).

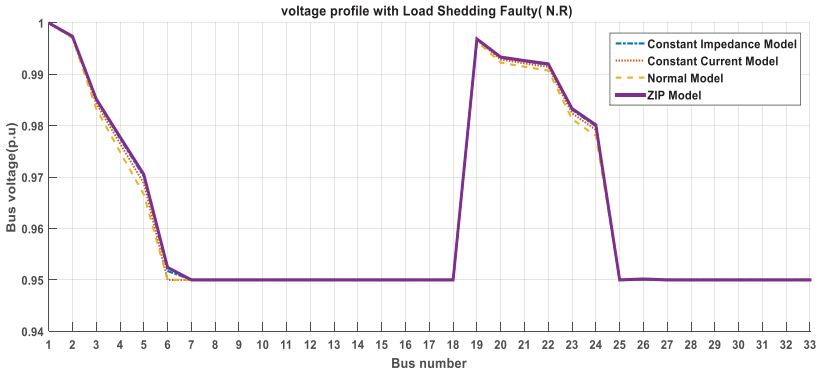

Fig. 11. Voltage profile with UVLS at faulty case by using (N.R.).

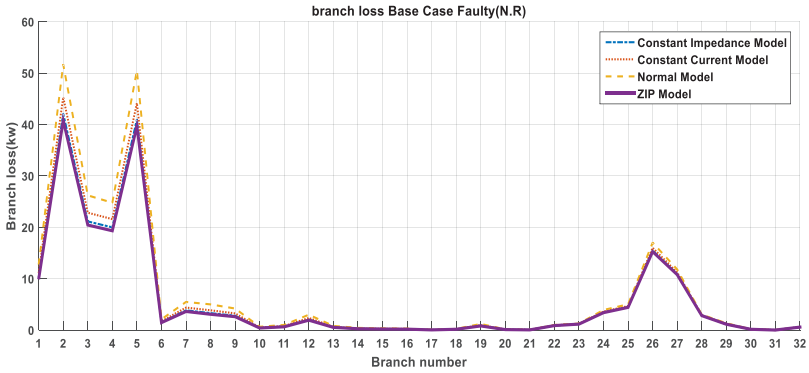

Fig. 12. Branch loss without UVLS at faulty case by using (N.R.).

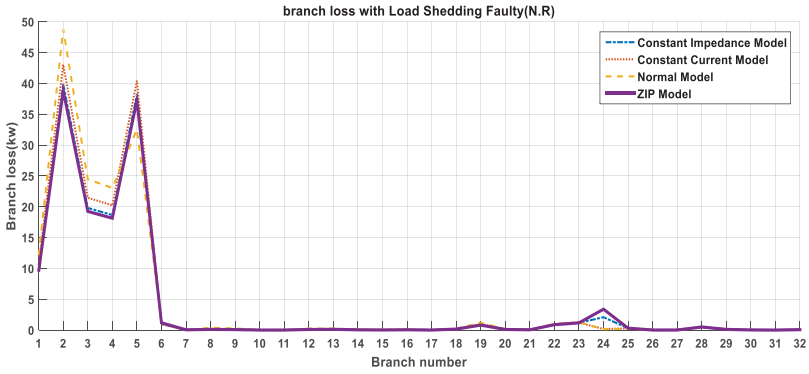

Fig.13. Branch loss of standard 33 bus network with UVLS at faulty case by using (N.R.).

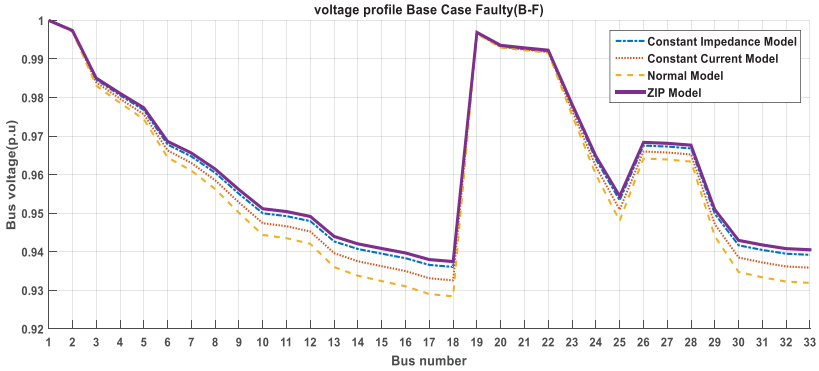

Fig.14. Voltage profile without UVLS at faulty case by using (B-F).

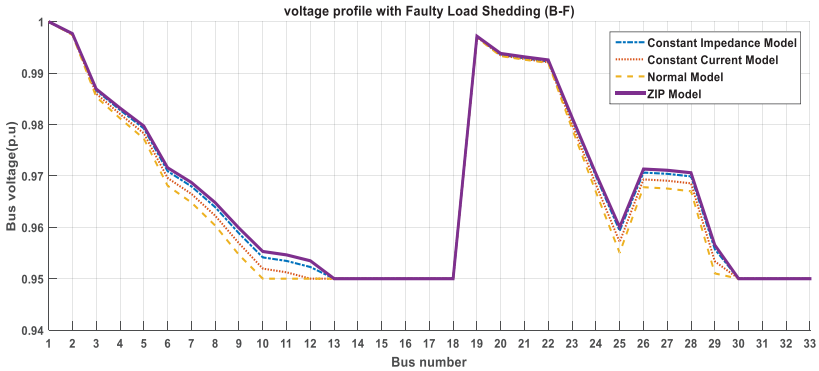

Fig. 15. Voltage profile with UVLS at faulty case by using (B-F).

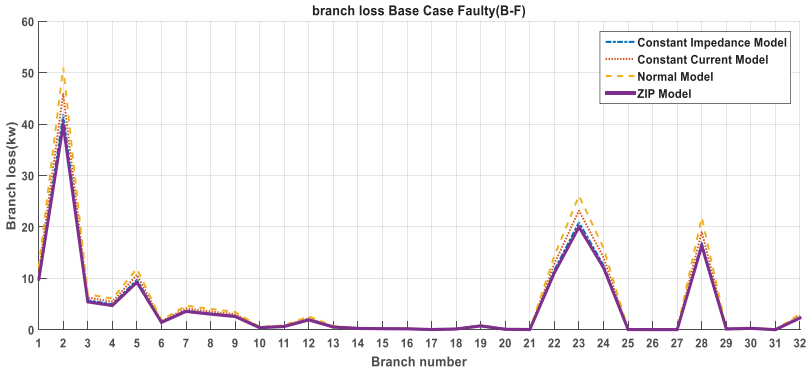

Fig. 16. Branch loss without UVLS at faulty case by using (B-F).

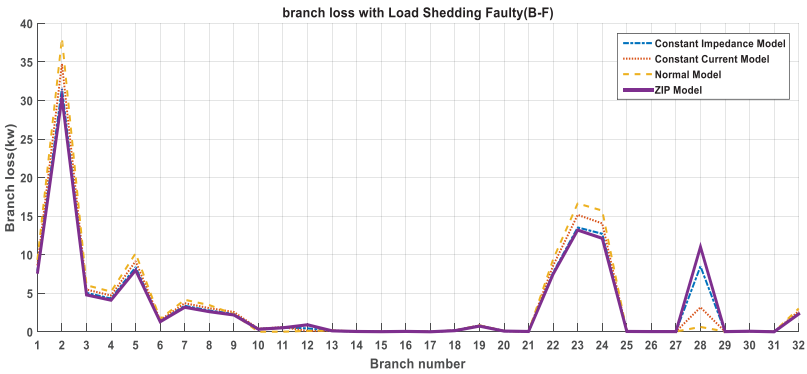

Fig.17. Branch loss with UVLS at faulty case by using (B-F).

9 Conclusions

To avoid voltage collapse, an under-voltage load shedding approach was adopted in this research. The DOA is used to determine the best placement and amount of load shedding for system buses in order to get the best voltage values (voltage profile) and losses reduction. In addition, based on the two-load flow methods Newton Raphson and Backward-Forward, comparison and assessment have been implemented among four different load models: constant I, constant Z, constant P, and ZIP models to identify the load model type that provided the most improvement in the voltage profile and loss reduction. The effectiveness of this method was validated through the 33-IEEE standard distribution power system under two cases health and fault. The outcomes show that the ZIP type is the superior model to provide the optimum resolution for load shedding strategy in comparison with other load models. Furthermore, the Backward-Forward load flow method outperforms the Newton Raphson method in terms of enhancing the voltage profile and increasing loss reduction.

References

[1] K. R. Gayathri and G. V. Maruteswar, "Frequency and Voltage Stability Assessment Applied to Load Shedding," International Journal of Engineering Trends and Technology, vol. 19, no. 2, pp. 106-115, 2015

[2] K. Lopez, S. Perez, and L. Rodrigues, "Optimal under voltage load shedding based on voltage stability index," Ingeieria E Investigation, vol. 36, No. 2, pp. 43-50, 2016.

[3] P. Chawla, and V. Kumar, "Optimal Load Shedding for Voltage Stability Enhancement by Genetic Algorithm," International Journal of Applied Engineering Research, vol. 7, no.11, pp. 2066-2070, 2012.

[4] R. M. Larik, M. W. Mustafa, S. H. Qazi, N. H. Mirijat, S. Shaikh, and A.R. Bhatti, "Under Voltage Load Shedding Scheme to Provide Voltage Stability," 4th International Conference on Energy, Environment and Sustainable Development 2016 (EESD 2016), pp1-7.

[5] N. A. Yusof, H. Mokhlis, M. Karimi, J. A. Laghari, H. A. Illias, and N. M. Sapari,"Under-Voltage Load Shedding Scheme Based on Voltage Stability Index for Distribution Network," Ingeniería e Investigación vol. 36, no. 2, pp. 43-50, 2016.

[6] I. K. Ashan, S. M. Taghi, M. Mortezaee, and T. Amaraee ,"A robust under voltage load shedding scheme against voltage instability," Turkish Journal of Electrical Engineering & Computer Sciences,

vol. 24, pp. 3309-3320, 2016.
[7] Raja M. Larik,M. W. Mustafa, and A.R. OkinoOtuoze,"A New Technique of Load Shedding to Stabilize Voltage Magnitude and Fast Voltage Stability Index by Using Hybrid Optimization," ARPN Journal of Engineering and Applied Sciences,vol. 13, no. 8, pp. 2734- 2745, 2018.
[8] J. Modarresi, E. Gholipour, and A. Khodabakashian," New Adaptive and Centralized Under-Voltage Load Shedding to Prevent Short –Term Voltage Instability," IET Generation, Transmission & Distribution,vol.12, no. 11, pp. 2530-2538, 2018.
[9] Z. M. Yasin, H. Mohamad , I. N. Samon, N. A. Wahab, and N. A. Salim, "Optimal Undervoltage Load Shedding using Ant Lion Optimizer," Journal of Applied and Fundamental Sciences, vol. 10, no. 5S, 2018, pp. 426-443.
[10] M. Klaric, I. Kuzle, and S. Tesnjak, "Example of Undervoltage Load Shedding Implimentation," IEEE 2007, Windhoek, South Africa, pp. 1-6, 2007
[11] N. M. Sapari, H. Mokhlis, J. A. Laghari, A. H. A Bakar, M. R. M. Dahalan,"Application of Load Shedding Schemes for Distribution Network Connected with Distributed Generation: A review," Renewable and Sustainable Energy Reviews, vol. 82, no.1 , pp. 858-867, 2018.
[12] F. Teng, "Implementation of a Voltage Sweep Power Flow Method and Comparison with Other Power Flow Techniques," Semester Thesis, Swiss Federal Institute of Technology, Zurich, 2014.
[13] H. K. Verma, and P. Singh, "Optimal Reconfiguration of Distribution Network Using Modified Culture Algorithm," Journal of the Institution of Engineers , vol. 99, no. 6, pp. 613–622, 2018.
[14] N. A. Roustami and M. O. Sadegh,"The effect of load modelling on load flow results in distribution systems," American Journal of Electrical and Electronic Engineering, vol. 6, no.1, pp. 16-27, 2018.
[15] U. Eminoglu, and M. H. Hocaoglu," A new power flow method for radial distribution systems including voltage dependent load models," Electrical Power System Research, vol. 76, no. (1-3), pp. 106-114, 2005.
[16] S. Mok, S. Elangovan, C. Longiian, and M. Salama," A new approach of power flow analysis of balanced radial distribution systems," Electric Machines Power System,vol. 28, no.24, pp.325-340, 2000.
[17] K. Lenin, B. R. Reddy, and M. S. Kalavathi,"Dolphin echolocation algorithm for solving optimal reactive power dispatch problem," International Journal of Computer, vol. 12, no.1, pp. 1-15, 2014.
[18] A. Kaveh, N. Farhoudi,"A new optimization method: Dolphin Echolocation," Advances in Engineering Software, vol. 59, pp. 53-70, 2013.
[19] T. q. Wu, M. Yao, and J. H. Yang," Dolphin swarm algorithm", Frontiers of Information Technology & Electronic Engineering, Frontiers of Information Technology & Electronic Engineering, vol. 17, no. 8, pp. 717-729, 2016.
[20] A. A. El-Fergany, and A.Y. Abdelaziz, "Artificial Bee Colony Algorithm to Allocate Fixed and Switched Static Shunt Capacitors in Radial Distribution Networks," Electric Power Components and Systems, vol. 42, no. 5, pp. 427–438, 2014.
[21] M. R. Haghifam, and O.P. Malik, "Genetic Algorithm-based Approach for Fixed and Switchable Capacitors Placement in Distribution Systems with Uncertainty and Time Varying Loads," IET Generation Transmission & Distribution, vol. 1, no. 2, pp. 244–252, 2007.
[22] R. S. Rao, S. V. L. Narasimham, M. R. Raju, and A. S. Rao, "Optimal Network Reconfiguration of Large-Scale Distribution System Using Harmony Search Algorithm," IEEE Transactions on Power Systems, vol. 26, no. 3, pp. 1080 - 1088, 2011.
[23] M. Sedighizadeh, M. Ghalambor, and A. Rezazadeh, "Reconfiguration of Radial Distribution Systems with Fuzzy Multi-Objective Approach Using Modified Big Bang-Big Crunch Algorithm," Arabian Journal for Science and Engineering, vol. 39, no.8, pp. 6287–6296, 2014.
[24] Zhe Chen," A Study of Power Distribution System Reconfiguration based on Reliability Indices", A Thesis Presented to the Faculty of the Graduate School at the University of Missouri-Columbia, 2016.

Doppler Shift Effect with Non-Orthogonal Multiple Access Technology for 5G System

Roaa Ali Hussein[1], Saad Ahmed Ayoob [2]
roaa.enp6@student.uomosul.edu.iq[1], sa_ah_ay@uomosul.edu.iq[2]

Electrical Engineering Department, University of Mosul, Mosul, Iraq [1], Electrical Engineering Department, University of Mosul, Mosul, Iraq [2]

Abstract. Non-orthogonal Multiple access (NOMA) is a 5G wireless connectivity technology. It aims to improve user (UE) service at cell edge (CE) by pairing with the UE at cell center (CC). User velocity is an important component of 5G communication systems. This paper investigates the presence of a Doppler shift effect (DSE) for the movement of a user in NOMA cell. Also, the emphasis in this search is on DSE for users (UEs) at the CC and on the user's velocity at 180km/h. The method used for the simulation, Link (LL) Level emulator for Vienna 5G. Through the NOMA principle, the results demonstrate that DSE was evident on the UE in center of the cellular network. When changing user's speed from 0 to 180 km/h, the user's efficiency changed from 4.937 Mbit/s to 0.6418 Mbit/s at transmitted Power of eNB equal 25dBm. In other expression, due to an increase in the UE's speed and DSE, the user's throughput decreases by nine times his efficiency at speed = 0 km / h. By increasing number of eNB antennas, MIMO (8X2) has achieved 4 times better user efficiency improvement than MIMO (2X2). The number of UE antennas is increased antennas to four and changing number of eNB antennas, MIMO (2X4) enables to maintain user's throughput at high speed and DSE. In this type of MIMO, the user's efficiency has reached a result close to that of UE when his motion is stationary.

Keywords: 5G, NOMA, MIMO, Doppler Effect, UEs, velocity.

1 Introduction

A large number of technologies have been specified for the 3G (3GPP) Partnership Project. This is aimed at achieving high data and high performance on mobile 4G systems [1]. Recent developments in the area of ICT (Information and Communication Technologies) have highlighted the current generation of wireless communication experiences. In future, smart things in intelligent homes, offices, streets and cities in the intelligent world are expected to be in the new generation [2].To meet these future communication requirements [3].

3GPP was a candidate for a 5G wireless communication system for submission to the International Telecommunications Union (ITU) of 5GNR new radio specification [4]. Along this development, 5G networks should support three major families of applications, including

IMDC-IST 2021, September 07-09, Sakarya, Turkey
Copyright © 2022 EAI
DOI 10.4108/eai.7-9-2021.2314871

enhanced (eMBB) mobile broadband, massive machine (mMTC) type communications and ultra-reliable and (URLLC) low-latency communications. Multiple access (MA) schemes are being explored to meet these new requirements [5]. The approaches can be classified orthogonally and non-orthogonally in MA techniques. Signals from different UEs are not interference in orthogonal approaches, and they can be accomplished by time- division, frequency-division and orthogonal-frequency division (TDMA, FDMA, and OFDMA)[6]. Orthogonal multiple access (OMA) technology used in 4G, which is the basis for the work of Long-Term Evolution (LTE) networks, and in 5G this technology and non-orthogonal multiple access technology are used [7].

The proposal was made, and is extensively studied, NOMA. In contrast to OMA, NOMA superposes multiple symbolic data sources by distinguishing their transmission power [3]. Furthermore, when compared to OMA schemes, NOMA can greatly increase user fairness and spectral performance [8]. NOMA allows access to multiple users who share a block of resources, such as time and frequency [9]. The allocated resources are shared in NOMA where the channel is shared between users by coupling the user at CE (has weak signal) with the user near from eNB (has strong signal) i.e. using same bandwidth (BW). As for the orthogonal multiple access (OMA) technology, the bandwidth is divided by the number of users, thus sub-carriers are divided and the transfer efficiency of the cell decreases [8]. Technologies and new ideas are required to improve capacity and provide high data rates. Because of their ability to split a frequency selective channel into several narrowband flat fading sub-channels, OFDM (Orthogonal Frequency Division Multiplexing) has been widely used in multi-carrier wireless systems [10].

High mobility communications were taken into account as part of 5G communications [11]. Mobility is the mobile station's maximum speed which fulfills a defined Quality of Service (km/h). The successful mobility evaluation will meet the packet error ratio and spectral efficiency threshold for mobility (120 and 500) km/h [4].

It is worth mentioning that the supremacy of NOMA over OMA is the importance of high speed in 5G. Therefore, the researchers were interested in this technology and examined it. Also, they presented challenges and addressed problems facing users within NOMA technology.

2 Related Work

E. A Feukeu et al. [12] analyzed and designed a Direct Development Method (DDM) for combating the effect on the vehicle network of Doppler shift (DS). DDM shows that the best communication connection of two mobile phones moving up to 250 km/h is possible if taking the prescribed threshold into account.

P. Fan et al. [13] sought to present a survey of 5G high-traffic wireless technologies. A key aspect of the research is to develop an optimal cell association metric taking into account various factors such as signal quality, interference, traffic loads and mobility. Traditional association metrics supported signal strength, but the signal-to-noise ratio wouldn't be sufficient for the longer term 5G high mobility HetNets.

T. Levanen et al. discussed several issues in [14]. They discussed ways to obtain high-resolution location information on high-speed train networks. An example of a high-speed train system with a carrier frequency of 30 GHz, the estimate of Doppler distortion is examining.

T. Ahmed et al. proposed the generally power allocated system (GPA) for different users. The simulated BER performance of the wireless system for NOMA using different modulation techniques has similar results to other conventional GPA formulation validation schemes [10].

D. Feng compared the performance of different NOMA schemes through tapped delay line (TDL) channel with typical and high UE speed. The simulation results display that NOMA schemes have a better BLER performance than OMA under these channel assumptions. The high UE speed channel conditions of BLER for NOMA schemes are different from normal speed conditions [15].

H. Ahmad et al. analyzed the study of the performance of NOMA in comparison with OMA in pedestrian and vehicle environments. Also, the performance of users is evaluated. NOMA performed 50% better for CC users than OMA, while OMA outperformed NOMA 56% for CE users [16].

This enables better connectivity of the paired NoUEs of NOMA. S. Mounchili et al. proposed a new NOMA user pairing program based on the user's distance [17]. Also, a common energy allocation strategy was subsequently proposed, which takes the conditions of its user channel into account. Around 80 percent of users have been paired with NOMA from the simulation results.

D. Deshmukh et al. [18] provided algorithm to allocate resources based on the resource block technique. The resource block provides the power allocated (PA) as per the user demand. It usually suppies equal power to all types of UEs. The simulation uses MATLAB software. The results show that the proposed approach is better than OFDM and the existing NOMA. The proposed approach achieves a 50% greater sum rate in terms of power and a 20% higher sum rate in terms of NoUEs.

B. E. Y. Belmekki et al. [19] studied performance and interference of vehicle communications (VCs) with the NOMA. They also compare VCs performance at crossings, roads and demonstrate that VCs performance at crossings is worse than on highways. VCs are also compared. Monte-Carlo simulations validate all the analysis results. The Doppler Effect appears when the user’s speed increases. This effect is in the throughput of UEs.

In this paper, NOMA is used to improve throughput for UEs and ensure their service at high speed. A NOMA downlink scenario for users with varying speeds is used. In addition, we show the effect of high speed on user efficiency in terms of the Doppler Effect. This paper focuses on the users at the cell center because they are most affected by the Doppler.

3 NOMA AND DOPPLER SHIFT

3.1 NOMA

The NOMA idea is presented toward future improvements of spectrum efficiency in lower frequency bands for downlink of 5G system [6]. When two users are paired by pairing methods in [20]. In NOMA system, the Superposition Coding (SC) is deployed at the transmitter and the Successive Interference Cancellation (SIC) is performed at the receiver [17],[21],[22],[23],[6]. NOMA techniques can mainly be divided into two categories, namely, code-domain NOMA and power- domain PD- NOMA [21]. in this paper, we focus on PD for DL. Power allocation takes into account two system preferences; users’ fairness and users’ QoS requirements. In order to make sure that all users are fair, UEs are ordered under channels; users with bad channel gains are assigned higher power levels and those with good channel gains are allocated less power levels [22].

3.2 DOPPLER SHIFT

The Doppler shift (DS) on the received signal will lead to a discrepancy between transmitter and receiver frequencies, and this is called carrier frequency offset (CFO). It should be noted that, even for systems without DS, small CFO may also occur due to the instability of oscillators in wireless transceivers. In multi-carrier systems such as OFDM, CFO will destroy the orthogonally among the subcarriers, and introduce inter-carrier interference (ICI). The performance of OFDM systems is seriously degraded by ICI. In addition, since the DS in high mobility systems change with respect to time, the CFO is time-varying, which is difficult to track and compensate[11].

This section addresses the Doppler shift effect (DSE) and related issues, one of the most challenging issues in the 5G network. Specifically, DE causes two problems, Doppler frequency offset (FO) (or CFO) and fast fading. Due to the movement between transmitter and receiver, the carrier frequency of the received signal will be shifted from its original value as shown in Fig. 1. [13]

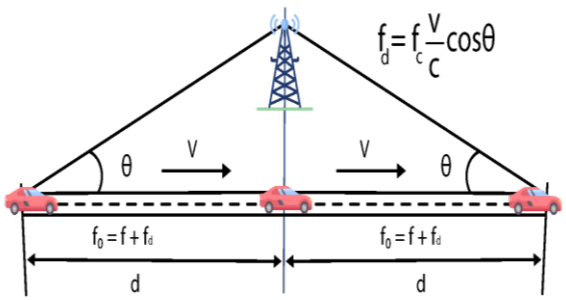

Fig. 1. Doppler effect.

The Doppler shift in frequency can be written as

$$f_d = \pm f_c \frac{V}{C} \cos\theta \quad . \tag{1}$$

Where f_d is the change in source frequency seen on the receiver, fc is the source frequency, V is the difference in velocity between transmitter and source, C is the speed of light and θ is the angle of speed vector. The frequency change is maximum if θ=0. The OFDM symbols are extremely sensitive for this change. The change in frequency is also known frequency shift [12].

4 Methodology and Simulation results

The LL simulator uses to show DSE on user throughput. The simulation model contains four users. Two users in the CC called near-users, and two users in the CE called far-users. The pairing used in a NOMA cell is of the different channel gain types. The emulator supports types of Doppler models, namely (uniform, discrete Jake, Jake). The Jake type is used when the user's velocity is greater or equal to zero. The distance between UE and eNB is determined by path

loss (PL) per link between them. The PL for the UE1, UE2, UE3 and UE4 is (80, 90, 100, 110) dB respectively.

In this section, the results obtained with the NOMA scenario LL simulator are reviewed. It also includes how the problem is noticed and how to treat it. The simulation shows the DE when high mobility for UE.

4.1 Change the velocity of UEs and DE (Doppler effect)

The velocity of UEs was altered from (0-36-72-108-144-180) km/hour as exposed in Table (1) with some transmitter and receiver antennas fixed to the number two (MIMO (2X2)) in each change for the velocity of UEs.

Table 1. The simulation model parameters.

parameter	value
Doppler model	Jake
TxPower eNB	43 dBm
Center frequency	2.5 GHz
MIMO	(2x2)
Velocity	0, 36km/h, 72km/h, 108 km/h ,144km/h, 180km/h
Bandwidth channel/subcarrier spacing frequency	1.4 MHz / 15 KHz
NOMA receiver	Minimum Mean (MMSE) Square-Error
Estimation channel model	Approximate-Perfect

The following Figures (2), (3), (4), (5), (6), (7) show the relationship of the eNB station's transmission power with the user's throughput in NOMA technology. The user moves at different speeds (0-36-72-108-144-180) km/h when moving a pedestrian and in a vehicle. Figure (2) shows that when UEs' speed is zero, the movement is stationary, there is no DE (no fluctuation) in the user's throughput.

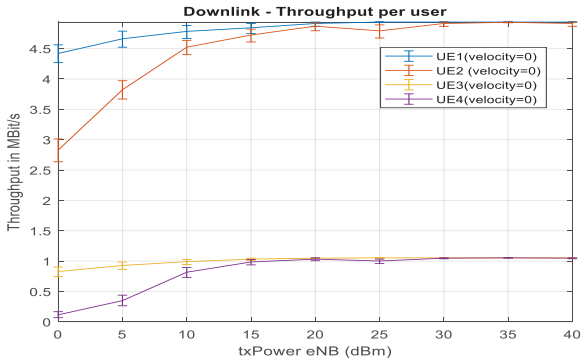

Fig. 2. Throughput of UEs when velocity=0

DE appears when UE speed increases, as exposed in Figures (3, 4, 5, 6, 7). For near users from eNB, their efficiency decreases and fluctuates. In far away, the speed of the users does not affect them due to the user's distance from the eNB station that makes the speed change relatively and has little effect. It can be seen that the DE is not only on efficiency fluctuation but also affects the amount of transport efficiency of users close to eNB.

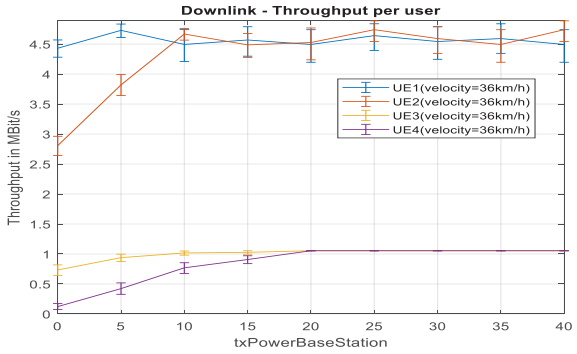

Fig. 3. Throughput of UEs when velocity=36 km/h

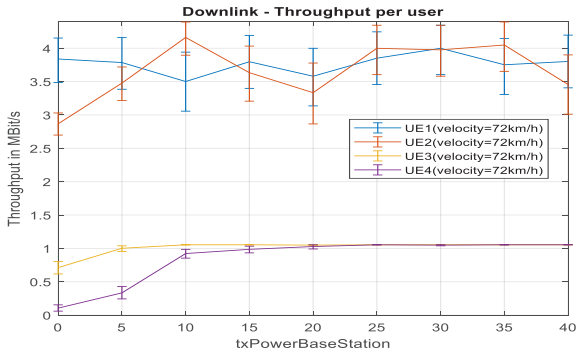

Fig. 4. Throughput for UEs when velocity=72km/h

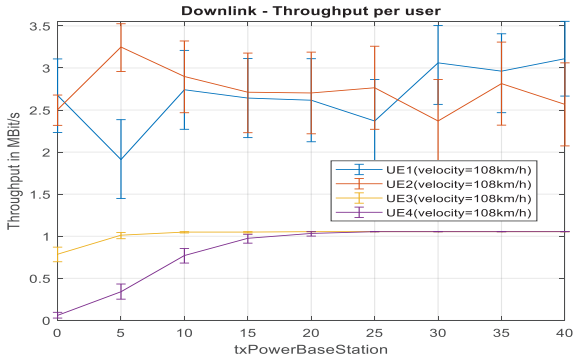

Fig. 5. Throughput for UEs when velocity=108km/h

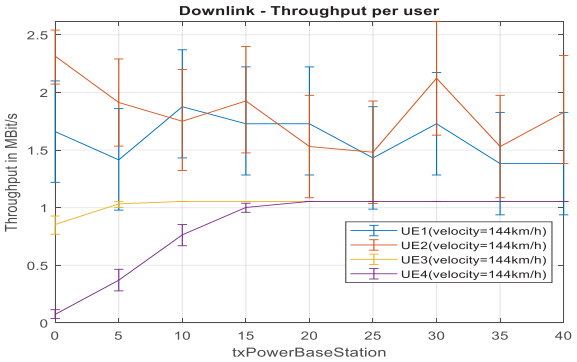

Fig. 6. Throughput for UEs when velocity=144km/h

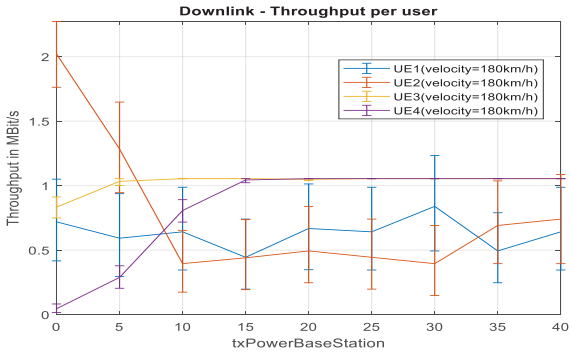

Fig. 7. Throughput for UEs when velocity=180km/h

From the previous results, it is clear that the Doppler effect appears strongly on users near the station. So the focus is on the results of nearby users who have a strong signal. The results of the first user are examined to show the effect. The DE observed as shown in Fig. 8. The problem of the first user has appeared. The same means the case for the second user then the Doppler is reduced on the whole NOMA cell.

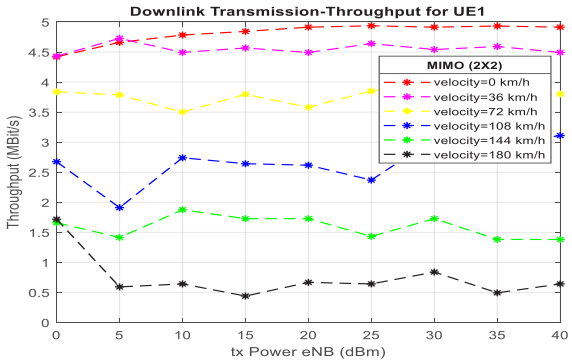

Fig. 8. Throughput for UE1 in different velocity

4.2 Increase the number of eNB antennas

It is proposed to increase the number of eNB antennas and indicate its effect on the transmission efficiency of the UE1. The number of eNB (NoeNB) antennas varies at different speeds for users shown in Table (2). The use of the same parameters which displayed in Table (1).

It is worthy of attention that the NoUE antennas are two and fixed. Different speeds were taken for each type of MIMO.

Table 2. The antenna numbers at the user's side equal two.

parameter	value
Number of user	4users (2user in CC , 2user in CE)
MIMO	(2x2),(4x2),(8x2),(16x2)
velocity	36km/h ,72km/h,180km/h

Figure (9) shows that when using MIMO (2X2), the first user near eNB suffers from DE at different speeds

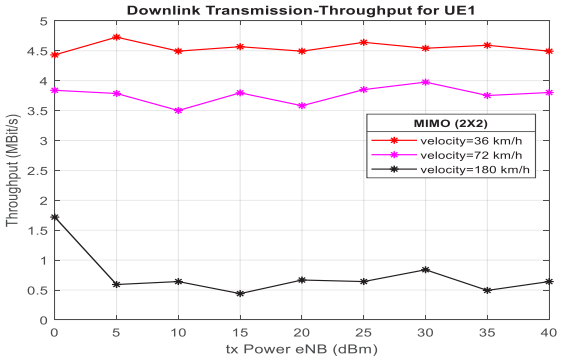

Fig. 9. relationship between txPowereNB and throughput using MIMO(2X2)

Figure (10) shows a noticeable improvement by reducing DE at velocity UE = 36, 72 km/h. In both Figures (11) and (12), DE is reduced by 100% at a user speed of (36, 72) km/h. It is interesting to see in the four figures (9), (10), (11), (12) that increasing the number of eNB antennas from 2 to 4 showed a decrease in DE at the user's speed (36, 72 km/h). However, when increasing the number of eNB antennas from 4 to 8 to 16. The DE doesn't reduce at the user's speed (180 km/h).

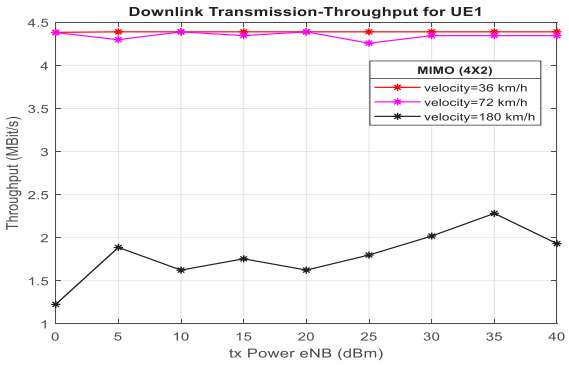

Fig. 10. relationship between txPower and throughput using MIMO(4X2)

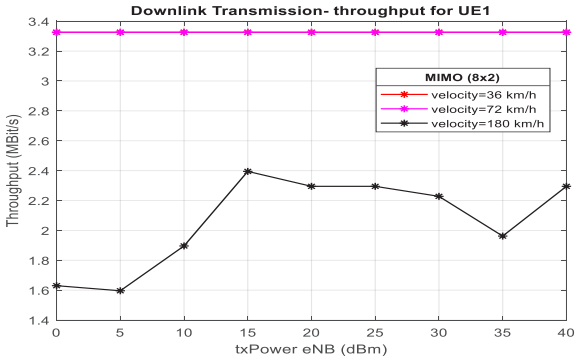

Fig. 11. relationship between txPower and throughput using MIMO(8X2)

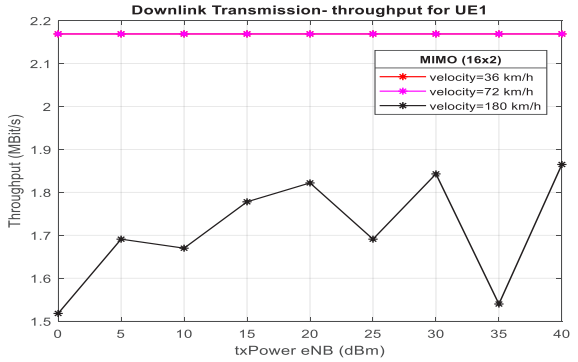

Fig. 12. relationship between txPower and throughput using MIMO(16X2)

In the previous Figures, the DE is observed. Figure (13) shows the value of the UE transmission efficiency by altering the user speed (36, 72, 180) km/h. The efficiency of the first user observed at txPower eNB = 30dBm for the different numbers of eNB antennas.

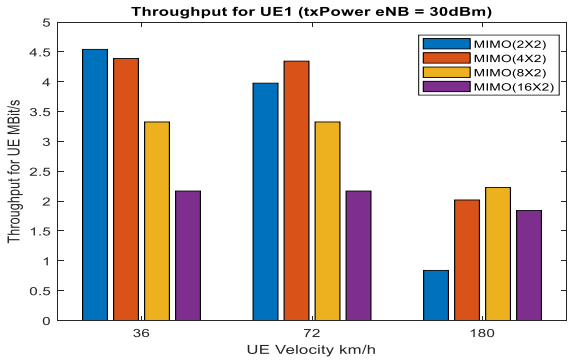

Fig. 13. compare throughput UE1 between different MIMO and different velocity

It is worthy that a user's efficiency is 4.542Mbps when used MIMO (2X2) and a speed equal to 36 km/h. Also, the efficiency decreases by 0.566Mbps at 72km/h. When increasing the speed to180km/h, the throughput decreases by 3.7027Mbps compared with 36km/h. In other words, the user's transmission efficiency is 4.345Mbps when used MIMO (4X2) and a speed equal to 36 or 72 km/h. At a speed of 180km/h, its efficiency is reduced by 2.326Mbps.
The UE's efficiency in MIMO (4X2) is less than MIMO (2X2) at 36km/h by a little 0.153Mbps. But at 72km/h, it is 0.369Mbps higher than MIMO (2X2), and the cause for the decrease and increase is the DE.

The decrease in user efficiency was also observed at MIMO (8X2) and (16X2). The DE is improved, but the cost is user efficiency. Therefore, it suggested increasing the number of UE antennas to four.

4.3 Increase the number of receiver antennas

The same constraints of Table (1) use with the parameters in Table (3). The number of UE antennas fixed to four. Besides, the number of eNB antennas varies (2-4-8-16) antennas.

Table 3. The antenna numbers at the user's side equal four.

parameter	value
MIMO	(2x4),(4x4),(8x4),(16x4)
velocity	36km/h ,72km/h , 180km/h

The users' speed is 180km/h to see the effect of MIMO on Doppler at this speed. Figure (14) shows the DE for the user at 180km/h with changing the number of eNB antennas. Very little DE was observed at MIMO (2×4). Despite the increase in txPower, a user efficiency decrease in MIMO (4X4), (8X4), (16X4) due to the occurrence of ICI.

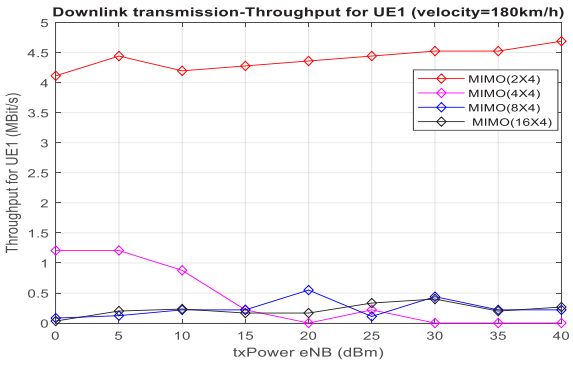

Fig. 14. Throughput UE1 using different MIMO and velocity=180km/h

4.4 Compare MIMOs for various sending and receiving antennas

Figure (15) shows a comparison of the DE for both MIMO (8X2) and MIMO (4X4). There is an effect on both but in terms of user service by eNB MIMO (8X2) is better than MIMO (4X4). At txPowereNB = 25dBm, MIMO (8X2) is more user-efficient (2.0756 Mbps) than MIMO (4x4).

Figure (16) compares the DE for the first user between MIMO (2x4) and MIMO (4x2). MIMO (2X4) achieved a UE transfer efficiency (2.644 Mbps) more than MIMO (4X2) at txPowereNB = 25dBm.

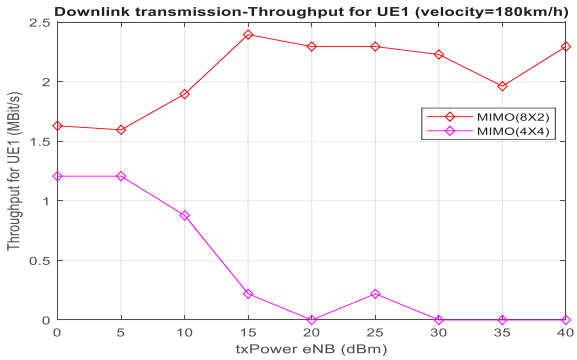

Fig. 15. Compare MIMO(8X2) and MIMO(4X4) in term of Doppler effect

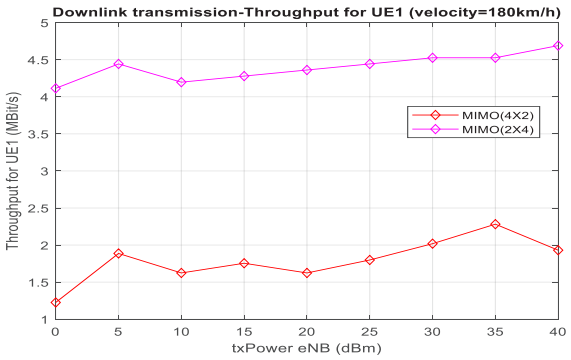

Fig. 16. Compare MIMO(4X2) and MIMO(2X4) in term of Doppler effect

A comparison was made for MIMO between speed and user efficiency at txPowereNB = 30dBm shown in Figure (17). In MIMO (4x4), a user efficiency at speed 36km/h (7.607Mbps). When increasing UE's speed to 180km/h, there is deterioration in the user service as his efficiency drops to 0.1Mbps. Same case in MIMO (8x4), (16x4).

At 180km/h, the user efficiency MIMO (2X4) increases by 4.1266, 4.0871, and 4.426Mbps over MIMO (4X4), (8X4), and (16X4) respectively.

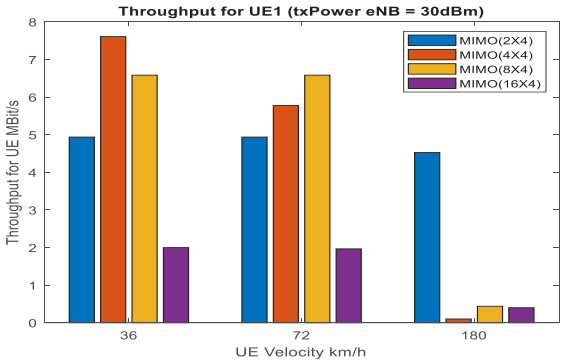

Fig. 17. Relationship Between throughput UE1 and velocity for different MIMO

5 CONCLUSION

In this section, simulating a NOMA scenario in the LL simulator is used to evaluate users 'performance at high speed. DSE appears when the user moves at a certain speed (user speed may be in a pedestrian or vehicle). The results show the DSE on NOMA technology, for users at CE at high speed, the fluctuation caused by the DSE reduced due to the limited space in which the user wanders at his speed. As for users in CC, the DSE was very high at high mobility. Thus, this affects cell efficiency which is dependent on the principle of NOMA technology. To maintain the permanency of the user's service in the cellular network, it proposed to increase the No. of eNB antennas from 2-4-8-16 antennas. DSE was reduced at speeds less than 180 km/h. At 180 km/h, the impact was evident despite the increased No. of eNB antennas. DSE addressed a speed equal to 180 km/h by proposing to increase the No. of UE antennas from 2 to 4. The simulation results express that MIMO (2X4) has better user efficiency performance than MIMO (4X4), (8X4), (16X4) at 180km/h. That is, MIMO turned out to be one of the ways to treat the DSE.

Acknowledgment

This work was supported by Electrical Department, Engineering College, Mosul University.

References

[1] Yan C, Harada A, Benjebbour A, Lan Y, Li A, Jiang H. Receiver design for downlink non-orthogonal multiple access (NOMA). In 2015 IEEE 81st Vehicular Technology Conference (VTC Spring); 11-14 May 2015; Glasgow, UK. IEEE Xplore: IEEE; 2015. p. 1-6.

[2] Zanella A, Bui N, Castellani A, Vangelista L, Zorzi M. Internet of things for smart cities. IEEE Internet Things J. 2014;1(1):22–32.

[3] Lin CH, Shieh SL, Chi TC, Chen PN. Optimal inter-constellation rotation based on minimum distance criterion for uplink NOMA. IEEE Trans Veh Technol. 2019;68(1):525–39.

[4] Henry S, Alsohaily A, Sousa E. 5G is real: Evaluating the compliance of the 3GPP 5G New Radio system with the ITU IMT-2020 requirements. IEEE Access. 2020;8:42828–40.

[5] Cai Y, Cui F, Qin Z, Li G, McCann J. Modulation and Multiple Access for 5G Networks. IEEE Commun Surv Tutorials. 2018;20(1):629–46.

[6] Anxin L, Yang L, Xiaohang C, Huiling J. Non-Orthogonal Multiple Access (NOMA) for Future Downlink Radio Access of 5G. China Commun. 2015;12(Supplement):28–37.

[7] HAMMODAT A.N. and AYOOB S.A. Studying the effect of increasing capacity using comp technology in lte-a networks. Journal of Engineering Science and Technology. 2021; 16(1): p. 556–570.

[8] Liang W, Ding Z, Poor HV. Key Technologies for 5G Wireless Systems. First. Cambridge university press; 2017. 6, Non-Orthogonal Multiple Access (NOMA) for 5G Systems; p. 109–32.

[9] KULKARNI AV, MOTADE SN. NOMA MULTIUSER DETECTION WITH MIMO FOR MAXIMIZING. J Eng Sci Technol. 2021;16(1):236–50.

[10] Ahmed T, Yasmin R, Homyara H and Hasan M.A.F.M. GENERALIZED POWER ALLOCATION (GPA) SCHEME FOR NON-ORTHOGONAL MULTIPLE ACCESS (NOMA) BASED WIRELESS COMMUNICATION SYSTEM. international J Comput Sci Eng Inf Technol. 2018;Vol.8(5/6):1–9.

[11] Wu J, Fan P. A Survey on High Mobility Wireless Communications: Challenges, Opportunities and Solutions. IEEE Access. 2016;4(c):450–76.

[12] Feukeu EA, Djouani K, Kurien A. Compensating the effect of Doppler shift in a vehicular network. In: 2013 Africon; 9-12 Sept. 2013; Pointe aux Piments, Mauritius. IEEE; 2013. p. 1-7.
[13] Fan P, Zhao J, I C-L. 5G high mobility wireless communications: Challenges and solutions. China Commun. 2016;13(2):1–13.
[14] Levanen T, Talvitie J, Wichman R, Syrjala V, Renfors M, Valkama M. Location-aware 5G communications and Doppler compensation for high-speed train networks. In 2017 European Conference on Networks and Communications (EuCNC); 12-15 June 2017; Oulu, Finland. IEEE; 2017. p. 1-6.
[15] Feng D. Performance comparison on NOMA schemes in high speed scenario. In 2019 IEEE 2nd International Conference on Electronics Technology (ICET) 2019; 10-13 May 2019; Chengdu, China. IEEE; 2019. P.112–16.
[16] Ahmad H, Mohd Ali D, Norsyafizan Wan Muhamad W, Syarhan Idris M. Performance analysis of NOMA in pedestrian and vehicular environments. In: Journal of Physics: Conference Series; 22-24 October 2019; Melaka, Malaysia. IOP Publishing; 2020. p. 1-6.
[17] Mounchili S, Hamouda S. Pairing Distance Resolution and Power Control for Massive Connectivity Improvement in NOMA Systems. IEEE Trans Veh Technol. 2020;69(4):4093–103.
[18] Deshmukh D, Kumar N, Mishra K. Non-Orthogonal Multiple Access System based on Resource Allocation Scheme in OFDM. In:2020 Fourth International Conference on Computing Methodologies and Communication (ICCMC); 11-13 March 2020; Erode, India. IEEE; 2020. p. 575-579.
[19] Belmekki BEY, Hamza A, Escrig B. On the performance of 5G non-orthogonal multiple access for vehicular communications at road intersections. Veh Commun. 2020;22:1–12.
[20] Shahab MB, Irfan M, Kader F and Shin SY. User pairing schemes for capacity maximization in non-orthogonal multiple access systems. Wirel Commun Mob Comput . 2016;2884–2894.
[21] Kucur O, Karabulut Kurt G, Shakir MZ, Ansari IS. Nonorthogonal Multiple Access for 5G and beyond. Wirel Commun Mob Comput. 2018;2018(12):2347–81.
[22] Liaqat M, Noordin KA, Abdul Latef T, Dimyati K. Power-domain non orthogonal multiple access (PD-NOMA) in cooperative networks: an overview. Wirel Networks . 2020;26(1):181–203.
[23] Islam SMR, Avazov N, Dobre OA, Kwak KS. Power-Domain Non-Orthogonal Multiple Access (NOMA) in 5G Systems: Potentials and Challenges. IEEE Commun Surv Tutorials. 2016;19(2):721–42.

A literature Survey on Well-known Algorithms of Optimum Power Flow

Baqer Atiyah Allamey[1], Falah Jaber Kshash[2], Warid Warid[3]
{dr.baqer_turki@stu.edu.iq[1] , hhs.falah@gmail.com[2] , warid.sayel@stu.edu.iq[3]}

Southern Technical University, Basra, Iraq[1,2,3]

Abstract. One of the most often researched non-linear optimization issues is the optimal power flow (OPF) problem. The performance of electricity production, transmission, and distribution must be improved under a variety of system needs and control restrictions in general (OPF). The compositions of OPFs and the methods used to apply them are quite diverse. Furthermore, as a result of recent power markets and the absorption of renewable resources, the character of OPF is evolving. Various OPF formulations have been dealt with using a variety of classical and meta-heuristic methods throughout the last three decades. This survey explores both traditional and intelligent OPF approaches to provide a strong background for the present status of OPF formulations and solutions approaches. The survey covers all of the optimization approaches that researchers have used to (OPF), with a focus on the advantages and disadvantages of each method for both traditional and intelligent OPF methods.

Keywords: Optimal Power Flow (OPF), classical Optimization methods, metaheuristic algorithm Optimization.

1 Introduction

Since Carpentier initially published a paper in 1962, the optimal power flow (OPF) problem has been one of the most extensively studied problems in power system operation. The goal of OPF formulation is to arrive at a steady-state solution that reduces generating costs, system losses, or optimizes societal welfare or system utilization, among other things while maintaining acceptable performance of the system active and reactive power constraints on generators, line flow limitations, and a maximum output of different compensating devices...etc. The generic OPF problem is a large-scale, non-convex, nonlinear optimization problem with both continuous and discrete control variables. Several OPF formulations have been created to solve specific examples of the problems, each with its own set of assumptions and choices of objective functions, system limitations, and controls. Generally, the OPF approach is frequently applied to several industrial applications such as restricted economic dispatch and voltage control problems [1]. In this survey, the OPF methods are broadly classified as conventional and intelligent methods. Solution methodologies can broadly be categorized into two groups: classical methods; several traditional methods used for solving OPF problems such as the Newtonian technique grid flow programming, linear programming, nonlinear programming, quadratic programming, and the interior point method. As the main shortcoming, these traditional methods are not suitable for large and difficult OPF problems. Because the

IMDC-IST 2021, September 07-09, Sakarya, Turkey
Copyright © 2022 EAI
DOI 10.4108/eai.7-9-2021.2314847

optimization framework is non-linear and multimedia in nature, these approaches may become trapped in local solutions. Traditional approaches are based on diverse mathematical programming frameworks and are used to answer a variety of sizes of OPF issues in order to meet the requirements of various objective functions, application types, and constraint natures. Traditional methods are inadequate for dealing with qualitative constraints. These approaches have weak convergence, can only identify one optimum solution in a single simulation run, become excessively slow when the number of variables grows big, and are computationally expensive when addressing a large system.. Intelligent methods; many meta-heuristic methods were used to solve OPF such as genetic algorithm (GA), particle swarm optimization (PSO), artificial neural network (ANN), bee colony optimization (BCO), differential evolution (DE), grey wolf optimizer (GWO), shuffled frog-leaping (SFL) and fuzzy logic (FL) method. Recently, to overcome the shortcomings of conventional methods, many intelligence optimization techniques based on various concepts such as evolutionary inspired algorithms, human-inspired algorithms, and naturally inspired algorithms were implemented to solve the OPF formulation. The main advantages of meta-heuristic optimization techniques are that they are relatively flexible in dealing with different qualitative constraints. As a result, they are well suited for solving multi-objective optimization problems. In most cases, they could also find the global optimal solution. It also has learning capability, is fast in convergence, and is suitable for non-linear modeling. However, there are some drawbacks such as high dimensionality and the selection of training methods [2]. In this article, the form of a table is used to review the scientific contributions of each method with its advantages and disadvantages. Also, a summary to review the conclusions is given.

2 Optimal Power Flow Methods

The traditional and modern optimization techniques that have been used to solve the OPF problem are depicted in Fig 1.

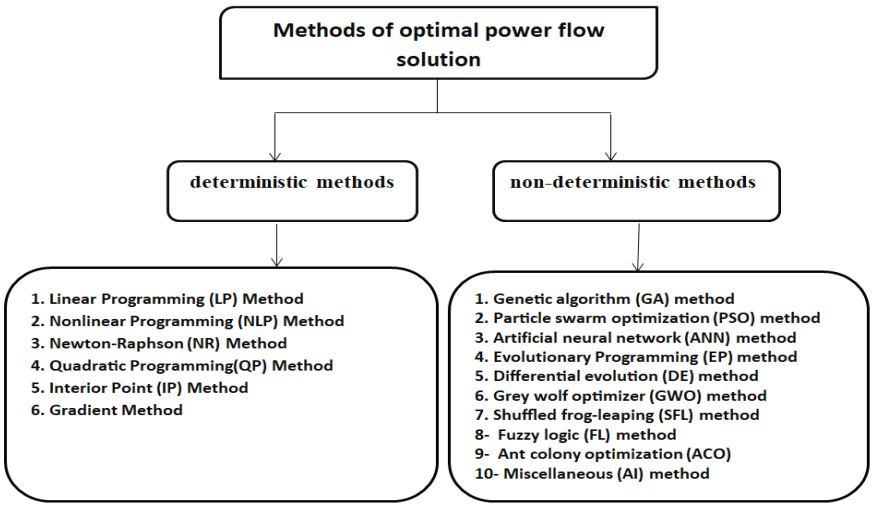

Fig. 1. Optimal Power Flow Solution Methods.

2.1 Classical Methods (Deterministic Methods)

2.1.1 Linear Programming (LP) Method

Several academics have used linear programming to tackle many problems involving optimal power flow. Linear programming formulation necessitates the linearization of the goal function as well as nonnegative variable constraints. Several nonlinear power system optimization issues are linearized using various linear programming-based methodologies [3]. In Table 1, the most important scientific contributions in this field were explained:-

Table 1. The LP approaches are used for solving the OPF problem.

Ref. No.	year	objective function	system	Scientific contribution
[4]	1996	the optimal cost and benefit.	14 bus system	provided a recursive linear programming-based method for reducing line losses and determining the best capacitor allocation in a distribution system.
[5]	2001	transmission losses and generator reactive outputs	the French, Portuguese, and Moroccan systems.	The method proposed is an iterative approach in which the objective function and constraints are linearized in each iteration. A set of tangent cuts is also used to represent the objective function..
[6]	2003	determines the number, position, and settings of phase shifters in a network. maximize system load ability	the IEEE 24-, 118-, and 300-bus systems, a 904-bus network	A recent mixed-integer linear programming (MILP) method was used.
[7]	1992	cost optimization	5-bus system	For optimum power flow, a linear programming-based optimization approach was presented.
[8]	2014	generation cost, P loss.	Iraqi 24 bus (400 kV) test system.	Linear Programming to cover the target fitness and constraints in each iteration.

In summary, we find that linear programming has several advantages and disadvantages which are mentioned briefly as follows:

Advantages:

1. The LP approach can easily deal with nonlinearity constraints.
2. It is effective in dealing with inequalities and it has a good convergence characteristic.
3. Efficiently handles local constraints.
4. It is capable of incorporating contingency constraints.

Disadvantages:

1. It suffers a lack of accuracy. Also, it is trapped in local minima.
2. Although LP approaches are quick and dependable, they have several drawbacks due to piecewise linear cost assumptions.

2.1.2 Nonlinear Programming (NLP) Method

Nonlinear programming (NLP) is a technique for solving problems with nonlinear goal and constraint functions. The fundamental benefit of NLP formulation for (OPF) is also that they correctly reflect the behavior of power systems. (NLP) techniques employ the reduced gradient technique with the Lagrange multiplier or the penalty function optimization method (2). In Table 2, the most important scientific contributions in this field were explained:

Table 2. The NLP approaches are used for solving the OPF problem.

Ref. No.	year	objective function	system	Scientific contribution
[9]	2001	Losses and cost	IEEE 30-bus system	Applied a new nonlinear convex programming (NLCNFP) model.
[10]	2006	maximize the system load ability	IEEE 24-bus	In the deregulated energy markets, a new method is applied to find the best number and position of TCSCs utilising a mixed-integer non-linear programming methodology.
[11]	2004	minimize active losses and load stability	from 30,57,118,300 to 2098 buses system	presents and compares the computational performance of smooth, non-smooth, and Jacobian smoothing nonlinear complementarity (NC) methods for solving nonlinear (OPF) problems.
[12]	2002	the total cost of VArs committed or the overall cost associated with the VAr requirement	the IEEE-I 18 bus system	The characteristics of optimal power flows (OPFs) based on linear programming (LP) and nonlinear programming (NLP) are examined.
[13]	1970	reduction in computer time, storage requirements	the IEEE 14, 30, 57, and 118bus systems	provides a decomposition methodology that may be combined with the Fletcher-Powell method to broaden the nonlinear programming method's application to huge systems.

In summary, we find that nonlinear programming has several outcomes as follows:

Advantages:

1. When compared to linear programming, the nonlinear programming (NLP) method is more accurate since it may be used for nonlinear objective functions and constraints.
2. Can be applied to large-scale problems.

Disadvantage:

1. some components of the system are not considered.

2.1.3 Quadratic Programming (QP) method

With a quadratic objective function and linear constraints, it is a type of nonlinear programming. In power systems, quadratic programming-based optimization is used to keep a specified voltage profile, maximise power flow, and lower generating costs [1]. In Table 3, the most important scientific contributions in this field were explained:-

Table 3. The QP approaches are used for solving the OPF problem.

Ref. No.	year	objective function	system	Scientific contribution
[14]	1989	Voltage deviation, cost, and losses	A 39-bus system	A generalized optimal power system flow problem has been formulated using a quadratic form of power systems. The (OPF) method is built with the feasibility, convergence, and optimality requirements in mind.
[15]	1998	Losses with many elements including reactive power.	the IEEE 30 and 278 bus systems	The method of successive quadratic programming (SQP) was used to develop a reactive power optimization model. The focus of this study is on the mathematical elements of reactive power optimization using the successive QP approach.
[16]	2000	total generation and transmission losses	the CIGRE system and the Italian EHV system	For security-constrained economic dispatch, dual sequential quadratic programming was recommended. By minimising transmission constraints and subsequently punishing constraint violations, the dual quadratic technique is utilised to produce a dual viable starting point. It features a quick calculating time and good precision.
[17]	2003	voltage stability and minimum reactive cost	the IEEE 14-bus system.	For competitive marketplaces, a method is proposed that integrates cost and voltage stability analysis using an OPF formulation.
[18]	2005	calculations of line flows and real losses	the CIGRE 63-bus system and Italian EHV network.	proposed SCOPF (security-constrained optimal power flow) to find the best UPFC and TCPAR settings and operation modes. The HP (Han-Powell) algorithm was used to find the solution to the OPF.

In summary, we find that QP could be summarized by:

Advantages:

1. In many cases, conditioned and divergent systems are solvable.
2. When compared to other recognized approaches, the accuracy of the QP approach is significantly better.
3. It has fast convergence characteristic.

Disadvantage:

1. Obtaining solutions to quadratic programming problems in reliable performance of approximating QP problems is difficult.

2.1.4 Interior Point (IP) Method

It's a novel method for computing large-scale linear programming problems quickly. Because it enhances search directions only within the limitations of the possible space, it is referred to as an internal technique. Interior Point Methods (IPMs) are a type of scaling approach that uses projections to solve linear and nonlinear optimization problems [3]. In Table 4, the most important scientific contributions in this field were explained:

Table 4. The IP approaches are used for solving the OPF problem.

Ref. No.	year	objective function	system	Scientific contribution
[19]	2002	fuel cost and power loss minimization	IEEE 14 and 57 buses standard test systems	presented an independent OPF methodology with IPBCM approach.
[20]	2001	cost and loss minimization	The IEEE 30 and 118 buses	For optimum power flow problems, new versions of interior-point techniques were introduced. A mixture of two approaches, affine-scaling and centralization, is used to get the optimal answer.
[21]	2005	generation cost and active power losses.	Nordic32 system , IEEE118 and IEEE300 systems	Two interior point (IP) based methods were compared to address various OPF issues: the infeasible 1 pure primal-dual method and the infeasible primal-dual predictor-corrector approach.
[22]	2006	Time, iterations, and power losses	IEEE Test Systems with various buses	A new transformer model is applied by ideal case and load impedance.
[23]	2020	the MSE-loss and total energy cost	The energy price data	The Linear Programming relaxation was given a log-barrier term, which makes it twice differentiable and is the usual procedure in Linear Programming when employing interior point methods.

In summary, we find that IP has unique outcomes such as:

Advantages:

1. It is one of the most effective algorithms available.
2. high accuracy, high convergence speed and reliability.

Disadvantages:

1. Due to the starting and ending conditions, there is a constraint.
2. If the step size is selected incorrectly, the solution is infeasible.

Finally, the disadvantages of traditional approaches might be summarized as three main drawbacks:

1. The optimum solution cannot be obtained and are frequently stuck at a local optimum.

2. All of these approaches are predicated on the assumption of objective function properties in which some of its elements are not attainable.
3. With discrete variables like transformer taps, none of these techniques can be used. It is observed that intelligent techniques are suitable methods to overcome the above drawbacks.

2.2 Artificial Intelligence (AI) Methods (Non-Deterministic Methods)

Intelligent search has become a widely used methodology. Several non-deterministic optimization approaches were discovered to address the global search methods in supporting the deterministic optimization algorithms. Many of these methods, such as the genetic algorithm, particle swarm optimization, artificial neural network, evolutionary programming, differential evolution, grey wolf optimizer, shuffling frog-leaping, fuzzy logic (FL) method, and ant colony optimization, have been utilised to tackle OPF problems. We will briefly mention the scientific contributions made by researchers to some of the methods above:

2.2.1 Genetic Algorithms

The genetic algorithm (GA) works with the problem parameters encoded binary string rather than the system's real parameters. GA employs an iterative process in which each iteration step three genetic factors (selection, crossover, and mutation) are applied to enhance the new selection of populations [3]. In Table 5, the most important scientific contributions in this field were explained:

Table 5. The GA approaches are used for solving the OPF problem.

Ref. No.	year	objective function	system	Scientific contribution
[24]	2005	fuel cost, P losses, and computing time	the electrical network in western Algeria	The Lagrange approach was used to construct a genetic algorithm solution in this paper.
[25]	2007	fuel cost, P losses	the modified IEEE 57 bus test system	To deal with OPF, a hybrid method is applied such as GA and mat power including the both active and reactive power dispatching.
[26]	2010	fuel cost, P losses and voltage stability enhancement	IEEE 30 bus system	The DQLF method is applied that is combined with an enhanced genetic algorithm to solve the OPF problem.
[27]	2014	minimization of cost, P losses, and emission	IEEE 30-bus test system	considers fuel cost and emission functions and proposes a solution to the severely constrained multi-objective involving competing objectives.
[28]	2018	fuel cost, P losses	two test systems, 15 benchmark functions	designs and suggests a real-coded genetic algorithm that is more efficient.

In conclusion, we discover that GA has a number of advantages and downsides, which are briefly listed below:

Advantages:

1. GA avoids the trap of local optimality, they can deliver a globally optimal solution.
2. GA can solve non-smooth, non-continuous, and non-convex problems.
3. Changeable, with the ability to create a large number of solutions and a fast convergence.

Disadvantages:

1. GA are stochastic algorithms which means that the solution isn't always optimal.
2. With increasing chromosomal length the run period and accuracy of the solution decrease.
3. Once the system model goes bigger, the GA might lead to a waste of computing efforts.

2.2.2 Particle Swarm Optimization (PSO) Method

PSO is a population-based stochastic optimization method. It is a natural phenomena like as bird flocks and fish schools that occur in socially organised colonies. PSO employs a crew of individuals to scour the search space for promising regions [3]. In Table 6, the most important scientific contributions in this field were explained :

Table 6. The person approaches are used for solving the OPF problem.

Ref .No.	year	objective function	system	Scientific contribution
[29]	2002	fuel cost, voltage deviation, and voltage stability	standard IEEE 30-bus test systems	For the best position of OPF problem control variables, the PSO method is utilised.
[30]	2013	fuel cost, P losses	IEEE 14 and 30 bus test systems.	To identify the lowest generation cost values, this innovative approach adds PSO to the Newton Raphson method.
[31]	2015	Fuel cost, P Losses, and L-index	standard IEEE 30-bus test system	Particle Swarm Optimization (PSO) was used to tackle the optimization problem for the FACTS device's power injection model.
[32]	2020	Cost ($/h) , P loss (MW) , VD and L max	standard IEEE 30 and 57 bus test systems	A multi-objective hybrid firefly and PSO (MOHFPSO) was developed for various multi-objective optimal power flow (MOOPF) challenges.
[33]	2020	Fuel cost, P Losses, VD and L-index	tested for IEEE 9 and 30 bus systems	The reactive power is solved using the PSO method and the MATPOWER 6.0 toolbox.

In summary, PSO could be briefly summarized by:

Advantages:

1. Capable of solving non-convex optimization problems on a large scale, such as OPF.
2. Simple concept, simple implementation, relative control parameter robustness, computing efficiency, and fast convergence speed.
3. Flexibility in balancing global and local search space exploration.

Disadvantage:

1. Slow convergence in detailed search stage (local search capability is limited).

2.2.3 Ant Colony Optimization (ACO) Method

It is based on ant foraging and the creation of a trail utilising pheromone communication. ACO is distinguished by using a probabilistic model to provide optimum solutions at hand [34]**.** In Table 7, the most important scientific contributions in this field were explained:

Table 7. The ACO approaches are used for solving the OPF problem.

Ref .No.	year	objective function	system	Scientific contribution
[35]	2004	Generating cost, Total cost	A universal moment generating function (UMGF) , three and ten generating units	A suggested ant colony optimization method with stochastic disruption activity (RPACO) with randomised technique towards the Unit commitment (UC) with stochastic spinning reserve calculation.
[36]	2013	the voltage stability	WSCC 9-bus test system.	The voltage stability margin feature was introduced and put into the load target function of an OPF using an ACS method.
[37]	2016	the total fuel cost and ecological emission	an IEEE 30 and 118 bus test system	The ideal power flow with ecological emission is resolved using an enhanced ant colony optimization technique.
[38]	2020	Power losses and Cost	the IEEE 30 and the IEEE 57 bus test cases	shows the use of mixed-integer AC optimization for power grid.
[39]	2020	fuel cost, p losses and voltage deviation	the IEEE-30 bus system	OPF is also solved using AC with single target function based on constraints.

In summary, we find that ACO has several advantages and disadvantages which are mentioned briefly as follows:

Advantages:

1. Intelligent search, global optimization, dependability, and positive feedback are all features.

2. Has the ability to compete with other optimization techniques.
3. The computational operators of the ACO algorithm are simple, with no crossover or mutation, resulting in low memory and calculation costs.
4. ACO is a gene selection that has the benefit of being able to be combined with other algorithms.

Disadvantages:

1. The convergence rate is very slow.
2. Over time, the pheromone gets overpowered.
3. It is simple to fall in the local optimal.
4. Theoretical analysis is difficult [40].

2.2.4 Fuzzy Logic (FL) Method

Fuzzy logic is based on fuzzy set theory, which deals with approximate rather than precise reasoning. It is utilised to solve the problem of load flow, resulting in a significant reduction in processing time. To express inexact relationships FL theory is a easy and appropriate tool [41]. In Table 8, the most important scientific contributions in this field were explained:

Table 8. The FL approaches are used for solving the OPF problem.

Ref. No.	year	objective function	system	Scientific contribution
[42]	1992	cost of energy generation	very small system the 6 bus/6 branch network	presented a fuzzy model to describe load and generation uncertainty as fuzzy numbers.
[43]	1997	operating cost and correction times	14-bus system	the creation of fuzzy membership functions and their objectives using a mechanism for expressing the tolerance parameters required.
[44]	2004	percentage Real and Reactive power curtailment and per unit generation cost	modified IEEE 30 bus test system	An effective and practical mixture model for overcrowding management for active and reactive power transactions has been created in the deregulated fuzzy environment of the power system.
[45]	2010	Fuel cost and emissions	the IEEE 14-bus system	the use of a fuzzy model to obtain a Pareto curve that reflects the (tradeoff) between two competing objectives.
[46]	2013	voltage deviations and Network Constraints	thestandardIEEE30-bustestsystem	introduce a new controller architecture that uses AFLC and SFLC techniques to regulate VAR flow in the power system network. A simulation software is used to introduce and test an adaptive fuzzy set.

In summary, we find that FL has several outcomes such as:

Advantages:

1. As a result, a fuzzy multi-objective approach like this is appealing for such problems in terms of cost and emissions.
2. Ease of use and flexibility, as well as a lower cost of development.
3. Is capable of modeling nonlinear functions of any complexity.
4. Has the ability to deal with data that is inaccurate or incomplete.

Disadvantages:

1- A large number of calculations are required on account of the matrix.
2- When large-scale networks exist, a straightforward implementation of these approaches becomes inefficient resulting in increased memory requirements and computational time [41].

2.2.5 Differential Evolution (DE) Method

DE is a direct random search technique that is based on a population. To get from a random starting population to a final solution, it combines simple arithmetic operators with the conventional evolutionary operators of crossover, mutation, and selection. It uses a greedy strategy rather than a stochastic method to solve the problem [3]. In Table 9, the most important scientific contributions in this field were explained:

Table 9. The DE approaches are used for solving the OPF problem.

Ref .No.	year	objective function	system	Scientific contribution
[47]	2007	the total fuel cost and P losses	two test systems	Proposes improved DE approaches for tackling the problem of economic load dispatch.
[48]	2008	fuel cost and transmission losses	6-bus and IEEE 30 bus systems	MDE technique to achieve optimal power flow (OPF).
[49]	2012	fuel cost, P losses, and L-index	IEEE 30 and 118 bus systems	provides a multi-objective differential evolution-based method for OPF.
[50]	2018	cost, power loss emission, voltage deviation and stability	IEEE 30, 57 and 118 bus systems	This research assesses the performance of appropriate CH, SF, SP, and joint of two of these.
[51]	2020	fuel cost, P losses, Vd, the emission, and the generation and emission cost	IEEE30-bus test system	A self-adaptive penalty constraint handling system with improved adaptive differential evolution (JADE).

In conclusion, we discover that DE offers a number of benefits and drawbacks, which are briefly discussed below:

Advantages:

1. When evaluated, it outperformed search heuristics.
2. It is a simple and effective evolutionary approach for optimising continuous-space functions.
3. The DE algorithm is a method for dealing with objective functions that are non-differentiable, non-linear, and multimodal.
4. It can search at random, requires fewer parameters to set is fast, and can be utilised to solve high-dimensional difficult optimization problems.

Disadvantages:

1. The DE has a number of drawbacks, including lengthy operations, stagnation, and poor searchability.
2. Takes into account recent times of unstable convergence and the ease with which a regional optimum could be reached [52].

1.2.6 Grey Wolf Optimizer (GWO) Method

heuristics method is applied by GWO, which helps us understand Gray wolf hunting technique and leadership structure. Omega wolves are preceded by scoffed kappa and lambda wolves, whereas alpha wolves make decisions, beta wolves help alpha wolves, delta wolves are the lowest, and sneered kappa and lambda wolves are the highest [3]. Table 10 summarises the most significant scientific achievements in this field:

Table 10. The GWO approaches are used for solving the OPF problem.

Ref .No.	year	objective function	system	Scientific contribution
[53]	2015	the total transmission loss, and voltage deviation	IEEE 30 and 118 bus systems	Best control elements are updated by GWO such as generator voltages, tap changing transformer ratios, and the number of reactive compensation devices.
[54]	2016	cost, Emission, total generation (MW), and percentage of losses	IEEE 30 bus system	Modifications to the exploration-exploitation balance in the original GWO algorithms, which search the solution space with a random localization, have been suggested for high-quality solutions.
[55]	2017	P loss (MW) and total cost	IEEE 30-bus test system.	The method is used to address the optimal power flow (OPF) problem in a system incorporating wind farms in order to reduce power grid losses and power production costs.
[56]	2018	quadratic fuel cost, P loss, L-index, and Vd	IEEE 30-bus.	The DGWO algorithm is proposed to improve this optimizer's search capabilities (DGWO).
[57]	2020	fuel cost, P losses, and L-index and Vd	IEEE 30 bus.	ORPD problems are computed using a unique nature-inspired metaheuristic optimization approach based on the Grey Wolf Optimization (GWO) algorithm.

In conclusion, we discover that GWO offers a number of benefits and drawbacks, which are briefly listed below:

Advantages:

1. Its ability to solve OPF problems in both single- and multi-objective optimization domains.
2. Due to its basic structure, it is straightforward to apply.
3. Requirements for storage and computation are reduced.
4. Convergence occurs faster since the search space is always shrinking and there are fewer choice criteria.
5. It is the capacity to avoid local minima and govern algorithm performance with only two control parameters, resulting in increased stability and robustness [58].

Disadvantages:

1. There is a lack of precision in solving problems.
2. Inadequate local search capability.
3. A slow rate of convergence [59].

1.2.7 Shuffled Frog- Leaping (SFLA) Method

To find a globally optimal solution, SFLA employs a heuristic search based on the evolution of memes carried by individuals and global information flow. It combines the advantages of PSM's local search tool with the concept of combining data from several local searches to arrive at a global solution (3)**.** In Table 11, the most important scientific contributions in this field were explained:

Table 11. The SFLA approaches are used for solving the OPF problem.

Ref .No.	year	objective function	system	Scientific contribution
[60]	2011	total cost	standard IEEE - 30bus system	Proposed a new way for distributing the power optimal distribution based on a shuffling frog jumping algorithm.
[61]	2017	total loss, total cost, and the Vd	IEEE 33 and 69 bus test systems	For optimal DG placement in the distribution system, the shuffled frog leaping algorithm (SFLA) is used.
[62]	2018	P loss	the IEEE33 node distribution system	A reconfiguration algorithm for a distribution network based on an improved shuffling frog leaping algorithm was developed using molecular dynamics theory and cloud simulation theory.
[63]	2021	P loss	standard IEEE 14,300 bus test system	The best frog information is used to augment the local search in each iteration of the proposed Advanced Frog Leaping Algorithm (EFLA).

In summary, we find that SFLA has some unique operational outcome in terms of

Advantages:

1. It adds the benefits of PSM's local search tool with the idea of merging data from multiple local searches to get a global solution.

Disadvantage:

1. Slow convergence, It's easy to get caught up in the local best answer, which leads to premature convergence.

Traditional methodologies are not always adequate and cannot guarantee a global solution since OPF issues are multimodal, nonlinear, or non-convex; therefore many heuristic methods were applied. By looking at the past studies stated above, the benefits of new optimization approaches may be summarized as follows:

1. These techniques can be used in systems of various sizes are available.
2. High dependability in obtaining the optimum solutions in a single simulation run.
3. These techniques rarely resulted in local minimum solutions.
4. When compared to traditional methods, these techniques converge quickly to the optimum solution.
5. Suitable in solving multi-objective optimization problems.
6. Able to handle various qualitative constraints.

3 CONCLUSION

This study examines a variety of optimization techniques for tackling OPF issues, including both classic and intelligent approaches. Even if classical methods have made significant progress, they still have drawbacks. For example, due to the relatively limited ability to handle real-world large-scale power system problems so mathematical formulations must be simplified to obtain solutions. Some needed linearization and differentiability may become entangled at a locally optimal. have poor convergence are ineffective in dealing with qualitative constraints and will be very slow if there are a lot of variables. But the main benefit of artificial intelligence approaches is their adaptability in organizing different qualitative constraints. The optimum solution can be performed using AI approaches in one computation. In the vast majority global solution can be approached. In this survey, the benefits and drawbacks of artificial intelligence methods were discussed. Also in this Paper, various popular techniques in optimum power flow researchers' contributions to each methodology have been presented clearly and concisely.

References

[1] A. Immanuel and C. Chengaiah, “A Comprehensive Literature Survey on Recent Methods of Optimal Power Flow,” *IOSR J. Electr. Electron. Eng. Ver. II*, vol. 10, no. 5, pp. 2278–1676, 2015, doi: 10.9790/1676-10520112.

[2] M. Ebeed, S. Kamel, and F. Jurado, *Optimal power flow using recent optimization techniques*, no. June. Elsevier Inc., 2018.

[3] A. Khamees, N. Badra, and A. Abdelaziz, “Optimal Power Flow Methods: A Comprehensive Survey,” *Ieejournal.Com*, vol. 7, no. 4, pp. 2228–2239, 2016, [Online]. Available: http://www.ieejournal.com/wp-content/uploads/Volume/Vol 7 No 4/Optimal Power Flow Methods A Survey.pdf.

[4] T. S. Chung and G. Shaoyun, “A recursive LP-based approach for optimal capacitor allocation with cost-benefit consideration,” *Electr. Power Syst. Res.*, vol. 39, no. 2, pp. 129–136, 1996, doi: 10.1016/S0378-7796(96)01103-0.

[5] E. Lobato, L. Rouco, M. I. Navarrete, R. Casanova, and G. López, “An LP-based optimal power flow for transmission losses and generator reactive margins minimization,” *2001 IEEE Porto Power Tech Proc.*, vol. 3, pp. 121–125, 2001, doi: 10.1109/PTC.2001.964894.

[6] F. G. M. Lima, F. D. Galiana, I. Kockar, and J. Munoz, “Phase shifter placement in large-scale systems via mixed integer linear programming,” *IEEE Trans. Power Syst.*, vol. 18, no. 3, pp. 1029–1034, 2003, doi: 10.1109/TPWRS.2003.814858.

[7] Mukherjee, Srijib K., Agustin Recio, and Christos Douligeris. "Optimal power flow by linear programming based optimization." Proceedings IEEE Southeastcon'92. IEEE, 1992.

[8] F. M. Tuaimah and M. F. Meteb, “A Linear Programming Method Based Optimal Power Flow Problem for Iraqi Extra High Voltage Grid (EHV),” *J. Eng.*, vol. 20, no. 4, pp. 23–35, 2014.

[9] J. Zhu and J. A. Momoh, “Multi-area power systems economic dispatch using nonlinear convex network flow programming,” *Electr. Power Syst. Res.*, vol. 59, no. 1, pp. 13–20, 2001, doi: 10.1016/S0378-7796(01)00131-6.

[10] A. K. Sharma, “Optimal number and location of TCSC and loadability enhancement in deregulated electricity markets using MINLP,” *Int. J. Emerg. Electr. Power Syst.*, vol. 5, no. 1, pp. 1–15, 2006, doi: 10.2202/1553-779X.1117.

[11] G. L. Torres, “Smooth , non-smooth and Jacobian smoothing nonlinear complementarity methods for solving optimal power flows,” no. December, 2014.

[12] D. Pudjianto, S. Ahmed, and G. Strbac, “Allocation of VAr support using LP and NLP based optimal power flows,” *IEE Proc. Gener. Transm. Distrib.*, vol. 149, no. 4, pp. 377–383, 2002, doi: 10.1049/ip-gtd:20020200.

[13] A. M. Sasson, “Decomposition Techniques Applied to the Nonlinear Programming Load-Flow Method,” *IEEE Trans. Power Appar. Syst.*, vol. PAS-89, no. 1, pp. 78–82, 1970, doi: 10.1109/TPAS.1970.292671.

[14] Momoh, James A. "A generalized quadratic-based model for optimal power flow." Conference Proceedings., IEEE International Conference on Systems, Man and Cybernetics. IEEE, 1989.

[15] N. Grudinin, “Reactive power optimization using successive quadratic programming method,” *IEEE Trans. Power Syst.*, vol. 13, no. 4, pp. 1219–1225, 1998, doi: 10.1109/59.736232.

[16] G. P. Granelli and M. Montagna, “Security-constrained economic dispatch using dual quadratic programming,” *Electr. Power Syst. Res.*, vol. 56, no. 1, pp. 71–80, 2000, doi: 10.1016/S0378-7796(00)00097-3.

[17] Lin, X., A. K. David, and C. W. Yu. "Reactive power optimisation with voltage stability consideration in power market systems." IEE Proceedings-Generation, Transmission and Distribution 150.3 (2003): 305-310.

[18] A. Berizzi, M. Delfanti, P. Marannino, M. S. Pasquadibisceglie, and A. Silvestri, “Enhanced security-constrained OPF with FACTS devices,” *IEEE Trans. Power Syst.*, vol. 20, no. 3, pp. 1597–1605, 2005, doi: 10.1109/TPWRS.2005.852125.

[19] X. Ding, X. Wang, Y. Song, and J. Geng, “The interior point branch and cut method for optimal power flow,” *PowerCon 2002 - 2002 Int. Conf. Power Syst. Technol. Proc.*, vol. 1, pp. 651–655, 2002, doi: 10.1109/ICPST.2002.1053623.

[20] E. D. Castronuovo, R. Salgado, and J. M. Campagnolo, “New Versions of Interior Point Methods

Applied to the Optimal Power FlowProblem," no. June 2014, pp. 1–6, 2001.

[21] F. Capitanescu, M. Glavic, and L. Wehenkel, "An interior-point method based optimal power flow," *Proc. ACOMEN Conf.*, no. June 2005, pp. 1–18, 2005.

[22] W. Yan, J. Yu, D. C. Yu, and K. Bhattarai, "A new optimal reactive power flow model in rectangular form and its solution by predictor corrector primal dual interior point method," *IEEE Trans. Power Syst.*, vol. 21, no. 1, pp. 61–67, 2006, doi: 10.1109/TPWRS.2005.861978.

[23] J. Mandi and T. Guns, "Interior Point Solving for LP-based prediction+optimisation," no. NeurIPS, 2020, [Online]. Available: http://arxiv.org/abs/2010.13943.

[24] R. Ouiddir, M. Rahli, and L. Abdelhakem-Koridak, "Economic dispatch using a genetic algorithm: Application to western Algeria's electrical power network," *J. Inf. Sci. Eng.*, vol. 21, no. 3, pp. 659–668, 2005.

[25] M. Younes, M. Rahli, and L. Abdelhakem-Koridak, "Optimal Power Flow based on Hybrid Genetic Algorithm," *J. Inf. Sci. Eng.*, vol. 23, no. 6, pp. 1801–1816, 2007, doi: 10.6688/JISE.2007.23.6.10.

[26] M. S. Kumari and S. Maheswarapu, "Enhanced Genetic Algorithm based computation technique for multi-objective Optimal Power Flow solution," *Int. J. Electr. Power Energy Syst.*, vol. 32, no. 6, pp. 736–742, 2010, doi: 10.1016/j.ijepes.2010.01.010.

[27] H. Aliyari, R. Effatnejad, and M. Savaghebi, "Economic Dispatch With Genetic Algorithm," *ICTPE Conf.*, no. September, pp. 82–87, 2014.

[28] J. K. Pattanaik, M. Basu, and D. P. Dash, "Improved real coded genetic algorithm for dynamic economic dispatch," *J. Electr. Syst. Inf. Technol.*, vol. 5, no. 3, pp. 349–362, 2018, doi: 10.1016/j.jesit.2018.03.002.

[29] M. A. Abido, "Optimal power flow using particle swarm optimization," *Int. J. Electr. Power Energy Syst.*, vol. 24, no. 7, pp. 563–571, 2002, doi: 10.1016/S0142-0615(01)00067-9.

[30] B. E. Turkay and R. I. Cabadag, "Optimal power flow solution using particle swarm optimization algorithm," *IEEE EuroCon 2013*, no. July, pp. 1418–1424, 2013, doi: 10.1109/EUROCON.2013.6625164.

[31] J. Praveen and B. S. Rao, "Single objective optimization using PSO with Interline Power Flow Controller," no. November, 2016.

[32] A. Khan, H. Hizam, N. I. Abdul-Wahab, and M. L. Othman, "Solution of optimal power flow using non-dominated sorting multi objective based hybrid firefly and particle swarm optimization algorithm," *Energies*, vol. 13, no. 6, 2020, doi: 10.3390/en13164265.

[33] M. T. Rabadiya and V. B. Patel, "REVIEW ON REACTIVE POWER DISPATCH USING PARTICLE SWARM OPTIMIZATION (PSO) AND GREY WOLF OPTIMIZER," vol. 7, no. 8, pp. 6674–6680, 2020.

[34] L. Slimani and T. Bouktir, "An Ant colony optimization for solving the Optimal Power Flow Problem in medium-scale electrical network," no. November 2014, 2005, doi: 10.13140/2.1.3402.2088.

[35] L. Shi, J. Hao, J. Zhou, and G. Xu, "Ant colony optimization algorithm with random perturbation behavior to the problem of optimal unit commitment with probabilistic spinning reserve determination," *Electr. Power Syst. Res.*, vol. 69, no. 2–3, pp. 295–303, 2004, doi: 10.1016/j.epsr.2003.10.008.

[36] L. Kanagasabai, B. R. Reddy, and M. S. Kalavathi, "Optimal Power Flow using Ant Colony Search Algorithm to Evaluate Load Curtailment Incorporating Voltage Stability Margin

Criterion," *Int. J. Electr. Comput. Eng.*, vol. 3, no. 5, 2013, doi: 10.11591/ijece.v3i5.2738.

[37] V. Raviprabakaran and R. C. Subramanian, "Enhanced ant colony optimization to solve the optimal power flow with ecological emission," *Int. J. Syst. Assur. Eng. Manag.*, vol. 9, no. 1, pp. 58–65, 2018, doi: 10.1007/s13198-016-0471-x.

[38] V. Suresh, P. Janik, and M. Jasinski, "Metaheuristic approach to optimal power flow using mixed integer distributed ant colony optimization," *Arch. Electr. Eng.*, vol. 69, no. 2, pp. 335–348, 2020, doi: 10.24425/aee.2020.133029.

[39] A. Qasim and L. Tawfeeq Al-Bahrani, "Constraint Optimal Power Flow Based on Ant Colony Optimization," *J. Eng. Sustain. Dev.*, vol. 24, no. Special, pp. 274–283, 2020, doi: 10.31272/jeasd.conf.1.30.

[40] L. Sun, X. Kong, J. Xu, Z. Xue, R. Zhai, and S. Zhang, "A Hybrid Gene Selection Method Based on ReliefF and Ant Colony Optimization Algorithm for Tumor Classification," *Sci. Rep.*, vol. 9, no. 1, pp. 1–14, 2019, doi: 10.1038/s41598-019-45223-x.

[41] Vlachogiannis, J. G. "Fuzzy logic application in load flow studies." IEE Proceedings-Generation, Transmission and Distribution 148.1 (2001): 34-40.

[42] Miranda, Vladimiro, and Joao P. Saraiva. "Fuzzy modelling of power system optimal load flow." IEEE Transactions on Power Systems 7.2 (1992): 843-849..

[43] J. J. Buckley and L. J. Jowers, "Fuzzy multiobjective LP," *Stud. Fuzziness Soft Comput.*, vol. 222, no. 3, pp. 81–88, 2008, doi: 10.1007/978-3-540-76290-4_9.

[44] N. P. Padhy, "Congestion management under deregulated fuzzy environment," *Proc. 2004 IEEE Int. Conf. Electr. Util. Deregulation, Restruct. Power Technol.*, vol. 1, no. April, pp. 133–139, 2004, doi: 10.1109/drpt.2004.1338481.

[45] V. C. Ramesh and X. Li, "Optimal power flow with fuzzy emissions constraints," *Electr. Mach. Power Syst.*, vol. 25, no. 8, pp. 897–906, 1997, doi: 10.1080/07313569708955784.

[46] A. M. Abusorrah, "Optimal power flow using adaptive fuzzy logic controllers," *Math. Probl. Eng.*, vol. 2013, no. August, 2013, doi: 10.1155/2013/975170.

[47] L. dos S. Coelho and V. C. Mariani, "Improved differential evolution algorithms for handling economic dispatch optimization with generator constraints," *Energy Convers. Manag.*, vol. 48, no. 5, pp. 1631–1639, 2007, doi: 10.1016/j.enconman.2006.11.007.

[48] S. Sayah and K. Zehar, "Modified differential evolution algorithm for optimal power flow with non-smooth cost functions," *Energy Convers. Manag.*, vol. 49, no. 11, pp. 3036–3042, 2008, doi: 10.1016/j.enconman.2008.06.014.

[49] M. A. Abido and N. A. Al-Ali, "Multi-Objective Optimal Power Flow Using Differential Evolution," *Arab. J. Sci. Eng.*, vol. 37, no. 4, pp. 991–1005, 2012, doi: 10.1007/s13369-012-0224-3.

[50] P. P. Biswas, P. N. Suganthan, R. Mallipeddi, and G. A. J. Amaratunga, "Optimal power flow solutions using differential evolution algorithm integrated with effective constraint handling techniques," *Eng. Appl. Artif. Intell.*, vol. 68, pp. 81–100, 2018, doi: 10.1016/j.engappai.2017.10.019.

[51] S. Li, W. Gong, L. Wang, X. Yan, and C. Hu, "Optimal power flow by means of improved adaptive differential evolution," *Energy*, vol. 198, p. 117314, 2020, doi: 10.1016/j.energy.2020.117314.

[52] Y.-C. Wu, W.-P. Lee, and C.-W. Chien, "Modified the performance of differential evolution algorithm with dual evolution strategy," *Int. Conf. Mach. Learn. Comput.*, vol. 3, pp. 57–63, 2009.

[53] M. H. Sulaiman, Z. Mustaffa, M. R. Mohamed, and O. Aliman, "Using the gray wolf optimizer for solving optimal reactive power dispatch problem," *Appl. Soft Comput. J.*, vol. 32, pp. 286–292, 2015, doi: 10.1016/j.asoc.2015.03.041.

[54] A. A. A. Mohamed, A. A. M. El-Gaafary, Y. S. Mohamed, and A. M. Hemeida, "Multi-objective Modified Grey Wolf Optimizer for Optimal Power Flow," *2016 18th Int. Middle-East Power Syst. Conf. MEPCON 2016 - Proc.*, pp. 982–990, 2017, doi: 10.1109/MEPCON.2016.7837016.

[55] M. Siavash, C. Pfeifer, A. Rahiminejad, and B. Vahidi, "An application of grey Wolf optimizer for optimal power flow of wind integrated power systems," *Proc. 2017 18th Int. Sci. Conf. Electr. Power Eng. EPE 2017*, 2017, doi: 10.1109/EPE.2017.7967230.

[56] M. Abdo, S. Kamel, M. Ebeed, J. Yu, and F. Jurado, "Solving non-smooth optimal power flow problems using a developed grey wolf optimizer," *Energies*, vol. 11, no. 7, pp. 1–16, 2018, doi: 10.3390/en11071692.

[57] R. Jamal, B. Men, and N. H. Khan, "A Novel Nature Inspired Meta-Heuristic Optimization Approach of GWO Optimizer for Optimal Reactive Power Dispatch Problems," *IEEE Access*, vol. 8, pp. 202596–202610, 2020, doi: 10.1109/ACCESS.2020.3031640.

[58] I. A. Hameed, R. T. Bye, and O. L. Osen, "Grey Wolf optimizer (GWO) for automated offshore crane design," *2016 IEEE Symp. Ser. Comput. Intell. SSCI 2016*, 2017, doi: 10.1109/SSCI.2016.7849998.

[59] N. Singh, "A Modified Variant of Grey Wolf Optimizer," *Sci. Iran.*, vol. 0, no. 0, pp. 0–0, 2018, doi: 10.24200/sci.2018.50122.1523.

[60] H. C. Nejad, "Applying Shuffled Frog Leaping Algorithm for Economic Load Dispatch of Power System," vol. 20, no. 20, pp. 82–89, 2011.

[61] M. C. V. Suresh and J. Belwin Edward, "Optimal placement of distributed generation in distribution systems by using shuffled frog leaping algorithm," *ARPN J. Eng. Appl. Sci.*, vol. 12, no. 3, pp. 863–868, 2017.

[62] X. Dong, Z. Wu, L. Chen, Z. Liu, and X. Xu, "Distribution Network Reconfiguration Method with Distributed Generators Based on an Improved Shuffled Frog Leaping Algorithm," *2018 IEEE PES/IAS PowerAfrica, PowerAfrica 2018*, pp. 102–107, 2018, doi: 10.1109/PowerAfrica.2018.8521095.

[63] K. Lenin, "Factual Power Loss Diminution by Enhanced Frog Leaping Algorithm," *J. Appl. Sci. Eng. Technol. Educ.*, vol. 3, no. 2, pp. 114–118, 2020, doi: 10.35877/454ri.asci112.

Characterization of Iraqi crude oil using Aspen Hysys

Fatimah Azer Naji[1], Adnan A. Ateeq[2], and Mohammed A. Al-Mayyahi[3]
{mscfatimah@gmail.com[1], adnan_ateeq@betc.edu.iq[2], moh1973may@gmail.com[3]}

Thermal Techniques Engineering Basra Oil Company-Basra-Iraq[1]
Basrah Engineering Technical College Southern Technical University, Basra, Iraq[2]
Chemical and Petroleum Refining Engineering Department Basra University for Oil and Gas Basra, Iraq[3]

Abstract. The economical value of crude oil is influenced by various chemical and physical properties, Therefore, enhancing the crude oil properties can be of great benefit for crude oil-exporting countries as Iraq. The process of enhancing crude oil properties can be carried out through the blending of different crude oils from different wells. In this research, we illustrate Iraqi crude oil enhancing through the blending of three different Iraqi oils, Nahran Umar Crude, Badra Crude, and West Qurna Crude. The blending process was carried out using a common industrially used simulator for the oil and gas field, Aspen HYSYS.

Keywords: Thermodynamic properties, crude oil, density, viscosity, specific heat, and thermal conductivity.

1 Introduction

Crude oil is a non-uniform admixture of different hydrocarbons, that in most cases would contain certain impurities including metals, chlorides, elemental nitrogen, nitrogen oxides, elemental sulfur, hydrogen sulfide, hydrogen oxides, and mercaptans. The presence of certain impurities would affect the oil quality. For example, crude oil can be classified as light, medium, or heavy crude according to its density which is directly influenced by the length and structure of the hydrocarbon chains, it may be also classified as sweet or sour based on sulfur content or classified as naphthenic, paraffinic or aromatic (Abdel-Raouf, 2012).

The API gravity of medium crude oils ranges from 22.3 to 31.1 above which the crude is classified as light crude otherwise it's considered heavy crude oil. The higher API gravity, the lower the sulfur content. Crude oil of sulfur content below 0.5% in weight is known as sweet oil otherwise is sour (Bennett,2016). Naphthenic, paraffinic, and aromatic nature can be estimated based on the Watson Characterization Factor (KW) with naphthenic oils in the range of 10 to 11, paraffinic in the range of 11 to 12.9 (Scherzer et al, 1996).

Taking into consideration that each refinery would have a unique design based on the feed specifications and produced petroleum products and that well production capacity and crude oil properties interface certain changes along well lifetime. Therefore, crude oil blending can be considered a must for certain refineries. Light crude distillation produces higher yields per unit mass of high-value products like gasoline compared to medium and heavy crudes consuming less energy in form of heat. On the other hand, transportation and storage costs of light crudes are relatively low which makes light oils more favorable for refineries (Speight, 2001). The purpose

IMDC-IST 2021, September 07-09, Sakarya, Turkey
Copyright © 2022 EAI
DOI 10.4108/eai.7-9-2021.2314846

of crude oils blending is to obtain a new blend with certain properties to ease transportation, meet feed specifications of certain plants, making use of lower grade oils by mixing a small portion with high-grade oils, etc (Demirbas, 2017).

Enhancing crude oil properties through blending processes has been studied for many years. García and Urbina (2003) characterized sixteen crude oils from Eastern Venezuela in terms of wax content, hydrocarbons distribution, and other factors, to study those factor effects on the flowing properties of these crudes and their blends. Some blends of those crudes showed significant improvement in oil flow decreasing the wax crystallization tendency.

Li et al. (2006) investigated the blending process of Cabinda oil and Oman oil to obtain the optimum blending ratio that would form a suitable feedstock for a certain refining operation. They studied the distillation products' yields showing an optimal blending ratio of 7:3 for the Cabinda oil and Oman oil respectively. They also validated relationships between yields, viscosities, and surface tension.

Centeno et al. (2011) reported seventeen mixing rules that were used for the prediction of crude oil viscosity and its fractions. The mixing rules were examined and validated by comparing estimated values with experimental viscosities of various crudes of various API gravities. It was reported that only four of the tested rules showed the good ability of crude prediction (Chevron, Walther, Einstein, and Power-law), while no rule was able to calculate the viscosity of all the crudes successfully, A fifth rule (Chririnos) showed good accuracy for the prediction of distilled products such as naphtha.

Hou et al. (2015) established a model for crude oil optimization and properties prediction for Shanbei crude blending, which aims to improve the total yield of fractions and to reduce the viscosity of the blend. The model was used to predict the results of two different blends. Blends were later prepared and distilled to validate the model.

Hernández et al. (2019) investigated important mixing rules to estimate the viscosity of blended crude oils. Experimental viscosity of various binary and tertiary crude oil blends was tested in labs and used to validate the mixing model and determine its accuracy. They proved that the mixing rule with 4 interaction parameters has the highest ever efficiency compared to conventional mixing rules. Interaction parameters were obtained by statistical techniques and sensitivity analysis.

Naji et al. (2021) investigated the blending process of different Iraqi oils and its effect on obtained blend API gravity and sulfur content. They also simulated the fractionation process of different blends to predict atmospheric distillation products' yields and quality. The aim of the research. Characterization and analysis of the thermodynamic properties, including density, viscosity, specific heat, and thermal conductivity of Iraqi crude oils. this is of great importance in the stage that comes after the extraction process, which is dealing with these oils in transportation and storage operations.

2 The Aim of the Research

In this research, we aim to characterize and analyse thermo-mechanical properties of three different Iraqi crude oils and their blends, including density, viscosity, specific heat, and thermal conductivity. The importance of such properties becomes clear during the early design stages of refineries.

3 Blending Process Simulation

The simulation process was carried out using two different software's "Aspen HYSYS ®" and "Aspen Plus ®" provided by Aspen Tech Inc. Both simulators have widely proved their ability to solve complex industrial models that handle material balance calculations, heat balance and heat transfer calculations, vapor-liquid equilibrium (VLE) calculations, hydraulics calculations. The two simulators contain built-in thermodynamic models known as "Fluid Packages''.

A. Fluid Package Selection

The selection of an adequate fluid package depends mainly on the process itself as well as the chemical components we would deal with, with Aspen Tech providing a "method assistant" the fluid package of "Peng-Robison (PR)" was selected.

According to the Aspen Tech user guide (Aspen Tech, 2000), Peng-Robinson (PR) model is the most used thermodynamic model for (VLE) calculations in Oil & Gas industries, especially when dealing with hydrocarbons at temperatures above -271 °C, below 900 °C, and pressures below 100,000 kPa.

B. Crude Oils Defining

The three crudes were imported to Aspen HYSYS ® and Aspen Plus ® in form of crude assays. Assay data type was selected as "True Boiling Point (TBP) weight basis" due to available crudes lab data. Imported assays included light ends (C1:C5) analysis, TBP curves, molecular weight curves, kinematic viscosity curves at 20 °C and 100 °C, density curves, sulfur content curves, and bulk properties like API gravities, Watson factors, and viscosities. Table 1 represents a classification summary of each crude oil.

Table 1. Crude Oils classification summary.

Crude Properties	Crude (1)	Crude (2)	Crude (3)
API gravity	42.9	35.5	22.8
Watson Factor	12	11.9	11.6
Sulphur Content wt%	1.19	2.31	4.13
Classification	Light, Paraffinic, Sour	Light, Paraffinic, Sour	Medium, Paraffinic, Sour

4 Results and Discussion

Data obtained through Aspen HYSYS ® was re-arranged and visualized using MATLAB ® software.

4.1 Heat Capacity

Specific heat capacity for a certain substance represents the amount of supplied energy required to increase the temperature of this substance one degree Celsius, and thus for a crude blend of high specific heat. Capacity would require much energy for the refining process.

i. Mass Heat Capacity

Results showed that increment blending percentage of crude (3) would significantly decrease the overall blend mass heat capacity while increasing the percentage of crude (2) would have no significant effect. This is due to the small difference between crude (1) and crude (2) mass heat capacities, 1.846 and 1.847 kJ/kg. respectively, and the low mass heat capacity of crude (3), 1.472 kJ/kg., compared to other crudes. Fig 1**.** illustrates the variation of mass heat capacity for different blending ratios.

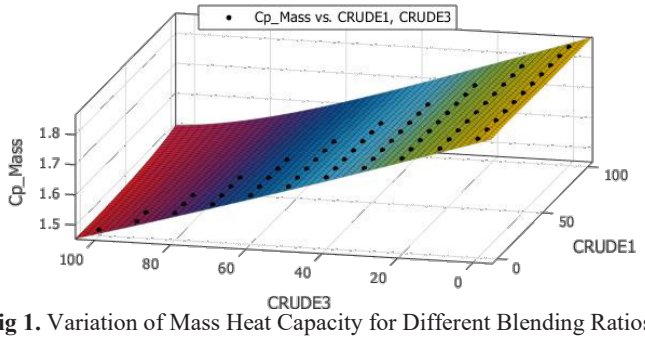

Fig 1. Variation of Mass Heat Capacity for Different Blending Ratios.

ii. Molar Heat Capacity

Molar heat capacities of crude (1), crude (2), and crude (3) were estimated as 293.6, 341.1, and 693.8 kJ/kmol.°C respectively. Unlike the variation scheme of mass heat capacity, increasing the blending percentage of crude (3) increases the molar heat capacity of the overall blend severely. On the other hand, increasing the blending percentage of crude (2) has a significant effect in increasing the blend molar heat capacity. Fig 2. shows the variation of molar heat capacity for tertiary blending.

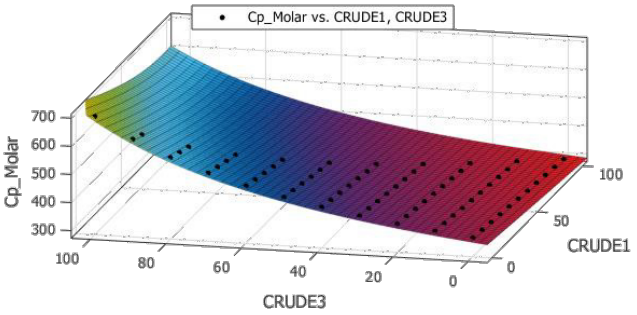

Fig 2. Variation of Molar Heat Capacity for Different Blending Ratios.

The irreconcilable behaviour of mass and molar heat capacities variation for tertiary blending is supposed to be due to the significant difference in molar mass of each blend which was reported to be 159, 184.7, and 471.2 kg/kmol for crude (1), crude (2) and crude (3) respectively.

4.2 Latent Heat of Vaporization

Standard heat of vaporization of various blending scenarios was analysed. The importance of such thermal property is summarized in estimating energy demands of atmospheric distillation units' re-boilers side by side with heat capacity. Results showed that increasing the blending percentage of crude (3) would lead to a severe increase in heat of vaporization of the obtained blend and thus the re-boiler duty. While increasing crude (2) blending percentage would increase the blend heat of vaporization but less sharply.

Specific heats of vaporization were estimated as 173.7, 230.6, and 453.1 MJ/kmol for crude (1), crude (2), and crude (3) respectively. Fig 3. shows the variation of molar heat of vaporization for tertiary blending.

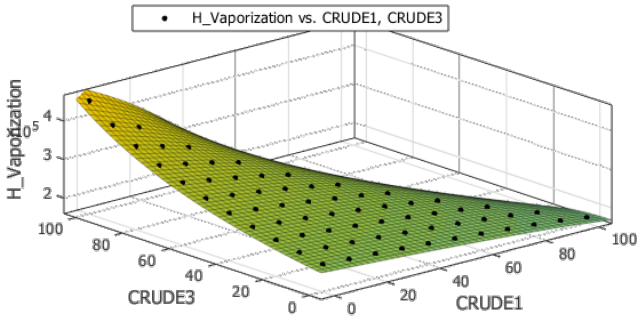

Fig 3. Variation of Heat of Vaporization for Different Blending Ratios.

4.3 Thermal Conductivity

The importance of thermal conductivity of the obtained blend is an accurate estimation of heat transfer coefficients for the refinery pre-heaters and boilers. Thus, variation of thermal conductivity of the blend was studied for various blending ratios. Fig 4. shows the variation of thermal conductivity in W/m.k for tertiary blending.

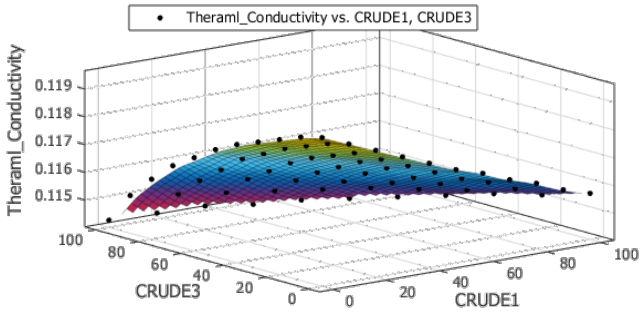

Fig 4. Variation of Thermal Conductivity for Different Blending Ratios.

4.4 Heat Capacity

Viscosity is one of the most used properties in calculations related to momentum transfer, fluid flow, and heat transfer. Thus, estimation of blend viscosity for various blending ratios is of great importance. Results collected from the Aspen HYSYS case study were analysed and plotted in Figs 5 & 6. Since viscosity is a temperature-dependent property, it's not easy to compute all viscosity variation possibilities. In this case, we study the viscosity variation due to variation of blending ratios at a constant temperature of 60 °F.

Results showed that increasing the percentage of crude (3) in the blend would increase both dynamic and kinematic viscosities of the blend severely. While increasing crude (2) percentage in the blend would have no significant effect on neither dynamic nor kinematic viscosities of the blend for low percentages of crude (3). For high percentages of crude (1), neither increasing crude (2) nor crude (3) percentages would have a significant effect on dynamic or kinematic viscosities.

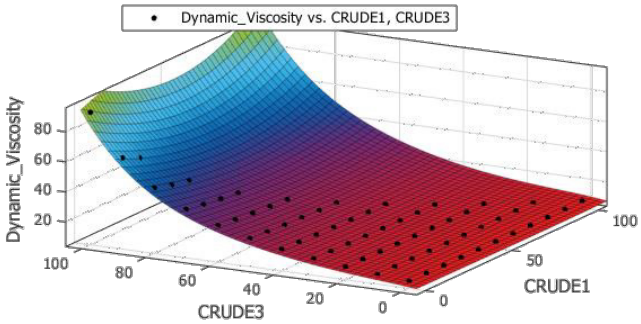

Fig 5. Variation of Dynamic Viscosity for Different Blending Ratios.

4.5 Adiabatic Index

The adiabatic index, also known as the isentropic expansion factor, is the ratio of heat capacity at constant pressure to heat capacity at constant volume, it's important in the evaluation of adiabatic expansion and compression of fluids, represented in fluid behaviour within distillation columns in this case.

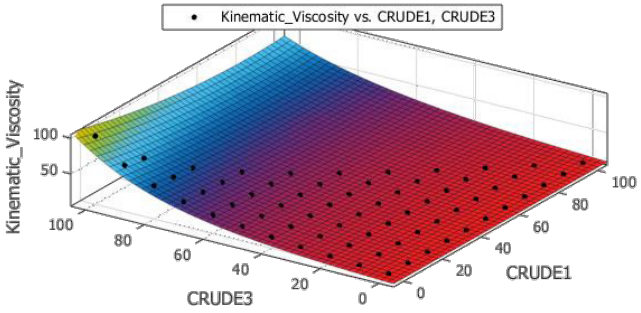

Fig 6. Variation of Kinematic Viscosity for Different Blending Ratios.

The adiabatic index for the blend was studied for various blending ratios and reported in Fig 7. Results showed that increasing the percentage of crude (3) in the blend would have a dramatic decrease in the adiabatic index of the blend while increasing crude (2) percentage has a small influence in decreasing the adiabatic index.

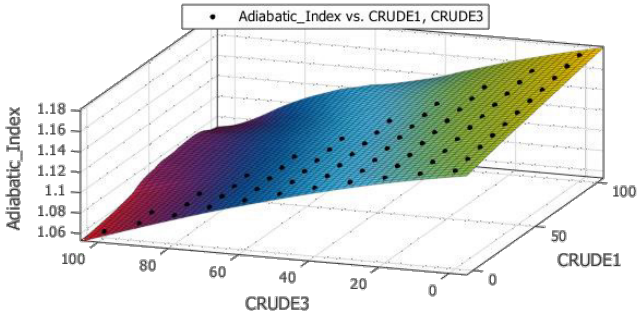

Fig 7. Variation of Adiabatic Index for Different Blending Ratios.

5 Conclusion

Depending on simulation results we conclude that the blending process of different grade crude oils can significantly enhance certain thermo-mechanical properties. With small changes in blend ratio, certain properties would change significantly and thus performing simulation studies for rating purposes of already installed petroleum refineries can be of great importance to prepare the optimum feed blend.

References

[1] Abdel-Raouf, M. Crude oil emulsions: Composition stability and characterization. (2012).
[2] Bennett, S. Medium/Heavy duty truck engines, fuel & computerized management systems. Cengage Learning. (2016).
[3] Scherzer, J., & Gruia, A. Hydrocracking science and technology. CRC Press. (1996).
[4] Speight, J. G., & Ozum, B. Petroleum refining processes. CRC Press. (2001).
[5] Demirbas, A., & Bamufleh, H. S. Optimization of crude oil refining products to valuable fuel blends. (2017). Petroleum Science and Technology, 35(4), 406-412.
[6] García, M. D., & Urbina, A. Effect of crude oil composition and blending on flowing properties. (2003). Petroleum Science and Technology, 21(5-6), 863-878.
[7] Li, S., Liu, J., Shen, B., Xu, X., Fan, Q., Chen, J., & Zhao, G. Distillation yields from blending Cabinda crude oil and Oman crude oil. (2006). Petroleum Science and Technology, 24(6), 737-747.
[8] Centeno, G., Sánchez-Reyna, G., Ancheyta, J., Muñoz, J. A., & Cardona, N. (2011). "Testing various mixing rules for calculation of viscosity of petroleum blends" Fuel 90(12), 3561-3570.
[9] Hou, J., Li, X., & Sui, H. (2015). The optimization and prediction of properties for crude oil blending. *Computers & Chemical Engineering*, *76*, 21-26.
[10] Hernández, E. A., Sánchez-Reyna, G., & Ancheyta, J. (2019). "Comparison of mixing rules based on binary interaction parameters for calculating viscosity of crude oil blends", Fuel 249, 198-205.
[11] F. A., Ateeq, A. A., & Al-Mayyah, M. A. (2021). Optimization of blending operation for the Iraqi oils. Journal of Physics: Conference Series, 1773(1), 012037.
[12] Aspen Technology, Inc. (2000). "ASPEN PLUS® User Guide", 169-180

Experimental Study of the Wet Cooling Tower using Different Packing Materials

Alaa H. Hussein[1], Safaa H. Faisal[2], Bassam A. Mohammed[3]
{alaahamel2@gmail.com[1], s_hfaisal100@stu.edu.iq[2*], Bassam.moh@stu.edu.iq}

Thermal Mechanical Engineering Department., Southern Technical University, Basra, Iraq[1,2,3]

Abstract. Three alternative materials are suggested to use in the wet cooling tower as a replacement to the standard plastic packing (PL). These are reed plants (RP), drinking water bottlenecks (WB), and chicken feathers (CF). Results show that increasing the airflow rate leads to an improvement in thermal performance together with an increase in pressure drop. Increasing the water flow rate negatively affects the thermal performance with a slight increase in the pressure drop. The increase in inlet water temperature does not show any effect on the pressure drop. It is found that the PL packing is the best in terms of thermal performance, followed by the RP packing. The CF packing comes in the next, and finally, the WB has the lowest performance. The WB packing is the best in terms of pressure drop, followed by CF packing and then the PL packing, while the RP has the highest pressure drop.

Keywords: Cooling tower, Counterflow, Packing, Tower efficiency, Pressure drop.

1 Introduction

Many air conditioning systems, industrial processes, and thermal power plants produce large amounts of waste heat that must be removed and dissipated. Water is the best environment used to remove that waste heat from the respective heat exchangers. This may be done by drawing a continuous stream of water from a nearby source of water, heating it during the process, and then draining it back to the same source of the cooling water. The idea of using cooling towers in many industrial establishments came to remove heat directly from the atmosphere, thus saving large quantities of cooling water and recycling it again [1]. The common working principle of the cooling tower is to remove the heat energy from the hot cooling water using direct contact with cold air and expel it to the atmosphere while some applications use indirect cooling. There are two types of cooling towers: natural cooling towers and mechanical cooling towers. The latter has two types: forced draft or induced draft. The cooling tower consists mainly of several important parts including the water spray system, fillers, and fans. The water spray system is located at the top of the tower, and it receives hot water. The packing function is to increase the surface area of water droplet precipitation and increase the period of contact with air. Fans are used to push air into or absorb it from the tower, which increases the process of evaporation and thereby boost heat dissipation [1].
Throughout the cooling tower, two processes occur between air and water streams which are heat and mass transfer. The properties of air entering the cooling tower plays an important role in the evaporation process. Many studies are introduced to improve and represent the thermal performance of the cooling tower.

IMDC-IST 2021, September 07-09, Sakarya, Turkey
Copyright © 2022 EAI
DOI 10.4108/eai.7-9-2021.2314845

Merkel's work [2] in (1925) can be considered a pioneer in this field as she combined the equations covering mass and energy transfer into the single equations based on enthalpy potential. Baker and Shryock[3] explained in detail Merkel's approach and applied it to several cases of cooling towers. Jaber and Webb[4] developed the effectiveness-NTU theory to be applied for designing the cooling tower. Elsarrag [5] used a burned clay as a filler in cooling towers and developed a correlation for mass transfer coefficient. Gharagheizi et al [6] studied and compared the cooling tower characteristics using two types of film fillers. It was concluded that the type and arrangement of packing influence the efficiency of the cooling tower. Mahmood et al [7] study the thermal performance of the counter flow cooling tower using three types of packaging, plastic sheets, aluminium sheets, and plastic balls. They found that aluminium packing gives the highest performance while the lowest is attained for plastic balls. Lemouari et al [8] conducted an experimental analysis of a cooling tower packed with galvanized sheets having a vertical grid in a zigzag form. They claimed that this arrangement possesses good mass and heat transfer characteristics comparing with other types of packing. Abbas[9] used a steel filler with two arrangements parallel and grid shapes in a counter flow cooling tower. He shows that the temperature of the water entering the tower has a great influence on the thermal performance. Kariem [10] study the possibility of reducing the evaporation rate from the dry-wet cooling tower combination system. Four corrugated packing shapes were adopted with all possible combinations. The results show that series configuration produces lower evaporation rates. Ghazani et al [11] used a laboratory-scale wet counter-flow cooling tower to examine the performance in the light of the first and second law of thermodynamic. The results showed that the irreversibility along the height of the tower depends on the mass ratio of water-to-air. Chen et al [12] compare the performance of cooling towers that used fresh bamboo mesh filler in the cooling tower with that in service for nine years. The results showed that although some mechanical properties of the used packing are decreased, it still met the normal requirements. Kong [13] used a foamed ceramic corrugated board packaging in a wet counter-flow cooling tower. They found that the range of cooling water and its efficiency decrease with increasing water to air flow mass ratio.

In this work, the performance of the counter flow wet cooling tower is studied and analysed experimentally using four different packing materials. The reference packing material is plastic packages (PL) and the suggested packing materials are reed plant (RP), drinking water bottlenecks (WB), and chicken feather waste (CF). These packings are chosen due to their low cost, lightweight, and local availability. Besides, the use of such alternative materials can solve an environmental and social problem, as it leads to a reduction in the level of pollution they cause.

2 Experimental Works

2.1 Experimental setup

The practical experiments of the present study are carried out using a laboratory-scale cooling tower. The apparatus as shown in Fig 1 is a counter flow, forced draught wet cooling tower. It can perform all operation conditions required by the present study. It mainly consists of:

1- Cooling tower column.

2- Basin to collect cold water exit from cooling tower column.
3- Hot water tank made of galvanized iron sheets and supplied with an electric heater.
4- Make up a water system to compensate for water losses during the evaporation process.
5- Hot water circulating pump.
6- Hot water spray system that is placed at the top of the tower column.
7- Forced draught Fan to push the air into the tower.
8- Water flow meter.
9- Eliminator.
10-Thermocouple sensors to measure 6 points of temperatures for air and water.

The specifications of each part of the cooling tower are given in Table 1, while the specifications of different measuring devices that have been used are given in Table 2.

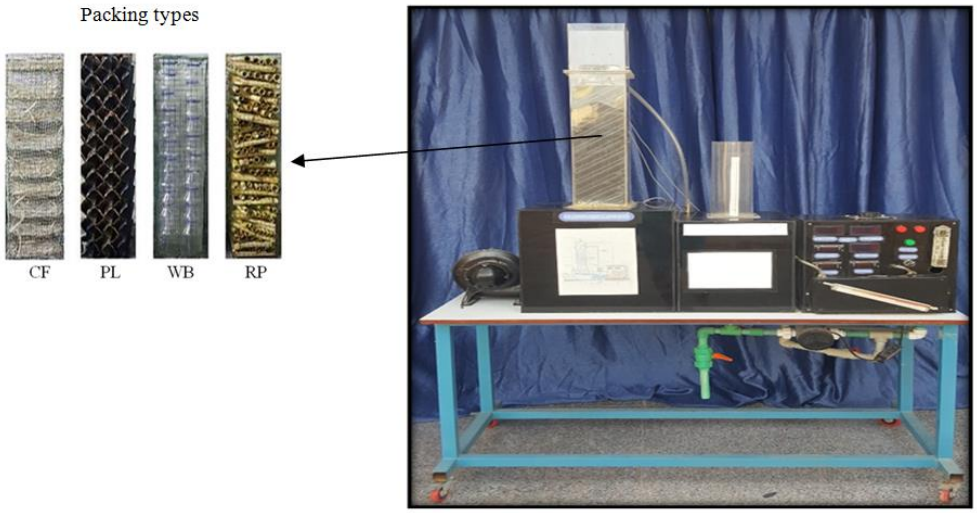

Fig. 1. Laboratory scale cooling tower and the used packing types.

Table 1. Specification of the cooling tower.

Part	Specification
Cooling tower column	Made of plastic sheet (15cm *15cm) *60cm high.
Circulating water pump	120 W,230V,50Hz, max capacity 0.067 kg/s.
Packing to be used	(14cm*14cm)*50cm high.
Main heater power	2.5 KW,230V,50Hz.
Forced draft fan	260 W, 230V, 50Hz, 3000 r.p.m, max capacity 0.086 kg/s.
Hot water tank	(31*28*28) cm.
Coldwater basin	(34cm*32)*12cm high.

Table 2. Specifications of different measuring devices.

Device	Type-Model	Range	Accuracy
Thermo-Anemometer	Turbine type-Model AN100	0.40-30 m/s	± 3% +0.20 m/s
Water flow meter	Float type	0 ~ 18 L.P.M	± 4%
Differential pressure drops	Digital type-model GM520	±35kPa, LCD display	+ 0.3% FSO

Humidity &Temperature Meter	Digital type-Model GM 1361	RH= 0 ~ 99.9 % T= -50 ~1200 ºC	±2.0 ºC ±0.4 ºC ± 5%

Referring to Fig 2. The description of air and water circuits found while the cooling tower in operation is as follows:

A. Water Circuit: The warm water is pumped from the main tank (supplied with heaters) and passes through the control valve to the top of the tower column. The water is sprayed via the water spray system and falls onto the packing. The water is cooled by exchanging heat and mass with air. Finally, it is collected in the water basin located down the tower column. Measurements include mass flow rate, inlet water temperature T_{in}, and exit temperature T_{out}. Make-up water is supplied automatically by a compensation system located near the tower column.

B. Air Circuit: The forced draught blows the air into the tower column from the left side. Measurement includes mass flow rate, dry bulb temperature at the inlet $T_{a1}$and exit T_{a2}, wet bulb temperature at the inlet T_{wb1} and exitT_{wb2}. As air flows through the packed column, the moisture content starts to increase, and the water will cool down. Before the air leaves the top of the column, it passes through an eliminator; and finally, the air is discharged to the atmosphere.

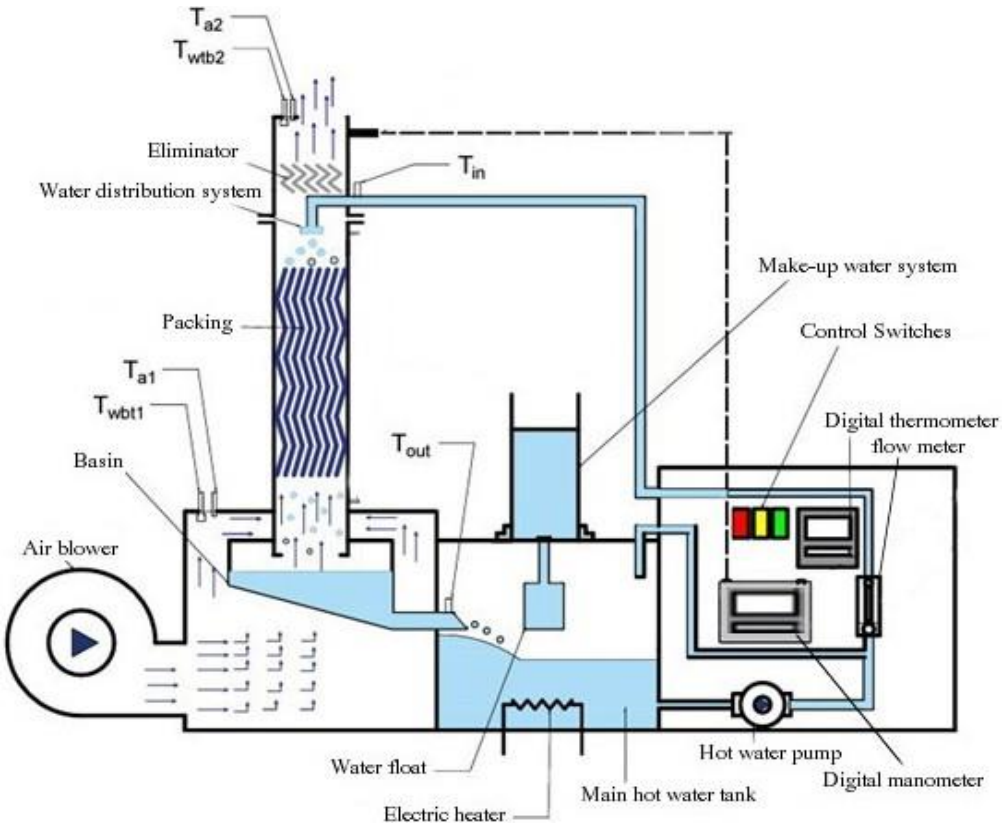

Fig. 2. Schematic diagram of the laboratory scale cooling tower.

2.2 Operation conditions

The operation condition covered by the present study includes hot water flow rates 0.025,0.033.0.05, and 0.0678kg/s, inlet hot water temperatures 45,47,and 49° C, and air mass flow rates 0.037,0.066,and 0.086 kg/m. The experiments were done at an ambient air temperature of 28° C dry-bulb temperature and 16° of wet-bulb temperature.

2.3 Experimental procedure

At first, the water in the main tank is heated before its ingoing the tower. After the required temperature of the water is attained, the pumping is started to the top of the tower at the required rate. At the same time, the fan mounted is started to force the required airflow rate into the tower. The steady-state is ensured by recognizing the water temperatures. When these temperatures are varying by just 0.1˚C, then steady-state has been achieved. The time interval needed is about 10-15 minutes. This procedure is repeated for other values of hot water temperature, water, and airflow rates.

2.4 Data reduction

The air mass flow rate G is calculated from the continuity equation as:

$$\mathrm{G} = \mathrm{V}.\mathrm{A}.\frac{\mathrm{P_{air}}}{287*(\mathrm{T_{a1+273}})} \quad (1)$$

Where V is the air velocity and A is the area of the fan duct. the value of atmospheric pressure $\mathrm{P_{air}}$ is assumed 101325 Pa.
The cooling tower range is the temperature difference between the hot water inlet and outlet:

$$\mathrm{Range} = \mathrm{T_{in}} - \mathrm{T_{out}} \quad (2)$$

The approach is the difference between the hot water outlet temperature and the ambient wet bulb temperature:

$$\mathrm{Approach} = \mathrm{T_{out}} - \mathrm{T_{wb1}} \quad (3)$$

The cooling tower efficiency η is the ratio of the actual temperature range to the ideal range, which is the sum of actual range plus approach [1]:

$$\eta = \frac{\mathrm{Range}}{\mathrm{Range+Approach}} = \frac{\mathrm{T_{in}-T_{out}}}{\mathrm{T_{in}-T_{wb1}}} \quad (4)$$

The heat load of cooling water Q is found by thermodynamic heat balance equation [1]:

$$\mathrm{Q} = \mathrm{L}.\,\mathrm{Cp_w}.\,(\mathrm{T_{in}} - \mathrm{T_{out}}) = \mathrm{G}.\,(\mathrm{h_{a2}} - \mathrm{h_{a1}}) \quad (5)$$

Where L is the water mass flow rate, $\mathrm{Cp_w}$ is the specific heat of hot, and $\mathrm{h_{a2}} - \mathrm{h_{a1}}$ is enthalpy difference of air at inlet and outlet.
The tower characteristic or so-called number of transfer units NTU is defined as [1]:

$$\mathrm{NTU} = \int_{\mathrm{T_{a1}}}^{\mathrm{T_{a2}}} \frac{\mathrm{Cp_w}}{(\mathrm{h_s}-\mathrm{h_a})}\,\mathrm{dT} \quad (6)$$

Where h_s is the enthalpy of saturated air and h_a is the enthalpy of unsaturated air.
The evaporation rate $\dot{\mathrm{m}}_{\mathrm{eva}}$ is found from:

$$\dot{\mathrm{m}}_{\mathrm{eva}} = \mathrm{G}.\,(\omega_{\mathrm{a2}} - \omega_{\mathrm{a1}}) \quad (7)$$

Where ω is the humidity content of the air.

3 Results and discussion

Fig 3. (a, b, c, and d) is for the number of transfer units and tower efficiency as they vary with air and water mass flow rates for the four tested packing s. All the curves are drawn for fixed inlet temperatures of the hot water and cold air.

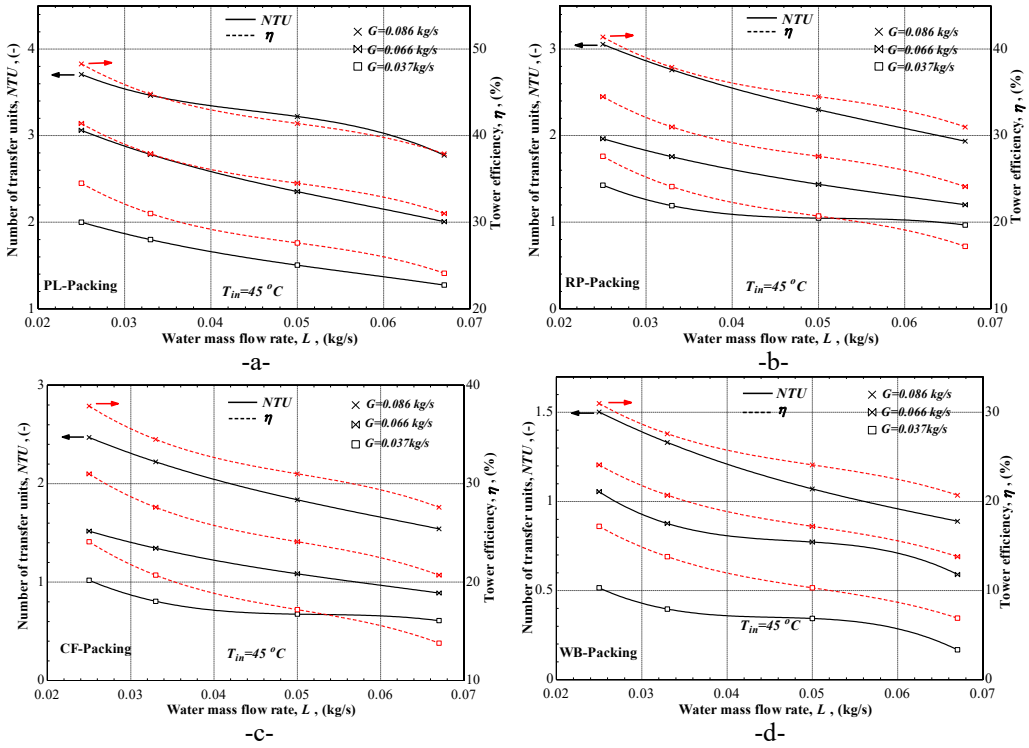

Fig. 3. The variation of NTU and tower efficiency with air and water mass flow rates (-a- PL, -b- RP , -c- CF, and -d- WB packing).

It is clear from the figure that increasing air mass flow rate has a positive effect while the water mass flow rate hurts both the NTU and tower efficiency for all the tested packing s. This is quite understood, and it coincides with the results found in the literature related to this subject. Increasing the airflow rate will improve the heat and mass transfer due to increasing the evaporative rate. More air will be in contact with less water and certainly, this is a good situation for the cooling tower. By fixing the inlet conditions of hot water and cold air, then the tower efficiency will be a function of tower range only. The sum of range and approach which is the ideal rage is constant in this case. The increase of the airflow rate will make the range higher due to declining the outlet temperature of the water. of course, this will increase the tower efficiency as the air mass flow rate increase. The figure shows that the standard PL packing shows the best performance concerning the value of NTU and tower efficiency. The lowest performance is observed for WB packing. The RP and CF packing being between these two limits. The worst performance of WB packing is attributed to the short contact time between the air and water. On the other side, the comparative performance of RP packing is related to the higher surface area, which maximizes the heat transfer.

Fig 4. (a, b, c, and d) shows the variation of pressure drop and evaporation rate with air and water mass flow rates for the four tested packings. Again, all the curves are drawn for fixed inlet temperatures of the hot water and cold air.

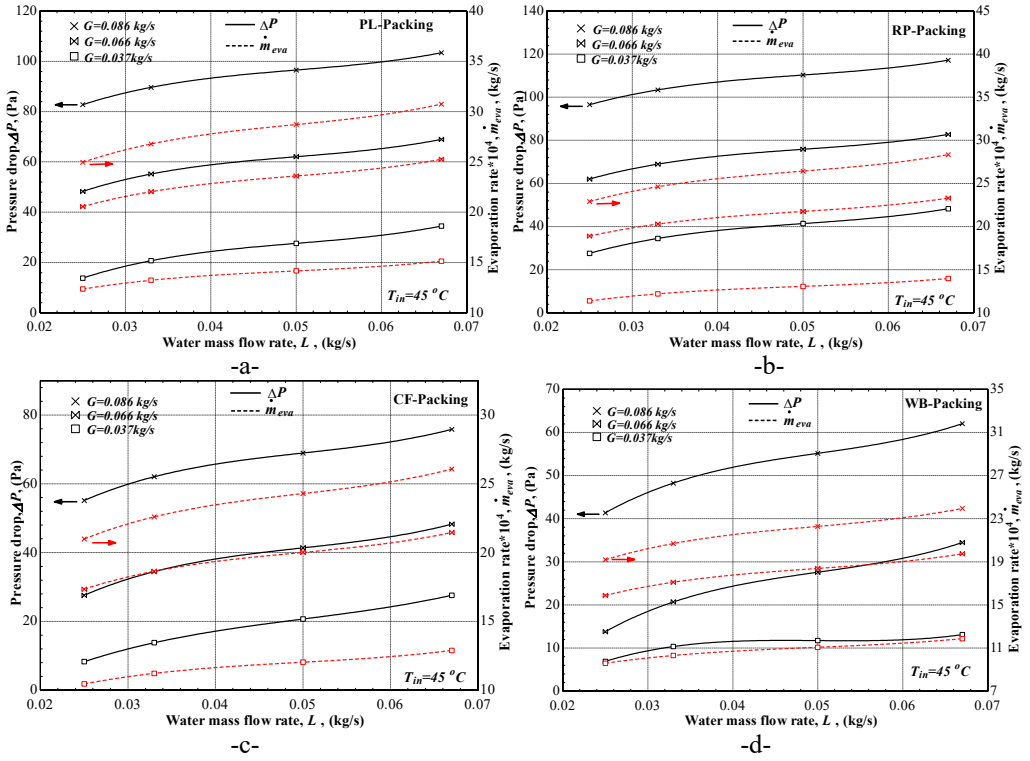

Fig. 4. The variation of pressure drop and evaporation rate with air and water mass flow rates (-a-PL, -b-RP , -c-CF, and -d- WB filling).

Increasing air mass flow rate will increase both pressure drop and evaporation rate due to raising the air velocity. Increasing the water flow rate will also increase the pressure drop and evaporation rates, but at lower levels than the effect of air. Rising the hot water flow rate imposes overwork on the tower and it represents an obstruction in the flow of air and so the pressure drop will increase. Generally, the pressure drops, and evaporation rate are in a small range due to the limited capacity of the tower. The figure shows that the RP packing has the largest value of the pressure drop, followed by PL packing, then CF packing, and WB has the lowest recorded pressure drop. Unfortunately, the low-pressure drop for the WB packing is accompanied by the worst thermal performance. The low-pressure drop is mainly due to uniform air distribution across the tower.

Fig 5. shows the effect of hot water temperature on the tower performance in terms of NTU and efficiency for the four tested packing s. The curves are drawn for the best situation of maximum tested air flow rate and minimum hot water flow rate. As the temperature of hot water increases from 45°C to 49° C, both NTU and tower efficiency will decrease due to the increase in heat load applied to the tower. However, the WB packing shows a less decreasing percentage of NTU comparing to the other types of packing.

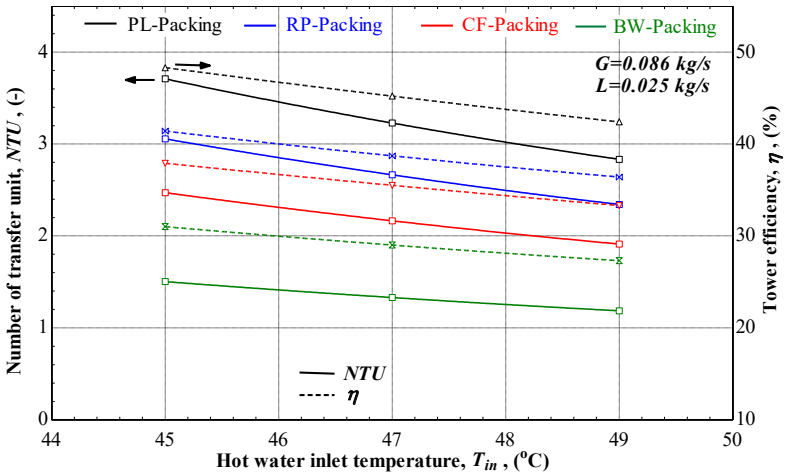

Fig. 5. The variation of NTU and tower efficiency with hot water temperature.

Fig 6. reveals the effect of hot water temperature on the pressure drop and evaporation rate for the four tested packing s. For the three tested hot water temperatures, the pressure drop is constant which is mainly due to the low-temperature range that causes no noticeable change in this parameter. As hot water rises, then the evaporation rate will increase for all the tested packing s due to the decrease in the latent heat of evaporation. The higher temperature is supposed to cause higher heat transfer since it is the driving force for this phenomenon. Since the air flow rate and its conditions are fixed, then this situation will not be attained.

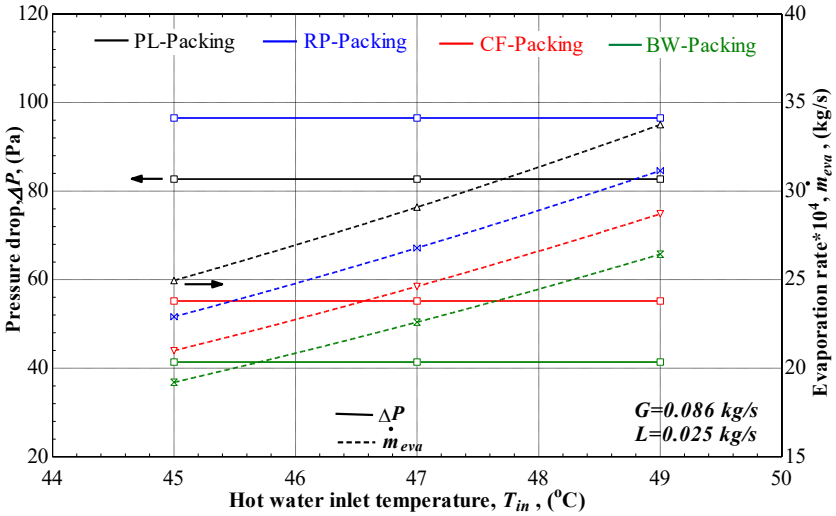

Fig. 6. The variation of pressure drops and evaporation rate with hot water temperature.

3 Conclusions

The present work introduces an experimental study for the performance of wet counter flow cooling using four types of packing PL, RP, CF, and WB. The following conclusions are revealed:

1. Increasing air mass flow rate causes better thermal performance of the tower but it also increases the pressure drop. Excessive rate of hot water flow rate caused the performance to degrade and so does its temperature.
2. The PL packing is still the most effective in terms of NTU and efficiency among the tested packings. The comparative packing is RP, then the CF packing comes next. The WB packing was the least performing of the packings. The thermal performance of the suggested packing belongs to its evaporative rate ability.
3. Higher pressure drop is recognized for the RP packing and the WB shows the lowest value of pressure drop.

Acknowledgments

The authors would like to express their gratitude to Basra Engineering Technical College, Basra, Iraq for their support to do this work.

References

[1] American Society of Heating, Refrigerating, and Air-Conditioning Engineers. ASHRAE Handbook Heating , Ventilating, and Air-Conditioning- Systems and Equipment. USA.2012.
[2] Merkel F. Verdunstungskuhlung. erste Ausgabe. Berlin: VDI-Verl, 1925.
[3] Baker DR, Shryock HA. A comprehensive approach to the analysis of cooling tower performance. ASME J of heat transfer. 1960; 83(3): 339-349.
[4] Jaber H and Webb RL. Design of cooling towers by the effectiveness-NTU method. J. Heat Transfer. 1989; 111(4): 837–843.
[5] Elsarrag E. “Experimental study and predictions of an induced draft ceramic tile packing cooling tower. Energy Convers. and Manag. 2006; 47: 2034–2043.
[6] Gharagheizi F, Hayati R, Fatemi S. Experimental study on the performance of mechanical cooling tower with two types of film packing. Energy Convers. and Manag. 2007; 48: 277–280.
[7] Mahmoud AF, Ahmed HH, Mahmoud RA. Experimental and theoretical study of cooling tower performance using different types of packing. J. of Eng. and Devel. 2009; 12(4): 21-43.
[8] Lemouari M, Boumaza M, Kaabi A. Experimental analysis of heat and mass transfer phenomena in a direct contact evaporative cooling tower. Energy Convers. and Manag. 2009; 50: 1610–1617.
[9] Abbas MN. Study the performance of different packing in open cooling towervs. J. of Eng. and Devel.2012; 16(2):193-210.
[10] Kariem NO. Effect of changing packing shapes on the evaporation rates using different combination arrangements of dry-wet cooling towers. Al-Qadisiyah J. for Eng. Sci. 2013; 6(2): 232-246.
[11] Ghazani MA, Hosseini AH, Emami MD. A comprehensive analysis of a laboratory scale counter flow wet cooling tower using the first and the second laws of thermodynamics. Appl. Therm. Eng. 2017; 125 :1389–1401.
[12] Chen LS, Fei BH, Ma XX, Lu JP, and Fang CH. Investigation of bamboo grid packing properties

used in cooling tower. Forests. 2018; 9 (762):1-9.
[13] Kong QJ, Liu DY, Wang P, Xie DQ, Wu Q, Zhao XY. Experimental study on the heat and mass transfer characteristics of a counter-flow wet cooling tower with foam ceramic packing. Thermophysics and Aeromechanics. 2019; 26 (2): 267-279.

Numerical Study of the Effect of Orientation Angles on Combined Convection in a Cavity Contain Rotation Cylinder

Sana.M.Shrama[1], Falah A. Abood[2], Sana.J.Yaseen[3], Amani J. Majeed[4]*
{sanamech77@gmail.com, dr.falah.abood@gmail.com,
sana.yaseen@uobasrah.edu.iq, ammani.majeed@uobasrah.edu.iq}

Mechanical Engineering department , Basrah University / Basrah, Iraq[1,2,3]
Petroleum Engineering department, Basrah University / Basrah, Iraq[4*]

Abstract. This study examines the influence of a rotating cylinder on heat transmitted by mixed convection in an air-filled square space. The appropriate mathematical models for continuous, incompressible, 2-dimensional, laminar flows with Boussinseq's approach are solved numerically, where constant fluid properties have been used. The most important parameters examined are: the angular velocity (Ω = 0 - 1000) and the angle of inclination (Θ = 0 – 90º), the study has been carried out with the Rayleigh number (Ra = 10^4), the Prandtl number (Pr = 0.7). The results show that the streamlines are affected by the angular velocity, where the forced convection becomes dominant at high values of angular velocity. The rotation of the cylinder has an effect on the heat exchange between the walls of the cavity and the fluid. Finally the average Nusselt number is increased with increases of angular velocity and decreases as inclination angles change from horizontal to vertical position. A good agreement has been achieved by comparing the results of this work with other previous work.Keywords: Inclined square cavity, rotating cylinder, mixed convection, numerical method.

Nomenclature

Cp	constant pressure specific heat
g	gravitational acceleration
H	height (width) of the enclosure
k	thermal conductivity
Nu	Nusselt number
p	pressure
Pr	Prandtl number
r	radius
R	radius at the surface of the cylinder
Ra	Rayleigh number
Ri	Richardson number
T	temperature
u,v	Cartesian velocity components
x, y	Cartesian co-ordinates

Greek symbols

α	thermal diffusivity
μ	dynamic viscosity
ν	kinematic viscosity
ρ	density
ψ	streamfunction
Ω	angular rotational velocity
φ	inclination angle

IMDC-IST 2021, September 07-09, Sakarya, Turkey
Copyright © 2022 EAI
DOI 10.4108/eai.7-9-2021.2314844

1 Introduction

Natural convection in enclosed spaces has been widely analyzed, because of its use in cooling electronic equipment, nuclear and chemical reactors, heat exchangers, and other applications [1]. The buoyancy force and partially heated enclosure walls cause natural convection, while the rotation of cylinder causes forced convection. Both of them influence the resulting flow and create mixed convection. The direction of rotation matching with forced and natural convection, therefore it is results in the strengthening or in the weakening of the convective flow. The free convection of a porous medium in a vertical square cavity was studied numerically [1], the Nu was increased with Ra. The mixed convection is studied in a square cavity with a concentric rotating cylinder studied numerically [2]. The impact of the cylinder's radius, rotational velocity, thermal capacity, and thermal conductivity were investigated. It can be noticed that the cylinder's size has a significant impact on the resulting flow and heat transfer process. Numerical simulations of 2D, laminar mixed convection, and steady-state in a sinusoidal corrugated vented cavity with a heat conducting cylinder were performed [3]. Richardson and Reynolds numbers are taken in the ranges 0–10 and 50–200, respectively; thermal conductivity ratio changed from 0.2 to 10. The results showed that the average Nusselt number increased, and the average temperature of the inside corrugated cavity decreased with increasing the diameter of the cylinder. A rotating circular with mixed convection inside a square cavity at different vertical places and different Richardson number was calculated numerically. The study showed that the temperature distribution and the flow field within the enclosure relied powerfully on the Richardson numbers and the location of the rotating cylinder, the great value of heat transfer rate obtained near the lowest wall of the enclosure [4]. The effect of mixed convection on triangular enclosure contains a rotating single or multi cylinders investigated numerically [5], three cases were examined: a single rotating cylinder, three rotating cylinders in the same and in different directions. The most important parameters examined were Rayleigh number with range of 102 - 105, angular velocity with range of (Ω = 0 - 1000) (for both cases). The result show that the mean Nu number for the single or multiple cylinders increased according to increasing Ra, and Ω. Also, the mean Nu number of a single cylinder was greater than that of multiple cylinders.

Mixed convection of a heated concentration cylinder with the enclosure studied numerically. The effect of different values of Lewis and Richardson numbers and buoyancy ratio were studied. It can be observed at the same Ri number the value of average Sherwood number raised as Lewis number growths. The mean Nu number about the cylinder reduced incrementally with the increase in buoyancy ratio at Ri number ¼ 0.01, the for all Lewis numbers except at ¼ 0.1 [6]. The effect of surface roughness on the turbulent flow through a rotating cylinder was calculated numerically [7]. The study was performed at three values of Reynolds numbers (5x105, 106 and 5x106) and fluctuation rates (1, 2 and 3). The study showed that the drag coefficient improved with increasing surface roughness and rate of rotation, but decreased with increasing Reynolds number.

The heat transfer of a rotating heated cylinder has been examined experimentally and numerically [8]. The experimental study was carried over to a range of Re and Gr numbers from 1880-6220 and 14,285-714,285, respectively, while numerical calculations were performed for different ranges of same numbers. For Re numbers greater than 8000, the Gr number had no effect on heat transfer rates and the results for unlike values of Gr are consistent. Heat transfer on a rotating cylinder was studied numerically [9]. The forced convection with a constant non-dimensional rotational speed between 0 and 6 for Re numbers from 20 to 200 and for a fixed Pr.

It has been found that the mean Nusselt number decreases with increasing rotational rate and increases with increasing Re.

Mixed convection heat transfer has been studied numerically in a trapezoidal cavity with a rotating heated cylinder [10]. The study concentrated on the influence of the variation of the inertia effect of the rotating cylinder on the parameters of the Re number for different Gr numbers ranging from 103 to 105 and for constant value of Richardson's number of 1.

The effect of a thin heated plate located in a square cavity was analyzed numerically [11]. The effect of inclination angle and Gr number on flow and heat transfer has been investigated, it can be noticed for low Gr numbers, the variation of the inclination angle has no influence on the heat transfer. While the behavior changed for higher value of Gr number. It was observed that for each case studied there was a direction that delivered best thermal performance.

Mixed convection heat transfer has been studied a long rotating cylinder for the range of the Ri number ($0 \leq Ri \leq 1$), the rotation angle ($\propto \leq 4$), the Re number range 1 - 40 and fixed value of the Pr number [12]. It was noticed that for the particular value of rotation angle, the average Nu number decreased with decreasing Re number, and with increasing the angle for fixed value of Ri and Re. Heat transfer using a nanofluid around a rotating cylinder with a constant nondimensional rotation rate varying from 0 to 5 was studied [13]. The study occurred at nanoparticle volume fractions range of 0–5%, Re number range of (5 – 40). It was noticed that the average Nu number was decreased with increasing value of the rotation rate for the fixed Re number.

The effects of a heated rotating cylinder in a cavity have been studied experimentally. The experiments were investigated for the bottom heated plate temperature ranging from 313 K to 333 K. The study showed that the heat transfer inside the cavity was improved due to the rotation of inner cylinder [14]. Mixed convective nanofluid flow within a triangular cavity with a flexible sidewall under the effect of an inner rotating cylinder was analyzed numerically [15]. It was noticed that the anti-clockwise rotation of the cylinder increased the heat transfer enhancements as compared to clockwise rotation. Also, it can be observed that adding nanoparticles resulted in 49.63% enhancement of heat transfer.

The heat transfer on a rotating cylinder was investigated for varying rotation rate, Re and Pr numbers [16]. It was noticed that for a constant Re and Pr numbers as the rotation rate decreased, the average Nu number was also decreased. Mixed convection heat transfer in a trapezoidal cavity was studied numerically [17]. It can be noticed as the Ri number increased the average Nu number increased for all aspect ratios, and it was reduced as the rotational angle increased. The laminar flow over a rotating cylinder within an enclosure were studied numerically [18]. It was observed that the local and average values of the Nusselt number improved as Reynolds number increased for a specific angle of rotation.

2 Physical Modeling

2.1 Model Presumptions and Equations

Fig. 1 shows the description of the problem for mixed convection in a 2D inclined square cavity, of width and height H, with the rotating cylinder, the cylinder was located at the center of the cavity. Both the vertical walls are completely insulated. The lower wall of the cavity is exposed to- uniform heat flux and the upper wall fixed at cold temperature, the rotating cylinder produces

a forced flow.The working fluid is air, incompressible fluid and the Boussinseq's approximation is used, the density of fluid is affected by temperature changes. A constant fluid properties are assumed for all remaining thermophysical fluid properties. Moreover, a laminar flow and neglect the thermal radiation heat transfer have been assumed. The governing equations can be applied on fluid flow mixed convection inside the enclosure, in its dimensionless form [19].

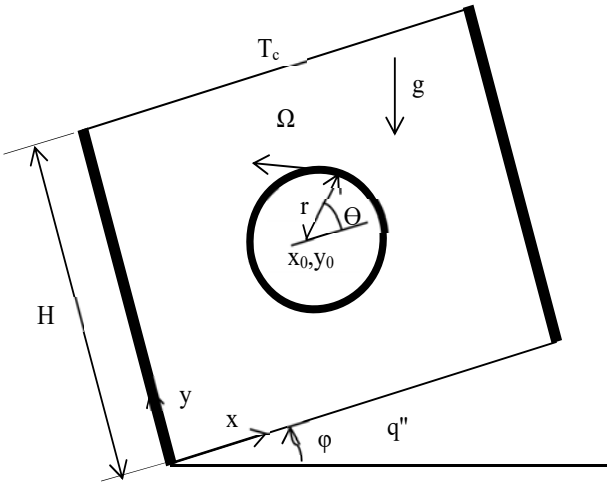

Fig. 1. The geometry and the physical model

$$\frac{\partial U}{\partial X}+\frac{\partial V}{\partial Y}=0 \tag{1}$$

The equations of momentum are:

$$U\frac{\partial U}{\partial X}+V\frac{\partial U}{\partial Y}=-\frac{\partial P}{\partial X}+\Pr\left(\frac{\partial^2 U}{\partial X^2}+\frac{\partial^2 U}{\partial Y^2}\right)+RaPrTgsin\varphi \tag{2}$$

$$U\frac{\partial V}{\partial X}+V\frac{\partial V}{\partial Y}=-\frac{\partial P}{\partial Y}+\Pr\left(\frac{\partial^2 V}{\partial X^2}+\frac{\partial^2 V}{\partial Y^2}\right)+RaPrTgcos\varphi \tag{3}$$

The energy conservation equation:

$$U\frac{\partial T}{\partial X}+V\frac{\partial T}{\partial Y}=\frac{\partial^2 T}{\partial X^2}+\frac{\partial^2 T}{\partial Y^2} \tag{4}$$

The parameters in a dimensionless form which are used in the previous equations can be clarified as following [19]:

The space coordinates:

$$(X,Y)=\frac{(x,y)}{H} \tag{5}$$

The velocity components:

$$(U,V)=\frac{(u,v)}{\alpha f/H} \tag{6}$$

The temperature:

$$T = (T* - T_c)/(T_h - T_c) \quad (7)$$

The driving pressure:

$$P = (p+\rho_o gy)/[\rho_{of} (\alpha_f/H)^2] \quad (8)$$

And the numbers of Prandtl and Rayleigh emerge as:

$$Pr = \nu/\alpha f \quad (9)$$

$$Ra = g \beta (T_h - T_c) H^3/(\nu\alpha) \quad (10)$$

The definition of heat transfer coefficient in terms of the local Nusselt number (*Nu*) and average Nusselt number (Nu_{avg}) is given as:

$$Nu = -\frac{\partial T}{\partial n} \quad (11)$$

$$Nu_{avg} = \frac{1}{L}\int_0^L NudL \quad (12)$$

The dimensionless governing parameters:

$$R = \frac{r}{H} \quad (13)$$

$$\Omega = \frac{\omega * H^2}{\alpha_f} \quad (14)$$

For the rotating cylinder, the dimensionless formula of velocity modules are explained below:

$$U = -\Omega (Y - Y_0) \quad (15)$$

$$V = (\Omega X - X_0) \quad (16)$$

The absolute value of velocity at any point of the cylinder can be evaluated as:

$$|V| = \sqrt{U^2 + V^2} = |\Omega| R \quad (17)$$

For the present study and dimensionless parameters:

$$Ri = \frac{RaPr}{4\Omega^2 R^4} \quad (18)$$

$$\frac{\partial \psi}{\partial X} = -v \quad (19)$$

$$\frac{\partial \psi}{\partial Y} = u \quad (20)$$

The boundary conditions used in this study are:

1- $\frac{\partial T}{\partial Y} = 1$ at bottom wall

2- $T=0$ at upper wall

3- $\frac{\partial T}{\partial Y} = 0$ at vertical walls (presumed to be insulated)

4- $\frac{\partial T}{\partial Y} = 0$ at the surface of the cylinder (are assumed to be insulated)

3 Result and Discussion

3.1 Numerical Scheme and code Validation

The flexPDF package used Galerkins weighted finite element remainder scheme to numerically solve the dominant Eq. (1) to Eq. (4). The values distribution of (∂U/∂X + ∂V/∂Y) through the domain is presented in Fig.2. It is clear that the continuity equation is exactly validated.

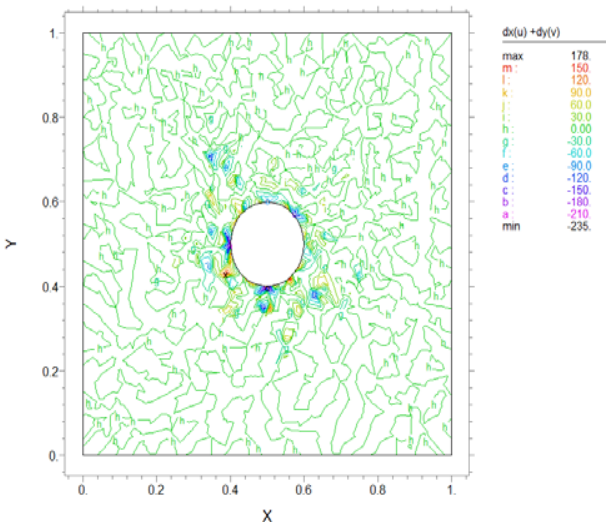

Fig. 2. Validation of continuity equation

For the developed model validation, simulations were performed to compare the mixed convection case of a heated rotating cylinder in a square cavity, as indicated in [19]. The summary of the comparison is shown in Table 1, a good agreement has been achieved by comparing the results of this work with other previous work [19].

Table 1. The comparison of the surface average present work Nusselt number with ($Ri = 10^3$, $L/R = 5$, $Pr = 0.71$) [19].

	Nu_{avg}	
Ra	Present work	Liao and Lin [19]
10^4	6.44	6.5
10^5	9.86	9.8

3.2 Flow field and Isotherms

The effect of tilt angle is examined for Θ=00, 300, 600, 900, the flow and thermal field in the cavity in the form of streamlines (right) and isotherms (left) for Ra=104 at Ω =1000 are shown in Figure 3.

In this figure, fluid flow takes place on the space between the cylinder and the enclosure, and it consists of longitudinal cells located in the gap area at the bottom and the upper of the cylinder this due to secondary flow. At tilt angle Θ=0º, there is a big circulating cell cover all the whole cavity, and a number of small cells surrounding the great cell at the core of the cavity. Figure shows a uniform temperature distribution near the lower wall and upper wall of the enclosure, and a weak heat transfer by natural convention is take place between the walls and the fluid.

With an increase in the tilt angle of hot surface, a recirculation cell develops in the gap area at the top of the cylinder and the other at the bottom of the cylinder leading to a significant change in the streamlines structure. The streamlines are very dense, thus indicating intense fluid flow, this an expected result due to the natural convection effects and rotation effects on the fluid motion. By observing Fig. 3, it is at angle 30° that flow changes its behavior from one pattern to the other. From angle Θ=30° to 90°, the flow field is a strong circulation moving to upward along the hot wall and moving to downward along the cold wall, so that the vortices merge above the cylinder to form a single longitudinal vortex, also the same vortex is take place near the bottom surface of the cylinder, which is located in the core of the enclosure.

For isotherms, the figures show that as the tilt angle of the heated surface increases towards the vertical position, the direction of the convection currents tends to become parallel to the hot surface and parallel to the direction of fluid movement at the angle θ =90o , where the isothermal pattern becomes thinner. There is a uniformity in the temperature distribution within the gap due to the effect of rotation, which is typical of convection problems in closed cavities. The streamlines are affected by the rotating cylinder, with increasing angular velocity the vortex pattern splits into many cells and thus forced convection becomes dominant.

The case of the anticlockwise rotating cylinder is shown in this figure. Isotherm are spread in the fluid where some thermal layers can be observed near the hot and cold walls. The significant expansion of the recalculating cell presses the flow path. Convective heat transfer associated with the cell causes a removal of heat from the heated wall. The convection heat transfer enhanced by the rotation of the cylinder plays an important role in the heat exchange between the walls of the cavity and the fluid. The heat transfer process is mainly dependent of the cylinder

motion. The thermal field represented by the temperature distribution are uniformly around the cylinder at the low and high values of angular velocity.

3.3 Nusselt number

The average Nusselt number changes with angular velocity at different inclination angles at $Ra=10^4$ is depicted in Fig. 5.

The general outcome from the plot is that Nu increases with angular velocity. For rotating velocities close to zero (nearly motionless cylinder), the situation corresponding to inclination angle $\Theta=90^0$ presents the minimum average Nusselt number. Apparently, there is only a small heat transfer between the walls of the enclosure and the fluid .From the figure it can be seen that the value of the Nusselt number increases with the increase in the angular velocity. For rotating velocities close to zero (a nearly motionless cylinder), the lowest value for the average Nusselt number occurs when the heated surface is in the vertical position where the least heat exchange occurs between the gap walls and the fluid.

When the rotational speed increases, the intensity of the flow lines increases and the thermal boundary layer covers the entire area of the gap, which leads to an improvement in heat exchange and an increase in the Nusselt number. When the angle $\Theta = 0^o$, the direction of the flow is perpendicular to the direction of the buoyant force , so the heat is transferred from the heated surface due to the effect of the buoyant force and with help of the rotation process which lead to an improvement in heat transfer coefficient . When the angle of inclination change from the horizontal to the vertical position, the direction of the convection currents resulting from the buoyant force gradually change until it becomes parallel to the direction of the fluid movement at $\Theta = 90^o$, so the heat transfer coefficient decreases with the increase of inclination angle.

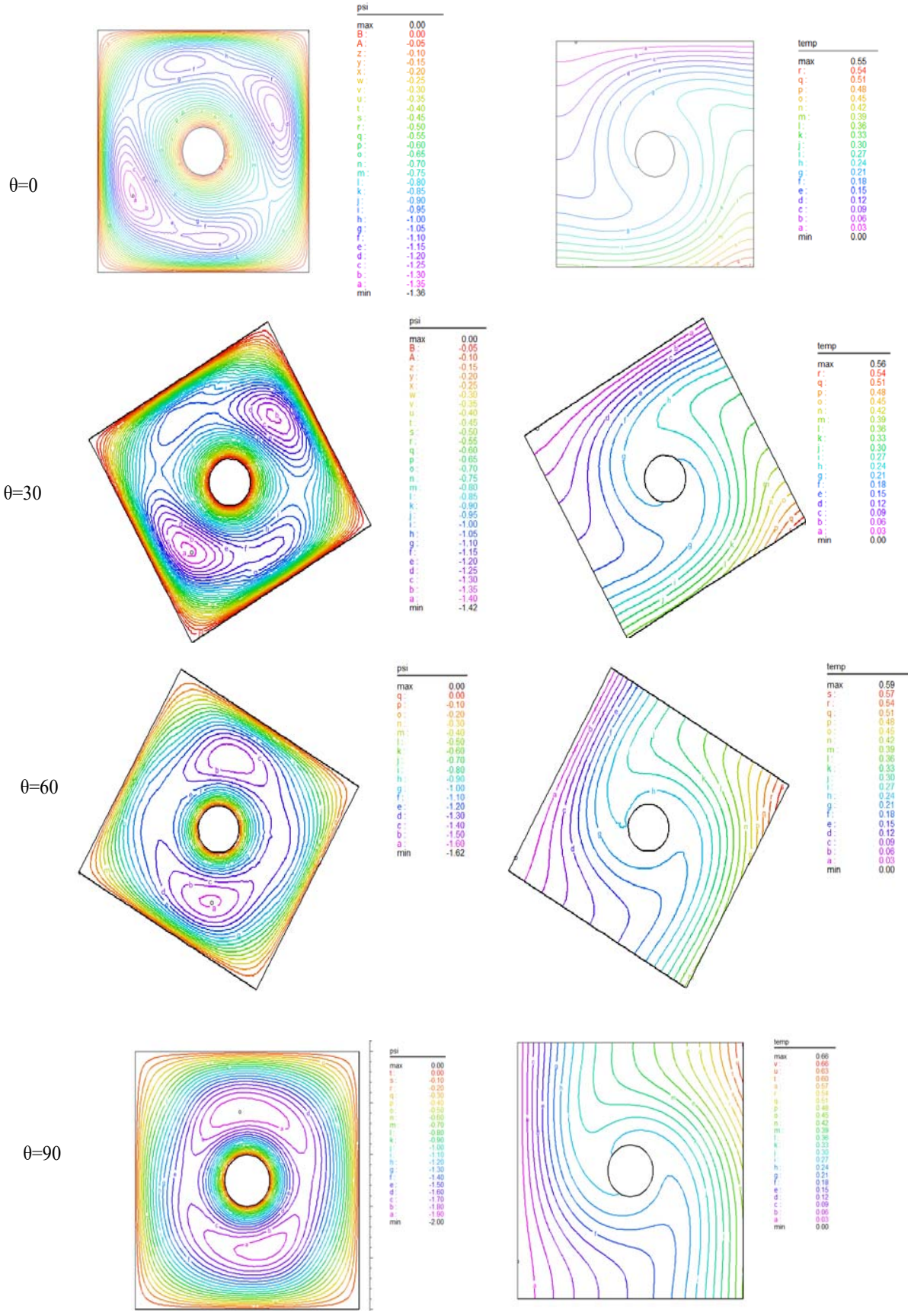

Fig .3: Isotherms and streamlines for different inclination angles at Ω =1000, Ra=10^4

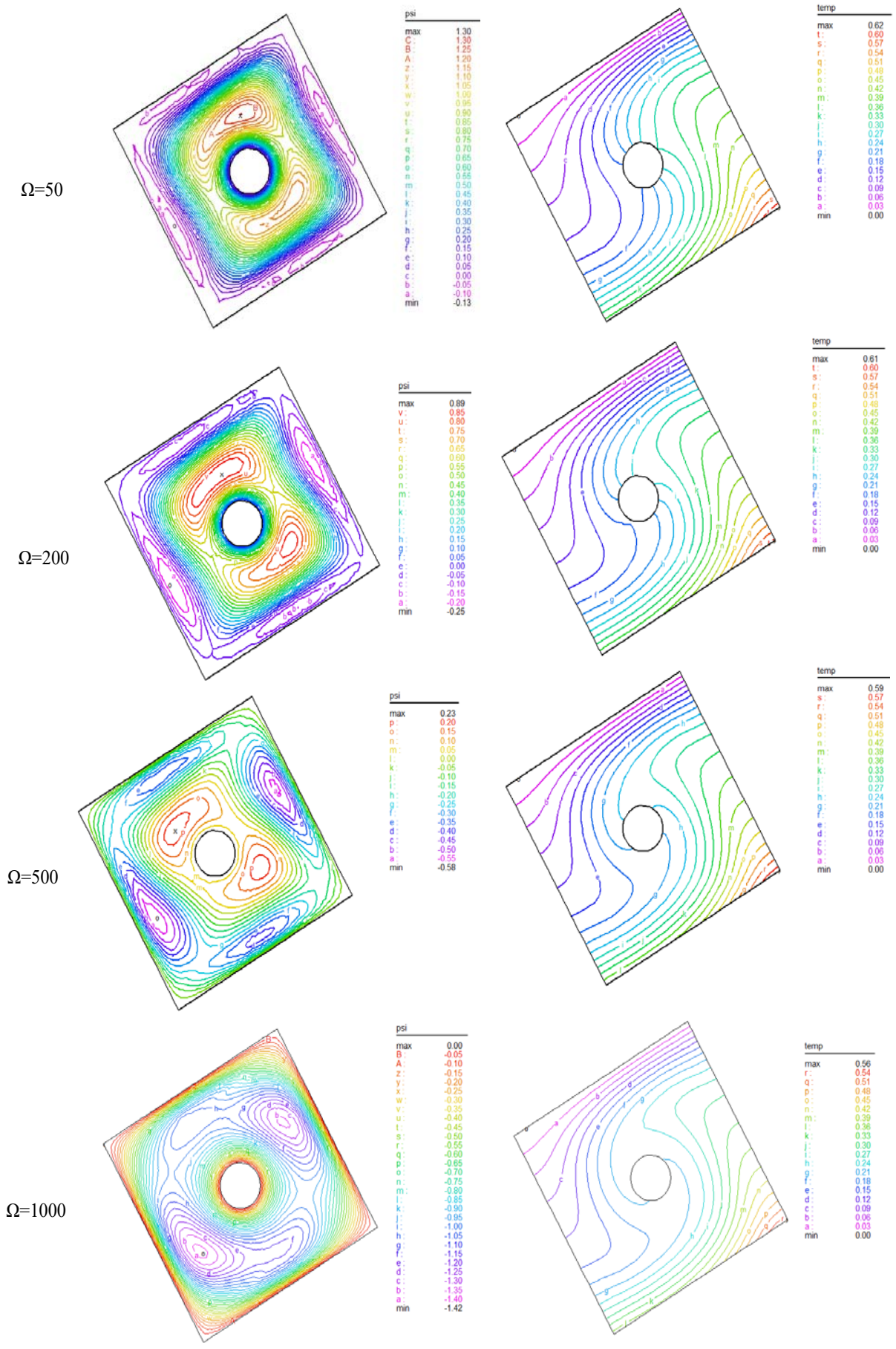

Fig.4: Streamlines and isotherms for different angular velocity at Θ=30° and Ra=10^4

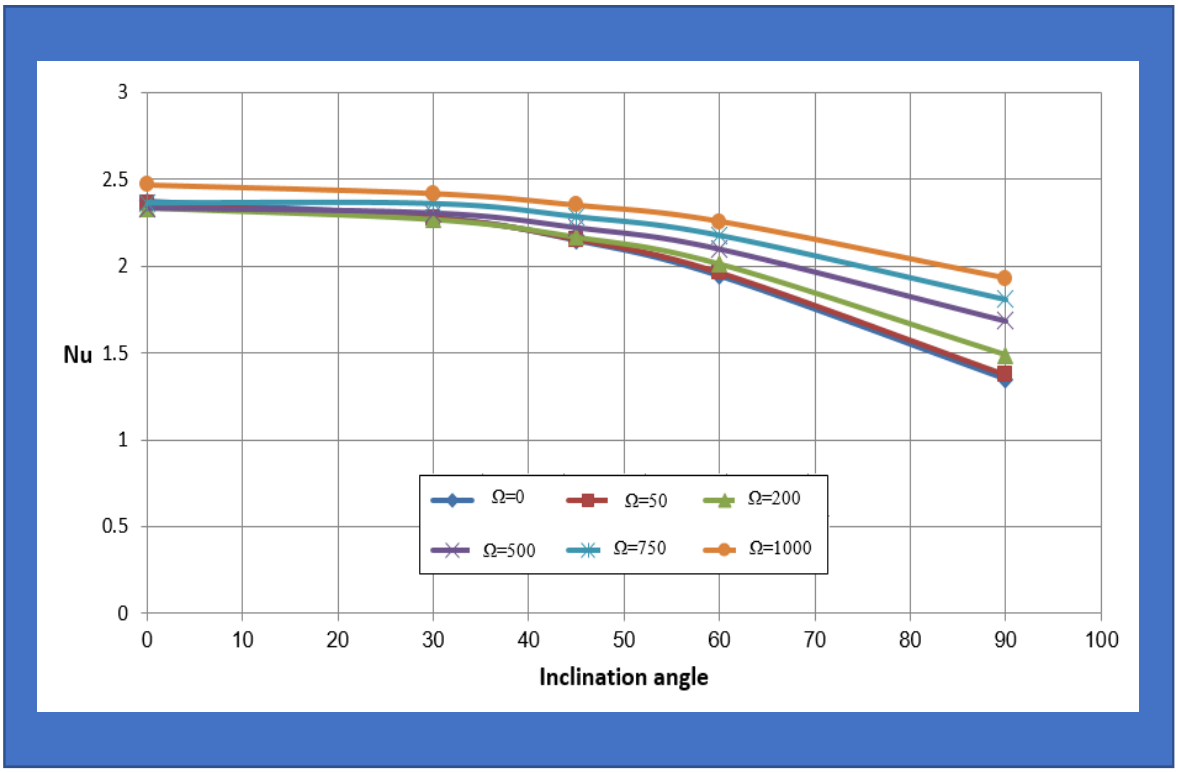

Fig. 5: The average Nusselt number changes with angular velosity at different inclination angles for Ra=10^4

4. Conclusions

The important conclusions for mixed convective heat transfer in a square enclosure of the flow can be drawn from the numerical simulation results as:

• The effect of circulating flow by the cylinder increases the density of the isotherm lines, making it cover most area of the cavity

• When the angular velocity is increased, the results showed a distortion in the streamline distributions near the surface of the cylinder due to the strong influence of the secondary flow.

• As the inclination angle increases, the buoyancy force increases and the thermal lines become more intense.

• Streamlines are affected by the angular velocity, where the forced convection becomes dominant at high values of angular velocity.

• The rotation of the cylinder has a strong effect on the heat exchange between the walls of the gap and the fluid

• At angle 30 ° and angle 60 °, the effect of angular velocity on the heat transfer process is small due to the effect of the direction of the convection currents.
• The value of Nusselt number increases with the increase in angular velocity and decreases with the change of the tilt angle of the hot surface from the horizontal to the vertical position.

5. References

[1] A. Barletta, S. Lazzari. (2005), 2D free convection in a porous Cavity heated by an internal circular boundary, The COMSOL Multiphysics User's Conference Stockholm. 2005.
[2]V.A.F. Costa, A.M. Raimundo. (2010), Steady mixed convection in a differentially heated square enclosure with an active rotating circular cylinder. International Journal of Heat and Mass Transfer 53 1208–1219, 2010.
[3] S. H. Hussain, Q. R. Abd-Amer. (2011) Mixed Convection Heat Transfer Flow of Air Inside a Sinusoidal Corrugated Cavity With a Heat Conducting Horizontal Circular Cylinder. Journal of Enhanced Heat Transfer, 18 (5): 433–447, 2011.
[4] F.H. Ali, (2011) Study of mixed convection in a square enclosure with a rotating circular cylinder at different vertical locations, The Iraqi Journal For Mechanical And Material Engineering, Vol.11, No.2,242-252, 2011.
[5] A. K. M. Alshara. (2012) Effect of Single or Multi Rotating Horizontal Cylinders on The Mixed Convection Heat Transfer Inside a Triangular Enclosure. Al-Qadisiya Journal for Engineering Sciences Vol. 5 No. 1. 2012.
[6] H. Xu, R. Xiao, F. Karimi, M. Yang, Y. Zhang, (2014), Numerical study of double diffusive mixed convection around a heated cylinder in an enclosure, International Journal of Thermal Sciences 78, 169e181, 2014.
[7] Everts, M, Ebrahim R., Kruger, J.P., Miles, Sharifpur M. and Meyer, J.P, (2014) Turblent flow a Cross a Rotating Cylinder with Surface Roughness, HEFAT, 10th International Conference on Heat Transfer, Fluid Mechanics and Thermodynamics. Orlando, Florida, 2014.
[8] R.I.(2014) Elghnam Experimental and numerical investigation of heat transfer from a heated horizontal cylinder rotating in still air around its axis, Ain Shams Engineering Journal 5, 177–185, 2014.
[9] R. Bouakkaz1, K. Talbi1, M. Ouazzazi, Y. Khelili1 and F. Salhi. (2015) Effect of Rotation Rates on the Laminar Flow and Heat Transfer Past a Circular Cylinder. Vol. 32, No. 02, pp. 519 - 529, April - June, 2015.
[10] M. Khan, A. A. Khanb, M. N. Hasan. (2016) Numerical study of mixed convection heat transfer from a rotating cylinder inside a trapezoidal enclosure. International Conference on Mechanical Engineering, 2016.
[11] N. Hamici, D. Sadaoul. 2017 Numerical Study of Mixed Convection and Thermal Radation in a Square Cavity with an Inside Inclined Heater. Lille, 28 Août au 1er Septembre, 2017.
[12] K.Yahiaoui1, D. Nehari, B.Draoui, (2017), The Investigation of the Mixed Convection from a Confined Rotating Circular Cylinder, Periodica Polytechnica Mechanical Engineering, *61(3), pp. 161-172, 2017*.
[13] R. Bouakkaza, F. Salhib, Y. Khelilic, M. Quazzazid, K. Talbi, (2017), Unconfined laminar nanofluid flow and heat transfer around a rotating circular cylinder in the steady regime, archives of thermodynamics,Vol. 38, No. 2, 3–20, 2017.
[14] M. F. Ejaz, S. Manzoor, (2018) Experimental Investgation of Heat Transfer in a Vertical Annulus with a Bottom Heated Rotating Inner Cylinder, International Journal of Heat and Technology, Vol, 36, No.2, 2018.
[15] F. Selimefendigil, Hakan F. Oztop, Ali. J. Chamkha. (2019) Analysis of mixed convection and entropy generation of nanofluid filled triangular enclosure with a flexible sidewall under the influence of a rotating cylinder. Journal of Thermal Analysis and Calorimetry, 135:911–923, 2019.
[16] V. Sharma, A. K. Dhimman, Heat Transfer from a Rotating Circular Cylinder in the Steady Regim: Effects of Prandtl Number.
[17] M. A. H. Mamun, T. R. Tanim,M. M. Rahman, R. Saidur and Shuichi Nagata, (2011) Analysis of Mixed Convection in a Lid Driven Trapezoidal Cavity, Convection and Conduction Heat Transfer,
[18] A. Anguraj and J. Palraj, Numerical study of fluid flow and heat transfer in a backward facing step with a rotating cylinder, Department of Mathematics, PSG College of Arts and Science, Tamil Nadu, INDIA.

[19] C. C. Liao and Lin. C. A, Mixed convection of a heated rotating cylinder in a square enclosure, Department of Power Mechanical Engineering, National Tsing Hua University, Hsinchu 30013, Taiw. International Journal of Heat and Mass Transfer 72 9–22, 2014.

5G Uplink Performance of Symbol-Based Schedulers with Network Slicing

Omar Ghanim Al Taee[1], Ali Othman Al Janaby[2], Younis M. Abbosh[3]
{omar.salim2019@stu.uoninevah.edu.iq[1], ali.mohammed@uoninevah.edu.iq[2],
younis.abbosh@uoninevah.edu.iq[3]}

Communication Department Ninevah university[1,2,3]

Abstract. One of the key elements of the 5G system is network slicing which is a talented technique to create adapted end-to-end logic network path including dedicated and shared resources. Resources scheduling and distribution of network slices show an essential effect on network performance, resource deployment, and load balancing. This paper compares many resources scheduling schemes in the 5G system with network slicing. We first compare many resource scheduling algorithms, best CQI (BCQI), Round Robin (RR), proportional fair (PF), to assess each scheme performance. Moreover, this paper proposes an adaptive scheduling scheme that dynamically chooses the scheduling algorithm among mentioned schemes to optimize the traffic, user throughput, and cell capacity. Finally, results anticipated assessed and concluded.

Keywords: 5G, Network slicing, Scheduler algorithms.

1 Introduction

5G systems are intended to support a wider range of applications and business models [1]. This is probable arises from some very high diversity requirement on network performance to achieve some important parameters; peak rates up to 10Gbps, and latency equal to 1 ms. To optimize the above network parameters for low latency with high user's throughput can achieve peak data rate comes with reduced spectral efficiency (SE). For this situation, utilizing the network slicing technique with a 5G system has become an initial necessity to enhance 5G system developers to comprise logical networks with precise functionality, without sacrificing the quality of the infrastructure [2]. This logical network, denoted as slices, can be personalized to achieve two purposes. First to provide a particular system behaviour through the utilization of control plane (CP) or user plane (UP) functions to enhance specific services domain (enhanced MBB (eMBB)), massive Machine Type Communication (mMTC), Ultra-Reliable and Low Latency Communication (URLLC). Second, to offer tenants a specified level of guaranteed network shared resources and isolation concerning the operation of other concurrent slices [2].

Service-defined networking (SDN) and network function virtualization (NFV) are two fundamental technologies for core network slicing [3]. SDN decouples network control and data forwarding, allowing network control operations to run independently in logically centralised controllers as applications [4]. Specific network functions are decoupled from dedicated and hardware platforms and transferred to general-purpose commercial hardware via NFV [5]. Furthermore, as a significant emerging technology in 5G, Mobile Edge Computing

IMDC-IST 2021, September 07-09, Sakarya, Turkey
Copyright © 2022 EAI
DOI 10.4108/eai.7-9-2021.2314842

(MEC) is projected to serve low-latency communication, which is one of the use cases in future 5G [6].
This paper will deal with the comparison of scheduling schemes used with network slicing. Also, the paper proposed a new scheme that adapts dynamically between different traffic services.

The rest of the paper covers the following: Section 2 debates the previous works, while section 3 overview the types for schedulers. Section 4 presents System Model and Configuration. Then, section 5 discusses Simulation Evaluation and Results Assessment. Section 6 presents the Proposed dynamic scheme. Finally, a conclusion is added at the end of the paper.

2 Related Works

Many resources allocation and scheduling schemes have been developed for LTE, LTE-A systems, and finally for 5G systems, at the uplink, by much research related to performance comparison in terms of packet delay, throughput and, fairness. Some articles as well, investigate the network performance at high-speed UE.

Authors in [7] investigated and measured the downlink performance of the RR, BCQI, and PF schemes in terms of throughput and Bit Error Rate (BER) representing the extreme cases in scheduling. The evaluation indicated that the BCQI scheme beats the other algorithms in terms of user throughput but on the expenditure of fairness to other UEs suffering from weak SNRs.
In [8], the authors evaluated the effects of high speed (UEs) on the throughput of different data rate services using four scheduling schemes in the uplink of the LTE system. The paper simulated 20 and 30 UEs switch at high mobility and different service demands.
The authors reported in [9] that the RR and PF schemes performed well in the downlink transmission mode. PF, on the other hand, gave good data rates for many transmission modes. Although RR gave superior compiled and non-BS individual data speeds, the absolute value of this data speed is not as great as the PF.
In [10] research has been carried out stating that, real-time and non-real-time UEs are scheduled individually. More, some UEs perhaps left without getting any resource blocks (RB)s.
Authors in [11] discussed the occasion that has arisen to deepen information in this field of study. This technology is included in phases of standardization and definitions, with every part of which each manufacturer the research group will undertake to refine by offering the most proper solution. One of these aspects is scheduling. The objective of the project is the 5G technology studio as its general construction is exposed for the longest time concerning LTE in cover one and cover two. Then there is concentration on the MAC undercoat to study different algorithm options scheduling that can be applied in the new telephone generation.
The authors of [12] propose a collaborative multi-user pre-emptive scheduling scheme technique to improve system spectral efficiency while lowering latency. Existing URLLC traffic was always given higher precedence during each scheduling opportunity. The supplied scheduler discovers acceptable URLLC-eMBB traffic in a multi-user transmission when irregular URLLC traffic appears during a transmission time interval (TTI). If the available spatial degrees of liberty within a TTI are limited, the URLLC traffic overwrites a portion of the ongoing eMBB transmissions to meet the URLLC latency requirements with little eMBB throughput loss.
In addition, the authors established several scheduling disciplines for public safety users who are required to intervene during exceptional events or in post-disaster areas in [13]. They

studied which of numerous scheduling methods, such as RR, PF, and others, performed better in this exceedingly difficult setting.

3 Schedulers Overview

This paper will compare the performance and delay of many types of scheduling schemes. This item presents a short review of resource allocation and packet scheduling schemes which are: RR, BCQI, and PF.

3.1 Round Robin (RR) Algorithm

RR scheme is a non-aware scheduling scheme that lets user equipment (UE) take tries in utilizing the common RBs, without considering the channel states while offering high fairness for all UEs in radio channel assignment. This will degrade the UE throughput [14].

3.2 Best CQI Algorithm

This system gives the UE with the highest SNR additional RBs. The channel condition is sent to the BS by the UEs to execute packet scheduling. The BS basically sends the UEs a reference signal (RS) in the downlink. These RSs are used by UEs for channel quality indicator measures (CQI). At the expense of fairness, the BCQI method can boost UE throughput and system capacity. UEs at the cell boundary are unlikely to be scheduled under this technique [15].

3.3 Proportional Fair (PF) Algorithm

PF is the scheme used with Time-frequency that was applied between multi-user system. Initially, it utilized Time Domain Scheduling (TDS) system and then Frequency Domain Scheduling (FDS) system. The main purpose of the combined FDS and TDS system is to improve the throughput and data-rate fairness among the UEs diversity [16]. The fairness and throughput are considered for a system model to operate between the BCQI and the RR schemes. The granularity of 1 resource block (RB is proposed to the scheduling algorithm [7].

4 System Model and Configuration

gNB controls the scheduling planning for uplink resources between the users. Considering the following gNB and UEs operations the UL transmissions could be shown in Table 1.

Table 1. Operation of gNB and UEs.

gNB	UEs
-Run the scheduling algorithm to assign uplink resour -Send the uplink assignment to the UEs -Receive the PUSCH transmissions from the UEs	-Send the pending buffer status report to the gNB. -Receive the uplink assignment from the UEs. -Adhere to the received uplink assignment from the gNB for PUSCH transmission.

Simulation studies are carried out using MATLAB. The simulation model data are integrated in Table 2.

Table 2. CONSTRAINTS DATA IN THE SIMULATIONS.

Parameters	Settings
Configurable	TDD pattern
UEs No.	3
UEs from gNB distances	UE1:100m, UE2:400m, UE3:700m
Simulation time	10000 ms
Scheduling	symbol-based
Scheduling strategy comparison between :	RR, BestCQI, PF
HARQ	16
Subcarrier spacing	15 kHz
Duration of the uplink pattern	5 ms
Periodicity at which the UL packets are generated by UEs	30
Size of the UL packets (in bytes) generated by UEs	2000
Sequence number field length (in bits) of the logical channel for each UE	6
Reassembly timer (in ms) of the logical channel for each UE	5
The length of Max buffer for logical channel for each UE	20000
Channel Update Periodicity	200 ms

5 Simulation Evaluation and Results Assessment

The simulation runs using the MATLAB codes is applied to 5G system model. It runs according to the system model parameters model. The MAC and RLC data results for 3 UEs are illustrated in Fig. 1 for the RR Scheduler Note in this algorithm that the distribution is fair according to the user's distance and priority.

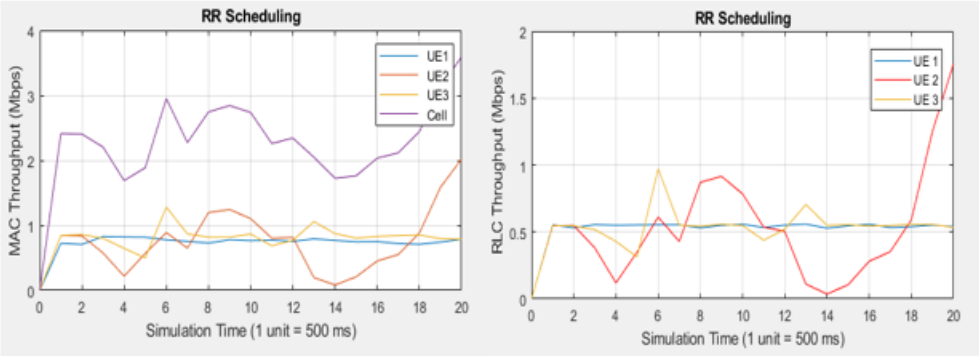

Fig 1. The evaluation user's MAC and RLC throughput with time (RR Scheduler).

According to the results of the user's throughput in Fig 1, it is found that the user's throughput is equal to or slightly more than the cell throughput. And the RLC throughput shown in the figure we found the nearest user is stable and constant with interval.

For the Best CQI scheduler MAC and RLC throughput shown in Fig 2 For this algorithm, the distribution is unfair, and the priority is channel quality.

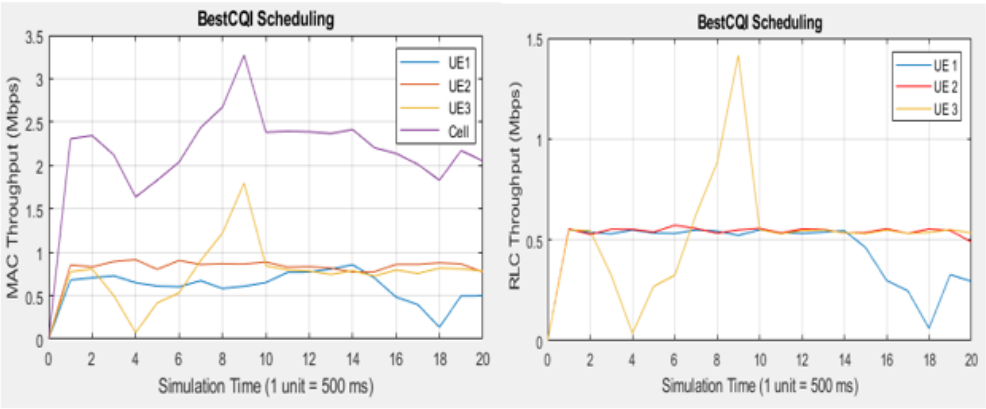

Fig. 2. The evaluation user's MAC and RLC throughput with time (Best CQI Scheduler).

Thus, the results Fig 2 we notice that the user who has higher throughput is the one who has the priority and stability with the interval. When the system uses the PF scheduler the result for MAC and RLC throughput shown in Fig. 3 is a good balance between the objective of maximizing cell throughput and fairness for all users.

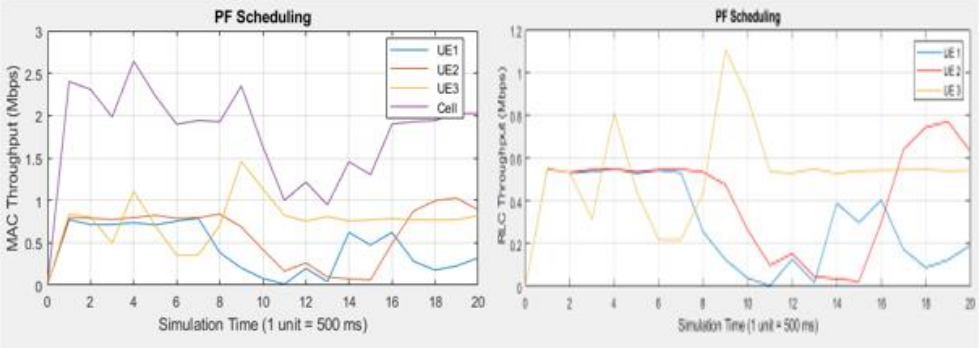

Fig. 3. The evaluation user's MAC and RLC throughput with time (PF Scheduler).

According to Fig 3, we notice balanced distribution among the users because the PF scheduler doesn't rely on interval and priority.

Through the previous results that you get, comparison of types of schedulers we notice that RR the priority is for the closest Best CQI The priority is for those who have higher CQI, PF all UE has the same opportunity.

To know the distribution of resources, share over time for the 3 type Scheduler, we observe Fig 4, 5 and 6.

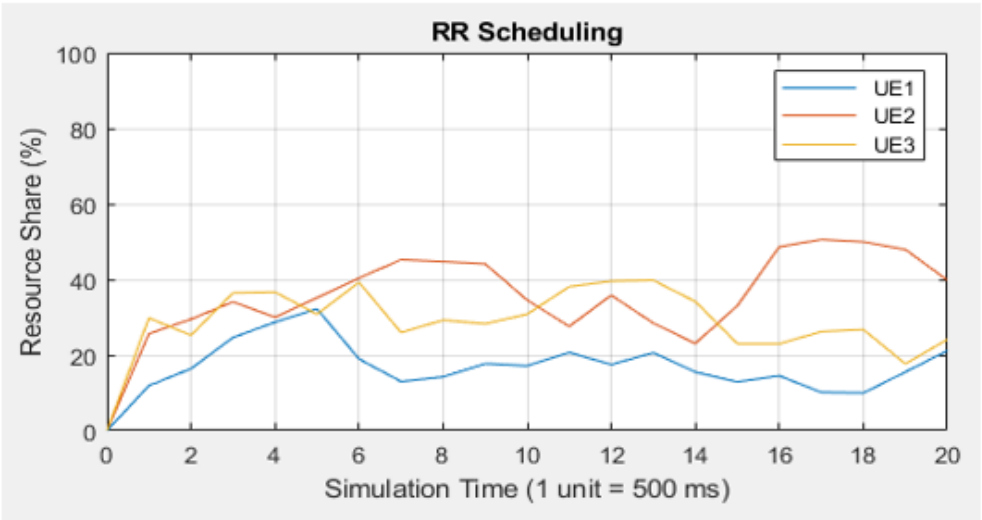

Fig. 4. Resources share with time for RR scheduling.

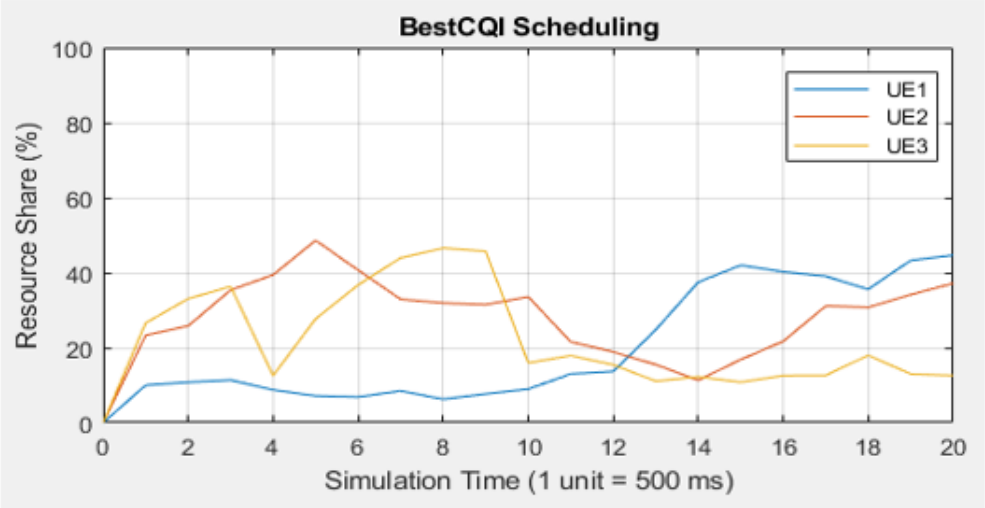

Fig. 5. Resources share with time for BCQI scheduling.

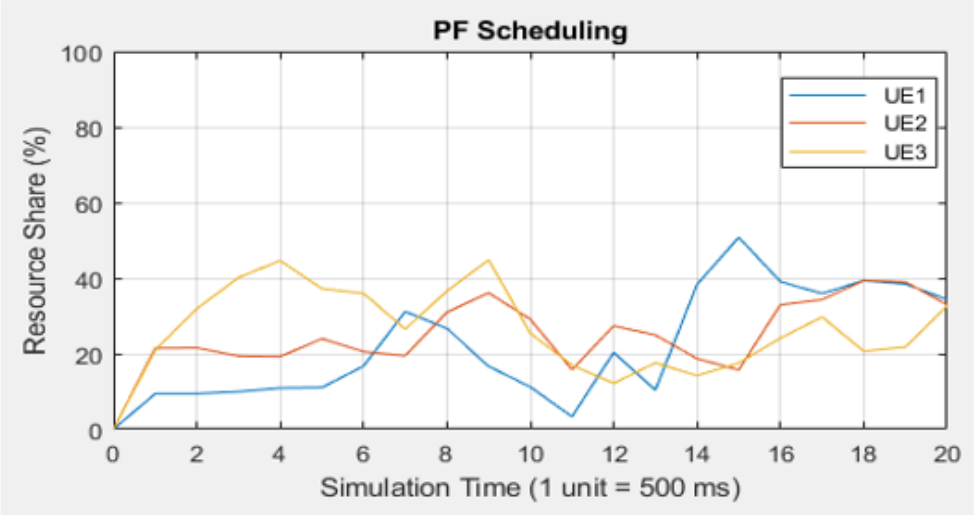

Fig. 6. Resources share with time for PF scheduling.

6 New Dynamic Proposed Scheme

According to the channel state for each user, adaptive scheduling can be made according to the users' conditions, for example, if the distance is close between them and the bit you saw is close, RR scheduling can be used, but if there is a miss with CQI and there is nothing emergency, best CQI scheduling can be used, and if there are lapses between users based on terms of capacity and reliability and need a fair procedure we use PF scheduling.

A scheduler is considered efficient according to the quality of service among UEs. The allocated RBs using BCQI time frame is assigned to the UE with the high CQI (best channel conditions). The BCQI algorithm can approve the system performance. In this scheduling, the eNB controls the located UEs based on the probability to grant resources. It is evidence that BCQI and RR, as well as all scheduling algorithms, could not provide the basis at the same time.
The proposed UL 5G system scheduler is based on this aspect to find a way to achieve the best performances. It leads to a new proposed dynamic UL 5G scheduler. This proposed scheme can switch among BCQI, PF, and RR schedulers since it adaptively add features of all time frames of the operated SNR, the appropriate scheduler for each slice selected according to 5G characteristics shown in Fig 7.

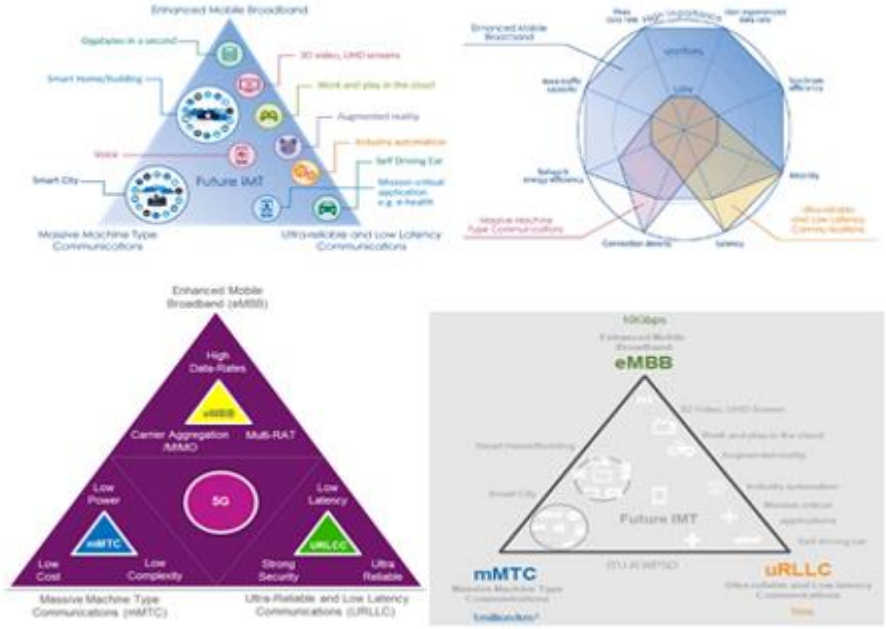

Fig 7. 5G key and Usage Scenarios (eMBB, mMTC, uRLLC).

6.1 The Dynamic Proposed Scheme Steps

The proposed adaptive scheme, as indicated in Fig. 8, can be presented as the following:
At each the SINR at the receiver for TTI time slot of all active UEs might be determined. The proposed adaptive scheme inserts a new process; the process is that to investigates whether the user application or service is a traffic type.
The investigation is to choose among traffic types; eMBB, and mMTC. Then, the system assigns the traffic type, a scheduler is adopted according to the following steps.

Step 1: Insert UE's packet into the system's queue.

Step 2: For each UE, the system finds out CQI, PMI, and RI while taking into consideration the traffic type, channel condition (SNR), and the quality of service (QoS) requirement.
Step 3: The preparation starts at each TTI.
Step 4: System chooses traffic model
Step 5: Each UE assigns his slice
Step 6: For eMBB slice using Best CQI scheduling for URLLC using PF scheduling for mMTC using RR scheduling.
Step 7: System waiting for packet acknowledgment, ACK.
Step 8: if ACK failed, use a hybrid automatic repeat request (HARQ).

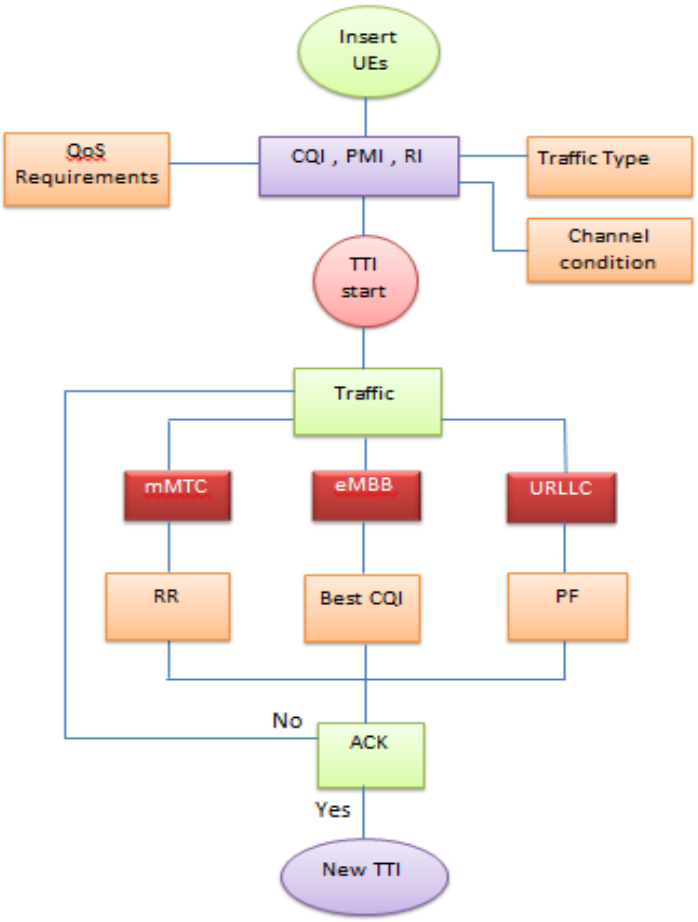

Fig 8. Flow chart of the proposed scheduling.

6.2 Anticipated Results

The proposed dynamic scheme is based on the traffic slicing technique to schedule the traffic user's applications. The adopted proposed scheme can be simulated, be implemented, and tested

efficiently. It can be real-time to evaluate the 5G system performance at uplink utilizing network slicing.

7 Conclusion

In this paper, comparative resource scheduling algorithms have been evaluated for the 5G system. The algorithms for resource allocation has been discussed towards the 5G era. The paper has compared many resource scheduling algorithms to justify the optimum scheme. Then, it was concluded the best resource allocation algorithms into the new 5G networks based on math models and typical examples.

References

[1] Alliance NG. 5G white paper. Next generation mobile networks, white paper. 2015 Feb 17;1.

[2] Ferrus R, Sallent O, Perez-Romero J, Agusti R. On 5G radio access network slicing: Radio interface protocol features and configuration. IEEE Communications Magazine. 2018 Jan 10;56(5):184-92.

[3] Li X, Samaka M, Chan HA, Bhamare D, Gupta L, Guo C, Jain R. Network slicing for 5G: Challenges and opportunities. IEEE Internet Computing. 2017 Sep 18;21(5):20-7.

[4] Sayadi B, Gramaglia M, Friderikos V, Von Hugo D, Arnold P, Alberi-Morel ML, Puente MA, Sciancalepore V, Digon I, Crippa MR. SDN for 5G Mobile Networks: NORMA perspective. InInternational Conference on Cognitive Radio Oriented Wireless Networks 2016 May 30 (pp. 741-753). Springer, Cham.

[5] Yousaf FZ, Bredel M, Schaller S, Schneider F. NFV and SDN—Key technology enablers for 5G networks. IEEE Journal on Selected Areas in Communications. 2017 Oct 6;35(11):2468-78.

[6] Al Janaby AO. 5G Downlink Throughput Enhancement by Beams Consolidating at Vacant Traffic. Journal of Communications Software and Systems. 2019 Dec 3;15(4):311-6.

[7] Habaebi MH, Chebil J, Al-Sakkaf AG, Dahawi TH. Comparison between scheduling techniques in long term evolution. IIUM Engineering Journal. 2013 Mar 4;14(1).

[8] Othman A, Othman SY, Al-Omary A, Al-Rizzo H. Comparative performance of subcarrier schedulers in uplink LTE-A under high users' mobility. International Journal of Computing and Digital Systems. 2015;4(04).

[9] Kawser MT, Farid HM, Hasin AR, Sadik AM, Razu IK. Performance comparison between round robin and proportional fair scheduling methods for lte. International Journal of Information and Electronics Engineering. 2012 Sep;2(5):678-81.

[10] Kumar N, Ahmad A, Awasthi S, Sharma K. Parameter aware utility proportional fairness scheduling technique in a communication network. International Journal of Innovative Computing and Applications. 2021;12(2-3):98-107.

[11] Davyt E, Muzante A, Rizzo M. A5iGnator: Framework para la Implementación de Algoritmos de Asignación de Recursos en 5G.

[12] Esswie AA, Pedersen KI. Multi-user preemptive scheduling for critical low latency communications in 5G networks. In2018 IEEE Symposium on Computers and Communications (ISCC) 2018 Jun 25 (pp. 00136-00141). IEEE.

[13] Gomez K, Goratti L, Granelli F, Rasheed T. A comparative study of scheduling disciplines in 5G systems for emergency communications. In1st International Conference on 5G for Ubiquitous Connectivity 2014 Nov 26 (pp. 40-45). IEEE.

[14] Kanagasabai A. *On Design and Analysis of Channel Aware LTE Uplink and Downlink Scheduling Algorithms* (Doctoral dissertation, Université d'Ottawa/University of Ottawa).

[15] Dikamba T. Downlink scheduling in 3GPP long term evolution (LTE).

[16] Cuesta CF. Resource Allocation and Time-Frequency Scheduling in LTE. InSeminar Mobile Communication, TUWEIN 2007 (Vol. 12).

Energy Management Optimization of Generators Using Modified Firefly Algorithm

Wafeeqa Abdulrazak Hasan[1], Issa Ahmed Abed[2], Diyah Kammel Shary[3]
{Wafeeqa.alibraheem@stu.edu.iq[1], issaahmedabed@stu.edu.iq[2], diyahpower@stu.edu.iq[3]}

Basrah Engineering Technical College, Southern Technical University, Iraq[1,2,3]

Abstract. The proposed microgrid system in island mode in this study is made up of a mix of conventional and renewable energy sources, including two diesel generators, two wind turbines, and three fuel cell plants. Using the artificial intelligence technology to manage its energy sources by optimization methods, to decide the scheduling of each generator's optimum power output per hour over 24 hours at a minimum total generation cost using MATLAB software package. For management of the energy of the proposed microgrid in an hour-to-day, such data should be specified in advance, including the planned load demand, the wind forecast for the next day for each hour, and the cost coefficients of each generator. To investigate the optimum performance, each algorithm will be executed for 30 runs at each hour within 24 hours. The methods of optimization used in this microgrid system suggest modified of the firefly algorithm (IFA) by hybridizing it with the local search algorithm and then using IFA in this study to manage the energy sources. Eventually, the results obtained that the IFA method enhances the performance of the energy scheduling with minimise the total generation cost of microgrid compared to the other optimization methods presented in this study, which IFA method produced better results compared to the used FA.

Keywords: Energy management; optimization; microgrid firefly algorithm; modified firefly algorithm.

1 Introduction

To optimise the use of Distributed Generators (DGs), the power system is being reconfigured to allow for higher penetration levels. Microgrids (MG) are small power systems made up of a number of dispersed micro-generators that can meet a considerable amount of a community's demand. MGs have a number of advantages for the system, including lower customer interruption costs, lower system losses, and better renewable resource penetration levels [1]. A microgrid is one of the electrical systems that supply electrical energy gained from renewable energy sources [2]. The best solution to the energy crisis is the MG group with renewable energy sources. [3]. Microgrids are classified according to the type of operation as grid-connected mode and an islanded mode where the distributed energy resources (DERs) are supplied the loads directly without being connected to the grid [4,5]. MGs energy management aims to increase energy efficiency and minimize losses of power. An optimal arrangement of units in the grid-connected type or stand-alone type MGs energy management is carried out to optimize benefits through the application of renewable DGs also the energy storage system (ESS) [6,7]. Management of energy for the microgrid is the control software that allows the system to operate optimally [8]. The use of artificial intelligence technology to tackle problems

IMDC-IST 2021, September 07-09, Sakarya, Turkey
Copyright © 2022 EAI
DOI 10.4108/eai.7-9-2021.2314839

with electricity source problems that use various sources due to their robustness and capability was active to handle easy use with complicated systems [3]. For these systems, the energy management system (EMS) would collect all the necessary information, solve an optimization problem, and communicate the correct allocation of energy into each distributed energy resource [9]. The proposed target concerns identifying the optimal hourly management for the ability to operate the proposed microgrid system to reach the required load demand profile at a minimum total cost of generation. Energy management strategies have always been known to be an important issue of research. Firstly, the approaches that have been suggested in the literature for optimal cost and scheduling power generation areas Sulaiman, et al. [10]. had presented an economic load dispatch issue paper that used a meta-heuristic firefly algorithm. K. Thenmalar and A. Allirani [11] presented a firefly algorithm that minimizes the total operating costs of the generator, the total emission costs as well as the scheduling of the generator units. M.N. Abdullah et.al. [12]. optimized the operation scheduling of microgrid by proposed a firefly algorithm (FA) which is used to find out the best energy production, provided the cost is as low as possible. A. Karthikeyan et.al [13] had given particle swarm optimization method (PSO) to solve the proposed economic dispatch problem which concerning the cost and emission are analysed for the 24-hour interval. F. Shariatzadeh et.al [14] proposed a solution to the problem of the shipboard microgrid electricity system (SMPS) for implemented particle optimization (PSO) approach and that the use of genetic algorithm (GA). M. Basu and A. Chowdhury [15] had been given a cuckoo search algorithm for solving both convex and no convex economic dispatch (ED) problems of fossil fuel-fired generators

This study used the optimization methods in the island microgrid system include the firefly algorithm (FA) which is an algorithm based on the original firefly algorithm and suggested modified of it (IFA) by hybridizing it with the local search algorithm to manage the energy sources in this system, also used to determine each generator's optimum power output within 24 hours at a minimal cost. Organizing the paper includes problem Formulation and microgrid system model in Section 2, Section 3 demonstrations the proposed optimization methods IFA, Next Section 4 Simulation performance and discussion. In the end, the conclusion was presented in Section 5.

2 Microgrid System Model

The main problem of the research is to determine the optimal scheduling of power generations in an hour - day with minimizing the total generation cost of microgrid systems while satisfying the constraints of load demand and limits generators. When a microgrid's generation consists of several sources with varying costs for each source, whether renewable or conventional, the difficulty becomes even greater. Although the running cost is the most important factor, the microgrid's performance must also be optimal. As a result, the firefly algorithm and a modified firefly method will be used to reduce the MG system's overall generating cost in island mode. The main model of a microgrid system is implemented, which includes two diesel generators, three wind turbines, and fuel-cell plants, as well as general operational and typical DERs' associated cost functions. The established plant is operating in an island microgrid system [12,15]. And this microgrid system is shown in Fig. 1.

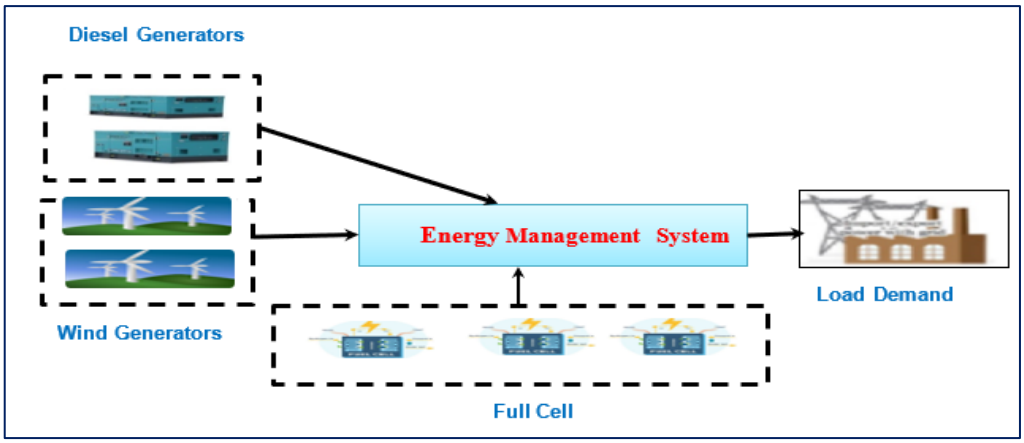

Fig. 1. The Model of a microgrid system.

2.1 Problem Formulation

The objective function represents the minimization of the total generation cost (FCtotal) of the microgrid, which is illustrated as follows: To evaluate the optimum power output of any generator in each hour to find the lowest cost within 24 hours of the considered microgrid, the objective function represents the minimization of the total generation cost (FCtotal):

$$FC_{total} = \sum_{t=1}^{T}(\sum_{i=1}^{N_{diesel}} F_{D,i}(t) + \sum_{i=1}^{N_{wind}} F_{W,i}(t) + \sum_{i=1}^{N_{fuel}} F_{F,i}(t)) \quad (1)$$

Where N_{diesel} ,$N_{wind,}$ and N_{fuel} are the numbers of diesel generators, wind turbines, and fuel cell plants. Parameter T is the scheduling time, and FC_{total} is the overall value of cost generation throughout time T. Two different types of restrictions depending on the issue of microgrid optimisation. The first restriction is power produced by all the distributed generations should also be balanced by the power load for each scheduled time (t), and the second restriction is each generator's output power should be within both the lower limit and the upper limit.

3 Modified Firefly Algorithm (IFA)

For firefly algorithms, the search depends entirely on random walks, so it is not possible to guarantee a fast convergence [16]. Local search is implemented to facilitate the algorithm's exploration and search abilities and ensure fast convergence of algorithms. Firefly algorithm has been allowed to search for a global optimum for the suggested target function [17]. Can use a local search technique to enhancement several of the target functions of features found in the population [18]. Within this development, programming codes are presents to solve the problem of optimization using IFA. Then it was implemented on the proposed MG's objective/fitness feature. In this study, the implement improved firefly algorithm. Here is a significant improvement, essentially, in the combination of a local search method with FA to speed up convergence. This makes the technique more applicable for a broader variety of practical energy management applications while retaining the attractive characteristics of its classical FA.

3.1 Local Search

The principle behind the local search is to replace the current candidate solution s with some adjacent candidate solutions within the S-search area of the complete candidate solution. Candidate solution N(s) neighborhood $s \in S$ is described by all candidate solutions which can be achieved through the application of specific solutions modifies to s, or "movements"[19]. The widest perturbing form of local search is a possibly iterative improvement (In the literature often referred to as iterated descent, hill climbing, etc.). Replaces the existing candidate solution with an improved neighbour solution, as well as repeats its steps till a locally optimal candidate solution, namely a candidate, is found a solution without neighbours improving [19]. To minimize FA's shortages and increase the FA's search capability, firefly has been improved and enhanced [20].

This technique requires no gradient knowledge to conduct the local operation search. We used this technique since we wanted to demonstrate that even with a simplistic one, the algorithmic approach provides better convergence properties [18]. The pseudo-code of the local search algorithm is as follows [18].

```
Con ←1
Long← δ ( max_k{ U_k − L_k } )
for i = 1 to m do
for k = 1 to n do
 λ1 ← U (0, 1)
while Con < LSITER do
x ← z^i
 λ2 ← U (0, 1)
if  λ1  > 0.5 then
 x_k ← x_k + λ2  (Long)
else
 x_k ← x_k − λ2  (Long)
end if
if f (x) < f(z^i) then
z^i ← x
Con ← LSIT ER − 1
end if
Con ← Con + 1
end while
end for
end for
z^best ← argmin {f(z^i), ∀i}
```

4 Simulation Results and Discussion

In this study for energy management issue of MG which is scheduling of optimum output power generators by running each method in (30 runs) per hour within 24 hours with the

minimum total generation cost for each generator, which must also satisfy the load demand and each generator must produce within its limits as shown in Fig. 2.
The microgrid in this study is made up of numerous traditional and renewable energy power plants, including two diesel generators, two wind generators, and three fuel cell plants.

4.1 Effect the Change of Population Sizes by Using IFA

When FA test is done (30 runs) at each hour within 24 hours to achieve the minimal cost, the findings of IFA are given a lower cost of the microgrid system at a population size of 100 compared to population sizes of (20) and (50). The cost for population size (100) is $30919.9526 dollars, which is the lowest cost when compared to other population sizes. In addition, Fig. 3 shows the distribution for the best power schedule in 24 hours. To further elucidate, Fig. 3 shows the convergence curve for various population sizes. Using IFA, Fig. 4 depicted the largest population size at the lowest cost.

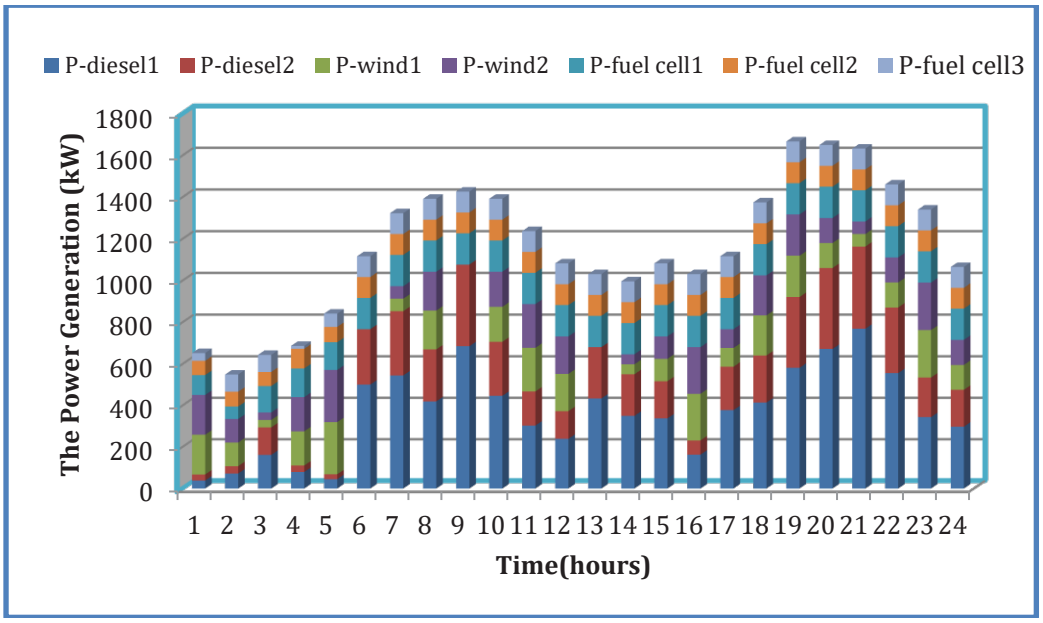

Fig. 2. Best plan of power generation of microgrid system by using IFA at (MaxIter 500) and (100 population size).

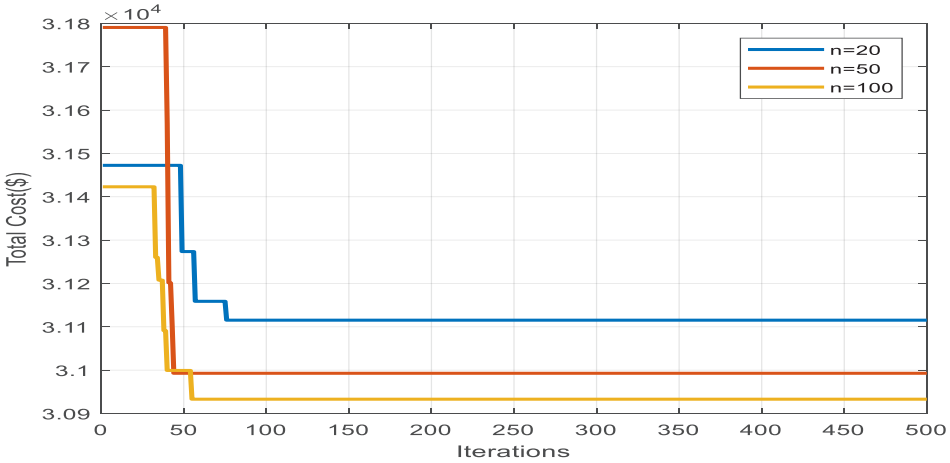

Fig. 3. Convergence curve for a number of population sizes using IFA for minimum cost.

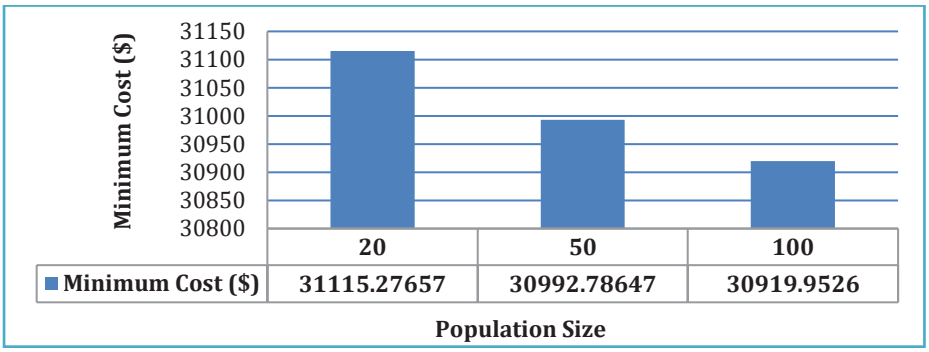

Fig. 4. Various population sizes and the lowest cost of using IFA (MaxIter 500)

4.2 Effect Change the Number of Iteration (MaxIter) by Using IFA

The optimization results show that the modified firefly algorithm is more effective at (100 population size) and high-value iteration than at other low-value iterations. At iteration (500), IFA performs the best operation for MG with the lowest generation cost compared to other cases (100) and (250) at system hourly load demand, as shown in Fig. 5. Fig. 6 shows the comparison of the generation power of the microgrid with that of the requested power in every hour of a day, which the results obtained from IFA. The power balance equation is seen to have been fulfilled because the power generations are in correspondence with the power demanded. There is a difference between the values of the power generation and the values of power demand for each hour because it is a very small value, so it is neglected. Fig. 7 displays the best cost at every hour after the IFA has been implemented for 30 attempts during each hour, and the sum of the best cost at each hour represents the best cost of generation within a day

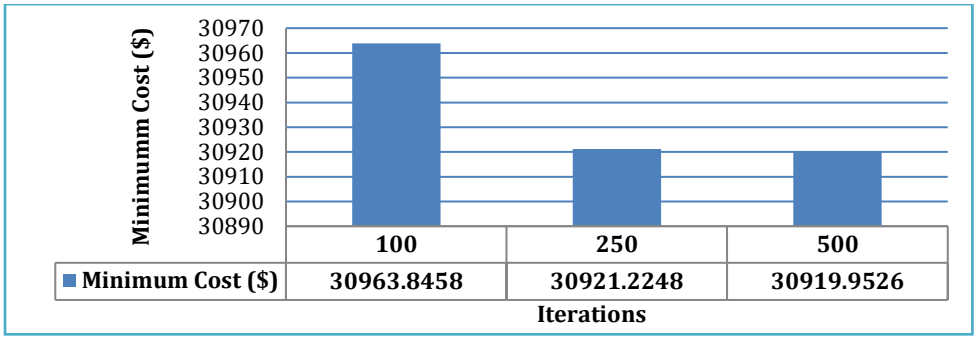

Fig. 5. Different Iteration and the minimum cost from using IFA at (population size100).

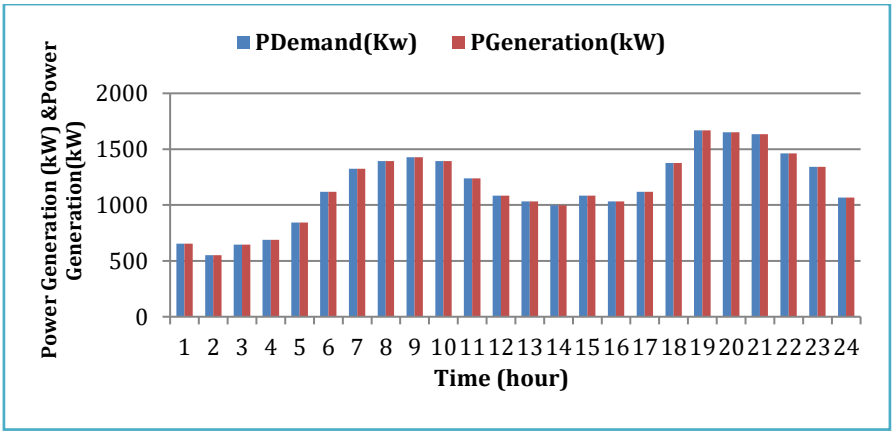

Fig. 6. Different Iteration and the minimum cost from using IFA at (population size100).

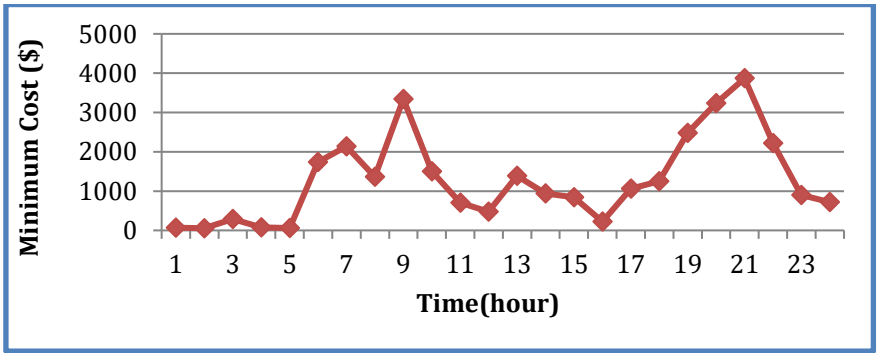

Fig. 7. Optimal hourly generation cost of the microgrid system by using IFA.

And then analyse the findings and compare them with various optimization approaches. In two cases as follows:

Case1: Change the Standard Parameters of the Algorithms

1. A Comparison of the Optimal Cost with Number of Iteration

The comparative results of optimal total generation cost for the proposed microgrid system by firefly algorithm and its modified algorithm that used at the different number of iterations are (500) and (100) with some populations is (100) and each algorithm is executed in (30 times) in each hour within 24 hours and the result as shown Table (1). In this comparison notice that at maximum iteration gives the less minimum cost by used IFA than the comparison of the results with FA. When increasing the number of iterations for the IFA the total generation cost of the microgrid system is decreased.

Table 1. Comparative results of optimal generation cost by the proposed optimization methods with several iterations at (population size100).

Iteration	IFA	FA
500	30919.9526	30968.1056
100	30963.8458	31021.754

2. Comparison of the Optimal Cost with Population Size

The results of optimal total generation cost at several iterations are (500) with a different number of populations is (20) and (100) at each algorithm are executed at 30 runs in each hour within 24 hours at (500 iterations) and the result as shown Table (2). In this comparison notice that at maximum iteration give the less minimum cost. When increasing the population size for the various algorithms the total generation cost of the microgrid system is decreased.

Table 2. Comparative results of optimal generation cost by various methods with population size at(500 iterations).

Population size	IFA	FA
100	30919.9526	30968.1056
20	31115.27657	31064.4187

Case2: Change the Number of Times of the algorithms Running.

Original FA and its modified are executed in (3 times) for each hour within 24 hours on the MG system at same parameters of iteration is (500) and several populations are (100), where the results of minimum total generation of cost listed in Table 3 to compare it with the results in running the original FA and IFA algorithms at (30 times). From the results obtained at the number of runs of the optimization algorithm in (30 times) are less than the results when runs the optimization algorithms in (3 times). So, when increase the number runs for the various algorithms the total generation cost of the microgrid system is decreases. Figs 8 and 9, give the speed convergences of the original FA and its modified optimization method in this test at (3 runs). From the comparison between the simulation results at a different number of executed runs, notice that the optimal results are found to increase the number of runs the modified FA.

Table 3. Comparative results of optimal generation cost by the proposed optimization methods with some iterations at (population size100).

Table 3. Comparative results of optimum generation output by various methods at (500 iterations and 100 population size).

Algorithms	IFA	FA
Run(30)times	30919.9526	30968.1056
Run(3)times	31919.7555	31921.6915

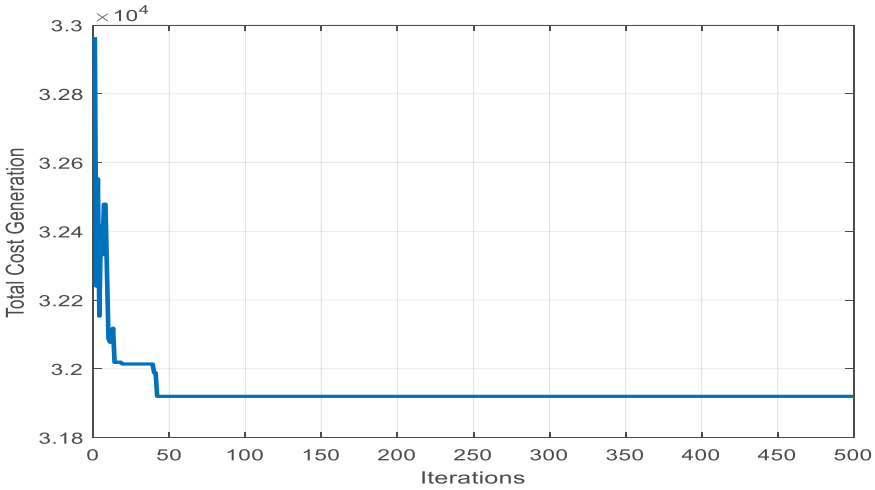

Fig. 8. Converges curve of used IFA method.

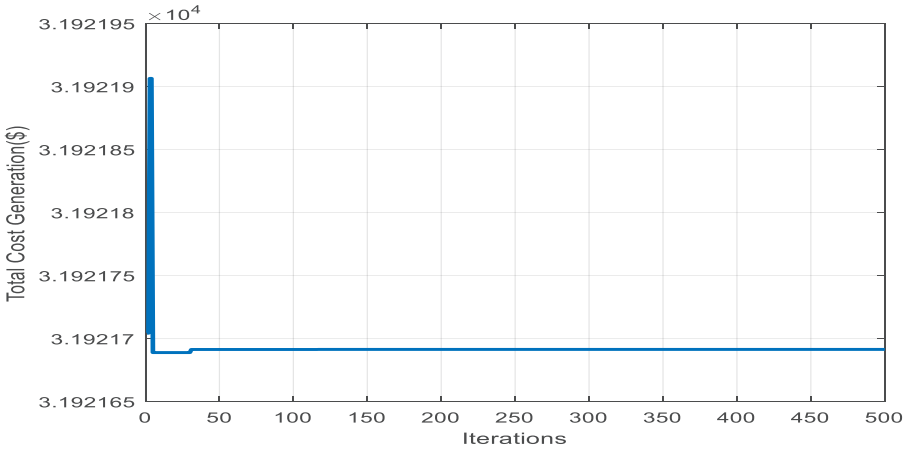

Fig. 9. Converges curve of used FA method.

5 Conclusion

The optimal cost of total generation in each hour within 24 hours and scheduling optimal power generation to lower total cost of generation by applying optimization methods such as firefly algorithm, improved firefly algorithm by hybrid FA with local search to enhanced FA are discussed in this study. Add for that, presents a new method is atom search algorithm and particle swarm optimization method. Where runs each method (30 times) for each hour through day and simulation the results of each proposed method at various values of iteration and population size, which find that when increase these standard parameters of the algorithm will find best results. The light absorption coefficient, attraction coefficient minimum value, and absorption coefficient of the Firefly algorithm are all dependent on the optimised problem, and we discovered that there are two methods for selecting the appropriate algorithm parameters for the problem: one is to tune the parameters, and the other is to modify the parameters while the algorithm is running. It can be observed from the results obtained that the IFA method enhances the performance of the energy scheduling by minimizing the total generation cost of microgrid compared to the other optimization methods presented in this study, which IFA method produced better results compared to the used FA. Additionally, it can also be concluded that if the number of operating times increases for the algorithm used in this study for each hour within 24 hours, an optimum power schedule can be found at a minimum of the overall cost of generation of the microgrid system.

Acknowledgments.

We are grateful to Southern Technical University, Engineering Technical College of Basra, and the Department of Electrical Power Engineering for their contributions to this paper.

References

[1] Ashoke K. B., Sunetra. C., &S. P. C.Impact of Strategic Deployment of CHP-Based DERs on Microgrid Reliability. Power Delivery, IEEE Transactions; 2010;25(3):1697-1705.

[2] Zhixin M, Ling X, V.Disfani, &L. Fan, An SOC-Based Battery Management System for Microgrids. IEEE Transactions on Smart Grid;2014;5(2): 966-973.

[3] Sharmistha S.,Subhadeep B., &Aniruddha B.Operation cost minimization of a Micro-Grid using Quasi-Oppositional Swine Influenza Model Based Optimization with Quarantine. Ain Shams Engineering Journal .2018; 9(1):45-63.

[4] Zein Alabedin, A. M., El-Saadany, E. F., & Salama, M. M. A. Generation scheduling in Microgrids under uncertainties in power generation. IEEE Electrical Power and Energy Conference; 2012; p.133-138.

[5] Emiliano D.A., Hao Z., & Georgios. B. G. Distributed Optimal Power Flow for Smart Microgrids .IEEE Transactions on Smart Grid;2013;4(3):1464–1475.

[6] Hossam A.G., & Abdelazeem A.A. Microgrid energy management in grid-connected and islanding modes based on SVC. Energy Conversion and Management. 2014 :86 ;964–972.

[7] Ashoke K. B., S.P. C, S. Chowdhury, and S. Paul. Microgrids: Energy management by strategic deployment of DERs—A comprehensive survey. Renewable and Sustainable Energy Reviews; 2011:15(9); 4348–4356.

[8] Wencong S. & Jianhui W. Energy Management Systems in Microgrid Operations. The Electricity Journal. 2012: 5(8);45–60.

[9] Alireza A. A Memory-Based Genetic Algorithm for Optimization of Power Generation in a Microgrid. IEEE Transactions on Sustainable Energy;2018: 9(3); 1081–1089.

[10] Sulaiman, M. H., Mustafa, M. W., Zakaria, Z. N., Aliman, O., & Abdul Rahim, S. R. Firefly Algorithm Technique for Solving Economic Dispatch Problem‖, IEEE International Power Engineering and optimization conference, Malaysia; June 2012: 6-7; 90-95.

[11] Thenmalar, K., & Allirani, A. Solution of firefly algorithm for the economic themal power dispatch with emission constraint in various generation plants‖, Fourth International Conference on Computing, Communications and Networking Technologies (ICCCNT); 2013.

[12] Mohd N. A. ,Nur.L.A. ,&Jasru J.J. Opyimal Power Generation in Microgrid System using Firefly Algorithm,IEEE 20176 th International Conference on Electrical Engeenering and Informatics(ICEEI);Langkawi;Malysia;2017.

[13] Karthikeyan, A., Manikandan, K., & Somasundaram, P.,Economic Dispatch of Microgrid with Smart Energy Storage Systems using Particle Swarm Optimization, in 2016 International Conference on Computation of Power, Energy Information and Commuincation (ICCPEIC), p. 783–789.

[14] Shariatzadeh, F., Kumar, N., & Srivastava, A. K. Optimal Control Algorithms for Reconfiguration of Shipboard Microgrid Distribution System Using Intelligent Techniques‖, IEEE Transactions on Industry Applications; 2017 :53(1), 474–482.

[15] Mousumi. B. ,&Anirban C. Cucko Search algorithm for economic dispatch ,Energy;2013:60;99-108.

[16] Gai-Ge W.,Lihong G.,Hong D. ,& Heqi W. A New Improved Firefly Algorithm for Global Numerical Optemization,Journal of Computational and Theortical Nanoscience;2014:11(2);477-485.

[17] Abhishek R. &T. M. Optimal reactive power dispatch using hybrid Nelder–Mead simplex-based firefly algorithm: International Journal of Electrical Power & Energy Systems;2015: 66 ; 9-24.

[18] Issa A. A. Photovoltaic Parameters Identification Using Optimization Algorithm. University of Thi-Qar Journal. 2017;12(2):47-64.

[19] Kwiecien J. & B.F. Firefly algorithm in optimization of queueing systems:Bulletin of The Polish Academy of Sciences Technical Sciences; 2012 : 60 (2) .

[20] Issa A. A. An Improved Technique Based on Firefly Algorithm to Estimate the Parameters of the Photovoltaic Model, Iraq, Journal Electronic Engineering ;2016:12(2);137-145.

A Survey on Monitoring Water Quality by Aid of IoT

Ali Hadi Abdulwahid[1]*, Muwaffaq Jameel Salih[2]
{dr.alhajjiali@stu.edu.iq[1], muwaffaq.jameel@stu.edu.iq[2]}

Southern Technical University/Engineering Technical College /Basra[1]
Southern Technical University/Faculty of Graduate Studies/ Basra[2]

Abstract. The many types of environmental surveillance systems connected to water quality are covered in this study. To explain each water monitoring system with diverse characteristics, many parameters are considered. Over the last years, the technology features of several approach methodologies linked to water quality monitoring, as well as their installation with the IoT component, have been studied. In this study, the process of various approaches to the technologies employed will be critically evaluated, as well as which techniques are focused on which parameters.

Keywords: Water, quality, Monitoring, IoT.

1 Introduction

This Water quality monitoring system comprehension and execution is now a very significant side of today's society. Typical approaches are mostly utilized to collect results, such as chemical samples, physical situations, and biological facts [1][2]. The most basic methods for these parameters are condition monitoring, which includes understanding problems or risks to assess specific causes of dysfunction and evaluate pollution inputs, and problem investigation monitoring, which requires understanding problems or risks to determine specific causes of dysfunction and evaluate pollution inputs[3]. Another method for surveillance of water goodness is to use the Internet of Things (IoT), and this study concentrates on the IoT element of surveillance of water goodness. The following are the factors that are primarily considered for water quality monitoring and are defined by WHO as shown in table 1. The rapid growth of industry, as well as a higher reliance on agricultural expansion, are two of the key causes of this problem[4]. Because of the non-uniform rainfall distribution, the situation might occasionally become worse. Droughts and floods, as well as insufficient knowledge and understanding among people, are other origins of polluted water. According to the World Water Assessment Program, almost two million tons of human waste are discharged into the water each day.
The different types of contaminants, many of which are human-made, make ensuring the safety of water a difficult task. Excessive use of natural resources is the primary cause of water pollution issues. Monitoring water quality continuously is an important aspect of determining water quality since it is impossible to determine how frequently water quality is affected.

IMDC-IST 2021, September 07-09, Sakarya, Turkey
Copyright © 2022 EAI
DOI 10.4108/eai.7-9-2021.2314822

Governments, communities, and corporations must now satisfy a variety of water quality objectives. As a result, a wide water quality monitoring system is often required.
This paper starts with giving Common chemical and physical water goodness parameters then in the next part a glance at the Internet Of Things (IoT) is given, after that The existing water monitoring systems are reviewed. Finally, there is the conclusion of the paper.

Table 1. IoT parameters of water quality monitoring

Parameters	**Units**	**Drinking water IS: 10500 - 1991**	
		Desirable	Maximum
Turbidity	NTU	5	10
pH value	-	6.5 to 8.5	No relaxation
Total hardness (as CaCO3)	mg/l	300	600
Iron	mg/l	0.3	1
Chlorides	mg/l	250	1000
Calcium	mg/l	75	200
Copper	mg/l	0.05	1.5
Manganese	mg/l	0.1	0.3
Sulphate	mg/l	200	400
Nitrate	mg/l	50	No relaxation

2 Common Chemical and Physical Water Goodness Parameters

A. pH: can be considered as a metric for determining how acidic or alkaline a liquid is. A pH of 7 is considered neutral, while pH values lower and above 7 are acidic and alkaline, correspondingly. A pH range of 6.0 to 9.0 is usually suggested for distribution systems.
B. Electrical conductivity: This parameter is a measurement of a liquid's ability to conduct electricity. The amount of conductive ions present in salt that is dissolved in liquid and other inorganic compounds is measured as conductivity. The higher the conductivity, the more salts are dissolved. The conductivity of drinkable water must be within 0 to 2500 S/cm.
C. Oxidation-reduction potential (ORP): The strength with which electrons are transported across different species in a liquid is measured by RP. This demonstrates water's ability to remove pollutants on its own. ORP measurements in healthy water are often very high.

D. Turbidity: This is measured in nephelometric turbidity units (NTU) and represents the density of suspended and colloidal particles in water. Turbidity of less than 1 NTU should be present in drinkable water.

3 Internet Of Things (IoT)

In numerous study domains, the IoT technique is used to track, acquire, and analyze data from remote sites. Because of the increase in data volume, monitoring systems are now becoming important aspects of decision-making. Sensors based on the Internet of Things (IoT) might be utilized to offer precise water quality management. The Internet of Things (IoT) is a new type of environment in which practically every computer and piece of equipment we use are connected to a network. It may be combined to execute complex duties requiring a high level of intellect. For this information and interconnectivity, IoT systems include integrated sensors, actuators, processors, and transceivers. The Internet of Things (IoT) has a significant influence on almost every aspect of human existence. IoT uses the functionalities of Wireless Sensor Network (WSN) technology to convert daily living into a common phenomenon.
The IoT architecture is made up of various levels, as shown in Fig 1.

A. The sensing layer is the physical layer with sensors and an actuator.
B. The transport layer is the networking layer (Network Layer). It delivers sensor readings from the physical layer to the layer of processing via networks different standards.
C. The processing layer sometimes referred to as the middleware layer, collects, analyzes, and manages vast volumes of data that come from the transport layer. It can accommodate and sustain a variety of resources. For big data analysis, it employs a variety of technologies, including databases, cloud storage, and modules.
D. As a result, the suggested system's purpose may be accomplished, and the application layer hosts an alarm system that can provide alert signals of water quality data to the decision-maker.

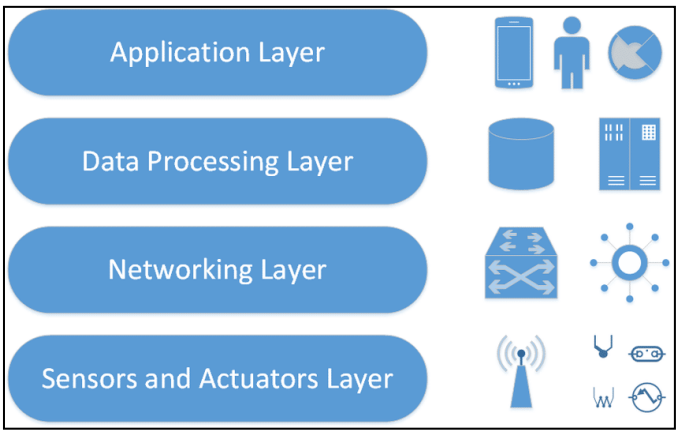

Fig.1. IoT architecture.

4 Water Monitoring Systems Review

Ali Hadi Abdulwahid implemented a system to monitor the physical characteristics of water, such as temperature, pH, turbidity, and electrical conductivity. Arduino board is used in this system as a core microcontroller. and ESP8266 module to transmit data to the Thingspeak server[1].

Abdallah Hammad, Talaat Salem, Mohie Omar designed and implemented IoT-based a low-cost Early Warning Framework (EWF) for water quality monitoring of the River Nile in real-time. The Prototype system is used to monitor three different water quality parameters (pH, Turbidity, and Temperature). WiFi technology is used to send data to the cloud. The cost was the main aspect for designers. So the overall cost was in the acceptable range of about 197$[5].

Brinda Das, P.C. Jain To assess water quality, the authors implemented a water quality control device to test water quality in real-time employing separate sensors (to sense the following parameters: electrical conductivity, pH, and temperature). In this system, the ZigBee module sends data collected by the sensors wirelessly to the processing unit, and the GSM module transfers the data wirelessly from the microcontroller to the Smartphone/PC. In the event of anyone attempting to pollute the water body, the device even has proximity sensors to warn officials by sending a message to them through the GSM module[6].

K. Spandana and V.R. Seshagiri Rao assumed that the method proposed reduces the complexity and improves the efficiency by gathering water parameter data such as level of water, Co_2 temperature, and pH. The gathered information is stored in a database site that can be accessed from anywhere in the world. Using a Wi-Fi module, the interconnection between sensors and the work is accomplished wirelessly[4].

The system implemented by Sathish Pasika and Sai Teja Gandla utilizes ultrasonic, pH, turbidity, and DHT-11 sensors, a microcontroller device as the processing unit, and a single ESP8266 Wi-Fi module (NodeMCU) data transmission unit. All sensors are data collected and processed by the MCU and transferred to the ThingSpeak server by the ESP8266 (NodeMCU) Wi-Fi data connectivity module to the central server[3].

The system that was built by Luo Hongpin, Li Guanglin, Peng Weifeng, Song Jie, Bai Qiuwei, utilizes solar panels and lithium cells as an energy source. For the control of aquaculture water quality parameters, the YCS-2000 dissolved oxygen sensor, pH electrode, Pt1000 temperature sensor, and ammonia nitrogen sensor were used; the STM32F103 chip was used for data processing; the ZigBee and GPRS modules were used for data transfer to the remote monitoring center, where the data was processed and displayed. The device was attached to an aerator to automatically regulate the concentration of dissolved oxygen. This system was built by using of WeMos D1 mini and (pH, turbidity, temperature, and ultrasonic) sensors[6].

The research team consists of Abdul Rauf Memon, Saadia Kulsoom Memon, Abdul Aziz Memon, and Tayab Din Memon implement a framework. WeMos D1 mini is an Arduino-like board for transmitting sensor information over the internet with built-in Wi-Fi capability. For water quality data collection, internet data transfer, reporting, documentation, and analysis, the overall experimental setup was developed and tested. It is experimentally noticed that it takes less than a minute for the machine to change its values[7].

The sensor data are obtained by an ATmega32U4 microcontroller in this device proposed by Nansong Wuand and Muhammad Khan transmitted to a LoRa transceiver module. The 915 MHz frequency band MicrochipRN2903 LoRa transceiver communicates with the LoRa gateway, which can either be linked to the backbone Internet through WiFi or a wired network. Then the LoRa gateway forwards the information to the TTN cloud[8].

Md. Mahbubur Rahman, Chinmay Bapery, Mohammad Jamal Hossain, Zahid Hassan, G.M. Jamil Hossain, Md. Muzahidul Islam. Concentrate on multiple parameters. Like pH, turbidity,

temperature, salinity, dissolved oxygen. Data from analog sensors is translated to digital data known as analog to digital converter(ADC). This information is processed through Arduino. The interpreted data is then sent to NodeMCU with Arduino and NodeMCU serial communications. Processed data parameters are then sent to the real-time Firebase servers[9].
The system proposed by Mourvika Shirode, Monika Adaling, Jyoti Biradar, Trupti Mate utilize conductivity, pH, turbidity, and temperature sensors, a microcontroller as a processing module, and the four sensors collect data in analog signals type. The ADC generates the digital format of these signals. Via a WiFi module, these digital data are sent to the processing unit (the microcontroller). The microcontroller processes analyze and further communicates the digital information through the WiFi module, which transfers the water quality parameter information to the mobile smartphone or personal computer, which is also displayed on the microcontroller's LCD[10].
Sivasankari G.G, Bineet Kumar Jha, Venugopal K.R. design device operate on the Cloud-based Ubidots network for data integration and dashboard integration have been suggested. The device has several sensors stored within the water tank. Using ZigBee/Wi-Fi technology, these sensors are attached to the microcontroller. To read the outcome, the microcontroller is linked directly to the LCD[11].

Table 2. A comparison of suggested node design for water quality surveillance systems.

No	Author(s)	Water Parameters	Controller	Communications	IoT Platform	Power Supply
1	Ali Hadi Abdulwahid	Temperature pH turbidity conductivity	Arduino	WiFi	ThingSpeak	not specified
2	Noha Kamal Abdallah Hammad Talaat Salem Mohie Omar	pH Turbidity Temperature	Raspberry Pi3	WiFi	not specified	not specified
3	Brinda Das P.C. Jain	pH conductivity temperature	LPC2138	Zigbee GSM	ThingSpeak	power supply adapter
4	K. Spandana V.R. Seshagiri Rao	pH level CO2	ESP8266	WI-FI	not specified	not specified
5	Sathish Pasika Sai Teja Gandla	pH turbidity	Arduino Mega	Wi-Fi	ThingSpeak	power supply adapter
6	Luo Hongpin Li Guanglin Peng Weifeng Song Jie Bai Qiuwei	pH Ammonia nitrogen, temperature	GPRS	Zigbee GPRS	not specified	battery solar panels

7	Abdul Rauf Memom	pH turbidity temperature level	Arduino	Wi-Fi	ThingSpeak	power supply adapter
8	Nansong Wu, Muhammad Khan	pH turbidity DO temperature	ATmega32U4	LoRa	TTN	not specified
9	Md. Mahbubur Rahman Chinmay Bapery Mohammad Jamal Hossain, , Zahid Hassan G.M. Jamil Hossain Md. Muzahidul Islam	pH Turbidity Temperature Dissolved Oxygen Salinity	Arduino	Wi-Fi	Firebase	not specified
10	Mourvika Shirode Monika Adaling Jyoti Biradar Trupti Mate	pH conductivity turbidity temperature	LPC2148	Wi-Fi	ThingSpeak	not specified
11	Bineet Kumar Jha Sivasankari G.G Venugopal K.R.	pH Turbidity Temperature Dissolved Oxygen Salinity	CC200	Wi-Fi	Ubidotes	not specified

5 Conclusion

The study gives a summary of recent research on water monitoring methods that have been developed and are now being employed in the effective monitoring of water quality systems. In the context of IoT technology, each study has its specific value. The papers examined are all aimed at improving the water quality monitoring system and advancing it to a higher level in some way.

References

[1] A. H. Abdulwahid, "IoT Based Water Quality Monitoring System for Rural Areas," *9th Int. Conf. Renew. Energy Res. Appl. ICRERA 2020*, pp. 279–282, 2020, doi:

10.1109/ICRERA49962.2020.9242798.

[2] S. M. G. Nikkam and V. R. Pawar, “Analyzing water quality for industrial application under IoT environment,” *Int. Res. J. Eng. Technol.*, vol. 3, pp. 882–885, 2016.

[3] S. Pasika and S. T. Gandla, “Smart water quality monitoring system with cost-effective using IoT,” *Heliyon*, vol. 6, no. 7, p. e04096, 2020.

[4] S. Shanthi, T. Gopi, and C. Vidhyesh, “IoT Based Water and Air Quality Monitoring System and Analysis,” *Int. J. Appl. Eng. Res.*, vol. 14, no. 6, pp. 1405–1409, 2019.

[5] N. Kamal, A. Hammad, T. Salem, and M. Omar, “EARLY WARNING AND WATER QUALITY, LOW-COST IOT BASED MONITORING SYSTEM,” *JES. J. Eng. Sci.*, vol. 47, no. 6, pp. 795–806, 2019.

[6] L. Hongpin, L. Guanglin, P. Weifeng, S. Jie, and B. Qiuwei, “Real-time remote monitoring system for aquaculture water quality,” *Int. J. Agric. Biol. Eng.*, vol. 8, no. 6, pp. 136–143, 2015.

[7] A. R. Memon, S. K. Memon, A. A. Memon, and T. D. Memon, “IoT Based Water Quality Monitoring System for Safe Drinking Water in Pakistan,” in *2020 3rd International Conference on Computing, Mathematics and Engineering Technologies (iCoMET)*, 2020, pp. 1–7.

[8] N. Wu and M. Khan, “LoRa-based Internet-of-Things: A Water Quality Monitoring System,” in *2019 SoutheastCon*, 2019, pp. 1–4.

[9] Z. Hassan, G. M. J. Hossain, and M. M. Islam, “Internet of Things (IoT) Based Water Quality Monitoring System,” *Educ. Res.*, vol. 2, no. 4, pp. 168–180, 2020.

[10] M. Shirode, M. Adaling, J. Biradar, and T. Mate, “IOT based water quality monitoring system,” *Int. J. Sci. Res. Comput. Sci. Eng. Inf. Technol.*, vol. 3, no. 1, pp. 1423–1428, 2018.

[11] B. K. Jha, G. G. Sivasankari, and K. R. Venugopal, “Cloud-Based Smart Water Quality Monitoring System using IoT Sensors and Machine Learning,” *Int. J.*, vol. 9, no. 3, 2020.

Design and implementation of control Cabinet Based Siemens S7-300 Programmable Logic Controller PLC

Basim Mohsin Abdulwahid Al-Najari
{pe21023@student.uniten.edu.my}

University Tenaga Nasional UNITEN, Malaysia

Abstract. The present proposal is to design and implement of control cabinet-based Siemens S7-300 programmable logic controller (PLC). Using PLC in industries is easy, resilient, and more compact than the classic system. The cabinet will be used in both training and research activities. It consists of two parts hardware and software. The hardware consists of several cards such as power supply, Central Processing Unit (CPU), digital input, digital output, analog input, and analog output. On the other hand, the software is the Totally Integration Automation (TIA) and it will be installed on a Personal Computer (PC). The TIA is the latest version of Siemens software, and it consists of two parts, logic builder (Step7) and Human Machine Interface (HMI) builder. In TIA, the logical diagram and HMI pages of the process can be designed to fabricate supervisory control and data acquisition (SCADA). An applied program will be written and loaded in the PLC to test the overall system.

Keywords: PLC, SCADA, CABINET, TIA, HMI, CPU, CCR.

1 Introduction

Programmable logic controllers (PLCs) have been used in industry in one form or another for the past twenty years. The PLC is designed as a replacement for the hardwired relay and timer logic to be found in traditional control panels [1]. In today's world, many industries are getting automated using PLC and thus it has become the main part of the industries [2]. It acts a major function in the automation field which tends to reduce complexity, increases safety, and be cost-efficient [3]. Input devices: for example, switches, and output devices, for example, motors, being controlled are connected to the PLC and then the controller monitors the inputs and outputs according to this program stored in the PLC [4]. In this paper, a programmable logic controller experiment set for education was designed [5]. These controllers are specially designed to survive in harsh situations and shielded from heat, cold, dust, and moisture, etc. PLC consists of a microprocessor that is programmed using the computer language. The program is written on a computer and is downloaded to the PLC via cable [6]. Automation is the delegation of human control functions to technical equipment [7]. This Laboratory Trainer and research setup system is fully integrated with PLC Motion Animation software. The software tool can be used as an offline and Online animation tool with its collection of sample HMI applications. The trainer can be used alternately for the operation and control of industrial manufacturing processes [8]. The PLCs consist of power supply, Central Processing Unit CPU, memory, and input & output modules. The input unit receives the field signals from the input devices and converts these signals to a form compatible with the CPU requirements. The output

IMDC-IST 2021, September 07-09, Sakarya, Turkey
Copyright © 2022 EAI
DOI 10.4108/eai.7-9-2021.2314820

unit (a set of relays, transistors, or Triac) translates the CPU orders to field actuators. Memory is used to save the user program, data, and configuration [9]. The advance of technology and electric drives raises the usage of PLC in industrial systems. The use of Programmable Controllers in automation things increases flexibility and reliability of processes and expands and enhances the production [10]. Wireless technologies are rapidly being adapted from simple monitoring and control to supervisory control and data acquisition (SCADA) systems. Wireless provides highly reliable data communications in a harsh and interference-heavy environment [11]. Recent developments in Human Machine Interface (HMI) have brought remarkable advances in performance, flexibility, and openness. Selecting an HMI interface for a PLC-based automation system that will meet the needs of the process over the projected lifetime of the control system requires consideration of many issues [12]. Hence it has become difficult to debug the failures in the system and it is a highly feasible job to facilitate alternate connections to the fault-tolerant systems in the relay logic [13]. In this task, the analytical compute model for optimizing the functions of the volume processing plant can handle all possible decision variables in the setup [14]. For complete control of the building, a proper SCADA implementation and optimization strategy must build [15]. This paper presents the design and implementation of control cabinet-based Siemens S7-300 PLC.

2 Cabinet Implementation

The Siemens PLC cabinet consists of two parts as below:

2.1 Hardware

2.1.1 Enclosure

The enclosure is used to contain the electrical modules and their connections to fabricate Siemens PLC rack type and it is 70cm *50cm*20cm dimensions.

2.1.2 Power Supply

The power supply is used to supply the voltage to the CPU and input-output modules. The type of this supply is Siemens PS 307 with output current equal to 5A, input voltage equal to (220) VAC, and output voltage equal to 24VDC. Fig 1. shows the wiring connection of this module.

2.1.3 Central Processing Unit CPU Module

The central processing unit (CPU) is the main part of the cabinet. it is modular and compact, versatile, a secure investment, and is powerfully fit for a full range of applications. A scalable and flexible design, a communication interface that fulfils the highest standards of industrial communication and a full range of powerful integrated technology functions make this CPU an integral part of a complete and comprehensive automation solution. It is standalone or dedicated to run one program that continuously monitors the state of the input devices and makes decisions based upon a custom program to manipulate logically the state of the output devices. The CPU that is used in this research is Siemens S7-300 model CPU315 2pn/dp. Fig 2. shows the CPU wiring connections.

2.1.4 Micro Memory Card (MMC)

The micro memory module is a permanent storage media. it is used as a part of PLC to store and backup programs and data without battery. The PLC is a battery-less device, and it loses its program in case of power off. When the PLC starts, it loads the user program from the MMC and stores it in its internal memory (RAM). The PLC is not operating without MMC. The type of MMC in this research is a FLASH EPROM and Its capacity is 512Kb.

2.1.5 Digital Input Module

The digital input module is used to input the safety devices signals such as pressure switch, level switch, flow switch, temperature switch, limit switch .ext. the model of this module is SIMATIC SM 321 DI32*DC24V. The number of input channels is (32) channel (from I0.0 to I3.7) and the signal level per channel is 24vdc. Sixteen (16) Snap switches are used to test the module inputs. Fig 3. shows the wiring connection of this module.

2.1.6 Analog Input Module

The analog input module is used to convert the analog input signal to digital or binary to be suitable for manipulation inside PLC. several types of signals can be measured through this module depends on their configuration. the signals can be bipolar voltage or current, unipolar voltage or current signal, Temperature or Resistance. The process signals that can be measured by this module such as pressure, level, flow, temperature, vibration, speed, weight, and so on. Table 1 shows the analog input signal and its limits. the model of this module is SIMATIC SM 331 AI8*13bit. The number of input channels is 8 channels, and the resolution of each channel is 13 bits. Table(4) shows the channel number and its address. Mill ampere supply is used to input analog input signal (4 to 20) mA to test the module in the laboratory. Fig 5. shows the wiring connection of this module.

A. Current-DATA Relation

If we suppose that the input signal is a unipolar current signal with a 4 to 20 mA range.
From table (1) we see that when the input signal is 4 mA, the data is 0 and when the input signal is 20 mA, the data is 27648 therefore the relationship between the current and the DATA is linear and can be represented by the equation below:

$D=(27648/16)*(I-4)$
Where:
D: DATA.
I: current.
mA: mill Ampere.
Fig 6. represents the relationship between current and data.

B. Resolution

The resolution is the value of the input that changes the DATA one BIT.
It is a ratio between changing in current and changing in data and equal $\Delta i/\Delta d=16/27648=578.7\mu A/bit$
That means 578.7μA current value changes the DATA one BIT.

Δi: changing in current.
Δd: changing in data.
µA: micro-Ampere.
bit: is the smallest cell in a digital system.

2.1.8 Analog Output Module

The analog input module is used to convert the digital or binary signal inside PLC to analog value to control the end device. two types of signals output from this module depends on their configuration. the signals can be bipolar voltage or current, unipolar voltage, or current signal. Table 2 shows the analog output signal and its limits. the model of this module is SIMATIC SM 332 AO8*12bit. The number of output channels is 8 channels, and the resolution of each channel is 12 bits. Table 5 shows the channel number and its address. Mill Ampere meter is used to read analog output current (4 to 20) mA to test the module in the laboratory. Fig 7. shows the wiring connection of this module.

A. Current-DATA Relation

If we suppose that the output signal is a unipolar current signal with a 4 to 20 mA range.
From Table 2 we see that when the DATA is 0, the output signal is 4 mA and when the DATA is 27648, the output signal is 20 mA therefore the relationship between the DATA and the current is linear and can be represented by the equation below:
I=(16/27648)*D+4
Where:
I: DATA.
D: current.
mA: Mill Ampere.
Fig 8. represents the relationship between data and current.

B. Resolution

The resolution is the value of DATA or numbers of bits that changes the output current one micro-Ampere (µA).
It is a ratio between changing in data and changing in current and equal Δd/Δi=27648/16=1.728 bit/µA.
That means 1.728-bit data value changes the current one micro-Ampere.
Δd: changing in data.
Δi: changing in current.
µA: micro-Ampere.
bit: is the smallest cell in the digital system.

2.1.9 Ethernet Cable

Ethernet cable is used for PC-PLC Profinet data communications. It is preassembled with two RJ45 connectors (10/100MB) and with (2) meter length. Download in the PLC and upload from the PLC instructions for programming and configuration can be done by using this cable.

2.1.10 Personal Computer (PC)

Personal Computer PC is used as a Siemens programmer (PG) for programming and configuration. In addition, it is used as a Siemens PC station for HMI page design and display. The Totally Integration Automation (TIA) portal is installed on the PC to do all
SCADA requirements. The connection between PC and PLC is a Profinet communication using Ethernet cable.

2.1.11 Rail

Rail is used to containing SIMATIC S7-300 modules. it is 480 mm in length. All S7-300 modules are mounted onto the rail. the module arrangement in the rail is according to the slot numbers. each module can be inserted in and removed from the rail easily. Table 3 shows the SIMATIC S7-300 module's horizontal arrangement in the rail.

2.2 Software

The software which is used in this research is the Integration Automation TIA portal V13 and it consists of two parts as below:

2.2.1 Logic Builder

The logic builder is the SIMATIC STEP7 V13. It is used to build the sequence of the process as instructions using ladder diagram language and store it in the PLC memory. When the PLC is in RUN mode, the sequence of the process stored in the PLC memory is executed to operate the process. The SIMATIC STEP7 V13 contains many instructions to fulfil all logical processes, mathematical processes, and batch functions.

2.2.2 HMI Builder

The HMI builder is the WinCC Advanced RT V13. It is used to build the HMI pages for the operator and store them on the PC. The HMI pages relate to the sequence of the process under the TIA portal environment to fabricate the SCADA system. the WinCC Advanced RT V13 contains many instructions to display the process on the computer screen. There are three types of HMI pages:

1. A graphic page is used to show the location of the device on the site and its current readings.
2. The alarm page is used to display the event's current state for each device on the site and to give an alert in case of abnormal states.
3. The trending page is used to display the signal's current values and their curves for the period such as (5 min,15 min,30 hours, and so on) according to the operator requirements.

3 Overall System

Fig 9. shows the block diagram of the overall system.
Fig 10. shows a photograph of the Siemens S7-300 cabinet front.
Fig 11. shows a photograph of the Siemens S7-300 cabinet inside.

4 Case Study

For commissioning the hardware and software, the practical example (Level measurement and monitoring) was designed and connected to the site to test the overall system in both hardware and software.

4.1 Level measurement and Monitoring

The case study is to measure the level of water vessel (V-604) with (4 meters) height and (20 meters) diameter in the water treatment unit of the factory (Fertilizer Plant). The old measuring and monitoring system consists of an electronic differential pressure transmitter as a level transmitter (LT-604) and level indicator (LIA-604) to display the level value in the central control room (CCR) for monitoring and to give alarm in case of low level. Fig 12. shows the water vessel. Fig 13. shows the block diagram of the old level measuring and monitoring system. Fig 14. shows the level transmitter in the site. Fig 15. shows the level indicator (LIA 604) in the central control room CCR. The cabinet was connected instead of a level indicator to display the level of the vessel on the computer screen in the central control room CCR. Two wires of the transmitter were connected to the cabinet for reading the analog input signal on pin2 of the module. The channel address is PIW256. Fig 16. shows the wiring diagram of the connection.

4.1.1 Level Calculations

For open tank calculations, the range of the transmitter can be calculated as below:
p=h*s.g.
s.g=density of object/density of water.
the density of water =1000 kg/m^3
the s.g of water=density of water/density of water=1, then
p=h
Δp=Hp-Lp ---------- the differential pressure=high pressure-low pressure
But Lp=0 then
Hp=head
Head=max-min
Δp=head
the head= 3 meters
Δp=3 mH_2O*1000
Δp=3000 mmH_2O
Then the transmitter range is from 0 to 3000 mmH_2O.
Where the range (0 to 3000 mmH2O) gives (4 to 20 mA) to the analog input module in the cabinet.
Where:
p: pressure
h: head
s.g: specific gravity.
Hp: high-pressure side.
Lp: low-pressure side.
Δp: differential pressure.

4.1.2 The Cabinet Commissioning

The cabinet was tested in the site (water treatment unit) for commissioning and the steps below were done:

1. The transmitter related to the cabinet, and this led to display the level of the vessel and equal to (78.8%) on the HMI pages.
2. The low-level set was entered in the HMI graphic page and equal to (70%).
3. The pump P-604 was started to decrease the level of the vessel and this led to minimizing the level of the vessel gradually.
4. When the level of the vessel reached less than the set (70%), the low-level alarm displayed on the HMI pages (graphic page and alarm page) informed the operator in the CCR about this abnormal state.
5. The pump P604 was stopped, and the valve was opened to maintain the standard level of the vessel.

4.2 Flowchart

A flowchart is a formalized graphic representation of a logic sequence. The purpose of a flow chart is to provide programmers with a common language or reference point when dealing with a process. The flowchart of the case study is read the level value through the level transmitter (LT 604), if the level value is less than 70% alarm will be displayed on the graphic page and alarm page for operators in the CCR, then the level value will be displayed on the pages of the HMI. Fig 17. shows the flowchart of the level measurement and monitoring system.

4.3 Ladder Diagram

The ladder is a diagram that shows actual component symbols and the basic wiring configuration of a relay logic circuit. The Ladder diagram in the case study is consist of always false and always true internal contacts, Scale function block to scale the transmitter analog input signal 4~20mA to 0~100% range, and the less than compare function to display the alarm on the cabinet lamp in case of level value less than 70%. Fig 18. shows the Ladder diagram of the level measurement and monitoring system.

4.4 HMI Pages

Three pages were designed as HMI pages for operators. Three command blocks are designed to move from one page to another. The HMI pages are as below:

4.4.1 Graphic Page

A graphic page was designed for level measurement and monitoring to display devices and their readings such as vessel and transmitter. The alarm object flickers in red colour in case of a level value less than 70%. Fig 19. shows the graphic page of the level measurement and monitoring system.

4.4.2 Trend Page

The trending page was designed for level measurement and monitoring to display the response of the level transmitter for (15 min) in addition to displaying the current value. Fig 20. shows the graphic page of the level measurement and monitoring system.

4.4 3 Alarm Page

The alarm page was designed for level measurement and monitoring to display the low-level alarm Tag, Date of alarm, Time of alarm, and its Status. Fig 21. shows the alarm page of the level measurement and monitoring system.

4.5 Profnet Topology (Network)

Profinet (Process Field Net) is an industry technical standard for data communication over Industrial Ethernet (IE), designed for collecting data and controlling, equipment in industrial systems. the network in the case study consists of two devices (PLC and PC) that were connected through (2) meters Ethernet cable. each device has an internet protocol (IP). Table 6 shows the device's internet protocols (IPs). Fig 22. shows the Profinet Topology (network) of the level measurement and monitoring system.

4.6 Cabinet Photographs

Fig 23. shows the photograph of the overall measurement and monitoring system.

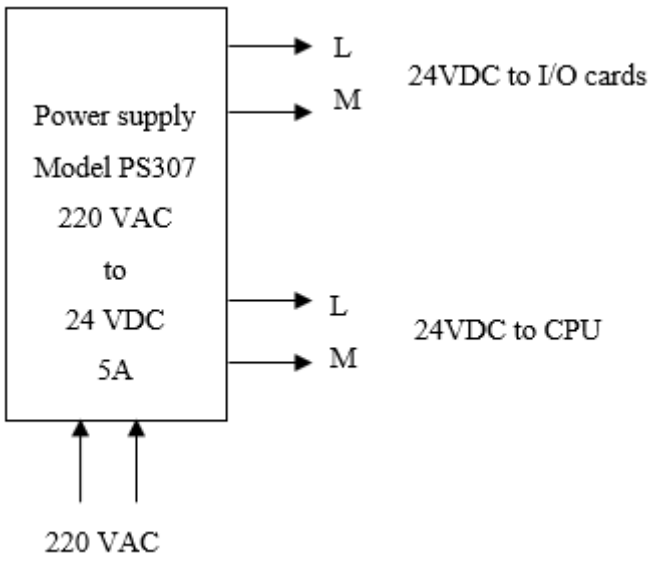

Fig 1. Power Supply.

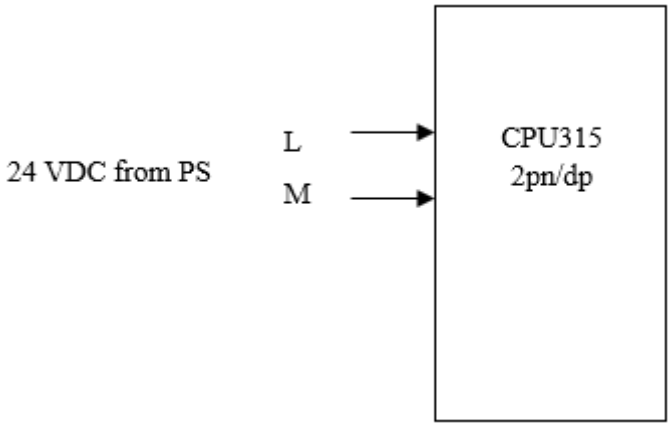

Fig 2. Central Processing Unit CPU.

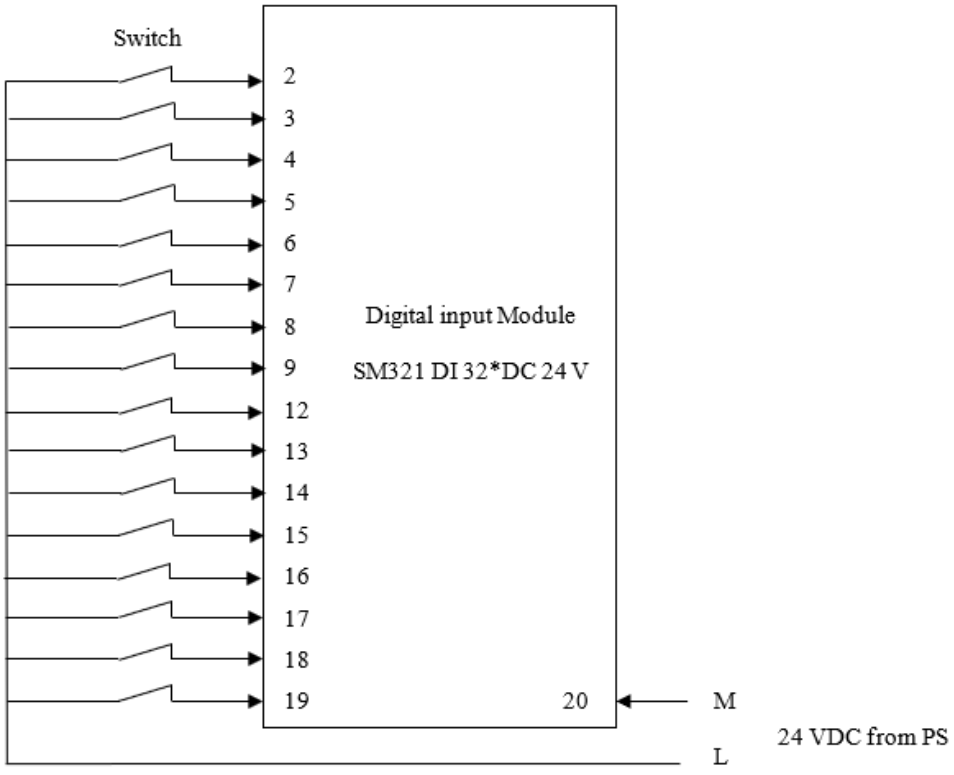

Fig 3. Digital input module. M = negative, L = positive.

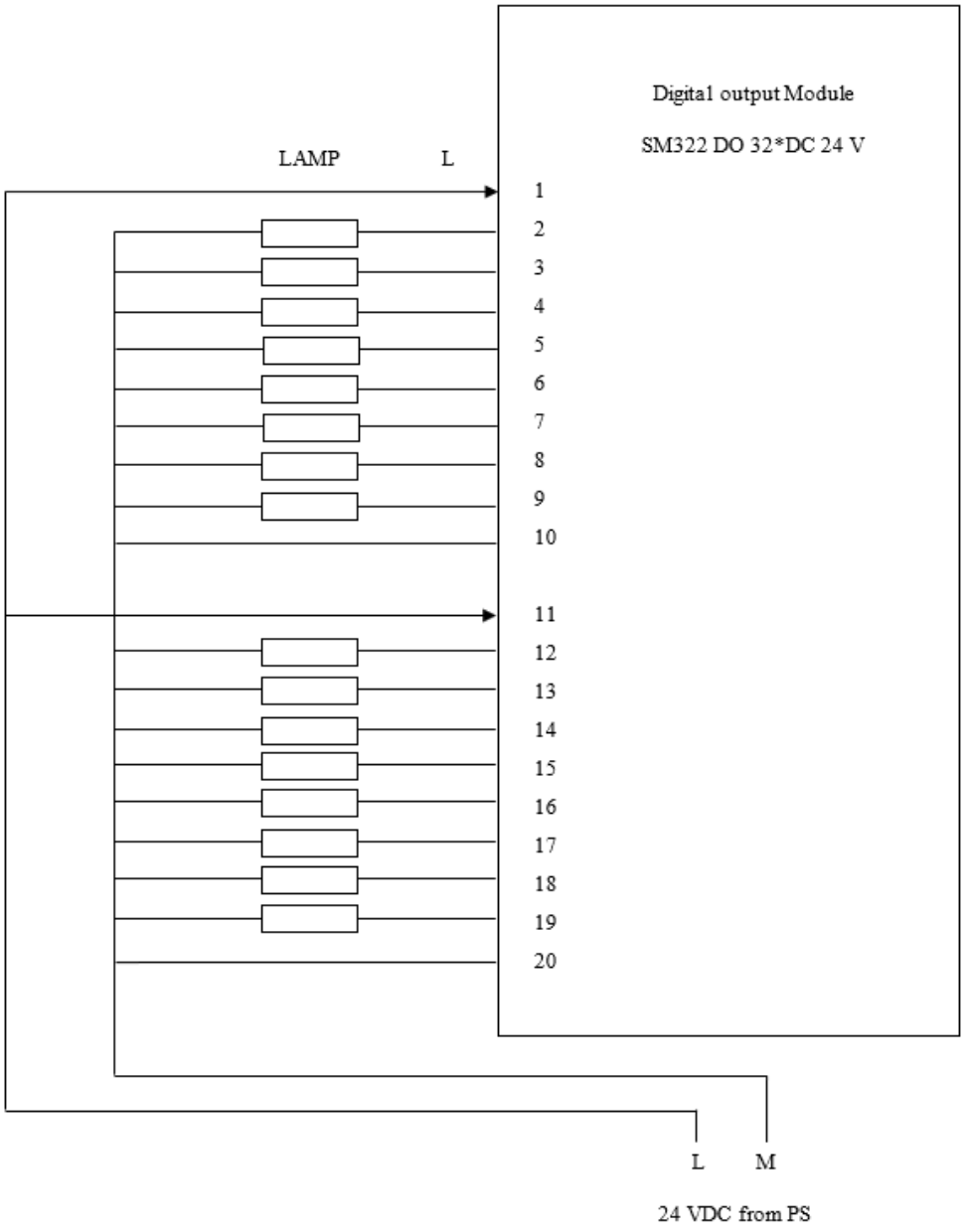

Fig 4. Digital output module, M = negative, L = positive.

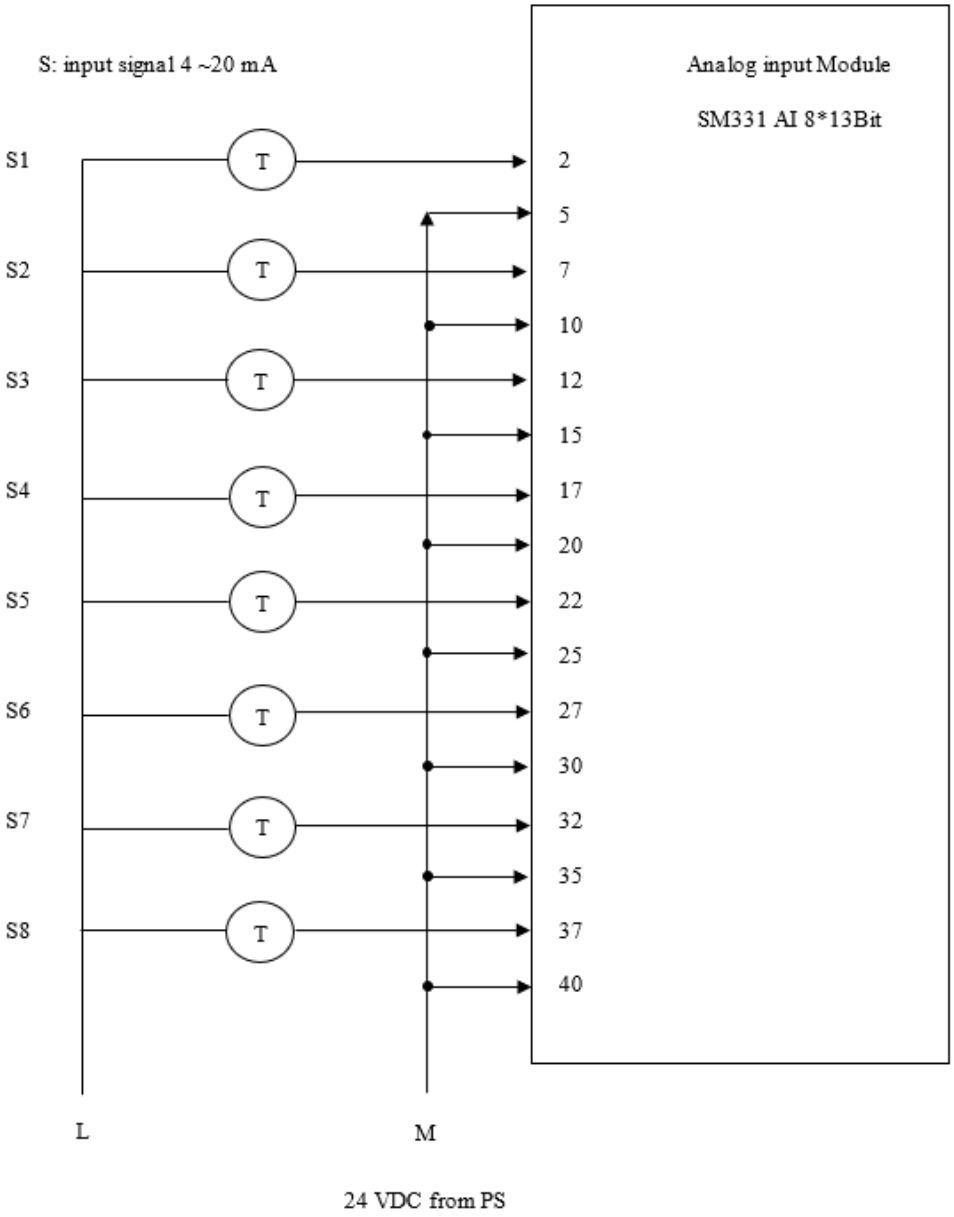

Fig 5. Analog input module, M = negative, L = positive, and T = Transmitter.

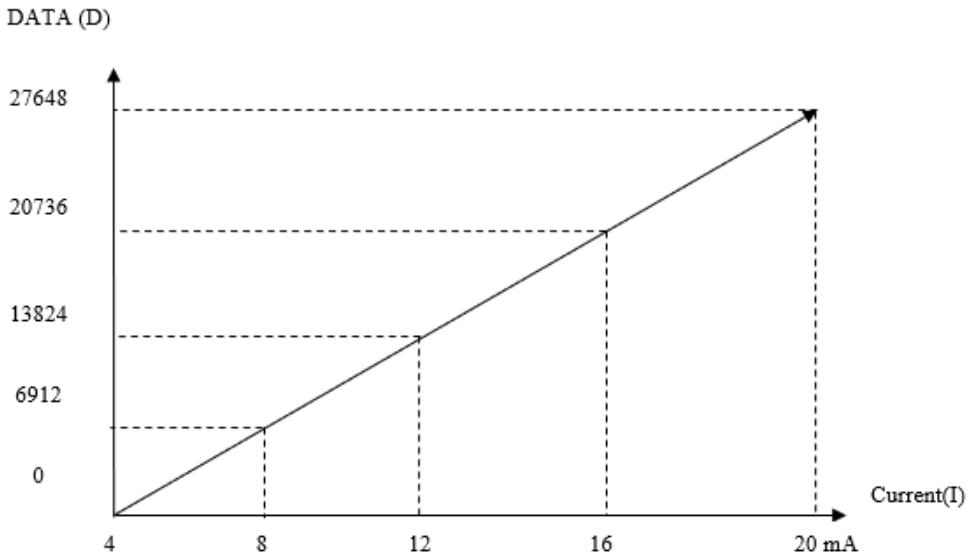

Fig 6. Current-DATA relation.

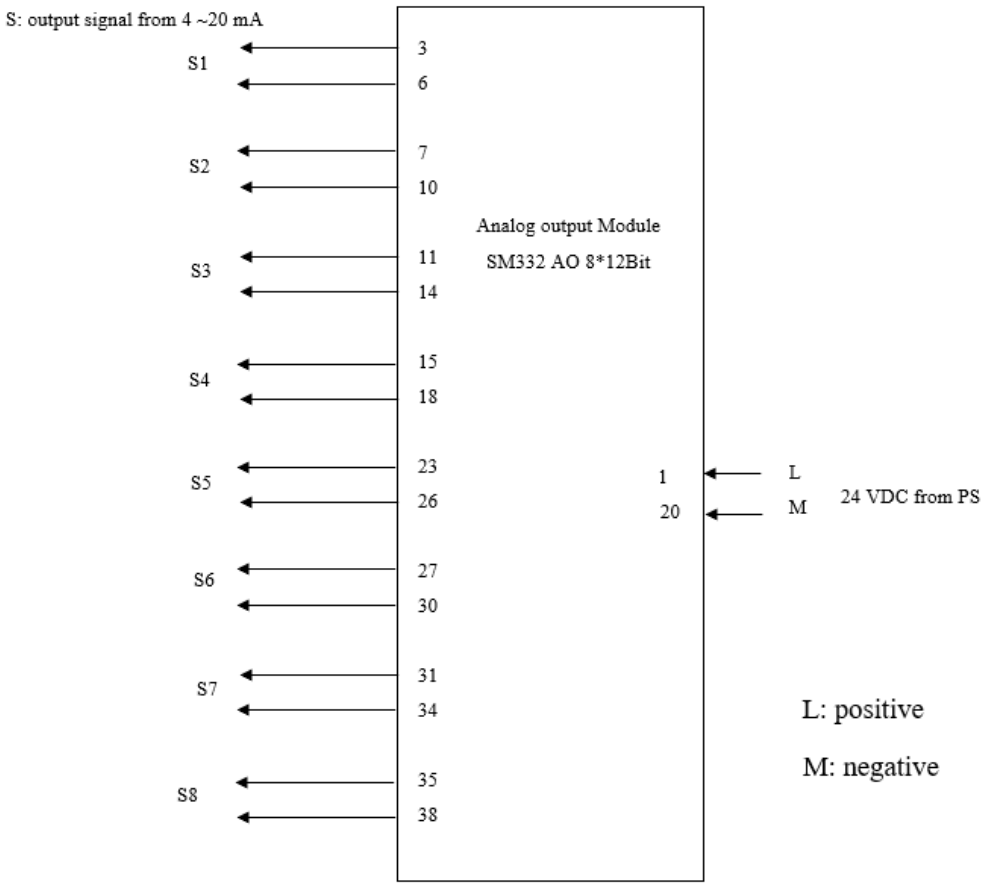

Fig 7. Analog output module.

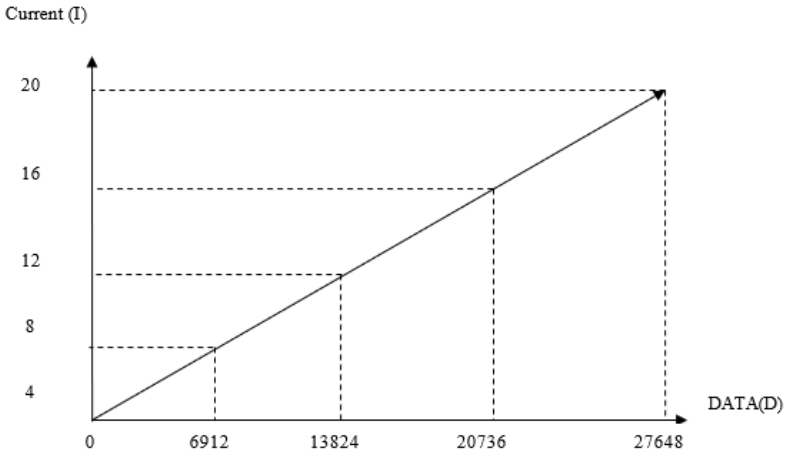

Fig 8. DATA-Current relation.

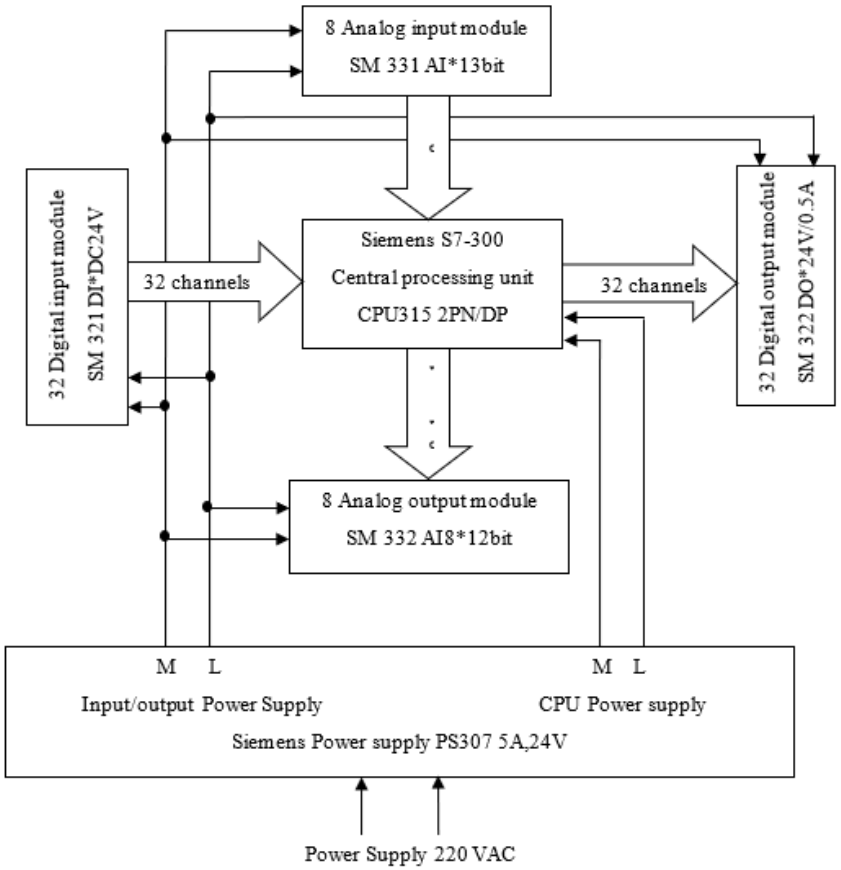

Fig 9. Block diagram of the S7-300.

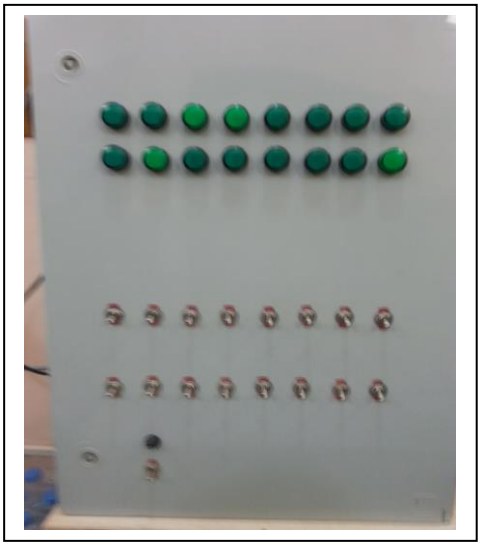

Fig 10. photograph of the Siemens S7-300 cabinet front.

Fig 11. photograph of the Siemens S7-300 cabinet

Fig 12. water vessel (V-604) in the water

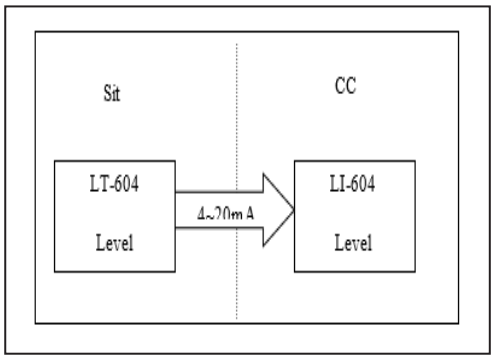

Fig 13. Block diagram of the old level measuring and monitoring system.

Fig 14. level transmitter (LT-604) in the water treatment unit.

Fig 15. level indicator (LI-604) in the water treatment unit.

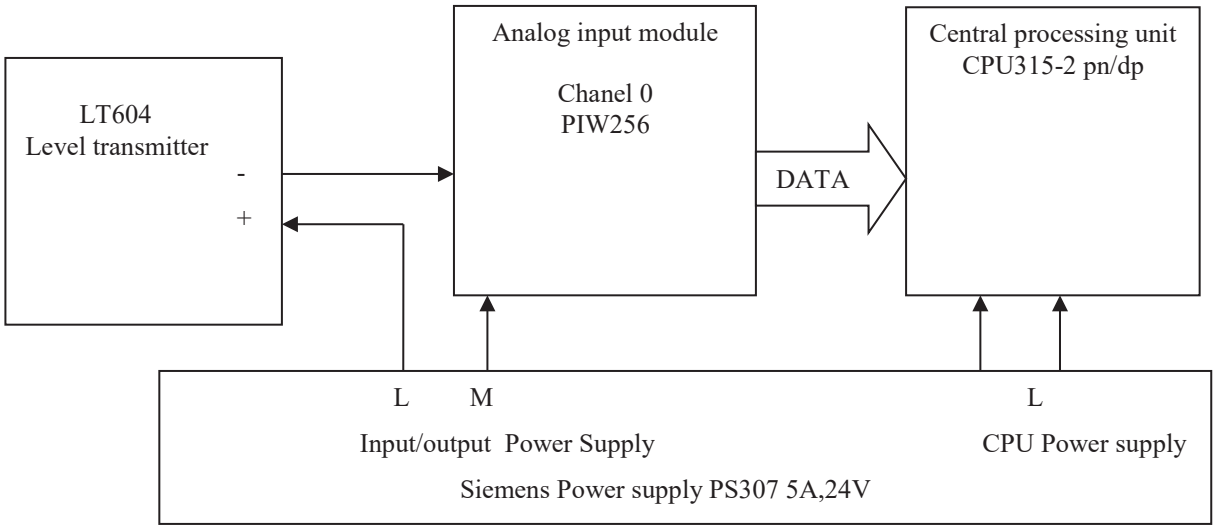

Fig 16. Block diagram of the new measuring and monitoring system

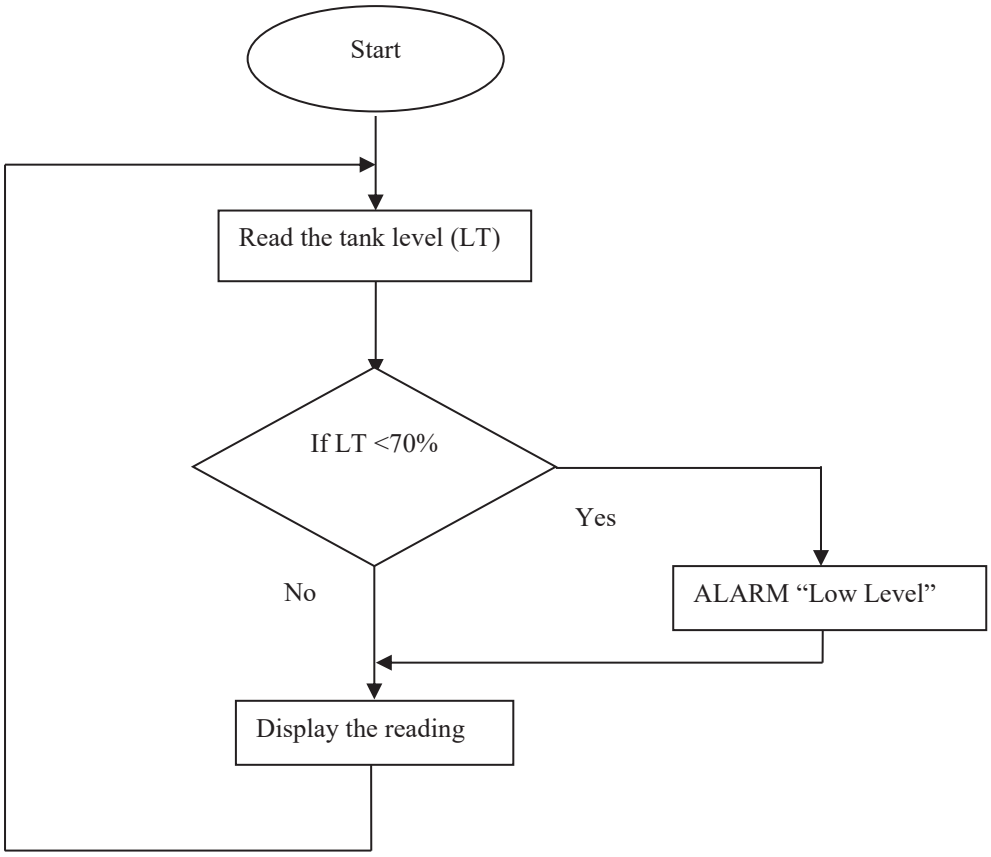

Fig 17. Level Measurement flow chart

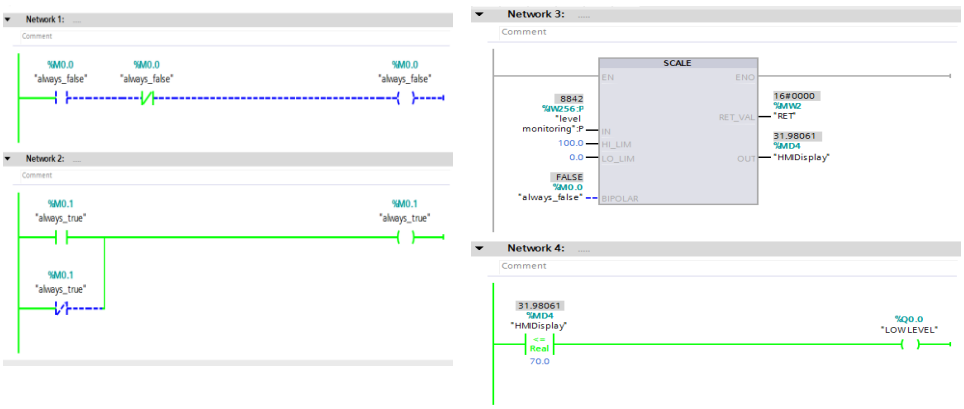

Fig 18. Ladder diagram of the Level Measurement.

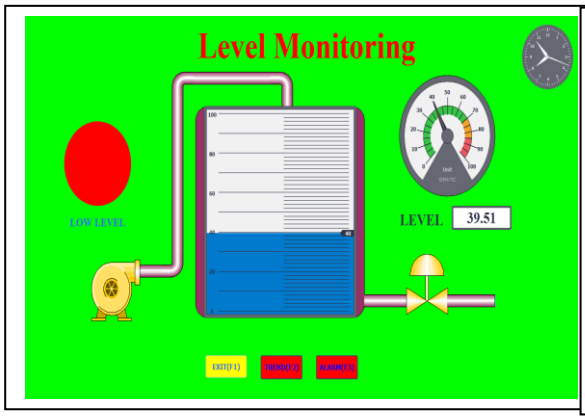

Fig 19. Graphic page of the Level Measurement

Fig 20. Trend page of the Level Measurement.

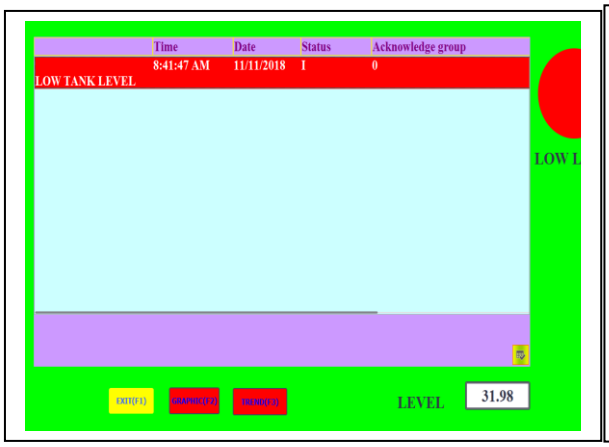

Fig 21. Alarm page of the Level Measurement.

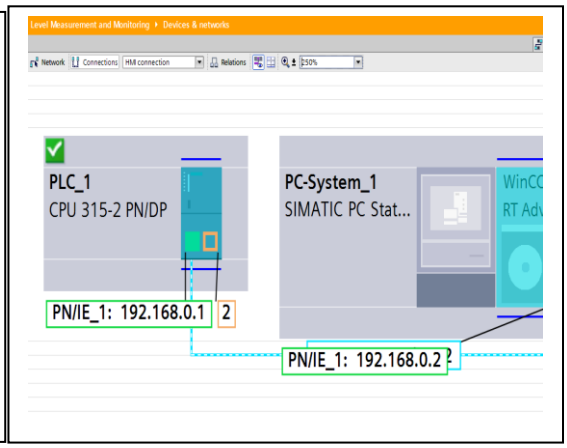

Fig 22. Profinet Topology of the Level Measurement.

Table 1. Analog input limits.

Index	Ratio	Input range (mA)	Value in HEX	Value in DEC
1	0%	4	0	0
2	25%	8	1B00	6912
3	50%	12	3600	13824
4	75%	16	5100	20736
5	100%	20	6C00	27648

Table 2. Analog output limits.

Index	Ratio	Value in DEC	Value in HEX	Output range (mA)
1	0%	0	0	4
2	25%	6912	1B00	8

3	50%	13824	3600	12
4	75%	20736	5100	16
5	100%	27648	6C00	20

Table 3. S7-300 modules arrangement inside the rail.

Slot 0	Slot 1	Slot 2	Slot 3	Slot 4	Slot 5
Power supply	CPU	Digital input	Digital output	Analog input	Analog output

Fig 23. Photograph of overall measurement and monitoring system.

5 Results and Discussion

In this present study, Siemen's control cabinet-based S7-300 PLC has been designed and implemented. Several Siemens modules were used to build the cabinet such as power supply, CPU, DI, DO, AI and AO. The latest software of Siemens is the TIA. The TIA was used to program the sequence of the process as a LADDER diagram in PLC and to design the HMI pages in the PC to fabricate the SCADA system. The cabinet has been tested in the water treatment unit of the factory for commissioning. Two-wire differential pressure transmitters were connected to the cabinet to measure the vessel level and to display the value on HMI pages. The results obtained that the practical level values are identical to the theoretical values and according to the equation of current-DATA relation. We found deviation in the reading of the

old monitoring system, but the reading of the new monitoring system was very accurate. Also, the HMI software gave the expected findings and we found that the new monitoring system is better than the old monitoring system. The experimental tests of the PLC set and HMI software are successfully done. The cabinet can be used as training and a research kit and many types of research in automation can be done by using this kit. We found that using of SCADA system instead of a classic system has several advantages such as reduce time consumption, reduce human resource consumption, Increase production, greater accessibility (remotely), Instantaneous alert on alarms or events, organized data records and report generation automatically, data analysis (real-time and historical data plotting of graphs, charts, trends, etc.), easy user interfaces for interaction (graphical HMI interface with animation for easy understanding), Automated calculation and easy of diagnosis and maintenance.

References

[1] P. Logic et al., "Chapter 8 : Programmable Logic Controller (PLC)," Ind. Electron. Control, vol. 485, no. 8, p. 1, 2106.

[2] V. M. Kantilal and A. P. Lakhlani, "ZIGBEE based Wireless Monitoring and Controlling of Automation System using PLC & SCADA," Int. J. Adv. Res. Electr. Electron. Instrum. Eng., vol. 3, no. 1, pp. 6768–6775, 2014.

[3] D.Baladhandabany, S.Gowtham, T.Kowsikkumar, and P.Gomathi, "PLC Based Automatic Liquid Filling System," Int. J. Comput. Sci. Mob. Comput., vol. 4, no. 3, pp. 684–692, 2015.

[4] Y. N. Burali, "PLC Based Industrial Crane Automation & Monitoring," Int. J. Eng. Sci., vol. 1, no. 3, pp. 01–04, 2012.

[5] E. Yilmaz and S. Katrancioglu, "Designing programmable logic controller (PLC) experiment set with internal experiment blocks," Procedia - Soc. Behav. Sci., vol. 28, pp. 494–498, 2011, doi: 10.1016/j.sbspro.2011.11.095.

[6] N. Thakur and M. Hooda, "A Review Paper on Digital Watermarking Techniques & Its Applications," Int. J. Sci. Res., vol. 5, no. 6, pp. 1864–1868, 2016, doi: 10.21275/v5i6.nov164699.

[7] V. M. Kumar, A. Sivasankar, G. Prabakaran, R. Dhanabal, and A. M. Krishnan, "Design and Implementation of PLC Based Control Panel for Hydraulic Assembly Press," pp. 1704–1711, 2017, doi: 10.15662/IJAREEIE.2017.0603097.

[8] P. Chakraborty, A. Hossain, and V. Pillarisetty, "Designing and assembling of a programmable logiccontrols (PLC) laboratory trainer and advanced research setup," ASEE Annu. Conf. Expo. Conf. Proc., vol. 2016-June, 2016, doi: 10.18260/p.26701.

[9] A. Thesis, "PLC Based Implementation of Solar Photovoltaic Energy Maximum Power Point Tracking Techniques," no. October, 2014.

[10] A. Thesis and S. To, "Dedicated to my parents , sisters , dear wife and lovely sons Arshed azeez saher," no. July, 2017.

[11] M. J.Marie, G. A. Al-Suhail, and H. T. Khadim, “Developing Al-Najaf Cement Plant using Wireless SCADA System,” Int. J. Comput. Appl., vol. 64, no. 13, pp. 17–23, 2013, doi: 10.5120/10693-5602.

[12] V. M. Koshti and S. M. Joshi, “Design of Human Machine Interface for Plc Based Automation System,” IFAC Proc. Vol., vol. 40, no. 18, pp. 343–346, 2007, doi: 10.3182/20070927-4-ro-3905.00057.

[13] A. M. Anusha and A. V Sutagundar, “Design of a PLC Based Elevator Control System,” vol. 6, no. 2, pp. 32–36, 2015.

[14] L. Chitra, S. Siranjeevi, A. Manikandan, and G. Saravanan, “Automation of Batch Production in Paint Industry using PLC,” Int. J. Innov. Technol. Explor. Eng., vol. 9, no. 2S4, pp. 435–440, 2019, doi: 10.35940/ijitee.b1207.1292s419.

[15] V. T. Samuel, “Control of Smart Building Using Advanced SCADA,” ,THESIS,University of South Florida, January, 2013.

A Comparison Study of Velocity Controller of Indirect Field Oriented Control of Linear Induction Motor Drive Using Model Predictive Controller

Fatimah F. Jaber[1], Diyah K. Shary[2] , and Haider Alrudainy[3]
{fatimah.jaber@stu.edu.iq[1], diyahpower@stu.edu.iq[2], h.m.a.Alrudainy@stu.edu.iq[3]}

Southern Technical University, Engineering Technical College, Basra, Iraq [1,2,3]

Abstract. Controlling the velocity of indirect field-oriented control of linear induction motor (LIM) drive is recently receiving significant attention. In this paper, a comparison study in connection to response time and resilience using two different controllers including PID and model predictive control (MPC) is extensively investigated. Two vector control systems for LIM drive are introduced in this study. The first drive mechanism uses a traditional PID controller to control the LIM's velocity. For effective control, whereas, MPC has been adopted to monitor the LIM velocity in the second drive system. Therefore, the performance of these controllers under parameters variation conditions and load disturbance has been compared. MATLAB simulation toolbox has been utilized, in this work, to demonstrate the feasibility of the two suggested schemes. The results showed that MPC based approach is superior to the traditional PID-based drive controller in terms of load disturbances and parameter variations.

Keywords: Linear induction motor (LIM), PID controller, indirect field-oriented control (IFOC), and model predictive control (MPC).

1 Introduction

Due to its remarkable advantages including direct producing thrust force, low cost, simple structure, high acceleration/deceleration, and easy maintenance, the linear induction motor is practical in areas that require linear motion. As a result, LIMs are still commonly utilized in a wide range of implementations, such as transportation, pumping of liquid metal, actuators, sliding door closers, conveyor systems, and so on [1]. The feedback linearization and field-oriented control (Vector Control) methods have made high-performance implementations of induction motor drives feasible owing to rapid progress in microelectronics and power electronic devices. Nevertheless, the motor's parameters must be precisely defined, and the correct flux data must be accurately measured to be effectively used in various applications. Besides, the performance of these motors is significantly impacted by the variations of motor parameters and unknown external disturbances [2], [3].

PID controllers are frequently utilized in industrial applications like motor control because of their simple construction and quick parameter adjustment [4]. The PID formulas are simple and can be easily applied to various controlled plants, but if the process is highly ordered and nonlinear, it may not yield good control results [5]. Both in the industry and the research control community, model predictive control (MPC) has advanced significantly in recent years. The model predictive control can find the optimum solution while keeping the constraints in mind

IMDC-IST 2021, September 07-09, Sakarya, Turkey
Copyright © 2022 EAI
DOI 10.4108/eai.7-9-2021.2314819

[6]. As a result, a plethora of exploratory research demonstrated that MPC can be significantly effective in such processes than the PID controller counterparts [7], [8].

This work provides a comparison of various controlling schemes for an IFOC drive of a linear induction motor. The major contributions of this work can be summarized as follow:

1- Various controls have been used to monitor the LIM drive's velocity.
2- To validate our schemes a computer simulation has been adopted.
3- To investigate which controller is resistant to load disturbances and motor parameter variations.

2 Background

Controlling the velocity of linear induction motors has been the subject of a slew of research papers in recent years, as seen in Table 1. In [9] the speed control of a single-side LIM using model fuzzy predictive force control (FPFC) is presented. This study [10] has been used a proposed controller dependent on an optimal recurrent wavelet neural network with a PID controller to control the velocity, thrust force, and the stator current of a 3-phase linear induction motor that considering the end effects. Using the particle swarm optimization technique, the proposed controller is tuned online. In [11] suggests a novel secondary field-oriented control model of LIM that depends upon a fuzzy self-adapting PI controller that takes the impact of the longitudinal end effect into account. This work [12] provides an optimal $P\ I^{\lambda}\ D^{\mu}$ controller with 2DOF and anti-windup strategies depend upon PSO Optimization, which is utilized to control the linear induction motor velocity. In [13] the LIM speed control method is proposed in this study, which leads to optimal control of motor characteristics like, flux, current, and thrust based on the DTFC method. DTFC is a more developed control approach that employs several PI controllers.

Table 1. Literature review of approaches used to control LIM.

Ref.	Approaches	Advantages	Disadvantages
[9]	Model fuzzy predictive force control (FPFC)	Lower force ripple and a faster convergence speed	The accurate measurement of force and flux is critical to the FPFC's successful service
[10]	RWNN+PID	Efficient and provides preferred and rigorous performance	Very complex
[11]	Fuzzy Self-adapting PI Controller	Robust and respond quickly to new dynamic procedures	One of the most frequently mentioned drawbacks of fuzzy logic methods is the lack of adequate resources for analysing the controller's results, such as stability, optimality, robustness, and so on
[12]	$P\ I^{\lambda}\ D^{\mu}$ + 2DOF+ anti-windup strategies depend upon PSO	Powerful in terms of improving the motor's performance	PSO has several drawbacks, including the inability to address scattering problems, the difficulty in defining initial design parameters, and the possibility of converging early and being stuck in a local minimum while dealing with complicated problems

[13]	DTFC with several PI	Reduced in the forcer thrust and flux ripple by around 0.8 percent	The coefficients of the PI controller must be adjusted correctly

3 LIM Model

The linear induction motor model can be studied by using the d-q axis equivalent circuit as shown in Fig 1. which considers the end effects? The q-axis circuit of LIM is analogous to the q-axis circuit of a rotating induction motor. Where the q-axis circuit parameters do not vary with the end effects. Because secondary direct-axis entrance currents reduce the direct-axis secondary flux linkage (λ_{dr}), the d-axis circuit of the rotary induction motor cannot be utilized in a LIM study when end effects are considered [14]:

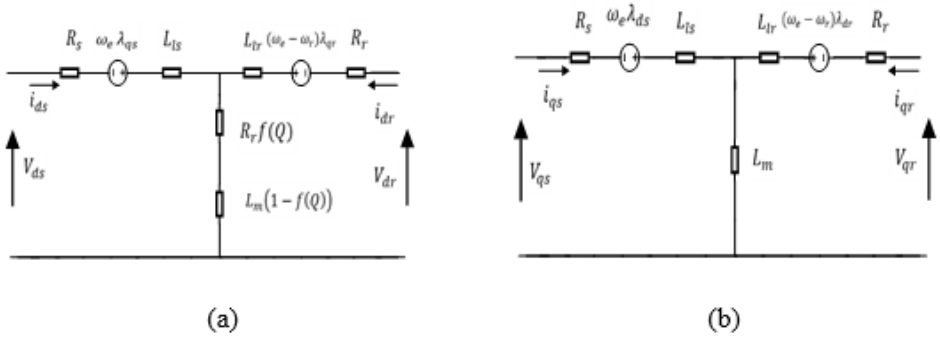

Fig 1. Demonstrates: (a) LIM's d-axis electrical circuit; (b) LIM's q-axis electrical circuit.

Based upon the d-q axis electrical circuit, the voltage equations of primary and secondary (linor) are described in differential equations in the synchronous reference frame given below [14]:

$$V_{ds} = R_s i_{ds} + R_r f(Q)(i_{ds} + i_{dr}) + p\lambda_{ds} - \omega_e \lambda_{qs} \quad (1)$$

$$V_{qs} = R_s i_{qs} + p\lambda_{qs} + \omega_e \lambda_{ds} \quad (2)$$

$$V_{dr} = R_r i_{dr} + R_r f(Q)(i_{ds} + i_{dr}) + p\lambda_{dr} - \omega_{sl} \lambda_{qr} \quad (3)$$

$$V_{qr} = R_r i_{qr} + p\lambda_{qr} + \omega_{sl} \lambda_{dr} \quad (4)$$

Where, (V_{ds}, V_{qs}) and (V_{dr}, V_{qr}) represents the primary and linor voltages in the direct-quadrature axis respectively, R_s and R_r represents the primary and linor resistance respectively, (i_{ds}, i_{qs}) and (i_{dr}, i_{qr}) represents the primary and linor direct-quadrature currents respectively, p represents the differential operator, $(\lambda_{ds}, \lambda_{qs})$ and $(\lambda_{dr}, \lambda_{qr})$ represents flux linkage of the primary and linor in direct -quadrature axis respectively, ω_e represents the angular velocity of the primary, ω_{sl} represents the slip frequency, and Q represents the factor linked to the primary length. $f(Q)$ is indicated as:

$$f(Q) = \frac{1-e^{-Q}}{Q} \quad (5)$$

Where,

$$Q = \frac{D*R_r}{L_r\, v_r} \tag{6}$$

Where, D, L_r, and v_r represents the LIM length, linor self-inductance, and LIM velocity respectively. The primary and secondary flux linkages can be described as [14]:

$$\lambda_{ds} = L_{ls} i_{ds} + L_m\big(1 - f(Q)\big)(i_{ds} + i_{dr}) \tag{7}$$

$$\lambda_{qs} = L_{ls} i_{qs} + L_m\big(i_{qs} + i_{qr}\big) \tag{8}$$

$$\lambda_{dr} = L_{lr} i_{dr} + L_m\big(1 - f(Q)\big)(i_{ds} + i_{dr}) \tag{9}$$

$$\lambda_{qr} = L_{lr} i_{qr} + L_m\big(i_{qs} + i_{qr}\big) \tag{10}$$

Where, $L_{ls}, and\ L_{lr}$ represents the leakage inductance of the primary and linor respectively, and L_m represents the mutual inductance. Thrust Force of linear induction motor can be described as [14]:

$$Fe = \frac{3\pi P}{2\tau_p\, 2}\big(\lambda_{ds} i_{qs} - \lambda_{qs} i_{ds}\big) = M.v' + B.v + F_L \tag{11}$$

Where P represents the number of poles, τ_p is the pole pitch, M is the total mass of the moving part, and B is the viscous friction.

4 Indirect Field-Oriented Control of LIM

The IFOC of LIM is not as simple as the rotary induction motor due to the new resistance and inductance in the excitation branch, both of which are dependent on the motor velocity. As a result, decoupling the thrust and speed is more difficult. In ideally field-oriented control, the secondary flux linkage axis is forced to align with the direct-axis, yielding in [15], [16]:

$$\lambda_{qr} = \frac{d\lambda_{qr}}{dt} = 0 \tag{12}$$

$$\lambda_{dr} = \lambda_r = constant \tag{13}$$

The thrust force demonstrated in (11) can be accurately expressed by the following equation using the IFOC method and given that the electrical time constant is much smaller than the mechanical time constant:

$$F_e = k_f . i_{qs} \tag{14}$$

Where;

$$k_f = \frac{3\pi}{2\tau_p} P \frac{L_m\big(1-f(Q)\big)}{L_r - L_m f(Q)}\ \lambda_{dr} \tag{15}$$

Furthermore, using (3) the feed-forward slip velocity signal is:

$$V_{sl} = \frac{\tau_p . L_m (1 - f(Q)) . i_{qs}^*}{\pi (\frac{L_r}{R_r} - \frac{L_{mf(Q)}}{R_r}) \lambda_{dr}} \tag{16}$$

The decoupling control method uses a dual current controller, that utilized to provide the required regulatory voltages to the space vector pulse width modulation inverter is given as:

$$V_{ds}^* = (current\ controller)(i_{ds}^* - i_{ds}) - \frac{\pi}{\tau_p} V_e L_\sigma(Q) i_{qs}^* \tag{17}$$

$$V_{qs}^* = (current\ controller)\left(i_{qs}^* - i_{qs}\right) + \frac{\pi}{t_p} V_e L_\sigma(Q) i_{ds}^* + \frac{P . L_m \pi}{L_r \tau_p} V_r \lambda_{dr} \tag{18}$$

Where $L_\sigma(Q)$ is the leakage inductance that represented by:

$$L_\sigma(Q) = L_S - L_m f(Q) - \left(L_m\left(1 - f(Q)\right)\right)^2 / (L_r - L_m f(Q) \tag{19}$$

5 A 3-Phase Inverter Depend on Space Vector Pulse Width Modulation

SVPWM (space vector pulse width modulation) is a popular way for controlling the three-phase voltage source inverters (VSI)in applications such as control of induction motors and permanent magnet synchronous motors. The main purpose beyond SVPWM is to divide the 2-dimensional plane into six similar areas, each area has named a sector as demonstrated in Fig 2. Each sector is determined by four vectors, two vectors from these four vectors (v_i, v_{i+1} where $i \epsilon \{1, \dots 5\}$) are named active vectors because when supplied these vectors to the power circuit will produce an output voltage larger than zero, while the other two vectors (V_0 *and* V_7) are named inactive vectors because the entire switches will be off or on [17], [18].

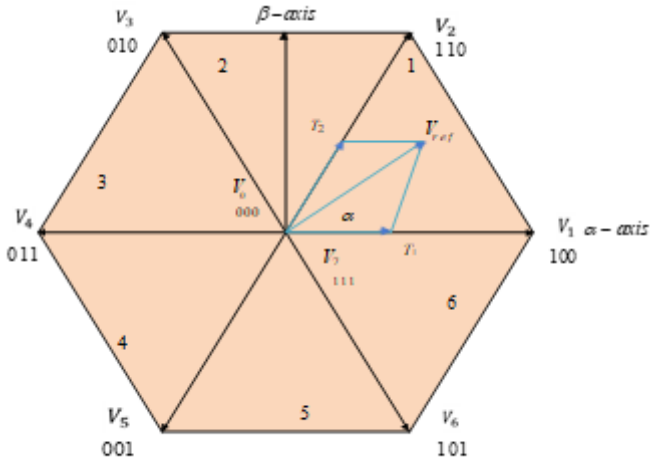

Fig 2. SVPWM 2-D plot.

6 Control Design

6.1 LIM Drive with PID as Velocity Controller

The PID controller will be used to regulate the velocity of the LIM in the first method of IFOC of the LIM drive. Fig 3. depicts the PID controller's principle [19]. PID controllers have 3 main control modes: proportional, integral, and derivative. A PID controller has no idea what performance is required to get the system to the set point. It directs the output in the direction of the process's potential to access the setpoint, and it relies on feedback to do so [20].

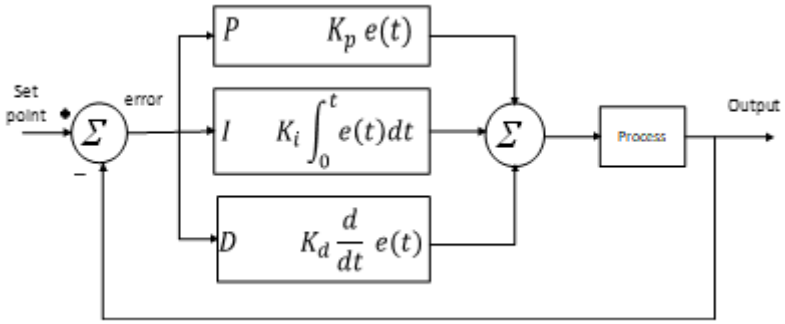

Fig 3. PID control circuit diagram.

6.2 Model Predictive Control as Velocity Controller for LIM Drive

MPC is a commonly used approach in the industry for dealing with control problems that are multivariable and constrained. The algorithm of the MPC is primarily based on [21]:

1. A dynamic internal model of the process,
2. The timeline of previous control actions, and
3. A cost function for optimizing over the prediction horizon.

Model predictive control's key theory is to select a control action by resolving an optimum control issue online repeatedly. This attempts to minimize a performance criterion over the future horizon, perhaps with restrictions on the manipulated inputs and outputs, where future behaviour is calculated using a plant model. There are problems engender with ensuring the stability of closed-loop, reducing online computations, and knob with the model uncertainty. The importance of this control technique becomes apparent when the system's path is determined in advance, as in the case of machine tools, chemical processes, or robots. An easy block diagram depicting the MPC controller's basic structure is demonstrated in Fig 4. In this diagram, a model is utilized to forecast future outputs of the plant using past and present values as well as suggested optimal future control behaviour. The optimizer calculates these actions considering the cost function (which considers future monitoring error) and restrictions. It's worth noting that the control signal is calculated using the system model's expected output and the actual error [21].

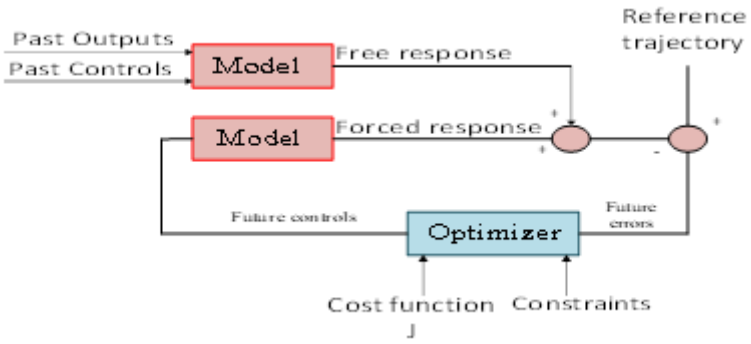

Fig 4. Shows the MPC controller's basic structure.

The overall goal is to reduce the output future error to zero with the least amount of input effort possible. In Generalized Predictive Control, for example, the cost function to be minimalized is a weighted sum of square expected errors and square future control values [21].

$$J(N_1, N_2, N_u) = \sum_{j=N_1}^{N_2} \beta(j)[y\hat{}(k+j|k) - w(k+j)]^2 + \sum_{j=1}^{N_u} \lambda(j)[u(k+j-1)]^2 \quad (20)$$

The J represents the cost function, which is concerned with the error signal minimization, the output's lower and upper prediction horizons denoted by N_1 *and* N_2 respectively, the control horizon is signified by N_u, $\beta(j)$ *and* $\lambda(j)$ denotes a weighting factor, $y\hat{}$ is the forecasting output, the reference trajectory over the future horizon is denoted by the ω, the control signal is represented by a latter u, and the predictive horizons are denoted by j. The sampling instant is denoted by the letter k and $j|k$ denotes that at time k, i will perform iteration j.

The control horizon permits for a reduction in the number of calculated future controls based on the relationship.

$$\Delta u(k+j) = 0 \; for \; j \geq N_u \quad (21)$$

The cost function can include constraints on the control signal, as well as changes in the control signal and output signal.

$$u_{min} \leq u(k) \leq u_{max} \quad (22)$$

$$\Delta u_{min} \leq \Delta u(k) \leq \Delta u_{max} \quad (23)$$

$$y_{min} \leq y(k) \leq y_{max} \quad (24)$$

While keeping the Constraints in mind, the solution of (20) offers the best control signal sequence over the horizon. The motor's transfer function can be calculated using the indirect field-oriented technique as follows:

$$Transfer \; Functiom = \frac{V}{F_e - F_L} = \frac{1}{Ms+B} \quad (25)$$

For ease of execution, the simplistic LIM linearized model defined by (25) is used in the MPC controller's structure.

7 Linear Induction Motor with Suggested IFOC

Fig 5. displays the block diagram of the LIM drive system, which contains the PID or MPC controllers. The measured velocity is utilized for closed-loop control that is being compared to the reference velocity to get the i_{qs}^{*}.

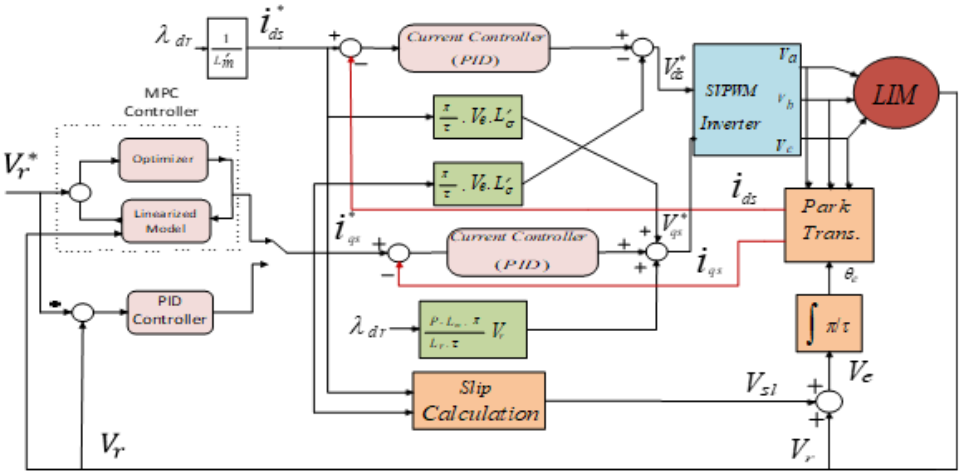

Fig 5. Linear induction motor drive with PID or MPC as a velocity controller.

8 Results and Discussion

To verify the feasibility of the suggested systems and to compare the two controllers' performances, computer simulations were used. This was done using the MATLAB / Simulink software kit. The LIM parameters utilize in this work are specified in Table 2.

Table 2. The parameters of LIM.

Parameters	values
P	4
τ_p (m)	0.0465
$R_s(\Omega)$	13.2
$R_r(\Omega)$	11.78
$L_s(H)$	0.42
$L_r(H)$	0.42
$L_m(H)$	0.4
M(kg)	4.775
B(kg/sec)	53

The response of the PID controller versus the MPC controller for LIM drive velocity control is seen in Fig 6. During the start-up time, the PID controller has a poor transient response. In contrast to the MPC controller, it gets a long time to rise. When there is a load disruption (200 N), the PID controller's response is greatly impacted, as seen in the figure. The suggested

controller is also investigated under parameter uncertainty. In this scenario, the secondary resistance is increased by 25% in the LIM model, although it is held at its nominal value in the slip calculator. Also, the mover mass rose by 50% in the motor model only, this case is showed in Fig 7.

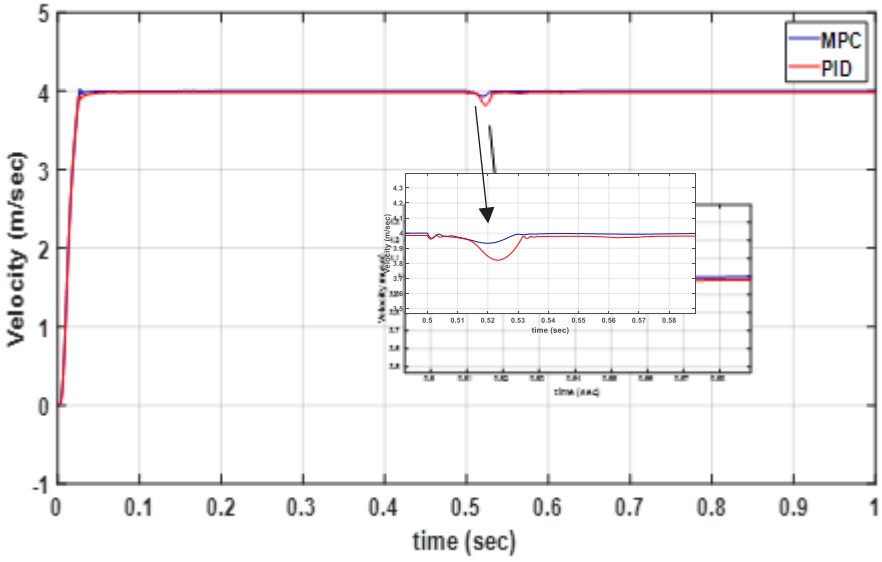

Fig 6. The MPC controller's response of velocity relative to the PID controllers at load disruption.

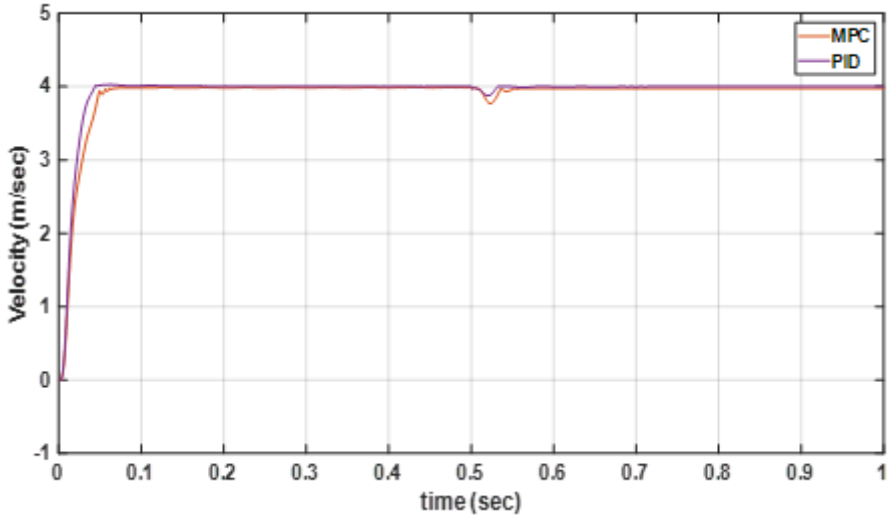

Fig 7. The MPC controller's response of velocity relative to the PID under change of load and parameters variation.

9 Conclusion

Using of the MPC and PID controllers as velocity controllers of the LIM drive has been successfully demonstrated in this study. In addition, the MPC's response is compared to that of a standard PID controller. In the simulation, the LIM drive's output with the model predictive control controller and the PID controller was evaluated. The findings revealed that the model predictive control controller has a fast response time and is resilient in the face of parameter instability and load disturbances.

References

[1] Hamzehbahmani H. Modeling and simulating of single side short stator linear induction motor with the end effect. Journal of electrical engineering. 2011;62(5):302-8.

[2] Hassan A, Mohamed YS, Mohamed TH, editors. Robust control of a field oriented linear induction motor drive. 2006 Eleventh International Middle East Power Systems Conference; 2006: IEEE.

[3] Mannan MA, Murata T, Tamura J, Tsuchiya T, editors. Indirect field oriented control for high performance induction motor drives using space vector modulation with consideration of core loss. IEEE 34th Annual Conference on Power Electronics Specialist, 2003 PESC'03; 2003: IEEE.

[4] Bendjedia M, Tehrani K, Azzouz Y. Design of RST and fractional order PID controllers for an induction motor drive for electric vehicle application. 2014.

[5] Huang Y, Yasunobu S, editors. A general practical design method for fuzzy PID control from conventional PID control. Ninth IEEE International Conference on Fuzzy Systems FUZZ-IEEE 2000 (Cat No 00CH37063); 2000: IEEE.

[6] Diab AAZ, Kotin DA, Pankratov VV, editors. Speed control of sensorless induction motor drive based on model predictive control. 2013 14th International Conference of Young Specialists on Micro/Nanotechnologies and Electron Devices; 2013: IEEE.

[7] Salem FM, Mosaad MI, Awadallah MA. A comparative study of MPC and optimised PID control. International Journal of Industrial Electronics and Drives. 2015;2(4):242-50.

[8] Efheij H, Albagul A, Albraiki NA, editors. Comparison of model predictive control and PID controller in real time process control system. 2019 19th International Conference on Sciences and Techniques of Automatic Control and Computer Engineering (STA); 2019: IEEE.

[9] Kazraji SM, Feyzi M, Sharifian MB, Tohidi S. Fuzzy Predictive Force Control (FPFC) for Speed Sensorless Control of Single-side Linear Induction Motor. Engineering, Technology & Applied Science Research. 2017;7(6):2132-8.

[10] Saleh AL, Obaid BA, Obed AA. Motion control of linear induction motor based on optimal recurrent wavelet neural network-PID controller. International Journal of Engineering & Technology. 2018;7(4):2028-34.

[11] Xu W, Zhang Y, Zeng C, Xiao X, editors. Rotor field oriented control of linear induction machine based on fuzzy self-adapting PI controller. 2012 IEEE International Symposium on Industrial Electronics; 2012: IEEE.

[12] Saleh AL, Obed AA, Al-Yasir YI, Elfergani IT, Rodriguez J, Clarke RW, et al. Anti-windup scheme based on 2DOF-PIλDμ controller for velocity tracking of linear induction motor. International Transactions on Electrical Energy Systems. 2019;29(12):e12134.

[13] Shadabi H, Sadat AR, Pashaei A, Sharifian M. Speed Control of Linear Induction Motor Using DTFC Method Considering end-effect Phenomenon. International Journal on Technical and Physical Problems on Engineering. 2014;6(4):75-81.

[14] Da Silva E, Dos Santos E, Machado P, De Oliveria M, editors. Vector control for linear induction motor. IEEE International Conference on Industrial Technology, 2003; 2003: IEEE.

[15] Boucheta A, Bousserhane I, Hazzab A, Sicard P, Fellah M. Speed control of linear induction motor using sliding mode controller considering the end effects. Journal of Electrical Engineering and Technology. 2012;7(1):34-45.

[16] Hamedani P, Shoulaie A, editors. Indirect field oriented control of linear induction motors considering the end effects supplied from a cascaded H-bridge inverter with multiband hystersis modulation. 4th Annual International Power Electronics, Drive Systems and Technologies Conference; 2013: IEEE.

[17] Hendawi E, Khater F, Shaltout A, Egypt G. Analysis, simulation and implementation of space vector pulse width modulation inverter. Power. 2006;4(T6):T2.

[18] Kubeitari M, Alhusayn A, Alnahar M. Space vector PWM simulation for three phase DC/AC inverter. World academy of science, engineering and technology. 2012;6(12):1402-7.

[19] Hartono H, Sudjoko R, Iswahyudi P, editors. Speed Control of Three Phase Induction Motor Using Universal Bridge and PID Controller. Journal of Physics: Conference Series; 2019: IOP Publishing.

[20] Devi K, Gautam S, Nagaria D. Speed control of 3-phase induction motor using self-tuning fuzzy PID controller and conventional PID controller. International Journal of Information & Computation Technology. 2014;4(12):1185-93.

[21] Diab AZ, Kotin D, Anosov V, Pankratov V, editors. A comparative study of speed control based on MPC and PI-controller for Indirect Field oriented control of induction motor drive. 2014 12th International Conference on Actual Problems of Electronics Instrument Engineering (APEIE); 2014: IEEE.

Comparative Performance of mmWave 5G System for many Beamforming Methods

Shaymaa A. Ahmed[1], Saad A. Ayoob[2], Ali Othman Al Janaby[3]
{shymaa.enp9@student.uomosul.edu.iq[1], Sa_ah_ay@uomosul.edu.iq[2],
ali.mohammed@uoninevah.edu.iq[3]}

The University of Al Mosul[1,2]
Ninevah University[3]

Abstract. With the massive propagation of the mobile phone traffic and demand for high data rate transmission has grown this day, the current cellular spectrum for bands less than 3 GHz is severely deficient and cannot convoy these requirements, which requires the search for suitable solutions for the application of the fifth generation 5G. The potential of millimetre-wave (mm-wave) to provide a high data rate (Gigabits per second) has attracted great interest to become a broadband candidate for the fifth generation of cellular communications networks. To increase the spectral efficiency of cellular networks, Massive multi-input multi output (MMIMO) is considered one of the most promising methods, by equipping the base station with antenna arrays with hundreds or thousands of active elements with the use of beamforming technology and conducting coherent processing on both sides of the transmitter and receiver. In this paper, two mm-wave frequencies(28GHz and 73GHz) have been compared in terms of spectrum efficiency using a massive MIMO using two beamforming methods: conjugate beamforming (CB) and zero-forcing (ZF).

Keywords: Beamforming, Massive MMIMO, mm-wave, CB, ZF, 5G.

1 Introduction

Increasing demands from users for an advanced communication mode, in addition to voice communication, have led to significant growth in the volume of data traffic with the increased use of video communications, social media communication, and access to cloud data. To meet these requirements, it was necessary to use higher frequencies than in the fourth generation, and thus use more bandwidth. The frequency range (30-300 GHz) has been receiving a lot of interest in the fifth-generation communications in recent times, as it was called the millimetre wave (mm Wave) because it has a short wavelength measured in millimetres. To meet the requirements of the fifth generation, the main key to success in achieving the required large data rates is expected to be using millimetre-wave in communications. But the main problem with the use of millimetre-wave is its short propagation distance, which leads to signal attenuation due to oxygen absorption, object blocking, and signal scattering problems as this can lead to the limited coverage of the eNodeB base station. To alleviate this problem, it was necessary to use a massive MIMO technology [1][2]. MIMO technology uses multiple antennas in transceivers to transfer more data simultaneously. Attenuation due to millimetre-wave weakening cannot be compensated with MIMO technology. Thus, more data rate can be provided in addition to more

IMDC-IST 2021, September 07-09, Sakarya, Turkey
Copyright © 2022 EAI
DOI 10.4108/eai.7-9-2021.2314818

power gain to compensate for millimetre-wave attenuation by adopting Massive multi-input multi-output (MMIMO)instead of MIMO technology [3].

The main contribution of this paper can be explained as follows:

1. We compute the spectral efficiency to the number of UEs k by proposing downlink MU massive MIMO on mm-wave channel with the two precoding schemes ZF, CB at indoor LOS environments by using two frequencies (28GHz and 73GHz).
2. We increase the number of BS antennas from 100 to 500 and show how this influences spectral efficiency.
3. Our results show that the spectral efficiency increases by increasing the number of BS antennas (N) for different linear precoding schemes. We also concluded that a better spectral efficiency can be obtained at 28GHz.

The other paragraphs of this paper will be prepared as follows; Section 2 reviews the related work. Section 3 overviews the 5G. Section 4 presents the proposed scheme. Finally, section 5 completes the simulation evaluation and conclusion.

2 Related works

In [4], the author presents a 3D statistical channel model for millimetre-wave communications LOS and NLOS for the link, local area, and tracking CIRs, with random carrier frequency, signal bandwidth, and antenna bandwidth, which is invaluable in the design of the fifth generation of cellular millimetre-wave networks. and random antenna frequency, they show good agreement between the model and the published RMS DS as well as a MATLAB-based statistical simulator was implemented to generate a large set of PDPs and 3D power angle spectra, which shows good agreement with field measurements, thus validating 3-D SSCM to design the next generation of wireless systems that will use sub-6 GHz and mm Wave models to design filters, multi-element antenna arrays, and mm Wave transceivers.
In [5], the researchers compared three large-scale propagation path loss candidate models for use over the entire microwave and millimetre-wave radio spectrum: the mm Wave alpha-beta-gamma (ABG) model, the near free space reference distance (CI) model, and the CI model with the exponent of frequency-weighted path loss (CIF).
In [6], the authors used a downlink multi-user mm Wave system with an efficient hybrid analogue/digital beamforming algorithm for systems. and demonstrated that massive multiuser MIMO could be an ideal candidate for a mm Wave communications system. And they proved that the proposed algorithm, through the simulation results, and with the increase in the number of users outperform the traditional hybrid beam configuration as it improved the sum rate and thus led to better performance for the bit error rate (BER).
In [7], the researchers presented specifics and applications of a new channel simulation software called NYUSIM, which can be used to configure actual temporal and spatial channel responses to uphold realistic physical layer simulations, link layer, and 5G cellular communication layout.
In [8], The researchers describe the results of an internal experimental validation test and discuss a multi-user 28 GHz multi-input (MIMO) output using of Active Digital MIMO System (AAS)

(360 elements) for application on a 5G base station. This report was the first experimental validation of a multi-user MIMO using 28 GHz digital AAS.
In [9], the researchers studied resource allocation as the need to increase capacity requires adding more antennas and the use of Massive multi-input multi-output (MMIMO) allows multiple users to be scheduled to use the same frequency resource simultaneously.
In [10], the researchers provided a comprehensive overview of the factors affecting millimetre-wave propagation such as the effects of the surrounding environment (atmospheric attenuation, free space path loss, rain and foliage attenuation, material penetration losses) In addition, many factors influence the propagation properties of the wave. The researchers discussed the radio-frequency spectrum, organizing 5G issues, and the methods of modelling for the channel. Current channel scaling campaigns and modelling methods for the most interesting 5G communication scenarios, such as millimetre-wave communications, massive multi-input communications, multiple access, and performance analysis were also presented
In [11], this thesis is the first to introduce deep learning (DL) frame for channel estimation in a large smart surface (LIS) with the help of a multi-input system (MIMO). Explain his superior performance.
In [12], the researchers proposed power distribution in the small cell to reduce path loss by specifying large power and controlling the distributed power to reduce the high cost and power consumption where millimetre wave hybrid beamforming exploits large bandwidth which reduces the large path loss in the Rayleigh fading channel.
In [13], this paper, the researchers propose an intelligent downlink reflective surface (IRS) supported by non-orthogonal mm Wave multiple access (NOMA) and MIMO Massive antenna with lens antenna array where individual antenna users are grouped without direct correlation but are connected to the base station (BS) with the help of the IRS as a single NOMA group. The performance of the millimetre-wave beam area-weighted sum average supported by non-orthogonal multiple access (NOMA) was verified by simulations.

3 An Overview of the Most Important 5G Technologies

In this section, an overview of the 5G system massive multi-input multi output (MMIMO) and Millimetre Wave and Beamforming schemes:

3.1 Massive MIMO Technique

Massive Multi-Input Multi Output (MMIMO) technology is now a cornerstone of upcoming 5G systems, where base stations are equipped with hundreds or a few thousand arrays of antennas that achieves a lot of performance gains in terms of reliability, security, and improved efficiency (spectrum and energy) relative to traditional MIMO [14]. One of the most important ways to increase the efficiency of the spectrum is by sending many simultaneous parallel focus beams to serve each user individually in place of using a sole omnidirectional beam for serving all users, this can be achieved by using Massive Multi-Input Multi Output (MMIMO) as shown in Fig 1 [15]. Massive Multi-Input Multi-Output (MMIMO) use is cheaper than conventional systems by replacing 50-watt super linear amplifiers with hundreds of mill watt low power amplifiers[15][16]. Massive Multi-Input Multi Output (MMIMO) provides high energy efficiency as BS concentrates the emitted power on exactly spatial directions where the user is located and thus Massive Multi-Input Multi Output (MMIMO) reduces limitations on the

linearity, accuracy, and RF gain requests of the amplifiers used [17]. It also reduces interference with other channels because it uses a tapered beam. The Massive multi-input multi-output (MMIMO) technology significantly reduces latency at the air interface because it uses many antennas and uses beamforming that solves the fading problem of the transmitted signal [15].

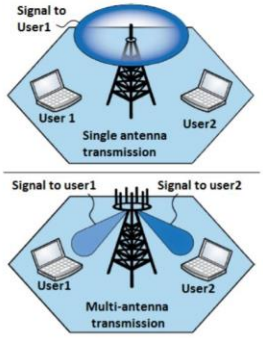

Fig. 1. Omnidirectional antenna and multi-directional antenna.

3.2 Millimetre wave

Millimetre-wave is one of the promising solutions to meet the unprecedented demands to provide a high data rate that keeps pace with the requirements of the fifth generation, due to its wide bandwidth [18]. The mm-wave contains frequency bands ranging from (30 - 300) GHz with wavelengths ranging from 1 to 100 mm and it has a basic 10Gb/s bandwidth access with the highest data rates [19][20]. However, due to its short wavelength, it suffers from large-signal attenuation caused by oxygen intake, object blocking, and signal scattering problems which lead to shortening of the wave propagation distance and thus shortening the coverage range of the eNodeB base station in mobile communications. Therefore, the use of Massive Multi-Input Multi-Output (MMIMO) and beamforming techniques is necessary to avoid the problems associated with using mm Wave [20].

3.3 Beamforming

The Massive Multi-Input Multi-Output (MMIMO) and mm Wave technologies provide solutions to many technical challenges facing the application 5G in the future. Spectrum and energy efficiency are enhanced in wireless communication networks by deploying a massive number of antennas in the transmitter and/or receiver (Massive Multi-Input Multi-Output (MMIMO)). To achieve the required performance gains in the environment in which the signal suffers from scattering, simple beamforming strategies must be used, such as the Transmission of the Maximum Rate (MRT) or Zero Forcing (ZF) [21]. Beamforming is a technique that focuses the signal on a beam in a specific direction towards a specific user rather than sending it equally in all directions. To increase the capacity, the beamforming technique must be applied, which leads to an increase in the strength of the received signal for each user while reducing the

strength of the interference signal from other users [22]. ZF precoding considers the interference between users and disregards the effect of noise, while in MRT, BS is trying to maximize SNR received regardless of the effect of multi-user interference(5). We use two conventional linear detectors MRC and ZF and they can be modelled as shown in equation (1) [16]:

$$A = \begin{cases} G & for\ CB \\ G(G^H G)^{-1} & for\ ZF \end{cases} \quad (1)$$

Where A is an (N × K) linear detector matrix that depends on channel G.
$H \in C^{Nt \times K}$
N is the number of antennas and K is the number of UEs [16].

4 Proposed Model

As we mentioned earlier, a millimetre-wave is one of the most important solutions to add a huge amount of bandwidth that is currently required. But there are important components of its modelling, most notably [18]:

1- Spatial Consistency: Shows incessant and actual channel progress accompanying the user's equipment path within the local zone [23] [24].
2- Human Blockage Shadowing Loss: this means loss due to somebody close to the mobile phone who may block the transmission signal. This loss may cause several hundreds of milliseconds [25].
3- Outdoor-to-Indoor (O2I) penetration: modern buildings are fabricated by material that induced a big permeation loss for mm-wave signal transferred from outdoor to indoor and in opposite direction [26]. The wave channel model components are shown in Fig 2:

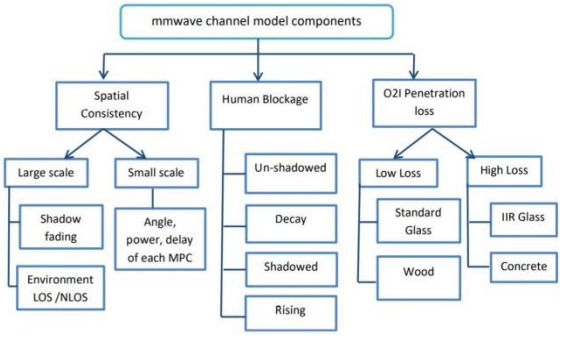

Fig. 2. mm-wave channel model components.

In addition to many important factors that go into calculating millimetre-wave path losses, such as barometric pressure, humidity, temperature, rain rate, polarization, and foliage loss [27]. We Propose a downlink multiuser Massive Multi-Input Multi-Output (MMIMO) with mm-wave

channel by using two precoding schemes ZF, MRT which is also called conjugate beamforming (CB). Perfect channel estimation and small-scale fading channels are assumed. The LOS MIMO channel matrix, G, is modelled as shown in equation (2):

$$G_l = \frac{\lambda}{4\pi R} \exp\left(-j\frac{2\pi}{\lambda}\, d_l\right) \quad (2)$$

Which contains the l_{th} column of the Nr × Nt.
Where G_l indicates the l_{th} transmit antenna vector which contains all channel routes between the l antenna and all receive antennas, and λ=c/f, where λ is carrier wavelength, and c is the speed of light, and f is the carrier frequency, and R represents the space between the transmitter antenna array and the receiver antenna array, and d_l is the distance vector between l transmit antenna and all receive antennas [28].

5 Proposed Model Configuration and Simulation

We study the performance of multi-user Massive multi-input multi output (MMIMO) mm Wave channels for the indoor environment by using MATLAB (m.file) and sketch spectral efficiency (SE) results concerning no. of UEs (K) by applying two beamforming methods, for example., Conjugate Beamforming (CB), Zero-Forcing (ZF) by using the assumptions in the Table 1.

Table 1. Simulation assumption.

Parameter	Setting
$\boldsymbol{d_l}$	0.5 λ
Transmit power	30dBm
Carrier frequencies	28GHz,73GHz
No.of base station antenna (N)	100,500
Noise variance	-80dBm
R	200m
Path loss exponent for 28GHz	1.8-1.9
Path loss exponent for 73GHz	2.0

Fig 3 shows the comparison between the spectral efficiency versus no. of users (k) for 28GHz and 73GHz for indoor LOS environments at N=100 and N=500 respectively.

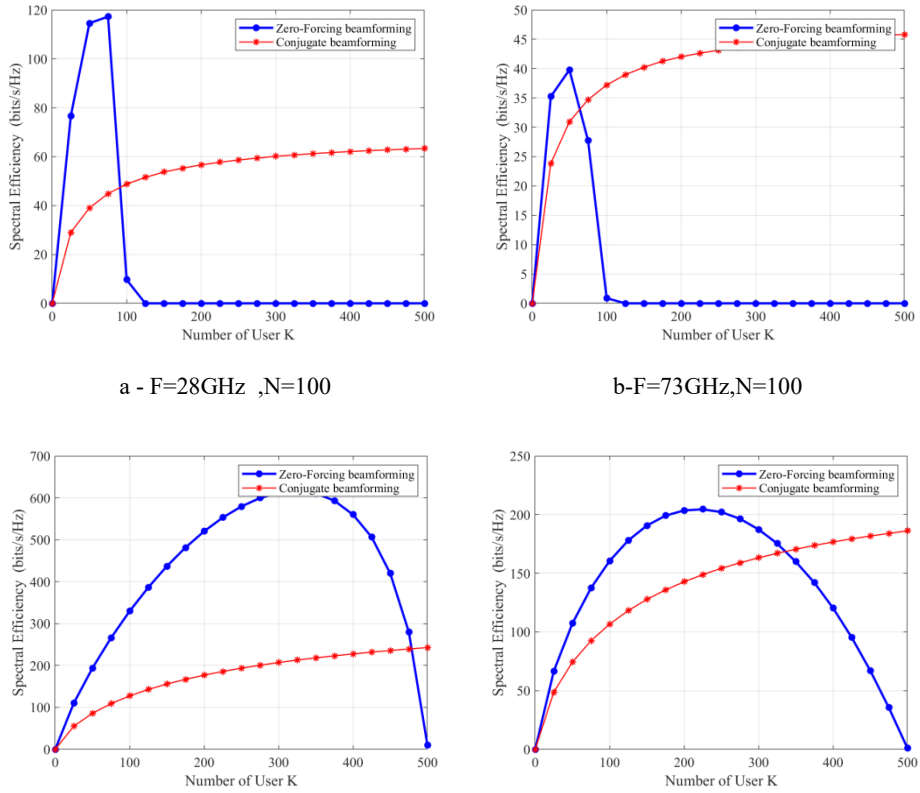

a - F=28GHz ,N=100

b-F=73GHz,N=100

c- F=28GHz, N=500

d-F=73GHz, N=500

Fig. 3. Comparison of spectral efficiency for different frequencies (28 and 73 GHz) and different no. of antennas concerning no. of UEs k.

We can summarize the above figures in the following Table 2:

Table 2. The maximum value of the spectrum efficiency for ZF precoding schemes.

Frequency (GHz)	No.of BS antennas	Spectral efficiency(bit/sec/Hz)
28	100	117.2
28	500	612.3
73	100	39.79
73	500	203.6

6 Conclusion

Massive multi-input multi-output (MMIMO) with mm-wave is the most enabling key for the next generation of communication. In this paper, we compare two mm-wave frequencies; for example, 28GHz and 73GHz by applying multi- user Massive Multi-Input Multi-Output (MMIMO) and obtain the spectral efficiency results by using Zero-Forcing (ZF) and conjugate beamforming precoding schemes. The results show that the spectral efficiency at 28GHz is better than it at 73GHz and show that there is a remarkable improvement in the spectral efficiency when the no. of BS antennas increased. We also note that the ZF precoding scheme outperforms the CB, but when no. of UEs increased we note that CB is better than ZF because its arithmetic burden scales as (MK) while ZF complexity scales as (MK^2).

Acknowledgement

This work was supported by the Electrical Department, Engineering College, Mosul University.

References

[1] Islam MS, Kamruzzaman M, Jessy T, Zahan MS, Hassan MS. Performance Analysis of Massive MIMO for 5G Wireless Communication Systems. International Conference on Computing, Communication, and Automation (ICCCA2016); 29-30 April 2016; Greater Noida, India. IEEE; 16 January 2017. p. 1579-1583.

[2] Poudel KN, Gangaju S. Spectral Efficiency, Diversity Gain, Multiplexing, Capacity Analysis for Massive MIMO, 5G Communication System. International Conference on Networking and Network Applications; 16-19 Oct. 2017; Kathmandu, Nepal. IEEE; 08 January 2018. p. 133-137.

[3] Phuangkor W, Uthansakul P. Gain Compensation of Massive MIMO for Shifting from 4G to 5G Mobile Communications. 2019 11th International Conference on Information Technology and Electrical Engineering (ICITEE) ; 10-11 Oct. 2019 ; Pattaya, Thailand. IEEE; 12 December 2019. p. 1-6.

[4] Samimi MK, Rappaport TS. 3-D millimeter-wave statistical channel model for 5G wireless system design. IEEE Transactions on Microwave Theory and Techniques. 2016 Jun 28;64(7):2207-25.

[5] Sun S, Rappaport TS, Thomas TA, Ghosh A, Nguyen HC, Kovács IZ, Rodriguez I, Koymen O, Partyka A. Investigation of prediction accuracy, sensitivity, and parameter stability of large-scale propagation path loss models for 5G wireless communications. IEEE Transactions on Vehicular Technology. 2016 Mar 16;65(5):2843-60.

[6] Jing J, Xiaoxue C, Yongbin X. Energy-efficiency based downlink multi-user hybrid beamforming for millimeter wave massive MIMO system. The Journal of China Universities of Posts and Telecommunications. 2016 Aug 1;23(4):53-62.

[7] Sun S, MacCartney GR, Rappaport TS. A novel millimeter-wave channel simulator and applications for 5G wireless communications. In2017 IEEE International Conference on Communications (ICC) ;2017 May 21 ; Paris, France. IEEE; 31 July 2017. p. 1-7).

[8] Manini M, Gueguen C, Legouable R, Lagrange X. Study of MIMO channel matrices correlation to optimize resource allocation algorithms in multi-users 5G. In2019 12th IFIP Wireless and Mobile Networking Conference (WMNC) ; 11-13 Sept. 2019; Paris, France. IEEE; 24 October 2019. p. 162-166 .

[9] Uwaechia AN, Mahyuddin NM. A comprehensive survey on millimeter wave communications for fifth-generation wireless networks: feasibility and challenges. IEEE Access. 2020 Mar 30;8:62367-414.

[10] Elbir AM, Papazafeiropoulos A, Kourtessis P, Chatzinotas S. Deep channel learning for large intelligent surfaces aided mm-wave massive MIMO systems. IEEE Wireless Communications Letters. 2020 May 11;9(9):1447-51.
[11] Abdullah Q, Salh A, MohdShah NS, Abdullah N, Audah L, Hamzah SA, Farah N, Aboali M, Nordin S. a Brief Survey and Investigation of Hybrid Beamforming for Millimeter Waves In 5G Massive MIMO Systems. arXiv preprint arXiv:2105.00180. 2021 May 1
[12] Liu P, Li Y, Cheng W, Gao X, Huang X. Intelligent Reflecting Surface Aided NOMA for Millimeter-Wave Massive MIMO with Lens Antenna Array. IEEE Transactions on Vehicular Technology. 2021 Mar 23.
[13] Ju S, Xing Y, Kanhere O, Rappaport TS. Millimeter wave and sub-terahertz spatial statistical channel model for an indoor office building. IEEE Journal on Selected Areas in Communications. 2021 Apr 23;39(6):1561-75.
[14] Larsson EG, Edfors O, Tufvesson F, Marzetta TL. Massive MIMO for next generation wireless systems. IEEE communications magazine. 2014 Feb 12;52(2):186-95.
[15] A.O.M. Al Janaby, "5G downlink throughput enhancement by beam consolidation at vacant traffic," Journal of Communications Software and Systems, vol. 15, no. 4, pp. 311–316, Dec. 2019.
[16] Ngo HQ, Larsson EG, Marzetta TL. Energy and spectral efficiency of very large multiuser MIMO systems. IEEE Transactions on Communications. 2013 Feb 7;61(4):1436-49.
[17] Rusek F, Persson D, Lau BK, Larsson EG, Marzetta TL, Edfors O, Tufvesson F. Scaling up MIMO: Opportunities and challenges with very large arrays. IEEE signal processing magazine. 2012 Dec 10;30(1):40-60.
[18] Ju S, Kanhere O, Xing Y, Rappaport TS. A millimeter-wave channel simulator NYUSIM with spatial consistency and human blockage. In2019 IEEE Global Communications Conference (GLOBECOM) ; 9-13 Dec. 2019 ; Waikoloa, HI, USA. IEEE ; 27 February 2020 . p. 1-6 .
[19] Budalal AA, Islam MR, Habaebi MH, Rahman TA. Millimeter Wave Channel Modeling–Present Development and Challenges in Tropical Areas. In2018 7th International Conference on Computer and Communication Engineering (ICCCE); 2018 Sep 19; Kuala Lumpur, Malaysia . IEEE; 19 November 2018. p. 23-28.
[20] Bogale TE, Le LB. Massive MIMO and mmWave for 5G wireless HetNet: Potential benefits and challenges. IEEE Vehicular Technology Magazine. 2016 Feb 3;11(1):64-75.
[21] Swindlehurst AL, Ayanoglu E, Heydari P, Capolino F. Millimeter-wave massive MIMO: The next wireless revolution. IEEE Communications Magazine. 2014 Sep;52(9):56-62.
[22] Ali E, Ismail M, Nordin R, Abdulah NF. Beamforming techniques for massive MIMO systems in 5G: overview, classification, and trends for future research. Frontiers of Information Technology & Electronic Engineering. 2017 Jun;18(6):753-72.
[23] Ju S, Rappaport TS. Simulating motion-incorporating spatial consistency into nyusim channel model. In2018 IEEE 88th Vehicular Technology Conference (VTC-Fall) ;2018 Aug 27 ; Chicago, IL, USA . IEEE; 15 April 2019 . p. 1-6.
[24] Ju S, Rappaport TS. Millimeter-wave extended NYUSIM channel model for spatial consistency. In2018 IEEE Global Communications Conference (GLOBECOM); 2018 Dec 9; Abu Dhabi, United Arab Emirates. IEEE; 21 February 2019 .p. 1-6.
[25] MacCartney GR, Rappaport TS, Rangan S. Rapid fading due to human blockage in pedestrian crowds at 5G millimeter-wave frequencies. InGLOBECOM 2017-2017 IEEE Global Communications Conference; 2017 Dec 4; Singapore.IEEE; 15 January 2018. p. 1-7.
[26] Haneda K, Zhang J, Tan L, Liu G, Zheng Y, Asplund H, Li J, Wang Y, Steer D, Li C, Balercia T. 5G 3GPP-like channel models for outdoor urban microcellular and macrocellular environments. In2016 IEEE 83rd vehicular technology conference (VTC spring);2016 May 15; Nanjing, China .IEEE; 07 July 2016 .p. 1-7.
[27] Liebe HJ, Hufford GA, Cotton MG. Propagation modeling of moist air and suspended water/ice particles at frequencies below 1000 GHz. In AGARD. 1993 Nov.
[28] Raed M, Abdelhamid A. Space modulation techniques. New Jersey, USA: Wiley; 2018 May 8.chapter 7, SMTs for Millimeter-Wave Communications; p. 171-183

PC/PLC Based Simultaneous Running of More than One Laboratory Experiments Using WxPython and Pymodbus

Jawad Radhi Mahmood[1], Ramzy Salim Ali[2]
{jawad.mahmood@uobasrah.edu.iq[1], ramzy.ali@uobasrah.edu.iq[2]}

Department of Electrical Engineering, College of Engineering, University of Basrah, Basrah 610001, Iraq[1]
Department of Electrical Engineering, College of Engineering, University of Basrah, Basrah 610001, Iraq[2]

Abstract. The Programmable Logic Controllers (PLCs) allow many industrial fields to input and output devices to be connected directly to their input and output points or modules. They also allow communication with more than one device through their communication ports. For these issues, the PLCs can be used to play an important role in supporting the education process. In this context, this paper introduces PC/PLC based laboratory platform to allow the simultaneous utilization of three experimental setups, one for Direct-On-Line (DOL) and star/delta starting of three-phase induction motor, one for the single-phase AC line controller, and one for the Inverse-Definite-Minimum-Time (IDMT) overcurrent protective relay. The first one allows the user to monitor and record the three-phase induction motor's current history under DOL and star/delta starting methods. The second one allows its user to understand the difference between the magnetic relay and Solid-State-Relay (SSR), run the AC line controller in ON/OFF, phase angle, and integral cycle modes of operations, and understand the basic construction and operation of soft starters. With the third setup, the user can test the various standard characteristic curves of the IDMT overcurrent relay. This platform uses three Personal Computers (PCs) and one Programmable Logic Controller (PLC). Each PC uses Wxpython (Graphic user interface toolkit of python programming language) and PyModbus communication utility to interface its related set-up to the central PLC.

Keywords: Direct-On-Line DOL, Solid-State-Relay (SSR), Programmable Logic Controller (PLC); WxPython; Pymodbus.

1 Introduction

An accurate account of engineering practice could help educators explain the relevance of coursework to students, helping to provide appropriate motivation for learning [1]. On the level of universities, the engineering practice could, to some extent, be achieved through instructional laboratories which form an essential part of the engineering curricula [2]. They allow students to engage with real hardware, components, material and validates their conceptual knowledge, and learn from trial and error [3]. They provide practical knowledge that goes beyond the mere theory[4]. In general, Most lecturers feel that laboratory work helps to develop personal skills [5]. From this satisfaction and understanding, some attempts have been done to develop engineering laboratories in engineering universities and colleges. As an example of these attempts, Yousif I. AlMashhadany[6] introduced programable logic controller-based platform for classical control laboratory. J.M. Fernandes & T. Van Niekerk [7] introduced a programmable logic controller-based laboratory for nonlinear systems (ball-on-wheel balancing

IMDC-IST 2021, September 07-09, Sakarya, Turkey
Copyright © 2022 EAI
DOI 10.4108/eai.7-9-2021.2314817

system). Mahmood et.al. [8] developed a PLC-HMI driven platform to control the speed of a three-phase induction motor using a fuzzy logic controller and the traditional Proportional-Integral-Derivative (PID) controller. Gerard Geaney and Tom O'Mahoney[9] introduced a remote laboratory for PLC education by using three PLCs (S7-1200 as a master PLC to allow the student to select either S7200 or Micrologic 1000 analog for programming). O ¨zgu¨ r Cemal O ¨ zerdem [10], Introduced two experimental setups using PLC (one for the elevator and the second for metal ball carrier). Luiz F Alves, Dennis Brand, and An Oliveira [11] discussed the use of a plant driven by four PLCs and allows the simultaneous running of three setups (water temperature in the plant, water level in two reservoirs, and water flow rate through the plant). Mahmood et al. [12] also presented a PLC/HMI-based real-time educational power system protective relay platform, to facilitate the understanding of the operating principle of the Inverse Definite-Minimum-Time relays (IDMT).

The current paper introduces an educational platform that allows the simultaneous utilization of three instructional setups through the cooperation of two computational platforms (the personal computer and the programmable logic controller) with the help of the well known Python programming language and its Wxpython graphic user interface kit and Pymodbus utility which is a full Modbus protocol implementation.

The Programmable logic controller (PLC) is a computer-based, solid-state, single-processor device[13]. It can accept digital and analog input and output signals coming from the industrial field input and output devices. PLC comes with built-in communication ports usually 9-pin RS232, RS-422, RS-485, and Ethernet [14]. PLC supports more than one operation mode, the repetitive or scan mode of operation which has been adopted in this work is the main operation mode that each PLC should have at least one of it. In this mode, the user application program is repetitively executed from its start statement to its end statement as long as the PLC is in the run mode. Here the program execution does not depend upon any condition. From the point of view of programming languages, all the PLCs support ladder language, and some of them in addition to the ladder language support function block and /or structured text programming languages. In this work, the structured text programming language has been used. This language is very close to the well-known Pascal language.

Wxpython is a cross-platform python programming language. Its library allows programmers to develop highly Graphical User Interfaces (GUI) for their programs using Menu bars, Menus, Panels, StaticText, TextCtrl, RedioItem, CheckItem, Button, ToggleButton, ComboBox, etc. In WxPython all the elements of a GUI are contained within top-level windows such as wx.Frame or wx.Dialog [15].

Modbus protocol is widely used in the industrial field. It supports client/server communication between field devices such as PLCs, VFDs, and smart input/output units. Modbus devices are provided with well defined Modbus memory map. Pymodbus is a full Modbus protocol implementation. It uses asynchronous communication over TCP/IP connections [16]. It allows reading of data from PLCs and writing data to PLCs over Ethernet connection[17]. The PLCs data can be accessed as bit(s) and word(s).

2 The Work Aim

Most of the students feel there is a gap between theory and practice and this untrue feeling hurts their cooperation with the teaching staff. So, to alleviate or eliminate this untrue feeling,

the teachers should show their students the concrete relationship between theory and practice through experimental work.
The present work aims to achieve the above target and increase the engineering teaching process efficiency through integrating what is explained in the classroom with the real-time behaviour of the covered items or topics.

3 The Proposed Platform Architecture

The proposed platform architecture consists of two parts. These are the hardware and the software parts.

3.1 The Hardware Part

As stated above, the proposed work supports the simultaneous running of three experiments. The details of this structure are shown in Fig 1 and Fig 2, where Fig 1 introduces the general layout, and Fig 2 details the wiring of each setup and its relation with the PLC input and output points.

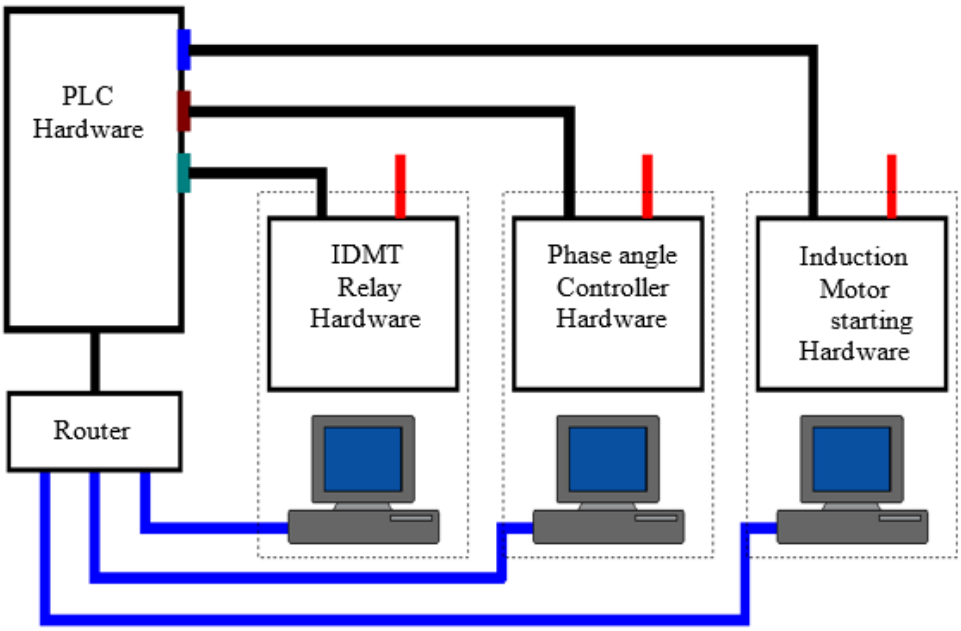

Fig 1. Hardware Setup.

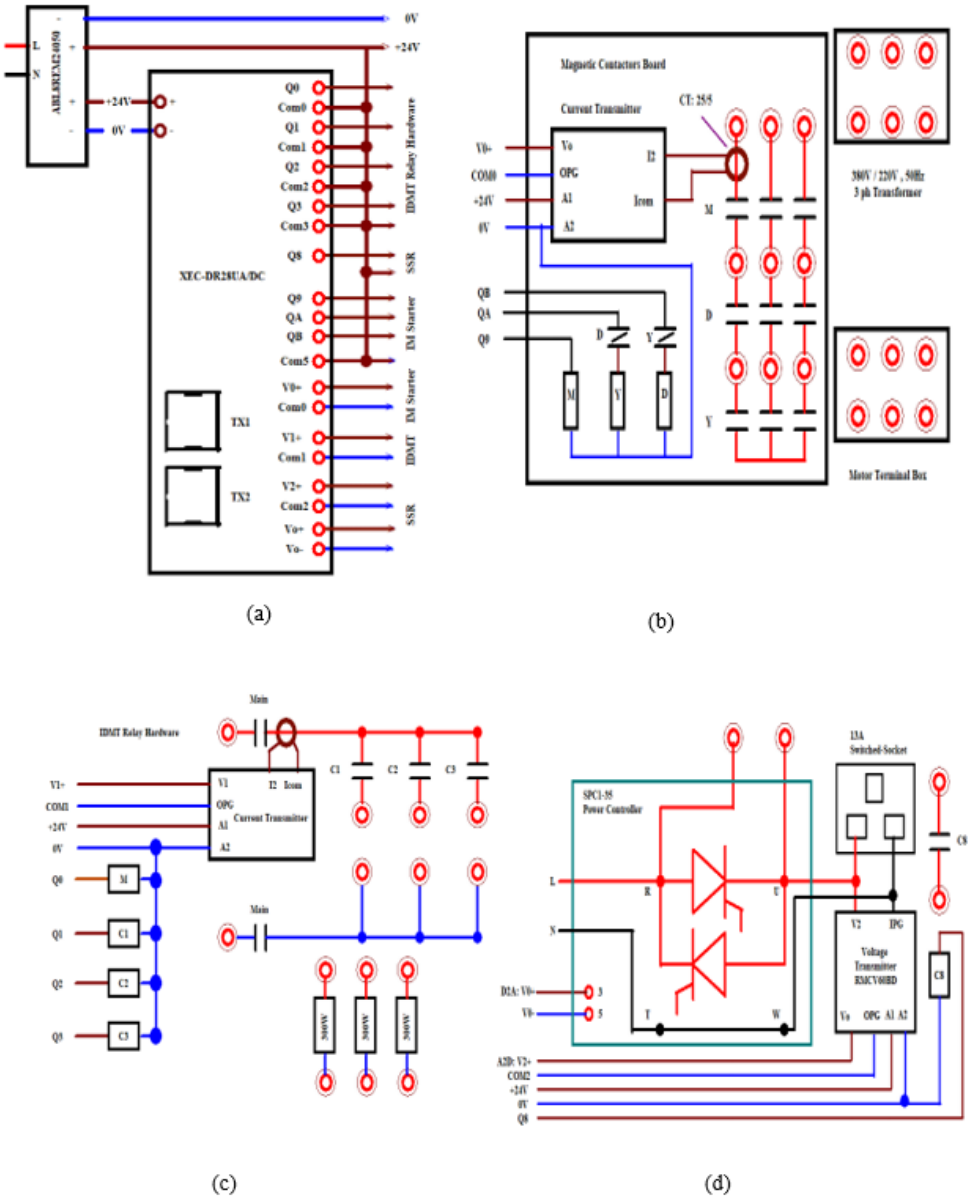

Fig 2. Wiring details of the platform.

3.2 The Software Part

The three-python programmed personal computers (PCs) and the programmable logic controller (PLC) share this part. Each PC is a Modbus TCP/IP client and plays the role of HMI, whereas the PLC is their Modbus TCP/IP server.

3.2.1 The WxPython Based Graphical User Interfaces

The proposed platform allocates one interfacing screen for each setup. Fig 3 represents that of the three-phase induction motor starting setup. Through this screen, the user can start the motor under direct -online and star-delta starting. The starting mode selection is done via the menu labelled “Mode of Operation”. The display labelled menu enables the real-time monitoring of the motor line current or displays the motor line current history. The ON /OFF commands are issued using “Start and Stop “for the Star-delta mode and “Main”, “Star”, and “Delta” for the direct-on-line mode of operation. The sampling time is user-defined, and this affects the recorded details of the current.
Fig 4 is the interfacing screen of the solid-state AC line controller (phase angle controller or power controller). Its “operation Mode” menu allows the user to select one of the supported modes represented by ON/OFF, Integral Cycle, phase angle, and soft starter control modes in addition to the independent switching of the magnetic contactor mode. The display labelled menu allows the real-time monitoring or displaying the history of the r.m.s value of the output voltage. This screen also gives an opportunity to the user to test different values for the ramp time (for soft starting mode), ON and OFF periods (for the integral cycle mode), and the firing angle (for phase angle mode).

Fig 5 is the screenshot of the IDMT overcurrent setup interfacing screen. Through its “IDMT Characteristics” labelled menu, this interfacing screen allows the user to run this setup under different standard characteristic curves (IEC Normal Inverse, IEC Very Inverse, IEC Extremely Inverse, IEEE Moderately Inverse, IEEE Very Inverse, IEEE Extremely Inverse). This screen involves two input boxes to set the Time Multiplier Setting (TMS), the pickup current (Is), 4 set switches (the green coloured), and 4 reset switches (the red coloured).

3.2.2 The PLC as a Modbus Server

The PLC as a Modbus device can be used as a client or server. In this work, it has been used as a server whereas the PCs take the roles of clients. The PCs as clients can do the following with the PLC:

- Read and write the PLC digital outputs as single or multiple
- Read the PLC digital inputs.
- Read the PLC storage memory as 16-bit register(s)
- Write the PLC storage memory as 16-bit register(s)
-

The read/write processes are executed for the server Modbus memory area. In PLC, this area can be configured by the programmer. In this work, the PLC Modbus memory setting is as shown in Table 1, and this means the three PCs will communicate with the PLC within this setting. They can read the PLC discrete inputs and outputs (coils), can write the PLC discrete outputs, can read the PLC memory words starting from %MW0, and can write the PLC memory words starting from %MW100 which is treated as register number 0 in the write registers commands. Table 2 details how the current three clients share this memory setting and command the PLC.

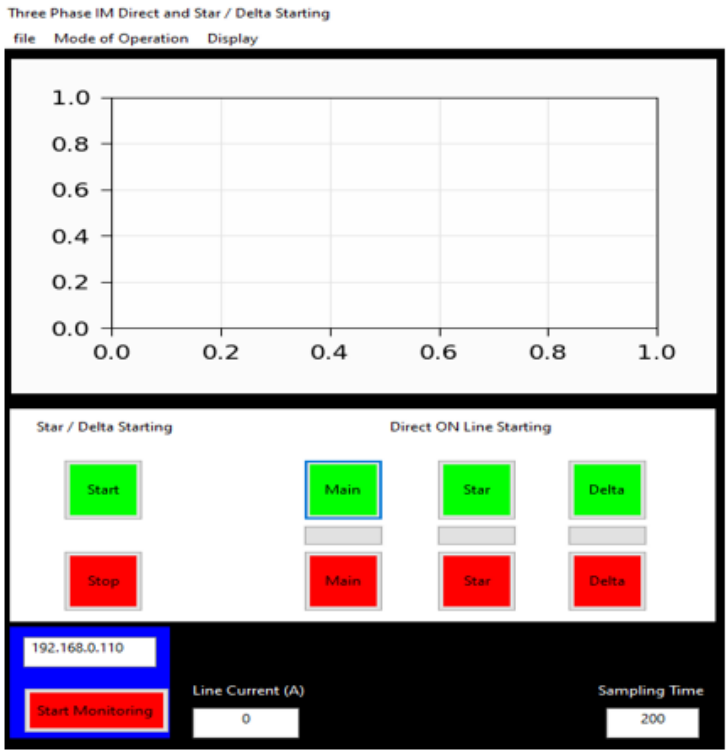

Fig 3. Induction motor startin setup inerfacing screen.

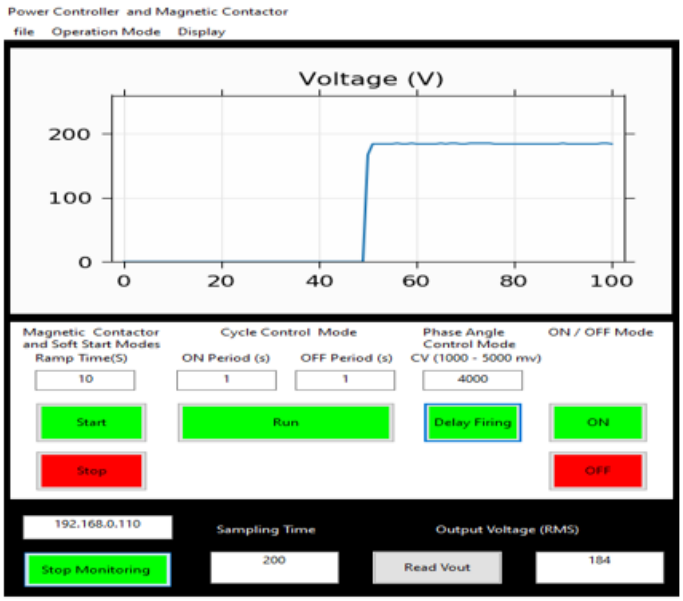

Fig 4. Solid-state AC line controller inerfacing screen.

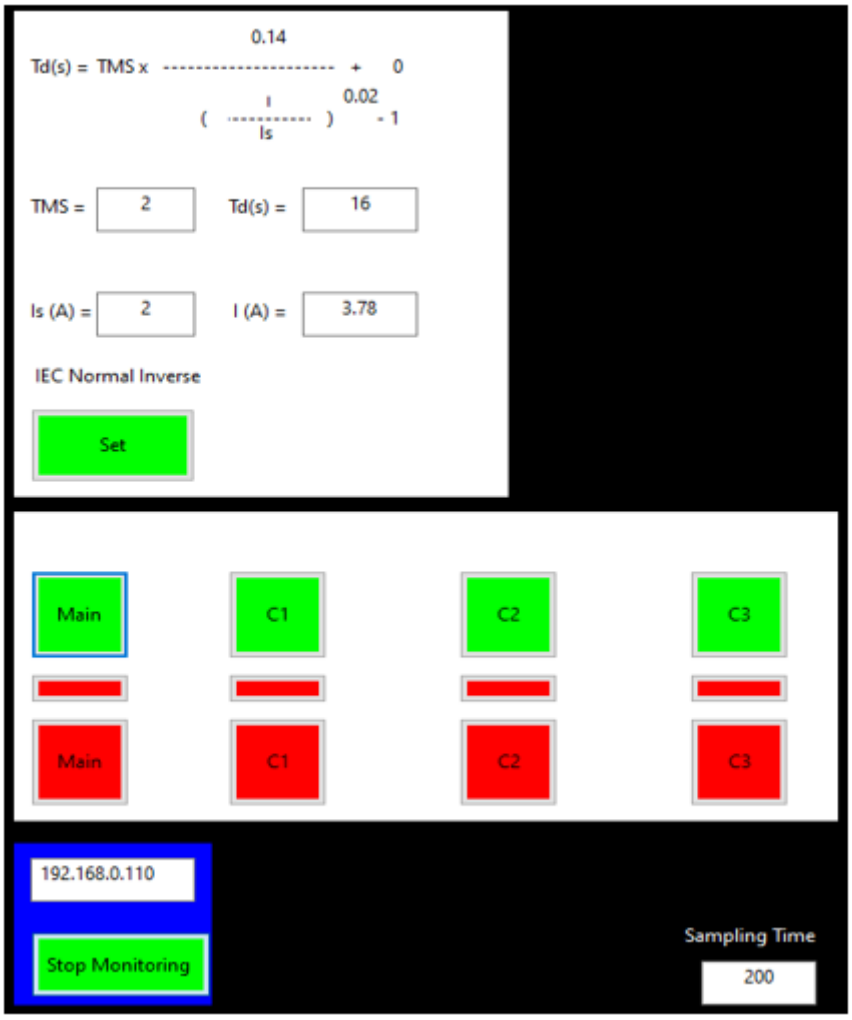

Fig 5. IDMT over current relay inerfacing screen.

Table 1. PLC Modbus Memory Setting.

Bit Read Area Address	**%IX0.0.0**
Bit Write Area Address	**%QX0.0.0**
Word Read Area Address	**%MW0**
Word Write Area Address	**%MW100**

Table 2. Modbus memory Map.

Setup	Client Command			PLC Memory	Comments
	Address(s)	Type	Value		
IM Starting	1	Write register	X	%MW101	X=1: Enable DOL starting, X=2: Start YD starter, X=3: Stop YD starter
	X	Write coil	Y	%QX0.0.X	X = 9: Q9=Y, X=10: QA=Y, X=B: QC=Y
	[9,10,11]	Read coils		%QX0.0.9, QX0.0.A, %QX0.0.B	Read the status of Q9 to QB
	10	Read Input registers		%MW10	Read line current (MW10 =UW0.1.3)
Phase angle controller	2	Write registers	X	%MW102	X=1: Q8 =1, X=2: Q8 =0;
	170	Write registers	ramp	%MW270	To set the soft starting period
	159	Write registers	X	%MW259	Set the operation mode: X=1 to 5
	160	Write registers	X	%MW260	Apply 5*X volt for the controller (X=1 or 0)
	60	Read input registers		%MW60	Read the controller output voltage MW60(MW60= UW0.1.4)/48)
	[161,162,163]	Write registers	A,B, C	%MW261,%MW262, %MW263	A to enable & disable the cycle mode, B & C set the mark and space periods.
	164	Write registers	alpha	%MW264	Set the firing angle equivalent value
IDMT relay	[131,132]	Write registers	Is, TMS	%MW231,%MW232	Set the pickup and TMS values
	130	Write registers	X	%MW230	Set the characteristic curve type (X=0 to 5)
	X	Write coil	Y	%QX0.0.X	X=0: Main , X=1: C1, X=2: C2, X=3: C3 magnet contactor

4 Discussion

The proposed platform allows three students groups to share one PLC to operate three experimental setups at the same time. Each setup allows the students to experimentally understand or verify certain topics of the classroom as follow:

4.1 Three Phase Induction Motor Starting Setup

With this setup, the students can sense the difference between direct-on-line and start delta starting. Fig 6 is a snapshot of the recorded motor line current data under star connection, delta connection, and star-start delta-run connection. As it is evident from the figure, this setup and through its recording facility can clearly show the students why a star-delta starter is necessary. This response belongs to a three-phase squirrel cage induction motor with a 3.0A full load current. With direct delta starting this motor draw about two times its rated current whereas with star-delta starter draw slightly more than its rated current.

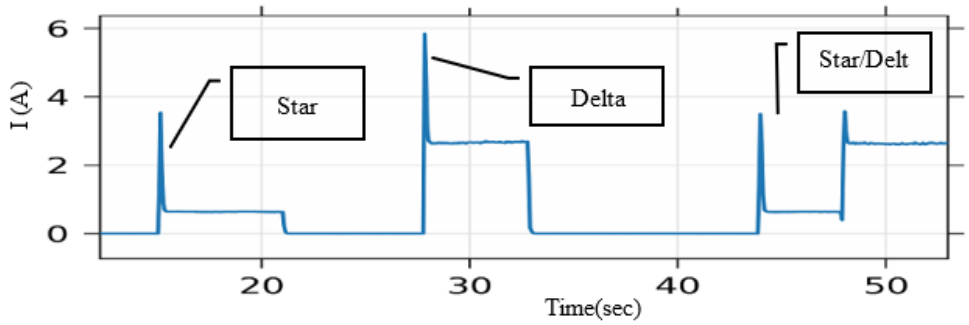

Fig 6. 3Ph IM starting current under Star, Delta , & Star/Delta starting.

4.2 Single Phase AC Line Controller Setup

A **s**ingle-phase AC line controller (power controller) consists of two anti-parallel connected thyristors. Industrially, AC line controllers are widely used with heating elements. These power electronic elements use an analogy signal to determine the firing delay to the zero crossing instants of the applied voltage. This structure allows these elements to be run in a different mode of operation like ON/OFF, Phase angle, and Integral Cycle control mode of operations. With this setup, the students have an opportunity to explore the physical meaning of each of these supported modes and to understand the difference between the magnetic contactor and AC line controller. Figs 7 to 9 are snapshots for the recorded data of the r.m.s values of the output voltage of the ac line controller under different modes. Fig 7 shows the operation of this device under cycle mode of operation in which the analogue control signal input terminal receives either its minimum value for the OFF state or maximum value for the ON state and the ON/OFF is cyclic. Fig 8 shows the difference between the ac line controller as a solid-state relay and the magnetic contactor. With ac line controller, the forward voltage drop across the thyristors is clear whereas there is no voltage drop in the case of the magnetic contactor. In Fig 9, the analogue control signal has been gradually increased from its minimum to its maximum values. This mode of operation is used for soft starting. With this setup which consists of a single-phase ac line controller, magnetic contactor, and r.m.s value voltage transmitter, the students can be introduced to the soft starting concept. Fig 9 shows the soft starting under two ramp slops, (a) belongs to 1 sec and (b) belongs to 10 sec. Table 3 lists the relation between the analogue control voltage setting, and the PLC digital to the analogue voltage applied to the controller analogue input control terminal

and the r.m.s value of the output voltage of the controller. As it is seen, the control voltage setting is the mv picture of the real voltage applied to the ac controller control terminal. Through this utility, the students can get an experimental idea about the relation between the control voltage setting and the output voltage r.m.s value as illustrated in Fig 10.

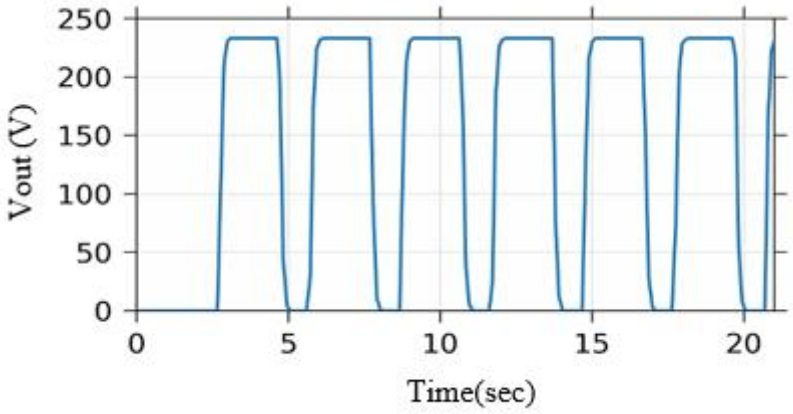

Fig 7. Controller output voltage under cycle mode.

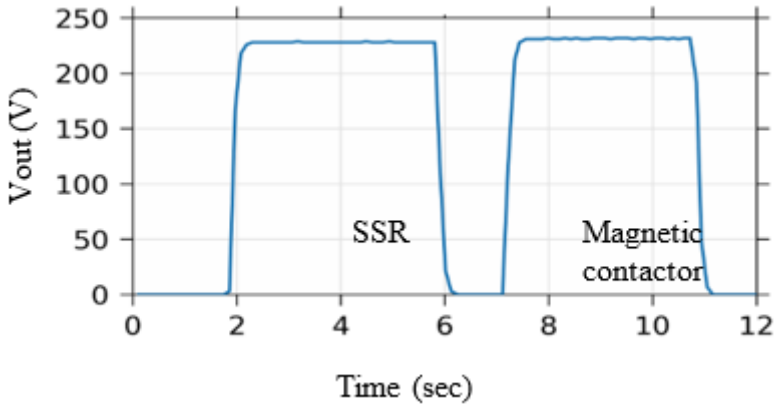

Fig 8. Controller output voltage with bypass contact.

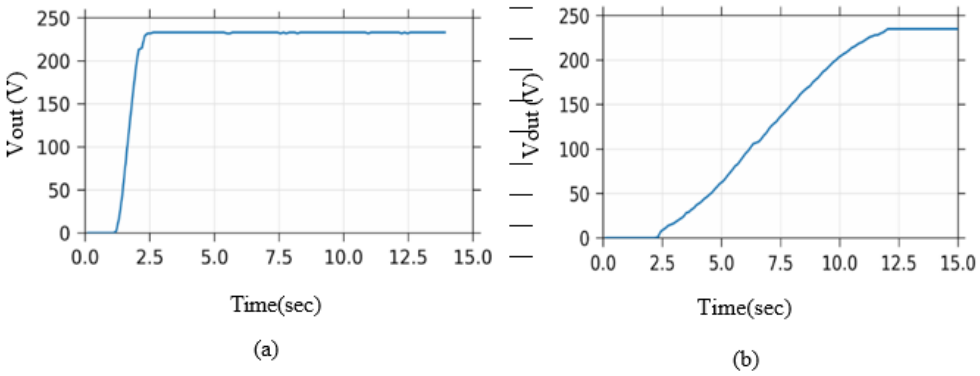

Fig 9. Controller output voltage under soft start mode. (a): 1 sec ramp period. (b): 10 sec ramp period.

Table 3. The relation between the analogue control voltage setting and the PLC digital to the analogue voltage applied to the controller analogue input control terminal

Analog Voltage user setting	Analog Voltage	R.M.S of Vout (V)
1000	1.200	0
1500	1.503	11
2000	2.005	37
2500	2.506	70
3000	3.007	112
3500	3.508	149
4000	4.000	184
4500	4.510	213
5000	5.010	227

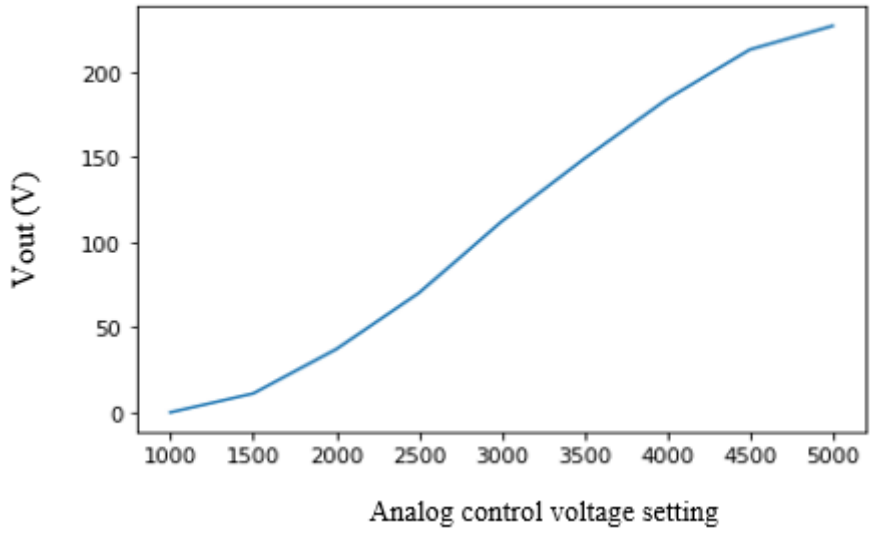

Fig 10. Control voltage setting versis Vout

4.3 IDMT Overcurrent Relay Setup

An inverse definite minimum time (IDMT) overcurrent relays are widely used in the protection of electrical equipment. The IDMT over-current relay characteristic is represented as in equation (1) [12]:

$$T = TMS \times \left\{ \left[\frac{k}{\left(\frac{I}{I_S}\right)^{a} - 1} \right] \right\} + c \quad (1)$$

With this platform, the students can sense the effect of the IDMT 's parameters (k, a, and c) on the tripping delay time in addition to the effect of the time multiplier setting (TMS). Table 4 shows the setup's outcome for different plug settings for the six standard characteristic curves.

Table 4. Trip delay time in sec.

	Plug Setting								
Curve Type	1	1.25	1.5	1.75	2	2.25	2.5	2.75	3
IEC normal Inverse	∞	32	17	12	10	08	07	07	06
IEC Very Inverse	∞	56	27	18	13	10	09	07	07
IEC Extremely Inverse	∞	53	24	15	10	07	06	04	04
IEEE Moderately Inverse	∞	12	06	05	04	03	03	03	02
IEEE Very	∞	35	16	10	07	05	04	03	03

Inverse									
IEEE Extremely Inverse	∞	50	22	14	09	07	05	04	04

5 Conclusions

In this paper, a PC/PLC-based platform for the simultaneous running of three laboratory experimental setups (using WxPython and Pymodbus) has been presented. The currently supported setups are three-phase induction motor starting, single-phase ac line controller and IDMT overcurrent relay setups. The platform offers an experimental opportunity to sense the undesirable value of the three-phase induction motor starting current under direct-on-line starting and compare the drawn current with that under star connection, understand the various operating mode of the single-phase ac line controller and the difference with the magnetic relay in addition to its cooperation with the magnetic contactor to construct soft starter, provide a cost-effective platform for understanding the overcurrent protective relays and their behaviour under different characteristic curve settings. The platform also offers real-time monitoring and history recording facilities. The real-time monitory facility functions as if it were an oscilloscope. The history recording facility allows the user to come across every instant in the operation journey of the setup under consideration. Through the history recording facility, the motor starting current can be seen as a situation that is difficult to be sensed by the traditional metering facilities. The overall cost can be highly reduced by using cheap second-hand PCs as clients.

References

[1] Trevelyan, J.P. Technical Coordination in Engineering Practice. *Journal of Engineering Education*, 2007. **96** (3): pp. 191-204.

[2] Luo Y., Jeevjyot Singh Chhabda J. S. Design and Implementation of a Virtual Lab in an Engineering Laboratory Course, 54th ASC Annual International Conference Proceeding (2018).

[3] Razali Z. B. and Trevelyan J. Valuable Experience in Engineering Laboratory: Enhance Understanding of Engineering Concepts. Regional Conference on Engineering Education (RCEE 2007).

[4] Rashid M., Imran A. T., Zia Y. I., Al-Turkistany M., and Rashid S. Evaluation of Engineering Laboratories. International Conference on Education and e-Learning Innovations (2012).

[5] Norrie S. E. The role of laboratory work in engineering education: student and staff perceptions. International journal of Electrical Engineering Education (2016).

[6] Al Mashhadany Y. I. Design and Implement of a Programmable Logic Controller (PLC) for Classical Control Laboratory. *Intelligent Control and Automation*, 2012, 3, pp. 44-49.

[7] Fernandes J.M. and Van N. T. A Programmable Logic Controller Based Laboratory: Analysis of Conventional and Intelligent Control Schemes for on linear Systems. Journal for New Generation Sciences, Volume 13 Number 3, 2015.

[8] Mahmood J. R., Ali R. S., Migdadi H., Abd-Alhameed R. A. and Ibrahim, E.M. Development of Educational Fuzzy Control Laboratory Using PLC, and HMI. In Proceedings of the Internet Technologies and Applications Conference (ITA15), Wrexham, UK, 8–11 September 2015; pp. 383–387.

[9] Geaney G. and O'Mahoney T. Design and evaluation of a remote PLC laboratory. The International Journal of Electrical Engineering and Education (2015).

[10] Ozerdem O. C. Design of two experimental setups for programmable logic controller (PLC) laboratory. International Journal of Electrical Engineering Education (2016).

[11] Alves L.F., Brandao D. and Oliveira A. A multi-process pilot plant as a didactical tool for the teaching of industrial processes control in electrical engineering course. International Journal of Electrical Engineering Education (2018).

[12] Mahmood J. R., Ali R. S., and Abd-Alhameed R. A. PLC/HMI-Based Implementation of a Real-Time Educational Power System Protective Relays Platform. electronics, MDPI, 2020, 9 (1), 118.

[13] Ryan E., Mohammed A. A review on applications of programmable logic controller. 2016, Renewable and sustainable energy reviews.

[14] Jeong Y., Ansari M. I., Shin W., Kang B., Lim J., Moon H., and Shim J. PLC and Arduino Interaction Based on Modbus Protovol. Journal of Korea Multimedia Society Vol.20, No.3, March 2017, pp. 511-519.

[15] John Hunt J. A Beginners Guide to Python 3 Programming. Springer Nature Switzerland AG 2019.

[16] PyModbus Documentation, Release 2.5.0 2021.

[17] Mehta K., Joshi R., Jadav H. M., and Kulkarni S. V. Integration of MODBUS/TCP master monitoring and control system using python for High power RF system. Conference: International Conference on Electrical, Electronics, Signals, Communication and Optimization (EESCO) – 2015.

Simulation of Indirect Field Oriented Control on 5-Phase Synchronous Reluctance Motor

Namariq Abdulameer Ameen*[1], Ali Kadhim Abdulabbas[2], Habeeb Jaber Nekad[3]
{nam.almo79@gmail.com[1], ali_univbasra75@yahoo.com[2], hjn24177@gmail.com[3]}

Department of Electrical Engineering, University of Basrah, Iraq [1'2'3]

Abstract. Nowadays, multiphase ac machine drives are taken into consideration for several applications because they offer many advantages when in contrast with their three-phase equivalent. Therefore, in various applications, there is expanding in the achievement of the five-phase machine in electric drive systems. This paper uses mathematical modelling to demonstrate the dynamic simulation of a five-phase Synchronous Reluctance Motor SynRM driven by a five-phase current-controlled space vector PWM inverter. The theory of reference frame has been employed to get the transformation of five-phase SynRM voltage equations for removing the inductances angular dependency. The pulses for an inverter are created by applying the five-phase Space Vector Pulse Width Modulation (SVPWM) method. Then, for a five-phase SynRM, an indirect rotor flux-oriented vector control technique is constructed. Furthermore, the control block diagram is also presented in this paper with performance behaviour discussion under different load conditions and variance reference speed. The equivalent controllers are appropriately proposed to provide independent torque control. Finally, the obtained simulation results are typical and demonstrated by using Matlab/Simulink.

Keywords: Field-Oriented Control, Electric Drive Systems, Reluctance Torque, Synchronous Reluctance Motor.

1 Introduction

The synchronous reluctance motor (SynRM) has piqued the interest of many scientists and gained more attention as a possible substitution for an induction drive in recent decades, which is treated as a suitable choice for several variable-speed drive systems [1], [2], [3]. SynRM and induction motor (IM) are similar in stator construction, but its rotor has no field windings which results in reduced losses and higher efficiency [4]. Since SynRM is free of magnets, it is cheaper than permanent magnet motors [5]. SynRM has many advantages like it has a simple rugged structure, easy maintenance compared with induction motors, a reduced manufacturing cost, a moment of inertia is minor and the torque per unit volume is higher [2], [6]. The SynRMs are more durable than brushless (BL) motors and have lower rotor assembly costs [7]. The SynRM has the only rotor being salient, so it is structurally simpler than switched reluctance motor(SRM) with a doubly salient structure. Furthermore, from the standpoint of torque ripple, it is superior in SRM [8], [9]. There are some drawbacks in SynRM like power factor poorness and reduced torque density (slightly acceptable). These issues can be overcome by properly manipulating the design parameters of SynRM or by proposing a suitable control technique [4]. Besides, increasing the number of SynRM phases to reduce the undesired increase in the torque ripple is considered an effective way [10], [11].

IMDC-IST 2021, September 07-09, Sakarya, Turkey
Copyright © 2022 EAI
DOI 10.4108/eai.7-9-2021.2314812

In recent years, multiphase synchronous reluctance machines are treated as a perfect choice with the modern power electronics advancement, so the five-phase machine(in particular) has gotten a lot of coverage [12]. Commonly, high phase number drives are often favoured over three-phase drives for a variety of reasons. such as the high torque density, and improved efficiency, superior fault tolerance, amplitude lessening, torque pulsations, frequency rising, diminished harmonic currents in rotor, current per phase is reduced, phase voltage is nearly stable, DC link current harmonics are adequate, and dependability is improved. Hence, increasing the number of phases for an identical volume machine will enhance the torque per r.m.s ampere [2], [4], [13]. Furthermore, by injecting the third harmonic into a five-phase system, torque can be increased further without enlarging copper losses, in three-phase devices. However, incorporating the third harmonic to raise torque is not doable. SynRM model which includes the third harmonic and its influence on machine torque was presented in [3], [14].
Multi-phase projects for drive systems have recently been managed in specific demanding high trustworthiness, such as hybrid vehicles, ship propulsion, aircraft appliances, and applications requiring high power. Accordingly, the necessity of multiphase systems with n separate drive units is not inequitable for huge drives since various components are acquired in the present designs as in [15], [16].
In this paper, reference frame theory is used to model five-phase SynRM. Only the outer broad vectors are realized in Simulink of the five-phase current-controlled space vector pulse width modulation (SVPWM) technique using MATLAB simulation software. Besides that, the fundamental harmonic of spatial field is only employed to develop motor torque in executing a high-performance indirect rotor flux-based vector control technique. For SynRM drives, there are various current vector control techniques; the most widely used is the constant direct-axis current control technique, which is adopted in this paper. The direct-axis current reference value is maintained constant in this technique, while the quadrature-axis current is used to control motor torque. Accordingly, by regulating the d and q-axis currents separately, the generated electromagnetic torque and rotor flux can be regulated. This paper is aimed to obtain the results by the current control technique, the electromagnetic torque and flux are fully decoupled. The speed for various loads, as well as different acceleration/deceleration and reverse modes, have been clarified.
The following sections of the paper are arranged as follows: Section II involves the system equations clarification and transformations needed for motor modelling. Section III demonstrates the five-phase space vector pulse width modulation(SVPWM) in operation. Section IV exhibits the implementation of the indirect flux-oriented vector control strategy by using MATLAB/SIMULINK. Section V and VI show the simulation implementation and simulation results, respectively. Finally, Section VII summarizes the paper with a brief conclusion.

2 System Equations and Transformation

Fig 1 illustrates a basic description model for a two-pole five-phase SynRM with concentrated winding in the stator and a salient pole rotor form created by the cut-out eliminated from around the rotor. The concentrated windings are the best choice in motor structure because the Distributed Windings stator (DW) outcomes in a high manufacturing cost resulted from the distributed winding difficulty [17].

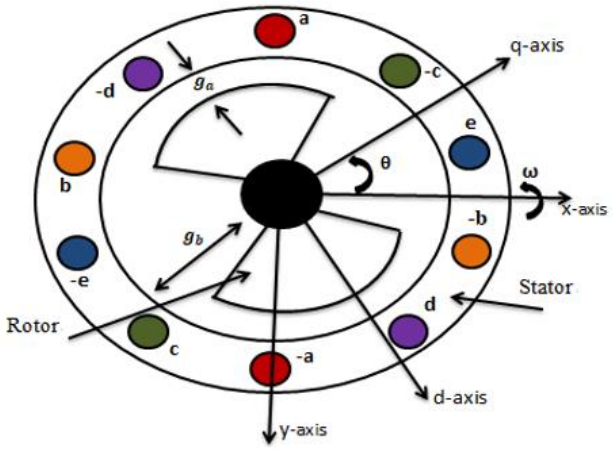

Fig 1. Five-phase synchronous reluctance motor prototype.

Motor phases are moved apart by 72° electrical degree [18]. The smallest air gap length that is shown in the figure is g_a , and the largest air gap length is denoted by g_b.Torque density is extremely influenced by the saliency ratio$\frac{g_b}{g_a}$. The rotor position θ is defined as the angle formed by the q-axis of the stator and the rotor. It is observed that the d-axis is phase-shifted from the q-axis by 90°.

The machine's dynamic behaviour can be described by parameter equations such as voltage, flux, and torque, which are time-varying variables. It is challenging to solve these differential equations, so variables with time-varying will be changed to time-invariant variables to decrease the motor voltage equations complexity caused by electric circuit relative motion. Iron saturation is neglected by assumption, and the fundamental component of air gap flux will only be kept in mind.

Generally, the following are the equations in the natural reference frame that describe the electrical characteristics of this machine in matrix form [2]:

Stator voltage equation:

$$V_s = R_s I_s + p\,\lambda_s \tag{1}$$

The equation for the Stator Flux Linkage is:

$$\lambda_s = L_{ss} I_s \tag{2}$$

Where p = d/dt and

$$I_S = [i_{as} \quad i_{bs} \quad i_{cs} \quad i_{ds} \quad i_{es}] \tag{3}$$

$$V_S = [v_{as} \quad v_{bs} \quad v_{cs} \quad v_{ds} \quad v_{es}] \tag{4}$$

$$\lambda_S = [\lambda_{as} \quad \lambda_{bs} \quad \lambda_{cs} \quad \lambda_{ds} \quad \lambda_{es}] \tag{5}$$

Also, $R_s = r_s I$ where r_s is the resistance for every stator coil, considering that all coils are the same, and I am a 5x5 character matrix. In stator, L_{ss} is a 5x5 symmetric inductance matrix with the pattern:

$$L_{ss}=\begin{bmatrix} L_{aa} & L_{ab} & L_{ac} & L_{ad} & L_{ae} \\ L_{ba} & L_{bb} & L_{bc} & L_{bd} & L_{be} \\ L_{ca} & L_{cb} & L_{cc} & L_{cd} & L_{ce} \\ L_{da} & L_{db} & L_{dc} & L_{dd} & L_{de} \\ L_{ea} & L_{eb} & L_{ec} & L_{ed} & L_{ee} \end{bmatrix} \quad (6)$$

Because the inductance matrix L_{ss} and the rotor position change together, the second expression of (1) be able to represent as

$$\frac{d\lambda_s}{dt}=L_{ss}\frac{dI_s}{dt}+\frac{dL_{ss}}{dt}I_s \ . \quad (7)$$

By applying the chain rule, the equation's second term can be represented as

$$\frac{dL_{ss}}{dt}I_s=\frac{dL_{ss}}{d\theta_{rm}}\frac{d\theta_{rm}}{dt}I_s. \quad (8)$$

θ_{rm} is the rotor mechanical position, so the rotor mechanical speed is

$$\omega_{rm}=\frac{d\theta_{rm}}{dt} \quad (9)$$

So,

$$\frac{dL_{ss}}{dt}I_s=\omega_{rm}\frac{dL_{ss}}{d\theta_{rm}}I_s \quad (10)$$

Equation (7) can be written in the form

$$\frac{d\lambda_s}{dt}=L_{ss}\frac{dI_s}{dt}+\omega_{rm}\frac{dL_{ss}}{d\theta_{rm}}I_s \quad (11)$$

By substituting equation (11) into (1), the voltage equation is a natural frame of reference abcde-the system is giving by:

$$V_s = R_sI_s + L_{ss}\frac{dI_s}{dt}+\omega_{rm}\frac{dL_{ss}}{d\theta_{rm}}I_s \quad (12)$$

A five-phase synchronous reluctance machine's transient and steady-state performance can be expressed using the previously established equation set. As a result of the coupling degree between windings, these equations are slightly confusing for the reader, so it is suitable to signify the machine by the easiest equations set. There are renowned transformations that can make the equations easier if the space harmonics are disregarded. The salient structure of the rotor causes variation in the inductance matrix L_{ss} concerning the rotor position.

A 5x5 transformation matrix T(θ) is recommended for simplifying the windings inductance matrix and converting the variables from a stationary (a-b-c-d-e) reference frame to a rotating (d-q-x-y-n) reference frame to abstract the inductance reliance [2], [8].

That is F_{dqxyn}= T(θ) F_{abcde}

F may be either $\boldsymbol{V_s}$ or $\boldsymbol{I_s}$

Therefore, the transformation matrix is as follow:

$$T(\boldsymbol{\theta})=\frac{2}{5}\begin{bmatrix} \cos\theta & \cos(\theta-\frac{2\pi}{5}) & \cos(\theta-\frac{4\pi}{5}) & \cos(\theta+\frac{4\pi}{5}) & \cos(\theta+\frac{2\pi}{5}) \\ \sin\theta & \sin(\theta-\frac{2\pi}{5}) & \sin(\theta-\frac{4\pi}{5}) & \sin(\theta+\frac{4\pi}{5}) & \sin(\theta+\frac{2\pi}{5}) \\ 1 & \cos\frac{2\pi}{5} & \cos\frac{4\pi}{5} & \cos\frac{4\pi}{5} & \cos\frac{2\pi}{5} \\ 0 & \sin\frac{2\pi}{5} & \sin\frac{4\pi}{5} & -\sin\frac{4\pi}{5} & -\sin\frac{2\pi}{5} \\ \frac{1}{\sqrt{2}} & \frac{1}{\sqrt{2}} & \frac{1}{\sqrt{2}} & \frac{1}{\sqrt{2}} & \frac{1}{\sqrt{2}} \end{bmatrix} \quad (14)$$

By employing the transformation in equation (14) to five-phase voltage matrix equation specified in (1), one can obtain the voltage equations denoted by the flux linkages in the synchronously rotating reference frame (d-g-x-y-n) as given below:

$$\boldsymbol{v_{qs}} = \boldsymbol{r_s}\, \boldsymbol{i_{qs}} + \boldsymbol{\omega}\ \ \boldsymbol{\lambda_{ds}} + \frac{d\lambda_{qs}}{dt} \quad (15)$$

$$v_{ds} = r_s\, i_{ds} - \omega\ \lambda_{qs} + \frac{d\lambda_{ds}}{dt}$$

$$v_{xs} = r_s\, i_{xs} + \frac{d\lambda_{xs}}{dt}$$

$$v_{ys} = r_s\, i_{ys} + \frac{d\lambda_{ys}}{dt}$$

$$v_{ns} = r_s\, i_{ns} + \frac{d\lambda_{ns}}{dt}$$

Fig 2 illustrates the five-phase reluctance machine equivalent circuits in balance operation. The x-axis, y-axis, and n-axis equivalent circuits are all zero equivalent circuits that do not participate in torque development. The q-axis and d-axis equivalent circuits, on the other hand, are dependable for generating torque and magnetizing flux. Additionally, because of the decoupling activity between the q-axis and d-axis equivalent circuits, developing a control protocol to control this five-phase SynRM is not tricky [5].

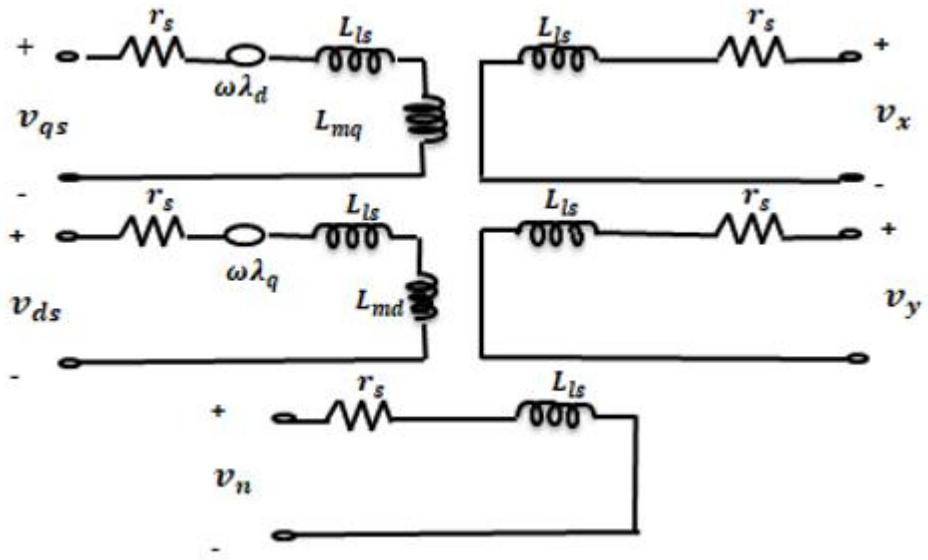

Fig 2. Five-phase SynRM equivalent circuit in the synchronous reference frame.

The electrical torque equation is attained from the magnetic co-energy W_{co} theory

$$T_e = \left(\frac{\partial W_{co}}{\partial \theta_r}\right) \tag{16}$$

The stored magnetic energy is equal to the co-energy of a linear magnetic system.

$$W_{co} = \frac{1}{2} I_s^t [L_{ss}] I_s \tag{17}$$

, and $T_e = \frac{P_{in}}{\omega} \frac{P}{2}$

$$P_{in} = \frac{5}{2} (L_{md} - L_{mq}) \omega \, i_{qs} i_{ds} \tag{18}$$

Where P_{in} represents the input power
P represents the number of poles
ω_m represents the mechanical angular velocity

$$T_e = \frac{5}{2} \frac{P}{2} (\lambda_{ds} i_{qs} - \lambda_{qs} i_{ds}) \tag{19}$$

$$= \frac{5}{2} \frac{P}{2} (L_{md} - L_{mq}) \, i_{qs} i_{ds}.$$

$$T_e = \mathrm{J} \frac{d \, \omega_m}{dt} + \mathrm{B} \, \omega_m + T_L \tag{20}$$

$$\therefore \omega_m = \frac{1}{J} \int (T_e - \mathrm{B} \, \omega_m - T_L) \tag{21}$$

Torque equation indicates that the torque is large when the saliency ratio $\frac{L_d}{L_q}$ is large, to enhance the torque density and improve the efficiency of synchronous reluctance motors, the saliency ratio must rise, and the difference $(L_d - L_q)$ must also be maximized in value. So far, such a ratio seems to have a physical limit with that structure, where the synchronous inductance is the maximum value of L_d and the stator leakage inductance is L_q.

3 Five-phase Space Vector Pulse Width Modulation Technique

Fig 3 illustrates a five-phase Voltage Source Inverter (VSI) that uses the space vector pulse-width modulation (SVPWM) method to create five-phase voltages for five-phase SynRM. In a five-phase inverter, there are five legs. Two power semiconductor switches (IGBTs) with anti-parallel diodes are connected within each switch on each leg. The DC voltage source of the inverter is split into two equal parts, and the junction between the two sources is joined to the ground as in reference for load balancing. The gating signal (pulse generated for switches) is advanced or delayed by 72°. The inverter DC voltage source is converted into a controllable AC voltage source with changeable frequency and amplitude values [19].

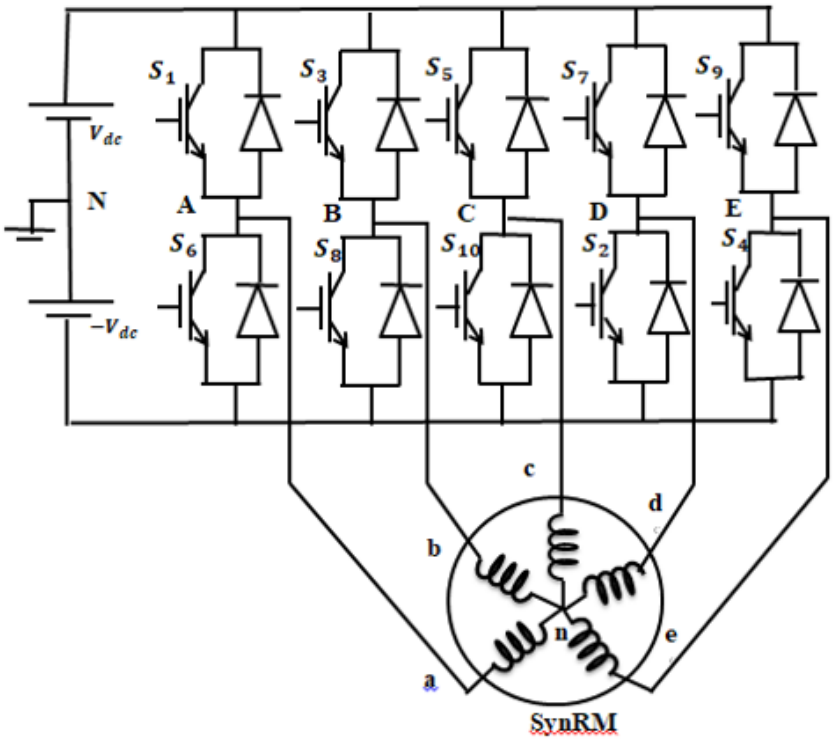

Fig 3. Five-phase Voltage Source Inverter.

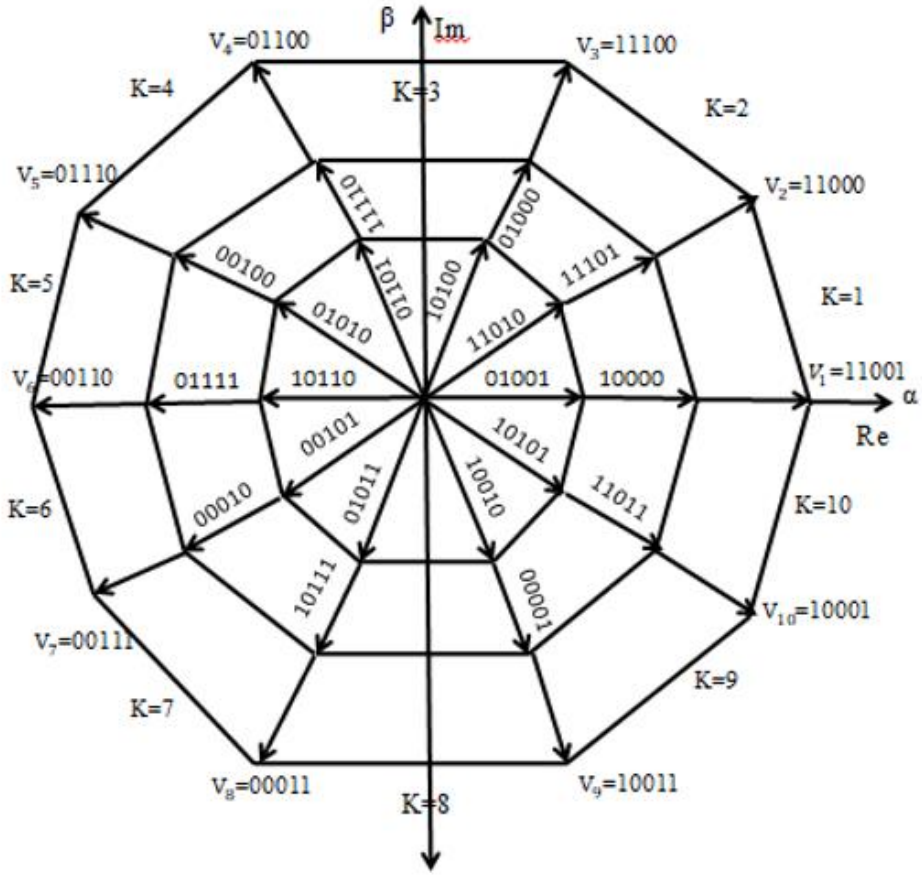

Fig 4. Switching vectors of all thirty-two states and voltage sectors.

Five-phase to neutral voltages transformation is as follows

$$\left.\begin{aligned} V_a &= \left(\tfrac{4}{5}\right)V_A - \tfrac{1}{5}(V_B + V_C + V_D + V_E). \\ V_b &= \left(\tfrac{4}{5}\right)V_B - \tfrac{1}{5}(V_A + V_C + V_D + V_E). \\ V_c &= \left(\tfrac{4}{5}\right)V_C - \tfrac{1}{5}(V_B + V_A + V_D + V_E). \\ V_d &= \left(\tfrac{4}{5}\right)V_D - \tfrac{1}{5}(V_A + V_B + V_C + V_E). \\ V_e &= \left(\tfrac{4}{5}\right)V_E - \tfrac{1}{5}(V_A + V_B + V_C + V_D). \end{aligned}\right\} \quad (22)$$

By using Clark's transformation, $V_\propto$ and V_β is as follows.

$$\begin{bmatrix} V_\alpha \\ V_\beta \end{bmatrix} = \frac{2}{5}\begin{bmatrix} 1 & \cos(2\pi/5) & \cos(4\pi/5) & \cos(4\pi/5) & \cos(2\pi/5) \\ 0 & \sin(2\pi/5) & \sin(4\pi/5) & -\sin(4\pi/5) & -\sin(\frac{2\pi}{5}) \end{bmatrix}\begin{bmatrix} V_a \\ V_b \\ V_c \\ V_d \\ V_e \end{bmatrix} \quad (23)$$

Then $|V_{ref}|$, and α can be determined as follows:

$$|V_{ref}|=\sqrt{{V_\alpha}^2 + {V_\beta}^2} \quad (24)$$

$$\alpha = \tan^{-1}\left(\frac{V_\beta}{V_\alpha}\right) = \omega t = 2\pi ft \quad (25)$$

Where f is the fundamental frequency.

There are thirty-two vectors that thirty of them are non-zero switching vectors. The remaining two vectors seem to be zero switching vectors. Fig 4 depicts the non-zero vectors. The apexes of the three decagons are equipped with all thirty non-zero vectors. These decagons are different in length of their sides where their amplitude ratio is $1:1.618:1.618^2$, starting from the least one to the largest one. Only one phase vector of the ten furthest vectors with the largest amplitudes will be switched from one vector in every two adjacent vectors. Therefore, these vectors are utilized to form five-phase currents, and these ten non-zero vectors shown in Fig 5 are the same as the six non-zero vectors in the three-phase inverters [20].

The constant switching frequency of SVPWM is a benefit. Accordingly, this technique is usually employed in three-phase systems, which are similarly developed for five-phase systems. If it is taken for one switching time interval T_s , the two non-zero vectors that are adjacent to the reference vectors V_{ref} and the two zero vectors are selected. These vectors will conduct for their predetermined periods ensuring that the specific voltage follows the reference voltage. The first and second non-zero vectors conduction time in addition to the zero vectors are given in equations (26)-(28) [21].

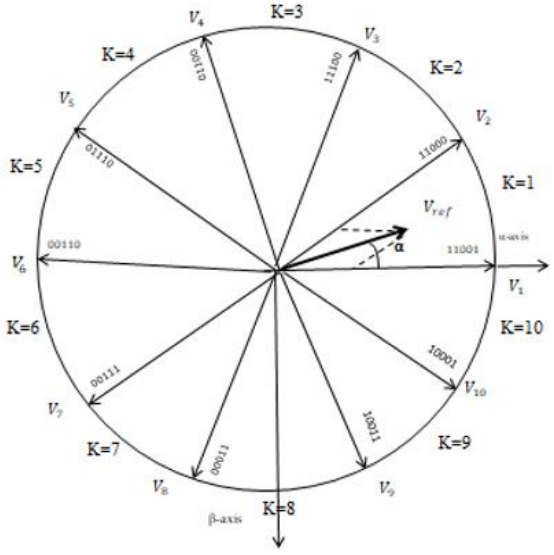

Fig 5. Ten switching vectors of five-phase SVPWM.

$$T_{1=} \frac{|V_{ref}| \sin(\frac{k\pi}{5}-\alpha)}{|V| \sin(\frac{\pi}{5})} T_s \quad (26)$$

$$T_2 = \frac{|V_{ref}| \sin(\alpha - \frac{(k-1)\pi}{5})}{|V| \sin(\frac{\pi}{5})} T_s \quad (27)$$

Where k =1,2 … 10 is the number of sectors that corresponds to the location of the reference vector.
, and

$$T_0 = T_s - T_1 - T_2 \quad (28)$$

Where $|V_{ref}|$ is reference space vector, and T_s is switching time which is equal to $\frac{1}{f_s}$.

Angle α represents the reference voltage vector angle and its range is between (0,2π).
In the next step, the switching period of every switching device is determined as shown in Fig 6. The total switching period T_s is divided into seven parts with zero state vector adopted in the first and the last quarter for the half zero state vector time, while active state vectors are employed in the second and third portions for half of the whole time of their vector. This sequence will be repeated in the second half of the switching cycle [18].

When the reference vector is situated at k is 1 in the first sector as illustrated in Figure 5, for reducing total switching, the two non-zero vectors V_1 and V_2 are conducting with two zero vectors as shown below: in the first time interval, the vector V_0(00000) is affected for the time $\frac{t_0}{2}$, then A and B will be switched on when V_2 (11000) is active at the period T_2. Next, E will be switched on, and the vector V_1(11001) is active during T_1 . In response to this, C and D will finally be switched on when V_{31} (11111) is activated at the time instant $\frac{T_0}{2}$.For subsequent time interval which is a mirror to the previous one, the conducting succession will be $\bar{V}_{31}$- $\bar{V}_1$- $\bar{V}_2$- $\bar{V}_0$ for $\frac{T_0}{2}$, T_1, T_2 and $\frac{T_0}{2}$ correspondingly; thereafter, If the reference vector is already in the first sector, this arrangement would be maintained. Figure 6 depicts the entire switching pattern. Each stage is only switched once throughout each time interval, and each time interval starts from zero vector $\bar{V}_0$ and finishes in zero vector $\bar{V}_0$ at the end of the following time interval that results in minimized total switching losses.

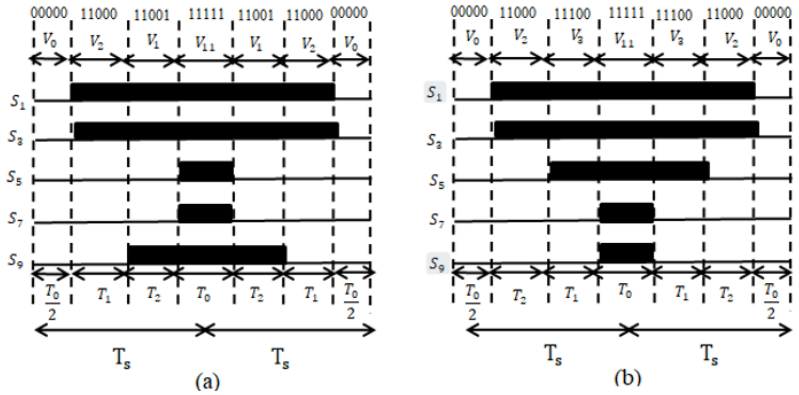

Fig 6. Five-Phase switching time interval, (a) sector-1, (b) sector-2.

Fig 7 illustrates a Simulink model of the SVPWM inverter with a five-phase SynRM. Clark transformation was applied to transfer five-phase reference frame to αβ-reference frame (v_α and v_β) which are utilized in the five-phase VSI's pulse generator block.

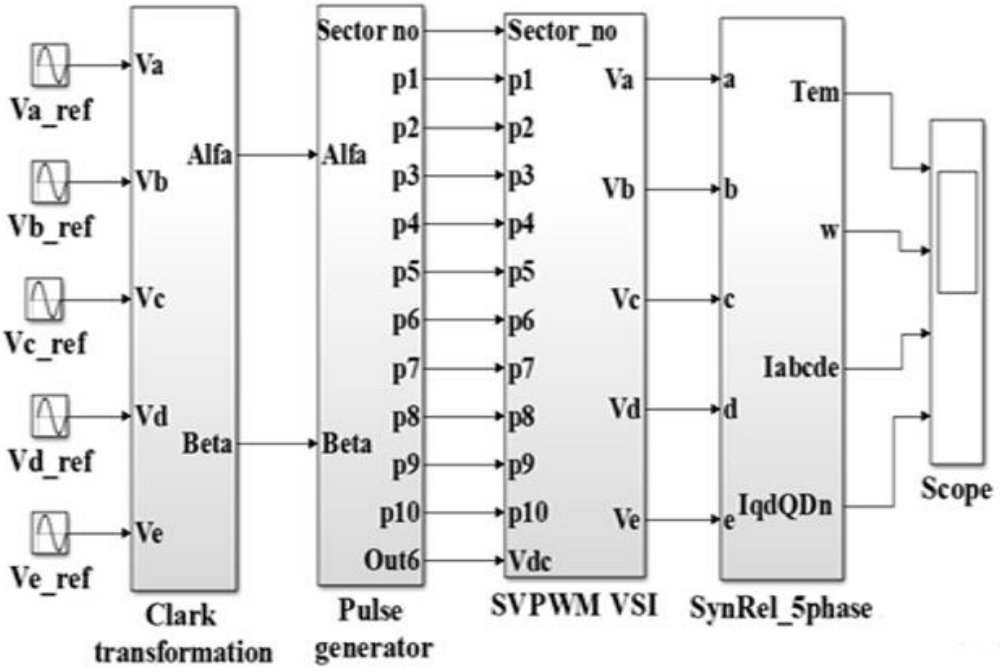

Fig 7. Simulink model of SVPWM Implementation on SynRM.

4 Rotor Flux Field Oriented Vector Control

Direct and indirect vector control methods are the two different types of vector control methods. Rotor flux-oriented vector control, stator flux-oriented vector control, and magnetizing flux-oriented vector control are the three types of indirect vector controls. The direct employment is dependent on the rotor, stator, or magnetizing flux linkage vector amplitude and location being directly measured or approximated. In comparison to direct methods, indirect methods are extremely reliant on system parameters. Scan coils tapped stator windings, or Hall-effect sensors aimed at flux sensing are used in traditional direct vector control algorithms. This will reveal any constraints imposed by the machine's structural and thermal environments. Since indirect control systems have less complicated hardware, they have increased overall efficiency at low speeds. The five-phase synchronous reluctance machine is regulated using a rotor-flux field-directed control approach, as shown below.
At steady state, the q-axis and d-axis voltage equations can be obtained from equations (15).

$$V_{qs} = r_s\, i_{qs} + \omega \;\; \lambda_{ds} + \frac{d\lambda_{qs}}{dt} \tag{29}$$

$$V_{ds} = r_s\, i_{ds} - \omega\ \lambda_{qs} + \frac{d\lambda_{ds}}{dt} \tag{30}$$

As shown in (19), the electromagnetic torque and q-axis current can be calculated:

$$\therefore\ T_e = \frac{5}{2}\frac{P}{2}\left(\lambda_{ds} i_{qs} - \lambda_{qs} i_{ds}\right) \tag{31}$$

Now, using rotor flux field-oriented technique, where λ_{qs} =0,

$$i_{qs} = \frac{T_{em}}{K_T \lambda_{ds}} \tag{32}$$

Where, $K_T = \frac{p}{2}\frac{5}{2}\left(1 - \frac{L_{qs}}{L_{ds}}\right)$

Only the reference quadrature axis current regulates the torque in this process, as shown in equation (32); the reference direct axis current is kept constant. The rotor flux field-oriented vector control of the five-phase synchronous reluctance motor is depicted in Fig 8, based on equations (29)-(32), where stator stationary axes represent α and β, and rotor synchronous rotating axes are d and q. Fig 9 illustrates the block diagram of the control system of this paper using the five-phase transformation in (19) and five-phase current regulated PWM by specific switching pattern selection to trigger the five-phase inverter IGBTs. A speed PI controller is used in the control block scheme, with the speed error as its input and the reference torque as its output. By utilizing (32), the q-axis current can be determined whose error is an input to another current PI controller. The d-axis current error is the input to the second current PI controller. The d-axis and q-axis demand voltages can be determined using (29) and (30).

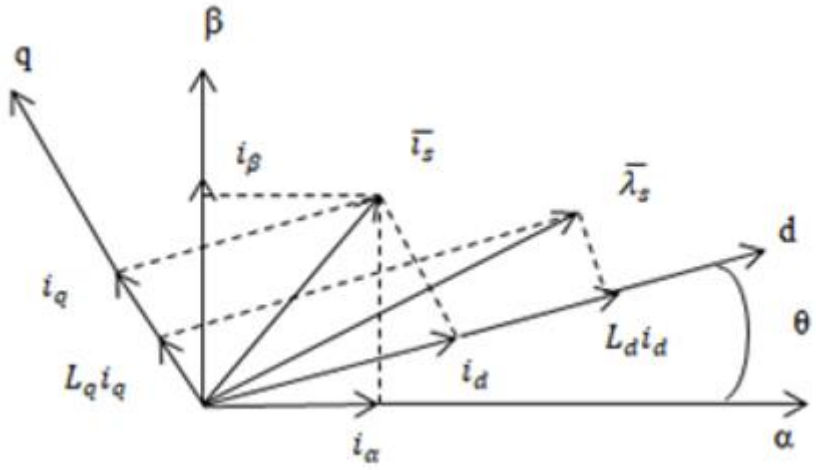

Fig 8. Rotor-oriented control of SynRM.

5 MATLAB/SIMULINK Implementation

The voltage, flux, and torque equations, and the transformation matrices built-in MATLAB, were used to simulate a five-phase SynRM model in [22]. The five-phase SVPWM is used to produce switching pulses for the IGBTs in the five-phase inverter. The overall control algorithm discussed previously with five-phase SynRM and five-phase current regulated SVPWM simulation is performed by MATLAB/SIMULINK program and described in Figure 9 [23]. The parameters listed in Table 1 are used to design and simulate the mathematical model of the concerned motor. Table 2 shows the PI parameters of the individual speed and current controllers.

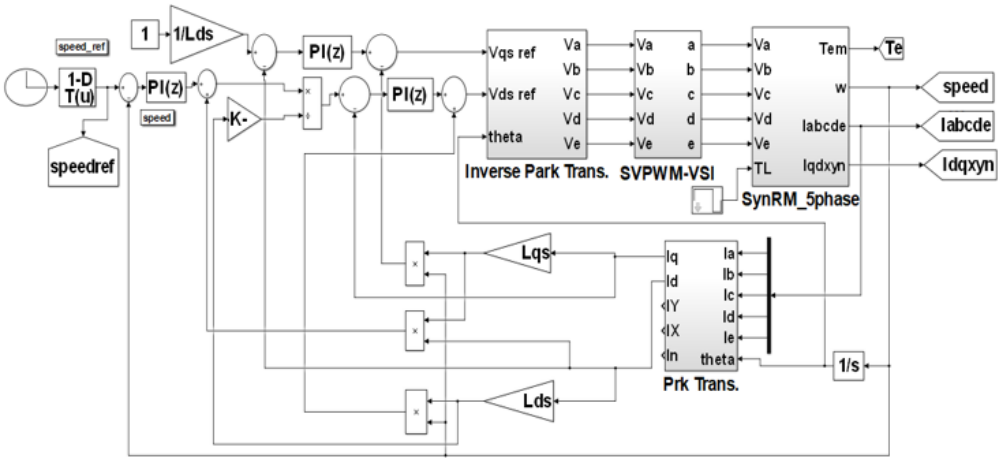

Fig 9. Field flux oriented control of five-phase SynRM simulation.

Table 1. Motor Parameters.

Parameters	Description	Values
L_d	inductance on d-axis	1.2 H
L_q	inductance on q-axis	0.1 H
V_{rated}	Voltage in Rated State	415 V
R_s	Stator resistance	4
J	Inertia	0.125 Kg.m2
B	Damping	0.009
P	Number of Poles	4

N_{rated}	Rated speed	1500 r.p.m
F	Frequency	50 Hz
f_s	Switching frequency	5 kHz

Table 2. PI controllers' parameters.

Parameters	Controller	
	Speed	Current
K_P	0.52	0.1
K_I	1.5	2.3

6 Simulation Results

A. MOTOR SPEED IN R.P.M

The five-phase SynRM's dynamic output is exanimated for operation under indirect rotor-field directed control. Acceleration transient starts from standstill to the rated speed 1500 r.p.m at t= 0.3 sec. till t=0.6 sec. After that speed is reversed till t=1 sec. at -1500 r.p.m as shown in Fig 10. It is worth noting that the actual speed in Fig 11 closely matches the reference speed, and the speed with reference speed is illustrated together in Fig 12. Rotor position in (rad), which is the integration of the speed is illustrated in Fig 13, and its variation concerning the speed variation is apparent.

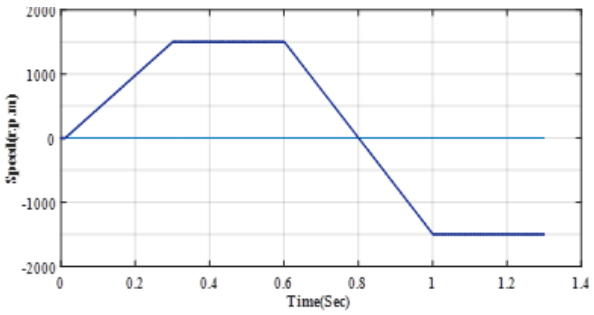

Fig 10. Motor speed in (r.p.m).

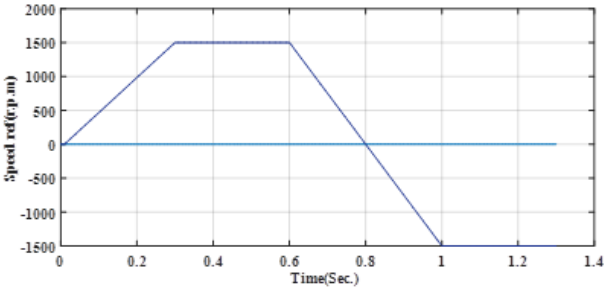

Fig 11. Reference speed (r.p.m).

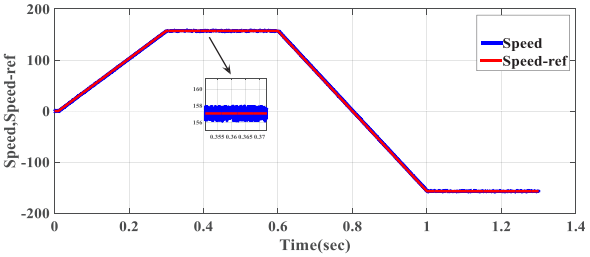

Fig 12. Speed with reference speed.

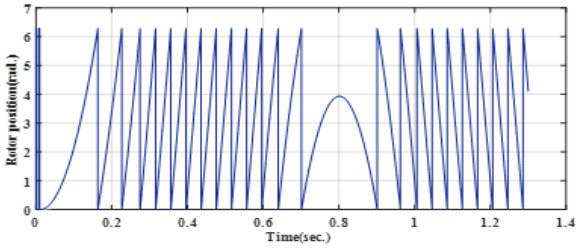

Fig 13. Rotor position (rad).

B. ELECTROMAGNETIC TORQUE AND LOAD TORQUE

Fig 14 displays load torque which is varied from zero to 20N.m at t=0.01 sec. till t=0.7 sec., then drop to -20 N.m at t=1 sec. The developed torque is assumed to be started from the rated torque 40 N.m and stabilized at the steady-state torque 20 N.m in the positive operation of the motor, and -20 N.m in the negative operation of the motor, as depicted in Fig 15.

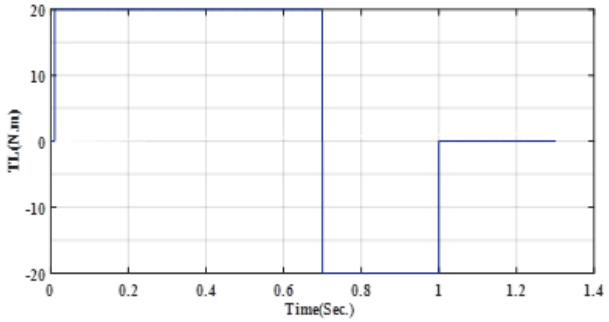

Fig 14. Load Torque (N.m).

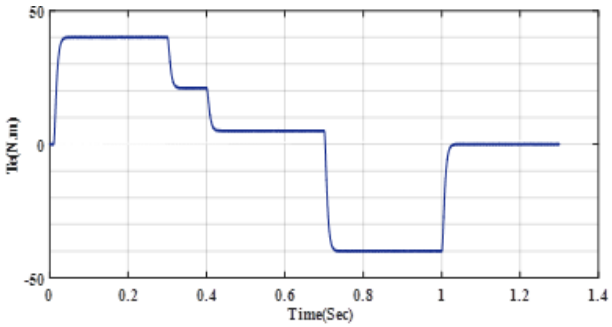

Fig 15. Electromagnetic Torque (N.m).

C. Direct Quadrature Axis Currents

According to the control strategy, the d-axis current is kept constant at 5A to obtain the machine's rated voltage as in Fig 16, while the q-axis current is varied with the developed torque as shown in Fig 17.

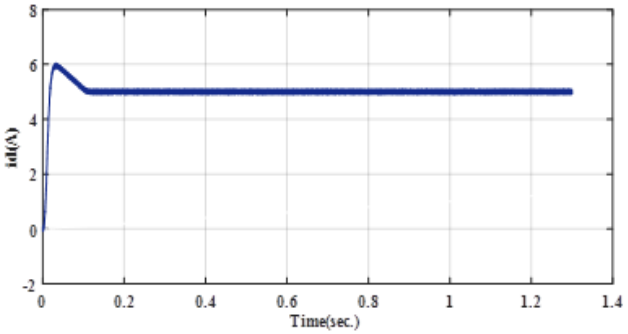

Fig 16. Direct-axis current (A).

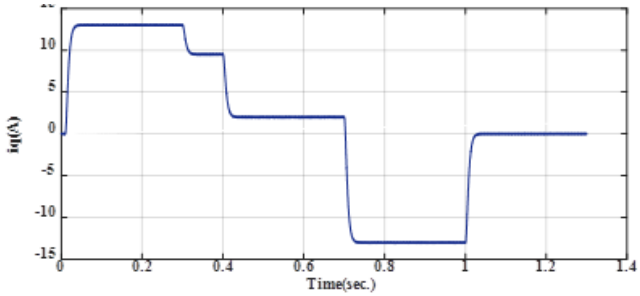

Fig 17. Quadrature-axis current (A).

D. Actual Five-Phase Currents

Fig 18 shows the real five-phase currents i_{abcde} obtained from the machine. These currents are achieved using inverse park transformation. When the motor alters its speed from 1500 r.p.m to -1500 r.p.m, these currents are inversed due to speed changing.

E. Stator Phase Voltages and Phase to Phase Voltage

The phase v_{abcde} terminal voltages of the stator are seen in Fig 19, while the line-to-line voltage waveform is shown in Fig 20.

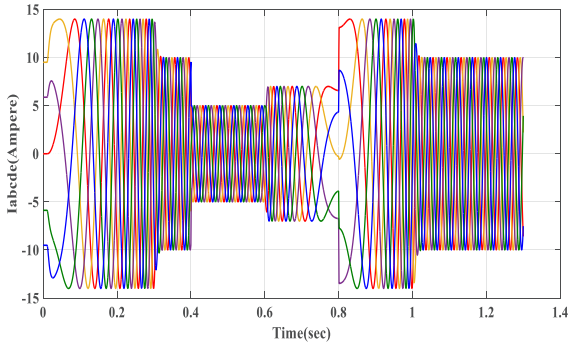

Fig 18. Stator phase currents i_{abcde} (A).

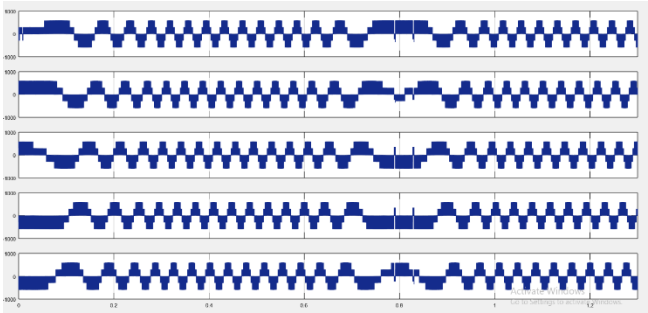

Fig 19. Phase voltages v_{abcde}(volt).

F. Stator Flux Linkage

The variance of stator flux in all situations is depicted in Fig 21. The d-axis and q-axis fluxes changing show that the stator flux is revolving along a predetermined direction, and the indications were typical.

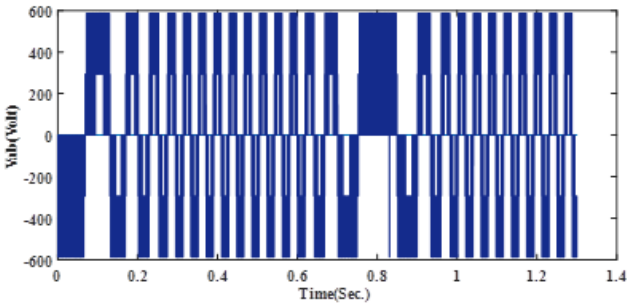

Fig 20. Line-line voltage v_{ab}(volt).

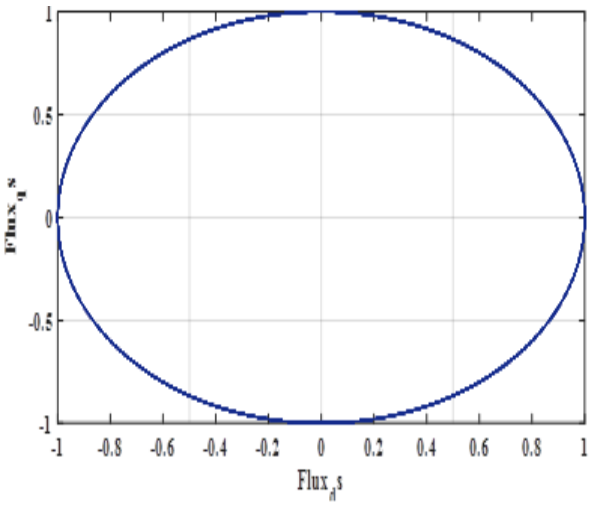

Fig 21. Stator Flux linkages.

7 Conclusions

The simulation models of a five-phase SynRM driven by a five-phase voltage source PWM inverter were recognized in this paper. According to a study in the field of multiphase machines, it is necessary to develop machines with a greater number of phases. Multiphase machines have many pros, such as high trustworthiness when the machines run incessantly even if one of its several phases is open or short-circuited without deficiency in performance as well as a smaller amount of current per phase which is a favorable characteristic exclusively in electric vehicles and analogous applications. This model is being used to create the indirect rotor flux field guided vector control of five-phase SynRM after it is used to implement a five-phase current-controlled SVPWM inverter, with outer speed closed-loop control and inner

currents loop control by using PI controllers. Thus, all simulation results approve the developed model legitimacy at all the transient, dynamics, and steady-state responses. Furthermore, the previous results verify that the proposed control system assurances stable and robust responses under a varied range of operating conditions. Consequently, it can be utilized for control applications with high-performance motion.

References

[1] H. A. Toliyat, S. P. Waikar, and T. A. Lipo, "Analysis and simulation of five-phase synchronous reluctance machines including the third harmonic of air gap MMF," *IEEE Transactions on Industry Applications*, vol. 34, no. 2, pp. 332-339, 1998.

[2] R. Shi, H. A. Toliyat, and A. El-Antably, "A DSP- based direct torque control of five-phase synchronous reluctance motor drive," *APEC 2001. Sixteenth Annual IEEE Applied Power Electronics Conference and Exposition*, pp. 1077-1082, 2001.

[3] R. Shi, H. A. Toliyat, and A. El-Antably, "Field oriented control of five-phase synchronous reluctance motor drive with flexible 3rd harmonic current injection for high specific torque," *IEEE Industry Applications Conference. 36th IAS Annual Meeting, Chicago, IL*, pp. 2097-2103, 2001.

[4] S. M. Ismaeel, S. M. Allam, E. M. Rasheed, "Current vector control techniques of five phase synchronous reluctance motor," *International Middle East Power Systems Conference (MEPCON),Cairo, Egypt*, pp. 1180-1185, 2019.

[5] R. Shi and H. A. Toliyat, "Vector control of five-phase synchronous reluctance motor with space vector pulse width modulation (SVPWM) for minimum switching losses," *APEC. Seventeenth Annual IEEE Applied Power Electronics Conference and Exposition, Dallas, TX, USA*, vol. 1, pp. 57-63, 2002.

[6] S. J. Mun, Y. H. Cho, & J. H. Lee, "Optimum design of synchronous reluctance motors based on torque/volume using finite-element method and sequential unconstrained minimization technique," *IEEE Transactions on Magnetics*, vol. 44, no. 11, pp. 4143-4146, 2008.

[7] T. J. E. Miller, Brushless Permanent-Magnet and reluctance motor drives, 2nd ed, Oxford university press, New York, 1989. Chapter three, Permanent-magnet materials and circuits; pp. 34-50.

[8] H. A. Toliyat, R. Shi, and H. Xu, "A DSP-based vector control of five phase synchronous reluctance motor," *IEEE Industry Applications Conference, Thirty-Fifth IAS Annual Meeting and World Conference on Industrial Applications of Electrical Energy, Rome, Italy*, vol. 3, no. 3, pp. 1759-1765, 2000.

[9] B. Bilgin, J. w. Jiang and A. Emadi, Switched Reluctance Motor Drives :fundamentals to applications, 1st ed, CRC Press, Taylor and francis group, 2019. Chapter two, Electromagnetic principle of switch reluctance motor; pp.35-90.

[10] Q. chen, Y. Yan, G. Xu and M. Xu, "Principle of Torque Ripple Reduction in Synchronous Reluctance Motors With Shifted Asymmetrical Poles," *IEEE Journal of Emerging and Selected Topics in Power Electronics*, vol. 8, no. 3, 2020.

[11] Q. Chen, X. Shi, G. Xu and W. Zhao, "Torque calculation of five-phase synchronous reluctance motors with shifted-asymmetrical-salient-poles under saturation condition," *CES Transactions on Electrical Machines and Systems, IEEE* , vol. 4, no. 2, 2020.

[12] A. Iqbal, "Dynamic performance of a vector-controlled five-phase synchronous reluctance motor drive: an experimental investigation, " *IET Electric Power Applications*, vol. 2, no. 2, pp. 298-305, 2008.

[13] A. Iqbal, E. Levi, M. Jones and Mohibullah, "Simulation studies of current regulated PWM VSI fed multi-phase AC machine drives, " *Proceedings Student Conference on Research and Development, Putrajaya, Malaysia, SCORED*, pp. 390-394, 2003.
[14] H. A. Toliyat, L. Xu and T. A. Lipo, "A five phase reluctance motor, with high specific torque, " *IEEE Transactions on Industry Applications*, vol. 28, no. 3, pp. 659-665, 1992.
[15] A. K. M. Arafat & S. Choi, "Optimal phase advance under fault-tolerant control of a five-phase permanent magnet assisted synchronous reluctance motor, " *IEEE Transactions on Industrial Electronics*, vol. 65, no. 4, pp. 2915-2924, 2017.
[16] S. S. R. Bonthu, S. Choi, J. Baek, "Comparisons of three-phase and five-phase permanent magnet assisted synchronous reluctance motor, " *IET Electric Power Applications* , vol. 10, no. 5, pp. 5- 2016.
[17] V. Bilyi, D. Bilyi, O. Moros, G. Dajaku and D. Gerling, "Synchronous reluctance Machine with multiphase stator cage winding, " *20th International Conference on Electrical Machines and Systems (ICEMS)*, *Sydney, NSW, Australia, 2017.*
[18] H. Abu-Rub, A. Iqbal & J. Guzinski, High performance control of AC drives with MATLAB/Simulink models, 1st ed., John Wiley & Sons, 2012.
[19] K.Chen and Y.Xie, "Reducing Harmonic Distortion in Five-Phase VSI Using Space Vector Based Optimal Hybrid PWM, " *IEEE Transactions on power electronics"* , vol. 32,no. 3, pp. 2098-2113, 2017.
[20] D.Raja and G.Ravi, "Design and implementation of Five-Phase Inverter With SVPWM Switching Technique for Induction Motor Drive," IEEE Fifth International Conference on Science Technology Engineering and Mathematics(ICONSTEM), vol. 1, no. 1, pp. 332-337. 2019.
[21] S.C.Rangari,H.M.Suryawanshi and B.Saha "Implementation of Large and Medium Vectors for Five-Phase Voltage Source Inverter"IEEE International Conference on Intelligent Computing and Control Systems(ICICCS), pp.751-756,2017.
[22]N. A. Ameen, A. K. Abdulabbas and H. J. Nekad, "Modelling and Simulation of Five-Phase synchronous Reluctance Motor Fed by Five-Phase Inverter", *Iraqi Journal for Electrical and Electronic Engineering(IJEEE*), vol.17, no.1, pp. 1-8 , 2021.
[23] J.Kacprzyk, Advanced Control of Electrical Drives and Power electronic Converters, 1st ed, vol.75, Springer, Press 2017. Chapter one, Sensorless control of polyphase induction machine; pp.3-26.

Network Utility Maximization for Information Frequency Adaptation in Vehicular Networks

Hayder M Amer[1], Hawraa H. Al Mohammed [2], Lyudmila Mihaylova[3], Marcos Rodrigues[4]
{hayder.amer@stu.edu.iq[1], hawraahm89@gmail.com[2], l.s.mihaylova@sheffield.ac.uk [3]}

Computer System Department, Technical Institute of Basra, Southern Technical University-Iraq[1]
Sheffield Hallam University, Computer and Networking department, Sheffield, United Kingdom[2]
Department of Automatic Control and Systems Engineering, University of Sheffield, Sheffield, United Kingdom[3]

Abstract. The increment in traffic jams in vehicular environments has a vital influence on the wireless channel. This is due to broadcasting many application messages among communicated vehicles. This has generated a data wireless channel congestion problem. This problem influences the efficiency and performance of the network due to the large data collision, high messages loss, and low throughput which in turn decreases the awareness and safety in the vehicular environments. In this paper, a new efficient broadcast approach has been developed based on the network utility maximization method to adjust vehicle broadcasting rate and mitigate overhead on the wireless channel. The results from the simulation scenario have shown that the developed broadcast protocol enhances vehicular network performance by reducing channel congestion and improves network attributes such as delay, throughput, messages loss, and total channel occupation time as compared to other tested approaches.

Keywords: Vehicular networks, IoV networks, Wireless channel congestion, Optimization approach.

1 Introduction

Intelligent Transportation Systems (ITSs) are considered a powerful system for enhancing vehicles mobility in smart cities [1]. Providing vehicles with communication devices has introduced a new concept for an innovative approach for the components of safety applications in the vehicular communication environment, path planning, and entertainment. This can happen with the incorporation of multiple technologies and devices installed inside the vehicle [2]. The ITSs consolidated a broad range of control schemes such as wireless communication tools and technologies that can be utilized to generate data and announcement of traffic messages to boost road infrastructure and vehicles mobility which in turn helps to improve awareness and safety drivers.

The Internet of Things (IoT) [3] has been regarded as an attractive challenge for the transportation study society and it presents a novel area for ITSs. IoT includes many connected devices and Vehicular Ad-hoc Networks (VANETs) are considered as one of the major elements. VANETs included different wireless communication systems such as Vehicle to Vehicle (V2V) and Roadside Units (RSU) or Vehicle to Infrastructure (V2I) communication systems [4]. These systems are wireless sensors installed inside vehicles or deployed on the

IMDC-IST 2021, September 07-09, Sakarya, Turkey
Copyright © 2022 EAI
DOI 10.4108/eai.7-9-2021.2314811

road segments to collect and broadcast traffic-related information. VANETs can be employed to observe the conditions of the vehicular environment such as accidents and vehicles flow on the road segments. The protocol that is used to govern and support the communication among connected vehicles is called the Wireless Access of Vehicular Environment (WAVE) protocol [5]. However, increasing the number of communicated messages among drivers leads to the problem of data channel congestion in VANETs. This occurs due to the absence of centralized and stable topology and sending many messages at a fixed rate through the communication channel. This also increments the amount of battled vehicles to obtain the communication channel which influences the time that is required to send the safety messages and leads to a decrease the awareness in the vehicular environments. The problem of channel congestion hurts the parameters and performance of the network [6].

Many protocols and approaches have been developed to improve vehicular network performance in the presence of roads congestion and dynamic scenarios. Periodic messages adaptation strategies have been developed in [7] and [8]. The authors in [7] have introduced a beacon adaptation strategy that utilizes the road lanes to optimize vehicles transmission rate. The more multiple lanes on the road segment, the less the sending rate of the nodes. However, this approach has not calculated the real number of vehicles on the road sections.

In [8], a decentralized beacon modification strategy has been proposed that employs the investigation of the effects of multiple performance measurements such as orientation, quantity, and vehicles transportation conditions on the adaptation of the beacon rate. Nevertheless, the implied approach examines the effects of these parameters separately on the channel congestion rather than joining these measurements to obtain the adapted transmission rates. Moreover, the improper drop of periodic information affects the traffic data that must be propagated among drivers.

The authors in [9] have proposed an adaptation model based on a theoretical analysis to indicate the performance of IEEE 802.11p WAVE protocol and a retransmission strategy of the traffic data is introduced to promote the reliability of VAENTs. Nevertheless, the retransmission is initiated once a failed delivery has occurred. This approach causes data redundancy and overloads the wireless communication channel.

In [10], an approach that is called Utility-Based Packet Forwarding and Congestion Control (UBPFCC) has been introduced to enhance the sending frequency of beacon messages. This approach uses the size and cost function of data to adapt the rate of beacon packets. The UBPFCC employs a cost function specified for every vehicle to dynamically determine the rest of sending frequency to the vehicles. This approach gives the vehicle with high-cost function a high sending rate while those with the lower values broadcast data at low rates. However, this strategy has not estimated the density of vehicles on the road sections when calculating the cost function which has significant effects on the broadcast rate of the traffic information.

A data rate adaptation approach that uses game theory has been presented in [11]. A non-cooperative game approach has been utilized to module the problem of channel congestion and the existence of the optimal solution has been proved mathematically. The optimal data rate solution has been estimated via the KKT-Lagrange multiplier method. However, this approach has not considered the mobility of vehicles in the formulated cost function which makes it valid for only dense scenarios while the awareness of vehicles has been affected in the sparse environment.

Hence, this paper develops a novel efficient broadcast rate strategy for VANETs by applying Network Utility Maximization (NUM) method. The developed strategy implements a broadcast protocol to regulate the problem of wireless congestion in the vehicular network by using traffic control to enhance adequately the performance and measurement parameters of the network.

The suggested strategy essential participation:

1. A novel strategy of information rate adaptation that is called NUM-Date Rate Control (NUM-DRC) has been developed. This strategy adapts the sending rate based on the optimization method to alleviate wireless channel congestion. The sending rate and channel occupancy time have been used in the cost function to obtain solicited balance.
2. 2. The presence of a single optimal solution has been proved in this work for the vehicular network.
3. Priorities for the transmitted applications have been considered in this work to differentiate between high priority messages and low priority messages.
4. Lagrange multipliers have been applied to resolve the optimization dilemma and KTT conditions are used to find the optimal solution (information optimal sending rate).
5. A comprehensive performance evaluation is carried out for the proposed approach. This involves measuring the proposed strategy over a highway scenario. The proposed strategy is compared with other implemented strategies from the literature. The obtained outcomes confirm that the suggested strategy is adjusted to efficiently optimize the rates of traffic information to mitigate the data congestion problem in a vehicular network.

The remainder of the paper is structured as follows: In Section 2 gives details of the optimization method. Section3 gives the data rate optimal solution calculation. The section shows 4 the simulation scenario and the evaluation of the proposed approach. Finally, Section 5 concludes the paper.

2 Information Rate Optimization Approach

The NUM optimization method has been applied in this paper to propose a novel adaptation approach of the disseminated information rate that is called NUM-DRC. This approach applies the theory of optimization problem to form the problem of information rate adaptation and the target is to maximize the cost function which leads to finding the optimal solution for each vehicle in the network. Here, let $V=\{v_j$, j=1, 2, ⋯, m$\}$ represent a group of communicated vehicles that are driving on the road segment and contended with each other to access the wireless channel to broadcast safety messages at a maximum rate in selfish behaviour. Therefore, this paper assumes that:

1. Each vehicle in the network has a sized buffer of B messages
2. Each communicated vehicle in the network has two kinds of safety application messages $A_p = \{ap_n; n = 1,2\}$ that are: (i) Periodic messages or beacon is sent periodically and include the information that is related to the traffic status, (ii) Emergency messages are transmitted once an accident occurs or emergencies appear and they disappear when the event fades.

According to the queuing theory [12], [13], the channel congestion and buffer overload happen when vehicles' broadcasting rate is higher than the channel capacity or many vehicles send data at the same time without considering other vehicles' buffer size or channel capacity limitation. Here, the problem is to send data at a rate in a significant approach that guarantees fairness

among nodes and reduces channel congestion without decreasing awareness among the drivers. This paper utilizes two factors in the formulated utility $UF_j(R_j^{ap_n})$ that are:

1. Messages rate $R_j^{ap_n}$: It depicts the broadcasting rate for each vehicle in the network. The utility functions have been formed by several representations for example exponential, logarithmic, and linear [14]. This paper utilizes the exponential function to represent the message rate function of vehicle profit. This is because the exponential function has a rigorous concave shape that makes it a distinctive property. In addition, the second derivative of this function is negative. Thus, the vehicle v_j message rate function is expressed as follows:

$$MS_j(R_j^{ap_n}) = (1 - e^{(1-R_j^{ap_n})}) \quad (1)$$

2. Price function: In the communication network, the pricing or penalty cost is considered as an effective approach to enhance the network resources utilization [15]. The suitable pricing strategy controls the redundant use of the network resources among contending nodes when the data channel congestion occurs in the network. Here, the Channel Occupancy Percentage (COP) has been utilized as a price that demands to be paid by every vehicle when the congestion happens. The COP has been estimated according to [16] as follows:

$$COP_j = \sum_{j=1}^{m} h_{kj} R_j^{ap_n} \quad (2)$$

where h_{kj} function depicts the likelihood that a definite transmission generates a received signal strength higher than threshold power transmission of the carrier sense at a specific location from the transmitter and it is given by:

$$h_{kj} = \frac{\Upsilon(m, \frac{mCS_T}{\Omega})}{\Upsilon(m)} \times T_{frame} \quad (3)$$

Where T_{frame} is the time needed to transmit a safety application packet, Υ is the gamma function, m is the Nakagami fading parameter, CS_T represents the threshold power transmission of the carrier sense and Ω represents the average received signal strength at a certain position which can be estimated as follows:

$$\Omega = P_t \frac{\varphi}{d_{kj}^{\eta}} \quad (4)$$

Where P_t is the power transmission of the sender, d_{kj}^{η} is the gap between the sender and the recipient node, the path loss factor is represented by η, and φ is given by:

$$\varphi = \frac{G_S G_r \lambda^2}{(4\pi)^2} \quad (5)$$

where G_s and G_r are the antenna gains of sender and receiver nodes, receptively. λ is the wavelength.

Therefore, each player will pay a cost based on its *COP* function, if the *COP* has a high value this affects the vehicle awareness due to increasing the congestion on the wireless channel. On the other hand, a lower *COP* value means a decrease in channel congestion and increases the opportunity to transmit traffic data at a high frequency.

The utility of the price function PR_f is given by:

$$PR_f(R_j^{ap_n}) = COP_j \tag{6}$$

Each vehicle v_j has a cost function represented by $CF_j\left(R_j^{ap_n}\right)$ as follows:

$$CF_j\left(R_j^{ap_n}\right) = \alpha_j\, MS_j\left(R_j^{ap_n}\right) - \mu_j\, PR_f(R_j^{ap_n}) \tag{7}$$

whereα_j and $\mu_j$are weight factors for vehicle v_j *the* cost function such that α_j and $\mu_j > 0$ for all $j = 1, 2, \cdots, m$. This paper has used the NUM model to formulate the specified problem as follows:

$$\begin{gathered} \max_{R_j^{ap_n}} \sum_{j=1}^{m} CF_j\left(R_j^{ap_n}\right), \\ subjet\ to\ \sum_{j=1}^{m} R_j^{ap_n} \le L, \\ 1 \le R_j^{ap_n} \le R_{max}^{ap_n} \quad \forall\, j=1, 2, \cdots, m. \end{gathered} \tag{8}$$

where $R_j^{ap_n}$ is a vector consisting of $R_1^{ap_n}, \cdots, R_j^{ap_n}, \cdots, R_m^{ap_n}$, L represents the maximum data load and $R_{max}^{ap_n}$ depicts the maximum broadcast rate of a single-vehicle.

3 Optimal Data Rate Calculation

The formulated utility function $CF_j\left(R_j^{ap_n}\right)$ has a robustly concave, property and it is unceasingly differentiable function over $R_j^{ap_n} \geq 0$ for all $j=1, 2, \cdots, m$. The formed optimization dilemma in equation (8) has a sole optimal solution according to the optimization theory [17]. Hence, two solutions can be utilized to find the optimal solution in the modeled optimization problem in (8) that are localized or distributed approaches. The localized approaches are efficient in practice because they can obtain the solution quickly [18]. However, this solution has a disadvantage that is an extra communication of cost messages among drivers which in turn drives to overload the channel of the wireless communication. The distributed strategies are more efficient due to the partitioning of the framework into segments that are locally solved to reduce the additional exchange of data among drivers in the network [19]. However, using these methods increase the CPU time that is required to obtain the optimal solution which requires to be rapid in VANETs. This work utilizes the beacon messages to send the congestion information [15]:

$$\psi_j, \zeta_j \geq 0,$$

$$\text{L-} \sum_{j=1}^{m} R_j^{ap_n} \geq 0,$$

$$\nabla \sum_{j=1}^{m} CF_j\left(R_j^{ap_n}\right) + \psi_j \nabla \left(R_{out}^{ap_n} - \sum_{j=1}^{m} R_j^{ap_n}\right) = 0, \tag{9}$$

$$\psi_j \left(\mathrm{L} - \sum_{j=1}^{m} R_j^{ap_n}\right), \zeta_j \left(R_{max}^{ap_n} - R_j^{ap_n}\right) = 0$$

To solve the equation in (9), three unknown's variables ($R_j^{ap_n}$, ψ_j, ζ_j) need to be found. Therefore, three states are estimated based on complementarity constraints optimization:
Case 1: $\psi_j = 0$, $\zeta_j = 0$ and ($1 \leq R_j^{ap_n} \leq R_{max}^{ap_n}$)

$$\alpha_j(0 - (-1)\, e^{(1 - R_j^{ap_n})}) - \mu_j h_{kj} = 0,$$

$$R_j^{ap_n} = \ln\left(\frac{\alpha_j}{\mu_j h_{kj}}\right) - 1$$

Case2: $R_j^{ap_n} = 1 \; and \; \zeta_j = 0$

$$\alpha_j(0 - (-1)\, e^{(0)}) - \mu_j h_{kj} - \psi_j = 0,$$

$$\psi_j = \alpha_j - \mu_j h_{kj}$$

The solution $R_j^{ap_n} = 1$ is considered if the condition ($\psi_j > 0$) satisfied and it is estimated as follows:

$$\alpha_j \geq \mu_j h_{kj} \quad \cdots condition\ 1$$

Case3: $R_j^{ap_n} = R_{max}^{ap_n} \; and \; \psi_j = 0$

$$\alpha_j(0 - (-1)\, e^{(1 - R_{max}^{ap_n})}) - \mu_j h_{kj} - \zeta_j = 0,$$

$$\zeta_j = \alpha_j(e^{(1 - R_{max}^{ap_n})}) - \mu_j h_{kj}.$$

The solution $R_j^{ap_n} = R_{max}^{ap_n}$ is founded, if the condition ($\zeta_j > 0$) satisfied and it is as follows:

$$\mu_j h_{kj} \leq \alpha_j(e^{(1 - R_{max}^{ap_n})}) \quad \cdots condition\ 2$$

Hence, the global optimum of information sending rate ($R_j^{ap_n^*}$) for player v_j; $\forall j \in V$.

$$R_j^{ap_n^*} = \begin{cases} 1 - \ln\left(\frac{\mu_j h_{kj}}{\alpha_j}\right) & otherwise \\ 1 & if\ condition\ 1 \\ R_{max}^{ap_n} & if\ condition\ 2 \end{cases} \tag{10}$$

4 Vehicles Broadcasting Rate Allocation Among Safety Application

VANETs applications require that each vehicle needs to be aware of the priorities of the transmitted messages. Here, this paper assumes that a vehicle, v_j hosts two applications

(beacon and warning messages) with different priorities where $AP = \{ap_n; n = 1, 2\}$.Here, ap_n denotes the priority of transmitted beacon or emergency messages by vehicles. Therefore, a vehicle with a low value of ap_n has a higher priority to transmit traffic information at a high frequency. Once each vehicle determines its transmitted rate ($R_j^{ap_n}$) by using the NUM model. Then, this value is disseminated among safety applications based on their priorities as follows:

$$R_j^{ap_n} = w_j \, R_j^{ap_n^*} \tag{11}$$

$$w_j = \begin{cases} \frac{\sum_{n=1}^{2} ap_n}{(n-1)\sum_{i=1}^{2} ap_n} & if\ n = 2 \\ 1 & if\ n = 1 \end{cases} \tag{12}$$

$$\sum_{n=1}^{2} w_j = 1 \tag{13}$$

Where $R_j^{ap_n}$ represents the transmitted rate of safety application *j* hosted in the vehicle v_j, w_j is preference weight parameter of an application ap and n denotes the number of safety applications.

5 Performance Evaluation

This paper employs Veins that is a vehicular network simulator [20]. Veins consolidate the network simulator OMNeT++ [21] with the traffic simulator Simulation for Urban Mobility (SUMO) [22]. This simulator can control the flow and interaction in vehicular networks. This paper implements a highway scenario to examine and assess the developed approach. A various number of vehicles has been estimated to depicts the effects of increasing density of vehicles on the performance of tested approaches. The rate of the traffic information has been set up to 10MHz and the broadcast spectrum has been declared from 300 to 1000 meters. Table I reveals the parameters of the examined simulation scenario. The vehicle's velocity is selected from 20-32 m/s in the motorway scenario.

Table I: Motorway Scenario configuration parameters

Parameters selection	Values
Dimension of motorway road	850 m motorway scenario
Speed of vehicles	20-32 m/s
Vehicles number	50, 100, 150, 200, 250, 300
Simulation time	250 s
The utilized protocol	WAVE
Range of Transmission	500 m
Rate of transmission	6 Mbps
Information frequency	10 *MHz*
α_j	5
μ_j	0.7

A. Parameters Selection of NUM-DRC

Figs 1 and 2 show the impact of varying preferences parameters in the utility function on information rate and COP. Here, when μ_j is fixed to constant values such as 0.7 and α_j has various states of (2.5, 5.0, and 10.0), respectively. Figs 1 and 2 show that the increasing sending rate of α_j will enhance the traffic information flow in the network but this comes at the cost of consuming the bandwidth due to the channel capacity limit and broadcasting a large amount of information.

However, improving the preference parameter of μ_j will reduce the damage of competition and will minimize the COP. This is due to apply low information frequency as presented in Figs 3 and 4. These two figures show the influence of increasing μ_j weight on the COP and information rate when α_j has a fixed constant value. Therefore, by adjusting the preference parameter μ_j the information rate and the COP will decline and vice versa. Here, values of the preference parameters (α_j and μ_j) have been determined to obtain a balanced approach that can settle the channel congestion conditions.

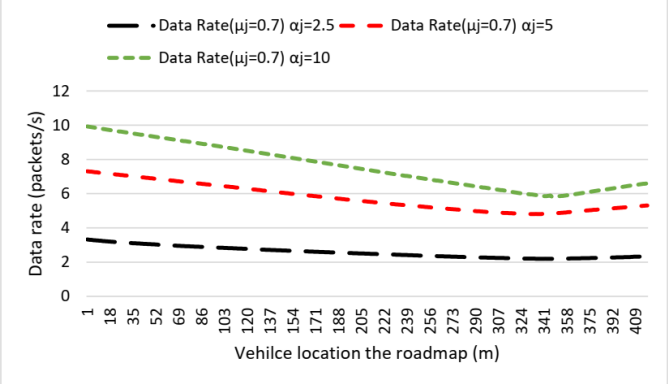

Fig. 1. α_j vs information rate

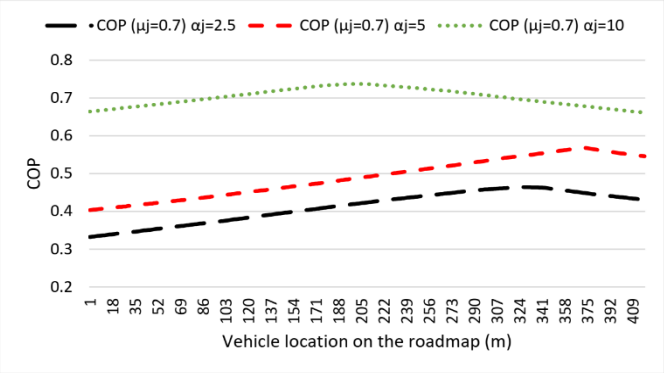

Fig. 2. α_j vs COP

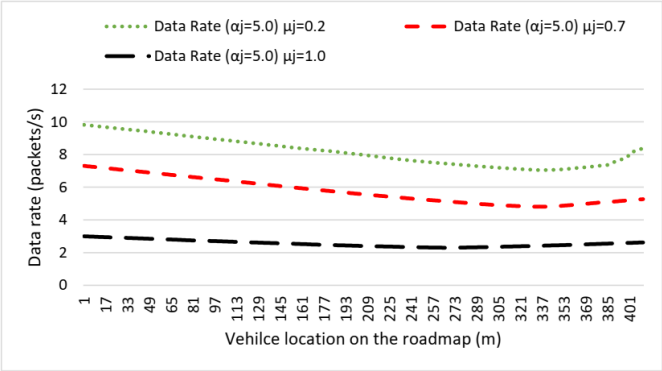

Fig. 3. $\mu_j$vs information rate

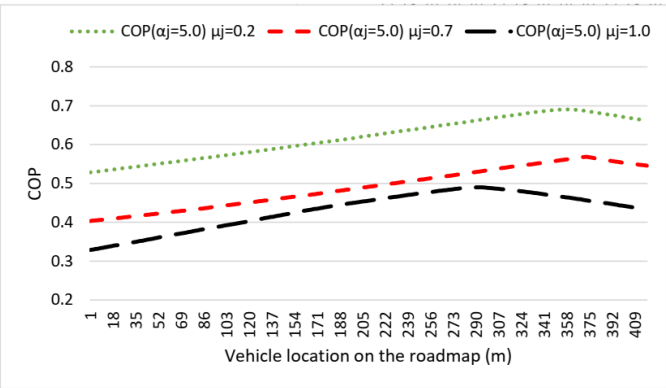

Fig. 4. $\mu_j$vs COP

B. Simulation experiment of NUM-DRC

The evaluation of performance is employed to determine the effectiveness and ability of the developed broadcast protocol. The common performance properties used by many developed congestion control schemes in VANETs are throughput, packet loss rates, occupancy time, and delay on the channel. A review of measurement parameters is displayed as follows.

1. Throughput: It measures the total amount of collected messages at the end node.
2. Delay: This parameter represents the required time to send a message successfully from the sender application layer to the receiver application layer.
3. Messages Loss: It describes the total amount of the channel and buffer lost messages during the simulation time.

Hither, to measure the performance of the suggested approach, a four-lane motorway road has been created in Veins. Fig 5 reveals the motorway scenario that is performed in Veins. Fig 6 illustrates the impact of increasing of flowing vehicles in the simulation scenario on the throughput. The figure records that there is a concrete connection between the density of communicated vehicles and the amount of successfully received messages at destination vehicles, the throughput rises with an increase of the density of the vehicle's number in the communication environment. It is undeniable that the recorded throughput by the NUM-DRC broadcast protocol is more reliable contrasted to the WAVE and GTACC approaches. This is

due to the applied efficient adjustment broadcast protocol that aids to alleviate congestion on the wireless channel and reduces the number of dropped traffic information. This supports improving the number of collected messages at the destination vehicles.

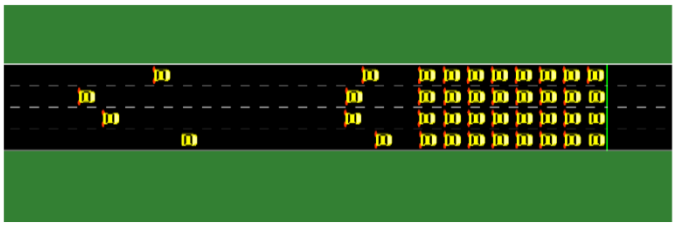

Fig. 5. Motorway scenario for tested approaches

Fig 7 demonstrates the average delay fluctuations effects with increments in the flowing vehicles reported by NUMDRC, WAVE, and GTACC, respectively. According to this figure, it is stated that the increasing density of communicated nodes affects the time delay. Fig 9 points that the time delay values boost when simulation scenario various vehicles number from 50 to 300. Moreover, this figure has shown that the average delay reported by NUM-DRC is more solid when compared to that one recorded by both the GTACC and WAVE.

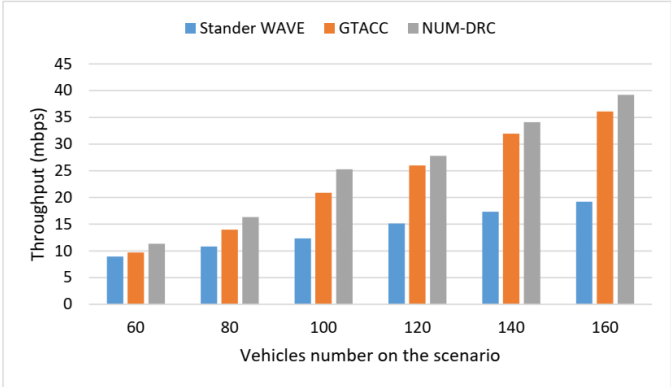

Fig. 6. Throughput of motorway scenario.

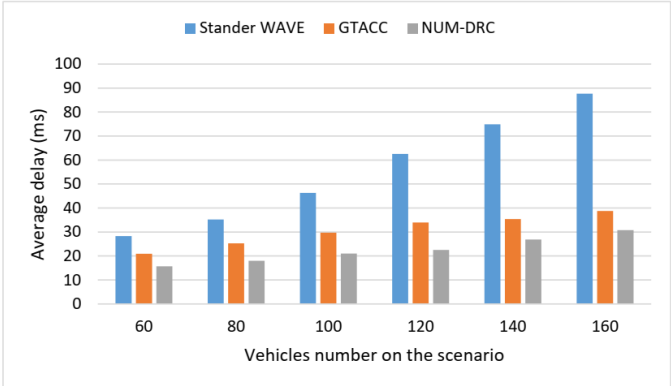

Fig. 7. Average delay of motorway scenario.

Fig 8 describes the mount of loss packets captured by examined approaches. In the dense environments, the amount of flowing vehicles increases which in turn raises the probability of messages loss. This is because of the increment in the competition among the communicated vehicles to obtain the network channel and transmit information simultaneously which causes to a broadcast storm and crash in data. Figure 10 shows that the NUM-DRC has fewer messages loss in contrasted other approaches due to the fair adjustment broadcast protocol of traffic information rate and considering the COP as an objective feature which aids to decline the congestion on the channel.

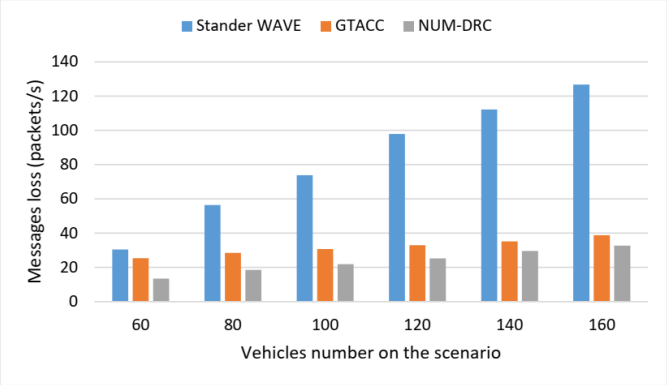

Fig. 8. Messages loss of motorway scenario.

6 Conclusion

As the density of communicated vehicles increases on the road segments, the number of disseminated traffic safety messages is also increased which generates channel congestion problem. This diminishes the vehicular network efficiency and quality of service parameters. Therefore, this work develops a novel broadcast rate adaptation strategy that can reduce channel congestion. This approach formulates channel congestion control in vehicular communication as an optimization problem by applying the network utility maximization method to overcome and alleviate the congestion problem. The significance of the developed broadcast protocol on the vehicular network achievement has been recorded by Veins simulation and tested across a motorway scenario as contrasted to the WAVE protocol and GTACC.

Acknowledgments

The authors are grateful for the support of the Iraqi Government, specialty the Ministry of Higher Education, Southern technical university, and the Technical Institute of Basra.

References

[1] C. C. C. Pang, W. W. L. Lam, and N. H. C. Yung, “A method for vehicle count in the presence of multiple-vehicle occlusions in traffic images,” *IEEE Transactions on Intelligent Transportation Systems*, vol. 8, no. 3, pp. 441–459, 2007.

[2] S. Sharma and S. Sebastian, “IoT based car accident detection and notification algorithm for general

road accidents." *International Journal of Electrical & Computer Engineering (2088-8708)*, vol. 9, 2019

[3] W. Viriyasitavat, T. Anuphaptrirong, and D. Hoonsopon, "When blockchain meets internet of things: characteristics, challenges, and business opportunities," *Journal of industrial information integration*, 2019.

[4] C. R. Storck and F. Duarte-Figueiredo, "A 5g v2x ecosystem providing internet of vehicles," *Sensors*, vol. 19, no. 3, p. 550, 2019.

[5] Z. Tong, H. Lu, M. Haenggi, and C. Poellabauer, "A stochastic geometry approach to the modeling of dsrc for vehicular safety communication," *IEEE Transactions on Intelligent Transportation Systems*, vol. 17, no. 5, pp. 1448–1458, 2016.

[6] J. Singh and K. Singh, "Congestion control in vehicular ad hoc network: A review," in *Next-Generation Networks*. Springer, 2018, pp. 489–496.

[7] L. Wischhof, A. Ebner, H. Rohling, M. Lott, and R. Halfmann, "Adaptive broadcast for travel and traffic information distribution based on intervehicle communication," in *Proceedings of the IEEE IV2003 Intelligent Vehicles Symposium, 2003*. IEEE, 2003, pp. 6–11.

[8] R. K. Schmidt, T. Leinmuller, E. Schoch, F. Kargl, and G. Schafer, "Exploration of adaptive beaconing for efficient intervehicle safety communication," *IEEE network*, vol. 24, no. 1, 2010.

[9] M. I. Hassan, H. L. Vu, and T. Sakurai, "Performance analysis of the ieee 802.11 mac protocol for dsrc safety applications," *IEEE Transactions on vehicular technology*, vol. 60, no. 8, pp. 3882 3896, 2011.

[10] D. Puthal, Z. H. Mir, F. Filali, and H. Menouar, "Cross-layer architecture for congestion control in vehicular ad-hoc networks," in *Proceedings of International Conference on Connected Vehicles and Expo (ICCVE), 2013*. IEEE, 2013, pp. 887–892.

[11] H. M. Amer, C. Tsotskas, M. Hawes, P. Franco, and L. Mihaylova, "A game theory approach for congestion control in vehicular ad hoc networks," in *Proceedings* of IEEE *Sensor Data Fusion: Trends, Solutions, Applications (SDF)*, 2017, pp. 1–6.

[12] F. Gebali, *Analysis of computer networks*. Springer, 2015, NewYork, USA.

[13] S. Keshav, *Mathematical foundations of computer networking*. Addison-Wesley, 2012, Iniana, USA.

[14] Q.-T. Nguyen-Vuong, Y. Ghamri-Doudane, and N. Agoulmine, "On utility models for access network selection in wireless heterogeneous networks," in *NOMS 2008-2008 IEEE Network Operations and Management Symposium*. IEEE, 2008, pp. 144–151.

[15] J. K. MacKie-Mason and H. R. Varian, "Pricing congestible network resources," *IEEE journal on Selected Areas in Communications*, vol. 13, no. 7, pp. 1141–1149, 1995.

[16] Q. Chen, D. Jiang, T. Tielert, and L. Delgrossi, "Mathematical modeling of channel load in vehicle safety communications," in *2011 IEEE Vehicular Technology Conference (VTC Fall)*. IEEE, 2011, pp. 1 5.

[17] D. P. Bertsekas and A. Scientific, *Convex optimization algorithms*. Athena Scientific Belmont, 2015.

[18] D. P. Palomar and M. Chiang, "Alternative distributed algorithms for network utility maximization: Framework and applications," *IEEE Transactions on Automatic Control*, vol. 52, no. 12, pp. 2254–2269, 2007.

[19] Q.-V. Pham and W.-J. Hwang, "Network utility maximization-based congestion control over wireless networks: A survey and potential directives," *IEEE Communications Surveys & Tutorials*, vol. 19, no. 2, pp. 1173–1200, 2016.

[20] Muniyandi RC, Qamar F, Jasim AN. Genetic Optimized Location Aided Routing Protocol for VANET Based on Rectangular Estimation of Position. Applied Sciences. 2020 Jan; 10(17):5759.

[21] Varga A. A practical introduction to the OMNeT++ simulation framework. InRecent Advances in Network Simulation 2019 (pp. 3-51). Springer, Cham.

[22] Behrisch M, Bieker L, Erdmann J, Krajzewicz D. SUMO–simulation of urban mobility: an overview. In Proceedings of SIMUL 2011, The Third International Conference on Advances in System Simulation 2011.

The effect of the electrode tool material type on the surface roughness and tool wear in EDM

Abbas Fadhil Ibrahim[1]
{70011@uotechnology.edu.iq[1]}

Production Engineering and Metallurgy, University of Technology-Baghdad-Iraq[1]

Abstract. Electrical discharge machining (EDM) is a nontraditional procedure for cutting brittle, hard materials and forming challenging forms. It is used to manufacture metal matrix compounds and very solid materials. This research focused on studying the effect of three different materials type of electrodes tool. The performance of electrodes produced from copper (Cu), graphite (Gr), and composite materials (Cu-Gr) specified is compared in assessing the roughness (Ra) of the workpiece and the electrode's wear (EW). These electrodes were used in a process to machine titanium alloy, aluminum alloy, and stainless steel 304 samples. Through the experiments and based on the data obtained, it has been proven that electrodes made of (Cu-Gr), some experiments, showed high performance and wear resistance (WR) than others, and to increase the electrical discharge machining processing efficiency of aluminum alloy and SS304, as well as for the processing of titanium alloy, concluded that it was suitable to use a tool produced of composite materials.

Keywords: EDM, electrodes wear (EW), Al- alloy, SS304, composite materials.

1 Introduction

One of the non-traditional machining's of electrostatic discharge machining (EDM) is mainly widely used frequently for cutting brittle, hard materials and for making difficult shapes [1]. Unwanted metals are separated and removed from the specimen by a series of repeated periodic electric sparks between the electrode and workpiece separated by a dielectric [2]. For the high-precision processing of all kinds of conductive materials, from alloys regardless of hardness, EDM is used in the manufacture of important parts, such as gearbox housings, copiers, and many others [3]. The main feature of this technology compared to other traditional machining methods is the ability of electrical discharge machining to machine any hard material, ensuring surface properties and high precision [4]. Determine the optimal solution and quality improvements of machined surface, with result in decreases in operating cost [5]. These components operate under variable loads and temperature conditions, high-strength materials are used, such as titanium-aluminum-tungsten-based alloys, thermally strengthened steel alloys, and others[6].

At present, several composite materials to wear resistance have been developed, which can enhance increase the WR of the tools compared to the materials used traditionally. The use of a composite material consisting of colloidal Cu-Gr containing less than 2% graphite is one of the most used materials to solve this problem [7]. Electrode tools made of composite materials are produced using the metallic powder method. Thus, it is possible to change the technological standards and chemical composition of the powders used in the development of compounds to

IMDC-IST 2021, September 07-09, Sakarya, Turkey
Copyright © 2022 EAI
DOI 10.4108/eai.7-9-2021.2314806

the electrode using this technique which makes it possible to greatly improve its properties [8]. Le Hong Ky et.al [9] designed some parameters and analyzed them according to the Taguchi method with an orthogonal array. Also, were investigated the input parameters such as Pon, Poff, Ip, and Sv. The effect of these factors on the Ra was estimated by analyzing variance. Using a Tungsten: Copper composite electrode, J Prasanna et al. [10] investigate tool wear rate (TWR) and material removal rate (MRR). The Ra of electrical discharge machine samples with Electrode Tool (ET) materials was examined by T Ablyaz et al [11]. Three distinct types of ETs were explored for the trials, each constructed of a different material: composite, copper, and graphite. The workpiece materials were chosen from aluminium, low alloy 35GS steel, and OT4 titanium alloy. Maradona and Wykes [12] used the Taguchi approach to provide a new way for optimising the removal rate of EDM using Cu-W tools, resulting in an increase in MRR. When Goyal et al. [13] compared the MRR and TWR of pure copper and copper tungsten tools, they discovered that composite material tools have better performance and wear resistance. Through a review of the literature, it was found that it is necessary to study the characteristics of tools produced from composite materials to enhancement machining dissimilar alloys Also, this paper aims to verify the performance of electrode tools to surface roughness and wear resistance when the operation of titanium alloy, aluminum alloy and stainless steel 304.

2 Experimental Procedure

Taguchi method was used to designed and analyzed the experiment's work. Also, five input parameters including the workpiece material, electrode material, Ip, Pon, and Poff, were selected for the investigation. CNC-based EDM machine (CHEMER CM 323C), as illustrated in Fig 1 was used in experiments. Copper, graphite, and composites containing copper and 2% graphite were used in the manufacture of the electrodes Fig 2. The physical properties of three types of electrodes as shown in Table 1 The workpiece of Ti- alloy, Al- alloy 6061, and SS 304 were prepared of dissimilar materials. The independent process factor levels for EDM are described in Table 2.

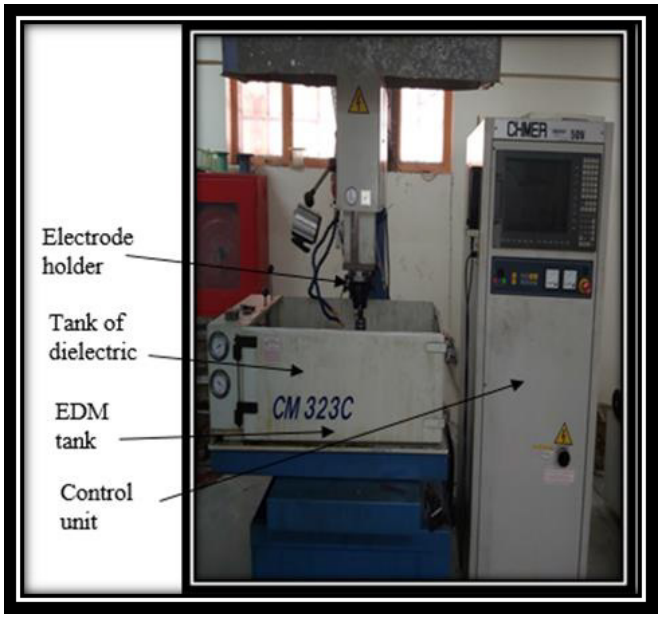

Fig 1. EDM CM323C CNC Machine.

Fig 2. Three types of electrode tools.

Table 1. Physical properties of copper, graphite, and copper-graphite electrode.

Physical properties	Copper	Graphite	copper - graphite
Electrical resisitively(μΩ/cm)	1.96	0.12	1.81
Electrical conductivity compared With Silver(%)	92	0.11	87
Thermal conductivity (W/mK)	380.7	160	367
Melting point(°C)	1083	455	1118
Specific heat(cal/g°C)	0.092	0.18	0.11
Specific gravity at 20°C(g/cm^3)	8.9	1.75	8.4

Coefficient of thermal Expansion($x10^{-6}{}^{o}C^{-1}$)	6.6	7.8	6.9

Table 2. Input process parameters for EDM.

Factor	Level		
	1	2	3
Workpiece material	Titanium alloy	Aluminum alloy	SS304
Electrode material	Copper	Graphite	Copper-graphite
Current (A)	10	20	30
Pulse on time (µsec)	100	150	200
Pulse off time (µsec)	6	12	18

An orthogonal matrix L27 (35) (27 tests, 5 factors, 3 levels) was created. After all of the studies, the surface roughness (Ra) was determined using a portable Maher Federals surface roughness gauge. The weight of the tool was also monitored in this experiment to track volumetric loss owing to abrasive wear as a result of machining.

3 Methodology

The Taguchi method and analysis of variance (ANOVA) were used to determine the influence and contribution of input factors in the experimental data analysis.

3.1 Taguchi

It is frequently used as a powerful programme for assessing process parameters in all applications [14]. In this study, a specially built orthogonal array from Taguchi was utilised to explore the impacts of processing factors in a small number of experiments, which requires less time.

3.2 Signal-to-Noise (S/N) ratio characteristics

The signal-to-noise ratio was employed to assess experimental design modifications. The term signal denotes a desired value, whereas the term noise denotes an unfavourable value [15]. The S/N ratio is calculated using the following equation to produce the least Ra and TW:

$$S/N = -10 \log\left[\frac{1}{n}\sum_{i=1}^{n}(y^2)\right] \quad (1)$$

Where n: number of replications.
yi: observed response value

4 Results and Analysis

According to the design of experiments (DOE) by the Taguchi method, the results of the experimental work for (Ra) and (ER) are presented in Table 3. The highest quality was obtained in evaluating the surface roughness of the machine surface by using an electrode tool made of

copper. The electrode produced from (Cu-Gr) possesses 2.5- and 1.1-times higher surface quality than the electrode produced from Cu and Gr respectively. By analyzing the wear resistance results of titanium samples, it was found that the copper-graphite electrode has a resistance of 1.2 times higher than that of the control. During the experiments, the parts of the particle were adhesion to the work of electrode surface and thus the weight of the graphite electrode increased after the operation.

Table 3. Design of experimental and the output response.

No.	Workpiece material	Electrode material	current(A)	Pon(µs)	Poff(µs)	Ra(µm)	Ew(gr)
1	Ti-alloy	Cu	10	100	6	2.386	0.0036
2	Ti- alloy	Cu	10	100	12	2.314	0.0032
3	Ti- alloy	Cu	10	100	18	2.311	0.0027
4	Ti- alloy	Gr	20	150	6	3.771	0.0000
5	Ti- alloy	Gr	20	150	12	3.655	0.0000
6	Ti- alloy	Gr	20	150	18	3.672	0.0000
7	Ti- alloy	Cu-Gr	30	200	6	4.923	0.0028
8	Ti-alloy	Cu-Gr	30	200	12	4.841	0.0026
9	Ti- alloy	Cu-Gr	30	200	18	4.872	0.0022
10	Al- alloy	Cu	20	200	6	7.438	0.0017
11	Al- alloy	Cu	20	200	12	7.116	0.0014
12	Al- alloy	Cu	20	200	18	6.846	0.0014
13	Al- alloy	Gr	30	100	6	6.845	0.0000
14	Al- alloy	Gr	30	100	12	6.822	0.0000
15	Al- alloy	Gr	30	100	18	6.607	0.0000
16	Al- alloy	Cu-Gr	10	150	6	8.117	0.0006
17	Al- alloy	Cu-Gr	10	150	12	7.593	0.0006
18	Al- alloy	Cu-Gr	10	150	18	7.734	0.0004
19	SS304	Cu	30	150	6	5.296	0.0037
20	SS304	Cu	30	150	12	5.246	0.0032
21	SS304	Cu	30	150	18	5.337	0.0025
22	SS304	Gr	10	200	6	4.978	0.0000
23	SS304	Gr	10	200	12	4.836	0.0000
24	SS304	Gr	10	200	18	4.811	0.0000
25	SS304	Cu-Gr	20	100	6	6.721	0.0004
26	SS304	Cu-Gr	20	100	12	6.744	0.0002
27	SS304	Cu-Gr	20	100	18	6.578	0.0002

From Table 3. It was observed that when operating the aluminum alloy, the wear resistance of the Cu-Gr electrode tool was increased by an amount3.3 times higher wear strength than the tool produced from Cu, but the Ra when using the tool produced from copper-graphite possesses was 0.4- and 0.7-times higher surface quality than the tool produced from copper and graphite respectively and enhanced significantly than other electrodes.

An analysis of the obtained data using SS304 showed that a tool produced from Cu-Gr possesses a wear resistance that is 4.5 times higher than that of a tool made of Cu. It also gives a lower surface quality than copper and graphite. While the highest surface quality obtained was when using the graphite tool.

The influence of parameters workpiece material, electrode material, (Ip), (Pon), and (Poff) on the surface roughness is shown in Fig 3. the Ra decreases upon decreasing the (Pon), and (Ip). Experiments have demonstrated that the workpiece and electrode material have an effect on improving surface roughness, with the titanium alloy as the workpiece and copper as the

electrode material reducing surface roughness. The depth of the EDM's drilling surface grows as peak current increases, resulting in a larger value of Ra. These variables affect the power input, and it's possible that a lower power input enhances the surface polish.

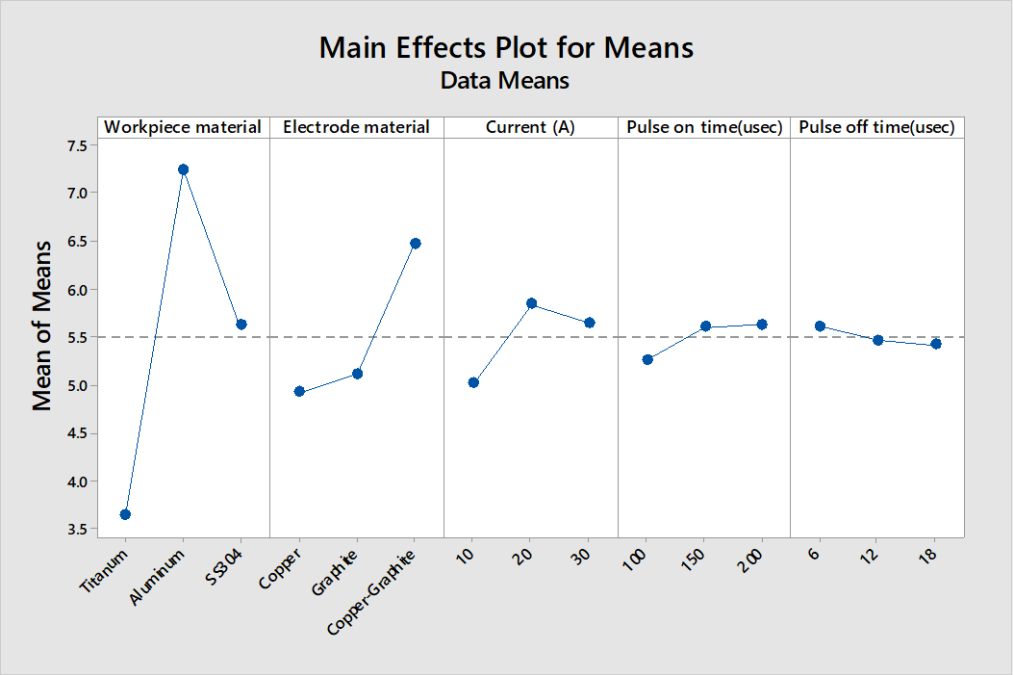

Fig 3. Main effects of each parameter on surface roughness.

The influence of process parameters on electrode wear is shown in Fig. 4. The electrode wear increases with using titanium alloy as workpiece and copper material as electrode tool increasing Pon, and Ip. Due to the increased cutting speed, more energy is delivered to the cutting process as the pulse duration increases. Increasing the current causes the Pon to rise, which improves the cutting rate even more.

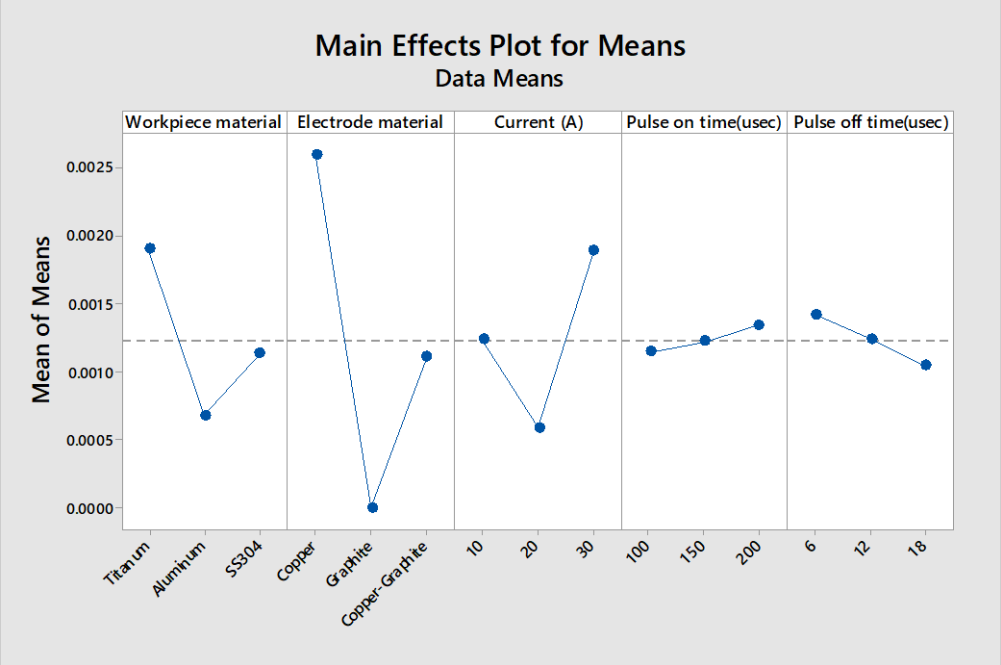

Fig 4. Main effects of each parameter on electrode wear.

5 Conclusions

Three types of electrode tool material on surface roughness and tool wear by using three dissimilar workpieces in EDM sinking by the Taguchi design method has been presented. Based on analyzing the data obtained from the experiments, it can be concluded that :

1- The highest surface quality obtained was when using the graphite tool, while the lower surface quality obtained was when using the composite electrode.

2-When a composite material is used for the electrode, some experiments, showed high performance and wear resistance than others and increase the electrical discharge machining processing efficiency of aluminum alloy and SS304, as well as for processing raw EDM of titanium alloy.

3- Concluded that it was suitable to use a tool produced of composite materials.

References

[1] K. Ojha, R. K. Garg, and K. K. Singh. MRR Improvement in Sinking Electrical Discharge Machining: A Review, Journal of Minerals & Materials Characterization & Engineering,2010, 9(8), p. 709-739.

[2] S. B. Chikalthankar, V. M. Nandedkar, S. V. Borde, 2013 Experimental Investigations of EDM Parameters, International Journal of Engineering Research and Development.2013, 7, p. 31-34.

[3] ShazarelShamsudin, Mohamed ShaikYusof. Electrical Discharge Machining (EDM) Of Beryllium Copper Alloys Using Design Of Experiment (Doe) Approach, International Engineering Convention, Damascus Syria.2009, 11, p. 257- 268.

[4] Yeliseyev Y, Savushkin B EDM of aerospace products (Moscow: MSTU him NE. Bauman),2010 , p 437.

[5] KapoorJatinder, Singh Sehijpal and KhambaJaimal, Effect of cryogenic treated brass wire electrode on material removal rate in wire electrical discharge machining, Proceedings of the Institutionof Mechanical Engineers, Part C: Journal of Mechanical Engineering Science. 2012, 226(11), p. 2750-58.

[6] A O Grisharin, N D Ogleznev, K R Muratov, T R Ablyaz, S B Preetkanwal and S SSarabjeet, Investigation of the machinability of composite materials electrode-tools while EDM,IOP Conf. Series: Materials Science and Engineering.2019, 510.

[7] Grisharin A, Ablyaz T and Ogleznev N 2017 Improving the efficiency of machining parts of hydraulic cylinders and special-purpose products through the use of electrode tools with enhanced electroerosion properties (Perm: Perm national research polytechnic university, University Press) p 151.

[8] Bains P, Payal H and Sidhu S 2017 Analysis of Coefficient of Thermal Expansion and Thermal Conductivity of Bi-Modal SiC/A356 Composites Fabricated via Powder Metallurgy Route doi:10.1115/ht2017-5122.

[9] Le Hong Ky1, Tran Thi Hong2, Nguyen Van Cuong3, Tran Thanh Hoang4, Do Thi Tam4, LuuAnh Tung4, Nguyen Thanh Tu4, Vu Ngoc Pi4, Effect of Electrical Discharge Machining on Surface Roughness of Cylindrical Shaped Parts , Key Engineering Materials, Vol. 853, pp 13-17,2020.

[10] N. Beri, S. Maheshwari , C. Sharma, and Kumar, “Optimization of electrical discharge machining process with CuW powder metallurgy electrode using grey relation theory”. International Journal of Machining and Machinability of Materials, Vol. 9, No.1/2, pp. 103 – 115, 2011.

[11] T Ablyaz1, E Shlykov1, K Muratov1, S Oglezneva1, V Karmanov1, I Osinnikov1, S S Sarabjeet2 and D Sahil, Experimental analysis of the EDM process of dissimilar materials, IOP Conf. Series: Materials Science and Engineering 754 (2020).

[12] P. Goyal, “Enhancement of MRR in EDM by composite material electrode on die steel,” International Journal of Science, Engineering and Technology Research (IJSETR), Vol 3, Issue 10, October 2014.

[13] J. Prasanna, S .Rajamanickam, K. O. Amit , and R. G . Karthick, “Sathya Narayanan P V. MRR and TWR evaluation on electrical discharge machining of Ti-6Al-4V using tungsten : copper composite electrode,” Frontiers in Automobile and Mechanical Engineering, IOP Conference Series: Materials Science and Engineering, PP. 197 – 012087, 2017.

[14] Abbas F. Ibrahim , Abdullah F. Huayier , Naeem A. Abdulhusein 2021 Influence of machining parameters on material removal rate in chemical machining of silicon carbide (SIC), Journal of Physics: Conference Series 1818 .

[15] Abbas Fadhil Ibrahim and Ali Mundher Mustafa 2019 Experimental investigation of machining parameters on material removal rate and surface roughness in chemical machining, IOP Conf. Series: Materials Science and Engineering 518 .

Optimum Design Parameters with the Lowest Cost of Basra Refinery Kettle Reboiler

Husam J. Alsaemre[1], Adnan A. Ateeq[2], and Ali N. Kalaf[3]
Eng.hussam1980@gmail.com[1], Adnan_ateeq@stu.edu.iq[2], alinasiralmajed@gmail.com[3]

Department of Thermal Mechanical Engineering, Southern Technical University, Basra, Iraq[1,2]
Department of Chemical Engineering, College of Engineering, University of Basra, Basra, Iraq[3]

Abstract: Operating a kettle reboiler on high efficiency has been the foci of this study. In this study, an attempt to choose the best design parameters and the optimal operating conditions to attain the highest efficiency while maintaining the annual cost at the lowest. Aspen plus® and Aspen exchanger design and rating (EDR)® software V10 were implemented for design simulation and optimization calculations to control those factors connected to heat transfer coefficient, which is an indication of the efficiency. The study used to apply techniques on the kettle reboilers available in enhancing the gasoline unit in Southern Refinery Company in Iraq. A conclusion found that cast iron is the best metal type while the suitable diameter is found 25.4 mm and optimum operating conditions was 493 k and 4 kg/s, the temperature of cold in-stream and mass flow rate of the fluid entering the hot stream respectively, this yields to increase the efficiency by 28.27%.

Keywords: Kettle reboiler, Aspen Plus®, Aspen EDR®, simulation, optimization, Heat exchanger.

1 Introduction

Reboilers are heat exchangers commonly used to heat the bottoms of industrial distillation columns are generally utilized in the petroleum industry. Since distillation is such a critical process in the petroleum, petrochemical, and chemical industries, the effective-reboiler operation is also necessary when a liquid might also need to be vaporized for various reasons, especially when a liquid feed is needed to be vaporized before entering a reactor. Normally, the liquid boils inside the shell by the effect of hot fluid flows in the tube side. The contact-liquid flows in the outer surface area of the tube will change their phase by receiving the latent heat transfer from the tube side, the vapor that produces will be used in the specific process for the reason which the reboilers was manufactured. The design of a reboiler is determined by the type and uses of the process to select the correct and suitable one. Reboiler classified according to the circulation type into forced and Natural circulation[1]. The use of a specific type of reboiler for a specific operation must first be through a full knowledge of the types of reboilers, their classification, advantages, and disadvantages of each type [2]. The simulation will now be carried out in almost all the areas of sciences and especially in engineering. It is important to improve and optimize the design, chemical, and physical properties used in the simulation program's approach can be calculated using statistical models. Heat exchangers with the same surface area but a different height and diameter produce a different average heat transfer coefficient [3]. a model for simulating the fluid dynamics and pillow plate thermal performance thermosiphon of reboilers' correlations for the single-phase heat transfer coefficient were used, the heat transfer coefficient with nucleate boiling was calculated [4]. Kettles reboiler with two phases flow was simulated in two dimensions, the one-fluid model was created. The one fluid model demonstrated that tube liquid evaporation can occur often at low heat flux than the earlier assumed and that the fluid kinetic energy required to cause tube vibrations was much lower than previously occurred [5]. A 241-tube thin slice kettle reboiler was used to study the two-phase flow phenomenon when boiling R113 and n-pentane, it was discovered that the height of the row pressure drop distribution in each column was unaffected by the mixture [6]. A kettle reboiler shell side thermal hydraulics simulation and analysis were shown. The computational fluid dynamics approach (CFD) was used to present the model. The main finding was that in mixture models, simulating the slip between liquid and gas-phase velocity, or simulating the interface friction model in two-fluid models, had a substantial influence on the void fraction distribution and two-phase flow area. [7]. Presented a simulation of a kettle reboiler. A hydrodynamic model has been developed using a rectangular tube sheet. Results demonstrate that the rate of the reboiler recirculation has been shown to differ with the heat flux and pressure. Furthermore, mass flux and heat transfer coefficient has shown steadily rising from the bottom to the top tube row of the package at a known value of heat flux and pressure vapor quality [8]. A simple model that split the evaporator into two parts (region for heating and evaporation) described the results of all of these parameters. The operating characteristics of these two zones are determined by the length differences of these two zones [9]. The

IMDC-IST 2021, September 07-09, Sakarya, Turkey
Copyright © 2022 EAI
DOI 10.4108/eai.7-9-2021.2314804

repercussions of these recasting for the Data from thin-sliced rigs were used to determine the design of full-scale kettle reboilers, moreover, Shell side evaporators recirculation was discussed, which has been done by used 241 tubes package kettle reboiler thin slice device [10]. Under the multiple objective optimizations scheme, an improved version of the genetic algorithm was used for this. This optimization method was used to locate a set of optimal points identified as the Pareto-optimal set [11]. Used the Aspen HYSYS simulation software to simulate and optimize a crude oil distillation plant in a refinery to increase the unit's performance. The simulation-derived optimum operating conditions improved the plant's performance, resulting in higher kerosene and naphtha produces [12]. An optimized model for dropping film from plate-fin condenser-reboilers, the suggested geometrical optimization method, and analysis results could provide technical guidelines for designing and optimizing actual falling film from plate-fin condensers-reboilers and other falling film type plate-fin heat exchangers for cryogenic device applications[13]. This research includes studying the influence of factors that affect optimal performance and the cost of kettle reboiler that is used in enhancing gasoline units in Southern Refinery Company in Iraq.

2 Process Description

Since the purpose of the study is to increase the performance and efficiency of the reboiler through simulation by using the Aspen Plus®, Aspen EDR® program V 10, the design of projects and the calculation of the equipment cost through AspenTech items depend on a predefined design and cost considerations, the costs are described in the cost estimate database of AspenTech, where the AspenTech program also identifies the construction metals, handling, and landing costs, in which the latest versions or with old versions, the AspenTech cost calculation foundation and database are updated usually.

For that reason, this study clarifies the relationship of all variables and factors that affect the increase in performance and efficiency, whether mechanical or thermal, to reach the optimal design, as well as taking into consideration the design cost, where a case study of a kettle reboiler was taken from Southern Refinery Company, the procedure done by the following steps:

1- Aspen Plus simulation for kettle reboiler: Aspen Plus V 10 was used to simulate a kettle reboiler, the chosen components in the hot stream (tube side) were benzene and hydrogen (1% mole fraction), and in the cold stream (shell side) was benzene, the table (1) represents the data of the operation condition (pressure, temperature, and mass flow rate) and the basic design information that has been taken from the case study in the enhancement benzene unit at the southern refinery company which is used as input for the simulation in the program. Benzene is a mixture of petroleum components that consists of 36 materials for the cold stream and 38 materials for the hot stream.

The components that were used were selected in the databank of the program and the ratio of composition of components was input for the cold and hot streams. The fluid package that was used in the simulation model was the Peng-Robinson equation of state, which is the suitable method that can be used to calculate the properties (such as the enthalpy, entropy, etc.) of fluid or fluid-mixture. **Figure (1)** show the simulation environment of the kettle reboiler and the input data in Aspen Plus.

Table 1: Data for Operation Conditions

Data for Hot Stream (Tube): BENZENE+H_2				
IN			OUT	
P	35.97	bar	35.928	bar
T	788	k	568	k
$\dot{m}$	3.055	kg/s (vap.)	3.055	kg/s (vap.)
Data for Cold Stream (Shell): BENZENE				
IN			OUT	
P	25.83788	bar	25.668	bar
T	503	k	505	k
$\dot{m}$	20.48	kg/s (liq.)	11.8675	kg/s (vap.)

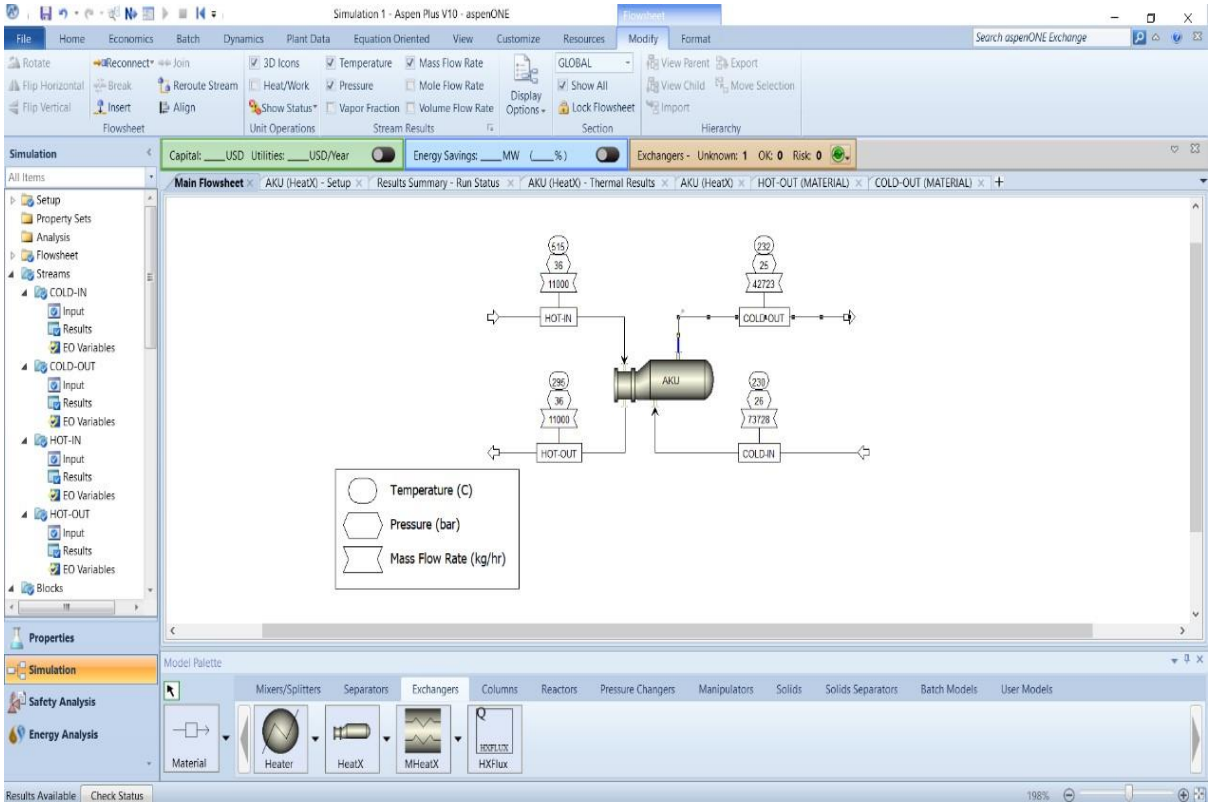

Fig. (1): The Simulation of Kettle Reboiler Using Aspen Plus.

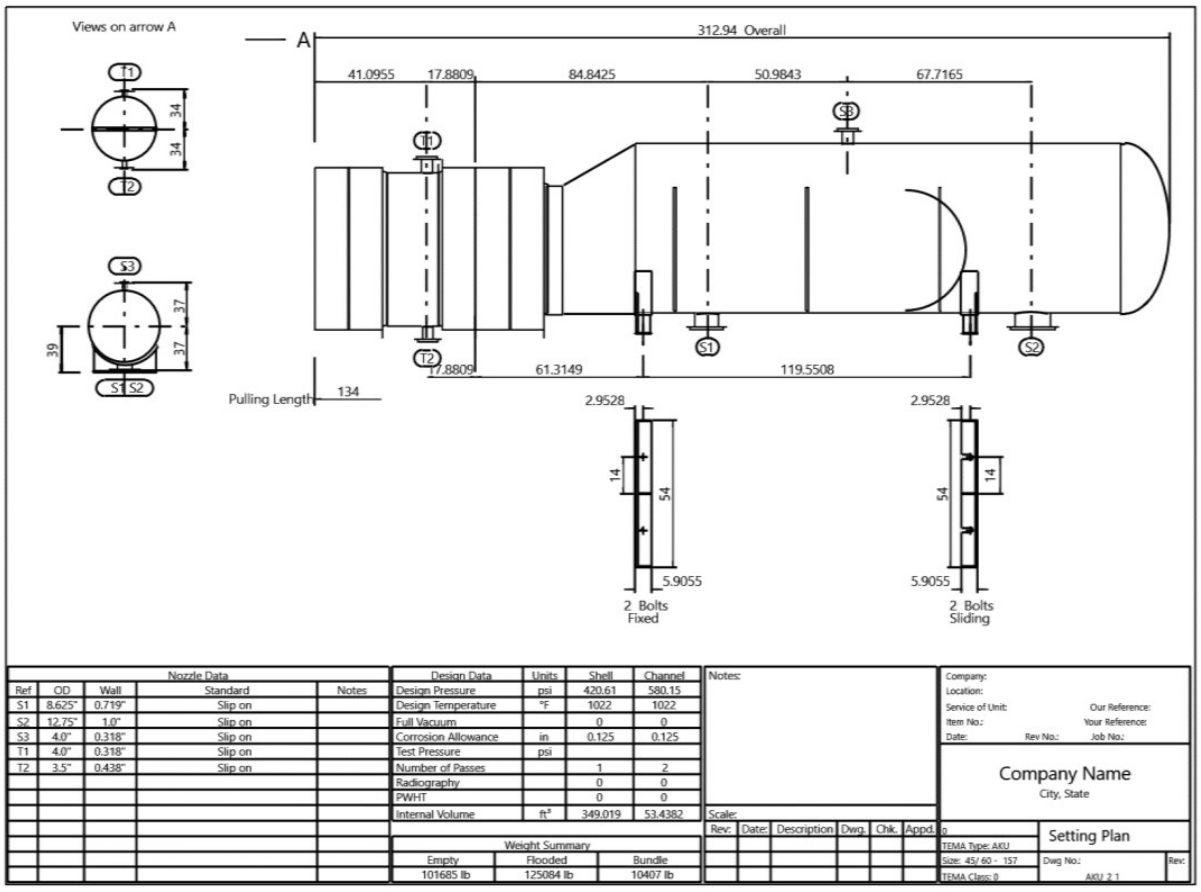

Fig. (2): The Simulation of Kettle Reboiler Using EDR.

2- Aspen exchanger design and rating (EDR): Critical methods are sizing new equipment and rating existing equipment to provide sufficient space and selecting the right exchanger type for given use as shown in Fig 2. At a given set of process parameters, this will result in the most cost-effective heat exchanger configuration. This broad variety of device requirements is addressed by Aspen EDR and they're useful for both the infrastructure contractor and the equipment fabricator, enabling models to be moved from prototype to practical troubleshooting. EDR is used to design the heat exchanger after the information data of the flow rate and temperature were obtained for the hot and cold streams in Aspen Plus where EDR used these data for calculations. The mechanical data that used in the modeling simulation in design the kettle reboiler by EDR is that for the internal and outside shell diameter is 1150 and 1200 mm respectively and for the tube, the number of the tube is 200 with an internal diameter of 25 mm and a thickness of 2.5 mm also 4000 mm length and using a tube pitch of 32 mm.

3- Simulation of design variable: In this research, the effect of a set of design and operational variables on the kettle reboiler was studied, take a case study of a kettle reboiler located in the Southern Refinery Company at the gasoline enhancing unit. Table (2) below represents the simulation result from the Aspen Plus program. The kettle reboiler design calculation equations were also compared with the results of the Aspen Plus program and EDR, and the effects of design variables on costs were also calculated during those operations.

Table 2: The Simulation Result by Aspen Plus.

Data for Hot Stream (Tube): BENZENE+H_2				
IN			OUT	
P	35.97	bar	35.928	bar
T	788	k	568	k
λ	170.3	kJ/kg		
ρ	5.721	kg/m³		
μ	0.023	cP		
=	0.000023	N.s/m²		
k	0.931	W/m. k		
C_p	3.932	kJ/kg.k		
$\dot{m}$	3.055	kg/s (vap.)	3.055	kg/s (vap.)
Data for Cold Stream (Shell): BENZENE				
	IN		OUT	
P	25.83788	bar	25.668	bar
T	503	k	505	k
$\dot{m}$	20.48	kg/s (liq.)	11.8675	kg/s (vap.)
P_c	33.83	bar		
P	25.837	bar		

4- Create a structure of a thermo-hydraulic design strategy (mathematical model), The mathematical model's purpose is to figure out the overall heat transfer coefficient, the heat exchanged area required, number of tubs, and heat duty for the kettle reboiler The design equation [14] that used as follows:

$$\text{Heat Duty } (Ø): Ø = \dot{m} * \lambda * 1.05 \quad (1)$$

Where (1.05=5% of heat losses)

$$\text{Mean temperature difference } (\Delta T_m): \Delta T_m = \Delta T_{ln} * F \quad (2)$$

$$\Delta T_{ln} = \frac{\Delta T1 - \Delta T2}{\frac{\Delta T1}{\Delta T2}} \quad (3)$$

The exchanger required area (A)

$$A = \frac{\emptyset}{U_{\circ}\,\Delta T_m} \tag{4}$$

No. of Tubes (Nt):

$$Nt = \frac{A}{\pi * Do * L} \tag{5}$$

The number of tubes pass (NP)

$$N\ pass = \frac{Nt}{2} \tag{6}$$

Cross-section area (AC)

$$A\ cross = \frac{\pi * (Di)^2}{4} \tag{7}$$

Area pass: Apass= Npass * A cross (8)

Velocity in tubes(v):

$$v = \frac{\dot{m}}{\rho * A\ pass} \tag{9}$$

Reynolds Number (Re):

$$Re = \frac{\rho * v * Di}{\mu} \tag{10}$$

Shell side boiling coefficient (h_o) from Mostinski Equation:

$$h_0 = 0.104 * Pc^{0.69} * \left(\frac{\emptyset}{A}\right)^{0.7} * \left[1.8\left(\frac{P}{Pc}\right)^{0.17} + 4\left(\frac{P}{Pc}\right)^{1.2} + 10\left(\frac{P}{Pc}\right)^{10}\right] \tag{11}$$

Prandtl Number (pr):

$$Pr = \frac{cp * \mu}{K} \qquad , where\ Nusselt\ number = \frac{hi * Di}{K} \tag{12}$$

Tube side heat transfer coefficient (*hi*)

$$\frac{hi * Di}{K} = 0.23 * Re^{0.8} * Pr^{0.3} \tag{13}$$

The overall heat transfer coefficient (U_o) :

$$U_0 = \frac{1}{\frac{1}{h_0} + \frac{1}{hod} + \frac{Do * \left(\ln\frac{Do}{Di}\right)}{2K_w} + \left(\frac{Do}{Di} * \frac{1}{hid}\right) + \left(\frac{Do}{Di} * \frac{1}{hi}\right)} \tag{14}$$

Where (K_w) is the thermal conductivity of tube metal.

5- Model validation: Validation is the procedure of verifying whether the simulating and the modeling and their related results are matching the results of the mathematical model, This comparison between the simulation and mathematical model is very important to verify these results. Table (3) shows a comparison between the Aspen Plus results obtained from the simulation and the mathematical model (design equation) we notice a great convergence between the results in the two cases, and this indicates that the simulation results are valid and reliable in design calculations, with an acceptable error margin of 7.1% for the overall heat

transfer coefficient, 1.3% for the heat exchanged, 0.43% for heat exchanged area and 0.25% for the number of tubes.

Table 3: The Model Validation

Design Parameters	Aspen Plus Calculations	Design Equation Calculations
Number of tubs	200	200
Heat exchanged area	62.3 m^2	62.57 m^2
Heat exchanged	2094.3 kW	2122.087 kW
overall heat transfer coefficient	361.7 $W/m^2.k$	335.76 $W/m^2.k$

3 Result and discussion

Many parameters affect the tube design of the kettle reboiler and that's led to reflected in the overall design and cost. In this section the mechanical and thermal variable design will discuss as follow:

3.1 Effect of tube diameter: The table below (4) shows that the change of tube diameter reflects on the area which makes a change in heat exchanged, overall heat transfer coefficient, mean temperature difference, which led to an impact on the cost. The marked with red row represents the simulation of the case study in which its result will be adopted in this study. And it's clear that the smaller the diameter of the tube is the greater heat exchanged and overall heat transfer coefficient as shown in **Figure (3)**. The cost calculation is shown in appendix (1) which demonstrates the cost calculation by the EDR program. Increasing the heat transfer coefficient as the tube diameter decreases, because reducing the tube diameter raises the fluid flow velocity, which increases the Reynolds number, thus boost the Nselt number, which increases the heat transfer coefficient.

Table 4: Tubes Diameter Change and Its Effects.

Tube Dia. mm	Area m^2	Heat Exchanged kW	U_o $W/m^2.k$	Total Cost USD$
12.7	31.8	2146.4	1133.6	275181
15.88	39.5	2138.4	782.5	275727
19.05	47.4	2124.7	572.7	276254
22.22	55.3	2108.1	438.8	276580
25.4	62.3	2094.3	361.7	277088
28.58	71.2	2076.7	288.2	277712

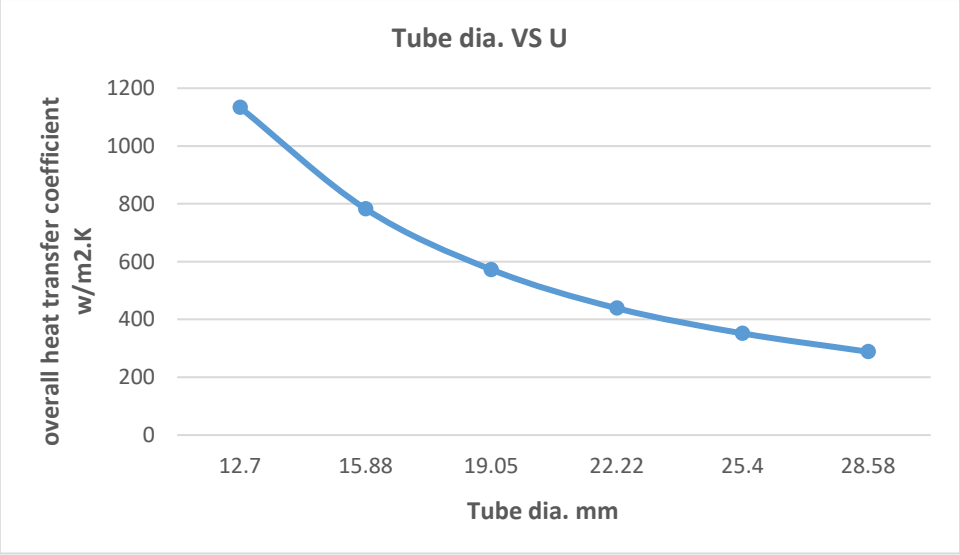

Fig. (3): Tubes Diameter and Its Relation With Overall Heat Transfer Coefficient

3.2 Effect of Reboiler metal: The difference in the metal of the reboiler has a great impact on the design due to the difference in the overall heat transfer coefficient for each metal as well the huge impact

on the cost as shown in Appendix (2) which clarify how the change in the metal effect on the overall cost of the reboiler which is calculated by the simulation in the EDR. While table (5) shows the effect of the change in the metal of the tubes on the heat exchanged, the mean temperature difference, the cost of the tubes, and the overall cost, on other hand, it doesn't affect the area and the number of tubes.

Table 5: Tubes Metal Change and Its Effects.

Tube Metal	Area m^2	Heat Exchanged kW	NO. Of Tubes	Tube Metal Cost USD$	Total Cost USD$	U $W/m^2.K$
Carbon steel	62.3	2094.3	200	3344	277024	361.7
SS-304	62.3	2088.5	200	8101	245880	353.6
Titanium	62.3	2087.5	200	66402	914185	352.3
3.5Ni steel	62.3	2093.6	200	23601	374867	360.9
Copper	62.3	2098.3	200	17300	661960	368.07
Aluminum 3003	62.3	2097.8	200	2955	436003	367.3
Al-Ni Bronze	62.3	2097.1	200	43080	799506	366.5
SS-321	62.3	2088.1	200	212390	317340	353.03

From **Figure (4)**, which shows the heat exchanged when changing the tube metal, and **Figure (5)** which shows the reboiler metal (the shell and tubes) against the cost, it is possible to choose the best type of metal that meets the requirements of the reboiler process and the lowest total cost. In addition, consideration must be given to values of the overall heat transfer coefficient which shows in **Figure (6)** for choosing the best metal for the design. Obviously, by comparing the cost with the values of the heat transfer coefficient, it becomes clear that cast iron is the best choice.

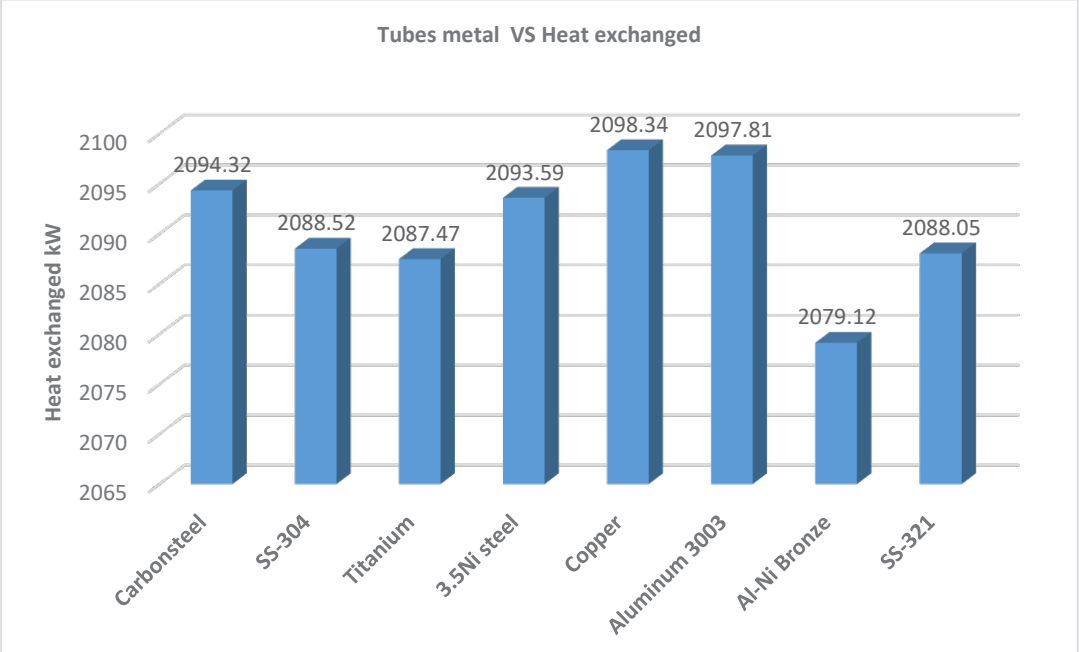

Fig. (4): Tubes Metal and Its Relation With Heat Exchanged.

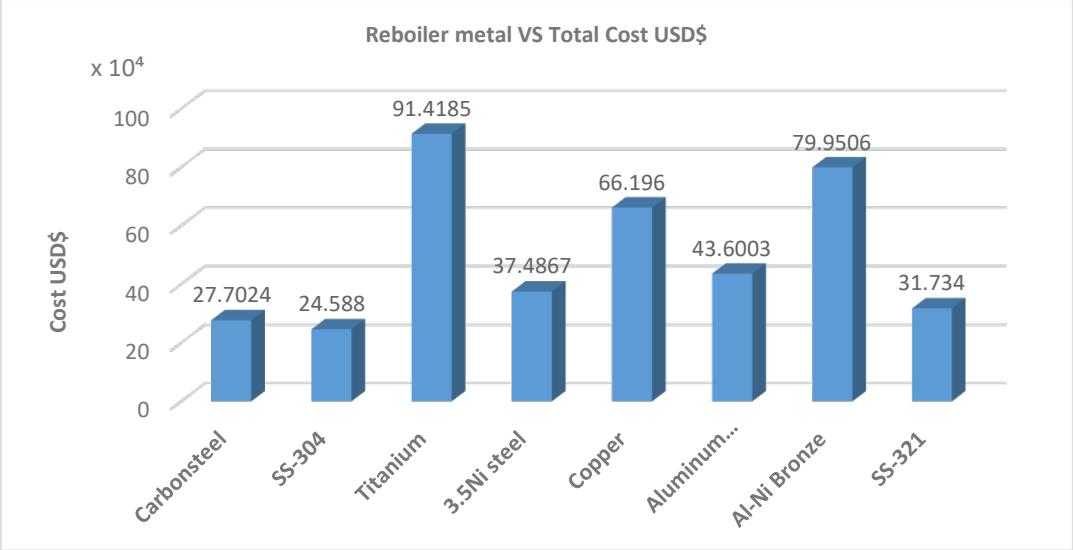

Fig. (5): Reboiler Metal and Its Relation with the Total Cost

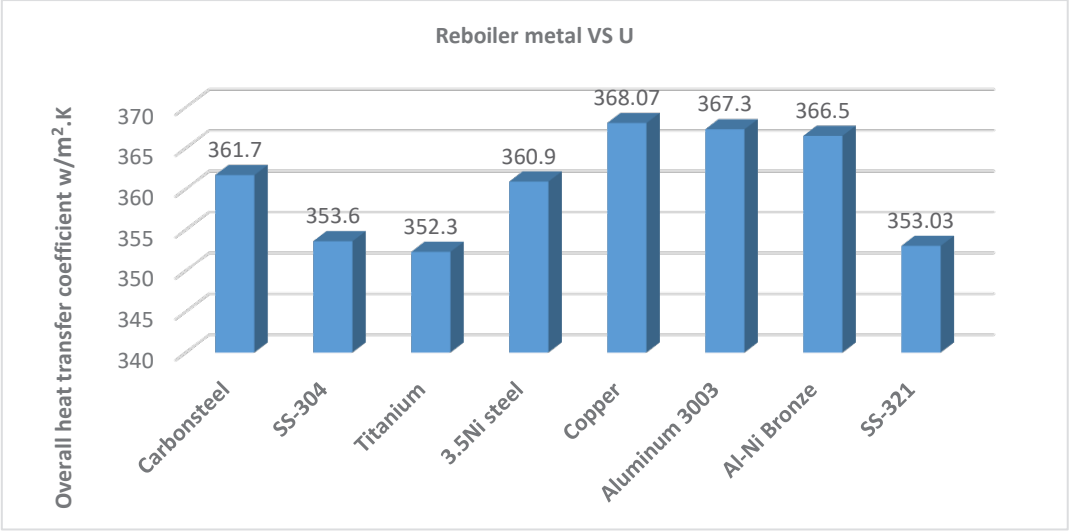

Fig. (6): Reboiler Metal and Its Relation with the Overall Heat Transfer Coefficient.

3.3 Effect of Mass flow rate: When the flow rate of the vapor in the hot stream increases, as showing in **Figure (7),** it is clear that the change is directly proportional, the heat exchange increases with the same design diameter of the tube, reaching a flow rate of 5 kg/s the warning of vibration appears, after access this flow rate and getting the 6 kg/s there is a failure in the implementation of the program due to the problems of vibration, therefore increasing the flow with the acceptable range will be enhancing the heat duty.

The same change in the mass flow rate was done and found the affected on the temperature of the hot out and cold out streams in the simulations, as shown in **Figures (8)** and **(9)**, the same failure was found after passing 4 kg/s because the problem of vibration and also the overall heat transfer coefficient will decrease, the result of the simulation discovered that the relationship was direct within the specified acceptable flow range and depend on the result shows in **Figures (10)** it's clear that the best flow is 4 kg/s. The increase in the flow rate leads to an increase in the flowing's: fluid velocity, Reynolds number, Nusselt number. Consequently, an increase in the overall heat transfer coefficient has resulted.

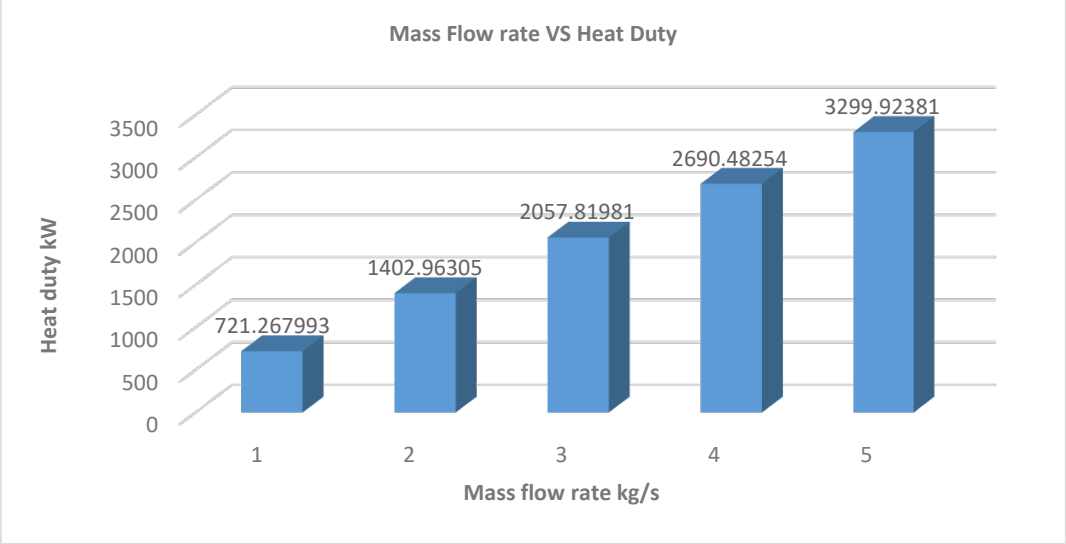

Fig. (7): Mass Flow Rate Change and Its Effect On Heat Duty

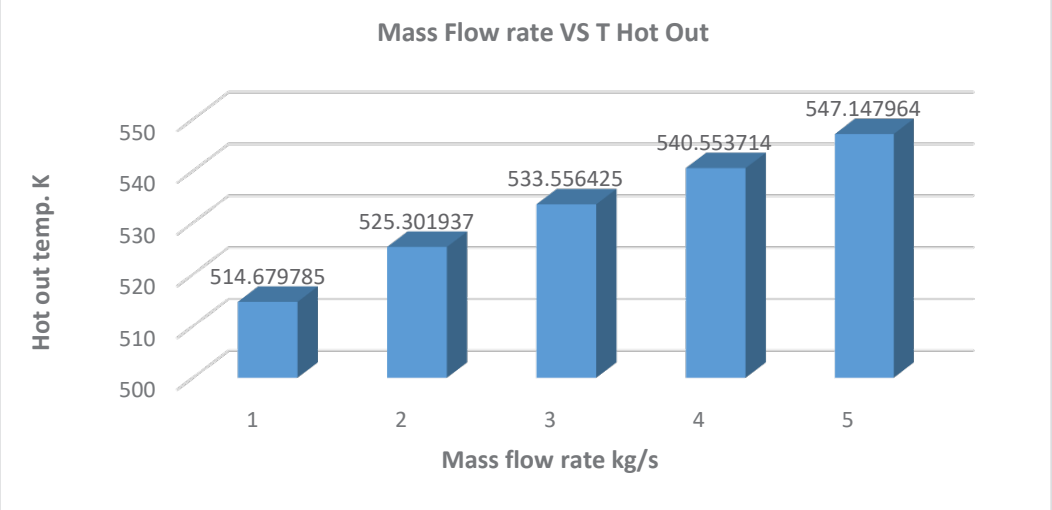

Fig. (8): Mass Flow Rate Change and Its Effect On The Temperature Of Hot Out

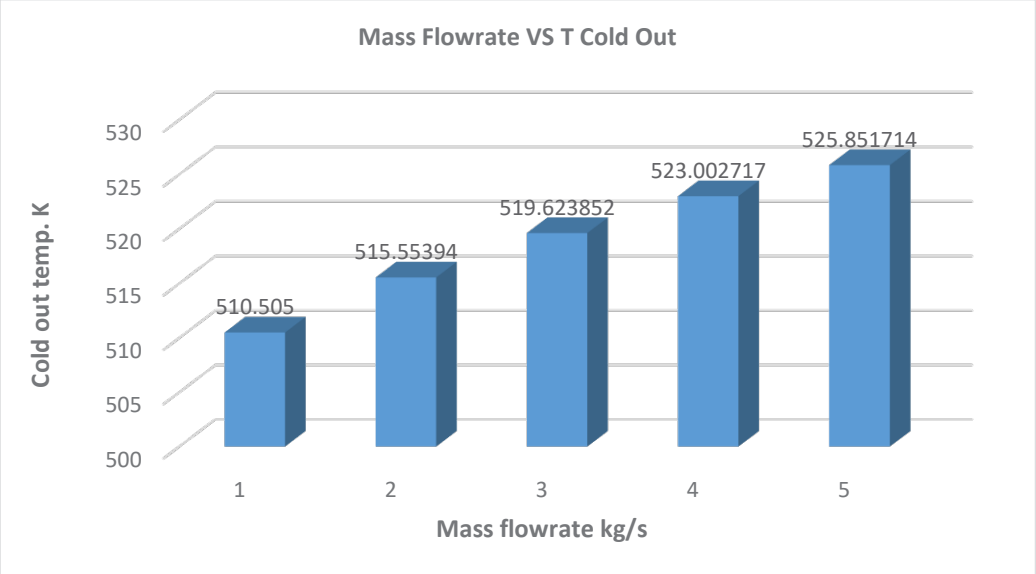

Fig. (9): Mass Flow Rate Change and Its Effect On The Temperature Of Cold.

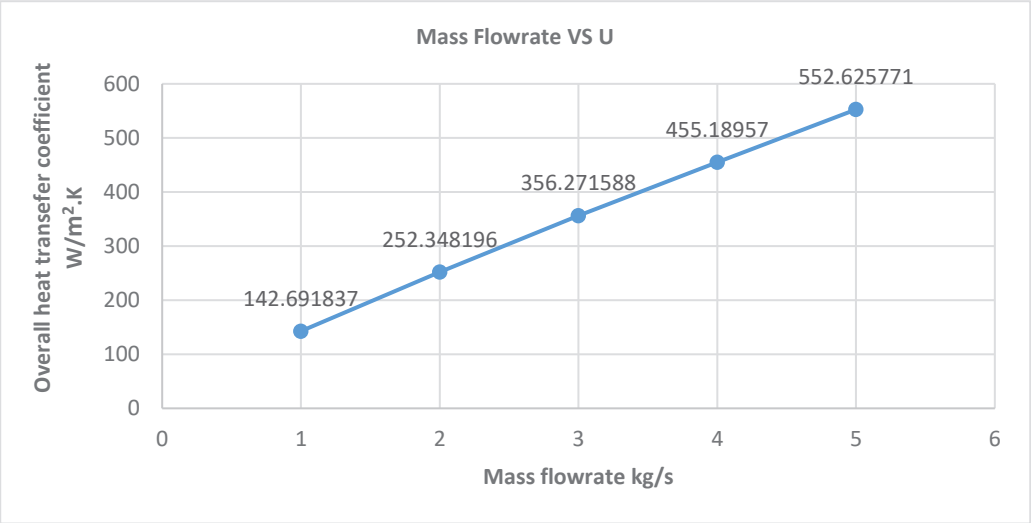

Fig. (10): Mass Flow Rate Change and Its Effect On The Overall Heat Transfer Coefficient.

3.4 Effect of inlet shell-side temperature: The effect of the temperature is very important to do the suitable design for the reboiler, while the temperature of the inlet of cold streams change when the simulation was done, it was affected the overall heat transfer coefficient, as shown in **Figure (11)** it's clear that when increasing the temperature of the cold stream from 473 k (an increase of 5 degrees whenever doing the simulation) until it reaches 503 k its effect on the overall heat transfer coefficient, and also the figure shows the best temperature that can be used to improve the efficiency which it is 493 k, while all the other operating condition remains as it is. In the same topic, **Figure (12)** shows the relationship between the tube length and the bulk temperature, which describes the bulk temperature distribution along the tube and the tube metal side temperature and tube side fouling surface temperature distribution along the tube.

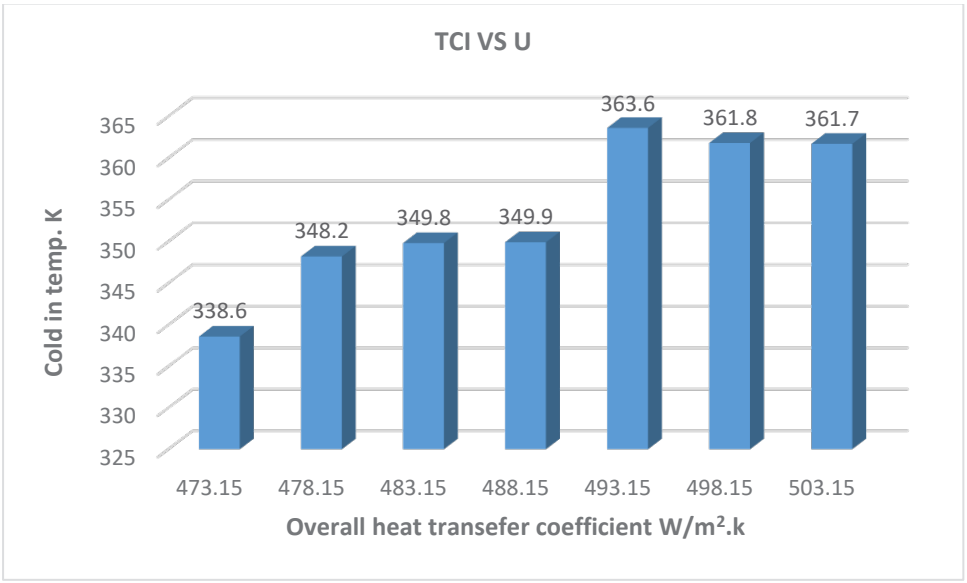

Fig. (11): The Change of the Cold Stream Inlet Temperature and Its Effect on the Overall Heat Transfer Coefficient.

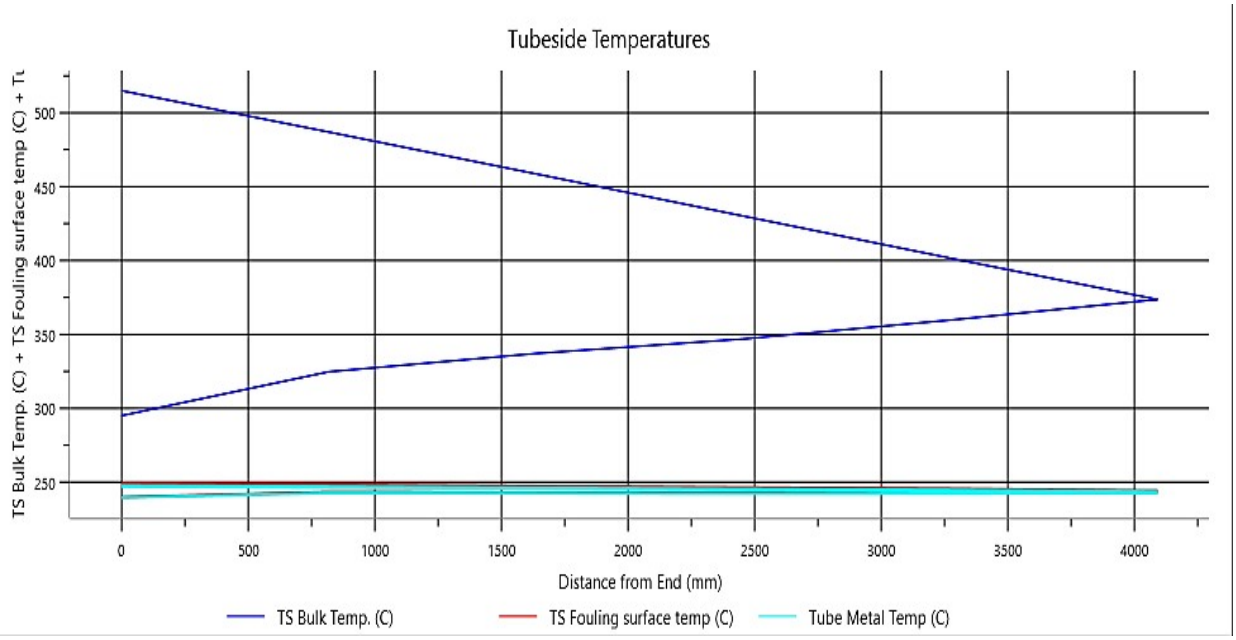

Fig. (12): The Change of Tube Side Temperature, Tube Side Bulk Temperature, and Tube Side Fouling Surface Temperature Distribution Along the Tube

4 General Notes for Kettle Reboiler Design:

1- For the predicted maximum flow, a safety coefficient of 0.7 is utilized.
2- To prevent vapor coverage, a tube pitch from 1,5 – 2,0 times the exterior diameter of the tube must be utilized.
3- tall narrow bundles are more effective than tiny chubby bundles.
4- The shell must be designed so that the vapor and the liquids may be disengaged. The necessary shell radius depends on the heat flow
5- At a minimum of 0.25 m space must be the float between both the fluid and the shell.
6- When a low vapor flow rate is needed, a vertical, cylindrical container must be used with a coil or heated jacket
7- If the temp fluctuates on both sides, it is essential to adjust the logarithmic difference in temperatures for variations in actual cross or counter-current flows.
8- The mean temperature difference must always be dependent on the boiling point of the fluid if the feeding is under-cooled.

4 Conclusion

Kettles reboiler heat exchanger was simulate using Aspen Plus and Aspen EDR to study the effect of the operation condition variables and choosing the optimum design specification at the lowest cost that was calculated by using Aspen EDR. By doing so, the optimization method can be divided into two steps:

1- Enhancing the model and its operating conditions by providing the optimal temperature and mass flow rates. This affected directly on the overall heat transfer coefficient yields to provide a clear indication of the efficiency.

By determining the optimal operating conditions which are 493.15 k for the cold stream inlet temperature and 4 kg/s for the hot stream flow rate of the reboiler. While performing the simulation above, it was found that the overall heat transfer coefficient has been positively increased by 28.27%.

2- By selecting the best suitable tube diameter as well as the best type of metal utilized, the best appropriate design and its influence on cost were investigated.

The optimum tube diameter was 25.4 mm, and the suitable tube metal was carbon steel, by using the Aspen EDR program for calculating their effect on the cost.

NOMENCLATURE

Symbol	Definition	Unit
P	Pressure	bar
T	Temperature	k
λ	Latent heat	kJ/kg
$\dot{m}$	Mass flow rate	Kg/s
ρ	Density	kg/m³
μ	Viscosity	N.s/m²
K_w	Thermal conductivity	W/m. k
c_p	Specific heat	kJ/kg.k
P_c	Critical Pressure	bar
Ø	Heat duty	kW
F	Correction factor	Dimensionless
A	Exchanger required area	m
U_o	Overall heat transfer coefficient	W/m².k
Nt	No. of Tubes	Dimensionless
Do	Outside tube diameter	m
L	Tube length	m
Np	Number of tubes pass	Dimensionless
AC	Cross-section area	m
Di	Inside tube diameter	m
v	Velocity in tubes	m/s
Re	Reynolds Number	Dimensionless
h_o	Shell side boiling coefficient	W/m².k
pr	Prandtl Number	Dimensionless
hi	Tube side heat transfer coefficient	W/m².k

LIST OF ABBREVIATIONS

Abbreviation	Definition
HEs	Heat exchanger
TEMA	Tubular Exchanger Manufacturers Association
LMTD	Log Mean Temperature Difference
EDR	Exchanger Design and Rating
Nt	No. of Tubes
Np	Number of tubes pass
Re	Reynolds Number
Pr	Prandtl Number

Appendix (1): Reboiler diameter change and its cost effects by EDR simulation.

Tube dia.					
0.5	12.7	**Weights**	kg	**Cost data**	Dollar(US)
		Shell	33658.4	Labor cost	174586
		Front head	7744.3	Tube material cost	1518
		Rear head	0	Material cost (except tubes)	99077
		Shell cover			
		Bundle	4306.1		
		Total weight - empty	45708.8	Total cost (1 shell)	275181
		Total weight - filled with water	56375.6	Total cost (all shells)	275181
0.625	15.88	**Weights**	kg	**Cost data**	Dollar(US)
		Shell	33658.4	Labor cost	174650
		Front head	7744.3	Tube material cost	1990
		Rear head	0	Material cost (except tubes)	99087
		Shell cover			
		Bundle	4439.1		
		Total weight - empty	45841.8	Total cost (1 shell)	275727
		Total weight - filled with water	56491.7	Total cost (all shells)	275727
0.75	19.05	**Weights**	kg	**Cost data**	Dollar(US)
		Shell	33658.4	Labor cost	174695
		Front head	7744.3	Tube material cost	2461
		Rear head	0	Material cost (except tubes)	99097
		Shell cover			
		Bundle	4563.2		
		Total weight - empty	45965.9	Total cost (1 shell)	276254
		Total weight - filled with water	56599.9	Total cost (all shells)	276254
0.875	22.22	**Weights**	kg	**Cost data**	Dollar(US)
		Shell	33658.4	Labor cost	174698
		Front head	7744.3	Tube material cost	2933
		Rear head	0	Material cost (except tubes)	98949
		Shell cover			
		Bundle	4626.2		
		Total weight - empty	46029	Total cost (1 shell)	276580
		Total weight - filled with water	56655	Total cost (all shells)	276580
1	25.4	**Weights**	kg	**Cost data**	Dollar(US)
		Shell	33658.4	Labor cost	174725
		Front head	7744.3	Tube material cost	3404
		Rear head	0	Material cost (except tubes)	98959
		Shell cover			
		Bundle	4733.7		
		Total weight - empty	46136.5	Total cost (1 shell)	277088
		Total weight - filled with water	56748.8	Total cost (all shells)	277088
1.125	28.58	**Weights**	kg	**Cost data**	Dollar(US)
		Shell	33658.4	Labor cost	174868
		Front head	7744.3	Tube material cost	3874
		Rear head	0	Material cost (except tubes)	98970
		Shell cover			
		Bundle	4832.5		
		Total weight - empty	46235.2	Total cost (1 shell)	277712
		Total weight - filled with water	56834.9	Total cost (all shells)	277712

Appendix (2): Reboiler metal change and its cost effects by EDR simulation.

Tube material				
Carbonsteel	**Weights**	kg	**Cost data**	Dollar(US)
	Shell	33658.4	Labor cost	174722
	Front head	7744.3	Tube material cost	3344
	Rear head	0	Material cost (except tubes)	98958
	Shell cover			
	Bundle	4720.7		
	Total weight - empty	46123.4	Total cost (1 shell)	277024
	Total weight - filled with water	56737.1	Total cost (all shells)	277024
SS-304	**Weights**	kg	**Cost data**	Dollar(US)
	Shell	8813.5	Labor cost	93685
	Front head	4131.3	Tube material cost	8101
	Rear head	0	Material cost (except tubes)	144094
	Shell cover			
	Bundle	4784		
	Total weight - empty	17728.9	Total cost (1 shell)	245880
	Total weight - filled with water	28342.8	Total cost (all shells)	245880
Copper	**Weights**	kg	**Cost data**	Dollar(US)
	Shell	14851.6	Labor cost	114826
	Front head	6502.8	Tube material cost	17300
	Rear head	0	Material cost (except tubes)	529834
	Shell cover			
	Bundle	5440.3		
	Total weight - empty	26794.7	Total cost (1 shell)	661960
	Total weight - filled with water	37402.2	Total cost (all shells)	661960
Aluminum 3003	**Weights**	kg	**Cost data**	Dollar(US)
	Shell	26631.3	Labor cost	174894
	Front head	13093.9	Tube material cost	2955
	Rear head	0	Material cost (except tubes)	258154
	Shell cover			
	Bundle	1666.3		
	Total weight - empty	41391.5	Total cost (1 shell)	436003
	Total weight - filled with water	52005.5	Total cost (all shells)	436003
Titanium	**Weights**	kg	**Cost data**	Dollar(US)
	Shell	8547.1	Labor cost	88283
	Front head	2944.4	Tube material cost	66402
	Rear head	0	Material cost (except tubes)	759500
	Shell cover			
	Bundle	2745.4		
	Total weight - empty	14236.9	Total cost (1 shell)	914185
	Total weight - filled with water	24844.4	Total cost (all shells)	914185
3.5Ni steel	**Weights**	kg	**Cost data**	Dollar(US)
	Shell	6471.3	Labor cost	82207
	Front head	3717.3	Tube material cost	23601
	Rear head	0	Material cost (except tubes)	269059
	Shell cover			
	Bundle	4665.7		
	Total weight - empty	14854.2	Total cost (1 shell)	374867
	Total weight - filled with water	25468.2	Total cost (all shells)	374867
Al-Ni Bronze	**Weights**	kg	**Cost data**	Dollar(US)
	Shell	10805.6	Labor cost	94486
	Front head	4183.9	Tube material cost	43080
	Rear head	0	Material cost (except tubes)	661939
	Shell cover			
	Bundle	4530.8		
	Total weight - empty	19520.2	Total cost (1 shell)	799506
	Total weight - filled with water	30127.7	Total cost (all shells)	799506
SS-321	**Weights**	kg	**Cost data**	Dollar(US)
	Shell	9248.6	Labor cost	95164
	Front head	4193.6	Tube material cost	9786
	Rear head	0	Material cost (except tubes)	212390
	Shell cover			
	Bundle	4784		
	Total weight - empty	18226.2	Total cost (1 shell)	317340
	Total weight - filled with water	28840.1	Total cost (all shells)	317340

References

[1] S. P. C, J. Parikh, and D. Jain, "' Design of A Vertical Thermosyphon Reboiler ,'" 1995.

[2] B. Kilkovsky, J. Kohoutek, Z. Jegla, and P. Stehlik, "Software application for supporting of CAE in process engineering: Automated choice of the suitable reboiler type," *Chem. Eng. Trans.*, vol. 18, no. January 2009, pp. 821–826, 2009, doi: 10.3303/CET0918134.

[3] Y. Susmiati, B. Purwantana, N. Bintoro, and S. Rahayoe, "Design and testing of vertical tubular baffle heat exchanger as an internal reboiler in the distillation device," *IOP Conf. Ser. Earth Environ. Sci.*, vol. 355, no. 1, 2019, doi: 10.1088/1755-1315/355/1/012001.

[4] R. Goedecke and S. Scholl, "Modelling and simulation of a pillow plate thermosiphon reboiler," *Heat Mass Transf. und Stoffuebertragung*, vol. 55, no. 1, pp. 95–104, 2019, doi: 10.1007/s00231-018-02543-4.

[5] D. A. McNeil, K. Bamardouf, and B. M. Burnside, "A one-fluid, two-dimensional flow simulation model for a kettle reboiler," *Int. J. Heat Mass Transf.*, vol. 53, no. 5–6, pp. 825–835, 2010, doi: 10.1016/j.ijheatmasstransfer.2009.11.042.

[6] D. A. McNeil, K. Bamardouf, B. M. Burnside, and M. Almeshaal, "Investigation of flow phenomena in a kettle reboiler," *Int. J. Heat Mass Transf.*, vol. 53, no. 5–6, pp. 836–848, 2010, doi: 10.1016/j.ijheatmasstransfer.2009.11.041.

[7] M. Pezo, V. Stevanovic, and Z. Stevanovic, "Simulations of the kettle reboiler shell side thermal-hydraulics with different two-phase flow models," *Therm. Sci.*, vol. 10, no. 2, pp. 127–140, 2006, doi: 10.2298/tsci0602127p.

[8] S. Kumar, A. Jain, B. Mohanty, and S. C. Gupta, "Recirculation model of kettle reboiler," *Int. J. Heat Mass Transf.*, vol. 46, no. 15, pp. 2899–2909, 2003, doi: 10.1016/S0017-9310(03)00015-2.

[9] S. Arneth and J. Stichlmair, "Characteristics of thermosiphon reboilers," *Int. J. Therm. Sci.*, vol. 40, no. 4, pp. 385–391, 2001, doi: 10.1016/S1290-0729(01)01231-5.

[10] B. M. Burnside, K. M. Miller, D. A. McNeil, and T. Bruce, "Heat transfer coefficient distributions in an experimental kettle reboiler thin slice," *Chem. Eng. Res. Des.*, vol. 79, no. 4, pp. 445–452, 2001, doi: 10.1205/026387601750282373.

[11] S. S. Parhi, G. P. Rangaiah, and A. K. Jana, "Optimizing reboiler duty and reflux ratio profiles of vapor recompressed batch distillation," *Sep. Purif. Technol.*, vol. 213, no. December 2018, pp. 553–570, 2019, doi: 10.1016/j.seppur.2018.12.066.

[12] F. Kamişli and A. A. Ahmed, "Simulation and Optimization of A Crude Oil Distillation Unit Ham Petrol D amıtma Ünitesinin Simülasyonu ve Optimizasyonu," vol. 14, no. 2, pp. 59–68, 2019.

[13] Y. Zhou and J. Yu, "Optimization design of falling film type plate-fin condenser/reboilers by minimizing specific entropy generation rate," *Cryogenics (Guildf).*, vol. 99, pp. 25–31, 2019, doi: 10.1016/j.cryogenics.2019.02.006.

[14] S. . Thakore and B. . Bhatt, *Introduction to Process Engineering and Design*, vol. 91. 2007.

Lightweight Authentication Protocol For Smart Healthcare

Saja A. Hussein[1], Issa Ahmed Abed[2] , Zaid Alaa Hussien[3]
{saja.abhadli5@gmail.com[1], issaahmedabed@stu.edu.iq[2], zaid.alaa@stu.edu.iq[3]}

Basrah Engineering Technical College, Southern Technical University, Iraq[1,2],
Management Technical College Basrah, Southern Technical University, Iraq[3]

Abstract. The application of modern technology to human health, is a hot research subject, especially in medical technology. In developing countries, the Telecare Medicine Information System (TMIS) is widely used in smart healthcare systems, allowing a physician to obtain patient-related information from a distance. The privacy of such data has been identified as a prominent obstacle to the widespread development of IoT. Because of the importance of this data, it must be transmitted between the patient and the cloud server. So, we proposed a lightweight and fast protocol to ensure data access and also, to prevent attackers from generating fake data, and we have proven that this protocol is more secure.

Keywords: Authentication, Lightweight, Smart Healthcare, IoT, Cloud.

1 Introduction

The availability and exchange of knowledge around the spectrum of medical care is a major problem for healthcare organizations. since healthcare data is usually distributed through multiple health systems in a bunch of locations. Many of these systems do not joint with one another, allowing data to remain separate inside silos. This anti-pattern results in clinical care knowledge shortages, data access inefficiencies, and increased costs for healthcare organizations. Data isolation is a major problem for healthcare organizations, as it prevents them from taking advantage of the latest IT technologies, such as cloud computing's data processing and analytics capabilities, which can help optimize treatment while lowering costs. Modern IT systems areto an increasing extent taking over cloud computing and transferring their workloads to the cloud to gain economic advantages, of scale, energy consumption, scalability, and elasticity[1]. The Popularity of long-term in-home smart healthcare Monitoring Systems has resulted from the aging population and the prevalence of chronic diseases[2]. In addition to the Coronavirus at present. Intelligent health monitoring IoT devices, such as ECG, blood pressure bands, pulse oximeters, and other devices, can capture health data and provide direct input to patients and hospitals, either as an alert of imminent medical emergencies or as a monitoring aid during workouts, thanks to the rapid advancement of sensing technology[3]. Patients use a variety of medical IoT devices to keep track of their health. The details received (personal health records) would be sent back to hospitals for diagnosis and prompt responses. However, since the tracked health data contains

IMDC-IST 2021, September 07-09, Sakarya, Turkey
Copyright © 2022 EAI
DOI 10.4108/eai.7-9-2021.2314798

personal information, there are significant protection and privacy breaches in terms of data privacy and identity authentication. As a result, the data must be well secured against unauthorized access[4]. A protected user authentication strategy is built around two or three main security components:(1) any information that is only identified by the user (e.g. passwords and PIN codes),(2) a physical entity, token, that is only held by the user (e.g. smart card and smart device), and(3) a physical attribute that reflects the user's specific biometrics (e.g. fingerprint)[5]. Several security protocols, such as authentication and access control protocols, that use public-key cryptographic systems have recently been proposed to improve privacy and security in the healthcare setting. As an example, Shehzad et al.[6] in 2017 proposed a protocol that is powerful enough to defend against all types of attacks, especially stolen smart devices and patient anonymity violations. Azad et al.[7] In 2020 proposed a scheme for a SIP-based next-generation network that relies on a low-entropy mutual password rather than a Public-Key Infrastructure PKI or a trusted third-party mechanism. Zahid et al.[8] 2019 proposed biometrics-based authentication and key agreement protocols for E-Health Services that are reliable and efficient. Tan et al.[9] 2017 proposed a scheme By combining biometrics, hash function operations, and an effective smart card-based password authentication. As healthcare systems can not afford high communication and computation overheads, authentication schemes should be as cost and transmission-efficient as possible while also maintaining high security. and this weakness was observed in previous protocols. As a result, we proposed in this paper a scheme that is more lightweight and secure against attacks by using a one-way-hash that cannot be decrypted, and we demonstrated the proposed scheme is lightweight, resulting in low communication and computation overheads.

2 System Model

The components of the proposed system are depicted in Fig 1. The main components can be classified into two categories, as seen in the figure: patients, and cloud server, and that will physicians/doctors connected with. The patients are supposed to be equipped with different sensors and monitors that record the physiological parameter values in real-time, like as heart rate and temperature, and so on. The data is then transmitted to the doctor through the open channel through a cloud server. This aids in the distance check of symptoms, the provision of online and without-complications care to patients. even so, the physiological data of patients is extremely important and can easily be compromised when transmitted through the internet. As a result, this paper introduces a practical mutual authentication scheme for establishing safe and trustworthy two-way communication between patients and medical servers. A patient's personality is defined by coded values. Nevertheless, these parameters can not be derived from transmitted messages because they are sent in a secret structure over the channel, All of this at a low cost of communication and computation overhead.

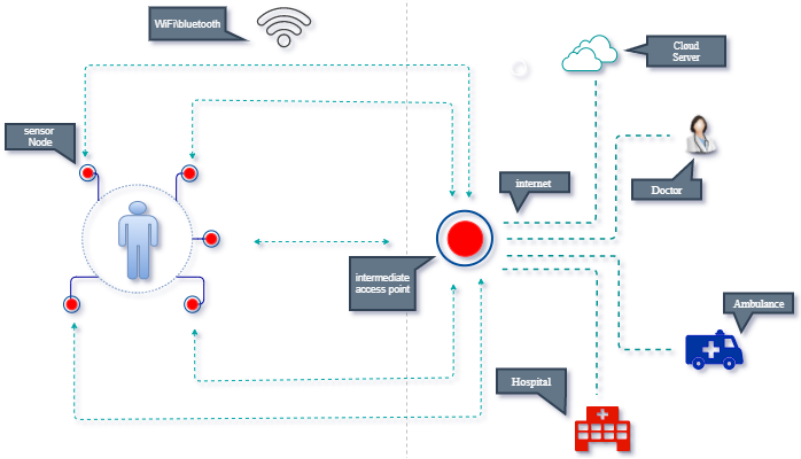

Fig 1. The components of the smart healthcare system.

3 Proposed Protocol

The authentication of the proposed protocol is divided into three different sections: A) Registration, B) login and C) Authentication. This section contains extensive details about these phases, which are as follows, **Table1.** represents the notations of the proposed protocol.

Table 1. Notations and their Description.

Notaion	Description
ID_u, PW_u	u-th user (patient)
Q_i, S	Random numbers
σ_i	Biometric secret key
ns_1	Server privet key
Z, ns_2	Random numbers
$\oplus$	XOR operation
||	Concatenation operation
h(.)	One-way-hash function
Sk_u	Session key between patient and server

3.1 Registration Phase

Throughout these steps, the patient uses the safe channel to register with the cloud server. Step 1. The Patient select an identity ID_u, password PW_u and scan (his or her) biometrics B_u (for example, fingerprint, and so on) on a smart device, and this SD will generate a random number Q_i. Then it will compute pseudo-identity and password respectively.

$$PID_i = h(ID_u \| Q_i) \quad (1)$$

$$HPW_i = h(PW_u \parallel Q_i) \quad (2)$$

After selected Biometric secret key σ_i then compute

$$X_i = h(B_u \parallel \sigma_i) \quad (3)$$

And this step will be finished with sending the message include the pseudo-identity and password $< PID_i, HPW_i >$ through a protected channel to the cloud server.

Step 2. When the cloud server is received the data include the registration request, then it's start compute

$$R_i = h(PID_i \parallel ns_1) \quad (4)$$

After the server secret key ns_1 is generated, and compute

$$g_i = R_i \oplus HPW_i \quad (5)$$

$$D_i = h(HPW_i \| PID_i \| R_i) \quad (6)$$

The server generates a random number S to compute

$$m_i = h(S \| ns_1) \oplus PID_i \quad (7)$$

Then store $< m_i, g_i, D_i, h(.) >$ in its database and send these values to the patient through a secure channel.

Step 3. On the patient side after it's received the values from the server, then start to compute

$$W_i = Q_i \oplus h(ID_u \parallel PW_u) \quad (8)$$

$$E_i = \sigma_i \oplus h(HPW_i \parallel PID_i) \quad (9)$$

and then store these values in the smart device, finally, the content of it will be $< W_i, m_i, g_i, X_i, D_i, E_i, h(.) >$. The sequence of steps performed by the cloud server and the patient is depicted in Fig 2.

3.2 Login Phase

Step 1. In this phase, the patient will insert (his or her) own parameters ID_u, PW_u, into the smart device and then imprints the biometric B_u in the same smart device. After that compute

$$Q_i^* = W_i \oplus h(ID_u \| PW_u) \quad (10)$$

$$HPW_i = h(PW_u \| Q_i^*) \quad (11)$$

$$PID_i = h(ID_u \parallel Q_i^*) \quad (12)$$

$$\sigma_i' = E_i \oplus h(HPW_i \parallel PID_i) \quad (13)$$

then compute

$$X_i' = h(B_u^* \| \sigma_i) \tag{14}$$

and check if

$$X_i' = X_i \tag{15}$$

Then the verification is passed and proceeds to the next steps. Else, try again to enter the parameters for two more attempts only, and after three failed attempts, the login will stop. When the condition is true then compute

$$R_i = g_i \oplus HPW_i \tag{16}$$

$$D_i' = h(HPW_i \| PID_i \| R_i) \tag{17}$$

and check if

$$D_i' = D_i \tag{18}$$

that's mean the pseudo-identity and password are each correct otherwise server terminates the session.

Step 2. The smart device will generate Z as a random number and calculates

$$L{=}m_i \oplus PID_i = h(S \| ns_1) \tag{19}$$

$$M_1 = h(R_i \| L \| PID_i) \tag{20}$$

$$M_2 = h(M_1 \| D_i \| t_1) \oplus Z \tag{21}$$

at the end of this step login request will send to the server content these values $< PID_i, M_1, M_2, t_1 >$.

3.3 Authentication Phase

Step 3. As the server receives the request message from the Patient, it checks the authenticity of the time stamp, if $t_2 - t_1 > \Delta t$ that's mean is the timestamp that has not expired then the server will calculate

$$R_i' = h(PID_i \| ns_1) \tag{22}$$

$$L1{=}m_i \oplus PID_i \tag{23}$$

$$M_1' = h(R_i' \| L1 \| PID_i) \tag{24}$$

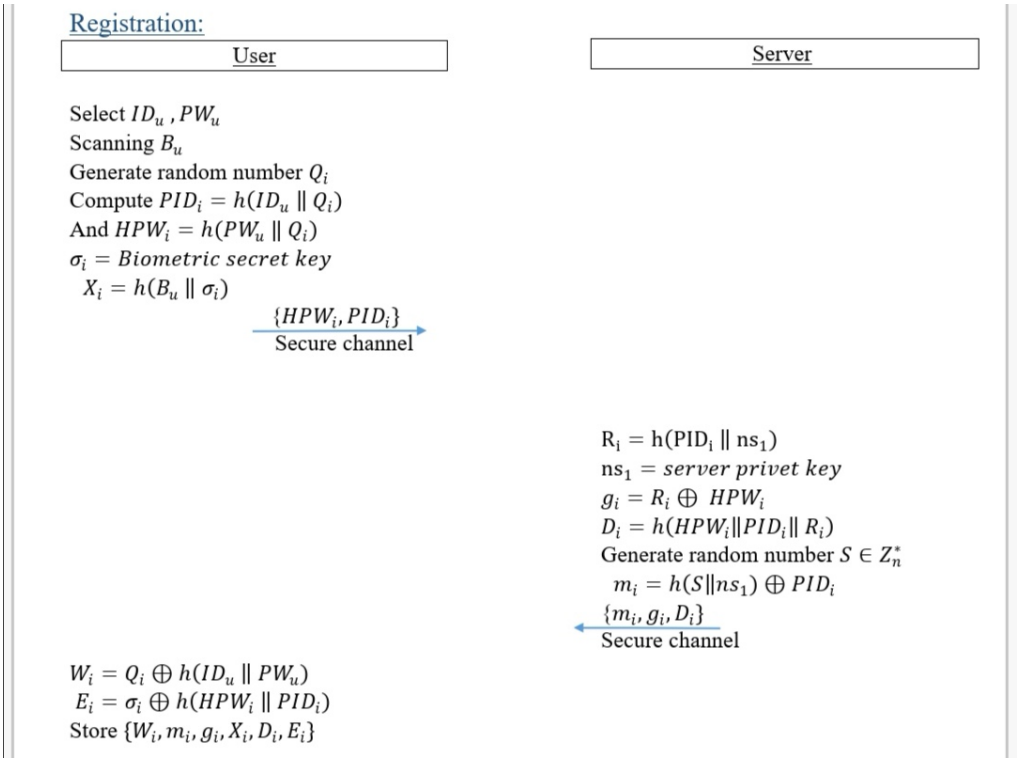

Fig 2. The registration phase for the proposed scheme.

and check if

$$M_1' = M_1 \tag{25}$$

then server generates a random number $ns_2 \in Z_n^*$ and compute

$$M_4 = ns_2 \oplus h(R_i' \| L1 \| PID_i) \tag{26}$$

$$M_5 = h(ns_2 \| R_i' \| L1 \| PID_i \| Z \| t_3) \tag{27}$$

After that server will send a message that contains the values $< M_4, M_5, t_3 >$ to the Patient. Otherwise, the session will terminate by the server.

Step 4. On the Patient side, it will get a time-stamp t_3 as well as checking the time interval; if $t_4 - t_3 > \Delta t$ and the session will terminate by the Patient if that condition is not verified, then calculate

$$ns_2' = M_4 \oplus h(R_i \| L \| PID_i) \tag{28}$$

$$M_5' = h(ns_2' \| R_i \| L \| PID_i \| Z \| t_3) \quad (29)$$

and then check if

$$M_5 = M_5' \quad (30)$$

then finally calculate the session key

$$Sk_u = h(ns_2' \| Z \| R_i \| L \| PID_i \| M_5) \quad (31)$$

Else, the session will terminate by the Patient. The last two phases are shown as under in Fig 3.

4 Security Analysis

This checklist of security systems covers different security attacks as well as advantageous security properties, and it is generally used in the documentation of multi-factor user authentication as a valuation criteria, as shown in Table 2.

1. Offline Guessing The Password Attack: Over the unreliable channel, the password of patient PW_u and identity ID_u are never conveyed in plain text. Furthermore, the one-way hash functions and concatenation operations are secure the Patient's password, identity, and biometric that are a part of the components of the saved parameter $\{W_i, m_i, g_i, X_i, D_i, E_i\}$. Therefore, the attacker would be unable to reverse it and know the password. As a result, the proposed protocol is resistant to guessing the password.
2. Stolen Smart device Attack: Assume that the Adversary will steal the patient's smart device and retrieve the data stored on it $\{W_i, m_i, g_i, X_i, D_i, E_i\}$. Even in this case, Adversary is unable to retrieve the Patient's credentials password PW_u and identity D_u. Since the password is concealed throughout the values are stored in a smart device, that is secured using one-way hash functions, As a result, Adversary would not be able to retrieve the Patient's credentials in a polynomial amount of time

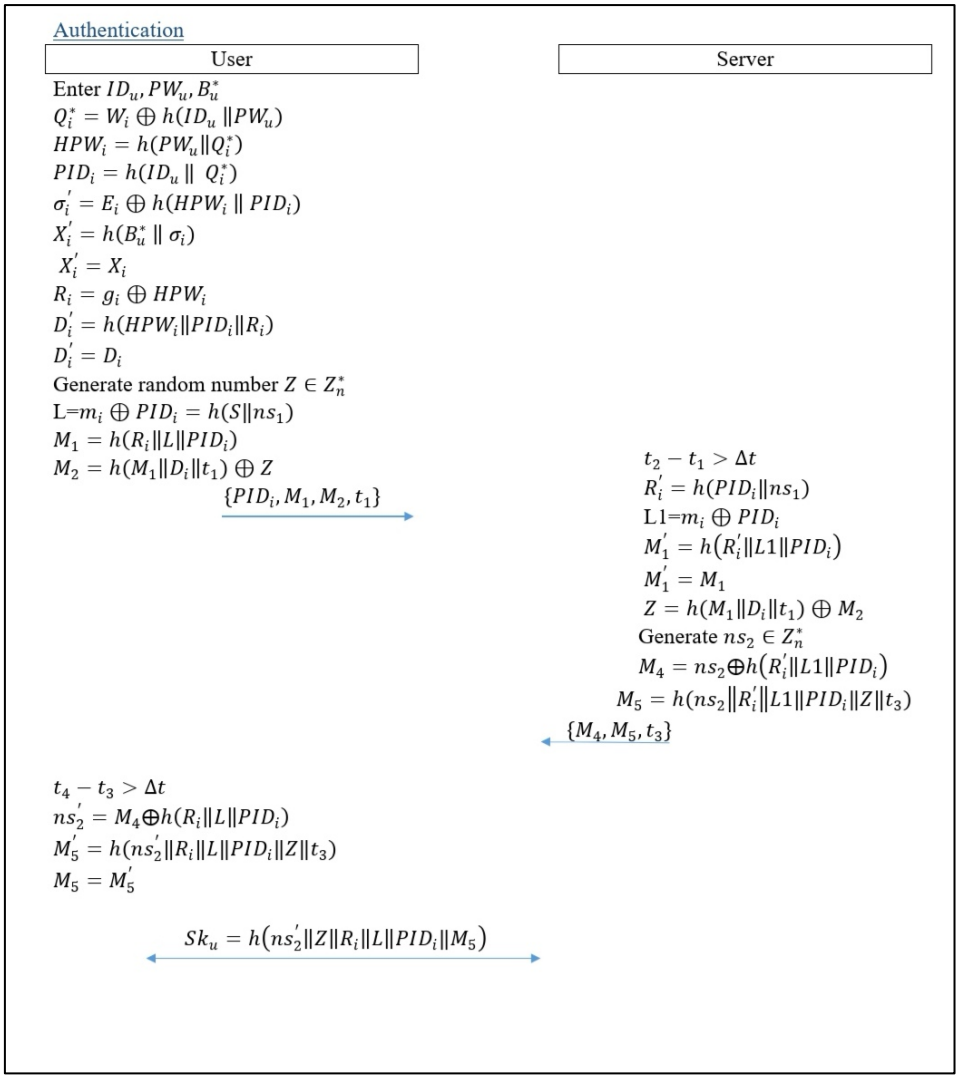

Fig 3. Login and Authentication phase for the proposed scheme.

3. Replay Attack: Replay attacks can resist the proposed protocol and ignore the data that have been replayed, and it guarantees this via the strength of random numbers and timestamps. To verify the novelty of the messages received, Time-stamps (t_1, t_3) are used.

4. Impersonation Attack: The protocol is designed to withstand imitation threats on both the Patient and the cloud server. An adversary will failure to vary the transmitted messages. The reason

for this is that median tokens require either the cloud server's or the patient's private key information. The intermediate tokens cannot be modified to impersonate the Patient's and server's identities without these values.

5. Privileged Insider Attack: At the registration process, and through the protected channel important information is transmitted from the patient side. Meanwhile, the Patient and the cloud server communication may intercept. even so, the intercepted information cannot be used to decipher the patient's identity (PID_i) and password (HPW_i) pseudo values. for the reason that The Adversary does not have access to the server's private key, nor does he have access to the random numbers.$ns_1$and ns_2 respectively.

6. Temporary Information Attack on Known Session: Assume that the Adversary obtains information about the random numbers (ns_2 , Z) used during the processing of session keys (Sk_u). Although these numbers are available, Adversary cannot calculate the Sk_u unless knowing R_i , PID_i and L.

7. Perfect Forward Secrecy: With the impossibility of accessing the session keys unless the private key is known, perfect forward secrecy will ensure.

8. Maintains Patient Anonymity: The contact between the cloud server and the patient is grounded on the parameters (ID_u,PW_u and B_u). A Patient's personality is defined by the mixture of these values. nevertheless, these parameters cannot be derived from transmitted messages since they are sent in a secret structure over the channel.

9. Resistance to Denial of Service attacks: At each point of the protocol, timestamps and different tokens are used to validate received messages. As a result, the Adversary is unable to deceive the legitimate parties and consume their resources.

10. Mutual authentication: On receiving the request message, $\{PID_i, M_1, M_2, t_1\}$ the server authenticates the Patient side in the proposed protocol. When validating the t_1 timestamp and comparing the Eq. (24) with Eq. (20) $M_1' = h(R_i'\|L1\|PID_i) = M_1$. Also, the server returns a message $\{M_4, M_5, t_3\}$ to patient. Similarly, It validates the newness of the t_3 and Eq.(29) with Eq.(27) $M_5' = h(ns_2'\|R_i\|L\|PID_i\|Z\|t_3) = M_5$ The authentication will be done if all values are identical. As a result, the current protocol achieves mutual authentication.

11. stolen verifier attacks: In the server database, the proposed scheme would not construct or save a verifier table. However, On the cloud server-side, the proposed protocol does not store a verification table, However, also an adversary with entry to the database server would be unable to verifiers the Patient analyses data.

12. man-in-the-middle attack: Mutual authentication between the Patient and the server is provided by the proposed scheme. The parameter in Eq. (20) $M_1 = h(R_i\|L\|PID_i)$ is used to authenticate the Patient. On the other side, the patient authenticates the server using Eq. (27) $M_5 = h(ns_2'\|R_i\|L\|PID_i\|Z\|t_3)$ *To* compute M_1 and M_5, the adversary on both sides requires R_i or the secret key ns_1. As a result, no adversary can be both a cloud server and a patient. Also, the session key computation Eq.(31) $Sk_u = h(ns_2'\|Z\|R_i\|L\|PID_i\|M_5)$ which needs the secret parameter of a patient R_i in addition to the random numbers (ns_2 , Z) provided by each participating server and Patient. Any attacker behaving like a man in the middle would be unable to have these random numbers. As a result, the proposed scheme is highly resistant to MitM attacks. We reviewed the potential attacks and compared them between our protocol and other protocols, and the next table shows that.

Table 2. Security parameters comparison.

	proposed	[9]	[8]	[10]
Offline Password Guessing Attack	✓	×	✓	×
Stolen Smart device Attack	✓	×	✓	✓
Replay Attack	✓	✓	✓	✓
Impersonation Attack	✓	✓	✓	✓
Privileged Insider Attack	✓	✓	✓	×
Temporary Information Attack on Known Session	✓	✓	✓	×
Perfect Forward Secrecy	✓	×	✓	×
Maintains Patient Anonymity	✓	×	✓	✓
Resistance to Denial of Service (DoS) attacks	✓	✓	✓	×
Mutual Authentication	✓	×	✓	✓
Stolen Verifier Attacks	✓	×	✓	✓
Man-In-The-Middle Attack	✓	×	✓	×

5 Performance Analysis

- The comparison of the proposed protocol has been accurate with current modern protocols such as [8], and [9], not just for performance but also for computation and communication. The following are the notations that are involved:
  t_h : secure one-way hash function for Computation cost
  t_E : symmetric encryption/decryption for Computation cost

The following is the computational cost from the above processes, according to the experimental results. Tan et al.[9] scheme takes $4t_h$ at operations carried out during registration and $12t_h + 2t_E$ at operations carried out during authentication, Zahid et al.[8] performs $4t_h + 1t_E$ and $15t_h + 2t_E$ for registration and authentication processes respectively, Kisung et al.[10] needs the computation cost $20t_h$ for both registration and authentication phases and that takes around $0{:}\,08\ ms$. In our scheme, Assume that executing a hash function t_h takes around $0{:}\,004\ ms$ and symmetric encryption/decryption t_E takes around $0{:}\,008\ ms$. **Table 3.** shows that the comparison of the result between the proposed protocol to recent related protocols [9] and [8]. The Table demonstrates that the protocol of Zahid et al has around 36% in contrast to the proposed protocol, there is an additional overhead, in the same time that our protocol has around 10% In terms of computation cost, there is an additional overhead as compared to the Tan et al protocol. Though, our protocol is more secure than another alternative scheme.

- The communication cost is compared in **Table 3.** During the login and authentication processes, the total bandwidth used, and the number of messages exchanged, will derive the communication cost. Assuming the random numbers, one-way hash function output is (160-bits) each, while timestamps expend (32-bits). The login phase from the proposed protocol is $\{PID_i, M_1, M_2, t_1\}$ needs (160 + 160 + 160 + 32) = 512 whereas the

authentication phase $\{M_4, M_5, t_3\}$content(160+160+32) = 352. As a result, the proposed scheme's total bit requirement is 864 bits.

From the previous analysis, we noticed that both protocols in [9] and [8] used encryption and this makes it possible to decrypt the data sent through the open channel between the server cloud and the patient, while on the other hand, in our protocol this cannot happen because we only use one-way-hash that cannot be decrypted, and this is what makes The proposed protocol is more lightweight and does not have high computational and communication overheads.

Table 3. Compare overheads and review proposed and current protocol.

Protocol	Computational cost		Running Time	Exchanged Messages	Communication cost
	Registration processes	Authentication processes			
Tan et al.[9]	4th	12th +2E	≈0:08ms	3	1184
Kisung et al.[10]	7th	13th	≈0:08ms	4	3008
Zahid et al.[8]	4th+1E	15th+2E	≈0:1ms	3	842
proposed scheme	8th	14th	≈0:088ms	2	864

6 Conclusion

In the proposed protocol, we have explained how it is resistant to many attacks like Offline Guessing the Password Attack, Stolen Smart device Attack, MitM Attack, Resistance to Denial of Service (DoS) attacks, and so on. against important patients' data, as it is transmitted through the open channel to the cloud server and vice versa. This paper also proved that Scheme. [9] has many security mistakes and does not prevent multiple attacks, including Stolen Smart device Attacks, Man-In-The-Middle attacks, Offline Password Guessing attacks, and so on. As well, the computation cost of [8] protocol has around 36% in contrast to the proposed protocol, there is an additional overhead. Therefore, to overcome these security flaws, we designed the protocol proposed in this paper.

References

[1] Rohit Ranchal, Paul Bastide, Xu Wang, Aris Gkoulalas-Divanis, Maneesh Mehra, Senthil Bakthavachalam, Hui Lei, Ajay Mohindra, "Disrupting Healthcare Silos: Addressing Data Volume, Velocity and Variety With a Cloud-Native Healthcare Data Ingestion Service,". In IEEE Journal of Biomedical and Health Informatics, Nov. 2020, vol. 24, no. 11, pp. 3182-3188.

[2] Zaid Alaa Hussien, Hai Jin, Zaid Ameen Abduljabbar, Mohammed Abdulridha Hussain, Ali A. Yassin, Salah H. Abbdal, Mustafa A. Al Sibahee, Deqing Zou, "Secure and efficient e-health scheme based on the Internet of Things,". In 2016 IEEE International Conference on Signal Processing, Communications and Computing (ICSPCC), 5-8 Aug. 2016, pp. 1-6.

[3] Pei Huang, Linke Guo, Ming Li, Yuguang Fang. "Practical Privacy-Preserving ECG-Based Authentication for IoT-Based Healthcare,". In IEEE Internet of Things Journal, Oct. 2019, vol. 6, no. 5, pp. 9200-9210.
[4] Sobhan Esmaeili, Seyed Reza Kamel Tabbakh, Hassan Shakeri. "A priority-aware lightweight secure sensing model for body area networks with clinical healthcare applications in Internet of Things,". In Pervasive and Mobile Computing, Nov. 2020, vol. 69, pp.1574-1192.
[5] Amal sammoud, Nicolas montavont, Mohamed Aymen chalouf, Ammar bouallegue, Omessaad hamdi, "A secure and lightweight three-factor authentication and key generation scheme for direct communication between healthcare professionals and patient's WMSN,". In: 2020 IEEE Symposium on Computers and Communications (ISCC), 2020, pp. 1-6.
[6] Shehzad Ashraf Chaudhry, Husnain Naqvi, Muhammad Khurram Khan. "An enhanced lightweight anonymous biometric based authentication scheme for TMIS,". Multimed Tools Appl 77, 2018,5503–5524.
[7] Muhammad Ajmal Azad, Samiran Bag, Charith Perera, Mahmoud Barhamgi, Feng Hao. "Authentic Caller: Self-Enforcing Authentication in a Next-Generation Network,". in IEEE Transactions on Industrial Informatics, May 2020, vol. 16, no. 5, pp. 3606-3615.
[8] Zahid Mehmood, Anwar Ghani, Gongliang Chen, Ahmed S. Alghamdi. "Authentication and Secure Key Management in E-Health Services: A Robust and Efficient Protocol Using Biometrics,". In IEEE Access, 2019, vol. 7, pp. 113385-113397.
[9] Zuowen Tan, "An efficient biometrics-based authentication scheme for telecare medicine information systems,". In Network, 2013, vol. 2, no. 3, pp. 200-204.
[10] Kisung Park, Sungkee Noh, Hyunjin Lee, Ashok Kumar Das, Myeonghyun Kim, Youngho Park, Mohammad Wazid. "LAKS-NVT: Provably Secure and Lightweight Authentication and Key Agreement Scheme Without Verification Table in Medical Internet of Things,". in IEEE Access, 2020, vol. 8, pp. 119387-119404.

Short Circuit and Stability Analysis of a Multi-Machine System with Wind Turbine Using the ETAP Program

Sara Ismail Abd-Al Huseen[1], Rushed Almansory[2]
{s.ismail@fgs.stu.edu.iq [1], r.s.almansory@stu.edu.iq[2]}

Southern Technical University, Technical Engineering College, Iraq, Basrah[1, 2]

Abstract. This study focuses on the effects of a multi-machine 12 bus system-connected wind power plant (WPP) on the impact of variations in turbulences happening on multiple buses during service. The DFIG-based wind turbine was considered in this paper to assess the presentation features of DFIG For load current study, Short circuit study then transient stability. ETAP program analyzed the imitation effects the outcomes of the imitation display that a system disturbance that happens in a wind turbine-connected multi-machine scheme does not lead to a reduction in the bus close the fault thendecreases the constancy.

Keywords: WPP, Multi-Machine, DFIG, ETAP.

1 Introduction

Turbines (WT) with initiation engines are commonly used to provide a native load and power directly to the grid. Transient phenomena can occur During the start and braking time of the WT [1]. Stability is contingent on both the initial state of activity and the intensity of the disruption. Vishal Vaman Mehtre, Shripad Ganapati Desai, Prof. Dr. D.S. Bankar [2] The functional features of DFIG were evaluated using power flow analysis, short circuit analysis, harmonic analysis, and ideal load flow evaluation in this paper. Aman J, Mukesh K, Abhinav K, Rahul K [3] They discuss the analysis of the stability and transients of a multi-machine system using the ETAP program and explain the effect of the stability of the power system (PSS). Archana R, Subramaniya Siva A [4] It presents an integrated system for wind energy in a transmission system (IEEE) 30 bus with photovoltaic energy. This idea came as a result of bad weather conditions, which have an impact on the system, where the voltage, stability, and level of harmonic distortion are controlled. B A Ashad, A Siswanto, I C Gunadin, and Yusran [5] This study provides a new step for modeling disturbances in multi-machine systems connected to wind turbines and the effects of wind power in a vector system 9 bus and argues that the error can have a small moment of inertia sufficient to make it unstable. When it comes to checking temperature boundaries or stable state frequency regulation, wind power is close to any other form of electricity generation. However, during and after disruptions, the activity of wind turbines is diverse from that of traditional generators [6]. Readings and studies to evaluate the behavior of a wind turbine power scheme through transient disruptions that can lead to loss of generation stability in reference [7]. On the other hand, Additional difficulties in

IMDC-IST 2021, September 07-09, Sakarya, Turkey
Copyright © 2022 EAI
DOI 10.4108/eai.7-9-2021.2314795

voltage/frequency regulation, as well as reactive capacity reparations, can arise as a result of the introduction of wind energy, power value (e.g. harmonic distortion and flicker), and delivery system safety. Wind energy can be shared with enough compensators to improve the power circulation device's process [1, 8]. Wind power is usually produced by wind generators, which can operate at either a fixed or variable speed. The latter is distinguishable as it has more power for a given speed, optimal mechanical stability, lower mechanical forces, and lower excessive noise [9]. There are usually four types of generators in the latest developments in wind power conversion. Kind 1 is a fixed speed induction generator, kind 2 is a variable rotor resistance induction generator, kind 3 is a partial-scale power converter variable speed wind turbine design, and kind 4 is a full-scale power converter variable speed concept. In this article, the generator form 3 is used [10]. ETAP is the most detailed and thorough power system analysis program available, analysis, tracking, application, regulator, efficiency, and optimization. Real-time simulation, dynamic load shedding, optimal load flow, and cost optimization are among ETAP's unique features [11]. The load flow and transient stability in a device consisting of a double-fed induction generator (DFIG) wind turbine and a synchronous generator were investigated in this study using ETAP software with a limit of 12 buses. In the second section of the research, how DFIG works is discussed, while in the third section the system model is explained in detail, and in the fourth section, the load flow and short circuit of the system are studied with some illustrations and results represented by the tables and discussed, and in the fifth, the transient stability test is conducted with the proposed model in the presence of And the absence of a wind turbine, and in the sixth, some special concepts of modeling and stability of the system are presented with the mention of mathematical equations, and finally, in the seventh, the research work is concluded with mentioning the advantages and disadvantages.

2 Induction generator with two feeds (DFIG)

The main energy source will no longer be controlled, the use of DFIG has Become a viable plus effective option for power production. Its feasibility and efficiency are attributable to the Capacity of the Converters to control the excitation of the system rotor field, as shown in Fig 1 [12]. A wound rotor generator and a PWM transformer operating on an AC/DC/AC IGBT are included in the DFIG. As compared to traditional wind generators, it has a higher dynamic performance throughout grid outages, the idea of a variable-speed wind turbine (VSWT) fitted with a doubly fed induction generator (DFIG) is gaining traction. The induction generator system (DFIG) is a more straightforward and cost-effective alternative to the synchronous machine. In the DFIG converter, a dc-link capacitor connects a rotor-side converter (RSC) and a grid-side converter (GSC). This converter's necessary rating is usually 25-30% of whole scheme capacity, which lowers converter costs, decreases harmonics infusion into the linked grid, and improves the wind turbine system's overall performance [13].DFIG’s key benefit lies in its capacity to work at very low wind speeds and high wind speeds. The reactive influence is fed into the grid to prevent Power absorption from the grid and thus voltage disruption is minimized, thus over-ruling the need for reactive power compensation [14]. With a little wind speed, DFIG is very powerful. DFIG is during fault conditions Capable of handling higher current values without disrupting the device [2]. A changeable wind turbine, particularly in light wind conditions, makes better use of the available wind resources than a fixed-speed wind turbine [4].

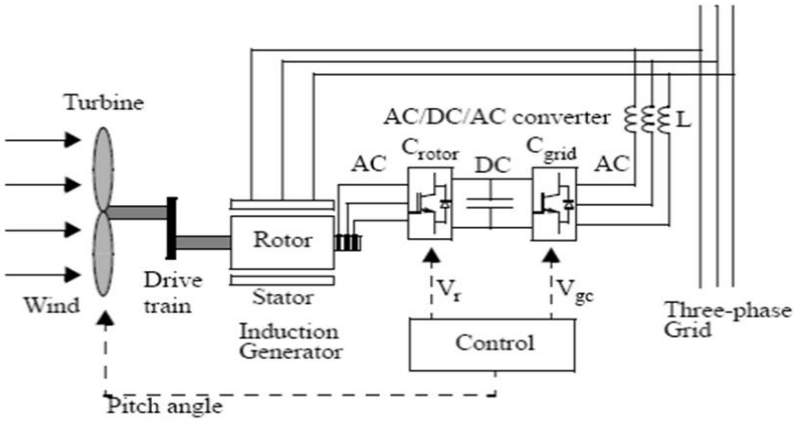

Fig. 1. Double fed induction generator

3 Model of Power System

Fig. 2 shows a single-line schematic of the model used to examine the performance of multi-machine interconnected wind turbines during unexpected short circuit events during simulation. This system involves a converter substation, 13.8 kV, and a three-sub feeder delivery system that is linked to a wide network via a 69 kV longitudinal cable. To retain voltage and frequency power, the 13.8 kV delivery power plant is fitted with a three-phase fixed shunt dc link. A transformer connects the grid to a 69 kV, 1000 MVA fault current storage bus. The scheme consists of three radial lines with four feeders L1 (1.082MVA), L2 (1MVA),L3 (0.5 MVA),L4 (0.5 MVA) .between bus 4 and 5, 11 and 12,considered two operated 13.8/0.48 KV , 1.5 and 1 MVA step-up transformers. And between bus 6 and bus 7, 9 and 10, considered two operated 13.8/2.4KV step-up transformer. Between bus 3 and 2 considered operated 69/13.8KV main step-up transformer. With one wind turbine generator (2.1 MW) at bus 4 and an asynchronous generator (4.25 MW) at bus 8.

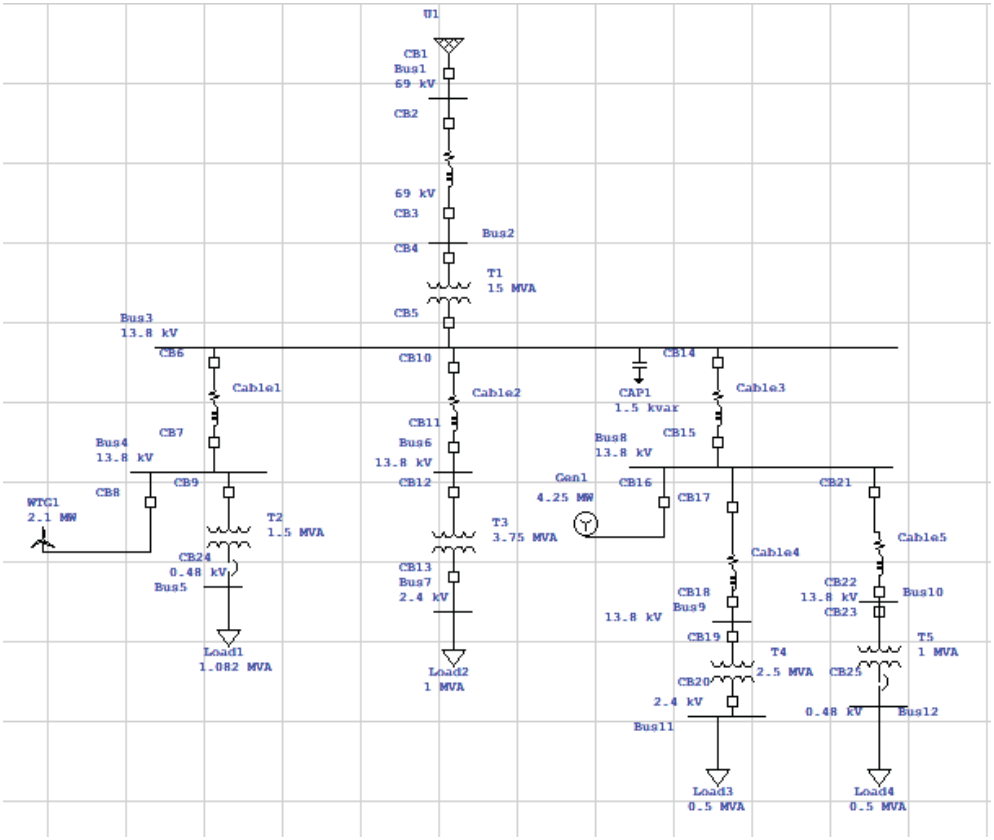

Fig. 2: 12-bus Multi-machine with wind turbine generator [12].

4 The system's load flow and short circuit study

4.1 Load Flow Study

Analysis of Load Flow has been tracked under the ETAP program. The Load Flow Analysis is capable of Separately Specifying and changing the device parameters for each event. ETAP has several options to identify the display options based on the load flow analysis needs and specifications of the user. In the 12 bus method, Power flow is measured using the adaptive Newton RAPHSON load flow algorithm. For analysis, Wind velocity is taken as the nominal. 963 KW and 82 KVAR are both real and reactive capacity close to the network as shown in Fig 3.

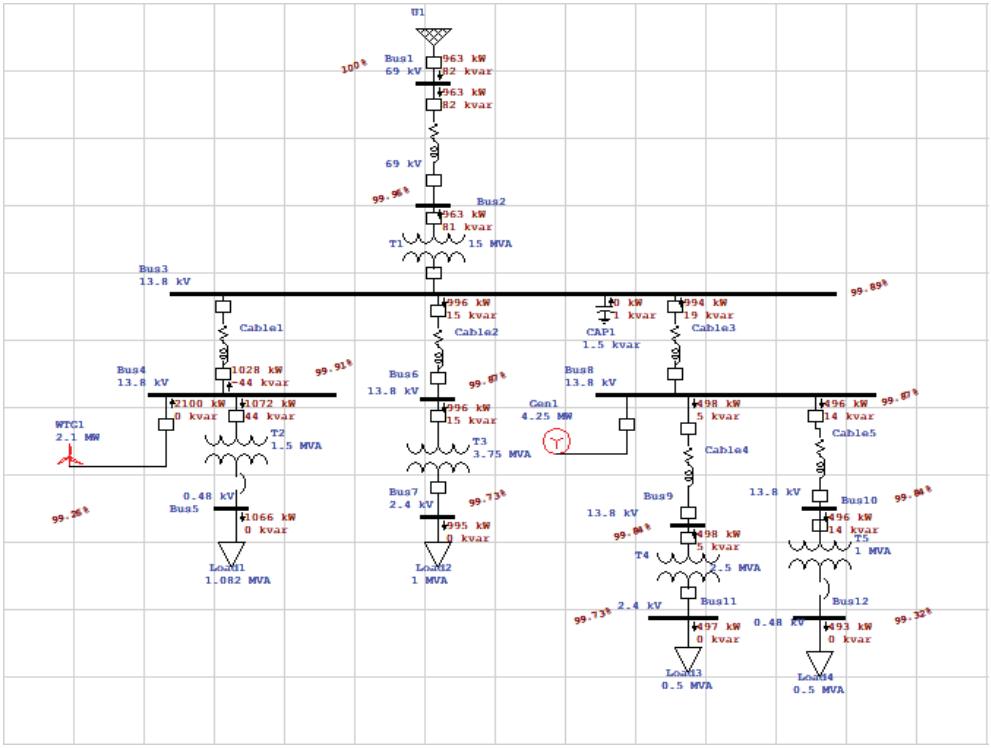

Fig. 3: Load flow (analysis result of the system).

Results of the load flow study of the 12-bus system has been observed that the bus voltages are increased by 100%, 99.959%, 99.890%, 99.914%, 99.866%, 99.728%, 99.867%, 99.843%, 99.843%,99.735% in bus no 1,2,3,4,6,7,8,9,10,11 respectively and decreased by 99.256% ,99.318 in bus no 5,12.

4.2 Short Circuit Analysis

For the circuit breaker study, the capacity of the ETAP program was measured. The willingness of the machine to adjust to its normal state, as well as the main protective equipment's ranking, Are the most important factors in short circuit research. The device is shown in Figs 4, 5 before joining the wind turbine introducing a 12 bus fleet, a generator for bus 8, loads for buses 5, 7, 10, and 12.

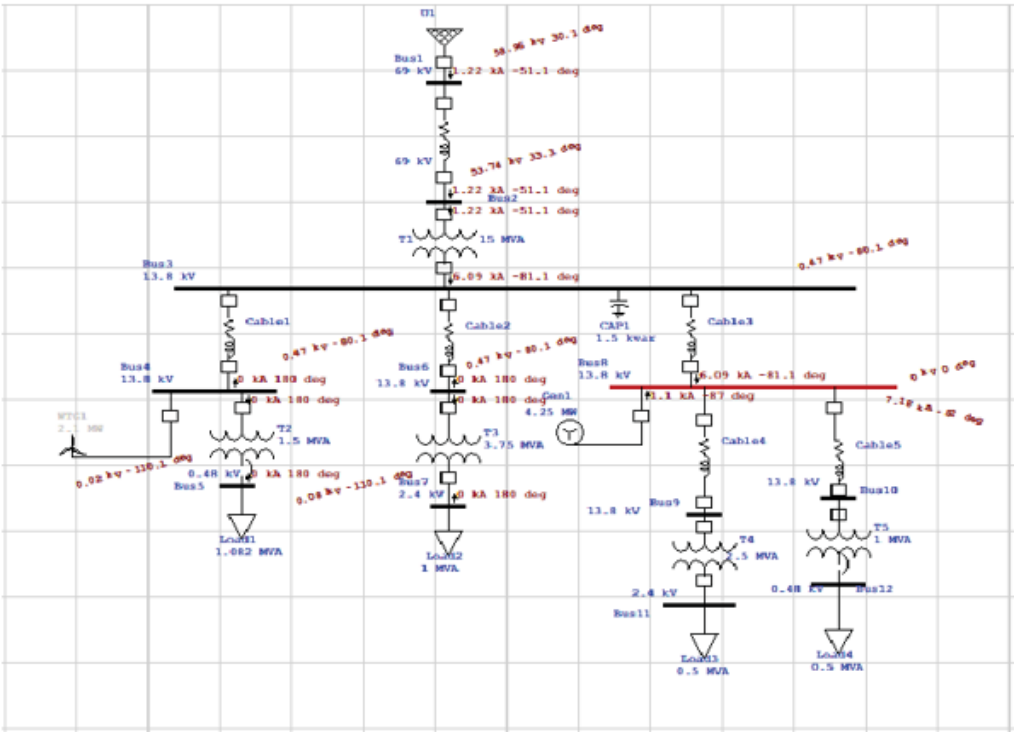

Fig .4: Error in bus bar 8.

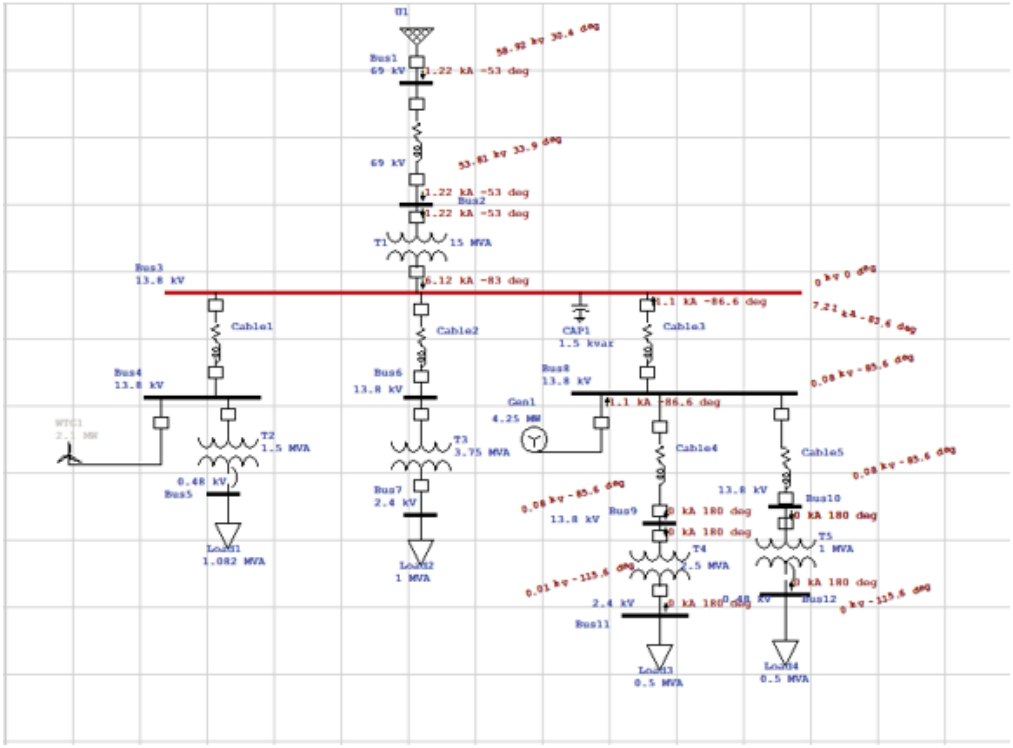

Fig. 5: Error in bus bar 3.

Table 1 . Voltages on each bus before entering a wind turbine

Buses	Voltages ofbuses	Error at bus 3	Error at bus 8
1	69 KV	58.92KV	58.96KV
2	69 KV	53.81KV	53.74KV
3	13.8 KV	0KV	0.47KV
4	13.8KV	-	0.47KV
5	0.48 KV	-	0.02KV
6	13.8 KV	-	0.47KV
7	2.4 KV	-	0.08KV
8	13.8 KV	0.08KV	0KV
9	13.8 KV	0.08KV	-
10	2.4 KV	0.08KV	-
11	13.8 KV	0.01KV	-
12	0.48 KV	0KV	-

Case 1: Absence of wind turbine and presence of a synchronous generator
Results of short circuit analysis in the absence of wind turbines are shown in Table 1, when a breakdown occurs on Bus No. 3, we note that the voltage results are higher on Bus No. 1 and drop to zero on Bus No. 12 and Bus No. 4,5,6,7 out of the work. Otherwise, when there is a fault

on Bus no 8, the results of the voltages are the Maximum on Bus No. 1 and the Minimum on Bus No. 5 and Bus No. 9, 10, 11, and 12 are out of the work.

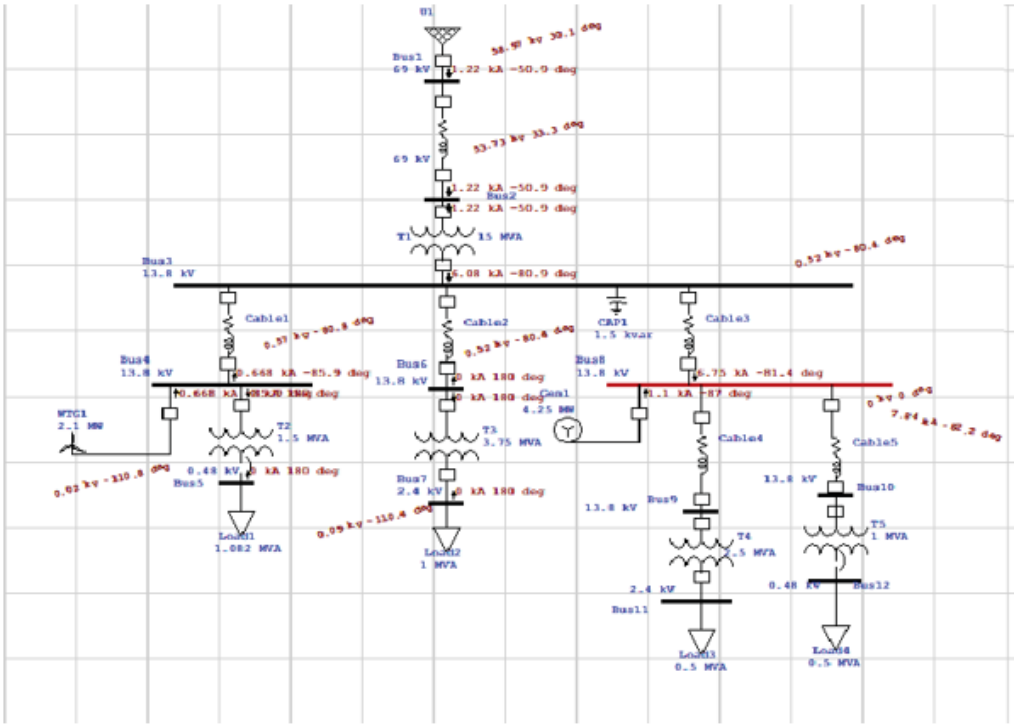

Fig .6: Error in bus bar 8.

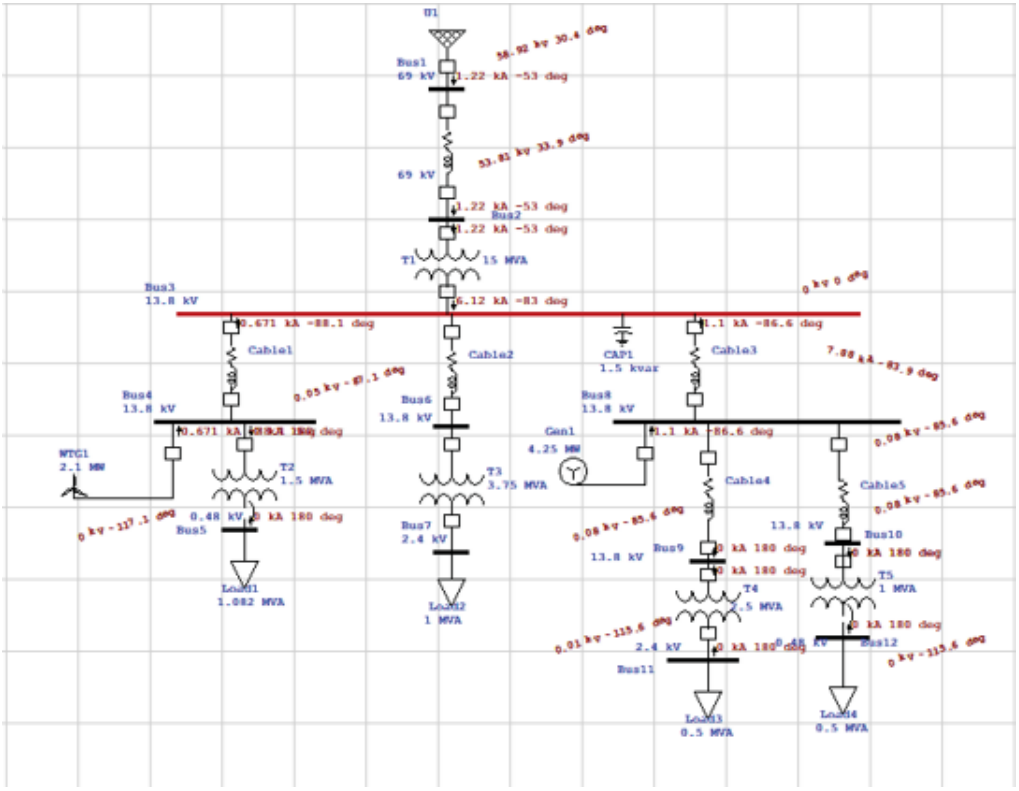

Fig. 7: Error in bus bar 3

Table 2. Voltages on each bus after entering a wind turbine

buses	Voltages of buses	Error at bus 3	Error at bus 8
1	69 KV	58.92KV	58.97KV
2	69 KV	53.81KV	53.73KV
3	13.8 KV	0K V	0.52KV
4	13.8 KV	0.05KV	0.57KV
5	0.48 KV	0KV	0.02KV
6	13.8 KV	-	0.52KV
7	2.4 KV	-	0.09KV
8	13.8 KV	0.08KV	0KV
9	13.8 KV	0.08KV	-
10	2.4 KV	0.08KV	-
11	13.8 KV	0.01KV	-
12	0.48 KV	0K V	-

Case2: wind turbine and sync generator are present

When a fault occurs on Bus No. 3, we observe that the voltage results are higher on Bus No. 1 and decrease to zero On Bus No. 5, 12, and Bus No. 6, 7 out of the work. Otherwise, when there is a fault on Bus no 8, the introduction of a wind turbine does not affect on results.

5. Transient Stability system under test Transient Stability Analysis event

At time t = 10 sec, the circuit breaker is triggered on bus 4 and cleared at time t = 10.5 sec. In the models, the 30-sec Simulations involve electromagnetic transients, but saturation is not included. When failure occurs, there is a large difference in voltage through transient conditions, and positive sequence current Fluctuations are often very strong. On the other hand, because of the combination of DG, these variations cannot be avoided. It injects the device with full reactive power and the voltage incomes to its usual range. When an error happens, the DG device supplies reactive power. Before installing a wind turbine, the fault in Figures 8 and 9 of Bus 4 has little effect on the major grid's real and reactive power.

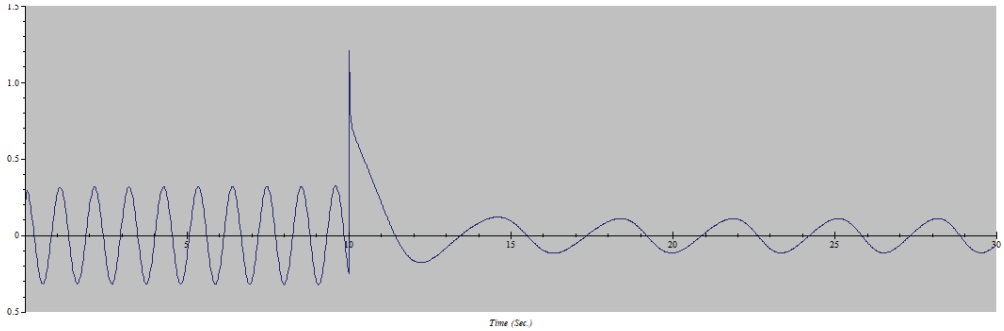

Fig. 8: bus 4. Synchronous Generator: Active power MW (Before adding a wind turbine)

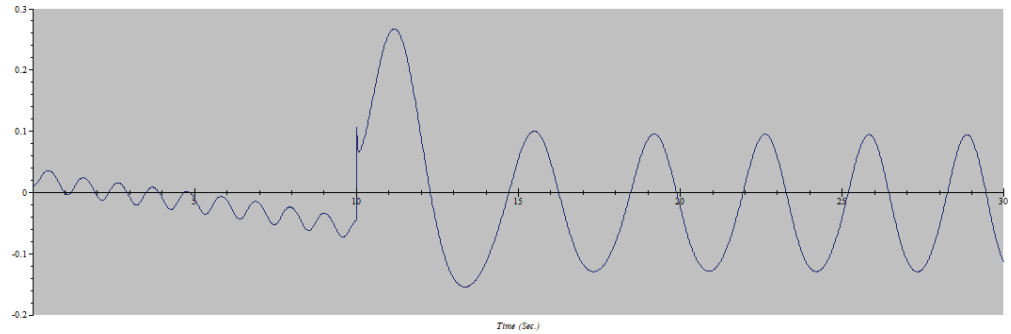

Fig. 9: bus 4. Synchronous Generator: Reactive power MVAR (Before adding a wind turbine)

Now when the synchronous wind turbine has been linked to the device, a short circuit case has been established on bus 8 for time t = 10 seconds and resolved at t = 10.5 seconds, The simulation has been run for 30 seconds, the wind turbine's power is 5 MW, and wind speed is the main factor, as shown in Figures 10 and 11. For simulation, the wind speed may vary from 8 m/s to 12 m/s. Due to the wind turbine itself delivering compensating VARs, the patterns in reactive and actual power are slightly different.

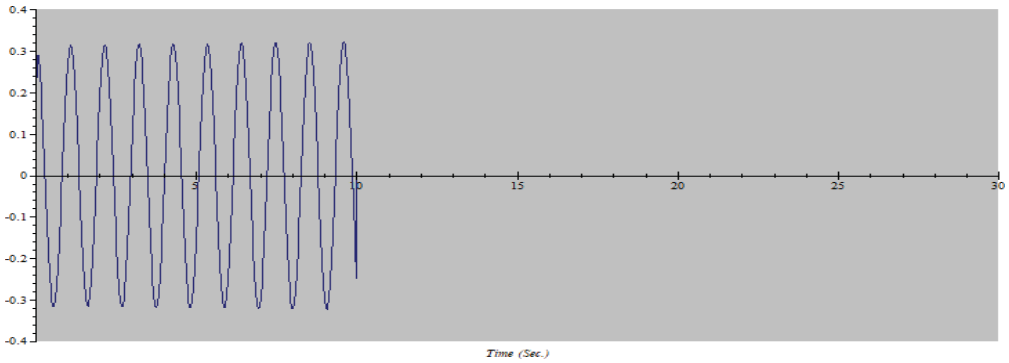

Fig .10: bus 8. Synchronous Generator: Active power MW (after adding a wind turbine)

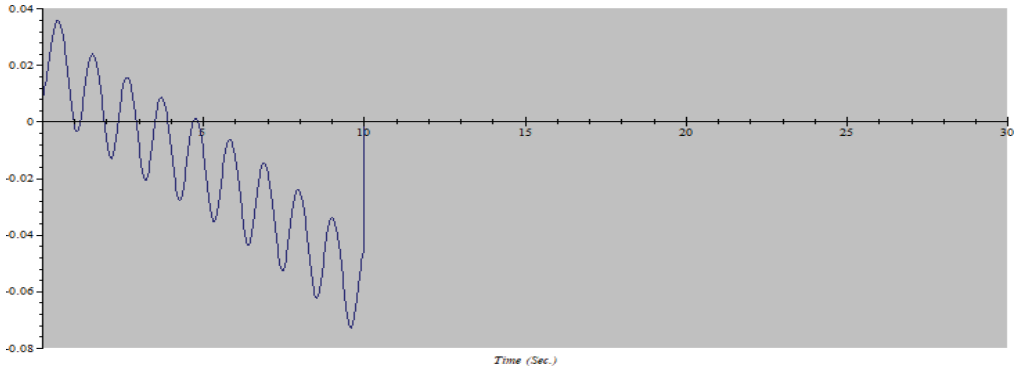

Fig .11: Bus 8. Synchronous Generator: Reactive power MVAR (after adding a wind turbine)

Remarks on the Result:

The studies of stability analysis are conducted in four situations. In table 3, the results of transient trials, events, and observations are listed.

Table 3. The study's overview reveals

Events	Due to a fault, the generation isdown.	Study
Event 1	Fault on bus 4	Since the synchronous can supply the load, the winding mechanism has no negative impact on the project.
Event 2	Fault on bus 8	Since the wind turbines are insufficient to supply the load, Generator G1 will quickly lose its balance.

6 Modeling Concerns for Wind Turbine and Stability Equations

Whenever a mechanism is disturbed, its stability refers to its ability to adjust to its stable state. As described earlier, Electricity is produced by synchronous machines which are in sync with the rest of the system. As a result, a Balancer can be described as the capacity of a power supply to restore to a stable equilibrium before losing equilibrium. Random variations in load and

production stages cause these minor disruptions. These slight changes may cause catastrophic failure in a power system network because they force the rotor angle to high voltage [15].
Multi-machine network disruption is a safety issue that causes changes in grid integration and voltage on the power system linked to the wind turbine, which affects multi-machine systems [5]. As shown in Fig 12, the wind turbine design with DFIG is made up of the following components: wind speed model, aerodynamic model, mechanical model, DFIG model, protection model for back-to-back multilevel inverters, and transformer. The following equations define the aerodynamic model.

$$\lambda = (\omega M R) / V \quad (1)$$

$$PM = (1/2) \rho \pi R2V3 \quad (2)$$

$$TM = PM / \omega M = (1/2 \lambda) \rho \pi R3V2CP \quad (3)$$

Where λ is the tip-to-ground speed ratio, ω is the blade angular velocity (rad/s), R is the blade radium (m), V is the wind speed (m/s), PM is the machine-driven power from wind (KW), ρ is the air strength (Kg/m3), CP is the Factor of strength. The power factor is greatest at a certain rate of the tip speed ratio. The maximum power Can be captured by a wind turbine with DFIG by achieving the optimum tip speed ratio under the valued wind Speed. Pitch regulation and DFIG control restrict the captured power to the valued energy overhead the valued wind speed, leaving the optimum power coefficient operation [16].

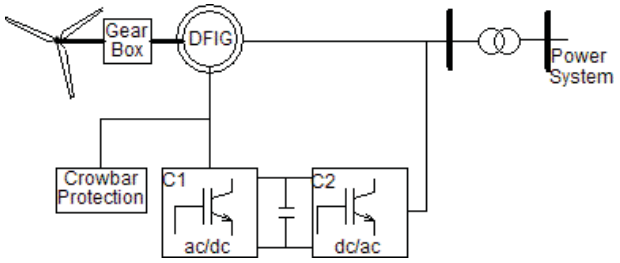

Fig. 12: Wind turbine with DFIG

When a system is exposed to significant or extreme disruptions, transient stability studies determine whether synchronism is maintained or not. A short circuit, a loss of a sudden large load, or a loss of generation is all examples of disturbances. A temporary stability testing aims to see if the load angle incomes to a stable value after the disruption have passed. To decide the constancy, nonlinear equations are solved. Transient stability is the focus of the Equal Area Criterion. It is, in reality, a very simple graphical method that is employed. It is used to determine the transient stability of a single machine or two-machine device in the presence of an infinite bus [3].
Swing Equation: The swing formula is a time-dependent expression for the gravitational attraction of the rotor with respect to the stator field.
For generator, Tag = T s – T e
=Input Torque – Out put Torque

For motor, Pa g = P s – P e
= Input Power – Out put Power
As angular displacement always varying so its measure is difficult w.r.t synchronously rotating axis
ɵ = Ws.t + ð
d ɵ/d t = d/d t (Ws.t+ð)
d2 ɵ/d t2= d2ð/d t2 = α
M d2ð/dt2= P s – P e = P s – P max sin ð

Where:
W s = angular velocity of the reference axis rotating synchronously
ð =angular displacement in electrical degree

7 Conclusion

The research performed in the program of the ETAP was useful in the DFIG wind turbine power demonstration. Originally, the results of the load flow clearly show that the DFIG can generate great output power at high wind speeds. In addition, by giving reactive Arrays to the grid, DFIG machines provide voltage stability. In the presented model assessment, two hypotheses are established. First, the micro-grid research system is expected to be equal, which means no single-phase demands or imbalanced three-phase demands are taken into account. Second, there is no interplay between both the Generating units and the network. Another thing to consider is the action that proceeds the tripping. Pre-fault results are the same, implying that fast transients do not cause safety relays and that long-term stability is unaffected. The simulation results revealed that the similarities between the results of the outcome of these two different evaluation systems support the feasibility of the usage of a double-fed induction generator to increase the multi-transient machine's stability. The system that has been created can simply be adapted to other big wind farm models that have been tested for erroneous running.

References

[1] C. S. Desmoulins, P. Demopoulos. “Electrical Transients of Wind turbines In A Small Power Grid”. IEEE Transactions on Energy Conversion. September 1996; Volume 11: No 3.

[2] Vishal Vaman Mehtre, Shripad Ganapati Desai, Prof. Dr. D.S. Banker. “Analysis of a Doubly Fed Induction Generator based Wind Farm”. IEEE International Conference on Technological Innovations in ICT For Agriculture and Rural Development. 2016: 7.

[3] Amman Jaiswal, Mukesh Kumar, Abhinav Kumar, Rahul Kumar. “Load Flow and Stability Analysis of Multi-Machine Power Systems in ETAP”. Maulana Abdul Kalam Azad University of Technology (MAKAUT) 2018.

[4] Archana R1, Subramaniya Siva A2. “A Perspective Analysis for the Impact of PV and Wind Hybrid Distributed Generation”. International Journal of Advanced Research in Electrical. April 2018; 7(4): 7.

[5] B A shad, A Siswanto, I C Gunadin, and Yusran. “Stability Analysis and Fault Changes on Wind Turbine Effect in Multi-Machine Power System”. Materials Science and Engineering. IOP Conference Series; 2019; Indonesia: B A Shad; 2020.p. 7.

[6] Thomas Ackermann. “Wind Power in Power Systems”. Edited by T. Ackermann: John Wiley & Sons; 2005. 684-745

[7] J. T. de Oliveira, M. F. de Medeiros Jr., and C. B. M. Oliveira. “Development of Modules for Transient Stability Studies of Power Systems with Wind Turbines in Different Simulation Platforms”. IEEE. 2006.

[8] B. Dong, S. Asgarpoor, and W. Qiao. “Voltage Analysis of Distribution Systems with DFIG Wind Turbines”. IEEE. 2009.

[9] T. A. and A. M., “Modeling Issues of Grid-Integrated Wind Farms for Power System Stability Studies,” Model. Control Asp. Wind Power Syst., 2013, doi: 10.5772/54612.

[10] Napalm, Prof. S.U Kulkarni. “PMSG Based Wind Farm Analysis in ETAP Software”. IJSRSET .2017; 3(3): 5.

[11] Hei Yan Lai, Weijie Mai, C. Y. Chung. “Educational Simulation Platform for Micro-grid”. IEEE.2014: 7.

[12] Vijay Ray, Summit Sahrawi, Kamet Pander. “Transient Stability Analysis of Wind Turbine Based MicroGrid using ETAP Software”. International Journal of Engineering Research & Technology (IJERT). April– 2014; 3(4):4.

[13] Prescient Debra, AK shay Kudu, M.R. Ram ekes, D.R. Tutakane. “Analysis of DFIG based Wind Energy System with Grid Integration under normal and abnormal conditions”. IOSR Journal of Electrical and Electronics Engineering (IOSR-JEEE). Mar – Apr. 2015; 10(2): PP 46-52.

[14] Vishal Vaman Mehtre, Shripad Ganapati Desai, Prof. Dr. D. S. Banker. “Power Comparability Analysis of DFIG And SCIG based Wind Farm”. IJSRSET. 2016; 2 (3): 5.

[15] M .Saleh Ebn Sharif, M. Monower Zahid Khan, M . Moniruzzaman, Anamika Bose. “Design, Simulation and Stability Analysis of Wind-PV-Diesel Hybrid Power System Using ETAP”. American Journal of Modern Energy .2017; 3(6): 121-130.

[16] Heping Zou, Hui Sun, Jiyan Zou. “Fault Ride-through Performance of Wind Turbine with Doubly Fed Induction Generator”. IEEE. 2007.

The Effect of Baffle Inclination on a Heat Recovery Ventilator Performance

Hawraa Imad Abdulhafedh[1], Saadoon Fahad Albahadili[2], Raed Sabri Hameed[3]
{eng_hawra5@yahoo.com[1], s.albahadili@stu.edu.iq[2], raed.hameed@stu.edu.iq[3]}

Engineering Technical College of Basra, Southern technical university, Basra, Iraq

Abstract. The current research focuses on numerical simulations of recovering low-grade airborne heat to co-save a portion of the energy used by household ventilation. The investigation of three-dimensional steady-state turbulent flow and heat transfer utilizing the CFD approach and the finite volume method with ANSYS software to solve the Naiver Stock and energy equations. The turbulent flow model is governed by the k-ε turbulence model with the SIMPLE-discretization algorithm. To enhance the recovering system thermal performance, two baffles are inserted into both inlet hot and cold channels with changing their inclination (45, 90, and 135°) respectively. The Thermo aerodynamic performance assessments are included velocity, temperature, and effectiveness distribution along with airflow from the leading edge to the end of the core, through the two baffles. The results reveal simply that the flow is characterized by significant deformations. When fixed inclination baffles (45°) are added inside the channel at a constant Reynolds number, the efficacy increases by 35%.

Keywords: Heat Recovery, Numerical Simulation, Plat heat exchangers, Baffles, CFD.

1 Introduction

Rapid increases in global energy consumption have raised questions about supply issues, energy depletion, and negative environmental consequences. Global change and ozone destruction, for example, have been major problems that people have had to contend with. Building energy consumption, including operation and maintenance, accounts for 40% of total global energy demand today. Furthermore, heating, ventilation, and air conditioning (HVAC) systems use 40–60 percent of a building's energy intake, depending on the environment. Meanwhile, this energy consumption results in a significant volume of greenhouse gas pollution, such as carbon dioxide emissions (CO2). As a result, governments are working to improve energy-efficient and environmentally sustainable construction technology. Because of their potential to deliver significant energy benefits for residential buildings, heat recovery systems are seen as a very promising technology. A heat recovery ventilator (HRV) is a heat recovery device that recovers heat from an air-to-air heat exchanger. It transfers heat or mass from one air stream to another by removing, recovering, or salvaging it. To put it another way, the air that would otherwise be discarded into the atmosphere is used to preheat or precool the incoming air of an HVAC device. Heat recovery systems usually recover 60 percent to 95 percent of the heat in the exhaust air, resulting in dramatic improvements in building energy efficiency [1].

IMDC-IST 2021, September 07-09, Sakarya, Turkey
Copyright © 2022 EAI
DOI 10.4108/eai.7-9-2021.2314793

A few studies have evaluated the potential of plate type on heat recovery performance. Han H et al [2] performed an experimental study to evaluate the influences of outdoor conditions variation on the thermal performance of the plate-type heat recovery ventilators. The results observed that the outdoor temperature decreasing as an enhancement influence on the heat recovery coil efficiencies.

Assuncao [1] did a simulation study to evaluate the influences of baffle geometry, and Reynolds number variation on the heat recovery ventilator performance. The results show that the height of the baffle has a positive influence on the overall ventilator performance. In the case of the Reynolds variations, the increase has the worst influences on the pressure drop, meanwhile, an augmented Nusselt number so as the heat transfer effectiveness. M.Ghazvini et al. [3] presented a simulation study to predict the influences of V-fin attack angle on the performance of heat recovery system, under different flow and wide range of attack angle (40°–80°). The study observed that under a high flow rate the attack angle of 40° shows the highest system performance. Kang et al. [4] investigated the effect of porous baffles, experimentally, on the average heat transfer coefficients for heated rectangular channels made up of aluminum foam. The results showed that porous baffles have enhanced influences on heat transfer by 300% compared to straight channels with no baffles. Hamidou et al. [5] Introduced a numerical procedure to study the effect of wavy baffle using a rectangular duct section on heat transfer for turbulent flow. The baffle was arranged in the duct wall to produce vortices. They concluded that wavy baffles using will increase the velocity more than four times the reference velocity. D. Saad et al. [6] evaluated the effect of the baffle's shape inside a corrugated square duct experimentally. The study includes various baffles shape flat, rectangular, semicircular, triangular, and trapezoidal. The results show that the baffles using have an enhanced effect on the average Nusselt-number compared to the smooth duct, meanwhile baffles leads to a substantial increase in friction factor over a plain duct; the trapezoidal baffle provides higher thermal performance than the other baffled. Waleed et al. [7] presented a numerical study for the v-corrugated channel angles influences on laminar forced convection heat transfer and fluid flow characteristics with angles variations from 0° to 60°. The results showed that the wavy angle increasing at constant Reynolds increases has an enhanced effect on heat transfer and pressure drop. The corrugated angle of 60 shows maximum heat transfer enhancement. Younes et al. [8] carried out a simulation analysis for cascaded rectangular-triangular baffle (CRTB) using FLUENT software. The results showed that the insertion of CRTBs in the channel has considerable enhancement on heat transfer rate meanwhile much high friction loss. Xinyi et al. [9] investigated experimentally and numerically the overall heat transfer performance and friction factor in a rectangular duct with ribbed and ribbed-grooved rib angle of 30°. With slopes angles of 30°, 45°, 60°, and 0°. The experimental results show that the grooved channel has enhanced positive influences on the overall thermal performance, the Nusselt number ratio, and the friction factor ratio. The numerical results show that the slope angles of 30° and 45° show superior thermal performance and overall thermo-hydraulic performance ratio compared with the cases for V-shape ribs. Y. Menni et al. [10] performed numerically the effect of complex obstacles within solar channels. Where two obstacles of the form '+' interlaced within a two-dimensional and rectangular channel have been placed. A Newtonian fluid, turbulent, incompressible, and of stable properties flows inside the channel. The effect of flow rate on temperature was investigated. the fluid dynamic analysis showed a considerable augmentation in the normalized friction factor with the Reynolds number, introducing large recirculation zones. where it was found that direct proportionality between the skin friction and the elevation of the Reynolds number. Prashanta et al. [11] presented an experimental investigation of the effect of baffles characteristics (orientation, perforation, and position) on local heat transfer and

friction factor in a rectangular duct. The study concluded that using two inclined baffles has a positive enhancement on both the overall heat transfer coefficient and the average Nusselt number compared to smooth duct, meanwhile having the worst effect on frictional head loss. To improve the performance of systems, Ameur [12] quantitatively evaluated the impact of the inclination angle of baffles and the direction of inclination on a rectangular channel heat exchanger. These studies discovered that the straight baffle produces a more intense and wider vortex than the inclined baffle. The opposite direction appears to be more promising in terms of heat transfer intensification in the case of the inclined baffle.

The purpose of this study is an enhancement of the turbulent heat transfer inside the plate-type (crossflow) heat recovery ventilator by installing two baffles along the airflow duct that are attached on the top and bottom sides of the hot and cold inlet ducts, as well as investigating three different baffle angles (45°, 90°, and 135°).
The paper is structured as follows: the numerical model is proposed in section 2 followed by showing the obtained results for four case studies in section 3. Finally, the paper is concluded in section 4.

2 Numerical models

HRV is visualized and simulated by numerical simulation using commercial CFD code by ANSYS Fluent version 20 program. The Fixed plate heat recovery system is the most widely used type, owing to the structure simplicity associated with efficiency enhancement. Which consist of thin plates stacked together. For better heat transfer, the plates may be flat, have baffles, or have other disturbances. [1]. The schematic of a crossflow fixed-plate heat recovery system with two channels with two baffles for both channels is shown in Fig. 1. with a heat exchanger dimension of 370mm width(w), 320 mm height(H), and L = 370 mm in length and dimension of the cold and hot channel are W = 370 mm in width, H = 320 mm in height and L = 1170 mm in length. The baffles have a high H = 137.28 mm.

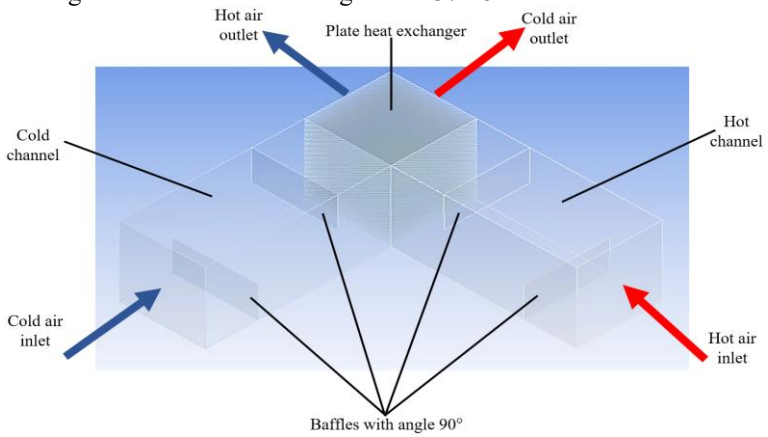

Fig. 1. The longitudinal section of the exchanger with hot and cold channels.

2.1 Assumptions

The current work uses the following:

- Reynolds number 12000 is used in the numerical simulation.
- The airflow should be turbulent and at a constant rate.
- Heat and flow transfer are three-dimensional processes.
- Gravity and radiation have no effect.
- Fluid and solid physical characteristics remain constant.
- The fluid is incompressible and Newtonian.
- The fluid has a steady velocity profile and a uniform temperature as it enters the channel; and
- The Shear-Stress Transport (SST) k-model is utilised to close the configuration under inquiry.

2.2 Boundary conditions

A uniform Three-dimensional profile of fluid velocity (u = Uin, v = Uin, w = Uin) at 25°C (Tin = 298 K) is in cold channel and (u = Uin, v = Uin, w = Uin) at 41°C (Tin = 314 K) in hot channel. an atmospheric pressure (P = Patm) outlet condition is applied at the channel outlet. The inlet turbulence intensity was kept constant at I = 2%. Impermeable boundary and no-slip wall criteria were applied to the channel's surfaces.

2.3 Governing equations

The Continuity Equation:

$$\frac{\partial u}{\partial x} + \frac{\partial v}{\partial y} + \frac{\partial w}{\partial z} = 0 \quad (1)$$

The Momentum Equations:

X-Direction:

$$\rho\left(u\ \frac{\partial u}{\partial x} + v\ \frac{\partial u}{\partial y} + w\ \frac{\partial u}{\partial z}\right) = -\frac{\partial P}{\partial x} + \mu\left(\frac{\partial^2 u}{\partial x^2} + \frac{\partial^2 u}{\partial y^2} + \frac{\partial^2 u}{\partial z^2}\right) \quad (2)$$

Y- Direction:

$$\rho\left(u\ \frac{\partial v}{\partial x} + v\ \frac{\partial v}{\partial y} + w\ \frac{\partial v}{\partial z}\right) = -\frac{\partial P}{\partial y} + \rho g_y + \mu\left(\frac{\partial^2 v}{\partial x^2} + \frac{\partial^2 v}{\partial y^2} + \frac{\partial^2 v}{\partial z^2}\right) \quad (3)$$

Z- Direction:

$$\rho\left(u\ \frac{\partial w}{\partial x} + v\ \frac{\partial w}{\partial y} + w\ \frac{\partial w}{\partial z}\right) = -\frac{\partial P}{\partial z} + \mu \quad (4)$$

The Energy equation:

$$\rho Cp \left(u \frac{\partial T}{\partial x} + v \frac{\partial T}{\partial y} + w \frac{\partial T}{\partial z}\right) = k \left(\frac{\partial^2 T}{\partial x^2} + \frac{\partial^2 T}{\partial y^2} + \frac{\partial^2 T}{\partial z^2}\right) \quad (5)$$

where u, v, and w are velocities in the x, y, and z directions, respectively; the volumetric density viscosity in a dynamic state; p the stress; T stands for temperature; Cp is the fluid's heat capacity at constant pressure, and k is its thermal conductivity [13].

For Turbulent flow k-epsilon model was used [11].

For turbulent energy k,

$$\frac{\partial(\rho u_j k)}{\partial x_j} = P_k - \beta^* \rho \varepsilon k + \frac{\partial}{\partial x_j}\left[\left(\mu + \frac{\mu_t}{\sigma_k}\right)\frac{\partial k}{\partial x_j}\right] \quad (6)$$

For specific dissipation rates ε:

$$\frac{\partial(\rho u_j \varepsilon)}{\partial x_j} = \alpha \frac{\varepsilon}{k} P_k - \beta \rho \varepsilon^2 + \frac{\partial}{\partial x_j}\left[\left(\mu + \frac{\mu_t}{\sigma_\omega}\right)\frac{\partial \varepsilon}{\partial x_j}\right] \quad (7)$$

The production of kinetic energy, P_k, for incompressible flows is expressed by:

$$P_k = \mu_t \left[\frac{\partial u_i}{\partial x_j} + \frac{\partial u_j}{\partial x_i}\right]\frac{\partial u_i}{\partial x_j} \quad (8)$$

2.4 Computational methodology

The ANSYS workbench is used to construct the model geometry and mesh, while FLUENT software is used to compute the main formulas for steady-state turbulent flow. To simulate hydrodynamic and heat transfer problems, computational fluid dynamics (CFD) is used as a volume control approach. The first step in the derivation of the flow domain in the finite volume approach is to divide it into cells, and then analyze it using the governing equations on control points on the cells. The mesh model is made up of 6,932,658 elements and was created using tetrahedral cells (see Fig. 2). The SIMPLE (Semi-Implicit Method for Pressure-Linked Equations) algorithm discretizes the convective terms in momentum and energy equations using a second-order upwind. Convergence absolute criterion is set by the continuity and momentum equations by 10^{-3} as for the energy equation 10^{-6}.

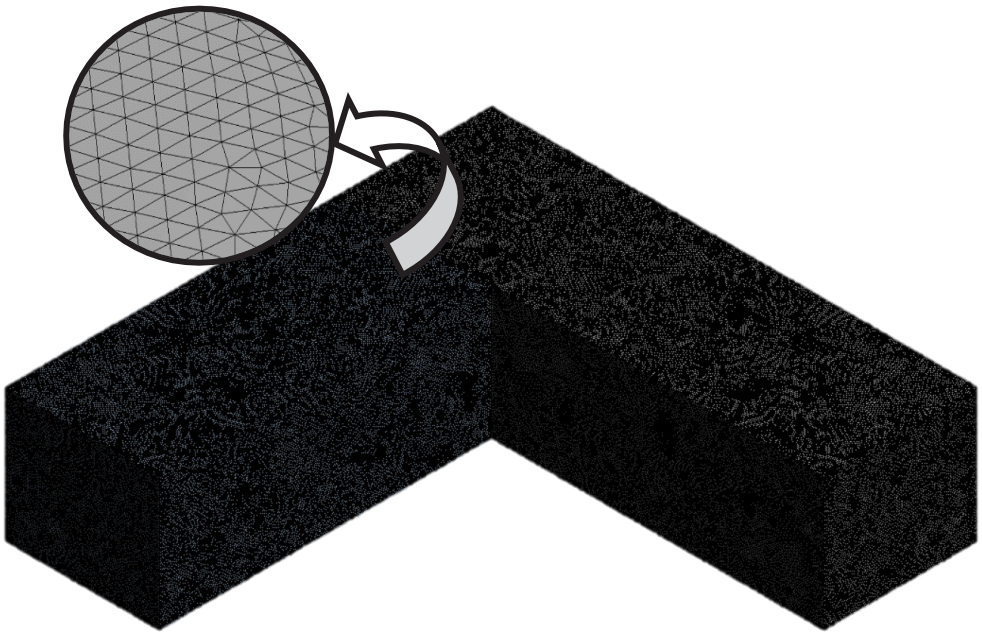

Fig. 2. The meshing of the computational model.

3 Results and discussion

The present section of this paper aims to demonstrate the effect of turbulence or circulation of air entering the core of the exchanger on its thermal performance through the distribution charts of velocity, the gradient of temperature, and efficiency.

Fig. 3, presents the Contour of velocity [m/s] for Re=12000 on the Y-Z plane along the cold channel only with four cases: case 1 without baffles, cases 2,3, and 4 with baffles at 45,90 and 135-degree baffle inclination respectively. Because the fluid is transported from the middle to the near-wall regimes, the emergence of longitudinal vortex flows can aid in increasing heat transfer in the square channel. The results show a high swirl with baffles at all angles inclination. At Case 3 maximum air velocity is reached 1.4m/sec, while 0.9 and 1.1 for 45 and 135-degree inclination angles.

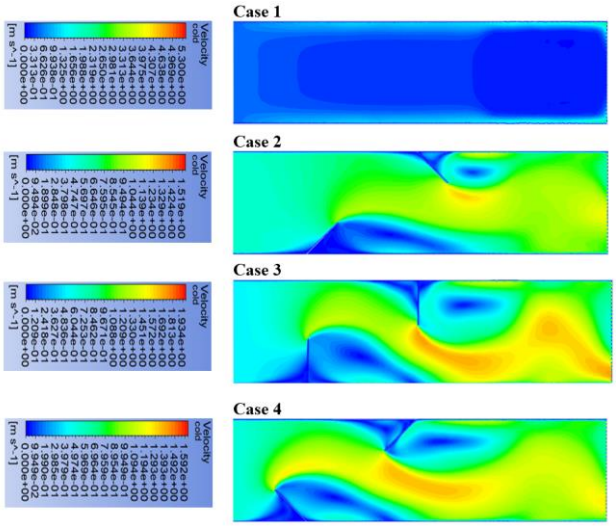

Fig. 3. The contour of velocity [m/s] for Re=12000 on the Y-Z plane in the cold channel.

Fig. 4, shows the contour of velocity [m/s] for Re=12000 on the X-Y plane in the hot channel only with four cases: case 1 without baffles, cases 2,3, and 4 with baffles at 45,90 and 135-degree baffle inclination respectively. The flow is accelerated and redirected near the baffles as the streamlines are compared at different baffle inclination angles. As the baffle approaches, the fluid is accelerated in the first zone, directly upstream of the two baffles, and reaches a velocity in the axial direction; the streamlines of fluid are deflected. The second zone, which is positioned between the end (the top) of each baffle and the channel wall, is characterised by relatively high velocities, which can reach values of the order of 440 percent of the entrance velocity. The results confirm there is a clear effect of the inlet air vortices on the gradient then the thermal performance inside the core will be enhanced. The results show a high swirl with baffles at all angles inclination. At Case 3 max air velocity reaches 1.4m/sec, while 0.9 and 1.1 for 45 and 135-degree inclination angles.

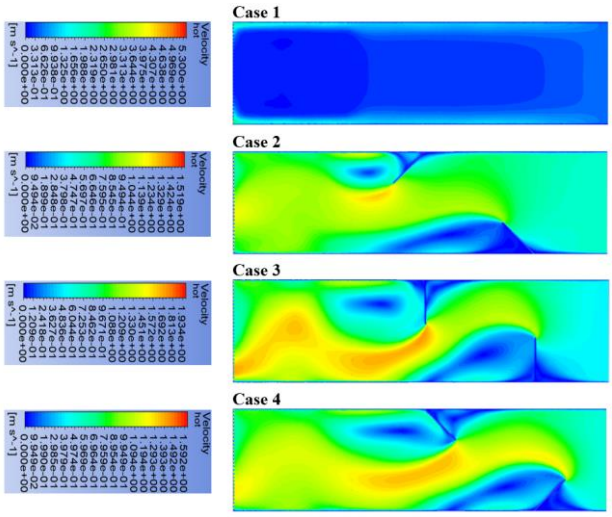

Fig. 4. The contour of velocity [m/s] for Re=12000 on the X-Y plane in the hot channel.

Fig. 5, presents the Contour of temperature [k] for Re=12000 on Y-Z plane in recovery core when fixed baffles inside the inlet cold channel with different angle inclination 45,90 and 135 degrees respectively. The value of the largest temperature gradient appears behind the core's interface wall as a result of variations in the direction of the flow caused by the baffles. It is obvious that as a result of the facilitated heat exchange, temperatures for high velocities drop significantly..

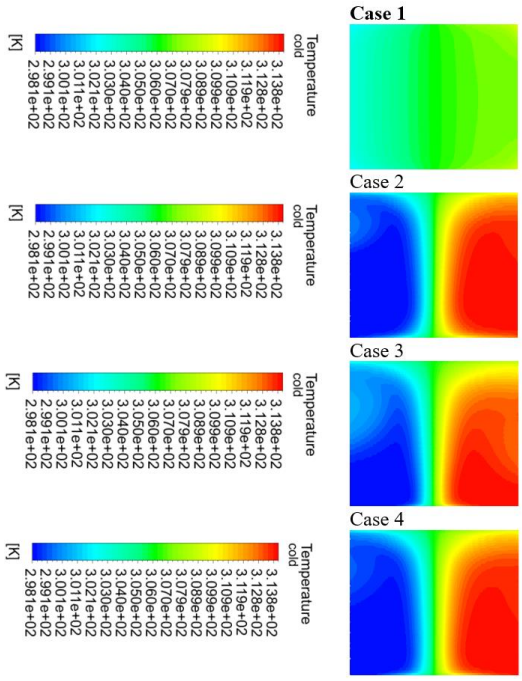

Fig. 5. The contour of temperature [k] for Re=12000 on the Y-Z plane in the core.

Fig. 6, presents the temperature gradient inside the core of the recovery at the hot side as the result of variation of baffles inclination inside the hot channel. Also, the results show the high effect of air swirl on the thermal perforation especially at angles 45 and 135 degrees. The results gave a higher effect for the baffle at an angle of 45 degrees more than the others.

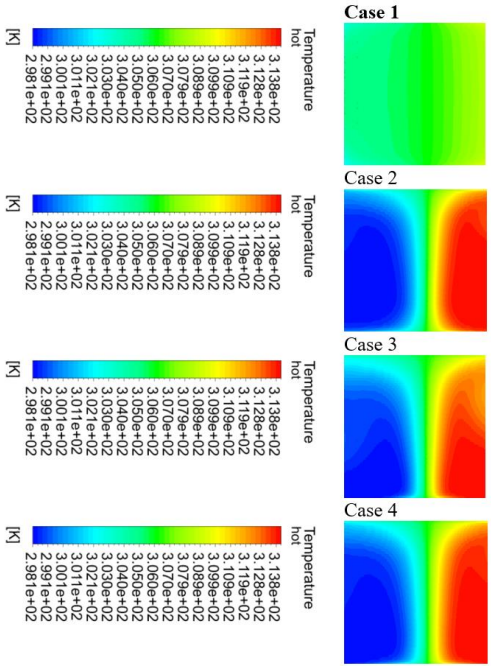

Fig. 6. The contour of temperature [k] for Re=12000 on the X-Y plane in the core.

Figure 7 depicts the fluid temperature profiles for a Reynolds number of 12,000 at various points along the hot and cold channel centerlines. The cold channel's inlet temperature is 298.15 k in all cases, but the outlet temperature varies between 308.4 k and 312.6 k. The highest temperature was found in case 2, which was 312.6 k. This means that the baffle has a temperature enhancement effect with a temperature increase of 4.2 k. However, in the hot channel, the inlet temperature is 314.15 k, and the heat exchanger's outlet temperature varies from 303.87 k to 299.74 k, with the lowest temperature in case 2 and the highest in case 1. In terms of heat transfer, this means that case 2 is the best angle.

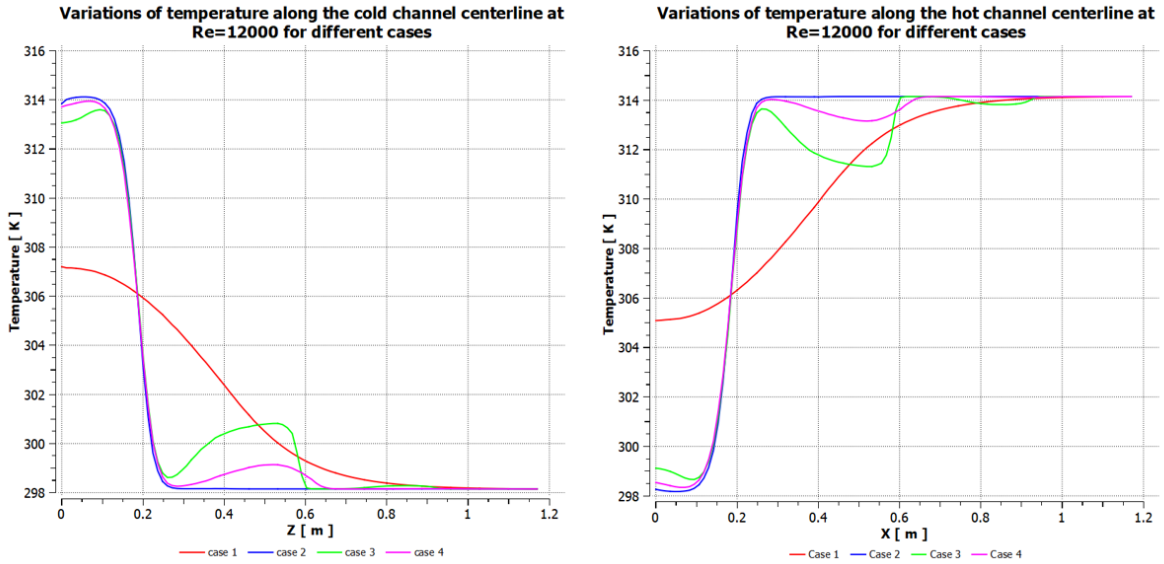

Fig. 7. Temperature variation along the hot and cold channel centerlines at Re=12000 for various instances.

Fig. 8, presents the average velocity profile along the hot and cold channel at constant Reynold number (Re=12000) for various cases. For both the hot and cold channels, the inlet velocity was 0.51 m/s. When placing the baffles, we noticed an increase in velocity along the channels, which increased by 0.2 m/s. Case 3 90^0) yielded the highest average velocity, which was 1.4 m/s.

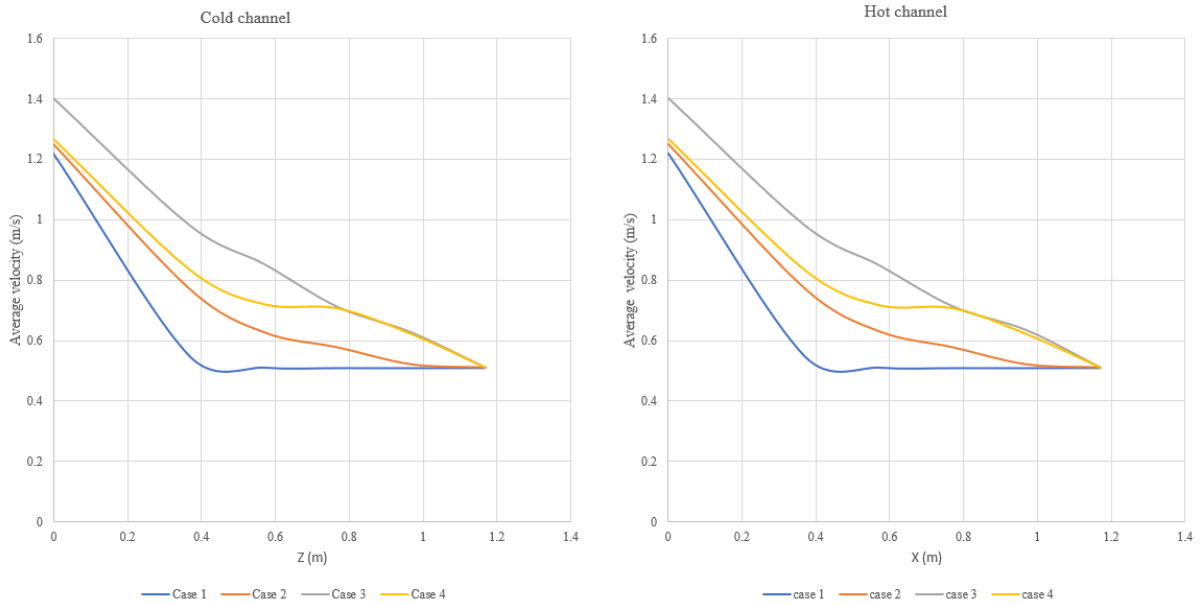

Fig. 8. Variation of average velocity along the hot and cold channel at Re=12000 for different cases.

For various situations with Re = 12000, Fig. 9 depicts the pressure drop fluctuation along the hot and cold channel at the centerlines level. As expected, as the angle of the baffles is increased, the pressure reduces. The pressure drops values range from 16.34 pascal, in case 1, to 18 pascals in case 4. Also, the results show the high-pressure drop occurs in case 4 (135°). In case 3, we observe a decrease in pressure drop near the first and second baffles due to high air vortices.

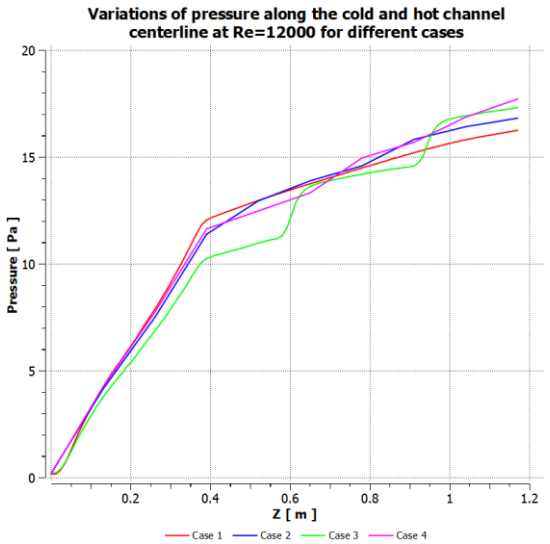

Fig. 9. Variation pressure along the hot and cold channel centerline at Re=12000 for different cases.

Fig. 10, illustrates the overall recovery system effectiveness in four cases at constant Re. The results notice the increase in effectiveness by increasing the inclination of angle. The results turn out that the effectiveness increased by 22% when the baffles were applied to the channel. It was found that the most effective angle was 45 degrees (case 2), with a 90 percent effectiveness. Furthermore, a review of our numerical results on axial velocity and temperature

fields for the entire region analysed reveals that the recovery effectiveness is linked to circulation velocity..

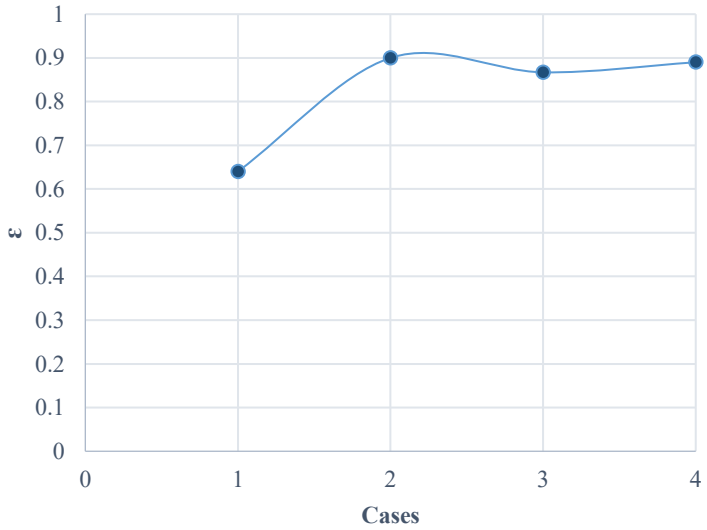

Fig. 10. Effectiveness for different cases at constant Re=12000.

4 Verification

Verification was carried out to ensure that the current numerical model is working properly through a comparison between the numerical of the current model and the experimental for the same model used. By making sure of its current results and applying the same experimental operating conditions in terms of flow, inlet temperature for the cold pass (25.1 °c) and inlet temperature for hot pass (41.6 °c), volume flow rate (139 m^3/h), and the number of passes (56). dimensions of core, length (370 mm), width (370 mm), height (320 mm), and thickness (0.6mm). There was a strong correlation between the obtained results and the experimental data, as shown in Fig. 11. The largest relative error between the numerical current work and the experimental current work is approximately 6.4 percent, as can be observed. Hence the comparison can be considered reasonable. This indicates the validity of the numerical model used in our current research.

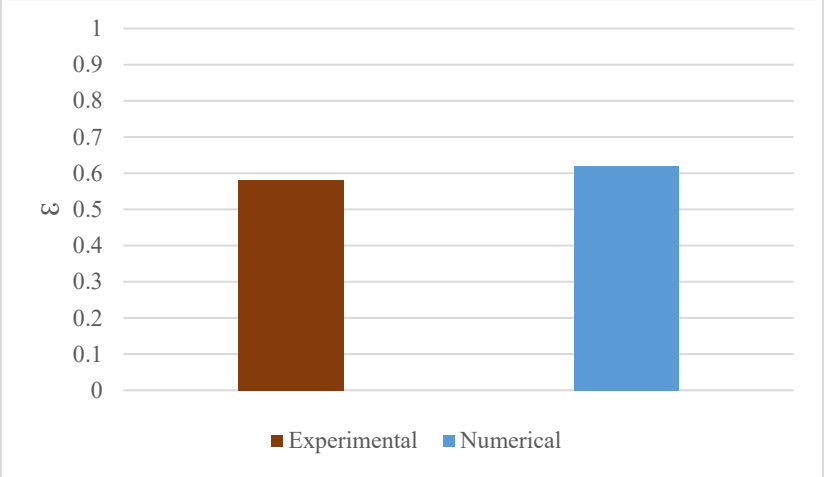

Fig. 11. Effectiveness tests with the change of numerical results and experimental results.

5 Conclusions

The heat transfer in an HRV with two baffles mounted to the top and bottom walls of the hot and cold duct at various angles is investigated numerically in this work.. The main conclusions of this study are drawn as follows:

1. When fixed baffles are mounted within the channel at a constant Reynolds number, the effectiveness increases by 35%. While maximum effectiveness is found about 90 percent for the 45° baffles angle.
2. The pressure drop increases with the increase in the baffles's angle, and the results notice the highest pressure drop occurs in case 4. At its maximum rated design flow, the pressure drop did not exceed 130 Pa, indicating that the thermal output could be improved.
3. In terms of temperature difference, case 2 shows enhancement influences on heat transfer performance.
4. Finally, Maximum velocity is found in case 3 where the velocity is about 1.4 m/s axial that found recovery effectiveness is related to the velocity of circulations.

References

[1] F. L. ASSUNCAO, "A NUMERICAL PERFORMANCE ANALYSIS OF HEAT RECOVERY VENTILATORS WITH STAGGERED-BAFFLE CHANNELS," Angew. Chemie Int. Ed., 2016.

[2] H. Han, Y. Choo, and Y. Kwon, "An experimental study on the effect of outdoor temperature and humidity conditions on the performance of a heat recovery ventilator," Proc. Clima, Well Being Indoors, 2007.

[3] Y. Menni, M. Ghazvini, H. Ameur, M. H. Ahmadi, M. Sharifpur, and M. Sadeghzadeh, "Numerical calculations of the thermal-aerodynamic characteristics in a solar duct with multiple

V-baffles," Eng. Appl. Comput. Fluid Mech., 2020.
[4] K. H. Ko and N. K. Anand, "Use of porous baffles to enhance heat transfer in a rectangular channel," Int. J. Heat Mass Transf., 2003.
[5] H. Benzenine, R. Saim, S. Abboudi, and O. Imine, "Numerical analysis of a turbulent flow in a channel provided with transversal waved baffles," Therm. Sci., 2013.
[6] D. Saad and M. S. Kassim, "Effect of Baffles Geometry on Heat Transfer Enhancement inside Corrugated Duct," Int. J. Mech. Eng. Technol., 2019.
[7] W. M. Abed, "Numerical Study Of Laminar Forced Convection Heat Transfer And Fluid Flow Characteristics In A Corrugated Channel Nomenclature : List of symbols," 2010.
[8] Y. Menni and A. Azzi, "Numerical analysis of thermal and aerodynamic fields in a channel with cascaded baffles," Periodica Polytechnica Mechanical Engineering, vol. 62, no. 1. pp. 16–25, 2018, doi: 10.3311/PPme.10613.
[9] X. Tang and D. Zhu, "Experimental and numerical study on heat transfer enhancement of a rectangular channel with discontinuous crossed ribs and grooves," Chinese J. Chem. Eng., 2012.
[10] Y. Menni, A. J. Chamkha, and A. Azzi, "Fluid flow and heat transfer over staggered + shaped obstacles," Journal of Applied and Computational Mechanics. 2020.
[11] P. Dutta and A. Hossain, "Internal cooling augmentation in rectangular channel using two inclined baffles," Int. J. Heat Fluid Flow, 2005.
[12] H. Ameur, "Effect of corrugated baffles on the flow and thermal fields in a channel heat exchanger," J. Appl. Comput. Mech., 2020.
[13] "Versteeg H., An Introduction to Computational Fluid Dynamics - The Finite Volume Method, 1995.pdf.".

Allocation and Sizing of the Distributed Generation for Power System Instability Prevention

Dhafer Mayoof Dahis
{ Eng.dafir@stu.edu.iq [1]}

Southern Technical University Basrah ,Iraq[1]

Abstract. Supplying customers regularly and network stability are some of the most essential tasks for power suppliers companies. In this paper, distributed generation resources (DGs) are used to increase the stability of the transmission network when the most critical line is eliminated. One of the major works in this paper is calculating the revenue of the network operators due to a reduction in purchasing real power from generation companies since using distributed generation resources. Moreover, the cost of these resources and the cost of environmental pollution, are all considered in this study. Categorizing the load into the three-time span, light, medium, and peak load, with variation in consumption, along with considering variation in purchasing power tariffs in the mentioned category, inflation rates, and annual interest rates, and the proper lifetime expectancy of distributed generation resources are other significant aspects of this paper. Mat-Power, in MATLAB, is used for load power flow equations and other network computations to find the optimum location and capacity of distributed resources. A 14 IEEE bus Reliability Test System is simulated to indicate the network stability of the power system in the presence of distributed generation sources.

Keywords: Priority of transmission lines; Distributed generation resources; Optimum allocation and sizing, Timespan, Interest rates, and inflation.

1 Introduction

Power system operation is done in the safest mode so that the elimination of each power line cannot create any obstacle in a normal operating state of the power system. To assess the safety of the power system, it is necessary to simulate the elimination of each power line to study power system performance in terms of voltage deviation for each load point and line overload [1]. Therefore, identifying the most critical power line, the line that its elimination either deliberately or unknowingly takes the power system more quickly to instability, over other lines is significantly essential. On the other hand, due to the competitive market among electricity industries, high and unprofitable investments are eradicated, and consequently, keeping the power system stable and secure is accompanied by a lot of stress [2,3].

Furthermore, the restructuring of the electricity industries changed the rules and economic criteria in the power system [4]. Applying distribution Generations (DGs) in power systems is one of the prominent phenomena that play an essential role in power system restructuring [5]. In this paper, the DG is meant to be a diesel generator unit with a quick launch in the

IMDC-IST 2021, September 07-09, Sakarya, Turkey
Copyright © 2022 EAI
DOI 10.4108/eai.7-9-2021.2314782

transmission network. The rapid loading rate of these resources is considered to be their significant benefit.

In most researches on the location and optimal sizing of distributed generations, these resources are addressed in Low and Medium-voltage (LV and MV), and the placement of DGs in the transmission network is rarely taken into consideration. In [6], the priority of the lines is based on the bus voltage only; due to the elimination of each of the lines various constraints of the power system are at risk and the prioritization of the lines cannot be considered from only one perspective. In [7], optimal allocation and sizing of distributed generation resources are aimed at reducing losses. In [8], placing DGs in the transmission and distribution system for proper scheduling the interruption of the loads, while interrupting the load should be the last way to prevent instability in the power system. In [9], the installation of distributed generation resources in the distribution system is done by considering the increase in voltage of the standard coupling points and the thermal constraints of the power lines .

In this paper, distributed generation resources are implemented to increase power system stability. Given the economic aspects of installing these resources, the optimal DGs allocation and sizing determination is significantly essential. This article generally has two stages:

- First step: power lines prioritization.
- The second step: optimal allocation and sizing determination of distributed generation sources to prevent the power system from instability after the most critical line identification and then elimination.

Significant features of this article include:

- Considering the costs of distributed generation resources along with the cost of environmental pollution.
- Considering the gained profit for the operators due to injecting real power via DGs and consequently reduction in purchasing power.
- Considering three-time span, light, medium, and peak load, with variation in consumption levels and variable purchasing power tariffs in specified periods.
- Consider the life expectancy for distributed generation resources along with inflation rate and annual interest rate.
- Simultaneous optimal allocation and sizing determination of DGs to make the simulation more realistic.

2 Prioritization of lines in the transmission network

In prioritizing the power line using specific performance indicators the effect of eliminating each power line on the entire system is described. An overview of the impact of cutting each of the power lines on power system operators is provided. Prioritization took place while indicators are arranged in numerical order and events that have a more extensive index creates more problems for the power system. The following two hands are presented in the following.

2.1 Real Power Flow Index

Consider a power system that works in a stable condition. If one or more transmission lines are eliminated other power lines will face overloading and these phenomena put the power system

security and stability in danger. They can lead the power system into unstable conditions. Real power flow index as presented in (1) [10].

$$PIw_i = \sum_{j=all\ other\ branches} \left(\frac{P_{flowj}}{P_j^{\max}} \right)^{2n} \quad (1)$$

Where:

PIw_i is efficiency related to the real power flow index when the transmission line is eliminated.

$P_{flow\ j}$ is power flow in the transmission line jth, after the ith transmission line is eliminated.

$P_j^{\max}$ is Maximum transmittable power in jth power line

n is an arbitrary natural number

3 Voltage Performance Index

After each line is eliminated, the voltage of every point of the power system faces variation, and consequently, there is a risk of a voltage security violation. Voltage deviation in the acceptable range is expressed by the voltage performance index in (2). This indicator represents the difference between the bus voltages before and after the power lines elimination relevant to the maximum allowable voltage deviation [10].

$$PIv_i = \sum_{k \in a} \left(\frac{\left(V_k^{pre} - V_k^{past} \right)}{\max vol\ drop} \right)^{2n} \quad (2)$$

In the above equation:

PIv_i is power system voltage performance index when ith power line is eliminated.

a is set buses whose voltage is beyond the limitation.

V_k^{pre} is kth bus voltage before ith transmission line is eliminated.

V_k^{past} is kth bus voltage after ith transmission line is eliminated.

4 Allocation and sizing of the distributed generation resources

Allocation and inappropriate sizing determination for distributed generation resources not only create more cost for the power system but also lead to undesirable effects on system performance [11]. Determining the allocation and optimal sizing of distributed generation in the transmission network can be presented as an optimization problem.

4.1 The objective function

Equation (3) express the objective function of the problem while its details are presented in equations (4) to (15).

$$Max \quad \text{Benefit-Cost}_{\text{total}} \tag{3}$$

Where:
Benefit represents the benefit of the system operators by reducing the consumed power from power plants.

$\text{Cost}_{\text{total}}$ Indicates the total charges imposed on the power system operators.

The Benefit function is computed from (4).

$$\text{Benefit} = BPV\ (B_1) \tag{4}$$

In the above equation:
BPV (B1) expresses the gained revenue from the reduction of the purchasing power from power plants over the proper lifetime of DG and is calculated from equation (5) [12].

$$\text{BPV}(B_1) = B_1 \times \sum_{t=1}^{T_{total}} \left(\frac{1+InfR}{1+IntR} \right)^t \tag{5}$$

In the above equation:
T_{total} is a proper lifetime of DG

$InfR$ is the annual inflation rate.

$IntR$ is the annual interest rate.

B1 is computed annual profit due to the reduction in the purchasing power from power plants, which is calculated from equation (6).

$$B_1 = \sum_{j=1}^{3} C_j^P \times \Delta Ploss_j \times T_j \tag{6}$$

In the above equation:

$j = 1,2,3$ expresses three light, medium, and peak load span times.

C_j^P is the cost of purchased active power from power plants.

T_j is duration related to the jth period.

$\Delta Ploss_j$ are losses of active power variation due to the absence and presence of DG in the j[th] time which can be calculated from equation (7).

$$\Delta Ploss_j = Ploss_j^{No\ DG} - Ploss_j^{With\ DG} \tag{7}$$

In the above equation:

$Ploss_j^{No\ DG}$ is active power losses without the presence of the DG at the jth time.

$Ploss_j^{With\ DG}$ is active power losses insight of the DG at the j[th] time. Function related to

$\text{Cost}_{\text{total}}$ can be calculated from (8).

$$\text{Cost}_{\text{total}} = \begin{pmatrix} \text{Cost}_{DG-Investment} + CPV\ (C_1) \\ + CPV\ (C_2) + CPV\ (C_3) \end{pmatrix} \tag{8}$$

$\text{Cost}_{DG-Investment}$ is DG investment cost which can be computed from (9).

$$\text{Cost}_{DG-Investment} = k_{DG-Inv} \times \sum_{i=1}^{N_{BUS}} \left[P_{DG_i} \right] \tag{9}$$

Where:

k_{DG-Inv} is investment cost for DG for generating 1MW of power per 1 Hour. P_{DG_i} is the generated power from DG which is connected to the ith bus.

N_{BUS} is a number of buses in a simulated power system. $CPV\ (C_1)$ represents the current value of the operation cost for DG, which is obtained from equation (10) [10].

$$CPV\ (C_1) = \text{Cost}_{\text{DG-Maintenance}} \times \sum_{t=1}^{T_{total}} \left(\frac{1 + InfR}{1 + IntR} \right)^t \tag{10}$$

Where:

$\text{Cost}_{\text{DG-Maintenance}}$ represents annual cost maintenance for DG from eq. (11)

$$\text{Cost}_{\text{DG-Maintenance}} = k_{\text{DG-Maintenance}} \times T \times \sum_{i=1}^{N_{BUS}} P_{DG_i} \tag{11}$$

$\text{k}_{\text{DG-Maintenance}}$ is the cost of maintenance for DG for generating 1MW per hour.

$CPV\ (C_2)$ is present value for DG operational cost and comes from eq. (12)

$$CPV\ (C_2) = \text{Cost}_{\text{DG-Operation}} \times \sum_{t=1}^{T_{total}} \left(\frac{1 + InfR}{1 + IntR} \right)^t \tag{12}$$

Where:

$\text{Cost}_{\text{DG-Operation}}$ is the DG annual operation cost computable using (13) [12].

$$\text{Cost}_{\text{DG-Operation}} = k_{\text{DG-Operation}} \times T \times \sum_{i=1}^{N_{BUS}} P_{DG_i} \tag{13}$$

In the above equation:

$k_{\text{DG-Operation}}$ is DG cost of operating per megawatt-hour

$CPV\ (C_3)$ is the current value of environmental pollution caused by DGs, which is obtained from equation (14).

$$CPV\ (C_3) = \text{Cost}_{\text{DG-Pollution}} \times \sum_{t=1}^{T_{total}} \left(\frac{1+InfR}{1+IntR} \right)^t \tag{14}$$

In the above equation:

$\text{Cost}_{\text{DG-Pollution}}$ shows the annual cost of environmental pollution caused by DG and is obtained from equation (15) [12].

$$\text{Cost}_{\text{DG-Pollution}} = T \times \sum_{i=1}^{N_{BUS}} \left[\begin{pmatrix} \rho_{NO_x} \times EF_{NO_x} + \\ \rho_{SO_2} \times EF_{SO_2} + \\ \rho_{CO_2} \times EF_{CO_2} \end{pmatrix} \times P_{DG_i} \right] \tag{15}$$

Where:

ρ_x is penalty price for producing x-type of pollutants.

4.2 Constraints on the issue

The voltage security limitation is expressed by (16).

$$|V_{\min}| \le |V_i| \le |V_{\max}| \quad i = 1,2,...,\text{N}_{\text{BUS}} \tag{16}$$

The thermal constraint of the feeders is expressed using equation (17).

$$|S_i| \le \alpha |S_i^{\max}| \quad i = 1,2,...,\text{N}_{\text{Branch}} \tag{17}$$

Where:

N_{Branch} Number of system branches

α reliability index for power line congestion.

Generation capacity limitation for each DG is expressed in (18).

$$P_{DG_i} \le P_{DG}^{\max} \quad i = 1,2,...,\text{N}_{\text{BUS}} \tag{18}$$

The limitation of reactive power generation using DG is given by (19)

$$Q_{DG_i}^{\min} \le Q_{DG_i} \le Q_{DG_i}^{\max} \quad i = 1,2,...,\text{N}_{\text{BUS}} \tag{19}$$

Limitation related to a maximum total capacity of DGs is expressed in (20).

$$\sum_{i=1}^{N_{BUS}} P_{DG_i} \le P_{DG}^{Max-Total} \tag{20}$$

5 Simulation results

5.1 Power lines prioritization

Using the mentioned indices expressed in Section 2, are a deterministic factor for power lines prioritization. In this study, the vulnerability of transmission lines is considered, in fact, by applying the performance indices, the effect of each power line's elimination on other lines in the transmission system is examined. The modified load in light, medium, and peak loading span time are shown in Table 1.

Table 1. Modified load for an IEEE 14 bus RTS.

Bus	Peak load P (MW)	Peak load Q (MVAr)	Medium load P (MW)	Medium load Q (MVAr)	Light load P (MW)	Light load Q (MVAr)
1	0	0	0	0	0	0
2	27.5	16.5	26.25	15/75	25	15
3	104.5	22	99.75	21	95	20
4	55	-4.4	52.5	-4.2	50	-4
5	11	5.5	10.5	5.25	10	5
6	16.5	11	15.75	10.5	15	10
7	0	0	0	0	0	0
8	0	0	0	0	0	0
9	33	16.5	31.5	15.75	30	15
10	11	16.5	10.5	15.75	10	15
11	33	5.5	31.5	5.25	30	5
12	44	16.5	42	15.75	40	15
13	60.5	33	57.75	31.5	55	30
14	33	16.5	31.5	15.75	30	15

To determine the efficiency index in equation (1), n =2 is considered, and the maximum transmitted power of each line is assumed to be 100 MW. In equation (2), n=1 is also considered. In Table 2, ten lines are identified which their elimination leads to the highest risk for the power system. Elimination of the 10^{th} and 13^{th} power lines leads to divergence in power load flow. According to the objectives of this paper elimination of the power lines that create a divergence in power load flow equations is excluded. Therefore Line 2 is the most critical in this power system.

Table 2. Prioritization of transmission lines based on actual power flow and voltage performance induces

Rank	Line	From bus	To bus	*PIv*	*PIw*
1	2	1	5	10.2	118.16
2	3	2	3	7.9	105.19
3	17	9	14	6.6	104.04
4	12	6	12	6.3	104.04
5	16	9	10	5.8	96.04
6	11	6	11	5.1	92.16
7	14	7	8	3.9	88.36
8	9	4	9	3.5	88.36
9	1	1	2	2.4	86.49
10	5	2	5	1.2	82.81

6 location and optimal sizing for distributed generation resources

According to the calculations carried out in the first stage, the calculations in this section are carried out without the presence of line number 2. The distributed generation resources are considered as negatively load with the ability to generate reactive and reactive power, and the maximum capacity for each DG is 80 megawatts. The parameters considered for the optimization problem are presented in Table (3).

Table 3 Input Parameters.

Parameters	Unit	Value
k_{DG-Inv}	$\$/MW$	3800
$k_{\text{DG-Maintenance}}$	$\$/MWh$	0.0075
$k_{\text{DG-Operation}}$	$\$/MWh$	0.08
T	$hour$	8760
$S_i^{\max}$	MVA	100
$\lvert V_{\min}\rvert$	$P.U.$	0.95
$\lvert V_{\max}\rvert$	$P.U.$	1.05
$P_{DG}^{Max-Total}$	MW	2500
$Q_{DG_i}^{\min}$	$MVAr$	-26.2947
$Q_{DG_i}^{\max}$	$MVAr$	+26.2947
T_{total}	$year$	20

InfR	%	8.5
IntR	%	13
$\cos\varphi_{DG}$	-	0.95
α	**%**	95

The different periods and tariffs for purchasing active power from power plants in a light, medium, and peak loading are given in Table (4). The values for environmental pollution are described in Table 5. Table (6) presents the results related to optimum allocation and sizing of the DGs.

Table 4. Data for a three-time span.

Time span	Period (hour / year)	Price ($/MWh)
Light load	2500	0.54
Medium load	5010	0.85
Peak load	1250	1.02

Table 5. Environmental Pollution Data [13].

Type of pollutant	Pollution coefficient (lb/MWh)	Cost of pollution ($/lb)
NO_x	0.00044	4.2
SO_2	0.000008	0.99
CO_2	0.001596	0.014

The voltage profile in light, medium, and peak loading periods is illustrated in Fig. 1. Moreover, active transmitted power in lines by considering different time spans in either presence or absence of the DGs and active and reactive losses are given in Table 7 and Table 8, respectively. Table (9) illustrates the profits and costs from DGs installation.

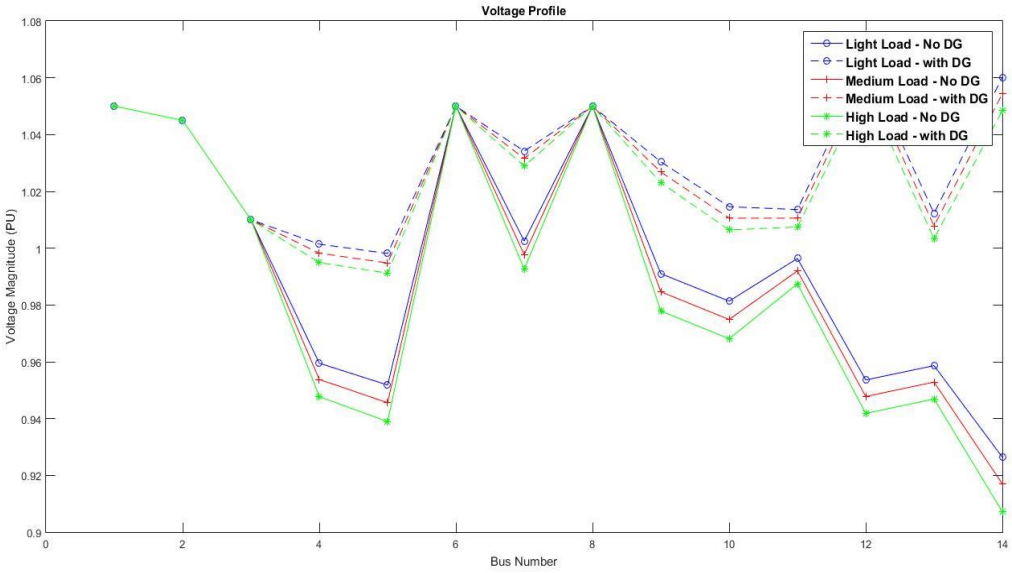

Fig 1. Voltage profile absence and presence of the DGs.

Table 6. Optimal Allocation and sizing of the DGs.

Bus	P (MW)	Q (MVAr)
3	11.856	3.896
12	69.149	22.728
14	69.935	22.986

Table 7. Actual transmitted power in lines.

Line	From bus	To bus	Peak Load (MW)		Medium load (MW)		Light load (MW)	
			*	**	*	**	*	**
1	1	2	182.1	6.4	156	27.7	130	48.5
2	2	3	0	0	0	0	0	0
3	2	4	157.1	90	149	83	141	76
4	2	5	158.3	86	150	78.9	142	71.9
5	3	4	20.8	6.1	19	7.07	17.8	7.86
6	4	5	1.33	19	0.64	19.1	0.03	19
7	4	7	68.56	27	65.4	24.6	62.2	21.6
8	4	9	38.76	16	37.1	14.1	35.3	12.4
9	5	6	135	52	128	46	121	40.1

10	6	11	11.26	19	10.6	19.1	9.97	18.5
11	6	12	41.15	5.6	39.1	7.42	37	9.15
12	6	13	66.13	21	62.7	18.5	59.4	15.7
13	7	8	67.07	22	58.5	33.4	80.9	60.8
14	7	9	68.56	27	65.4	24.6	62.3	21.6
15	9	10	34.68	25	33.1	23.6	31.5	22.1
16	9	14	39.65	15	37.9	16.3	36.1	18.1
17	10	11	23.28	14	22.2	12.9	21.2	11.9
18	12	13	5.47	19	5.28	19.7	5.08	19.9
19	13	14	4.10	21	4.11	20.9	4.10	20.7
*: Without DG				**: With DG				

Table 8. Active and reactive power losses in lines.

Losses	Peak Load		Medium Load		Peak Load	
	With -out DG	With DG	With -out DG	With DG	With -out DG	With DG
P_{Loss} (MW)	53	15.4	46.4	13.7	40.5	12.3
Q_{Loss} (MVAr)	194	18.3	166.7	10.3	141.4	3.8

Table 9. Review of Economic Measures.

Type		Value ($)
Benefit		3025900
Cost	Investment	573570
	Maintenance	133030
	Operation	1419000
	Environmental pollution	33315
	Total	2158915

7 Conclusion

Simulation results indicate in presence of the distributed generation resources (DGs), system stability is achievable. According to Figure (1) and Table (7), optimum allocation and sizing of DGs cause voltage security limitation and power line congestion for different periods. Table (8) also shows a significant reduction in active and reactive power losses over other time spans in presence of the DGs. Furthermore, with the reduction of active and reactive power losses due to the presence of the DGs, system operators can gain a prominent revenue. As a result, installing these resources will be economically justifiable.

References

[1] M. Amohadi and M. Fotuhi-Firuzabad, "Optimal Placement of Automatic Switching Equipment in Radial Distribution Networks Based on Protective Coordination", Journal of Electrical Engineering & Technology, vol. 14, no. 3, pp. 1127-1137, 2019.

[2] Ravishankar, Vijayendra, Veeramanju, "Voltage and power losses control using distributed generation and computational intelligence", Tehnicki vjesnik - Technical Gazette, vol. 23, no. 4, 2016.

[3] P. Pavani and S. Singh, "Placement of DG for reliability improvement and loss minimization with reconfiguration of radial distribution systems", International Journal of Energy Sector Management, vol. 8, no. 3, pp. 312-329, 2014.

[4] L. Jian, Z. Qian, Z. Liangang and Y. Mengkai, "Distributed economic dispatch method for power system based on consensus", IET Renewable Power Generation, vol. 14, no. 9, pp. 1424-1432, 2020.

[5] Marko Vukobratovic, Predrag Maric, "Evaluation of Distributed Generation Impact on Reliability of a Distribution System using DIg SILENT Power Factory", Regular, vol. 9, no. 10, pp. 381-389, 2020.

[6] U. Sultana, A. Khairuddin, B. Sultana, N. Rasheed, S. Qazi and N. Malik, "Placement and sizing of multiple distributed generation and battery swapping stations using grasshopper optimizer algorithm", Energy, vol. 165, pp. 408-421, 2018.

[7] O. Khoubseresht and H. Shayanfar, "The role of demand response in optimal sizing and siting of distribution energy resources in distribution network with time-varying load: An analytical approach", Electric Power Systems Research, vol. 180, p. 106100, 2020.

[8] . Kaushik Das, Antonios Nitsas, Mufit Altin, Anca D Hansen, Poul E. Sorensen, “Improved Load-shedding Schems Considering Distributed Generation”, IEEE Manchester, PowerTech, June 2017

[9] Desmond Okwabi Ampofo, Isaac Kofi Otchere, Emmanuel Asuming Frimpong, “An Investigative Study on Penetration Limits of Distributed Generation on Distributed Network”, IEEE PES, PowerAfrica, pp. 573-576, June 2017

[10] Z. Ghofrani-Jahromi, M. Abedi, G. Gharehpetian and M. Masjed-Jamei, "contingency ranking using analytical hierarchry process for calculating bus weighting factors ", International Journal of Power and Energy Systems, vol. 30, no. 2, 2010.

[11] Hijun Xing, Xin Sun, “Distributed Generation Locating and Sizing in Active Distribution Network Considering Network Reconfiguration”, IEEE Access, Vol 5, pp. 14768-14774, July 2017

[12] N. Khalesi, N. Rezaei, M.-R. Haghifam, “DG allocation with application of dynamic programming for loss reduction and reliability improvement,” ELSEVIER, Vol.33, No.2, pp. 288-295, 2011.

[13] G. Memarzadeh and F. Keynia, "A new index-based method for optimal DG placement in distribution networks", Engineering Reports, vol. 2, no. 10, 2020.

The Effect of Fins on the Performance of the Plate Heat Recovery Ventilator

Braihan Abdulwadood Salman*[1], Saadoon Fahad Albahadili [2], Raed Sabri[3]
{parehan.abdulwadood@stu.edu.iq[1], s.albahadili@stu.edu.iq[2], read.hameed@stu.edu.iq[3]}

Basra Engineering Technical College, Southern Technical University of Basra, Iraq[1'2'3]

Abstract. The present work focuses on modifying an existed commercial heat recovery ventilator unit. The heat exchanger (the core) of this unit is a fixed plate type operating in a crossflow arrangement without fins. The theoretical analysis is performed to investigate the effect of adding a suitable number of fins to the core in two conditions. These conditions are to investigate the effect of adding fins on the performance of the ventilation unit and the possibility of reducing the core size maintaining the original performance, provided that the added fins do not lead to exceeding the permissible pressure drop of 450 Pa at full capacity of 1000m^3/h air flow rate. The obtained results indicate that adding fins up to 144 fins per meter makes the heat recovery ventilator has its highest performance with an increase in effectiveness by 33.3%. The lowest volume that can be obtained without compromising the performance of the exchanger is 37% of the original volume by adding 120 fins/m.

Keywords: Heat Recovery Ventilator, Plate Heat Exchanger, Energy Saving.

1 Introduction

Mechanical ventilation is used to continually provide fresh air while recovering thermal energy [1]. Mainly, compact heat recovery ventilator (HRV) is adopted for better air distribution [2]. It consists of a heat exchanger that transfers heat between the hot fresh air with stale room air that has been thermally pre-treated but carries pollutants and needs to be disposed of. The plate heat exchanger as shown in Fig 1, represents the core of the HRV unit. It is constructed from several Aluminum layers or parting plates. The plates serve as the primary surface for heat transfer. They are stacked on each other, separated by spaces, to form two sets of passages through which fresh air and indoor air alternately flow and exchange heat due to temperature differences without mixing.

Among the many compact heat exchangers, the finned plate heat exchangers have their superior performance. They are distinguished by high efficiency, smaller size, low weight and reasonable cost [3]. The sensible effectiveness is close to 66% [4].

The most two important factors that affecting the effectiveness of heat exchangers are the heat transfer surface area and the convective heat transfer coefficient. Note that air is one of the low-level fluids in the values of the heat transfer coefficient. To compensate for this factor secondary surface areas like fins are used.

One of the important strategies in energy sustainability is to recover heat lost due to ventilation as efficiently as possible by using heat recovery ventilators. The benefit of the energy recovery ventilator was summarized by, reducing HVAC energy consumption, reducing peak demand,

IMDC-IST 2021, September 07-09, Sakarya, Turkey
Copyright © 2022 EAI
DOI 10.4108/eai.7-9-2021.2314781

improving humidity control, and providing appropriate ventilation. The magnitude of the benefits varies depending on climate [5]. The main parameters that affecting the HRV performance are the construction parameters and the operating parameters [6].

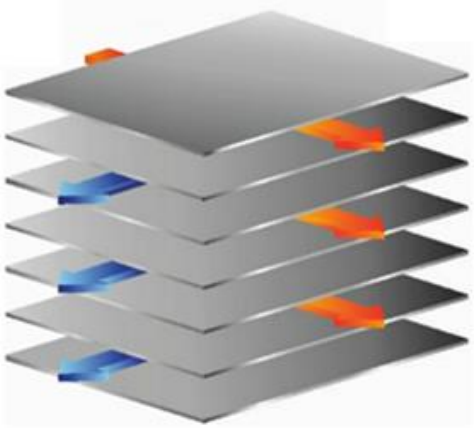

Fig 1. Plate HRV construction [5].

Mardiana et al [7] concluded that to study the performance of HRV in terms of heat duty and effectiveness, the following parameters should be considered: the dimensions which determine the core size, the core material, flow arrangement, airflow rate, and the permissible pressure drop.

Alireza Vali et. al [8] showed that the highest sensible effectiveness was obtained by using fins with a smaller aspect ratio. To achieve more than 60%, effectiveness, NTU should be larger than 3 with an aspect ratio less. than 0.3.

Ahmed A. Abduljabbar [9] showed that reducing the channel pitch of the core by increasing fin density acted as a motivation for better performance.

Ahmed Taha Al-Zubaidi [10] found that the effectiveness for corrugated fins was found 10% higher than the case of the pins type owing to the difference in surface area, passage length, and Reynolds number. The pressure drop in both cases was 11.02 Pa.

Ranganayakulu and K.N. Seetharamu [11] concluded that the heat transfer coefficient of the gases is smaller than liquids by 10 to 50 times. Therefore, enhancing the air-side heat transfer coefficient could have significantly reduced the heat exchanger size. It was possible to achieve this target by increasing the heat transfer surface area per unit volume by adding fin.

2 Theoretical Analysis

A commercial HRV is analyzed under climate similar to the climate in Basra City. The technical feature of the HRV is shown in Table 1. The HRV configuration parameters, operating parameters, and assumptions are first determined. then the dominant equations and formulas are discussed.

Table 1. The technical features of the HRV unit [5].

Character	Value	Character	Value

n, (fin/m)	0	Heat Transfer area (A)	7.615 m^2
a, (fin spacing)	--	$\sigma = (A_o/A_{fr})$	0.446 m^2/m^2
b, (Plate spacing)	5.1 mm	$\beta = (A/V_p)$	390.2 m^2/m^3
N_{plate}/side	28	$\alpha = (A/V)$	173.94 m^2/m^3
Rated air flow	1000 m^3/h	L_1 x L_2 x L_3	370 x 370 x 320 mm

2.1 Geometrical analysis

The compact air-to-air plate heat exchanger under investigation is shown in Fig 2. The exterior dimensions are L1, L2, and L3 as length, width, and depth respectively. Several plates are arranged to create adjacent overlaid cross-passage ways for air streams (both streams are unmixed).

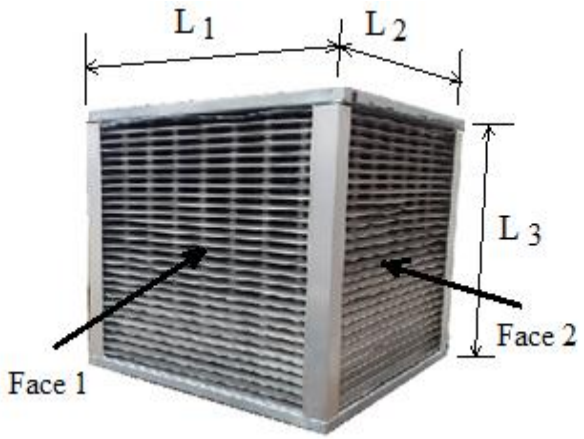

Fig 2. The core of the heat Recovery unit [5].

The specified data of the core is taken from Table 1.

The primary heat transfer area is,

$$A_p = \alpha V \quad (1)$$

The minimum flow area through the core is,

$$A_o = \sigma A_{fr} \quad (2)$$

The frontal area of each flow side, A_{fr}

$$A_{fr,i} = L_i L_3 \ , \quad (3)$$

The mass flow rate of air $\dot{m}$ is calculated as

$$\dot{m} = \rho \dot{V} \tag{4}$$

The secondary heat transfer surface is provided through the fins area,

$$A_f = 2(bL_j)\ nL_1\ N_{plate,} \tag{5}$$

The total heat transfer area for each flow face A is given by,

$$A = A_p + A_f \tag{6}$$

The hydraulic diameter D_h is given. by [12].

$$D_h = 4\frac{Ao}{\frac{A}{L_j}} \tag{7}$$

(A/L_j) is the wetted perimeter.

The ratio of minimum free flow area to frontal area for each flow face $\boldsymbol{\sigma}$, is given by,

$$\sigma = \frac{A_o}{A_{fr}} \tag{8}$$

The ratio of total surface area for a flow face relative to the void. volume is designated as β and is given by,

$$\beta = \frac{A}{V_p} \tag{9}$$

The heat transfer surface area for one flow face divided by the total apparent volume V of the exchanger is designated as α,

$$\alpha = \frac{A}{V} \tag{10}$$

2.2 Thermal analysis

The analysis is based on a set of heat exchanger dimensions and a specified volume air flow rate ($\dot{V}$) at predetermined temperatures of entering both hot and cold airstreams, $T_{h,i}\ and\ T_{c,i}$, respectively.

Assuming Steady. state heat transfer with no losses and the air is uniformly distributed. Air properties are evaluated in the first pass of calculation at the inlet. No condensation of moisture. The heat conductivity of the metal is constant.

The subscripts *c* and *h* denote cold and hot streams respectively, i and o denote inlet and outlet respectively.

The mass flow rate ($\dot{m}$) is expressed as,

$$\dot{m} = \rho\dot{\mathrm{V}}/3600 \text{ (kg/s)} \tag{11}$$

$\dot{\mathrm{V}}$ is the air volume flow rate (m^3/h)

The heat capacity, C is,

$C = \dot{m}c_p$ (W/K) (12)

C_{min} is the smaller of C_h and C_c.

The specific heat ratio is (C^*);

$$C^* = \frac{C_{min}}{C_{max}} \quad (13)$$

The maximum velocity (u_{max}) through the minimum flow area,

$u_{max} = \dot{m}/\rho A_o$ (m/s) (14)

The mass velocity G is given by,

$G = \dot{m}/A_o$ (kg/m^2.S) (15)

Re, is the Reynolds number,

$$Re = \frac{\rho\, u_{max}\, D_h}{\mu} \quad (17)$$

A modified practical correlation of Nusselt number is used [5],

$$Nu = (0.93 + 0.0001\, Re)\, [\, 0.274\, Re^{0.569} Pr^{0.333}] \quad (18)$$

The heat transfer coefficient h is given by,

$$h = Nu\, \frac{k}{D_h} \quad (19)$$

The efficiency of thin fins is given as [12],

$$\eta_f = \frac{\tanh\left(\sqrt{\frac{2h}{k_m\, t_f}}\, l_f\right)}{\sqrt{\frac{2h}{k_m\, t_f}}\, l_f} \quad (20)$$

k_m fin material thermal conductivity

L_f the fin length

The overall heat transfer coefficient, assuming no fouling layers is given as [13].

$$\frac{1}{UA} = \frac{1}{(\eta_o\, h\, A)_c} + \frac{t_{sh}}{k_m\, A_p} + \frac{1}{(\eta_o\, h\, A)_h} \quad (21)$$

$$\eta_o = 1 - \frac{A_f}{A}(1 - \eta_f) \quad (22)$$

The HRV effectiveness in terms of NTU is presented as, [14].

$$\varepsilon = 1 - \exp[\, \left(\frac{NTU^{0.22}}{C^*}\right) \{\exp(-C^* NTU^{0.78}) - 1\}\,] \quad (23)$$

$$NTU = \frac{UA}{C_{min}} \tag{24}$$

From the definition of the effectiveness (ε), the recovered heat is obtained as,

$$\dot{Q} = \varepsilon\, C_{min}(T_{h,i} - T_{c,i}) \tag{25}$$

Using the energy equation, the outlet temperature of the cold and hot streams can be determined as;

$$T_{c,o} = T_{c,i} + \varepsilon\, \frac{C_{min}}{C_c}\, (T_{h_i} - T_{c_i}) \tag{26}$$

$$T_{h,o} = T_{h,i} - \varepsilon\, \frac{C_{min}}{C_h}\, (T_{h_i} - T_{c_i}) \tag{27}$$

For the air to air heat cross-flow exchanger, since C*≈1, the arithmetic average temperature is given [12].

$$T_{m,h} = \frac{T_{h,i}+T_{h,o}}{2} \quad (℃) \tag{28}$$

$$T_{m,c} = \frac{T_{c,i}+T_{c,o}}{2} \quad (℃) \tag{29}$$

In this situation, it is necessary to recalculate the air properties and the thermal analysis steps have to be repeated based on the obtained mean air temperatures. If the resulting mean values of the mean temperature do not match the values of the last iterated, then the calculation should be repeated until they match.

2.3 Hydraulic analysis

The main pressure losses through the core only with uniform flow consist of:

- Contraction and Expansion losses at the entry and exit to the core.
- Friction losses along with the core [12].

$$\Delta P = 4f\left(\frac{L}{D_h}\right)\left(\frac{G^2}{2\rho}\right) + (K_c + K_e)\left(\frac{G^2}{2\rho}\right) \tag{30}$$

$K_c\ and\ K_e$ are the entrance and exit loss coefficient.

The recommended values of K_c and K_e are given by [13],

$$K_c = 0.5\,(1-\sigma) \tag{31}$$

$$K_e = (1-\sigma)^2 \tag{32}$$

A modified practical correlation of friction factor is used [5],

$$f = 37.6523\,\left(\frac{l_f}{D_h}\right)^{-0.384}\left(\frac{a}{b}\right)^{-0.092} Re^{-0.835} \tag{33}$$

3 Results and discussions

The analysis is conducted under the most frequent operating indoor air temperature 24°C. The ranges of temperatures for outdoor weather are mostly ranged from 30°C to 48°C for hot climate in Basra. There are extremely hot and humid conditions, but they are considered rare and excluded.

Adding fins to the heat exchanger divides the air passages into smaller channels while increasing the surface area of the heat exchange. As a result, many factors are affected, some of which have a negative or positive impact to different extent on the HRV performance. Table 2 shows the effect of adding many fins up to 270 fins per/m. The flow rate is kept fixed at the maximum rated value of 1000m3/h. The table demonstrates the change in most factors involved in the calculations of the performance. Relative comparison between the first case with no additional fins (row a), and the last case with 270 fin/m (row b). It is expected that an increase in the number of Reynolds will occur due to the decrease in the flow area A_o after adding fins, but the calculations showed that Re is subjected to a decrease due to a greater percent reduction in the hydraulic diameter. This effect has reflected on the value of the Nusselt number (Nu), which underwent some decrease. Nevertheless, the overall heat transfer coefficient (U) has increased due to the large increase in the surface area (A). The outcome of all these variables is an increase in the NTU value, which leads to an improvement in the effectiveness (ε) when increasing the number of fins.

Table 2. Fin effect on the HRV performance.

	n	Nf	A	Dh	Re,av	Ao	Nu	U	NTU	ε
a	0	0	7.62	0.0103	3248.4	0.0528	31.05	39.57	0.934	0.4556
	54	20	9.5	0.008	2604.4	0.0511	25.975	42.58	1.25	0.5209
1000 m3/h	108	40	11.4	0.0064	2175.6	0.0494	22.604	45.87	1.609	0.5745
	143	**53**	**13**	**0.0057**	**1969**	**0.048**	**20.97**	**48.1**	**1.86**	**0.603**
	162	60	13.2	0.0053	1868	0.0477	20.17	49.35	2.013	0.6183
	216	80	15.1	0.0045	1636.6	0.046	18.321	53.05	2.466	0.6541
b	270	100	17	0.0039	1456.2	0.0443	16.86	56.96	2.972	0.6835
*100% increase			**1.23**	**-0.6235**	**-0.552**	**-0.161**	**-0.457**	**0.439**	**2.182**	**0.5003**

	Th,i	Tc,i	Th,o	Tc,o	ΔTh	ΔTc	Qrec	ΔP	β	α
a	46	24	36	33.833	10.023	9.8326	3233.7	127.8	390.2	173.94
	46	24	34.5	35.298	11.461	11.298	3706.5	240.9	502.1	216.92
	46	24	33.4	36.508	12.639	12.508	4095.3	359.5	621.7	259.61
1000 m3/h	**46**	**24**	**33**	**37.166**	**13.28**	**13.17**	**4306**	**450**	**703**	**286.9**
	46	24	32.4	37.504	13.602	13.504	4414.1	507.1	750	302.31
	46	24	31.6	38.323	14.39	14.323	4675.6	691.8	887.8	345
b	46	24	31	39	15.037	15	4891	922.7	1036	387.7
*100% increase					**0.5003**	**0.5255**	**0.5125**	**6.221**	**1.656**	**1.2289**

One of the consequences of these variables is an increase in the amount of change in the temperature of hot and cold airstreams (ΔT_h and ΔT_c), which led to an increase in the amount

of the recovered heat (Q_{rec}). Although the exchanger kept its size, it became more compact by the substantial increase in values β and α. The only negative condition that accompanied the improvement in thermal performance is the increase in pressure drop (ΔP).

It is evident in Figs 3, 4, and 5 that adding fins causes an increasing ineffectiveness. The recovered heat and pressure drop are also increased. Adding up to 143 fins/m doses does not lead to exceeding the permissible pressure drop of 450 Pa. At this point, the effectiveness is 60.3% instead of its initial value of 45.6% (an increase of 33.3%). The recovered heat is increased by 34%. Further, an increase in fins resulting in exceeding the permissible pressure drop. However, the number of fins can be increased to obtain better performance, but at a flow rate less than the maximum rate. For example, adding 162 and 216 to 270 fins/m, the critical flow rates would be 904, 695, and 543.5 m^3/h to obtain an efficiency of 62.3%, 67.2%, and 71.1%, respectively. Operating the HRV at flow rates less than the critical at any added number of fins does not set limits on the number of fins. The area under the red dashed line indicates the safe field in terms of pressure drop for any number of fins below 144 fin/m. At a low flow rate with 270 fins/m, the effectiveness reaches the threshold of 80%.

Figs 6, 7, and 8 illustrate the effect of adding fins on the core volume relative to the original volume with no fins while maintaining its initial performance. The green point on the figures represents the exchanger condition at its original volume. It is clear from the figures that an increase in fins leads to an increase in all performance parameters. To keep these parameters unchanged, the volume of the exchanger should be reduced by a percent depends on the added number of fins. For example, when adding 20 fins/m, the volume must be reduced to about 82.8% of its original size, noting that the pressure drop is still below or at the permissible limit. Also, adding 40 fins/m allows reducing the size to 69% of the original without reservation.

The lowest volume that can be obtained without compromising the performance is 37% of the original volume by adding 120 fins/m. Extra fins do not lead to reduce the volume below 37% because it will lead to exceeding the maximum pressure drop. Adding 130 fins allows for a reduction in volume to 49%, but with better performance, the effectiveness improved by 10.4%, and the recovered heat increased by 11%. Adding 143 fin/m does not allow for any reduction in the size. At this point, the HRV has its highest performance with an increase in effectiveness and recovered heat by 33.3% and 34% respectively.

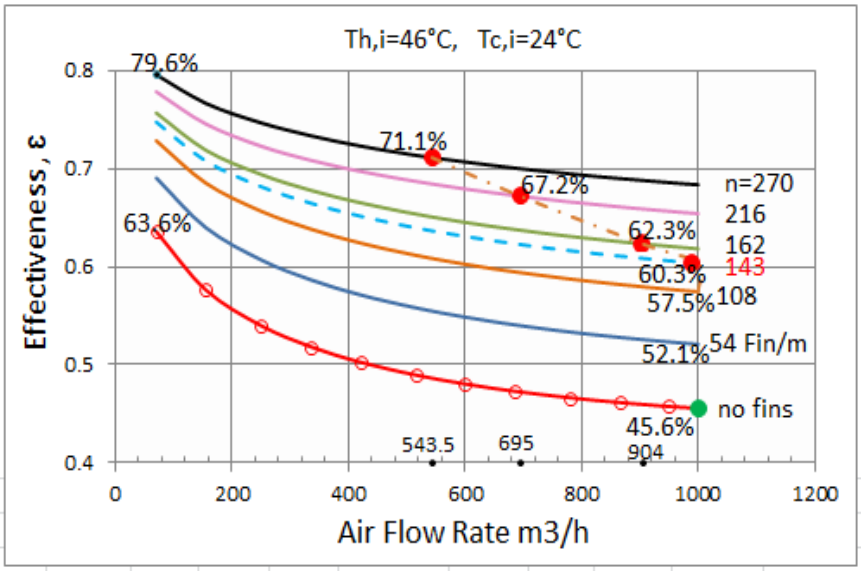

Fig 3. Effectiveness Vs flow rate.

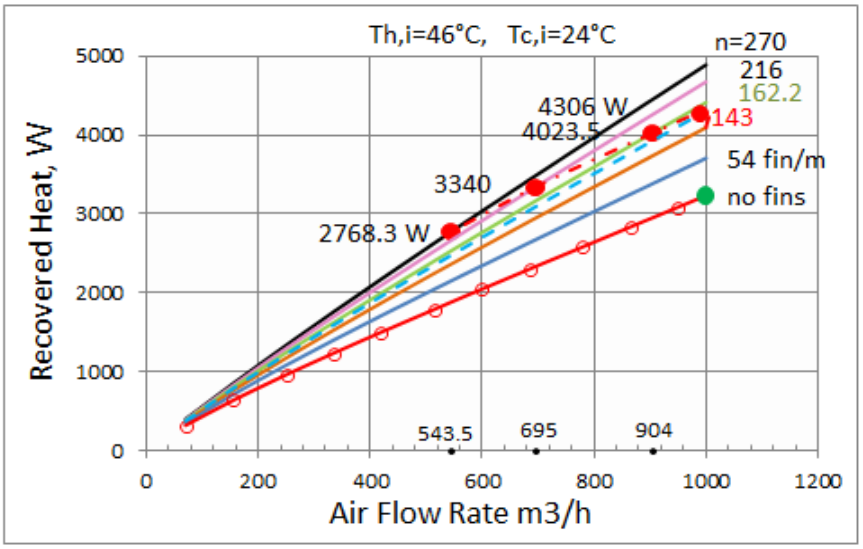

Fig 4. Recovered heat Vs flow rate.

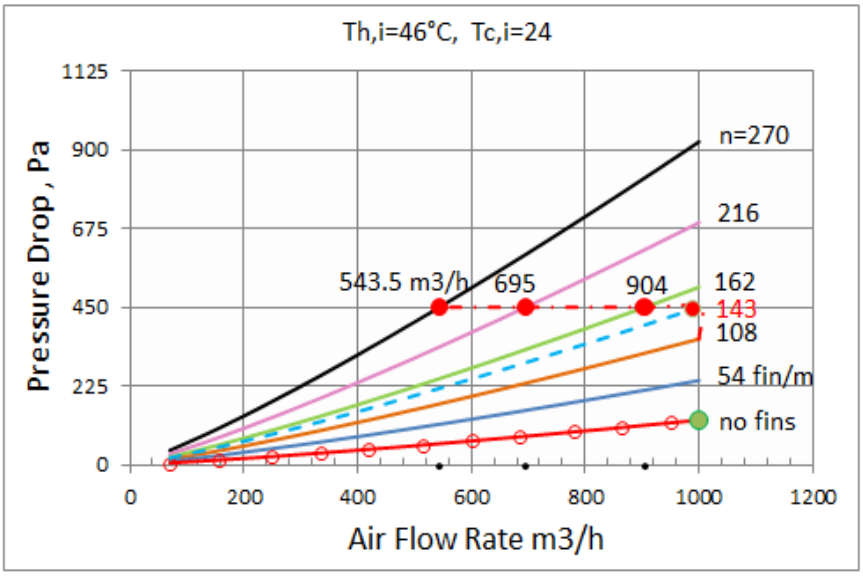

Fig 5. Pressure drupe Vs flow rate.

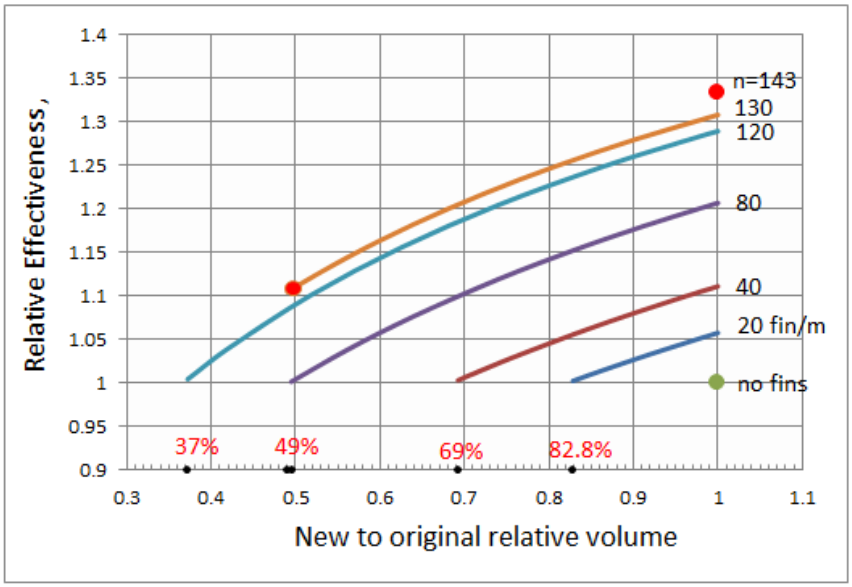

Fig 6. Effectiveness Vs relative volume.

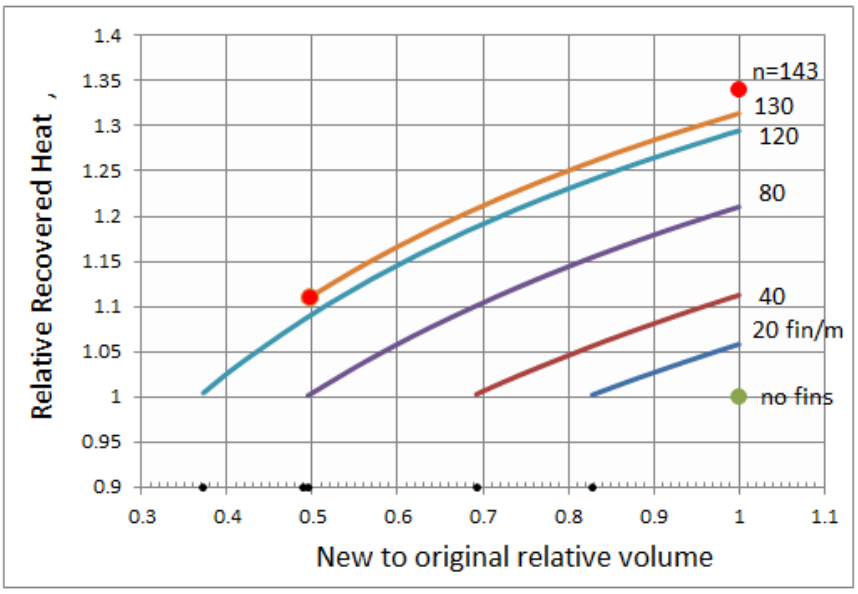

Fig 7. Recovered heat Vs relative volume.

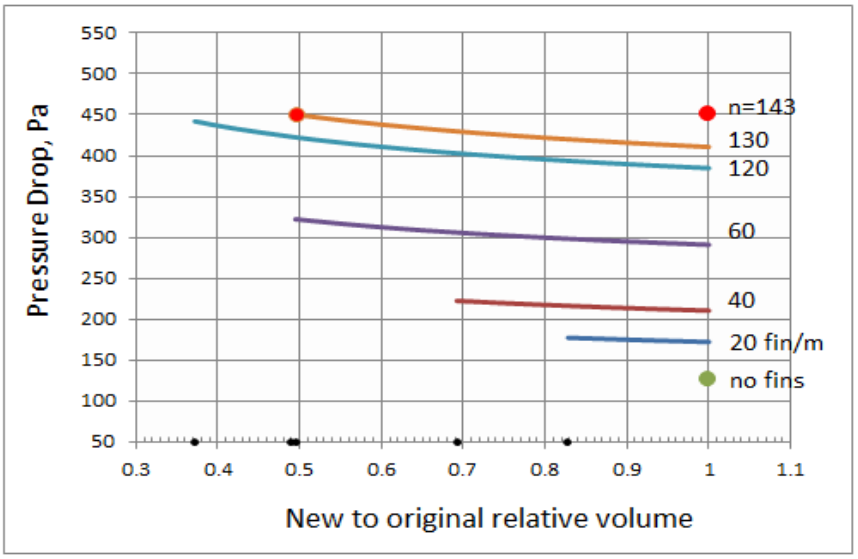

Fig. 8. Pressure drop Vs relative volume.

4 Conclusions

The following conclusions are extracted from the discussed results for the HRV performance:

1- While the heat recovery ventilator recovers low-quality heat, it indirectly provides high-quality energy to accomplish the same task by A/C systems without violating the second law of thermodynamics.

2- The pressure drop did not exceed 130 Pa at its maximum rated design flow, allowing improving the thermal performance.

3- Adding fins up to 143 fin/m, make the HRV has its highest performance with an increase in the effectiveness by 33.3% and an increase in the recovered heat by 34% with the condition of pressure drop not exceeding 450 Pa.

4- The HRV size can be reduced to 37 % of its original size without compromising its performance in terms of efficiency and heat duty by adding 120 fins/m with the condition of pressure drop not exceeding the permissible level.

References

[1]. Dominic O'Connor, John Kaiser. Calauti. "A Study of Passive Ventilation Integrated with Heat Recovery" Energy and Buildings, Volume 82, 2014.
[2]. Energy Efficiency In Canada, "Report to Parllament under the energy efficiency act 2017–2018" Energy Resource Canada.
[2]. Sidramappa Alur "Experimental Studies on Plate Fin-Heat-Exchangers". PhD thesis, Mechanical Engineering Department National Institute of Technology Rourkela 2012.
[4]. Ahmad Mardiana Idayu "Novel heat recovery systems for building applications" PhD thesis, University. of Nottingham 2011.
[5]. Braihan Abdulwadood Salman, "The Performance Evaluation of Energy Recovery Unit for Basra City" Master thesis in thermal technical engineering, Southern Technical University, Basra-Iraq 2020.
[6]. Ashrae-HVAC, fundamentals. Handbook 2001.
[7] Mardiana A. and S. B. Riffat, "Review on physical and performance parameters of heat recovery system for building applications" ELSEVIER, July 2013.
[8]. Alireza Vali, Carey J. Simonson, Robert. W. Besant, Gazi Mahmood "Numerical model and effectiveness correlations for a run-around heat recovery system with combined counter and cross flow exchangers" ELSEVIER, Journal of Heat and Mass Transfer 52 (2009) 5827–5840.
[9]. Ahmed. A. Abduljabbar "Energetic and Exergetic Study for Cross-Corrugated membrane-Based total Recovery Exchanger for Ventilation" PhD Thesis Cranfield University 2017
[10]. Ahmed Y Taha, Al-Zubaydi, Guang Hong and W. John Dartnall "CFD Modelling and Analysis of Different Plate-Heat Exchangers" ResearchGate 2017,
[11]. C. Ranganayakulu, K.N. Seetharamu "Compact Heat Exchangers–Analysis, Design and. Optimization using FEM and CFD approach" 2018 John Wiley & Sons.
[12]. Ramesh K. Shah, Dusan P. Sekulic "Fundamentals of heat exchanger design", John Wiley & Sons, Inc 2003.
[13]. J. P. Holman. "Heat Transfer" Tenth Edition, McGraw-Hill Series, 2010.
[14]. Eric M Smith "Advances in Thermal Design of Heat Exchangers, A Numerical Approach: Direct-sizing, step-wise rating, and transients" John Wiley & Sons, Ltd. 2005.

Position Control of the Surface Motor Based on Artificial Neural Network

Abdulhasan F. Abdulhasan[1], Rabee' H. Thejel [2], Diyah K. Shary[3]
{abd.allami@stu.edu.iq, rabee_alabbasi@stu.edu.iq, diyahpower@stu.edu.iq}

[1-3]Department of Electrical Power Techniques Engineering, Southern Technical University, Iraq

Abstract. The step movement of the switched reluctance planar motor (SRPM) has high oscillation, due to the nonlinear magnetic circuit behavior and high force ripples. Therefore, traditional linear controllers are insufficient in SRPM control, thus a closed-loop motor position control system based on Neural-PID controller is designed to obtain the optimum characteristics of operation for these motors.

Keywords: switched reluctance planar motor, neural network controller, PID controller, position control of the planar motor.

1 Introduction

The planar motor also named Surface Motor (SFM) uses electromagnetic force to achieve a high precision movement without friction [1]. The two-dimensional movement of the planar motor is accurate and fast and used in many laboratory and industrial applications. These motors offer certain benefits over the rotating motor due to the absence of the rotary-to-linear transformation mechanisms in their XY movements [2]. Consequently, the direct-drive surface motors can be expected that they will replace using the traditional XY movement that achieves two-dimensional movement by using a rotary machine with mechanical transformation or using two linear motors fixed one on the other [3]. The surface motor is the switched reluctance planar motor (SRPM) that consists of the mover (armature) part and the platen (stator) part [4]. It is a robust, low-cost, and simple motor. With the requirements of the simple converter and control, the SRPM is gaining much attention in the drive applications in the industry [5]. Due to the nonlinear magnetic circuit and high force ripples, the step position of SRPM has high oscillations and overshoots during the step movement, and it is difficult to reduce the oscillations and achieve the precision position without using a good control method.

Many control strategies were applied for SRPM to realize position control. In [5], the adaptive control based on the pole-placement method was designed and implemented with parameter setting online for SRPM. The performance of this controller has good position control over the PID controller in static, dynamic, and robustness to disturbances. In [6], improved the SRPM with an optimized structural design to reduce the electromagnetic force ripple. The results prove the optimized SRPM has a higher drive force and the optimization design of the SRPM is effective in reducing the ripple of the electromagnetic force. In [7], designed a DSP-based sliding mode controller of the SRPM for accurate locating applications. The position errors for X and Y directions are 0.016 and 0.029 mm, respectively. In [8], a predictive position control (PPC) of the PSRMs for XY movement systems is given. By reducing the cost function based on the PPC, the optimal control sequence is derived. The methods above have been applied to SRPMs drive, but there is no oscillation elimination for the position response of the SRPM.

In this paper, the Neural-PID controller is proposed and designed for the SRPM drive circuit to reduce the position oscillation.

2 The Modeling of SRPM

The modular of the switched reluctance planar motor consists of six phases of switched reluctance motor (SRM), three for the movement in X-direction (X_1, X_2, X_3) and three for movement in Y-direction (Y_1, Y_2, Y_3) [2]. The mathematical model of the SRPM for one phase in the X-direction that is given in [9], [10] can be implemented using Matlab/Simulink as is shown in Fig 1. Subsystem 1 and subsystem 2 of Fig 1 are shown in Figs 2 and 3, respectively. All other phases of SRPM can be implemented in the same way.

IMDC-IST 2021, September 07-09, Sakarya, Turkey
Copyright © 2022 EAI
DOI 10.4108/eai.7-9-2021.2314778

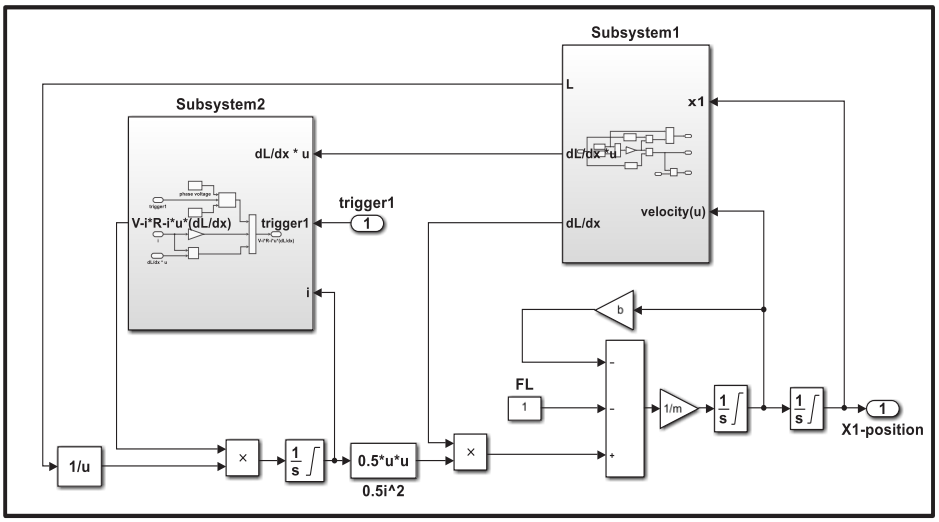

Fig 1. Implemented Simulink model of one phase of SRPM in the X-direction.

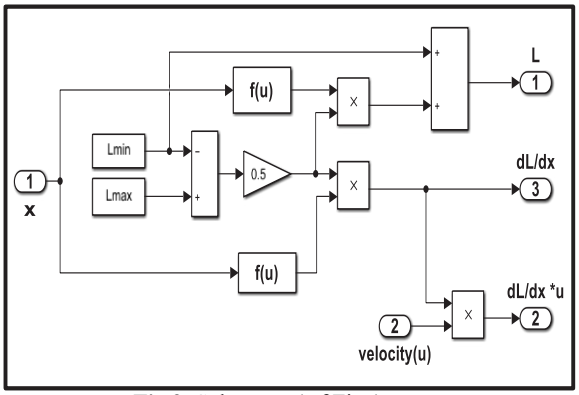

Fig 2. Subsystem1of Fig.1.

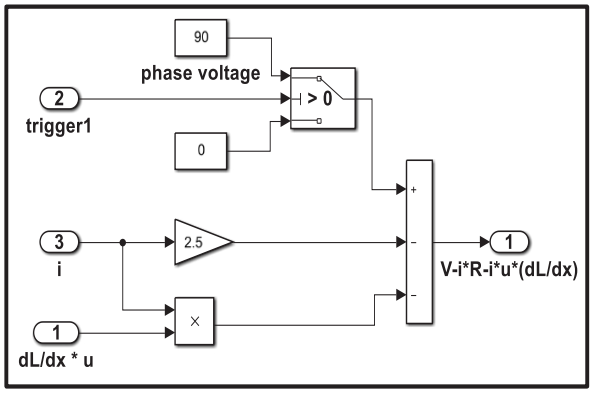

Fig 3. Subsystem2 of Fig.1

3 The SRPM Controller

The switched reluctance planar motor is a non-linear system. Therefore, it is not easy to obtain a good result for SRPM using the traditional linear control methods. Thus, the performance of the traditional PID controller has been insufficient due to the nonlinear structure of the surface motor. In this work, the performance and accuracy requirements of the SRPM position control system are done by integrating a neural network with a PID controller. The complete controller type position control-based surface motor drive system is proposed as shown in Fig 4. Where, X_{off} is the off-position of the mover in (m), X_{ref} is the reference position of the motor in (m), X is the actual (mover) position in (m), and e(t) is the error between the reference and actual positions.

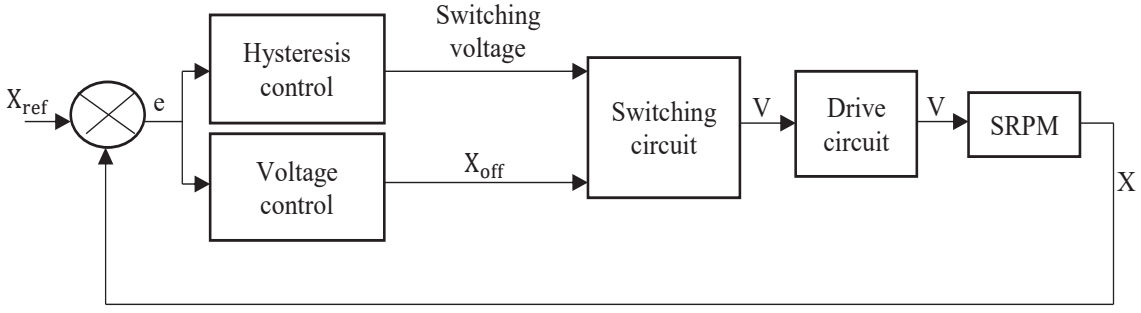

Fig 4. The configuration of SRPM with the proposed controller.

In this work, the controller contains two-controller blocks, the position-X_{off} controller (voltage control) and position-I_{ref} controller (hysteresis control). These controllers are supplied to a switching circuit as shown in Fig 5. A Neural Network (NN) controller is used to tune the parameters of PID controllers of hysteresis and voltage control.

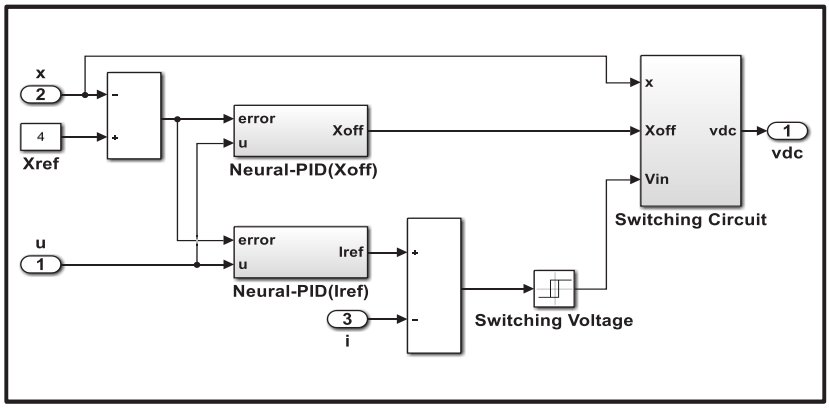

Fig 5. Position- X_{off} and position-I_{ref} controllers with switching circuit.

3.1 Position- I_{ref} controller (Hysteresis Control)

In this control method, the current is adjusted between two current levels equal to $I_{ref} \pm \Delta i$, where, Δi is the hysteresis band (chopping width) and I_{ref} is the reference current. The reference position X_{ref} is compared with the mover position X to give the position error. The position error signal is handled by the PID position controller to produce the reference current as shown in Fig 6. The errors estimate by comparing the reference current with the actuator current and it is used to limit the switching voltage that is supplied to the switching circuit as shown in Fig 5.

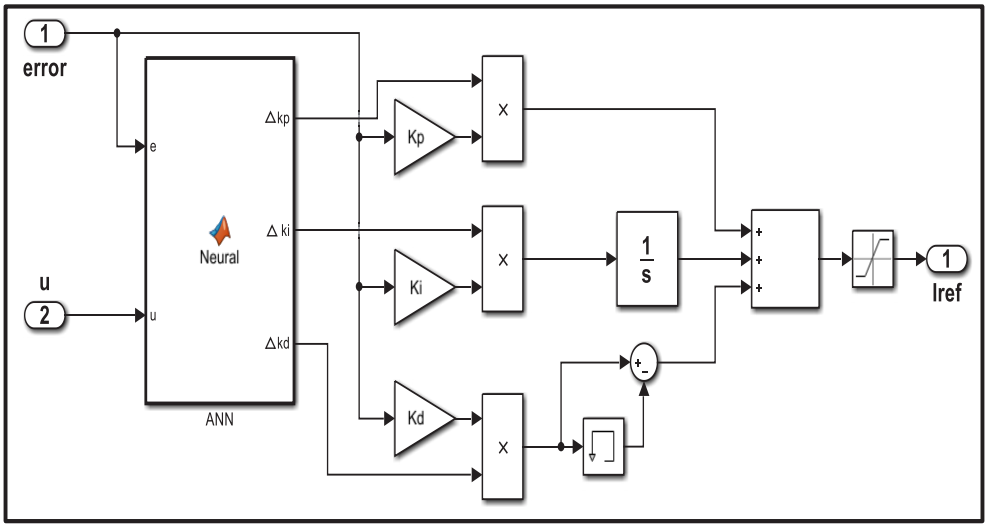

Fig 6. Implemented Simulink model of position-I_{ref} controller.

The switching logic of the current chopping controller is summarized as [11]:
if $(I_{ref} - i) \geq \Delta i$ then $Vin = V_{dc}$
if $(I_{ref} - i) \leq -\Delta i$ then $Vin = -V_{dc}$
else $e = 0$
Δi is chosen to be 0.1 and V_{dc} is 90 Volt.

where, i, and Vin are the phase current (actuator current), and the switching voltage, respectively.

The parameters of the PID controller are tuned online by the NN. In this paper two input neurons (error (e), velocity (u)), five hidden neurons, and three output neurons (the change in parameters gains of PID controller) have been chosen as shown in Fig 7.

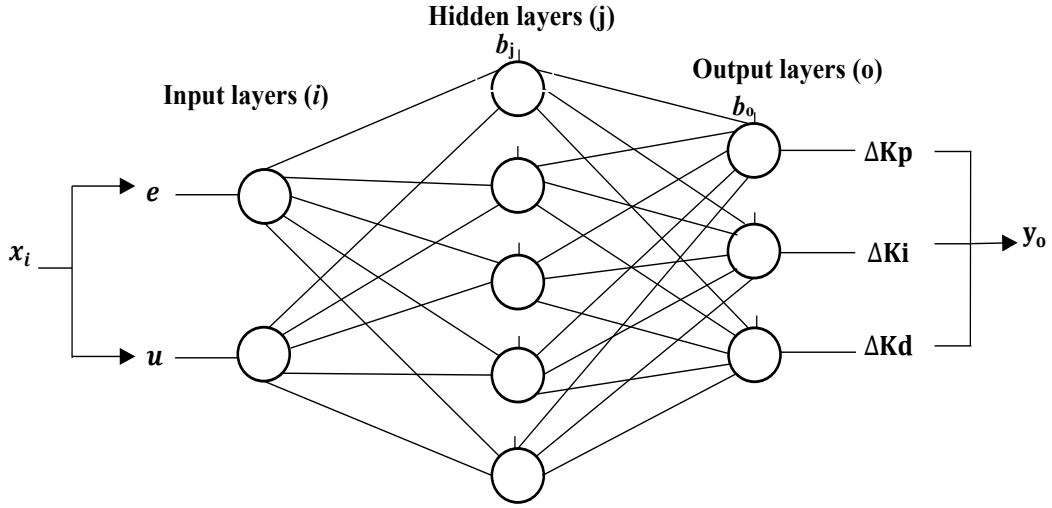

Fig 7. Structure of NN controller.

Where,

$x_i = \begin{bmatrix} e \\ u \end{bmatrix}$ and $y_o = \begin{bmatrix} \Delta Kp \\ \Delta Ki \\ \Delta Kd \end{bmatrix}$

The mathematical equation that describes the neural network can be calculated by the following equations [12]:

$$S_j^k = \sum_{i=1}^{N} w_{ji}^k . x_i^k + b_j^k \quad (1)$$

$$y_j^k = \frac{1}{1+e^{-S_j^k}} \quad (2)$$

$$S_o^k = \sum_{j=1}^{n} w_{oj}^k . y_j^k + b_o^k \quad (3)$$

$$y_o^k = \frac{1}{1+e^{-S_o^k}} \quad (4)$$

where, y_j^k, y_o^k, W_{ji}, W_{oj}, b_j^k, b_o^k, k, K are the output of hidden layers, the output of NN, the weights between the hidden and the input neurons, the weights between the output neuron and the hidden neurons, the bias of hidden layers, the bias of output layers, the present training set and k=1:K, and the total no. of the training sets, respectively.

In this work, the backpropagation training algorithm was used to train the weights of NN. The weights are altered in the backward direction by the delta rules equations of the backpropagation algorithm as follow:

$$\partial = y_o^k . (1 - y_o^k) . (d^k - y_o^k) \quad (5)$$

$$\partial_h = y_j^k * (1 - y_j^k) * w_{oj}^k * \partial \quad (6)$$

$$w_{oj}^{k+1} = w_{oj}^k + \partial * \eta * y_j^k \quad (7)$$

$$b_o^{k+1} = b_o^k + \partial * \eta \quad (8)$$

$$w_{ji}^{k+1} = w_{ji}^k + \partial_h * \eta * x_i^k \quad (9)$$

$$b_j^{k+1} = b_j^k + \partial_h * \eta \quad (10)$$

where η, e_{max}, ∂, ∂_h are the learning ratio which is chosen to be 0.5, the maximum error, the delta rule of the output neurons, and the delta rule of the hidden neurons, respectively.

The flow chart of the algorithm architecture of the backpropagation learning program is shown in Fig 8. The input data (x_i) is represented as a vector with rows equal to (K) and its columns equal to the number of input neurons. The desired output data (d) is expressed as a column vector with K rows.

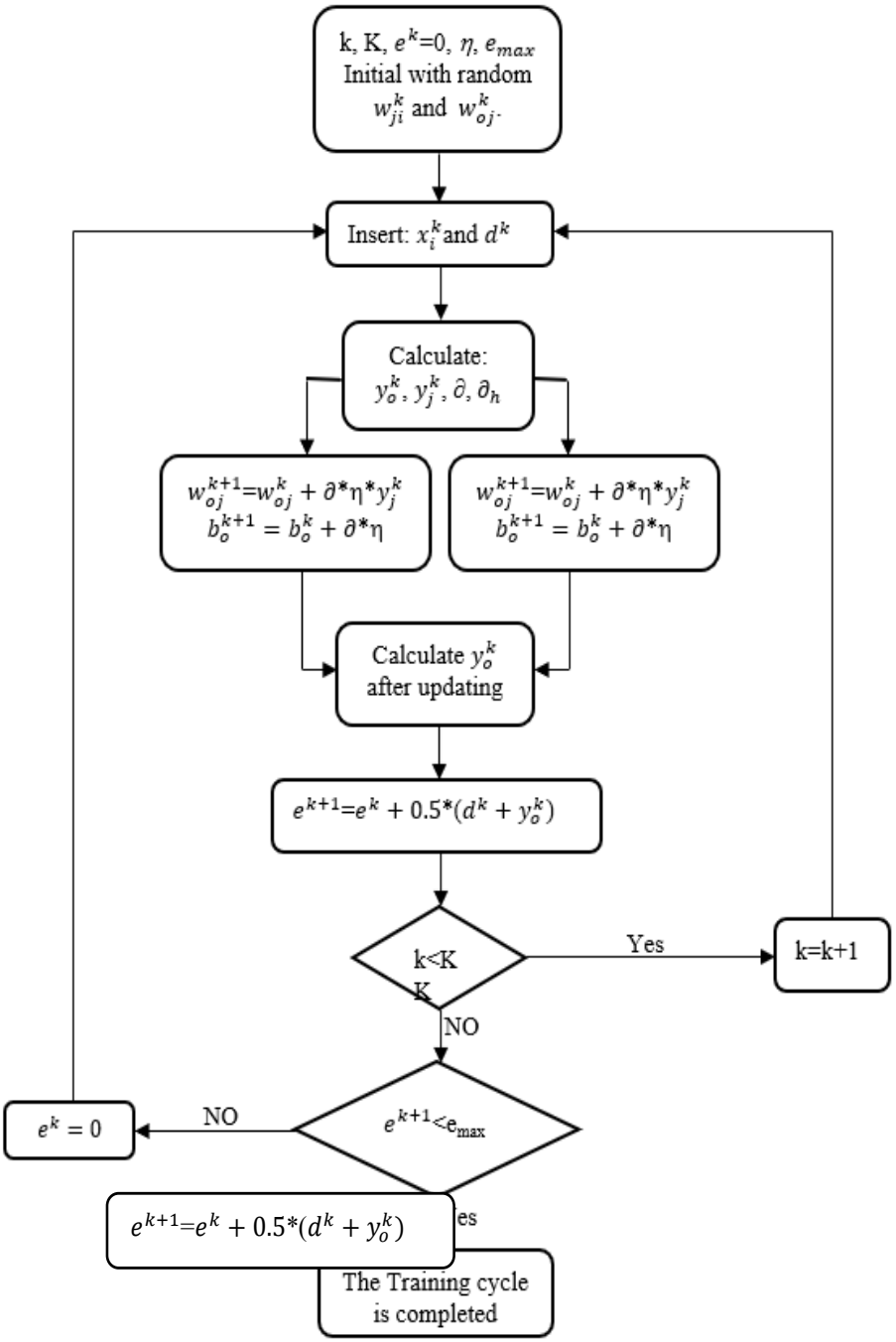

Fig 8. Flow chart of the backpropagation training.

The neural network parameters are:

1-The weights of the hidden layers:

$$w_{ji} = \begin{bmatrix} 0.7950 & 0.1905 \\ 0.8574 & 0.2478 \\ -1.0578 & 0.4141 \\ -0.9118 & 0.0548 \\ 0.3957 & 0.9090 \end{bmatrix} , h_j = \begin{bmatrix} 2.0662 \\ 1.8304 \\ -0.1093 \\ 0.8324 \\ 1.9222 \end{bmatrix}$$

2-The weights of the output layers:

$$w_{oj} = \begin{bmatrix} -1.7848 & -1.9092 & -0.1539 & -1.2367 & -1.6983 \\ -2.0520 & -0.8829 & 0.0322 & -0.6682 & -1.3627 \\ -1.8352 & -1.5920 & -0.0895 & -1.5324 & -1.8329 \end{bmatrix} , h_o = \begin{bmatrix} 12.0682 \\ 9.4067 \\ 6.2037 \end{bmatrix}$$

3.2. Position- X_{off} controller (voltage control)

This control occurs by applying a voltage on phases of SRPM from the turn-on position (X_{on}) period to a turn-off position (X_{off}) period. After that, the applied voltage is reversed completely until a certain demagnetizing position (X_q), which allows the return of the magnetic flux towards zero. The mover position at which the stator current becomes zero is called the demagnetizing position (X_q). The correct decision of the period-off position and the value of current determine the performance of SRM. In this controller, the Neural-PID controller is used to select the appropriate off-position of the motor as is shown in Fig 9. The output of this controller is supplied to a switching circuit as shown in Fig 5. The NN is used to tune the parameters of the PID controller. In this controller, the structure and learning algorithms of NN are the same that is used in position-I_{ref} controller.

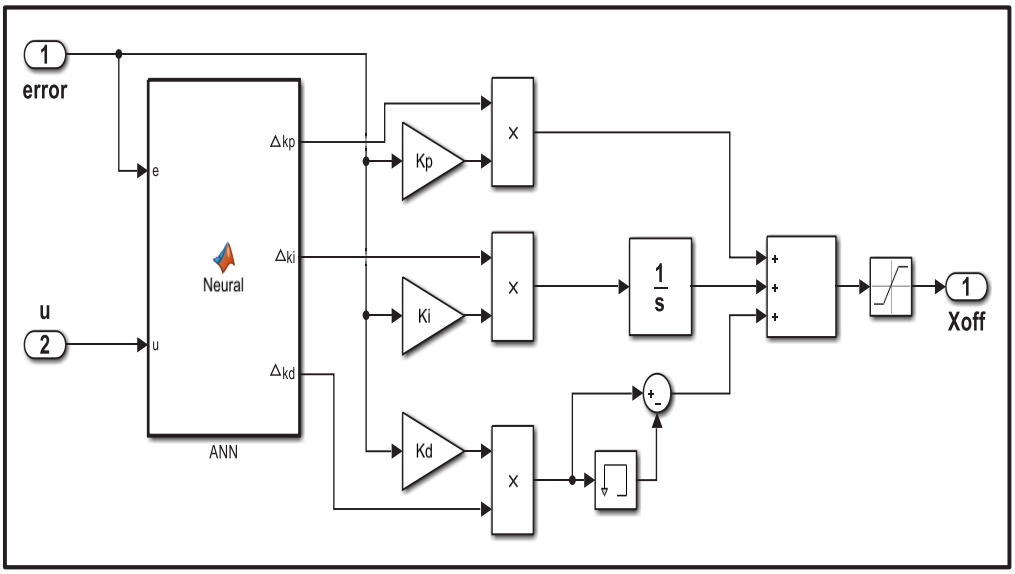

Fig 9. Implemented Simulink model of position-X_{off} controller.

The neural network parameters are:

1-The weights of hidden layers:

$$w_{ji} = \begin{bmatrix} 0.5265 & -23.0829 \\ 1.5274 & 19.9201 \\ 13.9150 & -13.9376 \\ 1.4507 & -18.8408 \\ 1.5747 & -1.0786 \end{bmatrix} , h_j = \begin{bmatrix} 6.7429 \\ -1.1446 \\ -0.2194 \\ 4.4439 \\ -2.5557 \end{bmatrix}$$

2-The weights of output layers:

$$w_{oj} = \begin{bmatrix} 2.4602 & -7.0001 & 39.7432 & 2.8495 & 15.5845 \\ 3.0966 & 2.9797 & -8.8762 & -3.4552 & -4.7579 \\ 7.2849 & -3.0789 & 3.8074 & 2.1286 & 5.8654 \end{bmatrix} , h_o = \begin{bmatrix} -19.2974 \\ 1.3311 \\ -3.9006 \end{bmatrix}$$

3.3 Switching Circuit

The movement of the SFM is achieved by energizing and de-energizing the phase windings. The selection of conduction positions plays important role in the force ripple and the power of SRPM. However, it is hard to pick the proper conduction position [11]. In this work, the switching circuit is used to compare the mover position (X) for each phase with the turn-on position, turn-off position, and demagnetizing position to give the appropriate voltage supply for SRM as shown in Fig 10. Currently, the performance of SRPM is done by keeping the on position constant and changing the off position of SRPM. X_{on} and X_q values are chosen to be 0 mm and 3 mm, respectively.

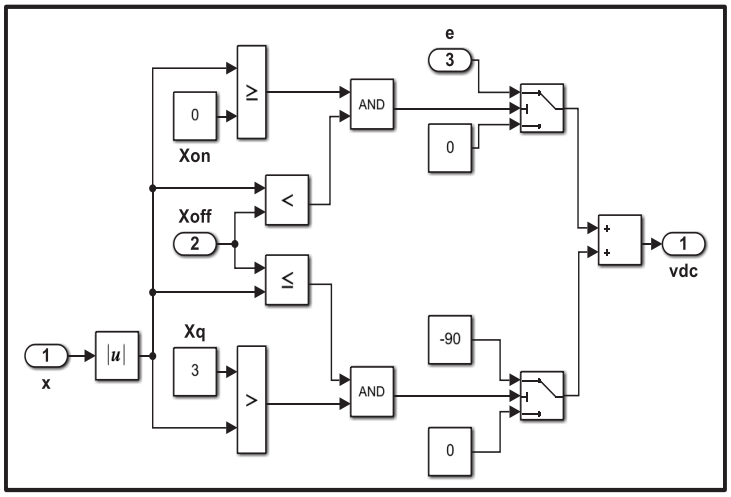

Fig 10. Switching circuit of the SRPM.

4 Simulation Results

The modeling with the control circuits of the SRPM was implemented using Matlab/Simulink software. The parameters of one phase of the surface motor are given in Table 1. The results of one phase in X-direction of the SRPM are adopted and the remaining phases of the motor will give the same results. Each phase of SRPM can step 4mm in X or Y direction. It can note that the high overshoots and oscillations in step response of SRPM are removed when utilizing the Neural-PID controller as shown in Fig 11. While Fig 12 shows the ability of the motor to work at different load conditions when using the Neural-PID controller. The thrust force is generated in one phase of SRPM in the X-direction is shown in Fig 13. This figure shows that the thurst force decrease until reach zero when the motor step movement is completed, which equals 4 mm also it shows that X_{off} will not exceed 3 mm. The position-inductance characteristic is shown in Fig 14. This figure proves the inductance starts at a minimum value and reaches a maximum value when the motor movement is completed. Figs 15 and 16 show the XY movement of SRPM when the motor is traveled through a rectangular and triangle target, respectively. These figures show the validity of the surface motor to achieve accurate tracing to the desired positions.

Table 1. The parameters of the SRPM.

Parameters	values
Pole width	6 mm
Pole pitch	12 mm
Phase separation	10 mm
Winding length	30 mm
Wind width	25 mm
Air gap width	0.5 mm
Phase resistance	2.5 Ω
Aligned inductance	19.2 mH
Unaligned inductance	11.5 mH
The mass of moving platform (m)	1.8Kg
Friction constant (b)	0.08N*s*m^{-1}

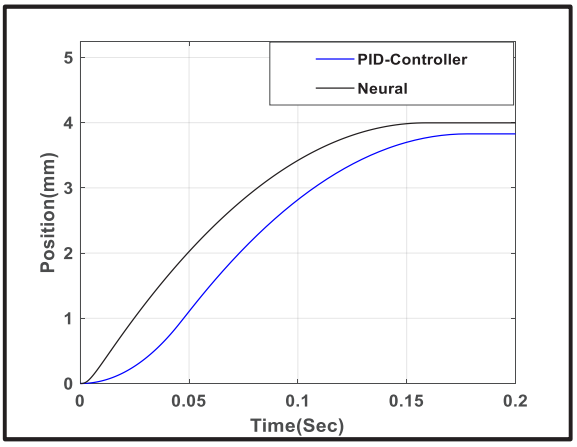

Fig 11. The Position response of one phase of SRPM in X-direction with m=1.8kg.

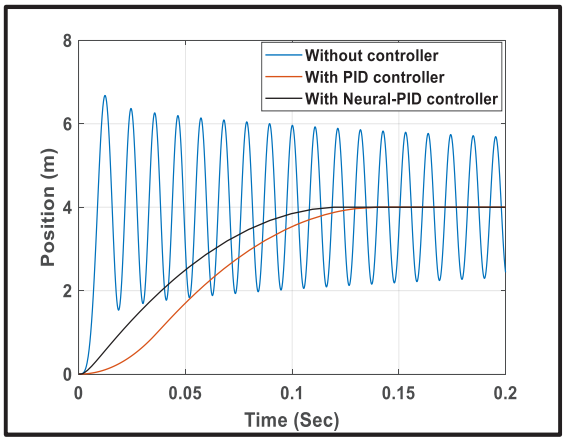

Fig 12. The Position response of one phase of SRPM in X-direction with m=3 kg.

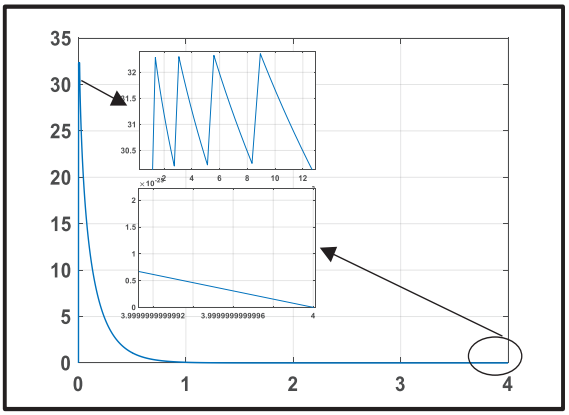

Fig 13. The force–position characteristic of one phase of SRPM in X-direction with Neural-PID controller at m=1.8 kg.

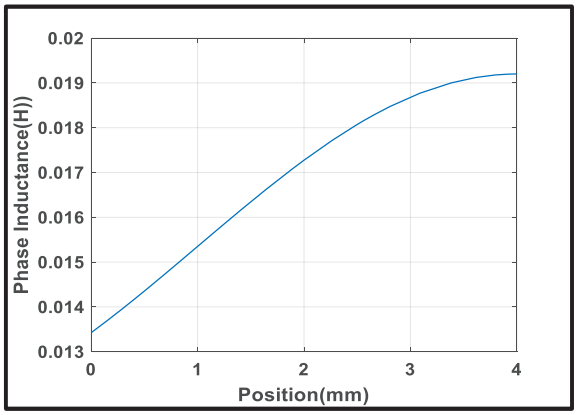

Fig 14. Phase inductance-position characteristics of the surface motor in X-direction with Neural-PID controller at m=1.8 kg.

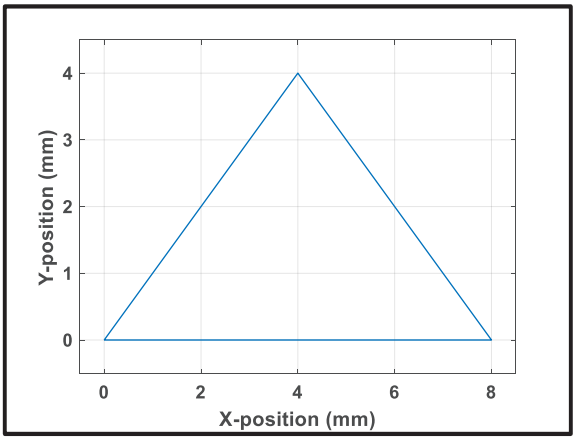

Fig 15. Square movement of the surface motor with Neural-PID controller.

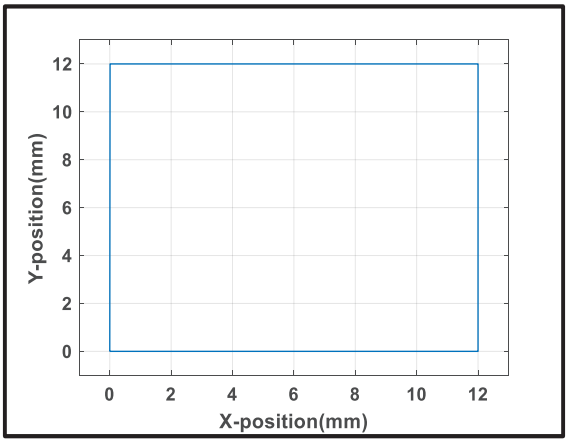

Fig 16. Triangle movement of the surface motor with Neural-PID controller.

5 Conclusions

The modeling of SRPM and the Neural-PID controller has been designed and tested using Matlab/Simulink software. The simulation results show that the control performance of the SRPM with the Neural-PID controller is

better than the PID controller. The SRPM performance with Neural-PID controller has no oscillation, no overshoot, short rise time, strong robustness to load variation, and smooth and precise final position. The simulation results prove the proposed Neural-PID controller is effective for the SRPM to compare with the traditional PID controller. The main results from this work are concentrated on position regulation with neural technique. Therefore, it would be interesting to focus on velocity control using traditional controller (PID), fuzzy and neural strategies.

References

[1] L. Xuepeng, M. Xuesong, and W. Xutang, "Model and Control of Novel Surface-Motor in Plane Motion," *Journal of the Korean Society for Industrial and Applied Mathematics*, vol. 8, no. 2, pp. 39-49, 2004.

[2] L. Szabo, D.-C. Popa, V. Iancu, E. Kovacs, and F. Toth, "On the Usefulness of Simulation in Designing a Permanent Magnet Modular Surface Motor for Advanced Mechatronic Systems," In *2006 IEEE International Conference on Mechatronics*, pp. 88-93: IEEE, July 2006.

[3] J. Pan, N. Cheung, W. Gan, and S. W. Zhao, "A novel planar switched reluctance motor for industrial applications, "*IEEE Transactions on Magnetics*, vol. 42, no. 10, pp. 2836-2839, October 2006.

[4] J. Pan, N. C. Cheung, and J. Yang, "High-precision position control of a novel planar switched reluctance motor," *IEEE Transactions on Industrial and Electronics*, vol.52, no.6, December 2005.

[5] J. F. Pan and N. C. Cheung, "An adaptive controller for the novel planar switched reluctance motor," *IET Electric Power Applications,* vol. 5, no. 9, pp. 677-683, November 2011.

[6] G. Z. Cao, J.-L. Fang, S.-D. Huang, J.-A. Duan, and J. F. Pan, "Optimization design of the planar switched reluctance motor on electromagnetic force ripple minimization," *IEEE Transactions on Magnetics*, vol. 50, no. 11, November 2014.

[7] H. J. Hu, G.-Z. Cao, S. D. Huang, Z.- Z. Xu, and C. Wu, "A DSP-based sliding mode controller for the planar switched reluctance motor," In *2017 IEEE International Electric Machines and Drives Conference (IEMDC)*, pp. 1-6, May 2017.

[8] Z.-Y. Hu, S.-D. Huang, G.-Z. Cao, L. Chen, G. Jing, and Y. Liu, "Predictive Position Control With Stable Control Parameters of Planar Switched Reluctance Motors," In *2020 10th Institute of Electrical and Electronics Engineers International Conference on Cyber Technology in Automation, Control, and Intelligent Systems (CYBER)*, pp. 318-321: IEEE, October 2020.

[9] J. M. Yang, Q. Zhong, N. C. Cheung, and S. W. Zhao, "On Control of Planar Switched Reluctance Motor," *Proceedings of the 17th World Congress, The International Federation of Automatic Control, Seoul, Korea,* vol. 41, no. 2, pp. 15702-15707, July 2008.

[10] W. Zaafrane, M. Dursun, and H. Rehaoulia, "Double-sided linear switched reluctance motor analysis and modeling including end-effect," in *2018 5th International Conference on Electrical and Electronic Engineering (ICEEE)*, pp. 124-128: IEEE, May 2018.

[11] S. Zhou and H. Lin, "Modeling and simulation of switched reluctance motor double closed-loop control system," *Proceeding of the 6th World Congress on Intelligent Control and Automation, Dalian, China,* PP. 6151-6155, June 2006.

[12] R. S. Burns, "Advanced control engineering", University of Plymouth, UK, pp.348-354, Elsevier,2001.

Thermal Enhancement for Solar Water Heating System by Using Phase-change Materials

1st Eng. Zahraa A. Abdalaali [1], 2nd Prof Dr. Saadoon F. Dakhil[2], 3rd Dr. Tahsien. A. Jabbar [3]
albadyzhra5@gmail.com [1], s.albahadili@stu.edu.iq [2], tahseen.ali@stu.edu.iq [3]

Fuel and Energy Department, College of Technical Engineering, Southern Technical University

Abstract: Thermal storage using phase-change materials PCMs is an efficient technique for enhancing the efficiency of solar energy utilization. This paper presents an investigation of solar thermal energy storage systems using an encapsulated PCM working in a realistic environment (Basra, Iraq). Numerical investigating the thermal performance of the heating system by using CFD technics with finite volume method .Water is used as the heat-transfer fluid HTF as well as sensible heat material. While paraffin wax packed in small cylindrical galvanized-iron capsules is used as the latent heat-PCM material. The capsules are integrated into a commercially cylindrical storage tank for hot water. First, the advantage of using flat plate solar collector FPSC and PCM is demonstrated on an insulated water tank. Finally, a turbulent-transient-3D model was developed using the ANSYS FLUENT 2020 R1 and compared with the experimental results. It was found in this case that the water temperature reaches above 50°C. Remained hot at least 25°C higher than the ambient temperature throughout 16 hours due to the presence of PCM. Parametric analyzes are performed to study the effect of the HTF flow rate (3 and 15lit/min) and the amount of PCM (5 and 10kg) on the PCM melting process, the charging time, and thermal storage energy of the water tank. The results indicate that the best performance can be obtained with the highest flow rate and the highest amount of PCM 15lit/min and 10kg, respectively, according to the current study. The results proved good agreement between the measured and numerical work.

Keywords: heat transfer-PCM-solar energy-FLUENT.

1 Introduction

Amongst many resources of alternative energy, solar energy is considered more promising because of its hygiene and availability in various places of the globe. The major component for any thermal storage application is the solar water heater collector (SWHC). With the use of a solar collector, the energy from solar radiation is converted to heat. Two types of storage systems are essentially built Sensible and latent heat storage. Both of them are combined to store a large amount of heat in a small unit volume thermal energy storage (TES) tank. Thermal energy storage in solar

IMDC-IST 2021, September 07-09, Sakarya, Turkey
Copyright © 2022 EAI
DOI 10.4108/eai.7-9-2021.2314777

water heaters has recently emerged as an effective means of capturing and storing solar energy. In solar energy applications the time delay and usable power between the energy supply or production and its consumption, as well understood from engineering practice, is a significant problem. The PCM is the best option to get rid of this problem, due to its low cost, ease of use, and high storage capacity[1]. It is possible to classify PCMs into four various types as seen below **Figure 1 [2]**.
Several researchers had experimentally and numerically improved the thermal performance of the PCM in terms of operating time and storage energy capacity under an acceptable temperature range by incorporating it into storage tanks[1],[3],[4],[5], the benefit of this technique is to increase the thermal storage capacity, as researchers filled spherical or cylindrical capsules with PCM and integrated them into the storage tank. Or with solar collectors[6],[7],[8], this technology is beneficial because it prevents the loss of heat and energy in pipes or duct networks, and also in terms of cost as storage tanks and insulation material become unnecessary. The PCM was also integrated with the heat exchanger to release and absorb harvested energy in domestic applications[9],[10],[11]. Some researchers summarized techniques to improve the heat transfer of the PCM, either by using different types of PCM or by supporting it with materials that improve its efficiency. Cabeza et al.[12] experimentally studied the behavior of PCM (compound of a granular PCM graphite) in a TES at the University of Lleida, The researcher concluded that this module is very promising, even without exterior energy supply this technique will provide hot water for a long time. Beyne et al.[13] experimentally improved the heat transfer by treating the PCM material with metal foam (Aluminum and Copper) to raise its thermal conductivity, The results showed that adding metallic foam reduces cooling time by at least 25% compared to PCM without foaming. Kulkarni et al. [14] experimentally study the feasibility of storing solar energy using paraffin wax as PCM. The use helps to reduce the cooling rate of water; thus, it hence improves the efficiency of the system. Al-Kayiem & Lin [15] experimentally verified the system performance consisting of a flat plate solar collector integrated with a thermal energy storage tank for heating water in three cases with and without PCM (paraffin wax) and with Cu-PCM nanoparticles. The efficiency of the collector was improved with paraffin wax and Nano-composite by (6.9% and 8.4%), respectively. Sathiyaraj et al. [16] experimentally improved the PCM thermal conductivity for thermal storage (use paraffin wax as PCM) by boosting it with graphite powder. The results showed that the paraffin/graphite powder compound had better performance in heat transfer due to the high thermal conductivity (300 to 550 W/mK). Lu et al. [17] experimentally and numerically studied the performance of the Water Storage Tank containing two types of PCMs(CH3COONa·3H2O and C12H24O2) with various melting points, the increase in the amount of PCM had a significant influence on the heat release of the water tank. And others cited a mathematical model of PCM and different solution methods to model the phase-change using computational fluid dynamics of ANSYS FLUENT software. Bouhal et al. [18]numerically developed two heat transfer models for testing a TES containing PCM integrated with SWHC for domestic applications, the apparent heat capacity Cp^{app}technique and the enthalpy method, the results showed that the enthalpy method resulted in more computing time than the Cp^{app} model,

and the apparent heat capacity Cp^{app} technique is suitable during the phase change process. Abdulrahman et al.[10]numerically verified the effect of the PCM melting process.
The present work aims to perform experimental and numerical verification to analyze the performance of thermal storage for the storage tank integrated with paraffin wax as a PCM is packed in cylindrical capsules used in the domestic hot water DHW system under environmental conditions (Iraq, Basra). Numerical simulations of the 3D turbulent flow transient model are performed by solving the governing equations. The experimental and numerical procedure is done by controlling the mass of PCM and the flow rate of HTF. Then comparing the results for verification.

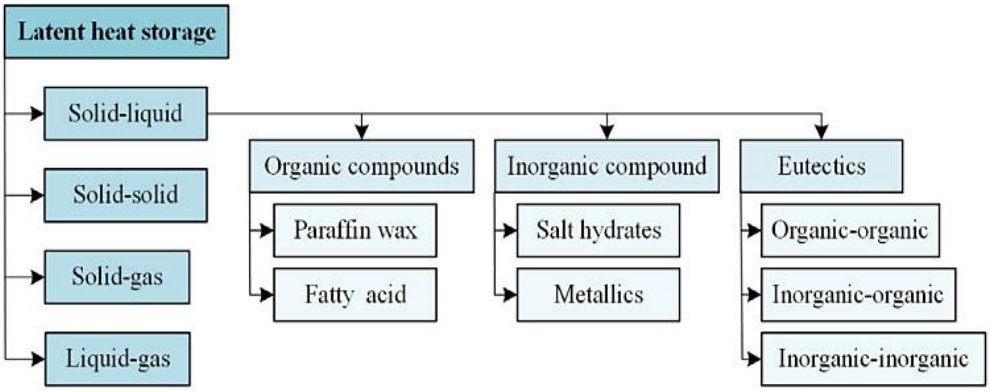

Fig. 1. Categories of LHS and classification of PCMs **[2].**

2 Experimental Discretion

2.1 Experimental setup

The photographic image and schematic diagram are seen in **Figures (2and 3)**, respectively, of the experimental setup. The setup is consisting of a flat plate collector (1*1) m^2 by a tilt angle of 30°. Which has a glass cover, absorber plate of galvanized steel with 0.01cm thick, 17 m of copper pipe, and an insulation frame with a thickness of 3 cm. Connected to the main supply of water and the storage tank (40cm diameter/120cm height with 138liters capacity). Integrated with cylindrical capsules (2cm diameter/25cm height). Paraffin wax is utilized as the PCM in this study, where 40 samples are used by a total of 10 kg of paraffin, 0.25kg of paraffin is packed in each cylindrical capsule and the material of the cylindrical capsules is galvanized iron. 22K-type thermocouples with an accuracy of (±0.1∘C) are placed at the inlet, outlet, and each three are distributed at the lower, middle, and upper sections of the tank. Five are inserted in a PCM capsule at equal interval space at the central section of the tank. Also, one to measure the temperature of ambient air. The accuracy of the flow-meter is (±0.2lit/min) to measure the heat transfer fluid rate.

2.2 Experimental procedure

The performance of TES to thermal storage is studied using (3lit/min and 15lit/min) flow rates. With varying inlet HTF temperatures and water volume 60liter with and without the PCM into the tank. Also, by controlling the amount of PCM. The readings are recorded during the day for 16hour which started at 9:00 am. Every 30minutes the PCM and HTF temperature are measured. The stored thermal energy within the capsules is kept until the PCM approaches its melting point. Finally, the PCM heats up to the point of being superheated, the energy is then deposited in liquid PCM as sensible heat. The experiments were conducted during November-2020 under the environmental conditions of Karma-Ali district at (Iraq/Basra), this site is located at 47.8°E and 30.5°N.

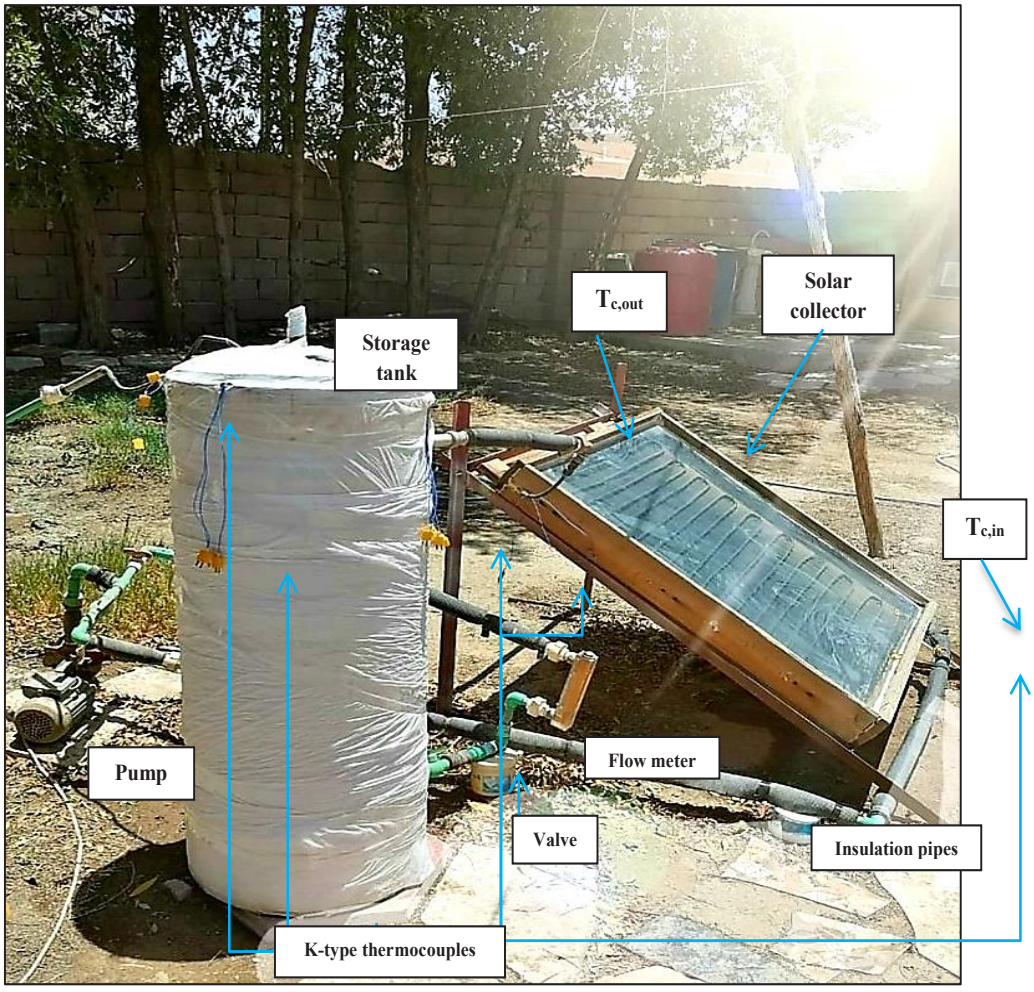

Fig. 2. Photograph view of the experimental setup.

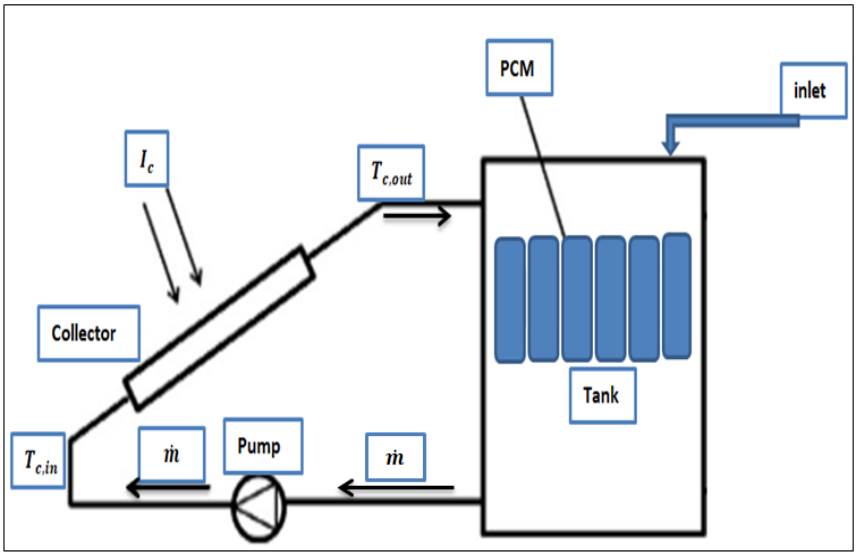

Fig. 3. Schematic diagram of the experimental test rig.

3 Theoretical Analysis

3.1 Mathematical Model

3.1.1 Physical descriptions

Figure 4. depicts a schematic 3D-computational model for the stored thermal energy. It consists of a TES tank integrated with PCM's cylindrical capsules with a dimension of 40cm diameter/48cm height of TES tank filled by water, and 2cm diameter/25cm height of capsules which are packed with paraffin wax as PCM material after melting to form the heat-absorbing part of the hot water. The cylindrical capsules of the PCM are arranged one level and spaced instead of one unit, to increase the surface area of the convection. Due to the transmission of heat from the HTF to the PCM, the PCM melts and turns from the solid phase to the liquid. Numerical simulation is performed by controlling the mass of paraffin wax (5kg and 10kg) and the water flow rate (0.05kg/s and 0.25kg/s).

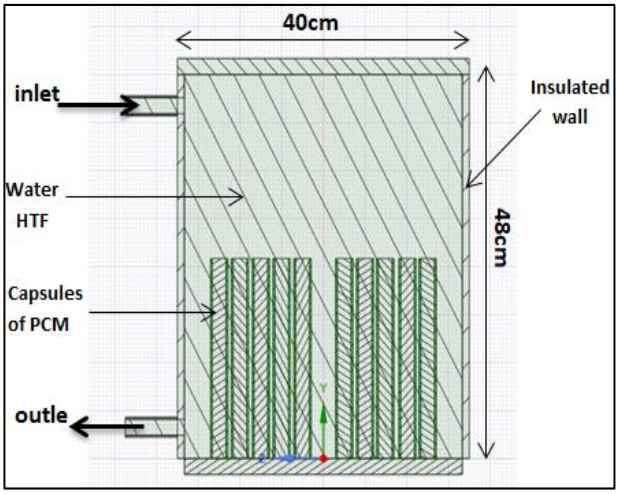

Fig. 4. Schematic of section mode 3D-computational model.

3.1.2 Assumption:

A transient flow model during the PCM melting process of the TES tank is developed using the following:

- PCM melting process is transient and 3D model with temperature variations is used.
- Flow is Turbulent.
- The fluid is Newtonian and Incompressible.
- The PCM is isotropic and homogeneous.
- For PCM and water, thermo-physical properties are constant.
- For PCM a negligible volumetric expansion.
- Heat transfer by radiation is neglected. Energy fluxes are exchanged between PCM and fluid, and loss through the wall of the tank.

PCM

$$m^{pcm} c^{pcm} \frac{dT^{pcm}}{dt} = \dot{Q}_{cond}^{pcm} + \dot{Q}_{\mathrm{w}} \quad (1)$$

Fluid

$$m^{w} c^{w} \frac{dT^{w}}{dt} = \dot{Q}^{flow} + \dot{Q}_{conv}^{pcm/w} + \dot{Q}_{loss} \quad (2)$$

where $\dot{Q}^{flow}$ is the energy change by the direct inlet-outlet flow counting the flow in both directions. upward/downward. $\dot{Q}_{loss}$ is the convection heat loss from the top and bottom of the cylindrical tank bases to the environment.

3.1.3 Governing equations:

The governing equations are applied based on Navier-Stokes and energy equations for the thermal storage tank these can be expressed as follows:

The continuity equation:

$$\nabla \cdot u = 0 \quad (3)$$

The momentum equation:

$$\rho_f \frac{\partial u}{\partial t} + (\rho_f \cdot u \cdot \nabla)u = -\nabla p + \nabla \cdot (\mu_f \cdot \nabla u) \quad (4)$$

The energy equation:

$$\rho_f \cdot C_f \cdot \frac{\partial T}{\partial t} + \rho_f \cdot C_f \cdot u \cdot \nabla T = \nabla \cdot (\lambda_f \cdot \nabla T) \quad (5)$$

The PCM phase transformation are solved by using the Enthalpy formulation method, this method assumes that enthalpy H is an amount of 'h' and latent heat 'ΔH'

$$\rho_p \cdot \frac{\partial H}{\partial \tau} = \lambda_p \cdot \nabla^2 \cdot T \quad (6)$$

$$H = h + \Delta H \quad (7)$$

$$h = h_{ref} + \int_{T_{ref}}^{T} C_p dT \quad (8)$$

where h_{ref} and T_{ref} are represented by the reference enthalpy and the reference temperature, respectively.

$$\Delta H = \beta \cdot L$$

$$\beta = \begin{cases} 0 & T < T_S \\ \frac{T - T_S}{T_L - T_S} & T_S < T < T_L \\ 1 & T > T_L \end{cases} \quad (9)$$

(10)

3.1.4 Initial and boundary conditions

In this study, two cases were investigated with amounts of PCM (5kg and 10kg) and water as a working fluid. The mass-flow was set as the boundary conditions of inlet and outlet. The initial temperature of the TES tank was 291 K, the inlet water temperatures were (313k and 323k), and the inlet mass-flow rates were (0.05 kg/s and 0.25 kg/s).

$t = 0,\ T_{(x,y,z,t=0)} = 291k$

(11)

On the wall, there was a no-slip condition. for example, the water velocity was zero near the wall:

u=v=w= 0

(12)

Keeping the wall, top, and bottom wall boundary conditions adiabatic.

$\frac{\partial T}{\partial x} = \frac{\partial T}{\partial y} = \frac{\partial T}{\partial z} = 0$

(13)

The limits for the inlet water are:

$t > 0, T = T_{in}\ , \dot{m} = \dot{m}_{in}$

(14)

3.2 Numerical analysis

Using ANSYS workbench 2020 R1 the geometry and mesh are constructed for the model and the Computational methodology is performed to solve the governing equations (3), (4), and (5) for transient turbulent flow using CFD (FLUENT) software. To simulate the heat transfer and hydrodynamic problems. Numerically, by using the finite volume method FVM the governing equations are solved. In the first step, the computational model is divided into elements. The mesh model is created by using tetrahedral cells and consists of 112633 elements. From solution methods SIMPLE (Semi-Implicit-Method for Pressure- Linked-Equations) algorithm is used for the pressure-velocity coupling and Second-order upwind is selected. Also, the turbulence models *k-epsilon* description and is solved in a pressure-based solver. The solution process based on convergence criteria 10^{-6} and for energy is within 10^{-3}. The residuals definition is shown as follow[19]:

$$R = \frac{\sum_{cellp} \left| \sum_{nb}\ a_{nb}\phi_{nb} + b - a_p\phi_p \right|}{\sum_{cellp} \left| a_p\phi_p \right|}$$

The utilized time step is set to 10s in calculations and the maximum number of iterations per time step is set as 20.

4 Result and Discussion

- **Energy calculation for the thermal water tank**

For investigating the influence of the PCM on the thermal energy storage $Q_{storage}$ in this study. The thermal energy when without and with PCM in the water tank is calculated according to follows, respectively:

Sensible heat stored $\longrightarrow$ $Q_{storage} = m \cdot C_p \cdot (T_{\text{hot}} - T_{\text{cold}})$ (15)

Latent heat stored $\longrightarrow$ $Q_{storage} = m \cdot c_{p,s} \cdot (T_m - T_i) + m \cdot \beta \cdot \Delta h_m + m \cdot c_{p,l} \cdot (T_f - T_i)$ (16)

The second term in equation (16) is solved depending on the relationship (10) mentioned above. This section includes analysis of experimental and computational results depending on the various variables based on their importance with 60lit of water.

i. Effect of the HTF Inlet temperatures by using FPSC

Figure 5. shows the time variation temperatures of the PCM, water at the tank, and the temperature of ambient air, on November 9 with flow-rate 15lit/min and 5kg of PCM. It can be noted that at the beginning of the operation, the water temperature rises at a quicker rate associated to the temperature of the PCM which is initially in the solid phase. Until it reaches a temperature of about 50°C, which is approximately equal to the aforementioned melting temp. From there, the PCM gradually turns into the liquid phase as a result of absorbing heat from the water. After turning off the system and closing the valves, the water temperature decreases by 2-3°C below the PCM temperature and continues to decrease. At this stage the PCM keeps releasing the heat into the water, thus reducing the rate of water temperature drop. From another aspect, we note the big difference in the ambient air temperature for water and PCM.

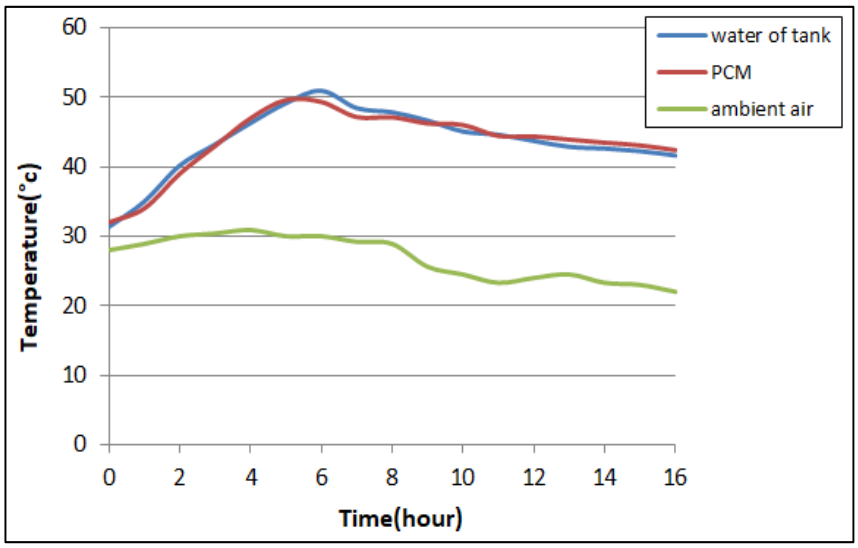

Fig. 5. Time variation temperatures of the PCM, the water of the tank, and the ambient air.

ii. Effect of the flow rates of HTF

Figure 6 illustrates the influence of changing HTF flow rates (15lit/min and 3lit/min) at (November 9 and 20), respectively, during system operation with 5kg of PCM into the tank and variable inlet temperatures of HTF. The effect of varying the flow rate can be observed on the melting process, the charging time, and thermal storage energy. As the graphs show that the time required for the PCM and the water to reach the maximum temperature is about 50-52°C less with a flow rate of 15lit/min compared to 3lit/min. Throughout the operation period, the rate of heat transfer from the HTF into the TES tank to the PCM and the water is slightly higher for the flow rate of 15lit/min. Concerning the PCM, the increase in the flow rate has a significant effect on the phase change of the PCM from the solid phase to the liquid, as the arrival time of the PCM to the melting point as shown in the graph is approximately 52°C with a flow rate of 15lit/min less compared to 3lit/min. This is attributed to an increase in the surface heat transfer coefficient of PCM-water. The flow rate effect is also evident in the thermal storage capacity. With an increase of 15lit/min the storage capacity increases to over 1000KJ compared to 3lit/min. All This means that the heat absorbed from the FPSC and transported by the HTF to the tank is affected by the HTF flow rate.

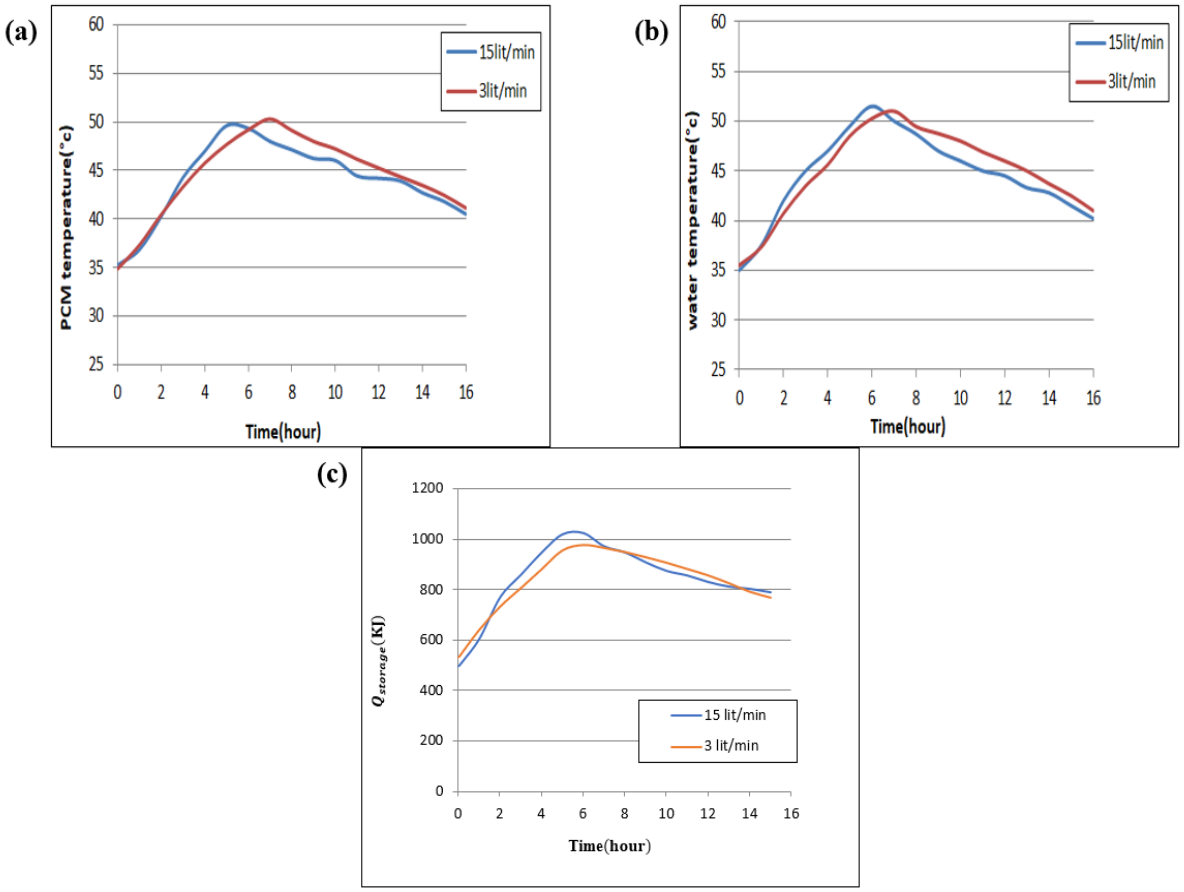

Fig. 6. Effect of HTF flow rate on (a) PCM melting process, (b) charging-time, and (c) thermal energy $Q_{storage}$ of the water tank.

iii. Effect of varying the PCM mass

The effect of using different PCM towards thermal storage is studied. 5kg and 10kg of paraffin wax were added to the storage tank with 60liters of water. The temporal variance of water temperatures is compared with (5and10kg) PCM and without it at (November 9, 20, and 23), respectively. As shown in **Figure 7**, although the maximum water temperature exceeds 50°C and is nearly close in all three cases. The water gains and loses heat at a faster rate without PCM during the first 6h of operating the system compared to the other cases. Whereas, water with 10kg PCM gains and loses heat at a slower rate compared to the other cases. This is due to the solid PCM absorbing heat from the water and turning it into the liquid phase during the charging period and releasing it during gradual solidification for PCM to water about 10h after switching off the system.

The storage tank with 10kg PCM is maintaining the water temperature better than the other two cases by 6-5°C.

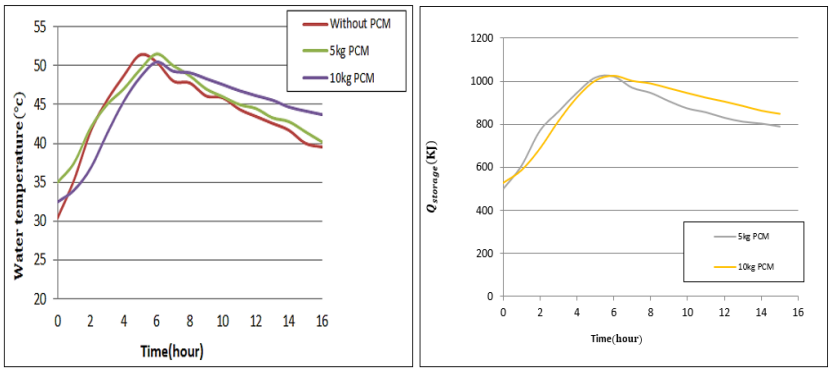

Fig. 7. Comparison of the water temperature difference and thermal energy $Q_{storage}$ for a variant amounts of the PCM.

iv. Comparison between the Experimental and Numerical Analysis

The same procedures were applied and used for both the experimental and numerical models. The volume of water inside the tank was 60liters with 5kg of PCM approximately 20capsules (2cm diameter/25cm height). The initial temperature of the TES tank was 291K, the inlet water temperatures were (313k and 323k), and the inlet mass-flow rates were (0.05kg/s and 0.25kg/s). The effect of changing the mass rate of HTF based on thermal energy was studied. **Figure 8(a)** and **(b)** compares the experimentally and numerically calculated thermal energy of the water tank according to equation (16), as a function of time for the different flow rates (0.05kg/s and 0.25kg/s). Where the outcomes indicate that the experimental results are identical to the results of the numerical simulation.

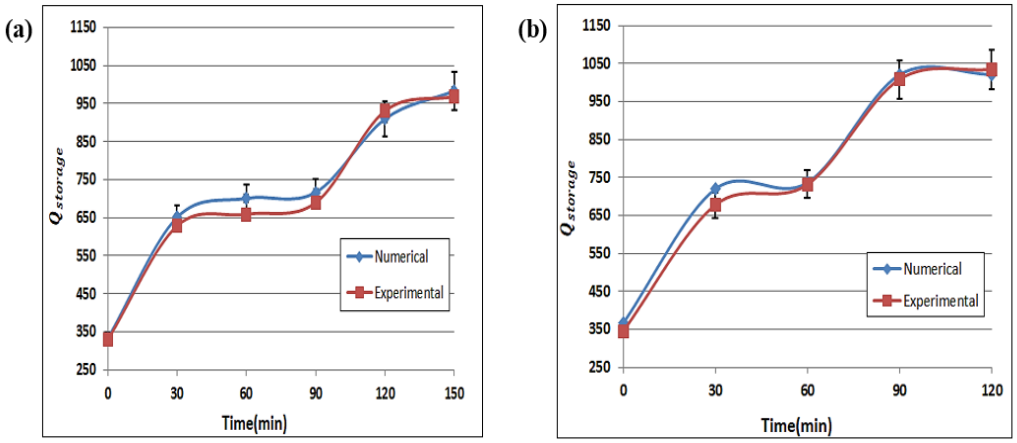

Fig. 8. Thermal storage energy $Q_{storage}$**(KJ)** of the TES tank as a function of time for the different flow rates, **(a)** at a flow rate ($\dot{m}$= 0.05 kg\s), **(b)** at flow rate ($\dot{m}$= 0.05 kg\s).

5 Conclusions

In this study, an experimental and numerical model was used to verify the thermal energy storage integrated with a PCM material of paraffin wax to using hot water for the DHW system to at an average temperature more than the nominal temperature. ANSYS FLUENT 2020 R1 is adopted to solve the governing equations of the transient-3D mathematical model. The following is concluded based on experimental and theoretical results:

1. Experimental results have proven the best performance of the TES system by using the solar collectors and PCM that to get hot water for a long time after the switch-off the system or the termination of the input heat energy. The water temperature was kept above 42°C in all climatic and operational conditions.
2. Flow rates of HTF have a significant effect on PCM melting process and charging time. Which were reduced by 2hour at the flow rate is increased from 3 to 15lit/min.
3. Thermal storage energy of water tank with PCM increases to over 1000KJ at 15lit/min.
4. It is observed, that the addition of PCM into a storage tank increases the energy stored and this raises with the amount of PCM. Based on the above results, 10kg paraffin wax achieves superlative PCM mass to be integrated with storage tank due to its potential to store large energy and maintain the water temperature better than cases of 5kg and without PCM by 6-5°C.References

[1] T. Kousksou, P. Bruel, G. Cherreau, V. Leoussoff, and T. El Rhafiki, “PCM storage for solar

DHW: From an unfulfilled promise to a real benefit," *Sol. Energy*, vol. 85, no. 9, pp. 2033–2040, 2011, doi: 10.1016/j.solener.2011.05.012.

[2] M. E. Zayed *et al.*, "Performance augmentation of flat plate solar water collector using phase change materials and nanocomposite phase change materials: A review," *Process Saf. Environ. Prot.*, vol. 128, pp. 135–157, 2019, doi: 10.1016/j.psep.2019.06.002.

[3] R. M. Reddy, N. Nallusamy, and K. H. Reddy, "The Effect of PCM Capsule Material on the Thermal Energy Storage System Performance," *ISRN Renew. Energy*, vol. 2014, pp. 1–6, 2014, doi: 10.1155/2014/529280.

[4] S. Aziz, N. A. M. Amin, M. S. Abdul Majid, M. Belusko, and F. Bruno, "CFD simulation of a TES tank comprising a PCM encapsulated in sphere with heat transfer enhancement," *Appl. Therm. Eng.*, vol. 143, pp. 1085–1092, 2018, doi: 10.1016/j.applthermaleng.2018.08.013.

[5] A. Shahsavar, J. Khosravi, H. I. Mohammed, and P. Talebizadehsardari, "Performance evaluation of melting/solidification mechanism in a variable wave-length wavy channel double-tube latent heat storage system," *J. Energy Storage*, vol. 27, no. November 2019, p. 101063, 2020, doi: 10.1016/j.est.2019.101063.

[6] A. J. N. Khalifa, K. H. Suffer, and M. S. Mahmoud, "A storage domestic solar hot water system with a back layer of phase change material," *Exp. Therm. Fluid Sci.*, vol. 44, pp. 174–181, 2013, doi: 10.1016/j.expthermflusci.2012.05.017.

[7] M. Chaabane, H. Mhiri, and P. Bournot, "Thermal performance of an integrated collector storage solar water heater (ICSSWH) with phase change materials (PCM)," *Energy Convers. Manag.*, 2014, doi: 10.1016/j.enconman.2013.07.089.

[8] E. Kifaya, P. Saadoon, F. Dakhil, and O. Ibraheem, "Improving Heat Transfer through Paraffin Wax for Sustainability Heat Pump," vol. 6, no. 5, pp. 138–143, 2018.

[9] J. Soibam, "Numerical Investigation of a Heat Exchanger using Phase Change Materials (PCMs)," no. October, 2017.

[10] R. S. Abdulrahman, F. A. Ibrahim, and S. F. Dakhil, "Development of paraffin wax as phase change material based latent heat storage in heat exchanger," *Appl. Therm. Eng.*, vol. 150, no. December 2018, pp. 193–199, 2019, doi: 10.1016/j.applthermaleng.2018.12.149.

[11] C. Pagkalos, G. Dogkas, M. K. Koukou, J. Konstantaras, K. Lymperis, and M. G. Vrachopoulos, "Evaluation of water and paraffin PCM as storage media for use in thermal energy storage applications: A numerical approach," *Int. J. Thermofluids*, vol. 1–2, p. 100006, 2020, doi: 10.1016/j.ijft.2019.100006.

[12] L. F. Cabeza, M. Ibáñez, C. Solé, J. Roca, and M. Nogués, "Experimentation with a water tank including a PCM module," *Sol. Energy Mater. Sol. Cells*, 2006, doi: 10.1016/j.solmat.2005.08.002.

[13] W. Beyne *et al.*, "Experimental investigation of solidification in metal foam enhanced phase change material," *IOP Conf. Ser. Mater. Sci. Eng.*, vol. 251, no. 1, 2017, doi: 10.1088/1757-899X/251/1/012112.

[14] M. M. V Kulkarni, D. S. Deshmukh, and A. Professor, "Improving Efficiency of Solar Water Heater Using Phase Change Materials," *Pratibha Int. J. Sci. Spirituality, Bus. Technol.*, vol. 3, no. 1, pp. 2277–7261, 2014.

[15] H. H. Al-Kayiem and S. C. Lin, "Performance evaluation of a solar water heater integrated with a PCM nanocomposite TES at various inclinations," *Sol. Energy*, vol. 109, no. 1, pp. 82–92, 2014, doi: 10.1016/j.solener.2014.08.021.

[16] R. Sathiyaraj, R. Rakesh, N. Mithran, and M. Venkatesan, “Enhancement of heat transfer in phase change material using graphite-paraffin composites,” *MATEC Web Conf.*, vol. 172, pp. 9–11, 2018, doi: 10.1051/matecconf/201817202001.

[17] S. Lu, T. Zhang, and Y. Chen, “Study on the Performance of Heat Storage and Heat Release of Water Storage Tank with PCMs,” *Energy Build.*, 2017, doi: 10.1016/j.enbuild.2017.10.059.

[18] T. Bouhal, T. El Rhafiki, T. Kousksou, A. Jamil, and Y. Zeraouli, “PCM addition inside solar water heaters: Numerical comparative approach,” *J. Energy Storage*, vol. 19, no. August, pp. 232–246, 2018, doi: 10.1016/j.est.2018.08.005.

[19] Y. Qin *et al.*, “The effect of phase change material balls on the thermal characteristics in hot water tanks: CFD research,” *Appl. Therm. Eng.*, vol. 178, p. 115557, 2020, doi: 10.1016/j.applthermaleng.2020.115557.

Three-Stage Charging of Lead Acid Batteries by Artificial Intelligence Fuzzy Logic Controller

Dr. Abdullah J. H. Al Gizi [1*], Wadullah Hatem [2]
(abdullal.algizi.@stu.edu.iq, waadallahmhhawes@gmail.com)
[1]Thi-Qar technical collage Electromechanical Southern Technical University, Iraq
[2]Southern Technical University / Engineering Technical College/Basra

Abstract. The traditional methods of charging lead-acid batteries depend on stabilizing the current or voltage through simple electronic circuits, which causes the shorten the life of the batteries due to damage to the electrodes or the hot and dry batteries. To achieve the best charging efficiency, this paper has adopted artificial intelligence represented by (Fuzzy Logic Control (FLC)) to achieve three charging stages through which the current and voltage are controlled together. Using three algorithms of this type, the batteries are charged when a constant voltage source is available, while the charge is discharged when the source is cut off while preserving the nominal voltage and current limits of the battery to prevent damage.

Keywords: Fuzzy logic control(FLC), state of charge (SOC), lead-acid battery,

1 Introduction

In remote areas that lack the electricity grid, the facility that needs an emergency power source, or in electric cars and other uses, the need for batteries has emerged as source of energy storage [1]. Lead-acid batteries of all kinds are relatively cheap and can be produced in large quantities with high power and capacity [2], so they are preferred over other types of batteries, especially in photovoltaic systems. Using diesel generators despite their low initial cost, but they are considered expensive in the long run due to the cost of fuel and maintenance in addition to pollution [3]. In this paper, artificial intelligence is used as an algorithm that checks for optimal battery charging to keep batteries safe from damage and to increase battery life. In the research presented by [4], he relied on charging, discharging, or standby without specifying the charging stages that ensure that the battery is not damaged. Despite the research presented by [5], artificial intelligence was used to obtain the maximum power from a photoelectric cell (using P&O algorithm), but the algorithm that he used to charge the battery was not considered efficient because it did not use artificial intelligence as it either passes or does not pass a signal from (P & O algorithm circuit) to (Plus with Modulation (PWM)) where it is compared with zero or one always. Although the paper presented by [6] reviews different methods of charging batteries, it is traditional and does not include any artificial intelligence or taking into account the charging stages to control the amount of current and voltage according to the manufacturer's data. It also did not take into account the (MPPT) of the photovoltaic cell, as it will not benefit from about 40% of the solar energy.

In this paper, three stages of charging and one stage of discharging were used using (Fuzzy Logic Control), and it was taken into account that the current is fixed at the beginning of charging to avoid the large surge of current at the beginning of charging. Upon reaching 80% of the charging state, the voltage is fixed because the current starts to reach the saturation state and decreases with the increase in the state of charge (SOC) as it approaches a full charge. When the (SOC) reaches 100%, the voltage is reduced to the limits that allow only the battery to remain always charged during the standby period without causing damage to the battery. The method used allows charging and discharging according to the state of the source if it is connected or disconnected through an algorithm that connects three stages of (FLC). The DC source can be replaced by a photovoltaic cell with a Maximum Power of the circuit or any other power source.

IMDC-IST 2021, September 07-09, Sakarya, Turkey
Copyright © 2022 EAI
DOI 10.4108/eai.7-9-2021.2314776

2 Solar batteries

In most cases, batteries are used to store the energy generated by photovoltaics(PV), in order to be used later when the sun sets or on cloudy days, especially in remote areas that are not connected to the electrical grid. Although some loads can operate on a non-constant voltage, such as water pumps or fans, etc., other loads such as lighting require a constant voltage, so batteries (in addition to storage) are used to produce a constant voltage for the loads. The batteries also help make the photovoltaic cell operate at its maximum power point(MPP) while supplying the load with the high current when needed without being restricted by the capacity of the PV. A charge controller is used to protect the batteries from (overcharging) and (undercharging). Batteries are also used in emergencies, such as hospitals, when the batteries are always charged with a full charge, they are supplied with a small current whenever their charge is reduced to preserve the plates from damage, taking into account activating them with a high charge from time to time and this method of charging is called (float charge).

Batteries generally consist of two electrodes conducting electricity from two different materials immersed in a solution called electrolyte, where one of the electrodes becomes negative and the other positive. The potential difference between the electrodes depends on the material the electrodes are made of and the electrolyte solution used.[7]

3 Types of rechargeable batteries

a- Lead acid batteries
b- Nickel-cadmium (Ni-ca) batteries
c- Nickel-Metal hydride (Ni MH) batteries
d- Lithium ion batteries
e- Lithium polymer batteries

Today, due to their low cost, ease of manufacture, durability, low self-discharge, and not need maintenance, especially gel type. lead-acid batteries are widely used in photovoltaic systems. We will cover this type of cell in this chapter [3, 4, 7, 8].

4 Lead acid batteries

The anode consists of lead dioxide (pbo2), while the negative electrode consists of sponge lead, and both of them are immersed in a solution of sulfuric acid with water at a ratio of (400-480 g / 1) and a density of (1.24-1.28 kg / 1). The nominal voltage of a single cell of 2 volts drops to 1.8 volts when it loses its full charge and rises to (2.3-2.5) volts when fully charged. The voltage of the 6-cell battery becomes (12, 10.8, (13.8-15) volts, respectively, for each case [7].

4.1 Types of lead-acid batteries

There are many types of lead-acid batteries and they can be classified in several forms and several ways, and for the sake of knowing them clearly, they can be classified first into two main sections, open or closed sealed. Both types are made from plates. These plates are divided into two types, flat and tubular plates. Plates can be thin (as in car batteries) or as thick as in batteries that are used to store the energy generated from photovoltaics. Car batteries use a large number of thin plates to produce a high current to power the car, so they are not suitable for storing energy for a long time, while the plates in storage batteries are thick and have a small number.

Sealed Lead-acid batteries have three types, absorbent glass mat type (AGM), gel type and valve-regulated lead-acid (VRLA).

4.2 Battery parameters and variants

1- The capacity of the battery (Ah)
2- Battery voltage
3- State of charge (SOC) and Depth of discharge (DOD)

4- Battery life cycle
5- Self-discharge
6- Rate of charge or discharge

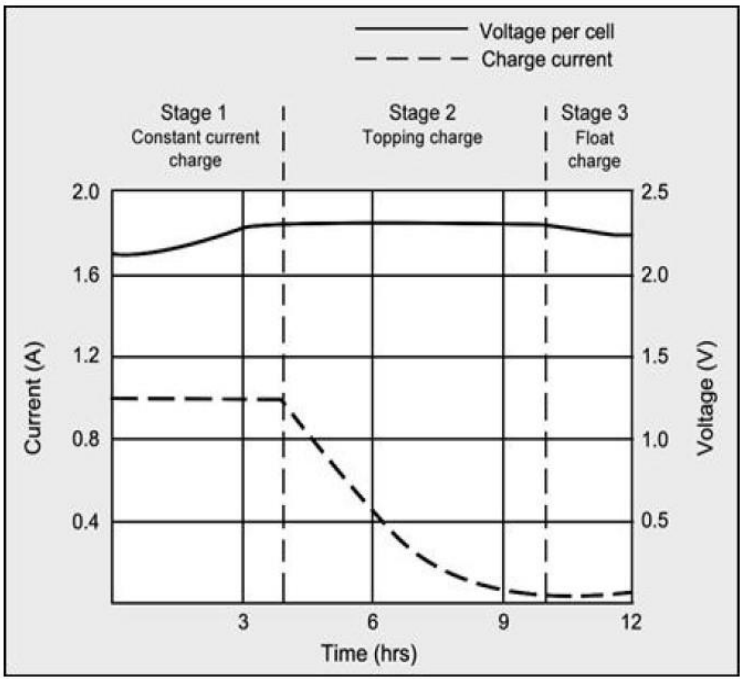

Figure *1* shows three charging stages. The area or first stage represents (constant current charge), the second stage represents (topping charge) and the third stage represents (float charge). The first stage (the constant current charging stage) represents the bulk of the charging of the battery in half the charging time, where approximately 70% of the battery capacity is charged within (5 to 8) hours and the remaining 30% is charged in the second stage at a time of another (7 to 10) hours. The importance of the second stage lies in improving the performance of the battery, without which the battery cannot reach a full charge. After reaching a full charge the third stage maintains this full charge from the self-discharge effect. The charging current decreases when the charge saturation of the battery begins, and the battery reaches full charge when the current reaches only 3% of the total current. When storing, batteries must be fully charged and recharged every 6 months, with a guarantee that the voltage of each cell will not drop below 2.1 volts [7, 8].

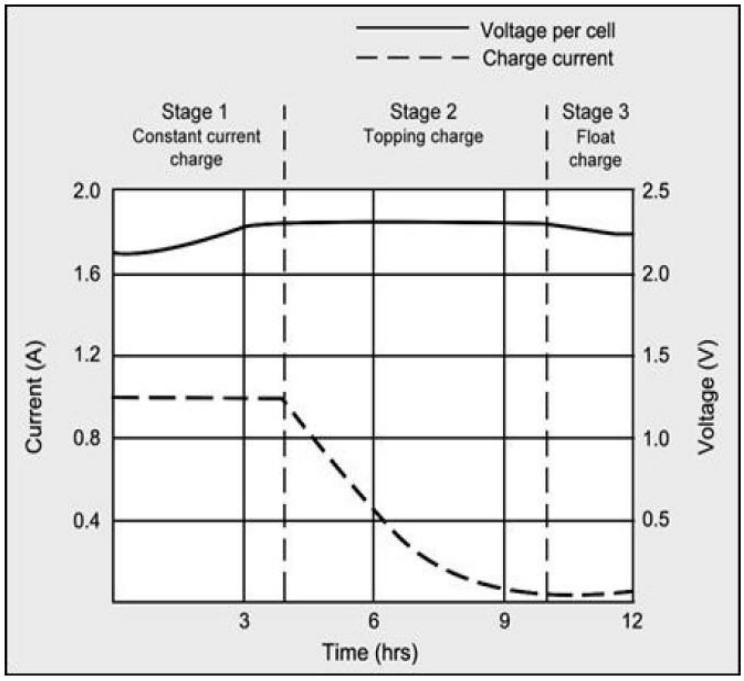

Figure 1: Charging stages of the lead-acid battery [7]

5 Methodology of the proposed bidirectional buck-boost convertor

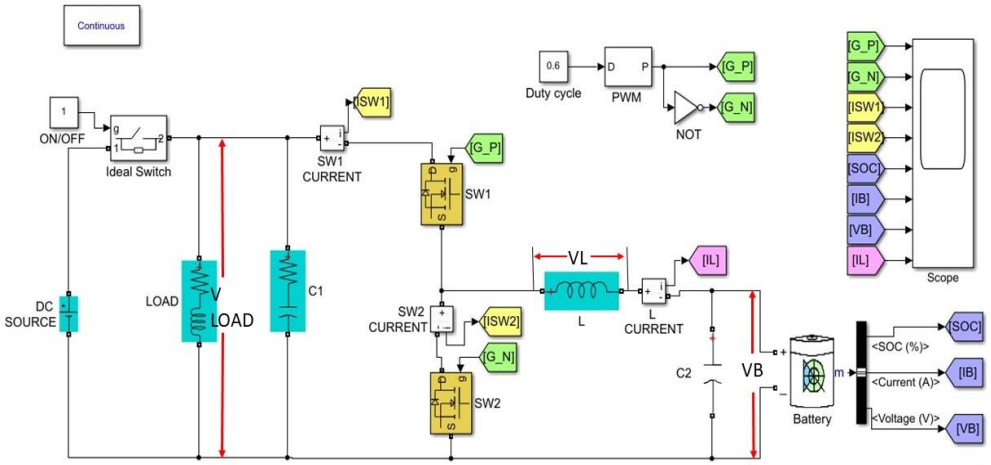

Figure 2 shows a Bidirectional buck-boost convertor. it can be understood how it works by transferring power from the DC source to the load and the battery when the Ideal Switch is on (this means that the DC source has sufficient voltage and is connected to the circuit). When the SW1 is (on) at a time t =0.6T (T=Ton+Toff), the SW2 is (off), (this means that the SW1 is 60% (on) and 40% (off), SW2 is 60% (off) and 40% (on) from the total time (T). The current in the inductor does not change suddenly but depends on the time constant ($\tau = L / R$), where the current increases gradually in the inductor until the SW1 becomes (off). As for the voltage across the inductor, it is (VLOAD – VB), the voltage across the SW1 is zero because it is a short circuit, while the voltage across the SW2 is the source voltage because it is an open circuit and becomes (VLOAD). The inductor at this stage stores energy in the form of a magnetic field that depends on the value of the inductor (L) and the change in current. In the second stage, when the SW1 (off) and the SW2 (on), the inductor returns the stored energy to the circuit, and since the current is not reflected in the inductor, the polarity of the inductor is reversed and the voltage across it becomes negative and its value is (-VB). The output current remains constant because the capacitor is stored and discharges the charge according to its value, and the output voltage approaches a constant value whenever the capacitive value (C2) is large. The values of inductor and capacitor can be calculated from the following equations [1, 9].

$$D = \frac{V_B}{V_{LOAD}} \tag{1}$$

$$\mathrm{L} = \frac{\mathrm{V_B}\times(1-\mathrm{D})}{\mathrm{fs}\times\Delta\mathrm{IL}} = \frac{\mathrm{V_B}\times(\mathrm{V_{LOAD}}-\mathrm{V_B})}{\mathrm{fs}\times\Delta\mathrm{IL}\times\mathrm{V_B}} \tag{2}$$

$$\Delta\mathrm{IL} = \frac{(\mathrm{V_{LOAD(max.)}}-V_B)\times\mathrm{D}}{\mathrm{fs}\times\mathrm{L}} = \mathrm{I_{L(max.)}} - \mathrm{I_{L(min.)}} \tag{3}$$

To estimate the value of an inductor ripple ΔIL, it is selected between (0.2 to 0.4) of the output current [10]

$$\Delta\mathrm{IL} = (0.2 \text{ to } 0.4) \times I_{LOAD(max.)} \tag{4}$$

$$\mathrm{C_{2(min.)}} = \frac{\Delta\mathrm{IL}}{8\times\mathrm{fs}\times\Delta\mathrm{V_B}} \tag{5}$$

Where:- V_B = Battery voltage, D=duty cycle, V_{LOAD}=input voltage, L=inductor, I_{in}=input current ΔIL=estimated inductor ripple current, I_B=output Battery current, fs=switching frequency, $V_{LOAD(min)}$=minimum input voltage, $I_{L(max.)}$=maximum inductor current, $I_{L(min.)}$=minimum inductor current, $C_{2(min.)}$=minimum output capacitor, ΔV_O=desired output ripple voltage.

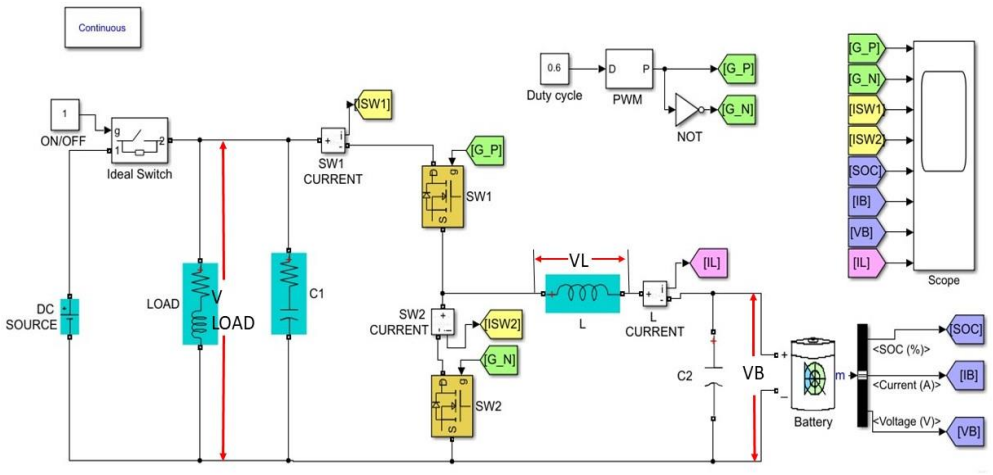

Figure 2: Bidirectional buck-boost converter circuit diagram.

When the ideal switch becomes off, the power is transferred from the battery to the load. When the duty cycle (D=Ton), the SW2 becomes on and SW1 off. Where (T = Ton + Toff). When the SW2 is (on) and because it is an electronic switch, it becomes a short circuit and the voltage across it becomes zero. The inductor will be connected directly to the Battery for a period of (0.4T). The current in the inductor does not change momentarily but depends on the (time constant: $\tau = L / R$). The current continues to increase through Inductance during a period (0.4T). A magnetic field in the coil is formed in the form of stored energy proportional to the value of inductance and the change in current. In this case, the SW1 is off (open circuit). In the second stage (Toff = 0.6T), the SW1 is on and SW2 is off. When the SW1 is on (closed circuit), the coil will become connected in series with the SW1, at this moment the coil signal will be inverted because the current remains in the same direction where the coil energy will be discharged into the Capacitor and the load over the period of 0.6T and the inductor voltage will be VL = -(VB-VLOAD). The output voltage (load voltage) will be the sum of the input voltage and the inductance voltage, so this circuit is a step-up converter [1, 9]

The following equations show how to find the inductor and capacitor of a boost converter.

$$V_{LOAD} = \frac{1}{1-D} V_B \tag{6}$$

$$L = \frac{V_B \times D}{fs \times \Delta IL} = \frac{V_B \times (1-D) \times D}{fs \times \Delta IL} = \frac{V_B \times (V_{LOAD} - V_B)}{fs \times \Delta IL \times V_{LOAD}} \tag{7}$$

$$\Delta IL = \frac{V_{B(min)} \times D}{fs \times L} = I_{B(max.)} - I_{B(min.)} = I_{L(max.)} - I_{L(min.)} \tag{8}$$

In order to estimate the value of an inductor ripple ΔIL, it is selected between (0.2 to 0.4) of the output current[11].

$$\Delta IL = (0.2 \text{ to } 0.4) \times I_{LOAD(max.)} \times \frac{V_{LOAD}}{V_B} \tag{9}$$

$$C_{O(min.)} = \frac{I_{LOAD(max.)} \times D}{fs \times \Delta V_{LOAD}} \tag{10}$$

Where:- V_{LOAD} = output voltage , D=duty cycle , V_B=battery voltage, L=inductor, I_B=battery current ΔIL=estimated inductor ripple current , I_{LOAD}=output current, fs=switching frequency $V_{B(min)}$=minimum battery voltage, $I_{B(max.)}$=maximum battery current $I_{B(min.)}$=minimum battery current, $I_{L(max.)}$=maximum inductor current, $I_{L(min.)}$=minimum inductor current, $C_{1(min.)}$=minimum output capacitor, ΔV_O=desired output ripple voltage

6 Fuzzy logic control as a controller

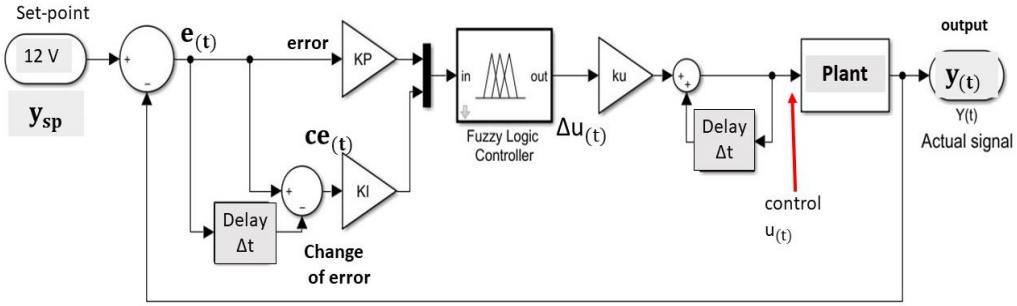

Figure 3: A block diagram of a PI fuzzy control system

In order to achieve the charging stages of a lead-acid battery shown in

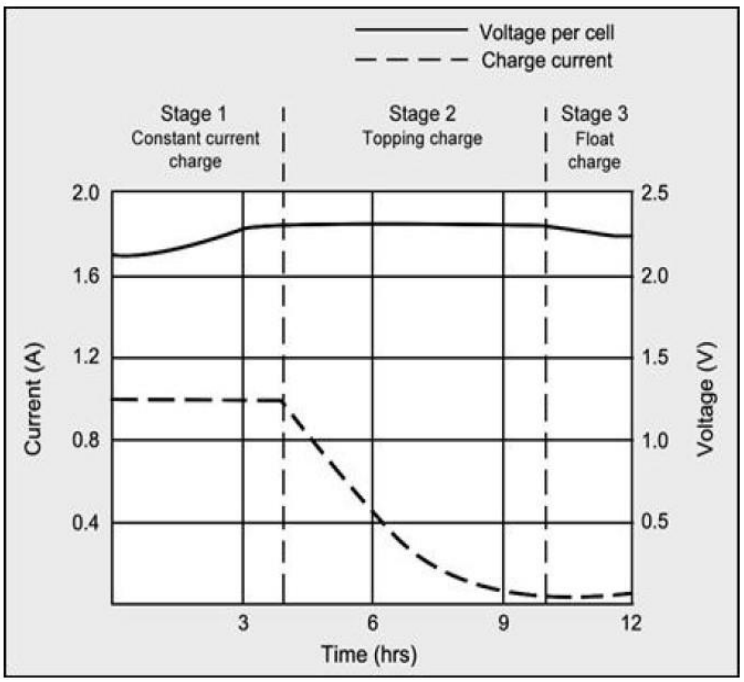

Figure *1*, it requires controlling the amount of the duty cycle so that the current is stabilized first (bulk charge approximately from 10 to 30% of the battery capacity) until the state of charge (SOC) reaches 80%. Then the voltage is installed (topping charge) at the limits (from 2.30 to 2.45 volts per cell). After the battery is fully charged, either the battery is disconnected from the source or it continues charging at a voltage of approximately 2.25 volts/cell (float charge) to protect the battery from damage [7]. To achieve all of these Conditions require one of the control methods, and we will use in this paper the Fuzzy Logic Control (FLC) to control the battery charge. The reason for choosing this type of control system is that it does not need any information about the system and does not require that the system be linear or non-linear [12].

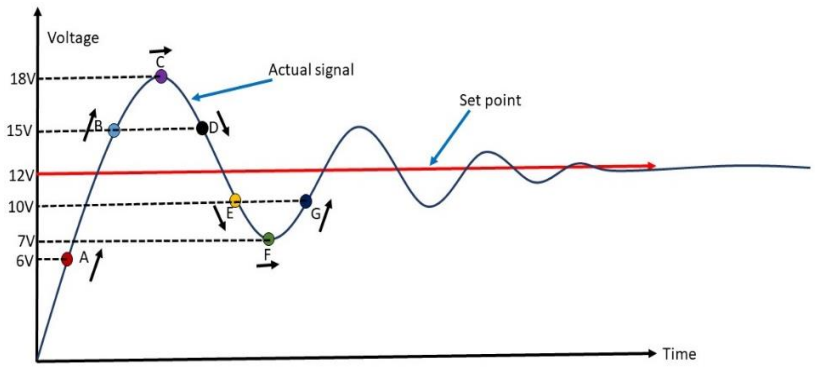

Figure 4: set point and actual signal for the system.

The Fuzzy control circuit shown in Figure 3 is based mainly on comparing the error e(t) with the change of error when comparing the actual signal coming out of the system with the desired reference signal. To understand how the circuit works, the signals are analyzed in Figure 4. In point A, the (12-6=6) volt error is positive because the reference signal is greater than the actual signal, while in point B the error is (15-12=-3) volt. Thus, the value of the remaining points can be calculated in the same way by subtracting the value of the actual signal from the reference signal. In this way, the value of the error can be determined, but the direction of its movement can only be known by comparing the current error with the previous error with a new parameter called the change of error ce(t). For example, when moving from point A to point B, the magnitude of the change of error will be (-3-6= - 9). So we will have the following cases. The points that fall above the reference signal all have the error amount negative, while for all the points below the reference signal the error magnitude is positive. The amount of change in error is below and above the reference signal, either negative or positive, depending on the movement of the point. For example, points A, B, and G are negative while points D and E are positive. And C, F is zero because slop is zero.

$$e_{(t)} = y_{sp} - y_{(t)} \tag{11}$$

$$ce_{(t)} = e_{(t)} - e_{(t-1)} \tag{12}$$

Where: - $e_{(t)}$=the error, y_{sp}= set-point or reference point or desired value, $y_{(t)}$=actual output value.
$ce_{(t)}$=the change of error, $e_{(t-1)}$= the previous error.
Case (1):- If $e_{(t)}$ is negative $y_{sp} - y_{(t)} < 0$, then $y_{sp} < y_{(t)}$.
case (2):- If $e_{(t)}$ is positive $y_{sp} - y_{(t)} > 0$, then $y_{sp} > y_{(t)}$. For both cases $ce_{(t)}$ it can have a positive or negative value
$ce_{(t)} = e_{(t)} - e_{(t-1)} = y_{sp} - y_{(t)} - [\, y_{sp} - y_{(t-1)} \,]$. y_{sp} is constant because it is the reference voltage.
$ce_{(t)} = -(\, y_{(t)} - y_{(t-1)})$. Now if $ce_{(t)}$ is negative $-(\, y_{(t)} - y_{(t-1)}) < 0$, then $y_{(t-1)} < y_{(t)}$. if $ce_{(t)}$ is positive $-(\, y_{(t)} - y_{(t-1)}) > 0$, then $y_{(t-1)} > y_{(t)}$.

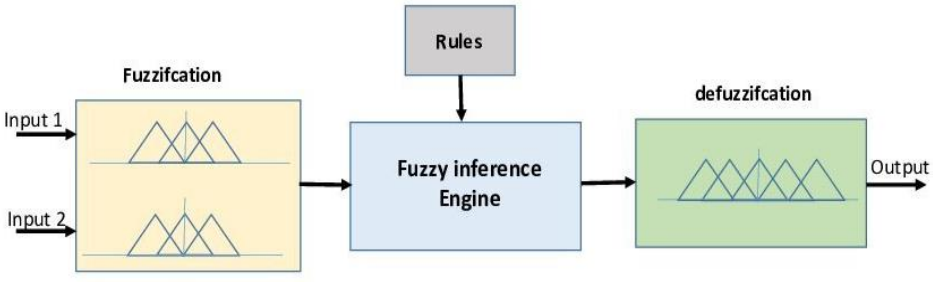

Figure 5: General structure of fuzzy logic control.

After determining the error values and the change in error, they are entered into the Fuzzy circuit shows in

Figure 5 is the block diagram which is converted into linguistic values, and take for example the error values (positive big(PB), positive medium (PM), positive small (PS), zero, negative small (NS), negative medium (NM), and negative big (NB)). In the same way, the values of the change of error and output control

u(t) are converted into linguistic values, then they are compared with each other through a rule table specifying the conditions discussed in Figure 4, according to the relationships shown below.

If e(t) positive and ce(t) negative, then u(t) positive

If e(t) negative and ce(t) negative, then u(t) negative

If e(t) negative and ce(t) positive, then u(t) positive

If e(t) positive and ce(t) positive, then u(t) negative

Table 1 shows the relationship between error and change of error, and variables from 1 to 49 represent the linguistic value of the control signal required to correct the actual signal in order for it to apply to the reference signal [12, 13]. Finally the defuzzification by returning the linguistic values to a crisp value.

Table 1: Rule base.

$ce_{(t)}$ / $e_{(t)}$	NB	NM	NS	ZE	PS	PM	PB
NB	1 NB	2 NB	3 NB	4 NB	5 NM	6 NS	7 ZE
NM	8 NB	9 NB	10 NB	11 NM	12 NS	13 ZE	14 PS
NS	15 NB	16 NB	17 NM	18 NS	19 ZE	20 PS	21 PM
ZE	22 NB	23 NM	24 NS	25 ZE	26 PS	27 PM	28 PB
PS	29 NM	30 NS	31 ZE	32 PS	33 PM	34 PB	35 PB
PM	36 NS	37 ZE	38 PS	39 PM	40 PB	41 PB	42 PB
PB	43 ZE	44 PS	45 PM	46 PB	47 PB	48 PB	49 PB

The circuit in Figure 2 is controlled by replacing the Duty Cycle constant with the circuit shown in Figure 6, which is a two-stage charging stage and a discharging stage

6.1 Charging stage

When the state of charge (SOC) is less than 80%, Switches 1 and 2 pass the actual current and reference current shows in Figure 6. As for switches 5 and 3 in Figure 7, they pass the voltage and thus we achieve the

first condition for the charge status of the lead-acid batteries shown in

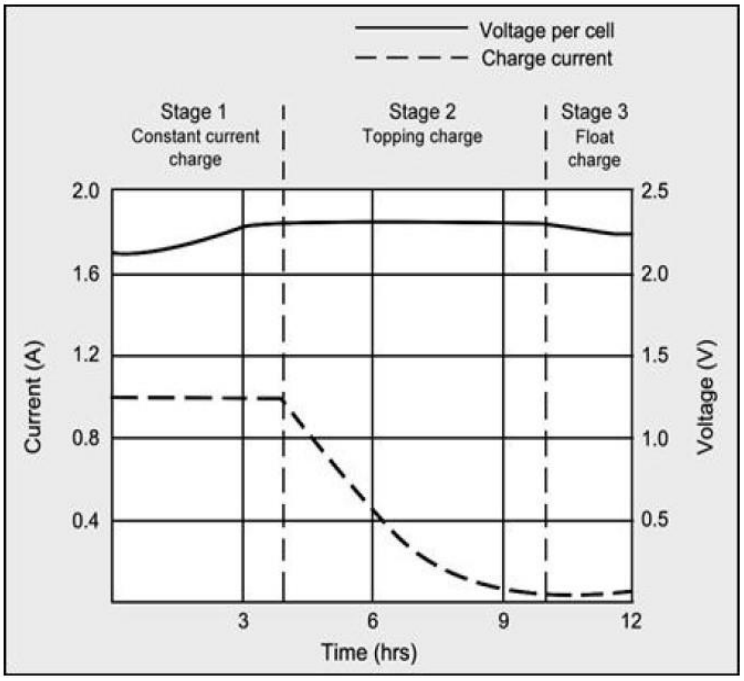

Figure *1*, provided that switch 4 is in case 1, meaning that the source is connected to the circuit. When the charging state reaches 80% or more, the previous state will be reversed and the voltage is connected through switches 1 and 2, while the current is connected through switches 3 and 5. After the charging state reaches 100%, the voltage is reduced to 13.1 volts by switch 6, which is the voltage that prevents self-discharge. Fuzzy Logic Controller 1 and 2 is a double-loop feedback control by controlling the voltage and current when the converter is in the (buck converter) state. The current or voltage is controlled when the output of the first controller becomes a reference for the second controller so that under no circumstances is it allowed for the voltage or current to rise to a greater extent than the nominal battery values.

6.2 Discharging stage

When the DC power supply is disconnected, the switch 4 state becomes off in Figure 6, where the charge controller 1,2 is disconnected. The FLC discharging control is connected via the converter when it is in the boost converter state. The voltage of the load is fixed to 24 volts through the Fuzzy controller. The rule base table is the same as Table 1. Only the rules are reversed for the fact that the relationship of the input voltage to the output of the (boost converter) is inverse according to Equation No. 6, while in the (buck converter) it is positive according to Equation No. 1.

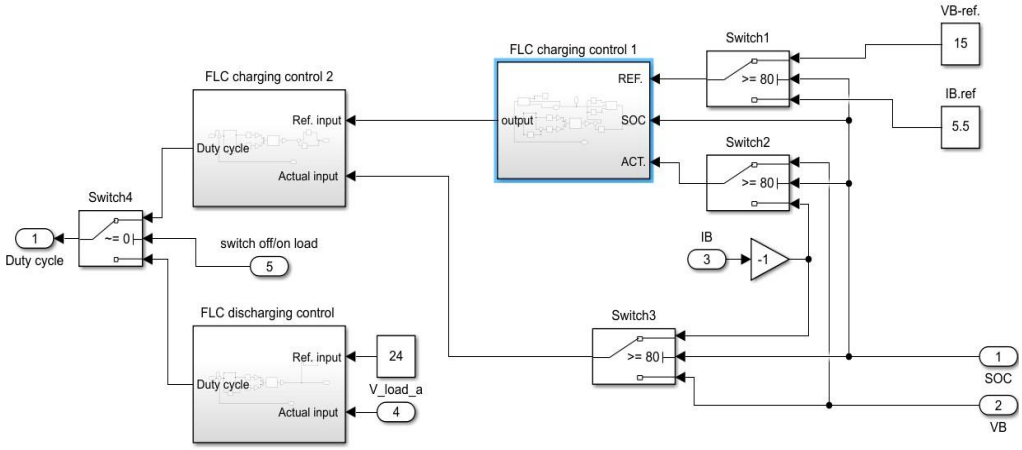

Figure 6: the main controller circuit to control the duty cycle.

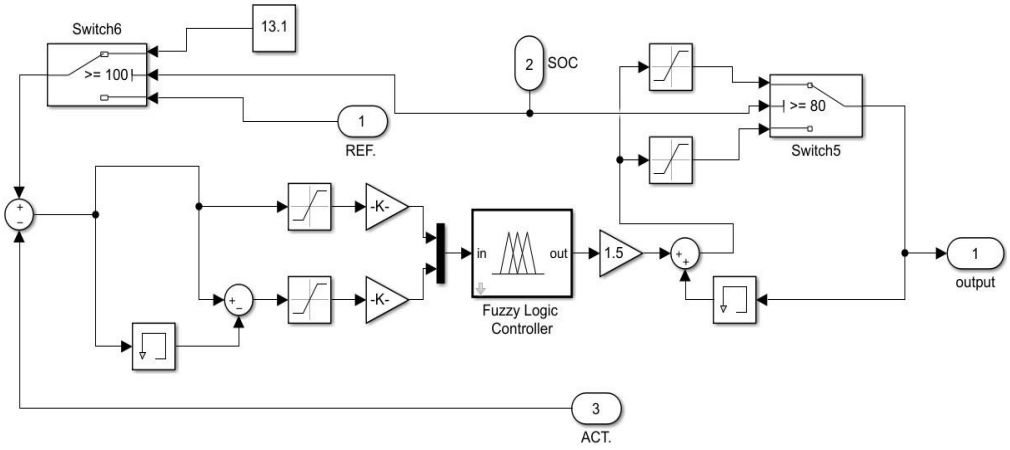

Figure 7: FLC charging controller 1.

7 Results and discussion

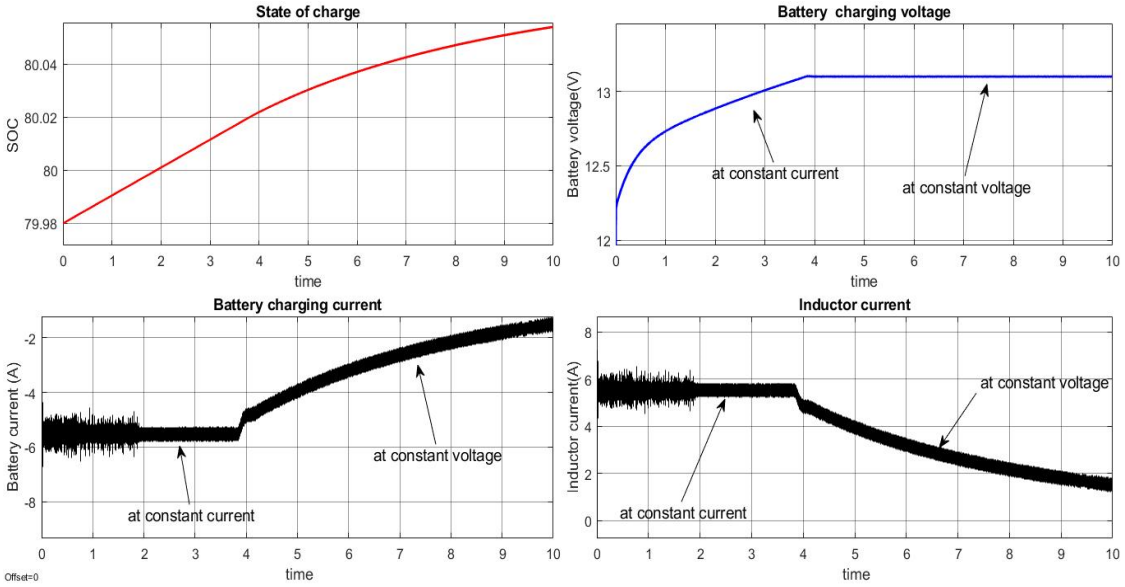

Figure 8: Charging stage results.

The battery used in this experiment has the following specifications (12 volts nominal, 5.5-ampere max. charge/discharge current, 13.08-volt full charging, cycle use 14.4-14.5 volt, standby use 13.1-13.5 volt) as it was adopted from MATLAB. When the charge is less than 80%, the lead-acid batteries are charged with a constant current equal to the charging and discharging current as shown in Figure 8. In order to avoid damage to the positive electrode, battery overheating, gases and water evaporation from the battery, the voltage is fixed at 15 volts after the charging state reaches 80%. Finally, when the battery is fully charged, the voltage is reduced to 13.1 volts, which is slightly higher than the full charge voltage, to ensure the battery remains charged in the standby state

In the case of discharging when the source is cut off from the load, as in Figure 9, the load is supplied with a constant voltage of 24 volts via the boost converter. All of this is achieved through the artificial intelligence of the Fuzzy logic control that was used in this research.[1]

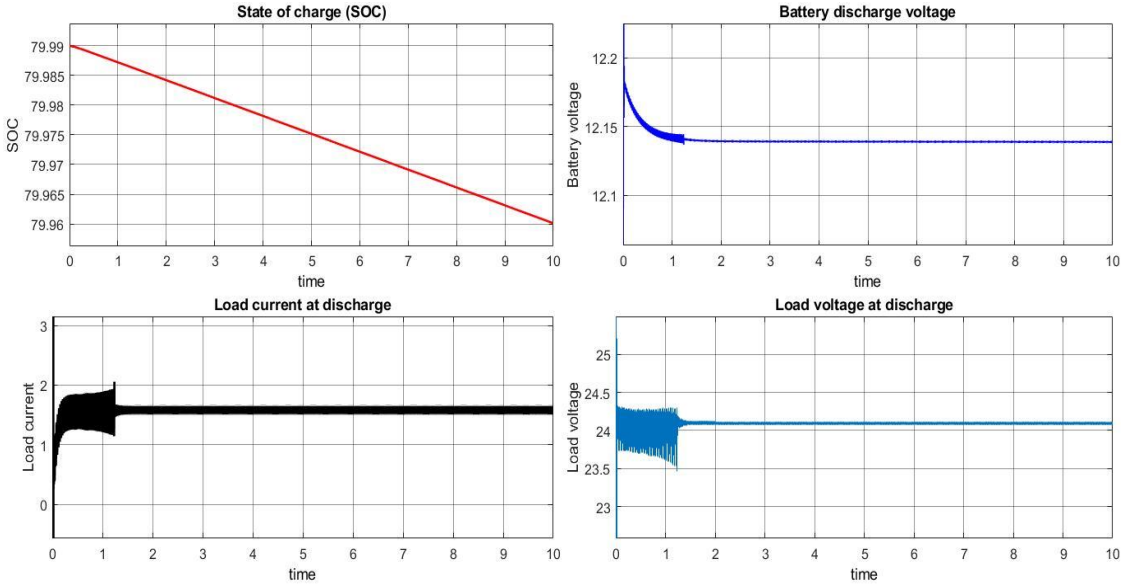

Figure 9: discharging stage results.

8 Conclusion

A new method has been applied in this research to charge lead-acid batteries using artificial intelligence, taking into account the characteristics of batteries represented by the charging current and voltage in order to preserve the battery from damage on the one hand and reduce the charging time on the other hand.

Acknowledgment

We are thankful to my supervisor for his main valuable suggestion and critical reading of the manuscript.

References

[1] V. Viswanatha, "Microcontroller based bidirectional buck–boost converter for photo-voltaic power plant," *Journal of Electrical Systems and Information Technology,* vol. 5, no. 3, pp. 745-758, 2018.

[2] M. Hoque, M. Hannan, A. Mohamed, and A. Ayob, "Battery charge equalization controller in electric vehicle applications: A review," *Renewable and Sustainable Energy Reviews,* vol. 75, pp. 1363-1385, 2017.

[3] P. Manimekalai, R. Harikumar, and S. Raghavan, "An overview of batteries for photovoltaic (PV) systems," *International Journal of Computer Applications,* vol. 82, no. 12, 2013.

[4] M. I. Hlal, V. K. Ramachandaramurthy, A. Sarhan, A. Pouryekta, and U. Subramaniam, "Optimum battery depth of discharge for off-grid solar PV/battery system," *Journal of Energy Storage,* vol. 26, p. 100999, 2019.

[5] R. H. Tan, C. K. Er, and S. G. Solanki, "Modeling of Photovoltaic MPPT Lead Acid Battery Charge Controller for Standalone System Applications," in *E3S Web of Conferences*, 2020, vol. 182: EDP Sciences, p. 03005.

[6] M. LokeshReddy, P. P. Kumar, S. A. M. Chandra, T. S. Babu, and N. Rajasekar, "Comparative study on charge controller techniques for solar PV system," *Energy Procedia,* vol. 117, pp. 1070-1077, 2017.

[7] I. Buchmann, "Batteries in a portable world: a handbook on rechargeable batteries for non-engineers," 2001.

[8] E. Banguero, A. Correcher, A. Pérez-Navarro, F. Morant, and A. Aristizabal, "A review on battery charging and discharging control strategies: Application to renewable energy systems," *Energies,* vol. 11, no. 4, p. 1021, 2018.

[9] M. Barrenetxea Iñarra, I. Baraia-Etxaburu Zubiaurre, I. Larrazabal Bengoetxea, and I. Zubimendi Azaceta, "Power electronic converter design handbook," 2018.

[10] T. Instruments, "Basic calculation of a buck converter's power stage," *Application Report-SLVA477B, Rev,* 2015.

[11] T. Instruments, "Basic calculation of a boost converter's Power Stage," *Application Report SLVA327B,* 2009.

[12] G. Chen, T. T. Pham, and N. Boustany, "Introduction to fuzzy sets, fuzzy logic, and fuzzy control systems," *Appl. Mech. Rev.,* vol. 54, no. 6, pp. B102-B103, 2001.

[13] L. Reznik, *Fuzzy controllers handbook: how to design them, how they work*. Elsevier, 1997.

A PV generation system based on P&O MPPT algorithm and SVPWM inverter for standalone applications

Duha Khalf[1], Kadhim H. Hassan[2], Diyah K. Shary[3]
{duhakareem249o0ll@gmail.com[1],k.hassan@stu.edu.iq[2], diyahpower@stu.edu.iq[3] }

[1,2,3] Basra Engineering Technical College, Southern Technical University, Iraq

Abstract. The output of photovoltaic cells continues to change with surrounding environments, therefore, the maximum power point of the solar cell relies on the amount of solar irradiation and environment temperature. Maximum Power Point Tracking (MPPT) technology is utilized in photovoltaic systems to take entire advantage of output power for Photovoltaic cells. Power Inverters also is an important side of Photovoltaic power generation. This paper proposed a Perturb and Observe (P & O) MPPT algorithm with space vector pulse width modulation (SVPWM) control method for a three-phase complete stand-alone Photovoltaic generation system. The proposed PV generation system is implemented into Matlab / Simulink. Simulation results show the proposed stand-alone Photovoltaic system can achieve the excellent execution of MPPT and get the output voltage in high quality. The system is tested and verified using a solar cell Kyocera Solar KD215GX-LPU PV module.

Keywords: Photovoltaic system (PV); Maximum PowerPoint Tracking (MPPT); Space vector pulse width modulation (SVPWM)

1. Introduction

Because of the increasing demand for energy, pure, environmentally and sustainable energy is required. Solar energy, a type of renewable energy indicating a lot of interest in meeting growing load demands. Most of the solar energy sources that can be used to produce clean electricity are available for free everywhere, despite the cost of composition is high, the cost of operation is very low [1].

Solar cells are variable current or voltage sources because they depend on the variation in temperature, irradiation, and load. Due to the solar cells have a low efficiency, Maximum power point tracking (MPPT) technology is utilized to supply the output of the solar cell effectively. The technology can source maximum power from different sources by utilizing a controlled DC-DC boost, converter with a tracking algorithm inserted between the solar cell and the load [2]. In this paper, Perturb and Observe (P & O) Technique is used due to its low cost, easy implementation, and good execution [3].

In photovoltaic power generation systems, inverters that convert DC power from solar cells into AC power for grids are becoming more popular every day. Inverters are an important unit in the power regulation part of PV systems that use a variety of DC to AC converters. Inverter tasks in a power generation system including DC to AC conversion, system control, and output power quality assurance with various protection mechanisms [4]. Multi-level inverters with Pulse Width

IMDC-IST 2021, September 07-09, Sakarya, Turkey
Copyright © 2022 EAI
DOI 10.4108/eai.7-9-2021.2314775

Modulation (PWM) control are becoming more important. They have many additional advantages over other topologies and are extra efficient [5].

In [6] proposed a switched ZSI to achieve higher voltage gain than a conventional inverter. A better pulse width modulation (PWM) was applied [7-8]. In this work, a structure of a photovoltaic generator system is proposed based on the perturb and observe optimised algorithm and space vector pulse width modulation technique for 3-phase pulse width modulation inverter. The simulation result shows an increase in output power with better performance in output voltage and current.

2. Photovoltaic modeling

Solar cells convert the sun's rays into DC power. This is a process known as the photoelectric. A Photovoltaic consists of multiple PV cells might found in parallel and series to increase the voltage and current in the array. There are many types of solar cell modules. A solar cell using a single diode model, is shown in Figure 1 [6] [3].

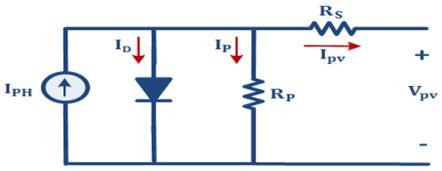

Figure 1. The single-diode model [7]

$$I_{PV} = I_{PH} - I_D - I_p \quad (1)$$

$$I_{PH} = I_P \frac{G}{1000} + K_I(T - T_{ref}) \quad (2)$$

$$I_O = I_{do}\left(\frac{T}{T_{ref}}\right)^2 e^{\left[\frac{qEg}{nk}\left(\frac{1}{T_{ref}} - \frac{1}{T}\right)\right]} \quad (3)$$

$$I_P = \frac{\frac{V_{PV}}{N_S} + I_{PV}R_S}{R_P} \quad (4)$$

The output current of the Photovoltaic model is given as [8]

$$I_{PV} = N_P I_{PH} - N_P I_O \left[e^{\frac{q\left(\frac{V_{PV}}{N_S} + I_{PV}R_S\right)}{nKT}} - 1 \right] - I_P \quad (5)$$

Where V_{PV}: photovoltaic voltage, I_O: diode reverse saturation current, I_{PV}: photovoltaic cell output current, I_{PH}: photogeneration current, I_{SC}: short-circuit current, I_D: diode current, k: The constant of Boltzmann that equal to ((1.38) * 10 $^{-23}$ J / K), q: the charge of electrons (1.602 * 10 ^ -19 °C), R_S: Series resistance of solar cells, R_P: Parallel resistance of solar cells, n is diode emission coefficient, T is Kelvin unit Ambient temperature, T_{ref} the reference absolute temperature, E_g : the silicon bandgap energy (1~3) eV, K_i : the current temperature coefficient in a short circuit and I_{do}: Reverse current of the diode [9].

In the ideal case, Rs is equal to zero and Rp is infinite. Industrialists try to reduce the effects of both resistances to improve the product [9]. In this paper, a solar cell module of the type Kyocera Solar KD215GX-LPU PV is considered, in which the table parameter is listed below:

Table 1. Parameters of the Kyocera Solar KD215GX-LPU PV panel used in this task.

Quantity	Value
$\mathbf{V_{mpp}}$	26.6 V
$\mathbf{I_{mpp}}$	8.09A
$\mathbf{P_{mpp}}$	215.194W
$\mathbf{V_o}$	33.2V
$\mathbf{I_{sc}}$	8.78A
$\mathbf{K_i}$	(0.02 ± 0.015) %/℃
$\mathbf{K_v}$	$-(93 \pm 10)$ mV/℃
$\mathbf{N_S}$	54

3. The Perturb and P&O Algorithm

The MPPT technology is utilized from solar panels to get maximum power efficiency. PV modules are not constantly concerning the power supply and the V-I characteristics are non-linear making them difficult to use. This is observed using a DC-DC boost converter by changing the duty cycle of the entire MPPT algorithm. A flow chart for the P & O MPPT is seen in Figure 2 [3]. Over the last few years, many techniques have relied on MPPT. Many MPPT algorithms are reported [10]. In our PV generation system, we used the Perturb and Observe (P & O) algorithm. The P & O algorithm is the most well-known used algorithm due to its low cost, good execution, and simple implementation. As shown in Figure 3, the algorithm has a small disturbance, at the start, the solar cell voltage, current, and power P1 are acquired, after which the operating voltage of the photovoltaic model is perturbed by a slight increase. It then generates a new power P2. Therefore, the change in power ΔP is measured by the variation between P1 and P2. If the fluctuation is equal to the positive sign, the operating point will approach MPP due to the disturbance of the operating voltage. In this case, the maximum PowerPoint P_{MPP} can be obtained and the applicable voltage V_{MPP} can be measured. Therefore, extra perturbations can be inserted in the same direction to achieve MPP. On the other side, if the variation is equal to negative, the algorithm decides to inverse the whole operation. The change in power must be in the same direction for more perturbations [2], [11], [12].

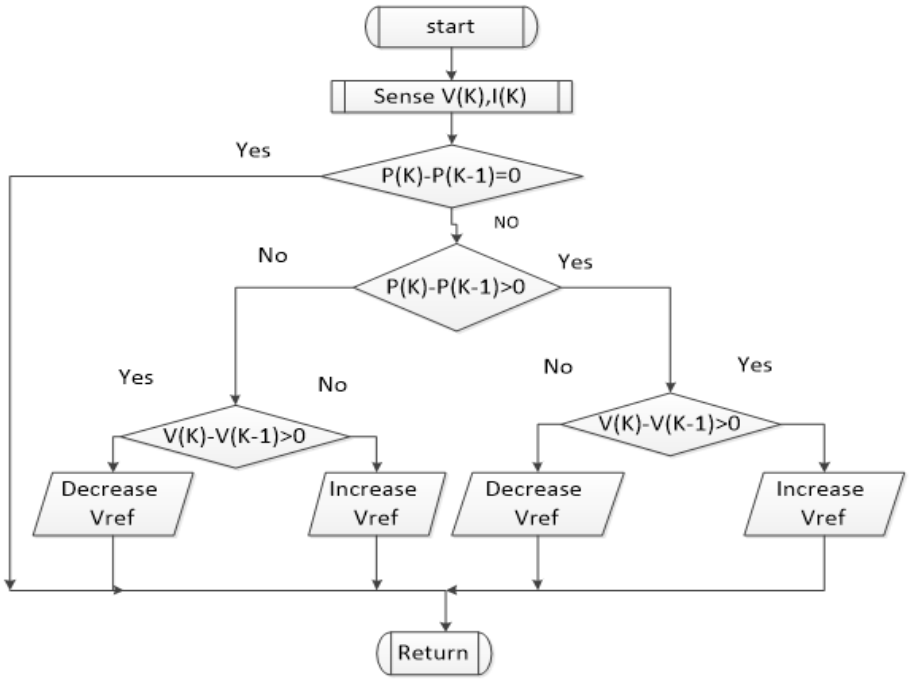

Figure 3. The P&O MPPT algorithm

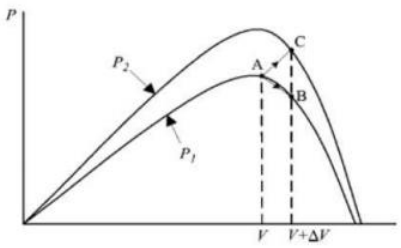

Figure 2. The hill-climbing for the 'P&O' algorithm

4. Principle of three-phase Space Vector Pulse Width Modulation (SVPWM)

The 3-phase Voltage Source Inverter (VSI) principle is controlled by utilizing the switching signal generated by SVPWM technology. For the top switch on the same leg is turned,on whenever the bottom switch, is turned off, so it is used to set the inverter. Figure 4 indicates the voltage waveform of the inverter leg. One leg of the inverter will change its state and will remain fixed at 60° for the next cycle (360 °). There are 6 discrete values of leg voltage so that one cycle is (360 °). The eight switching cases on the inverter leg needed to code the upper arm case are binary switched to 3 bits. Table (2) lists the switching cases. Here, the switch is on for a bit (1) while the switch for a bit (0) is off [13][14].

Table 2 shows the spatial vectors that exemplify the eight switching cases of VSI. The six non-zero vectors (V1 to V6) are divided into six sections of the hexagon in the complex plane with the center of the hexagon between the two zero vectors. (Null vector) as seen,in Figure 5 [11]. The angle, for non-zero vectors is 60. The reference voltage vector ($Vref$) is generated by switching between two closer active space vectors and one zero vector. This exemplifies the three-phase AC voltage of the space vector power width modularity method. The VSI is varied by changing the magnitude and frequency of $Vref$. SVPWM based on,the voltage of the fixed $\alpha\beta$ reference,frame by converting the 3-phase voltage of the ABC reference of the fixed reference,frame utilizing Clark's transformation. The maximum capacity of the output voltage can be obtained by SVPWM technology. It is shown thatt he radius,of the largest,circle formed into the,hexagon. [15]. Three steps should be applied to perform the SVPWM [13].

1- determine , $V\beta$, $Vref$ and angle,α.

2- calculate,the time,durations T_1, T_2, and T_0.

3- calculate the switching states based on the above step

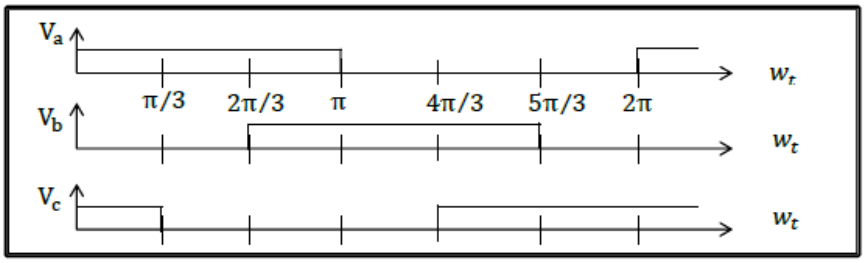

Figure 4. The voltages waveform of the 3-ph VSI

Table 2. The switching table and output voltages of the VSI

Voltage vectors	Switching vectors			Phase voltages (p.u)			Line volages (p.u)		
	A	B	C	V_{an}	V_{bn}	V_{cn}	V_{ab}	V_{bc}	V_{ca}
V_0	0	0	0	0	0	0	0	0	0
V_1	1	0	0	2/3	-1/3	-1/3	1	0	-1
V_2	1	1	0	1/3	1/3	-2/3	0	1	-1
V_3	0	1	0	-1/3	2/3	-1/3	-1	1	0
V_4	0	1	1	-2/3	1/3	1/3	-1	0	1
V_5	0	0	1	-1/3	-1/3	2/3	0	-1	1
V_6	1	0	1	1/3	-2/3	1/3	1	-1	0
V_7	1	1	1	0	0	0	0	0	0

Step-1 calculates the switching $V\alpha$, and $V\beta$ by using Clark's transformation[15].

$$\begin{bmatrix} V\alpha \\ V\beta \end{bmatrix} = \frac{2}{3}\begin{bmatrix} 1 & \frac{-1}{2} & \frac{-1}{2} \\ 0 & \frac{\sqrt{3}}{2} & \frac{-\sqrt{3}}{2} \\ \frac{1}{2} & \frac{1}{2} & \frac{1}{2} \end{bmatrix}\begin{bmatrix} V_A \\ V_B \\ V_C \end{bmatrix} \quad (6)$$

Then that calculates $|\bar{V}ref|$ and α from Figure 6 as following.

$$|\bar{V}ref| = \sqrt{V\alpha^2 + V\beta^2} \quad (7)$$

$$\alpha = tan^{-1}\left(\frac{V\beta}{V\alpha}\right) = 2*\pi* f * t \quad (8)$$

(f) is the fundamental operating frequency.

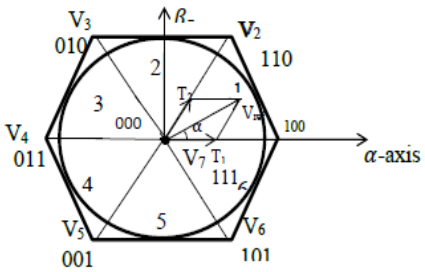

Figure 5. Switching voltage, sectors.

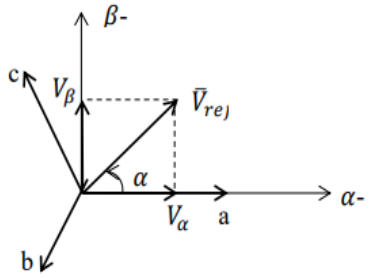

Figure 6. Voltage,vector

Step-2: For sector one of the hexagon seen in Figure (5), the time duration T_1, T_2 and T_0 can be determined:

$$T_1 = \frac{\sqrt{3}\,T_Z|V_{ref}|}{V_{dc}}\, sin\left(\frac{pi}{3} - \alpha\right) \quad (9)$$

$$T_2 = \frac{\sqrt{3}\,T_Z|V_{ref}|}{V_{dc}}\, sin(\alpha) \quad (10)$$

$$T_0 = T_Z - (T_1 + T_2) \quad (11)$$

The switching time for any sector is[16].

$$T_1 = \frac{\sqrt{3}\,T_Z|V_{ref}|}{V_{dc}}\, sin\left(\frac{k\pi}{3} - \alpha\right) \quad (12)$$

$$T_2 = \frac{\sqrt{3}\,T_Z|V_{ref}|}{V_{dc}}\, sin\left(\alpha - \frac{k-1}{3} * \pi\right) \quad (13)$$

$$T_0 = T_Z - (T_1 + T_2) \quad (14)$$

where: Tz is;the;switching time ($Tz = 1/fz$); k is the;number;of,sectors (from 1 to 6), $0 \le \alpha \le 60°$.

Step-3: the time located to switching devices is calculated. As seen in Table (3), the, whole swtiching slot Tz can be divided into 7 parts by applying the zero, state vector of the first, part to the $1/4^{th}$ from state time. In the 2nd and 3rd parts of the time, apply the active state vector to half of the total time for the vector, then the $1/4^{th}$ zero of the state vector slot. This sequence is repeated during the switching period. [17].

Table 3. Switching time for each sector

Sectors (n)	Upper switching (S1, S3, S5)	Lower switching (S4, S6, S2)
1	S1 = T1 + T2 +T0/2 S3 = T2 +T0/2 S5 =T0/2	S4 =T0/2 S6 = T1 +T0/2 S2 = T1 + T2 +T0/2
2	S1 = T1 +T0/2 S3 = T1 + T2 +T0/2 S5 =T0/2	S4 = T2 +T0/2 S6 =T0/2 S2 = T1 + T2 +T0/2
3	S1 =T0/2 S3 = T1 + T2 +T0/2 S5 = T2 +T0/2	S4 = T1 + T2 +T0/2 S6 =T0/2 S2 = T1 +T0/2
4	S1 =T0/2 S3 = T1 +T0/2 S5 = T1 + T2 +T0/2	S4 = T1 + T2 +T0/2 S6 = T2 +T0/2 S2 =T0/2
5	S1 = T2 +T0/2 S3 =T0/2 S5 = T1 + T2 +T0/2	S4 = T1 +T0/2 S6 = T1 + T2 +T0/2 S2 =T0/2
6	S1 = T1 + T2 +T0/2 S3 =T0/2 S5 = T1 +T0/2	S4 =T0/2 S6 = T1 + T2 +T0/2 S2 = T2 +T0/2

5. Simulink model design

The PV Simulink model including the P & Q controller, based on MPPT, is shown in Figure 7. Optimal PV systems include PV panels, boost converters with MPPT algorithms, and inverters. The basic purpose of the MPPT is to adjust 'the convertor duty cycle. This allows the converter to provide maximum power to the inverter at, any irradiance and temperature. Boost convertor impedance gives the requirement to maximize maximum power) is determined using, the following, equation [12]:

$$R_I = (1 - D)^2 R_O \quad (15)$$

To keep the output impedance constant, MPPT technology is used to change the duty cycle so that the source input impedance shown is equal to the full load impedance. By training and optimizing the parameters of the P & Q controller, we will get the best output in terms of minimum average error. The output of the P & Q controller is then validated to the high; frequency carrier signal to obtain the desired duty-cycle that synchronized with P_{max} with changing weather conditions [18].

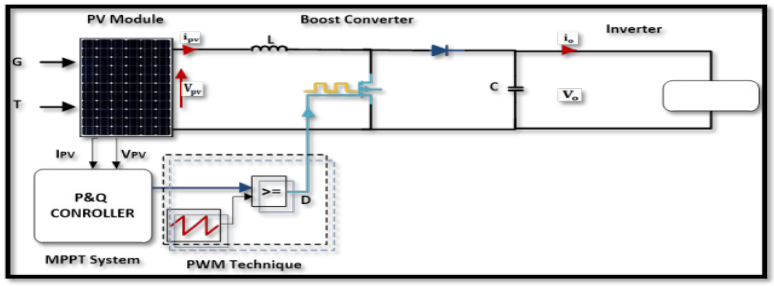

Figure 7. The PV‘model with a P&Q controller.

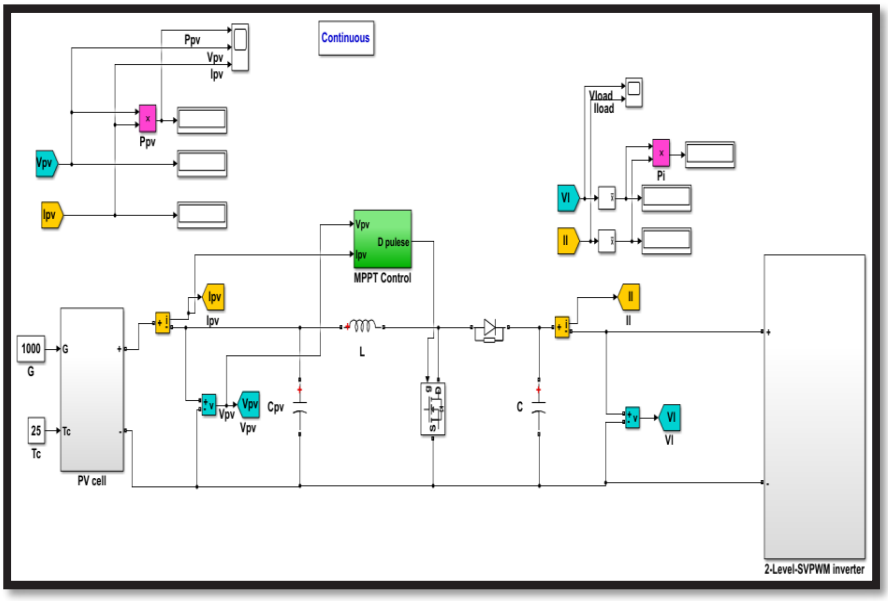

Figure 8. The PV system model with a P&Q controller.

6. Simulation Results

As shown in Figure 8, the PV system with the P & Q controller MPPT method and an SVPWM control scheme for a 3-phase power pulse width modulation inverter is implemented in the Matlab / Simulink software package. The Simulink model of the PV module is designed according to the mathematical formulas is shown in Figure 9. The Kyocera Solar KD215GX-LPUPV module has the characteristics shown in Table (1) and consists of 72 polycrystalline silicon solar cells. The Simulink models of the boost converter are illustrated in Figure 10 [3]. The boost converter inductance and capacitor values are 0.01MH and 700µF respectively while the output load value is 78 ohms. The complete Simulink model of a 3-phase power supply PWM inverter and the SVPWM control method is shown in Figure 8.

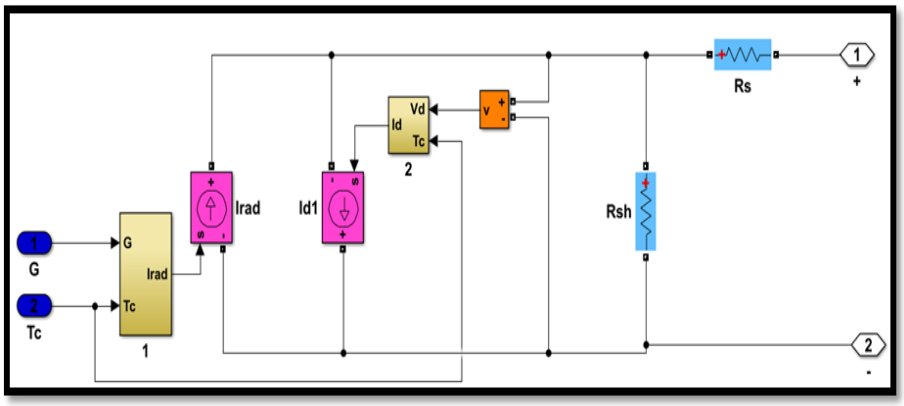

Figure 9. The PV system model

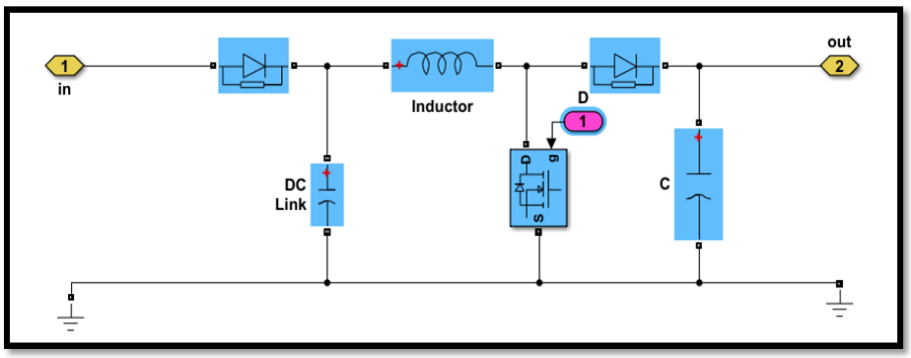

Figure 10. The Boost'converter model

Using arbitrary values of temperature and irradiance supplied to the solar panel, it is necessary to calculate the value of input impedance R_i in order 'to get the MPPT after choosing the optimsed input resistance value for the total probability of sun temperature and irradiance. By fixing the output impedance to 78 ohms, the value of duty ratio D can be calculated using equation (15). The temperature values are:25℃, and 50 ℃ and the irradiance is changing as $600W/m^2$., $800W/m^2$., and $1000W/m^2$. 'The duty ratio supplied to the boost converter for maximum power at all temperatures and irradiance values should be optimum. The values of irradiance and .temperature are used as inputs for training' data' of P & Q control, the desired output is the duty cycle. The operation test of the Photovoltaic system in simulation including the Photovoltaic system response, The outputs of the boost converter under different values in irradiance are shown in Figures 11,12,13,14,15, and 16, and temperature are shown in Figures 17, 18, and 19. For example, If the load is connected directly to the PV panel at T = 25 ° C, G = 10^3 W/m^2 and the power is 213.9

Watts, while the power 202.5 W when connected to PV via a boost' converter. Therefore, the P & Q controller is efficient at extracting MPPT in the context of temperature and irradiation changes.

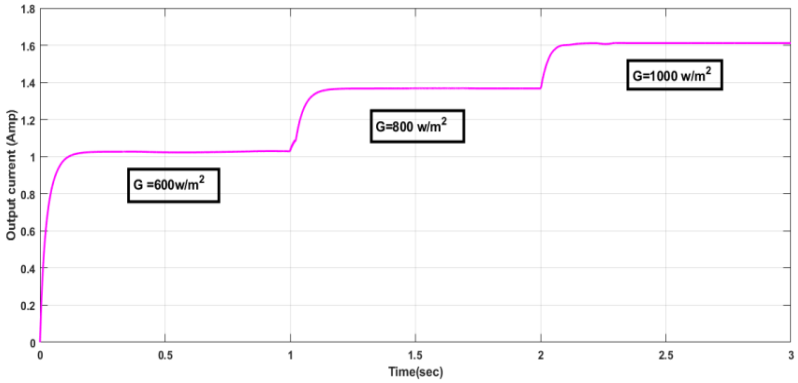

Figure 11. The output current response for boost' converter T =25 ℃

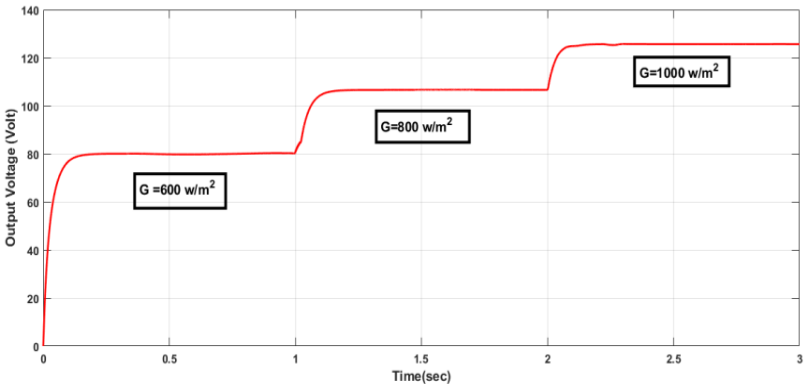

Figure 12. The output voltage response for boost' converter T =25 ℃

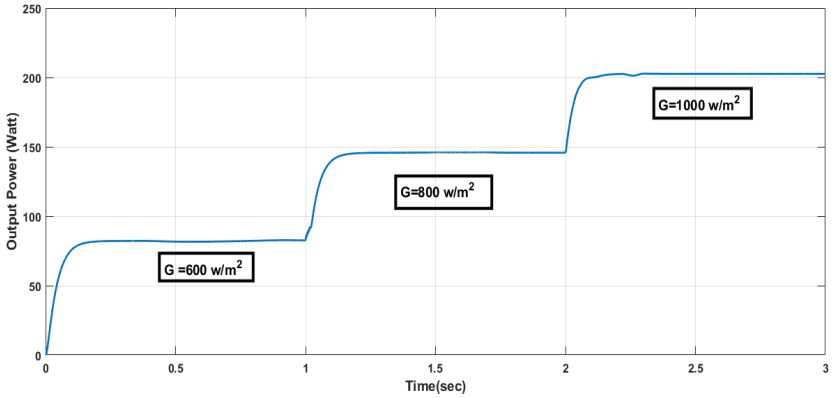

Figure 13. The output power response for boost' converter T =25 ℃

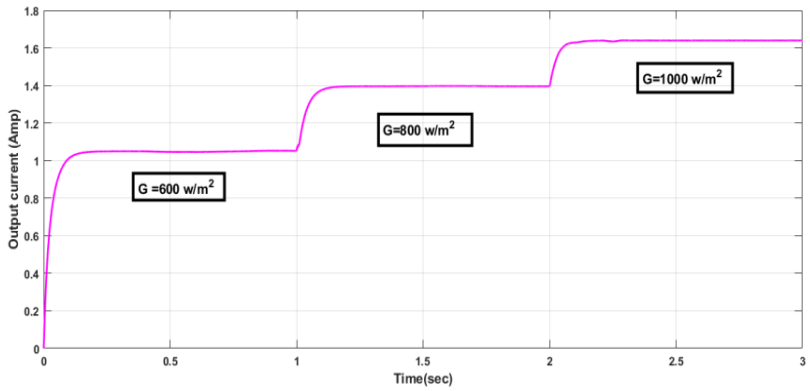

Figure 14. The output current response for boost' converter T =50 ℃

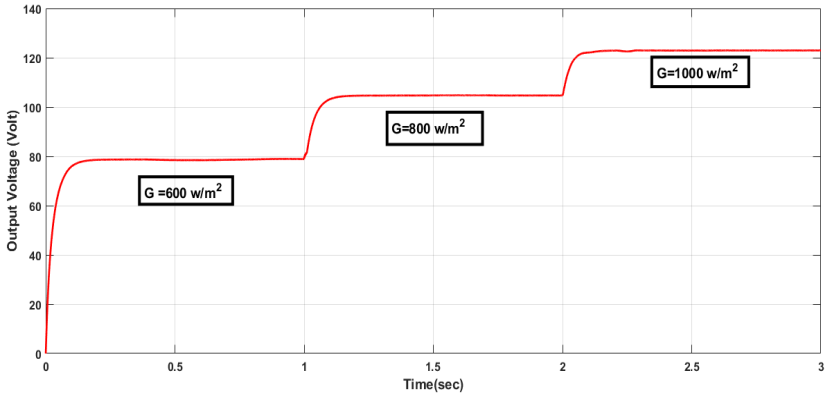

Figure 15. The output voltage response for boost' converter T =50 ℃

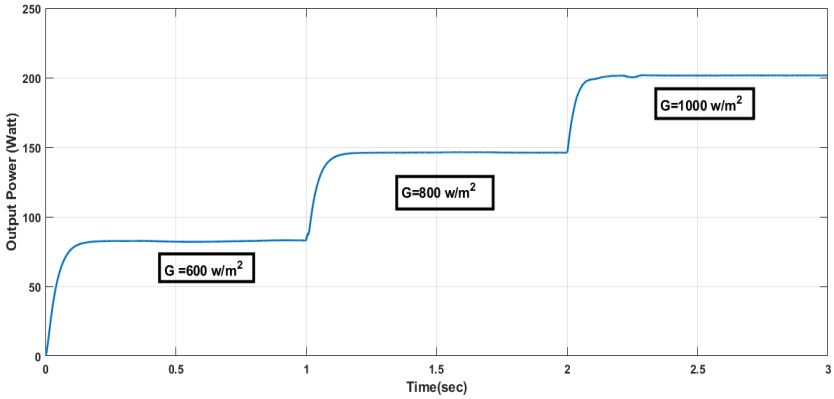

Figure 16. The output power response for boost' converter T =50 ℃

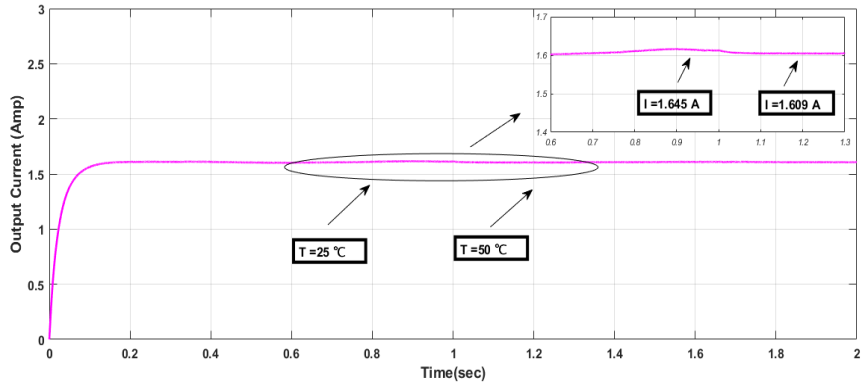

Figure 17. The output current response for boost' converter at changing Temperature at G=1000 W/M^2

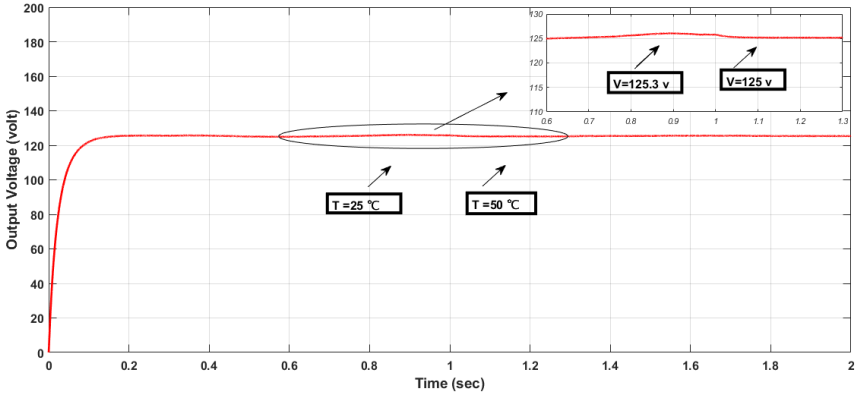

Figure 18. The output voltage response for boost' converter at changing Temperature at G=1000 W/M^2

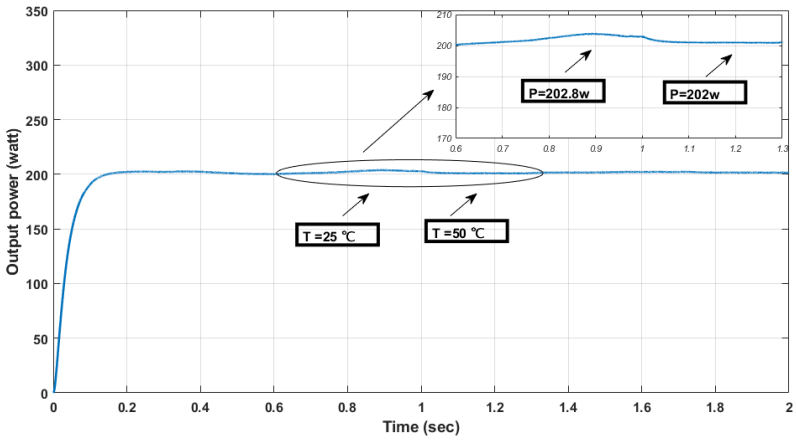

Figure 19. The output power response for boost' converter at changing Temperature at G=1000 W/M^2

The output of the SVPWM is produced from the Simulink model illustrated in Figure 20 in which including positioning the based on the f = 50 Hz, and fs = 10 kHz. Figure 21 shows a Simulink diagram of the switching time of the SVPWM pulse waveform. It can be seen that the shape of the inverter output voltage is determined depending on the modulation index.

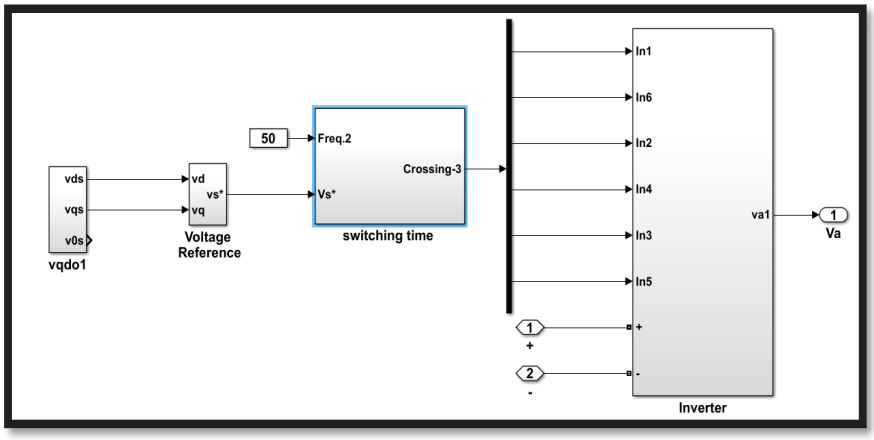

Figure 20. The Simulink block diagram for SVPWM

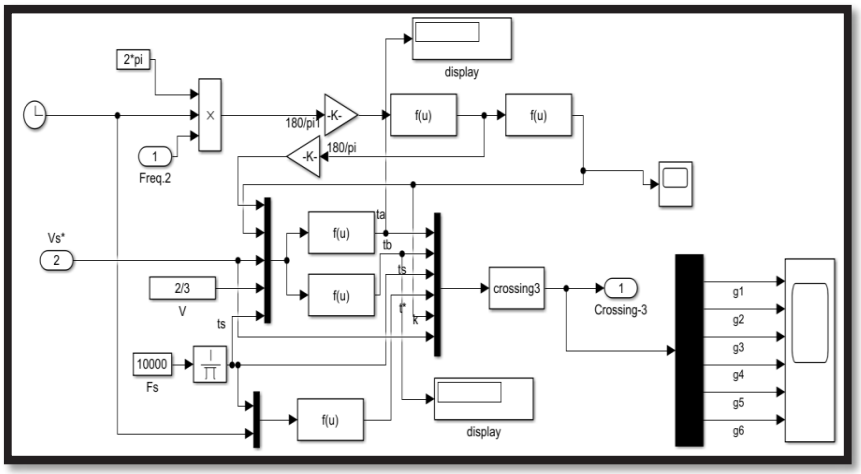

Figure 21. The simulation block diagram for switching time

The output voltages of SVPWM in case of T = 25 °C and G= 1000 W/M^2 is shown in Figure 22. The output voltages of SVPWM in case of changing the irradiance at T = 25°C are shown in Figure 23 and the output voltages at T = 50 °C are shown in Figure 24. The whole output voltage based on Harmonic Distortion is seen in Figure 25.

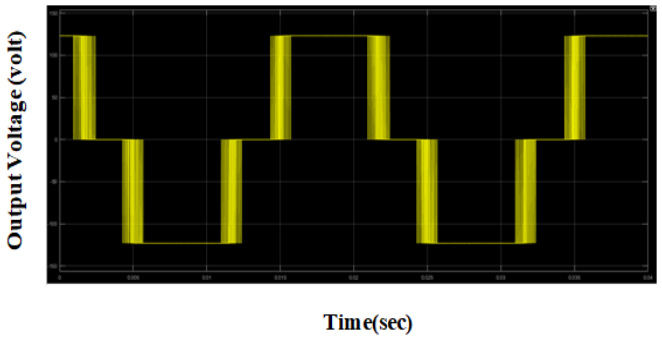

Figure 22. The output voltage for G=1000 w/m^2 and T=25℃

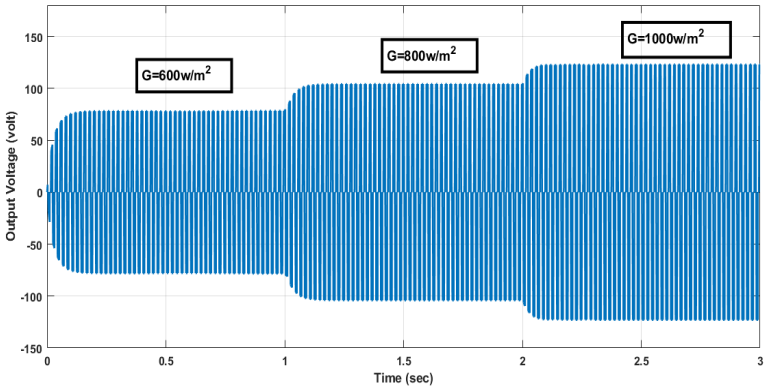

Figure 23. The output voltage for various different irradiation at T=25℃

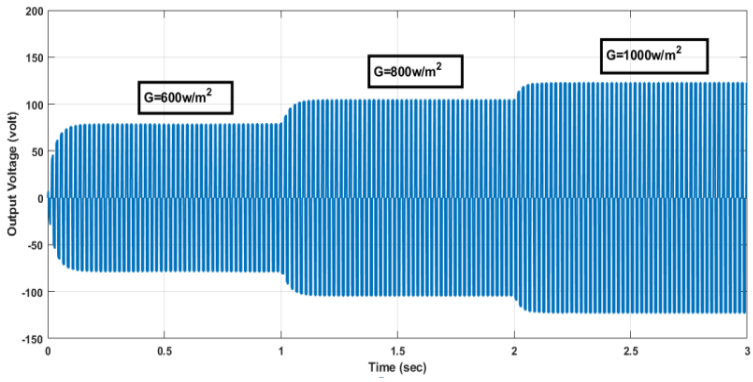

Figure 24. The output voltage for various irradiation at T=30℃

Figure 25.The THD of output line voltage for space vector pulse width modulation

7. Conclusion

The stand-alone Photovoltaic power generation system has been proposed. The design depends on the (P & Q) MPPT and SVPWM methods for a 3-phase PWM inverter. The P & Q MPPT algorithm is implemented in Matlab / Simulink. The simulation results show that the P&Q MPPT algorithm can simultaneously get better performance of the dynamic and steady-state performance of Photovoltaic systems. At the same time, the output result of the inverter using the SVPWM has improved power quality. The results also show that the proposed Photovoltaic system has a reliable and effective response under variation atmospheric conditions. Therefore, a stand-alone Photovoltaic power generation system based on the P & Q MPPT method for a 3-phase voltage source pulse width modulation inverter and SVPWM control is practical and effective. The designed system produces the ability to operate at lower switching frequencies with less dv/dt the voltage stress on the switching device. Space vector pulse width modulation is the best selection of inverter switching states that improves the DC link voltage employment. This outperform other traditional pulse width modulation methods.

References:

[1] A. Pandey, N. Dasgupta, and A. K. Mukerjee, “High-performance algorithms for drift avoidance and fast tracking in solar MPPT system,” *IEEE Trans. Energy Convers.*, vol. 23, no. 2, pp. 681–689, 2008, doi: 10.1109/TEC.2007.914201.

[2] P. Shaw, “Modelling and analysis of an analogue MPPT-based PV battery charging system utilising DC-DC boost converter,” *IET Renew. Power Gener.*, vol. 13, no. 11, pp. 1958–1967, 2019, doi: 10.1049/iet-rpg.2018.6273.

[3] W. I. Hameed, A. L. Saleh, B. A. Sawadi, Y. I. A. Al-Yasir, and R. A. Abd-Alhameed, “Maximum power point tracking for photovoltaic system by using fuzzy neural network,” *Inventions*, vol. 4, no. 3, 2019, doi: 10.3390/inventions4030033.

[4] B. M. Hasaneen and A. A. E. Mohammed, “Design and simulation of DC/DC boost

converter," *2008 12th Int. Middle East Power Syst. Conf. MEPCON 2008*, pp. 335–340, 2008, doi: 10.1109/MEPCON.2008.4562340.

[5] M. Chen and D. Sun, "A unified space vector pulse width modulation for dual two-level inverter system," *IEEE Trans. Power Electron.*, vol. 32, no. 2, pp. 889–893, 2017, doi: 10.1109/TPEL.2016.2585223.

[6] H. C. Lu and T. L. Shih, "Design of DC/DC boost converter with FNN solar cell maximum power point tracking controller," *Proc. 2010 5th IEEE Conf. Ind. Electron. Appl. ICIEA 2010*, no. 1, pp. 802–807, 2010, doi: 10.1109/ICIEA.2010.5515085.

[7] A. M. Dakhil, A. R. Hussein, and A. L. Saleh, "Transformer-less Single-phase Inverter Based on SPWM Technique for Standalone PV Application," *Solid State Technol.*, vol. 63, no. 3, pp. 4088–4101, 2020.

[8] P. K. Pathak and A. K. Yadav, "Design of battery charging circuit through intelligent MPPT using SPV system," *Sol. Energy*, vol. 178, no. July 2018, pp. 79–89, 2019, doi: 10.1016/j.solener.2018.12.018.

[9] S. Wadhankar and B. Charjan, "Design and Simulation of Photovoltaic Water Pumping System," no. September, pp. 83–92, 2019, doi: 10.1007/978-981-13-6148-7_9.

[10] M. A. Eltawil and Z. Zhao, "MPPT techniques for photovoltaic applications," *Renew. Sustain. Energy Rev.*, vol. 25, pp. 793–813, 2013, doi: 10.1016/j.rser.2013.05.022.

[11] V. Janaki Ramaiah and S. Keerthipati, "Hybrid PWM Scheme for Pole-Phase Modulation Induction Motor Drive Using Carrier-Based Hexagonal and Octadecagonal SVPWM," *IEEE Trans. Ind. Electron.*, vol. 67, no. 9, pp. 7312–7320, 2020, doi: 10.1109/TIE.2019.2946537.

[12] S. J. Yaqoob, A. Raisan Hussein, and A. L. Saleh, "Low Cost and Simple P&O-MPP Tracker Using Flyback Converter," no. November, 2020, [Online]. Available: www.solidstatetechnology.us.

[13] M. Valan Rajkumar, P. S. Manoharan, and A. Ravi, "Simulation and an experimental investigation of SVPWM technique on a multilevel voltage source inverter for photovoltaic systems," *Int. J. Electr. Power Energy Syst.*, vol. 52, no. 1, pp. 116–131, 2013, doi: 10.1016/j.ijepes.2013.03.022.

[14] S. Chatterjee, "A multilevel inverter based on SVPWM technique for photovoltaic application," *Int. J. Power Electron. Drive Syst.*, vol. 3, no. 1, pp. 62–73, 2013, doi: 10.11591/ijpeds.v2i4.403.

[15] A. M. Nazlee, N. H. Hamid, F. A. Hussin, and N. B. Z. Ali, "Space Vector PWM for PMSM simulation using Matlab Simulink," *IEEE Asia-Pacific Conf. Circuits Syst. Proceedings, APCCAS*, pp. 1127–1130, 2010, doi: 10.1109/APCCAS.2010.5774974.

[16] K. A. Chinmaya and G. K. Singh, "Experimental analysis of various space vector pulse width modulation (SVPWM) techniques for dual three-phase induction motor drive," *Int. Trans. Electr. Energy Syst.*, vol. 29, no. 1, pp. 1–15, 2019, doi: 10.1002/etep.2678.

[17] K. Agrawal, A. Gandhi, M. T. Shah, and M. V. Gojiya, "Design, analysis and realization of SVPWM using embedded code generation technique for a three phase, two level inverter," *Int. Conf. Electr. Power Energy Syst. ICEPES 2016*, pp. 377–382, 2017, doi: 10.1109/ICEPES.2016.7915961.

[18] W. I. Hameed, B. A. Sawadi, and A. M. Fadhil, "Voltage tracking control of DC-DC boost converter using fuzzy neural network," *Int. J. Power Electron. Drive Syst.*, vol. 9, no. 4, pp.

1657–1665, 2018, doi: 10.11591/ijpeds.v9n4.pp1657-1665.

Design of a Hexagonal Printed Monopole Antenna with Circular Slot for UWB Breast Cancer Imaging Applications

Salamatu Abubakar Ibrahim[1], Isah Musa Danjuma[1], Mohamed Abdul-Al[2], and Raed Abd Alhameed[1,2]
{s.a.ibrah2@bradford.ac.uk, I.M.Dasnjuma@bradford.ac.uk, M.Abdul-Al@bradford.ac.uk, and R.A.A.Abd@bradford.ac.uk}

[1]School of Electrical Engineering and Computer Science, University of Bradford, Bradford BD71DP, United Kingdom
[2]Faculty of Engineering and Informatics, University of Bradford, Bradford, BD7 1DP, UK.

Abstract. A low profile hexagonal printed monopole antenna with circular slot is presented for ultra-wide band (UWB) breast cancer imaging application. The sensor was designed to operate in the UWB band frequency range of 3.1-10.6 GHz. The antenna dimensions are 30x30x1.6 mm^3. FR4 substrate is used between ground and radiating patch having a relative permittivity of 4.6, and loss tangent of 0.0025. The antenna is designed using Computer Simulation Technology Software (CST). The simulation results reveals that the antenna bandwidth can be increased using the slots configurations.

Keywords: Microwave imaging, UWB antenna, monopole antenna, Breast cancer detection.

1 Introduction

Antenna design with the use of ultra-wideband communications has garnered a lot of considerations by researchers all over the world. These recognitions are due to low cost, low power consumption, small size, wide impedance bandwidth, omnidirectional characteristics, easy fabrication, and high data transmission rate [1]. These inherent qualities have made monopole antenna a good candidate for this research. Additionally, it could also be used for many communication applications such as radar application, position and tracking systems, microwave imaging application particularly for breast cancer imaging application [2].

By making certain changes to the antenna construction, monopole antennas are now being used for ultra-wideband technology. The technique for expanding bandwidth of ultra-wide band antennas by using slot methods of various shapes and configurations in the patch of the antenna, such as rectangular, partially circular, triangular, and hexagonal, is extensively considered for investigating impedance matching [3]. The effects of the slots on impedance bandwidth evaluation, radiation pattern characteristics, gain performance, and radiation efficiency were

IMDC-IST 2021, September 07-09, Sakarya, Turkey
Copyright © 2022 EAI
DOI 10.4108/eai.7-9-2021.2315502

discovered by simulation testing.

Non-ionizing and non-destructive testing are two advantages of using a microwave imaging sensor as a medical imaging tool for breast cancer screening. In comparison to x-ray mammography, microwave imaging has advantages of cheap cost, low complexity, high data rate, and no breast compression [4]. The antenna is employed as a sensor in microwave imaging to transmit and receive microwave signals into the breast tissues.

Changes in electrical characteristics of various tissues, such as relative permittivity and conductivity, provides the basis for this theory. The antenna's dispersed signal is utilized to identify the difference in dielectric characteristics between normal and malignant tissue in a more efficient, effective, safe, and precise manner. The difference in water content between normal and malignant tissues is used to detect the tumor in this approach. Microwaves can distinguish between healthy and unhealthy tissue. The presence of strong water within the malignant tissues is used as a tumor diagnostic factor. As a result, imaging using microwave antennas is another option for early breast cancer diagnosis, potentially saving a lot of lives. For microwave imaging measurements, a variety of UWB antennas have been proposed, including the bow tie and Vivaldi antennas [5, 6].

In the near field of the breast phantom, the use of a monopole antenna for the microwave-imaging provides a very effective and efficient performance [7]. Over the UWB band, antenna basics such as return loss, VSWR, and radiating pattern are well defined.

In this paper, a novel, low profile, low cost, enhanced impedance bandwidth and high-performance monopole antenna for breast cancer microwave imaging is presented. The antenna is small and uniform in size suitable for the microwave imaging application. In this study, the antenna was analysed, and the simulation results indicate good signal transmission and reception. The remaining of the paper are as follows: Section II presents the antenna geometry and optimization design, while Section III analyses the antenna performance measurements and conclusion are drawn in Section IV.

2 Antenna Geometry And Optimisation Design

2.1 Antenna Geometry

The proposed antenna has a uniform geometry of 30 x 30 mm^2 on a FR-4 substrate with thickness of 1.6 mm, permittivity of 4.6, and loss tangent of 0.0025. The basic antenna structure consists of a hexagonal patch with a circular slot, a feed line and 2 uniform rectangular planes acting as a partial ground. The hexagonal patch parameters were defined as follows: Substrate length (SL), Substrate width (SW), Patch length (PL) Microstrip length (ML), Microstrip width (MW), short side (SS), Long side (LS), radius (R), and angle (a^0), as shown in Fig.1 and Fig. 2 respectively. The values of UWB antenna parameters are tabulated in Table1. These parameters were optimized to get the optimum result used for the microwave imaging sensor and the antenna was fed with a 50 Ω coaxial transmission.

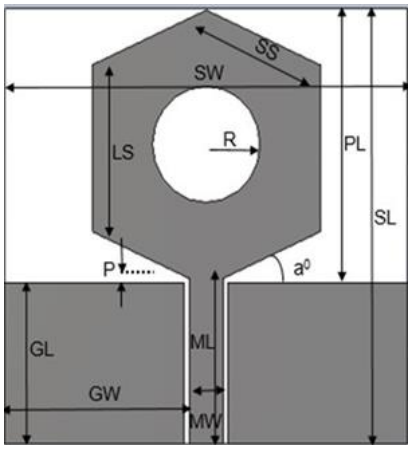

Fig.1. Geometry layout of the hexagonal monopole antenna.

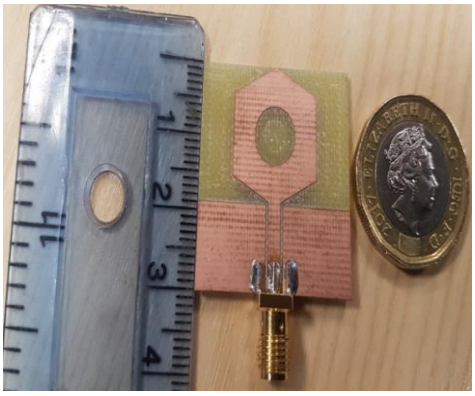

Fig.2. Physical implementation of the hexagonal monopole.

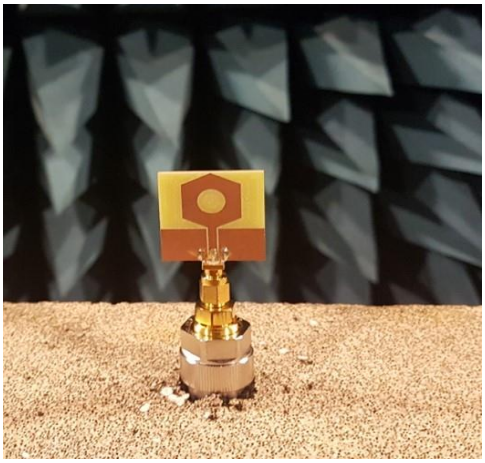

Fig.3. Far field Measurement of the proposed antenna in the anechoic chamber.

Table 1: Dimensions specification of the proposed antenna

Parameter	Dimensions in mm
Substrate width (SW)	30
Substrate length (SL)	30
Substrate thickness (ST)	1.6
Microstrip length (ML)	11.40
Microstrip width (MW)	2.50
Microstrip gap (MG)	0.4
Long Side (LS)	11.49
Short Side (SS)	9.30
Radius (R)	4
Angle (a^0)	25
Partial ground length (GL)	11.10
Partial ground width (GW)	13.35

2.2 Optimization Design

All engineering designs require optimization to enable engineers obtain the greatest outcomes from the parameters of their designs. Small changes in a system's size can have a multiplier effect on the system overall efficiency. Interactions can be time-consuming in a system with numerous variables, making it impracticable to determine their optimal value. Computer simulation technology (CST) was utilized for this design, and the optimization was done with the particle swam optimisation method.

The algorithm takes the advantage of S-parameter sensitivity information used to reduce the number of simulations needed and speed up the optimization process [8]. It is the most robust of the optimization algorithms. The parameters that affect the performance of the proposed monopole UWB antenna are the gap between the 2 uniforms rectangular antenna planes acting as the partial ground, the partial ground length (GL and the angle at the bend of the corners of the ground plane (a^0). These parameters affect the proposed antenna radiation pattern, return loss and the impedance matching and hence, optimized to achieve better antenna performance as indicated in the return loss of Fig. 4 and 5 respectively.

3 Antenna Performance Measurements

The simulation results of the hexagonal monopole antenna have been analysed and optimized using CST microwave studio. Mat lab software was used to plot the simulated result, and Agilent technologies N5242 was used to acquire the measured results with the use of a vector network analyzer that covers the 10 MHz to 26 GHz frequency range. The simulated measurement is shown in Fig.4, while the simulated and measured return loss results are indicated in Fig.5.

The proposed antenna's -10 dB operational bandwidth spans the UWB spectrum from 3.1 to 10.6 GHz. The first resonance occurs at 3.99 GHz, the second at 6.5 GHz, and the maximum resonance occurs at 10.6 GHz. The lower frequency bandwidth is significantly influenced by

the slot in the monopole antenna's patch.

The current flow will follow the curvature of the slot if the slot is etched on the radiating patch. As a result, the slot shape has an impact on the distribution of surface current as indicated in Fig. 6. The course of the surface current is controlling the antenna's radiation [9]. Although, the proposed antenna design is simple and compact in size, it achieves the overall impedance bandwidth of the UWB spectrum, and the simulated and measured results are in good agreements.

The breast phantom electrical properties were taken from [4] and the modelling of skin and fat phantom were taken from CST's material library. The skin and fat have the following dimensions: skin with radius 82 mm, thickness of 2 mm and depth of 32 mm, fat with radius 80 mm and depth of 32 mm. The plastic layer was modelled around the breast phantom as it was used in [5] to support the antenna. The plastic layer has a dimension including relative permittivity of $\varepsilon_r = 3$, conductivity of $\sigma = 0.0015$ s/m, radius = 92 mm, thickness = 8 mm, and depth of 32 mm.

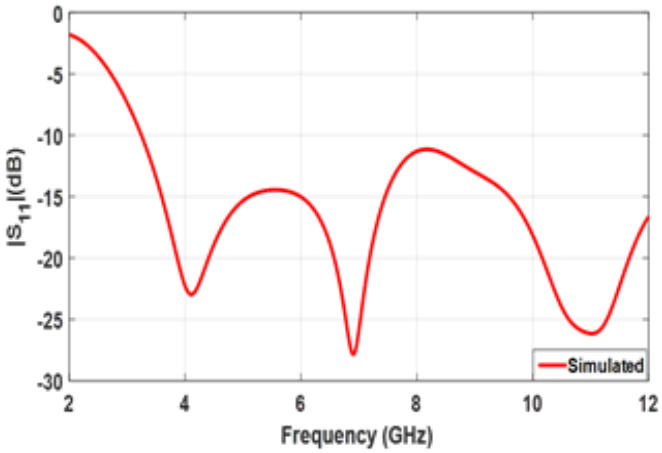

Fig.4. Simulated results with optimized parameters of gap 4mm and partial ground length GL = 11.10 mm and angle of 25^0**.**

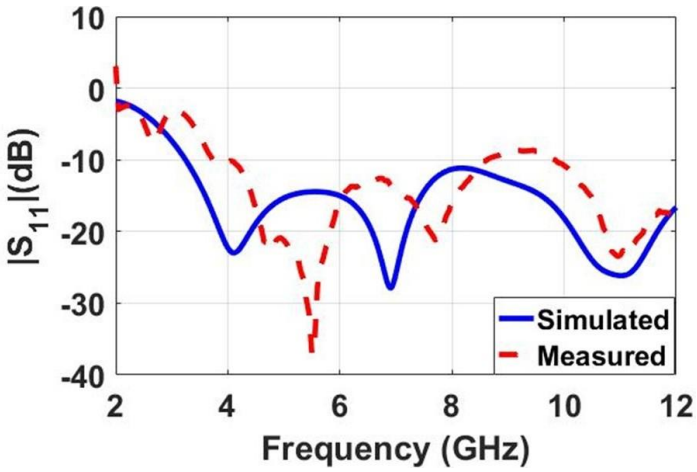

Fig. 5. Simulated and measured results of the proposed antenna.

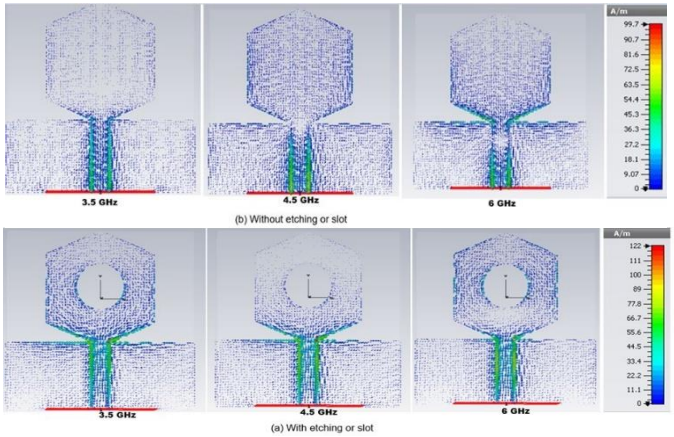

Fig.6. Surface current densities of the Proposed antenna.

4 Conclusion

An experimental investigation of a small UWB antenna was carried out for breast cancer microwave imaging. The antenna's low profile and simple construction make it an excellent option for microwave imaging applications. The excellent result between the simulated and measured results of the antenna is used to assess antenna performance. The antenna's uniform size of 30 x 30 mm2 is suitable for use in a wide range of microwave imaging applications.

References

[1] Haraz, O. and A.-R. Sebak, *UWB antennas for wireless applications.* Advancement in microstrip antennas with recent applications, 2013: p. 125-152.

[2] Adnan, S., et al., *Simulation and experimental measurements for near field imaging.* Progress In Electromagnetics Research, 2012.p. 433.438.

[3] Mohamed S. Soliman., et al., The Effect of the Ground Slots up on the Bandwidth Performance for UWB Antenna, in 18th Mediterranean Microwave Symposium,2018: p.227-230.

[4] Mirza, A.F., et al., *An active microwave sensor for near field imaging.* IEEE Sensors Journal, 2017. **17**(9): p. 2749-2757.

[5] I.M Danjuma, et al., Design and optimization of a bowtie dipole adjacent to dielectric material for through the wall imaging using hybrid electromagnetic computational analysis techniques. in 2017 Internet Technologies and Applications (ITA). 2017. IEEE.

[6] Danjuma, I., et al., *Design of a taper slot low profile Vivaldi antenna for ultra-wideband microwave breast imaging applications.* Journal of Multidisciplinary Engineering Science and Technology (JMEST).

[7] Danjuma, I.M., et al., *AT slot monopole antenna for UWB microwave imaging applications.* 2018.

[8] Liu, B., et al., *Efficient global optimisation of microwave antennas based on a parallel surrogate model-assisted evolutionary algorithm.* IET Microwaves, Antennas & Propagation, 2018.

[9] Yaghjian, A. et al., *Equivalence of surface current and aperture field integrations for reflector antennas.* IEEE Transactions on antennas and propagation, 1984. **32**(12): p. 1355-1358.

Low profile Substrate Integrated Waveguide (SIW) wideband antenna for Ku-band Applications

Faris Mohammed Ali[1], Ahmed Ghanim Wadday[1], Aseel Hameed Al_Nakkash[2], Ali Najah Al-Shamani[1]

fanmnm2018@gmail.com

[1] Department of Communications Techniques Engineering, Engineering Technical College, Al-Furat Al-Awsat Technical University, Al-Najaf 31001, Iraq
[2]Middle Technical University/ Electrical Technical Engineering College, Iraq

Abstract: For wireless applications, a low-profile circular slot with a substrate integrated waveguide (SIW) antenna is given. For bandwidth augmentation, the proposed antenna structure consists of a microstrip antenna with two circular-shape slots etched on the top of the radiation plane and stacked one on top of the other. An FR-4 substrate with a dielectric constant of 4.3 and a thickness of 1.5 mm was used to create this antenna. The optimised antenna design has a 13.2 GHz operating frequency, a 4.913 percent bandwidth, and a peak gain of roughly 6.05 dB over the operating frequency, making it appropriate for wireless communication applications with good matching characteristics. CST Microwave Studio is used to compute the design model and performance evaluation of a proposed antenna..

Keywords: Wideband, low profile, a slot antenna vias, substrate integrated waveguide (SIW)

1. Introduction

In recent years, wireless communication systems which operate at microwave frequencies have evolved rapidly, where this area attracted many industrial and academic fields [1, 2, 3, 4]. substrate integrated waveguides SIWs technology has been replaced the conventional transmission lines over the old ones due to its desirable propagation characteristics and simple construction [5]. SIW technology has been introduced as one of the techniques available to provide low-cost implementation such as waveguide Components by using a standard PCB printed circuit board [6, 7], (SIW) have many advantages over conventional bulky metallic counterparts, such as low cost, small size and easy manufacturing along with the difficult characteristics of the waveguide including high power handling capability and low insertion losses and integration with planar circuits [8,9]. SIW configuration is a mixture of dielectric material embedded in linear arrays of metal vias along with upper and lowest conductive surfaces [10,11, 12].

Cassivi et al. were the first to present a substrate integrated waveguide cavity, which was implemented in a planar substrate using four rows of metallic vias [13]. Later The SIW technique has been used for designing and fabrication filters and slot antennas [14, 15, 16,17]. low profile designs antenna are achieved by using SIW technique for high gain and wideband [18, 19, 20, 21]. Impedance bandwidth was improved to up to 13.89% with moderate gain and unidirectional radiation characteristics in [22].

In this study, substrate integrated waveguide technology is applied to a traditional microstrip antenna with two circular slots etched on the antenna's top metallic surface for satellite applications. The classic rectangular waveguide, with SIW's periodic metallic vias serving as the standard waveguide's sidewall. As a result, this study presents a SIW antenna with two circular slots, which corresponds to a filling dielectric rectangular waveguide with two etched slots cut in the top wall of the waveguide [23].

2. SIW Microstrip Antenna Design Procedure

As illustrated in Fig.1, the SIW antenna is made by sandwiching two conductive layers between dielectric substrates that are connected on both sides by cylindrical metallic array vias and activated with inset feeding.

IMDC-IST 2021, September 07-09, Sakarya, Turkey
Copyright © 2022 EAI
DOI 10.4108/eai.7-9-2021.2315363

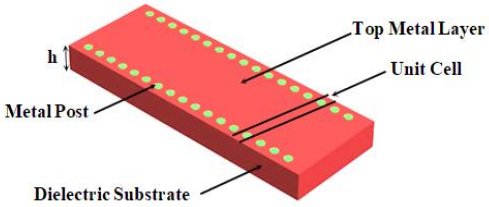

Fig. 1. SIW structure

The SIW's operating principle contains the artificial channel to Guiding the Wave inside the substrate. This is achieved by drilling the metal vias on the substrate that function as side walls to SIW structure Fig. 2 The SIW structured by choosing suitable dielectric material and that Just at the beginning of the antenna design stage should be considered taking into account parameters such as antenna bandwidth, size, gain, impedance matching, etc. and other Structure requirements.

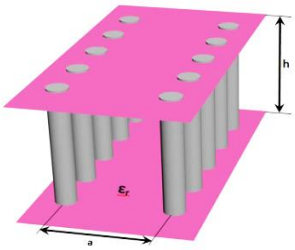

Fig. 2. SIW structure (conventional rectangular waveguide)

At the beginning, the dimensions of The antenna with microstrip patch in Fig. 3 A patch length (Lp) and patch width (Wp) can be obtained by equations below. [24] .

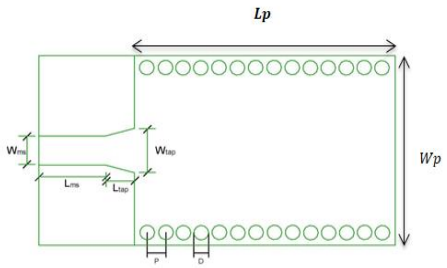

Fig. 3. Design geometry of the SIW antenna

Where

$$wp = \frac{c}{2f_o\sqrt{\frac{(\epsilon_r+1)}{2}}} \qquad (1)$$

$$lp = \frac{c}{2f_o\sqrt{\epsilon_{reff}}} - 2\Delta l \qquad (2)$$

C: Light speed within free space.

f_o: The frequency of resonances.

ϵ_r : The substrate dielectric constant.

ΔL: the extended increase of patch length

Can measure the effective dielectric constant as:

$$\epsilon_{reff} = \frac{\epsilon_r+1}{2} + \frac{\epsilon_r-1}{2}\left[1 + 12\frac{h}{w}\right]^{\frac{1}{2}} \qquad (3)$$

ϵ_r : Dielectric constant of the substrate.

$\in_{reff}$: Effective dielectric constant.
h: thickness of dielectric substrate.
w: the patch the width.
SIW's calculations include numbers of design equations and their design rules to ensure minimal losses from leakage between metalized via gaps in the structure of SIW [6]. Effects of p (pitch: distance between two vias) and d (diameter of hole) on those difficulties were explored in order to ensure that the waveguide section becomes free of leakage loss or radiation less [25].

$$d < \frac{\lambda_g}{5} \quad (4)$$

$$p \leq 2d \quad (5)$$

λg : Waveguide wavelength.
So, the cut off frequency (fc) of arbitrary mode for a rectangular waveguide, is found by the following formula:

$$fc = \frac{c}{2\pi}\sqrt{\left(\frac{m\pi}{a}\right)^2 + \left(\frac{n\pi}{b}\right)^2} \quad (6)$$

a, b: dimensions of the waveguide.
m, n: number of modes.
At fundamental mode, this can be simplified by:

$$f\,c = \frac{c}{2a} \quad (7)$$

For Dielectric filled waveguide width at the similar cut off frequency, dimension "ad" is given by:

$$a_d = \frac{a}{\sqrt{\in_r}} \quad (8)$$

We can now proceed to the SIW design equations after determining the dimension "a" for the Dielectric filled waveguide:

$$w = a_d + \frac{d^2}{0.98\,p} \quad (9)$$

Where d: diameter of via.
p: pitch (distance between two vias)

$$w = a_d - 1.08\frac{d^2}{p} + 0.1\frac{d^2}{a_d} \quad (10)$$

The SIW structure can be presented as simply rectangular waveguide as shown in Fig. 2 through the so-called equivalent width a_{eq}. This is stated as:

$$a_{eq} = asiw - \frac{d^2}{0.95\,p} \quad (11)$$

$$l_{eff} = l_{siw} - \frac{d^2}{0.95\,p} \quad (12)$$

3. The Proposed Antenna Configuration

The proposed SIW antenna construction has overall dimensions of 35mmx18mm and was developed as a single layer on FR-4 substrate with a relative permittivity of εr= 4.3, loss tangent of = 0.025, and a thickness of h=1.5 mm. It is fed by a 50 Ω microstrip line. 1.08mm and 1.20mm are the diameter and period of the metallic via, respectively. 15.8 mm is the equal distance between two rows of metallic vias. Equations (11) - (13) are used to calculate the SIW cavity dimensions (12). The suggested SIW antenna's geometry is depicted in Fig. 4, and the overall antenna dimensions are listed in Table 1.

Table 1: Parameter and dimension of SIW radiator.

Parameter Values (mm)	Parameter Values (mm)
The total length (L)	35
The total width (W)	18
Via's diameter (D)	1.08
Pitch between two vias (P)	1.20
Equavelent width of SIW (Asiw)	15.8
Microstrip Width (Wms)	1.56
Microstrip Length (Lms)	3.10
Taper 's width (Wtap)	3.58
Taper's length (Ltap)	4.90
Diamrter of circular slot(Dc)	12.5
Width of circular slot(Wc)	0.5
Distance between slots(S)	2

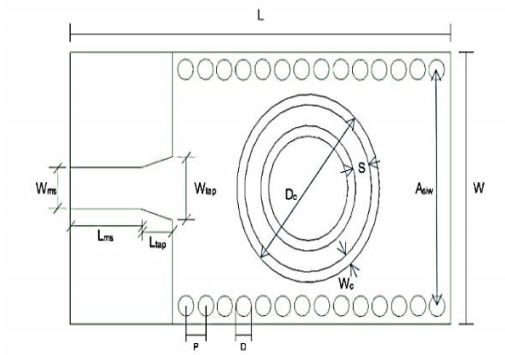

Fig. 4. Geometry of the proposed antenna

4. Results and Discussion

To assess and compare our results, we developed the first proposed antenna without SIW and slot, as shown in Fig. (5a). The antenna was created using the specified substrate. As illustrated in Fig. (5b), the antenna gives a single band resonance within the sweep frequency range of (9-20) GHz, with a resonant frequency of around 10 GHz. However, this behaviour does not rule out the potential of other resonances occurring outside of this frequency range.

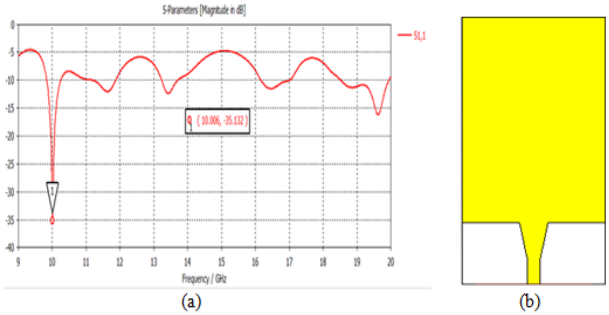

Fig. 5:(a) geometry of first proposed antenna (b) Simulated return loss response of antenna without SIW

Fig. 6 illustrates the computed two-dimensional directivity patterns of this antenna. The measured omnidirectional directivity is 8.8 dB with a peak gain 2.07 dB and fractional bandwidth (4.1%).

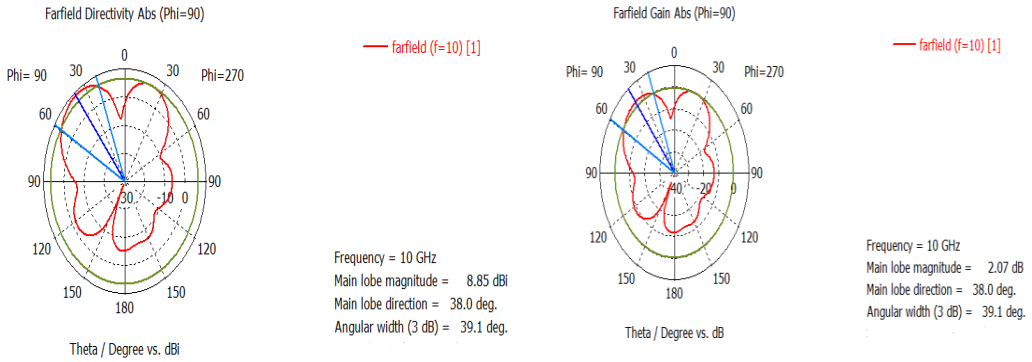

Fig. 6 simulated two-dimensional directivity radiation patterns

From the results, it was found that the proposed antenna doesn't satisfy the goal of frequency band, gain and bandwidth requirements for satellite applications, to achieve antenna match with Ku-band range application and satisfy these requirements, SIW antenna has accomplished. Where, SIW technique is applied with prescribed calculated dimensions of via and equivalent distance between vias to enhance the bandwidth and gain. Circular slot is added to increase the bandwidth, directivity, gain, and enhance the antenna matching. After executed above procedure, the proposed SIW antenna for one, two and three circular slot have done as shown in Fig. 7 (a to d).

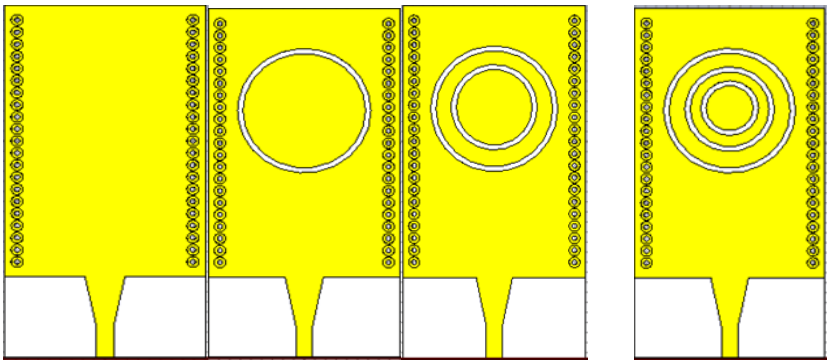

(a) (b) (c) (d)

Fig. 7: (a) SIW antenna without slots, (b) SIW with one circular slot.
(c) SIW with two circular slot. (d) SIW antenna with three circular slot.

The result in Fig. 7a shows that, when SIW applied on the conventional microstrip antenna, the antenna gives two resonant frequencies (14.8 and 19.22) GHz. Where the upper resonant frequency can satisfy the requirement range with peak directivity of (8.43 and 9.74) dBi , respectively for two resonance. As well as, the gains and bandwidth are (2.99 and 2.26) dB, (1.086% and 1.349%) GHZ respectively. Fig. 8 show the directivity and gain of the two resonance frequencies in polar form for the antenna shown in Fig. (7a).

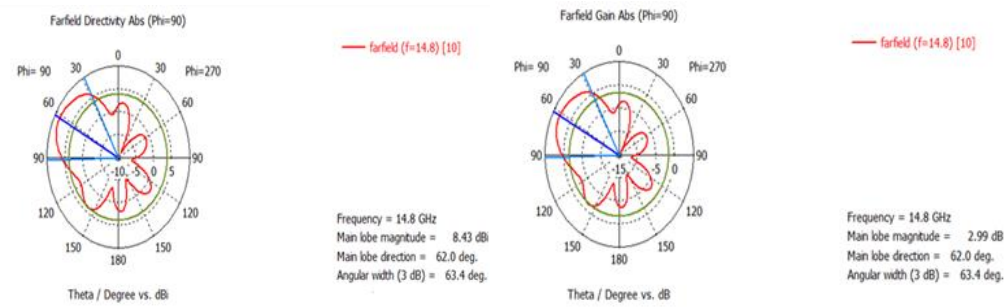

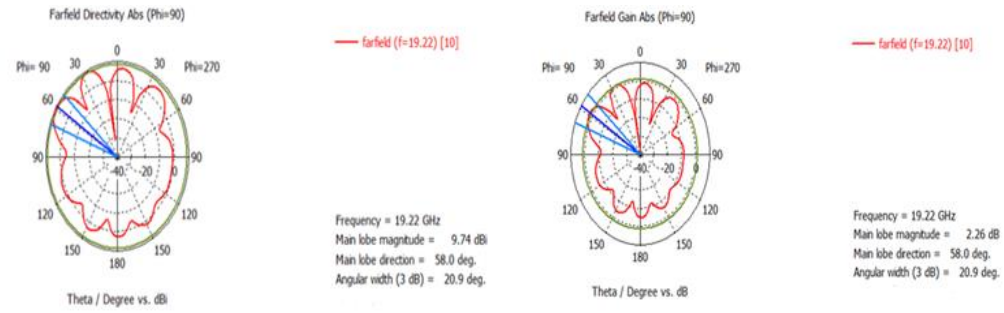

Fig. 8 directivity and gain of SIW antenna without slots for(14.8 and 19.22) GHz

While, Fig. 7b shows that when etched one circular slot on the one top of the antenna gives three resonant frequencies which are (11.20, 13.18, 19.53) GHz, the middle is at the required range, the peak directivities are (7.66, 8.34,10.1)dBi, respectively for (13.18)GHz. While the peak gain for the triple-band is (4.74, 5.53, 3.44) dB with fractional bandwidth about (502 , 1.001, 3) respectively. Fig. 9 show the directivities and gains of SIW one slot antenna in polar form.

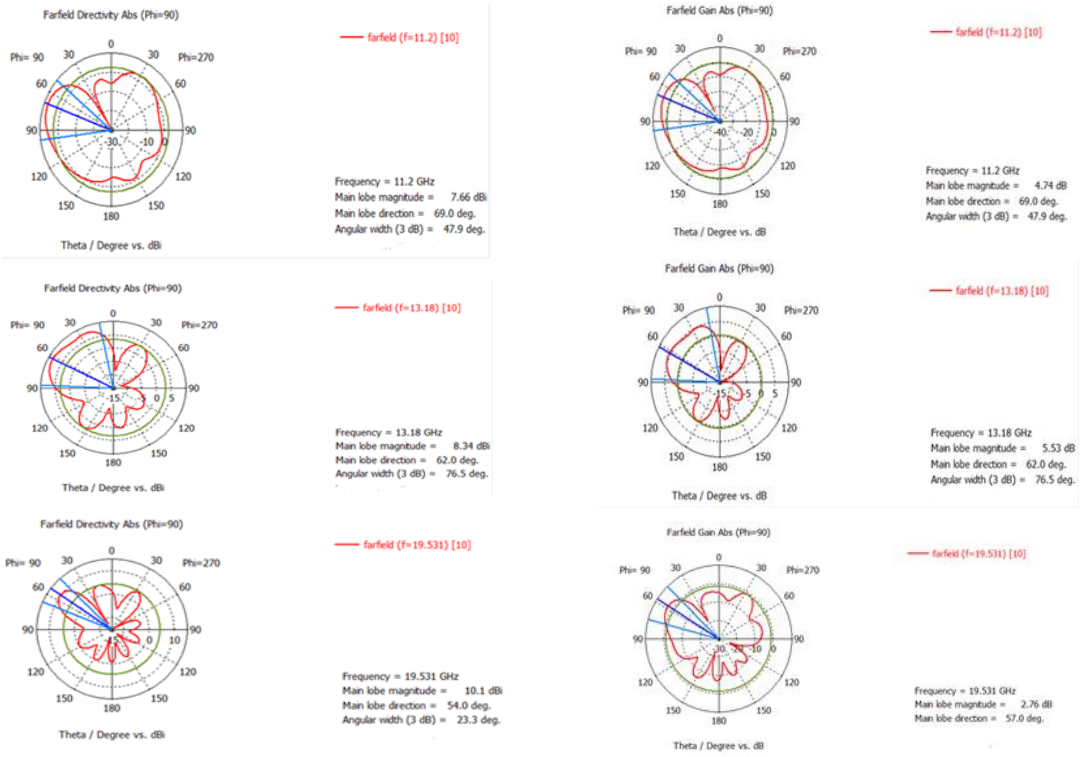

Fig. 9 Directivities and gains of SIW radiator with one circular slot

Meanwhile, results of the SIW radiator with two slot shows that etched two circular slots on the one top of the antenna give one resonant frequency about (13.2) GHz which is the required range. The directivity and gain are (8.56) (6.06) dB with a bandwidth about (4.913) GHZ. Fig. 10 shows the directivity and gain in polar form.

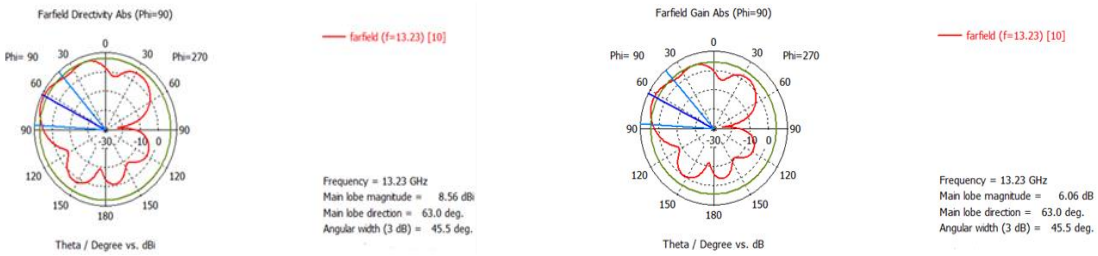

Fig. 10. Directivities and gains of SIW antenna with two circular slot

Finally, when the third slot is included the frequency is still about (13.2) GHz is in the required range, the directivity is 8.78 dBi, the gain is 6.28 dB with a bandwidth of about (3.568) GHz. Fig. 11 shows the directivity and gain in polar form.

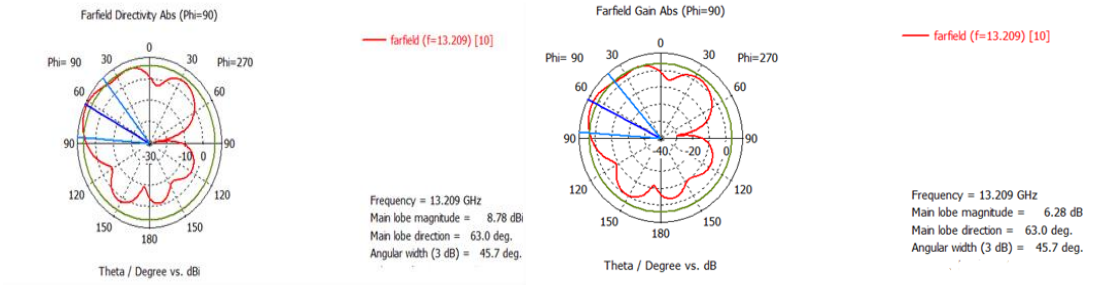

Fig. 11. Directivities and gains of SIW antenna with three circular slot

From the results, we can show that the antenna with two slots has properties that satisfy the requirement of the Ku-band. Therefore, to compare between results of SIW antennas, Fig. 12 illustrates the compression of s11 parameter for these SIW antennas.

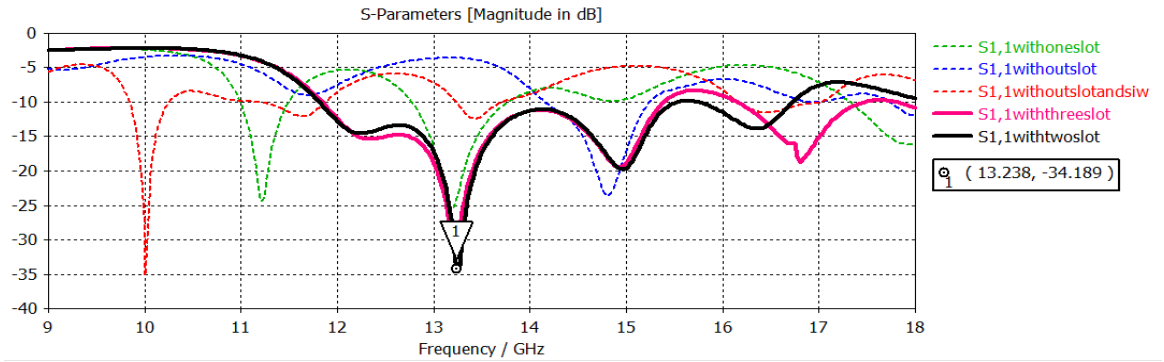

Fig. 12 S11 parameter for antennas without slots and with slots, one, two slots and three

5. Conclusion

According to the result of the first proposed antenna (without SIW and slot) has low gain and narrowband, when SIW technique and slots are added to the antenna structure to gives best radiation performances. Single circular slot etched on the top metallic layer as shown Fig.(7b) give triple-band resonant frequency while the gain is increased when the second slot is added, the antenna offers a wide band with higher gain reached to (4.9 GHZ). Finally when etched the third slot, the result improved slightly. This will lead to making the antenna with two circular slots satisfy the requirement of satellite application by improving the bandwidth, gain and directivity.

REFERENCES

[1] P. S. Newsletter, “Slotted Waveguide Antenna Arrays Hung Yuet Yee and Philip N . Richardson,” no. December, pp. 4–8, 1982.

[2] R. R. Shah, A. Patel, and V. E. D. V. Dwivedi, “Design, development and fabrication of post coupled band pass waveguide filter at 11.2GHz for radiometer,” *Microw. J.*, pp. 1–10, 2008.

[3] A. Patel, Y. P. Kosta, N. Chhasatia, and K. Pandya, “Multiple band waveguide based microwave resonator BraodBand Microstrip Fratcal Antennas View project Phase detection system based on digital signal processing in millimeter wave interferometer for fusion plasma diagnostics View project 58 PUBLICATIONS 157 CITATIONS SEE PROFILE IEEE-INTERNATIONAL CONFERENCE ON ADVANCES IN ENGINEERING, SCIENCE AND MANAGEMENT.”

[4] F. Mira, M. Bozzi, F. Giuppi, L. Perregrini, and A. Georgiadis, “Efficient design of SIW filters by

using equivalent circuit models and calibrated space-mapping optimization," *Int. J. RF Microw. Comput. Eng.*, vol. 20, no. 6, pp. 689–698, Nov. 2010, doi: 10.1002/mmce.20478.

[5] D. Deslandes and K. Wu, "Integrated Microstrip and Rectangular Waveguide in Planar Form," 2001.

[6] T. Djera, A. Doghri, and K. Wu, *Handbook of Antenna Technologies*, no. Salmon 2004. 2014.

[7] E. G. Turitsyna and S. Webb, "Simple design of FBG-based VSB filters for ultra-dense WDM transmission ELECTRONICS LETTERS 20th January 2005," *Electron. Lett.*, vol. 41, no. 2, pp. 40–41, 2005, doi: 10.1049/el.

[8] H. Y. Chien, T. M. Shen, T. Y. Huang, W. H. Wang, and R. B. Wu, "Miniaturized bandpass filters with double-folded substrate integrated waveguide resonators in LTCC," *IEEE Trans. Microw. Theory Tech.*, vol. 57, no. 1, pp. 1774–1782, 2009, doi: 10.1109/TMTT.2009.2022591.

[9] R. Arora, S. B. Rana, and S. Arya, "Performance analysis of Wi-Fi shaped SIW antennas," *AEU - Int. J. Electron. Commun.*, vol. 94, pp. 168–178, Sep. 2018, doi: 10.1016/j.aeue.2018.07.002.

[10] Z. Xu, J. Liu, S. Huang, and Y. Li, "Gain-enhanced SIW cavity-backed slot antenna by using TE410 mode resonance," *AEU - Int. J. Electron. Commun.*, vol. 98, pp. 68–73, Jan. 2019, doi: 10.1016/j.aeue.2018.10.039.

[11] H. A. Ali, E. Massoni, L. Silvestri, M. Bozzi, L. Perregrini, and A. Gharsallah, "Increasing the bandwidth of cavity-backed SIW antennas by using stacked cavities," *Int. J. Microw. Wirel. Technol.*, vol. 10, no. 8, pp. 956–967, Oct. 2018, doi: 10.1017/S1759078718000478.

[12] C. Zhang, J. Wang, M. Chen, Z. Zhang, and Z. Li, "A new kind of circular polarization leaky-wave antenna based on substrate integrated waveguide," *Int. J. Antennas Propag.*, vol. 2015, pp. 1–7, 2015, doi: 10.1155/2015/397960.

[13] O. Caytan *et al.*, "Half-Mode Substrate-Integrated-Waveguide Cavity-Backed Slot Antenna on Cork Substrate," *IEEE Antennas Wirel. Propag. Lett.*, vol. 15, pp. 162–165, 2016, doi: 10.1109/LAWP.2015.2435891.

[14] Y. Cassivi, L. Perregrini, K. Wu, and G. Conciauro, "Low-Cost and High-Q Millimeter-Wave Resonator Using Substrate Integrated Waveguide Technique."

[15] K. Mahant and H. Mewada, "A novel substrate integrated waveguide (SIW) based highly selective filter for radar applications," *J. Electromagn. Waves Appl.*, vol. 33, no. 13, pp. 1718–1725, Sep. 2019, doi: 10.1080/09205071.2019.1632747.

[16] L. Yan, W. Hong, G. Hua, J. Chen, K. Wu, and T. J. Cui, "Simulation and experiment on SIW slot array antennas," *IEEE Microw. Wirel. Components Lett.*, vol. 14, no. 9, pp. 446–448, Sep. 2004, doi: 10.1109/LMWC.2004.832081.

[17] S. Mukherjee, A. Biswas, and K. V. Srivastava, "Broadband substrate integrated waveguide cavity-backed bow-tie slot antenna," *IEEE Antennas Wirel. Propag. Lett.*, vol. 13, no. c, pp. 1152–1155, 2014, doi: 10.1109/LAWP.2014.2330743.

[18] A. M. Hamzah, L. Audah, and N. Alkhafaji, "H-Shaped Fractal Slots Based Highly Miniaturized Substrate Integrated Waveguide Metamaterial Bandpass Filters for C-Band Applications," vol. 86, no. March, pp. 139–158, 2020.

[19] P. E. Navamani and A. Swaminathan, "Low profile high gain circular SIW antenna for L and S band applications," *Microw. Opt. Technol. Lett.*, vol. 61, no. 11, pp. 2482–2490, 2019, doi: 10.1002/mop.31922.

[20] M. Asaadi and A. Sebak, "High-Gain Low-Profile Circularly Polarized Slotted SIW Cavity Antenna for MMW Applications," *IEEE Antennas Wirel. Propag. Lett.*, vol. 16, pp. 752–755, 2017, doi: 10.1109/LAWP.2016.2601900.

[21] G. Q. Luo, Z. F. Hu, W. J. Li, X. H. Zhang, L. L. Sun, and J. F. Zheng, "Bandwidth-enhanced low-profile cavity-backed slot antenna by using hybrid SIW cavity modes," *IEEE Trans. Antennas Propag.*, vol. 60, no. 4, pp. 1698–1704, 2012, doi: 10.1109/TAP.2012.2186226.

[22] A. Gupta, D. K. Srivastava, and J. P. Saini, "Modified e-slotted patch antenna for WLAN/Wi-Max satellite applications," *TELKOMNIKA (Telecommunication Comput. Electron. Control.*, vol. 18, no. 1, p. 258, Feb. 2020, doi: 10.12928/telkomnika.v18i1.12959.

[23] A. Kumar and S. Raghavan, "Broadband SIW cavity-backed triangular-ring-slotted antenna for Ku-band applications," *AEU - Int. J. Electron. Commun.*, vol. 87, pp. 60–64, Apr. 2018, doi: 10.1016/j.aeue.2018.02.016.

[24] Balanis et al., "ANTENNA THEORY ANALYSIS AND DESIGN ",1938, "Modern antenna hand book / Constantine A. Balanis. , Published by John Wiley & Sons, Inc., Hoboken, New Jersey,, 4th

ed,2016.

[25] K. Wu, D. Deslandes, and Y. Cassivi, “The substrate integrated circuits-A new concept for high-frequency electronics and optoelectronics,” *6th Int. Conf. Telecommun. Mod. Satell. Cable Broadcast. Serv. TELSIKS 2003 - Proc.*, vol. 1, 2003, doi: 10.1109/TELSKS.2003.1246173.

Seismic Performance Assessment and Upgrading of Al-Karamah Teaching Hospital Building under 2017 Halabjah Earthquake

Haider A. Abass[1], Husain K. Jarallah[2]
{hiaderaabass@uomustansiriyah.edu.iq[1], khalfdce@uomustansiriyah.edu.iq[2]}

Department of Civil Engineering, College of Engineering, Mustansiriyah University, Baghdad – Iraq[1,2]

Abstract. Seismic evaluation and retrofitting are considered very important issues in the maintenance and strengthening in terms of buildings resistance against earthquake loads. The study aims to apply a practical way, such as the seismic assessment of the Al-Karamah Teaching Hospital -Thalassemia Centre Building in Baghdad, Iraq. It is involving the analysis and converts 2017 Halabjah earthquake records to the response spectrum. By using the pushover analysis, the results were compared with results of (Design Basis Earthquake (DBE), and Maximum Considered Earthquake (MCE)) elastic response spectrum of the Iraqi Seismic Code (ISC-2017). The results were carried out in terms of capacity curves, performance level according to ATC-40, and the plastic hinge mechanism. Regarding the practical method aforementioned, the results illustrated that the plastic hinges formed in the primary elements (structural elements). The retrofitting mechanism was conducted by joining two parts of the Thalassemia Centre Building to be one entity. This technique leads to an increase in the base shear to (61.77%, 51.51%, 28.51%, and 70.85%) for two parts in the two directions (X and Y) respectively, a decrease in the roof displacement to (8%, 27%, 108.16%, and 387%) for two parts in the two directions (X and Y) respectively, neglecting the torsion effect, a decrease in the story drift and change the performance level of the building to the Immediate Occupancy (IO) level.

Keywords: Response Spectrum, Moment- Curvature Analysis, Iraqi Seismic Code, 2017 Halabjah Earthquake, Plastic Hinge.

1 Introduction

A complete study of the seismic evaluation will be much too wide for this study to undertake. However, several excellent references can be used as a starting point for the seismic evaluation such (ATC 40 [1]), (FEMA-365 (2)], and (FEMA-273 (3)]. The recent contributions of the seismic evaluation and previous efforts are most closely linked to the current project's requirements. For performance assessment, selecting suitable damage parameters is critical. Overall lateral deflection, inter-story drift, and plastic hinge rotation are the most commonly utilized damage parameters. Overall defection isn't usually a sign of damage, but inter-story drift is a good indicator of lateral load-resisting system deterioration [4]. They are also good damage guidelines since the maximum values of a member's or joint's rotations, curvature, and ductility factors are directly related to the element deformation capabilities. However, using merely the maximum value of each of these factors to calculate the total damage caused by a cyclic reversal of deformation may be insufficient [5]. For such cases, damage measures that account for both full deformation and cyclic effects have been developed. Both indices may be used to assess the

IMDC-IST 2021, September 07-09, Sakarya, Turkey
Copyright © 2022 EAI
DOI 10.4108/eai.7-9-2021.2315297

overall state of a structure [6]. Many existing systems are vulnerable, which may explain structural vulnerabilities and low ductility. Common structural weaknesses include lakes in the load direction, strength and rigidity dislocations, (perpendicular, lateral, and weight) abnormalities, weak column and strong beam, and eccentricity. Insufficient shear reinforcement, poor confinement, and a lack of anchorage length of the beam-reinforcement bars are all examples of low ductility details [7]. Other displacement-based damage metrics include curvature and ductility factors, lateral drift or roof displacement, inter-story drift, member or joint rotations, and other displacement-based damage parameters. Inter-story drift and lateral drift are two often utilized criteria that are part of the direct development of performance level. IDR (inter-story drift) is a key engineering response quantity and structural performance indicator. It's calculated by dividing the difference in translational displacement for two consecutive floors by the story height. While the maximum values of displacement-based damage parameters provide a good measure of damage, they ignore the damage caused by cyclic deformation reversal during earthquakes [8]. This study is concerned to implement a practical way of seismic evaluation and rehabilitation on the Al-Karamah Teaching Hospital-Thalassemia Centre building. This building was impacted by the 2017 Halabjha earthquake, and the main elements were damaged. The study analyzed the building by using pushover analysis. The results were carried out within capacity curves (Base shear versus Roof displacement), performance level, and plastic hinge mechanism. The technique that used in this study was more effective to retrofit the building, it decreases the story drift to the acceptable limits, neglects the torsion effect, and changes the performance level of the building to Immediate Occupancy IO level.

2 General Description

2.1 Description of the Thalassemia Centre Building

Al-Karamah Teaching Hospital is a large hospital to a very big population in the side of Al-Karkh (the western shore of the Tigris River as it ran through Baghdad) of Baghdad city in Iraq. It is considered one of the oldest and most famous major hospitals in Iraq. This hospital was established in 1927 with an area of 1.25 Hectare (72000 ft2) of capacity (445) beds. The hospital includes the consulting, emergency building, and departments (internal, surgical, private ward, urinary tract, eyes, ear, nose, throat, burns center, gynecology, obstetrics department, pediatrics department, fractures, and bones). The buildings already constructed are (1) Al- Hayat Dialysis Centre, (2) Thalassemia Centre, (3) Respiratory Care Centre, Nadori Surgery Centre, (4) Stem Cell Centre, (5) Centre for Diseases and dialysis (children), laboratories, unitsof supportive examinations. The hospital receives more than (18000) thousand patients per month and provides medical and health services to all citizens from all Iraqi provinces. In 2016, the Thalassemia Centre Building, which houses 195 patient beds, was completed. The center building is a six-story structure with a total area of around 1400m2. From an architectural standpoint, the first story is for consultants, the second story is for laboratories, the third flooris for hospital administration, and the other floors are designated as patient admissions corridors. The expansion joint divides the building into two sections. An expansion joint connects each block. The outside dimensions of the structure are approximately (50.4 x 32.4) m. The first component is rectangular in plan and has overall plan dimensions of 50.4 x 15.6 m. The second part is L shape in the plane, the first length is 21.6 m and the second length is 14.4 m, while the

width is 32.4 m. The first story height is 6.7 m, the second and third story is 5.7m, and the typical 4th,5th, and 6th story height is 4 m. **Fig 1** illustrates the interfaces of the Thalassemia Centre Building. From the structural point of view, Thalassemia Centre Building is on a raft foundation resting on medium-stiff soil. The foundation was meant to be 1.37 meters beneath the original ground level. The foundation slab is 0.9 meters thick. Under the raft foundation, a 50 mm thick lean concrete has been laid. Using a slab steel frame, the first, second, and third stories are divided to 1.8 m from the bottom slab level, and the secondary stories are used to fix the mechanical components (ducts, e.g.). A system of slabs and beams supported by columns carries the weight of the entire structure as well as the weight superimposed on the building. The slab system is a two-way waffle slab with a 70mm concrete slab on all floors. Between the two sections, there is a 175 mm clean gap. The plan with the column orientation is shown in **Fig.2**.

Fig. 1. Thalassemia Center Building Interfaces.

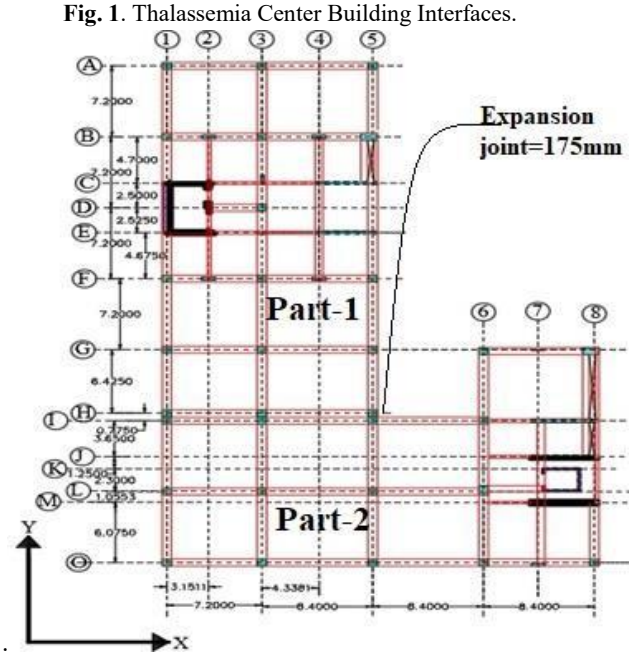

Fig. 2. Floor Framing Plan (All Dimensions in Meter Unit).

2.3 Description of 2017 Halabjah Earthquake

On November 12th, 2017, at 18:18:15 GMT, one of the greatest earthquakes was recorded struck the Iraq-Iran region. According to the US Geological Survey, the earthquake had a magnitude of 7.3 degrees on the Richter scale. The earthquake was named Halabjah earthquake, a city in Iraq's Kurdistan region because the epicenter was only 32 kilometers south of Halabjah city. Although the epicenter was near Kermanshah province in Iran, at 34.840°N latitude 45.924°E longitude, **Fig 3** depicts the location of the Halabjah earthquake.

Fig. 3. Regional Map Showing November 12, 2017, Earthquake.

2.4 Field Investigations

The Thalassemia Centre Building was damaged in the 2017 Halabjah earthquake, according to an inquiry. Figure 4 depicts the building's structural and non-structural damages.

Fig. 4. Damages in Thalassemia Centre Building. a) Structural Elements Damages and b) Non-Structural Elements Damages.

3 Materials Properties

The material parameters acquired from the structural drawings are shown in **Table** 1. The specified (default values) are translated to 'anticipated' values by a factor greater than one, according to ACI 369 R-11 [9].

Table 1. Materials Properties

	Concrete		Reinforcing Steel	
Member	Specified cylinder strength (MPa)	Expected cylinder strength (MPa)	Specified yield strength (Mpa)	Expected yield strength (Mpa)
Beam	30	45	420	525
Column	30	45	420	525

4 Building Modelling

4.1 Nonlinear Modeling of Beam-Column Frames

As frame elements, the centerlines of beams and columns are connected at nodes. There are five beam-column frames in the transverse direction and seven beam-column frames in the longitudinal direction. The first, second, and third stories' steel frames were computed and distributed as a concentrated force on the columns. The weight of the two-way waffle slabs with ribs was distributed to the surrounding main beams in triangular and trapezoidal segments.

4.1.1 Moment Curvature Analysis

A nonlinear geometrical model is used to model the beam-column frames. Using SAP 2000 Section Designer [10].

4.1.1.1 Results of Moment Curvature Analysis

Section Designer in SAP 2000 generated a moment-curvature analysis of beams sections [10]. Positive and negative moment-curvature of the beams have been established in three locations, two at the end span and one in the middle. The moment-curvature connection was idealized linearly [11,12]. The moment-curvature of beam-1 is shown in **Fig 5**, and the remaining beams have been defined using the same way.

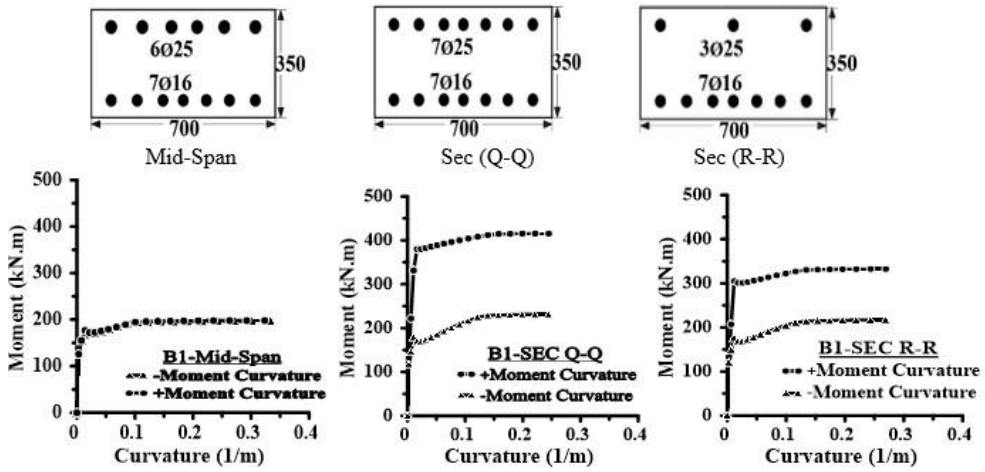

Fig.5. Moment-Curvature Relationship of Beams.

4.1.3 Results of Columns-Interaction

The moment-curvature and columns interaction relationship of the building columns is defined using SAP2000 Section Designer [10]. The results of existing column-1 interaction curves with various angles are shown in Fig 6, and the other columns were defined using the same way.

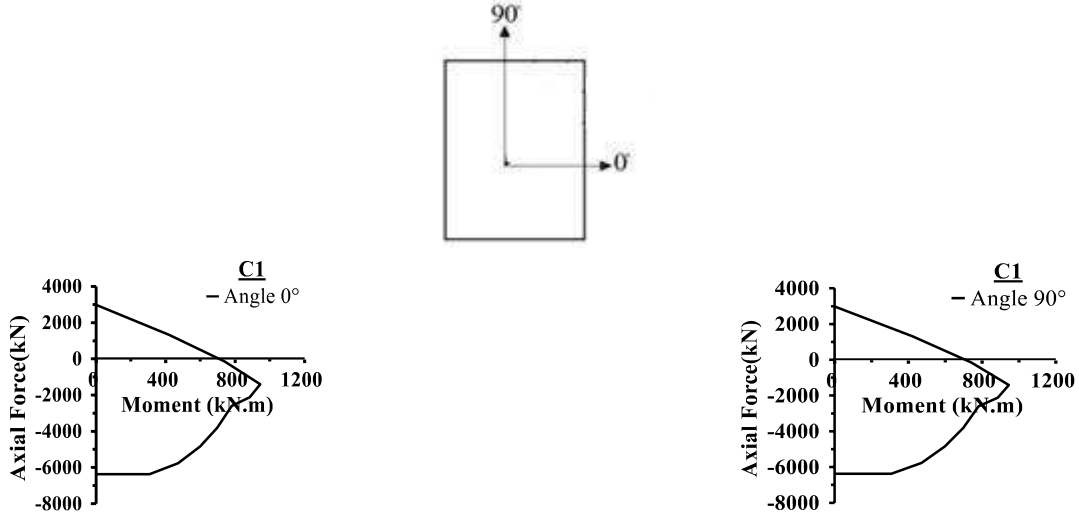

Fig.6. Existing Column-1 Interaction Diagram.

4.1.4 Nonlinear Modeling of Shear Wall

This study defines the shell component by using a multi-layered. This technique gives a better understanding of the seismic behavior of the shear wall. According to the mechanics of composite material, the shell element was defined by this technique. Several layers of varied thickness make form the shell element. Concrete and steel rebar components were assigned to different levels based on their qualities. In SAP2000 [10], the multi-layered shell element is shown in Fig 7. The reinforcing bars are distributed into two layers according to an existing shear wall of the hospital structure. The strain and curvature of the other layers are computed during finite element computations [13]. The stress will be calculated based on the material's constitutive relationships.

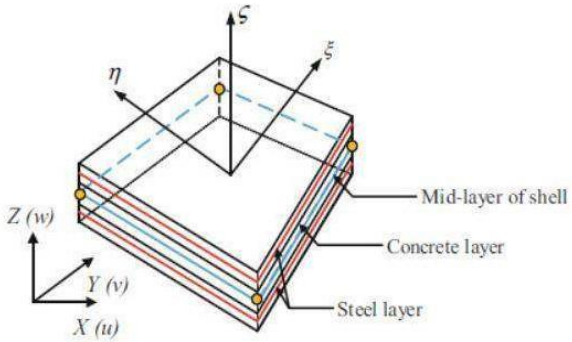

Fig.7. Multi-Layered Shell Element in SAP2000.

4.2 Properties of Nonlinear Plastic Hinges

Fig 8 shows the plastic deformation curve that are specified if it satisfies the point definitions. The origin is always Point A and cannot be adjusted. The whole deformation from Point A to Point B takes place within the frame element. The symbol B stands for yielding. The deformation at B is always zero since the hinges in this investigation are rigid plastic. As a result, there will be no deformation at B, and the hinge will only show plastic deformation beyond B. The ultimate capacity is specified as point C, and the residual strength is defined as point D. Point E denotes complete failure. As demonstrated in the figures, the load will be reduced to zero force/moment beyond E.

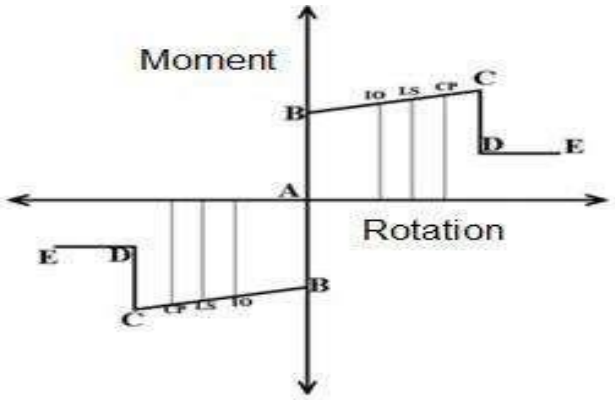

Fig.8. The curve of Actual Rigid- Used for Hinges.

4.2.1 Implementation of Moment- Rotation Relationship in Models

In SAP 2000 [10], the plastic deformation curve for hinges was implemented. On a moment-rotation diagram, A, B, C, D, and E must all be points. Where plasticity in the member is expected to occur, the curvature must be checked with a defined plastic hinge length, Lp. According to Park and Pualy [14] calculation, the plastic hinge length was assumed in (1).

$$L_p = 0.5 * H \quad (1)$$

For all section types with an expected shear wall, the length of the plastic hinge was calculated to equal half the depth of the member. The depth of each member and the lengths of plastic hinges employed are summarized in Table 2.

Table 2. Member Depths and Plastic Hinge Lengths.

Section	Depth (mm)	Hinge Length (mm)
Beams		
B (1-15)	350	175
B (12)	500	250
Columns		
C (1,4)	600	300
C (2,5)	1250	625
C3	1000	500
C6	500	250

4.3 Elastic Response Spectrum and Ground Motions

ISC-2017 [15] was used to determine the MCE and DBE elastic response spectra. To get the desired MCE, the established design spectral accelerations, Sa, were multiplied by 1.5. R, 0), Cd), and I have values of 4.5, 2.5, 5, and 1.5, respectively. The Halabjah earthquake's acceleration records were obtained from the Iraqi seismic network at the Iraqi Meteorological Organization and seismology (IMOS). In this study, two components were considered: X and Y components, which reflected the building's planning axis. The two components were analyzedand the response spectrum was conducted using PRISM software, as shown in **Fig 9**.

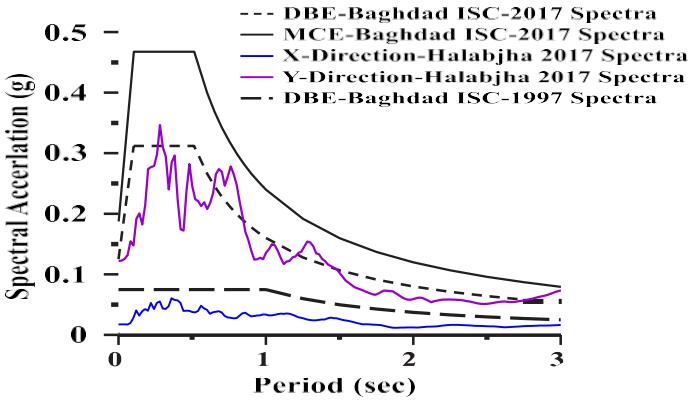

Fig.9. Response Spectrum Used in the Study.

4.4 Effect of Pounding

4.4.1 Studying of the Pounding Effect of Thalassemia Centre Building

Thalassemia Centre Building consists of two parts as shown in Fig 10. The expansion joint width is equal to 175 mm between the two parts of the building. According to ISC-2017, The maximum inelastic response displacement (δxt) must be allowed by separations. δxt shall be determined at critical locations using the following equation, taking into account the structure's translational and torsional displacements, as well as torsional amplifications, where applicable:

$$\delta_x = \frac{C_d \delta_{max}}{I_e} \tag{2}$$

Where δx denotes the max. elastic displacement at the critical point. Adjacent structures must be separated by at least δx, which is calculated as follows:

$$\delta_{xt} = \sqrt{(\delta_{x1})^2 + (\delta_{x2})^2} \tag{3}$$

where δx_1 and δx_2 are neighboring structures maximum inelastic response displacements at their adjacent edges. In this study, eight cases have considered its effect to study the pounding effect on the building, the eccentricity, and the orthogonal direction of the seismic loads. Table3 presents the seismic loading example that was applied.

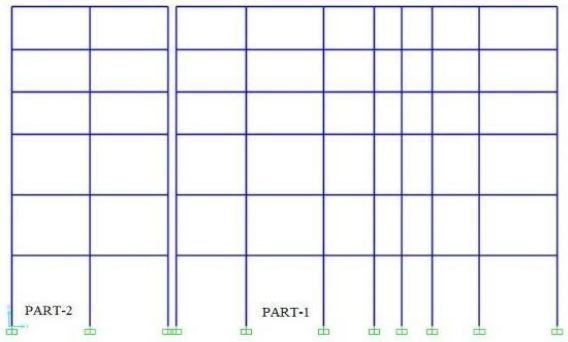

Fig. 10. Expansion Joint Between Two Parts of Building.

Table 3. Seismic Loads Cases.

Seismic Load Case	Eccentricity	Seismic Load Case	Eccentricity
EQ-X1	0.05	EQ-Y1	0
EQ-X2	-0.05	EQ-Y2	0
EQ-X3	0	EQ-Y3	0.05
EQ-X4	**0**	EQ-Y4	-0.05

Eight seismic load combination is considered to study the pounding effect on the building as follows:

1- EQ1=EQ-Y1+0.3EQ-X1 .....(4 a)
2- EQ2=0.3EQ-Y1+EQ-X1 .....(4 b)
3- EQ3=0.3EQ-Y2+EQ-X2 .....(5 a)
4- EQ4=EQ-Y2+0.3EQ-X2 .....(5 b)
5- EQ5=0.3EQ-Y3+EQ-X3 .....(6 a)
6- EQ6=EQ-Y3+0.3EQ-X3 .....(6 b)
7- EQ7=0.3EQ-Y4+EQ-X4 .....(7 a)
8- EQ8=EQ-Y4+0.3EQ-X4 .....(7 b)

4.4.2 Pounding Effect Results

Fig 11 and Table 4, present the results of the pounding effect on the thalassemia center building by various seismic load cases. From Figure, the pounding will have happened from two combination load cases (EQ-5 and EQ-6) between the two parts of the building.

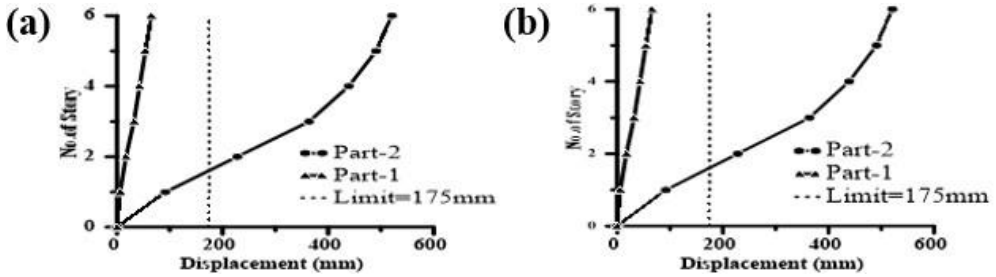

Fig.11. Pounding Effect Between Two Parts of Building. a) 1st Load Combination Case and b) 3rd Load Combination Case.

Table 4. Pounding Values between Two Parts.

Seismic Combination Load Case	Building		Maximum Elastic Displacement ($\boldsymbol{\delta_{xt}}$)(mm)	Limit (mm)
	Part-1	Part-2		
	$\boldsymbol{\delta_x}$(mm)	$\boldsymbol{\delta_x}$(mm)		
1st Load Combination Case	124	470.4	486.47	175
3rd Load Combination Case	118	450.2	465.40	175

4.5 Modelling of Diaphragm

The floor slabs of the buildings were modelled as a 'rigid diaphragm'. Based on pounding effects, the rigid diaphragm represented two parts of the building as one part. In the present work, such diaphragms were modelled for every story of the building.

4.6 Model Analysis and Dynamic Characteristics

By using SAP 2000 [10], the model analysis has been performed. **Fig. (12)** presents the dynamic characteristics of the whole building. The first mode shape represents displaced sway,with a higher inter-story drift at the bottom and a decreasing inter-story drift as the structure rises as shown in **Fig 12**.

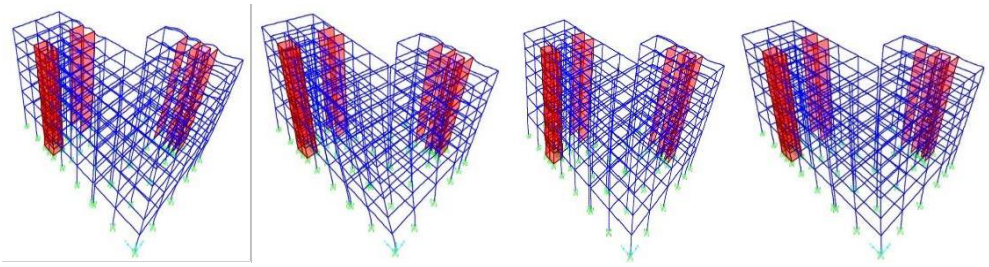

Mode-1, T=0.33sec Mode-2, T=0.27sec Mode-3, T=0.24sec Mode-4, T=0.19sec

Fig. 12. Modes Shape of Thalassemia Centre Building.

4.7 Lateral Load Distributions

By calculating the base shear forces and displacements connected to the advancement of yielding in building elements at various phases, the pushover study determines the building levels. According to equation (8), lateral forces are applied in proportion to the story masses and the square height of the floor.

$$F_i = \frac{m_i h_i^k}{\sum_{j=1}^{n} m_j h_j^k} \quad (8)$$

The mass and height of the i^{th} floor are represented by m_i and h_i.
The original load distribution was employed in the analyses for each direction. Pushover analyses in both directions use the same lateral load distribution Fig 13.

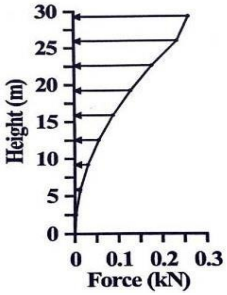

Fig. 13. Distribution of the Lateral Load for Pushover Analysis.

4.7.1 Implementation of Pushover Analysis and Results

After the gravity pushover, the lateral pushover analysis in the two directions X- and -Y was done under displacement control. The structure is pushed to one side until a collapse mechanism occurs. As a bare frame, the models used in the pushover analysis.

4.7.1.1 Pushover Analysis Results

In the real situation of the Thalassemia Centre Building, the implementation of pushover analysis in two parts of the building has been performed. Fig 14 shows the Part-1, Part-2, and 2parts together of the Thalassemia Centre Building.

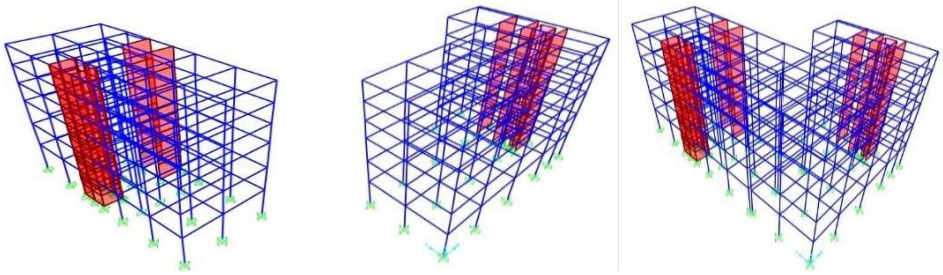

a) Part-1 b) Part-2 c)2Parts together

Fig. 14. Thalassemia Centre Building under study.

4.7.1.1.1 Capacity Curve Results

Under the effect of the 2017 Halabjha earthquake, the building (for the two parts) was impacted by the earthquake. Fig 15 illustrated the capacity curves of the real situation of the building with the suggested retrofitted technique.

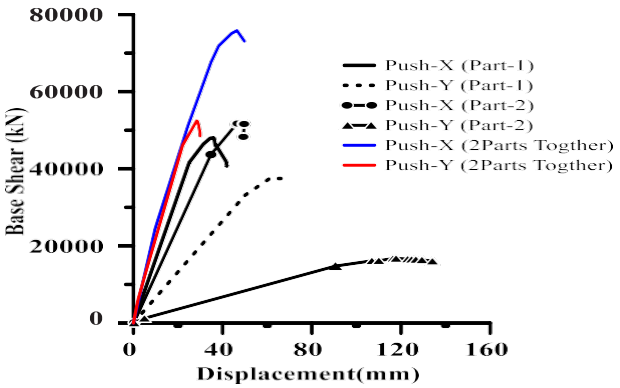

Fig. 15. Capacity Curves of Thalassemia Center Building Parts.

4.7.1.1.2 Performance Point Results According to ATC-40

Figure 16 and Table 5 demonstrate the building's performance level using the capacity spectrum technique based on ATC-40 [1] with 5% initial dampening.

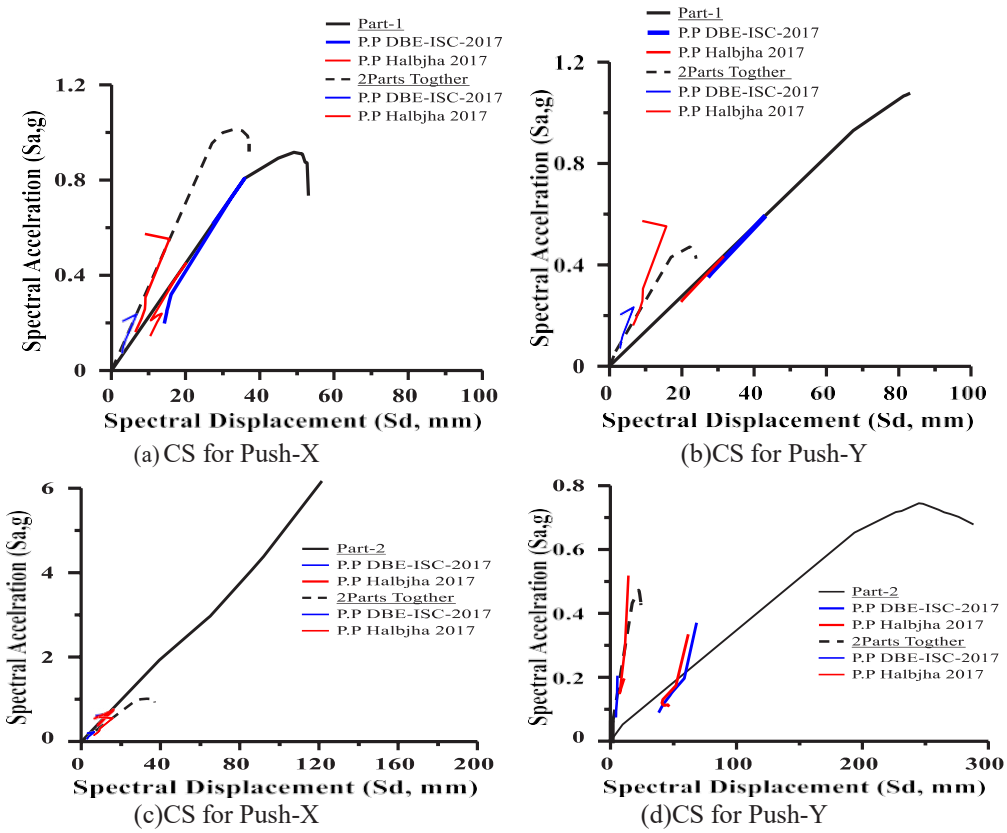

Fig. 16. Capacity Spectrum for Push-X and Push-Y for Part-1(DBE, ISC-2017and Halabjah-2017).

Table 5. States of Performance Points According to ATC-40 for Part-1

		Part-1		Part-2		2Parts together	
Direction and Earthquake level		**Vb (kN)**	**Roof Displacement Δroof(mm)**	**Vb (Kn)**	**Roof Displacement Δroof(mm)**	**Vb (k N)**	**Roof Displacement Δroof(mm)**
X	DBE ISC-2017	31792.38	19.12	10097.43	8.19	55723.46	21.00
	MCE ISC-2017	43422.36	27.4	16458.34	13.22	98396.72	38.00
Y	DBE ISC-2017	21161.60	31.95	5313.338	30.80	42356.10	33.00
	MCE ISC-2017	31372.08	17.36	7509.58	24.68	50630.50	27.00
X	Halabjah 2017	17759.30	10.69	9504.60	7.72	43116.06	16.00
Y	Halabjah 2017	15521.95	23.43	4852.9	27.89	33707.38	28.00

4.7.1.1.3 Plastic Hinge Mechanism

Fig 17 presents the plastic hinge mechanism for Part-1, Part-2, and 2 parts together, it shows that the plastic hinge is formed in the structural elements, this reflects that the two parts cannot be insufficient to resist the Halabjha earthquake as a bare frame.

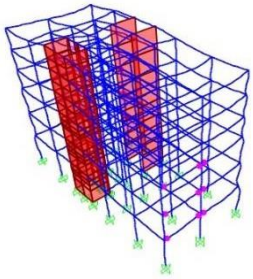

a) X-.Direction (DBE), Part-1

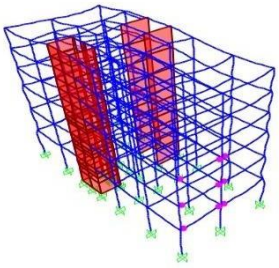

b) Y-.Direction (DBE),Part-1

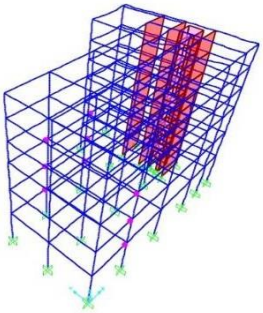

c) X-Direction (DBE),Part-2

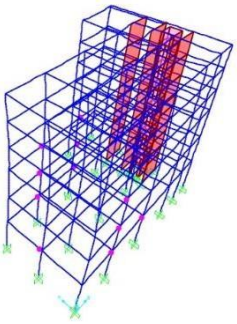

b) X-Direction (DBE), Part-2

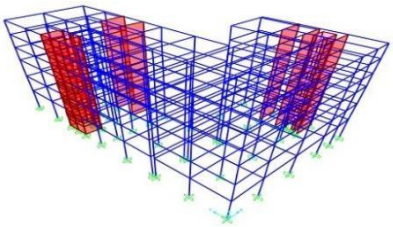

d) X-Direction (DBE),2Parts togther

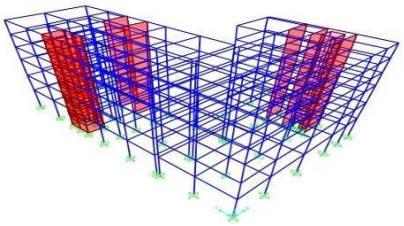

e) X-Direction (DBE), 2Parts together

Fig. 17. Plastic Hinge at Performance Point.

5 Conclusions

It can be concluded, based on the limitations of assessment codes and testing procedures, that:

1. The technique leads to an increase in the base shear to 61.77% and 51.51% higher than the base shear of Part-1 in the X and Y directions respectively, on other hand, it leads to a decrease in the roof displacement to 8% and 27% less than the roof displacement of Part-1 in the X and Y directions respectively.
2. In the X and Y directions, the mechanism causes the base shear to increase to 28.51 percent and 70.85 percent higher than the base shear of Part-2, respectively; on the other hand, it causes the roof displacement to decrease to 108.16 percent and 387 percent less than the roof displacement of Part-2, respectively.
3. The results of the plastic hinge mechanism clarified that Thalassemia Centre Building (as one entity) doesn't form any plastic hinge with the Halabjah response spectra and MCE of ISC-2017, and the building was in Immediate occupancy.
4. The torsion effect, the results explained that no torsion effect on the building.
5. The inter-story drift, the result showed that the inter-story drifts within acceptable limits.
6. According to ISC-2017, the values of spectral response acceleration at short and 1 sec periods were suitable and appropriate for use in seismic analysis and design. According to the DBE response spectrum of ISC-2017, the rise in base shear in X and Y directions was 22.62 percent and 20.42 percent higher than the values of Halabjah earthquake spectra, respectively.
7. According to the DBE response spectrum, the roof displacement increased by 23.80% and 20% in the X and Y directions, respectively, compared to the Halabjah earthquake spectra. [9] According to the MCE response spectrum of ISC-2017, the increase in base shear was 56.18 percent in X directions and 33.42 percent in Y directions, respectively, compared to the values of Halabjah earthquake spectra.
8. In the X and Y directions, the increase in roof displacement was 57.89 percent and 40.74 percent higher than the values of Halabjah earthquake spectra, respectively.
9. This Technique of retrofitting will apply to Thalassemia Centre Building becausethe Ministry of Health has not taken any previous or current action of rehabilitation.

Acknowledgments

The authors would like to express their gratitude to Mustansiriyah University (www.uomustansiriyah.edu.iq) in Baghdad, Iraq, for their assistance with this project.

References

[1] Applied Technology Council, "Seismic Evaluation and Retrofit of Concrete Buildings", Report No. SSC 9601: ATC-40, Vol.1, Redwood City, California,1996.

[2] Federal Emergency Management Agency, "Pre Standard and Commentary for the Seismic Rehabilitation of Buildings", FEMA-356, Washington, D.C, 2000.

[3] Federal Emergency Management Agency, “NEHRP Guidelines for the Seismic Rehabilitation of Buildings”, FEMA-273”, Washington, D.C, 1997.
[4] Deng, M.K., Liang, X.W., Wang, Q.L. and Cai, D.Y., “Research on Calculating Methods of Story Drift for Reinforced Concrete Shear Wall Structures”, Journal of Earthquake Engineering and Engineering Vibration 28:3, 95-103, 2008.
[5] Just, G., Koch, I., Brod, M., Jansen, E., Gude, M. and Rolfes, R. “Influence of Reversed Fatigue Loading on Damage Evolution of Cross-Ply Carbon Fibre Composites. Materials”, 1153, doi:10.3390/ma12071153, 2019.
[6] Bagchi, A., “Evaluation of The Seismic Performance of Reinforced Concrete Buildings”, Ph.D., dissertation to Civil and Environmental Engineering, Carleton University, Ottawa, Canada, 2001.
[7] He, H., Cong, M. and Lv, Y., “Earthquake Damage Assessment for RC Structures Based on Fuzzy Sets”, Mathematical Problems in Engineering, Hindawi Publishing Corporation, Article ID 254865, 2013.
[8] Dumaru, R., “Seismic Performance Assessment and Strengthening Techniques for Existing Reinforced Concrete in Nepal”, Ph.D., dissertation to the Faculty of Engineering of the University of Porto, Portuguese public,2018.
[9] Guide for Seismic Rehabilitation of Existing Concrete Frame Building and Commentary (ACI 369R-11), Reported by ACI Committee 369,2011.
[10] Computers and Structures, SAP2000 v22 Integrated finite element analysis and design of structure basic analysis reference manual, 2012.
[11] Bolander, J., “Investigation of Torsional Effects on Thirteen-Story Reinforced Concrete Frame-Wall Structure Modeled in ETABS and SAP2000 Using Linear and Nonlinear Static and Dynamic Analyses”, M.Sc. thesis submitted to civil engineering, University of California, San Diego, 2014.
[12] Kasimzade, A., Nematli, E., Mammadzada,V. and Atmaca,G., “New Design Criteria in Performance Based Earthquake Engineering”, International Journal of Trend in Scientific Research and Development (IJTSRD), Vol: 4, 2020.
[13] Fahjan, Y.M, Kubin, J., and Tan, M.T., “Non-Linear Analysis Methods for Reinforced Concrete Buildings with Shear Walls”, 14 European Conference on Earthquake Engineering, 2010.
[14] Park, R. and Paulay, T., “Reinforced Concrete Structures”. New York: John Wiley & Sons, 1975.
[15] Ministry of housing and construction, Iraq "Iraqi seismic code requirement for buildings",2017.

Effect of Imperfection Factors on Simulation of the Slender RC Columns Strengthened by SFR Using ABAQUS

Wameedh I. Braidi[1], Mohammed S. Al-Helfi[2]
{wameedhissa@uomisan.edu.iq[1], mohmsce1974@stu.edu.iq[2]}

University of Misan, Dep. Of Civil Engineering[1]
Southern Technical University, Technical Institute of Amara[2]

Abstract. Due to geometric effects rather than material failure, buckling is the most typical failure mode of slender RC columns. Real columns are never perfect, and their flaws have a big effect on their stability, therefore, to use FEA software to study slender RC columns, requires a number for this imperfection, known as the imperfection factor. By checking experimental fields, codes provide some imperfection factor values to utilize in design and analysis these factors cover all kinds of imperfection that means they will be a flexible value. On the other hand, numerical fields like FEA software manuals dose note give a clear way to specify the imperfection factor according to experimental references especially material imperfection dependency. The results of the analytical model of the slender RC columns are presented in this work. The investigation includes the creation of an analytical model based on the finite element approach using ABAQUS/Standard 2020 software to see how material variation affects the value of the imperfection factor. The analytical model was compared to the experimental work utilizing similar properties to validate the results. All columns were axially loaded. The experimental and finite element results were in good agreement. From the relationship between SFR variation and the imperfection factor, a second-order equation could be suggested.

Keywords: Buckling, Slender RC column, FE analysis, ABAQUS, Imperfection.

1 Introduction

Buckling is a physical phenomenon in which a relatively straight, slender member (or body) bends laterally (typically suddenly) from its longitudinal position due to compression [1]. Buckling, rather than material failure, is a loss of stability caused by geometric effects. However, if the resulting deformations are not controlled, the material can fail and collapse [2]. Real columns are never perfect, and defects in them have a significant impact on their stability. The real columns buckle before the buckling force because of these defects from the perfect shape or material [3]. The material yielding or the column buckling can both cause a column to fail. It is of interest to the engineer to determine when this changeover takes place. In slender columns, buckling is a more common mode of failure. Imperfection refers to the trait or state of being imperfect. These imperfections are divided into geometric imperfection, thickness imperfection, material imperfection, and boundary imperfections [4]. Local and overall (bow, global, or out-of-straightness) geometric imperfections are the two basic categories of initial geometric imperfections. Initial local geometric imperfections can be discovered on the outer or

IMDC-IST 2021, September 07-09, Sakarya, Turkey
Copyright © 2022 EAI
DOI 10.4108/eai.7-9-2021.2314928

inner surfaces of metal structural members in perpendicular directions to the member surfaces. Initial overall geometric imperfections, on the other hand, are global profiles for the entire structural member throughout its length in any direction. An eccentricity of

$$e_j = l_0 /400 \quad (1)$$

where l_0 is the effective length

maybe used as a simplified alternative for walls and isolated columns in braced systems to cover imperfections associated with normal execution variations [5]. Or the eccentricity equal of:

$$e_0 = \alpha m \, L / 500 \quad (2)$$

where L is the span of the bracing system

$$\text{and } \alpha_m = \sqrt{0{,}5(1 + \frac{1}{m})} \quad (3)$$

in which m is the number of members to be restrained [6]. Equivalent geometric imperfections, with values that reflect the impacts of both global and local imperfections, should be utilized. From the previous equations (1,2) Eurocodes offered a similar range for the imperfection factor in concrete and steel structures. In this study, because of the columns subjected to the concentric load, therefore the eccentricity (e) is equal to the imperfection factor (IMF). Perturbations in geometry are the most common source of imperfections. Abaqus allows you to define an imperfection in three ways: as a linear superposition of buckling eigenmodes, via static analysis displacements, or by directly providing the node number and imperfection values. The perturbations utilized are usually a few percent of a relative structural dimension like a beam cross-section or shell thickness [7]. Nessa Yosef Nezhad Arya in 2015 studied the second-order FE analysis of axial loaded concrete members according to Eurocode 2, the nonlinear analysis focused on concrete material modelling and its nonlinear behaviour, by comparing the FEA results of a benchmark experiment, the finite element model was confirmed [8]. Alaa Hussein Al-Zuhairi & Safaa Qays Abdulrahman in 2020 studied the performance of slender reinforced concrete columns with different cross-sectional shapes, the study aimed to use nonlinear finite element analysis to explain the structural performance of slender SSRC columns both experimentally and numerically [9]. Four samples were selected “first one normal concrete and the other three was strengthened with SFR” from an experimental study where don by Al-Helfi & Allami (the strengthening effect of SFR and CFRP on a part or whole of the of slender RC columns) one was a reference and others were compared [10] to investigate the material variation effect on the imperfection factor using ABAQUS/Standard 2020.

2 Experimental Programs

All columns were axially loaded, with dimensions of 2000 mm in length and 120 mm x 60 mm in cross-section, column top, and bottom ends were supported by load plate working as a hinge, and the major longitudinal reinforcement was symmetrically 2 x 3Ø6. The stirrups were Ø6 @ 50 mm along with 300 mm from the ends of the column, with 150 mm in the remaining length. The first reference column (SC11) tested was not strengthened, whilst the other columns were strengthened using SFR as detailed in Table 1.

Table 1. Summary of Experimental Results.

Column ID	Strengthened Materials	Length of Strengthened	Fcu (Mpa)	EC (Mpa)	Ultimate Load Test Result (KN)
SC11	Non	Non	35	24870	182
SC21	SFR	L	55	31176	261
SC22	SFR	L/2	55	31176	260
SC23	SFR	L/3	55	31176	244

3 Finite Element Analysis

Because laboratory studies require expensive equipment and tools, as well as a specialized laboratory with qualified workers to complete the experiments, they do not cover a large variety of factors. As a result, the finite element method (FEM) is the most suited tool for expanding the range of parameters to be investigated. A three-dimensional nonlinear numerical analysis has been carried out to simulate the imperfection factor effect on RC columns buckling.

3.1 Analysis Procedure

There are two types of research methods in Abaqus: linear and nonlinear. Because the buckling behaviour cannot be obtained, the nonlinear analysis couldn't depict axially loaded slender column real behaviour in this paper, for both static general and dynamic analysis produced by Abaqus software. This development occurred because of two aspects. First, all FEM equations are based on the equilibrium of stresses and strain compatibility, which means that these equations are impossible to solve due to the discontinuous response at the buckling point. Second, up until final collapse, A perfect (ideal) column is used to illustrate the FE model. Instead of bifurcation, Abaqus handles the discontinues problem by displaying a geometric imperfection mode in the perfect (ideal) geometry of the model. In Abaqus, there are numerous approaches for defining an imperfection. One of these techniques is to use the *IMPERFECTION keyword to directly apply the imperfection in the input file. This necessitates data like eigenvalues and buckling modes, which were provided via linear elastic buckling analysis. In a brief, the FE simulation of the provided specimens necessitated the creation of two models for the same mesh: To determine the likelihood of collapse, an initial model for elastic buckling analysis was developed as shown in Fig 1. This model was analysed with linear elastic buckling to get possible buckling mode and Eigenvalue of this mode which represent the critical load. The plastic model then imports imperfection data (buckling mode,

Eigenvalue) from the linear analysis to do the nonlinear analysis of slender RC columns [7]. The input file of both models has been altered as shown in Fig 2.

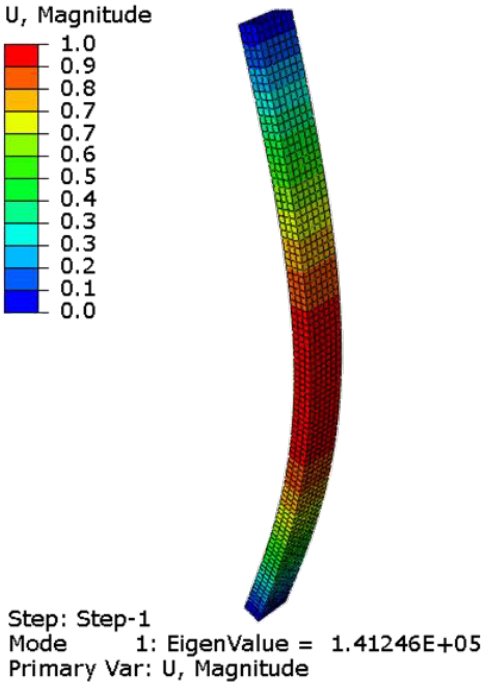

Fig. 1. Linear analysis (buckling mode).

```
**OUTPUT REQUEST
**
*Restart, write, frequency=0
**
**FIELD OUTPUT: F-Output-1
**
*Output, field, variable=PRECELECT
*NODE FILE
U
*End Step
```

(a) Elastic model

```
**- - - - - - - - - - - - - - - - - - - - - - - - - - - - -
- -
*IMPERFECTION, FILE=Job-1,
STEP=1
1,4
**
**STEP: Step-1
**
*Step, name= Step-1, nlgeom= YES
*Dynamic, Explicit
,1.
```

(b) Plastic model

Fig. 2. The input file of imperfection factor (highlighted characters).

3.2 Material Properties

Plain concrete's nonlinear behaviour in compression and tension was simulated using the concrete damage plasticity model (CDPM), which took damage characteristics into account. To explain the response of plain concrete with uniaxial and compound stresses, CDPM employs two types of parameters. The reinforcing steel bars were also modelled using Abaqus' plasticity model, which used a bilinear model to characterize the stress–stress relationship of reinforcement. Up to the yielding point, the bilinear model is elastic, and between the yielding point and the start of strain hardening, it is ideal plastic as shown in Fig 3.

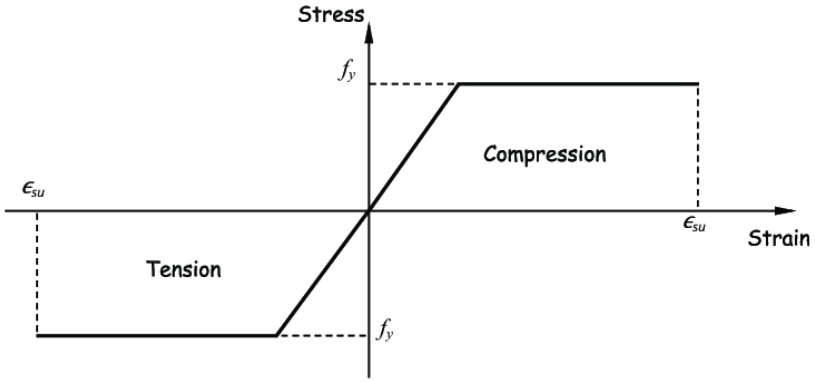

Fig. 3. Stress-strain curve for steel reinforcement.

3.3 FEA model boundary conditions, interaction, and meshing

Both ends of the samples were treated as pinned ends in the nonlinear analysis, identical to the test condition. Reference points (RP) were used to simulate the pin ends conditions. At both ends, the movement was constrained in all axes, except the axial movement at the top end was allowed. Although all rotations in all axes were allowed. To ensure a complete link between the reinforcing bars and the concrete, the interactions were represented as an embedded region. In the linear and nonlinear analyses, a mesh size of 20 mm was chosen for concrete and reinforcement. Concrete was modelled using C3D8 element, 8-node linear brick. The steel reinforcement was modelled using D3T2, a two-node linear three-dimensional truss as shown in Fig 4.

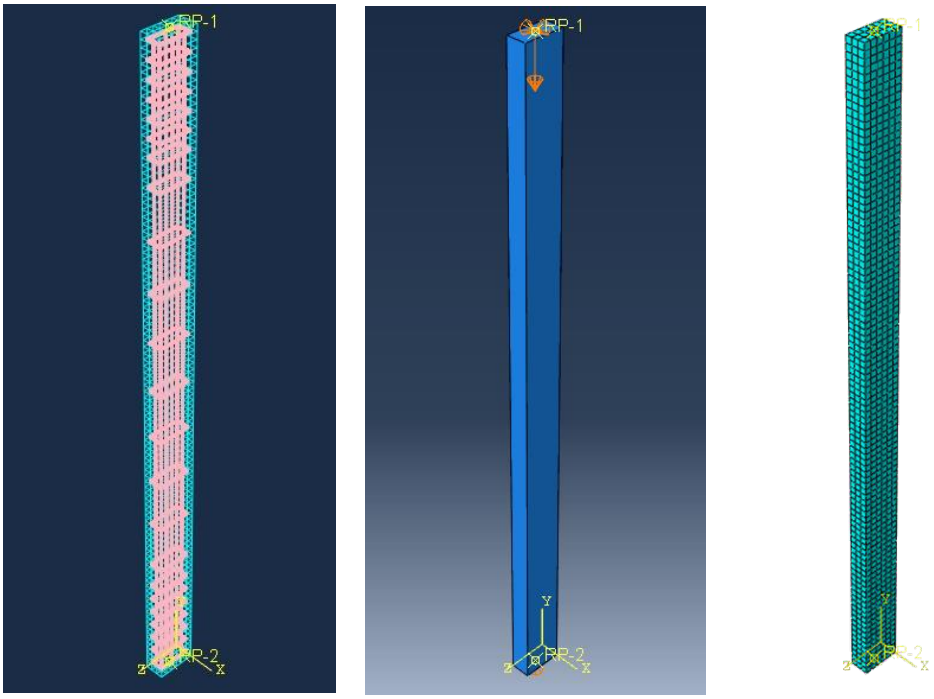

(a) Boundary conditions (b) Interaction (c) Meshing

Fig. 4. Slender RC column modelling.

4 Analysis Results and Discussion

4.1 Imperfection Factor Check

In this section two verification are presented: first, check to see which imperfection factors provided by Eurocodes give satisfying results for the reference model, and the second check by choosing different imperfection factor values in addition to reference model imperfection factor to investigate SFR strengthened effect.

4.1.1 Reference Model

Using the numerical method highlights the fact that the results may not be precise because of material properties and modelling errors. Referring to Eurocode 2 [8] and Eurocode 3 [9], two values will be tested through the simulation respectively to compare with the experimental reference model (normal concrete) results:

$$L = \text{clear length of column} = 2000\text{mm}$$

From equation (1)

Imperfection factor = L / 400 = 2000 / 400 = 5 mm

From equation (2)

Imperfection factor = L / 500 = 2000 / 500 = 4 mm

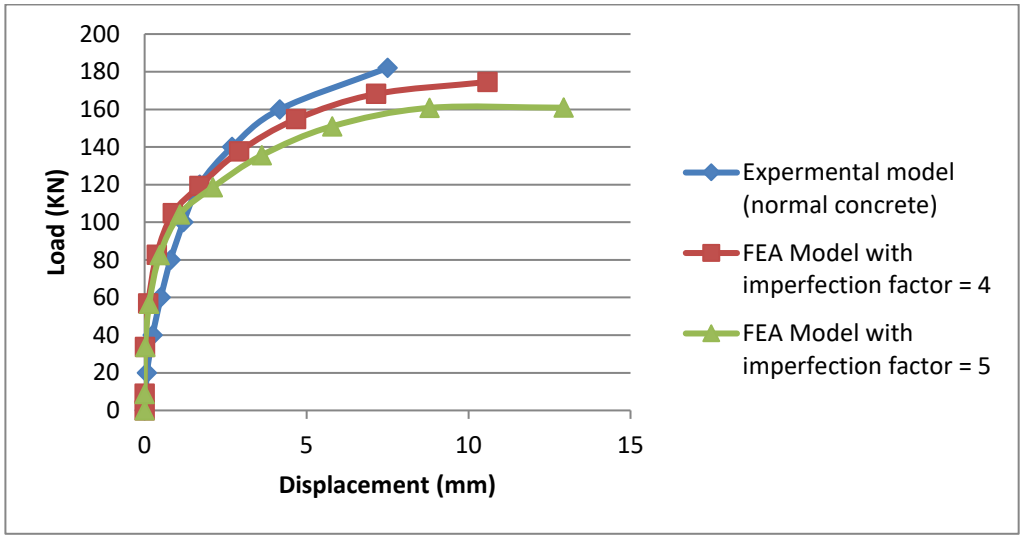

Fig. 5. Comparison between two different imperfection factor values of the load-deflection curve for FEA model and experimental model.

As illustrated in Fig 5. Which shows that the imperfection factor (4) is considered satisfactory.

4.1.2 SFR Strengthened Models

As mentioned previously, there are no imperfection factor values within the specifications, considering the effect of SFR, two values will be tested in addition to reference column imperfection factor value (1.5, 2.5, 4) to see how well the results match the experimental work as shown in Fig 6.

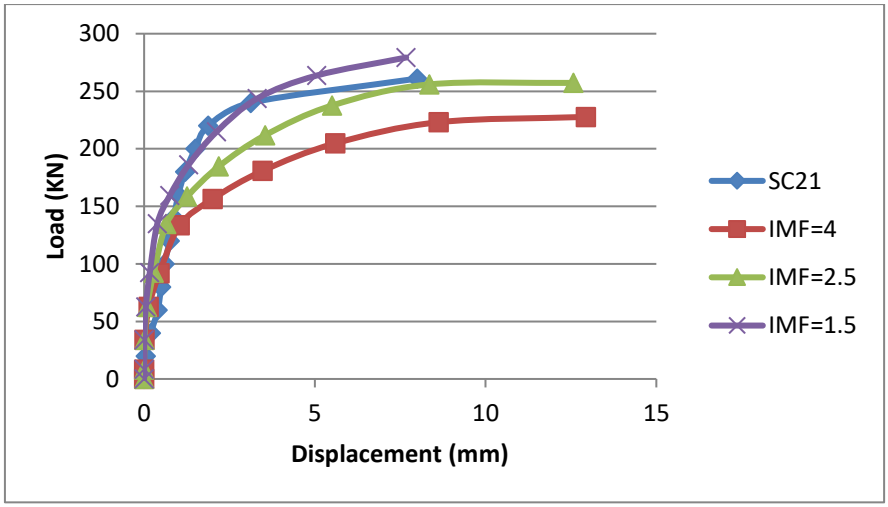

(a) SC21 (All lengths of the column strengthened with SFR).

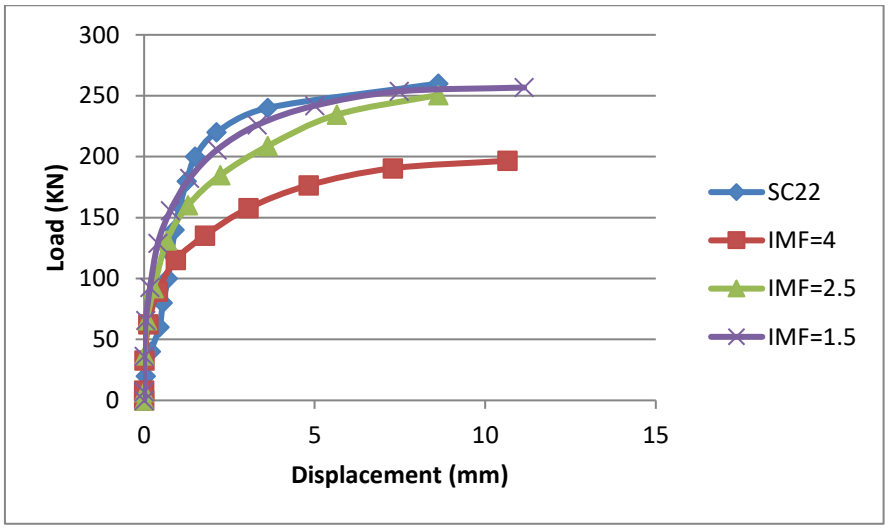

(b) SC22 (L/2 of the column strengthened with SFR).

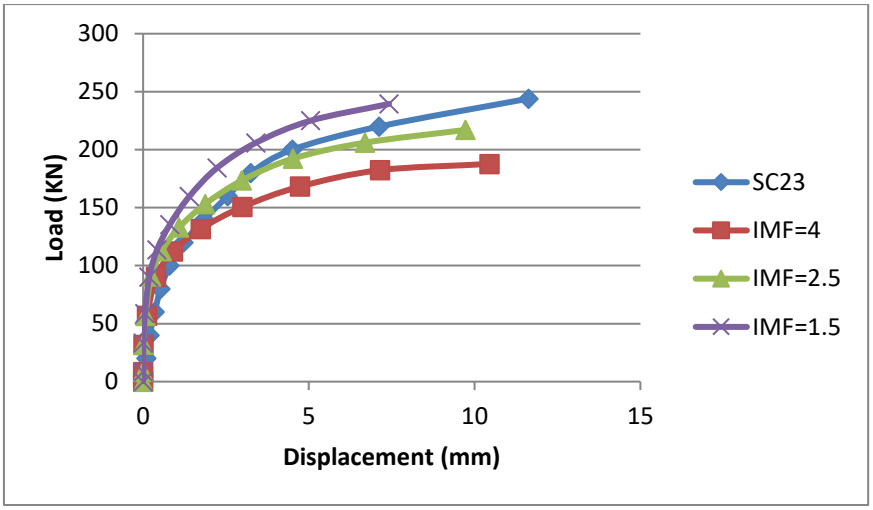

(c) SC23 (L/3 of the column strengthened with SFR).

Fig. 6. SFR effect on the imperfection factor for each strengthened column

Fig 6-a shows the comparison between load-deflection curve for each experimental (all length of the column strengthened with SFR) and FE model, FE model tested with three different values of imperfection factors to see which is the nearest to experimental results, also Figure 6-b and 6-c show the comparison between experimental and FE model for each L/2 SFR strengthened column and L/3 SFR strengthened column respectively. Table 2. showing the best values for the imperfection factor that apply to the behaviour of the real columns tested in the laboratory.

Table 2. Columns IMF values.

Column	IMF
SC11	4
SC21	1.5
SC22	1.5
SC23	2.5

4.1.3 IMF-SFR relationship

Fig 7. illustrates the relationship between the imperfection factor and SFR distribution length by a curve showing different values for this factor which gives a clear idea about the material deviation imperfection factor.

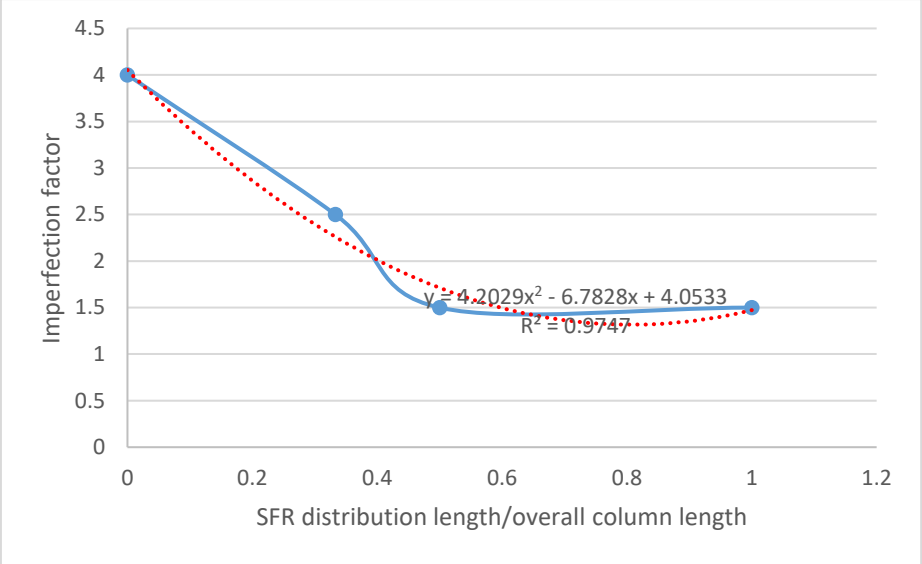

Fig. 7. IMF-SFR relationship.

Although, by getting a graphical relationship it's easy to convert to a mathematical equation that can be used to determine imperfection factor for RC slender column strengthened with SFR of any distribution length.

Since y = IMF (imperfection factor)

x = SFRL (steel fibre reinforcement distribution length)

The suggested equation will be

$$IMF = 4.2029\ SFRL^2 - 6.7828\ SFRL + 4.0533 \quad (4)$$

4.2 Deformation Diagram

Most compressed structural elements are designed using Euler's theory of buckling, or one of Euler's adjustments to account for inelastic behaviour . The practical applicability of these ideas is typically assessed by comparing them to buckling loads acquired using a traditional mechanical or hydraulic testing machine. A half sinewave will buckle a column with hinged ends, the deformation diagrams of slender RC column at failure load are shown in Fig 8.

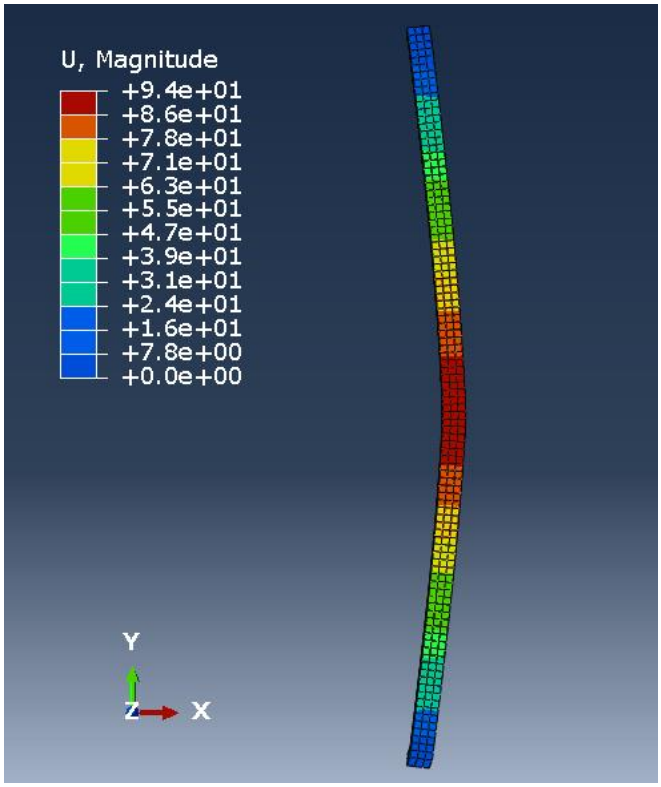

Fig. 8. Slender RC column deformations.

4.3 Failure mode

The inception of cracks is seen at the mid-height of the column as the load increased until failure, Fig 9b shows the failure mode in the slender RC column that has been analysed and which also gave good compatibility with the experimental model shown in Fig 9a.

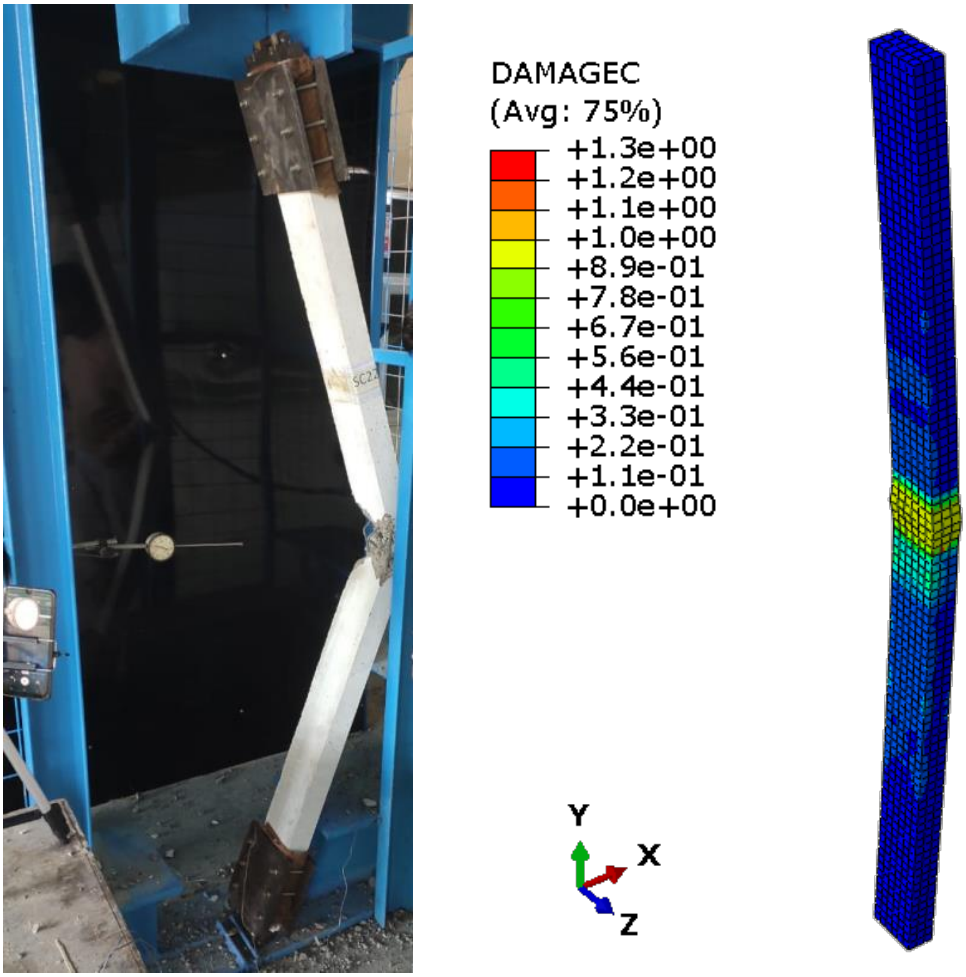

(a) Experimental failure mode **(b)** Analytical failure mode

Fig. 9. Failure mode.

4.4 Failure Load

The comparison of ultimate load and maximum deflection between finite element and experimental results are shown in Table 3. which shows that the agreement between finite element and experimental results is quite good.

Table 3. Ultimate load and deflection results.

Column ID	Ultimate load (KN)		Maximum deflection (mm)	
	EXP.	FEM	EXP.	FEM
SC11	182	174	7.5	10.5
SC21	261	279	8	7.7

SC22	260	256	8.6	11.1
SC23	244	217	11.6	9.7

The presence of SFR distribution deviation affected the values of the failure load which reflecting the difference of the imperfection factor for every case.

5 Conclusion

Geometrical nonlinearity of slender RC column makes buckling the most common failure mode when it analysed using a suitable FEA software, ABAQUS one of the powerful software for this purpose, Abaqus user manual mentions to the geometric imperfection without considering material perturbation effects on this factor, the nonlinear FEA prosses depends on constant imperfection factor provided to the input data of the FEA models if they have the same geometry and material, but the factor will be variable if the material variation distribution through column length changes from a model to another, this variation could be written as a suggested second-order equation resulted from representing load-deflection curve relationship for all models, the analytical model was compared to the experimental work and the results were in good agreement.

References

[1] Chai H. Yoo, Sung C. Lee. Stability of Structures Principles and Applications. Butterworth-Heinemann: Elsevier; 2011. P1.
[2] Ever J. Barbero, Finite Element Analysis of Composite Materials Using Abaqus. Taylor & Francis Group; 2013. P177.
[3] Tjorvi, B. Structural Analysis of Columns with Initial Imperfections. Master's Thesis, University of Iceland, Reykjavik, Iceland, 2017. P 13-14.
[4] J. N. S. Suryanarayana Raju, M. Venkata Rao, G. Sabarish, P. Venkateswara Rao. Effect of Imperfections on Stability of Column and Frame. International Journal of Engineering Research & Technology (IJERT). 2016; Vol. 5 (issue 11).
[5] Eurocode 2: Design of concrete structures - Part 1-1: General rules and rules for buildings, BS EN1992-1-1:2004, P.56.
[6] Eurocode 3: Design of steel structures - Part 1-1: General rules and rules for buildings, BS EN1993-1-1:2005, P.36.
[7] Abaqus Analysis User's Manual, v6.7, Introducing geometric imperfections.
[8] Nessa Yosef Nezhad Arya, Second-order FE Analysis of Axial Loaded Concrete Members According to Eurocode 2. Master theses, royal institute of technology (KTH), Stockholm, Sweden; 2015.
[9] Alaa Hussein Al-Zuhairi & Safaa Qays Abdualrahman. A Comparative Study of the Performance of Slender Reinforced Concrete Columns with Different Cross-Sectional Shapes. Fibers: 2020. P 5.
[10] Mohammed Al-Helfi, Ali Allami. Experimental Work to Study the Strengthening Effect of SFR and CFRP on a Part or Whole of the Length of Slender RC Columns. Civil and Environmental Engineering. 2021; Vol. 17 (issue 1): P 9-22.

Flexural Behaviour of Recycled Demolition Waste Reinforced Concrete Beams

Husham Mohammed Rashid[1], Hasan Jasim Mohammed[2]
{hushammoh99@st.tu.edu.iq[1], dr.hassanjassim@tu.edu.iq[2]}

Department of Civil Engineering, Faculty of Engineering,
Tikrit University, P.O. Box (42) Tikrit, Iraq[1,2]

Abstract. The experimental study investigates the effect of using recycled demolition aggregate (RDA) on the flexural behaviour of reinforced concrete beams. The beams were 1400 mm long, 150 mm wide and 200 mm deep, with the same longitudinal and shear reinforcement. The replacement ratios of recycled demolition aggregate are 0 %, 25 %, 50 %, 75 %, and 100 % of the coarse aggregate weight. The results presented that the deflections of the beams were reduced by up to 15 % and 43 % of 75 % RDA and 100% RDA, respectively when compared to the control beam. Furthermore, at 100% RDA, ductility, stiffness, and toughness were reduced by approximately 24 %, 10 %, and 34 %, respectively. At the same stage of loading, RDA beams cracked faster than normal aggregate beams.

Keywords: Recycled demolition waste, Reinforced concrete, Flexural, Beams, Coarse aggregate.

1 Introduction

It is important to understand the effect of recycled demolition aggregate (RDA) on the behaviour of reinforced concrete (RC) beams under flexural strength to assess the material's potential use in structural elements. Numerous studies have been conducted to evaluate the use of RDA in structural elements, beams, slabs, columns, and so on. This topic is also relevant given the anticipated increase in perceptible coarse aggregate consumption [1]. The mechanical properties of natural coarse aggregate replaced with recycled concrete aggregate (RCA) or recycled clay brick aggregate are being investigated. There are five replacement rate ratios considered: 0%, 25%, 50%, 75%, and 100%. The reduction in compressive strength is about 13 % for replaced with 100 % replacing [2]. Properties of concretes made with higher strengths than their parallel made with normal concrete [3]. Several previous studies have demonstrated that using recycled demolition aggregates in concrete reduces workability, strength, and durability issues [4], [5], [6], [7], [8], [9]. In most cases, RCA has two interfacial transition zones (old and new). It is the weakest part of the concrete. As a result, failure is often the result. Furthermore, Fig 1 showed the failure shapes of natural aggregate concrete, recycled aggregate concrete upon compressive strength, and split tensile strength tests [10].

IMDC-IST 2021, September 07-09, Sakarya, Turkey
Copyright © 2022 EAI
DOI 10.4108/eai.7-9-2021.2314922

Fig. 1. The failure shape for NA and RCA [14].

The research aim is to investigate the flexural behaviour of RC beams with different recycled demolition aggregate ratios. The replacement ratios of recycled demolition aggregate are 0 %, 25 %, 50 %, 75 %, and 100 % of the coarse aggregate weight. The effect study is concerned with the flexural strength of RC beams, as well as the crack pattern and failure modes. The ductility, stiffness, and toughness of these RC beams were then evaluated.

2 Experimental Program

This study looks at the flexural behaviour of reinforced concrete beams made with various percentages of recycled demolition aggregate.

2.1 Sample Design of RC Beams

Five RC beams were created (one normal aggregate (NA) and four RDA). Beams have a variety of RDA ratios (0 %, 25 %, 50 %, 75 % and 100 %) of the coarse aggregate weight. All the beams were designed to fail in flexural, with shear reinforcements added to prevent shear failure and meet the requirements of ACI 318-19. As shown in Fig 2, the dimensions of all RC beams are 1400 mm long, 150 mm width, and 200 mm depth.

2.2 Materials

Ordinary Portland cement type (I) with a compressive strength of 41 MPa at age 28-day was used. The cement passed the ASTM C150 / C150M-19a test. Natural river sand with a water absorption rate of about 1% and with an oven-dry relative density of 2.66 was used. Moreover, it has a moisture content of 2.8 %, fineness modulus is 2.68 of sand used, and all results meet ASTM C778-17 specifications. Natural coarse aggregate with a maximum size of 12.5 mm, an absorption of 0.45%, an oven-dry relative density of 2.6, and a moisture content of coarse aggregate of 1% was used, and all outcomes conformed to the ASTM C33 / C33M-18 specifications. The recycled demolition aggregate (RDA) with an angular shape (12.5 mm maximum size), absorption of 2.56%, and oven-dry density are 2.52 was used RDA composition as presented in Fig. 3 includes the RDA component percentages of 78.7 %, 11.9

%, 8.9 %, and 0.8 % of recycled concrete aggregate, masonry, tiles, and gypsum, respectively. It passed the ASTM C33 / C33M-18 tests. The plasticizer used is a high-performance, hydrophobic material that meets ASTM C-494-Type B requirements. A quantity of plasticizer, 1.78% of the weight of the cement was applied. The longitudinal reinforcement in the tension zone is 2 ø8 mm and in the compression, the zone is 2 ø6 mm, also the shear steel reinforcement is ø6 mm @ 80 mm for all beams were used. It was passed the ASTM A615/A615M-15a tests. The mixes included replacing 0 %, 25 %, 50 %, 75 %, and 100 % of the coarse aggregate weight with recycled RDA. The normal concrete was mixed in the same ratio (1:1.5:2.0) specified by ACI code requirements (ACI 211). While the RDA concrete was replacing the ratio of the coarse aggregate weight by RDA.

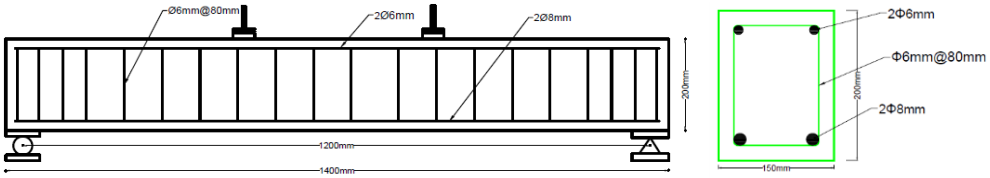

Fig. 2. Details of RC beams used in the experimental program.

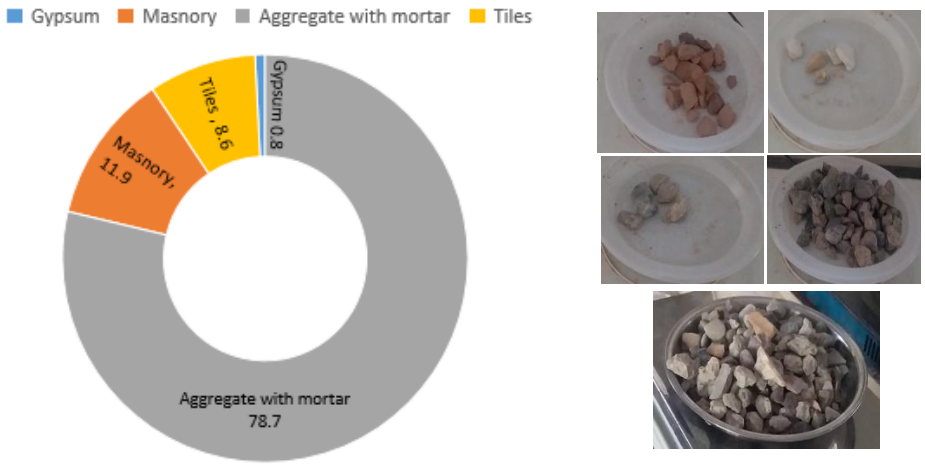

Fig. 3. Recycled demolition aggregate composition.

2.3 Test Setup and Instrumentation

Under a static load, all RC beams were tested to failure. In the mid-span, one LVDT that measures mid-span deflection was installed. A 200-ton load cell measures the load on beams from the universal machine. The data logger collects information from the LVDT and the load cell. The load applied to the beam was gradually increased at a rate of 2 mm/min. A white colour paint directly on each beam marked the propagation of cracks. A four-point loading test

was performed on the simply supported RC beams, which were supported using steel rods and subjected to two loads. The maximum load, deflection, and crack pattern of the first major crack were recorded.

3 Experimental Results and Discussion

3.1 Flexural Behaviour of RC Beams

Table 1 displays the results of the RC beam tests. The load-deflection curves of all tested RC beams are shown in Fig 4, which describes the behaviour of RDA/NA RC beams from the beginning of loading until complete failure. The flexural strength of RC beams with NA and RC beams with RDA exhibit nearly identical elastic behaviour in the first stage of loading. In addition, the occurrence of a behaviour changes load-deflection curve in the second stage of loading revealed that the load-carrying capacities of the RDA concrete beams are slightly lower than of the NA concrete beams. The test results show that the ultimate flexural strength of RC beams containing 25% and 50% recycled demolition aggregate is not reduced when compared to NA beams. While the replacement ratio was increased from 75% to 100%, there was a 15% and 43% decrease in ultimate flexural strength, respectively. This reduction in RDA beams is because the weaker aggregate has a greater effect on the strength of the concrete, after a reduction in the ultimate strength of the RC beam.

Table 1. Results of Tested RC beams.

Group. No.	Beam Designation	Py (kN)	Pu (kN)	Deflection (mm)		Pu Change %
				δy	δu	
Beam with NA	BR-0%	46.5	69.62	4.8	30.92	---
Beams with RDA	BR-25%	49.83	69.95	5.66	31.4	+0.47
	BR-50%	46.7	68.55	5.20	26.86	-1.56
	BR-75%	40.9	60.71	5.95	29.59	-14.67
	BR-100%	31.23	48.61	4.35	21.19	-43.22

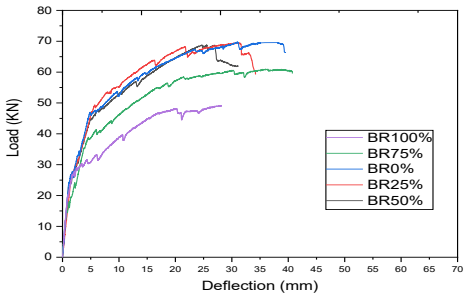

Fig. 4. Load-deflection curves of tested RC beams.

3.2 Crack Pattern and Failure Modes for Flexural RC Beams

Fig 5 shows the propagation of RC beams with the main wide cracks located in the centre of the beam's mid-span. The width of the cracks gradually decreases as they spread towards the top chord until they reach the top layer. Before the appearance of cracking, the linear elastic behaviour of the RC beams was observed until the cracking load. Curve fractures occur because of the beginning of cracking in the beams as loading increases. The number of cracks and crack width is greater in RDA beams than in NA beams. In addition, as the percentage of RDA in RC beams increased, so did the number and width of cracks.

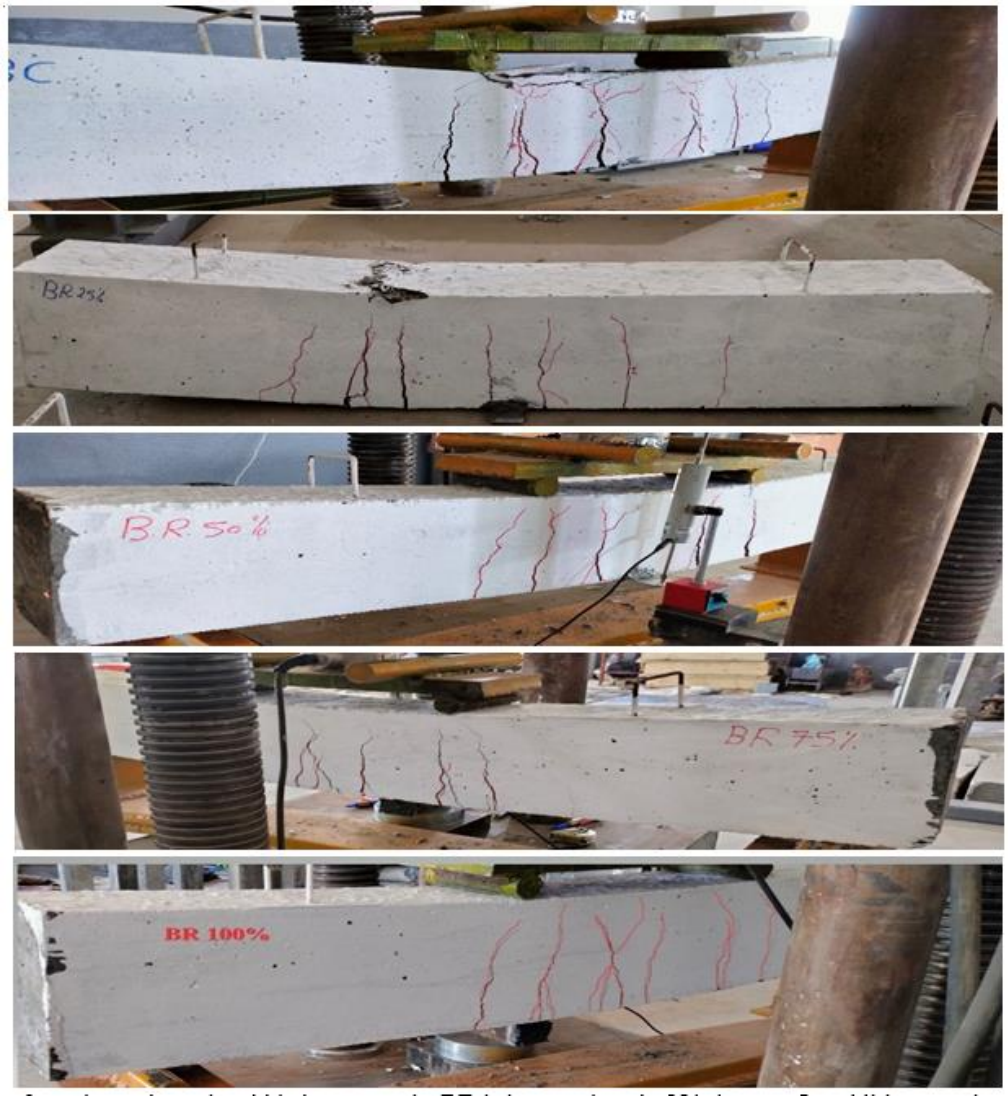

Fig. 5. The crack pattern of all tested RC beams.

3.3 Ductility Behaviour

Depending on the type and proportion of the replaced aggregate, substituting the RDA may increase or decrease the ductility index. According to Fig.6, the ductility values for RDA beams decreased because they had less deflection at the failure loading and more deflection value at the elastic limit. All ductility index values decreased because of the decreased ultimate deflection of the RDA beams. Furthermore, the test results show a reduction in ductility index of (15, 20, 23, and 24) % as RDA replacement was increased from (25, 50, 75, and 100) %, respectively. The decrease in ductility is caused by the tensile strength of RDA concrete, which gradually decreases as the proportion of replaced aggregates increases.

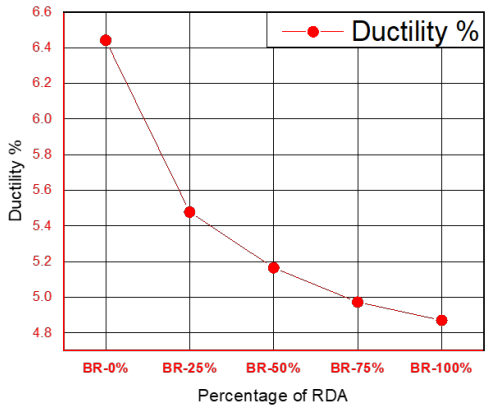

Fig.6. Ductility of RC beams.

3.4 Stiffness Behaviour

Fig 7 illustrates the stiffness values of RC beams. The value of stiffness beams with RDA is found to be lower than the value of the NC beam. The stiffness results show a slight reduction in stiffness of (0.55, 1.89, 6.8, and 10.45) % as the RDA replacement was increased from (25, 50, 75, and 100) %, respectively. Decreasing in stiffness due to the lower strength of concrete with RDA, as well as fractures in the load-deflection curve, the higher the reason for this is that the strength of RDA is weak and the presence of two interfacial transition zones compared to normal aggregates.

3.5 Toughness Behaviour

Fig 8 shows that the flexural toughness values for (BR25 %, BR50 %, BR 75%, and BR100%) beams decreased because they had less deflection at the failure loading and more deflection value at the elastic limit. All flexural toughness values decreased due to a decrease in the load-deflection curve of the RDA beams. Furthermore, the test results show a decrease in flexural toughness of (0.4, 11.9, 27.8, and 33.9) % as RDA replacement was increased from (25, 50, 75, and 100) %, respectively.

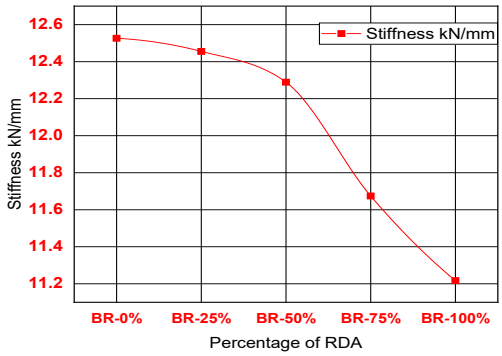

Fig.7. Stiffness of RC beams.

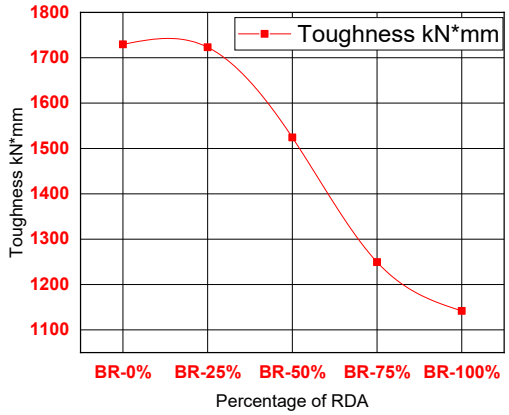

Fig.8. Toughness of RC beams.

4 Conclusions

The experimental study looks at how using recycled demolition aggregate (RDA) affects the flexural behaviour of reinforced concrete beams. The beams were 1400 mm long, 150 mm wide, and 200 mm deep, and they were reinforced longitudinally and shear. The replacement ratios of RDA are 0%, 25%, 50%, 75%, and 100% of the coarse aggregate weight.

1. For high ratio of RDA replacement, the flexural strength of the RC beam decreased. While the flexural strength low percentage of RDA replacement decreased slightly.
2. At the ultimate load, RC-RDA beams showed less deflection than the control beam.
3. The ductility values of RDA beams varied depending on the maximum and elastic limit deflection values. The reduction in ductility of (15, 20, 23, and 24) % as RDA replacement was increased from (25, 50, 75, and 100) %, respectively.

4. RDA beams stiffness was lower than normal beam stiffness about 10.48% at 100% RDA replacement.
5. At 100 % RDA replacement, RDA beam toughness was about 33.9% lower than normal beam stiffness.

Acknowledgments

Tikrit University has provided support for this study. The authors would like to express their appreciation to the university specialists who assisted them with this study. This study is not applicable for funding.

References

[1] Bai G., Zhu C., Liu C., and Liu B., An evaluation of the recycled aggregate characteristics and the recycled aggregate concrete mechanical properties. Construction and Building Materials. 2020; 240: 117978.
[2] Chaocan Zheng, Cong Lou, Geng Du, Xiaozhen Li, Zhiwu Liu and Liqin Li. Mechanical properties of recycled concrete with demolished waste concrete aggregate and clay brick aggregate. Results in Physics. 2018; 9: 1317-1322.
[3] Arezoumandi M, Drury J, Volz JS, and Khayat KH. Effect of recycled concrete aggregate replacement level on shear strength of reinforced concrete beams. ACI Mater. J. 2015; 112(4).
[4] Shirani Bidabadi M., Akbari M., and Panahi O.,. Optimum mix design of recycled concrete based on the fresh and hardened properties of concrete. Journal of Building Engineering. 2020; 32: 101483.
[5] Peng L., Zhao Y., and Zhang H.,. Flexural behaviour and durability properties of recycled aggregate concrete (RAC) beams subjected to long-term loading and chloride attacks. Construction and Building Materials. 2021; 277:122277.
[6] Zhu C., Liu C., Bai G., and Fan J.,. Study on long-term performance and flexural stiffness of recycled aggregate concrete beams. Construction and Building Materials. 2020; 262: 120503.
[7] Sadowska-Buraczewska B., Barnat-Hunek D., and Szafraniec M.,. Influence of Recycled High-Performance Aggregate on Deformation and Load-Carrying Capacity of Reinforced Concrete Beams. Materials. 2020; 13: 186.
[8] Rahal K., and Elsayed K.,. Shear strength of 50 MPa longitudinally reinforced concrete beams made with coarse aggregates from low strength recycled waste concrete. Construction and Building Materials. 2021; 286: 122835.
[9] Arezoumandi M, Smith A, Jeffery AS and Khayat H. An experimental study on flexural strength of reinforced concrete beams with 100% recycled concrete aggregate. Engineering Structures. 2015; 88: 154-162.
[10] Lee GC and Choi HB. Study on interfacial transition zone properties of recycled aggregate by micro-hardness test. Construction and Building Materials. 2013; 40: 455-460.

Risk Factors of Glycaemia Control among Children and Adolescents with Type 1 Diabetes in Basra City/Iraq

Shukur Abdulkareem Mahmood[1] , Majid A. Maatook[2] , Dhaigham E. Aatwan[3]
{shukurcomm@gmail.com[1], m.maatook@stud.edu.iq[2] dhaigh1977@gmail.com[3]}

Southern Technical University/College of Health & Medical Technology, Basra/Iraq[1,2]
Al Basra Health Directorate/Faiha Specialized Diabetes, Endocrine, and Metabolism Centre/Iraq[3]

Abstract. Little is known about risk factors and levels of glycaemic control for poor-controlled hyperglycaemia in Iraq children and adolescents with type 1 diabetes mellitus. The study aims to determine the glycaemic control and risk factors of poor control hyperglycaemia in children and adolescents with type 1 diabetes mellitus patients. A cross-sectional study was 209 type 1 diabetics. Glycaemic control of type 1 diabetes varies widely among children and adolescents in Basra/Iraq, risking microvascular complications. Only (36) 17.2% of children and adolescents with type 1 diabetes mellitus were good-controlled diabetes, (25) 69.4%, was compliance with insulin therapy in good-controlled type 1 diabetes mellitus patients, females were higher than males and in the age group (1-6) years, higher than the other age groups. The major risk factors for poor-controlled hyperglycaemia are noncompliance with insulin therapy, not checking daily glucometer blood glucose and irregular clinic visits for follow-up.

Keywords: Glycaemic Control, Adolescents, Children, Insulin, Basra City.

1 Introduction:

Diabetes is a chronic disease of huge morbidity and mortality; regular medical treatments and self-entraining are needed to ensure optimum glycaemic control that is critical in decreasing the long-term risk of diabetes-related complications and mortality [1]. Good-controlled patients with type 1 diabetes mellitus in paediatric patients are critical not only for reducing complications and delaying progression but also for normal growth and development [2]. However, glycaemic regulation is insufficient in the majority of clinical settings. According to one study, only 37% of adults with diabetes mellitus have an HbA1c level of 7% [3]. Further, in one paediatric study, the mean level of HbA1c was found to be 8.8% [4], indicating that the majority of children did not meet the recommended target level of HbA1c less than 7.5% [5]. Poor-controlled hyperglycaemia may be caused by failure to take medication on time, eat too much and exercise too little. Some episodes of hyperglycaemia occur for no apparent cause. Illness may also cause a rise in blood glucose levels. Hyperglycaemia can damage the kidneys, nerves, blood vessels, eyes, teeth, and gums over time [6]. Hyperglycaemia-related neurocognitive complications have also been reported [7]. During a nationwide Iraq project conducted between 1 January 2012 and 31 December 2016, 818 new cases of type 1 diabetes were found, coinciding with a worldwide rise in the incidence of diabetes. Males made up 417 of these (50%). The annual incidence rate of type 1 diabetes was 7.4 per 100,000, and the prevalence rate of type 1 diabetes in people aged less than 40 was 87 per 100,000 in 2016 [8]. However, few studies in Iraqi children and adolescents with glycaemic control scale type 1 diabetes as well as risk factors associated with uncontrolled hyperglycaemia have been carried out in Iraq.

2 Methods

A cross-sectional study was carried out from 1st. September 2020 until the 15th. May of 2021 to determine the glycaemic control and risk factors of poor control hyperglycaemia in children and adolescents with type 1 diabetes mellitus in Basra city, for the study sample which

IMDC-IST 2021, September 07-09, Sakarya, Turkey
Copyright © 2022 EAI
DOI 10.4108/eai.7-9-2021.2314899

was 209 type 1 diabetics, selected randomly from the visitors of a Faiha Specialized Diabetes, Endocrine, and Metabolism Centre (FDEMC). The American Diabetes Association assigned target HbA1c levels to patients based on their age groups. A comparison has been made between good-controlled patients and poor-controlled hyperglycaemia patients. To assess each risk factor's role in uncontrolled type 1 diabetes hyperglycaemia, the Odds Ratios, was calculated. At the time of the study, we followed the American Diabetes Association (ADA) 2014 Guidelines. The data of all patients were obtained from interview patients and the digital records of (FDEMC) as it has an internal network system and Microsoft Access program for documenting all patients' information and investigations. Statistical analysis: Together, study data are shown as frequency and percentages (%). The variations between the groups of the study were established by the Chi-square test, the Odds Ratios were calculated. Statistical significance is designated by a value of P. < 0.05. All statistical investigates were attained by utilizing IBM SPSS (version 25).

3 Results

3.1 Distribution of the Glycaemic Control of the Sample

The study included a total of 209 type 1 diabetic,36 (17.2%) with good-controlled diabetes and 173 (82.8%) with poor-controlled hyperglycaemia diabetes, who were already diagnosed as type 1 diabetes mellitus as shown in Fig 1.

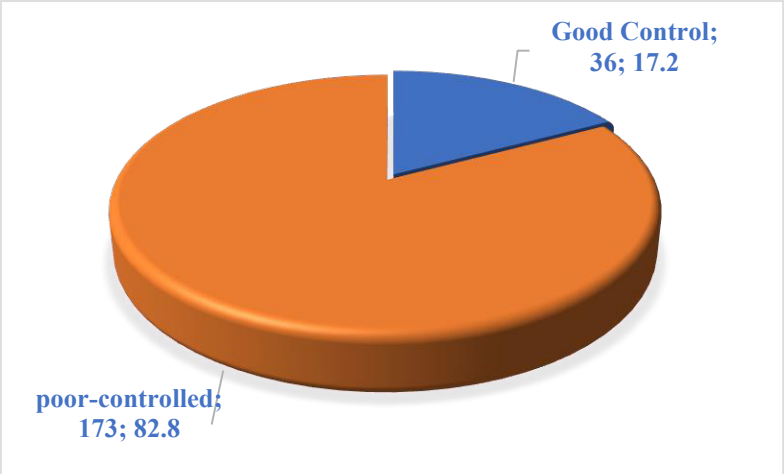

Fig 1. Distribution of the glycaemic control of the sample.

3.2 Distribution Glycaemic Control According to the Age Group of the Sample

A total of 209 types 1 diabetic, 108 (51.7%) males and 101 (48.3%) females who are already diagnosed as type 1 diabetes patients aged (2 – 18) years were included in the present study. The results show that the patient's males, 59 (54.6%) in (13 – 18) years and females, 44 (43.6%) in (13 – 18) years as appear in Fig 2.

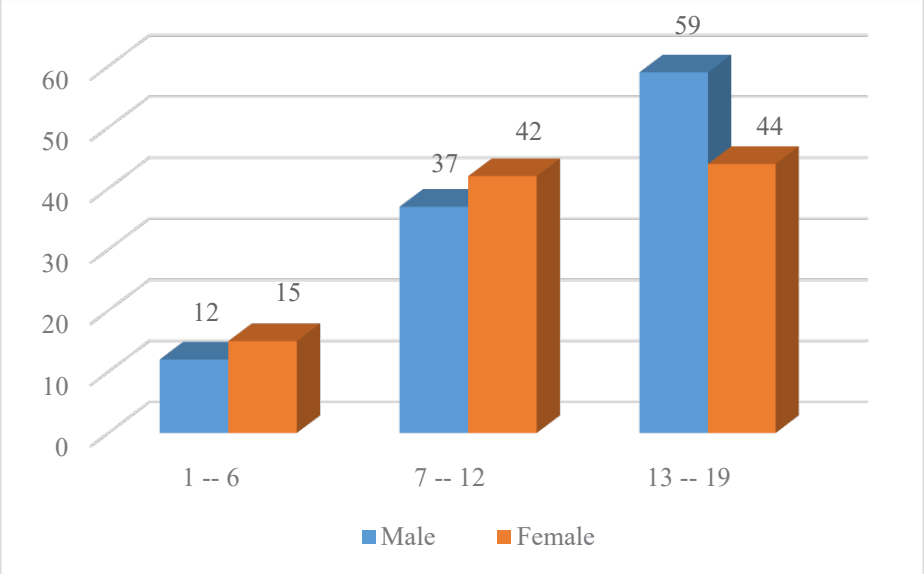

Figure 2. Distribution of the gender according to age grouping of the sample.

3.3 Distribution Educational Level of Patients and Patients' Parents According to Glycaemic Control of the Sample

The distribution educational level of patients and patients' parents according to Glycaemic Control is represented in Table 1.

The present study found that in poor-controlled hyperglycaemia type 1 diabetes patients, 77 (44.5%) had secondary school level, 12 (6.9%) uneducated patients, whereas in good-controlled diabetes with type 1 diabetes patients, 15 (41.7%) had a primary school level, 2 (5.6%), uneducated patients. Regarding parents' education levels, the present study found that among uncontrolled hyperglycaemia diabetes T1DM (paternal) patients 96 (55.5%) had a primary school, 35 (20.2%) high educated level (university), whereas in well control diabetes with T1DM paternal patients 16 (44.4%) had a primary school, 4 (11.2%) was secondary school level, 16 (44.4%) high educated level (university). According to parents' education levels, the present study found that among uncontrolled hyperglycaemia diabetes T1DM (maternal) patients 1 (0.5%) uneducated, 116 (67.1%) had a primary school, whereas in well control diabetes with T1DM paternal patients, 15 (41.7%) was secondary school level, 7 (19.4%) high educated level (university) as shown in Table 1.

Table 1. Distribution educational level of patients and patient's parents according to Glycaemic Control of the sample:

Parameters		Glycemic Control No. = 209				P. Value
		P|oor-controlled HG (N = 173)		Good-Control (N = 36)		
		N	%	N	%	
Patient Education	Child	16	9.3	7	19.4	0.282
	Primary	68	39.3	15	41.7	
	Secondary	77	44.5	12	33.3	
	Other	12	6.9	2	5.6	
Paternal Education	Primary	96	55.5	16	44.4	0.006
	Secondary	42	24.3	4	11.2	
	University	35	20.2	16	44.4	
Maternal Education	Illiterate	1	0.5	0	0	0.008
	Primary	116	67.1	14	38.9	
	Secondary	32	18.5	15	41.7	
	University	24	13.9	7	19.4	

3.4 Distribution Monitoring of Hba1c, Blood Sugar and Medical Follow–Up of T1DM According to Glycaemic Control of the Sample

According to blood glucose level checking daily, this shows that in poor-controlled hyperglycaemia type 1 diabetes patients, 106 (61.3%) unchecking blood glucose level daily, whereas, in good-controlled type 1 diabetes patients, 25 (69.4%) check blood glucose level daily. Regarding the monitoring of HbA1c, this shows that in poor-controlled hyperglycaemia type 1 diabetes patients, 113 (65.3%) check HbA1c every three months, whereas, in good-controlled type 1 diabetes patients, 35 (97.2%) checking HbA1c every three months.
Regarding the monitoring of ketone in urine, this shows that in poor-controlled hyperglycaemia type 1 diabetes patients, 118 (68.2%) had not checked ketone in urine, whereas, in good-controlled type 1 diabetes patients, 20 (55.6%) check ketone in urine. According to regular medical follow-up, this shows that in poor-controlled hyperglycaemia type 1 diabetes patients, 131 (75.7%) lack regular clinic visits for medical follow-up, whereas, in good-controlled type 1 diabetes patients, 32 (88.9%) had regular clinic visits for medical follow-up.
Regarding availability for a telephone consultation, this shows that in poor-controlled hyperglycaemia type 1 diabetes patients, 155 (89.6%) unavailability for a telephone consultation, whereas, in good-controlled type 1 diabetes patients, 13 (36.1%) availability for a telephone consultation, 23 (63.9%) unavailability for a telephone consultation. According to diabetes-related education received, this shows that in poor-controlled hyperglycaemia type 1 diabetes patients, 69 (39.9%) received education from an endocrinologist, 54 (31.2%) did not receive any education from another person, whereas, in good-controlled type 1 diabetes patients, 28 (77.8%) received educated from an endocrinologist, 1 (2.8%) not received any educated from another person as appears in Table 2.

Table 2. Distribution monitoring of HbA1c, blood sugar and medical follow–up of T1DM according to Glycaemic Control.

Parameters			Glycemic Control No. = 209				OR(95% CI)	P. Value
			P|oor-controlled HG (N = 173)		Good-Control (N = 36)			
			N	%	N	%		
Do you daily glucometer blood glucose check?		Yes	67	38.7	25	69.4	0.28(0.13-0.6)	0.001
		No	106	61.3	11	30.6	-	
Monitor HbA1c	Every 3 months		113	65.3	35	97.2	0.05(0.01-0.4)	<0.001
	Every 6 months		60	34.7	1	2.8	-	
Do you check your urine for ketones?		Yes	55	31.8	20	55.6	0.37(0.18-0.78)	0.007
		No	118	68.2	16	44.4	-	
Do you regular clinic visits for follow-up		Yes	42	24.3	32	88.9	0.04(0.01-0.12)	<0.001
		No	131	75.7	4	11.1	-	
Availability for telephone consultation		Yes	18	10.4	13	36.1	0.19(0.07-0.54)	<0.001
		No	155	89.6	23	63.9	-	
Diabetes related education received from	Family Physician		6	3.5	0	0	-	<0.001
	Endocrinologist		69	39.9	28	77.8	-	
	Nurse		16	9.2	0	0	-	
	Nutritionist		2	1.2	0	0	-	
	Internet		26	15.0	7	19.4	-	
	No Education		54	31.2	1	2.8	-	

3.5 Relationship Between Insulin Therapy Characteristics and Glycaemic Control of the Sample

According to the insulin regimen, 64 (94.8%), using multiple injections of insulin injections daily in poor-controlled hyperglycaemia type 1 diabetes patients, whereas 8 (22.2%), using twice injections of insulin injections daily in good-control type 1 diabetes patients, with a significant statistical difference between poor-controlled hyperglycaemia type 1 diabetes patients, and good-control type 1 diabetes patients, was found (P. = 0.001). The present study found that the type of insulin injection used in poor-controlled hyperglycaemia type 1 diabetes patients, 133 (76.1%) was vial injection, whereas in good-control type 1 diabetes patients, 31 (86.1%) vial injection, the results showed no significant statistical difference between good-control diabetes and poor-controlled hyperglycaemia diabetes was found (P = 0.22). The current study discovered that the way of insulin storage in poor-controlled hyperglycaemia type

1 diabetes patients, 168 (97.1%), was good storage of insulin through the transformation from the centre to home, whereas in good-controlled type 1 diabetes patients, 32 (88.9%). The current study discovered that compliance with insulin therapy in poor-controlled hyperglycaemia type 1 diabetes patients was 146 (84.4%), whereas compliance with insulin therapy in good-controlled type 1 diabetes patients was 25 (69.4%).

The present study found that injection areas that are often used in insulin injection therapy, in poor-controlled hyperglycaemia type 1 diabetes patients, 83 (48.0%) was insulin injection in the arm with insulin therapy, whereas, in good-controlled type 1 diabetes patients, 18 (50.0%) was the insulin therapy injection in the more than site, the results showed no significant statistical difference between good-controlled type 1 diabetes and poor-controlled hyperglycaemia type 1 diabetes was found (P = 0.854). The current study found that the rotation sites with each insulin injection, in diabetic patients with poor-controlled type 1 diabetes patients, 118 (68.2%) did not have a rotation position with each insulin injection treatment, while in diabetics who were good-controlled type 1 diabetes patients, 18 (50.0%)%) The site was rotated with each insulin injection treatment, the results showed a significant statistical difference between good-controlled type 1 diabetes and poor-controlled hyperglycaemia type 1 diabetes was found (P. = 0.037).

According to the insulin injector among patients with poor-controlled hyperglycaemia of type 1 diabetes patients, 82 (47.4%) was patients self-injected, 90 (52.0%) was injected by parents, 1 (0.6%) was injected by others, while in the control condition of diabetes with type 1 diabetes patients 11 (30.6%) was patients self-injected 25 (69.4%) was injected by the parent. The results showed no significant statistical difference between good-controlled type 1 diabetes patients, and poor-controlled hyperglycaemia type 1 diabetes patients, was found (P = 0.153).

According to the educational level of insulin injector among patients with poor-controlled hyperglycaemia of type 1 diabetes, 84 (48.6%) had a primary school, 76 (43.9%) was at the secondary school level, 13 (7.5%) High educational level (university), while in the control condition of diabetes with type 1 diabetes patients 12 (33.3%) had a primary school, 17 (47.3%) was at the secondary school level, 7 (19.4%) High level of education (university).

Regarding the educational level of insulin injectors in poor-controlled hyperglycaemia type 1 diabetes patients and good-controlled type 1 diabetes patients, the results showed a significant statistical difference between poor-controlled hyperglycaemia type 1 diabetes patients and good-controlled type 1 diabetes patients, (P. = 0.05).

Table 3. Relationship between Insulin therapy characteristics and Glycaemia control:

Parameters		**Glycemic Control No. = 209**				**OR(95% CI)**	**P. Value**
		P|oor-controlled HG (N = 173)		**Good-Control (N = 36)**			
		N	%	N	%		
Types of insulin regimen	Twice Daily	9	5.2	8	22.2	0.19(0.07-0.54)	0.001
	Multiple daily	164	94.8	28	77.8	-	
Type of insulin	Pen	40	13.9	5	13.9	1.87(0.68-5.11)	0.220
	Vial	133	76.1	31	86.1	-	
Syringe reuse	Every injection	21	12.2	12	33.3	-	0.002
	Every 2-3 injections	58	33.5	14	38.9	-	
	More 4 injections	94	54.3	10	27.8	-	
Way of storage insulin	Good	168	97.1	32	88.9	4.20(1.07-16.5)	0.027
	Bad	5	2.9	4	11.1	-	
Compliance with insulin therapy	Yes	146	84.4	25	69.4	2.38 (1.05-5.4)	0.034
	No	27	15.6	11	30.6	-	
Injection areas that are often used:	Arm	83	48.0	16	44.4	-	0.854
	Thigh	9	5.2	1	2.8	-	
	Abdomen	6	3.5	1	2.8	-	
	More than 1 site	75	43.3	18	50.0	-	
Do you rotate sites with each injection?	Yes	55	31.8	18	50.0	0.47(0.23-0.97)	0.037
	No	118	68.2	18	50.0	-	
Insulin injector	Patient	82	47.4	11	30.6	-	0.153
	Parent	90	52.0	25	69.4	-	
	Other	1	0.6	0	0	-	
	Primary	84	48.6	12	33.3	-	0.050

Educational level	Secondary	76	43.9	17	47.2	-
of insulin injectors	University	13	7.5	7	19.5	-

4 Discussion

The study included a total of 209 type 1 diabetic,36 (17.2%) with good-controlled diabetes and 173 (82.8%) with poor-controlled hyperglycaemia diabetes, who were already diagnosed as type 1 diabetes mellitus patients and corresponds with the study [9]. Diabetic patients with poor-controlled hyperglycaemia diabetes are at a higher risk of complications, such as cardiovascular disease, even at a young age, and have a poorer health-related quality of life than non-diabetic patients [9]. The present study found that in poor-controlled hyperglycaemia type 1 diabetes patients, 77 (44.5%) had secondary school level, 12 (6.9%) uneducated patients, whereas in good-controlled diabetes with type 1 diabetes patients, 15 (41.7%) had a primary school level, 2 (5.6%), uneducated patients, the results showed that no significant statistical difference between well-controlled diabetes with T1DM patients and uncontrolled hyperglycaemia diabetes T1DM patients was found (P. = 0.282). The results showed that a significant statistical difference between well-controlled diabetes with T1DM patients and uncontrolled hyperglycaemia diabetes with T1DM patients was found (P. = 0.006); (P. = 0.008) and corresponds with a study by [9]. According to blood glucose level checking daily, this shows that in poor-controlled hyperglycaemia type 1 diabetes patients, 106 (61.3%) unchecking blood glucose level daily, whereas, in good-controlled type 1 diabetes patients, 25 (69.4%) check blood glucose level daily. The results showed a significant statistical difference between poor-controlled hyperglycaemia and good-controlled type 1 diabetes patients (P. = 0.001) in agreement with this study [10]. Regarding the monitoring of HbA1c, this shows that in poor-controlled hyperglycaemia type 1 diabetes patients, 113 (65.3%) check HbA1c every three months, whereas, in good-controlled type 1 diabetes patients, 35 (97.2%) checking HbA1c every three months.

The results showed a significant statistical difference between poor-controlled hyperglycaemia and good-controlled type 1 diabetes patients (P. < 0.001) which is confirmed with this study [11]. Regarding the monitoring of ketone in urine, this shows that in poor-controlled hyperglycaemia type 1 diabetes patients, 118 (68.2%) had not checked ketone in urine, whereas, in good-controlled type 1 diabetes patients, 20 (55.6%) check ketone in urine.

The results showed a significant statistical difference between poor-controlled hyperglycaemia and good-controlled type 1 diabetes patients (P. = 0.007) which agrees with this study [12]. According to regular medical follow-up, this shows that in poor-controlled hyperglycaemia type 1 diabetes patients, 131 (75.7%) lack regular clinic visits for medical follow-up, whereas, in good-controlled type 1 diabetes patients, 32 (88.9%) had regular clinic visits for medical follow-up. The results showed a significant statistical difference between poor-controlled hyperglycaemia and good-controlled type 1 diabetes patients (P. < 0.001) which agrees with this study [9]. Regarding availability for a telephone consultation, this shows that in poor-controlled hyperglycaemia type 1 diabetes patients, 155 (89.6%) unavailability for a telephone consultation, whereas, in good-controlled type 1 diabetes patients, 13 (36.1%) availability for a telephone consultation, 23 (63.9%) unavailability for a telephone consultation. The results showed a significant statistical difference between poor-controlled hyperglycaemia and good-controlled type 1 diabetes patients (P. < 0.001) which agrees with this study [9]. According to diabetes-related education received, this shows that in poor-controlled hyperglycaemia type 1 diabetes patients, 69 (39.9%) received education from an endocrinologist, 54 (31.2%) did not receive any education from another person, whereas, in good-controlled type 1 diabetes patients, 28 (77.8%) received educated from an endocrinologist, 1 (2.8%) not received any educated from another person. The findings revealed a significant statistical difference between poor-controlled hyperglycaemia and good-controlled type 1 diabetes patients (P. < 0.001). This may be attributed to a continued lack of public knowledge about diabetes mellitus in children, as well as among primary healthcare providers [10]. According to the insulin regimen, 64 (94.8%), using multiple injections of insulin injections daily in poor-controlled hyperglycaemia type 1 diabetes patients, whereas 8 (22.2%), using twice injections of insulin injections daily in good-control type 1 diabetes patients. This result shows that the insulin regimens in poor-controlled hyperglycaemia type 1 diabetes patients, were higher than in good-controlled type 1 diabetes patients, with a significant statistical difference between good-controlled diabetes and poor-controlled hyperglycaemia diabetes was found (P. = 0.001), which agrees with other

studies like these by [13],[15]. Traditional insulin regimens of two insulin injections a day, on the other hand, can still be an effective therapeutic choice for children under the age of six, particularly for families who cannot afford intensive insulin therapy.

The present study found that the type of insulin injection used in poor-controlled hyperglycaemia type 1 diabetes patients, 133 (76.1%) was vial injection, whereas in good-control type 1 diabetes patients, 31 (86.1%) vial injection, the results showed no significant statistical difference between good-control diabetes and poor-controlled hyperglycaemia diabetes was found (P = 0.22). Compared with patients who used pen insulin injection, had 1.87 times (95% CI = 0.68-5.11) higher odds of poor-controlled hyperglycaemia diabetes patients, and good-controlled diabetes patients, an indicator of high risk for poor-controlled hyperglycaemia diabetes. The present study found that the times type of reuses insulin syringes every injection in poor-controlled hyperglycaemia diabetes patients, 94 (54.3%) was insulin syringe reuses 4 times or more than the injection, whereas, in good-controlled diabetes patients, 14 (38.9%) insulin syringe reuses every 2 – 3 injections, the results showed a significant statistical difference between good-controlled diabetes and poor-controlled hyperglycaemia diabetes was found (P = 0.002). The current study discovered that the way of insulin storage in poor-controlled hyperglycaemia type 1 diabetes patients, 168 (97.1%), was good storage of insulin through the transformation from the centre to home, whereas in good-controlled type 1 diabetes patients, 32 (88.9%), was good storage of insulin from the centre to home, with the results showing a significant statistical difference between good-controlled type 1 diabetes patients and poor-controlled hyperglycaemia type 1 diabetes patients was found (P. = 0.027). The current study discovered that compliance with insulin therapy in poor-controlled hyperglycaemia type 1 diabetes patients was 146 (84.4%), whereas compliance with insulin therapy in good-controlled type 1 diabetes patients was 25 (69.4%). The results revealed a significant statistical difference between good-controlled type 1 diabetes patients and poor-controlled hyperglycaemia type 1 diabetes patients was found (P. = 0.034) which is confirmed with this study [16]. Compared with patients' compliance with insulin therapy, had 2.38 times (95% CI = 1.05-5.40) higher odds of poor-controlled hyperglycaemia type 1 diabetes patients, and good-controlled type 1 diabetes patients, an indicator of high risk for poor-controlled hyperglycaemia type 1 diabetes patients. The present study found that injection areas that are often used in insulin injection therapy, in poor-controlled hyperglycaemia type 1 diabetes patients, 83 (48.0%) was insulin injection in the arm with insulin therapy, whereas, in good-controlled type 1 diabetes patients, 18 (50.0%) was the insulin therapy injection in the more than site, the results showed no significant statistical difference between good-controlled type 1 diabetes and poor-controlled hyperglycaemia type 1 diabetes was found (P = 0.854) which is in agreement with this study [17]. The current study found that the rotation sites with each insulin injection, in diabetic patients with poor-controlled type 1 diabetes patients, 118 (68.2%) did not have a rotation position with each insulin injection treatment, while in diabetics who were good-controlled type 1 diabetes patients, 18 (50.0%)%) The site was rotated with each insulin injection treatment, the results showed a significant statistical difference between good-controlled type 1 diabetes and poor-controlled hyperglycaemia type 1 diabetes was found (P. = 0.037) which is in agreement with this study [18]. According to the insulin injector among patients with poor-controlled hyperglycaemia of type 1 diabetes patients, 82 (47.4%) was patients self-injected, 90 (52.0%) was injected by parents, 1 (0.6%) was injected by others, while in the control condition of diabetes with type 1 diabetes patients 11 (30.6%) was patients self-injected 25 (69.4%) was injected by the parent. The results showed no significant statistical difference between good-controlled type 1 diabetes patients, and poor-controlled hyperglycaemia type 1 diabetes patients, was found (P = 0.153). According to the educational level of insulin injector among patients with poor-controlled hyperglycaemia of type 1 diabetes, 84 (48.6%) had a primary school, 76 (43.9%) was at the secondary school level, 13 (7.5%) High educational level (university), while in the control condition of diabetes with type 1 diabetes patients 12 (33.3%) had a primary school, 17 (47.3%) was at the secondary school level, 7 (19.4%) High level of education (university). Regarding the educational level of insulin injector in poor-controlled hyperglycaemia type 1 diabetes patients and good-controlled type 1 diabetes patients, the results showed a significant statistical difference between poor-controlled hyperglycaemia type 1 diabetes patients and good-controlled type 1 diabetes patients, (P. = 0.05) which agrees with this study [19].

References

[1]. Johnson EL, Feldman H, Butts A, Chamberlain J, Collins B, Doyle-Delgado K, et al. Standards of medical care in diabetes—2020 abridged for primary care providers. Clin Diabetes. 2020;38(1):10–38.

[2]. Fogel JL, Raymond JK. Implementing Telehealth in Pediatric Type 1 Diabetes Mellitus. Pediatr Clin North Am [Internet]. 2020;67(4):661–4.

[3]. Juarez DT, Ma C, Kumasaka A, Shimada R, Davis J. Failure to reach target glycated A1c levels among patients with diabetes who are adherent to their antidiabetic medication. Popul Health Manag. 2014;17(4):218–23.

[4]. Archinkova M, Konstantinova M, Savova R, Iotova V, Petrova C, Kaleva N, et al. Glycaemia control in type 1 diabetes mellitus among Bulgarian children and adolescents: the results from the first and the second national examination of HbA1c. Biotechnol Biotechnol Equip [Internet]. 2017;31(6):1198–203.

[5]. DiMeglio LA, Acerini CL, Codner E, Craig ME, Hofer SE, Pillay K, et al. ISPAD Clinical Practice Consensus Guidelines 2018: Glycaemia control targets and glucose monitoring for children, adolescents, and young adults with diabetes. Pediatr Diabetes. 2018; 19:105–14.

[6]. Eid S, Sas KM, Abcouwer SF, Feldman EL, Gardner TW, Pennathur S, et al. New insights into the mechanisms of diabetic complications: role of lipids and lipid metabolism. Diabetologia. 2019;62(9):1539–49.

[7]. Streisand R, Monaghan M. Young children with type 1 diabetes: Challenges, research, and future directions. Curr Diab Rep. 2014;14(9).

[8]. Almahfoodh D, Alabbood M, Alali A, Mansour A. Epidemiology of type 1 diabetes mellitus in Basrah, Southern Iraq: A retrospective study. Diabetes Res Clin Pract. 2017 Nov 1; 133:104–8.

[9]. Sayed MH, Hegazi MA, Abdulwahed K, Moussa K, El-Deek BS, Gabel H, et al. Risk factors and predictors of uncontrolled hyperglycaemia and diabetic ketoacidosis in children and adolescents with type 1 diabetes mellitus in Jeddah, western Saudi Arabia. J Diabetes. 2017;9(2):190–9.

[10]. Markowitz JT, Butler DA, Volkening LK, Antisdel JE, Anderson BJ, Laffel LMB. Brief screening tool for disordered eating in diabetes: Internal consistency and external validity in a contemporary sample of pediatric patients with type 1 diabetes. Diabetes Care. 2010;33(3):495–500.

[11]. Hanberger L, Åkesson K, Samuelsson U. Glycated haemoglobin variations in paediatric type 1 diabetes: The impact of season, gender and age. Acta Paediatr Int J Paediatr. 2014;103(4):398–403.

[12]. Singh H, Saroch A, Pannu AK, Sachin HJ, Sharma N, Dutta P. Clinical and biochemical profile, precipitants and prognostic factors of diabetic ketoacidosis: A retrospective study from a tertiary care center of north India. Diabetes Metab Syndr Clin Res Rev [Internet]. 2019;13(4):2357–60.

[13]. Rosenbauer J, Dost A, Karges B, Hungele A, Stahl A, Bächle C, et al. Improved metabolic control in children and adolescents with type 1 diabetes: A trend analysis using prospective multicenter data from Germany and Austria. Diabetes Care. 2012;35(1):80–6.

[14]. Al-Agha A, Ocheltree A, Hakeem A. Metabolic control in children and adolescents with insulin-dependent diabetes mellitus at King Abdul-Aziz university hospital. JCRPE J Clin Res Pediatr Endocrinol. 2011;3(4):202–7.

[15]. Craig ME, Jones TW, Silink M, Ping YJ. Diabetes care, Glycaemia control, and complications in children with type 1 diabetes from Asia and the Western Pacific Region. J Diabetes Complications. 2007;21(5):280–7.

[16]. Alahmadi S, Ragaban A, Alblowi S, Aljumail E, Zarif H. Diabetic ketoacidosis; Annual Incidence and Precipitating Factors at King Abdulaziz Medical city, Jeddah. 2018;72(July):4831–5.

[17]. Tsadik AG, Atey TM, Nedi T, Fantahun B, Feyissa M. Effect of Insulin-Induced Lipodystrophy on Glycaemia Control among Children and Adolescents with Diabetes in Tikur Anbessa Specialized Hospital, Addis Ababa, Ethiopia. J Diabetes Res. 2018;2018.

[18]. Cunningham MT, McKenna M. Lipohypertrophy in insulin-treated diabetes: Prevalence and associated risk factors. J Diabetes Nurs. 2013;17(9):340–3.

[19]. Tsadik AG, Atey TM, Nedi T, Fantahun B, Feyissa M. Effect of Insulin-Induced Lipodystrophy on Glycaemia Control among Children and Adolescents with Diabetes in Tikur Anbessa Specialized Hospital, Addis Ababa, Ethiopia. J Diabetes Res. 2018;2018.

Implementation of LTE in Mosul city: problems and solution

Mahmood Samir Sadoon[1], Saad Ahmed Ayoob[2]
{mahmoodenp135@student.uomosul.edu.iq[1], sa_ah_ay@uomosul.edu.iq[2]}

Electrical Engineering Department, University of Mosul, Mosul, Iraq[1,2]

Abstract. The selection of cell tower locations is an essential step in designing any cellular system network. The sites are selecting according to the specifications of that system. In addition, each cellular system has optimal geographic locations appropriate to the frequency and design of that system. For example, the sites of the second-generation (2nd G) system towers may not be compatible with the sites of the fourth generation (4th G) system towers for long-term evaluations (LTE) technology in terms of design and location. However, most companies that provide cellular service choose the same locations as the 2nd generation towers to prepare 4th generation service to save operating and construction costs. After operating 4th generation service in the same locations of the 2nd generation towers in the city of Mosul, many problems appeared in the cellular coverage. In this paper, these problems are discussing and comparing with the results of the Atoll software. Methods have been proposing to solve these problems and improve cellular coverage by up to 7% of the area covered.

Keywords: LTE, 2nd generation model, 4th generation model, Coverage, Gaps, Atoll.

1 Introduction

Cellular communication systems have developed in the past decades and their data speed has increased from the first, second, third, and fourth to fifth generation (1G, 2G, 3G, 4G, and 5). Fig 1. Shows a comparison between the generations of cellular communication systems in terms of data download speed and the technologies used [1], [2], [3].

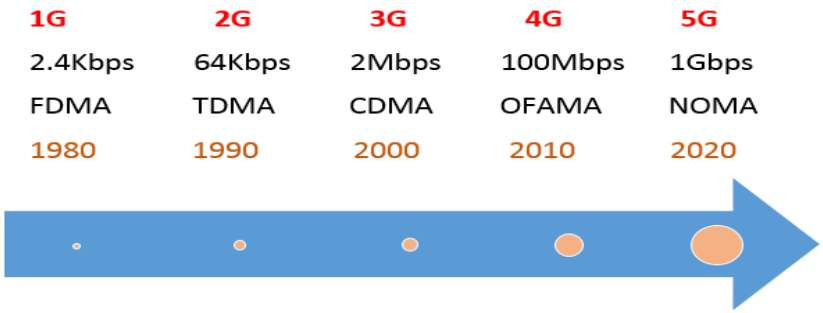

Fig. 1. Technologies used for mobile phone systems and download speed.

With the increasing request of high data transmission rates, 4th generation system with LTE technology have developed, which uses Multi Input Multi Output –Orthogonal Frequency

IMDC-IST 2021, September 07-09, Sakarya, Turkey
Copyright © 2022 EAI
DOI 10.4108/eai.7-9-2021.2314878

Divisions Multiplex (MIMO-OFDM) technology to achieve these requirements as it provides high spectral efficiency with high data rate in multipath [4]. The principle of operation OFDM technology depends on the fragmentation of the signal to be sent into several parts. Each part is sent on a narrow frequency channel called the carrier so that each carrier is orthogonal to the neighbouring carriers on its two ends; for example, when the carrier has the greatest value, the adjacent carriers have a zero value as shown Fig 2. [5], [6].

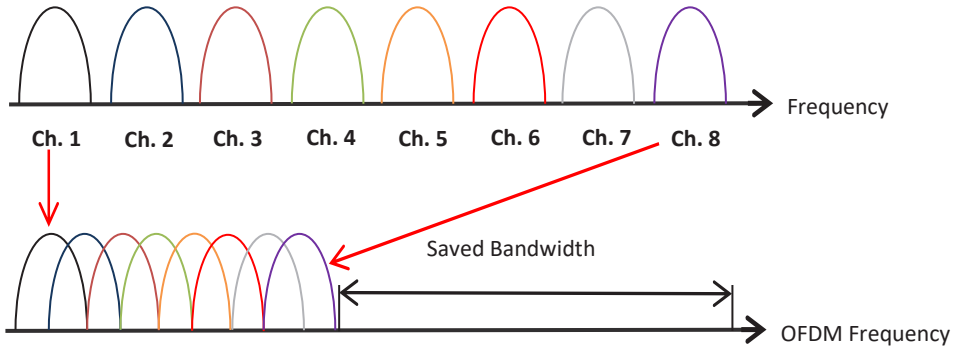

Fig. 2. Orthogonality characteristic of sub-carrier frequencies in OFDM systems.

Although 5th generation technologies have become faster than 4th generation technologies in transmitting data, they are still limited to use due to the high prices of mobile phones that work with this technology [7], and some researchers claim there is a relationship between short frequencies of 5th generation technologies and appearance of the Coronavirus (Covid 19)[8]. Other research denied this claim [9], While other studies are still ongoing on this subject, which may restrict the spread of this technology at present time. Research aimed to identify the problems of cellular coverage of mobile phone networks operating with 4th generation -LTE technology in the city of Mosul and to present some practical proposals to solve these problems and improve cellular coverage in the city of Mosul using the Atoll simulation method.

2 Previous Work

The central design was used to improve the quality of service for LTE technology for a specific computational area using the Atoll program, where the optimum value of the azimuth angle (-8.7 degrees), mechanical inclination (0 degrees), antenna gain (20 dB) and antenna height (27.5 meters) were achieved. The average signal coverage across the region increased from -78.56 dBm to -76.31 dBm [10]. Another study discussed the increase in the number of users on the 4G cellular network in Indonesia. And simulating the deployment of the 4G LTE-Advanced network in Central Jakarta with a frequency spectrum of 2100MHz. The study concluded that the network deployment in Central Jakarta requires at least 109 sites to cover all regions [11]. A new proposal was presented to plan a cellular network working 4G technology using meta-heuristic algorithms and to choose the best locations for the towers by covering the cell with the minimum required power and calculating the average number of users by using Monte-Carlo simulations [12].

In a study conducted to design and simulate a cellular system downtown Phnom Penh. LTE system was building with peak data rate and low latency. In addition to determining the dimensions of the coverage areas and the transmitting power of the city of Phnom with it on the map, measuring the signal level and knowing the interference areas [13]. Another study was conducted for a cellular system using (2^{nd}, $3^{rd,}$ and 4^{th} generation) technology and measuring the received signal strength at Ondokuz Mayis University (OMU) using the "Netmonitor" application on Android phones. The results showed that the 2^{nd} generation signal is higher than the signal receiving from the 3^{rd} and 4^{th} generation [14]. The growth of subscribers to 2025 for a cellular network (LTE) in Denpasar was predicting using Atoll's Monte Carlo simulation and determination of the maximum subscribers connected to the LTE network at 1800MHz. The simulation results showed that in 2017, 99.8% of subscribers connect successfully and only 0.2% of users were rejecting while in 2025, 99.3% of users connect successfully and only 0.7% of users are rejected [15]. A study was conducted to find the best design for a cell operating with LTE technology to improve the quality of communication and coverage in urban areas and rural suburbs and reduce the path loss for the Okumura Hata model for MATLAB by using the Atoll program, where the results were comparing, and the best model was knowing for each region [16].

3 LTE Architecture

LTE architectures were designed to increase the data transfer rate, reducing the waiting period, achieving optimal radio access for the data packet, and achieve smoother roaming service and quality, LTE systems consist of radio and non-radio networks, where the radio network called Evolved- UMTS (Universal Mobile Telecommunications Systems) Terrestrial Radio Access Networks (E-UTRAN), While the non-radio part called Evolved Packets Cores (EPC) networks which connect to Packet Data Networks (PDN). Fig 3. shows the architecture of the LTE system with different interfaces for each link [17],[18].

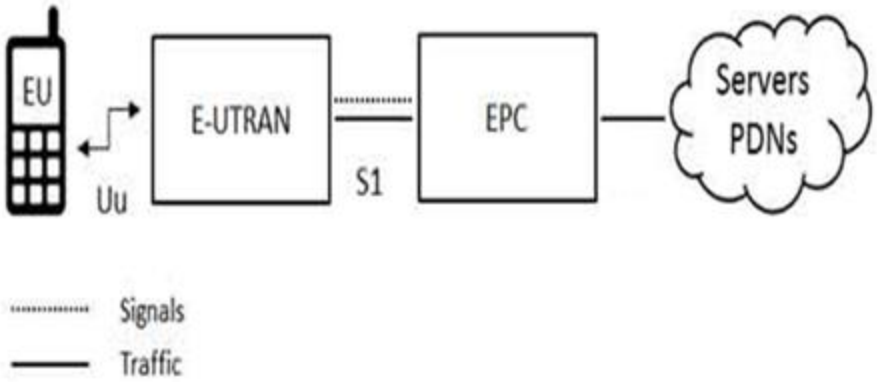

Fig. 3. LTE Architecture.

The E-UTRAN architecture consists of eNodeB (eNB) which are advanced base stations. These base stations are connecting Equipment users (EU) devices to a network. E-UTRAN is a distributed architecture because it doesn't contain central controllers, Fig 4. is showing that the E-UTRAN architecture consists of a network of advanced base stations that are connecting to other eNB via (x2) link and connects to the core of EPC via the (S1) link, while it is connecting to user's devices via the Uu link. All the following radio functions are operated by (E-UTRAN):

1. Compress the IP packet headers.
2. Data encryption and protection.
3. Connects to EPC networks, which include selecting signals and configuring a path for carrying and routing data.

Radio Resources Management (RRM) includes all functions of radio carriers such as access control, mobile control, user resource allocation, and radio load control. The main function of a radio network is to control the user and establish carriers. It also provides effective and true terminals with (Quality of services QOS), protection, mobility, management, and finally, it allows communication with external IP packet networks [19],[20].

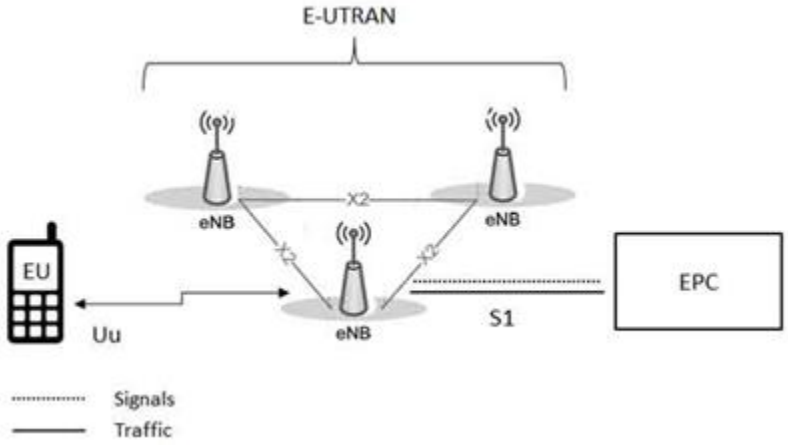

Fig. 4. E-UTRAN Architecture.

Fig 4. shows that the access network is responsible for the cellular coverage through a group of towers (eNB), and each tower covers a certain geographical area in which there are several users' equipment (EU), and the cellular coverage must cover all geographical areas without any coverage gaps between regions (towers) to make all users connect to the cellular network and improves the efficiency and performance of the cellular network.

4 Simulation Model for LTE 4th Generation

With the development and spread of cellular networks, many simulation programs have appeared to represent these networks, Atoll is one of these programs that is using to simulate cellular networks. In this model, a cellular communication network used both 2nd generation and 4th generation with LTE technologies was simulated in the city of Mosul. Six sites for one of the companies operating in the city were selecting, represented, and simulated in the Atoll

program, and their properties were studying to find out the reasons for the poor cellular coverage of the 4thG network in the city.

4.1 Assumptions

The 2ndG model and the 4th generation model depended on some assumptions:

1. The frequency of the 2nd generation is 900 megahertz (MHz).
2. The frequency of the 4th generation is 1800 MHz
3. Six towers (sites) for the 2nd generation model.
4. Six towers for the 4th generation model.
5. Each tower consists of three cells (three sectors).
6. The coordinates and locations of the towers are identical to the real coordinates of the towers of a company operating in the city.
7. The characteristics of the tower in the simulation programs for height, direction, antenna tilt, and transmitting power are like the real characteristics of the tower.

4.2 Variables

The variables that we are using for the 2nd generation and 4th generation models are showing in Table 1. Note that the transmitting power used is 43 dBm and the antenna tilt angle is 0 degrees.

Table 1. Coordinates and site properties for simulation models**.**

Site	longitude	Latitude	Antenna high for sector 1	Antenna high for sector 2	Antenna high for sector 3	Antenna azimuth sector 1	Antenna azimuth sector 2	Antenna azimuth sector 3
Zuhor	43.1923	36.3754	18	16	18	0	120	240
Zuho1	43.1978	36.3759	19	19	19	0	120	240
Zuho2	43.2026	36.3777	18	18	16	0	120	240
Zuho3	43.195	36.3825	16	18	16	0	120	240
Zuho4	43.2026	36.3822	18	18	18	0	120	240
Zuho5	43.1963	36.3885	22	22	22	0	120	240

5 Simulation and Results

The level of a signal receiving in a cellular system considers one of the characteristics of system efficiency, and the efficient system has a better signal level. To test the efficiency of cellular networks in the city of Mosul, a simulation of 2nd and 4th generation's networks were madding for a group of towers, for one of the provided service cellular networks in the city. According to the assumptions that were mentioning previously and using the Atoll, program at

greater than -70 dbm receiving signal. The level of a signal receiving for the 2nd generation shows in Fig 5. While the level of the received signal for the 4th generation is showing in Fig 6.

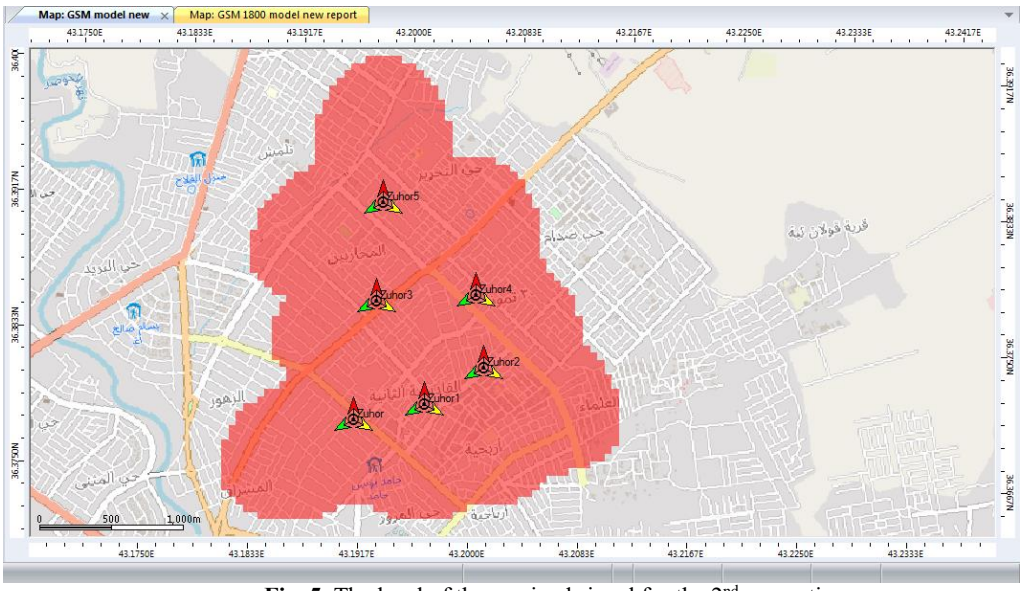

Fig. 5. The level of the received signal for the 2nd generation.

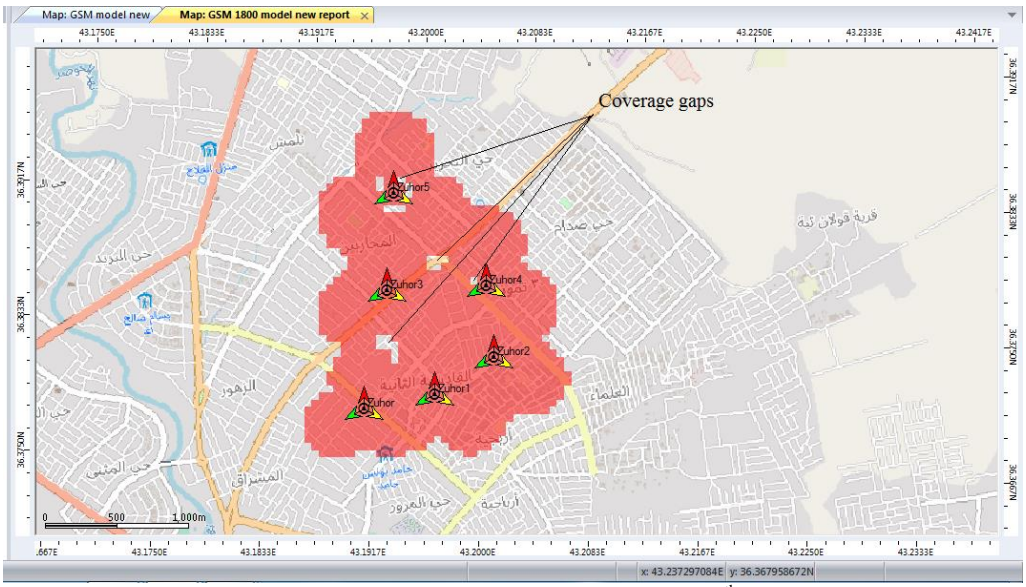

Fig. 6. The level of the received signal for the 4th generation.

The red colour in Figs 5 and 6. Are showing the areas covered by the cellular network consisting of six towers distributed on the geographical map of an area in Mosul city using the simulation

program Atoll, in Figure 6. which represents the signal level for the 4th generation were near areas from towers but without coverage (gaps), and that means several users, despite their proximity to the towers, but they have poor cellular service, while the same areas in Figure 5. Are completely covering by the signal because it works with the technology of the 2nd generation, whose frequency is less than the frequency of the 4th generation therefore the coverage of the 2nd generation is higher than the coverage of the 4th generation. The companies that provided cellular service in the city of Mosul have used the same sites of the 2nd generation towers to prepare the 4th generation service to save the cost, but this procedure led to the existence of problems and gaps coverage for the 4th generation. To solve coverage problems and fill the gaps, there are a set of proposals that we can show:

1. Change some of the towers' locations
2. Increase antenna height
3. Change tilt of the transmitter antenna
4. Change azimuth of the transmitter antenna

Each proposal has characteristics that depend on the structure of cellular systems and the nature of the geographical areas that the network operates. Mosul city has population density and urban nature and closed area so that most of the communication towers are building with few heights above the rooftops. To increase the height of the antennas, we need to change the structure of the tower, and this proposal does not proportionate with the nature of the small areas of the rooftops in the city, so the proposal to change antenna height cannot be used in all areas of the city. As for the proposal to change the azimuth antenna should not be used in urban areas that suffer from poor coverage in most directions because it increases coverage in one direction and decreases it in the other. The proposal to change some tower locations for the cellular network in the city of Mosul, despite its cost, but it the best choice to cover areas and fill coverage gaps. As will proposal for change antenna tilt can also be used to increase coverage in nearby areas, if it does not have a significant impact on coverage of distant areas. It is also possible to take the proposal to change some sites and the proposal to change the antenna tilt to obtain the best cellular coverage and at a low cost.
By using the proposal to change antennas tilt with the proposal to change some tower's location for a simulation model of 4th generation network, the coordinates of two sites (Zuhor and Zuhor4) of the six tower sites were changed and change antennas tilt in one tower (Zuhor5) only, as shown in Table 2.

Table 2. Changing the coordinates and antennas tilt for some sites for simulation models.

Site	longitude	Latitude	Antenna Tilt for sector 1	Antenna Tilt for sector 2	Antenna Tilt for sector 3
Zuhor	43.1911441	36.3791889	same	same	same
Zuhor4	43.2026371	36.3839493	same	same	same
Zuho5	same	same	add 4 degree	add 4 degree	add 4 degree

After using the suggestions in Table 2. For the simulation model, the level of the received cellular signal was increasing for the 4th generation, coverage gaps are filling in the 4th generation model, and both second and fourth generation areas became completely covered by cellular coverage, as showing in Figs 7 and 8.

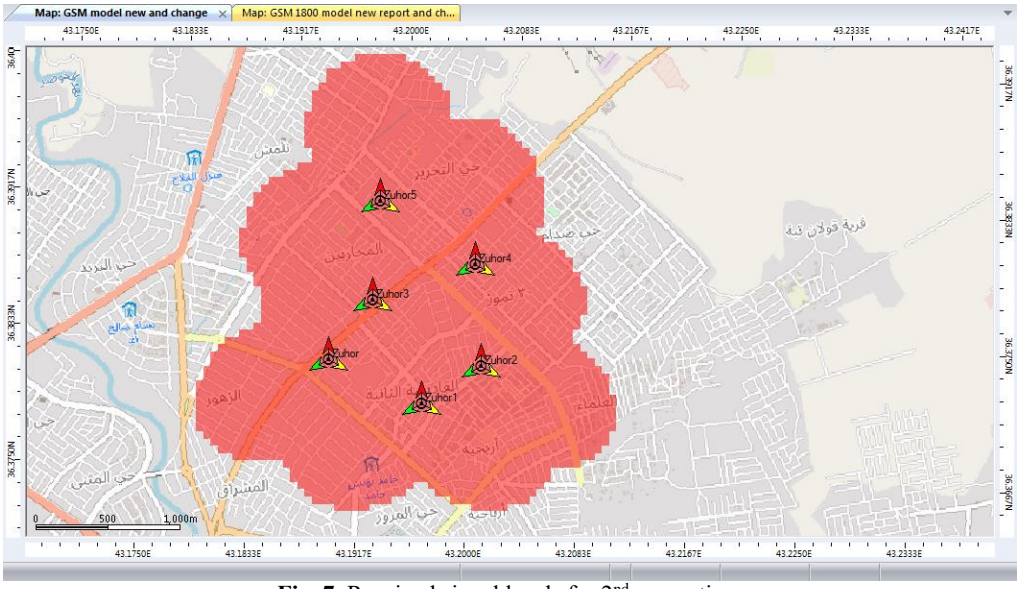

Fig. 7. Received signal levels for 2nd generation.

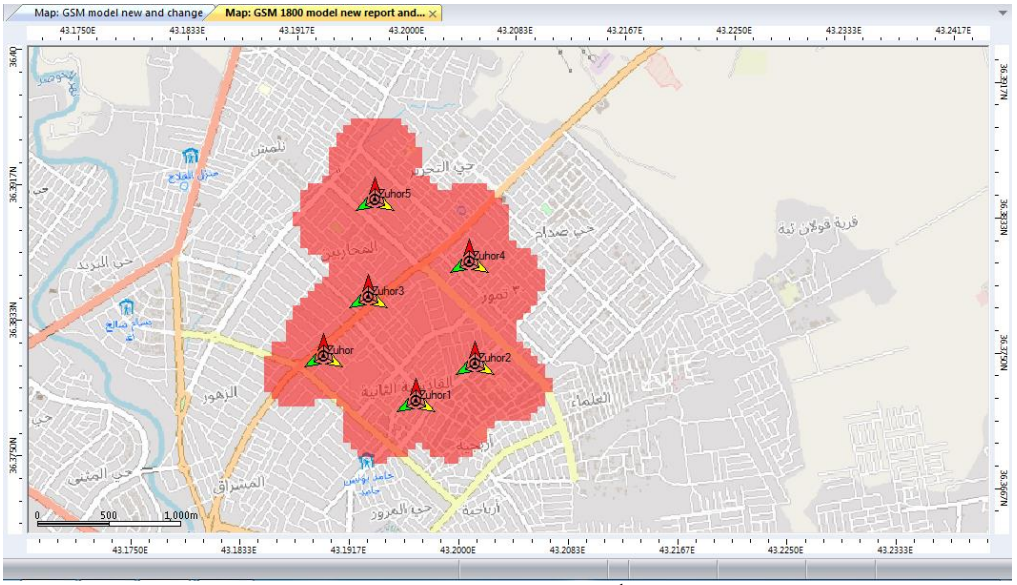

Fig. 8. Received signal levels for 4th generation.

Figs 7 and 8. Show the improvement in coverage. Therefore, the total coverage areas increased in addition to closing coverage gaps. In the 4th generation model, a total covered area by a cellular signal of the smaller signal level -70 dbm increased from 2.93 square kilometres to 3.14 square kilometres, as shown in Fig 9 and 10.

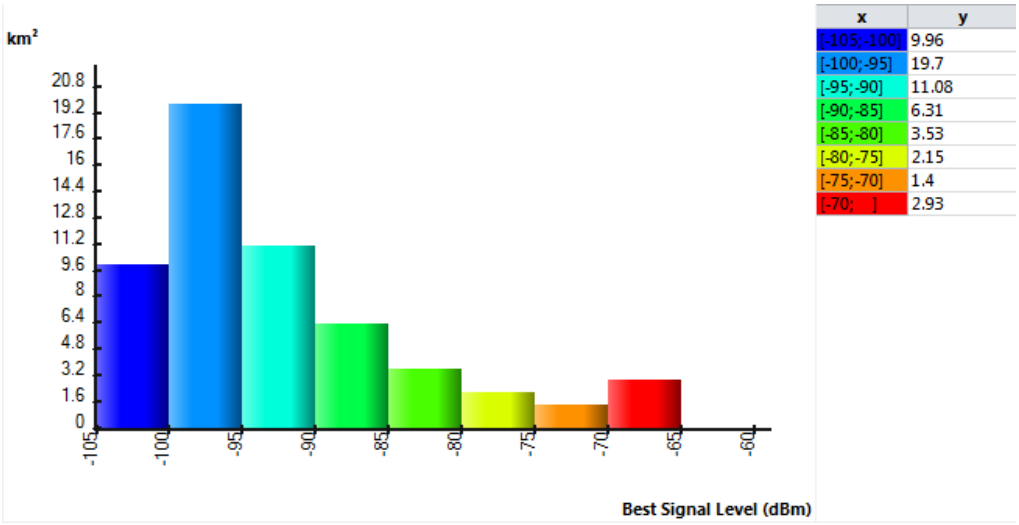

Fig. 9. Covered areas for 4th generation technology before change towers location and antennas tilt.

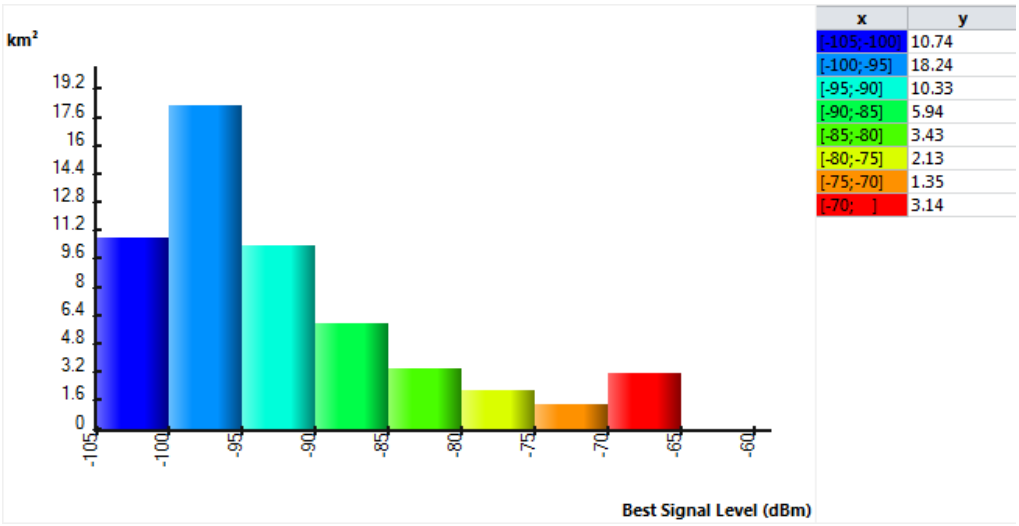

Fig. 10. Covered areas for 4th generation technology after change tower's location and antennas tilt.

Figs 9 and 10. Are showing the levels of a received signal for each area in a square kilometre, where the additional covered areas by a signal level greater than -70 dbm are 0.21 Km^2, which is equivalent to an increase of 7% of the total coverage area, in addition, other levels of the

signal coverage decreased, and that reduces the interference and handoff process (hand over). Increasing coverage area, closing the gaps, and reducing interference come after using proposal of change positions of some towers and change of antennas tilt for 4th generation simulation model.

6 Comparison with Previous Works

Most of the previous works dealt with the topics of designing virtual cellular networks using the fourth-generation technology for choosing the optimal values for these networks in terms of tower locations, transmitted power, capacity, number of users, and traffic density. while in this study, real problems were referred to in a cellular fourth-generation network operating in Mosul city as will proposals to solve those problems and improve cellular coverage in the city were referred in the study.

7 Conclusions

A simulation model of 4th generation system was built which consisting of a group of tower sites for one of the cellular service companies in Mosul city. The 4th generation system services were adding to the same sites (coordinates) of the 2nd generation system, and each site became equipped with both the 4th generation and 2nd generation services. The simulation model showed that there are gaps in the cellular signal received greater than -70 dBm for the 4th generation, which has a higher frequency than the 2nd generation, and that affects the efficiency of cellular service. In this study, a set of proposals were presented to close the coverage gaps and improve cellular coverage by up to 7% of the area covered for the 4th generation cellular service. A proposal to change some tower locations and a proposal to change antenna tilt was chosen as the best suggestions, where it compact with the geographical nature of Mosul city and the nature of the structure of the cellular network. our future work will be to make Drive Test (DT) during a call for the cellular networks that provide cellular services in the city of Mosul and roaming between the locations of the cell towers to improve the 4th generation service in the city.

Acknowledgment

This work was supported by Electrical Department, Engineering College, Mosul University

References

[1] Vora L J. EVOLUTION OF MOBILE GENERATION TECHNOLOGY: 1G TO 5G AND REVIEW OF UPCOMING WIRELESS TECHNOLOGY 5G. IJMTER. 2015. Volume 02(Issue 10): page 281-290.

[2] C S Patil, R R Karhe, M A Aher. Development of Mobile Technology: A Survey. IJAREEIE. November 2012. Volume 1(issue 5).page 374 -379.

[3] Gawas A U. An Overview on Evolution of Mobile Wireless Communication Networks:1G-6G. IJRITCC. May 2015. Volume 3(Issue 5). Page 3130- 3133

[4] Venkateswarlu P, Nagendra R. "Channel Estimation Techniques in MIMO-OFDM LTE Systems. IJERA. July 2014. Volume 4(Issue 7). Page 157-161.

[5] Agarwal A, Agarwal K. Implementation and Performance Evaluation of OFDM System in Diverse Transmission Channel Using Simulink. AJEEE. 2015. Volume 3. Page 117-123.

[6] Dixit S, Katiyar H. Performance of OFDM in time selective Multipath fading channel in 4G Systems. Fifth International Conference on Communication Systems and Network Technologies. 2015. Page 421-424.

[7] Bega D, Gramaglia M, Bernardos C J, Banchs A, Costa-Perez X. Towards the network of the future: from enabling technologies to 5G concepts. Transaction on Emerging telecommunication technologies. August 2017. Volume 28(Issue8).Page 1-13.

[8] Fioranelli M, Sepehri A, Roccia M G, Jafferany M, Olisova O Yu, Lomonosov K M, Lotti T. 5G Technology and induction of coronavirus in skin cells. Journal of biological regulators and homeostatic agents.2020. Volume 34. Page 3-10

[9] Uthman M, Shaibu F E, Najashi B G, Labran I F, Sadiq A. 5G Radiation and COVID-19: The Non-Existent Connection. IJRECE. June 2020. Vol 8(Issue 2). Page 34-38.

[10] Amit Bhagat and Nanda Bikram Adhikari, “Optimization of QoS key parameters in LTE network by using central composite design (CCD)”, Research Journal of Engineering Sciences, Vol. 10(1), January 2021.

[11] P. A. Fadhila and M. I. Nashiruddin, "Planning & Simulation Analysis of 4G LTE-Advanced Mobile Network Deployment Using 2100 MHz Frequency Spectrum in Dense Urban Area: Case Study in Central Jakarta," *2021 IEEE Asia Pacific Conference on Wireless and Mobile (APWiMob)*, 2021, pp. 8-14.

[12] Ghazzai H, Yaacoub E, Alouini M-S, Dawy Z, Adnan A-D. Optimized LTE Cell Planning with Varying Spatial and Temporal User Densities. IEEE. 2015.

[13] Seven S, Astuti R P, Prasetya B.Design and Simulation of LTE Radio System for Broadband Wireless Access in Central Phnom Penh. e-Proceeding of Engineering. 2015. Volume 2. Page 3884-3889.

[14] Engiz B K, Kurnaz Ç. Comparison of Signal Strengths of 2G/3G/4G Services on a University Campus. IJAMEC. 2016. Page 37-42.

[15] Rahmatia S, Azzahra A A, Ismail M, Astharini D, Samijayani O N. Subscriber Growth Forecasting of LTE Network 1800 MHz FDD at Denpasar City using Monte Carlo Simulation. JET. 2019. Volume 19.

[16] Maswood M M S, Dey U K, Uddin Md A, Ghosh A K, Mamun Md M, Sonia S S, Alharbi A G . A Novel Approach to Design the Cell of LTE Cellular Network to Improve the Call Quality and Coverage Area in Rural and Suburban Area. IEEE. 2021.

[17] Dahlman E, Parkvall S, Sköld J. 4G LTE/LTE-Advanced for Mobile Broadband. UK: Academic Press is an imprint of Elsevier; 2011. Page 109,110.

[18] Holma H, Toskala A. LTE-ADVANCED. Finland: Nokia Siemens Networks; 2012. Page 22, 23.

[19] Dima Dababneh, B.SC.,"LTE Traffic Generation and Evolved Packet Core (EPC) Network Planning", Ottawa-Carleton Institute for Electrical and Computer Engineering (OCIECE) Department of Systems and Computer Engineering Carleton University Ottawa, Ontario, Canada, March 2013.

[20] Alexander Kukushkin, "4G- Long Term Evolution (LTE) System," in *Introduction to Mobile Network Engineering: GSM, 3G-WCDMA, LTE and the Road to 5G* , Wiley, pp.205-291, 2018.

Wireless Sensor Networks Applications, Challenges, and Security Requirements

Ali Hadi Abdulwahid[1*], Muwaffaq Jameel Salih[2]
{dr.hajjiali@stu.edu.iq, muwaffaq.jameel@stu.edu.com[2]}

Southern Technical University/Engineering Technical College /Basra[1]
Southern Technical University/Faculty of Graduate studies/ Basra[2]

Abstract. Wireless sensor networks (WSNs) are a type of network that consists of connected sensor nodes that communicate wirelessly to gather data about the environment. WSNs have grown in popularity, but they have several major limits and security issues that must be carefully considered while building and implementing them. An overview of WSN and common communications standards are given in this paper, and as a result of the wide range of WSN applications, these applications are briefly discussed with focusing on Designing challenges and key security goals.

Keywords: Wireless, sensor node, network, mote, sink, ZigBee, LoRa.

1 Introduction

As a result of considerable advances in the fields of telecommunications, and computer technology, we currently have a new computing and networking architecture known as wireless sensor networks (WSNs). Traditionally, installing wired sensors in restricted appliance areas only yielded poor results. Meanwhile, compared to wired sensor nodes, the practice of adopting wireless technology created sensor nodes that formulated more viable solutions. Recently, there has been a measurable advantage associated with the considerable possibility of linking multiple devices and networks in an eloquent attempt to solve critical issues and challenges. The first wireless sensor network was a sound surveillance system created by the US navy in the 1950s to identify and monitor enemy submarines.[1]. Today, this servicing technology is used to detect undersea biodiversity and volcanic activity. With the rapid growth of the aforementioned WSN, this technology can now be easily applied around the world[2].

2 Overview on Wireless Sensor Networks

Small individual sensor nodes form up a wireless sensor network. When a node is linked to other nodes, this number will rise to hundreds of thousands of nodes, depending on the application scenario. Depending on the network deployment, every sensor node in a wireless sensor network observes its environment and transmits the collected data to a single or group of sink stations utilizing a wireless connection. Sensor nodes have three main functions: the first is to sense their surrounding environment, the second is to process the data that was initially detected, and the third is to communicate or interact with other sensor nodes or sink stations in the network. The most critical of the above specifications are sensing the environment. WSNs may be organized in a variety of ways, including centralized, distributed, and ad hoc. The general communication structure of a WSN is demonstrated in Fig 1 Sensor field, a sink node, and user or task management component are the main components. A sensor field is a collection of sensor nodes deployed in a certain area. Each sensor node in the sensor field can sense its phenomenon and send the data to the sink through a multi-hop link A sink is a type of sensor node that gathers data from the sensor field and either performs the necessary operations or simply transfers the data to the user or task monitor node. It also sends queries to the network's sensor nodes and retrieves the information required. Finally, each sensor node in

IMDC-IST 2021, September 07-09, Sakarya, Turkey
Copyright © 2022 EAI
DOI 10.4108/eai.7-9-2021.2314823

the sensor field is assigned by the user or task manager node. Regardless, the sink node communicates with the user or task monitor node over the Internet or via satellite [1][2].

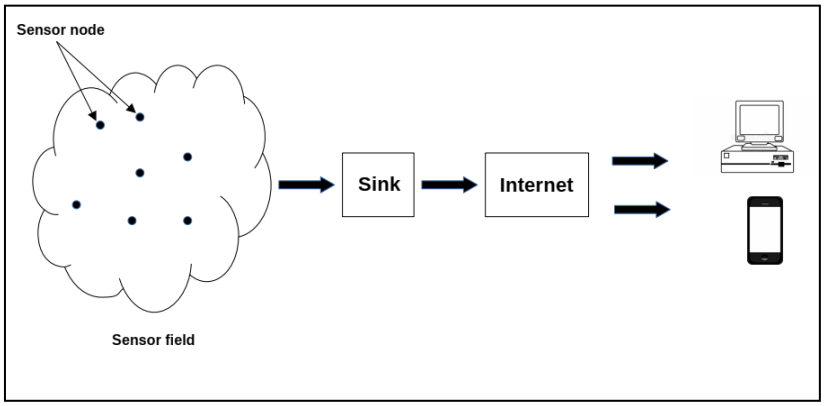

Fig.1. The communication architecture of wireless sensor network

3 Sensor Node Description

A sensor node can be defined as a small system with four main hardware components: sensing, processing, transceiver, and power generator. A global positioning system (GPS) and a mobilizer are both used by the sensor node for location purposes. Fig 2 depicts the basic architecture of a sensor node[3].

Sensing Unit: A sensing device collects information (such as temperature, pressure, light, and displacement) from its surroundings and produces an optical or electrical signal in response. The two fundamental components of a sensing network are a sensor and an analog to digital converter (ADC). One or more sensors generate analog signals in the sensor section, which are then converted to digital signals by the ADC and fed into a processing unit for supplementary operations. Sensor nodes are categorized as thermal, optical, acoustic, or mechanical sensors based on the phenomenon observed or gathered[3].

Processing Unit*:* A processing unit is made up of two components: storage and a processor. Sensed data is temporarily stored in a storage component that functions as nonvolatile memory for programming instructions. On occasion, it will also store processed data. The sensor node's processor enables it to collaborate with other network nodes to finish the task. The microcontroller of a sensor node conducts tasks, processes data, and manages the sensor node's other operations. Microcontrollers are used in sensor nodes because of their unique characteristics, such as low cost, ease of attachment to auxiliary apparatuses, ease of training, and squat power utilization. Because of their power-saving features, ATMEL, At super 128L, and MSP430 are the most widely used microcontrollers. The MSP 430 has six power modes, ranging from fully powered up to powered down. These kinds of power-saving techniques extend the system's lifetime and extend the sensor node's life[3].

Transceiver Unit: The transceiver connects the node to the rest of the network. It combines a transmitter and receiver into a single unit that operates on a particular radio frequency (RF). Modulation, filtering, multiplexing, band bass, and demodulation are all needed for the RF message, making it more complicated and costly. Sensor nodes depend on industrial science medical bands (ISM), which provide a free radio band with wide accessibility. Optical communication, infrared, and radio frequency are the three transmission systems available in wireless transmission. For starters, optical communication requires low power, sightlines, and

squatting in ambient conditions. Second, whereas infrared communication does not necessitate the use of antennae, it has a limited broadcasting range. Third, since it offers free bandwidth at 173, 433, 868, and 915 MHz and 2.4 GHz, radio frequency communications are the most appropriate medium best suited for wireless transmission. The IEEE 802.15.4 specification is used by the majority of sensor nodes to create low-rate wireless personal area networks. The transceiver is standard in that it has four operating modes: send, receive, idle, and sleep. The transceiver consumes the same amount of power in both receive and idle modes. When the transceiver is not actively running, it can go into sleep mode rather than being left in idle mode, as this wastes a lot of energy. It will simply transition from sleep to active broadcast or receive mode[3].

Power Unit: The sensor node is a small micro-electrical device that consumes very little power. The sensor node is kept alive by the power unit in a harsh and unforgiving world where changing batteries is costly and difficult. Sensor nodes primarily use energy for sensing, transmission, and data aggregation. The transmission of information uses the most energy of the aforementioned operations as compared to the others. The sensor node's lifespan, on the other hand, will be determined by the application scenario. Scientists monitoring the presence or age of ice (particularly in the form of glaciers) or ocean bed slides, for example, need sensors that can operate continuously. Finding the temperature in a specific area can take several hours or days when sensors are deployed on the battlefield. Previously, vanadium and molybdenum oxide were used to make the batteries for tiny sensor nodes. Since sensor nodes worked in a variety of locations, future energy exploration from the atmosphere is possible. Sensor node batteries should be as small as possible and as effective as possible. Electrochemical objects made of nickel-zinc, lithium-ion, and nickel-metal hydride are used as electrodes. Furthermore, since sensor nodes are typically installed in unconditional areas and must collaborate with other sensor nodes about their current location for data transmission, certain routing protocols and particular applications require the location of a sensor node, which is made possible by a location-finding device. A mobilizer is an optional part of a sensor node's definition that moves the sensor node from one location to another to complete the mission[3].

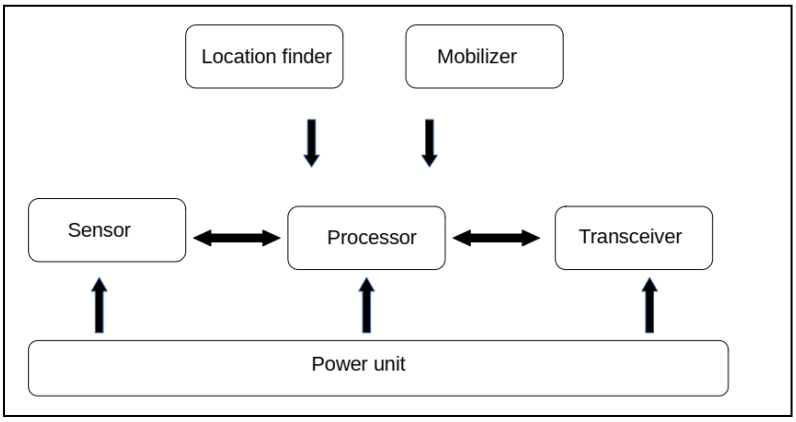

Fig.2. A sensor node's basic configuration

4 Applications of WSN

WSNs can be used for military, industrial, medical, and environmental monitoring, to name a few. Since these applications have different operational needs, they prefer to use different WSN architectures. High bandwidth, high security, and good coverage are the most critical criteria for military surveillance. WSN solutions that are stable, reliable, robust, and real-time

are required for industrial monitoring applications. In medical applications, security and network stability are generally valued, and environmental monitoring typically needs strong, energy-efficient, and independent sensor nodes[4]–[6]. Fig 3 shows some of the Wireless sensor network applications.

Environmental surveillance*:* The progress of humankind has had enormous environmental effects, and all efforts to promote environmental protection have been conducted with zeal. Environmental monitoring is an example of a large effort that allows for the monitoring of various physical characteristics to control or limit environmental pollution. Manual data collection was required in traditional environmental monitoring systems, which were eventually declared unsuccessful due to their need for human intervention and lack of early detection ability for pollution cases. Digital data loggers were introduced a few years ago to help improve the geographical and temporal quality of environmental monitoring, but they missed real-time data analyses. With the development of micro-electromechanical systems (MEMS), low-power WSN systems were introduced, and environmental surveillance could be done remotely as well as in real-time. Since then, this strategy has favored a proactive approach to environmental pollution. In the field of environmental monitoring, sensor nodes provide the following services [7], [8]:

A. Pollution Monitoring.
B. Forest Fire Detection.

Fig 4 shows a forest fire detection system by using WSN.

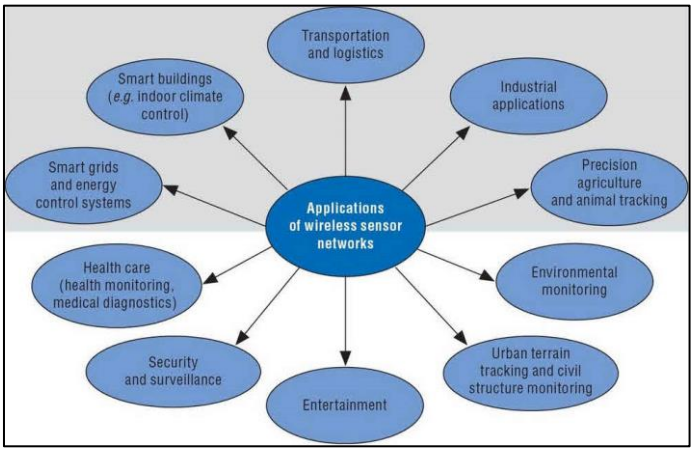

Fig.3. Wireless sensor network applications**.**

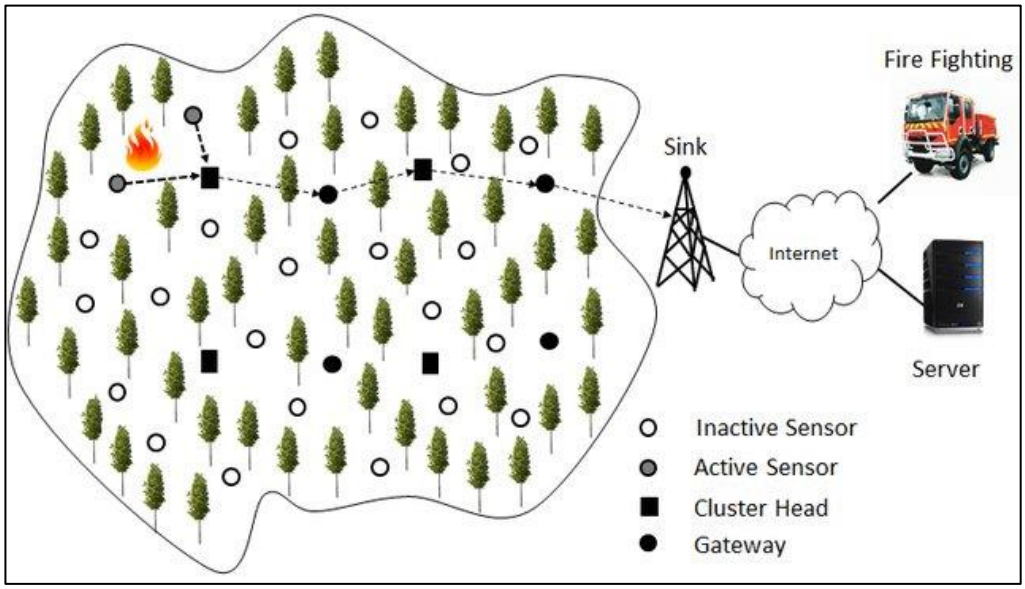

Fig.4. Wireless sensor Network applications in forest fire detection systems**.**

Military Applications: With the formation of The Defense Advanced Research Projects Agency (DARPA) and enemy monitoring, wireless sensor network development largely started with military applications. The destruction of specific sensor nodes by hostile activities has little consequence on or influence on military action because sensor nodes are extensively placed. As a result, sensor nodes are suitable for use on the battlefield. Identification of enemy forces, movement detection, analysis, and progress of their movement can all be accomplished using appropriate sensors in a particular network region. On the battlefield, sensor nodes have the following functions [9]:

A. Battlefield Surveillance.
B. Targeting.
C. Intrusion Detection.
D. Monitoring Forces.
E. Target Classification.
F. Battle Damage Evolution.

Industrial Monitoring: Wireless sensor networks are primarily used by industries to determine the degree of output quality in their operations as well as in cost-cutting procedures. Sensors are used to measure the water level in the tank and the temperature and pressure in refrigerators in nuclear power plants, for example. The monitoring of machine health is another important application of sensor networks. This application aims to find faulty equipment parts that need to be repaired or replaced. Inventory management is another major issue in large businesses. Larger industries' globalization makes it difficult to handle their equipment and goods, so these companies' management is accomplished by wireless sensor networks[10].

Agriculture Monitoring: In the agricultural research community, the use of wireless sensor networks is increasingly growing. Sensor nodes in agricultural production measure elements including temperature, wetness, moisture levels of soil, and sunlight, allowing stakeholders to take the necessary precautions to maximize harvest. In potato fields, the LOFAR-Agro project is used for crop monitoring. Wireless sensor networks are used to identify diseased potatoes in this experiment. The use of pesticides is reduced and limited to vulnerable areas by locating

those areas[10]. Fig 5 below demonstrate using Wireless sensor Network applications in Agriculture.

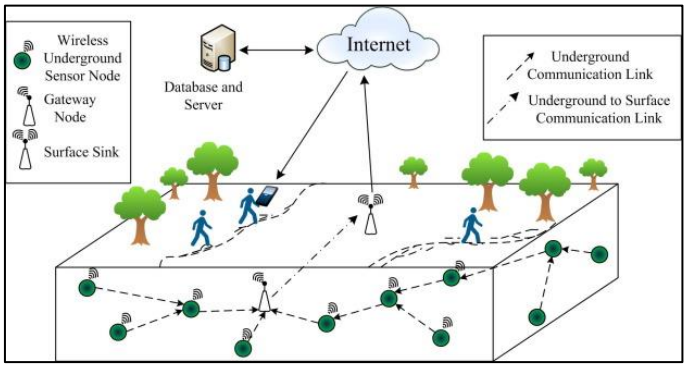

Fig.5. Wireless sensor Network applications in Agriculture**.**

Health Monitoring: Patients are fitted with collective sensors on specific points of their body in this application, which tracks patient measurements such as blood pressure, heart rate, and so on. Some of the applications that benefit from health monitoring include home-based wireless ECG monitoring systems that use Zigbee technology. Such techniques, in addition to occasional supervision by a general practitioner, can be useful for supervising patients in their homes. Electrocardiograms (ECG) are important for detecting abnormalities in heart disease. While clinical ECG equipment is useful for short-range inspection, it is impractical for home health care. Wireless ECG monitoring systems have recently been developed that are compliant with both Bluetooth and Zigbee protocols. A ZigBee device will support an unfailing multi-hop, self-organizing, and mesh network, which keeps the IEEE 802.15 plus ZigBee alliance's appliance software layers stable. ZigBee can provide low-energy networking and a low rate for equipment that requires a long battery life[10].

Smart Home: The use of certain integrated, specially built sensor nodes allows for remote control of home applications. Sensor nodes can be used in household appliances such as microwaves and washing machines, and they can be maintained without human intervention. In intelligent home projects, sensor nodes share resources such as water, heaters, and electricity.

Power Grids*:* Wireless sensor nodes used in power grid applications provide essential information about eclectic use, allowing them to operate more efficiently. Sensor nodes are used to control the entire surrounding environment by measuring and monitoring energy output and consumption. If any irregular positions are observed, the nodes will send diagnostic information to a central authority for resolution.

Automobiles: For a long time, sensor networks have been used to control and track vehicles. Video cameras that are mounted in a specific location to monitor traffic are a typical example. The videos are sent to a human operator, and small sensor nodes are used to track traffic as a low-cost alternative to video cameras. Sensor nodes capture images of traffic and send them to a human operator or automated controllers, as well as receiving control signals. Sensor nodes are placed in specific vehicles to track and control their movements.

5 WSN communication standards

WSNs often employ the Wireless Personal Area Network (WPAN) or Low Power Wide Area Network (LPWAN) standards to transport gathered data to the sink. These standards include IEEE 802.15.4, Sigfox, and low-power Bluetooth. There is no specific networking standard that is deemed perfect for all WSNs, and the standard that is adopted is based on the communication requirements and resource restrictions of a particular function. Table 1 shows some of the most important elements to think about when selecting a wireless communication solution[8]. The following are common communication standards for WSNs*:*

ZigBee: On the highest part of the IEEE 802.15.4 specification, ZigBee is a WPAN standard that covers the networking and device layers. With a maximum bandwidth of 250 kbps, ZigBee devices may transmit over several hundreds of meters and build mesh, a cluster tree, and star network architectures.[11], [12].

Bluetooth low energy (BLE): BLE is a low-energy edition of the Bluetooth protocol that can transmit data at up to 1 megabit per second over a distance of 30–80 meters. [11][12].

Long-range wide area network (LoRaWAN): LoRaWAN is a network protocol designed for applications that send limited quantities of data across great distances only a few times per 24 hours. Its low-power technology allows it to run for up to ten years without recharging[13].

SigFox: SigFox may be considered the first cellular network depend specialized to low-bandwidth Machine-to-Machine (M2M) and Internet-of-Things (IoT) applications. Its unique Ultra Limited Band (UNB) technology uses unlicensed frequency bands to transfer data over an extremely narrow spectrum. SigFox has a range of up to 40 kilometers in open space.[8].

Table 1. Considerations in the selection of a WSN connectivity standard.

Item	Description
Frequency	For low-cost deployment, WSNs frequently use unlicensed ISM frequency channels. Several of these bands are susceptible to channel blockage and interference of signals, making them unsuitable for mission-critical applications.
Range	Nodes are placed in remote locations in some WSN applications, necessitating connectivity technologies with long-range capability. good planning of network coverage needs is required when choosing the suitable solution.
Data Rate	The type and volume of data that will be delivered through a WSN will influence the connectivity mode used. In comparison to another type of data signal, multimedia signals necessitate high-speed data solutions.
Power	All WSNs have a finite amount of energy, but various applications need a various degree of autonomy, therefore the connectivity standard chosen should meet the related power needs.
Security	Different levels of protection are available in WSN connectivity specifications. Sensors that support mission-critical applications will have to take this into account.

6 Designing challenges for WSNs

The following are some design challenges for WSNs[2], [4], [14], [15]:

Fault Tolerance: Based on the application, the number of sensor nodes can reach thousands. A few sensor nodes can stop working or become blocked as a result of physical damage or environmental changes. The fault-tolerance problem's trustworthiness is determined by the failure nodes' ability to adjust the sensor network's entire task. Fault tolerance refers to the ability to extend the functionality of a sensor network, excluding any interruptions caused by sensor node failure. There are several fault tolerance and energy-efficient algorithms that can be used to extend the network's lifespan. As a result, losing one node has no impact on the network's results. Consider some sensor nodes installed in the office to monitor temperature and humidity; the toleration value must below.

Production Cost: Sensor network design aims to have the least expensive sensor nodes possible. WSNs have a large number of sensors to calculate or estimate network costs, but the outlay of each sensor node is more significant. We can purchase 10 Bluetooth devices for the price of one sensor node. Bluetooth devices are considered to be low-cost devices. Consider the sensor node in Fig 1, which includes additional units such as a sensing device, a processing unit, a position finding system, and a mobilizer, all of which add to the sensor node's cost. As a result, with all of the application criteria, the expense of the sensor node becomes a challenge.

Scalability: Sensor nodes may be monitoring thousands of operations at any given time. To complete the application, the number could reach tens of thousands. Adding more nodes to an established network does not affect the sensor network's continuous efficiency. The density of the nodes is calculated using how many nodes are in a specific region, with densities variable depending on the node function and where the sensor nodes are placed.

Network Topology*:* A sensor network's geographical configuration is known as network topology, and it must have a high-density value. *Pre-deployment*, *post-deployment*, and *re-deployment* are the three topologies that make up a wireless sensor network. Pre-deployment is the first step of sensor node deployment, which is accomplished by throwing or positioning each sensor node in the network field one after the other. This deployment method involves manually or mechanically placing nodes one by one (released from plane, rocket, missile, etc.). Even though these sensor nodes are distributed according to engineering measurements, the schemes used for initial deployment nodes in the network are inserted in the factory. Using the above methods comes at a high price tag: encouraging self-organization and avoiding fault tolerance, eliminating the need for any pre-deployment, and re-planning generally lowers the initialization cost. Post-deployment occurs after the initial deployment of sensor node topology, which can change due to substantial operations on the sensor network, such as jamming or sensor nodes moving from one location to another to complete the assigned task, resulting in changes in vacant energy, reachability, task specifics, and malfunctioning. Due to energy shortages or other causes, device failure is typical in any network design. As a result, the geometrical and spatial relationships of sensor networks are horizontal to the implementation challenges. If certain sensor nodes fail to function properly due to changes in the environment, re-deployment is used. As a result, certain auxiliary sensor nodes can be re-deployed in place of shattered nodes at any time, as well as necessary adjustments in assignment dynamics. The addition of new nodes could necessitate network reorganization.

Data Delivery Mode: Reactive, proactive, hybrid, query-driven, and event-driven data is the most typical type of wireless sensor network data; however, in the application of wireless sensor networks, only one data delivery model is required.

Global Identification: The setup of wireless sensor networks has many sensor nodes, yet this does not prevent global identification. A GPS provides location data to adjacent sensor nodes, but it relies on line-of-sight from many satellites. However, sensors installed within a building, underwater, or beneath deep foliage, or those jammed by eavesdroppers, make this impossible in some cases.

Storage and Retrieval: Sensor networks investigate environmental changes and generate a significant volume of raw data in a continuous time series. Traditional database management is not suitable for wireless sensor networks, even though data is continuous. In wireless sensor nodes, three forms of memory are used: flash memory, fuse bits, and electrically erasable programmable read-only memory (EEPROM).

Area Coverage*:* WSNs are made up of a few sensor nodes. With a few homogenous sensor nodes, area coverage tends to expand across the entire region. WSNs are traditionally made up of two processes: (1) area coverage and (2) computational complexity. The first is after discreetly organizing into pre-defined sections. Sensor nodes keep track of environmental data indefinitely. Furthermore, even though this type of sensor consumes a lot of energy, sensed substances are transferred to a base station via a communication component, either directly or through additional nodes.

In-Network Processing: In wired and wireless networks, transport protocols are used to ensure that data transmitted from senders to receivers is not modified by intermediary nodes until it reaches its destination or receiver. To eliminate information redundancy, wireless sensor network data can be changed or aggregated by intermediate nodes.

Latency: The time required for a packet to pass from the sender to the receiver and be correctly received is known as latency. Because the environment changes so quickly, sensor data is only valid for a limited time. As a result, receiving sensed data in a timely and latency-free way is critical.

Network Lifespan: Because the sensor node is a small electrical device with limited resources and energy, the network's lifespan is limited. When all of the nodes in a network are inactive, it is said to be effective. When networking is running well, it can monitor the entire region and gather data utilizing a variety of superior services. Appropriate practices aim to limit energy usage and increase the life of the network.

6 Basic Security Requirements

The goal of security in a sensor network is to safeguard specific sensor nodes as well as the entire network from malicious attacks from both within and outside the network. The most important security needs for protecting a network's integrity are listed below[16]:

Data confidentiality: This is usually the most important purpose, and it concentrates on preventing unauthorized individuals from accessing the sensor through activities like eavesdropping. This is especially critical for applications like WBANs that use several sensor streams. Correlating data streams allows attackers to deduce information about an individual. The most popular method for protecting data is to encrypt it with ciphers.

Data integrity*:* The focus is on ensuring that the data received has not been tampered with in any way throughout the transmission process, whether deliberately or accidentally.

Authentication: Authentication helps the sensor node to confirm the identity of the sensor node it is communicating with. Authentication can be done in many ways, including the interchange of authentication keys or the use of digital signatures. These tactics can be used by a party to validate its identity. They also protect against impersonation and forgeries.

Non-repudiation: The principle of non-repudiation ensures that a sensor node cannot reject sending a message it has already sent.

Authorization: Due to authorization, only permitted nodes will reach network services or certain destinations.

Freshness: The freshness of sensor data messages is examined to ensure that they are fresh, sorted, and unduplicated. This prevents an attack from replaying previous messages from a security point of view. Freshness is commonly implemented by using sequence numbers and timestamps in the data sent by the sensor.

7 Conclusion

Many applications can benefit from the use of wireless sensor networks. Their main advantage is their low cost and flexibility to take measurements remotely and in real-time. These networks, however, face resource constraints in terms of fault tolerance, production cost, scalability, and area coverage, among other issues. These restrictions, if not addressed appropriately, might reduce the efficacy and efficiency of using WSN applications.

References

[1] I. F. Akyildiz, W. Su, Y. Sankarasubramaniam, and E. Cayirci, "Wireless sensor networks: a survey," *Comput. networks*, vol. 38, no. 4, pp. 393–422, 2002.

[2] S. K. Gupta and P. Sinha, "Overview of wireless sensor network: a survey," *Telos*, vol. 3, no. 15μW, p. 38mW, 2014.

[3] H. T. T. Binh and N. Dey, *Soft computing in wireless sensor networks*. CRC Press, 2018.

[4] M. Bhende, S. J. Wagh, and A. Utpat, "A quick survey on wireless sensor networks," in *2014 fourth international conference on communication systems and network technologies*, 2014, pp. 160–167.

[5] C. Buratti, A. Conti, D. Dardari, and R. Verdone, "An overview on wireless sensor networks technology and evolution," *Sensors*, vol. 9, no. 9, pp. 6869–6896, 2009.

[6] G. Zhao, "Wireless Sensor Networks for Industrial Process Monitoring and Control: A Survey.," *Netw. Protoc. Algorithms*, vol. 3, no. 1, pp. 46–63, 2011.

[7] L. M. L. Oliveira and J. J. P. C. Rodrigues, "Wireless sensor networks: A survey on environmental monitoring," *J. Commun.*, vol. 6, no. 2, pp. 143–151, 2011, doi: 10.4304/jcm.6.2.143-151.

[8] M. Pule, A. Yahya, and J. Chuma, "Wireless sensor networks: A survey on monitoring water quality," *J. Appl. Res. Technol.*, vol. 15, no. 6, pp. 562–570, 2017.

[9] B. Shahi, S. Dahal, A. Mishra, S. B. V. Kumar, and C. P. Kumar, "A review over genetic algorithm and application of wireless network systems," *Procedia Comput. Sci.*, vol. 78, pp. 431–438, 2016.

[10] H. T. T. Binh, N. T. Hanh, and N. Dey, "Improved cuckoo search and chaotic flower pollination optimization algorithm for maximizing area coverage in wireless sensor networks," *Neural Comput. Appl.*, vol. 30, no. 7, pp. 2305–2317, 2018.

[11] V. C. Gungor and G. P. Hancke, "Industrial wireless sensor networks: Challenges, design principles, and technical approaches," *IEEE Trans. Ind. Electron.*, vol. 56, no. 10, pp. 4258–4265, 2009.

[12] J.-S. Lee, Y.-W. Su, and C.-C. Shen, "A comparative study of wireless protocols: Bluetooth, UWB, ZigBee, and Wi-Fi," in *IECON 2007-33rd Annual Conference of the IEEE Industrial Electronics Society*, 2007, pp. 46–51.

[13] A. Augustin, J. Yi, T. Clausen, and W. M. Townsley, "A study of LoRa: Long range & low power networks for the internet of things," *Sensors*, vol. 16, no. 9, p. 1466, 2016.

[14] P. Papageorgiou, “Literature survey on wireless sensor networks.” Citeseer, 2003.
[15] R. Soua and P. Minet, “A survey on energy efficient techniques in wireless sensor networks,” in *2011 4th Joint IFIP Wireless and Mobile Networking Conference (WMNC 2011)*, 2011, pp. 1–9.
[16] M. J. McGrath, C. Ni Scanaill, and D. Nafus, *Sensor technologies: healthcare, wellness, and environmental applications*. Springer Nature, 2013.

Look-up Table Reduction for Subcarrier Activation in OFDM with Index Modulation Systems

Abdulrahman Ikram Siddiq[1], Hussein Nadhem Fadhel[2]
{draisiddiq@ntu.edu.iq[1], h.fadil@ntu.edu.iq[2]}

TECK, Northern Technical University, Kirkuk, Iraq[1,2]

Abstract. Orthogonal frequency division multiplexing with index modulation (OFDM-IM) is a promising multi-carrier communication technique. A limited set of k out of n available subcarriers are activated and modulated by constellation symbols. The selection of the subcarrier activation pattern is performed according to data mapped via Look-up Tables (LUTs) or equivalent iterative mathematical algorithms. The complexity of mapping data to active subcarrier indices can rise dramatically with n, and then limit the applicability of OFDM-IM. Therefore, in this paper, a new subcarrier activation scheme is proposed, where smaller size LUTs are used. A reduction ratio in LUT overall size of about 84% is achieved for $(n, k) = (8, 4)$, and this ratio increases with n. The presented analysis and simulation show that an OFDM-IM exploiting the proposed scheme is an identical less complex version of classical OFDM-IM, with a very close BER performance.

Keywords: Orthogonal frequency division multiplexing, subcarrier index modulation, subcarrier encoding, subcarrier activation pattern.

1 Introduction

Orthogonal Frequency Division Multiplexing (OFDM) is the multicarrier transmission a technique that has become a popular signaling format in high-speed wireless communications [1]. OFDM is adopted in many standards, such as Asymmetric Digital Subscriber Line (ADSL), Wi-Fi, Worldwide Inter-operability for Microwave Access (WiMax), Long Term Evolution (LTE) [2]. The reason is the advantages of OFDM including its high resistance to frequency selective fading, ease of implementation, high data rate, and high spectral efficiency [1,2].
OFDM with Index Modulation (OFDM-IM) systems are the result of applying the concept of spatial modulation (SM) to the subcarriers of OFDM [3]. The growing interest in OFDM-IM is due to its many advantages over OFDM. Advantages such as transmit power-saving [4-6], better BER performance [3,7], and a trade-off between system performance and spectral efficiency (SE) [4,7], have made OFDM-IM a possible alternative to OFDM in future communication standards [8,6].
Moreover, SM has been successfully applied in multiple antenna communication systems. That is, among a set of available transmit antennas, a unique antenna is selected to transmit constellation symbols. The selected antenna number is used as an information-bearing unit [9]. Index modulation is also used in a decision gathering scheme for cluster-based wireless sensor networks [10]. It is reported that this scheme outperforms conventional schemes in terms of overall decision error rate. In [11], a differential subcarrier index modulation scheme is proposed to eliminate the need to channel state information knowledge at the receiver.

IMDC-IST 2021, September 07-09, Sakarya, Turkey
Copyright © 2022 EAI
DOI 10.4108/eai.7-9-2021.2314821

To increase the SE of OFDM-IM, the Multiple-Mode OFDM-IM is proposed to convey data through the use of multiple distinguishable constellations and their full permutations. The system achieves a better BER performance than OFDM-IM [12].
A modification to the data to the SAP mapping scheme is proposed in [13] such that the subcarriers are activated with an equal probability. The equiprobable subcarrier activation (ESA) involves iterative arithmetic operations and requires the small table to store SAPs in the transmitter and receiver. The complexity of ESA is comparable with the classical combinatorial scheme. The Generalized Precoding aided Quadrature Spatial Modulation (GPQSM) is proposed in [14]. It is applied on both phase and quadrature components of the signal in MIMO systems. It is shown that the improvement in BER performance of GPQSM is at the expense of an increased decoding complexity as compared with traditional MIMO. Two methods are proposed in [15] to enhance the SE and the diversity of OFDM-IM. The combinatorial data to the SAP mapping scheme is modified and applied to the in-phase and quadrature components of the signal. It is shown that the proposed methods enable low complexity detection and better error performance over classical OFDM-IM.
In more detail, the basic idea in OFDM-IM is that only a subset of the available subcarriers are selected according to the data and used to carry constellation symbols while the other subcarriers in the OFDM block are just turned off. Being selected according to data, the indices of active subcarriers also convey information [3]. To avoid high complexity, an N-subcarrier OFDM block is divided into g subblocks of n subcarriers in each. Subcarrier activation is applied to these subblocks independently, usually with a fixed activation ratio, k/n. That is k of the subcarriers out of n in a subblock are activated [4,16]. However, there are $C_k^n (= \frac{n!}{k!(n-k)!})$ possible subcarrier activation patterns (SAPs). An SAP is selected according to p_1 bits of data, where $p_1 = \lfloor \log_2 C_k^n \rfloor$ and $\lfloor \ \rfloor$ is the greatest lower integer operator. Then, the k active subcarriers are modulated by $p_2 = k \log_2 M$ bits of data, where M is the signal constellation order. As a result, a total of $p = (p_1 + p_2)$ bits are loaded to each OFDM-IM subblock [4,15]. The p_1 to SAP mapping/demapping is implemented via Look-up Tables (LUTs) whose size becomes dramatically high for large n [3,4,6,7]. In [3], it is proposed to use combinatorial number theory to map data to subcarrier indices instead of LUTs for large n. The combinatorial algorithm selects the active subcarrier indices by calculating the binomial coefficients many times. The scheme also involves binary-to-decimal and decimal-to-binary conversion at the transmitter and receiver, respectively, therefore, the complexity is still not low. Additionally, it can give a catastrophic result in some error cases.
In this paper, a new subcarrier activation scheme is proposed where LUTs smaller in size as compared to classical OFDM-IM are used. The advantage of the proposed scheme is twofold, it reduces system complexity and avoids the need to use the combinatorial scheme. The rest of this paper is organized as follows. In Section II, the details of subcarrier encoding, decoding, and LUT sizes of the proposed subcarrier activation scheme, are described. The BER performance of an OFDM-IM exploiting the proposed scheme is evaluated in Section III. Finally, conclusions are given in Section IV.

2 System Model

An OFDM-IM system conveys $m\ (= gp)$ bits by the transmission of each N-subcarrier frequency domain block denoted as $\boldsymbol{x} = [x_0, x_1, \ldots, x_{N-1}]^T$. That is, $\boldsymbol{x}$ is the result of the subcarrier activation/deactivation and symbol modulation according to a stream of m bits, as

described in Section 1. Then, as in ordinary OFDM systems, $\boldsymbol{x}$ undergoes the processes of IFFT, Cyclic Prefix (CP) addition, transmission through the channel, CP removal and FFT, whose output is an estimate of $\boldsymbol{x}$ denoted as $\boldsymbol{y} = [y_0, y_1, \ldots, y_{N_1}]^T$. In this work, a slowly time-varying multipath Rayleigh fading channel is assumed. The equivalent frequency domain relation between $\boldsymbol{x}$ and $\boldsymbol{y}$ can be expressed as

$$\boldsymbol{y} = \boldsymbol{H}x + \boldsymbol{w}$$

Where $\boldsymbol{H} = diag(h_0, h_1, \ldots, h_{N-1})$ and h_i is the channel fading coefficient at the $(i+1)^{th}$ subcarrier with $h_i \sim \mathcal{CN}(0,1)$. The independent additive white Gaussian noise (AWGN) is $\boldsymbol{w} = [w_0, w_1, \ldots, w_{N-1}]^T$ such that $w_i \sim \mathcal{CN}(0, N_o)$.

3 Proposed Scheme

The proposed scheme aims to reduce the complexity of p_1 to SAP mapping/demapping in OFDM-IM systems. The idea is to split p_1 into two segments, namely, p_{11} and p_{12}, and map each segment to a corresponding part of the SAP in different ways.

3.1 Subcarrier Encoding

Subcarrier encoding is the activation/deactivation of the subcarriers of a subblock according to p_1. In the proposed scheme, the binary word p_1 is divided into two smaller size words p_{11} and p_{12}. Such that, p_{11} are the first d bits of p_1, where

$$d = \min(k, n-k)$$

and p_{12} is the remaining bits of p_1. It can be shown that $p \geq d \; \forall \; n, k$. The bits of p_{11} are used to directly determine the state of the first d lhs subcarriers of the subblock. Whereas, p_{12} is used to select the activation pattern for the remaining $n-d$ rhs subcarriers, such that the total number of active subcarriers in the subblock is k.

The $2^{p_{11}}$ possible codes of p_{11} can be classified into $d+1$ categories in terms of the number of 1s in p_{11}, denoted by $n_1(p_{11})$. Each category consists of C_i^d codes, where, $i = n_1(p_{11})$ and $0 \leq i \leq d$. The total number of codes in all of these categories is

$$\sum_{i=0}^{d} C_i^d = 2^{p_{11}}$$

According to the proposed scheme, for each p_{11} code with i ones, there must be $k-i$ ones, active subcarriers, in the rhs SAP. Then, for each such p_{11} code, there are actually C_{k-i}^{n-d} rhs SAPs. On the other hand, to achieve a total of 2^{p_1} SAPs, then for each p_{11} code there must be at least $2^{p_{12}}$ different rhs SAPs to be assigned to the $2^{p_{12}}$ possibilities of p_{12}. This necessitates that

$$C_{k-i}^{n-d} \geq 2^{p_{12}}, \qquad 0 \leq i \leq d$$

However, Eq.(4) is not valid for all values of i. That is, for some i values, such as 0 and d, C_{k-i}^{n-d} is less than $2^{p_{12}}$. While, fortunately, it is greater than $2^{p_{12}}$ for other i values such as $d/2$ or $(d+1)/2$ for even and odd d, respectively. The residual $C_{k-i}^{n-d} - 2^{p_{12}}$ SAPs can be used to

complete the required number of rhs SAPs in the cases of $C_{k-i}^{n-d} < 2^{p_{12}}$. This can be correct, and hence the proposed scheme is valid for all n and k, if the total number of generated SAPs by the proposed scheme is equal or greater than the total number of SAPs required in the system, 2^{p_1}. Generally, in the proposed scheme, there are C_{k-i}^{n-d} rhs SAPs for each p_{11} code of i ones, i. e., $C_i^d C_{k-i}^{n-d}$ rhs SAPs for each category of p_{11}. Then, summing over the $d+1$ categories, yields C_k^n, which is by definition greater than 2^{p_1}.

$$\sum_{i=0}^{d} C_i^d C_{k-i}^{n-d} = C_k^n$$

Next, the p_{12} to rhs SAP mapping is performed by $d+1$ LUTs each of size $2^{(p_{12})}(n-d)$ bits. That is, for a given p_{11} with $n_1(p_{11})$ ones, a LUT is used to mapping the associated p_{12} to $(n-d)$- element rhs SAPs of $k - n_1(p_{11})$ ones. A total of Q_{prop} bits of memory is required to store the LUTs.

$$Q_{prop} = 2^{(p_{12})}(n-d)(d+1)$$

Whereas, in conventional OFDM-IM p_1 is mapped to n- bit SAPs by a Q_{conv} - bit LUT.

$$Q_{conv} = 2^{p\,1} \times n$$

Bearing in mind that p_{11} is directly mapped to lhs SAPs, Table 1 shows the superiority, defined by the percentage $r = (Q_{conv} - Q_{prop}\,/Q_{conv})) \times 100$ %, of the proposed subcarrier activation scheme over conventional OFDM-IM. In Table 1, $k = n\,/\,2$ which produces the largest C_k^n and p_1 representing the worst-case LUT size for a given n. The percentage advantage is about 84 % at $n = 8$, and $k = 4$, and most importantly, it becomes greater at larger n. However, smaller size LUTs lead to less memory consumption, faster response, and less system complexity.

Table 1. LUT size comparison

n	2	4	6	8	10	12	16	32
Q_{conv}	4	16	96	512	1280	6144	131072	1.7E+10
Q_{prop}	2	6	24	80	120	336	2304	2228224
r %	50	62	75	84	90	94	98.24	99.99

As an example, consider the case of $n = 8$ and $k = 4$. Then, $C_4^8 = 70$, $p_1 = 6$ bits, p_{11}=4 bits and p_{12}=2 bits. According to the number of ones, $0 \leq n_1(p_{11}) \leq 4$, there are 5 categories of p_{11} codes, with $C_{n_1(p_{11})}^{d} = C_{n_1(p_{11})}^{4} = 1,4,6,4$ and 1, p_{11} codes in each category. The number of available rhs SAPs for each p_{11} code depends on its $n_1(p_{11})$ and is given by $C_{k-n_1(p_{11})}^{n-d} = C_{4-n_1(p_{11})}^{4} = 1,4,6,4$ and 1, for the five categories, respectively. There must be $2^{p_{12}} = 4$ rhs SAPs for each possible p_{11}, and this is not fulfilled for the first and fifth categories. But for the third category, there are rhs SAPs more than the required number, and can be used by the first and fifth categories as long as the total number of SAPs, $\sum_{i=0}^{4} C_i^4 C_{4-i}^4 = 70$, is greater than $2^{p_1} = 64$. That is, in the third category, there are $C_{k-2}^{n-d} - 2^{p_{12}} = 2$ unused rhs SAPs for each possible p_{11} code in this category, which are $C_2^4 = 6$ possible codes. Then, there are 12 unused SAPs in this category that can be used to complete the set of rhs SAPs in the first and fifth categories.

The p_{12} to rhs mapping LUTs can be designed as follows. There are five LUTs, a LUT for each p_{11} category. The LUTs of the second, third and fourth categories are as given in Table 2.

Table 2. p_{12} to rhs SAP mapping of the second, third and fourth LUTs.

p_{12}	rhs SAP 2nd LUT	rhs SAP 3rd LUT	rhs SAP 4th LUT
00	1110	0011	0001
01	1101	0110	0010
10	1011	1100	0100
11	0111	1001	1000

Note that, the patterns 1010 and 0101 are possible rhs SAPs for the $n_1(p_{11}) = 2$, not needed in the third LUT and are reserved to be used with the first and fifth LUTs of $n_1(p_{11}) = 0$ and 4, as shown in Table 3.

Table 3. p_{12} to rhs SAP mapping of the first and fifth LUTs.

p_{12}	1stLUT		5thLUT	
	lhs SAP	rhs SAP	lhs SAP	rhs SAP
00	0000	1111	1111	0000
01	0011	1010	0011	0101
10	0110	1010	0110	0101
11	1100	1010	1100	0101

The first LUT is used with a single p_{11} possibility of 0000. Then, accordingly, the only possible rhs SAP is 1111. This is used when $p_{12} = 00$. For the other three p_{12} possibilities, the rhs SAP 1010 is used and to distinguish between these latter cases and the rhs SAPs of $n_1(p_{11}) = 2$, the lhs SAP is replaced by three different patterns of two ones each, to conserve a total of $k = 4$ ones in the SAP. Note that these modified lhs SAPs will not interfere with the cases of $n_1(p_{11}) = 2$ since the latter does not use the 1010 nor 0101 rhs SAPs. Similarly, the unused r h s SAP 0101 can be used to complete the fifth LUT. That is, the fifth LUT is used when p_{11} is 1111. Then, for $p_{12} = 00$, an all zeros (0000) rhs SAP is used. For the other three p_{12} possibilities, the rhs SAP is selected as 0101, with the lhs SAP cannot be left as 1111. To have a total of k(=4 in this example) ones, then the lhs SAP must be replaced by three different 4 - bit codes with 2 ones in each, as shown in Table 3. Such that the decoder can rely on this lhs SAP to determine p_{12}.

3.2. Decoding

The subcarrier decoder demands the received SAP to estimate replicas of p_{11} and p_{12}, denoted as p'_{11} and p'_{12}, respectively. In low complexity detectors, the received SAP is detected by determining the state of each subcarrier. A better detector than simple thresholding [6] is when the k highest energy subcarriers out of n within a received subblock are recognized as active. This scheme ensures that the detected SAP is one of the C_k^n SAPs with k active subcarriers and discards the $2^n - C_k^n$ invalid possibilities.

For simplicity, let a detected SAP be represented by an n- bit binary word, denoted by SAP'. The proposed subcarrier decoding scheme is as follows. The segment of $n - d$ rhs bits of SAP' is compared with the reserved rhs patterns that are used in the LUTs of $C_{k-n_1(p_{11})}^{n-d} < 2^{p_{12}}$. If a

match is found, then the corresponding LUT is selected to be used to estimate p'_{12} depending on the lhs d bits of SAP', and p'_{11} is the p_{11} code associated with this
LUT. Otherwise, the LUT to be used is that of $n_1(p_{11}) = n_1(p'_{11})$, where p'_{11} is the segment of the lhs d bits of SAP'. Then, the $n - d$ pattern of SAP' is searched for in this LUT to determine p'_{12}

For the example of $n = 8$ and $k = 4$, let SAP' $= 11011000$. The rhs SAP' does not match any of the reserved patterns (1010 and 0101). Then, p'_{11} is the lhs SAP'$(= 1101)$ and $n_1(p'_{11})(= 3)$ selects the fourth LUT, from which the rhs SAP' is demapped to $p'_{12} = 11$. Another example is when SAP'$= 00111010$. The rhs SAP' matches the reserved pattern 1010. Then, the first LUT is selected resulting in $p'_{11} = 0000$, and the lhs SAP$'$ is demapped to $p'_{12} = 01$.

However, there are $C_k^n - 2^{p_1}$ unused SAPs according to the classical OFDM-IM [4,11]. In the proposed method these unused SAPs are those whose r h s SAP matches a reserved rhs pattern while their lhs SAPs do not match any of the cases in the corresponding LUT. For $n = 8$ and $k = 4$, there are six unused SAPs. Their rhs SAP is either 1010 or 0101, and their lhs SAP is one of the patterns 1001,1010 or 0101. If such an SAP appears in the detection, due to wrong subcarrier state detection, the decoder will just consider it as an invalid SAP and discards it just like what happens in classical OFDM-IM. That is, for SAP$' = 10011010$, the rhs SAP matches the reserved pattern 1010. Then, the first LUT is selected and p'_{11}=0000. But, the demapping of the lhs SAP' from this LUT fails, resulting in the rejection of the whole SAP'.

4. BER Performance

The BER performance of an OFDM-IM system exploiting the proposed subcarrier encoding scheme is evaluated by computer simulation. The k maximum energy (ME) subcarrier state detection method is used, where the k highest energy subcarriers are considered as active within the received subblock. ME is adopted due to its simplicity and it ensures that a received SAP always belongs to the space of C_k^n patterns of k active subcarriers.

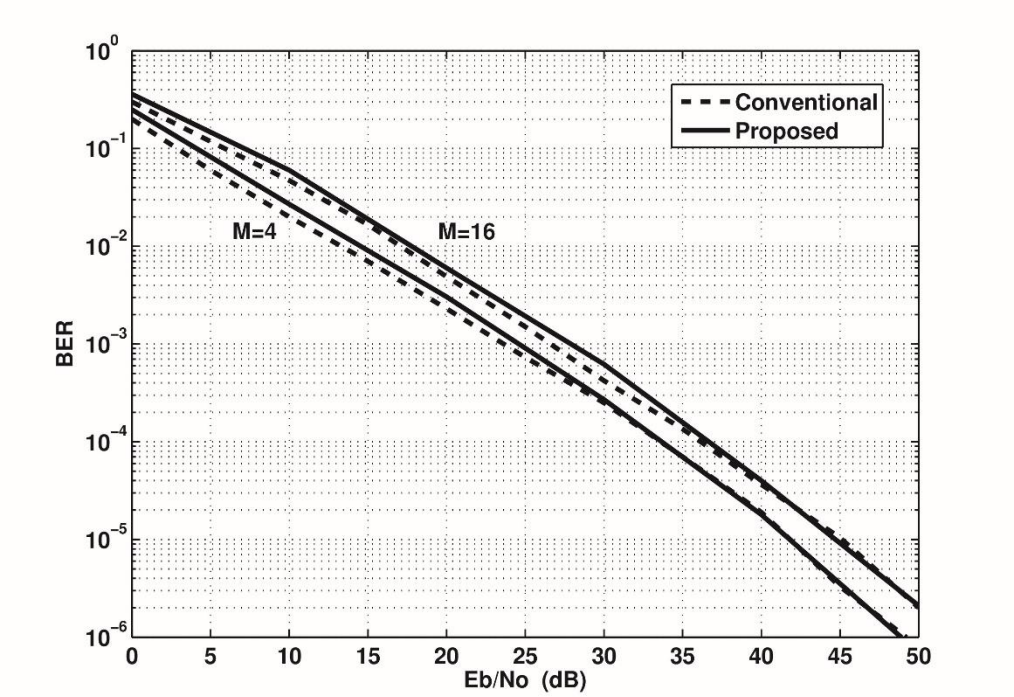

Fig 1. BER performance of OFDM-IM exploiting conventional LUT and proposed subcarrier encoding

Generally, errors in the OFDM-IM receiver result from erroneous SAP detection and de-modulation of modulated active subcarriers. For proposed and classical OFDM-IM systems equivalent in terms of n, k, and SAP detection, a slight difference in subcarrier decoding error performance can happen due to SAP detection errors. This difference is because of the dependence in the demapping of both sides of SAP' in the proposed scheme, unlike in classical OFDM-IM. But at high enough SNR, when the state of the received subcarriers is correctly estimated, this difference should decrease and the BER performance of both systems becomes almost identical. However, active subcarrier demodulation is the same in these systems for a given SAP'. The BER is shown in Figs. 1 and 2 for (n, k) of (8,4) and (10,5), respectively, both with $N = 128$, $M = 4$ and 16, over a frequency selective fading Rayleigh channel. Bearing in mind that the OFDM-IM based on the proposed subcarrier encoding scheme is identical to classical OFDM-IM in terms of spectral and energy efficiency, then it can be considered as a lower complexity alternative with a closely equivalent BER performance.

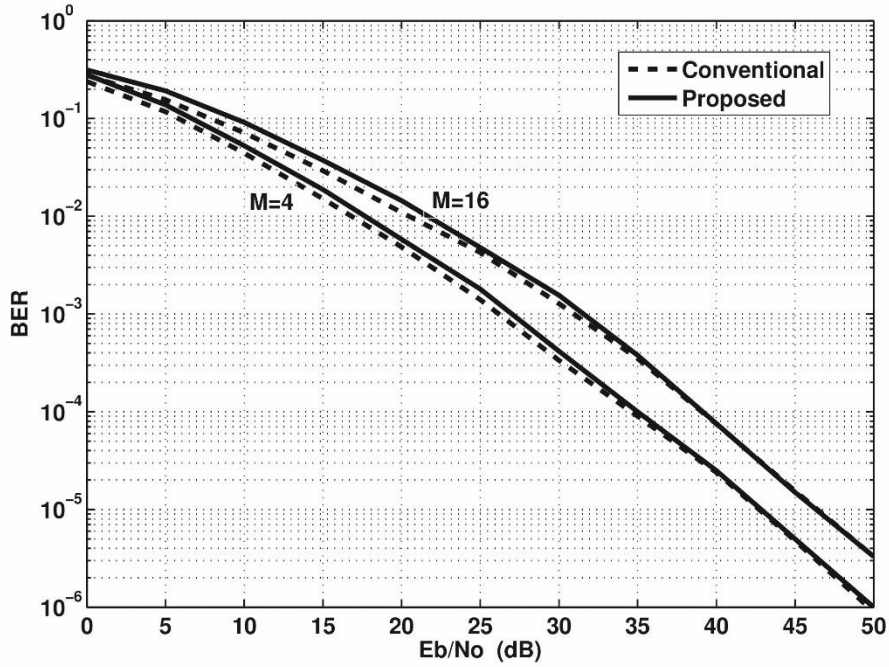

Fig 2. BER performance of OFDM-IM exploiting conventional LUT and proposed subcarrier encoding.

5 Conclusion

In this paper, a new subcarrier encoding scheme is proposed for OFDM-IM systems. Unlike classical OFDM-IM where a code of p_1 data bits are mapped via a LUT to an SAP, or by equivalent relatively complicated mathematical operations, it is proposed to use part of p_1 to directly activate/deactivate part of the subblock. The remaining bits of p_1 are mapped by LUTs to SAPs for the remaining part of the subblock. That is, a shorter data code is mapped and hence smaller LUTs are used concerning the LUT of an equivalent classical OFDM-IM. In the proposed scheme, the data-to-SAP mapper/demapper does not need to run an exhaustive search to the contents of a huge LUT to locate a match, but instead, one of the $(d + 1)$ smaller size LUTs need to be searched. Moreover, the 1's complement symmetry between pairs of the $(d + 1)$ LUTs could be invested to implement hardware realizations with further reduction in the complexity of the proposed scheme. However, such realizations are feasible as long as their hardware implementation is more efficient as compared with the combinatorial algorithm of the same n and k. This comparison depends on hardware implementation parameters which are beyond the scope of this paper. Simulation tests show the close equivalence of the proposed and conventional OFDM-IM in terms of BER performance. The proposed method can be used in OFDM-IM and its derivatives as a lower storage memory demanding alternative to the conventional LUT scheme of index bits to SAP mapping.

References

[1] Ahmad, J., Jehad, H., Huseyin, A., 2020. OFDM With Hybrid Number and Index Modulation. IEEE ACCESS. 8, 55042-55053.

[2] Liu, H., Cong, W., Wang, L., Li, D., 2017. Symbol error rate performance of nonlinear OFDM receiver with peak value threshold over frequency selective fading channel. AEU-Int J Electron Commun. 74, 163-170.

[3] Basar, E., Aygolu, U., Panayirci, E., Poor, H., 2013. Orthogonal frequency division multiplexing with index modulation. IEEE Trans Signal Process. 61 (22), 5536-5549.

[4] Basar, E., Wen, M., Mesleh, R., Renzo, M., Xiao, Y., Haas, H., 2017. Index modulation techniques for next-generation wireless networks. IEEE Access. 5. 16693-16746.

[5] Siddiq, A., 2017. E_ect of subcarrier activation ratio on the performance of OFDM-IM over rayleigh fading channel. IEEE Commun Lett. 21 (6), 1293-1296.

[6] Mrkic, J., Kocan, E., Pejanovic-Djurisic, M., 2017. Index modulation techniques in OFDM relay systems for 5G wireless networks. IEEE 40th International Conference on Telecommunications and Signal Processing (TSP), 208-211.

[7] Fan, R., Yu, Y., Guan, Y., 2015. Generalization of orthogonal frequency division multiplexing with index modulation. IEEE Trans Wireless Commun, 14 (10), 5350-5359.

[8] Basar, E., 2016. Index modulation techniques for 5G wireless networks. IEEE Commun Mag. 54 (7), 168-175.

[9] Mesleh, R., Haas, H., Sinanovic, S., Ahn, C., Yun, S., 2008. Spatial modulation. IEEE Trans Veh Technol. 57 (4), 2228-2241.

[10] Althunibat, S., Mesleh, R., 2008. Index modulation for cluster-based wireless sensor networks. IEEE Trans Veh Technol. 67 (8), 6943-6950.

[11] Althunibat, S., Mesleh, R., Basar, E., 2008. Differential subcarrier index modulation. IEEE Trans Veh Technol. 67 (8), 7429-7436.

[12] Li, Q., Wen, M., Basar, E., Poor, H., Zheng, B., Chen, F., 2018. Diversity enhancing multiple-mode OFDM with index modulation. IEEE Trans Commun. 66 (8),3653-3666.

[13] Wen, M., Zhang, Y., Li, J., Basar, E., Chen, F., 2016. Equiprobable subcarrier activation method for OFDM with index modulation. IEEE Commun Lett. 20 (12), 2386-2389.

[14] Li, J., Wen, M., Cheng, X., Yan, Y., Song, S., Lee, M., 2017. Generalized precoding aided quadrature spatial modulation. IEEE Trans Veh Technol. 66 (2), 1881-1886.

[15] Wen, M., Ye, B., Basar, E., Li, Q., Ji, F., 2017. Enhanced orthogonal frequency division multiplexing with index modulation. IEEE Trans Wireless Commun. 16 (7), 4786-4801.

[16] Siddiq, A., 2016. Low complexity OFDM-IM detector by encoding all possible subcarrier activation patterns. IEEE Commun Lett. 20 (3), 446-449.

A review of Effect the Zinc Oxide deposition on Crystalline Silicon Solar Cells

Ali Kadhim Naser[1]*, Dhafer Manea.Hachim[2], Qahtan A Abed[3]
{alikadhim558@gmail.com[1], coj.dfr@atu.edu.iq[2], qahtan.abed@atu.edu.iq[3]}

Engineering Technical College / Najaf, Al-Furat Al-Awsat Technical University, 31001 Najaf, Iraq[1,2,3]

Abstract. Zinc oxide (ZnO), a direct bandgap semiconductor, provides tremendous promise in various applications, such as optical waveguides, clear conductive oxides, and chemical gas sensors. It is also used in UV-light emitters, piezoelectric transducers. ZnO is in various forms, such as nanoparticles, Nano-belts, Nano-rods, nano-tubes, and nanowires. The purpose of this research is to review a general overview of ZnO and its application, the use of ZnO as an anti-reflection coating with various styles on the solar cells, and the conventional and unconventional techniques that had been used to coating the anti-reflection layers on the solar cell will be reviewed. This is based on a review of previous studies related to applications of anti-reflective coatings of ZnO and make a comparison of practical results was obtained with different semiconductor materials (SIC, TiO2, ZnS, SiO2, SiN4).

Keywords: zinc oxide, anti-reflection coating**.**

1 Introduction

Renewable energies are relevant because they are created instead of conventional production from environmentally friendly [1]. A fossil-fuel-based technology source, and cause pollution to the atmosphere. Solar power is a perfect source of renewable energy that is clean, safe, and unrestricted. The Sun uses a thermonuclear process to turn 650,000,000 tons of hydrogen into helium to provide its energy. This system produces heat and electromagnetic radiation. That flows then through the atmosphere in all directions. Just 57 percent reaches the earth's surface in these radiations, which are 1.6 x 1018 units of sun energy [1].

The wavelength of a photon and its energy values are strictly relative to each other. Sunlight consists of a 44-percent amount of visible light, a 3-percent portion of ultraviolet light at ground level, and the rest is infrared light. Although the overall volume of UV radiation hitting the planet is 77 percent of the total solar UV radiation, only infrared light does contact the earth. High-frequency radiation is absorbed by photovoltaic cells, including ultraviolet (UV) and visible light, which converts it into energy. Although low-frequency radiation is infrared radiation, it is usually converted into heat or thermal radiation [2].

The first type of photovoltaic developed was silicon solar cells. In Sun PV, crystalline cells have to be played within two respects, with CPF in the monocrystalline cell and CIGS in the polycrystalline cell. As their manufacturing processes are quick and low-cost, polycrystalline

IMDC-IST 2021, September 07-09, Sakarya, Turkey
Copyright © 2022 EAI
DOI 10.4108/eai.7-9-2021.2314810

cells are more comprehensive than monocrystalline cells. Monocrystalline cell production is 15-20%, whereas polycrystalline cell output is 12-17% [3][4].
There are essentially two explanations for a solar panel's decreasing efficiency: soil and reflection. The sunlight gets to the panel's surface above a certain angle, passes via the glass panel, and then enters the cell. 8-10percentage of the light was reflected from a glass surface and was not transmitted to the cell. About 35 to 36 percent of light hitting the solar cell silicon substrate reflects. An optical, electrical power loss occurs from the absorption of the Sun's rays[5]. Consequently, decreasing optical losses are factors that improve the performance of PV cells. This paper investigates the application of anti-reflective coatings (ARC) to silicon and glass substrates to minimize solar cell optical losses, investigates the physics of ARC, fabrication techniques for ARC, and compares zinc oxide and different semiconductors materials with Nano sizes as antireflection coatings. Naji et al. (2021) investigated the blending process of different Iraqi oils and its effect on obtained blend API gravity and sulfur content. They also simulated the fractionation process of different blends to predict atmospheric distillation products' yields and quality.

2 Literature Studies

As an important ARC for energy conversion efficiency enhancement, this study investigates the synthesis of zinc-oxide nanowire arrays on Si micro pyramids. As a result, this structure indicates suppressing bandwidth reflection in the 300-1200 nm range, with a 3.2 percent scale weighted reflectance. The conversion efficiency was 16.0%, which is the highest for most solar cells[2]. Method of preparation of ZnO for easy and inexpensive chemical bath deposition Nanorod arrays (NRAs) and their use as an anti-reflective coating in polycrystalline silicon cells. The zinc oxide NRAs have been shown to have a full crystalline wurtzite structure of about 40-50 nm diameter. The conversion efficiency increases from 2.27 percent to 6.61 percent after the deposition of ZnO NRAS antireflection coating [3]. The use of ZnO thin films as antireflective solar cell layers is seen in this study. The thin film was synthesized by sol-gel and then, using the spin-coating technique, placed on a P-N silicon substratum. The results showed that a nanostructured zinc oxide layer with hexagonal crystalline phase and particle sizes 30-50 nm was successfully grown on this silicone substrate. ZnO nanorods were produced using hydrothermal methods as an antireflection coating in a commercially available microwave oven (ARC). Relative improvement is more than 65 percent in the reflectivity was investigated via ZnO nanorods for both textured and planar Si surfaces, lifetime (miteff) measurement was presented, and test to be increased. As compared to the ARC of ZnO nanorods. [4] This research shows that ZnO nanopyramid structures on Si substrates are manufactured through an electrochemical low-temperature deposition the nanostructures were investigated concerning nanorods and planar ZnO texture on Si substrates for their antireflection (AR) properties. Reflectance spectra observe that the texture based on nanopyramid reduced light reflections from 380 to 1000 nm in a broad-spectrum and is far more efficient than planar textures and nanorod [5]. Using the Zno granulate source thermal chemical vapor deposit, ZnO nanowires are synthesized to increase significant Si-solar cell output using a simple and cost-effective process. The nanowires are generated at different levels of O2 flow. Notice that spectral reflectivity reduction and downshifting process as well as photon trapping reduction also enhance the efficiency of Si-solar cells and enhance the fill factor of ZnO nanowires of different diameters have different effects on the characteristics of silicon solar cells [6]. Enhancement by zinc oxide nanowhisker of silicon solar cells, thereby improving solar cell characteristics. The zinc oxide

Nanowire array coated with the solar cell has a broadband reflection of 500 to 1,100 nm, and the lowest possible reflection of less than 3 percent can be easily achieved [7]. This research examines Nanocrystalline Zinc oxide film applied by the ultrasonic spray-on substrate of textured silicon as an antireflective sheet. It was noted that the ZnO film crystallites' favored growth orientation is along the c-axis with a hexagonal wurtzite phase and a small tensile strain value of 0.26%. The combination of a ZnO film as an anti-reflex coating minimizes reflection to 2.57 percent [8]. In this research, a vertically aligned nanorod array was mounted in the antireflection (AR) layer on the Si solar cells' substrate. We found that nanorod morphology, driven by synthetic chemistry, significantly impacts the AR layer's efficiency. We also showed that the performance of light-harvesting in solar cells increased greatly from 10.4 to 12.8 percent by using zinc oxide Nano-rod as the ARC in a multi-crystalline silicon solar cell [9]. This paper study Synthesized nanoparticles through a microwave process and developed a spin-coating technique to manufacture thin film on a silicon substrate, and examined the efficiency of a ZnO nanoparticle covered silicone solar cell doped with iron differing (0-20 percent). Both J-V and EQE specification for the 180.29 mm thick of Zinc oxide was observed for improved silicon solar cell performance. and The efficiency of power conversion was improved by about 30 percent iron-doped ZnO thin film and the same thick ZnO layer [10]. The anti-reflective coating properties of zinc oxide Nano-needles for Silicon solar cells are being investigated. After using ZnO, the reflection spectrum induces more light emission due to low reflection around the spectral spectrum of the visible field [11]. Easy-low temperature precipitation 46-87 nm Nano diameters synthesis in this study and investigation of silicon solar cell coating with un-doped and cobalt-doped zinc oxides (5 percent, 10 percent, 15 percent, and 20 percent), A simple spin has put doped and undoped zinc oxide thin films silicon solar cell coating technique. Improvement in PV cell characteristics and external quantum efficiency was observed with increasing optical bandgap with increase ZnO coating [12]. In this research, we have developed multi-scaled hierarchical ZnO nanostructures on plasma-enhanced chemical vapor deposited in silicone nitride-coated textured single-crystalline silicon solar cells for antireflective purposes, The multi-scaled hierarchical ZnO doped Er nanostructures looked like needles Nanotip arrays and hydrothermal have been built. The effect of the growth time on EZO NTAs microstructures has been studied, The EZO NTAs, growing for 60 minutes, demonstrated the best photovoltaic and antireflective efficiency. The conversion efficiency was established to be raised from 15.64% to 17.41%[12].

3 Basic Concept Anti-Reflection Coating

L. Rayleigh unintentionally discovered the idea of the antireflective coating. In 1917, however, Fraunhofer developed the first genuine anti-reflector in the 19th century.[7]
Coating, the substratum surface with a transparent material with the optical path variance decreases the reflection. These coatings are called "coatings against reflection." The reflected light is built as disruptive interference, whereas the transmitted light is constructive interference. Construction interference increases the light intensity transmitted, whereas the disruptive interference of the light reflected prevents light transmission[1].
Some applications require antireflection coatings not only for the reduction of reflection but also for a substantial increase in transmission [6]. When two light waves interact with a π phase difference, the waves interfere destructively. If all waves have the same magnitude, the net amplitude will be zero. In this situation, the incident light reflectance may be decreased or even reduced to zero with disruptive interference [7]. The reflection loss at an interface is

minimized by the two surrounding media if a thin material layer has a refractive index value, The possible configuration is seen in Fig 1.
If there is light from a refractive index medium (n0) to another medium (n2) with a thin intermediate refractive index layer (n1), two interfaces are formed. Consequently, both interfaces reflect. The difference in path length between the two reflected rays, which Is based on the middle layer's optical Thickness, induces a phase difference resulting in constructive or destructive interference. If the middle layer is one-quarter wavelength thick, the path difference results in a π phase difference that contributes to harmful interference. Thus, The wavelength and very poor reflectance too particles the nearby wavelengths decrease towards non reflected [8].
Anti-reflex coatings can range from a single layer with virtually zero reflectance at just a single wavelength to a multilayer system with a more extensive layer, with almost zero reflection over a range of wavelengths [9].

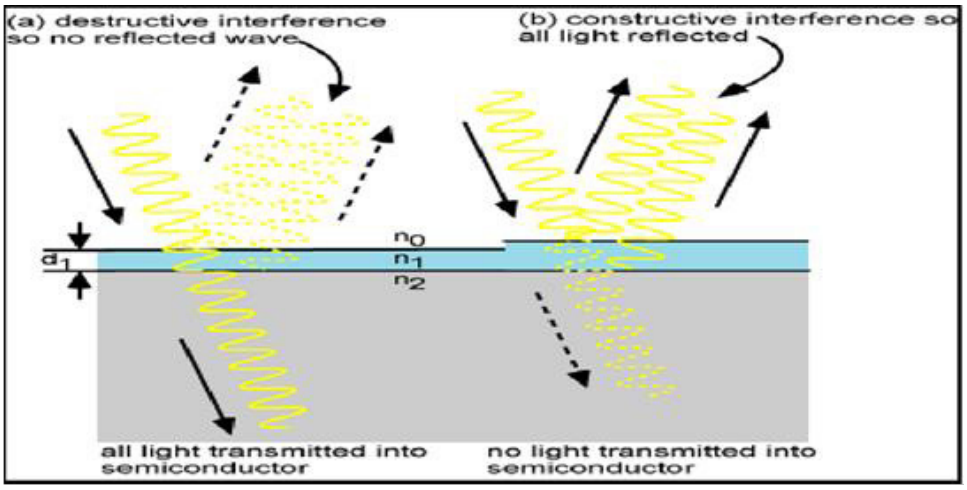

Fig 1. Shows prospective configurations [8].

4 Anti-Reflecting Coating Styles

4.1. ARC Single-Layer

A single-layer ARC aims to achieve destroying Light incident interference by generating an optical path gap of $\pi/2$. Single-layer ARC was considered moderately, Restriction of reflection at a specified wavelength. The substrate used for silicon solar cells can be suitable for single-layer ARC [6]. Titanium dioxide, silica, zinc oxide, and so forth. Were studied to reduce reflectivity and improve their performance. Here, it must be noted that the use of an anti-reflective film on glass with a relatively low refractive index (n=1.22) poses a challenge to finding a material that has a lower refractive index than the glass to reduce the reflection losses on the glass [6][10].

4.2. The Multi-Layer ARC

Multiple layers of ARC are meant to remove reflectance over a broader range than the ARC single layer. For example. with the same optical effect, two layers or bilayer ARC will perform zero reflectance " (n1d1 = n2d2 = λ/4) " Thickness [11], If a high index coat is used, for example, a polycrystalline aluminum oxide (n=1.69) is present before a low index (n= 1.05) coated interface where the index convergence is high (such as a refractive index magnesium fluoride 1.38). The double-layer alternating RC reflects a V-shaped dip. The three-layer ARC achieved reflection reduction across a far more extensive spectrum, from thin films to membranes and other polymer-ceramic biomaterials. [6]. Figure.2, The glass substrate's patterns define 2 The reflecting single layer, double layer, and tri-layer. Reflection is taken from a single layer on a glass substrate. , A, B, C, respectively [6].

5 Anti-Reflecting Coating Techniques

Most nanotechnology ARCs can be fabricated by either subtractive top-down or bottom-up manufacturing methods. Fig 2, Denote A comparison of particle-deposition methods used to prepare AR coatings.

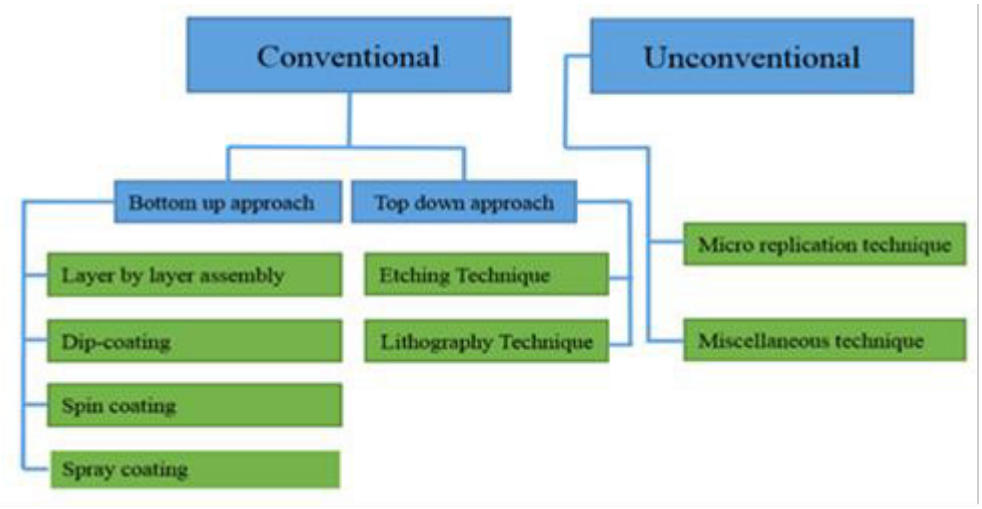

Fig 2. anti-reflecting coatings fabrication process [5].

5.1 Sol-Gel Process

The most popular strategies for adsorption and recovery of ARC are dip-coating and spin-coating. The substrate is dipped into a precursor solution in the dip method coating system and withdrawn at a controlled speed [6]. In contrast, spin-coating involves rotating the substrate at a steady rate, while a precursor is dispensed on its surface. The precursor is mixed in an organic solvent that contains the metal-organic compound. The solution is either spun onto the

substrate or dipped onto the substrate and then dried away with the solvent's evaporation.[14]. The film then undergoes a final heat treatment in which the organic residue is removed, causing the film to be either metal oxide or fluoride. The sol-gel method has been utilized to produce commercial-scale amounts of ARC-grown glasses for over 40 years [6].

5.2 Vapor deposition process

The most widely used industrial method for manufacturing anti-reflective coatings is the vapor deposition technique [11]. Plasma-enhanced deposition of chemical vapor (PECVD) is a technology used to deposit semiconductors onto silicon wafers. This method is widely used in ARC manufacture silicon (NaNx: H) coatings on textured silicon solar cells. In which, it is apparent that SiNx is a coating on crystalline silicon solar cells textured. The silicon nitride coatings are usage an antireflection layer and a Passivation layer of surface for silicon solar cells [10]. For example, in the deposition method often a palladium species is used with ammonia or amine. The first volatile chemical is poured onto a hot board. Unique technologies such as plasma-assisted evaporation (PAD) and plasma modified evaporation processes can apply to strongly clean transparent glass substrates (e.g., dielectrics), GaN substrates have been produced as polymer substrates. To decrease or stop scratching from occurring, industries worldwide have looked at different ways to eliminate the presence of scratches, building coatings composed of reflective and scratch resistance [15]. A vapor deposition technique has been utilized to deposit the GRIN ARC on Si. like the technology which is using a new method called glancing angle deposition (GLAD).

5.3 Etching

Techniques like etching have been employed to produce near-field optical coatings and optical colloids like moth's eye-like structures to offer antireflective characteristics. This method has been standard for many years, using masks or particles that mimic masks [16][17]. As an illustrative case, a monolayer of self-assembled nanostructures such as silicon nanoparticles acted as a mask to etch a silicon substrate to fabricate interconnected ARCs [18]. To build the mask on Si substrates and conducted an SF6 dry etching to produce Moth's eye nanomaterials. It was calculated that the quantity of reflectance for silicon substrates was reduced to 2.5% and the measurements of the Moth's eye nanostructures on the substrate were found to be of the same size as well as the same duration of the etching [19].

6 Comparison of the Impact of Different Semi-Conductor Materials as ARC-Layers

As depicted in Table1, shows the comparison with practical results in terms of various semi-conductors were used and the relationship between reflection value and layer thickness, wavelength, and consequently the solar cell’s electrical characteristics related to the reflection value was obtained.

The film thickness of the anti-reflection layer deposited on the solar cell plays the main role in the reflection value and so on it is not easy to be adjusted to obtain the fit layer thickness, Film thickness must be optimized to get an optimal level of VOC and ISC. According to table 1, for example, the optimum thickness of SiC ARC was 36.159 nm, and so on the maximum efficiency was 16.06 percent has been achieved for that thickness. The highest performance

was achieved with maximum VOC and ISC values of 0.6779 V and 2.807 A. The optimum thickness and efficiency for solar cells made of TiO2, ZnO, ZnS, SiO2, and Si3N4 ARC are 62.396, 78.411, 63.479, 101.351, and 74.257 nm, respectively. have, 19.73 percent, 20.34 percent, 19.83 percent, 18.99 percent, and 20.35 percent, respectively. The reduction in light reflection is the explanation for the increased efficiency [59]. As reflection increases, VOC, ISC, and solar cell efficiency decrease. As a result, thickness optimization played the main role to achieve the lowest reflectance and the best VOC, ISC, and consequence performance.

Table 1- Data of various semi-conductor - ARC –layers.

	ARC-SIC [60]					ARC-TIO2[61]					ARC-ZNO[62]				
λ	n	Thick nm	I_{SC}	V_{OC}	η %	n	Thick nm	I_{SC}	V_{OC}	η %	n	Thick nm	I_{SC}	V_{OC}	η%
250	3.25	19.2	2.6	0.6765	15.14	2.46	25.4	2.78	0.67	15.9	2.38	26.17	2.79	0.677	16.00
300	3.52	21.2	2.6	0.6765	15.10	3.32	22.5	2.71	0.67	15.4	2.404	31.198	2.937	0.679	16.84
400	3.51	28.4	2.7	0.6774	15.72	2.68	37.2	3.31	0.675	18.0	2.114	47.304	3.269	0.682	18.82
500	3.45	36.1	2.8	0.6779	16.06	2.48	50.4	3.43	0.683	19.3	1.968	63.516	3.467	0.683	20.01
600	3.40	44.0	2.8	0.6777	16.03	2.42	62.3	3.42	0.681	19.7	1.913	78.411	3.523	0.684	20.34
700	3.35	52.1	2.7	0.6786	15.86	2.36	74.0	3.37	0.683	19.4	1.883	92.937	3.473	0.683	20.04
800	3.31	60.3	2.7	0.6777	15.63	2.34	85.3	3.24	0.682	18.8	1.863	107.296	3.359	0.682	19.36
900	3.28	68.4	2.7	0.6776	15.44	2.32	96.7	3.15	0.681	18.2	1.851	121.556	3.226	0.681	18.56
1000	3.24	76.9	2.6	0.6777	15.34	2.31	108.0	3.06	0.680	17.7	1.841	135.810	3.109	0.680	17.86
1100	3.21	85.1	2.6	0.6777	15.47	2.30	119.3	2.99	0.679	17.3	1.833	150.027	3.023	0.679	17.35

	ARC- ZNS [63]					ARC- SiO_2 [64]					ARC- Si_3N_4 [65]				
λ	n	Thick	I_{SC}	V_{OC}	η	n	thick	I_{SC}	V_{OC}	η	n	thick	I_{SC}	V_{OC}	η
250	2.60	24.0	2.7	0.677	15.8	1.52	41.12	2.75	0.6774	15.7	2.28	27.3	2.8	0.677	16.00
300	2.57	29.1	2.9	0.678	16.6	1.51	49.67	2.87	0.6785	16.4	2.16	34.6	2.9	0.679	16.9
400	2.56	39.0	3.1	0.681	18.2	1.5	66.67	3.09	0.6805	17.7	2.07	48.3	3.2	0.682	18.8
500	2.42	51.6	3.3	0.683	19.5	1.482	84.35	3.24	0.6818	18.6	2.03	61.5	3.4	0.683	20.0
600	2.3	63.4	3.4	0.6836	19.8	1.48	101.3	3.29	0.6823	18.9	2.02	74.2	3.5	0.684	20.3

700	**6 2.33**	**75.0**	**3.9**	**0.6831**	**19.5**	**1.474**	**118.7**	**3.26**	**0.682**	**18.7**	**2.0**	**87.3**	**3.4**	**0.683**	**20.0**
800	**2.32**	**86.0**	**3.2**	**0.6821**	**18.8**	**1.473**	**135.7**	**3.18**	**0.6813**	**18.2**	**1.99**	**100**	**3.3**	**0.682**	**19.3**
900	**2.31**	**97.4**	**3.1**	**0.6811**	**18.1**	**1.472**	**152.8**	**3.07**	**0.6803**	**17.6**	**1.99**	**113**	**3.2**	**0.681**	**18.5**
100	**2.30**	**107.6**	**3.0**	**0.6803**	**17.6**	**1.471**	**169.9**	**2.98**	**0.6795**	**17.1**	**1.9**	**125**	**3.1**	**0.680**	**17.8**
1100	**2.29**	**119.7**	**2.9**	**0.6796**	**17.2**	**1.47**	**187.0**	**2.91**	**0.6788**	**16.6**	**1.98**	**138**	**3.0**	**0.679**	**17.4**

6. A short review of zinc oxide.

The semiconductor known as zinc oxide possesses considerable potential in many applications, including optoelectronic devices and organic LED whiteners. [20]. It may also be used for a variety of chemical gas sensors and spin practical instruments. For UV-light emitters, it is often used, piezoelectric transducers, and chemical sensors. For light-emitting diodes and UV or blue-spectrum photonic applications, ZnO's large bandgap makes it a promising material. While high exciton binding energy (60 meV) will guarantee a broad range of emission characteristics even at room temperature, in addition to being far greater than that of GaN (25 meV) (RT) [21]. ZnO has several benefits as a metal oxide with a large bandgap. A higher breakdown voltage and the capacity to manage significant electrical noise and high power operation are available. Zinc oxide's piezoelectric properties and semiconducting nature make it useful for devices such as piezoelectric generators that collect electricity.[22].

A semiconducting characteristic activates the essential metal oxide for doping. aluminum-doped Zinc oxide is a wide-area node consisting of an n-type material; additives in ZnO alter its optical properties that can be used to tune the emission color[23]. ZnO is in various forms, As well as nano-engineered, nano-sized, nanostructured, and nano-building materials. And by controlling the nanostructure's morphology and size, it is easy to alter its properties. They have excellent optical and electrical properties and can be easily synthesized into different shapes, so they are possible candidates for photovoltaic (PV) implementations[24]. Some of the ZnO nanoparticles have low reflectivity, increasing the light absorption; ZnO nanostructures are typically applied as the PV systems' antireflection layer. Nanostructures of Al and ZnO are also preferable, such as metal oxide (TCO) for solar panels [21]. Table 2. Represents much of the features of zinc oxides.

Table 2. zinc oxide properties [25].

Chemical formulation	ZnO
Energy gap (Eg) at room temperature	3.37 EV
Appearance	Solid
Colour	White

Crystalline structure	Hexagonal and Cubic
Point of melting	1975°
Density	5.606 g/cm3
Electron mass effective	Me* = 0.24 mo
mass effective	Mh* = o.59 mo

7.1. Crystalline ZnO structure

Gold, indium, and zinc are essential semiconductor materials. ZnO can be crystallized in the wurtzite, cubic Zn, and cubic rock salt systems. [27], as displayed in Fig 3. The cubic patterned structure of rock salt can be obtained at relatively high zinc oxide temperatures and pressures, Only cubic substrates may stabilize the cubic zinc blend structure. They are not known to be a standard system belonging to ZnO in the atmospheres. Four O atoms encircle each Zn atom at the corners of a tetrahedron and vice versa in both its hexagonal wurtzite and cubic Zn blend arrangement. [26]. The Sp3 covalent bond, eclipsed for hexagonally wurtzite, and staggered for the cubic zinc blending structure, is distinguished by this tetrahedral coordination. The ionic character of ZnO is also, and This leads to increased bandgap energy beyond what the strictly covalent bonding predicted.[20]
Fig 3 [28] shows the hexagonal cell with two grid constants, a and c is the wurtzite structure; the c/a ratio of a complete hexagonal structure is 1,6333. The system is composed of two hexagonally enclosed interpenetrating sublattices. One consists of Zn atoms, whereas the other consists of O atoms. They interpenetrate with each other along the c-axis with a value of u 0.3755 in an optimal hexagonal configuration. Where u is defined as the bond length of Zn-O parallel with the c-axis, which is equivalent to (u= [(1/3). (a/c)2)+1/4]). X-ray diffraction or transmission electron microscopy at room temperature typically investigates the constants in nature (HRTEM). The surface region ranges from 3.24 to 3.25 Angstroms for a and from 5.20 to 5.25 Angstroms for c [27].

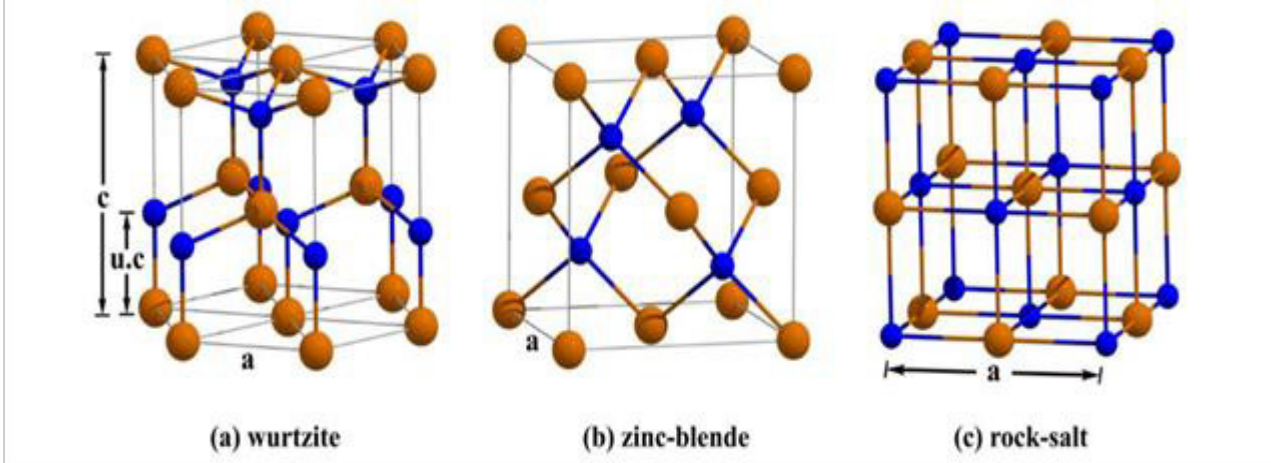

Fig 3. Zinc oxide crystalline [28].

7.2 ZnO Nanostructures Category

From a morphological perspective, Nano-materials can be sub-divided into four categories: 0-dimension (Nano-particles), one- dimension (N-tube, NW, NRs), two-dimension (Nano-layers, Nano-plates), and three-dimension (Nano-tetrapods, Nano-flowers) [29] .There are some kinds of Nano-structures, even more exotic, like forming nano-organ-like structures. Deposition and development strategies had a significant influence on morphological developments. Morphology specifically depends on Material composition, temperatures of formation, and diffusion [30].

7.3 Zinc Oxide Nanostructure in Solar Cell

Nanostructure of a single dimension applies to NW, Nano-fibres, Nano-cables, NT, Nano-belt, and more[30], which are extended in one specific direction. Because of its distinctive electronic and optical properties, ZnO semiconducting NWs must develop nano-electronic devices. , Conversion and storage of energy (photovoltaic cells, storage systems, condensers, hydrogen storage systems), Emitting light diodes, catalysis, delivery of drugs, nano generation and piezoelectric power, A chemical growth aqueous and CVD strategies verify that a large part of the Nanowire in the array comes into close communication with the substratum [31]. Therefore, ZnO nanowires have an ongoing pathway for the transport of electric carriers. This is important for increasing the efficiency of other devices of this nature based on nanomaterials. ZnO Nanowire's vertical focus has excellent optoelectronic properties. Thus, the design of light-emitting diodes and photovoltaic panels has been studied; Excluding p-n junctions and dye-sensitive solar panels, modules dye-sensitized solar panels. Also, ZnO's piezoelectric and semiconductor properties lead to potential employed devices with gas sensors [32]

8. Solar Cells

An electrical instrument that transfers light energy to the electricity directly via a photovoltaic rection. Its photoelectric cell form is described as a device whose electrical character, for example, voltage, current, and resistance, changes in light intensity[35]. Solar cells are the main parameters of PV modules, or they are also classified as solar panels. They may be used as a photodetector, like infrared detectors, light detection, and nearby electromagnetic radiation Visible spectrum of light intensity measurement. Sir Alexander-Edmond Becquerel first coined the photovoltaic (PV) effect in 1839, Russel Ohl developed the first current silicon solar cell in 1946. Thin silicon wafers are photovoltaic solar cells that convert solar power into energy in advance. [36]. The latest photovoltaic (PV) development is focused on the idea of each cell system forming an electron-hole, which consists of two kinds of wafers (p and n types) of the semiconductor. The various materials for solar cell photovoltaic systems are primarily used in silicon (Sc, Mc crystallines, and amorphous silicon), Telluride of cadmium, selenide copper-indium-gallium, and indium-gallium-sulfide of copper. photovoltaics solar cell systems are classified into different groups based on these materials, as shown in Figure. 4 [37] [38].

8.1 Single/Mono-Crystalline Silicon Solar Cell

Single-crystal silicon is used as the base material with all silicon wafers equipment nowadays [39]. Monosilicon is a structural component of photovoltaic cells used in solar power production. It is a single crystal in which all of the lattice structure is continuous, uninterrupted, and devoid of grain boundaries. Mono-Si can be prepared with pure silicon or doped, containing very little to no additional elements to alter its conductivity [40]. The Czochralski method produces most silicon crystals, with crystals up to several meters long and well over a hundred kilograms in weight; The crystals are then cut down into thin, thin wafers are then further processed[41]. Single-crystal silicon is, without a doubt, the most important technological material over the last few centuries, the "silicon era" because of its accessibility at a fair cost, which has been crucial to the growth of electronic devices on which we rely today. Monocrystalline single-crystalline silicon solar efficiency Cells ranging from 17 to 18 percent[36].

8.2.Solar Cell of Polycrystalline Silicon (Poly-Si or Mc-Si)

Polycrystalline silicon, also known as polysilicon, Is a pure silicon form used in photovoltaic solar and electronics technology as a natural resource [39]. Polysilicon, developed through a chemical filtration system called the Siemens method, is purified from metallurgical-grade silicon. The distillation method includes the dissolution and decomposition at high temperatures of volatile silicon compounds and the subsequent release of silicon. Emerging technology in the refining process uses a fluidized bed process [42]. The solar PV industry also usages metallurgical processes rather than chemical processes to purify their products. Polysilicon used in electronics has impurities under one portion per billion, while when used for solar cell production, fewer grade purities were needed. The large polysilicon rods, usually broken into small chunks, are directly cut into individual cuboids; these individual cuboids are then cast into multi-crystalline ingots or processed to develop single crystal boules. These materials are then cut into thin silicon chips and used to manufacture solar cells, integrated circuits, and other semiconductor devices [43]. Small crystals make up polysilicon, Identified as crystallites also. Both polysilicon and multi silicon can be used interchangeably to describe silicon-based compounds; multi-crystalline usually describes crystals that are more than 1mm in size. Polycrystalline Silicon solar cells are now the most commonly known Sun cells. In 2008 they were thought to account for up to 48 percent of solar cell production worldwide. Even though they are cheaper to manufacture than monocrystalline silicon solar panels, their efficiency is ~12–14 percent and hence, they are less efficient than monocrystalline [44][45].

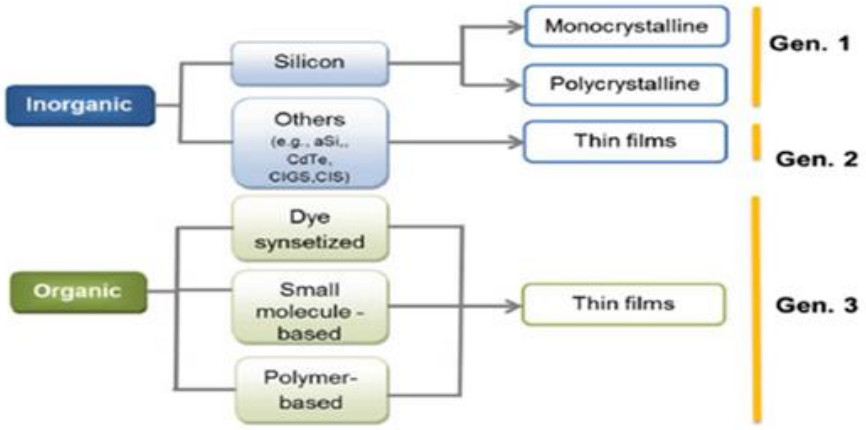

Fig. 4. Photovoltaic Solar Cell Type [37].

9 Conclusions

ZnO Nano sizes have high carrier density and mobility, which improves the energy efficiency of solar cells. This review discusses recent advances in ARC coatings, especially coatings containing ZnO nanoparticles. The development of ARC coatings is still fraught with challenges in terms of choosing the right material and ideal thickness. Anti-reflective coatings must have unique properties, for example; Thermal and mechanical stability, for use in various conditions and over long periods. The mechanical and electrical properties of ZnO according to published studies made it possible to use ZnO to create multifunctional materials with improved anti-reflection and self-cleaning properties. It can be used in solar cell components to provide high-energy conversion while also lowering costs. ZnO's high strength and durable surfaces make it ideal for anti-reflective and self-cleaning applications, allowing manufacturers to use it to enhance the mechanical strength of their products.

References

[1] Z. Yao, " ZnO Nanoparticles as a Luminescent down-shifting Layer for Solar Cells," pp. 1–165, 2015

[2] U. Bach, "Solid-state dye-sensitized mesoporous TiO2 solar cells," EPFL, 2000.

[3] Z. Yao, "T. Nyamwanza, vol. 2014, no. June, pp. 1–2, 2014

[4] Y. Liu et al., "Hybridizing ZnO nanowires with micro pyramid silicon wafers as superhydrophobic high-efficiency solar cells," Adv. Energy Mater., vol. 2, no. 1, pp. 47–51, 2012.

[5] Y. Qu et al., " Chemical bath deposition produced ZnO nanorod arrays as an anti-reflective layer in the polycrystalline Si solar cells," J. Alloys Compd., vol. 698, pp. 719–724, 2017.

[6] P. Anurang, O. Demircioglu, F. Es, and R. Turan, "HE Unalan," J. Am. Ceram. Soc., vol. 96, no. 4, p. 1253, 2013.

[7] X. Jin et al., "Preparation of K2Ti6O13 fibers by electrospinning for near-infrared reflectivity," Ceram. Int., vol. 45, no. 11, pp. 14198–14204, 2019.

[8] X. Yu, D. et.al, "improvement of silicon solar cells efficiency by ZnO nanowhisker array coating," Nanoscale Res. Lett., vol. 7, no. 1,2012.

[9] S. Sali, M. et.al, “zinc oxide Nano-crystalline film deposited by ultrasonic spray on a silicon substrate textured as the anti-reflection coating,” Phys. B Condens. Matter, vol. 407, no. 13, pp. 2626–2631, 2012

[10] J. Y. Chen, et.al, “Growth of vertically aligned znic oxide nano-rod arrays as antireflection coating on silicon solar cells,” Sol. Energy Mater. Sol. Cells, vol. 94, no. 5, 2010.

[11] G. R. Neupane, A. Kaphle, and P. Hari, “Microwave-assisted Fe-doped ZnO nanoparticles for enhancement of silicon solar cell efficiency,” Sol. Energy Mater. Sol. Cells, vol. 201, p. 110073, 2019.

[12] M. Al-Fandi, Y. F. Makableh, M. Khasawneh, and R. Ready, “Near-zero reflection by nanostructured antireflection coating design for Si substrates,” Superlattices Microstruct., vol. 117, pp. 115–120, 2018.

[13] A. Kaphle et.al, “Enhancement the power conversion efficiency of silicon solar cells by doped zinc oxide nano-particle thin-film layers,”, vol. 657, pp. 76–87, 2018.

[14] B. Liu, S. Qiu, R. Hu, Y. Liao, N. Chen, and G. Du, “Multiscaled hierarchical nanostructures for enhancing the conversion efficiency of crystalline silicon solar cells,” Appl. Surf. Sci., vol. 259, pp. 705–710, 2012.

[15] H. Hanalei, et al., "Highly efficient antireflective, self-cleaning coatings that incorporate carbon nanotubes into solar cells " vol. 59, pp. 620–635, 2016, DOI: 10.1016.

[16] A. Jalali, M. Reza, V. Nima, N. Fariba, T. Abadi, and A. Eftekhari, “Investigating the effect of sol-gel solution concentration on the efficiency of silicon solar cells : role of ZnO nanoparticles as an anti-reflective layer,” Chem. Pap., no. 0123456789, 2019, DOI: 10.1007/s11696-019-00872-0.

[17] H. K. RAUT, "Studies on nanostructured antireflective coatings," 2014.

[18] K. L. Morgan, D. E. Brocker, S. D. Campbell, D. H. Werner, and P. L. Werner, "Transformation-optics-inspired antireflective coating design for gradient index lenses," Opt. Lett., vol. 40, no. 11, pp. 2521–2524, 2015.

[19] P.-F. Fu, E. S. Moyer, and C. R. Yeakle, "Method for forming an anti-reflective coating." Google Patents, Sep. 27, 2011.

[20] J. K. Holt, et al "Hotwire chemical vapor deposition of a high hydrogen content nitride for solar cell passivation, antireflection applications,", vol. 430, no. 1–2, 2003

[21] S. Chattopadhyay, et.al, "Anti-reflecting and photonic nanostructures," Mater. Sci. Eng. R Reports, vol. 69, no. 1–3, pp. 1–35, 2010.

[22] B. Sheldon, J. S. Haggerty, and A. G. Emslie, "Exact computation of the reflectance of a surface layer of arbitrary refractive-index profile and an approximate solution of the inverse problem," JOSA, vol. 72, no. 8, pp. 1049–1055, 1982.

[23] P. G. Verly, et.al, "Fourier-transform method for the design of wideband antireflection coatings," vol, 31, no. 19. 1992.

[24] D. Chen, "Anti-reflection made by sol-gel processes: a review," Sol. Energy Mater. Sol. Cells, vol. 68, no. 3–4, pp. 313–336, 2001.

[25] Z.-P. Yang, L. Ci, J. A. Bur, S.-Y. Lin, and P. M. Ajayan, "Experimental observation of an extremely dark material made by a low-density nanotube array," Nano Lett., vol. 8, no. 2, pp. 446–451, 2008.

[26] K. C. Sahoo et al., "Fabrication of antireflective sub-wavelength structures on silicon nitride using nanocluster mask for a solar cell application," Nanoscale Res. Lett., vol. 4, no. 7, p. 680, 2009.

[27] Z. Huang, et.al “a review assisted Metal chemical etching of the silicon: Ulrich Gösele,” Adv. Mater., vol. 23, no. 2, 2011.

[28] H. L. Chen, et.al, "Using lithography colloidal for optimizing sub-wavelength pyramidal and honeycomb structures in solar cells," Opt. Express, vol. 15, no. 22, 2007.

[29] H. Xu et al., "Biomimetic antireflective Si nanopillar arrays," Small, vol. 4, no. 11, 2008.

[30] Z. Yao, "ZnO Nanoparticles as a Luminescent down-shifting Layer for Solar Cells," pp. 1–165, 2015, [Online]. Available: http://theses.insa-lyon.fr/publication/2015ISAL0090/these.

[31] B. Chen et al., "Graphene coated ZnO nanowire optical waveguides," Opt. Express, vol. 22, no. 20, pp. 24276–24285, 2014.

[32] M.-J. Chenet.al, "ZnO- ultraviolet light-emitting and nanostructures fabricated by atomic layer deposition," Semicond. Sci. Technol., vol. 27, no. 7, 2012.

[33] B. Kumar and S.-W. Kim, "Energy harvesting based on semiconducting piezoelectric ZnO nanostructures," Nano Energy, vol. 1, no. 3, pp. 342–355, 2012.

[34] S. Xu and Z. L. Wang, "One-dimensional ZnO nanostructures: solution growth and functional properties," Nano Res., vol. 4, no. 11, pp. 1013–1098, 2011.

[35] C. F. Klingshirn, et.al, ZnO: fundamental properties towards the novel applications, vol. 120. Business Media & Springer Science 2010.

[36] Ü. Özgür, and H. Morkoç Zinc oxide: device technology and fundamentals, materials, John Wiley & Sons, 2008.

[37] H. Daniel, et.al, "An integrated method to realizing high-performance liquid junction sensitized solar cells quantum dot," Nat. Commun., vol. 4, no. 1, 2013.

[38] T. Wonglakhon, "Interaction potentials for modeling GaN precipitation and solid-state polymorphism," 2020.

[39] V. V Pokropivny, et.al." Classification of nanostructures by dimensionality, the concept of forms engineering in nanomaterial science," Mater. Sci. Eng. C, vol. 27, no. 5–8, 2007.

[40] V. Cauda et al., Nanostructured Zinc oxide Materials: Synthesis, and Applications. 2014.

[41] B. Weintraub, et.al, " synthesis of one-dimensional zinc oxide Nanosize and the applications," Nanoscale, vol. 2, no. 9, pp. 1573–1587, 2010.

[42] X. S. Shen, et.al," silver Nanoparticles: agglomeration, control the surface morphology, and application as SERS substrates," Phys. Chem. Chem. Phys., vol. 11, 2009.

[43] Y. Zhu et al., "Multiwalled carbon nanotubes beaded with ZnO nanoparticles for ultrafast nonlinear optical switching," Adv. Mater., vol. 18, no. 5, pp. 587–592, 2006.

[44] Q. Lu, Z. Wang, et.al, " photoluminescent properties of zinc oxide encapsulated in mesoporous silica SBA-15 fabricated by two-solvent strategy," Nanoscale Res. Lett., vol. 4, no. 7, 2009.

[45] M. RPSGOI and A. Yadav, "improve the efficiency of the photovoltaic through P&O algorithm,". Res. Eng., vol. 2, pp. 2642–2644, 2015.

[46] K. H. Raut D. W. Deshmukh, " Comparative of the Studies of Diverse Generation in Solar Cell :" vol. 1, no. 3, pp. 1–9, 2018.

[47] A. S. Sarkın, et.al, "A review of self-cleaning and anti-reflection on the solar cells -," Sol. Energy, vol. 199, no. June 2019, pp. 63–73, 2020, DOI: 10.1016/j.solener.2020.01.084.

[48] R. N. Castellano, PV panel processing. Archives contemporaines, 2010.

[49] A. Mohammad Bagher, " Solar Cells Types, Application," Am. J. Opt. Photonics, vol. 3, no. 5, DOI: 10.11648/j.ajop.2015

[50] S. Dimitrijevic, Principles of semiconductor devices. Oxford university press New York, 2012.

[51] W. Hwang and K. H. Zaininger, "Silicon: the semiconductor material," in Silicon, Springer, 2004, pp. 25–42.

[52] F. C. Krebs, "Polymer solar cell modules prepared using roll-to-roll methods: knife-over-edge coating, slot-die coating and screen printing," Sol. Energy Mater. Sol. Cells, vol. 93, no. 4, pp. 465–475, 2009.

[53] C. J. Brabec, et.al, “Sol. Energy Mater,” Sol. Cells, vol. 30, no. 83, p. 273, 2004.

[54] T. Saga, "Nanoparticles Materials 2, 96-102 (2010)." 2010.

[55] C. Bosserelle, E. S. Reddy, and E. J. Krüger, “WavesE andE Coasts inE theE Pacific.”

[56] A. Jalali, M. Reza, V. Nima, N. Fariba, T. Abadi, and A. Eftekhari, “Investigating the effect of sol-gel solution concentration on the efficiency of silicon solar cells : role of ZnO nanoparticles as an anti-reflective layer,” Chem. Pap., no. 0123456789, 2019, DOI: 10.1007/s11696-019-00872-0.

[57] B. Kumaragurubaran and S. Anandhi, “Reduction of reflection losses in a solar cell using anti-reflective coating,” in 2014 International Conference on Computation of Power, Energy, Information and Communication (ICCPEIC), 2014, pp. 155–157.

[58] S. R. info. [Online]. https ://refra ctive index .info/ and tmp/data/main/SiC/Larru quert . txt. A. 14 J. 2018, “SiC.” .
[59] T. R. info. [Online]. https ://refra ctive index .info/ and tmp/data/main/TiO2/Siefk e. txt. A. 14 J. 2018, “TIO2 refractionindex.” .
[60] L. Fanni et al., “the porosity of zinc oxide electrodes: from dense to Nano-pillar coating,” Mater. Res. Express, vol. 2, no. 7, 2015.

Enhancing Battery Recharge Performance through an Intelligent MPPT for Photovoltaic Solar Panels

Baqer Turki Atiyah[1], Naeib Faisal[2], and Ali Idham Alzaidi[3]
{ dr.baqer_turki@stu.edu.iq[1], naeibabase@gmail.com[2], dr.alizaidii@stu.edu.iq[3]}

Southern Technical University, Thiqar Technical College, Nasiriyah, Iraq[1,2,3]

Abstract. Fuzzy Logic MPPT (Maximum Power Point Tracking) is one of the most powerful boosting techniques for photovoltaic panels. One of the main challenges of a Photovoltaic Device enhanced with a fuzzy circuit control is the fact that it requires the photovoltaic panels to work at their maximum power point while having a high performance. In this study, an intelligent MPPT system is proposed that aims to enhance the performance of the recharge factor as well as decrease the resource spent to complete the task. To accomplish this, a fuzzy logic technique is proposed that uses a three-step charging factor. MATLAB SIMULINK is used to simulate and validate the results in a numerical experiment. Ultimately the results indicate that a three-step charge enhances the recharge factor and decreases the cost whilst improving the performance.

Keywords: PI-Fuzzy Control, Charge Control, PV Panels, MPPT, Intelligent Systems.

1 Introduction

The rise in energy consumption around the world, as well as the fact that fossil fuels are slowly running out, has led to the rise of clean renewable energies. Solar energy is one of the top contenders for the renewable energy category, especially in Middle Eastern countries that have an inordinate amount of sunlight exposure. One of the most popular solar-sourced energy production is via photovoltaic solar panels [1]. Although this technique has several benefits associated with renewables, it does also have its drawbacks. First, the daily energy conversion rate for solar panels is between 9% to 17%, which is considered very low. This is further exasperated by the fact that factors such as temperature and irradiance play a major role in the energy conversion rate, making the process even more unreliable than it already is [2]. The maximum power point output of the photovoltaic system is heavily dependent on the climate, the maximum power input, and the voltage associated with the photovoltaic panels. The climate itself is not controllable, albeit predictable if the panels were to be located in places that have a high percentage of sun exposure. However, besides the issue of the climate, other attributes such as the system efficiency can directly impact the output of the Photovoltaic system. To cut costs of a PV system, while also maximizing its efficiency, the system would need to operate at its peak power point [3]. There are several existing algorithms in the literature that are based on MPPT, such as Perturb & Observe, Inc. Conductance [4], and Fuzzy Logic. Each MPPT algorithm has its own set of pros and cons. While some are efficient in their processing, they are at the same time very expensive to execute. PV power systems include DC-DC converters, buck-type DC-to-to-DC converters a duality. MPPT algorithms extract voltage and current from the polarity of photovoltaic panels and monitor the service cycle of PWM (Pulse width Modulation) applied to the switch (MOSFET, IGBT, and so on) of DC-DC converters to

IMDC-IST 2021, September 07-09, Sakarya, Turkey
Copyright © 2022 EAI
DOI 10.4108/eai.7-9-2021.2314808

regulate the converter's voltage and current. However, the Fuzzy Logic Control method is considered very reactive depending on the environment they are set up in. Additionally, the FLC does not require device parameters to operate. Current and voltage are continuously changing after the boost converter is initiated due to the changing environmental conditions and the characteristics of the circuit elements [5]. To charge the battery quickly and efficiently, a constant current is required, as well as a sufficient voltage while charging. [6]. However, charging the battery quickly may affect the lifecycle of the batter adversely.

The charge controller loads the battery in stages to ensure that it is fully charged without causing damage to the battery due to unnecessary charge gassing and overheating [7]. Numerous previous works of literature cover the study of various MPPT algorithms, their modelling, and implementation in Simulink [8]. These publications, however, do not evaluate the MPPT tracking performance in terms of tracking time or tracking quality. Additionally, there is no discussion about how to combine this MPPT with a battery charge controller.

Tauhid Latif and co-Furs in 2014 [9] studied a SEPIC/PI process for enhancing control voltage, which was compared to a device that only used a buck converter and a battery with Incremental conductance. The proposed system is different, and the boost converter only has one circuit, so the losses are lower with the FLC MPPT method; because the system isn't being analysed, the number of components is significantly fewer, and the design is simpler. But it can also double as a boost converter or as well as a buck converter.

Hari Shankar Suresh and colleagues [10] investigated a device in 2014 that used Perturb & Observe MPPT methods and a buck-boost converter to regulate the current and voltage of a photovoltaic panel, as well as an open circuit method to monitor the battery charge. With the proposed device, Pert & Observe oscillates about maximum power point, and as a result, this causes power loss, The proposed system is schematized in **Error! Reference source not found.**.

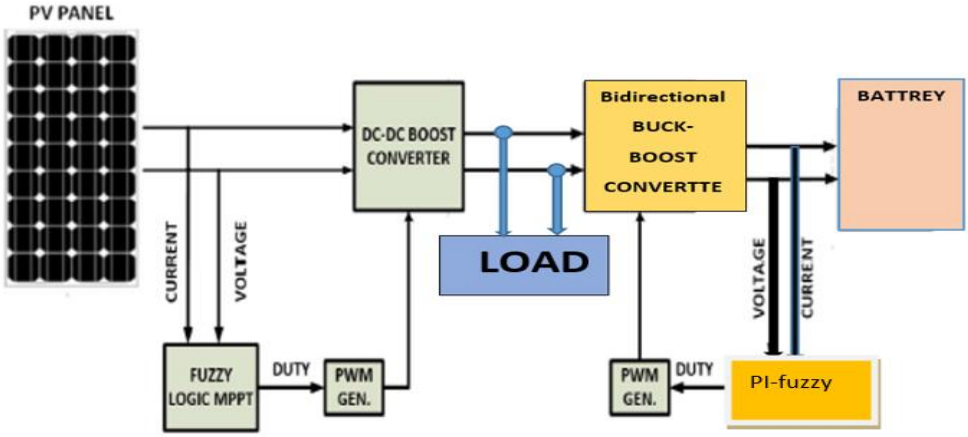

Fig 1. PV system MPPT algorithm and PI –fuzzy control charge circuit.

2 Methodology

Error! Reference source not found. demonstrates the basis for the stand-alone photovoltaic power generation system's power converter system. This framework integrates a

maximum power point monitoring controller with a bidirectional buck-boost converter with charge and discharge control. The battery charge and discharge controllers use a bidirectional buck-boost converter that possesses both buck and boost converter characteristics [11].
In the end, the output of energy conversion has been significantly increased. Additionally, this converter acts as a battery energy storage device within the system structure but also enables an auxiliary power supply at the load terminal. The power supply can be regulated and operated by implementing the device characteristics described previously.
The Fuzzy Logic MPPT algorithm is more challenging to implement but offers better PowerPoint locating capability. You are not required to understand the system's model; all inputs to an MPPT controller must be either error or change. It includes the following equations that illuminate the principles of E and EC [12].

$$E(k) = \frac{\Delta P}{\Delta I} = \frac{P(k) - P(k-1)}{V(k) - V(k-1)} \tag{1}$$

$$\mathrm{EC(k)} = \mathrm{E(k)} - \mathrm{E(k-1)} \tag{2}$$

In equation (1), P stands for power, while V is the voltage associated with the photovoltaic panel. The logic of the equation dictates that to calculate the principles of E, which takes the values of the previous power and voltage, to get the absolute values for them. If the equation is positive, meaning and the current power and voltage are higher than the previous power and voltage, then this means that based on the Fuzzy Logic MPPT, the voltage should be increased. This process is illustrated in Fig 2. The voltage is increased, so long as the relationship remains positive. The relationship is set up in such a way that a positive change in power, would require a negative change in voltage to keep the point at its maximum value possible [5].

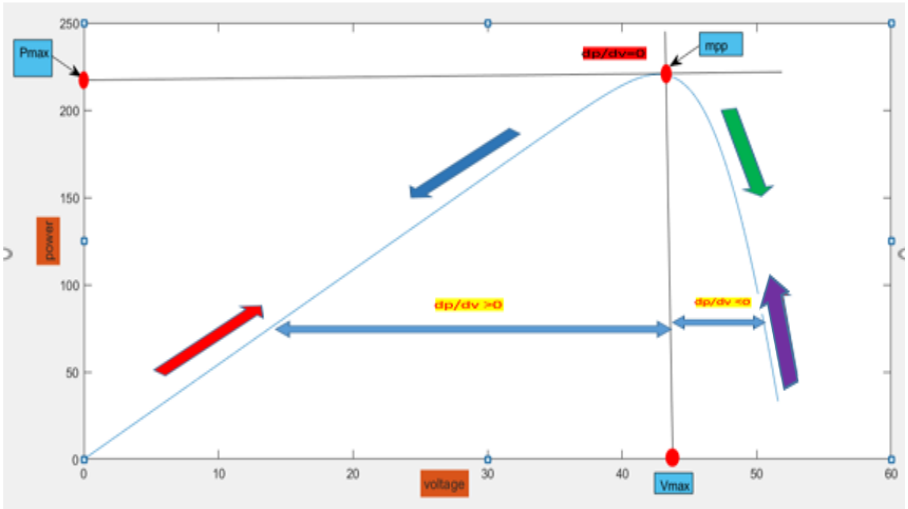

Fig 2. Voltage Power Relationship on the FLC Algorithm for the PV System.

This figure establishes what is required for the system to do to reach its MPP. Thus, establishing the logic behind the simulation as well as the corrective course for the photovoltaic panels.

3 Proposed Converter and Controller

This research proposed a bidirectional buck-boost converter as illustrated in Fig 3 for managing the storage and supply of energy across photovoltaic and battery systems. Due to the bidirectional nature of the circuit layout of a bidirectional converter, two operating modes can be selected depending on which way of the power flow boost and buck types. The boost mode also knowns as the discharging mode, the converter is either open or closed depending on the state of the switch-mode power supply (SMPS). In the buck mode also knowns as the charging mode, the proposed power flows from the DC bus to the battery bank to charge the battery [13].

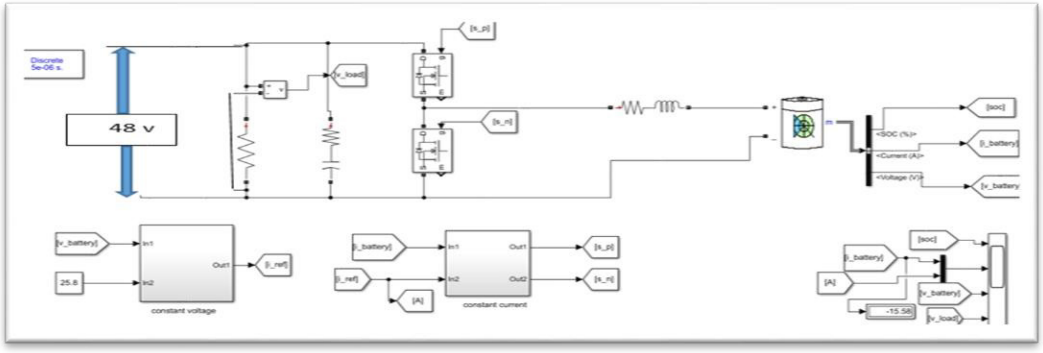

Fig 3. Proposed Bidirectional Buck-Boost Converter.

Regarding the proposed battery charge controller, it was developed using a lead-acid battery with three-state charging methods of constant current charging, constant voltage charging, and float charging. The flowchart illustrated in Fig 4 elaborates on the inner workings of the proposed three-stage battery controller. The controller measures the state of charge (SoC), if the value is at full capacity, meaning 100%, then the system is sent to float charging where the batter is aimed at maintaining 100%. However, if the SOC is lower than 80% then two conditions apply, either bulk charging or absorption charging. The bulk-charging scenario works when SOC is lower than 80%, thus the battery is charged at its rated capacity based on the MPPT. The absorption charging works when the SOC is valued at above 80%. In this scenario the MPPT is disabled, and the battery is charged at a constant voltage. The float charging ensures that the SOC does not go over 100% and thus prevents any excessive uncontrolled charge.

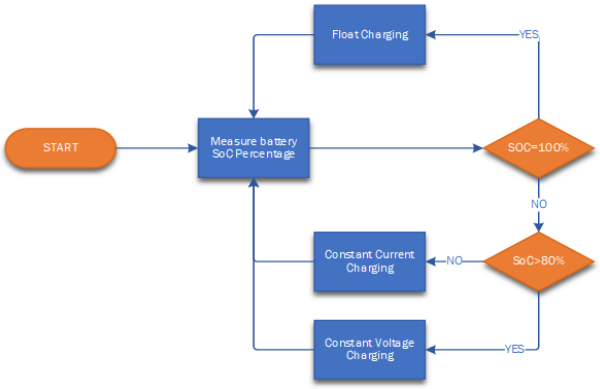

Fig 4. Three-stage lead-acid battery charge controlled flowchart.

4 Results of the Simulation

Applying both the MPPT, with the FLC as well as the three-stage charging lead-acid battery resulted in improved performance. The results are illustrated in Figure 5. It is indicated that when the lead-acid battery type is used in conjunction with using a 24 volt and 100 AH capacity with a 99.7% charging using the three-stage charging. During the one minute that the simulation was running, there was an indication that the photovoltaic array produced 1066 W of power.

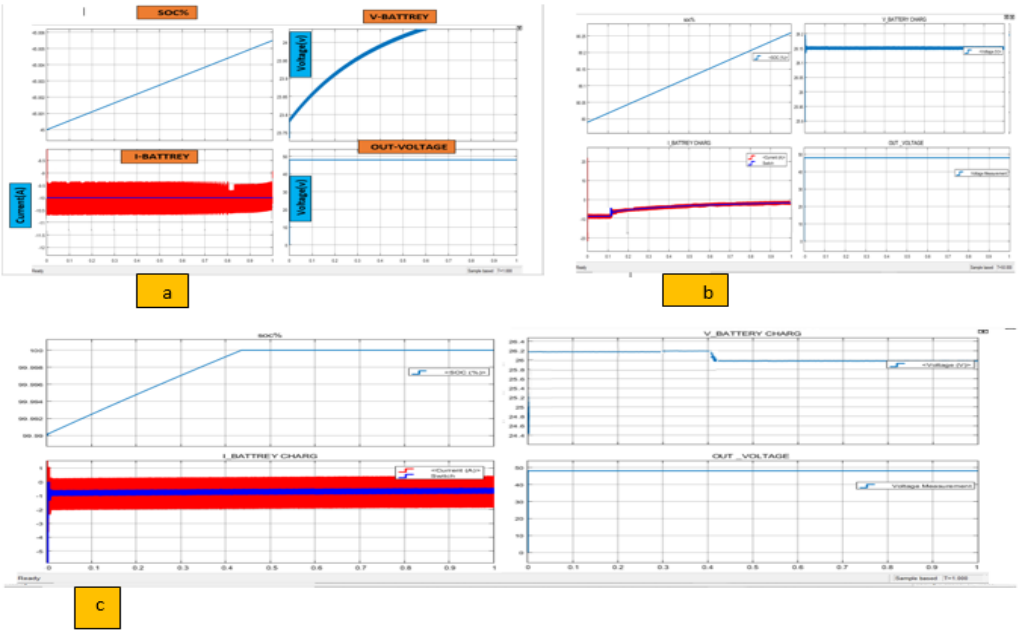

Fig 5. Scheming the charge of a lead-acid battery in three states of (a) constant current, (b) constant voltage, and (c) float charging.

5 Conclusion

In this study, a photovoltaic control circuit was proposed based on a combination of Fuzzy Logic and MPPT. Using Simulink to numerically simulate and validate the results on a photovoltaic system modelling circuit. This system was made using a module with simulations that included the MPPT FLC algorithm, the boost converter, and the three-stage charge controller. The results of the simulation indicate that the MPPT battery charger is capable of charging a 24 V lead-acid battery, using a three-stage charging strategy. This system tracks the maximum power produced by a 1.2 kW PV array source. The overall efficiency of the system reached 99.3%, which is on par with currently commercially sized high-end PVs.

References

[1] P.-C. Chen, P.-Y. Chen, Y.-H. Liu, J.-H. Chen, and Y.-F. J. S. E. Luo, "A comparative study on maximum power point tracking techniques for photovoltaic generation systems operating under fast-changing environments," vol. 119, pp. 261-276, 2015.

[2] B. Subudhi and R. J. I. t. o. S. E. Pradhan, "A comparative study on maximum power point tracking techniques for photovoltaic power systems," vol. 4, no. 1, pp. 89-98, 2012.

[3] M. P. Raj and A. M. Joshua, "Design, implementation, and performance analysis of a LabVIEW based fuzzy logic MPPT controller for stand-alone PV systems," in 2017 IEEE International Conference on Power, Control, Signals and Instrumentation Engineering (ICPCSI), 2017, pp. 1012-1017: IEEE.

[4] M. Rebhi, O. Abdelkhalek, B. Bousmaha, and M. Yaichi, "Variable Step Size Techniques for Conventional MPPT Algorithms," in International Conference in Artificial Intelligence in Renewable Energetic Systems, 2020, pp. 822-830: Springer.

[5] U. Yilmaz, A. Kircay, S. J. R. Borekci, and S. E. Reviews, "PV system fuzzy logic MPPT method and PI control as a charge controller," vol. 81, pp. 994-1001, 2018.

[6] J. Jana, K. D. Bhattacharya, and H. Saha, "Design & implementation of MPPT algorithm for battery charging with the photovoltaic panel using FPGA," in 2014 6th IEEE Power India International Conference (PIICON), 2014, pp. 1-5: IEEE.

[7] N. Karami, N. Moubayed, R. J. R. Outbib, and S. E. Reviews, "General review and classification of different MPPT Techniques," vol. 68, pp. 1-18, 2017.

[8] M. A. Enany, M. A. Farahat, A. J. R. Nasr, and S. E. Reviews, "Modeling and evaluation of main maximum power point tracking algorithms for photovoltaic systems," vol. 58, pp. 1578-1586, 2016.

[9] T. Latif and S. R. Hussain, "Design of a charge controller based on SEPIC and buck topology using modified Incremental Conductance MPPT," in 8th international conference on Electrical and Computer Engineering, 2014, pp. 824-827: IEEE.

[10] H. Suresh et al., "Efficient charging of battery and production of power from solar energy," in 2014 International Conference on Embedded Systems (ICES), 2014, pp. 231-237: IEEE.

[11] P. N. Thang and V. T. J. I. E. J. Vinh, "A Flexible DC-DC Converter for the Battery-DC Bus Renewable Energy System," vol. 20, no. 4, 2020.

[12] T. S. Cheema, J. J. I. J. o. I. R. Kaur, Development, and ISSN, "Fuzzy logic based MPPT algorithm for solar PV systems," vol. 211, p. 3.5, 2014.

[13] V. J. J. o. E. S. Viswanatha and I. Technology, "Microcontroller based bidirectional buck-boost converter for photo-voltaic power plant," vol. 5, no. 3, pp. 745-758, 2018.

Speed Control of Permanent Magnet Synchronous Motor Using SVPWM Vector Control

Doaa AL-Mansory[1], Issa Ahmed Abed[2], Diyah AL-Thammer[3]
{doaasalihnaser@gmail.com[1], issaahmedabed@stu.edu.iq[2], diyahpower@stu.edu.iq[3]}

Engineering Technical College, Southern Technical University, Iraq[1'2'3]

Abstract. This article discusses how to regulate the speed of a Permanent Magnet Synchronous Motor (PMSM). Depending on the field-oriented control principle, which is among the most often used AC motor drives accessible in the industry, a new approach to regulating the PMSM using pulse width modulation of space vectors (SVPWM) is suggested. The entire framework is designed on the MATLAB /Simulink platform (vector control). The whole system, using the speed loop outside and the interior current loop, using two control loops are simulated based on synchronous motor speeds using power electronics and microelectronic technology have advanced. The AC servo device for PMSM is applied based on control methods that are used more often.

Keywords: PMSM, SVPWM, field-oriented control, controlling vector.

1 Introduction

In many industrial applications, the ability to control the speed of electric motors is necessary, just like robots, computer numerical control (CNC), traction engines, air conditioning, pumping systems, etc. Permanent magnet synchronous motors (PMSM) have been widely used recently increasing, substituting the Induction motor due to the requirement for greater efficiency and smaller size in an application, for example, vehicles and appliances for homes [1, 2]. This machine is now commonly used in servo systems with high-efficiency applications such as actuators in robotics and aerospace, as no external excites are provided to the rotor, reduction of damages, and highly effective PMSM. There are primarily two types of PMSM drive in the industry, one shows the distribution of sinusoidal flux in a PMSM, while the other is the distribution of trapezoidal change in a brushless DC machine [3]. Due to complexity compared to field-oriented induction motor drive control, PMSM drives are usually favored in servo systems. The principle of vector control is used in this work to achieve a linear transient response, along with decoupled regulation of the transient response of the AC three-phase unit, such as the separately excited DC motor [4, 5]. The vector control-based proportional-integral (PI) control method (field-oriented control) is widespread and useful for the regulation of PMSM with an accurate mathematical model [6]. PMSM vector control was performed using the space vector pulse width modulation (SVPWM) inverter output voltage methods generation rather than a traditional sinusoidal modulation of the width of the pulse. The flux (i_d) as well as Torque (i_q) of the system, it is possible to function independently in the same period in this scheme [7]. The SVPWM technology ensures optimum voltage of DC input utilization and less harmonic distortion. Multilevel inverters and two-level inverters are usually known as an inverter. In contrast to the two-level inverters, one of the benefits of multilevel

IMDC-IST 2021, September 07-09, Sakarya, Turkey
Copyright © 2022 EAI
DOI 10.4108/eai.7-9-2021.2314439

inverters is decreased harmonic distortion. Sometimes known as the control of decoupling or vectors, the field-oriented rule came in late 1960; the research field of ac drives was prominently developed in 1980 to resolve the challenges of synchronous motor drive and induction inverter-fed oscillating flux and torque response. Numerous authors have modelled and simulated such a drive. The author in [8] described the modeling and simulation of a PMSM drive system that depends on FOC. The work in [9] presented a MATLAB/Simulink implementation of a vector-controlled PMSM drive utilizing the SVPWM method.

This paper is structured it is as follows: the PMSM basic mathematical model developed in Section II. The suggested methodology of vector control is provided in Section III. Section IV describes the implementation of the SVPWM algorithm on a systematic basis. Design of two-level inverter in section V. Results of the simulation for section VI are discussed Section VII contains the conclusion.

2 Proposed System

The magnetic field is a permanent magnet. The field is excited by permanent magnets that produce sinusoidal back EMF in a synchronous motor, which is one form of AC synchronous motor. It uses a permanent magnet to generate a magnetic field. The d-q rotor reference frame principle was used to construct the motor axis. In this model, a speed and current closed-loop control method have been used, with the SVPWM formula in the inner loop that accounts for the strong coupling, time-varying, as well as non-linearity properties, and also the PI speed controller with the outer loop to improve robustness and anti-interference efficiency.

2.1 Mathematical Model of PMSM

Generally, the wound rotor synchronous motor's stator is quite similar to the permanent magnet synchronous motor's stator. The main difference is that the high-performance permanent magnet PMSM rotor is constructed from new magnetic materials of rare earth with high levels of surface or rotor conductivity. The winding of the three-phase stator creates through the air gap, a rotating magnetic field. The relationship in the space between the stator and the electromagnetic field of the rotor generates electromagnetic Torque that drives the synchronization of the rotor. The following ones are the assumption in the derivation process is made [10], [11]:

- Saturation and variance of parameters are ignored.
- Stator windings are balanced with sinusoidal mediated EMF.
- The loss of eddy current and hysteresis is negligible.
- No current field dynamics are available.

PMSM stator voltage equations can be written as a rotating reference frame in d, q with the assumptions as follows [12],[13],[14],[15],[16],[17],[18],[19],[20]:

$$V_q = R_s i_q + \omega_r \lambda_d + \rho \lambda_q \tag{1}$$

$$V_d = R_s i_d - \omega_r \lambda_q + \rho \lambda_d \tag{2}$$

Where, V_q and $V_d$the stator voltage is the d, q reference frame, i_d and i_q are the d, q rotating reference frame stator current in, λ_d and λ_q are the d, q axis stator flux relation, R_s is the winding resistance of the stator as a result of the permanent magnets., the flux linkage may be used to express as a flux linkage λ_f. ρ: operator $\frac{d}{dt}$. Flux Linkages equations:

$$\lambda_q = L_q i_q \tag{3}$$

$$\lambda_d = L_d i_d + \lambda_f \tag{4}$$

Where L_q and L_d the inductance of the d and q axis stator and the rotor permanent magnet flux is λ_f. Substituting eqn. (3), eqn. (4) in eqn .(1), and eqn. (2) we get the voltage as:

$$V_q = R_s i_q + \omega_r\left(L_d i_d + \lambda_f\right) + \rho L_q i_q \tag{5}$$

$$V_d = R_s i_d - \omega_r L_q i_q + \rho\left(L_d i_d + \lambda_f\right) \tag{6}$$

And we arranged them in matrix format we get:

$$\begin{bmatrix} V_q \\ V_d \end{bmatrix} = \begin{bmatrix} R_s + \rho L_q & \omega_r L_d \\ -\omega_r L_q & R_s + \rho L_d \end{bmatrix} \begin{bmatrix} i_q \\ i_d \end{bmatrix} = \begin{bmatrix} \omega_r \lambda_f \\ \rho \lambda_f \end{bmatrix} \tag{7}$$

In the above equation, ω_r is the rotor electrical speed, where ω_m is the mechanical rotor velocity in rad/sec,

$$\omega_m = \omega_r \left(\frac{2}{p}\right) \tag{8}$$

The formula of electromagnetic Torque generated can be written as:

$$T_e = \frac{3}{2}\left(\frac{p}{2}\right)\left[\lambda_f i_q + \left(L_d - L_q\right) i_d i_q\right] \tag{9}$$

If, P, the number of poles. By setting i_d equal to zero and $L_d = L_q$ at in type Surface Permanent Magnet Synchronous Motor (SPMSM). The torque equation is as follows:

$$T_e = \frac{3}{2}\left(\frac{p}{2}\right) \lambda_f i_q \tag{10}$$

The mechanical equation of Torque for modeling of PMSM express the relationship between the electromagnetic Torque T_e , load torqueT_l, and electrical speed ω_r as follows, the mechanical Torque equation:

$$T_e = T_l + B\omega_m + J\frac{d\omega_m}{dt} \tag{11}$$

Solving the mechanical velocity of the rotor from the equation:

$$\omega_m = \int \left(\frac{T_e - T_l - B\omega_m}{J}\right) dt \tag{12}$$

J the inertia of the rotor, B the value of the coefficient of viscous friction, and T_l the Torque of the load.

2.2 Park and Clarke Transformations

The amounts of AC motors in the three phases can be evaluated in two-phase equivalent rules αβ coordinate frame for complex space vectors. They can be converted further into a relation of two-phase rotating dq reference time frame invariant. The PMSM dynamic performance in the reference frame, dq it can be used to describe the features of the transient and steady-state. The transformation of Clark is used to convert the quantities of three-phase abc into equivalent amounts of two stages of αβ quantity as in eqn. (12). To transform the space vectors αβ frame into a rotating frame that is time-invariant dq frame in eqn. (13), Park converting is used. The various techniques of transformation are explained below in matrix form:

1) Transformation by Clark (abc-to-αβ):

$$\begin{bmatrix} i_\alpha \\ i_\beta \end{bmatrix} = \frac{2}{3} \begin{bmatrix} 1 & \frac{-1}{2} & \frac{-1}{2} \\ 0 & \frac{\sqrt{3}}{2} & \frac{-\sqrt{3}}{2} \end{bmatrix} \begin{bmatrix} i_a \\ i_b \\ i_c \end{bmatrix} \tag{13}$$

2) Transformation of Park (αβ-to-dq):

$$\begin{bmatrix} i_d \\ i_q \end{bmatrix} = \begin{bmatrix} cos\theta & sin\theta \\ -sin\theta & cos\theta \end{bmatrix} \begin{bmatrix} i_\alpha \\ i_\beta \end{bmatrix} \tag{14}$$

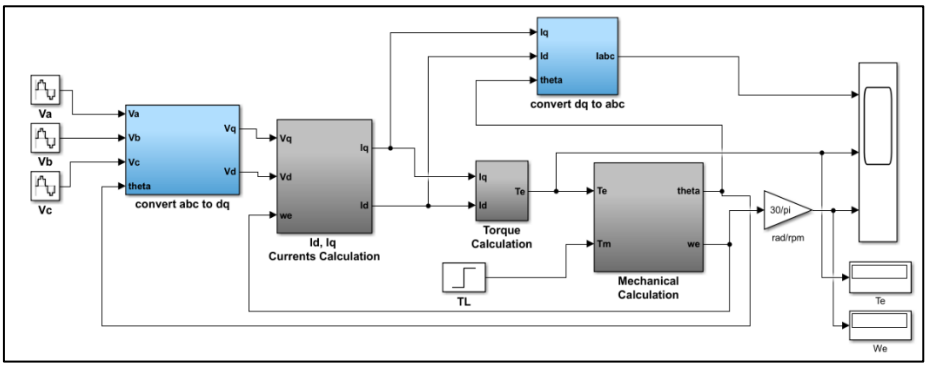

Figure 1. a) the Implementation of PMSM, MATLAB/Simulink program Simulink model with drive circuit; b) Simulink model of PMSM drive circuit

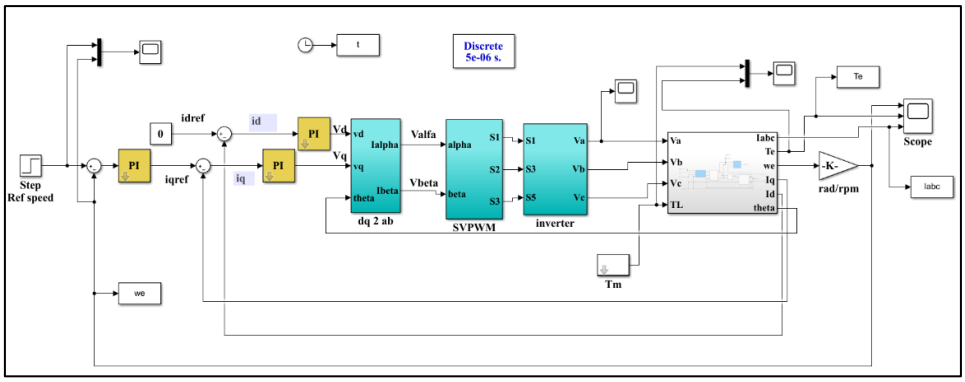

Figure 2. Simulink model of PMSM drive circuit.

3 Vector Control Theory for PMSM

The system of method of vector control is an intelligent method of regulating the drive to PMSM, using the field-oriented concept to regulate magnetic circuit controls of the space vector. Utilizing Park and Clarke transforms, with two orthogonal elements i_{sq} andi_{sd}, 3-phase currents of stators are converted into two-phase currents. The regulation of vectors is supposed to separately control torque and flux. Here, i_{sq} is it the component creating Torque, and i_{sd} is the component making flux [21]-[22]. Therefore, there are two distinct loops for control:

1. Velocity loop: the outer circle that regulates the motor speed and produces the reference signal for the current controller with the q-axis.
2. The Current loop: the inner circle was the motor that governs the motor's flux and Torque.

For a motor drive system with maximum speed range, the speed control loop consists of a motor, an inverter, a controller that measures the discrepancy between the speed of reference and real velocity that produces an error that is fed to the controller of the PI. For the motion control system, PI controllers are commonly used. They include a proportional gain, which has results proportional to the failure input and integration for a step-change in information to make the steady-state error zero.

4 Space Vector Technique of Pulse Width Modulation

Modulation of Space vector pulse width (SVPWM) is a digital adjustment method that aims to produce, on average, PWM load line voltages equal to the reference load line [23]. In reality, SVPWM is just an algorithm for modulation that transforms the reference from control to phase voltage (phase to neutral) should be applied to the specified PWM modulation times/duty-cycles. In the power electronics and drive systems industry, these methods of PWM switching have usually been employed. The purpose of the pulse width is modulated to provide an inverter-regulated voltage output after the output voltage's harmonic content is reduced. One of the different forms of modulation techniques is Space Vector Modulation Techniques. However, SVPWM is becoming a primary method of realizing PWM due to the benefits, including.

- Lower current ripple power.
- Better use of buses.
- Lower order harmonics, along with its output voltage power, can be removed or minimized.

The inverter can have eight space vector outputs depending on the eight possible switching combinations, of which six are active vectors (V1-V6), and two zero vectors (V0 and V7). As in the case of a regular hexagon, six sectors compose the space vector path. A maximum reachable voltage is the circle radius, i.e. ($1/\sqrt{3}$) Vdc, as seen by Fig. 3. The distance of 60 degrees between any two non-zero vectors adjacent to them. In the SVPWM approach, the reference voltage ($Vref$) is a vector created through switching between one and two nearest zero vectors active space vectors, representing the three-phase AC voltage [24].

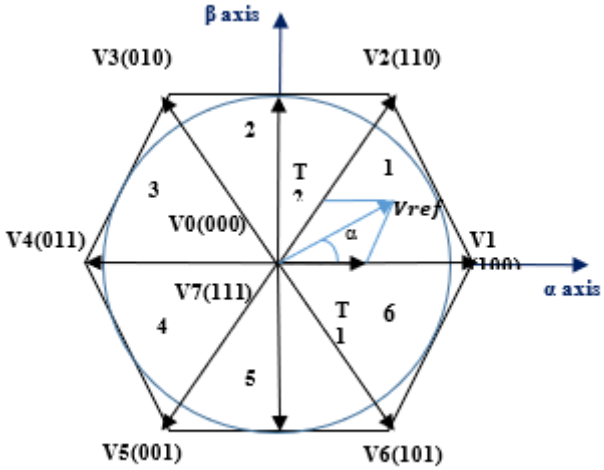

Figure 3. Basic switching vectors and six sectors for SVPWM [24].

Step1: The sector can be determined according to the relationship between Vα, Vβ in each sector, and$Vref$. Sector judgment model the following technique is used to determine the sector it is based on the expression voltage $\alpha - \beta$ coordinate for control implementation as follows: [25]

When, $V_\beta > 0$, After that, A=1, else A=0 (15)

$\sqrt{3}\ V_\alpha - V_\beta > 0$, After that, B=1, else B=0 (16)

$-\sqrt{3}\ V_\alpha - V_\beta > 0$, After that, C=1, else C=0 (17)

V_α ,V_β , they first converted from 3-phase to 2-phase stationary frame voltage.

Determination $V\alpha$ and Vβ from Clark's transformation as this:

$$\begin{bmatrix} V_\alpha \\ V_\beta \end{bmatrix} = \frac{2}{3}\begin{bmatrix} 1 & -\frac{1}{2} & -\frac{1}{2} \\ 0 & \frac{\sqrt{3}}{2} & -\frac{\sqrt{3}}{2} \end{bmatrix}\begin{bmatrix} V_a \\ V_b \\ V_c \end{bmatrix} \quad (18)$$

Then determine$|\overline{V_{ref}}|$, and angle α from **Fig. 4:**

$$|\overline{V_{ref}}| = \sqrt{{V_\alpha}^2 + {V_\beta}^2} \qquad ; \alpha = \tan^{-1}\left(\frac{V_\beta}{V_\alpha}\right) = 2\pi f t \quad (19)$$

Where (f) is the fundamental frequency

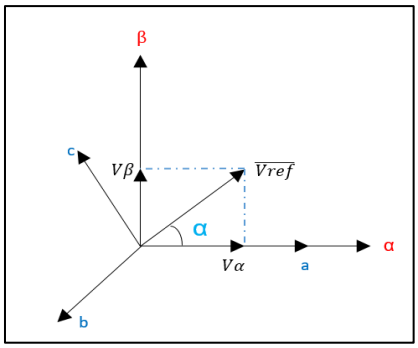

Figure 4. Reference Voltage of SVPWM for PMSM.

Step2: Vector estimation switching period T1, T2

T1 and T2 The operating time of the current sector's corresponding voltage vector. You can measure the active time as follows:

$$X = \sqrt{3}\,\frac{T}{V_{dc}}\,V_\beta \tag{20}$$

$$Y = \frac{3}{2}\,\frac{T}{V_{dc}}\left(V_\alpha + \frac{1}{\sqrt{3}}\,V_\beta\right) \tag{21}$$

$$Z = \frac{3}{2}\,\frac{T}{V_{dc}}\left(\frac{1}{\sqrt{3}}\,V_\beta - V_\alpha\right) \tag{22}$$

Where T denotes the total amount of time spent switching. It will now determine the operation time based on the data in Table 1.

Table 1. Assessment of T1 and T2 for SVPWM.

The No. sector	1	2	3	4	5	6
T1	-z	Y	X	Z	-y	-x
T2	x	Z	-y	-x	-z	Y

Step3: Determining the points for vector switching, the switch of the voltage vectors, the PWM symmetrical series, can be used. it can measure the vector switching points as follows:

$$T_a = \frac{T_0}{4} \tag{23}$$

$$T_b = \frac{T_0}{4} + \frac{T_1}{2} \tag{24}$$

$$T_c = \frac{T_0}{4} + \frac{T_1}{2} + \frac{T_2}{2} \tag{25}$$

Where T is the whole time period. In the current sector, T1 and T2 are the voltage vector's operating times. Where $T_0 = T - T_1 - T_2$.

Now, the points for vector switching Tcm1, Tcm2, and Tcm3 can be discovered in Table 2.

Table 2. Switching with Points vector

	Sector					
Point switching vector	1	2	3	4	5	6
Tcm1	Ta	Tb	Tc	Tc	Tb	Ta
Tcm2	Tb	Ta	Ta	Tb	Tc	Tc
Tcm3	Tc	Tc	Tb	Ta	Ta	Tb

Step 4: created PWM puls
Now, pulses of PWM can be generated by comparing Tcm1, Tcm2, and Tcm3 with Isosceles' triangle wave. To receive PWM2, PWM4, PWM6, it can be set on NOT service on PWM1, PWM3, and PWM5. The PWM waveform symmetrical space vector, which is used in 3-phase VSI. Below is the procedure for the design of the SVPWM method. The switching frequency (fs) of the SVPWM used in this control is (5 kHz), and the sampling time (Ts) is (0.0002 sec), and the dc input voltage is 200v.

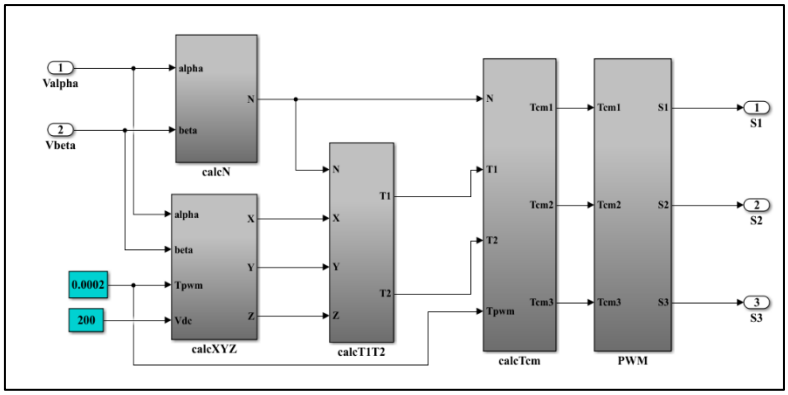

Figure 5. ign steps of SVPWM.

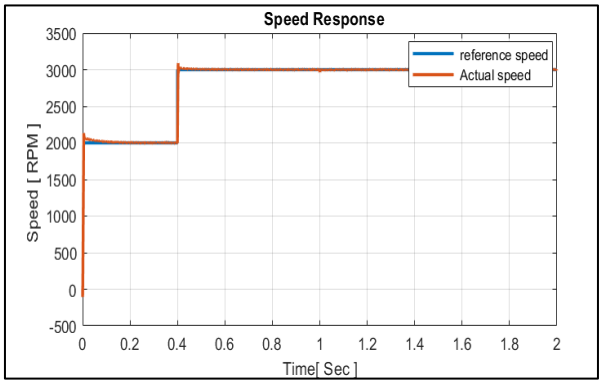

Figure 6. Speed response with reference to PMSM.

5 Space Vector Technique of Pulse Width Modulation

In this work, the vector control system incorporating the strategy of SVPWM for voltage inverting the supply from DC to AC is verified. A fundamental requirement with respect to the vector control system to the PMSM drive is SVPWM, which mainly a rotating vector that depends on a similar sinusoidal three-phase variable voltage. Using some examples of reference values, the motor torque and speed are regulated to check the vector control system drive for PMSM, and the findings indicate that the motor variables are almost tracking their reference. The torque and speed are displayed in **Figure 6** and **Figure 7** respectively. The measured motor speed of 3000-rpm constant speed, which is when any disturbance is shed the controller

responds to the reference speed variables (step Ref). Speed and torque responses at full load torque (1.27 N.m) as illustrated below:

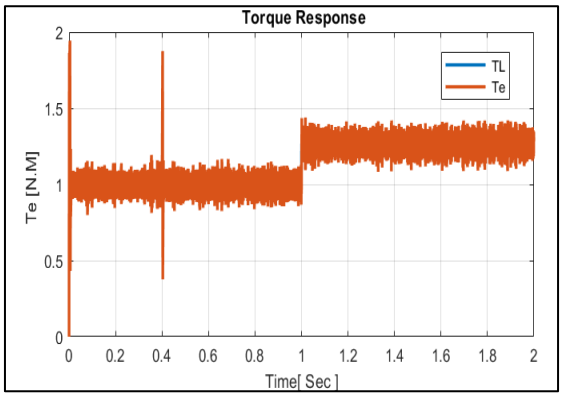

Figure 7. Electromagnetic torque with torque load..

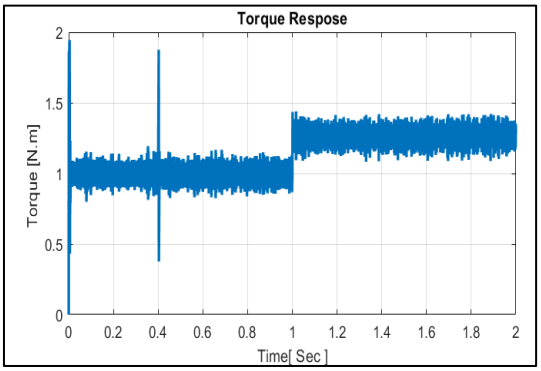

Figure 8. Three-phase stator current with PI controller.

The sinusoidal current flowing through a three-phase stator is seen in **Figure.8**. This value is updated during the velocity adjustment. The value of the rated phase current is used to verify the stator current's response (2.7A RMS) in table 4. That is when the load at its maximum value of the load torque TL is (1.27 N.m), at shown in **Figure.9**. The current value is (2.7 A RMS) at full load, and the torque response graph with the PI controller in the PMSM is show.

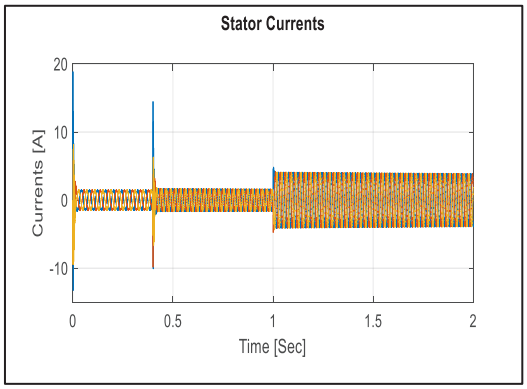

Figure 9. Torque response of the PMSM with PI controller.

A proportional-integral (PI) controller must be used to remove steady-state error [26]. This error is a result of a comparison between both the measured and reference motor speeds. This error must be equal to zero to produce tracking results as shown in **Figure. 10**. The settings of a traditional proportional-integral (PI) speed controller are controlled by manually adjusted to maintain the reference speed tracking [27]. Error resulting from a difference between the actual and desired speeds of the output. A proportional Kp parameter is utilized to reduce the time required for the rise time, and the integral parameters Ki are employed to reduce settling time and overshoot [28].

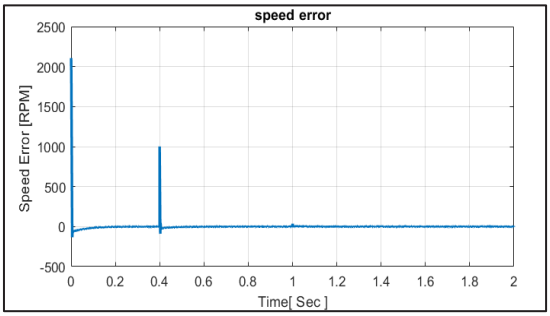

Figure 10. Error between reference speed and actual speed.

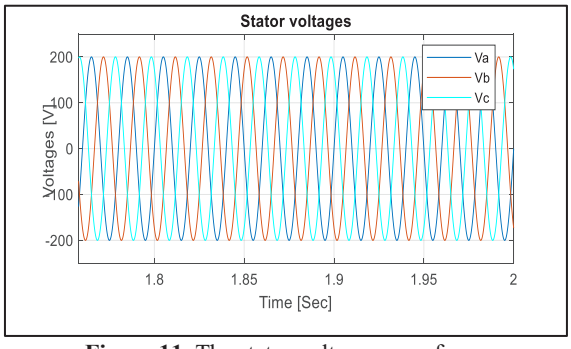

Figure 11. The stator voltages waveform.

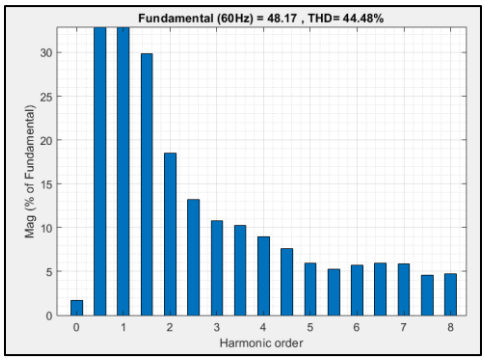

Figure 12. The total harmonics distortion for different starting time (0.6s and 1s).

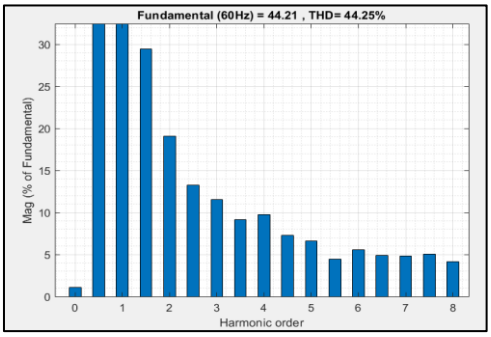

Figure 13. Percentage of Magnitude versus teh harmonic order.

Table 3. Nominal Parameters of the PMSM.

Variable	Value
Rated current	2.7 A_{rms}
Rated voltage	200 V_{rms}
Speed rated	3000 rpm
Torque rated	1.27 N.m
Number of pairs of poles the	4
Resistance to Stator winding (Rs)	2.7Ω
Stator inductance (L=Ld=Lq) (SPMSM)	8.5mH
Constant Torque	0.301 N.m/A
Linkage of flux	0.0615 Wb
Moment of Inertia	31.69e^{-6} kg.m²
Viscous friction B	52.79e^{-6} N.m.s/rad
Static Nominal friction	0.289

6 Conclusion

Vector control schemes using the SVPWM method in the MATLAB/SIMULINK framework has been simulated and tested. For vector transformation, PMSM was decoupled into torque and excitation elements can be performed. In order to convert the three-step sinusoidal frame to reference frames and vice versa, Clark and park transformation are utilized with its inverses. The PMSM, however, has a robust nonlinear characteristic, which results in a discrepancy

between the parameters built and the actual parameters. The simulation model of the PMSM vector control system, which is based on closed-loop flux and current in PMSM vector control systems, proposes and designs the simulation model of the PMSM vector control system using the SVPWM method in this work, which effectively simulates the complete system.

References

[1] Linares-Flores, Jesús, et al. "Robust back stepping tracking controller for low-speed PMSM positioning system: design, analysis, and implementation." *IEEE Transactions on industrial informatics* 11.5 (2015): 1130-1141.

[2] Duc-Do, Ton, et al. "θ-D approximation technique for nonlinear optimal speed control design of surface-mounted PMSM drives." *IEEE/ASME* Transactions *on Mechatronics* 20.4 (2014): 1822-1831.

[3] Kumar Mahto, Rajesh, et al. "Vector Control of Permanent Magnet Synchronous Machine with Reduced Switch Five-Level Voltage Source Inverter." *2019 IEEE 21st Electronics Packaging Technology Conference (EPTC)*. IEEE, 2019.

[4] Vindel, David, et al. "Field-oriented control of a PMSM drive system using the dSPACE controller." *2012 IEEE International Electric Vehicle Conference*. IEEE, 2012.

[5] Wang, Aimeng, et al. "A new exponential reaching law of sliding mode control to improve performance of permanent magnet synchronous motor." *IEEE Transactions on Magnetics* 49.5 (2013): 2409-2412.

[6] Sarkar, Prasanta, et al. "SVPWM based vector control of PMSM drive in the delta domain." *2017 International Conference on Electrical, Computer, and Communication Engineering (ECCE)*. IEEE, 2017.

[7] Kamalaselvan, A., et al. "Modeling simulation and analysis of closed-loop speed control of the PMSM drive system." *2014 International Conference on Circuits, Power and Computing Technologies [ICCPCT-2014]*. IEEE, 2014.

[8] Amin, Faisal, et al. "Modelling and simulation of field oriented control based permanent magnet synchronous motor drive system." Indonesian Journal of Electrical Engineering and Computer Science 6.2 (2017): 387-395.

[9] Saiyad Mahammad soaib, M.,"Vector controlled PMSM drive using SVPWM technique-A MATLAB/simulink implementation." Electrical, Electronics, Signals, Communication and Optimization (EESCO), 2015 International Conference. 2015.

[10] Kumar Chakraborty, Ajoy, et al. "Control of permanent magnet synchronous motor (pmsm) using vector control approach." *2016 IEEE/PES Transmission and Distribution Conference and Exposition (T&D)*. IEEE, 2016.

[11] Suman, Kumari, et al. "Speed control of permanent magnet synchronous motor drive system using PI, PID, SMC and SMC plus PID controller." *2018 International Conference on Advances in Computing, Communications and Informatics (ICACCI) IEEE, 2018.*

[12] Kaiqi, Zhao. "The study of an improved PI method for PMSM vector control system based On SVPWM." *2011 IEEE Industry Applications Society Annual Meeting*. IEEE, 2011.

[13] Aktas, Mustafa, et al. "Comparison of DC link current and stator phase current in inverter switching faults detection of PMSM drives in HEVs." *Engineering Science and Technology, an International Journal* 21.4 (2018): 664-671.

[14] Amin, Faisal, et al. "Modelling and simulation of field-oriented control based permanent magnet synchronous motor drive system." *Indonesian Journal of Electrical Engineering and Computer Science* 6.2 (2017): 387-395.

[15] Wang, Xudong, et al. "Simulation of PMSM field-oriented control based on SVPWM." *2009 IEEE Vehicle Power and Propulsion Conference*. IEEE,2009.

[16] Pandey, Richa, et al. "Multilevel Inverter Fed Permanent Magnet Synchronous Motor Drive with Constant Torque Angle Control." *Advance in Electronic and Electric Engineering, Research India Publications, ISSN* (2013): 2231-1297.

[17] Al-Khatat, Majid K., et al. "Study and compare the performance of sensor less control of PMSM drive system." *Engineering and technology journal* 32.10 Part (A) Engineering (2014): 2528-2547.

[18] Suman, Santosh Kumar, et al. "Novel approach of speed control of PMSM drive using neural network controller." *2016 International Conference on Electrical, Electronics, and Optimization Techniques (ICEEOT)*. IEEE, 2016.

[19] Dwivedi, Sanjeet, et al. "Vector Control Vs. Direct Torque Control comparative evaluation for PMSM drive." *2010 Joint International Conference on Power Electronics, Drives and Energy Systems & 2010 Power India*. IEEE, 2010.

[20] Gajanan Petkar, Sagar, et al. "A Modified Model Predictive Current Control of Permanent Magnet Synchronous Motor Drive." *IEEE Transactions on Industrial Electronics* (2020).

[21] Boby, Kiran, et al. "Mathematical modelling of pmsm vector control system based on SVPWM with pi controller using Matlab." *International Journal of Advanced Research in Electrical, Electronics and Instrumentation Engineering* 2.1(2013).

[22] Bida, Vladislav M., et al. "PMSM vector control techniques—A survey." *2018 IEEE Conference of Russian Young Researchers in Electrical and Electronic Engineering (EIConRus)*. IEEE, 2018.

[23] Bhaskar Reddy, Naga, et al. "Comparison of modulation techniques for multilevel inverter fed permanent magnet synchronous motor." *International Journal of Engineering Science and Technology* 2.10 (2010): 5206-5214.
[24] Mohammed, Laith A., et al. "Permanent Magnet Synchronous Motor Drive Based on Maximum boost control Z-source SVPWM." *Zanco Journal of Pure and Applied Sciences* 31. s3 (2019): 176-181.
[25] Saiyad Mahammadsoaib, M., et al. "Vector controlled PMSM drive using SVPWM technique-A MATLAB/simulink implementation." *Electrical, Electronics, Signals, Communication and Optimization (EESCO), 2015 International Conference*. 2015.
[26] Utomo, Wahyu Mulyo, et al. "Speed tracking of field oriented control permanent magnet synchronous motor using neural network." International Journal of Power Electronics and Drive System (IJPEDS) 4.3 (2014): 290-298.
[27] Fadhil, Ghaith Majd, et al. "Improved Control Method for Three Phase Induction Motor Based on Optimization DTC Technique." 2020 International Conference on Electrical, Communication, and Computer Engineering (ICECCE). IEEE, 2020.
[28] Odhafa, Thaer A., et al. "Controlling of Boost Converter by Proportional Integral Controller." (2021).

Improved Path Planning of Mobile Robot using Atom Search Optimization Algorithm

Shahad M.Majeed[1], Issa Ahmed Abed[2], and Alaa A. Al-Saffar[3]
shahadmohammed@stu.edu.iq[1], issaahmedabed@stu.edu.iq[2], alaaasaffar@stu.edu.iq[3]

Basrah Engineering Technical College, Southern Technical University, Iraq

Abstract. Robots have found applications in a variety of settings, ranging from speeding up manufacturing processes for completing complex jobs in hazardous and hostile areas. Path planning for mobile robots is one of the most difficult challenges in robotics. Robot route planning is a difficult optimization issue that must be tackled in a variety of applications. In this paper, we proposed the Atom search optimization (ASO) algorithm to improve the mobile robot path with free, static and dynamic obstacles environments and compare the results with the particle swarm optimization (PSO) algorithm**.** The "atom search optimization" algorithm is a novel algorithm that was used for the first time in this study to plan the route of a mobile robot. This algorithm has improved the path and the execution time(time required for the robot to reach the destination) was reduced. The authors checked the proposed method with several cases using MATLAB2020a software. It has been demonstrated that the suggested strategy, rather than PSO, found better, more consistent, and smoother pathways with a shorter computation time.

Keywords. Mobile robot route planning, Atom search optimization algorithm, particle swarm optimization.

1 Introduction

Rapid technological advancements open up new and better prospects in a variety of areas. Robotics is now one of the most exciting developments [1]. The primary aim of robotic technology is to develop machines that can perform such human tasks. They are commonly used in a variety of circumstances to speed up a process or work in and exploring aggressive, hazardous, and inaccessible environments [1]. Forward kinematics and, later, inverse kinematics is necessary for the design of any work in robotics systems [2]. In this work Forward kinematics is considered. One issue is how the mobile robot determines the shortest path to the target while avoiding collisions. In mobile robot work, the path planning issue is crucial. To plan the course of the robot from one point to another, robotic systems employ intelligence algorithms. Path planning's main objective is to determine a robot's permissible movement in a given setting with obstacles. From the start position to the target position, these motions require a collision-free direction [2]. A smart mobile robot route planning system can save a lot of time while also lowering the robot's wear and capital expenditure

IMDC-IST 2021, September 07-09, Sakarya, Turkey
Copyright © 2022 EAI
DOI 10.4108/eai.7-9-2021.2314437

[3]. Researchers all around the world have developed a variety of meta-heuristic search algorithms to address complicated global optimization issues and approaches to improve them during the last few decades [5]. A constrained optimization problem can be used to overcome the difficulty of route planning. Depending on the environment and tasks that the robot must do, the goal or fitness function of the problem can be presented in a variety of ways [1].

In this paper, For tackling mobile robot path planning in two-dimensional space with static and dynamic impediments, the (ASO) technique was introduced. The results are compared with a PSO algorithm in the same manner. The suggested technique is a novel type of atom dynamics-based meta-heuristic global optimization methodology. ASO is a population-based iterative heuristic global optimization algorithm that that can be applied to a wide range of optimization issues. ASO is a simple and straightforward method that mathematically describes and replicates nature's atomic motion concept, where atom interaction forces emerging from the Lennard-Jones potential and constraint forces arising from the bond-length potential interact with each other. To investigate the problem of mobile robot path planning, the ASO method is utilized. In path planning issues, The findings of the experiments indicate that ASO can outperform other well-known techniques such as (PSO) and that it is competitive with its rivals..

2 Robot path planning

The fundamental purpose of robot route planning using optimization criteria is to identify a path from start to finish that is free of collisions [5]. In its most basic form, path planning attempts to build a collision-free path for the robot from its starting place to the destination location while staying away from the strewn about the workspace, using some knowledge about the environment [6]. There are some assumptions made in this work before exploring and proposing a solution to this issue:

• The proposed environment was designed with 200 x 200 pixels.
• The proposed environment was designed with three scenarios free, static &dynamic obstacles.
• The obstacles are represented by an equally size circular shape.
• The speed of the dynamic obstacles was fixed.

• The mobile robot movement was omnidirectional at any time.
• Minimizing the distance function yields the shortest distance. $f(x, y)$[7].

$$f(x,y) = \sqrt{(x_d - x_s)^2 + (y_d - y_s)^2} \quad (1)$$

where: The next position is represented by x_d, y_d , and the current position is represented by x_s, y_s.

• The shortest path planning was obtained by applying PSO &ASO algorithms, then compared the results between them.

3 Atom Search Optimization

ASO approach is fundamental molecular dynamics. The notion of molecular dynamics was developed in theoretical physics and has since been applied to domains like chemistry, biology, and materials science; where atomic motion is governed by classical mechanics. Newton's second law is that, if F_i is the interaction force and G_i is the constraint force acting on the i^{th} atom and the atom has mass m_i then the acceleration of the atom is [8], [4]:

$$a_i = \frac{F_i + G_i}{m_i} \tag{2}$$

The interaction force operating on the Lennard-Jones potential (L-J potential) is employed on i^{th} atom from the j^{th} atom in the d^{th} dimension at t time, which can be represented as[8], [4]:

$$F_{ij}^{d}(t) = \frac{24\varepsilon(t)}{\sigma(t)}\left[2\left(\frac{\sigma(t)}{r_{ij}(t)}\right)^{13} - \left(\frac{\sigma(t)}{r_{ij}(t)}\right)^{7}\right]\frac{r_{ij}(t)}{r_{ij}^{d}(t)} \tag{3}$$

And

$$F'_{ij}(t) = \frac{24\varepsilon(t)}{\sigma(t)}\left[2\left(\frac{\sigma(t)}{r_{ij}(t)}\right)^{13} - \left(\frac{\sigma(t)}{r_{ij}(t)}\right)^{7}\right] \tag{4}$$

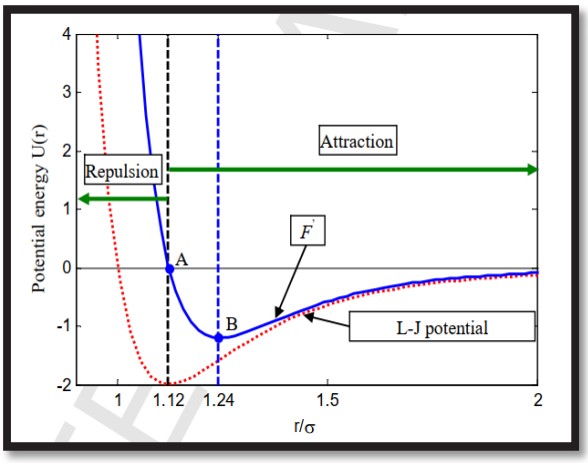

Fig. 1. Atoms force curve

Figure 1 depicts the atoms' force curve for molecular dynamics [4]. It can be demonstrated that due to repulsion or attraction, atoms retain a constant relative distance that fluctuates within a given range, and the repulsion shift relative to the equilibration distance (r=1.12σ) is substantially larger than the attractiveness. As a result, the repulsion is positive, while the attraction is negative. thus,

atoms will not converge to a single spot. As a result, equation (4) cannot be directly used to the solution of optimization problems. This equation has been updated to the following as: [8], [4]:

$$F'_{ij}(t) = -\eta(t)\left[2\left(h_{ij}(t)\right)^{13} - \left(h_{ij}(t)\right)^{7}\right] \quad (5)$$

Where the depth function is η(t) that can be used to modify the repulsion or attraction zone, defined as [8], [4]:

$$\eta(t) = \alpha\left(1 - \frac{t-1}{T}\right)^{3} e^{-\frac{20t}{T}} \quad (6)$$

Where the maximum number of iterations is T and a is the depth weight and the function behaviors of F' with different values of η corresponding to the values of h ranging from 0.9 to 2 are depicted in Figure 2.

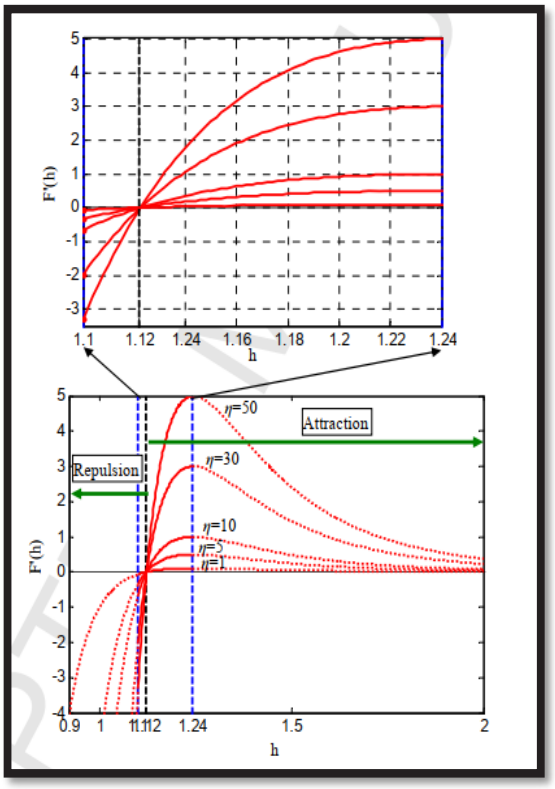

Fig. 2. F' function behavior with various values of η

According to Figure 2, repulsion develops when h values are in a certain range of 0.9 to 1.12, attraction takes place when h values range from "1.12 to 2".The equilibration takes place when h values range from 1.12 to 2. The attraction steadily grows h from equilibration " h=1.12 " to maximum " h=1.24 " and then starts to reduce. If h is greater than or equal to 2, the attraction is about equivalent to zero. As a result, in ASO, to encourage exploration, with a smaller function value, the lower limit of repulsion is set to h= 1.1, while with a bigger function value, the higher limit of attraction is set to h= 1.2. With a larger function value, the upper limit of attraction is set at "h =2.4", therefore h is expressed as [4]:

$$h_{ij}(t) = \begin{cases} h_{min} \text{ if } \frac{r_{ij}(t)}{\sigma(t)} < h_{min} \\ \frac{r_{ij}(t)}{\sigma(t)} \text{ if } h_{min} \leq \frac{r_{ij}(t)}{\sigma(t)} \leq h_{max} \\ h_{max} \text{ if } \frac{r_{ij}(t)}{\sigma(t)} > h_{max} \end{cases} \quad (7)$$

h_{max} and h_{min} are the upper and lower limits of h_{ij} respectively. The length scale σ(t) is described as follows [8], [4]:

$$\sigma(t) = \left\| x_{ij}(t), \frac{\sum_{j \in KBest} x_{ij}(t)}{K(t)} \right\| \quad (8)$$

Where: K_{Best} denotes the subset of K atoms with the best function fitness values [8], [4].

$$\begin{cases} h_{min} = g_0 + g(t) \\ h_{max} = u \end{cases} \quad (9)$$

where u is the upper limit and g is a drift function that aids the algorithm in drifting from exploration to exploitation [8], [4]:

$$g(t) = 0.1 \times \sin\left(\frac{\pi}{2} \times \frac{t}{T}\right) \quad (10)$$

The weighted sum of components of the forces in the d^{th} dimension is now the total force acting on the i^{th} atom from all other atoms. [8], [4]:

$$F_i^d(t) = \sum_{j \in KBest} \text{random}_j F_{ij}^d(t) \quad (11)$$

where random j is a number in the range [0,1] [8], [4].

The geometric restriction plays a crucial role in atom motion in molecular dynamics. For the sake of simplicity, each atom in ASO is assumed to have a covalent link with the best atom, the best atom

exerts a restriction force on each atom. The constraint force operating on the i^{th} atom in the d^{th} dimension is defined as [4]:

$$G_i^d = \lambda(t)\left(x_{\text{best}}^d(t) - x_i^d(t)\right) \tag{12}$$

where, the Lagrangian multiplier is λ(t), which is described as:

$$\lambda(\mathrm{t}) = \beta \mathrm{e}^{-\frac{20\mathrm{t}}{\mathrm{T}}} \tag{13}$$

Where: the multiplier weight is β.

As a result, the i^{th} acceleration of an atom at time t can be expressed as [8]:

$$\begin{aligned} \mathrm{a}_\mathrm{i}^\mathrm{d}(\mathrm{t}) = {} & \frac{\mathrm{F}_\mathrm{i}^\mathrm{d}(\mathrm{t}) + \mathrm{G}_\mathrm{i}^\mathrm{d}(\mathrm{t})}{\mathrm{m}_\mathrm{i}} \alpha \left(1 - - \frac{\mathrm{t}-1}{\mathrm{T}}\right)^3 \mathrm{e}^{\frac{-20\mathrm{t}}{\mathrm{T}}} \\ & * \sum_{\mathrm{j} \in \mathrm{KBest}} \frac{\mathrm{random}_\mathrm{j}\left[2\left(\mathrm{h}_{\mathrm{ij}}(\mathrm{t})\right)^{13} - \left(\mathrm{h}_{\mathrm{ij}}(\mathrm{t})\right)^7\right]}{\mathrm{m}_\mathrm{i}(\mathrm{t})} \\ & \frac{\left(\mathrm{x}_\mathrm{j}^\mathrm{d}(\mathrm{t}) - \mathrm{x}_\mathrm{i}^\mathrm{d}(\mathrm{t})\right)}{\left\|\mathrm{x}_\mathrm{i}(\mathrm{t}), \mathrm{x}_\mathrm{j}(\mathrm{t})\right\|_2} \\ & + \beta \mathrm{e}^{-\frac{20\mathrm{t}}{\mathrm{T}}} \frac{\mathrm{x}_{\mathrm{best}}^\mathrm{d}(\mathrm{t}) - \mathrm{x}_\mathrm{i}^\mathrm{d}(\mathrm{t})}{\mathrm{m}_\mathrm{i}(\mathrm{t})} \end{aligned} \tag{14}$$

At the t^{th} repetition, the mass of the i^{th} atom is $m_i(t)$. It is determined as follows [8]::

$$M_i(t) = e^{-\frac{Fit_i(t) - Fit_{\text{best}}(t)}{Fit_{\text{worst}}(t) - Fit_{\text{best}}(t)}} \tag{15}$$

$$\mathrm{m}_\mathrm{i}(\mathrm{t}) = \frac{\mathrm{M}_\mathrm{i}(\mathrm{t})}{\sum_{\mathrm{j}=1}^{\mathrm{N}} \mathrm{M}_\mathrm{j}(\mathrm{t})} \tag{16}$$

Where: $\mathrm{Fit}_{\text{best}}(\mathrm{t}) = \min_{\mathrm{i}=\{1,2,\ldots,\mathrm{n}\}} \mathrm{Fit}_\mathrm{i}(\mathrm{t})$ and $\mathrm{Fit}_{\text{worst}}(\mathrm{t}) = \max_{\mathrm{i}=\{1,2,\ldots,\mathrm{n}\}} \mathrm{Fit}_\mathrm{i}(\mathrm{t})$

The i^{th} atom's location and velocity at time(t + 1) are given by [8]:

$$v_i^d(t+1) = \text{ random}_i^d v_i^d(t) + a_i^d(t) \tag{17}$$

$$x_i^d(t+1) = x_i^d(t) + v_i^d(t+1) \tag{18}$$

Each atom must communicate with as many atoms as feasible that have a better fitness value than its K neighbors to improve the exploration in the first stage of the ASO algorithm. The atoms must associate with as few atoms with a higher fitness value as feasible as their K neighbors to improve exploitation in the last stage of iterations[4]. The distance ratio r_{ij} to the length scale σ controls

whether Attraction or repulsion is the attraction or repulsion interaction force acting on each atom from its neighbors. The length scale σ reflects the distance between each atom and its K neighbors' average location. As a result, K is a time-dependent function that decreases with the number of repetitions, and K may be determined [4], [8]:

$$K(t) = N - (N-2) \times \sqrt{\frac{t}{T}} \tag{19}$$

4 Simulation Results

TO plan the path of a "mobile robot", the proposed ASO algorithm was implemented utilizing MATLAB R2020a. Experiments were carried out On the platform with Intel® Core™ i7-8550U CPU at 1.99GHz, Windows 10 Home OS. A number of pre-tests were used to identify the parameters for the suggested procedures as in **Table** 1. In order to discover the shortest pathways for free, static and dynamic obstacle environments 5 random points were generated. The maximal number of iterations was 20. To resolve the path planning issue, ASO was proposed and compared with a particle swarm optimization algorithm. The study was testing our proposed ASO in three environments (free, Static & Dynamic obstacles) as in figures3,4,5 & 6. Search space was 200 × 200 grid with three obstacles. The maximal number of iterations was 20. The proposed method was run by taking four cases in each environment as in **Tables** 2,3 & 4. From the obtained result, it can be concluded that the execution time(the time required to travel the robot from the current point to the goal) and the minimum path(minimum cost) in ASO were reduced as compared with PSO algorithms. This demonstrates the Atom Search optimization algorithm's strength.

Table 1. parameters for ASO and PSO

Optimization algorithm	parameters				
	Maximum iteration	alpha(α)	Beta(β)	Limda(λ)	m
ASO	20	20	0.5	1	1
	parameters				
PSO	Maximum iteration	W	C1	C2	Population size
	20	1	1.5	1.5	50

5 conclusion

This work looked at the challenge of mobile robot path planning in a two-dimensional workspace. Atom Search optimization algorithm and Particle Swarm Optimization search methods were proposed for finding the shortest path in the space were employed to select the best path with free

static and dynamic obstacles. Only the path length was used as objective by using Euclidian distance. The method that has been proposed is ASO was tested in three different settings and shown to be capable of determining the best path with minimum time as compared with PSO. In further research, instead of using ASO, the Butterfly algorithm can be used to optimize the robotic path.

Table 2. comparative between ASO and PSO for free obstacles environment

cases	Start point	target	minimum cost (Shortest path in pixels for ASO)	minimum cost (Shortest path in pixels for PSO)	Execution time for ASO (second)	Execution time for PSO (second)
Case1	(20,20)	(180,70)	165	173	36.0142	38.7519
Case2	(20,20)	(180,190)	175	210	41.2211	42.7239
Case3	(20,10)	(137,95)	122	162	25.5928	32.4814
Case4	(20,20)	(30,160)	145	146	29.9424	32.0411

The best path for ASO	The best path for PSO	The cost for ASO	The cost for PSO
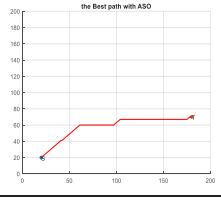	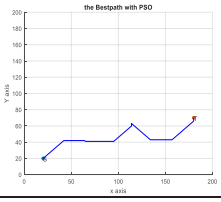	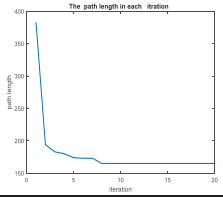	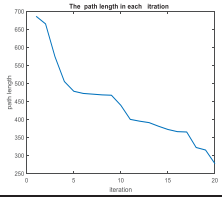
Start point (20,20) &target(180,70)	Start point (20,20) &target(180,70)	cost=165	cost=173
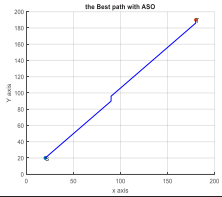	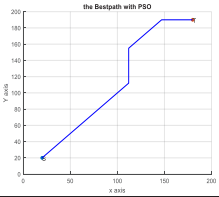	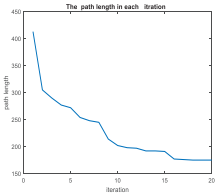	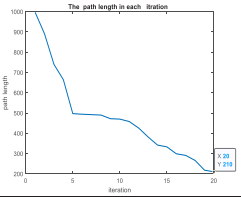
Start point (20,20) &target(180,190)	Start point (20,20) &target(180,190)	cost=175	cost=210
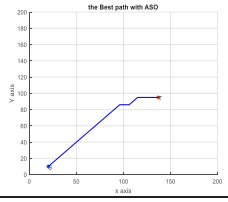	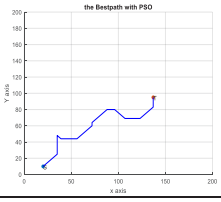	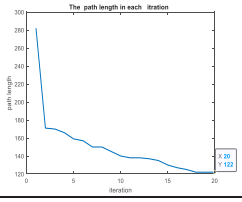	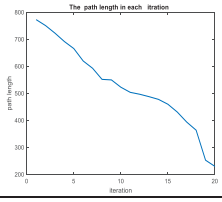
Start point (20,10) &target(137,95)	Start point (20,10) &target(137,95)	cost=122	cost=162

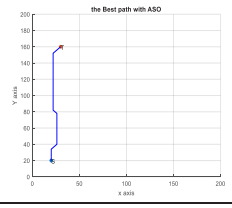	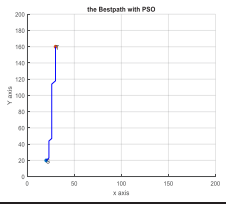	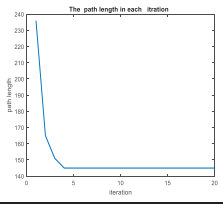	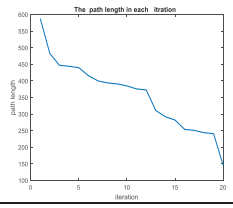
Start point (20,20) &target(30,160)	Start point (20,20) &target(30,160)	cost=145	cost=146

Fig.3. the best path ,the cost in each iteration for ASO & PSO in free obstacles environment

Table 3. comparative between ASO and PSO for static obstacles environment

cases	Start point	target	minimum cost (Shortest path in pixels for ASO)	minimum cost (Shortest path in pixels for PSO)	Execution time for ASO (second)	Execution time for PSO (second)
Case1	(20,20)	(180,70)	166	167	31.367	35.5854
Case2	(20,20)	(180,190)	195	196	36.5991	37.2071
Case3	(20,10)	(137,95)	123	139	23.5234	26.3468
Case4	(20,20)	(30,160)	147	149	27.9884	28.9725

The best path for ASO	The best path for PSO	The cost for ASO	The cost for PSO
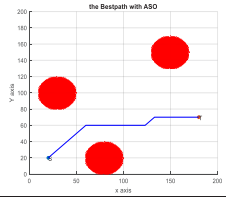	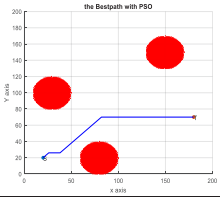	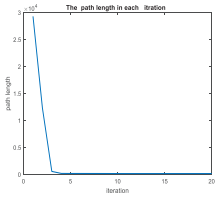	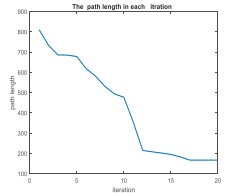
Start point (20,20) &target(180,70)	Start point (20,20) &target(180,70)	cost=166	cost=167
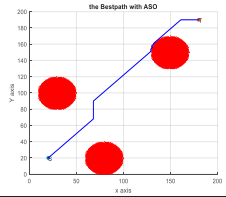	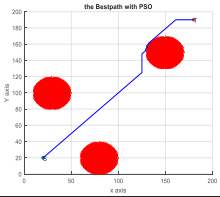	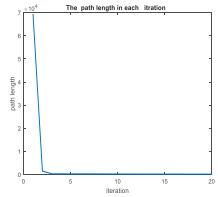	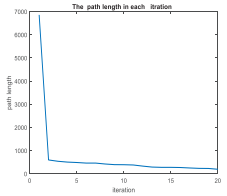
Start point (20,20) &target(180,190)	Start point (20,20) &target(180,190)	cost=195	cost=196

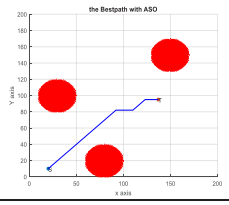	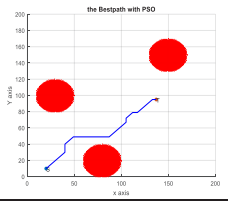	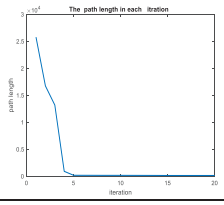	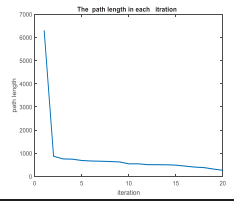
Start point (20,10) &target(137,95)	Start point (20,10) &target(137,95)	cost=123	cost=139
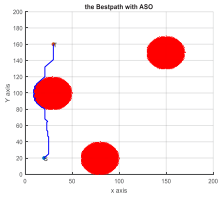	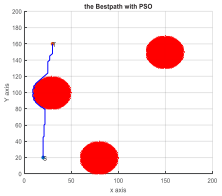	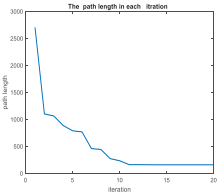	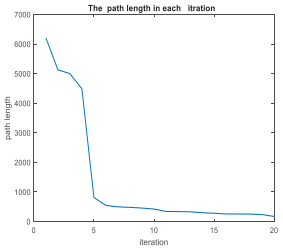
Start point (20,20) &target(30,160)	Start point (20,20) &target(30,160)	cost=147	cost=149

Fig. 4. The best path, the cost in each iteration for ASO & PSO in static obstacles environment

Table 4. comparative between ASO and PSO for dynamic obstacles environmen

cases	Start point	target	minimum cost (Shortest path in pixels for ASO)	minimum cost (Shortest path in pixels for PSO)	Execution time for ASO (second)	Execution time for PSO (second)
Case1	(20,20)	(180,70)	165	169	24.5218	27.9011
Case2	(20,20)	(180,190)	195	268	20.2752	22.4291
Case3	(20,10)	(137,95)	121	161	6.6995	15.7852
Case4	(20,20)	(30,160)	145	151	27.5628	50.9255

The motion of robot using ASO algorithm			
Case1	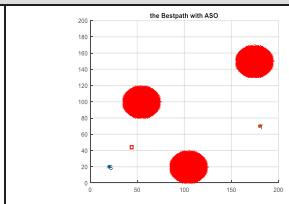	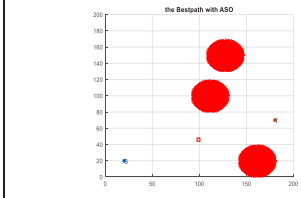	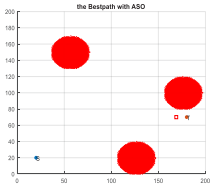
Case2	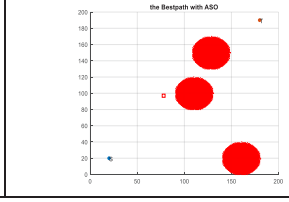	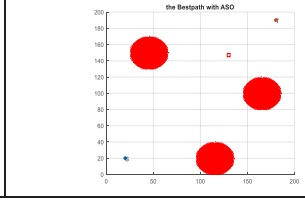	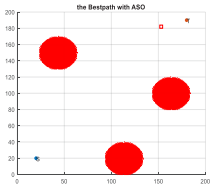

Case3	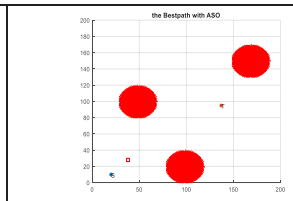	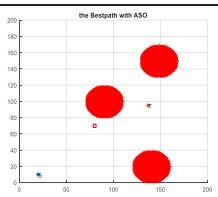	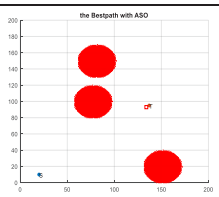
Case4	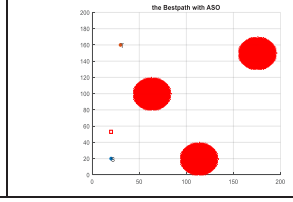	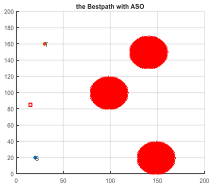	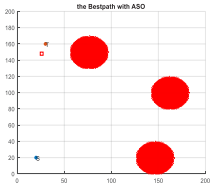

Fig. 5. The robot's motion from start point to end point in each case using ASO

The motion of robot using PSO algorithm			
Case1	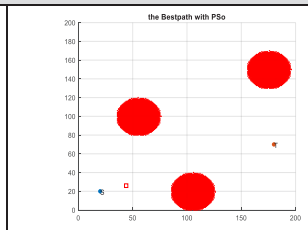	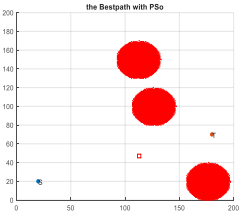	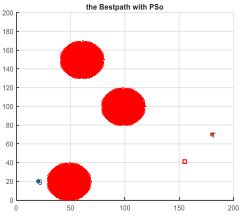
The motion of robot using PSO algorithm			
Case2	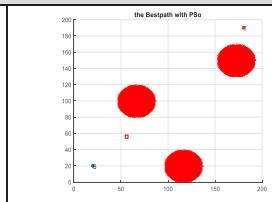	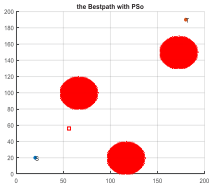	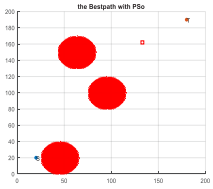
Case3	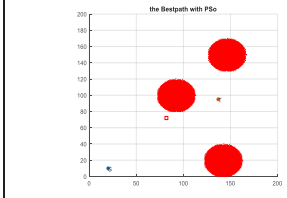	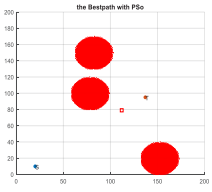	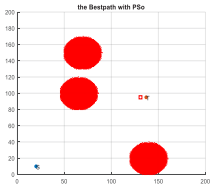

Case4	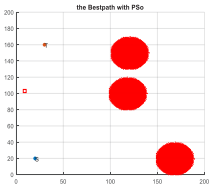	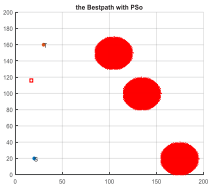	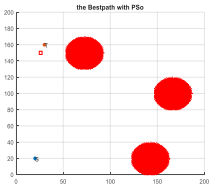

Fig. 6. The robot's motion from start point to end point in each case using PSO

References:

[1] Tuba E, Strumberger I, Zivkovic D, Bacanin N, Tuba M. Mobile Robot Path Planning by Improved Brain Storm Optimization Algorithm. 2018 IEEE Congr Evol Comput CEC 2018 - Proc. 2018; (July): 1–8.

[2] Abed, I. A., Koh, S. P., Sahari, K. S. M., Tiong, S. K., & Yap, D. F. (2012). Comparison between genetic algorithm and electromagnetism-like algorithm for solving inverse kinematics. *World Applied Sciences Journal*, *20*(7), 946-954.

[3] Yüzgeç U, Doğan L. Robot Path Planning using Gray Wolf Optimizer. 2019; (May 2018).

[4] Zhang H, Lin W, Chen A. SS symmetry Path Planning for the Mobile Robot : A Review. 2018;

[5] Tan, J. D., Dahari, M., Koh, S. P., Koay, Y. Y., & Abed, I. A. (2016). An improved electromagnetism-like algorithm for numerical optimization. *Theoretical Computer Science*, *641*, 75-84.

[6] Zhao, W., Wang, L., & Zhang, Z. (2019). A novel atom search optimization for dispersion coefficient estimation in groundwater. *Future Generation Computer Systems*, *91*, 601-610.

[7] Wang Y, Cai F, Wang Y. "Dynamic path planning for mobile robot based on particle swarm optimization Dynamic Path Planning for Mobile Robot based on Particle Swarm Optimization". 2017;020024(August).

[8] Châari I, Koubâa A, Bennaceur H, Trigui S, Al-Shalfan K., SmartPATH: A hybrid ACO-GA algorithm for robot path planning. 2012 IEEE Congr Evol Comput CEC 2012. 2012;(1):10–5.

[9] Ibraheem IK, Ajeil FH, Khan ZH. Path planning of an autonomous mobile robot in a dynamic environment using modified bat swarm optimization. arXiv. 2018; (July).

[9] Ghosh KK, Guha R, Ghosh S, Bera SK, Sarkar R. Atom search optimization with simulated annealing-A hybrid metaheuristic approach for feature selection. arXiv. 2020.

Multi-level Chaos-Shift-Keying for Non-Orthogonal Multiple Access with Physical Layer Security

Walid A. Al-Hussaibi[1], Israa M. Al-Musawi[2], Falah H. Ali[3]
{alhussaibi@stu.edu.iq[1], israa.almusawii@gmail.com[2], f.h.ali@sussex.ac.uk[3]}
{[1,2]BETC, [1]BTI}, Southern Technical University, Basrah, Iraq
[3]Communications Research Group, University of Sussex, Brighton, UK

Abstract. To address the key issue of users' privacy in future wireless communications, this work presents a generalized uplink secure code-domain non-orthogonal multiple access (SCD-NOMA) based on multi-level chaos-shift-keying (MCSK) signalling over Rician propagation environment. To have cost-effective physical layer security (PLS), the proposed scheme is designed by employing chaotic drive systems at the users' side and a chaotic response system at the base station (BS) receiver. The transmitted signals are estimated efficiently at the BS through integrated maximum likelihood (ML) and chaos demodulation techniques. The efficacy of the proposed SCD-NOMA system is validated by intensive simulation results of the realized error rate, connectivity, and security gap, in comparison to the reference systems. Besides, the proposed scheme provides a huge key-space to increase the system's PLS and compact exhaustive brute-force attacks.

Keywords: code-domain NOMA; chaotic signals; physical layer security; CSK; wireless fading channels.

1 Introduction

The rapid advancement in modern technologies has initiated an incredible growth in the number of wirelessly connected devices worldwide. Therefore, new wireless networks like 5G and beyond are required to attain the critical issues of massive connectivity, reliability, security, and affordability [1]-[4]. In the same context, non-orthogonal multiple access (NOMA) is one of the attractive communication techniques that have been designed over the past years to achieve the next-generation targets by investing in power-domain NOMA (PD-NOMA) and code-domain NOMA (CD-NOMA). In such schemes, the connected users' performance outperforms the traditional orthogonal multiple access (OMA) schemes utilizing spectral efficiency and connectivity, however, at the cost of increased co-channel interference [5]-[7].

In wireless networks, the possibility of signal interception from unauthorized receivers is quite high owing to the open transmission nature [8]. Besides, the remarkable increase in the number of served users and related data traffic in the NOMA schemes may result in additional data security leakage [7]-[9]. Consequently, using the common security techniques based on cryptographic methods at the network upper layers becomes ineffective owing to cost, complexity, and power limitations [3], [4], [7]. Thus, physical layer security (PLS) emerges as a cost-effective alternative technique by utilizing the main channel features like noise, interference, diversity, and fading, to expand the realized security gap between the illegal and the legal receiver [8]-[10]. Moreover, PLS may be used jointly with other cryptography-based methods to further enhance the overall system security [4].

IMDC-IST 2021, September 07-09, Sakarya, Turkey
Copyright © 2022 EAI
DOI 10.4108/eai.7-9-2021.2314409

In the literature, many PLS systems have been presented by exploiting the properties of the chaotic signal in chaos-based secure communication (CBSC) like its wideband spectrum, unpredictable operation performance, and its high sensitivity to the changes in initial conditions (ICs) [7], [9], [11]-[16]. Moreover, the parameters of the chaotic system can provide an enormous key-space that remarkably enhances the system security against eavesdroppers brute-force attacks [14]. For example, various CBSC systems based on NOMA approaches have been studied such as [9], [16] over Gaussian channels and [6], [12], [17] over fading channels with multiple-input multiple-output (MIMO) technique integrated with orthogonal frequency division multiplexing (OFDM) method [11].

The realized security gap based on the performance of bit-error-rate (BER) emerges as an efficient and practical PLS measure to evaluate the achieved PLS instead of the information theoretic-based measures such as the secrecy throughput, secrecy outage probability, and secrecy rate [3], [9]-[14], [18]. Secure communications may be achieved by expanding the realized gap between the BER performance of legal and illegitimate receivers [17]-[20]. Other important metrics are considered also like the key-space which is employed to assess the computational efforts required by an external eavesdropper to guess the secret keys correctly. Moreover, the key mismatch between the transmitter and the receiver shows the capability of the illegal receiver to correctly guess the secret keys using extensive search computations [7], [12]-[14].

The major contributions for this paper may be highlighted as follows:

1) A generalized uplink multiuser communications system design of secure CD-NOMA (SCD-NOMA) is presented over the environment of a realistic channel. Composite large-scale propagation and small-scale Rician fading are adopted rather than the simple Gaussian channel in [9] and [16] or the small-scale Rayleigh fading in [3], [12], and [17].
2) Multi-level chaos-shift-keying (MCSK) modulators and demodulators are used at the communication ends rather than the binary CSK in [3], [12], [16], and [17] to create an effective PLS with a large key-space advantage and higher spectral efficiency. At the receiving base station (BS), maximum likelihood (ML) and chaotic demodulation are used together for multiuser detection (MUD).
3) The realized results of the proposed SCD-NOMA are verified and compared with the reference schemes, by extensive simulations for security gap, BER, key-space metrics, and user connectivity. Moreover, the OMA gains like MIMO [8] and OFDM [11] are excluded to have a realistic performance evaluation. The realized results utilizing multiple system configurations, ICs, and chaotic sequence lengths, are attractive and show many valuable tradeoffs.

The rest of this paper is arranged as follows. In Section 2, a concise chaotic communications technical background is discussed. Section 3 shows the system design of the proposed SCD-NOMA. The designed system results and simulations are highlighted in Section 4, meanwhile, conclusions are presented in Section 5.

2 Chaotic Communications

Various modulation methods are used in CBSC such as the conventional CSK technique [12]. In this method, the involved chaotic signals can be generated from different mathematical models that reveal a nonlinear dynamical behaviour like the two-dimensional equations of the discrete-time Henon chaotic system (HCS) [6]:

$$x(n+1) = y(n) + 1 - ax^2(n)$$
$$y(n+1) = bx(n) \tag{1}$$

where n is the time instance for the chaotic attractor, $a = 1.4$, and $b = 0.3$. By using simple hardware electronic circuits or different software tools (e.g. MATLAB), the chaotic signals (x and y) of HCS can be found with high sensitivity to ICs ($\approx 10^{-15}$/state).

In CBSCs, the data can be encrypted and sent to the receiving end with high secrecy levels by using the attractive characteristics of chaotic signals. In this case, at the receiver side, it is hard to correctly decode the transmitted signals without previously knowing the parameters of the chaotic system such as the ICs, code length (β), chaotic sequence length ($\mathcal{L}$), number of chaotic states ($\mathcal{D}$), and modulation level (M). The integration of those parameters can form an essential robust key-space set $\mathcal{S} = \{\text{ICs}, \beta, \mathcal{L}, \mathcal{D}, M\}$. As a result, potential eavesdroppers using brute-force attacks will not be able to easily discover the transmitted signals owing to the need for exhaustive efforts of computations (more than 2^{100}) to scan and break the key-space $\mathcal{S}$ [13], [14]. Hence, effective PLS can be granted in CBSCs since only planned receivers with the exact system parameters are capable of decoding the transmitted data accurately.

3 System Design of SCD-NOMA

Consider a multiuser SCD-NOMA with MCSK modulation/demodulation as given in Fig. 1, in a single-cell cellular system. The proposed scheme consists of K single-antenna users communicating simultaneously with a single-antenna BS over a wireless fading propagation channel. For the MCSK units at the user's end and BS receiver, an accurate drive-response synchronization mechanism is assumed [15]. In addition, the BS is assumed to have complete channel state information (CSI) to perform efficient equal power control and MUD.

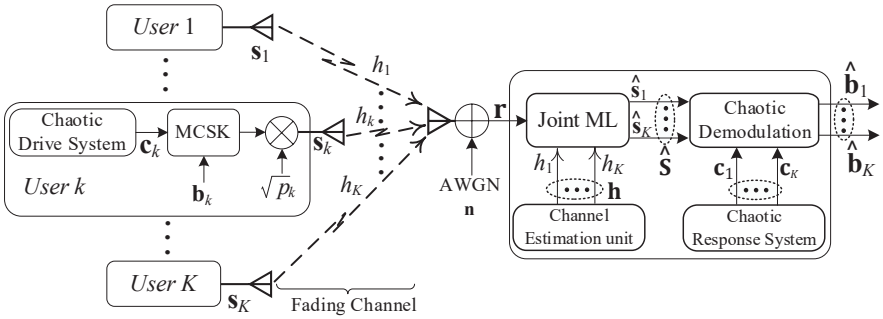

Fig. 1. General system design of SCD-NOMA over wireless fading channel environment.

3.1 Signal Model

For the considered SCD-NOMA scheme, the digital data symbol of user k is shown as $\mathbf{b}_k = [b_{k,1} \dots b_{k,U}]$ with $U = \log_2(M)$ binary bits. It has an alphabet set $\mathbf{B}_k = \left\{\mathbf{b}_k^{(1)}, \dots, \mathbf{b}_k^{(i)}, \dots, \mathbf{b}_k^{(M)}\right\}$

of size M, where $\mathbf{b}_k^{(i)} = \left[b_{k,1}^{(i)} \dots b_{k,U}^{(i)}\right]$ denotes the i^{th} possible data symbol. For each user k, a certain chaotic codebook is assigned as $\mathbf{C}_k = \left\{\mathbf{c}_k^{(1)}, \dots, \mathbf{c}_k^{(i)}, \dots, \mathbf{c}_k^{(M)}\right\}$, where $\mathbf{c}_k^{(i)} = \left[c_{k,1}^{(i)} \dots c_{k,\beta}^{(i)}\right]$ and $c_{k,j}^{(i)}$ is the j^{th} chip of i^{th} chaotic code of length $\beta \ll \mathcal{L}$. The active users utilize MCSK as $\mathbf{b}_k^{(i)} \rightarrow \mathbf{c}_k^{(i)}$ for $k = 1, \dots, K$ and $i = 1, \dots, M$. Throughout this work, is presumed that $T_{\mathbf{b}}$ the symbol duration is β times the chip duration T_c. Subsequently, user k transmitted signal is given with equal power allocation p_k as $\mathbf{s}_k = \left[s_{k,1} \dots s_{k,\beta}\right] \in \mathcal{R}^{1\times\beta}$ which represents one of the possible elements from the overall set $\mathbf{S}_k = \left\{\mathbf{s}_k^{(1)}, \dots, \mathbf{s}_k^{(i)}, \dots, \mathbf{s}_k^{(M)}\right\}$. The received composite signal at the BS $\mathbf{r} = \left[r_1 \dots r_\beta\right] \in \mathcal{C}^{1\times\beta}$ is modelled by

$$\mathbf{r} = \sum_{k=1}^{K} h_k \mathbf{s}_k + \mathbf{n} \tag{2}$$

where $\mathbf{n} = \left[n_1 \dots n_\beta\right] \in \mathcal{C}^{1\times\beta}$ stands for the vector of the AWGN with zero-mean and σ_n^2-variance coefficient, and h_k is the fading channel of user k given as [21],

$$h_k = \sqrt{\xi_k}\left[\sqrt{\frac{\mathcal{K}}{\mathcal{K}+1}}\,\bar{g}_k + \sqrt{\frac{1}{\mathcal{K}+1}}\,\breve{g}_k\right] \tag{3}$$

where $\bar{g}_k$ is a complex-valued line-of-site (LOS) coefficient, $\breve{g}_k$ is the scattered fading of zero-mean unit-variance elements and it is presumed to be fixed over the symbol duration $T_{\mathbf{b}}$, $\mathcal{K}$ is the Rician fading coefficient, and $\xi_k = \ell_k^{-\vartheta}$ stands for large-scale path loss, ℓ_k is the distance of user k from the BS, and ϑ denotes the path loss exponent.

3.2 Receiver Design

Signal estimation is carried out jointly at the BS using the optimal ML receiver and chaotic demodulator. For the considered MCSK, there is a set of $\Omega = M^K$ probable elements for transmitted signals as $\mathbb{S} = \left\{\mathbf{S}^{(1)}, \dots, \mathbf{S}^{(l)}, \dots, \mathbf{S}^{(\Omega)}\right\}$, where $\mathbf{S}^{(l)} = \left[\mathbf{s}_1^{(l)} \dots \mathbf{s}_k^{(l)} \dots \mathbf{s}_K^{(l)}\right]^{\mathrm{T}}$, and $\mathbf{s}_k^{(l)}$ is the l^{th} likely transmitted signal vector from user k. Therefore, MUD can be performed as

$$\hat{\mathbf{S}} = [\hat{\mathbf{s}}_1 \dots \hat{\mathbf{s}}_k \dots \hat{\mathbf{s}}_K]^{\mathrm{T}} = \arg\min_{\mathbf{S}^{(l)}\in\mathbb{S}} \left\|\mathbf{r} - \mathbf{h}\mathbf{S}^{(l)}\right\|^2 \tag{4}$$

where $\|.\|$ represents the Euclidean vector norm. The output of estimated signals can be sent then to the chaotic modulator to find the detected data as $\hat{\mathbf{b}}_k = \left[\hat{b}_{k,1} \dots \hat{b}_{k,U}\right]$ for $k = 1, \dots, K$.

4 Results and Security Evaluations

In this section, simulation experiments are accomplished to demonstrate the SCD-NOMA system performance by terms of the realized security gap, BER, and the users' connectivity for any considered OMA resource dimension. The effects of parameter β and mismatch of the secret keys on the BER performance are also studied. The Key-space analysis is shown to validate the SCD-NOMA improved resistance to fight the brute-force attacks from potential unauthorized receiver devices. The considered parameters for simulations are: cellular network radius of

300 m; $\vartheta = 4$; $K = 2, 3,$ and 4; $\mathcal{L} = 10^4$; $M = 4$; $\beta = 50$; and the ICs utilized in the chaotic drive/response systems are $\{x_0 = 0.0, y_0 = 0.0\}$. The legal BS employs perfect ICs meanwhile the illegitimate receiver device owns inaccurate secret keys (ICs) of 10^{-15} accuracy. The BER outcomes are compared for fairness with the reference system of quadrature phase-shift keying NOMA (QPSK-NOMA) and averaged over 10^6 channels.

4.1 BER Performance and Achieved Security Gap

In **Figure 2**, the BER curves of the 2-user scheme as a function of the signal-to-noise ratio (SNR) are given considering different Rician factors. The presented results of all scenarios show that the legal receiving end achieves a substantial performance gain for all connected users in comparison to the 2-user QPSK-NOMA reference owing to the extra code diversity. For example, at BER target of 10^{-5} the BERs of SCD-NOMA outperform the references by 21 dB, 27.5 dB, and 26 dB when $\mathcal{K} = 0$, $\mathcal{K}$ =4, and $\mathcal{K}$ =8, respectively. Moreover, it is clear that with the increase of $\mathcal{K}$ from $\mathcal{K} = 0$ to $\mathcal{K} = 8$, the attained security gap also significantly increases. It is noted that the unauthorized receiver BERs reveals an obvious error floor due to imperfect ICs.

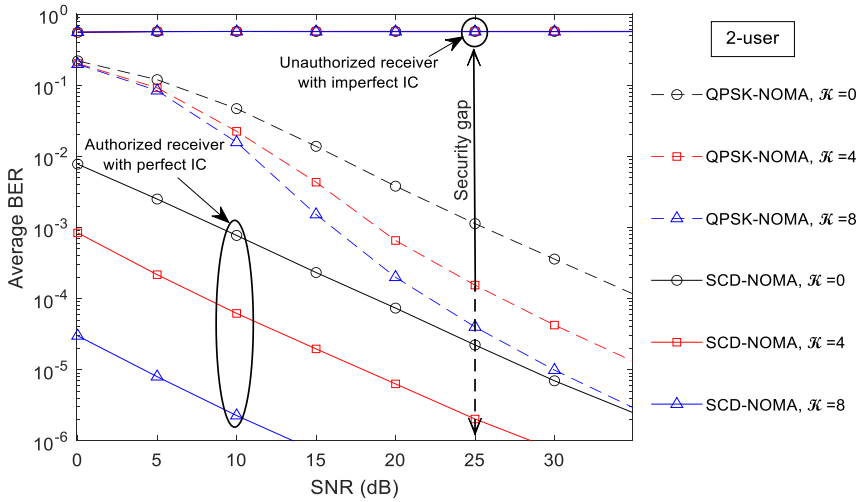

Fig. 2. Average BER of 2-user SCD-NOMA using $\beta = 50$ and different Rician factors of $\mathcal{K} = 0, \mathcal{K} = 4$, and $\mathcal{K} = 8$.

Figures 3 and **4** show the BERs of 3 and 4-user schemes, respectively as a function of SNR considering different Rician factors. The BERs of the authorized receiver for all Rician factor scenarios display a significant performance compared to the benchmark references over the entire SNR range. Moreover, the best performance among all considered scenarios with a remarkable security gap is noticed when $\mathcal{K} = 0$. The BERs of the illegal receiver for those cases also achieve an error floor over the whole range of SNR. A summary for the attained gains in dB is presented in **Table 1** considering target BER of 10^{-5}. As it can be seen the 4-user realizes a huge dB gain and for all Rician factors compared to the reference systems.

Table 1. SNR gain for the considered scenarios at target BER of 10^{-5} compared with the considered reference systems.

Rician Factor	2-user scenario	3-user scenario	4-user scenario
$\mathcal{K} = 0$	21 dB	36.2 dB	45.7 dB
$\mathcal{K} = 4$	27.5 dB	28.4 dB	44.6 dB
$\mathcal{K} = 8$	26 dB	31 dB	45.8 dB

4.2 Effect of code length and User Connectivity

Figure 5, shows the BER curves of 2, 3, and 4-user schemes as a function of the code length β for two SNR values of 15 dB, 25 dB, and $\mathcal{K} = 0$ Rician factor. It is noticed that the increased values of β have a direct influence on enhancing the BER performance and the level of PLS, however, at the cost of an increased receiver complexity. Moreover, the increased level of β has no impact on data rate degrading compared to the OMA systems since $T_{\mathbf{b}} = \beta T_c$. On the other hand, the unauthorized receiver BERs with imperfect ICs also reveal an obvious error floor over the entire range of β. The obtained results are based on a very tiny difference in the ICs of about 10^{-15}. So, the choice of the appropriate parameters for SCD-NOMA allows cost-effective information security with robust error rate performance.

The user connectivity effect on the performance of the SCD-NOMA system can also be noticed from **Figure 5** where the BER performance shows very close results as K increased from 2 to 4. This is a remarkable finding since the BERs are demonstrating high robustness to the number of users increase in contrast to the considered reference of QPSK-NOMA. Therefore, the nonorthogonal users who can be served reliably in this scenario are only limited by the target BER. However, the complexity of BS receiver will be increased as K increased resulting in ML search effort of $\mathcal{O}(M^K)$. This provides a significant tradeoff between the achieved BER performance, user connectivity, and the required SNRs.

4.3 Effect of Secret Key Mismatch

In **Figure 6,** the secret key mismatch effect on the BER system performance is illustrated as a function of the sensitivity to ICs (10^{-x}) considering 2, 3, and 4-user schemes with $\mathcal{K} = 0$ and two SNRs values of 15 dB and 25 dB. It may be noticed that all configurations' signals reveal a clear error floor up to 10^{-16} accuracy. Moreover, the BER performance of all served users can achieve a reliable link at BER target of 10^{-3} when ultra-high sensitivity levels of $\leq 10^{-16}$ is used.

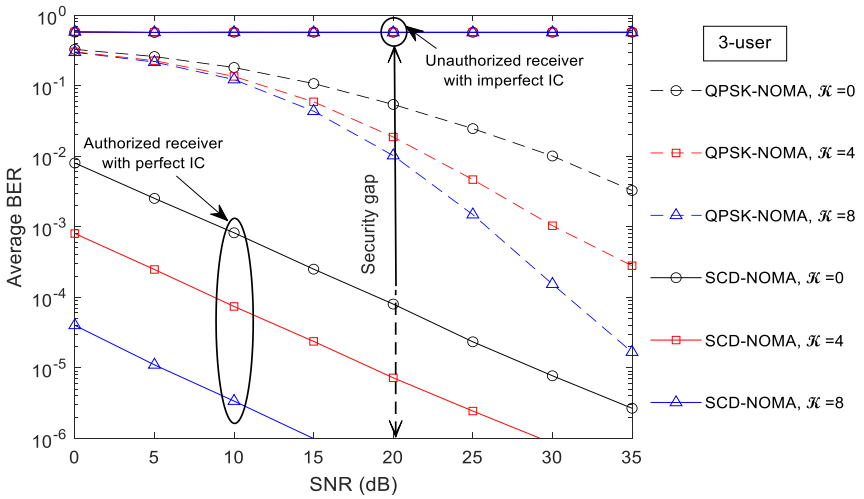

Fig. 3. Average BER of 3-user SCD-NOMA using $\beta = 50$ and different Rician factors of $\mathcal{K} = 0, \mathcal{K} = 4$, and $\mathcal{K} = 8$.

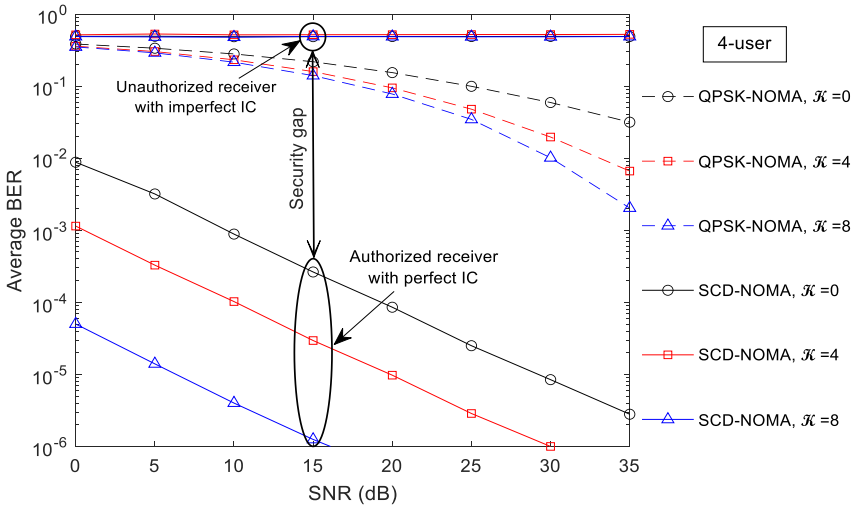

Fig. 4. Average BER of 4-user SCD-NOMA using $\beta = 50$ and different Rician factors of $\mathcal{K} = 0, \mathcal{K} = 4$, and $\mathcal{K} = 8$.

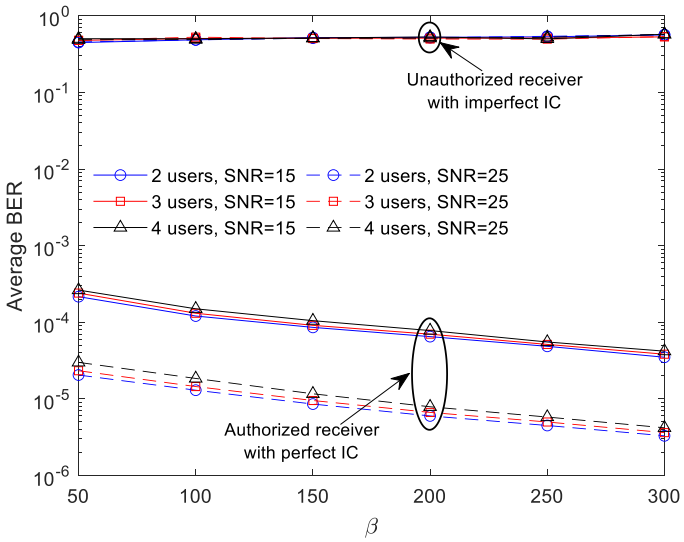

Fig. 5. Average BER performance of 2, 3, and 4-user SCD-NOMA as a function of β using $\mathcal{K} = 0$.

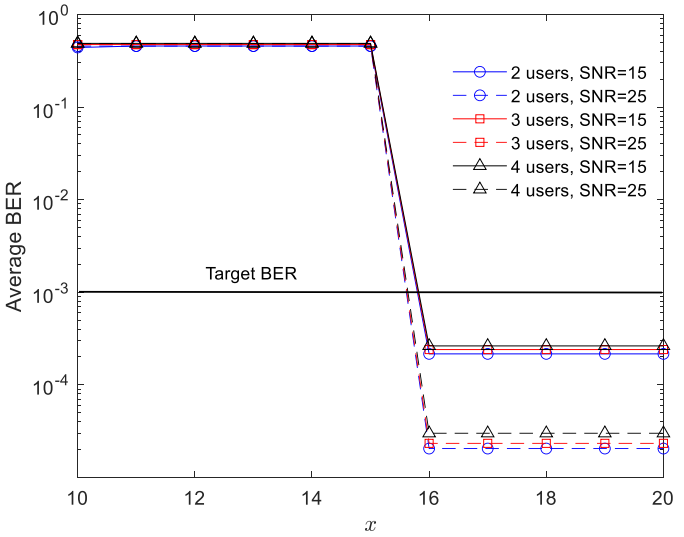

Fig. 6. Average BER performance of 2, 3, and 4-user SCD-NOMA as a function of the sensitivity to ICs (10^{-x}) using $\beta = 50$ and Rician factor of $\mathcal{K} = 0$.

4.4 Key-Space

The SCD-NOMA system's robustness against possible brute-force attacks may be estimated according to the attained key-space. Many essential parameters are considered in the designed system that can efficiently provide powerful secret keys with a key-space set $\mathcal{S} = \{K, \beta, \mathcal{L}, \mathcal{D}, M, \text{ICs}\}$. For example in HCS, the employed ICs with $10^{-16}/\text{state}$ accuracy will attain a key-space of $10^{2\times16} = 10^{32}$. Moreover, when any of the K-served users employ different chaotic codes of length β from any $\mathcal{D}$-state chaotic system, the realized key-space will be increased to $K \times M \times \beta \times \mathcal{L} \times \mathcal{D}$ times. For example, the key-space for PLS will be of order $\mathcal{O}(10^8 \times 10^{32} = 10^{40}) \approx \mathcal{O}(2^{133})$, which is larger than the bound limit of 2^{100} in [14].

5 Conclusion

An efficient uplink system design for SCD-NOMA is presented in this work over Rician channel environments with large-scale and small-scale fading. At the users' sides, a general MCSK system has been used while ML and chaos demodulation have been employed for MUD at the receiving BS. The realized security gap and BER result considering different SCD-NOMA scenarios have confirmed the effectiveness of the proposed scheme in comparison to the QPSK-NOMA reference with many appealing tradeoffs. Furthermore, a massive key-space of order $\mathcal{O}(2^{133})$ is attained to fight the intensive brute-force attacks. The designed system robustness may lead to possible future integration with the existing OMA techniques for modern secure wireless communications.

References

[1] Makki B., Chitti K., Behravan A., Alouini M.S.: A Survey of NOMA: Current Status and Open Research Challenges. IEEE Open Journal of Communications Society. Vol. 1, 179-189 (2020)

[2] Khan L., Yaqoob I., Imran M., Han Z., Hong C.: 6G Wireless Systems: A Vision, Architectural Elements, and Future Directions. IEEE Access. Vol. 8, 147029-147044 (2020)

[3]Almusawi I., Al-Hussaibi W., Tahir Y.: Wireless Nonorthogonal Chaotic Communications: Opportunities, Challenges, and Future Directions. IMDC-SDSP. Antalya, Turkey (2020)

[4] Hamamreh J., Furqan H., Arslan H.: Classifications and Applications of Physical Layer Security Techniques for Confidentiality: A Comprehensive Survey. IEEE Communications Surveys & Tutorials. Vol. 21, 2, 1773-1828 (2019)

[5] Islam S., Avazov N., Dobre O., Kwak K.: Power-Domain Non-Orthogonal Multiple Access (NOMA) in 5G Systems: Potentials and Challenges. IEEE Communications Surveys & Tutorials. Vol. 19, 2, 721-742 (2017)

[6] Almusawi I., Al-Hussaibi W., Tahir Y.: Chaos-Based NOMA for Secure Wireless Communications over Rayleigh Fading Channels. IMDC-SDSP. Antalya, Turkey (2020)

[7] Al-Musawi I., Al-Hussaibi W., Tahir Y. H., Ali F.: Chaos-Based Physical Layer Security in NOMA Networks over Rician fading Channels. Accepted in IEEE ICC'2021. Canada, (2021)

[8] Xiao K., Gong L., Kadoch M.: Opportunistic Multicast NOMA with Security Concerns in a 5G Massive MIMO System. IEEE Communications Magazine. Vol. 56, 3, 91-95 (2018)

[9] Okamoto E., Horiike N., Yamamoto T.: Sparse chaos code multiple access scheme achieving larger capacity and physical layer security. 2017 20th International Symposium on Wireless Personal Multimedia Communications (WPMC). 604-610, (2017)

[10] Cao K., Wang B., Ding H., Lv L., Tian J., Gong F.: On the Security Enhancement of Uplink NOMA Systems With Jammer Selection. IEEE Trans. Commun. Vol. 68, 9, 5747-5763 (2020)

[11] Masuda Y., Okamoto E., Yamamoto T.: Low Complexity Decoding of Downlink Chaos NOMA Scheme with Physical Layer Security. 2020 IEEE 17th Annual Consumer Communications & Networking Conference (CCNC). 1-6, Las Vegas, NV, USA (2020)
[12] Al-Musawi I., Al-Hussaibi W., Tahir Y. H., Ali F.: Chaos-Based Secure Power-Domain NOMA for Wireless Applications. 2020 23rd International Symposium on Wireless Personal Multimedia Communications (WPMC). 1-6, Okayama, Japan (2020)
[13]Elfiqi A., Khallaf H., Hegazy S., Elsonbaty A., Shalaby H., Obayya S.: Chaotic Polarization-Assisted *L*DPSK-MPPM Modulation for Free-Space Optical Communications. IEEE Transactions on Wireless Communications. Vol. 18, 9, 4225-4237 (2019)
[14] Bi M., Fu X., Zhou X., Zhang L., Yang G., Yang X., Xiao S., Hu W.: A Key Space Enhanced Chaotic Encryption Scheme for Physical Layer Security in OFDM-PON. IEEE Photonics Journal. Vol. 9, 1, 1-10 (2017)
[15] Al-Hussaibi W.: Effect of filtering on the synchronization and performance of chaos-based secure communication over Rayleigh fading channel. Communications in Nonlinear Science and Numerical Simulation. Vol. 26, 1-3, 87-97 (2015)
[16] Tam W., Lau F., Tse C.: Analysis of bit error rates for multiple access CSK and DCSK communication systems. IEEE Transactions on Circuits and Systems I: Fundamental Theory and Applications. Vol. 50, 5, 702-707 (2003)
[17]Lau Y., Jusak J., Hussain Z.: Blind Adaptive Multiuser Detection for Chaos CDMA Communication. IEEE TENCON 2005. 1-5, Melbourne, Australia (2005)
[18] Hamamreh J., Basar E., Arslan H.: OFDM-Subcarrier Index Selection for Enhancing Security and Reliability of 5G URLLC Services. IEEE Access. Vol. 5, 25863-25875 (2017)
[19] Hamamreh J., Arslan H.: Secure Orthogonal Transform Division Multiplexing (OTDM) Waveform for 5G and Beyond. IEEE Communications Letters. Vol. 21, 5, 1191-1194 (2017)
[20] Christopher R., Borah D.: Physical Layer Security for Weak User in MISO NOMA Using Directional Modulation (NOMAD). IEEE Communications Letters. Vol. 24, 5, 956-960 (2020)
[21] Sanguinetti L., Kammoun A., Debbah M.: Theoretical Performance Limits of Massive MIMO With Uncorrelated Rician Fading Channels. IEEE Trans. Commun. Vol. 67, 3, 1939-1955 (2019)

The Prevalence of Cryptosporidium in rivers water in Basra Province

Mahmoud S. Thamer[1], Maitham H. Shanoot[2], Wathiq A. Al-Rmadhan[3]
{mahmood.Thamir@stu.edu.iq[1], maitham.altai@stu.edu.iq[2], wathiq.alrmadhan@stu.edu.iq[3]}

Technical Institute, Environmental Pollution Research, Southern Technical University, Basra, Iraq[1,2,3]

Abstract. The study included testing 300 liters of water from five rivers in Basra from December 2012 to November 2013 for detection of *Cryptosporidium spp* oocysts in rivers water (Al-Ashar, Al-Ribat, Al-khandiq, Alkhora and Shatt Al-Arab), each sample was concentrated and Stained with A modified Zheil-Nielson. The results revealed that the prevalence of *Cryptosporidium* oocysts was (13.7%). The percentages of prevalence with Cryptosporidium were in high rate in Al-khandiq river (6.41%) while the low rates were in Al-Ribat river (2.42%). This first study shows the occurrence of Cryptosporidium oocysts in rivers in Basra Province.

Keywords: Cryptosporidium, Rivers Basra.

1 Introduction

Within the past decades, the epidemiology of protozoan waterborne diseases has changed. There has been an upsurge in the incidence of waterborne outbreaks, sometimes known as cholera outbreaks. This is not only to increased susceptibility to diseases but also to the emergence of newly recognized waterborne parasites [5, 9]. Outbreaks caused by drinking water were attributed to several factors; contamination of the water source by heavy rainfall, snow melts, or agricultural runoffs which wash parasites from land areas into surface water, and contamination of water wells and canals by soil or by dead animal's carcasses thrown into them [10]. Cryptosporidium sp. is a worldwide infection that is expected to be more prevalent in developing nations, particularly among youngsters [4]. Insects play a crucial role in Oocyst transmission through a variety of pathways, including direct contact with infected people or animals, consumption of contaminated food (foodborne transmission), and water (waterborne transmission) [2]. Exoskeletons and digestive tracts of house flies, cockroaches, beetles, and synanthropic flies can all spread oocysts [3]. Numerous studies show that polluted water is a significant risk factor for cryptosporidiosis. Cryptosporidiosis accounts for up to 15% of gastrointestinal illnesses among children in impoverished countries, with seroprevalence rates ranging from 25% to 35 percent [8]. The goal of this study was to find out how common Cryptosporidium spp. were in some river resources.

IMDC-IST 2021, September 07-09, Sakarya, Turkey
Copyright © 2022 EAI
DOI 10.4108/eai.7-9-2021.2315643

2 Materials and Methods

2.1 Samples Water for Test

Water samples were taken in Basra province from December 2012 to November 2013. A total of 300 litters of water samples were collected from rivers (Al-Ashar, Al-Ribat, Al-khandiq, Al-khora, and Shatt Al-Arab) and placed in polyethylene containers, which were then delivered to the parasitological laboratory at the university of Basra's college of education. The water of the river was collected from the surface twenty monthly samples were taken from each type of river.

2.2 Oocyst Detection

To detect Cryptosporidium oocysts, a modified Zehil Neelson stain method was used. Water samples were centrifuged, and a drop was taken from each deposit with a Pasture pipette and smeared on a glass slide. The smears were then fixed transiently over a flame and stained with a strong carbol fuchsin solution for 5 minutes. The slide was heated until steam formed, but not to the point of boiling, and an extra stain was applied if the slide became dry. The smear was stained, then washed under running tap water for 1-2 minutes before being decolorized in 5% sulphuric acid for 30 seconds. The smears were rinsed in tap water for 1-2 minutes before being counterstained for 1 minute with 3 percent methylene blue stain. Finally, the smears were rinsed in tap water, air-dried, and inspected microscopically for Cryptosporidium oocysts under oil immersion (100). The following formula was used to compute the percentage of contaminated samples:

$$\text{Percentage of infected samples} = \frac{\text{Number of infected samples}}{\text{Total number of samples}} \text{ x } 100 \quad (1)$$

2.3 Statistical Analysis

After data cleaning, the data was transferred to a Microsoft Excel Spreadsheet for statistical analysis, and then into the SPSS (Statistical Package for the Social Sciences version 15.) package software application. For all variables, descriptive statistics (%) were performed, as well as analytical statistics to determine the relationships between the variables. Chi-square statistical tests were used to determine the relationship between variables.

3 Results

As shown in Figures 1 and 2, and Table 1, Cryptosporidium oocysts were identified in 37 of 300 litters of water samples, for a total prevalence of 31.25 percent.

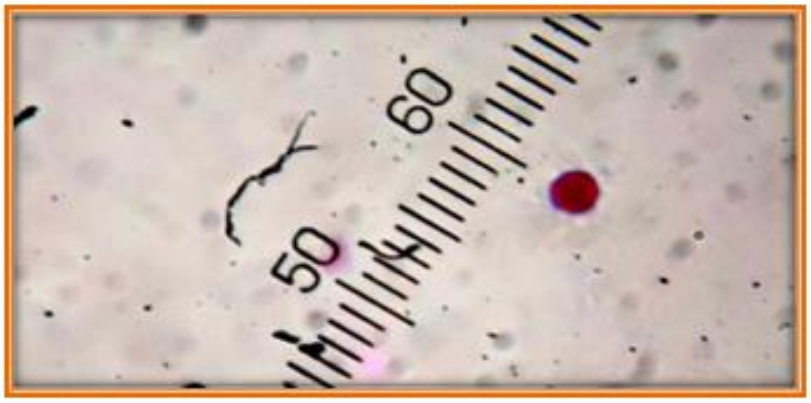

Fig 1: Zeihl Neelsen modified staining of cryptosporidium oocysts at 100X.

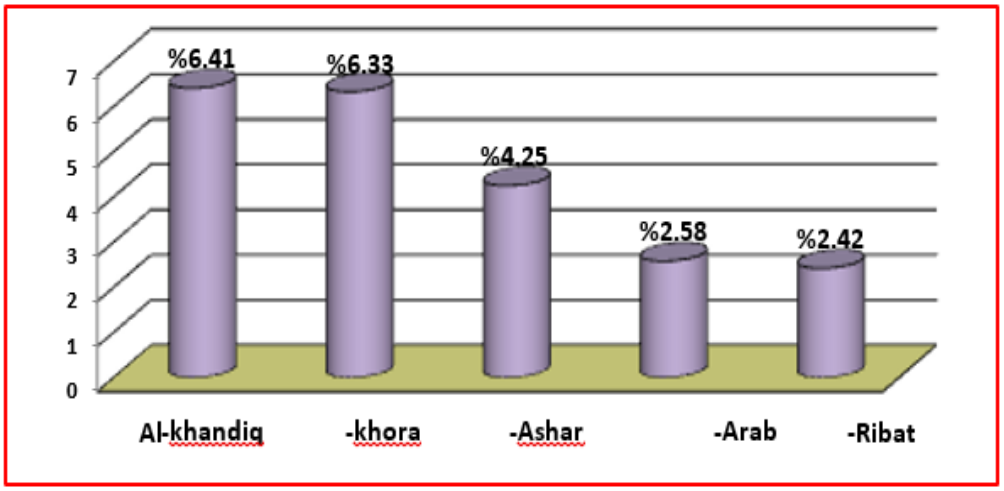

Fig 2: Prevalence of Cryptosporidium oocysts in some rivers water.

Table 1: Cryptosporidium's Overall Prevalence.

Name of Parasite	No. of Examined samples / L	No. of infected samples	Average oocyst /L	Percentage of infected samples
Cryptosporidium	300	37	4.4	13.7%

4 Discussion

Cryptosporidiosis is one of the most common diarrheal disorders caused by protozoan parasites, and it is a serious public health concern globally [7], however epidemiological research for this parasite are few in Iraq [1]. The importance of water and food in the spread of this disease is now widely acknowledged; water is likely to be the most common pathway for large-scale outbreaks of the disease, as a result of contamination of either raw or processed water [6].

In this study, we found that from (300) L water samples examined (37) L were positive for oocyst of *Cryptosporidium* with the rate of (13.7%), this result agrees with [5] who found the parasite in water samples collected from (Al-Ashar, Al-Ribat, Al-khandiq, Al-khora, and Shatt AlArab) in Basra province which is in access of animals and contamination those rivers with faecal materials which come from sewage water, our result disagrees with (Ali, 1998) he did not find the oocyst of the parasite in lake water in Basra province this might be due to the different source of study be carried out on lake water from housing and animal treading.

The present study revealed that no significant difference between the five rivers although the high rate was recorded in Al-khandiq river (6.41%), while the low rate was recorded in Al-Ribat river (2.42%).

References

1. Al-Baytee, A. J.; Jawad, S. Q. and Mehdi, H. S. (2012). Prevalence of Cryptosporidium oocysts in different types of water in Al-Mansoria diala Province. J. Al-Nahrain Univ., 1(15): 103-107.
2. Ali, N. H. (1998). Prevalence of Cryptosporidiosis with zoonotic aspect., M.Sc.
3. Thesis, Coll. Med. Univ. Basrah.
4. Al-Shamiri , A.H.; Al- Zubairy, A.H.; Al-Mamari, R. F.(2010). The Prevalence of Cryptosporidium spp. in Children, TaizDistrict, Yemen. Iranian, J .Parasitol: Vol. 5(2), PP. 26-32.
5. Collins, P.A; Wright, M.S. (1997). Emerging intestinal protozoa: A diagnostic dilemma. Clin Lab Sci, 10(5):273-8.
6. Hvnter, P. R. and Thompson, R.C. (2005). "The zoonotic transmission of Giardia and Cryptosporidium". Int. J. Parasitol.; 35: 1181-1190.
7. Johason, D. W; Pieniuazek, N.J.; Griffin, D.W.; Mispner, L. and Rose, J. B. (1995). "Development of a PCR protocol for sensitive detection of Cryptosporidium oocysts in water samples". App. Environ. Microbiol. 61; 3849-3855.
8. Juranek , D. D.(2000). Cryptosporidiosis. In: Hunter's Trop. Med. and Emerging Infectious Disease. Strickland, G. Thimas (Editor) 8th ed. WB Saunders Company Ltd. London, P. 594 - 600.
9. Leclerc, H.; Schwartzbrod, L.; Dei-Cas, E. (2002). Microbial agents associated with waterborne diseases. Crit. Rev. Microbiol.; 28(4):371-409.
10. Mac Kenzie, W.R.; Hoxie, N.J.; Proctor, M. E. (1994). A massive outbreak in Milwaukee of Cryptosporidium infection transmitted through the public water supply. Engl. J. Med.; 331(3): 161-7
11. Meinhart, P.L.; Casemore, D.P; Miller, K.B.(1996). Epidemiologic Aspects of human cryptosporidiosis and the role of waterborne transmission. Epid Rev.; 18(2):118-36.

Detection of Cryptosporidium spp. in Animals' Zoo of Basra City

Mahmoud S. Thamer[1], Wathiq A. Al-Rmadhan[2], Maitham H. Shanoot[3]
{mahmood.Thamir@stu.edu.iq[1], wathiq.alrmadhan@stu.edu.iq[2], maitham.altai@stu.edu.iq[3]}

Technical Institute, Environmental Pollution Research, Southern Technical University, Basra, Iraq[1,2,3]

Abstract. The detection of Cryptosporidium Spp. from faecal samples collected from several animals at the Basra Zoo is part of this research. The total infected percentage reach to (52.9%, 28.6%, 16.7%, 12.5%, 6.7%, 0.0%, 0.0%, 0.0%, 0.0%) in bears, cat, lions, pigs, camels, banshee, horse, tigers, and hyena respectively. The results showed that the total infected percentage was (13%). The average oocyst size was found to be within the typical range of Cryptosporidium Spp oocyst sizes. The average oocyst size was found to be within the range of Cryptosporidium spp. oocyst sizes.

Keywords: Cryptosporidium, Zoo, Basra.

1 Introduction

Parasitic illnesses in caged animals are one of the most common causes of severe diarrhoea and even death [4]. Many researchers have been tracking various parasites in captive and wild animals at zoological gardens across the world, and many zoos, conservation parks, and wildlife rehabilitation centres have expressed worry about the current state and level of contamination of their animal collections. A zoo is predisposed to the spread of infections due to the concentration of numerous animal species in a small space, as well as the stress induced by imprisonment and contact with humans [3].

Cryptosporidiosis is a zoonotic and anthropologic disease caused by protozoan parasites of the genus Cryptosporidium. It has a worldwide distribution and is one of the four leading pathogens causing diarrheal disorders in children, according to most surveys [8]. The goal of this study was to identify certain zoonotic protozoa and determine their prevalence in various hosts.

2 Materials and Methods

2.1 Collection of Water Samples

This study has been performed from September until November 2013. Nine types of these animals Zoo of Basra city (bears, lions, camels, pigs, banshee, horse, tigers, hyena, and cats) all

IMDC-IST 2021, September 07-09, Sakarya, Turkey
Copyright © 2022 EAI
DOI 10.4108/eai.7-9-2021.2315519

the sample were put in polyethylene containers water which delivered to the laboratory parasitological to detect of oocyst of *Cryptosporidium* spp.

2.2 Oocyst Detection

To detect Cryptosporidium oocysts, the faecal samples were concentrated using the formalin method [6], a drop was taken from each deposit using a Pasture pipette and smeared on a glass slide, then the smears were fixed transiently over a flame and stained for 5 minutes with a strong carbol fuchsin solution. The slide was heated until steam formed, but not to the point of boiling, and an extra stain was applied if the slide became dry. The smear was stained, then washed under running tap water for 1-2 minutes before being decolorized in 5% sulphuric acid for 30 seconds. The smears were rinsed in tap water for 1-2 minutes before being counterstained for 1 minute with 3 percent methylene blue stain. Finally, the smears were rinsed in tap water, air-dried, and inspected microscopically for Cryptosporidium oocysts under oil immersion (100). The following formula was used to compute the percentage of contaminated samples:

$$\text{Infected Percent} = \frac{\text{Infected samples}}{\text{Total samples}} \text{ x } 100 \qquad (1)$$

2.3 Statistical Analysis

After data cleaning, the data was transferred to a Microsoft Excel Spreadsheet for statistical analysis, and then into the SPSS (Statistical Package for the Social Sciences version 15.) package software application. For all variables, descriptive statistics (%) were performed, as well as analytical statistics to determine the relationships between the variables. Chi-square statistical tests were used to determine the relationship between variables.

3 Results

Air-dried slides were examined under light microscopy at 100 X magnifications, oocyst of *Cryptosporidium* were found as pink coloured round and spherical body as shown in Figure 1.

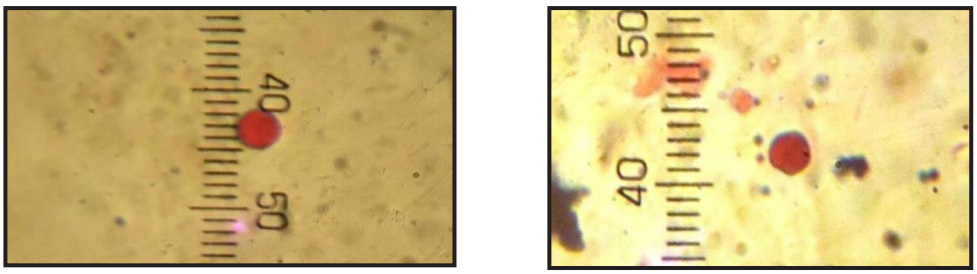

Fig 1: Cryptosporidium oocyst staining with a modified Zeihl Neelsen 100 X**.**

90 inspected animals with 15 (13%) were disease-ridden with Cryptosporidium spp. nine types of these animals Zoo (bears, lions, camels, pigs, banshee, horse, tiger, hyena, and cat) were delivered to the laboratory parasitological to detect oocyst of Cryptosporidium spp. As represented in Table 1.

Table 1: The percentage of animals infected with Cryptosporidium Basrah Zoo is a zoo in Basrah, Iraq.

	Examined animals	Infected animals	Percentage of infected one
bears	**17**	**9**	**52.9%**
lions	**12**	**2**	**16.7%**
camels	**15**	**1**	**6.7%**
pigs	**8**	**1**	**12.5%**
banshee	**11**	**0**	**0.0%**
horse	**6**	**0**	**0.0%**
tiger	**7**	**0**	**0.0%**
hyena	**7**	**0**	**0.0%**
cat	**7**	**2**	**28.6%**
Total	**90**	**15**	**13%**

Discussion

Table 1 shows the overall prevalence of Cryptosporidium Spp. in animals at Basra Zoo (1). 90 (13%) of the (9) tested animals were contaminated with Cryptosporidium oocyst. Six types of these animals are bears, lions, camels, pigs, and cat; each had infected with oocyst of the parasite, while banshee, horse, tiger, hyena none. This is result is quite agree with [7] which recorded (21.9%) in confined animals in Al- Zawra Zoo in Baghdad city, but disagreement with [7] who identified oocysts of *Cryptosporidium* spp. in deer at caged animals of one park in Baghdad (100%), and with [1] who recorded Percentage (58.7%) in the north zoo of Iraq cities and worldwide prevalence of parasite which was 19.5% [5] at a zoo in southern Brazil. The variations between these findings and those of other research are related to the diagnostic technique utilised or the fact that parasite prevalence varies from year to year and from one region to another within the same country [2].

4 Recommendation

1. The use of a routine microscopically diagnostic procedure is advised, and technical medical personnel must be trained to diagnose Cryptosporidium and other parasites in caged animals in Iraq.
2. More research into the detection of Cryptosporidium in captive animals' workers.
3. To account for all sociocultural influences, a more complete epidemiological investigation is necessary.
4. Introduce parasite species diagnosis using molecular techniques, genotyping, and subtyping in captive animals.

References

1. Al-Obaidi, W. A. (2006). Detection of Cryptosporidium Spp. in zoo of Mosul and Dohuk cities Vet. Sc., 2(20): 203-212.
2. Amin, O. M. (2007). Prevalence, distribution and host relationships of *Cryptosporidium* parvum (protozoa) infections in the United States, 2003-2005. Parasitol. Cent. Inc. (PCI) explores 16(1): 22-28.
3. Appelbee A. J., Thompson, R. C., Olson, M. E. 2005. *Giardia* and *Cryptosporidium* in mammalian wildlife current status and future needs. Trends Parasitol, 21:370-376.
4. Cordon, G. P., prados, A. H., Romero, D., Moreno, M.S, pontes, A., Qsuna, A . and Rpsales, M.J. (2008) Intestinal parasitism in the animals of the zoological garden "Pena Escrita(AlMunecar , Spain).Vet. Parasitol. 156: 302-309.
5. Ludwig, R. and Marques, S. .Occurrence of *Cryptosporidium* Spp. oocysts in mammals at a zoo in southern Brazil Rev. Ibero-Latinoam. Parasitol. (2011); 70 (1): 122-128.
6. Nasser, S. K. (2014). The distribution of *Cryptosporidium* in Some Resources of Water, Vegetables and Animals Feces in Basra Province. M. Sc. Thesis, College of Education for pure sciences, Basra Univ., 88 pp.
7. Radhy, A.M., and Hassan, I. Q. (2012) Investigation about some parasites in feces of captive animals in AL- Zawraa zoo. J. Anbar.Vet.Sc., 5(1): 139-150.
8. Xiao, L.; Morgan, U. M.; Fayer, R.; Thompson, R. C.; Lal, A. A, (2000). *Cryptosporidium* systematics and implications for public health. Parasitol. Today, 16: 287–292.

Ameliorating effect of Alteplase in bleomycin-induced pulmonary fibrosis in adult rats

Mahdi M.Thuwaini[1], Hanaa S.Kadhem[2], Ali Esmail Al-Snafi[3], Maha K.Abrahem[4]
[1] Department of laboratory Investigation, College of Medical and Healthy Techniques/ Southern Technical University,
[2]Department of pathological analysis, College of Science, Basra University, [3] Department of Pharmacology, College of Medicine, Thi qar University- Iraq
mahdi.murshd@stu.edu.iq

Abstract, The goal of this study was to see if alteplase may help adult rats suffering from bleomycin-induced lung fibrosis. Alteplase 0.9mg/ kg i.p. as a single dose daily for 3weeks, significantly ameliorated the declined serum levels of SOD and GSHpx, and significantly, decrease the elevated level of hydroxyproline in (BLM) treated rats. The bulk of the alveolar walls were filled by collagenous fibres with diffuse cellular infiltration, bands of collagen fibres, and increased macrophages and fibroblast cells in sections of lung tissue from BLM-treated rats. The lung of rats treated by alteplase in combination with (BLM) revealed that fibrotic lesions appeared less, with mild inflammatory cells, minimum blood vessels congestion and most parenchyma tissue appeared similar to a normal structure. As a result, the findings could provide one treatment option for preventing lung fibrosis caused by anticancer therapy.

Keywords: Alteplase, Bleomycin, Pulmonary fibrosis, rats, GSH, SOD, HYP

1. Introduction

In a reparative process, fibrosis is the production of extra fibrous tissue in tissue [1]. Interstitial lung injury with tissue fibrosis and a loss of lung elasticity characterise pulmonary fibrosis (PF). PF can be caused by a variety of disorders or it might be idiopathic, meaning there is no recognised cause. There were three forms of lung tissue fibrosis as well: Replacement fibrosis, which happens in fibrosing alveolitis (IPF) and extensive allergy alveolitis [2], localised fibrosis in reaction to irritants, such as coal dust and silica, and diffuse parenchymal lung disease (DPLD), which occurs in fibrosing alveolitis (IPF) and extensive allergic alveolitis. There are a variety of methods for modelling (PF) and/or inducing lung tissue damage in animal models to obtain a realistic picture of human disease. Because there are pathologic similarities between fibrotic reactions in human and rodent lungs, animal models are an excellent tool for investigating pathologic changes in vivo. [3-4]. Various animal models of (PF) have been developed, however, to examine potential therapeutics for

IMDC-IST 2021, September 07-09, Sakarya, Turkey
Copyright © 2022 EAI
DOI 10.4108/eai.7-9-2021.2315497

the disease (PF). Chemical induction by bleomycin (BLM) is the most commonly used model in rodents (mouse, rats and hamster) [3]. Most of pulmonary fibrosis inducing models were stimulated lung-injury in response to oxidative stress.
Bleomycin, the anticancer drug, caused lung cell damage and fibrosis by inducing lipid peroxidation, independent from its effect on DNA. Therefore, one of the serious side effects of BLM in humans has been observed in the lungs, which may progress to fatal diffuse (PF) [5-8].

This research was designed to investigate the ameliorating effect of alteplase in bleomycin-induced pulmonary fibrosis in adult rats

2. Material and methods

2.1 Animals

Albino Wister male rats (Rattus norvegicus) weighing 200-250 g were obtained from Thi-Qar University's College of Science's animal centre. All animals were provided free access to food and water, and were kept at a constant temperature of 22±3 degrees Fahrenheit with a 12-hour light/dark cycle.

2.2 Experimental design

Animals were randomly assigned to one of four groups (10 rats each). The rats in group 1 (Control group) were given 0.5ml/animal/daily i.p. of sterile saline solution (the vehicle). For three weeks, Group 2 got bleomycin 15mg/ kg/ i.p. three times weekly. Group 3 received alteplase 0.9mg/ kg i.p. as a single dose daily for 3weeks (Benoitet al., 2010). Group 4 received bleomycin and alteplase simultaneously at doses, periods and administration similar to that mentioned in the groups 2 and 3. All the treatments were dissolved in normal saline and were administered for 3 weeks (9). The rats were anaesthetized with chloroform and venous blood samples were taken via direct heart puncture into sterilised tubes at the conclusion of the experiment. Sera was kept in a deep freezer.

2.3 Estimation of GSHpx, SOD and HYP

According to the kit instructions, serum glutathione peroxidase (GSHpx), superoxide dismutase (SOD), and hydroxyproline (HYP) were tested (Cusabio Eliza kit, catalo no. CSB-E 121144r).

2.4 Histopthological examination

Lung tissue samples were taken from sagittal lung slices, fixed in 10% formalin for 24 hours, then washed, dehydrated, clarified, and embedded in paraffin; sections of around 4m were stained with Hematoxylin-Eosin for microscopic analysis.

2.5 Statistical analysis

The paired students T-test was used to assess differences between groups. $P<0.05$ was used to determine whether differences were statistically significant.

3. Results

The serum level of SOD in the control was 9.42±1.08 Pg/ml, administration of alteplase did not induce significant changes in the serum SOD (9.270±0.591 Pg/ml), however, SOD was significantly declined in bleomycin group (7.77±0.644 Pg/ml) ($P<0.01$), while administration of alteplase with bleomycin significantly restored the serum SOD level to the normal. The level of seum GSHpx was also decreased significantly in bleomycin treated group (17.04±1.52 MIU/ml) compared with control (33.18±3.444 MIU/ml) ($P<0.001$), while alteplase did not affected the level of GSHpx when administered alone (30.62±3.92 MIU/ml) but it restored the level of GSHpx to normal limit when administered with bleomycin (30.07±2.00 MIU/ml). On the other hand, the serum level of hydroxyproline was 1.44±0.20 µg/ml in the control group, it was did not change by alteplase (1.67±0.19 MIU/ml), but it was significantly increased by bleomycin (2.86±0.12 MIU/ml) ($P<0.0001$), while alteplase significantly ameliorated the effect of bleomycin on hydroxyproline (1.54±0.34 MIU/ml) (Table 1).
Normal architecture, a spongy appearance of the lung with thin alveolar septa, clear alveolar cavities, and normal alveolar ducts were observed microscopically in the control group's rat lung sections. The alveoli were evenly dispersed and the lung tissue appeared normal. The alveolar epithelial tissue lining and loose connective tissue included a large capillary network around the alveoli, forming the interalveolar septa. The alveolar ducts have several alveoli openings along their length, and the alveolar sacs form at the end of the ducts (Figure 1). The histological evaluation of lung sections from rats given alteplase revealed normal histological characteristics, which were similar to the sections from the control group (Figure 2).

The bulk of the alveolar walls were filled by collagenous fibres with diffuse cellular infiltration, as well as bands of collagen fibres, with an increase in macrophages and fibroblast cells in BLM-treated rats' lung sections (figure 3). The sections of the lung of rats treated by alteplase in combination with (BLM), revealed that fibrotic lesions appeared less, with mild inflammatory cells, minimum blood vessels congestion and most parenchyma tissue appeared similar to normal structure (figure 4 & 5).

Table 1: Alteplase's effect on superoxide (SOD), glutathione peroxidase (GSHpx), and hydroxyproline (HYP) in blood serum of rats with bleomycin-induced pulmonary fibrosis.

Groups	SOD Pg/ml	GSHpx MIU/ml	HYP µg/ml
Control	9.42±1.08[a]	33.18±3.44[a]	1.44±0.20[a]
Bleomycin	7.77±0.644[b]	17.04±1.52[b]	2.86±0.12[b]
Alteplase	9.27±0.591[a]	30.62±3.92[a]	1.67±0.19[a]
BLM+Alteplase	9.08±1.09[a]	30.07±2.00[a]	1.54±0.34[a]

Vertically similar letter means not significant

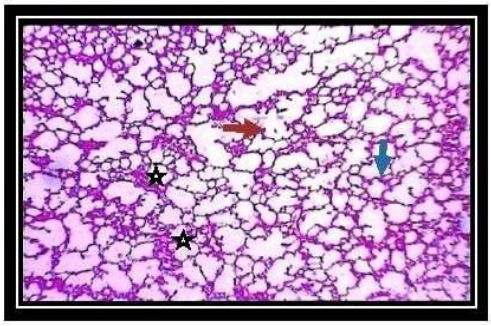

Figure1: Section in normal lung tissue showing that alveoli were homogeneously distributed ( ) with normal interalveolar septa ( ) and capillary network around alveoli ( ) **(H&E 40X)**.

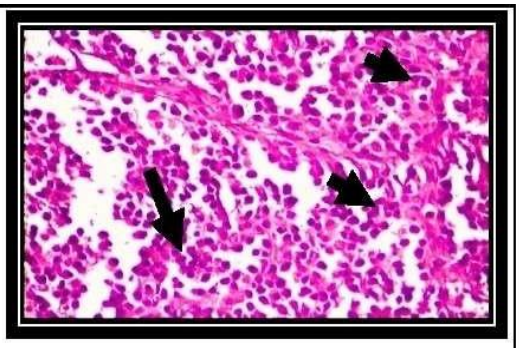

Figure 2: Section of the lung of rats treated with alteplase showed heavily invasion of lung tissue with mononuclear cells prominently macrophages ( ) , lymphocytes with fewer other inflammatory cells, also fewer fibroblast infiltrate interalveolar septa **(H&E. 400X).**

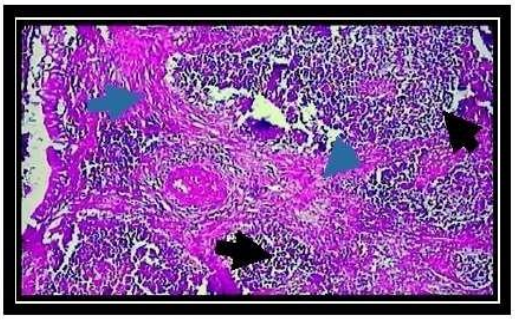

Figure 3: Section of the lung of bleomycin-treated rat, revealed an increase in cellularity of alveolar septum, look-like lymphatic nodule ( ) and intra-alveolar fibrosis with collagenous bands accompanying great septal thickness ( ) **(H&E. 100X).**

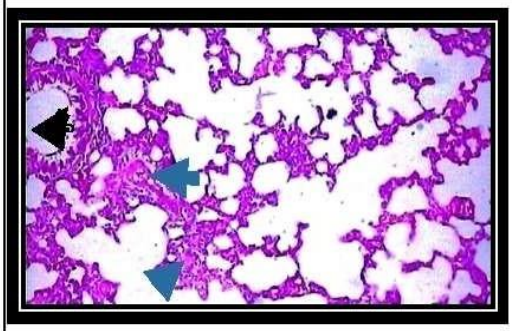

Figure 4: Section in the lung of rat treated with (bleomycin and alteplase) showed mild inflammatory cells, less than other groups, limited areas of fibrosis ( ) and collapse, with clear lumen of bronchioles lining with normal folded epithelium ( ) **(H&E. 100X).**

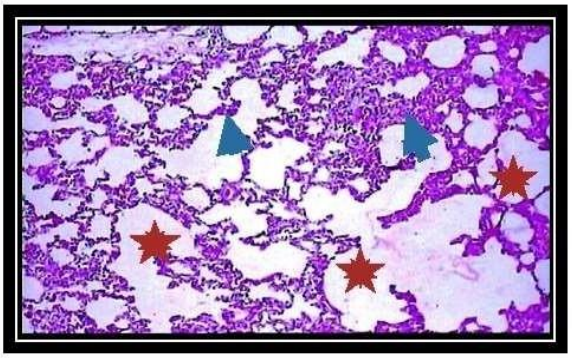

Figure 5: Section in the lung of rat treated with (bleomycin and alteplase) showed more patent alveolar space ( ) and reduced both inflammatory cells infiltration and thickness of the interalveolar septa ( ) **(H&E. 40 X).**

4. Discussion

Antineoplastic medicines frequently produce pulmonary fibrosis as a side effect. The goal of this investigation was to see if alteplase had any protective properties. To examine potential therapeutics for pulmonary fibrosis, various animal models of pulmonary fibrosis have been established (PF). The most frequent model for PF is bleomycin-induced lung fibrosis, which has a characteristic inflammatory pattern. In mice and rats (mouse, rat and hamster). Usuki and Fukua (10) observed that giving bleomycin to rodents causes histological changes that are nearly identical to those seen in human pulmonary fibrosis.

As in our results, the previous studies also showed that rat serum hydroxyproline was significantly increased, in bleomycin induced pulmonary fibrosis in rats (11-15). Furthermore, bleomycin induced significant deleterious changes in antioxidant status. The declined antioxidant status in our study was also recorded by many workers (12, 16). They discovered that a healthy balance of oxidants and antioxidants was one of the most critical factors in maintaining lung homeostasis, protecting the lungs from a variety of pathological diseases, and promoting normal healing.

The histopathological lesions that appeared with bleomycin in this study were similar to those recorded by many authors (17- 18). The histopathological lesions induced by bleomycin confirmed that injurious effects of bleomycin. Bleomycin–treated animals showed prominent parenchymatous disruption manifested by the appearance of over-expanded alveoli with thinning, destruction of the interalveolar septa and connection of many alveoli together. These finding, were similar to the picture of the emphysematous lung previously described (19). These could be attributed to proteolytic parenchyma destruction. Furthermore, it was reported that damage of the interstitial tissue could be followed by alveolar and interstitial edema, inflammation and breakdown of connective tissue (20-21), all these findings matched with our histological results. In the current study, the treatment with alteplase has been proven beneficial as it attenuated lung pathology induced by bleomycin. Where it reduced pulmonary inflammation, reduced extensive areas of collagen deposition whether interalveolar, around alveoli or peribronchioleoli, around blood vessels and subpleura zone. It also decreased inflammatory cells infiltration, re-epithelization of cellular lining alveoli. The effect of alteplase could be attributed to its fibrin dissolving characteristics and its antioxidant effects in BLM-induced pulmonary damage, where ROS led to the depletion of glutathione and oxidant/antioxidant imbalance, subsequently. Alteplase blocked this process and eventually improved the case of the lung.

5. Conclusion

According to our results, alteplase decreased hydoxyproline which elevated in pulmonary fibrosis induced by bleomycin. It also increase the antioxidant status which declined by bleomycin. Furthermore it ameliorated the histological alterations in the lung. Accordingly, the results confirmed the protective effects of fibrinolytic drugs in pulmonary fibrosis.

References

1. Wynn TA. Common of unique mechanizes regulate fibrosis in various fibro proliferative diseases. J Clin Merest. 2007;117 (3): 524-529.
2. Belloli EA, Beckford R, Hadley R and Flaherty KR. Idiopathic non-specific interstitial pneumonia. Respirology. 2016; 21(2):259-68.
3. Moeller A, Ask K and Warburton D. Gauldie, J. and Kolb, M. The bleomycin animal model: a useful tool to investigate treatment options for idiopathic pulmonary fibrosis. Int J Bio Chem Cell Biol 2008; 40(3): 362-382.
4. Antje M, Juan C, Rodriguez Z, Linggiaow L, Jack G and Martin K. Models of pulmonary fibrosis. Respir. Diseases. 2006; 3(3): 243-249.
5. Epstein E. Intralesional bleomcin and Raynaud's phenomenon. J Am Acad Dermatol 1991; 24 (9): 3-6.
6. Epstein JB, Gorsk M, Wong FL and Millnery A. Topical bleomcin for the treatment of dysplastic oral leukoplakia. Cancer. 1998; 83: 629-634.
7. Fasske E and Morgenroth K. Experimented bleomycni lung in mice a contribution to the pathogenesis of pulmonary fibrosis. New York, 1983: 133-146.
8. Gartner LP and Hiatt JL. Color textbook of histology: Respiratory system. 3rd ed. Sanders an Imprint of Elsevier Inc, 2007; 15: 345-365.
9. Mahdi M. Thuwaini, Ali E. Al-Snafi, Hanaa S. Khadem. Ameliorating effect of urokinase in bleomycin- induced pulmonary fibrosis in rats. International Journal of Pharmaceutical Research. 2021; 13(2): 2980-2983.
10. Usuki J and Fukuda Y. Evolution of three patterns of intra-alveolar fibrosis produced by bleomycin in rats Pathol Int. 1995; 45(8):552-564.
11. Avissar N, Finkelstein JN, Horowitz S, Willey JC, Coy E, Frampton MW, Watkins RH, Khullar P, Xu YL and Cohen HJ. Extracellular glutathione peroxidase in human lung epithelial lining fluid and in lung cells. Am J Physiol. 1996; 270:L173-L182.
12. Fattmann CL, Chu CT and Oury TD. Experimental models of asbestos-related diseases. In: Roggliv, Oury TD, Sporn, TA. (Ed.). Pathology of asbestos associated diseases. 2nd ed. New York: Springer- Verlag, 2005; 256-308.
13. Yao HW, Zhu JP, Zhao MH and Lu Y. Losartan attenuates bleomycin-induced pulmonary fibrosis in rats. Respiration. 2006; 73:236-242.
14. Molina-Molina M, Serrano-Mollar A, Bulbena O, Fernaftdez-Zabalegui L, Closa D, Marin-Arguedas A, Torrego A, Mullol J, Picado C and Xaubet A. Losartan attenuates bleomycin induced lung fibrosis by increasing prostaglandin E2 synthesis. J Thorax. 2006; 61: 604-610.
15. Giri SN, Chen ZL, Younker WR and Schiedt MJ. Effects of intratracheal administration of bleomycin on GSH-shuttle enzymes, catalase, lipid peroxidation, and collagen content in the lungs of hamsters. Toxicol Appl Pharmacol. 1983; 71(1):132-141.
16. Rahman I and MacNee W. Oxidative stress and regulation of glutathione in lung inflammation. Eur Respir J. 2000; 16(3):534-554.
17. Cooper J, Zitnik R and Mathay R. Mechanisms of drug induced pulmonary disease. Annu Rev Med. 1988; 39: 395- 494.
18. Izbicki G, Segel MG, Christensen TG, Conner MW and Brener R. Time course of bleomycin-induced lung fibrosis. Int J Exp Path. 2002; 83(3):111-119.

19. Borzone G, Moreno R, Urrea R, Menese M, Oyarzun M and Lisboa C. Bleomycin-induced chronic lung damage does not resemble idiopathic pulmonary fibrosis. Am J Respir Crit Care Med. 2001;163:1648-53.
20. Sullivan JB, Krieger GR. Clinical environmental health and toxic exposures. 2nd ed. Philadelphia: Lippincott Williams & Wilkins, 2001.
21. Jafarian D, Rabbani TG, MirMohammed Sadeghi H, Moghaddam N, Alvavis A, Mahmodi F and Safacian L. Development and time- course of bleomycin-induced pulmonary fibrosis in mice. DARU. 2007; 15(1): 1-6.

Assess the Extent to Which Nursing Staff Adhere to Safety and Prevention Measures Against the Corona Virus at Basra General Hospital / Iraq

[1] Farzdq Fakhir Gatae Al-husseinawi

[1]Southern Technical University, Iraq,Department of Nursing Technologies, Technical Institute Basra, Southern Technical University, Iraq.

{farazdaq.fakhir@stu.edu.iq[1]}

Abstract. This study was conducted during the month of February 2021 until June 2021, and the first aims to Nurses commitment level to safety and prevention measures during coronavirus of Basra general hospital / Iraq and the second aims to create a safe work environment to nurse staff . The risks that workers are exposed to, by using appropriate preventive and personal measures to avoid work injuries and diseases that they are exposed to, and the latter aims to create awareness among workers about safe methods and the importance of adhering to safety and prevention measures. We used the descriptive and analytical approach to collect the necessary data using observation checklist with images used and observed for nurse work during hospital. The target population of the study consists of nursing cadres in Basra General Teaching Hospital. As the number of samples reached (130) distributed over the hospital lobbies. Participation included (129). SPSS Statistical Package 23 was used to analyze and arrive at the analyzed results and to apply descriptive statistics for methods, frequencies, and percentages. The largest participants were females more than males, and the participating ages were 20-30 years old, the most among the groups. One of the most important recommendations of the study is to keep pace with global changes and achieve safety requirements in hospital halls. The nurse also needs to deal safely by committing to wearing personal equipment inside the hospital to avoid injuries.

Keywords: Assessment , nursing ,staff , corona virus ,safety

1 Introduction

Coronavirus is a family of viruses that causes respiratory infections including the new coronavirus (SARS-CoV-2) discovered in December 2019 in China. [1]. COVID-19 is a new illness that can affect your lungs and airways. This new virus and disease were unknown before the outbreak began in Wuhan, China, in December 2019 [2].

In the end of 2019 appeared in Wuhan, the capital of Hubei Province Chinese what is known as the new corona virus COVID-19 [3]. The coronavirus pandemic has led to the exposure of all groups of societies to an unprecedented change in a short period of time, forcing a change in their lifestyle, destroying the economy of many countries, affecting health care systems in all countries of the world, preventing movement and flight times, The world has become a prisoner of the Corona virus [4].

IMDC-IST 2021, September 07-09, Sakarya, Turkey
Copyright © 2022 EAI
DOI 10.4108/eai.7-9-2021.2315496

This has also been reinforced by the strict home quarantine measures, travel restrictions, examination and continuous monitoring that have been imposed on most of the world's population, in addition to the large amount of misinformation circulating in social media.[5]

Not to mention the feeling of alienation, and psychological distress embodied in depressive symptoms, and even a state of boredom in general, which may later develop into severe symptoms at times.[6]

The new corona virus is that virus that belongs to viruses .The well-known corona virus that may cause disease to humans and animals, which was described by WHO. The global health pandemic, which appeared recently in the Chinese city of Yuhan at the end of 2019, and its pathological symptoms are manifested in fever, fatigue, dry cough and pain, as This virus is transmitted to humans through small droplets scattered from the nose or Mouth when an infected person coughs or sneezes, and the virus can also be transmitted For humans, causing this disease state through droplets scattered on surfaces surrounding the person. .[7]

Healthcare personnel, who are key to controlling and eliminating outbreaks of severe infectious diseases, are at high risk of infection. During the outbreak of SARS, Ebola virus disease, and Middle East respiratory syndrome, hundreds of health care workers were infected and even died.[8]

1.1 Objective

This study aims to know the nurses' commitment to the level of safety and prevention measures during Corona at Basra General Hospital in Iraq. So that we can complete it and work on evaluating the safety for the best in the event of injuries and preserving the lives of the nurses. The study aims to:

1-Explanation of the extent of commitment of nursing staff to personal protective equipment in the hospital during the Corona virus pandemic.

2-Providing the nursing staff with background information on safety and personal protection during Corona.

3-Emphasizing the role of training and awareness among nurses regarding safe ways to preserve people, and this will enhance the safety of everyone, raise their morale and increase their self-confidence.

2. Methodology

2.1 Study design

Due to its usefulness and effectiveness for descriptive and assessment purposes, the cross-sectional study design was adopted, in addition to evaluating the cause and effect at the same time.

2.2 Study Population and sampling

Based on the study problem and its objectives, the study population includes nursing staff in Basra Hospital In order to gather information about the current situation. Participation included (130) of nurse. and 129 were received

2.3 Data collection instrument

The researchers collected data using a checklist , which included nurses working in words Basra general hospital, and analyzed the data. In addition working take picture to observe the

nursing staff.The checklist included general information including (sex, age, Academic achievement ,Years of service, some of the questions about the checklist).And the answer to the checklist placed was yes or no. Its purpose is to know the health system followed by nurses, hospital and patients. The results are discussed and appropriate solutions and recommendations presented in case of wrong or inappropriate behavior.

2.4 Period of the study

This study was conducted from 24 February 2021 through the end of July 2021.

2.5 Data analysis

The statistical program (Spss) (Statistical Package for Social Sciences) /version 23 was used to analyze and reach the results analyzed and applying descriptive statistics (Data analysis: SPSS 23 (Statistical Package for the Social Sciences) was used, and the analysis was by frequency, mean, percentage, and Std. Deviation)

3. Result & Discussion

This summarized as follows:

1. Sample distribution by age

The age group 20-30 reached (40.3%),age group 31-40 reached (27.9%).while age 41-50 reached (21.7%).and age 50 or more reached (10.1%)

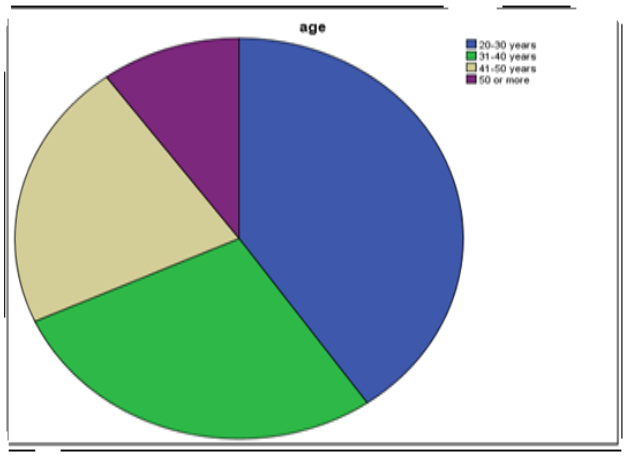

Fig .1. The distribution by age

2. Sample distribution by sex

It appears from analyzing data that the percentage of females which was (56.6%) is more than Males which was(43.4%)

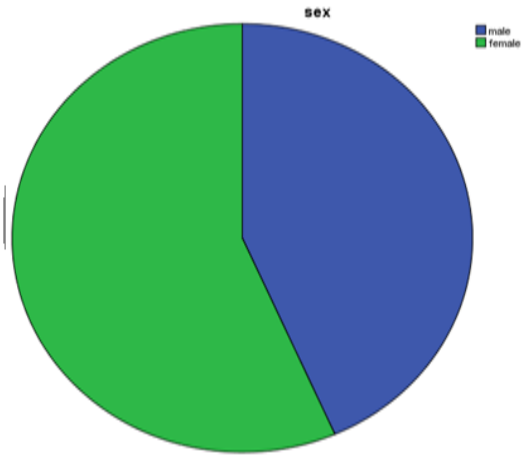

Fiq. 2.The distribution by sex

3. Sample distribution by academic achievement

In appears from analyzing data that the percentage of middle school was (4.7%).Preparatory reached (50.4%).Diploma (40.3%) .and Bachelor (4.7%) .

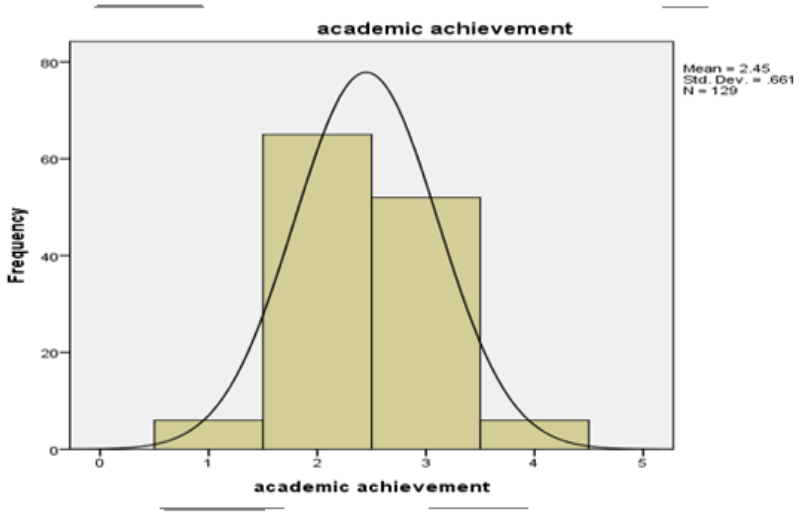

Fig.3. Sample distribution by academic achievement

4. sample distribution by years of service

About the years of service 1-10 years reached (38.8%).and 11-20 years was (27.1%).also 21-30 years was (20.2%).and 30 years or more reached (14%).

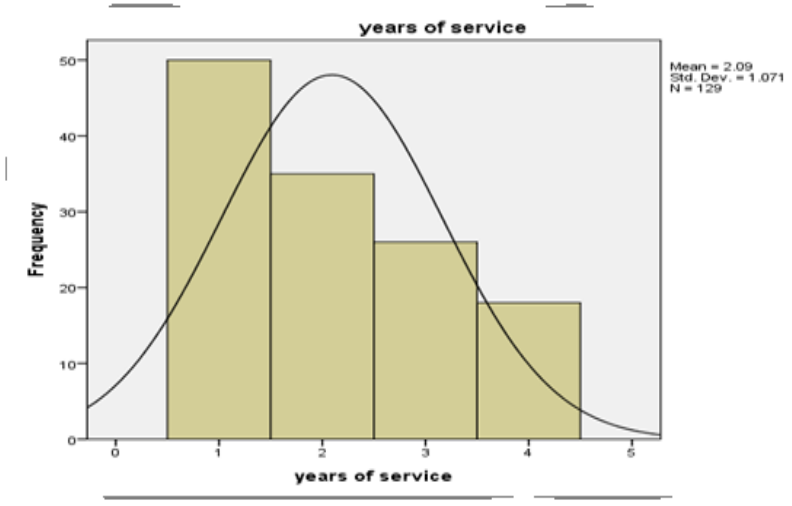

Fig.4. sample distribution by years of service

5 . Mean , standard deviation, frequency and percentage of participant answers of checklist

According to the answers of the questionnaire it shows there's some questions been answered with (no) more than yes or in very close percentages such as The first question was answered with no 50.4% , and question 15 was (53.5%) no . Other data shows some issues that need to pay attention for , such as sterilizing or types of used masks and health care for both patients and nurses.

Table:.1 . Mean , standard deviation, frequency and percentage of participant answers of checklist

	Q	YES & NO Freq & (%)		Mean	Std. Deviation
1	Is there a booth for sterilizing? before entering the ward?	64 49.6%	65 50.4%	1.50	.502
2	Is there sterilization materials in the ward?	122 94.6%	7 5.4%	1.05	.227
3	Is there distance between the nurses and the patient ?	91 70.5%	38 29.5%	1.29	.458
4	Nurses are not allowed to the ward except after wearing a mask ?	114 88.4%	15 11.6%	1.12	.322
5	A temperature is taken for the patient's companion before entering the ward ?	66 51.2%	62 48.1%	1.48	.502
6	The gown is to be worn before entering the ward ?	112 86.8%	17 13.2%	1.13	.340
7	Wearing gloves in the ward?	120 93.0%	9 7.0%	1.07	.256
8	The patient wear gloves and mask ?	89 69.0%	40 31.0%	1.31	.464
9	Sterilizing the ward before entering	87 67.4%	42 32.6%	1.33	.470
10	Sterilizing the ward after finishing	76 58.9%	52 40.3%	1.41	.493
11	The type of the mask is N95	79 61.2%	50 38.8%	1.39	489
12	Is the mask type a surgical type?	91 70.5%	38 29.5%	1.29	.458
13	Are the items and clothes of patients infected with Corona sterilized?	75 58.1%	54 41.9%	1.42	.495

14	Is it possible to sterilize and reuse medical and disposable face masks?	56 43.4%	73 56.6%	1.57	.498
15	Gathering patients suspected or confirmed to have coronavirus in the same room	60 46.5%	69 53.5%	1.53	.501
16	The presence of special waste to dispose of the belongings of the patient with Corona	102 79.1%	27 20.9%	1.21	.408
17	Using disposable gown	109 84.5%	20 15.5%	1.16	.363
18	Patients are educated about the dangers of Corona	109 84.5%	20 15.5%	1.16	.363
19	The patient's companion is prevented from entering the ward if his temperature is high	86 66.7%	42 32.6%	1.33	.471
20	Preventing the nurse from entering the ward if his temperature is high	93 72.1%	36 27.9%	1.28	.450
21	The ward has adequate ventilation	89 69.0%	40 31.0%	1.31	.464
22	Ward space is suitable for social distancing	91 70.5%	38 29.5%	1.29	.458
23	The used masks are disposed of in a healthy and safe way	113 87.6%	16 12.4%	1.12	.331
24	Gloves are disposed of in a healthy and safe way after leaving the ward	113 87.6%	16 12.4%	1.12	.331
25	Are the nursing staff examined by their colleagues to ensure their safety from the Corona virus?	81 62.8%	47 36.4%	1.37	.484

6. pictures taken by researchers during the study (by researcher)

The test lab and researchers contributed to the present study.

Fig. 5. Test lab and people contributed to this study.

4. Conclusion

We can conclude the following:

1. The study is the first of its kind in Basra Governorate, which relates to Nurses commitment level to safety and prevention measures during coronavirus of Basra general hospital Iraq .

2. Urging such useful studies of population and for all medical and health cadres, not just nursing, to preserve and prevent injuries, as well as equip hospitals with personal protective equipment.

3. Hospital nurses use personal equipment materials to protect themselves from dangers, but the shortage of some personal protective equipment important to hospital safety.

4. Female participants were more than males and The highest age group 20-30 reached (40.3%)

Our recommendations

1. All nurses (male and female) of different educational levels should be involved in more obligatory roughness to develop and achieve optimum level of knowledge regarding their tasks as caregivers especially those working in medical-surgical words.
2. Activating continuous education units in hospitals to educate nurses to enrich their knowledge of such diseases in addition to peptic ulcers.
3. Further studies should be conducted on large samples relating to the educational levels of nursing as a whole.

Acknowledgments.

We would like to express my sincere thanks and thanks to all the nursing staff at Basra General Teaching Hospital, for their continuous cooperation during the research period and for allowing picture to be taken.

References

(1) Pereira, L. J., Pereira, C. V., Murata, R. M., Pardi, V., & Pereira-Dourado, S. M. (2020). Biological and social aspects of Coronavirus Disease 2019 (COVID-19) related to oral health. *Brazilian Oral Research*, *34*.

(2) UNRWA. (2020, 3 5). *The emerging corona virus (COVID-2019).* Retrieved from http://archive.org: https://www.who.int/ar/emergencies/diseases/novel-coronavirus-2019

(3) Chan, J. F., Lau, S. K., To, K. K., Cheng, V. C., Woo, P. C., & Yuen, K. Y. (2015). Middle East respiratory syndrome coronavirus: another zoonotic betacoronavirus causing SARS-like disease. *Clinical microbiology reviews*, *28*(2), 465-522.

(4) Viswanath, A., & Monga, P. (2020). Working through the COVID-19 outbreak: Rapid review and recommendations for MSK and allied heath personnel. *Journal of clinical orthopaedics and trauma*, *11*(3), 500-503..

(5) Banerjee, D. (2020). The COVID-19 outbreak: Crucial role the psychiatrists can play. *Asian journal of psychiatry*, *50*, 102014.

(6) Zhai, Y., & Du, X. (2020). Mental health care for international Chinese students affected by the COVID-19 outbreak. *The Lancet Psychiatry*, *7*(4), e22.

(7) World Health Organization. (2005). Statement on the second meeting of the International Health Regulations (2005) Emergency Committee regarding the outbreak of novel coronavirus (2019-nCoV).

(8) Lujan, M. (2019). O2 'Free health/free die': investigating women's health in post-ebola rural sierra leone

Estimate some immunoglobulin's and complement cascade in pregnant women suffering from urinary tract infection

Fidan Fikrat Ahmed

Northern Technical University, Health and Medical Technical College/ Kirkuk, Iraq.
fidanfikrat1972@ntu.edu.iq

Abstract, The objective of this study is a measurement of some immunoglobulin's (IgM and IgG) and complement cascade (C3, C4) in pregnant women suffering from urinary tract infections (UTI) by single radial Immunodiffusion test 30 samples of urine and the blood were collected from pregnant female infected by UTI and 10 specimens were collected from healthy pregnant women in the period from December 2020 to June 2021 the samples were taken from pregnant female and they're aged ranging from 18 to 30 years. The results of the study showed that the levels of IgG is higher in those with UTI the mean is in the three trimesters respectively than in control and there's a statistically significant in the first trimester only with $P \leq 0.05$. In UTI patients, the results appeared a elevate in the level of C3 and C4 in those with UTI is higher in the first and third trimester, however, it's slightly lower in UTI patients than in control in the second trimester, there's no statistical significance between those with UTI and control. Otherwise, the results demonstrated that the level of hepcidin in UTI patients increased compared with control in the first, second and third trimesters respectively.

Keywords: Urinary tract infection; immunoglobulin; complement cascade

1. Introduction

The infections of the urinary tract (UTIs) are described as bacterial infections, and affect about 150 million people per year universally [1]. UTI is generally caused by different types of bacteria, and also various microorganisms like fungi and some viruses [2]. The type of UTI infection is usually classified as complicated and uncomplicated infections. The uncomplicated UTI type happens in the absence of functional or structural deformity within the urinary system. The complicated infections are happening in presence of deformity urinary tract that elevated the sensitivity to bacterial infection [3-4]. The family of *Enterobacteriaceae* is responsible for the infections of the urinary tract in man. *E. coli* is classified as the most frequent uropathogen [5]. the immunoglobulins describe as a category of proteins found in serum that play a significant role as antimicrobial activity in urinary tract infections where the IgM type represents an indicator of new infection with pathogens, the levels of IgG were elevated in the chronic infections, and IgA consists of the secretory part that assists in decreasing the infections

IMDC-IST 2021, September 07-09, Sakarya, Turkey
Copyright © 2022 EAI
DOI 10.4108/eai.7-9-2021.2315491

of mucosal membrane and secretory based. However, the role of the complement system especially for C3 in recurrent UTIs is still debatable [6]. UTIs in pregnant females continue to demonstrate a clinical issue [7]. Although the occurrence of bacteriuria in pregnant women is slightly higher compared with a non-pregnant female, its effects for mother and fetus are more severe [8-9].

2. Materials & Methods

2.1. Sample Collections

The study was performed during the period from December 2020 to June 2021 with the collection of 70 samples of serum and urine from pregnant women with ages ranging from 18-30 years. 50 of them were suspected to be infected with UTI and 20 pregnant women without any infection symptoms as the control group. The last menstrual period and the number of times they had a pregnancy were all recorded.

2.2. Microscopic examination

The samples of urine were collected from pregnant women in clean disposable cups and a portion of the sample is placed in a test tube and centrifuged at 400 x g for 5-10 minutes and the sediment was examined under the light microscope for the presence of pus cells and RBC [10].

2.3. Radial Immunodiffusion test

Single Radial Immunodiffusion (SRID) tests were used for the quantitative determination of many human serum proteins such as IgG, IgM, and C3, C4 complements. The sera were removed from freezing and equilibrated to room temperature. Plates were getting refrigerator then the zip lock bag and lid removed, wells were inspected for moisture. The serum of infected women and control were shaken (in their containers) by inversion, each sample was dispensed onto the wells. Each well-required 5µl of serum. After the lid was replaced, it was incubated in an incubator at 37 c. Incubation time was 72 hours. Immunoprecipitation ring diameters were measured by hand lens (0.1 mm precision). The calculated diameters were compared to the standard diameter to conclude the concentrations of serum humoral factors [11].

2.4. Hepcidin measurement

The levels of hepcidin were measured inpatient and control serum by using an Enzyme-linked immunosorbent assay (ELISA) depending on the technology of the biotin double antibody sandwich

2.5. Statistical analysis

The results and the data of current work were analysed by utilizing the program called Statistical Package for Social Sciences (SPSS-17), and significant changes between the means of studied groups were compared at the level of probability $P < 0.05$

3. Results and discussion

Out of 70 pregnant females, 50 (71.4%) had UTI and 20(28.6%) women as control. the isolation of bacteria from the urine samples including *E. coli, S. aureus, Klebsiella, and proteus*

[12]. In the present work, the incidence of UTI was significantly high. The high percent of infection may be back to the majority of females in current work belonged to socioeconomic with lower and/or middle levels; this theory is supported by various studies that referred that the UTI has happened at a higher rate among pregnant females living in status with poor socioeconomic [13-14]. The isolated bacteria from the urine sample in the present work was *E. coli* and this agreed with the findings of previous studies [15-18]. The flora located in faeces serves as the source of *E. coli* that colonizes the introitus of the vagina and urethra to bladder infection [19].

4. Immunological study

The samples of serum from infected women with UTI and those who were healthy were tested to diagnose IgM, IgG, C3, and C4 by immunodiffusion plates, and the findings of this work were demonstrated that the IgG, IgM, C3 and C4 levels in infected pregnant with UTI and control subjects without UTI are showed in the table (1) expressed as mean ± SD. Also, the estimates of hepcidin levels were done according to the procedure of the kit.

Table 1: Serum Immunoglobulin's (IgG and IgM) in pregnant women infected with UTIs compared with control subjects.

Parameter	Months	Control (mean±SD)	Patients With UTI (mean±SD)
IgM mg/d	1-3	134.4 ± 10.23 b	206.1 ±14.45 a
	4-6	151.3 ± 5.19 b	283.12± 8.03 a
	7-9	103.5 ±13.42 b	238.33 ± 10.52 a
IgG mg/d	1-3	1026.6 ± 19.51 a	911.5 ± 11.5 b
	4-6	1146.3 ± 27.62 a	824.9 ± 61.4 b
	7-9	973 ± 18.72 a	793.1 ±13.4 b

The results in Table (2) show the mean concentrations of **(C3, C4)** for each of the positive patients (pregnant women which suffering from UTIs) and also for control (without UTI), according to the trimesters of pregnancy. Otherwise, the present results show a significant increase in UTI patients compared with the control group, as shown in table (3).

Table 2: Serum Complement components (C3 and C4) in pregnant women infected with UTIs compared with control subjects.

Parameter	Months	Control (mean±SD)	Patients With UTI (mean±SD)
C3 (mg/d)	1-3	94.21 ± 8.2 b	152.5±3.08 a
	4-6	84.2 ± 4.28 b	104.35 ± 6.14 a
	7-9	71.73 ± 6.5 b	93.31 ± 4.01 a
C4 (mg/d)	1-3	134.8 ± 8.01 b	193.3 ± 9.8 a
	4-6	131.3 ± 12.4 b	197.33 ±13.82 a
	7-9	128.22 ± 9.36 b	184.1 ± 8.42 a

Table 3: Serum hepcidin in pregnant women infected with UTIs compared with control subjects.

Parameter	Months	Control (mean±SD)	Patients With UTI (mean±SD)
Hepcidin ng/ml	1-3	12.64 ± 1.04 b	14.6±1.16 a
	4-6	13.27 ± 1.62 b	18.83 ± 0.72 a
	7-9	15.18 ± 1.74 b	25.17 ± 2.61 a

The present work demonstrated elevated levels of IgG in UTI patients; others have reported the same investigation in their works about the protective immunity role against infection of the parasite [20]. The important and protective act of IgG versus pathogens explains the significantly elevated levels of IgG found in the UTI women in the current study, since it is the immunoglobulin synthesis and secreted during the secondary immune response. Elevate the values of IgM as recorded in patients of UTI, the same observation was reported by another study [21]. Elevate in complement's element may show by a variety of explanations, one interesting activity depends on outcomes of [22]. UTI infection attributed the increase of complement component production to the stimulation of the inflammatory mediators [23]. The immunity of maternal is altered during pregnancy time to favour implantation and growth of the embryo. The study suggests that immune response is modulated by humoral immune response

[24]. The present findings demonstrated significant elevate in patients with UTI, where the level of hepcidin elevates in the infection, thus limiting iron produced and released into the blood and disrupting pathogen growth [25]. The current findings agree with [26] who referred that hepcidin and the levels of ferritin were significantly elevated, whereas the levels of iron significantly reduced in the children with a bacterial infection.

References

1. Flores-Mireles, A. L.; Jennifer N. W.; Michael C. and Scott J. H. (2015). Urinary tract infections: epidemiology, mechanisms of infection and treatment options. Nat. Rev. Microbiol. 13(1): 1-17.
2. Olin SJ, Bartges JW (2015) Urinary tract infections: treatment/comparative therapeutics. Vet Clin North Am Small Anim Pract 45:721–746
3. Bazzaz, B. S. F.; Sareh D. F.; Reza A. and Bahman K. (2021). Deep insights into urinary tract infections and effective natural remedies. Afr J Urol. 27(6): 1-13.
4. Sheerin NS, Glover EK (2019) Urinary tract infection. Medicine 47:546–550.
5. Dlakhal, Z. A. (2013). Bacterial isolates associated with urinary tract infections in children. Misan J. Aca. Stu. 12(22): 56-60.
6. Hooton TM. Uncomplicated urinary tract infection. New Engl J Med. 2012; 366: 1028-1037
7. Hannan TJ, et al. Host-pathogen checkpoints and population bottlenecks in persistent and intracellular uropathogenic Escherichia coli bladder infection. FEMS Microbiol Rev. 2012; 36: 616-648.
8. Soman N. Abraham & Yuxuan Miao. The nature of immune responses to urinary tract infections. Nature Reviews Immunology volumel5 (2015); pages655–663.
9. Foxman B. Epidemiology of urinary tract infections: incidence, morbidity, and economic costs. Am J Med 2002; 113: 5-13.
10. Schnarr J, Smaill F. Asymptomatic bacteriuria and symptomatic urinary tract infection in pregnancy. Eur J Clin Invest 2008; 38 (Suppl. 2): 50-7
11. Mazor-Dray E, Levy A, Schlaefer F, Sheiner E. Maternal urinary tract infection: is it independently associated with an adverse pregnancy outcome? J MaternFetal Neonatal Med 2009; 22: 124-32.
12. Bolton M, Horvath DJ, Li B, et al. Intrauterine growth restriction is a direct consequence of localized maternal uropathogenic Escherichia coli cystitis. Plus, ONE 2012; 7: 1-9.
13. Vandepitte, Jozef, Engbaek, Kraesten, Rohner, P, Piot, Peter, Heụck, Claus C. et al. (2003). Basic laboratory procedures in clinical bacteriology / J. Vandepitte L. 2nd ed. Geneva: World Health Organization.
14. Franklin, R.; Matthew, A.; Karen, B.: Michael, N. George M; Dwight, J. et al. Performance Standards for Antimicrobial Susceptibility Testing: Twenty-First Information Supplement. Clinical and laboratory standards institute (CLSI) sl. (2011); Vol.31 (1).
15. Schaeffer, A.J. Infections of the urinary tract. In: Walsh, P.C.; Retik, A.B.; Vaughan, E.D.; Wein, A.J.; Campbells Textbook of Urology. 7th Edn. WB. Anders company: London; (1998); p: 534 614.

16. Sheikh, M.A.: khan, M.S.; khatoon, A. and Arain, G.M. Incident of urinary tract infection during pregnancy. Eastern Mediterranean Health Journal. (6), (2000); p: 265-271.
17. McCormick, T.; Ashe, RG.; Kearney, PM Urinary infection tract in pregnancy. The Obstetrician and Gynaecologist; 10: (2008): 156-62
18. Moghadas, AJ and Irajian, G. Asymptomatic urinary tract infection in pregnant women Iranian journal of pathology (3), (2009) p 105-108.
19. Suman, E. Bhat, GK and Hegde, BMBacterial adherence and immune response in recurrent urinary tract infection. J Gynec Obstet. (75) (2001); p: 263-268.
20. Colgan, R.; Nicolle, LE.; McGlone. A.and Hooton, TM Asymptomatic bacteriuria in adults. Am Fam Physician.; 74 6 (2006): p985-90
21. Hernandez BF Lopez Carmona JM Rodriguez M Peralta Pedrero ML Rodriguez Gutierrez RS and Ortiz Aguirre AR in pregnant women bacteria Asymptomatic and uropathogenic in vitro antimicrobial sensitivity GinecolObstet Mix 75 (6) (2007) p: 325–31.
22. Stamey, TA Pathogenesis and treatment of urinary tract infections. The Williams and Wilkins Co., Baltimore, Maryland.
23. Ramirez, R.M.; Ceballos, E.; Alarcon de Noya, B.; Noya, O. and Bianco, N. The immunopathology of human schistosomiasis III immunoglobulin isotype profiles and response to praziquantel. Men. Inst. Oswaldo Cruz. (91). (1996); p: 593-599.
24. Arinola, O.G.; Salawu, L. and Ojurongbe, O. Immunoglobulin classes (IgG, IgA, and IgM) and acute-phase proteins in the pregnant woman with urinary schistosomiasis. WAJM. (24) 1. (2005); P: 44-48.
25. Miletic, VD.; Hester, CG and Frank, MM) Regulation of complementary activity by immunoglobulin. I. Effect of immunoglobulin isotype on C4 uptake on antibody-sensitized sheep erythrocytes and solid-phase immune complexes. J Immunol. 15612) (1996); p: 749-57.
26. Botto, M.; Kirschfink, M.; Macor, P.; Pickering, M.C.; Wurzner, R. and Tedesco, F. Complement in human (2009).
27. Wegmann, T.G., Lin, H.; Guilbert, L. and Mosmann, T. R. Bidirectional cytokine interactions in the maternal-fetal relationship: is successful pregnancy a TH2 phenomenon? Immunology Today: (14): (1993); 353-3566.
28. Rishi G, Wallace DF, Subramaniam VN. Hepcidin: regulation of the master iron regulator. Biosci Rep 2015;35. pii: e00192.
29. Kossiva L, Gourgiotis DI, Tsentidis C, Anastasiou T, Marmarinos A, Vasilenko H, et al. Serum hepcidin and ferritin to iron ratio in evaluation of bacterial versus viral infections in children: a single-center study. Pediatr Infect Dis J 2012;31: 795e8.

Virulence Characteristics and Antibiotic Resistance of *Klebsiella pneumoniae* Isolated from Clinical Sources

Mohammed Hussein Amer[1], Hasan Abd Ali Khudhair[2] and Khwam R Hussein[3]
[1]Faculty of Graduate Studies, Southern Technical University, Iraq
[2-3]Al-Nasiriyah Technical Institute, Southern Technical University, Iraq
[1]mohu19761976@gmail.com, [2]hasanabdali89@stu.edu.iq, [3]krhussein@stu.edu.iq

Abstract Klebsiella pneumoniae (K. pneumoniae) is a Gram-negative capsulated bacterium that causes a variety of human diseases. This study was to investigate the prevalence and antibiotic susceptibility pattern of K. pneumoniae isolated from diverse clinical samples, as well as to discover some of the bacteria's virulence components using a molecular approach. One hundred and eighty patients suffering from respiratory, urinary, wounds and burns infections were enrolled in this study and evaluated for the presence of K. pneumoniae infection via culturing, microscopical, motility and biochemical characteristics as well as API 20E and VITEK 2 systems. Molecular technology was used for detection the presence of K1 and K2 genes as well as the presence and sequencing 16S ribosomal ribonucleic acid (16S rRNA) gene. The results showed that a low prevalence of K. pneumoniae (27.8%) in Iraqi patients with higher positivity rate in sputum samples (42%) compared to other clinical samples.. According to the results of phylogenetic tree construction of 16S rRNA gene, we identified six mutated clinical isolates of K. pneumoniae that were deposited in GenBank under the accession numbers of MW642198, MW642199, MW642200, MW642201, MW642202 and MW642203. The mutated 16S rRNA gene stains exhibited a significantly higher resistance to all antibiotics types that used in this study.

Key Words: *Klebsiella pneumoniae*, Antibiotics Resistance, *K1* and *K2* Genes.

1. Introduction

Klebsiella pneumoniae is a Gram-negative capsulated bacterium that is abundant in the environment and causes a variety of human infections including bloodstream infection (BSI), urinary tract infection (UTI), surgical-site infection, and pneumonia. It is a major pathogen for nosocomial pneumonia and a major source of sepsis [1]. In the healthcare setting, these infections are particularly problematic in infants, the elderly, and immunocompromised persons [2]. These infections are distinguished by their tendency to spread metastatically and their high morbidity and mortality [3].

The hypermucoviscosity trait [4] appears to be associated with the invasiveness of K. pneumoniae strains, as evidenced by the excessive "stickiness" of their colonies on agar plates. Due to an increase in the number of illnesses and an increase in the number of strains resistant to antibiotics, K. pneumoniae is receiving attention. More than a third of K. pneumoniae isolates reported to the European Centre for Disease Prevention and Control were resistant to at least one antimicrobial class, with the most common resistance phenotype being combined resistance to fluoroquinolones, third-generation cephalosporins, and aminoglycosides [5]. Furthermore, antibiotic-resistant genes have been found in Klebsiella species, which can spread to other gram-negative bacteria. In fact, Klebsiella was the first organism to discover many of the antibiotic-resistant genes presently found in multidrug-

IMDC-IST 2021, September 07-09, Sakarya, Turkey
Copyright © 2022 EAI
DOI 10.4108/eai.7-9-2021.2315374

resistant organisms [6]. Smooth lipopolysaccharide (LPS with O antigen), pili for adherence to host cells, anti-phagocytic capsules (K antigen), and siderophores that aid the bacterium in its competition with the host are all produced by K. pneumonia [7]. The capsule serotypes K1 and K2, which are the most virulent to humans, have been the focus of research into the virulence determinants of K. pneumoniae [8]. As a result, determining medication resistance in two key pathogenicity serotypes, K1 and K2, requires studying the resistance of this gram-negative bacterium isolated from clinical specimens. The most common method for characterising K. pneumoniae isolates is molecular capsular typing, which has great repeatability in differentiating clinical isolates [9].

Many sequenced virulence genes have been discovered in K. pneumonia, including 16S RNA analysis and sequencing of sections within the 16S rRNA gene, which can increase the speed and effectiveness of estimating the variety of bacteria helpful for pathogen and identification [10]. The purpose of this work is to assess the prevalence and antibiotic susceptibility pattern of K. pneumoniae isolated from clinical samples (urine, sputum, wound smears, and burn smears), as well as to identify some virulence factors of K. pneumoniae using a molecular technique.

2. Materials and Methods

One hundred and eighty patients with age ranged from 16-55 years whom attending Al-Hussein Teaching, Mohammed Al-Mosawy and Al-Habbobi Hospitals during the period from beginning of October 2020 to end of March 2021. A written consent was obtained from each patient to fulfill the international research ethical criteria. The patients were classified according their suffering into; 42 patients with UTI, 33 patients with wounds, 15 patients with burn and 90 patients with respiratory tract infection (RTIs). From each subject with UTI or RTI; a fresh urine and sputum samples were obtained, respectively, and placed in the sterile suitable containers, whereas from each subject with wound or burn; a fresh swabs were taken from the sites of injuries. All collected samples were quickly transported to laboratory for culturing.

Klebsiella pneumoniae isolates were performed using blood and MacConkey agar as the method that illustrated via [11]. The primary detection of *K. pneumoniae* was assesses via culturing, microscopical, motility, and biochemical tests (catalase, indole, oxidase, citrate utilization, urease and glucose) characteristics according to the methods that mentioned in [11, 12]. The confirmatory diagnosis of this bacterium was done using API 20E system and VITEK 2 system (Bio-Merieux, France). Antimicrobial susceptibility test was done using disc diffusion method according to [13] with following antibiotics; doxycycline, rifampicin, ciprofloxacin, gentamycin, cefuroxime, ceftazidime, amikacin, imipenem, ceftriaxone and levofloxacin. The inhibition zone sizes were measured with calipers and the findings were calculated in reference to the clinical and laboratory standards institute guidelines [13].

Deoxyribonucleic acid (DNA) was extracted from bacterial isolates using bacterial DNA extraction kit (Anatolia, Turkey). The genes 16*S rRNA*, *K1* and *K2* were detected by polymerase chain reaction (PCR) technique using specific primers (Table 1) with using PCR thermo cycler system (Eppendrof, UAS). The method was preceded according to instructions of the company. After PCR amplification, the reaction product was separated by electrophoresis on agarose gel (1%) and then the PCR product image was taken [14].

Table 1. The primers that used in the study

Genes		Primer Sequences (5′————3′)	Product Size	References
16S rRNA	F	AGAGTTTGATCCTGGCTCAG	1500 bp	[15]
	R	GGTTACCTTGTTACGACTT		
K1	F	GGTGCTCTTTACATCATTGC	1283 bp	[16]
	R	GCAATGGCCATTTGCGTTAG		
K1	F	CAACCATGGTGGTCGATTAG	531 bp	[17]
	R	TGGTAGCCATATCCCTTTGG		

16*S rRNA:* *16S ribosomal ribonucleic acid*, **F:** Forward, **R:** Reverse and **bp:** base pair

The 16*S rRNA* gene was subjected to nucleotide sequencing with an automated DNA sequencing machine at Bio-Service unit (National Science and Technology Development Agency). The 16*S rRNA* gene sequences determined were aligned along with the sequences of type strains obtained from Multiple Sequence Alignment program CLUSTAL X (version 1.82) [18, 19].

Frequency distribution of categorical variables within the groups of the study was performed using Chi-Square method. Statistics were regarded as statistically significance at p-value <0.05.

3. Results

The results showed that out of 180 clinical samples, only 50 (27.8%) samples were detected as *K. pneumoniae* infections. In Figure 1, the results of *K. pneumoniae* were reported in sputum 21/50 (42%) followed in urine 14/50 (28%) and then wounds 8/50 (16%).

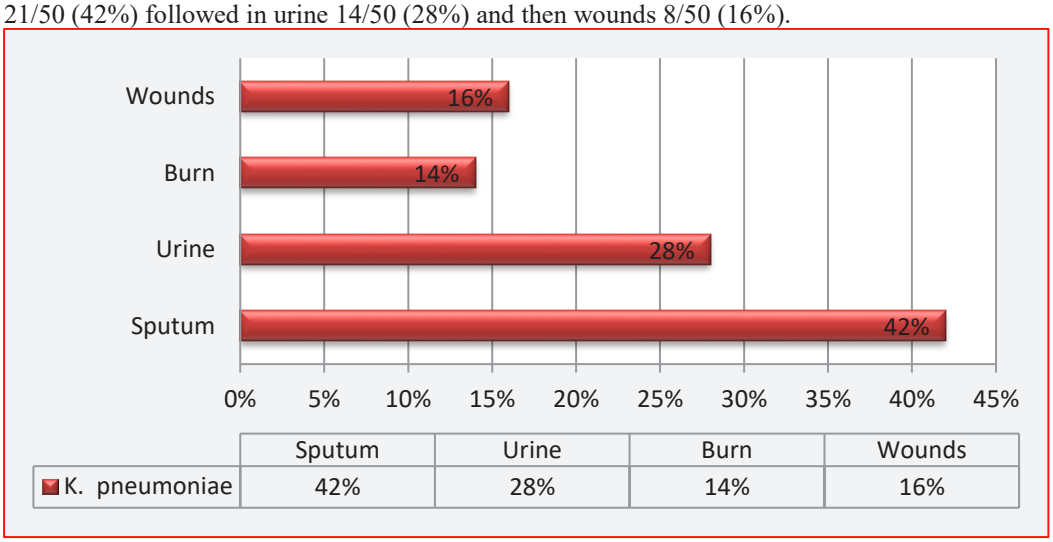

Figure 1: Prevalence of *K. pneumoniae* according to clinical samples

Klebsiella pneumoniae isolates susceptibility to antibiotics was illustrated in Table (2). For Imipenem, ciprofloxacin, levofloxacin, doxycycline and rifampicin antibiotics, the results of antibiotics assay of *K. pneumoniae* isolates was revealed a significantly ($P<0.05$) high frequency % of resistance (96%, 82%, 76%, 72% and 70%, respectively). In the same table, the results of *K. pneumoniae* isolates susceptibility to ceftazidime, ceftriaxone, and cefuroxime, showed that 33/50 (66%), 29/50 (58%) and 23/50 (46%) were found to be resistant to these antibiotics, respectively. For antibiotics susceptibility to gentamycin and amikacin, the results showed that 29/50 (58%) and 22/50 (44%) of isolates were sensitive to former two antibiotics, respectively.

Table 2: Antibiotics susceptibility pattern of *K. pneumoniae* isolates

Antibiotics/ Isolates	Resistance		Intermediate		Sensitive	
	NO	%	NO	%	NO	%
Doxycycline	36	72	5	10	9	18
Rifampicin	35	70	4	8	11	22
Ciprofloxacin	41	82	6	12	3	6
Gentamycin	10	20	11	22	29	58
Cefuroxime	23	46	16	32	11	22
Ceftazidime	33	66	9	18	8	16
Amikacin	22	44	6	12	22	44
Imipenem	48	96	1	2	1	2
Ceftriaxone	29	58	4	8	17	34
Levofloxacin	38	76	8	16	4	8

P.Value <0.05 For all except amikacin , N=Number and %=Percentage.

Regarded to molecular characterization, the current study results showed that out of 19 *K. pneumoniae* isolates, 7 isolates (36.8%) were positive for *K1* gene (Figure 2) and 6 isolates (31.6%) were positive for *K2* gene (Figure 3) ,whereas 6 isolates (31.6%) were neither *K1* nor *K2*.

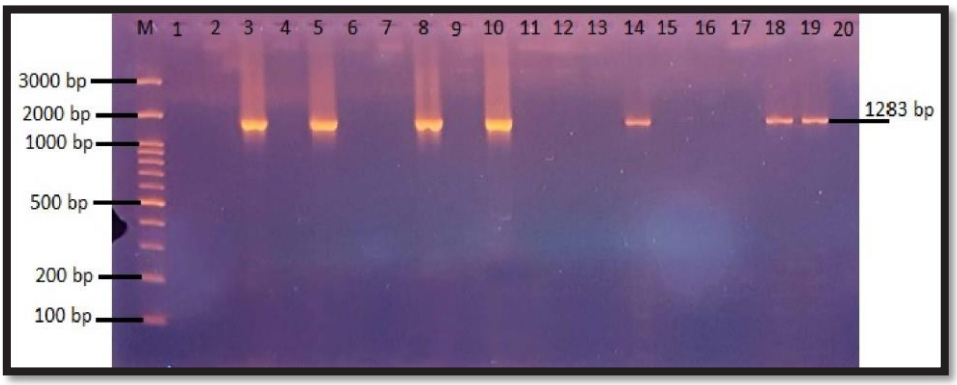

Figure 2: Polymerase chain reaction product (1283 base pair) of *K. pneumoniae K1* gene

Figure 3: Polymerase chain reaction product (531 base pair) of *K. pneumoniae K2* gene

The correlation between the antibiotics resistance and the present of *K1* and *K2* genes in 19 bacterial isolates is illustrated in Table (3). The results of gentamycin and amikacin revealed a significantly ($p<0.05$) high frequency % of antibiotics resistance among *K1* (71.4% for both) and *K2* (50% and 83.3%, respectively) positive isolates compared to *K1* and *K2* negative isolates (16.7% and 33.4%, respectively), whereas other antibiotics types revealed higher resistance rate, but without significant differences ($P>0.05$).

Table 3. Association between antibiotics resistance and the present of *K1* or *K2 K. pneumoniae* isolates

Antibiotics/ Isolates		*K1* positive (N=7		*K2* positive (N=6)		Non-*K1* and *K2* (N=6)		P.value
		NO	%	NO	%	NO	%	
Doxycycline	R	7	100	6	100	6	100	>0.05
Rifampicin	R	7	100	5	83.3	5	83.3	>0.05
	I	0	0	1	16.7	0	0	
	S	0	0	0	0	1	16.7	

Ciprofloxacin	R	6	85.7	5	83.3	5	83.3	>0.05
	I	1	14.3	1	16.7	1	16.7	
Gentamycin	R	5	71.4	3	50	1	16.7	<0.05
	I	0	0	3	50	5	83.3	
	S	2	28.6	0	0	0	0	
Cefuroxime	R	6	85.7	5	83.3	4	66.7	>0.05
	I	1	14.3	1	16.7	1	16.7	
	S	0	0	0	0	1	16.7	
Ceftazidime	R	6	85.7	6	100	6	100	>0.05
	S	1	14.3	0	0	0	0	
Amikacin	R	5	71.4	5	83.3	2	33.4	<0.05
	I	1	14.3	0	0	2	33.3	
	S	1	14.3	1	16.7	2	33.3	
Imipenem	R	7	100	6	100	6	100	>0.05
Ceftriaxone	R	6	85.7	4	66.7	5	83.3	>0.05
	I	0	0	1	16.7	0	0	
	S	1	14.3	1	16.7	1	16.7	
Levofloxacin	R	6	85.7	4	66.7	5	83.3	>0.05
	I	1	14.3	1	16.7	1	16.7	
	S	0	0	1	16.7	0	0	

R: Resistance, I: Intermediate, S: Sensitive and N: Number.

According to the results of the PCR and gene sequencing (phylogenetic tree construction) of *16S rRNA* gene of 19 *K. pneumoniae* isolates (data not shown), we identified six mutated clinical strains of *K. pneumoniae* that were deposited in GenBank under the accession numbers of MW642198, MW642199, MW642200, MW642201, MW642202 and MW642203. Therefore Table 4 shows the antibiotics susceptibility findings of these isolates, which revealed that the majority of the isolates 6 (100%) were resistance for all antibiotics, except gentamycin and amikacin were 5/6 (83.3%). The differences were significant ($p<0.05$) for all mentioned antibiotics.

Table 4. Antibiotics susceptibility pattern of 16*S rRNA K. pneumoniae* isolates.

(6S rRNA Positive Mutated Isolates (N=6))

Antibiotics/ Isolates	Resistance		Intermediate		Sensitive	
	NO	%	NO	%	NO	%
Doxycycline	6	100	0	0	0	0.0
Rifampicin	6	100	0	0	0	0
Ciprofloxacin	6	100	0	0	0	0
Gentamycin	5	83.3	0	0	1	16.7
Cefuroxime	6	100	0	0	0	0
Ceftazidime	6	100	0	0	0	0
Amikacin	5	83.3	1	16.7	0	0
Imipenem	6	100	0	0	0	0
Ceftriaxone	6	100	0	0	0	0
Levofloxacin	6	100	0	0.0	0	0

P. Value <0.05 For all **, N=**Number, **%=**Percentage and **16S rRNA=**16S ribosomal ribonucleic acid.

4. Discussion

Klebsiella pneumoniae is one of the most common enteric bacteria, accounting for up to 10% of all nosocomial infections and causing severe morbidity and death in pneumonia and urinary tract infections [20]. The present study was found a low prevalence of *K. pneumoniae* (27.8%) in total included clinical samples. The result was in consistent with 19.6% and 24% as estimated respectively, via [21] along with [22] and seems to be lower than that reported by [23] in clinical samples, who reported a frequency % of *K. pneumoniae* positivity is 73.3%. The discrepancies in prevalence rates could be accounted in part by changes in the study population, sample collecting method, and isolation and diagnosis methodologies.

Klebsiella pneumoniae is a common cause of pneumonia, urinary tract infections, skin infections, soft tissue infections, bacteremia, and septicemia, all of which have significant morbidity and death rates [24]. In this investigation, 50 isolates of K. pneumoniae were gathered from several clinical sample sources. Among the patients, *K. pneumoniae* infection was the higher microorganism isolated from the sputum samples (42%), followed by the urine samples (28%) and wound swabs (16%), whereas the lowest prevalence was reported in burns swabs (14%) (Figure 1) which was in line with above mentioned findings. Our results were closer to a previous studies carried out by [25] who reported that the *K. pneumoniae* was the predominant gram negative bacilli (60%) in RTIs, [26] who recorded a 26.79% of UTIs were

K. pneumoniae [27], and [28] whom reported that 23.3% of wounds and 16% burns swabs were diagnose as *K. pneumoniae* infection, respectively. The varied frequencies of K. pneumoniae isolation from different samples could be attributable to sample size differences, as well as different geographical and clinical situations with associated risk factors.

Drug resistance in human pathogenic bacteria like K. pneumoniae is a common occurrence around the world. Because of the widespread use of antibiotics in medical practise, this is considered a serious problem in both poor and developed countries [29]. We studied K. pneumoniae isolated from various clinical specimens in Al-Nasiriyah City to see if there was a variation in medication resistance (Iraq). The present study was reported a significantly higher frequency % of imipenem resistance (96%) among *K. pneumoniae* isolates (Table 2), a result with high consistency with the [17] who reported that 93.3% of *K. pneumoniae* isolates were resistant to imipenem. Result of this study revealed that *K. pneumoniae* had higher resistance to ciprofloxacin (82%). In consistent with this finding, another study [30] observed that *K. pneumoniae* bacterial types are generally insensitive to ciprofloxacin (88%). High resistance rate to imipenem and ciprofloxacin in the present study might be due to uncontrolled consumption of these antibiotics in Iraq. Antibiotic resistance in K. pneumoniae has numerous mechanisms, including quinolone drugs like ciprofloxacin and levofloxacin. These techniques involved modulating the target sites that bind with antibiotics by causing chromosomal genetic mutations in the genes encoding for DNA grease or resulting in the development of antibiotic-resistant enzymes [31]. Coinciding with these evidences this study results (Table 2) exhibited high resistance for ciprofloxacin and levofloxacin (82% and 76%, respectively). In this study, doxycycline antibiotic had bad activity against *K. pneumoniae* isolates (Table 2). Matching to our findings, another study [32] verified that only 6% of *K. pneumoniae* isolates were sensitive to this antibiotic. Rifampin was found to be effective against gram-negative bacteria in the majority of cases. Rifampin monotherapy, on the other hand, is not recommended in clinical practise since rifampin-resistant mutations arose soon after treatment began [33]. In compatibility with these findings, current study revealed (Table 2) a low activity of this antibiotic against *K. pneumoniae* isolates. Previous findings have found an elevated level of resistant of *K. pneumoniae* isolates to third generation cephalosporin such as ceftazidime and ceftriaxone [34]. A previous study had reported that the rate of *K. pneumoniae* isolates insensitive to ceftazidime and ceftriaxone is 52% and 65%, sequently [35].

In harmony with current study findings, another study verified that 74.3% of *K. pneumoniae* isolates were resist to ceftazidime drug [36] and 65.8% were resist to ceftriaxone drug [29]. In the present research, the results of susceptibility of *K. pneumoniae* isolates to cefuroxime antibiotic showed that 46% of the isolates were resistance to this drug (Table 2). Consistent with this finding, previous studies showed that a 37.5% [37] and 89.47% [38]. These findings concluded that there is urgent need to test the antibiotics activity against patient's isolates before therapy initiation. Regarded to aminoglycosides antibiotics, results of present study confirmed that *K. pneumoniae* isolates were more sensitive to gentamycin (58%) and amikacin (44%) compared to other mentioned above antibiotics. In agreement with our findings, another study observed that *K. pneumoniae* bacterial types had low resistance to gentamycin (15%) and amikacin (33.3%) antibiotics [17].

The findings revealed that 36.8% and 31.6% of the *K. pneumoniae* isolates had *K1* and *K2* genes, respectively (Figures 2 and 3) and 31.6% of the remaining isolates were not carry either of them. In line with our results, another previous study [39] recorded an elevated prevalence of *K1* gene compared to *K2* gene or absent of both genes. According to this study, all bacterial isolates that positive for *K1* and/or *K2* genes were found to be resistance to all current study used antibiotics (Table 3). According to these findings, isolates carrying these

genes become more virulent than others, and the presence of these virulence factors combined with a high level of drug resistance should make bacteria a highly infectious agent and result in treatment failure [40].

The bacterial 16S rRNA gene has nine "hypervariable regions" (V1-V9), which show significant sequence variability among bacteria [41]. When individual antibiotics target a shared or partially overlapping binding site on the ribosome, simultaneous loss of antibiotic sensitivity after acquisition of a single rRNA nucleotide mutation to combinations of structurally separate antibiotics may occur. When the mutated nucleotide is directly involved in the antibiotic binding site, minor structural changes may suffice to yield resistance; however, resistance mutations can also occur at sites that are not involved in antibiotic binding but where mutation causes structural perturbations that propagate toward the antibiotic binding site [42]. The findings of the present study (Table 4) confirmed the evidence of impaired antibiotics activity against a mutated identified clinical *16S rRNA* gene *K. pneumoniae* strains. A better explanation for these findings is that methylation of nucleotides implicated in the binding of 16S rRNA to antibiotics causes a decrease of affinity, leading in high-level antibiotic resistance [43]. In clinical isolates of gram-negative bacteria, several plasmid-encoded 16S rRNA methylases have been discovered [44].

The limited sample size (n=50) was the primary limitation of this study. Furthermore, the study was mostly conducted in Al-Nasiriyah City, and patients under the age of 16 were not evaluated. Finally, the molecular tests were performed for 19 isolates only which may be increase the bias of sample selection.

In conclusions, the prevalence of *K. pneumoniae* was higher among patients with respiratory system diseases compared to other. The presence of *K1*, *K2* and mutated *16S rRNA* genes consistent with elevation the rate of *K. pneumoniae* isolates resistance to antibiotics. As a result, continuing antimicrobial resistance monitoring, cautious antimicrobial agent use, and the construction of a surveillance system are all critical for preventing the spread of antibiotic resistance strains in Iraq.

References

1. Bengoechea JA, Sa Pessoa J. Klebsiella pneumoniae infection biology: living to counteract host defences. FEMS microbiology reviews. 2019 Mar;43(2):123-44.
2. Magill SS, Edwards JR, Bamberg W, Beldavs ZG, Dumyati G, Kainer MA, Lynfield R, Maloney M, McAllister-Hollod L, Nadle J, Ray SM. Multistate point-prevalence survey of health care–associated infections. New England Journal of Medicine. 2014 Mar 27;370(13):1198-208.
3. Paczosa MK, Mecsas J. Klebsiella pneumoniae: going on the offense with a strong defense. Microbiology and Molecular Biology Reviews. 2016 Sep 1;80(3):629-61.
4. Dubey D, Raza FS, Sawhney A, Pandey A. Klebsiella pneumoniae renal abscess syndrome: a rare case with metastatic involvement of lungs, eye, and brain. Case reports in infectious diseases. 2013 Aug 5;2013.
5. European Centre for Disease Prevention and Control. European Centre for Disease Prevention and Control. Antimicrobial resistance surveillance in Europe 2015. Annual Report of the European Antimicrobial Resistance Surveillance Network (EARS-Net). 2017.
6. Xu L, Sun X, Ma X. Systematic review and meta-analysis of mortality of patients infected with carbapenem-resistant Klebsiella pneumoniae. Annals of clinical microbiology and antimicrobials. 2017 Dec;16(1):1-2.

7. Izquierdo L, Merino S, Regué M, Rodriguez F, Tomás JM. Synthesis of a Klebsiella pneumoniae O-antigen heteropolysaccharide (O12) requires an ABC 2 transporter. Journal of bacteriology. 2003 Mar 1;185(5):1634-41.
8. Zacharczuk K, Piekarska K, Szych J, Zawidzka E, Sulikowska A, Wardak S, Jagielski M, Gierczyński R. Emergence of Klebsiella pneumoniae coproducing KPC-2 and 16S rRNA methylase ArmA in Poland. Antimicrobial agents and chemotherapy. 2011 Jan 1;55(1):443-6.
9. Siu LK, Fung CP, Chang FY, Lee N, Yeh KM, Koh TH, Ip M. Molecular typing and virulence analysis of serotype K1 Klebsiella pneumoniae strains isolated from liver abscess patients and stool samples from noninfectious subjects in Hong Kong, Singapore, and Taiwan. Journal of clinical microbiology. 2011 Nov 1;49(11):3761-5.
10. Esmaeel JR, Sadeq JN. Detection virulence factors of Klebsiella pneumonia from cattle by using PCR tec. Kufa Journal For Veterinary Medical Sciences. 2017;8(1).
11. Goldman E, Green LH, editors. Practical handbook of microbiology. CRC press; 2015 Jun 4.
12. Mahon CR, Manuselis G, editors. Textbook of diagnostic microbiology. WB Saunders company; 2000.
13. Balouiri M, Sadiki M, Ibnsouda SK. Methods for in vitro evaluating antimicrobial activity: A review. Journal of pharmaceutical analysis. 2016 Apr 1;6(2):71-9.
14. Sambrook J, Rusell DW. Vectors and bacterial strains. Molecular cloning. 2001;3:A3.
15. Embaby AM, Heshmat Y, Hussein A, Marey HS. A sequential statistical approach towards an optimized production of a broad spectrum bacteriocin substance from a soil bacterium Bacillus sp. YAS 1 strain. The Scientific World Journal. 2014 Jan 1;2014.
16. Turton JF, Baklan H, Siu LK, Kaufmann ME, Pitt TL. Evaluation of a multiplex PCR for detection of serotypes K1, K2 and K5 in Klebsiella sp. and comparison of isolates within these serotypes. FEMS microbiology letters. 2008 Jul 1;284(2):247-52.
17. Anis RH, Ahmed SM, Esmaeel NE. Virulence determinants associated with biofilm formation by Klebsiella pneumoniae causing hospital-acquired bloodstream infection. Microbes and Infectious Diseases. 2021 May 1;2(2):317-25.
18. Björkroth KJ, Schillinger U, Geisen R, Weiss N, Hoste B, Holzapfel WH, Korkeala HJ, Vandamme P. Taxonomic study of Weissella confusa and description of Weissella cibaria sp. nov., detected in food and clinical samples. International Journal of Systematic and Evolutionary Microbiology. 2002 Jan 1;52(1):141-8.
19. Phalakornkule C, Tanasupawat S. Characterization of lactic acid bacteria from traditional Thai fermented sausages, 2006.
20. Nourbakhsh F, Borooni S, Tajbakhsh E, Daneshmand D. Frequency and Antimicrobial Susceptibility of Multidrug-resistant Klebsiella pneumoniae Isolated From Wound Samples in Isfahan, Iran. Avicenna Journal of Clinical Microbiology and Infection. 2020 Jun 30;7(2):40-4.
21. Fatima S, Liaqat F, Akbar A, Sahfee M, Samad A, Anwar M, Iqbal S, Khan SA, Sadia H, Makai G, Bahadur A. Virulent and multidrug-resistant Klebsiella pneumoniae from clinical samples in Balochistan. International Wound Journal. 2021 Jan 21.
22. Chakraborty S, Mohsina K, Sarker PK, Alam MZ, Karim MI, Sayem SA. Prevalence, antibiotic susceptibility profiles and ESBL production in Klebsiella pneumoniae and Klebsiella oxytoca among hospitalized patients. Periodicum biologorum. 2016 Mar 16;118(1).
23. Zhang Y, Wang Q, Yin Y, Chen H, Jin L, Gu B, Xie L, Yang C, Ma X, Li H, Li W. Epidemiology of carbapenem-resistant Enterobacteriaceae infections: report from the

China CRE Network. Antimicrobial agents and chemotherapy. 2018 Feb 4;62(2):e01882-17.

24. Azar SL, Ebadi AR. Examining the pattern of susceptibility and antibiotic resistance in Klebsiella pneumoniae strains isolated from urine samples of children with urinary tract infections from the children's hospital of Tabriz in 2015. Br Biomed Bull. 2017;5(3):1-3.

25. Saha A, Debnath J, Das PK, Das NS, Tripathi P. Prevalence and antibiotic susceptibility pattern of multidrug resistant gram negative bacilli in lower respiratory tract Infections in a tertiary care hospital of Tripura. Indian Journal of Microbiology Research. 2020 Dec 15;5(4):538-42.

26. Soni P, Nerurkar A, Gandhi V. Klebsiella Pneumoniae, an Important Uropathogen: Prevalence and Antimicrobial Susceptibility Pattern. Pathology Update: Tropical Journal of Pathology & Microbiology. 2019; 5(3):171-176.

27. Abbas HA, El-Masry EM, Shaker GH, Mohsen I. Bacterial etiology and antimicrobial resistance of burn wound infections in a burn unit in Hehia General Hospital in Egypt. Int. J. of Biol. Ph. Research. 2013;4(12):1251-5.

28. Aljanaby AA, Alhasani AH. Virulence factors and antibiotic susceptibility patterns of multidrug resistance Klebsiella pneumoniae isolated from different clinical infections. African Journal of Microbiology Research. 2016 Jun 14;10(22):829-43.

29. Naqid IA, Hussein NR, Balatay AA, Saeed KA, Ahmed HA. The Antimicrobial Resistance Pattern of Klebsiella pneumonia Isolated from the Clinical Specimens in Duhok City in Kurdistan Region of Iraq. Journal of Kermanshah University of Medical Sciences. 2020 Jun 30;24(2).

30. Sonia SJ, Afroz S, Rasheduzzaman M, Uddin KH, Shamsuzzaman SM. Prevalence and Antimicrobial Susceptibility Pattern of Klebsiella Pneumoniae Isolated from Various Clinical Specimens in a Tertiary Care Hospital in Bangladesh. Medicine Today. 2020 Aug 29;32(2):95-9.

31. Ahmed RZ, Hadi TF, Abdullah RM. Bacteriological and Molecular Study of Klebsiella Pneumoniae Isolated from Patients with Urinary Tract Infections from Several Hospitals in Baghdad. Medico Legal Update. 2020 Nov 18;20(4):2049-55.

32. Chen A, Smith KP, Whitfield BA, Zucchi PC, Lasco TM, Bias TE, Kirby JE, Hirsch EB. Activity of minocycline against Klebsiella pneumoniae carbapenemase (KPC)-producing Enterobacteriaceae clinical isolates, with comparison to doxycycline and tigecycline. Diagnostic microbiology and infectious disease. 2017 Aug 1;88(4):365-7.

33. Zhang Y, Li P, Yin Y, Li F, Zhang Q. In vitro activity of tigecycline in combination with rifampin, doripenem or ceftazidime against carbapenem-resistant Klebsiella pneumoniae bloodstream isolates. The Journal of antibiotics. 2017 Feb;70(2):193-5.

34. Gupta V, Kumarasamy K, Gulati N, Garg R, Krishnan P, Chander J. AmpC β-lactamases in nosocomial isolates of Klebsiella pneumoniae from India. The Indian journal of medical research. 2012 Aug;136(2):237.

35. Namratha KG, Sreeshma P, Subbannayya K, Dinesh PV, Champa H. Characterization and antibiogram of Klebsiella spp. isolated from clinical specimen in a rural teaching hospital. Sch. J. App. Med. Sci. 2015;3(2E):878-83.

36. Nourbakhsh F, Borooni S, Tajbakhsh E, Daneshmand D. Frequency and Antimicrobial Susceptibility of Multidrug-resistant Klebsiella pneumoniae Isolated From Wound Samples in Isfahan, Iran. Avicenna Journal of Clinical Microbiology and Infection. 2020 Jun 30;7(2):40-4.

37. Assafi MS, Ibrahim NM, Hussein NR, Taha AA, Balatay AA. Urinary bacterial profile and antibiotic susceptibility pattern among patients with urinary tract infection in duhok

city, kurdistan region, Iraq. International Journal of Pure and Applied Sciences and Technology. 2015 Oct 1;30(2):54.

38. Saha A, Debnath J, Das PK, Das NS, Tripathi P. Prevalence and antibiotic susceptibility pattern of multidrug resistant gram negative bacilli in lower respiratory tract Infections in a tertiary care hospital of Tripura. Indian Journal of Microbiology Research. 2018 Dec 15;5(4):538-42.

39. Al-Jailawi MH, Zedan TH, Jassim KA. Multiplex-PCR assay for identification of Klebsiella pneumoniae. Int J Pharm Sci Rev Res. 2014;26(1):112-7.

40. Adwan GM, Owda DM, Abu-Hijleh AA. Prevalence of Capsular Polysaccharide Genes and Antibiotic Resistance Pattern of Klebsiella pneumoniae in Palestine. Jordan Journal of Biological Sciences. 2020 Dec;13(4): 475-482.

41. Ibrahim IA, Kareem TA, Azeez YM, Falhi HK. Phylogenetic tree analysis based on the 16S sequence alignment for Klebsiella spp. isolated from different sources. Iraqi Journal of Science. 2019 Dec 29:2618-28.

42. Cocozaki AI, Altman RB, Huang J, Buurman ET, Kazmirski SL, Doig P, Prince DB, Blanchard SC, Cate JH, Ferguson AD. Resistance mutations generate divergent antibiotic susceptibility profiles against translation inhibitors. Proceedings of the National Academy of Sciences. 2016 Jul 19;113(29):8188-93.

43. Yan JJ, Wu JJ, Ko WC, Tsai SH, Chuang CL, Wu HM, Lu YJ, Li JD. Plasmid-mediated 16S rRNA methylases conferring high-level aminoglycoside resistance in Escherichia coli and Klebsiella pneumoniae isolates from two Taiwanese hospitals. Journal of Antimicrobial Chemotherapy. 2004 Dec 1;54(6):1007-12.

44. Yamane K, Doi Y, Yokoyama K, Yagi T, Kurokawa H, Shibata N, Shibayama K, Kato H, Arakawa Y. Genetic environments of the rmtA gene in Pseudomonas aeruginosa clinical isolates. Antimicrobial agents and chemotherapy. 2004 Jun 1;48(6):2069-74.

Assessment of Hepatitis C virus (HCV) associated with hemodialysis patients in Thi-Qar province, Iraq

Ali Abdulhussein Khalaf [1], Khwam R Hussein[2]
{alialhussein222@gmail.com[1], krhussein@stu.edu.iq[2]}
Faculty of Graduate Studies, Southern Technical University, Iraq[1]
Al-Nasiriyah Technical Institute, Southern Technical University, Iraq[2]

Abstract: Hepatitis is liver inflammation that can lead to many fatal health problems. Hepatitis C virus (HCV) is a blood-borne virus. Hemodialysis patients are at greater risk of acquiring HCV infection and this is a major global health problem. The study included 120 samples from patients who underwent dialysis at the age range of 20 to 87 years; males were 58.3% while 41.7% were females. The study confirmed that the percentage of HCV infection among Hemodialysis patients was 30%, the high rate was in age groups 50-59 years (33.3 %), in males is high than females. There was an association between blood transfusion and HCV infection (P value=0.037). Also, the high percentage was in patients who remained more than 36 months 50.0% and twice sessions per week at 61.1%. Six isolates were recorded in the global GenBank with accession numbers: MW947494-MW947499. History of blood transfusions and a long period of Hemodialysis treatment were major risk factors for anti-HCV positive. HCV RNA testing should be conducted on all patients prior to Hemodialysis and blood before transfusion using PCR.

Keywords: HCV, Hemodialysis patients, PCR, NS5B and 5'UTR

1. Introduction

Hepatitis is a liver inflammation that can cause various health complications and death. Hepatitis C virus (HCV) is a virus that spreads through the bloodstream. This virus can cause both acute and chronic hepatitis. More than 170 million people are thought to be infected with the hepatitis C virus worldwide. An estimated 399 000 people died of hepatitis C virus in 2016. However, 1,75 million new HCV infections have been reported worldwide in 2015 [1]. Hemodialysis (HD) is the most common method used for the treatment of advanced and permanent renal failure [2]. Hemodialysis patients are more likely to get HCV infection, which is a serious global health issue. Risk factors for HCV infection in patients with dialysis include the number of time a blood transfusions, HD period and dialysis mode, dialysis unit prevalence of HCV infection, prior organ transplantation, intravenous drug use, male sex, old age and HD unit nosocomial HCV transmission [3]. The prevalence of HCV infection among HD patients in various parts of the world ranges from 1 % to 90 % in a wide range. The prevalence rate is less than 5% in northern Europe, about 10% in southern Europe and the United States, and between 10% and 70% in many northern African, Asian and South American countries [4]. However, it is high in

IMDC-IST 2021, September 07-09, Sakarya, Turkey
Copyright © 2022 EAI
DOI 10.4108/eai.7-9-2021.2315370

developing countries: 18% in Brazil; 21% in Turkey; 24% in Tunisia; 45% in Saudi Arabia; and 78% in Morocco [5]. In Egypt between 52.3% and 82.3% [6]. In Iraq, in 2014, 42.6% [7]. HCV is a small single-stranded RNA virus (approximately 55–65 nm) in size, with a genome containing 9600 nucleotides HCV segments are both nonstructural (NS; P7, NS2, NS3, NS4A, NS4B, NS5A, and NS5B) and structural (core, E1, and E2)[8]. The viral RNA genome consists of 341 nucleotides in the 5 'untranslated region (5'UTR), a single long open reading frame (ORF) carrying 3010-3040 amino acids in a big viral polypeptide, and the 3' untranslated region (3'UTR) of varying length [9]. HCV can be categorized into at least seven major genotypes and various subtypes (a, b, c, etc.) based on genomic sequence variation [10].
HCV infection diagnosis is based on the diagnostic tests for two types of laboratory testing: serological tests for the identification of anti-HCV antibodies and molecular tests for detecting viral particulates. The HCV-RNA test polymerase chain reaction (PCR) confirm diagnosis and quantity of viral copies of the blood [11]. On the other hand, this study is aimed to evaluate the hepatitis C virus infection rates among dialysis patients in dialysis units in Thi-Qar province, south of Iraq as well as to assess the main risk factors that may contribute to the transmission of this virus among dialysis patients. In addition, study the non-structural 5B (NS5B) gene and the 5' untranslated region (5'UTR).

2. Materials and Methods

The current study (case control study) was carried out after the approval of the Ministry of Health, Thi-Qar Health Directorate. The samples were taken from Al-Hussein Center for kidney Dialysis at Al-Hussein Teaching Hospital in Thi-Qar province, south of Iraq for the period from 1st of September 2020 to 31st of March 2021. The samples were collected from 120 Iraqi patients who underwent dialysis at age range 20-87 years, 70 (58.3%) were males and 50 (41.7%) were females. A direct interview (questionnaire) was completed with each patient to record the following personal information (patient name, age, address, gender, Occupation, Marital Status). Also, associated risk factors that included (History of HCV diagnosis, the date of the first dialysis, the number of times dialysis, family history of HCV, blood donation, the date of the blood donation, blood transfusion, the date of the blood transfusion, renal transfusion, the date of renal transfusion, previous surgery, the date of the previous surgery). In addition, chronic diseases as hypertension and diabetes were included. Blood samples (5ml) were drawn from each hemodialysis patients in this study (positive group and negative group of HCV) and collected in a sterile plastic tube. The blood samples were allowed to clot for 30 minutes at room temperature then centrifuged at 2000 gx for 15 minutes for clear separation of serum. The serum was saved in sterile tube and analyzed by ELISA assay to detect anti HCV antibody using commercially available kits (RecombiLISA HCV Ab ELISA Kit, Biotech, USA). The serum was stored at -20 °C until the future test by reverse transcription-PCR technique. HCV RNA was extracted from serum HD patients with anti-HCV positive using (QIAamp® Viral RNA Mini Kit, QIAGEN, Germany) according to manufacturer's instructions. RNA samples were converted to cDNA using (OneScript® Hot cDNA Synthesis Kit, abm, Canada). PCR was carried out to amplify the 5'UTR region (241bp in size) by the forward primer 5'-ACTCCACCATAGATCATCCC-3' [12] and the reverse primer 5'-AACACTACTCGGCTAGCAGT-3'. In addition, amplify the NS5B gene (826 bp in size) using the forward primer 5'-CAATWSMMACBACCATCATGGC-3' and the reverse primer 5'-CAGG ARTTRACTGGAGTGTG-3' [13].
Amplification of cDNA was carried out in a final volume of 25 µl reaction mixture using (GoTaq® Green Master Mix, Promega, USA) Which contains 5 µl cDNA samples, GoTaq®

Green Master Mix 12.5 µl, forward primer 1.5µl, reverse primer 1.5 µl and Nuclease free water 4.5 µl. PCR amplification conditions were 1 cycle of pre- denaturation at 94ºC for 5min and 35 cycle of denaturation at 94ºC for 30 sec, annealing at 56ºC for 30 sec, extension at 72 ºC for 30 sec and 1 cycle of final extension at 72ºC for 7min. Amplicon (10 µl) was mixed with (2µl) bromophenol blue (loading buffer) and loaded in the wells of the 1.5% agarose gel. The cathode was connected to the well side of the unit and the anode to the other side. The gel was run at 80 V until the bromophenol blue tracking dye migrated to the end of the gel. The cDNA was observed by staining the gel with ethidium bromide and viewed with UV transilluminator. Also, the purified NS5B gene PCR products were directed to Bioneer Company in Korea for achieved the DNA sequencing by AB DNA sequencing system. Phylogenetic study was done based on national center for biotechnology information -basic local alignment search tool (NCBI-Blast) alignment documentation. The phylogenetic tree was created by using the Neighbor-Joining method and evolutionary analyses was performed in molecular evolutionary genetics analysis (MEGA X) program. The data was analyzed using the statistical software that was available statistical packages for social science-version 26 (SPSS). The Chi-Square (X2) test was used to evaluate these significant differences at level $p<0.05$.

3. Results

The study included 120 cases of hemodialysis patients, using ELISA technique. The results were positive for HCV infection in 36 (30%) of those while 84 (70%) were negative for HCV infections (Figure 1).

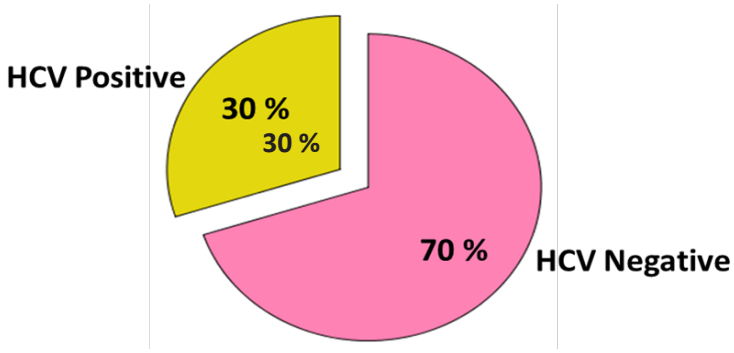

Fig. 1. Prevalence of hepatitis C virus infection among hemodialysis patients

The results showed that the high rate of infections with HCV among hemodialysis patients was in the age groups 50-59 years (33.3 %) and, 60-69 years 22.2% then 40-49 years was 19.4%. Also, the results confirmed that males were high than females, where the percentage of males was 58.3 % (n=70) while the incidence in females was 41.7% (n=50).where there were not significant differences (P = 0.419) as shown in Table (1,2).

In addition, the number of study patients who received a blood transfusion was 73 (60.8 %), where 27 (22.5%) of them were anti-HCV positive. The statistical analysis showed significant differences (P =0.037). Also, the period of hemodialysis was high percentage (50.0%) in patients who remained more than 36 months with significant differences (P =0.001) Table (3). The high number of sessions per week for hemodialysis patients with HCV infection was twice per week

61.1% (n=22), followed by three times a week at a rate of 33.3% (n=12), where it appeared significant differences (P=0.003) (Table 4).

Table 1: Distribution of hemodialysis patients with anti-HCV positive according to gender

Variables	groups	All patients		HCV +ve	
		NO.	%	NO.	%
Gender	Male	70	58.3	19	52.8
	Female	50	41.7	17	47.2
	Chi-Square	=0.653	df=1	P-value	=0.41

Table 2: Distribution of hemodialysis patients with anti-HCV positive according to age group

Variables	groups	All patients		HCV +ve	
		NO.	%	NO.	%
Age group (years)	20-29	13	10.8	2	5.6
	30-39	11	9.2	5	13.9
	40-49	14	11.7	7	19.4
	50-59	36	30.0	12	33.3
	60-69	31	25.8	8	22.2
	70-79	14	11.7	2	5.6
	> 80	1	0.8	0	0
	20-29	13	10.8	2	5.6
	Chi-Square	=7.765	df=6	P-value	0.256
Gender	Male	70	58.3	19	52.8
	Female	50	41.7	17	47.2
	Chi-Square	=0.653	df=1	P-value	=0.41

Table 3. Risk factors among hemodialysis patients with HCV infection

Risk factors	groups	All patients		HCV +ve	
		NO.	%	NO.	%
Length of time on hemodialysis	>12 months	35	29.2	7	19.4
	12-24 months	39	32.5	7	19.4
	25-36 months	14	11.7	4	11.1
	< 36 months	32	26.7	18	50.0
	Total	120	100.0	36	100.0
	Chi-Square	=17.356	df=3	P-value	0.001
History of blood transfusion	Yes	73	60.8	27	22.5
	NO	47	39.2	9	7.5
	Chi-Square	=4.332	df=1	P-value	0.037

Table 4. Relationship between the number of hemodialysis sessions per week and HCV infections

NO. of hemodialysis sessions per week	All patients		HCV +ve	
	NO.	%	NO.	%
Once	9	7.5	2	5.6
Twice	92	76.7	22	61.1
Three times	18	15.0	12	33.3
Four times	1	0.8	0	0
Total	120	100.0	36	100.0

The results of PCR were performed after the amplification process. The positive results were distinguished when the cDNA band base pairs of sample equal to the target product size [14], then the products were visualized by UV trans-illuminator and using digital camera for photographing as in Figures (2 and 3).

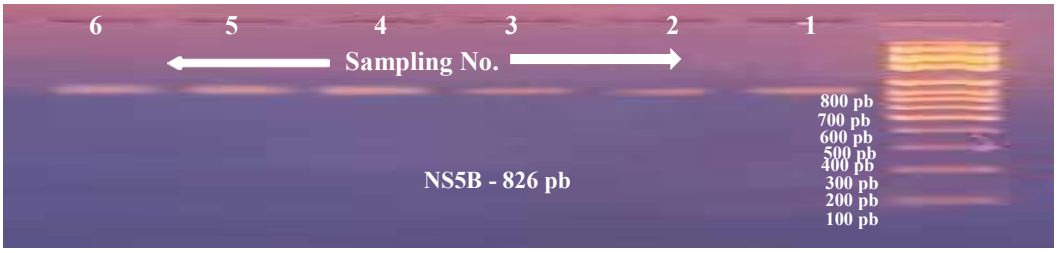

Fig. 2: Gel electrophoresis for PCR product from patients with hepatitis C, M: 100 bp DNA ladder, samples 1- 6: represent samples positive for NS5B.

Fig. 3. Gel electrophoresis for PCR product from patients with hepatitis C M: 100 bp DNA ladder, samples 1- 6: represent samples positive for 5UTR.

In addition, after carried out viral RNA extraction for several samples and cDNA conversion then amplification have been completed, the study succeeded in getting 6 accession numbers then recorded them in the global GenBank as shown in Table (5). Also, The results of the current study, and through the Phylogenetic trees, showed isolates similar sequences to previously recorded isolates from neighboring countries such as Saudi Arabia and Iran, as well as isolates from countries of the world as the United Kingdom (UK),Thailand and the Netherlands Figure (4).

Table 5. Results sequence analysis for non-structural 5B (NS5B) Gene

Sequences	Accession number	Genotypes
Sq1	MW947494	1a
Sq2	MW947495	5b
Sq3	MW947496	1a
Sq4	MW947499	3a
Sq5	MW947497	5b
Sq6	MW947498	1a

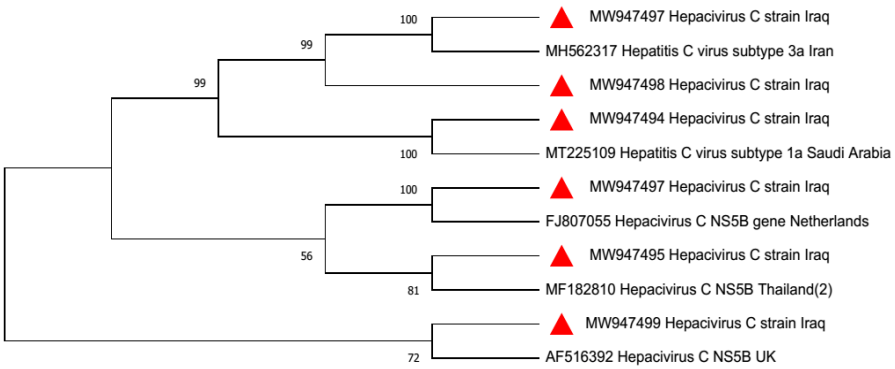

Fig. 4. Phylogenetic tree of studied isolates of HCV NS5B Gene with reference HCV strains in Genbank. Symbol ref▲ to local isolated have recorded.

4. Discussions

The prevalence of HCV in hemodialysis (HD) patients around the world ranges between 1 and 90%, and the risk of HCV infection due to dialysis is estimated at 2% annually [4]. The results of study were that compared to previous studies from other regions of Iraq like in Basra was 42.6% [7], in Baghdad 40.3% [15], but they were high than from other part of Iraq such as in Sulaimani was 26.7% [16], Al-Anbar was 11.7 % [17].In Iran were 8.1% and in Palestine were 24.7% [18], [19] but they were lower rate than Jordan 34.6% [20] and in Egypt 39.7% [21]. Also, other part of the world in the USA, and Southern Europe around 10% while below 5% in more countries of Northern Europe [22]. This variance due to differences in the risk factors that could impact HCV infection rates, or it because differences in the degree to which universal measures to avoid nosocomial transmission are implemented [23]. The results showed that the highest rate of infections was between the ages of 40-69 years, this occur because the older people have a high rate of renal failure diseases and need HD. This finding is agreement with previous studies [24]. Also, the study confirmed that males were high incidence than females this due to the males are more likely to be at risk and having anti-HCV positive than females [25]. The results are agreement with a previous studies have reported in Iraq [26], and in Iran [27]. But they were disagreement with the other study in Egypt [28]. Also, there were not significant differences ($p > 0.05$) between sex and anti-HCV positive in the study, this similar to another previously reported study [29]. HCV infections in HD patients have been significantly decreased when the number of blood transfusions has been reduced [30]. Several studies reported a significant relationship among history of blood transfusion and anti-HCV positive in HD patients [31]. The results were in agreement with the result of the current study that confirmed there was an association between blood transfusion and HCV infection, as the statistical analysis showed significant differences ($p < 0.05$). The statistical analysis showed that HCV infection depending on the length of a period on hemodialysis, where significant differences ($p < 0.05$) in the current study. The high percentage was in patients who remained more than 36 months. This result was similar to the findings of many studies conducted in different countries[32], who reported that the risk of contracting HCV infection increases significantly with the length of dialysis, this due to increase virus exposure, the long of period patients are in contact with hemodialysis equipment, or due to a lack of adequate anti-HCV antibody screening [33]. In addition, hemodialysis patients have weakened immune systems,

and any minor lapse in universal control of HCV infection could expose them to the virus [34]. The results of the number of sessions per week for hemodialysis patients with HCV infection were an agreement with previous study showed that HD patients who had a history of sharing hemodialysis devices frequently weekly were at an increased risk of HCV infection, which due to all these HD patients had more potential to be exposed to HCV-contaminated medical equipment, HCV-contaminated objects, or the HCV-contaminated hands of medical staffs, possibly leading to nosocomial infections [35].

On the other hand, non-structural 5B (NS5B) Gene is a suitable gene region for studying the molecular epidemiology of HCV. HCV genotyping through nucleotide sequence analysis of NS5B is a reliable method for distinguishing between HCV subtypes [36]. Phylogenetic analysis of HCV genotypes and subtypes is a helpful molecular method for scientists to identify or estimate evolutionary relationships between individuals or organisms groups [37]. However, the 5'untranslated region (5'UTR) is the most conserved region in the genome. It is often the best strategy for HCV genome detection [38]. For this reason, using the 5'UTR Gene for the purpose of HCV-RNA recommends for detection. The region controls genome replication and translation, and it can be used to diagnose this virus [39].

5. Conclusions

A history of blood transfusions as well as a longer period of HD treatment was the major risk factors for the development of anti-HCV positive. The 5'UTR Gene is often the best approach for detection of HCV-RNA and HCV genotyping across nucleotide sequence analysis of NS5B is a reliable manner for differentiating among HCV subtypes. In addition, HCV RNA easy should be performed on all patients prior to Hemodialysis patient and blood transfusion using PCR.

References

[1] Organization World Health, *Global hepatitis report 2017*. World Health Organization, 2017.

[2] B. H. Scribner, J. E. Z. Caner, R. Buri, and W. Quinton, “The technique of continuous hemodialysis,” *ASAIO J.*, vol. 6, no. 1, pp. 88–103, 1960.

[3] E. Nicolardi, A. Grieco, G. L. Rapaccini, and M. Pompili, “Natural history, diagnosis and treatment of chronic hepatitis B and C in hemodialysis patients,” *G. Ital. di Nefrol. Organo Uff. Della Soc. Ital. di Nefrol.*, vol. 27, no. 3, pp. 262–273, 2010.

[4] S. Marinaki, J. N. Boletis, S. Sakellariou, and I. K. Delladetsima, “Hepatitis C in hemodialysis patients,” vol. 7, no. 3, pp. 548–558, 2015, doi: 10.4254/wjh.v7.i3.548.

[5] F. Fabrizi and P. Martin, “Health care-associated transmission of hepatitis B and C viruses in hemodialysis units,” *Clin. Liver Dis.*, vol. 14, no. 1, pp. 49–60, 2010.

[6] A. Afifi, “The Egyptian Renal Registry,” *9th Annu. Rep. year*, 2008.

[7] S. S. Shihab, H. A. Al-Hmudi, H. S. Al-Edani, and K. H. Mahdi, “Viral hepatitis infections in Basrah haemodialysis unit: serological diagnosis and viral loading,” *Eur. J. Exp. Biol.*, vol. 4, no. 2, pp. 106–112, 2014.

[8] C. Alpers *et al.*, “KDIGO clinical practice guidelines for the prevention, diagnosis, evaluation, and treatment of hepatitis C in chronic kidney disease: introduction,” *Kidney Int.*, vol. 73, no. suppl. 109, pp. S6–S99, 2008.

[9] T. S. Gritsun and E. A. Gould, “The 3′ untranslated regions of Kamiti River virus and Cell fusing agent virus originated by self-duplication,” *J. Gen. Virol.*, vol. 87, no. 9, pp. 2615–2619, 2006.

[10] D. A Hassan, S. Q Maulud, R. H Saeed, and B. F Nore, "Seroprevalence and Genotypic Distribution Patterns of Hepatitis C Virus among Infected Patients from Erbil Province: Kurdistan/Iraq," *Diyala J. Med.*, vol. 14, no. 1, pp. 84–93, 2018, doi: 10.26505/djm.14013640911.

[11] M. Jadoul *et al.*, "Prevalence, incidence, and risk factors for hepatitis C virus infection in hemodialysis patients," *Kidney Int.*, vol. 95, no. 4, pp. 939–947, 2019, doi: 10.1016/j.kint.2018.11.038.

[12] H. L. Zaaijer, H. T. M. Cuypers, H. W. Reesink, I. N. Winkel, P. N. Lelie, and G. Gerken, "Reliability of polymerase chain reaction for detection of hepatitis C virus," *Lancet*, vol. 341, no. 8847, pp. 722–724, 1993, doi: 10.1016/0140-6736(93)90488-3.

[13] S. Akkarathamrongsin *et al.*, "Geographic distribution of hepatitis C virus genotype 6 subtypes in Thailand," *J. Med. Virol.*, vol. 82, no. 2, pp. 257–262, 2010, doi: 10.1002/jmv.21680.

[14] V. Sgaramella, "YAC protocols. Methods in molecular biology, vol. 54," *FEBS Lett.*, vol. 398, no. 2–3, pp. 338–338, 1998, doi: 10.1016/0014-5793(97)81273-2.

[15] A. S. Malik and H. M. H. AL-Rubaie, "Seroconversion rate of hepatitis C virus infection among haemodialysis patients in Al-Kadhimiya Teaching Hospital (dialysis unit)," *Iraqi J. Med. Sci.*, vol. 9, no. 4, pp. 343–349, 2011.

[16] Z. S. Ramzi, A. A. Abdulla, A.-H. Tariq, and N. G. Al-Tawil, "Prevalence and risk factors for hepatitis C virus infection in hemodialysis pateints in Sulaimani," *Zanco J. Med. Sci. (Zanco J Med Sci)*, vol. 14, no. 1 Special, pp. 44–50, 2010.

[17] J. I. Al-Mashhadani, "Hepatitis C virus infection among haemodialysis patients in Al-Anbar governorate," *IRAQI JOURNALOF COMMUNITY Med.*, vol. 20, no. 1, pp. 20–23, 2007.

[18] H. Al Zabadi, H. Rahal, and R. Fuqaha, "Hepatitis B and C prevalence among hemodialysis patients in the West Bank hospitals, Palestine," *BMC Infect. Dis.*, vol. 16, no. 1, pp. 1–5, 2015.

[19] R. Tajbakhsh, "Prevalence of hepatitis C and B virus infections among hemodialysis patients in Karaj, Iran," *Saudi J. Kidney Dis. Transplant.*, vol. 26, no. 4, p. 792, 2015.

[20] M. A. Daw and A. A. Dau, "Hepatitis C virus in Arab world: a state of concern," *Sci. World J.*, vol. 2012, 2012.

[21] H. A. Ahmed, Y. S. Yassine, A. R. Tawafe, and M. M. Ebazaway, "Epidemiological study of patients on regular haemodialysis at the Kafer El-Shakh Governorate, Egypt," *Menoufia Med. J.*, vol. 28, no. 2, p. 267, 2015.

[22] C. Gómez-Gutiérrez, N. C. Chávez-Tapia, G. Ponciano-Rodríguez, M. Uribe, and N. Méndez-Sánchez, "Prevalence of hepatitis C virus infection among patients undergoing haemodialysis in Latin America," *Ann. Hepatol.*, vol. 14, no. 6, pp. 807–814, 2015, doi: 10.5604/16652681.1171751.

[23] M. Al-Jamal, A. Al-Qudah, K. F. Al-Shishi, A. Al-Sarayreh, and L. Al-Quraan, "Hepatitis C virus (HCV) infection in hemodialysis patients in the south of Jordan," *Saudi J. Kidney Dis. Transplant.*, vol. 20, no. 3, p. 488, 2009.

[24] S. Ashkani-Esfahani, S. M. Alavian, M. Salehi-Marzijarani, and et al Mahmood, "Prevalence of hepatitis C virus infection among hemodialysis patients in the Middle-East: A systematic review and meta-analysis," *World J. Gastroenterol.*, vol. 23, no. 1, p. 151, 2017.

[25] I. I. Sarhan and C. R. Kamel, "Prevalence of hepatitis C virus seroconversion among hemodialysis patients in Egypt," *Egypt. Liver J.*, vol. 5, no. 2, pp. 34–39, 2015, doi: 10.1097/01.ELX.0000463167.48017.41.

[26] Hasanain MH AL-Rubaie1 et al, "Seroconversion Rate of Hepatitis C Virus Infection among Haemodialysis Patients in AL-Kadhimiya Teaching Hospital (Dialysis Unit)," *Iraqi JMS Publ. by Al-Nahrain Coll. Med.*, no. 1681–6579, pp. 343–349, 2011.

[27] M. J. Zahedi, S. D. Moghaddam, S. M. Alavian, and M. Dalili, "Seroprevalence of hepatitis viruses B, C, D and HIV infection among hemodialysis patients in Kerman Province, South-East Iran," *Hepat. Mon.*, vol. 12, no. 5, p. 339, 2012.

[28] S. A. Senosy and E. M. El Shabrawy, "Hepatitis C virus in patients on regular hemodialysis in Beni-Suef Governorate, Egypt," *J. Egypt. Public Health Assoc.*, vol. 91, no. 2, pp. 86–89, 2016, doi: 10.1097/01.EPX.0000484091.57255.c0.

[29] R. B. Fissell *et al.*, "Patterns of hepatitis C prevalence and seroconversion in hemodialysis units from three continents: the DOPPS," *Kidney Int.*, vol. 65, no. 6, pp. 2335–2342, 2004.

[30] M. P. Halle *et al.*, "Hepatitis B, hepatitis C, and human immune deficiency virus seroconversion positivity rates and their potential risk factors among patients on maintenance hemodialysis in Cameroon," *Iran. J. Kidney Dis.*, vol. 10, no. 5, p. 304, 2016.

[31] M. Espinosa *et al.*, "Marked reduction in the prevalence of hepatitis C virus infection in hemodialysis patients: causes and consequences," *Am. J. kidney Dis.*, vol. 43, no. 4, pp. 685–689, 2004.

[32] F. Joukar, S. Besharati, H. Mirpour, and F. Mansour-Ghanaei, "Hepatitis C and hepatitis B seroprevalence and associated risk factors in hemodialysis patients in Guilan province, north of Iran: HCV and HBV seroprevalence in hemodialysis patients," *Hepat. Mon.*, vol. 11, no. 3, p. 178, 2011.

[33] W. A. Alashek, C. W. McIntyre, and M. W. Taal, "Hepatitis B and C infection in haemodialysis patients in Libya: prevalence, incidence and risk factors," *BMC Infect. Dis.*, vol. 12, no. 1, pp. 1–8, 2012.

[34] A. Kashem *et al.*, "Hepatitis C virus among hemodialysis patients in Najran: prevalence is more among multi-center visitors," *Saudi J. Kidney Dis. Transplant.*, vol. 14, no. 2, p. 206, 2003.

[35] G. Cai *et al.*, "Factors Correlating to the Development of Hepatitis C Virus Infection in Hemodialysis Patients—Findings Mainly from Asiatic Populations: A Systematic Review and Meta-Analysis," *Int. J. Environ. Res. Public Health*, vol. 16, no. 8, p. 1453, 2019.

[36] D. G. Murphy, B. Willems, M. Deschênes, N. Hilzenrat, R. Mousseau, and S. Sabbah, "Use of sequence analysis of the NS5B region for routine genotyping of hepatitis C virus with reference to C/E1 and 5′ untranslated region sequences," *J. Clin. Microbiol.*, vol. 45, no. 4, pp. 1102–1112, 2007.

[37] D. Mutimer *et al.*, "EASL Clinical Practice Guidelines: management of hepatitis C virus infection," *J. Hepatol.*, vol. 60, no. 2, pp. 392–420, 2014.

[38] K. Hesamizadeh, S. M. Alavian, A. N. T. Shabankareh, and H. Sharafi, "Molecular tracing of hepatitis c virus genotype 1 isolates in iran: a NS5B phylogenetic analysis with systematic review," *Hepat. Mon.*, vol. 16, no. 12, 2016.

[39] G. K. Alagoz *et al.*, "Hepatitis C virus genotype distribution in Turkey remains unchanged after a decade: performance of phylogenetic analysis of the NS5B, E1, and 5'UTR regions in genotyping efficiency," *Turk J Gastroenterol*, vol. 25, no. 4, pp. 405–410, 2014.

Evaluation the Diagnostic Values of Direct and Indirect Non-invasive Biochemical Markers of Liver Fibrosis in Patients with Chronic Hepatitis B Virus

Dawood Salman Mahdi[1], Hamid Jaddoa Abbas[2] and Mostafa Salman Hasan[3]
{ dr.dawds@stu.edu.iq[1]}

Southern Technical University, Health and Medical technology College. Iraq, Basra[1]
Al-Faiha'a Teaching Hospital, Iraq, Basra[2]

Abstract. To investigate hepatic fibrosis in chronic hepatitis B patients using non-invasive direct and indirect biomarkers, as well as to assess the diagnostic accuracy of these biomarkers. There are 119 people in a case-control study: 50 healthy people served as controls, whereas 69 individuals with chronic hepatitis B were diagnosed using the PCR method. In addition to cholesterol, the direct biomarkers (serum fibronectin, haptoglobin, and TNF alpha) and indirect biomarkers (serum total bilirubin, direct bilirubin, aspartate aminotransferase AST, alanine aminotransferase ALT, alkaline phosphatase ALP, albumin, and gamma-glutamyl transferase - GGT) are For liver function tests and a fibrotic marker, there was a significant difference ($P < 0.05$) between control and HBV patients: fibronectin (168.56± 98.47 control vs. 98.24 ± 74.87 HBV) and TNF alpha (121.96+124.8 control vs. 56.03±48.39 HBV). The haptoglobin and cholesterol revealed no differences between males or females when compared with control. The sensitivity of fibrotic markers: fibronectin, TNF alpha, and haptoglobin cannot be calculated. These biomarkers could be used instead of a liver biopsy to track the progression and therapy of liver fibrosis.

Keywords: Hepatitis B virus, liver fibrosis, Liver Biopsy.

1 Introduction

The creation of an excessive quantity of scar tissue in the liver is known as hepatic fibrosis. It occurs when the liver strives to repair and replace damaged cells. The liver can be injured by a variety of factors. Fibrosis itself causes no symptoms, but severe scarring can lead to cirrhosis. The persistence of liver viral infection causes chronic damage and excessive extracellular matrix formation by hepatic stellate cells in the liver, which can lead to cirrhosis and malignancy. The liver is a multilobed reddish-brown glandular organ that occupies most of the upper right section of the human abdominal cavity, just below the diaphragm. It is in charge of metabolism, immunity, digestion, detoxification, and storage, among other things [1]. It also has the responsibility of regulating the flow and safety of substances absorbed from the digestive system prior to their distribution to the systemic circulatory system. The importance of the liver is reflected by the fact that complete loss of hepatic function can result in death within minutes [2]. Hepatitis is an inflammation of the liver which results in damage to hepatocytes with subsequent cell death (necrosis) [3]. Liver fibrosis is a complicated fibrogenic and inflammatory process that develops as a result of chronic liver injury and is a precursor to liver cirrhosis [4].

IMDC-IST 2021, September 07-09, Sakarya, Turkey
Copyright © 2022 EAI
DOI 10.4108/eai.7-9-2021.2315367

2 Materials and Methods

119 participants took part in the case-control study: 50 healthy controls (26 men and 24 women) and 69 patients with chronic hepatitis type B for at least 6 months (36 males and 33 females). Al-Faiha'a Gastrointestinal Centre in Barah, Iraq, treated the patients. Full clinical examinations and laboratory tests were used to diagnose the patients. The Patients, who had chronic diseases except for patients in our study were excluded from the study. The parameters Haptoglobin is the measurement by Abbott C4000 autoanalyzer. The ELISA technique was used to measure fibronectin and TNF alpha. Cobas INTEGRA plus 400 auto analysers for liver function testing and cholesterol measurement.

2.1 Statistical Analysis

Statistical significance was defined as p-values less than 0.05 using IBM SPSS Statistics 22.0.

3 Results

3.1 Control and Hepatitis B Patients

This work was observed that the age, sex, and haptoglobin did not show statistical differences between the control group and hepatitis B patients (P-value >0.05), While all the other variables were shown significant differences (P <0.05) as represented in Table 1.

Table 1. Data on healthy people and individuals with hepatitis B.

Variables		Control (N= 50)	Hepatitis B (N= 69)	P-Value
Age		42.2 ± 15.7	43.0 ± 15.9	0.784
Sex	Male	36 (52.2%)	26 (52.0%)	0.912
	Female	33 (47.8%)	24 (48.0%)	
	Total	69 (100%)	50 (100%)	
Bilirubin- T		0.41 ± 0.17	2.58 ± 2.27	0.0001
AST		16.24 ± 4.61	60.37 ± 56.11	0.0003
ALT		29.90 ± 10.26	74.73 ±71.5	0.0002
ALP		75.12 ± 15.09	115.4 ± 73.78	0.0001
GGT		17.65 ± 7.81	88.19 ± 83.06	0.0001
Albumin		4.28 ± 0.24	4.11 ± 0.51	0.001
Haptoglobin		156.20 ± 54.33	159.82 ± 59.09	0.731
Fibronectin		168.56 ± 98.47	98.24 ± 74.87	0.0001
TNF		121.96 ± 124.83	56.03 ± 48.39	0.0001

3.2 Comparison Between Control and Hepatitis B Patients According to Gender

Table 2 shows the gender contrast between control and hepatitis B patients. In the current study, all variables (P <0.05) in male and female patients with hepatitis B were substantially different from the control group, with the exception of haptoglobin (P > 0.05).

Table 2. Control and hepatitis B patients data according to sex.

Variables	Males			Females		
	Control (N= 26)	Hep. B (N = 36)	P. Value	Control (N = 24)	Hep. B (N = 33)	P. Value
Bilirubin-T	0.47 ± 0.13	2.61 ± 2.32	0.0001	0.35 ± 0.18	2.55 ± 2.25	0.0001
AST	17.98 ± 4.79	57.20 ±49.9	0.005	14.36 ± 3.65	63.81 ±62.7	0.007
ALT	32.80 ± 9.79	85.05 ± 83.9	0.0003	26.88± 10.06	63.48 ± 53.9	0.0045
ALP	74.07 ± 14.80	108.13 ±82	0.012	76.25 ± 16.85	123.49 ± 63	0.001
GGT	21.88 ± 8.08	73.13 ± 69.3	0.0003	13.06 ± 4.2	74.21 ± 67.8	0.001
Albumin	4.38 ± 0.18	4.23 ± 0.48	0.032	4.37 ± 0.3	3.99 ± 0.53	0.001
Haptoglobin	162.84 ± 46.64	150.22 ± 49	0.830	149 ± 61.81	170.3 ± 67.2	0.645
Fibronectin	120.47 ±101.16	68.9 ± 70.14	0.0001	220.66 ± 63.93	130.25 ± 67.13	0.001
TNF	72.84 ± 67.88	48.67 ± 31.87	0.004	175.16 ± 150.	64.06 ± 61.13	0.002

3.3 ROC Analysis for the Hepatitis B

Table 3 shows the ROC for the identification of liver fibrosis in hepatitis B. According to the findings of this investigation, fibronectin and TNF had the lowest AUC.

Table 3. ROC for liver fibrosis detection with hepatitis B.

Variables	The area under the ROC curve	p-value (AUC0=0.5)	Best cut-off criterion	Sensitivity (%)	Specificity (%)	Efficiency	PPV	NPV
Haptoglobin	0.519	0.772	-	-	-	-	-	-
Fibronectin	0.278	0.0001				-	-	-
TNF	0.374	0.020	-	-	-	-	-	-

3.4 Identification of people with hepatitis B

According to the findings of this investigation, no parameters had statistically significant differences (P>0.05). The size of the odds ratios, on the other hand, differed. Table 4 shows that GGT and AST were optimum.

Table 4. Detail of people with hepatitis B who are at risk of developing liver fibrosis.

Variables	P. Value	Odd ratio	95% Confidence Limits	
			Low	Upper
Bilirubin T	0.917	0.0001	0.0001	*
AST	0.966	11.781	0.0001	66.0
ALT	0.933	0.028	0.0001	1.790
ALP	0.967	0.545	0.0001	12.000
GGT	0.959	20.141	0.0001	3.400
Albumin	0.999	0.080	0.0001	*
Haptoglobin	0.930	1.939	0.0001	511.000
Fibronectin	0.931	0.579	0.0001	12.000
TNF	0.944	1.389	0.0001	130.0

3. 5 Correlations Patients Results

Table 5 shows the associations between the factors for patients. A correlation coefficient of 0.6 or higher was regarded significant in this study as an indicator of correlation between binary variables. All other factors were not significant except for ALT and AST.

Table 5. Correlations over patients.

	Bilirubin D	AST	ALT	ALP	GGT	Albumin	Hepato.	Fibron.	TNF	Cholesterol
Bilirubin T	**0.92**	**0.461**	**0.581**	**0.401**	**0.521**	**0.361**	**0.061**	**0.081**	**0.072**	**0.16**
AST			**0.631**	**0.351**	**0.211**	**0.081**	**0.021**	**0.131**	**0.101**	**0.08**
ALT				**0.351**	**0.311**	**0.151**	**0.041**	**0.081**	**0.071**	**0.13**
ALP					**0.521**	**0.401**	**0.031**	**0.091**	**0.061**	**0.12**
GGT						**0.361**	**0.011**	**0.171**	**0.121**	**0.09**
Albumin							**0.081**	**0.101**	**0.091**	**0.01**
Hepato.								**0.061**	**0.021**	**0.01**
Fibronectin									**0.721**	**0.12**
TNF										**0.02**

4 Discussion

The deposition of ECM produced by HSC and other hepatic cells is directly involved in liver fibrosis markers, as well as indirect liver function assessments. Hepatic injury is linked to a disruption of several metabolic activities, that helps with the biochemical analysis of liver illness. The current study revealed the haptoglobin in HBV patients (159.82) was a non-significant difference when compared with control, this result appeared due to begin to decrease the haptoglobin concentration after it was elevated at the onset of infection because

of the progress of hepatocyte damage and synthesis of fibrosis this result was an agreement with [5]. The fibronectin levels in hepatitis B were significant low (98.24) compared with control, the decreased level of fibronectin due to decrease releasing from hepatocytes in patients with chronic hepatitis this result was an agreement with [6], the fibronectin serum level increases with the advancement of liver fibrosis but finally decreases in patients with cirrhosis due to hepatic dysfunction which agreement with [7] and [8]. In dendritic cells, the viral core proteins induce immunological tolerance and overproduce IL-10, which can suppress the production of pro-inflammatory cytokines. The viral core proteins, which induce immunological tolerance in dendritic cells and overproduce IL-10, which can suppress the production of pro-inflammatory cytokines, appeared to be responsible for this result (TNF-α). The result was an agreement with [9]. The current study revealed the mean of haptoglobin, fibronectin, and TNF alpha in the male (150.22, 68.9, 48.67) respectively lower than female this indicter the liver fibrosis in the male more progress than female, this result agreement with [10]. Estrogens are important for preserving homeostasis and making the liver less vulnerable to a variety of chronic liver disorders, according to [11]. Feminine immune responses are greater than male immune responses in adulthood, which resulting in a decreased risk of infection and a superior ability to clear viral infection in women, according to [12]. ROC curves are used to diagnose liver fibrosis caused by hepatitis B. The results showed that haptoglobin, fibronectin, and TNF had an area under the ROC less than 0.6, therefore sensitivity and specificity could not be calculated. The risk of liver fibrosis was determined using multivariable logistic regression analysis. The outcomes were shown that some variables in the model were non-significant(P value>0.05), but the odds ratios in these parameters are more risk compared with other parameters, this result is an agreement with [13].

4 Conclusion

Hepatic fibrosis can be predicted directly and indirectly using direct and non-invasive biochemical markers in patients with chronic hepatitis B virus, as well as the progression and management of fibrosis.

References

[1] Vasimahmed Lala, Amandeep Goyal, Pankaj Bansal and David A. Minter, 2021, Liver Function Tests, StatPearls ; 12.
[2] Morini, S., Carpino, G., Carotti, S., & Gaudio, E. (2020). Anatomy and Embryology of the Liver. In Liver Diseases Springer. (pp. 3–16).
[3] Marc Ringehan, Jane A. McKeating and Ulrike Protzer, 2017, Viral hepatitis and liver cancer, journal the royal society.
[4] Joon-Il Jun and Lester F. Lau, 2018 , Resolution of organ fibrosis , the journal of clinical investigation ; 128(1):97-107
[5] Erturk, Erkan, Ozkurt, Parlak & Cure, M. C. (2014). Serum fibronectin levels in acute and chronic viral hepatitis patients. The Malaysian Journal of Medical Sciences, 21(1): 29.
[6] Safaei, Oskouie, Mohebbi, Razaghi, Z., & Nejadi, N. (2020). Proteomic study of advanced cirrhosis based on HCV to reveal potential biomarkers. Gastroenterology and Hepatology From Bed to Bench, 13(1):113.
[7] Younesi, S., & Parsian, H. (2019). Diagnostic accuracy of glycoproteins in the assessment

of liver fibrosis: A comparison between laminin, fibronectin, and hyaluronic acid. The Turkish Journal of Gastroenterology, 30(6): 524.

[8] Sarvari, Mojtahedi, Kuramitsu, Malek-Hosseini; et al (2011). Differential expression of haptoglobin isoforms in chronic active hepatitis, cirrhosis and HCC related to HBV infection. Oncology Letters, 2(5): 871–877.

[9] Rosen, H. R., & Golden-Mason, L. (2020). Control of hcv infection by natural killer cells and macrophages. Cold Spring Harbor Perspectives in Medicine, 10(9).

[10] Jamal Sarvari, Zahra Mojtahedi, Yasuhiro Kuramitsu and Seyed-Ali Malek-Hosseini 2011, Differential expression of haptoglobin isoforms in chronic active hepatitis, cirrhosis and HCC related to HBV infection, Oncology Letters, 2(5): 871–877

[11] Ezhilarasan, D. (2020). Critical role of estrogen in the progression of chronic liver diseases. Hepatobiliary & Pancreatic Diseases International, 19(5): 429-434

[12] Henze, L., Schwinge, D., & Schramm, C. (2020). The Effects of Androgens on T Cells: Clues to Female Predominance in Autoimmune Liver Diseases? Frontiers in Immunology, 11:1567.

[13] Karsdal, Morten A, Hjuler, Rasmussen;et.al (2019). Assessment of liver fibrosis progression and regression by a serological collagen turnover profile. American Journal of Physiology-Gastrointestinal and Liver Physiology, 316(1): 25–31.

Investigating the Gene Expression Profiles of Immune Checkpoints in Breast Cancer Microenvironment and Peripheral Blood: A Comparative Study

Howraa J Bakal[1], Khairallah A.S Mohammed[2], Naael H. Ali[3]
{horaa.j.al@gmail.com[1], dr.kmohammed@stu.edu.iq[2], nhali66@yahoo.com[3]}

Department of Medical Lab Technology, College of Health and Medical Technology, Southern Technical University, Iraq[1,2]
College of Medicine, University of Basra, Iraq[1]

Abstract. The goal of this study was to compare and assess the expression of immunological checkpoints (FOXP3 and CTLA-4) in the tumour microenvironment and peripheral blood in breast cancer patients. The CTLA-4 and FOXP3 transcripts was measured using real-time PCR after total RNA was splitted from blood and tissues from 36 women with breast cancer and 15 women with breast benign tumours. CTLA-4 expression was considerably higher in the tissues of breast cancer patients than in the blood ($P<0.02$). CTLA-4 expression was considerably lower in blood from individuals with breast cancer compared to blood from the benign group ($P<0.001$). There was no difference in CTLA-4 mRNA expression in tissues and blood in a breast benign tumour. FOXP3 was higher in tissue from breast cancer than in blood, although it was equivalent in both tissues and blood from benign breast tumours.

Keywords: Checkpoints, Gene Expression, CTLA-4, FOXP3, Breast Cancer (BC)

1 Introduction

BC is one of the most frequent cancers in women, and it has a high fatality rate. Breast cancer was predicted to be responsible for 29 percent of cancer diagnoses and 15 percent of cancer-related deaths [1, 2]. The host immune response appears to play a substantial influence in the prognosis of malignant tumours, according to accumulated data [3]. The relevance of the host immune response and immunological tolerance in the development of neoplastic illness was revealed by these findings [4]. Normally, the immune system plays a vital role in defence against malignant tumours so that the compromised patients have an increasingly significant incidence of malignancy [5]. Based on the evidence, the immune system's primary function is to recognise and kill cancerous cells as soon as they arise [6]. Unfortunately, tumour cells can evade immune detection through a variety of methods, including down-regulation of immune responses [7]. Some cancerous cells can protect themselves from killing by the immune system through stimulating immune checkpoints. Immune checkpoints are important in the self-tolerance process because they restrict the immune system from attacking cells randomly [8]. Those immunological checkpoints are currently being exploited as cancer therapeutic targets. Clinical trials using checkpoint inhibitors of solid tumours revealed a clear response that could not be replicated by other medication [9, 10]. Cancer immunotherapy aims to improve the immune system's ability to

IMDC-IST 2021, September 07-09, Sakarya, Turkey
Copyright © 2022 EAI
DOI 10.4108/eai.7-9-2021.2314941

recognise tumour cells by disrupting the mechanisms that tumour cells use to escape and suppress immunological responses [11]. One of the main immune regulatory molecules is Treg cells regulatory. These cells play an essential role in the regulation of immune activities and keep the effect of self-antigens. This can be achieved by different techniques, ex. suppression of antigen-presenting cells via CTLA-4 and secretion of immunomodulatory cytokines (IL-10, TGF-β, and IL-35) [12, 13]. Forehead Box P3 (FOXP3) is a master transcription factor that controls Treg cell development, maintenance, and suppressor activity [14, 12, 15]. Treg cells are crucial immune-mediated inflammation, but they've also been important mediators of active immune evasion; reducing these cells can boost endogenous anti-tumour immunity and immunotherapy efficacy. Many researchers have looked into Treg cell are immunosuppression in cancer patients [16, 17]. Treg cells suppress immune cells such as CD8+ T, NK, B cells, and APCs [18, 19]. The chemokine CCL22, which is released by tumour cells, collects them in tumour tissues [18, 19]. Increasing the number of Treg cells promotes cancer progression by weakening the immune system and allowing tumour cells to avoid detection and elimination by the immune system. Tumor growth may be aided by suppressing cell-mediated immunity and increasing the number and/or function of Treg cells [16]. Some indicators, such as FOXP3, Cytotoxic T lymphocyte antigen-4 (CTLA-4) and glucocorticoid-induced TNFR family-related gene (GITR), alter Treg cells' immunosuppressive capabilities [20, 21]. Despite the fact that numerous studies have been done on measuring FOXP3 and CTLA-4 expression in the peripheral blood of breast cancer patients [22, 23], there has been little research done on measuring FOXP3 and CTLA-4 in malignant tissues. The goal of this study was to compare and assess the expression of FOXP3 and CTLA-4 in the tumour microenvironment and peripheral blood of breast cancer patients.

2 Materials and Methods

2.1 Participants

Between August 2020 and February 2021, a total of 51 women, aged 30 -63 years with breast cancer who attended cancers centre/AL-Sadr teaching hospital, Basra, Iraq, were involved in the present study. Permission from the doctor was acquired, and each participant signed a consent form. The patients had just been diagnosed with cancer and were included in the trial before starting chemotherapy, radiation, or immunotherapy. Expert oncologists confirm the diagnosis of breast cancer based on specific surgical and pathological findings. To validate the diagnosis, all patients completed a medical status questionnaire. The questionnaire asked about sex, age, the presence or absence of another chronic disease, family history, and drug use.

Two millilitres of venous blood samples and tissue specimens (Formalin fixation and paraffin embedding, FFPE) were collected from all participants including 36 patients (malignant cases) and 15 women with breast benign tumour as a positive control.

2.2 Extraction and Transcription of Real-Time PCR

PB (peripheral blood) and FFPE (Formalin-Fixed Paraffin-Embedded) specimens using the Geneaid kit, the RNA is extracted (Geneaid, Taiwan) and PROMIGA kit (PROMIGA, USA)

based on producer's recommendations. A Nanodrop spectrophotometer was used to assess the purity and concentration of total RNA in all samples. To make cDNA from extracted RNA, a complementary DNA (cDNA) synthesis kit (OptiScriptTM RTSystem ONE-STEPRT-PCRPreMix, Korea) was employed. The reverse transcription process includes adding a reverse transcription enzyme, heating it to 45°C for 35 minutes, and then cooling it to 95°C for 5 min, for reversing halt transcription enzyme from working.
The gene of FOXP3 - CTLA-4 was investigated using a real-time PCR apparatus (Applied Biosystems, USA) with 10 litres of SYBR green master mix, 2 litres of template cDNA, 1 litre of particular primers (10 pmol stock), and 6 litres of nuclease-free water. Bioneer Company synthesised the primers (Korea). Table 1 lists the primer sequences that were employed. 95°C for 1 min, 40 cycles of 95°C for 15 sec, 55-60°C for 1 minute, 95°C for 15 seconds was the thermal cycler's schedule.
The GAPDH gene was utilised as an internal control to normalise the amplified target genes. The quantity of FOXP3 and CTLA-4 in PB or FFPE expressed as a percentage of the amount of GAPDH determined using the $2^{-\Delta\Delta CT}$ algorithm.

Table 1. PCR Primers for amplification of the genes encode CTLA-4 and Foxp3.

Gene	Primers	Sequence	Reference
CTLA4	Forward	5-GCCCTGCACTCTCCTGTTTTT-3	(Khalife et al. 2018) [24]
	Reverse	5-GGTTGCCGCACAGACTTCA-3	
Foxp3	Forward	5-GTGGCCCGGATGTGAGAAG-3	
	Reverse	5-GGAGCCCTTGTCGGATGATG-3	
GAPDH	Forward	5-TTCCAATATGATTCCACCCA-3	
	Reverse	5-GATCTCGCTCCTGGAAGATG-3	

2.2 Statistical Analysis

The data concluded the average, Std Dev., and standard error. The arithmetic comparison was done using (SPSS version 25) and the ANOVA and Mann-Whitney U tests, where needed. When P is less than 0.05 the data are statistically significant.

3 Results

The expression of CTLA-4 and FOXP3 was determined in tissues (FFPE) and peripheral blood (PB) of 36 women with BC and 15 positive controls (breast benign tumour) with mean age: 47 ± 7.8 and 42 ± 10 ((P > 0.05) years, respectively. The quantity of FOXP3 and CTLA-4 expression in the PB or FFPE expressed as a percentage of the amount of GAPDH expression determined using the $2^{-\Delta\Delta CT}$ method.

3.1 The Expression of CTLA4 By Tissues and Blood

Table 2 and Fig 1 show the fold change in CTLA-4 gene in tissues and blood of women with BC and a positive control group (breast benign tumour).
CTLA-4 in the tissues was substantially higher than in blood in control BC with ($P<0.02$). There was no difference in CTLA-4 mRNA in tissues or blood in the group with breast benign tumours.
CTLA-4 expression was considerably lower in blood from individuals with breast cancer compared to blood from the benign group ($P<0.001$). In addition, CTLA-4 expression in breast cancer tissues was lower than in the benign group, but the difference was not significant.

3.2 The Expression of FOXP3 by Tissues and Blood

The amount of the FOXP3 mRNA was in tissue from BC non-control was higher than the expression in blood but with less significant level (Fig. 2 and Table 2). FOXP3 mRNA was similar in both tissues and blood from breast benign tumours (positive control) and higher compared with breast cancer patients (Fig 1 and Table 2).

Table 2. The CTLA-4 and FOXP3 in blood and tissues from patients with BC and positive control group (Breast benign tumour).

Group	Source of mRNA	CTLA-4 expression	FOXP3 expression
Breast cancer N=36	Blood	0.032373 ± 0.21	0.318797 ± 0.42
	Tissue	0.265997 ± 0.27	0.697323 ± 0.26
Positive control group N=15	Blood	0.998159 ± 0.49	1.003004 ± 0.47
	Tissue	1.010447 ± 0.28	1.000194 ± 0.30

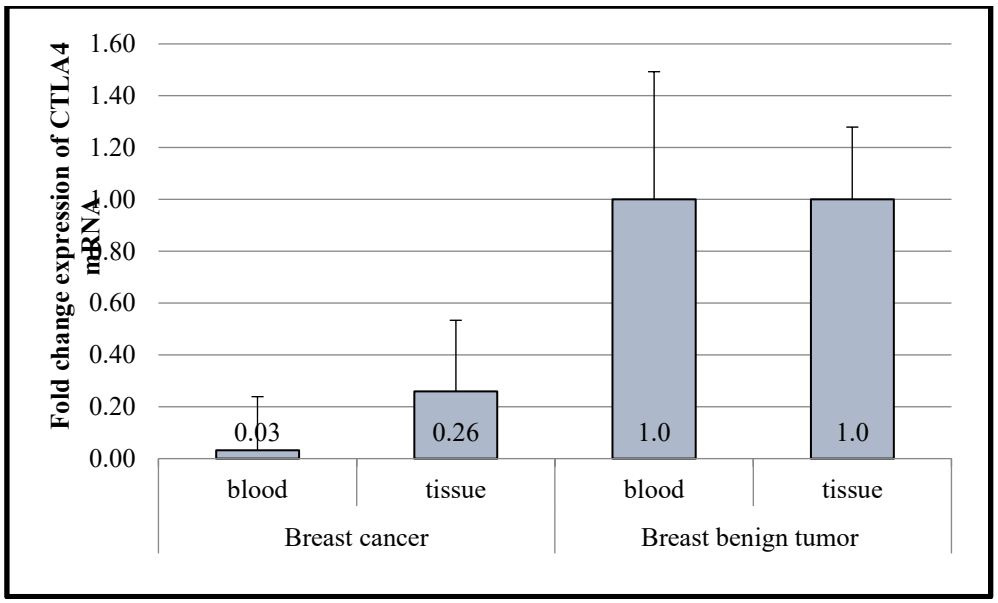

Fig 1. CTLA-4 mRNA in tissues and blood from BC non-control a positive control group (breast benign tumour). CTLA-4 in the tissues of breast cancer patients was substantially higher than in the blood.

No difference in CTLA-4 mRNA expression in tissues and blood in a breast benign tumour. CTLA-4 expression in the blood and tissues of BC non-control detected as less than the benign group.

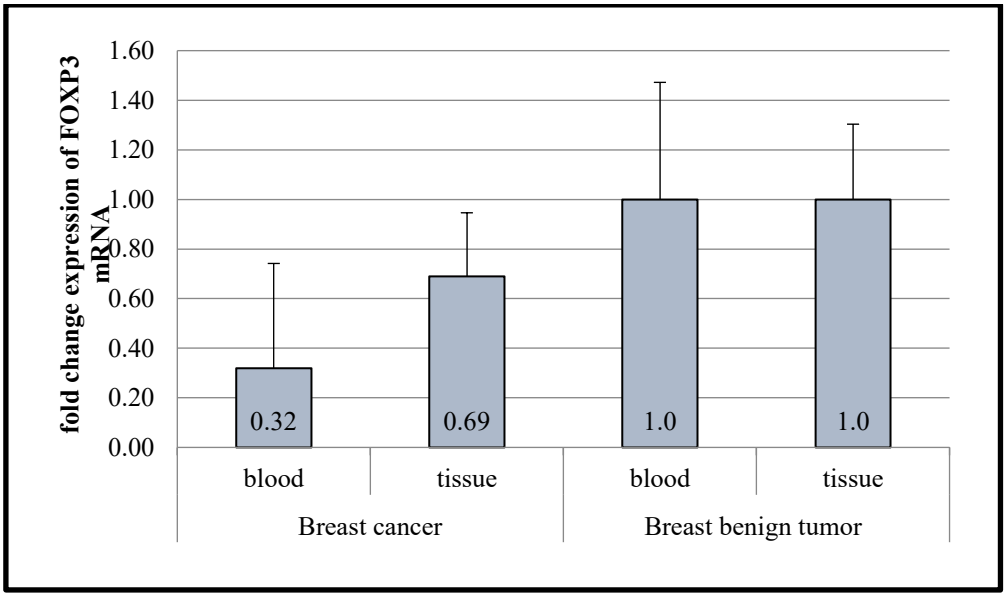

Fig 2. The mRNA of FOXP3 by tissues and blood from patients with BC and positive control group (breast benign tumour). The FOXP3 in tissue from BC was higher than the expression in blood, while it was similar in both tissues and blood from breast benign tumours. The expression of FOXP3 in blood and tissues from patients with BC was lower compared with the benign group.

4 Discussion

In breast cancer, the tumour microenvironment is becoming more well recognised as a significant role in tumour growth and a possible therapeutic target. Multiple cell types are seen in both intratumor (in the breast) and distant (metastatic) tumours. An extracellular matrix, soluble components (cytokines, growth factors, hormones, and enzymes), and physical features (pH and oxygen concentration) are also present [25]. soluble factors and cells of suppressive immune work synergistically to obstruct efficient antitumor immunity and promote breast cancer development and spread. Immunological suppressive systems such as immune checkpoints have evolved in the immune system to defend against autoimmunity by developing tolerance to self-antigens. Tumors use immunosuppressive pathways to dampen antitumor responses, allowing them to avoid identification and eradication by the immune system [26, 27]. The immune checkpoints that we investigated is CTLA-4 and Foxp3 were recruited by the immune system as regulatory molecules and used or induced by tumour cells to escape from immune surveillance. We compare the expression of CTLA-4 and Foxp3 in tissue microenvironment and peripheral blood. This study achieved with needs for breast biopsy as a specimen from malignant or benign tumours. Given such an invasive method a comparative study between expression of immune checkpoints in microenvironment tissue and peripheral blood was arising. According to our knowledge, such studies are rare and sparse. The study of checkpoints expression is useful not only for avoiding intrusive procedures, but also for identifying key aspects in tumour genesis and growth in terms of a metric of therapy response. Changes in epigenetic could lead to aberrant gene in tumour microenvironment cells [25], and gene expression profiles obtained from tumour stroma can predict clinical prognosis [26]. In light of these recent findings, the BC environment is gaining popularity and thus a possible therapeutic and new medicines could be targeted.

The present study showed that CTLA-4 gene expression in breast cancer tissues was significantly higher than peripheral blood and lower than the expression in tissues and blood from the control group (benign tumour). These discoveries will aid in early detection, and the development of therapeutic methods for BC. However, tissue biopsy for breast cancer tissues is still required. Using the ELISA approach, Isitmangil G et al. [28] got the serum level of CTLA-4 higher in non-control than in controls. CTLA-4 expression was shown to be high in tumour cells but very mildly positive or negative in normal breast tissue by Moa et al [29].

FOXP3 was the other immune checkpoint studied here. Its sign in in breast cancer tissues is expected higher in blood but it is not at the significant level, which could be owing to the limited sample size. Foxp3 expression in tumours, on the other hand, was linked to a lower overall survival rate, and risk rose as Foxp3 expression increased. Foxp3 was also a good predictor but not as reappearance risk.

Finally, we hope that our findings will be useful in early detection of BC.

Acknowledgments

Authors thank Ms. Zahraa H Abdulkareem for her excellent technical help.

References

1. Mattiuzzi, C., & Lippi, G. Current cancer epidemiology. Journal of epidemiology and global health. 2019; 9(4), 217.
2. Siegel, R. L., Miller, K. D., & Jemal, A. Cancer statistics, 2016. CA: a cancer journal for clinicians. 2016; 66(1), 7-30.
3. Chen, D. S., & Mellman, I. Oncology meets immunology: the cancer-immunity cycle. Immunity. 2013; 39(1), 1-10.
4. Galon, J., Mlecnik, B., Bindea, G., Angell, H. K., Berger, A., Lagorce, C., ... & Pagès, F. Towards the introduction of the 'Immunoscore'in the classification of malignant tumours. The Journal of pathology. 2014; 232(2), 199-209
5. Casey, S. C., Li, Y., & Felsher, D. W. An essential role for the immune system in the mechanism of tumor regression following targeted oncogene inactivation. Immunologic research. 2014; 58(2-3), 282-291.
6. Monzavi-Karbassi, B., Pashov, A., & Kieber-Emmons, T. Tumor-associated glycans and immune surveillance. Vaccines. 2013; 1(2), 174-203.
7. Spranger, S. Mechanisms of tumor escape in the context of the T-cell-inflamed and the non-T-cell-inflamed tumor microenvironment. International immunology. 2016; 28(8), 383-391.
8. Pardoll, D. M. The blockade of immune checkpoints in cancer immunotherapy. Nature Reviews Cancer. 2012; 12(4), 252-264.
9. Tanday, S. Nivolumab for recurrent or metastatic head and neck cancer. The Lancet Oncology. 2016; 17(11), e483.
10. Wang, X., Bao, Z., Zhang, X., Li, F., Lai, T., Cao, C., ... & Ying, S. Effectiveness and safety of PD-1/PD-L1 inhibitors in the treatment of solid tumors: a systematic review and meta-analysis. Oncotarget. 2017; 8(35), 59901.
11. Sheikhi, A., Jafarzadeh, A., Kokhaei, P., & Hojjat-Farsangi, M. Whole tumor cell vaccine adjuvants: comparing IL-12 to IL-2 and IL-15. Iranian Journal of Immunology. 2016; 148-166.
12. Jafarzadeh, A., Jamali, M., Mahdavi, R., Ebrahimi, H. A., Hajghani, H., Khosravimashizi, A., ... & Daneshvar, H. Circulating levels of interleukin-35 in patients with multiple sclerosis: evaluation of the influences of FOXP3 gene polymorphism and treatment program. Journal of Molecular Neuroscience. 2015c; *55*(4), 891-897.
13. Takeuchi, Y., & Nishikawa, H. Roles of regulatory T cells in cancer immunity. International immunology. 2016; 28(8), 401-409.
14. Etesam, Z., Nemati, M., Ebrahimizadeh, M. A., Ebrahimi, H. A., Hajghani, H., Khalili, T., ... & Jafarzadeh, A. Altered expression of specific transcription factors of Th17 (RORγt, RORα) and Treg lymphocytes (FOXP3) by peripheral blood mononuclear cells from patients with multiple sclerosis. Journal of Molecular Neuroscience. 2016; 60(1), 94-101.
15. Szylberg, Ł., Karbownik, D., & Marszałek, A. The role of FOXP3 in human cancers. Anticancer research. 2016; 36(8), 3789-3794.
16. Hatanaka, H., Ishizawa, H., Nakamura, Y., Tadokoro, H., Tanaka, S., Onda, K., ... & Hirano, T. Effects of vitamin K3 and K5 on proliferation, cytokine production, and regulatory T cell-frequency in human peripheral-blood mononuclear cells. Life science. 2014; 99(1-2), 61-68.
17. Tohyama, N., Tanaka, S., Onda, K., Sugiyama, K., & Hirano, T. Influence of anticancer agents on cell survival, proliferation, and CD4+ CD25+ Foxp3+ regulatory T cell-frequency in human peripheral-blood mononuclear cells activated by T cell-mitogen. International immunopharmacology. 2013; 15(1), 160-166.
18. Jafarzadeh, A., Fooladseresht, H., Minaee, K., Bazrafshani, M. R., Khosravimashizi, A., Nemati, M., ... & Ghaderi, A. Higher circulating levels of chemokine CCL22 in patients with breast cancer: evaluation of the influences of tumor stage and chemokine gene polymorphism. Tumor Biology. 2015a; 36(2), 1163-1171.
19. Muenst, S., Läubli, H., Soysal, S. D., Zippelius, A., Tzankov, A., & Hoeller, S. The immune system and cancer evasion strategies: therapeutic concepts. Journal of internal medicine. 2016; 279(6), 541-562.
20. Nasser, A., Khosravi, A., & Azizian, R. The role of T regulatory lymphocytes in lymphoma. Middle East Journal of Cancer. 2014; 5(2), 55-66.

21. Rathod, S. B., Das, R., Thanapati, S., Arankalle, V. A., & Tripathy, A. S. Suppressive activity and altered conventional phenotype markers/mediators of regulatory T cells in patients with self-limiting hepatitis E. Journal of Viral Hepatitis; 2014; 21(2), 141-151.
22. Jaberipour, M., Habibagahi, M., Hosseini, A., Habibabad, S. R., Talei, A., & Ghaderi, A. Increased CTLA-4 and FOXP3 transcripts in peripheral blood mononuclear cells of patients with breast cancer. Pathology & Oncology Research. 2010; 16(4), 547-551.
23. Kawaguchi, K., Suzuki, E., Yamaguchi, A., Yamamoto, M., Morita, S., & Toi, M. Altered expression of major immune regulatory molecules in peripheral blood immune cells associated with breast cancer. Breast Cancer. 2017; 24(1), 111-120.
24. Khalife, E., Khodadadi, A., Talaeizadeh, A., Rahimian, L., Nemati, M., & Jafarzadeh, A. Overexpression of regulatory T cell-related markers (FOXP3, CTLA-4 and GITR) by peripheral blood mononuclear cells from patients with breast cancer. Asian Pacific journal of cancer prevention: APJCP. 2018; 19(11), 3019.
25. Coleman RE, Gregory W, Marshall H, Wilson C, Holen I: The metastatic microenvironment of breast cancer: clinical implications. Breast 2013; 22(suppl 2): S50–S56.
26. 26- Folgueira MA, Maistro S, Katayama ML, Roela RA, Mundim FG, Nanogaki S, de Bock GH, Brentani MM: Markers of breast cancer stromal fibroblasts in the primary tumour site associated with lymph node metastasis: a systematic review including our case series. Biosci Rep 2013; 33: e00085.
27. Finak G, Bertos N, Pepin F, Sadekova S, Souleimanova M, Zhao H, Chen H, Omeroglu G, Meterissian S, Omeroglu A, Hallett M, Park M: Stromal gene expression predicts clinical outcome in breast cancer. Nat Med 2008; 14: 518–527.
28. Isitmangil G, Gurleyik G, Aker FV, Coskun C, Kucukhuseyin O, Arikan S, Turan S, Talu CK, Dogan MB, Farooqi AA, Yaylim I. Association of CTLA4 and CD28 Gene Variants and Circulating Levels of Their Proteins in Patients with Breast Cancer. In Vivo. 2016 Jul-Aug;30(4):485-93.
29. Mao H, Zhang L, Yang Y, Zuo W, Bi Y, Gao W, Deng B, Sun J, Shao Q, Qu X. New insights of CTLA-4 into its biological function in breast cancer. Curr Cancer Drug Targets. 2010 Nov;10(7):728-36.

Evaluation of Some Biomarkers in the Diagnosis and Severity Identification of Patients with COVID-19

Haider Nasser Jabber[1], Mahdi Murshid Thuwaini[2], Hamed Jaddoa Abbas[3]
{haiderhh198@gmail.com[1], Hayder9015@yahoo.com[2], hamed@uobasrah.edu.iq[3]}

College of Medical and Health Technology / Southern Technical University - Basrah, Iraq[1,2]
Al-Fayhaa Teaching Hospital – Al- Zahraa Medical college- Basrah University, Basrah, Iraq[3]

Abstract. This work shows how effective the biomarkers D dimer, C-reactive protein (CRP), and Lactate Dehydrogenase (LDH) were at diagnosing COVID-19 and how severe it was. A case-control research included (136) Covid-19 patients and (48) healthy people as a control group. Kits used to measure D dimer, CRP, and LDH. The outcomes are shown that there was a highly significant increase (P-value < 0.01) in the levels in COVID-19 patients compared to the control group for the biomarkers: D dimer, CRP, and LDH. There was a highly significant increase (P-value < 0.01) in COVID-19 patients with severe disease compared to other groups for the following biomarkers: D dimer and LDH. The study also showed that that the sensitivity values of the markers were 88%, 85%, and 79, for D-dimer, CRP, and LDH, D respectively; while specificity values were: 63%, 61%, and 66% respectively. These markers might be used in detection of COVID-19.

Keywords: COVID-19, SARS-CoV-2, D-dimer, CRP, LDH.

1 Introduction

SARS-CoV and Middle East respiratory syndrome coronavirus-2 (MERS-CoV) have generated epidemics in the previous two decades, with mortality rates of 9.5 percent and 34.4 percent, respectively. COVID19 has been identified as the third highly epidemic disease, having a lower mortality rate than SARS and MERS and a wide range of symptoms from one country to the next. Until the time of writing this study, more than 185 million cases have been officially registered as positive cases in about 222 countries all over the world, while the deaths exceed 4 million worldwide. The largest number of cases have been recorded in the United State of America (USA) with more than 34 million followed by India which recorded more than 30 million. The United States has the most deaths (about 600000), but Peru has the greatest mortality rate (approximately 5790 deaths per million of population) [1]. Inflammatory damage patterns in SARS and COVID-19 patients are comparable. Proinflammatory cytokines such as interleukin (IL)-1, IL6, IL12, interferon-gamma (IFN), IFN-induced protein 10 (IP10), macrophage inflammatory proteins 1A (MIP1A), and monocyte chemoattractant protein-1 (MCP1) have been associated to pulmonary infection and severe lung damage. These are identified in the serum of persons who have been diagnosed with SARS (D-dimer, CRP, and LDH).COVID-19 emergency warning indications include constant discomfort or pressure in the chest, difficulty breathing, disorientation, and pale lips or face, all of which require rapid medical attention. Pneumococcal infection develops as the situation worsens, and the incubation

IMDC-IST 2021, September 07-09, Sakarya, Turkey
Copyright © 2022 EAI
DOI 10.4108/eai.7-9-2021.2314940

period has yet to be calculated because the virus was only recently discovered. Symptoms could develop as soon as three days after exposure or as late as 13 days later, according to the new information. According to recent studies, the incubation period is roughly five days on average [2].
The importance of the lab outcomes in detection and follow-up of Covid-19 patients cannot be overstated. The biomarkers for Covid-19 have been the subject of numerous studies. Complete blood count (CBC), tests studying coagulation and fibrinolysis flows such as prothrombin time (PT) and activated partial thromboplastin time (aPTT) and D-dimers, and inflammation-related parameters are the most common routine assays requested by COVID-19 clients (procalcitonin, CRP, ESR, and ferritin). Because the virus has the potential to severely impair multiple key organs, including the liver, kidneys, and heart, doctors can determine the functioning processes of these organs by analysing biochemical indicators [3].

2 Materials and Methods

The work included (136) people diagnosed with Covid-19 (71 male and 65 female) and (48) healthy subjects as a control group. Who visited Al-Basra Teaching Hospital in Basra, Iraq? All patients in this research were diagnosed by specialist physicians and confirmed clinical and laboratory investigations, throughout the period from October 2020 to May 2020. The practical research was conducted at Southern Technical University in Basra's Medical Laboratory Technology department. D dimer (BioMérieux, France), CRP (Roche Diagnostics, Switzerland), and LDH (Roche Diagnostics, Switzerland) were also measured using kits (Roche Diagnostics, Switzerland).

2.1 Statiastical Analysis

The data is expressed in terms of averages and Std Dev. (SD). The t-test (for means) and the chi-square test were used to see if there were any differences between the groups (for frequencies). SPSS for Windows was used to conduct all statistical analyses (version 23, USA). ANOVA was employed as normal distribution based on $P < 0.05$ and $P > 0.05$ as the significant. and non-significant respectively.

3 Results and Discussion

3.1. Demographic Characteristics of the Study Groups

Table 1. Statistical distribution (frequency and percentage) of study groups (patients and control) by their age and gender.

Items	Sub-groups	COVID-19 patients (N= 136)		Control Group (N= 48)		Chi Square (P value) Sig.
		Freq.	%	Freq.	%	
Age	17-31	6	4.4	0	0.0	4.13 (0.24) NS
	32-46	34	25.0	16	33.3	
	47-61	54	39.7	24	50.0	
	62-76	31	22.8	8	16.7	

Mean ± SD	**77-91**	**11**	**8.1**	**0**	**0.0**	
		54.13 ± 14.55		**51.46 ± 8.27**		**T-test = 1.12 (0.06) NS**
Gender	**Male**	**71**	**52.2**	**24**	**50.0**	**0.07 (0.79) NS**
	Female	65	47.8	24	50.0	

Table 1 showed statistical distribution (frequency and percentage) of study groups (patients and control) by their age and gender. This table explained that the highest percentage of the age subgroup is (47-61) years which constituted (39.7%) for the patient's group, and (50%) for the control group (figure 4.1), the same table revealed that the male percentage of patients are (52.2%), while gender is equally distributed among the control group (50% for each).

Table 2. Differences in the measurement of serum biomarkers between COVID-19 patients and control group

Biomarkers		**Patients (N= 136)**	**Control Group (N= 48)**	**T Test P value**
D dimer	**Mean**	**2418.01**	**466.33**	**7.18 0.000 HS**
	SD	**3093.01**	**409.10**	
CRP	**Mean**	**30.71**	**4.74**	**11.49 0.000 HS**
	SD	**24.10**	**6.35**	
LDH	**Mean**	**595.32**	**139.88**	**6.49 0.000 HS**
	SD	**811.59**	**58.38**	

HS: at P≤0.01; NS: at P≤0.05; SD: Std. Dev.

Table 2 shows the differences in the measurement of serum biomarkers between COVID-19 patients and the control group. This table exhibited that there is a highly significant increase (P-value < 0.01) in the levels in COVID-19 cases relative to the control for the following biomarkers: D dimer, CRP, and LDH.

3.2. Measurement of Biomarkers

Table 3. ANOVA table for Differences in the measurement of routine markers among patients' subgroups classified based on severity.

Biomarkers		**The severity of the Disease**			**F Test P-value**
		Mild (N= 42)	**Moderate (N=70)**	**Severe (N=24)**	
D dimer	**Mean**	**878.55 A**	**2843.98 B**	**3869.62 B**	**9.59 0.000 HS**
	SD	**1284.79**	**3425.50**	**3305.92**	
CRP	**Mean**	**23.40**	**33.94**	**34.10**	**2.87 0.06 NS**
	SD	**23.98**	**24.30**	**21.68**	
LDH	Mean	415.30 A	533.10 A	1091.86 B	6.17 0.000 HS
	SD	242.98	267.91	1793.71	

HS: at P≤0.01; NS: at P>0.05; SD: Std, Dev.; ANOVA: Analysis of Variance Different letters refer to a significant difference.

Table 3 Revealed differences in the measurement of serum biomarkers among different severity subgroups of COVID-19 patients. This table showed that there is a highly significant increase (P-value < 0.01) in COVID-19 people with severe illness compared to other groups for D dimer and LDH.

3.3. Receiver-Operating Characteristics of the Biomarkers

Table 4. ROC and AUC of the biomarkers for the diagnosis of breast cancer.

Biomarkers	(AUC)	Sig. p-value	Cut-off Point	Sensitivity (%)	Specificity (%)	PPV	NPV
D-dimer	**0.81**	**0.01**	**6.34**	**88**	**63**	**83**	**73**
CRP	**0.66**	**0.08**	**6.34**	**85**	**61**	**63**	**53**
LDH	**0.84**	**0.06**	**375.74**	**79**	**66**	**82**	**06**

AUC; PPV; NPV.

The work also showed that that the sensitivity values of the markers were 88%, 85%, 79% for D-dimer, CRP, and LDH, D respectively; while specificity values were: 63%, 61%, 66% respectively (Table 4 and Fig 1)

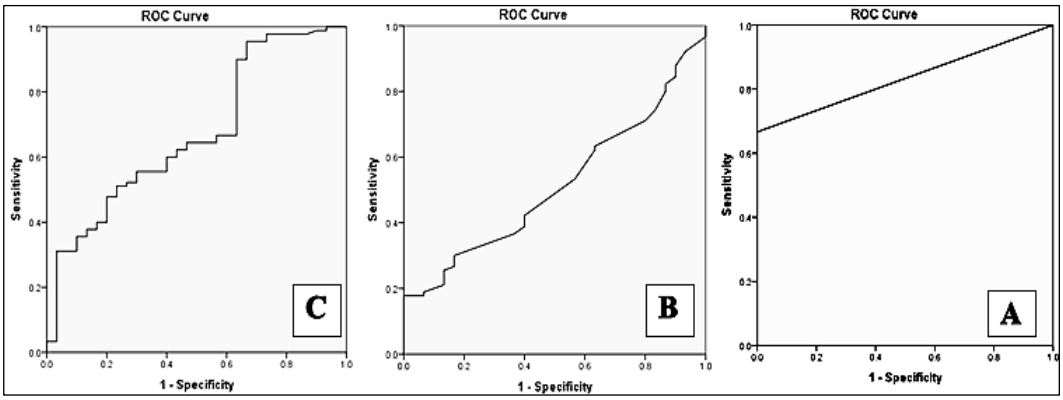

Fig 1. Diagonal segment of the ROC curve for (A) : D-dimer , (B) : CRP, (C) : LDH

The current study agrees with Rostami and Mansouritorghabeh [4] and Spiezia et al. [5] in terms of D-dimer. D-dimer was described as most effective lab results in Covid-19 people who need to be admitted to the hospital. No survivors had a considerably greater 2.12 µg/mL D-dimer according to Guan and his co-authors, who looked at 1099 people in lab with Covid-19 of 550 hospitals. Similarly, aberrant coagulation findings, particularly markedly high D-dimer, have been detected in deaths with Covid-19; a reflective investigation of 191 COV-Pat. showed 1g/mL Dimer when intended to hospital [7].

Although elevated D-dimer concentrations and dead-space ventilation may be caused by processes other than micro cloths, previous research suggests that intravascular disease plays a

key role in expanding dead space and producing hypoxemia in COVID-19-related ARDS [8]. According to Malik et al, greater D-dimer ranks are linked to a roughly threefold increased jeopardy of weak results in COVID-19 people [9].

Concerning CRP, the results agreed with Liu et al. they showed that CRP is raised in patients compared to control healthy people [10]; Patients with Covid-19 had high C-reactive protein (58.3 percent, 95 percent CI 21.8–94.7 percent), according to Rodriguez-Morales et al. (2020). RP is a sensitive biomarker of inflammation, infection, and tissue damage produced by the non-specific acute-phase protein IL-6 in the liver. CRP levels are generally low, but they spike dramatically during acute inflammatory responses [11]. CRP rises alone in conjunction with viral or bacterial infections. This work presents the balance of CRP in COVID-19 and detected CRP > 41.8 mg/L were more likely to cause more illness [12]. CRP levels are strongly related to the degree of inflammation and the severity of the condition. As a result, it is a significant biomarker in the diagnosis and assessment of infectious illness severity [9].

Regarding LDH, the results agreed with Liu et al., they showed that LDH was studied in 19 patients compared to control healthy subjects [10]; Rodriguez-Morales et al. counted the patients with Covid-19 showed high C-reactive protein (57.0%, 95%CI 38.0–76.0) [11]; Huang et al. reported that LDH levels were high in 73% of non-control; Liu et al. (2020C) found that CRP and LDH in 85% of non-control [13]; it was found that abnormal LDH levels observed, both at admission and hospitalization (LDH 37.6%), it is believed that lactate dehydrogenase (LDH) is released in large quantities of inflammatory and indicators of cell damage of the illness growth, activity, and movement [14].

CRP and LDH levels were found to be favourably linked with lung injury Murray scores in previous research [10]. Hypoalbuminemia, lymphopenia, and CRP ≥4 mg dL–1 revealed to be prognostic markers for pneumonia development to respiratory failure in MERS-CoV infected patients, while higher dehydrogenase was associated with severe acute respiratory syndrome (SARS-CoV) on entering to the hospital. As a result, a combination of hypoalbuminemia, lymphopenia, and elevated CRP and LDH concentrations in 2019-nCoV infected individuals to the hospital that might have acute lung problems [10].

Regarding D-dimer kits fluctuates between 93-95 percent [4]; Demelo-Rodrguez et al. also found that the D-dimer had a sensitivity of 95.7 percent, 29.3 percent specificity, and AUC of 0.729 with a cut-off point of 1.57 (μg/ml). Cui et al. studied the frequency of VTE in 81 ICU hospitalised people COVID-19 [16] and established such criteria for the detection of silent DVT [15]. They discovered that D-dimer with a cut-off point of 1.5 (μg/mL) had an 85% sensitivity and an 88.5 percent specificity for VTE prediction; Liu et al. calculated computed the optimal values markers that was 32.1 pg/ mL, 41.8 mg/L, and 0.07 ng/mL for IL-6, CRP, and PCT, respectively [10].

4 Conclusion

D dimer, CRP, and LDH levels are higher in COVID-19 patients, and D-dimer and LDH levels are higher in patients with severe COVID-19 infection. In the diagnosis of COVID-19, D-dimer and CRP had quite high sensitivity and specificity.

References

[1] Mohamadian, M., Chiti, H., Shoghli, A., Biglari, S., Parsamanesh, N., & Esmaeilzadeh, A. (2021). COVID-19: Virology, biology, and novel laboratory diagnosis. The journal of gene medicine, 23(2), e3303.

[2] Hafeez A, Ahmad S, Siddqui S, Ahmad M, Mishra S. A (2020) Review of COVID-19 (Coronavirus Disease-2019) Diagnosis, Treatments, and Prevention. EJMO.; 4(2): 116-125 .

[3] Kumar D, Malviya R, Kumar Sharma P. (2020) Corona Virus: A Review of COVID-19. EJMO;4(1):8–25.

[4] Rostami, M., & Mansouritorghabeh, H. (2020). D-dimer level in COVID-19 infection: a systematic review. Expert review of hematology, 13(11), 1265–1275.

[5] Spiezia, L., Boscolo, A., Poletto, F., Cerruti, L., Tiberio, I., Campello, E., Navalesi, P., & Simioni, P. (2020). COVID-19-Related Severe Hypercoagulability in Patients Admitted to Intensive Care Unit for Acute Respiratory Failure. Thrombosis and haemostasis, 120(6), 998–1000.

[6] Guan, W. J., Ni, Z. Y., Hu, Y., Liang, W. H., Ou, C. Q., He, J. X., Liu, L., Shan, H., Lei, C. L., Hui, D., Du, B., Li, L. J., Zeng, G., Yuen, K. Y., Chen, R. C., Tang, C. L., Wang, T., Chen, P. Y., Xiang, J., Li, S. Y (2020). Clinical Characteristics of Coronavirus Disease 2019 in China. The New England journal of medicine, 382(18), 1708–1720 .

[7] Zhang, L., Yan, X., Fan, Q., Liu, H., Liu, X., Liu, Z., & Zhang, Z. (2020B). D-dimer levels on admission to predict in-hospital mortality in patients with Covid-19. Journal of thrombosis and haemostasis : JTH, 18(6), 1324–1329.

[8] Grasselli, G., Tonetti, T., Protti, A., Langer, T., Girardis, M., Bellani, G., Laffey, J., Carrafiello, G., Carsana, L., Rizzuto, C., Zanella, A., Scaravilli, V., Pizzilli, G., Grieco, D. L., Di Meglio, L., de Pascale, G., Lanza, E., Monteduro, F., Zompatori, M., Filippini, C (2020). Pathophysiology of COVID-19-associated acute respiratory distress syndrome: a multicentre prospective observational study. The Lancet. Respiratory medicine, 8(12), 1201–1208.

[9]. Malik, P., Patel, U., Mehta, D., Patel, N., Kelkar, R., Akrmah, M., Gabrilove, J. L., & Sacks, H. (2021). Biomarkers and outcomes of COVID-19 hospitalisations: systematic review and meta-analysis. BMJ evidence-based medicine, 26(3), 107–108.

[10] Liu, Y., Yang, Y., Zhang, C., Huang, F., Wang, F., Yuan, J., Wang, Z., Li, J., Li, J., Feng, C., Zhang, Z., Wang, L., Peng, L., Chen, L., Qin, Y., Zhao, D., Tan, S., Yin, L., Xu, J., Zhou, C.Liu, L. (2020A). Clinical and biochemical indexes from 2019-nCoV infected patients linked to viral loads and lung injury. Science China. Life sciences, 63(3), 364–374.

[11] Rodriguez-Morales, A. J., Cardona-Ospina, J. A., Gutiérrez-Ocampo, E., Villamizar-Peña, R., Holguin-Rivera, Y., Escalera-Antezana, J. P., Alvarado-Arnez, L. E., Bonilla-Aldana, D. K., Franco-Paredes, C., Henao-Martinez, A. F., Paniz-Mondolfi, A., Lagos-Grisales, G. J., Ramírez-Vallejo, E., Suárez, J. A., Zambrano, L. I., Villamil-Gómez, W. E., Balbin-Ramon, G. J., Rabaan, A. A., Harapan, H., Dhama, K., (2020). Clinical, laboratory and imaging features of COVID-19: A systematic review and meta-analysis. Travel medicine and infectious disease, 34, 101623.

[12] Liu, F., Li, L., Xu, M., Wu, J., Luo, D., Zhu, Y., Li, B., Song, X., & Zhou, X. (2020B). Prognostic value of interleukin-6, C-reactive protein, and procalcitonin in patients with COVID-19. Journal of clinical virology : the official publication of the Pan American Society for Clinical Virology, 127, 104370.

[13] Huang C, Wang Y, Li X. (2020) Clinical features of patients infected with 2019 novel coronavirus in Wuhan, China. Lancet;395: 497e506.

[14] Farhana A, Lappin SL. Biochemistry (2021) Lactate Dehydrogenase. [Updated 2021 May 7]. In: StatPearls [Internet]. Treasure Island (FL): StatPearls Publishing; 2021 Jan-. Available from: https://www.ncbi.nlm.nih.gov/books/NBK557536/

[15] Demelo-Rodríguez, P., Cervilla-Muñoz, E., Ordieres-Ortega, L., Parra-Virto, A., Toledano-Macías, M., Toledo-Samaniego, N., García-García, A., García-Fernández-Bravo, I., Ji, Z., de-Miguel-Diez, J., Álvarez-Sala-Walther, L. A., Del-Toro-Cervera, J., & Galeano-Valle, F. (2020). Incidence of asymptomatic deep vein thrombosis in patients with COVID-19 pneumonia and elevated D-dimer levels. Thrombosis research, 192, 23–26.

[16] Cui, S., Chen, S., Li, X., Liu, S., & Wang, F. (2020). Prevalence of venous thromboembolism in patients with severe novel coronavirus pneumonia. Journal of thrombosis and haemostasis : JTH, 18(6), 1421–1424.

Assessment of Physical and Chemical hazards Among Health Care Workers in Wasit Governorate

Nassa Sattar Yaqoob Al-mayahi[1], Shrouk Abdulrazk Hassan Alibraheem[2], Alaa Kadhim Jasim[3]
{ nsystar09@ gmail.com [1], shrouk.alibraheem@stu.edu.iq [2], alaa-alderawi@stu.edu.iq[3]}

Southern Technical University, Health and Medical Technical College, Community Health Techniques and Medical Laboratory Department/Iraq[1,2,3]

Abstract. Health care workers are on the front lines of this worldwide pandemic, with the significant burden of identifying and treating an increasingly expanding number of severely sick patients, sometimes making vital decisions under physical and psychological stress. This study is descriptive; a cross-sectional study conducted at four hospitals in Wasit governorate. The data collection started from December 2020 till March 2021. The Data were collected by direct interview with the health worker by the researcher, by using a self-reporting questionnaire from the occupation hazard dimension, which includes two domains: physical hazards and chemical hazards. The statistical method used includes Mean, Standard Deviation, and Chi-square. Statistical significance was considered whenever the P-value was equal to or less than 0.05. The current study found that the highest percentage 254 (57.6%) were in the age group <30 years, there was a distinct female's preponderance of 242(54.9%). There is a highly significant positive correlation (P-value <0.01) between physical hazards and prevention and control methods (r= 0.144*); a highly significant positive correlation (P-value <0.01) between chemical hazards, and prevention and control methods (r= 0.770*).where the chemical hazard reached to241(54.6%) while followed physical hazards reached to 196(44.4%) the results also showed Weighted Mean for physical hazard equal 3.28±0.67which is within the medium level risk.

Keywords: Assessment, Physical, Chemical hazards, Health care workers.

1 Introduction

Occupational hazard in Iraq poses a danger to the individual in the working environment in addition to the consequences such as fatal accidents, minor to serious injuries and immediate allergic and systemic effects [1]. Occupational hazard is the risk, harm, or danger that an individual is exposed to at the workplace. Workers are exposed to a variety of risks throughout work times, virtually as many as the diverse types of labour, including physical, biological, mechanical, chemical, psychological, and ergonomic issues. These are to account for one of many negative health effects[2]**.** In the health sector at present, many health workers and other workers are exposed to the risks of ionizing and non-ionizing radiation that are used in daily use in medical tasks. It is considered of importance at the diagnostic and therapeutic levels [3]. Health workers, who are estimated to number more than two million, deal with radiation as a result of related practices, exposing half of this number to artificial and ionizing radiation [4]. The risks posed by chemicals are processed, produced, processed, and transported and they have an environmental and human health impact. A chemical hazard is a form of chemical exposure occupational hazard. Chemical occupational exposure can have short-term and long-term health

IMDC-IST 2021, September 07-09, Sakarya, Turkey
Copyright © 2022 EAI
DOI 10.4108/eai.7-9-2021.2314929

effects. Neurotoxins, immunologic agents, dermatologic agents, carcinogens, toxic substances, reproductive substances, systemic toxins, asthma genes, and sensitizers, to mention just a few, are toxic substances [5]. In health-care environments such as hospitals, doctor's offices, and clinical labs, personal protective equipment (PPE) is done routinely. Personal protection equipment (PPE) acts as a barrier between infectious elements such as viruses and bacteria and the body, mouth, nose, and eyes (mucous membranes) when worn properly. PPE can stop contaminants from being spread by blood, bodily fluids, or respiratory secretions [6].

1.1 Aims of the Study

1. To assess physical and chemical hazards among health care workers in Wasit governorate.
2. To find out the relationship between physical and chemical hazards and health workers' demographic information and some related factors.
3. To find out the relationship between physical and chemical hazards and prevention and control methods.

2 Methodology

This study is a descriptive cross-sectional study conducted at four hospitals in Wasit governorate which are AL-zahraa teaching hospital, AL-suwaira hospitals, AL-naemania hospitals, and AL-shaheed fairooz hospital. Data were collected during the period starting from December 2020 till March 2021. The worker's participation in the study were441 workers in these hospitals. Data were collected using direct interviews of health workers using a questionnaire. the questionnaire from consists of four-part: First part socio-demographic characteristic of the studied health worker regarding age, gender …etc. The second part is the occupational characteristic of the studied health worker regarding professional, years of expertness, and place work. The third part the occupational hazard dimensions which include four domains: Physical hazard (14 items), Chemical hazard (11 items), and prevention and control methods (23 items) was assessed by using a five Likert scale. Analysis of data was carried out using the available statistical package of SPSS-25 (Statistical Packages for Social Sciences- version 25). Data were presented in simple measures of frequency, percentage, mean, standard deviation, and range (minimum-maximum values). The significance of difference for different percentages (qualitative data) was tested using the Pearson Chi-square test (χ2-test). Statistical significance was considered whenever the P-value was equal to or less than 0.05.

3 Results

Table 1 represents the Socio-demographic characteristics of the study population. The results found that the mean ± SD of their ages was 30.8±8.12 years, the age range of the health worker in the study was between 20-56 years, The highest percentage 254(57.6%) were in the age group <30 years. There was a distinct female preponderance242 (54.9. As for residence and educational level, the study revealed that most participants in studied hospitals from urban regions 394 (89.3%), while the highest percentage 354 (80.3%) of health workers have an educational level (institute and College) followed by 74(16.8%) had secondary educational level the result of this study indicated that 265(60.1%) of the study population were married and

161(36.5%) of participation were single in the study hospital. The study demonstrated that the first rank of health care workers were nurses 125 (28.3%) followed by 107(24.3%) of medical assistants, laboratory assistants, and radiology assistants in all studied hospitals. While the overall frequency of Technicians was 86(19.5%) in all hospitals. Which found that most participants had years' experience ≥5 is 244(55.3%). The result of this study indicated that the highest proportion of participants were 117(26.5%) working in medical Laboratories followed by 82 (18.6%) working in admission units for patients in all studied hospitals.

Table 1. Socio-demographic characteristics of health care workers.

Socio-demographic characteristics		No	Percent
age groups	<30 years	254	57.6
	≥30 years	187	42.4
	Mean ±SD(Range)	30.83±8.123 (20-56)	
Gender	Male	199	45.1
	Female	242	54.9
Residence	Urban	394	89.3
	Rural	47	10.7
Educational level	Primary	4	0.9
	Intermediate	9	2.0
	Secondary	74	16.8
	Institute and College	354	80.3
social status	Married	265	60.1
	Single	161	36.5
	Others	15	3.4
experience years	<5 years	197	44.7
	≥5 years	244	55.3
	Mean ±SD(Range)	7.83±7222 (1-35)	
Place of working	Administrative units	22	5.0
	consulting unit	10	2.3
	Radiology department	16	3.6

	Admission unit for patients	82	18.6
	Health units	45	10.2
	Pharmacy unit	44	10.0
	Emergency	36	8.2
	Operation department	45	10.2
	Blood bank	9	2.0
	Medical Laboratories	117	26.5
	Maternity hall	15	3.4
Professional	Physicians	29	6.6
	Pharmacists	34	7.7
	Technicians	86	19.5
	Nurse	125	28.3
	Biologist and Chemist	33	7.5
	Medical assistant and laboratory assistant and Radiology	107	24.3
	Administrative employees	27	6.1

Table 2 represent the distribution of HCW according to physical hazards in. showed that the mean of for question (1) (conditioning is available in the workplace and suitable for use), was (3.57), for question (11) (the electrical lifts are in good and safe condition) was (2.59), for question (12) (enough lighting is available at the workplace)was (3.74). While the stander deviation for question (1)was (1.369), for question (11) was(1.323), was(1.176),for question(12) was (1.208).

Table 2. The Distribution of Healthcare Workers According to Physical Hazards.

Physical **hazard**	Strongly agree		Agree		Neutral		Disagree		Strongly Disagree		Mean	SD
	No	%	No	%	No	%	No	%	No	%		

1.Air conditioning is available in the workplace and suitable for use	120	27.2	182	41.3	33	7.5	40	9.1	66	15.0	3.57	1.369
2.Central ventilation systems are available in the work environment	76	17.2	143	32.4	75	17.0	79	17.9	68	15.4	3.18	1.334
3.Windows is available in the work environment and help to enter lighting and air circulation	146	33.1	163	37.0	35	7.9	42	9.5	55	12.5	3.69	1.349
4.A sterilization gate is available at the entrances to the health institution	100	22.7	107	24.3	59	13.4	94	21.3	81	18.4	3.12	1.445
5.Cleaning workers put a warning sign when the start sanitizing work floors	55	12.5	121	27.4	89	20.2	95	21.5	81	18.4	2.94	1.313
6.Protective barriers are available to be placed on doors and windows to prevent direct contact with patients	78	17.7	96	21.8	78	17.7	96	21.8	93	21.1	2.93	1.409
7.There are indications on the floors for social distancing of 2 meters or one and a half meters	51	11.6	69	15.6	90	20.4	112	25.4	119	27.0	2.59	1.339
8.Wash basins(sink)are available at the exits of the rooms	63	14.3	133	30.2	98	22.2	84	19.0	63	14.3	3.11	1.275
9.The work environment is suitable for personal protective equipment to wearing throughout the working hours	85	19.3	179	40.6	93	21.1	44	10.0	40	9.1	3.51	1.176

10.Follow up of preventive methods when using lifts as wearing a mask and sterilization	115	26.1	157	35.6	73	16.6	43	9.8	53	12.0	3.54	1.300
11.The electrical lifts are in good and safe condition	57	12.9	113	25.6	114	25.9	66	15.0	91	20.6	2.95	1.323
12.Enough lighting is available at the workplace	128	29.0	177	40.1	75	17.0	16	3.6	45	10.2	3.74	1.208
13-Availability of personal protective equipment (PPE) in the workplace to prevent exposure to medical radiation.	79	17.9	147	33.3	86	19.5	62	14.1	67	15.2	3.25	1.319
14.Fire extinguishers are available	149	33.8	200	45.4	32	7.3	18	4.1	42	9.5	3.90	1.193
Weighted Mean= 3.28±0.67												
positive phrases mean <2.60 low, mean 2.60-3.39mediumand mean ≥3.40high, while negative mean <2.60 high, mean 2.60-3.39medium, and mean ≥3.40 high												

Table 2.1, the result of the found that study the highest percentage 71(74.7%) of the study population had a good score (low risk) about physical hazards in Al- Zahraa teaching hospital followed by 58.3% in Al-Shaheed Fairooz hospital. While the overall percentage of physical hazards in the studied hospitals were reached 245 (55.6%) (Low risk) and high risk reached 196(44.4%) The differences between the four hospitals concerning the scoring level were statistically significant P value equal 0.05.

Table 2.1. The Relationship between the Study Hospitals and Total Risk Score of The Physical Hazards.

Name hospital			Total Score		P. Value
			Poor (High Risk <42)	Good/Acceptable (Low Risk ≥42)	
	Al-Zahraa hospital	No	24	71	0.000*
		%	25.3%	74.7%	
	Al-Shaheed Fairooz	No	48	67	
		%	41.7%	58.3%	

	Al-swiara	No	75	54	
		%	58.1%	41.9%	
	al-Nuamania	No	49	53	
		%	48.0%	52.0%	
Total		No	196	245	
		%	44.4%	55.6%	

Table 2.2 represents the relationship between the demographic characteristics of the studied sample concerning all questions was not statistically significant P>0.05, except social status P value equal 0.047, professional P value equal 0.025, and experience years P value equal 0.026 were significant.

Table 2.2. The Relationship between Demographic Characteristics of Healthcare Workers and The Total Risk Score About Physical Hazards.

Association	Total Physical Hazards Score		
Socio-demographic	**DF**	**Chi-Square (X^2)**	**P. value**
age groups	1	0.314	0.575
Gender	1	0.440	0.507
Residence	1	0.934	0.334
Educational level	3	6.079	0.108
social status	2	6.129	0.047*
Professional	6	14.480	0.025*
experience years	1	4.962	0.026*
Place of working	10	17.329	0.067

Table 3 Represent the distribution of HCWs according to chemical hazards. The results of this study indicated that the mean regarding (labels are placed to explain which detergents to avoided mix with other chemicals it may cause toxic gas) was (3.73) were rest on agreed respond level. While the SD of (1.462).

Table 3. The Distribution of Healthcare Workers According to chemical Hazards.

Chemical hazard	Strongly agree		Agree		Neutral		Disagree		Strongly Disagree		Mean	SD
	No	%	No	%	No	%	No	%	No	%		
1. Sterilizers and disinfects are used	120	27.2	116	26.3	44	10.0	80	18.1	81	18.4	3.26	1.485
2.Guidance labels are placed	55	12.5	87	19.7	89	20.2	116	26.3	94	21.3	2.76	1.325

for sterilizers to explain their safe use												
3-labels are placed to explain which detergents to avoided mix with other chemicals it may cause toxic gases	198	44.9	96	21.8	40	9.1	46	10.4	61	13.8	3.73	1.462
4.Observation of the production and expiration date of the sterilizing materials and cleaning materials are done frequently	56	12.7	91	20.6	28	6.3	86	19.5	180	40.8	2.45	1.498
5. led the use of sterilizers or cleaning materials to irritates the eye, nose, and throat.	179	40.6	70	15.9	9	2.0	98	22.2	85	19.3	2.64	1.628
6.Did inhalant long-standing aesthetic gas sterilization or cleaning materials cause your poisoning.	180	40.8	84	19.0	33	7.5	94	21.3	50	11.3	2.43	1.474
7. you suffer from allergies and burn in the skin as a result of using sterilizers.	59	13.4	70	15.9	70	15.9	164	37.2	78	17.7	3.30	1.299
8. You suffer from sensitive skin as a result of using latex gloves or any medicinal substance that contains latex.	52	11.8	76	17.2	92	20.9	115	26.1	106	24.0	3.33	1.326
9. Did use cleaning and sterilization	52	11.8	64	14.5	97	22.0	136	30.8	92	20.9	3.34	1.282

materials use your causes suffocation or shortness of breath.												
10.The oxygen bottles are stored in suitable places and maintained permanently	33	7.5	86	19.5	28	6.3	100	22.7	194	44.0	2.24	1.380
11.Did there warning signs and symbols for chemicals	53	12.0	91	20.6	22	5.0	90	20.4	185	42.0	2.40	1.489

Table 3.1 Represent the total score percentage of chemical hazards level was found poor score 241(54.6%) and high score200 (45.4%) in the study. The association between the four hospitals concerning the scoring level was statistically significant P value equal to 0.047.

Table 3.1. The Relationship between the Study Hospitals and Total Risk Score of the Chemical Hazards.

					P. Value
Name hospital			Total Score		
			Poor (High Risk <33)	Good/Acceptable (Low Risk ≥33)	0.047*
	Al-Zahraa hospital	No	64	31	
		%	67.4%	32.6%	
	Al-Shaheed Fairooz	No	58	57	
		%	50.4%	49.6%	
	Al-swiara	No	67	62	
		%	51.9%	48.1%	
	al-Nuamania	No	52	50	
		%	51.0%	49.0%	
Total		No	241	200	
		%	54.6%	45.4%	

Table 3.2 Represent the Relationship between the demographic characteristics of the studied sample concerning all questions was not statistically significant P>0.05, as appear in Table 7. Except gender was significant P-value equal 0.049.

Table 3.2. The Relationship between Demographic Characteristics of healthcare workers and the Total risk Score about Chemical hazards.

Association	**Total Chemical Hazards Score**		
Socio-demographic	**DF**	**Chi-Square (X^2)**	**P. value**
age groups	1	0.866	0.352
Gender	1	3.882	0.049*
Residence	1	0.045	0.832
Educational level	3	5.289	0.152
social status	2	2.213	0.331
Professional	6	2.717	0.843
experience years	1	0.495	0.482
Place of working	10	11.186	0.343

Table 4 Represent the distribution of HCW according to prevention and control methods in health institutions. The mean for question (1)(training courses are conducted to educate health care workers about coronavirus)was(2.24), for question(21) (the first aid kit is available and usable) was(3.74), were resting on agree to responses level. While SD for question (1) was(1.380) , for question (21)was(1.060).

Table 4. Distribution of Healthcare Workers according to the Prevention and Control Methods.

Prevention and Methods	Strongly agree		Agree		Neutral		Disagree		Strongly Disagree		M	SD
	No	%	No	%	No	%	No	%	No	%		
1.Training courses are conducted to educate health care workers about corona virus	33	7.5	86	19.5	28	6.3	100	22.7	194	44.0	2.24	1.380
2.instruction on infection prevention and control is available on coronavirus	53	12.0	91	20.6	22	5.0	90	20.4	185	42.0	2.40	1.489
3.Discouraging a direct contact with employees(hugging and shaking hand)	61	13.8	88	20.0	27	6.1	83	18.8	182	41.3	2.46	1.519

4.the workplace shall be disinfected at appropriate intervals	56	12.7	91	20.6	28	6.3	86	19.5	180	40.8	2.45	1.498
5. the medical devices are disinfected before and after use	85	19.3	98	22.2	9	2.0	70	15.9	179	40.6	2.64	1.628
6.soap and tissue paper are provided e near the handwashing basin	50	11.3	94	21.3	33	7.5	84	19.0	180	40.8	2.43	1.474
7.hands washing before entering the work environment and after takeoff the personal protective equipment and when leaving the work environment	58	13.2	96	21.8	9	2.0	85	19.3	193	43.8	2.41	1.532
8.Avoidance frequent contact with common surfaces where possible (leaving doors open where possible)	111	25.2	231	52.4	71	16.1	22	5.0	6	1.4	3.95	1.857
9.prevent the gatherings in elevators or elevators for transporting people which is considered unsafe under the current conditions of the coronavirus and beware of contact points in elevators	85	19.3	199	45.1	93	21.1	42	9.5	22	5.0	3.64	1.052
10. the employees and auditors who enter the health institution are examined searching for symptoms of coronavirus	33	7.5	86	19.5	28	6.3	100	22.7	194	44.0	2.24	1.380
11.Availability of adequate quantities of personal protective equipment(mask, gloves, eyeglasses, boots, work suit)	53	12.0	91	20.6	22	5.0	90	20.4	185	42.0	2.40	1.489
12.Provide personal protective equipment in appropriate sizes for	61	13.8	88	20.0	27	6.1	83	18.8	182	41.3	2.46	1.519

every employee or person visiting the workplace												
13.Prevention equipment is examined periodically and maintained and replaced when needed	56	12.7	91	20.6	28	6.3	86	19.5	180	40.8	2.45	1.498
14.Personal prevention equipment is eliminated in safe ways do not pollute the work environment and others	85	19.3	98	22.2	9	2.0	70	15.9	179	40.6	2.64	1.628
15.the wounds are covered before the laboratory enter	50	11.3	94	21.3	33	7.5	84	19.0	180	40.8	2.43	1.474
16. the jewelry is covered(it should not affect the gloves)and removed before entering any workplace where this is required	58	13.2	96	21.8	9	2.0	85	19.3	193	43.8	2.41	1.532
17.portable electronic devices are kept in areas that cannot be contaminated and disinfected frequently	103	23.4	220	49.9	69	15.6	33	7.5	16	3.6	3.82	0.993
18. A warning signs exist in biological laboratories have	101	22.9	178	40.4	95	21.5	39	8.8	28	6.3	3.65	1.117
19.Records of waste removal destruction and treatment are available	84	19.0	183	41.5	100	22.7	40	9.1	34	7.7	3.55	1.129
20.waste workers are being drawn to coronavirus-related waste	110	24.9	190	43.1	77	17.5	36	8.2	28	6.3	3.72	1.117
21.first aid kit is available and usable	99	22.4	209	47.4	79	17.9	28	6.3	26	5.9	3.74	1.060
22.A published contingency plan is available	33	7.5	86	19.5	28	6.3	100	22.7	194	44.0	2.24	1.380

23.A workplace response plan is an available case someone develops symptoms of coronavirus and employees are aware of them	53	12.0	91	20.6	22	5.0	90	20.4	185	42.0	2.40	1.489
Weighted Mean= 2.81±0.78												

Fig 1 Represent the total score prevention and control methods. The highest percentage of the studied sample which reached 266(60.0%) had a poor score (high risk) regarding prevention and control methods, while reached to175 (40.0%%) of them had a good score (low risk) toward it.

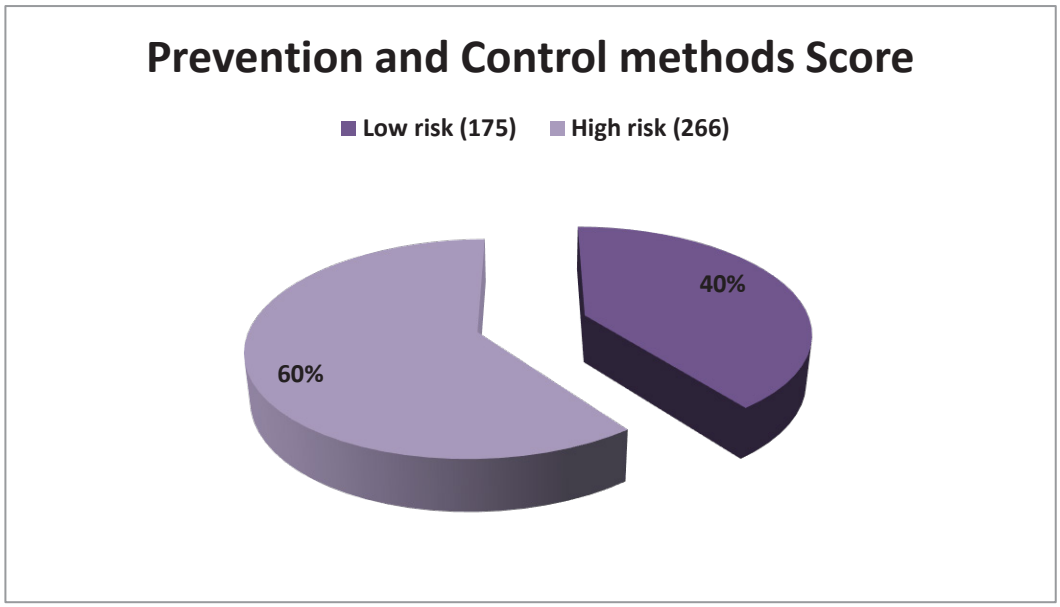

Fig 1. The total score of the Prevention and Control Methods.

Table 5 represents Pearson's correlation coefficients physical hazards, and prevention and control methods. It shows that there is a highly significant positive correlation (P-value <0.01) between physical hazards and prevention and control methods (r= 0.144**).

Table 5. Pearson's correlation coefficients physical hazards, and prevention and control methods.

		physical hazard
Prevention and control methods	Pearson Correlation	0.144**
	Sig. (2-tailed)	0.002

	N	441

Table 6 represents Pearson's correlation coefficients chemical hazards, and prevention and control methods. It shows that there is a highly significant positive correlation (P-value <0.01) between chemical hazards and prevention and control methods (r= 0.770*).

Table 6. Pearson's correlation coefficients chemical hazards, and prevention and control methods.

		Chemical hazards
Prevention and control methods	Pearson Correlation	0.770**
	Sig. (2-tailed)	0.000
	N	441

4 Discussion

The present study found that 254(57.6%) were in the age group of health care workers <30 years. These results are consistent with the previous study was done in Palestine hospitals [7], which found that 60% of the study participants fall included the age group (20-30 years) This may be due to the increasing number of graduates from medical institutes and colleges in Iraq and Their enrolment in the direct job more than before. in this study, there was a distinct female's preponderance 242(54.9%). These results agreed with the study findings done in Nigeria [6], which found that most of the participants were females, and another similar study in India [9] revealed that the highest percentage (80%) of the study samples were females. Furthermore, these results are consistent with the study findings done in Riyadh, Saudi Arabia [10], which found the participants proportion in the study for females higher than males. But, these results differ from the findings study in Palestine [11] who found that most participants were males. The results of this study indicated that 265(60.1%) of the study population were married, and 161(36.5%) of Participants were single in studied hospitals. These results are consistent with the study done in Nigeria[8], which revealed that the highest percentage (63.0%) of the study samples were married. The current findings that the first rank of health care workers were nurses 125 (28.3%) followed which reached to 107(24.3%) of medical assistants, laboratory assistants, and radiology assistants in all studied hospitals. While the overall frequency of Technicians was 86(19.5%) in all hospitals. This may be due to the increasing number of private and government colleges that graduate large number of nurses .These results agreed with the study conducted in the Northern West Bank Hospital Palestine [12], which found that the first rank of health care workers were practical nurses (46.4%).
In this study, most of the participants respond with "agree and strongly agree" regarding" the electrical lifts are in a good and safe condition" and" enough lighting is available at the workplace". These findings agreed with the previous study in Egypt[13]. Which found that most of HCWs reported that electrical installations and lighting were in good condition

This study revealed there are differences between the four hospitals concerning the physical hazards level were statistically significant P value equal 0.05. These findings were agreed to the study conducted in a Greek hospital [14], which found that most participants declared low to

medium levels of risk concerning physical hazards. But, these results disagreed with the study conduct in Egypt[15], which found that physical hazards were the first rank among radiation health teams compared to other occupational hazards.
The association between the four hospitals concerning the chemical hazard scoring level was statistically significant P value equal to 0.047. These results disagree with another study conducted in Benin-city, Nigeria [16], which found that chemical hazards levels were 68% among health care workers and the association between the study hospitals concerning the exposure level were statistically significant P value equal 0.005.
The study was done in Palestine, Almurr, 2013who reported that respondents do not take training regarding safety practices [12]. Also, a study, conducted in a European Gaza hospital Saqer, 2014) found there is a lack of occupational training for health care providers towards knowledge of occupational health and safety risks at European Gaza Hospital. The finding agreed with our result in this study [17].
In Palestine, a study revealed that only (27.3%) of health care personnel indicated the lack of infection-prevention equipment such as gloves, hats, closed shoes, and work suits. This result disagreed with the study of our findings in Palestine [18]. A study conduct in Gaza [19], who showed apparent progress in adherence of healthcare workers in the implementation of infection prevention. This finding disagrees with our results in this study.

5 Conclusion

There are some following conclusions:

1- The study showed that the hazards in hospitals were moderate for chemical hazards followed by physical hazards.
2- The study revealed that the less commitment to prevention and control methods, the greater the risks to workers.
3- The study revealed that the relationship between the study sample and the physical hazards with the regarded to demographic characteristics are (social status, professional and experience years) $p>0.05$.

References

[1] Younis, NM., Hussein, AA., Ahmed, MM., & Younis, NM**.** Quality of life and occupational hazards among cement factory workers in Mosul city. QoL and Occupational Hazards among Cement Factory Workers.2021, 24(2), 1–8.
[2] Abdel-Wahed, A., Alazab, RM., Elsaidy, W H., Imam, M E.-H., & Ghandour, A A. Risk assessment of physical health hazards in Al-Azhar University Hospital in new Damietta, Egypt. The Egyptian Journal of Hospital Medicine.2013 , 53(1), 1019–1035.
[3] Khamtuikrua C, Suksompong S. Awareness about radiation hazards and knowledge about radiation protection among healthcare personnel: A quaternary care academic center–based study. SAGE open Med. 2020;8:1–8.
[4] Erkan I, Yarenoglu A, Yukseloglu EH, Ulutin HC. The investigation of radiation safety awareness among healthcare workers in an education and research hospital. Int J Radiat Res. 2019;17(3):447–53.
[5] Bhusnure OG, Dongare RB, Gholve SB, Giram PS. Chemical hazards and safety management in pharmaceutical industry. J Pharm Res. 2018;12(3):357–69.
[6] United State Food and Drug Administration. Personal Protective Equipment for Infection Control [Internet]. 2020 [cited 2021 Apr 14]. Available from: https://www.fda.gov/medical-devices/general-hospital-devices-and-supplies/personal-protective-equipment-infection-control

[7] Al-Khatib IA, El Ansari W, Areqat TA, Darkhawaja RA, Mansour SH, Tucktuck MA, et al. Occupational safety precautions among nurses at four hospitals, Nablus district, Palestine. Int J Occup Environ Med. 2015;6(4):243–6.
[8] Seidat Moyosore Ogunnaike MOA. Occupational hazard preventive measures among nurses in a Nigerian tertiary health institution. Nurs Care Open Access J [Internet]. 2020;7(1):20–5. Available from: https://medcraveonline.com/NCOAJ/NCOAJ-07-00212.pdf
[9] Chelladurai UM, Suga SSD, Myneni S, Sivagananam P, Ravikumar D, Kumar MR, et al. KNOWLEDGE, ATTITUDES ON OCCUPATIONAL HEALTH HAZARDS AND SAFETY (OHHS) AMONG THE HEALTHCARE WORKERS IN A TERTIARY CARE HOSPITAL. J Crit Rev. 2020;7(14):1540–8.
[10] Alshalani AJ, Salama KF. Assessment of Occupational Safety Practices Among Medical Laboratory Staff in Governmental Hospitals in Riyadh, Saudi Arabia. J Saf Stud. 2019;5(1):1–23.
[11] Alqam TIS. Occupational hazards among laboratory workers in Palestinian governmental hospitals in the West Bank.Al- Quds University [Internet]. Master Thesis; 2013. Available from: https://core.ac.uk/download/pdf/287328913.pdf
[12] Almurr BJ. Knowledge and Practice of Standard Precaution and Sharp Injures among Nurses in the Northern West Bank Hospitals; Palestine [Internet]. 2013. Available from: https://repository.najah.edu/bitstream/handle/20.500.11888/7825/Bushra AlMurr_0.pdf?sequence=1&isAllowed=y
[13] Abdel-Wahed A, Alazab RM, Elsaidy WH, Imam ME-H, Ghandour AA. Risk assessment of physical health hazards in Al-Azhar University Hospital in new Damietta, Egypt. Egypt J Hosp Med. 2013;53(1):1019–35.
[14] Tziaferi SG, Sourtzi P, Kalokairinou A, Sgourou E, Koumoulas E, Velonakis E. Risk assessment of physical hazards in greek hospitals combining staff's perception, experts' evaluation and objective measurements. Saf Health Work. 2011;2(3):260–72.
[15] Eliwa SM, Sorour AS, Mahmoud SF. Occupational Health Hazards and Protective Measures among Radiation Health Team. Zagazig Nurs J. 2018;14(2):48–63.
[16] Omoijiade EN. An assessment of laundry workers exposure to workplace hazards in secondary and tertiary health facilities in Benin-city, Nigeria. MOJ public Heal. 2018;7(5):252–9.
[17] Saqer AM. Assessment of Health and Safety Risk among Health Care Providers in European Gaza Hospital. (Thesis) Islamic University-Gaza,Faculty of Science - Environmental Health. 2014.
[18] El Attar SM. Assessment of health and safety risk among health care providers at Al Shifa Medical Complex [Internet].2016. Available from: https://iugspace.iugaza.edu.ps/bitstream/handle/20.500.12358/21320/file_1.pdf?sequence=1&isAllowed=y
[19] Aldirawi A, Aljerjawy M, abu Mustafa A. Adherence to infection prevention and control protocol in neonatal intensive care units in governmental hospitals in Gaza Strip-A comparative study. Int J Recent Acad Res. 2019;1(7):300–4.

Development of a wireless power transfer system for electric vehicle charging using an E-Class power amplifier

Ali Nasser Hussain[1], Sadik Kamel Gharghan[2], Rasha Majid Abd Al-nabe[3]
{alinasser1974@yahoo.com[1], sadik.gharghan@mtu.edu.iq[2], bcc0024@mtu.edu.iq[3]}

Electrical Engineering Technical College, Middle Technical University, Baghdad, Iraq[1, 3], Electrical Engineering Technical College, Middle Technical University, Baghdad, Iraq[2]

Abstract. Wireless transmission technology is considered one of the advanced and advanced technologies at present, through which complexity in electrical wiring is avoided, as well as its valuable use in difficult-to-reach places such as high places, roads, etc., in this research a wireless power transmission system was designed using electromagnetic induction technology to charge the battery of electric cars wirelessly and with a high transmission efficiency of up to 90% where an E-type power amplifier was used that includes an IRFP250 switch and a throttle coil of 325μH. The intrinsic is 67μH. and its internal resistance is 32mΩ. This system was implemented using the MATLAB program. As for the receiving side, a receiving coil was designed to be equal and equivalent to the transmitter coil with the size and inductive value, and the distance between the two coils was 20cm. After implementing the program, an excellent quality factor was obtained, high efficiency, and very little power loss.

Keywords: WPT, Class E, Electric Vehicle charger, Battery, inductive coupling.

1 Introduction

In recent years, interest in wireless transmission technology has begun to grow rapidly. The technology can be used for wireless charging of the mobile or any other electronic device. This method is important and useful when transmission by wires is not possible. Today, there is some vital and daily application that require Wireless Power Transfer (WPT). Wireless energy can be transmitted in various ways a technique such as resonant inductive coupling and capacitive coupling based on electromagnetic radiation, microwaves [1], [2]. One of the major challenges and difficulties facing researchers in this field is how to improve capturing the largest possible amount of energy using the techniques mentioned earlier. This process is known as energy harvesting. In 1891 Nikola Tesla made the wireless energy transmission using the resonant radio frequency transformer called Tessa's coils that produced high-frequency alternating currents, high voltage, and low output current [3]. After a short period, studies had shown that high-frequency currents can be used in medical applications because these high-frequency currents are not harmful to the human body and can pass through them without any danger [4]. Since the invention of wireless devices, this technology has evolved. In wet

IMDC-IST 2021, September 07-09, Sakarya, Turkey
Copyright © 2022 EAI
DOI 10.4108/eai.7-9-2021.2314927

environments, wireless charging pads for devices such as electric razors and electric toothbrushes are utilized to reduce the risk of harmful electric shock. It has also been clarified when the turns of a coil are deployed and distributed inside its diameter, the coupling coefficient of flowing between the magnetically wrapped coils con be amplified and the situation is reversed when distributed at the circumference [5]. Using a strongly coupled system, the experimental results [6] showed that 60w were transferred with an efficiency of about 40% at a distance of 2m. That experimental model in its time was considered sufficient to interpret this technique. The helical transmitter and receiver used in that system were identical and had one copper ring with a radius of 25cm. The resonance frequency was 9.9 MHz Capacitors paralleled with a coil were used to achieve resonance between transmitter and receiver coils which in turn consisted of two large coils, each with a diameter of 30cm at a distance of 3.8 cm from each other [7]. The power was transferred up to 50% with a frequency of about 8.3 MHz showed that the efficiency and distance between transmitter and receiver could be enhanced in the WPT system by using an intermediate coil between the transmitting and receiving antennas [8]. The efficiency of that system was better and exceeded 90% at a resonance frequency of 1.25 MHz Various types and sizes of transmitter and receiver coils used at a frequency of 13.56 MHz were introduced [9]. The wireless power transfer and harvesting were obtained using magnetic resonance. The transmitter coil diameter was 60 and 20 cm apart from the receiver coil. The transmission efficiency was 80%. Next, the transmission efficiencies ranged from 40-75% at distances ranging from 20-50 cm were achieved keeping the size of the receiver like the size of the iPhone 4. The printed coil inductors were used at 13.56 MHz and implemented with implanted sensors [10]. The transmission of power was 15 mW at 6mm while at 17mm, the transmission of power had approached 1.17 mW. The wireless power transmission and harvesting system with Tesla's resonators was introduced [11] To obtain an efficiency above 75% with a resonator's frequency extending from (503-525) KHz, the resonators were arranged in a domino-like axis at a distance of 3m, 8W LEDs were used in that research. Eventually, it was concluded that the distances (spaces) between resonators are worse when they are not arranged. In a prototype introduced [12], the power transfer efficiency was enhanced to 64.2% at a separating distance of 15 cm, and the power transferred to load was also enhanced to 5.26 W with 10 V excitation voltage. In the systems introduced inductive magnetic resonance coupling was adopted to provide very high energy at short distances which can be used for wireless charging of electric such as cars and Handicapped vehicles [13] [14]. This paper begins with the WPT system and then proposes the inductive wireless power transfer technology and gives an overview of IWPT technology to solve the problem of power transfer with small distances and high efficiency, as well as concern for human safety by eliminating wire problems. The theory of WPT in electric vehicle applications has gained wide acceptance in the world. We hope that researchers will be interested in WPT theory because it contributes to the development of technology.

2 Materials and Methods

The proposed power harvesting system: The proposed WPT system is shown in Fig. 1. It represents a resonant inductive WPT system built of a transmitting circuit which includes an AC power transmitting coil driven by a power amplifier and a receiving circuit consisting of receiving coil connected power harvesting coil followed by a suitable rectifying circuit and driving a certain electrical load.

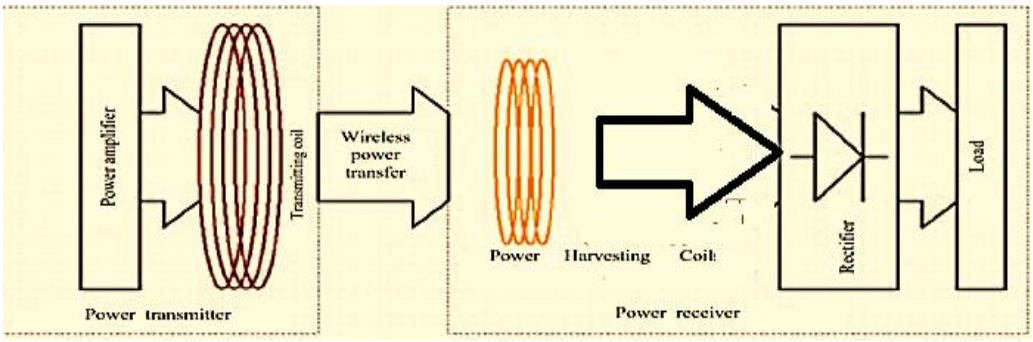

Fig. 1. The block diagram of a proposed power harvesting system having one transmitting antenna and one receiving antenna.

The AC transmitting circuit consists of a Class-E power amplifier driving a planar spiral transmitting coil T_x. The receiving coil R_x is also a planar spiral coil located axially and perpendicularly with the transmitting coil on an axis passing through their centre points as shown in Figs 2 to 4.

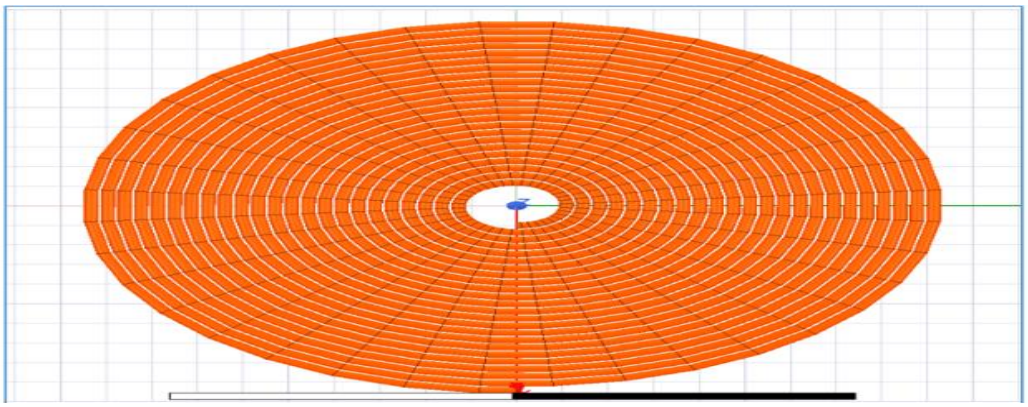

Fig. 2. The power transmitting coil in the proposed WPT system.

Fig. 2 shows the number of turns of the coil, the inner diameter of the coil, and the outer diameter of the coil. The coefficient of coupling k=0.02194 between two planar spiral coils located as shown in fig.6 is given [15]:

$$K=\frac{1}{[1+\sqrt[3]{4}\left[\frac{h}{\sqrt{r_t * r_r}}\right]^2]^{\frac{3}{2}}} \quad (1)$$

Where:
r_t and r_r : Radii of transmitter and receiver coils.
h: Distance between the centers of the two coils.
The inductance and low-frequency resistance of the planar spiral coil is given [15] :

$$L=\frac{(0{\cdot}3937)\times(a\times N)^2}{(8\times a)+(11\times b)} \quad (2)$$

$$R_{low\ frequency} \approx \frac{1}{\sigma\pi a^2}[1+\frac{1}{48}\times[\frac{a}{\delta}]^2] \quad (3)$$

Where:
N: Coil Number of turns
δ: Skin depth
σ : Conductor material conductivity
At operating frequency 100kHz.
a, b and $\delta$are given by:

$$a=\frac{r_0+r_i}{2} \quad (4)$$

$$b=r_0-r_i \quad (5)$$

$$\delta=\frac{1}{\sqrt{\mu\pi\sigma f}} \quad (6)$$

Where:
$r_i$and r_0: Inner and outer radii of the spiral coil
μ=μ_0. μ_r= Permeability
f = WPT system operating frequency
The transmitting coil is designed and implemented using a copper tube of diameter of 6.35 mm and length of 15 m. the outer and inner diameters are 360 and 60 mm, respectively as shown in Fig 2, according to Eq. 2, the self-inductance L_T of the transmitting coil Tx is 67 uH, the value of the self-inductance L_T determined according to the analysis program (ANSYS electromagnetics Software 2016) is 67 uH. Using Eq. 3, the low-frequency resistance R_1 of the transmitting coil is calculated as 0.032 Ω. Each receiving coil is wound of a copper tube of a diameter of 6.35 mm and length of 15 m. Using the same methodology for inductance and resistance calculations, the self and resistances of receiving coils are listed in Table 1.

Table 1. Calculated parameters of transmitting and receiving coils.

Parameter	Inductance	Resistance	r_i	r_o	N
L_t	67 uH	0.032 Ohm	30 mm	180 mm	23
L_r	67 uH	0.032 Ohm	30 mm	180 mm	23

In this table, transmitter coils L_t and R_t are corresponding to receiving coils, L_r and R_r respectively. In Table 1, the inductances are listed. Using Eq. 2 and the parameters of the designed transmitting and receiving coils.

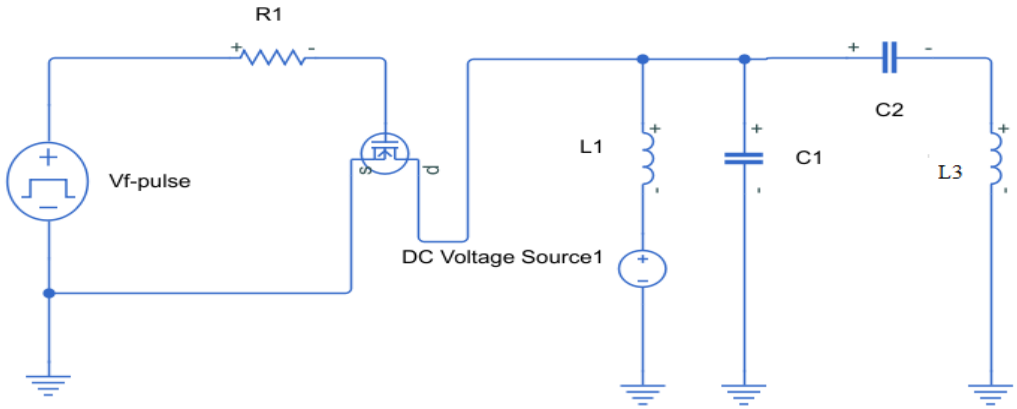

Fig. 3. The proposed Class-E power amplifier.

Fig 3 shows the circuit design of a Class-E power amplifier, DC voltage source, and Vf-pulse at the operating frequency.

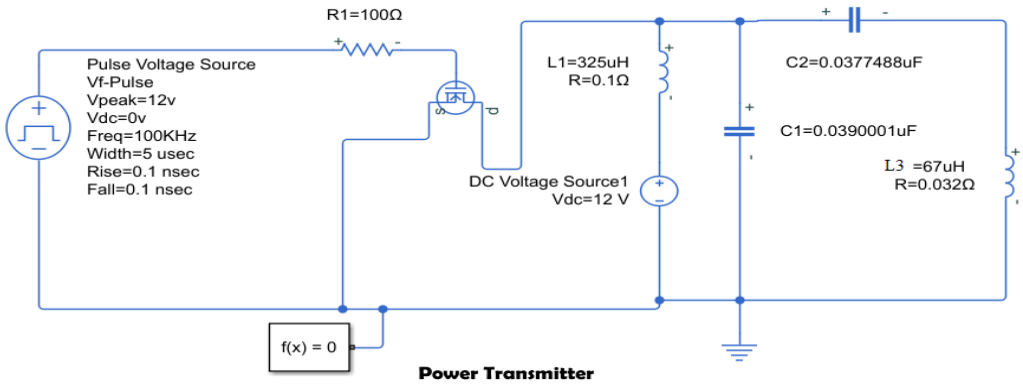

Fig. 4. The circuit design power transmitter of a proposed WPT system.

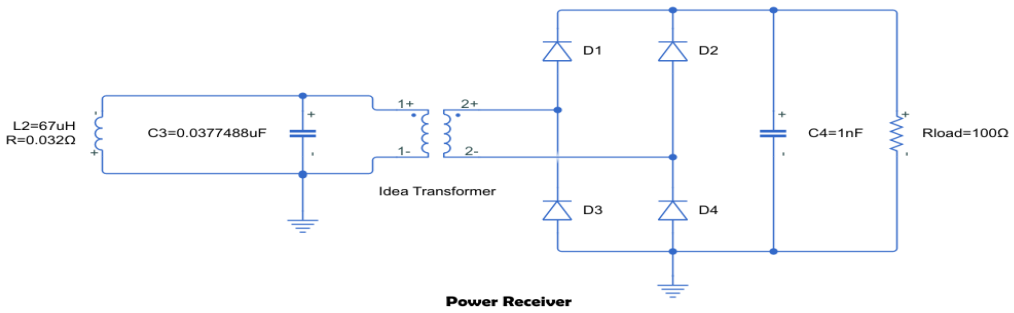

Fig. 5. The circuit design power receiver of a proposed WPT system.

Fig.5 shows the design of the receiver circuit containing the full-wave rectifier circuit.

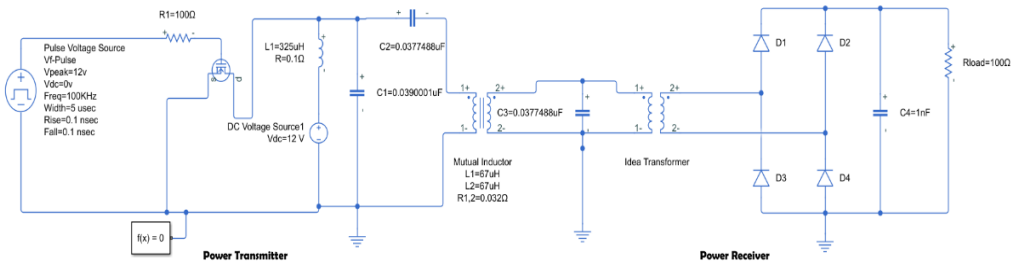

Fig. 6. The circuit design of a proposed WPT system.

2.1 Power amplifier design

In the WPT system, several techniques are used in the transmitter to increase the amount of transmitted energy and thus increase the spreading of magnetic flux in the area to be covered. The most efficient of these technologies is the Class-E power amplifier which is a switch-mode amplifier having high efficiency and high output power, thus, it is suitable to be used in the WPT system to enhance the power transmission efficiency. To increase the power output of the transmitter, connected MOSFET of the type IRFP250 are chosen as the main switching device of the Class-E power amplifier. The series Capacitor C_2 and transmitter inductance L_3 are tuned to a resonance frequency slightly less than the proposed WPT frequency which is 100 kHz. The shunt or parallel Capacitor C_1 is determined such that the parallel combination constituted by L_3 and C_1 resonates at 100 kHz which complies with the MOSFET transition frequency specified in its datasheet. The inductance of the radio frequency choke LRFC is chosen to be

very much >L_3. The amplifier DC Voltage is 12 V. Figure 3 shows the complete circuit diagram of the Class-E power amplifier which is designed on the MATLAB program.

2.2 Circuit design of the proposed WPT system

This system is built of a Class-E power amplifier with a planar spiral coil as a transmitting circuit and receiving coil connected planar spiral power harvesting coil followed by a rectifying circuit driving a certain load as receiving circuit. The proposed system is designed on MATLAB program as shown in Fig. 4, Fig. 5, Fig. 6. The receiving coil power harvesting coil is tuned to resonate at a frequency of 100 kHz by the Capacitor C_2, which is set to 0.0377 uF, and C_1, which is set to 0.039 uF. The Class-E power is the same as that specified in Fig. 3 and is driven by a 12 V DC supply and triggered by a square wave of a positive level of 12 V and having a frequency of 100 kHz.

3 Results and Discussion

The performance of the power amplifier proposed in Fig. 3 was tested on the MATLAB program. The triggering voltage Vs to the switching device is shown in Fig. 6. The DC supply voltage level of 12 V is shown in Fig. 7 and the switching MOSFET drain voltage is shown in Fig.8. The DC I_{Dc} is drawn by the power amplifier shown in Fig. 9 and the AC I_t is flowing in the transmitting coil is shown in Fig. 10.

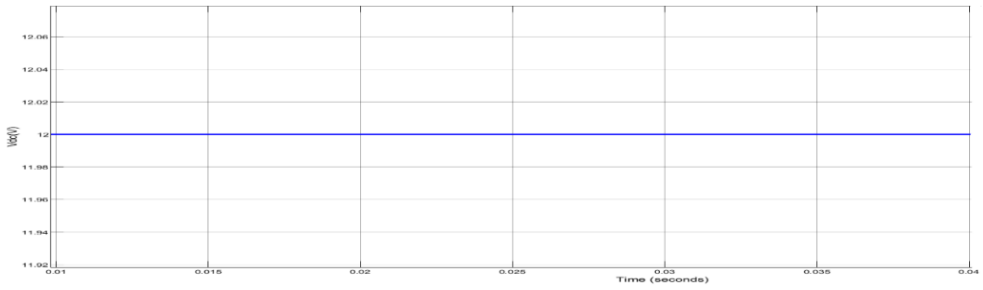

Fig. 7. The DC supply voltage.

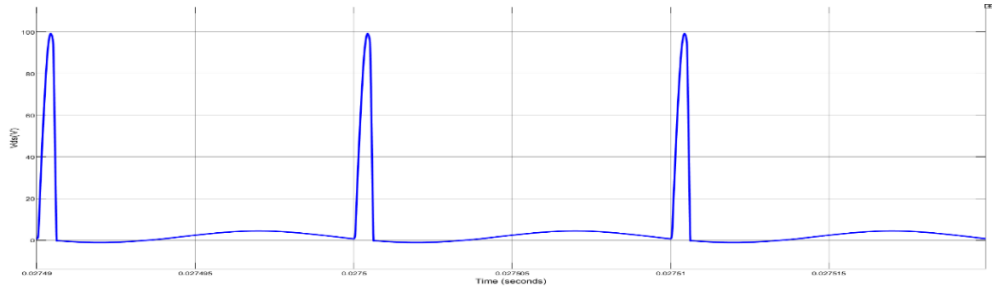

Fig. 8. The DC voltage MOSFET drain voltage of the Class-E power amplifier.

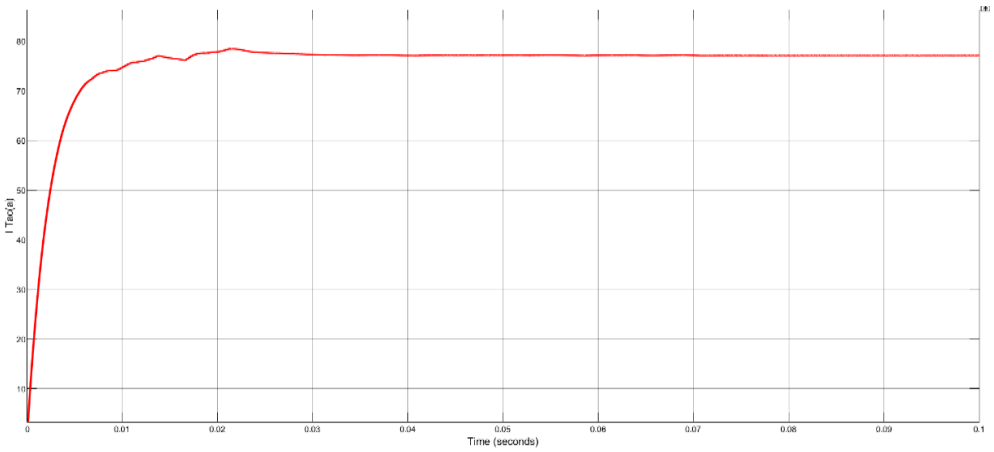

Fig. 9. The DC of the Class-E power amplifier.

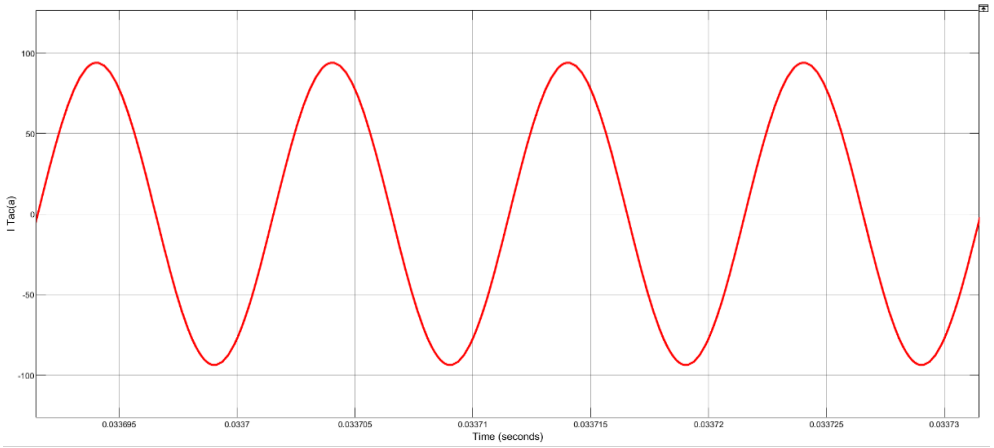

Fig. 10. The AC transmitting coil current of Class-E power amplifier.

The AC voltage V_t across the terminals of the transmitting coil is in shown Fig. 11. The amplitude of the AC voltage across the terminals of the transmitting coil is about 3Kv.

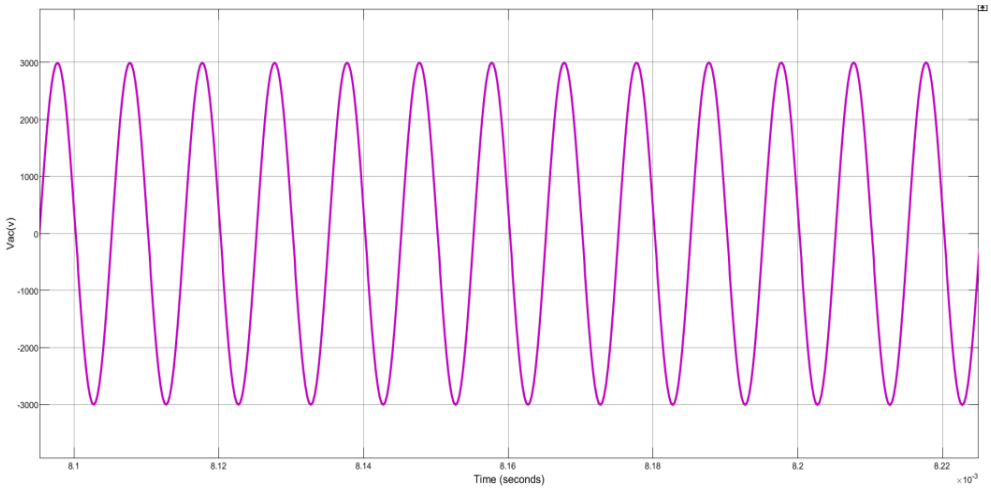

Fig. 11. The AC voltage transmitting coil of Class-E power amplifier.

The performance of the proposed WPT system shown in Fig. 6 was tested on the MATLAB program. The AC and DC voltage outputs of the receiving circuit for a load resistance of 100 Ω are shown in Fig. 12, Fig.13.

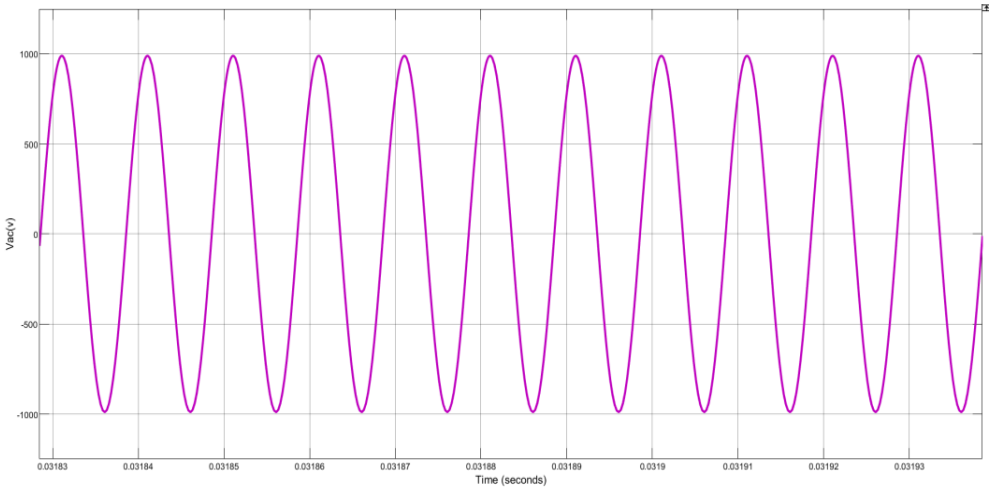

Fig. 12. The AC output voltages of the WPT system receiving a spiral power harvesting coil.

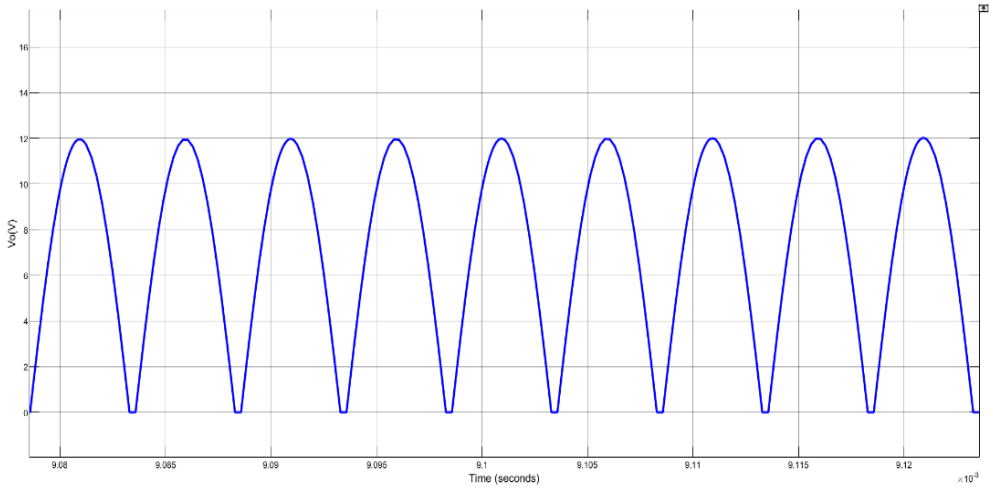

Fig. 13. The DC output voltages of the WPT system having connected spiral power harvesting coil RL=100Ω.

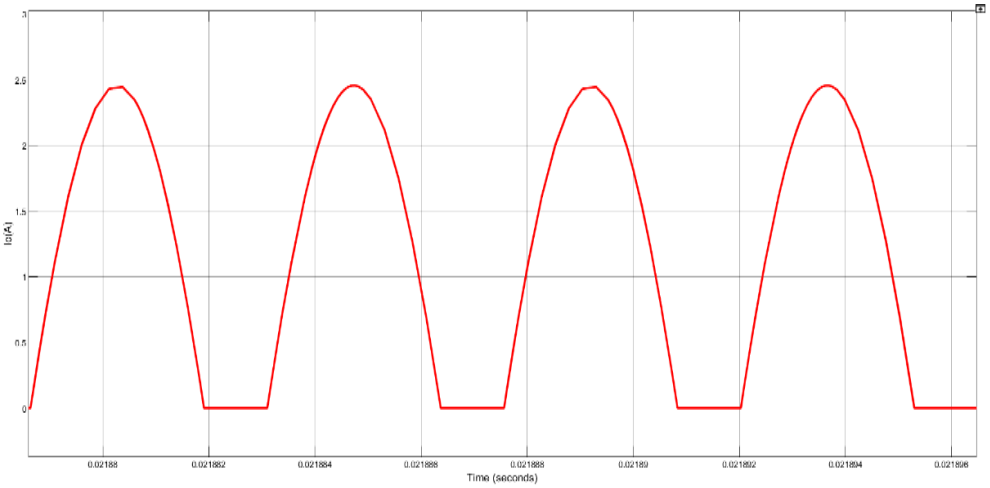

Fig. 14. The DC charging current of the 12V DC battery in the WPT system having connected spiral power harvesting coils.

Fig. 14 shows a DC charging the battery with a value of 2.5 Amps. The power consumed by the Class-E power amplifier driving the planar spiral transmitting coil of 67 uH is 29.4w (2.45A×12 V). The efficiency of a WPT is measured by how much power it is capable to harvest from a certain transmitting Source.

Table 2. Comparison between the WPT system and previous works.

Ref.	Frequency (KHz)	Distance (mm)	Efficiency (%)
[16]	40	300	85
[17]	100	300	81
[18]	60	200	82
[19]	20	160	80
[20]	31.6	200	74.8
This work	100	200	90

4 Conclusion

The wireless power transmitting system that uses electromagnetic induction technology to charge the electric vehicle battery has two coils, the first is transmitter coil and the second is the receiver coil, both of which have the same value of 67 μH and internal resistance of 32 mohm. A Class-E power amplifier type was used on an IRFP 250 switch and a 325 μF throttle switch. Implementation of this system using MATLAB program. The distance between the two coils was 20 cm. After implementing the program, an excellent quality factor was obtained, high efficiency up to 90%, and very little power loss.

Parameters

L= Inductance
N=Number of Turns of coil
C = Capacitance
R= Resistance
F = Operating frequency
P= Power
Q= Quality Factor
K= Coupling Factor
r_o= outer Radius of coil
r_i= inner Radius of coil
L_l= Inductance chock LRFC
T_X= Transmitting coil
R_X= Receiving coil
V_O= Output voltage/ Secondary coil voltage
Io = Output current/ Secondary coil current

References

[1] Kim, K.Y., Wireless power transfer-principles and engineering explorations. 2012.
[2] Chen, W.-T., et al., A 36 W wireless power transfer system with 82% efficiency for LED lighting applications. 2013. **6**(1): p. 32-37.

[3] Valenta, C.R. and G.D.J.I.M.M. Durgin, Harvesting wireless power: Survey of energy-harvester conversion efficiency in far-field, wireless power transfer systems. 2014. **15**(4): p. 108-120.
[4] Nagoorkar, V., Midrange Magnetically-Coupled Resonant Circuit Wireless Power Transfer. 2014.
[5] Zierhofer, C.M. and E.S.J.I.t.o.B.E. Hochmair, Geometric approach for coupling enhancement of magnetically coupled coils. 1996. **43**(7): p. 708-714.
[6] Kurs, A., et al., Wireless power transfer via strongly coupled magnetic resonances. 2007. **317**(5834): p. 83-86.
[7] Cannon, B.L., et al., Magnetic resonant coupling as a potential means for wireless power transfer to multiple small receivers. 2009. **24**(7): p. 1819-1825.
[8] Kim, J., et al., Efficiency analysis of magnetic resonance wireless power transfer with intermediate resonant coil. 2011. **10**: p. 389-392.
[9] Choi, J., J.-K. Cho, and C. Seo. Analysis on Transmission efficiency of wireless energy transmission resonator based on magnetic resonance. in 2011 IEEE MTT-S International Microwave Workshop Series on Innovative Wireless Power Transmission: Technologies, Systems, and Applications. 2011. IEEE.
[10] Zhong, W., C.K. Lee, and S.R.J.I.t.o.i.e. Hui, General analysis on the use of Tesla's resonators in domino forms for wireless power transfer. 2011. **60**(1): p. 261-270.
[11] Olivo, J., et al., A study of multi-layer spiral inductors for remote powering of implantable sensors. 2013. **7**(4): p. 536-547.
[12] Ahn, D., M. Kiani, and M.J.I.t.o.m. Ghovanloo, Enhanced wireless power transmission using strong paramagnetic response. 2013. **50**(3): p. 96-103.
[13] Song, C., et al., Low EMF and EMI design of a tightly coupled handheld resonant magnetic field (HH-RMF) charger for automotive battery charging. 2016. **58**(4): p. 1194-1206.
[14] Luo, Z. and X.J.I.T.o.I.E. Wei, Analysis of square and circular planar spiral coils in wireless power transfer system for electric vehicles. 2017. **65**(1): p. 331-341.
[15] Lee, Y.J.A., Microchip Technology Inc, Antenna circuit design for RFID applications. 2003.
[16] Covic, G.A., J.T.J.I.J.o.E. Boys, and S.t.i.p. electronics, Modern trends in inductive power transfer for transportation applications. 2013. **1**(1): p. 28-41.
[17] Dai, Z., et al., A witricity-based high-power device for wireless charging of electric vehicles. 2017. **10**(3): p. 323.
[18] Zeng, H., S. Yang, and F.Z.J.I.T.o.P.E. Peng, Design consideration and comparison of wireless power transfer via harmonic current for PHEV and EV wireless charging. 2016. **32**(8): p. 5943-5952.
[19] Gao, Y., et al. Misalignment effect on efficiency of wireless power transfer for electric vehicles. in 2016 IEEE Applied Power Electronics Conference and Exposition (APEC). 2016. IEEE.
[20] Nayak, P.S.R. and D. Kishan. Design and analysis of SS resonant IPT system with computed mutual inductance through FEM model. in 2018 International Conference on Power, Instrumentation, Control and Computing (PICC). 2018. IEEE.

Isolation and Identification of Dermatophytesis and Fungal Factors Samples from Infected Patients in Basra – Iraq

Ahmed Hamid Dawood Alatbee[1], Entiha abdulzahra abdulkareem[2], Shafeeqa Abdusayed Obaid[3]
{ahmed.dawood@stu.edu.iq[1], intihaa.abdulkareem@stu.edu.iq[2], Shafeeqa .abdulsayed@stu.edu.iq[3]}

Southern Technical University, Technical Institute of Basra Department of Anesthesia and Medical Laboratories Techniques, - Iraq[1,2,3]

Abstract. Fifty samples were collected from patients who showed symptoms of Fungal infection in private clinics and government hospitals. After examining, samples found 20 patients with fungal skin. The study showed an increase in dermatophytosis at an earlier age, as well as increased rates of infection in more rural areas compared to downtown. Where the study confirmed a higher rate of Tinea infections was Tenia corperis 50% followed by after that Tenia pedis 25% while the lowest rate of infection tinea capitis 15%. While two infections appeared by pityrs Versicolor is.

Keywords. Microsporum, Dermatophytes, candidia spp ,Tenia infection, Trichophyton spp.

1 Introduction

The recent incidence of tinea pedis and the spread of one major causative agent, T. rubrum, increased. It is usually not taken care of despite its great impact on the environment and human health.[1] Dermatophytes are a group that can invade the keratinized tissues (hair, skin, and nails) of humans and other animals to produce an infection known as dermatophytes, commonly referred to as a ringworm. [2] Fungal skin infection in the general population of developing countries The World Health Organization has reported a prevalence of up to 19.7% [3] Some species (e.g., Epidermal- phyton floccosum, Trichophyton rubrum, Trichophyton mentagrophytes,) are distributed worldwide, whereas others have a partial geographic restriction (e.g., Trichophyton Sudanese, violaceum, Trichophyton schoenleini, Trichophyton Trichophyton concentric,) [4] Some fungal pathogenic fungi are free to live and cause disease through the entry of their spores through wounds or inhalation and others are part of the normal flora of the human body such as, yeast, Candida. [5] Droplet's cause damage due to toxins and the enzymes they produce because they provoke an allergic reaction and penetrate directly into the tissues [6] The epidemiology of tinea capitis and tinea pedis (with onychomycosis) experienced the most dramatic changes. Changes in the prevalence of tinea corporis, tinea corporis, tinea corporis, and tinea cruris have been less extensively studied. Reflects the spread of dermatophytes responsible for causing local

IMDC-IST 2021, September 07-09, Sakarya, Turkey
Copyright © 2022 EAI
DOI 10.4108/eai.7-9-2021.2314919

tendencies in the head and ringworm, which is believed to be the source of infection. [7] . Sometimes the infection spreads to the skin in other parts of the body (or may have started for the first time in another area, such as sports foot (foot feed.) Usually deepens fungal infection in the body deep in body and is not serious [8].

2 Materials and Method

Samples were collected from skin clinics and government hospitals

2.1 Materials

1. Wire Loop
2. Potassium Hydroxide Has A Concentration Of 10%
3. Slides
4. Baker
5. Benzene Burner
6. Small Size Shower
7. Stain
8. Stick
9. Swap
10. Cover Slid

2.2 Method

2.2.1 Preparation of Sabouraud Dextrose Agar (SDA)

1. Suspend 65 g of the medium in one litter of distilled water
2. Heat with frequent agitation and boil for one minute to completely dissolve the medium.
3. Autoclave at 121° C for 15 minutes.
4. Cool to 45 to 50°C and pour into petri dishes or tubes for slants.

Hair or skin scrapings were inoculated on the sterilization (SDA`(SDA+Cycloheximide +chloramphenicol then incubate at 30 ± 1 o C and examined every 2-3 days.

3 Result and Discussion

Fifty samples were collected from patients who showed symptoms of Fungal infection in private clinics and government hospitals. Fig 1 it found Positive cultural examination 40%people infected with various ages fungal skin infection while the negative cultural examination was 60%. Fig 2 Dermatomycosis infections in the age group(1-10) highest 40% followed by age group (11-20) years which was (30%) than age group (21-30) years then age group(31-40) and age group (41-50) each was (10%). The study also showed that women are more affected than men. Fig 3 show that the higher rate of tinea infections was tenia corperis 50% followed by tenia pedis 25% while the lowest rate of infection tinea tenia capitis 15%. While two infections appeared by pityrs Versicolor. Fig 4 shows that the rates of infection with dermatophytes in males 30% Were less than females 70% Which matches the results that have been reached by Kaddouri (2008) [9]This result was not near that found by Tan (2005) [10], which found that the incidence rate for females was higher males in Tikrit[9]. The study also found an increase in the rate of fungal infection in rural areas compared to the city center, where 75% of the total infections were found in rural areas where culture and health care were low, while 25% of the total infections were found. In the city, this indicates a very important difference between the level of infections between the countryside and the city and the need to focus on raising the level of health and medical culture in rural areas to avoid fungal infections Fig 5.

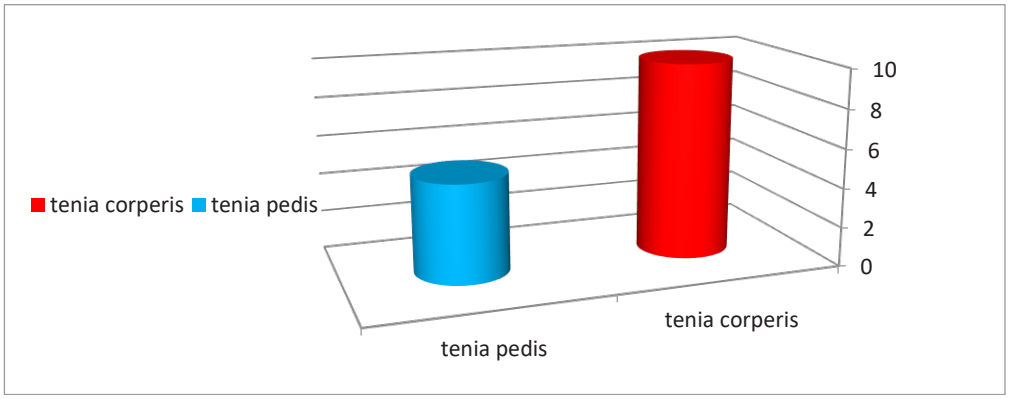

Fig 1. Show the percentage of positive and negative infections.

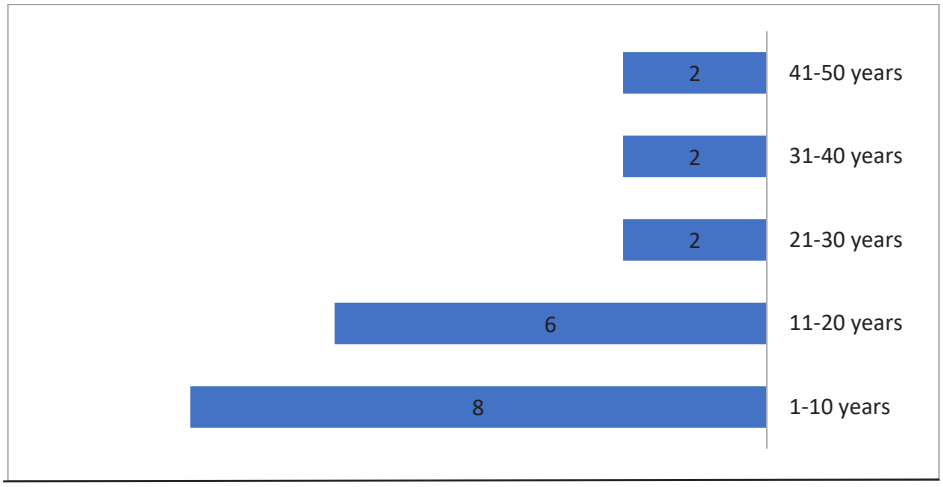

Fig 2. Show the percentage of dermatophytes Infections at different age groups.

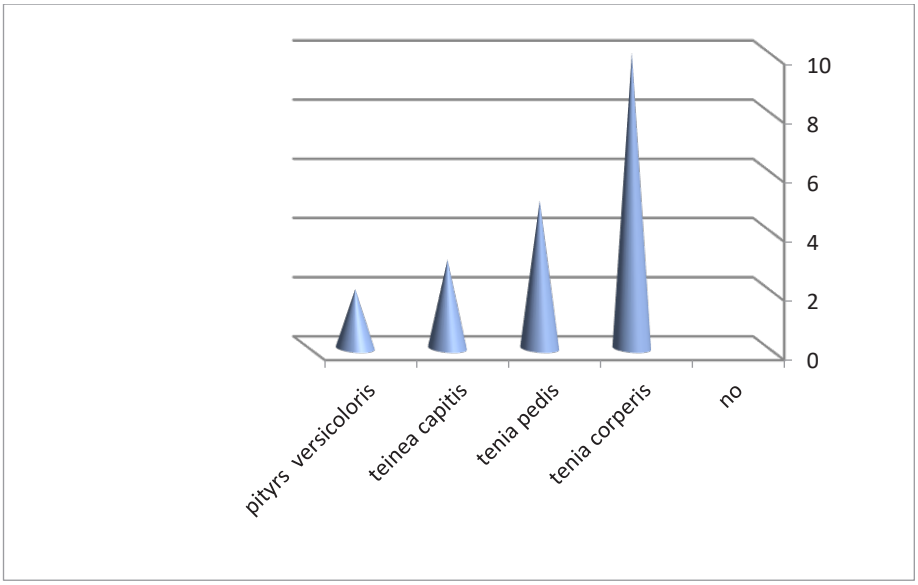

Fig 3. Show The percentages of dermatophytes (tinea) Infections.

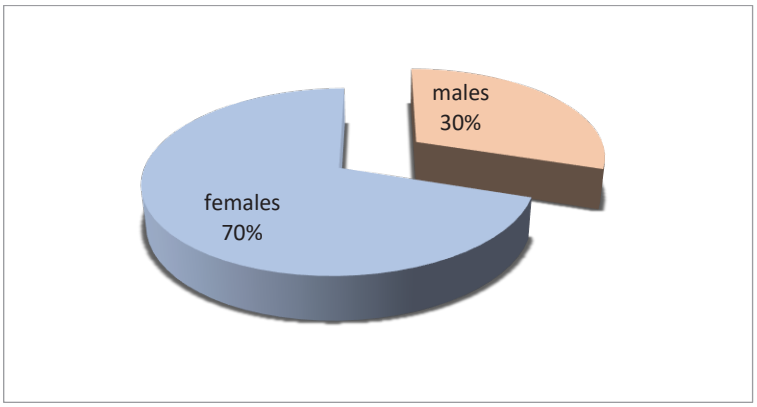

Fig 4. Show that the infection rates with dermatophytes in males and females

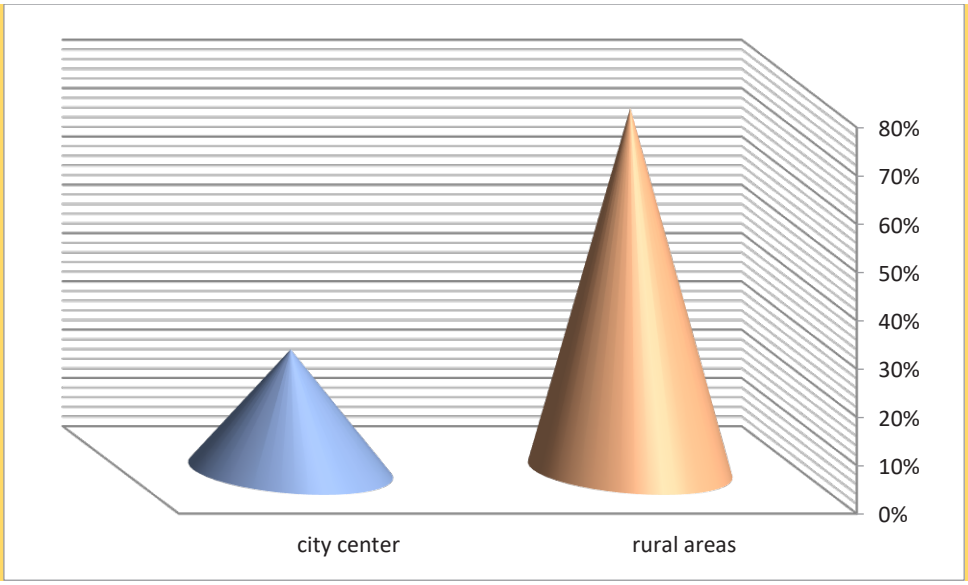

Fig 5. It explains the difference between rural areas and the city centre

4 Conclusion and Recommendation

The most important conclusions of the research: Determine the rate of infection with skin fungi and the most types of fungi that affect the skin in Basra Governorate, in addition to determining the most affected age groups, which has a very important role in reducing infection rates. One of the most important recommendations that we recommend in the future is to expand the scope of the study to include all districts and sub-districts in Basra, due to the increased infection of skin fungi, which may be transmitted from one person to another in Basra.

References

1. Jonathan B. Losos, Kenneth A. Mason, Susan R. Singer, Peter H. Raven, George B. Johnson, McGraw-Hill : biology book : Publisher Obeikan Publishing, 2014 : Number of pages 1378 pages
2. Dr. Harish C. Gugnani : Department of Medical Mycology : Vallabhbhai Patel Chest Institute,University of Delhi, Delhi-110007, India : (2000)
3. Kieran Sweeney and Iona Heath; address : British joumal of General practice .
4. Affiliations : Fungi that Infect Humans
5. Willey, Joanne M; Sherwood, Linda; Woolverton, Christopher J; Prescott, Lansing M. Microbiology : Prescott, Harley, and Klein's microbiology : Publication date 2008 : Publisher New York : McGraw-Hill Higher Education : Collection folkscanomy; additional_collections
6. Gerard Tortora , Berdell Funke, Christine Case , Derek Weber , Warner Bair III : Microbiology: An Introduction 13th Edition : Publisher : Pearson; 13th edition (January 8, 2018) : Hardcover : 960 pages
7. Sunil Dogra1, Dipika Shaw2, Shivaprakash M Rudramurthy2 : Antifungal drug susceptibility testing of dermatophytes: Laboratory findings to clinical implications

8. Year : 2019 | Volume : 10 | Issue : 3 | Page : 225-233 Publication of IADVL in India
9. medical editors : Mayo Clinic Marketplace : Nail fungus : June 09, 2011.

10. The Inhibition Effect of some Plant's extracts on growth of dermatophytes isolation fro m patients : Qadory, A. G. : 2008 : College of Science. Uni. of Tikrit. Iraq.

11. Superficial fungal infections seen at the National Skin Tan H. H (2005). Centre, Singapore

Assessment of Preventive Measures Among Health Care Workers Regarding Nosocomial Infections in Kut City Hospitals

Qasim Abbas Khyoosh Al.Eqabi[1], Shrouk Abdulrazak Hassan Al.Ibraheem[2], Tareq Mahdi AL.Qassab[3]
{ qasim.abbas.kh@gmail.com[1], shrouk.albraheem@stu.edu.iq[2], tareq.mahdi@mtu.edu.iq[3] }

Community health Techniques/ Al-Furat Al-Awsat Technical University-Iraq[1]
Medical laboratories techniques/ Southern Technical University-Iraq[2]
Community Health Technology/ Middle Technical University-Iraq[3]

Abstract. The aim is to assess the preventive measures of HCWs and determine the relationship between preventive measures and the demographic characteristics of HCWs. Methods: Cross-sectional study conducted among 500 HCWs in Wasit governorate hospitals. This sample was distributed throughout four hospitals include, AL-Zahra, AL-Karama teaching hospitals, AL-Kut gynecology hospital, and Martyr Fairouz general hospital, for the period of October 15th, 2020, to May 15th, 2021. Through self-report and questionnaires, data were collected and analysed through descriptive and inferential statistics. Results: Findings depict that majority of age groups among those who are 20-29 years old 63.2%, 50.2 were male residence in urban areas, 36.2 were medical assistance, and hold a diploma, work less than 10 years and within adequate training. Finding reveals that the majority of 49.8% were poor preventive measures. There was a significant relationship between preventive measures with age, and years of experience of HCWs. Conclusion: Poor preventive measures towards NIs, more years of experience, and more training the staff help raising professionals' health workers.

Keywords: Health care workers (HCWs), Preventive measures, Nosocomial Infections (NIs).

1 Introduction

Health-care workers are the cornerstone of healthcare systems; a healthy and professional workforce is a must for a healthy community, and this is especially important in times of crisis like the COVID-19 pandemic[1]. Health care workers should also be well-informed about the disease and take precautions to protect themselves and the population as a whole[2]. It is the responsibility and duty of all healthcare workers to prevent healthcare-associated infections, professionals in infection control need evidence-based educational content to decrease HAIs[3]. Therefore, to achieve optimal prevention and control of HAI as a regulatory goal, most hospitals have recognized and reached written measurable standards for preventing this infection[4]. Hand cleaning, adequate personal protective equipment, aseptic procedures to prevent patient exposure to microbes, and the monitoring of sharps, blood spills, linen, and garbage to ensure a safe environment are all standard precautions[5]. According to the Centers for Disease Control and Prevention, universal precautions are a set of precautions designed to avoid pathogen transmission when providing health care[6]. Using personal safety barriers such as gloves can reduce exposure accidents to a great extent[7]. In addition to the use of face masks, goggles,

IMDC-IST 2021, September 07-09, Sakarya, Turkey
Copyright © 2022 EAI DOI 10.4108/eai.7-9-2021.2314879

overhead caps, and gowns, washing hands after disposing of gloves, not returning needles, sanitary disposal of medical waste, sterilization of surgical tools[8]. Hand hygiene is a simple, easy-to-implement habit and an effective method that can help to reduce the risk of infection[9]. The most important intervention in infection prevention is still washing hands[10].
Hand hygiene is measured by the World Health Organization's five moments of hand hygiene, which include washing hands before touching the patient, before clean/sterile operations, after exposure to the risk of body fluids, after touching the patient, and after touching the patient's area[11]. Health workers should always wear personal protective equipment, such as gowns, gloves, goggles, face shields, surgical masks, cardiopulmonary resuscitation masks, head coverings, respirators, and shoe cover because they establish a physical barrier that protects health workers from meeting contaminated or contagious materials[12], In addition to protect patients and visitors from threats to their health[13]. Therefore, this study amid to assess preventive measurements of HCWs; and determine the relationship between preventive measures and demographic characteristics of HCWs.

2 Methodology

A descriptive cross-sectional study through the use assessment approach and questionnaire items is conducted to explore preventive measures is conducted among 500 healthcare workers selected throughout the use of non-probability sampling approach at four hospitals in kut city divided as follows 135 from AL-Zahra teaching hospital, 125 from AL-Karama teaching hospital, 110 from AL-Kut gynecology obstetric and paediatrics hospital, and 130 from Martyr Fairouz general hospital, to explore preventive measures about nosocomial infections among health care workers. The study was conducted from October 15th2020 to May 15th2021. Data was collected using a questionnaire and self-report technique, A questionnaire was created through a related comprehensive review of the literature, which was used as a data collection tool that included socio-demographic characteristics; and preventive measures composed of (20) items. Data was collected using a questionnaire "self-administrative" health worker. The researcher introduced himself to the participants and explained the purpose of the study to get oral agreement. The questionnaire fills out an answer by the participants (health workers). "Through used SPSS-ver. 24 to analyse and evaluate the study data used descriptive analysis to describe the study variables: frequencies and percentages; and inferential statistic include Chi-square “test.

3 Results and Discussion

3.1 Part I: Socio-Demographic Characteristics

The results of the study appeared that 500 samples who participated in this study their age ranged from 20-29 years old and constituted 63.2% as a high percentage at mean + Sd.=30.18+8.620, while the age<20 years composed the lowest percentage out a total of the study sample, as shown in table 1. These results come due to the increasing number of graduates from medical institutes and colleges in Iraq and their enrolment in the direct job more than before. These findings agreed with the study conducted by Tripura deals with hospital-acquired infection knowledge. Findings depict most of the study participants were from 18 to 25 years age group 70.7% [14].

The distribution of gender in this study composed 50.2% were male and 49.8% were female, due to the male more responses to participants in the study. findings come in the same line with a study conducted in Gondar and deals with health care workers regarding infection prevention. Their findings depict that most of the study participants were male, constituted 50.7% were male[15].

The results that urban residents were predominant, it constituted 96.2% out a total number of the study population, as being the hospitals covered by the study are in urban areas so, the health care workers residents in those areas. These results agree with the findings of a study conducted in the Wasit governorate. Found that most of the study participants 94.7% of health workers in two hospitals were residing in an urban area [16].

The results reveal the distribution of study sample according to specialty, findings depicts that most of the study participants were medical assistant, it constituted 36.2% out the total number. Science specialization was the lowest among the results. Being the specialist was considered the major proportion of staff in a health organization, due to the large number of institutions that graduate from such departments. While in a study that found the highest proportion of health workers in Al-Kut hospital 39.1% were nurses compared to 36.8% of health workers in Al-Karamah teaching hospital were technicians [16].

The results that diploma graduated were more than half of the study sample. It constituted 56.8% of the total number of the study population. While the high diploma is the lowest percentage. The presence of institutes in most of the governorates and the graduation of batches of morning and evening study in large numbers in addition to the presence of several departments and various specialties.

Some previous studies agreed with this result, Okwii, found diploma health care workers constituted 48.9% as a majority. In Middle East hospitals found that most respondents depict to have a diploma which indicates 63.6% [17].In regarding the years of experience, results indicate that 73.4% had less than 10 years as predominant findings. As is most of them find new appointments. Because of new hires and the exploitation of young energies among those with working experience >5 years were about 85 respondents 43.4% in a study conducted in Yemen and assessed the standard precautions and nosocomial infection[18].

The results that most of the study participants work less than 8 hours daily, constituted 88.4% out the total number of the study population due to result indicates that the health workers work in the morning shift, as stated in the study cross-sectional study conducted in northwest Ethiopia deals with Knowledge, attitude, and practice of healthcare professionals regarding infection prevention at Gondar University referral hospital. Their findings depict that working hour among health care workers per day are 8 hours 63.8%[15].

Results indicate that laboratories workers were predominant among the study population, which composed 28.8% of the total number. Because of their large numbers and the diversity of their specialties. While in the study Okwii, stated that 30.7% of the respondents were from the medical ward, 26.1% were from paediatrics, 21.6% from surgery, and 21.6% from accident and emergency[19]. Distribution of the study sample according to the training course, most of them had one session of training and composed 32.2% out the total number. Participation in a training session in Iraq is diminished due to the political and economic limitations and this is controlled by the policy of the minister of health of Iraq. These results matched with a cross-sectional study conducted by Yazie et al., who found that more than half 55.3% of the study participants were untrained, is only 44.7% of them were taken training regarding infection prevention and safety in northwest Ethiopia[15].

Table 1. Descriptive statistics of demographic variables.

Variables	Rating	N=500	%
Age	<20 years old	5	1.0
	20-29 years old	316	63.2
	30-39 years old	121	24.2
	40-49 years old	39	7.8
	50 and older	19	3.8
Gender	Male	251	50.2
	Female	249	49.8
Residences	Urban	481	96.2
	Rural	19	3.8
Specialty	Physician	52	10.4
	Nurse	151	30.2
	Medical technologies	96	19.2
	Medical assistance	181	36.2
	Sciences	20	4.0
Education attainmen	Preparatory	30	6.0
	Diploma	284	56.8
	Bachelors	156	31.2
	Higher diploma	11	2.2
	Master and above	19	3.8
Years of experience	<10 years	367	73.4
	10-20 years	115	23.0
	21-30 years	18	3.6
Work hours	≤8 hours	442	88.4
	>8 hours	58	11.6
Workplace	Emergency department	58	11.6
	Consulting department	84	16.8
	Surgical wards	45	9.0
	Medical wards	53	10.6
	Maternity wards	43	8.6
	Pediatric wards	35	7.0
	Laboratories	144	28.8
Training course	No training	146	29.2
	One session	161	32.2
	Two sessions	108	21.6
	More than two sessions	85	17.0

3.2 Part II: Preventive Measures Towards Nosocomial Infections

The findings presented the overall health care workers' preventive measures toward nosocomial infections in Wasit governorate hospitals. Finding reveals that the majority of 49.8% were poor preventive measures at the low level of mean, due to the lack of monitoring by authorities, in addition to the shortage of medical facilities, we find a great shortage of personal protective equipment in hospitals. On the other hand, most of the training courses are theoretical presentations without practical application**,** Fig.1. show the status**.** Our results are consistent with those of an Iranian study conducted in Yazd, the practice among health care staff was poor,

the negative results were 49% from the total, due to staff deficiency failing health personnel to comply with medical instructions. Our results are consistent with those of an Iranian study conducted in Yazd, the practice among health care staff was poor, the negative results were 49% from the total, due to staff deficiency failing health personnel to comply with medical instructions [20]. Study in Yemen among healthcare workers to assess the preventive measures of nosocomial infections, their results show that over half 53.9% have poor practice and 46.1% of them had a good level practice. The poor practice returns to disparities in their education this result shows that there is a gap between the theoretical and practical aspects, which indicates that it is necessary to link between the theoretical and practical aspects about infection and its control[21]. Also, findings concerning preventive measures for nosocomial infections, found that 33.3% have practiced while 66.7% do not practice preventive measures for nosocomial infection, because of the shortage in availability of medical facilities[22].

At the University of Gondar comprehensive specialized hospital in northwest Ethiopia, most respondents have poor infection control practices 64% when it comes to HAI prevention. This lower result may be due to variations in the study sites' sanitary facilities and logistical requirements for HAI prevention activities. Other factors associated with the good practice were also not positively applied by HCWs, indicating that equipment and materials are inaccessible[23].

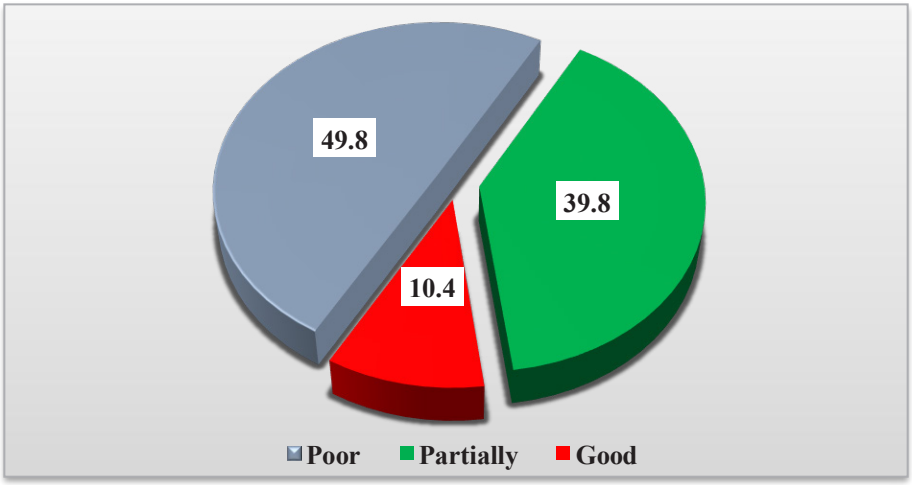

Fig 1. Overall preventive measures towards nosocomial infections.

3.3 Part III: Relationship Between Preventive Measures of Nosocomial Infections and Demographic Characteristics

Findings depict there was no significant relationship between health care workers preventive measures towards nosocomial infections and demographic characteristics at p-value >0.05 (χ^2obs > χ^2cri) except, health workers age and years of experience has been significantly associated at p-value ≤0.05 (χ^2obs < χ^2crit). The strong positive association could be because as the number of years of service increases, healthcare workers are repeatedly exposed to infection prevention principles and became more experienced, Table 2 results showed that the status. Our results are consistent with those of a study conducted in Palestinian hospitals, shows a comparison of mean practice scores about socio-demographic characteristics of the studied

sample. It displays that high mean practice scores were found among those who were in the age group of 20-30 and who attended training courses[24]. It is clear that age is an important factor in infection prevention practice, showing that healthcare staff who are over 30 years of age or older have around twice times to application of infection prevention practices appropriately as opposed to those who are less than 30 years of age this may be due to advanced age and long years of service, which over time leads to improvement in their practices, in addition to age, long work experience, and educational status were significantly associated with infection prevention practice[25]. The practice of preventing hospital-acquired infection is significantly associated with the educational level and work experience of health care staff at (p=0.027 and 0.044 respectively)[23]. Findings from Trinidad and Tobago confirmed that there was no significant association between socio-demographic variables with their practices (p>0.05)[26].

Table 2. The statistical relationship between health care workers' preventive measures and their demographic characteristics.

Variables	Rating	Preventive measures			Total	D.f	*Sig.*	
		Poor	Partially	Good				
Age	<20years old	0	5	0	5	8	χ^2obs.= 37.912 χ^2 crit.= 15.507 P-value=0.000	HS
	20-29years old	163	121	32	316			
	30-39years old	54	49	18	121			
	40-49years old	13	24	2	39			
	50and older	19	0	0	19			
	Total	249	199	52	500			
Gender	Male	129	101	21	251	2	χ^2obs.= 2.286 χ^2 crit.= 5.991 P-value=0.319	NS
	Female	120	98	31	249			
	Total	249	199	52	500			
Residences	Urban	239	193	49	481	2	χ^2obs.= 0.919 χ^2 crit.= 5.991 P-value=0.632	NS
	Rural	10	6	3	19			
	Total	249	199	52	500			
Specialty	Physician	27	20	5	52	8	χ^2obs.= 4.417 χ^2 crit.= 15.507 P-value=0.818	NS
	Nurse	75	58	18	151			
	Medical technologies	47	41	8	96			
	Medical assistance	89	75	17	181			
	Sciences	11	5	4	20			
	Total	249	199	52	500			
Education attainment	Preparatory	15	13	2	30	8	χ^2obs.= 3.749 χ^2 crit.= 15.507 P-value=0.879	NS
	Diploma	143	113	28	284			
	Bachelors	77	63	16	156			
	Higher diploma	5	4	2	11			
	Master and above	9	6	4	19			
	Total	249	199	52	500			
Years of experience	<10years	196	132	39	367	4	χ^2obs.= 11.107 χ^2 crit.= 9.488 P-value=0.025	S
	10-20years	44	58	13	115			
	21-30years	9	9	0	18			
	Total	249	199	52	500			

Work hours	≤8 hours	223	170	49	442	2	χ^2obs.= 3.765 χ^2 crit.= 5.991 P-value=0.152	NS
	>8 hours	26	29	3	58			
	Total	249	199	52	500			
Workplace	Emergency depart.	25	27	6	58	14	χ^2obs.= 12.277 χ^2 crit.= 23.685 P-value=0.584	NS
	Consulting depart.	40	37	7	84			
	Surgical wards	23	14	8	45			
	Medical wards	30	17	6	53			
	ICU	15	16	7	38			
	Maternity wards	21	18	4	43			
	Pediatric wards	21	12	2	35			
	Laboratories	74	58	12	144			
	Total	249	199	52	500			
Training course	No training	76	59	11	146	6	χ^2obs.= 7.619 χ^2 crit.= 12.592 P-value=0.267	NS
	One session	71	72	18	161			
	Two sessions	54	38	16	108			
	More than two	48	30	7	85			
	Total	249	199	52	500			

" χ^2obs. = Chi-square observer, χ^2crit. = Chi-square critical, D.f= Degree of freedom, P-value= Probability value, S= significant, NS= non-significant, S= significant, HS= high significant".

4 Conclusion

This study found that with preventive measures concerning nosocomial infections, health care workers were poor preventive measures due to limitation of training and shortage of health resources. More years of experience and more training the staff on infection control programs by local officials help to raise professionals' health workers preventive measures. As well as, Provide the facilities and exploiting young energies of health staff which indeed help to develop their practice.

References

[1] Shi Y, Wang J, Yang Y, Wang Z, Wang G, Hashimoto K, Zhang K, Liu H. Knowledge and attitudes of medical staff in Chinese psychiatric hospitals regarding COVID-19. Brain, Behavior, & Immunity-Health. 2020 Apr 1;4:100064.

[2] Huynh G, Nguyen TN, Vo KN, Pham LA. Knowledge and attitude toward COVID-19 among healthcare workers at District 2 Hospital, Ho Chi Minh City. Asian Pacific Journal of Tropical Medicine. 2020 Jun 1;13(6):260.

[3] Biberaj P, Gega M, Bimi I. Knowledge and source of information among health care students on nosocomial infections. Proceedings of the in Proceedings of the International Journal of Humanities Social Sciences and Education (IJHSSE. 2014 Jul;1:46-51.

[4] Sarani H, Balouchi A, Masinaeinezhad N, Ebrahimitabs E. Knowledge, attitude, and practice of nurses about standard precautions for hospital-acquired infection in teaching hospitals affiliated to Zabol University of Medical Sciences (2014). Global journal of health science. 2016 Mar;8(3):193.

[5] Kretzer D. STANDARD PRECAUTIONS (INCLUDING HAND HYGIENE AND USE OF PPE). Policy. 2018 Jan 18.

[6] Asmr Y, Beza L, Engida H, Bekelcho T, Tsegaye N, Aschale Y. Assessment of knowledge and practices of standard precaution against blood borne pathogens among doctors and nurses at adult emergency room in Addis Ababa, Ethiopia. Emergency medicine international. 2019 Apr 23;2019.
[7] Buowari OY. Universal Precautions: A Review. Nigerian Health Journal. 2012;12(3):68-74.
[8] Johnson OE, Asuzu MC, Adebiyi A. Knowledge and practice of universal precautions among professionals in public and private health facilities in Uyo, Southern Nigeria-a comparative study. Ibom Med. 2013;5(1):9-19.
[9] Vermeil T, Peters A, Kilpatrick C, Pires D, Allegranzi B, Pittet D. Hand hygiene in hospitals: anatomy of a revolution. Journal of Hospital Infection. 2019 Apr 1;101(4):383-92.
[10] Zakeri H, Ahmadi F, Rafeemanesh E, Saleh LA. The knowledge of hand hygiene among the healthcare workers of two teaching hospitals in Mashhad. Electronic physician. 2017 Aug;9(8):5159.
[11] Saito H, Kilpatrick C, Pittet D. The 2018 World Health Organization SAVE LIVES: clean your hands campaign targets sepsis in health care.
[12] Swan J, McDonald M. Infection Control Training for New York State Healthcare Professionals.
[13] Brown L. Use of personal protective equipment in nursing practice. Nursing Standard. 2019 May 1;34(5).
[14] Datta A, Nag K, Karmakar N, Chakraborty T. An epidemiological study on knowledge, attitude and practice of injection safety among health care personnel in a tertiary care hospital of Tripura. International Journal of Community Medicine and Public Health. 2018 Sep;5(9):4128-34.
[15] Yazie TD, Sharew GB, Abebe W. Knowledge, attitude, and practice of healthcare professionals regarding infection prevention at Gondar University referral hospital, northwest Ethiopia: a cross-sectional study. BMC research notes. 2019 Dec;12(1):1-7.
[16] Daham, F. H. ASSESSMENT OF OCCUPATIONAL HAZARDS ON HEALTH WORKERS OF TWO HOSPITALS (AL-KUT AND AL-KARAMA) IN WASIT GAVERNORATE. A thesis for partial Fulfillment master Degree/ Southern Technical University.2020,P.37-79.
[17] Mohd-Nor N, Bit-Lian Y. Knowledge, attitude and practices of standard precaution among nurses in middle-east hospital. SciMedicine Journal. 2019 Dec 1;1(4):189-98..
[18] Gawad A. Assessment of knowledge about standard precautions and nosocomial infection among nurses working in hospitals of Sana'a city, Yemen. International Journal of Caring Sciences. 2017 Jan 1;10(1).
[19] Okwii M. *Knowledge, Attitude And Practices Of Nurses On Prevention And Control Of Hospital Acquired Infections In Soroti Regional Referral Hospital* (Doctoral dissertation, International Health Sciences University).
[20] Mohammadzadeh M, Behnaz F, Parsa S. Knowledge, practice and attitude towards standard isolation precautions in nurses, auxiliary nurses and midwives of Shahid Sadoughi Hospital, Yazd, Iran. Int J Infect Control. 2013;9(1):1-8.
[21] Alrubaiee G, Baharom A, Shahar HK, Daud SM, Basaleem HO. Yemeni Nurses' Knowledge and Practices of Nosocomial Infection. Control Measures at Baseline: An Intervention Study. Global Journal of Medical Research. 2018;18(1):1-0.
[22] Maynard, E. Knowledge and Practice of Preventive Measures for Nosocomial Infections among Health Workers in Primary Health Care Center in Aluu , Rivers State, 2019.
[23] Bayleyegn B, Mehari A, Damtie D, Negash M. Knowledge, Attitude and Practice on Hospital-Acquired Infection Prevention and Associated Factors Among Healthcare Workers at University of Gondar Comprehensive Specialized Hospital, Northwest Ethiopia. Infection and Drug Resistance. 2021;14:259.
[24] Ayed A. Knowledge and practice of nursing staff towards infection control measures in the Palestinian hospitals.
[25] Desta M, Ayenew T, Sitotaw N, Tegegne N, Dires M, Getie M. Knowledge, practice and associated factors of infection prevention among healthcare workers in Debre Markos referral hospital, Northwest Ethiopia. BMC health services research. 2018 Dec;18(1):1-0.
[26] Unakal CG, Nathaniel A, Keagan B, Alexandria B, Lauralee B, Varun C, Akpaka PE. Assessment of knowledge, attitudes, and practices towards infection prevention among healthcare workers in Trinidad and Tobago. International Journal of Community Medicine and Public Health. 2017 Jul;4(7):2240-7.

Molecular Characterization of Staphylococcus Haemolyticus Isolated from Vaginitis and Some of Their Virulence Factors

Enas R. Alwaily[1], Ruaa M. Khazaal[2], Mohammed H. Flaih[3*] and Khwam R. Hussein[4]
{Enas.Kazem@alayen.edu.iq[1], Ruaa.m1982@stu.edu.iq[2], moh.alqurayshi@stu.edu.iq[2*], krhussein@stu.edu.iq[3]}

College of Pharmacy, Al-Ayen University, Al-Nasiriyah, 64001, Iraq[1]
Department of Medical Laboratory Techniques, Al-Nasiryah Technical Institute, Southern Technical University, Al-Nasiriyah, 64001, Iraq[2,3]
Department of Nursing, Al-Nasiryah Technical Institute, Southern Technical University, Nasiriyah, 64001, Iraq[4]

Abstract: Vaginitis is still considered to be a global health problem for females. It is mainly occurred by bacterial vaginosis, trichomonal, candidal, and gonococcal vaginal infections. This study is aimed identify Staphylococcus haemolyticus in females infected with vaginitis and determine some of their virulence genes. A total of 250 vaginal swabs were collected from females with vaginitis. Of the 250 vaginal swabs, 40 isolates were showed bacterial growth of S. haemolyticus. In susceptibility testing, S. haemolyticus isolates were sensitive to some antibiotics, whereas other isolates were resistant. The amplified 16S rRNA gene was in all isolates, using conventional PCR, icaA, blaz, mecA, and SodA genes were detected in 30, 23, 32, and 24 samples, respectively. The sequencing analysis of all local isolates appeared slight mismatching in their sequencing. The PCR products of virulence factors of S. haemolyticus showed slight variations. This may explain different clinical manifestations and the infection severity.

Keywords: 16S rRNA, S. haemolyticus, antimicrobial susceptibility, resistance genes, virulence genes.

1 Introduction

Vaginal infections (vaginitis) are mainly included bacterial vaginosis, trichomonal, candidal, and gonococcal vaginal infection which are a global problem for females [1]. This infection is characterized by symptoms such as vulvovaginal pain, itching, and burning. The diagnosis of the disease depends on the presence of yellow purulent WBCs (10 cells per field), and the existence of endocervical bleeding resulting from ersioned tissue [2]. The molecular diagnosis of vaginitis causative agents has proven that practical and can increase the accuracy more than cultures, also for detecting low levels of fungi [3], [4]. The molecular diagnosis approaches of the three major common causes of vaginitis are now available, depending on the collection of 1-2 vaginal swabs [4]. Staphylococci consider as bacterial normal flora that colonizes the human skin and mucosal membranes and cause opportunistic infection. However, S. haemolyticus returns to the Staphylococcus epidermidis group [coagulase-negative Staphylococci] that is mostly isolated from the axillae, perineum, also from human inguinal areas [5]. It can cause a local or systemic infection. Since its high antibiotic-resistant phenotype and the ability to the formation of biofilms make S. haemolyticus more resistant to the drug [6], [7]. However, S. haemolyticus biofilms are polysaccharide intercellular adhesin [1] that may be used for determining S. haemolyticus isolates from biofilm structure [8], [9].

IMDC-IST 2021, September 07-09, Sakarya, Turkey
Copyright © 2022 EAI
DOI 10.4108/eai.7-9-2021.2314816

S. haemolyticus genome contains a chromosome and three plasmids. The size chromosome is near form S. aureus and S. epidermidis and has a G+C similar content [5]. S. haemolyticus genome also contains many insertion sequences [ISs], those elements may promote frequent genomic rearrangements which accelerate the diversification of the species. Theoretically, these adaptations might help S. haemolyticus overcome the adverse effects of chemical exposure [10]. In molecular diagnosis, the 16S rRNA gene is mostly used to the identity of bacteria spp. for many reasons, [i] nearly, it is found in all bacteria [ii] the function of the 16S rRNA gene does not change with overtime, this meaning random sequence changes are a more accurate measure of evolution and [iii] the 16S rRNA gene (1, 500 bp) is a large fragment enough for informatics purposes [11]. Generally, there is little information about a molecular aspect of vaginitis causative agents, so the current study is aimed to identify and to characterize S. haemolyticus isolated from females, as the main causative of vaginitis and define some of the genetic determinants of virulence factors of these isolates.

2 Materials and methods

2.1 Samples Collection

Vaginal swabs were collected from 250 female patients who attended the consulting clinic at Bint Al-Huda Hospital of the Maternity and Children in Al-Nasiriyah city at Thi-Qar province southern Iraq, from the beginning of February to the end of December 2020. The age of the patients is ranged between 17-50 years. However, two vaginal swabs were taken from each patient, then transported to the laboratory after inoculating these swabs into sterile tubes containing a transport medium, one of the swabs was directly exanimated via staining with Gram stain and wet mounted film, and another swab was used for inoculation onto the SDA medium, CHROM agar for Candida, CHROM agar orientation CHROM agar for Staphylococci, Eosin methylene blue agar, MacConkey's agar, for microbiological investigation and phenotypic diagnosis. The biochemical tests were accomplished by Vitek 2 system. The susceptibility test was carried out using the disk diffusion method according to CLSI [12].

2.2 Ethical Agreement

It was obtained from University Committee (Al-Ayen University). Participants in the study were volunteers. The written consent was taken from all patients who were free to withdraw at any time.

2.3 Genomic Extraction

All of S. haemolyticus isolates were subculture in BHI broth (10 mL) and incubated at 37℃ overnight, then centrifuged (8000 xg). The sediment was collected to extract the genomic DNA according to kit user manual guidelines (Geneaid, Taiwan). Using a Nanodrop spectrophotometer, DNA concentration and purity were checked. The extracted DNA was preserved by freezing at -20°C until used in PCR amplification.

2.4 Molecular Diagnosis and DNA Sequencing

Using NCBI-Gene Bank database and Primer 3 design online, all PCR primers of blaz, icaD, mecA, and SodA genes were designed and supplied by Macrogen Company, Korea. The 16S rRNA gene forward primer: CGTGGAGGGTCATTTGGGAA, and reverse primer: GTTTGTCACCGGCAGTCAAC (559bp), SodA gene F: TCTGCAGTTGAGGGAACAGA, R:AACCTGAACCGAAACGAGCT (262bp), icaA gene F: ATGGTCAAGCCCAGACA GAG, R: ACAAACAAACTCATCCATCCGA (236bp), blaz gene F: TGCTTCGACTTCA AAAGCGA, R:GGTTCAGATTGGCCCTTAGGA (564bp), and mecA gene F: TGGCCAA TACAGGAACAGCA, R: CGTCAACGAT TGTGACACGA (426bp). The PCR master mix was provided by AccuPower®PCR PreMix kit (Bioneer, Korea). The PCR master mix

components included 5 µl of DNA template, 1.5 µl of each F and R primers, and 12 µl of nuclease-free water that was placed in a standard PCR tube. The PCR thermocycler conditions were an initial denaturation set at 95°C for five min, then 30 cycles as followed denaturation set at 95°C for 20 s., annealing was 60°C for 20 s. of 16Sr RNA, fnbA, icaD genes, 58°C for 20 s. of Sod A, MecA genes and 61°C for 20 s of blaz gene and extension set at 72°C for one min. The final extension was at 72°C for five min. PCR products were electrophoresed with Agarose gel (1%) and bromide ethidium (0.25µg/ml). DNA ladder (100 bp) (Bioneer) was used as a molecular marker for each gel. The gel was photographed at a UV Transilluminator [13].
The DNA sequencing was applied as a confirmative identification for PCR positive samples and to analyse the phylogenetic relationships. The visualized gene isolates were purified using a gel purification kit and then sent to Macrogen Company in Korea to perform the sequencing of DNA. The phylogenetic tree analysis was performed using the Maximum Likelihood Process and Molecular Evolutionary Genetics Analysis using MEGA V. 6 software.

2.5 Statistical Analysis

The study data were analysed with SPSS version 23 [the chi-square test]. A statistical significance was accepted if $p \leq 0.05$.

3 Results and discussion

Of the 250 vaginal swabs, 130 isolates were showed bacterial growth and 100 isolates were showed fungal growth, whereas 20 isolates did not appear any growth. A total of 40 out of 250 cultured vaginal swabs were classified as S. haemolyticus isolates. A high number of the isolates were observed as sensitive for meropenem, imipenem, ciprofloxacin, cefotaxime, cefixime. Additionally, another number of antibiotic-resistant isolates is showed in Table (1). Most of the S. haemolyticus isolates were sensitive to fluoroquinolones, carbapenems, quinolones. The statistical analysis data showed insignificant differences (P=0.00). However, high multidrug resistance may return to difficulty in biofilm penetration (protective nature of biofilm) by antibiotics, the slow growth rate of the bacteria, and the presence of antibiotic degradation mechanisms [15]. These findings are like the study of Goldenberg et al. [14], also agree with the results of Guta [16] but vary on other S. haemolyticus strains that were isolated from non-vaginal environments [17]. The high antibiotic resistance may return to the random and excessive use of antibiotics that leads to creating the resistant strains, these results are very important when the physician begins prescribing the correct antibiotic for treatment. The antibiotic resistance is occurred by increased Biofilm formation that mostly leads to persistent infections [18], [19].

3.1 Molecular Identification and Sequencing of 16S rRNA Gene

The amplification of 16S rRNA products appeared in all 40 bacterial isolates of S. haemolyticus at 559 bp as shown in Fig 1. The 16S rRNA gene contains the 30S subunit region of the ribosome of prokaryotic and is a universal gene where find in all bacteria spp. It is very useful for the reconstruction of phylogenies because of the evolutionary slow rate of this gene. 16S rRNA is used for conferring the relatedness of diverse bacteria and for the determination of the species. The similarity percentage of 16S rRNA among species (to define them as identical species) is 98.7%. In Staphylococci, the 16S rRNA gene is very similar across species, as a result, two different species can have identical 16S rRNA sequences [20],[21]. The guidelines of bacterial classification proposed the strains that have lower than 97% 16S rRNA sequence identity be considered as different bacterial species [22]. The sequencing analysis of local isolate [MW485615] revealed that there were differed in only two nucleotides in their linear sequenced DNA, and the 16S rRNA sequence showed a very high similarity (99%) between these two local isolates and NCBI-BLAST S. haemolyticus SH1 strain [MK886483.1], this result is agreed with the study of Ghebremedhin et al. [23]. Both local isolates were recorded in NCBI BLAST GenBank as a global scientific website with accession numbers MW485614 and MW485615

respectively. The phylogenetic tree as represented in Fig 2 revealed high bootstrap values of 99% with MK886483.1 isolate.

Table 1. Antimicrobial resistance to S. haemolyticus isolated from vaginitis.

Antimicrobial	*S(%)	R(%)
Penicillin group:		
Amoxicillin, clavulanicacid,AMC	15(37.5)	25(62.5)
Methicillin	6(15)	34(85)
Cephalosporins:		
cephalothin, KF	10(25)	30(75)
cefixime, CFM	31(77.5)	9(22.5)
Cefotaxime, CTX	17(42.5)	23(57.5)
ceftriaxone, CRO	26(65)	14(35)
Tetracycline-class :		
doxycycline, DO	25(62.5)	15(37.5)
Aminoglycoside :		
gentamicin, CN	20(50)	20(50)
Amikacin, AK	19(47.5)	21(52.5)
Netilmicin, NET	23(57.5)	17(42.5)
Nitrofurantoin, NI	16(40)	24(60)
Carbapenems:		
Imipenem, IPM	33(82.5)	7(17.5)
Meropenem, MEM	31(77.5)	9(22.5)
Quinolones:		
Ciprofloxacin, CIP	25(62.5)	15(37.5)
Levofloxacin, LEV	26(65)	14(35)
Glycopeptide:		
Vancomycin, V	23(57.5)	17(42.5)
Sulfonamides:		
Trimethoprim/sulfamethoxazole, TS	21(52.5)	19(47.5)
Lincosamide:		
Lincomycin, L	25(62.5)	15(37.5)

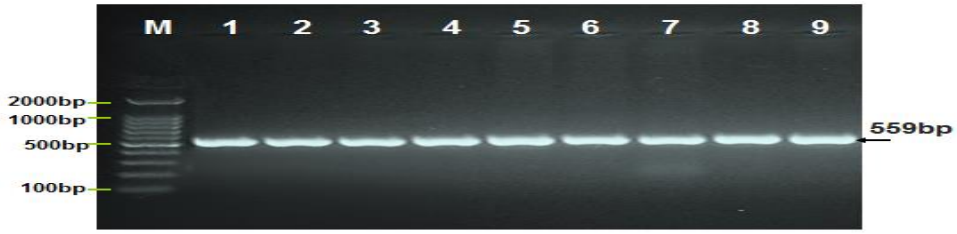

Fig. 1. Agarose gel electrophoresis of 16S rRNA gene of S. haemolyticus isolates. Where Marker ladder [2000-100bp], lanes [1-9] were positive at 559bp.

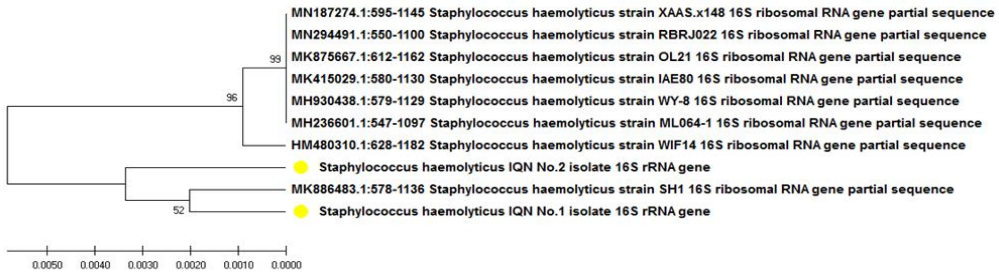

Fig. 2. Phylogenetic analysis of 16S rRNA gene partial sequence in local S. haemolyticus MW485614 and MW485615 [IQN. No.1 and IQN. No.2] isolates at total genetic changes (0.005-0.001%).

The gel electrophoresis for PCR products of icaA, blaz, mecA, and SodA genes of S. haemolyticus was recorded in 30 (75%), 23(%57.5), 32(80%), and 24 (60%) at 583, 564, 426, 262 bp, respectively as represented in Fig 3. The sequence alignment analysis of the icaA gene in local isolates (MW940832 and MW940833) revealed that were 5 substitutions in their linear sequenced DNA, the identities for this isolate were 99%. The phylogenetic analysis showed that two local S. haemolyticus isolates that showed a close genetic relationship with NCBI-BLAST S. aureus intercellular adhesion locus at total genetic changes (0.04-0.01%) as shown in Fig 4. This result agrees with the results of Barros et al. [24] and with the study of Panda and Singh [25] that identified icaA operon in S. haemolyticus that isolated from ocular infections and showed a role this operon in the formation of biofilms in S. haemolyticus isolates.

The sequence alignment analysis of the blaz gene in the local isolate (MW940836) revealed that were 10 nucleotide substitutions in its linear sequenced DNA, while in the local isolate (MW940837) showed 9 substitutions, the identities for this isolate was 98%. The phylogenetic analysis based on blaz gene partial sequence in local S. haemolyticus isolates revealed that showed a close genetic relationship with NCBI-BLAST S. aureus strain A7 at total genetic changes (0.04-0.01%) as shown in Fig 5. The results were consistent with Olsen et al. [26] who have confirmed that all penicillin resistance strains were carried the blaZ gene and showed a similar organization of blaR1 and blaZ. The sequence alignment analysis of the mecA gene in local isolate (MW940834) was shown only 4 substitutions in its linear sequenced DNA, while in local isolate (MW940835) was included 3 substitutions in its linear sequenced DNA, the identities for this isolate was 99%.

The phylogenetic analysis based on mecA gene partial sequence in local S. haemolyticus isolates were showed a close genetic relationship with NCBI-BLAST S. haemolyticus at total genetic changes (1.5-0.5%) as shown in Fig 6. The current result was consistent with Hussain et al. [27] study who showed that 83.3% of S. haemolyticus were positive for the mecA gene, whereas inconsistent with the study of Xu et al. [28] that proved only 22% of S. haemolyticus isolates were carriage this gene. The sequence alignment analysis of the SodA gene in the local isolate (MW940838) was shown only 2 substitutions in its linear sequenced DNA, while in another isolate (MW940839) was contained 3 substitutions in its linear sequenced DNA, the identities for this isolate was 99%. The phylogenetic analysis based on SodA gene partial sequence in local S. haemolyticus isolates were showed a close genetic relationship with NCBI-BLAST S. haemolyticus at total genetic changes (0.04-0.01%) as showed in Fig 7. The result was consistent with the study of Poyart et al. [6] that showed the sodA gene constitutes a highly discriminative target sequence for differentiating closely related bacterial species. Generally, all phylogenetic analyses that showed in Figs 4 to 7 revealed high bootstrap values of 98-99%.

4 Conclusion

The 16S rRNA gene is very useful to phylogenies reconstruction because of its evolutionary slow rate, the 16S rRNA sequence showed slight variation. The presence or absence of virulence genes in the S. haemolyticus genome and the variation of DNA sequencing among the isolates may explain the differences of the clinical manifestations or reflect the disease severity.

Acknowledgments

The authors would also like to thank the staff of Bint Al-Huda Hospital for their assistance during the sample collection. The study was not financially supported.

Conflict of interests: The authors declared that no conflict of interests among them.

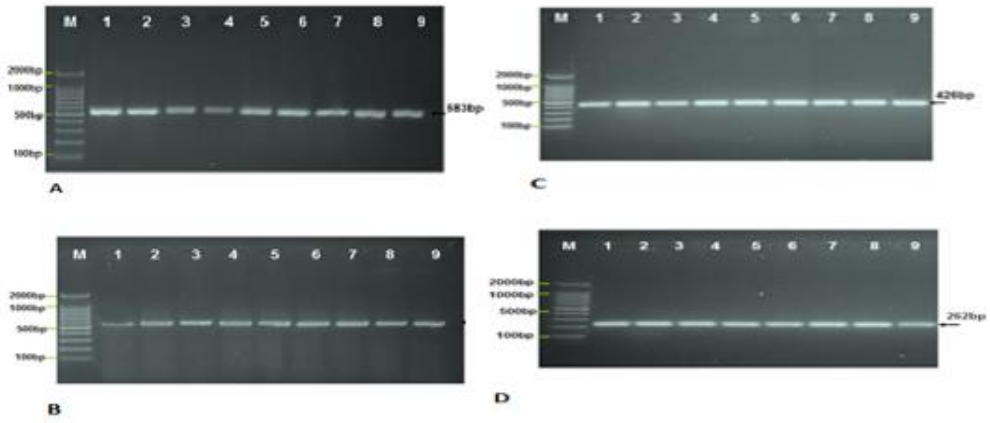

Fig. 3. The PCR product analysis of S. haemolyticus genes. Where Marker ladder [2000-100bp], lanes [1-9] were positive of: [A] icaA gene at 583bp.[B]: blaz gene at 564bp. [C]: mecA gene at 426bp.[D]: sodA gene at 262bp.

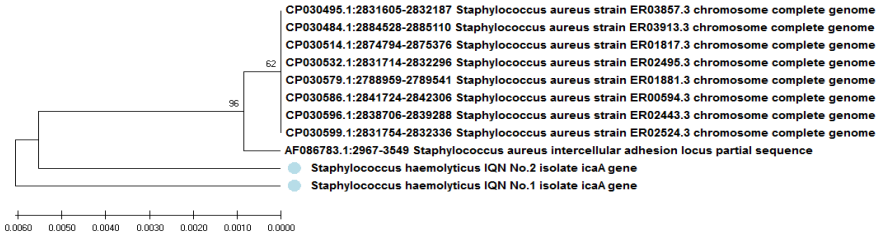

Fig. 4. Phylogenetic tree analysis of icaA gene partial sequence in local S. haemolyticus MW940832 and MW940833(IQN No.1-No.2) isolates at total genetic changes (0.04-0.01%).

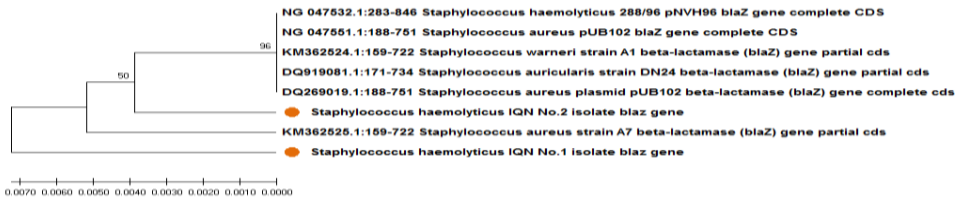

Fig. 5. Phylogenetic analysis of blaz gene partial sequence in local S. haemolyticus MW940836 and MW940837 (IQN No.1-No.2) isolates at total genetic changes (0.04-0.01%).

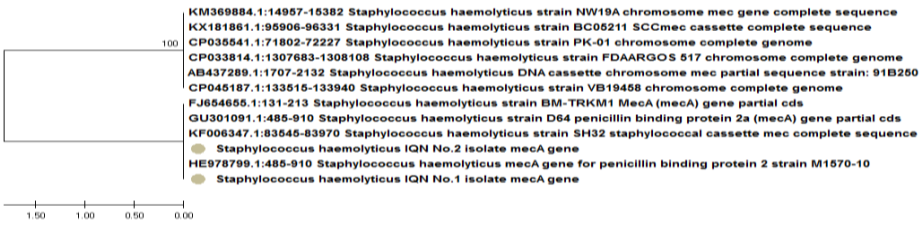

Fig. 6. Phylogenetic analysis of mecA gene partial sequence in local S.haemolyticus MW940834 and MW940835 (IQN No.1-No.2)isolates at total genetic changes (1.5-0.5%).

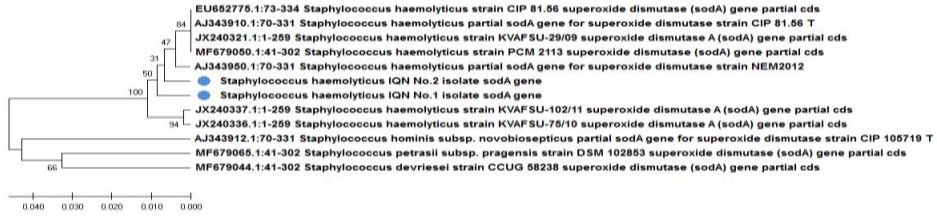

Fig. 7. Phylogenetic analysis of sodA gene partial sequence in local S. haemolyticus MW940838 and MW940839 (IQN No.1-No.2) isolates at total genetic changes (0.04-0.01%).

References

[1] Mulu W, Yimer M, Zeneb Y, Abera B. Common causes of vaginal infections and antibiotic susceptibility of aerobic bacterial isolates in women of reproductive age attending at Felegehiwot referral Hospital, Ethiopia: a cross-sectional study. BMC Women's Health .2015; 15 [42]: 1-9.

[2] Sánchez A, Rivera A, Castillo F, Ortiz S. Cervical erosion as result of infectious vaginitis. European Journal of Experimental Biology. 2012; 2[5]:1659-1663.

[3] Sherrard J. Evaluation of the BD MAXTM Vaginal Panel for the detection of vaginal infections in a sexual health service in the UK. Int J STD & AIDS. 2019; 30[4]:411-4.

[4] Baptista P V, Eleutério J. Diagnosis of vaginitis: time to improve and move on. Jornal Brasileiro de Doenças Sexualmente Transmissíveis. 2020; 32. e203214: 1-3.

[5] Takeuchi F, Watanabe S, Baba T, Yuzawa H, ItoT, MorimotoY, Kuroda M, Cui L, Takahashi M, Ankai A, Baba S, Fukui S, Lee J C, Hiramatsu H. Whole-Genome Sequencing of Staphylococcus haemolyticus Uncovers the Extreme Plasticity of Its Genome and the Evolution of Human-Colonizing Staphylococcal Species. Journal of Bacteiology. 2005; 187[21]: 7292–7308.

[6] Poyart C, Quesne G, Boumaila C, Trieu-Cuot P. Rapid and accurate species-level identification of coagulase-negative staphylococci by using the sodA gene as a target. Journal of clinical microbiology. 2001; 39:4296–4301.

[7] Falcone M, Giannella M, Raponi G, Mancini C, Venditti M. Teicoplanin use and emergence of Staphylococcus haemolyticus: is there a link. Clinical Microbiology and Infectious Diseases. 2006; 12:96–97.

[8] Al Laham NH, Rohde G, Sander A, Fischer M, Hussain C, Heilmann D, Mack R, Proctor G, Peters K, Becker C, von E. Augmented expression of polysaccharide intercellular adhesin in a defined Staphylococcus epidermidis mutant with the small-colony-variant phenotype. J. Bacteriol. 2007; 189:4494–4501.

[9] Fredheim E, Aarag G, Klingenberg C, Rohde H, Frankenberger S, Gaustad P, Flægstad T, Sollid J E. Biofilm Formation by Staphylococcus haemolyticus. JOURNAL OF CLINICAL MICROBIOLOGY. 2009; 47[4]: 1172–1180.

[10] Bouchami O, Achour W, Mekni MA, Rolo J, Ben H A. Antibiotic resistance and molecular characterization of clinical isolates of methicillin-resistant coagulase-negative staphylococci isolated from bacteremic patients in oncohematology. Folia Microbiol. [Praha] .2011; 56. 122–130

[11] Patel JB. 16S rRNA gene sequencing for bacterial pathogen identification in the clinical laboratory. Mol. Diagn. 2001; 6:313–321.

[12] Clsi. Performance Standards for Antimicrobial Susceptibility Testing. 2010. Twentieth Informational Supplement. Clinical and Laboratory Standards Institute, Wayne.

[13] Sambrook J, Green M R. Molecular Cloning: A laboratory manual. Cold Spring Harbor, NY: Cold Spring Harbor Laboratory press. 2012; 1-34.

[14] Goldenberg R, Thompson C. The infectious origins of stillbirth. Am J Obstet Gynecol. 2003; 189[3]: 861-873.

[15] Ohadian S M, Reza M P, Aminharati F. Biofilm formation and antimicrobial resistance in methicillin-resistant Staphylococcus aureus isolated from burn patients, Iran. The Journal of Infection in Developing Countries.2014; 8[12]:1511-7.

[16] Guta C D. Microbiological study of antepartum and postpartum vaginal flora. Clinical and laboratory research and therapeutical particularities. 2013. Doctoral thesis, University of Medicine &Pharmacy of Cralova, Faculty of Medicine.

[17] Koeijers J, Verbon A, Kessels A, Bartelds A, Donkers G, Nys S, Stobberingh E. Urinary tract infection in male general practice patients: uropathogens and antibiotic susceptibility. Urology. 2010; 76: 336-340.

[18] Cerca N, Martins S, Cerca F, Jefferson KK, Pier GB, Oliveira R, Azeredo J. Comparative assessment of antibiotic susceptibility of coagulase-negative staphylococci in biofilm versus planktonic culture as assessed by bacterial enumeration or rapid XTT colorimetry. J Antimicrob Chemother. 2005; 56 [2]: 331–336.

[19] Namvar AE, Asghari B, Ezzatifar F, Azizi G, Lari AR Detection of the intercellular adhesion gene cluster [Ica] in clinical Staphylococcus aureus isolates. GMS Hyg Infect Control. 2013; 8[1]: Doc03.

[20] Ash C, Farrow J A, Dorsch M, Stackebrandt E, Collins MD. Comparative analysis of Bacillus anthracis, Bacillus cereus, and related species based on reverse transcriptase sequencing of 16S rRNA. Int. J. Syst. Bacteriol. 1991; 41: 343–346.

[21] Trebesius K, Harmsen D, Rakin A, Schmelz J, Heesemann J. Development of rRNA-targeted PCR and in situ hybridization with fluorescently labelled oligonucleotides for detection of Yersinia species. J. Clin. Microbiol. 1998; 36: 2557–2564.

[22] Janda JM, Abbott SL. 16S rRNA gene sequencing for bacterial identification in the diagnostic laboratory: pluses, perils, and pitfalls. Journal of Clinical Microbiology. 2007; 45:27614.

[23] Ghebremedhin B, Layer F, Ko¨nig W, Ko¨nig B. Genetic Classification and Distinguishing of Staphylococcus Species Based on Different Partial Gaps, 16S rRNA, hsp60, rpoB, sodA, and tuf Gene Sequences. Journal of clinical microbiology. 2008; 46[3]: 1019–1025.

[24] Barros EM, Lemos M, Souto-Padrón T, Giambiagi-deMarval M. Phenotypic and genotypic characterization of biofilm formation in Staphylococcus haemolyticus. Curr. Microbiol. 2015; 70: 829–834.

[25] Panda S, Singh DV. Biofilm Formation by ica-Negative Ocular Isolates of Staphylococcus haemolyticus. Frontiers in Microbiology. 2018; 9[2687]: 1-9.

[26] Olsen JE, Christensen H, Aarestruo F M. Diversity, and evolution of blaZ from Staphylococcus aureus and coagulase-negative staphylococci. Journal of Antimicrobial Chemotherapy. 2006; 57:450–460.

[27] Hussain Z, Stoakes L, Massey V, DiagreD, Fitzgerald V, El Sayed S. Correlation of oxacillin MIC with mecA gene carriage in coagulase-negative staphylococci. Journal of Clinical Microbiology. 2000; 38[2]:752–4.

[28] Xu Z, Shah HN, Misra R, Chen J, Zhang W, Liu Y, Cutler R, Mkrtchyan H V. The prevalence, antibiotic resistance and mecA characterization of coagulase-negative staphylococci recovered from non-healthcare settings in London, UK. Antimicrobial Resistance and Infection Control. 2018; 7[73]: 1-10.

Detection of Mutations in the 81 Bp RRDR of Rpob Gene in Mycobacterium Tuberculosis Clinical Isolates Using Xpert®MTB/RIF in Basra/Iraq

Ghorob S Khudhair[1], Khairallah A.S Mohammed[1], Dheyaa Bekheet Al-Rabeai[2]
{ghorob64@gmail.com, dr.kmohammed@stu.edu.iq, Dheyaabukheet@yahoo.com}

Department of Medical Lab Technology, College of Health and Medical Technology, Southern Technical University, Iraq[1]
Advisory Clinic for Chest Diseases and Respiratory/ Basra[2]

Abstract. In Iraq, the Xpert® MTB/RIF test is now being utilised to detect rifampicin-resistant Mycobacterium tuberculosis (MTB) isolates. Rifampicin resistance is assessed using five overlapping probes in the Rifampicin Resistant Determinant Region (RRDR) of the rpoB gene (A, B, C, D, E). From January 2016 to December 2020, data was gathered from specimens obtained and evaluated using conventional methods and the Xpert® MTB/RIF assay at the Advisory Clinic for Chest Diseases and Respiratory in Basra province. Among the 2542 positive samples for MTB, rifampicin resistance was detected in 57 (2.24%) specimens, of which full data for 44 RR–TB patients is available. Of the 44 RR-TB patients, 35 (79.5%) were retreatment cases, and the most common *rpoB* mutations were in the region of Probe E (70.5%), followed by Probe B (11.3%), Probe A, and D (9.1%) for each. Mutations in Probe C were not observed.

Keywords: Rifampicin-resistance, *rpoB*, Xpert® MTB/RIF assay, Basra.

1 Introduction

Tuberculosis (TB) is one of the most infectious bacterial diseases causing a public health threat. It is estimated that 10.0 million at a rate of 132 per 100000 population new cases of TB occurred in 2019 with high mortality, resulting in 1.2 million (16 per 100000 population) death globally [1]. According to the WHO report (2019), the incidence of TB in the Middle East is 810000 at a rate of 115 per 100 000 population and in Iraq 16 000 at a rate of 42 per 100000 population [1]. Rifampicin is possibly the utmost important drug in the control and treatment of tuberculosis (TB) [2]. Treatment of TB has become more difficult since the emergence and spreading of multidrug-resistant (MDR) strains [2]. In 2019, WHO reported that the global MDR/RR-TB incidences are 484000 at a rate of 6.4 and in Iraq 11 00 at a rate of 2.9 per 100000 population. Hence, to launch a proper effective treatment, it is of great importance to promoting fast and reliable diagnostic assay to detect and to assess the resistance of *M. tuberculosis* strains against main drugs. Conventional methods were commonly used to identify multidrug-resistant (MDR) strains. However, many limitations of the traditional methods of diagnosis of RR-TB such as time-consuming, lack of laboratory infrastructures, and biosafety make them difficult to be applicable, especially in rural settings [3]. WHO endorsed a molecular assay (Xpert assay) which can detect *Mycobacterium tuberculosis* and rifampicin resistance within a few hours and does not require high technical expertise and a high standard of biosafety measures [4]?

IMDC-IST 2021, September 07-09, Sakarya, Turkey
Copyright © 2022 EAI
DOI 10.4108/eai.7-9-2021.2314814

In this study, we studied the prevalence of RIF-resistant TB and the dominant site mutation types at RRDR in the *rpoB* gene of rifampicin-resistant MTB strains isolated from specimens of patients diagnosed to have TB in Basra/Iraq, using Xpert® MTB/RIF assay.

2 Materials and Methods

The research was carried out in Basra, Iraq's third largest city, with a population of over 3 million people. The data for the study came from the Advisory Clinic for Chest Diseases and Respiratory (ACCDR), the sole health centre in Basra province, Iraq, that deals with tuberculosis patients. From January 2016 to December 2020, data was gathered from specimens obtained and evaluated using the Xpert® MTB/RIF assay at the Advisory Clinic for Chest Diseases and Respiratory (ACCDR) in Basra province. The patients were clinically diagnosed in CCDR, and sputum samples were examined microscopically for *acid-fast bacilli* (AFB), cultured on Lowenstein-Jensen solid medium, and subjected to conventional drug susceptibility tests [5]. Following that, the samples were run through the GeneXpert MTB/RIF test according to the manufacturer's recommendations (Cepheid, Sunnyvale, CA, USA). Molecular beacons are used in five overlapping areas of the rpoB DNA region by the GeneXpert MTB/RIF. The probes can detect mutations in codons 507-511 (Probe A), 511-518 (Probe B), 518-523 (Probe C), 523-529 (Probe D), and 529-533 (Probe E) (Probe E). The Basra Health Authority's Research and Development Committee approved the study..

3 Results

Mycobacterium tuberculosis was found in 2542 samples between 2016 and 2020, with the highest frequency (35%) in the 15-34 year old age group. Rifampicin resistance was found in 57 of the samples positive for Mycobacterium tuberculosis (2.24 percent). Only 44 RR–TB patients have complete data (Table 1). As shown in Table 1, out of 44 patients diagnosed with RR-TB, 35 (79.5%) were retreatment cases, with the largest frequency (36.4%) occurring in individuals aged 15 to 34 years. Table 2 reveals that the most common rpoB mutations were found in Probe E (31, 70.5 percent), Probe B (5, 11.3 percent), Probe A, and Probe D for each of the four probes (4, 9.1 percent). Probe C mutations were not found, and no combination of two probes was found in any case.

Table 1. Demographic and clinical characteristics of study RR – TB patients (n=44).

Characteristics	New cases (n= 9)	Relapse (n=35)
	Age	
≤14	0	0
15 – 34	4	16
35 – 54	3	12
≥ 55	2	7
	Sex	
Female	3	19
Male	6	16
	Region	

Rural	4	14
Urban	5	21

Table 2. Probe types were distributed among clinical variables in 44 RR-TB patients.

Probe types	Treatment history		Sex		Age (year)			Region	
	New	Relapse	Male	Female	15 – 34	35 – 54	≥ 55	Rural	Urban
A	0	4	0	4	3	1		1	3
B	1	4	2	3	2	1	2	2	3
C	ND*	ND	-	-	-	-	-	-	-
D	1	3	2	2	1	3	0	3	1
E	7	24	18	13	14	10	7	12	19
Total	9	35	22	22	20	15	9	18	26

*ND = not detected

4 Discussion

The present results showed that during the study period (2016 – 2020), Mycobacterium tuberculosis was detected in 2542 samples at an average of 508.4 per year. World Health Organization stated a target for tuberculosis case detection for the last 5 years rate at about 43/100,000 population in Iraq [6]. Given that Basra's overall population is expected to be 2,985,073 in 2019 [7], the expected tuberculosis cases will be around 1,253 people. The average number of diagnosed cases reported in this study was 508.4, which is less than half of the expected figure. This could be due to a lacklustre screening programme or an erroneously high anticipated case detection target.

The age group 15 - 34 years showed the highest frequency of TB (35%) and RR-TB (75%) among tuberculous patients diagnosed in this study. The high prevalence of TB in adolescence and early adulthood could be because they have a much wider range of social contacts outside of the household increasing the risk of exposure to Mycobacterium tuberculosis [8]. According to previous research, the risk of Mycobacterium TB infection is highest during adolescence and young adulthood [8, 9, 10]. As a result, in addition to suffering from tuberculosis, teenagers and young adults may also contribute to the disease's continuous spread. Furthermore, numerous medical disorders linked to tuberculosis develop throughout adolescence, such as HIV infection, diabetes, mental health issues, or exposure to hazardous chemicals like tobacco [8, 9]. Furthermore, many young women encounter health issues related to pregnancy and delivery, which may raise their TB risk [10, 11].

Out of 2542 samples, 57 (2.24%) samples were resistant to rifampicin. World Health Organization stated a target for MDR/RR-TB, for the last 5 years rate at about 3/100,000 population in Iraq [6]. Based on the estimated population in Basra, then the predictable cases of MDR/RR-TB would be about 86.57 patients. The number of patients diagnosed in this study was 57, which is significantly fewer than the projected amount. This could be due to a lacklustre screening programme or an erroneously high anticipated case detection target. The incidence rate of resistance to Rifampicin documented in this study (2.24%) is lower than that reported by Mohajeri et al. in Iran (14.28%) [12], Abdel Dayem et al. in Egypt (8%) [11], Al Ammari et al. in Saudi Arabia (5.9%) [14] and Al-Mussawi et al. in Basra (7.56% [15]. These differences could be due the to sample size or using different detection methods. The present results showed that 79.5% of RR-TB were retreatment cases. These findings were like what has been reported by Liu et al. [16]. The significant rate of rifampicin resistance among retreatment cases seen in

this study could be attributable to a large number of resistant strains circulating in the community as a result of the large number of previously treated cases.
Rifampicin resistance was identified in this study using the Xpert® MTB/ RIF assay and rpoB gene mutations in the 81 bp-RRDR. The most prevalent mutation was found in codons 529–533, which is represented by Probe E (31, 70.5 percent), followed by Probe B, D, and A. These results are compatible with many other studies done in African and Asian countries which reported that sequence 529-533 (probe E) are the most prevalent codons related to RIF-resistance [17, 18,19, 20]. However, according to another study conducted in Malawi, the majority of RR cases discovered by the Xpert® MTB/RIF assay were linked to probe B (23/64) and probe E (23/64) [21]. In addition, no RIF resistance related to Probe C was found in this investigation. Probe C was only seen once, in the study by Metcalfe et al. in Zimbabwe [22], which could be due to the fact that this specific location within RRDR is likely to be less susceptible to drug resistance-causing genetic changes.
The data on the probes that confer RR could be utilised to track drifts over time, identify transmission hotspots, and investigate outbreaks, especially when the RR is lower than mutations outside the Probe E zone. In addition, studies on mutations can aid in the development of new TB medicines. The key limitation of our work was that the rpoB gene was not sequenced, so we were unable to determine the exact rpoB mutations.

5 Conclusion

The Probe E region mutations were discovered to be the most prevalent rpoB gene mutations. Probe C-related RIF resistance was not found. The importance of using the Xpert MTB/RIF assay for detecting MTB and rifampicin-resistant bacteria from suspected TB/MDR cases in a timely manner was highlighted in this study. It may provide preliminary information on the mutation pattern of MTB strains resistant to rifampicin. To discover the exact rpoB mutations, more molecular research is required.

References

[1] Global tuberculosis report 2019. Geneva: World Health Organization; 2019. License: CC BY-NC-SA 3.0 IGO.

[2] Connell D.W., M. Berry, G. Cooke, O.M. Kon Update on tuberculosis: TB in the early 21 century. European Respiratory Review June. 201; 20 (120) 7184.

[3] Parsons, L. M., Somoskövi, A., Gutierrez, C., Lee, E., Paramasivan, C. N., Abimiku, A., Spector, S., Roscigno, G., & Nkengasong, J. Laboratory diagnosis of tuberculosis in resource-poor countries: challenges and opportunities. Clinical microbiology reviews. 2011; 24(2):314–350.

[4] Lawn, S. D. and M. P. Nicol, "Xpert MTB/RIF assay: development, evaluation and implementation of a new rapid molecular diagnostic for tuberculosis and rifampicin resistance, Future Microbiology. 2011; vol. 6, no. 9, pp. 1067–1082.

[5] Mankhi, A. S., Supervised by Hashem, Z. S. Guidelines of Laboratory manual work of tuberculosis in Iraq , Prepared by Ministry of Health. Iraq. Baghdad, 2009.
[6] World Health Organization, *Global Tuberculosis Report 2015-2019*, World Health Organization, Geneva, 2015, 2016, 2017, 2018, and 2019.

[7] Central Statistical Organisation. Ministry of Planning. Republic of Iraq. http://cosit.gov.iq/ar/2018-2019.

[8] Nduba V, Hoog AH, Mitchell E, et al. Prevalence of tuberculosis in adolescents, western Kenya: implications for control programs. Int J Infect Dis 2015; 35: 11–17.

[9] Comstock GW, Livesay VT, Woolpert SF. The prognosis of a positive tuberculin reaction in childhood and adolescence. Am J Epidemiol 1974; 99: 131–138.

[10 Mathad JS, Gupta A. Tuberculosis in pregnant and postpartum women: epidemiology, management, and research gaps. Clin Infect Dis 2012; 55: 1532–1549.

[11] Rendell NL, Batjargal N, Jadambaa N, et al. Risk of tuberculosis during pregnancy in Mongolia, a high incidence setting with low HIV prevalence. Int J Tuberc Lung Dis 2016; 20: 1615.

[12] Mohajeri P, Norozi B, Atashi S, Farahani A. Anti tuberculosis drug resistance in west of Iran. J Global Infect Dis 2014; 6:114-7.

[13] Abdel Dayem AM, Sharkawy SH, Mohammed Fathy RM, Hassanin OM, Ali A. Detection of drug-resistant *Mycobacterium tuberculosis* using Geno Type MTBDR plus assay in smear positive cases. Egypt J Chest Dis Tuberc. 2019; 68:284-9.

[14] Al Ammari M, Al Turaiki A, Al Essa M, Kashkary AM, Eltigani SA, Ahmed AE. Drug resistant tuberculosis in Saudi Arabia: an analysis of surveillance data 2014-2015. Antimicrob Resist Infect Control. 2018 Jan 22;7:12.

[15] Al-Mussawi Abdulameer Abuallh, Naael Hussein Ali, Alaa Hussein Abed. Molecular quantification of Rifampicin-resistance in *Mycobacterium tuberculosis* Egypt J Chest Dis Tuberc. 2017; 66, 425-427.

[16] Liu, Z., Zhang, M., Wang, J., Chen, S., Wu, B., Zhou, L., Pan, A., Wang, W., & Wang, X. Longitudinal
Analysis of Prevalence and Risk Factors of Rifampicin-Resistant Tuberculosis in Zhejiang, China. BioMed research international. 2020; 3159482-8.

[17] Tadesse M, Aragaw D, Dimah B, Efa F, Abdella K, Kebede W, Abdissa K, Abebe G. Drug resistance-conferring mutations in *Mycobacterium tuberculosis* from pulmonary tuberculosis patients in Southwest Ethiopia. Int J Mycobacteriol. 2016 Jun;5(2):185-91.

[18 Ochang EA, Udoh UA, Emanghe UE, Tiku GO, Offor JB, Odo M. Evaluation of rifampicin resistance and 81-bp rifampicin-resistant determinant region of *rpoB* gene mutations of *Mycobacterium tuberculosis* detected with Xpert MTB/RIF in Cross River state, Nigeria. Int J Mycobacteriology. 2016; 5:145–6.

[19] Mboowa G, Namaganda C, Sengooba W. Rifampicin resistance mutations in the 81 bp RRDR of *rpoB* gene in *Mycobacterium tuberculosis* clinical isolates using Xpert® MTB/RIF in Kampala, Uganda: a retrospective study. *BMC Infect Dis.* 2014;14:481.

[20] Rahman A, Sahrin M, Afrin S, Earley K, Ahmed S, Rahman SM, Banu S. Comparison of Xpert MTB/RIF Assay and GenoType MTBDRplus DNA Probes for Detection of Mutations Associated with Rifampicin Resistance in *Mycobacterium tuberculosis*. PLoS One. 2016 Apr 7;11(4):e0152694.
[21] Chikaonda T, Ketseoglou I, Nguluwe N, Krysiak R, Thengolose I, Nyakwawa F, Rosenberg NE, Stanley C, Mpunga J, Hoffman IF, Papathanasopoulos MA, Hosseinipour M, Scott L, Stevens W.

Molecular characterisation of rifampicin-resistant *Mycobacterium tuberculosis* strains from Malawi. Afr J Lab Med. 2017;6(2):463.

[22] Metcalfe JZ, Makumbirofa S, Makamure B, Sandy C, Bara W, Mason P, Hopewell PC. Xpert(®) MTB/RIF detection of rifampin resistance and time to treatment initiation in Harare, Zimbabwe. Int J Tuberc Lung Dis. 2016;20(7):882-9.

Effect of Parvovirus B19 in Diabetes Mellitus Type 1

Ahmed Hasan Mohammed[1*] and Alzahraa Albatool Ibrahim saber[2]
(ahmedhasan5@sci.utq.edu.iq[1] , alzahraan25@yahoo.com[2])

[1] University of Thi-Qar, College of Science, Pathological Analysis Department, Nasiriyah, Iraq
[2] Higher Health Institution, Thi-Qar Health Directorate, Nasiriyah, Iraq

Abstract. Type 1 diabetes mellitus (T1D) is one of the complicated diseases and many studies indicated the contribution of viruses in the consequences of T1D. The present study aimed to detect of Parvovirus B19 *NS1* gene in the sera of T1D patients by using conventional PCR. Forty-five patients with T1D have been conducted in this study based on clinical examination and laboratory evaluation of random blood sugar, fasting blood sugar, and glycated hemoglobin. Viral genome extraction was made according to the kit manufacture's manual then conventional PCR and gel electrophoresis was performed to detect the target genome. The results showed the presence of *NS 1* gene in 7 (14%) of 45 patients included in this study, so conclude that the detection of viral genome in the blood samples of T1D patients is not sufficient to prove that human Parvovirus B19 has a role in the pathogenesis and consequences of T1D.

Keywords: Parvovirus B19, type 1 diabetes mellitus, PCR, fasting blood sugar.

1. Introduction

Type 1 diabetes (T1D) is an autoimmune disorder that usually strikes individuals at almost any age. It is caused by autoreactive T cells [1]. The 2019 International Diabetes Federation (IDF) states that T1D incidence, prevalence, and mortality estimates for children < 15 years for all 211 countries. The estimated cases were about 600,900 and incident cases around 98,200. So many countries were continuing to be affected and remain to have the highest rate and others have seen lowest rate as in East and South-East Asia. Generally speaking 3-4% per year there is an increase of incidents for such type of illness. On top of that T1D mortality has drastically decreased, , especially in people with diabetic nephropathy [2].
It is known that genetic and environmental factors could affects the major contribution for the development of the disease. Viruses may consider the main onset of T1D [3]. It is found in some cases there is a link between T1D and viruses including DNA viruses from families Herpesviridae and Parvoviridae and RNA viruses of families Togaviridae, Paramyxoviridae, Retroviridae, and Picornaviridae. There is a strong relationship between T1D and enteroviruses [4]; wherever, there is the uncertainty of the relation of diabetes to enteroviruses [3]. Multi models applied in some cases to highlight the triggering to beta-cell pancreatic destruction however, there is no indication of introducing other viruses [5]. Parvovirus B19 (B19V), is a member of enteroviruses that belongs to the family Parvoviridae, genus Erythroparvovirus may have a role in the development of T1D. Several cases of autoimmune disease that occur after

IMDC-IST 2021, September 07-09, Sakarya, Turkey
Copyright © 2022 EAI
DOI 10.4108/eai.7-9-2021.2314785

acute infection with B19V have been reported. Kasuga *et al*. reported an association between T1D and infection with parvovirus B19in young adults who showed serum levels of B19 IgM and antibodies to the diabetic autoantigen IA-2 were significantly elevated [6,7]. Whereas rat virus parvovirus Kilham showed autoimmune diabetes in rats [8] for which T1D had not clarified [6]. This work targeted the presence of B19V in T1D patients by detection of the B19V *NS1* gene in the blood sample of T1D patients using conventional PCR.

2. Patients and Method

2.1. Study Design

A study was covered with 45 T1D patients attending the Special Center of the Endocrine Glands and Diabetes in Al-Nasiriyah city, south of Iraq. Known cases of T1D patients (males and females) of age range 3-16 years with their demographic or clinical information regarding age, sex, weight, the duration of the disease, insulin therapy (Number of doses during the day and type of insulin), family members with T1D and T2D and clinical history of the patients were mandatory for inclusion criteria.

2.2. Sample Collection

Five milliliters of venous whole blood were withdrawn by 5.0 ml syringe sterile disposable. About 1.0 ml was separated in the EDTA tube for the HbA1c test and the remaining (4.0 ml) of the blood samples was collected in a sterile gel tube, subsequently allowed to clot, and centrifuged at 3000 rpm for 10 min for serum separation to perform the blood sugar tests and extraction of the viral genome.

2.3. Blood Sugar Tests

The blood sugar test was done by using the RANDOX kit/ UK. Glucose oxidase and hydrogen peroxide were considered and formed the basis for tests requirements.

2.4. HbA1c Test

It is a test to count 2 to 3 months' average blood sugar level. It is based on the principle of fluorescence immunoassay technology by using the Finecare HbA1C Rapid Quantitative test kit/China. The test uses a sandwich immunodetection method.

2.5. Viral genome extraction and PCR

The viral genomic DNA was considered from serum samples using the viral nucleic acid extraction kit from Qiagen/USA, according to the manufacturer's protocol. The conventional PCR technique has been used in this study for amplification of the NS1 gene of B19

V and the primers designed by (Alpha DNA/ Canada) include: (Forward primer 5’-GCC GCC AAG TAG AGG AA-3’ and reverse primer 5’-CCA CGA TGC AGC TAC AA-3’). The PCR reaction mix consisted of 5µl of extracted DNA, 1µl of forward and reverse primers, and 13µl distilled water. All these components were placed in the PCR tubes that contents all other components and the final volume in the reaction tube was 20µL. The extension for the PCR product was at 72°C for 7 min. The PCR was validated over 2% gel electrophoresis with Green Star™ Nucleic Acid Staining solution I upon preparation.

3. Results

The present study included 45 patients having T1D with age range 3 – 16 years old. Demographic data for those patients showed that the percentage of males among T1D patients was (35.5%) and the percentage of females was (64.5%). While the age and the bodyweight of all subjects representing by mean ± SD are as follows, (10.02 ± 3.14) and (31.85 ± 11.73), respectively.

The biochemical test results of fasting blood sugar, random blood sugar, and HbA1c test for patients group represented by mean ± SD were (217.02 ± 107.61), (328.87 ± 117.92) and (10.74 ± 3.43) respectively table (1).

The results of the PCR technique detected the presence of the B19V *NS1* gene in only 7 (14%) of T1D patients, whereas the others (86%) gave negative results (figure 1). This study evaluates the effect of the presence of B19V on clinical data which was measured for T1D patients, and the results showed there was no effect for the B19V on each of fasting blood sugar, random blood sugar, and glycated hemoglobin. On the other hand, the results also showed, and weight in the presence or absence of the B19V table (2).

Table 1. List of elements of diabetes mellitus type 1.

Demographic or Clinical data	Percentage or Mean (± SD)
Sex	Male: 35.5% Female: 64.5%
Age	10.02 ± 3.14
Weight	31.85 ± 11.73
FBS	217.02 ± 107.61
RBS	328.87 ± 117.92
HbA1c	10.74 ± 3.43

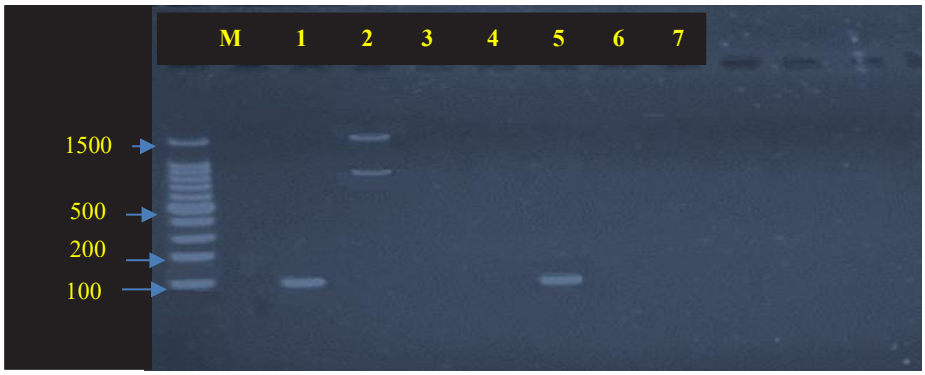

Fig 1. Detection of Parvovirus B9 (NS1) Gene by Conventional PCR. NS1Gene molecular position 120bp, lines (2, and 6) in this image and other samples are negative.

Table 2. Type 1 diabetes mellitus patients according to PCR results.

Item	PCR positive	PCR Negative	P-value
	Mean ± SD	Mean ± SD	
Age	10 ± 2.1	10 ± 3.3	P = 0.978
Weight	35 ± 11.5	31 ± 11.8	P = 0.452
FBS	194.5 ± 100	221 ± 109.7	P = 0.540
RBS	298 ± 41.7	334.5 ± 126.6	P = 0.168
HbA1c	10.5 ± 2.4	11 ± 2.3	P = 0.587

4. Discussion

For a long time, there are many studies have been suggested that viruses such as Coxsackie B, Rubella, Mumps, Cytomegalo viruses, Epstein Barr virus, Parvovirus B 19, Hepatitis C virus, Retrovirus, Rotavirus, and HIV appear to play a vital role among the numerous environmental factors, which together with the genetic susceptibility, may be implicated in the pathogenesis of T1D [9, 10, 11, 12, 13].

The present study included some of the demographic parameters (such as sex, age, and body weight) and biochemical parameters (such as F.B.S, R.B.S, and HbA1c) to give a clear picture of the epidemiological and clinical situation of T1D patients, who included in this study. A large proportion of patients with T1D was females (64.5%) compared with males (35.5%). This result corresponds with the results of studies conducted in Australia, Oman, Saudi Arabia, Libya, and Egypt [14] but, it differs from other studies in Kuwait, Tunisia, and Basra city which showed that T1D was higher in males than females [15, 16].

Patients in this study were selected from the age of children and adolescents with a mean of (10.02 ± 3.14) for early detection of the virus would be easier and more possible than the patients if they were older. In addition, T1D is frequently diagnosed during childhood and adolescence [17]. The epidemiological trends reported the number of children and adolescents with T1D at school are continued to increase [18, 19]. where the average global incidence rate increasing by 3% to 4% per annul [20]. Many countries have also reported that children are much younger at the time of diagnosis [21,22]. While another study showed an increase [23].

This study also included biochemical tests such as (F.B.S, R.B.S, and HbA1c). They are one of the basic tests approved by the World Health Organization (WHO) since they have an essential role in determining the management of diabetes mellitus. Also, a very young child does not always show clear symptoms [24,25]. The results of these tests in the present study showed significant elevation than the normal value because the patients with T1D have a disturbance in the pancreas, so a little or no insulin is released, resulting in glucose accumulation in the bloodstream and, as a result, an increase in glucose concentrations in diabetic patients [26].

The molecular diagnosis represented by the PCR assay of the current study showed the presence of the B19V *NS1* gene in 7 (14%) of T1D patients. Although this is a small percentage, it may show a potential relationship between B19V infection and T1D consequences [27-28]. However, we cannot assert an association between current or past B19V infection and the development of T1D in these patients and required further investigations.

Acknowledgment: thanks should go to the Center of Diabetes and Endocrine Glands in Al-Nasiriyah city, Iraq for their collaboration during samples collection.

References

1. Giwa AM, Ahmed R, Omidian Z, Majety N, Karakus KE, Omer SM, *et al*. Current understandings of the pathogenesis of type 1 diabetes: Genetics to environment. World J Diabetes. 2020;11(1):13–25.
2. Tuomilehto J, Ogle G, Lund-Blix N, Stene L. Update on Worldwide Trends in Occurrence of Childhood Type 1 Diabetes in 2020. Pediatr Endocrinol Rev. 2020;17: 198–209.
3. Report C, Sunumu O, Bir P, Diyabetik H, Fulminan A. Parvovirus Infection in a Child Complicated with Diabetic Ketoacidosis and Acute Fulminant Hepatitis: A Case Report. 2017;11(2):92–4.
4. Yeung W-CG, Rawlinson WD, Craig ME. Enterovirus infection and type 1 diabetes mellitus: systematic review and meta-analysis of observational molecular studies. BMJ. 2011; 342.
5. Wamsingh A, Chapman N, Tracy S. Coxsackieviruses and diabetes. Bioessays, 1997; 19(9): 793-800.
6. O'Bryan TA, Beck MJ, Demers LM, Naides SJ. Human parvovirus B19 infection in children with new onset Type 1 diabetes mellitus. Diabet Med. 2005;22(12):1778–1779.
7. Kasuga A, Harada R, Saruta T. Insulin-dependent diabetes mellitus associated with parvovirus B19 infection. Ann Intern Med. 1996;125(8): 700–701.
8. Ellerman KE, Richards CA, Guberski DL, Shek W, An L. Kilham Rat Virus Triggers T-Cell-Dependent Autoimmune Diabetes in Multiple Strains of Rat. Diabetes. 1996;45(5): 557–562.
9. Blomqvist M, Juhela S, Erkkila S, Korhonen S, Simell T, Kupila A, *et al*. Rotavirus infections and development of diabetes-associated autoantibodies during the first 2 years of life. Clin Exp Immunol. 2002;128(3): 511–515.
10. Christen U, Herrath M. Infections and Autoimmunity--Good or Bad? J Immunol. 2005; 174(12): 7481–7486.
11. Fujinami R, Herrath M, Christen U, Whitton J. Molecular Mimicry, Bystander Activation, or Viral Persistence: Infections and Autoimmune Disease. Clin Microbiol Rev. 2006; 19(1): 80–94.
12. Saber AZABI, Mohammed AH. The roles of human cytomegalovirus and Epstein-Barr virus in type 1 diabetes mellitus. Ann Trop Med Public Heal. 2019; 22(09): 90-99.
13. Mohammed AH, Saber AA. THE possible association between Epstein-barr virus and type 1 diabetes mellitus. Iraqi JMS. 2019;17(3&4):175–82.

14. Shah V, Wu M, Polsky S, Snell-Bergeon J, Sherr J, Cengiz E, *et al*. Gender differences in diabetes self-care in adults with type 1 diabetes: Findings from the T1D Exchange clinic registry. J Diabetes Complications. 2018 Aug 1;32(10): 961-965.
15. Zayed H. Genetic Epidemiology of Type 1 Diabetes in the 22 Arab Countries. Curr Diab Rep. 2016;16(5): 37.
16. Almahfoodh D, Alabbood M, Alali A, Mansour A. Epidemiology of Type 1 diabetes mellitus in Basrah, Southern Iraq: a retrospective study. Diabetes Res Clin Pract. 2017;133: 104-108.
17. Atkinson MA, Eisenbarth GS, Michels AW. Type 1 diabetes. Lancet. 2014;383(9911):69–82.
18. Särnblad S, Berg L, I D, Jönsson Å, Forsander G. Diabetes management in Swedish schools: A national survey of attitudes of parents, children, and diabetes teams. Pediatr Diabetes. 2014;15(8): 550-556.
19. Bixo A, Akesson K, Ilvered R, Forsander G, Särnblad S. Self-care management of type 1 diabetes has improved in Swedish schools according to children and adolescents. Acta Paediatr. 2017;106(12): 1987-1993.
20. Patterson C, Gyürüs E, Rosenbauer J, Cinek O, Neu A, Schober E, *et al*. Trends in childhood type 1 diabetes incidence in Europe during 1989-2008: Evidence of non-uniformity over time in rates of increase. Diabetologia. 2012; 55(8): 2142–2147.
21. Bendas A, Rothe U, Kiess W, Kapellen T, Stange T, Manuwald U, *et al*. Trends in Incidence Rates during 1999-2008 and Prevalence in 2008 of Childhood Type 1 Diabetes Mellitus in GERMANY - Model-Based National Estimates. PLoS One. 2015; 10(7): e0132716.
22. Vehik K, Ajami NJ, Hadley D, Petrosino J, Burkhardt B. The Changing Landscape of Type 1 Diabetes: Recent Developments and Future Frontiers. Curr Diab Rep. 2013;13(5): 642-650.
23. Piffaretti C, Mandereau-Bruno L, Guilmin-Crépon S, Choleau C, Coutant R, Fosse-Edorh S. Trends in childhood type 1 diabetes incidence in France, 2010 – 2015. Diabetes Res Clin Pract. 2018;149: 200-207.
24. World Health Organization. Laboratory diagnosis and monitoring of diabetes mellitus. World Health Organization, 2003.
25. Suliman H. The relation of age to the severity of Type I diabetes in children. J Family Community Med. 2010;17(2): 87–90.
26. Ramanathan K, Karthick H, Arun N. Structure Based Drug Designing for Diabetes Mellitus. J Proteomics Bioinforma. 2010;3(11):310–313.
27. von Poblotzki A, Gerdes C, Reischl U, Wolf H, Modrow S. Lymphoproliferative responses after infection with human parvovirus B19. J Virol. 1996;70(10):7327–7330.
28. Munakata Y, Kodera T, Saito T, Sasaki T. Rheumatoid arthritis, type 1 diabetes, and Graves' disease after acute parvovirus B19 infection. Lancet. 2005;366(9487):780.

Assessment of Existing Bond-Slip Models of Adhesively Bonded CFRP-Steel Joints

Mohammed J. Altaee[1], Majid M.A. Kadhim[2], Sarmed A.S. Altayee[3] and Akram Jawdhari[4]
{ mohammed.altaee@uobabylon.edu.iq[1], majid.mohammed@uobabylon.edu.iq[2],
eng.sarmed.salih@uobabylon.edu.iq[3], akram.hassan@uky.edu [4]}

Environmental Research and Studies Center, University of Babylon, Hilla, Iraq[1]
College of Engineering, University of Babylon, Hilla, Iraq[2,3]
Queen's University, Kingston, ON, Canada[4]

Abstract Strengthening of steel structures with fibre-reinforced polymer (FRP) composites has attracted great attention due to their desirable mechanical properties, non-corrosive nature, and ease of application. The bond between an FRP laminate and steel substrate plays a significant role in ensuring the effectiveness of the strengthening system. Various bond-slip (τ-δ) relations for FRP-steel joints have been developed, mainly from experimental tests on single or double-lap shear specimens. However, existing models employ different stress-slip relations and mathematical expressions, suggesting that their predictions of failure load, mode and other interface properties, might be inconsistent. In this study, a comprehensive finite element (FE) model, comprising all parts of the FRP-steel joint in a double-lap configuration, has been developed to evaluate several commonly used (τ- δ) models. The FE model is able to capture all probable failure modes including interfacial failure (debonding), FRP rupture and steel yielding. In addition, a new trapezoidal τ- δ law has been coded into the FE software by the authors and compared with other existing models. The FE model was then used to simulate a large number of double-lap tests from literature containing different material and geometric properties and varying by the (τ- δ) relation from examined theoretical models. Comparisons with experimental data showed a large scatter of failure loads and joint behavior, due to difference in (τ- δ) models. The models that best align with test results and those that deviate, were identified and discussed.

Keywords: FRP-steel joint, finite element, bond-slip model, ABAQUS, double strap joint.

1 Introduction

Fibre reinforced polymer (FRP) composite has been widely employed in civil engineering strengthening applications due to their excellent material properties such as resistance to harsh environment and high tensile strength. Previous studies illustrated that the use of FRP in strengthening/repair of steel members subjected to static [1–5], cyclic [6], [7] and impact loads [8], [9] offers a promising alternative to conventional rehabilitation techniques. Thus, several manuals and guidelines (e.g., [10]) have been proposed for strengthening steel structures with FRP materials. Despite the large body of research on this discipline, few studies have been conducted on the bond-slip response between FRP and steel substrate.

Analysis of FRP strengthened members are usually undertaken by analytical or finite element (FE) methods [11–18]. FE method provides a powerful tool to expand investigations

IMDC-IST 2021, September 07-09, Sakarya, Turkey
Copyright © 2022 EAI
DOI 10.4108/eai.7-9-2021.2315490

into the effectiveness of FRP strengthening technique without the need to perform repetitive, expensive and time-consuming tests. However, use of this method in studying the bond of FRP-steel joint is conditional to using a bond-slip (τ- δ) model capable of representing the joint's interfacial behavior and predicting the failure load. The τ- δ model is typically implemented in FE analysis as a material input for cohesive elements that define the interface between dissimilar parts [13,14].

Several τ-δ models have been suggested in previous research studies [19–21] to represent the bond response between FRP and steel substrate. Xia and Teng [20] model was one of the first trails in developing bond-slip model for FRP-steel joints. Another model was proposed by Fawzia et al.[19] and was developed based on a few specimens of double strap joints. Both of above models can be used for linear adhesive materials. Fernando [21] proposed two models, including a triangular (bilinear) and trapezoidal models, which can be used for linear (brittle) and nonlinear (ductile) adhesive materials, respectively.

In this research, a robust FE model has been developed for 21 FRP-bonded double-strap steel specimens tested by other researchers, constituting a wide range of geometrical and material characteristics, including a bond length (Lf) from 30 to 250 mm; an FRP elastic modulus (Ef) from 159 to 479 GPa corresponding to normal, high and ultra-high modulus laminates; two types of adhesive, brittle and ductile (nonlinear); and three types of failure modes, namely: debonding at FRP-steel interface, FRP rupture, and delamination. The FE model was used to test the predictions of several τ- δ relations that commonly used for FRP-bonded steel, by implementing each of those relations within the numerical framework and comparing the model's results with those from tests. In addition, the study developed and implemented a trapezoidally shaped (τ- δ) model into ABAQUS software. In contrast to the linear (τ- δ) model currently available in ABAQUS and typically implemented for brittle adhesives, the trapezoidal model can be used to accurately model the behavior of steel members bonded to FRP composites by ductile or nonlinear adhesives.

2 Bond-slip models

As previously mentioned, several bond-slip models proposed in the literature, to predict the bond behaviour of FRP-steel joints, have been examined in this study. While other models might be available in literature, the three above models were selected due to their popularity among research on FRP bonded steel members. The mathematical details and key parameters of each model considered in this research are listed in Table 1. The first model in the table was developed by Xia and Teng [20] which based on experimental data of 13 single shear tests. The variables considered in the model are the adhesive type and adhesive thickness (ta). The model is bilinear in shape as can be seen in Fig. 1, with key parameters of maximum shear strength (τ_f), slip at maximum shear (δ_1), slip at complete debonding (δ_f), and fracture energy (G_f). The key parameters are related to the mechanical properties of the adhesive, including its tensile strength ($f_{t,a}$), thickness (ta), and fracture energy (G_a). The model only considers the cohesive failure within the adhesive layer while neglecting interface debonding.

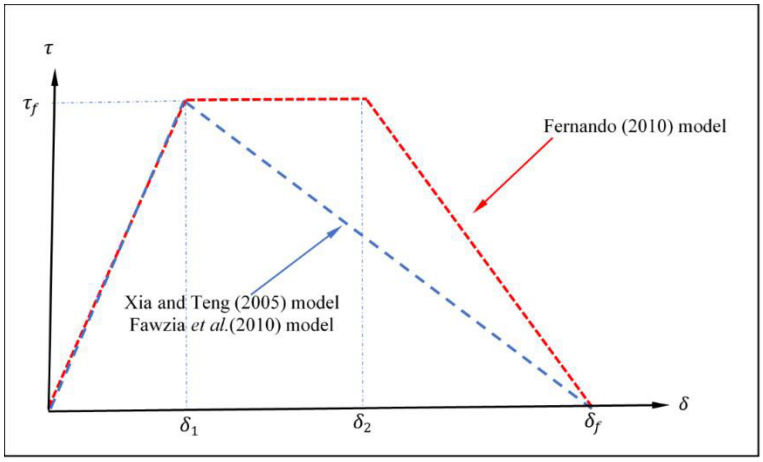

Figure 1. Bond-slip shapes of [19], [20] and [21].

The second model in Table 1, by Fawzia et al. [19] was derived from analysis 26 double shear joints tests. A number of parameters were investigated including the modulus of carbon FRP (CFRP) sheet considering two types, normal and high modulus; type of adhesive, considering three commercially available adhesive (Araldite420, MBrace saturant and Sikadur30); number of CFRP layers, either 3 or 5; and bond length (lf) ranging from 80 to 250 mm. This model is bilinear also (Fig. 1) and dependent on the adhesive properties alone. Fernando [21] tested 18 single-shear bond specimens and developed two τ-δ models, a bilinear and trapezoidal models, as shown in Fig. 1. The parameters examined were the adhesive type, testing four types, namely: Sikadur 30, Sikadur330, Araldite420 and Araldite 2015; adhesive thickness, trying three values for ta =1.5, 2 and 3mm; and CFRP modulus (Ef), using two values for Ef = 235 and 340 GPa.

3 Finite element modelling

ABAQUS software [22] was employed to model the FRP-steel double lap joints. Solid elements C3D8R were used to represent the steel plates. FRP laminates were modelled using linear three-dimensional four-node shell elements with reduced integration and membrane strain (S4R). The bond region between FRP and steel was modelled using eight-node three-dimensional cohesive elements (COH3D8). Elements with mesh size of 1 mm were used in the bond region for all parts (steel, FRP and adhesive material) as shown in Fig 2. The mesh was then gradually increased to a maximum size of 5 mm, for regions outside the bond area. Since the explicit solver was used in the current research which overcomes the convergence problem that normally occurs in the case of contact or material complicities, less care was paid to use smaller element size as a treatment of convergence aspects. The total number of elements for simulated joints ranged from 13544 to 6147 elements based on the bond length.

Table 1. Details of bond-slip models from literature.

Bond-slip model	τ_f	δ_1	δ_2	δ_f	G_f
Xia and Teng [20]	$0.8f_{t,a}$	$\tau_f . t_a$/Ga	-	$\frac{2G_f}{\tau_f}$	$\frac{31}{\tau_f}\left(\frac{f_{t,a}}{G_a}\right)^{0.56} {t_a}^{0.27}$
Fawzia et al. [19]	$f_{t,a}$	$\frac{t_a}{10}$	-	$\frac{t_a}{4}\ for\ t_a = 0.1 - 0.5\ mm$ $0.125 + \frac{t_a - 0.5}{10}\ for\ t_a = 0.5 - 1\ mm$	-
Bilinear model Fernando [21]	$0.9f_{t,a}$	$0.3\left(\frac{t_a}{G_a}\right)^{0.65} f_{t,a}$	-	$\frac{2G_f}{\tau_f}$	$628\ {t_a}^{0.5}R^2$
Trapezoidal model Fernando [21]	$0.9f_{t,a}$	0.081 mm	0.8 mm	$\frac{2(G_f - \tau_f(\delta_2 - \frac{\delta_1}{2}))}{\tau_f} + \delta_2$	$628\ {t_a}^{0.5}R^2$

G_f: Interfacial fracture energy, R: the area under stress (MPa) strain curve of the adhesive material, τf: allowable shear strength of adhesive, t_a: adhesive thickness, $f_{t,a}$: allowable tensile strength of adhesive. G_a: adhesive shear modulus. δ_1: damage initiation of adhesive in bilinear model, δ_2:damage initiation of adhesive in trapezoidal model.

Due to geometrical and material symmetry of specimens in x, y and z axes, only one eighth portion of the full-scale specimens was modelled. For the FRP-steel joint consists of two interfaces (FRP-to-adhesive interface and adhesive-to-steel interface), a surface-to-surface contact elements were used in either interface, along with pure master to slave contact algorithm. Due its small stiffness compared to steel and FP, the adhesive layer was assumed to be the slave surface. In addition, the adhesive layer was modelled as a discrete layer, with mechanical properties and layer thickness taken from the corresponding experimental tests. The steel plates were modelled as a linear elastic material defined by the elastic modulus (Es) and Poisson's ratio (ν), assuming values of Es =200 GPa and ν =0.3. The linear elastic model was selected in lieu of a plasticity-based model because no yielding was reported for the steel plates in the experimental studies. FRP was modelled using a lamina model which is suitable to model unidirectional FRP composites. In order to model the rupture failure of FRP, Hashin failure criteria [23] was used as a damage initiation criteria when the laminate's stress exceeds its tensile strength. After damage initiation, the laminate stiffness is assumed to degrade to a very small value, simulating a brittle failure.

A traction-separation model is used to define the adhesive layer in ABAQUS, based on recommendations of previous research on FRP strengthened steel or concrete members [8], [13–16], [18][24]. The traction-separation model contains three stages, an ascending linear stage, damage initiation in stage two, and damage progression in the last stage. In the first stage, Young's or shear moduli of the adhesive layer were divided by its thickness to obtain the stiffness of the linear elastic response in the normal and two shear directions, respectively [22]. Then, a quadratic nominal stress criterion was used to define the onset of debonding (damage) for the second stage. The quadratic criterion considers the mixed mode debonding process due to normal (peeling) and shear and is widely used in studies on FRP-steel bond problems such as

[13], [14]. In the last stage, the interface debonding process is modelled in ABAQUS by cohesive zone model (CZM), considering three options, a bilinear form applicable to (τ- δ) models by Xia and Teng [20] and Fawzia et al. [19]; a trilinear form applicable to the bilinear (τ- δ) model by Fernando [21]; and a tubular form applicable to the trapezoidal (τ- δ) model by Fernando [21].
Numerical values for the key inputs of the traction-separation law, namely: τ_f, δ_1, and δ_f, were obtained from the theoretical (τ- δ) models examined in this study using available material and geometric properties of the experimental specimen. The FE model of each double-strap specimen was run four times, according to the (τ- δ) models examined in Table 1.

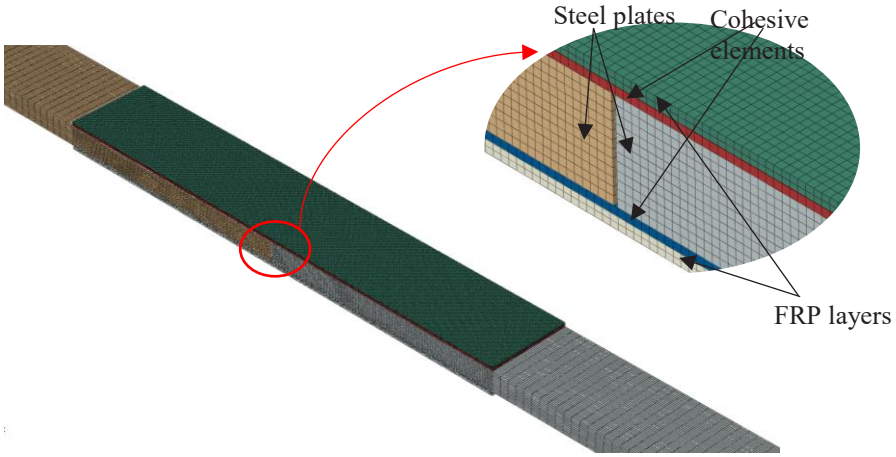

Figure 2. Typical FE model for double-strap FRP-steel joints.

4 Summary of experiments

To evaluate predictions of the (τ- δ) models considered in this study, FE models were generated and compared with 21 double-strap joint tests obtained from four sets of experiments from [13], [14], [19] , and [25]. The experimental tests contained specimens with various bond lengths, bond widths, material and geometric properties for the FRP laminate and adhesive layer, as can be noticed in Table 2. The specimens were selected to assess the models' ability in capturing the behavior of different FRPs, specimen dimensions, and failure modes. Table 3 list the mechanical properties of FRP composite and adhesive layer for each experiment, as reported in the experimental research.

Table 2. Details of experimental specimens and key results summary.

Reference	Specimen Id	L_f mm	Failure load (Pult.), kN				Failure mode (FM)			
			Pult-exp.	Pult-FE1.	Pult-FE2.	Pult-FE3.	FM-exp.	FM-FE1.	FM-FE2.	FM-FE3.
	S3-30	30	41.0	12.4	20.8	33.9	D	D	D	D

Al-Mosawe et al. [14]	S3-60	60	69.1	13.4	22.6	68.3	D	D	D	D
	S3-90	90	93.6	13.5	22.7	102.1	D	D	D	D
	NS-30	30	41.9	12.7	22.5	34.2	D	D	D	D
	NS-60	60	69.8	15.3	26.0	68.4	D	D	D	D
	NS-90	90	94.2	15.5	26.1	101.9	D	D	D	D
	UHS-30	30	31.8	19.2	29.7	34.2	F	D	D	D
	UHS-60	60	64.1	22.6	38.4	57.3	F	D	D	D
	UHS-90	90	73.2	24.6	41.1	73.2	F	D	D	D
	S2-30	30	15.5	6.1	10.6	17.1	F	D	D	D
	S2-60	60	27.6	6.6	11.1	34.0	F	D	D	D
	S2-90	90	31.1	6.7	11.1	51.0	F	D	D	D
Wu et al. [25]	A50	50	137.2	59.0	98.7	141.8	F	D	D	D
	A100	100	250.6	61.2	108.4	232.3	F	D	D	F
	A250	250	267.3	61.6	109.9	232.3	F	D	D	F
Al-Zubaidy et al [13]	CF-1-A-10	10	19.8	12.2	17.5	25.9	D	D	D	D
	CF-1-A-20	20	37.8	12.5	19.1	28.8	D	D	D	F
	CF-1-A-30	30	45.2	12.7	19.1	28.8	F	D	D	F
Fawzia et al. [19]	NA80	80	86.1	31.8	51.6	134.2	D	D	D	F
	NA150	150	77.8	31.8	81.1	136.4	D	D	D	F
	NA250	250	93.2	31.8	81.1	141.7	D	D	D	F

where: L_f= FRP bond length; Pult-exp.= ultimate load from test; Pult-FE1., Pult-FE2., and Pult-FE3. = ultimate load from FE model and using (τ- δ) models from Xia and Teng [20], Fawzia et al. [19], and Fernando [21], respectively; FM-exp.= failure mode from test; FM-FE1., FM-FE2., and FM-FE3. = failure mode from FE model and using (τ- δ) models from Xia and Teng [20], Fawzia et al. [19], and Fernando [21], respectively; D = FRP debonding; F= FRP rupture or delamination.

Table 3. Mechanical properties of FRP and adhesive materials.

Ref.	Specimen ID	FRP laminate				Adhesive	
		Modulus E_f , GPa	Strength σf, MPa	Width W_f, mm	Thickness t_f, mm	Modulus E_a, GPa	Thickness t_a, mm
Al-Mosawe et al. [14]	S3	159	2854	20	1.4	3.2	0.5
	NS	203	2861	20	1.4	3.2	0.5
	UHS	450	1602	20	1.2	3.2	0.5
	S2	159	2854	10	1.4	3.2	0.5
Wu et al. [25]	A50	479	1500	50	1.45	1.9	0.36
	A100	479	1500	50	1.45	1.9	0.31
	A250	479	1500	50	1.45	1.9	0.38
Al-Zubaidy et al. [13]	C-F-A	205	1644	50	0.18	2.23	0.5
Fawzia et al. [19]	NA	640	2650	50	0.53	4.0	0.47

5 FE Results

Results of FE models, generated by utilizing either of the three (τ-δ) models examined in this study, were compared with experimental data from 21 FRP–steel double-strap joint tests. The

comparisons were made for ultimate load ($P_{ult.}$) and failure mode (FM) as listed in Table 2. Furthermore, the results were compared in graphical forms, representing plots of P_{ult} against bond length (L_f), bond width (W_f) and modulus of elasticity of FRP (E_f). The following sections discuss the obtained results.

Ultimate load vs. bond length

Table 2 lists the ultimate load from experiments ($P_{ult\text{-}exp}$) and those from FE models ($P_{ult\text{-}FE}$) obtained by utilizing either of the three (τ-δ) models discussed earlier. Fig. 3 plots the relation between the experimental and numerical ($P_{ult.}$) versus the bond length (Lf). It can be seen from the figure, that the models by Xia and Teng [20] and Fawzia et al. [19] were unable to accurately predict Pult. for most specimens and bond lengths and their predictions were divergent from the experimental values by 13 to 83 %. On the other hand, the model by Fernando [21] yielded much better results in comparisons with most test points, except for few cases of divergence. Most importantly, this model was able to capture the variation of $P_{ult.}$ with Lf for most samples and predict the effective bond length (L_{eff}), a length at which the ultimate load becomes constant when Lf reaches a certain value. Fig. 3 (d, e) shows for experimental specimens UHS tested by Al-Mosawe et al., [14]and specimens tested by Wu et al., [25], L_{eff} is 60 and 100 mm, respectively. The FE model implementing (τ-δ) model by Fernando [21] predicted identical values for L_{eff}.

5.1 Failure modes

The predictive capability of the three (τ-δ) models can be assessed by examining their predictions for the failure mode and comparing with that from the tests, as can be seen in Table 2. It can be noticed that most of models were not able to capture the failure mode correctly for all specimens. The models by Xia and Teng [20] and Fawzia et al. [19] predicted only a debonding failure, regardless of the bond length. In the experimental tests, the failure mode is typically by debonding when Lf is smaller than L_{eff}, and FRP rupture or delamination for larger values of Lf. This trend was only captured when the (τ-δ) model by Fernando [21] is used, although for some specimens, the model still failed by debonding.

5.2 Bond width

The capability of (τ-δ) models in capturing the effects of FRP bond width (W_f) was assessed by comparing the FE models with two experimental specimens from refrence [14], specimens S2 and S3 in Table 2, corresponding to W_f of 10 and 15 mm, respectively. Fig. 4 plots the relation between $P_{ult.}$ and $W_{f.}$, comparing test results with those from the FE models for the three examined (τ-δ) models. Similar to the comparison for the bond length, the model by Fernando [21] was able to simulate the effects of W_f, with a maximum divergence from test results by 17 %. While the other two models were not able to capture W_f, and their predictions of $P_{ult.}$ ranged from 50 to 85%.

5.3 FRP modulus

Al-Mosawe et al. [14] also studied experimentally the effects of FRP elastic modulus (Ef), by testing three values, 159, 203, and 450 GPa, corresponding to three classes of moduli; normal, high, and ultra-high, respectively. In order to evaluate the capability of (τ-δ) models in capturing the effects of Ef, the results of FE analysis from either of these theoretical models were

compared with those from Al-Mosawe et al. [14] tests for the different values of FRP modulus. Fig. 5 plots the relation between Pult. and Ef., comparing test results with those from the FE models for the three examined (τ-δ) models.

Similar to previous comparisons for other parameters, the model by Fernando [21] was able to simulate the effects of Ef. , with a maximum divergence from test results by 17 % as was in the FRP width study and the other two models were also not able to capture Ef, and their predictions of Pult. ranged from 50 to 85%. A noticeable trend from either the experimental tests or FE models corresponding to the (τ-δ) model by Fernando [21], is seen in Fig. 4, where Pult. seems to decrease with the increase of Ef. , perhaps as a result of high stress concentrations developed in stiff laminates as noticed by other researches [6], [13].

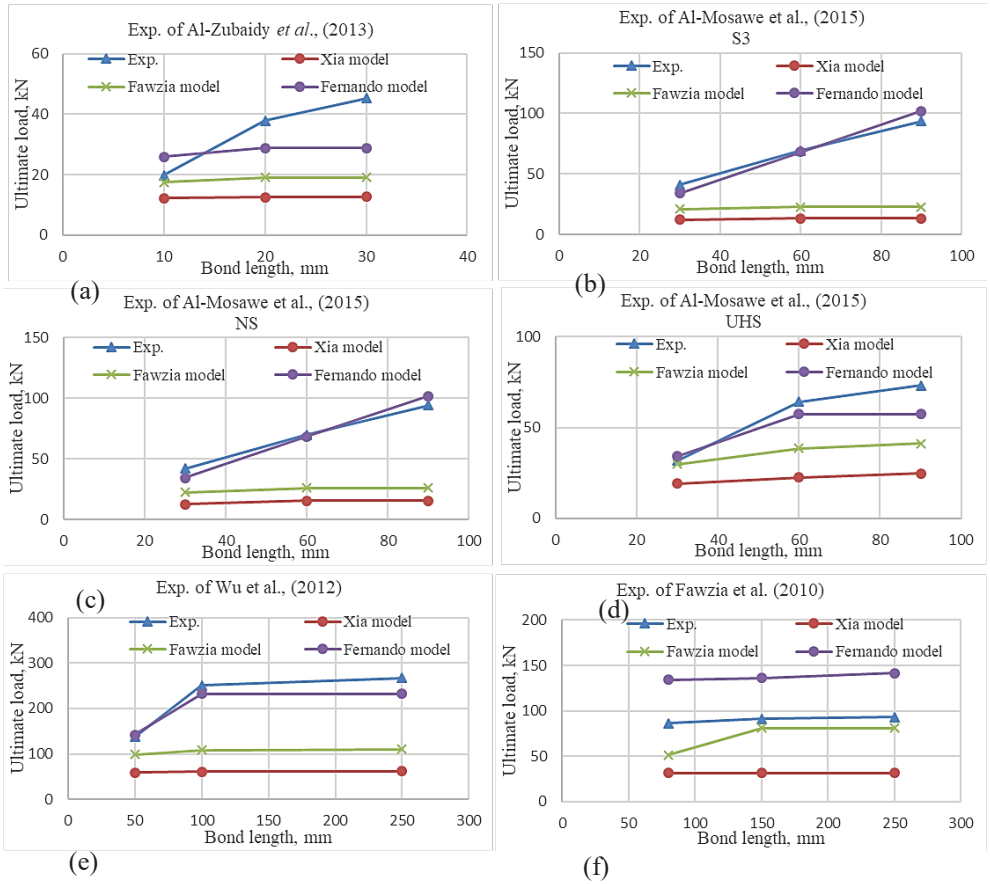

Figure 3. Ultimate load vs. bond length from tests and FE models using different (τ-δ) models.

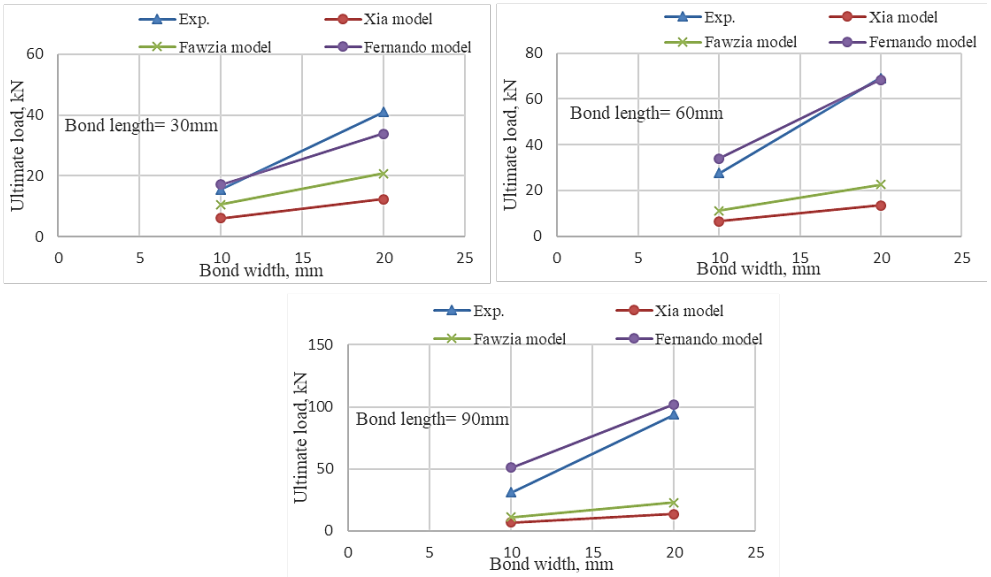

Figure 4. Ultimate load vs. bond width from tests by Al-Mosawe et al., [14] and FE models using different (τ-δ) models.

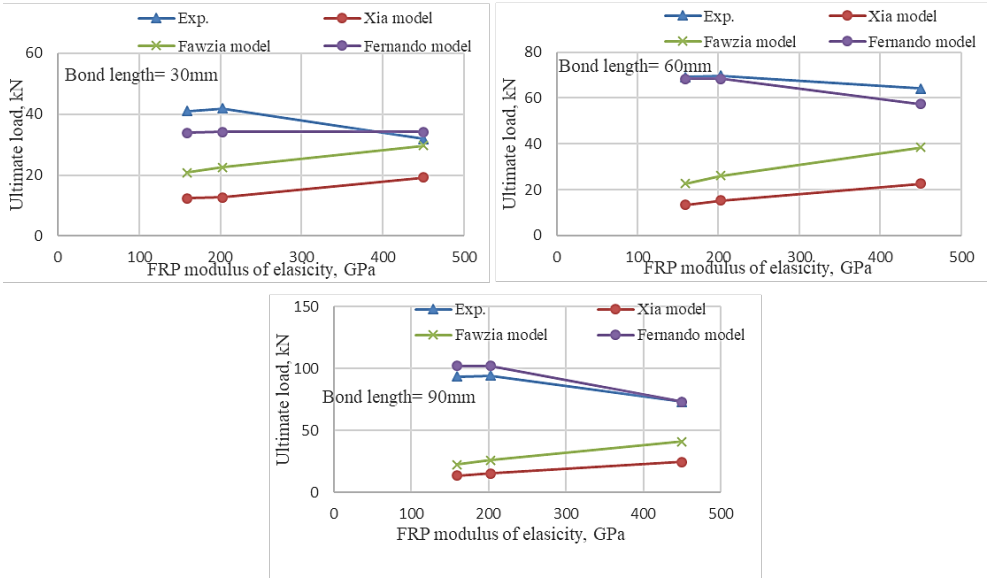

Figure 5. Ultimate load vs. FRP elastic modulus, from tests by Al-Mosawe et al., [14] and FE models using different (τ-s) models.

6 Conclusions

In this study, the predictive capability of three bond-slip (τ-δ) models that widely used in literature for FRP-steel bond joints has been examined using finite element (FE) analysis. A robust FE model comprising all the joint parts and probable failure modes, was developed and compared with results from 21 double-strap FRP-steel tests from literature, constituting a wide range of material and geometric properties. Interfacial properties such as maximum shear stress and accompanying slip required for the FE model were obtained from the theoretical bond-slip models, allowing for results comparison between (τ-δ) models and experiments, in terms of ultimate load (P_{ult}) and failure mode. Based on the results obtained, the following conclusions can be drawn:

1. Compared to (*τ-δ*) models by Xia and Teng [20] and Fawzia *et al.* [19], the model by Fernando [21] had much better calibrations with most test specimens in regards to P_{ult}. and to capture the effects of effective bond length and the corresponding failure mode in some specimens.
2. The model by Fernando [21] was also able to capture the ultimate load when either the bond width or FRP elastic modulus were varying from 10 to 20 mm, and 159 to 450 GPa, respectively. The other two models were not able to simulate the effects of these two parameters.
3. A trapezoidal traction-separation relation was implements in ABAQUS software which provided an accurate representation for the bond-slip model from Fernando [21].
4. Regardless of the success seen from some of the (*τ-δ*) models, much effort is still needed to develop a model capable of simulating a wide range of material and geometric variables for the FRP-steel joint.

References

[1] Deng J, Lee MMK. Behaviour under static loading of metallic beams reinforced with a bonded CFRP plate. Compos Struct [Internet]. 2007 Apr;78(2):232–42. Available from: DOI: 10.1016/j.compstruct.2005.09.004

[2] Colombi P, Poggi C. An experimental, analytical and numerical study of the static behavior of steel beams reinforced by pultruded CFRP strips. Compos Part B Eng [Internet]. 2006 Jan;37(1):64–73. Available from: DOI: 10.1016/j.compositesb.2005.03.002

[3] Kadhim MMA. Effect of CFRP plate length strengthening continuous steel beam. Constr Build Mater [Internet]. 2012 Mar;28(1):648–52. Available from: DOI: 10.1016/j.conbuildmat.2011.09.020

[4] Altaee MJ, Cunningham LS, Gillie M. Experimental investigation of CFRP-strengthened steel beams with web openings. J Constr Steel Res [Internet]. 2017 Nov;138:750–60. Available from: DOI: 10.1016/j.jcsr.2017.08.023

[5] Altaee MJ, Cunningham LS, Gillie M. Experimental investigation of CFRP-strengthened steel beams with web openings. J Constr Steel Res [Internet]. 2017 Nov;138:750–60. Available from: DOI: 10.1016/j.jcsr.2017.08.023

[6] Deng J, Lee MMK. Behaviour under static loading of metallic beams reinforced with a bonded CFRP plate. Compos Struct [Internet]. 2007 Apr;78(2):232–42. Available from: DOI: 10.1016/j.compstruct.2005.09.004

[7] Kim YJ, Harries KA. Fatigue behavior of damaged steel beams repaired with CFRP strips. Eng Struct. 2011;33(5):1491–502.

[8] Kadhim M, Wu Z, Cunningham L. FE modelling of CFRP strengthened steel members under impact loads. In: Proceedings of the 24th UK Conference of the Association for Computational Mechanics in Engineering. Cardiff University Cardiff, UK; 2016. p. 343–6.
[9] Kadhim MMA, Wu Z, Cunningham LS. Experimental study of CFRP strengthened steel columns subject to lateral impact loads. Compos Struct. 2018;185:94–104.
[10] Schnerch D, Dawood M, Rizkalla S, Sumner E. Design guidelines for the use of HM strips: strengthening of steel-concrete composite bridges with high modulus carbon fiber reinforced polymer (CFRP) strips. Tech. report No. IS-06-02. Constructed Facilities Laboratory. North Carolina State University; 2006.
[11] Seleem MH, Sharaky IA, Sallam HEM. Flexural behavior of steel beams strengthened by carbon fiber reinforced polymer plates–Three dimensional finite element simulation. Mater Des. 2010;31(3):1317–24.
[12] Kadhim MMA, Mohammed MJ, Chabuk AJ. Effect of prestressed CFRP plate location on behavior of RC beam strengthened with prestressed CFRP plate. J Univ Babylon. 2012;20(1):105–13.
[13] Al-Zubaidy H, Al-Mahaidi R, Zhao X-L. Finite element modelling of CFRP/steel double strap joints subjected to dynamic tensile loadings. Compos Struct [Internet]. 2013 May;99:48–61. DOI: 10.1016/j.compstruct.2012.12.003
[14] Al-Mosawe A, Al-Mahaidi R, Zhao X-L. Experimental and Numerical Study on Strengthening of Steel Members Subjected to Impact Loading Using Ultrahigh Modulus CFRP. J Compos Constr [Internet]. 2016 Dec;20(6):04016044. Available from: DOI: 10.1061/(ASCE)CC.1943-5614.0000703
[15] Al Taee M, Cunningham L, Gillie M. Novel Technique for Strengthening Steel Beams with Web Penetrations. In: Proceedings of the MACE PGR Conference. Manchester: University of Manchester; 2016. p. 9–11.
[16] Al Taee M, Cunningham L, Gillie M. CFRP Strengthening of Steel Beams with Web Openings. In: Proceedings of Structural Faults & Repair 2016: 16th International Conference. Edinburgh; 2016. p. 1754.
[17] Kadhim M, Wu Z, Cunningham L. Modelling impact resistance of polymer-laminated steelwork. Proc Inst Civ Eng Comput Mech. 2017;170(1):7–24.
[18] Altaee M, Cunningham LS, Gillie M. Practical Application of CFRP Strengthening to Steel Floor Beams with Web Openings: A numerical Investigation. J Constr Steel Res [Internet]. 2019 Apr;155:395–408. Available from: DOI: 10.1016/j.jcsr.2019.01.006
[19] Fawzia S, Zhao X-L, Al-Mahaidi R. Bond–slip models for double strap joints strengthened by CFRP. Compos Struct. 2010;92(9):2137–45.
[20] Xia SH, Teng JG. Behaviour of FRP-to-steel bonded joints. In: Proceedings of the international symposium on bond behaviour of FRP in structures. International Institute for FRP in Construction; 2005. p. 419–26.
[21] Fernando ND. Bond behaviour and debonding failures in CFRP-strengthened steel members. The Hong Kong Polytechnic University; 2010.
[22] Dassault Systèmes DS. Abaqus analysis user's guide. Technical Report Abaqus 6.14 Documentation, Simulia Corp; 2016.
[23] Hashin Z. Failure criteria for unidirectional fiber composites. 1980;
[24] Kadhim M., Adheem A., Jawdhari A., Altaee MJ., Predictive Capability of Existing Confinement Models for FRCM Composites Confined Concrete. IMDC-SDSP EAI. 2020.
[25] Wu C, Zhao X, Duan WH, Al-Mahaidi R. Bond characteristics between ultra high modulus CFRP laminates and steel. Thin-Walled Struct. 2012;51:147–57.

Effect of Ginger on Oxidative Stress Induced by Hydrogen Peroxide in Male Quail

Abdullah F. Abdul-Majeed*[1], Saeb Y. Abdul-Rahman[2], Hassan A. Al-krad[3]
{E. mail: dr.abdullah@uomosul.edu.iq [1] , E. mail: dr.saeb.y@uomosul.edu.iq [2]}

[1,2] Department of Animal Production, College of Agriculture and Forestry, University of Mosul / Iraq, [3] Department of physiology, College of Vet. Medicine, Hama / Syria.

Abstract. This study was conducted to investigate the effect of Ginger (*Zingiber officinale*) as an antioxidant and its ability to prevent the effect of H_2O_2-induced oxidative stress and its reflections on blood parameters and antioxidant status of male quail. 120 local male quail on 21 days aged were randomly distributed according to complete randomized design into 4 groups and reared until 56 days age as follows: Control group, H_2O_2 group (tap water with 0.5% H_2O_2), Ginger group (1000 mg ginger/kg ration), H_2O_2 with Ginger group (1000 mg ginger/kg ration and tap water with 0.5% H_2O_2). Results revealed that the H_2O_2 induced oxidative stress retracted the blood parameters and serum antioxidant status (decrease glutathione 1.10 µmol/l and increase malondialdehyde 1.79 nmol/ml), while the ginger enhanced the blood parameters and serum antioxidants status (elevation glutathione 2.92 µmol/l and decline in malondialdehyde 0.41 nmol/ml) compared to the control group (1.58 µmol/l, 0.74 nmol/ml respectively). In conclusion, ginger prevented the oxidative stress effects and returned most of the biochemical values to normal values as in the control group.

Keywords: *Zingiber officinale*, H_2O_2, Malondialdehyde, Glutathione, *Coturnix coturnix*.

1 Introduction

Oxidative stress is defined as an imbalance between the production of reactive oxygen species (ROS) and the ability of defensive biological systems (body antioxidants) to remove them or repair their destructive effects [1]. Therefore, the superior production of reactive oxygen species and their free radicals leads to oxidation of poly-unsaturated fatty acids (PUFA) in cellular membranes, thus it disturbs membrane permeability due to lipid peroxidation [2], and formation of the Malondialdehyde (MDA), which is one of its most important products, and it's used as an indicator of cellular membranes damage. The antioxidant systems in the cell work to reduce/or remove the oxidative damage by scavenging those free radicals or inhibiting the process of lipid peroxidation [3].

Many plants has an antioxidant capacity that prevents or reduce the oxidative stress. Ginger (*Zingiber officinale*) is one of these plants that has antioxidant capacity [4]. The antioxidant effect of ginger is due to its active ingredient as camphene, shogaols, zingiberol, and vitamin C and E [5].

* Part of PhD. dissertation submitted by the first author.

IMDC-IST 2021, September 07-09, Sakarya, Turkey
Copyright © 2022 EAI
DOI 10.4108/eai.7-9-2021.2315485

Shanoon [6] has indicated that ginger has an antioxidant effect similar to/ or greater than vitamin C or E. Al-kattan *et al.* [7] also indicated that ginger preserves the cells that suffer from oxidative stress whether it is pathologically or chemically induced by H_2O_2 with drinking water.

One of the reasons for choosing males in the study is that the males are usually subjected to high level of oxidative stress during spermatogenesis due to the high levels of polyunsaturated fatty acids of spermatozoa membrane [19, 27].

The present study aimed to evaluate the effect of crushed dry ginger roots (*Zingiber officinale*) role as an antioxidant, and its preventive ability against the hydrogen peroxide-induced oxidative stress.

2 Materials and Methods

This study was conducted on 120 male quail (*Coturnix coturnix*) for the period 21 to 56 days of age. The requirements of lighting, ventilation and temperature were taken into consideration according to the bird's age. The birds were distributed randomly into four groups (30 males/group) in ground cages with dimensions 2.0 x 2.5 x 3.0 m for length, width and height, respectively. Ginger roots (*Zingiber officinale*) were cleaned, dried and crushed, then it was mixed with the ration at a concentration of 1000 mg/kg, that was formed according to the poultry nutrition requirement [8] and which included a starter ration (24.6% crude protein and 2838 kcal/kg of energy, then replaced with a finisher ration at 42 days aged (22.00% crude protein and 2942 kcal/kg of energy). Water and ration were allowed *ad libitum* throughout the study. The study treatments were as follows:

T_1: Control group: birds were reared on standard ration and tap water.

T_2: Hydrogen peroxide group (H_2O_2): birds were reared on a standard ration and tap water with 0.5% hydrogen peroxide.

T_3: Crushed ginger group: birds were reared on a standard ration with crushed ginger (1000 mg / kg of ration) and tap water.

T_4: Crushed ginger and hydrogen peroxide group: birds were reared on standard ration with crushed ginger (1000 mg/kg of ration) and tap water with 0.5% hydrogen peroxide.

At the end of the study (at 56 days aged), six birds were slaughtered from each group, and the blood was collected in tubes without anticoagulants, then the serum was isolated, and kept at -20°C until biochemical tests were performed, that included determination of serum glucose, cholesterol, triglycerides, Aspartate transaminase (AST), Alanine transaminase (ALT) (Biosystem Kits, Spanish made), serum glutathione GSH level, according to the modified Burtis and Ashwood method [9], and serum MDA level which was estimated by using the modified Thiobarbituric Acid Reaction Assay method [10].

Serum corticosterone hormone level was determined by AssayMax Corticosterone Elisa Kit (manufactured by AssayMax American company), using the ELISA Micro Plate Reader Type Bio-Rad Model 550 (Japanese made).

Statistical analysis:

Statistical analysis was carried out using the Statistical Analysis Statics program [11]. The experiment was designed according to the complete randomized design (CRD), and the

data were analyzed by using one-way analysis of variance, and to determine the differences between the means ($P \leq 0.05$), we used the Duncan's Multiple Range Test [12], according to researchers Steel and Torrie [13].

Results and Discussion

Table 1 indicates that the addition of hydrogen peroxide with drinking water (T_2) led to a significant increase in serum glucose (338.73 mg/dl) compared to the two groups of ginger T_3 (278.05 mg/dl) and T_4 (308.88 mg/dl), as well as a significant increase in the concentration of cholesterol and triglycerides compared to all study groups at ($P \leq 0.05$). These results are in agreement with Salah [14] who said that the addition of 0.5% hydrogen peroxide in drinking water led to a significant increase in blood glucose in broiler breeder males (Arbor Acers) compared to the control group after 4 and 8 weeks of treatment.

It was found that oxidative stress increases the secretion of corticosterone from the adrenal cortex, which stimulates the gluconeogenesis process [15]. Further, reinforcing this opinion is the presence of a significant increase in the blood corticosterone level of birds of the hydrogen peroxide group (Table 3).

The elevated serum cholesterol when administering hydrogen peroxide may be due to disturbances in the metabolic processes of lipids or in the digestive processes, which led to changes in the absorption and excretion of steroid [16]. This is consistent with what Ameen Agha [17] observed of elevated cholesterol concentration in the group of chickens that consumed H_2O_2 with drinking water.

Table 1. Effect of hydrogen peroxide and crushed ginger on blood glucose, cholesterol and triglycerides of male quails at 56 days aged (Means ±SE).

Parameters / Treatments	Glucose mg/dl	Cholesterol mg/dl	Triglycerides mg/dl
T_1 (Control)	320.00 ±4.84 AB	208.35 ±8.75 B	163.62 ±8.31 B
T_2 (H_2O_2)	338.73 ±4.90 A	247.68 ±7.49 A	220.25 ±20.70 A
T_3 (Ginger)	278.05 ±12.39 C	166.80 ±8.25 C	122.55 ±12.21 B
T_4 (Ginger + H_2O_2)	308.88 ±4.75 B	221.62 ±6.12 B	147.72 ±13.53 B

- Different letters in each column indicate a significant difference at ($P \leq 0.05$).
- H_2O_2 = 0.5% and Ginger = 1000 mg/kg of ration.

The high level of cholesterol in H_2O_2-stressed birds may be due to a decrease in the activity of the thyroid gland (Hypothyroidism), as the decrease of the thyroxine in stressed birds has a negative effect on the excretion of cholesterol with the bile, thus increasing its level in the blood [18].

On the other hand, the significant increase in triglycerides was in parallel with the cholesterol increase due to the positive correlation between both parameters [19].

Table 1 also shows the role of crushed ginger (T_3), which led to a significant decrease ($P \leq 0.05$) in the glucose (278.05 mg/dl) and cholesterol (166.80 mg/dl) concentration compared to other groups, and the triglycerides (122.55 mg/dl) compared to the hydrogen peroxide (220.25 mg/dl) group of quail.

Our results were consistent with the results of Saeid *et al.* [20] who gave the ginger aqueous extract with drinking water in two concentrations 0.4 and 0.6% significantly reduced

glucose level compared to the control group, while the study did not agree with Malekizadeh *et al.* [21] who indicated in a study on laying hens that dietary addition of ginger powder in 1 and 3% did not have a significant effect on glucose concentration compared to the control group.

The ability of ginger to reduce blood glucose levels may be due to its phenolic components which classified as hypoglycemic compounds [22], or perhaps due to presence compounds that stimulate insulin secretion, which increases the entry of glucose into the cells and thus leads to a decrease in its level in the blood. This is agreed with Elshater *et al.* [23] who said that ginger had a significant hypoglycemic effect on blood glucose of alloxan-induced diabetes mellitus compared to the control group.

As for the ability of ginger to reduce the cholesterol and triglyceride levels in the blood, it is in agreement with the findings of Han *et al.* [24], who stated that it may be due to the inhibition of lipid absorption in the intestine, because the high fiber content of ginger, as well as the oleo-resin compounds [25], which works to inhibit the absorption of bile salts in the intestine, which stimulates the liver to convert cholesterol into new bile salts, which results in a decrease its level in the blood [26].

It was also noted from Table 1 that the addition of ginger with hydrogen peroxide (T_4) led to reducing the effect of hydrogen peroxide to elevate the level of glucose (308.88 mg/dl), cholesterol (221.62 mg/dl) and triglycerides (147.72 mg/dl), and the values remained at the control group values (320.00, 208.35 and 163.62 mg/dl respectively). This is due to the antioxidant activity of ginger, which is returned to the phenolic substances in it [5].

From Table 2 it was noticed that the addition of hydrogen peroxide led to a significant increase in the level of both AST (353.73 U/L) and ALT (12.59 U/L) enzymes in the blood compared to the control group (301.87 and 9.69 U/L respectively) at ($P \leq 0.05$). This result was in agreement with Taha [27] when he treated broiler breeder males with hydrogen peroxide, and it also agreed with the results of Al-kattan [28], as it recorded a significant increase in both AST and ALT in the blood of laying hens when given H_2O_2 in drinking water at 0.5% concentration compared to the control group.

The high level of AST and ALT in the blood may be attributed to the oxidative stress induced by hydrogen peroxide, which leads to increased cellular oxidative stress, and produce many ROS which oxidizes the polyunsaturated fatty acids in cellular membranes and damage the channels and pumps in it [29], as a result, the membrane loses its selective permeability, due to the lipid peroxidation of the cell membrane and the leaching of these enzymes to the outside of cells [30]. The validity of this assumption is further enhanced by an increase of MDA (1.79 nmol/ml) level and a decrease in GSH (1.10 µmol/L) level in the blood of quail that were given hydrogen peroxide (T_2) (Table 3).

Table 2. Effect of hydrogen peroxide and crushed ginger on blood AST and ALT of male quails at 56 days aged (Means ±SE).

Parameters Treatments	AST U/L	ALT U/L
T_1 (Control)	301.87 ±9.77 B	9.69 ±0,43 BC
T_2 (H_2O_2)	353.73 ±16.48 A	12.59 ±0.63 A
T_3 (Ginger)	246.88 ±11.85 C	8.43 ±0.39 C
T_4 (Ginger + H_2O_2)	255.77 ±8.84 C	10.92 ±1.02 AB

- Different letters in each column indicate a significant difference at ($P \leq 0.05$).
- H_2O_2 = 0.5% and Ginger = 1000 mg/kg of ration.

As it can be seen from Table 2 that the addition of crushed dry ginger (T_3) led to a significant decrease in the concentration of both ALT (246.88 U/L) and AST (8.43 U/L) enzymes compared to the control group (301.87 and 9.69 U/L respectively). The results of our research are in agreement with Malekizadeh *et al.* [21] who stated that the addition of ginger powder at 1 and 3% to the diet has a significant decreasing effect on AST and ALT in the blood of white Leghorn chicken compared to the control group. It also agreed with Shanoon [6] who found a significant decrease in the level of AST and ALT in the blood of broiler breeders when adding 5 and 10% of the ginger aqueous extract to drinking water compared to the control group.

This may be due to the high level of phenolic compounds in ginger, including Gingerols, Shogaols and Zingerone, which gave ginger its effective role as an antioxidant [31, 32], as well as vitamin A and C, which leads to the inhibition of the lipid peroxidation. Accordingly, the cell membranes were protected from the oxidation processes, and these membranes retained their selective permeability property, and the cells conserved their contents and not filtered out of the cell, including these enzymes, therefore their level in blood serum decreased [33].

The addition of ginger with hydrogen peroxide (T_4) prevented the effect of peroxide stress, and this was evident from the decrease of the enzyme levels of AST (255.77 U/L) and ALT (10.92 U/L) compared to the hydrogen peroxide group (353.73 and 12.59 U/L respectively). This is due to the antioxidant effects of ginger, which that previously mentioned, as well as its lowering effect of the corticosterone level (Table 3).

It is also noticed from Table 3 that the hydrogen peroxide-induced oxidative stress, as it is clear in the significant increase of MDA (1.79 nmol/ml) and corticosterone (15.93 ng/ml) (stress hormone) level, and the significant decrease in the level of glutathione (1.10 µmol/L) in the quail blood of H_2O_2- treated group (T_2) compared to all the study groups.

Table 3. Effect of hydrogen peroxide and crushed ginger on blood Glutathione, Malondialdehyde and Corticosterone of male quails at 56 days aged (Means ±SE).

Parameters Treatments	Glutathione (GSH) µmol /L	Malondialdehyde (MDA) nmol /ml	Corticosterone ng /ml
T_1 (Control)	1.58 ±0.06 C	0.74 ±0.04 B	2.54 ±0.12 C
T_2 (H_2O_2)	1.10 ±0.04 D	1.79 ±0.12 A	15.93 ±0.77 A
T_3 (Ginger)	2.92 ±0.13 A	0.41 ±0.05 C	1.52 ±0.18 C
T_4 (Ginger + H_2O_2)	2.00 ±0.09 B	0.74 ±0.05 B	4.56 ±0.57 B

- Different letters in each column indicate a significant difference at ($P \leq 0.05$).
- H_2O_2 = 0.5% and Ginger = 1000 mg/kg of ration.

Pravda [34] and Ayed *et al.* [35] stated that hydrogen peroxide depletes the glutathione in the blood and tissues and causes a decrease in its level in the body and that its decrease is associated with an increase in the level of malondialdehyde, which is considered one of the main indicators of the occurrence of the lipid peroxidation. This finding was in line with AL-Ma'atheedi and Hassan [36] in their study on adult roosters exposed to oxidative stress, and Taha [27] who reported that the addition of hydrogen peroxide to drinking water at 0.5% of broiler breeder males led to a significant increase in malondialdehyde level, and a significant decrease in the glutathione level in testicular tissue compared to the control group, also was referring to that by Ameen Agha [17] in broilers.

The elevation of corticosterone level in the H_2O_2 group (T_2) (Table 3) in response to stress induced by H_2O_2. This is consistent with Abdul-Majeed [15] who said that the oxidative stress induced by H_2O_2 leads to an increase in the secretion of the corticosterone (Stress hormone) from the adrenal cortex in response to stress and mentioned that the hydrogen peroxide with drinking water led to a significant increase in corticosterone level of quail compared to the control group at ($P \leq 0.05$).

It is also evident from Table 3 that the dietary addition of ginger (T_3) improved and significantly increased serum glutathione level (2.92 µmol/L) compared to the control group (1.58 µmol/L), and with the other study groups at ($P \leq 0.05$). And when ginger was given with hydrogen peroxide (T_4), it was able to prevent the effect of stress caused by hydrogen peroxide and improve the serum antioxidant status, as it raised the level of glutathione significantly (2.00 µmol/L) compared to both groups of hydrogen peroxide and control (1.10 and 1.58 µmol/L respectively).

And in regard to MDA, it was significantly decreased when ginger was added to the feed (T_3) (0.41 nmol/ml) compared to the control group (0.74 nmol/ml) and the other study groups at ($P \leq 0.05$), and it was at the level of its values in the control group when ginger was added with hydrogen peroxide (T_4) (0.74 nmol/ml). Ginger was able to prevent the effect of stress-induced by hydrogen peroxide and returned the MDA values to the level of its values in the control group, and it was even significant with the hydrogen peroxide group at ($P \leq 0.05$) (Table 3).

Our results are agreed with Ogbuewu *et al.* [37] who indicated that ginger acts to protect the cells because it contains gingerols and shogaols that play an essential role in protecting cells from oxidative damage resulting from the free radicals. Also, our results agree with the results of researcher Shanoon [6] who found a decrease in the level of malondialdehyde and an increase in the level of glutathione in the groups of broiler breeder chickens that consumed a diet containing 2.5 g ginger/ kg of feed compared to the control group.

The ability of the ginger plant to raise the level of glutathione and reduce the level of malondialdehyde is consistent with all of the Tohma *et al.* [38], Zidan *et al.* [39] and Zhang *et al.* [40] when they indicated that the ginger is one of the plants that possess an antioxidant capacity due to its high phenolic contents. Also, the ginger's ability in decreasing corticosterone may be related to its vitamin C content which inhibits 11-ß Hydroxylase and 21-Hydroxylase, so it reduces corticosterone production by the adrenal cortex [19].

To confirm the validity of this assumption, when was given the ginger alone (T_3), it reduced or decreased the level of the stress hormone (corticosterone) (1.52 ng/ml) than it was in the control group (2.54 ng/ml), and when it was added with the hydrogen peroxide (T_4) (4.56 ng/ml), there was a significant decrease in its level compared to the hydrogen peroxide group (T_2) (15.93 ng/ml), because it reduced and suppressed the effect of stressful hydrogen peroxide and raised the level of the corticosterone hormone (Table 3).

Conclusion

We conclude, our study revealed that the hydrogen peroxide was heavily impacting on all of the studied parameters of the blood, and the addition of a substance that has an antioxidant capacity as ginger (*Zingiber officinale*) prevented the negative effects of oxidative stress induced by hydrogen peroxide, also that the ginger has an ability or role to improve or enhance the antioxidant status in the body, and returned most of the parameter values and antioxidant status to their values in the control group.

Acknowledgments

The authors thanks specially the University of Mosul and the College of Agriculture and Forestry for their assistance and support to carrying out this research.

Conflict of Interest

The authors declare that there are no conflicts of interest regarding the publication of this manuscript.

References

[1] Pizzino G, Irrera N, Cucinotta M, Pallio G, Mannino F, Arcoraci V, Squadrito F, Altavilla D, Bitto A. Oxidative Stress: Harms and Benefits for Human Health. Oxid. Med. Cell. Longev., 2017, ID 8416763, 13 pages, https://doi.org/10.1155/2017/8416763

[2] Gianazza E, Brioschi M, Martinez Fernandez A, Casalnuovo F, Altomare A, Aldini G, Banfi C. Lipid peroxidation in atherosclerotic cardiovascular diseases. Antioxid. Redox Signal., 2021 Jan 1;34(1):49-98. https://doi.org/10.1089/ars.2019.7955

[3] El-Beltagi HS, Mohamed HI. Reactive oxygen species, lipid peroxidation and antioxidative defense mechanism. Not Bot Horti Agrobot Cluj Napoca. 2013, 41(1):44-57. https://doi.org/10.15835/nbha4118929

[4] Mbaveng AT, Kuete V. *Zingiber officinale*. InMedicinal Spices and Vegetables from Africa 2017 Jan 1 (pp. 627-639). Academic Press. https://doi.org/10.1016/B978-0-12-809286-6.00030-3

[5] Mao QQ, Xu XY, Cao SY, Gan RY, Corke H, Li HB. Bioactive compounds and bioactivities of ginger (*Zingiber officinale* Roscoe). Foods. 2019; 8(6):185. https://doi.org/10.3390/foods8060185

[6] Shanoon AK. *Effect of Ginger Zingiber officinale and Thyme Thymus vulgaris on Reproductive and Reproduction performance of broiler breeder chickens Ross 308* (Doctoral dissertation), College of Agriculture, University of Tikrit, Tikrit: Iraq. 2011.

[7] Al–Kattan M, Al–Annaz R, Al–Sarrag I. Effect of *Zingiber officinale* plant and H_2O_2 on some physiological, histological and biochemical parameters in local male rabbits. Mesopotamia J. of Agric. 2007, 35(1):36-42. http://dx.doi.org/10.33899/magrj.2007.26468

[8] Dale N. National research council (NRC). Nutrient requirements of poultry–ninth revised edition (1994). J Appl Poult Res. 1994, 3(1):101. https://doi.org/10.3382/japr.2014-00980

[9] Gault VA, McClenaghan NH. Tietz textbook of clinical chemistry and molecular diagnostics. Elsevier Saunders, Missouri, USA; 2006.

[10] Buege JA, Aust SD. [30] Microsomal lipid peroxidation. In Methods in Enzymology 1978, 52:302-310. Academic press, London. https://doi.org/10.1016/S0076-6879(78)52032-6

[11] Statistical Analysis Systems (SAS) Institute. Software, SAS User's Guide: Version 9.2 Review Edition. SAS Institute Inc, Cary, North Carolina, USA. 2008.

[12] Duncan DB. Multiple range and multiple *F* tests. Biometrics. 1955 Mar 1;11(1):1-42. https://doi.org/10.2307/3001478

[13] Steel RG and Torrie JH. Principles and procedures of statistics. McGraw- Hill Book. Co., Inc., New York. 1960, Pp 481.

[14] Salah SI. *Effect of using Vitamin C, A and Fenugreek seeds on some physiological and histological parameters of male Arber Acers Breeder* (MSc Thesis) College of Agriculture and Forestry, University of Mosul, Mosul, Iraq. 2008.

[15] Abdul-Majeed AF. *Effect of H_2O_2–Induced Oxidative Stress, Ginger and Vitamin C on the Antioxidant Level, Physiological and Productive Performance of Quail and its Progeny* (Doctoral dissertation, Ph. D Thesis). College of Agriculture and Forestry, University of Mosul, Mosul: Iraq. 2013,37-39. https://orcid.org/0000-0001-7331-9969

[16] Hassan SM, Al-Kennany ER, Al-Hafez HA. Hydrogen peroxide-induced atherosclerosis in chickens: effect of vitamin C. Iraqi J. Vet. Sci.. 2000;13(2):249-70. https://www.cabdirect.org/cabdirect/abstract/20003002291
[17] Ameen Agha, FKhT. *Effects of Coriander, Thyme, Vanadyl Sulfate and Sodium Tungstate and Their Interactions on Some Physiological and Biochemical Aspects in Broiler Chickens.* (Doctoral dissertation, Ph. D Thesis). College of Veterinary Medicine, University of Mosul, Mosul: Iraq. 2002. https://orcid.org/0000-0003-0616-2177
[18] Duntas LH, Brenta G. A renewed focus on the association between thyroid hormones and lipid metabolism. Front. Endocrinol. 2018 Sep 3;9:511. https://doi.org/10.3389/fendo.2018.00511
[19] Abdul-Majeed, AF., AL-Krad, HA, Abdul–Rahman, SY. Effect of Zingiber, Vitamin C and Hydrogen Peroxide on Some Physiological and Productive Parameters in Male Quails. AL-Furat University Journal for Researches and Scientific Studies. 2013, 7(25),218-242. http://journal.alfuratuniv.edu.sy/downloads/files/1549064891_12.pdf
[20] Saeid JM, Mohamed AB, AL-Baddy MA. Effect of aqueous extract of ginger (*Zingiber officinale*) on blood biochemistry parameters of broiler. Int. J. Poult. Sci.. 2010; 9(10):944-7. https://dx.doi.org/10.3923/ijps.2010.944.947
[21] Malekizadeh M, Moeini MM, Ghazi S. The effects of different levels of ginger (*Zingiber officinale* Rosc) and turmeric (*Curcuma longa* Linn) rhizomes powder on some blood metabolites and production performance characteristics of laying hens. J. Agric. Sci. Technol. 2012;14(1):127-134. https://www.sid.ir/en/journal/ViewPaper.aspx?id=283764
[22] Khazaei MR, Makalani F, Ghanbari E, Fayzemahdavi M, Khazaei M. An overview of effective herbal and antioxidant compounds on diabetes. J. Contemp. Med. Sci.. 2018 Sep 26;4(3):126-133. http://www.jocms.org/index.php/jcms/article/view/450/240
[23] Elshater AE, Salman M, Moussa M. Effect of ginger extract consumption on levels of blood glucose, lipid profile and kidney functions in alloxan induced-diabetic rats. Egyptian Academic Journal of Biological Sciences. A, Entomology. 2009 Jun 1;2(1):153-62. https://dx.doi.org/10.21608/eajbsa.2009.15515
[24] Han LK, Gong XJ, Kawano S, Saito M, Kimura Y, Okuda H. Antiobesity actions of *Zingiber officinale* Roscoe. Yakugaku zasshi: J. Pharm. Soc. Jpn. 2005 Feb 1;125(2):213-7. https://pubmed.ncbi.nlm.nih.gov/15684576/
[25] Srinivasan K. Ginger rhizomes (*Zingiber officinale*): A spice with multiple health beneficial potentials. Pharma Nutrition. 2017 Mar 1;5(1):18-28. https://doi.org/10.1016/J.PHANU.2017.01.001
[26] Cohen DE. Balancing cholesterol synthesis and absorption in the gastrointestinal tract. J. Clin. Lipidol. 2008 Apr 1;2(2):S1-3. https://www.ncbi.nlm.nih.gov/pmc/articles/PMC2390860/
[27] Taha, AT. *Effect of Some Antioxidant on Reproductive and Physiological Performance in Broiler Breeder Males.* (Doctoral Dissertation), College of Agriculture and Forestry, University of Mosul, Mosul: Iraq.2008.
[28] Al-kattan, MMD. *Effect of Using Some Antioxidants on Production Performance and Some Physiological Characters in Laying Hens.* (Doctoral Dissertation), College of Agriculture and Forestry, University of Mosul, Mosul: Iraq. 2006.
[29] Walia M, Kwan CY, Grover AK. Effects of free radicals on coronary artery. Medical Principles and Practice. 2003;12(1):1-9. https://doi.org/10.1159/000068159
[30] Catalá A, Díaz M. Impact of lipid peroxidation on the physiology and pathophysiology of cell membranes. Front. Physiol. 2016 Sep 22;7:423. https://doi.org/10.3389/fphys.2016.00423
[31] Sekiwa Y, Kubota K, Kobayashi A. Isolation of novel glucosides related to gingerdiol from ginger and their antioxidative activities. J. Agric. Food Chem. 2000 Feb 21;48(2):373-7. http://dx.doi.org/10.1021/jf990674x
[32] Zancan KC, Marques MO, Petenate AJ, Meireles MA. Extraction of ginger (*Zingiber officinale* Roscoe) oleoresin with CO2 and co-solvents: a study of the antioxidant action of the extracts. J. Supercrit. Fluids. 2002 Sep 1;24(1):57-76. https://doi.org/10.1016/S0896-8446(02)00013-X

[33] Al-Katib SM, Al-Khashab EM, Kalo MS, Hamdoon AA. The Antioxidant Effects of Flavonoids and non Flavonoid Part Extracted from Ginger (*Zingiber officinale*) Roots. Rafidain journal of science. 2009 Sep 1;20(6):18-31. http://dx.doi.org/10.33899/rjs.2009.39940
[34] Pravda J. Hydrogen peroxide and disease: towards a unified system of pathogenesis and therapeutics. Molecular Medicine. 2020 Dec;26(1):1-0. https://doi.org/10.1186/s10020-020-00165-3
[35] Ayed HS, Khalaf AS, Mohammed TM. Effect of Aqueous Extract of Truffle on Some Antioxidants in Rats Exposed to Oxidative Stress induced by Hydrogen peroxide. In IOP Conference Series: Earth and Environmental Science, Volume 735, 2nd Virtual International Scientific Agricultural Conference 21-22 January 2021, Iraq. Pp 1-6. https://iopscience.iop.org/article/10.1088/1755-1315/735/1/012019/pdf
[36] AL-Ma'atheedi, MS and Hassan, AA. Effect of vitamin c and selenium on some physiological and reproductive characters in adult roosters exposed to oxidative stress induced by hydrogen peroxide. Iraqi J Vet Med. 2012 Mar 4;36(0A):32-42. https://jcovm.uobaghdad.edu.iq/index.php/Iraqijvm/article/view/352
[37] Ogbuewu IP, Mbajiorgu CA, Okoli IC. Antioxidant activity of ginger and its effect on blood chemistry and production physiology of poultry. Comp. Clin. Path. 2019; 28(3):655-60. https://doi.org/10.1007/s00580-017-2536-x
[38] Tohma H, Gülçin İ, Bursal E, Gören AC, Alwasel SH, Köksal E. Antioxidant activity and phenolic compounds of ginger (*Zingiber officinale* Rosc.) determined by HPLC-MS/MS. J. Food Meas. Charact. 2017 Jun;11(2):556-66. https://doi.org/10.1007/s11694-016-9423-z
[39] Zidan DE, Kahilo KA, El-Far A, Sadek KM. Ginger (*Zingiber officinale*) and thymol dietary supplementation improve the growth performance, immunity and antioxidant status in broilers. Glob. Vet. 2016;16(6):530-8. https://www.idosi.org/gv/gv16(6)16/3.pdf
[40] Zhang GF, Yang ZB, Wang Y, Yang WR, Jiang SZ, Gai GS. Effects of ginger root (*Zingiber officinale*) processed to different particle sizes on growth performance, antioxidant status, and serum metabolites of broiler chickens. Poult. Sci. 2009 Oct 1;88(10):2159-66. https://doi.org/10.3382/ps.2009-00165

Screening of extracellular polymeric substance producing bacteria isolated from environmental sources and testing their ability to seal fractures zones of oil reservoir rocks

Asaad Faraj Hamzah[1], Wijdan Hussein Al-Tamimi [2]
{asaadfaraj@yahoo.com [1] , wijdanhussien@gmail.com [2]}

Technical institute of Basrah , Southern Technical University, Basrah, Iraq [1].
Departments of Biology, Science Collage, University of Basrah, Basrah, Iraq [2].

Abstract. In this study, 21 environmental bacterial isolates isolated from different environmental sources in Basra Governorate identified phenotypically and genetically based on 16 rRNA gene sequence analysis were screened to reveal their ability to produce biopolymer based on the viscosity scale formed in the cultural media and use of Sudan Black stain. Six isolates showed their ability to produce biopolymer, and the two isolates of *Bacillus licheniformis* strain CC91, Bacillus thuringiensis strain LU3 recorded the best results. The isolate of the *Bacillus licheniformis* strain CC91 was tested in the process of sealing fractures and openings with high permeability for samples of oil reservoir rocks.

Keywords: biopolymer, byproducts, MEOR, petroleum microbiology.

Introduction

Biopolymers are polymers produced derived from natural renewable resources synthesized by either microorganisms under different environmental conditions or chemically synthesized from a biological material [1][2]. Biopolymers they are composed by monomeric units covalently linked to form larger structures of Biopolymers [3].Often the production of polysaccharides biopolymer by bacteria for the purpose of protecting from desiccation conditions or the risk of predation by other microbes as well as to assist in adhesion to surfaces [4][5]. Ates ,2015 [6] mentioned that in 1861 Pasteur was the first noticed the production of dextran polymer in wine by bacteria, the first person to identify this bacterium Leuconostoc mesenteriodes was Van Tieghem in the year 1878. Bio-polymers have now gained much attention due to their importance in industrial sectors all over the world [7][8]. Many bacteria can produce different types of biopolymers such as Bacillus sp. produce Levan [9], Xanthomonas sp. produce Xanthan gum [10], Sclerotium sp. Produce Scleroglucan ([11] and many others [4]. The proposed processes of biopolymers in microbial enhanced oil recovery (MEOR) are application in indirectly reducing water mobility towards undesirable zones due to the ability of some microorganism to produce viscous biopolymers (Nwidee *et al*., 2016 [12] ; Song *et al*.,2020[13]). Because these zones take the majority of the injected aqueous flow, it is expected that they will be successfully stopped, forcing water floods into the less permeable regions [4] [14] [15]. The current study aimed at screening a number of

IMDC-IST 2021, September 07-09, Sakarya, Turkey
Copyright © 2022 EAI
DOI 10.4108/eai.7-9-2021.2315380

bacterial isolates for their ability of biopolymer production and selecting the most efficient one in production to test the ability of the product to close the high permeability openings of the oil reservoir rocks.

Material and methods

Screening of biopolymer production

In this study, 21 diagnosed bacterial isolates were used [16] which were isolated from various oil sources. for screening of biopolymer production activity 2 ml of overnight broth culture of each isolates were add to 250 ml Erlenmeyer flask containing 100 ml of sterilized biopolymer producing media modification of [17] including (per litter distilled water) 40 g sucrose as a carbon source, 0.5 g $NaNO_3$, 1.0 g yeast extract, 0.5 g KH_2PO_4, 0.25 g $MgSO_4 \cdot 7H_2O$, pH 7.0. 1 ml stock solution was composed of (g/L): $FeCl_3$.$6H_2O$ 0.08, $CuSO_4$ $5H_2O$ 0.075, H_3BO_3 0.15 solid media were prepared by the addition of 15 g·L-1 agar. Wet and viscous colonies were selected and identified as the bacteria that produce biopolymers.

The Erlenmeyer flask was infected with 2% 12 hour old inoculum and incubated for 72 hours at 30 °C on a shaker at 180 rpm. The culture was centrifuged for 30 minutes at 12,000 rpm, and the exopolysaccharide-containing cell-free supernatant was used to assess viscosity.

.

Viscosity measurement

Biopolymers production was detected by measuring the viscosity of supernatant solution using a glass capillary viscometer at 25°C in a refrigerated bath and circulator. The sample broth was first cooled in a refrigerated bath for 2 minutes before viscosity was measured [18].

Sudan black stain

The biopolymer production by the microbes can be confirmed by staining with Sudan black stain in two methods:-

- **Slide Method**

After heat fixing the smear, the slide was submerged in 5 percent Sudan Black (w/v in 70% ethanol) staining for 5 minutes and allowed to dry in air, the excess stain was de-stained using xylene several times and blot dried with absorbent paper, safranin was added for 30 seconds and washed with tap water and dried. Under an oil immersion microscope, the stained cells were examined. The biopolymer granules appeared as blue black droplets and cytoplasm part of microorganisms appeared as pink color [19]**.**

- **Plate Method**

In this method grown colonies on agar plates were flooded with 3% of Sudan Black (w/v in 70% ethanol) solution for 20 min. Later, the ethanol solution was added as a dye remover solution of Sudan black stain .Finally the solution was drained off and observed for screening of biopolymer producers as black mucous colonies [20].

Extraction of Crude biopolymer:

Centrifugation of broth culture yielded cell-free supernatant, which was then treated with half volume of distilled water before being placed in a shaking incubator at 30 oC for one hour. To precipitate the extracellular protein fractions, 7% trichloroacetic acid (TCA) was added to the cell-free supernatant. The protein fractions were then collected by centrifugation at 9,000 rpm for 30 minutes at 4°C. To the clear supernatant, an equal volume of 100%

ethanol was added. Precipitation was gathered around the glass rod. Four to five times the dissolving and precipitation process was repeated until uniform white precipitates were obtained. Vacuum desiccators were used to dry the sample. The crude biopolymer was dialyzed and lyophilized against distilled water [21].

Characterization of polymer using Fourier Transform Infra-Red (FTIR)

To determine the basic functional groups of the two partial purified polymer, Fourier Transform Infra-Red (FT-IR) spectroscopy analysis in the Chemistry department /College of Sciences/ University of Basra was used. 1 mg of dried biopolymer was milled with 100 mg of KBr to form a very fine powder to be analyzed by FT-IR spectra at the wavelength of 400–4000 cm−1 [22].

Production of extracellular polymeric substance to seal fracture zones in tested cores

Three oily saturated cores having high permeability zone and deep cracks were selected in this experiment, the core plugs were dried in a hot air oven at 65°C for 24 h and mass of each dray core was measured using a sensitive balance then saturated with crude oil using vacuum pump .each core was placed separately to 500 ml Erlenmeyer flask contain 250 mL of sterile polymer production medium which mentioned previously. Each flask was inoculated with 2% of the bacterial suspension of broth culture of ***Bacillus licheniformis*** **strain CC91** and incubated at 30 ° C for 7 days. One of cores treated as control without bacteria.

Results and discussion

Screening of biopolymer producing bacteria

Twenty-one of bacterial isolates were tested for the biopolymer production. Ten isolates were observed in sucrose containing media. Many researchers showed using sucrose as carbon source in biopolymer production media [23] [24] [25].Each colony was grown clearly on the nutrient and give appositive result in screening test .the best result showed with two gram positive strains ***Bacillus licheniformis*** **strain CC91** and ***Bacillus thuringiensis*** **strain LU3**. Biopolymer was reported to be created by a huge number of gramme positive bacteria in prior studies. [26],[27],[28].

3.7.2.1 Viscosity measurement

After an incubation period of 3-5 days, a viscosity was observed in the medium containing the polymer-forming bacteria that could be distinguished during shaking of the bottle, as well as the presence in **Figure** 1. Supernatant viscosity test for all isolates indicated that there are 6 isolates with the highest values ranged between (3.7643-2.4543 c.st) **Table 1** .The two highest values recorded (3.7643 c.st) and (3.6942 c.st) for ***Bacillus licheniformis*** **strain CC91** , ***Bacillus thuringiensis*** **strain LU3** respectively, as shown in **Figure 2**. The results of the viscosity measurement in our study were identical to the results reported by Illias *et al*. [29] in the viscosity measurements of several biopolymers production strains of the genus ***Bacillus*** spp. used in their study. According to Lee & Tripathi, (2005) [30], the viscosity measuring approach is very relevant in many chemical, biological, and medicinal applications where sample numbers are limited..

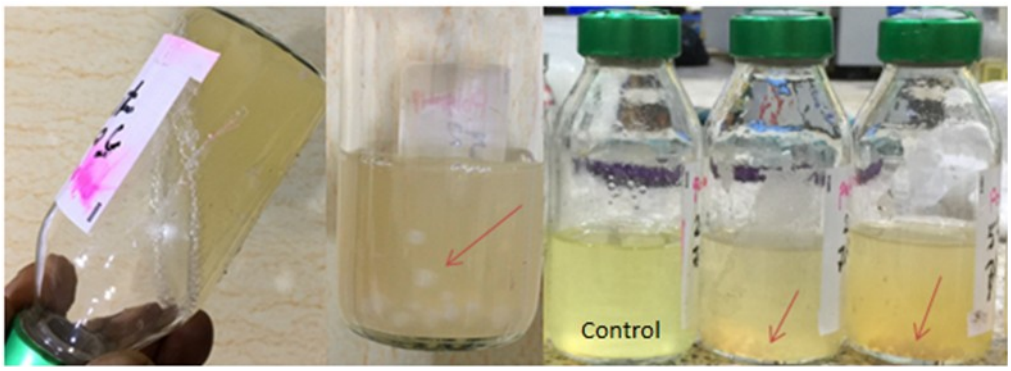

Fig. 1. Viscosity of biopolymer producing

Table 1: Viscosity measurements of isolates

Strain		Viscosity centistokes (c.st)	Sudan black stain
1	Control	0.8334	-
2	*Bacillus cereus strain ASWISA1*	1.5432	-
3	*Lysinibacillus boronitolerans strain SWTPB36*	0.9987	-
4	*Bacillus subtilis strain HDZK-BYSB7*	1.0876	-
5	*Bacillus thuringiensis strain ASWISA2*	2.2655	+
6	*Enterobacter aerogenes strain B19*	1.6543	-
7	*Bacillus sonorensis strain ASWISA3*	1.8766	-
8	*Bacillus licheniformis strain CC91*	3.7643	+
9	*Bacillus cereus strain ASWISA4*	1.2333	-
10	*Bacillus subtilis ASWISA5*	1.4432	-
11	*Bacillus subtilis ASWISA7*	1.4236	-
12	*Pseudomonas stutzeri strain ASWISA6*	1.6675	+
13	*Bacillus cereus strain A*	1.8776	-
14	*Bacillus cereus ASWISA8*	0.9877	-
15	*Bacillus cereus Strain US04*	0.8776	-
16	*Bacillus thuringiensis strain LU3*	3.6942	-

17	*Bacillus paramycoides strain ASWISA9*	2.4543	+
18	*Bacillus paramycoides strain ASWISA10*	2.5655	+
19	*Brevibacillus brevis strain ASWISA11*	1.0987	+
20	*Enterobacter cloacae strain ASWISA12*	0.8766	-
21	*Enterobacter cloacae strain FC1375*	1.0432	-
22	*Bacillus cereus strain LDPE1*	0.9232	-

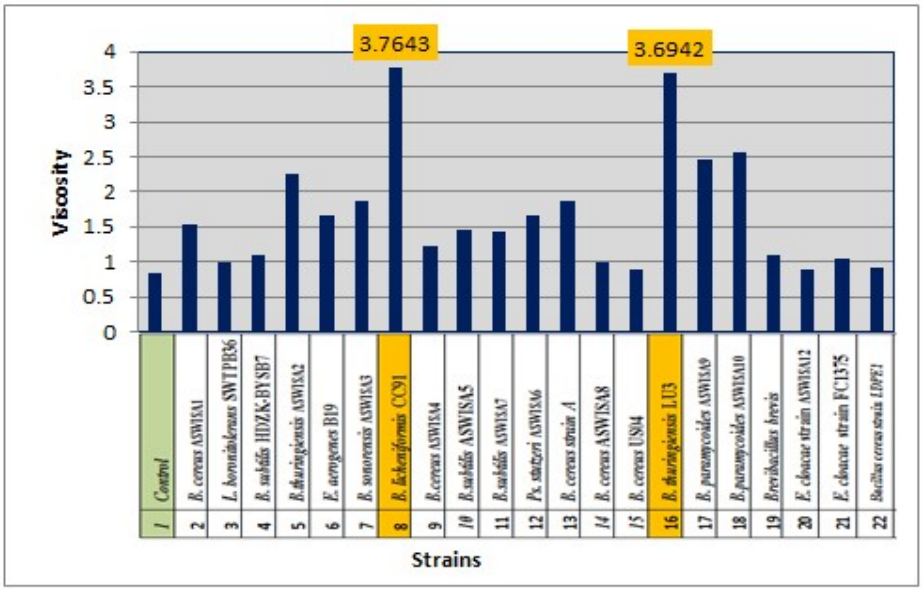

Fig. 2. Viscosity values for supernatant of isolates

Sudan black stain

Use of Sudan black stain in slides and plate method gave positive results similar to all isolates that gave positive results of viscosity measurements testing. **Figure 3** shows the black color of sticky colonies growing on the plates for both isolates for ***Bacillus licheniformis* strain CC91**, ***Bacillus thuringiensis* strain LU3**. As well as spores stained in black color while the cells stained in red color in slide stain method **Figure 4.** Yasin & Al-Mayaly,2020 [31] had the same finding, showing granules loaded with black staining, as biopolymer granules can be seen as dark spots under the light microscope.

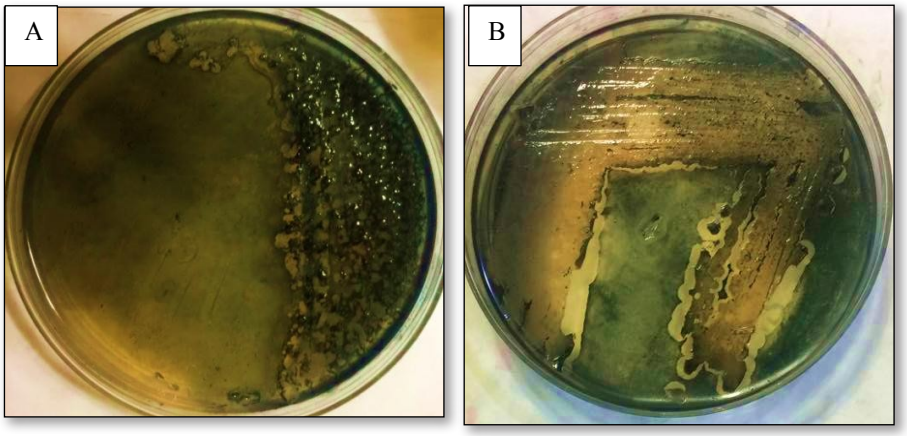

Fig. 3. Sudan black stain plate methods (A)
Bacillus licheniformis strain CC91(B) of *Bacillus thuringiensis* strain LU3

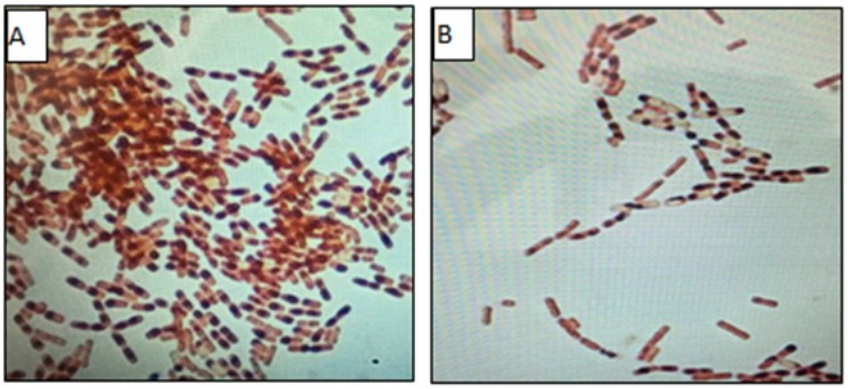

Fig. 4. Sudan black stain slide methods (A) *Bacillus licheniformis* strain CC91(B) *Bacillus thuringiensis* strain LU3

Extraction of Crude biopolymer

The results of the extraction of biopolymer using solvents are shown to separate the top layer containing the polymer for each of the three isolates: ***Bacillus licheniformis*** **strain CC91(8) ,** ***Bacillus thuringiensis*** **strain LU3**as shown in the **Figure 5.**

Fig.5. -Extracted of biopolymer with solvents

Characterization of polymer using Fourier Transform Infra-Red (FTIR)

Figure 6 illustrates FTIR studies of extracted biopolymer produce by ***Bacillus licheniformis*** **strain CC91** Which was chosen as the best isolate for the production of biopolymers. The OH (Hydroxyl) group is represented by band 3471, while the C=O (Carbonyl) and COO (ester) groups are represented by band 1743. The band at 1458 represents CH, which has asymmetrical stretching and bending vibrations in the CH3 group, while the band at 1377 represents the COH bond. C-O bonding was seen in bands stretching from 1095 to 1283. The investigated results confirmed that the recovered biopolymer component was Polyhydroxybutyrates, as reported by Arun et al. (2009) [32]. (PHB). Alarfaj et al. (2015) [28] also came to the same conclusion.

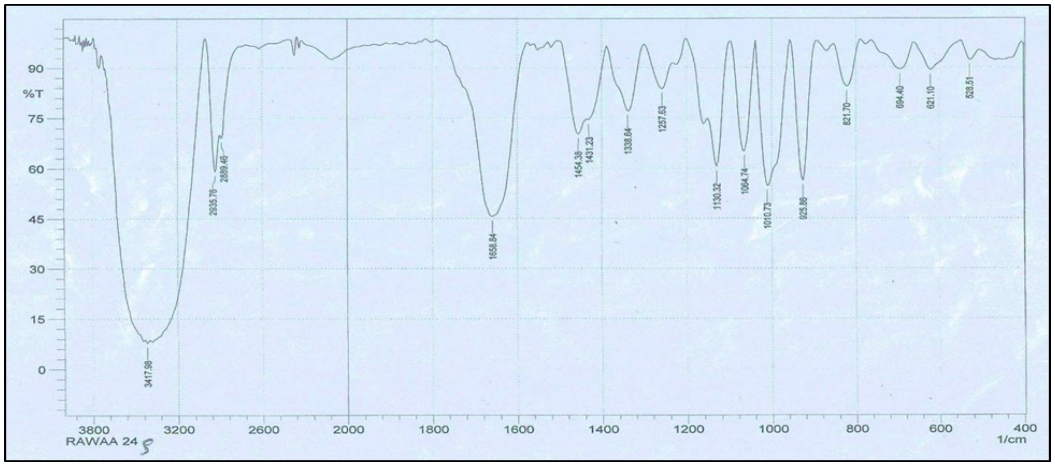

Fig.6. FTIR of extracted biopolymer produce *by Bacillus licheniformis* strain CC91

Production of extracellular polymeric substance to seal fracture zones in tested cores

The results of the inoculated of ***Bacillus licheniformis*** **strain CC91** bacteria in biopolymer production culture medium with the presence of the cores selected from the oil fields that contain cracks and fractures showed a sticky layer of extracellular polymer and the biomass of bacteria growing in all the cracks and fractures to form a sticky layer to close these openings as in the **Figure 7** that shows the nature of the cores before (A) and after culturing (C) comparing with the core treated without bacteria (B) . Several studies have indicated the use of various bacterial strains in the process of reducing high permeability areas of oil reservoir that follow the mechanism of water injection in oil recovery processes to increase oil recovery. Bacillus licheniformis strain BNP29 was able to produce considerable volumes of biomass, polymer with selective plugging, and boosted oil recovery from 9.3 to 22.1 percent, according to Yakimov et al. (1997)[33]. Suthar et al. (2009) [34] utilised Bacillus licheniformis TT33 in the sand pack to exhibit bacterial growth and biofilm formation, resulting in a 27.7±3.5 oil recovery.

Fig. 7. A- The cores before culturing B- without bacteria C- The cores after culturing

Conclusion

In the current study, biopolymer production was investigated for 22 environmental bacterial isolates, six of which showed the possibility of biopolymer production related to the viscosity measurement of the medium, as well as the use of Sudan black stain for the growth bacterial colonies or fixed cells. The isolate ***Bacillus licheniformis*** **strain CC91** was chosen from one of twenty environmental isolates genetically diagnosed as the best isolates that have the ability to produce biopolymers.

FTIR studies of extracted biopolymer produce by ***Bacillus licheniformis strain CC91*** confirming that the extracted biopolymer compound was Polyhydroxybutyrate (PHB).

The isolate ***Bacillus licheniformis*** **strain CC91** showed ability to produced extracellular polymeric substance to seal fracture zones in tested core samples taken from an oil reservoir that may subsidize to the processes of microbial oil recovery (MEOR).

References

[1] Smith, A. M., Moxon, S., & Morris, G. A. Biopolymers as wound healing materials. (2016). In Wound healing biomaterials (pp. 261-287). *Woodhead Publishing*.

[2] Xia, S., Zhang, L., Davletshin, A., Li, Z., You, J., & Tan, S. Application of Polysaccharide Biopolymer in Petroleum Recovery. (2020). *Polymers*, 12(9), 1860.

[3] Hovland, B. (2015). Assessment of the biodegradability of xanthan in offshore injection water (*Master's thesis, The University of Bergen*).

[4] Sen, R. Biotechnology in petroleum recovery: the microbial EOR. (2008). *Progress in energy and combustion Science*, 34(6), 714-724.

[5] Costa, O. Y., Raaijmakers, J. M., & Kuramae, E. E. Microbial extracellular polymeric substances: ecological function and impact on soil aggregation. (2018). *Frontiers in microbiology*, 9, 1636.

[6] Ates, O.. Systems biology of microbial exopolysaccharides production. (2015). *Frontiers in bioengineering and biotechnology*, 3, 200.

[7] De Vuyst, L., De Vin, F., Vaningelgem, F., & Degeest, B. Recent developments in the biosynthesis and applications of heteropolysaccharides from lactic acid bacteria. (2001). *International Dairy Journal*, 11(9), 687-707.

[8] Shaaban, M. T., & Mowafy, E. I. (2012). Studies on incubation periods, scale up and biodisintegration of poly-β-hydroxybutyrate (PHB) synthesis by Stenotrophomonas (pseudomonas) maltophilia and Pseudomonas putida. Egypt. *J. Exp. Biol*.(Bot.), 8, 133-140.

[9] Goodman, S. H. Investigation into the Potential Application of Microbial Enhanced Oil Recovery on Unconventional Oil: (2018). *A Field Specific Approach (Doctoral dissertation, University of Liverpool*).

[10] De Vuyst, L., & Vermeire, A. Use of industrial medium components for xanthan production by Xanthomonas campestris NRRL-B-1459. (1994). *Applied microbiology and biotechnology*, 42(2), 187-191.

[11] Sandford, P. A. Exocellular, microbial polysaccharides. (1979). *Advances in carbohydrate chemistry and biochemistry*, 36, 265-313.

[12] Nwidee, L. N., Theophilus, S., Barifcani, A., Sarmadivaleh, M., & Iglauer, S. EOR processes, opportunities and technological advancements. (2016). *Chemical Enhanced Oil Recovery (cEOR)*-a Practical Overview, 2-52.

[13] Song, C., Chen, Y., & Wang, J. Plugging high-permeability zones of oil reservoirs by microbially mediated calcium carbonate Precipitation. (2020). *ACS omega*, 5(24), 14376-14383

[14] Guo, S., Nighot, M., Al-Sadi, R., Alhmoud, T., Nighot, P., & Ma, T. Y. Lipopolysaccharide regulation of intestinal tight junction permeability is mediated by TLR4 signal transduction pathway activation of FAK and MyD88. (2015). *The Journal of Immunology*, *195*(10), 4999-5010.

[15] Sabooniha, E., Rokhforouz, M. R., & Ayatollahi, S. Pore-scale investigation of selective plugging mechanism in immiscible two-phase flow using phase-field method. (2019). *Oil & Gas Science and Technology*–Revue d'IFP Energies nouvelles, 74, 78.

[16] Hamzah, A. F., Abd-Alsahib, W. H., & Mahdi, S. S. Isolation and identification new bacterial strains isolated from different sources of Al-Rafidiyah oil field in Iraq. (2020). *Catrina: The International Journal of Environmental Sciences*, 21(1), 15-22.

[17] She, Y. H., Zhang, F., Xiang, T. S., Liu, B. B., Zhao, L. P., Zhou, L. G., & Shu, F. C. Microbial diversity in petroleum reservoirs analyzed by PCR-DGGE. (2005). *Acta Ecologica Sinica*, 25(2), 237-242.

[18] Illias, R. M., Ooi, S. W., Idris, A. K., & Rahman, W. A. W. A.. Isolation and characterization of halotolerant aerobic bacteria from oil reservoir. (2001). *Jurnal Teknologi*, 1â-10.

[19] Wei, Y. H., Chen, W. C., Huang, C. K., Wu, H. S., Sun, Y. M., Lo, C. W., & Janarthanan, O. M. (2011). Screening and evaluation of polyhydroxybutyrate-producing strains from indigenous isolate Cupriavidus taiwanensis strains. *International journal of molecular sciences*, *12*(1), 252-265.**.**

[20] Mehta, V., Patel, E., Vaghela, K., Marjadi, D., & Dharaiya, N. Production of biopolymer from dairy waste: an approach to alternate synthetic plastic. (2017). *Int. J. Res. Biosci*., 6(4), 1-8.

[21] Jamil, N., & Ahmed, N. Production of biopolymers by Pseudomonas aeruginosa isolated from marine source. (2008). *Brazilian archives of Biology and Technology*, 51(3), 457-464.

[22] Aparna, A., Srinikethan, G., & Smitha, H. Production and characterization of biosurfactant produced by a novel Pseudomonas sp. 2B. (2012) . *Colloids and Surfaces* B: Biointerfaces, 95, 23-29.

[23] Jiang, G., Hill, D. J., Kowalczuk, M., Johnston, B., Adamus, G., Irorere, V., & Radecka, I. Carbon sources for polyhydroxyalkanoates and an integrated biorefinery. (2016). *International journal of molecular sciences*, 17(7), 1157.

[24] Ahmad, S., Amir, A., Zafaryab, M., Osama, K., Faridi, S. A., Siddiqui, M. H., ... & Khan, M. A.. Production and characterization of polyhydroxybutryrate biopolymer from Azohydromonas australica using sucrose as a sole carbon source.(2017*). J. Microb. Biochem. Technol*., 9, 82-86.

[25] Jeong, M. S., Noh, D. H., Hong, E., Lee, K. S., & Kwon, T. H. Systematic modeling approach to selective plugging using in situ bacterial biopolymer production and its potential for microbial-enhanced oil recovery. (2019). *Geomicrobiology Journal*, 36(5), 468-481.

[26] Mergaert, J., & Swings, J. Biodiversity of microorganisms that degrade bacterial and synthetic polyesters.(1996). *Journal of industrial microbiology*, 17(5), 463-469.

[27] Verlinden, R. A., Hill, D. J., Kenward, M. A., Williams, C. D., & Radecka, I. Bacterial synthesis of biodegradable polyhydroxyalkanoates. (2007). *Journal of applied microbiology*, 102(6), 1437-1449.

[28] Alarfaj, A. A., Arshad, M., Sholkamy, E. N., & Munusamy, M. A.. Extraction and Characterization of Polyhydroxybutyrates (PHB) from Bacillus thuringiensisKSADL127 Isolated from Mangrove Environments of Saudi Arabia.(2015). *Brazilian Archives of Biology and Technology*, 58(5), 781-788.

[29] Illias, R. M., Ooi, S. W., Idris, A. K., & Rahman, W. A. W. A. Isolation and characterization of halotolerant aerobic bacteria from oil reservoir.(2001). *Jurnal Teknologi*, 1â-10.

[30] Lee, J., & Tripathi, A. Intrinsic viscosity of polymers and biopolymers measured by microchip. (2005). *Analytical chemistry*, 77(22), 7137-7147.

[31] Yasin, A. R., & Al-Mayaly, I. K. Isolation and identification of polyhydroxyalkanoates producing bacteria from biopolymers waste in soil. (2020). In IOP Conference Series: *Materials Science and Engineering* (Vol. 928, No. 6, p. 062014). IOP Publishing.

[32] Arun, A., Arthi, R., Shanmugabalaji, V., & Eyini, M.. Microbial production of poly-β-hydroxybutyrate by marine microbes isolated from various marine environments. (2009). *Bioresource technology*, 100(7), 2320-2323.

[33] Yakimov, M. M., Amro, M. M., Bock, M., Boseker, K., Fredrickson, H. L., Kessel, D. G., & Timmis, K. N. The potential of Bacillus licheniformis strains for in situ enhanced oil recovery. (1997). *Journal of Petroleum Science and Engineering*, 18(1-2), 147-160.

[34] Suthar, H., Hingurao, K., Desai, A., & Nerurkar, A. Selective plugging strategy based microbial enhanced oil recovery using Bacillus licheniformis TT33. (2009). Journal of microbiology and biotechnology, 19(10), 1230-1237.

Study the Extent of The Relationship Among Hormonal Disturbance, Vitamin D Deficiency and Age in Women with Polycystic Ovary Thiqar City, Southern Iraq

Shalan H. Al-Saedy[1], Ali E. Al-Snafi[2*], Mahdi M. Thuwaini[3]
{aboahmad61@yahoo.com[1], dr.aliasm@utq.edu.iq[2]}

College of Medical and Healthy Techniques, Southern Technical University- Basrah[1,3]
College of Medicine, University of Thi-Qar- Iraq[2]

Abstract. The goal of this study was to see if there was a link between LH, FSH, testosterone, oestradiol, progesterone, and metabolic markers, including AMH and vitamin D, in a woman.. PCOS patients had significant increases in serum levels of LH (P <0.01), FSH (P 0.05), LH/FSH ratio (P <0.05), testosterone (P <0.01), progesterone (P <0.05), antimalaria (P <0.001), glucose (P <0.01), total cholesterol (P 0.01), triglycerides (P <0.001), LDL (P <0.01), VLDL (P <0.05), and Vitamin D (P <0.01). AMH appeared to be favourably connected with higher levels of LH, FSH, LH/FSH ratio, testosterone, progesterone, hyperglycemia, total cholesterol, triglycerides, LDL, and VLDL, and un-correlated with oestradiol and HDL. We can conclude that AMH can potentially be applicate as a diagnostic marker for PCOS, the results also showed vitamin D deficiency is related to pathophysiology of PCOS. Vitamin D serum levels showed an inverse correlation with hyperglycaemia, hyperlipidaemia, and hormonal disturbances in PCOS.

Keywords: Hormonal disorders, metabolic disorders, PCOS, Vitamin D, AMH

1 Introduction

PCOS is a complicated endocrine condition that affects women of reproductive age and is thought to be the leading cause of infertility due to anovulation. [1-2]. It has been described as a syndrome characterised by oligomenorrhea and polycystic ovaries, as well as hirsutism, acne, and obesity [3]. Excess secretion of androgen associated with changes in ovarian morphology represented the main pathological factor in PCOS. Hyperlipidaemia, insulin resistance, and psychosocial dysfunction are part of the symptoms and signs of PCOS [4]. PCOS is diagnosed by the presence of oligo amenorrhoea, polycystic ovaries morphology, and hyperandrogenaemia [5].

Anti-Mullerian hormone (AMH), a glycoprotein secreted by the granulosa cells of ovarian early developing follicles, has also been used in the diagnosis of PCOS [6]. PCOS is defined by an overabundance of tiny antral follicles in the ovaries and high levels of AMH in the blood [7]. Vitamin D insufficiency is frequent among women with PCOS, according to numerous research [8]. Low vitamin D levels were linked to menstrual abnormalities, ovulation issues, and

IMDC-IST 2021, September 07-09, Sakarya, Turkey
Copyright © 2022 EAI
DOI 10.4108/eai.7-9-2021.2315371

infertility [9-10]. Vitamin D insufficiency has also been linked to increased insulin resistance and and other factors [10-11]. Vitamin D receptors were found in a variety of human tissues, including the ovary and endometrial, indicating that vitamin D plays an active function in female reproductive organs [12-13]. The researchers wanted to see if there was a link of serum vitamin D levels, hormonal irregularities, and age in individuals with PCOS.

2 Materials and Methods

Fasting of 60 blood samples were composed from married infertile women (20-40 years) with PCO attending Al-Shatra hospital, Bint AL-Hoda, and Al-Hussein teaching hospital in Thi-Qar governorate- Iraq, who diagnosed by gynaecologists, through the period from 1 September 2020 until the end of November 2020. Patients with androgen-secreting tumours, hyperprolactinemia, The study excluded women with Cushing syndrome, congenital adrenal hyperplasia, contraceptives, hypoglycemic drugs, lipid-lowering therapy, or hormonal prescriptions. To serve as a control, fasting blood samples were taken from 30 healthy non-pregnant women of similar ages. The study was permitted by Thi-Qar governorate's health directorate and the South technical university's ethical board. All participants gave their informed consent. Glucose and lipid profile were determined by using Cobas C311 photometric assays and ion-selective electrode measurements (Kits and instrument Roche- Germany), while, LH, FSH, oestradiol, progesterone, testosterone, AMH, and vitamin D were determined by using Cobas 411 immunoassay analysis (Kits and instrument Roche- Germany) [14-15]. All data is presented as a mean ±SE. Student t-tests were used to analyse differences in mean values for specific hormone measures.

3 Results

In the group aged 20-25 years, PCO patients showed significantly elevated serum levels. While the serum level of oestradiol, HDL cholesterol, and vitamin D were significantly declined. Table 1 shows vitamin D levels were positively connected with oestradiol and HDL cholesterol while being negatively correlated with LH, FSH, LH/FSH ratio, total testosterone, progesterone, AMH, hyperglycemia, total cholesterol, triglycerides, and VLDL cholesterol.

Table 1: Data in PCOS patients aged 20-25 years in comparison with aged-matched control.

Parameter studied		Control (15)	PCOS patients (37)	Significancy
LH (IU/L)		4.99±o.62	15.86±0.96	P< 0.001
FSH (IU/L)		3.42±0.32	4.68±0.45	P< 0.05
LH/FSH		1.45±0.08	3.38±0.12	P< 0.05
Total testosterone (ng/ml)		0.46±0.08	0.58±0.06	P< 0.05
Oestradiol (pmol/l)		116.64±8.62	106.33±9.32	P< 0.05
Progesterone (nmol/ml)		0.67±0.06	1.44±0.09	P< 0.05
AMH(ng/ml)		2.40±0.12	10.00±0.23	P< 0.001
Glucose (mg/dl)		94.60±3.23	109.02±4.32	P< 0.05
Lipid profile	Total cholesterol (mg/dl)	170.00±6.16	176.00±7.22	P< 0. 05
	Triglycerides (mg/dl)	150.66±5.56	175.81±6.32	P< 0.01
	LDL (mg/dl)	98.81±3.51	97.17±4.12	NS
	VLDL (mg/dl)	30.76±1.45	35.18±1.94	P< 0.05
	HDL (mg/dl)	48.93±1.66	45.91±1.57	P< 0.05
Vitamin D (ng/ml)		16.95±0.96	14.26±0.84	P< 0.05

In the group aged 26-30 years, serum biochemical analysis of PCO patients revealed significant elevation of serum levels were illustrated. While the serum level were significantly declined in comparison with control. As indicated in Table 2, vitamin D levels were positively connected with oestradiol testosterone and HDL cholesterol, but negatively correlated with LH, FSH, LH/FSH, total testosterone, AMH, hyperglycemia and etc.

Table 2: Similar to Table 1 but for patients aged 26-30 years.

Parameter studied		Control (6)	PCOS patients (11)	Significancy
LH (IU/L)		5.67±	9.58±	P< 0.01
FSH (IU/L)		3.79±	5.37	P< 0.05
LH/FSH		1.49±	1.78±	P< 0.05
Total testosterone (ng/ml)		0.42±	0.48±	P< 0.05
Oestradiol (pmol/l)		107.90±	74.33±	P< 0.05
Progesterone (nmol/ml)		0.84±	0.76±	NS
AMH(ng/ml)		5.35±	8.96±	P< 0.01
Glucose (mg/dl)		97.80±	101.00±	P< 0.05
Lipid profile	**Total cholesterol (mg/dl)**	190.00±	196.00±	P< 0. 05
	Triglycerides (mg/dl)	184.00±	211.50±	P< 0.01
	LDL (mg/dl)	91.00±	99.70±	P< 0.05
	VLDL (mg/dl)	41.20±	45.60±	P< 0.05
	HDL (mg/dl)	53.80±	40.72±	P< 0.01
Vitamin D (ng/ml)		21.96±	17.28±	P< 0.05

In PCO non-control aged 31-35 years, serum levels of LH were considerably higher. Serum levels of oestradiol were significantly lower in the experimental group than in the control group. Vitamin D levels were positively related to oestradiol and HDL cholesterol, but negatively related to LH, FSH, LH/FSH, as indicated in Table 3.

Table 3: Similar to Table 1 but for patients aged 31-35 years.

Parameter studied		Control (5)	PCOS patients (7)	Significancy
LH (IU/L)		4.13±0.31	11.17±0.73	P< 0.001
FSH (IU /L)		3.44±0.05	4.71±0.08	P< 0.05
LH/FSH		1.20±0.05	2.37±0.06	P< 0.01
Total testosterone (ng/ml)		0.47±0.02	0.55±0.03	P< 0.05
Oestradiol (pmol/l)		119.32±4.62	90.39±3.78	P< 0.05
Progesterone (nmol/ml)		0.37±0.03	0.54±0.04	P< 0.05
AMH(ng/ml)		2.41±0.07	11.27±0.26	P< 0.001
Glucose (mg/dl)		82.00±3.54	113.857±6.23	P< 0.05
Lipid profile	**Total cholesterol (mg/dl)**	198.00±7.82	205.00±9.63	P< 0. 05
	Triglycerides (mg/dl)	200.00±8.82	257.85±10.64	P< 0.001
	LDL (mg/dl)	101.25±3.62	105.83±3.82	P< 0.05
	VLDL (mg/dl)	44.50±1.28	56.83±1.64	P< 0.05
	HDL (mg/dl)	58.00±2.68	42.00±1.98	P< 0.01
Vitamin D (ng/ml)		20.51±2.82	14.96±1.64	P< 0.01

PCO patients aged 31-35 years had significantly higher serum levels when compared to the control group. The serum levels of oestradiol, on the other hand, all decreased significantly. Vitamin D levels were linked with oestradiol and HDL cholesterol, but adversely associated with LH, FSH, LH/FSH, total testosterone, AMH, hyperglycemia, total cholesterol, triglycerides, and LDL cholesterol, as indicated in Table 4.

Table 4: Similar to Table 1 but for patients aged 36-40 years.

Parameter studied		Control (4)	PCOS patients (5)	Significancy
LH (IU/L)		6.54±0.42	10.32±0.85	P< 0.01
FSH (IU/L)		4.40±0.12	5.28±0.24	P< 0.05
LH/FSH		1.48±0.12	2.03±0.15	P< 0.05
Total testosterone (ng/ml)		0.52±0.06	0.68±0.08	P< 0.05
Oestradiol (pmol/l)		92.00±4.62	60.00±3.32	P< 0.01
Progesterone (nmol/ml)		0.82±0.06	0.84±0.04	NS
AMH(ng/ml)		1.47±0.09	3.90±0.13	P< 0.01
Glucose (mg/dl)		104.66± 4.58	165.40±6.51	P< 0.001
Lipid profile	**Total cholesterol (mg/dl)**	180.00±8.72	227.00± 12.64	P< 0. 001
	Triglycerides (mg/dl)	156.66±8.62	210.00±10.28	P< 0.001
	LDL (mg/dl)	127.25±6.23	142.20±7.52	P< 0.01
	VLDL (mg/dl)	45.33±6.43	47.25±6.67	NS
	HDL (mg/dl)	46.00±2.12	42.80±1.23	P< 0.05
Vitamin D (ng/ml)		29.11±1.34	14.84±0.98	P< 0.01

4 Discussion

All tables showed that the results of all age subgroups of the control group were similar, furthermore the results of all age subgroups in PCO patients were also identical. The results agreed with many previous studies [16], [17], [18], which mentioned that there were no variations in the level of pathological markers among age groups in PCO women.

The hormonal disturbances recorded in PCOS in this study could be attributed to hypothalamic dysfunction. Hypothalamic dysfunction may be a primary or secondary cause of abnormal steroid feedback. In either case serum LH level, rises and increased levels are observed clinically in approximately 50% of PCOS women [19]. In roughly 60% of individuals with PCOS [20], the ratio between FSH and LH levels, which is ordinarily around 2 to 1, becomes reversed and occasionally even higher (2 or 3 to 1) as a result of this derangement [20], as shown in the current study. Increased androgen production is caused by an increase in LH hormone, which is further boosted by insulin resistance associated with this disease [21].

The current study showed that AMH was positively correlated with the elevated LH, FSH, LH/FSH ratio, testosterone, progesterone, glucose, and lipid profile and negatively correlated with oestradiol, and HDL. While vitamin D was negatively correlated with AMH. These results agreed with many studies [22], [23], [24]. In addition, giving vitamin D tablets to PCOS patients restored their serum AMH levels [23], [24].
Vitamin D deficiency was discussed in which greater levels of total testosterone and dehydroepiandrosterone sulphate in PCOS patients [25], [26]. Deficiency was connected to higher levels of LH, FSH, LH/FSH ratio and etc.
Vitamin D receptors (VDRs) have been found in a variety of human tissues, including the ovary and endometrium, proposing vitamin D roles in female reproductive tissues [26], [27], [28]. PCOS has been associated to metabolism of calcium and phosphate, as well as low vitamin D levels [26] [29].
25(OH) D has been identified in women with PCOS in numerous investigations, ranging from 11 to 31 ng/ml, of (67–85 percent) having values below 20 ng/ml. Many research [30], [31] have proven the link between vitamin D levels and excessive LH and testosterone, as well as PCOS symptoms (infertility, hirsutism, and insulin resistance).
Vitamin D helps to boost the activity of steroidogenic enzymes such 3b-HSD. The corpus luteum is formed by luteinized human granulosa cells throughout the menstrual cycle, which produces a lot of progesterone (and a few oestrogens) and causes endometrial changes such decidualization in order to sustain a pregnancy. Increased progesterone synthesis by 1,25-dihydroxy vitamin D3 potentiates granulosa cell luteinization, resulting in a healthier endometrial environment [24].
In contrast, vitamin D is associated to many factors of which are common in PCOS and have been linked to ovulatory dysfunction [31], [32]. After supplementing PCOS patients with vitamin D, they showed an improvement in insulin sensitivity [33], [34].

5 Conclusion

Vitamin D insufficiency and PCOS pathogenesis are clearly linked, according to the research. In PCOS patients, vitamin D may play a role in the development of hormonal and metabolic problems. Furthermore, vitamin D's ovarian action may encourage its usage as an adjuvant medication in the treatment of PCOS.

Ethical considerations
The ethics committee of the Thi-Qar governorate's health directorate, as well as the ethical board of the South technical university in Iraq, gave its approval to the study.

References

1. Bellver J, Rodríguez-Tabernero L, Robles A, Muñoz E, Martínez F, Landeras J, García-Velasco J, Fontes J, Álvarez M, Álvarez C, Acevedo B; Group of interest in reproductive endocrinology (GIER) of the Spanish fertility society (SEF). Polycystic ovary syndrome throughout a woman's life. J Assist Reprod Genet 2018; 35(1):25-39.
2. de Melo AS, Dias SV, Cavalli Rde C, Cardoso VC, Bettiol H, Barbieri MA, Ferriani RA and Vieira CS. Pathogenesis of polycystic ovary syndrome: multifactorial assessment from the foetal stage to menopause. Reproduction 2015; 150(1): R11-24.
3. Azziz R and Adashi EY. Stein and Leventhal: 80 years on. Am J Obstet Gynecol 2016; 214(2):247.

4. Macut D, Damjanovic S, Panidis D, Spanos N, Glisic B, Petakov M, Rousso D, Kourtis A, Bjekic J and Milic N. Oxidised low-density lipoprotein concentration - early marker of an altered lipid metabolism in young women with PCOS. Eur J Endocrinol 2006;155(1):131-136.
5. Rotterdam ESHRE/ASRM-Sponsored PCOS consensus workshop group. Revised 2003 consensus on diagnostic criteria and long-term health risks related to polycystic ovary syndrome (PCOS). Hum Reprod 2004; 19(1):41-47.
6. Victoria M, Labrosse J, Krief F, Cédrin-Durnerin I, Comtet M and Grynberg M. Anti müllerian hormone: More than a biomarker of female reproductive function. J Gynecol Obstet Hum Reprod 2019; 48(1):19-24.
7. Stracquadanio M, Ciotta L, Palumbo MA. Relationship between serum anti-Mullerian hormone and intrafollicular AMH levels in PCOS women. Gynecol Endocrinol 2018; 34(3):223-228.
8. Javed Z, Papageorgiou M, Deshmukh H, Kilpatrick ES, Mann V, Corless L, Abouda G, Rigby AS, Atkin SL, Sathyapalan T. A Randomized, controlled trial of vitamin D supplementation on cardiovascular risk factors, hormones, and liver markers in women with polycystic ovary syndrome. Nutrients 2019;11(1):188.
9. Rashidi BH, Gorginzadeh M, Aalipour S, Sills ES. Age related endocrine patterns observed in polycystic ovary syndrome patients vs. ovulatory controls: descriptive data from a university based infertility center. Arch Endocrinol Metab 2016; 60(5):486-491.
10. Shalan B Al-Saedy, Mahdi M. Thuwaini, Ali E. Al-Snafi. Vitamin D, hormonal and metabolic disturbances in polycystic ovary syndrome. International Journal of Pharmaceutical Research 2021;13(2):3067- 3072.
11. Rashidi H, Ghaderian SB, Moradi L. The effect of vitamin D3 on improving lipid profile, fasting glucose and insulin resistance in polycystic ovary syndrome women with vitamin D deficiency. Middle East Fertility Society Journal 2018; 23(3): 178–183.
12. Murshid RM, Abdulrazaq AA, Muhammed EM. Association between vitamin D level and polycystic ovarian syndrome in premenopausal Iraqi women. Indian Journal of Public Health Research & Development 2019; 10(2): 698.
13. Ngo DT, Chan WP, Rajendran S, Heresztyn T, Amarasekera A, Sverdlov AL, O'Loughlin PD, Morris HA, Chirkov YY, Norman RJ, Horowitz JD. Determinants of insulin responsiveness in young women: impact of polycystic ovarian syndrome, nitric oxide, and vitamin D. Nitric Oxide 2001; 25: 326–330.
14. Al-Snafi AE. Study the efficacy of anti-estrogenic drugs in the treatment of poly cystic ovary induced in female rats by estrogen valerate. World J Pharm Sci 2014; 2(4): 313-316.
15. Al Snafi AE, Al-Fartosi KG, Al-Yasiry ZQ. Study the effect of PG E1 and PGF2α on male rat reproductive functions. Immun Endoc & Metab Agents in Med Chem 2018; 18: 1-4.
16. Al-Mulhim AA, Abul-Heija AA, Al-Talib AA, Al-Turki HA and Gasim TG. Hormonal, metabolic and clinical profile of Saudi women with polycystic ovary syndrome. Saudi Journal of Medicine and Medical Sciences 2013; 1(1): 30.
17. Da Silva Feuser CS, Barbosa JS, da Silva EB, de Medeiros SF. Current insights into gonadotropic pituitary function in the polycystic ovary syndrome. Asian Pacific Journal of Reproduction 2014; 3(1): 64–70.
18. Crisosto N, de Guevara AL, Echiburú B, Maliqueo M, Cavada G, Codner E, Paez F, Sir-Petermann T. Higher luteinizing hormone levels associated with antimüllerian hormone in postmenarchal daughters of women with polycystic ovary syndrome. Fertility and Sterility 2019; 111(2): 381–388.
19. Ambiger S, Patil SB, Rekha M, Dhananjaya S. Role of leutinizing hormone LH and insulin resistance in polycystic ovarian syndrome. International Journal Reprode Contracept Obstet Gyncol 2017; 6(9): 3892–3896.
20. Saxena P, Prakash A, Nigam A, Mishra A. Polycystic ovary syndrome: Is obesity a sine qua non? A clinical, hormonal, and metabolic assessment in relation to body mass index. Indian Journal of Endocrinology and Metabolism 2012; 16(6): 996.
21. Rosenfield RL, Ehrmann DA. The pathogenesis of polycystic ovary syndrome (PCOS): the hypothesis of PCOS as functional ovarian hyperandrogenism revisited. Endocrine Reviews 2016; 37(5): 467–520.
22. Merhi Z, Doswell A, Krebs K, Cipolla M. Vitamin D alters genes involved in follicular development

and steroidogenesis in human cumulus granulosa cells. Journal of Clinical Endocrinology & Metabolism 2014; 99(6):1137-1145.
23. Merhi Z, Seifer DB, Weedon J, Adeyemi O, Holman S, Anastos K, Golub ET, Young M, Karim R, Greenblatt R, Minkoff H. Circulating vitamin D relationship ships with serum antimullerian hormone levels in latereproductive- age women: women's Interagency HIV Study. Fertil Steril 2012; 98: 228–234.
24. Irani M, Merhi Z. Role of vitamin D in ovarian physiology and its implication in reproduction: a systematic review. Fertility and Sterility 2014; 102(2): 460-468.
25. Ostadmohammadi V, Jamilian M, Bahmani F, Asemi Z. Vitamin D and probiotic co-supplementation affects mental health, hormonal, inflammatory and oxidative stress parameters in women with polycystic ovary syndrome. Journal of Ovarian Research 2019; 12(1): 5.
26. Fang F, Ni K, Cai Y, Shang J, Zhang X, Xiong C. Effect of vitamin D supplementation on polycystic ovary syndrome: A systematic review and meta-analysis of randomized controlled trials. Complement Ther Clin Pract 2017; 26:53-60.
27. Thomson RL, Spedding S, Buckley JD. Vitamin D in the aetiology and management of polycystic ovary syndrome. Clinical Endocrinology 2012; 77(3): 343–350.
28. Hilger J, Friedel A, Herr R, Rausch T, Roos F, Wahl DA, Pierroz DD, Weber P, Hoffmann K. A systematic review of vitamin D status in populations worldwide. British Journal of Nutrition 2014; 111(1): 23–45.
29. Lin MW, Wu MH. The role of vitamin D in polycystic ovary syndrome. The Indian Journal of Medical Research 2015; 142(3): 238.
30. Li HW, Brereton RE, Anderson RA, Wallace AM, Ho CK. Vitamin D deficiency is common and associated with metabolic risk factors in patients with polycystic ovary syndrome. Metabolism 2011; 60(10): 1475-1481.
31. Yildizhan R, Kurdoglu M, Adali E, Kolusari A, Yildizhan B, Sahin HG, Kamaci M. Serum 25-hydroxyvitamin D concentrations in obese and nonobese women with polycystic ovary syndrome. Arch Gynecol Obstet 2009; 280: 559–563.
32. Muscogiuri G, Policola C, Prioletta A, Gian Pio Sorice G, Mezza T Lassandro A. Low levels of 25 (OH) D and insulin-resistance: 2 unrelated features or a cause-effect in PCOS? Clinical Nutrition 2012; 31(4): 476-480.
33. Karadag C, Yoldemir T and Yavuz DG. Effects of vitamin D supplementation on insulin sensitivity and androgen levels in vitamin-D-deficient polycystic ovary syndrome patients. J Obstet Gynaecol Res 2018; 44(2):270-277.
34. Kensara OA. Prevalence of hypovitaminosis D, and its association with hypoadiponectinemia and hyperfollistatinemia, in Saudi women with naive polycystic ovary syndrome. J Clin Transl Endocrinol 2018; 12: 20-25.

Investigation of the Effect of Diabetes on Lower Limb Muscles with Surface Electromyography (EMG)

Mahmoud I. Al-Kadi[1]
{mahmoudalkadi67@kecbu.uobaghdad.edu.iq/mahmoudalkadi67@yahoo.com}

Biomedical Engineering Department, Al-Khawarizmi College of Engineering, University of Baghdad[1]

Abstract. The ELECTROMYOGRAM (EMG) is a signal that indicates the muscle power and strength, It varies according to its type, location, and size of the muscle and other effectors, and in this project, it shows the muscle also affected by diseases like diabetes. The signals recorded were about 20 signals of cases (10 signals for normal cases and 10 signals for diabetes patients) after choosing three muscles in the lower limb (vastus lateralis (VL), TIBIALIS ANTERIOR (TA), and GASTROCNEMIUS medialis (GM)), each case apply three tests (standing, walking and stand over one foot) to know when the muscle affected greatly in which test and when the fatigue occurs. These signals were filtered carefully to eliminate the interface of other signals using three different stages according to the EMG frequencies (0.1 - 450) Hz. Three kinds of features were extracted (mean, standard deviation, and Shannon entropy) from EMG signals. The results show the variance between control muscles and patient muscles in amplitude and power where this variance increases whenever the duration and severity of the diabetes are increased.

Keywords: Diabetes, Muscles, EMG, Features.

1 Introduction

The muscular system is in charge of the human body's mobility. About 700 identified muscles are attached to the bones of the skeletal system, accounting for nearly half of a person's total weight. Each muscle is a separate organ made up of skeletal muscle tissue, blood vessels, tendons, and nerves [1]. The muscular system's tasks include movement, vasoconstriction and vasodilatation (constriction and dilation of blood vessel walls), peristalsis (wavelike motion in the digestive tract), and vasodilatation (constriction and dilation of blood vessel walls). Cardiac motion, posture maintenance (skeletal muscle activation maintains body posture and muscular tone), and heat generation (about 75% of ATP (adenosine triphosphate) energy required in muscle contraction is dissipated as heat). Skeletal muscle, smooth muscle, and heart muscle are the three types of muscles [2].
Diabetes, for example, damaged the muscle and the nerve that supplied it. Diabetes mellitus is a collection of metabolic illnesses defined by high blood sugar levels (hyperglycemia) caused by insulin secretion, insulin action, or both. Chronic hyperglycemia has been linked to microvascular and macrovascular consequences, including blindness, renal disease, nerve damage, amputations, heart disease, and stroke [3].
Type I diabetes is caused by a lack of insulin production in the body, necessitating daily insulin injections. Type II diabetes is caused by a lack of insulin production in the body, necessitating

IMDC-IST 2021, September 07-09, Sakarya, Turkey
Copyright © 2022 EAI
DOI 10.4108/eai.7-9-2021.2315286

daily insulin injections. This type is caused by the immune system attacking the pancreas' beta cells. This variety can appear at any age, however it is more prevalent throughout childhood and adolescence. Genetic predisposition and environmental triggers (infection or stress) are contributing variables in the emergence of these kinds [4]. Type II diabetes develops when the body fails to produce enough insulin. Reduced food intake, greater physical exercise, and finally oral medicines or insulin are used to treat high blood glucose levels. Many factors contribute to this category. First, there's insulin resistance in the liver and skeletal muscle, as well as increased glucose production in the liver, fat cell overproduction of free fatty acids, and insulin insufficiency. Second, as beta-cell loss progresses, insulin secretion diminishes. Obesity, age, and lack of physical exercise, genetic susceptibility, and conditions associated with insulin resistance are all contributing factors that lead to this type of diabetes [5]. Gestational diabetes is the last kind of diabetes. When a lady gets pregnant, this kind appears. Insulin resistance can be caused by hormones produced by pregnant women. Late in pregnancy, all women develop insulin resistance. Gestational diabetes develops when the pancreas does not produce enough insulin during pregnancy. Women who are overweight or obese are more likely to develop gestational diabetes. Additionally, gaining too much weight during pregnancy may increase your risk of gestational diabetes. After the baby is born, gestational diabetes usually goes away. A woman with gestational diabetes, on the other hand, is more likely to develop type I diabetes later in life. Obesity and type diabetes are more frequent in babies delivered to mothers who had gestational diabetes. All of these types are divided into three categories: mild, moderate, and severe [3,6,7].

2 Muscle and Diabetes

Type I Diabetes Mellitus (TIDM) impairs muscle growth and development, resulting in decreased muscle mass and myofiber size, poor metabolic regulation, and a switch to a glycolytic phenotype. While initial human TIDM research found no differences in capillary density, studies in TIDM animals show that the disease is linked to a decrease in skeletal muscle capillarization and angiogenesis [8]. As previously demonstrated, changes in muscle structure and metabolism are frequently associated with reductions in muscle function. In addition to growth and function, TIDM has been shown to impair the ability to repair damage, as evidenced by studies of muscle regeneration using chemical and genetic models of TIDM. Overall, these investigations show that TIDM has a deleterious influence on skeletal muscle and its ability to grow, maintain, and repair [9]. Muscle growth and development are significantly impaired in Type I Diabetes Mellitus (TIDM), resulting in reduced muscle mass and myofiber size, poor metabolic control, and a switch to a glycolytic phenotype. While initial studies in human TIDM reported no difference in capillary density, investigations in TIDM mice illustrate that the disease is associated with a decline in skeletal muscle capillarization and angiogenesis These alterations to muscle structure and metabolism often are associated with reductions in muscle function, as previously demonstrated in addition to growth and function, the capacity for repair from damage is also adversely affected by TIDM, as indicated by studies of muscle regeneration using chemical and genetic models of TIDM Collectively, these studies highlight the negative impact TIDM is having on skeletal muscle and its potential for growth, maintenance, and repair. Muscle atrophy can be caused by a variety of factors, including extended inactivity, ageing, and chronic diseases like Type II Diabetes Mellitus (TIIDM). Muscle atrophy occurs when the pace of contractile protein production and breakdown is out of equilibrium. Muscle atrophy

combined with inactivity can reduce the ability to perform everyday activities, lower quality of life, and increase mortality under catabolic situations. Damaged or unfolded proteins must be degraded in order to maintain cellular homeostasis in healthy muscle. However, in atrophic situations such as disuse or diabetes, persistent elevated activity of these pathways increases the rate of contractile protein breakdown, eventually leading to muscle atrophy and decreased protein synthesis [10].

3 Methodology

This section illustrates the steps adopted as shown in figure 1. The recorded EMG data are divided into two types: data acquired from a group of diabetic's patients aged 20-60 years in different levels of diabetes while the other data was acquired from normal persons (as control signals). Some of the patients had severe diabetes (treatment through the injection of insulin) and others had recently been diagnosed with diabetes ((treatment through tablets). The consent form and the agreement were taken from the patients before recording their EMG signals for scientific research.

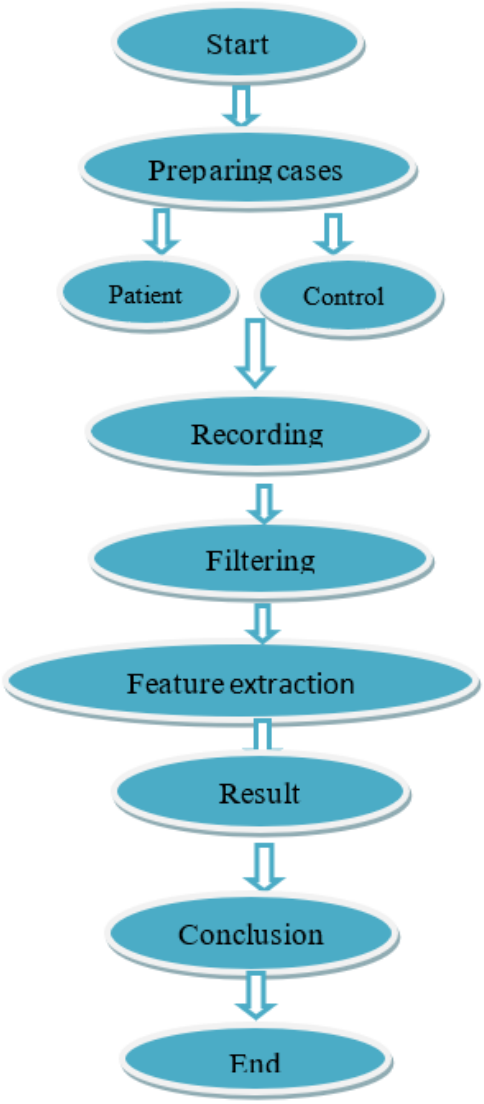

Fig.1. The steps of the methodology.

4 Acquiring the EMG Signals

MyoTrace 400 was used for recording the EMG signals with three channels. The goal of this system is to measure and quantify muscle biopotential signals alone or in combination with other kinematic signals. Channels 1,2 and 3 are connected to the EMG electrodes on the patient muscles in the locations tibialis anterior (TA), gastrocnemius medialis (GM) and vastuslateralis (VL) respectively for one lower limb while the ground electrodes were connected to the knee bone as shown in figure 2 [11,12].

Fig 2. The location of EMG electrodes.

The EMG signals were recorded from 20 samples, 10 signals for normal cases and 10 signals for diabetes patients. Each signal is recorded with the following sequence: stand on a single foot for 1 minute, walk for 5 minutes, stand for 1 minute then record another 5 minutes [13]. All recorded EMG signals were acquired in biomedical labs of Al-Khwarizmi College, Baghdad University. This research was committed based on ethical process of the University of Baghdad. The ethics approval is taken before recording the EMG signal. The study also conforms to the principles of the Declaration of Helsinki (Good Clinical Practice (GCP) 2008), which is the declaration on ethical principles in conducting human trials, adopted at the 18th World Medical Association (WMA) held at Helsinki, Finland in 1964 [14,15].

5 Feature Extraction

The features are chosen carefully according to their ability to describe the muscle signal changes at different levels of diabetes, considering the execution speed and the efficiency in classifying the EMG signals. Some of these features depend on sub-band coefficients, while the others depend on the wave of the sub-bands (i.e., reconstruction of the sub-band to generate a new time series for each sub-band) [16,17,18].

5.1 Mean Square Error (MSE)

This criterion is used to follow the variation of EMG bands after removing the noise and artifacts that overlapped with the time-series elements. This feature is defined as follows:

$$MSE = \frac{1}{N}\sum_{n=1}^{N}[(x(n) - \hat{x}(n)]^2 \quad (1)$$

where$x(n)$is the contaminated time series and $\hat{x}(n)$ is the filtered time series.

5.2 Standard Deviation of the Wavelet Coefficients (SD)

This feature calculates the standard deviation of each EMG. The variation of this feature is utilized to follow the level of diabetes.

$$STD = \left(\frac{1}{NS-1}\sum_{i=1}^{NS_{jk}}(x_i - \bar{x})^2\right)^{\frac{1}{2}} \quad (2)$$

5.3 Time Series Shannon Entropy

Shannon entropy is the first concept of entropies in information theory literature. This type of entropy is used to quantify the disorders in the time series and to measure the flatness of the energy spectrum in the wavelet domain. This entropy quantifies the regularity of a time series and predicts new values according to previous observations. The probability density function of Shannon entropy "ShaEnt" was calculated:

$$ShEn_{jk} = -\sum_{n=1}^{NS_{jk}} p_{jk} \ln p_{jk} \quad (3)$$

6 Results and Discussion

Ascertaining the effectiveness of denoising techniques, feature extraction, and EMG signal classification is of prime importance. This section describes the validation process for the proposed methodologies. The methodologies that were employed to characterize the EMG signals for the muscle that is affected by a chronic disease such as type I and II Diabetes Mellitus (TIDM /TIIDM) were validated by using the data that were acquired in the lab of Al-Khwarizmi engineering college. The first stage of signal processing of the recorded signal is the noise removal process. This stage includes three sub-stages to remove the noise and artifacts from the recorded EMG signals. Conventional filters are the first approach that is used to denoise the EMG signals which consist of two types of filters: notch filter (NF) and bandpass filter (BPF). NF is used in all EMG recording devices to eliminate the effects of the AC line and its harmonics (50 Hz). This filter ensures the complete removal of this type of noise from the frequency of EMG signals. BPF with order 4 has been used to specify the effective frequencies that represent an EMG signal, which is confined between 50 and 450 Hz. The filter also removes the DC level that is generated by electronic equipment. The third filter is a wavelet filter. This technique removes artifacts that overlapped with the recorded EMG signals. In this work, the three channels of EMG signals are filtered by this technique second by second using MWT db4 with order 4. Figure 3a shows the three channels of EMG signals before and after undergoing the NF, BPF, and WT denoising process of the control signals. Figure 3b shows the three channels of EMG signals before and after undergoing the BSF, BPF, and WT denoising process of the patient's signals. The most of artifacts and noise that overlapped with the recoded signal are removed without affecting the details of the EMG signals.

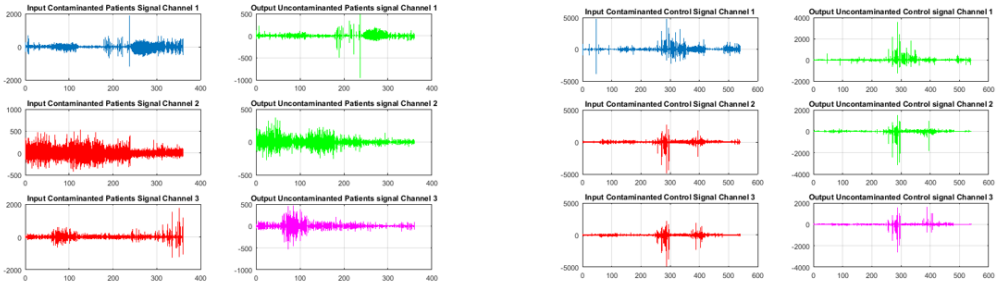

(a) **(b)**

Fig.3. Three channels of the EMG signal filtered by NF, BPF and WT technique (a) Control signals (b) Patients signals.

As mentioned before, three features were extracted from the EMG signal. All functions were chosen carefully according to their ability to describe the EMG signal changes when the power of the muscle due to diabetes. All features were extracted from EMG signal second by second. These features are Mean (MEAN), Standard deviation (STD), and finally Shannon entropy (ShaEnt). The next section will discuss these features for both (control signals and diabetes signals) for finding the effect of this disease on the effectiveness of the muscle. According to Figure (4), the mean value for each second rises by (40mv) in the healthy muscles (control signal) while the mean value of the EMG signals is reduced to (20mv) in the infected muscles. this feature gave good evidence that the muscles are affected efficiently by diabetes where the EMG signals are reduced with the severity of the disease.

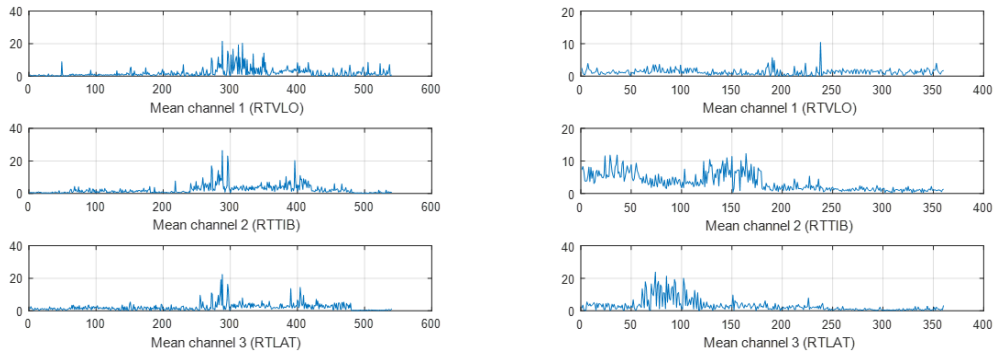

(a) **(b)**

Fig.4. The Mean of three channels of the EMG signal
(a) Control signals (b) Patients signals.

The standard deviation (SD) is one of the best ways to determine the dispersion. It is based on calculating the deviation from the average either by divergence or convergence. Figure (4) shows the deviation for normal muscles and infected muscles. Figure 5a shows SD of the normal muscle where it is normally distributed around the mean and the sample value is reached to (200) while the deviation values for the infected muscles are less than (100) and not distributed

around the mean (chaotic signal) as illustrated in figure 5b. In the same meaning, the signal of the infected muscles has many variations along the time comparing with normal muscle.On the other side, this feature didn't observe a significant variation in channel one that means the Vastus lateralis muscle (RTVLO) does not have essentially affected by diabetes.

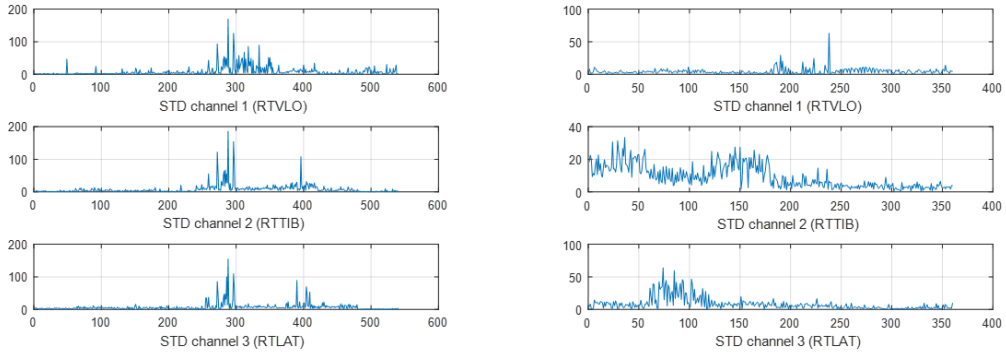

(a) **(b)**

Fig.5. The standard deviation of three channels of the EMG signal
(a) Control signals (b) Patients signals.

Generally, the entropy function is used to illustrate the randomness of the samples of the recorded signals. Figure 6a shows the Shannon entropy of the control signal while figure 6b shows the signal entropy of the infected muscles. these figures show the disparity between the entropies where the entropy of the control signal gives a high distribution and higher in value (10^8) while the entropy of the that recorded from the infected muscle low distribution and lower in value (10^7) (weak muscles) which means the muscles would work regularly when they are not affected by diabetes.

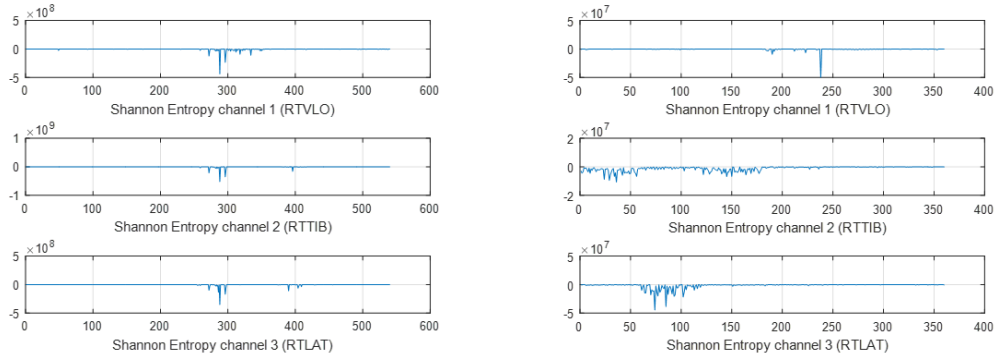

(a) **(b)**

Fig.6. The Shannon Entropy of three channels of the EMG signal
(a) Control signals (b) Patients signals.

6 Conclusion

After observation of the results and figures, it is clear that the muscle of diabetes mellitus has been affected by a significant impact as the muscle tends to lose or damage, as the reduction of the effectiveness of insulin increases the level of sugar and lose muscle insulin effect, which strengthens and rebuild, and the real problem of the disease that the patient gradually loses the ability to move, that he suffers wasting reduces movement and prevents him from serving himself and even from the work of exercises that strengthen his muscles.

References

[1] Dr.Ebneshahidi , Muscle Physiology, 2004 Pearson Education, Inc., publishing as Benjamin Cummings.

[2] Anne Buckley MD PhD Neuropathology, Diseases of Skeletal Muscle,2004.

[3] Emily Loghmani ,diabetes mellitis: type 1 and type 2, 2005.

[4] American Diabetes Association.Economic consequences of diabetes mellitus in the U.S. in 1997. Diabetes Care 1998;21(2):296-309.

[5] Rosenbloom AL, Joe JR, Young RS, Winter WE. Emerging epidemic of type 2 diabetes in youth. Diabetes Care 1999;22(2):345-354.

[6] Pinhas-Hamiel O, Dolan L, Daniels SR, Standiford D, Khoury PR, Zeitler P. Increased incidence of noninsulin-dependent diabetes mellitus among adolescents. J Pediatr 1999;128:608-615.

[7] American Diabetes Association.Type 2 diabetes in children and adolescents.Pediatrics 2000;105(3 Pt 1):671-680.

[8] H Yki-Järvinen [1], H Vuorinen-Markkola, L Koranyi, R Bourey, K Tordjman, M Mueckler, A M Permutt, V A Koivisto, Defect in Insulin Action on Expression of the Muscle/ Adipose Tissue Glucose Transporter Gene in Skeletal Muscle of Type 1 Diabetic Patients , Journal of Clinical Endocrinology and Metabolism, 1992 Sep;75(3):795-9. doi: 10.1210/jcem.75.3.1517369.

[9] Santos, A. J. C. A., Silva, E. L. A., Albuquerque, Y. M. L., Oliveira, B. D. R. and Caiaffo, V., Effects of diabetes mellitus type I on skeletal muscle: an integrative review, Journal of Morphological Sciences 33(2):118-120 · January 2016

[10] Jing He and David E. Kelley, Muscle glycogen content in type 2 diabetes mellitus, Department of Medicine, University of Pittsburgh School of Medicine, Pittsburgh, Pennsylvania, 1 July 2004.

[11]Ricky Watari1 , Cristina D Sartor1 , Andreja P Picon1 , Marco K Butugan1 , Cesar F Amorim2 , Neli RS Ortega3 and Isabel CN Sacco, Effect of diabetic neuropathy severity classified by a fuzzy model in muscle dynamics during gait, Journal of NeuroEngineering and Rehabilitation 2014, 11:11.

[12] Perry BD, Caldow MK, Brennan-Speranza TC, Sbaraglia M, Jerums G, Garnham A, Wong C, Levinger P, AsrarUlHaq M, Hare DL, Price SR, Levinger I , Muscle atrophy in patients with Type 2 Diabetes Mellitus: roles of inflammatory pathways, physical activity and exercise, ExercImmunol Rev. 2016; DOI:22:94-109.

[13] Sacco IC, Amadio AC: Influence of the diabetic neuropathy on the behaviour of electromyographic and sensorial responses in treadmill gait. ClinBiomech (Bristol, Avon) 2003, 18(5):426–434

[14] Kwon OY, Minor SD, Maluf KS, Mueller MJ: Comparison of muscle activity during walking in subjects with and without diabetic neuropathy. Gait Posture 2003, 18(1):105–113

[15] Petrofsky J, Lee S, Bweir S: Gait characteristics in people with type 2 diabetes mellitus. Eur J ApplPhysiol 2005, 93(5–6):640–647.

[16] Gomes AA, Onodera AN, Otuzi ME, Pripas D, Mezzarane RA, Sacco IC: Electromyography and kinematic changes of gait cycle at different cadences in diabetic neuropathic individuals. Muscle Nerve 2011, 44(2):258–268.

[17] Sawacha Z, Spolaor F, Guarneri G, Contessa P, Carraro E, VenturinA, Avogaro A, Cobelli C: Abnormal muscle activation during gait in diabetes patients with and without neuropathy. Gait Posture 2012, 35(1):101–105.

[18] Jason L. Rucker, Stephen D. Jernigan, Joan M. McDowd and Patricia M. Kluding,Adults with diabetic perfral neuropathy exhibit impairments an multitasking and other executive functions , J NeurolPhysTher. 2014 Apr; 38(2): 104–110.

Clinical Significance of Some Tumour Biomarkers in the Diagnosis of Breast Cancer in Comparison with Histopathological Biopsy

Adil Nadhim Radhi [1], Mahdi Murshd Thuwaini[2], Hamed Jaddoa Abbas[3]
{adilalasadi86@gmail.com[1], Hayder9015@yahoo.com[2], hamed@uobasrah.edu.iq[3]}

College of Medical and Health Technology / Southern Technical University - Basrah, Iraq[1,2]
Al-Fayhaa Teaching Hospital – Al- Zahraa Medical college- Basrah University, Basrah, Iraq[3]

Abstract. This study aimed to assess the diagnostic power of tumour biomarkers (Serum CA15-3, CA27.29, and CA549) in the diagnosis or confirming the breast cancer (BC) in comparison with histopathological biopsy. A case-control study consisted of (60) female patients with breast cancer and (30) healthy subjects as control. Kits were used to measure serum CA15-3, while Enzyme-Linked Immunosorbent Assay (ELISA) was used to measure Serum CA27.29 and CA549. The current study showed that there were highly significant increases in the levels of CA15-3, CA27-29 with BC cases. It was also a highly significant increase in the levels of CA15-3, CA27-29, in BC patients with stage IV compared to another state. The study also showed that the sensitivity values of the markers were: 87%, 36%, 56% for the markers CA15-3, CA27-29, and CA 549 respectively. The study also reveals that specificity values of the markers were: 62%, 36%, 40% for the same markers respectively. It could be concluded these markers could be used in the diagnosis of BC.

Keywords: BC, Tumour Markers, CA 15-3, CA 27.29, CA 549

1 Introduction

Breast cancer is the most common cancer in women of all ages, including those under 35 years old, and it continues to be the leading cause of cancer-related death. Women under the age of 50 are not screened, therefore cancer diagnosis is made based on clinical signs and symptoms, which can be inconvenient and postponed [1].

BC is a worldwide health problem; it is the leading for death among females allover the world and too expensive to treat. Because health-care assets are limited, decisions about BC treatments are made on "value for money" [2].

Invasive breast cancer incidence is steadily rising since 2004. According to a recent study, rises in body mass index (BMI) and decreases in the average number of births per woman (both BC risk factors) have recently contributed to rise in incidence. In 2017, an estimated 231,840 women in the USA would be detected with BC. This is also the 2nd largest reason of death in women, after lung cancer [3]. It causes early mortality in females. When a tumour is tiny and treatable, breast cancer usually has no symptoms, which is why screening is critical for early identification.. A painless lump is the most prevalent physical indication. Even before the primary breast tumour, breast cancer can migrate to underarm lymph nodes and generate a lump

IMDC-IST 2021, September 07-09, Sakarya, Turkey
Copyright © 2022 EAI
DOI 10.4108/eai.7-9-2021.2314939

or swelling [4]. Early detection, determining prognosis, predicting response or hard to treat medicines, surveillance following primary surgery, and monitoring therapy with all possible uses of markers serum in BC [4]. The major goal of this study was to compare the rate of diagnostic of tumour biomarkers (Serum CA 15-3, CA 27.29, and CA 549) with histopathological biopsy in diagnosing primary breast cancer.

2 Materials and Methods

60 women was considered and diagnosed with breast cancer. In the study, population age ranged from (30-74 years) old. The study also included (30) healthy women as control. Who visited Al-Basra Oncology Centre in Al-Sadr Teaching Hospital in Basra? All patients in this research were diagnosed by oncologist Al-Basra Oncology Centre in Al-Basra Teaching Hospital and confirmed by all clinical and laboratory investigations throughout the period from October 2020 to May 2020. The practical analyses of the study were carried out in the department of Medical Laboratory at STU, Basra. Kits were used to measure serum CA 15-3 (Roche Diagnostics- Switzerland), while Enzyme-Linked Immunosorbent Assay (ELISA) was applied to measure Serum CA 27.29 and CA 549

2.1 Statistical Analysis

Mean and variance (SD) of the data were computed. The t-test (for means) and the chi-square test were used to see if there were any differences between the groups (for frequencies). SPSS for Windows was used to conduct all statistical analyses (version 23, USA). ANOVA was employed for normally distributed data. Example is when $P < 0.05$ was statistically considered significant, while $P > 0.05$ was judged non-significant.

3 Results and Discussion

3.1. Features of the Groups suggested

Table 1. showed statistical distribution (frequency and percentage) of study groups (patients and control) by their age and breast cancer characteristics. This table explained that the highest percentage of the age subgroup is (41-51) years which constituted (50%) for the patient's group, and (5.7%) for the control group. This same table revealed that the highest percentage of patient's subgroup are those with Grade II (62.2%), Stage II (68%).

Table 1. Statistical distribution (frequency and percentage) of study groups (patients and control) by their age and breast cancer characteristics.

Items	Sub-groups	BC Patients (N= 60)		Control Group (N= 30)		Chi Square (P value) Sig.
		Freq.	%	Freq.	%	
Age	30-40	11	18.3	4	13.3	2.05 (0.56) NS
	41-51	30	50.0	17	56.7	
	52-62	16	26.7	9	30.0	

	63-73	3	5.0	0	0.0	
Grade	I	0	0.0	-	-	-
	II	37	62.2	-	-	
	III	23	37.8	-	-	
	IV	0	0.0	-	-	
Stage	I	0	0.0	-	-	-
	II	45	75.6	-	-	
	III	12	20.0	-	-	
	IV	3	4.4	-	-	

NS: at P value>0.05; SD: Stand. Dev.

3.2. Measurement of Biomarkers

Table 2. Differences in the measurement of serum biomarkers between BC patients and control group.

Biomarkers	BC Patients (N= 60)		Control Group (N= 30)		T Test P value
	Mean	SD	Mean	SD	
CA 15-3	130.19	66.2	6.83	1.61	4.58 0.000 (HS)
CA 27-29	10.89	9.58	6.09	1.89	3.69 0.000 (HS)
CA 549	0.22	0.05	0.20	0.04	1.21 0.22 (NS)

HS: at P≤0.01; NS: at P≤0.05; SD: Stan. Dev.

Table 2. exhibited differences in the measurement of serum biomarkers between BC patients and the control group. This table shows that there is a highly significant increase (P-value < 0.01) in the levels in BC patients compared to the control group for the biomarkers: CA 15-3 and CA 27-29.

3.3. Measurement of Biomarkers During Different Stages of Breast Cancer

Table 3. ANOVA table for Differences in the measurement of biomarkers among various states of BC.

Biomarkers	Stage Sub-groups			F Test P-value
	Stage 2 (N= 68)	Sage3 (N= 18)	Stage4 (N= 4)	

CA 15-3	Mean	99.05 A	58.94 A	157.00 B	10.92
	SD	127.81	55.78	20.38	0.000 (HS)
CA 27-29	Mean	9.48 A	13.59 A	22.88 B	3.10
	SD	10.27	14.91	17.97	0.05 (S)
CA 549	Mean	0.21	0.23	0.23	0.66
	SD	0.05	0.03	0.05	0.52 (NS)

HS: at P≤0.01; SS at P≤0.05; NS: at P>0.05; SD: Standard Deviation; ANOVA: Analysis of Variance; Different letters refer to the significant difference among stages.

Table 3. revealed differences in the measurement of biomarkers among patients' subgroups classified according to the stage of breast cancer. This table showed that there is a highly significant increase (P-value < 0.01) in the levels of CA 15-3 and CA 27-29 in BC non-control with stage IV as compared to stage II and stage III.

3.4. Receiver-operating characteristics of the Biomarkers

Table 4. ROC and AUC of the biomarkers for the detection of BC. AUC: Area Under the curve; Positive Predictive Value (PPV); Negative Predictive Value (NPV).

Biomarkers	(AUC)	Sig. p-value	Cut-off Point	Sensitivity (%)	Specificity (%)	PPV	NPV
CA 15-3	0.83	0.000	6.33	0.87	0.62	0.82	0.72
CA 27-29	0.51	0.81	6.1	0.36	0.36	0.53	0.21
CA 549	0.58	0.15	0.20	0.56	0.40	0.65	0.30

Figure 1 and Table 4 It was about biomarker full area (is well AUC) and (ROC) curve examination for breast cancer diagnosis. The sensitivity values for the markers CA 15-3, CA 27-29, and CA 549 were 0.87%, 0.36 %, and 0.56%, respectively, as shown in the table. The same table revealed that sensitivity values of the markers were: 62%, 36%, and 40% for the same markers respectively.

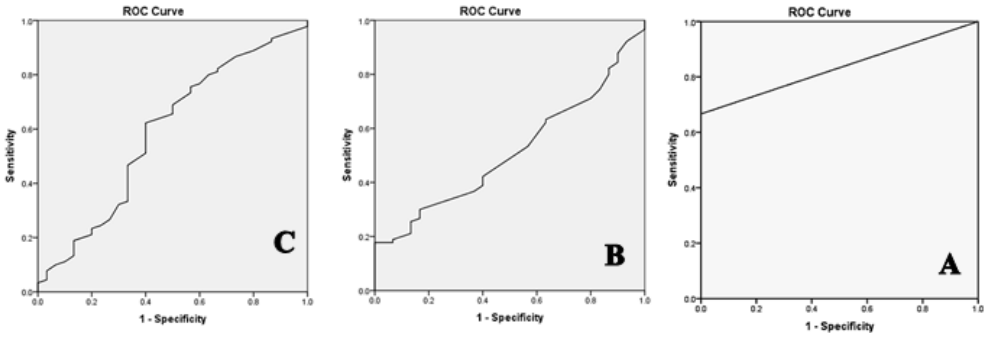

Fig 1. Diagonal segment of the ROC curve for (A) : CA 15-3 (B) : CA 27-29 (C) : CA549

Regarding CA-15-3, the results agreed with, the current study agrees with Hussain et al., they showed a highly significant elevation (mean value = 35.450 U/ml) in Ca15-3 serum levels in BC patients in comparison with the control group (mean value = 8.180 U/ml) and this increasing

due to increased secretion of Ca15 – 3 from cancer cells [6]. This result also come in agreement with Hassan et al. that showed increased CA 15-3 in BC patients. Previous research revealed the tumour marker CA 15-3 is the most commonly used tumor-tagging the suitable diagnosis and clinical practise of BC patients' monitoring and follow-up [7]. It was also suggested that elevated levels of the tumour marker with 1% CA 15-detection rate of control and 3%: -20% of benign breast changes, 36%: -40% of hepatitis, and 14 percent -70 percent of gastric cancer patients. CA15-13 appears to play a role in the malignancy of breast cancer, as it was discovered that CA15-3 has significantly elevated serum levels but not with benign tumours; in addition, Fu and Li discovered that malignant tumours all over the stages had high CA15-3, especially in advanced stages [9].

The current study's findings concurred with Atom et al., who observed substantial changes in in the level of CA15-3 of various stages of BC [10], but differed from Moazzezy et al., who discovered that serm level of CA15-3 and CEA were unrelated to BC staging [11]. CA15-3 is significantly correlated with BC in all stages (Stage I: SMD=2.03, Stage II: SMD=3.88, Stage III: SMD=5.12), according to a large meta-analysis conducted by Zhang et al. While all malignant tumours have elevated levels of CA15-3, it was discovered that the level of CA15-3 keeps rising tumour progresses. These findings show that monitoring CA15-3 levels rather than early diagnosis may be more effective for monitoring advanced tumours [2]. CA15-3 is a mucinous glycoprotein that is one of the Mucin1 (MUC-1) gene's products. MUC-1 is frequently linked to malignancies of the colon, breast, ovary, lung, and pancreas. The levels of CA15-3 and CEA in the blood were found to be strongly linked with the chance of developing malignant breast cancer in a meta-analysis research [9].

In the case of CA 27-29, the findings of this study agree with Chan et al., the authors of a previous study. An immunoradiometric technique was used to analyse 1721 patients with benign and malignant breast cancer in a multicentre investigation of CA549, a breast cancer marker. A 95 percent combined specificity was achieved. The specificity for benign breast disorders was 94.8 percent, and 88.2 percent for other benign diseases, for a total of 90.1 percent. The combined specificity for patients with malignant (non-breast) disorders was 75.6 percent; the findings correspond with Kabel (2017), who discovered the MUC-1 gene. CA 27.29 is strongly linked to breast cancer, with an elevated CA 27.29 level found in 80% of women with breast cancer. CA 27-29, on the other hand, can be discovered in patients with various cancers, as well as benign breast, liver, and kidney problems, and ovarian cysts. [12].

According to preliminary study, each signal has limited sensitivity and specificity in detecting early metastatic disease following breast cancer surgery [13]. Regarding CA 15-3, which is the most commonly used tumour marker in the diagnosis of breast cancer, Zaleski et al. investigated improved sensitivity for breast cancer detection using a combination of miR-34a and tumour markers CA 15-3 or CEA, and discovered that the AUC, sensitivity, and specificity for CA 15-3 were 0.72, 0.95, and 0.36, respectively [14]. CA15.3 is the most commonly utilised breast tumour marker, according to a recent study this is not applicable and prognosis in individuals who have already been diagnosed [3].

4 Conclusion

The researchers discovered that patients with breast cancer had higher levels of the following biomarkers: CA 15-3, CA 27-29. CA 15-3 and CA 27-29 are two biomarkers that have increased in correlation with advanced stages of breast cancer. In the diagnosis of breast cancer, CA 15-3 had a good sensitivity and specificity.

References

[1] Seidler S. J. and Huber D.E. Overview of Diagnosis and Treatment of Breast Cancer in Young Women. EC Gynaecology, 2020, SI.02: 18-25.

[2] Zhang X, Xing C, Guan W, Chen L, Guo K, Yu A, Xie K. Clinicopathological and prognostic significance of nestin expression in patients with breast cancer: a systematic review and meta-analysis. Cancer Cell Int. 2020, 14;20:169.

[3] Aglan, S. A., Elsammak, M., Elsammak, O., El-Bakoury, E. A., Elsheredy, H. G., Ahmed, Y. S., Sultan, M. H., & Awad, A. M. (2021). Evaluation of serum Nestin and HOTAIR rs12826786 C>T polymorphism as screening tools for breast cancer in Egyptian women. Journal of medical biochemistry, 2020, 40(1), 17–25.

[4] Wolff AC, Tung NM, Carey LA. Implications of Neoadjuvant Therapy in Human Epidermal Growth Factor Receptor 2-Positive Breast Cancer. J Clin Oncol. 2019, 2019;3.

[5] Li J, Guan X, Fan Z, Ching LM, Li Y, Wang X, Cao WM, Liu DX. Non-Invasive Biomarkers for Early Detection of Breast Cancer. Cancers (Basel). 2020 ,12(10):2767.

[6] Hussain A. M., Ali H. A. and Mohammed H. L. The Ca 15-3, Ca 27.29 And Amh Biomarkers For Breast Cancer In Iraqi Patients . Biochemical And Cellular Archives, 2020, .20 : 1119 .

[7] Hassan H. AB-H, Tauma A. M. and Ataimish SH. H. Determination of Some Biochemical Markers for Breast Cancer Women in Baghdad. AL - Ma'mon Collage J., 2016, 1 (28), 317 – 327.

Kabel, A. M. Tumor markers of breast cancer : New prospectives . Journal of Oncological Sciences., 2017, 3 : 5-11 .

[8] Laessing D, Nagel D, Heinemann V, Untch M, Kahlert S, Bauerfeind I. Importance of CEA and CA 15-3 during disease progression in metastatic breast cancer patients. Anticancer Res., 2017,27 (4A):1963-8.

[9] Fu Y, Li H. (2016) Assessing Clinical Significance of Serum CA15-3 and Carcinoembryonic Antigen (CEA) Levels in Breast Cancer Patients: A Meta-Analysis. Med Sci Monit. 2016; 22:3154-3162 .

[10] Atoum M, Nimer N, Abdeldayem S, Nasr H. Relationships among Serum CA15-3 tumor marker, TNM staging, and estrogen and progesterone receptor expression in benign and malignant breast lesions. Asian Pac J Cancer Prev, 2012, 13(3): 857–60 .

[11] Moazzezy N, Farahany TZ, Oloomi M, Bouzari S. Relationship between pre¬operative serum CA 15-3 and CEA levels and clinicopathological parame¬ters in breast cancer. Asian Pac J Cancer Prev, 2014, 15(4): 1685–88 .

[12] Chan, D. W., Beveridge, R. A., Bhargava A., Wilcox, P. M. Kennedy, J. Schwartz, M. K. Breast Cancer Marker CA549: A Multicenter Study . American Journal of Clinical Pathology, 1994, 101(4) :465–470 .

[13] Nicolini A, Carpi A, Ferrari P, Morganti R, Mazzotti V, Barak V, Duffy MJ. An individual reference limit of the serum CEA–TPA–CA 15-3 tumor marker panel in the surveillance of asymptomatic women following surgery for primary breast cancer. Cancer Manag Res., 2018, 10:6879-6886 .

[14] Zaleski, M., Kobilay, M., Schroeder, L., Debald, M., Semaan, A., Hettwer, K., Uhlig, S., Kuhn, W., Hartmann, G., & Holdenrieder, S. (2018). Improved sensitivity for detection of breast cancer by combination of miR-34a and tumor markers CA 15-3 or CEA. Oncotarget, 9(32), 22523–22536.

Determination of ϒ-aminobutyric acid (GABA) in Ziziphus Tuffahi fruit & Earmotiun

Firas Jameel Jabbar[1],
{firas.alassadi@stu.edu.iq[1]}

Department of Pharmacy, Southern Technical University, Basra, Iraq[1]
College of Agriculture University of Basra[1]

Abstract. This study was conducted during the season 2020-2021 in the laboratories of the College of Agriculture, the University of Basra, and the Technical Institute of the Southern Technical University to study two types of buckthorn fruits, namely Tuffahi and Earmotiun fruits, and the concentration of GABA was estimated in both varieties before maturity and full maturity. (HPLC) was used to determine the concentration of this vital substance and the results showed the presence of this acid in a higher concentration in the fresh phase of both cultivars, while the concentration of GABA in the pome fruit was higher than in the Emotion fruit. and microorganisms. It has many important and health-promoting functions. There are not many studies about this acid and its presence in plants, so this study aimed to confirm the presence of this acid in the fruits of buckthorn.

Keywords: GABA, HPLC, Ziziphus, Tuffahi, Earmotiun, ZT1, ZE2.

1 Introduction

GABA (Gamma-Aminobutyric Acid) is a non-protein, four-carbon amino acid found in plants, animals, and microbes. This acid is an inhibitory neurotransmitter in the brain that affects personality and stress management. It is a metabolic product of plants and microorganisms created by decarboxylation of glutamic acid [1-3]. Detected in a variety of traditional foods resulting from microbial fermentation, these foods are safe and environmentally friendly. It also has the potential to offer new health-beneficial products rich in GABA. Since glutamate decarboxylase catalyses the synthesis of GABA, the best fermentation conditions are largely determined by the biochemical properties of the enzyme [4-7]. In a study tea leaves, mulberry leaves, tomatoes, animals, lactic acid bacteria (LAB), yeasts, and melds all were found to contain GABA. [8-10]. Tempeh (fermented soybeans) Dade (fermented buffalo milk), Assam durian (fermented durian), bar singsong (fermented cassava), ikan budu (fermented fish), sake, sake yogurt, sourdough, raspberry beer, kimchee cheese, and zeltar All are examples of fermented foods and drinks that contain GABA [11-12]. The presence of ϒ-aminobutyric acid (GABA) has also been detected in the fruits of sea buckthorn, which is widely cultivated in the warm tropical regions of Asia, Africa, and Europe [13]. The fruits contain many important chemical compounds in addition to nutrients, such as vitamins, sugars, organic acids, alkaloids, polyphenols, and saponins [14]. Buckthorn fruits are popular with a taste that is acceptable to most people. It is widely consumed in Asian countries as a food, in addition to being used as a folk medicine for thousands of years [15] used to relax and improve sleep [16]. In the past few years, the fruit has been commonly used to treat tiredness, fatigue, and anaemia. Several studies have emerged confirming the use of buckthorn in the treatment of some tumours, as an anti-

IMDC-IST 2021, September 07-09, Sakarya, Turkey
Copyright © 2022 EAI
DOI 10.4108/eai.7-9-2021.2314934

inflammatory, memory improvement, and liver preventative, in addition to its calming effect [17-20]. Minerals such as potassium, calcium, sodium, and others are known for their importance to human health. To live a healthy life, these components must be present in sufficient proportions in the human diet [21]. The chemical composition of jujube, which plays an essential function in human health, is unknown. There has been little research on the mineral composition of jujube fruit and leaves [22, 23]. The majority of studies focused on the content of the pulp and seed oil. These oils constitute 12.35 percent and 37.5 percent of the dry weight of the pulp and seeds, respectively, and are used for medicinal and pharmaceutical applications (blood pressure, antioxygen, hypothermic) [24-26]. The present study was conducted to determine the concentration of the active substance GABA (gamma-aminobutyric acid) in two cultivars of buckthorn fruits during the pre-ripening and full-ripening phases, that is, in February and March, respectively. The fruits were collected from the trees of the Hartha orchard, north of Basra Governorate, and the two cultivars Al-Tuffahi and Al-Armouti.

2 Chemicals and Equipment

Sigma-Aldrich provided the ϒ--aminobutyric acid (GABA) (St Louis, MO, USA). Methanol, ortho-phthalaldehyde (OPA), β-mercaptoethanol (BME), sodium tetraborate, ascorbic acid, formic acid, and other analytical grade chemicals were obtained via HPLC from Media Company, Inc (Fairfield, USA). J&K Chemical Ltd provided the information (Shanghai) A Shimadzu liquid chromatography system comprising an LC-20AD solvent delivery system (pump), an SPD-20A photodiode array reagent, and a SIL-20ACHT injector with a 50 µl ring volume was used for HPLC chromatography. For data collection and processing, use LC version 1.25. (Shimadzu, Japan). For this study, a Princeton SPHER C18 (25 cm 4.6 mm ID, 5) was used. Preparation of samples.

2.1 Preparation of Samples

To estimate the concentration of ϒ-aminobutyric acid (GABA) in both pre-ripening and fully ripened buckthorn cultivars, samples were collected from both Tuffahi and Earmutiun cultivars in February and March from one of the Hartha orchards. In the north of Basra Governorate. The samples were kept in special bags and transported directly to the laboratory at room temperature. The samples were washed in distilled water, then cut into small strips, then dried, and ground into a powder using an electric mill. Finally, all samples were wrapped in straw bags and stored at (-20 °C) for the analysis process.

2.2 Extraction of Samples For Analysis Using Sonication Technology

To perform the analysis process using HPLC technology, samples must be extracted from the two cultivars used in this study, Tuffahi and Earmutiun, deionized water is added to the pre-crushed samples and sonication is performed at room temperature for 60 minutes, thousands of Vacuum small bubbles in the solution during sonication. Cavitation is the process of bubbles breaking down in a solution. This causes intense vibrational vibrations in the cavity field, shattering chemical connections like those between water molecules, separating clumps of molecules, and enabling mixing. When dissolved gas is vibrated, for example, gas bubbles clump together and exit the solution more easily. The sound waves' energy causes friction in the solution, which produces heat. To stop a sample from heating up and insulting. After the sonication was terminated, the extract was centrifuged at 3000 rpm for 20 min. The supernatant was separated and stored at 0°C for analysis by HPLC technology.

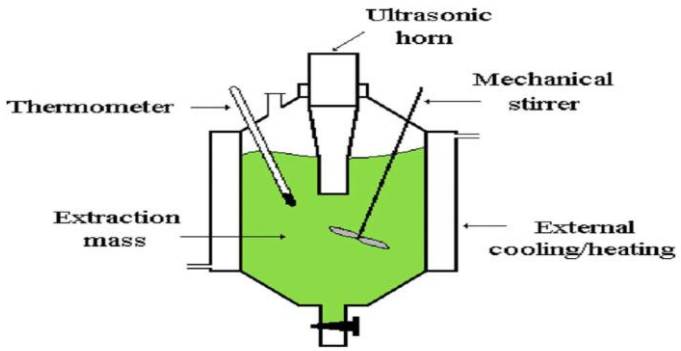

Fig 1. Sonication instrument for extraction of GABA.

2.3 Preparation of Derivatization Reagent

A derivation reagent has been made. As follows, 150 mg o-phthaldialdehyde was combined with 3 mL methanol, 27 mL 0.1 M tetraborate sodium (pH 9.5), 500 µl-mercaptoethanol, and 30 mg ascorbic acid in a mixture that included 3 mM methanol.

a) HPLC Analysis

500 µl of sample was combined with an equivalent volume of derivatization reagent, vortexed for 20 seconds, filtered, and injected into the HPLC apparatus for analysis. At 336 nm, the GABA spectrum was obtained. Methanol (a) and 0.05 percent formic acid were used as rinse solvents (b). The injection volume was 12 µl and the flow rate was 0.6 ml per minute. The gradient programme went like this: 0-14 minutes: 30% - 25% of b; 14-19 minutes: 24% - 32% of b; 19-25 minutes: 34% of b; 19-25 minutes: 34% of b.

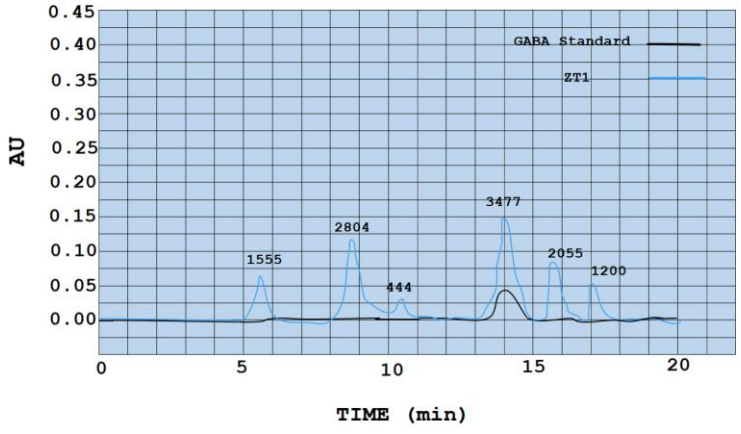

Fig 2. HPLC chromatograms of GABA from standard and ZT1 fruit.

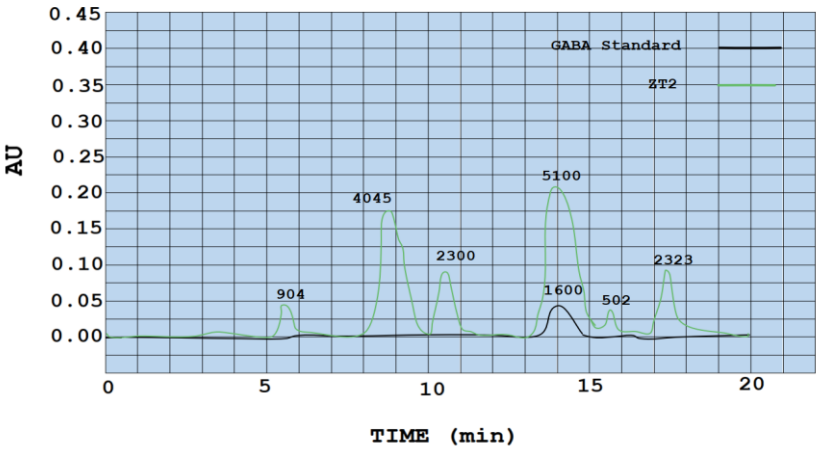

Fig 3. HPLC chromatograms of GABA from standard and ZT2 fruit.

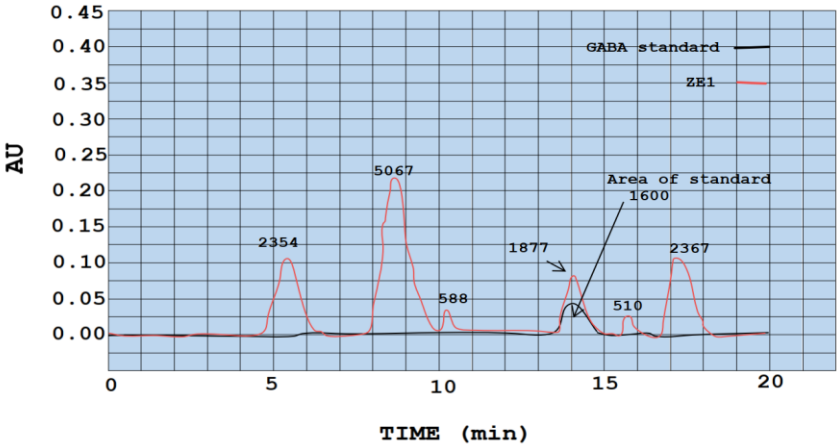

Fig 4. HPLC chromatograms of GABA from standard and ZE1 fruit.

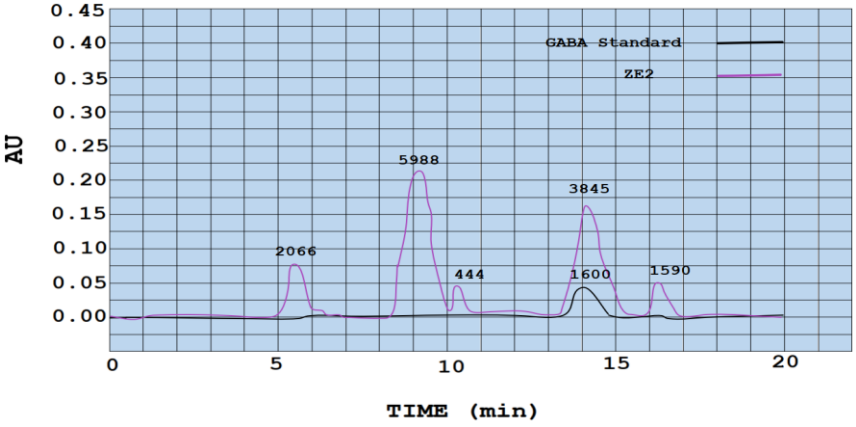

Fig 5. HPLC chromatograms of GABA from standard and ZE2 fruit.

2.4 Preparation of standard solution

Methanol was used to make the stock standard solution with 230 µg/mL beta-aminobutyric acid (GABA).

b) Calibration of GABA.

For the linearity studies, nine different concentrations of ϒ-aminobutyric acid (GABA) were used. Peak area versus concentration showed a linear calibration curve for all samples in the 100–900 µg/ml concentration range. The linear regression equations for GABA are found to be Y = 5.5947X + 278.67. The calculated regression coefficient values (0.9983) indicated a high degree of linearity.

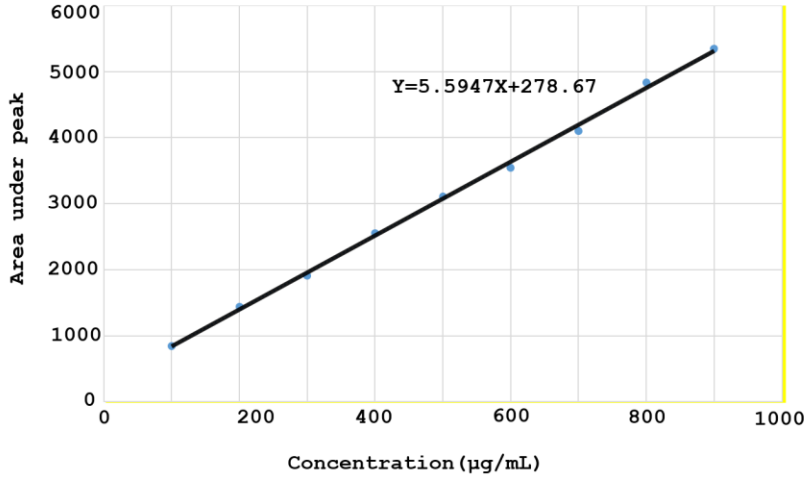

Fig 6. Shown the calibration curve of GABA.

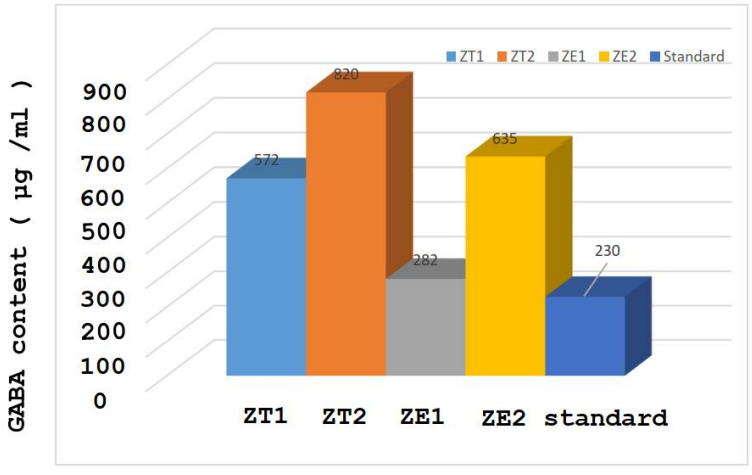

Fig 7. Shown the GABA content in several ziziphus fruits.

3 Results and Discussion

Figures (2-5) show the chromatography of the GABA standard and four samples (ZT1, ZT2, ZE1, and ZE2), and the results of HPLc are shown in Table (1). The concentration of GABA in ripe Tuffahi and Earmutin was higher than that in unripe sea buckthorn fruits where the concentrations were all the following [ZT1 (572 µg/ml), ZT2 (840 µg/ml), ZE1 (282 µg/ml) and ZE2 (635) micrograms/ml.

Table 1. Show the concentration of GABA in Ziziphus fruit.

Samples	The area under the curve (AUC)	Conc of GABA (µg/ml)
ZT1	3477	572
ZT2	5100	840
ZE1	1877	282
ZE2	3845	635
GABA Standard	1600	230

As a result, the therapeutic effect of GABA depends on the amount of sea buckthorn consumed during food. For example, Diana presented her research on the amount of (GABA) a person consumes to influence blood pressure reduction and discovered that a daily intake (10-70 mg) is effective in lowering blood pressure. The same study also found that eating an amount (200 g) of ripe buckthorn has a significant sedative effect [27]. In another study conducted by (Okay) and others on several volunteers, each of them ate an amount (26.4 g) of (GABA) and found that this substance leads to a reduction in sleep disturbances, insomnia, and depression. (65%) of them [28]. The researcher (Lnoue) conducted a study on 39 patients with moderately high blood pressure, ranging in age from (28 - 81) years, with an average of (54). Year. They were given a dose of GABA with fermented milk. And the researcher found a decrease in their blood pressure within (2 - 4) weeks [29].

5 Conclusion

From the current study, we find that GABA is present in the fruits of Tuffahi and Earmotiun. We also found that "the percentage of (GABA) substance increases during the stages of the growth process to reach the peak concentration at the freshness and full maturity. Also, it was found in this study that there is a greater percentage of (GABA) in the fruits of Tuffahi compared to the fruits of Earmotiun.

References

[1]. Adeghate, E.; Ponery, A.S. (2002). GABA in the endocrine pancreas: cellular localization and function in normal and diabetic rats. *Tissue Cell* 34, 1-6.

[2]. Aoki, H.; Uda, I.; Tagami, K.; Furuya, Y.; Endo, Y.; Fujimoto, K. (2003). The production of a new tempeh like fermented soybean containing a high level of γ- aminobutyric acid by anaerobic incubation with *Rhizopus. Biocsi. Biotechnol. Biochem* 67(5), 1018-1023.

[3]. Blanc, P.J.; Loret, M.O.; Santerre, A.T.; Pareilleux, A.; Prome, D.; Prome, J.C.; Laussac, J.P.; Goma, G. (1994). Pigment of *Monascus J. Food Sci.* 59, 862-865.

[4] Li, H.; Qiu, T.; Huang, G.; Cao, Y. (2010). Production of gamma-aminobutyric acid by *Lactobacillus brevis* NCL912 using fed-batch fermentation. *Microb. Cell Fact.* 9, 85.
[5] Li, H.; Qiu, T.; Gao, D.; Cao, Y. (2010). Medium optimization for production of gamma-aminobutyric acid by *Lactobacillus brevis* NCL912. *Amino Acids* 38, 1439-1445.
[6]. Li, Q.; Yao, H.Y.; Zhang, H. (2004). Studies on Screening for γ -aminobutyric acid producer and optimization of fermentation conditions. *Chin. J. Amino Acids Biotic Res.* 26(1), 40-43.
[7]. Lu, X.; Xie, C.; Gu, Z. (2008). Isolation of γ-aminobutyric acid-producing bacteria and optimization of fermentative medium. *Biochem. Eng. J.* 41, 48-52.
[8] Wu .C, Hsueh .Y.H, Kuo . G.H , Liu . S. J , Characterization of a potential probiotic Lactobacillus brevis RK03 and efficient production of γ -aminobutyric acid in batch fermentation, Int. J. Mol. Sci. 19 (143) (2018) 1–16.
[9] Hong . J , Kim . K, Biochemical and Biophysical Research Communications Crystal structure of g -aminobutyrate aminotransferase in complex with a PLP-GABA adduct from Corynebacterium glutamicum, Biochem. Biophys. Res. Commun. 514 (3) (2019) 601–606.
[10] Diana. M, Quílez. J, Rafecas .K , "Gamma-aminobutyric acid as a bioactive compound in foods : a review, J. Funct. Foods 10 (2014) 407–420.
[11] Kim.M.K.K, Isolation and identification of γ -aminobutyric acid (GABA)-producing lactic acid bacteria from kimchi, J. Kor. Soc. Appl. Biol. Chem. 55
(2012) 777–785.
[12] Zhang.Q, Qing.S, T. Xiao, Z. Shuming, Z. Lin, T. Jie, X. Wenliang, Characterizatio of γ -aminobutyric acid (GABA) -producing Saccharomyces cerevisiae and coculture with Lactobacillus plantarum for mulberry beverage brewing, J. Biosci. Bioeng. 129 (4) (2019) 447–453.
[13] Hernández, F., Noguera-Artiaga, L., Burló, F., Wojdyło, A., Áa, C.-B.,Legua, P. (2016). Physico-chemical, nutritional, and volatile composition and sensory profile of Spanish jujube (Ziziphus jujuba Mill.) fruits. Journal of the Science of Food and Agriculture, 96(8), 2682–2691.Huang, B. (2017). The Chinese Rural Statistc Yearbook. Beijing: China Statistic Press.
[14] Zhan, R., Xia, L., Shao, J., Wang, C., & Chen, D. (2018). Polysaccharide isolated from Chinese jujube fruit (Zizyphus jujuba cv. Junzao) exerts anti-inflammatory effects through MAPK signaling. Journal of Functional Foods, 40, 461–470.
[15] Finotti, E., Bersani, E., Del Prete, E., & Friedman, M. (2015). Application of a functional mathematical index (FMI) for predicting effects of the composition of jujube fruit on nutritional quality and health. Journal of Food Composition and Analysis, 42, 164–170.
[16] Chen, J., Zhonggui, L., Maiwulanjiang, M., Zhang, W. L., Zhan, J. Y. X.,Lam, C. T. W., … Tsim, K. W. K. (2013). Chemical and biological assessment of Ziziphus jujuba fruits from China: Different geographical sources and developmental stages. Journal of Agricultural and Food Chemistry, 61(30), 7315–7324.
[17] Bai, L., Zhang, H., Liu, Q., Zhao, Y., Cui, X., Guo, S., … Bai, N. (2016).Chemical characterization of the main bioactive constituents from fruits of Ziziphus jujuba. Food & Function, 7(6), 2870–2877.
[18] Li, X., Li, X., Zhou, B., Man, S., Gao, W., & Jing, S. (2017). Study on the bioactive constituents and in vitro antioxidant and in vivo anti-inflammatory activities of extracts from the fruits of ziziphus jujuba mill. cv. jinsixiaozao hort. Food Science and Technology Research, 23(3), 417–426.
[19] Pu, Y., Ding, T., Wang, W., Xiang, Y., Ye, X., Li, M., & Liu, D. (2018). Effect of harvest, drying and storage on the bitterness, moisture, sugars, free amino acids and phenolic compounds of jujube fruit (Zizyphus jujube cv. Junzao). Journal of the Science of Food and Agriculture, 98(2),628–634.
[20] FNIC, (Food and nutrition information center) (internet addresses). http://warp. nal.usda.gov/ fnic/etext/000105.html (2008).
[21] Sena.L.P , D.J. Vanderjagt, Rivera.C, Tsin .A.CT.C , Muhamadu.I, Mahamadou.O, Millson.M , Pastuszyn.A and Glew. R.H, Plant Foods Human Nutr. , 52, 17 (1998).
[22] Al-Kindy .S.M.Z , Abdulnour.A.O and M.M. Al-Rasbi, Sci. Technol., 6, 39 (2001).
[23].Montiel-Herrera.A , Campista-Leon .S , Camacho-Hernandez.I.L , Rios-Morgan .A and Delgado-Vargas.F , Int. J. Food Sci. Nutr., 56, 587 (2005).
[24] Elaloui, M., Mguis, K., Laamouri, A., Albouchi, A., Cerny, M., Mathieu, C., Vilarem, G.,Hasnaoui, B., 2011. Fatty acids and sterols oils compositions of four Tunisian ecotypes of Ziziphus zizyphus (L.). H. Karst. Acta Bot. Gallica 159, 25–31.
[25] Elaloui, M., Laamouri, A., Albouchi, A., Cerny, M., Mathieu, C., Vilarem, G., Hasnaoui,B., 2014a. Chemical compositions of the Tunisian Z jujuba oil. Emir. J. Food Agric. 26, 602–608.

[26] Elaloui, M., Laamouri, A., Fabre, J., Mathieu, C., Vilarem, G., Hasnaoui, B., 2014b. Distribution of free amino acids: polyphenols and sugars of Ziziphus jujube pulps harvested from plants grown in Tunisia. Nat. Prod. Res. 29, 94–97.
[27] Diana, M., Quilez, J., & Rafecas, M. (2014). Gamma-aminobutyric acid as a bioactive compound in foods: A review. Journal of Functional Foods, 10, 407–420.
[28] Okada, T., Sugishita, T., Murakami, T., Murai, H., Saikusa, T., Horino, T., …Takahashi, T. (2000). Effect of the defatted rice germ enriched with GABA for sleeplessness depression, autonomic disorder by oral administration. Journal of the Japanese Society for Food Science and Technology, 47(8), 596–603.
[29] Inoue, K., Shirai, T., Ochiai, H., Kasao, M., Hayakawa, K., Kimura, M., & Sansawa, H. (2003). Blood-pressure-lowering effect of a novel fermented milk containing γ-aminobutyric acid (GABA) in mild hypertensives. European Journal of Clinical Nutrition, 57, 490–495.

Paediatric Germ Cell Tumours: Case Study Oncology Centre of Basra Between 2004-2015

Nayef J. Farhan Al-Khafaji[1], Wasan H. Saud Al-Ibadi[2], Aqila A. Sahi Kadhim[3]
{nayef_farhan@yahoo.com[1], wasanhameed27@yahoo.com[2], akilaabood@yahoo.com[3]}

Basra Special Children Hospital, Basra, Iraq[1,2]
Gynecologist in Basra general hospital[3]

Abstract. The incidence of germ cell tumours (GCT) was 2.9% in all malignant tumours of children less than 16 years old with the occurrence of GCT in male to female ratio was 1.0:1.1. The main aim of this study is to exhibit the outcome and treatment of children less than 16 years old in Basra Oncology Centre in Iraq between 2004-2015. In the oncology Centre of Basra 45 cases of GCT age 1 to 156 months (mean 78.5 months). The sample divide as a following, female 24 (46.7%) and male 21(53.3%) with gonadal 21(46.7%) testes 9(20%) and ovary 12(26.7%). Histologically, in our data, the most common GCT was teratomas 2 mature teratomas these two cases were excluded from the current study, 20 cases immature 44.4%, followed by yolk sac tumours nineteen cases (n:19=42.2%), dysgerminoma (n: 4=8.9%) and embryonal carcinoma (n: 2=4.4%). Based on the results, about 5 years overall survival (OS) is 88.9%. During the previous years, the surgical, chemotherapy, and radiotherapy guidelines for (GCT) have been purified to decrease the early and late morbidities and associated with improving survival. Used of Platinum (carboplatin /cisplatin) the outcome of children with (GCT) has improved 5-year survival.

Keywords: Germ cell tumours, Platinum, children, Basra

1 Introduction

Germ cell tumour (GCT) incidence is approximately 2-3% of paediatric malignancies. The prevalence of Germ Cell Tumours in white children is 2.5 per million in and in African American children is 3.0 per million under 15 years of age. comparison the incidence of GCT in male: female the ratio was 1.0:1.1[1].

GCTs are highly occurrence in the gonadal (ovaries and testes) follow by extragonadal sites like mediastinum, pineal and sacrococcygeal regions, and retroperitoneum [1, 2]. The germ cells are the source and origin of sperm and ova and after fertilization then produce all the embryonic and extraembryonic structures of the developing embryo. totipotential germ cell is the origin of Yolk sac tumours which is differentiated to extraembryonic structures while Teratomas are origin from the second type of cell which produces the embryonic tissues so that neoplasms contain tissues from all three germ layers (ectoderm, endoderm, and mesoderm) so Teratomas are either begin or malignant depending on present or absent of malignant germ cell elements (embryonal carcinomas, germinomas, endodermal sinus tumours or choriocarcinomas) or primitive neuroectodermal tumours which is a rare malignant somatic element in paediatric[1, 3].

IMDC-IST 2021, September 07-09, Sakarya, Turkey
Copyright © 2022 EAI
DOI 10.4108/eai.7-9-2021.2314945

GCTs show numerous histologic subtypes. The features of each histologic subtype are independent of presenting clinical characteristics; tumour biology depends on the site of origin and the clinical behaviour vary with state, site of origin, and age of the patient. The introduction of platinum-based chemotherapy(carboplatin and cisplatin) increased the overall survival by more than 80%, even in late stages [2, 4].
This project aimed to display our oncological centre experience with the epidemiological and clinical characteristics, handling, management, and outcome in germ cell tumours (GCTs) over 12 years.

2 Materials and Methods

Forty-five children with GCT were admitted to our oncological centre between 2004 and 2015. The pause date for analysis of these patients was February 2016 and only follow members in our study for five years. Their pathologic features, clinical characteristics, methods of treatment, relapse, and survival outcomes were retrospectively evaluated. The tumours were stratified according to the Dehner system[5]. In our study, two mature teratoma patients were diagnosed and excluded. Table 1 shows the Children's Oncology Group (COG) classification system for staging was used[5, 6].

Table 1. Children's Oncology Group (COG) staging system.

Stage I	Complete surgical removal associated with margins tumour-free.
Stage II	Microscopic residual tumour or persistently raised tumour markers, with negative lymph nodes.
Stage III	Biopsy only, or gross residual disease, lymph node involvement.
Stage IV	Metastatic tumour.

The quantitative variables were described using median and range; qualitative variables were described using frequency and percentages. We used the chi-square test to examine the relationship between pairs of variables. Overall survival (OS) and relapse-free survival (RFS) distributions were estimated by the method of Kaplan-Meier survival analyses. Using the Cox proportional hazards regression model, multivariate analyses were performed to determine the variables that were independently predictive of prognosis.

3 Results

Throughout twelve years, forty-five patients with GCTs were admitted to the Oncology Centre of Basra. Distribution data of the 45 patients according to the sex 24 were female and 21 were male, as illustrated in Table 2.

Table 2. Sex incidence in GCT patients in our study.

Sex	**No.**	**%**

Female	24	53.3
Male	21	46.6

Their median age was 78.5 months (1-156 months). The children society classified according to the age to the following group[7]:

- Neonates: birth up to 1 month.
- Infants: 1 up to 24 months; (1months to 2years)
- Children: 24 up to 144 months; (2 years to12 years)
- Adolescents: 144 up to 192 months;(12 years to 16 years) [7]

Table 3. Age distribution in GCT and percentage.

Age	NO.	percentage
birth up to 1 month	1	2.2
1 up to 24 months	14	31.1
24 up to 144 months	29	64.4
144 up to 192 months	1	2.2

As shown in Table 3, the most common age associated with GCT were 24 up to144 months of age (64.4%). The sex distribution in GCT in Oncology Centre of Basra was female more than male; the female was 24(53.3%) and the male was 21 (46.6%); male; female (1:1.1). in all age groups either same or female more than male. The abdominal or pelvic mass associated with abdominal distension was present in 20 patients(43.5%) which is identical to other signs included sacrococcygeal mass in 20 patients (43.5%). Abdominal pain was the second most frequent symptom, reported in 19 patients (41.3%) either acute, chronic, or both. The third important symptom was increased testicular size with a palpable mass in 10 patients (21.7%). Other symptoms and signs included constipation, precocious puberty, urinary symptoms, nausea, vomiting.

Table 4. Occurrence of signs and symptoms in GCT.

Symptoms and Signs	No.	%
Abdominal distension	20	43.5
Sacrococcygeal mass	20	43.5
Abdominal pain	19	41.3
Increase testicular size	10	21.7

The abdomen ultrasound and Computed tomography which were the most common investigation used diagnosis and follow-up of patients with GCT. abdominal ultrasound, which was the most common investigation, used in all patients. Computed tomography was performed for most patients. Magnetic resonance imaging was not performed. Serum alpha-fetoprotein (AFP) level:

1) Normal (<20IU/ml)
2) Moderate (20-399IU/ml)
3) Elevated (≥400IU/ml)

Alpha-fetoprotein (AFP) was measure in 27 (60%) patients in the oncology Centre of Basra. four cases were normal <20IU/ml (8.9%) ,thirteen cases Moderate 20-399IU/ml (28.8%) and ten cases Elevated ≥400IU/ml (22.2%). AFP measurement according to the tumour histopathology Teratoma 14 patients (31.1%), yolk sac 12 patients (26.6%), and embryonal carcinoma one case (2%). Unfortunately, eighteen cases (40%) with GCT did not measure the tumour markers because of socio-economic difficulties.

Table 5. Alpha fetoprotein level evaluation in GCT.

AFP level	No.	%
Not measure	18	40
Normal (<20IU/ml)	4	8.9
Moderate (20-399IU/ml)	13	28.8
Elevated(≥400IU/ml)	10	22.2

The most common site for the presence of GCT was the extragonadal site 24 patients (53.3%) extragonadal (4 retroperitoneum, 20 sacrococcygeal) as presented in Table 5, the second place was ovaries 12 patients (26.6%) and the testes were lesser site 9 patients (20.1%).

Table 6**.** GCT site distribution.

Location	No.	%
extragonadal	24	53.3
ovaries	12	26.6
testes	9	20.1

The testicular tumour mainly occurs at age 1month to 2 years(5cases 11.1%), the ovarian tumours most common in 2 to 12 years(11 cases 24.4%), and also the extragonadal tumour commonly in 2-12 years old (14 cases 31.1%). Histologically, teratomas were found most frequently (2 mature, 20immature 44.4%), followed by yolk sac tumours (n:19=42.2%), dysgerminoma (n:4=8.9%), and embryonal carcinoma (n: 2=4.4%), as illustrated in Table 7.

Table 7**.** GCT histological occurrence.

Histology	No.	%
teratomas	20	44.4
yolk sac tumours	19	42.2
dysgerminoma	4	8.9
embryonal carcinoma	2	4.4

The distribution of GCT according to the age; teratomas are most frequently in 2-12 years old patients and yolk sac tumours occur mostly in less than 2 years old patients, as shown in Fig 1.

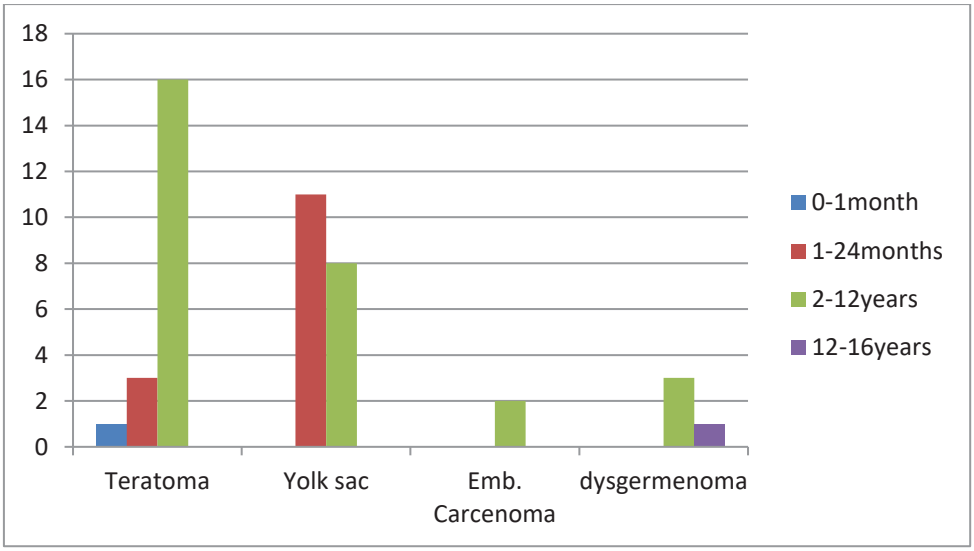

Fig 1. GCT histological distribution according to the age.

In the oncology Centre of Basra found teratomas most frequently occur in females while the yolk sac occurs mostly in males.

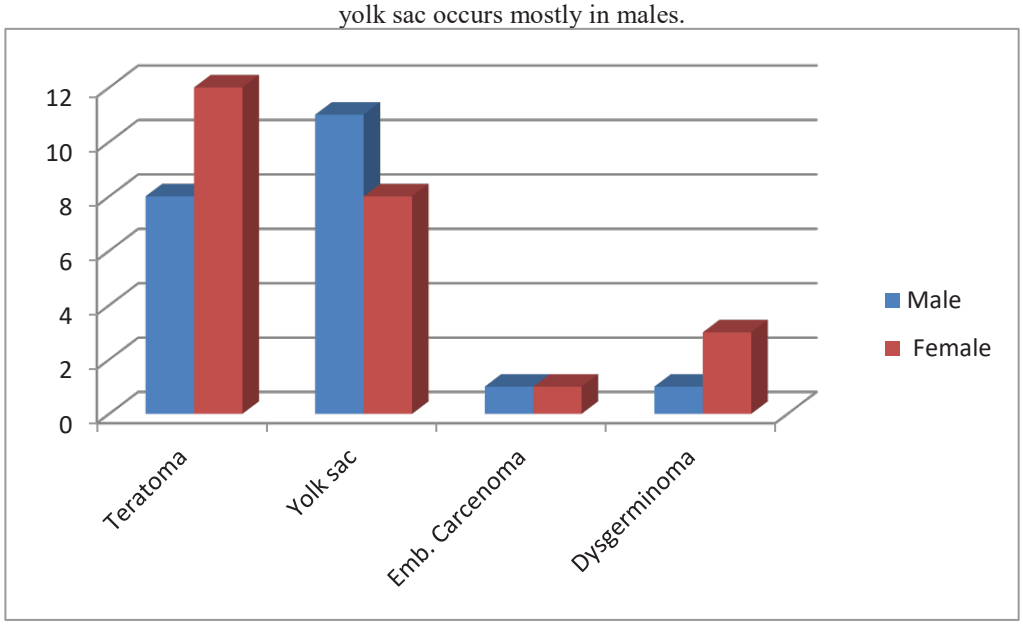

Fig 2. GCT histological distribution according to the sex.

The prevalence staging in GCT in the oncology Centre of Basra the most common was stage III 23 cases (51.1%) follow by stage II was 10 cases (22.2%) then stage I was 7 cases (15.6%) and the last one was stage IV 5 cases (11.1%).

Table 8**.** Allocation of GCT according to the stagging system.

Stage	No,	%
I	7	15.6
II	10	22.2
III	23	51.1
IV	5	11.1

Management of the GCT in all patients was surgical excision either for treatment or for biopsy followed by chemotherapy. Previously before the start, our collection of data in the oncology Centre of Basra used VAC (vincristine, actinomycin, cyclophosphamide) protocol .while in a period of our study used BEP protocol (cisplatin, bleomycin, and etoposide) as four to six courses depending on the stage of the disease.
Finally, the outcome of GCT in oncology Centre of Basra overall survival (OS) was 86.7%, that during five years (60 months) follow up and the outcome Exitus six cases (13.3%) two of them during treatment and the remainder four died during follow up, all of them were at a late stage (stage IV).

Table 9. Outcome of GCT in oncology Centre of Basra overall survival (OS)

Outcome	No.	%
overall survival	39	86.7
Exitus	6	13.3

4 Discussion

Paediatric germ cell tumours (GCTs) are uncommon and various tumours are hypothesized to occur as a result of events in the uterus although that largely take place of unknown ethology[8]. GCT arises due to variation from normal differentiation of germ cells and includes a heterogeneous group of neoplasms with remarkable variability concerning histology and site of presentation: immature GCTs, malignant and Benign can be present in paediatric group with different rates, also according to age. The GCT histopathological types and sites differed with age and sex groups. The clinical characteristics found in this study are similar to other national and international studies related to the issue[9].
The most common age of occurrence of GCT was below 24 months 21 patients (46.6%). second, the peak incidence of GCT occurs 1-23 months age group. This step of the result is like a study conducted by Özdemir, et al. Where the first peak was observed during the first 2 years of life. At less than one year old GCT was more incidence in females than males (M: F 1:2.5) there was a highly significant difference between the incidence of GCT in females than females in the first two years of life. While in 2-5 years old the female more involvement than male (F: M 1:1.1). The finding of this study agreed with Özdemir, et al., [2]. The teratoma was most patients 20 cases (44.4%) mainly immature teratoma. Teratoma occurs highly incidence in females (26.6%) and males (17.7%) follow by yolk sac 19 cases (42.2%) commonly occur in male patients 11

cases (24.4%) and female 8 patients(17.7%). We excluded two patients who were diagnosed with mature teratoma and eliminated them in the evaluation of survival, staging, and follow regularly. Extragonadal site of origin was the most common (Sacrococcygeal and retroperitoneal regions) in 24 patients (53.3%). the Sacrococcygeal was the most frequent extragonadal GCTs 20 cases(44.4%), diagnosed during the first two years of life, half (50%) occurred at the sacrococcygeal region.
The outcome in the oncology Centre of Basra has highly improved OS (86.6%) as in Gobel U, et al. The prognosis in GCTs did not improve until the late 1970s when the VAC regimen became the standard chemotherapy in GCTs. Since the introduction of platinum-based agents(carboplatin and cisplatin) in paediatric chemotherapy protocol, the survival rates for children with malignant GCTs ranging from 75% to more than 90% [10]. In our follow up the OS was higher than another centre can explain by a little number of patients.

5 Conclusion

Our study demonstrates a correlation between tumour stage and survival. This can be explained by most Exitus patients associated with stage IV. The number of candidates in our series was little because our infrastructure capacity was very limited and depend on limited facilities. must be in the future used value of microRNAs as markers for enhancing the diagnosis and follow up the GCT and Elevated AFPand B-HCG level at the time of diagnosis and follow up had a beneficial effect on prognosis. In advanced stage and poor prognosis GCT advice used neoadjuvant (preoperative) chemotherapy to try to improve outcome.

References

[1] J. D. Fish, *et al.*, *Lanzkowsky's manual of pediatric hematology and oncology*: academic press, 2016.

[2] S. İncesoy-Özdemir, *et al.*, "Clinical and epidemiological characteristics of children with germ cell tumors: A single-center experience in a developing country," *The Turkish journal of pediatrics,* vol. 59, pp. 410-417, 2017.

[3] S. M. C. de Sousa Lopes, *et al.*, "Proximal visceral endoderm and extraembryonic ectoderm regulate the formation of primordial germ cell precursors," *BMC Developmental Biology,* vol. 7, pp. 1-9, 2007.

[4] M. J. Murray, *et al.*, "Identification of microRNAs from the miR-371∼373 and miR-302 clusters as potential serum biomarkers of malignant germ cell tumors," *American Journal of Clinical Pathology,* vol. 135, pp. 119-125, 2011.

[5] L. Dehner, "Gonadal and extra gonadal germ cell neoplasms: teratomas in childhood," *Pathology of neoplasia in children and adolescents,* 1986.

[6] F. Shaikh, *et al.*, "Paediatric extracranial germ-cell tumours," *The Lancet Oncology,* vol. 17, pp. e149-e162, 2016.

[7] I. Mahmood, "Prediction of drug clearance in children: impact of allometric exponents, body weight, and age," *Therapeutic drug monitoring,* vol. 29, pp. 271-278, 2007.

[8] J. N. Poynter, *et al.*, "Trends in incidence and survival of pediatric and adolescent patients with germ cell tumors in the United States, 1975 to 2006," *Cancer,* vol. 116, pp. 4882-4891, 2010.

[9] M. Büyükpamukcu, *et al.*, "Malignant sacrococcygeal germ cell tumors in children: A 30-year experience from a single institution," *Tumori Journal,* vol. 99, pp. 51-56, 2013.

[10] U. Göbel, *et al.*, "Germ-cell tumors in childhood and adolescence," *Annals of oncology,* vol. 11, pp. 263-272, 2000.

Evolution the Correlation Between the Severity of Cytomegalovirus Infection among Aborted Women with Vitamin D and Oxidative Stress Biomarkers

Batool A. Hussein*[1], Khalid M. Dakhel*[2], Raid M. H. Al-Salih*[3]
{batoolhussein100@gmail.com[1]}

Ministery of health – AL-Shatraa General Hospital[1]
Southern Technical University - Nassiriah Technical Institute - Community Health Department[2]
University of Thi-Qar - College of Science- Department of Chemistry[3]

Abstract. The most common complication of early pregnancy is abortion. Embryo-fatal infections have been documented to cause less than 4% of spontaneous abortions (SAs). Viruses, notably cytomegalovirus, appear to be the most frequently involved pathogens. The study is a case-control study conducted in Bint Al-Huda Teaching Hospital in the period between October 2020 to March 2021. One hundred subjects enrolled in this study and divided into (25) aborted CMV^+ women, (25) aborted CMV^- women, (25) non- aborted CMV^+ women as patients' groups, and (25) non- aborted women with cytomegalovirus seronegative test as a control group. This study was designed to assess the correlation between the severity of CMV infection among aborted women with VD levels and oxidative stress biomarkers (Malondialdehyde, Ceruloplasmin, and transferrin). Anti-cytomegalovirus antibody was positively correlated with vitamin D, MDA, and ceruloplasmin and negatively correlated with transferrin as an oxidative stress biomarker.

Keywords: Aboration, *Cytomegalovirus*, vitamin D, Oxidative stress

1 Introduction

Expulsion or evacuation of the embryo or foetus weighing less than 500 g, which is comparable to around 20–22 weeks of gestation, is classified as miscarriage or spontaneous abortion. It is the most common early pregnancy problem [1]. 6–15 percent of all clinically confirmed pregnancies end in spontaneous abortion, according to estimates [2].
Genetic variables, anatomic factors, autoimmune illnesses, endocrine dysfunction, thrombophilia, lifestyle issues, and maternal infections all have a role in spontaneous abortion. However, in up to 50% of instances, the underlying cause remains unknown [3]. Embryo-fatal infections have been documented to cause less than 4% of spontaneous abortions (SAs). The creation of harmful metabolic by-products, as well as lethal or placental infection, are all conceivable mechanisms [4]. Viruses appear to be the most commonly involved pathogens, and CMV is a common virus that can reach the placenta by viremia, which can occur after both primary and recurrent infection, or via an ascending route from the cervix, which is the most common route [5].

IMDC-IST 2021, September 07-09, Sakarya, Turkey
Copyright © 2022 EAI
DOI 10.4108/eai.7-9-2021.2314930

After viral infections, reactive species are frequently generated. Reactive species are protected by antioxidant defences, which include both enzymatic and non-enzymatic components. Oxidative stress is defined as an imbalance in the creation of reactive species and the body's incapacity to detoxify these reactive species [6].
Vitamin D is a secosteroid hormone that helps maintain mineral balance and bone metabolism [7]. Vitamin D regulates the immune system in addition to its physiological role [8]. Low vitamin D levels during pregnancy may increase the risk of obstetrical problems [9]. A substantial percentage of RSA patients are said to be vitamin D deficient[10], and low vitamin D levels have been linked to an increased risk of miscarriage in the first trimester [11].

2 Materials and Methods

2.1 Sample collection

25 aborted women with CMV seropositive (A), 25 aborted women with CMV seronegative (B), and 25 non-aborted women with CMV seropositive (C) with an age range from (16-43) years were selected from those attending the Teaching Hospital of Bint Al-Huda at Thi-Qar province during the time between October 2020 and March 2021 were included in this study as patient groups. Another group of 25 healthy individuals (D) with an age range from (16-43 years) was included in this study as a control group.

2.2 Exclusion Criteria

Women with diabetes and cardiovascular illnesses, could be a good cause of abortion however, this has been excluded from this study**.** A 3-5 ml from each subject, as peripheral blood was collected by vein puncture. The collected samples were placed in a gel vacuum tube and allowed to clot at room temperature, and then the samples were centrifuged at 3600 rounds per minute (min) (RPM) for 10 min for serum separation. The collected sera were transferred to the different tubes and frozen at $^{-}$20 °C to be analysed later unless used immediately. Homolysis samples were discarded.

2.3 Determination of Anti-Cytomegalovirus IgG and IgM Antibodies

Bioactive Diagnostical used enzyme-linked immunosorbent test (ELISA) kits to measure CMV IgG and IgM. (Germany).

2.4 Determination of Total Vitamin D

Monobind Inc's enzyme-linked immunosorbent assay (ELISA) kit was used to detect total vitamin D. (USA).

2.5 Determination of Malondialdehyde

Sunlong used an enzyme-linked immunosorbent test (ELISA) kit to measure malondialdehyde (MDA) (China).

2.6 Determination of Ceruloplasmin

Ceruloplasmin (Cp) was tested by a biochemical method based on the Cp-catalysed oxidation of colourless paraphenylenediamine (PPD) to blue-violet oxidize form.

2.7 Determination of Transferrin

Transferrin was measured by measuring both iron concentration and total iron-binding capacity (TIBC) and using the following formula

$$TF\left(\frac{g}{l}\right) = TIBC(\mu g/L)X0.007 \quad (1)$$

2.8 Statistical Analysis

Version 22 of the Statistical Package for Social Sciences (SPSS) was used. The correlation between continuous variables was determined using Pearson correlation coefficient analysis. P-values of less than or equal to 0.05 are deemed significant ($p<0.05$).

3 Results

Table 1 shows the correlation between IgG titer and VD3 in all study groups. There was a positive non-significant Pearson correlation amongst IgG titer and VD in the aborted group with CMV, non-aborted with CMV and control groups, and a negative non-significant correlation between IgG titer and VD in an aborted group with non-CMV.

Table 1. Correlation between IgG titer and total VD in all study groups.

Study Items	**Statistic Relation**	**Statistics**							
		A		B		C		D	
		IgG	Sig	**IgG**	Sig	**IgG**	Sig	**IgG**	Sig
VD3	Pearson correlation	.148	.47	-.078-	.71	.113	.59	.154	.46
No.		25		25		25		25	

Table 2 shows the correlation between IgG and MDA levels in all study groups. Positive non-significant correlation between IgG titer and serum MDA in aborted with CMV and control groups. Table 2 also shows a negative correlation between IgG titer and serum MDA in aborted with non CMV and non-aborted with CMV groups.

Table 2. Correlation between *cytomegalovirus* IgG titer and serum MDA in all study groups.

Study Item	Statistic Relation	Statistics							
		A		B		C		D	
		IgG	Sig	**IgG**	Sig	**IgG**	Sig	**IgG**	Sig
MDA	Pearson correlation	.236	.25	-.003-	.99	-.375-	.06	.063	.76
No.		25		25		25		25	

Table 3 shows the correlation between IgG titer and serum ceruloplasmin level in patients and control groups. A positive non-significant Pearson correlation between IgG titer and ceruloplasmin in aborted with CMV and non-aborted with CMV groups. A negative non-significant correlation between IgG titer and ceruloplasmin in aborted with non CMV and control groups.

Table 3. Correlation between *cytomegalovirus* IgG titer and serum ceruloplasmin in all study groups.

Study Item	Statistic Relation	Statistics							
		A		B		C		D	
		IgG	Sig	**IgG**	Sig	**IgG**	Sig	**IgG**	Sig
CP	Pearson correlation	.048	.81	-.224-	.28	.224	.28	-.196-	.34
No.		25		25		25		25	

Table 4 shows the correlation between IgG titer and serum transferrin level in patients and control groups. A negative non-significant Pearson correlation amongst IgG titer and serum transferrin level is observed in aborted with CMV and control groups. A positive significant correlation between CMV IgG titer and transferrin level in aborted group with non CMV and positive non-significant correlation in a non-aborted group with CMV was revealed in the same table.

Table 4. Correlation between *cytomegalovirus* IgG titer and serum transferrin in all study groups.

Study Item	Statistic Relation	Statistics							
		A		B		C		D	
		IgG	Sig	**IgG**	Sig	**IgG**	Sig	**IgG**	Sig
TF	Pearson correlation	-.166-	.427	.526	.007	.085	.685	-.057-	.786
No.		25		25		25		25	

4 Discussion

Vitamin D has been shown to promote the immune system and antiviral responses by inducing autophagy and the creation of antimicrobial peptides such as catholicising, and it is thought to play a role in protecting the developing foetus from infections during pregnancy [12]. Many cells in the body, including those in the placenta, have the vitamin D receptor, and many of them can convert 25-hydroxyvitamin D (25(OH)D), the predominant circulating form of vitamin D, to its bioactive form, 1,25-dihydroxy vitamin D (1,25(OH)D2) [13]. In the presence of particular conditions or stimuli, this enables for local synthesis of 1, 25 (OH)D2 and subsequent vitamin D-dependent antimicrobial immune responses [14].

Lower levels of the bioactive form of vitamin D, calcitriol (1, 25(OH) D2), have been linked to an increase in both congenital and peri/postpartum CMV infections in perinatally exposed but HIV-uninfected infants born to non-breastfeeding HIV-positive women [15], which is completely consistent with the current study.

During viral infection, inflammatory cells such as macrophages, neutrophils, and dendritic cells identify, envelop, and phagocytose the virus. The pathogens boost the generation of RS by activating the NADPH oxidase complex and nitric oxide synthase in phagocytic cells [16]. Viruses produce RS in different ways, but they all share a similar pathogenic route that emphasises RS generation and antioxidant depletion [17]. Stehbens, (2004) had reported viral infection to induce server oxidative stress in agreement with my current study [17].

ROS upregulates HCMV lytic replication in fibroblasts via extracellular and intracellular pathways, according to Xiao et al., (2015). Furthermore, antioxidant pre-treatment reduces HCMV replication in vitro and in vivo [18], which explains the positive correlation between IgG titer and MDA serum level in the current study.

The antioxidant is expressed at levels capable of sustaining tolerable amounts of ROS within the cells under non-stressed conditions, allowing redox-sensitive activities to function [19]. Some of the effects of stress response induction can help the viral infection, while others can be harmful. The human cytomegalovirus has a number of mechanisms to deal with the negative features of cellular stress responses while keeping the positive ones [20]. According to Tilton et al. (2011), virally infected cells boost the synthesis of antioxidant enzymes that can swiftly remove ROS and maintain redox equilibrium. The current investigation supported Tilton et al., (2011) findings that CMV infection raises antioxidant levels [21].

Transferrin and other antioxidant inhibit viral infection. Kotelnikova *et al*., (2011) that worked on the effectiveness of antioxidants as CMV infection inhibitors in the cell culture of human embryonic fibroblast. This study found that adding antioxidants to the cells reduces viral protein concentrations in the cells to levels similar to those found in non-infected cell cultures [22]. This study agreed with the current study regarding the aborted group with CMV.
Anti-CMV IgM antibodies level among patients' groups in the current study was too low indicating no acute infection with CMV among aborted women which consider as a limitation for the study.

5 Conclusion

The severity of *cytomegalovirus* infection positively correlated with vitamin D, MDA, and ceruloplasmin and negatively correlated with transferrin as oxidative stress biomarkers.

References

[1] Baek KH, Lee EJ, Kim YS. Recurrent pregnancy loss: the key potential mechanisms. Trends in molecular medicine. 2007 Jul 1;13(7):310-7.

[2] Zheng D, Li C, Wu T, Tang K. Factors associated with spontaneous abortion: a cross-sectional study of Chinese populations. Reproductive health. 2017 Dec;14(1):1-9.

[3] El Hachem, Hady, Vincent Crepaux, Pascale May-Panloup, Philippe Descamps, Guillaume Legendre, and Pierre-Emmanuel Bouet. "Recurrent pregnancy loss: current perspectives." *International journal of women's health* 9 (2017): 331.

[4] Landolfo S, Gariglio M, Gribaudo G, Lembo D. The human cytomegalovirus. Pharmacology & therapeutics. 2003 Jun 1;98(3):269-97.

[5] Nigro G, Mazzocco M, Mattia E, Di Renzo GC, Carta G, Anceschi MM. Role of the infections in recurrent spontaneous abortion. The Journal of Maternal-Fetal & Neonatal Medicine. 2011 Aug 1;24(8):983-9.

[6] Camini FC, da Silva Caetano CC, Almeida LT, de Brito Magalhaes CL. Implications of oxidative stress on viral pathogenesis. Archives of Virology. 2017 Apr;162(4):907-17.

[7] Tamblyn JA, Hewison M, Wagner CL, Bulmer JN, Kilby MD. Immunological role of vitamin D at the maternal–fetal interface. Journal of Endocrinology. 2015 Mar 1;224(3):R107-21.

[8] Mott KR, Maazi H, Allen SJ, Zandian M, Matundan H, Ghiasi YN, Sharifi BG, Underhill D, Akbari O, Ghiasi H. Batf3 deficiency is not critical for the generation of CD8α+ dendritic cells. Immunobiology. 2015 Apr 1;220(4):518-24.

[9] Urrutia RP, Thorp JM. Vitamin D in pregnancy: current concepts. Current opinion in obstetrics & gynecology. 2012 Mar;24(2):57.

[10] Ota K, Dambaeva S, Han AR, Beaman K, Gilman-Sachs A, Kwak-Kim J. Vitamin D deficiency may be a risk factor for recurrent pregnancy losses by increasing cellular immunity and autoimmunity. Human reproduction. 2014 Feb 1;29(2):208-19.

[11] Martorell R, Ascencio M, Tacsan L, Alfaro T, Young MF, Addo OY, Dary O, Flores-Ayala R. Effectiveness evaluation of the food fortification program of Costa Rica: impact on anemia prevalence and hemoglobin concentrations in women and children. The American journal of clinical nutrition. 2015 Jan 1;101(1):210-7.

[12] Campbell GR, Spector SA. Vitamin D inhibits human immunodeficiency virus type 1 and Mycobacterium tuberculosis infection in macrophages through the induction of autophagy. PLoS pathogens. 2012 May 10;8(5):e1002689.

[13] Liu N, Kaplan AT, Low J, Nguyen L, Liu GY, Equils O, Hewison M. Vitamin D induces innate antibacterial responses in human trophoblasts via an intracrine pathway. Biology of reproduction. 2009 Mar 1;80(3):398-406.

[14] Walker VP, Zhang X, Rastegar I, Liu PT, Hollis BW, Adams JS, Modlin RL. Cord blood vitamin D status impacts innate immune responses. The Journal of Clinical Endocrinology & Metabolism. 2011 Jun 1;96(6):1835-43.

[15] Bearden A, Van Winden K, Frederick T, Kono N, Operskalski E, Pandian R, Barton L, Stek A, Kovacs A. Low maternal vitamin D is associated with increased risk of congenital and peri/postnatal transmission of Cytomegalovirus in women with HIV. PloS one. 2020 Feb 13;15(2):e0228900.

[16] Camini FC, da Silva Caetano CC, Almeida LT, de Brito Magalhaes CL. Implications of oxidative stress on viral pathogenesis. Archives of Virology. 2017 Apr;162(4):907-17.

[17] Stehbens WE. Oxidative stress in viral hepatitis and AIDS. Experimental and molecular pathology. 2004 Oct 1;77(2):121-32.

[18] Go YM, Jones DP. Redox control systems in the nucleus: mechanisms and functions. Antioxidants & redox signaling. 2010 Aug 15;13(4):489-509.

[19] Alwine, J.C., 2008. Modulation of host cell stress responses by human cytomegalovirus. *Human cytomegalovirus*, pp.263-279.

[20] Tilton C, Clippinger AJ, Maguire T, Alwine JC. Human cytomegalovirus induces multiple means to combat reactive oxygen species. Journal of virology. 2011 Dec 1;85(23):12585-93.

[21] Kotel'nikova RA, Faingol'd II, Poletaeva DA, Mishchenko DV, Romanova VS, Shtol'ko VN, Bogdanov GN, Rybkin AY, Frog ES, Smolina AV, Kushch AA. Antioxidant properties of water-soluble amino acid derivatives of fullerenes and their role in the inhibition of herpes virus infection. Russian Chemical Bulletin. 2011 Jun;60(6):1172-6.

Investigation of Vertical Ground Reaction Force during Walking with the Exoskeleton for Patient with Unilateral Lower Limb Weakness

Niaam Kh. Al-Hayali[1], Jumaa S. Chiad[2], Somer M. Nacy[3], and O. Hussein[4]
{neaam@kecbu.uobaghdad.edu.iq[1], jumaachiad@gmail.com[2], somernacy@googlemail.com[3]}

Biomedical Engineering Department, Alkhwarizmi College of Engineering, University of Baghdad[1]
Mechanical Engineering Department, College of Engineering, Al-Nahrain University[2]
Biomedical Engineering Department, Alkhwarizmi College of Engineering, University of Baghdad[3]

Abstract. Using lower extremity exoskeletons in the healthcare field like for rehabilitation is a substantial application. Lower limb exoskeletons can help in performing specific functions like gait assistance, and physical therapy support for patients who are lost their ability to walk again. The ground reaction force characteristics during human walking can be an important descriptor of gait disorders. The purpose of this study is to reveal the effect of the designed lower limb exoskeleton on the patient with right lower limb weakness based on the investigation of the ground reaction force. Results show that dynamic asymmetry practically disappears in the vertical GRF between the left and right legs during walking using the exoskeleton. The symmetry between the left and right limbs when walking using the exoskeleton for the maximum vertical GRF (first peak) is 98.9%, the minimum vertical GRF (the valley) is 99%, and the maximum vertical GRF (second peak) is 97.48%.

Keywords: Exoskeleton, quasi-passive, ground reaction force, gait analysis, rehabilitation.

1 Introduction

Lower extremity exoskeletons have recently been extensively developed as helpful and rehabilitation aids for patients with lower-limb diseases [1-3]. Lower extremity exoskeletons may be defined as wearable systems that are worn by a patient and work in harmony with the patient's movements [4][5]. Lower extremity exoskeletons are used to assist rehabilitation training by providing functional motion assistance for patients with neurological and age-related disorders [3][6-8]. The features of ground reaction force (GRF) during human walking can be a useful diagnostic of abnormal gait. Exoskeletal ambulation can be investigated using GRF analysis to see how the exoskeleton affects the patient with lower limb weakness. The GRF acting on the body during upright movements is a major external force [9] which acts on the foot by a supporting horizontal surface during standing, walking, or running [10] with the same magnitude and in opposite direction to the force applied by the body [11] as shown in Fig 1.

IMDC-IST 2021, September 07-09, Sakarya, Turkey
Copyright © 2022 EAI
DOI 10.4108/eai.7-9-2021.2314896

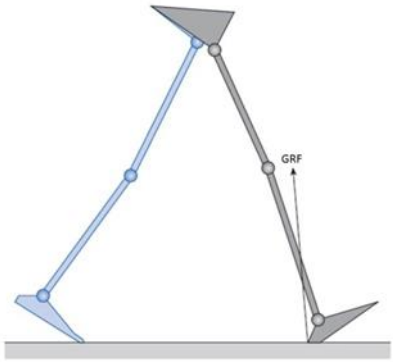

Fig. 1. GRF vector during the heel strike transient [12].

A mechanical sensor system [13] called a force plate is utilised to monitor GRF [14]. This plate is based on Newton's third law of motion [15][16]. Many professional and sophisticated computer systems include GRF measurement, which can be easily collected during normal clinical gait analysis [17]. This force is three-dimensional and consists of a single vertical [18] component plus two horizontal shear components [10]. Each component assesses a distinct aspect of the activity. The vertical component is mostly caused by the body's vertical acceleration [19]. The forces in the anterior-posterior and medial-lateral planes are represented by the two horizontal components [20]. The vertical component of the GRF, which is the force with the greatest magnitude that the earth reacts on the body, receives the most attention [21]. A typical vertical GRF profile of a single walking stride is shown in Fig 2. In a fraction of a second, the vertical GRF of contact with the ground heel strike (HS) will drop to zero and rise abruptly to virtually body weight. The body mass is travelling downhill and settling on the leg at the instant of foot flat (FF). It will be essential to apply a vertical force greater than body weight on the foot to decrease this downward motion while still supporting the body weight. The subject's foot is bearing 120 percent of his body weight at this time. The movement of the body's centre of mass is upward in mid-stance (MS). This action causes an upward acceleration, allowing the body to be supported by a force less than its own weight. At MS, this person has a body weight of 63 percent. The body mass is accelerated forward and upward at heel off (HO), preparing for the stance phase of the other leg. This indicates that the body will need to be supported by more than its own weight. Finally, toe-off (TO) is the point at which the foot loses contact with the ground and the force equalises. The M-shaped graph, also known as a double peak graph, depicts the fluctuation of force in relation to body weight and is typical of normal gait [22]. The purpose of this paper is to study the effect of the designed lower limb exoskeleton on a patient with lower limb weakness by investigated the vertical ground reaction force.

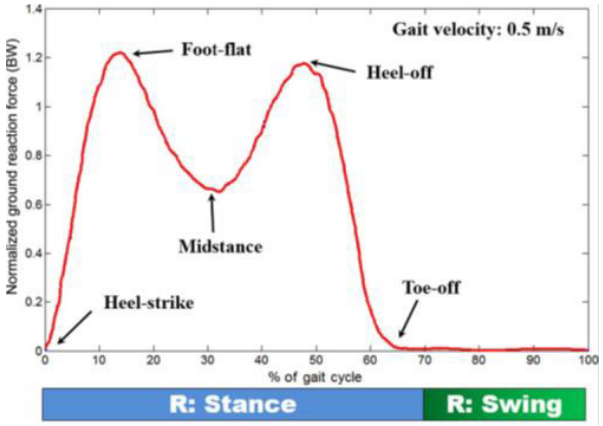

Fig. 2. GRF in a normal walking stage [17].

2 Materials and Methods

2.1 Subject

Within Biomedical Engineering Department of the faculty of Al-Khawarizmi College of Engineering, University of Baghdad, all tests were carried out. The study was conducted on one subject, 21 years old female suffering from right side lower limb weakness. The weight of the subject was (59 Kg), and the length was (1.67 m). The individual was given a thorough description of the study's purpose and process, as well as verbal instructions. The subject was chosen based on the projected exoskeleton's allowable length and shoe size range.

2.1 Procedure

Before the study began, the participant had approximately 15 minutes of acclimatization to the exoskeleton device. Later for walked subject, four or five tests were carried to ensure the exoskeleton with contented body fit. For providing rehabilitation of the right gait for the patient including to keep the control of the exoskeleton that might be difficult and thus sagittal plane motion is the most important plane during human walking is only considered and simplifies the hip joint and knee joint as one degree of freedom hinge. A 2 degree of freedom (DOF) quasi-passive lower limb exoskeleton is designed to improve gait rehabilitation, as shown in Fig 3. In addition to its lightweight, the exoskeleton's links can be adjusted in size to align the exoskeleton's joints with the patient's joints. The exoskeleton's components were chosen after studying the kinetics and kinematics of human walking.

Fig. 3. The proposed lower limb exoskeleton components.

As demonstrated in Fig 4a, the patient begins walking without the exoskeleton at a sufficient distance from the force plate to achieve the self-selected speed before the foot contacts the force plate's centre. The ground reaction force was measured by the force plate as the walking procedure was repeated fifteen times. AMIT's Bioanalysis programme helped with the analysis, data processing, and evaluation. Soon these tests finished the trials, the truest data based on the intact left leg was chosen in the calculation results. The same experimental protocol was repeated for the patient when walking using the proposed exoskeleton as shown in Fig 4b.

Fig. 4. The participant walking on a force plate (a) without the exoskeleton (b**)** using the exoskeletal device.

3 Results and Discussion

The ground reaction force has widely employed for medical and clinical tests for patient examination. The features of the GRF during human walking can be a useful diagnostic of abnormal gait. The variation of the vertical GRF for both limbs during walking without and with the designed exoskeleton is presented in Fig 5. The figure shows asymmetrical patterns in the vertical GRF of the L and R lower limb during the walking of the patient without using the exoskeleton. The time taken for posture stage is equal to 1.08s and 1.1s for left and right legs, respectively. The extreme values of the vertical GRF whne the legs are not considered the weights on L-R legs. The patient's left leg is normal and does not suffer from any problems; therefore, the vertical GRF for this leg has the normal two peaked form and the mid-stance valley. On moving downward and landed supported by the leg, the value of the first peak is equal to 457.69N, the mid-stance valley is 400N, and for forward and upward movements for the posture stage of the other leg, the second peak is equal to 445.25N. In comparison with the left leg, the weak right leg has a significant irregular reduction in all the extreme values of the vertical GRF. Shortly after the right heel strike and when the body mass moving downward, the vertical GRF rises to its first peak which is equal to 372.56N. The mid-stance has an irregular curve shape, and it has a hill with a peak value equal to 365.088N. The second elevation value during heel off is equal to 355.17N. When walking without using the exoskeleton, the symmetry between the two legs for the maximum vertical GRF (first peak) is 77.15%, the minimum vertical GRF (the valley) is 90.44%, and the maximum vertical GRF (second peak) is 74.64%. Dynamic asymmetry practically disappears in the vertical GRF between the two lower limbs during walking using the exoskeleton. The duration of the stance phase for both legs is increased and is equal to 1.32s for the left leg and 1.18s for the right leg. Increasing stance duration when walking with the exoskeleton will provide static stability [23]. The extreme values of the vertical GRF of the right leg are increased and the curve shape has become close to normal. So, the value of the first peak comprises 423.9N in L-Leg, 419.216N in R-Leg, the value of the mid-stance valley is 396.7N for L-Leg, 392.9N for R-Leg, and the value of the second peak is 426.37N for the left leg and 415.9N for the right leg. For the vertical GRF, the symmetry between the left and right limbs when walking using the exoskeleton for the maximum vertical GRF (first peak) is 98.9%, the minimum vertical GRF (the valley) is 99%, and the maximum vertical GRF (second peak) is 97.48%.

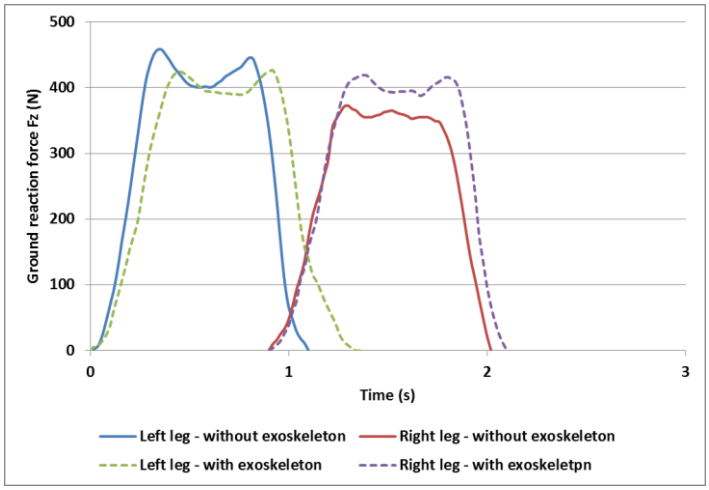

Fig. 5. Vertical walking GRFs of the subject with lower limb weakness before and after wearing the designed exoskeleton.

4 Conclusion

Ground reaction forces (GRFs) are employed to evaluate joint kinetics in biomechanical analysis, that mostly is considered to conclude many gait disorders. Investigating vertical ground reaction forces makes it possible to certain exoskeleton on people with lower limb weakness. The results show that the asymmetrical patterns in the vertical GRF between the left and the right leg disappear during walking using the designed exoskeleton which indicates that the designed exoskeleton help in performing gait improvement for a patient with unilateral lower limb weakness and providing static stability by increasing the stance duration.

References

1. M. Cestari, D. Sanz-Merodio, F.C. Arevalo, E G. ARES, a variable stiffness actuator with embedded force sensor for the ATLAS exoskeleton. Industrial Robot: An International Journal; 2014. p. 518–26.
2. Kong K, Jeon D. Design and control of an exoskeleton for the elderly and patients. IEEE/ASME Trans Mechatronics. 2006;11(4):428–32.
3. Sanchez-Villamañan MDC, Gonzalez-Vargas J, Torricelli D, Moreno JC, Pons JL. Compliant lower limb exoskeletons: A comprehensive review on mechanical design principles. J Neuroeng Rehabil. 2019;16(1):1–16.
4. Stopforth R. Customizable rehabilitation lower limb exoskeleton system. Int J Adv Robot Syst. 2012;9:1–7.
5. Krut S, Benoit M, Dombre E, Pierrot F. MoonWalker, a lower limb exoskeleton able to sustain bodyweight using a passive force balancer. Proc - IEEE Int Conf Robot Autom. 2010;2215–20.
6. Lyu M, Chen W, Ding X, Wang J, Bai S, Ren H. Design of a biologically inspired lower limb exoskeleton for human gait rehabilitation. Vol. 87, Review of Scientific Instruments. American Institute of Physics Inc.; 2016.
7. Huo W, Mohammed S, Amirat Y, Kong K. Active Impedance Control of a lower limb exoskeleton to assist sit-to-stand movement. Proc - IEEE Int Conf Robot Autom. 2016;2016-June:3530–6.
8. Chen B, Ma H, Qin LY, Gao F, Chan KM, Law SW, et al. Recent developments and challenges of lower extremity exoskeletons. J Orthop Transl [Internet]. 2016;5:26–37. Available from: http://dx.doi.org/10.1016/j.jot.2015.09.007
9. Chockalingam N, Healy A, Needham R. Interpreting Ground Reaction Forces in Gait. Handb Hum Motion. 2017;
10. Winter DA. Biomechanics and Motor Control of Human Movement: Fourth Edition. Biomechanics and Motor Control of Human Movement: Fourth Edition. 2009. 1–370 p.
11. Beckham G, Suchomel T, Mizuguchi S. Force Plate Use in Performance Monitoring and Sport Science Testing. New Stud Athl. 2014;29(3):25–37.
12. Whittle M. Gait analysis : an introduction. Butterworth-Heinemann; 2007. 255 p.
13. Lamkin-Kennard KA, Popovic MB. Sensors: Natural and Synthetic Sensors [Internet]. Biomechatronics. Elsevier Inc.; 2019. 81–107 p. Available from:

http://dx.doi.org/10.1016/B978-0-12-812939-5.00004-5
14. Karatsidis A, Bellusci G, Schepers HM, de Zee M, Andersen MS, Veltink PH. Estimation of ground reaction forces and moments during gait using only inertial motion capture. Sensors (Switzerland). 2017;17(1):1–22.
15. Baldovino RG, Jamisola RS. A Survey in the Different Designs and Control Systems of Powered Exoskeleton for Lower Extremities. J Mech Eng Biomech. 2017;1(4):103–15.
16. Knudson D. Fundamentals of Biomechanics. Second Edi. Springer Science+Business Media, LLC. 2007.
17. Winiarski S, Rutkowska-Kucharska A. Estimated ground reaction force in normal and pathological gait. Acta Bioeng Biomech. 2009;11(1):53–60.
18. Fineberg DB, Asselin P, Harel NY, Agranova-Breyter I, Kornfeld SD, Bauman WA, et al. Vertical ground reaction force-based analysis of powered exoskeleton-assisted walking in persons with motor-complete paraplegia. J Spinal Cord Med. 2013;36(4):313–21.
19. Wardoyo S, Hutajulu PT, Togibasa O. A Development of Force Plate for Biomechanics Analysis of Standing and Walking. J Phys Conf Ser. 2016;739(1).
20. Headon R, Curwen R. Recognizing movements from the ground reaction force. ACM Int Conf Proceeding Ser. 2001;15-16-Nove:37.
21. Vaverka F, Elfmark M, Svoboda Z, Janura M. System of gait analysis based on ground reaction force assessment. Acta Gymnica [Internet]. 2015;45(4):187–93. Available from: https://doi.org/10.5507/ag.2015.022
22. Alamdari A, Krovi VN. A Review of Computational Musculoskeletal Analysis of Human Lower Extremities. Human Modeling for Bio-Inspired Robotics: Mechanical Engineering in Assistive Technologies. 2017. 37–73 p.
23. EV P. Investigation of biomechanical parameters of walking in the exoskeleton in patients with complete lower palsy. Int J Biosens Bioelectron. 2018;4(3):138–40.

Time Trends of Noncommunicable Diseases Mortality in Basra province During 2010-2019

Sadiq A. Rahmah[1], Shrouk Abdulrazak Hassan Alibraheem[2], Rajaa A. Mahmoud[3]
{altyye149@gmail.com[1], shrouk.albraheem@stu.edu.iq[2], rahmedmahmoud@gmail.com[3]}

Department Community Health Techniques, College of Health & Medical Tech/Basrah, South Technical University, Iraq[1]

Southern Technical University/College of Health & Medical Technology, Basra/Iraq[2]

University of Basra/ Al Zahraa College of Medicine, Basra/Iraq[3]

Abstract. Chronic Noncommunicable diseases are a primary cause of illness and deaths worldwide, that responsible for 41 million deaths out of 57 million each year that represent 71% of all causes of death worldwide. To estimate the cause-specific death rate due to noncommunicable diseases in Basra province during the period 2010-2019. This study is a descriptive, retrospective study including all deaths due to noncommunicable diseases recorded in Official Statistical records in Basra health Directorate during the period 2010-2019. The time trend of death due to non-communicable diseases is increasing due to the rise of cause-specific death rate from 238 per 100000 in 2010 to 240 per 100000 in 2019. The highest death rate of non-communicable diseases is a cardiovascular disease that has a death rate equal to 213per100000 in 2010 to 227per100000 in 2019 compared with other selected non-communicable diseases in this study found the cardiovascular diseases first cause of death in non-communicable found to be in this study

Keywords: Chronic Diseases, Noncommunicable Diseases, Deaths of Basra Province.

1 Introduction

Chronic Noncommunicable diseases are a leading source of mortality and morbidity worldwide, that responsible for 41 million deaths each year that represent 71% of all causes of death worldwide[1]The burden of NCDs has been rise as a concern globally, has long been a source of concern in developed countries; however, they are causing increasing concern in developing countries due to their demographic and epidemiological transition, the impact of globalization on consumption habits, and the aging of populations. It has been identified as one of the biggest challenges to the health of the 21st century[2]. The reasons for this increased by 20.5% from 2009 to 2019, which represented 7.1 million deaths in 2019 compared to 2009[3] There are four leading causes of NCD deaths, that including the first one Cardiovascular disorders with reach to 17.9 million deaths annually, fallowing be the second cancers that kill more than nine million, while the mortality from respiratory diseases that reached to 3.9 million, for diabetes annual death equal to1.6 million, NCD deaths accounting for more than 80% of all premature death[4]. Additionally, approximately 15 million people aged 30–69 die prematurely because of NCDs Surprisingly, developing countries, which account for half of all premature NCD deaths, have more problems than developed countries. Furthermore, within countries, poor people are more likely to suffer from NCDs.[5] chronic noncommunicable diseases have been a

IMDC-IST 2021, September 07-09, Sakarya, Turkey
Copyright © 2022 EAI
DOI 10.4108/eai.7-9-2021.2314873

major public health concern in Iraq, as they are responsible for most deaths, responsible for more than 55% of all mortality and 30% were premature death in 2016[6]. Despite the limited information regarding the true prevalence of non-communicable diseases in Iraq the main impediments include prevention and regulation treatment and diagnostic materials as well as the lack of cooperation between the public and private sectors, other challenges were the limited institutional and human resources[7]. In Iraq, NCD_s are estimated to account for 55% of all deaths where (27% cardiovascular diseases, 11% Cancers, 4% Diabetes,2% chronic respiratory diseases) while 11% for Other NCDs compared with 17% Communicable, maternal, perinatal, and nutritional conditions and 28% Injuries [8]. the Objectives of this study was to estimate the cause-specific death rate due to noncommunicable diseases in Basra province during the period 2010-2019.

2 Materials and Methods

This study is a descriptive retrospective study including all patients fulfilling due to noncommunicable diseases that were recorded in Official Statistical records in Basra health Directorate during the period 2010-2019. The sample size includes 52008 patients who died from the most prevalent non-communicable diseases (cardiovascular diseases, cancer, diabetes, hypertension, asthma, and Epilepsy). Data was collected from the Basra health directorate depending on the death certificate and forensic medicine reports for the above diseases. Furthermore, data were analysed by using Visual Foix Bro 7 and Microsoft Excel 2016 to the estimation of the cause of death rate from data shown in Table 1.

Table 1. Distribution of NCDs mortality in total population during the period between 2010-2019.

N	Years	Total population	Non-communicable deaths
1	**2010**	2467531	4455
2	**2011**	2788470	4799
3	**2012**	2591153	4645
4	**2013**	2672425	4803
5	**2014**	2744758	4878
6	**2015**	2818803	5323
7	**2016**	2894594	5517
8	**2017**	2972166	5820
9	**2018**	2908491	5776
10	**2019**	2985073	5992

The following equation calculating the Cause-Specific Death Rate due to non-communicable diseases [9].

$$\text{CSDRs} = \frac{\text{number of death due to a specific cause in a specific period}}{\text{Total population in the midpoint of a period}} \times \mathbf{100000}$$

3 Results

Time trends of deaths due to non-communicable diseases during 2010-2019. Regarding the Cause-Specific Deaths Rate of non-communicable diseases. the results show an increase in the death rate of NCDs during 2010-2019.for each year death rate decrease from 328.2 per 100000 in 2010 to 323.2 per 100000 in 2014 that represent the lowest death rate after that increase to 356per 100000 in 2017 that represent as highest death rate and gradual dropping to 340.2 per 100000 in 2019 as shown in Fig.1

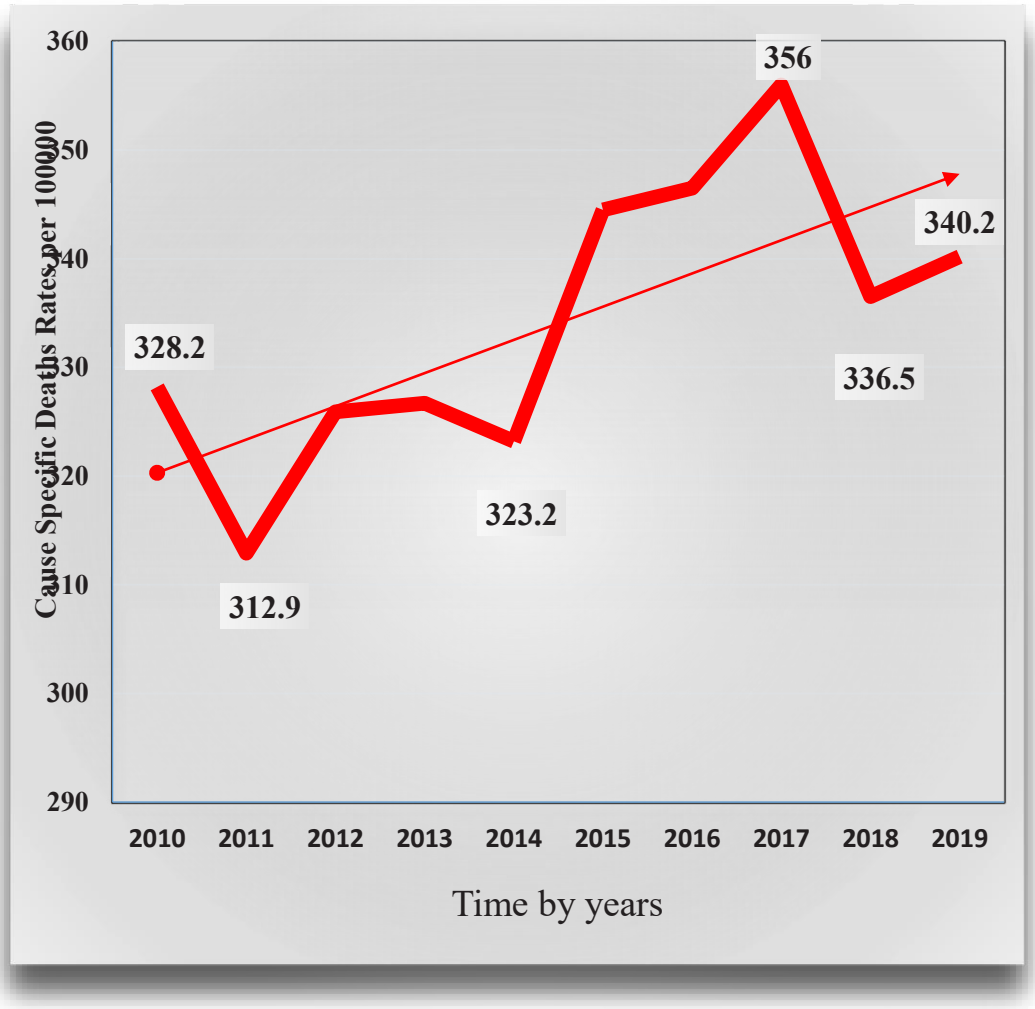

Fig 1. Time trend of death due to NCDs (overall) during 2010-2019.

Concerning to most preventable non-communicable diseases, the study found the cardiovascular diseases first cause of death in non-communicable diseases with the death rate from 213.2 per 100000in 2010 to 227 per 100000 in 2019 followed by cancer as the second cause of death with a death rate of 64.9 per 100000 in 2010 to 66.6 per 100000 in 2019 compared to those of others (diabetes mellitus, hypertension, asthma, and Epilepsy) during the period 2010-2019 as available in Fig.2

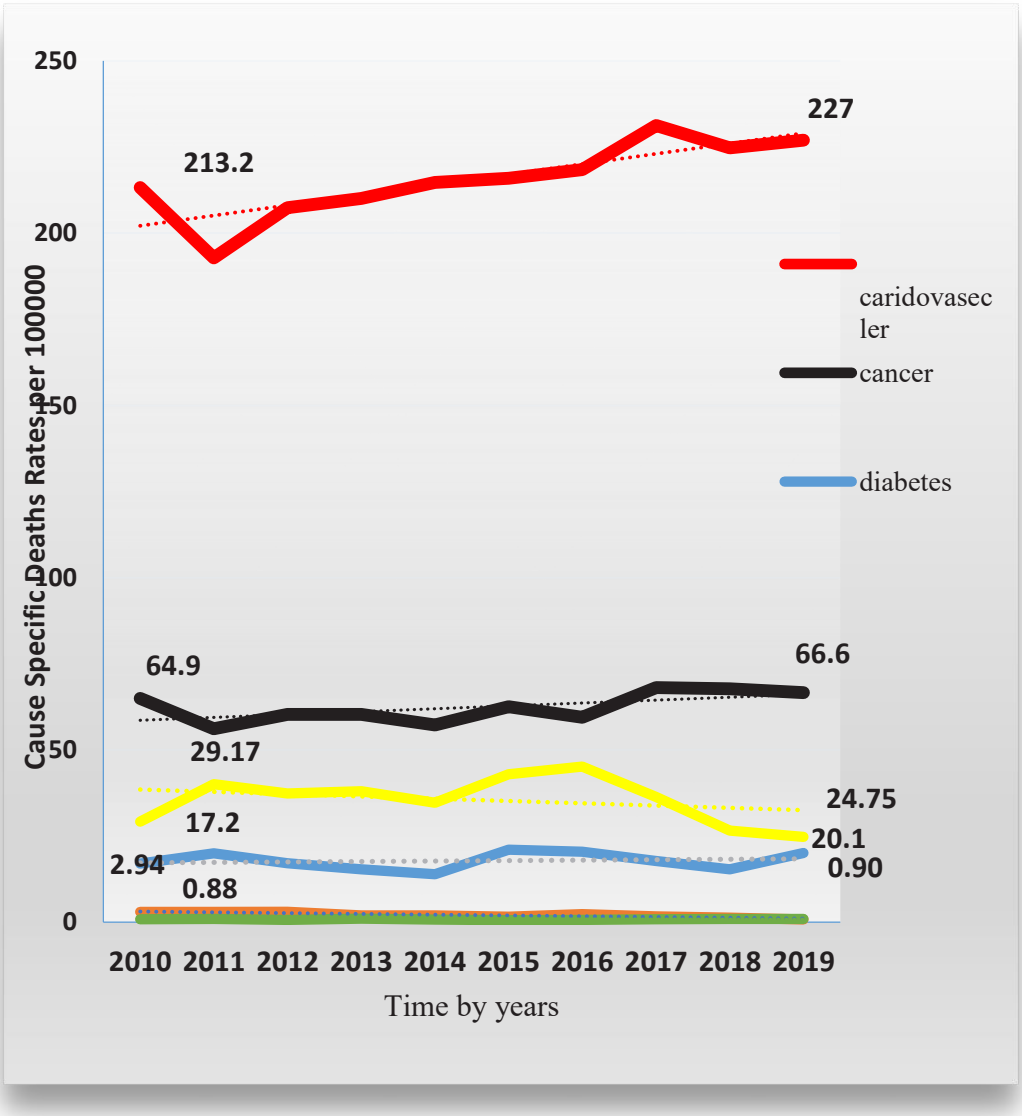

Fig 2. Time trend of death due to NCDs (Separately)during 2010-2019.

4 Discussion

This study is conducted to assess time trends of death due to Noncommunicable diseases in Basra during 2010-2019. The results show an increase in mortality due to noncommunicable diseases in the last ten years. The Eastern Mediterranean area, which ranks worst in the area in terms of mortality from NCDs, is confronted with a slew of health issues stemming from violent wars and political upheavals.[10] However, this is descriptive research, not an evaluation of specific governmental policies, actions, or changing national circumstances. The interpretation of these trends in NCD-related premature avertable mortality should be done with extreme care. It is critical, for example, to determine the relative contributions of NCD incidence and survival rates. Competition from fatalities from non-NCD causes, particularly those at early ages, will impact mortality attributed to premature avertable mortality from NCDs, which is especially concerning in conflict contexts. There may also be temporal gaps between the decrease of amenable mortality and the implementation of remedies and policies.[5] Cause of. Death Information System is a critical component of the monitoring and evaluation of health interventions to prevent and reduce non-communicable diseases and related risk factors[11] can expanse this increase due to Mortality of noncommunicable diseases in Basra according to cause of death registration has increased in the past decade using several data sources to collect information about the cause of death. In the context of the comprehensive ICD-10 coding system, the quality of cause of death is also improving, and a priority of public health policy is to improve the diagnosis of the cause of death by providing death certificates from adult coroners[12] Combined with the WHO report, interventions that focus on multiple risk factors, such as eating a balanced diet, regular physical exercise, and avoiding tobacco products, can prevent at least 80% of premature heart disease, stroke, and diabetes. 2, 40% of malignancies.[13] In future investigations of NCD-related premature avertable mortality, a more detailed study of these consequences is required. the WHO global recommendation to reduce premature deaths from major non-communicable diseases with a goal of 25x 25(reduce 25% of the premature death by 2025) still some developing countries such as Iraq do not achieve this goal by increasing the death rate over time, it may be due to the increased level of risk factors for non-communicable diseases, as most people are not aware of the impact of non-communicable diseases and association with their risk factors and the weak healthcare system in this country[14].

5 Conclusion

Noncommunicable diseases remain a major and persistent problem in Basra due to the high mortality rate during the past ten years, and this confirmed that Basra is still far from the global target of the World Health Organization to reduce deaths due to non-communicable diseases by25x2025.

References

[1] World Health Organization. "WHO package of essential noncommunicable (PEN) disease interventions for primary health care." (2020).

[2] Global Health Policy. The U.S. Government and Global Non-Communicable Disease. Availableathttps://files.kff.org/attachment/fact-sheet-The-US-Government-and-Global-Non-Communicable-Disease-Efforts (accessed 30 April 2021) Published: Jan 29, 2019

[3] Qiao J, Lin X, Wu Y, Huang X, Pan X, Xu J, Wu J, Shan PF, Ren Y. Global Burden of Non-

Communicable Diseases Attributable to Dietary Risks in 1990-2019.
[4] Bigna JJ, Noubiap JJ. The rising burden of non-communicable diseases in sub-Saharan Africa. The Lancet Global Health. 2019 Oct 1;7(10):e1295-6.
[5] Kazemi E, Khosravi A, Aghamohamadi S, Shariati M, Kazemeini H. Trends in premature mortality in the Islamic Republic of Iran: probability of dying between ages 30 and 70 years. Eastern Mediterranean Health Journal. 2021;27(1):33-40.
[6] Pengpid S, Peltzer K. Overweight and obesity among adults in Iraq: prevalence and correlates from a National Survey in 2015. International Journal of Environmental Research and Public Health. 2021 Jan;18(8):4198.
[7] Naser RN, Al-Ghuzi AA. PREVALENCE OF NON-COMMUNICABLE DISEASES AMONG GERIATRIC POPULATION IN AL-NASIRIYAH CITY 2015. University of Thi-Qar Journal Of Medicine. 2016;11(1):1-23.
[8] World Health Organization. Noncommunicable diseases country profiles 2018.
[9] Friis, R. and Sellers, T. 'Measures of Morbidity and Mortality Used in Epidemiology', Epidemiology for PublicHealthPractice,p.50.Availableat:http://samples.jbpub.com/9781284103717/9781449651589_CH03 _Friis.pdf (2013)
[10] World Health Organization. Monitoring Health in the Sustainable Development Goals: 2017 update.
[11] Peykari N, Hashemi H, Dinarvand R, Haji-Aghajani M, Malekzadeh R, Sadrolsadat A, Sayyari AA, Asadi-Lari M, Delavari A, Farzadfar F, Haghdoost A. National action plan for non-communicable diseases prevention and control in Iran; a response to emerging epidemic. Journal of Diabetes & Metabolic Disorders. 2017 Dec;16(1):1-7.
[12] World Health Organization. The impact of chronic disease in the islamic republic of Iran. Genouva: Organization. 2002.
[13] Eyre H, Kahn R, Robertson RM, ACS/ADA/AHA Collaborative Writing Committee, ACS/ADA/AHA Collaborative Writing Committee Members, Clark NG, Doyle C, Hong Y, Gansler T, Glynn T, Smith RA. Preventing cancer, cardiovascular disease, and diabetes: a common agenda for the American Cancer Society, the American Diabetes Association, and the American Heart Association. Circulation. 2004 Jun 29;109(25):3244-55.
[14] World Health Organization. Global NCD target: reduce premature deaths from NCDs. World Health Organization; 2016.

Influence of Genetic polymorphism of IL-2 and IL-6 on susceptibility to Helicobacter pylori infection and prognosis of Gastroduodenal Diseases

Khairallah A.S Mohammed[1], Methaq M. Neamah AL-Hilfi[2], Naael H. Ali[3], Ali Dawood AL-Hilfi[4]
{dr.kmohammed@stu.edu.iq[1], meethaqnama@gmail.com[2], nhali66@yahoo.com[3]}

Department of Medical Lab Technology, College of Health and Medical Technology, Southern Technical University, Iraq[1,2]
College of Medicine, University of Basra, Iraq[3]
Al -Sader Teaching Hospital, Basra, Iraq[4]

Abstract. We wanted to see if there is a link between IL-6 -174G/C and -572G/C, IL-2 330T/G and +114T/G to the aetiology of H. pylori infections. In 24 H. pylori-positive patients (5 chronic gastritis, 17 peptic ulcer, 2 stomach cancer) and 13 healthy people, PCR, DNA sequencing, and the ELISA technique were employed to describe the IL-2 and IL-6 polymorphisms and evaluate their serum levels. The IL-6 -174GG genotype was shown to be the most common (75%) among patients with high rate of getting gastric cancer (OR: 4.8, P <0.05). A high prevalence of IL-6-572GG genotype (66.7%) was observed among patients with a possible high rate of getting gastric cancer in subjects carrying GC genotype (OR: 2.7, P >0.05). IL-2 -330TT and +114TG genotypes were most frequent (58.3%, 50% respectively) among patients, of gastric cancer in patients carrying IL-2-330GG (OR: 2.4) and IL-2+114TT genotype (OR: 2.26). The serum levels of ILs -2/6 were varied about genetic variation.

Keywords: Helicobacter pylori, interleukin 6, interleukin 2, polymorphism

1 Introduction

Helicobacter pylori is a common pathogenic agent linked to chronic gastritis, peptic ulcer disease, and gastric cancer. The virulence factors of H. pylori and the host immune response are responsible for the development and prognosis of H. pylori infections. Interleukin 2 (IL-2) and interleukin 6 (IL-6) are significant members of the host immune system that play a critical role in the pathophysiology of H. pylori-induced gastro-duodenal disorders [1, 2]. Variations in the genes encoding these cytokines may modify their production or interaction with H. pylori virulence factors, resulting in the severity of inflammation and perhaps influencing immunopathology [2, 3]. IL-2 is an immunoregulatory cytokine that plays a role in cell-mediated immunity [1, 2]. T cells make it when mitogens activate them, or when antigen-presenting cells interact with them [1]. IL-2 also functions as the growth factor of T-cell and modulates the immune response by influencing T-cell differentiation into Th1 and Th2 effector subsets. [1]. It aids in the recruitment and spread of inflammatory immunological responses, such as H. Pylori-associated gastro-duodenal illness [2]. IL-2 polymorphisms related to the

IMDC-IST 2021, September 07-09, Sakarya, Turkey
Copyright © 2022 EAI
DOI 10.4108/eai.7-9-2021.2314840

growth of atrophic gastritis, peptic ulcers, and stomach cancer in numerous investigations [3]. In the IL-2 gene, two polymorphisms have been discovered: - 330T/G and + 114T/G. The -330T/G polymorphism is found in the IL-2 gene's promoter region and related to high variety of inflammatory illnesses and malignancies [4].

Monocytes, lymphocytes, macrophages, endothelium, and intestinal epithelial cells, among other immune and non-immune cells, release IL-6, a multifunctional cytokine. It functions as a link between the innate and adaptive immune systems, increasing IFN production in T cells and increasing immunoglobulin release in activated B cells [5]. Interleukin-6 is a cytokine that can be either pro-inflammatory or anti-inflammatory. Its functions include triggering an immunological response, combating infection, and responding to specific microbial compounds, as well as regulating body temperature and driving muscular contraction [6]. IL-6 gene polymorphisms have been linked to H. pylori-mediated gastroduodenal illness in several investigations [7, 8, 9]. Many SNPs were discovered in the IL-6 promoter's 5' flanking region, including -174, -572, -1363, -597, and +634 [2]. IL-6-174 and IL-6 -572 have been linked to H. pylori-mediated gastro-duodenal illness in other investigations [10]. The goal of this investigation was to see if there was a link between polymorphisms in the genes that encode IL-2 and IL-6 and the immunological response that resulted from such genetic changes and the development of H. pylori-mediated illnesses.

2 Materials and Methods

2.1 Study Population

The study showed in the Endoscopy Unit of a specialist centre for the digestive system and liver at Al Sadr Teaching Hospital, Basra – Iraq on 24 patients with Gastro-duodenal Diseases (suspected H. pylori infection) and 13 healthy individuals. Appropriate consent was agreed with patients. All individuals were tested for H. Pylori faecal antigen and the positive results were confirmed by rapid urease test (helicotechUT PLUS, Strong Biotech Corporation, Taiwan). The eligible patients had been confirmed to have H. pylori with chronic gastritis or peptic ulcer by clinical and endoscopic examinations, and histopathologically confirmed to have gastric cancer by endoscopic biopsy.

2.2 Assessment of Serum IL-2 and IL-6 Levels

Each participant had three millilitres of venous blood drawn and centrifuged at 4000 RPM for 15 minutes to collect serum. IL-2 and IL-6 levels in the blood were assessed using enzyme-linked immunosorbent assay (ELISA) kits (KOMA ELISA KIT, KOMABIOTECH, KORA, IL-2 Lot No:42223, IL-6 Lot No:46223). The tests were carried out as directed by the manufacturer.

2.3 DNA Extraction

DNA purification kits (PROMIGA, USA) were used to separate genomic DNA from completely fresh blood collected in EDTA anticoagulant tubes for molecular research, according to the producer's directions.

2.4 PCR Technique

Using specified primers, the PCR technique was employed to amplify definite sections of IL6 and IL2 (Table 1). 2 µl DNA, 1 µl per primer, 12.5 µl master mix , and 8.5 l nuclease-free water made up the reaction mix. An initial denaturation stage of 5 minutes at 94oC was followed by 37 cycles of 30 seconds at 94ºC, a 45-second annealing step at 58oC for primer A and 60ºC for primer B, and a 1-minute extension step at 72ºC, followed by an 8-minute final extension at 72ºC. Agarose gel electrophoresis was used to visualise the amplified products.

2.5 DNA Sequencing

20 µl of PCR product were sent for sequencing with appropriate primers according to business instructions (Macrogen firm, South Korea). Bio Edit [11] and Nucleotide search (https://blast.ncbi.nlm.nih.gov/Blast.cgi?PAGE TYPE=BlastSearc) were used to analyse and align the sequences retrieved.

Table 1. The primers utilised in this study.

IL	Gene	Primer	Classification	Size bp	Reference
IL-2	*A (IL-2 -330 T/G)*	*AF*	*5'ATTCACATGTTCAGTGT AGTTCT3'*	130	Song *et al* [4]
		AR	*5' GTGATAGCTCTAATTCAT GC3'*		
	B L-2 +114 T/G)	*BF*	*5' ATGTACAGGATGCAACTC CT 3'*	261	Song *et al* [4]
		BR	*5' TGGTGAGTTTGGGATTCT TG3*		
IL-6	A L-6-572 G/C)	AF	5'CTCCTCTAAGTGGGCT GAAG3'	212 B	Zhang et al. [10]
		AR	5'CAGCCTGGGATTATG AAGAA3'		
	B L-6-174 G/C)	BF	5'TTGTCAAGACATGCCA AAGTG3'	300	Matos *et al* [12]
		BR	5'TCAGACATCTCCAGTC CTATA3'		

2.6 Statistical Analysis

The SPSS Version 25 software was considered to conduct the statistical limits $P \leq 0.05$ that was regarded important in all tests, and the relevant P-value was determined as an indication of significance. Odds ratios (OR) with a 95 percent confidence interval (CI) were calculated to investigate the association between cytokine gene polymorphisms and gastroduodenal diseases and H. pylori infection.

3 Results

Polymorphisms in the IL-6 and IL-2 genes are referred to by allelic and genotypic, as well as their blood levels in H. pylori-positive patients and healthy people, are shown in Tables 2 to 5. For the IL-6 -174 SNP, the typical sequencing results of IL-6 (300 BP) revealed three genotypes: GG, GC, and CC (figure 1). As shown in Table 2, the IL6 polymorphisms -174 GG genotype and G allele are the most frequent (75%, OR: 4.8, P<0.05 and 84.5%, OR: 2.6 respectively) among H. pylori-positive patients of a significant gastric cancer risk. The results of Table 3 show a high prevalence of IL-6-572 GG genotype (66.7%) among patients of a possible gastric cancer in subjects carrying GC genotype (OR: 2.7, P >0.05). Tables 4 and 5 show that IL-2-330 TT and IL-2+114 TG genotypes are most frequent (58.3%, 50%, respectively) among patients, of similar risk in patients carrying IL-2-330 GG (OR: 2.4, p> 0.05) and IL-2+114 TT genotype (OR: 2.26, P>0.05). All the genotypes of IL -6 and IL -2 which presented a possible high risk in developing H. pylori infections produced high serum levels of these cytokines as represented from Table 2 to 5.

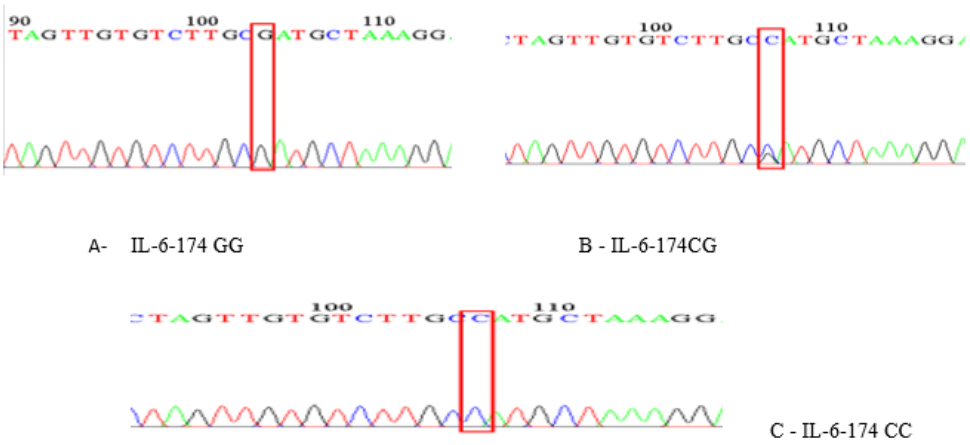

Fig 1. Sequencing results of IL-6 (300 BP) showing three genotypes for IL-6 -174 SNP.

4 Discussion

Human genetic variations are related to various illnesses [10]. The genotype at polymorphic regions in the gene encoding interleukins is hypothesised to determine their time variant that

contributes to the growth of disorders in which interleukins have been involved. In normal subjects, the G allele at position -174 found to be related to amount of plasma IL-6 than the C allele [13]. Other investigations have found that a high level of IL-6 is linked to gastric cancer and the tumor's development pattern [14]. Furthermore, a high level of IL-6 that was linked to angiogenesis in gastric carcinoma, as well as speeding up the activity and spread of cancer cells [15]. IL-6-174, -572 SNP has been linked to a variety of illnesses, breast cancer [16], irritable bowel syndrome [17], lung cancer [18], and prostate malignancies [19].

Table 2. Alleles and genotypes frequencies of IL-6-174 G>C and serum level of IL-6 in the *H. pylori*-positive patients and healthy people.

IL-6-174 G>C		*Patients versus healthy people*			Endoscopic findings			IL-6 serum level Median (pg/ml)	
		H. Pylori patient (n=24) N(%)	Healthy people (n=13) N(%)	OR 95% CI P-value	Chronic gastritis (n=5) N(%)	Peptic ulcer (n= 17) N(%)	Gastric cancer (n=2) N (%)	Patients	Healthy people
Genotype	***GG***	***18(75)***	***5(38.5)***	***4.8 1.13-20.5 0.034***	***3 (60)***	***13 (76.5)***	***2 (100)***	***169***	**10**
	CG	5(20.8)	8(61.5)	0.16 0.037-0.73 0.017	2 (40)	3 (17.6)	0 (0)	112	
	CC	1(4.2)	0(0)	1.7 0.062-45.3 0.74	0 (0)	1 (5.9)	0 (0)	94	
Allele	***G***	***41(85.4)***	***18(69.2)***	***2.603 0.82-8.3 0.104***					
	C	7(14.6)	8(30.8)	0.38 0.12-1.22 0.104					

Table 3. Alleles and genotypes frequencies of IL-6-572 G>C and serum level of IL-6 in the *H. pylori*-positive patients and healthy people.

IL-6- 572 G>C		Patients versus healthy people			Endoscopic findings			IL-6 serum level Median (pg/ml)	
		H. Pylori patient (n=24) N(%)	Healthy people (n=13) N(%)	OR 95% CI P-value	Chronic gastritis (n=5) N(%)	Peptic ulcer (n= 17) N(%)	Gastric cancer (n=2) N (%)	Patients	Healthy people
Genotype	GG	16(66.7)	11(84.6%)	0.36 0.065 - 2.05 0.25	4 (80)	12 (70.6)	0 (0)	132	**10**
	GC	**8(33.3)**	**2(15.4)**	**2.75 0.49 - 15.5 0.25**	**1 (20)**	**5 (29.4)**	**2 (100)**	**181**	
	CC	------	----------	---	-----	----	----	-----	
Allele	G	40(83.3)	24(92.3)	0.42 0.082 - 2.13 0.29					
	C	**8(16.7)**	**2(7.7)**	**2.4 0.47 - 12.5** 0.29					

Table 4. Alleles and genotypes frequencies of IL-2+114 T>G and serum level of IL-2 in the *H. pylori*-positive patients and healthy people.

IL-2+114 T>G		Patients versus healthy people			Endoscopic findings			IL-2 serum level Median (pg/ml)	
		H. Pylori patient (n=24) N(%)	Healthy people (n=13) N(%)	OR 95% CI P-value	Chronic gastritis (n=5) N(%)	Peptic ulcer (n= 17) N(%)	Gastric cancer (n=2) N (%)	Patients	Healthy people
Genotype	**TT**	**7(29.2)**	**2(15.4)**	**2.26 0.39-12.9 P=0.36**	**1(20)**	**4(23.4)**	**2(100)**	**58**	
	GG	5(20.8)	6(46.2)	0.3 0.07-6.3 P=0.115	0 (0)	5 (29.4)	0 (0)	52	31.1
	TG	12(50)	5(38.5)	1.6 0.4-6.3 P=0.5	4 (80)	8 (47.1)	0 (0)	49.1	
Allele	**T**	**26(54.2)**	**9(34.5)**	**2.23 0.83-5.99 P=0.11**	-	-	-		
	G	22(45.8)	17(65.4)	0.45 0.17-1.2 P=0.11	-	-	-		

Table 5. Alleles and genotypes frequencies of IL-2-330 T>G and serum level of IL-2 in the *H.* pylori-positive patients and healthy people.

IL-2-330 T>G		Patients versus healthy people			Endoscopic findings			IL-2 serum level Median (pg/ml)	
		H. Pylori patient (n=24) N(%)	Healthy people (n=13) N(%)	OR 95% CI P-value	Chronic gastritis (n=5) N(%)	Peptic ulcer (n= 17) N(%)	Gastric cancer (n=2) N (%)	**Patients**	**Healthy people**
Genotype	TT	14(58.3)	8(61.5)	0.87 0.22-3.5 0.85	3 (60)	11 (64.7%)	0 (0)	49.7	31.1
	TG	6(25)	4(30.8)	0.7 0.17-3.4 0.71	1 (20)	5 (29.4%)	0 (0)	49	
	G G	**4(16)**	**1(7.7)**	**2.4 0.24-24.1 0.46**	**1 (20)**	**1 (5.9%)**	**2 (100)**	**81.7**	
Allele	T	34 (70)	20(76.9)	0.73 0.24-2.2 0.574					
	G	**14 (29)**	**6 (23.1)**	**1.37 0.45-4.14 0.574**					

In this study, we detected a high frequency of IL-6-174 and -572 SNPs in patients with gastro-duodenal disease associated with H. pylori. We found that gastric cancer was associated with GG genotype of -174 and GC genotype of -572 SNP which are like other studies [7], [20]. On other hand, the GG genotype in both SNPs was more frequent among people who have a peptic ulcer or chronic gastritis. These results agree with those found by Gatti et al. 2007 [7]. Furthermore, we investigated the polymorphisms of IL-6 gene -572 and -174 SNPs about their serum levels. We found high serum levels associated with IL-6-174 G/G (169 pg/ml) and -572 G/C (181 pg/ml) genotypes, both genotypes detected in cancer patients. Chae et al. (2016) found that IL6-174 polymorphisms affect IL-6 expression in G allele carriers and are linked with greater plasma concentrations [16]. The connection between interleukin-6 polymorphisms and serum levels has been studied in several research [21]. The GG genotype gene was discovered to be responsible for manufacturing more IL-6 than the IL-6 -572 GC genotype [22]. Mucosal injury is caused by the insusceptible activity and assimilated immunity in gastro-duodenal disease caused by H. pylori. CD4 cells release a variety of cytokines that are involved in pathophysiology in which the disease had been found to cause inflammation of the gastro-duodenal disease-associated H. pylori [23]. By affecting the transcriptional control of the IL-6 gene, IL-6 gene polymorphisms may affect inter-individual variability in blood levels of IL-6 expression [24]. According to Barisani et al. (2006), polymorphism at locations -174 and -572 influences IL-6 expression [25]. Overall, the present findings demonstrate the odds of developing H. pylori infections (gastritis, peptic ulcer, and gastric ulcer) were highest in those people with high producer polymorphism (GG genotype) while that the low production of IL-6 (CC genotype) seemingly provides some protection against the susceptibly and development of H. pylori infections.

Furthermore, as compared to healthy people, the prevalence of IL-2 +114 TT genotype, T allele, and IL-2 -330 GG genotype, G allele is significantly greater in H. pylori-infected patients. In these patients, these SNPs could be taken for the growth of gastroduodenal illness. Also, the present data showed that +114GG genotype, G allele, and -330 TG genotype, T allele could be protective against the susceptibly and development of H. pylori infections. These findings corresponded with those in another research [26]. However, a bigger sample size is required to corroborate the findings.

The present results showed high levels of IL 2 in serum associated with IL-2 -330 SNP GG genotype (81.7 pg/ml**)** and with +114 TT genotype (58 pg/ml). Many studies considered that having the IL-2-330 GG and 114 TT genotype increases the risk of a variety of illnesses, including B-Cell Non-Hodgkin Lymphoma [27] and Gastric cancer [28, 29]. Changes in gene promoter activity usually cause changes in gene expression levels, and the IL-2 gene that is clarified by its impact on cytokine [30].
Overall, the current data imply that genetic variants in the IL-6 and IL-2 genes are biologically relevant in the development of H. pylori-induced gastro-duodenal illness. The influence of ILs gene polymorphism on cytokine expression elucidates the biological relevance of ILs gene polymorphism. The study's biggest limitation was the small number of patients, most of whom had stomach cancer. However, many samples is required for additional research to confirm the link between IL-6 and IL-2. More understanding of such association would be of importance in determining the clinical implications of these genetic variations about H. pylori-induced gastroduodenal disorders.

References

1. Owen, J. Punt, J. and Stranford, S. Kuby Immunology.7th edition. New York : W.H. Freeman; 2013:116- 118.

2. Sugimoto, M.Yamaoka, Y. and Furuta, T.. Influence of interleukin polymorphisms on development of gastric cancer and peptic ulcer. World J Gastroenterol. 2010; 16(10): 1188-1200.

3. Rudnicka K, Backert S, Chmiela M. Genetic Polymorphisms in Inflammatory and Other Regulators in Gastric Cancer: Risks and Clinical Consequences. Curr Top Microbiol Immunol. 2019;421: 53-76.

4. Song H, Chen L, Cha Z, Bai J. Interleukin 2 gene polymorphisms are associated with non-Hodgkin lymphoma. DNA Cell Biol. 2012;31(7):1279-1284.

5. Hein TM, Sander P, Giryes A, Reinhardt JO, Hoegel J, Schneider EM. Cytokine Expression Patterns and Single Nucleotide Polymorphisms (SNPs) in Patients with Chronic Borreliosis. *Antibiotics (Basel)*. 2019;8(3):107.

6. Luo Y, Zheng SG. Hall of Fame among Pro-inflammatory Cytokines: Interleukin-6 Gene and Its Transcriptional Regulation Mechanisms. *Front Immunol*. 2016;7:604.

7. Gatti LL, Burbano RR, Zambaldi-Tunes M, de-Lábio RW, de Assumpção PP, de Arruda Cardoso-Smith M, Marques-Payão SL. Interleukin-6 polymorphisms, Helicobacter pylori

infection in adult Brazilian patients with chronic gastritis and gastric adenocarcinoma. Arch Med Res. 2007;38(5):551-5.

8. Chakravorty, M. de Datta,D Choudhury, A. et al. Association of specific haplotype of TNF withα Helicobacter pylori-mediated duodenal ulcer in eastern Indian population. J Genet. 2008; 87:299–304.

9. Hwang IR, Hsu PI, Peterson LE, Gutierrez O, Kim JG, Graham DY, Yamaoka Y. Interleukin-6 genetic polymorphisms are not related to Helicobacter pylori-associated gastroduodenal diseases. Helicobacter. 2003;8(2):142-8.

10. Zhang WG, Bai XJ, Chen DP, Lv Y, Sun XF, Cai GY, Bai XY, Chen XM. Association of Klotho and interleukin 6 gene polymorphisms with aging in Han Chinese population. J Nutr Health Aging. 2014;18(10):900-4.

11. Hall TA. BioEdit: a user-friendly biological sequence alignment editor and analysis program for Windows 95/98/NT. Nucl Acids Symp Ser. 1999;41:95–98.

12. Matos MF, Lourenço DM, Orikaza CM, Bajerl JA, Noguti MA, Morelli VM. The role of IL-6, IL-8 and MCP-1 and their promoter polymorphisms IL-6 -174GC, IL-8 -251AT and MCP-1 -2518AG in the risk of venous thromboembolism: a case-control study. Thromb Res. 2011;128(3):216-20.

13. Fishman D, Faulds G, Jeffery R, Mohamed-Ali V, Yudkin JS, Humphries S, Woo P. The effect of novel polymorphisms in the interleukin-6 (IL-6) gene on IL-6 transcription and plasma IL-6 levels, and an association with systemic-onset juvenile chronic arthritis. J Clin Invest. 1998 Oct 1;102(7):1369-76.

14. Kai H, Kitadai Y, Kodama M, Cho S, Kuroda T, Ito M, Tanaka S, Ohmoto Y, Chayama K. Involvement of proinflammatory cytokines IL-1beta and IL-6 in progression of human gastric carcinoma. Anticancer Res. 2005;25(2A):709-13.

15. Ashizawa T, Okada R, Suzuki Y, Takagi M, Yamazaki T, Sumi T, Aoki T, Ohnuma S, Aoki T. Clinical significance of interleukin-6 (IL-6) in the spread of gastric cancer: role of IL-6 as a prognostic factor. Gastric Cancer. 2005;8(2):124-31.

16. Chae JW, Ng T, Yeo HL, Shwe M, Gan YX, Ho HK, Chan A. Impact of TNF-α (rs1800629) and IL-6 (rs1800795) Polymorphisms on Cognitive Impairment in Asian Breast Cancer Patients. PLoS One. 2016;11(10):e0164204.

17. Bashashati M, Moradi M, Sarosiek I. Interleukin-6 in irritable bowel syndrome: A systematic review and meta-analysis of IL-6 (-G174C) and circulating IL-6 levels. Cytokine. 2017; 99:132-138.

18. Chen J, Liu RY, Yang L, Zhao J, Zhao X, Lu D, Yi N, Han B, Chen XF, Zhang K, He J, Lei Z, Zhou Y, Pasche B, Li X, Zhang HT. A two-SNP IL-6 promoter haplotype is associated with increased lung cancer risk. J Cancer Res Clin Oncol. 2013;139(2):231-42.

19. Song H, Chen L, Cha Z, Bai J. Interleukin 2 gene polymorphisms are associated with non-Hodgkin lymphoma. DNA Cell Biol. 2012 Jul;31(7):1279-84.

20. Kang JM, Kim N, Lee DH, Park JH, Lee MK, Kim JS, Jung HC, Song IS. The effects of genetic polymorphisms of IL-6, IL-8, and IL-10 on Helicobacter pylori-induced gastroduodenal diseases in Korea. J Clin Gastroenterol. 2009;43(5):420-8.

21. Ma Y, Tang RK, Yang X, Peng GG, Liu Y, Wang XM, Wu BH, Yu JM. Lack of an association between interleukin-6 gene promoter polymorphisms (-174G/C, -572G/C) and ischemic heart disease and/or ischemic stroke: a meta-analysis. Hum Immunol. 2011;72(8):641-51.

22. Jerrard-Dunne P, Sitzer M, Risley P, Buehler A, von Kegler S, Markus HS. Inflammatory gene load is associated with enhanced inflammation and early carotid atherosclerosis in smokers. Stroke. 2004; 35(11):2438-43.

23. Bagheri N, Razavi A, Pourgheysari B, Azadegan-Dehkordi F, Rahimian G, Pirayesh A, Shafigh M, Rafieian-Kopaei M, Fereidani R, Tahmasbi K, Shirzad H. Up-regulated Th17 cell function is associated with increased peptic ulcer disease in Helicobacter pylori-infection. Infect Genet Evol. 2018; 60:117-125.

24. Qi L, van Dam RM, Meigs JB, Manson JE, Hunter D, Hu FB. Genetic variation in IL6 gene and type 2 diabetes: tagging-SNP haplotype analysis in large-scale case-control study and meta-analysis. Hum Mol Genet. 2006;15(11):1914-20.

25. Barisani D, Ceroni S, Meneveri R, Cesana BM, Bardella MT. IL-10 polymorphisms are associated with early-onset celiac disease and severe mucosal damage in patients of Caucasian origin. Genet Med. 2006;8(3):169-74.

26. Abdiev S, Ahn KS, Khadjibaev A, Malikov Y, Bahramov S, Rakhimov B, Sakamoto J, Kodera Y, Nakao A, Hamajima N. Helicobacter pylori infection and cytokine gene polymorphisms in Uzbeks. Nagoya J Med Sci. 2010;72(3-4):167-72.

27. Abdel Rahman HA, Khorshied MM, Reda Khorshid OM, Mourad HM. Association of Interleukin-2-330T/G and Interleukin-10-1082A/G Genetic Polymorphisms with B-Cell Non-Hodgkin Lymphoma in a Cohort of Egyptians. Turk J Haematol. 2018;35(2):99-108.

28. Melchiades JL, Zabaglia LM, Sallas ML, Orcini WA, Chen E, Smith MAC, Payão SLM, Rasmussen LT. Polymorphisms and haplotypes of the interleukin 2 gene are associated with an increased risk of gastric cancer. The possible involvement of Helicobacter pylori. Cytokine. 2017;96:203-207.

29. Hoffmann SC, Stanley EM, Darrin Cox E, Craighead N, DiMercurio BS, Koziol DE, Harlan DM, Kirk AD, Blair PJ. Association of cytokine polymorphic inheritance and in vitro cytokine production in anti-CD3/CD28-stimulated peripheral blood lymphocytes. Transplantation. 2001;72(8):1444-50.

30. Świątkowska-Stodulska R, Kitowska A, Skibowska-Bielińska A, Wiśniewski P, Sworczak K. Hageman factor C46T promoter gene polymorphism in patients with hypercortisolism. Horm Metab Res. 2014;46(7):510-4.

Comparison of toxic effects of some nonsteroidal anti-inflammatory medications on the kidney and lung tissues of rats

Manal N. Al-Hayder[1], Tamadir H. W. Aledani[2]*, Rafid A. Doulab[3]
{Manal.Abd-AlHassan@uobasrah.edu.iq[1], tamadir.wadi@uobasrah.edu.iq[2], rafid.doulab@uobasrah.edu.iq[3]}

Department of Pharmacology & Toxicology, College of Pharmacy, University of Basrah[1], Department of Clinical Laboratory Sciences, College of Pharmacy, University of Basrah[2], Central laboratory, College of Pharmacy, University of Basrah[3]

Abstract, Nonsteroidal anti-inflammatory drugs that include diclofenac sodium and naproxen are frequently and widely used. Nevertheless, they cause adverse deleterious effects on multiple organs. This work represents a comparative study of the toxic effects of diclofenac sodium and naproxen in rats that is almost nonexistent.The methodology is applied on 15 rats orally administered nonsteroidal drugs for three weeks. The hematopathological and histopathological effects were evaluated. Abnormal hematological profile in both diclofenac sodium and naproxen treated groups comparing to the control is illustrated. Interestingly, the statistical comparison between the two treated groups revealed that in the naproxen group the red blood cells count, hemoglobin, and mean corpuscular hemoglobin concentration were significantly lower, while the platelets and plateletcrit significantly increased more than another group. The histopathological micrographs demonstrated the harmful effects of both drugs in the kidney and lung tissues. We concluded that a high dose of naproxen potentially generates higher toxic effects compared to a lower dose of diclofenac sodium as habitually used.

Keywords: Blood parameters, histopathology, nonsteroidal anti-inflammatory drugs, toxic effects.

1 Introduction

Nonsteroidal anti-inflammatory drugs (NSAID) are known as cyclooxygenase inhibitors and are widely used as analgesics, anti-pyretics, anti-inflammatory and anti-cancer drugs to treat different types of cancer, chronic pain, postoperative pain, rheumatoid arthritis, osteoarthritis, and spasms [1, 2, 3]. As well as, there are many recent speculations to use NSAID in the therapy of COVID-19 such as indomethacin for blocking coronavirus RNA synthesis. It is also shown that it is possible to use celecoxib and diclofenac for inhibiting cyclooxygenase-2 which is promoted by SARS coronavirus [4]. Although this considerable therapeutic use of the NSAID, they cause adverse harmful effects on multiple organs such as gastrointestinal, cerebral, cardiovascular, renal, hepatic, and pulmonary pathologies that can lead to the risk of organ damage especially when they are daily used in high dose and for long term [1, 2]. Thus, diclofenac sodium and naproxen among the NSAID are the most available, cheapest, and most extensively and frequently used. Several studies have shown their toxicities in the rats including gastrointestinal ulceration, gastric damage, severe lesions in the liver and cerebrum, hepato-renal damage, and acute pulmonary toxicity [5, 6, 7, 8, 9, 10].

IMDC-IST 2021, September 07-09, Sakarya, Turkey
Copyright © 2022 EAI
DOI 10.4108/eai.7-9-2021.2314408

Regarding the systematic reviews and meta-analysis to compare between the effects of diclofenac sodium and naproxen in the human [11, 12, 13], the comparative study of their toxic effects in the rats is almost nonexistent according to our knowledge. Therefore, the aim of the present study is to shed more light on the hematopathological and histopathological effects of diclofenac sodium and naproxen in the kidney and lung tissues of the rats as a comparative study.

2 Materials and methods

2.1 Experimental animals and design

In this study, fifteen males of the albino rats, 5 weeks old and weighing 70-80g, were used. These animals were housed under typical conditions of the temperature and lighting in the animals' house of Pharmacy College, University of Basrah, Iraq. Then they were distributed to three groups: control, treated with diclofenac sodium and treated with naproxen in each group of five rats.

All animals were weighed weekly and orally administered by gavage every day for three weeks. The second group was administered 5mg/kg body weight (b.w.)/day of the 50mg diclofenac sodium tablet. Whereas, the third group was administered 50mg/kg b.w./day of the 500mg naproxen tablet. Both diclofenac sodium and naproxen were dissolved in 5% dimethyl sulfoxide (DMSO). Thus, the control group was administered 0.1ml DMSO/day.

2. 2 Hematological estimation

At the termination of the third week, using chloroform the rats were anesthetized to collect blood samples by cardiac puncture in collection tubes containing ethylenediaminetetraacetic acid (EDTA) as an anticoagulant. The automated blood cell analyzer (Genex, Florida, USA) was used for evaluation directly all blood parameters (total white blood cell count, granulocytes, mean corpuscular volume, monocytes count, red cell distribution width, platelet large cell ratio, plateletcrit, platelets, lymphocytes, red blood cells count, hematocrit, mean corpuscular hemoglobin concentration, hemoglobin, and mean corpuscular hemoglobin).

2. 3 Histopathological examination

After euthanasia and dissection, kidneys and lungs were preserved in 10% formaldehyde until embedding in the paraffin wax. The rotary microtome was used to cut the tissue samples into 5 µm sections. Subsequently, for microscopic examination, a haematoxylin and eosin (H&E) stain was utilized.

2.4 Hematological data analysis

Statistical GraphPad Prism software using one-way analysis of variance then Bonferroni's multiple comparison test analyzed the hematological results. Also, an unpaired t-test was used for comparison between diclofenac sodium and naproxen. The significance was assessed at $p<0.05$.

3 Results

3.1 Hematological parameters

As shown in Figure (1), the hematological profile of the treated rats in comparison with the control showed abnormalities in the whole blood picture for both diclofenac sodium and naproxen. The values of total white blood cell count, granulocytes, mean corpuscular volume, monocytes count (MID), red cell distribution width, platelet large cell ratio (P-LCR), plateletcrit (PCT), and platelets (PLT) were elevated. This elevation was significant for MID, PLT and PCT in the rats treated with diclofenac sodium and those treated with naproxen. Whereas P-LCR was significantly affected only in the rats treated with naproxen.

In contrast, the values of lymphocytes, red blood cells count (RBC), hematocrit (HCT), mean corpuscular hemoglobin concentration (MCHC), hemoglobin (HGB) and mean corpuscular hemoglobin (MCH) were decreased compared to the control. Significantly, RBC was diminished in the rats treated with diclofenac sodium and in those treated with naproxen. For lymphocytes, its significant decreased value was remarked only in the diclofenac sodium-treated rats. While HGB, HCT, MCH, and MCHC were significantly impacted only in the rats treated with naproxen (Figure 1).

Remarkably, the statistical analysis showed that the values of RBC, HGB, and MCHC were significantly lesser in the rats administered naproxen than with diclofenac sodium. Also, PLT and PCT were significantly augmented in the naproxen-treated rats than those with diclofenac sodium (Figure 2).

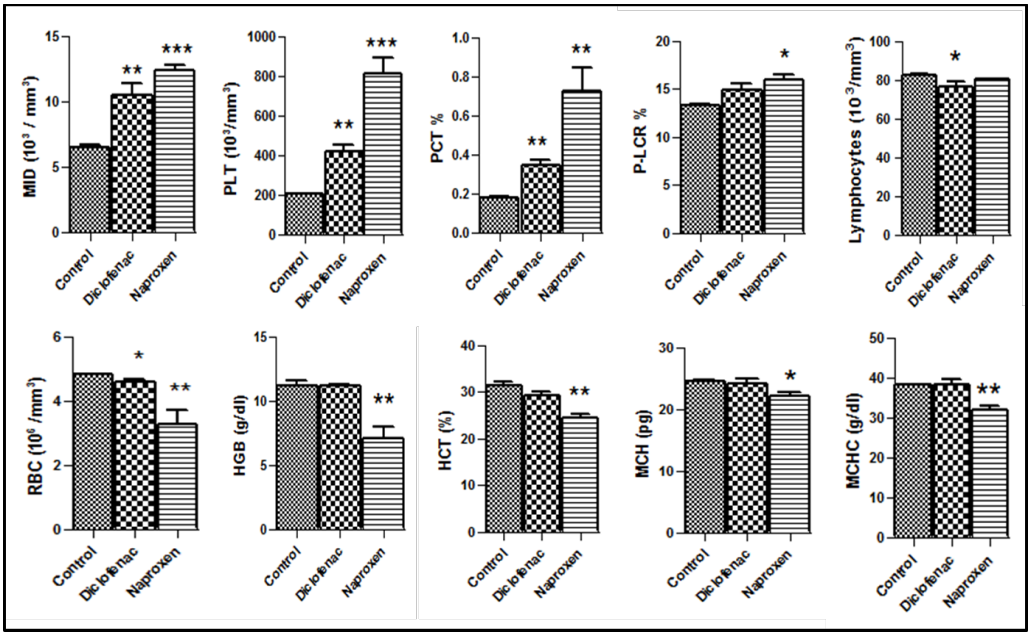

Figure 1. Significant impact of diclofenac sodium and naproxen on blood parameters compared to the control in the albino rats. MID: monocytes count, PLT: platelets, PCT: plateletcrit, P-LCR: platelet-large cell ratio, RBC: red blood cells count, HGB: hemoglobin, HCT: hematocrit, MCH: mean corpuscular hemoglobin, and MCHC: mean corpuscular hemoglobin concentration. For expressing the significant values; * for $p<0.05$, ** for $p<0.01$, and *** for $p<0.001$as mean ± SEM values.

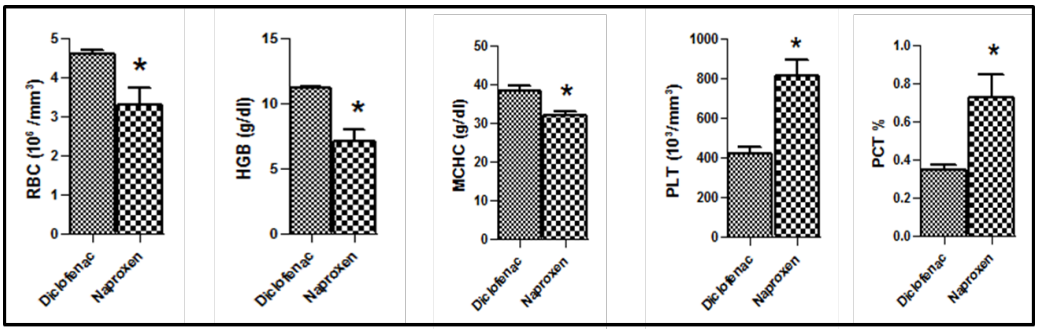

Figure 2. Significant impact of naproxen on some hematological parameters in comparison with diclofenac sodium in the albino rats. RBC: Red blood cells count, HGB: hemoglobin, MCHC: mean corpuscular hemoglobin concentration, PLT: platelets, and PCT: plateletcrit. Mean ± SEM expresses the values; the significance is expressed as * $p<0.05$.

3.2 Histopathological findings

Histological examination of the kidney tissue in the control group exhibited normal glomeruli, proximal and distal tubules. In contrast, the kidneys' sections of both groups treated with diclofenac sodium and with naproxen illustrated harmful changes including necrosis in the epithelial tissue of tubules, shrinkage of the glomeruli, and enlargement of the Bowman's space (Figure 3).

Moreover, the photomicrographs of the lung tissue also revealed evident pathological changes in both treated groups involving alveoli surrounded by thickening walls, and intra- alveolar hemorrhage comparing to the control which showed normal architecture of lung tissue as normal bronchioles and alveoli structure with thin inter-alveolar walls (Figure 4).

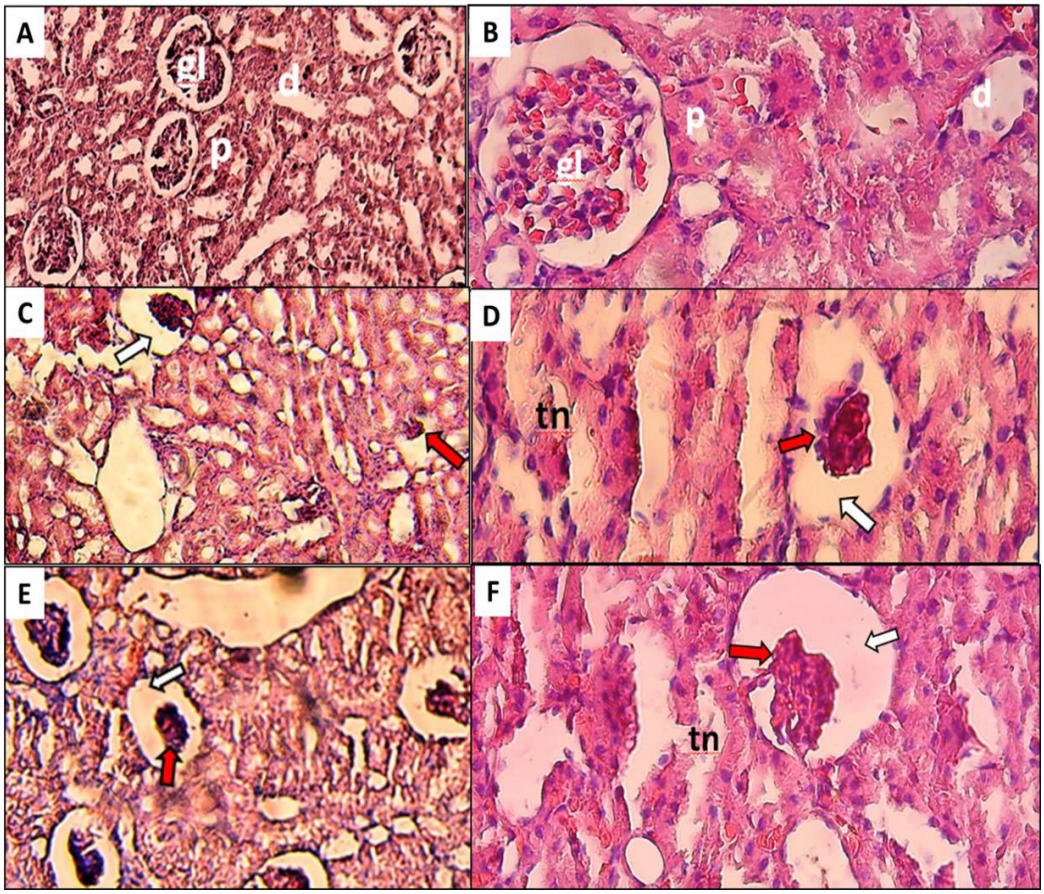

Figure 3. Photomicrographs of the kidney tissue in albino rats. (A&B) Control group showed normal kidney histology: normal glomerulus (gl), proximal (p) and distal tubules (d). (C&D) Diclofenac sodium-treated group revealed glomerular shrinkage (red arrow), Bowman's space enlargement (white arrow), and tubular necrosis (tn). (E&F) Naproxen-treated group also exhibited glomerular shrinkage (red arrow), Bowman's space

enlargement (white arrow), in addition to tubular necrosis (tn). Using H&E stain and magnifications 100x and 400x.

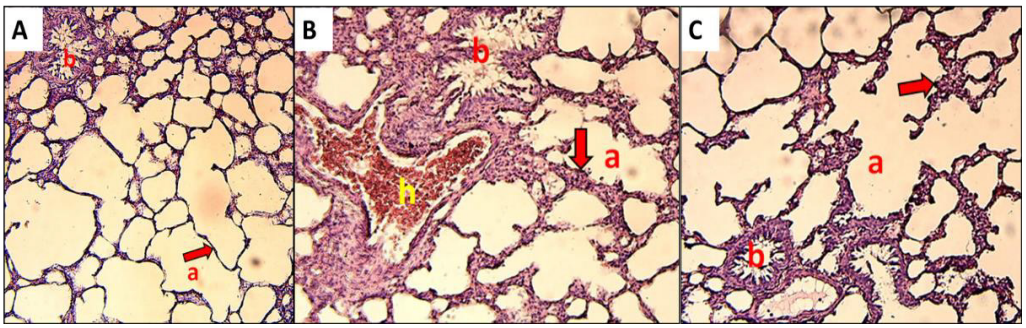

Figure 4. Photomicrographs of the lung tissue in albino rats. (A) Control group displayed normal lung histology: normal structure of the alveoli (a) enclosed by thin septa (red arrow), and normal bronchioles (b). (B) and (C) Diclofenac sodium-treated group and naproxen-treated group respectively elucidated thickened alveolar septa (red arrow), and intra- alveolar hemorrhage (h). Using H&E stain and magnification 200x.

4 Discussion

The increasing demand for the NSAID to treat a broad spectrum of diseases encourages investigating the least harm and toxicity for different organs. In this regard, NSAID can cause increasing and dysregulation of inflammatory response that induce pathologic harms [14]. Thus, the findings for both diclofenac sodium and naproxen demonstrated hematological alterations that were represented by significant elevation of MID, PLT, and PCT in comparison to the control. The significant increase in the platelets may indicate their aggregation to prevent potential bleeding in the site of the damage. Also, there was a significant decrease in lymphocytes, RBC, HCT, MCH, HGB, and MCHC. According to previous studies [15, 16, 17], the significant decrease in the RBC, HGB, HCT, MCH, MCHC, and lymphocytes considers as an indicator of hemolytic anemia and it is correlated with toxicity.

On the other hand, the histopathological findings of this study confirmed the toxic effects of both diclofenac sodium and naproxen. The hemorrhage in the tissues possibly interprets the significant decrease in the RBC and hemoglobin parameters; also it could explain the significant increase in the platelets. For diclofenac sodium, the results of lung histopathology are similar to those obtained by Aljuhani et al. [10], but they intraperitoneally administered the albino rats with overdose (200 mg/kg b.w.) of diclofenac. Also, the diclofenac-induced nephrotoxic injury in the kidney tissue was achieved in the albino rats by intraperitoneal administration with 50mg/kg b.w. [9, 18]. In this context, there are no obtainable data around the histopathological effects of naproxen in kidney and lung tissues of the rats for supporting the interpretation of our results. Despite that, naproxen-induced renal toxicity and lung lesions in humans are well known [19, 20, 21, 22]. There is a case report of 17 years old girl taken 4 times/day of 250 mg naproxen for 4 days; the biopsy from her

kidney appeared interstitial nephritis and necrosis in the papillae and tubules [23].

5 Conclusion

Diclofenac sodium and naproxen had shown deleterious hematopathological and histopathological effects in the rats.The hematopathological changes could cause and reflect tissue damage involving the kidney and the lung. Furthermore, both drugs had certain convergent effects. However, the outcomes suggest potential toxic effects of naproxen more than diclofenac sodium as a consequence of using it in a higher dose than diclofenac; that was evident from the statistical significance.

Acknowledgments. All authors thank the deanship of the College of Pharmacy, University of Basrah.

References

[1] Dong Y-H, Chang C-H, Wu L-C, et al. Comparative cardiovascular safety of nonsteroidal anti-inflammatory drugs in patients with hypertension: a population-based cohort study. *Br J Clin Pharmacol* 2018; 84: 1045–1056.

[2] Bindu S, Mazumder S, Bandyopadhyay U. Non-steroidal anti-inflammatory drugs (NSAIDs) and organ damage: A current perspective. *Biochem Pharmacol* 2020; 180: 114147.

[3] Liggett JL, Zhang X, Eling TE, et al. Anti-tumor activity of non-steroidal anti-inflammatory drugs: cyclooxygenase-independent targets. *Cancer Lett* 2014; 346: 217–224.

[4] FitzGerald GA. Misguided drug advice for COVID-19. *Science* 2020; 367: 1434.

[5] Kim J-H, Kim Y-S, Song G-G, et al. Protective effect of astaxanthin on naproxen-induced gastric antral ulceration in rats. *Eur J Pharmacol* 2005; 514: 53–59.

[6] Silva RO, Santana APM, Carvalho NS, et al. A sulfated-polysaccharide fraction from seaweed Gracilaria birdiae prevents naproxen-induced gastrointestinal damage in rats. *Mar Drugs* 2012; 10: 2618–2633.

[7] Ekundi-Valentim E, Mesquita FP, Santos KT, et al. A comparative study on the anti-inflammatory effects of single oral doses of naproxen and its hydrogen sulfide (H2S)-releasing derivative ATB-346 in rats with carrageenan-induced synovitis. *Med Gas Res* 2013; 3: 24.

[8] Lojo N, Rasic Z, Zenko Sever A, et al. Effects of Diclofenac, L-NAME, L-Arginine, and Pentadecapeptide BPC 157 on Gastrointestinal, Liver, and Brain Lesions, Failed Anastomosis, and Intestinal Adaptation Deterioration in 24 Hour-Short-Bowel Rats. *PLoS One* 2016; 11: e0162590.

[9] Mostafa RE, El-Marasy SA, Abdel Jaleel GA, et al. Protective effect of royal jelly against diclofenac-induced hepato-renal damage and gastrointestinal ulcerations in rats. *Heliyon* 2020; 6: e03330.

[10] Aljuhani N, Elkablawy MA, Elbadawy HM, et al. Protective effects of Ajwa date extract against tissue damage induced by acute diclofenac toxicity. *J Taibah Univ Med Sci* 2019; 14: 553–559.

[11] McGettigan P, Henry D. Cardiovascular risk with non-steroidal anti-inflammatory drugs: systematic review of population-based controlled observational studies. *PLoS Med* 2011; 8: e1001098.

[12] van Walsem A, Pandhi S, Nixon RM, et al. Relative benefit-risk comparing diclofenac to other traditional non-steroidal anti-inflammatory drugs and cyclooxygenase-2 inhibitors in patients with osteoarthritis or rheumatoid arthritis: a network meta-analysis. *Arthritis Res Ther* 2015; 17: 66.

[13] Coxib and traditional NSAID Trialists' (CNT) Collaboration, Bhala N, Emberson J, et al. Vascular and upper gastrointestinal effects of non-steroidal anti-inflammatory drugs: meta-analyses of individual participant data from randomised trials. *Lancet* 2013; 382: 769–779.

[14] Maseda D, Zackular JP, Trindade B, et al. Nonsteroidal Anti-inflammatory Drugs Alter the Microbiota and Exacerbate Clostridium difficile Colitis while Dysregulating the Inflammatory Response. *mBio*; 10. Epub ahead of print 8 January 2019. DOI: 10.1128/mBio.02282-18.

[15] Orinya OA, Adenkola AY, Ogbe RJ. Haematological and biochemical studies on the effect of diclofenac sodium on Wistar *Rattus norvegicus*. *Int J Bio Chem Sci* 2017; 10: 2231.

[16] Agha FE, El-Badry MO, Hassan DAA, et al. Role of Vitamin E in Combination with Methionine and L- carnosine Against Sodium Fluoride-Induced Hematological, Biochemical, DNA Damage, Histological and Immunohistochemical Changes in Pancreas of Albino Rats. *Life Science Journal* 2012; 9: 1260–1275.

[17] Khan AM, Dubey N, Raina R, et al. *TOXIC EFFECTS OF DELTAMETHRIN AND FLUORIDE ON HEMATOLOGICAL PARAMETERS IN RATS*. Research Report 46(1), Jammu, India: Department of Pharmacology and Toxicology, Faculty of Veterinary and Animal Sciences, Shere-Kashmir University of Agricultural Sciences and Technology.

[18] Peter S J, Basha S K, Giridharan R, et al. Suppressive effect of Spirulina fusiformis on diclofenac-induced hepato-renal injury and gastrointestinal ulcer in Wistar albino rats: A biochemical and histological approach. *Biomed Pharmacother* 2017; 88: 11–18.

[19] Hörl WH. Nonsteroidal Anti-Inflammatory Drugs and the Kidney. *Pharmaceuticals (Basel)* 2010; 3: 2291–2321.

[20] Whelton A, Schulman G, Wallemark C, et al. Effects of celecoxib and naproxen on renal function in the elderly. *Arch Intern Med* 2000; 160: 1465–1470.

[21] Ogawa H, Kurashima K, Namura M, et al. Pulmonary infiltrates with eosinophilia due to naproxen. *Jpn J Med* 1991; 30: 32–34.

[22] Guerrero Gómez DA, París Zorro S, Aponte Barrios W, et al. Drug reaction with eosinophilia and systemic symptoms (DRESS) with severe and atypical lung involvement. *Radiol Case Rep* 2020; 15: 2178–2182.

[23] Kovacevic L, Bernstein J, Valentini RP, et al. Renal papillary necrosis induced by naproxen. *Pediatr Nephrol* 2003; 18: 826–829.

Response of Apricot Trees to Ground Fertilization and Foliar Spraying

Raad Taha Mohammed Ali[1], Akram Abdul-Kadhim Hadi[2], Mawahib Midhat Hussein[3]
{Raadbalaket87@gmail.com, com.akr@atu.edu.iq, mawaheb.hussen@atu.edu.iq}

AL-Furat Al-Awsat Technical University, Iraq[1'2'3]

Abstract. The response of the apricot tree to combinations of fertilization with Qrop Complex and foliar spraying with seaweed extract (Alge-Zone) and their interactions in some chemical and yield traits are discussed. This includes the content of leaves Of chlorophyll and nutrients, Fruit weight (g), yield per tree kg. tree -1, percentage of total soluble solids (T.S.S). The randomized complete block design (R.C.B.D) was used with three replicates including the least significant difference (LSD) to compare the means at the 0.05 probability level. The results showed that the ground fertilizer with Qrop Complex gave an increase in the studied characteristics, and the foliar spraying with seaweed extract (Alge-Zone) had a positive effect on each of the leaves' content of chlorophyll and nutrients (nitrogen, phosphorous, potassium, boron and iron). Fruit Weight (g), The yield of one tree kg. tree -1, the percentage of total soluble solids (T.S.S). As for the interaction treatment, the ground fertilization with Qrop Complex fertilizer (600 g.tree-1) and foliar spraying with seaweed extract (Alge-Zone) at a concentration of 3 ml. L-1 significantly excelled in giving the best results in the studied traits which the content of leaves Of chlorophyll (54.67 SPAD), content of leaves Of nutrients (nitrogen, phosphorous, potassium, boron, and iron) of (1.60%, 0.47 %, 1.59, 50.30 mg.kg-1 and 251.67 mg.kg-1) respectively, Fruit weight of (16.96 g), yield per tree (15.77 kg. tree -1) and percentage of total soluble solids (T.S.S) of (15.66).

Keywords: Apricot, Alge-Zone, Foliar Spraying, Ground Fertilization.

1 Introduction

Follow the apricot Prunus armeniaca L. of the Rosaceae family. It is a fruit of the temperate region and the Mediterranean basin, which needs a period of cooling during the autumn and winter seasons to end the dormancy phase in the trees [1]. It was believed that the original home of the apricot is Armenia, but recent studies have shown that it is likely that its origin country is West and Central Asia [2]. It extends eastward to China, and from these areas, it moved to Greece and some European countries, then moved from it to Syria and some North African countries, North America, and Australia [3]. The word Apricot dates to the Greeks, where it was called AL-Praecox, which means early fruit [4]. Apricot is one of the summer fruits of high nutritional value that enters beside fresh consumption in many food industries, the most important of which are juices, jams, and apricot chips, which increase its economic value [5].
Ground feeding with nutrients for crops is one of the most important foundations of agricultural production and plant life preservation and providing nutrients in a balanced manner positively affects the growth and development of plants [6]. The compound fertilizer KPN is one of the

IMDC-IST 2021, September 07-09, Sakarya, Turkey
Copyright © 2022 EAI
DOI 10.4108/eai.7-9-2021.2314870

important nutrients to improve the type of fruits and increase production in fruit trees through ground addition or spraying on trees and within the concentrations recommended by the companies producing it is important. Apricots, such as nitrogen, phosphorous, and potassium, in addition to containing small mineral elements to grow well, increase their yield and improve the quality of their fruits [7]. Studies also indicated that the availability of potassium in appropriate quantities plays an important role in improving the quality and productivity of trees. The importance of potassium comes in that it enters many vital processes in plant cells and is based on regulating the osmotic pressure of cells [8]. It increases the plant's ability to retain water and contributes to the process of opening and closing plant stomata [9], as well as its role in stimulating and activating the work of plant enzymes and many other vital processes [10]. seaweed extract is one of the basic materials that can be added or sprayed to the plant and the soil to provide the plant with the basic elements because it contains the necessary macro and micronutrients, some hormones, and growth regulators such as auxins, gibberellins and cytokinin's [11] , These compounds increase the growth of roots and vegetative system and increase the amount of The yield , improving its quality, and increasing the aging of the fruits Plant resistance to biotic and abiotic stress[12], Also these extracts increase Efficient nutrient absorption in apples and increases the content of chlorophyll in leaves and increases From the processes of photosynthesis and respiration, and these compounds May act as an antioxidant because it contains alpha-tocopherol and Beta-carotene, niacin, thymine and ascorbic acid Through its role in increasing the activity of enzymes glutathione reductase Superoxide ascorbate peroxidase and dismutase[13], The aim of this research is to know the role of Qrop Complex fertilizer and seaweed extract in improving the quality and quantity of fruits.

2 Materials and Methods

The experiment was conducted in 2018-2019 private orchards in the Awfi region / Babylon province to study the effect of fertilization with Qrop Complex as shown in Table 1 and foliar spraying with seaweed extract (Alge-Zone) table and their interactions on some chemical traits and the result such as the content of chlorophyll in leaves (SPAD) and (nitrogen, phosphorous, potassium, boron and iron), average fruit weight (g), yield per tree kg.tree-1, percentage of total soluble solids (TSS)at the age of 6 years and almost homogeneous in length and size and planted with dimensions of 4 * 3 for this cultivar grafted on the seed origin. 48 trees were elected and all the required service operations for trees such as irrigation, fertilization, weeding, and control were conducted equally. In this experiment, two factors were used, the first being the ground fertilization with Qrop Complex fertilizer at four levels (control treatment, 200 g.L-1, 400 g.L-1, 600 g.L-1). The second factor is foliar spraying with seaweed extract (Alge-Zone)) at four concentrations (the control treatment, 1 ml.L-1, 2ml.L-1, 3ml.L-1) and accordingly it is a factorial experiment 4*4 = 16 treatments. The Randomized Complete Block Design (RCBD) with three replicates and one tree for the experimental unit, seaweed extract sprays were conducted at two dates after flowering and after flowers set. At the 0.05 probability level, the findings were statistically analysed using the least significant difference (LSD) to compare the means [3].

Table 1. The contents of the fertilizer Qrop Complex.

So3	Mgo	Ca^{++}	K^{+}	P	N

14	2	3	24	6	12

3 Studies Traits

1- Chlorophyll content of leaves (SPAD): The chlorophyll concentration was estimated in leaves when they are on trees using the manual scale SPAD meter [14].
2- Content of leaves of nutrients (N, P, K, B, and Fe):
Each seedling and replicate had leaf samples obtained, which were then rinsed with distilled water and placed in perforated paper bags. Then, for 48 hours and until confirmed, it was dried in an electric oven at 65 degrees Celsius. The samples were then pulverised, and 0.5 g of the powdered sample (dry leaves) was obtained. According to Black, 1965, the nitrogen concentration was calculated using the Microkjedhal apparatus and it was digested by concentrated 96% sulfuric acid (15) ml and (3 g) of the mixture (copper sulfate 0). 2 + potassium sulfate 0.8) with heating for an hour, then transfer the digestion solution to a volumetric flask with a capacity of 50 cm 3 and complete the volume with distilled water in the amount of (20) ml and then wiped using a standard hydrochloric acid 0.1 Then the nitrogen percentage was calculated according to the equation.
a- Nitrogen content of leaves (%): it was estimated using the Microkjedhal device according to the method [15].
b- The phosphorous content of the leaves (%): was also estimated by the method of soft digestion by using ammonium molybdate and ascorbic acid using a spectrophotometer Where (10) ml of the solution of the digested sample was taken and placed in a volumetric flask, then (0.1) g of ascorbic acid was added and (4) ml of ammonium molybdate solution for each sample, after which the contents of the beaker were heated on a hot plate for one minute, so the colour of the solution became blue, then read along the wavelength of 620 nm. At the same time, the samples of standard prepared solutions were read at the same time and method of preparing the digested sample, then the ratio was calculated Percentage of phosphorous according [15], [16].
c- Potassium content of the leaves (%): using a photometer flame as mentioned in [17]
d- Boron content of the leaves (mg.kg-1): it was determined by a Spectrophotometer Absorption Atomic device according to the method of [18], [19].
e- The iron content of the leaves (mg.kg-1): It was determined by a Spectrophotometer Absorption Atomic device according to the method of [18], [19]
7- Average weight of the fruit (g): according to the average weight of the fruit, weighing 10 fruits from each experimental unit, using a sensitive electric scale of the Metller type, then extracting the average weight of the fruit, estimated in grams.
8- The yield of one tree kg. tree -1: According to the yield of one tree by multiplying the average weight of one fruit by the number of fruits per tree, estimated in kilograms.
9- Percentage of total soluble solids (T.S.S): The percentage of total soluble solids in fruits was measured by taking a drop of fruit juice for each experimental unit using the Refractometer Hand device directly on the device.

4 Results

4.1 Chlorophyll Content (SPAD)

Table 2 shows that there are significant differences in the average chlorophyll content of leaves (SPAD) due to the effect of adding Qrop Complex fertiliser at an average of 600 g. tree-1, which resulted in the highest average chlorophyll content of leaves (51.32 SPAD) compared to the control treatment, which resulted in the lowest average of chlorophyll content of leaves (51.32 SPAD) (35.45 SPAD). As for the foliar spraying treatment with seaweed extract, the concentration of 3 ml.L-1 was excelled on the rest of the concentration and gave the highest rate of (45.67 SPAD) compared to the control treatment, which gave the lowest average for that trait reached (40.27 SPAD), As for the interaction treatments, the treatment of Qrop Complex fertilizer at an average of 600 g.tree-1 Alge-Zone seaweed extract at a concentration of 3 ml.L-1 was excelled and it gave the highest significant average in the chlorophyll content of leaves, which amounted to (54.67 SPAD) compared to the control that gave) 32.67 SPAD), which is the lowest average for this trait.

Table 2. Effect of ground fertilization and foliar spraying with seaweed extract on Leaf content of chlorophyll (SPAD) for apricot trees cultivar Zaini.

Ground Fertilization	Foliar Spraying with Seaweed Extract				Average
	A0	A1	A2	A3	
F0	32.63	35.01	36.33	37.81	35.45
F1	38.00	41.45	42.36	42.88	41.17
F2	42.97	44.41	45.34	47.30	45.01
F3	47.49	50.84	52.27	54.67	51.32
average	40.27	42.93	44.08	45.67	
L.S.D0.05	F= 4.920		A= 4.920		F*A= 9.840

4.2 Nitrogen Content of Leaves (%)

Table 3 indicated that the fertilization using Qrop Complex fertilizer at an average of 600 g.tree-1 had a significant effect on the average nitrogen content of the leaves of the apricot trees understudy, where these trees excelled and give the highest average for that trait amounted to (1.53%). Compared to the control treatment that gave the lowest average (1.19%). It is also noted from the same table that the trees differ among themselves in the nitrogen content of leaves. The trees sprayed with seaweed extract Alge-Zone at a concentration of 3 ml.L-1 excelled on the rest of the concentrations and gave (1.42%) compared to the control treatment that gave (1.32%). In terms of the interaction between the Qrop Complex fertiliser and the seaweed extract Alge-Zone, the same table's data show that the interaction trees Qrop Complex fertiliser excelled at an average of 600 g. Tree-1 with a 3 ml concentration of seaweed extract. When compared to the control therapy, which delivered the lowest average for the same attribute (1.60 percent), L-1 gave the highest average for the same trait (1.60 percent) (1.12 percent).

Table 3. Effect of ground fertilization and foliar spraying with seaweed extract on leaves content of Nitrogen (%) for apricot trees cultivar Zaini.

Ground Fertilization	Foliar Spraying with Seaweed Extract				Average
	A0	A1	A2	A3	

F0	1.12	1.18	1.22	1.27	1.19
F1	1.29	1.33	1.35	1.36	1.33
F2	1.39	1.41	1.43	1.46	1.42
F3	1.47	1.49	1.55	1.60	1.53
average	1.32	1.35	1.39	1.42	
L.S.D0.05	F= 0.161		A= 0.161		F*A= 0.323

4.3 The Phosphorous Content of The Leaves (%)

The results in Table 4 indicate that there are significant differences between the average phosphorous content of leaves (%) due to the fertilizer treatments. The trees were significantly excelled to the fertilizer treatment with Qrop Complex at an average of 600 g.tree-1 on the rest of the treatments (0.42%) When the control treatment gave the lowest average (0.16%). It is also evident from the same table that the trees showed significant differences among themselves in the phosphorous content of leaves (%) when sprayed with seaweed extract Alge-Zone. The trees sprayed with a concentration of 3 ml.L-1 excelled in the leaves content of phosphorous (%) and gave (0.33%)) compared to the control treatment that gave the lowest average for this trait (0.26%). The interaction of the Qrop Complex fertiliser treatment with Alge-Zone seaweed extract had a substantial impact on the leaves' phosphorous content (percent). The Qrop Complex fertiliser application at an average of 600 mg, according to the same table's results. Interaction of Tree-1 with Alge-Zone seaweed extract. The trees sprayed with a concentration of 3 ml.L-1, which yielded the greatest rates of (0.47 percent), outperformed the control treatment, which yielded the lowest average of (0.35 percent) (0.12 percent).

Table 4. Effect of ground fertilization and foliar spraying with seaweed extract on leaves content of phosphorous (%) for apricot trees cultivar Zaini.

Ground Fertilization	Foliar Spraying with Seaweed Extract				Average
	A0	A1	A2	A3	
F0	0.12	0.16	0.17	0.19	0.16
F1	0.22	0.25	0.27	0.28	0.26
F2	0.30	0.32	0.34	0.37	0.33
F3	0.38	0.40	0.44	0.47	0.42
average	0.26	0.29	0.31	0.33	
L.S.D0.05	F= 2.674		A= 2.674		F*A= 5.349

4.4 Potassium content of leaves (%)

Table 5 demonstrates that when the potassium content of leaves was given 600 g.tree-1, ground fertilisation with Qrop Complex fertiliser had a substantial effect. This treatment had the highest average rate for this feature (1.54 percent), while the control treatment had the lowest average

rate (1.24 percent) for apricot trees. When it came to spraying treatments, the trees treated with Alge-Zone seaweed extract, sprayed at a concentration of 3 ml.L-1, performed exceptionally well. In comparison to the control treatment, which had the lowest average (1.54 percent), this had the greatest average (1.54 percent) (1.24 percent). The interaction had a substantial influence on the potassium content of leaves, according to the same table, as it achieved the maximum average potassium content in leaves when treated with Qrop Complex fertiliser at an average of 600 g. Alge-Zone, a seaweed extract, interacts with tree-1. Qrop Complex, at a concentration of 600 g, was applied to the trees. Tree-1 interaction with spraying 3 ml.L-1 seaweed extract produced the highest average of (1.44 percent) when compared to the control treatment, which produced the lowest average for that attribute (1.09 percent).

Table 5. Effect of ground fertilization and foliar spraying with seaweed extract on Potassium content of leaves (%) for apricot trees cultivar Zaini.

Ground Fertilization	Foliar Spraying with Seaweed Extract				Average
	A0	A1	A2	A3	
F0	1.09	1.26	1.29	1.31	1.24
F1	1.33	1.35	1.36	1.39	1.36
F2	1.42	1.43	1.45	1.47	1.44
F3	1.48	1.52	1.56	1.59	1.54
average	1.33	1.39	1.42	1.44	
L.S.D0.05	F= 0.186		A= 0.186		F*A= 0.382

4.5 Boron Content of Leaves (mg.kg^{-1})

Table 6 showed significant differences between the average boron content of leaves for apricot trees, cultivar Zaini under study because of adding high-potassium fertilizer. The trees differed significantly and excelled among trees treated with Qrop Complex at a concentration of 600 g.tree-1 and Which gave the highest average of boron content of leaves (48.04 mg.kg-1) while the control treatment gave (30.88 mg.kg-1). The trees under research varied among themselves in their effect on the boron content of leaves when sprayed with seaweed extract, as shown in the same table. The trees treated with 3 ml.L-1 Alge-Zone performed best and produced the greatest average of (41.82 mg.kg-1). The trees that had not been treated had the lowest average for this attribute, which was (37.48 mg.kg-1). As shown in the same table, the interaction between the fertiliser treatment Qrop Complex and Alge-Zone seaweed extract had a substantial impact on the boron content of the leaves. The trees treated with Qrop Complex fertiliser at a dosage of 600 g.tree-1 and foliar spraying with seaweed extract Alge-Zone at a concentration of 3 ml.L-1 had the greatest average boron content in leaves (50.30 mg.kg-1) When the control treatment was used, the leaves had the lowest average boron level (28.61 mg.kg-1).

Table 6. Boron concentration of leaves (mg.kg-1) for apricot trees cultivar Zaini after ground fertilisation and foliar spraying with seaweed extract.

Ground Fertilization	Foliar Spraying with Seaweed Extract				Average
	A0	A1	A2	A3	

F0	28.61	29.18	31.96	33.75	30.88
F1	34.72	35.11	36.96	38.45	36.31
F2	39.73	42.73	43.53	44.77	42.69
F3	46.86	47.20	47.80	50.30	48.04
average	37.48	38.56	40.06	41.82	
L.S.D0.05	F= 9.838		A= 9.838		F*A= 19.676

4.6 Iron Content of Leaves (Mg.Kg-1)

Because of the ground addition of the fertiliser Qrop Complex, significant variations in the average iron content of leaves are shown in Table 7. At a concentration of 600 g.tree-1, the fertiliser considerably improved the trees. As indicated in Table 7, apricot trees differed in their average iron content of leaves when sprayed with seaweed extract, with the highest average for this feature (231.18 mg.kg-1), and the lowest average for the same trait (control treatment without spraying) (216.34 mg.kg-1). The interaction of Qrop Complex and seaweed extract in the leaves had a clear influence on the iron content of the leaves. Trees were given a 600 g fertiliser treatment, with tree-1 interfering with a 3 ml concentration of seaweed extract. When compared to the control treatment, which delivered the lowest average for the same attribute (251.67 mg.kg-1), L-1 excelled and gave (251.67 mg.kg-1) (185.00 mg. kg- 1).

Table 7. Effect of ground fertilization and foliar spraying with seaweed extract on Iron content in the leaves (mg.kg-1) for apricot trees cultivar Zaini.

Ground Fertilization	Foliar Spraying with Seaweed Extract				Average
	A0	A1	A2	A3	
F0	185.00	190.00	199.00	208.33	195.58
F1	211.67	217.67	222.00	226.00	219.34
F2	227.67	231.67	234.00	238.67	233.00
F3	241.00	246.67	248.67	251.67	247.00
average	216.34	221.50	225.92	231.18	
L.S.D0.05	F= 2.674		A= 2.674		F*A= 5.349

4.7 Fruit Weight (g)

Table 8 shows that a high potassium fertiliser, Qrop Complex, was used at an average rate of 600 g.tree-1. It had a substantial influence on the fruit weight of apricot trees of cultivar Zaini, where these plants excelled and gave the greatest average of that feature of (16.14 g) when compared to the control treatment, which offered the lowest average of that attribute (11.97 g). The table also shows that the weight of the fruit varies between the trees. The trees sprayed with

Alge-Zone seaweed extract at a concentration of 3 ml.L-1 outperformed the other concentrations, averaging 14.66 g, compared to the control treatment, which had the lowest average for the same attribute. (13.48 g)   The significance of the apricot trees with the soil fertiliser at an average of 600 g is indicated by the results of the interaction between the treatment of the Qrop Complex fertiliser with the seaweed extract Alge-Zone, as shown in the table. The interaction of Tree-1 with seaweed extract at a concentration of 3 ml.L-1 produced the highest average for the same characteristic. (16.69 g) in comparison to the control therapy, which produced the lowest average for this feature of (11.18 g).

Table 8. Effect of ground fertilization and foliar spraying with seaweed extract on Fruit weight (g) for apricot trees cultivar Zaini.

Ground Fertilization	Foliar Spraying with Seaweed Extract				Average
	A0	A1	A2	A3	
F0	11.18	12.02	12.15	12.51	11.97
F1	12.94	13.04	13.68	13.88	13.39
F2	14.20	14.74	15.01	15.30	14.81
F3	15.61	15.93	16.06	16.96	16.14
average	13.48	13.93	14.23	14.66	
L.S.D0.05	F= 1.771		A= 1.771		F*A= 3.543

4.8 The Yield of One Tree (Kg^{-1})

Because of the use of this fertiliser, Table 9 demonstrated changes in the yield average of one tree for apricot trees, cultivar Zaini under research. The trees differed, with the trees fed with Qrop Complex fertiliser at a concentration of 600 g excelling. The tree with the highest average yield per tree was Tree-1 (15.05 tree .kg-1). The control therapy, on the other hand, produced the lowest average for the same feature, which was (11.78 tree .kg-1). The trees under research differ in their effect on the yield of one tree when sprayed with seaweed extract, as shown in the same table. The trees treated with 3 ml.L-1 Alge-Zone performed best and produced the greatest average of (13.95 tree .kg-1). While the untreated trees had the lowest average for that attribute (12.88 tree.kg-1), the interaction between the Qrop Complex ground fertiliser and the seaweed extract Alge-Zone altered the output of one tree. As shown in the same table, trees treated with Qrop Complex fertiliser at a concentration of 600 g.tree-1 in combination with foliar spraying with seaweed extract Alge-Zone at a concentration of 3 ml.L-1 yielded the highest average of yield per tree (15.77 tree.kg-1), while the control treatment yielded the lowest average for this trait (15.77 tree.kg-1) (10.65 tree .kg-1).

Table 9. Effect of ground fertilization and foliar spraying with seaweed extract on the Tree yield (kg^{-1}) for apricot trees cultivar Zaini.

Ground Fertilization	Foliar Spraying with Seaweed Extract				Average
	A0	A1	A2	A3	
F0	10.65	11.84	12.10	12.51	11.78
F1	12.77	12.87	13.02	13.23	12.97

F2	13.50	13.74	14.01	14.30	13.89
F3	14.59	14.84	15.01	15.77	15.05
average	12.88	13.32	13.54	13.95	
L.S.D0.05	F= 1.902		A= 1.902		F*A= 3.804

4.9 Percentage of Total Soluble Solids (T.S.S)

The percentage of total soluble solids (TSS) for the apricot trees understudy was significantly affected by fertilising with Qrop Complex fertiliser at an average rate of 600 g.tree-1, as shown in Table 10. These trees outperformed the control treatment, yielding the greatest average for that attribute (15.29 percent) compared to the control treatment, which yielded the lowest average (13.41 percent). The proportion of total soluble solids (TSS) differs among the trees in the same table, with the trees sprayed with seaweed extract Alge-Zone at a concentration of 3 ml having the highest TSS. L-1 surpassed the other concentrations, yielding (14.69 percent) compared to 14.13 percent for the control. The relevance of the trees that were fertilised with the fertiliser Qrop Complex at an average of 600 gm is indicated by the findings of the same table for the interaction between the treatment of the Qrop Complex fertiliser with the seaweed extract Alge-Zone. When compared to the control treatment, which had the lowest average for this feature (15.66 percent), the highest average in percentage of total soluble solids (TSS) was (15.66 percent) (13.04 percent).

Table 10. Effect of ground fertilization and foliar spraying with seaweed extract on the percentage of total soluble solids (T.S.S) for apricot trees cultivar Zaini.

Ground Fertilization	Foliar Spraying with Seaweed Extract				Average
	A0	A1	A2	A3	
F0	13.04	13.29	13.57	13.74	13.41
F1	13.90	14.07	14.25	14.38	14.15
F2	14.57	14.63	14.72	14.96	14.72
F3	15.04	15.17	15.27	15.66	15.29
average	14.13	14.29	14.45	14.69	
L.S.D0.05	F= 1.428		A= 1.428		F*A= 2.857

5 Discussion

5.1 Effect of Ground Fertilization on The Leaves Content of Chlorophyll and Mineral Elements (N, P, K, B, Fe)

Tables from 2-7 show the significance of trees fertilized with this fertilizer on the control treatment (without adding). The reason for the increase in this trait maybe since this fertilizer contains nutrients necessary for growth, especially potassium, which works to stimulate enzymes related to physiological processes such as photosynthesis. It also helps in the movement and transfer of food manufactured in the leaves to other plant tissues, which increased

the manufacture of food manufactured in the leaves as a result of containing good quantities of major elements, which increased the content of the leaves of chlorophyll and mineral elements, as the increase of these elements in the plant as a result of processing and absorption from before the plant, Fertilizing of fruit trees with compounds containing one or more nutrients necessary for plants to improves their nutritional status as well as their growth, nitrogen is the main component in mineral fertilizers that are added to plants, it encourages vegetative and root growth of plants and strengthens the root group, It's a necessary part of cell protoplasm. It accounts for 2-4 percent of the plant's dry matter after water. It's found in a wide range of chemical molecules, including amino acids, proteins, nucleic acids, enzymes, and plant hormones. It also forms an essential part of the dye for photosynthesis (chlorophyll) and gives the plant a green colour, While phosphorous is necessary for several vital processes such as photosynthesis, carbohydrates, energy transfer within the plant and cell division, it enters the composition of nucleic acids, energy-carrying compounds, and some enzymes, accelerates the early formation of roots and increases their growth and spread in the soil, as well as accelerating the flowering of trees and comes in second place After nitrogen in terms of the quantities needed by the plant, and potassium is necessary for several physiological processes within the plant such as building sugars, starch, proteins and cell division [20].

5.2 The Effect of Ground Fertilization on The Weight of The Fruit, The Yield of One Tree, and The Percentage of Total Soluble Solids

The data in Tables 8-10 show that this is the case, and the explanation for this could be related to improved tree vegetative growth. As a result of the growth in processed foodstuffs that develop leaves and collect them in the fruits, the number of fruits left on the tree at harvest increased. As a result of digesting nutrients and boosting their absorption from the soil, this had a favourable impact on tree yields, resulting in a rise in the trees' benefit from them in terms of improving their vegetative and fruit growth [20].

.

5.3 Effect of Seaweed Extract on Chlorophyll Content and Mineral Elements (N, P, K, B, Fe) In Leaves.

Tables 2-7 show that foliar spraying with seaweed extract had a clear effect on the attributes studied. These compounds increase the growth of the vegetative system, increase the quantity of yield, improve its quality, delay the aging of fruits, and increase plant resistance to biotic and abiotic stress. [21]. These extracts also have a great role as primary products of organic materials, and synthetic materials such as seaweed extract cells consist of many important compounds such as sugars, amino acids, RNA, DNA, and enzymes, as well as proteins [22]. Vitamins and minerals are significant molecules because of their involvement in boosting the efficiency of the photosynthetic process, increasing the produced materials in the leaves, and increasing the mineral content of the leaves [23].

5.4 Effect of seaweed extract on fruit weight, yield per tree, and percentage of total soluble solids:

It is evident from the results presented in Tables 8-10 to the increase that occurred when spraying with seaweed extract. The reason for this may be due to the improvement of the vegetative growth of trees and thus the increase in processed foodstuffs that grow leaves and combine them with young fruits in an increase in yield. Which led to an increase in the number

of fruits remaining on the tree when harvesting, which was positively reflected on the yield of trees because of processing nutrients and increasing their absorption from the soil, which led to an increase in the trees' benefit from them in improving their vegetative and fruit growth. When trees are treated with seaweed extracts, the quality of orange fruits improves as the percentage of sugars in them increases [24]. Also, these extracts increase the efficiency of nutrient absorption, increase the processes of photosynthesis and respiration, and these compounds may act as an antioxidant because they contain alpha-tocopherol, beta-carotene, niacin, thymine, and ascorbic acid, and through their role in increasing the activity of many enzymes [22]. As for the treatment of the interaction between the Qrop Complex fertilizer and the seaweed extract, its effect was clear in giving the best results. The reason may be due to the result of their interaction, thus giving a clear surge in the studied characteristics.

References

[1] Taha Sheikh Hassan. 2002 . Encyclopedia of almond fruit. first edition. Aladdin House Publications. Syria. p. 352.

[2] Punia, M.S .2007. Wild Apricot. National Oil Seeds and Vegetable Oils Development Board. Ministry of Agriculture, Govt. of India

[3] Al-Douri, Ali and Adel Al-Rawi. 2000. Fruit production. first edition. Book publishing house. University of Al Mosul. p. 528.

[4] Janick, J . 2005 .The origin of fruits, Fruit growing and Fruit breeding. Plant Breeding. Rev.25: 255-320.

[5] Bal, J. S .2005 . Fruit Growing. 3th edt. Kalyani Publishers, New Delhi. India.

[6] Prasad, R. and Power, J.F. 1997. Soil Fertility Management for Sustainable Agriculture. Lewis Publishers in an Imprint of CRC Press, 243.

[7] Jassim M. A. Al-Aa'reji and Jihad Sh. K. Perot .2017. Effect of some liquid organic and (NPK) fertilizers on growth and fruiting of apricot trees "Prunus armeniaca L. "cv. Royal . Collage of Agriculture and Forestry/ University of Mosul

[8] HUSSEIN,M.M. ,M.M.SHAABAN AND A.K.M.EL-SAALY . 2008 . Response of cowpea plant grown under salinity stress to n p,k-foliar application .American J.of plant physiology 3 (2) ,2008, 81-88 .

[9] Al-Sahaf, Fadel Hussein. (1989). Applied plant nutrition. University of Baghdad - Ministry of Higher Education and Scientific Research.

[10] TISDALE, S.L., NELSON, J. AND D. BEATON. 1993 . Soil Fertility and Fertilizer. Prentice Saddle River. New Jersey. USA.1993, P. 220.

[11] O'Dell, C. 2003. Natural Plant Hormones are Biostimulants Helping Plants Develop High Plant Antioxidant Activity for Multiple Benefits. Virginia Vegetable, Small Fruit and Specialty Crops. 2 (6): 1-3.

[12] Demir,N.;B.Dural&K.Yildirim.2006.Effec to of seaweed suspensions on seed germination of tomato,pepper and aubergine. J.Biol.Sci.6:1130-1133.

[13] Ayad,J.Y.1998.TheEffect of SeaweedAscophyllumnodosumExtract on Antioxidant Activities and Drought Tolerance of Tall Fescue FestucaarundinaceaSchreb .Ph.D.thesis. agronomy department. Texas Tech.University.Pp.158.

[14] Felix Loh, j. G. and B. Nina. 2000. Use of the Minolta SPAD- 502 to determine chlorophyll concentration in ficus benjamina L. and populus deltoid's Marsh leaf tissue . Hort. Science. 35 (3) :p.423.

[15] Black, C.A. 1965.Methods of Soil Analysis.Part 2.Amer.Soc.of Agron.Inc.U.S.A.

[16] Olsen, S.R.;C.V.Coil;F.S.Watanabe, and L.A.Dean. 1954. Estimation of available phosphorus in soil by extraction with sodium bicarbonate. USDA-Circular, 939:1-9.

[17] Richards, L.A. 1954 .Diagnosis and Improvement of Saline and Alkali Soils.U.S.D.A.Handbooks No.60.
[18] Chapman , H. D and F.P pratt. 1961. Methods of analysis for soils, plants and water . univ. of calif. Div. Davision of Agric. Sci. p.309.
[19] Al-Nuaimi, Saadallah Najm. 1999 . Fertilizers and soil fertility. Ministry of Higher Education and Scientific Research, University of Mosul. House of books for printing and publishing.
[20] Nijjar, G. S. 1985. Nutrition of Fruit Trees. Published by Mrs Usha Rajumar for Kalyani, India, New Delhi, pp: 10-52.
[21] Demir,N.;B.Dural&K.Yildirim.2006.Effec to of seaweed suspensions on seed germination of tomato,pepper and aubergine. J.Biol.Sci.6:1130-1133..
[22] Doug ,S; L..Change ;C.F.scagel and L.H.Fuchigami .2005 .Timing of urea applactioneffects leaf and root N uptake in young fugi / M.9 apple trees.
[23] Al-Mayah, Abdel Reda Amwan and Ibrahim Hameem Flyer. 1991. Aquatic plants and algae. The first part. Ministry of Higher Education and Scientific Research. Albasrah university
[24] Fornes,F.;M.Sanchez& J.L.Guardiola.2002 Effect of a seaweed extract on the productivity of"deNules"Clementine Mandarin and Navelinaorange.Botanica Marina.45(5):487-489.

Flow Field Simulation between Angle Vane and Cylinder

[1]Rafi M. Qasim, [2]Tahseen A. Jabbar, [3]Ihsan A. Abdulhussein

{rafi.mohammed@stu.edu.iq[1], tahseen.ali@stu.edu.iq[2], drengihssan@stu.edu.iq[3]}

[1,2]Fuel and Energy Department, Basrah Engineering Technical College, Southern Technical University, Basra, Iraq

[3]Basra Engineering Technical College, Southern Technical University, Basra, Iraq

Abstract. Water flow around cylinder represents a noticeable problem in fluid mechanics. The computational fluid dynamic is employed to study numerically the turbulent flow field around a cylinder without vane and with vane respectively. The vane configuration and direction are considered in the numerical study. The analysis is done in two dimensions by using ANSYS software. The finite volume method is used to model and simulate the cases study. The numerical study concentrates on strain rate, stream function, swirling, vorticity, velocity in the flow direction, radial velocity, pressure distribution, pressure coefficient and drag coefficient. It is recognizing that the vane changes the flow field hydraulic response. It is found from the result that the vane more reduces the value of the drag coefficient as compared with the value of the drag coefficient when the cylinder is alone. The stream function reveal how much the fluid suffer from deformation while the strain rate reveal how much t5he flow velocity change with distance. Also, vorticity illustrate a dramatic hydraulic response especially in the case of the vane existence. The study shows that the vane has direct effect on the flow separation zone and dissipation the turbulent intensity before it passes the cylinder.

Keywords: Cylinder, Flow Field, Fluid-Structure Interaction, Vane.

1 Introduction

One of the most dominant problems of flow-cylinder structure interaction is the turbulent flow around a circular cylinder which is placed vertically or in inclined position inside the flow respectively. Such a pier radically changes the flow around it. It is very important to study the flow field around a cylinder under different conditions like placing an obstacle, for example vane, before the cylinder at upstream to reduce the turbulence and separation zone of the flow. Many papers dealt with the problem of flow around a cylinder like flow around bridge pier, pile and pile groups. Sowoud et al. [1] investigated the turbulence model applicability in the engineering practice for the case of subcritical flow and examined the variation of Reynolds number on the characteristics of the flow. ANSYS FLUENT (19.1) is used to perform the numerical simulation in two dimensions. Majtaba Daneshi [2] did a numerical investigation for the flow characteristics at the downstream of a circular cylinder, ANSYS Fluent and the two-dimensional finite volume

IMDC-IST 2021, September 07-09, Sakarya, Turkey
Copyright © 2022 EAI
DOI 10.4108/eai.7-9-2021.2315181

method is used to perform the numerical analysis. Here, the characteristics are investigated under the following conditions: laminar and turbulent unsteady incompressible flow. The characteristics include drag force, pressure distribution and velocity fields. Also, the effect of Reynolds number on the flow parameter is investigated. Kartik Chandra Bhagat et al. [3] carried out a numerical and an experimental work to obtain the pressure coefficient and drag force for various aspect ratio (L/D). The numerical analysis is performed by adopting ANSYS Fluent 14.5 to investigate the pressure distribution around a circular cylinder and point of the flow separation. Yuce and Kareem [4] made a numerical investigation to investigate the flow field around the cylinders with the same characteristic length under the same flow conditions with the ranging from the laminar flow to the turbulent flow. The simulation is performed in two dimensions. The flow field was found to be affected by the shape of the cylinder, wake downstream of the square cylinder was found to be much more turbulent than that of the circular one. Also, the increased in Reynolds number will reflect on the turbulence of the wake flow and its length at the downstream of the cylinders. Wei and Aode [5] used the method of large-eddy simulation to investigate numerically the scour and the turbulent flow field around a circular pier. From the result they found decreasing in shear stress with increase in the scour depth, also a gradual increase occurred in the gradient of vertical pressure and turbulent intensity. Davis and Moore [6] investigated numerically the flow which pass a rectangular cylinder. Dependent on the mean inlet flow velocity and the cylinder height, they mentioned the forces which are acting on the cylinder and the structure of the wake with different aspect ratio and the angles of the attack at two values of the Reynolds number. Oudheusden et al. [7] carried out an experimental to investigate the vorticity near a square cylinder by adopting PIV technology, where the Reynolds which is adopted in the experiment work has the values of 4000, 10000 and 20000. Gera et al. [8] investigated two dimensional unsteady flows by using the finite element method around a cylinder with quadrilateral shape, and Reynolds number range from 50 to 250. Bai and Li [9] used a computational fluid dynamic technique to simulate unsteady flow around circular cylinder in two dimensions with Reynolds number equal to the 200. The very reliable values of the pressure distribution coefficients, the coefficients of friction and buoyancy, and the Strouhal number were found. Richardson et al. [10] investigated the flow around the bridge pier without and with the scour hole. Also, they made a comparison with experimental result. They discover that the flow patterns around a pier of the bridge are well simulated by Flow3D hydrodynamic model. Chang el al. [11] adopted the model of large eddy simulation to find the solution of the flow equations around the pier of the bridge with a fixed bed and no scour.

The hydraulic functionality of the vane nearby a cylinder, concentrated on create a hydraulic field around the vane. Here, when the flow passes the vane and becomes ready to enter the upstream region of the cylinder, the turbulence at the upstream of the cylinder is not strong as compared with turbulence at the vane upstream region. Because of the vane destroy strongly and dissipate the flow energy and this occurs suddenly when the flow encounters the vane. Also, the flow separation will rise owing to the presence of the vane. The presence of the vane at the upstream of the cylinder, play an important role in civil engineering application like the presence of the vane at the upstream of the bridge pier will reduce the scour depth around the pier at high efficiency and this will lead to increase the serviceability life of the pier and avoid the hydraulic failure owing to the scour around the pier. The target of the present paper concentrates on the investigation the

influence of vane configuration and direction on the neighboring cylinder. Here the vane is placed at the upstream of the cylinder. This subject deal with challenge problem happens between the vane and the cylinder under the turbulent flow condition. This challenge emerged from the interference which happens between flow and vane in addition to vane and flow field around the cylinder. This interference reveals a noticeable situation with appear clear due to the existence of the vane.

2 Numerical modeling and solution

The current paper deals with three different cases. The first case is a cylinder without vane, while in the second and third case respectively the cylinder is nearby the vane. The modeling and simulation are performed in two-dimensions (2D) by utilizing the software ANSYS (fluent). Based on the geometry which is generated by ANSYS, fine meshes range from 29900 to 29993 elements. The numerical analysis depends on finite volume method. **Figure 1** illustrate the three different cases, **Figure 1** contains all the following dimensions cylinder diameter, vane length and width, also domain length and width. **Figure 2** illustrate the computational grids for the three cases which used in this paper. The assumption which are adopted in the modeling and simulation of the current problem are listed below:

1- The flow material is water.
2- Water is considered as incompressible material.
3- The physical properties of water are considered constant.

Table 1 shows the water properties. Table 2 reviews the boundary condition of the hydraulic system. The channel bed described as horizontal, flat and fixed, while the walls is considered vertical. Both the vane and a cylinder are considered submerged. The adopted velocity of water is equal to the 0.1 m/sec and the time of analysis equal to 8 second.

Table 1. Water Properties [12,13].

Density ( )	Viscosity (kg/m.s)
998.2	0.001003

Table 2. Boundary Condition of the Hydraulic System. The numerical analysis deals with the studying of

Inlet	Velocity at inlet
Outlet	Pressure at outlet
Cylinder	No slip-Wall

Vane	No slip-Wall
Channel bed	No slip-Wall
Channel sides	No slip-Wall
Top surface of flow	Atmospheric Pressure

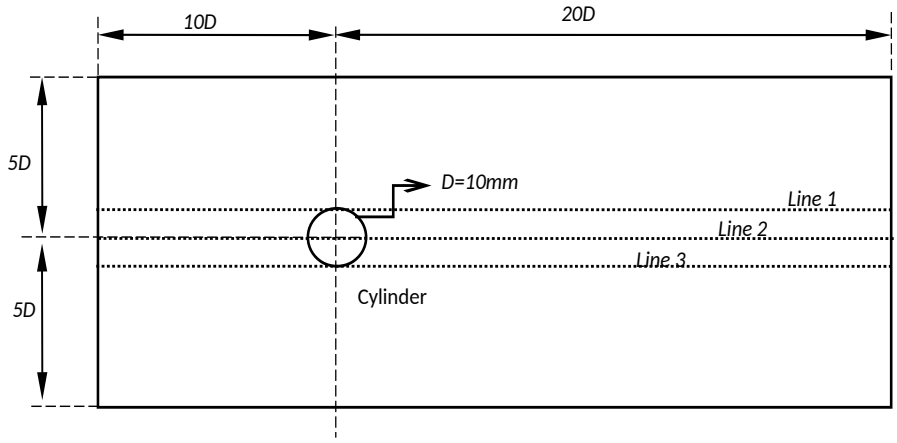

Case (1)

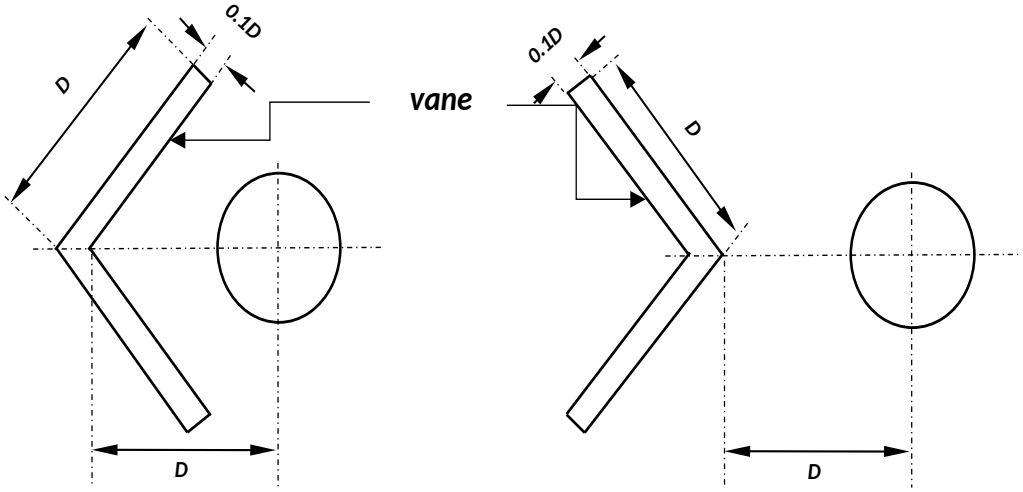

Case (2) Case (3)

Figure 1. Shows the configuration and direction of vane neighboring to a cylinder, also shows a cylinder alone.

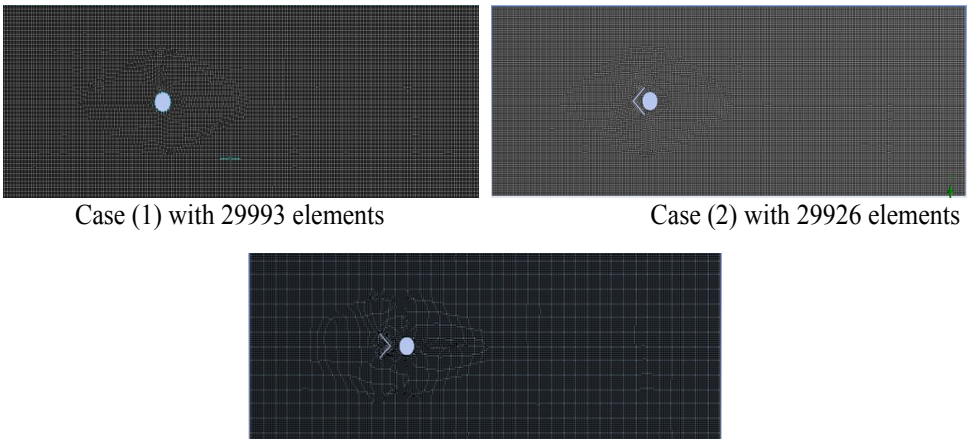

Case (1) with 29993 elements Case (2) with 29926 elements

Case (3) with 29900 elements

Figure 2. Shows the mesh of the different cases.

The CFD governing equations that will be used for the simulation are the conservation of momentum equation and incompressible fluid continuity equation is shown in equations (1) to (4), respectively.

(1)

(2)

(3)

(4)

Verification

It is very important to undergo verification in the software before adopting it in solving the present problem. So, the fluent software is used for analysis of the case study in reference [12] and the results which have been obtained from the analysis are compared with the previous results that have been obtained in the reference [12]. Case studied in reference [12] concentrated on the flow field around a square. Three-dimensional analysis is used in the simulation of the reference [12] case studied. Table 3 reviews the information of reference [12] case studied, while Table 4 shows the obtained value of the drag coefficient from the study in reference [12] and the drag coefficient value from the current study.

Table 3. Case study information

D (m)	V (m/s)	H (m)		Re (no unit)
1	0.292	2	1.225	20000

Table 4. Comparison between the previous study [12] and current problem.

Reference studies	Reynolds Number	Setup	
Zaid et al. [12]	20000	Numerical	2.1951
Present study	20000	Numerical	2.15

3 Result and Discussion

The simulation of the current problem is done by the finite volume method and is explained briefly in this section.

Strain Rate: **Figure 3** concentrates on the contour variation of strain rate for different case studies. Generally, strain rate refers to the gradient of the flow velocity. The velocity gradient increases from case to case. It is obvious from figure, case (2) has high strain rate as compared with the cases (1) and (3). for case (2) high separation of water will happen at the vane front and this separation makes a reduction in water flow velocity before it passes the cylinder and this reduction continues with increase in distance, therefore, the gradient of flow velocity increasing at the cylinder downstream. In case (2) the obstruction which is provided by the vane play an important role in reducing the flow velocity and increases the strain rate or flow velocity gradient, while case (3) has less effect as compared with case (2). In case (1) there is no obstruction which confines and dissipates water flow, therefore, there is no noticeable shortage in the value of flow velocity when the flow past the cylinder, so there is no significant alter in strain rate at the downstream region of the cylinder. **Figure 4** shows the variation in strain rate in the direction of the flow, the **Figure 4** adopts three lines in longitudinal direction one of the lines pass at the center of the cylinder while the remainder pass at the edge of the cylinder. Figure shows for all cases, that the maximum value of the strain rate always occurs in case (2) at each line which passes at the center and the edge of the cylinder. While the strain rate in case (1) and case (3) has moderate values. For all cases when the flow passes the cylinder the strain rate vanishes.

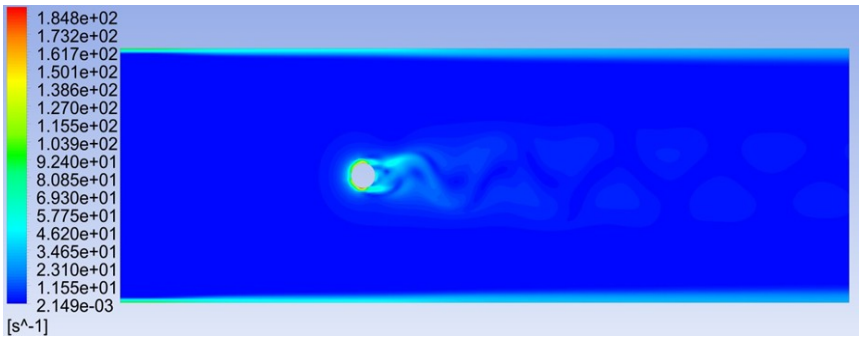

Case (1)

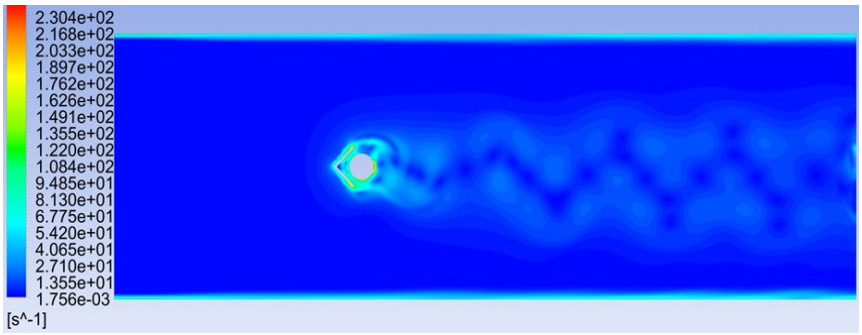

Case (2)

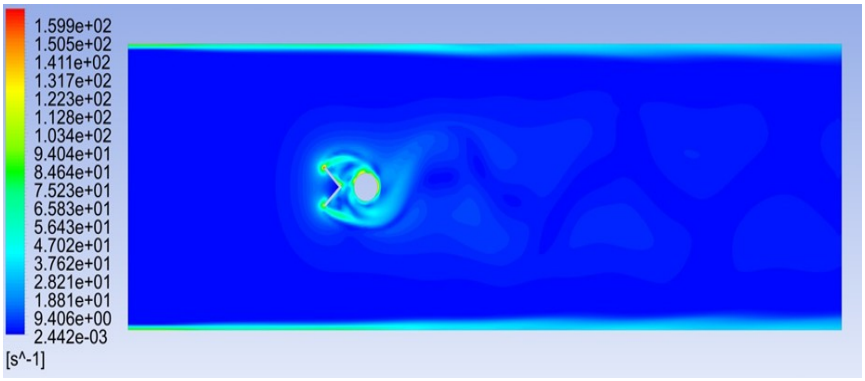

Case (3)

Figure 3. Shows the change in strain rate for different cases.

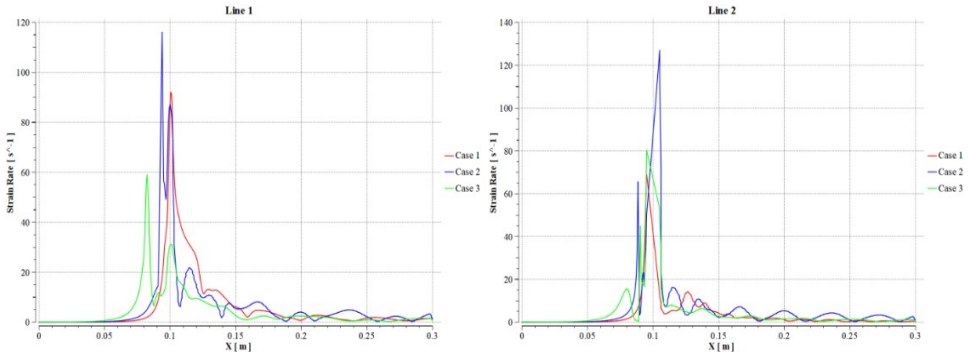

(a) (b)

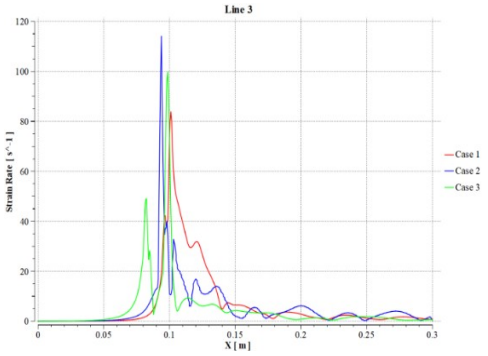

(c)

Figure 4. Shows the change in strain rate for different line in the direction of the flow (a) Line 1, (b) Line 2 and (c) Line 3.

Figure 5 concentrates on the contour variation of stream function for different case studies. The stream function is used to describe the stream line which generates around the body like the cylinder and the vane. When the cylinder is alone case (1), the stream line which is generated at the cylinder downstream has small amplitude. While in case (2) the effect of the vane on the stream line appears clearly. Here, the vane separate, dissipate and work to deflect the flow direction, therefore, all these processes will reflect on the shape of the stream line around the cylinder, while case (3) has moderate hydraulic response between case (1) and case (2). Generally, the change in stream line depends mainly on the flow velocity and volumetric flow. In case (2) the water undergoes more deformation as compare with the other cases.

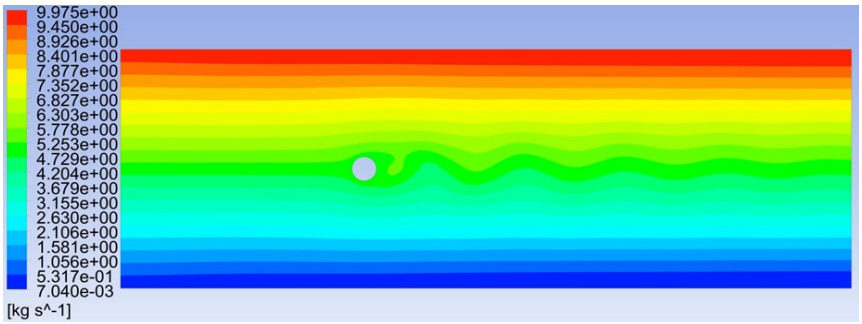

Case (1)

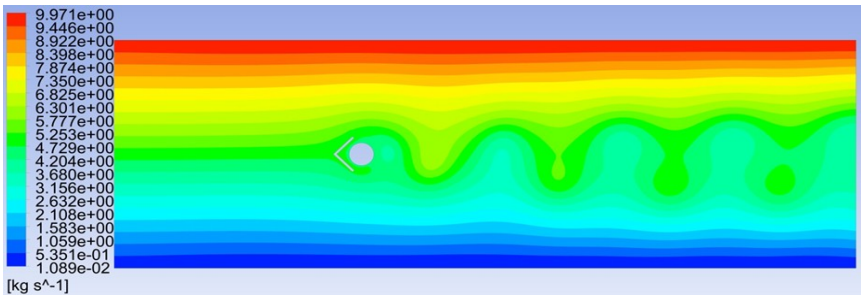

Case (2)

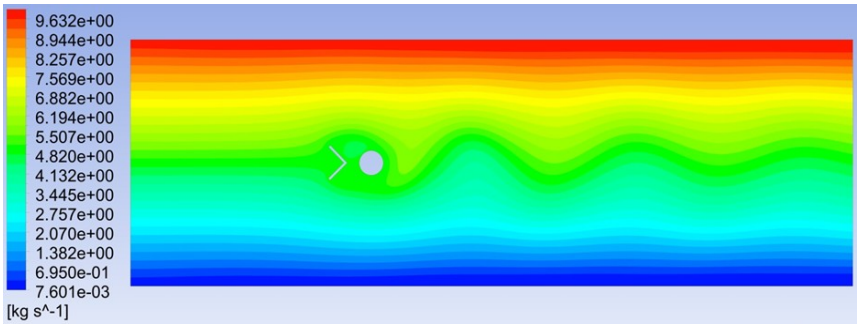

Case (3)

Figure 5. Shows the change in stream function for different cases.

Figure 6 concentrate on the contour variation of swirling for different case studies. Generally swirling refers to the eddy which generates near the obstacle. Here, the obstacle is the cylinder and the vane. For all cause, it is obvious normal swirling (eddy) and this means that the turbulence which create the eddy is not high. In this figure the swirling is normal to the xy-plane because the problem is analysis in two dimensions.

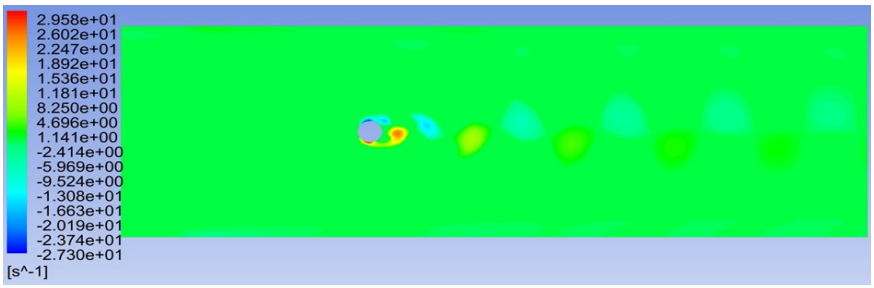

Case (1)

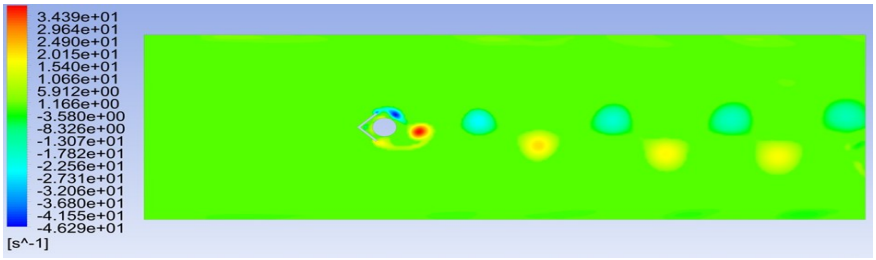

Case (2)

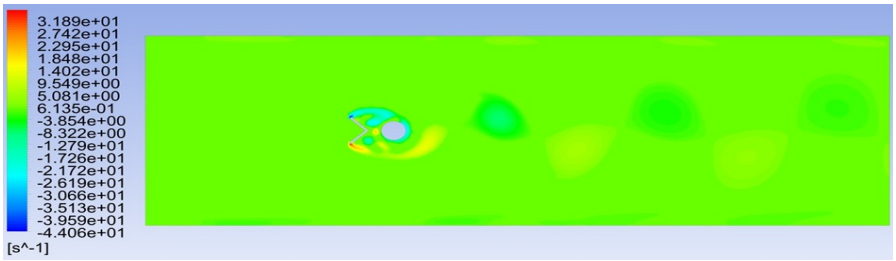

Case (3)

Figure 6. Shows the change in swirling normal to z.

Figure 7 illustrate the flow velocity contour in the direction of the flow for all cases. We observe a strong eddy occur in case (2) when the cylinder is near by the vane as compare with case (1) and case (2). Also, at the near lateral side of the cylinder in case (1), we observed a strong oscillatory flow representing by the two vortexes at the side of the cylinder. For cases 2 and 3 the oscillatory will develop at the downstream of the cylinder. The oscillatory flow at the downstream of case (2) can be described as stronger as compared with other cases.

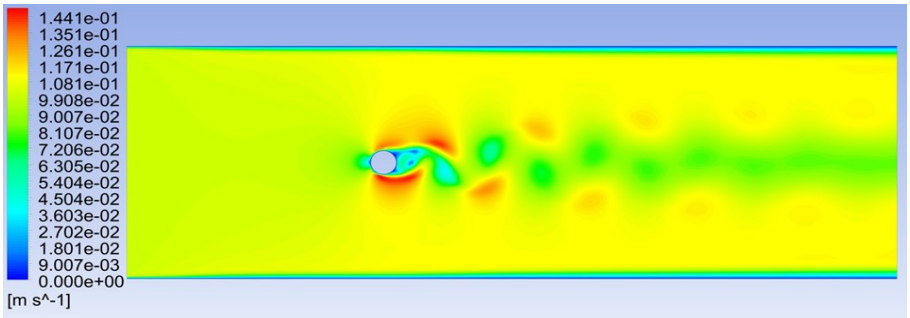

Case (1)

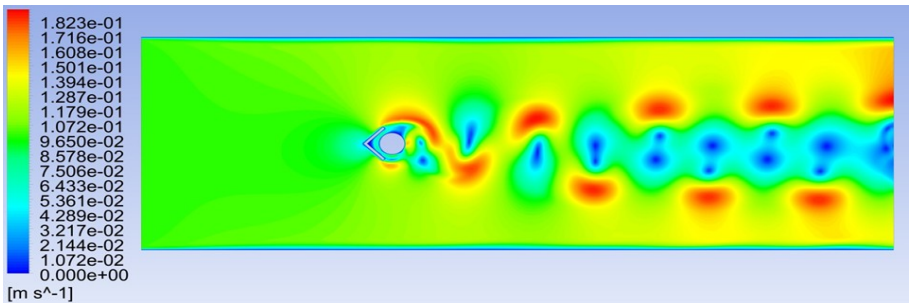

Case (2)

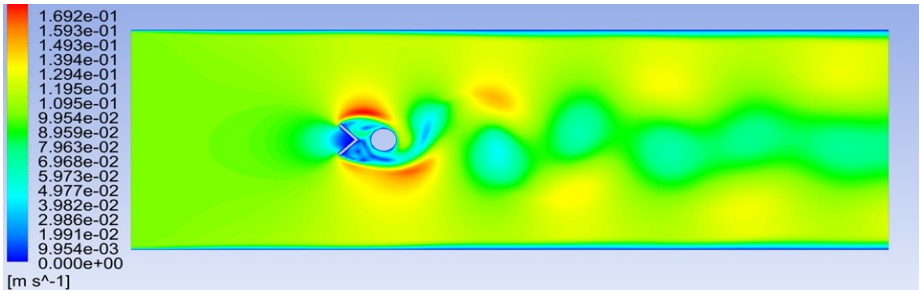

Case (3)

Figure 7. Shows the counter of flow velocity magnitude.

Figure 8 illustrate the variation in the radial flow velocity for different cases. It is evident from the figure when the flow passes the cylinder (case -1) or the cylinder which is nearby the vane (case -2 and case-3) the turbulence and the eddy grow and develop gradually, regardless of especially the direction and the configuration. Dramatic alter happens in radial velocity relies on the points of the fluid separation, turbulent dissipation and the flow velocity gradient with distance. The radial flow velocity at the downstream of case (2) can be described as more alter as compared with other cases.

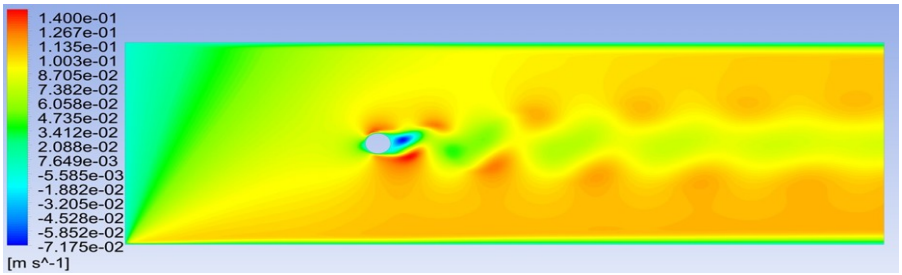

Case (1)

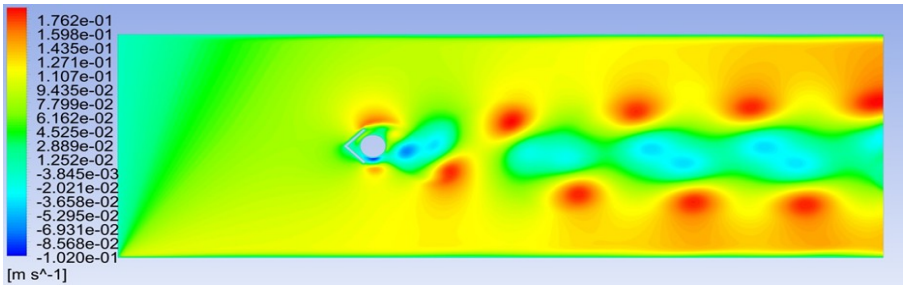

Case (2)

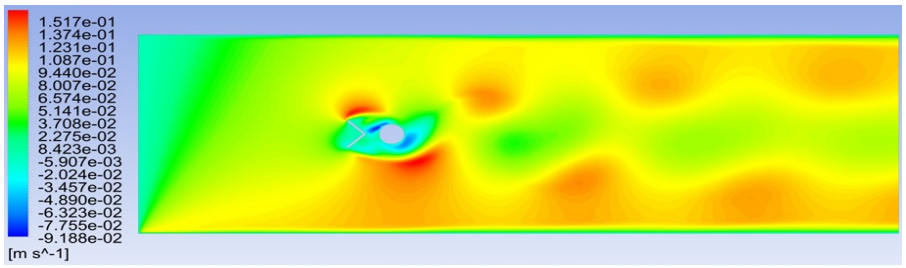

Case (3)

Figure 8. Shows the counter of radial flow velocity magnitude.

Figure 9 illustrates the vorticity contours map around a cylinder without vane and with vane respectively. Here, the mode of the vortex formation depends on the pressure around the cylinder or the pressure around the vane. In case (1) thick layers are composed mostly of vorticity of small magnitude around the cylinder surface, while in cases (2 and 3) the thick layers will be created around the vane instead of the cylinder surface. For all cases the vorticity will develop strongly at the downstream of the cylinder especially in case (2) as compared with other cases. The projection area of the cylinder and the vane, also the location of the flow separation point represent the major factors which control the vorticity. **Figure 10** illustrate the pressure contour variation around alone cylinder (case-1) and around cylinder which nearby the vane respectively. The pressure values change form positive at upstream region to the negative values at the downstream region with significant fluctuation depends on the case study. Generally, for all cases, the contour refers to the maximum and positive values of pressure will be happened at the upstream regardless the existence of the vane, while the minimum and negative values will be dominate at the downstream regardless the existence of the vane. The existence of the vane leads to the variation in pressure values and makes a difference between the upstream values and downstream values.

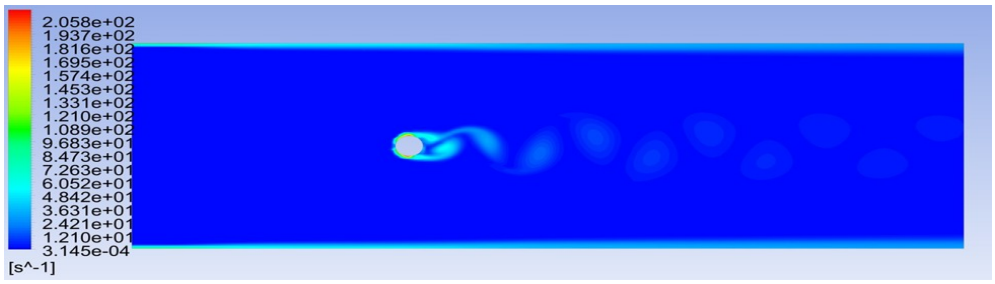

Case (1)

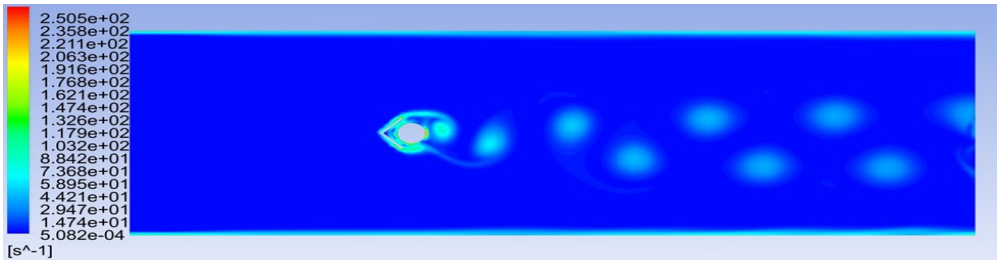

Case (2)

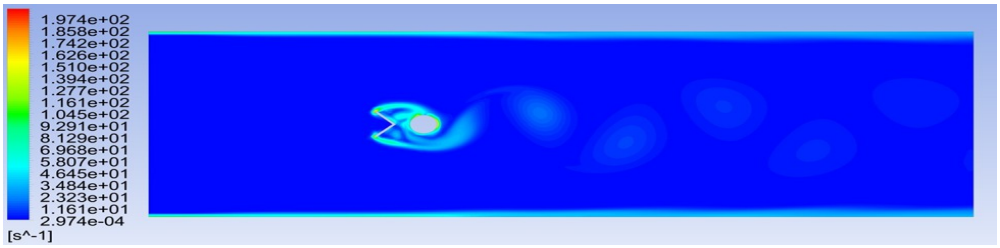

Case (3)

Figure 9. Shows the contour of vorticity

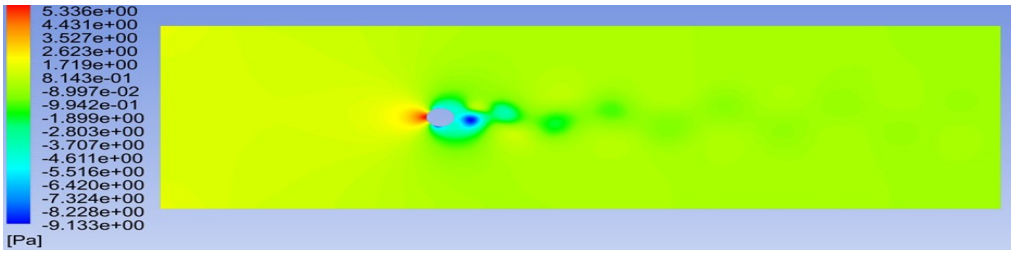

Case (1)

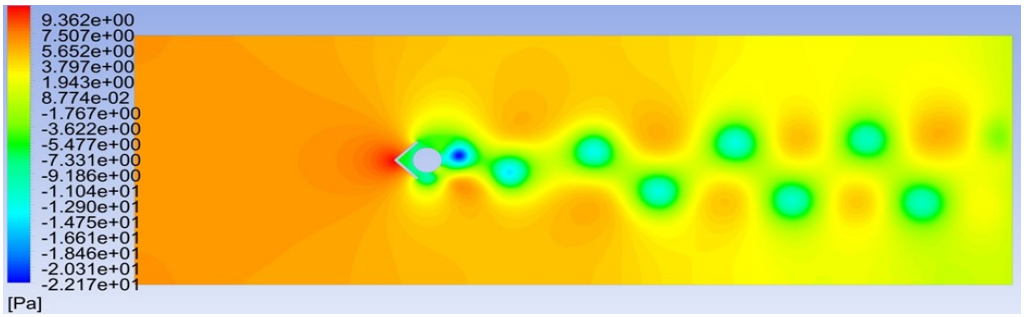

Case (2)

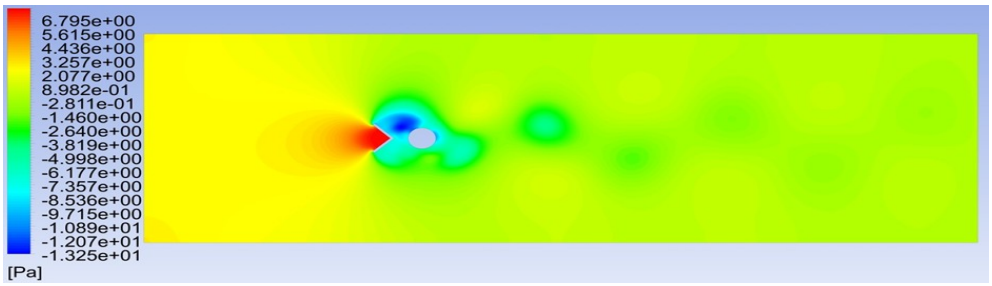

Case (3)

Figure 10. Shows the pressure contour variation.

Figure 11 reviews the pressure coefficient contour variation. The pressure coefficient values change from positive at upstream to the negative at the downstream. Regardless of the vane's presence, this happen owing to the influence of water flow separation and water velocity losses which happen when the flow past the vane.

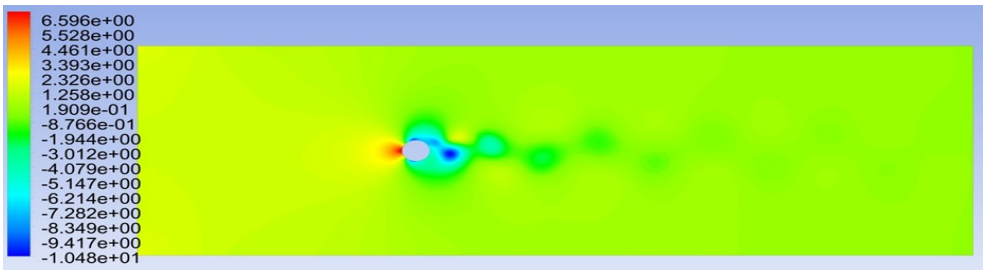

Case (1)

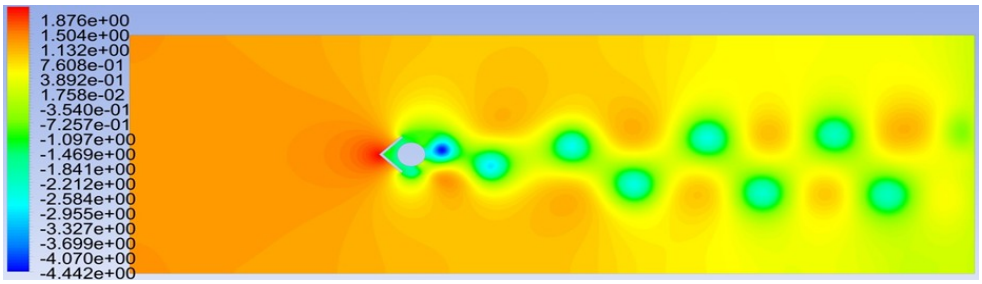

Case (2)

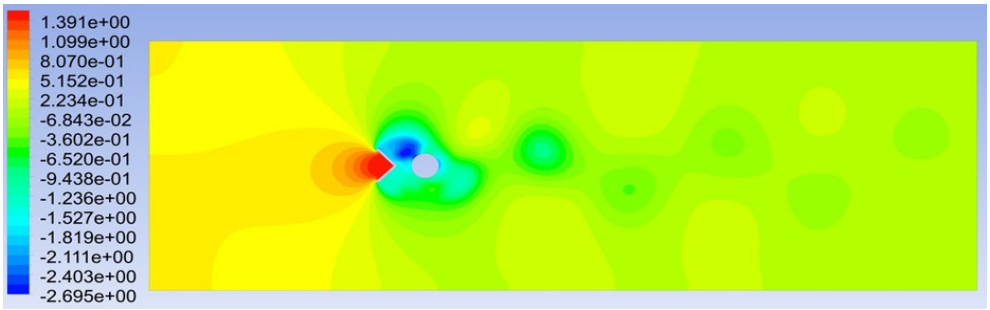

Case (3)

Figure 11. Shows the pressure coefficient contour variation.

Figure 12 shows the variation in the pressure, **Figure 12** adopts three lines in longitudinal direction one of the lines pass at the center of the cylinder while the remainder pass at the edge of the cylinder. Figure shows for all cases, case (3) always represents the upper limit in positive and case (2) always represent the lower limit in negative values respectively, while case (1) always represents the moderate limit in positive and negative values respectively. It is clear from the figure that the pressure always positive at the upstream of the cylinder and the pressure always negative at the downstream of the cylinder. The variation in pressure occurs owing to high flow separation by the vane and the cylinder, also the dissipation in flow velocity will reflect on the pressure distribution.

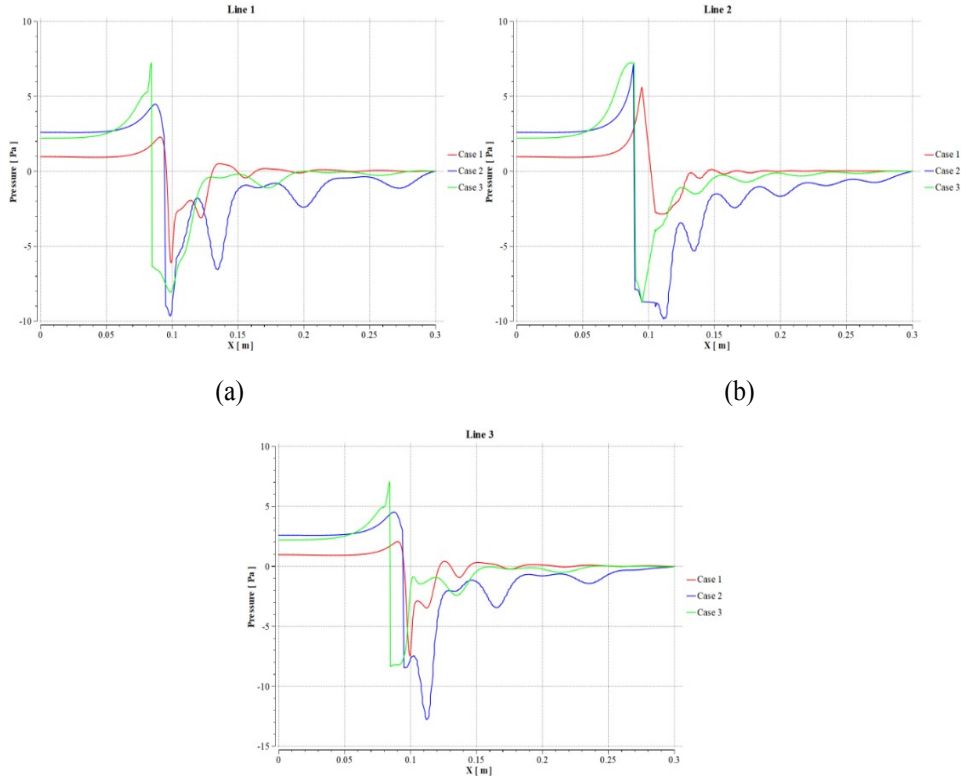

Figure 12. Shows the pressure variation at different lines (a) Line 1, (b) Line 2 and (c) Line 3.

Figure 13 shows the variation in drag coefficient with time, generally for all cases the drag coefficient has periodic response. The presence of vane neighboring to the cylinder reduce the drag coefficient as compared with alone cylinder regardless the direction and configuration of the vane, because of the separation zone occur at the vane instead of the cylinder this will reduce the vortex separation from the cylinder surface. Negative drag coefficient on a cylinder appears to be counter-intuitive in spite of there is no principle or law that prohibits it. The pressure variation plays a vital role in produce the negative drag.

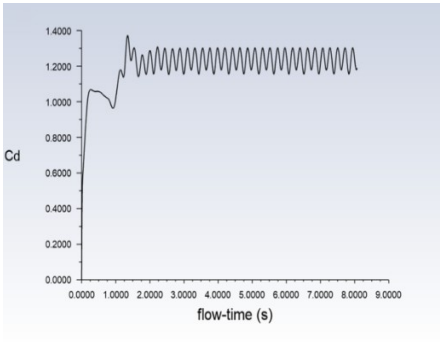

Case (1) Cd= 1.1899269

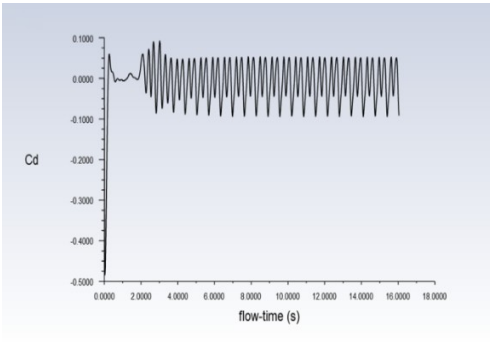

Case (2) Cd= -0.091996409

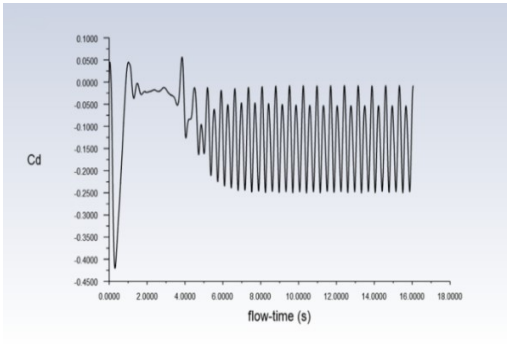

Case (3) Cd= -0.0093440274

Figure 13. Show the variation of drag coefficient with time.

4 Conclusion

Flow field around cylinder without vane and with vane had been studied in this paper. Studying covers the influence of strain rate, stream function, flow velocity, radial velocity, swirling, vorticity, pressure, pressure coefficient and drag coefficient. From this study it is found that the vane direction and configuration have a major impact on the flow field around a cylinder. It is found that the vane has significantly affect in reduce the drag coefficient to the reasonable and satisfactory value as compare with drag coefficient without vane. It is found that the pressure distribution and pressure coefficient are more sensitive to the presence of the vane at the upstream of the cylinder. The flow velocity gradient controls the strain rate while the stream function expresses how much the flow suffer deformation when it passes the obstructions. The velocity field has allowed the showing of the eddy zone, vortex zone and recirculation zone. The vorticity is affected by the pressure and flow separation zone. The response of flow field around the cylinder is more sensitive to the existence of the vane.

References

[1] Sowoud, K.M., AL-Filfily, A.A., Abed, B.H., "Numerical Investigation of 2D Turbulent Flow past a Circular Cylinder at Lower Subcritical Reynolds Number". IOP Conf. Series: Materials Science and Engineering 881 (2020) 012160, doi:10.1088/1757-899X/881/1/012160.

[2] Mojtaba D, 2016 "Numerical Investigation of the Fluid Flow around and Pas a Circular Cylinder by ANSYS Simulation" International Journal of Advanced Science and Technology 92 49- 58.

[3] Bhagat, K. C., Soren, S. K. and Chaudhary, S. K., 2016 "Experimental and Numerical Analysis of Different Aerodynamic Properties of Circular Cylinder". International Research Journal of Engineering and Technology (IRJET) 3(9) 1112-17.

[4] Yuce, M.I., Kareem, D.A., A "Numerical Analysis of Fluid Flow around Circular and Square Cylinders" Journal American Water Works Association, http://dx.doi.org/10.5942/ jawwa.2016.108.0141, (E546- E554).

[5] Zhao Wei, Huhe Aode, "Large-Eddy Simulation of Three-Dimensional Turbulent Flow around a Circular Pier" Journal of Hydrodynamics. Ser. B, 2006,18(6):765-772.

[6] Davis, R.W., Moore, E. F., Purtell, L.P. "A numerical-experimental study of confined flow around rectangular cylinders" Phys Fluids 1984;27(1):46-59.

[7] B.W.V. Oudheusden, F. Scarano, N.P.V. Hinsberg, D.W. Watt "Phase-Resolved Characterization of Vortex Shedding in the Near Wake of a Square Section Cylinder at Incidence" Experiments in Fluids, Vol. 39, pp. 86-98, 2005. https://doi.org/10.1007/s00348-005-0985-5

[8] B. Gera, P.K. Sharma, R.K. Singh "CFD Analysis of 2D Unsteady Flow Around a Square Cylinder" International Journal of Applied Engineering Research, Vol. 1, No. 3, pp. 602- 610, 2010.

[9] H. Bai, J.W. Li" Numerical Simulation of Flow Over a Circular Cylinder at Low Reynolds Number" Advanced Material Research, Vols. 255-260, pp. 942-946, 2011. https://doi.org/10.4028/www.scientific.net/AMR.255-260.942 .

[10] Richardson, J.S., Pancheng V.G. "Three dimensional simulation of scour inducing flow at bridge piers" J.Hydrau. Eng. ASCE 1998:124(5)

[11] Chang, WY., Lai JS, Yen CI "Simulation of scour depth evolution at pier nose" In: Proceedings of the 1999 international water resources publications, LLC, Highlands Ranch, CO.:1999.

[12] Zaid M., Yazdanfar Z., Chowdhury H., Alam F.”Numerical modeling of flow around a pier mounted in a flat and fixed bed” Energy Procedia, 160: 51-59, 2019.

NoSQL: Will it be an alternative to a relational database? MySQL vs MongoDB comparison

Basit alyasiri[1], Bushra Sahi[2], Nassir AL-Khafaji[3]
{alyasirib@gmail.com[1], bushrasahi69@gmail.com[2], nassir.farhan@stu.edu.iq[3]}

Nasiriya Technical Institute, Southern Technical University, Iraq[1'2'3]

Abstract. NoSQL databases and related technologies are rapidly evolving and are commonly used in a variety of scenarios (consistency, availability, partition tolerance), and this has sparked controversy in the database world in several, so this paper aims to shed light on the characteristics that determine the use of databases. By discussing the challenges and studying the differences in depth and trying to answer the question related to the future use of the database, we started by discussing both relational and non-relational databases, shortcomings, and challenges, then we chose a model of both types, and we studied the differences in practice in the query process by installing database servers, it is an important part of the data handling process. We also discussed the popularity of the two models adopted for several considerations and concluded that non-relational databases, despite the challenges, tend to be the first choice soon.

Keywords: Relational Database, Nosql, Database, CAP, Mongodb, Mysql Queries.

1 Introduction

Information management systems have increased in importance nowadays because of the importance of modelling and organizing the data that we need to use in the right way and at the right time. These systems provide a very efficient way of dealing with different types of data. Currently, organizations are dealing with applications that generate large amounts of data daily, so their size is growing exponentially and that is why the thinking of using a database goes beyond the limits of the relational database in use which has evolved over decades. But because there are certain limits to the use of these rules, including their limitations in dealing with big data, as well as their unsuitability for the unstructured and diversified data found in many companies, and because of their inability to update.

And add other schemes that we need to add as the work develops, and from Here comes the need to use non-relational databases that have adopted many characteristics to deal with large, structured, or unstructured data. It may also can accept the addition of new updates depending on business variables, but many organizations have not dispensed with the relational database because they work one way or the other. To manage their data because it has advantages that compete with non-relational database, which are among the challenges for NoSQL that can discuss solutions and deal with their use, Where previous works were investigated and we found that most of them focused on one topic, which is how to choose database by studying differences between different models of them, so our study was heading towards whether it is possible to

IMDC-IST 2021, September 07-09, Sakarya, Turkey
Copyright © 2022 EAI
DOI 10.4108/eai.7-9-2021.2314925

solve NoSQL instead of a relational database in all cases.

2 Related Study

There have been a lot of discussions lately about the performance of SQL and NoSQL databases. However, there have been few studies comparing the performance of SQL and NoSQL databases.

[4]This paper discusses database storage structures, concepts, and differences, as well as insertion, update, deletion, and selection processes. A set of the non-relational database was selected for evaluation, and their performance was successively compared with no relational database, and it was concluded that the performance of the relational database is stronger in small data, versus big data. Non-relational databases are preferred.

[7]This paper compares the efficiency of different queries and commands in both relational database and NoSQL systems using two different sets of data of different sizes to highlight the advantages of NoSQL database and over the relational database and especially when investigating big data. The study concluded that differences in execution time were observed and demonstrated using graphs. In all cases, it can be inferred that NoSQL databases outperform relational databases.

[9] This article introduces the main types and characteristics of NoSQL data models, as well as detailed and synthetic comparison between the relational model and the NoSQL data models and concluded that The Relational Model and NoSQL Models are not mutually exclusive, but rather complement each other, and Each has advantages and disadvantages in a particular context. They represent solutions of different scenarios and coexistence within companies.

[12] This paper compares the concepts of NoSQL and Relational databases then their limitations. And address the advantages and types of NoSQL databases. . From these comparisons, the conclusion was that a relational database might be a great choice if you have structured data and need a traditional relational database. If you have unstructured and/or structured data with the potential for rapid growth, NoSQL would be the best choice.

[15]This paper did a comparative analysis to discover that non-relational databases work better than a relational database. Looking at the dataset used for the experiment, the hypothesis is that MongoDB works better only for insertion, deletion, and selection, while Oracle still does better with the update process in the available environment.

3 Database

The database has played an important role in society for centuries, and anything that carries information constantly is a type of database. Cave drawings, stone slabs, and papyrus are all true examples of the database. The history of the database is largely due to the desire to create structures that can meet the requirements of storing information accurately and permanently over long periods while enabling users to easily search for information within the stored data.

The introduction of computers opened new possibilities for database technology, which allowed to quickly generate, and access information stored on the disk; However, the mere existence of a computerized system does not automatically make the data strongly interactive. But it needs systems to manage it and languages for the processes of interacting with data in terms of querying, adding, speaking, and other operations that you perform on the database to get the required [1].

4 Relational Database

The relational database has become an integral part of most software applications, and, in the opinion of most programmers, they cannot be dispensed with due to their ease of use, organization of data, and constant storage, which enables constant data retrieval while allowing multiple users to access the same data concurrently with the ability to modify that data. Most current relational database programs are written by separate teams of programmers and are then reused by other applications [13]. SQL databases are Database Management Systems (RDBMS). Microsoft SQL Server, Oracle Database, MySQL, and IBM DB2 have historically been the most popular of these. Except for MySQL, this is also used to store data for Web applications.

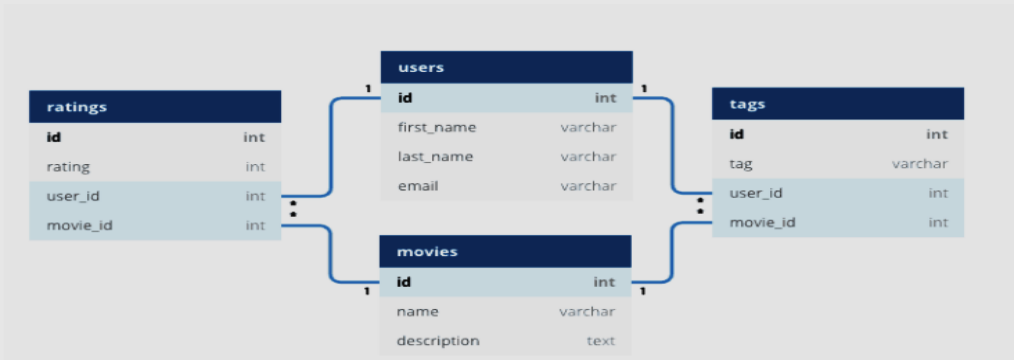

Fig 1. Example of a relational database.

4.1 The ACID Properties

The ACID properties ensure that transactions are reliable in a relational database. Atomicity, Consistency, Isolation, and Durability (ACID) are acronyms for Atomicity, Consistency, Isolation, and Durability. The ACID properties are usually followed by the RDBMS database.

1. Atomicity: A transaction must be done in its entirety or none.
2. Consistency: All transactions ensure that the database's credibility is maintained. After a transaction, the database is not left in an invalid state.
3. Isolation: Each transaction must be run in isolation to ensure that any data inconsistencies do not a fact other transaction.
4. Durability: A completed transaction's modifications must be retained, An ACID-compliant database ensures that only successful transactions are

completed, which provides data integrity for the database as well as the ability to recover from system failures. [12]

4.2 Challenges Faced by Relational Database

Since the 1980s, the relational model has dominated the computing industry, mostly for data storage and retrieval. After a while, relational databases began to lose their importance due to facing some challenges, and the most important of them [4]:

1. Big Data: The development of big data applications, particularly web applications, has become increasingly important in recent years. Indeed, a growing number of organizations across a variety of sectors depend on information gleaned from vast quantities of data. However, when dealing with large amounts of data, conventional relational database systems and platforms are inefficient, with slow response times and a lack of scalability, performance, and accuracy. To address the complexity of big data problems. [11]
2. Unstructured data: Difficulty dealing with relational database with unstructured data While relational databases take advantage of SQL, which has been optimized to work with structured data, SQL can become very complex when dealing with unstructured data.[12]
3. Data schema modification and development: With application creation and development, the relational database schema cannot be modified over time, and modifications cannot accommodate different types of data [14]. It became clear that conventional relational databases were incompatible with the requirements of a variety of applications and their data. This resulted in the introduction of a new technology known as NoSQL among commercial organizations and businesses.[12]

5 NoSQL Database

The current meaning of the term NoSQL was given by Eric Evans, in June 2009, at a meeting in San Francisco, organized by Johan Oskarsson for discussions on a new open-source distributed database. In October of the same year, Emil Efren, the founder, and CEO of Neo4J described, in a message on Twitter, the term NoSQL as “Not Only SQL Today, but NoSQL is also used as an alias for ”Next-Generation Database Management Systems mostly addressing some of the points: (being non-relational, distributed, open-source and horizontally scalable”) [9].

5.1 NoSQL Database Types

NoSQL data is stored in one of four data architecture patterns.

1. Key-Value Store Database
2. Column Store Database
3. Document Database
4. Graph Database

Fig. 2. Example of a key-value store**.**

Fig. 3. Example of a Document Store.

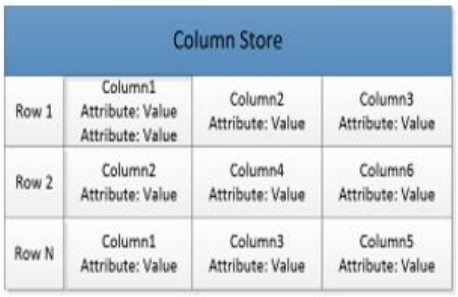

Fig. 4. Example of a Column Store.

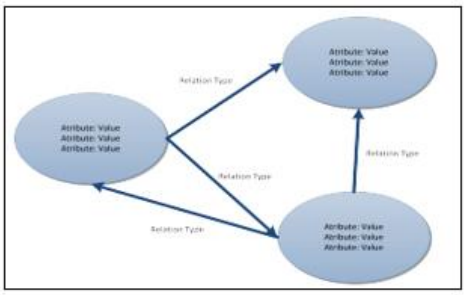

Fig. 5. Example of a Graph Store.

5.2 Characteristics of NoSQL Database

1. Big data: is a term that refers to a group of vast amounts of structured and semi-structured data. It is used in many organizations and in various web applications and research to make critical decisions. Efficient storage in processing this large volume of data and extracting critical information with a short response time is one of the requirements in today's competitive environment. Relational databases, which have dominated storage technology for a long period, seem unsuitable for mixed data formats. Data in tables cannot be expressed only in terms of rows and columns. NoSQL enables the development of a variety of storage formats that are easily compatible with high-speed, large, and varied data [3].
2. Scalable Horizontally scalable refers to the fact that, unlike relational database that can be scaled mainly vertically, by increasing the capacities of highly specialized and very expensive servers, NoSQL database can be distributed on multiple commodity servers, thus offering the possibility to add new servers in the system architecture, at any time, as needed.
3. The CAP Theorem Instead of ACID restrictions for a relational database, the NoSQL database, which emerged to achieve horizontal scalability, and access to data with the help of multiple nodes are based on CAP theory. CAP theory has been named based on the principles of consistency, availability, and partition tolerance. Consistency refers to having the same data at the same time on all nodes as the data is distributed. In the event of any changes,

it ensures that updates are made to all nodes and ensures that users have access to the same data. Ensure that all requests directed to the database with the help of the principle of access do not go unanswered even if some nodes (nodes) are not available [5].

4. Partitioning Tolerance allows data to be distributed to multiple nodes and create a block, even if some nodes are corrupted. Is that the system can continue to work? Also, the CAP theory, A system contains no more than two of the three principles mentioned at the same time. He expresses his ability to present it. Hence, a database System can be CA, AP, or CP at the same time [6].

5. Non-relational means that the data are represented by principles other than those used by the relational model [8].

6. Distributed refers to the fact that, unlike a relational database, NoSQL databases are used efficiently and flexibly in distributed systems with multiple servers and different environments [5].

7. Open-source means that, unlike most RDBMSs, NoSQL is open-source to provide solutions for complex applications at lower costs, although many of these systems today also offer commercial variants [2].

6 Comparison Between a Relational Database and NoSQL Stores

To study database, the general and future trend, and the best choice considering the rapid developments in the use of data in terms of type and quantity, and the best mechanism to obtain the best results. We performed a comparison between the MySQL relational database type and the NoSQL type (MongoDB). The comparison was according to the following aspects:

1. Comparison of general characteristics. Between MySQL vs MongoDB.
2. Comparison of the quality of queries Between MySQL vs MongoDB.
3. Comparison According to the CAP theorem. Between MySQL vs MongoDB.
4. Comparison by popularity Between MySQL vs MongoDB.

6.1 Comparison of characteristics Between MySQL vs MongoDB.

We provide a description and comparison of the main characteristics of relational databases and NoSQL stores according to the paragraphs mentioned in Table 1.[17]

Table 1. Comparison of the main characteristics of relational databases and NoSQL stores [17].

Name of properties	MongoDB	MySQL
Description	One of the most popular documents stores available both as a fully managed cloud service	Widely used open-source RDBMS
License	Open Source	Open Source
Data scheme	schema-free	Yes
SQL	Read-only SQL queries via the MongoDB Connector for BI	yes
Partitioning methods	Shading	horizontal partitioning, shading with MySQL Cluster
Replication methods	Multi-Source deployments with MongoDB Atlas Global Clusters	Multi-source replication
MapReduce	Yes	No
Consistency concepts	Eventual Consistency Immediate Consistency	Immediate Consistency
Foreign keys	no	yes
Transaction concepts	Multi-document ACID Transactions	ACID
Concurrency	Yes	yes
Durability	yes	Yes

6.2 Compare the Quality of Queries Between MySQL vs MongoDB.

To test the advantages of operations between relational and non-relational databases, a comparison was made between the two databases, MySQL and MongoDB in the four

1. Insert
2. Select
3. Update
4. Delete

And because the results that we obtain for testing operations in the different databases need to determine the performance and specifications of the computer used, so we used in these tests a computer that has the following characteristics, an Intel Core i5 processor and an Intel Core i5 processor (2.8 GHz) And 4 GB RAM. And Windows 10 64-bit, for that, we needed MySQL database by installing AppServ9.3.0 into MongoDB database through installing 4.4 MongoDB Compass Create and develop the same database in MySQL server and MongoDB server, and we created the same tables in both databases,

6.2.1 Insert

In the data entry test, 10,000 records were first entered into tables that do not contain data from the MySQL and MongoDB databases, organized by some tables for the hiding process, whose databases were created. The time it takes to enter.

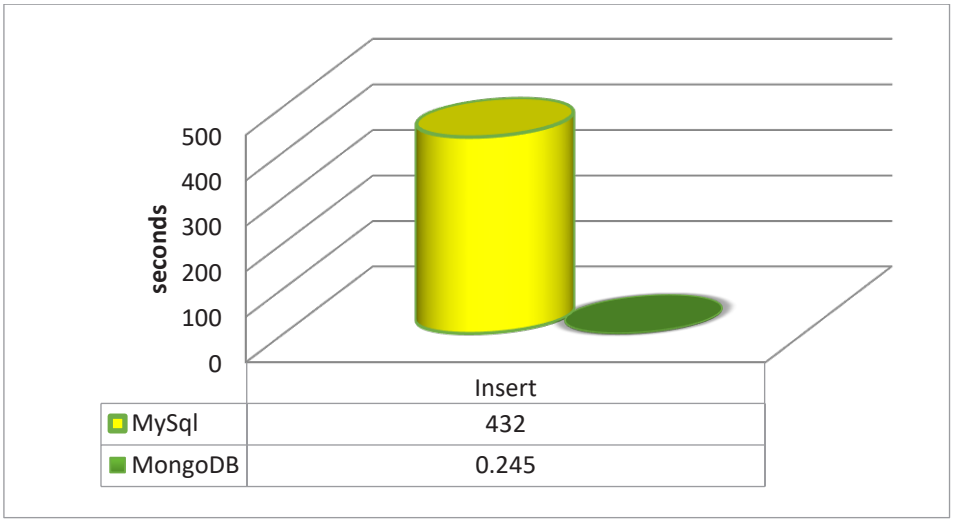

Fig 6. MySQL vs. MongoDB Insert.

Through the results, the MongoDB database took 0.245 seconds to enter 10,000 records, while the result of entering the same number of records in MySQL was 432 seconds. Hence, we conclude that MongoDB is the best performer in the process of entering a large group of records at once as shown in Fig 6.

6.2.2 Select

In the case of the record display test, two queries were executed,

1. The first is to choose all records and respond to the time required to execute this query.
2. The second is to query specific records on the condition that the time required to be executed for both rules is also calculated.

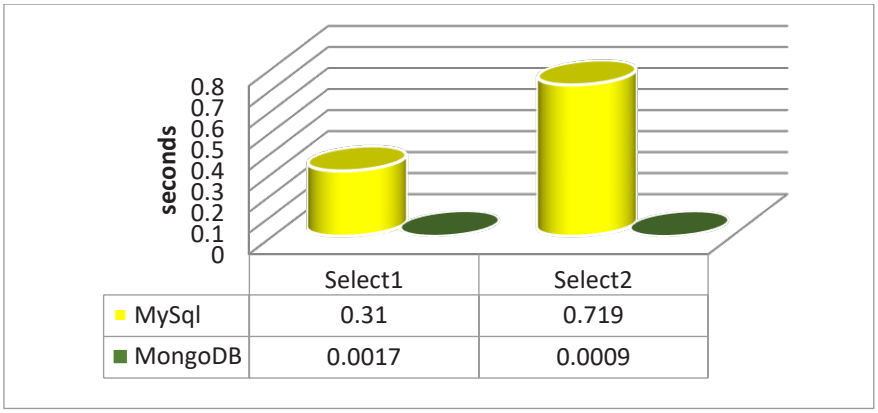

Fig 7. MySQL vs. MongoDB select.

As shown in Fig 7 the results of the first test, the query for all records took 0.31 seconds for the MySQL database, while the MongoDB database took 0.0017 seconds in the second test, the query result for specific records for the MySQL database took 0.719 seconds, and for the MongoDB database, the query result For specific records 0.0009 seconds, so the MongoDB database is the fastest in the case of displaying records in different modes and terms of the number of records tested.

6.2.3 Update

In the database update test, two operations were performed:

1. Username update test
2. Update test in the comment field for the user

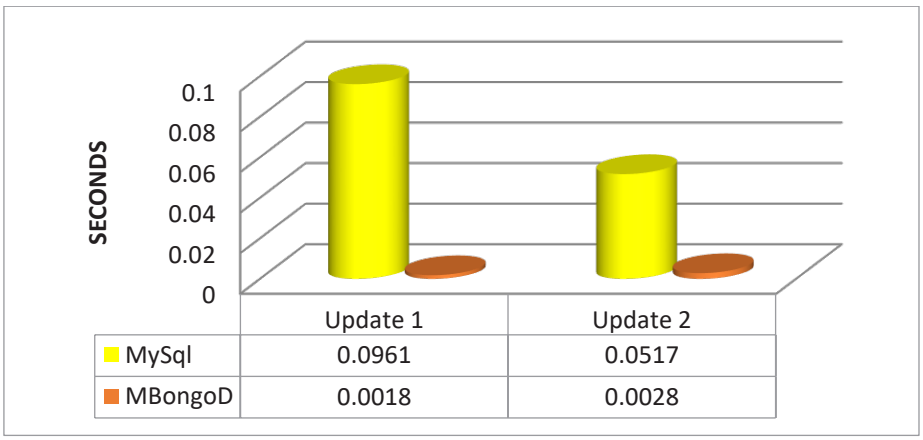

Fig 8. MySQL vs. MongoDB update.

The results shown in Fig 8 showed that the first update process took 0.0961 seconds in the MySQL database, and in the MongoDB database, the update process took 0.0018 seconds, while the second query needed 0.0517 seconds in the MySQL database to complete the update process, and MongoDB database needed to 0.0028 seconds, and from here we can say that the update process in MongoDB is better than the two mentioned queries.

6.2.4 Delete

In the process of deleting records, we have two queries:

1. Query deletes all user comments.
2. Query Delete some users' comments.

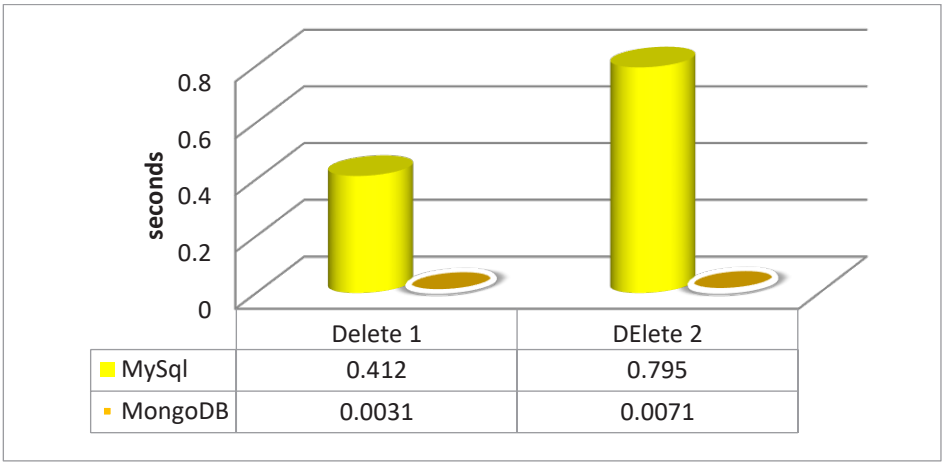

Fig 9. MySQL vs. MongoDB Delete.

In the results of the deletion process for both queries, it was shown that the first query completed the deletion process to 0.0412 seconds for the MySQL database, while for the MongoDB database, the time to delete was 0.0031, for the second query, the time to remove comments of specific users in the MySQL database was 0.795 seconds while the MySQL database was the time The deletion process took 0.0071 seconds, and from here it was found that the MongoDB database is the fastest in the deletion process, especially in deleting large data as shown in Fig 9.

6.3 Comparison According to the CAP Theorem Between MySQL vs MongoDB

According to CAP theory, a NoSQL database is in a CA state where it is ensured that all changes made in the database are visible in all nodes at the same time and that the system responds to all requests. However, if some nodes are damaged, the system can crash. But in MongoDB, the system in a CP state ensures that it continues to work and responds to requests even if nodes are corrupted so if the system is in this state, the system continues to work even if a section of the nodes are damaged, and

also ensures that the data is updated or consistent across all nodes But it may not respond to all requests because availability is not guaranteed in this type of database.
Therefore, MongoDB has an advantage when used in most systems that need these features [5][6].

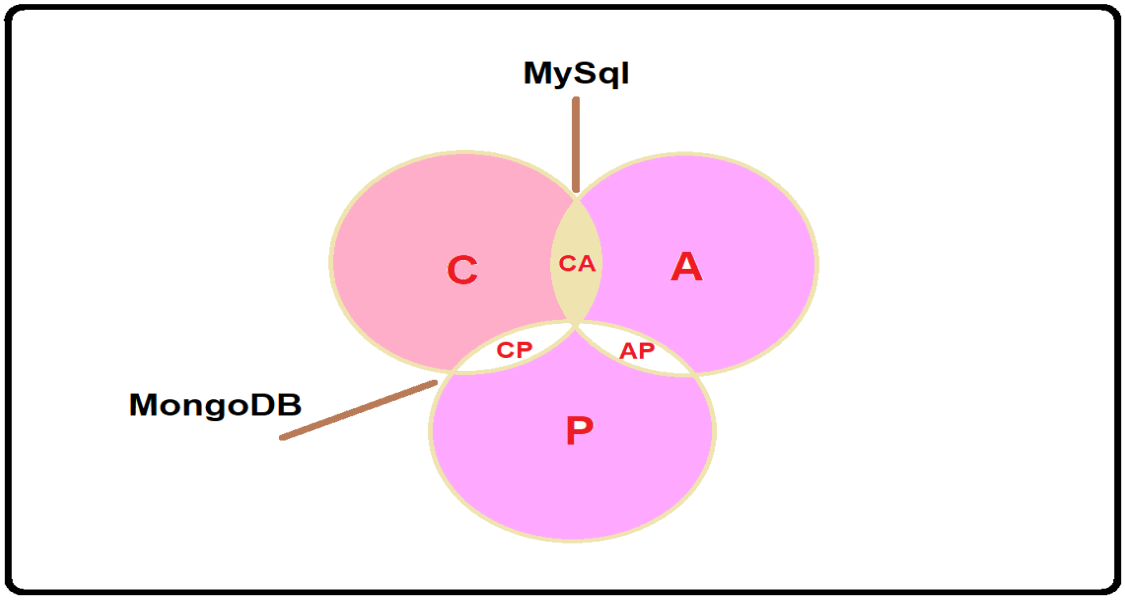

Fig 10. Classification of CAP and Databases.

6.4 Comparison by popularity Between MySQL vs MongoDB

Here we review the difference between MongoDB and MySQL concerning CAP theory MongoDB: The CAP theorem chooses Consistency and Partition Tolerance for the MongoDB database such as CP. What exactly does this imply? This ensures that all clients will be able to see the same clear view of the database. Users of one node, on the other hand, would have to wait for all other nodes to consent before being able to read or write to the database. In this case, continuity takes precedence over availability.

By various dates, a distinction was made between the MySQL database and MongoDB database, which were categorized by popularity [16]. The following parameters were used to determine the popularity of each system:

1. The number of times the system has been mentioned on the internet, as determined by the number of times the system has been mentioned in search engine queries.

2. For the time being, we're measuring with Google and Bing. To ensure that only valid results are counted. The system has a lot of people interested in it. Google Trends uses to count search frequency.

3. The frequency of technical discussions about the system. On the IT FAQ pages, I used the number of related questions and the number of users interested. Some job offers for the system. They are the offers on the leading professional search engines

4. The number of personal files in professional networks.
5. The importance of social networks. Tweets that refer to the system count.[16]

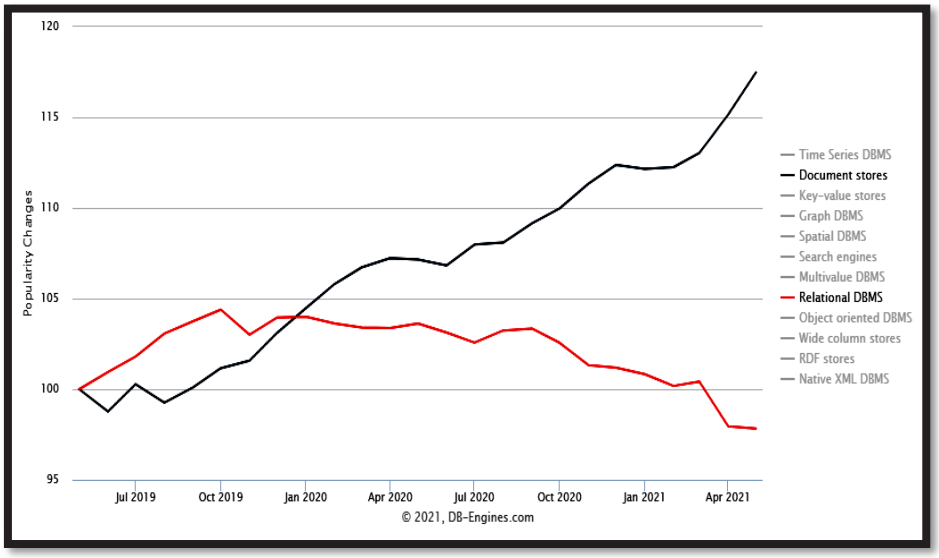

Fig 11. the historical trend of the two categories' popularity (Relational DBMS vs Document stores) from (2013-2021) [17].

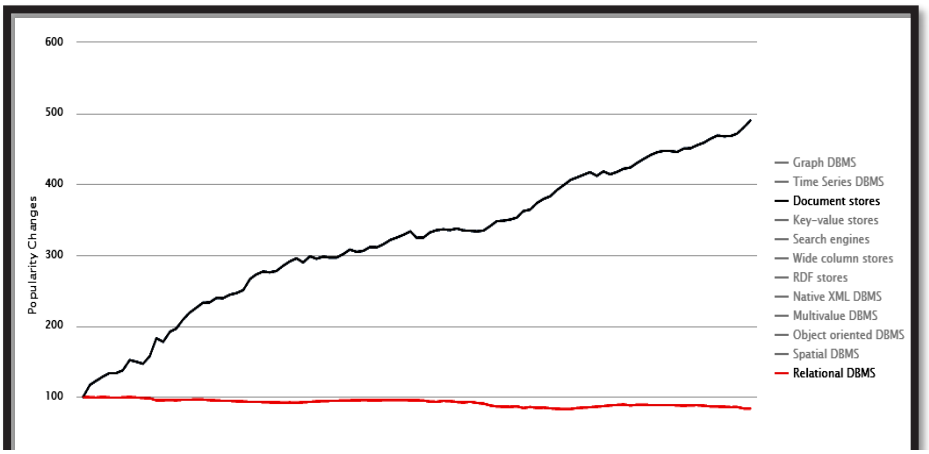

Fig 12. the historical trend of the two categories' popularity (Relational DBMS vs Document stores) from (2019 - 2021) [17].

The graph in Fig 11 shows the historical trend of popularity for the category (DBMS Relational and Document Stores) from (2013-2021). According to the criteria we mentioned for determining popularity, it showed a rise in the popularity of document stores versus relational DBMS.

The graph in Fig 12 shows the historical trend of popularity for the category (DBMS Relational and Document Stores) from (2019-2021). According to the criteria we mentioned for determining popularity, it showed a rise in the popularity of document stores versus relational DBMS.

7 Conclusion

After reviewing the challenges and differences, especially by analysing the query test comparison between MySQL and MongoDB databases, where we used servers with modern versions and a work environment that simulates the impact, we found that one of the reasons that lead us to believe in moving to NoSQL is the high performance in the four processes (input, selection, deletion, and update) which are important elements in the effectiveness of databases. By studying the analysis of the growth of the popularity of MySQL and MongoDB databases (such as discussions or job offers and other considerations), we found that MongoDB is more growing over years (from 2013 to 2021). This is an early indicator that precedes widespread use and that follows a factor Given time, it can be a logical decision to put the non-relational database at the forefront of the choice of enterprise data management, although it is currently facing challenges, according to the data of growth in the technology of this type, the data, and systems used, the increasing popularity and scope of use, the trend towards their use will not be far. After we have reviewed several studies and the ideas provided by a lot of research on selecting the right database between relational and non-relational databases, we found most of them conclude that selecting the right database follows the organization's need for how to manage its data robustly. And its success despite the existence of future problems, solutions, and frameworks that are moving towards modern databases. We found that one of the important

reasons not to use non-relational databases is the lack of experience in managing this type compared to relational databases. We suggest taking the inquiries of this study and researching more in different aspects to clarify the future of databases and thus build plans according to an outlook.

References

[1] Chapter 2 - relational database. In Peter Mccaffrey, editor, An Introduction to Healthcare Informatics, pages 17–29. Academic Press, 2020.

[2] Wajid Ali, Muhammad Usman Shafique, Muhammad Arslan Majeed, and Ali Raza. Comparison between sql and nosql database and their relationship with big data analytics. Asian Journal of Research in Computer Science, pages 1–10, 2019.

[3] Gourav Bathla, Rinkle Rani, and Himanshu Aggarwal. Comparative study of nosql database for big data storage. International Journal of Engineering & Technology, 7(2.6):83–87, 2018.

[4] Roman Cereˇsˇn´ak and Michal Kvet. Comparison of query performance in relational a ˇ non-relation database. Transportation Research Procedia, 40:170–177, 2019.

[5] Raif Deari, Xhemal Zenuni, Jaumin Ajdari, Florije Ismaili, and Bujar Raufi. Analysis and comparison of document-based database with sql relational database: Mongodb vs mysql. In Proceedings of the International Conference on Information Technologies (InfoTech 2018), pages 1–10, 2018.

[6] Tuˇgba Beril Doˇgu¸c and Ahmet Arif Aydın. Cap-based examination of popular nosql database technologies in streaming data processing. In 2019 International Artificial Intelligence and Data Processing Symposium (IDAP), pages 1–6. IEEE, 2019.

[7] Benymol Jose and Sajimon Abraham. Performance analysis of nosql and relational database with mongodb and mysql. Materials today: PROCEEDINGS, 24:2036– 2043, 2020.

[8] Sarah H Kamal, Hanan H Elazhary, and Ehab E Hassanein. A qualitative comparison of nosql data stores. Int. J. Adv. Comput. Sci. Appl, 10(2):330–338, 2019.

[9] Gianina Mihai. Comparison between relational and nosql database. Annals of the University Dunarea de Jos of Galati: Fascicle: I, Economics & Applied Informatics, 26(3), 2020. 13

[10] Anasuodei Moko and Prince Oghenekaro Asagba. Big data and nosql database architecture: A review. 2020.

[11] Ahmed Oussous, Fatima-Zahra Benjelloun, Ayoub Ait Lahcen, and Samir Belfkih. Big data technologies: A survey. Journal of King Saud University-Computer and Information Sciences, 30(4):431–448, 2018.

[12] Sowndarya Palanisamy and P SuvithaVani. A survey on rdbms and nosql database mysql vs mongodb. In 2020 International Conference on Computer Communication and Informatics (ICCCI), pages 1–7. IEEE, 2020.

[13] Shaymaa Ahmed Razoqi. Reasons of the transformed toward nosql database and its data models. JOURNAL OF EDUCATION AND SCIENCE, 29(2):82–100, 2020.

[14] Kosovare Sahatqija, Jaumin Ajdari, Xhemal Zenuni, Bujar Raufi, and Florije Ismaili. Comparison between relational and nosql database. In 2018 41st international convention on information and communication technology, electronics and microelectronics (MIPRO), pages 0216–0221. IEEE, 2018.

[15] B Sirish Shetty and KC Akshay. Performance analysis of queries in rdbms vs nosql. In 2019 2nd International Conference on Intelligent Computing, Instrumentation and Control Technologies (ICICICT), volume 1, pages 1283–1286. IEEE, 2019

[16] Link of related {https:// medium .com /edureka/ sql-vs-nosq l-db-5d9b69ace6ac}

[17] Link of related {https://db-engines.com/en/ranking_definition}

Evaluating The Effect of Intent Factors on the Student's Intention to Register for External Exams via The Internet: Directorate of Education in Dhi-Qar as A Case Study

Mohammed Jaber Farhan[1], Bushra Sahi Chassab[2] and Nassir Jabir Al-Khafaji[3]
{809895@gmail.com[1], bushrasahi69@gmail.com[2], nassir.farhan@stu.edu.iq[3]}

Directorate of Education, Thi-Qar, Iraq[1]
Nassriyah Technical Institute, Southern Technical University, Iraq[2,3]

Abstract. This study seeks to identify the affected factors that impact the behavioural intention of students on online external exams registration in the directorate of education in Thi-Qar. The study also intended to identify whether students prefer online external exam registration in terms of attitude, subjective norms, and whether website design has an impact on them. Additionally, the current study looked at how students evaluate these criteria in terms of relevance when registering for external exams online. A basic random sampling procedure was used, and 347 people were given questionnaires. A total of 304 questionnaires were gathered, with 304 of them being deemed to be usable. Several statistical methods were used to examine the data, including descriptive analysis, regression test, reliability analysis, and correlation test. The findings demonstrated that students' attitudes, subjective norms, and website usability were all strongly associated. Furthermore, the outcomes of the study revealed that the most essential element was regarded to be website usability, with other characteristics having a moderate impact on student intention to register electronically. The findings of the present study may be useful in persuading officials at the Thi-Qar Directorate of Education to use online technology to speed up office operations.

Keywords: Website Usability, Subjective Norm, Attitude, Student Intention.

1 Introduction

The Internet has a significant impact on everyone's lifestyle, altering how people work, live, and learn. Hasan, et al. [1], Public lifestyles have altered dramatically as a result of the rapid rise of Internet technology. Salamat, et al. [2] Governments in developing nations attempt to give services to citizens using information technology and communications methods. As a result, ICT has introduced several changes to government services, such as online voting, driver's license renewal, voter registration, and so forth. COVID -19 affected the handling based on face-to-face on all the world. As well as, the spread of COVID-19 has left universities and educational institutions in a predicament[3]. Additionally, COVID-19 has affected Most businesses in the world, and employees and citizens are encouraged or forced to do business from home remotely. In addition, the demand for appropriate technology is growing. [4]. This leads us to the conclusion that students will have a greater opportunity to advocate for their

IMDC-IST 2021, September 07-09, Sakarya, Turkey
Copyright © 2022 EAI
DOI 10.4108/eai.7-9-2021.2314923

continued enrolment in educational institutions, as well as for how successfully educational programs and services meet students' service expectations.[5].Developing countries such as Iraq have pushed to adopting online systems to overcome the implications of a pandemic in various fields. On this orientation, the directorate of education in Thiqar suggested adopting an online system to end suffering the students in registration of external exams. The online registration of external exams made students more independent of bureaucracy and reduce the lines of crowds. Every year more than 20 thousand come from Nasiriyah and districts to present on the external exam with a long line and spent a long time to complete their application without knowing if the result is accepting or not. Furthermore, the students who desires to register in the external exams come from different backgrounds and levels in technological skills. According to Hasbullah, et al. [6] Knowing about consumer behaviour and understanding what they require is critical for improving and attracting online customers. Depend on interview with manager of external exam department (Waleed, personal communication, January 4, 2021) stated that the online registration is a crucial and corner stone to rid of the crowds of student, enquiries about the conditions and have accurate database to search the documents. The objective of this study is to identify the effected factors that impact behavioural intention of student on online external exams registration to improve the services and less complaints issued from students in directorate of education in Thiqar.

2 Literature Review

2.1 Theory of Reasoned Action (TRA)

Fishbein and Ajzen [7] developed the TRA, which states that a person's intention to engage in a specific activity is the strongest predictor of whether they engage in that behaviour (2011). According to the TRA, consumer behaviour is influenced by their attitude and subjective norms toward the activity in question, as well as their behavioural intention. [8] and that based on these variables, it is possible to forecast customer behaviour. The study's guiding framework was the theory-reasoned-action (TRA) framework. The TRA was preferred to choose it from the TAM and TPB for a variety of reasons. Researchers are interested in researching theories that are less commonly used than the TAM, which was consistently applied in prior studies. Even though the Technology acceptance model has advantages For instance extensive use in the field of IT area, researchers are interested in researching theories that are less commonly used than the TAM[9]. Icke Ajzen and Martin Fishbein, the authors of the TRA theory, think that people make conscious judgments about how they act and that they are in control of most of their behaviour. According to this theory, humans make rational decisions about how to act. Even if a person is highly motivated by her views and subjective norms, if activities are not fully within volitional control, intervening contextual variables may prevent her from performing the behaviour.

2.2 The Relationship between Attitude on trust and Intention to Online Registration

Students can be persuaded or encouraged to use the online system to register if they have a trusting attitude. represents a consensus among experts on online trust that the nature and essential meaning of online trust are identical to that of face-to-face trust [10-13]. Online trust has been identified as an important factor since it reduces perceived risk and generates good

recommendations, both of which influence a customer's decision [14-16]. According to [17] Trust inspired motivation to engage and contribute. Additionally, online trust increases the interactions of the individuals in the system [18]. Trust in the online system belongs to the government has a vitally important effect in adopting and using that service. As a result, propose the following hypothesis: Hypothesis 1: There is a positive relationship between attitude towards intention online external exams registration among students in the directorate of education in Thiqar

2.3 The Relationship Between Subjective Norm And Intention to Online External Exams Registration.

Ajzan & Driver (1980) Subjective norms are defined as the perceived pressure exerted by others, such as neighbours, peers, friends, and those involved in the activity of interest, on the respondent's behaviour, either directly or indirectly. The subjective norm (SN) is a tool for measuring people's perceptions of whether or not other people with similar attitudes would or will not behave in the same way when it comes to technology.[19]. Aboelmaged and Gebba [20] According to the data, there was a favourable association between subjective norms and system adoption. In Kim, et al. [21] Subjective norms have a favourable association with the behaviour intention to utilize an online system, according to a study. This finding can be regarded as indicating that recommendations have a significant impact on a student's intention. As a result, propose the following hypothesis: Hypothesis 2: There is a significant relationship between subjective norm towards intention online external exams registration among students in the directorate of education in Thiqar.

2.4 The Relationship Between Website Usability and Intention to Online External Exams Registration Among Students in The Directorate Of Education In Thi-Qar Province

In their study, Barnes and Vidgen [22] Consumers perceive the website to be simple to operate and learn, navigate, and use, with clear and understandable interactions, which operationalized the concept of usability. As the usage of online systems grows more common in everyday life, system usability has become increasingly critical.[23]. Alam and Yasin [24] said that one component of usability that has been investigated and proven to be crucial is website design. Alam et al. [29] recognized that the design of the website is considering one of the distinctive features in the internet world. As well, Shergill and Chen [25] referred to those design elements of the website were selected as the most important factor influencing consumer views of online systems. The usability of the system reflects the degree of user satisfaction. Moreover, satisfaction plays a significant role in positive behavioural intention [26]. More useful websites tend to foster more positive attitudes toward online systems, whereas websites that are less accessible have the reverse impact [27]. According to Belanche, et al. [28] Usability has a favourable impact on consumers' willingness to use a website. As a result, it is proposed that a website's usability is positively associated with a student's intention to use the internet. As a result, propose the following hypothesis:
Hypothesis 3: There is a significant relationship between usability towards intention online external exams registration among students in the directorate of education in Thiqar.

3 Research Methodology

Fishbein and Ajzen[7] developed a theoretical framework. There are three constructs, the first and second of which are based on Fishbein and Ajzen's Theory Reasoned Action (1980). Alam, et al. [29] added another variable to the research to make it more robust. It was proposed by Alam et.al [29] where it was determined that website usability is one of the factors that has been studied and found to be important. The TRA has been used to evaluate a range of behavioural intents in the past, Blood donation, bone marrow donation, and internet shopping are all options. [30]. The data reveal whether or whether this profile can alter the nature of those relationships, as well as the magnitude of the influence. Further investigation will identify the dominating personality trait that has the most impact on relationships. The researchers hope to acquire a better understanding of the goal of online registration and contribute new information to the corpus of knowledge on online systems by combining the frameworks.

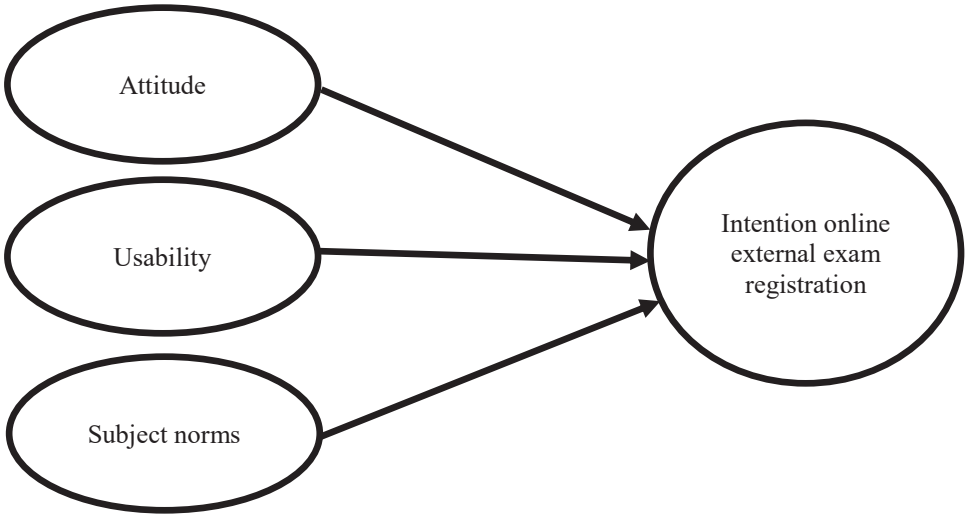

Fig 1. Framework for Research adopted from [6].

4 Analysis & Findings

The sampling was taken from the students who use the online external exams registration in the directorate of education in Thiqar. The questionnaires were distributed on 347 students and only 305 questionnaire was return and valid. The Statistical Package for Social Science (SPSS 20) was used as an instrument to analyse the collected data that return from the students who participated in this study and their data were valid.

4.1 Descriptive Statistics

Table 1. Descriptive Statistics.

Variables	Std. Deviation	Mean
Attitude	0.50168	4.3843

Subject norms	0.47020	4.3704
usability	0.36558	4.3889
Intention online registration	0.65570	4.1574

According to table 1, the mean values for all variables range from 4.3889 to 4.1574. Website usability has the greatest mean (4.3889) and the smallest standard deviation (0.36558), Attitude and subjective standards come in second and third, with mean values of 4.3843 (SD=0.50168) and 4.3704 (SD=0.4702, respectively. This indicates that responders have a high level of agreement on the subjective norm, attitude, and website usability. All of the variables had a standard deviation of less than one, the results were closely clustered around the mean, indicating that they were closely clustered around the mean.

4.2 Reliability Analysis

Table 2. Reliability Analysis.

Variables	Cronbach Alpha	Number of items
Attitude	0.737	4
Subject norms	0.717	4
usability	0.700	4
Intention online registration	0.827	4

The results of four sets of reliability testing are shown in table 2. The test began with a question about trust. There are four aspects to attitude. On these four items, the reliability test was used, and Cronbach's alpha value was 0.737. Subjective norm testing was the next step in the process. The subjective norm consisted of four items, with a reliability test result of 0.717 for subjective norm support. After that, the reliability test moved on to the third variable, which was website usability. There are four things in the website usability category that have a dependability value of 0.7. The final run was to determine whether you intended to quit. In this study, the intention to register online was measured using a four-item questionnaire. The intention to register online has a dependability score of 0.827.

4.3 Correlation Analysis

Table 3: Person correlation for variables.

			Attitude	Subject norms	usability	Intention online registration
	Attitude	Person Coefficient	1.000			
		Significance (2-tailed)	.			
	Subject norms	Person Coefficient	.508**	1.000		

		Significance (2-tailed)	0.000	.		
	usability	Person Coefficient	. 427**	.417**	1.000	
		Significance (2-tailed)	.000	.000	.	
	Intention online registration	Person Coefficient	.512**	.541**	.552**	1.000
		Significance (2-tailed)	0.000	0.000	0.000	.

According to the findings, the correlation coefficient between subjective norms and attitude is 0.508, or 50.8 percent at the 99% confidence interval; website usability and attitude are 0.427, or 42.7 percent at the 99% confidence interval, and intention to register online and attitude is 0.512, or 51.2 percent at the 99% confidence interval. This means that the Pearson's correlation between all of the variables and attitude was less than 0.70, implying that each of the variables and attitude is the independent variable. In terms of relationship strength, the findings point to a moderate relationship. Since all variables are significant at 0.00, attitude is significant to all of them. According to the findings, the correlation coefficient between website usability and the subjective norm is 0. 417, or 41.7 percent at the 99% confidence interval, and intention to register online and the subjective norm is 0.541, or 54.1 percent at the 99% confidence interval. In terms of relationship strength, subjective norm and attitude indicate a moderate association, whereas intention to register online and website usability indicates a moderate relationship. Because all variables are significant at 0.00, the subjective norm is significant for all of them. The value of the correlation coefficient between website usability and intention to register online is 0.552 or 55.2 percent at the 99 percent confidence range, according to the findings. This means that the Pearson's correlation between website usability and all of the variables was less than 0.70, implying that attitude and each of the variables are separate variables. In terms of relationship strength, the results of website usability and attitude indicate a moderate association, whereas subjective norm and online intention register indicate a significant relationship. Since all variables are significant at 0.000, All variables are affected by website usability.

4.4 Regression Analysis

Table 4. Regression analysis.

Independent Variables	Significance value	Beta
Attitude	0.009	0.177
Subject norms	0.000	0.337
usability	0.004	0.348
R^2	SIG.	F VALUE
0.419	0.000	12.014

Table 4 shows that the association between attitude and intention to register online is significant at the 99 percent confidence level, with a positive beta value of 0.177. This suggests that a good

attitude toward taking an external exam has a considerable impact on the desire to register online. Hypothesis 1 is so accepted. The results also reveal that subjective norms have a substantial positive connection (beta value = 0.337) to register online at a confidence level of 99 percent (sig=.1). As a result, hypothesis 2 is supported, which states, "There is a substantial association between subjective norm and intention to register for online external exams among students in the directorate of education in Thiqar.". This suggests that a student's social influence is greater. In other words, students are more likely to accept a trusted individual's behaviour, which boosts their desire to perform it. Typically, students seek information from their most trusted sources, such as peers and friends. A student's close friends and family members may be able to persuade him or her to take the recommended action. The association between the intention to register online and website usability was determined to be significant (sig=.000) at the 99% significant level, with a positive beta of 0.348. This shows that the desire to register online is strongly linked to the usability of a website. As a result, the third hypothesis is now considered valid. This hypothesis is significant because students are more likely to register online when the website provides information that is simple to understand. The more appealing a website is, the more likely people are to register online. The R2 for this study is 0.419, implying that website usability, subjective norm, and attitude, and can explain 41.9 percent of the variation in online registration intention. This suggests that the study's findings were almost average in explaining registration intent to register online, with other factors accounting for the remaining 58.1 percent.

Hypothesis	Remarks
There is a positive relationship between attitude towards intention online external exams registration	Accepted
There is a positive relationship between subjective norm towards intention online external exams registration	Accepted
There is a positive relationship between usability towards intention online external exams registration	Accepted

The hypothesis testing results from the Regression Analysis are summarized in Table 5. The first hypothesis, that there is a positive association between intention to register for external tests online and attitude, is validated, as is the second hypothesis, that there is a positive association between intention to register for external exams online and subjective norm. However, the third hypothesis, ‘There is a positive relationship between usability and intention to register for external exams online,' is also well supported. It demonstrates that in this investigation, all three hypotheses are accepted.

5 Discussion and Conclusion

According to the findings, one's attitude toward online registration has a substantial positive correlation with one's desire to register online. This attribute in this study relates to the online registration for external exams. They have a positive attitude toward their conduct as it pertains to online registration to encourage students to register. In other words, students will be more likely to register if the online external exam registration has a constructive approach toward their demands. The results were in line with TRA (Fishbein and Ajzen, 1980), which revealed a positive link between behaviour and attitude. Because students are invisible and have no face-to-face contact, online registration and student trust are critical. Students would be attracted to online registration if the greatest services were provided to them. Hypothesis 2 was

likewise accepted, in which subjective norm was found to have a positive and significant relationship with the desire to register online. The value of the Person correlation is 0.541, showing that the factor influences the intention to register online by approximately 50%. According to Ajzen and Fishbein (1975), A person's subjective norm is linked to their normative belief, which is described as a fear of a relevant referent individual or group accepting or disapproving of the person's behaviour. To put it another way, advances in normative thinking will improve subjective norms, which will indirectly boost a person's registration intention. This conclusion, like attitude, was corroborated by Theory Reasoned Action (Fishbein and Ajzen, 1975), which revealed a relationship between subjective norms and conduct. This study focused on friends and peers because they use and spend far more time online than family and relatives. The findings were also in line with what had been seen in prior studies. Karaiskos (2011) stated that among the social variables, the subjective norm has been deemed a crucial determinant of intention. It reveals that encouraging group remarks have a significant impact on those closest to students' acceptance. Students will seek counsel from a trusted referent individual or group, such as friends and peers, because the information from others may be distorted. The third hypothesis looked at the link between website usability and online registration intent, and it was shown to be true. This suggests that as the website becomes more user-friendly, the likelihood of students registering for external exams online will rise. In online registration, website usability refers to the student's expectation that the website would be simple to use and understand. Page loading, navigation, content, security, efficiency, and consumer focus are five important factors that should be addressed while developing a website, according to Osama et al. (2010). Aidil, (2010) reinforced this research by identifying website design characteristics as a dominating or powerful component that influences people's attitudes toward online systems because websites play a key role in attracting people to the system. The first impression and entry point for student online registration for external exams is the website.

References

[1] H. F. A. Hasan, A. Ilias, R. A. Rahman, and M. Z. A. Razak, "Service quality and student satisfaction: A case study at private higher education institutions," *International Business Research,* vol. 1, no. 3, pp. 163-175, 2008.

[2] M. A. Salamat, S. Hassan, and M. S. Muhammad, "Electronic participation in Malaysia," *Journal of e-Government Studies and Best Practices,* vol. 2011, no. 270543, pp. 1-11, 2011.

[3] M. Calbi *et al.*, "The consequences of COVID-19 on social interactions: an online study on face covering," *Scientific reports,* vol. 11, no. 1, pp. 1-10, 2021.

[4] F. M. E. Sepasgozar, U. Ramzani, S. Ebrahimzadeh, S. Sargolzae, and S. Sepasgozar, "Technology acceptance in e-governance: A case of a finance organization," *Journal of Risk and Financial Management,* vol. 13, no. 7, p. 138, 2020.

[5] Y. Chen and F. Q. Fu, "The behavioral consequences of service quality: An empirical study in the Chinese retail pharmacy industry," *Health marketing quarterly,* vol. 32, no. 1, pp. 14-30, 2015.

[6] N. A. Hasbullah, A. Osman, S. Abdullah, S. N. Salahuddin, N. F. Ramlee, and H. M. Soha, "The relationship of attitude, subjective norm and website usability on consumer intention to purchase online: An evidence of Malaysian youth," *Procedia Economics and Finance,* vol. 35, pp. 493-502, 2016.

[7] M. Fishbein and I. Ajzen, *Predicting and changing behavior: The reasoned action approach*. Taylor & Francis, 2011.

[8] T. Hansen, M. S. Risborg, and C. D. Steen, "Understanding consumer purchase of free-of cosmetics: A value-driven TRA approach," *Journal of consumer behaviour,* vol. 11, no. 6, pp. 477-486, 2012.

[9] H. Amin, "An analysis of online banking usage intentions: an extension of the technology acceptance model," *International Journal of Business and Society,* vol. 10, no. 1, p. 27, 2009.

[10] C. L. Corritore, B. Kracher, and S. Wiedenbeck, "On-line trust: concepts, evolving themes, a model," *International journal of human-computer studies,* vol. 58, no. 6, pp. 737-758, 2003.

[11] Y. H. Fang, C. M. Chiu, and E. T. Wang, "Understanding customers' satisfaction and repurchase intentions: An integration of IS success model, trust, and justice," *Internet research,* 2011.

[12] S. L. Jarvenpaa and V. S. Rao, "Trust in online consumer exchanges: Emerging conceptual and theoretical trends," in *E-Commerce and the Digital Economy*: Routledge, 2015, pp. 255-272.

[13] V. Shankar, G. L. Urban, and F. Sultan, "Online trust: a stakeholder perspective, concepts, implications, and future directions," *The Journal of strategic information systems,* vol. 11, no. 3-4, pp. 325-344, 2002.

[14] Y. H. Chen and S. Barnes, "Initial trust and online buyer behaviour," *Industrial management & data systems,* 2007.

[15] M. Fan, Y. Tan, and A. B. Whinston, "Evaluation and design of online cooperative feedback mechanisms for reputation management," *IEEE Transactions on Knowledge and Data Engineering,* vol. 17, no. 2, pp. 244-254, 2005.

[16] K. Hassanein and M. Head, "Manipulating perceived social presence through the web interface and its impact on attitude towards online shopping," *International Journal of Human-Computer Studies,* vol. 65, no. 8, pp. 689-708, 2007.

[17] W. C. Kim and R. Mauborgne, "Fair process: Managing in the knowledge economy," *Harvard business review,* vol. 81, no. 1, pp. 127-136, 2003.

[18] M. Turilli, A. Vaccaro, and M. Taddeo, "The case of online trust," *Knowledge, Technology & Policy,* vol. 23, no. 3-4, pp. 333-345, 2010.

[19] R. S. Al-Maroof, S. A. Salloum, A. E. Hassanien, and K. Shaalan, "Fear from COVID-19 and technology adoption: the impact of Google Meet during Coronavirus pandemic," *Interactive Learning Environments,* pp. 1-16, 2020.

[20] M. Aboelmaged and T. R. Gebba, "Mobile banking adoption: an examination of technology acceptance model and theory of planned behavior," *International Journal of Business Research and Development,* vol. 2, no. 1, 2013.

[21] E.-J. Kim, J. J. Kim, and S.-H. Han, "Understanding Student Acceptance of Online Learning Systems in Higher Education: Application of Social Psychology Theories with Consideration of User Innovativeness," *Sustainability,* vol. 13, no. 2, p. 896, 2021.

[22] S. J. Barnes and R. T. Vidgen, "An integrative approach to the assessment of e-commerce quality," *J. Electron. Commerce Res.,* vol. 3, no. 3, pp. 114-127, 2002.

[23] L.-M. N. Tchouakeu, M. K. Hills, M. H. Jarrahi, and H. Du, "On-line course registration systems usability: a case study of the e-Lion course registration system at the Pennsylvania State University," *International Journal of Information Systems and Social Change (IJISSC),* vol. 3, no. 4, pp. 38-52, 2012.

[24] S. S. Alam and N. M. Yasin, "An investigation into the antecedents of customer satisfaction of online shopping," *Journal of Marketing Development and Competitiveness,* vol. 5, no. 1, pp. 71-78, 2010.

[25] G. S. Shergill and Z. Chen, "WEB-BASED SHOPPING: CONSUMERS'ATTITUDES TOWARDS ONLINE SHOPPING IN NEW ZEALAND," *Journal of electronic commerce research,* vol. 6, no. 2, p. 78, 2005.

[26] R. L. Oliver, *Satisfaction: A behavioral perspective on the consumer: A behavioral perspective on the consumer*. Routledge, 2014.

[27] S. A. Becker and F. E. Mottay, "A global perspective on web site usability," *IEEE software,* vol. 18, no. 1, pp. 54-61, 2001.

[28] D. Belanche, L. V. Casaló, and M. Guinalíu, "Website usability, consumer satisfaction and the intention to use a website: The moderating effect of perceived risk," *Journal of retailing and consumer services,* vol. 19, no. 1, pp. 124-132, 2012.

[29] S. S. Alam, Z. Bakar, H. B. Ismail, and M. Ahsan, "Young consumers online shopping: an empirical study," *Journal of Internet Business,* no. 5, 2008.

[30] S. Chuchinprakarn, "Application of the theory of reasoned action to on-line shopping," *Knowledge Center E-paper Bangkok University,* pp. 1-7, 2005.

Precipitation Forecast for Thi-Qar Province of Iraq Utilizing Machine Learning Approaches

Anwar Alnawas[1], Nassir Jabir Al-Khafaji[2], Hayder Hussein Azeez[3]
{anwar.alnawas@stu.edu.iq[1], nassir.farhan@stu.edu.iq[2], hayder.hussein@stu.edu.iq[3]}

Nassriyah Technical Institute, Southern Technical University, Iraq[1,2,3]

Abstract. Rainfall is considered a main to provide water in rivers along with Iraqi territory. The unpredictable amount of rainfall due to climate change can cause either overflow or dry in the rivers. Although, there are a lot of electronic devices that have harnessed the prediction of precipitation using weather conditions such as humidity pressure, and temperature. Regrettably, these classical methods cannot work efficiently, so exploiting machine learning techniques can predict accurate outcomes. Therefore, predictions of data-based models using deep learning algorithms are promising for these purposes. This empirical study seeks to build a precipitation prediction model using a deep learning mechanism through utilizing historical weather data. Deep learning outperformed other classifiers based on the findings collected. The current study's experiment yielded accurate findings of up to 91.59% when testing the model with actual weather data within the specified period.

Keywords: Machine Learning, Data Mining, RapidMiner, Rainfall Rate, Thi-Qar

1 Introduction

Precipitation prediction is one of the important topics of interest to researchers in the world. Where, the rainfall is a major influence in the economic and social aspects of human life [1], such as health, agriculture, transportation, and others. For this purpose, our study found the need to build a model to understand climate indicators predict rainfall. Weather forecasting equipment such as satellites, balloons, aircraft, buoys, ground stations, and radar systems are used to gather and update atmospheric data [2]. Using this historical data provided by these tools, weather, and rainfall forecast models can be designed using a machine learning approach. One of the key steps in a machine learning approach is to extract a specific set of data that is useful for making predictions and correlations between different parameters. Therefore, data mining provides this to analyse data and devise bases for weather forecasts. Data mining techniques are separated into categorization and grouping procedures, with the data being saved and structured in a database. A data extraction method called classification is used to categorize unknown samples [3]. Using classification algorithms, it is simple to forecast precipitation [4]. Aggregation is a method of grouping objects based on information. In Iraq, agriculture is one of the most important areas affected by rain, many crops need to know the times of rain. In Iraq, agriculture is one of the most important areas affected by rain. The Ministry of Agriculture-Iraq has installed many automatic weather stations in various agricultural areas in Iraq to measure many weather factors that influence agriculture such as air temperature, relative humidity of the air, the intensity of solar radiation, atmospheric pressure, and others. Automatic weather stations

IMDC-IST 2021, September 07-09, Sakarya, Turkey
Copyright © 2022 EAI
DOI 10.4108/eai.7-9-2021.2314897

provide daily data that can be used to create rain forecast models. In this study, data provided by automatic weather stations were used to construct a rain forecast model using the Deep Learning (DL) technique.
The rest of the study is organized as follows. in Section 2. , related works are explained. In Section 3. , the proposed methodology is described. Section 4. , describes how the experiments are conducted. Section 5. , the results are investigated and discussed. Finally, Section 6. , concludes the paper and remarks on key findings.

2 Related works

In present years, the utilize of machine learning algorithms for precipitation forecasting has attracted considerable attention. Drought prediction is a useful technique for analysing the negative effects of drought occurrences on important water supplies, agriculture, ecosystems, and hydrology. [5]. Therefore, a better rainfall predicting model is crucial for early warning that can reduce hazards to life and property and better manage agricultural farms. Using machine learning we can harness the historical data analysis of precipitation data and can forecasting rainfall in the coming seasons. For a comprehensive look at previous studies related to this topic, several previous studies on machine learning used in rainfall prediction are discussed.
Thirumalai, Harsha [6] discusses the rainfall rate in past various seasons based on the harvest seasons and predicts the rainfall for future years. Different types of real data were measured by linear regression method for two cropping seasons for early prediction. In this study, Kharif and Rabi were taken as the main variable where if one variable was given then the other can be predicted using linear regression. Thirumalai's study also calculated Mean and Standard deviation to predict future crop seasons. The results of the Thirumalai study help farmers to make the right decision to harvest a particular crop according to the crop seasons.
Chatterjee, Datta [7] also conducted an empirical study in India. In this paper, a Hybrid Neural Network (HNN) model is proposed to foretell rainfall rate according to several features for instance temperature, relative humidity, vapor content, and atmospheric pressure. The data has been collected by meteorological stations in West India over the period from 1989 to 1995. The findings of the present paper have suggested that feature selection can reasonably improve the performance of any classifier while predicting rainfall. In the same context, Kar, Thakur [8] have used the fuzzy logic technique to predict the rainfall, given the temperature of that particular geographical location.
Another study conducted by Moon, Kim [9], suggests a method for an effective early warning system (EWS) for very short-term heavy rainfall with machine learning techniques. The tests of EWS were run for 652 locations in South Korea from 2007 to 2012. The empirical results showed that the pre-processing methods improved the prediction quality and logistic regression works well on heavy rainfall nowcasting in terms of F-measure and equitable threat score.
Because agriculture is the backbone of the Indian economy, many studies seek to utilize sophisticated technologies to predict the climate. While agriculture is also more important to many Middle Eastern countries such as Iraq. But unfortunately, few studies take advantage of machine learning models to predict rainfall rate.
Another study related to aspects of precipitation prediction was discussed by Moulana, Roshitha [10]. They discuss a model used to predict long-term precipitation. Machine learning was harnessed for rainfall prediction purposes. The dataset was collected for rainfall prediction from the year 1901-2015 and consecutive for 3 months for each state in India. The results of this study

highlighted that the rate of rainfall is reasonably good in various states of India in the main three months (March, April, and May). Abdel-Kader, Abd-El Salam [11] ware considered as a recent study that proposed a powerful hybrid technology has been implemented to predict rainfall by combining Particle Swarm Optimization (PSO) and Multi-Layer Perceptron (MLP) which is the popular kind used in Feed Forward Neural Network (FFNN). The proposed hybrid technique has two phases, in the first phase is developed neural network by determining the number of neurons for input layer, neurons for hidden layer, and number of neurons for output layer; in the second phase PSO mainly used for automatic generation of optimized weights which used in the first phase for training network.

3 Methodology

Process for analysing weather using data extraction techniques, all standard steps that contain data selection for evaluation is performed. Throughout the process, the dataset is cleaned, formatted, and prepared for mining and interpretation. Fig 1. It shows the main steps in the proposed model for forecasting rain using the DL approach.

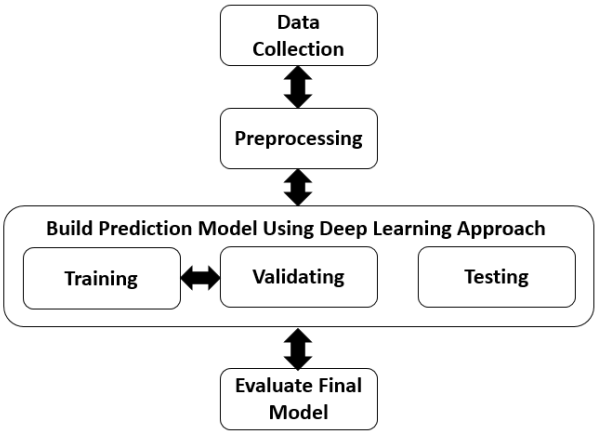

Fig. 1. The proposed model for forecasting rain using the DL approach.

3.1 Data Collection

Machine learning needs a suitable data source to build a correct prediction model. Determining the source of the data is one of the main steps to predict rainfall rate. Therefore, the data provided by the Iraqi Agrometeorological network in the Ministry of Agriculture-Iraq was used as a source of data for this study. Before making any forecasts, it is essential to understand the current weather conditions and their consequences. This process is done by examining a large amount of monitoring data.

3.2 Data Pre-Processing

After collecting the raw data, pre-processing of data aims to improve the quality of this raw data. The data provided contains 2,191 instances and 9 attributes, to predict the occurrence of rainfall. Noise reduces data quality. Therefore, noise must be removed from within the dataset using pre-processing techniques before mining tasks begin [12]. To obtain satisfactory results, a set of filters has been applied appropriately to process the data before further analysis.

3.2 Build Model

The availability of big data and the rapid development of neural network architectures, as well as increasing computational tasks, have contributed to the success of the DL concept. It pushed for its use to replace machine learning more efficiently than conventional networks. In this essential stage of methodology, DL was used to identify exact patterns in the existing dataset. Through, discovering cognitive associations, changes, and important structures from the weather dataset.

3.2 Evaluation

The evaluation stage of the prediction model is considered one of the important stages [13]. Through the evaluation, the accuracy of the model can be measured. The evaluation was based on a confusion matrix. It provides a set of evaluation factors such as Accuracy (Acc), Precision (P), and Recall (R) to evaluate data mining classifiers.

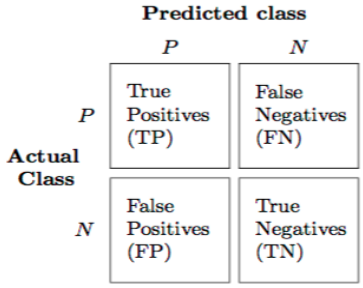

Fig. 2. Confusion matrix model.

For a binary classifier [14], lists of rates that are often computed from a confusion matrix are:

1. **Accuracy**: Indicates the correctness of the model.

$$Acc = \frac{TP+TN}{TP+TN+FP+FN} \quad (1)$$

2. **Recall**: Indicates the sensitivity of the model or how many TPs are returned.

$$R = \frac{TP}{TP+FN} \quad (2)$$

3. **Precision**: Indicates the result of relevancy or how often predicted TP is correct

$$P = \frac{TP}{TP+FP} \tag{3}$$

4 Experimental

RapidMiner was used as the main tool for data processing and analysis. It provides an integrated environment for data collection, formatting and processing, machine learning, DL, and results in presentation. It also provides a graphical interface to facilitate access to all available tools and functions. RapidMiner is used for commercial, educational, training, validation, models improvement, and visualization of results. In this study, RapidMiner studio (V 9.9) Educational Edition was used.

4.1 Data Collection

The official website of the Iraqi Agrometeorological Network provides access to meteorological data. Many stations provide data daily. The source of the data was Souk Al-Shuyoukh station (located at 30.95° N, 46.56° E), for the period from 1/1/2014 to 31/12/2019. While completing the request through the website to obtain the data, the data is submitted in CSV format. Table 1 shows the distribution of the dataset that used in this study, both quantitatively and descriptively.

Table 1: Distribution of the dataset that used in the study.

Attributes	Description	Measuring unit	Instances	Missing data	Data type
Date	Date	Date	2,191	91	date
Rain	Rain	mm	2,191	0	real
AT Avg	Average of temperature	C°	2,191	0	real
AT Max	Maximum of temperature	C°	2,191	0	real
AT Min	Minimum of temperature	C°	2,191	0	real
RH Max	Relative Humidity	%	2,191	0	real
RH Min	Relative Humidity	%	2,191	1	real
SLR Total	Total Solar Radiation	Mj/m2	2,191	0	real
WS Avg	Wind Speed	m/s	2,191	0	real
WS Max	Wind Speed	m/s	2,191	0	real
ET	Evapotranspiration	mm	2,191	0	real

Fig 3 below illustrates the distribution of raw data and visualization of attributes that were collected at the specified periods before pre-processing. The ten major attributes were represented in Fig 3, date attribute was not used since the date scale was not suitable for this study.

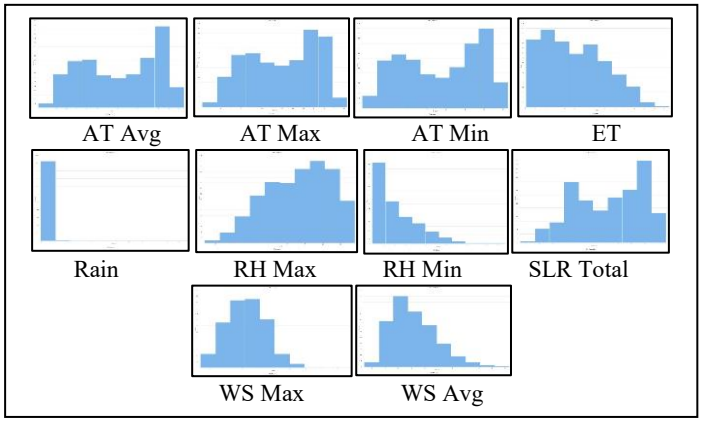

Fig. 3. The representation of attributes before pre-processing.

4.2 Data Pre-Processing

Pre-processing is an important process that reduces data inaccuracy. To obtain the best accuracy of results, the data used must be effective. In this study the following processing was used:

1. **Remove missing values:** Some instances do not have values recorded in several attributes. All instances that contain missing values are ignored.
2. **Data transformation:** Real number values changed to binary for rain attribute. Because it represents the "label" in the classification model. Where the amount of rain greater than 0 mm is represented by "1". The amount of rain equal to zero is represented by "0".
3. **Remove duplicates:** All attributes with the same values are removed.

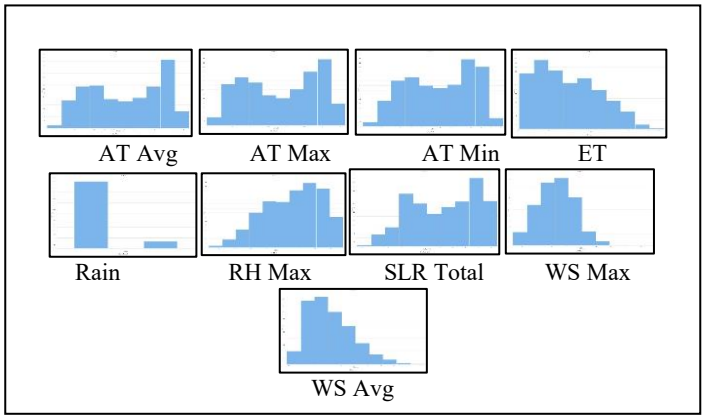

Fig . 4. The representation of attributes before pre-processing.

Fig 4 presents the attributes after pre-processing. The ten attributes have been formatted and normalized. Fig 3 and 4 show the difference in the distribution of the data representation, for example, there is a difference in the representation of rain attribute in Figs 3 and 4. The reason

for this difference is the rain theme contains missing data before processing. Datasets are divided into training and test datasets with 70:30.

4.3 Build a Prediction Model

Through several pre-processing steps, the dataset was formatted for use in building a prediction model. At this stage, DL plays an important role in bridging the gap by representing data to create a prediction model. Due to arithmetic developments and the benefit of various observations, DL has seen continuous improvement in its capabilities. Currently, Three-dimensional (3D-Var) and four-dimensional (4D-Var) variation approaches, as well as ensemble methods, are used in DL systems (commonly Kalman filter). A single deterministic state is estimated using the 3D-Var method by minimizing a cost function that includes the three terms background, observation, and model error. In addition, 4D-Var records variations in observation across time.
RapidMiner provides the ability to model prediction using layouts. The DL operator is based on a multi-layer forward-fed artificial neural network that is trained using random gradient descent by back-propagation. This network contains many hidden layers that are made up of neurons with tanh, rectifier, and maxout activation functions.
An artificial neural network can use the DL operator to select among a variety of activation functions. To be able to construct nearly any form of the artificial neural network today, all of the key training parameters are also available. The following settings have been made:

1. Activation function: Rectifier.
2. Hidden layers: 5 layers hidden by 50 artificial neurons each.
3. Epochs: 10.
4. Loss function: Automatic.
5. Max w2: 0 (maximum value of the sum of the square roots of the inputs of a neuron, set to zero allows any value without limits, by default it is set to the value 10).

5 Results and Discussion

The multiplicity of weather monitoring parameters enriches the analysis results[15]. By going through the confusion matrix, we can display the results obtained using the proposed model. Using variable epoch values to study its effect on the results, Table 2 shows the behaviour of the model using these values.

Table 2. performance results using different Epochs values

Epochs	Acc	R	P
10	0.90	0.72	0.72
20	0.90	0.71	0.71
30	0.90	0.80	0.73
40	0.90	0.66	0.72
50	0.90	0.76	0.73

60	0.91	0.70	0.74
70	0.90	0.78	0.72
80	0.92	0.73	0.77
90	0.92	0.74	0.74
100	0.92	0.73	0.76

The results above show the higher epoch value gives higher performance results for the evaluation factors Acc, R, and P. The performance of two types of classifiers were also compared with the DL approach. Which are Naïve Bayes and Decision Tree. Table 3 shows the result of the comparison.

Table 3. performance results using different classifiers

Classifiers	Acc	R	P
DL	91.59	73.39	76.1
Decision Tree	89.52	62	68.07
Naïve Bayes	67.62	72.56	58.38

Based on the results obtained compared with other classifiers (Decision Tree and Naïve Bayes) in this study, it is possible to rely on the use of DL approaches to design prediction models for weather conditions in general and rain. To ensure the validity of the prediction models, they must be applied to more than one case and different datasets.

6 Conclusion

The study of weather has become a magnet in recent years for researchers. This discipline regulates a variety of fields, including agriculture, and governments select the sorts of crops that are dependent on the state of the weather. Therefore, it is important to be aware of the weather forecast for the next few days so that measures may be taken. In this study, the DL approach was used to build a rainfall prediction model. The main steps of building a model were data collection, pre-processing, model building, and model evolution. To understand and implement the workflow, the Rapid Miner program was used to implement the proposed approach. According to the obtained results, DL achieved better results compared to other methods. The performance of the model reached an accuracy of 91.59%. The results obtained from the model help us to understand and predict the times of rain, the model can be used for transportation, agriculture, or any field affected by rain.

Acknowledgments

The authors are deeply grateful to the Iraqi agrometeorological network Ministry of Agriculture-Iraq, to provide weather data and information that used in this study.

References

[1] Anwar MT, Nugrohadi S, Tantriyati V, Windarni VA. Rain prediction using rule-based machine learning approach. Advance Sustainable Science, Engineering and Technology. 2020;2(1):1-6.

[2] Kunjumon C, Nair SS, Suresh P, Preetha S. Survey on weather forecasting using data mining. Conference on Emerging Devices and Smart Systems (ICEDSS); 2-3 March 2018; Tiruchengode, India: IEEE; 2018. p. 262-4.

[3] Thushika N, Premaratne S. A data mining approach for parameter optimization in weather prediction. International Journal of Data Science. 2020;1(1):1-13.

[4] Schultz M, Betancourt C, Gong B, Kleinert F, Langguth M, Leufen L, et al. Can deep learning beat numerical weather prediction? Philosophical Transactions of the Royal Society A. 2021;379(2194):1-22.

[5] Juneja A, Das NN. Big data quality framework: Pre-processing data in weather monitoring application. International Conference on Machine Learning, Big Data, Cloud and Parallel Computing (COMITCon); 14-16 Feb. 2019 Faridabad, India IEEE; 2019. p. 559-63.

[6] Thirumalai C, Harsha KS, Deepak ML, Krishna KC. Heuristic prediction of rainfall using machine learning techniques. International Conference on Trends in Electronics and Informatics (ICEI); 11-12 May 2017; Tirunelveli, India: IEEE; 2017. p. 1114-7.

[7] Chatterjee S, Datta B, Sen S, Dey N, Debnath NC. Rainfall prediction using hybrid neural network approach. 2nd International Conference on Recent Advances in Signal Processing, Telecommunications & Computing (SigTelCom); 29-31 Jan. 2018; Ho Chi Minh City, Vietnam IEEE; 2018. p. 67-72.

[8] Kar K, Thakur N, Sanghvi P. Prediction of rainfall using fuzzy dataset. International Journal of Computer Science and Mobile Computing. 2019;8(4):182-6.

[9] Moon S-H, Kim Y-H, Lee YH, Moon B-R. Application of machine learning to an early warning system for very short-term heavy rainfall. Journal of Hydrology. 2019;568:1042-54.

[10] Moulana M, Roshitha K, Niharika G, Sai MS. Prediction of rainfall using machine learning techniques. International Journal of Scientific & Technology Research. 2020;9(1):3236-40.

[11] Abdel-Kader H, Abd-El Salam M, Mohamed M. Hybrid machine learning model for rainfall forecasting. Journal of Intelligent Systems and Internet of Things. 2021;1(1):5-12.

[12] Suryanarayana V, Sathish B, Ranganayakulu A, Ganesan P. Novel weather data analysis using hadoop and mapreduce–a case study. 5th International Conference on Advanced Computing & Communication Systems (ICACCS); 15-16 March 2019; Coimbatore, India: IEEE; 2019. p. 204-7.

[13] Tharun V, Prakash R, Devi SR. Prediction of rainfall using data mining techniques. Second International Conference on Inventive Communication and Computational Technologies (ICICCT); 20-21 April 2018; Coimbatore, India: IEEE; 2018. p. 1507-12.

[14] Yadav SA, Sahoo BM, Sharma S, Das L. An analysis of data mining techniques to analyze the effect of weather on agriculture. International Conference on Intelligent Engineering and Management (ICIEM); 17-19 June 2020 London, UK: IEEE; 2020. p. 29-32.

[15] Yasmin RY, Sakya AE, Merdijanto U. A classification of sequential patterns for numerical and time series multiple source data—a preliminary application on extreme weather prediction. International Conference on Data and Software Engineering (ICoDSE); 1-2 Nov. 2017; Palembang, Indonesia: IEEE; 2017. p. 1-5.

Smart Energy Metering Based on Arduino, GSM, and Raspberry pi3 as Server

Doaa.S.Al-sehail[1], Osama Y.K Al-Atbee.[2], Ali Marhoon[3]
{doaa.alsehail28@gmail.com[1], usama.khader@uobasrah.edu.iq[2], alifm60@gmail.com[3]}

[1,2,3]Electrical Engineering Department, University of Basrah, Basrah, Iraq

Abstract. This paper proposed and implement a microcontroller-based smart meter that utilizes the GSM as wireless communication with the utility server. The scheme aims to build a low-cost smart power meter that improves the electric grid and prevents electricity loss, making life more comfortable for the consumer and utility. Raspberry Pi3 server equipped with programmed systems in highly efficient and reliable languages (PHP and Python) and secure databases (MySQL) to set up an automatic metering and billing system. The proposed system provides exchange information between the consumer and the utility, where the consumer can access his data through a web page. Issuing a monthly bill and sending it to the consumer by e-mail and SMS as well as disconnecting the power source in case the consumer fails to pay his bill.

Keywords: Smart Meter, Arduino Mega 2560 Micro-Controller, GSM SIM900A, Raspberry pi3, RTC

1 Introduction

Electricity has become one of the vital technology in human daily life. It is an important part of factories and homes. The world development leading to more electricity demand and consumption. With such development, calculating the power consumptions by the energy supplier's companies and producing bills using the old-style reading of the traditional meters became ineffective. There are many defects, including the complete dependence on the meter readers, as well as human errors that occur that cannot be avoided, and the time required to accomplish whole area data reading and billing. Also, there is a great chance of theft and the consumer not getting an update about the amount of energy consumed at a regular interval [1]. So the demand has increased effectively for meters that collect readings electronically, but this method has become ineffective and expensive because it requires a visit to collect the readings by a specialized employee by the company. This means a lot of time and many employees, and sometimes the consumer is not present at his house. To improve the way of collecting the meter reading, the smart meter plays an important role in eliminating the problems that were previously raised. Smart Energy Meters (SEM) are measurement devices used by utilities to deliver billing information to all customers and operating their electric systems. This is the main reason behind companies targeting SEMs, as reading and remote control help reduce workforce costs. It has become an important national strategy related to the standard of living and individual safety, as SEM can contact the individual and let him know how his money was spent on electricity. SEM is designed and implemented on a large scale and is stable in various scenarios and methods to achieve optimal cost efficiency on the electrical system [2]. Some researchers used wireless networks to establish a connection between meters and control centers to obtain the best strategy [2]. The main feature that distinguishes smart meters from other meters is their ability of two-

IMDC-IST 2021, September 07-09, Sakarya, Turkey
Copyright © 2022 EAI
DOI 10.4108/eai.7-9-2021.2314803

way communication between the consumer and the utility [3]. There are many communication technologies currently used for smart metering systems, but (CDMA, GSM, WIMAX, ZigBee, and WLAN) are among the most widespread communication technologies in the world, the above methods except GSM are very expensive to implement and operate requires complex infrastructure setup, short remote operation and still requires field intervention from human operators or is prone to error and reliability problem due to noise in a transmission line or weather condition [4]. GSM is the best technology currently used because it is widely available, very reliable, and inexpensive compared to means of communication. Other SEM automation based on GSM [4] uses a current sensor to measure the value of current consumed by the load and PIC to convert the value that gets from the sensor to a digital unit. Automatic power metering using ZigBee and GPRS [5]. A pic18le4620 microcontroller was used with the cc2430 as a communication function and supports the Zigbee protocol, as it can transmit data up to 10 meters indoors and about 200 meters outdoors. This data is collected by Zigbee and sent via GPRS using sim300 to the service provider, but one of the drawbacks of this work is that the bill is not presented to the consumer. IoT Energy monitoring system [6] It is suggested that data be sent every 20 seconds to the Raspberry Pi 3 server via Wi-Fi type esp8288, where the user can access the information used about the energy consumed over the internet to that server as well as use josn (Java Object Script Notation) and also the data is processed through Server to calculate the amount of energy consumed during the day. Zigbee power meter [7]. An SEM is designed to calculate the voltage, current, and power factor and to send the obtained data to the home compliant gateway via the Zigbee protocol, but one of the disadvantages of this method is that it cannot be used in long distances. Prepaid energy meter based on GSM and RFID [8] a design of master card reader and energy meter that informs the consumer about his energy consumption via GSM. Smart meter with deployment network [9] presented system consists of energy meter installed in each home and raspberry pi as a server. The consumed power will be compared with the available balance for the same home at the server. The drawback of this system is the use of a power line carrier (PLC) which is expensive and not always available. This paper presents a wireless smart energy meter topology to overcome the drawbacks and improves the traditional energy meters system. An Arduino microcontroller with the GSM as a communication tool with the Raspberry Pi server and other peripherals are utilized to propose a smart energy metering system. the developed system can provide a detailed measurement of power usage and energy consumption patterns. Thus, the consumer can Understand their electricity usage patterns so they can adapt their behavior to reduce their energy profile.

2 Proposed system

The main function of the SEM is its ability to communicate the meter reading to the resource via the communication network. For a fast and efficient means of data collection, it is preferable to use a GSM network in the proposed system for communication purposes between consumers and the utility service. The main reason for choosing GSM is due to the large network coverage, low cost, and negligible maintenance, sending data to a web server through it becomes a useful and easy-to-use tool. The Arduino-based smart metering system consisting of a smart power meter and Raspbian Linux version available for Raspberry Pi3 Model B provides the full functionalities needed for servers [10]. The data sent by the smart meter are stored on the MYSQL database within the Raspberry server which includes multiple tables. The flowchart and overall block diagram for this project are presented in Fig. 1 and Fig. 2 respectively.

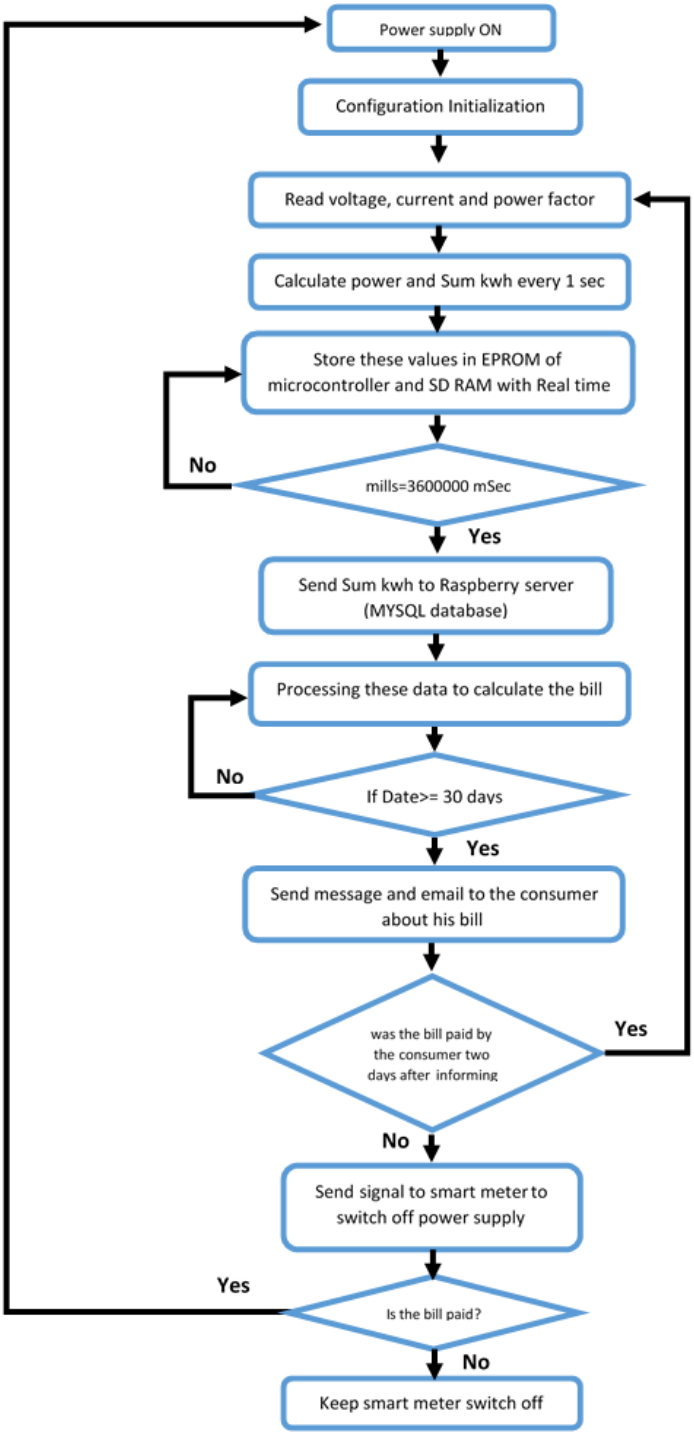

Fig. 1. The flowchart of the proposed system.

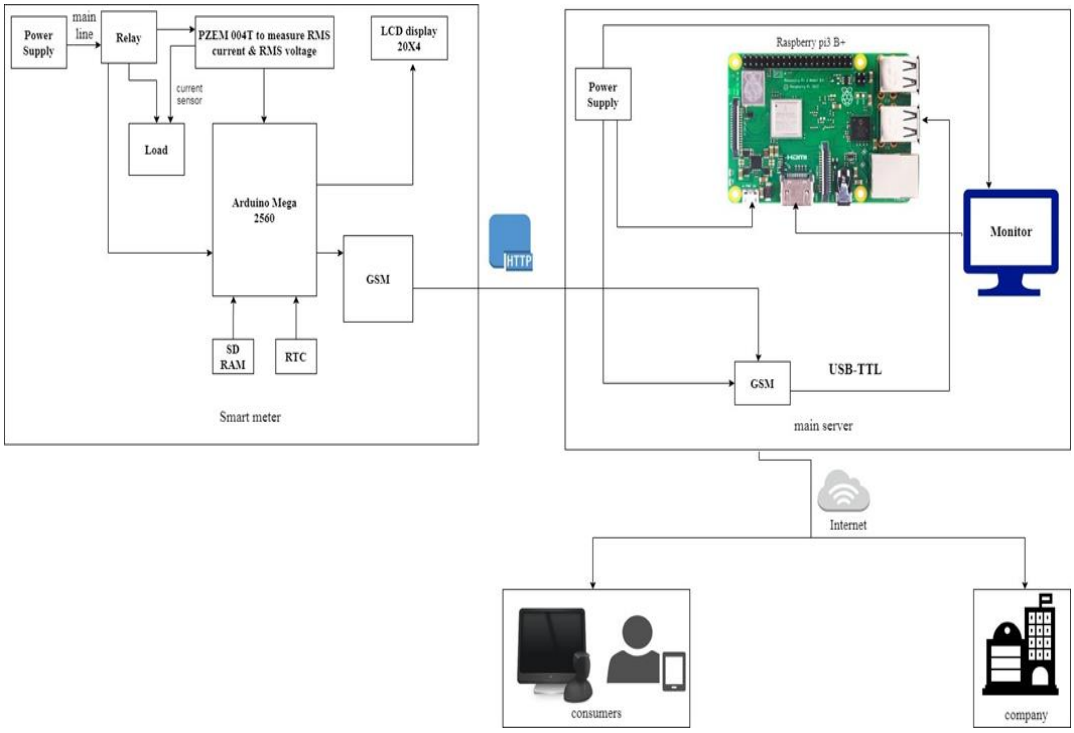

Fig. 2. The block diagram of the proposed system.

3 Function of the proposed energy meter

The designed meter measures RMS values for current and voltage. The measurement of RMS of the discrete signal is as follows [12]:

$$V_{RMS} = \sqrt{\frac{1}{N} \sum_N v^2(n)} \quad (1)$$

$$I_{RMS} = \sqrt{\frac{1}{N} \sum_N i^2(n)} \quad (2)$$

Where, and are discrete values of voltage and current. N is that the number of samples during a single period of the discrete signal. The real power of the discrete-time signal is measured as follows:

$$P = V_{RMS} \times I_{RMS} \times p.f \quad (3)$$

4 Implementation

A. Software Implementation

The project was simulated in proteus 8.0. First, it needs to add a library in proteus software because the software does not support Arduino boards by default. The hex. A file of code is uploaded in Arduino boards in Proteus. The simulation of the smart Energy meter consists of the following parts:

- Voltage measurement circuit.
- Current measurement circuit.
- Relay to connect or disconnect the load.

After uploading the Arduino code, the results can be shown on the LCD as shown in Fig. 3.

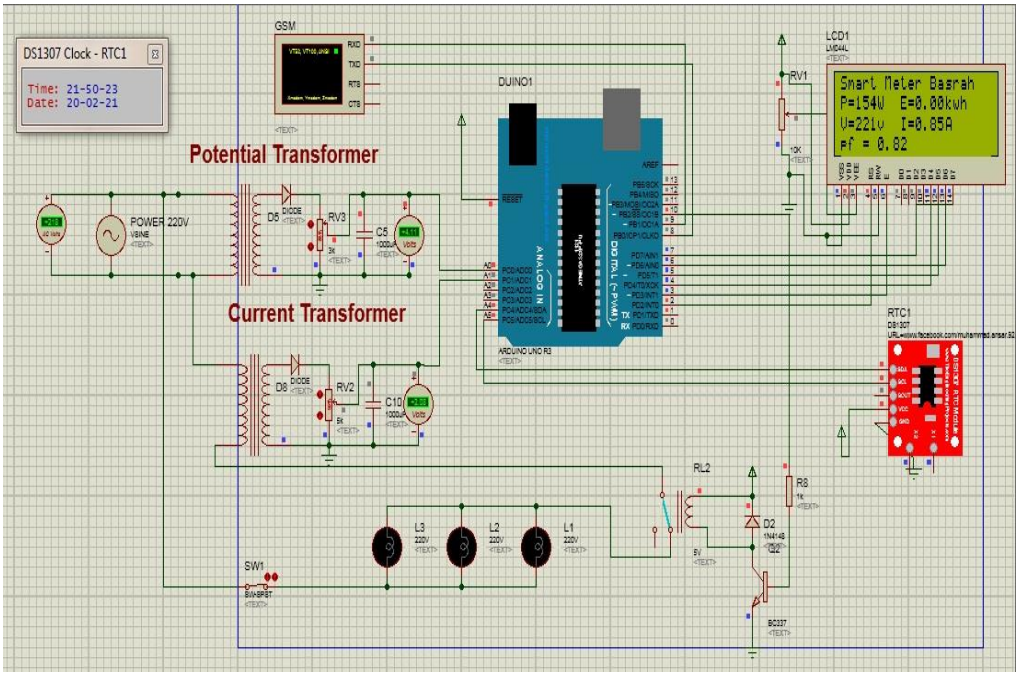

Fig.3. the simulation of the proposed system.

B. Hardware Implementation

The main components that have been used in the project are:

- Arduino Mega 2560

Arduino Mega 2560 is an ATMEGA 2560 based microcontroller board. It contains a total of 54 pins. Of the 54 I / O pins, 16 are analog input/output data pins and 4 are UART serial communication pins. The advantage of Arduino Mega over other microcontrollers is its higher

graphic memory and bigger size of RAM that makes it a fast processing controller. The microcontroller needs a DC power supply of 5 V, 1 A rating [13].

- Pzem 004T sensor

The module as shown in Fig. 4 is used to measure the AC voltage, current, active power, frequency, power factor, and active power, and this module is read through the TTL interface. The measuring current range of this module (10A-100A) and the voltage range (80V-380V).

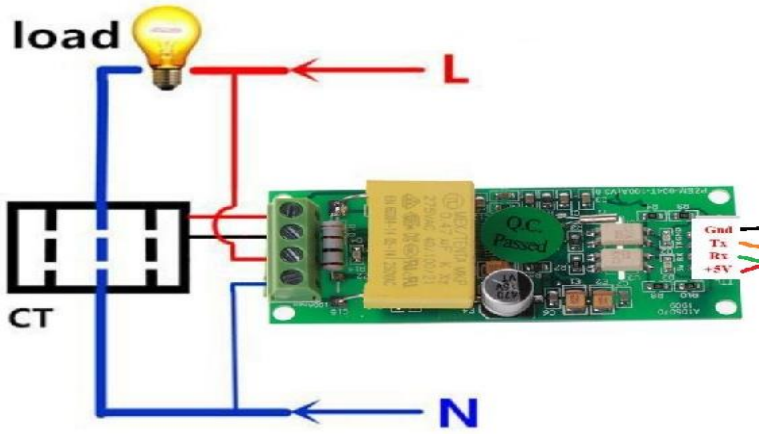

Fig. 4. PZEM 004T.

- GSM Module SIM900A

SIM 900A is a dual-band GSM / GPRS (900/1800 MHz) module. It communicates with controllers by using AT commands. As it can control the meter by sending a signal through GSM that is connected to Raspberry Pi server to the GSM located in the Smart Meter to control it and send notifications by the utility and displaying them on LCD or sending them to the consumer's mobile.

- Liquid Crystal Display (LCD)

This component is responsible for displaying consumption data in kilowatts as well as displaying tariffs and notifications sent by the approval authority and measuring power quality.

- SD Card

The Micro SD card unit is used to store the values so that the meter readings are not lost in the event of a malfunction or a problem in sending data to the server.

- Relay

In the proposed design, a relay was included to handle remote requests by utilities, to control the connection between the main and the load. The model identified in this design is a single-chain 5V-10A power unit.

- Real-Time Clocking (RTC)

Real-Time Clock Module DS3231 used in this project is a low cost and high fidelity unit as it saves hours and minutes of Information in seconds, dates, days, months, and years. Date month which ends in less than 31 days, are automatically adjusted, including a leap year.

- Raspberry pi3 B+

It is a small, powerful, and inexpensive computer board that works the same way as a standard computer and requires a keyboard to enter commands, a display unit, and a power source. Raspberry pi 3 is used as a server because is a small single-board computer. It is ideal for use as a basic Linux desktop, media center computer, development machine, or any number of projects. It is preferable due to its low power consumption and respectable processing capabilities [10]. Databases were installed in high-level languages, MySQL, and the system was programmed in reliable languages such as PHP, and Python to control and process all data sent to this server and sending information from the server to the consumer such as invoices and other notifications about the meter status or in the event of maintenance on the electrical grid.

C. Prototype Design

As mentioned earlier, the Arduino Mega 2560 was used as a micro-controller with GSM to provide communication between the consumer, the smart meter, and the server, as the GSM communicates with the network and sends the data and in the event of an error such as non-payment of the bill, a message appears on the LCD in the meter and the mobile.
Fig. 5 shows the output of SEM of the proposed system. It sends SMS to the user monthly with the number of consumed units and how much money a consumer will have to pay for the utility.

Fig. 5. Smart meter implementation.

Fig. 6 shows the all components implemented in the proposed system. An integrated system has been designed in high-level programming languages such as (PHP, Python) to calculate the bill and send it via e-mail and SMS to the customer's mobile at the beginning of each month as shown in **Fig. 7**. If the bill is not paid, the electricity is disconnected from the meter through the server, and the electricity is also returned to the meter remotely. This system can also issue reports for each customer and know the status of the device, is it active or inactive. **Fig. 8** shows the login page of the system that is programmed to manage the received data and processed it to control the smart meter.

Fig. 6. The implementation of the proposed system.

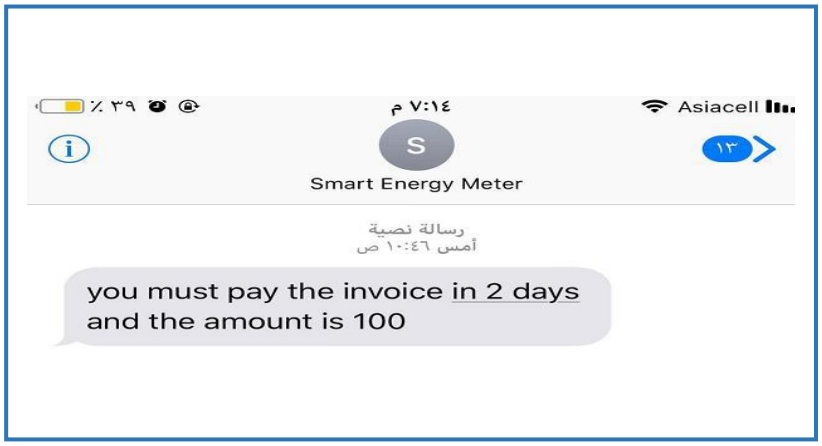

Fig. 7. Text message (SMS) sent to the consumer with the value of the monthly bill.

Fig.8. Login page of the system.

Fig. 9 shows the management of the smart meter webpage, the webpage has software built in PHP and PYTHON languages, the function of each icon in Fig.9 is:

- Users: the users can be added to the system to manage the system, control Meters, and adding new meters if there are new consumers.
- Customer: Adding a new customer to the system in the event of submitting an additional request, and includes recording the entire customer's data such as his name, address, phone number, e-mail, and the unique identifier of the meter. All details can also be modified in the event of a change in the added information.

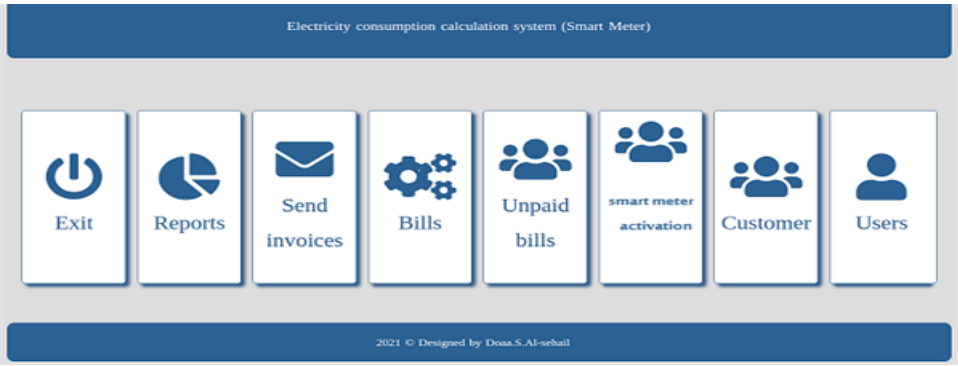

Fig. 9. Smart meter page management.

- Smart meter activation: Revitalize the meter if it was cut off upon non-payment of the bill and the period allowed for the consumer to pay has been exceeded.
- Unpaid bills: Report of unpaid bills after exceeding the time allowed for payment.
- Bills: Issuing invoices to the consumer at the beginning of each month where the system has been programmed to issue an invoice if the server date refers to the first day of the month or when the consumer requests the bill.
- Reports: Includes all consumer reports, invoices (daily and monthly), and counter status (active or not).

Fig. 10 shows the amount of kilowatt-hour was received by the My-SQL server for two consumers that were previously added to the energy consumption system through the consumer's page within the designed system, the date and time of the consumption.

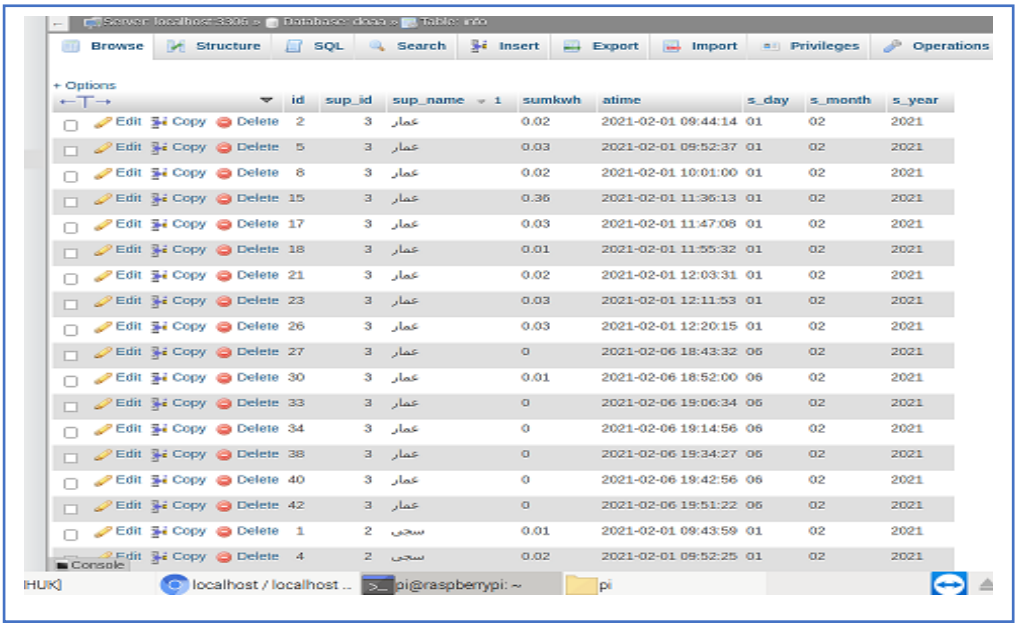

Fig. 10. The data was received from the smart meter for two consumers.

Table 1 shows a watt reading comparison of the smart meter between the simulation and the experimental setup for different load sets.

Table 1. Smart-Meter Reading.

Load steps	Power measurements (Watt) simulation	Power measurements (watt) Experimental
1	21	21.3
2	263	262.13
3	444	444.5
4	695	693.4

5 Conclusion

This paper presents a smaller, cheaper, faster scale, and wireless smart energy meter instead of the outdated energy meters. It is also relatively economical and direct to use, and at the same time provides high reliability. With the recent wireless meter system, it is possible to plan to read the values and monitor the meter readings continuously, and disconnected the power supply by the control center every time the user fails to pay the required bill on time without the need for human intervention. This feature is well managed by connected the consumer smart meter to a central control unit wirelessly. Moreover, it helps in avoiding the wrong readings that sometimes occur because of the local electricity meter readers' mistakes. Leading to save time, effort, and reduces the cost of maintenance. The designed meter provides many features that help the consumer knowing the amount of energy consumed, the bill, and the actual time for consumption. the consumer can access his account at any time he wants through his phone or Web page. All in all, the system simulation, and the smart energy meter implementation worked effectively and proves that they can replace the traditional electricity meters.

References

[1] A. S. Metering, S. Visalatchi and K. K. Sandeep, "Smart energy metering and power theft control using arduino & GSM," 2017 2nd International Conference for Convergence in Technology (I2CT), Mumbai, 2017, pp. 858-961, doi: 10.1109/I2CT.2017.8226251.

[2] M. Burunkaya and T. Pars, "A smart meter design and implementation using ZigBee based Wireless Sensor Network in Smart Grid," 2017 4th International Conference on Electrical and Electronic Engineering (ICEEE), Ankara, 2017, pp. 158-162, doi: 10.1109/ICEEE2.2017.7935812.

[3] Danielly B. Avancini, Joel J.P.C. Rodrigues, Simion G.B. Martins, Ricardo A.L. Rabelo , Jalal Al-Muhtadi d ,and Petar Solic " Energy meters evolution in smart grids: A review" Journal of Cleaner Production 217 (2019) 702e715

[4] H. G. R. Tan, C. H. Lee and V. H. Mok, "Automatic power meter reading system using GSM network," 2007 International Power Engineering Conference (IPEC 2007), Singapore, 2007, pp. 465-469.

[5] L. Quan-Xi and L.Gang "Design of remote automatic meter reading system based on ZigBee and GPRS"2010 ACADEMY PUBLISHER.

[6] K. Chooruang and K. Meekul, "Design of an IoT Energy Monitoring System," *2018 16th International Conference on ICT and Knowledge Engineering (ICT&KE)*, Bangkok, 2018, pp. 1-4, doi: 10.1109/ICTKE.2018.8612412.

[7] D. Balsamo, G. Gallo, D. Brunelli and L. Benini, "Non-intrusive Zigbee power meter for load monitoring in smart buildings," *2015 IEEE Sensors Applications Symposium (SAS)*, Zadar, Croatia, 2015, pp. 1-6, doi: 10.1109/SAS.2015.7133611.

[8] E. I. Abbas, M. E. Safi and M. A. Jaber, "Design and Implementation Prepaid Energy Meter Supported by RFID and GSM Technologies," 2018 International Conference on Advanced Science and Engineering (ICOASE), 2018, pp. 216-220, doi: 10.1109/ICOASE.2018.8548870.

[9] N. T. Surajudeen-Bakinde, S. O. Ayodele, N. T. Surajudeen-Bakinde, T. David Oloruntoba, A. O. Otuoze and N. Faruk, "Development of an Internet based prepaid energy meter," 2017 IEEE AFRICON, 2017, pp. 1370-1373, doi: 10.1109/AFRCON.2017.8095681.

[10] M. Istifanos, I.Tekahun " performance evaluation of Raspberry pi3 B and web server" faculty of computing, bleking institute of technology, SE-371 79 Karlskrona Sweden,2020

[11] K. Ashna and S. N. George, "GSM based automatic energy meter reading system with instant billing," *2013 International Mutli-Conference on Automation, Computing, Communication, Control and Compressed Sensing (iMac4s)*, Kottayam, India, 2013, pp. 65-72, doi: 10.1109/iMac4s.2013.6526385.

[12] "IEEE Standard Definitions for the Measurement of Electric Power Quantities Under Sinusoidal, Nonsinusoidal, Balanced, or Unbalanced Conditions," in *IEEE Std 1459-2010 (Revision of IEEE Std 1459-2000)* , vol., no., pp.1-50,19March2010,doi: 10.1109/IEEESTD.2010.5439063.

[13] M.Tahir,S.Muneeb , M.S.Jan and M.Hassan "Smart Energy Meter with Advanced Features and Billing System" *2019 4th International Electrical Engineering Conference(IEEC2019).*

Estimation of the parameters by using non-Bayesian in Modified Weibull Extension Distribution

Shaima'a B. Yass[1], Iden H. Al Kanani[2]
{shai.bader@yahoo.com[1], Iden_alkanani@yahoo.com [2]}

Al-Iraqia University, College of Engineering, Networks Engineering Department[1],
University of Baghdad, College of Science for Women, Department of Mathematics[2]

Abstract. In this paper, studying the modified Weibull extension model, and derive the estimators of three parameters by using maximum likelihood method, and ordinary least squares estimator method. Then by utilizing Monte Carlo method in simulation procedure for generate many various of samples sizes with many various of replicate the sample size. Finally, finding that the maximum likelihood method are the best values from the ordinary least squares method.

Keywords: Modified Weibull extension, Classical distribution methods, Newton Raphson method.

1 Introduction

There are number of application of Weibul distributions and modified Weibull distribution to modeling the test data in scientific research and life experiments. Also, number of research dealing with these models to estimate the parameters.

In 2002, Xie et al. [6], generalized the Weibull distribution to a modified Weibull extension, model with three parameters, and in 2005 [4], Nadarajah driving explicit algebraic formulas for the kth moment of the distribution. Furthermore , in 2012, Peng et al. [5], proposed comparative analysis to prove that the modified Weibull extension distribution is more accurate and flexible in modeling the satellite reliability than the classical Weibull distribution. The accuracy and convenience of the modified Weibull extension distribution indicates its practical application in health of living organisms and engineering designs. In 2018, Al Kanani and Kalt [3] using simulation to studied classical distribution methods of the modified Weibull distribution. In 2019, Al Kanani and Jalil [2] discussed some estimation method for new distribution (mixture distribution) to estimate the parameters. In 2021, Al Kanani and Ali [1] dealing with exponentiated Weibull as a special case of Weibul distributions for estimate the parameters. By the way, the aim of this research is estimating all the three parameters of the modified Weibull extension model, by using maximum likelihood estimator method, and ordinary least squares estimator method to show the best values of parameters.

This paper is organized as follows. In section 2 recalling the information of modified Weibull extension, such as probability density function, Cumulated distribution, the reliability function, and hazard function. Section 2, and section 3 are devoted to the parameter estimation, Maximum Likelihood Estimator, and Ordinary Least Squares Estimator, respectively. Some sample sizes are generating for the simulation procedure in section 4, to illustrate the application of the modified Weibull extension model. Finally, comparative studies by using mean square error are used in section 5.

IMDC-IST 2021, September 07-09, Sakarya, Turkey
Copyright © 2022 EAI
DOI 10.4108/eai.7-9-2021.2314887

2 Modified Weibull Extension Model

The probability density function of this model is:

$$f(x) = \theta\,\gamma\left(\frac{x}{\delta}\right)^{\gamma-1} e^{\left(\frac{x}{\delta}\right)^{\gamma} + \theta\delta\left(1-e^{\left(\frac{x}{\delta}\right)^{\gamma}}\right)}; \text{ for } x, \delta, \theta, \gamma > 0 \tag{1}$$

Where the shape parameter is γ, the scale parameters are δ, $and\ \theta$. And, the Cumulated distribution function is:

$$F(x) = \int_0^x f(t)dt = 1 - e^{\,\theta\delta\left(1-e^{\left(\frac{x}{\delta}\right)^{\gamma}}\right)},\ x > 0 \tag{2}$$

Where, the reliability function is:

$$\mathrm{R}(x) = \int_x^{\infty} f(t)dt = e^{\,\theta\delta\left(1-e^{\left(\frac{x}{\delta}\right)^{\gamma}}\right)},\ x > 0 \tag{3}$$

And, the hazard function:

$$h(x) = \frac{f(x)}{R(x)} = \theta\gamma\left(\frac{x}{\delta}\right)^{\gamma-1} e^{\left(\frac{x}{\delta}\right)^{\gamma}},\ x > 0 \tag{4}$$

3 Maximum Likelihood Estimator Method (MLE)

This method is one of the most widely utilizing in statistical estimation. It used to estimate the parameters of discrete and continuous distribution. The idea of this method is to find an estimate to parameter , say $\widehat{\boldsymbol{\theta}}(\boldsymbol{X})$, that maximize the likelihood (joint) function.
Taking the likelihood function of three parameters modified Weibull extension distribution to get:

$$L(\delta, \theta, \gamma;\ x_i) = \prod_{i=1}^{n} f(x_i\ ;\ \delta, \theta, \gamma) \tag{5}$$

That is:

$$L(\delta, \theta, \gamma;\ x_i) = \theta^n\,\gamma^n \prod_{i=1}^{n}\left(\frac{x_i}{\delta}\right)^{\gamma-1} e^{\sum_{i=1}^{n}\left[\left(\frac{x_i}{\delta}\right)^{\gamma} + \theta\delta\left(1-e^{\left(\frac{x_i}{\delta}\right)^{\gamma}}\right)\right]} \tag{6}$$

Taking the natural logarithm for the above function, to obtain:

$$LnL = n\,Ln\theta + n\,Ln\gamma + (\gamma-1)\sum_{i=1}^{n} Ln\left(\frac{x_i}{\delta}\right) + \sum_{i=1}^{n}\left[\left(\frac{x_i}{\delta}\right)^{\gamma} + \theta\delta\left(1-e^{\left(\frac{x_i}{\delta}\right)^{\gamma}}\right)\right] \tag{7}$$

The partial derivatives for the logarithm likelihood function with respect to parameters δ , θ and γ are :

$$f_1(\delta) = \frac{\partial Ln\,L}{\partial\delta}$$

$$f_1(\delta) = \frac{n}{\delta} - \frac{n\gamma}{\delta} + \sum_{i=1}^{n}\left[-\frac{\gamma}{\delta}\left(\frac{x_i}{\delta}\right)^{\gamma} + \theta\left(1-e^{\left(\frac{x_i}{\delta}\right)^{\gamma}}\right) + \theta\gamma\left(\frac{x_i}{\delta}\right)^{\gamma} e^{\left(\frac{x_i}{\delta}\right)^{\gamma}}\right] \tag{8}$$

$$g_1(\theta) = \frac{\partial Ln\, L}{\partial \theta} = \frac{n}{\theta} + \sum_{i=1}^{n}\left[\delta\left(1 - e^{\left(\frac{x_i}{\delta}\right)^{\gamma}}\right)\right] \tag{9}$$

$$h_1(\gamma) = \frac{\partial Ln\, L}{\partial \gamma}$$
$$= \frac{n}{\gamma} + \sum_{i=1}^{n} Ln\left(\frac{x_i}{\delta}\right) + \sum_{i=1}^{n}\left[\left(\frac{x_i}{\delta}\right)^{\gamma} Ln\left(\frac{x_i}{\delta}\right) - \theta\delta e^{\left(\frac{x_i}{\delta}\right)^{\gamma}}\left(\frac{x_i}{\delta}\right)^{\gamma} Ln\left(\frac{x_i}{\delta}\right)\right] \tag{10}$$

The above equations (8), (9), and (10), are system of non-linear equations, can be solved by using Newton – Raphson method. Thus we need the Jacobian matrix J_{K1}, which is:

$$J_{K1} = \begin{bmatrix} \frac{\partial f_1(\delta)}{\partial \delta} & \frac{\partial f_1(\delta)}{\partial \theta} & \frac{\partial f_1(\delta)}{\partial \gamma} \\ \frac{\partial g_1(\theta)}{\partial \delta} & \frac{\partial g_1(\theta)}{\partial \theta} & \frac{\partial g_1(\theta)}{\partial \gamma} \\ \frac{\partial h_1(\gamma)}{\partial \delta} & \frac{\partial h_1(\gamma)}{\partial \theta} & \frac{\partial h_1(\gamma)}{\partial \gamma} \end{bmatrix}$$

Where the pratial derivative are getting as follows:

$$\frac{\partial f_1(\delta)}{\partial \delta} = \frac{\partial^2 Ln\, L}{\partial^2 \delta}$$
$$\frac{\partial f_1(\delta)}{\partial \delta} = \frac{-n}{\delta^2} + \frac{n\gamma}{\delta^2} + \frac{\gamma}{\delta^2}\sum_{i=1}^{n}\left(\frac{x_i}{\delta}\right)^{\gamma} + \frac{\gamma^2}{\delta^2}\sum_{i=1}^{n}\left(\frac{x_i}{\delta}\right)^{\gamma} + \frac{\theta\gamma}{\delta}\sum_{i=1}^{n} e^{\left(\frac{x_i}{\delta}\right)^{\gamma}}\left(\frac{x_i}{\delta}\right)^{\gamma}$$
$$-\frac{\theta\gamma^2}{\delta}\sum_{i=1}^{n} e^{\left(\frac{x_i}{\delta}\right)^{\gamma}}\left(\frac{x_i}{\delta}\right)^{\gamma} - \frac{\theta\gamma^2}{\delta}\sum_{i=1}^{n} e^{\left(\frac{x_i}{\delta}\right)^{\gamma}}\left(\frac{x_i}{\delta}\right)^{2\gamma} \tag{11}$$

$$\frac{\partial f_1(\delta)}{\partial \theta} = \frac{\partial^2 Ln\, L}{\partial \theta \partial \delta}$$
$$\frac{\partial f_1(\delta)}{\partial \theta} = n - \sum_{i=1}^{n} e^{\left(\frac{x_i}{\delta}\right)^{\gamma}} + \gamma\sum_{i=1}^{n} e^{\left(\frac{x_i}{\delta}\right)^{\gamma}}\left(\frac{x_i}{\delta}\right)^{\gamma} \tag{12}$$

$$\frac{\partial f_1(\delta)}{\partial \gamma} = \frac{\partial^2 Ln\, L}{\partial \gamma \partial \delta}$$
$$\frac{\partial f_1(\delta)}{\partial \gamma} = \frac{-n}{\delta} - \frac{1}{\delta}\sum_{i=1}^{n}\left(\frac{x_i}{\delta}\right)^{\gamma} - \frac{\gamma}{\delta}\sum_{i=1}^{n}\left(\frac{x_i}{\delta}\right)^{\gamma} Ln\left(\frac{x_i}{\delta}\right) - \theta\sum_{i=1}^{n} e^{\left(\frac{x_i}{\delta}\right)^{\gamma}}\left(\frac{x_i}{\delta}\right)^{\gamma}$$

$$Ln(\frac{x_i}{\delta}) + \theta \sum_{i=1}^{n} e^{(\frac{x_i}{\delta})^{\gamma}} \left(\frac{x_i}{\delta}\right)^{\gamma} + \theta\gamma \sum_{i=1}^{n} e^{(\frac{x_i}{\delta})^{\gamma}} \left(\frac{x_i}{\delta}\right)^{\gamma} Ln(\frac{x_i}{\delta}) +$$

$$\theta\gamma \sum_{i=1}^{n} e^{(\frac{x_i}{\delta})^{\gamma}} \left(\frac{x_i}{\delta}\right)^{2\gamma} Ln(\frac{x_i}{\delta}) \tag{13}$$

$$\frac{\partial g_1(\theta)}{\partial \delta} = \frac{\partial^2 Ln\, L}{\partial \delta \partial \theta} = \frac{\partial f_1(\delta)}{\partial \theta} \tag{14}$$

$$\frac{\partial g_1(\theta)}{\partial \theta} = \frac{\partial^2 Ln\, L}{\partial \theta^2} = \frac{-n}{\theta^2} \tag{15}$$

$$\frac{\partial g_1(\theta)}{\partial \gamma} = \frac{\partial^2 Ln\, L}{\partial \gamma \partial \theta} = -\delta \sum_{i=1}^{n} e^{(\frac{x_i}{\delta})^{\gamma}} \left(\frac{x_i}{\delta}\right)^{\gamma} Ln(\frac{x_i}{\delta}) \tag{16}$$

$$\frac{\partial h_1(\gamma)}{\partial \delta} = \frac{\partial^2 Ln\, L}{\partial \delta \partial \gamma} = \frac{\partial f_1(\delta)}{\partial \gamma} \tag{17}$$

$$\frac{\partial h_1(\gamma)}{\partial \theta} = \frac{\partial^2 Ln\, L}{\partial \theta \partial \gamma} = \frac{\partial g_1(\theta)}{\partial \gamma} \tag{18}$$

$$\frac{\partial h_1(\gamma)}{\partial \gamma} = \frac{\partial^2 Ln\, L}{\partial \gamma^2}$$

$$\frac{\partial h_1(\gamma)}{\partial \gamma} = \frac{-n}{\gamma^2} + \sum_{i=1}^{n} \left(Ln(\frac{x_i}{\delta})\right)^2 \left(\frac{x_i}{\delta}\right)^{\gamma} - \theta\delta \sum_{i=1}^{n} \left(Ln(\frac{x_i}{\delta})\right)^2 \left(\frac{x_i}{\delta}\right)^{\gamma} e^{(\frac{x_i}{\delta})^{\gamma}}$$

$$-\theta\delta \sum_{i=1}^{n} \left(Ln(\frac{x_i}{\delta})\right)^2 \left(\frac{x_i}{\delta}\right)^{2\gamma} e^{(\frac{x_i}{\delta})^{\gamma}} \tag{19}$$

Thus, all above equations in section 3, proved that the Jacobian matrix J_{K1} is non-singular symmetric matrix, therefore:

$$\begin{bmatrix} \delta_{k+1} \\ \theta_{k+1} \\ \gamma_{k+1} \end{bmatrix} = \begin{bmatrix} \delta_k \\ \theta_k \\ \gamma_k \end{bmatrix} - {J_{K1}}^{-1} \begin{bmatrix} f_1(\delta_k) \\ g_1(\theta_k) \\ h_1(\gamma_k) \end{bmatrix}$$

4 Ordinary Least Squares Estimator Method (OLS)

This method is one of the most popular technique, to estimate the parameters when the models is linear and nonlinear in variables. The idea of this method is to minimize the sum squared differences between observed sample and the expected sample, as follows:

$$\sum_{i=1}^{n} {\epsilon_i}^2 = \sum_{i=1}^{n} [Y_i - E(Y_i)]^2 \tag{20}$$

Now, applying this method to minimize the sum squared difference between the estimate of cumulative distribution function, and the empirical cumulative distribution function, thus:

$$\sum_{i=1}^{n} {\epsilon_i}^2 = \sum_{i=1}^{n} \left[F(x_i) - \hat{F}(x_i)\right]^2 \tag{21}$$

Where empirical cumulative distribution function is:

$$F(x_i) = \frac{i - 0.5}{n} \tag{22}$$

Thus:

$$\sum_{i=1}^{n} {\epsilon_i}^2 = \sum_{i=1}^{n} [\frac{n - i + 0.5}{n} - e^{\theta\delta(1-e^{\left(\frac{x_i}{\delta}\right)^\gamma})}]^2 \tag{23}$$

The partial derivatives for the logarithm likelihood function with respect to parameters δ , θ and γ are :

$$f_2(\delta) = \frac{\partial \sum_{i=1}^{n} {\epsilon_i}^2}{\partial \delta}$$

$$f_2(\delta) = -2\theta \sum_{i=1}^{n} \left[\frac{n - i + 0.5}{n} e^{\theta\delta(1-e^{\left(\frac{x_i}{\delta}\right)^\gamma})} - e^{2\theta\delta(1-e^{\left(\frac{x_i}{\delta}\right)^\gamma})}\right]\left[1 - e^{\left(\frac{x_i}{\delta}\right)^\gamma} + \gamma e^{\left(\frac{x_i}{\delta}\right)^\gamma} \left(\frac{x_i}{\delta}\right)^\gamma\right] \tag{24}$$

$$g_2(\theta) = \frac{\partial \sum_{i=1}^{n} {\epsilon_i}^2}{\partial \theta}$$

$$g_2(\theta) = -2\delta \sum_{i=1}^{n} \left[\frac{n - i + 0.5}{n} e^{\theta\delta(1-e^{\left(\frac{x_i}{\delta}\right)^\gamma})} - e^{2\theta\delta(1-e^{\left(\frac{x_i}{\delta}\right)^\gamma})}\right](1 - e^{\left(\frac{x_i}{\delta}\right)^\gamma}) \tag{25}$$

$$h_2(\gamma) = \frac{\partial \sum_{i=1}^{n} {\epsilon_i}^2}{\partial \gamma}$$

$$h_2(\gamma) = 2\theta\delta \sum_{i=1}^{n} \left[\frac{n - i + 0.5}{n} e^{\theta\delta(1-e^{\left(\frac{x_i}{\delta}\right)^\gamma})+\left(\frac{x_i}{\delta}\right)^\gamma} - e^{2\theta\delta(1-e^{\left(\frac{x_i}{\delta}\right)^\gamma})+\left(\frac{x_i}{\delta}\right)^\gamma}\right] \left(\frac{x_i}{\delta}\right)^\gamma Ln\left(\frac{x_i}{\delta}\right) \tag{26}$$

The above equations (24), (25), and (26) are system of non-linear equations, can be solved by using Newton – Raphson method. Thus we need the Jacobian matrix J_{K2}, which is:

$$J_{K2} = \begin{bmatrix} \frac{\partial f_2(\delta)}{\partial \delta} & \frac{\partial f_2(\delta)}{\partial \theta} & \frac{\partial f_2(\delta)}{\partial \gamma} \\ \frac{\partial g_2(\theta)}{\partial \delta} & \frac{\partial g_2(\theta)}{\partial \theta} & \frac{\partial g_2(\theta)}{\partial \gamma} \\ \frac{\partial h_2(\gamma)}{\partial \delta} & \frac{\partial h_2(\gamma)}{\partial \theta} & \frac{\partial h_2(\gamma)}{\partial \gamma} \end{bmatrix}$$

Where the pratial derivative are getting as follows:

$$\frac{\partial f_2(\delta)}{\partial \delta} = \frac{\partial^2 \sum_{i=1}^{n} {\epsilon_i}^2}{\partial^2 \delta}$$

$$\begin{aligned} \frac{\partial f_2(\delta)}{\partial \delta} = -2 \sum_{i=1}^{n} \Bigg[& \left\{ \frac{n-i+0.5}{n} e^{\theta\delta\left(1-e^{\left(\frac{x_i}{\delta}\right)^{\gamma}}\right)} \left(\theta\left(1-e^{\left(\frac{x_i}{\delta}\right)^{\gamma}}\right) + \theta\gamma\, e^{\left(\frac{x_i}{\delta}\right)^{\gamma}} \left(\frac{x_i}{\delta}\right)^{\gamma} \right) \right. \\ & \left. - e^{2\theta\delta\left(1-e^{\left(\frac{x_i}{\delta}\right)^{\gamma}}\right)} \left(2\theta\left(1-e^{\left(\frac{x_i}{\delta}\right)^{\gamma}}\right) + 2\theta\gamma\, e^{\left(\frac{x_i}{\delta}\right)^{\gamma}} \left(\frac{x_i}{\delta}\right)^{\gamma} \right) \right\} \left\{ \theta\left(1-e^{\left(\frac{x_i}{\delta}\right)^{\gamma}}\right) + \theta\gamma \right. \\ & \left. e^{\left(\frac{x_i}{\delta}\right)^{\gamma}} \left(\frac{x_i}{\delta}\right)^{\gamma} \right\} + \left\{ \frac{n-i+0.5}{n} e^{\theta\delta\left(1-e^{\left(\frac{x_i}{\delta}\right)^{\gamma}}\right)} - e^{2\theta\delta\left(1-e^{\left(\frac{x_i}{\delta}\right)^{\gamma}}\right)} \right\} \left\{ \frac{\theta\gamma}{\delta} e^{\left(\frac{x_i}{\delta}\right)^{\gamma}} \left(\frac{x_i}{\delta}\right)^{\gamma} \right. \\ & \left. - \frac{\theta\gamma^2}{\delta} e^{\left(\frac{x_i}{\delta}\right)^{\gamma}} \left(\frac{x_i}{\delta}\right)^{2\gamma} - \frac{\theta\gamma^2}{\delta} e^{\left(\frac{x_i}{\delta}\right)^{\gamma}} \left(\frac{x_i}{\delta}\right)^{\gamma} \right\} \Bigg] \end{aligned} \tag{27}$$

$$\frac{\partial f_2(\delta)}{\partial \theta} = \frac{\partial^2 \sum_{i=1}^{n} {\epsilon_i}^2}{\partial \theta \partial \delta}$$

$$\begin{aligned} \frac{\partial f_2(\delta)}{\partial \theta} = -2 \sum_{i=1}^{n} \Bigg[& -e^{2\theta\delta\left(1-e^{\left(\frac{x_i}{\delta}\right)^{\gamma}}\right)} \delta\left(1-e^{\left(\frac{x_i}{\delta}\right)^{\gamma}}\right) \left(\theta\left(1-e^{\left(\frac{x_i}{\delta}\right)^{\gamma}}\right) + \theta\gamma e^{\left(\frac{x_i}{\delta}\right)^{\gamma}} \right. \\ & \left. \left(\frac{x_i}{\delta}\right)^{\gamma} \right) + \left(\frac{n-i+0.5}{n} - e^{\theta\delta\left(1-e^{\left(\frac{x_i}{\delta}\right)^{\gamma}}\right)} \right) e^{\theta\delta\left(1-e^{\left(\frac{x_i}{\delta}\right)^{\gamma}}\right)} \delta\left(1-e^{\left(\frac{x_i}{\delta}\right)^{\gamma}}\right) \left(\theta\left(1-e^{\left(\frac{x_i}{\delta}\right)^{\gamma}}\right) \right. \\ & \left. + \theta\gamma e^{\left(\frac{x_i}{\delta}\right)^{\gamma}} \left(\frac{x_i}{\delta}\right)^{\gamma} \right) + \left(\frac{n-i+0.5}{n} - e^{\theta\delta\left(1-e^{\left(\frac{x_i}{\delta}\right)^{\gamma}}\right)} \right) e^{\theta\delta\left(1-e^{\left(\frac{x_i}{\delta}\right)^{\gamma}}\right)} \left(1-e^{\left(\frac{x_i}{\delta}\right)^{\gamma}}\right) + \\ & + \left(\frac{n-i+0.5}{n} - e^{\theta\delta\left(1-e^{\left(\frac{x_i}{\delta}\right)^{\gamma}}\right)} \right) e^{\theta\delta\left(1-e^{\left(\frac{x_i}{\delta}\right)^{\gamma}}\right)} \gamma\, e^{\left(\frac{x_i}{\delta}\right)^{\gamma}} \left(\frac{x_i}{\delta}\right)^{\gamma} \Bigg] \end{aligned} \tag{28}$$

$$\frac{\partial f_2(\delta)}{\partial \gamma} = \frac{\partial^2 \sum_{i=1}^{n} {\epsilon_i}^2}{\partial \gamma \partial \delta}$$

$$\frac{\partial f_2(\delta)}{\partial \gamma} = 2\theta \sum_{i=1}^{n} \left[\frac{n-i+0.5}{n} e^{\theta\delta\left(1-e^{\left(\frac{x_i}{\delta}\right)^{\gamma}}\right)} \theta\delta e^{\left(\frac{x_i}{\delta}\right)^{\gamma}} \left(\frac{x_i}{\delta}\right)^{\gamma} Ln\left(\frac{x_i}{\delta}\right)(1 \right.$$

$$-e^{\left(\frac{x_i}{\delta}\right)^{\gamma}}) + \frac{n-i+0.5}{n} e^{\theta\delta\left(1-e^{\left(\frac{x_i}{\delta}\right)^{\gamma}}\right)} \theta\delta\gamma\, e^{2\left(\frac{x_i}{\delta}\right)^{\gamma}} \left(\frac{x_i}{\delta}\right)^{2\gamma} Ln\left(\frac{x_i}{\delta}\right) - 2$$

$$e^{2\theta\delta\left(1-e^{\left(\frac{x_i}{\delta}\right)^{\gamma}}\right)} \theta\delta e^{\left(\frac{x_i}{\delta}\right)^{\gamma}} \left(\frac{x_i}{\delta}\right)^{\gamma} Ln\left(\frac{x_i}{\delta}\right) (1 - e^{\left(\frac{x_i}{\delta}\right)^{\gamma}}) - 2\theta\delta\gamma e^{2\theta\delta\left(1-e^{\left(\frac{x_i}{\delta}\right)^{\gamma}}\right)}$$

$$e^{2\left(\frac{x_i}{\delta}\right)^{\gamma}} \left(\frac{x_i}{\delta}\right)^{2\gamma} Ln\left(\frac{x_i}{\delta}\right) + \frac{n-i+0.5}{n} e^{\theta\delta\left(1-e^{\left(\frac{x_i}{\delta}\right)^{\gamma}}\right)} e^{\left(\frac{x_i}{\delta}\right)^{\gamma}} \left(\frac{x_i}{\delta}\right)^{\gamma} Ln\left(\frac{x_i}{\delta}\right) -$$

$$\frac{n-i+0.5}{n} e^{\theta\delta\left(1-e^{\left(\frac{x_i}{\delta}\right)^{\gamma}}\right)} e^{\left(\frac{x_i}{\delta}\right)^{\gamma}} \left(\frac{x_i}{\delta}\right)^{\gamma} - \frac{n-i+0.5}{n} e^{\theta\delta\left(1-e^{\left(\frac{x_i}{\delta}\right)^{\gamma}}\right)} \gamma e^{\left(\frac{x_i}{\delta}\right)^{\gamma}}$$

$$\left(\frac{x_i}{\delta}\right)^{2\gamma} Ln\left(\frac{x_i}{\delta}\right) - \frac{n-i+0.5}{n} e^{\theta\delta\left(1-e^{\left(\frac{x_i}{\delta}\right)^{\gamma}}\right)} \gamma e^{\left(\frac{x_i}{\delta}\right)^{\gamma}} \left(\frac{x_i}{\delta}\right)^{\gamma} Ln\left(\frac{x_i}{\delta}\right) - e^{2\theta\delta\left(1-e^{\left(\frac{x_i}{\delta}\right)^{\gamma}}\right)}$$

$$e^{\left(\frac{x_i}{\delta}\right)^{\gamma}} \left(\frac{x_i}{\delta}\right)^{\gamma} Ln\left(\frac{x_i}{\delta}\right) + e^{2\theta\delta\left(1-e^{\left(\frac{x_i}{\delta}\right)^{\gamma}}\right)} e^{\left(\frac{x_i}{\delta}\right)^{\gamma}} \left(\frac{x_i}{\delta}\right)^{\gamma} + \gamma e^{2\theta\delta\left(1-e^{\left(\frac{x_i}{\delta}\right)^{\gamma}}\right)} e^{\left(\frac{x_i}{\delta}\right)^{\gamma}}$$

$$\left. \left(\frac{x_i}{\delta}\right)^{2\gamma} Ln\left(\frac{x_i}{\delta}\right) + \gamma e^{2\theta\delta\left(1-e^{\left(\frac{x_i}{\delta}\right)^{\gamma}}\right)} e^{\left(\frac{x_i}{\delta}\right)^{\gamma}} \left(\frac{x_i}{\delta}\right)^{\gamma} Ln\left(\frac{x_i}{\delta}\right) \right] \tag{29}$$

$$\frac{\partial g_2(\theta)}{\partial \delta} = \frac{\partial^2 \sum_{i=1}^{n} {\epsilon_i}^2}{\partial\delta\partial\theta} = \frac{\partial f_2(\delta)}{\partial \theta} \tag{30}$$

$$\frac{\partial g_2(\theta)}{\partial \theta} = \frac{\partial^2 \sum_{i=1}^{n} {\epsilon_i}^2}{\partial\theta^2}$$

$$\frac{\partial g_2(\theta)}{\partial \theta} = -2\delta^2 \sum_{i=1}^{n} (1 - e^{\left(\frac{x_i}{\delta}\right)^{\gamma}})^2 e^{\theta\delta\left(1-e^{\left(\frac{x_i}{\delta}\right)^{\gamma}}\right)} \left[\frac{n-i+0.5}{n} - 2e^{\theta\delta\left(1-e^{\left(\frac{x_i}{\delta}\right)^{\gamma}}\right)} \right] \tag{31}$$

$$\frac{\partial g_2(\theta)}{\partial \gamma} = \frac{\partial^2 \sum_{i=1}^{n} {\epsilon_i}^2}{\partial\gamma\partial\theta}$$

$$\frac{\partial g_2(\theta)}{\partial \gamma} = 2\delta \sum_{i=1}^{n} \left[\frac{n-i+0.5}{n} \theta\delta\, e^{\left(\frac{x_i}{\delta}\right)^{\gamma}} \left(\frac{x_i}{\delta}\right)^{\gamma} Ln\left(\frac{x_i}{\delta}\right)(1 - e^{\left(\frac{x_i}{\delta}\right)^{\gamma}}) \right.$$

$$e^{\theta\delta\left(1-e^{\left(\frac{x_i}{\delta}\right)^{\gamma}}\right)} - 2\theta\delta e^{2\theta\delta\left(1-e^{\left(\frac{x_i}{\delta}\right)^{\gamma}}\right)} e^{\left(\frac{x_i}{\delta}\right)^{\gamma}} \left(\frac{x_i}{\delta}\right)^{\gamma} Ln\left(\frac{x_i}{\delta}\right)(1 - e^{\left(\frac{x_i}{\delta}\right)^{\gamma}}) +$$

$$\left. \frac{n-i+0.5}{n} e^{\theta\delta\left(1-e^{\left(\frac{x_i}{\delta}\right)^{\gamma}}\right)} e^{\left(\frac{x_i}{\delta}\right)^{\gamma}} \left(\frac{x_i}{\delta}\right)^{\gamma} Ln\left(\frac{x_i}{\delta}\right) - e^{2\theta\delta\left(1-e^{\left(\frac{x_i}{\delta}\right)^{\gamma}}\right)} e^{\left(\frac{x_i}{\delta}\right)^{\gamma}} \left(\frac{x_i}{\delta}\right)^{\gamma} Ln\left(\frac{x_i}{\delta}\right) \right] \tag{32}$$

$$\frac{\partial h_2(\gamma)}{\partial \delta} = \frac{\partial^2 \sum_{i=1}^{n} {\epsilon_i}^2}{\partial \delta \partial \gamma} = \frac{\partial f_2(\delta)}{\partial \gamma} \tag{33}$$

$$\frac{\partial h_2(\gamma)}{\partial \theta} = \frac{\partial^2 \sum_{i=1}^{n} {\epsilon_i}^2}{\partial \theta \partial \gamma} = \frac{\partial g_2(\theta)}{\partial \gamma} \tag{34}$$

$$\frac{\partial h_2(\gamma)}{\partial \gamma} = \frac{\partial^2 \sum_{i=1}^{n} {\epsilon_i}^2}{\partial \gamma^2}$$

$$\begin{aligned}\frac{\partial h_2(\gamma)}{\partial \gamma} = 2\theta\delta \sum_{i=1}^{n} Ln(\frac{x_i}{\delta}) \Big[\Big\{-\theta\delta(\frac{n-i+0.5}{n})\, e^{\theta\delta(1-e^{\left(\frac{x_i}{\delta}\right)^{\gamma}})} e^{2\left(\frac{x_i}{\delta}\right)^{\gamma}} \left(\frac{x_i}{\delta}\right)^{\gamma} Ln(\frac{x_i}{\delta}) \\ + \frac{n-i+0.5}{n} e^{\theta\delta(1-e^{\left(\frac{x_i}{\delta}\right)^{\gamma}})} e^{\left(\frac{x_i}{\delta}\right)^{\gamma}} \left(\frac{x_i}{\delta}\right)^{\gamma} Ln(\frac{x_i}{\delta}) + 2\theta\delta e^{2\theta\delta(1-e^{\left(\frac{x_i}{\delta}\right)^{\gamma}})} \\ e^{2\left(\frac{x_i}{\delta}\right)^{\gamma}} \left(\frac{x_i}{\delta}\right)^{\gamma} Ln(\frac{x_i}{\delta}) - e^{2\theta\delta(1-e^{\left(\frac{x_i}{\delta}\right)^{\gamma}})} e^{\left(\frac{x_i}{\delta}\right)^{\gamma}} \left(\frac{x_i}{\delta}\right)^{\gamma} Ln(\frac{x_i}{\delta})\Big\}\Big\{\left(\frac{x_i}{\delta}\right)^{\gamma}\Big\} \\ + \frac{n-i+0.5}{n} e^{\theta\delta(1-e^{\left(\frac{x_i}{\delta}\right)^{\gamma}})} e^{\left(\frac{x_i}{\delta}\right)^{\gamma}} \left(\frac{x_i}{\delta}\right)^{\gamma} Ln\left(\frac{x_i}{\delta}\right) - e^{2\theta\delta(1-e^{\left(\frac{x_i}{\delta}\right)^{\gamma}})} e^{\left(\frac{x_i}{\delta}\right)^{\gamma}} \\ \left(\frac{x_i}{\delta}\right)^{\gamma} Ln(\frac{x_i}{\delta})\Big]\end{aligned} \tag{35}$$

Thus, all above equations in section 4, proved that the Jacobian matrix J_{K2} is non-singular symmetric matrix, therefore:

$$\begin{bmatrix}\delta_{k+1}\\ \theta_{k+1}\\ \gamma_{k+1}\end{bmatrix} = \begin{bmatrix}\delta_k\\ \theta_k\\ \gamma_k\end{bmatrix} - {J_{K2}}^{-1} \begin{bmatrix}f_2(\delta_k)\\ g_2(\theta_k)\\ h_2(\gamma_k)\end{bmatrix}$$

5. Simulation Results

The Monte Carlo method is most popular method in simulation techniques using to generate the observations (samples) for any distribution. The simulation process is flexibility, and gave ability for the test and experimenting by frequency many time.

1- To apply Monte Carlo method for modified Weibull extension, we use the cumulative distribution function as follows:

$$F(x) = 1 - e^{\theta\delta(1-e^{\left(\frac{x}{\delta}\right)^{\gamma}})} \tag{36}$$

By substitute $F(x)$ as u, with a random number, then $u = F(x)$, that is $x = F^{-1}(u)$. Thus

$$e^{\theta\delta(1-e^{\left(\frac{x}{\delta}\right)^{\gamma}})} = 1 - u$$

$$\theta\delta(1 - e^{\left(\frac{x}{\delta}\right)^{\gamma}}) = Ln(1-u)$$

$$(1 - e^{\left(\frac{x}{\delta}\right)^{\gamma}}) = \frac{Ln(1-u)}{\theta\delta}$$

$$e^{\left(\frac{x}{\delta}\right)^{\gamma}} = 1 - \frac{Ln(1-u)}{\theta\delta}$$

$$\left(\frac{x}{\delta}\right)^{\gamma} = Ln(1 - \frac{Ln(1-u)}{\theta\delta})$$

$$x^{\gamma} = \delta^{\gamma} Ln(1 - \frac{Ln(1-u)}{\theta\delta})$$

$$x = \left(\delta^{\gamma} Ln(1 - \tfrac{Ln(1-u)}{\theta\delta})\right)^{\frac{1}{\gamma}} \quad (37)$$

2- Selected many different sample size
(n = 10, 20, 30, 50, 100).
3- Replicate to each experiment as (m =1000, 2500, 5000).
4- Plot a system of six-nonlinear equations,

$\begin{bmatrix} f_1(\delta) \\ g_1(\theta) \\ h_1(\gamma) \\ f_2(\delta) \\ g_2(\theta) \\ h_2(\gamma) \end{bmatrix} = \begin{bmatrix} 0 \\ 0 \\ 0 \\ 0 \\ 0 \\ 0 \end{bmatrix}$, For one of above sample sizes, for example, taking samples sizes (n =100), and sample replications (m =5000), can assist in finding initial approximations for both estimator methods, to find the values of parameters in two estimator methods. The plot is depicted in **Fig.1.**

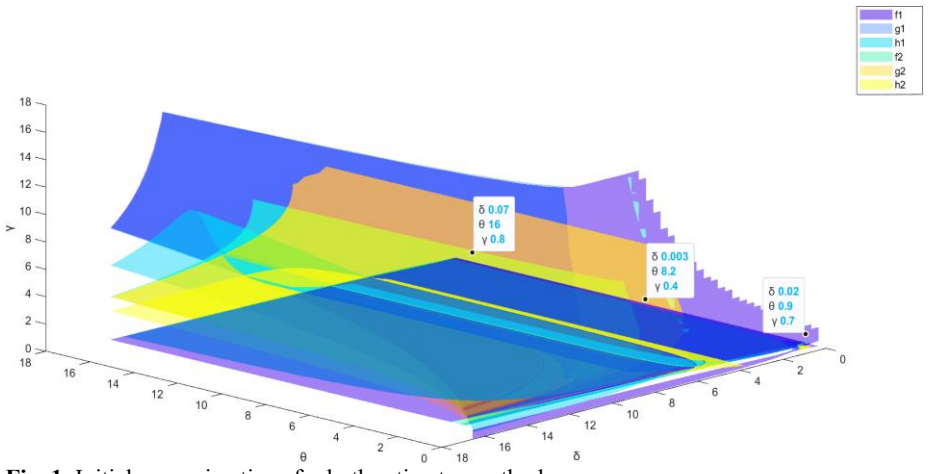

Fig. 1. Initial approximations for both estimator methods.

5-Selected the assumed values for the parameters
$\boldsymbol{\delta}$ = 0.07, 0.003, 0.02
$\boldsymbol{\theta}$ = 16.0, 8.2, 0.9
$\boldsymbol{\gamma}$ = 0.8, 0.4, 0.7.
6- To employ mesure of mean square error to compare between two methods of estimation given by the following formula $MSE(\hat{\theta}) = \frac{1}{m}\sum_{i=1}^{m}(\hat{\theta}_i - \theta)^2$, where $\hat{\theta}$ is the estimate of δ, θ, γ

7- For illustrating the basics of the process in MLE, explaining the first iteration for finding the first estimating of $\boldsymbol{\delta_1}$, $\boldsymbol{\theta_1}$, $\boldsymbol{\gamma_1}$, at first initial guess in Simulink as follows, with m=5000, n=100

Finding J_{K1} at first initial guess $\boldsymbol{\delta_0 = 0.02}$, $\boldsymbol{\theta_0 = 0.9}$, $\boldsymbol{\gamma_0 = 0.7}$, And finding $\begin{bmatrix} f_1(\delta) \\ g_1(\theta) \\ h_1(\gamma) \end{bmatrix}$ at first initial guess $\boldsymbol{\delta_0}$, $\boldsymbol{\theta_0}$, $\boldsymbol{\gamma_0}$, And applying

$J_{K1} \begin{bmatrix} \boldsymbol{\delta_1} \\ \boldsymbol{\theta_1} \\ \boldsymbol{\gamma_1} \end{bmatrix} - \begin{bmatrix} f_1(\delta) \\ g_1(\theta) \\ h_1(\gamma) \end{bmatrix} = 0$, which determined as $f(z) = \begin{bmatrix} a_1\boldsymbol{\delta_1} + a_2\boldsymbol{\delta_{1+}}a_3\boldsymbol{\delta_{1+}}a_4 \\ a_5\boldsymbol{\theta_1} + a_6\boldsymbol{\theta_1} + a_7\boldsymbol{\theta_1} + a_8 \\ a_9\boldsymbol{\gamma_1} + a_{10}\boldsymbol{\gamma_1} + a_{11}\boldsymbol{\gamma_1} + a_{12} \end{bmatrix} = 0$

After solving the above equation, adding the result with the first initial guess, to obtain the estimator for the first parameter $\boldsymbol{\delta_1}$, the second parameter $\boldsymbol{\theta_1}$, and the third parameter $\boldsymbol{\gamma_1}$, then finding the first iteration of mean square error for parameters, the process is depicted in **Fig.2.** By the same way for the process in OLS.

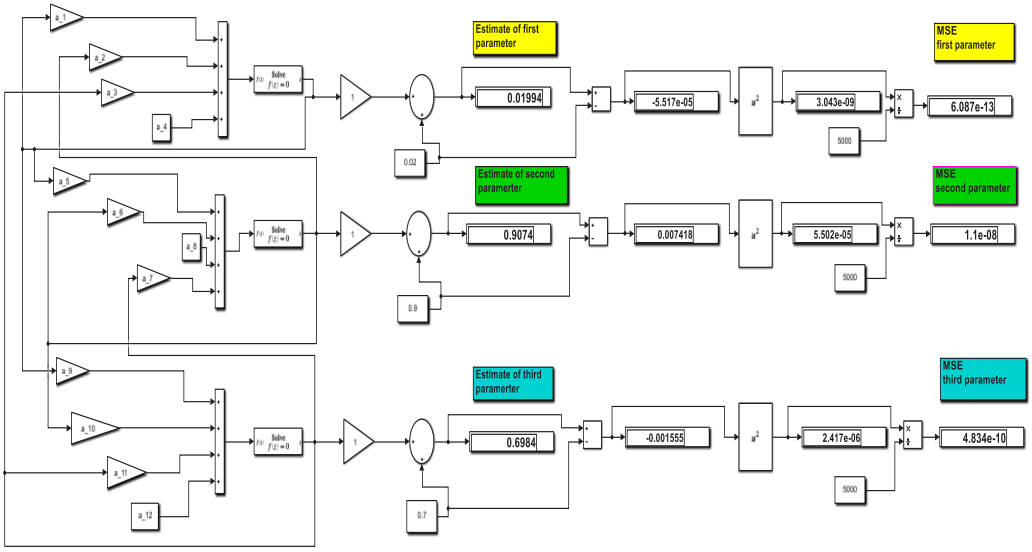

Fig. 2. The process in MLE, for the first iteration.

Table 1. MSE for the estimation of δ at **E1 {' δ = 0.02'} {' θ = 0.9'} {' γ = 0.7'}.**

m	n	MLE	OLS	best
1000	10	7.4699 e-09	1.5353 e-05	MLE
	20	7.7755 e-09	1.5102 e-05	MLE
	30	7.8831 e-09	1.4979 e-05	MLE
	50	7.6583 e-09	1.4895 e-05	MLE
	100	7.6147 e-09	1.4833 e-05	MLE
2500	10	7.5737 e-09	1.5424 e-05	MLE
	20	7.7216 e-09	1.5101 e-05	MLE
	30	7.593 e-09	1.4972 e-05	MLE
	50	7.579 e-09	1.4853 e-05	MLE
	100	7.7307 e-09	1.4796 e-05	MLE
5000	10	7.7353 e-09	1.5498 e-05	MLE
	20	7.6006 e-09	1.5054 e-05	MLE
	30	7.5871 e-09	1.4974 e-05	MLE
	50	7.7125 e-09	1.4878 e-05	MLE
	100	7.6811 e-09	1.4812 e-05	MLE

Table 2. MSE for the estimation of θ at **E1 {' δ = 0.02'} {' θ = 0.9'} {' γ = 0.7'}.**

m	n	MLE	OLS	best
1000	10	0.00010051	0.19623	MLE
	20	0.00010313	0.1969	MLE
	30	0.00010396	0.19737	MLE
	50	0.00010201	0.19756	MLE
	100	0.00010189	0.19773	MLE
2500	10	0.00010155	0.19588	MLE
	20	0.00010273	0.19692	MLE
	30	0.00010175	0.19724	MLE
	50	0.00010163	0.19761	MLE
	100	0.00010301	0.19788	MLE
5000	10	0.00010276	0.1958	MLE
	20	0.00010164	0.19709	MLE
	30	0.00010169	0.1973	MLE
	50	0.00010264	0.1963	MLE
	100	0.00010242	0.19783	MLE

Table 3. MSE for the estimation of γ at **E1** {' δ = 0.02'} {' θ = 0.9'} {' γ = 0.7'}.

m	n	MLE	OLS	best
1000	10	5.5494 e-06	0.011528	MLE
	20	5.7568 e-06	0.011417	MLE
	30	5.8284 e-06	0.011367	MLE
	50	5.6752 e-06	0.011326	MLE
	100	5.6499 e-06	0.011296	MLE
2500	10	5.6224 e-06	0.011555	MLE
	20	5.7213 e-06	0.011418	MLE
	30	5.6361 e-06	0.011356	MLE
	50	5.6267 e-06	0.011302	MLE
	100	5.7311 e-06	0.011278	MLE
5000	10	5.7288 e-06	0.011596	MLE
	20	5.6381 e-06	0.011395	MLE
	30	5.6318 e-06	0.011359	MLE
	50	5.715 e-06	0.011317	MLE
	100	5.6945 e-06	0.011287	MLE

Table 4. MSE for the estimation of δ at **E2** {' δ = 0.003'} {' θ = 8.2'} {' γ = 0.4'}

m	n	MLE	OLS	best
1000	10	4.151 e-09	9.7399 e-07	MLE
	20	4.265 e-09	9.6521 e-07	MLE
	30	4.2976 e-09	9.6219 e-07	MLE
	50	4.2103 e-09	9.5829 e-07	MLE
	100	4.2078 e-09	9.5573 e-07	MLE
2500	10	4.1923 e-09	9.7461 e-07	MLE
	20	4.2451 e-09	9.6549 e-07	MLE
	30	4.2011 e-09	9.598 e-07	MLE
	50	4.1966 e-09	9.558 e-07	MLE
	100	4.2524 e-09	9.5453 e-07	MLE
5000	10	4.2445 e-09	9.7905 e-07	MLE
	20	4.1962 e-09	9.637 e-07	MLE
	30	4.1972 e-09	9.6058 e-07	MLE
	50	4.2403 e-09	9.5771 e-07	MLE
	100	4.2296 e-09	9.5536 e-07	MLE

Table 5. MSE for the estimation of θ at **E2** {' δ = 0.003'} {' θ = 8.2'} {' γ = 0.4'}

m	n	MLE	OLS	best
1000	10	0.084508	1.675	MLE
	20	0.08583	1.723	MLE
	30	0.086261	1.747	MLE
	50	0.085138	1.768	MLE
	100	0.08535	1.78	MLE
2500	10	0.085168	1.671	MLE
	20	0.085797	1.722	MLE
	30	0.085291	1.753	MLE
	50	0.085382	1.774	MLE
	100	0.085841	1.79	MLE
5000	10	0.08567	1.655	MLE
	20	0.085215	1.735	MLE
	30	0.08517	1.751	MLE
	50	0.085642	1.77	MLE
	100	0.085582	1.783	MLE

Table 6. MSE for the estimation of γ at **E2** {' δ = 0.003'} {' θ = 8.2'} {' γ = 0.4'}

m	n	MLE	OLS	best
1000	10	3.0392 e-05	0.0063268	MLE
	20	3.1084 e-05	0.0063016	MLE
	30	3.1287 e-05	0.0062922	MLE
	50	3.0746 e-05	0.0062786	MLE
	100	3.0759 e-05	0.0062706	MLE
2500	10	3.0666 e-05	0.0063294	MLE
	20	3.0983 e-05	0.006303	MLE
	30	3.0723 e-05	0.0062827	MLE
	50	3.0705 e-05	0.0062693	MLE
	100	3.1034 e-05	0.0062654	MLE
5000	10	3.0968 e-05	0.006346	MLE
	20	3.0684 e-05	0.0062955	MLE
	30	3.0694 e-05	0.006286	MLE
	50	3.0947 e-05	0.0062767	MLE
	100	3.0888 e-05	0.0062691	MLE

Table 7. MSE for the estimation of δ at E3 {'δ = 0.07'} {'θ = 16.0'} {'γ = 0.8'}.

m	n	MLE	OLS	best
1000	10	3.0821 e-07	0.00034378	MLE
	20	2.2765 e-07	0.000332	MLE
	30	1.9724 e-07	0.00032659	MLE
	50	1.7103 e-07	0.00032311	MLE
	100	1.468 e-07	0.00032067	MLE
2500	10	3.1315 e-07	0.00034643	MLE
	20	2.2851 e-07	0.0003319	MLE
	30	1.988 e-07	0.00032654	MLE
	50	1.7004 e-07	0.00032179	MLE
	100	1.4464 e-07	0.00031935	MLE
5000	10	3.2276 e-07	0.00034953	MLE
	20	2.2595 e-07	0.00033012	MLE
	30	1.9861 e-07	0.0003266	MLE
	50	1.7072 e-07	0.00032264	MLE
	100	1.452 e-07	0.00031988	MLE

Table 8. MSE for the estimation of θ at E3 {'δ = 0.07'} {'θ = 16.0'} {'γ = 0.8'}.

m	n	MLE	OLS	best
1000	10	0.062166	1.756	MLE
	20	0.052586	2.113	MLE
	30	0.048369	2.346	MLE
	50	0.044588	2.399	MLE
	100	0.040646	2.484	MLE
2500	10	0.062834	1.571	MLE
	20	0.05279	2.098	MLE
	30	0.048731	2.236	MLE
	50	0.044351	2.402	MLE
	100	0.040172	2.572	MLE
5000	10	0.063675	1.561	MLE
	20	0.052417	2.214	MLE
	30	0.048696	2.282	MLE
	50	0.044472	2.458	MLE
	100	0.040279	2.542	MLE

Table 9. MSE for the estimation of γ at E3 {'δ = 0.07'} {'θ = 16.0'} {'γ = 0.8'}.

m	n	MLE	OLS	best
1000	10	2.1727 e-05	0.024765	MLE
	20	1.6545 e-05	0.024225	MLE
	30	1.4526 e-05	0.023989	MLE
	50	1.2769 e-05	0.023815	MLE
	100	1.1106 e-05	0.023693	MLE
2500	10	2.2051 e-05	0.024879	MLE
	20	1.6609 e-05	0.024225	MLE
	30	1.4642 e-05	0.023963	MLE
	50	1.2695 e-05	0.023737	MLE
	100	1.0948 e-05	0.023629	MLE
5000	10	2.2629 e-05	0.025043	MLE
	20	1.6438 e-05	0.024136	MLE
	30	1.4629 e-05	0.023971	MLE
	50	1.2742 e-05	0.023788	MLE
	100	1.0987 e-05	0.023658	MLE

6.Conclusion

Noting from all above tables that Mean Square Error values for Maximum likelihood estimator method is less than Mean Square Error values for ordinary least squares estimator method, thus we found that the best method for estimating the parameters is Maximum likelihood estimator method.

References

[1] Ali, A. H. and Al Kanani, I. H. "Classical methods to estimate the parameters of exponentiated weibull distribution,". Iraqi Academics Syndicate International Conference for Pure and Applied Sciences, Journal of Physics: Conference Series 2021; 1818 012078, doi:10.1088/1742-6596/1818/1/012078

[2] Jalil, M. and Al Kanani, I. H. " Some estimation methods for new mixture distribution with simulation and application," 2019 IOP conference , series: materials science and engineering 571(2019) 012014.

[3] Kalt, H G. and Al Kanani, I. H. " A comparison of MLE method and OLS for the estimation of modified Weibull distribution parameters by using the simulation ," ARPN Journal of Engineering and Applied Sciences, 2018; sept 13(17), ISSN 1819-6608.

[4] Nadarajah, S. "On the moments of the modified Weibull distribution," Reliability Engineering and System Safety, Elsevier, 2005; vol. 90(1), pages 114-117.

[5] Peng, W. Zhang, H. Huang, H. Gong, Z. and Liu,Y. "Satellite reliability modeling with modified Weibull extension distribution," 2012 International Conference on Quality, Reliability, Risk, Maintenance, and Safety Engineering, 2012; pp. 195-199, doi: 10.1109/ICQR2MSE.2012.6246218.

[6] Xie, M. Tang, Y. and Goh, T. N. "A modified Weibull extension with bathtub-shaped failure rate function," Reliability Engineering & System Safety, 2002; vol. 76, no. 3, pp. 279–285.

A Theoretical Study of the Supercontinuum Generation for the Photonic Crystal Fibre

Mohammed Salim Jasim[1], Nadia Al-Aboody[2]
{msjadr72@gmail.com[1], nadia.alaboody@stu.edu.iq[2]}

Ministry of Education, Missan Directorate of Education, Gifted Secondary School, Iraq[1]
Southern Technical University, Amara Technical Institute, Computer System Dep, Iraq[2]

Abstract. This work describes how numerical simulations based on the generalized nonlinear Schrödinger equation (GNLSE) have opened the way for a comprehensive physical understanding of the fundamental complex dynamics of supercontinuum generation (SCG) and Soliton fission (SC). SC was generated in optical fibres and fibre lasers that pumped by watt and kilowatt pulse sources, as well as in continuous-wave sources (CW) Light sources with increased spontaneous emission. An efficient approach for creating a continuous-wave source of soliton fission in the optical fibres pumped by CW light has been discovered. The ability to generate supercontinuum opens the door to a wide range of applications, from medicine to telecommunications.

Keywords: Photonic Crystal fibres (FCFs), Soliton, Generalized Nonlinear Schrödinger Equation (GNLSE), Supercontinuum generation (SCG), Continuous-Wave (CW).

1 Introduction

Photonic crystal fibre (PCF) technology has advanced steadily in recent years, attracting considerable interest from researchers [1-10]. In general, they are constructed of a single substance, such as silica, with tiny air holes running the length of their fibre. To obtain desirable optical features, such as indefinitely single-mode operation, several factors can be modified, including air hole arrangement, air hole pitch and diameter, air hole size, and the refractive index of the fibre material [5-11]. J. Wang et al. [12] proposed that PCFs be guided via a bandgap using elliptical air holes. H. Hassan [13] established two types of optical solid-core PCFs: total internal reflection and photonic bandgap. As a result, it appears that the suggested fibre is rather simple to produce. One of the most common uses of PCFs is supercontinuum generation (SCG) [14-16]. The spectral and temporal structure of a brief optical pulse changes as it passes through a Kerr nonlinearity and chromatic dispersion result in a transparent material. Apart from the invariant phase delay per unit propagation length, there are a few other factors to consider, the effects of dispersion and Kerr nonlinearity will perfectly cancel one another out, ensuring that even at long distances, the temporal and spectral structure of the pulses is retained [17]. While propagating in the nonlinear parameter n_2 should be positive in a lossless medium, and the chromatic dispersion should be positive, and the pulse must have the same temporal form as an unchipped sech2 pulse. The generalized nonlinear Schrödinger (GNLSE) equation describes the propagation of pulses in a nonlinear index of refraction with a dispersive medium. The supercontinuum is created by nonlinearities operating on the ultra-shot as it passes through a (PCF) with a highly nonlinear structure that separates into fundamental solitons, emitting

IMDC-IST 2021, September 07-09, Sakarya, Turkey
Copyright © 2022 EAI
DOI 10.4108/eai.7-9-2021.2314883

dazzling white light. Induced Raman scattering allows the first–order solitons to migrate to the side of longer wavelengths as they pass through the fibre, resulting in a process known as induced Raman scattering (SSFS), with a much broader scope [18]. As shown in Fig 1 [19], the following behaviours indicate the mechanism of supercontinuum production via soliton fission based on the (GNLSE). To overcome the bandgap, this work proposes a spherical air hole with one solid core, emphasizing the importance of dimensions represented by the long wave.
The remaining of this paper is organized as follows: the next subsections include a detailed explanation for the soliton types, section II illustrates the achieved results, and section III demonstrates the conclusion of this work.

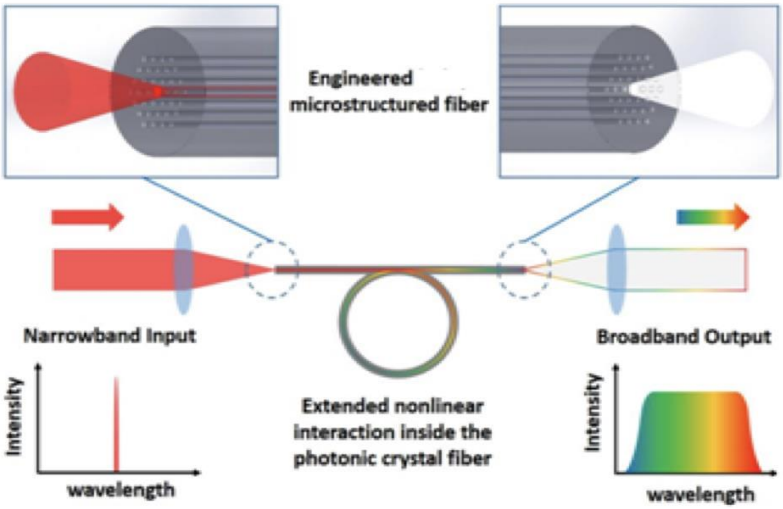

Fig 1. Supercontinuum generation.

1.1 Optical Soliton

Because of the medium's balance of dispersive and nonlinear effects, a soliton is an optical field that does not change during propagation. The two forms of optical solitons are spatial and temporal solitons [20-21]. When the electromagnetic field is spatially limited (as in optical fibres), temporal solitons develop, and the pulse form (in time) Because dispersion balances nonlinear effects, nothing changes. [22]. Nonlinear processes (self-focusing) balancing out diffraction would create spatial solitons [23-25] When the electromagnetic field is not locally restricted yet the form of the pulse in space does not change with the transmission. Fig 2 [19] illustrates this.

1.2 Soliton fission

Solitons are a fascinating representation of the nonlinear dynamics in nature that may be observed in a wide range of physics fields[24-25]. Solitons developing within optical fibres have gotten the most interest in the world of optics. With the development of new types of fibres, this fission mechanism has grown more relevant in recent years due to their nonlinear and dispersive properties, such as photonic-crystal fibres (PCF) [26].

Raman scattering, self-steepening, and cubic dispersion will all help to promote high-order soliton fission. These results, on the other hand, make it impossible to control the fission mechanism. Variation of chromatic dispersion between transmission lines (dispersion management) has been suggested as a method of regulating soliton dynamics [27-28]. Even when the spectrum of input pulses is just a few micrometres high, supercontinuum may be generated by ultrafast optical pulses traveling through such fibres (SC), and it can cover a broad spectral range from violet to infrared [29-30]. The fission of higher-order solitons is thought to be the fundamental physical mechanism causing SC creation in the anomalous-dispersion region [31].

(a) (b)

Fig 2. Linear and nonlinear effects on Gaussian pulses. (a) temporal soliton, (b) spatial soliton.

The generalized Schrödinger equation was used to achieve soliton fission and supercontinuum generation [32-33].

$$\frac{\partial A}{\partial z} = -\frac{\alpha}{2} - \sum_{m=2}^{M} i^{m-1} \frac{\beta_m}{m!} \frac{\partial^m A}{\partial t^m} + i\left(\gamma + i\gamma_1 \frac{\partial}{\partial t}\right) \left(A(z,t) \int_0^{\infty} R(t') \left| A(z, t-t')^2 \right| dt' \right) \quad (1)$$

α represents the losses in the fibre since the duration of fibre used in supercontinuum generation is too short (only a few meters), these losses may be ignored in the computational simulation. R (t') is a nonlinearity function, which incorporates both electrical and nuclear components and makes use of the following formula.

$$R(t') = (1 - f_R)\,\delta(t - t_e) + f_R h_R(t) \quad (2)$$

Because the electronic submission is treated as appearing instantly in this analysis, so $t_e \approx 1\,fs$. The Raman response feature, h_R (t), provides details on the vibration of silica molecules. Since this is better determined experimentally, an empirical form of $h_R(t)$ exists (Blow and Wood, 1989), This is determined by the equation (3) [34].

$$h_R(t) = \frac{\tau_1^2 + \tau_2^2}{\tau_1 \tau_2^2} e^{\left(\frac{-t}{\tau_2}\right)} \sin\left(\frac{t}{\tau_1}\right) \quad (3)$$

Blow and Wood's(1989), experimental results indicate that f_R=0.18, τ_1=12.2 fs, and τ_2=32 fs, When the approximations α =0 and $\tau_1 = \frac{\gamma}{\omega_\circ}$ are added to equation (1), the following results are obtained:

$$\frac{\partial A}{\partial z} = -\sum_{m=}^{M} 2\, i^{m-1} \frac{\beta_m}{m!} \frac{\partial^m A}{\partial t^m} + i\gamma \left(1 + \frac{i}{\omega_\circ} \frac{\partial}{\partial t}\right) \left(A(z,t) \int_0^{\infty} R(t') \left| A(z, t-t')^2 \right| dt' \right) \quad (4)$$

Substituting equation (2) into the integral of equation (4) gives:

$$\int_0^{\infty} R\,(t')\,\left|A\,(z,t-t')^2\right|dt' = (1-f_R)\int_0^{\infty}\delta\,(t-t_e)\,\left|A(z,t-t')^2\right|\mathrm{d}t' +$$
$$f_R\int_0^{\infty} h_R\,\left|A(z,t-t')^2\right|dt'$$
$$\int_0^{\infty} R\,(t')\,\left|A\,(z,t-\square')^2\right|\,dt' = (1-f_R)\left|A\right|^2 + f_R\int_0^{\infty} h_R\,\left|A(z,t-t')^2\right|dt'$$

Therefore, equation (4) becomes:

$$\frac{\partial A}{\partial z} = -\sum_{m-2}^{M} i^{m-1}\frac{\beta_m}{m!}\frac{\partial^m A}{\partial t^m} + i\gamma\,A\left(1+\frac{i}{\omega_\circ}\frac{\partial}{\partial t}\right)\left((1-f_R)\left|A\right|^2 +\right.$$
$$\left. f_R\int_0^{\infty} h_R\,\left|A\,(z,t-t')^2\right|dt'\right)$$
$$\frac{\partial A}{\partial z} = -\sum_{m-1}^{M} i^{m-1}\frac{\beta_m}{m!}\frac{\partial^m A}{\partial t^m} + i\gamma\,(1-f_R)\left(A\left|A\right|^2 + \frac{i}{\omega_\circ}\frac{\partial}{\partial t}\left(A\left|A\right|^2\right)\right) +$$
$$i\gamma\,f_R\,(A\int_0^{\infty} h_R\,\left|A(z,t-t')^2\right|dt' + \frac{i}{\omega_\circ}\frac{\partial}{\partial\,t}\left[A\int_0^{\infty} h_R\,\left|A(z,t-t')^2\right|dt'\right]) \quad (5)$$

1.2.1 Split step Fourier Method (STFM) for Solving the GNLSE

Equation(5) can be solved using the SSFM. This method focuses on distinguishing between the equation's dispersive and nonlinear components. This means that over a limited distance, these pieces can be regarded as autonomous. As a result, we can write equation (5) as follows: [19]:

$$\frac{\partial A}{\partial z} = \left(\widehat{D}+\widehat{N}\right)A \quad (6)$$

Equations (7) and (8) give the dispersive term $\widehat{D}$ and the nonlinear terms $\widehat{N}$

$$\widehat{D} = -\sum_{m=2}^{M} i^{m-1}\frac{\beta_m}{m!}\frac{\partial^m}{\partial t^m} \quad (7)$$

and

$$\widehat{N} = i\gamma\,(1-f_R)\,(\left|A\right|^2 + \frac{i}{\omega_\circ A}\frac{\partial}{\partial t}\left(A\left|A\right|^2\right) + i\gamma\,f_R\,(\int_0^{\infty} h_R\,\left|A\,(z,t-t')^2\right|dt' +$$
$$\frac{i}{\omega_\circ A}\frac{\partial}{\partial t}\left[A\int_0^{\infty} h_R\,\left|A(z,t-t')^2\right|dt'\right]) \quad (8)$$

Equation (6) when solved yields

$$A(z+h,t) = \exp\left[h\left(\widehat{D}\;+\;\widehat{N}\right)\right]A(z,t) \quad (9)$$

And

$$\exp(h\,\widehat{D})\exp(h\,\widehat{N}) = \exp(h\left[\widehat{D}+\;\widehat{N}\right] + \frac{h^2}{2}\left[\widehat{D}\widehat{N}-\;\widehat{N}\widehat{D}\right]+\cdots) \quad (10)$$

By disregarding the h^2 and higher components of the exponential, the following description may be derived.

$$\exp(h\left[\widehat{D}+\ \widehat{N}\right] \approx \exp\left(h\widehat{D}\right)\exp(h\,\widehat{N}) \tag{11}$$

As a result, the pulse envelope solution would be:

$$A(z+h,t)\ \approx \exp\left(h\widehat{D}\right)\exp(h\,\widehat{N})\ A(z,t) \tag{12}$$

equation (12), was determined by

$$A(z+h,t) \approx \exp(\frac{h}{2}\widehat{D}\,)\ \exp\,(\ \int_{z}^{z+h}\widehat{N}(z')dz'\ )\ \exp(\frac{h}{2}\widehat{D})\ A(z,t) \tag{13}$$

Equation (13) would be accurate to around third order.

2 The Achieved Numerical Results

The results were obtained using MATLAB OdE45. Table 1 lists the model parameters utilized in this study.

Table 1. Parameters for simulation.

Parameters	Values
Photonic Parameters	
Air hole diameter (d)	1.4 μm
Pitch (^)	1.6 μm
Pitch length	0.15 m
Number of holes	6
Wavelength	835 nm
Zero Dispersion Wavelength (ZDW)	780 nm
Nonlinearity (γ)	$0.11W^{-1}m^{-1}$
Fractional Raman Contribution (f_r)	0.18

First, computational effects with standard experimental parameters and an anomalous GVD regime are presented using the complete GNLSE in equation (1), which was considered as in Table 1, depending on the global dispersion in Table 2.

Table 2. Coefficient values of the Taylor series for the PCF's GVD used in simulation, expansion at 835 nm.

Coefficient	Value ($\frac{ps^2}{km}$)	Coefficient	Value ($\frac{ps^2}{km}$)
β_2	-11.830	β_3	8.1038×10^{-2}
β_4	-9.5205×10^{-5}	β_5	2.0737×10^{-7}
β_6	-5.3943×10^{-10}	β_7	1.3486×10^{-12}
β_8	-2.5495×10^{-15}	β_9	3.0524×10^{-18}
β_{10}	-1.7140×10^{-21}		

In the simulation, the initial infused pulse exhibits a hyperbolic secant field profile is $A(0,T), which\ is\ equal\ to\ P_0$ sech $\left(\frac{T}{T0}\right)$, , $T_0 = 28.4$ fs with P_0= 500W input power and all other simulation results assume hyperbolic secant input pulses. The PCFs selection and the input pulse parameters selected were to enable us to explore the SCG process in conditions that are representative of numerous real-world scenarios.

The dynamics of the spectral and the temporal evolution are shown in the first set of results. This is investigated using the numerical solution provided in Eq. 5. Fig 3 represents the findings of PCF propagation across a 0.15m length.

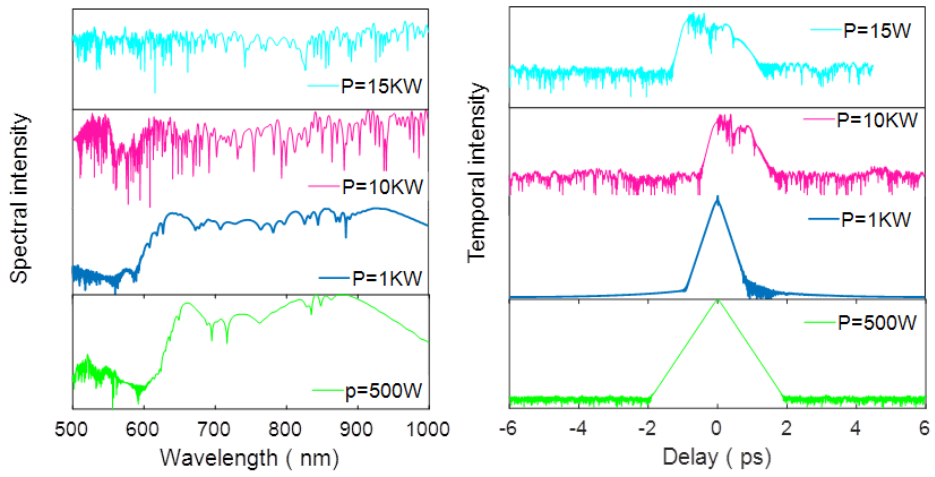

Fig 3. Supercontinuum generation across 0.15m fibre.

Fig 3 shows the results of simulations at various power levels using an 835 nm pump wavelength. one, plot spectral and temporal slices as seen at representative propagation distances to demonstrate the fine structure of the resulting spectrum, and on a logarithmic scale, the SC spectra are displayed. Understanding the underlying physics, on the other hand, involves considering the dynamical progression of the initial pulse toward the output SC, which is a very complicated process. Moreover, the use of discrete layers has only captured a portion of the intricacy of these dynamics, and the density plot representation which is illustrated in Fig 4.
In this work, to describe both the spectral and the temporal intensity, the use of the logarithmic density scale is related to the highest value. The spectral broadening becomes asymmetric over this range, with discrete peaks of spectral emerging on both sides of the injected pump's long and short wavelengths, which are linked to the formation of separate peaks of temporal on a background with minimal amplitude. The logarithmic density chart shows the time backdrop. Although most spectral widening occurs early in the transmission process, subsequent phases are marked by a distinct continuous red-shift of the high-wavelength parts and temporal transform of distinct peaks in the time domain. The SCGs short wavelength edge does not expand in response to this constant shift to high wavelengths. On the other hand, the SCG's low-wavelength side does not propagate any further. All these features may be explained by describing the SCG manufacturing process physically. It is also self-evident that a simple and fundamental explanation for such complex dynamics, in terms of well-known characteristics of soliton transmission, The essential characteristics of the SCG development shown in the preceding figures may be easily understood.

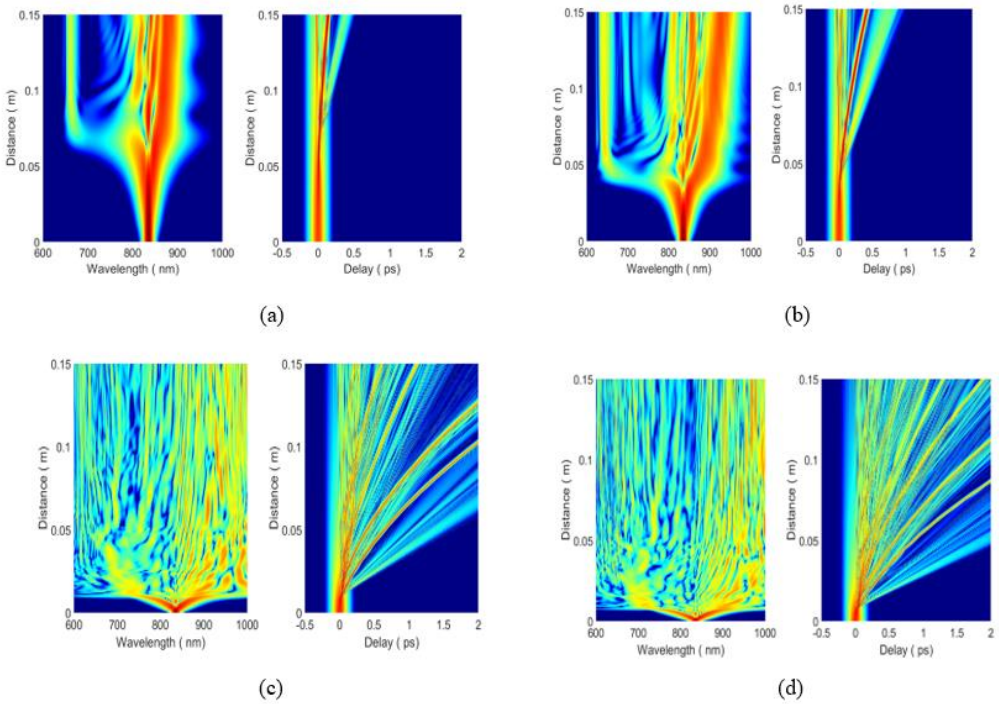

Fig 4. The density of the temporal and spectral development of SCG by ultra-short pulses with input powers of (a) 500W, (b) 1KW, (c) 10KW, and (d) 15KW are the results of numerical simulations. The input pulse wavelength is 850nm and the FWHM duration is 50 fs.

In Fig 4, the soliton fission process dominates supercontinuum generation with increased input power pumping. Even though pulse breakup and decay signals may be seen at such a high-power level, at a lower power level, the fundamental physics may be illustrated more clearly. Raman scattering and Higher-order dispersion are the two most critical phenomena in the femtosecond range that might disturb such perfect periodic growth by causing pulse breakage owing to soliton fission. The input pulse power decides which of the two effects is dominant; however, the input pulse bandwidth is low enough for input pulses of 500W that the Raman perturbation frequently wins out. Furthermore, the pulse breakdown is generated by the dispersive disturbance for pulses with a power greater than 15 KW. Singular solitons are expelled from the input pulse one at a time in a methodical way, and the ejected solitons are sorted in ascending order by peak power, with the highest peak power at the top. The point at which fission begins is usually the same as when the injected higher power reaches its maximum value The temporal and spectral properties are very complex, as shown in figure 4, the spectrum exhibits substantial modulation behaviour across short distances, although this can be explained simply as the result of spectral interference between several solitons on a linear scale, whose bandwidths continue to converge at this moment.

3 Conclusion

Supercontinuum creation is a complicated procedure, and any measurable description in terms of the basic physics, regardless of application, must take into consideration a variety of

fibre and pulse characteristics. Understanding the physics behind the SCG creation process is frequently more essential than knowing how to efficiently select a pump source and fibre type to produce an SCG with certain desired characteristics.
Looking into the SC generation in fibre lasers and photonic crystal fibres pumped by various power levels, ranging from 500W to 15KW. A ring laser with nanostructure nonlinear fibre shows SC production within a 650-950 nm spectral bandwidth of 500W. While the bandwidth grew to more than 600-1000nm at 15KW. Also, this study suggested and demonstrated a novel design method for producing a CW SC in an optical fibre pumped by CW light. This type of spectral expansion has more important in many modern applications including medical, industrial, and military, and play an important role in communication systems.

References

[1] Knight JC, Birks TA, Russell PS, Atkin DM. All-silica single-mode optical fibre with photonic crystal cladding: errata. Optics Letters. 1997 Apr 1;22(7):484-5.
[2] Russell P. Photonic crystal fibres. science. 2003 Jan 17;299(5605):358-62.
[3] Chiang JS, Wu TL. Analysis of propagation characteristics for an octagonal photonic crystal fibre (O-PCF). Optics Communications. 2006 Feb 15;258(2):170-6.
[4] Akowuah EK, Gorman T, Ademgil H, Haxha S, Robinson GK, Oliver JV. Numerical analysis of a photonic crystal fibre for biosensing applications. IEEE Journal of Quantum Electronics. 2012 Aug 17;48(11):1403-10.
[5] Hossain M, Maniruzzaman M. Prospect of Photonic Crystal Fibre (PCF) In Medical Science. InProceedings of 4th Global Engineering, Science and Technology Conference, BIAM Foundation, Dhaka, Bangladesh 2013 (pp. 1-5).
[6] Dash JN, Jha R. Graphene-based birefringent photonic crystal fibre sensor using surface plasmon resonance. IEEE Photonics Technology Letters. 2014 Apr 7;26(11):1092-5.
[7] Morshed M, Arif MF, Asaduzzaman S, Ahmed K. Design and characterization of photonic crystal fibre for sensing applications. European Scientific Journal. 2015 Apr 1;11(12).
[8] Kumar P, Fiaboe KF, Roy JS. Highly birefringent do-octagonal photonic crystal fibres with ultra flattened zero dispersion for supercontinuum generation. Journal of Microwaves, Optoelectronics and Electromagnetic Applications. 2019 Mar;18(1):80-95.
[9] Agbemabiese PA, Akowuah EK. Numerical analysis of photonic crystal fibre of ultra-high birefringence and high nonlinearity. Scientific Reports. 2020 Dec 3;10(1):1-2.
[10] Van Le H, Nguyen HT, Buczynski R, Kasztelanic R. Supercontinuum generation in photonic crystal fibres infiltrated with tetrachloroethylene. Optical and Quantum Electronics. 2021 Apr;53(4):1-8.
[11] Graydon O. Single-mode operation. Nature Photonics. 2018 Aug;12(8):443-.
[12] Wang J, Jiang C, Hu W, Gao M. High birefringence photonic bandgap fibre with elliptical air holes. Optical Fibre Technology. 2006 Jul 1;12(3):265-7.
[13] Hassan HF. Studying Enhancement of Humidity Sensor Based on Photonic Crystal Fibre Interferometer (Doctoral dissertation, University of Baghdad).
[14] Sharafali A, Nithyanandan K. A theoretical study on the supercontinuum generation in a novel suspended liquid core photonic crystal fibre. Applied Physics B. 2020 Apr;126(4):1-2.
[15] Le Canh T, Le Van H, Pysz D, Dinh TB, Nguyen DT, Dinh QH, Klimczak M, Kasztelanic R, Pniewski J, Buczynski R, Dinh KX. Supercontinuum generation in all-normal dispersion suspended core fibre infiltrated with water. Optical Materials Express. 2020 Jul 1;10(7):1733-48.
[16] Kumar P, Fiaboe KF, Roy JS. Design of nonlinear photonic crystal fibres with ultra-flattened zero dispersion for supercontinuum generation. ETRI Journal. 2020 Apr;42(2):282-91.
[17] Zhao S, Sun X. Soliton dynamics in an all-normal-dispersion photonic crystal fibre with frequency-dependent Kerr nonlinearity. Physical Review A. 2020 Sep 16;102(3):033514.

[18] Scheibinger R, Lüpken NM, Chemnitz M, Schaarschmidt K, Kobelke J, Fallnich C, Schmidt MA. Higher-order mode supercontinuum generation in dispersion-engineered liquid-core fibres. Scientific reports. 2021 Mar 5;11(1):1-1.
[19] Mohammed Salim Jasim, Soliton and Supercontinuum Generation in Photonic Crystal Fibres, PhD. thesis, University of Basrah,Iraq. 2019
[20] López-Zubieta BA, Jarque EC, Sola ÍJ, San Roman J. Spatiotemporal-dressed optical solitons in hollow-core capillaries. OSA Continuum. 2018 Nov 15;1(3):930-8.
[21] Al Qarni AA, Alshaery AA, Bakodah HO. Optical solitons for the Lakshmanan-Porsezian-Daniel model by collective variable method. Results in Optics. 2020 Nov 1;1:100017.
[22] Englebert N, Arabí CM, Parra-Rivas P, Gorza SP, Leo F. Temporal solitons in a coherently driven active resonator. Nature Photonics. 2021 May 10:1-6.
[23] Tiofack CG, Ndzana FI, Mohamadou A, Kofané TC. Spatial solitons and stability in the one-dimensional and the two-dimensional generalized nonlinear Schrödinger equation with fourth-order diffraction and parity-time-symmetric potentials. Physical Review E. 2018 Mar 9;97(3):032204.
[24] Bagri M, Kumar S. Solitons transmission system: A dynamic shift in optical fibre communication. Indian Jour-nal of Science and Technology. 2020 Aug 19;13(30):2193-202.
[25] Blair SM. Optical soliton-based logic gates. University of Colorado at Boulder; 1998.
[26] Golovchenko EA, Dianov EM, Prokhorov AM, Serkin V. Decay of optical solitons. ZhETF Pisma Redaktsiiu. 1985 Jul;42:74.
[27] Tai K, Hasegawa A, Bekki N. Fission of optical solitons induced by stimulated Raman effect. Optics letters. 1988 May 1;13(5):392-4.
[28] Wai PK, Menyuk CR, Lee YC, Chen HH. Nonlinear pulse propagation in the neighborhood of the zero-dispersion wavelength of monomode optical fibres. Optics letters. 1986 Jul 1;11(7):464-6.
[29] Genty G, Lehtonen M, Ludvigsen H. Effect of cross-phase modulation on supercontinuum generated in microstructured fibres with sub-30 fs pulses. Optics express. 2004 Sep 20;12(19):4614-24.
[30] Adamu AI, Habib MS, Smith CR, Lopez JE, Jepsen PU, Amezcua-Correa R, Bang O, Markos C. Noise and spectral stability of deep-UV gas-filled fibre-based supercontinuum sources driven by ultrafast mid-IR pulses. Scientific reports. 2020 Mar 18;10(1):1-0.
[31] Zhou R, Huang R, Li Q, Fu HY. Raman soliton at 2 μm in picosecond pumped supercontinuum by a weak CW trigger. Optics express. 2019 Apr 29;27(9):12976-86.
[32] Dudley JM, Genty G, Coen S. Supercontinuum generation in photonic crystal fibre. Reviews of modern physics. 2006 Oct 4;78(4):1135.
[33] Travers JC. Blue extension of optical fibre supercontinuum generation. Journal of Optics. 2010 Oct 29;12(11):113001.
[34] Blow KJ, Wood D. Theoretical description of transient stimulated Raman scattering in optical fibres. IEEE Journal of Quantum Electronics. 1989 Dec;25(12):2665-73.

A Survey on Physical Layer Security for FSO Communication Systems

Wafaa Mohammed Ridha Shakir [1], Ruwaida A. Abdulkareem[2]
{inb.wfa@atu.edu.iq[1], engrawada8888@gmail.com[2]}

Department of Computer Systems, Technical Institute of Babylon, Al-Furat Al-Awsat Technical University, Babil 51015, Iraq[1,2]

Abstract. Physical layer security (PLS), which uses information-theoretic techniques to protect data secrecy, has recently received a lot of academic attention. As wireless communications progresses to 5G and beyond, physical layer security research faces new hurdles. Because existing Radio-Frequency (RF) networks are unable to meet increasing data rate demands, optical wireless communication (OWC) based on free-space optical (FSO) techniques has been proposed as a viable approach to overcome RF spectrum limitations. Because of the small coverage offered by the narrow optical beam and the fact that they work properly only in the presence of line-of-sight components, FSO networks are more secure and less sensitive to eavesdropping than RF networks. However, the presence of an aggressive eavesdropper may undermine the secrecy performance of FSO networks. This document summarises all of the research that has been done on physical layer security in free space optical networks. In addition, the study suggests a number of open problems in these networks in order to improve and optimise security performance.

Keywords: Physical layer security, free-space optical, secrecy metrics.

1 Introduction

The increased demand for high-data-rate services and applications has prompted researchers to concentrate their efforts on using the unregulated optical spectrum for communications to meet the traffic demands of 5G and beyond networks. RF networks are proving insufficient to meet the growing need for data rate services [1], so optical wireless communication (OWC) has arisen as a promising alternative or supplement to existing RF networks to meet the anticipated traffic demand. Free-space optical (FSO) is regarded as one of the most promising OWC techniques due to its merit criteria. Due to its extensive bandwidth, free licences, strong security, low implementation costs, and other appealing properties, FSO technology enables the realisation of many applications [2]. Another feature of FSO is that the transmission can only function successfully when LOS component is present. To put it another way, if the LOS component is lacking, the channel suffers greatly. As a result of the extremely directional optical beam of the laser transmitter diode and the fact that they only work properly in the presence of LOS components, FSO networks are more secure and less sensitive to eavesdropping as compared to RF networks. Security in FSO networks, on the other hand, remains a concern, especially when a wiretapper or eavesdropper is hidden at the same building's top as the main receiver [3]. An eavesdropper is a user who attempts to obtain confessional information from a legitimate user. This is primarily due to the laser beam

IMDC-IST 2021, September 07-09, Sakarya, Turkey
Copyright © 2022 EAI
DOI 10.4108/eai.7-9-2021.2314809

spreading through the atmosphere, which causes the beam at the receiver to be substantially larger than the receiver size [4]. As a result, when the eavesdropper is in the divergence area of the transmitted optical beam, one possible eavesdropping occurs. By collecting radiated power across long FSO distances, the eavesdropper has a better chance of eavesdropping.

Using noise randomization, channel state information (CSI), and other resources (such as multiantenna and cooperative nodes), physical layer security (PLS) has emerged as a viable technique for minimising the amount of information received by eavesdroppers [5], [6]. In most wireless networks, the PL is utilised to facilitate reliable communication to approved destinations, while the top layers are used to protect and secure the communicated data [7]. The secrecy capacity measure was established by Wyner [8] to evaluate system secrecy performance. It was defined as the maximum source information that can be effectively recovered by the legitimate destination while keeping eavesdroppers as uninformed of this information as feasible. The eavesdroppers were believed to be completely aware to ensure an accurate evaluation [8].

Physical layer security techniques for FSO networks have the following advantages over cryptography approaches: Computing expense isn't a factor in physical layer security. Physical layer security, in contrast to traditional top-layer encryption systems, does not require a secret key because it relies on the properties of fading channels to ensure absolute secrecy [5]. As a result, safe and reliable communications can be established even if eavesdroppers (unauthorised smart devices) in FSO networks have powerful computer equipment. On the other hand, the security of computation-based encryption systems will be jeopardised if the eavesdroppers' equipment has enough processing power to solve challenging mathematical problems. Security in FSO systems is currently viewed as an open, demanding subject by the research community for all of these reasons.

We examine the research that has been done on securing FSO systems using PLS approaches in this work. Solutions offered in RF cannot be implemented in FSO systems due to the unique characteristics of this technology. As a result, a number of researchers have focused their efforts on how to improve the PLS in FSO systems by considering these factors. To our knowledge, only a small amount of research has looked into the security issue in FSO systems that use PLS approaches [9]. The aim of this study is to provide a extensive overview of PLS on FSO enablement technologies. The essential ideas for understanding PLS in FSO networks, as well as broader FSO systems for PLS model description, are first introduced. The key PLS performance measures of the FSO system are also defined. There is also some background information on these measurements. Second, we look at the PLS strategies that are often employed to improve secrecy performance. Then we go over some of the open difficulties in PLS for FSO systems, as well as some closing thoughts.

2 Fundamentals of Physical Layer Security in FSO Systems

The essential elements for comprehending PLS in FSO wireless communication systems are introduced in this section. The optical spectrum is used in FSO systems to deliver high data rates over long distances of up to ten kilometres between two stationary stations [10]. FSO lines have significantly more accessible bandwidth than RF links, resulting in higher data speeds. Because FSO systems operate at frequencies greater than 300 GHz, they do not require a licence. Because they use limited laser beams to transmit data, they are more secure than RF. They also

offer improved interference rejection and a high reuse factor, allowing the frequency to be reused multiple times. Eavesdroppers can obtain a version of the supplied data via atmospheric turbulences (AT), pointing error (PE), scattering channels, and laser-beam divergence, on the other hand [9].

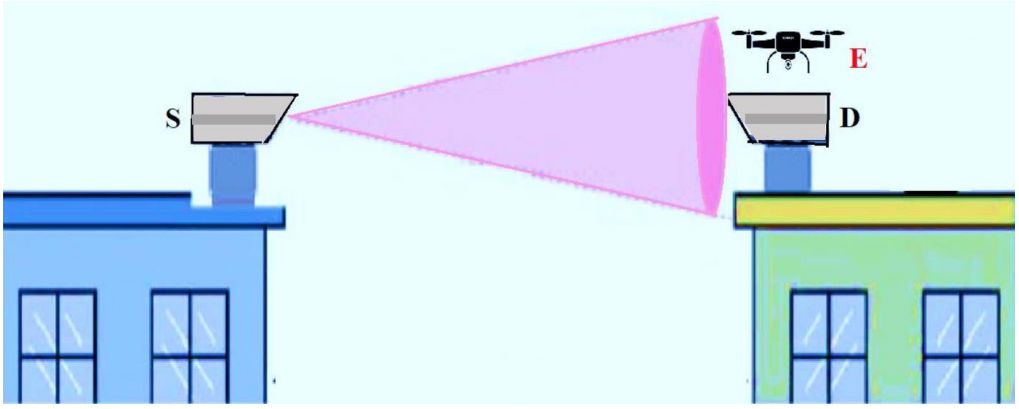

Fig. 1. FSO security communications over the physical layer.

2.1 The FSO System's General PLS Model

As illustrated in Fig. 1, the overall PLS for the FSO system is made up of three primary communication nodes. The FSO transmitter or source (S) node, the legitimate receiver or destination (D) node, and the eavesdropper (E) node are the first three nodes (also known as Eve). Laser diodes are commonly used as transmitters in FSO systems, and receivers must include photodetectors that can convert the received light intensity into an electrical signal. The legal channel is the FSO link between Alice and Bob, while the wiretap channel is Alice and Eve's FSO link. Alice sends confidential data to Bob across a legal FSO link in this system configuration. As a result, Alice's goal is to establish a communication route through which the secret information can be conveyed to Bob while assuring that the information is not intercepted by Eve. To accomplish secrecy in FSO wireless, PLS uses of specific features of the channel, such as fading, noise, and interference, among others. The availability of channel status information at all nodes is another crucial factor in the wiretap channel. CSI may be complete, partial, or even null at the nodes. Because the transmitter selects whether or not to broadcast and at what pace, CSI is critical from a security aspect. As a result, the system's secrecy performance will significantly enhance as a result of this fact.

The PLS for FSO systems, unlike its RF counterparts, is not yet mature, and its eavesdropping situations, which can be separated into active and passive eavesdropping, are currently being debated. When active eavesdropping is used, the eavesdropper may transmit jamming optical signals to legitimate receivers, clogging his receiver with unwanted noise [11]. Eve is supposed to passively intercept the genuine channel around Alice's transmitter [12], in the middle of the FSO connection [3], and near Bob's receiver [12]-[15] in the passive eavesdropping. This can also be applied to mixed RF-FSO relaying networks [16]-[17], where Eve is placed near Bob in the FSO link. In actuality, Eve's ability to intercept in the middle of the link is considerably hampered by the optical beamwidth of FSO systems, which is extremely tiny and invisible. As

a result, it's more realistic to limit the FSO channel, therefore modelling it as an FSO rather than a wiretap channel [17].

Eve is considered to be a fully passive eavesdropper positioned somewhere on or behind Bob's reception plane, attempting to tap the diverging optical beam's side lobs [17], [18]. This FSO over a wiretap channel model has also been used to improve secret-key rates (SKRs) in free-space quantum key distribution (QKD) systems [19], [20]. [12], [21] have also studied the correlated link channels.

2.2 PLS Performance Metrics for FSO Systems

The most often used secrecy performance measures in the literature are clarified in this section. The mean secrecy capacity (ASC), secrecy outage probability (SOP), and strictly positive secrecy capacity (SPSC) have closed-form formulas.

2.2.1 ASC

The mean secrecy capacity is one of the performance metrics for the free-space optical link in WOC. Data transmission is secure when the legitimate receiver's instantaneous SNR is much larger than the eavesdropper's SNR. As a result, the greatest data transfer rate that can be achieved without being hacked by an eavesdropper is defined as the mean secrecy capacity. The maximum achievable secrecy rate is denoted by (C_s) and may be defined as follows [22].

$$C_s(\gamma_{sd}; \gamma_{se}) = \max\{W \log_2(1+c\,\gamma_{sd}) - W \log_2(1+c\,\gamma_{se}); 0\} \quad (1)$$

where (γ_{sd}; γ_{se}) denote the electrical SNR of legitimate link (source to legal destination) and wiretap link (source to eavesdropper), and W denotes the bandwidth of the corresponding channel, and $\log_2(1+c\,\gamma_{sd}) = C_{sd}$ is main channel capacity, and $\log_2(1+c\,\gamma_{se}) = C_{se}$ is the wiretap capacity, respectively, while, c is a constant.

2.2.2 SOP

The possibility that the achievable secrecy capacity Cs falls below a predefined threshold rate Rs in information-theoretic security is described by SOP, a crucial parameter in physical layer security. In this case, the lawful channel's capacity is lower than the wiretap channel's, resulting in a security outage as defined by [22]:

$$SOP = P_r\{C_s(\gamma_{sd}; \gamma_{se}) < R_s\} \quad (2)$$

where $P_r\{.\}$ denotes the probability, R_s is the threshold secrecy rate.

2.2.3 SPSC Probability

SPSC, is the probability which may be thought of as a special instance when the target secrecy rate, Rs = 0 [22]. Insecure communications, SPSC can be characterized the system performance, as the following of having precisely positive secrecy capacity

$$SPSC = P_r\{C_s > 0\} = P_r\{\gamma_{sd} > \gamma_{se}\} \quad (3)$$

3 Physical Layer Security Techniques in FSO Systems

Min and Jams suggested a physical layer architecture in [23] to improve security in single input single output (SISO) FSO communication utilizing deflectors of acousto-optic (AODs) and gratings of synthetic holographic, in which the transmitter distributes packets along distinct beam pathways between two legitimate peers. The authors showed in [23] that the radius and intensity of the transmitted optical beam have a direct impact on security and that these parameters may be modified by altering the AODs parameters under various turbulence strength conditions. Lopez-Martinez et al. [12] investigated FSO communication with an external eavesdropper from the point of view of PLS. The processes of eavesdropping and the influence of disturbance-induced variations were explored in [12]. When the eavesdropper is closer to the intended receiver, the combined beam divergence and fading on received radiation allows the eavesdropper to penetrate the genuine communication link. Furthermore, the authors obtained closed-form formulations of the SPSC as the performance measure in [12], which found that the eavesdropper may penetrate the communication when close to the transmitter. In [14], the authors provide experimental data on optical transmission through the FSO link at a safe wavelength using Tokyo FSO Testbed. With a 7.8-kilometer link, this testbed comprises of one sender terminal and two reception ports, of legal recipient. The purpose of the testbed was to investigate PLS security approaches (such as secure message transmission and secret key) in real-world FSO lines across Tokyo. Furthermore, under true fading conditions, the secrecy performance of such a testbed is calculated using secrecy rate, outage probability, and predicted code length [14]. In [24], the authors looked into the dangers to sensitive data provided over the FOS link in the presence of eavesdropping out of the laser beam, where the eavesdroppers pick up information through a Non-LOS scattering channel. The authors examined FSO communication secrecy using the orbital angular momentum multiplexing technique. As it has been shown in [24], this technique provides a high level of security under certain disturbance conditions. This approach, as demonstrated in [24], gives a high level of security under particular disturbance situations. Using OOK modulation and threshold detection, the authors constructed a closed-form formula for an ASC and lower bound of ASC of the FSO system that suffers from turbulence-induced fading in [25]. In another paper, the authors used the intensity-modulation/direct-detection (IM/DD) technique over Malaga-M turbulence to develop formulas for the FSO system [15]. Because of their higher turbulence resiliency, the authors of [26] used numerical simulations and experiment results to verify that Bessel-Gaussian beams with spatial light modulators can improve the FSO link in weak to medium turbulence conditions than their Laguerre-Gaussian counterparts in weak to medium turbulence conditions. [27] investigates throughput of MIMO under-attack of a multiple-apertures eavesdropper (MIMO-ME) for coherent FSO.Furthermore, to analyse the overall system performance across the turbulence fading channel, adaptive and fixed transmission rate techniques are examined depended on the availability of the CSI at the transmission side constrained by the probability of a secrecy outage [27]. The authors of [28] performed an experiment utilizing Bessel–Gaussian (BS) beams to emulate data transmission across an eavesdropping channel under various AT conditions. Even when the eavesdropper can perform optical beam-splitting attacks in the channel to compromise PLS, and even when the legitimate transmitter and receiver do not use a shared key for communications, this study focused on achieving secure FSO communication by exploiting the

noisy and degraded channel conditions [28]. Under diverse AT settings, the authors of [19] combine FSO with the secret key agreement (SKA) to identify information security concerns and achieve secret key rates high-speed communications via FSO link. Another study [29] fragmented optical data into small fragments in order to provide secure communication over an FSO link under varied air turbulence conditions. The authors of [4] looked at how the secrecy of the FSO link was affected by turbulence-induced fading channels with pointing errors. Under two different weather situations, the authors of [30] compare the effective secrecy throughput of legal links and multi eavesdroppers with multiple-input-multiple-output relay supported. When the transmitter instantaneous CSI of the legitimate channel is available, the effect of using multiple relays on EST performance was investigated using two mechanisms: adaptive scheme with selective relaying, and fixed rate with all-active relaying, when the instantaneous CSI is not available at the transmitter [30].A framework for the secrecy analysis of a terrestrial FSO link considering the eavesdropper's location, under misalignments and atmospheric turbulence conditions is established in [31]. From a security standpoint, the IM/DD FSO system with CV-QKD technique was investigated [31]. In various recent works of literature [33]-[36], the inherent benefits of employing FSO based on transmitter spatial diversity [32] have been extended to improve PLS in FSO. In addition, [37]-[39] explored the security implications of hybridization between FSO and RF link. The hybrid FSO/RF system's main idea is to send identical signals across both connections at the same time and combine the received signals using a single diversity combining technique to benefit both technologies [39]. In these aforementioned studies, it was assumed that only the RF link was attacked by the eavesdropper considering the high security of the FSO link and broadcasting nature of wireless RF channels, which makes the RF link vulnerable to eavesdropping attack. The hybrid FSO/RF systems differ greatly from mixed FSO-RF relay systems because the FSO connection is only part of the mixed FSO-RF relay system. The current research on the PLS of mixed FSO-RF systems [40]–[56] is primarily limited to the RF link alone attack by an eavesdropper, according to a complete open literature survey. Table 1 outlines the current research trends in PLS approaches in FSO systems that have been applied by various researchers in their studies.

Table 1. The PLS trends in FSO techniques.

System Type	Reference	Focus of the work	Contribution and Research Direction	Channel conditions	Metrics
SISO FSO	[23]	Enhancing the data security based on AOD.	Formulating a transmitter beam setting by varying AOD's parameters.	Various AT	Secondary GSM transmitting beam
	[12]	Evaluating the FSO link security in presence of the eavesdropper.	The mechanisms of eavesdropping based on the eavesdropper location and the effect of joint laser-beam divergence were stated.	Various AT	SPSC
	[14]	Emulating a typical scenario of PLS security of the real-field FSO link.	Real-life experimental FSO links was considered with the influence on the instantaneous secrecy rate and the code lengths is analysed.	Various AT	Secrecy rate, SOP, the code lengths

	[24]	Impact of eavesdropper's were studied.	Formulating the security metrics considering the visibility of the link and different positions of eavesdropper taking into account two-dimensional space around the laser beam.	Various AT	ASC, SOP
	[25]	Secure communication over FSO links suffering from turbulence-induced fading.	Apply OOK to enhance the secrecy in FSO link and various channel models.	Various AT	ASC
	[26]	Secure FSO communications based on Bessel-Gaussian orbital angular Momentum	This paper provides a proved of the superiority of Bessel-Gaussian beams over the Laguerre-Gaussian beams in resilience to AT effects based on ASC.	weak to medium AT	ASC
	[28]	Creating an experiment to emulating an optical wiretap channel to extended Wyner's wiretap channel model.	Achieve reliable secrecy over noisy communications over and degraded channel conditions.	Various AT	ASC
	[19]	Experimental investigations for eavesdropping risks of several kilo meters.	A secure high-speed key FSO link, with a practical representation of the wiretap channel model, is established	Various AT	Asymptotic key rate
	[29]	Enhancing the security of FSO link concerning the channel changes	A testbed to view and approve the FSO link between two buildings	In Lab AT	Intercept possibility
	[4]	Proposing a misalignment error model based on a non-orthogonal optical beam	A two-axis misalignment pointing error effect is modelled and the effect of such type of error is investigated on the security performance of the FSO link.	AT with PE	SOP, SPSC
	[31]	Ggeneralised misalignments model is considered of a terrestrial FSO link.	Taking the account of the drops on the system operation including the transceiver misalignments and other system performances.	AT with PE	SOP
MIMO-ME FSO	[27]	Characterized the MIMO-ME oertaion over coherent transmissions. .	In this paper, CSI on two schemes were considered.	AT with PE	EST

MIMO-FSO Relay	[30]	Evaluating the EST of MIMO with relay stations.	An adaptive scheme with selective relaying depending on CSI that is available in the sender is present.	AT foggy weather	EST
MISO-FSO	[36]	Enhancing the ASC via MISO schemes.	To decrease the fading effects in FSO channels, use spatial diversity at the transmitter.	generalized misalignment and AT	ASC
Hybrid FSO/RF	[39]	Analysing the PLS of hybrid FSO/RF scheme	Different system and channel parameters, are formulated with derivative security metrics for analysing the PLS.	AT with PE	ASC, SOP, SPSC
Mixed RF-FSO	[52]	Passive eavesdropper of secure dual-hop RF-FSO.	Assessment of the capabilities of the hyper-Gamma RF and G-G FSO mixed systems against malevolent passive eavesdropper assaults.	AT	ASC, SOP, SPSC

4 Research Issues in FSO Systems that are Still Unsolved

Despite the past literature, the issues that might be tackled in future research, these various recommendations and open issues will aid in development of the PLS in FSO schemes:

1- PLS evaluation in multiuser mixed FSO-RF scheme. The multiple users' optical signals are sent via FSO links from the relay node to the destination side via an RF link. The relay could be applied with a laser diode and capable of receiving and converting multiple optical signals into a radio frequency signal of another type. Studying PLS in multiuser mixed FSO-RF systems differs from studying PLS in single FSO link-based systems due to the specific features of such systems.

2- Increasing the secrecy rate in mixed FSO-RF systems by optimising relays beamforming. The distribution of RF and the distribution of genuine users and eavesdroppers may affect the optimization problem.

3- Investigating the PLS in hybrid RF/FSO schemes, in which many eavesdroppers can target either RF or FSO link, or both links at the same time. Data is sent over both links simultaneously in hybrid RF/FSO systems. As a result, from a security standpoint, it is critical to research and investigates this system model while several eavesdroppers target both links at the same time.

4- NOMA in FSO systems is an important open research area. Several recent studies have focused on using PLS to safeguard NOMA in RF networks, but no research has been done to date on PLS in NOMA-FSO. It is vital to optimise and analyse the PLS in NOMA-FSO based systems due to the unique properties of FSO systems.

5- A study of the security-reliability tradeoff in multiuser FSO user scheduling. In the literature, the multiuser FSO with opportunistic user scheduling systems is rarely researched and examined. Furthermore, trade-off analysis of reliable security for this type of FSO system has never been examined before, to the author's knowledge.

5 Conclusion

FSO provides many advantages over conventional existing radio or microwave techniques. FSO systems are more secure than transmitting radio systems due to the extremely directional optical beam, the limits of the eavesdropper location, and the practicality of its operating technique. The FSO, on the other hand, is particularly sensitive to atmospheric turbulence, and bad weather will result in FSO transmission interruptions and a significant reduction in overall system performance. Both the information-theoretic and security mechanisms components of FSO systems are addressed by the solutions given here. SISO FSO link-based systems, mixed FSO-RF, and hybrid FSO/RF systems were among the FSO systems examined. We also looked at how input signalling techniques, the FSO network's atmospheric turbulence parameters, the location of eavesdroppers, and the availability of CSI at the sending nodes all influence secrecy performance. Furthermore, we identified a number of outstanding research problems with significant potential for improving the security of current FSO systems.

References

[1] Yongpeng W., Khisti A., Xiao C., Caire G., Wong K-K., Gao X. A Survey of physical layer security techniques for 5G wireless networks and challenges ahead. IEEE Journal on Selected Areas in Communications. 2018; 36(4): 679-695.

[2] Shakir W.M.R. Performance analysis of the hybrid MMW RF/FSO transmission system. Wireless Personal Communications. 2019; 109(4): 2199-2211.

[3] Sun X., Djordjevic I. B. Physical-layer security in orbital angular momentum multiplexing free-space optical communications. IEEE Photonics Journal. 2016; 8(1): 1-10.

[4] Rubén B-R., García-Zambrana A., Castillo-Vázquez B., Qaraqe K. Secure communication for FSO links in the presence of eavesdropper with generic location and orientation Optics Express. 2019; 27(23): 34211-34229.

[5] Zhou X., Zhang Y., Song L. Physical layer security in wireless communications. CRC Press, 2016.

[6] Obeed M., Mesbah W. Efficient algorithms for physical layer security in two-way relay systems. Physical Communication. 2018; 28: 78–88.

[7] Massey J. L. An introduction to contemporary cryptology. Proceedings of the IEEE. 1988; 76(5):533–549.

[8] Wyner A. D. The wire-tap channel. Bell Labs Technical Journal. 1975; 54(8):1355–1387.

[9] Obeed M., Salhab A. M., Alouini M.-S, Zummo S. A. Survey on physical layer security in optical wireless communication systems. *Proceedings of Seventh International Conference on Communications and Networking (ComNet)*: 2018, Hammamet, Tunisia: 2018, p. 1-5,

[10] Kim I. I., Korevaar E. Availability of free-space optics (FSO) and hybrid FSO/RF systems. Optical Wireless Communications IV, E. Korevaar, ed., *Proceedings of SPIE*. 2001. Bellingham WA USA. 4530(1): p-84–95.

[11] Paul P., Bhatnagar M. R., Jaiswal A. Jamming in free space optical systems: mitigation and performance evaluation. IEEE transactions on communications. 2020; 68(3): 1631–1647.

[12] Lopez-Martinez F. J., Gomez G., Garrido-Balsells J. M. Physical layer security in free-space optical communications. IEEE Photonics Journal. 2015; 7(2).

[13] Endo H., Han T. S., Aoki T., Sasaki M. Numerical study on secrecy capacity and code length dependence of the performances in optical wiretap channels. IEEE Photonics Journal. 2015; 7(5): 1–18.

[14] Endo H., Fujiwara M., Kitamura M., Ito T., Toyoshima M., Takayama Y., et al. Free-space optical channel estimation for physical layer security. Optics express. 2016; 24(8): 8940–8955.

[15] Saber M. J., Sadough S. On secure free-space optical communications over Malaga turbulence channels. IEEE wireless communications letters. Lett. 2017; 6(2): 274–277.

[16] Pan X., Ran H., Pan G., Xie Y., Zhang J. On secrecy analysis of DF based dual hop mixed RF-FSO systems. IEEE Access. 2019; 7: 66725-66730.

[17] Pattanayak D. R., Dwivedi V. K., Karwal V. Physical layer security of a two-relay based mixed RF/FSO network in presence of multiple eavesdroppers. Optics communications. 2020; 463: 125429.
[18] Fujiwara M., Ito T., Kitamura M., Endo H., Tsuzuki O., Toyoshima M., et al. Free-space optical wiretap channel and experimental secret key agreement in 7.8 km terrestrial link. Optics express. 2018; 26(15): 19513–19523.
[19] Endo H., Fujiwara M., Kitamura M., Tsuzuki O., Ito T., Shimizu R., et al. Free-space optical secret key agreement. Optics express. 2018; 26(18): 23305–23332.
[20] Legre M., Huttner B. Quantum-enhanced physical layer cryptography: a new paradigm for free-space key distribution. *Proceedings of International Conference in Quantum Crypto. (QCRYPT)*. Cambridge, UK, Sept. 2017, p. 1–3.
[21] Ai Y., Mathur A., Verma G. D., Kong L., Cheffena M. Comprehensive physical layer security analysis of FSO communications over Málaga channels. IEEE Photonics Journal. 2020; 12(6): 1-17.
[22] Sánchez J.D.V. et.al. Survey on physical layer security for 5G wireless networks. Annals of Telecommunications. 2021; 76: 155–174.
[23] Eghbal M., Abouei J. Security enhancement in free-space optics using acousto-optic deflectors. IEEE/OSA Journal of Optical Communications and Networking. 2014; 6(8), 684–694.
[24] Zou D., Xu Z. Information security risks outside the laser beam in terrestrial free-space optical communication. IEEE Photonics Journal. 2016; 8(5): 1–9.
[25] Zhu J., Chen Y., Sasaki M. Average secrecy capacity of free-space optical communication systems with on-off keying modulation and threshold detection. *Proceedings of IEEE International Symposium on Information Theory and Its Applications (ISITA)*, 30 Oct.-2 Nov. 2016, Monterey, CA, USA, 2016, p. 616–620.
[26] Wang T.-L., Gargano J. A., Djordjevic I. B. Employing Bessel- Gaussian beams to improve physical-layer security in free-space optical communications. IEEE Photonics Journal. 2018; 10(5).
[27] Monteiro M. E. P., Revelator J. L., Souza R. D., Briante G. Maximum secrecy throughput of MIMOME FSO communications with outage constraints. IEEE Transactions on Wireless Communications. 2018; 17(5): 3487–3497.
[28] Wang T.-L., Djordjevic I. B. Physical-layer security of a binary data sequence transmitted with Bessel-Gaussian beams over an optical wiretap channel. IEEE Photonics Journal. 2018; 10(6).
[29] Huang Q., Liu D., Chen Y., Wang Y., Tan J., Chen W. et al. Secure free-space optical communication system based on data fragmentation multipath transmission technology. Optics Express. 2018; 26(10):13536–13542.
[30] Monteiro M. E. P. et al. Effective secrecy throughput analysis of relay-assisted free-space optical communication. Physical communication.2019; 35: 100731.
[31] Trinh, P. V., Carrasco-Casado, A., Pham, A. T., & Toyoshima, M. Secrecy analysis of FSO systems considering misalignments and eavesdroppers location. IEEE Transactions on communications. 2020; 68(12): 7810-7823.
[32] García-Zambrana A, Boluda-Ruiz R, Castillo-Vázquez C, Castillo-Vázquez B. Novel space-time trellis codes for free-space optical communications using transmit laser selection. Optics express. 2015;23(19):24195-211.
[33] Boluda-Ruiz R, García-Zambrana A, Castillo-Vázquez B, Castillo-Vázquez C. On the capacity of MISO FSO systems over gamma-gamma and misalignment fading channels. Optics express. 2015;23(17):22371-85.
[34] Boluda-Ruiz R, C. Castillo-Vázquez B, García-Zambrana A, Qaraqe K. On the average secrecy capacity for FSO wiretap channels with nonzero boresight pointing errors. *Proceedings of 2018 IEEE 88th Vehicular Technology Conference (VTC-Fall)*, 2018, Chicago, IL, USA, 2018, p. 1–5.
[35] Boluda-Ruiz R, Tokgoz SC, Garcia-Zambrana A, Qaraqe K. Asymptotic average secrecy rate for MISO free-space optical wiretap channels. *Proceeding of 2019 IEEE 20th International Workshop on Signal Processing Advances in Wireless Communications (SPAWC)*. IEEE; 2019, p. 1–5.
[36] Boluda-Ruiz R, Tokgoz SC, Garcia-Zambrana A, Qaraqe K. Enhancing secrecy capacity in FSO links via MISO systems through turbulence-induced fading channels with misalignment errors. IEEE photonics journal. 2020; 12(4): 1–13.

[37] Ai Y, Mathur A, Lei H, Cheffena M, Ansari IS. Secrecy enhancement of RF backhaul system with parallel FSO communication link. Optics communications. 2020; 475:126193.
[38] Kafafy M, Fahmy Y, Khairy M, Abdallah M. Secure backhauling over adaptive parallel mmWave/FSO link. *2020 IEEE International Conference on Communications Workshops (ICC Workshops)*. IEEE; 2020. Dublin, Ireland, June, 2020, p 1-6.
[39] Shakir WMR. Physical layer security performance analysis of hybrid FSO/RF communication system. IEEE access. 2021;9:18948-61.
[40] Abd El-Malek AH, Salhab AM, Zummo SA, Alouini M. Security-reliability trade-off analysis for multiuser SIMO mixed RF/FSO relay networks with opportunistic user scheduling. IEEE transactions on wireless communications. 2016;15(9):5904-18.
[41] Lei H., Dai Z., Ansari I. S., Park K. H., Pan G., Alouini M. S. On secrecy performance of mixed RF-FSO systems. IEEE Photonics Journal. 2017; 9 (4): 1–14.
[42] Abd El-Malek AH, Salhab AM, Zummo SA, Alouini M. Effect of RF interference on the security-reliability tradeoff analysis of multiuser mixed RF/FSO relay networks with power allocation. Journal of lightwave technology. 2017;35(9):1490-505.
[43] Yang L, Liu T, Chen J, Alouini M. Physical-layer security for mixed η-μ and M- distribution dual-hop RF/FSO systems. IEEE transactions on vehicular technology. 2018;67(12):12427-31.
[44] Lei H, Luo H, Park KH, Pan G, Ren Z, Alouini M. On secrecy performance of mixed RF-FSO systems with channel imperfection. IEEE Photonics Journal. 2018; 10(4): 1-13.
[45] Lei H, Dai Z, Park K, Lei W, Pan G, Alouini M. Secrecy outage analysis of mixed RF-FSO downlink SWIPT systems. IEEE transactions on communications. 2018; 66(12): 6384-95.
[46] Odeyemi KO, Owolawi P.A. Physical layer security in mixed RF/FSO system under multiple eavesdroppers collusion and non-collusion.Optical and Quantum Electronics. 2018; 50(7): 1-19.
[47] Saber MJ, Keshavarz A, Mazloum J, Sazdar AM, Piran MJ. Physical-layer security analysis of mixed SIMO SWIPT RF and FSO fixed-gain relaying systems. IEEE systems journal. 2019;13(3):2851-8.
[48] Ai Y, Mathur A, Cheffena M, Bhatnagar M, Lei H. Physical layer security of hybrid satellite-FSO cooperative systems. IEEE Photonics Journal. 2019; 11(1): 1–14.
[49] Lei H, Luo H, Park K, Ansari IS, Lei W, Pan G, et al. On secure mixed RF-FSO systems with TAS and imperfect CSI. IEEE transactions on communications. 2020;68(7):4461-75.
[50] Pan X, Ran H, Pan G, Xie Y. Zhang J. Secrecy analysis for multi-relaying RF-FSO systems with a multi-aperture destination. IEEE Photonics Journal. 2020; 12(2): 1-11.
[51] Pattanayak DR, Dwivedi VK, Karwal V, Ansari IS, Lei H, Alouini M., On the physical layer security of a decode and forward based mixed FSO/RF cooperative system. IEEE Wireless Communications. Letters. 2020; 9(7): 1031-1035.
[52] Pattanayak DR, Dwivedi VK, Karwal V. On the physical layer security of hybrid RF-FSO system in presence of multiple eavesdroppers and receiver diversity. Optics Communications. 2020; 477: 126334.
[53] Tubail D, El-Absi M, Salhab A, Ikki S, Zummo S, Kaiser T. Physical layer security of interference aligned mixed RF/unified-FSO relaying network. IET Communications. 2020; 14(14): 2282–2293.
[54] Wang Z, Shi W, Liu W, Zhao Y Kang K. Performance analysis of full duplex relay assisted mixed RF/FSO system. Optics Communications. 2020; 474: 126170.
[55] Islam S. et al. On secrecy performance of mixed generalized Gamma and Málaga RF-FSO variable gain relaying channel. IEEE Access. 2020; 8: 104127-104138.
[56] Sarker N. et al., Secrecy performance analysis of mixed Hyper-Gamma and Gamma-Gamma cooperative relaying system. IEEE Access. 2020; 8: 131273-131285.

A Recent update of phase change materials (PCM's) in cooling application

Ahmed H. N. Al-Mudhafar [1], Ali Lateef Tarish [2]
{E-mail address: alalahmed@stu.edu.iq[1], alialali@stu.edu.iq[2]}

Thermal Mechanics Eng. Dept., Eng. Technical College-Basra, Southern Technical University, Basra, Iraq[1,2]

Abstract. The use of indirect evaporative cooling in dry weather conditions to charge phase change materials (PCMs) storage systems can reduce overall energy consumption. Lower thermal conductivity is the main limitation of PCM, so a suitable technique must be used to enhance thermal conductivity.. Studies showed that the selection of PCMs for free cooling applications is critical because it depends on the outside temperature at the charging period. Therefore, the outside temperature should be lower than the solidification temperature of the PCMs during charging, and the melting temperature should be lower than the inside temperature during the discharging process. The objective of this review article is to evaluate current phase change materials applications in cooling systems. The investigations about the application of PCMs in cooling systems undertaken by different researchers will be described in this article. Free cooling and heating system using building envelop, free cooling and heating using Air Handling Unit latent heat thermal storage systems, air conditioning, and refrigeration systems are discussed briefly. About 35% of these studies used PCMs used in roofs, ceilings, and attics. Moreover, 6% of studies used PCMs on the floor, so there is a need for future studies about the application of PCMs on the floor to storage energy at off-peak load hours and release it at peak load hours to reduce energy consumption costs. The results in the literature showed that using PV-PCM in the attic can reduce up to 55% of the attic cooling load. PCMs can store a large amount of coldness during the phase change process which takes place at a constant temperature, so it is appropriate to use in the building.

Keywords: PCMs; thermal storage; building envelop; free cooling; air conditioning.

1 Introduction

Nearly 40% of worldwide carbon dioxide emissions and energy consumption result from the urban sector [1]. Most of the energy used is towards cooling and heating, thus reducing such consumption could improve the emissions of greenhouse gases in terms of using phase change materials (PCMs) to store and release thermal energy [2]. PCMs are materials that have strong heat performances and constant temperature [3-4]. As the substance changes its phase from liquid to solid or from solid to liquid thermal energy is released or absorbed [5]. PCMs are capable of storing a large amount of energy, therefore it is appropriate for use in buildings [6]; and improving heat energy storage [7] and their related discharing process using PCMs [8, 9]. The low thermal conductivity is one of the main drawbacks of the PCMs which reduce their heat transfer efficiency [10]. There are many advantages of integrating PCMs in the building that can be found in [11-13]. Cooling systems derived by solar is an attractive technology because of its availability and friendliness to the environment. Cooling produced by solar-driven equipment cannot correspond to the demand because of the periodic nature of solar energy [14]. To increase the efficiency of the system thermal energy storage (cold or hot) system is needed

IMDC-IST 2021, September 07-09, Sakarya, Turkey
Copyright © 2022 EAI
DOI 10.4108/eai.7-9-2021.2314779

to integrate with the solar cooling system [15, 16]. LHTES is more suitable than sensible energy storage because of the large storage energy densities with a small variation of volume and temperature [17, 18].

This paper focuses on latent heat thermal storage systems which are used to store heat or cold in PCMs. The purpose of this article is to review the current application of PCMs in cooling systems. These applications are divided into four groups, namely: free cooling and heating system using building envelope, free cooling and heating using air handling unit based on heat thermal storage, air conditioning, and refrigeration systems.

2 Free cooling and heating concept with applications

The operating principle of free cooling using PCMs is by storing heat from the building interior in the day time and then releasing heat in the night as shown in Fig. 1 which takes place at the relatively low-temperature difference. The PCMs solidified the operation process from daytime and night [19]. This process shows its importance in Iraq in which 15 degrees difference could exist [1, 20]. The next section discusses the applications of PCMs in-wall, roofs, ceilings, attic, and floors.

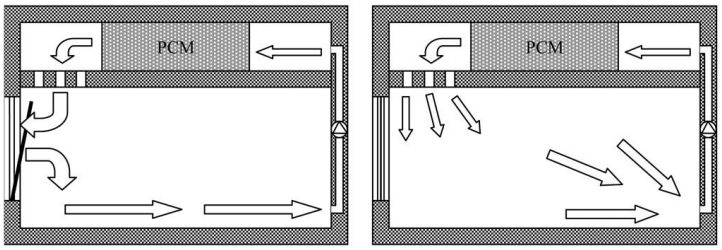

Fig. 1. PCM "free-cooling system": (left) PCM at night, (right) during the day.

2.1. Application of PCM in walls

Gracia et al. [21] experimentally tested two similar buildings one only one with ventilated façade to drop the thermal variations to prevent overheating or used to storage free cold at night. To change the operating mode of the façade six automatic opening gates were used. The study highlighted the efficiency of night-free cooling in reducing building cooling load. The system could provide air temperature below the set point temperature during summer conditions. Diarce et al. [22] used Fluent software to develop a 2D CFD model to study ventilated façade containing PCM on its outer surface as represented in Fig. 2. Moreover, a test room was built and integrated with a ventilated façade. The results indicated that for the ventilated façade it was suitable to consider PCM as a solid material with variable specific heat and neglect the effect of its phase-change during solidification and melting. The developed CFD model could be used to model ventilated façade with or without PCM with good accuracy compared to experimental data.

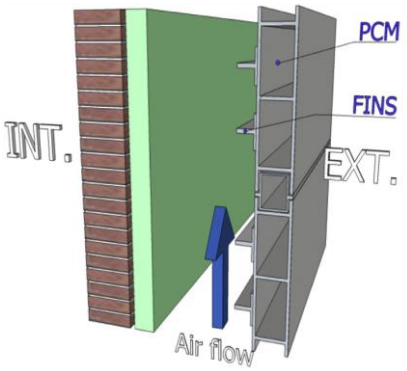

Fig. 2. The developed façade [22].

Building of light weight discussed by Barzin et al. [23] using PCM-impregnated gypsum boards in New Zealand for two tests. Charging coldness by utilizing night ventilation and free cooling enhanced the efficiency of using PCM as a cold storage system. The results showed that 73% of electricity was saved during one week period by using this method. The study recommended using this method to store cold energy in office buildings by using night ventilation during off-load hours. EnergyPlus software is used by Lei et al. [24] to illustrate the thermal variations in tropical weather (Singapore), in which the results achieved 21-32% of heat gain. The proper selection process of suitable phase change temperature is critical for PCM. The study highlighted that installing PCM in the exterior surface of exterior walls is preferred in tropical regions compared to interior location because it uses outside free night cold to solidify which lead to a reduction in cooling energy consumption. The results highlighted the advantage of using PCMs in tropical areas compared to other regions because it can reduce the cooling load through building envelop during the whole year, while in other regions PCM is only active in specific seasons. Experimental results by Principi and Fioretti [25] were compared with numerical results and showed similar dynamic performance. Sayyar et al. [26] developed composite nano-PCM and incorporated it into gypsum wallboard by using sandwich construction. The experimental results showed that using nano-PCM wallboard shifts the peak load and reduces the temperature fluctuations inside the room (18.5–26.5◦C) compared to (13–32◦C) for a room that used commercial drywall panels.

Lachheb et al. [27] developed a new gypsum matrix integrated with PCM to improve thermal storage in building materials. The gypsum matrix developed by Lachheb et al. [27] was produced by placing 24 copper tubes inside an aluminum mold (Fig.3 left), then a pasty mixture of gypsum and water was poured into the mold. The formed composite PCM-gypsum board has 20*20*1 cm^3 dimension as demonstrated in Fig. 3 right. The energy storage performance of the PCM-integrated gypsum board was experimentally evaluated to compare it with conventional gypsum board without PCM by using the transient guarded hot plates method. Moreover, PCM leakage during the liquid state was prevented by using copper tubes. Evola et al. [28] proposed a new methodology to study the effect of using PCM on improving building thermal performance in the summer season. This methodology was based on some statistical indicators which included: frequency of thermal comfort (FTC) and intensity of thermal discomfort (ITD) for occupants. To test this methodology EnergyPlus program was used to simulate the summer thermal performance of using PCM panels in three partitions walls of a central room located in a lightweight office building by using Chambéry (France) weather conditions. The simulation was performed twice for the same building, the first simulation was for building without using

a PCM panel in its partition and the second was by using PCM on the interior surface of its partition. Simulation results showed that the ITD reduced by about 35% by using PCM panels with a suitable night ventilation strategy, while the FTC reached 60% at (8 ACH) compared to 52% for a case without PCM. Researchers highlighted that the proposed methodology is suitable to help in choosing the suitable PCM depending on thermal comfort requirements and climate conditions. Castell and Farid [29] experimentally validated the previous four indicator methodology used by Evola et al. [28], which tested only for simulation results. The methodology was validated experimentally by incorporating PCM in concrete, timber, and brick. The results showed that the methodology was effective for lightweight buildings without insulation and high heat gain. But it failed for well-insulated massive buildings with low heat gain. The intensity of thermal discomfort (ITD) indicator was found to be the most effective indicator to evaluate the benefits of using PCM compared to other parameters used in the proposed methodology. Additionally, the ITD indicator was modified to take into account a range of temperature levels for thermal comfort depending on the season rather than a single set temperature. The frequency of thermal comfort (FTC) indicator was not suitable for buildings conditioned by the HVAC system, since these systems provide thermal comfort for all hours.

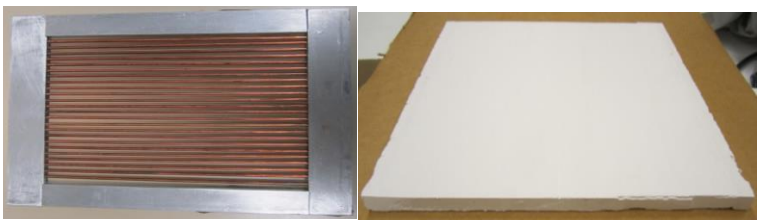

Fig. 3. Copper tubes included inside the mold (left); Copper tubes filled with PCM (paraffin) integrated inside gypsum panel (right).

2.2. Application of PCM in roofs, ceiling, and attic

Thermal stabilities were studied by Chung et al. [30] using different PCM-doped tile roof. Experiments were carried out in artificial summer weather conditions and actual winter conditions in South Korea. The results showed that PCM-doped roof tile can reduce the cooling load in the summer season and also reduce the heating load in winter conditions. Additionally, it reduces the indoor temperature in summer and increases in winter. Dong et al. [31] investigated the same subject but in roofs of residential buildings and compared to others. Many factors, such as roof slope, melting temperature and latent heat of PCM and PCM layer thickness were studied. The results showed that the PCM roof delays the time of peak temperature 3 hours compared to the common roof. By increasing the slope of the roof, the solid fraction of the PCM layer increases, and the heat flux and the average temperature of the roof decrease. The increase in the PCM layer thickness leads to an increase in the delay time of peak temperature. Kos´ny et al. [32] tested the thermal variations of PV-PCM attic and then establish a new control asphalt shingle roof. This roof work as a passive solar collector during winter, where store solar heat during the day and release it during the night. Kos´ny et al. [33] used the ESP-r program to present the effects of attic insulation encompassing and its condensed and dispersed PCM for the residential building located in Arizona, USA. The outcomes of this study showed that the best location of condensed PCM was under the attic floor insulation. Combination of PCM with attic insulation reduce the peak cooling load by more than 25% and shift it compared to the roof

without PCM with equivalent R-value. The blends of thermal insulation with PCM showed its potential for thermal energy storage. Simulation results showed that compared to non-PCM insulation the thick layers of PCM-enhanced insulation can produce a passive cooling effect by reversing the direction of heat flow. Kong et al. [34] studied the thermal performance of integrating PCMs in building envelopes. Results showed that the walls can keep the inside room temperature lower than the reference room without utilizing PCM. Zhou et al. [35] numerically simulated using shape-stabilized phase change materials (SSPCM) with 76% improvement in terms of power consumption with the case without night ventilation and SSPCM. The fan electrical COP for night ventilation increased from 6.5 to 7.5 by using SSPCM. Passive control cooling system for residential buildings was found more effective by Jiao et al. [36] using the Energy Plus program. The computed results in terms of one layer PCM was effective compared to a multi-layer PCM ceiling. Additionally, the phase change temperature of PCMs closer to the monthly average outside air temperature (27 ◦C in this case) leads to lower indoor temperature. Moreover, superior heat transfer was achieved by using PCM with high thermal conductivity and low thickness.

2.3. Application of PCM in floor

The energy consumption can be reduced using PCM but this relatd heavily on the weather conditions, the position of PCM, the melting point, and the daytime and night temperature. Ceramic tiles were embedded with PCM to enhance building thermal levels by Novais et al. [37]. Test data presented shows a 22% reduction in temperature and improve thermal performances. The wrong use of PCM could lead to an increase in energy consumption. The use of PCM might decrease the load and leads to reducing the cost of air conditioning devices. The night ventilation enhances the performance of PCM by utilising free cooling from the outside air. The use of PCM integrated with a building envelop outperforms thermal stability during the operations hours in the daytime. This has also confirmed the surface temperature in urban areas can be reduced.

3 Air Handling Unit latent heat thermal storage systems

Thermal storage technique can store and release coldness inside indoor environment during day time or used to store hotness at daytime and then released. The electric energy can be reduced in the future building when load demands at the off-peak are conisdered.

3.1. PCM-cooling storage unit charged by using outside cold at night

The thermal enactment of a window of an office using a PCM-cooling unit is discussed by Xiang and Zhou [38]. The unit is used to store the free outside cold and release it to the interior during the day. The operation principle of this unit is shown in Fig. 4. The effects showed that the optimum size with night ventilation could decrease inside the room by 3.3 ◦C with an 8.7 energy efficiency ratio. Compared to a conventional AC system of similar with the same size, the system could save 1.9 kW in 1 h that can be recorded as agood advantage.

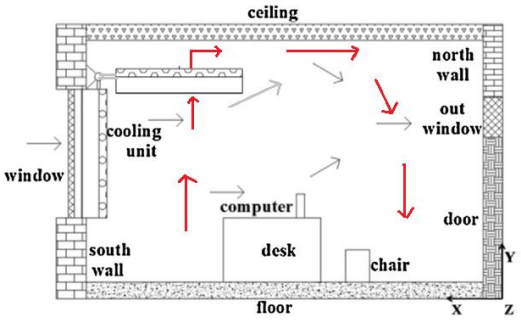

Fig. 4. Cooling unit (grey arrows for air movement and red arrows for air movement in day mode.

The thermal performance of using latent heat thermal storage is investigated by Osterman et al. [39] in an office building. It is observed that high variation of solar heat of about 142 kWh of annual energy consumption could be saved in office buildingstested the thermal performance is studied using multi-PCM by Mosaffa et al. [40-41].. Results showed that decreasing air inlet temperature during the cold charging process increases exergy efficacy. Navarro et al. [42] experimentally studied incorporating PCMs in a new prefabricated concrete slab (active slab) system to use it as a cold storage unit for active cooling. The active slab contains PCM inside its hollows. During the daytime, the cold is released to the interior ambient air by heat exchange with PCM. The results showed that between 15%-55% of cooling energy could be saved by using this technology compared to reference slabs without PCM. Sun et al. [43-45] developed latent heat PCM-cold storage unit to store free cold at night and used it to cool telecommunications-based stations (TBSs). A mathematical model was developed to simulate the application of this system in different weather conditions. Results showed that 50% of annual cooling energy consumption was reduced in the different climatic regions. Raj and Velraj [45] considered the PCM by applying shell and tube heat. The results showed the module improves the heat transfer 1 m/s heat velocity and an increased of 2 m/s of the solidification time. Tyagi et al. [46] tested the thermal performance of using PCM thermal energy storage for space cooling or heating of building at the typical climate in India. Calcium chloride hexahydrate was used as a PCM. The results showed that (TMS-I) was more effective for space cooling compared to the (TMS-II), While the (TMS-II) was more effective compared to (TMS-I) for space heating. Hasse et al. [47] studied using an aluminum honeycomb panel filled with PCM in which the the thermal inertia of honeycomb samples filled with PCM was larger compared with water or air-filled samples.

3.2. PCM cold storage unit charged by using indirect evaporative cooling

Using a concealed heat thermal energy storage system can decrease cooling energy consumption and restore comfort. However, this system depends on the local weather data and it is preferred to use in locations with high-temperature fluctuations between daytime and night in summer. Jaber and Ajib [48] studied the performance of the cooling scheme using a PCM called indirect evaporative and storage unit (IESU). This system consisted of a heat exchanger filled with PCM and an indirect evaporative cooling system. This unit with optimum size could reduce the cooling energy by 80% from the conventional AC system. The optimum PCM melting temperature to use in this system for Amman climate was 20 ◦C. The use of evaporative cooling to charge PCMs cold storage systems can reduce energy consumption, especially in dry

weather conditions. There is a need to produce a prefabricated cold storage system integrated with PCMs because it is easy to integrate into the building structure. Due to the low energy consumption of PCMs cold storage systems compared to conventional schemes, that is operated by a portable generator. So it can be used in locations that are not served by the electrical network.

4 Air conditioning and refrigeration systems

Thermal cold storage systems by using PCMs can be used for storage of cooling for off-peak cycles [49]. This reduces energy consumption and makes the system more energy efficient. This improves the peak cooling load and the ability of the cooling system including cost [50]. They also applied for the storage of cold energy from air conditioning systems when operating from solar energy sources and the stored cooling can be used during sunset.

4.1 Application of PCM in the freezer and refrigerated vehicle

Oro´ et al. [51] investigated food storage champers using PCM to state the system operation faults. Liu et al. [52, 53] tested a new cooler system using PCM thermal storage unit (PCTSU). Simulation results indicated that temperature or mass flow rate increased linearly with heat transfer fluid leads to a faster melting process of PCM and increases the heat transfer rate. The PCTSU is represented in Fig. 5. The results showed that the cosr reduced by 86.4% compared to nominal systems.

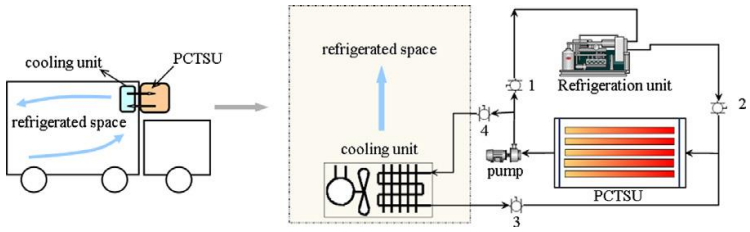

Fig. 5. Proposed refrigeration system [50].

4.2. Application of PCM store off-peak cooling from cooling systems

Bruno et al. [54] numerically studied using off-peak PCM-thermal storage and how the heat transfer passed through tubes and the tank. The unit was used to store cold from the chiller at the off-peak cycle. The result stated that 13.5% of cooling energy was saved with melting temperature of 10 ˚C. The increasing cold discharging is also found important for load shifting. Li et al. [55] studied the new type of PCM (HS-E2) used in direct contact PCM-cold storage tank to store cold for air conditioning unit. It is observed that charging time and charging capacity increased by decreasing the heat transfer fluid inlet temperature and increasing the PCM flow rate. DSC measurements for this new PCM (HS-E2) showed 173.5 kJ/kg latent heat and its solidification temperature was 7.03 ˚C, so it is suitable to use for thermal storage with conventional AC systems. Experimental data showed a similar trend with numerical results and their variation was about 7%. Moreno et al. [56] included the heat pump to shift peak cooling load for building by store cold at an off-peak time. The TES tank was used to store cold from the heat pump and use this cold for building cooling. The result showed that PCM storage tank

supply 14.5% colder and keep the inside temperature within 20.65% thermal comfort. The charging time of the PCM tank with 4.55 times the charging time. Chen et al. [57] experimentally investigated using a PCM cold storage tank coupled with an evaporator of an ejector cooling unit. The results showed that the ejector cooling COP was stabilized by using a storage tank. Additionally increasing heat transfer fluid flow rate was led to reducing the effectiveness of charging and discharging. Zhai et al. [58] developed a PCM-cold storage unit by using (lauric and capric acid) PCM with (14.97 ◦C) melting temperature. The PCM testbed operated with a pipe of copper finned with a diameter of 2 cm surrounded by a cylindrical container with 50cm long and 11cm diameter. The outcomes showed that the experimental finned unit was reduced by more than 70%. The TC of PCM is powered by using fins and this reduces the phase changes.

5 Conclusions

The use of PCMs in building envelopes was more beneficial since heat from the building takes place through the building envelope. The main reason for using PCM in building envelop is its capability to storing heat with fixed temperature. PCMs used in walls, roofs, ceilings, attic, and floor. More than 50% of these studies used PCMs in walls due to their large surface areas and higher energy consumption in walls. About 35% of these studies used PCMs in roofs, ceilings, and attics. And 6% of studies used PCMs on the floor, so there is a need for future studies about the application of PCMs on the floor to store energy at off-peak load hours and release it at peak load hours to reduce energy consumption costs. The thermal performance of PCMs depends on the climatic condition, so PCM should be carefully selected depending on its melting and solidification temperature suitable for local climate conditions. In most of these studies, the cooling energy consumption was reduced and in some of them, the reduction reached 100%. The peak load was reduced by more than 20%. And indoor temperature fluctuation reduced by more than 20%. The application of PCMs in a building depends on weather conditions and in the previous studies presented in this paper about 50% of these studies were conducted in the USA and European countries and more than 30% in China. So for future studies, there is a need for more studies in other climate regions like Middle East countries. There are many simulation programs used in the previous studies from this programme: Fluent, Energy-Plus, COMSOL, and ESP-r. Fluent was used for more than 30% of numerical simulation studies and the Energy-Plus programme used more than 30% of these studies.

By using PCM as a storage system for free cooling applications in buildings, the outside cold can be stored in the PCM and this cold can be released to the indoor during the hot day hours. This technology can lead to reducing consumption of the energy and the gases emission of greenhouses. But to apply the free cooling technique variation between night and day temperatures must be found. So the free cooling systems depend on the weather data and the melting temperature of the PCM used for storage cooling. For free cooling applications by using building envelop PCMs melting temperature used in the literature range from (16-30 ◦C). Using PCM to store cooling and heating can lead to reducing the cost of electricity bills by reducing energy consumption in cooling or heating and by shifting the peak load to off-peak hours. Charging the cold storage system which contains PCM during the coldest part of the night can reduce the energy consumption of the system because the cooling system which is used for charging works more efficiently at night. For free cooling applications by using latent heat thermal storage PCMs phase change temperature used in the literature range from (2-15 ◦C). Using indirect evaporative cooling in dry regions to charge PCMs in cooling can reduce up to

80% of energy consumption compared to the traditional system. The literature showed that using PV-PCM in the attic can reduce up to 55% of the attic cooling load. PCMs can store of coldness while in teh change process which takes place at un-varied levle of temperature, so it is appropriate to use in the building.

References

[1] Almudhaffar, Mujtaba, Ali A Monem, and Ahmed H Naseer. "Standardizing the Annual Electric Energy Consumption for a Residential Building in Basrah City." *Basrah Journal for Engineering Science* 14, no. 2 (2014): 162-175.
[2] Guarino, Francesco, Sonia Longo, Maurizio Cellura, Marina Mistretta, and Vincenzo La Rocca. "Phase change materials applications to optimize cooling performance of buildings in the Mediterranean area: a parametric analysis." *Energy Procedia* 78 (2015): 1708-1713.
[3] De Gracia, Alvaro, and Luisa F. Cabeza. "Phase change materials and thermal energy storage for buildings." *Energy and Buildings* 103 (2015): 414-419.
[4] Al-Mudhafar, Ahmed HN, Andrzej F. Nowakowski, and Franck CGA Nicolleau. "Performance enhancement of PCM latent heat thermal energy storage system utilizing a modified webbed tube heat exchanger." *Energy Reports* 6 (2020): 76-85.
[5] Osterman, Eneja, V. V. Tyagi, Vincenc Butala, N. Abdul Rahim, and Uroš Stritih. "Review of PCM based cooling technologies for buildings." *Energy and Buildings* 49 (2012): 37-49.
[6] Alizadeh, M., and S. M. Sadrameli. "Development of free cooling based ventilation technology for buildings: Thermal energy storage (TES) unit, performance enhancement techniques and design considerations–A review." *Renewable and Sustainable Energy Reviews* 58 (2016): 619-645.
[7] Zhou, Dan, G. S. F. Shire, and Yuan Tian. "Parametric analysis of influencing factors in Phase Change Material Wallboard (PCMW)." *Applied energy* 119 (2014): 33-42.
[8] Abdulrahman, Ruslan, Farah Ibrahim, Ahmed Al-Mudhafar, and Sadoun Dakhil. "Numerical study of PCM melting processes in trapezoidal channel." In *Journal of Physics: Conference Series*, vol. 1773, no. 1, p. 012017. IOP Publishing, 2021.
[9] Zafar, Sayem, Ibrahim Dincer, and Mohamed Gadalla. "Experimental testing and analysis of R134a clathrates based PCMs for cooling applications." *International Journal of Heat and Mass Transfer* 91 (2015): 756-765.
[10] Tay, N. H. S., M. Belusko, M. Liu, and F. Bruno. "Investigation of the effect of dynamic melting in a tube-in-tank PCM system using a CFD model." *Applied Energy* 137 (2015): 738-747.
[11] Zhang, Yinping, Guobing Zhou, Kunping Lin, Qunli Zhang, and Hongfa Di. "Application of latent heat thermal energy storage in buildings: State-of-the-art and outlook." *Building and environment* 42, no. 6 (2007): 2197-2209.
[12] Kamali, Saeed. "Review of free cooling system using phase change material for building." *Energy and Buildings* 80 (2014): 131-136.
[13] Tyagi, V. V., D. Buddhi, Richa Kothari, and S. K. Tyagi. "Phase change material (PCM) based thermal management system for cool energy storage application in building: An experimental study." *Energy and Buildings* 51 (2012): 248-254.
[14] Cheng, Xiwen, Xiaoqiang Zhai, and Ruzhu Wang. "Thermal performance analysis of a packed bed cold storage unit using composite PCM capsules for high temperature solar cooling application." *Applied thermal engineering* 100 (2016): 247-255.
[15] Diaconu, Bogdan M., Szabolcs Varga, and Armando C. Oliveira. "Numerical simulation of a solar-assisted ejector air conditioning system with cold storage." *Energy* 36, no. 2 (2011): 1280-1291.
[16] Al-Abidi, Abduljalil A., Sohif Bin Mat, K. Sopian, M. Y. Sulaiman, C. H. Lim, and Abdulrahman Th. "Review of thermal energy storage for air conditioning systems." *Renewable and Sustainable Energy Reviews* 16, no. 8 (2012): 5802-5819.

[17] Al-Mudhafar, Ahmed HN, Andrzej F. Nowakowski, and Franck CGA Nicolleau. "Thermal performance enhancement of energy storage systems via phase change materials utilising an innovative webbed tube heat exchanger." *Energy Procedia* 151 (2018): 57-61.
[18] Tarish, Ali Lateef, and Naseer T. Alwan. "Experimental Study of Paraffin Wax-Copper Nanoparticles Thermal Storage Material." *International Journal of Modern Studies in Mechanical Engineering* 3.3 (2017): 11-17. http://dx.doi.org/10.20431/2454-9711.0303002
[19] Stritih, Uroš, and Vincenc Butala. "RETRACTED: Experimental investigation of energy saving in buildings with PCM cold storage." (2010): 1676-1683.
[20] Tarish, Ali Lateef, Mushtaq Talib Hamzah, and Wasan Assad Jwad. "Thermal and exergy analysis of optimal performance and refrigerant for an air conditioner split unit under different Iraq climatic conditions." *Thermal Science and Engineering Progress* 19 (2020): 100595. https://doi.org/10.1016/j.tsep.2020.100595
[21] De Gracia, Alvaro, Lidia Navarro, Albert Castell, Álvaro Ruiz-Pardo, Servando Álvarez, and Luisa F. Cabeza. "Thermal analysis of a ventilated facade with PCM for cooling applications." *Energy and buildings* 65 (2013): 508-515.
[22] Diarce, G., Á. Campos-Celador, K. Martin, A. Urresti, A. García-Romero, and J. M. Sala. "A comparative study of the CFD modeling of a ventilated active façade including phase change materials." *Applied Energy* 126 (2014): 307-317.
[23] Barzin, Reza, John JJ Chen, Brent R. Young, and Mohammed M. Farid. "Application of PCM energy storage in combination with night ventilation for space cooling." *Applied Energy* 158 (2015): 412-421.
[24] Lei, Jiawei, Jinglei Yang, and En-Hua Yang. "Energy performance of building envelopes integrated with phase change materials for cooling load reduction in tropical Singapore." *Applied energy* 162 (2016): 207-217.
[25] Principi, Paolo, and Roberto Fioretti. "Thermal analysis of the application of pcm and low emissivity coating in hollow bricks." *Energy and Buildings* 51 (2012): 131-142.
[26] Sayyar, Mohammad, Rankothge R. Weerasiri, Parviz Soroushian, and Jue Lu. "Experimental and numerical study of shape-stable phase-change nanocomposite toward energy-efficient building constructions." *Energy and buildings* 75 (2014): 249-255.
[27] Lachheb, Mohamed, Mustapha Karkri, and Sassi Ben Nasrallah. "Development and thermal characterization of an innovative gypsum-based composite incorporating phase change material as building energy storage system." *Energy and Buildings* 107 (2015): 93-102.
[28] Evola, G., L. Marletta, and F. Sicurella. "A methodology for investigating the effectiveness of PCM wallboards for summer thermal comfort in buildings." *Building and Environment* 59 (2013): 517-527.
[29] Castell, Albert, and Mohammed M. Farid. "Experimental validation of a methodology to assess PCM effectiveness in cooling building envelopes passively." *Energy and Buildings* 81 (2014): 59-71.
[30] Chung, Min Hee, and Jin Chul Park. "Development of PCM cool roof system to control urban heat island considering temperate climatic conditions." *Energy and Buildings* 116 (2016): 341-348.
[31] Li, Dong, Yumeng Zheng, Changyu Liu, and Guozhong Wu. "Numerical analysis on thermal performance of roof contained PCM of a single residential building." *Energy conversion and management* 100 (2015): 147-156.
[32] Kośny, Jan, Kaushik Biswas, William Miller, and Scott Kriner. "Field thermal performance of naturally ventilated solar roof with PCM heat sink." *Solar Energy* 86, no. 9 (2012): 2504-2514.
[33] Kośny, Jan, Ali Fallahi, Nitin Shukla, Elizabeth Kossecka, and Ramin Ahbari. "Thermal load mitigation and passive cooling in residential attics containing PCM-enhanced insulations." *Solar Energy* 108 (2014): 164-177.
[34] Kong, Xiangfei, Shilei Lu, Yiran Li, Jingyu Huang, and Shangbao Liu. "Numerical study on the thermal performance of building wall and roof incorporating phase change material panel for passive cooling application." *Energy and Buildings* 81 (2014): 404-415.
[35] Zhou, Guobing, Yongping Yang, and Hong Xu. "Energy performance of a hybrid space-cooling system in an office building using SSPCM thermal storage and night ventilation." *Solar Energy* 85, no. 3 (2011): 477-485.
[36] Jiao, Feifei, and Peng Xu. "Simulation and feasibility analysis of PCM based passive cooling technique in residential house." *Procedia Engineering* 121 (2015): 1969-1976.

[37] Novais, Rui M., G. Ascensão, M. P. Seabra, and J. A. Labrincha. "Lightweight dense/porous PCM-ceramic tiles for indoor temperature control." *Energy and buildings* 108 (2015): 205-214.
[38] Xiang, Yutong, and Guobing Zhou. "Thermal performance of a window-based cooling unit using phase change materials combined with night ventilation." *Energy and Buildings* 108 (2015): 267-278.
[39] Osterman, Eneja, Vincenc Butala, and Uroš Stritih. "PCM thermal storage system for 'free'heating and cooling of buildings." *Energy and buildings* 106 (2015): 125-133.
[40] Mosaffa, A. H., L. Garousi Farshi, CA Infante Ferreira, and M. A. Rosen. "Energy and exergy evaluation of a multiple-PCM thermal storage unit for free cooling applications." *Renewable Energy* 68 (2014): 452-458.
[41] Mosaffa, A. H., CA Infante Ferreira, F. Talati, and M. A. Rosen. "Thermal performance of a multiple PCM thermal storage unit for free cooling." *Energy Conversion and Management* 67 (2013): 1-7.
[42] Navarro, Lidia, Alvaro de Gracia, Albert Castell, and Luisa F. Cabeza. "Experimental evaluation of a concrete core slab with phase change materials for cooling purposes." *Energy and Buildings* 116 (2016): 411-419.
[43] Sun, Xiaoqin, Quan Zhang, Mario A. Medina, and Shuguang Liao. "Performance of a free-air cooling system for telecommunications base stations using phase change materials (PCMs): in-situ tests." *Applied Energy* 147 (2015): 325-334.
[44] Raj, V. Antony Aroul, and R. Velraj. "Heat transfer and pressure drop studies on a PCM-heat exchanger module for free cooling applications." *International Journal of Thermal Sciences* 50, no. 8 (2011): 1573-1582.
[45] Sun, Xiaoqin, Quan Zhang, Mario A. Medina, Yingjun Liu, and Shuguang Liao. "A study on the use of phase change materials (PCMs) in combination with a natural cold source for space cooling in telecommunications base stations (TBSs) in China." *Applied Energy* 117 (2014): 95-103.
[46] Tyagi, V. V., A. K. Pandey, D. Buddhi, and S. K. Tyagi. "Exergy and energy analyses of two different types of PCM based thermal management systems for space air conditioning applications." *Energy conversion and management* 69 (2013): 1-8.
[47] Hasse, Colas, Manuel Grenet, André Bontemps, Rémy Dendievel, and Hébert Sallée. "Realization, test and modelling of honeycomb wallboards containing a Phase Change Material." *Energy and Buildings* 43, no. 1 (2011): 232-238.
[48] Jaber, Samar, and Salman Ajib. "Novel cooling unit using PCM for residential application." *international journal of refrigeration* 35, no. 5 (2012): 1292-1303.
[49] Zamfirescu, C., and A. Bejan. "Tree-shaped structures for cold storage." *International journal of refrigeration* 28, no. 2 (2005): 231-241.
[50] Tay, N. H. S., M. Belusko, and F. Bruno. "An effectiveness-NTU technique for characterising tube-in-tank phase change thermal energy storage systems." *Applied Energy* 91, no. 1 (2012): 309-319.
[51] Oró, Eduard, Laia Miro, Mohammed M. Farid, and Luisa F. Cabeza. "Thermal analysis of a low temperature storage unit using phase change materials without refrigeration system." *International journal of refrigeration* 35, no. 6 (2012): 1709-1714.
[52] Liu, Ming, Wasim Saman, and Frank Bruno. "Development of a novel refrigeration system for refrigerated trucks incorporating phase change material." *Applied Energy* 92 (2012): 336-342.
[53] Liu, Ming, Frank Bruno, and Wasim Saman. "Thermal performance analysis of a flat slab phase change thermal storage unit with liquid-based heat transfer fluid for cooling applications." *Solar Energy* 85, no. 11 (2011): 3017-3027.
[54] Bruno, Frank, N. H. S. Tay, and M. Belusko. "Minimising energy usage for domestic cooling with off-peak PCM storage." *Energy and buildings* 76 (2014): 347-353.
[55] Li, Xiao-Yan, Qiao-Qiao Zhao, and Dong-Qi Qu. "Investigation on the dynamic characteristics of a direct contact thermal energy storage charging process for use in conventional air-conditioning systems." *Applied Thermal Engineering* 91 (2015): 172-180.
[56] Moreno, Pere, Albert Castell, Cristian Sole, Gabriel Zsembinszki, and Luisa F. Cabeza. "PCM thermal energy storage tanks in heat pump system for space cooling." *Energy and buildings* 82 (2014): 399-405.
[57] Chen, Xiangjie, Mark Worall, Siddig Omer, Yuehong Su, and Saffa Riffat. "Experimental investigation on PCM cold storage integrated with ejector cooling system." *Applied Thermal Engineering* 63, no. 1 (2014): 419-427.

[58] Zhai, X. Q., X. W. Cheng, C. Wang, and R. Z. Wang. "Experimental investigation and performance analysis of a fin tube phase change cold storage unit for high temperature cooling application." *Energy and Buildings* 89 (2015): 9-17.

Fuel Cell 3D Contour Simulation of Serpentine Flow Field Inside Cubic Channels

Akeel M. Ali Morad[1], Hala E. Obeed[2], Fatima A. Khalaf[3], Noor H. Jawad[4], Zahraa K. Jabar[5], Mariam A. Moustafa[6]
{akeel@stu.edu.iq [1], zah78567@gmail.com [2], jhussein907@gmail.com[3]}

Southern Technical University, Basra Eng. Technical College, fuel and energy eng. Deprt[1]
Southern Technical University, Basra Eng. Technical College, fuel and energy eng. Deprt[2,3,4,5,6]

Abstract. In this study, we described the behavior of the serpentine flow field inside the fuel of a proton exchange membrane fuel cell (PEMFC). Pressure drop, inlet velocity, oxygen and gas diffusion layer (GDL), and current density determine the design of the fuel cell. The other parameters predicted in the open literature, such as temperature, humidity, etc., are not taken into account here. COMSOL Multiphysics 5.4 Software was used to simulate and test the electrochemical reactions governing equations. Three inlet velocities and three of (1.5, 2.5, and 3.5 m/sec) cubic channels are used to show the effect of a turbulent flow without wall slip. By analyzing the results, it can be concluded that the serpentine flow field enhances the performance of fuel cells with cubic channel geometry. We found a good correlation between the current density and cell voltage at different inlet velocities.

Keywords: Serpentine Flow Field, 3D Contour Analysis, Fuel Cells, Cubic Channels.

1 Introduction

Fuel cells have recently attracted more researchers' attention. Applications in the industrial sector, due to global warming and fuel cost problems [1-5]. The last fifty years have seen many studies focused on compiling the use of water with another electrolyte to produce voltages and currents [6- 9]. All these parameters played an important role in the design of the fuel cell membrane and the flow, whether single or two-phase [10-12]. The Serpentine flow is well known in the field of the fuel cell as a modern style of flow inside the channels. The designers developed new arts for the competitions of the fuel cell at serpentine flow. Recently published papers used the geometry of the channel as (M) [13]. In the catalyst layer and gas diffusion layer on the cathode side, they found a constant oxygen molar concentration. [14] uses a multi-serpentine with slots and hybrid geometry. The best electrical performance was achieved with less pressure drop inside the geometry, and therefore, less noise was generated. Through a three-dimensional wave flow channel, the channel geometry accelerates electrochemical reactions in the catalytic layer [15]. Their work results on the optimal flow channel are at minimum depth. The reaction inside the flow channel is observed more sensitive with relative humidity which showed by [16]. The experimental results shown at the increase in the humidity level, the performance of the cell increased.
In this study, we organized to preset the effect of the 3D serpentine flow field inside the three cubic channels of the fuel cell. The simulation is done used the free demo of the modern

IMDC-IST 2021, September 07-09, Sakarya, Turkey
Copyright © 2022 EAI
DOI 10.4108/eai.7-9-2021.2314813

software COMSOL Multiphysics 5.4. Most of the effective parameters were shown and compared with opened pieces of literature.

2 Problem Formation

The design for fuel cells depends upon the type of fuel utilized, current density, mass of the oxygen diffused and reacts with (GDL), and the pressure drop in each channel of the cell. The modern way is approached to use serpentine flow field and predicted with three parallel of equal lengths channels to an aligned of reactant distributed at fluid over the electrode area to identical in resistance flow. Nevertheless, this design may induce some gratuitously in the high-pressure drops with low-temperature fuel cells, obstructing because some of the water will be condensed which occurred in the bends. This design for serpentine channel to function used the cross-flow through channel-to-channel, to plot the essential convection in the porous material layer, and moderated it instead of a large cross-flow due to lead stagnant zones. The modern way is approached to use serpentine flow field and predicted with three parallel of equal lengths channels to an aligned of reactant distributed at fluid over the electrode area to identical in resistance flow.

This design for the serpentine channel used the cross-flow through channel-to-channel, to plot the essential convection in the porous material layer, and moderated it instead of a large cross-flow due to lead stagnant zones. The cathode is conditioned at the bottom of the GDL domain, while, the description of voltage used a lumped resistance, the anode, membrane, and GDL which arranged as shown in Fig 1. The design is consists of three inlets and three outlets cubic channels and the underlying is the GDL domain and faced the cathode at the bottom.

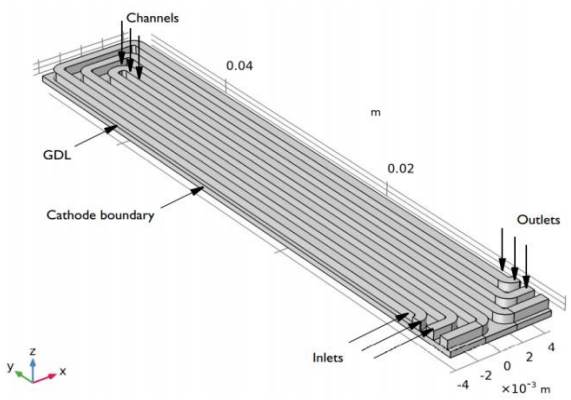

Fig 1. Model geometry.

Table 1. Shows all the input parameters to the simulated model.

Item	Expression
Rib width	0.7 (mm)
Channel width	0.8 (mm)

Plate width	50 (mm)
Channel height	0.8 (mm)
GDL height	0.5 (mm)
Channel-to-channel space	1.5 (mm)
Channels Number	3
Channel inner radius at corners	0.25 (mm)
Cell Voltage (V)	0.4
Open circuit voltage (V)	1.23
Lumped anode + membrane resistance	0.285 (ohm*cm^2)
Cell temperature (K)	180+273.15
GDL porosity	0.4
Inlet mass fraction of H_2O (cathode)	0.023
Inlet mass fraction of oxygen (cathode)	0.228

2.1 Governing equations

The reactions occurring in the cell are described by the following formulas of the porous cathode reaction according to[13]:

$$O_2 + 4H^+ + 4e^- \leftrightarrow 2H_2O \quad (1)$$

Where, O_2 is oxygen, H hydrogen, H_2O is water.

The cumulative response in PEMFC fuel cell to calculate local current density, *iloc* which depend upon the oxygen concentrated according to the kinetic expression below[1]:

$$\boldsymbol{i_{loc} = i_O\left(exp\left(\frac{\alpha_a}{RT}F\varphi_C\right) - \left(\frac{c_{O_2}}{c_{O_{2.ref}}}\right)exp\left(-\frac{\alpha_C}{RT}F\varphi_C\right)\right)} \quad (2)$$

Where, R= universal gas constant, Temperature, α = transfer coefficient for cathode and anode, F= Faraday constant equal (96487 C mol^{-1}), φ = cathode overpotential, Local oxygen concentration and the reference concentration of oxygen.
The combinations for both boundaries of the electrolyte-electrode Interface set up the mass flow boundaries according to the stoichiometric coefficient of the electrodes reactant. The flow is assumed without wall slip used for the wall of the channel, while the wall slip conditions are considered for the GDL walls.

The cathode potential φ , is calculated by relating the various parts of the cell according to:

$$\varphi_C = \boldsymbol{E_{cell} - E_{OCV} - R_{iloc}} \quad (3)$$

Where E_{cell} is the cell potential, E_{OCV} is the open circuit cell voltage and R is the lumped resistance of membrane, anode, and the GDLs.
the 3D flow of continuity equation is [1] :

$$\frac{\partial(\rho u)}{\partial x} + \frac{\partial(\rho v)}{\partial y} + \frac{\partial(\rho w)}{\partial z} = -\frac{\partial \rho}{\partial t} \tag{4}$$

Where, ρ=density, u, v,w are the velocity components of the x, y, and z respectively.
In porous electrodes, the momentum equation can be written as:

$$\nabla.(\varepsilon\rho \underset{\upsilon}{\rightarrow} \underset{\upsilon}{\rightarrow}) = -\varepsilon\nabla p + \nabla\varepsilon\tau + Sm \tag{5}$$

The momentum equation in the x-direction is :

$$u\frac{\partial(\rho u)}{\partial x} + v\frac{\partial(\rho u)}{\partial y} + \omega\frac{\partial(\rho u)}{\partial z} =$$

$$-\frac{\partial p}{\partial x} + \frac{\partial}{\partial x}\left(\frac{\mu\,\partial u}{\partial x}\right) + \frac{\partial}{\partial y}\left(\frac{\mu\,\partial u}{\partial y}\right) + \frac{\partial}{\partial z}\left(\frac{\mu\,\partial u}{\partial z}\right) + Sm \tag{6}$$

Where S_m is mass sink term. It can use the expression for y and z-direction (just changed the composition of each direction).
Diffusion mass flux vectored can calculate from Fick's equation is :

$$\underset{j}{\rightarrow}_{i} = \sum_{j=1}^{N-1} \rho\, Dij \nabla \underset{yi}{\rightarrow} \tag{7}$$

Where Dij is the diffusivity of species.
The heat is transferred due to the chemical source, the Brinkman Equations is[17] :

$$\frac{1}{\epsilon_P}\rho(u.\nabla)u\frac{1}{\epsilon_P} = \nabla.[-pI + K] - \left(\mu K^{-1} + \beta_F|u| + \frac{Q_m}{\epsilon_P^2}\right)u + F \tag{7}$$

$$\nabla.(\rho u) = Q_m,\ K = \mu\frac{1}{\epsilon_P}(\nabla u + (\nabla u)^T - \frac{2}{3}\mu\frac{1}{\epsilon_P}(\nabla.u)I \tag{8}$$

Where k is the conductivity of the polar plate. And for Transport of Concentrated Species is:

$$\nabla.j_i + \rho(u.\nabla)\omega_i = R_j \tag{9}$$

$$j_i = -(\rho D_i^m \nabla\omega_i + \rho\omega_i D_i^m \frac{\nabla M_n}{M_n} - j_{c,i} + D_i^T \frac{\nabla T}{T} \tag{10}$$

$$D_i^m = \frac{1-\omega_i}{\sum_{k\neq i}\frac{Xk}{D_ik}},\quad M_n = (\sum_i \frac{\omega_i}{M_i})^{-1} \tag{11}$$

2.2 Physical Model

To run the model, the proton exchange membrane fuel cell (PEMFC) was designed and tested successfully by COMSOL Multiphysics 5.4 software**.** Fig 2 shows the three inlet cubic channels with three cubic outflow channels. All dimensions and the operating parameters that were input to the run are shown in Table1**.** The model test with three different inlet velocities ranged as (1.5, 2.5, and 3.5 m/sec). Table 2 shows the element quality of the fuel cell domain. Fig 3 and Fig 4 show the mesh of the whole fuel cell and the test of the mesh.

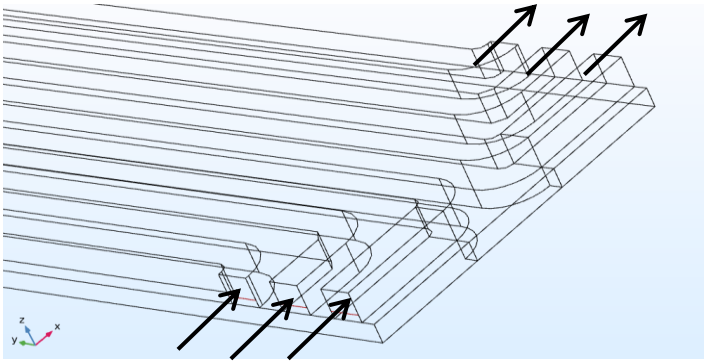

Fig 2. Dimensions of simulated.

Table 2. Statistical of element quality.

Description	Value
Min. element quality	0.08319
Average element quality	0.673
Tetrahedron	83113
Triangle	46997
Edge element	5041
Vertex element	140
Nu. of elements	251489
Element volume ratio	0.01344

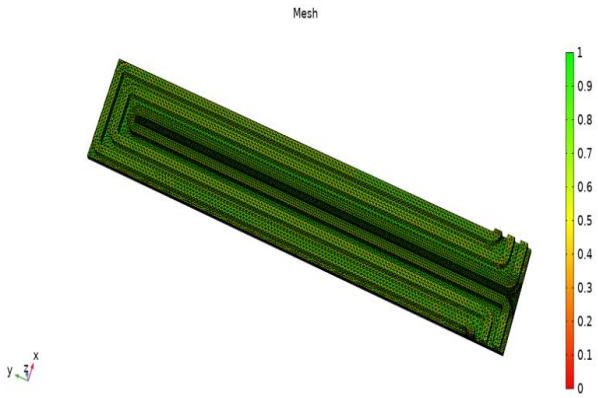

Fig 3. 3D mesh domain test.

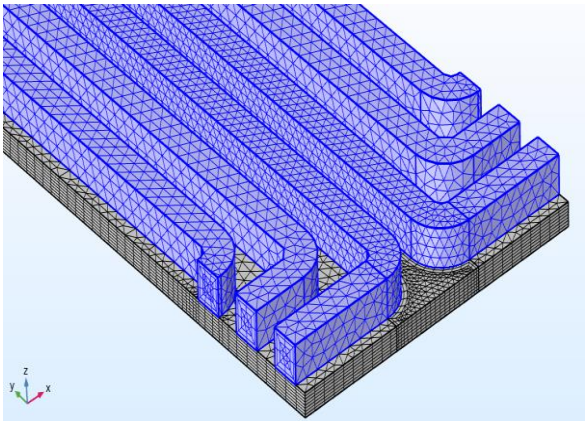

Fig 4. 3D snapshot for inlet and outlet meshing domain test.

3 Results and Discussions

3.1 Model Validation

Fig 5, explained the comparison of present work with previous work which was obtained from the experiment data's [1]. Their data compared at the ranged of the current density approximately from (0.22 to 1.07 A/cm^2). Our results are simulated at the inlet velocity of (1.5 m/sec). The Figure illustrates the current is slight decreases with varying cell voltage. While for previous work, the clear slop of line increased the current density vs cell voltage.

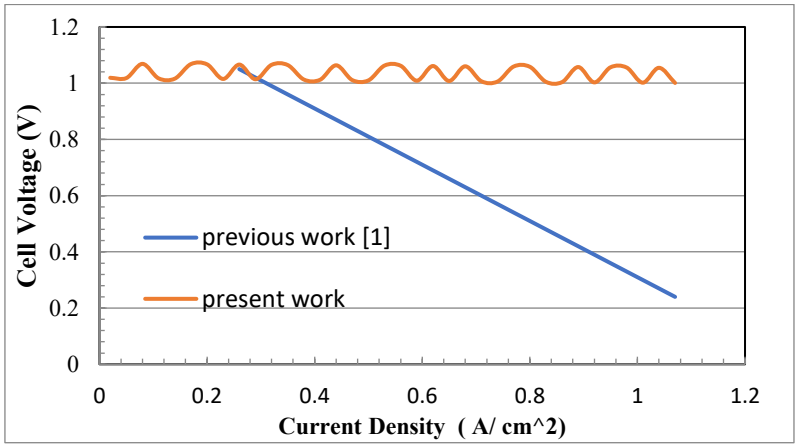

Fig 5. The comparison between present work with [1].

3.2 Oxygen distribution

Fig 6 shows the oxygen distribution in the fuel cell channels in 3D. Oxygen concentration is higher at the inlet of each channel, and then gradually decreases towards the outlet. With opened pieces of literature, the reduction in oxygen concentration leads to a slower reaction rate of the cell. In the channels, the oxygen mass fraction is significantly higher. As inlet velocity increases,

the high concentration value of oxygen starvation is remarkably reduced at the cell's outlet. In Figure 6, the oxygen distribution is shown at an inlet velocity of (1.5 m/sec) while Figs 6-b and 6-c show inlet velocities of 2.5 and 3.5 m/sec.

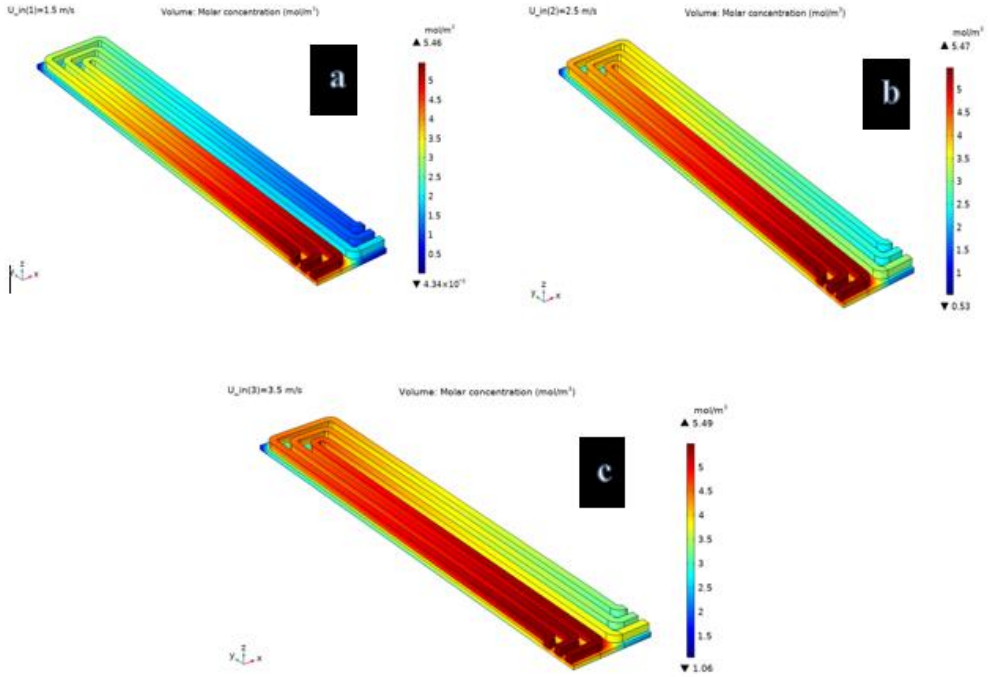

Fig 6. Distribution of oxygen concentration.

3.3 Velocity Distribution

Fig 7 shows the 3D velocity distribution of the water inside the fuel cell channels. Each cell of the channel displays a serpentine flow field. The distribution inside the channel changed as velocity increased at the inlet. The more reaction between gas and diffusion layer, the more reliable the reaction. In addition to the velocity distribution, the pressure distribution can also be used to show the behavior inside the fuel channel. As inlet velocity increases, the pressure increases and gradually decreases until it reaches a lower value at the outlet as shown in Fig 8.

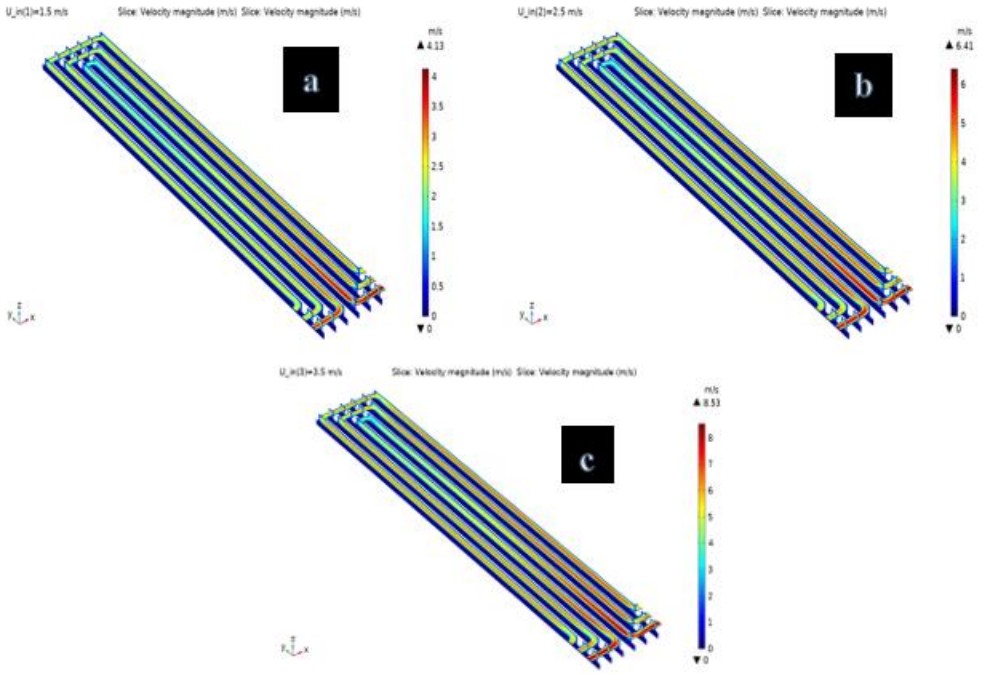

Fig 7. 3D velocity distribution at three inlet velocities.

3.4 Current Density

Fig 9 illustrates the current density distribution at the cathode base. The most uniform distribution of current density is seen at serpentine flow fields, as is the distribution of oxygen molar concentration. Gas diffusive layers in the cathode release more reactants and can participate in the electrochemical reaction of the catalyst layer, as shown in Fig 10. These results can be used to improve and implement serpentine flows in fuel cell PEMFCs.

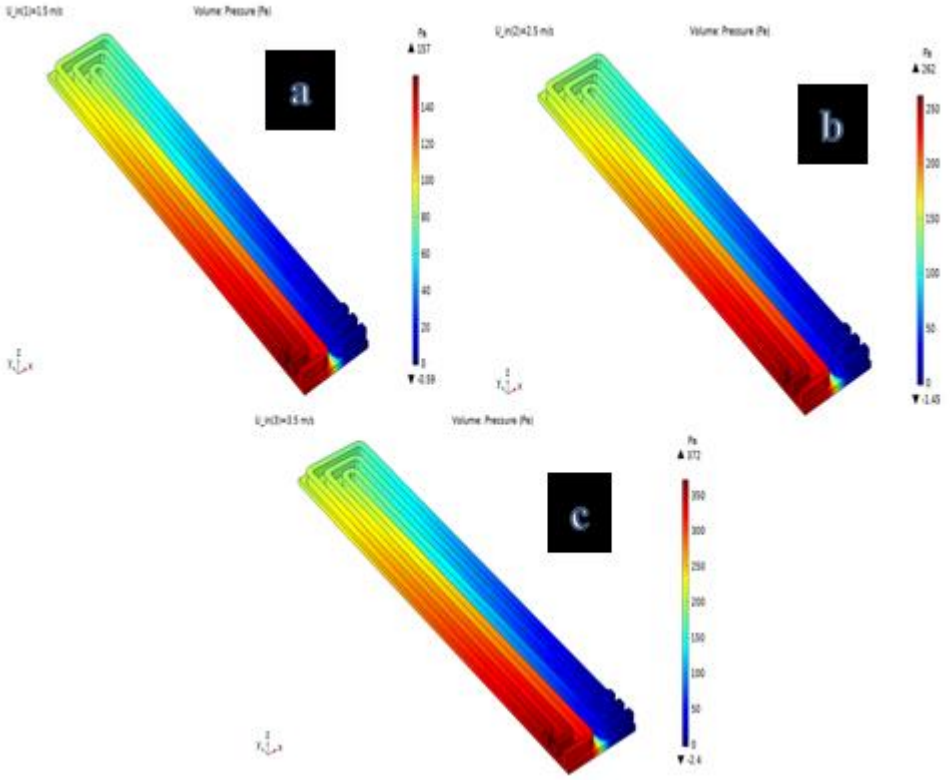

Figure 8. 3D pressure drop distribution at three inlet velocities.

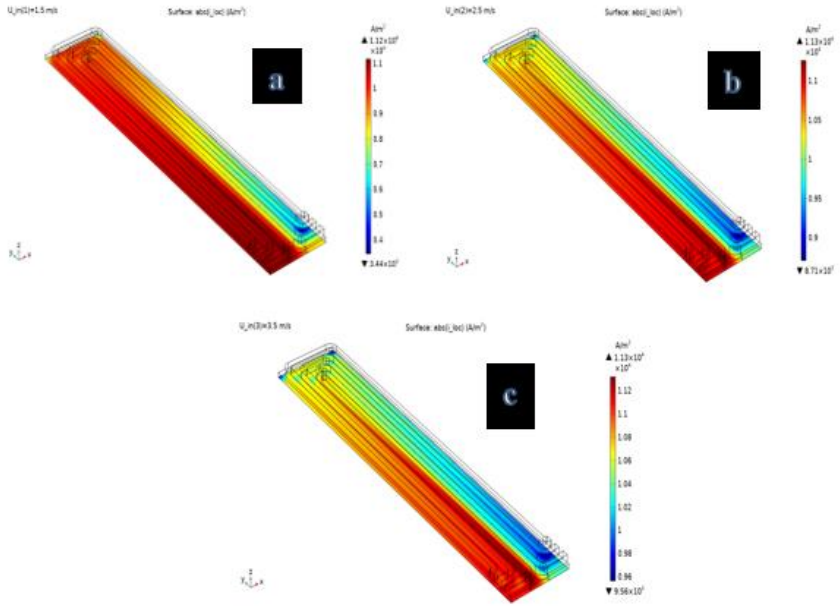

Fig 9. 3D current density distribution at the cathode at three inlet velocities.

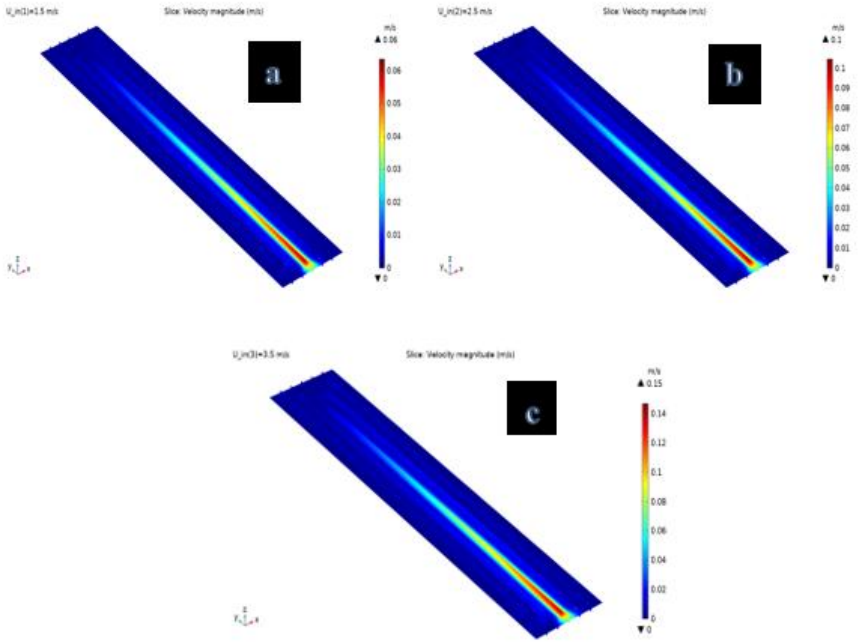

Fig 10. 3D gas diffusion layer (GDL) distribution at the cathode at three inlet velocities.

4 Conclusion

Three different inlet velocities were used to model the serpentine flow field in 3D. We use three cubic channels with inlet and outlet dimensions of (0.8*0.8 mm with average plate width of 50mm), all other parameters are listed in Table 1. By using the COMSOL Multiphasic 5.4 software (Free Demo), the model of the simulation is successfully run to test the effects of varying the inlet velocity on the performance of the fuel cell. The following conclusion follows:

1. The higher performance to produce the current density with serpentine flow field arrangement is obtained in the present work and so for observed by the former researchers.
2. 3D oxygen distribution uniformly at higher values inlet and gradually reduction it to outlet due to decreases the mass fraction when it reacts with GDL.
3. 3D current density distributed at the cathode is observed that the most uniform at serpentine flow field. The gas diffusive layer in the cathode is more reactant given participated the catalyst interchanged.
4. The increases in inlet velocities that lead to high-pressure drop values were observed through the inlet and outlet of each channel.

References

[1] Fatemeh Hashemi, Soosan Rowshanzamir, Mashallah Rezakazemi. CFD simulation of PEM fuel cell performance: Effect of straight and serpentine flow fields. (2012). Mathematical and Computer Modelling.Volume 55, Issues 3–4, Pages 1540-1557.

[2] Li X, Sabir I. Review of bipolar plates in PEM fuel cells: flowfield designs. Int J Hydrogen Energy 2005;30:359e71.
[3] Nik Suhaimi Mat Hassan, Wan Ramli Wan Daud, Kamaruzzaman Sopian, Jaafar Sahari. Water management in a single cell proton exchange membrane fuel cells with a serpentine flow field. (2009). Journal of Power Sources 193. 249–257.
[4] B. Rismanchi, M.H. Akbari, Performance prediction of proton exchange membrane fuel cells using a three-dimensional model. (2008). International Journal of Hydrogen Energy 33 439–448.
[5] Fan L, Zhang G, Jiao K. Characteristics of PEMFC operating at high current density with low external humidification(2017). Energy Convers Manage;150:763–74.
[6] A. Alaswad, A. Baroutaji b, H. Achour, J. Carton, Ahmed Al Makky, A.G. Olabi. Developments in fuel cell technologies in the transport sector. (2016). International Journal of Hydrogen Energy Volume 41, Issue 37, 5, Pages 16499-16508.
[7] Zhongying Shi, Xia Wang. A numerical study of flow crossover between adjacent flow channels in a proton exchange membrane fuel cell with serpentine flow field. (2008). Journal of Power Sources .185, 985–992.
[8] Lin L, Zhang X X, Feng H T, et al. Optimization of a serpentine flow field with variable channel heights and widths for PEM fuel cells. (2010). Sci China Tech Sci, 53: 453–460, DOI: 10.1007/s11431-010-0009-4.
[9] P.V. Suresh, S. Jayanti, A.P. Deshpande, P. Haridoss. An improved serpentine flow field with enhanced cross-flow for fuel cell applications. (2011). International Journal of Hydrogen EnergyVolume 36, Issue 10, Pages 6067-6072.
[10] Morad, A. M. A. A Two-Phase Pressure Drop Model for Homogenous Separated Flow for Circular Tube Condenser, Examined with Four Modern Refrigerants. (2018). Journal of Advanced Research in Fluid Mechanics and Thermal Sciences, 52 (2), 274–287.
[11] Andrew Higier, Hongtan Liu. Direct measurement of current density under the land and channel in a PEM fuel cell with serpentine flow fields. (2009). Journal of Power Sources 193 (2009) 639–648.
[12] Kush Chadha, Serguei Martemianov, Anthony Thoma. Study of new flow field geometries to enhance water redistribution and pressure head losses reduction within PEM fuel cell. (2021). International Journal of Hydrogen Energy Volume 46, Issue 10, 8, Pages 7489-7501.
[13] Chen Yang, Zhongmin Wan, Xi Chen, Xiangzhong Kong, Jing Zhang, Taiming Huang, Xiaodong Wang. Geometry optimization of a novel M-like flow field in a proton exchange membrane fuel cell(2021). Energy Conversion and Management Volume 228, 15, 113651.
[14] Xi Chen, Zhengkun Yu, Chen Yang, Yao Chen , Chao Jin , Yuejiao Ding, Wenbin Li, Zhongmin Wan. Performance investigation on a novel 3D wave flows channel design for PEMFC. (2021). International Journal of Hydrogen Energy Volume 46, Issue 19, 16, Pages 11127-11139.
[15] Mehrdad Ghasabehi , Moosa Ashrafi , Mehrzad Shams. Performance analysis of an innovative parallel flow field design of proton exchange membrane fuel cells using multiphysics simulation. (2021). FuelVolume 285, 1 February 2021, 119194
[16] Aezid-Ul-Hassan Najmi, Ikechukwu S. Anyanwu, Xu Xie, Zhi Liu, Kui Jiao. Experimental investigation and optimization of proton exchange membrane fuel cells using different flow fields. (2021). Energy Volume 217, 15, 119313.
[17] R.Byron Bird, Warren E. Stewart, Edwin N. Lightfoat. Transport Phenomena. 2nd Edition, (2002). Wiley International Edition.

Experimental and Theoretical Study to Improve the Spark Ignition Engine Performance

Ali R. Badr[1], Saadoon Fahad Albahadili [2], and Tahseen A. Jabbar[3]
{ ali.nabhani313@gmail.com[1], s.albahadili@stu.edu.iq[2], and tahseen.ali@stu.edu.iq[3]}

Fuel and Energy Department, College of Technical Engineering, Southern Technical University, Iraq[1,2,3]

Abstract. One of the most important components affecting performance in internal combustion engines(ICE) is the intake manifold. The present work presents an improvement of Spark Ignition (SI) engine performance by adding a swirl generator (mixer) within the inlet port. Experiments were applied on a single-cylinder, four-stroke, GREEN CUT AV3500 gasoline engine. Exhaust emissions compositions and fuel consumption are recorded. To understand the behaviour of airflow through the intake port with and without the swirl generator, a 3D model was analysed using Computing Fluid Dynamic (CFD) by ANSYS Fluent 2020 R1. Results show an enhancement of engine performance especially fuel consumption by 24%, and the concentration of CO in exhaust emissions by 67%. As well as, computationally, pressure drop improved with intake port equipped with the mixer.

Keywords: Internal Combustion Engine, Intake Manifold, CFD simulation, Swirl Motion, Experiment.

1 Introduction

Improving performance (power and torque),fuel-saving, and reducing pollutant emissions have intensified efforts to gain better design of an internal combustion engine manufacturing field [1]. One of the most crucial factors in achieving this is the optimization of the intake manifold design [2]. the inlet manifold is responsible for uniform air distribution inside the runner and preparing a homogeneous air-fuel mixture [3] inlet manifold geometry plays an important role in air motion phenomenon inside the intake manifold, which governs the engine performance of spark ignition engines [4] Generally, In a typical intake manifold, airflow is laminar during the induction stroke, resulting in weak homogeneity of fuel atomization. Meanwhile, creating turbulent flow decreases pressure drop through the intake port which increases air density to get better air-fuel mixing and complete combustion [5],[6]. Since the intake manifold plays an important role in engine performance, different techniques were studies to improve engine performance. J.Bayas, et.al. [7] conducted a study of the effect of intake manifold length on internal combustion engine performance. A single-cylinder, four-stroke intake manifold with various intake lengths mounted on the engine has been tested Length of the intake manifold is changed for a speed range of 1200-2000 rpm and the other parameters are kept constant. The first test was carried out with the typical intake manifold length of the engine under study 250mm and 45mm diameter, then the intake manifold length was changed

IMDC-IST 2021, September 07-09, Sakarya, Turkey
Copyright © 2022 EAI
DOI 10.4108/eai.7-9-2021.2314807

as per the calculations done by using empirical relationships and the data were recorded. Results show that the volumetric efficiency, toque, and brake power can be improved by varying the intake manifold length. The optimum engine performance was achieved when the length of the intake manifold decreased at high engine speeds. Och et. al. [8] investigates the effect of the intake manifold length on engine performance. The study is carried out on a single-cylinder diesel engine. The authors applied the stochastic optimization technique called Differential Evolution to find optimal duct lengths to optimize the engine performance. Results showed that the length of the intake manifold plays a role key in the engine outputs. Mohammed K. et al. [9] experimentally and numerically investigates the effect of the curvature of the inlet port on the engine performance. Various angles(0º,90º,180º,180º NP,135º NE) of curved intake port are applied on a single-cylinder four-stroke gasoline engine, the analysis of data shows the optimal angle of curvature is 135º, at which air velocity and pressure are improved resulting in enhancement of air/fuel ratio, the mass of fuel consumed and the emissions of exhaust gases. D.Ramasamy et. al.(10)conducted a study of performance improvement in Air Intake System (AIS) of 1.6L Engine by adding guide vane in the inlet plenum of the air filter, It was found that the pressure drop improved by 12.01% for the rpm speed of 1000 to 7000 With Guide Vanes, this results in air-fuel mixing and fuel combustion process to improvement in airflow behaviour. Sunaryo et. al. [6] presents a CFD analysis of adding a gasket mixer shaped between the carburettor and intake manifold in order to optimize the airflow behavers, researchers found that Adding an insulator mixer inside the air duct can improve the airflow characteristics, such as pressure and turbulence intensity, resulting in increased volumetric efficiency. In the same context, S.L.V. Prasad et.al. [11] Reported that The effect of air swirl created by directing airflow in the intake manifold on the engine outputs. Turbulence is created in the inlet manifold by grooving it with a helical groove that is 1 mm wide and 2 mm deep with different pitches to guide the airflow. Experiments are carried out on a single-cylinder, light-duty, direct injection diesel engine. As a result, the brake thermal efficiency was increased with an increase in brake power and specific fuel consumption and soot emission level were reduced. moreover, A.K. Mohiuddin [12] investigates the swirl effect on engine performance by inserting a swirl adapter. The experiment has been carried out on the protons CAMPRO engine model of 1.6 litters. In swirl device adapter blade angle is maintained at 30º placed in the intake port. The GT-SUITE software was used which has a standard swirl flow embedded in it. It is found that a swirl factor is an important tool in the reduction of fuel consumption and influences volumetric efficiency improvement. In this study, a swirl generator is applied in the intake port in order to improve the airflow characteristic

2 Materials and Methods

Figs 1 and 2 show the Schematic diagram and photographic experimental setup used for the investigations. A four-stroke, single-cylinder, SI engine is coupled to a dynamometer for measuring brake power. Fuel consumption of the engine is measured with the burette method, Engine speeds are measured with a tachometer, while exhaust gases are analysed by INFRARED 4 GAS ANALYZER model: FLUX-2000-4. A pipe of 90cm long is cut into 9 parts connected to the inlet port of the carburettor. At the beginning of the experiments, the engine was run at full load at 2760 rpm. When the engine reached the steady-state conditions, the first experiment was conducted to locate the best position for fixing the swirl generator. Then tests were carried out with various engine speeds and loads, with and without swirl generator.

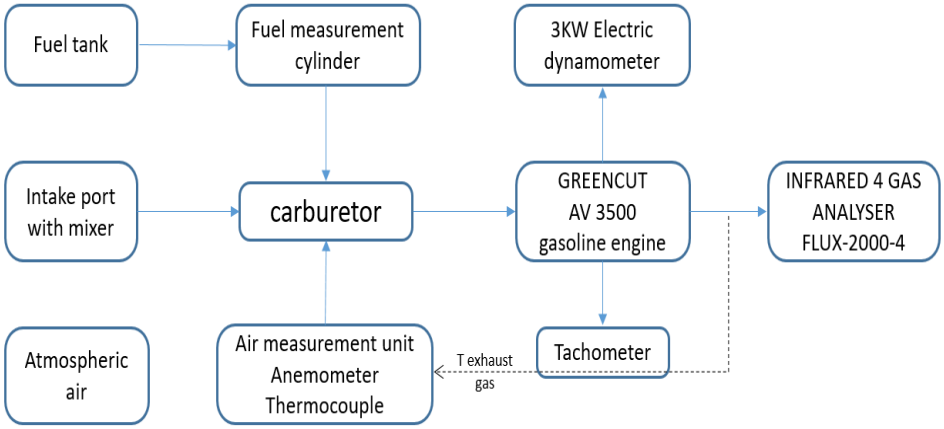

Fig. 1. Overall experiment instruments layout.

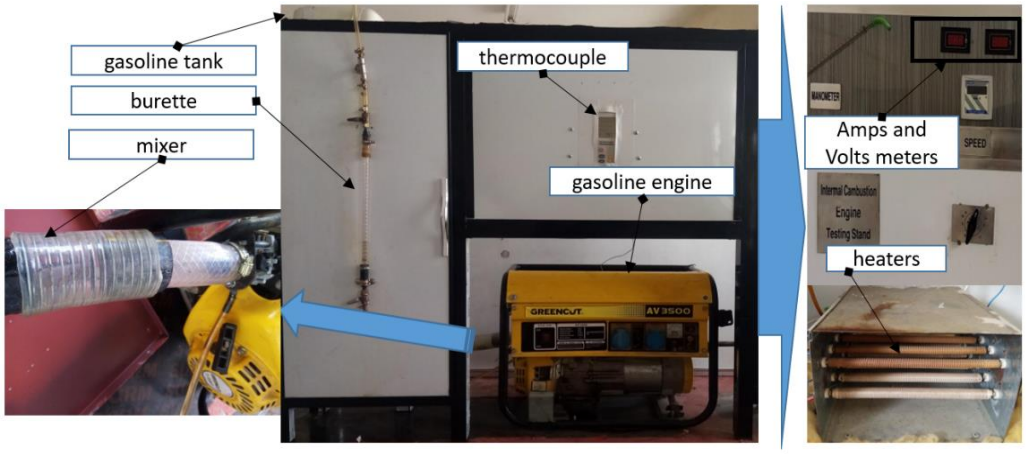

Fig. 2. Test equipment's photograph.

3 Computational Analysis

3.1 CFD Process Setup

Fig. 3 illustrates the 3D model of the engine geometry. Combustion chamber, intake and exhaust ports, intake and exhaust valves were established by using the Pre-processor design modeler of internal combustion engine IC Engine (Fluent) tools. After meshing the model by using the mesh tool to discretize the solution equations, the model is transferred to a Fluent setup, the air is used as a working fluid. k-ε turbulence model was used in the CFD model. Four models of mixer are simulated as shown in Figure (9), 20mm diameter,0.2mm thickness for each one, and 12mm depth of model (a)and (c),72mm^2 passing cross-section area.

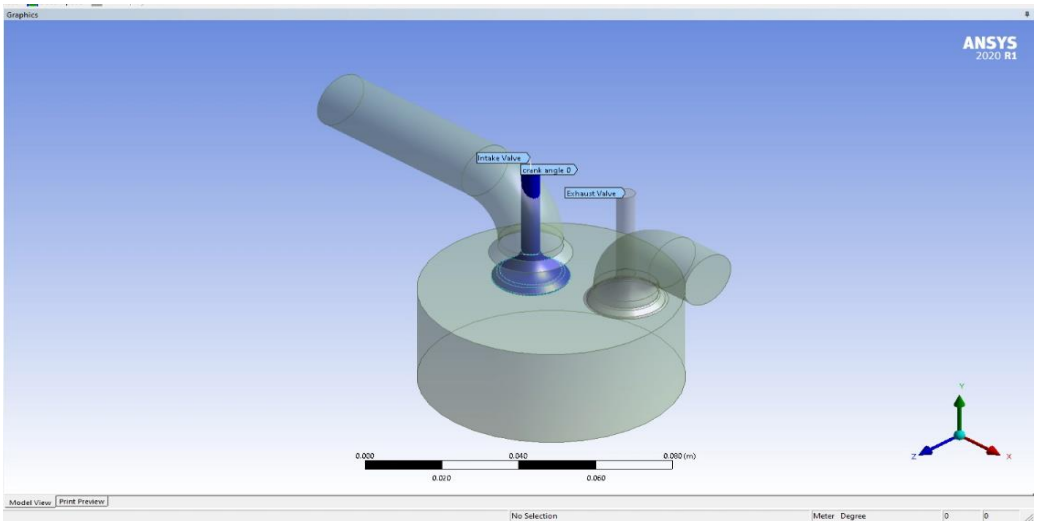

Fig. 3. Geometry model created in fluent.

3.2 Mathematical Equations

CFD generally solves fluid motion by solving the Navier-Stokes equation of mass, momentum, and energy equation. (13).

Continuity equation

$$\frac{\partial \rho}{\partial t} + \frac{\partial (\rho.\mathrm{u})}{\partial \mathrm{x}} + \frac{\partial (\rho.\mathrm{v})}{\partial \mathrm{y}} + \frac{\partial (\rho.\mathrm{w})}{\partial \mathrm{z}} = 0 \tag{1}$$

X-Momentum Equation

$$\rho \frac{\partial \mathrm{u}}{\partial t} + \rho u \frac{\partial \mathrm{u}}{\partial \mathrm{x}} + \rho v \frac{\partial \mathrm{u}}{\partial \mathrm{y}} + \rho w \frac{\partial \mathrm{u}}{\partial \mathrm{z}} = \rho g_x - \frac{\partial \mathrm{p}}{\partial \mathrm{x}} + \mu \frac{\partial^2 \mathrm{u}}{\partial \mathrm{x}^2} + \mu \frac{\partial^2 \mathrm{u}}{\partial \mathrm{y}^2} + \mu \frac{\partial^2 \mathrm{u}}{\partial \mathrm{z}^2} \tag{2}$$

Y-Momentum Equation

$$\rho \frac{\partial \mathrm{v}}{\partial t} + \rho u \frac{\partial \mathrm{v}}{\partial \mathrm{x}} + \rho v \frac{\partial \mathrm{v}}{\partial \mathrm{y}} + \rho w \frac{\partial \mathrm{v}}{\partial \mathrm{z}} = \rho g_y - \frac{\partial \mathrm{p}}{\partial \mathrm{y}} + \mu \frac{\partial^2 \mathrm{v}}{\partial \mathrm{x}^2} + \mu \frac{\partial^2 \mathrm{v}}{\partial \mathrm{y}^2} + \mu \frac{\partial^2 \mathrm{v}}{\partial \mathrm{z}^2} \tag{3}$$

Z-Momentum Equation

$$\rho \frac{\partial \mathrm{w}}{\partial t} + \rho u \frac{\partial \mathrm{w}}{\partial \mathrm{x}} + \rho v \frac{\partial \mathrm{u}}{\partial \mathrm{y}} + \rho w \frac{\partial \mathrm{w}}{\partial \mathrm{z}} = \rho g_z - \frac{\partial \mathrm{p}}{\partial \mathrm{z}} + \mu \frac{\partial^2 \mathrm{w}}{\partial \mathrm{x}^2} + \mu \frac{\partial^2 \mathrm{w}}{\partial \mathrm{y}^2} + \mu \frac{\partial^2 \mathrm{w}}{\partial \mathrm{z}^2} \tag{4}$$

3.3 The Standard k-ε Model

The standard k-ε model has two model equations one for the turbulence kinetic energy (k) and one for dissipation rate (ε). The model transport equation for k is derived from the exact

equation, while the model transports equation for ε was obtained by using the physical analysis. The standard model uses the following transport equations for k and ε (14).

The turbulent kinetic energy (k):

$$\frac{\partial}{\partial x_i}(\rho k u_i) = \frac{\partial}{\partial x_i}\left[\left(\mu + \frac{\mu_t}{\sigma_k}\right)\frac{\partial k}{\partial x_i}\right] + G_k - \rho\varepsilon \quad (5)$$

The energy dissipation rate (ε):

$$\frac{\partial}{\partial x_i}(\rho \varepsilon u_i) = \frac{\partial}{\partial x_i}\left[\left(\mu + \frac{\mu_t}{\sigma_\varepsilon}\right)\frac{\partial \varepsilon}{\partial x_i}\right] + C_{1\varepsilon}\frac{\varepsilon}{k}G_k - \rho C_{2\varepsilon}\frac{\varepsilon^2}{k} \quad (6)$$

Where:

G: Turbulent production term of kinetic energy.

$$\mu_t = \rho C_\mu \frac{k^2}{\varepsilon} \quad (7)$$

model constants

$C_{1\varepsilon} = 1.44, C_{2\varepsilon} = 1.92, C_\mu = 0.09\,, \sigma_k = 1.0\,, \sigma_\varepsilon = 1.3$

3.3 Boundary Conditions

The simulation work of this study has been applied on four models of the combustion chamber, including the intake port with mixer, piston, exhaust port, inlet valve, and exhaust valve. The boundary conditions were set as the velocity inlet and pressure outlet.

Boundary conditions at the inlet

$$\left.\begin{array}{l} u = u_{in} \\ v = w = 0 \end{array}\right\} \quad (8)$$

Boundary conditions at the outlet

The pressure outlet is zero**.**

$$\frac{\partial u}{\partial x} = \frac{\partial v}{\partial y} = \frac{\partial w}{\partial z} = 0 \quad (9)$$

$$\frac{\partial k}{\partial x} = \frac{\partial \varepsilon}{\partial x} = 0 \quad (10)$$

Boundary conditions at the solid walls

A No-slip boundary condition is applied to all of the wall surfaces.

$$u = v = w = 0 \quad (11)$$

4 Results and Discussion

4.1 Experimental Results

This analysis of data is carried out based on variable engine speeds with and without the mixer. The approach of this data analysis is carried out to study the output data behaviour towards the manipulation of engine speed and loads. Figs 4 and 5 demonstrate the effect of the mixer position through the intake port on fuel consumption and exhaust gas emissions in constant engine speed at 2760 rpm, nine points are investigated with 10cm each and moved forward, results show the distance of 20cm between the carburettor inlet hoe and mixer is the more effective distance in which fuel consumption enhanced by 24% which is from 14.7ml/min without mixer to 11.1ml/min with mixer. While The carbon monoxide volume percentage is lower on the condition with mixer 0.82%volume. and higher on the condition without mixer 2.46% volume with 67% improvement. This means that the closest mixer position causes high turbulence air motion through the carburettor, carrying a large volume of fuel and forming a rich air-fuel mixture; on the other hand, the further away swirl created slightly decreases through the pipe length, so the swirl position should be carefully selected. BSEC was lower with swirl flow as shown in Fig, 6, as well as carbon monoxide composition decreased as shown in Fig 7.

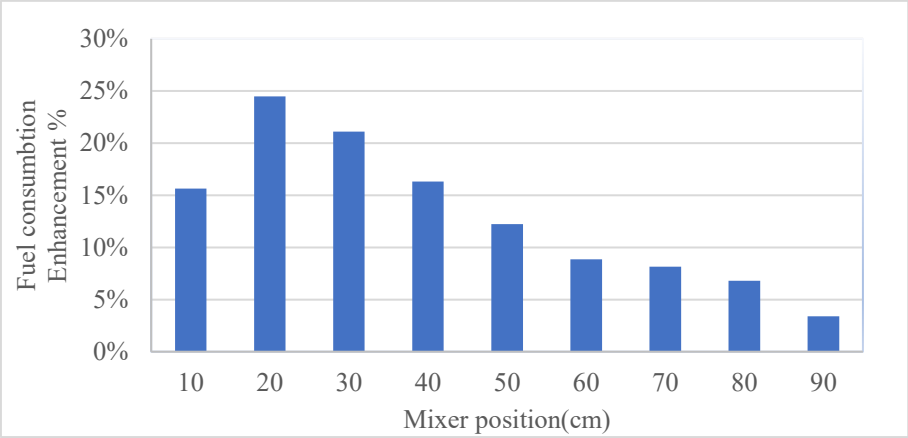

Fig. 4. Fuel consumption enhancement at various points intake pipe.

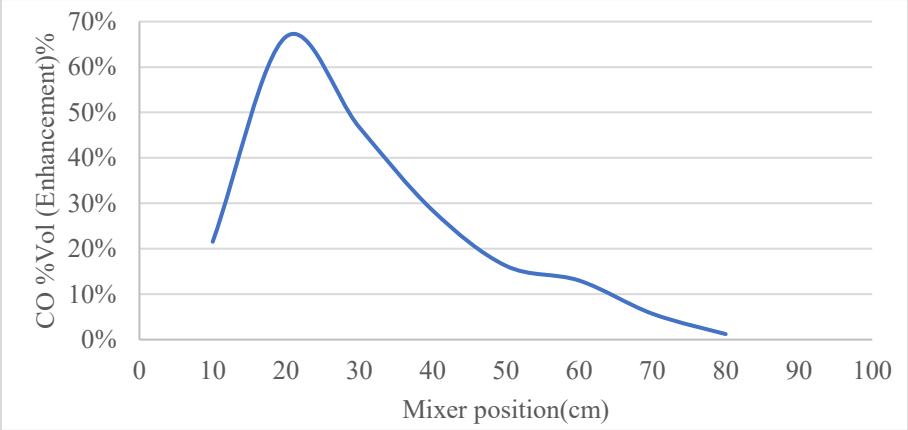

Fig. 5. CO % vol. Enhancement at the various points intakes pipe.

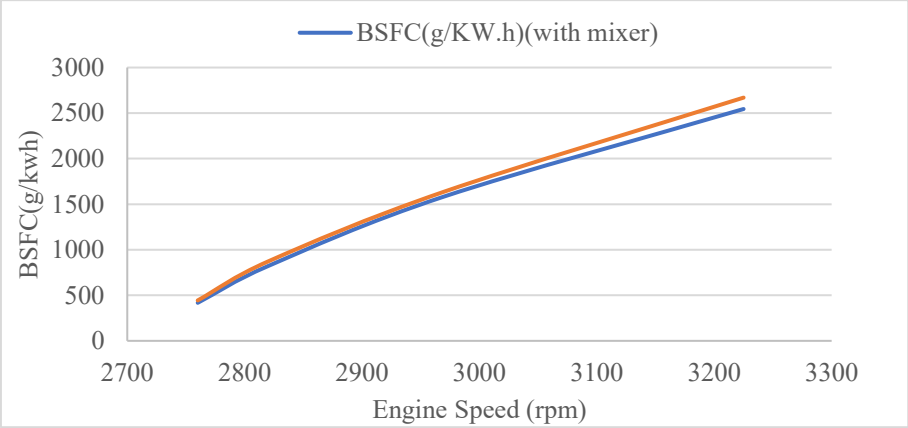

Fig. 6. Effect of different intake manifold configurations on BSFC for various engine speeds.

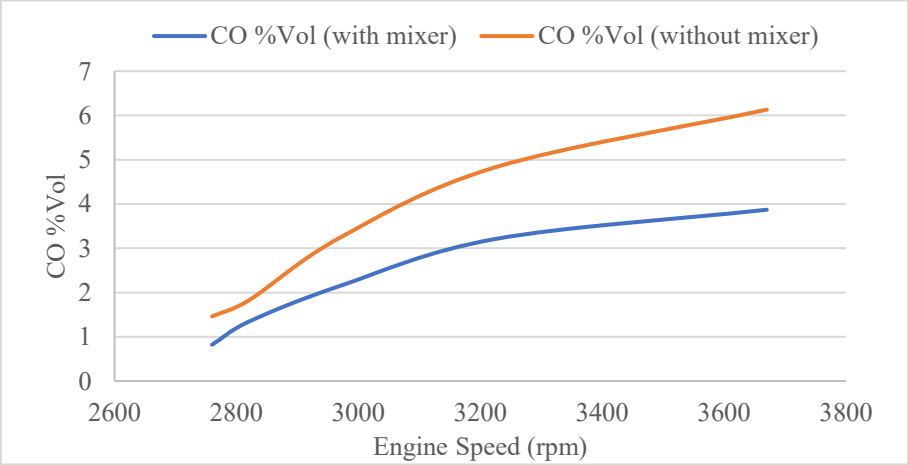

Fig. 7. Effect of different intake manifold configurations on CO emission for various engine speeds.

4.2 Theoretical Results

A higher intake air pressure is preferred to increase air density which allows for better combustion in a shorter time, improve fuel consumption, power output, and reducing of exhaust pollutants level. Fig. 9 demonstrates the turbulence intensity for four models of swirl generators. Based on Fig. 8 model 2 has the greatest turbulence intensity as well as the pressure drop. The higher the turbulence intensity, the higher the pressure drop. In this case, the more efficient model 1can be applied to increase the air pressure entering the combustion chamber which improves the air-fuel mixing process which leads to improving the combustion process.

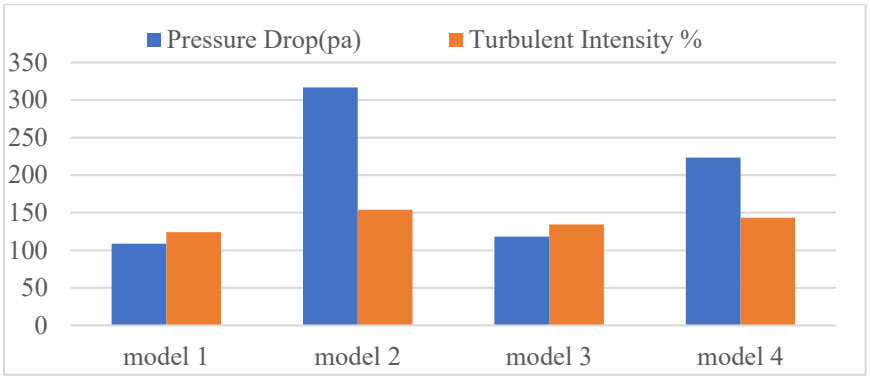

Fig. 8. Pressure drops across the mixer and turbulent intensity created by the mixer for four designs of mixed

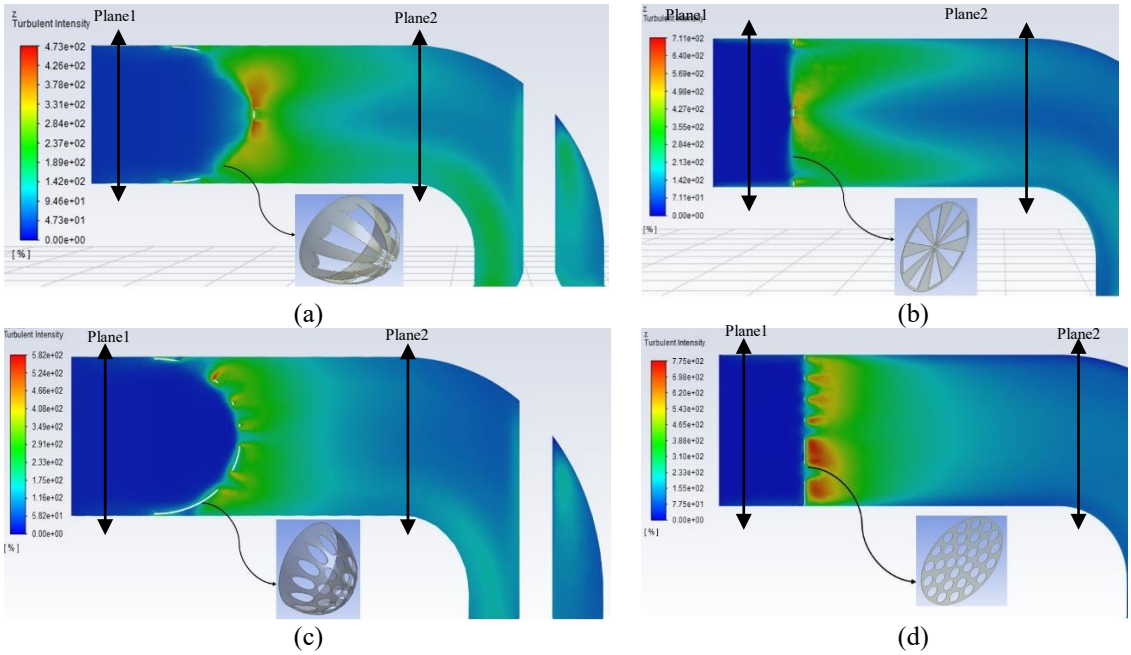

Fig. 9. Visualization of CFD simulations: Turbulence intensity for various shapes of m

5 Conclusion

Based on the experimental and numerical results it can be concluded that:

1- adding a swirl generator to the air intake port can improve the characteristics of the airflow, especially on the pressure and turbulence intensity.
2- Test with an intake port equipped with a swirl generator approved an improvement of fuel consumption and CO emission level.
3- CFD analysis shows that the shape of the swirl generator, blade number, blade area have a significant role in the airflow pattern.
4- CFD analysis can be applied to optimize the intake port of an IC engine.

Nomenclature

ICE	Internal Combustion Engine
SI	Spark Ignition
BSEC	Break specific fuel consumption
CFD	Computing Fluid Dynamic
k-ε	Turbulence model (k: turbulent energy, ε: Turbulent dissipation energy)
CO	Carbon monoxide
Model 1,2,3,4	Figurer (9). a, b, c, d respectively

References

1. Mallikarjuna JM. Characterization of Flow through the Intake Valve of a Single Cylinder Engine Using Particle Image Velocimetry. 2010;(July).
2. Singla S. Study of Design Improvement of Intake Manifold of Internal Combustion Engine. 2015;3(March):234–42.
3. Heywood-jb-internal-combustion-engine-fundamentals.pdf.
4. Mechanics F, Kumar M. Turbulence Modeling in CFD Simulation of Intake Manifold for a 4 Cylinder Engine. 2012;(July):1747–53.
5. Al-kayiem HH, Wahhab HAA. Computational Analysis of Flow Characteristic in Inlet and Exhaust Manifolds of Single Cylinder Spark Ignition Engine Research Article 2017;(June).
6. Sunaryo, Irfan A, Setiyo M, Amin N. Design and simulation of mixer insulators to improve turbulence in intake manifold. J Phys Conf Ser. 2020;1517(1).
7. Bayas J, Jadhav NP, Technical S, Society E, Enhancement HT. Effect of Variable Length Intake Manifold on Performance of IC Engine. Int J Curr Eng Technol. 2016;(June).
8. Och SH, Moura LM, Mariani VC, Coelho L dos S, Velásquez JA, Domingues E. Volumetric efficiency optimization of a single-cylinder D.I. diesel engine using differential evolution algorithm.

9. Rishack QA, Dakhil SF, Obaid MK. Theoretical and Experimental Study of the Intake Manifold Effect on the SI Engine Performance. Basrah J Eng Sci. 2014;14(2):200–15.

10. Ramasamy D, Zamri M, Mahendran S, Vijayan S. Design optimization of Air Intake System (AIS) of 1.6L engine by adding guide vane. Proc Int MultiConference Eng Comput Sci 2010, IMECS 2010. 2010;(September 2014):999–1003.

11. Prasad V, Rangadu VP. Reduction of emissions by intensifying air swirl in a single cylinder di diesel engine with modified inlet manifold

12. AKM M. Investigation of the Swirl Effect on Engine Using Designed Swirl Adapter. IIUM Eng J. 2011;12(3).

13. Y HKH, N J. Port flow simulation of an ic engine. Int J Innov Eng Res Technol. 2015;2(9):1–9.

14. ANSYS. ANSYS Fluent Theory Guide. ANSYS Inc, USA . 2013;15317(November):814.

Accounting Education and Its Role in Light of Contemporary Trends in The Accounting Profession - An Applied Study

Jenan Abd AL-Abbas Al Dulamy[1], Ade Ghani Hamadi[2]

{Jenan.aldulamy@atu.edu.iq[1], ade.ghani@mustaqbal-college.edu.iq[2]}
Babylon Technical Institute AL-Furat AL-Awsat Technical University1
Al Mustaqbal University College 2

Abstract. The value of research is in examining the evolution of the accounting profession and determining how to address modern challenges to the accounting profession through education, training, and re-consolidation and reformulation. The internationalization of the work environment necessitates are the development of accounting education in line with those developments through the introduction of changes in accounting curriculum programmes and learning methods based on the use of a questionnaire that is devoted to the above purpose through a survey. The samples collected from university teaching staff have reached a set of conclusions, this includes the development in accounting has grown calls for the development of accounting education. For a profession, and the available possibilities for continuing education, it is critical to the profession's capacity to fulfil the tasks given to it, and from here, the trends in accounting education followed play a significant part in the profession's continuance and development.

Keywords: Accounting Education, Contemporary Trends In The Accounting Profession.

1 Introduction

The study dealt with a very important topic, which is accounting education, and because of its importance in advancing the accounting profession, as it works to increase the confidence of users of financial reports and investors in the quality of the outputs of those reports and their impact on decision-making. The efficiency of the outputs of the accounting system is related to its ability to issue financial statements of quality and transparency. High on the safety of accounting procedures, the efficiency of management and the appropriateness of its policies, and accounting education is the basis on which the scientific and professional staff are built capable of measuring and communicating economic events and the availability of appropriate

IMDC-IST 2021, September 07-09, Sakarya, Turkey
Copyright © 2022 EAI
DOI 10.4108/eai.7-9-2021.2315378

information for decision-making, which requires the preparation and qualification of accountants and providing them with the knowledge and professional skills necessary to perform their role and this can only be achieved through Education, curriculum and skills. In light of the rapid and continuous changes in the business environment, on the one hand, globalization and the development of information and communication technology systems, which have become pressures, the accounting profession must respond to them to be up to the challenge imposed by the new circumstances and to enhance transparency, disclosure, and accountability, and ensure the quality of outputs. The accounting thought has witnessed development since the emergence of accounting in four stages, the first of which was the technical or professional stage, then the academic stage followed, then the third stage came to include the stage of information systems, and the fourth stage was the stage of social responsibility, which requires attention to accounting education to keep pace with contemporary trends in the profession Accounting. Based on the foregoing and to achieve the research objectives, the research was divided into several axes in addition to the introduction, as the first axis deals with the methodology of research and a review of some previous studies and the contributions made to the current research, and the second axis deals with a theoretical approach that includes accounting education and contemporary trends in accounting professions and accounting education and its role in qualifying accountants According to contemporary trends in the accounting profession, while the third axis dealt with presenting the results of the field study, while the fourth topic dealt with the most important conclusions and recommendations that have been reached.

2 Research Methodology

2.1 Research problem

Accounting is an integral part of the activities of economic units, and this is due to the importance of the services they provide, in addition to being the language of business and an information system that affects and is affected by the internal and external environment surrounding it, which is witnessing many rapid and continuous changes, so the quality of the accounting outputs Of great importance because it affects the decisions of users, and the quality of these outputs is mainly related to the efficiency of the accountant and the integrity of the accounting rules prepared on its basis, so the development of the accounting profession requires a focus on developing the capabilities of accountants, and higher education institutions are at the forefront of the responsible authorities for preparing qualified accountants who are available to them. The scientific and practical skills that enable them to practice the profession, and to meet the business needs of accounting, it was necessary to pay attention to accounting education and develop it to prepare accounting cadres capable of meeting the needs of the increasing demand for accounting arising from developments in the work environment, and the research problem in developing accounting education To meet the requirements of contemporary trends in the accounting profession, and work to provide graduates with skills and experiences a That required by the accounting labour market through accounting education.

2.2 Objectives of the Research

The research seeks to achieve the following objectives:

1. Learn about the concept of accounting education, its importance, and the factors affecting it, as well as the obstacles facing accounting education.
2. Shedding light on contemporary trends in the accounting profession.
3. Identify the basic requirements to face the contemporary challenges of the accounting profession.
4. Presenting some recommendations that prepare the future ambition of the field of developing accounting education to be in line with contemporary trends in the accounting profession.
5. Survey the opinions of a sample of lectures in the accounting departments in Iraqi universities and their reflection on the development of accounting education.

2.3 The importance of Research

The importance of research lies in reviewing the developments that the accounting profession has undergone and how to face contemporary challenges to the accounting profession through education, training, and reformulating and reorganizing the accounting profession. The continuous development in the business sector has led to the emergence of new topics that require follow-up of accounting thought for Responding to global economic changes in the work environment, which requires the development of accounting education in line with these developments through the creation of changes in accounting curricula programs and learning methods, and an emphasis on integration between accounting education acquired field experience and the requirements of the labour market.

2.4 Research Hypotheses

The research seeks to achieve the following hypotheses:

1. The possibility of developing accounting education.
2. Recent trends have affected the accounting profession.
3. There are basic requirements to face the contemporary challenges of the accounting profession.

2.5 Research Method

The descriptive-analytical method was adopted to verify the research hypotheses, adopt the inductive method for scientific research, in addition to adopting the analytical and interpretive method for the results obtained from the sample opinions.

3 Literature Review

A local study: (Jabbar, 2015) Titled (The reality of accounting education in Iraq and its compatibility with international accounting education standards - an applied study of a sample of universities)]1] The study aimed to highlight the importance of the interaction of Iraqi universities that offer to account educational programs with the requirements of practicing the accounting profession. Through relying on accounting education programs that simulate the requirements of international accounting education standards, and in a way that is reflected in the development of the reality of the practice of the profession, the study used an analytical

method using a questionnaire form, and the study reached the need to review the curricula and formulate them according to the requirements of the labour market in line with developments and provide training and education for lectures Undergraduates on methods of active education being the main pillar in accounting education programs, and for students' absorption to be according to the absorptive capacity of accounting departments.

An Arab study: A study (Medukh, 2014): Titled (The reality of the evolution of the accounting profession between the professional and technological qualification of accountants in companies operating in the Gaza Strip))]2] This study aimed to demonstrate the impact of accounting and technological qualification on the actual reality of the accounting profession in the Gaza Strip, and also Demonstrating the importance of qualifying the accountant and his knowledge of information technology in facing the challenges that accompany the accounting profession, in addition to emphasizing the role of knowledge management and information technology in developing and improving accounting qualification. For this axis (67.4%), through the companies' use of computers in accounting work, to achieve many advantages for them, and the results showed that obstacles are facing the process of developing the accounting profession in the Gaza Strip due to the lack of awareness of the company's owners about the accounting profession.

A Foreign Study: A Study (Bui & Porter, 2010): Titled (The Expectation-Performance Gap in Accounting Education: An Exploratory Study))]3]: This study came to explore and analyse the accounting education gap, since the mid-1980s, professional accounting bodies, employers and academics alike have expressed their regret at the failure of universities to equip accounting graduates with the competencies required for the modern business environment. Despite the introduction of changes to accounting education, the gap between the competencies that employers expect and that graduates possess remained, so the study aimed to determine the dimensions of the accounting education gap, and the research concluded with a proposal for a framework to reduce the expectation gap and the performance gap for accounting education in universities. New Zealand, after conducting interviews with students, academics, graduate trainees, and employers, while the study recommended the need for accounting departments in universities to update curricula and provide students with the necessary skills in line with the requirements of the modern business environment.

4 The Contribution Made by The Current Research

The previous studies agree that it was concerned with developing accounting education in universities and institutes and was adopted to achieve its goals on the questionnaire. As for the current study, it focused on developing accounting education in universities in line with contemporary trends in the accounting profession, which is supposed to be its first step in Developing education and improving outcomes to be able to meet the requirements of the labour market in the new work environment.

5 Theoretical Entrance

5.1 Accounting Education

Accounting education occupies a distinct position as it represents the reflective mirror of financial and economic performance and the backbone of economic units. The presence of accountants who possess the professional skills necessary to transform economic events into accurate information that meets the needs of their users is one of the indicators of the utmost care that accounting education receives in a way that ensures meeting the needs of the growing demand for Accountability, especially in light of the many and continuous changes in the sectors (financial, economic, ... and others) arising from the successive developments that surround it from all sides.

A. The Concept of Accounting Education

The definitions given by the writers and authors of the term Accounting Education have varied and varied. Accounting education is viewed as an organized process carried out by the responsible authorities, primarily universities, and through this process, the learner is provided with basic knowledge and the necessary scientific and practical capabilities that enable him. From the practice of the accounting profession]4], it becomes clear that the definition focused on providing the student (the learner) with knowledge and gaining the ability to practice accounting work, while Mudokh believes that accounting education is to provide the labour market needs of qualified and trained manpower Scientifically and practically, through which it can keep pace with the economic and social development plans that countries seek to achieve]2], it is clear that the definition focuses on providing the labour market needs of graduates who have experience, skills, and knowledge in accounting and auditing work.

Based on the above, it is clear that accounting education refers to providing the labour market needs of qualified and trained manpower to keep pace with economic and social development plans, as well as harmony with the changes in the business environment.

The importance of accounting education stems from the importance of accounting and the benefits it can provide to the community within which it operates, and the importance of accounting education is represented in]4]:

1. Contributes to the preparation and qualification of accounting staff, by providing them with various accounting knowledge.
2. Providing the accounting staff working in various economic units with the most important developments that accompany the profession.
3. Assist in determining the needs of the economic units in terms of programs and training courses, as well as solving the problems that these units face.
4. contribute to the development of the accounting profession by developing scientific curricula by modern developments.

B. Factors Affecting Accounting Education

Many factors affect the success of the accounting education program, which are reflected in the following]5]:

1. Personal factors: These factors relate to the student's abilities, qualities, motivation, and effort.
2. Direct environmental factors: related to the immediate environment that has a clear impact on the student, and these factors include (family circumstances, financial circumstances, and study time).
3. The factors of the professional accounting education program: These include the nature of the program and the competencies that must be present to complete the program.
4. Work environment factors: They are related to the business environment and the role that a professional accountant aspires to in the field of accounting, and this includes (the public's expectations of the role that an aspiring professional accountant will play in the accounting profession).

C. Obstacles to Accounting Education

The education systems in most developing countries, including higher education in Iraq, face many challenges in our contemporary world that are characterized by accelerated scientific and technological progress, at a time when there are still many obstacles faced by these systems, the most prominent of which is the incompatibility of the absorptive capacity of higher education institutions with growth Population and the failure to keep pace with modern curricula and technologies in research and education, in addition to the limited interaction and partnership between higher education institutions with state departments and the private sector]6]. Accounting education faces many obstacles, which are reflected in]7]:

1. The study plans focus on the cognitive aspects more than on the technical aspects and experiences that are required for accounting students.
2. An outlook prevails in the accounting departments in universities indicating that research and education are two competing activities and not complementary activities and that continuing to establish this view will lead to bad consequences in the two activities, which makes accounting research not understood by professionals or that it does not serve them.
3. The extreme exaggeration in focusing on specialization in accounting departments, as studies have shown for the Accounting Standards Board of the Institute of Chartered Accountants in which 100 universities around the world that offer a basic program in accounting education have shown that the required credit hours range from 120-130 credit hours, and 25 % Of them are related to non-accounting courses, i.e., they range from (30-35) credit hours.
4. The weak relationship between professionals and academics, as the relationship between the graduate and the university often breaks off after his graduation.
5. The methods of teaching accounting in universities are still traditional and do not keep pace with the spirit of the modern era in which technology prevails.
6. The accounting curriculum lacks the characteristic of suitability because it does not provide the graduate with the skills and expertise needed for the labour market. Accountants do it in practice, and what skills are there in practice]8].

5.2 Contemporary Trends in The Accounting Profession

The development of accounting thought since the inception of accounting has witnessed four stages, the first of which was the technical or professional stage, then the academic stage followed, then the third stage came in which the information systems stage entered, and the fourth stage was the social responsibility stage. In the technical or professional stage, the double-entry theory appeared in 1494. The accounting focused on recording notes and financial dealings in the records, and the accounts were organized, describing accounting at this stage as being an art and the American Accounting Association (AAA) defined the art of recording and classifying operations and events of a financial nature and interpreting the results of these operations and events.

And in the academic stage that began at the beginning of the nineteenth century, interest in accounting was described A science and social sciences for two main reasons. The first is the emergence of the Industrial Revolution and so on Its owner increased production and wealth, which prompted academics to lay down rules and foundations to preserve the capital and the distinction between income and capital, the second of which was the emergence of joint-stock companies and the resulting separation of management from the owners (owners of capital) to express the theory of agency, which led to the development of hypotheses consistent with the nature of The activities of the joint-stock companies, such as imposing the moral personality and imposing continuity, periodicity and harmony, as well as adopting generally accepted principles such as the interview, disclosure and recognition, and the stage of information systems, which is a tremendous development in accounting thought since the beginning of the twentieth century, has come as managerial accounting and quantitative and statistical methods have emerged to provide Data useful to management in the decision-making process.

At this stage, the definition of accounting came by the American Accounting Association (AAA) in 1971, describing it as a system for providing quantitative information on economic units and that this information is useful in terms of making and making decisions. Finally, the last stage of the development of the accounting thought came so that the focus at this stage is on the social responsibility of the economic units by measuring the cost and return and disclosing them to all the groups benefiting from the accounting information. The accounting definition of the American Accounting Association came in 1977 that accounting provides information that is useful in the decision-making process in a manner that leads to greater social welfare. Accordingly, the majority of contemporary studies have focused on the social, economic, and financial issues facing the various sectors. These studies have used information technology, methods and models that contribute to solving the problems faced by local and international economic units]9].

5.2.1 The Basic Requirements to Face Contemporary Challenges to The Accounting Profession

The basic requirements are [10]:

1. Education: Rapidly reviewing the Curriculum education in the fields of accounting and management in universities to allow achieving goals of motivation, understanding, and

application to meet the rapid development in the field of information technology and the increasing needs of management and other bodies outside the organization to additional reports that include useful information on areas that were not of interest. From before.

2. Training: To formulate integrated training programs for both professional accountants and management personnel to provide them with basic knowledge related to the effects of information technology on the nature of their work and the increased ability to meet the current needs of financial information.

3. Scientific Research: The fields of scientific research in the field of accounting and management in universities or elsewhere must be linked to the contemporary challenges facing the production and delivery of valuable financial information to users and find appropriate solutions for them.

4. Legislation: The speedy review of existing legislation that defines the patterns and size of the two information that must be provided in financial reports allows granting freedom to produce and provide more financial reports that provide valuable information to their users, especially since these two legislations represent a basic constraint in this aspect, as well as Its inflexibility to keep pace with the changes and formulate them at a time completely different from the contemporary time in terms of the existing challenges, including companies laws, capital law, law organizing the accounting profession and others.

5. Reorganizing and strengthening the accounting profession: by encouraging serious initiatives that are concerned with studying the existing problems and how to confront them and giving the profession an obligation force for members to adhere to the general charter for the profession.

5.3 Accounting Education and Its Role in Qualifying Accountants According to Contemporary Trends in The Accounting Profession

University institutions play an important role in preparing qualified accounting competencies possessing the scientific and applied skills that enable them to practice the accounting profession, through what they want to be in place, adapt and keep pace with competency-based education methods, there is no doubt that the successive and accelerating change and developments that accompanied the environment Business has a clear impact on the development of many sciences and professions, including accounting]11], in addition to the studies that deal with the professional and academic development of accounting confirm the existence of two inherent characteristics, namely, as continuity indicates that there are many One of the elements of thought and application whose usefulness has been proven and stabilized with time and has become what is known as conventional wisdom. As for the characteristic of change, it embodies the dynamic nature of accountability and the ability to keep pace with the continuous development of the surrounding environmental factors]12], As a result of the development in accounting, the demands for the development of accounting education increased, as the quality and development of the accounting profession is positively related to

the quality of accounting education, the way in which accountants learn and the degree of development of the education they receive, the professional and educational requirements that must be met to join the profession, and the available opportunities to continue Education has a decisive importance for the profession in terms of its ability to advance the responsibilities entrusted to it, and from here the trends of accounting education followed have a decisive role in the continuation and development of the accounting profession around the world and in turn this affects the efficiency and growth of the national and global economy]13]. Distinguish between two entries for accounting education:

1. The traditional approach: It is represented in the traditional method of teaching accounting or what is known as (indoctrination method), as accounting is studied according to this method without interconnection between the two sides (theoretical and applied), so it is unable to capture the professional requirements or application needs of the work environment.

2. The modern approach: It focuses on analytical abilities and skills in accounting, as it is concerned with skills in communication, information systems, decision-making, leadership, reliance on learning style, motivating students and urging them to search for science and accounting knowledge, and trying to find logical solutions to accounting problems, as well as It is about practicing practical cases and applications that do not have specific answers or typical solutions, which develops in them the faculty of thinking and brainstorming.

In the same context, there is a need to develop accounting skills in a way that can meet the required needs and according to the form that affects the increase in the interest of users, as the traditional image of the accountant as a number mill is no longer suitable for the profession, and the accountant is placed behind a table to collect huge columns of numbers to be presented to others from to make decisions, it is a non-vital issue that wastes effort and time, not to mention the mistakes that can occur. Computers and other types of modern technology and their tools have freed accountants from the tedious tasks of manual collection of financial information, so the future accountant is supposed to become more efficient and effective, taking upon himself a role The decision-maker and personal judgment through the experience and competence that he possessed in using his time for analysis and logical management regarding financial information, and he plays an active and effective role in the decision-making strategy within economic units]14], which requires a shift from the traditional method in Education to the method of transferring the skills that professional organizations, most notably the International Federation of Accountants, called for the need to move according to this direction, that is, the skills that They are developed during the different educational stages that can benefit their acquired when moving to the stages of work, in addition to the practically developed skills that help accountants in transferring them to different work environments.

Within this perspective, there have been many opinions on how to develop the accounting profession. From the point of view of Scott 1970, the development of accounting information is required to meet the requirements of the internal and external users of accounting reports of institutions on the one hand, while the other side is represented in the set of legislations and laws that regulate the work of accounting, During the existence of a deliberate curriculum based on standards for accounting education. Others have argued that the development of the accounting profession by adopting the systems approach is done by changing the curricula of

accounting education, provided that accounting is divided according to the following elements: The accounting function in the private sector, the local accounting profession, the accounting function in educational institutions, and the accounting in the government sector]15].

Based on the above, we see that the development of the accounting profession due to its role in the planning process and economic development to achieve sustainable development, which requires setting a general framework for accounting that seeks to achieve those goals while taking into consideration the conditions of the economic and social business environment, as well as developing the elements of the accounting system by adopting Systems Entrance.

6 Presenting the Results of the Field Study

6.1 Description of the Research Community and Research Sample

The research community represents the teaching staff in the accounting departments in Baghdad and the governorates. As for the sample size, it reached (67) lectures, and they were chosen intentionally and deliberately and by (60%) of the total community, Where the questionnaire is distributed to many teachers at the University of Baghdad, Al-Mustansiriya University, Al-Furat Al-Awsat Technical University, Babylon University, Future University College, Al-Hilla University College, Al-Qadisiyah University, Kufa University, Karbala University, Middle Technical University, Al-Muthanna University, in addition to publishing The link to the questionnaire in many accountants' groups and those who hold a science degree in accounting,

Table1 The forms distributed and returned from the research sample.

Distributed forms	Returned forms	Percentage%
67	60	90

A. Research tool

The questionnaire was adopted as one of the tools adopted in collecting data. The questionnaire included two parts, the first of which was devoted to the demographic information of the research sample and the second part was concerned with the main axes of the research variables (accounting education, contemporary trends in the accounting profession) through three groups of questions.

B. Statistical methods

A set of statistical methods were used according to the (SPSS) program and the following: (percentage and frequencies to describe the research sample, the arithmetic mean, and the standard deviation), as well as the Cronbach's alpha test to find out the stability of the paragraphs of the questionnaire, and it turned out that the reliability coefficient was (0.8938), which is a good stability coefficient, and the Pearson correlation coefficient was adopted to calculate the internal consistency of the paragraphs of the questionnaire, and the correlation coefficients had a significant level of significance of (0.05), in addition to the value of (R) calculated greater

than the tabular value of (R) at a degree of freedom (28) which is equal to (0.38) Accordingly, the paragraphs of the questionnaire are true to what they were measured for.

C. Analysis of the Characteristics and Characteristics of the Research Sample

The first part of the questionnaire contained a set of questions related to the demographic characteristics of the nature of the individuals responding to the questionnaire, and the aim of that was to give the impression that reinforces the confidence of the results that have been reached, and as in Table 2:

Table 2. Characteristics and characteristics of the research sample

The paragraphs	Duplicates	Percentage
Sex		
Males	42	%70
Female	18	%30
Total	60	%100
Qualification		
Master's degree or equivalent	24	%40
PhD or equivalent	36	%60
Total	60	%100
The scientific title		
assistant lecture	9	%15
Lecture	15	%25
Assistant Professor	24	%40
Professor	12	%20
Total	60	%100

From the table, it becomes clear that the research sample constitutes a high percentage of males (70%) and hold a doctorate by (60%), and that the percentage of respondents holding the title of assistant professor with a percentage (40%), followed by those holding the title of a lecture at a rate of (25%), followed by a small assumption They hold the title of professor (20%) and assistant lecture (15%).

6.2 The Results of the Field Study and Their Interpretation

The second part of the questionnaire questions was devoted to a group of questions that were classified into three directions related to testing the research hypotheses:

Analysing and discussing the results of the research hypothesis test: To test research hypotheses, the questions were formulated for three sections, the first related to the reality of accounting education and included (12) paragraphs, while the second section included criteria for contemporary trends in the accounting profession and included (10) paragraphs, and the third section included the basic requirements to face Contemporary challenges to the accounting profession, knowing that the scale area was divided as a percentage for each degree as follows: (Totally 100% -80% agree, 79% -60% agree, neutral 59% -40%, 39% -20% disagree, 19% don't agree completely).

Table 3. shows the results of the research sample responses for the first section of the questionnaire questions

	The paragraphs	Arithmetic mean	standard deviation	percentage
1	There is a balance between the theoretical and applied accounting education	3.75	0.84	75.00%
2	The accounting applications course is insufficient to qualify a graduate of the Accounting Department to join the labour market	3.80	0.61	76.00%
3	The educational curricula are not updated periodically	3.65	0.92	73.00%
4	There is no coordination between the economic and educational institutions to exchange ideas and opinions regarding the needs of the labour market and follow up the accounting education process	4.50	0.60	90.00%
5	Accounting education works to prepare outputs that are compatible with the requirements of the analytical and technical processes in accounting and auditing	4.15	0.66	83.00%
6	Current teaching methods do not motivate students to search for solutions to accounting problems using several sources	4.25	0.77	85.00%
7	Current training methods are not conducive to leadership and teamwork development	4.60	0.49	92.00%
8	Current educational methods are not conducive to developing communication and communication skills in the work environment	4.25	0.63	85.00%
9	Accounting education helps in developing aspects of accounting functions, including financial reporting, administrative control, and auditing	4.00	0.55	80.00%
10	The current educational curricula do not assist in the graduate's acquisition of intellectual, technical, personal, social, and organizational skills	4.65	0.58	93.00%
11	Accounting education curricula help the graduate in acquiring ethics and professional behaviour during the education program	4.35	0.58	87.00%
12	Accounting education contributes to improving accounting and financing practices, procedures, and financial policies	4.35	0.66	87.00%
	Total	4.19	0.6575	**%84**

The first research hypothesis: Table 3 shows the results of the research sample responses for the first section of the questionnaire questions

It is evident from Table (3) that the arithmetic average of the research sample for the accounting education axis is (4.19) and represents (84%) of the area of (for the quintet of Curt) used. That is, the first research hypothesis was accepted that accounting education in the local environment suffers from a weakness that requires its development, and the answers of the research sample can be analysed according to the following questionnaire questions:

1- The answers of the research sample regarding the balance between the theoretical and applied accounting education method amounted to (75%) towards the agreement, and the value of the arithmetic mean was (3.75) in the same direction and by (76%) and with an

arithmetic average (3.8) the sample agreed that the subject of accounting applications is insufficient. To qualify a graduate of the Accounting Department to join the labour market.

Table 4. The results of the first section of the questionnaire

	The paragraphs	Arithmetic mean	Standard deviation	Percentage
1	The technical or professional stage appeared when accounting focused on recording notes and financial dealings in the records and organizing accounts	**4.**88	**0.**76	97.5**0%**
2	The academic stage, which began at the beginning of the nineteenth century, was concerned with accounting as a science of social sciences	**4.**92	**0.**80	98.5**0%**
3	The emergence of the Industrial Revolution and its accompanying increase in production and wealth helped, prompting academics to lay down rules and foundations for preserving capital and differentiating between income and capital.	**4.**90	**0.**78	98.**00%**
4	The emergence of joint-stock companies and the resulting separation of management helped to formulate assumptions consistent with the nature of the activities of joint-stock companies	**4.**94	**0.**84	99.**00%**
5	The stage of information systems, which is considered a tremendous development in accounting thought, as managerial accounting and quantitative and statistical methods appeared to provide data that benefit management in the decision-making process	**4.**90	**0.**78	98.**00%**
6	The emergence of social responsibility for economic units helped in conducting cost-benefit measurement and disclosure for all groups benefiting from accounting information.	**4.**92	**0.**80	98.5**0%**
7	The successive and accelerating changes and developments that accompanied the business environment have a clear impact on the development of many sciences and professions, including accounting.	4.**3**5	0.67	8**4**.00%
8	Embody the dynamic nature of accounting and the ability to keep pace with the continuous evolution of the surrounding environmental factors	4.25	0.63	8**7**.00%
9	The quality and development of the accounting profession positively correlates with the quality of accounting education	4.20	0.68	8**6**.00%
10	The professional and academic development of accounting confirms the existence of two interrelated properties, continuity and change	4.45	0.**70**	**90**.00%
	Total	4.671	0.744	**% 94**

2- The sample members believe that the current educational curricula are not updated at appropriate intervals and with an agreement rate (73%) and an arithmetic average (3.65). Individuals of the sample agreed that there is no coordination between the economic and educational institutions in Iraq to exchange ideas and opinions regarding the needs of the labour market and follow-up The accounting education process, a percentage (90%) and an arithmetic average (4.5), and a percentage (38%) of the sample members agreed that accounting education works on preparing outputs that are compatible with the requirements of the analytical and technical processes in accounting and auditing.

3-The research sample agreed that the current teaching methods do not motivate the student to search for solutions to accounting problems using several sources at a rate of (85%) and with an arithmetic average (4.25). Developing the spirit of leadership and teamwork, with a mean of (4.6).

The second research hypothesis: Table (4) shows the results of the research sample responses regarding contemporary trends in the profession of financial accounting:

It is evident from Table (4) that the arithmetic means of the answers of the sample members amounted to (4,671), which represents (94%) of the Kurt five-year scale used, so the aforementioned percentage falls in the area of complete agreement (100-81%), on contemporary trends in the profession Accounting, and according to that, the second research hypothesis is accepted.

The third research hypothesis: The third hypothesis: Table (5) shows the results of the responses of the research sample regarding the basic requirements to face contemporary challenges to the accounting profession, which states that:

Table 4. The results of the first section of the questionnaire

	The paragraphs	Arithmetic mean	Standard deviation	Percentage
1	The technical or professional stage appeared when accounting focused on recording notes and financial dealings in the records and organizing accounts	**4.**88	**0.**76	97.**50%**
2	The academic stage, which began at the beginning of the nineteenth century, was concerned with accounting as a science of social sciences	**4.**92	**0.**80	98.**50%**
3	The emergence of the Industrial Revolution and its accompanying increase in production and wealth helped, prompting academics to lay down rules and foundations for preserving capital and differentiating between income and capital.	**4.**90	**0.**78	98.**00%**
4	The emergence of joint-stock companies and the resulting separation of management helped to formulate assumptions consistent with the nature of the activities of joint-stock companies	**4.**94	**0.**84	99.**00%**
5	The stage of information systems, which is considered a tremendous development in accounting thought, as managerial accounting and quantitative and statistical methods appeared to provide data that benefit management in the decision-making process	**4.**90	**0.**78	98.**00%**
6	The emergence of social responsibility for economic units helped in conducting cost-benefit measurement and disclosure for all groups benefiting from accounting information.	**4.**92	**0.**80	98.**50%**
7	The successive and accelerating changes and developments that accompanied the business environment have a clear impact on the development of many sciences and professions, including accounting.	4.**35**	0.67	8**4**.00%
8	Embody the dynamic nature of accounting and the ability to keep pace with the continuous evolution of the surrounding environmental factors	4.25	0.63	8**7**.00%
9	The quality and development of the accounting profession positively correlates with the quality of accounting education	4.20	0.68	8**6**.00%
10	The professional and academic development of accounting confirms the existence of two interrelated properties, continuity and change	4.45	0.**70**	**90**.00%
	Total	4.671	0.744	**% 94**

Table 2. The results of the third section of the questionnaire

	The paragraphs	Arithmetic mean	standard deviation	percentage
1	Legislation: The speed of reviewing the existing legislation that defines the patterns and volume of information that must be provided in financial reports allows granting the freedom to produce and provide more financial reports that provide valuable information to their users.	4.25	0.54	85.00%
2	Training: To formulate integrated training programs for both professional accountants and management personnel to provide them with basic knowledge related to the effects of information technology on the nature of their work and what it requires to increase the ability to meet the current needs of financial information	4.55	0.67	91.00%
3	Scientific Research: The fields of scientific research in the field of accounting and management in universities or elsewhere must be linked to the contemporary challenges facing the process of producing and communicating financial information	4.40	0.59	88.00%
4	Reorganizing and strengthening the accounting profession: by encouraging serious initiatives that study the existing problems and how to face them	4.50	0.60	90.00%
5	Education by reviewing the educational curriculum in the fields of accounting and management in universities to allow achieving goals of motivation, understanding, and application to meet the rapid development in the field of information technology and the increasing needs of management	4.70	0.46	94.00%
	Total	4.48	0.572	% 90

It is clear from Table (5) that the arithmetic average of the answers of the sample members is (4.48), which represents (90%) of the area of the scale used because it is located in the area of complete agreement (100-81%), that is, some obstacles prevent the development of accounting education in the environment. The fifth question in the axis related to the third hypothesis achieved the highest percentage of answers, with a percentage (94%) and an arithmetic average (4.70), which indicates the individual respondents agree to education by reviewing the education curriculum in the fields of accounting and management in universities to allow achieving the goals of motivation, understanding, and application. To meet the rapid development in the field of information technology and the increasing needs of management, and accordingly, the third hypothesis is accepted.

7 Conclusion

The research came out with many conclusions, which are:

1. The importance of keeping pace with accounting with professional developments at the international level, through which accounting organizations seek to serve the community,

by applying international accounting education standards that help to develop accounting education curricula, which is reflected in educational outputs and the preparation of efficient accounting cadres to practice the profession of accounting, which is reflected Positively on the financial statements of economic units.

2. A deficiency in accounting education curricula due to reliance on traditional methods of teaching, and the inconsistency of accounting education programs and curricula in terms of linking the theoretical and applied aspects by focusing on the theoretical side, as well as not keeping pace with technological developments.

3. As a result of the development in accounting, there have been increasing demands for the development of accounting education, as the quality and development of the accounting profession is positively related to the quality of accounting education, how accountants learn and the degree of development of the education they receive, the professional and educational requirements that must be met to join the profession, and what is available from Opportunities for continuing education are of crucial importance to the profession in terms of its ability to fulfil the responsibilities entrusted to it, and from here the trends of accounting education followed to have a decisive role in the continuation and development of the accounting profession.

4. The sample members agreed that the quality and development of the accounting profession positively correlates with the quality of accounting education.

There are three recommendations:

1. The importance of adopting the development of accounting education from an integrated perspective by developing educational curricula in accounting and contributing to the development of the profession by setting up a strategic framework for this development that takes into account the goals of accounting education and linking those goals with the needs of society and the requirements of practicing the accounting profession, and on the other hand linking the objectives Financial and moral requirements and needs, studying the causes of the gap between them, and suggesting accounting solutions.

2. Commitment to the continuous updating of accounting education curricula in line with the development of global accounting thought and contemporary trends of the accounting profession.

3. Developing the education philosophy to provide graduate students with broad accounting skills and knowledge, and to focus on developing analytical and innovative thinking.

References

[1] Jabbar, Nazem, The reality of accounting education in Iraq and its compatibility with international accounting education standards - an applied study of a sample of Iraqi universities -, Al-Muthanna Journal of Administrative and Economic Sciences,2015, pp. 110-131.

[2] Madhoukh, Khayyam Muhammad Kamel, The Reality of the Development of the Accounting Profession between the Professional and Technological Qualification of Accountants in Companies Operating in the Gaza Strip, Master's Thesis in Accounting and Finance, Faculty of Commerce, Islamic University, Palestine, 2014.
[3] Bui & Porter, The Expectation-Performance Gap in Accounting Education: An Exploratory Study, Accounting Education journals, No.19, 2010.
[4] Bou Azria, Hajira, The reality of accounting education in Algerian universities in light of the trend towards implementing International Financial Reporting Standards (IFRS) - a questionnaire study at the Jilali University in General, a master's thesis in financial and accounting sciences in the Faculty of Economic, Business and Management Sciences , Algeria, 2017.
[5] IAESB, International Accounting Education Standards Board, Development and Management of Written Examinations Based on the Practices of Selected IFAC Member Bodies, Information, 2014.
[6] Saad, Salma Mansour, The role of benchmarking in developing curricula for accounting departments in Iraqi universities, a research published in the Journal of Accounting and Financial Studies, Volume VII, Issue 20, 2012.
[7] Al-Ani, Safaa Ahmed Muhammad, Requirements for activating the quality of the university accounting education system in light of ISO standards, Al-Muhasibi Journal for Accounting and Auditing Sciences Quarterly scientific journal issued by the Syndicate of Accountants and Auditors, General Center Baghdad - Iraq, Volume 23, Issue 45, 2006.
[8] Srdar, Nujoud Abdulhadi Srdar, The Gap Between Learning And Teaching In Accounting Education: The Saudi Arabian Experience, The Thesis Is Submitted In Partial Fulfilment Of The Requirements For The Award Of The Degree Of Doctor Of Philosophy Of The University Of Portsmouth –UK , 2017.
[9] Al-Amiri, Saud Jaid Mashkour, Entrances to the Evolution of Accounting Thought, House of Approaches for Publishing, First Edition, Amman – Jordan , 2020.
[10] Al-Naghi, Mahmoud El-Sayed , Accounting Theory - Contemporary Introduction, Series of Accounting Knowledge 2, The Modern Library, Arab Republic of Egypt, 2017.
[11] Belkaoui, Ahmed Riahi Accounting theory ,2002.
[12] Al-Shirazi, Abbas Mahdi, Accounting Theory, Dhat Al-Salasil House, Kuwait ,1990.
[13] Al-Rubaie Jabbar Jassim, Factors of Building Technical Accounting Skills for Technical Education Authority Students, Technical Journal, Volume 20, Second Issue, Baghdad-Iraq ,2007.
[14] Al-Hubaity, Qasim Mohsen and Yahya, Ziad Hashem, "The Impact of Developments in Business Environment on Management Accounting in the Twenty-first Century", a research published in the Journal of Future Research, No. (13), 2006.
[15] Al-Mansouri, Jaber Hussein and Al-Mashkour, Emad Abdul Sattar, The extent of the contribution of the components of the accounting profession in raising the efficiency of accountants to rationalize investment decisions, Journal of Economic and Administrative Sciences - University of Karbala, Volume 1, Issue 3, 2012 ,pp. 48 -66.

The effect of using fair value accounting in activating the Iraqi stock market (A field study on companies registered in the Iraqi market for financial markets)

Nahla Ghalib Abdul Rahma[1], Abdulhussain Tofeeq Shibli[2], Jalil Ibrahim Salih
(nahla.jalee@stu.edu.iq[1], Husainshibli@yahoo.com[2], jalil.ibrahim@stu.edu.iq[3])

Southern Technical University, Technical Institute of Basrah, Iraq[1], University of Basrah, Economic & Administration College, Iraq[2], Southern Technical University, Technical College of Administration, Basrah, Iraq[3]

Abstract, The study aims to know the reflection of the application of fair value accounting on revitalizing the market and increasing its efficiency through the opinions of preparers, analysts, and users of financial information for companies listed on the Iraqi Stock Exchange. The research provided a framework of knowledge for the concept of fair value and its importance in the stock market based on the descriptive analytical approach by preparing a questionnaire prepared for this matter. Furthermore, A random sample was selected that includes a group of specialists in the aspects of financial analysis and investment, and the conclusion that was reached is the existence of a relationship of using fair value accounting by companies registered in the Iraqi Stock Exchange and increasing the market capitalization of the market.

Keywords: Fair value, Iraq stock market, Indicators of active markets

1 - Introduction

The principle of historical cost is one of the accounting principles that the accounting theory still adheres to in the accounting measurement, and it is considered one of the most important principles on which the contemporary accounting model relies as a basis for evaluating each of the assets and liabilities (Yang, 2021), and (Galassi, 2020) believes that the principle of historical cost is based on several justifications, as it provides a large degree of objectivity in the measurement and the figures are comparable and facilitate the process of accurate verification of historical cost data and thus give a high degree of confidence in the accounting information. (Alexander & Fasiello, 2020) indicates that historical cost has continued to be used as a basis for measurement and recording due to its dependence on facts that have already occurred and are supported by documents and are not subject to differences in personal judgment and judgment, and are easy to verify, and are measured by the amount paid for them in cash or its equivalent at the time their occurrence. (Freeman, 2020) confirms (Gardi, 2021) despite those justifications on which the principle of historical cost is based and its consistency with the generally accepted accounting assumptions and principles, but it raised many criticisms

IMDC-IST 2021, September 07-09, Sakarya, Turkey
Copyright © 2022 EAI
DOI 10.4108/eai.7-9-2021.2315376

about the limited usefulness of using the resulting financial statements and reports, especially "Criticism about the inadequacy of accounting information for decision-making, and this means that in cases of inflation, historical values become unrealistic and therefore the financial statements do not represent the true financial position of economic enterprises, as well as" the difficulty of comparing financial positions during several successive accounting periods, especially with the change in economic conditions that it is characterized by a constantly changing and volatile dynamic movement and a change in the purchasing power of the monetary unit. (Hajiyev, 2021) believes that after the increasing criticism of data and financial information users of the historical cost principle and their low confidence in the financial information prepared on its basis, the trend towards fair value accounting began, and the replacement of traditional historical cost accounting measurement with fair value measurement was considered an important issue in light of Prioritize the characteristics that must be available in the information, especially reliability, suitability, caution, and caution. furthermore, (Smith, 2021) indicates at the end of the eighties and the beginning of the nineties of the second millennium and as a result of the criticisms that faced the application of the principle of historical cost in accounting, the opinions in favor of the direction of accounting on the basis of fair values began to increase, especially for the items of assets and financial investments, which are usually called "market value." However, With the end of the twentieth century and the world's tendency towards the new world order (globalization), the emergence of major multinational companies and the economic openness between countries, and the interconnection of their economies with each other, especially in the areas of global trade and freedom of commercial and financial dealings, all of this led to pressures on the accounting profession and affecting some of the principles on which it is based, including the historical cost principle, which is facing severe criticism in the direction of the transition to the application of fair value (Nordlund, 2021). And (Pandya, 2021) indicates that as a result of these pressures, the trend towards applying fair value accounting as a basic requirement in proving the treatment of financial events and operations began to be more accurate and closer to the actual reality in accordance with the prevailing conditions in order to achieve the efficiency and reliability of the published financial statements, which prompted the specialized professional bodies to issue Accounting standards that meet the continuing needs that coincide with the great development on the international financial level, especially with regard to the application of fair value. (He et al, 2018) confirms that many specialized professional bodies issued the foundations that require recognition of some changes that occur in financial instruments and the impact of many Items with those changes such as items (income statement, change in shareholders' equity and cash flow (including the Financial Accounting Standards Board and the International Accounting Standards Board).

2- Literary survey:

The researchers reviewed a number of literature and studies that discussed the topic of fair value, including a study (Al-Khadash & Abdullatif, 2009), which aims to analyze the impact of applying fair value accounting for financial instruments on the financial performance of companies registered in the Jordanian stock market and the return on earnings per share. The study included the financial statements of a selected sample of Jordanian banks registered in the Jordanian stock market for a period of 4 years, and the published results were compared using the fair value and those calculated using the historical cost for the same years. The study found that the financial performance of banks is greatly affected by the evaluation of financial instruments at fair value, as there was a very high positive value of the earnings per share when applying the fair value compared to the return when deleting the gains or losses of financial instruments according to the historical value basis. As for the study (Christensen & Nikolaev,

2013), it aims to clarify the circumstances of the application of fair value accounting as an alternative to the historical cost model. The study found a set of results, including that the application of fair value to non-financial assets such as buildings and equipment is less efficient for decision-makers if compared to historical cost, and that the Financial Reporting Standards (IFRS) provided an advantage that was not provided by the previous standards, as it allowed companies to choose between the historical cost and the fair value for non-financial assets, with an obligation to remain consistent in the disclosure of the accounting policy used. While the study (Elfaki & Hammad, 2015) aims to identify the impact of the application of fair value on accounting information and its quality, and this study was applied to a group of companies listed on the Sudanese stock market, and the researchers relied on the questionnaire to achieve the objectives of the study, and the data were analyzed using the statistician program SPSS, and the study concluded that there is a relationship and an impact between the application of fair value and the appropriateness and reliability of accounting information and its quality. A study (Flayyih, 2015), which aimed to identify the method of fraud under the fair value approach. The study reached conclusions, the most important of which is that there are many doubts about the reliability of the prepared statements in light of the fair value. Also, the use of the fair value of companies listed in the Iraqi market may lead to delaying the issuance of financial statements in a timely manner, which will lose the benefit of those statements, as companies with the application of historical costs delay the issuance of financial statements.

The study (Fontes et al, 2018) indicates the extent to which the measurement of banking assets at fair value contributes to reducing information asymmetry between users of financial statements and investors in shares in the stock market, and the extent of the impact of recognizing credit risk gains and losses when adopting fair value in financial statements. The study indicates that the information asymmetry is less for banks that enjoy measuring their banking assets at fair value and that the recognition of credit risk gains and losses has a significant impact when presenting financial statements at their fair value. As for the study (Hsu et al, 2019), it aims to identify the extent to which the recognition of the fair value of investment properties is related to the risks of a collapse in stock prices. This study was conducted in China, and the study sample was represented by a number of Chinese companies that own investment properties in the Chinese stock market for the period from 2007 to 2011, and the study reached several conclusions, the most important of which was that companies registered in the Chinese stock market that recognize and register their investment properties at their fair value face greater risks in their stock prices compared to companies that present their financial statements at historical cost, and that the risks of the collapse of the shares of Chinese companies It has been reduced and mitigated in companies that apply a strict corporate governance system.

The study (Chirkova et al, 2018) aims to identify the problems and difficulties in determining the fair value of intellectual property in the structure of financial market assets and to provide a model that determines the intellectual property of a trademark in accordance with the "fair value to protect the interest between the licensee and the owner of the right to the trademark because the elements of intellectual property and other intangible assets are either undervalued or overvalued, and this study was conducted in the Russian financial markets, and the study concluded that the adoption of a mathematical model allows an alternative assessment of intangible intellectual assets in the ownership structure of financial markets, the model was used to analyze the activities of individual financial markets operating within the Russian national economic system.

The study (Queku, 2020) indicates the importance of adopting fair value as a criterion for the stock prices of banks listed on the Ghana Stock Exchange, and the financial statements for the period from 2008-2018 were adopted in this study, and the study found that there is a difference

in profits between financial statements prepared according to “historical cost” and prepared according to fair value. And that the fair value makes the profits and the book value close to the economic reality, and there is a weak correlation in the average difference between the book value of property rights at the historical cost and the fair value. In Panama, the study (Adegboyegun et al., 2020) aims to identify the impact of fair value dependence on the reports of companies listed on the Nigerian Stock Exchange. In their study, the researchers relied on a questionnaire to achieve the objectives of the study, the data collected was analyzed by relying on the SPSS statistical program. The study concluded that there is a strong correlation between the fair value and reporting of Nigerian companies and that the fair value contributed to the assessment of amounts and prediction of corporate profits and the uncertainty of future cash flows in the reports of companies that depend on their reliability.

3- Theoretical framework for research / fair value

3.1 The concept of fair value

The introduction of the principle of fair value came to address the shortcomings in the historical cost that could not express the financial position of the unit in a reliable manner and in view of what the large expansions in investments imposed on the accounting function about the need for investors and shareholders to stand up to the reality of the real financial position of the economic unit and what is happening to their money from changes, the traditional accounting based on historical cost has become unable to meet these requirements, which promotes the shift towards fair value (Guo et al, 2021 Guo,). Nevertheless, the traditional accounting based on historical cost has become unable to meet the requirements of investors and shareholders to help them identify the reality of the financial position of the economic unit and the changes taking place in their money, so it was necessary to take another approach and shift towards the fair value approach (Ahn et al, 2020). (Kulish et al, 2018) indicates that there is no specific agreement for the concept of fair value by accountants, professionals, professional organizations, and researchers, but there are several concepts of fair value issued by the organization, and some of them are issued within international and American accounting standards.

(Adegboyegun et al, 2020) defined the fair value since its inception as an input to the accounting measurement, which is “the value of the cash expected to be obtained if the asset is sold on the date of preparing the financial statements.” While (Filip, 2021) considers that the International Accounting Standards Board (IASB) defined it as “the amount with which an asset can be exchanged or a liability paid between knowledgeable and willing parties to deal on a purely commercial basis or in a balanced framework or under normal conditions or between two independent parties, where the transaction takes place in a balanced framework.” (Filip) adds that the balanced transaction in this framework is defined as any transaction that takes place between unrelated or dependent parties and takes place between a willing buyer and a willing seller, and both of them work to obtain the greatest benefit for themselves, and pricing is based on such transactions are based on fair market values.

(Sangchan, 2020) indicates that the US Internal Revenue Service in March 1959 defined it as the amount that makes ownership change between a willing buyer and a seller willing to sell when the first is not compelled to buy and the second is not forced to sell and that both parties have knowledge reasonable facts relating to the transaction. (Falkenheim, 2021) confirms that the Financial Accounting Standards Board "FASB" defined it as the amount accepted by knowledgeable parties who have a desire to exchange an asset or settle a liability in operations that do not include related parties.

(Adwan, 2020) considers that fair value has been addressed in its concept in International Accounting Standard No. (39) As “the value by which an asset is exchanged or a liability is settled between knowledgeable and willing parties, which operate under normal market conditions.” As for (Nordlund, 2021) it indicated that the International Valuation Standards Committee (IVSC) defined the fair value in the third criterion for valuing assets for the purposes of preparing financial statements and related accounts as “an estimated amount in exchange for an asset exchange on the valuation date between a buyer and seller, and both are willing to conclude a deal in the light of a neutral market, as each of them has sufficient information and has complete freedom and without coercion to complete the deal.
However, (Pandya, 2021) indicates that the Accounting Standards Committee in England and Wales has defined the fair value of assets as “the price at which the asset can be sold in free transactions away from the parties involved in the buying and selling process.” Furthermore, in Iraq, Accounting and Regulatory Standards Board (2001) defined the fair value within accounting rule no. (14) Accounting for investments as "the acceptable value that can be exchanged for an existing by a buyer and seller who are knowledgeable and willing to deal with the same policy of dealing with third parties."

3.2 Reasons for interest in fair value

Some many reasons and motives led to the interest in fair value, including the following: (Nigro & Stahl, 2021) (McInnis & Yust, 2018).
1- The shortcomings of traditional accounting and its inability to show the true fair value of companies in order to provide appropriate information to decision-makers.
2 - The need for accounting disclosure of intangible assets, which are usually not recognized under traditional accounting when a company is offered for sale or merger, (for the goodwill of the store).
3 - It is considered an efficient measurement tool, especially when it comes to stock prices in general.
4 - The fair value is linked to the concept of preserving the in-kind capital, which gives the actual picture of the institution's performance.
5 - The fair value is linked as a whole to the concept of comprehensive income, which is considered as one of the new measures of income, which gives more benefit to users of financial statements, especially in financial institutions.
6- It helps in improving the financial analysis process because it shows the actual reality of the institution's performance.

3.3 Objectives of the fair value approach:

The fair value approach aims to show the items of the financial statements at the value closest to reality at the date of preparing the budget. Companies in general and banks, in particular, apply the fair value approach in order to achieve the following objectives (Menicucci, 2020) (Dakheel et al, 2021):
1 - Making rational investment and commercial decisions related to the sale or purchase of investments, merger decisions that take place between units, or decisions of acquisition (purchase) of a unit, as these decisions are based on highly reliable financial information.
2 - Corporate business planning.
3 - Show the current value of each of the shareholders, investors and lenders.

4 - Managing and measuring the risks surrounding the economic unit, taking into consideration the expected financial risks inherent in investment decisions that may result from changes of an economic dimension in market values, currency rates, interest and the situation of debtors.
5- Determining the amount of capital that should be devoted to various business lines.

3.4 Advantages and Criticisms of Fair Value:

3.4.1 Advantages of fair value:

The use of the fair value approach is the best alternative to address the shortcomings witnessed by the historical cost principle, and this approach has several advantages, represented by the following (Flayyih, 2015) (Dakheel et al, 2021) (Beigman et al, 2021):
1 - The fair value reflects the economic reality of the company and is closer to the fair expression of the financial statements about the financial position, business result, cash flows, and changes in property rights.
2 - If the assets and liabilities are valued on the basis of fair value, they represent economic income, as market prices are taken into consideration.
3- The application of fair value is consistent with the concept of capital preservation.
4 - This entry provides an accurate measure of the concept of the value and economic profit for the company.
5- The fair value approach takes into account the changes in the purchasing power of the monetary unit.
6- The use of the fair value approach is more suitable for making decisions and performing financial analyzes and a better basis for forecasting business results and cash flows.
7- Information based on fair value helps in making comparisons between similar companies that use fair value.
8 - Using the fair value approach provides investors with awareness and a predictive outlook for the value of the company.
9- The fair value approach is an efficient and effective measurement tool, as fair value information is widely used for commercial purposes, especially in making decisions about financial instruments, and in determining the company's general financial position.
10 - The fair value approach helps in improving the financial analysis because it shows the actual reality of companies' performance.

3.4.2 Criticisms of fair value:

Despite the advantages that the fair value approach possesses, there are many criticisms directed at this approach, including the following (Sellhorn & Stier, 2019) (Ahn et al, 2020):
A- Lack of impartiality and accuracy of the accounting measurement of the fair value approach, due to bias and differing personal opinions and judgments, due to its partial dependence on arbitrary measurement methods.
B - This approach requires additional costs, which leads to an increase in the cost over the benefit achieved.
C- It is difficult to determine the fair value according to this approach for a number of the company's assets when there are no active or regular markets.
D - The preparation and presentation of financial statements and statements according to this approach require a longer period of time, which may lead to the loss of the information contained in these data on the timing feature.
e- Multiple accounting measurement approaches to the fair value approach lead to results that differ according to the measurement outputs of each of the accounting measurement inputs.

F- The values calculated according to this approach are fluctuating at each re-evaluation and treatment of evaluation differences in different ways, which makes the expression of values in the records less stable.
G - The use of this approach when preparing the financial statements provides accountants with a wide scope to manipulate the results of the company's business, as well as to respond to the interests and desires of the company's board of directors and to manipulate revenues.

4 - The approaches to determining the fair value:

There are several approaches to determining fair value. The American Standard No. (157) for measuring fair value, issued in September 2006 and effective in November 2007, identified three approaches, represented by the market entrance and the present value entrance, as well as the "cost entrance, as follows: 2021) (DeFond et al, 2020).

A- Market Entrance: The market entry depends on the market value of the item or item being evaluated, provided that this item has an active and efficient financial market. Market entry is used when evaluating observable prices available from appropriate information, including similar market operations. Comparing Market Entry applications requires information on comparable transactions.
Furthermore, the market is active when the following conditions are present (Spulbar & Birau, 2019):
1. Mutual assets shall be uniform and homogeneous.
2. The buyer and seller are willing to exchange existing assets most of the time.
3. The prices are general and common and known to all.

b- Present value entry:

This approach depends on finding the present value of the expected cash inflows and outflows from the items under evaluation during their lifetime by transferring future interests such as cash flows or profits to a single amount allocated (Siriop, 2021). One of the valuation methods according to this approach is options pricing models, and the income approach is used when evaluating to convert future amounts to a single discounted present value (present value methods) depending on the assumption that market partners are the reason for those future amounts, the income approach is the most common for valuing long assets term, which is directly applicable because most long-term assets result from an economic benefit accruing to the owner of the asset (Louche e called the modified cost, or the replacement cost entrance, and t al, 2019).
c- Cost entry: This entry is called the modified cost, or the replacement cost entry, and this approach depends on determining the current cost of replacing the asset after settling it due to obsolescence factors (Wermers, 2020).

3.5 The concept of active/efficient financial markets:

Financial markets are the widest and most comprehensive system of markets whose activity is centered on securities, so in most cases, the financial market is classified according to the purposes of financing, some of which are allocated to financing economic projects, and some of them finance operations (Yliheljo, 2021). However, (Mamais, 2021) defines financial markets as "the framework that ensures the meeting between money offerors and money seekers, regardless of the means by which this meeting is achieved or the place in which it takes place, but provided that there are channels of communication between dealers in the market". (Runtev, 2020) believes that the financial market is a "mechanism through which financial

assets are traded in buying and selling, and it enables the efficient transfer of financial resources from economic sectors with financial surplus to economic sectors that suffer from financial deficit". (Dakila, 2020) indicates that the financial market is described as efficient or active when the prices of securities, such as stocks, "reflect all the information made available to investors, and thus the financial market has played the desired role, in which no investor can exploit information or spread rumors with the aim achieving an additional return over the accepted average, and according to (Schär, 2021) there are some conditions that must be met in active or efficient markets, including the following:

-Availability of fully competitive conditions between investors or those who enter this market.

- The available information or data must be correct, whether it is financial or non-financial, and that this information is issued by companies through financial statements, budgets, and others.

-Disclosure of information and its availability in a timely manner, that is, as quickly as possible and at the lowest cost of obtaining it, and it must be available to all market entrants without exception.

However, (Heaton, 2019) defined the active or efficient financial market as "the market that contains a sufficient and increasing number over time of: the number of traded securities and the value of these securities, buy and sell orders for securities, the number of companies registered in the market, in addition to the total market capital, in addition to the presence of a large number of investors, whether individuals and institutions or their representatives in the trading process, such as brokerage and financial brokerage companies. (Steriotis et al, 2018) indicates that active or efficient financial markets are defined as "the markets in which a large number of knowledgeable participants trade on rational judgment, aiming to maximize profits, competitors, free and active competition, and who seek to come up with expectations about future stock prices, So that all information is available and available to everyone equally and without any costs". (Malceniece, 2019) defines active or efficient financial markets as "those markets that enjoy a high degree of flexibility, and allow a quick response in stock prices, as a result of changes in the results of the analysis of information and data flowing to the market, which ultimately leads to the achievement of parity between the market value and the real value of the security". (Mamaysky, 2020) defines active or efficient financial markets as "those markets that determine the correct price of securities, i.e. the price that reflects the true value of these securities, and the real value of the security is the amount that he obtains or pays for this paper in view of the return that can check it out."

3.6 Characteristics of Active or Efficient Financial Markets:

There are characteristics of the financial markets that are characterized by the highest levels of efficiency, which distinguish them from other financial markets that lack efficiency, and they are as follows: (Kubic, 2021) (Filip et al, 2019) (De Santis et al, 2018)

a - The efficient financial market includes investors who make rational and rational decisions in their investment directions, which motivates them to always increase their wealth.

b - An active/efficient financial market in which information is available without any additional costs to obtain it, whether it is information for lenders or investors, or administrative authorities in the market, or government regulatory authorities.

c - An active/efficient financial market is free from tax fees for the trading of securities, and no costs imposed on the trading process itself.

d - The efficient financial market includes a large number of investors, in order to ensure that none of them is able to influence prices.

e - The active/efficient financial market does not allow the investor to achieve a large return, but the return will be within the accepted rate.

f - The active/efficient financial market must have information based on informational elements that disclose the real data that would direct the investor to compare between the various investment opportunities, as it will reflect the real value of the securities.

3.7 Indicators of active markets as a measure of their efficiency:

The market index is a numerical value that measures the changes taking place in the stock market. The index is configured and its value is determined at the starting stage or period, and then its value is compared at any point in time, thus it is possible to identify market movements, whether up or down so that the index reflects the prices of the market and its trend (Wang, 2021). (Tan et al, 2020) believes that a market index is a tool for measuring the evolution of the prices of the securities registered in it in a continuous and regular manner. While (Klaus & Koser, 2021) confirms that stock market indicators are a technique that allows giving a numerical result by means of a relationship showing the evolution of quantities and prices over time in order to identify the performance of the market, a particular economic sector, or a financial portfolio with the possibility of comparing it with its counterpart in the same market or other financial markets. nevertheless, there are a number of very important metrics and indicators that can be invoked to measure the activity of the stock market, and these indicators are as follows (Pervaiz, 2021) (Mutize et al, 2020):

1 - The general index of stock prices: with the presence of a number of shares in each stock market, and due to the difficulty of measuring the general trend of market activity, it was necessary to reach a special index for each financial market, which represents the average stock prices (for companies listed in the market) per day. It is based on daily trading operations, and therefore it is noted that each market has its own indicator.

2 - Market size: The market size is measured by two main indicators (Biondi & Olla, 2020):

a- Market capitalization index (market capitalization rate): the market capitalization means the total shares listed in the market multiplied by their average prices at the end of the period. It also refers to the total value of the securities listed in the market. The market capitalization rate is measured by dividing the market value of the registered shares. This indicator is a mirror that reflects the level of market activity, as the higher the value of this indicator, the higher the volume of the market.

b - Number of companies index: This indicator refers to the number of companies listed in the stock market, as the increase in the number of companies reflects the development in the financial market in general, but this indicator may lose its value if it is not accompanied by the use of the market value indicator, the number of listed companies may be large, but the total market value of the shares of those companies is small.

3 - Market liquidity: Market liquidity m[illegible]lity to buy and sell securities easily in the secondary market, and there are two indic[illegible]asure it: (Benton & Philips, 2020)

a - Trading volume index: Trading volume means the value of what is traded in shares and bonds at various prices during a period of time. This rate is measured by dividing the total shares traded in the market by the gross domestic product.

b - Turnover Index: This indicator indicates the percentage of the shares of a particular company or the shares of a group of companies within one sector during a certain period of time. The turnover rate can be extracted by dividing the total shares traded by the market capitalization during the year or during any period of time.

4- The degree of concentration indicator: It means the degree of trading concentration, whether the trading volume is concentrated in a specific number of listed companies or distributed over a large number of them. Nevertheless, the degree of concentration can be measured by calculating the share of the top ten companies in the total market capital and the

total trading value, that is, it is calculated by measuring the market capitalization of the ten largest companies in the market in proportion to the total market capitalization.

4 - Hypotheses

Despite the positives and economic and financial achievements witnessed by business organizations in the last three decades that may be achieved by the application of the principle of historical cost, which cast a negative shadow on the reality and safety of accounting measurement in accordance with this principle (historical cost), which led to a deficiency in the usefulness of the information provided by the financial reports which is unable to provide financial indicators that express the financial position and business results of these institutions, which strongly supported the tendency to apply other alternative measurement bases (Samih, 2020). However, many professional organizations interested in formulating financial accounting standards have called for the use of the "fair value" method as a main entry point for measurement, which sparked controversy when differentiating between the fair value method and other alternative measurement methods, and that the changes resulting from the application of historical cost made those bodies turn to the concept of fair value, which has become an important basis and measure for recognition and measurement when accounting for transactions, and then disclosed (Bryan, 2021). Furthermore, the application of fair value in the Iraqi stock market achieves high efficiency in directing resources as centers for attracting and accumulating capital from savers to employ them in various and appropriate investment activities, which is positively reflected on the economy of the state as a whole.

Accordingly, the research problem can be posed through the following question: Is the adoption of the use of fair value accounting as a basis for accounting measurement by companies registered in the Iraqi market for securities would have a direct positive impact on the activation of the market and thus its efficiency. In order to answer this question and accurately treat the research variables, the following hypotheses were formulated.

H1: There is no significant correlation between the use of fair value accounting by companies registered in the Iraq Stock Exchange and the increase in the market capital of the market.

H2: There is no significant correlation between the use of fair value by companies registered in the Iraq Stock Exchange and the increase in the number and value of buy and sell orders.

5- Methodology:

5.1 Sample:

The research population consists of the number of financial analysts and investors in the Iraq Stock Exchange, and the number of distributed questionnaires reached (105) questionnaires and distributed equally to the research sample. It was distributed by hand and with the help of a number of researcher assistants, and (86) questionnaires were returned from them, thus the response rate is approximately (81.90%), and this percentage is considered acceptable to generalize its results to the research population.

2.5 Data collection methods:

The researcher adopted the questionnaire as a method of research, which is one of the main means of collecting the necessary data necessary to achieve the objectives of the research and test its hypotheses using the SPSS statistical program. The questionnaire was prepared by the researcher depending on the theoretical aspect that was put forward in the research, and the

questionnaire included (14) questions, and the strength of the answer was determined through the use of the five-point Likert scale to express the opinions of each member of the sample. Each of the cases has a weight consistent with its importance, as it was assigned to the answer strongly agree (5) points, agree (4) points, neutral (3) points, disagree (2), and strongly disagree (1) point, and then test and analyze the results according to Appropriate statistical methods to prove the two hypotheses of the research.

6- Statistical methods used:

A number of statistical methods will be used and employed for the purpose of describing and analyzing the data of the study variables and testing its hypotheses through the help of the computer to extract the results and based on the ready-made application software package (20) SPSS V. The arithmetic mean and standard deviation were also used to describe the variables.

7- Descriptive results and hypothesis testing:

7.1 Descriptive results:

This group includes a description of the results of the answers of all respondents to the research questionnaire, using the arithmetic mean and standard deviation. The research included (14) factors that could have an impact on the fair value and these factors were selected through the theoretical side of the research. The respondents were asked to determine the importance of each factor using a Likert scale from 1 to 5 where (5) indicates (strongly agree) and (1) to (strongly disagree).

A - Results related to the first hypothesis: There is no significant correlation between the use of fair value accounting by companies registered in the Iraqi Stock Exchange and the increase in the market capital of the market. After analyzing the answers of the research sample individuals on the questionnaire, the arithmetic averages and standard deviations of these hypotheses, and the results were as in Table (1) below:

Table (1)
Descriptive statistical analysis of the axis of the extent to which fair value accounting is used and the increase in market capitalization of the market

Influencing factors	Arithmetic mean	standard deviation	ranking	Importance
1 - The International Accounting Standards Implementation Guide and its annexes provide a full explanation of the requirements for applying fair value.	**4,80**	**0,96**	**1**	High
2 - The advantages of using fair value outweigh the disadvantages.	**4,17**	**0,83**	**4**	High
3- The companies registered in the Iraq Stock Exchange have qualified cadres capable of understanding the requirements of applying fair value.	**3,97**	**0,90**	**6**	High
4 - There are experts and appraisers available in the Iraq Stock Exchange that	**3,90**			

can be used to determine the values of some assets and liabilities for which it is difficult to find a fair value.		**0,75**	**7**	High
5- Adopting the application of fair value helps in providing financial reports that are characterized by reliability, honesty of expression and comparability.	**4,42**	**0,65**	**3**	High
6- Preparing financial statements according to the fair value approach is more beneficial than those prepared according to historical cost.	**4.49**	**0.64**	**2**	High
7- The accounting information published in the financial statements according to the fair value approach affects the decisions of investors in joint stock companies.	**4.15**	**0.86**	**5**	High
all paragraphs	**4.27**	**0.84**		

Table (1) above indicates that the answers of the research sample ranged between (4.80 - 3.90) arithmetic averages, and respondents believe that the guide to applying international accounting standards and its annexes provide a full explanation of the requirements for applying fair value and preparing financial statements according to the fair value approach is more benefit of that prepared according to the "historical cost", and the adoption of the application of the fair value helps in providing financial reports characterized by reliability, honesty of expression and comparability. These paragraphs are of high importance because the arithmetic means of the answers of the individuals of the research sample for each of them is more than (3.5), and these items were occupied the three rank paragraphs are as shown in Table (1) above, and the arithmetic mean of the general sum was (4.27), either the standard deviation was (0.84), and this deviation indicates the extent to which the values of this axis are dispersed from the arithmetic mean of all paragraphs.

B - Results related to the second hypothesis: there is no significant correlation between the use of fair value by companies registered in the Iraqi Stock Exchange and the increase in the number and value of buying and selling orders.

After analyzing the answers of the research sample individuals on the questionnaires, the arithmetic averages and standard deviations of this hypothesis were found, and the results were as in Table (2) below:

Table (2)

Descriptive statistical analysis of the axis of using fair value and increasing the number and value of buying and selling orders

Influencing factors	Influencing factors	Influencing factors	Influencing factors	**Influencing factors**
1 - The adoption of fair value accounting would make the Iraqi market for financial markets	3,48	1,03	6	medium

more integrated with financially efficient markets.				
2 - The adoption of fair value by companies registered in the Iraq Stock Exchange had a clear role in increasing the number of investors, individuals or institutions.	4,42	0,65	1	High
3 - It is expected that in the future, many foreign companies will offer their securities through the Iraqi market for the financial markets after the spread and succession of applying the fair value approach.	3,83	0,81	5	High
4 - Reliance on fair value is a strong incentive for foreign indirect investments to enter the Iraqi financial market.	4,00	0,88	3	High
5 - The use of fair value has a positive effect on information users in rationalizing them in making their decisions, which increases the confidence of dealers in the market.	4,17	0,83	2	High
6- Dependence on fair value is a decisive factor in the increase and development of market response speed indicators, such as the ratio of trading value to GDP and market capital.	3,85	0,75	4	High
7 - The increase in the number of investors, whether local or foreign, individuals and institutions has a direct positive impact on the increase in the number of brokerage and financial brokerage companies.	3,40	0,89	7	medium
all paragraphs	3.88	0.83		

Table (2) above indicates that the answers of the research sample ranged between (4,42 - 3.40) arithmetic averages, and the respondents believe that the adoption of fair value by companies registered in the Iraq Stock Exchange had a clear role in increasing the number of investors, individuals or institutions, that the use of fair value has a positive impact on information users in rationalizing them in making their decisions, which increases the confidence of dealers in the market, and the reliance on fair value is a strong incentive for the entry of indirect foreign investments into the Iraqi market for financial markets. These paragraphs are of high importance

because the arithmetic means of the answers of the individuals of the research sample for each of them is more than (3.5), and these paragraphs occupied the three ranks as shown in Table (2) above, and the arithmetic mean of the general total reached (3.88), either the standard deviation has been It reached (0.83), and this deviation indicates the dispersion of the values of this axis from the arithmetic mean of all paragraphs.

Second: Hypothesis testing:

The research hypotheses were tested through the data of the actual responses to the survey of the research group, which is represented by a number of financial analysts and investors in the Iraqi Stock Exchange, using the (Z) test and at a level of significance (0.05), and the two hypotheses of the research will be verified according to the sequence that was mentioned in the chapter The first search is as follows:

(a) The test of the first hypothesis, which states the following:

There is no significant correlation between the use of fair value accounting by companies registered in the Iraqi Stock Exchange and the increase in the market capitalization of the market, and to prove the validity of error of this hypothesis in the framework of the results of the statistical analysis, a (Z) test was conducted on the arithmetic mean, which shows Its results are data in Table No. (3).

Table (3) Results of the (Z) test

Arithmetic mean	Sample volume	Z		test results
		calculated	tabular	The first hypothesis
4.27	81	13.523	1,979	reject the hypothesis

It was found through statistical analysis that the calculated (Z) value is (13.523), which is greater than its tabular value of (1,979). Therefore, it rejects the null hypothesis and accepts the alternative hypothesis that there is a significant correlation between the use of fair value accounting by companies registered in the Iraqi market Securities and increase the market capitalization of the market

b- The test of the second hypothesis, which states the following:

There is no significant relationship between the use of fair value by companies registered in the Iraqi Stock Exchange and the increase in the number and value of buy and sell orders. In order to prove the validity of this hypothesis or its error within the framework of the results of the statistical analysis, a (Z) test was conducted on the arithmetic mean, the results of which show the data of Table No. (4).

Table (4) Results of the (Z) Test

Arithmetic mean	Sample volume	Z		test results
		calculated	tabular	The first hypothesis
3.88	81	3.514	1,979	reject the hypothesis

It was found through statistical analysis that the calculated (Z) value is (3.514), which is greater than its tabular value of (1,979). Therefore, it rejects the null hypothesis and accepts the alternative hypothesis that there is a significant relationship between the uses of fair value by companies registered in the Iraqi Stock Exchange. Finance and increase the number and value of buying and selling orders.

Conclusions and Recommendations:

First, the conclusions:

1 - The information published at fair value in the financial statements of companies registered in the Iraq Stock Exchange is important to the decisions of investors and the activation of the market.
2 - The use of fair value accounting requires the availability of laws and legislation that contribute to controlling the ethics of the management of companies applicable to them, as well as the availability of qualified technical personnel to deal with fair value.
3 - The use of fair value accounting in accounting measurement helps users of financial information to make better decisions.
4 - There is a relationship between the use of fair value accounting by companies registered in the Iraq Stock Exchange and the increase in the market capital.
5 - There is a significant correlation between the use of fair value by companies registered in the Iraq Stock Exchange and the increase in the number and value of buying and selling orders.

References

[1] Adegboyegun, A. E., Ben-Caleb, E., Ademola, A. O., Madugba, J. U., & Eluyela, F. D. (2020). Fair value accounting and corporate reporting in Nigeria: A logistics regression approach. International Journal of Financial Research, 11(2), 301-310.

[2] Adwan, S., Alhaj-Ismail, A., & Girardone, C. (2020). Fair value accounting and value relevance of equity book value and net income for European financial firms during the crisis. Journal of International Accounting, Auditing and Taxation, 39, 100320.

[3] Ahn, J., Hoitash, R., & Hoitash, U. (2020). Auditor task-specific expertise: The case of fair value accounting. The Accounting Review, 95(3), 1-32.

[4] Alexander, D., & Fasiello, R. (2020). Prudence and directive 34–reality and rhetoric in accounting regulation. Accounting in Europe, 1-17.

[5] Al-Khadash, H., & Abdullatif, M. (2009). Consequences of fair value accounting for financial instruments in the developing countries: The case of the banking sector in Jordan. Jordan journal of business administration, 5(4), 533-551.

[6] Beigman, E., Brennan, G., Hsieh, S. F., & Sannella, A. J. (2021). Dynamic Principal Market Determination: Fair Value Measurement of Cryptocurrency. Journal of Accounting, Auditing & Finance, 0148558X211004134.

[7] Benton, A. L., & Philips, A. Q. (2020). Does the@ realDonaldTrump really matter to financial markets?. American Journal of Political Science, 64(1), 169-190.

[8] Biondi, Y., & Olla, S. (2020). Financial accumulation implies ever-increasing wealth inequality. Journal of Economic Interaction and Coordination, 1-9.

[9] Bryan, S., Lilien, S., Sarath, B., & Yan, Y. (2021). Evolving Standards of Fair Value and Acquisition Accounting. In Information for Efficient Decision Making: Big Data, Blockchain and Relevance (pp. 525 .

[10] Chirkova, L., Chirkova, P., & Shkolik, O. (2018, December). The problems of determining the fair value of intellectual property in the structure of assets of financial institutions. In Journal of Physics: Conference Series (Vol. 1141, No. 1, p. 012013). IOP Publishing .

[11] Christensen, H. B., & Nikolaev, V. V. (2013). Does fair value accounting for non-financial assets pass the market
test?. Review of Accounting Studies, 18(3), 734-775.
[12] Dakheel, A. F., Kadhummatrood, A., & Abbas, A. H. (2021). THE EFFECT OF FAIR VALUE ESTIMATES ON THE
AUDITOR'S REPORT UNDER CONDITIONS OF UNCERTAINTY. PalArch's Journal of Archaeology of
Egypt/Egyptology, 18(1), 3487-3500.
[13] Dakila Jr, F. G. (2020). The development of financial markets in the Philippines and its interaction with monetary policy
and financial stability. José Vicente Romero, Hernando Vargas, Pamela Cardozo and Andrés Murcia..... 8 3 From float
to currency floor and back to float: the Czech National Bank's temporary exchange rate commitment, 219 .
[14] De Santis, F., Greco, G., & Cenciarelli, V. G. (2018). External audit and fair value measurements. External audit and fair
value measurements, 1-102.
[15] DeFond, M., Hu, J., Hung, M., & Li, S. (2020). The effect of fair value accounting on the performance evaluation role of
earnings. Journal of Accounting and Economics, 70(2-3), 101341.
[16] Elfaki, A. A. A., & Hammad, S. M. E. (2015). The impact of the application of Fair Value Accounting on the quality of
accounting information. An empirical study on a group of companies listed on the Khartoum stock exchange. International
Journal of Academic Research in Accounting, Finance and Management Sciences, 5(1), 148-160.
[17] Falkenheim, M. (2021). Fair-Value Cost Estimation and Government Cash Flows: Working Paper 2021-05 (No. 57062).
[18] Filip, A., Hammami, A., Huang, Z., Jeny, A., Magnan, M., & Moldovan, R. (2019). The Relevance of the Fair Value
Measurement Hierarchy: A Holistic Perspective. Available at SSRN 3504756.
[19] Filip, A., Hammami, A., Huang, Z., Jeny, A., Magnan, M., & Moldovan, R. (2021). The Value Relevance of Fair Value
Levels: Time Trends under IFRS and US GAAP. Accounting in Europe, 1-22.\
[20] Flayyih, H.H. (2015). The Fraud under the fair value Exploratory St. journal of Economics And Administrative
Sciences, 21(86).
[21] Fontes, J. C., Panaretou, A., & Peasnell, K. V. (2018). The impact of fair value measurement for bank assets on
information asymmetry and the moderating effect of own credit risk gains and losses. The Accounting Review, 93(6),
127-147.
[22] Freeman, G. (2020). A Comprehensive Study of Accounting Principles and Applications through Analysis of Case
Studies.
[23] Galassi, G. (2020). Economic income, historical costing income and conservatism. An integrated approach. De Computis-
Revista Española de Historia de la Contabilidad, 17(2), 28-42.
[24] Gardi, B. (2021). Investigating the effects of Financial Accounting Reports on Managerial Decision Making in Small
and Medium-sized Enterprises. Available at SSRN 3838226.
[25] Guo, K., & Zhang, A. (2021). Effect of Fair Value Measurement on Earnings Management of Chinese Real Estate Listed
Companies. Proceedings of Business and Economic Studies, 4(1).

[26] Hajiyev, H. (2021, January). Accounting and tax accounting for the accrual of depreciation of fixed assets and ways of convergence. In SHS Web of Conferences (Vol. 92, p. 02020). EDP Sciences.
[27] He, L. Y., Wright, S., & Evans, E. (2018). Is fair value information relevant to investment decision-making: Evidence from the Australian agricultural sector?. Australian Journal of Management, 43(4), 555-574.
[28] Heaton, J. B. (2019). On the (Significant) Possibility of Informationally-Efficient Markets. Available at SSRN 3412568.
[29] Hellmann, A., Patel, C., & Tsunogaya, N. (2021). Foreign-language effect and professionals' judgments on fair value measurement: Evidence from Germany and the United Kingdom. Journal of Behavioral and Experimental Finance, 30, 100478.
[30] Hsu, A. W. H., & Wu, G. S. H. (2019). The fair value of investment property and stock price crash risk. Asia-Pacific Journal of Accounting & Economics, 26(1-2), 38-63.
[31] Klaus, J., & Koser, C. (2021). Measuring Trump: the Volfefe index and its impact on European financial markets. Finance Research Letters, 38, 101447 .
[32] Kubic, M. (2021). Time to get it Right: An Examination of Post-Acquisition Fair Value AdjustmentsTime to get it Right. Journal of Financial Reporting.
[33] Kulish, N. V., Sytnik, O. E., Tunin, S. A., Frolov, A. V. E., & Germanova, V. S. (2018). Approaches to the valuation of biological assets at fair value. Research journal of pharmaceutical, biological and chemical sciences, 9(3), 746-750.
[34] Louche, C., Busch, T., Crifo, P., & Marcus, A. (2019). Financial markets and the transition to a low-carbon economy: Challenging the dominant logics. Organization & Environment, 32(1), 3-17.
[35] Malceniece, L., Malcenieks, K., & Putniņš, T. J. (2019). High frequency trading and comovement in financial markets. Journal of Financial Economics, 134(2), 381-399.
[36] Mamais, K. (2021). Evaluating investment strategies among the International Financial Markets: three essays on investment decisions.
[37] Mamaysky, H. (2020). Financial markets and news about the coronavirus. Available at SSRN 3565597.
[38] McInnis, J. M., Yu, Y., & Yust, C. G. (2018). Does fair value accounting provide more useful financial statements than current GAAP for banks?. The Accounting Review, 93(6), 257-279.
[39] Menicucci, E. (2020). Fair Value Accounting and Earnings Quality. In Earnings Quality (pp. 107-137). Palgrave Pivot, Cham.
[40] Mutize, M., Tefera, E., & Nkhalamba, M. (2020). The development of financial markets in Africa: trends, challenges and prospects. Journal of Economics and Behavioral Studies, 12(1 (J)), 46-54.
[41] Nigro, C. A., & Stahl, J. R. (2021). Venture Capital-Backed Firms, Unavoidable Value-Destroying Trade Sales, And Fair Value Protections. European Business Organization Law Review, 22(1), 39-86.
[42] Nordlund, B., Lorentzon, J., & Lind, H. (2021). A note on auditing fair value of investment properties. Journal of Property Investment & Finance.

[43] Pandya, A., van Zijl, W., & Maroun, W. (2021). Fair value accounting implementation challenges in South Africa. Journal of Accounting in Emerging Economies.

[44] Pervaiz, K., Virglerová, Z., Khan, M. A., Akbar, U., & Popp, J. (2021). Sovereign credit ratings and Asian financial markets. E a M: Ekonomie a Management.

[45] Queku, Y. N. (2020). Value Relevance of Fair Value Measurement and Stock Price Predictability: Incremental Effect and Synergetic Analysis of Listed Banks in Ghana. ADRRI Journal of Arts and Social Sciences, 17(7 (5)), 85-110.

[46] Runtev, Miki. "The Impact Of Digitization On Financial Markets And Their Tendency On Global Growth." Economic Development/Ekonomiski Razvoj 22 (2020).

[47] Samih, O., Alqtish, A. M., & Qatawnh, A. M. (2020). The Impact of Fair Value Accounting on Earnings Predictability: Evidence from Jordan. Asian Economic and Financial Review, 10(12), 1466-1479.

[48] Sangchan, P., Habib, A., Jiang, H., & Bhuiyan, M. B. U. (2020). Fair value exposure, changes in fair value and audit fees: evidence from the Australian real estate industry. Australian Accounting Review, 30(2), 123-143.

[49] Schär, F. (2021). Decentralized finance: On blockchain-and smart contract-based financial markets. FRB of St. Louis Review.

[50] Sellhorn, T., & Stier, C. (2019). Fair value measurement for long-lived operating assets: Research evidence. European Accounting Review, 28(3), 573-603.

[51] Siriopoulos, C. (2021). Financial Markets are Not Efficient: Financial Literacy as an Effective Risk Management Tool. The International Journal of Business and Management Research, 9(1), 65.

[52] Smith, M. K. S., Smit, I. P., Swemmer, L. K., Mokhatla, M. M., Freitag, S., Roux, D. J., & Dziba, L. (2021). Sustainability of protected areas: Vulnerabilities and opportunities as revealed by COVID-19 in a national park management agency. Biological Conservation, 255, 108985.

[53] Spulbar, C., & Birau, R. (Eds.). (2019). Emerging research on monetary policy, banking, and financial markets. IGI Global.

[54] Steriotis, K., Tsaousoglou, G., Efthymiopoulos, N., Makris, P., & Varvarigos, E. M. (2018). A novel behavioral real time pricing scheme for the active energy consumers' participation in emerging flexibility markets. Sustainable Energy, Grids and Networks, 16, 14-27.

[55] Tan, X., Sirichand, K., Vivian, A., & Wang, X. (2020). How connected is the carbon market to energy and financial markets? A systematic analysis of spillovers and dynamics. Energy Economics, 90, 104870.

[56] Wang, J., Sun, T., Liu, B., Cao, Y., & Zhu, H. (2021). CLVSA: A convolutional LSTM based variational sequence-to-sequence model with attention for predicting trends of financial markets. arXiv preprint arXiv:2104.04041.

[57] Wermers, R. (2020). Active investing and the efficiency of security markets. The Journal of Investment Management.

[58] Yang, Y., Jia, Y., Ling, S., & Yao, C. (2021). Urban natural resource accounting based on the system of environmental

economic accounting in Northwest China: A case study of Xi'an. Ecosystem Services, 47, 101233.
[59] Yliheljo, E. (2021). The Variable Nature of Ownership of Emission Units in the Intersection of Climate Law, Property
Law, and the Regulation of Financial Markets. Climate Law, 11(1), 45-75.

The Active Role of Servant Leadership to Improve Performance of employees

Manal Abdel Hamid Abdel Majid[1], Haider jare mahsen[2]
{Manal.abdulmajeed@stu.edu.iq[1], haider.jare@stu.edu.iq[2]}

Technical Institute, Southern Technical University, Iraq[1,2]

Abstract. The study expressed the problem through a set of questions focused on whether there is a correlation and effect relationship between the modern leadership patterns based on a hypothetical model of 60 members as leaders and heads of departments at the University of Basra. The members are appointed from various colleges such as Arts, Administration, Economics, Education for Girls, and Law. The study considers a descriptive-analytical approach based on a questionnaire consisting of three sections. The first concerns the personal data of the respondents. The second includes servant leadership with its six dimensions represented by trust, participation in decision-making, empowerment, vision, providing guidance, and helping subordinates to Success and growth. Finally, the third deals with the performance of employees, measured by the following variables: job satisfaction, creativity, absence, and finally productivity. A statistical programme is written to justify the outcomes of this study. It is found that the orientation to servant leadership is one of the best trends as it is a new style based on positive ideas and principles that create a method of work.

Keywords: Servant leadership, performance employees, Al Basra University

1 Introduction

Leaders' roles have changed dramatically in the past few years, so many successful leaders have changed their ways of working, through making moving from the center of the group to its periphery, working as team members rather than leaders or managers, and becoming the new leaders They work on understanding the human behavior of individuals to direct this behavior to achieve the goals of the organization. Therefore, successful leadership is the one who works to spread the spirit of cooperation and teamwork among the workers, and it is the one who realizes the importance of raising the morale of subordinates, identifying their desires, and completing the work entrusted to them to achieve the goals Servant leadership also plays a key role in planting confidence among subordinates within the university formations and their participation in decision-making, providing guidance and helping them to grow and succeed. Finally, the research was divided into four sections. The first topic was devoted to the research methodology and deals the second topic with the theoretical aspect represented in the concept of leadership. The maid with its six dimensions, in addition to the variables of workers' performance, the third topic includes the practical aspect, and finally deals the fourth topic with the Conclusions and recommendations.

1.1 The Study Problem

The researchers found, through the exploratory study of the colleges under study, that there are some organizational problems related to the behavior of workers that lead to confusion as a

IMDC-IST 2021, September 07-09, Sakarya, Turkey
Copyright © 2022 EAI
DOI 10.4108/eai.7-9-2021.2315375

result of not choosing leadership patterns that help raise the performance and efficiency of workers, but the contrary, negatively affect their performance. Among these influences is the low level of Mutual trust between superiors and subordinates because they believe that leaders prefer their interests over the interests of workers and the goals of the organization, which leads to their sacrificing the values of justice and equality, frequent complaints by subordinates about how the work is managed, feelings of dissatisfaction and anxiety, low productivity within the work environment, and thus the need appears To study the influential leadership styles, especially the servant leadership philosophy, which is one of the most prominent types of contemporary leaders, and the research problem can be diagnosed by answering the following questions:

a) To what extent can servant leadership affect organizational citizenship behavior and change the direction of employees' performance positively towards achieving the organization's goals?
b) Does the application of the servant leadership philosophy reduce the negative indicators in the organizations?

1.2 The Study Aim

The main objectives of the study can be identified as follows:
Recognizing the extent to which the administrative leaders practice to remove the servant leadership from the point of view of the faculty members. Evaluating the level of administrative leaders in the organizations under study concerning the application of the dimensions of servant leadership and the performance of employees Clarify the nature of the relationship and the impact between servant leadership and the performance of workers for the organizations surveyed. To present some suggestions and recommendations to the surveyed organizations about the interest in removing the effect of servant leadership on the performance of the employees. Determine whether there is an influence relationship between the dimensions of servant leadership and the performance of employees.

1.3 The Importance of the Study

The importance of the study comes from the importance of servant leadership as one of the patterns of its leaders capable of helping organizations to overcome their internal problems, through its policies in taking care of the interests of workers and helping them solve their problems, raising the efficiency of their performance and developing their abilities and skills, which leads to raising the efficiency of the organization's performance, which helps it Facing the challenges of the external environment and building society as a whole**.**

1.4 Hypothesis of the Study

The research is based on two main hypotheses:

a) There is a positive statistically significant correlation between servant leadership and the performance of employees at the University of Basra.
b) There is a positive and statistically significant effect of servant leadership on improving the performance of employees at the University of Basra.

1.5 The Study Model

The model was designed to represent the basic idea on which the study is based and to clarify the nature of the relationship between the study variables. The scheme included two main variables:

1. the independent variable (x) is represented by servant leadership.
2. the dependent variable (y) is represented by the performance of workers.

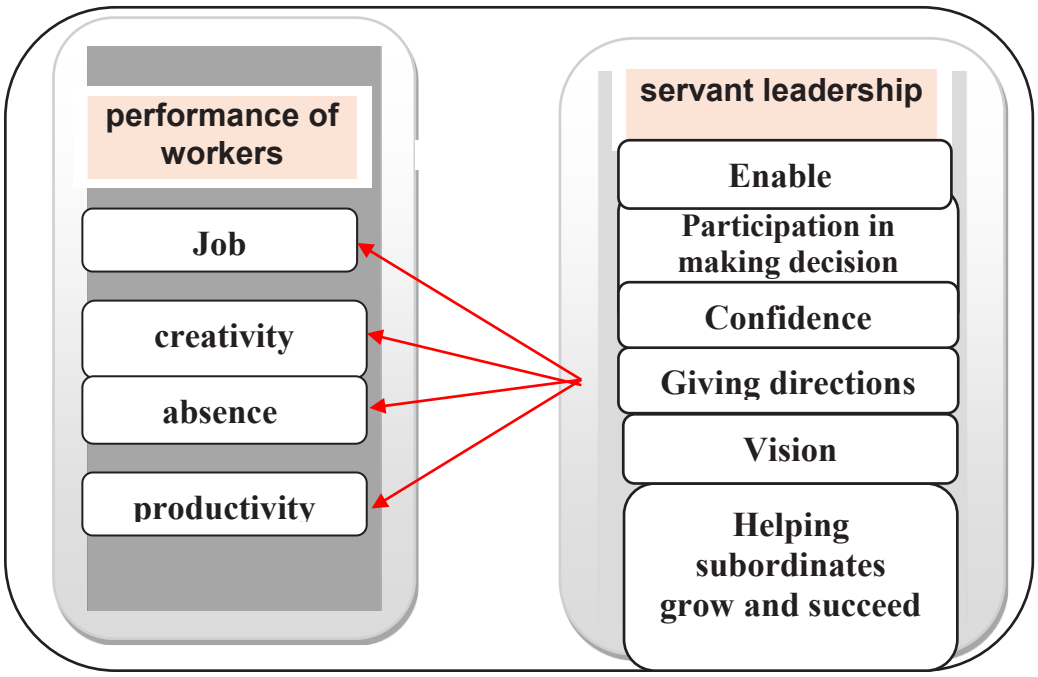

Fig 1. The Study model.

1.6 The study Community and Sample

The researchers chose the University of Basra as a community for the study, and it was determined in light of the researchers' inventory of several faculties that serve the objectives of the study, taking into account the diversity in the scientific and human aspects. College of Arts, College of Education for Girls, and College of Law). The following reasons were behind choosing the mentioned colleges:

1. The clarity of the role of leadership patterns in the mentioned colleges as a result of the great role in which Iraqi universities play and their important impact on society, is a service organization, which provides the requirements for advancement in various aspects of life for any country. It is one of the most homogeneous organizations in its activities. Diversity in its sectors of work.
2. This study has adopted the double sample method to obtain the data required for the analysis. The sample included deans, assistant deans, and heads of departments in some faculties of the University of Basra, while the second sample included faculty members in the mentioned faculties. A questionnaire that measures the role of servant leadership in improving the performance of employees was distributed to faculty members. The

researchers distributed (80) forms to the respondents in their workplaces, and the retrieved and valid forms for analysis were (60) forms.

1.7 Methods of Data Analysis and Measurement

1. Conducting validity tests using factor analysis and testing reliability through Alpha Cranach's to measure the accuracy of sample answers.
2. The normal distribution using statistical methods using the program (SPSS 25. v).
3. Descriptive statistics using (arithmetic mean, standard deviation, relative importance).

2 Servant Leadership Concept

Servant leadership is one of the contemporary theories in organizational behavior, which has a positive impact on the behavioral patterns of employees, such as job satisfaction, job commitment, organizational confidence, organizational culture, empowering workers, so we can clarify several concepts from the point of view of several researchers:
Olesia defined servant leadership as ((a leadership style upside down, i.e. the leader who transcends his interests and prefers serving the needs of others, as it helps them achieve growth and development and allows them to achieve what they aspire to financially and emotionally, taking into account the work to achieve the goals of the organization)).[1] (as mentioned by Northouse) as it is the relationship between the leader and the follower, and it is one of the forms of moral leadership because it reflects the aspect of privileging others over the self and what is known about its concerns with the needs of subordinates and its focus on moral considerations in the relationship of the leader with his followers who are in power And the end of that relationship is [2]. And Blanchard shows that servant leadership means influencing people so that they participate willingly and voluntarily in the pursuit of common goals beneficial to all parties with all their hearts, minds, souls, creativity, excellence, and all other resources they possess[3]While Patterson sees (the concept of servant leadership by focusing on the relationship between the leader and the follower, it is a type of leadership that requires focusing on the followers first and foremost [4.]From the foregoing and after reviewing the researchers' views, it becomes clear that the concept of servant leadership is a strategy and a model of work through the positive influence of the leader on the behavior and organizational culture of workers to change their attitudes and help them achieve their interests without any conflict with the interests and objectives of the organization as a whole through altruism, sacrifice, humility and achieving trust among them. Justice and equality.

2.1 Dimensions of Servant Leadership:

There is a discrepancy in the views of researchers about the dimensions of servant leadership, which differ according to the field and nature of work. Most of the dimensions agreed upon by all researchers were chosen, which may bear different names, but they carry the same content, which is as follows:

2.2.1 Confidence:

1. Trust is one of the most important dimensions of servant leadership, which is represented by the leader's high morals and credibility in dealing and implementing

promises with others, it has a fundamental impact on the relationship between the boss and subordinates, as the lack of trust leads to a negative feeling among employees, which affects their behavior and job performance, and from an organizational perspective, trust can be defined It is any behavior in a way that makes professional roles secondary when the individual is a leader, where confidence revolves around self-honesty and is accurately represented, privately and publicly, in the leader's internal intentions and commitments towards followers [5]

2. Al-Atwi & Al-Shaibani consider (it is the positive feeling that the individual possesses towards the other party in terms of his confidence in carrying out the agreed actions and actions, and it can be said that it is a mental state that cannot be measured directly and cannot be verified at present, but it is possible to see its results in the future, and it can be measured by behavior, which is A movement that includes voluntary work between two people, so the first must show his confidence for the other party to trust him, otherwise the two will remain distrustful of each other, the concept of trust is one of the most important concepts that is difficult to define without research and scrutiny, as it represents a basic element for organizations of all kinds)[6] .

2.2.2 Participation in Decision-Making

Participation in decision-making The decision-making process goes through several stages, and the process of employee participation in the decision-making process is the most important stage by motivating workers and giving them self-confidence and power to make decisions. It is psychological, political, economic, and social, and therefore the decision-making process is carried out through teamwork, and therefore we find that the decision-making process includes all the stages before the issuance of the decision, including the final stage. [7]

2.2.3 Empowerment

Empowerment is one of the basic characteristics of servant leadership, as it is based on a basic idea that (the authority to make decisions must be delegated to employees to enable them to respond effectively to the needs of customers. This idea in its previous sense forces the leadership to abandon its old method based on the idea of guidance and adopt a new method based on consultation and participation[8]. Empowerment is closely related to the previous dimension, with the leader empowering and developing workers in several aspects, including training, creativity in the field of work, information exchange, self-confidence, and decision-making, each according to his work.

2.2.4 Vision

All organizations begin their work by setting a clear vision to achieve their strategic goals, which are laid by leaders mainly and their abilities to succeed in communicating these visions and influencing the trends and behavior of employees to achieve the goals of the organization. And (Russell) sees that The most important thing that distinguishes a servant leader from others in terms of a sense of the unknown and the ability to provide a strategic vision for the organization and make others believe in his abilities to predict what is difficult to predict to achieve the desired goals[9]. We also find that the success of leaders depends on their vision of their

organizations, as well as the ability of leaders to formulate a good vision that positively affects their ability to influence workers.10]

2.2.5 Giving Directions

These are the characteristics that affect the workers and that the servant leadership seeks by providing the necessary support and guidance in how they perform their work, which is concerned with developing their efficiency to achieve their goals, which are aimed at achieving goals of the organization. Therefore, Abdullah believes that the servant leader should provide directions and instructions to subordinates to be Introducing them to what is required of them and what is beneficial to both the workers and the organization, as well as making the tasks move dynamically towards achieving the goals of the organization, and from this direction, providing directions means providing a degree of health for the issue through which the servant leader can push his subordinates to work with high-quality performance and to the maximum of their energies in A framework through which to satisfy their needs and desires and achieve their personal goals of servant leadership.[11].

2.2.6 Helping Subordinates Grow and Succeed

The human resource is one of the most important assets of organizations in its various specializations and sectors, and it has a significant impact on its success and progress. Therefore, leaders of organizations should pay attention to workers, appreciate their support for them, facilitate their tasks and satisfy their needs.[12] a believes that the servant leader for subordinates is a present and future value in sound organizations and the leader expresses his responsibility to take care of others towards achieving their full potential. Individuals can be developed in any organization by creating a dynamic learning environment as the mistakes of others lead to a vision new and are viewed as learning opportunities[13] .

2.3 Employees Performance

The best way to achieve the goals of the organization is to raise the performance of the individual worker by providing appropriate conditions for the nature of work, and the most important of these conditions is the nature of the interaction between the leader and subordinates (administrative behavior) because it is the most interactive relationship than the workers' dealing with other things such as machines, equipment or other things. Such as administrative, marketing ells. (Russell) defined the performance of workers in organizations as (the set of managerial behaviors that express the individual employee's performance of his work, which includes the quality and level of performance, capabilities, and skills required such as communication skills and interaction with the organization's customers and the extent of commitment to and response to administrative systems[14] that the performance of employees refers to all behaviors that contribute to the completion of basic work in the organization, such as production and marketing, and it is possible to identify sub-paragraphs through which it is possible to determine the efficiency of the performance of employees in any organization as follows:

2.3.1 Job Satisfaction

Job satisfaction is meant the positive feeling that employees feel towards the leader and the organization, which leads to outstanding performance as a result of what the organization offers them. Therefore, job satisfaction has been defined as the degree of positive or negative feeling of members of the organization towards their work and tasks in the organization [15] The job satisfaction is explained as the pleasant psychological or emotional state that the working individual reaches when he attains a certain degree of satiation. Therefore, it is the responsibility of the organization to encourage them and their participation in the various affairs of the organization, such as allowing their participation in defining job descriptions and limits, contributing to the performance evaluation procedure, and participating in decision-making. A distinguished organization values its employees and allows for mutual benefit to be achieved between the organization's goals It also develops the employees' capabilities to promote justice and equality[16.]

2.3.2 Creativity

Creativity is meant to generate and develop new ideas to benefit from them in the performance of employees, and there is a set of definitions of creativity, as[17]sees that creativity means the application of a good idea as a beginning or improvement of a product, process or service, and explain[18] that creativity is a complex process that is easy to identify as being of fundamental importance in achieving organizational success, but it is difficult to manage it. If the international competition intensifies and the product life cycles are shortened, the pressure on the necessity of creativity multiplies, and thus creativity means renewal as it depends mainly on initiative and starting from ideas and knowledge. New and innovative things are created that were not previously through interaction and blending, so creativity is a process characterized by it When the individual encounters situations, he gets excited and experiences them deeply, then responds to them in a manner consistent with himself, the response is different from the response of others and is singular. This process includes service products, technologies, new work, new administrative tools, and processes, or new ideas methods. Here, the organization's management must adopt a policy that Motivates and encourage appropriate development of creativity and help invest the energy of talented by providing the appropriate atmosphere for them at all levels.[19].

2.3.3 Absence

Absence is the worker's failure to attend work at the time he is expected to attend to participate in the production according to the work program. If the person is on an official vacation or Holiday, this is not considered an absence, even if this situation reduces the number of people available to work, the lesson is the person's absence To work even though he is restricted in the work schedule [20]

2.3.4 Productivity

The improvement in productivity in terms of quantity, type, and cost occur if one of the following indicators is achieved (increasing outputs while remaining the same inputs, reducing outputs by less than the proportion of reducing inputs, increasing outputs by a greater proportion than increasing inputs, obtaining the same outputs but with fewer inputs)[21] As some researchers see, the high performance of the organization is achieved through the interaction of five main components:(employee involvement, self-directed team, total quality management, organizational education, integrated production technology[22] in the framework presented.

The active role of servant leadership with all its variables and its direct impact on the individual worker, considering it the most important input to productivity and performance, is one of the basics necessary to achieve any success and high efficiency.

3. The Practical Side

In this topic, the information resulting from the analysis of the data collected using the questionnaire designed in the light of the five-point Liked scale will be interpreted, their sub-dimensions and to test the study hypotheses using descriptive statistics methods and inferential.

3.1 Questionnaire Validity Test (Reliability and Validity)

The reliability test was conducted by the (half-splitting) method to know the stability value of the questionnaire (the scale), which means the stability of the results obtained (that the scale gives the same results if it is re-applied), and also the validity was tested by the (self-authenticity) method to know the validity of the scale Which means does the scale measure what it is designed to measure (how well the test represents the behavior to be represented).

Table 2. Shows the values of the reliability and validity coefficients for the scale.

Dimension/Variable	Stability coefficient value split half	The value of the self-honesty coefficient)square root of stability coefficient(
Servant Leadership	0.90	0.94
Employee performance	0.87	0.93
Total Scale (Resolution)	0.91	50.9

It is clear from the values of the reliability coefficients above that all of them are greater than (0.67), and therefore the scale is characterized by high stability, and the values of the self-honesty coefficient were high and close to the correct one, which indicates that the scale is characterized by acceptable honesty and stability and is suitable for relying on the outputs obtained from it.

3.2 Characteristics of the Study Sample (Demographic Information)

In this paragraph, we show the characteristics of the demographic study sample, which includes (gender, age, years of service in the job, academic achievement) and as in the following table:

Table 3. Demographic Information.

Identification Information	Categories	Frequency	Percentage
Gender	Male	30	%50
	Female	30	%50
Total		60	%100

Age	**year 20 -25**	**18**	**%30**
	year26 -30	**14**	**%23.3**
	35 year 31-	**16**	**%26.7**
	More than40 year	**12**	**%20**
Total		**60**	**%100**
years of service in the job	**5years or less**	**18**	**%30**
	6-10 year	**12**	**%20**
	11-15 year	**16**	**%26.7**
	More than 15 year	**14**	**%23.3**
Total		**60**	**%100**
Achievement	**Bachelor**	**16**	**%26.7**
	Higher Diploma	**14**	**%23.3**
	M.A.	**16**	**%26.7**
	PhD	**14**	**%23.3**
Total		**60**	**%100**
Source: Prepared by researchers based on the outputs of the spss v25 program			

Through the above table, it is clear that the characteristics of the research sample were representative of the male and female categories in equal proportions, while the years of service in the job for all groups were in close proportions for the researched sample, which means that there is a good diversity in the members of the selected sample that will give good perceptions to achieve the goal of the study. The ages of the selected study sample were medium and close for all groups. As for academic achievement, the highest percentage of holders of a bachelor's degree and a master's degree was in equal proportions, amounting to (26.7%), while it was for holders of doctorate degrees and higher diploma in equal percentages also at a rate of (23.3%), which are all percentages They are close, indicating that the scientific level of the study sample includes multiple categories that will give greater credibility to its outputs.

3-3-Sample trends about the study variables and their sub-dimensions

To know the trends of the sample members about the research variables and their sub-dimensions, the researchers used for this purpose the weighted arithmetic means, standard deviations, and the relative importance (agreement ratio) to measure and evaluate the degree obtained related to the responses of the study sample members, to identify the extent of consistency and compatibility in the opinions of the sample and their perceptions of variables The study, in general, is as follows: Perceptions of the sample members about the independent variable (servant leadership) and its dimensions: The servant leadership variable was measured with six sub-dimensions including (trust, participation in decision-making, empowerment, vision, providing guidance, helping subordinates to success and growth) and each dimension consisted of several paragraphs (questions) included in the study questionnaire and the statistical outputs were as in the table following:

Table 4. Shows the responses of the sample members and their perceptions of servant leadership and its sub-dimensions.

Statistical Indicators / Diensions		Arithmetic mean	Standard deviation	Agreement percentage (%)	Sort by importance
Dimensions of the independent variable	Giving directions	2.98	0.57	59.7	First
	Helping subordinates succeed and grow	3.01	0.72	60.2	Second
	Participation in decision making	2.98	0.67	59.7	Third
	Vision	2.99	0.63	59.8	Fourth
	Confidence	3.04	0.74	60.9	Fifth
	Empowerment	3.03	0.63	60.7	VI
	Total servant leadership	3.01	0.20	60.1	

Source: Prepared by researchers based on the outputs of the spssv25 program

1. Evident from the above table that the percentage of agreement among the study sample members is very close to the dimensions of the servant leadership variable, and it was arranged according to the arithmetic mean (trust, participation in decision-making, empowerment, foresight, providing guidance, helping subordinates to success and growth) respectively, where the percentage of agreement was (The relative importance) for each of them is about (59%-60%), which is an agreed percentage indicating close importance to the study sample for all dimensions of the independent variable, and the arithmetic mean values of the servant leadership variable and its dimensions indicate a neutral trend when classified on a five-graded Liked scale, and that their answers This is evident from the small standard deviation value, where all dimensions were less than one.
2. The sample members' perceptions of the dependent variable (workers' performance) and its dimensions:

a) The employee performance variable was measured with four sub-dimensions including (job satisfaction, creativity, absence, productivity) and each dimension consisted of several paragraphs (questions) included in the research questionnaire form and the statistical outputs were as in the following table:

Table 5. Shows the responses of the sample members and their perceptions of the employees' performance and its sub-dimensions.

	Statistical Indicators / Diensions	Arithmetic mean	Standard deviation	Agreement percentage (%)	Sort by importance
Dimensions of the dependent variable	Productivity	3.12	0.69	62.3%	First
	Creativity	3.06	0.52	61.2%	Second
	Absence	3.04	0.48	60.8%	Third
	Job Satisfaction	3.06	0.58	61.2%	Fourth
	total employees performance	3.07	0.38	61.4%	
Source: Prepared by researchers based on the outputs of the spssv25 program					

Evident from table (4) above that the percentage of agreement among the study sample members is very close to the dimensions of the variable performance of employees, and it was arranged according to the arithmetic mean (productivity, creativity, job satisfaction, absence) respectively, where the percentage of agreement (relative importance) for each of them is about (60%-62%), which is an agreement percentage indicating close importance to the study sample for all dimensions of the dependent variable, and the arithmetic mean values of the variable performance of workers and its dimensions indicate a neutral trend when classified on a five-graded Liked scale, and that their answers are homogeneous on these dimensions, and this is evident from the value of little standard deviation where all dimensions were less than one.

3.4 Measuring, Testing, and Analysing the Correlation and Effect Relationships Between the Study Variables (Testing the Study Hypotheses)

To test the hypotheses of the study, the researchers used inferential statistics methods (normal distribution test, linear correlation, Pearson coefficient, simple linear regression) as follows:

3.4.1 Normal Distribution Test

Conducting the statistical analysis of the data requires the availability of certain conditions, the most important of which is the normal distribution of the data. The (Kolmcrof-Smirnov) test and the (Shapiro-Wilk) test have been conducted for the independent variable and the dependent variable, where the null hypothesis that indicates a normal distribution of data is tested against the alternative hypothesis that indicates The data does not follow a normal distribution, as shown below:

Table 6. Shows the results of the Kolmcrof-Smirnov (K-S) test and the (Shapiro-Wilk) (S-W) test for a normal distribution.

Variable	Sample size (n)	(Kolmcrof-Smirnov) test (K-S)	(Shapiro-Wilk) test S-W)(
X:Servent leader ship	60	.101**0	.968**0
Y: employees performance		.162**0	0.933**
The mark (**) indicates that the test value is significant assuming a level of significance (0.01), meaning that the (P_ value) is greater than (0.01).(			
Source: Prepared by researchers based on the outputs of the spss v25 program((			

Through the above table, it is clear that the independent variable and the dependent variable follow a normal distribution, where the null hypothesis is accepted, which indicates that the data follow a normal distribution where the (P_value) of the two tests above was greater than (0.01) and the histogram below shows the curve of the normal distribution of the two variables:

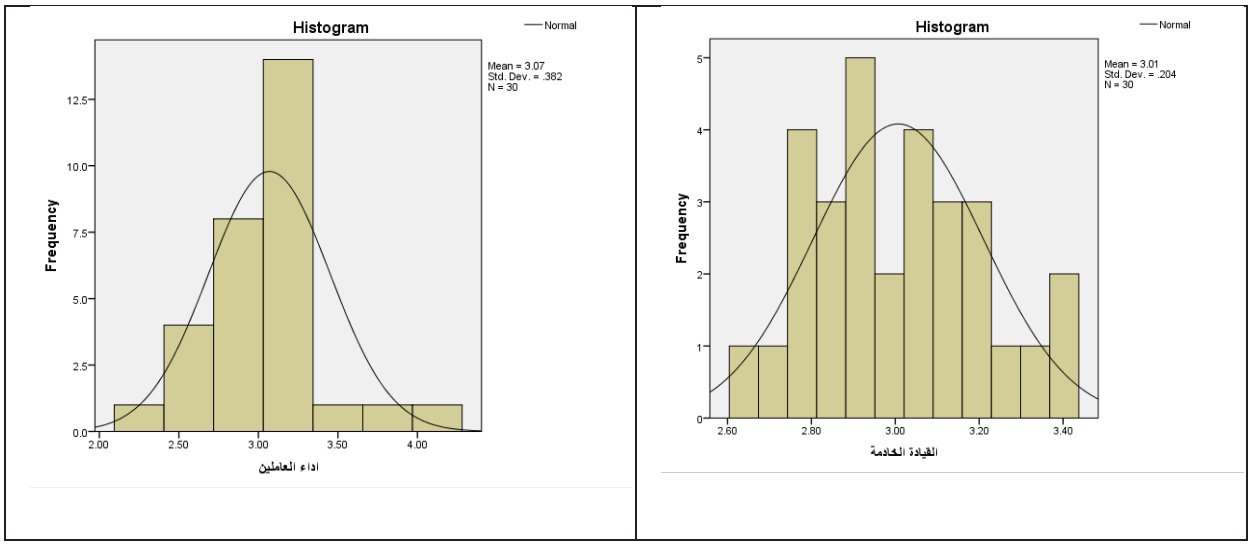

Fig 2. Normal Distribution Curve.

3.4.2 Testing the Existence of a Correlation Between the Research Variables

To test the first hypothesis which states (there is a positive statistically significant correlation between servant leadership and the performance of employees at the University of Basra), the simple linear correlation coefficient was calculated between the variable (servant leadership) and the variable (worker performance) as in the table below:

Table 7. Correlation coefficient (Pearson) between research variables.

Y / X	Employees performance: Y	p-value
X:servent leadership	**0.77	0
The sign (**) above the value of the correlation coefficient indicates that the correlation is significant (statistically significant) assuming a level of significance (0.01), meaning that the (P_value) of the (t) test is less than (0.01)		
Source: Prepared by researchers based on the outputs of the spss v25 program		

It is clear from the above table that the correlation between servant leadership and the performance of employees is significant (statistically significant) below the level of morality (0.01), which is a direct (positive) and strong correlation, which means that the first hypothesis is accepted and that the increase in the presentation of the servant leadership model in Basra university institutions will cause an increase in performance staff.

3.4.3 Testing the Existence of an Effect of the Independent Variable (Servant Leadership) on the Dependent Variable (the Performance of Employees)

To test the second hypothesis which states (there is a positive and statistically significant effect of servant leadership on improving the performance of employees at the University of Basra), a simple linear regression analysis was used to determine whether the independent variable (servant leadership) affects the dependent variable (the performance of employees) and what is the size of the effect. As in the table below:

Table 8. Test values (F), coefficient of determination (R2), and regression coefficients.

Y: employees performance				
Y / X	value (F) Calculated	Coefficient of determination (R^2)	Regression constant (A)	Regression coefficient (B)
X:servent Leadership	33.45**	%60	2.21	90.4
The sign (**) with the highest value (F) indicates that the effect is significant (statistically significant) assuming a level of significance (0.01), meaning that the (P_value) is less than (0.01).				
The significance of the regression model is tested through the value (F), while the value of the coefficient of determination (R2) represents the explanatory power of the independent variable for the changes that occur in the dependent variable.				
Source: Prepared by researchers based on the outputs of the spss . v25 program				

There is a significant effect (statistically significant) below the level of significance (0.01) for the servant leadership variable in the variable of employee performance. The servant leadership variable explained about (60%) of the changes that occur in the performance of workers, and the rest is due to other variables and the random error factor, which means accepting the second hypothesis. And that the performance of employees is improved by applying the servant leadership model in the institutions of the University of Basra. The regression equation of the dependent variable (the performance of the workers) on the independent variable (the servant leadership), which was equal to: (the performance of the workers = 2.21 + 0.49 of the servant leadership).), and in the case that the servant leadership is equal to zero, the renewal of the performance of the workers will be equal to (2.21).

3.4.4 Discussing the Results

1. The majority of the sample members agreed with the availability of the elements of servant leadership in the colleges under study, but there is a lack of interest in some important aspects of the dimensions of servant leadership represented in ((trust, participation in decision-making, empowerment, vision, providing guidance, and helping subordinates to succeed and grow)). This generates a feeling of dissatisfaction and injustice, which may push the workers to take other aspects of work called informal organizations, which may conflict with the directions of the management
2. Most of the sample members agree that there is no real desire on the part of the senior management to formwork teams and encourage workgroups because they believe that assigning such an approach will reveal problems and provide solutions that the higher management may not understand, or it may consider it an additional failure that weakens its authority.
3. It was also shown that the senior management in the college's understudy was not aware of such leadership patterns and its impact on identifying the problems and tendencies of the workers, as the worker is a person with feelings and interests, which are closely linked with his colleagues and with the external environment that cannot be separated from them, which indicates the lack of understanding of the higher management aspects Psychological and social, which works to organize the relationship of the individual with others so that he can perform his tasks in achieving his goals and the goals of the organization together
4. The presentation and analysis showed the validity of the hypothesis (there is a positive and statistically significant effect of servant leadership on improving the performance of employees at the University of Basra).

4 Conclusions and Recommendations

As a result of the indicators of the study, the following conclusions were reached:

1. The results showed the presence of the constituents of servant leadership in the sample under study, in addition to the existence of a correlation and an effect for the two variables (independent and dependent) in some university formations, whether at the macro or sub-level.
2. The emergence of a significant and positive effect of the two main variables

3. The working individuals are instinctively inclined to form relationships with colleagues and superiors through which they seek to achieve their goals
4. The servant leadership style focuses on the positive psychological aspects by raising individual motives in addition to focusing on the material aspects by identifying the interests of the workers - and working to achieve them - which are mostly material rather than psychological or social, which all lead to improving the performance of workers.
5. The realization of the faculty members in the faculties of the University of Basra that the leadership vision is a distinctive characteristic of its leadership.
6. The results of the study show that the leaders' orientation towards establishing teamwork with its various practices, as well as the issue of providing the opportunity for others to participate in decision-making was at a weak or not prominent level, and this simply explains the absence of some trends and practices that are emphasized in the management literature regarding strengthening the teamwork process within organizations.
7. It is clear from the practical side that the percentage of agreement among the study sample members is very close to the dimensions of the servant leadership variable, and it was arranged according to the dimensions (trust, participation in decision-making, empowerment, vision, providing guidance, helping subordinates to success and growth), which indicates a positive and influential trend Which leaders work in the faculties understudy
8. As it is clear that the percentage of agreement among the study sample members is very close to the dimensions of the employee performance variable, and it was arranged according to the arithmetic mean (productivity, creativity, job satisfaction, absence), respectively, where the percentage of agreement was average, which is an agreement percentage indicating close importance to the study sample for all dimensions of the dependent variable.
9. The values of the arithmetic means indicate the variable performance of workers and its dimensions.

We recommend decision-makers in the college's understudy to invest their energies and expertise and to move towards adopting the servant leadership style.

1. Spreading the spirit of cooperative work among employees by placing servant leaders in the college's understudy on the one hand and adopting work teams, which creates a positive feeling of belonging and loyalty to those teams, which leads to raising the performance of organizations and achieving their goals.
2. Consolidating the concept of service and sympathy among employees within the university in a way that creates a conducive atmosphere for service and personal assistance towards each other.
3. Adopting the concept of servant leadership as it is one of the most popular leadership styles in encouraging followers and helping them to learn, develop and adopt the philosophy of continuing education, which positively and directly affects the performance of employees.

4. There must be an awareness for the senior management of the positive impact of servant leaders on the performance of employees and achieving success and development. Therefore, it must start with planning and the correct selection of leaders, and the preparation of servant leaders on a scientific basis.
5. It was found through presentation and analysis that there is a weak relationship between participation and providing guidance, which made there a need to focus on the importance of the participation of employees until a balance is achieved between leadership and subordinates within the organizational environment.

References

[1]-Olesia weeks s. & namusonge G.s. & iravo. Mike "Role of servant leadership on organizational commitment: An Exploratory survey of state corporation in Kenya"International Journal of Humanities and social science. 2013 . Vol 3. N.13 p87

[2] -Northouse, P. G "Leadership: Theory and practice" (Fourth ed.), Thousand Oaks: Sage Publications. 2001. p257

[3]-Blanchard h, K, Relections on encourage the hert .in J. M.Kouzes ,&B.Z.poster (Eds.)Christian" reflections on the leadership challenge" sanfrancisco. Jossey -Bass .2004. p33

[4]-Patterson, K." A servant leadership A theoretical model (Doctoral dissertation, Regent university retrieved from proQuest Digital Dissertations Databas. 2003. p2

[5]Peterson C., & Seligman, M. E. Character strengths and virtues: A handbook and classification Oxford University Press. 2004. Vol. 1. p112

[6] - Al-Atawi, Amar and Al-Shaibani, the important “the role of leadership support and trust in building organizational commitment for workers”, an exploratory research, the opinions of a sample of employees of the General Directorate of Karbala Education, Karbala University Scientific Journal. 2010. Issue 3 Vol 2 . p131

[7]- Al-Aghbreen, "The Contemporary Planning and Organizational Dimension" Beirut, Dar Al-Nahda Al-Arabiya. 2000. p167

[8]-Adams. s"The relationships among adulf attachment" general self-disclosure. and perceived organizational trust. unpublished dissertation of doctor of human development. faculty of the Virginia polytechnic Institute and state University. 2004. p51

[9] Russell .R.F.& Stone ,A,G, A" review of servant leadership "attributes leadership & organization Development Journal .(2002) 23(3/4)p157-145)

[10] -Joseph, E. E., & Winston B. E.). A correlation of servant leader ship trust, and organizational trust. Leadership & Organization Development Journal(2005.vol 26.1.p 6-22

[11]-Abdullah, Ron Faridoun " The role of servant leadership in achieving job engagement" An analytical study of the opinions of a sample of faculty members at the University of Sulaymaniyah. 2018. Issue.1.vol (8) p9

[12] -Liden. Robert c, Wayne. S. j, zaho. Hao & Henderson. D, "servant leadership: Development of a multidimensional measure and multi-level Assessment", leadership Quarterly. 2008. V.19, N.2 p16

[13] Spears Larry (2005). The Understanding and Practice of Servant, studies .regent university

[14]- confirmed Gibbs, John "Performance Measure Properties and Incentives- Institute for the Study of Labor. (2004). No.(1356). On Line, Available at:" www.alazhar.edu.ps/library/aattachedFile.asp

[15]-Schermerhon, Jr, John.R. and James G. Hunt &Richard N; Os Born".Organizational Behavior"7ed.New York Wiley &sons. 2000. INC,p57

[16]- Haddad, Shafiq Ibrahim, Judeh, Mahfouz Ahmed, the extent to which ministries and institutions winning the King Abdullah II Award for Excellence in Government Performance and Transparency achieve a culture of excellence from the point of view of their employees and service recipients, The Jordanian Journal of Business Administration. 2015. Issue 2, Vol 11.p 253-282.

[17]-Robbins, Stephen. Business. Today: The new world of Business. U.S.A Harcourt College publisher. 2001 .p11
[18] Terziovski ,mile &Samson. Professor Danny and Glassop, Linda Greating" core competence through the management of organizational innovation". 2001. p24
[19] -Kaplan, Soren & Winby Stu, (2007), "Organizational Models for Innovation Organizational Design that Support Strategic Innovation and Growth,p19 On-Line, Available at:" www.innovation-point.com
[20]- Cascio, W.F. Managing human resources Productivity, quality of work life. Profits "6 ed, McGraw-Hill: Boston, MA 2003. p24
[21]- Al-Hamami, Sana Muhammad Rashid Daoud, "Methods of conflict management and their impact on the performance of workers, a master's thesis" University of Baghdad (2006) p24
22-Tarr, D, " The strategic toughness of servant-leadership ", In L. C. Spears (Ed.), Reflections on leadership, How Robert K. Greenleaf's theory of servant-leadership influenced today's top management thinkers. New York.1995. :p7

Using Time Driven-Activity Based Costing TD-ABC approach for controlling

Jaber H. Ali [1], Doa'a Qahtan[2]
{ drjaber@stu.edu.iq [1] }
Management Technical College, Southern Technical University, Basra, Iraq[1]
Faculty of Graduate Studies, Southern Technical University, Basra, Iraq [2]

Abstract: The aim of this research to reach the possibility of using TD-ABC approach and its ability to determine unused capacity and actual time of activities, which leads to the effectiveness of the control system. In addition, the Process Mapping (PM) that enhances of controlling the implementation of activities. The research was represented case study in Ibn Majid Co., which still depend on traditional accounting systems. Where contemporary accounting systems have emerged to handling the shortcomings in the traditional systems, and the problems they face and to overcome inaccuracies in calculating product/service costs and allocating indirect costs. The study relied on the approach Time Driven-Activity based costing TD-ABC and its role in the control process by providing accurate information on the actually time on per activity, the costs of exploited resources and the exclusion of unused capacity. The researchers concluded the application of the TD-ABC approach led to the allocation of indirect costs more accurately and relatively, in addition to determining the practical Capacity and determining the time consumed by each activities, which enables the system to control costs and operations.

Keywords: Activity Based Costing (ABC), Time Driven-Activity based costing (TD-ABC), Controlling, Process Mapping (PM).

1. Introduction:

The focus has become on the manufacturing of success and continuity, including improving quality, cost reduction, determining real time, constant innovation and other basic demands adopted by economic units to maintain their competitive position in the market. In order to succeed, companies have to react quickly and produce a top quality with low-cost product in appropriate time[1].The companies to manage cost reduction in production processes should preform efficient accounting systems so as to calculate the influnce of refinements on the cost of products, as well as to control costs, Process and this to ensure continuity and development [2]. Traditional cost accounting has received attention, which has led to many methods of calculating it and differing in the way it deals with costs, which are focused mainly on manufacturing costs towards the determination of the manufacturing cost per unit, dynamic cost management approach involves modern managerial accounting methods focused on the total costs through the whole product life cycle [3]. The study significance arise in the importance of the approach Time Driven- activities Based costing TD-ABC, as it is one of the contemporary

IMDC-IST 2021, September 07-09, Sakarya, Turkey
Copyright © 2022 EAI
DOI 10.4108/eai.7-9-2021.2315373

approaches that work to enhance the cost accounting system for the economic unit and provide more accurate information by determining the actual time spent of activities, which affects the effectiveness of the control system [4].The TD-ABC approach emerged to overcome the defects of the activity-based cost approach (ABC) because of the difficulties faced by this approach, especially in terms of the high costs of its application, its need for many data and details, and to solve the problem of imprecise allocation of indirect costs by relying on many cost drivers [5]. Whereas, the TD-ABC approach provides an intact methodology for measuring the cost of companies' products, which helps management in performing its basic functions in controlling and making appropriate decisions, and thus the possibility of evaluating the performance of companies' activities.

2. literature review:

2.1 THE TRADITIONAL & CONTEMPORARY ACCOUNTING SYSTEMS:

Kaplan & Cooper 1998 had been analyzed many inserted cost system it listed to grow profitability and performance. which was the traditional costing systems that used at most previously and its no longer in financial reporting procedures. Direct costs in the traditional costing system are attributed directly to the cost objects. In an inversion, indirect costs have been allocated to each cost object using one or a few cost drivers on the basis of volume (ex. direct labor, machine hours, units of production, ...etc) [6]. The traditional costing system has been used (DM, DL & OH) to assign the cost of product. Nevertheless easy using, traditional costing system hasn't allocated duly overhead costs for various products "average allocation of OH costs" [7]. Cost systems have attended a several of developments that resulted in a reconsideration of the traditional cost accounting systems, which have been subjected to many criticisms because of the information presented that lacks accuracy and appropriateness in under of the modern environment. In addition, cost-reduction and cost-control activities to improve performance are necessary to warranty profit margins and increasingly as a component of competitiveness of modern economic units, that tended to operate in the global market under strong competition [8]. An approach that distinguish the activities which needed to produce a specific service/product and assigns the cost of each activity resource to operations according to the actual consumption is called activity Activity-Based Costing ABC . it's One of the best tools for refining a costing system, an approach to address indirect costs has refines, and one of the best tools for improving the costing system.The ABC is allocat cost out of two stages 1) processes consume activities, 2) activities consume costs. Subsequntly the overhead costs of operations were allocated based on the activities consumed within the provision of those services, as the (ABC) approach improves the costing system by identifying individual activities as the primary cost purposes. Because of criticism directed at the traditional costing system, in achieving effective control over indirect costs, in planning and making sound decisions, and in the deceptive results and data shown by the traditional costing system [9] [10]. On the other side, the overhead costs are determined the allocated of the supplied resources costs for activities which based on drivers relevant to those activities. Therefore, the costs of products /services that used a huge amount of activities will be higher than products /services that do not **[11].** In 2003-2004 and more comprehensively in 2007, Kaplan & Anderson reference to the

main implementing troubles of the traditional ABC as following:(1)Time consuming and costly were result to the interviewing and surveying process (2)The ABC approch data have been subjective ,complicated to validate and expensive to store, process and report (3) Most ABC approach was local and hadn't provided an completed vision of institution-wide profit opportunities (4)The ABC approach was theoretically incorrect because it preclouded the possiblity for unused capacity **[4]**.

2.2 TIME DRIVEN- ACTIVITY BASED COSTING (TD-ABC):

To overcome the difficulties presented in ABC approach (Kaplan & Anderson) developed what is called TD-ABC approach [6]. TD-ABC approach can into implemented proportionality speedily because only estimates of two parameters are required: (1) the unit cost of supplying capacity (ex: cost per min.); (2) the time required to perform an activity [9]. TD-ABC approach emulate the actual processes used to perform work throughout a project. It can therefore capture far more difference and complexity than a traditional ABC approach, without creating an exploding request for storage, data estimates, or processing abilities. Using TD-ABC, a company can adopt complexity rather than being forced to use inaccurate, simplified ABC models of its complex businesses [12]. Acorn Systems onset workout more delicate with used the time estimates rate & time equations. An equations have been fed already from Enterprise Resource Planning system (ERP) with information collected from transaction coils [6]. And many researchers have defined TD-ABC's cost approach TD-ABC, the initial of them [12] defined it as "it is a cost estimation approach in which time is the only driven and its purpose is to provide activity costs with the basis of time consumption for each activity." [13] added that TD-ABC is "a modified version of activity-based costing (ABC), a cost accounting approach that relies on employee reported data to determine the percentage of time consume by activities, or on activity time sheet. Existing. Data generated in this way can be time-consuming and expensive to collect as well as difficult to validate." The procedures for applying the TD-ABC approach are the following steps [14], as shown in **Fig.1**. below:

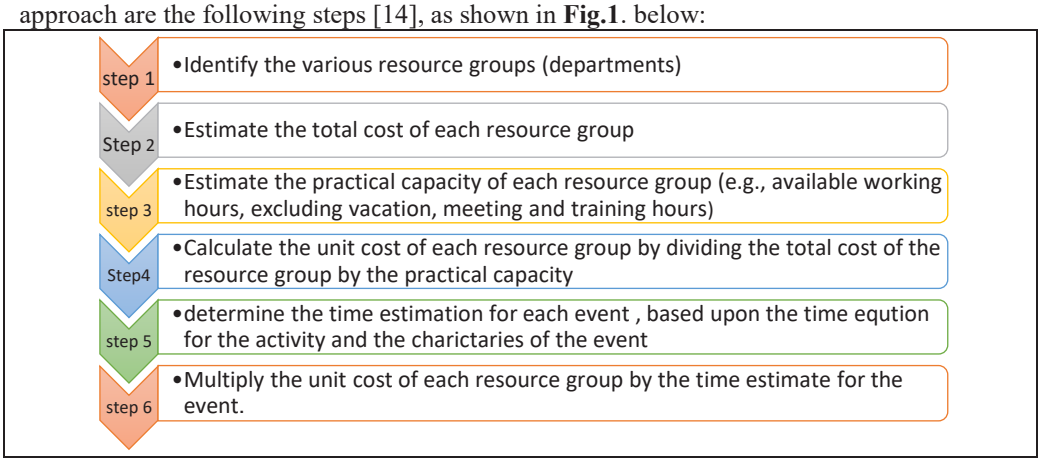

Fig.1. Steps of implemention TD-ABC approach

An approach TD-ABC calculates cost by concentricity on two elements:(1) the cost of each unit of time (2) the quantity of time required for each stage or process to be completed [15].

Total cost is known as "the cost of all the resources supplied to the process or department" resources such as: personnel, supervision, equipment, infrastructure and technology.Practical capacity is known as "the amount of time employees work non-stop" which represent first parameter is sum by dividing the total cost of supplying the resource capacity by practical capacity [12]. There were two methods to get this a mount: a proportion of theoretical capacity 1) Assuming practical capacity is about 80%-85% to labor (due to rests, arrival and departure, meetings and training) and for machines (due to repair, maintenance and schedule change) with full theoretical capacity, 2) Calculate the adjusted real values of the company and that the accuracy is not objective, because the approximate reilability is enough because critical errors going to be reveal either unexpected excess or in lack of allocated resources [16].

2.3 THE ROLE OF CONTROLLING FOR TD-ABC APPROACH:

Controlling pointed out to management efforts to effect the actions of persons in charge of performing functions, afford costs and growing revenue. In this respect, (Robert et al.,1997) considered management as two-stages process: 'planning' indicate to the method that management plans and individuals want to carry out, 'control' indicate to the excutions used to locate whether real performance is consistent with these plans. Meantime management sets the comperhensive aims the company, defines the center of accountability (responsibility) and layout evaluation, reporting procedures and standards [17]. The application of effective methods to support output enformant control plays an important role in the success of each manufacturing system. Without the implementation of sophisticated output performance control system, the prosperite of all productions planning activities is in suspicion. Looking forward to the current status of study in both of them detect the fact that minimal important has been paid to the development of production performance control systems [18]. The Cost Control Systems (CCS) are formated of methods and steps in order to help controlling at the operation costs and ensures that cost dosen't exceed a certain level. Cooper & Dart in the fileds of Target Costing (TC) and value analysis, Activity Based Costing (ABC), Time Driven- Activity based costing (TD-ABC) . All of these approaches are driven to controlling a enterprise cost to improve firm performance. These processes have been systematized became an inserted (CCS). Enterprise performance reflects the cumulative result of efforts of a firm, it has transfred different understanding to various individuals. That Resulting to convey from financial (conventional) to non financial (Contemporary) measures of performance, The non-financial part measured was on customer value "the difference between realization and sacrifice" in idioms of lead time to delivery and defect or reduction level and market share [19] [20]. The TD-ABC approach provides accurate information about the real time, cost of the actual resources consumed for each activity, as well as assist allocate indirect costs on products/ services based on the time driven and provides the necessary measures of the exploited and unutilized production capacity for each activity, as it works to determine a more equitable and objective product cost which serves as a control tool to determine the implementation process in real time using time equations and the process mapping of the TD-ABC approach can be used as a controlling tool to track the implementation of strategies [13]. Process Mapping (PM) is a explain for an analysis of the process flow by display between how did work do and how had did it, jobs of the system must be perform from how does the system build to perform those substantial functions since received the order to delivery it the customer [21]. The Process Map (PM) determins for each stage of the project process. In any stage, the time required to do each activity is estimated. Then, the required resource costs for each stage is calculated by assignment the cost for per unit capacity [22].

Afterwards, having the knowlge in the intended field of work and the results to be obtained, we are identifing activities to be performed and the facilities to be utilized to producting the suggested result for the project. Then we draw the (PM) of activities identify their dependencies, and estimated actual time, resources and time restriction. After that, the operational budget is evolved, determining the (direct & indirect) costs, founding the base plan to monitoring and controlling the output process [23].

3. Methodology:

Study Problem: In light of the increasing competition in the markets, companies seek to adopt firm accounting systems, as they are one of the most important systems that produce the necessary information that helps management to take the necessary decisions and enable the control system. Therefore, it should always aim to keeping effective cost systems to ensure the company's continuity in the market. Where the problem of the study is that the case study company adopts traditional cost accounting systems based on actual costs that do not take into account the factors of time and theoretical capacity or reduce costs. Which leads to bearing the product at relatively high costs that negatively affect competitiveness in the market and limited the process of controlling costs and operations operational. The study problem is framing with the following questions: (1) what is the importance of applying the TD-ABC approach in determining the actual time of activities, which contributes to accurate cost calculation? (2) Does the use of the TD-ABC approach help identify the unused capacity, which helps the effectiveness of the control system for production processes?

Study Hypothesis: The study was based on a main hypothesis that: (The use of the approach TD-ABC enables the system of control on costs and activities by determining the real time consumed of each activities and unused capacity, which enhances the process of cost control).

Study data collection: To raise data and information for realize the theoretical and practical side of the study the researcher was adopted on books and articles that dealt with research variables, in addition documents, records, and official reports of the case study that were collected directly or indirectly through unstructured visits and interviews, as well benefiting from some of the basic observations that crystallized during the discussion with Engineers and project administrators for the company beneath study.

Study methods: It relied on the inductive and deductive approach in achieving the objectives of the study. The following equations Table 1. were using to reach the results that would address the problem of the study and achieve appropriate control over activities [24] [1] [4] [11].

Table 1. Equations of the application case Study by using TD-ABC

$AR = \text{Capacity cost rate} = \frac{\text{Cost of all resources supplied}}{\text{Practical capacity}}$ …….. (1)
$Tt = \beta 0 + \beta i Xi$ …… (2) Where: Tt = Time must to perform an activity per Min. β0 = The standard time to perform the basic activity per Min. βi = The estimated time to perform the incremental activity per Min.

Xi = The quantity of incremental activity (Time).

Total Cost Of Each Activity = Capacity Cost Rate (AR) × Time required for the Activity (STi) …… (3)

STi = Estimated Unit Time for Each Activity X Actual Quantity of Each Activity ……..(4)

TC of production = DMC + DLC + OHC ……..(5)
Where :
TC = Total Costs
DMC = Direct Material Costs
OHC = Overhead Costs

4. Previous Studies:

A study [25] entitled: "Development of a real-time TDABC model for production activities A case study at a manufacturing company". The study aimed to clarification the influence of utiliza the TD-ABC approach precise real-time production activity data rather than estimated values or direct observation. The study rely on the deductive and inductive approach, the study sample was conducted as a case study at the Swedish startup battery manufacturing company Northvolt, and the data were collected by conducting 8 irregular interviews with different employees within the company under study. The results of the study show that TD-ABC approach with components of automated activities directly refer to the production cost accounting is automated, and this means that when a cost is applied to a cost object through this apprach, this cost is calculated automatically and accurately in the system. It is not necessary to update the production cost for each product. Retrospectively or randomly calculated but automatically calculated in real time. The study recommends that exploring the necessary data that enhances the traceability of activities, as the resources to perform activities consist of materials for cost purposes for the resources they consume, which contribute to supporting automated management. A study **[1]** entitled: "TDABC for a manufacturing environment: A case study" This study aimed to Implementation of TD-ABC in a furniture manufacturing company to estimate product costing and compare the cost obtained from TDABC with the traditional costing system. As well as the management, effect of TDABC in a small manufacturing environment. The results of the study showed the TDABC system assistances the directors, department bosses to differentiate, and analyzing the implicit activities that drive the overhead costs. This model also identifies the operational improvement, to help the company to diminishing the cost of the production. The study recommended the application of TDABC in small manufacturing industries as it helps to discuss the results and its usefulness in small scale manufacturing industries. It provides useful information for making decisions about future investment and expansion of the manufacturing setup. A study [26] entitled " The Impact of Applying Time Driven Activity-Based Costing on Improving the Efficiency of Performance in Jordanian Industrial Corporations: A Survey Study". The study aimed to display the importance of applying TD-ABC approach to improving performance efficiency in Jordanian industrial companies by using the descriptive analytical method. A survey list has been prepared; the data collected and processed to a sample of 73 participants in different management positions from 30 industrial companies listed on the Amman Stock Exchange (ASE). The survey analyzed by using SPSS program. The results of the study refer to the company that applied TD-ABC approach benefited of technological developments based on activity diagrams and its ability to help management see the whole view of the activities' performance and evaluate the company's competitive strategy, which was reflected in improving pricing decisions for different products. The study recommends the necessity of applying TD-ABC in companies as it has proven its effect on reducing product costs and increasing corporate profitability through industrial companies' activities plans. A study **[5]** entitled "Application of the TDABC Model in the Logistics Process Using Different Capacity Cost Rates". The study aimed to design and application (TD-ABC) technology for the logistics process using different capacity cost rates, and aims to description and analysis detail of the resources economic unit, its activities and cost objects that constitute the logistics process in order to develop an appropriate model of TD-ABC. The results of the study using the TD-ABC approach helps to

adequately reflect the logistic function and these activities have specific resources allocated and can be measured by different outputs because it is supported by a string of time equations. The study recommends the TD-ABC model developed in this case study can used in similar cases and as a basis for analysis of logistics costs in other logistics operations. Moreover, managers can depend on the proposed approach to analyze product profitability and logistics cost structure.

5. THE APPLICATION OF TD-ABC APPROACH:

Ibn Majid Company is a leading company in heavy engineering industries, especially the manufacture and installation of oil and industrial equipment that meets the needs of the companies of the Ministry of Oil, Industry, Electricity and the private sector of these products. A case study began by collecting data related to the pipelining project within the company, recording notes about the stages of the production process and the timing of each phase, in addition to data related to machinery and equipment, their depreciation, cost of consumed DM, DL and all OH. After collecting the data, a process flow chart was created to provide an overview of the production stages of the company under study, as shown in **Fig. 2.** below:

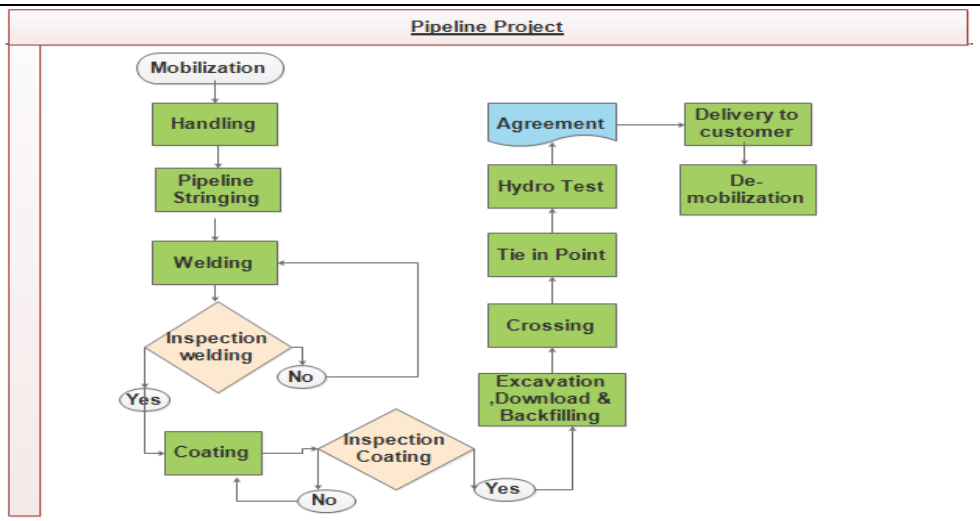

Fig. 2. Pipeline project process mapping at the case study company

To calculate costs using the TD-ABC approach, there are steps that must be followed, starting with the activities being determined ,then estimated the costs of whole resources utilized, and the accepted theoretical Capacity to calculate the Capacity cost rate, Time equation must established for every activity, after that estimated time is determined. per activity, the Total Cost (TC) is determined, as follows:

5.1 Production activities used: The first step taken with the TD-ABC approach is analyze and locate the industrialization activities that occur, in order that comprehend their area and the specific series of events occurring, for whole actions differ however, it has the same purpose. At Ibn Majid State CO. for a case study of the piping project, the activities are

represented by (Mobilization, Handling, Pipeline Stringing, welding, Inspection welding including "visual and x-ray inspection", coating process, the process of drilling, Excavation -Download & Backfilling, Crossing, Tie in points , hydro- test, and Demobilization). The project was handed over to the beneficiary under the supervision of the project manager, site engineer and others, and then an order was issued. Raise the work site represented by equipped office caravans and their accessories, in addition to machines and other equipment.

5.2 Estimated Total Cost (TC) of the resources utilized: If the all resources utilized gradient beneath the similar activities, the costs can assigned to the activity directly. Nevertheless, if the resources are utilized for multiple activities, an apportionment method based the suitable cost driver should use. In this research, resources are assign based on the kinds of resources utilized for per activity, and they are divided to (labor wage, equipment & machinery costs, depreciations, training and qualification costs, and other costs). As shown in Table 2.

Table 2. Statement of resource supplied

No.	Activity	Direct Labor (IQD)	Factory Overhead (IQD)	cost of all resource supplied (IQD)
1	Mobilization	3,350,000.000	18,758,055.556	22,108,055.556
2	Handling	5,950,000.000	6,500,000.000	12,450,000.000
3	Pipeline Stringing	5,860,000.000	1,200,000.000	7,060,000.000
4	Welding	651,424,000.000	83,775,000.000	735,199,000.000
5	Inspection welding (Visual, X-ray)	4,750,000.000	81,000,000.000	85,750,000.000
6	Coating	23,700,000.000	8,250,000.000	31,950,000.000
7	Excavation, Download & Backfilling	6,250,000.000	2,600,000.000	8,850,000.000
8	Crossing	4,900,000.000	1,430,000.000	6,330,000.000
9	Tie in Point	2,600,000.000	1,335,000.000	3,935,000.000
10	Hydro Test	5,500,000.000	900,000.000	6,400,000.000
11	Demobilization	1,150,000.000	1,958,055.556	3,108,055.556
	Total	715,434,000.000	207,706,111.111	923,140,111.111

5.3 Estimated practical capacity (acceptable cap.): Hours of project working inside the site it take 6 days in a week, from 7 a.m. to 3 p.m. The employees are working an average 8 hours a day, and 250 days a year. 20% is a rate of these deductions for breaks, training and maintenance of these working hours, this mean the employees have a practical cap. Of 96,000.00 minutes per a year.

5.4 Calculation of the capacity cost rates: In this step, the unit cost rate was calculated for the time required to perform each activity of the project. This value is obtained by dividing

the estimated total cost of each activity the conversion cost (direct labor costs and overhead costs) specified in the first step by the process capacity specified in step previous .The cap. Cost rate (per minute) able to acquire using the following equation (1).

$$\text{AR} = \text{Capacity cost rate} = \frac{\text{Cost of all resources supplied}}{\text{Practical capacity}} \qquad (1)$$

Table 3. Illustrate summary of the Cap. cost rate of each activity for pipeline project activity.

Table 3. Cap. Cost Rate

No.	Activity	cost of all resource supplied	Practical Capacity supplied min/Y	Capacity Cost Rate (IQD/min)
1	Mobilization	22,108,055.556	96,000	206.334
2	Handling	12,450,000.000	96,000	98.438
3	Pipeline Stringing	7,060,000.000	96,000	52.708
4	Welding	735,199,000.000	96,000	7,798.948
5	Inspection welding	85,750,000.000	96,000	934.896
6	Coating	31,950,000.000	96,000	289.063
8	Excavation, Download & Backfilling	8,850,000.000	96,000	81.771
9	Crossing	6,330,000.000	96,000	55.521
10	Tie in Point	3,935,000.000	96,000	20.156
11	Hydro Test	6,400,000.000	96,000	56.250
12	Demobilization	3,108,055.556	96,000	21.959
	Total	923,140,111.111		

5.5 Activity time equation: TD-ABC time equation can combine all the time needed to undertake all activities in each activity within a single equation, and the mathematical model used to establish TD-ABC time equation is shown below equation (2):

$$\mathbf{Tt = \beta_0 + \beta_i X_i} \qquad \mathbf{(2)}$$

Where:

Tt = Time must to perform an activity per Min.
β0 = The standard time to perform the basic activity per Min.
βi = The estimated time to perform the incremental activity per Min.
Xi = The quantity of incremental activity (Time).

5.6 Determination of the estimated time for each activity: A time equation was needed to develop to calculate the estimated production time. The estimated time for each activity

was determined based on the Motion and Time study principles. As shown in Table 4. , Time required for each Activity defined in Table 5.

Table 4. Volume of cost-drivers for the project Pipe line

Var.	Activity	Driver	Quantity (per day for 1 groups)
X1	Mobilization	No. of round	1
X2	Handling	No. of round	1
X3	Pipeline Stringing	km	1
X4	Welding	No. of joint	8
X5	Inspection welding	No. of sample joint	5
X6	Coating	No. of round	5
X7	Excavation ,Download & Backfilling	km	1
X8	Crossing	No. of Gross	2
X9	Tie in Point	No. of point	2
X10	Hydro Test	km	5
X11	Demobilization	No. of round	1

Table 5. Time estimated for each Activities

No.	Activity	No. of Work days (1)	Quantity (2)	Available capacity per minute (3)=(1)*(8H*60 min)	practical capacity (min) (4)=(3)*80%	Time required for the Activity (5)=(4)*(1)
1	Mobilization	15	1	7,200.00	5,760.00	5,760.00
2	Handling	20	1	9,600.00	7,680.00	7,680.00
3	Pipeline Stringing	25	1	12,000.00	9,600.00	9,600.00
4	Welding	35	8	16,800.00	13,440.00	107,520.00
5	Inspection welding (Visual , X-ray)	25	5	12,000.00	9,600.00	48,000.00
6	Coating	30	5	14,400.00	11,520.00	57,600.00
7	Excavation ,Download & Backfilling	30	1	14,400.00	11,520.00	11,520.00

8	Crossing	15	2	7,200.00	5,760.00	11,520.00
9	Tie in Point	15	2	7,200.00	5,760.00	11,520.00
10	Hydro Test	25	5	12,000.00	9,600.00	48,000.00
11	Demobilization	15	1	7,200.00	5,760.00	5,760.00
	Total	250		120,000.00		324,480.00

5.7 Calculation of cost per product unit (unit cost):

Total Cost Of Each Activity = Capacity Cost Rate (AR) × Time required for the Activity (STi) **(3)**

$$\text{AR=Capacity Cost Rate} = \frac{\text{Cost of all resources supplied}}{\text{Practical Capacity of Resources Supplied}} \quad \textbf{(1)}$$

STi = Estimated Unit Time for Each Activity X Actual Quantity of Each Activity **(4)**

Table 6.Calculate the Total Conversion costs of each activity

No.	Activity	Time Driven (1)	Time required for the Act. Sti (min) (2)	Cap. Cost Rate(AR) (3)	TC Of Each Act.(4) = AR(3) × Sti (2)	Allocating costs unit to each activity (5)=(4)/(1)
1	Mobilization	1	5,760.00	230.29	1,326,483.333	1,326,483.333
2	Handling	1	7,680.00	129.69	996,000.000	996,000.000
3	Pipeline Stringing	1	9,600.00	73.54	706,000.000	706,000.000
4	Welding	8	107,520.00	7,658.32	823,422,880.000	102,927,860.000
5	Inspection welding (Visual , X-ray)	5	48,000.00	893.23	42,875,000.000	8,575,000.000
6	Coating	5	57,600.00	332.81	19,170,000.000	3,834,000.000
8	Excavation, Download & Backfilling	1	11,520.00	92.19	1,062,000.000	1,062,000.000
9	Crossing	2	11,520.00	65.94	759,600.000	379,800.000
10	Tie in Point	2	11,520.00	40.99	472,200.000	236,100.000
11	Hydro Test	5	48,000.00	66.67	3,200,000.000	640,000.000
12	Demobilization	1	5,760.00	32.38	186,483.333	186,483.333
	Total Conversion costs (IQD)				894,176,646.667	120,869,726.667

5.8 The total cost of production: able to obtain through the equation below:

TC of project = DMC + DLC + OHC (5)

Where :

TC = Total Costs
CDM = Direct Material Costs
OHC = Overhead Costs

TC of Pipeline project = 45,696,000.000 + 894,176,646.667 = 939,872,646.667 IQD

6. RESULTS AND DISCUSSION:

TD-ABC provides the detailed analysis of the cost. From the above data, it can be seen that The TD-ABC approach using the process mapping Fig.1. Helps to define the steps of the pipelining project and the sequence of operations, thus enhancing the process of controlling the implementation. It is noted that the utilize of resources for various activities as seen (Table 2.), the resources were assigned depend on the kind of resources utilized for each activity. Which achieves the process of controlling the consumed resources and allocating them to activities in a real and fair manner, leading to a more accurate calculation of the cost of project. The TD-ABC approach using in allocating the indirect costs represented as wages (transportation, training, qualification, safety courses. etc.) by calculating the capacity cost rate as see (Table 3.) by using Equation (1) . The total actual indirect costs lead about to a reduction the indirect costs and the unit cost of each activity as see (Table 6.)by using Equation (3) and (4), which support management in controlling costs leads to an improve Profitability. TD-ABC is using time as the cost driver. Therefore, more production time is responsible for the higher cost. The time of the activity is estimated using Time Equations (see Table 4.).It indicated that the time consumed by activity is based on the (No. of round, No. of gross, No. of Tie in point, KM, etc.). The production help managers can control on parameters of activities to reduce the time and the cost. In this way, it helps the management to identify the waste in manufacturing that causes high production time and high manufacturing cost. The TD-ABC approach was related to the time equation as see (Table 5.) the Time estimated for each Activities by using Equation (2). Which provides detailed and clear information to the management about the distribution of time on activities and the identification of activities that consume more time, in addition to making decisions related to reducing time, which is reflected on production processes, which are necessary for the control process and the provision of cost information. Direct Labor is relatively high as see (Table 2.), and this appears especially during welding activities because the company case study relies on daily wage employees from outside the company because there are no specialized employees with experience and certificates of competency in accordance with the Welding Procedure Specification WPS required within the contract. Therefor the researcher recommends Employees Designation Specialized experienced and efficient to for reduce activities that consume high costs. The cost of raw materials (for pipeline project represent the low amount because the Customer supplied Pipes with fittings, this, in turn, reduces the inventory space within the company case study, and reduces waste of raw materials and exposure to spoilage during storage. That cost of raw materials represents the raw materials consumed and supporting the production process such as (welding wire -cutting stone -lifting pods ... etc.).That were provided from the local markets in quantities that suit the needs of the work, which leads to a reduction in the cost of preparing resources compared to foreign markets and reducing the period Import and processing which are non-value-adding activities.
This research provides a contribution to the TD-ABC literature by developing an integrated framework. That expands understanding of how TD-ABC contribute to the allocation of indirect costs more accurately and relatively, in addition to determining the practical capacity and

determining the time consumed by each activity, unlike previous studies that were limited to studying the impact of one variable of the current study. On the other hand, the practical contributions involve The application of the case study helps the practitioners and administrators of the company under study to reconsider the method of calculating costs and enhance control over unit costs and production processes.

7. CONCLUTION:

With growing of industry and rising competition in the manufacturing environment, companies are developing cost accounting systems accompanied with effective control systems to provide feedback of data (financial and non-financial) that are relevant and objective which helps the management in making the necessary decisions to keeping market share. TD-ABC be the substitutional tool for administration to utlized for competence non-HR and HR management and to Improving the process of cost control and operational control. In light of the results obtained, the researchers concluded that the use of the TD-ABC approach in the case study of Ibn Majid Company contributed to the control process, with time equations that led to determining the actual time of activities, and the effect of the consumed resources and time for each activity. According to these result that administrator will control of the real cost driver such as direct material,mostly which is the cost driver for the cost of resources and the activity that consumes the highest cost, as direct labor appeared relatively high, especially during welding activities due the case study's company of dependence on daily wage workers. Wherefore researchers recommend training or hiring competent, experienced and particular worker to perform work efficiently to reduce cost- consuming activities. In addition, the researchers concluded that the non-financial information provided by the TD-ABC approach by determine practical capacity (for workers and machines) and excluding unused capacity enhances operational control for production processes. Based on the previous conclusions, the researchers recommend the need for the company to embrace contemporary accounting methods, the most important of which is the Time Driven- activity based costing (TD-ABC) and it's easy to implement, which provides information that helps management in controlling. In addition, the need to educate companies about the TDABC approach to solve the problem of allocating indirect costs better and distributing them more equitably, as well as to overcome the disadvantages of the traditional method based on time equations. These conclusions confirm the validity of the study hypothesis.

References:

[1] Ganorkar, Ashwin B., Ramesh R. Lakhe, and Kamalkishor N. Agrawal. **"TDABC for a manufacturing environment: A case study."** Tékhne 16.2 (2018): 2-10.

[2] ALDANIYAZOV, Korkembay. **"Factors and Ways to Reduce Product Costs."** Espacios 38.46 (2017): 37-37.

[3] Perčević, Hrvoje, and Mirjana Hladika. **"Movement from traditional to modern cost accounting methods in manufacturing companies."** Muhasebe ve Finans Tarihi Araştırmaları Dergisi 10 (2016): 155-180.

[4] Namazi, Mohammad. **"Time Driven Activity Based Costing: Theory, Applications and Limitations."** Iranian Journal of Management Studies 9.3 (2016): 457-482.

[5] Afonso, Paulo, and Alex Santana. **"Application of the TDABC model in the logistics process using different capacity cost rates."** Journal of Industrial Engineering and Management (JIEM) 9.5 (2016): 1003-1019.
[6] Guzman, Lorena Siguenza, Alexandra Van den Abbeele, Joos Vandewalle, Henri Verhaaren and Dirk Cattrysse**"Recent evolutions in costing systems: A literature review of Time-Driven Activity-Based Costing."** Review of Business and Economic Literature 58.1 (2013): 34-64.
[7] Alami & ElMaraghy, Darwish, and Waguih . **"Traditional and Activity Based Aggregate Job Costing Model."** Procedia CIRP 93 (2020): 610-615.
[8] Santana, Alex, and Paulo Afonso. **"Analysis of Studies on Time-Driven Activity Based Costing (TDABC)."** The International Journal of Management Science and Information Technology (IJMSIT) 15 (2015): 133-157.
[9] Akhavan, Sina, Lorrayne Ward, and Kevin J. Bozic. **"Time-driven activity-based costing more accurately reflects costs in arthroplasty surgery."** Clinical Orthopaedics and Related Research® 474.1 (2016): 8-15.
[10] Horngren ,Datar, Srikant M., and Madhav V. Rajan. **Horngren's cost accounting: a managerial emphasis**. Pearson, 2018.
[11] Ramida, P. O. N. G. W. A. S. I. T., and CHOMPU-INWAI Rungchat. **"Analysis of wooden toy manufacturing costs through the application of a time-driven activity-based costing system."** Vol. 65, presented at the Symposium on Mechanical Engineering, Industrial Engineering, and Robotics. 2015.
[12] Kaplan, Robert S., and Steven R. Anderson. **Time-driven activity-based costing: a simpler and more powerful path to higher profits**. Harvard business press, 2007.
[13] Cidav Zuleyha , David Mandell , Jeffrey Pyne, Rinad Beidas, Geoffrey Curran and Steven Marcus:**"A pragmatic method for costing implementation strategies using time-driven activity-based costing."** Implementation Science 15 (2020): 1-15.
[14] Din ,Kakrona ,Duangpun Kritchanchai,Atchara Dokkulab **"Time Driven Activity Based Costing in Outpatient Logistics"** , Proceedings of the International Conference on Industrial Engineering and Operations Management Bangkok, Thailand, March 5-7, 2019.
[15] Koolmees, Dylan, et al. **"Time-Driven Activity-based Costing for Anterior Cruciate Ligament Reconstruction: A Comparison to Traditional Accounting Methods."** Arthroscopy, sports medicine, and rehabilitation 3.1 (2021): e39-e45.
[16] Yonpae ,Park, Yonpae, Sungwoo Jung, and Yousef Jahmani. **"Time-Driven Activity-Based Costing Systems for Marketing Decisions."** Studies in business and economics 14.1 (2019): 191-207, DOI 10.2478/sbe-2019-0015.
[17] LAWYER, CHUKWUMA OBARA (PhD), "Cost Control and Accountability for Effective Budget Implementation ",SENIOR LECTURER / HEAD, DEPARTMENT OF ACCOUNTANCY, RIVERS STATE UNIVERSITY OF SCIENCE AND TECHNOLOGY PORT HARCOURT.5.21 (2014): 199-202.
[18] Zohoori et al. ,Bahareh Zohoori , Alexander Verbraeck, Morteza Bagherpour & Masoud Khakdaman ,**"Monitoring production time and cost performance by combining earned value analysis and adaptive fuzzy control."** Computers & Industrial Engineering 127 (2019): 805-821. https://doi.org/10.1016/j.cie.2018.11.019
[19] Mutya ,Tomasi Mutya, **"Cost Control: A Fundamental Tool towards Organisation Performance"**, Department of Business and Management Studies, Kumi University, Kumi, Uganda , Journal of Accounting & Marketing ,Journal of Accounting & Marketing ,ISSN: 2168-9601 Mutya, J Account Mark 2018, 7:3 ,DOI:10.4172/21689601.1000283.

[20] Cooper & Dart , Philip C. & Eleanor D.,**"Change in the Management Accountant's Role: Drivers and Diversity"**,University of Bath, School of Management, Working Paper Series ,Bath (2009).

[21] Nyemba & Mbohwa, Wilson R., and Charles . **"Process mapping and optimization of the process flows of a furniture manufacturing company in Zimbabwe using machine distance matrices."** Procedia Manufacturing 8 (2017): 447-454.

[22] Anzai, Yoshimi,**"Dissecting costs of CT study: application of TDABC (time-driven activity-based costing) in a tertiary academic center."** Academic radiology 24.2 (2017): 200-208. **http://dx.doi.org/10.1016/j.acra.2016.11.001**

[23] Oliveira ,Rosário Oliveira **:"Monitoring and Control of Schedule and Cost Performance in Facade Conservation"**,First International Symposium on Risk and Safety of Complex Structures and Components ,Department of Civil Engineering, School of Engineering, Polytechnic of Porto, 4200-485 Porto, Portugal 2019.

[24] Ostadi, Bakhtiar, Reza Mokhtarian Daloie, and Mohammad Mehdi Sepehri. **"A combined modelling of fuzzy logic and Time-Driven Activity-based Costing (TDABC) for hospital services costing under uncertainty."** Journal of biomedical informatics 89 (2019): 11-28.

[25] Rude, Hampus, and Aleksandar Balicevac. **"Development of a real-time TDABC model for production activities: A case study at a manufacturing company."** (2019).

[26] Al-Halabi, Nabil Bashir, and Yazan Mjahed Al-Mnadheh. **"The Impact of Applying Time Driven Activity-Based Costing on Improving the Efficiency of Performance in Jordanian Industrial Corporations: A Survey Study."** International Journal of Economics and Finance 9.12 (2017): 24-31.

Visual Management and its Impact on Reducing Wastage (3M) According to the Perspective of the Agile 7S Methodology: An Applied Study in Al-Rayan Company

Hasshim Nayef Hashim[1], Hussam Abdulameer Mohammed Alsalman[2]
{hashim.naif@stu.edu.iq[1], h.a.alsalman@stu.edu.iq[2]}

Technical College of Management Basra, Southern Technical University[1,2]

Abstract. The main objectives of this study are to:1) Determine the requirements for applying visual management strategies, and their relevance to the reduction of (3M) waste through the (7S) methodology:2) Recognizing the impact of each dimension of visual management on reducing waste and arranging them in terms of the level of importance. This research was carried out in (35) persons from the technical and administrative staff in the study sample company. and questionnaires were used to collect data. SMART-PLS 3.0 was used to test the hypothesis. The findings result proved that there is a correlation between visual management of (0.64) with the (7S)methodology, and it is significant at the level of significance (0.05). and Working individuals realize that drawing up a set of strategic plans in the company's departments is one of the priorities of administrative work and a basic requirement of visual management to reduce the waste and waste that occur in all the company's business.

Keywords: Visual Management, VM, Visual Management Strategies, VMS, 7S, Waste 3M.

1 Introduction

Visual management is a modern method of management and one of the most important reasons for the success of the Japanese experience, which calls for achieving several goals, such as increasing the level of transparency and the ability to communicate between the general personnel of the organization, as well as stimulating and raising morale among working individuals [1], [18]. The success of the application of visual management depends on some of the requirements in industrial organizations. [2] such as leadership, commitment, work team…etc. So, visual management (VM) is a workplace where all working individuals understand and manage their work in a safe, clean and orderly environment that promotes open communication and continuous improvement, as the visual management (VM) provides real-time information on the state of the workplace through a set of means of visual information Simple and effective, which allows working individuals to understand their effects on work as well as improve organizational performance, and this is in line with the (7 S) methodology that consists of seven stages: classification, arrangement, cleanliness, standardization, self-discipline, safety and team spirit (cooperation) as it works. Each stage continuously improves the performance of the organization by eliminating all forms of waste and maintaining a clean and safe work environment, which is reflected in improving the morale of workers. Improving the morale of workers is a qualitative form responsible for reducing the manufacturing lead time [8]. (All of this helps to get rid of all kinds of waste related to uncertainty and time Waiting and searching for relevant information and so on by eliminating what is unnecessary and leaving everything clear and predictable, as well as reducing clutter as the necessary elements are always in the same places and work is easier and faster and this contributes to achieving the goals of the organization and reducing waste. Muda (losses), Mura (difference), and Muri (overload-strain) and complete assigned tasks quickly and accurately [13].

IMDC-IST 2021, September 07-09, Sakarya, Turkey
Copyright © 2022 EAI
DOI 10.4108/eai.7-9-2021.2315372

2 Research Methodology

2.1 The research Problem

The concept of visual management and its strategies has received great attention by researchers and writers, as a modern and effective administrative method in enhancing the culture of the organization with modern productive approaches that are in line with the developments of the era characterized by dynamic changes and high speed in providing products and services. Realizes the concept and importance of Visual Management (VM) and its strategies based on clear scientific foundations, which will reduce waste and improve resource utilization, hence the researchers' desire to know the role played by visual management in reducing waste using the (7S) methodology. so, the research problem is reflected in the following main question : (What is the effect of visual management in reducing waste (Muri, Muda, Mura) using the (7S) methodology)?

2.2 The Importance of Research

The importance of the research is trying to bridge the knowledge gap in the literature in one of the controversial topics in the field of production and operations management by linking the variables (Visual Management, 3M, 7S) to achieve a clear understanding of the concepts used, and determine their importance and objectives, Besides measure the extent to which the visual management strategies are applied in the company under study, and to determine the role that the visual management plays in the company to reduce waste (3M) through the use of the (7S) methodology in the Iraqi environment.

2.3 Research Objectives

1. Defining the concept of visual management by providing scientific and cognitive material that helps researchers in the field of production and operations management.
2. Determine the requirements for applying visual management strategies, and their relevance to the reduction of (3M) waste through the (7S) methodology.
3. Recognizing the impact of each dimension of visual management on reducing waste and arranging them in terms of the level of importance.
4. Introducing industrial companies to one of the modern methods of quality systems, specifically the (7S), by proving its benefits in a clear practical way.

2.4 Proposed Conceptual Model

The. The model consists of three main dimensions (visual management, 3M & 7S), the independent dimension (visual management) consists of three sub-dimensions, namely (strategy of setting work rules, purification strategy, strategy to eliminate waste), and the dependent dimension consists of (3M).) from three sub-dimensions (Muri, Muda, Mura), and the mediating variable is the (7S) methodology as shown in Figure (1) the hypothetical research model.

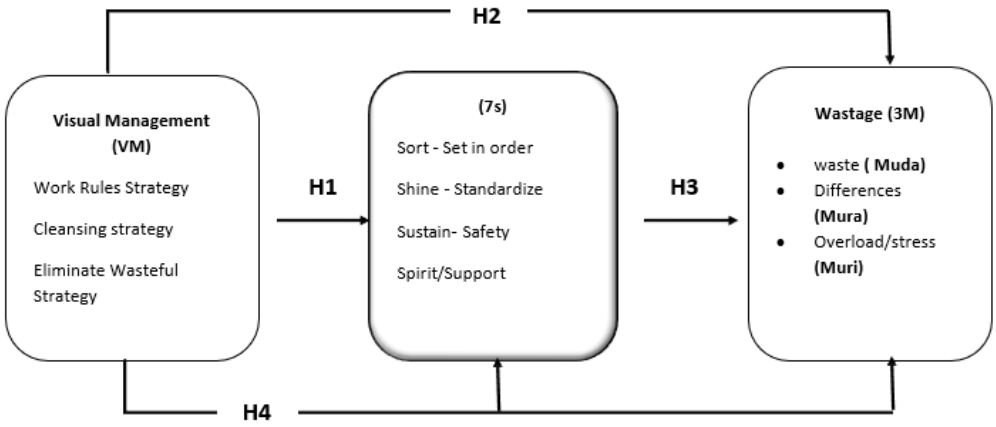

Fig 1. Proposed Conceptual Model.

2.5 The Following Hypotheses were Tested

1. The first main hypothesis: There is an influential relationship between the visual management strategies (VM) and the (7S) methodology.
2. The second main hypothesis: There is an effective relationship between visual management strategies (VM) and waste reduction (3M).
3. The third main hypothesis: There is an effective relationship between the (7S) methodology and waste reduction (3M).
4. .The fourth main hypothesis: There is an influence relationship between visual management (VM) and waste reduction (3M) using the (7S) methodology.

2.6 Research Methodology

The study used the descriptive-analytical method to achieve the goal of the study by verifying the relationship between visual management (VM) and wastage(3M) through the mediating variable(7S) methodology in Al Rayan Dairy Production. The questionnaire was used as the main tool for data collection. It was distributed to the study sample, which numbered (35) heads of departments and workers in the production department, and a five-point Likert scale was applied.

3 Theoretical Frameworks

3.1 Visual Management

Visual management (VM) is one of the core practices of an agile production system and an important management approach to information sharing and more transparency of work, as the reliance on vision during the execution of tasks has been observed by humans even before research confirms its importance [14]. In particular, [7] showed the contribution of each of the five senses to the processes of learning and analysis and found that sight contributed up to 75 percent of human perception, learning, and activity, with the visual system being the system with the highest ability to process information Of all the functions of the human brain, these findings could explain why many organizations, especially industrial organizations, advocate the use of simple and clear visual tools to communicate with workers [7]. Thus, visual management (VM) has constituted a new dimension of the processes, systems, and structures that make up an organization based on the use of graphical visualization techniques to increase focus on performance, according to [18]. There is a conflict of terminology when describing the use of visual methods to support management throughout Organization, some of the terms used are visual management, visual workplace, visual control, visual factory, visual aids, and visual communication [7].

The term visual management is used, which defines it [10] as "a management system that attempts to improve organizational performance by linking and aligning organizational vision,

core values, goals, and culture with other management systems, stakeholders, processes as well as the workplace, using stimuli, which address Direct one of the five senses (sight, hearing, feeling, smell, and taste)". Thus, visual management is "a self-interpreting, self-regulating work environment, where it happens, what is supposed to happen, at what time, day or night, which is a term It is used to refer to the method that makes work procedures visible to improve workflow,". As he knows it, It is [18] that "it is a management strategy that proposes to share relevant and easily understandable sensory information".

3.1.1 The Dimensions of visual management

Three important strategies can be summarized as follows: [4,1,2].

a) **Work Rules Strategy:** It is the organization's rules or a set of practical procedures that it sets and that are clear and specific in a way that serves its mission optimally to constantly improve and develop work. These rules are characterized by being scalable and adjustable to become simple and effective and keep pace with the culture of speed that describes the new world order, which includes defining tasks, practical procedures for implementation, methods, and standards for performance and evaluation through an objective study and a simple and clear scientific approach.

b) **Cleaning Strategy:** An important strategy that refers to organizing work and eliminating obstacles by diagnosing the organization's problems and accurately identifying performance gaps and their causes, so that it can develop appropriate solutions and develop plans to improve performance in the light of specific criteria, and of course it may be among the methods of solutions The dimensions of some leaders that impede the progress of work, and this strategy does not stop at this point, but extends to addressing the various tools, methods, and policies, as it is characterized as the most important means of continuous development and accordingly, change must be one of the values and concepts necessary to meet the challenges of the future.

c) **Eliminate Wasteful Strategy:** This strategy aims to get rid of unnecessary activities and procedures that do not add anything real to the work output and to introduce the value of speed into the culture of the organization, as there are many ways to waste material and human resources despite their scarcity, including wasting time Which is one of the most important types of waste, and it is through taking some routine administrative decisions in several days or even months, which hinders the interest of the organization and employees and disrupts the workflow. Those working behind it gain nothing but fear, doubt, hesitation, slowdown, complexity, and obstruction.

3.2 The Concept of the(7S) Methodology

The 7S methodology is rooted in the Japanese 5S methodology of sorting, arranging, brilliance, standardization, and self-discipline. In recent years, two pillars have been added, safety and team spirit (cooperation). The 5S methodology arose in the aftermath of World War II as part of the quality movement In Japan, the term was formally coined by Takashi Osada in 1980 [6]. [5] sees the 5S methodology as "a stage of workplace organization that has an impact on the efficiency, quality, and safety of workers." (5S) is one of the ways to create a comfortable and safe work environment within the organization so that the working individuals have a good work culture. [13] refers to it as "a valuable methodology to enhance and improve the productivity of organizations as it can enhance communication and help workers to be effective.", and generate concepts that contribute to reducing downtime, delivery times, inventory, defects, and related expenses." According to Japanese organizations, the 5S methodology has two aspects, the first is a high level of supervision of its proper implementation which explains the ideal performance, and the other is the provision of management Good and tools required, on Although the 5S methodology works to provide a clean and healthy workplace, it supports improving productivity and raising the performance of organizations, so the 5S methodology is one of the most well-known methodologies in the industrial environment [11].

6S, as an extension of 5S, is described as a team-oriented methodology, and this concept can be applied to achieve desired results within industrial organizations, as the basic idea of expanding the methodology from 5S to 6S is to provide continuous improvement by creating safety awareness Reducing the number of accidents and injuries in work environments [11] It provides a continuous improvement as well as enhances safety awareness. [16] sees the 6S methodology as "an advanced technology aimed at achieving a safe working environment for workers", is a methodology 6S is an essential measure for discipline and encouraging a culture of continuous improvement, and the main goal of the (6S) methodology is to reduce all faults in the industrial environment, which increases the productivity of organizations, achieving better quality products and a safe work environment, as well as meeting the needs and desires of customers. (6S) in any organization that seeks to improve its performance by reducing (80-90%) of the time in handling materials and searching for tools in the workplace, which gives a quick response to any problem that occurs in the workplace and works to solve it very quickly.

As a result of the developments, this methodology has become composed of seven pillars after adding the spirit of cooperation between team members, which is the (7S) to the (6S) methodology, which enhances the cohesion of the work team. [11] sees the (7S) methodology as "a methodology Continuously improve the work environment by classifying and arranging materials and tools, extensive cleaning, standardization and (self-discipline) maintaining what has been achieved by compiling work instructions and standard operating procedures for working personnel, eliminating most accidents in the workplace (occupational safety). [8] considers it "a simple and practical approach to building a culture of quality in the workplace that is relatively easy to do and requires few additional resources. The investment in time and effort pays off much more when results are achieved and maintained".

3.2.1 Dimensions of (7S) Methodology

This methodology includes seven main dimensions as follows [17,13,11]:

a) **Sort:** It is the process of removing all items that are not necessary for the current production from the work area; for example, distinguishing between what is needed and not wanted in the work area and getting rid of what is not needed, selecting and sorting workplace items into two main categories, important and unimportant An attempt to eliminate unused or rarely used items that pile up and cause disruptions.

b) **Set in order:** Arrange and distinguish items in such a way that they are easy to find and use, while sorting helps us identify what items are needed, order helps us decide how they should be placed; for example, everything should be placed according to its position so that it is ready for use when needed.

c) **Shine:** Refers to the need to keep the workplace clean. In Japanese industrial organizations, cleaning is a daily activity. At the end of each work, the work area is cleaned, and everything is returned to its place.

d) **Standardize:** Create a consistent way to carry out tasks and procedures, and this is done to ensure that the situation does not deteriorate back to the state it was in before the implementation of 1S, 2S, and S3, and the purpose of standardization is to ensure that everyone in the organization follows the same procedure, the same Item names, same size signs/floor marks, shapes, colours, and so on.

e) **Sustain-Self-Discipline:** Sustainability also means discipline which denotes commitment and preservation of the system and past practices in 1S, 2S, S3, and S4 as a way of life and the main objective is to give workers the commitment and motivation to follow each step, day in and day.

f) **Safety:** The condition of being protected from any kind of physical, social, spiritual, financial, political, emotional, occupational, psychological, or educational consequences.

g) **Spirit/support-Collaboration:** It is the desire to work and cooperate between senior management and individuals working in a team spirit.

3.3 Waste 3 M (Mura, Muri, Muda)

There are three types of waste, which are as follows [9]:

a) **Overload/stress (Muri):** Muri is defined as "the stress to which working personnel or equipment are subjected and refers to any action related to an appreciable physical or psychological stress" [15]. Examples of Muri include workers repeatedly bending over due to work, lifting Heavyweights, or repetition of tiring mental and physical actions, with client deadlines that are too short compared to the individual skill level of the workers [3].

b) **Differences (Mura):** (Mura) is the differences and discrepancies that occur in the process such as misalignment and irregularity of tasks, and if there is (Mura) in the organization it means there is a high possibility of overloading workers or machines (Muri) [9]. This (Mura) identifies differences and asymmetries in the process, for example, irregular use of the individual worker or machine, which must be reduced or eliminated to avoid the occurrence of (Muri) in any value-added production resource that causes (Muda). [15].

c) **Waste (Muda):** (Muda) Waste caused by (Muri, Mura) is any activity or process that does not add value and is a physical waste of time, resources, and money. Muda covers seven forms of wastage categorized by Taiichi Ohno within the Toyota Production System: Overproduction, Inventory, transportation, waiting, movement, additional processing, defects in the product, and recently the eighth type of loss has appeared: untapped talent [15].

4 The Practical Side

4.1 Analysing the Results of the Correlation Between the Dimensions and Variables of the Research

This paragraph aims to verify the extent of the validity of the main research hypotheses and the sub-hypotheses emanating from them using the (Smart PLS) program .Main and several sub-hypotheses that test a correlation between visual management and its dimensions and the (7S) methodology, and test correlations between visual management and wastage, as well as testing a correlation between the (7S)and wasted methodology. Table 1 shows the matrix of correlations between the dimensions and variables of the research.

Table 1. Correlations between research dimensions and variables.

Correlations									
Y	Y3	Y2	Y1	M	X	X3	X2	X1	
-.236**	-.261**	-.046	-.250**	.226**	.160**	.005	.388**	1	**X1**
-.404**	-.226**	-.181**	-.339**	.106*	.572**	.259**	1		**X2**
-.287**	-.113*	-.219**	-.210**	.439**	.313**	1			**X3**
-.411**	-.262**	-.224**	-.323**	.639**	1				**X**
-.626**	.183**	.332**	-.300**	1					**M**
.104*	.472**	.432**	1						**Y1**
.238**	.412**	1							**Y2**
.168**	1								**Y3**
1									**Y**
****. Correlation is significant at the 0.01 level (2-tailed).**									
***. Correlation is significant at the 0.05 level (2-tailed).**									

Source: Prepared by the researchers based on the results of (SmartPls).

According to the results of Table 1, the hypotheses will be tested as follows:

a) **The first hypothesis:** The results proved that there is a correlation between visual management of (0.64) with the (7S) methodology, and it is significant at the level of significance (0.05). The results also proved that there is a correlation between the strategy

of setting business rules of (0.23) with the (7S)methodology, which is significant at the level of significance (0.05). There is also a correlation between the purification strategy of (0.11) and the (7S)methodology, which is significant at the level of significance (0.05). As for the correlation between eliminating waste, it was (0.44) with the (7S) methodology, and it is significant at the level of significance (0.05).

b) **The second hypothesis:** The results proved that there is an inverse correlation between the visual management of (-0.41) waste, which is significant at the level of significance (0.05). The results also proved that there is an inverse correlation between the strategy of setting business rules of (-0.24) waste, which is significant at the level of significance (0.05). There is also an inverse correlation between the purification strategy of -0.40, which is significant at the level of significance (0.05). As for the inverse correlation of wastage elimination, it was (-0.29), and it was of significant significance at (0.05).

c) **The third hypothesis:** The results proved that there is an inverse correlation between the (7S)methodology of (-0.63) waste, which is significant at the level of significance (0.05).

4.2 To Test the Hypotheses of the Two Dimensions and Variables of the Research

a) **The first hypothesis:** The researcher assumes the existence of a positive influence relationship for visual management and its dimensions. the results appear in each of Figure (2), the effect coefficient. Between visual management and the (7S)methodology, and figure (3) presents the influence coefficient for the dimensions of visual management in the (7S)methodology, and the results will be presented in Table (2), which are as follows:

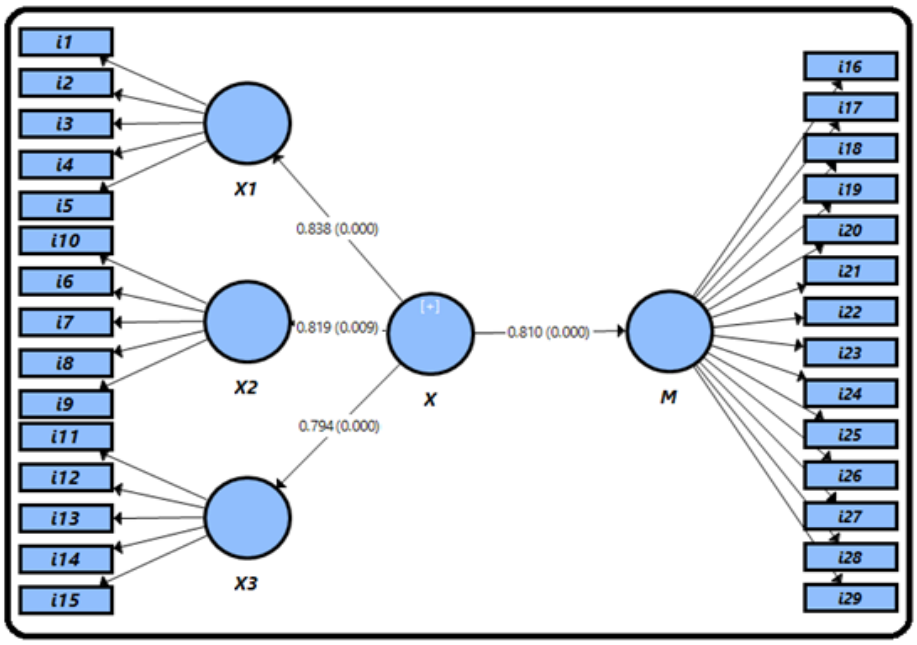

Fig 2. Impact factor for visual management in the (7S) methodology
Source: Prepared by the researchers based on the results of (SmartPls).

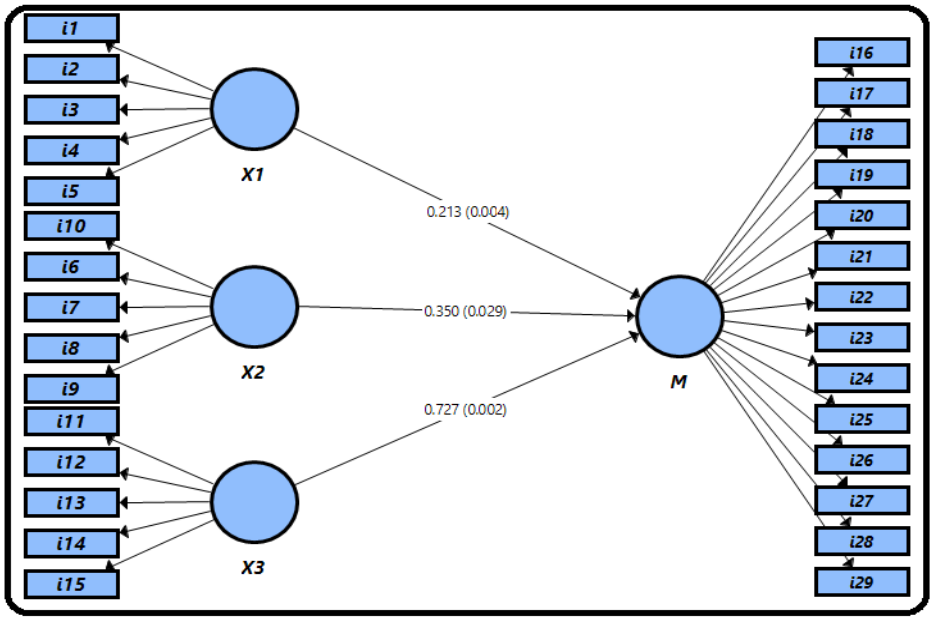

Fig 3. The influence coefficient for the dimensions of visual management in the (7S) methodology.

Source: Prepared by the researchers based on the results of (SmartPls).

Table 2. Some tests for the impact factor of visual management and its dimensions in the 7S methodology.

	Original Sample (O)	R^2	Standard Deviation (STDEV)	T Statistics (|O/STDEV|)	P Values
X -> M	0.810	0.66	0.092	8.852	0.000
X1 -> M	0.213		0.085	2.494	0.004
X2 -> M	0.350		0.036	9.777	0.029
X3 -> M	0.727		0.096	7.598	0.002

Source: Prepared by the researchers based on the results of (SmartPls).

According to Figs 2, 3, and Table 2, visual management explains the amount of (0.66) of the variation occurring in the (7S)methodology, and the visual management's effect in the (7S)methodology has been estimated at (0.81), which is significant at the level of significance (0.05). As for the effect of the visual management dimensions in the (7S)methodology, the effect of the strategy of setting business rules in the (7S)methodology was estimated at (0.21), which is significant at the level of significance (0.05). The effect of the purification strategy in the (7S)methodology was estimated at (0.35), which is significant at the level of significance (0.05). As for the effect of the strategy to eliminate waste in the (7S)methodology, it was estimated at (0.73), which is significant at the level of significance (0.05).

b) **The second hypothesis:** The researcher assumes the existence of a negative influence relationship for the visual management and its dimensions (strategy of setting business rules, purification strategy, strategy to eliminate waste) on waste, and it will be tested according to simple and multiple regression and the results appear in each of Fig 4 the influence coefficient between management As for the Fig 5 displays the impact factor for the dimensions of the visual management in the waste, and the results will be presented in Table 3, which are as follows:

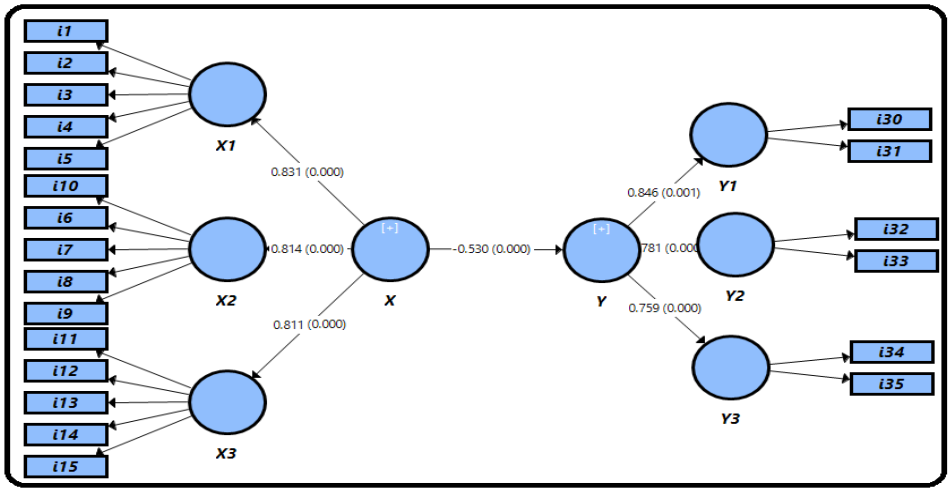

Fig 4. Impact factor for visual management on waste.
Source: Prepared by the researchers based on the results of (SmartPls).

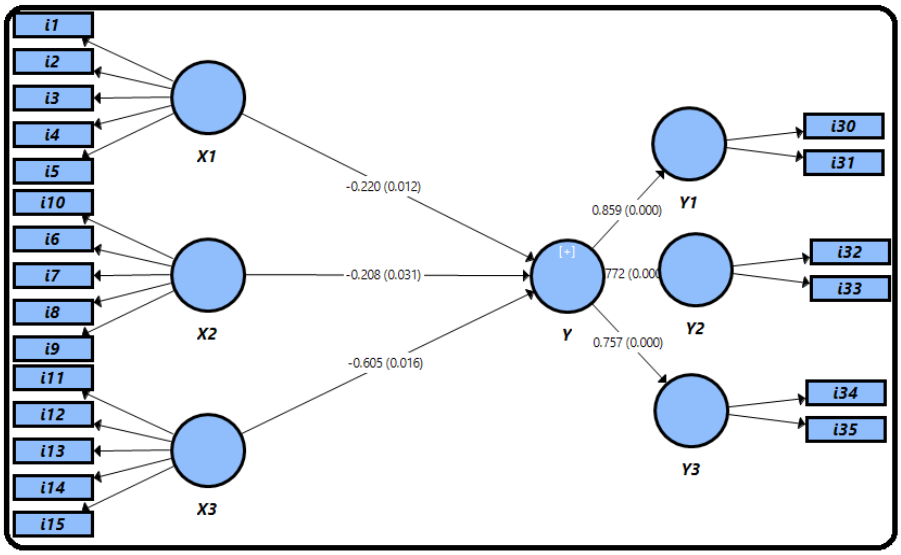

Fig 5. Impact factor for the dimensions of visual management in waste

Source: Prepared by the researchers based on the results of (SmartPls).

Table 3. Some tests for the impact factor of visual management and its dimensions in waste

	Original Sample (O)	R^2	Standard Deviation (STDEV)	T Statistics (|O/STDEV|)	P Values
X -> Y	-0.530		0.139	-3.818	0.000
X1 -> Y	-0.220		0.112	-1.967	0.012
X2 -> Y	-0.208		0.104	-2.000	0.031
X3 -> Y	-0.605		0.200	-3.027	0.016

Source: Prepared by the researchers based on the results of (SmartPls).

According to Figs 4 and 5 and Table 3, the visual management explains the amount of (0.28) of the variance in the waste, and the effect of visual management on the waste has been estimated at (-0.53), which is significant at the level of significance (0.05). . As for the effect of the visual management dimensions on waste, the effect of the business rule-setting strategy on waste was estimated at (-0.22), which is significant at (0.05). The effect of the purification

strategy on waste was estimated at (-0.21), which is significant at the level of significance (0.05). As for the effect of the strategy to eliminate waste on waste, it was estimated at (-0.61), which is significant at the level of significance (0.05).

c) **The third hypothesis:** The researcher assumes that there is a negative impact relationship between the (7S)methodology in loss, and it will be tested according to simple regression. Come:

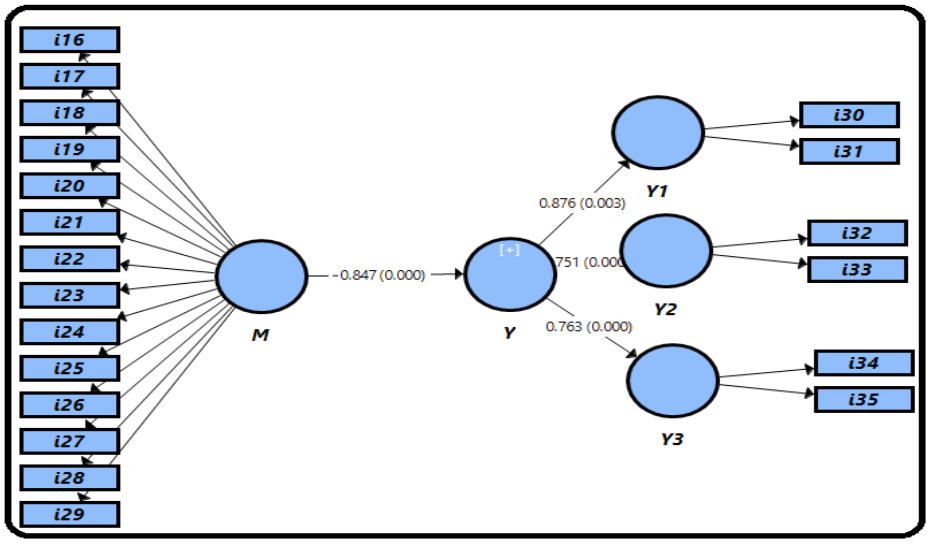

Fig 6. Impact Factor, (7S) Lost Methodology.

Source: Prepared by the researchers based on the results of (SmartPls).

Table 4. Some tests of the effect factor of the 7S methodology and its dimensions on Waste

	Original Sample (O)	R^2	Standard Deviation (STDEV)	T Statistics (|O/STDEV|)	P Values
M -> Y	-0.847	0.72	0.051	-16.608	0

Source: Prepared by the researchers based on the results of (SmartPls).

According to Fig 6 and Table 4, the (7S)methodology explains the amount of (0.72) of the variation in the waste, and the effect of the (7S)methodology on the waste has been estimated at (-0.85), which is significant at the level of significance (0.05).

d) **The fourth hypothesis:** The researcher assumes the existence of a negative influence relationship of visual management on waste through the 7S methodology, and it will be tested according to path analysis. The results appear in each of Fig 7 the influence coefficient between visual management and waste through the 7S methodology, and the results will be presented in Fig 7 The results in Table 5 are as follows:

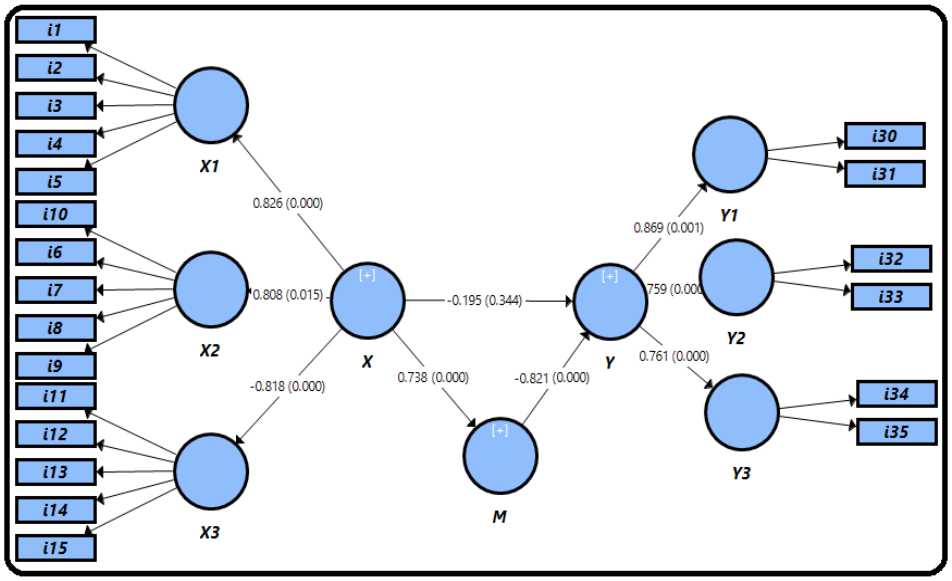

Fig 7. Impact coefficient for visual loss management.

Source: Prepared by the researchers based on the results of (SmartPls).

Table 5. Some tests for the impact factor of visual management and its dimensions in waste through the (7S)methodology

	Original Sample (O)	R^2	Standard Deviation (STDEV)	T Statistics (|O/STDEV|)	P Values
X -> Y	-0.195	0.75	0.206	-0.947	0.344
X -> M	0.738		0.147	5.014	0.000
M -> Y	-0.821		0.155	-5.283	0.000
X -> M->Y	-0.606		0.023	-26.487	0.000

Source: Prepared by the researchers based on the results of (SmartPls).

According to Fig 7 and Table 5, the visual management and the (7S)methodology explain the amount of (0.75) of the variance in the waste, and the direct impact of the visual management on the waste was estimated at (0.19), which is not significant at the level of significance (0.05). As for the overall effect of visual management on waste through the (7S)methodology, it reached (-0.61), which is significant over the level of significance (0.05), and this indicates that the independent variable will further reduce the waste.

5 Conclusions and Recommendations

The following lists are conclusions:

1. The possibility of applying the visual management strategies in the company under study to reduce waste and waste according to the (7S) methodology, through the results of the average sample answers about the main and sub-variables of the research.
2. The company's senior management is not interested in developing appropriate mechanisms to reward distinguished employees.
3. Working individuals realize that drawing up a set of strategic plans in the company's departments is one of the priorities of administrative work and a basic requirement of visual management to reduce the waste and waste that occur in all the company's business.
4. There is a limitation in guiding working individuals to enhance their abilities and skills, as well as encouraging individual initiatives towards creativity and innovation in the company under study.
5. The company under study focuses continuously on developing the competitive position at the local level, and this was confirmed by the answers of the sample most of the individuals working in the company under study are not interested in performing their

duties without supervision or control, which reflects the lack of ability to assume work responsibilities.

6. Through the analysis and interpretation of the results, it was found that the new (7S) methodology can have significant positive results on the performance of the organization when implemented effectively, by reducing various waste, organizing work areas, and enhancing hygiene in addition to team cohesion, and it is impossible to imagine 7(S) gains full value in the company if there are too many hurdles that cannot be addressed and removed.

The following lists are some recommendations:

1. Work on removing all obstacles that weaken the possibility of applying visual management strategies, by spreading the culture of visual management and making it in line with the values, beliefs, norms, and organizational expectations in the company
2. Ensuring the provision of the basic requirements that have an influential role in the process of improving leadership styles in light of this administrative style.
3. The need for senior management to support and encourage working individuals to present individual ideas and initiatives that would push the company towards creativity and innovation.
4. Emphasis on the visual management(VM) trends that call for the involvement of workers more in the decision-making process and work in a team spirit, as a large part of the success of applying the (7S) methodology is due to the management's ability to encourage employees to participate in the work team.
5. Forming higher control committees that adopt agreed performance standards to follow up on the progress of work in the company.
6. Develop appropriate mechanisms to reward distinguished workers by organizing competitions between departments within the company and evaluating workers in it to encourage them to develop and improve work.

References

[1] Al-Hadhali, Wajid bin Matar (2015) The Possibility of Applying Visual Management in Education Offices in the Makkah Al-Mukarramah Region and its Relationship to Employee Motivation, Master's Thesis in Educational Administration and Planning, Umm Al-Qura University, Kingdom of Saudi Arabia.

[2] Alqahtani, R. T. M. B. Z. (2019). A framework for the Saudi universities governance to achieve competitive advantage in decision making according to the aspirations of Vision 2030.

[3] Arezes, P., Carvalho, D., & Alves, A. C. (2010). Threats and opportunities for workplace ergonomics in lean environments. EurOMA.

[4] Fathi Al-Waishi (2013), Leadership styles for human resources: administrative ethics, strategies for change, the Arab Group for Training and Publishing, Cairo.

[5] Gapp, R., Fisher, R., & Kobayashi, K. (2008). Implementing 5S within a Japanese context: an integrated management system. Management Decision.

[6] HungLing, C. (2011). 5S implementation in Wang Cheng industry manufacturing factory in Taiwan. The Graduate School, University of Wisconsin-Stout, May.

[7] Jaca, C., Viles, E., Jurburg, D., & Tanco, M. (2014). Do companies with greater deployment of participation systems use Visual Management more extensively? An exploratory study. International Journal of Production Research, 52(6), 1755-1770.

[8] Joshi, A. A. (2015). A Review on (7S) as a tool of Workplace Organization. International Journal of Innovations in Engineering and Technology, 6(2), 19-26.

[9] Klimecka-Tatar, D. (2017). Value Stream Mapping as Lean Production tool to improve the production process organization–case study in packaging manufacturing. Production Engineering Archives, 17(17), 40-44.

[10] Liff, S., and P. A. Posey. 2004. Seeing is Believing: How the New Art of Visual Management can Boost Performance throughout your Organization. New York, NY: Amacom Books.

[11] Mahlaha, K., Sukdeo, N., & Mofokeng, V. (2020). A lean 7S methodology framework to improve efficiency and organisational performance: A review study in an SME organisation. In International Conference on Industrial Engineering and Operations Management (pp. 9-12).

[12] Management." International Research Symposium, Salford, UK.

[13] Purba, H. H., Jemali, S. E., & Nugeroho, A. A. U. (2018). Productivity improvement with implementation of 5S: a case study in mining services industry in the general services department. Int J Res Eng Sci Manag, 1, 1-7.
[14] Reinbold, A., Seppänen, O., & Peltokorpi, A. (2020). THE ROLE OF DIGITALIZED VISUAL MANAGEMENT TO EMPOWER SELF-MANAGED CREWS IN CONSTRUCTION PROJECTS. In Annual Conference of the International Group for Lean Construction.
[15] Romero, D., Gaiardelli, P., Thürer, M., Powell, D., & Wuest, T. (2019, September). Cyber-Physical Waste Identification and Elimination Strategies in the Digital Lean Manufacturing World. In IFIP International Conference on Advances in Production Management Systems (pp. 37-45). Springer, Cham.
[16] Sukdeo, N. (2017). The application of 6S methodology as a lean improvement tool in an ink manufacturing company. In 2017 IEEE International Conference on Industrial Engineering and Engineering Management (IEEM) (pp. 1666-1671). IEEE.
[17] Sureja, J. V., Rajpurohit, G. J., Valand, S. U., & Prajapati, D. B. (2017). Prof. Vivek A Deshpande5, Pritesh Shah6, Nikunj Shah7, BE Final Year Students, 5Asst. Professor of Mechanical Engineering, GH Patel College of Engineering & Technology, VV Nagar, -388120, Gujarat, India. In Proceedings of 2nd International Conference on Emerging Trends in Mechanical Engineering.
[18] Tezel, A., & Aziz, Z. (2017). Visual management in highways construction and maintenance in England. Engineering, Construction and Architectural Management.

A Comparison Between the International Standards PRINCE2 and PMBOK in Project Management

Sana`a Hassan Zubon[1], Maher Kadhim Taher[2]
{sanaahassanalenzi@stu.edu.iq[1], Maher.altameemi@stu.edu.iq}

Southern Technical University/Technical Institute/Basra/Department of mechanical Technologies, Iraq[1,2]

Abstract. PRINCE2 developed the short for Projects IN Controlled Environments through observations and a summary of experiences of project management professionals, concerned users, and review committees from hundreds of organizations from the public and private sectors. This has produced a flexible tool for best practices in project management. To suit and adapt to the institution or organization and to be used and applied. With success regardless of the type or size of the projects to be managed. To specify the limits of delegated authority, the PRINCE2 project specified tolerances for each project objective. PRINCE2 lists variations set there are time, cost, quality, scope, risks, and benefits. The Project Management Framework, which is based on the PMBOK Quid is a prominent project technique from PMI In the United States, this method is very popular, but PRINCE2 is very popular and folk in Europe. PRINCE2 is a project management method that is based on seven principles. PMBOK Project Management Body of Knowledge a Guide to Project Management is PMP Project Management Professional from PMI standards Institute. PRINCE2 new method in Project Management to Future jobs.

Keywords: PRINCE2, PMBOK, IT, EIA ,CCTA, ISO, AXELOS, PMI, PMP, CPM.

1 Introduction

PRINCE2 dates back to 1989, when the British government developed it through the Central Computer and Communications Agency (CCTA), after developing it from a previous methodology for Project Management Technology called (PROMPT) under the Project Guide (PRINCE1), and after that, it became (PRINCE2) A government specification adopted by the United Kingdom for managing IT(Information and Communication Technology) projects, and its program and curriculum are prepared by the British Governmental Commercial Office. It is also used very widely in European countries, especially in IT projects and for all projects. PRINCE2 is a general project management method apply to big or small, it is popular in United Kingdom (UK).

The project is defined as "a set of tasks that must be completed in order to achieve a specified goal." A project, according to PRINCE2, is a temporary organization formed to introduce one or more business products under a business case.

The program is a flexible, temporary organizational structure designed to coordinate, organize, and monitor the implementation of a collection of connected projects and activities to achieve the organization's strategic goals and objectives.

It is the process of assessing a proposed project's possible environmental consequences (both positive and negative).

IMDC-IST 2021, September 07-09, Sakarya, Turkey
Copyright © 2022 EAI
DOI 10.4108/eai.7-9-2021.2315307

The objective of this procedure is to provide decision-makers with the information they need to determine whether or not to proceed with the project.
A natural, chemical, biological, cultural, or socioeconomic effect on the ecosystem as a result of the project's operations is characterized as an environmental impact. Environmental impact assessment is training on what will be done before any project, for the main activities, or what will be done to ensure that no means will harm the environment in the short or long term, and it is the process by which the environmental impacts of an activity are predicted and described [1][2][15].

2 Research problem

One of the activities that must be performed and completed throughout a project is preparing for a project being the first to take place in PRINCE2 .Its purpose is to answer the question “Is this project feasible and deserving to be implemented?” And will the project succeed by being environmentally friendly?
Every project starts with an idea, but it might not be a good idea. During this process, sufficient information is provided to the project management committee to do its part in selecting the good ideas and eliminating the bad ones. Well-prepared projects will lead to good results and thus achieve the desired return on investment for the organization. This process occurs before the project has begun, and thus can be referred to as the pre-project process. When and how to do the appropriate methods is selected for the small or big projects? Skill, Tools, and Techniques PMBOK or PRINCE2?

3 The Importance of Research

The PRINCE2 method one of project management
PRINCE2 is a special method of project management in which all project steps are defined at the beginning, and PRINCE2 is based on dividing down a project into procedures, such as the first step (hiring the team)
The second step (supplying ...), and so on.
The PRINCE2 methodology is used to manage various projects, while it was initially intended for PRINCE2 projects.
PRINCE2 is new Knowledge so can use in Small Projects and Big Projects, learning from previous experience, All of Team of Project contributes to its success.

4 Environmental Impact Assessment

Determine the positive and negative environmental impacts, analyze these impacts, and benefit from the positive project environment.
Analyzing these effects to determine the most important effects on the environment and the extent of their influence on the work and surrounding environment. The long-term and short-term impacts, direct and indirect effects, and potential risks must also be taken into consideration.

- Prediction & Mitigation: Environmental impact assessment monitoring is the planned and systematic collection of environmental data to meet specific environmental goals and needs.
- Technical, scientific, structure, and environmental information.

- Data on the economic and technological features of the environment EIA (Environmental Impact Assessment) [2].

5 Standards in Projects

Standards are considered the norm and samples of objects that can be compared with such other phenomena. We can call the document level that specifies the rules, regulations, and requirements to assess adherence to them in the workforce only between the first and second definitions. The first important distinction is consistent with the ideal and the second contains only a recommendation on how to deal with her.
Where there was a variety of project management methodology and standards to summarize the requirements and quality of work.
The development of various techniques for project management has been conducted on this basis. Logically, there is a need to define what qualities and skills are the most important steps that must be taken for the project manager to be a successful leader [4][15].

5.1 Types of standards

To define project management standards, best practices have been analyzed and synthesized. To achieve this, management uses two components:
The existence of a self that considers individual projects and the entire company along with the requirements for qualifying project managers as follows:

- Define and understand the terminology, aspects of the activity in this area, and the role of all participants in the project.
- Ensure development and management professionals who practice design types of activity and increase the efficiency of these projects. The project management criteria can be divided into four types: International, national, industry, and enterprise.

5.1.1 PMI Standards Institute:

Project management technology was developed that began in the United States of America in the 1960s and was affected by several factors, the most important of which became the nuclear age and the competition with the Soviet Union to invade space and develop new defense strategies that were there based on PMI standards around the world. PMP is a registered mark of the Project Management Institute Foundation [3].

5.1.2 ISO standard

It is the oldest and strongest international organization dedicated to standardizing almost all areas of business and technology. It is the leader in restriction at the global level. It has the right to introduce any new standards into the system. ISO International Organization for Standardization [5].

5.1.3 The PRINCE2 standard

It stands for (Project Management in Controlled Environments) as a general framework for project management and is suitable for managing any type of project and in any industry. Project management has set another standard in the UK owned by AXELOS Limited (a joint venture with the UK government) and set clear instructions for reliability restrictions for effective project implementation despite the limited scope of the standard set in England in the IT industry (PRINCE1) design and development and the launch of a market for new products in engineering and the public sector.
The PRINCE2 methodology uses stage management and margin of tolerance as the main elements of project control. Margins of tolerance allow management to be exempt, that is, when these margins are exceeded and an exception occurs, the project board cannot make the necessary decisions on a case-by-case basis.
The base methodology includes sectors, plans, organization, quality, and risks, among other things in the application of this project. Quality management standards for groups that need to be monitored. There is a continuous adjustment of the environment, and a generation of products are often used on seven principles, subjects, and processes it is considered the most widespread professional certificate in project management [6][1][20].

6 Learning from experience

In PRINCE2, the recording and transfer of experiences must take place throughout the project, by documenting any lessons that could be learned from applying them to other projects.Clearly defined roles and responsibilities within the PRINCE2 project the roles and responsibilities of each are defined within a clear organizational structure that takes into account the interests of investors, users, and suppliers. PRINCE2 helps control an ever-changing project environment by providing the necessary tools to the Project Manager [4][12],[18],[23].

7 PRINCE2 Themes

This criterion has seven axes: business condition, organization, quality, plans, risks, change, and progress of work. Fig. 1 six performance objectives/Themes PRINCE2.

Fig. 1. Themes / Processes PRINCE2 (Web site)

PRINCE2 is a project management method that covers all six project variables: timelines, prices, quality, benefits, scope, and risks. Six factors are referred to as competing project constraints in the PMBOk [9][16][17].

7.1 Structure of PRINCE2

The PRINCE2 method is divided into four components, each of which is represented by the term Elements (sometimes known as integrated elements). Principles, characteristics, methods, and procedures are examples of these components.
Operations: Procedures and activities are being carried out during the project and also processes that answer the question of "What products do they wish to generate and when?"
The specialized aspects highlight the fact that PRINCE2 is a highly general framework that can be used for any project. As a result, PRINCE2 does not provide specific project-specific knowledge, such as the optimum way to build a financial project organization or how to maximize the benefits of a specialized financial product.
Detailed techniques: Many techniques, such as the (CPM) critical path method or the best way to run a brainstorming workshop, can be used during a project. PRINCE2 suggests that you choose the proper technologies for your project, but it doesn't tell you how to do it. Product-based planning and the quality review approach are covered in PRINCE2.[26],[27]

7.2 Benefits of Using PRINCE2

Benefits to applying the project management technique to PRINCE2:

- Best Practice: PRINCE2 has been used in hundreds of projects for over 30 years, and it continues to learn from them. As a result, all of the comments, recommendations, and learning from other techniques and conversations have helped PRINCE2 become a best practice.
- PRINCE2 is a project management method that may be used for a range of tasks. As a result, PRINCE2 may be applied for both small and large projects, such as election management, conference planning, bridge building, and IT projects.
- PRINCE2 establishes a framework for functions and responsibilities (also known as "Tasks roles and responsibilities"). Everyone in the team of the project has to understand what is expected this is especially crucial for project managers, who have a responsibility to ensure that activities are done according to plan.
- PRINCE2 concentrates on the product that is clearly defined at the start of the project and is fully understood by all stakeholders. As a result, everyone is on the same page regarding what they're working on and what the final product should be.
- PRINCE2 employs exception management. This permits the project manager to resolve some project difficulties, but once one of the tolerance issues is bypassed, the situation

should be escalated to the next higher management layer. There will be less management. [10][29],[27].

- Throughout the project life cycle, PRINCE2 continues to evaluate the project's viability from the viewpoint of the Business Case. If at any time throughout the project, the projected return on investment is no longer possible, the project should be discontinued.
- For reporting and management products, PRINCE2 has a well-defined structure. PRINCE2 refers to any document generated to aid in project management as "Management Products," which includes the Project Brief, Business Case, Project Plan, Recognition Reports, and End-of-Stage Report.
- PRINCE2 supports professional development and a strong belief (also known as 'lessons learned). We encourage you to learn from other projects at the start of the project to add a lesson log during the project transfer the lessons to future projects at the end of the project.[28],[30].

8 Principles

8.1 Persistence of Business Justification

The PRINCE2 project should have a continuous justification for the business reason for starting the project should make sense from the business point of view and there must be a clear return on investment. For example, the project will cost 20,000 euros, but during the first two years, it will save the company 80,000 euros. Does the project have commercial justifications?
The business case document explains the complete business case details, explaining the reason for implementing the project, expected costs and benefits, and timelines. Business Justification Information is another name for these resources. Because the business case is one of the first documents generated for a project, it will prevent certain initiatives from being started from real benefits for the firm. The business justification is then validated throughout the project's life cycle. This might happen, for example, at the end of each step.[7][15],[16].

8.2 Learning From Experience

The PRINCE2 project team must learn from past projects, therefore they must take the initiative to uncover past lessons learned and use them throughout the project's life.
As previously said, each project is unique, which means there is always something new to consider, which adds to the risk factor.
PRINCE2 encourages project teams to take the lead. It is necessary to learn from similar projects that may have been carried out within the same company, and if not, to get advice from other external sources (for example, bring in outside consultants).[22],[25].

8.3 Defined Roles and Responsibilities

According to PRINCE2, a project's roles and responsibilities should be established and agreed upon within an organizational structure that includes the interests of business stakeholders, users, and suppliers.
Because projects might include employees from many departments or organizations, Critical that the project has defined in team structure managing the project may be impossible.
Business sponsors, users, and suppliers are the project's three major stakeholders, according to PRINCE2.

- Business sponsors ensure that a business provides good value.
- Users are who will use the products once they have been developed and will receive the benefits.
- Suppliers provide resources and experience to the project and product development process.

The three primary stakeholders must be properly represented on the project management team.[21]

8.4 Management of stages

A good way to do any big task or project is to break it down into manageable parts. In PRINCE2 we refer to the manageable parts as stages. They are called management stages. The PRINCE2 project is planned, monitored, and controlled stage basis. These are referred to as the management stages.
The project board analyzes the performance of the previous stage, the feasibility study, and the plan for the next stage after each stage and determines whether to advance to the next step. When a project includes a lot of phases, the project board has greater influence over it, but it also means they have more work. Because there are fewer stages in the project, top management will have less influence and the project board will have fewer jobs.[[17][27]

8.5 Focus Products

Detailed product descriptions will guide the project, build correct expectations, and help deliver the desired products. The PRINCE2 manual states the following: The PRINCE2 project focuses on the identification and delivery of products, in particular, their quality requirements.
Good product descriptions provide clarity because they define the purpose, composition, derivation, and formatting of the product, quality standards, and quality method. A good product description also facilitates the identification of resource requirements, approvals, and activities.

8.6 plan for the current stage

Ascertain that future stage plans can benefit from previous and past tasks, for example, if one team produces its products faster than planned, this may be factored into the following stage's planning.
There are at least two management phases in a project: the initiation phase and another management phase the project closing process is part of the second phase in a two-stage project.

8.7 Management via Exception

PRINCE2 may not be familiar with, but it is important to understand that, according to the PRINCE2 definition project manager has some flexibility in dealing with factors time, cost, and scope before having to notify the project board if there is or maybe a problem (for example, the cost can change by 10%). If the problem is small and still within allowance (for example, cost increase by 5% - less than allowance 10%).
The project manager has to deal with it and he does not have to alert the project board and take their time. Management by exception is used by each level in the project organization to manage the level below. The layer below should notify the above management layer only if there is a major problem outside the scope of the PRINCE2 name for a major issue which means that the problem outside the agreed tolerance is an exception.
Now imagine that you are sitting on the project board if everything is going well, Project manager except for regular reports during the phase and at the end of the phase, unless there is an exception, hence the term "management by exception".

- Quality permitting: creating a new GSM and must keyboard to work for the average user for seven years but you have a tolerance of ± 5%.
- Permission range: GSM requirements have mandatory requirements in addition to "nice to have" requirements. So, the project can decide the "nice be" requirements to be included, but it must include the milestones.
- Permit feature: A benefit is a measurable improvement that occurs as a result of one or more stakeholders' initiatives. These are advantages for project participants. Increase marketing share by 5%, for example, or develop a new profitable market segment. Is the project still on schedule to deliver the promised benefits? is one of the questions posed during the project.
- Permission Risks: Again, using the GSM example, there will be a certain level of risk tolerance, and if you hear about something higher than that, you will notify the project board. For example, you discover that the risk is now very high - one provider cannot provide a five mega camera pixel with the correct integration specifications. This might generate more problems for your project [7],[8],[24],[26].

8.7.1 Coordination or coordination in proportion to the project environment

A PRINCE2 project should be designed for the size, environment, complexity, relevance, capabilities, and risks of the project. You must customize PRINCE2 to match your project, whether it's a small project like hosting a workshop. PRINCE2 can be used for every type of project.
An introduction to the knowledge of an organization
Let's take a look at what will be covered in this topic of organization.

- The knowledge included in the subject matter organization's purpose
- Some definitions of the organization, what is the project, what is the program.
- The three categories of stakeholders.
- The project board's duties and roles.
- Role of the project manager, description, and required skills. Other project responsibilities include authority change, team manager, and project support. [28]

9 What happens in the real world?

Project manager, it's more important to start developing products as soon as possible. You depend on others to make decisions, supply information and perform tasks for you. As a result, it is critical. If you don't get this down on paper and approve it.
The first task a project manager must complete in a project is to determine who is in charge of the project and what their roles and functions all tasks responsibilities are. Start with the executive, who might need a reminder that he's in charge of the project [7],[8].

9.1 PMBOK Guide

The PMBOK looks at the project through the eye of the project manager only. The PMBOK is concerned with explaining the skills, touching on the types of tools and techniques that can be used in the project, how and when to use them, and why they are used. PMBOK does not focus much on the nature of other functions in the project but rather focuses on Mainly on the job of the project manager and how this manager deals with other functions, the PMBOK does not discuss too many topics such as governance or benefits realization (with simple explanations of it in the book, and its extensive presence in the Program Management Manual and other PMI publications) [9][10].

9.2 PMBOK Guide: Strengths

One of the main strengths of the PMBOK Guide is that it provides a comprehensive set of useful tools and techniques. In total (119) tools and technologies are described or referenced. The Time Management Knowledge Area, for example, has 25 different tools and techniques. This compares with only about forty tools and techniques referenced in the Manual as a whole PRINCE2.
In the PMBOK Guide, knowledge domains can be treated in isolation. Therefore, if the project manager needs to have a better understanding of the earned value analysis to better manage project cost, he can focus on the cost management knowledge area in the PMBOK Guide I would not suggest that simply controlling the project's cost is insufficient; a project that would benefit from the application of the PMBOK Guide's value-earning techniques would still benefit, thus the PMBOK Guide is an excellent resource for a variety of project management programs [9],[10].

9.3 PMBOK Guide: Weaknesses

One of the weaknesses is the lack of specific responsibilities for the Project Management Team members. This is vaguely defined as the project team members who directly undertake its management activities.
The overly complex and detailed explanation of some of the elements is the second weakness. Complexity is always a hindrance and delay factor and does not provide aid and assistance, and as just mentioned above, there is anecdotal evidence that might suggest this PMBOK Guide does not do itself well. A small example of this can be found in the section detailing the cost management plan, where it indicates that the plan may define the amount of control by which activity cost estimates are rounded up and down. In my opinion, this detail is not important if we comprehensively look at things. On the other hand, since this evidence is a cognitive guide, the writers may have thought that they might not be able to leave this detail without mentioning it [11].

9.4 PRINCE2: Weaknesses

The lack of tools and techniques in PRINCE2 is the biggest weakness. PRINCE2 describes two techniques in great detail, namely the Quality Review Method and the Product Based Planning approach. The latter was incorporated into PRINCE activities to develop plans for Guide PMBOK [12]. On other hand, many proven and proven planning and control techniques (such as critical path analysis and value-earning analysis) have been well documented elsewhere, and thus do not need to be replicated in the PRINCE3.

9.5 PRINCE2: Strength

The focus on the business case to drive and drive the project decision-making process is PRINCE2's main strength. This helps to ensure that projects continue to notice and realize the desired benefits that they are working on achieving, thus ensuring a return on investment and we find that 'continue/stop' decisions will be taken as a result. The usage of management stages is required to review the updated business case. Another strength of Quality Assurance in Prince2 because of the focus on protection [13].[14][30]

Fig. 2. PRINCE2 Quality Assurance (Web site).

10 Practical Side to PRINCE2

They differ in the fact that the first focuses on the information, techniques, and skills that the project manager needs in his work, while the second focuses on the methods and controls required for project management.

PMBOK is considered more comprehensive by covering a greater number of knowledge domains. How to manage schedules and costs and thus increase the percentage of acquired skills for the degree holder.

PRINCE2 focuses on how to successfully manage the project with the lowest level of requirements, and even calls projects that apply the lower levels required by PRINCE2 projects, so PRINCE2 is concerned that the recipient can change his way well according to the nature of his project and his needs, so the PRINCE2 method is more flexible and more adaptable. Accepting the different implementation methods, PRINCE2 usually expects that the powers of

the project manager are limited and framed in the powers of the executive (the executive position is hardly present in the PMBOK)
The Team of the project in PRINCE2 is responsible for the success project in Scope Time and Quality and Risk, The Product sets out.
Information of Experience previous projects take the Team practical background for a new project that done.[15],[19],[20].

11 Conclusions

The following are the summarized remarks of the present work:
1. One of the advantages of working with PRINCE2 is the study of the realistic project environment and the orientation in the investments needed to achieve the expected benefits.
2. The study of the project environment is a study from the bottom of its organizational structure and the study of the external factors surrounding it and the factors that affect the success or failure of the project.
3. Is One of the most important advantages of working with PRINCE2 is the experiences and reports of previous projects, especially those that are similar in the business environment.
4. The work team considers the integrated picture of the success of the project, and it is not the responsibility of the project manager, any experiences are circulated by everyone.
5. project is appropriate to the Iraqi community environment where the changing environment and estimates of project success must be more proportional than failure.
6. More successful in small projects and more flexible to find alternatives that chive project success.

Any worker in any profession always makes sure the necessary tools are in the tool kit. Project management does not differ from this example much, just as there are strengths and weaknesses in both the PMBOK Guide and the PRINCE2 Manual, and project management practitioners must learn any "tool" It would be better to use it depending on the surrounding conditions and idea.

References

[1]AXELOS 2014 UK (wikipedia)
[2] Environmental impact assessment (EIA) ,Lenzen,M,Murray,S.;Korte B.;Dey,C.:A^Guide to best professional practices.
[3] PMBOK® Guide 7.0 from (PMI) Project Management Instiute (United State)
[4] PRINCE2, Meshaal Almanie 2018 10 November / Transformation Stattragy Progect Lenked in 2021.
[5] Basic Guide PRINCE2 for Dummies /Nic Graham
[6] PRINCE2, for Beginners Btyan Mathis
[7] Frank Turley Practitioner Level. The PRINCE2 Coach
[8] PMBOK Guide ver 7.0 2017,PMI
[9] PMBOK Guide ver 7.0 2017,PM
[10] PMBOK Guide ver 3.0 2013,PMI
[11] PMBOK, http//www.pmi.org
[12] PRINCE2 Sudy Guide bu Divide Hinde 5 june 2018 web sit id.Loc.gov.Isbn 10:111942089978-111942089608.
[13] PRINCE2 Guide Registerd Practitioner AMBCS, Yassin Abbas 2015, Knowledge TRAIN July 30/7 PPM

[14]PRINCE2 Process Map:English ,web:www.ilxgroup.com;AXLOS 2009-2014.
[15]Managing Successful Project with Prince2 :6th edittion Auther :AXELOS.,Great Britain Office.2014 UK,(Wikipedia).
[16]basic Guide /Prince2 for Dummies/Nic Graham
[17]http//www.axelos.com
[18]http:www.goodelearning.com
[19]info@longhallconsulting.com by Longhall Consulting limited Plot 1-7,Muri Okunola street,Victoria Island.
[20]www.Kowledggetrain.com.
[21]https://ae.linkedin.com.
[22]ABAD network for Training ,abadnet.com.sa
[23]www.simplilecarn.com
[24]PRINCE2 Foundation,6th edition ,https://www.peopecert.org
[25]https://www.quora.com
[26]https://www.prince2.com ,UK
[27]www.Knowledgetrain.com
[28]Prince2 Methodology in Project Management –A Complete Overview ,published on September 24,2021.project copyright 2021 Kissflow.Inc .
[29]Managing Successful Project with Prince2 ,Great Britain Office,number 9.
[30]Prince2 Key benfet ,21 Jul 2021 by Simon Buehring

Analytical Procedures and Their Impact on Reducing Audit Risks in the Auditor's Report

Sawsan Fadel jassim [1] , Alaa Fareed Abdulahad [2]

{sawsan.alansary@fgs.stu.edu.iq [1], alaabotto@stu.edu.iq [2]}

Faculty of Graduate Studies , Southern Technical University , Basra , Iraq [1] , Management Technical College, Southern Technical University, Basra, Iraq [2]

Abstract : The research aims to identify the concept of analytical procedures in the audit process, and the impact of their various uses in reducing audit risks in the auditor's report. The research sample was represented by a groupof auditors 'reports for a number of mixed and private joint stock companies listed in the Iraqi Securities Commission . In its practical and applied side, the study found that the diversity in the use of analytical procedures contributes to reducing the audit risk in the auditor's report, by increasing the confidence of the beneficiaries of the financial statements that they are free from the risks of discovering fundamental misstatements that affect the fairness of presenting that data. Where the use of different analytical procedures reduces the various risks to whichthe financial statements are exposed and enhances the honesty and fairness of their presentation.

Keywords : audit, analytical procedures , risk, Basra

1. Introduction

Analytical procedures as an audit method have recently attracted the interest of practitioners, academics, and standard setting committees. This is partly due to auditors' search for appropriate ways to reduce audit costs without sacrificing the high quality of audit services [1] . Also, the application of analytical procedures is one of the methods available to the auditor to obtain a deeper view of the entity , and can lead to more efficient and effective audits [2]. In addition, analytical procedures have the ability to provide critical information in order to evaluate past and present performance, as well as to identify warnings about the entity under audit in order to take appropriate action [3] . Moreover, one of the factors that oblige auditorsto use analytical procedures in auditing are the constraints imposed by the time frame of audit work and the great development of computing tools available to auditors [4] . Analytical procedures play an important role in a risk-based audit approach. It directs attention to areas of high risk and helps identify audit issues that the detailed audit procedures have not been able to detect. It also helps in evaluating the final audit results and providing objective evidence. Analytical procedures can also be a relatively inexpensive way to increase the auditor's confidence in the validity of the balances that are disclosed. Analytical procedures

IMDC-IST 2021, September 07-09, Sakarya, Turkey
Copyright © 2022 EAI
DOI 10.4108/eai.7-9-2021.2315296

can range from surveying and comparing information by an experienced auditor to applying different statistical models , Analytical procedures are also of critical importance in assessing the level of risk so that the auditor can use this risk assessment to design procedures for gathering appropriate audit evidence and reducing risks when expressing his neutral technical opinion on the financial statements [5].

2. Research Methodology

2.1 Research Problem: Analytical procedures are one of the means to obtain proof of evidence in the auditing process that the auditor practices in performing the audit task of the entity, especially in the most important pillar of auditing, which is examination and evaluation. These procedures help in analyzing the entity's activity and the extent of potential risks, as well as identifying areas of potential errors in the financial statements, and enabling the auditor to express his neutral technical opinion on the extent of the sincerity and fairness of the financial statements. Accordingly, the research problem can be summarized by the following question: To what extent does diversity in the use of analytical procedures contribute to reducing audit risks in the auditor's report?

2.2 Research Importance: The importance of this study stems from the fact that it sheds light on the topic of analytical procedures, which is one of the most important tools and methods for gathering evidence. This is because it is applied in all stages of the audit (planning, examination, expressing an opinion), as well as drawing the auditor's attention to unusual matters in the financial statements, and its role in reducing risks.

2.3 Research Aims: The main objectives of the research can be identified as follows: (1) Understand the concept of analytical procedures in the audit process. (2)The effect of using various analytical procedures to reduce audit risks.

2.4 Research Hypothesis: In light of the problem and objectives of the research, the following main hypothesis can be formulated: The diversity in the use of methods of analytical procedures leads to reducing the risk of auditing the auditor's report.

2.5 The Research Sample: The research sample was represented by a number of auditors' reports for the Office of Financial Supervision and private auditing offices issued by the Securities Commission inIraq for mixed and private shareholding companies for the fiscal years 2018-2019.

3. Previous Studies:

A study (Samaha & Hegazy2010)[1] entitled:" An Empirical Investigation Of The Use Of ISA 520 “Analytical Procedures” Among Big 4 Versus Non-Big 4 Audit Firms In Egypt" This study aimed to study International Auditing Standard No. 520 related to analytical procedures and to adapt it to analytical procedures in the context of the Egyptian audit environment. It also aimed to examine the extent to which analytical procedures are used in Egypt during the

three audit stages, according to the size of the entitys and the number of their employees. The results of the study showed that there is a relative decrease in the use of analytical procedures by account auditors in Egypt. The study also foundthat despite the auditors' conviction in Egypt of the usefulness of using analytical procedures during theaudit process, they doubted the feasibility of using them during the detailed testing phase. The auditors in Egypt also indicated that the international auditing standard 520 did not affect the audit profession in Egypt so much. The study recommended educating the auditors in Egypt by using analytical procedures in the audit process. Pinho (2014)[4] study entitled: (The Usefulness of Analytical Procedures - An Empirical Approach in the Auditing Sector in Portugal) The study aimed to identify the practices adopted in Portugal by the entities responsible for conducting financial audits (auditing firms or individual auditors), in terms of the use of analytical audit procedures during the various auditing stages. A survey was prepared and sent by e-mail to the auditors regarding the implementation aspect. This study found that account auditors in Portugal use analytical procedures frequently in the planning .A study (Al-Abdoun et al. 2018)[6] entitled "Analytical procedures in auditing and their implications for the continuity of establishments according to the perspective of the quality of financial reports - a field study on external audit offices operating in Iraq."stage, and not in the other two auditing stages. The study aimed to identify in a comprehensive way the role played by the analytical procedures by the auditing offices operating in Iraq in achieving the quality of financial data and its reflection in the possibility of judging the continuity of entities by the auditor. The application of analytical procedures has a positive role in achieving the quality of the financial statements, ensuring the ability to judge the continuity of entities by the auditor on the financial entities subject to audit. A study (Hryhoruk, et al, 2019)[7](Organization Of Analytical Procedures At The Audit Of Continuity Of The Enterprise Activity) The study aimed at theoretical proof and the development of methodological recommendations to improve the organization of analytical procedures in auditing the continuity of the entity. The study concluded that analytical procedures should be implemented in all stages of auditing financial statements through different methodological methods of economic analysis. Their types, contents and size depend on manyfactors. The study also concluded that the auditor should follow the required quality control policies and procedures to ensure that the audit procedures are carried out in accordance with the professional standards of auditing.

4. The Theoretical Framework for the Analytical Procedures, Auditing Risks, and the Auditor's Report

4.1 The Concept of Analytical Procedures : They are tests or procedures aimed at verifying the reasonableness of the carrying value of one of the items of the financial statements in light of the valueestimated by the auditor for that item [8], and it also defined as the science of detecting and analyzing patterns, identifying anomalies, and extracting other useful data in the basic data or related to the subject of auditing through analysis, modeling and visualization for the purpose of planning or conducting an audit[9] , and others defined it as a procedure consisting of analyzing important results and studying deviations and correlations, as well as diagnosing the development of entity trends[7].The researchers believe that the analytical

procedures are the various analytical methods, indicators and ratios that contribute to converting data into audit evidence that can be used in making audit decisions represented in the auditor's opinion on the entity's financialstatements.

4.2 The Importance of Analytical Procedures : Analytical procedures are very important in the auditprocess, and their importance is highlighted by the following [10] : (1) Analytical audit procedures are one of the means that an auditor may resort to in order to identify the weaknesses and strengths of the entity subject to auditing. (2) Assisting the auditor in improving the quality of the audit process. (3) The auditor can, through analytical procedures, evaluate the performance of his assistants, uncover shortcomings in their work, search for their causes and correct them.(4) Increasing theauditor's ability to detect errors. (5) It has great importance in managing the entity, as it helps it discoverthe deficiencies within the entity, and then correct them.

4.3 Types of Analytical Procedures : There are many types of analytical procedures as follows [11] : (1) Comparing the data of the entity subject to the audit with the data of the entities practicing the same activity. (2) Comparing the data of the entity subject to auditing with the corresponding data in the previous period. There are several types of comparisons in this type of analytical procedures, which are as follows: A - Comparing the balance of the current year with its equivalent in the previous year. B - Comparing the detail of the total balance with the equivalent in theprevious year. C - Calculations of percentages and financial ratios of the relations and compare them with previous years. (3) Comparing the data of the audited entity with its expectations. (4) Comparing the data of the entity subject to the audit with the expectations of the auditor.(5) Comparing the data ofthe entity subject to auditing with expectations using non-financial data. The researchers believe that the use of a specific type of analytical procedures depends largely on the personal judgment of the auditor, through his experience and the extent to which they can be employed in choosing the appropriate type of analytical procedures that are commensurate with the subject to auditing.

4.4 Methods of Analytical Procedures: Three levels of analytical procedures can be used [12] : (1) Descriptive analytical procedures (non-quantitative): for example, inquiring and obtaining expectations from previous audit results, auditing external (non-quantitative) information, and auditing internal (non-quantitative) information. (2) Simple quantitative analytical procedures: It isalso several types, including analysis of financial ratios such as (liquidity, activity, profitability, financing ratios, etc.), horizontal analysis, vertical analysis, estimated trend analysis, predictive testing, and budget deviation analysis. (3) Advanced quantitative analytical procedures methods: These methods include regression analysis, time series analysis, financial planning model and cash flow model.

5. Audit Risks:

5.1 The Concept of Audit Risk : Audit risk is the risk that the auditor will issue an unqualified opinion when the financial statements of the entity contain material misstatements [13] , And others also defined it as the risks of an auditor expressing an inappropriate audit opinion when the financial statements are materially misstated [14] . Auditrisk has also been defined as the risk that an auditor may make mistakes in expressing his opinion about the accuracy and correctness of the information presented in the financial statements [15] .

5.2 Types of Audit Risks : (1) Inherent Risk: (IR) The inherent risk is defined as the susceptibility of aparticular account balance or a particular type of transaction to error, which would be material if it is combined with errors in other balances or other types of transactions, with the absence of internal control procedures related to it [16] . (2) Control Risks: (CR) It is the process of estimating the auditor's probability of discovering errors that exceed the acceptable limit in a certain setof data in a timely manner by the internal control system [17] . (3) Detection Risks: (DR) Detection risk is defined as the risk that the auditor's objective procedures do not discover a misstatement existing in the account balance or a class of transactions that may be major, individuallyor when combined with misstatements in other balances or classes [18] .

5.3 Assessment of Audit Risks : There are four audit risk assessment tasks, which are as follows[18]: (1) Identify risks by developing an understanding of the entity and its environment, including relevant controls relating to risks, analysis of strategic risks and categories of significant transactions. (2) Relate the identified risks to what could misstate management's assertions about the existence, evaluation and measurement of transactions or assertions about rights, obligations,presentation and disclosure. (3) Determine whether the risks are of such a magnitude that they could lead to a material misstatement of the financial statements. (4) Considering the possibility that risks may lead to material misstatement of the financial statements and their impact on classes of transactions, account balances and disclosures.

5.4 Audit Risk Model (ARM) The three components of audit risk can be expressed in a theoretical model designed to help auditors understand how the assessment of each component affects the overall audit risk faced by the engagement [19] . The audit risk model that provides a framework for assessing the relationship between overall audit risk, inherent risk, control risk, and discovery risk suggests that even when deficiencies in internal control are identified, auditors can still provide an unqualified opinion by increasing their objective testing [20] . The interdependence of the three components of the audit risk model can be expressed in the figure below, which expresses the amount of audit evidence to be collected (or not collected) by the auditor for the purpose of providing reasonable assurance [21] .

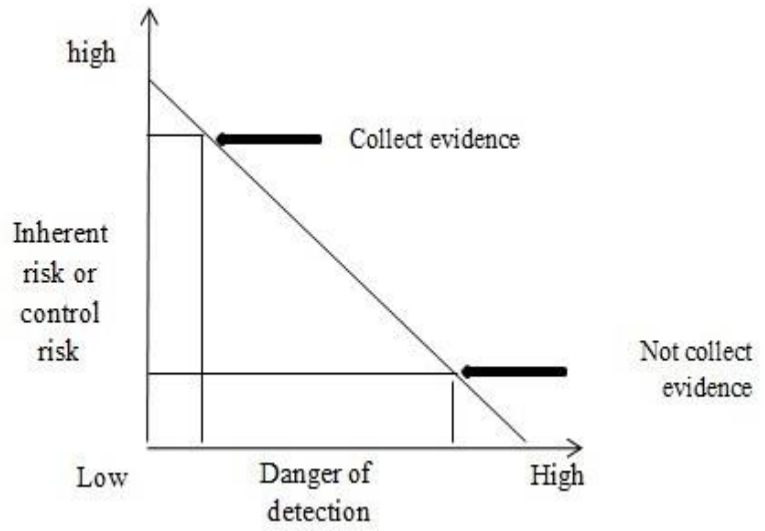

Figure (1): The relationship between inherent risks, control risks, and detection risks[21]

6. The Auditor's Report

6.1 The concept of the Auditor's Report : The auditor's report is a report that provides an opinion onwhether the entity's financial statements and related disclosures are presented in accordance withgenerally accepted accounting principles, and this opinion is based on the control tests and objective procedures that were performed during the audit process [19] . It is also defined asthe auditor's opinion as to whether the annual financial statements give a true and fair view in accordance with the appropriate framework and, where appropriate, and whether the annual financial statements comply with the legal requirements [22].

6.2 Types of the Auditor's Report : The auditors may express four types of opinions [19] : (1) Unreserved opinion: the auditor concludes that the financial statements present the financial position, results of operations and cash flows in accordance with generally accepted accounting principles. (2) Reserved opinion: The conclusion is that, with the exception of one or moreissues, the financial statements present the financial position, results of operations and cash flows in accordance with generally accepted accounting principles. Qualified opinions use the phrase except to describe issues that lead to a reservation. (3) Negative opinion: in which the auditor concluded that thefinancial statements do not present the financial position, results of operations, and cash flows in accordance with generally accepted accounting principles. (4) Refusal to express an opinion: the auditors do not express an opinion on the fairness of the entity's financial statements .

7. The Applied Aspect of Research

This axis extrapolates the most important observations, reservations and clarifications found in the auditors' reports for the research sample, which was represented by a number of mixed and private joint-stock companies. It will deal with both the reports of the Federal Office of Financial Supervision concerning mixed joint-stock companies and the reports of the private audit offices, which concern the private joint-stock companies for the two fiscal years 2018-2019. This axis will be a practical identification of the types of analytical procedures that are used by the auditors in their reports and theirreflection in reducing audit risks.

7.1 Extrapolation of the auditors' reports (Ban of Financial Supervision / Mixed Joint Stock Companies) : Report of the Financial Supervision Bureau of the Iraqi Company for the Production andMarketing of Meat and Field Crops.

7.1.1 Notes, reservations and clarifications for the fiscal year 2018

Note (1): The management report's lack of many indicators required to disclose the reality of the company's activity and the extent of developments taking place in it, contrary to the requirements of Accounting Rule No. (6) issued by the Accounting and Regulatory Standards Board in the Republic of Iraq regarding (disclosure of information related to financial statements and accounting policies) . Analytical procedure: The analytical procedure used in this note represents a descriptive (non- quantitative) analytical procedure by referring to the accounting rules.The risks it limits: Referring to the accounting rules as an analytical procedure contributes to reducing the risks of discovering violations of the requirements of the rules that should be applied.

Note (2): The company's delay in holding the general assembly meeting for the purpose of discussing and approving the company's financial statements for the year ended on 31/12/2017 issued by the Federal Office of Financial Supervision by virtue of its book No. (B 8/29/27/10438) on 5/20/ 2018 fora period of 159 days. The meeting was held on December 29, 2018 of Article (135) of the Companies Law No. (21) of 1997 (amended), as explained in paragraph (5-a-first) of the report on page (7).

Note (3): The company was late in approving the planning budget, as it approved it on 4/16/2018, contrary to Article (117 fourth) of the amended Companies Law No. (21) of 1997. As explained in paragraph (5-a-third) of the report on page (8). Analytical procedure: The analytical procedure used in the previous notes also represents a descriptive (non-quantitative) analytical procedure, but by referringto the applicable laws represented by the Companies Law. Risks Reduced: This analytical procedure contributes to reducing the risk of discovering violations of the laws for which financial statements should be prepared in accordance with their requirements.

Note (4): The Company has not performed tax accounting for its activities for the fiscal year/2017, in violation of Income Tax Law No. (113) for the year 1982 (as amended). } As

explained in paragraph (5-b) of the report on page (8) Analytical procedure: The analytical procedure used represents a descriptive (non-quantitative) analytical procedure, but by referring to the applicable laws represented by the tax law. The risks it limits: This analytical procedure contributes to reducing the risks of discovering violations of the laws that must be adhered to.

Note (5): There is no proportionality between the allowance account for doubtful debts, the balance of which is (5123) thousand dinars (five million, one hundred and twenty-three thousand dinars) and revolved from previous years, and the balance of the debtors account amounting to (5072629) thousanddinars (five billion seventy-two million Six hundred and twenty-nine thousand dinars as on December 31, 2018. Analytical procedure: The analytical procedure used in the two previous notes represents a simple quantitative analytical procedure (horizontal analysis) by comparing the balances of the year subject to audit with the balances of previous years. Risks that it limits: This analytical procedure contributes to reducing the risk of discovering material misstatements in the account balances referred to in the previous two paragraphs.

7.1.2 Notes, reservations and clarifications for the fiscal year 2019

1. **Financial statements:** By matching the financial statements and analytical statements with the trial balance for the year under audit. We noticed an increase and decrease between the balances recorded in the financial statements presented to us. And the trial balance, despite the reference to it in our report for the previous year, shows the number (B/8/29/27/12584) on 30/5/2019 regarding the financial statements for the year 2018. 30/6/2020 and indicated that it will address these differences in the following year, as shown in the table below.

Table 1: Differences in account balances for the Iraqi company for the production and marketing of meat and field crops for the year 2019 .

the difference /dinars	Balance undertrial balance	Balance under dinars	List name or statement	Account name	Accounting guide number
(1)	2538992359	2538992358	fixed assets	12/31building cost	112
1	520272358	520272359	fixed assets	machinery and equipment12/31	113
2	132472981	132472983	Fixed assets	The cost of transportation in 12/31	114
1	1058779742	1058779743	Fixed assets	Building allowance balance in12/31	2312
1	1700492582	1700492583	Fixed assets	Accumulated depreciation allowance	231
(1)	3034028353	3034028352	reserves	Reserves	22

Source: The Iraqi Securities Commission

Analytical Procedure: In this note, two types of analytical procedures were used. The first is a simple quantitative analytical procedure by comparing data and discovering differences, while the second is a non-quantitative procedure represented by inquiry from the responsible authorities in the company . **The Risks That it Limits:** The analytical procedures used in this note contribute to reducing the risks of discovering major misstatements in the account balances referred to in the previous table.

2. **Management Report:** The report of the Board of Directors submitted on the company's activity for the year ended December 31, 2019 still lacks some information and indicators, which constitutes a violation of Accounting Rule No. (6) issued by the Accounting and Regulatory Standards Board in the Republic of Iraq regarding (disclosure of information related to financial statements And the policies and below are the most important of those indicators: (1) Disclosure ofthe investment return with a statement of its development for at least three years. (2)A statement ofthe debts owed by others and the amounts collected during the year.(3) activities and expansions during the year and in the near future.Analytical procedure: The analytical procedure used is a descriptive (non-quantitative) procedure, which is to review the accounting rules to ensure their application.The risks it limits: This procedure limits the risks of discovering a major misstatement,which is a violation of accounting rules.

3. **The Result of the Company's Activity:** The result of the activity for the current operations (the first phase of the operational activity showed a surplus of) (366,468) thousand dinars (three hundred and sixty-six million four hundred and sixty-eight thousand dinars), an increase of (5,301)thousand dinars (five million three hundred and one thousand dinars, at a rate of 15% over the previous year of (361167) one thousand

dinars (three hundred and sixty-one million, one hundred and seven Sixty thousand dinars) while the result of the activity in (the second phase / total activity) was a surplus of (640552) one thousand dinars (six hundred and forty million five hundred and fifty two thousand dinars) with an increase of (201515) one thousand dinars (one hundred eighty million one hundred and thirty five thousand dinars)) at a rate of (39%) for the previous year, which amounted to (640418) thousand dinars (sixty-four million four hundred and eighteen thousand dinars. Our study of the results of the activity showed the following indicators:

(A) An increase in the current activity revenue account by (152452) thousand dinars (one hundred and fifty-two million four hundred and fifty-two thousand dinars) and at a rate of (15%) over the previous year of (1017,836) thousand dinars (one billion and seventeen million eight hundred and thirty-six thousand dinars). The increase in the account of the revenue from the sale of waste, the revenue of various services, the rent of fixed assets (except for lands), and the increase in the interest on the lease of credit lands as a result of the company fixing its dues.Analytical procedure: The procedure used in this note is the horizontal comparison between two years for the same account.The risks it limits: This measure contributes to limiting the detection of major misstatements in the account in question.

(B) The results of implementing the planning budge**t:** The table below shows the revenues, expenses and profit achieved from the company's activity compared to what is planned under the company's planning budget for the year subject of the report:

Table 2 : Comparing the planned and actual revenues and expenses of the Iraqi company for the production and marketing of meat and field crops for the year 2019.

(% 1/3per.)	difference / Thousand dinars(3)	Actual amount/ Thousand dinars (2)	planned amount /Thousand dinars (1)	Statement
(88)	(684443)	1463364	778921	Revenues
(54)	(288337)	822812	534475	Expenses
(162)	(396106)	640552	244446	Profit

Source: The Iraqi Securities Commission

It is evident from the above table that: Inaccuracy in preparing the planned estimates for some accounts, as shown in the table below, according to the company's response to our inquiry No. (2) on 9/3/2020:

Table 3: The company's answer to the inquiry of the Office of Financial Supervision .

Company's answer	per,) 1/3 (%	Difference thousand dinars	Actual amount thousand dinars (2)	Planned no. thousand (1) dinars	Name of account	No. Of guide
The reason for this is due to the settlement of some amounts related to the fiscal year 2014	(11)	2292	19458	21750	transfer expenses	38
The reason is due to the calculation of profits received from the Iraqi Company for Seed Production at a rate of (50%), while profits were received at a rate of (20%) .only	(33)	(29478)	61142	90620	Benefits and rentals	46

Source: The Iraqi Securities Commission

Analytical procedure: The analytical procedure used in the above paragraph is to compare the data of the entity under audit with its expectations by comparing the planning budget figures with the actual figures in order to verify the correctness of the balance.**The risks that it limits**: This analytical procedure contributes to reducing the risks of discovering major deviations in the actual account balances from what is planned.

7.2 Extrapolating the auditors' reports (private auditing offices / private joint stock companies)

(A) Report of the auditor of the Iraqi Company for Carpets and Furniture

Notes, reservations and clarifications for the fiscal year 2018

Note (1): The management report is in agreement with the Companies Law No. 21 of 1997 as amended. Analytical procedure: The analytical procedure used in the analysis of this illustration represents a descriptive (non-quantitative) analytical procedure through reference to the applicable laws. The risks that it limits: This analytical procedure contributes to reducing the risks of discovering violations that include misrepresentation in the financial statements as a result of non-compliance with laws.

Note (2) : The stock of the finished production was evaluated at the end of the period at the cost of manufacture. As for the incomplete production, it was evaluated according to the stages of production, according to the principles adopted in this field and based on the accounting rule No. (5) issued by the Accounting Standards and Rules Board in the Republic of Iraq**.**

Analytical procedure: This clarification refers to the auditor's reference to the accounting rules as a descriptive (non-quantitative) analytical procedure**. The risks it limits:** This procedure contributes to reducing the risks of discovering major violations resulting from non-

compliance with accounting rules.

Note (3) : The results of executing the company's production plan showed that no actual results were achieved for the planned quantities of carpet products, floor furnishings, and filters, noting that the planning was done for the entire available capacity and the following table shows:

Table 4: The planned and actual production capacity of the Iraqi Company for Carpets and Furniture for the years 2017-2018

2017		2018		measuring unit	Product Type
outlet	Planed	outlet	Planned		
-------	2000	--------	2000	M^2	Carpet
-------	3000	--------	3000	M^2	Furniture and flooring
2200	5000	2200	5000	M^2	Filters

Source: The auditor's report published in the Iraqi Securities Commission

Analytical Procedure: In the above note, a comparison between the planned figures is used in theentity's estimated and actual budget. Another procedure is used, which is horizontal analysis by comparing two different years for the same accounts**. Risks that it limits:** The aforementioned procedure contributes to reducing the risk of differences between what is planned and the actualnumbers, and thus discovering deviations, if any.

Notes, reservations and clarifications for the fiscal year 2019.

Note(1): The management report is in agreement with the Companies amended Law No. 21 of 1997. Analytical Procedure: The previous analytical procedure represents a descriptive (non-quantitative) analytical procedure by referring to the applicable laws and comparing them with the data of the entity subject to auditing. Risks that it limits: This procedure contributes to reducing the risk of discovering violations that include material misstatement of the financial statements as a result of non-compliance with laws.

Note(2): The stock of finished production was evaluated at the end of the period at the cost of manufacture. As for the incomplete production, it was evaluated according to the stages of production according to the principles adopted in this field and based on the accounting rule No. (5) issued by the Accounting Standards and Rules Board in the Republic of Iraq. Analytical procedure: This clarificationindicates that the auditor performed a descriptive (non-quantitative) analytical procedure, represented by indicating the extent of compliance with the accounting rules. The risks that it limits: This procedurewill enhance the confidence of the users of the financial statements that the company has carried out itsbusiness in accordance with the accounting rules, and also contributes to reducing the risks of discovering material violations resulting from non-compliance with the accounting rules.

Note(3): The results of the implementation of the company's production plan showed that no actual results were achieved for the planned quantities for each of the carpet products, floor furnishings and filters, noting that planning was done for the full available capacity and the following table shows:

Table 5 : The planned and actual production capacity of the Iraqi Company for Carpets and Furniture for the years 2018-2019

2018		2019		Measure unit	Product type
outlet	planned	outlet	Planned		
-------	2000	--------	2000	M^2	Carpet
-------	3000	--------	3000	M^2	Carpet and floor
2200	5000	3000	5000	M^2	Filters

Source: The auditor's report published in the Iraqi Securities Commission

Analytical procedure: The comparison between the planned and the actual is the procedure used in the previous note in addition to the comparison between two consecutive years. Risks that it limits: The aforementioned procedure contributes to reducing the risk of discovering differences between what is planned and the actual numbers, and thus discovering deviations, if any.

(B) The report of the auditor for Al-Zorah Financial Investment Company / private shareholding

Notes, reservations and clarifications of the financial statements for the year 2019

Note (1) The result of the company's activity for the current year showed a deficit of (5,777,981) dinars, thus the accumulated deficit amounted to (479474) 121 dinars, and after adding the amount (704445243) dinars, which represents the decrease in the allowance for depreciation in the value of investments, the total accumulated deficit becomes (825924717) Dinars, at a rate of (72% of the capital), which requires observing the first paragraph of Article (76) of the amended Companies Law No. 21 of 1997. Analytical Procedure: A descriptive (non-quantitative) analytical procedure was used, represented by reference to the applicable laws, which is the Companies Law. Risks limits: The use of the previous analytical procedure contributes to reducing the risk that the financial statements include violations of laws.

Note (2) The company has taken adequate measures to prevent money laundering or terrorism financing, and these measures are being implemented in accordance with the Money Laundering Law No. 39 of 2015 and the regulations and instructions issued by the Central Bank of Iraq. Analytical Procedure: A descriptive (non-quantitative) analytical procedure represented by reference to the applicable laws, which is the Money Laundering Law. Risks limits: The use of the previous analytical procedure contributes to reducing the risk that the financial statements may include violations of laws.

8. Conclusion

In light of the analyzed data, the researchers conclude that the diversity in the use of analytical procedures contributes to reducing the audit risk in the auditor's report, by increasing the confidence ofthe beneficiaries of the financial statements that they are free from the risks of discovering fundamentalmisstatements that affect the fair presentation of that data. The use of different analytical procedures reduces the various risks to which the financial statements are exposed and enhances the truthfulness and fairness of their presentation. In addition, the researchers also conclude that there is a discrepancy between the use of analytical procedures in preparing reports by auditors in the Office of Financial Supervision, and their use by auditors in private audit offices. As methods of quantitative and non- quantitative analytical procedures are used on a larger scale in the reports prepared by the auditors in the Office of Financial Supervision, while their use in private audit offices is limited to minor observations, and there is a weakness in the use of quantitative analytical procedures, as most of the procedures used are They are descriptive (non-quantitative) procedures. Based on the previous conclusions, the researchers recommend the necessity of using analytical procedures by the account auditors when auditing the financial statements of the entities subject to auditing, and the diversity in theiruse, taking into account that they are compatible with the accounts balances that are being audited. Thisconfirms the validity of the research hypothesis.

References

[1]Samaha , K. & Hegazy, M. (2010). "An Empirical Investigation Of The Use Of ISA 520 "Analytical Procedures" Among Big 4 Versus Non-Big 4 Audit Firms In Egypt." Managerial Auditing Journal.

[2] Kritzinger, J. A. (2016) " The application of analytical procedures in the audit process " (Doctoral dissertation, University of Pretoria).

[3] Moolman , A. M. (2017). "The usefulness of Analytical Procedures, other than ratio and trend Analysis, for Auditor decisions ". International Business & Economics Research Journal (IBER), Vol (16) , NO (3) .

[4] Pinho , C. (2014) . " The Usefulness of Analytical Procedures - An Empirical Approach in the Auditing Sector in Portugal " 24-33 .

[5] Lusk , E. J., & Halperin , M. (2016) " Client risk calibration in PCAOB audits: an analytical procedures panel risk assignment protocol." International Journal of Auditing Technology 3.1: 1-21.

[6] Al-Abdoun, H. F. & Mansour, Abdul Rahman Al-Bakri & Hussein, Sat Salih(2018). " analytical procedures in auditing and their implications for the continuity of enterprises according to the perspective of the quality of financial reports - a field study on external audit offices operating in Iraq" Journal of Graduate Studies / Al-Nilein University, Volume (11), Issue (42).

[7] Hryhoruk, P. M., Perevozova, I. V., Prystupa, L. A., Abesinova, O., & Melnyk, N. (2019)." Organization of analytical procedures at the audit of continuity of the enterprise activity".

[8] Abu Samhadana, N. A.(2006) . " The fields of contribution of the use of analytical review in planning and performing the audit process - an analytical study of the opinions of auditors in audit offices and companies inthe Gaza Strip – Palestine" Master Thesis of the Islamic University - Gaza / Faculty of Commerce.

[9] Li, H., Dai, J., Gershberg, T., & Vasarhelyi, M. A. (2018). "Understanding usage and value of audit analytics for internal auditors: An organizational approach. International Journal of Accounting Information Systems, 28, 59-76.

[10] Musa, Ali M. (2013). (Analytical review procedures and their role in rationalizing the personal judgment of the references), The Whole Journal, Issue (2), Volume (15).

[11] Arens , Alvin A , Randal J. Elder , Mark S. Beasley , Chris. E. Hogan.(2017). " Auditing And Assurance Services - An Integrated Approach " 16 TH Edition Prentice Hall .
[12] Ayat, Asma. (2015). " the use of analytical procedures in auditing and the quality of financial reports - a case study of the Sidi Arghis Mills Foundation" (Master Thesis of Umm El-Bouaghi University / College of Economic Sciences, Business Sciences and Management Sciences .
[13] Willekens , M. (2011) . " Discussion of "Short Interest as a Signal of Audit Risk " Contemporary Accounting Research , Vol (28) , No (4): 1298-1303.
[14] Okeyo & Awino , L. (2014) . " Audit risk assessment and detection of misstatement in annual reports for audit firms registered by Rab in Nairobi County " , Kenya Okeyo, Inda. Diss. Egerton University.
[15] Nikolovskia , P. & Zdravkoskib , I. & Menkinoskic , G. & Dičevskad , S. & Karadjova , V.(2016). " The concept of audit risk " International Journal of Sciences: Basic and Applied Research (IJSBAR) , Vol (27) , No (1): 22-31.
[16] Al-Quraishi, I. R. (2011). " external audit / scientific, theoretical and applied approach", Al-Muizz House for Printing and Publishing / Depository Number in Dar Al-Kutub in Baghdad 716.
[17] Younes, Z. & Issa, Z.(2016). (The risks of the audit profession on the quality of the audit - an analytical study of the opinions of a sample of external auditors in Algeria) Economic Visions Journal / University of the Martyr Hama Lakhdar, El-Oued, Algeria Issue (11) .
[18] Hayes , R. & Dassen , R. & Schilder , A. & Wallage, P . (2005). " Principles Of Auditing - An Introduction to International Standards on Auditing " 2TH Edition .
[19] Louwers , T.J. & Blay , A. D. & Sinason , D. H. & Strawser , J. R. & Thibodeau , J. C. 2018. " Auditing & Assurance Services " 7TH Edition .
[20] Hogan, C. E., & Wilkins , M. S. (2008). " Evidence on the audit risk model: Do auditors increase audit fees in the presence of internal control deficiencies? " Contemporary Accounting Research , Vol (25) , No (1): 219-242.
[21] Zaiceanu, A. & Hlaciuc, E. & Lucan , A. N.C. (2015) . "Methods for risk identificationand assessment in financial auditing." Procedia Economics and Finance , Vol (32): 595-602 .
[22] Muñoz – Izquierdo , N. & Segovia-Vargas, M. J. & Pascual-Ezama , D. (2019). " Explaining the causes of business failure using audit report disclosures" Journal of Business Research Vol (98) : 403 – 414.

The Role of Internal Control in Reducing Administrative and Financial Corruption Applied Research at the Technical Institute / Nasiriya

Hamida Athab Khudair[1], Ali Khalaf Gatea[2]
{Hameedah.athab@stu.edu.iq[1], ali.khalaf83@stu.edu.iq[2]}

Southern Technical University - Technical Institute / Nasiriya[1,2]

Abstract. The research aims to identify the role of internal control in reducing administrative and financial corruption, the necessity of diagnosing its causes, how to eliminate or reduce the phenomenon of corruption, and how to optimally use the institution's resources, as a questionnaire was designed to determine the nature of the relationship between internal control and administrative and financial corruption. Supporting the research hypotheses and reaching the most important conclusions that support the objectives of the research, which states that corruption negatively affects the stability of the social and political system and limits its ability to respect citizens' rights, equality, and equal opportunities. The research also recommended the necessity of paying attention to social upbringing and instilling the prevailing cultural values that establish morals and positive behaviour in society and spreading the advanced civilizational awareness that rejects corruption of all kinds.

Keywords: Internal Control, Individuals, Organizational Structure, Legal Reform, Administrative Procedures.

IMDC-IST 2021, September 07-09, Sakarya, Turkey
Copyright © 2022 EAI
DOI 10.4108/eai.7-9-2021.2314937

1 Introduction

The issue of administrative and financial corruption is a complex topic. Researchers differ on how to diagnose, analyse and suggest appropriate solutions to combat it. Corruption has become a global phenomenon at the level of states and individuals, in addition to its negative effects in reducing the effectiveness of political decisions, weakening the moral and ethical authority of society, and reducing the phenomenon of corruption. The administrative system will be a goal and a means to reach other goals related to the judiciary or mitigating the severity of this phenomenon because of its societal impact, and if governments are interested in fighting administrative corruption and rationalizing money management, and developing means of control and accountability, the success of this depends on the efficiency of the administrative system that is concerned with setting Objectives, control plans and evaluation, which help to achieve this, so internal control is the starting point at which the auditor begins his work. And financial - and a study of the internal control system and its role in reducing administrative and financial corruption.

2 Previous Studies

A Study (Andersson & Vilo, 2016) "How do Internal Auditors Become Comfortable in Their Role within Risk Management": The study aims at the extent to which the environment surrounding the work of the internal auditor affects the peace of work within the organization, and the provision of assurance, guarantee, and management consultancy services to the higher authorities within the organization, and what are the concerns that they may face, when providing a neutral technical opinion, which can add value to the organization, As a result, adequate safeguards must be provided to protect them from the consequences of expressing an opinion inside and outside the work environment, to make them feel comfortable when performing their role.

A study (Claros, 2013) "Removing Impediments to Sustainable Economic Development the Case of Corruption (removing obstacles to economic development, corruption as a model": The study aims to search for the causes and results of corruption in the process of economic development, by reviewing some of the factors that turned corruption into an influential factor in economic development, by studying the data of a selected group of countries working to combat corruption, over the past two decades and in cooperation with the World Bank. Corruption affects public finances, the characteristics, and the performance of the private sector, and it causes distortions in resource allocation and supply chains.

A study (Samieh & Bastanioour, 2016)" Against Administrative Corruption within Governmental Organizations from Motto to Practice": The study aims to provide solutions to combat administrative corruption by classifying workers, based on explaining the relationship between their awareness and their commitment to the complex situations they face during the performance of their job duties, and relied on a survey of the views of several workers, about patriotism and organizational culture, and the results of the research concluded that the perpetrators of The crime of corruption can be divided into three categories, a category that

includes employees who realize that corruption is a positive phenomenon and do not see it as an ominous and ominous phenomenon, and the category of employees who realize and feel that corruption is a negative phenomenon, and the third category is employees who realize that corruption is a negative phenomenon, but their feeling is uncertain. and commit it.

3 Literature Review

3.1 The Concept of Internal Control

There was no firm agreement on the nature of internal control, as a commercial concept for the provisions of control over private sector activities, or a financial accounting sense, aimed at preserving public property in the public sector[9], but the American Institute of Certified Public Accountants (AICPA) and the Securities and Exchange Commission (SEC) set a starting point in 1934, as an internal control was defined as an independent activity that divides the work of internal controls for organizations and provides advice to achieve goals at the lowest possible cost, and at the same time contribute to improving its operations and uses its controls to verify the risks inherent in the organization. [12], as defined as a process implemented by the board of directors and its delegated personnel to provide reasonable assurance to achieve the highest efficiency and effectiveness of operations within the organization, reliability of financial reporting, and compliance with applicable laws and regulations, [13], while it defines it [6]. It is an evaluation activity that is established within the organization, as a service whose functions include examining, evaluating, and monitoring the adequacy and effectiveness of accounting systems. While we see that internal control is the commitment to the standards, measures, and procedures set by the administration to preserve its assets, and to ensure the accuracy of its records, in addition to achieving the organization's goals related to the reliability of financial reporting.

3.1.1 Internal Control Objectives

The main objectives of the internal control system in auditing practices can be summarized as follows: [9]

a. Managing its business in an orderly and effective manner, including adherence to internal policies.
b. Protecting the organization's assets
c. Prevention and detection of fraud and error
d. Accuracy and completeness of accounting records.
e. Preparing financial information promptly.

3.1.2 Dimensions of Internal Control

There is a set of dimensions that control the effectiveness of the internal control systems within the organization, including the following:

a) Organizational structure: Its presence is the basis of the control process in the organization, to achieve functional independence between the different departments, as well as the separation of functional responsibilities to protect against intentional errors, which must have sufficient flexibility, to allow for adjustments required by

changes in policies and objectives of the organization, and to meet the objectives of internal control [3].

b) Individuals: Individuals are one of the most important factors affecting the effectiveness of internal control systems, whether workers within the organization or individuals with interests and who are involved in acts of corruption, which can be part of the solution in eliminating administrative and financial corruption by evaluating the costs and benefits of their work and making nutrition Reversible to internal control procedures and thus corruption can be effectively controlled [11].

3.1.3 Components of the Internal Control System

The internal control system helps the organization achieve its goals by providing a systematic and disciplined approach to assessing risk management and improving governance processes [4]. The internal control system in small organizations may be less formal and unstructured than in large organizations. The internal control system is as follows [1]:

a. Control environment: The internal control environment is the basic component for all other components because it requires management and employees to demonstrate commitment, integrity, and ethical values.
b. Risk assessment: is the practice of identifying, analysing, and managing risks that could prevent the organization from achieving its goals.
c. Control activities: There is a set of different control activities that can be applied to enhance the application of strong internal control systems, including preventive activities such as the separation of duties, and investigative activities such as bank reconciliations.
d. Information and Communication: Relevant and qualitative information is identified, captured, and communicated promptly, in a way that allows employees to perform their responsibilities, and the organization's management must ensure the immediate link between information related to internal control, which is necessary to improve supervisory performance.

3.2 Administrative and Financial Corruption

There is a consensus that corruption is harmful to society, as it distorts and affects the distribution of income and hinders investment, as well as causes inefficiency, waste of resources, and damage to society. and its organizations and violating regulatory instructions [5]. While corruption was defined in the administrative aspect as the result of illegal acts, deviant bureaucratic behaviour, and the exploitation of workers for their positions and tasks, that is, the exploitation or misuse of the public service for personal gain [2]. From the foregoing, we see that financial corruption is an illegal behaviour related to wasting public money and exploiting it to achieve private interests. As for administrative corruption, it is a behaviour related to administrative and functional deviations in violation of regulations, laws, and controls, to achieve personal interest at the expense of the public interest. Thus, administrative, and financial corruption is a distant behaviour for legal legislation aims to achieve private interests.

3.2.1 The Basics of Reducing Administrative Corruption

There are important basics that help reduce administrative and financial corruption, the most important of which are the following:

a) Administrative procedures: The administrative apparatus is the first affected by corruption, and some measures can reduce the demand for services contaminated with corruption, which make individuals or the private sector resort to illegal activities, and this is done by cancelling or reducing administrative procedures, to facilitate Work in various social and economic fields, and the demand for corrupt activities can also be reduced by enhancing public awareness, as the lack of knowledge and learning is one of the main factors that help in the spread of corruption, so promoting awareness of its harmful effects and the need to combat corruption is among the things It is the optimum achievement of the set goals and is considered one of the contents of internal control to preserve assets from embezzlement and misuse [11].

b) Legal reforms: Legal reform is a process represented in studying existing laws, calling for changes in legal systems and instructions for their implementation, to enhance societal justice or efficiency and integrity in providing services. This term is closely related to law reform bodies or law committees. And work on developing laws to keep pace with the challenges facing the work of organizations, whether in the public or private sectors [14].

3.2.2 Causes of Corruption (Practices)

The causes of corruption in practice must be identified, and special attention will be paid to economic, political, and agency interpretations [5].

a. Economic interpretation: The specific economic variables that have an impact on corruption are very diverse, and are often discussed in the so-called corrupt dependency theories in third world countries, and are caused by the weak level of control as a result of capitalist exploitation, in addition to political tyranny and weak economic development, and the existence of corruption Linked to economic underdevelopment and economic crises that reflect common causes of increased corruption, and thus the debate remains about how economic growth can limit administrative and financial corruption.

b. Political interpretation: The level of corruption is also affected by the political system that deals with it, and among these different political systems there is a general assumption that the level of democracy, leads to reducing or limiting the level of corruption, and this is what Friedrich says in that the degree of corruption varies inversely With the degree of compatibility of the authority, the greater the legitimacy of the authority in society, the less corruption is, while the practices of administrative and financial corruption spread to a large extent in the least democratic countries.

4 Research Methodology

4.1 Research Problem

Phenomena arose related to the improper behaviour of the individual, which is represented by the lack of integrity of individuals (behaviourally, functionally, materially), which is one of the phenomena with a negative impact on the economy, and that weak control makes it an obstacle in the way of progressing development and achieving the set goals, and the research problem lies in the following questions**:**

a) Is administrative and financial corruption practiced in a systematic and coordinated manner in public jobs?
b) Have the causes of administrative and financial corruption been diagnosed?
c) Can successful solutions be developed to address or reduce administrative and financial corruption?

4.2 Research Importance

Corruption in government units leads to waste of resources, slows down the process of economic growth and quality of life, and reduces the value of credibility for state agencies and their sound concepts that were developed for them. Finding means to combat the scourge of financial and administrative corruption, whether at the state level or the level of the organization and the individual.

4.3 Research Object

The research aims to answer the questions of the problem, which can be summarized as follows:

a) Identify the encouraging factors for the spread of the phenomenon of administrative and financial corruption.
b) Identify the role of internal control in diagnosing corruption cases.
c) Coming up with results that help develop successful solutions and eradicate the phenomenon of corruption.

4.4 Research Hypothesis

To reach sound answers and scientific solutions to the problems raised in this research, and to achieve the desired goal, the research seeks to test the following hypotheses:
H1: There is a significant correlation relationship between the dimensions of the independent variable internal control and the dimensions of the dependent variable, administrative and financial corruption.
H2: There is a significant effect relationship between the dimensions of the independent variable internal control and the dimensions of the dependent variable, administrative and financial corruption.

4.5 Limits and Sample Research

a) Relevant supervisory and administrative units at the Technical Institute / Nasiriya.
b) The research sample is represented by (heads of departments, units and divisions, teachers, technicians, and administrators).

4.6 Research Model

Based on the intellectual framework of the literature and considering the research problem and its objectives, it required the construction of a proposed comprehensive model, to diagnose the

relationship between internal control processes, administrative and financial corruption, and the trends of influencing them. The research model included two types of variables, which are as follows:

a) Independent variables: represented by the internal control variables, including (organizational structure, individuals)
b) The approved variables: represented by the administrative and financial corruption variables. Two of these variables have been selected, namely (legal reform, administrative procedures).

5 Data Collection and Analysis

The data processing was relied on the statistical program (spss) to obtain the following:

a. Frequency and percentages and their purpose are to describe the research sample.
b. The arithmetic mean is used to analyse data related to the role of internal control in reducing administrative and financial corruption.
c. Standard deviation to measure the degree of dispersion of the response value of service providers from the arithmetic mean.
d. Correlation coefficient to measure the strength of the relationship between the study variables.

5.1 Describe The Characteristics of The Study Sample

The questionnaire was conducted at the Technical Institute in Dhi Qar Governorate, and the Institute consists of eleven scientific departments and several administrative units, including scientific, financial, self, and other units, and it employs about 400 employees with various certificates. Table (1) indicates the number of forms distributed and retrieved by respondents. The number of the distributed forms was (40), and the number of the retrieved form was (40), which means that the retrieval rate was (100%), and the study sample included some employees of the Technical Institute in Nasiriya. the results were subjected to a statistical analysis based on the outputs of the (SPSS) program and the impact and correlation it contains significant significance at the degree of freedom (0.05), which was as follows :

Table 1. Case Processing Summary.

		N	%
Cases	Valid	40	100.0
	Excluded[a]	0	.0
	Total	40	100.0

Listwise deletion based on all variables in the procedure.
Table (1) shows the SPSS program entries, which were 100% correct.

Table 2. Study sample by gender.

Target	sample variables	Frequency	percentage
gender	Male	**20**	50%
	Female	20	50%
total		40	100%

Prepared by researchers based on the outputs of the spss program

The statistical results presented in Table (2) showed that the percentage of males in the surveyed sample is equal to the percentage of females. As for the age group, the statistical results are shown in Table (3) showed that the percentage of (52.5%) of the sample members was between (31-40) and represented the highest percentage, then came the category (41-50), where it reached The percentage of this category (30%), and the category (51-60) reached (12.5%), then the category (21-30) at the rate of (5%), and the category (25 years and less) reached (3.3%), and the lowest percentage was As for the category (50 years and over), its percentage was zero.

Table 3. The research sample by age group.

Variables	target sample	repetitions	percentage
Age group	-20	0	% 0
	30 – 21	2	% 5
	40 – 31	21	% 52.5
	50 – 41	12	% 30
	60 – 51	5	% 12.5
Total		40	100%

Prepared by researchers based on the outputs of the spss program

Table 4. Description of the research sample by academic qualification.

Variables	target sample	Frequency	percentage
Educational Qualification	Secondary	**1**	2.5 %
	Technical Diploma	16	40 %
	Bachelor	13	32.5 %
	Higher Diploma	2	5%
	M.A.	**6**	**15 %**
	PhD	2	5 %
Total		40	100%

Prepared by researchers based on the outputs of the spss program

The statistical results contained in Table (5) showed that the percentage of department heads in the respondents was (15%), while the percentage of teachers was (17.5), and the percentage of employees in the sample amounted to (67.5)

Table 5. Description of the research sample by job position.

Variables	target sample	Frequency	percentage
job position	Heads of Departments	6	% 15
	Administrators	7	% 17.5
	employee	27	% 67.5
Total		40	100%

Prepared by researchers based on the outputs of the spss program

As for the number of courses that the research sample benefited from in developing supervisory skills, the statistical results contained in Table (6) showed that (52.5%) of the sample individuals participating in the courses ranged between (4-6) and represented the highest percentage, then Then comes the courses that range between (1-3), where the percentage of these courses reached (20%), the courses (10 and more) reached (15%), and then courses (7-9) with a rate of (12.5%).

Table 6. Study sample by the number of courses.

variables	target sample	Frequency	percentage
	-	0	% 0
	3 – 1	8	% 20
Subscribed courses	6 – 4	21	% 52.5
	9 – 7	5	% 12.5
	10 -	6	% 15
Total		40	% 100
Prepared by researchers based on the outputs of the spss program			

5.2 Presenting The Results Related To The Role of Internal Control and The Basics of Reducing Administrative and Financial Corruption

Based on the answers of the study sample members to the questionnaire items to identify the differences in their opinions and provide a comprehensive perception of their views on the nature of these variables, the frequency distribution tables, percentages, and arithmetic means were used to estimate the levels and standard deviations, and to estimate the extent of dispersion in the answers around the arithmetic means (as It is shown in Table (3-1), and light of the statistical treatment presented by the mentioned table, it is clear that the opinions and attitudes of the study sample members tend towards the positive direction, based on the Likert quintuple scale, as it reflects arithmetic means higher than the hypothetical arithmetic mean of the scale (3), as next one:

a. Organizational Structure (x1): The percentage of those whose answers were in agreement on this stage was (8.53%) of the sample, with arithmetic mean (52.3), and a standard deviation (542.0), and in contrast, the percentage of The lack of agreement on this stage for the answers of the study sample members is (10%), and the percentage sometimes reached (2.36%), which indicates that more than half of the sample support the existence of an effective and clearly defined organizational structure
b. Individuals and the organization's work (x2): The percentage of those whose answers were in agreement in the stage reached (3.38%) of the sample, and in contrast, the percentage of disagreement among the respondents' answers is (4.28%), and sometimes (3 33%), and the arithmetic mean amounted to (2.3), with a standard deviation of (833.0), which means that less than half of the sample members indicate the presence of influential individuals in the effectiveness of internal control systems.
c. The basics of reducing administrative and financial corruption (legal reform y1), and the percentage of those whose answers, when agreeing on the formula for reducing corruption (legal reform), were (8.48%) of the sample, with an arithmetic mean of (31.3), and a standard deviation of (89.0), and in contrast, the percentage of

disagreement among the answers of the study sample members reached (2.26%) and sometimes (25%). The above percentages indicate that less than half of the sample confirms the availability of the legal reform factor to increase the Effectiveness of reducing administrative and financial corruption

d. The basics of reducing administrative and financial corruption (administrative procedures y2), and the percentage of those whose answers were in the case of agreement on the basics of reducing corruption (administrative procedures) reached (50%) of the sample, with arithmetic mean (5.3), and a standard deviation (98.0), in contrast, the percentage of disagreement and sometimes the answers of the sample members represent only (7.18%) and (3.31%), respectively, and these percentages indicate that half of the study sample members confirm here the existence of administrative procedures that help organization to make rational decisions that are in the public interest.

The opinions of the study sample members and their attitudes towards the role of internal control and the basics of reducing administrative and financial corruption in the institute, the study sample

Table 7. Summary severely.

answer scale / Dimensions	I do not agree		disagree		Sometimes I agree		Agreed		Strongly		mean	Std. d
	FR.	PR.	FR.	PR.	FR.	PR.	FR.	PR.	FR.	PR.		
X1	2	8,0	22	2,9	87	2,36	106	2,44	23	6,9	52,3	542,0
X2	5	5,4	29	2,24	40	3,33	31	8,25	15	5,12	2,3	833,0
Y1	9	6,5	33	6,20	40	25	55	4,34	23	4,14	31,3	89,0
Y2	10	2,6	20	5,12	50	3,31	46	7,28	34	3,21	5,3	98,0
Prepared by researchers based on the outputs of the spss program												n =40

5.3. Correlation Analysis of The Role of Internal Control in Reducing Administrative and Financial Corruption

Here it is necessary to verify the hypothesis whose content states that there is a significant correlation between internal control and the basics of reducing administrative and financial corruption. Based on this, the Pearson correlation coefficient is used to find the strength of the relationship between the study variables. The results reveal the existence of a positive significant relationship between internal control (x) in terms of all its dimensions and its impact on reducing corruption (y) and in terms of the basics of reducing administrative and financial corruption completely, where the value of the correlation between the two variables reached (691,0), which is a positive value that indicates the strength of the relationship between the two variables. The correlation coefficient between internal control and the basics of reducing administrative and financial corruption was as follows:

a. Organizational Structure (x1): Legal reform (0,574) and administrative procedures (0.636) which is a positive moral value indicating that the technical institute (the study sample) can highlight the general framework of the organizational structure
b. Individuals and business of the organization (x2): Legal reform (0.411), and administrative procedures (0.500), which is a positive value indicating that the technical institute (the study sample) possesses individuals who abide by administrative and legal procedures, regulations, and instructions, From the foregoing, the study concludes that the test results for the relationship between internal control in terms of all its dimensions, and the reduction of corruption in terms of the basics of building it in a complete and moral sense, and between the role of internal control, and the basics of reducing administrative and financial corruption are moral, and this proves the validity of the hypothesis whose content states that there is a relationship Morale between internal control and the basics of reducing corruption.

Table 8. Values of Pearson correlation coefficient between research variables.

	X	
Y	0.691*	
	X1	X2
Y1	0.574**	0.411**
Y2	0.636**	0.500**

Table 9. Reliability Statistics.

N of Items	Cronbach's Alpha Based on Standardized Items	Cronbach's Alpha
39	.829	.829
The reliability coefficient of the questionnaire items is .829, which is an excellent percentage for measuring the validity of the questions that were included within the questionnaire.		

6 Conclusions and Recommendations

In light of the results presented and analysed in the theoretical and applied frameworks of the studies, the following conclusions were reached:

a. Corruption negatively affects the stability and reputation of the political system and limits its ability to respect citizens' rights, equality, and equal opportunities
b. The internal control goes beyond the financial and accounting issues and the protection of the assets of the establishment, as it is a comprehensive system for the mechanisms of the control provisions set by the administration.
c. The internal control is designed to provide reasonable, logical, and not absolute assurances related to the achievement of all the objectives of the enterprise, which include protecting the enterprise's resources from misuse, relying on reports and

financial statements, and achieving efficiency and effectiveness for all enterprise activities.

d. Internal control is not a goal in itself, but a means to achieve a set of goals and is an integral part of administrative functions.

e. Effective internal control depends on the availability of appropriate accounting systems, and the accounting system depends on providing documents and records appropriate for those accounting systems to reveal the locations of administrative and financial corruption.

f. Despite the presence of internal control, the phenomenon of administrative corruption in government agencies in many developing countries is almost general and tangible, and it is present in developed countries, but to a lesser degree than in developing countries.

g. Corruption is an old phenomenon, and it was the main factor in the collapse and fall of most civilizations and regimes, and the engine of wealth and uprisings, old and new.

Considering the presented conclusions, we suggest the following recommendations:

a. Paying attention to social upbringing and instilling the prevailing cultural values that establish ethics and positive behaviour in society, and the dissemination of advanced civilizational awareness that rejects corruption of all kinds

b. The necessity of giving the internal control the attention of the various administrative bodies and establishing special units for internal control in the organization and linking them with the higher management to give it a sufficient degree of independence

c. The necessity of paying attention to the supervisory methods, which are essential tools for the supervisory work, and one or more methods can be used in one unit of the units.

d. Encouraging cooperation between the Supreme Audit Institutions in the field of computer insertion in the supervisory work and encouraging the Supreme Audit Institutions to develop work manuals and guidelines for use in examining the effectiveness of internal control.

e. The necessity of adhering to the general standards issued by the Internal Control Standards Committee, with interest in developing those standards that must be adhered to under automated systems.

References

[1] Abou. Z, Ramy, (2016), Master s Degree Project Internal Control Application , Empirical Evidence from Swedn.

[2] Al – Frijawy , Jawad & Militaru , Constantin , & Ali ,methaq Hashim , 2018 , The Phenomenon of the Spread of Administrative and Financial Corruption in IRAQ Despite the Multiplicity of Oversight Bodies , American Scientific Research Journal for Engineering Technology, and Sciences, Issn (Print) 2313 – 4410 , Issn (Online) 2313 – 4404 .

[3] AL – Hosseini , Murtadha Mohammed , & AL – Tamimi , Layth Ali , & Kadhim , Ezzaddin Hasan , 2019 , Reducing Financial and Administrative Corruption Through the Ingredients of the Internal Control System , Research Journal of Finance and Accounting , VOL. 10 , No . 16 .

[4] Andersson , Jessica , & Vilo , Tuulikki , 2016 , How do Internal Auditors Become Comfortable in their Role within Risk Management , Master s Thesis , Department of Business Studies , Uppsala University .

[5] Basem , Artimi , & saeh ,Mohamed , 2019 , the Impact of Corruption on some Aspects of the Economy , article in International Journal of Economics and Finance , Doi: 10.5539 / ijef.v5n8p1.
[6] Bubilek , Olga , 2017 , International Business Degree Thesis Bachelor of Business Administration , Degree Program : International Business , Identification number 15474 .
[7] Claros , Augusto Lopez , 2013 , Removing Impediments to Sustainable Economic Development the Case of Corruption , Policy Research Working Paper .
[8] Grigore, Ana-Maria, & Dragan, Irin Mehrdad , 2016 , against Administrative Corruption within governmental Organizations from motto to Practice , Journal " Problems and Perspectives in management " Founder LLC " Consulting Publishing Company " Business Perspectives .
[9] Moeller , Robert R. 2009 , Brink s Modern Internal Auditing A Common Body of knowledge , Published by John Wiley & Sons , Inc. , Hoboken , New Jersey , 7th Edition .
[10] Moeller , Robert R. **2014** , Executive s Guide to Cosa Internal Control Understanding and Implementing the New Framework , Published by John Wiley & Sons , Inc. , Hoboken , New Jersey .
[11] Mousavi , Parvenu , & Pourkiani , Masood , Administrative Corruption : Ways of tacklin the Problem , Natural and Social Sciences Vol. 2 , No. 3 (s) , PP. 1178 – 187Issn 1805 – 3602 .
[12] Paraskevi , Theodoridou , 2016 , The Effectiveness of Internal Audit and Internal Control Systems in Greek Banks, School of Economics , Business Administration & Legal Studies A thesis Submitted for the Degree of Master of Science (NSC) in International Accounting .
[13] Peteres , Michel , 2016 , Accounting Auditing and Control , thesis does an Association Exist between the Personal determinants of the CEO and CFO and Corporate internal Control Quality , Erasmus University Rotterdam .
[14] http://libguides.csu.edu.au>c.php.

The Role of the Ethical Responsibility of Management in Promoting Financial Disclosure

Ali Khalaf Gatea[1], Zina Hamza Gali[2], Amal Essa Abdullah[3]
{ali.khalaf83@stu.edu.iq[1], zena992@stu.edu.iq[2], amal.esaa34@stu.edu.iq[3]}

Southern Technical University Technical Institute / Nasiriya, Iraq[1'2'3]

Abstract. The research deals with the importance of the moral responsibility of management in disclosing financial and non-financial data, and in line with the reality of the company's economic activity in light of the global crisis that the economy is going through, as a result of the (Coved-19) pandemic, which caused the suspension of many production and service activities, and the role of Administration in providing stakeholders with credible and reliable data for decision-making, the research found the importance of administrative ethics with its dimensions (Credibility, Fairness, Objectivity, Responsibility) on disclosure in the financial statements, and the research recommends the need to tighten kinship on the management's actions regarding the nature of the information it discloses There is no conflict of interest with the beneficiaries.

Keywords: Administrative ethics, disclosure, financial statements.

1 Introduction

Ethics is the basis for building societies as it is essential for political, social, and economic decision-making. And talking about management ethics takes multiple directions and opinions commensurate with the culture of peoples, the way of their civilization, and their political, economic, and social identity, and the existence of ethics is not limited to a society without other societies. From an accounting point of view, management ethics is related to the extent to which the company responds to the needs expressed by stakeholders for information relevant to decision-making, which reflects the reality of the company's economic and financial activity.
Administrative ethics refers to ethical standards, which distinguish between right and wrong, or specific principles that benefit society because of the management's conduct of business [3].
While [8] defines it as the use of religious, political, or social teachings to create criteria by which the quality of public administration, in general, can be judged, and these criteria include (honesty, responsiveness, efficiency, effectiveness, merit).
Research on ethics, in general, has focused on the relationship between service providers and their customers, as there is a need for the service sector to have a developed ethical sense, given their dealings with various segments of society [2]. In the field of business, managers in some companies may resort to behaviours that violate the ethics of administrative work, to achieve their interests, such as manipulating financial statements and beautifying income, and as a result, harming external parties benefiting from the financial statements. In this field and response to corporate scandals, the US Congress passed the SOX Act to help prevent loopholes in internal

IMDC-IST 2021, September 07-09, Sakarya, Turkey
Copyright © 2022 EAI
DOI 10.4108/eai.7-9-2021.2314889

control, and one of its results was to clarify the responsibility of senior management for the company's financial statements, as CEOs and financial officials must certify, that Financial statements and fair disclosure of the company's operating results and financial condition, in addition; The company must maintain an adequate system, of internal controls, to protect the company's assets and ensure the accuracy of financial reports. The second consequence of the SOX Act is that companies now pay more attention to the formation of the audit committee of the board of directors, as the members of the Board of Directors must consist of Management is entirely independent (i.e., non-employees), and must include at least one financial expert. As a result, the law increases penalties for misconduct and guides management accountants [12].

2 The Concept of Disclosure in the Financial Statements

The financial statements are a mirror for every business company as they represent a mediator between the company and other parties through the information provided on the company's financial position and the success of its business, and these data are primarily used by external parties, which make various decisions based on this information, and to be able to make decisions, the information contained in financial statements must be accurate and reliable, however, most companies nowadays are increasingly resorting to smoothing financial statements to present a more attractive picture to the largest possible number of investors [5]. Transparently presenting accounting information to stakeholders, helps them make informed financial decisions, and that the conceptual framework of financial accounting, clarifies that the financial objective of the data is "to provide accurate information about the financial statements and that the result of the performance helps users in making economic decisions, so any event Likely to affect the company's current financial position or future risks, should be reflected in the financial statements [4], [11] states the requirements of IFRS 8 that the disclosure of segment information should include the following:

1. That the disclosure should include at least the following: revenue from external customers and transactions with other operating segments, interest income and interest expense, depreciation and amortization, "exceptional" items, income or expense tax, other material non-monetary items.
2. Types of products and services offered by the company.
3. Profit and loss measure for each sector.
4. The measure of liabilities for each segment is to be reported.
5. Total assets.
6. Profit or loss adjustments.

As for [5], [7] it lists the determinants of the Financial Accounting Standards Board for the qualitative characteristics of accounting information that characterize information more useful for decision-making purposes, which include:
Relevancy: For the information to be relevant, it must have an impact on the decisions used, for this information must also help the user to predict the future and confirm or correct past expectations through performance feedback.

1. **Reliability:** that is, the information is free from errors and biases, and it must accurately represent the company's events and activities.
2. **Comparison:** The information that is measured and reported to different institutions is comparable, as the comparison feature should allow users to identify aspects of

compatibility and fundamental differences in economic phenomena, if these aspects are not hidden using similar accounting methods.

3. **Consistency:** The principle of consistency means that the institution applies the same accounting standard for the same accounting events, from one accounting period to another. This does not mean that the company cannot move to another method, and the transition is made if the new method is better than the old one.
4. **Completeness:** Completeness means that the information includes important elements related to the events and activities
5. Timeliness: Information must be prepared in time before deciding to be useful to it.
6. **Verifiable:** This means that the same information is obtained by independent individuals.
7. **Accessible:** Refers to providing information to users when they need it appropriately.

2.1 Previous Studies

1. A study (Mukhlasin & Nur,2018): "Internal Control Disclosure Ethics Disclosure and Earnings Management as Signal to Detect Fraudulent Financial Reporting" study aims to prove the impact of the management's commitment to the company's internal controls, on the accuracy of financial reports. It also studies the relationship between management's intentions and interest in its interests, and fraudulent financial reports, by analysing the non-financial data of companies listed on the Indonesia Stock Exchange, and the most important conclusions reached, the possibility of improving the quality of information, By following the voluntary disclosure method, that is, disclosing internal control and management ethics, as it was found that following voluntary disclosure significantly reduces the preparation of fraudulent reports.
2. A study (Kim & Jo,2008): "Ethics and Disclosure: A Study of the Financial Performance of Firms in Seasoned Equity Offerings Market" study aims to know the role of administrative ethics in preventing profit manipulation and beautifying income, to obtain better performance in the long run, and its impact on financial disclosure, and damage to the interests of shareholders. The financial statements and consequently the company's lost gradually.
3. A study (Mansour & Salem,2017):" Importance of Management and Administrative Ethics on Corporate Success, and Sustainability" study aims to show the importance of the management’s commitment to administrative ethics, in sustainability, success, and continuous growth of companies, in the Arab world.

3 Research Methodology

1. **Research problem:** Disclosure, in general, is one of the most important matters for stakeholders because it represents a graph to know the business results of the economic unit and to enhance the effectiveness of investment decision-making and future forecasting, and the management practices in disclosing financial statements are one of the factors affecting the reliability and credibility of those data Accordingly, the research problem discusses the extent of the administration's commitment to ethical standards in disclosing financial statements, exercising its influence, and how to control over them.

2. **The importance of the research:** the importance of knowing the standards that govern administrative ethics and their role in disclosing information with transparency and credibility in the financial statements, the aim of which is to protect the wealth of shareholders and investors because some senior management disclose information that achieves their interests, and this is reflected negatively on the market value for the company.
3. **Research objectives:** The research aims to present the theoretical framework of the concept of management ethics and the standards that govern the ethical practices of senior management in financial and non-financial disclosure, and the relationship between administrative ethics in accounting disclosure and the value of the company. Considering the awareness of management ethics standards and their impact on financial and non-financial disclosure.
4. **Research hypothesis:** The research is based on the main hypothesis that states: " There is a significant statistically significant relationship between management's commitment to ethical standards and disclosure in the financial statements" Sub-hypotheses are derived from it:

H1: There is a significant relationship with statistical significance between the credibility of management and disclosure in the financial statements.
H2: There is a significant relationship with statistical significance between the fairness of management and disclosure in the financial statements.
H3: There is a significant relationship with statistical significance between the objectivity of management and disclosure in the financial statements.
H4: There is a significant statistically significant relationship between management responsibility and disclosure in the financial statements.

3.1 Data Collection and Analysis

For data collection, a questionnaire was designed based on the principles and standards of administrative ethical responsibility issued by the Council of Administrative Accountants, which contained four main axes including (credibility, justice, objectivity, responsibility), which was distributed to a selected group of employees in Iraqi companies listed in The Iraqi Stock Exchange, as well as the beneficiaries of the financial statements published by those degrees, and to measure the relationship between the proposed axes, the results were subjected to a statistical analysis based on the outputs of the (SPSS) program and the impact and correlation it contains significant significance at the degree of freedom (0.05), which was as follows:

Table 1. Case Processing Summary.

		N	%
Cases	Valid	76	100.0
	Excluded[a]	0	.0
	Total	76	100.0
Listwise deletion based on all variables in the procedure.			

Table 1 shows the SPSS program entries, which were 100% correct.

Table 2. Reliability Statistics.

Cronbach's Alpha	Cronbach's Alpha Based on Standardized Items	N of Items
.829	.841	19

Table 2 shows the reliability coefficient of the questionnaire items is .829, which is an excellent percentage for measuring the validity of the questions that were included within the questionnaire.

Table 3. Item Statistics.

	Mean	Std. Deviation	N
Credibility	3.8789	.33796	76
Fairness	3.8421	.35525	76
Objectivity	3.9474	.14373	76
Responsibility	3.8263	.28160	76

Table 3 shows the aggregated data for each variable, the arithmetic mean, and the number of valid entries.

Table 4. ANOVA.

		Sum of Squares	Df	Mean Square	F	Sig
Between People		11.789	75	.157		
Within People	Between Items	.661	3	.220	3.609	.014
	Residual	13.739	225	.061		
	Total	14.400	228	.063		
Total		26.189	303	.086		

Grand Mean = 3.8737
It is clear from Table 4 that the value of P. Value is 0.014, which is less than the 5% level of significance, and therefore we accept the program's analytical outputs because there are significant differences between the research variables.

Table 5. One-Sample Kolmogorov-Smirnov Test.

		credibility	Fairness	Objectivity	Responsibility
N		76	76	76	76
Normal Parameters[a,b]	Mean	3.8789	3.8421	3.9474	3.8263
	Std. Deviation	.33796	.35525	.14373	.28160
Most Extreme Differences	Absolute	.377	.328	.511	.363
	Positive	.360	.328	.357	.269

Negative	-.377-	-.321-	-.511-	-.363-
Test Statistic	.377	.328	.511	.363
Asymp. Sig. (2-tailed)	.000[c]	.000[c]	.000[c]	.000[c]

Test distribution is Normal. b. Calculated from data. c. Lilliefors Significance Correction.
Table 5 reflects the normal distribution of the drawn research sample based on the answers obtained according to the (Kolmogorov-Smirnov) test to test the moderation of the parameter test in proportion to the researcher's hypothesis, as we find that the P. Value is equal to 0.000 which is less than the level of significance 5%, and therefore we accept Statistical analysis results.

Table 6. One-Sample Test.

	Test Value = 0					
	T	df	Sig. (2-tailed)	Mean Difference	95% Confidence Interval of the Difference	
					Lower	Upper
credibility	100.059	75	.000	3.87895	3.8017	3.9562
Fairness	94.285	75	.000	3.84211	3.7609	3.9233
objectivity	239.416	75	.000	3.94737	3.9145	3.9802
responsibility	118.456	75	.000	3.82632	3.7620	3.8907

It is clear from Table 6 that the value of P. Value is 0.000, which is less than the level of significance 5%. Therefore, we accept the research hypotheses that there is an impact of management ethics with its variables (credibility, fairness, objectivity, responsibility.

Table 7. Correlations.

		credibility	Fairness	objectivity	Responsibility
Credibility	Pearson Correlation	1	.931**	.109	.012
	Sig. (2-tailed)		.000	.350	.921
	N	76	76	76	76
Fairness	Pearson Correlation	.931**	1	.086	.127
	Sig. (2-tailed)	.000		.461	.273
	N	76	76	76	76
objectivity	Pearson Correlation	.109	.086	1	.219
	Sig. (2-tailed)	.350	.461		.057
	N	76	76	76	76
responsibility	Pearson Correlation	.012	.127	.219	1

	Sig. (2-tailed)	.921	.273	.057	
	N	76	76	76	76

**. Correlation is significant at the 0.01 level (2-tailed).

Table 7 represents the correlation coefficient between the research variables, which is evident through the value obtained at the degree of freedom of 0.05.

Table 8. Summary Statistics questioners.

Details	N	Mean	Std. Deviation
The management adopts the strategic directions and main objectives of the company and supervises their implementation	76	3.9474	.32227
Communicate information fairly and objectively	76	3.8158	.45345
Develop a written policy that regulates the relationship with stakeholders to protect their rights	76	3.9737	.16114
Management refrain from drifting in any ethical behaviour that reduces the performance of the company	76	4.0000	.00000
The management shall refrain from engaging in or supporting any activity that would tarnish the reputation of the profession	76	3.9211	.27145
Contribute to the formation of a positive ethical culture and commitment to the integrity of the profession leads to the disclosure of objective and transparent information	76	3.8684	.47165
The commitment of the members of the Board of Directors to avoid conflict of interests with related parties.	76	3.9737	.16114
Maintain an appropriate level of professional leadership and experience by enhancing knowledge and skills	76	3.9211	.35640
Perform professional duties by regulations and laws related to professional standards.	76	3.6053	.71328
Provide accurate, clear, and concise information and recommendations to investors to support their decisions and identify future risks	76	3.8684	.41125
Maintain confidentiality of information except when disclosure is authorized or legally required	76	3.7632	.58580
Providing the necessary documents to shareholders to assist them in voting on decisions.	76	3.9474	.32227
Refrain from using confidential information for unethical or illegal advantages	76	3.9737	.16114
Publication of the Board of Directors' report and the auditor's report	76	3.6842	.57063
Provide all relevant information that is expected to affect a user's understanding of the reports, analyses, or recommendations	76	3.9211	.35640

Reporting by management of any delay or lack of information, processing, or internal controls.	76	3.8947	.38571
The administration sets electronic systems through which the company's financial and non-financial information is disclosed	76	3.8158	.45345
The company's management appoints an official to manage the company's disclosure methods and respond to investors	76	3.9211	.35640
The company's management discloses any proposed change in the financing or capital structure	76	3.8158	.50887
Report any restrictions that affect the success of the company's financial performance	76	3.8421	.49133
credibility	76	3.8789	.33796
Fairness	76	3.8421	.35525
objectivity	76	3.9474	.14373
responsibility	76	3.8263	.28160
Valid N (Listwise)	76		

4 Conclusion and Recommendations

In this article, we address the issues related to the ethical responsibility of management in its dimensions (Credibility, Fairness, Objectivity, Responsibility). And its relationship to disclosure in financial reports, from the point of view of the beneficiaries and stakeholders. and whether disclosure decisions are free from unethical manipulation of income or earnings smoothing. It was found that disclosure is directly related to the ethical responsibility of management. This supports the research hypothesis, which states that there is a significant relationship with statistical significance between the management's commitment to ethical standards and disclosure in the financial statements. According to the following:

1. There is a positive correlation with a moral significance between the credibility of the administration and the accounting disclosure in terms of table 6 at the level of morale less than (5%).
2. There is a positive correlation with a moral significance between the fairness of the administration and the accounting disclosure in terms of table 6 at the level of morality less than (5%).
3. There is a positive correlation with a moral significance between the objectivity of management and the accounting disclosure in terms of table 6 at the level of morale less than (5%).
4. There is a positive correlation with a moral significance between management responsibility and accounting disclosure in terms of table 6 at the level of morale less than (5%).
5. The administration's tendency to follow behaviours that violate work ethics, which may significantly affect the quality of financial information and, as a result, harm the related parties who benefit from the reports issued by the company.
6. The management's commitment to ethical standards leads to the disclosure of accurate and consistent information, and this leads to the company's long-term continuity and sustainability.

There are some recommendations as following:

1. The administration should be keen to disclose information accurately without any bias or temptation for their interests.
2. The higher authorities in the state should tighten oversight over the management of companies to comply with the standards of administrative ethics.
3. The necessity of stressing kinship on the management's actions regarding the nature of the information it discloses and the absence of a conflict of interest with the beneficiaries.
4. Spreading cultural awareness to investors to find out or detect any manipulation in the company's financial statements and thus take a correct decision.

References

[1] Aly M., Athmar S., (2017), Importance of Management and Administrative Ethics on Corporate Success, and Sustainability" International Journal for Innovation Education and Research, Vol.5 No.3.

[2] Brudney, J. L., Martinez, J. M., (2010), Teaching administrative ethics in nonprofit management: Recommendations to improve degrees, certificates, and concentration programs. Journal of Public Affairs Education, 16(2), 181-206.

[3] Chandio, A. R., Iqbal A. B., S. A., Ali, M., & Gadhi, G. N., (2019), administrative ethics with special reference to islam. GSJ, 7(7).

[4] Elliott B. , Elliott J., Financial Accounting and Reporting", 16 ed, Pearson Education Limited, 2013.

[5] Hachem B., Sujud H., (2019), Effect of the Quality of the Accounting Information System Outputs on Customer Satisfaction in Lebanese Commercial Banks, Issue 176.

[6] Kim, Y. & Jo, H., (2008). Ethics and disclosure: A study of the financial performance of firms in the seasoned equity offerings market. Journal of Business Ethics, 80(4), 855-878.

[7] Kieso D.E., Weygandt Jerry J., Warfield T. , Intermediate Accounting, 16ed, John Wiley & Sons, Inc. 2016

[8] Marume, S. B. M , Chikasha A. S., (2016), Administrative Ethics, International Journal of Business and Management Invention, Vol. 5 Issue 8.

[9] Mukhlasin M. , Nur A., (2018), Internal Control Disclosure, Ethics Disclosure, and Earnings Management as Signal to Detect Fraudulent Financial Reporting" Nur Anissa Vol. 5, No.6.

[10] Remenarić, B., Kenfelja, I., & Mijoč, I. (2018). Creative accounting-motives, techniques and possibilities of prevention. Ekonomski vjesnik, 31(1), 193-199.

[11] Spiceland D. , Nelson M., Thomas W. ,Intermediate Accounting, 8ed, Published by McGraw-Hill Education,2018.

[12] Weygandt J., Wisconsin M. , Kieso D. E., Accounting principal"13 ed, John Wiley & Sons, Inc, 2018.

[13] Mansour, A., & Alsalem, A. (2017). Importance of Management and Administrative Ethics on Corporate Success and Sustainability.

Box-Jenkins Modelling and Forecasting of WTI Crude Oil Price

Maitham A. Rodhan[1] , Adnan H. Jaaz[2]
{Maitham.Rodhan@buog.edu.iq[1], adnan.hadi@buog.edu.iq[2]}

Basra University for Oil and Gas. College of Industrial Management For oil and Gas[1,2]

Abstract. Oil is such an important commodity that its price and volatility have a significant impact on everyone's lives. Oil has a significant impact on economic growth. Unexpected changes in oil prices have an impact on both supplier and production countries' economic stability. As a result, estimating crude oil prices is critical. Trend, regression, moving average, and other methods are all used to model and forecast time-series data. The ARIMA approach is used to forecast the following year in this research. ARIMA approaches are used to analyse time-series data and are mostly utilised for loading forecasting because of their accuracy, mathematical soundness, and flexibility (due to the inclusion of AR and MA factors over a regression analysis). From March 1990 to March 2021, data on WTI prices was acquired from the US Energy Information Administration (EIA). The data is evaluated for stationarity and autocorrelation before using residuals procedures to choose amongst different ARIMA models for analysis. The outcomes of many models were evaluated, and the ARIMA (1,1,4) model was shown to be the most accurate forecasting model. The tables and figures below provide a full explanation of the above and summarise it.

Keywords: WTI crude oil, ARIMA Model, Stationarity, Oil Price Forecast, JEL Codes: C22, C51, E37, P28, G12

1 Introduction

Oil is one of the primary sources of energy consumption. Global consumption of crude oil and other petroleum products in 2014 for example reached more than 34 billion barrels, and its value exceeded $ 3.3 trillion. Therefore, the price of oil affects the world economy. Sudden variations in crude oil prices can have enormous economic implications; falls in crude oil prices hinder economic activity, while price booms produce severe inflation. As a result, energy academics, corporate leaders, and regulators are interested in modelling and forecasting crude oil prices. Both governments and corporations rely on accurate forecasting to make economic strategy decisions, yet it is difficult to foresee because to its chaotic and unpredictable nature.

Because there are so many variables that change over time, it's difficult to model the price of oil. As seen in Figure 1, the price of oil can fluctuate drastically in a short period of time, making it impossible to forecast. Oil has gone through some ups and downs during the last three decades.. The Asian Financial Crisis, combined with Iraq's decision to increase oil production,

IMDC-IST 2021, September 07-09, Sakarya, Turkey
Copyright © 2022 EAI
DOI 10.4108/eai.7-9-2021.2314841

caused oil prices to plummet in early 1999. However, the market rapidly adjusted and in November of 2000, it had hit approximately US$ 35. The global economy then began to regain momentum, resulting in a period of bullishness lasting a few years. As a result, oil prices have been rising. The price of oil reached an all-time high of US$ 133.88 in June 2008. In the same year, the United States had a housing bubble, which led to an unprecedented credit crisis. This pushed the prices to drop below $ 40 a barrel within a few months, but the prices improved after that until they exceeded $ 100 in 2014, but it did not last long, as it decreased to the level of $ 30 in 2016 due to the increased supply of crude oil, in 2020, due to the repercussions of Covid-19, prices fell to their lowest level in two decades, reaching $ 16.55 in April. So, all these fluctuations complicate the process of forecasting crude oil prices in general.

There are different types of oil, including West Texas Intermediate (WTI) crude. WTI is very high quality. It is the main benchmark for crude oil in the Americas. In this study, we will choose West Texas Intermediate crude oil to predict its price because it is the main benchmark for crude oil in the US, which is the largest consumer of crude oil in the world, as it consumes more than 20% of the total global consumption of crude oil, as well as the largest producer of crude oil in the world. Finally, we can say that forecasting crude oil prices is a very complicated matter because many factors affect prices. So, we will limit our paper to forecasting for one year to achieve the highest possible accuracy. Medium and long-term forecasts usually lack accuracy based on the origin nature of the global oil market.

The goal of this project is to discover factors that influence oil prices and develop an accurate oil price forecast model.

2 Factors Affecting Oil Prices

Crude oil is the most volatile supplies in terms of price due to a variety of factors such as the dollar's exchange rate, the prices of other energy sources such as natural gas, coal, and renewable energy sources of all kinds, supply and demand for oil, crude oil market speculation, and weather factors. As well, an important factor that affects crude oil prices is the geopolitical factor, which is a very important variable. Crude oil production centers, in general, are in areas experiencing continuous political turmoil. And thus, these disturbances affect crude oil supplies and hence prices. So, studying these variables can help us a lot in understanding the mechanism for determining prices for crude oil and thus enables us to find a more accurate predictive model.

2.1 Economic Factors

Oil demand and consumption by all sectors rises in response to economic, industrial, and population growth, and falls in response to economic downturns. Supply and demand play a role on oil pricing. When demand increases (or supply decreases), prices should rise, and when demand decreases, prices should fall (or supply increases). The pricing of gas and oil reserves reflect supply and demand pressures from a specific time period. Prices change to maintain future supply levels while taking current production levels into account when demand for crude

oil products is high. High prices, on the other hand, encourage production, hence boosting supply and lowering the price of oil and its derivatives[1].

2.2 Exchange Rate

Crude oil is exchanged in US dollars all over the world, but petroleum products are purchased in local currencies. As the dollar depreciates against other currencies, countries with non-dollar appreciating currencies profit from cheaper oil, whilst customers in USD-pegged countries pay a greater price for the same barrel of oil. As a result, changes in the value of the US dollar will affect global oil demand. When the US dollar depreciates versus other currencies, the cost of acquiring a dollar decreases. This will increase demand for crude oil in currencies other than the US dollar, driving up prices. As a result, a negative correlation is expected between the US Dollar exchange rate and crude oil price movements[2].

2.3 Geopolitical Events

Political upheaval has had a significant impact on oil supply and prices, particularly in oil-producing regions such as the Middle East. Long-standing historic rivalries between governments and tribes, religious differences, and ownership of critical resources such as petroleum could all contribute to such tensions. The highest oil prices in history have been connected to tensions with Iran; Iraq's production has been lowered in recent decades due to protracted war periods. Nigerian oil production is harmed by violence and insurgency activity in the Niger Delta. Nigeria's production output has been lowered due to frequent abductions of foreign employees, pipeline attacks, and sabotage of oil infrastructure. Venezuela's political unrest and nationwide strike harmed oil exports and had a direct influence on the international oil market. Libya experienced the same thing. The price of crude oil is rising as a result of all of this upheaval[3] .

2.4 Climatic Factors

Seasonal weather changes affect the oil demand. In the winter, more heating oil is consumed, whereas in the summer, more gasoline is consumed. As a result, the price of oil varies according to the season. Hurricanes, tsunamis, and thunderstorms, especially in major oil-producing areas, can cause physical damage to production facilities and infrastructure, disrupting oil supply and raising prices[4].

American oil production stopped after Hurricane ‘Evan’, which deprived the United States of America of more than 10 million barrels of production in September 2004. In addition to the suspension of production in some fields of Mexico due to the damage caused by this hurricane, which continued to stop production for more than 3-4 months. And based on the above, this hurricane caused a decrease in oil supplies to the markets. The price of a barrel of oil increased by $13m when Hurricane 'Katrina' hit the southern United States in 2005, affecting 19% of the US oil supply. The flooding of the Mississippi River in May 2011 caused oil prices to fluctuate[5].

2.5 Future Market Speculation

Future pricing above spot prices, which lead to anticipation of higher future prices, can persuade oil producers to keep their oil and sell it later for a bigger profit. This might diminish the existing supply of oil and have a significant impact on pricing[6]. Only about 3% of futures transactions result in the buyer of the futures contract getting possession of the commodity being exchanged, hence most futures trading is done by speculators. Furthermore, market sentiment plays an important part in determining oil prices. When speculators and hedge funds buy oil future contracts, for example, the simple concept that oil demand will rise dramatically at some point in the future might lead to a big surge in oil prices now[7].

2.6 Technological Development and Renewable Energies

The reliance on crude oil has been reducing as other energy technologies have advanced and their capital costs have continued to fall. To meet diverse areas of the world's energy needs, crude oil and other energy sources such as renewables, natural gas, and hydroelectric power are employed. While crude oil is still the most abundant significant energy source, it is largely utilised to make transportation fuels, whereas renewable energy is primarily used to generate power (electricity). As a result, because crude oil has no direct substitutes, demand for the other energy source does not always increase when the price of one rises[8] .

3 ARIMA Model

The ARIMA model combines autoregression (AR) and moving average (MA). AR makes use of the dependent relationship between an observation and a set of lagged observations. The term "integrated" refers to the use of raw observation differencing to keep a time series stable. MA is a model that takes into account the link between an observation and a residual error from a lagged moving average model.
AR (p) stands for autoregressive of order (p), that is:

$$Y_t = \phi_0 + \phi_1 Y_{t-1} + \phi_2 Y_{t-2} \ldots\ldots\ldots\ldots \phi_p Y_{t-p} + \varepsilon_t \quad (1)$$

Where, *Yt* - dependent variable at time *t*; *φ0*, *φ1*, *φ2*, --- *φp*- the predicted factors, *εt* – the error. an error describing the effects of variables that are not considered in the model. The term MA (q) stands for a q-order moving average model and is represented by:

$$Yt = \mu + \varepsilon_t - \omega_1 \varepsilon_{t-1} - \omega_2 \varepsilon_{t-2} - \ldots\ldots + \omega_q \varepsilon_{t-q} \quad (2)$$

Where, Yt-dependent variable at time t; -constant process average; t-error at time t; 1, 2,---, q-estimated coefficients

The ARMA (p, q) model is a mixture of AR (p) and MA (q) models that is represented by:

$$Y_t=\mu+ \phi_1 Y_{t-1} + \ldots. + \phi_p Y_{t-p} - \omega_1 \varepsilon_{t-1} \ldots. - \omega_q \varepsilon_{t-q} + \varepsilon_t \quad (3)$$

The above-mentioned t is a AWGN. That is, it is a set of variables with a zero mean, a two-variable variance, and a zero correlation across time, for example, E (ε_u- ε_v) = 0 if u ≠ v. They are also independent and identically distributed.
To obtain ARIMA, the ARMA model can be used to differentiate the time series for d times to achieve a stationary instance (p,d,q). The standard difference is:

$$\text{regular difference} = (1-B)^d \ X_t \quad (4)$$

B is for backward operator, while d stands for non-seasonal order of differences.

Although the differencing procedure can be repeated numerous times in theory, only one or two differencing operations are employed in practise[9]. To determine stationarity, utilise the Dickey-Fuller test, whose null hypothesis is that time-series data is nonstationary. The critical p-value was set to 0.05, which indicates that if the test p-value is greater than 0.05, the Dickey-Fuller null hypothesis, claiming that data is stationary, will be accepted.

4 Box-Jenkins Methodology

Box and Jenkins presented a time series analysis methodology for determining the optimum time function to create future projections. There are four steps to the methodology:

1. Identification.
2. Estimation
3. Diagnostic testing of the indicated model's suitability for simulating an event
4. Model application, such as forecasting.

For time series analysis and forecasting, the Autocorrelation Function (ACF) and the Partial Autocorrelation Function (PACF) are the two most important analytical tools (PACF). They look at statistical correlations between observations in a particular data collection. ACF has the advantage of allowing you to measure the level of linear dependence between observations in a time series separated by a lag k. The PACF image shows how many automobiles regressive keywords are needed to uncover one or more time lags with substantial correlations. The behaviour of the various models on the ACF and PACF can be seen as follows:

Table 1 Details of ACF and PACF Patterns.

Model	ACF	PACF
AR(p)	Tail off	Cut off after lag p
MA(q)	Cut off after lag q	Tail off
ARMA(p,q)	Tail off	Tail off

There may be more than one option for the final model in some cases. In this instance, we may want to select the most suited model using an alternative strategy based on information criteria. This is accomplished by employing the criteria outlined below.

4.1 Akaike Information Criterion AIC

It should be emphasised that for successful models, the model with the fewest variables delivers the best predicting results, for example, for a time series with multiple successful ARIMA models. In this scenario, the classical AR and/or MA should be selected. This is accomplished by selecting the best ARIMA model among successful models using Akaike's Information Criterion (AIC) (Akaike, H. 1974). The AIC value with the least value should be picked.

Akaike's Information Criterion (AIC) may be written as:

$$AIC(p, q) = \ln(\sigma^2) + 2(p + q) / T \quad (5)$$

Where σ^2 is the white noise variance's maximum likelihood estimate, sample size is T, and the total number of parameters found in the ARMA (p, q) model is (p + q). The correct model is then found by selecting the set of p and q values that minimise the AIC (p, q). To avoid over parametrization, the term 2 (p+q) T could be used as a penalty term..

4.2 Bayesian Information Criterion (BIC) / Schwarz Criterion (SC)

The BIC is given by[9] .

$$BIC(p, q) = \ln(\sigma^2) + \ln(T)(p + q)/T \quad (6)$$

with $\ln(T) / T > 2 / T$ for all $T \geq 8$

4.3 Determination Coefficient R^2 (R-squared)

The coefficient of determination shows how near the constructed model is to the optimum constant. If the model incorporates a free term, the determination coefficient can range from 0 to 1. (constant). It can be read as the proportion of the variance of the dependent variable Yt that can be explained using the independent and lag variables in the model, in the form that they exist in the model, in this case. If this is not the case, the coefficient of determination may be negative..

4.4 Adjusted Coefficient of Determination R^2_{adj}

Because the computed R^2 will not decrease as more lags are added to the assessed model, it cannot be used as a good indicator of the model's quality. For additional regressors, a fine is applied when calculating the adjusted determination coefficient (lag variables). As a result, the adjusted determination coefficient values do not surpass those of the standard determination coefficient. R2adj can be decreased by adding more variables to the model.

4.5 Standard Regression Error (s.e.regr)

The Standard Regression Error represents the variation of the time series in reference to the generated model. Adjusted R-squared, AIC value, SC value, and S.E. of regression are some of the model selection criteria. For rating and selecting the best model, the AIC and SC criteria are most typically utilised. The higher the coefficient of determination, the smaller the AIC, SC, and residual variance are. The ARMA (p,q) model that corresponds to it is superior.

4.6 Residual Analysis

If the Box - Jenkins model is good enough for time series data, we anticipate the residual to be a realisation of white noise. The residual, in other words, must be self-contained and conform to the normal distribution. This is visualised using the time series residual plot, residual correlogram, and Q-Q plot. The Ljung-Box test is also utilised, which is predicated on the autocorrelation being greater than zero. This hypothesis is supported by the Ljung-Box test with test statistic Q^{10}:
H0: independently distributed
H1: not independently distributed.

5 ARIMA Model

5.1 Data Description and Sources

The model is based on the West Texas Intermediate crude oil spot price. Time series data for Monthly WTI prices from Jan-1990 to Mar- 2021is used in this paper. This data was obtained from **the** US Department of Energy. As shown in Fig 1.

5.2 Stationarity Test

The PWTI data series (Jan-1990 to Mar- 2021) is shown in Fig 1.

Fig 1. The PWTI Data (Jan-1990 to Mar- 2021).

The outcomes result of the stationarity process is stated in Table 2.

Table 2. ADF Test on PWTI.

Null Hypothesis: Unit root assigned to PWTI

Exogenous: Constant

maxlag=16

		t-Statistic	Prob.*
Dickey-Fuller		-2.464102	0.1252
Used data:	1%	-3.447675	
	5%	-2.869071	
	10%	-2.570849	

From Table 2, the original non-stationary PWTI sequence is illustrated. Figure 2 Oil prices have a large difference when considering the highest and lowest, so by taking the natural logarithm we can reduce the variation of original PWTI data but it is also still nonstationary as

demonstrated in Table 3. Therefore, we take the first-order difference, and now it is stationary as represented in Table 4.

Table 3. ADF Test on LPWTI.

Null Hypothesis: LPWTI has a unit root

Exogenous: Constant

maxlag=16

		t-Statistic	Prob.*
Dickey-Fuller		-2.101028	0.2445
Values that must be tested:	1%	-3.447675	
	5%	-2.869071	
	10%	-2.570849	

Table 4. ADF Test on D(LPWTI).

Null Hypothesis: D(LPWTI) has a unit root

Exogenous: Constant

maxlag=16

		t-Statistic	Prob.*
Dickey-Fuller		-14.34564	0.0000
Test data:	1%	-3.447675	
	5%	-2.869071	
	10%	-2.570849	

5.3 Select the Model

The AC and PAC Graphs of the DLPWTI are shown in Table 5.

Table 5. AC and PAC Graphs of the DLPWTI.

Date: 04/28/21 Time: 01:10
Sample (adjusted): 1990M02 2021M03
Included observations: 374 after adjustments

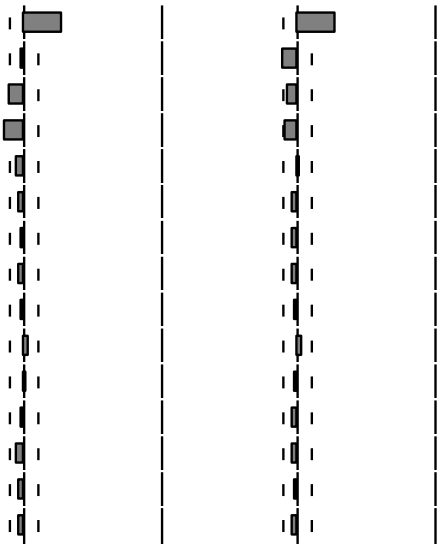

Autocorrelation	Partial Correlation		AC	PAC	Q-Stat
		1	0.286	0.286	30.841
		2	-0.022	-0.113	31.029
		3	-0.112	-0.080	35.817
		4	-0.143	-0.097	43.600
		5	-0.060	-0.001	44.977
		6	-0.030	-0.037	45.327
		7	-0.023	-0.031	45.524
		8	-0.030	-0.039	45.864
		9	-0.024	-0.020	46.085
		10	0.034	0.035	46.529
		11	0.021	-0.016	46.702
		12	-0.024	-0.040	46.918
		13	-0.053	-0.042	48.021
		14	-0.037	-0.010	48.568
		15	-0.030	-0.031	48.918

From Table 5. The q can be taken 1 or 3 or 4. And p can be taken 1 or 2. Therefore, we have multiple ARMA models. By following Adj-R^2, AIC, SC, and S.E. of relapse It appears that the most accurate model is ARMA (1,4).

5.4 Model Estimation

Table 6 summarized the data computation:

Table 6. Summarized Results.

Dependent Variable: D(LPWTI)
ARMA and OPG - BHHH
Date: 05/07/21 Time: 23:23
No. of data: 1990M02 2021M03
observations: 374

Variable	Coefficient	Std. Error	t-Statistic	Prob.
AR(1)	0.273944	0.019719	13.89264	0.0000
MA(4)	-0.123079	0.061020	-2.017036	0.0444
SIGMASQ	0.008837	0.000302	29.28794	0.0000

R-squared	0.094494	Mean dependent var.	0.002682
Adjusted R-squared	0.089612	S.D. dependent var.	0.098923
S.E. of regression	0.094387	Akaike info criterion	-1.874468
Sum squared resid	3.305211	Schwarz criterion	-1.842990
Log-likelihood	353.5254	Hannan-Quinn criteria.	-1.861969
Durbin-Watson stat	1.936439		

Inverted AR Roots	.27			
Inverted MA Roots	.59	.00-.59i	-.00+.59i	-.59

The final model is ARIMA (1, 1, 4), and specific form of the model is shown in Equation (7)

$$DLPWTI = 0.273226 \quad DLPWTI_{t-1} - 0.1236 \quad e_{t-4} \tag{7}$$

From Fig 2 we can see that the AR roots and all MA roots lie inside the united cycle. So, the ARIMA covariance is stationary and invertible and now we can forecast with this model.

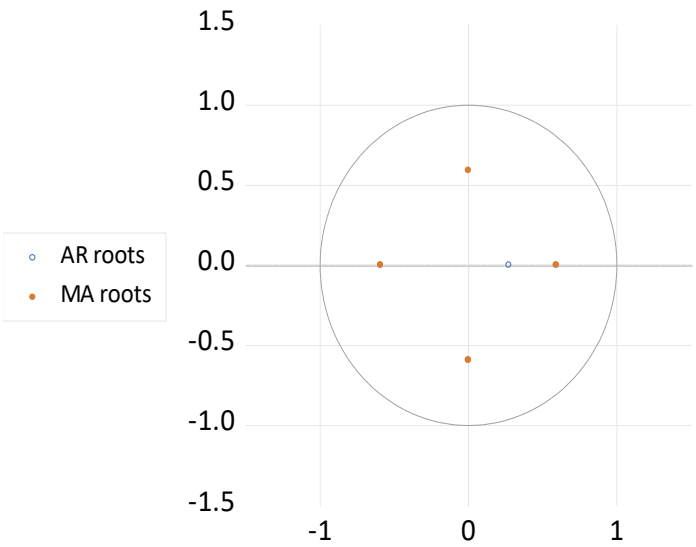

Fig 2. AR/MA Polynomials.

5.5 Forecasting

The PWTI values are predicted using this model from November 2021 to October 2022. Table 7 summarises the findings.

Table 7. PWTI Forecast from November 2021 to October 2022.

Nov 2021	Dec	Jan	Feb	Mar	Apr	May	Jun	Jul	Aug	Sep	Oct 2022
58.18	58.34	58.49	58.64	58.80	58.95	59.10	59.26	59.41	59.57	59.72	59.88

6 Conclusion

The ARIMA model has been used to predict the price of WTI crude oil, and two primary features were studied that affects the Oil prices. The study looked at 375 months of WTI crude oil price data from January 1990 to March 2021. The time series is unit root nonstationary, according to the Dickey-Fuller test. When comparing the greatest and lowest oil prices, we can see that there is a significant difference. We use the log of the original PWTI data to lessen the data's fluctuation and better fit it into the model. We can see from the log that the processed data has a general rising trend, and that the price differences between early and recent years have narrowed substantially, making data analysis and model training easier. First-order differencing was employed to convert the non-stationary time series into a stationary one, allowing the univariate box- Jenkins modelling approach to be used. The time series, ACF, and PACF plots of the first-order difference of the WTI crude oil price data revealed many ARMA (p, q) models with p (1,2) and q (1,3). (1,3,4). The ARIMA (1,1,4) model, which has the minimum AIC, BIC S.E. of regression statistics, emerges as the optimal model for the underlying generating process of WTI crude oil price data and was utilised to create a forecast.

References

Akaike, H: A new look at the statistical model identification. Transactions on Automatic Control, Vol.19, No.16, (1974), 723., Available on http://bayes.acs.unt.edu:8083/BayesContent/class/Jon/MiscDocs/Akaike_1974.

Clover Global: “Ten Factors that Affect the Price of Oil”, Clover Global Solutions, 2012, webpage, *https://c1wsolutions.wordpress.com/2012/04/30/factors-affect-price-of-oil/*. Accessed: May 1, 2021.

Francis, X.: On the power of Dickey-Fuller tests against fractional alternatives,” Business Cycles: Durations, Dynamics and Forecasting, Princeton University Press.1999 p.258.

Henry, d- Acquah, G Comparison of Akaike information criterion (AIC) and Bayesian information criterion (BIC) in the selection of an asymmetric price relationship, Journal of Development and Agricultural Economics Vol. 2(1), January 2010,p6.

King, K.- Deng, A.- Metz, D: “An Economic Analysis of Oil Price Movements: The Role of Political Events and Economic News, Financial Trading, and Market Fundamentals”, *Bates White Economic Consulting*, Washington DC, 2011,p14.

Kwasi,E :Box-Jenkins modelling and forecasting of Brent crude oil price, Munich Personal RePEc Archive,2015,p6.

Le, B. : “Crude Oil’s Impact on Renewable Energy: Energy Alternative or Energy Staple?”,2015, *http://www.altenergymag.com/article/2015/06/crude-oil%E2%80%99s-impact-on-renewable-energy-energy-alternative-or-energy-staple/20384*. Accessed: April 28, 2021.

Lioudis, N. : “The Determinants of Oil Prices”,2021: Investopedia webpage, http://www. investopedia.com/ask/answers/012715/what-causes-oil-prices-fluctuate.asp. Accessed: May 3, 2021.

Olimb, M- Ødegård, : “Understanding the Factors Behind Crude Oil Price Changes A Time-varying Model Approach”*, 2010,Unpublished MSc Thesis Report*, Norwegian University of Science and Technology, p8.

Olimb, M- Ødegård, T.: “Understanding the Factors Behind Crude Oil Price Changes A Time-varying Model Approach”*, Unpublished MSc Thesis Report*, Norwegian University of Science and Technology,2010, p11.

Pankratz, A : Forecasting with Univariate Box-Jenkins Models Concepts and Cases. John Wiley & Sons, Inc. New York, USA,1983, p: 414.

Salas, J- Delleur, J- Yevjevich, V and Lane, Applied : Modeling of Hydrologic Time series. Water Resources Publication, Michigan, USA.1980, P44.

Seth, S.: Do Oil and Natural Gas Prices Rise and Fall Together”,2015, Investopedia webpage, *http://www.investopedia.com/articles/active-trading/032515/do-oil-and-natural-gas-prices-rise-and-fall-together.asp*. Accessed: May 5, 2021.

U.S. EIA,: Cushing, OK WTI Spot Price FOB U.S. Energy Information Administration (EIA)2021.https://www.eia.gov/dnav/pet/hist/LeafHandler.ashx?n=PET&s=RWTC&f=M. accessed 14 April,

Bankruptcy Prediction: Evidence-based Experiences in the Banks

Sanaa Hasan Hilo[1], Khelood A. Mkalaf[2]
{sanahsanhelo@gmail.com[1], Hwhit27@gmail.com[2]}

Techniques of Materials Management, Department, Institute of Administration - Rusafa
Middle Technical University, Baghdad[1],
Techniques of Materials Management Department, Technical Institute for Administration
Middle Technical University, Baghdad[2]

Abstract. This study aims to predict the bankruptcy of private banks by adopting Altman Z-score's model. The financial position of these banks had been classified into three zones: safe zone, gray zone, and distress zone. Five of the famous private banks were selected that achieved the research objectives. The most important result of this study is to determine the financial position of these private banks that are located in the failure zone and financial hardship area. A major suggestion is needed to apply the Altman Z-score's models to avoid and reduce financial risks. It also contributes to identifying the weaknesses and strengths of the bank's financial position. As it assists bank managers in solving these problems in time.

Keywords: Altman Z-score's model, Financial distress, Predicting failure, Financial ratios, Bankruptcy, Private banks.

1 Introduction

Currently, the majority of the previous studies that focus on analyzing the financial failure of companies had a traditional theoretical character. [33], [37]. Where more than 90 years ago, previous studies indicated that the majority of companies were interested in studying the prediction of financial failure to survive, grow, and continue in market competition [3], [8]. Many of the financial analysis approaches have been used [9], [10], however, the most important ones are Altman's model due to its accuracy in detecting the early bankruptcy of companies [3], [14], [35]. In the context of the prediction of financial failure at banks, frequently, the annual financial reports are the main source for evaluating the performance of banks [2], [23]. Which, it mostly depends on the data on the income statements and the balance sheet [9]. As the annual financial position gives bank management the ability to achieve its goals and the possibility of survival, growth, and competition in the labor market [31]. The global economic challenges facing banks have imposed the need to adopt realistic scientific financial analysis methods that contribute to predicting the potential risks that banks face [27], [38]. As well as, determining its financial position, whether it is within the safe zone, the area of financial hardship, it will face financial failure or bankruptcy [29].

In the UK financial crisis, Almamy et al., (2016) study has proven that the predictive power of the Z-score model was (82.9%), which is consistent with Taffler's (1982) UK model [3]. Similarly, the importance of this model is increased with the financial crisis of the Kazakhstan

IMDC-IST 2021, September 07-09, Sakarya, Turkey
Copyright © 2022 EAI
DOI 10.4108/eai.7-9-2021.2314783

banking system. As, it had face sharp devaluation, high level of non-performing loans, and low liquidity level accompanied by constant state support using budgetary funds to stabilize the financial system according to The National Bank of the Republic of Kazakhstan: Financial Stability Report of Kazakhstan dated 2014. The risk of this bank's bankruptcy had been estimated at 4.3% up to 8.7%. But, the Kazakhstan banking system is powerfully supported by the government policy that is working to maintain of stability of the financial system in this country [13]. On the other hand, this model contributed to solving the financial crises that facing "Greece's systemic banks". For the prevention of full-scale banking collapse, it had imposed capital controls. Also, it covered the capital shortfall by attracting fresh capital from investors and shareholders. Its capital was raised by a collection of equity offerings, bong swaps, and the sales of foreign subsidiaries [24]. For this reason, this study applied Altman Z-score's model to a sample of private Iraqi banks listed on the Iraq Stock Exchange.

2 Methodology

In this study, Altman Z-score's model was used to predict financial failure and determine its position. Where five of the famous Iraqi private banks listed with the Iraq Stock Exchange were selected to accomplish the study objectives. Besides, these banking activities may expose it to financial risks due to the trading of stocks and financial instruments in the stock market. The data was collected by approving the financial statements of these banks for the five years between 2014-2018. Also, the income statement and balance sheet for each bank were used in the annual reports published by the Securities Commission. Figure 1 shows a summary of the Iraqi private banks selected. The data had been analyzed by using financial criteria financial ratios. Based on the quantitative statistical methods such as Pearson Coefficient, general trend. Ethics approval had been obtained for the application of this study in selected Iraqi Private Banks

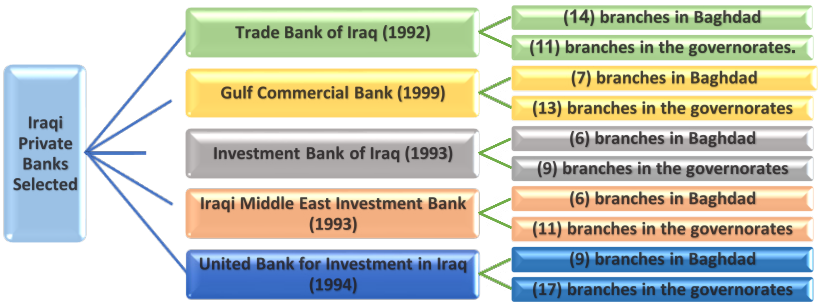

Fig. 1. Shows a summary of the Iraqi Private Banks selected.

3 Altman Z-score's Model

Currently, financial risk is one of the most significant problems facing local and international banks [26]. Where, majorities of banks are facing different challenges in the stock market and threats of financial speculation [9], such as decrease or increase in the price of

financial stocks, debt defaults, profitability, liquidity, interest, tax, financial distress, the deficit in debt payments, *etc.*[12]. Accordingly, banks need to reduce financial risk ratios by using financial analysis methods that can help their management in determining their financial position. Besides survival, growth, and continuation of competition in the stock market [11]. For this reason, many previous studies indicated that an "AltmanZ-score's model" is one of the most common models used for financial failure analysis [8], and determining the financial position of any company based on adopting Z-score's indicators [36]. It contributes to predicting bankruptcy or predicting failure for companies by carrying out multivariate analysis with the relative importance of each factor in the discriminatory and analyzed [10]. That adopted mathematical equations to investigate the performance of companies [6], [36]. Altman has developed this model for more than 50 years [4]. The Altman model has adopted variables like "Z-score" to identify the financial failure for the companies. That had been used by the Beaver (1966) model. Then, the financial failure analysis model based on the Altman-Z-Score had a new development by Toraman and Karaca (2016) study. Their study classifies the company position into three zones concerning their calculated Z-Scores namely [6], [8]:

(1) Safe zone when ($Z>3$) this referring there no risk of financial failure,
(2) Grey zone when ($1.81<Z<3$) is displays as neutrality, and
(3) The distress zone when ($Z<1.81$) is referring to high risk.

In the context of prediction of financial failure for banks, this model has been used by multiple studies due to its effectiveness in determining their financial position [9]. One of the most important risks is financial bankruptcy, which it will be exposed to in the future. Due to its reliable contribution for the third parties, it also can obtain the benefiting from these results, such as bank directors, agencies, distressed companies, the banking industry, shareholders, and the main provider of financing [32]. Whereas, these entities are particularly interested in reducing the level of bad loans to maximize profitability on credit activity. Therefore, banks seek to reduce the risk of default and, on the other hand, pay attention to capital adequacy. Investors also need reliable tools to help them make the right choice for their portfolios [6], [17]. For example, Fadhilah and Kurniawati's (2018) study applied the size of liquidity ratio of working capital to total assets for evaluated bankruptcy prediction in the National Private Banks Foreign Exchange listed in the Indonesian Stock Exchange. Banks insolvent were (29%) between 2010 - 2013. Comparing with banks that are in the gray area (71 %) in 2010 and 2013, and (67 %) in 2011 and 2012. The safe bank was (5 %). As a result, a Z-score on bankruptcy prediction for these banks appears similarly [16].

3.1 Financial Ratios Based on the Altman Z-score's Model

Altman Z-score's model uses the financial ratios for the income statement and the balance sheet to assess a company's liquidity, profitability, and efficiency. It can predict the financial position of a company if it is within the safety zone or risky zone [28]. Predicting financial failure or bankruptcy helps companies make the right decisions and procedures to avoid this risk [5]. Accordingly, financial ratios are among the forecasting techniques that are affected by multiple factors [27], such as financial leverage, solvency, revenues, and profitability that enable an estimate of the company's market strength [34]. Altman, (2019) study has indicated that the company's valuation depends on; Classifying the company within the database of markets that provide feedback about the current company's position in the market, evaluating the company's repayment potential through bonds, loans, and commercial papers, and development of business

performance by using financial analysis transforms and changes in the company, which are the most vital characteristics in determining the level of the company's position. So, in this study, the Altman Z-score model had adopted to predict the financial failure of the selected banks. It can assist the administration in identifies its financial position based on an assessment of the level of potential future risk. However, in this study, only four variables were adopted to estimate the financial position of the selected banks specifically: Networking capital, percentage of earnings retained, incomes power, and market ratio.

4 Results

4.1 Study Model

Altman Z-score's model had been adopted as an efficiency measurement tool to predict the financial failure of selected banks, and to determine their current financial position within the stock market. Table (1) illustrates the model and its linear equation [6], [7], [29]. Altman Z-score's model consists of four key variables, comparing with the original model that consists of five variables. Where the fifth variable (X5) represents sales to total assets, it's usually using to measure the potential losses of industrial companies by determining the impact of the percentage of their sales in the market [30]. The results of the modified Altman model showed that the success rate for determining Z-score was 90.9%. Besides, the possibility of predicting the company's bankruptcy date one year before its bankruptcy. The accuracy rate of these results was 97% [7]. So, the financial ratios adopted from the financial statements are significant in the analysis process to determine bankruptcy risks, analyze risks at the levels of operation, and perform the finance activities [32]. These include measuring profitability, liquidity, self-financing capacity, and debt. It is often useful to find out the ability to pay interest and pay off loans [30].

Table 1. Altman Z-score's Model (1983).

Altman Z-score's Model (1983)		
Z=6.56x1+3.26x2+6.72x3+1.05x4		
Varibles	Symbol	Equation
Z	Z	Overall index
X1	WC/TA	Working Capital/Total Assets
X2	RE/TA	Retained Earnings /Total Assets
X3	EBIT/TA	Earnings before Interest & Taxes/ Total Assets
X3	MC/TL	Market Value of Equity/Book Value of Total Liabilities
Source; (Altman et.al.,2016; Anjum,2012; Manaseer & Al-Oshaibat, 2018)		

4.2 Classification of Selected Banks Based on the Discrimination Zones

The financial position for the selected Iraqi banks based on the average of the Z- Scores has described in Table 2. As it shows from the (5) private Iraqi banks that were selected, there are (4) banks located within the safe zone. Accordingly, the percentage of banks within the safe zones was (80%), except for the Middle East Bank. As, its located in the gray area According to the average value of (z) as it reached (1.84), which requires taking caution and caution on the

part of the bank in the future for the possibility of financial hardship and taking measures to ensure that it becomes within the safe zone.

Table 2. Results Discrimination zones for Selected Iraq Private Banks

Iraq Private Banks	Ave. Z- Score	Discrimination zones
Commercial Bank of Iraq	5.25	"Safe" zone
Gulf Commercial Bank	3.04	"Safe" zone
Investment Bank of Iraq	3.93	"Safe" zone
Iraqi Middle East Investment Bank	1.84	"Grey" zone
United Bank for Investment in Iraq	2.79	"Safe" zone

The results of the trend analysis for the z value during the period 2014-2018 had shown in Table (3). Its shows that the financial position for each Iraqi Commercial Bank, the Gulf Commercial Bank, and the Investment Bank of Iraq are located within the safe zone and have a high value (z). Which is enhances the financial position of these banks. Whereas it indicated that the Middle East Bank has been located within the "Grey Zone" since 2015, and it has turned into financial hardship in recent years. So, it is an indication that the financial position of this bank is in danger. Which is may affect investors and the bank shares. Thus, the financial standing of this bank will be in doubt. On the other hand, the financial performance position of the United Investment Bank during the first four years had located within the safety zone. Nevertheless, it became within the financial distress zone in the last year. So, this requires the bank's management to take the needed measures to reduce the risk and correct its strategies to maintain its market value.

Table 3. Shows Z- Score for the Iraq Private Banks Selected

Discrimination Zones of the selected Iraq Private Banks						
Iraq Private Banks	Years					Z- Score
	2014	2015	2016	2017	2018	
Commercial Bank of Iraq	5.20	5.34	5.37	5.17	5.17	Safe
Gulf Commercial Bank	3.35	2.83	2.60	3.23	3.19	*Grey 2016*
Investment Bank of Iraq	4.28	4.12	4.01	3.74	3.52	Safe
Iraqi Middle East *Investment* Bank	2.83	2.38	1.60	0.66	1.74	Grey *Distress 2017*
United Bank for Investment in Iraq	3.83	3.94	4.09	3.59	0.00	*Distress 2018*

4.3 Pearson Correlation Matrix

Pearson correlation matrix is applied to find whether there is a significant relationship between the research variables. Also, to identify the most variable that has affected the financial performance for selected banks. As it appears in Table 4, there is a significant relationship between the measured research variables. The results have proved that there is a strong positive correlation of (0.930) between the value of (z) and (x1), which represents working capital to total assets as they reached. Also, there is a strong significant correlation (0.806) between the value of (z) and (x2), which represents retained earnings to total assets. While, there was a weak positive correlation (0.277) between the value of (z) and (x3), which represents earnings before

interest and taxes to total assets. Finally, there was a strong correlation of (0.643) between the value of (z) and (x4), which represents the book value of equity to total liabilities.

Table 4. Shows the Pearson correlation matrix Results

The Results of the Pearson Correlation Matrix					
	X1	X2	X3	X4	Z
X1	1				
X2	0.742	1			
X3	0.169	0.251	1		
X4	0.680	0.407	-0.081	1	
Z	0.930	0.806	0.277	0.643	1

4.4 Analysis of the Financial Ratios Based on the Altman Z-Score Model

In this study, the final results show there were two from five banks selected has located at the Distress Zone. While the third one has been placed at the Grey Zone for many reasons as indicated below:

Net Working Capital: The results of the position financial analysis for the networking capital shown that:

- The United Bank for Investment in Iraq is threatened with bankruptcy during 2018 for several reasons. As it appears from Figure 2, the fixed assets have started to decline since the year 2016, by an amount respectively were (0.014, 0.020, and 0.026). Also, the working capital adequacy was rising to (36%) in 2018, which is more than the minimum permissible percentage in the Iraqi banking system (12%).
- The financial activities of the Iraqi Middle East Investment Bank for the period 2014-2018 indicated threatened with bankruptcy during 2017. In addition to the dispersion and instability of the financial position since 2015 for several reasons, as shows in Figure 3.

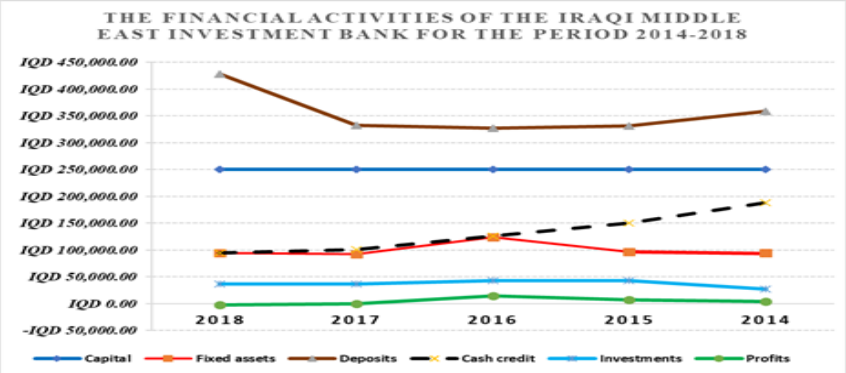

Fig. 2: The financial activities of the United Bank for Investment in Iraq for the period 2014-2018

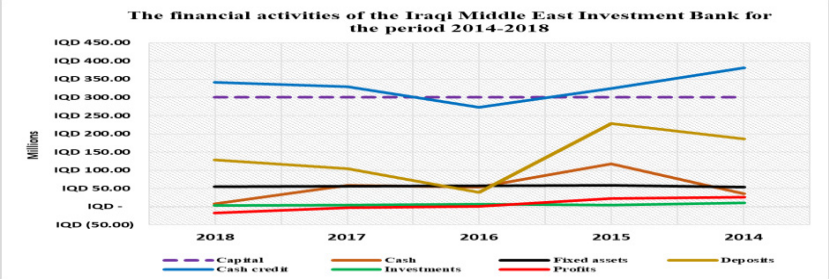

Fig. 3: The financial activities of the Iraqi Middle East Investment Bank for the period 2014-2018

As it appears from Figure 3, the fixed assets have started to decline since the years 2015, 2016, and 2018 by an amount respectively were (0.034, 0.20, and 0.021). Also, the working capital adequacy was rising to (110%) in 2018, which is more than the minimum permissible percentage in the Iraqi banking system (12%). That has indicated a high investment rate. That is means there is higher dispersion, higher risk ratios, and instability due to the increase and decrease in the trend of all variables due to the lack of a good strategy for management in planning and execution.

The Banks Financial Leverage: The financial leverage for the banks selected was demonstrations as following:-

- The United Bank for Investment in Iraq indicated that the percentage of earnings retained from 2014-2018 as respectively (-6.9%) in 2014, (1.5%) in 2015,(0.3%) in 2016,(-8.5%) in 2017, and (2.1%) in 2018.
- The percentage of earnings for the Iraqi Middle East Investment Bank retained from 2014, 2015, and 2016 as respectively (1.4%, 2.1%, and 4.8 %). Then, it's started to decline to (-0.2) during 2017 and decline to (-0.9) in 2018. Consequently, the bank was unable to distribute profits to shareholders because of the loss.

Incomes Power: The results of this study confirmed the reason that lead to the bankruptcy of these banks was the weakness in achieving profits.

- The United Bank for Investment in Iraq exposed a continuing high percentage of losses in profits since 2014. The loss ratio was (0.081) in 2018, compared to (0.096) in 2017, (18.187) in 2016, (0.015) in 2015, and (0.041) in 2014.
- The Iraqi Middle East Investment Bank has suffered from profit inability since 2014. Earning power was increased to (0.35) in 2015 and to (0.53) in 2016. Then, it was a decline (-0.23) in 2017. and (-0.71) in 2018.

Market Value: The results of the study showed that the financial leverage for these banks was as follows:

- The financial leverage ratio of The United Bank for Iraqi Investment has reached since 2014, respectively (59%) in 2014, (71%) in 2015, (43%) in 2016, (%35) in 2017, (42%) in 2018. As a result of the high debt ratios of the bank.

- The financial leverage ratio of Iraqi Middle East Investment Bank has reached since 2014, respectively (117%) in 2014, (120%) in 2015, (116%) in 2016, (123%) in 2017, (164%) in 2018. As a result of the high debt ratios of the bank.

5 Discussion

This study confirms the applicability of Altman Z-score's model to predict the financial failure of selected Iraqi private banks. A result of this study revealed that the performance of the Middle East Bank has continued to decline. Its financial position had located within the Grey zone during the years 2015, 2016, and 2018. Therefore, in 2017, it faced financial risk as a result of an increasing decline in its performance. Its financial position had located in the Distress zone. Although the result of the z-score shows the financial position for each of the Iraqi Commercial Bank, Iraqi Investment Bank, and Al Khaleej Commercial Bank within the safety zone area, still, they had suffered from high dispersion in financial performance and uncertainty. While the result of z-sore has shown the performance of The United Investment Bank located within the safe zone during the early years of its works, however, It is performance dropped to be in the Distress zone in 2018. Consequently, this financial insolvency is an indication of the bankruptcy of this bank, its inability to perform its financial obligations towards shareholders and investors, and its inability to repay debts.

Bank bankruptcy or financial failure is considered a critical threat to the national economy more than business company failures due to its harmful and negative impact on other banks' systemic risk [36]. Therefore, Therefore, it must detect banking failures before it occurs to correct bank performance and avoid bankruptcy [25]. Equity investors also focus on preserving capital to obtain returns and profits. Therefore, they avoid investing in the securities of companies experiencing financial distress. It adopts strategies in selecting companies that have continuous growth in the stock market, a strong investment budget, the ability to repay debts, and the ability to generate profits [4]. Consequently, Altman Z-score's model is the most widely used technique for analyzing financial failure because it reveals early on the company's financial distress [8]. It has been used by scholars as a standard to measure credit risk in many empirical studies and practical applications [5]. Where these results of this study agree with the Manaseer & Al-Oshaibat, (2018) study. It is confirmed the need to adopt the Altman model in predicting the financial position of banks to avoid bankruptcy and correct deviations in their financial performance in time.

6 Conclusion

Presently, the increasing global economic crisis has affected the performance of Iraqi private banks. The administration of these banks should review their financial policy for borrowing and interest, select the right strategy that assists to offer cash liquidity, and achieve profits and returns. In addition to taking suitable procedures to correct deviations in financial performance. So, it can contribute to avoiding risk and financial bankruptcy. The most important proposal of this study is that the Central Bank of Iraq can adopt the "Altman Z-Score model" as a control tool to measure the financial risks that will be exposed to banks in the future. Thus, it can be taking appropriate measures to correct the banking business before reaching bankruptcy. This model is considered a standard for measuring banking performance, as it contributes to identifying efficient banks with continuous growth activities in the stock market.

Based on this, it's necessary to adopt the variables of this model in banking studies because of their importance in determining the ability of banks to operate in a business environment without reaching high risks and avoiding bankruptcy. Furthermore, applying this model to the rest of the other governmental and private Iraqi banks that have defaulted in their financial performance, to help them avoid reaching bankruptcy.

Finally, for the future researchers in this area; (1) to conduct advanced studies that include adding additional financial indicators to measure the bank's performance and the potential financial risks that may be exposed in the future. (2) to apply this model in the industrial, service, commercial, or investment sectors due to its importance in determining the competitive position of companies. As well as the possibility of their survival in the business market. (3) to expand the application of this model on larger samples to include local and international sectors.

References

[1] Abou-El-Sood H. Are regulatory capital adequacy ratios good indicators of bank failure? Evidence from US banks. International Review of Financial Analysis. 2016 Dec 1; 48: 292-302.

[2] Adeusi SO, Akeke NI, Adebisi OS, Oladunjoye O. Risk management and financial performance of banks in Nigeria. Risk Management. 2014;6(31):123-9.

[3] Almamy J, Aston J, Ngwa LN. An evaluation of Altman's Z-score using cash flow ratio to predict corporate failure amid the recent financial crisis: Evidence from the UK. Journal of Corporate Finance. 2016 Feb 1;36:278-85.

[4] Altman EI. Applications of distress prediction models: What have we learned after 50 years from the Z-score models?. International Journal of Financial Studies. 2018 Sep;6(3):70.

[5] Altman EI, Hotchkiss E, Wang W. Corporate financial distress, restructuring, and bankruptcy: analyze leveraged finance, distressed debt, and bankruptcy. John Wiley & Sons; 2019 Mar 26.

[6] Altman EI, Iwanicz-Drozdowska M, Laitinen EK, Suvas A. Financial distress prediction in an international context: A review and empirical analysis of Altman's Z-score model. Journal of International Financial Management & Accounting. 2017 Jun;28(2):131-71.

[7] Anjum S. Business bankruptcy prediction models: A significant study of the Altman's Z-score model. Available at SSRN 2128475. 2012 Aug 13.

[8] Apan M, Öztel A, İslamoğlu M. Comparative empirical analysis of financial failures of enterprises with altman Z-score and VIKOR methods: BIST food sector application. Australasian Accounting, Business and Finance Journal. 2018;12(1):77-101.

[9] Badea I, Matei G. The Z-Score Model for Predicting Periods of Financial Instability. Z-Score Estimation for the Banks Listed on Bucharest Stock Exchange. Finance: Challenges of the Future. 2016 Jan 1;16(18).

[10] Bandyopadhyay A. Managing Portfolio Credit Risk in Banks. Cambridge University Press; 2016 May 9.

[11] Berger AN, Klapper LF, Turk-Ariss R. Bank competition and financial stability. InHandbook of Competition in Banking and Finance 2017 Sep 29. Edward Elgar Publishing.

[12] Bitar M, Pukthuanthong K, Walker T. The effect of capital ratios on the risk, efficiency and profitability of banks: Evidence from OECD countries. Journal of international financial Markets, Institutions and Money. 2018 Mar 1;53:227-62.

[13] BOLAT A. Evaluating the current financial state of banking sector in Kazakhstan using Altman's Model, Bankometer Model. Revista Espacios. 2017 Oct 18;38(48).

[14] Chiaramonte L, Liu H, Poli F, Zhou M. How accurately can Z-score predict bank failure?. Financial markets, institutions & instruments. 2016 Dec;25(5):333-60.

[15] Delen D, Kuzey C, Uyar A. Measuring firm performance using financial ratios: A decision tree approach. Expert systems with applications. 2013 Aug 1;40(10):3970-83.

[16] Fadhilah S, Kurniawati I. ANALISIS PREDIKSI KEPAILITAN PADA BANK UMUM SWASTA NASIONAL DEVISA YANG TERDAFTAR DI BURSA EFEK INDONESIA TAHUN 2010–2013. Jurnal REKSA: Rekayasa Keuangan, Syariah dan Audit. 2018 Jul 4;4(1):93-112.

[17] Hardinata L, Warsito B. Bankruptcy prediction based on financial ratios using Jordan Recurrent Neural Networks: a case study in Polish companies. InJournal of Physics: Conference Series 2018 May 1 (Vol. 1025, No. 1, p. 012098). IOP Publishing.
[18] Iraqi Securities Commission: The annual financial statements of Commercial Bank of Iraq for the years 2014 to 2018.
[19] Iraqi Securities Commission: The annual financial statements of Gulf Commercial Bank for the years 2014 to 2018.
[20] Iraqi Securities Commission: The annual financial statements of the Investment Bank of Iraq for the years 2014 to 2018.
[21] Iraqi Securities Commission: The annual financial statements of the Iraqi Middle East Investment Bank for the years 2014 to 2018.
[22] Iraqi Securities Commission: The annual financial statements of United Bank for Investment for the years 2014 to 2018.
[23] Kiliç M, Kuzey C, Uyar A. The impact of ownership and board structure on Corporate Social Responsibility (CSR) reporting in the Turkish banking industry. Corporate Governance.2015 Jun 1.
[24] Kokkoris I, Anagnostopoulou M. Altman Z-Score Bankruptcy Analysis in the Greek Banking Sector. International Corporate Rescue. 2016;13(1).
[25] Le HH, Viviani JL. Predicting bank failure: An improvement by implementing a machine-learning approach to classical financial ratios. Research in International Business and Finance. 2018 Apr 1;44:16-25.
[26] Lepetit L, Strobel F. Bank insolvency risk and Z-score measures: A refinement. Finance Research Letters. 2015 May 1;13:214-24.
[27] Liang D, Lu CC, Tsai CF, Shih GA. Financial ratios and corporate governance indicators in bankruptcy prediction: A comprehensive study. European Journal of Operational Research. 2016 Jul 16;252(2):561-72.
[28] Lord J, Weech-Maldonado R, Davlyatov G. Predicting financial distress in nursing homes: An application of the Altman Z-Score model. Innovation in Aging. 2017 Jul;1(Suppl 1):185.
[29] Manaseer S, Al-Oshaibat SD. Validity of Altman Z-score model to predict financial failure: Evidence from Jordan. International Journal of Economics and Finance. 2018 Jul 20;10(8).
[30] Maricica M, Georgeta V. Business failure risk analysis using financial ratios. Procedia-Social and Behavioral Sciences. 2012 Oct 24;62:728-32.
[31] Mostofa M, Rezina S, Hasan M. Predicting the financial distress in the banking industry of Bangladesh: A case study on private commercial banks. Australian Academy of Accounting and Finance Review. 2016 Jan;2(1).
[32] Niresh J, Pratheepan T. The application of altman's z-score model in predicting bankruptcy: Evidence from the trading sector in sri lanka. International Journal of Business and Management. 2015 Nov 25;10(12).
[33] North D, Baldock R, Ullah F. Funding the growth of UK technology-based small firms since the financial crash: are there breakages in the finance escalator?. Venture Capital. 2013 Jul 1;15(3):237-60.
[34] Trejo Pech CO, Noguera M, White S. Financial ratios used by equity analysts in Mexico and stock returns. Contaduría y administración. 2015 Sep;60(3):578-92.
[35] Sironi A, Resti A. Risk management and shareholders' value in banking: from risk measurement models to capital allocation policies. John Wiley & Sons; 2007 Apr 30.
[36] Sudiyatno B, Puspitasari E. Tobin's q dan altman z-score sebagai indikator pengukuran kinerja perusahaan. Kajian Akuntansi. 2010;2(1):247233.
[37] Sun J, Li H, Huang QH, He KY. Predicting financial distress and corporate failure: A review from the state-of-the-art definitions, modeling, sampling, and featuring approaches. Knowledge-Based Systems. 2014 Feb 1;57:41-56.
[38] Verlekar RP, Kamat MS. Application and Recalibration of Altman Z-score Model for Forecasting Banking Bankruptcy in India. Wealth: International Journal of Money, Banking & Finance. 2019 Jul 1;8(2).

An Integrated Approach to Improving Strategic Performance Management in Higher Education: University of Kufa is a model from developing countries

1st Ahmed Maher Mohammed Ali[1], 2nd Yasir Sahib Malik[2], 3rd Hassnain Kadhem Ojah[3]
{ahmedm.fadhil@uokufa.edu.iq[1], yasirs.abdali@uokufa.edu.iq[2],
hassnink.alshahmani@uokufa.edu.iq[3]}

[1,2,3]Faculty of Administration and Economics, University of Kufa, Iraq

ABSTRACT. Improving Strategic Performance Management in the contemporary competitive environment has given way to Higher education to regulate their processes, resources, policies, employees, and systems to Strategic advantages and objectives. The present paper studies the Improving Strategic Performance Management with reference to its development, application, and applicability of Improving Strategic Performance Management in Higher education by literature review. The use of Strategic Performance Management in Higher Education is revealed by a survey of the literature; nevertheless, it must be redefined and tailored to the demands and standards of the institutions. The present trends in Strategic Performance Management in Higher Education are approved and recommended by the review. The theme of emerging research focuses on the Integrated Approach of Strategic Management in improving Higher Education performance, Providing a holistic view, it emphasizes the quality of processes to achieve customer satisfaction in return for achieving quality education. as well as integrating various steps to enable the achievement of the improving Strategic Performance Management in Higher Education. This paper adds to previous value relevance literature and Improving Strategic Performance Management by throwing light on the University of Kufa sector in developing countries.

Keywords: Strategic Performance Management, Higher Education, University of Kufa.

1. Introduction

In recent years, research on the relationship between Strategic Performance Management (SPM) and Business Units has grown in importance. Many academics assume that (SPM) must explicitly be advantageous to assist business activities to boost competitive advantage and performance [1]. There is evidence that the Integrated Approach behavior of stakeholders, business processes, internal processes, and Strategic performance measurement systems can result in Higher Education organizations Improving Strategic Performance [2].

Although the phrase Strategic Performance Management (SPM) has been around since the beginning, little research has been done on it at universities. It was solely conducted at university about the control system [3], [4]. Following that, strategic costing, strategic planning, control systems, and strategic performance assessment systems [5] were discussed. This is remarkable given that educational reforms began at the close of the twentieth century, and the old management of higher education has become obsolete [6]. Experiential research on (SPM) and performance has taken a contingency approach, with researchers searching for systematic links between certain (SPM) aspects and Improving performance in Higher Education [7]. Even though many countries have implemented the concept of (SPM) on a large scale, it has been accepted and realized that it is not appropriate, and it will be seen through this study how adjustments might aid in the establishment of a strong infrastructure for the future [8], [2]. The purpose of this article is to demonstrate the value of higher education institutions in developing countries, as well as their objectives and strategies for achieving these goals. As a result, they are required to give information on their priorities and resource allocation to determine the extent to which they are fulfilling their social responsibilities in light of their strategic performance [9], [3], [4]. Everyone now wants data and guidance on how to make higher education institutions more effective. As

IMDC-IST 2021, September 07-09, Sakarya, Turkey
Copyright © 2022 EAI
DOI 10.4108/eai.7-9-2021.2314436

a result, higher education institutions compete for money and market share [10]. They are now working to improve the quality of academic staff recruitment, training, as well as the system for rewarding, motivating, and utilizing them. [11]. These factors all contribute to higher education institutions' strategic performance, and as a result of these new needs, there is a greater demand than ever before for an integrated approach to strategic performance management [12], [13]. The research focuses on using the analysis method of the data from previous studies to demonstrate the role of an integrated approach to managing Strategic performance in higher education [14].

2. Literature Review

Although much research has been done on the benefits and drawbacks of traditional and modern strategic management, Little is known about their uses and catalysts for developing successful and helpful systems [15]. When reviewing the literature on dis topic, it emerged that there is little interest in managing actual performance along with implementing the human resource management philosophy in Higher Education Institutions [16]. Is this to say that higher education administrators have several options for implementing the Performance Management strategy to be the best in the industry? Or are there other, non-monetary reasons for implementing this method? [17], [3], [4].

An important question that should be asked in the case of Performance Management: If the practices were implemented in the higher education institution, what could be said about the actual results of these practices and the follow-up of these processes? [18]. According to the opinion of a number of specialists, one of the biggest obstacles is the use of performance results and their monitoring after implementation [19]. The problem of performance results is mostly an evaluation from a financial perspective only [20], [9]. So financial metrics showed difficulty in evaluating Performance Management actually in implementing and evaluating Measures of performance management and implementing This is such a unique and novel practice [21]. The autonomy of higher education institutions has been exploited [22]. However, new pressures on the environment, as well as other economic pressures such as worldwide opposition, marketization, and shifting government functions, depict a different picture [23]. They play a critical role in the development of human resources and manpower, which contribute to a country's social and economic growth and strengthen its position in the global economy [24]. To put this into another way, the university's input, in this case, our students and teachers are the processes, and the result is the number of students graduating with quality [10]. Performance management is one of Improving's attributes [3]. Through the effective implementation of Strategic Performance Management [25], this process can be improved and generate better results.

This western approach of Strategic Performance Management [26] can likewise assist developing countries. Higher education, which is a portion of Human Resource Management policies, and other tertiary education services [27] are the two distinct domains in this topic. Higher education produces two types of outputs: high-quality students and research papers produced as a result of teaching input [28]. These institutions are powered by good outputs in the form of graduates and research publications [4], rather than productivity and revenues. Strategic Performance Management (SPM) is a process for generating a shared understanding of what needs to be accomplished and how it should be accomplished, as well as an integrated strategy to developing and managing people to improve individual, team, and organizational performance [16], [15]. It is one of the most important applications in the field of human resource management, and because of its simplicity in the real world, it is easy to implement and control [12]. Higher education institutions must embrace these Strategic Management strategies to stay competitive and address any compliance and accountability issues that may arise [13]. Furthermore, if not followed correctly, (SPM) has been seen as a flaw [26]. When integrated into an organization's fundamental human resource initiatives, these approaches are effective [17]. HRM has been shown to help Strategic Performance Management and the right Human Resource Management policies that can help an employee's performance in studies and research [11]. In reality, there is a strong link between (SPM) and HRM, and it has been discovered that the correct HRM methods can improve current and future performance [9]. This aids the entire approach to the necessary Improving (SPM) model [22]. There are three different models for strategic performance. The first is to use the model to manage institution performance, and the second is to use the model to measure individual employee's Strategic Performance [24]. The third area is concerned with the integration of employee performance with the organization's overall Strategic Performance [29]. Strategic Performance Management, according to research, is a very powerful instrument that cannot be separated from any other management system [27]. It assists line managers in defining responsibilities and managing people most effectively to get the most out of them [10]. Employee stimulation, pleasure, and obligation are the outcomes of excellent project

management, all of which, at the very least, contribute to superior results from the start [3]. It is critical to introduce (SPM) to Higher Education Institutions because it aids. evaluate performance using supplied metrics and assists in recognizing employee success to reward them as well as provide opportunities for advancement through performance evaluation and feedback [2]. However, for SPM to function correctly at Higher Education Institutions, it must be modified. Some studies [6] offer a unique perspective on (SPM) practice in Higher Education Institutions. Traditional approaches (SPM), for example, are not suitable for Higher Education Institutions, according to a survey [15], [18]. As a result, existing (SPM) systems must be brought into compliance with Higher Education Institutions' duties for a compatible system that allows for progress and modification. These findings are consistent with those of other studies in the field [14]. The focus should be on academic motivation and progress. Furthermore, they assert for specific significant findings for (SPM) in Higher Education Institutions that there is a divide between the rhetoric of (SPM) and the real world at universities, especially in the research [28].

3. METHODOLOGY ADOPTED

The study focuses on how to acquire data using this method, and analyze from the research conducted earlier on the role of Strategic Performance Management in higher education from various sources such as scholarly articles, journals, books, online articles, and so on, and considering the constraints related to the realization, the study is focused on using the approach to collect data and analyze from the research conducted earlier on the role of Strategic Performance Management in higher education from various sources such as scholarly articles, journals, books, online articles, and so on. As the authenticity of the study has been verified in past studies, researchers have determined that this form of research is more appropriate for the observationally-based view and provides the objective of recommending distinguished concepts and measures for adoption. . Using the previous studies provided at the time, the analysis approach is assisting in the structure of a stronger point of view. This type of research aids in assessing the role of Strategic Performance Management in an educational system without jeopardizing ethical concerns. Previously, research on the role of higher education institutions in strategic performance management in developed and developing countries was conducted. The study has been focused on making visuals and charts from the output in a wide manner, with no opinions added. The authors stressed the importance of qualitative research and defined models for implementation, and only those were used. In addition, the variables for Strategic Performance Management have been designed to keep the path clear and free of obstructions. the amalgamation of Improving Strategic Performance Management Indicators are grouped into six viewpoints in this approach:

(1) **Educational and learning distinction:** According to research, learners can only benefit from education if they are given enough assistance and autonomy to make key decisions. Education also has a good impact on successful learning processes, as well as better and more current learning approaches. Improved student projects, courses that are more relevant to industry practices, motivation to conduct research in certain areas, and improved outcomes. Teaching, learner assistance, instructor support, learning materials, curriculum, assessment, feedback, and improvement are all consistently and continually focused on learning.

(2) Scientific research distinction: Members of the faculty and students must participate in research activities at various levels and are obligated to do so in diverse ways at each level. Scientific research in higher education focuses on integrating information at all levels and applying it to educational aims and objectives.

(3) Community participation, environment development, and stakeholders: Educational institutions serve an important role not only in the development of human resources but also in the development of society. It is the key contributor to the development of human resources to meet social requirements, and it must be included in development plans. In terms of stakeholders, educational institutions should play an important role. Encourage international relationships, practical experiences, and training programs to improve the capacity for sustainable development.

(4) Human and material resources: Should be made accessible Books, nonmaterial audio education environment in an academic environment to facilitate education administration, and all forms of related materials used in the learning process to make learning very easy according to the resources in educational institutions in development.

(5) Financial resources: It is expected that distributing cash to institutions with the best performance will achieve a balance in the quality of academic activities by the latter in contrast to the former. This guideline can be used as a motivational principle in Strategic Performance Management.

(6) Quality and Institutional capacity: To design procedures and requirements for the plan, three layers of quality were required: primary, institutional, and quality-oriented culture. As a result, intellectual, behavioral, and management competencies must be developed. It necessitates creating awareness about the need of obtaining excellence. As a result, to achieve true educational quality and institutional capability, the following factors must be considered:

- The objectives of the educational performance, the qualifications level, and the curricula;
- The competence and qualifications of the teaching staff, the study environment, and the technical assistant staff.
- The independent assessment of, on the one hand, the educational and research activity and, on the other hand, the students' results.

According to Integrated Approach to Improving Strategic Performance Management, Chancellors' staff were interviewed and Vice-Chancellors to managers on the front lines. the data collected was linked with the Integrated Approach to Improving (SPM). It was found out in the research that the University of Kufa tends to adopt a Central financial and a more administrative-based strategy that focuses on the evaluation of performance traditional instead of the Strategic Performance Management stewardship approach. There is political pressure on Iraqi universities to abide by laws traditional, they could not handle the pressure, therefore it tries to remain within the global ranking of educational institutions in developed countries. Short-term goals are more important, which can jeopardize research excellence and do not align with Higher Education Institutions' long-term goals of providing knowledge for society. Kufa University operates in a context characterized by Weak competitiveness as a result of the public financing system that allocates resources, not based on performance, in other words, the performance of each the university is yearly assessed by The Ministry of Higher Education and Scientific Research. which, subsequently, distributes the public funds to Unfairly. Such a mechanism is based on a Lack of merit principle of resource allocation and, at the same time, its application encourages a performance constancy among all national educational institutions in terms of education quality, research output, and management efficiency. These institutions' research outputs are being held back by the loss of vital education professionals. Furthermore, it limits the quality of instruction provided in the facilities. All of these significant challenges, both for improving outputs and for further growing their staff and policies, exist in the higher education scene of developing countries.

4. CONCLUSION

In Higher Education Institutions, the notion of (SPM) is present. However, it must be part of an Integrated Approach to Improving Higher Education Institutions' Vision. Traditional performance management and strategic performance management must be understood by higher education institutions. However, both of these phrases are frequently used interchangeably. Traditional performance management can be seen as a component of Strategic Performance Management systems. Higher education institutions must establish (SPM) methods to improve teacher and student performance by aligning objectives and goals with educational strategic goals. This will be an integrated approach to improving the overall performance of educational institutions so that they can achieve their goals. Strategic performance management at educational institutions must consider the performance of all members of the organization. This covers performances by faculty members as well as administration. The attention, however, Members of the academic and administrative communities should be treated equally.

The most essential indications for Strategic Performance Management, on the other hand, should be the same. The presence of a well-functioning Quality Assurance Department in educational institutions can be extremely beneficial to Higher Education in terms of implementing and designing an effective (SPM) for reviewing and saving results records. Universities should make use of emerging approaches to improve strategic performance management, such as a 360° assessment and the balanced scorecard, as evidenced by the research. In the context of Higher Education, these strategies of an integrated approach to (SPM) are advised to be used. Furthermore, the results of an integrated approach (SPM) should be used, and faculty members should be satisfied, committed, and motivated, as well as assist the university in understanding job strategic performance through metrics and recognized by correct and deductive feedback.

In conclusion, it was also noted that the central financial and administrative-based method does not work effectively and that the oversight approach is more appropriate. This, however, does not make things any easier to grasp, as professional staff and faculty members always prefer a strategic

performance management system that is more oriented toward targets and has a clear measuring technique. Most proponents of the specified approach deemed strategic performance feedback and approach certainty to be the most important factors to consider. However, in a world where knowledge and research-creation are valued, this is not the case. As a result, a number of authors have proposed the hybrid Integrated approach as the best strategic performance management system for higher education.

The strengths of both the central financial and administrative-based approach and the monitoring approach will become part of the ideology, giving universities a clear choice. The central financial and administrative strategy gives clarity, but the monitoring method promotes confidence. The university's knowledge habit process will be unaffected, and the personnel will be at ease because the Integrated method will work for their well-being and ensure high-quality long-term strategic performance from their end as well. Iraqi universities are currently compelled to use a central financial and administrative-based method to implement performance management, but with a clear path laid out, it is more probable that a hybrid Integrated approach will prove to be the best option for them.

Strategic performance management should have been a coordinated multilateral effort that drew on the expertise and experiences of both academics and support staff and went beyond typical higher education criteria. With the ultimate goal of being fruitful, the improvement of these perplexing systems must draw on the abilities of management, support, and faculty members. The findings also suggested that traditional commercial approaches to strategic performance management would not work in higher education. As a result, existing performance management methodologies and models should be customized to higher education institutions' visions, with the Integrated approach, which considers a process of institutional reform and systemic change, gradually expanding.

5. REFERENCES

[1] Samantha Evans, A. P. (2017). What are the consequences of a managerial approach to union renewal for union behavior? A case study of USDAW, Employee Relations, 39, 1, 2.

[2] Soledad Moya, D. P.-P. (2015). Performance-based Incentives and the Behavior of Accounting Academics: Responding to Changes, Accounting Education,24, 3, 208.

[3] Toke Bjerregaard, C. J. (2014). Organizational Responses to Contending Institutional Logics: The Moderating Effect of Group Dynamics, British Journal of Management, 25, 4, 651.

[4] Ramunė Kasperavičiūtė-Černiauskienė, D. S. (2016). The adoption of ISO 9001 standard within higher education institutions in Lithuania: innovation diffusion approach, Total Quality Management & Business Excellence, 1.

[5] Denise Thursfield, K. G. (2016). Exploring performance management in four UK trade unions, Employee Relations, 38, 5, 789.

[6] Jardioui, Meriam, Patrizia Garengo, and Semma El Alami. (2017). The impact of organizational culture on performance measurement system design, implementation and use: Evidence from Moroccan SMEs. Paper presented at IFIP International Conference on Advances in Production Management Systems, Hamburg, Germany, September 3–7; Cham: Springer.

[7] Kotkova Striteska, Michaela, and Viktor Prokop. (2020). Dynamic Innovation Strategy Model in Practice of Innovation Leaders and Followers in CEE Countries—A Prerequisite for Building Innovative Ecosystems. Sustainability 12: 3918.

[8] Nordiawan, Deddi, Eko Prasodjo, and Sudarsono Hardjosoekarto. (2017). Reconstruction of performance-driven culture: Application of soft systems methodology at East Java Province, Indonesia. Paper presented at 16th European Conference on Research Methodology for Business and Management Studies, Dublin, Ireland, June 22–23; Dublin: Academic Conferences and Publishing International Limited, pp. 277–86.

[9] Prokop, Viktor, Samuel Amponsah Odei, and Jan Stejskal. (2018). Propellants of University-Industry-Government synergy: Comparative study of Czech and Slovak manufacturing industries. Ekonomický ˇcasopis SAV 66: 987–1001.

[10] Smith, Marisa, and Umit S. Bititci. (2017). Interplay between performance measurement and management, employee engagement and performance. International Journal of Operations & Production Management 37: 1207–28. Striteska, Michaela, David Zapletal, and Lucie Jelínková. (2016). Performance management systems in czech companies: Findings from a questionnaire survey. E+M. Economics and Management 4: 44–55.

[11] Samantha Evans, A. P. (2017). What are the consequences of a managerial approach to union renewal for union behavior? A case study of USDAW, Employee Relations, 39, 1, 2.

[12] Muhammad Tanveer, and Asif Mahbub Karim. (2018). Higher Education Institutions and the Performance Management. Library Philosophy and Practice, e-journal, at University of Nebraska-Lincoln,1;23.

[13] Elizabeth Bates, L. K. (2014). Exploring the Impact of the Increased Tuition Fees on Academic Staffs' Experiences in Post-92 Universities: A Small-Scale Qualitative Study, Education Sciences,4, 4, 229.

[14] Achim Krausert. (2017). HR differentiation between professional and managerial employees: Broadening and integrating theoretical perspectives, Human Resource Management Review, 27,3, 442.

[15] Adelien Decramer, C. S. (2013). Employee performance management culture and system features in higher education: relationship with employee performance management satisfaction, The International Journal of Human Resource Management 24, 2, 352.
[16] Adelien Decramer, M. A. (2015). Does performance management affect nurses' well-being? Evaluation and Program Planning, 49, 98.
[17] Adelien Decramer, S. G. (2013). The impact of internationalization on volume and quality of scholarly publication performance, Public Money & Management, 33, 2, 111.
[18] Nieves Arranz, F. U. (2016). The effect of curricular and extracurricular activities on university students' entrepreneurial intention and competences, Studies in Higher Education, 1.
[19] Melinde Coetzee, J. M.-M. (2014). Human resource practices as predictors of engineering staff's organizational commitment, SA Journal of Human Resource Management,12, 1.
[20] Kamel Mellahi, J. G. (2016). Performance management practices within emerging market multinational enterprises: the case of Brazilian multinationals, The International Journal of Human Resource Management, 27, 8, 876.
[21] Layland, A., & Redding, S. (2020). Strategic performance management with a communication lens. Rockville, MD: National Comprehensive Center at Westat, f this publication can be downloaded from https://www.compcenternetwork.org.
[22] Layland, A., & Redding, S. (2017). Casting a statewide strategic performance net: Interlaced data and responsive supports. San Antonio, TX: Building State Capacity and Productivity Center.
[23] Lewis, L. (2019). Organizational change: Creating change through strategic communication. Hoboken, NJ: John Wiley & Sons.
[24] Redding, S., & Layland, A. (2017). Strategic performance for your branch: Organizing people and their work in an LEA or SEA Division or strand. San Antonio, TX: Building State Capacity and Productivity Center.
[25] Zavadsky, H., Berry, T., & Savage, T. (2017). BSCP center strategic communications toolbox. San Antonio, TX: Building State Capacity and Productivity Center at Westat.
[26] Michaela Kotkova Striteska & David Zapletal. (2020). The Role of Corporate Culture in Performance Measurement and Management Systems, international journal of Financial Studies, 2;12.
[27] Gochhayat, Jyotiranjan, Vijai N. Giri, and Damodar Suar. (2017). Influence of organizational culture on organizational effectiveness: The mediating role of organizational communication. Global Business Review 18: 691–702.
[28] Halaskova, Martina, Renata Halaskova, and Viktor Prokop. (2018). Evaluation of efficiency in selected areas of public services in European Union countries. Sustainability 10: 4592
[29] Kamel Mellahi, J. G. (2016). Performance management practices within emerging market multinational enterprises: the case of Brazilian multinationals, The International Journal of Human Resource Management, 27, 8, 876.

Sensitivity analysis of air-intake temperature on the performance of a gasoline engine of Daewoo prince (1800 cc)

Hayder Mnati[1], Asaad Almayyahi[2] and Mudhar Al-Obaidi[1]
{hhadermtm@mtu.edu.iq [1], o8l1ubad6j@gmail.com [2],
dr.mudhar.alabedt@mtu.edu.iq [1]}

[1] Middle Technical University, Technical Institute of Baquba, Baquba, Dayala-Iraq
[2] General Directorate of Vocational Education, Al Hartha Industrial School-Iraq

Abstract. The gasoline engine and especially the four-stroke engine can be considered as one of the best and well-known engine brands that attracted the interest of consumers due to its effectiveness compared to other alternative engine types. The current study has experimentally investigated the performance and fuel economy of the gasoline engine at various intake air temperatures. In this work, a four-cylinder gasoline engine of Daewoo prince (1800 cc) was selected. The air intake temperature was taken between 40 °C to 58 °C at a constant speed and load gasoline. The results confirmed that an increase in the air intake temperature causes incomplete combustion that is associated with an increase in fuel consumption. Therefore, there was a noticeable increase in fuel consumption at increased air intake temperature with an advanced and shorter combustion duration.

Keywords: Gasoline engine, Sensitivity analysis, Air-intake temperature, Fuel consumption.

1 Introduction

The internal combustion engine is characterised by converting chemical energy into mechanical energy. This is a very fast oxidising process, which chemically merges fuel and oxygen in an atmospheric air pressure that discharges massive heat energy [1]. In other words, this process burns all combustible components in the fuel by merging oxygen with carbon and hydrogen. Hosting more air into the air-fuel mixture would advance the efficiency of combustion and boost the engine performance. Simply, the ignition incident is an engine operation period where the charge ignites and speedily oxidises through the chemical reaction to discharge heat energy [2,3]. Therefore, efficient combustion would completely burn all the combustible chemical constituents in the fuel. In the same context, incomplete combustion is recognised when there is unburned fuel or left constituents. Equation (1) describes the consequence of incomplete combustion such as C, H_2, CO, or OH [4]

$$CH4 + 2(O2 + 3.76\ N2) \longrightarrow CO2+2H2O + 7.52\ N2$$

In other words, a high-performance engine of a complete mixing process can significantly limit exhaust emissions. This is attributed to the existence of closed-loop control for the fuel injection unit that aids to regulate the quantity of injected fuel considering the limited volume of intaking air. However, the air intake temperature can be considered as an alternative option to significantly improve the engine performance and fuel consumption as referred by George

IMDC-IST 2021, September 07-09, Sakarya, Turkey
Copyright © 2022 EAI
DOI 10.4108/eai.7-9-2021.2314435

and Patterson [5]. This is basically because of air temperature on the oxygen concentration of the air charged into the system that influences the combustion process through ignition delay and fuel burning rate. It is affirmed that the colder air is denser than hotter air and contains a high amount of oxygen. Several experimental studies can be found in the open literature that investigated the impact of air intake temperature on the performance of several types of gasoline engines. For instance, Kamil and Bakar [6] and Taylor and Fayette [7] explored the simplest way to improve the engine performance by changing the air intake temperature to reduce the fuel consumption at lower exhaust emissions. Abdullah et al. [8] studied the influence of air intake temperature variation between 20 °C to 30 °C on the performance indicators of naturally aspirated gasoline engines (1.6 L) include the fuel consumption and exhaust emissions at variable engine speeds and fixed load. The experimental data confirmed the growth of the fuel consumption and the emission of unburned hydrocarbons (UHCs) and carbon monoxide (CO) emissions as a result of increasing air intake temperature.

The main target of this study is to classify the best features of air intake temperature for a selected four-cylinder gasoline engine of Daewoo prince (1800 cc) that can fulfil a high-efficient engine performance at the possible low fuel consumption. This will be addressed by allocating the fuel consumption of the selected gasoline engine at a specified air intake temperature. Therefore, several experiments were carried out on the air intake system in an appropriate and protected environment to secure less polluted air.

2 Experimental setup and procedure

This section is devoted to measuring the performance indicators of a four-cylinder gasoline engine type Daewoo prince (1800 cc) water-cooled at a fixed power and operating time as a result to varying the air intake temperature between 40 °C to 58 °C. The measuring of the fuel consumption, density of the intake air, mass flow rate of intake air, and mass flow rate of fuel are considered for each run. The intake air temperature and humidity are measured using a hydro-thermometer. This is specifically carried out via the use of a sensor positioned near the air filter. However, the atmospheric pressure is assumed constant throughout the entire experiment. Also, the spark plug and filter are continuously cleaned to maintain engine consistency. Figure 1 demonstrates the schematic diagram of the gasoline engine while Table 1 reports the main characteristics of the deployed engine.

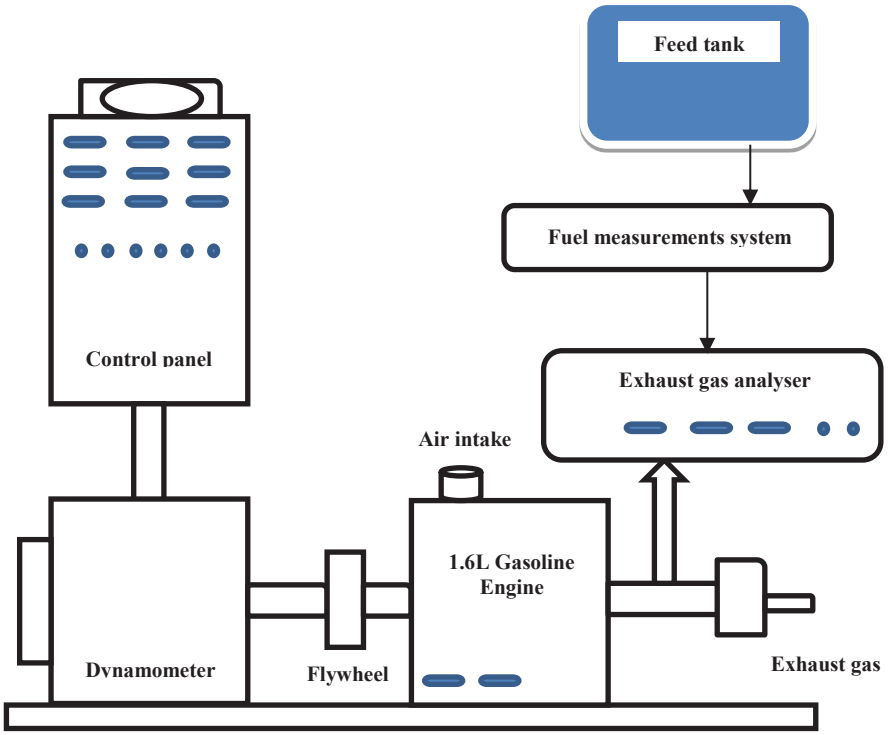

Fig. 1. Schematic diagram of four-cylinder four-stroke gasoline engine

Table 1. Specification of the four-cylinder four-stroke engine

Model and make	Daewoo prince/South Korea
General	Four-stroke/Spark ignition
Number of cylinders	Four-inline engine
Displacement	1800 cc
Bore (diameter of each cylinder)	84.8 mm
Stroke	79.5 mm
Diameter of orifice	55 mm
Max power	80 kw
Max. Rpm	5400
Fuel system	Injection
Cooling	Water

3 Modelling of fuel consumption at different air intake temperatures

Modelling of any industrial process especially gasoline engine is important to conceive the influence of operating conditions on the process performance metrics. This section exhibits a set of simple equations that have been used to characterise the calculation of air mass flow rate, air density, fuel mass flow rate, and fuel consumption.

The air mass flow rate (ma^0) (kg/s) of the engine is calculated by Eq.1

$$ma^0 = Aa\ cd\ \sqrt{2\ \rho_a\ (p_1 - p_2)} \quad (1)$$

Aa (m²) is the fixed area of the air intake orifice of the engine as illustrated in Eq. 2

$$Aa = \frac{\pi}{4} d^2 \quad (2)$$

d (m) is the diameter of the orifice of the engine. cd is the coefficient of discharge unit (-), ρ_a (kg/m3) is the air density

$$\rho_a = \frac{p_1}{R\ T} \quad (3)$$

p_1 and p_2 are the manometer pressure of the engine (atmospheric pressure), and manometer pressure of the air intake, respectively. R is the real gas constant (atm cm^3/mole K), and T (K) is the absolute temperature.

Fuel mass flow rate (mf^o) (kg/s) is calculated based on Eq. 4

$$mf^o = \rho_f\ \frac{v}{t} \quad (4)$$

$\rho_f, v,$ and t are the fuel density (kg/m^3), volume of consumed fuel (m^3), and operating time (s), respectively. In this regard, fuel consumption has been basically calculated from the consumed volume of fuel divided by the operating time.

4 Results and discussion

Table 2 presents a set of experimental data that demonstrate the variation of air intake temperature between 40 to 58 ºC at a fixed speed engine of 1500 rpm with the calculation of air density, air mass flow rate, fuel mass flow rate, and fuel consumption at a fixed operating time of 60 s for each experiment. It is important to mention that the above calculations were made at specific assumptions of fixed fuel density and fixed air intake pressure of 876.5 kg/m^3 and 1 atmosphere, respectively. These assumptions are plausible because these parameters were insignificantly changed along with the considered variation of air intake temperature.

Table 2. The experimental data of the Daewoo prince engine at fixed 1500 rpm of speed engine

Experiment No.	T (C°)	ρ_a (kg/m^3)	ma^0 (kg/s)	mf^o (kg/s)	Fuel consumption (L/hr)
1	40	1.127	0.0813	0.0009	3.72
2	43	1.117	0.0809	0.00092	3.78
3	45	1.11	0.0807	0.00093	3.84
4	47	1.103	0.0804	0.00094	3.9
5	48	1.099	0.0803	0.00096	3.96
6	50	1.093	0.0801	0.00099	4.08
7	53	1.082	0.0797	0.00102	4.2
8	55	1.076	0.0794	0.00105	4.32
9	56	1.073	0.0793	0.00109	4.5
10	58	1.066	0.0791	0.00112	4.62

A detailed discussion of the influence of air intake temperature on the air density, air mass flow rate, and fuel consumption is detailed in the next sections.

4.1 Air density

Air density is an important engine performance indicator. Basically, it is dependent on several parameters such as temperature and humidity. The air density values at different air intake temperatures are calculated using Eq. 3. In this regard, Table 2 affirmed that air density decreases with the increase of air intake temperature of a gasoline engine. More specifically, Figure 2 shows a steady-state reduction of air density as a result of an increase in air intake temperature. Increasing air temperature would increase the maturity of air particles and increase the space between them which may interpret the reduction of a number of particles per cubic meter, i.e., decreases the air density.

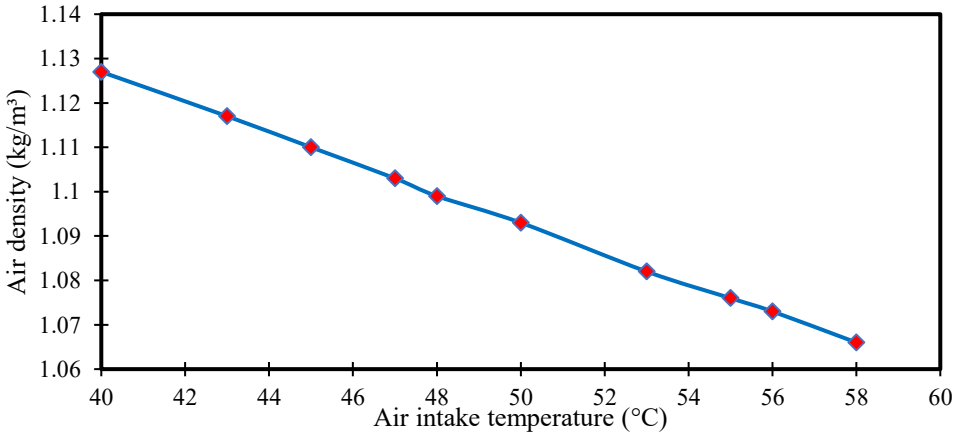

Fig. 2. Air intake temperature against air density

4.2 Air mass flow rate

Air mass flow rate was measured in kg per cubic meter of the engine at different air intake temperatures. Figure 3 depicts a noticeable decrease in the air mass flow rate due to increasing air intake temperature between 40 °C to 58 °C. This phenomenon can be attributed to the existence of lower oxygen concentration at higher temperatures. Taylor and Fayette [7] indicated that increasing of air intake temperature of the gasoline engine would create more placing between the gas molecules at fixed operating pressure. This means a higher air volume that entails increasing air temperature, which consequently results in reduced overall air mass flow rate across the sensor. Therefore, it is fair to claim the reduction of air mass flow rate as a result of increasing the air intake temperature.

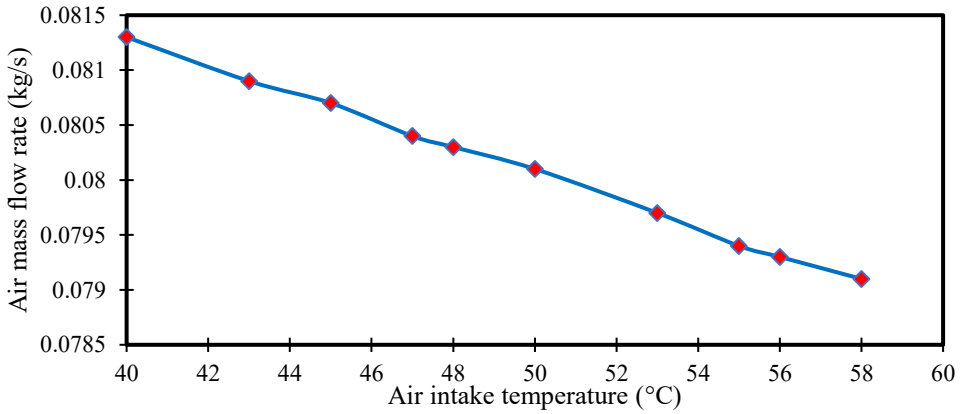

Fig. 3. Air mass flow rate against the air intake temperature

4.3 Fuel consumption

Fuel consumption is another fundamental engineering indicator of engine performance, which is directly related to volumetric fuel saving. Fuel consumption can be defined as the amount of consumed fuel for driving a given distance. This parameter has been calculated using a graded cylinder for a specified operation time.

The impact of increasing air intake temperature on the fuel consumption of gasoline engines can be seen in Figure 4. This showed a decrease in fuel consumption as a result of increasing the air intake temperature. This would confirm that lower air intake temperature delivers more oxygen to be joined with fuel components, which improved the combustion process of lower fuel consumption. Therefore, it is fair to mention that applying a lower air intake temperature can increase the engine performance better than a higher air intake temperature.

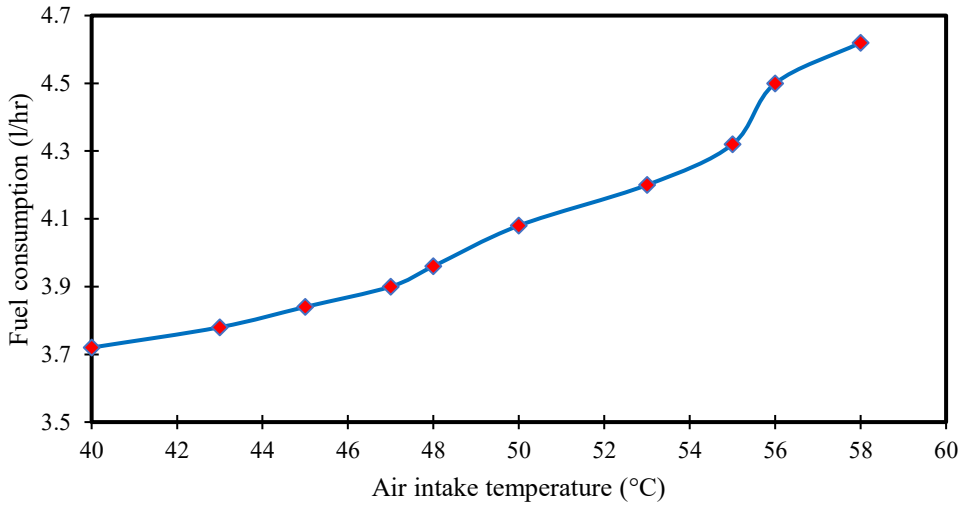

Fig. 4. Air intake temperature against the fuel consumption

Interestingly, any decrease in the air intake temperature would increase the air mass flow rate (higher oxygen concentration) as can be seen in Figure 3. Undoubtedly, the increase of charged air temperature will reduce the concentration of oxygen in the air that affects the combustion process by delaying the ignition and fuel burn rate. This is specifically compared to a higher oxygen concentration at the lower air intake temperature, which causes a complete mixing process and complete combustion. Therefore, lower fuel consumption is confirmed at a lower air intake temperature as presented in Figure 5. Therefore, a higher oxygen concentration at a low air intake temperature leads to a complete mixing process and complete combustion. Therefore, a lower air intake temperature results in improved and reduced fuel consumption. Up to this point, it is concluded that there is a significant and direct correlation between fuel consumption and air-fuel ratio. The current results corroborate the whole findings of Abdullah et al. [8] who experimentally concluded that lower air intake temperature would result in reduced fuel consumption of 1.6 L gasoline engines.

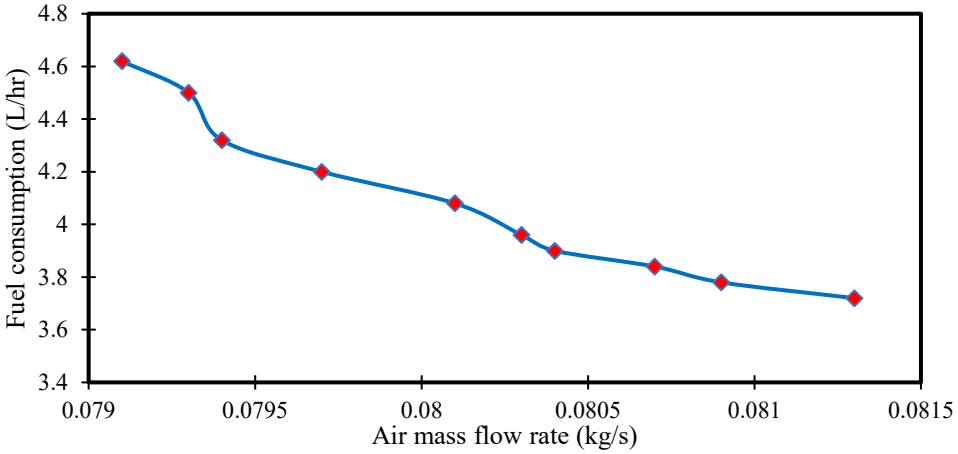

Fig. 5. Fuel consumption against the air mass flow rate

5 Conclusions

This research focused on experimentally studying the effect of air intake temperature on the engine performance, and fuel consumption of a four-cylinder gasoline engine of Daewoo prince (1800 cc). In this regard, the tests were performed at fixed engine speed and engine load with different air intake temperatures between 40 °C to 58 °C. The results confirmed an increase in fuel consumption due to a decrease in air intake temperature. Specifically, the lowest value of specific fuel consumption dominantly occurred at 40 °C of air intake temperature. This is attributed to higher combustion at lower air intake temperature of higher oxygen concentration compared to a higher air intake temperature. Moreover, other important variables were measured to systematically interpret this behavior such as air density, air mass flow rate, and fuel mass flow rate besides the fuel consumption. These variables are apparently decreased when the temperature of the inlet air increases. Therefore, it can be concluded that a lower air intake temperature would improve the fuel economy by hosting a leaner air-fuel mixture. In other words, the cold air is denser and contains a large amount of oxygen that showed rich combustion. Thus, it is recommended to control the air intake temperature to mitigate the fuel consumption of gasoline engines.

References

[1] Saber, H.A., Al-Barwari, R.R.I. and Talabany, Z.J.: Effect of ambient air temperature on specific fuel consumption of naturally aspirated diesel engine. Journal of science and engineering, 1(1), 1-7 (2013).
[2] Radcliff, R., Roark, L., and Koloski. R.: Small engines, 3 ed., American Technical Publishers (2009)
[3] Abdullah, N.R., Mamat, R., Rounce, P., Tsolakis, A., Wyszynski, M.L. and Xu, H.M.: Effect of injection pressure with split injection in a V6 diesel engine (No. 2009-24-0049). SAE Technical Paper (2009).

[4] Baker, P. and Najafi, G.: The effect of methanol-diesel blended ratio on engine performance. International Journal of Automotive and Mechanical Engineering, 8, 1385-1395 (2013).
[5] George, S., Patterson, D.: Engine Emissions: Pollutant Formation and Measurement Plenum press. New York London (2013).
[6] Kamil, M., Bakar, R.A.: Performance evaluation of external mixture formation strategy in hydrogen fueled engine. Journal of Mechanical Engineering and Sciences, 1, 87-98 (2011).
[7] Taylor, B. and Fayette, C.: The internal-combustion engine in theory and practice: Combustion, fuels. Volume 2, M.I.T. press (2012).
[8] Abdullah, N.R., Ismail, H., Michael, Z., Rahim, and A.A., Sharudin, H.: Effects of air intake temperature on the fuel consumption and exhaust emissions of natural aspirated gasoline engine. Journal Teknolog, i 76(9) (2015).

The Effect of Adopting Technology in Intellectual Capital

Mustafa Abdullah Mohammed[1], Abbas Ali Muhammad[2], Alhamzah Alnoor[3], Marwa Al-Maatoq[4]
{m.abdulla@stu.edu.iq[1], ma425770@gmail.com[2], alhamzah.malik@stu.edu.iq[3], marwamousa993@gmail.com[4]}

Southern Technical University, Management Technical College-Iraq[1,4]
Office of High Commissioner for Human Rights, Basrah, Iraq[2]
School of Management, Universiti Sains Malaysia, 11800 Pulau Pinang, Malaysia[3]

Abstract. This research seeks to provide a practical and theoretical framework on the subject of "the impact of the use of information technology in enhancing the performance of human resources." The hypothetical study plan was tested in the private sector in the province of Basra, and it includes several contracting companies. The questionnaire and the personal interview were used as a data collection method for the study, and the sample size was 213 employees. Several statistical methods were used to test the study hypotheses. The results concluded that there is an impact of information technology on the performance of human resources. Some studies have addressed these variables in the service sector because of their importance in all countries. Further studies in other sectors and the introduction of other variables are needed.

Keywords: Information technology, performance, human resources

1 Introduction

All organizations operating in various economic, industrial, commercial, and service sectors private as well as public depend on today to a large extent on information technology to accomplish their tasks and achieve their goals, through the ability of information technology to achieve many opportunities for all organizations represented by (reducing costs and making a decision, analysis, communication, and feedback) that are employed by those organizations in the field of (accounting, finance, research and development, operations management, marketing, human resource management) or any other business function (Alpar & Kim, 1990).
Also, the developments in the field of (IT) and its low costs helped organizations a lot to adapt and employ it in their work by investing very large amounts in the field of IT, which proved its ability to give economic value to the business (Raymond & Paré, 1992). Expressed by increasing competitiveness and high productivity, and thus increasing returns. In some developed countries, their budgets have shown the number of large sums invested in the field of (IT) (Hyvönen, 2007). In 2010, the United States of America spent more than $562 billion on (hardware, software) software, wired and non-wired telecommunications equipment) as well as its intention to spend $800 billion on business consulting, management, and services, much of which involves redesigning corporate business processes to take advantage of this new technology (Otim et al., 2012; Ding, 2014). Accordingly, based on the importance of the topics

IMDC-IST 2021, September 07-09, Sakarya, Turkey
Copyright © 2022 EAI
DOI 10.4108/eai.7-9-2021.2314900

of the study, and in continuity with previous research efforts in increasing intellectual enrichment in these topics, this study came to focus on the following question: "what extent is information technology available in contracting companies that enhances the performance of human resources?"

2 Literature Review

2.1 Information technology

The use of the word technology has increased dramatically during the twentieth century until this concept expanded and included several concepts of technology (Kim & Lee, 2006). It includes tools, machines, equipment, weapons, all means and material tools for technical performance. Thus, all the experiences that were created for technical and artistic innovation are the know-how. Moreover, it is what people do, their skills, the methods they use, the procedures they perform, the routine of work. In addition, it is the manufacture and use of things, which include people themselves and other things as a group or as a combination (one unit). According to (DeLone & McLean, 2016) as the material means, methods, technical processes, and skills to transform inputs such as (materials, knowledge, capital, energy) into outputs represented by (goods and services). The word technology may be of two syllables, the first TECHNO meaning (art, workmanship, technical). As for the second syllable, it is LOGY meaning (doctrine, science, theory). If the two words meet in one word, we find that every art or craft must be framed by science or a certain scientific theory (Grigoriev & Teleshevskii, 2011). It is an effective tool for the achievement and development of administrative processes in all organizations and includes a set of devices, equipment, software, communications, and the human element, whose adoption entails collecting and processing data on the activities of the organization, storing information, processing, retrieval and updating it at an economic cost, high flexibility, and relatively fast speed to respond to the requirements of its beneficiaries to form Competitive advantage of the organization (Segars, 1997).
Information technology represents the physical components of devices and their accessories such as the monitor, keyboard, printer, and others. Also, computer software, which are invisible components that manage computer resources, process, store, retrieve and transfer data. A computer consists of the following main parts, the physical components of a computer system (Agarwal & Prasad, 1998). However, the central processing unit (CPU) is one of the most important parts of the computer, where the computer is linked with the input and output units, and its most important functions are to perform arithmetic and logical operations, storage, control, monitoring and routing (Nguyen, 2009). On the other hand, the software consists of computer programs of the System Software category and the Application Software category. Investment in the field of information technology and its applications in various business fields requires directing resources towards the communication network that links data processing systems, operations, database management systems, and direct service points to the end beneficiary. Therefore, the Internet is a global network of information that includes large pockets of erased networks distributed throughout the world (McAfee, 2002). The Intranet is a private corporate network that uses internet technologies that are designed to meet the needs of employees for internal information or the exchange of data and information about operations and activities of the organization (Rad et al., 2018).

2.2 HR Performance

Performance reflects the organization's ability to achieve its near and long-term goals, which are represented in survival, growth, and adaptation by using its available resources, with high efficiency and effectiveness, and based on quality and reaching the satisfaction of stakeholders (Soltani et al., 2014). There is no agreement on the concept of performance among researchers in management science, and this difference is reinforced by the different criteria and standards adopted in the study and measurement of performance (Chow, 2012). The concept of performance is defined as the management's ability to transform the inputs into the organization's own into several outputs with specifications and the lowest possible cost. Based on previous studies it is the outcome of using the available inputs in a group of activities accomplished by the working individual, which are carried out consciously and consciously during a specific time measured by the prevailing unit of work (Wright et al., 2003). Also, it referred to the concept of performance as obligating the technical and administrative workers to provide their best achievement (Van De Voorde & Beijer, 2015).
Researchers differed in determining the dimensions of human resource performance. And productivity, liquidity ratio, and turnover ratio (Soltani et al., 2014), while others depended on the link between behavioural and economic indicators, including social responsibility, increasing profits, work turnover, sales growth, and market share (Al-Musadieq et al., 2018). The performance of human resources consists of two basic dimensions, which are the organizational dimension, which means the methods and mechanisms adopted by organizations in the organizational field to achieve their goals. As for the social dimension of management, it refers to the extent to which satisfaction is achieved among stakeholders in the organization (Beltrán-Martín & Bou-Llusar, 2018). In conclusion, the dimensions of human resource performance consist of Efficiency, which is the ability and perfection to achieve the specified goal, meaning to increase to the highest possible extent the results or outputs compared to the inputs. Effectiveness is immediate efficiency, adaptability to future goals, meaning doing the right things. Finally, quality is the production of a product or service that meets the needs and recommendations of customers, i.e., the solution to the satisfaction achieved by stakeholders because of meeting their needs (Khoreva & Wechtler, 2018).

2.3 The Relationship Between Information Technology and HR Performance

Research and studies have shown a positive relationship between information technology and decision-making (Kryscynski et al., 2018). Where the positive results were on the various dimensions and levels of decisions. The positive impact of information technology was reflected on the quality of the decision (Kassar & Singh, 2019), as well as on the decision-making process. Through its role in providing accurate and timely information in a way that enhances the positive interaction between the members of the organization and the data collected. IT can also affect the stage of mental thinking, as well as its impact on the stages of the decision-making process such as design, selection, and implementation (Van De Voorde & Beijer, 2015). This is due to the ability of information technology to reduce bias by providing objective and logical information (Sharma & Sharma, 2017). It also has a role in providing managers with the necessary information at the various necessary administrative levels.
IT has a fundamental and renewed role in increasing the effectiveness of organizational communication by reducing the time it takes to access information for decision making (Kryscynski et al., 2018). Through its great impact on internal communications, so that it increases its efficiency and effectiveness and transcends the limits of time and place (Silva et

al., 2017). Besides, the use of IT is positively related to horizontal communication patterns to increase the effectiveness of empowerment and to enable managers to make decisions at the lower level (Brockbank et al., 2018). IT helps to pass quickly access to large amounts of information faster and easier than before (Gupta et al., 2019), especially considering the development of e-mail as one of the communication channels emanating from information technology. The close relationship between IT and the means of organizational communication, as the linking of hardware components (computers), software and their applications, and networks of IT with systems such as the Internet and Intranet to create a computerized environment for easy access to information, thus, creating effective and rapid communication and information exchange (Sekhar et al., 2017). Hence, the study assumes that IT affects organizational communication and its sub-dimensions: official books, e-mail, intranet, meetings (Al Qalhati et al., 2020). Based on the previous discussion, it can be assumed:

H1: There is an influence relationship between information technology and efficiency.
H2: There is an influence relationship between information technology and effectiveness.
H3: There is an influence relationship between information technology and

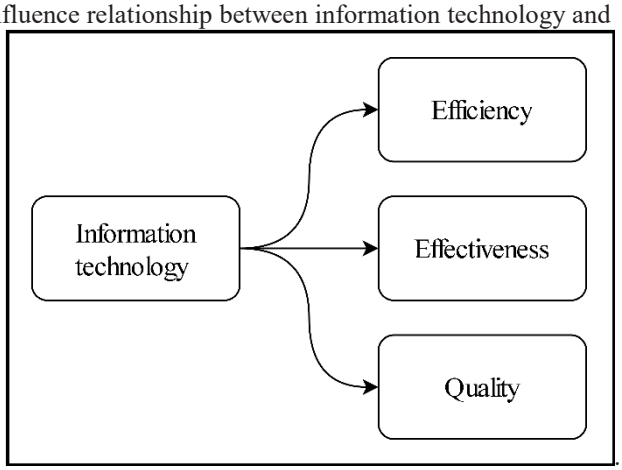

Fig. 1. Conceptual Framework.

3 Methodology

Through a review of the previous administrative literature, the researcher found a few studies that employed this approach (the use of information technology) in studying the performance of human resources, especially in the private sector, so this study is a new contribution within the Iraqi environment. In addition, most of the previous studies tried to focus on single dimensions such as the relationship between the use of information technology and organizational citizenship behaviour or the use of information technology and human resource performance, while this study will present an integrative model. Therefore, this study targeted an exploratory design. The design of the study indicates that it is the development of plans to collect information based on time and the research question, which provides evidence for data and information collection, and establishes a framework for determining the relationships between variables. The problem posed is that the design of this study adopted an exploratory design. Moreover, the hypothetical study plan was tested in the private sector in the province of

Basra, and it includes several contracting companies. The questionnaire and the personal interview were used as a data collection method for the study, and the sample size was 213 employees. The questionnaire is the basic source for data collection, which is a set of questions that the respondent records his answer to, usually by choosing one of the specified alternatives. The questionnaire was relied upon due to the researcher's accurate knowledge of what was required and how to measure the variables to be studied, and the (Likert) quintuple scale was relied upon, which is graded according to the following answers (strongly disagree "1", disagree "2", agree to some extent "3", Agree "4", strongly agree "5"). This study has used a scale of information technology based on (Luftman et al., 2017), to measure information technology and included 12 items, while the dependent variable (i.e., human resource management) was measured by adopted12 items (Alnoor, 2020). Hence, the final sample consisted of 124 administrators and 89, representing 64% of males and 36% of females. Those with a diploma represented the majority at a rate of 32%, while the percentage of those who obtained a bachelor's degree was 47% of the sample, masters, and doctorates were 21%.

4 Data analysis

We have used SEM-Modelling structural equations (SEM) in the current study to evaluate the Model-fit. It is by confronting the models dependent on multiple indicators and choose the better model. The results in Table 1 were obtained through Amos v .23. The reliable indicators are, first, RMSEA-root mean square error of approximation, and SRMR-standardized root means square residual, which both must be lower than 0.08 (Arbuckle, 2006). Secund, CFI-comparative fit index; IFI-incremental fit index; and NFI-normed fit index, its value must ≥ 0.90. Third, the ratio between X2Chi-square and df-degree of freedom, which must be lower than 2.5 (Arbuckle, 2006). We were an exam the single-factor (M1) this is done by linking all the variables to a single latent factor; the results were (X2/df= 2.109; CFI=.646; IFI= .496; NFI=.785; RMSEA=.163, Then, we was exam the two-factor (M2), innovation was identified as the first latent factor and the rest of the variables loading on innovation, the results were (X2/df= 1.468; CFI=.962; IFI= .957; NFI= .952; RMSEA= .078). Table 1 summarizes the results for three models, as a model (M3) comparing other models is better.

Table 1. Assessing the model's fit.

Models	CFI	IFI	NFI	RMSEA	X^2/df
M1	.646	.496	.785	.163	2.109
M2	.962	.957	.952	.078	1.468

In Table 2, the results show descriptive statistics that have means, SD-standard deviations, and correlations test between the study variables. Correlation coefficients between the variables are lower than (0.5). They thus do not indicate the multicollinearity problems; this also suggests that the independent variables do not overlap, which leads to the difficulty of measuring the effect of the independent variable on the function. Also, the Cronbach's alpha test was used to verify the reliability of study measures and their internal consistency. Table 2 shows that the values of Cronbach's alpha are more significant than 0.70; they are statistically acceptable in

managerial and behavioural studies (Pallant, 2020). Finally, these results support the hypotheses of the study.

Table 2. Descriptive statistics, correlations, and reliability

Variables	Mean	SD	1	2	3	4
1-Information technology	3.34	.864	1			
2- Efficiency	3.56	.903	.386**	1		
3- Effectiveness	3.35	.922	.332**	.129**	1	
4-Quality	3.57	.996	.595**	.306**	.465**	1

Amos was used to analysing the hypotheses of the current study model. Also, the Bootstrapping tool was used to test the level of significance of the indirect effects, and it is a robust tool and is widely used in similar studies.

Table 3. Testing hypotheses.

Path			Estimate	C.R	P	Label
Information technology	→	Efficiency	0.328	5.246	0.000	Supported
Information technology	→	Effectiveness	0.210	8.609	0.000	Supported
Information technology	à	Quality	0.127	9.336	0.000	Supported
Information technology	à	Human resource	0.278	9.085	0.000	Supported

Based on the path coefficients built in the above table using PLS-SEM, it is clear that most of the study hypotheses are supported as the critical success factors. Hence, there is a positive impact of information technology on human resource performance.

5 Discussion

The results reached by the researcher were based on answering the objectives and hypotheses of the research, which were formulated by reviewing the literature related to this topic, and through the data collected through the use of each of the private interviews with several general managers in contracting companies, as well as data collection through The questionnaire form, which included general managers and their assistants, department managers and divisional officials in several companies. Therefore, the results indicated the great role that information technology plays in the college, the study sample, in good proportions. The answers of the sample members for all the paragraphs related to this axis and its sub-dimensions were in good agreement, which indicates the companies' use of software related to their activities and their possession of devices, equipment, technical human resources, and communication networks to accomplish the basic college tasks, and thus provide an acceptable service. The results also showed the existence of a correlation and impact relationship between information technology in its dimensions and the performance of human resources, and these results are consistent with the results reached by each, as information technology currently contributes significantly to the completion of the basic tasks, functions, and activities of the college by providing data and information with the required speed and accuracy. The results of the current study reinforced the results of previous studies regarding the existence of a positive correlation

and the impact of information technology with its dimensions on the performance of human resources, as it helped to transcend the limits of spatial and temporal considerations and fundamentally affected the mechanism of companies' work, by enhancing the role of organizational communications represented by the intranet and e-mail (Internet), and it was consistent with the findings of the study by increasing the volume of the transmitted information and the possibility of disseminating it to wider ranges in a very short time. And then, through observation and interviews with several general managers, heads of departments, and people, there appeared the response of the organizational structures of the research sample companies to information technology within their organizational structures. Finally, the results showed the existence of an indirect positive correlation and impact of information technology on organizational performance and thus making accurate and objective decisions. While through complexity, information technology helps to provide information from various functional departments and administrative levels quickly and accurately, thus overcoming the obstacles facing decision-makers due to the diversity and complexity of tasks.

6 Limitation and Future Research

This study includes some limitations, as in other studies that can be handle in future studies. The current study focused on the contracting industry sector, there is a need to conduct more studies on other areas such as other industrial sectors or the service sector. The current study is cross-sectional, so longitudinal studies are required to support the results of the present study with more reliable results. Regarding the variables, it is possible to think about variables that fall outside the employee's mind or composition such as leadership or entrepreneurial culture, and therefore there is a need to support the current model with influencing environmental variables. These are the condition for learning and innovation. The aim of the study was the changes that occurred in the contracting industry in southern Iraq, a comparative study between the results of the current research and education in other countries that are culturally different from Iraq will provide us with more results to clarify the problem. This study includes some limitations that can be handle in future studies. The current study focused on the electric power projects industry sector, so there is a need to conduct more studies on other industries or the service sector. The other limitation is the lack of data. The panel data analysis could bring more accurate results. The current study is cross-sectional, so longitudinal investigation would be more advanced to support the results of the present study with more reliable results.

7 Conclusion

It is possible to identify the most important recommendations that resulted from the study and based on the results of the study analysis and the conclusions that were reached, we recommend the importance of directing the higher departments in the college under research towards expanding the adoption of information technology, as it is a tool that leads to making its organizational structures more flexible to adapt to current and future work requirements, through Providing its administrative units with administrative and technical competencies capable of playing its pivotal role, and enhancing its annual budget so that it can improve its systems of hardware components (computers) and advanced software, and grant it sufficient independence in making its decisions regarding its activities and tasks. We suggest expanding

reliance on the use of the Internet, intranet, and other information technology tools, to approximate the distance between the college headquarters and the affiliated departments and geographically dispersed in the governorates of the country on the one hand, and the other hand, working on the most accurate data and information in the fastest time and at the lowest cost. Because of the negative result of the study of the weak influence of communication networks on decision-making, and through personal interviews, it is due to the companies under research, or rather all Iraqi organizations, relying on the official books issued by the ministry or other ministries when taking an action or decision. Without relying on the intranet or the Internet as an official tool to transfer correspondence between them. Moreover, based on the results of the analysis of the weak relationship and negative impact value between data and organizational communication, so we suggest that the relevant authorities pay attention to databases in terms of data volume and quality, and by enhancing them with appropriate software capable of processing information with appropriate speed and accuracy. And the use of organizational communication as a primary channel for transmitting data to be invested in making quick and accurate decisions. Also, because the human element represents the effective tool in the perpetuation of the role of information technology in the work of the researched companies, so we recommend paying attention to the establishment of specialized courses in the field of information technology to raise the level of skill and knowledge capabilities to address technical problems and make updates in the operating systems. Finally, this study suggests an attempt to raise the level of the role of information technology from being a tool used to overcome obstacles and enhance opportunities for the college to improve the services provided, and because of its positive impact on all functional departments in the researched companies to making it a real partner in all programs from preparing strategic plans and setting policies and executive programs.

References

[1] Agarwal, R., & Prasad, J. (1998). The antecedents and consequents of user perceptions in information technology adoption. Decision support systems, 22(1), 15-29.

[2] Al Qalhati, N., Karim, A. M., Al Mughairi, B., Al Hilali, K., & Hossain, M. I. (2020). Technology and HR Practices in Educational Sector in Sharqiya Governate of Oman. International Journal of Academic Research in Business and Social Sciences, 10(10), 435-443.

[3] Al-Musadieq, M., Nurjannah, N., Raharjo, K., Solimun, S., & Fernandes, A. A. R. (2018). The mediating effect of work motivation on the influence of job design and organizational culture against HR performance. Journal of Management Development.

[4] Alnoor, A. (2020). Human capital dimensions and firm performance, mediating role of knowledge management. International Journal of Business Excellence, 20(2), 149-168.

[5] Alpar, P., & Kim, M. (1990). A microeconomic approach to the measurement of information technology value. Journal of Management Information Systems, 7(2), 55-69.

[6] Arbuckle, J. (2006). Amos 7.0 user's guide. Springhouse, PA: Amos Development Corporation.

[7] Beltrán-Martín, I., & Bou-Llusar, J. C. (2018). Examining the intermediate role of employee abilities, motivation and opportunities to participate in the relationship between HR bundles and employee performance. BRQ Business Research Quarterly, 21(2), 99-110.

[8] Brockbank, W., Ulrich, D., Kryscynski, D. G., & Ulrich, M. (2018). The future of HR and information capability. Strategic HR Review.

[9] Chow, I. H. S. (2012). The roles of implementation and organizational culture in the HR–performance link. The International Journal of Human Resource Management, 23(15), 3114-3132.

[10] DeLone, W. H., & McLean, E. R. (2016). Information systems success measurement. Foundations and Trends® in Information Systems, 2(1), 1-116.

[11] Ding, F. (2014). Hierarchical estimation algorithms for multivariable systems using measurement information. Information Sciences, 277, 396-405.

[12] El-Kassar, A. N., & Singh, S. K. (2019). Green innovation and organizational performance: the influence of big data and the moderating role of management commitment and HR practices. Technological Forecasting and Social Change, 144, 483-498.
[13] Grigoriev, S. N., & Teleshevskii, V. I. (2011). Measurement problems in technological shaping processes. Measurement techniques, 54(7), 744-749.
[14] Gupta, S., Kumar, S., Kamboj, S., Bhushan, B., & Luo, Z. (2019). Impact of IS agility and HR systems on job satisfaction: an organizational information processing theory perspective. Journal of Knowledge Management.
[15] Hyvönen, J. (2007). Strategy, performance measurement techniques and information technology of the firm and their links to organizational performance. Management Accounting Research, 18(3), 343-366.
[16] Khoreva, V., & Wechtler, H. (2018). HR practices and employee performance: the mediating role of well-being. Employee Relations.
[17] Kim, Y., & Lee, K. (2006, November). A quality measurement method of context information in ubiquitous environments. In 2006 International Conference on Hybrid Information Technology (Vol. 2, pp. 576-581). IEEE.
[18] Kryscynski, D., Reeves, C., Stice-Lusvardi, R., Ulrich, M., & Russell, G. (2018). Analytical abilities and the performance of HR professionals. Human Resource Management, 57(3), 715-738.
[19] Luftman, J., Lyytinen, K., & Zvi, T. B. (2017). Enhancing the measurement of information technology (IT) business alignment and its influence on company performance. Journal of Information Technology, 32(1), 26-46.
[20] McAfee, A. (2002). The impact of enterprise information technology adoption on operational performance: An empirical investigation. Production and operations management, 11(1), 33-53.
[21] Nguyen, T. H. (2009). Information technology adoption in SMEs: an integrated framework. International Journal of Entrepreneurial Behavior & Research.
[22] Otim, S., Dow, K. E., Grover, V., & Wong, J. A. (2012). The impact of information technology investments on downside risk of the firm: Alternative measurement of the business value of IT. Journal of Management Information Systems, 29(1), 159-194.
[23] Pallant, J. (2020). SPSS survival manual: A step by step guide to data analysis using IBM SPSS. Routledge.
[24] Rad, M. S., Nilashi, M., & Dahlan, H. M. (2018). Information technology adoption: a review of the literature and classification. Universal Access in the Information Society, 17(2), 361-390.
[25] Raymond, L., & Paré, G. (1992). Measurement of information technology sophistication in small manufacturing businesses. Information Resources Management Journal (IRMJ), 5(2), 4-16.
[26] Segars, A. H. (1997). Assessing the unidimensionality of measurement: A paradigm and illustration within the context of information systems research. Omega, 25(1), 107-121.
[27] Sekhar, C., Patwardhan, M., & Vyas, V. (2017). Causal modelling of HR flexibility and firm performance in Indian IT industries. Journal of Modelling in Management.
[28] Sharma, A., & Sharma, T. (2017). HR analytics and performance appraisal system. Management Research Review.
[29] Silva, A., Varajão, J., Pinto, C. S., & e Sá, J. O. (2017, April). Who can assess HR performance in IT/IS projects: a review. In World Conference on Information Systems and Technologies (pp. 779-789). Springer, Cham.
[30] Soltani, E., Gennard, J., Van der Meer, R. B., & Williams, T. (2004). HR performance evaluation in the context of TQM. International Journal of Quality & Reliability Management.
[31] Van De Voorde, K., & Beijer, S. (2015). The role of employee HR attributions in the relationship between high-performance work systems and employee outcomes. Human Resource Management Journal, 25(1), 62-78.
[32] Wright, P. M., Gardner, T. M., & Moynihan, L. M. (2003). The impact of HR practices on the performance of business units. Human resource management journal, 13(3), 21-36.

Questionnaire

A. Information technology

1. The devices used in information technology are the best and most modern currently.
2. The devices used are commensurate with the company's business and functions.
3. The computer helps a lot in solving the problems that I face in my work.
4. Computer programs are suitable for carrying out the company's tasks.
5. I find it easy to use computer programs.
6. The applied software helps to achieve in college.
7. I can get the required information within the databases.
8. I use the database to search for information.
9. You find the existing database useful to you and your department.
10. The available communication allows the exchange of information between employees
11. I can use the Internet to get things done more quickly
12. The use of the Internet helps to facilitate the completion of work.

B. Human resource performance

1. Complete the work according to the available resources.
2. Reducing the wastage of all kinds of resources.
3. Complete the work within the time.
4. A reduction in labor-related costs.
5. The ability to adapt to various environmental conditions.
6. Achieving well-established general goals.
7. Have plans and procedures that can positively deal with changes.
8. Encouraging senior management to support and disseminate quality.
9. Have the necessary human resources to help support quality.
10. Assisting in setting quality as a criterion for determining the value of individual.
11. Develop and implement long-term plans to provide high quality services to customers.
12. The company provides support for the implementation of strategic plans.

The influence of financial critical success factors on project success: Evidence from several electric power projects in Iraq

Aymen Raheem Abdulaali[1], Alhamzah Alnoor[2], Dr. Hadi Al-Abrrow[3], Hasan Oudah Abdullah[4], Sammar Abbas[5]
{aymen.abdulali@stu.edu.iq[1], alhamzah.malik@stu.edu.iq[2], hauni_2000@yahoo.com[3], hasan_oudah@yahoo.com[4], sabbas@kust.edu.pk[5]}

Southern Technical University, Management Technical College-Iraq[1]
Southern Technical University, Management Technical College-Iraq, School of Management, University Sains Malaysia, 11800 Pulau Pinang, Malaysia[2]
Department of Business Administration, College of Administration and Economics, University of Basrah, Iraq[3]
Department of Business Administration, Basrah University College for Science and Technology, Iraq[4]
Institute of Business Studies, Kohat University of Science and Technology, Pakistan[5]

Abstract. This research seeks to provide a practical and theoretical framework on "The Impact of Critical Success Factors on the Project's Success." The questionnaire and the personal interview were used as a data collection method for the study, and the sample size was 15 employees. Several statistical methods were used to test the study hypotheses. The results showed a positive effect of the critical success factors on the success of the project and their clarification of the existence of a positive correlation between the essential elements of success in the success of the project. The novelty of the context under the given circumstances of Covid-19 adds to the originality of this study. Several previous studies have also emphasized the need for this type of study in other contexts. The findings can call managers' attention to a critical issue of project success in electric power projects.

Keywords: critical success, project success, electric power projects

1 Introduction

The variables that appeared in the work environment and their impact put pressure on organizations to perform efficiently and effectively to compete in the market, the most important of which is globalization (Alias et al., 2014). The restrictions were abolished, and this made organizations face severe and continuous changes in the work environment. Marketing gaps became under attack, so the various departments resorted to formulating cautious strategies and implementing them accurately. Any mistake can cause a severe crisis and a threat of failure (Westerveld, 2003). These errors may be caused by a group of factors characterized by being the most critical to getting rid of loss called the essential factors of success, which are the entrance that was established and popularized over the past thirty years and since then it has been the focus of the attention of writers and researchers to this day because it can be considered as a warning sign and alert about the dangers facing the organization (Thi & Swierczek, 2010). Accordingly, and based on the importance of the topics of the study, and in continuity with

IMDC-IST 2021, September 07-09, Sakarya, Turkey
Copyright © 2022 EAI
DOI 10.4108/eai.7-9-2021.2314877

previous research efforts in increasing intellectual enrichment in these topics, this study came to focus on the following question: “To what extent do critical success factors contribute to the success of project management?”.
The previous regime - due to the lack of serious interest in construction and services, and spending most of the country’s resources in wars and problems that the previous administrations created or were involved in, and the result was that the cities of Iraq became like cities, devoid of the manifestations of reconstruction and lacking the simplest services, and they are to the villages closer than to the cities - despite the presence of disparity in that, between a town and another for incorrect considerations - and after the fall of the regime, people rejoiced in the new situation, perhaps changing something from this bad reality, but with all the regret, things did not go as they should be for many reasons, most of which are unconvincing, despite the magnitude of the defect left by the former regime that exists in construction and services in the governorates and the need for huge and exceptional funds and efforts to address this imbalance, and the impossibility of implementing this in a short time, but the process of reconstruction and implementation of government projects is going in many cases. We have wrong aspects of it, which made us call it the title of the problem (Al-Abrrow et al., 2019). The problem of construction and implementation of government projects is not a single problem. Still, it addresses a group of issues that led to the emergence of reconstruction and services in the current bad manner. Through field visits to electric power projects and reviewing the completion rates of projects implemented by private companies, it was found that many problems led to the resulting delay of a large part of these projects (Alnoor, 2020).

2 Literature Review

2.1 Critical success factors

Critical Success Factors The approach that was established and popularized among people over the past thirty years by several researchers and writers, where consultants and various departments have increasingly used this approach as a means of support for strategic planning, which led to an increasing and great interest in it from analysts and researchers (Ahmadabadi & Heravi, 2019). In 1961, Ronald Daniel launched the term success factors and used this term to define the information needed in the performance of administrative duties. It also suggested that information systems in the organization should focus on the success factors in most industries from three to six factors (Müller & Jugdev, 2012). Munro & whether defined it as the success or failure of the organization's effort to form the strategic plan and identify the main problems that arise from the strategic implementation process (Zwikael & Globerson, 2006). While a potential or actual crisis, decision, or plan that, if left unresolved, affects the application of the driving force of the organization or any of the essential elements of the strategy such as competitive advantage, key capabilities, the desire to enter new systems, or expectations of return and growth. It may have a big role in the organization's failure (Gemuenden & Lechler, 1997). The critical success factors are those components required to create an environment for the success and excellence of projects. The project's success is usually recognized through the recognition of customer satisfaction, which has become increasingly important due to the competitive nature of the market and the uncertainty of the environment (Ika et al., 2012).
Through the previous presentation of the concept of critical success factors (CSFs) and their nature, we noted the role and importance of these factors in organizations in general and the

project's success. Therefore, this topic has received the attention of academic and professional organizations on the one hand, and writers and researchers, on the other hand, to reach the full benefit of the application—this method by identifying the various aspects related to it. Through the desk tracking of these efforts, the researcher got a set of reasons behind the importance of critical success factors (CSFs) for organizations. These reasons are:

1. Critical Success Factors (CSFs) are closely related to the organization's long-term goals. If these factors are effectively identified, the organization will be in a better position to achieve these goals (Belout & Gauvreau, 2004).
2. The success of applying critical success factors in different organizations and fields such as health care, academic institutions, industrial organizations, social institutions, and others (Pinto & Slevin, 1989) and their importance to individuals within those organizations and at various administrative levels.
3. Critical Success Factors (CSFS) focus on determining the information of strategic planning and management control required from senior management and then linking this method to determining the strategic direction of organizations (Ika et al., 2012).
4. These factors constitute the vital elements of organizations, meaning that the failure of these factors will lead to the loss of those organizations. Accordingly, they are - that is, the factors critical failure factors for organizations (Andersen et al., 2006).

Most researchers also agree on the importance of the critical elements of success and the need to define them as a prerequisite for competitive success and as a top priority in the analytical aspect because the organization needs to know which resources have a higher competitive value and what are the elements of sustainable competitive success to be able to direct its strategy in the right direction and devote its energy to excellence in one or More than these factors as an opportunity to obtain a sustainable competitive advantage (Fan, 2010). Therefore, successful organizations must face the fact that everything is changing, and that yesterday's world is gone, and organizations must adopt the method of a rapid transition in the stage. Thus, the critical elements of success are one of the most important tools for identifying information needs, which is the first crucial step in the development, design, or process of choosing a system (Rosacker & Olson, 2008).

2.2 Project success

Success is shrouded in ambiguity, as it is an extended term with multiple directions and implications. The confusion in the views around it confirms this ambiguity because “success is unknown by its nature.” Nevertheless, it has become clear that success is an important and complex expression to explore (Mavi & Standing, 2018). Most of this difference lies in two important things: the factors that cause success in organizations and the measures used to measure success in them, as effectiveness and efficiency are criteria for measuring the organization's success through its quest to continue its activities achieve its goals. And organizational success is a composite measure that combines them, and therefore, it is more comprehensive than either of them (Bradley, 2008).

All organizations of all kinds, objectives, and activities need to use criteria to judge the organization's success. However, that only one criterion can be determined to judge the success of the organization. It is no longer acceptable to believe that there is one global standard to evaluate the success of organizations. It is difficult to find an organization that is successful in

all aspects or a failure in everything. The criteria of efficiency and effectiveness can be used to judge the organization's success (Tsiga et al., 2017). Efficiency and effectiveness are two sides of the same coin: the successful or effective organization. The source of this relationship is their direct relationship to achieve goals and maintain the organization's survival, growth, and development. And suppose effectiveness is the basis of the success of the organization. In that case, efficiency is a condition for its survival, after it has achieved success because the first is the essence of the organization. A guide for its managers in the performance of organizational activities, then increase returns and effective investment of capital, in a way that is reflected on the welfare of society and its members, because this is linked to the provision of goods and services with high quality, providing job opportunities for individuals, giving a clear view of the health of the organization's work (Banihashemi et al., 2017). The concept of efficiency is inherent in the idea of effectiveness, but it cannot be mutual. The organization may be effective but not efficient. It achieves its goals but with a loss, and the organization's inefficiency negatively affects its effectiveness. The higher the costs of achieving a particular purpose, the lower the chances of the organization's ability to survive and succeed (Haq et al., 2019). Efficiency can be used as a long-term measure, while efficiency can be considered as a short-term measure. Effectiveness is the basis of success; Efficiency is the minimum condition for survival after success (Vrchota et al., 2021).

For an organization to be successful, it must be run as an open system. The organization must find and obtain the necessary resources, interpret, and act on environmental threats and opportunities, distribute products and services, and control and coordinate internal activities in the face of external changes and uncertainty. Organizations can increase their success by providing appropriate methods and tools to enhance success (Osei-Kyei & Chan, 2017). Furthermore, successful organizations must balance their needs, aspirations, and constraints against the greater interests of the communities in which they operate. At the same time, internal resources determine organizational success. These resources can be either tangible or intangible assets or capabilities, such as accumulated knowledge and skills. Intangible resources are more important than substantial resources for the effectiveness and success of organizations (Belout & Gauvreau, 2004).

Determining the main features of project success is one of the important topics for project owners and contractors to achieve effective success in project implementation. However, studies indicate that there is a difference between various researchers to choose the basic features to determine the success of the project, not that there is almost agreement between researchers in identifying three basic factors that represent the essential dimensions for the success of the project (Zwikael & Globerson, 2006; Al-Abrrow et al., 2019).

1. Scheduling

All projects are restricted to a specific period for project completion. Completing the project on time is a major challenge for project management and a major criterion for project success by the owner, contractor, and consultant.

2. Cost

Financial resources are a key factor in the continuity of project implementation, as the owner (the project owner) is considered the lower the project's costs, the higher its profits. Hence, many owners evaluate and choose offers based on the price offered by the contractor.

3. Quality

Quality is the approved standards for accepting the final product or project, implementation stages, and compliance with the required specifications. Based on the previous discussion, it can be assumed H1 to H21: There is an influence relationship between the dimensions of the independent variable critical success factors and the dimensions of the dependent variable project success. Fig 1. shows the proposed study model based on what was mentioned in the previous sections.

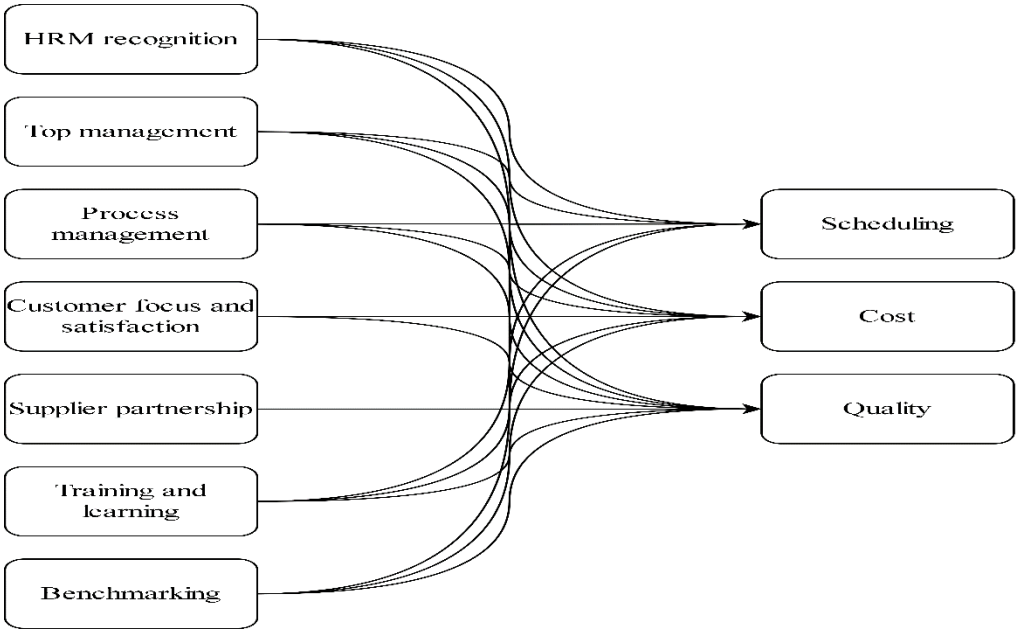

Fig. 1. Conceptual Framework.

3 Methodology

In this study, the opinions of several individuals working in several electric power projects were surveyed, and the study sample was represented by 233 individuals who were chosen randomly, based on Roscoe (1975), who believes that the sample size between (30-500) is suitable for various studies. Of the 233 questionnaires that were sent online with the help of human resource managers in the projects, 221 questionnaires were obtained. Furthermore, the response rate for this study was 94%. The questionnaire was translated and distributed for understanding by the respondents (the intended sample of the research). The questionnaire was relied upon because the researchers had accurate knowledge of what was required and how to measure the variables to be studied. And the (Likert) quintuple scale was relied on, which is graded according to the following answers (not completely agree “1”, disagree “2”, agree to some extent “3”, agree “4”, completely agree “5”)

The issue of bias is just normal in human resources research, particularly concerning questionnaires geared toward self-reports. As an answer to the problem, some preventive measures were implemented, such as guaranteeing the confidentiality of information for respondents, inversion of scale items (back translation) was formulated, and separate sources of data on the independent and dependent variables were used, 360-degree employee evaluation surveys were constructed to deal with bias (Podsakoff, MacKenzie, Lee, & Podsakoff, 2003). The 28 items were adopted according to the Hietschold et al. (2014) scale, which was used to measure sustainable performance. In addition, the project success was estimated based on (Al-Abrrow et al., 2019). Therefore, this study has been used nine times for project success. The final sample consisted of 74 administrators and 147engineers, representing 44% of males and 54% of females. Those with a diploma represented the majority at a rate of 65%, while the percentage of those who obtained a bachelor's degree was 15% of the sample, masters, and doctorates were 20%. The age group between 35-45 was the largest percentage, 67%.

4 Results

This study relied on several standards used previously in the management literature, characterized by stability and high credibility. Therefore, loading factor, Cronbach's alpha (CA), average variance extracted (AVE), composite reliability (CR) was adopted for the convergent validity test. The AVE value must be greater than 0.5, while consistency reliability (CR) must be greater than 0.7. In addition, the loading factor should be more than 0.7 (Hair et al., 2019). Table 1 shows that all criteria were met, indicating the model's reliability, as the AVE was greater than 0.5 and the CR was greater than 0.7, while the loading factors were greater than 0.7.

Table 1. assessment of the measurement model.

Construct	Items	Loadings	CR	AVE
HRM recognition	Q1	0.832	0.836	0.625
	Q2	0.835		
	Q3	0.896		
	Q4	0.864		
Top management	Q5	0.838	0.885	0.735
	Q6	0.880		
	Q7	0.833		
	Q8	0.873		
Process management	Q9	0.864	0.848	0.783
	Q10	0.812		
	Q11	0.830		
	Q12	0.844		
Customer focus and satisfaction	Q13	0.836	0.895	0.664

	Q14	0.875		
	Q15	0.879		
	Q16	0.957		
Supplier partnership	Q17	0.915	0.846	0.784
	Q18	0.947		
	Q19	0.859		
	Q20	0.947		
Training and learning	Q21	0.789	0.754	0.631
	Q22	0.794		
	Q23	0.895		
	Q24	0.835		
Benchmarking	Q25	0.776	0.789	0.673
	Q26	0.753		
	Q27	0.847		
	Q28	0.795		
Scheduling	Q1	0.803	0.884	0.664
	Q2	0.827		
	Q3	0.789		
Cost	Q4	0.894	0.783	0.825
	Q5	0.806		
	Q6	0.784		
Quality	Q7	0.918	0.936	0.774
	Q8	0.904		
	Q9	0.784		

In this study, the discriminant validity can be assessed using the one measures Fornell and Larcker (1981). Thus, the square roots of the AVE should be more than the correlations among the latent constructs—table 2 shown the discriminant validity result of this study.

Table 2. Discriminant validity result.

	Variables	1	2	3	4	5	6	7	8	9	10
1	**HRM recognition**	**0.79**									
2	**Top management**	0.42	**0.86**								
3	**Process management**	0.53	0.35	**0.88**							
4	**Customer focus and satisfaction**	0.32	0.54	0.24	**0.81**						

5	**Supplier partnership**	0.65	0.36	0.57	0.45	**0.89**					
6	**Training and learning**	0.22	0.39	0.22	0.67	0.48	**0.79**				
7	**Benchmarking**	0.52	0.43	0.43	0.35	0.13	0.33	**0.82**			
8	**Scheduling**	0.24	0.24	0.63	0.29	0.46	0.42	0.57	**0.81**		
9	**Cost**	0.65	0.57	0.25	0.24	0.63	0.69	0.44	0.34	**0.91**	
10	**Quality**	0.46	0.12	0.10	0.48	0.58	0.14	0.35	0.39	0.25	**0.88**

Table 2 shows the AVE's square roots for all constructs above the correlations among the latent constructs that indicate this study has sufficient discriminant validity. Descriptive statistics and correlations are presented in Table 3. The results suggested that the arithmetic averages of the variables were greater than the hypothetical average of (3.5), and this indicates the support of the research sample members regarding the vital role played by the critical success factors in increasing the success of the project and the standard deviation of the variables showed slight variations among the respondents' opinions as well as the fact that all the relationships among the basic variables are at the level of significance (0.05).

Table 3. Descriptive statistics and correlations.

	Variables	Mean	SD	1	2	3	4	5	6	7	8	9	10
1	**HRM recognition**	3.53	0.94	1									
2	**Top management**	3.65	0.89	0.42	1								
3	**Process management**	3.24	0.83	0.53	0.35	1							
4	**Customer focus and satisfaction**	3.73	0.84	0.32	0.54	0.24	1						
5	**Supplier partnership**	3.63	0.99	0.65	0.36	0.57	0.45	1					
6	**Training and learning**	3.89	0.95	0.22	0.39	0.22	0.67	0.48	1				
7	**Benchmarking**	3.21	0.83	0.52	0.43	0.43	0.35	0.13	0.33	1			
8	**Scheduling**	3.75	0.98	0.24	0.24	0.63	0.29	0.46	0.42	0.57	1		
9	**Cost**	3.07	0.87	0.65	0.57	0.25	0.24	0.63	0.69	0.44	0.34	1	
10	**Quality**	3.26	0.85	0.46	0.12	0.10	0.48	0.58	0.14	0.35	0.39	0.25	1

The correlation coefficients in Table 3 indicate a positive relationship between the variables and dimensions of the study. In addition to that, these results suggest that the data is valid for conducting other statistical analysis, especially testing the study hypotheses because the correlation was less than 0.9.

Since the type of hypotheses for this study are the hypotheses of an impact relationship (measurement of direct effects between variables), the researcher will use the Smart PLS program to test the hypotheses by path analysis, as the coefficients of this type of analysis are like the regression analysis coefficients in the sense that the path analysis provides the same results that it provides. Regression analysis So, there is no reason to present the same results again by regression analysis. Path analysis is based on the idea of least squares used in regression analysis. Table 4 shows the influence relationships between the study variables.

Table 4. Testing hypotheses.

Path			Estimate	C.R	P	Label
HRM recognition	→	Scheduling	0.042	4.506	0.000	Supported
Top management	→	Scheduling	0.099	7.374	0.000	Supported
Process management	→	Scheduling	0.118	5.102	0.000	Supported
Customer focus and satisfaction	→	Scheduling	0.085	4.381	0.000	Supported
Supplier partnership	→	Scheduling	0.155	7.578	0.000	Supported
Training and learning	→	Scheduling	0.104	3.088	0.000	Supported
Benchmarking	→	Scheduling	-0.004	8.876	0.000	Supported
HRM recognition	→	Cost	0.349	6.245	0.000	Supported
Top management	→	Cost	0.144	4.253	0.000	Supported
Process management	→	Cost	0.193	4.352	0.000	Supported
Customer focus and satisfaction	→	Cost	0.356	8.698	0.000	Supported
Supplier partnership	→	Cost	0.325	7.067	0.000	Supported
Training and learning	→	Cost	0.323	3.457	0.000	Supported
Benchmarking	→	Cost	0.270	3.364	0.000	Supported
HRM recognition	→	Quality	0.349	9.855	0.000	Supported
Top management	→	Quality	0.144	4.554	0.000	Supported
Process management	→	Quality	0.193	3.475	0.000	Supported
Customer focus and satisfaction	→	Quality	0.356	2.447	0.000	Supported
Supplier partnership	→	Quality	0.325	4.357	0.000	Supported
Training and learning	→	Quality	0.323	4.802	0.000	Supported
Benchmarking	→	Quality	0.270	5.092	0.000	Supported

Based on the path coefficients built in the above table using PLS-SEM, most of the study hypotheses are supported as the critical success factors. Their dimensions positively impact the success of the project and its dimensions.

5 Discussion

The findings of this study were based on answering the objectives and hypotheses of the research, which were formulated by reviewing the literature related to this topic, and through the data collected using each of the private interviews with several managers working for several electric power projects, as well as collecting data through the questionnaire form. The results of the study analysis revealed that the senior management and project managers in the organization need to observe and follow up on a set of important characteristics such as leadership roles. Hence, the results demonstrate team building and participation and team mental models to aid in developing the project team. Thus, this indicates that project managers need to learn basic

skills and the technical skills required to lead the project management, related to understanding the other side of the benefits achieved by project management. On the other hand, the results showed a direct positive impact relationship between the critical success factors and their dimensions and the project's success and dimensions. This explains that the reasons for this are due to effective distribution leading to increased quality, cost, and scheduling levels. Finally, the results showed a significant correlation between critical success factors and project success, due to the role of essential elements of success in providing solutions to work problems using various means such as administrative and statistical methods and technical standards.

6 Limitation and Future Research

This study includes some limitations that can be handle in future studies. The current study focused on the electric power projects industry sector, so there is a need to conduct more studies on other industries or the service sector. The other limitation is the lack of data. The panel data analysis could bring more accurate results. The current study is cross-sectional, so longitudinal investigation would be more advanced to support the results of the present study with more reliable results.

Regarding the variables, there is a lack of variables that fall outside the employee's mind or composition, such as leadership or entrepreneurial culture. Therefore, there is a need to support the current model with influencing environmental variables. These are the condition for learning and innovation. Because other variables represent personal readiness variables for learning, for example, curiosity and intellectual perseverance, we suggest lengthening the current model to become more accurate in the reached results. The aim of the study was the changes that occurred in the electric power projects industry in southern Iraq, so a comparative study between the results of the current research and learning in other countries that are culturally different from Iraq will provide us with more products to clarify the problem.

7 Conclusion

Considering the discussion of the results that have been reached, there is the importance of stimulating the vision and collective participation in drawing the picture of the future that the individuals and the organization aspire to achieve, developing the spirit of cooperation among all the contributors to the project and urging teamwork that serves the success of the project. Thus, to overcome the obstacles and obstacles facing the success of project management through continuous education of the need to choose the most efficient contractors to overcome the problems that hinder the completion of projects and public education that the project is of general interest that achieves the effective contribution of the parties related to the implementation of the project from ministries and government agencies. In addition, treatments must be provided for some cases of delay, in addition to improving the quality and cost through a few series of administrative reviews, activating the subject of the economic and technical feasibility study by the governorate directorates, and placing the necessary tools and machines for work close to the worksite. Hence, the necessity of empowering workers and giving them the freedom to make decisions can solve problems quickly and before they escalate by giving them more powers than it is now.

References

[1] Ahmadabadi, A. A., & Heravi, G. (2019). The effect of critical success factors on project success in Public-Private Partnership projects: A case study of highway projects in Iran. Transport Policy, 73, 152-161.

[2] Al-Abrrow, H., Alnoor, A., & Abbas, S. (2019). The effect of organizational resilience and CEO's narcissism on project success: Organizational risk as mediating variable. Organization Management Journal, 16(1), 1-13.

[3] Al-Abrrow, H., Alnoor, A., & Abbas, S. (2019). The effect of organizational resilience and CEO's narcissism on project success: Organizational risk as mediating variable. Organization Management Journal, 16(1), 1-13.

[4] Alias, Z., Zawawi, E. M. A., Yusof, K., & Aris, N. M. (2014). Determining critical success factors of project management practice: A conceptual framework. Procedia-Social and Behavioral Sciences, 153, 61-69.

[5] Alnoor, A. (2020). Human capital dimensions and firm performance, mediating role of knowledge management. International Journal of Business Excellence, 20(2), 149-168.

[6] Andersen, E. S., Birchall, D., Jessen, S. A., & Money, A. H. (2006). Exploring project success. Baltic journal of management.

[7] Banihashemi, S., Hosseini, M. R., Golizadeh, H., & Sankaran, S. (2017). Critical success factors (CSFs) for integration of sustainability into construction project management practices in developing countries. International Journal of Project Management, 35(6), 1103-1119.

[8] Belout, A., & Gauvreau, C. (2004). Factors influencing project success: the impact of human resource management. International journal of project management, 22(1), 1-11.

[9] Bradley, J. (2008). Management based critical success factors in the implementation of Enterprise Resource Planning systems. International Journal of Accounting Information Systems, 9(3), 175-200.

[10] Fan, D. (2010, July). Analysis of critical success factors in IT project management. In 2010 2nd International Conference on Industrial and Information Systems (Vol. 2, pp. 487-490). IEEE.

[11] Fornell, C., & Larcker, D. F. (1981). Evaluating structural equation models with unobservable variables and measurement error. Journal of marketing research, 18(1), 39-50.

[12] Gemuenden, H. G., & Lechler, T. (1997, July). Success factors of project management: the critical few-an empirical investigation. In Innovation in Technology Management. The Key to Global Leadership. PICMET'97 (pp. 375-377). IEEE.

[13] Hair, J.F., Risher, J.J., Sarstedt, M. and Ringle, C.M. (2019), "When to use and how to report the results of PLS-SEM", European Business Review, 31(1), 2-24.

[14] Hietschold, N., Reinhardt, R., & Gurtner, S. (2014). Measuring critical success factors of TQM implementation successfully–a systematic literature review. International Journal of Production Research, 52(21), 6254-6272.

[15] Ika, L. A., Diallo, A., & Thuillier, D. (2012). Critical success factors for World Bank projects: An empirical investigation. International journal of project management, 30(1), 105-116.

[16] Mavi, R. K., & Standing, C. (2018). Critical success factors of sustainable project management in construction: A fuzzy DEMATEL-ANP approach. Journal of cleaner production, 194, 751-765.

[17] Müller, R., & Jugdev, K. (2012). Critical success factors in projects: Pinto, Slevin, and Prescott–the elucidation of project success. International journal of managing projects in business.

[18] Osei-Kyei, R. and Chan, A.P.C. (2017), "Perceptions of stakeholders on the critical success factors for operational management of public-private partnership projects", Facilities, Vol. 35 No. 1/2, pp. 21-38

[19] Pinto, J. K., & Slevin, D. P. (1989). Critical success factors in R&D projects. Research-technology management, 32(1), 31-35.

[20] Rosacker, K. M., & Olson, D. L. (2008). Public sector information system critical success factors. Transforming Government: People, Process and Policy.

[21] Thi, C. H., & Swierczek, F. W. (2010). Critical success factors in project management: implication from Vietnam. Asia Pacific Business Review, 16(4), 567-589.

[22] Tsiga, Z., Emes, M., & Smith, A. (2017). Critical success factors for projects in the petroleum industry. Procedia Computer Science, 121, 224-231.
[23] ul Haq, I., Ali, S. M., & Nawaz, M. T. (2019, March). An analysis of the critical success factors in ICT sector of Pakistan. In 2019 5th International Conference on Information Management (ICIM) (pp. 45-53). IEEE.
[24] Vrchota, J., Řehoř, P., Maříková, M., & Pech, M. (2021). Critical Success Factors of the Project Management in Relation to Industry 4.0 for Sustainability of Projects. Sustainability, 13(1), 281.
[25] Westerveld, E. (2003). The Project Excellence Model®: linking success criteria and critical success factors. International Journal of project management, 21(6), 411-418.
[26] Zwikael, O., & Globerson, S. (2006). From critical success factors to critical success processes. International journal of production research, 44(17), 3433-3449.

Design, Simulation and Implementation High DC-DC Converter with 1-Phase Inverter Feeding Load from a Single Photovoltaic Panel

Khalid Badr Yas[1]
khalidbaderyass@gmail.com
Ministry of Education, Iraq. Baghdad[1]

Abstract. A DC/DC converter is used in a traditional single-phase two-stage grid-connected micro-inverter for photovoltaic (PV) applications to acquire the most DC power from the PV module. The rising voltage of the PV module to a grid voltage level is limited to a specified value in this inverter. Furthermore, the two-stage inverter is less efficient due to the lack of separation between the input and output. To supply an alternating current (AC) to the load, a single-stage Push-Pull PV micro-inverter was designed, simulated, and constructed in this research. To keep the produced power as high as possible, a microcontroller PIC 16F877A is used to track the highest power point of the panel and compute the appropriate pulse width of the converter. Sinusoidal pulse width modulation is employed for this purpose. The incremental conductance algorithm and maximum power point tracking (MPPT) technique are implemented using the PIC microcontroller. The PV module is tested using Matlab/Simulink software under varied solar irradiance (G) and ambient temperature (T) conditions. Experimentation results from a lab prototype are also given. The prototype will become a system that feeds a single-phase AC load with a clean sinusoidal current waveform from a single panel. The key advantage of this model is that it includes a real microcontroller, just like in real life, so that the MPPT algorithm code used in simulation will be used in real life.

Keywords: Photovoltaic Panel, Push-Pull DC-DC Converter, Micro-Inverter, Incremental Conductance, Matlab Simulink, Microcontroller.

1 Introduction

Solar energy will have a huge impact on its long-term benefits, which will be widely spread throughout the world because it is clean, inexhaustible, an independent resource, and its development is affordable because it is climate-friendly and an ideal power source for energy-deficient areas, making it advantageous [1]. There are many application fields for the conversion of solar energy into electrical energy such as vehicular, naval, residential, aircraft, and space applications [1-3]. As a result, solar energy is likely to play a significant part in global electric power generation in the next decades. A photovoltaic (PV) system can be used to harvest this energy. PV systems can be used either as stand-alone systems or in conjunction with the utility grid. In this study, stand-alone PV systems are designed to function independently of the electric utility grid, and they are often planned and sized to serve specific DC and/or AC electrical needs. Only a PV array may be used to power these systems. A direct-coupled system, in which the DC output of a PV module or array is directly connected to the converter, is the most basic sort of stand-alone PV system. Because direct-coupled systems need electrical energy storage (batteries), the load functions only during daylight hours, making

IMDC-IST 2021, September 07-09, Sakarya, Turkey
Copyright © 2022 EAI
DOI 10.4108/eai.7-9-2021.2315180

them ideal for typical applications like ventilation fans, water pumps, and small circulation pumps for solar thermal water heating systems [4-5]. The rapidly falling cost of stand-alone PV modules, advances in power electronics, and government incentives for PV systems make it critical that PV system penetration on the utility grid continues to rise, particularly on low and medium voltage grids [6]. Nowadays, more and more complex PV systems are being studied for designing and implementation of efficient PV system strategies. The input voltage to DC/DC converters varies substantially in regulated switch mode power supplies, notably in the case of PV supply sources due to unpredictable and rapid variations in solar irradiation and cell operating temperature. Several switching system connection topologies have been presented [7] with the goal of achieving the appropriate voltage level for specific applications such as pumps, motors in general, and power supply at various times of the day. The application in this case is to provide power to the load. This is accomplished by employing an inverter to convert the DC electric power generated by the PV array to AC electricity. The load is supplied with the inverter's output power. The (PV) array feeds a power optimizer, which is a DC/DC converter. It will supply its output power to the load or inverter. The power optimizers can extract maximum power from PV systems by continuously tracking the maximum PowerPoint. This is done by individually tuning the performance of the panel through (MPP). A power optimizer is ideal for treating PV arrays during the variation in irradiance and temperature. Maximum power point tracking is a technique usually utilized with a photovoltaic (PV) array system to track the point of maximum power. This is done by adjusting the pulse width of the DC/DC converter's electronic switch, to reach the maximum power point at different conditions [8-9]. In this work, a step-up (Push-Pull) DC/DC converter is used to fulfill the requirement of the inverter. It consists of five components: transformer, electronic switch, diode, and an input and output capacitor. The choice of the (DC/DC) Push-Pull converter configuration provides the lowest cost and the higher efficiency [10]. The maximum power point tracker has numerous algorithms such as incremental conductance, perturb and observe method, constant voltage, and constant current, etc. The selection between them is based on the operating conditions of the PV and the advantages of one of them due to many requirements and conditions. The incremental conductance algorithm is the most often utilised because of its great adaptability and accuracy throughout all seasons [11]. It is based on changes in light and temperature. On the power curve of a photovoltaic (PV) array, the MPP is found at the zero slope point. MPP has a negative on the right and a positive on the left. The terminal voltage of a photovoltaic (PV) array is always adjusted according to the MPP [12]. The (PV) array voltage and current must be monitored to estimate the conductance and incremental conductance. The maximum power point (MPP) is tracked in real-time using a microcontroller in this paper to solve the aforementioned drawbacks. A microcontroller has the advantage of not oscillating close to MPP. This type of control is only found in the Push-Pull converter, which uses a high-frequency transformer to create galvanic isolation between the input and output sides as well as a high conversion ratio. The PV module has been modeled and simulated based on the one-diode PV model using Matlab/Simulink software. The system to be simulated and implemented is shown below. It is composed of three main parts; the first part is the photovoltaic (PV) panel, which is intended to convert solar energy to electric energy. The second part is represented by the DC to DC converter triggered by using the Max-mum Power Point Tracker (MPPT) algorithm. Because photovoltaic (PV) arrays have a poor efficiency, the MPPT is used to extract maximum power and improve efficiency under various conditions. The third part is a 1-phase inverter switched by the sinusoidal pulse width modulation (SPWM) technique to provide sinusoidal voltages supplying the 1-phase electric load.

2 System Description

2.1 One-diode PV Cell Model

A PV cell model is represented by the corresponding circuit in Fig 1. A one-diode model [13] is another name for this concept. The output voltage and current of PV are Vpv and Ipv, which are coupled in parallel and series, respectively. Is is the diode saturation current, and Isource is the photocurrent source. The basic equation that represents the I–V characteristic of the ideal PV cell is [14] derived from semiconductor theory.

$$I_{source} - I_d - \frac{V_d}{R_p} - I_p = 0 \quad (1)$$

$$I_d = I_s \left[\exp\left(\frac{q V_d}{Nkt}\right) - 1\right] \quad (2)$$

$$V_{PV} = V_d - R_{se} . I_{PV} \quad (3)$$

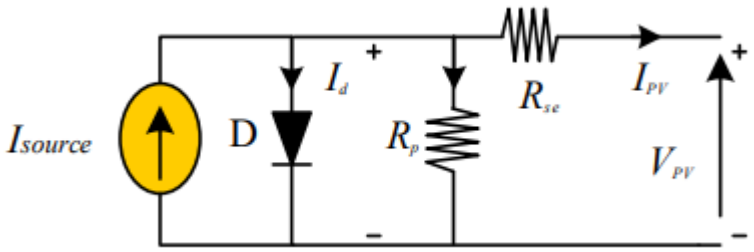

Fig. 1. Equivalent circuit of one–diode model for PV cell.

2.2 MPPT

As demonstrated in the flowchart in Fig 2, the incremental conductance method is utilised to change the duty cycle of the converter to follow the MPP. The I_C's algorithm has many topologies, but all that depends on the ΔV and ΔI. The naming came from the term $(\Delta I/\Delta V)$ which is known as incremental conductance [15]. This value makes the algorithm go in the right direction and achieving the goal at which $\{(\Delta P/\Delta V) = 0\}$ means reaching the maximum power point, as seen in Fig 3. The I-C algorithm catches the maximum power point exactly and still observing the system by observing the ΔV and ΔI, if they have any changes, then it will repeat the procedure to catch the maximum power point again. After calculating the ΔV and ΔI through the new condition, if the $\Delta V \neq 0$ this means the algorithm point is somewhere, but not on biggest power point, so the algorithm looking again at the sign of the new $(\Delta P/\Delta V)$, whether it is positive or negative for pursuing the right direction to reach the MPP again.

Assuming it catching up the maximum power point (MPP) at certain weather condition if the condition change suddenly the ΔV not change and still equal to zero, but the ΔI has greatly changed, that makes the algorithm to operate again and so on. The magnitude of the increment controls how quickly the MPP is tracked [16]. It is possible to increase the increment size, but

at the expense of accuracy [17]. Figure 4 depicts the algorithm's responsiveness to changing weather conditions.

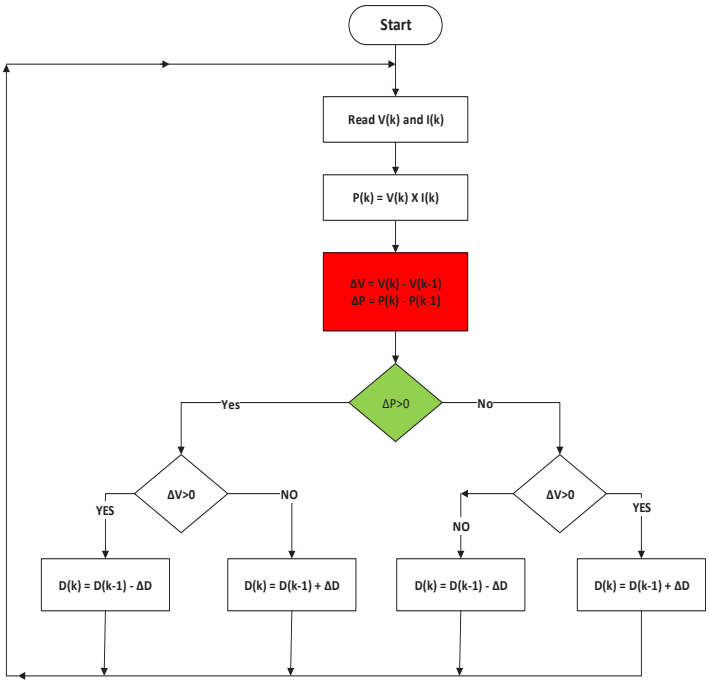

Fig 2. I_C's algorithm.

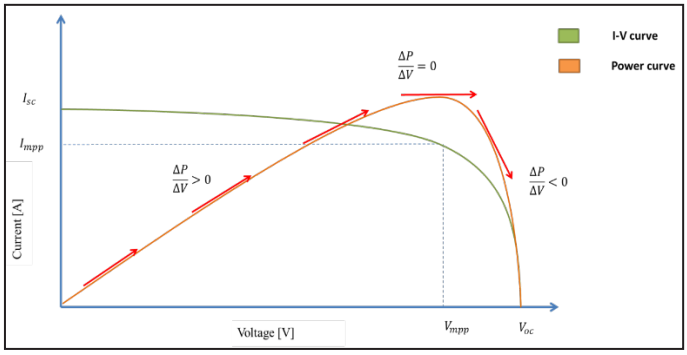

Fig 3. Operation of I_C Algorithm.

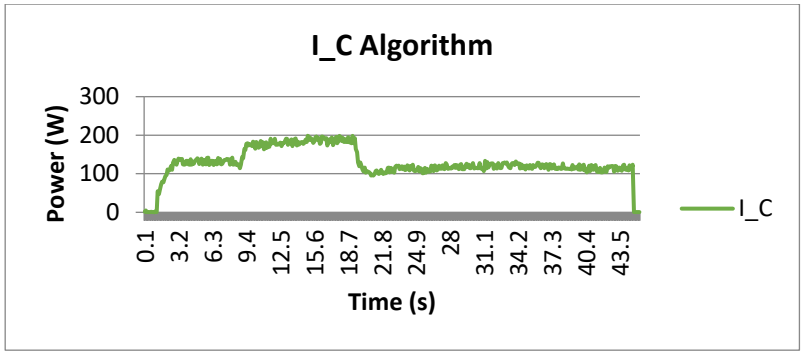

Fig 4. I_C Response

2.3 DC/DC Converter

A step-up DC/DC Push-Pull converter must be utilised to feed a 1-phase, 50Hz, 220 V AC load from low voltage (PV) panels, as shown in Fig. 5. This converter feeds the 1-phase inverter by the required voltage. The DC/DC converters are widely used to step up the DC voltage or to regulate (PV) array voltage. The input of these converters is a fluctuated DC voltage, which is supplied by the PV panels. So the mean DC output voltage should be adjusted to be equal to the required value. The quantity of energy absorbed from the PV and given to the inverter is continuously adjusted to accomplish output voltage regulation in the DC/DC converter. The maximum power point tracker (MPPT) algorithm adjusts the duty cycle for these two essential processes of energy absorption and injection.

The output from PIC is a PWM signal with a variable duty cycle ratio that is applied to the main IGBT through the optocoupler. Two optocouplers are used for the two IGBTs SAC_1 and SAC_2. The PV module voltage and current are sensed using a voltage divider and a current sensor, respectively. The signals of these sensors are fed to the microcontroller to implement the MPPT algorithm. A bank of input electrolytic capacitors consists of 2400µF connected across the PV input side.

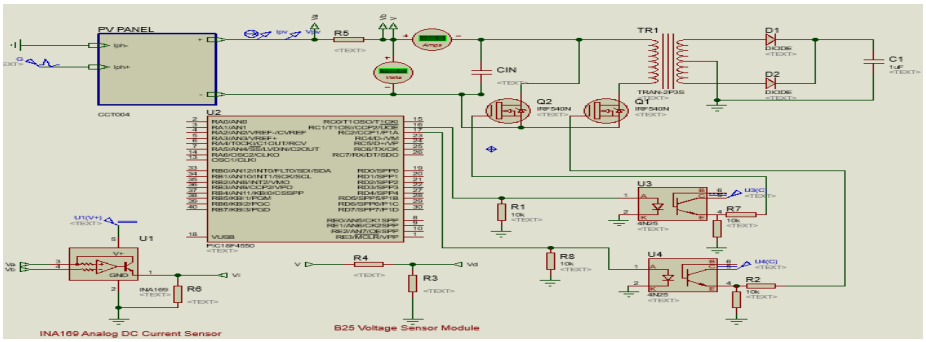

Fig 5. The Power Optimizer Simulation Typical Connection.

2.4 Inverter

The main purpose of a DC/AC full-bridge converter (inverter) is to produce alternating voltage and current waveforms from a DC power source. These types of power waveforms are found into many methodologies according to the load requirement. Hence, the output waveform parameters like magnitude and frequency can be controlled. Inverters can be divided into two types: voltage source inverter (VSI) and current source inverter (CSI). The voltage source inverters are most commonly used with a V/f control of Ac load, as seen in Fig 6. The PWM signals of the IGBTs generated by the microcontroller. The gate driver is implemented using an IR2110 integrated circuit. These drives are ideally suited for driving power IGBTs and used in inverter applications.

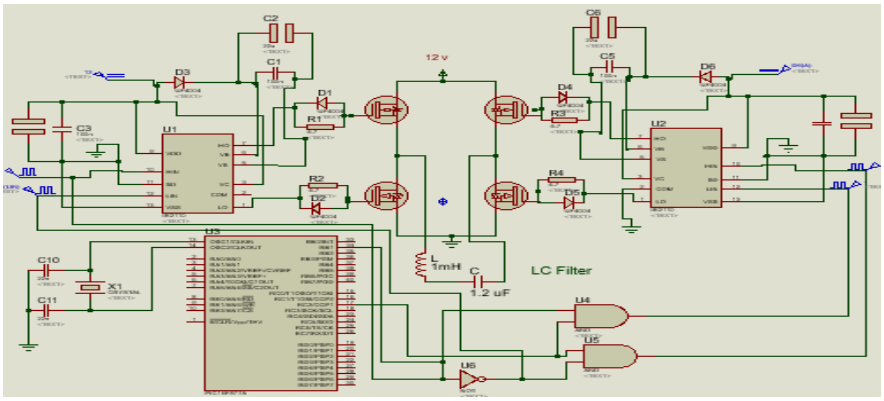

Fig. 6. Circuit of a Power Inverter with an LC Filter.

2.5 Microcontroller Based SPWM

This system's basic control circuit is a microcontroller that was designed to generate two digital SPWMs that are 180 degrees apart. The SPWM switching technique is used to provide a clean sine wave. This approach uses the same switching pattern as the DC-to-AC two-leg inverter. The SPWM is a dependable method. It's used in a variety of power electronics applications, including motor drivers, UPS systems, and renewable energy systems. Following the original sine wave amplitude, SPWM switching techniques are described as constant amplitude pulses with a variable duty cycle for each period. The most frequent way to make this signal is to compare a sinusoidal and a triangular waveform, as seen in Fig 7. We use a peripheral interface controller (PIC) microcontroller to replace the traditional technique in this study. Using the built-in PWM module, the microcontroller can stack commands to generate the required pulse width modulation waveform. Using the PIC16F877A system, the microcontroller generates a variable pulse width modulation signal that regulates the applied voltage on the gate drive. The microcontroller is simple and adaptable, allowing for real-time control algorithm changes without requiring any hardware changes. This inverter could be used in a stand-alone balanced load system or a grid-connected system powered by a photovoltaic panel.

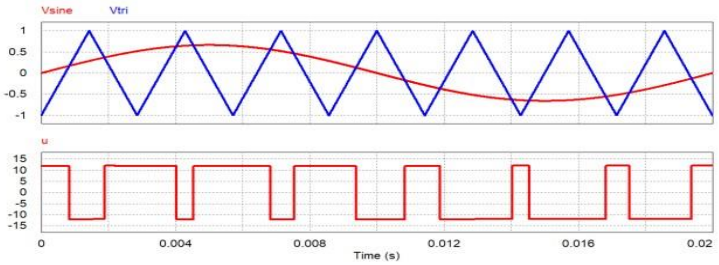

Fig 7. SPWM Generational Method.

Table 1. illustrates all of the criteria that were considered as well as the final design [18, 19].

NO.	Parameter	Value
1	Converter parameters	
2	V_{pv}	34-38V
3	I_{pv}	8A
4	P_{out}	290W
5	D_{max}	0.5
6	f_s	30 kHz
7	C_{in}	2400 uF
8	N	12
9	V_{out}	640V
10	η	0.85
11	Transformer design parameters	
12	N_p	7
13	N_s	84
14	PIV	800 V
15	Inverter Parameters	
16	IGBT's PIV	1800 V
17	Filter Parameters	
18	L	1 mH
19	C	1.2 uf

3 Simulation Results

The simulation results, as shown in Figs below show the P–V and I–V characteristics of the PV module for the one-diode model. The PV module has been tested by Matlab/Simulink as seen in figures 8 and 9 based on its datasheet parameters. To show the effects of the solar irradiation and ambient temperature on PV module characteristics, they illustrate and verify the nonlinear PV and IV PV output characteristics module. The PV module is tested for various solar irradiation and ambient temperature. To demonstrate the influence degree of each parameter on the characteristics of the PV module, the solar irradiation and ambient temperature should be varied independently. In addition, to demonstrate the impact of ambient temperature and solar irradiance on PV module properties. They demonstrate and verify the non-linear IV

and PV of PV output characteristic, and it has been tested under different solar irradiation and temperature. The solar radiation and ambient temperature must be changed autonomously to show the effect degree of each parameter on the characteristics of the PV module. Figs 10 and 11 show the IV and PV variations of one-diode model under varying temperature levels (0, 25, 55°C) and constant irradiation (1000 W/m²). When the temperature of the PV array is raised at constant solar irradiation, the voltage of the PV array falls, and the current rises, resulting in a decrease in the PV array's generated power.

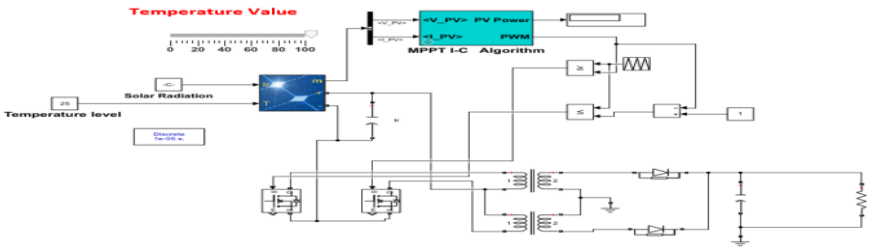

Fig 8. Simulated of the photovoltaic system under fixed irradiation and various temperature.

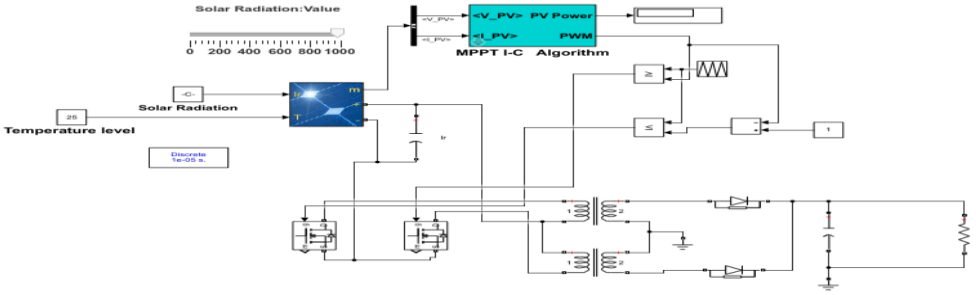

Fig 9. Simulated of the photovoltaic system under fixed temperature and various irradiation.

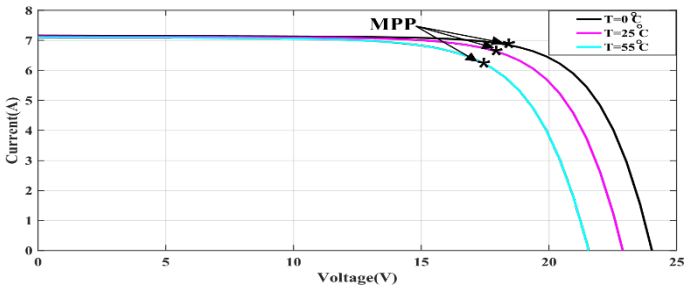

Fig 10. I-V curve under fixed irradiation and various temperature.

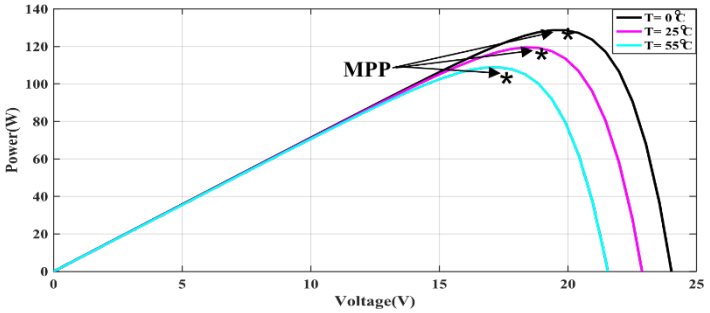

Fig 11. P-V curve under constant irradiation and various temperature.

The I-V and P-V characteristics of the one-diode model are shown in Figs 12 and 13 for different irradiation levels (1000, 800, 600 W/m^2) and constant temperature (25°C). The results displayed in the figures below show that when solar radiation is reduced from a constant temperature of 25°C, the PV array's voltage drops from V, the current drops, and the PV array's generated power drops.

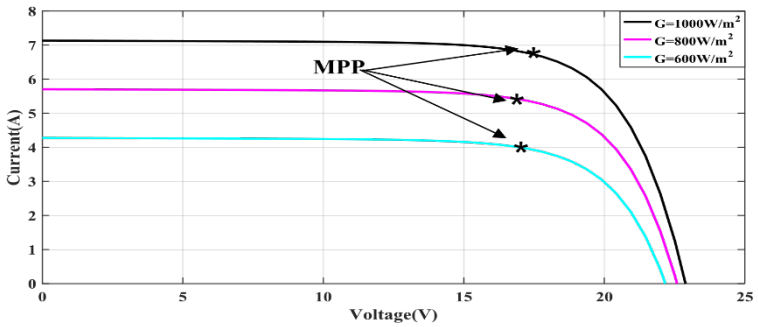

Fig 12. I-V curve under varied irradiation and constant temperature.

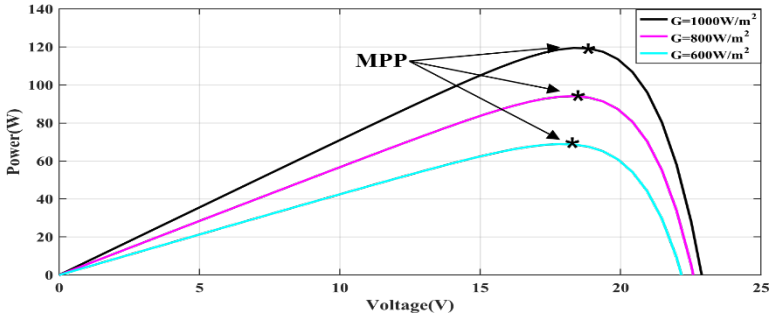

Fig 13. P-V curve under varied irradiation and constant temperature.

4 Experimental Implementation

The hardware power stage circuit for the proposed system is implemented using the design specification above. The voltage of the PV module has a range between 34-38V that is connected to the input terminals DC/AC inverter via Pull-Pull converter power circuit. The practical testbed of the converter is illustrated in Fig 14. While the practical inverter circuit implementation is in Fig 15. The results without and with filter are shown in Fig.16 and Fig. 17 respectively. The output voltage of the inverter is 220 V.

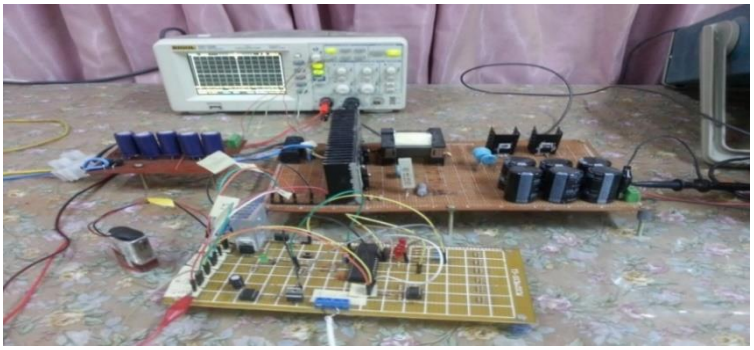

Fig 14. Practical Prototype of the Converter Power Circuit.

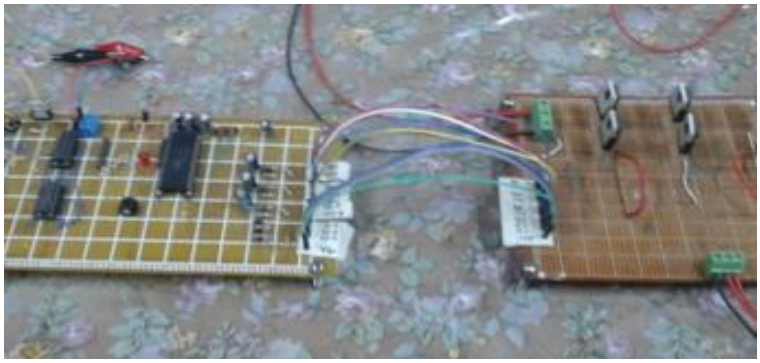

Fig 15. Inverter Practical Circuit.

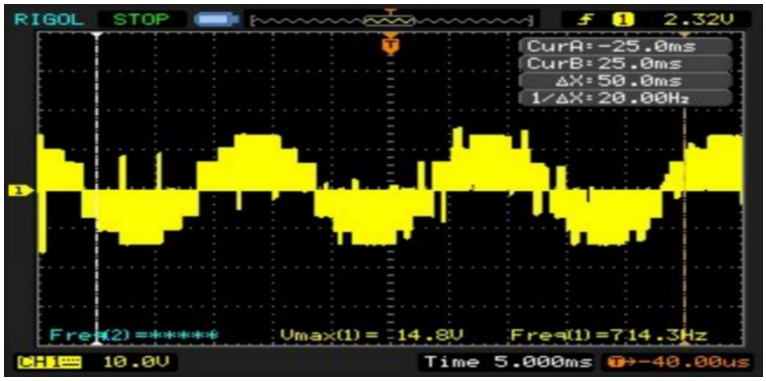

Fig 16. Output Sinusoidal Current Signal without Filter 24 Volt DC Input.

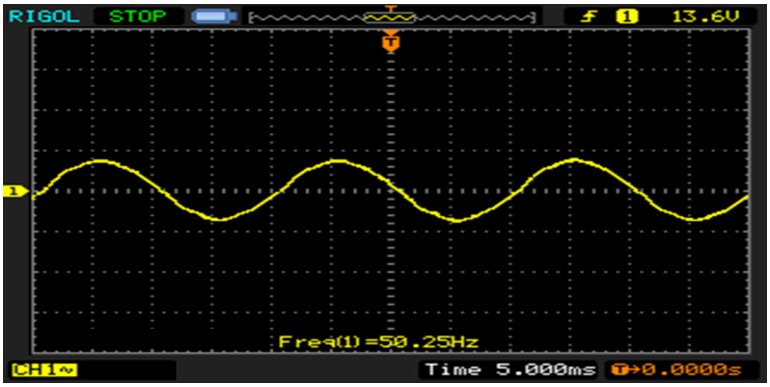

Fig 17. Filter and 540 Volt DC Input Output Sinusoidal Voltage Signal Across the Resister Load (Current waveform).

5 Conclusion

In this paper, a single-phase Push-Pull PV micro-inverter operating in DCM has been designed and implemented to feed alternating current to the load from a 250 W photovoltaic module. The PV module has been modeled and simulated based on the one-diode PV model using Matlab/Simulink software. DC/DC at 30 kHz The PV array's voltage is raised from PV DC at full power to 640 V DC using a Push-Pull converter. The MPPT controller uses the Incremental Conductance (I-C) technique to optimise the duty ratio. The duty ratio of this MPPT system is automatically varied to extract the most power. The inverter device will handle the DC to AC conversion. The output power optimizer voltage (up to 640 volts) will be used to generate 1-phase 220 volts at 50Hz. Furthermore, all of the plans are put into practise in the lab.

References

[1] B. Hachim, D. Dahlioui, and A. Barhdadi, "Electrification of Rural and Arid Areas by Solar Energy Applications," 2018 6th International Renewable and Sustainable Energy Conference (IRSEC), Rabat, Morocco, 2018, pp. 1-4, doi: 10.1109/IRSEC.2018.8702978.

[2] R. Dqg et al., “Control and implementation of a standalone solar photo-voltaic hybrid system.” pp. 1–8, Page 1 of 8 2015-IACC-0393 2015.

[3] L. An and D. D. C. Lu, “Design of a single-switch DC/DC converter for a PV-battery-powered pump system with PFM+PWM control,”IEEE Trans. Ind. Electron., vol. 62, no. 2, pp. 910–921, 2015.
[4] W. Priyono, D. F. Wijayan and E. Firmansyah, "Study and Simulation of a Hybrid Stand-alone PV System for Rural Telecomunications System," 2018 3rd International Conference on Information Technology, Information System and Electrical Engineering (ICITISEE), Yogyakarta, Indonesia, 2018, pp. 418-422, doi: 10.1109/ICITISEE.2018.8721000.
[5] "IEEE Recommended Practice for Sizing Lead-Acid Batteries for Stand-Alone Photovoltaic (PV) Systems," in IEEE Std 1013-2019 (Revision of IEEE Std 1013-2007) , vol., no., pp.1-50, 20 Sept. 2019, doi: 10.1109/IEEESTD.2019.8845030.
[6] Z. M. Salameh, “on the Performance of a Pv-Powered VolumetricWater Pump,” IEEE Transactions on Energy Conversion, vol. 5, no. 4, December 1990.

[7] S. Sukatjasakul and S. Po-Ngam, "The micro-grid connected single-phase photovoltaic inverter with simple MPPT controller," 2017 International Electrical Engineering Congress (iEECON), Pattaya, 2017, pp. 1-4, doi: 10.1109/IEECON.2017.8075751.
[8] L. Callegaro, M. Ciobotaru, J. E. Fletcher, P. A. Rios and D. J. Pagano, "Design of cascaded control loop for solar power optimizer based on a buck-boost converter," 2016 IEEE 2nd Annual Southern Power Electronics Conference (SPEC), Auckland, 2016, pp. 1-6, doi: 10.1109/SPEC.2016.7846136.
[9] K. B. and T. Morey, "Switching Power Supply Design Third Edition. Third Edition, McGraw-Hill Companies", New York, 2011.
[10] M. H. Rashid, "POWER ELECTRONICS Academic Press Series in Engineering". 2001.
[11] M. Seyedmahmoudian, B. Horan, R. Rahmani, A. M. T. Oo, and A.Stojcevski, “Efficient photovoltaic system maximum power point tracking using a new technique,” Energies, vol. 9, no. 3, pp. 1–18, 2016.
[12] M. Seyedmahmoudian et al., “State of the art artificial intelligence-based MPPT techniques for mitigating partial shading effects on PV systems – A review,” Renew. Sustain. Energy Rev., vol. 64, pp. 435– 455, 2016.
[13] V. K. Viswambaran, A. Ghani and E. Zhou, "Modelling and simulation of maximum power point tracking algorithms & review of MPPT techniques for PV applications," 2016 5th International Conference on Electronic Devices, Systems and Applications (ICEDSA), Ras Al Khaimah, 2016, pp. 1-4, doi: 10.1109/ICEDSA.2016.7818506.
[14] Y. Hsieh, L. Yu, T. Chang, W. Liu, T. Wu and C. Moo, "Parameter Identification of One-Diode Dynamic Equivalent Circuit Model for Photovoltaic Panel," in IEEE Journal of Photovoltaics, vol. 10, no. 1, pp. 219-225, Jan. 2020, doi: 10.1109/JPHOTOV.2019.2951920.
[15] P. K. Vineeth Kumar and K. Manjunath, "Analysis, design and implementation for control of non-inverted zeta converter using incremental conductance MPPT algorithm for SPV applications," 2017 International Conference on Inventive Systems and Control (ICISC), 2017, pp. 1-5, doi: 10.1109/ICISC.2017.8068662.
[16] R. A. Messenger and J. Ventre, "Photovoltai Systams Engineering," No claim to original U.S. Government works International Standard Book Number 0-8493-1793-2 Library of Congress Card Number 2003053063, ISBN 0-203-50629-4 Master e-book ISBN, 2005.
[17] T. K. Ghosh and M. A. Prelas, "Energy Resources and Systems", Volume 2, vol. 1. 2009.
[18] keng chin wu Pulse Width Modulated DC/DC Converters
[19] C. W. T. Mclyman, “Transformer and Inductor Design Handbook,” Third Edition, Revised and Expanded, ISBN:0-8247-5393-3, California, U.S.A, 2004.

Examining Mechanical Properties of Recycled Aggregate Concrete

Ali Alsalman[1], Jamal Khudair[2], Rahman S. Kareem[3*], Lateef Assi[4], Canh N Dang[5], José R. Martí-Vargas[6]
{alialsalman609@gmail.com[1], ali.mohamed@almaaqal.edu.iq [2], rahman.s.kareem@edu.stu.iq[3], lassi@email.sc.edu[4], dncanh86@gmail.com[5], jrmarti@cst.upv.es[6]}

Tatum-Smith-Welcher Engineers, Inc., 3100 S Market St., Rogers, AR 72758, USA[1]
College of Engineering, Civil Engineering Department, Al Maaqal University, Basra, Iraq[1]
College of Engineering, Civil Engineering Department, University of Basra, Basra, Iraq[2]
University of Arkansas, Department of Civil Engineering, 4190 Bell Engineering Center Fayetteville, AR 72701, USA[3]
Department of Structure, Shatrah Technical Institute, Southern Technical University, Shatrah, Dhi Qar, Iraq[3]
Department of Civil and Environmental Engineering, University of South Carolina, Columbia, USA[4]
Department for Management of Science and Technology Development, Ton Duc Thang University, Ho Chi Minh City, Vietnam[5]
Faculty of Civil Engineering, Ton Duc Thang University, Ho Chi Minh City, Vietnam[5]
Institute of Concrete Science and Technology (ICITECH), Universitat Politecnica de Valencia, Valencia, Spain[6]

Abstract. Several mid-strength recycled aggregate concrete (RAC) combinations are developed in this study. Three groups are studied in the experimental section. Natural aggregate concrete (NAC) combinations, for example, employed 100 percent natural gravel aggregate. The second group (RAC-I) mixed natural gravel aggregate with recycled concrete aggregate (30 percent per total weight of coarse aggregates). The compressive strength of the parent concrete was 20-30 MPa. The third group (RAC-II) had a similar and larger percentage of recycled concrete aggregate replacement, ranging from 30% to 100%. The compressive strength of the reference concrete was 30-40 MPa. The results showed that using 30% recycled concrete aggregate had no effect on the workability and mechanical qualities of the concrete. At 112 days, the shrinkage of RAC-I combinations is 40 percent higher than that of NAC mixtures. Based on the results of the emissions analysis, RCA appears to be a viable alternative for reducing CO2 emissions.

Keywords: Sustainable Construction; Recycled Concrete Aggregate; Recycled Aggregate Concrete; Compressive Strength; Modulus Of Elasticity; Shrinkage; CO_2 Emission.

1 Introduction

Construction and demolition wastes account for a large portion of solid wastes. The generation of these wastes has been increasing rapidly worldwide. The annual amount of wastes produced from construction and demolition is about 859 million tons in the EU [1] and about 230-530 million tons in the USA [2]. The most conventional method of disposing of these

IMDC-IST 2021, September 07-09, Sakarya, Turkey
Copyright © 2022 EAI
DOI 10.4108/eai.7-9-2021.2314894

wastes has been through its disposal in landfills [3], which is a key contributor to environmental pollution. Some countries have established laws to prohibit or applied specific taxes for generating waste areas [3]. For decades in the construction industry, concrete has been the most popular material and consequently generated a major portion of demolition wastes; the annual consumption of concrete globally is approximately 10 billion tons [4]. It is well known that a typical concrete mix consists of ordinary Portland cement (OPC), water, and aggregates. The primary aggregates that are used in the concrete industry are sand and gravel (crushed rocks can be used instead of gravel). The continuous use of such materials might yield irreversible influence on the natural resources and environment as well (e.g., agricultural losses and rainforest devastations); globally, the construction industry uses approximately 48.3 billion tons of aggregates annually [5]; this number is anticipated to double over the next two decades if the rate of consumption stays the same [6]. Thus, recycling of demolished concrete has been recognized as a promising solution, not only to preserve the natural resources but also to offer a cleaner and sustainable practice (e.g., reduce the CO_2 emission) for the construction industry [7].

Different kinds of solid wastes have been utilized as aggregates in concrete, such as recycled concrete aggregate (RCA), discarded tire rubber, and waste glass [8–10]. Among these materials, RCA gets a strong interest due to its readiness in a great amount, being available worldwide, and can partially or fully replace coarse and fine aggregates in new concrete [11–13]. RCA is processed from crushed, graded inorganic materials that are sourced from construction and demolition debris, such as buildings, roads, bridges, and sometimes even from catastrophes like wars or earthquakes [14, 15]. In terms of applications, RCA has been used in sub-base for road construction and permeable bases and concrete mixtures, such as sidewalks, curbs, bridge substructures, and building superstructures, concrete shoulders, and residential driveways [3, 16].

The utilization of RCA to develop recycled aggregate concrete (RAC) is locally oriented to fully reach its advantages. The aggregates are supposed to be collected, classified, and recycled within a small geographic region (e.g., a construction site, a city, or a town). This practice saves transportation costs, minimizes the burden on transportation infrastructures, and preserves energy. In this study, the researchers develop RAC mixtures from the demolition wastes of old buildings in the city of Basra. The wastes from the concrete account as the main source of construction and demolition wastes in Iraq due to the demolition from wars. The authors in this study aim to encourage design engineers in Basra to specify RAC in their design at least in non-structural concrete by presenting several tests to examine the performance of RAC. On the other hand, this study validates the applicability of existing design code equations for predicting mechanical properties.

2 Literature Review

In terms of concrete workability, several studies have been performed to examine the effect of RCA. It was reported that as the RCA content increased, the workability decreased [6]. When RCA was used as coarse aggregate, 5% mixing water was additionally needed for achieving workability similar to that of natural coarse aggregate. [17] stated that the concrete slump, which ranged from 50-100 mm, was achievable by using superplasticizers. [18], however, observed that the initial slump of RAC was slightly affected by the relatively high-water absorption of RCA. On the other hand, the rate of slump loss increased as the water absorption capacity of

RCA increased.

In terms of concrete mechanical properties, Younis and Mustafa [19] compared the mechanical properties of RAC to those of natural aggregate concrete (NAC). The investigated compressive strength ranged from 30.2 to 41 MPa at 28 days. The compressive strength of RAC was approximately 84% of the NAC. On the other hand, the splitting tensile strength was 93% of the NAC. Similar findings were reported by Ismail et al. [20] and Yaba et al. [21]. Zhou and Chen [22], nevertheless, informed that the compressive and flexural strengths of RAC were similar and even exceeded the strengths of NAC. The observation was attributed to the high water absorption capacity of RCA, which resulted in the improvement of the bond strength between aggregate and cement paste matrix [22].

The parent concrete of RCA is influential to the service performance and durability of concrete. [23] evaluated the long-term mechanical properties of RAC containing coarse RCA. RCA produced from high-strength parent concrete (the compressive strength of parent concrete equal to 110 MPa) could result in slightly higher strength in comparison to conventional high-strength concrete for the same water/binder ratio (*w/b*). However, the modulus of elasticity and splitting tensile strength of these high-strength RAC mixtures were similar to those of NAC at all ages. [24] pointed out that the utilization of RCA made from the parent concrete having a compressive strength of 50 MPa or greater did not affect the mechanical properties of RAC.

The shape of RCA is influential since it affects the bond between the cement paste matrix and coarse aggregate. The experimental results reported by [25] showed that the shape (i.e., angular or round shape) of RCA and replacement level up to 100% of natural aggregate had a minimal impact on the compressive strength of RAC. On the other hand, the authors concluded that the splitting tensile strength of RAC was influenced by the RCA properties (i.e., shape, surface texture, and crushing procedure) and replacement level.

The incorporation level of RCA influences the mechanical properties of RAC. [26] found that concrete compressive strength of 30-45 MPa was achievable with 25% of coarse RCA using the same amount of cement as in NAC. The modulus of elasticity of RAC was lower in comparison to that of NAC, and the tensile strength of RAC might be higher than that of NAC. [13] prepared RAC with different levels of replacement of natural coarse aggregate by RCA (20%, 40%, 60%, 80%, and 100%). The average reduction in compressive strength, splitting tensile strength, modulus of elasticity, and flexural strength were 10%, 14%, 11%, and 9%, respectively. Several studies stated that mechanical properties were not affected if RCA was incorporated by up to 30% of the natural coarse aggregate [11, 27–29]. On the other hand, the study conducted by [30] indicated that replacing all coarse aggregate with 100% of RCA had minimal influence on the performance. In terms of the correlation between compressive strength and other mechanical properties such as modulus of elasticity, flexural strength, and splitting tensile strength, several studies have reported the findings [22, 31, 32].

In terms of concrete deformation, several studies demonstrated that the incorporation of RCA increased concrete shrinkage. This increase was attributed to the high deformability of the attached mortar of RCA [25]. [33] reported that concrete mixtures prepared with RCA produced from high-strength parent concrete had lower drying shrinkage and higher resistance to chloride-ion penetration in comparison to the mixtures made with RCA produced from normal-strength parent concrete. The finding was confirmed by [34]. Also, [35] developed a drying shrinkage model for RAC containing both fine and coarse RCA. Test results showed that both fine and coarse RCA had a substantial influence on shrinkage, and the influence of fine RCA decreased with the content of coarse RCA increased. Moreover, [36] indicated that the internal curing effect of RCA delayed the development of free shrinkage at an early age.

3 Experimental Program

3.1 Materils Properties

The cementitious material was the ordinary type I Portland cement [37]. Fine aggregate was natural gradation sand and used for all concrete mixtures [38]. Two types of coarse aggregate were used: natural gravel aggregate with a maximum aggregate size of 20 mm and RCA, as shown in Fig 1. The RCA was divided into two types based on the reference concrete: Type I - obtained from a structural concrete source with 28-day compressive strength of 20-30 MPa, and Type II -obtained from a structural concrete source with 28-day compressive strength of 30-40 MPa. Both types of RCA were sourced from demolition wastes of concrete buildings. The demolition wastes were crushed, sieved, and stored in buckets for ready use. The gradation curves, along with specific gravity (bulk oven-dried, bulk saturated surface dry, and apparent), water absorption, and unit weight of natural sand, natural gravel aggregate, and RCA are presented in Fig 2 and Table 1, respectively [39–41].

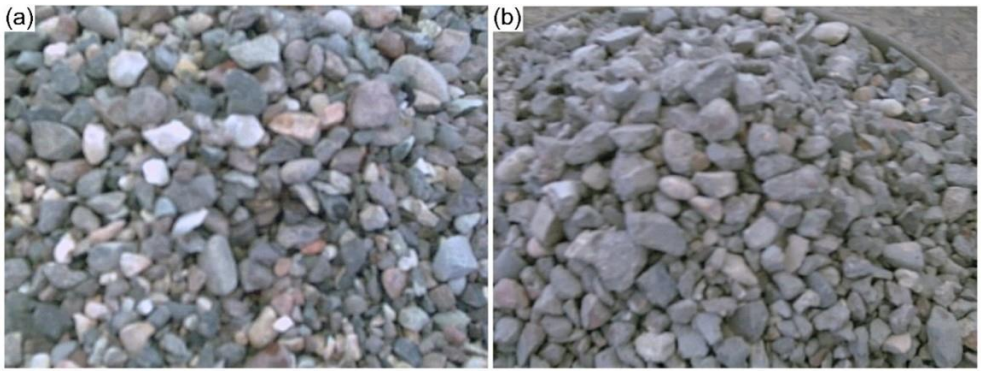

Fig 1. COARSE AGGREGATES: (A) NATURAL GRAVEL AGGREGATE (NGA) AND (B) RECYCLED CONCRETE AGGREGATE (RECYCLED CONCRETE AGGREGATE TYPE I)

The specific gravity of RCA was about 63% of the natural gravel aggregate on average. Previous studies indicated that the specific gravity of RCA ranges from 1.91 to 2.70 [42]. The average water absorption capacity of RCA was 3.9%, which is more than 4 times higher than that of natural gravel aggregate. Literature has reported values in the range of 0.5% to 14.75% [42]. On average, the unit weight of RCA was 84% of the natural gravel aggregate. The reduction in specific gravity and unit weight and the increase in water absorption capacity are attributed to the existence of loose paste in demolished construction wastes [11, 43].

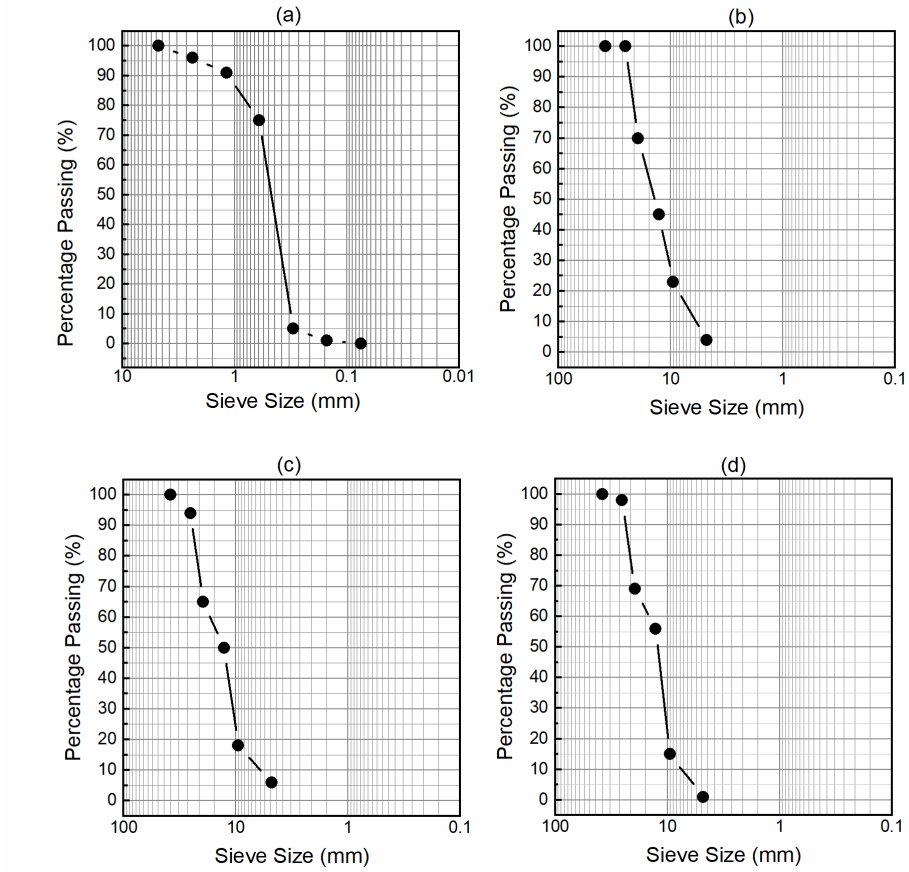

Fig 2. GRADATION OF AGGREGATES: (A) NATURAL SAND, (B) NATURAL GRAVEL, (C) RECYCLED CONCRETE AGGREGATE TYPE I, AND (D) RECYCLED CONCRETE AGGREGATE TYPE II.

Table 1. Properties of aggregates

Property	Natural Sand	Natural Coarse Aggregate	RCA Type I	RCA Type II
Specific gravity				
Bulk oven-dried	2.61	2.65	1.64	1.66
Bulk SSD	2.63	2.68	1.69	1.72
Apparent	2.68	2.70	1.70	1.75
Absorption (%)				
	1.29	0.90	3.83	3.90
Unit weight (kg/m^3)				
Loose	1400	1204	989	999
Compacted	1478	1266	1073	1092

3.2 Mixture Proportions

Table 2 summarizes the mixture proportions for three groups of concrete mixtures. For Group 1, mixtures NAC-1 to NAC-9 contained only natural aggregates (sand and natural gravel aggregates). Different *w/c* ratios and aggregate to cement (*Agg/C)* ratios were used to cover a wide range of strength and workability. For Group 2, mixtures RAC-1 to RAC-9 investigated the effect of RCA Type I, which was incorporated by 30% of the total weight of coarse aggregate. The replacement ratio was selected based on the recommendation of previous research studies [11, 27, 28, 43]. For Group 3, three subgroups were considered to investigate the effect of RCA Type II, as follows: (i) mixtures RAC-10, 13, and 16 examined the influence of the parent concrete grade on compressive strength (for the same replacement ratio in Group 2 -30%); (ii) mixtures RAC-11, 14 and 17 examined the effect of 50% replacement on concrete properties; and (iii) mixtures RAC-12, 15, and 18 examined the effect of 100% replacement on concrete properties. It should be noted that the content of cement is presented as an absolute amount, while the content of other concrete components is presented as a proportion to the cement content.

Table 2. Mixture proportions

Mixture	Cement kg/m^3	Weight Proportion					Ratio		
		Portland cement	Natural sand	Natural coarse aggregate	Recycled concrete aggregate		*w/c*	*Agg/C*	Recycle concrete aggregate / Total coarse aggregate
					Type I	Type II			
Group 1. NAC (mixtures including natural gravel aggregate)									
NAC-1	523	1	1	2	-	-	0.40	3	-
NAC-2	517	1	1	2	-	-	0.45	3	-
NAC-3	511	1	1	2	-	-	0.50	3	-
NAC-4	383	1	1.5	3	-	-	0.50	4.5	-
NAC-5	380	1	1.5	3	-	-	0.55	4.5	-
NAC-6	376	1	1.5	3	-	-	0.62	4.5	-
NAC-7	303	1	2	4	-	-	0.60	6	-
NAC-8	301	1	2	4	-	-	0.65	6	-
NAC-9	299	1	2	4	-	-	0.70	6	-
Group 2. RAC-I (mixtures including RCA Type I)									
RAC-1	523	1	1	1.4	0.6	-	0.40	3	0.3
RAC-2	517	1	1	1.4	0.6	-	0.45	3	0.3
RAC-3	511	1	1	1.4	0.6	-	0.50	3	0.3
RAC-4	383	1	1.5	2.1	0.9	-	0.50	4.5	0.3
RAC-5	380	1	1.5	2.1	0.9	-	0.55	4.5	0.3
RAC-6	376	1	1.5	2.1	0.9	-	0.62	4.5	0.3
RAC-7	303	1	2	2.8	1.2	-	0.60	6	0.3
RAC-8	301	1	2	2.8	1.2	-	0.65	6	0.3
RAC-9	299	1	2	2.8	1.2	-	0.70	6	0.3
Group 3. RAC-II (mixtures including RCA Type II)									

RAC-10	517	1	1	1.4	-	0.6	0.45	3	0.3
RAC-11	517	1	1	1	-	1	0.45	3	0.5
RAC-12	517	1	1	-	-	2	0.45	3	1
RAC-13	380	1	1.5	2.1	-	0.9	0.55	4.5	0.3
RAC-14	380	1	1.5	1.5	-	1.5	0.55	4.5	0.5
RAC-15	380	1	1.5	-	-	3	0.55	4.5	1
RAC-16	301	1	2	2.8	-	1.2	0.65	6	0.3
RAC-17	301	1	2	2	-	2	0.65	6	0.5
RAC-18	301	1	2	-	-	4	0.65	6	1

(Notes: NAC: Natural Aggregate Concrete; RAC: Recycled Aggregate Concrete; RCA: Recycled Concrete Aggregate; *Agg/C* = coarse aggregate to cement ratio; *w/c* = water to cement ratio).

3.3 Concrete Testing

The concrete was mixed using a tilting drum mixer. All dry materials were added and mixed for about one minute and then the water was added gradually to the mixer. The total mixing time was in a range of 3-5 minutes. The rheology of the concrete mixtures was evaluated by performing two tests: slump test and compacting factor test according to ASTM C143/C143M (2020) and [45], respectively. The slump test provides an approximate measurement of concrete consistency. In practice, the slump test is widely used as an indicator to evaluate consistency due to its simplification [46]. The compaction factor test, on the other hand, is more sensitive and accurate than the slump test and particularly beneficial for concrete mixtures with low workability and dry mixtures. The test can indicate significant differences in workability over a wide range since it is very sensitive and provides consistent results [47].

Cube specimens, 100 mm x 100 mm x 100 mm, were cast to determine the compressive strength. Prism specimens, 100 mm x 100 mm x 500 mm were cast to measure flexure strength and drying shrinkage. Cylindrical specimens, 150 mm x 300 mm, were cast to evaluate the splitting tensile strength and modulus of elasticity. The specimens were covered with damp canvas cloth and left in the laboratory for 24 hours. The specimens were then de-moulded and moist cured at 21ºC until the day of testing. Compressive strength was determined at 7 and 28 days of age according to EN B 2019 12390-3 [48], in which the 28-day compressive strength is the strength of interest in this study. Flexure strength, splitting tensile strength, and modulus of elasticity was determined at 28 days of age according to [49], [50], and [51], respectively.

Concrete shrinkage was investigated by measuring the linear change (swelling and shrinkage) according to [52]. Several concrete prisms (100 mm x 100 mm x 285 mm) were cast and moist cured at 21ºC for 14 days, then stored under laboratory general facilities conditions. Subsequent readings were recorded at intervals of 1 day, and at 3, 7, 10, and 14 days submerged in water, and after that at intervals of 3, 7, 14, 21, 28, 42, 56, 70, 84, and 98 days stored in air at a temperature ranging from 16 to 30ºC. The test was terminated after 112 days. It should be noted that all tests were conducted for NAC and RAC-I mixtures, while the only compressive test was conducted for RAC-II mixtures since recycled concrete aggregate Type II was difficult to

obtain. Most of the old buildings utilized concrete with compressive strength ranging from 20-30 MPa.

4 Experimental Results and Discussions

4.1 Fresh Concrete Properties

The measured slump and compacting factor result for NAC and RAC-I mixtures are shown in Figure 3. It can be noted that for a given *w/c* and *Agg/C* ratio, the RAC-I mixtures experienced lower workability, both in the measured slump and compacting factor. This observation is associated with the higher water absorption capacity of RCA (refer to Table 1), which results in a reduction in the net water content effective to the concrete workability. A similar finding is indicated by [11, 43]. Furthermore, RCA particles have rougher surface texture and additionally contain old mortar attached to the particles in comparison to natural gravel aggregate indicated in Figure 1, thus more work is needed to overcome the increased internal friction [11].

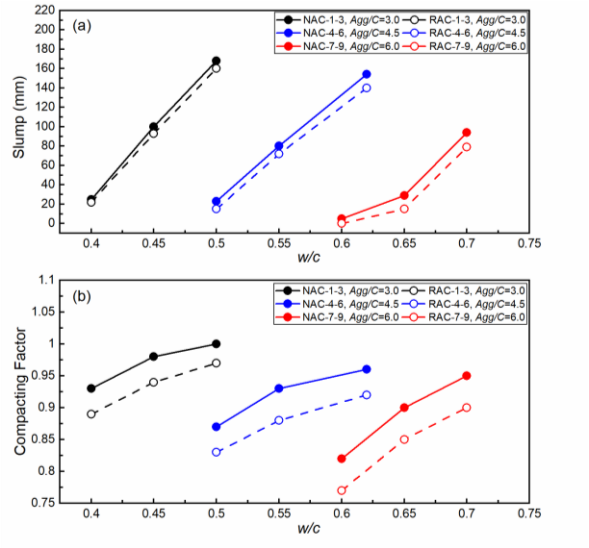

Fig 3. MEASURED (A) SLUMP AND (B) COMPACTING FACTOR

The effect of RCA types and replacement levels on the slump and compacting factor is indicated in Figure 4. For the same replacement level, the types of RCA have minimal influence on the slump and compacting factor, indicated by the results of the RAC-I and RAC-II mixture with 30% of RCA replacement. However, increasing the replacement level of RCA Type II from 30% to 50% reduced the slump and compacting factor by 22% and 3%, respectively. Replacing all coarse aggregate with RCA Type II decreased slump and compacting factor by 56% and 5%, respectively. This observation indicates that additional mixing and energy are needed for the concrete mixtures using 100% coarse RCA. Matias *et al.* [25] stated that the low workability mixtures contained RCA can be improved to be comparable to natural aggregate mixtures by using superplasticizers with dosage ranges from 0.42 to 0.5% by weight of the cement.

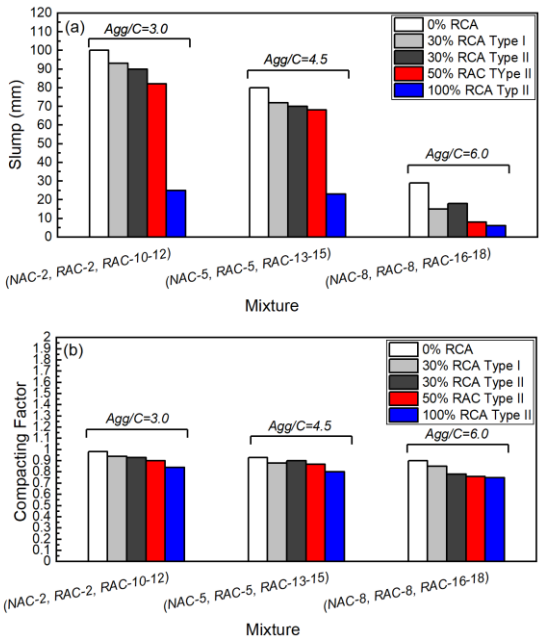

Fig 4. Effect of recycled concrete aggregate type and replacement level on (a) slump and (b) compacting factor.

4.2 Hardened concrete properties

4.2.1 Compressive strength

Aggregate in concrete represents the unit weight, modulus of elasticity, and dimensional stability of concrete (i.e., shrinkage and creep) [53]. The measured compressive strength at 28 days of the age of the NAC and RAC-I mixtures is presented in Figure 5. Overall, the NAC and RAC-I experienced a similar trend regarding the concrete strength reduction when the *w/c* ratio increased indicated by the dashed lines in the figure. This observation is apparent since the *w/c* ratio plays an important role in controlling the concrete compressive strength. The amount of coarse aggregate is another factor governing the concrete strength. As indicated in Figure 5, the compressive strength decreases as the *Agg/C* increases. In particular, the compressive strength of the concrete mixtures having *Agg/C* of 6.0 is nearly a half in comparison to the strength of the mixtures having *Agg/C* of 3.0. Figure 5 indicates the different effects of the RCA on the concrete compressive strength. For an *Agg/C* ratio of 3.0, the RAC-I mixtures had lower compressive strength than comparable NAC mixtures. The average reduction was 4%. This reduction may be attributed to the lower density and specific gravity of RCA as compared to natural gravel aggregate. A similar observation was found by [27, 28, 43]. As the aggregate content increased, RAC-I mixtures showed higher strength. The average increase was 12% and 20% for an *Agg/C* ratio of 4.5 and 6.0, respectively. The reason is related to the fact that RCA particles have an angular and rough surface texture and residual cementitious materials on the surface, which result in a better bond with cement paste matrix in comparison to natural gravel aggregate particles [24]. This observation is not in alignment with the one for *Agg/C* of 3.0.

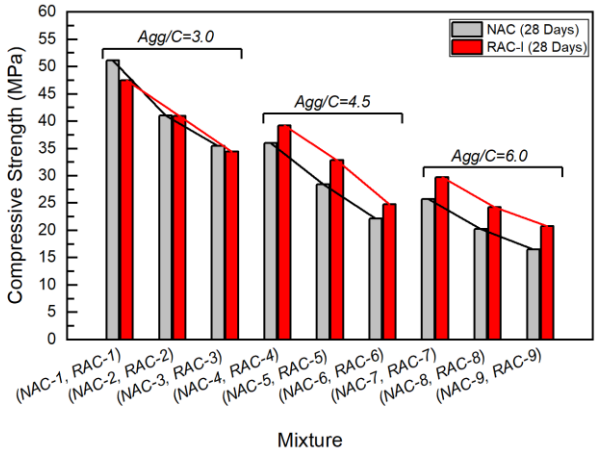

Fig 5. Measured 28-day compressive strength.

The effect of RCA type (Type I and Type II) and replacement level on compressive strength is presented in Figure 6. The RAC-II mixtures showed higher compressive strength than the comparable NAC and RAC-I mixtures. In comparison to the NAC mixtures, the increase was 20% on average. When the replacement of RCA Type II increased to 50% and 100%, strength increased by 33% and 27% in comparison to the NAC mixtures, respectively. In comparison to the RAC-I mixtures, the strength increase was 7%, 18%, and 14% for the replacement of 30%, 50%, and 100%, respectively. This finding is consistent with earlier research studies regarding the effect of parent concrete strength on the compressive strength of RAC [23, 26, 36, 54, 55]. The compressive strength of the parent concrete affects the quality of the RCA. This is the possible reason why RAC-II yielded higher compressive strength than RAC-I.

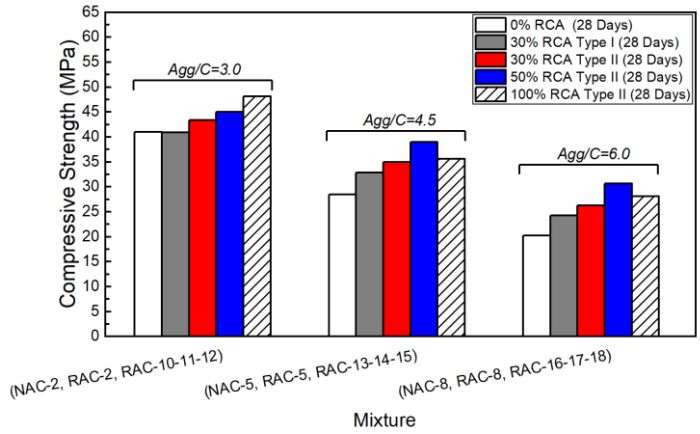

Fig 6. Effect of recycled concrete aggregate type and replacement level on compressive strength.

4.2.2 Modulus of Rupture (Flexural Strength)

Flexural strength depends on the aggregate type that affects the bond strength between cement paste matrix and coarse aggregate. The flexural strength results at 28-day of the age of the NAC and RAC-I mixtures are presented in Figure 7. For an *Agg/C* ratio of 3.0, the NAC and RAC-I

had similar flexural strength. The difference was 2% on average. The flexural strength of RAC-I mixtures was 12% and 22% higher than that of the NAC mixtures when the *Agg/C* ratio increased to 4.5 and 6.0, respectively. These results are consistent with the findings by [26]. The high water absorption capacity of the adhered mortar that exists on the RCA surface can strengthen the bond between the coarse aggregate and cement paste matrix [24].

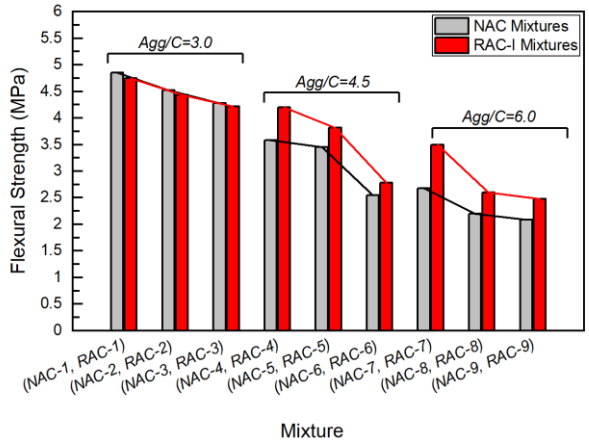

Fig 7. Flexural strength (Modulus of rupture)

The measured flexural strength of the NAC and RAC-I mixtures are compared to the predicted values by [56] as shown in Figure 8. Using the least-squares estimation method, the flexural strength of the NAC mixtures is represented by an equation $f_b = 0.19(f'c)^{0.84}$ with the coefficient of determination R^2 of 0.94. As shown, the ACI 318 equation provides a conservative prediction of flexural strength for the concrete mixture having compressive strength equal to or greater than 32.5 MPa, where 32.5 MPa as shown in Figure 8. For the mixtures having a compressive strength of less than 32.5 MPa, the ACI 318 equation overestimates the experimental values, which is unconservative in design. Similarly, the flexural strength of the RAC-I mixtures is represented by the equation $fb = 0.17(f'c)^{0.88}$ with the coefficient of determination R^2 of 0.95. The ACI 318 equation provides a conservative prediction for the mixtures.

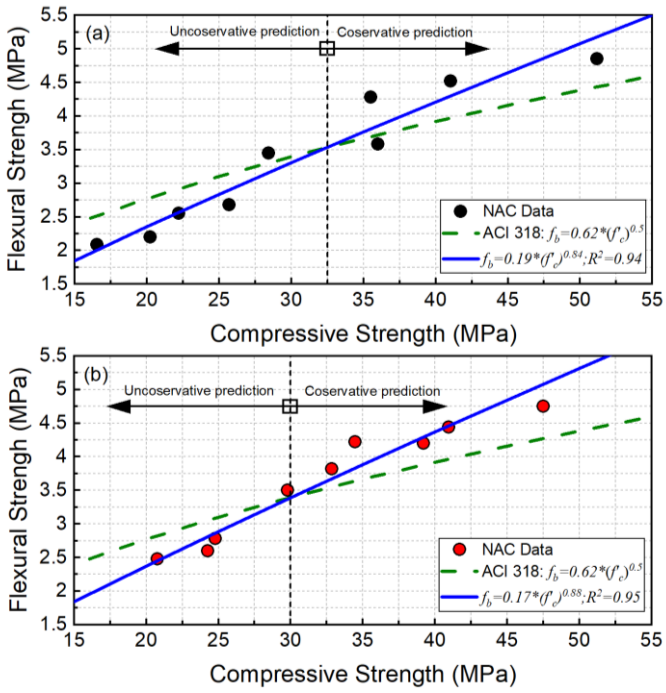

Fig 8. Flexural strength and compressive strength for (a) NAC and (b) RAC-I.

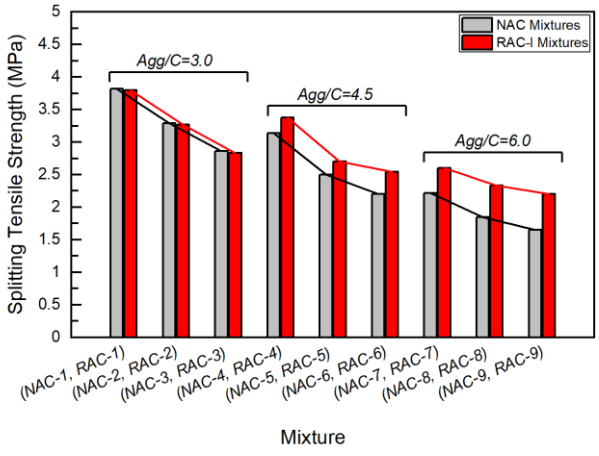

Fig 9. Splitting tensile strength.

4.2.3 Strength of Splitting Tensile

Like the flexural strength, the aggregate type can influence the tensile strength. The splitting tensile strength results at 28-day of the age of the NAC and RAC-I mixtures are presented in Figure 9. For an *Agg/C* ratio of 3.0, the RAC-I mixtures yielded approximately the same strength as the NAC mixtures. As the *Agg/C* ratio increased to 4.5 and 6.0, the RAC-I mixtures showed higher tensile strength by 10% and 25% in comparison to the NAC mixtures, respectively. The enhancement in the bond between the new cement matrix to the old one present on the surface of RCA particles is the source of the observation, which is like the one observed in the flexural

strength results. The verification of the experimental values against the design code is presented in Figure 10. Using the least-squares estimation method, the experimental data of the NAC and RAC-I mixtures are represented by $f_t = 0.20(f'c)^{0.76}$ and $f_t = 0.31(f'c)^{0.64}$ with the coefficient of determination R^2 of 0.98 and 0.94, respectively. As shown in the figure, on average, the ACI 318 equation overestimates the tensile strength of all NAC and RAC-I mixtures.

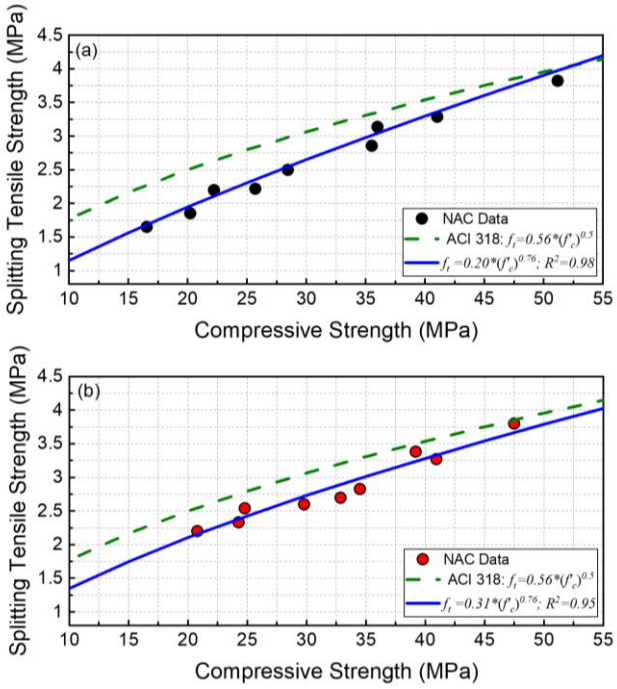

Fig 10. Relationship between splitting tensile strength and compressive strength (a) NAC and (b).

4.2.4 Modulus of Elasticity

The aggregate type is influencing the modulus of elasticity of concrete [53]. The modulus of elasticity test results of the NAC and RAC-I mixtures are presented in Figure 11. For an *Agg/C* ratio of 3.0, the RAC-I mixtures showed a lower modulus of elasticity in comparison to the NAC mixtures. The reduction was about 6%. The observed reduction is consistent with previous findings [11, 22]. Previous studies indicated that 30% incorporation of RCA by the total weight of coarse aggregate has minimal influence on the modulus of elasticity of RAC-I [11, 27–29, 43]. The minimal effect can be attributed to the fact that the modulus of elasticity. The concrete modulus of elasticity and concrete compressive strength is depicted in Figure 12. As can be observed, the ACI 318 equation captures the variation trend of the experimental data of the NAC and RAC-I mixtures. The experimental data of the NAC and RAC-I mixtures are represented by equation $Ec = 4520(f'_c)^{0.5}$ and $4520(f'_c)^{0.56}$ with the coefficient of determination R^2 of 0.99 and 0.97, respectively. On average, the ACI 318 equation overestimates the measured modulus of elasticity of the NAC and RAC-I mixtures by 5% and 14%, respectively. The lower density of RCA led to a reduction in stiffness. Furthermore, the natural gravel aggregate might participate in decreasing elasticity of concrete [28], at which the ACI 318 equation provides a fairly accurate prediction.

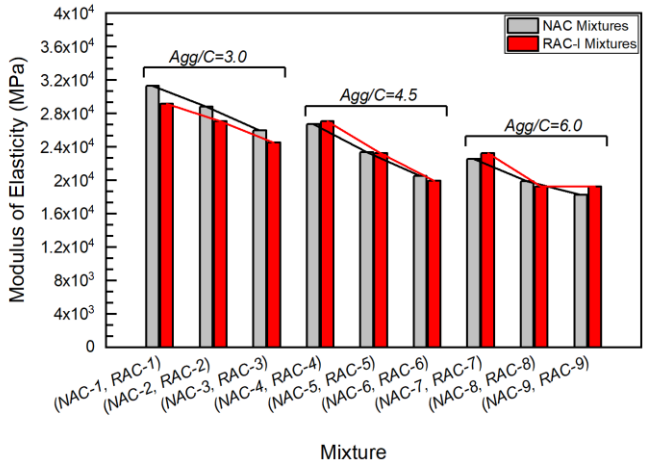

Fig 11. Modulus of elasticity.

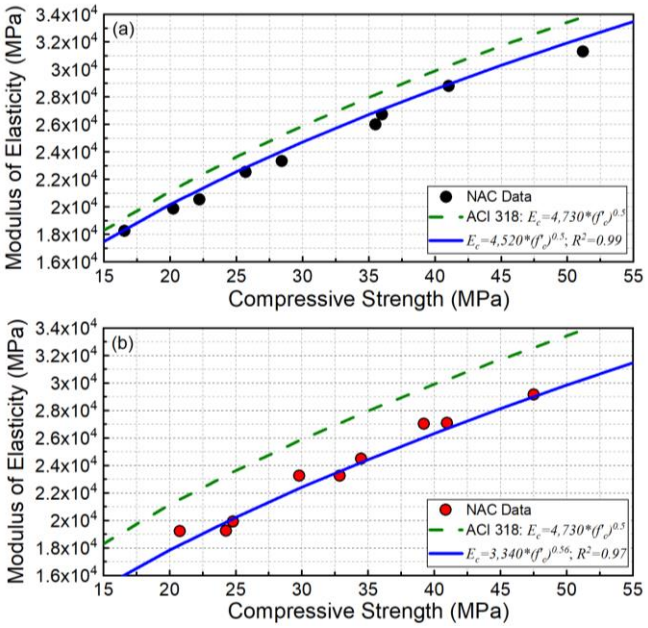

Fig 12. ELASTICITY AND COMPRESSIVE STRENGTH FOR (A) NAC AND (B) RAC-I.

4.2.5 Linear Change (Swelling and Shrinkage)

The error bars are based on a 95% confidence interval. On average, the expansion of the RAC-I mixtures at 3, 7, 10, and 14 days is 130%, 121%, 107%, and 116% higher than that of the NAC mixtures, respectively. The RAC-I mixtures exhibited higher shrinkage in comparison to the NAC mixtures regardless of *Agg/C* and *w/c* ratios. The difference in shrinkage between NAC and RAC-I mixtures tends to be consistent over time. The shrinkage of the RAC-I mixtures was 40% higher. This observation is accounted for the higher porosity and water absorption

generated by the existing mortar present on the surface of RCA particles [25].

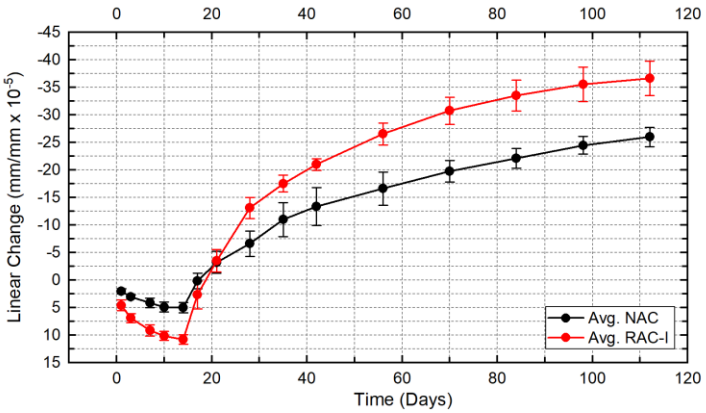

Fig 13. AVERAGE LINEAR CHANGE: SWELLING AND SHRINKAGE FOR NAC AND RAC-I.

4.2.6 CO_2 Emission of Concrete Mixtures

Because of the energy consumption during the process of manufacturing the raw materials of concrete, CO_2 is emitted into the atmosphere. Table 3 presents the resultant CO_2 emission of each component of the concrete.

Table 3. Emission factors of materials[1]

Material	kg-CO_2/kg	Reference
OPC	0.840	Sanjuán et al. [57]
Natural sand	0.0048	Hammond et al. [58]
Natural coarse aggregate	0.0048	Hammond et al. [58]
Recycled concrete aggregate (RCA-I & RCA-II)	0.0020	Alnahhal et al. [7] and García-Segura et al. [59]

[1] value of emission does not account for the emission resulted from transportation.

Table 3 summarizes the CO_2 emission for all concrete mixtures for one cubic meter of concrete as the functional unit. The highest CO_2 emission was observed with NAC-1 (447 kg-CO_2/m^3) and the lowest was RAC-18 (257 kg-CO_2/m^3). That OPC is the main contributor to the emission of all mixtures. On the other hand, the 100% replacement of natural coarse aggregate by RCA-II yielded an average reduction of the emission by 1.3%..

Table 4. Emission for one cubic of concrete.

Emission kg-CO_2/m^3						
Mixture	Cement	Sand	Gravel	RCA-I	RCA-II	Total
NAC-1	439	3	5	0	0	447
NAC-2	434	2	5	0	0	442
NAC-3	429	2	5	0	0	436
NAC-4	322	3	6	0	0	330
NAC-5	319	3	6	0	0	328
NAC-6	316	3	5	0	0	324
NAC-7	255	3	6	0	0	263
NAC-8	253	3	6	0	0	262

NAC-9	251	3	6	0	0	260
RAC-1	439	2	3	1	0	445
RAC-2	434	2	3	1	0	440
RAC-3	429	2	3	1	0	435
RAC-4	322	2	3	1	0	328
RAC-5	319	2	3	1	0	326
RAC-6	316	2	3	1	0	322
RAC-7	255	3	4	1	0	261
RAC-8	253	3	4	1	0	260
RAC-9	251	3	4	1	0	258
RAC-10	434	2	3	0	1	440
RAC-11	434	2	2	0	1	440
RAC-12	434	2	0	0	2	438
RAC-13	319	2	3	0	1	326
RAC-14	319	2	2	0	1	325
RAC-15	319	2	0	0	2	323
RAC-16	253	3	4	0	1	260
RAC-17	253	3	26	0	1	282
RAC-18	253	2	0	0	2	257

To examine the efficiency of each mixture, the ratio of the CO_2 emission to the compressive strength at the age of 28 days is considered as shown in Figure 14. It can be noticed that RAC-16 is the most efficient (5.4 kg-CO_2/MPa) which is 50% less compared to the corresponding with natural coarse aggregates (mixture NAC-8). In general, for medium-high strength concrete, mixtures with 30% of RCA-I showed less efficiency compared to NAC mixtures (NAC-1 and RAC-1, NAC-2 and RAC-2, NAC-3 and RAC-3). For medium and low strengths, RAC mixtures with 30% of RCA-I were more efficient; efficiency was 14% higher than NAC mixtures. Similarly, mixtures contained 50% and 100% of RCA-II showed higher efficiency with low strength concrete mixtures; the efficiency was 44% and 29%, respectively compared to NAC mixtures.

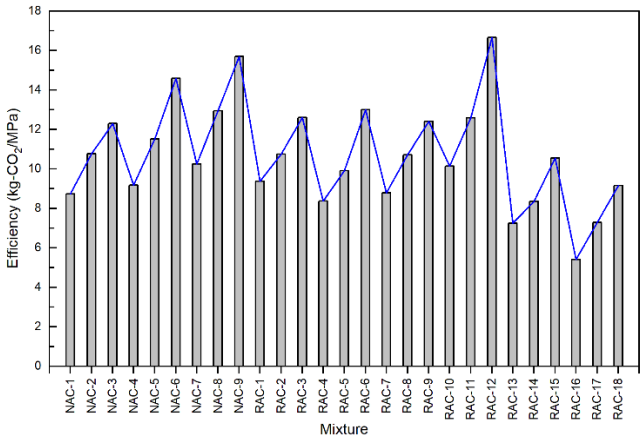

Fig 14. The EFFICIENCY OF CONCRETE MIXTURES.

5 Conclusion

The following list are the conclusions for the results:

1. RAC mixtures batched with 30% recycled concrete aggregate show lower workability than the NAC mixtures. The difference in workability between the two types of mixtures is more apparent as the *Agg/C* ratio increases.
2. For an *Agg/C* ratio of 3.0, the NAC mixtures show marginally higher compressive strength, flexural strength, splitting tensile strength, and modulus of elasticity as compared to those of the RAC mixtures. The average increase was 3%, 2%, 1%, and 7%, respectively.
3. For an *Agg/C* ratio of either 4.5 or 6.0, the NAC mixtures show lower compressive strength, flexural strength, and splitting tensile strength as compared to those of the RAC mixtures. The average reduction was 10%, 16%, and 17%, respectively. The modulus of elasticity, however, did not follow the same trend; both NAC and RAC mixtures show approximately the same values for an *Agg/C* ratio of 4.5 and 6.0.
4. Using RCA originated from a parent concrete with compressive strength of 30-40 MPa enhanced the RAC compressive strength by approximately 7% as compared to RCA originated from a parent concrete with compressive strength of 20-30 MPa at the same level of replacement. In comparison to NAC, the enhancement was 20% on average.
5. ACI 318 overestimates the measured splitting tensile strength and modulus of elasticity for all RAC and NAC mixtures. Regarding the flexural strength, ACI 318 overestimates the NAC and RAC mixtures having compressive strength less than 32.5 MPa and 30 MPa, respectively. Otherwise, the ACI 318 provides a conservative prediction.
6. The incorporation of 30% of recycled concrete aggregate increased swelling and shrinkage. The difference in shrinkage between the RAC and NAC mixtures tended to be consistent over time. At the age of 112 days, the difference was about 40%.
7. OPC is the main contributor to the CO2 emission of concrete, and it is responsible for approximately 97% of the total CO_2 emission.
8. The use of RCA can reduce the CO_2 emission generated from one cubic meter of concrete for low-strength concrete mixtures. As an average, mixtures contained 30%, 50, and 100% showed 14%, 44%, and 29%, respectively.

References

[1] European Commission. Directorate General for Internal Market, Industry, Entrepreneurship and SMEs. *Development and implementation of initiatives fostering investment and innovation in construction and demolition waste recycling infrastructure.* LU: Publications Office, https://data.europa.eu/doi/10.2873/11837 (2018, accessed 13 May 2021).

[2] United States Environmemtal Protection Agency. *The State of the Practice of Construction and Demolition Material Recovery-Final Report*. EPA/600/R-17/231, https://nepis.epa.gov/Exe/ZyPDF.cgi/P100SSJP.PDF?Dockey=P100SSJP.PDF (2017).

[3] Malešev M, Radonjanin V, Marinković S. Recycled concrete as aggregate for structural concrete production. *Sustainability* 2010; 2: 1204–1225.

[4] Aprianti S E. A huge number of artificial waste material can be supplementary cementitious material (SCM) for concrete production – a review part II. *Journal of Cleaner Production* 2017; 142: 4178–4194.

[5] Bostanci SC, Limbachiya M, Kew H. Use of recycled aggregates for low carbon and cost effective concrete construction. *Journal of Cleaner Production* 2018; 189: 176–196.

[6] Visintin P, Xie T, Bennett B. A large-scale life-cycle assessment of recycled aggregate concrete: The influence of functional unit, emissions allocation and carbon dioxide uptake. *Journal of Cleaner Production* 2020; 248: 119243.
[7] Alnahhal MF, Alengaram UJ, Jumaat MZ, et al. Assessment on engineering properties and CO2 emissions of recycled aggregate concrete incorporating waste products as supplements to Portland cement. *Journal of Cleaner Production* 2018; 203: 822–835.
[8] Kim J-H, Sung J-H, Jeon C-S, et al. A study on the properties of recycled aggregate concrete and its production facilities. *Applied Sciences* 2019; 9: 1935.
[9] Thomas BS, Gupta RC. Properties of high strength concrete containing scrap tire rubber. *Journal of Cleaner Production* 2016; 113: 86–92.
[10] Letelier V, Henríquez-Jara BI, Manosalva M, et al. Combined use of waste concrete and glass as a replacement for mortar raw materials. *Waste Management* 2019; 94: 107–119.
[11] Rahal K. Mechanical properties of concrete with recycled coarse aggregate. *Building and environment* 2007; 42: 407–415.
[12] Verma SK, Ashish DK. Mechanical behavior of concrete comprising successively recycled concrete aggregates. *Advances in concrete construction* 2017; 5: 303–311.
[13] Hamad BS, Dawi AH. Sustainable normal and high strength recycled aggregate concretes using crushed tested cylinders as coarse aggregates. *Case Studies in Construction Materials* 2017; 7: 228–239.
[14] McNeil K, Kang TH-K. Recycled concrete aggregates: A review. *International journal of concrete structures and materials* 2013; 7: 61–69.
[15] Zhang J, Shi C, Li Y, et al. Performance enhancement of recycled concrete aggregates through carbonation. *Journal of Materials in Civil Engineering* 2015; 27: 04015029.
[16] Gupta N, Kluge M, Chadik PA, et al. Recycled concrete aggregate as road base: Leaching constituents and neutralization by soil Interactions and dilution. *Waste Management* 2018; 72: 354–361.
[17] Somna R, Jaturapitakkul C, Chalee W, et al. Effect of the Water to Binder Ratio and Ground Fly Ash on Properties of Recycled Aggregate Concrete. *J Mater Civ Eng* 2012; 24: 16–22.
[18] Yang K-H, Chung H-S, Ashour AF. Influence of Type and Replacement Level of Recycled Aggregates on Concrete Properties.
[19] Younis KH, Mustafa SM. Feasibility of Using Nanoparticles of SiO2 to Improve the Performance of Recycled Aggregate Concrete. *Advances in Materials Science and Engineering* 2018; 2018: e1512830.
[20] Ismail A, Younis KH, Maruf S. Recycled Aggregate Concrete Made with Silica Fume: Experimental Investigation. *Civil Engineering and Architecture* 2020; 8: 1136–1143.
[21] Yaba HK, Naji HS, Younis KH, et al. Compressive and flexural strengths of recycled aggregate concrete: Effect of different contents of metakaolin. *Materials Today: Proceedings*. Epub ahead of print 10 February 2021. DOI: 10.1016/j.matpr.2021.01.164.
[22] Zhou C, Chen Z. Mechanical properties of recycled concrete made with different types of coarse aggregate. *Construction and Building Materials* 2017; 134: 497–506.
[23] Gholampour A, Ozbakkaloglu T. Time-dependent and long-term mechanical properties of concretes incorporating different grades of coarse recycled concrete aggregates. *Engineering Structures* 2018; 157: 224–234.
[24] Tabsh SW, Abdelfatah AS. Influence of recycled concrete aggregates on strength properties of concrete. *Construction and Building Materials* 2009; 23: 1163–1167.
[25] Matias D, de Brito J, Rosa A, et al. Durability of Concrete with Recycled Coarse Aggregates: Influence of Superplasticizers. *J Mater Civ Eng* 2014; 26: 06014011.
[26] Etxeberria M, Vázquez E, Marí A, et al. Influence of amount of recycled coarse aggregates and production process on properties of recycled aggregate concrete. *Cement and Concrete Research* 2007; 37: 735–742.
[27] Limbachiya MC, Marrocchino E, Koulouris A. Chemical–mineralogical characterisation of coarse recycled concrete aggregate. *Waste Management* 2007; 27: 201–208.

[28] Limbachiya M, Meddah MS, Ouchagour Y. Use of recycled concrete aggregate in fly-ash concrete. *Construction and Building Materials* 2011; S0950061811003771.
[29] Silva RV, de Brito J, Dhir RK. Establishing a relationship between modulus of elasticity and compressive strength of recycled aggregate concrete. *Journal of Cleaner Production* 2016; 112: 2171–2186.
[30] Gomes M, de Brito J. Structural concrete with incorporation of coarse recycled concrete and ceramic aggregates: durability performance. *Mater Struct* 2009; 42: 663–675.
[31] Younis KH, Amin AA, Ahmed HG, et al. Recycled Aggregate Concrete including Various Contents of Metakaolin: Mechanical Behavior. *Advances in Materials Science and Engineering* 2020; 2020: 1–17.
[32] Bui NK, Satomi T, Takahashi H. Mechanical properties of concrete containing 100% treated coarse recycled concrete aggregate. *Construction and Building Materials* 2018; 163: 496–507.
[33] Kou S, Poon C. Effect of the quality of parent concrete on the properties of high performance recycled aggregate concrete. *Construction and Building Materials* 2015; 77: 501–508.
[34] Wang Q, Geng Y, Wang Y, et al. Drying shrinkage model for recycled aggregate concrete accounting for the influence of parent concrete. *Engineering Structures* 2020; 202: 109888.
[35] Zhang H, Wang Y, Lehman DE, et al. Time-dependent drying shrinkage model for concrete with coarse and fine recycled aggregate. *Cement and Concrete Composites* 2020; 105: 103426.
[36] Bendimerad AZ, Delsaute B, Rozière E, et al. Advanced techniques for the study of shrinkage-induced cracking of concrete with recycled aggregates at early age. *Construction and Building Materials* 2020; 233: 117340.
[37] ASTM C150 / C150M. *Specification for Portland Cement*. ASTM International. Epub ahead of print 2020. DOI: 10.1520/C0150_C0150M-20.
[38] ASTM C136 / C136M. *Test Method for Sieve Analysis of Fine and Coarse Aggregates*. ASTM International. Epub ahead of print 2019. DOI: 10.1520/C0136_C0136M-19.
[39] ASTM C29 / C29M. *Test Method for Bulk Density (Unit Weight) and Voids in Aggregate*. ASTM International. Epub ahead of print 2017. DOI: 10.1520/C0029_C0029M-17A.
[40] ASTM C127. *Test Method for Relative Density (Specific Gravity) and Absorption of Coarse Aggregate*. ASTM International. Epub ahead of print 2015. DOI: 10.1520/C0127-15.
[41] ASTM C128. *Test Method for Relative Density (Specific Gravity) and Absorption of Fine Aggregate*. ASTM International. Epub ahead of print 2015. DOI: 10.1520/C0128-15.
[42] Verian KP, Ashraf W, Cao Y. Properties of recycled concrete aggregate and their influence in new concrete production. *Resources, Conservation and Recycling* 2018; 133: 30–49.
[43] Limbachiya MC, Leelawat T, Dhir RK. Use of recycled concrete aggregate in high-strength concrete. *Mat Struct* 2000; 33: 574–580.
[44] ASTM C143 / C143M. *Test Method for Slump of Hydraulic-Cement Concrete*. ASTM International. Epub ahead of print 2020. DOI: 10.1520/C0143_C0143M-15A.
[45] EN B. 12350-4 Testing fresh concrete-Part 4: Degree of compatibility. *Brit.Standards Institution*.
[46] Gambhir ML. *Concrete technology*. New Delhi: Tata McGraw-Hill, 2006.
[47] Koehler EP, Fowler DW. *Summary of concrete workability test methods*. 2003.
[48] EN B. 12390-3: 2019. Testing Hardened Concrete. *Compressive Strength of Test Specimens; British Standard Institute: London, UK*.
[49] ASTM C78 / C78M. *Test Method for Flexural Strength of Concrete (Using Simple Beam with Third-Point Loading)*. ASTM International.
[50] ASTM C496 / C496M. *Test Method for Splitting Tensile Strength of Cylindrical Concrete Specimens*. ASTM International. Epub ahead of print 2017. DOI: 10.1520/C0496_C0496M-17.
[51] ASTM C469 / C469M. *Test Method for Static Modulus of Elasticity and Poissons Ratio of Concrete in Compression*. ASTM International. Epub ahead of print 2014. DOI: 10.1520/C0469_C0469M-14.
[52] ASTM C157 / C157M. *Test Method for Length Change of Hardened Hydraulic-Cement Mortar and Concrete*. ASTM International. Epub ahead of print 2017. DOI: 10.1520/C0157_C0157M-17.
[53] Mehta PK, Monteiro PJM. *Concrete: microstructure, properties, and materials*. 3rd ed. New York: McGraw-Hill, 2006.

[54] Dodds W, Goodier C, Christodoulou C, et al. Durability performance of sustainable structural concrete: Effect of coarse crushed concrete aggregate on microstructure and water ingress. *Construction and Building Materials* 2017; 145: 183–195.
[55] Ajdukiewicz A, Kliszczewicz A. Influence of recycled aggregates on mechanical properties of HS/HPC. *Cement and Concrete Composites* 2002; 24: 269–279.
[56] ACI Committee 318, American Concrete Institute. *ACI 318-19: Building code requirements for structural concrete : ccommentary on building code requirements for structural concrete (ACI 318R-19)*. Farmington Hills, MI: American Concrete Institute, 2019.
[57] Sanjuán MÁ, Andrade C, Mora P, et al. Carbon dioxide uptake by cement-based materials: A Spanish case study. *Applied Sciences* 2020; 10: 339.
[58] Hammond G, Jones C, Lowrie F, et al. *Embodied carbon: the Inventory of Carbon and Energy (ICE)*. Bracknell: BSRIA, 2011.
[59] García-Segura T, Yepes V, Alcalá J. Life cycle greenhouse gas emissions of blended cement concrete including carbonation and durability. *Int J Life Cycle Assess* 2014; 19: 3–12.

Design for Sustainability & Product Differentiation An Empirical Study at SALSAL factory for Purified Water

Abdul Salam Ibrahim Obeyed[1], Hamid Shakir Mahmoud[2]
{abdulsalam.abrahem@stu.edu.iq[1], h.s.mhmood@stu.edu.iq[2]}

Technical College of Management Basra, Southern Technical University[1,2]

Abstract. This research aims to analyse and investigate the impact of design for sustainability (D4S) in terms of all three components of sustainability (economy, environment, and society) on product competitiveness in term of cost , quality , flexibility, and delivery . The main questions of this research focus are: how can design for sustainability affect product differentiation? The importance of this research is to focus on the new interest of literatures on sustainability which represent the a critical and strategic challenge for business organizations . Sustainability becomes the most source of competitive advantage in current business environment. method is useful in comparing various competitive products of the same family. This technique uses a visual representation of PSI to give an overview of the product's inherent and built-in sustainability levels in a simple and effective manner. The results of this paper improve our hypotheses related to the interactive roles of (PLS) stages with (PSI) (Social, environmental, and economic) .

Keywords: Design for Sustainability (D4S), Product Differentiation (PD).

1 Introduction

Contemporary literature in the field of production and operations management has shown a growing interest in the challenges facing traditional product design systems, specifically the challenges of integrating sustainability with design and manufacturing systems at the product and process levels. The subject of Design for Sustainability has received great attention in many contemporary studies and knowledge contributions. Due to the shift in the logic of competition from economies of scale and cost advantages towards sustainability and the advantages of flexibility and acceleration in response to the rapid changes in the industry environment. Several studies confirmed that design for sustainability means considering environmental, social and economic considerations in the initial stages of design, which will have positive effects in improving the competitiveness of the product. The research problem was represented in the question: How can design for sustainability contribute to improving the competitiveness of the product in the field of achieving the advantages of flexibility, cost, delivery, and cost domestically? The research sample included a comprehensive survey of all workers in the factory, including engineers and administrators, whose number (20) was distributed to a questionnaire that was developed and tested for its validity and stability using many statistical measures. The research included four sections, the first section was devoted to the research methodology and previous studies, while the second section was devoted to presenting and

IMDC-IST 2021, September 07-09, Sakarya, Turkey
Copyright © 2022 EAI
DOI 10.4108/eai.7-9-2021.2314938

discussing contemporary knowledge contributions in the field of design for sustainability and product competitiveness.

2 Research Methodology

The first section of the research was devoted to presenting the paragraphs of the approved methodology, the most important of which is the research problem, questions, objectives, and importance, as well as the research model and hypotheses, data collection tool, and statistical analysis methods. The following is a brief discussion of the research methodology paragraphs:

2.1 Problem Statement and Questions

According to the researcher's review of the literature related to design for sustainability, which showed that business organizations face great challenges as a result of growing competition and acceleration in providing designs that have the ability to respond to changes in the needs and desires of customers, as well as the transformation of sources of competitive advantage from cost advantages and economies of scale to advantages of creativity, flexibility and economics The scope, as Design for Sustainability (D4S) has become one of the most prominent methodologies that have achieved great successes in activating the ability of organizations to achieve flexibility and rapid response to the rapid changes in the industry environment and market dynamics to ensure the improvement of product competitiveness and an important source for strengthening the capabilities of adaptation and strategic creativity and based on the results of field coexistence with the reality The product design activities in the laboratory under research and the results of unstructured interviews conducted with workers in the field of design, research and development ** The research problem was formulated and developed according to the following questions:

1. What is the role of the Design for Sustainability (D4S) approach in achieving product competitiveness?
2. Does the management of the laboratory under consideration have a clear vision of the design methodology for sustainability and its role in activating the competitiveness of the product? To what extent does it adopt that methodology as a competitive advantage?
3. What are the dimensions of the requirements for implementing the design methodology for sustainability in the laboratory under investigation?
4. What are the requirements to achieve product competitiveness in the laboratory under investigation?
5. How does the Design for Sustainability methodology contribute to activating the research organization's ability to achieve product innovations and improve its competitiveness?

2.2 Research Objectives

The research seeks to achieve the following main objectives:

1. Presentation and discussion of contemporary knowledge contributions related to Design for Sustainability

2. Presentation and discussion of contemporary knowledge contributions related to product competitiveness
3. Analyse and diagnose the role of the Design for Sustainability methodology in improving product competitiveness
4. Diagnosing the reality of the Design for Sustainability methodology and its requirements in the research organization
5. Analysis of the reality and indicators of product competitiveness in the research organization
6. Presenting recommendations and proposals that contribute to strengthening the capacity of the organization under consideration by activating the requirements for successfully implementing the Design for Sustainability methodology to improve its competitiveness by improving product competitiveness
7. Testing the correlation between the Design for Sustainability methodology and product competitiveness
8. Testing the relationship between the design for sustainability methodology and product competitiveness.

2.3 Proposed Conceptual Model

Contemporary literature has shown an accelerated interest in the design methodology for sustainability as one of the contemporary strategies in strengthening the ability of business organizations to improve their competitiveness, not in the field of creativity in developing new products and processes, but in creating a balance between the advantages of cost, quality, recommendation, and sustainability, which contributes to improving the flexibility and speed of the organization's response to changes in Industry environment and hence the importance of the research are represented in two dimensions, the first is theoretical. For sustainability in the organization under discussion and its role in improving and activating the competitiveness of the product, as well as providing suggestions and recommendations that contribute to improving the organization's ability to employ the design methodology for sustainability in improving the competitiveness of its products.

2.4 Theoretical Research Model

Considering the theoretical trends of the study, which are based on the opinions of a group of researchers and their field implications, a hypothetical research model was formulated that identifies the most important relationships and influences between the variables addressed in the research. It was based on two types of variables, which are as follows:
The independent variable, which represents the Design for Sustainability methodology, whose study includes the adoption of a set of work stages that express its role as an independent variable in the hypothetical scheme of the research. Design for sustainability includes three dimensions: the environmental dimension of design, the economic dimension of design, and the social dimension of design, according to the Triple Bottom Line model. The variable adopted in the research hypothesis is (Dependent Variable).
This is represented by the product competitiveness variable, which was measured according to the model (Pasi Ojala, 2004) and considering the following indicators:

1. Cost competitiveness: It is measured by the ability of the company's products to compete with the cost advantage.

2. Quality competitiveness: It is measured by the product's ability to achieve quality advantages or quality competitiveness
3. Competitive flexibility: It is measured by the product's ability to achieve diversity and respond to changes in customers' tastes.
4. Competitive delivery: It is measured by the organization's ability to achieve the advantages of on-time delivery. Fig 1 shows the hypothesis of the research:

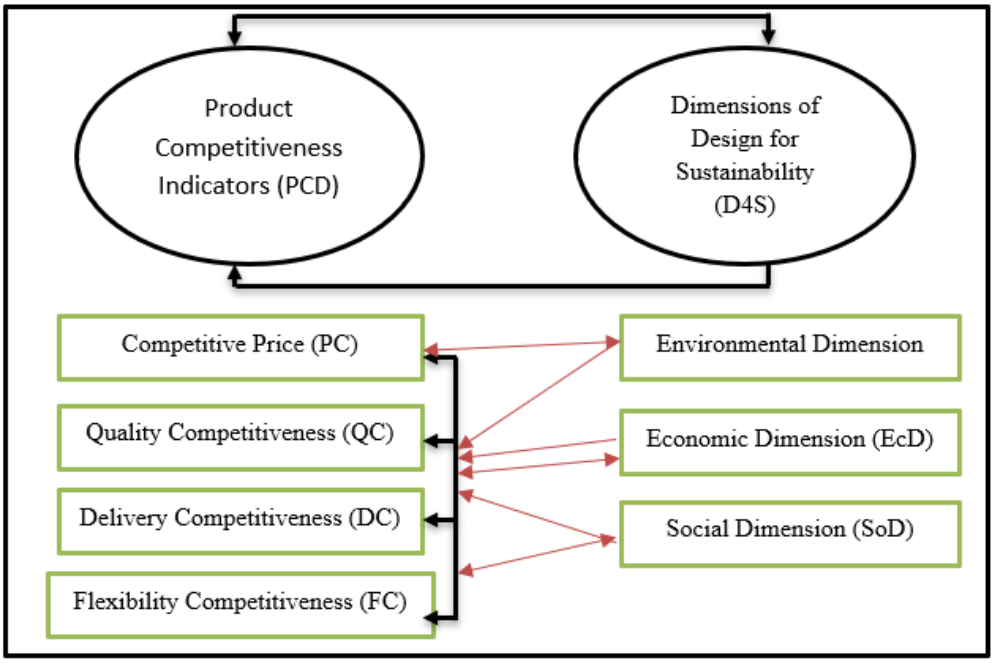

Fig 1. The hypothesis of the research.

2.5 The Following Hypotheses were Tested

H1: A statistically significant correlation between the objectivity of sustainability and product competitiveness, from which the following sub-hypotheses are derived:
H11: a statistically significant correlation, the environmental dimension of the design methodology for sustainability and product competitiveness
H12: a statistically significant correlation, the economic dimension of a methodology for sustainability and product competitiveness
H13: a statistically significant correlation with the social dimension of the design methodology for sustainability and product competitiveness
H2: The variance in the product can be explained in terms of dimensions of sustainability.
H21: The variance in who the product is for can be explained in terms of the environmental dimension
H22: The discrepancy can be explained by whom it is produced for
H23: The discrepancy in who the product is for can be explained in terms of the social dimension for sustainability.

2.6 Study Borders

The limits of the study were as follows:

1. **Place Boundaries:** The researcher elected Salsil Mineral Water Factory in Basra as a field to test hypotheses and a model as one of the organizations facing severe competition in the field of design and production through the availability of competing products in the local markets. Governorate.
2. **Time Borders:** The research period was determined by the period from (1/7/2018) to (1/9/2017), as this period was sufficient for the process of distributing and collecting the questionnaire and conducting many unstructured interviews with department managers and officials of different units to collect the necessary information about the reality of the situation. Study variables in the laboratory under study.
3. **Conceptual Borders:** The intellectual treatments of the topic of research extend to the field of production and operations management, specifically in the fields of design for sustainability and creative design, as they are among the emerging topics that have received noticeable interest from researchers and practitioners in the recent period.

2.7 Research Field and Data Collection

The Silsil Laboratory, which specializes in the production and filling of filtered and sterilized water with ozone, was selected. The laboratory holds standard specifications from specialized laboratories and the ISO (9000) certificate. It was established in 2009. The goal of the laboratory is to develop national products and compete with local and foreign products. The laboratory has a specialized staff of engineers and technicians, and the number of workers in the laboratory (60) workers, as the factory produces three sizes of water bottles, large and medium, and a small mug. To implement the research methodology, several methods were employed in obtaining data and information. The available references, periodicals, and the Internet were used to cover the theoretical aspect. While the questionnaire was adopted in the practical aspect, which was considered the main means, as its paragraphs were formulated in line with the research variables by taking advantage of the literature that dealt with these two variables. Simplicity and clarity were considered in drafting the questionnaire's paragraphs, as well as subjecting it to scientific and objective tests to measure its stability and apparent sincerity. Consistency) in terms of Cronbach's alpha, as the value of the tested coefficient for all paragraphs of the questionnaire was (0.76 α), which is greater than the standard value of the scale of (0.7), which confirms the acceptance of the level of internal consistency of the measurement tool as well as the significance of the correlations between the paragraphs of the tool measurement.

3 Intellectual Framework

The traditional approaches to product design and manufacturing are based on a set of product characteristics, including (functionality, performance, cost, time-to-market) and others. Contemporary literature in the new millennium has addressed many cognitive problems and challenges, including the integration between life-cycle data and design for sustainability. (D4S) for the product and process (Product / Process Sustainable) and its contents to provide innovative designs and products that contribute to improving the competitiveness of the product

and its ability to achieve the added value of the customer. These techniques can be employed in the design of products of an industrial or consumer nature in small sizes and large diversity (low volumes and large varieties Hence, the upcoming design and manufacturing practices require industrial organizations to realize the contemporary changes and challenges to shift from those practices to technologies that achieve expanding the traditional life cycle ranges from the perspective of the multi-stage life cycle (multiple life-cycles) towards the product / exchanged materials cycle. Perpetual Product/Material Life). The premise of design for sustainability is to reduce emissions and outputs as the negative impacts on the environment by adopting skilful, sensitive design and that achieving this requires renewable resources, reducing environmental impacts, and linking workers to the natural environment. In addition to reducing negative impacts, sustainable design must generate meaningful creative projects that can change Behaviour. The dynamic balance between environmental and social concerns generates long-term relationships between the user and the service/product and finally considers the environmental and social differences. (M). The principle that all trends of progress run out, and terminate with diminishing returns, is evident in the typical 'S' curve of the life cycle of technology and the useful life of any system as discussed in Industrial Environment and Life Cycle Assessment. Diminishing returns are the result of reaching normal limits. The common practice of business management is to read the diminishing returns in any direction of the effort as evidence of diminishing opportunities and the possibility of accelerating decline and an indication of the creation of new opportunities elsewhere.

Innovative design methodologies and innovative manufacturing techniques must be developed to create synchronization between traditional product characteristics and the life cycle to achieve the following basic objectives:

1. Reduction of manufacturing costs
2. Reduction of product development time
3. Reduction of material use
4. Reduction of energy consumption
5. Increased operational safety
6. Enhanced societal benefits
7. Reduction of industrial waste
8. Repair, reuse, recovery, and recycling of used products/materials
9. Consideration of environmental concerns
10. Education and training of the workforce

The accelerated transformations in the intellectual construction of the contemporary literature in the field of product design and manufacturing aim towards optimizing methodologies integrating environmental considerations, energy efficiency, product design, and manufacturing techniques for sustainability with product maintenance, reassembly, reuse of materials, remanufacturing, and recycling considerations. Contemporary design and manufacturing techniques have promoted new systems of thinking in the development of designing new products and processes and focused on the need to pay attention to the interests of all partners and stakeholders in the industry environment, which in turn requires the development of design methodologies, manufacturing processes, post-use processes, and resource planning systems (ERP) to simultaneously achieve multiple goals, including factory profitability, the rapid launch of products to the market, and conservation of environmental resources in line with environmental considerations.

Sustainability studies, in general, have shown a clear focus on the environmental, social, economic, and technical dimensions, including the problems of public health, community welfare, and the environment across the full business cycle, which is defined as the period from the start of the process of extracting and reducing raw materials to the complete product. Fig 2 shows the dimensions of design for sustainability with the presentation that most of the literature reviewed by the researcher agreed on three dimensions (environmental, social, and economic), while some knowledge contributions showed the technical dimension as the fourth dimension of sustainable design (Nagel, Pappas, and Olga Pierrakos) [1].

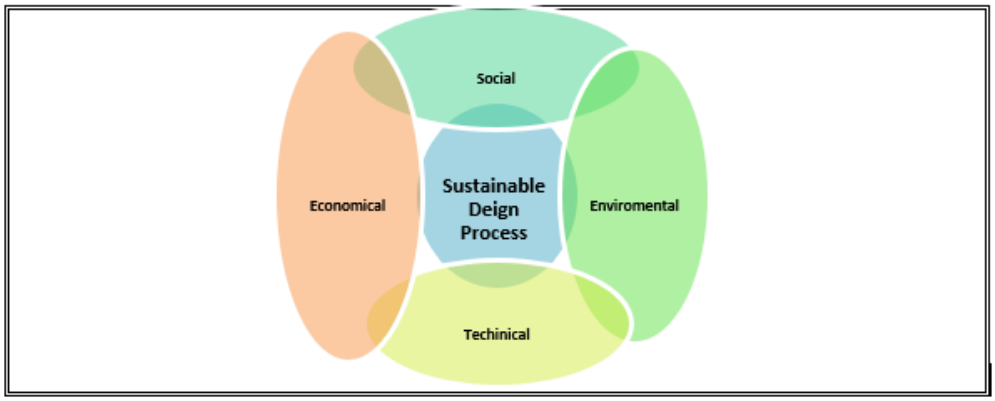

Fig 2. Integration of environmental, technical, social, and economic dimensions to generate sustainable design. Source: Robert L. Nagel, Eric C. Pappas, and Olga Pierrakos, 2012 "On a Vision to Educating Students in Sustainability and Design—"http://www.mdpi.com/journal/sustainability.PP: 72-91

As for sustainable products, they are generally defined as those products that achieve environmental, social, and economic benefits in conjunction with the protection of public health, welfare, and the environment during their total commercial life cycle, starting from the start of reducing materials and ending with the final product, taking into account the needs of future generations. Completely with nature throughout its entire life cycle[2]. . From a traditional perspective, the economic and environmental analysis of products usually focuses on analyzing the impact of these products on society. It is mostly a development to analyze the life cycle of an individual product, and that many other aspects, such as recycling in conjunction with multiple reuse opportunities, coincide with many economic, social, and environmental gains, which are The most important in contemporary manufacturing practices. The idea of recycling, reuse, and remanufacturing at present has come in conjunction with great interests in developing innovative manufacturing systems and processes in the field of products and materials to create products with multiple life cycles (Multiple). life-cycle products), which has become the reality in many applications in the fields of product manufacturing. The traditional concept that includes the study of the life of the product from cradle to grave ("from cradle to grave" has been transformed in the manufacturing literature to from cradle to cradle) from cradle to cradle") [3] and it is an important conceptual shift in the science of manufacturing, which has taken an important knowledge space at the level of the intellectual model of contemporary literature. This is due to environmental efficiency and concerns that coincided with reducing toxic emissions in air and water, and production with a minimum amount of waste, a minimum amount of energy, and at all levels. The literature in the past few years in the field of product and process sustainability has been concerned with attempts to develop

methodologies for assessing and evaluating the level of sustainability in the various stages of the product life cycle, and that this type of evaluation has helped manufacturing organizations to explore unsustainable components and elements at any stage of the product life cycle. Many types of research and studies presented qualitative or descriptive results about the product life cycle, which confirmed the difficulty of quantifying the results of those stages [3,4] and most of these studies are non-analytical and non-scientific in terms of the perceived value of their contributions. However, product sustainability does not mean or does not cover only simple assessment. The environment, as a measure of contribution, includes a comprehensive and simultaneous assessment of the environmental, economic, and social impact. These indicators are overlapping and interrelated and have an impact on each of the stages of the product life cycle with different levels of impact in the various stages. Legal legislation is also one of the most important factors motivating the manufacture of sustainable products. Among the international legislation in this regard is (i) Waste Electrical and Electronic Equipment (WEEE) legislation [6], (ii) legislation to reduce the use of hazardous materials (RoHS) [7], (iii) End-of-life-cycle legislation (ELVs) [8], which are legislation that aims to determine the responsibility of the extent to which products conform to specific sustainability goals across their life cycle directly, either to producers, manufacturers or exporters. As for the other incentives for the sustainability of the crown, they are represented in the positive social expectations and economic gains. In our current research, two scenarios will be adopted, the first includes the economic stimulus and the other social, both of which work within the framework of the environmental stimulus. The main objective of the research is to try to shed light on the importance of product design for sustainability by focusing on the real need to create sustainable products to achieve economic, social, and environmental benefits. The new framework for the comprehensive assessment of product sustainability will be presented in the research, and this new methodology includes the four stages of the product life cycle (before manufacturing, during manufacturing, during use, and after use) to cover the three components of sustainability (economic, environmental and social), all of which are integrated into an ordinal system to reach a scale Formulated for product sustainability:

3.1 Total Life-Cycle of Manufactured Products – Four Stages:

The industrial product life cycle includes four stages in the closed channel system (CLS):

a) Pre-manufacturing
b) Manufacturing
c) Use
d) Post-Use

3.2 The concept of '6R' Methodology

When looking at the flow of materials in the life cycle of sustainable products, three “patterns” (3R) [11] are noted, which are Reduce, Reuse, and Recycle, which are usually referred to as strategies for treating the product at the end of the life cycle. However, by adopting a more comprehensive and integrated perspective, it is possible to add three more "patents". These are Recover, Redesign, and Remanufacture, where the reduction activity is to reduce activities that seek to simplify the current design of a particular product to facilitate future post-use activities. , As for reuse, it refers to achieving the lowest environmental impact, mainly because it usually involves relatively fewer manufacturing processes [12]. Recycling refers to a series of activities

that include dismantling, smelting, and separating. Take-back represents the activity of collecting products at the end of the product's life cycle for subsequent use activities. It also refers to the dismantling of specific components of products at the end of their life. Re-design means integration with a reduction in that it involves re-designing the product due to the simplification of post-use processes in the future. Re-manufacturing is similar to manufacturing. However, the difference is that it is not made on virgin materials but on products that are already used. The 6R methodology aims in the product life cycle to reach a state of constant or permanent flow of materials, which in turn means reducing post-use activities [13, 14]. Closed Loop vs. Open Channel Lifecycle Systems. Open Loop Life-cycle Systems Fig 2 shows the closed channel (cradle to cradle) for the life cycle of the product, which is the opposite of the open channel (cradle to grave) (cradle to grave). Products are consumed and are considered obsolete at the end of the product life cycle. According to this scenario, the Material resource, waste output, energy consumed, and the rest of the system emissions are all a function of customer demand. To shift towards a closed channel system, three criteria for sustainable product recycling are required. These criteria are:

1. Reducing the energy and material resources required for the product to perform its primary function to achieve customer demand
2. Optimizing the resources used
3. Reducing or eliminating the adverse effects of waste and emissions

The closed-channel product system must meet two of the aforementioned criteria (i and ii) [15]. In such a manufacturing system, the activities of reuse, recycling, and recycling are the ones that rotate materials in the product system. These activities reduce the requirements for the need to extract new materials to feed the product system, which contributes to reducing the total energy input required and necessarily emissions per unit at production and consumption [16].

3.3 Product Differentiation

Product differentiation is a well-defined theoretical concept that is based on two conditions. First, buyers must realize that the goods ("brands") that belong to a product category are close substitutes for each other, but only find relatively poor substitutes with goods outside that category. At the same time, these brands must be sufficiently imperfect substitutes for each seller to see that his brand faces a downward-sloping demand curve. Research on industrial organization often refers to differentiated products, but the empirical correlates of structural differentiation have not received much attention [20].

We first define the conditions that are theoretically sufficient to cause the downward sloping demand curves faced by individual sellers. We then use factor analysis to determine whether these ground rules are attributable to the observed characteristics of the products and the ways that buyers choose. Upon reaching a positive result, we show that price adjustments in a cross-section of industries respond to factors in the way expected from the theoretical foundations of differentiation, as a test of this device for measuring differentiation. At least two models seem to provide conditions sufficient to link downward-sloping demand curves for individual producers to underlying characteristics of demand and technology.[21]

This output set is not attainable, however, if fixed costs or scale economies are present in the production of each distinct bundle. In that case, only some of the many possible bundles are produced. The typical buyer finds no attribute bundle that matches exactly the one he would

choose under the idealized conditions just defined. Relative prices determine the bundle chosen from among those offered. Although each buyer may make discrete switches between brands as relative prices change, buyers generally differ in their reservation prices for a given configuration. Therefore, downward-sloping demand curves are likely to result when the preferences of individual buyers are aggregated.[22]
The other theoretical model linking downward-sloping demand curves to ambient structural conditions comes from the literature on consumer information and transactions costs [20].

4 Statistical Analysis and Test Results

To enhance the theoretical side of the study, the statistical practical aspect was based on the study plan and its hypotheses. The third section was devoted to presenting and discussing the model and research hypotheses.

4.1 Model Test Results and Hypotheses

The current paragraph is devoted to presenting and discussing the results of the scheme test and the research hypotheses in terms of the indicators of descriptive and inferential statistical analysis and according to the following paragraphs.

4.1.1 Test Statistical Analysis of The Descriptive Results of The Research Variables (Statistical Descriptive Analysis)

Table 1 presents the results of the descriptive statistical indicators tests for the main and secondary research variables in terms of the weight mean (xw) and standard deviation (σ), as this paragraph aims to verify the level of response of the research sample to the approved variables and their clarity and dispersion from the arithmetic mean of the measurement tool.

Table 1. Rresults of the descriptive statistical analysis of the research variables.

N	Research Variables	Mean	standard deviation	Relative importance

				c e
1	Design for Sustainability (independent dimensions)			
A	The environmental dimension of the design	3.851	0.72	1
B	Economic dimension of design	3.242	0.67	3
C	The social dimension of design	3.630	0.85	2
	General mean	3.546	1.02	-
2	Design and Manufacturing for the Environment (Intermediate)	3.221	0.86	-
3	Product competitiveness			
	Cost Competitive	3.630	0.64	2
	Quality Competitive	3.560	0.85	3
	delivery Competitive	2.240	0.46	4
	Flexibility Competitive	3.8	0.72	1

		5 1		
	General mean	3 . 0 2 2	0 . 7 8	

statistical program (Spss). (N=47)

As is evident from the results of the descriptive statistical analysis of the research variables, the dimensions of the design methodology for sustainability came according to the relative importance of the research sample in the following order:
The dimension of flexibility competitiveness ranked first in terms of its relative importance with an arithmetic mean of (3.85) and a standard deviation of (0.72). This means that the laboratory adopts standard or standard designs, followed in terms of importance by the dimension of cost competitiveness for a weighted average of (3.630) and with a standard deviation of (3.630) Its value is (0.85), followed by the dimension of quality competitiveness with a weighted mean of (3.56) and a standard deviation (0.04), and finally the dimension of delivery with a weighted mean of (3.24) and a standard deviation of (0.67).

4.1.2 Results of the Correlation Test (Variables Correlations Test)

Table 2 presents the results of the test of simple and multiple correlations between independent and dependent research variables within the framework of the intermediate variable represented by design and manufacture for the environment in terms of (Spearman) correlation coefficients for ranks and using the (SPSS) system.

Table 2. Matrix of correlations between research variables.

	1	2	3	4	5	6	7
1	-						
2	0 . 7 4 1 *	-					
3	0 . 8 4 2 *	0 . 7 4 3 *	-				
4	0 .	0 .	0 .	-			

	7 8 5 *	7 1 6	8 9 4 *				
5	0 . 4 1 1 *	0 . 5 2 1	0 . 4 2 9	0 . 7 9 6 *	-		
6	0 . 4 6 7 *	0 . 4 0 4	0 . 5 6 2 *	0 . 4 8 5	0 . 3 9 4 *		
7						0 . 4 4 3 * *	-

Key to significant test: * p ≤ 0.05, : p ≤ 0.05** Source: - The results of the (SPSS)

The results of the correlation matrix will be commented on within the limits of the current research hypotheses, which stipulated the existence of significant correlations between the design for sustainability methodology and the competitiveness of the product in the context of the laboratory's pursuit of sustainability. All dimensions of product competitiveness for products were the most obvious. The correlation relationship between the economic dimensions of design for sustainability with a correlation coefficient of (0.540), followed in terms of strength, the correlation between the social dimension of design for sustainability, and then the relationship with the economic dimension with a correlation coefficient of (0.425) and all of them significantly significant at a confidence level (0.05). The variable design for sustainability also achieved significant correlations, the most obvious of which was the correlation with a psychological one, and its value was (r = 0.460) at a significant level of (0.05). The results of the previous analysis verify the validity of the correlation hypotheses adopted in the research.

4.1.3 Analysis of The Results of The Impact of Design For Sustainability on Product Competitiveness

The content of this analysis represents the test of the second main research hypothesis that indicates the existence of a significant effect of Design for Sustainability (SPD) in terms of its combined dimensions in achieving product competitiveness. The coefficient of determination

(2r) of the general model, which indicates that (0.56) of the variance in the competitiveness of the product is explained by the components of the design for sustainability combined, and this is supported by the value of (F) which reached (102.4), which is greater than its tabular value at the level of significance (0.05) and two degrees of freedom (4.42).

To explain the relative importance of the partial effects of each component of the design for sustainability in achieving product competitiveness, it is possible to follow the regression coefficients (beta) and the values (t) calculated for each of them. (0.39) of the variance in achieving product competitiveness is supported by the calculated value (t) of (5.42) which is greater than the tabular at the level of significance (0.05), followed by the components (environmental dimension and social dimension) in terms of its regression coefficients of (0.35, 0.28, 0.25).) respectively and (t) values calculated for each of them compared to the tabular.

It is inferred from the results of the previous analysis that the competitiveness of the product that organizations seek derives its basic components to a large extent from the components of design for sustainability, as the more organizations own this technology, the more they can achieve institutional leadership within their work environment, and thus the second main research hypothesis was achieved.

Table 3. Results of the impact of design for sustainability on product competitiveness.

	Components of Designing for Sustainability				
Independent variable	The environmental dimension of	The Economic Dimension of	The social dimension of de	R 2	F

		ionofthedesignforsustainability	DesignforSustainability	signingforsustainability		
Productcom	B	0.26	0.39	0.28	*0.56	102.4

p e t i t i v e n e s s	T	* 4 . 7 3	* 5 . 4 2	* 4 . 8 5		

Prepare the table in light of the results of the Computer d.f 4, 42 < 0.05 *N = 3

5 Conclusions and Recommendations

The research reached several conclusions, the most important of which are:

1. The dimensions of design for sustainability did not achieve real substantive results in the researched laboratory in terms of many of the standards adopted in the research, as the most important dimension of the dimensions of design for sustainability, which received the attention of the research sample, was the economic dimension of product sustainability.
2. In the same direction, the product competitiveness indicators of the laboratory products did not exceed the standard limits of the scale adopted in the research by much. This conclusion is supported by the fact that the products of the laboratory lag behind in the standards of sustainability compared to similar products in international companies.
3. The results of the statistical analysis showed the existence of a significant correlation between the level of implementation of the design methodology for sustainability and the competitiveness of the product for the products of the laboratory in question.
4. The results of the statistical analysis proved that the Design for Sustainability methodology can explain the variation in product competitiveness indicators for the factory products, and its impact increases with the presence of the design variable for the environment as an intermediate variable.
5. The results of many field indicators showed that all the laboratory practices examined need further development and modernization to take advantage of the design for sustainability and design for the environment methodology to support the competitiveness of their products.

The most important recommendations reached by the research:

1. The necessity of activating the laboratory practices of the design methodology for sustainability, as it is one of the contemporary entrances to improve the competitiveness of products, a strategy for survival, and improve profitability.
2. Develop and update the capabilities of the factory workers to adopt the design methodology for the environment as a vital approach to improve product competitiveness indicators for competing products in the market.
3. Activate and update manufacturing and production technology in the factory to meet the requirements of the design methodology for sustainability and design for the environment to improve the competitiveness of the product.
4. Activate integration and coordination mechanisms between production and service departments to improve their ability to optimize the dissemination and exchange of information related to the successful implementation of the Design for Sustainability methodology.
5. The need for the laboratory management to pay attention to the availability of infrastructure and the material and human requirements to improve the indicators of the sustainability of the products and processes of the laboratory.

References

[1] Bhamra, T., & Lofthouse, V. (2016). Design for sustainability: a practical approach. Routledge.
[2] Ceschin, F., & Gaziulusoy, I. (2016). Evolution of design for sustainability: From product design to design for system innovations and transitions. Design studies, 47, 118-163.
[3] Ceschin, F., & Gaziulusoy, İ. (2019). Design for Sustainability (Open Access): A Multi-level Framework from Products to Socio-technical Systems. Routledge.
[4] Yıldız, S., Kıvrak, S., Gültekin, A. B., & Arslan, G. (2020). Built environment design-social sustainability relation in urban renewal. Sustainable Cities and Society, 60, 102173.
[5] Yıldız, S., Kıvrak, S., Gültekin, A. B., & Arslan, G. (2020). Built environment design-social sustainability relation in urban renewal. Sustainable Cities and Society, 60, 102173.
[6] Shabbir, M. S., Mahmood, A., Setiawan, R., Nasirin, C., Rusdiyanto, R., Gazali, G., ... & Batool, F. (2021). Closed-loop supply chain network design with sustainability and resiliency criteria. Environmental Science and Pollution Research, 1-16.
[7] Changede, S., Thomas, L., & Walker, S. (2021, March). Learning from Traditional Practices and Products in India to inform Design for Sustainability. In Fifteenth International Conference on Design Principles and Practices.
[8] Pan, S. L., Li, M., Pee, L. G., & Sandeep, M. S. (2021). Sustainability design principles for a wildlife management analytics system: Action design research. European Journal of Information Systems, 30(4), 452-473.
[9] Xia, B., Xiao, J., Ding, T., & Zhang, K. (2021). Probabilistic sustainability design of structural concrete components under climate change. Structural Safety, 92, 102103.
[10] Fonseca, J. D., Commenge, J. M., Camargo, M., Falk, L., & Gil, I. D. (2021). Multi-criteria optimization for the design and operation of distributed energy systems considering sustainability dimensions. Energy, 214, 118989.
[11] Schwaninger, M. (2018). Systemic design for sustainability. Sustainability Science, 13(5), 1225-1234.
[12] Park, H. S., Hwang, J. W., & Oh, B. K. (2018). Integrated analysis model for assessing CO2 emissions, seismic performance, and costs of buildings through performance-based optimal seismic design with sustainability. Energy and Buildings, 158, 761-775.
[13] Siu, K. W. M., & Xiao, J. X. (2020). Public facility design for sustainability: Participatory action research on household recycling in Hong Kong. Action Research, 18(4), 448-468.

[14] Mihelcic, J. R., & Zimmerman, J. B. (2021). Environmental engineering: Fundamentals, sustainability, design. John wiley & sons.
[15] Seidel, S., Chandra Kruse, L., Székely, N., Gau, M., & Stieger, D. (2018). Design principles for sensemaking support systems in environmental sustainability transformations. European Journal of Information Systems, 27(2), 221-247.
[16] Pan, S. L., Li, M., Pee, L. G., & Sandeep, M. S. (2021). Sustainability design principles for a wildlife management analytics system: Action design research. European Journal of Information Systems, 30(4), 452-473.
[17] Seidel, S., Chandra Kruse, L., Székely, N., Gau, M., & Stieger, D. (2018). Design principles for sensemaking support systems in environmental sustainability transformations. European Journal of Information Systems, 27(2), 221-247.
[18] Ebenezer, O. (2019). Graphic Design Principles and Theories Application in Rendering Aesthetic and Functional Installations for Improved Environmental Sustainability and Development. International Journal of Engineering and Manufacturing, 9(1), 21.
[19] Cortina, J.M. (1993). "What is coefficient alpha? An examination of theory and applications". Journal of Applied Psychology. 78: 98–104.
[20] Chen, J., Wang, X., & Chu, Z. (2020). Capacity sharing, product differentiation and welfare. Economic research-Ekonomska istraživanja, 33(1), 107-123.
[21] ROSEN, S., 1974, 'Hedonic Prices and Implicit Markets: Product Differentiation in Pure Competition', Journal of Political Economy, 82 (January/February), pp. 34-55.
[22]ARCHIBALDG, . C., EATON, B. C. and LIPSEY,R . G., 1983, 'Address Models of Value Theory', Institute for Economic Research, Queen's University, Discussion PaperNo.495

Synthesis and Study the Mechanical Properties for New Interpenetrating Polymer Network Based on HBPU/ECA

Firas Jameel Jabbar[1]
{firas.alassadi@stu.edu.iq[1]}

Department of Pharmacy, Southern Technical University, Basrah, Iraq

Abstract. New types of interpenetrating polymer networks (IPNs) were created in this study, which included highly crosslinked polyurethane (HBPU) with Ethylcynoacrylate (ECA), with different polyurethane percentages (10, 20, 30,40 % wt.). After the success of the preparation process of these polymers, they were identified by (FTIR) and (^{1}H NMR) spectroscopic to ensure the validity of the prepared polymeric structures. A device (Instron 5566) was used to study the mechanical properties of the prepared polymers and the following functions were obtained: Tensile strength, % elongation at break, impact strength. The impact of increasing the HBPU prepolymer fraction on the mechanical properties of the interpenetrating polymer network was investigated in this study. Impact strength improved significantly, while tensile strength gradually decreased as the percentage of polyurethane in IPNs rose.

Keywords: Hyperbranched polyurethane, HBPU ECA, impact strength, elongation, tensile strength.

1 Introduction

The short-chain cyanoacrylate (methyl or ethyl cynoacrylate) compounds are among the groups that belong to vinyl monomers known for their ability to polymerization by free radicals, which is famous for its unique properties, for example, its ability to fast adhesion and high effectiveness, as it has entered multiple industrial applications, especially " super glu" [1-3]. While long-chain cyanoacrylate compounds (butyl or hexylcyano acrylate) have been found to have distinguished medical applications in the field of leather and tissue adhesives [4-6]. The World Health Organization has permitted the use of these compounds in the biological and medical fields due to their biodegradability and low toxicity [7-9]. Also, "cyanoacrylate vapour has unique and important uses in forensic science to detect fingerprints by tracing the amino acids present in the fingerprint [10,11]. The presence of the double bond in some cyanoacrylate compounds, for example (allyl 2-cynoacrylate), gave it an important advantage to enter crosslinking reactions at high temperatures, and this characteristic enabled this type of unsaturated compounds to be used as thermally resistant adhesives {12,13]. Cyanoacrylate polymers have relatively poor thermal stability, and the mechanical properties deteriorate when thermal decomposition occurs, and its polymeric chains break down. The decomposition process often occurs by depolymerization at temperatures lower than the glass transition. Therefore, the idea of the current research is to improve the mechanical properties of cyanoacrylate polymers by preparing an interpenetrating polymer network with polyurethane, which has unique mechanical and thermal properties.[14-16].Smart polymers that can change their shape in response to external conditions and stimuli, such as sunlight, humidity, and pH ... have gained "great" attention from the academic and industrial circles, as they have widely entered into medical uses, space, and tissues [17-19]. Polyurethane is considered more popular

IMDC-IST 2021, September 07-09, Sakarya, Turkey
Copyright © 2022 EAI
DOI 10.4108/eai.7-9-2021.2314882

for "smart polymers" uses and has become a "research" topic for many researchers around the world because of its unique, distinct, and comprehensive properties[20-22]. However, the low strength of these polymers will limit their use in areas that require high mechanical properties, for example, materials used in outer space. Many researchers were able to improve the thermal and mechanical properties of polyurethane by adding organic or inorganic materials [23,24].
Fu et al . successfully developed the thermal properties of polyurethane by adding 1,3,5,7-tetrahydroxy adamantane [25]. While A.V et al . prepared a new type of polyurethane with nanotechnology by inserting nanoparticles into the pores of the PU film. The findings revealed that these nanoparticles could boost the polyurethane's blocking effectiveness at the expense of the PU film's memory performance because of these nanoparticles, which are considered one of the types of fillers that work to impede the movement of Polymer chains, which lead to a delay in the process of restoring the shape of the film, and this, in turn, will lead to the depletion of the effect of the shape memory[26]. Therefore, medicating the polymer shape without fillers demands for Shape memory polymers[27-29].
Interpenetrating polymer networks (IPNs) are an overlap of two or more polymers in networks where a partial interlacing on the molecular scale is present in the matrix [30-32]. There is no covalent bonding and therefore the polymers cannot be isolated unless the chemical bonds are crashed [33,34]. Thus, the mixtures of two prepared polymers, networked without any interlacing, are not generally considered to be IPNs, although many researchers have treated them as such IPNs are of different types, viz. sequential, simultaneous, and semi IPNs [35-37]. As their names suggest, sequential IPNs are formed sequentially by more than one IPN in a process, whereas simultaneous IPNs are formed simultaneously. However, semi-IPNs are formed by the polymerisation of a monomer in the presence of a polymer. All the types of IPN listed earlier are found in vegetable oil-based polymers. These IPNs have some advantages over polymer blends or cross-linked polymers[38-40]. Ballestero et colleagues discovered that chemical bonding points formed between two networks of polyurethane and acrylic/ester in interpenetrating polymer networks have a significant effect in minimizing phase separation in the polymeric system. [41]. Chen et al. were able to manufacture a new type of IPNs composite that includes the reciprocal solubility property of polyurethane/epoxy resin of both polymers was utilized to improve their outstanding damping performance [42]. Yu et al. have been preparing a type of IPNs that include polyurethane and epoxy, and they found that these polymers have distinct mechanical properties that include both tensile strength and impact strength. Besides, interpenetrating polymer network can improve the intelligent property of the shape through the formation of the network of entanglement, and therefore IPNs composite is considered an important attractive composite material as many specialized studies have appeared mainly on the mechanical properties and damping properties. While not looking at studies specialized in improving the performance of shape memory[43]. Because polyurethane is highly interlaced, it is considered one of the basic materials that exhibit damping behaviour in ranges of frequency, heat, and distinct thermal stability. Therefore, this type of polymer was used in the manufacture of ships and submarines, as it provided a low cost and improved operational performance compared to metal materials that are used for the same purpose[44]. Therefore, these advantages of polyurethane were taken advantage of to improve some properties of cyanoacrylate by preparing types of (IPNs).
In this work, a new type of interpenetrating polymer network type semi-IPNs has been prepared from mixing hyperbranched polyurethane (HBPU) with the s-triazine unit in the structure, which has a large number of functional groups on its surface, and the other part of IPNs included ethyl cyanoacrylate (ECA), which has a high adhesion strength resulting from the presence of a strong electron-withdrawing nitrile (CN) group and an ester group (CO2R) groups attached to the α-carbon of the double bond, but the weak property in this type of polymer is the weak thermal stability, which is close to the glass transition temperature (Tg). To make the HBPU/ ECA IPNs composite, several composition ratios of HBPU prepolymer and ECA were employed. The effect of HBPU content on the mechanical characteristics of IPNs composites was investigated.

2 Experimental

2.1 Materials and Instrument

Ethyl cyanoacrylate monomer (, viscosity; 6 cps, contains 0–0.3% hydroquinone as an inhibitor) was obtained from K&R international. polytetramethylene ether glycol (PTMEG) with Mw of 2000 g mol−1 was obtained from Jining Letian Crafts Co., Ltd, China. MDI (98% purity) and 1,3,5-Tris (2-hydroxyethyl) isocyanurate (THEIC) were obtained from Sigma-Aldrich (Milwaukee, WI, USA) and were used without any further purification. The IR spectra were registered using a PerkIn-El mer 16 F PCFTIR spectrometer (PerkinElmer Cetus, Norwalk, CT). CDCl3 as a solvent in an ECX 200-JEOL ^{1}HNMR spectrometer. The Tensile tests were conducted as specified by ASTM D638, while the flexural strength test was conducted as specified by ASTM -D790-10. An Instron- 5566 (Instron, Canton. MA.USA) was used for the tensile and flexural tests e film specimens were made in a dog bone shape according to ISO.527-2./1BB standards, with dimensions of 38 mm x 2 mm (centre) x 0.4 mm. To achieve average values, at least five specimens were tested. Multimode3 Atomic Force (AFM) microscope-(Brooke. the USA).

2.2. Preparation of HBPU/ECA IPNs

Scheme 1 shows the detailed synthesis procedure for the HBPU/ ECA IPNs hybrid. To begin, (PIMEC) was put to a reaction vessel with three necks, to which substance (MDI) was added in the following molar ratios (3: 7) and the reaction was stirred for 2 hours under a nitrogen atmosphere at a temperature of (60 °C). Then, according to the following molar ratio (1:8), a mixture of (THEIC) and (MDI) is made, and it is introduced to the reaction vessel with three necks and mixed for 5 hours at (80 ºC) to obtain HBPU prepolymer. After the period for forming the (pre-prepared polymer) has passed, an equivalent amount of (ECA) is added to the (prepolymer) and thoroughly mixed. Finally, (HBPU/ECA) is poured into the meld and treated in the oven at a temperature of (130 ºC) for 8 hours for the curing process to be done accurately. The HBPU/ECA IPNs with 10, 20, 30, 40 wt % HBPU were defined as IPN-1, IPN-2, IPN-3, IPN-4, respectively.

Table 1. Show the ratio of component HBPU, ECA in IPNs

IPNs	IPN-1	IPN-2	IPN-3	IPN-4
%HBPU/ECA	10/90	20/80	30/70	40/60

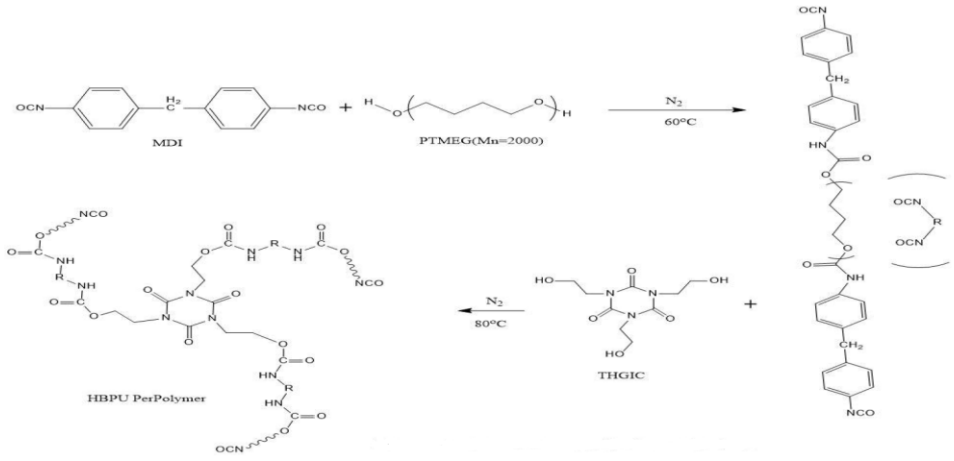

Scheme 1. Detailed synthesis route of the HBPU prepolymer

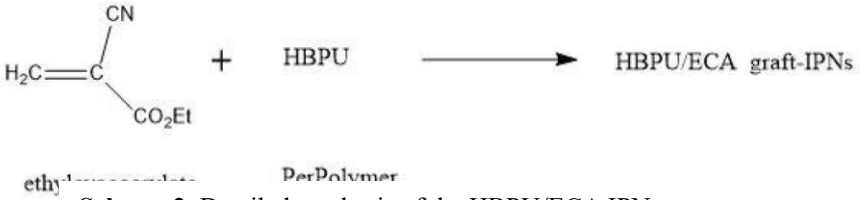

Scheme 2. Detailed synthesis of the HBPU/ECA IPNs

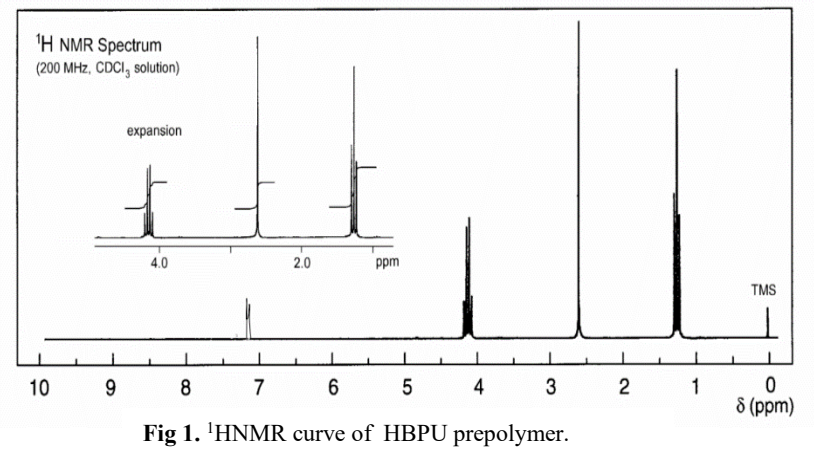

Fig 1. [1]HNMR curve of HBPU prepolymer.

To confirm the formation of the interpenetrating polymer network, spectroscopy FTIR and H^1 NMR were adopted to document the validity of the formed polymers. The ^{1}H NMR spectrum of the HBPU prepolymer is shown in Fig 1. Two peaks appear at (1.25 δ) and (2.70 δ), which are attributed to –CH_2—and –O—CH_2-- in PTMEG respectively, while prominent bands appear at (4.1 δ) attributable to--CH_2 which connected with a triazine ring, and this confirms the occurrence of the formation HBPU prepolymer as a result of the reaction between NCO group in MDI with the terminal hydroxyl group in compound THELC as shown in scheme (1). As for the bands appearing in position (7.1 δ) they belong to the protons of the benzene

ring located in MDI. Also, to prove the formation of the interpenetrating polymer networks that include ECA and HBPU, the FTIR technique was used to confirm the validity of the formation of these polymers. Fig 2 shows the spectra of three samples, which are respectively (ECA), (HBPU), and (IPN-4). The appearance of the stretch band at cm^{-1} for the group ($CH=CH_2$) in the monomer spectrum ECA and its disappearance in the spectrum IPNs proves the polymerization of the monomer and the formation of IPNs. Two peaks of HBPU prepolymer were identified, located at 3400 cm^{-1} and 1750 cm^{-1}, belonging to the group –NH stretching vibration and strong stretching C=O, respectively, and this is proof of the generation of urethane linkage, in addition to a peak at 2300 cm^{-1} attributed to group (NCO) terminal unreacted of HBPU prepolymer, the disappearance of this group when preparing all interpenetrating polymer networks confirms the success and validity of the preparation method.

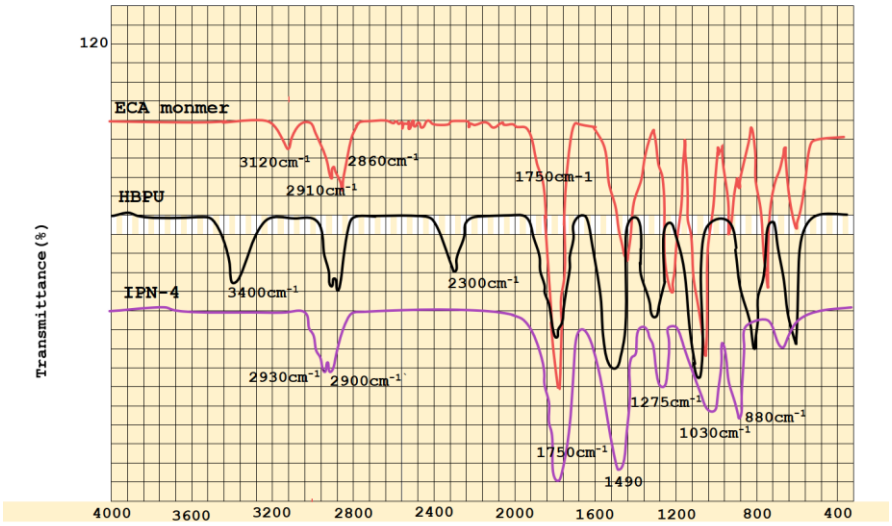

Fig 2. FTIR spectrum of ECA monmer, HBPU prepolymer and IPN-4.

3.1 Mechanical Properties

In polymers, stress-strain relationships are called dynamic dependencies and are not linear. The stress-strain curve was used to assess tensile characteristics (tensile strength at yield, impact strength, % elongation, and flexural stress). The (stress-strain) curve of IPN-1, IPN-2, IPN-3, IPN-4, and HBPU was shown in Fig 1 as an example of the effect of HBPU on the mechanical properties of IPNs based on HBPU/ECA. The tensile strength (TS) data of the various IPNs prepared in this study are shown in Fig 2. As DMTA data for IPNs is analysed, it can be shown that increasing HBPU causes a significant decrease in tensile strength from 51 MPa to 20 MPa and flexure stress from 481.4 MPa to 59.6 MPa, respectively. For all IPNs, the data indicate a slight increase in the Impact strength and a significant increase in % elongation at break from 15 to 65. This behaviour may be explained by a rise in interpenetration network formation.

Table 2. mechanical properties data of HBPU/ECA IPNs with different %wt.

Samples	Tensile strength (MPa)	% Elongation at break	Impact strength KJ/m^2	Flexure stress MPa
IPN-1	51	15	3.88	81.4
IPN-2	45	25	3.98	70.2
IPN-3	27	50	4.12	65.2
IPN-4	20	65	4.26	59.6
ECA polymer	75	10	3.84	66.0

HBPU	15	330	3.46	------

Another cause is the creation of crosslinking sites between HBPU and ECA, which makes the polymer chains less prone to slip at room temperature due to external forces. Elongation at break increases as HBPU content in HBPU/ECA IPNs increases, whereas tensile strength and Flexure stress steadily decrease. The results are like those seen in AFM's phase diagram Fig (9), indicating that the continuous hard phase of ECA in IPN-1 causes brittleness and that the elongation at break increase as the HBPU content rises. However, as HBPU content is increased, the number of PU domains in the composites grows, and as is well known, increasing the amount of polyurethane with a soft molecular chain reduces tensile strength. These findings imply that forming crosslinking sites between HBPU and ECA can improve mechanical strength and elastic modulus, which is dependent on the ECA/HBPU %wt. It also lays the groundwork for the HBPU-based IPNs shape memory polymer to have good mechanical properties. The technique (AFM) is one of the important and common techniques in distinguishing the phase separation in different polymeric materials and this is evident in the different shapes of the overlapping in interpenetrating polymer network .this appears in Fig (9A-D), which represents (IPN1-4), where we note that the incandescent parts represent the solid phase while the dark parts represent the soft phase. In Fig (9A), which shows the special morphology of the polymer (IPN-1) with a polyurethane ratio of 10%, there is a large overlap and compatibility between polyurethane and the monomer Ethyl Cynoacrylate and the appearance of the glowing parts representing the solid phase, which are about (10 nm) dimensions, while the compatibility begins to decay at increasing the proportion of polyurethane, where the dimensions are about (60nm), 150 nm and 200 nm for each of IPN2, IPN3 and IPN4 respectively.

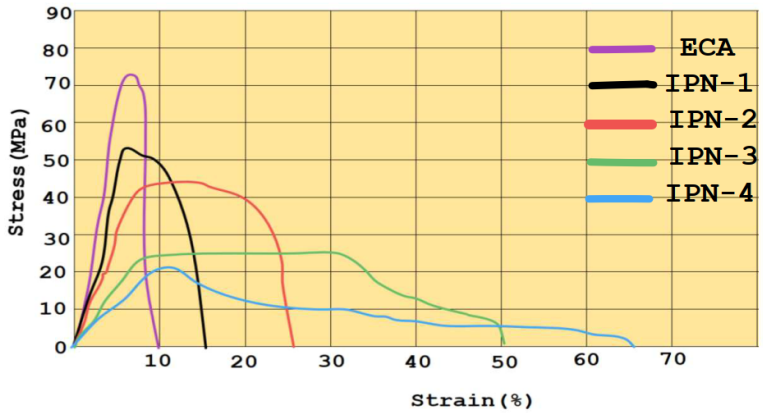

Fig 3. The representative stress-strain curves of HBPU/ECA IPNs with different composition ratios.

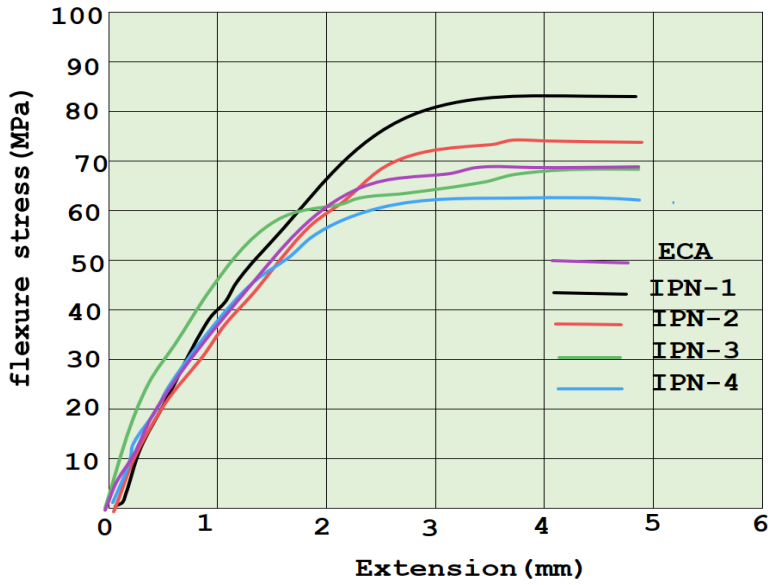

Fig 4. Show the flexture stress with Extension for IPNs.

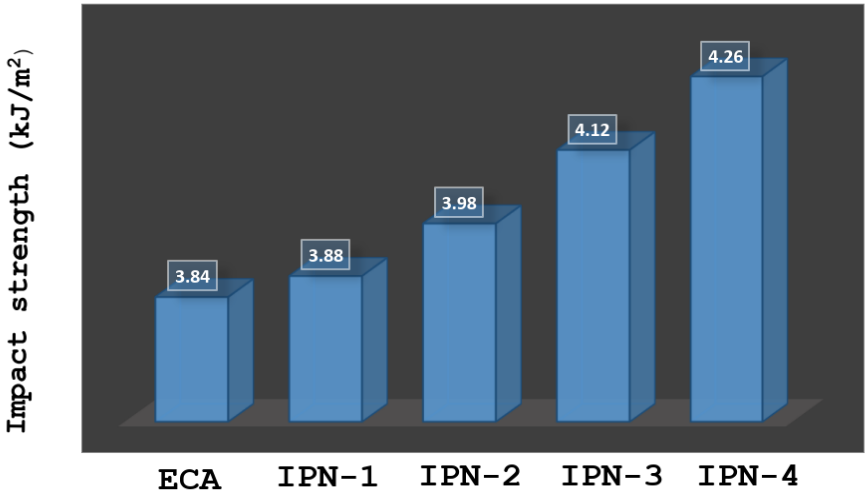

Fig 5. Show the Impact strength for ECA & IPNs.

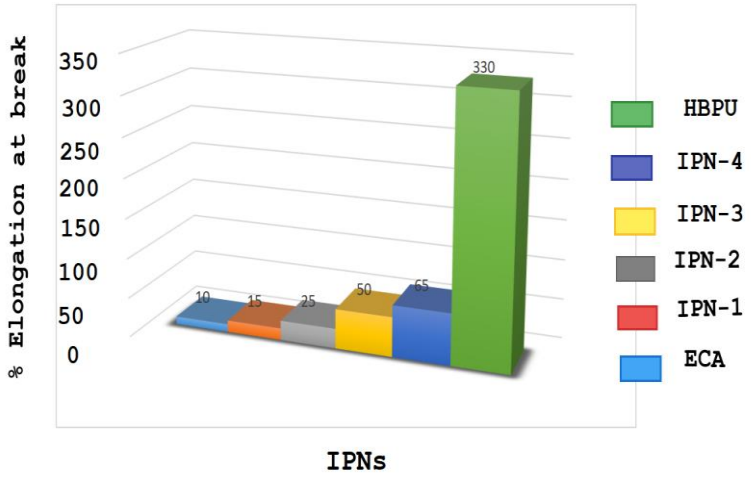

Fig 6. Show the % Elongation at break for HBPU, ECA & IPNS.

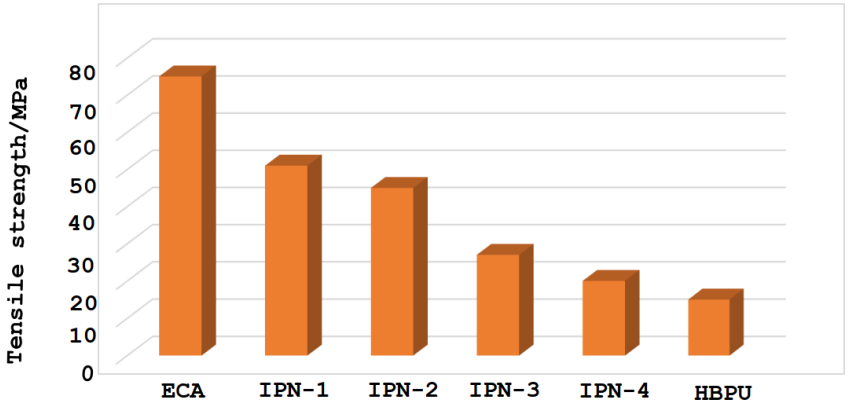

Fig 7. Show the Tensile strength for ECA, HBPU & IPNs

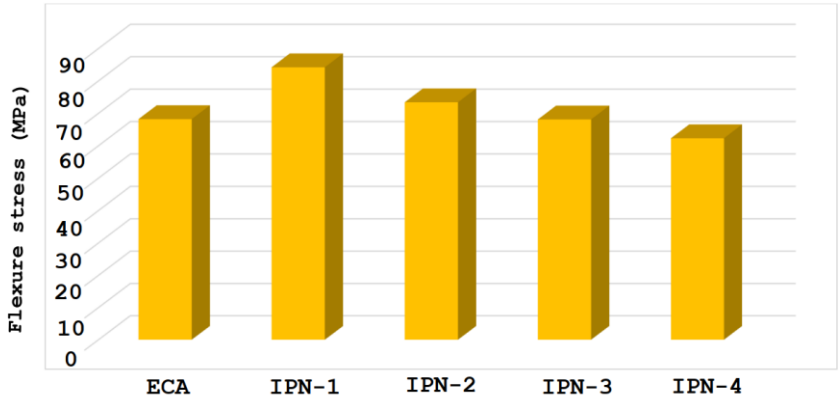

Fig 8. Show the Fleure stress for ECA & IPNs

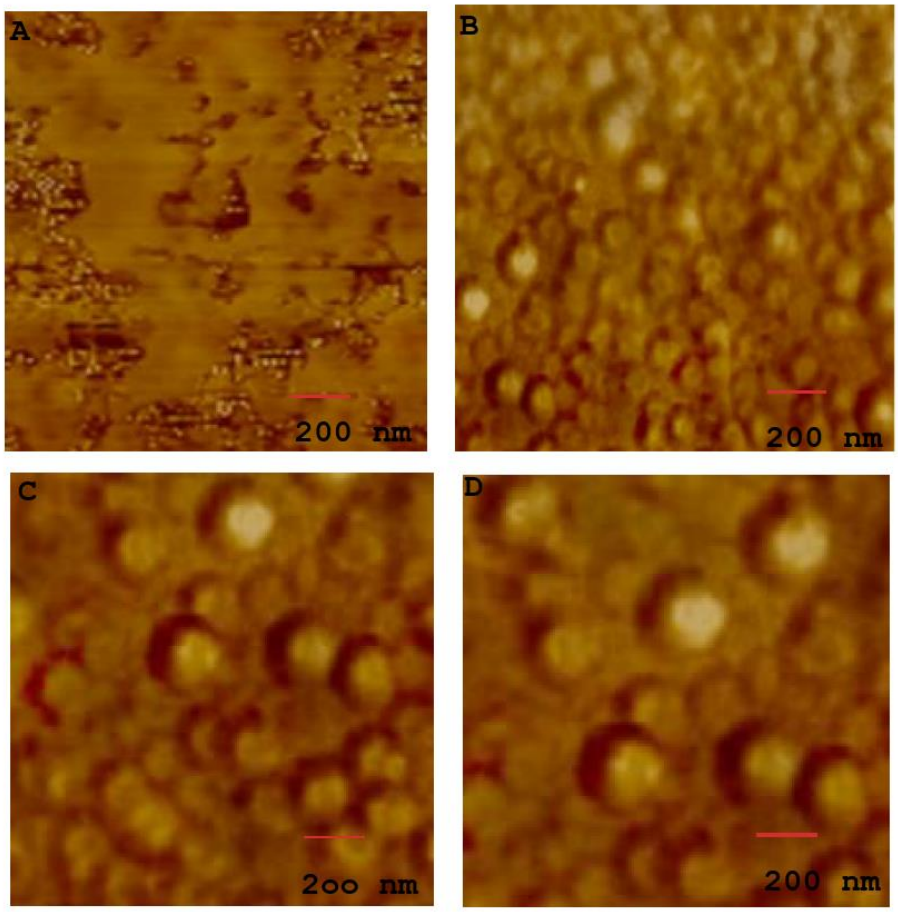

Fig 9. AFM micrographs of the IPNs samples: (A) IPN-1 and (B) IPN-2 (C) IPN -3 (D) IPN-4.

4 Conclusions

IPNs were produced by grafting HBPU and ECA together, resulting in an HBPU prepolymer with a triazinyl ring structure. The effects of the HBPU percentage on the mechanical properties of the IPNs were investigated. We can conclude that there are some considerable trends. As a result, the elastomeric IPN-4 sample indicated the highest value of impact strength (4.26 kJ/m^2) and the value of (65) for %elongation at break. . A decrement of modulus and tensile strength with a resultant increment of elongation for the elastomeric samples from (51 MPa) for IPN-1 to (20 MPa) for IPN-4 were observed.

References

[1]Klemarczyk, P.; Guthrie, J. Advances in anaerobic and cyanoacrylate adhesives. In advances in Structural Adhesive Bonding, 1st ed.; Dillard, D., Ed.; Woodhead Publishing Limited: Cambridge, UK, 2010; pp. 96–131, ISBN 978-1-84569-435-7.
[2] Shantha, K.L.; Thennarasu, S.; Krishnamurti, N. Developments and applications of cyanoacrylate adhesives.J. Adhes. Sci. Technol. 1989, 3, 237–260. [CrossRef]
[3] Fink, J.K. Chapter 13—Cyanoacrylates. In Reactive Polymers Fundamentals and Applications, 2nd ed.; Fink, J.K., Ed.; Elsevier: London, UK, 2013; pp. 317–330, ISBN 978-1-4557-3149-7.

[4] Singer, A.J.; Thode, H.C., Jr. A review of the literature on octylcyanoacrylate tissue adhesive. Am. J. Surg.(2004), 187, 238–248. [CrossRef] [PubMed].
[5] .Singer, A.J.; Quinn, J.V.; Hollander, J.E. The cyanoacrylate topical skin adhesives. Am. J. Emerg. Med. 2008,26 , 490–496. [CrossRef] [PubMed].
[6] Shivamurthy, D.M.; Singh, S.; Reddy, S. Comparison of octyl-2-cyanoacrylate and conventional sutures in facial skin closure. Natl. J. Maxillofac. Surg. 2010, 1, 15–19. [CrossRef] [PubMed]
[7] .Hynes, S.J. Biomedical applications of 2-cyanoacrylates. Irish Chem. News 2009, 25, 24–28.
[8] Nicolas, J.; Couvreur, P. Synthesis of poly(alkyl cyanoacrylate)-based colloidal nanomedicines. Wiley Interdiscipl. Rev. Nanomed. Nanobiotechnol. 2009, 1, 111–127. [CrossRef] [PubMed]
[9] Vauthier, C.; Dubernet, C.; Fattal, E.; Pinto-Alphandary, H.; Couvreur, P. Poly(alkylcyanoacrylates) as biodegradable materials for biomedical applications. Adv. Drug Deliv. Rev. 2003, 55, 519–548. [CrossRef].
[10] 17. Bumbrah, G.S. Cyanoacrylate fuming method for detection of latent fingermarks: a review. Egypt J. Forensic Sci. 2017, 7, 4. [CrossRef] [PubMed]
[11] Tahtouh, M.; Kalman, J.R.; Reedy, B.J. Synthesis and characterization of four alkyl 2-cyanoacrylate monomers and their precursors for use in latent fingerprint detection. J. Polym. Sci. Part A Polym. Chem. 2011, 49, 257–277. [CrossRef]
[12]Graf, A.; McDowell, A.; Rades, T. Poly(alkycyanoacrylate) nanoparticles for enhanced delivery of therapeutics—Is there real potential? Expert Opin. Drug Deliv. 2009, 6, 371–387. [CrossRef] [PubMed]
[13] Yordanov, G. Poly(alkyl cyanoacrylate) nanoparticles as drug carriers: 33 years later. Bulg. J. Chem. 2012, 1,61–73.
[14] Arias, J.L.; Gallardo, V.; Ruiz, M.A. Chapter 4—Multifunctional anticancer nanomedicine based on a magnetically responsive cyanoacrylate polymer. Methods in Enzymol. 2012, 508, 61–88. [CrossRef]
[15]Bumbrah, G.S. Cyanoacrylate fuming method for detection of latent fingermarks: a review. Egypt J. Forensic Sci. 2017, 7, 4. [CrossRef] [PubMed]
[16] Tahtouh, M.; Kalman, J.R.; Reedy, B.J. Synthesis and characterization of four alkyl 2-cyanoacrylate monomers and their precursors for use in latent fingerprint detection. J. Polym. Sci. Part A Polym. Chem. 2011, 49,257–277. [CrossRef]
[17] Liu.C, Qin.H, Mather.P.T, Review of progress in shape-memory polymers, J.
Mater. Chem. 17 (16) (2007) 1543.
[18] Sun.L, Huang .W.M, Ding . Z, Zhao . Y, Wang .C.C , Purnawali . H, Tang . C, Stimulus-responsive shape memory materials: A review, Mater Des. 33 (2012) 577–640.
[19] Hu. J, Zhu . Y, Huang . H, Lu . J , Recent advances in shape–memory polymers:Structure, mechanism, functionality, modeling and applications, Prog. Polym. Sci.37 (12) (2012) 1720–1763.
[20] Sharmin, E.; Zafar, F. Polyurethane: An Introduction; InTech: London, UK, 2012.
[21] Polyurethane Global Market Size Forecast 2021. Available online: https://www.statista.com/statistics/720449/global-polyurethane-market-size-forecast/ (accessed on 13 September 2018).
[22] Polyurethane Production, Pricing and Market Demand. Available online: https://www.plasticsinsight.com/resin-intelligence/resin-prices/polyurethane/ (accessed on 13 September 2018).
[23] Polo.M, Sponton. M, Jaramillo. F, Estenoz .D, Meira. G (2018) Linear segmented polyurethanes: I. A kinetics study. J Appl Polym Sci 135(4): 45747.
[24] Akbulut .H, Yoshida. Y, Yamada. S, Endo .T (2019) Synthesis and physical properties of poly(urethane)s using vicinal diols derived from acrylate and styrene monomers. J Polym Sci Part A, Polym Chem 57(7): 799-805.
[25] Fu. S, Zhu . J, Zou . F, Zeng . Z, Chen . S , A novel adamantane-based polyurethane with shape memory effect, Mater. Lett. 229 (2018) 44–47.
[26] Menon .A . V , Madras . G , Bose . S , Shape memory polyurethane nanocomposites with porous architectures for enhanced microwave shielding, Chem. Eng. J. 352 (2018) 590–600.
[27] Meng .H , Li . G , A review of stimuli-responsive shape memory polymer composites, Polymer 54 (9) (2013) 2199–2221.
[28] Hager . M . D , Bode . S , Weber . C , Schubert . U . S , Shape memory polymers: Past, present and future developments, Prog. Polym. Sci. 49–50 (2015) 3–33.
[29] Wang. L , Yang . X , Chen . H , Gong . T , Li . W , Yang . G , Zhou . S , Design of triple-shapemmemory polyurethane with photo-cross-linking of Cinnamon groups, ACS Appl. Mater. Inter. 5 (21) (2013) 10520–10528.

[30] Chen, S., Wang, Q., Wang, T., 2011. Hydroxy-terminated liquid nitrile rubber modified castor oil based polyurethane/epoxy IPN composites: Damping, thermal and mechanical properties. Polym. Test. 30, 726–731.
[31] Chen, S., Wang, Q., Pei, X., Wang, T., 2010. Dynamic mechanical properties of castor oil based polyurethane/epoxy graft interpenetrating polymer network composites. J. Appl. Polym. Sci. 118, 1144–1151.
[32] Sangermano M, Cook WD, Papagna S, Grassini S (2012) Hybrid UV-cured organic–inorganic IPNs. Eur Polym J 48:1796–1804.
[33] Hoffman, T., Khademhosseini, A., and Langer, R. (2019). Chasing the paradigm: clinical translation of 25 years of tissue engineering.Tissue Eng–Part A 25: 679–687.
[34] Dragan, E.S. (2014). Design and applications of interpenetrating polymer network hydrogels. A review. Chem. Eng. J. 243: 572–590.
[35] Kaczmarek, H., Vukovil-Kwiatkowska, I.,"Preparation and characterization of interpenetrating networks based on polyacrylates and poly (lactic acid)" eXPRESS Polymer Letters, 6, 1, 2012, 78-94.
[36] Shivashankar, M., Mandal, B., "A Reviewon Interpenetrating Polymer Network",Int JPharm Pharm Sci, 4, Suppl 5, 2012, 1-7.
[37] Kamal, M., "Camphor and poly (antimony acrylate) based interpenetrating network: Synthesis and Characterization",India Journal of Chemical Technolog , 18, July2018, pp. 284-290.
[38] Pan .J, Zhu . L , Han .J , and Hickner . M . A , "Mechanically tough and chemically stable anion exchange membranes from rigid-flexible semi-interpenetrating networks," Chemistry of Materials, vol. 27, no. 19, pp. 6689–6698, 2015.
[39] Lin . J, Yan . X , He . J , "Thermoplastic interpenetrating polymer networks based on polybenzimidazole and poly (1, 2-dimethy-3-allylimidazolium) for anion exchange membranes," Electrochimica Acta, vol. 257, pp. 9–19, 2017.
[40] Wang .Y, Wan . J , Wang . D , Wang . J, Wang . L and Feng . F "Preparation and characterization of a semi-interpenetrating network alkaline anion exchange membrane," Fibers and Polymers, vol. 19, no. 1, pp. 11–21, 2018.
[41] Ballestero .R , Sundaram .B.M , Tippur . H.V , Auad . M.L , Sequential graft-inter-penetrating polymer networks based on polyurethane and acrylic/ester copolymers,eXPRESS Polym. Lett. 10 (3) (2016) 204–215.
[42] Chen .S ,Wang . Q , Pei .X , Wang . T , Dynamic mechanical properties of castor oil-based polyurethane/epoxy graft interpenetrating polymer network composites, J.Appl. Polym. Sci. (2010) n/a-n/a.
[43] Yu .P, Li . G, Zhang . L , Zhao . F , Chen . S , Dmitriev . A . I , Zhang .G , Regulating microstructures of interpenetrating polyurethane-epoxy networks towards high-per-formance water-lubricated bearing materials, Tribol. Int. 131 (2019) 454–464.
[44] Mouritz A.P., Gellert E., Burchill P., Challis K.: Composite Structures 2001, 53, 21.

The physical properties of the addition of reinforcement metals of Aluminum and silica microparticles with unsaturated composite materials

Najah Rustum Mohsin[1], Ahmed Sahib Mahdi[2] , Ayad abdul ameer abdul hussein[3], Mohammad Sukri Mustapa [4]
{ najahr2000@stu.edu.iq[1], ahmed.altaei@stu.edu.iq[2], Ayad.abdulameer@stu.edu.iq[3], sukri@uthm.edu.my[4]}

Southern Technical University (STU), Iraq[1,2,3]
Universiti Tun Hussein Onn Malaysia (UTHM)[4]

Abstract. The absorption has a destructive effect on the mechanical and physical characteristics of the composite materials with a polymer base. It causes a reduction in the mechanical property values due to slight bonds between the matrix and the fibers. In the current paper, unsaturated polyester (UP) composite immersed in water, acidic solution (HCl), and the alkaline solution (KOH) were studied to investigate the effect of reinforcement on the thermal conductivity and absorption percentage values. Aluminum, Silica dioxide microparticles (SiO_2), and glass fibers (GF) were adopted as reinforcing materials. Three types of composite material were prepared: (C1) UP only, (C2) UP reinforced with 15% aluminum particles and 15% GF, and (C3) UP reinforced with 15% aluminum particles and 15% SiO_2. The empirical results displayed that, large values of thermal conductivity were obtained with the specimen C2 composite, and it reduced when the immersion time increased. On the other hand, when immersed in water, acid or alkaline solutions, the absorption of the non-reinforced composite was less than that of the reinforced composite, but with increasing the period of immersion it is noticed that the absorbance value increases for the non-reinforced composite while it decreases for the reinforced composite.

Keywords: Aluminum particles, Silica dioxide Unsaturated polyester, Glass fiber, Absorption, Immersion.

1 Introduction

Composite materials are characterized by their lightweight, high resistance, and flexibility in design, which made them play an important role in all engineering applications such as building aircraft, satellites, spacecraft, etc. Composite materials consist of polymers, plastic material, or light resins such as epoxy as a base material (matrix) immersed in its high strength fibers (synthetic fibers or natural fibers) such as Kevlar, glass, jute, sisal, etc. Where the matrix material works to transfer and distribute applied forces and stresses between the fibers, as well as working to collect and preserve those fibers from any harmful external Things. Fibers can be designed according to the load's direction; this will lead to weight reduction with the optimum use of materials. In recent years, a major importance to use the reinforcement of natural fibers in composite materials due to their superior properties such as density, low cost, corrosion

IMDC-IST 2021, September 07-09, Sakarya, Turkey
Copyright © 2022 EAI
DOI 10.4108/eai.7-9-2021.2314805

resistance, the biodegradability of non-toxic materials, and other unique characteristics [1,2,3]. George et.al.[4] elaborated the effect of some parameters of flax fiber on the epoxy composites intended by the autoclave molding method. H. Rashed et.al. [5] 2006 used jute fibers with different lengths and weight ratios to reinforce the polypropylene. P. N. Khanam [6] improved tensile and flexure strength by reinforcing unsaturated polyester by adding carbon and sisal fibers. M. R. Ismail et.al. [7] Used straw fibers as reinforcement, they obtained modulus of elasticity, impact strength, and flexural strength will be progressed with the rising of polymer ratio, while the water absorption is reduced with rising the polystyrene content in the same installation. V. Mittal et.al. [10] reinforced the epoxy with bagasse fibers and wheat straw fibers in different weight ratios and studied the influence of this on thermal, mechanical, and absorption properties.

In the current paper, unsaturated polyester resin (UP) was reinforced with Aluminum particles, glass fibers (GF), and silica dioxide (SiO_2) particles. For those samples, the influence of immersing duration of the water, acid solution (HCl), and the alkaline solution (KOH) on the thermal conductivity and absorption percentage were investigated.

2. EXPERIMENTAL WORK

2.1 Material used

2.1.1 Aluminum particles

Aluminum particles are used in a variety of applications in the industry, such as Cement, solid fuel, paint, and another coating. Aluminum is characterized by its lightweight and its high resistance to external stresses, good surface area, high hardness compares with polymer. Particle size (50-100) µm was used in this paper. The density of aluminum is 2.7 g \ cm^3 [14].

2.1.2 Silica particles

Silica particles have good resistance to acid and alkaline solutions, good surface area, high hardness, reduces thermal expansion of the polymer, and are cheap. Micro-silica particles with (50-100) µm size and density are 2.2 g/cm3 from BASF Company were used in this paper [15].

2.1.3 Glass fibers

Glass fibers (type E-glass) with properties reported in Table 1 were used as reinforced material.

Table 1: Mechanical Properties of E-glass fibers [12].

Tensile strength MPa	Modulus of elasticity GPa	Density g \ cm^3	Poison's ratio
3450	72.4	2.54	0.2

2.1.4 Unsaturated polyester

The unsaturated polyester resin is widely used in the industry because it has good physical and mechanical properties as well as ease of use and low cost. It is a transparent, viscous liquid and thermosetting resin, which is characterized by its high efficiency and low in both density and viscosity. In the current research, the unsaturated polyester resin was used as a polymer matrix. Methyl-ethyl-ketone peroxide with mixing ratios of 2% was used as a catalyst (hardener material). Both are manufactured by Industrial Chemicals & Resins Co. Ltd. Some properties of this resin are presented in Table 2.

Table 2: properties of unsaturated polyester resin [11, 12].

Tensile strength MPa	Modulus of elasticity GPa	Density g\ cm^3	Elon. %	Fracture toughness MPa- $m^{0.5}$	Thermal conductivity w/m.k	Poison's ratio	Thermal expansion coeff. 10-6/c°
34.5-103	2.1-3.4	1.1-1.4	2.6	0.6	0.17	0.37-0.4	100-180

2.2 Sample Preparation

Since it is simple, easy, and cheap, the proceeding of Hand Lay-up (HLU) was used to prepare the samples. Glass mold with dimensions (250 x 250 x 6) mm were used with wax to avoid sticking to it and having smooth faces. The volume fractions were calculated according to the relations:

$$V_r = \frac{M_r}{M_r+(1-M_r)\frac{\rho_r}{\rho_m}} \quad (1)$$

$$V_m = \frac{M_m}{M_m+(1-M_m)\frac{\rho_m}{\rho_r}} \quad (2)$$

$$V_r + V_m = 1 \quad (3)$$

Where V, M, ρ, m, and r represent volume fraction, mass, density, matrix, and reinforcement respectively. The specimens were cut into standard dimensions according to American specifications (ASTM-D 790-1984). The abbreviations and designation used in this study to address the different composite specimens are presented in Table 3.

Table 3: Abbreviations and details of the specimens Content.

Abbreviation	Description	Total Vr%	Total Vm%
C1	Pure unsaturated polyester resin	0	100
C2	15% Al + 15%GF + 70%UP	30	70
C3	15% Al + 15% Micro SiO_2 + 70%UP	30	70

2.3 Samples immersion in the solutions

Three types of solutions were used, which were tap water, hydrochloric acid (HCl) (Acidic solution), and potassium hydroxide (KOH) (Alkaline solution) with the normality of (1 N). The samples were weighed at room temperature by a sensitive balance with an accuracy of 0.0001.

2.4 Specimens absorption

Absorption is defined as the penetration of a liquid into a solid during a certain period. The absorption percentage (Weight gain percentage) can be extracted from the following relationship [10]:

$$M\% = \frac{(M_2 - M_1)}{M_2} \times 100\ \% \quad (4)$$

Where: M%: is the absorption percentage, M_1 and M_2: is the weight before and after immersion in solution respectively.

2.5 Thermal conductivity of specimens

Thermal conductivity represents the measurement of heat flow per unit time out of a unit area of a substance. It can be measured in several ways, in this paper; Lee's disc (made by Griffen and George) was used to study the effect of immersion time in the water on the value of thermal conductivity. Ideally, thermal conductivity is governed by Fourier's Law of thermal conductivity shown in the following related:

$$q = -K \frac{dT}{dx} \quad (5)$$

Where: q: Thermal flux, K: thermal conductivity coefficient, dT / dx: thermal gradient
When using Lee's disc, Thermal conductivity values can be extracted from the following two equations [16]:

$$K \left[\frac{T_B - T_A}{ds}\right] = e \left[T_A + \frac{2}{r}\left[d_A + \frac{1}{4} d_A\right] T_A + \frac{1}{2r} d_S T_B\right] \quad (6)$$

Where: (DA, DB, DC): represent to a thickness of disks A, B, and C, respectively, (T_A, T_B, T_C): temperatures of A, B, and C disks, respectively, r: disk radius and e refer to the amount of thermal energy that passes through the disk per second and can be calculated by using the equation:

$$e \left[d_A T_A + ds \left(\frac{T_A + T_B}{2}\right) + d_B T_B + d_C T_C\right] \quad (7)$$

Where: I: current through the heated coil (I = 0.25 A), V: the potential difference at both ends of the heater coil (V = 6 V), and ds: specimen thickness.

3. RESULT AND DISCUSSION

It is important to examine the immersion effect of polymeric materials in chemical solutions and water. In this paper, the unsaturated polyester resin was strengthened by using glass fibers, aluminum particles, and silica particles as a reinforced material with the percentages shown in Table 3. The influence of immersion in water on the coefficient of thermal conductivity was investigated, as well as the effect of immersion time in the water, acidic and basic solutions on the absorption percentage were studied. All treatments were performed by immersing the specimens at room temperature for periods of different times (3, 5, 7, 9, 11, and 13 weeks) for each solution.

3.1 Effect of immersion time in the water on thermal conductivity

Fig 1 displays the relationship between the values of thermal conductivity against the period of immersion of samples in water for a period of 3 to 13 weeks. It can be seen that the coefficient of thermal conductivity of C2 is greater than that of C3, which in turn is greater than that of C1, is because adding the fibers and aluminum in C2 raised the value of thermal conductivity of the composite, but the addition of silica particles and aluminum particles in C3 led to reducing it because the particles - usually - are porous, and when the material contains air spaces, it becomes less conductive because the gases are poor thermal conductivity. On the Other hand, when the immersion time increased, the coefficient of thermal conductivity decreased for all specimens, due to the spread of water through the interface region, cracks, and the weakly bonded areas, and this all reduces the binding forces. Moreover, when the immersion time increases, the degradation increases and thus leads to the failure of the material, as the water fills the existing voids and distances and thus act as a means of decomposition and disintegration.

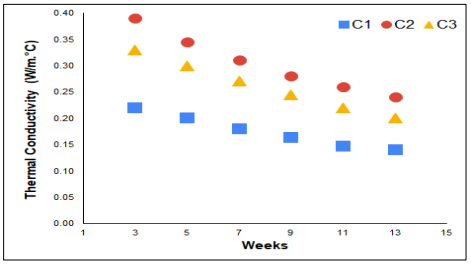

Fig. 1. Immersion time in the water on thermal conductivity.

3.2 Effect of immersion time in the water on absorption percentage

The process of absorption of all composite materials when exposed to moisture from the surrounding atmosphere or when immersed in water or chemical solutions follows Fick's law of the diffusion, meaning that the absorbed mass of water or solutions increases gradually and slowly with the square root of time until reaching a state saturation. The absorption by water or solution hurts the mechanical properties of composite materials because water and solutions weaken the bonds between the matrix and reinforcement materials.
Fig 2 shows the relationship between the absorption percentage for the three samples C1, C2, and C3 when immersed in water for 3 to 13 weeks at room temperature. It can be spotted that, the composite reinforced by aluminum particles and glass fibers has the greatest absorption

percentage, followed by the composite reinforced by aluminum and silica particles, and then, to a lesser extent, the non-reinforced composite. The poor compatibility and bonding between the matrix and the fibers (whether synthetic or natural) is a major reason for increasing water absorption and weakening mechanical properties while the particles work to reduce pores and thus lead to reduced absorbency. It can be discovered that there was a slight increase in the absorbance value of all samples when immersed in water for 13 weeks.

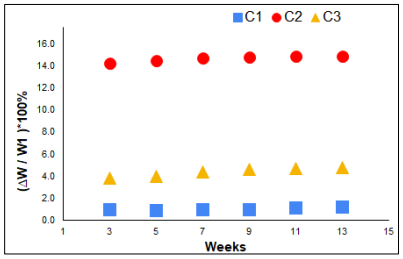

Fig. 2. Immersion time against absorption percentage (in water).

3.3 Effect of immersion time in acidic and alkaline solution on absorption percentage

Figs 3 and 4 show the relationship between the absorbance of the samples under investigation when immersed in an acidic solution (HCl) and alkaline solution (KOH) with normality (1N) for 3, 5, 7, 9, 11, and 13 weeks. During the first 3 weeks, it was evident that the absorption of sample C2 and C3 was approximately equal and much greater than that of sample C1, but as the submersion time increased, the absorbance of sample C1 increased while the absorbance of the other samples decreased. The containment of samples C2 and C3 on the discontinuous phase, including fibers, particles in addition to the presence of the interface leads to an increase in the penetration of the solution in them, and thus they reach saturation during the first three weeks, after that, a decrease in absorbance occurs based on the Fick's principle, furthermore, forming a coat from silica oxide that covering the specimen type 3 and operates as a protection layer and prevents from dissolving silica particles. Sample C1 contains continuous phase causes them to be slow to absorb solutions and thus their absorbance value increases with increasing the period of immersion. The specimens differ in the saturation event and that depends on various parameters such as the matrix model, the reinforced materials, the immersion period, and the volume fractions for reinforced materials.

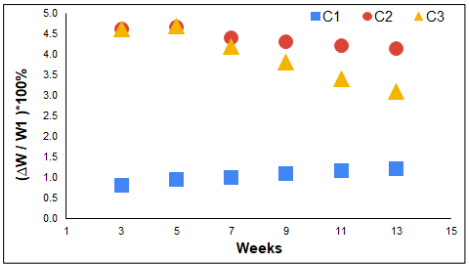

Fig. 3: Immersion time against absorption percentage (in acidic solution (HCl)).

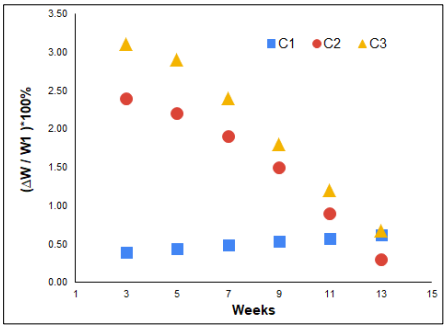

Fig. 4: Immersion time against absorption percentage (in alkaline solution (KOH)).

3.4 Effect of reinforcement type in absorption percentage

Figs 5, 6, and 7 show the relationship between the type of reinforcing material and the absorption percentage when samples are immersed in water, acidic and alkaline solutions for 3, 5, 7, 9, 11, and 13 weeks. An overview for all figures shows that the absorbance of composition material without reinforced is less than that the absorbance percentage when the composition material is reinforced with fibers or particles, especially when immersed in the alkaline solution, where the absorption rate does not exceed 0.6%. On the other hand, the specimen of composition materials reinforced with aluminum particles and glass fibers has the highest absorbance that occurs (14.9%) when immersed in water for 13 weeks. Furthermore, the absorption rate was decreased when increased the immersion period in the acidic and alkaline solution of the samples was fortified with fibers or reinforced with fibers and particles, while it increases for other cases. Increasing the immersion period in water leads to a large water penetration, which contributes to weakening the structure of the composite material thus the absorbance increases. Increasing the immersing period of the composite materials reinforced with fibers or particles in acidic or basic solutions leads to an increase in the digging of the surfaces of the fibers and particles, which increases the roughness of their surface and also increases their surface area, which increases the bonding strength and cohesion of them with the matrix material, This strengthens the composite structure and closes the voids and gaps, for this reason, the penetration of solution was reduced.

Over and above, C2 and C3 samples increased absorption suddenly after (3) weeks immersion in the acidic or alkaline solution, after that, it begins to drop. C1 samples suffered from deformation and obvious swells, but C2 and C3 it was less apparent. The microscopic pictures of the specimens that water immersion, HCl, and KOH after 7 weeks are shown in Figure (8). We can notice the changes in the samples by comparing the specimen's pictures before and after immersion.

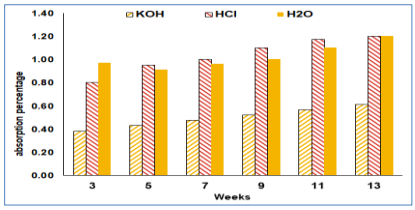

Fig. 5. Non-reinforced composite materials (C1) on absorption percentage.

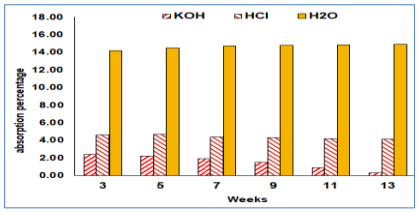

Fig. 6. Composite reinforced with aluminum particles and glass fibers (C2) on absorption percentage.

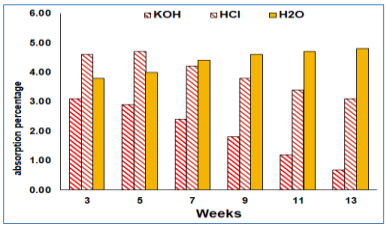

Fig. 7. Composite reinforced with aluminum particles and silica particles (C3) on absorption percentage.

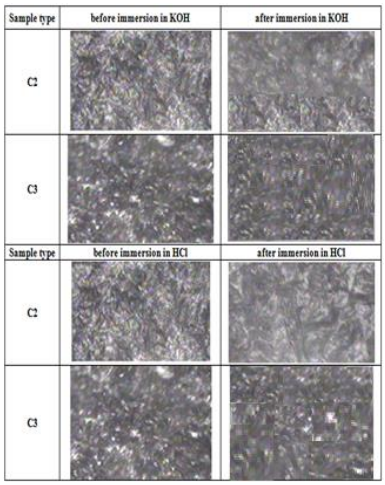

Fig. 8. Microscopic pictures (X10) for the samples before and after immersion in acidic and alkaline solution.

4. CONCLUSIONS

Based on the results of practical experiments in the current research, it can be observed, the absorption was increased until it reaches the saturation state, after that, it begins to drop. The specimens differ in the saturation event and that depends on various parameters such as the matrix model, the reinforced materials, the immersion period, and the volume fractions for reinforced materials.

The values of the thermal conductivity coefficient decrease for all samples when increasing the immersion time, noting that the highest value of it is found in composite reinforced with aluminum particles and glass fibers. On the other hand, the absorption of the non-reinforced composites was lower than that of the reinforced composites. The highest percentage of absorption was obtained when composite materials reinforced with aluminum particles and glass fibers were immersed in water for 13 weeks. Furthermore, the absorption percentage of composites reinforced with fibers or particles was decreased with increasing the immersion period in the acidic and basic solutions, while it increases for non-reinforced samples.

Immersion of the composite reinforced with fibers or particles in acidic or basic solutions for a long time leads to increased drilling and roughness of the surfaces of the fibers and particles as well as, increases their surface area, bonding strength, and cohesion with the matrix material which leads to closes the gaps and reduces the solution penetration.

ACKNOWLEDGEMENTS

I extend my sincere thanks and appreciation to the technicians in the laboratories of the Technical Institute in Nasiriyah / Southern Technical University / Iraq for their assistance in completing this paper.

REFERENCES

[1] NAHAS M. N. (2005). New Development in Composite Materials - Recyclable and Environment-Friendly Composite Materials. Journal of King Abdulaziz University-Engineering Sciences. Vol. 16(1).

[2] Kalia S., & Kaith B.S. (2009). Pretreatments of Natural Fibers and their Application as Reinforcing Material in Polymer Composites A Review. Polymer engineering and science/ Wiley. Vol. 49(7).

[3] Nabi D. S. , & Jog J. P. (1999). Natural fiber polymer composites: A review. Advances in Polymer technology. Vol.18(4).

[4[George J., Ivens J., & Verpoest I. (2000). Mechanical properties of flax fiber reinforced epoxy composites. Die Angewandte Makromolekulare Chemie. Vol. 272(12).

[5] Rashed H., Islam M., & Rizvi F. (2006). Effects of process parameters on tensile strength of Jute Fiber Reinforced Thermoplastic Composite. Journal of Naval Architecture and Marine Engineering. Vol.3(1).

[6] Khanam P. N. (2010). Sisal / carbon fiber reinforced hybrid Composites: tensile, flexural & chemical resistance properties. Journal of polymer and the environment. Vol. 18(4).

[7] Ismail M. R., Ali A. M., & Afify M. S. (2011). Mechanical Properties of Rice Straw Fiber-Reinforced Polymer Composites, Fibers and Polymers. Vol. 12(8).

[8] Salem A., & El-Tayeb N.S.M. (2014). The Impact of Rice Straw Microfibers Reinforced Epoxy Composite on Tensile Strength and Break Strain. International Journal of Scientific & Engineering Research. Vol. 5(10).
[9] Mittal V., & Sinha S. (2017). Effect of alkali treatment on the thermal properties of wheat straw fiber reinforced epoxy composites. Journal of Composite Materials. Vol. 51(3).
[10] Mittal V., & Sinha S. (2018). Mechanical, thermal and water absorption properties of wheat straw/bagasse-reinforced epoxy blended composites. Advances in Polymer Technology. Vol. 37(7).
[11] Data Sheet (2020). Industrial chemicals & resins Co. Ltd. Dammam, Saudi Arabia.
[12] Mallick P. K. (2007). Fiber Reinforced materials, Manufacturing and Design. 3rd Ed.
[13] Geodicke S., Kalleder A., Reinhard R., & Schmidt S. (1999). Nano binders for Natural Composites, Book of Abstracts of NATO Advanced Research Workshop on Polymers and Composites for Special Applications, Poznan. Poland.
[14] Ahmed Sahib Mahdi, (2018), the effect of geometrical profile of direct extrusion die on the process efficiency using Visio plasticity method, Journal of Engineering and Applied Sciences, Vol. 14, No 13, pp, 11064-11067.
[15] Seymour R. B. (1990). Polymeric Composite. Alden Press. London.
[16] Krishna A. R., & Krishna B. R. (2004). Thermal Analysis of Epoxy Based Fiber-Reinforced. IE (I) Journal – MC. Vol.84.

The effect of electronic collective scientific conversations on developing creative thinking and the ability of discussion among technical university students

Ethar Abdul muhsin Qasim Al- Mayyahi[1] and Mowaffaq Abdulaziz Al-Hisnawi[2]

[1]University of Kufa, Faculty of Education #
[2]Southern Technical University - Technical Institute in Nasiriyah
ethara.almayyahi@uokufa.edu.iq, Pdmh2005@stu.edu.iq

Abstract, This research aims to know the effect of electronic collective scientific conversations in developing the creative thinking and the ability to debate among technical university students. The research sample consisted of (46) male and female students for the academic year (2017-2018). They are divided into two groups of equal number with equivalent number of variables based on test and control. Five subjects of theoretical electrical installations were chosen during the second semester, the teaching plans were prepared, as well as the research tools, which are the test (experimental) of creative thinking and the form for noticing the ability was discussed and their psychometric properties extracted. The research outcomes the students of the test group who used electronic collective scientific conversations were superior in creative thinking and the ability to debate over the students of the control group who used the usual method. In light of this, the researchers concluded that there is a positive effect of electronic collective scientific conversations, and they recommended their use in the process of teaching students in technical universities. The effective of the electronic group scientific chatting to the growth of the creative thinking and the ability to the discuses to the technical university students

Keywords: Electronic conversations, Creative thinking,

1. The research problem and its importance

1.1 - the research problem:

As a result of scientific and technological developments and the emergence of the Internet, new technologies and methods for learning and social communication have emerged [1-5]. New fields of social, cultural and scientific communication have been created that were not previously familiar among individuals of various segments and institutions in various disciplines and goals, which made it possible to communicate in electronic group conversations via the Internet in which individuals participate to make groups with different goals close to the reality. The Educators have thought about

IMDC-IST 2021, September 07-09, Sakarya, Turkey
Copyright © 2022 EAI
DOI 10.4108/eai.7-9-2021.2315461

the importance of using all the data and results of scientific and technological development and benefiting from them in enhancing the positive role of the student in the learning process, because it is the basic base on which the development and construction process in society is based in the present and the future [6-8].

The effective use of social networks and electronic conversations between students and teachers have become necessary in educational institutions, including university institutions, in order to achieve desirable positive goals that are precisely defined and planned in advance, including working to develop thinking of its various types, including creative thinking, and developing the ability to debate among university students, especially the students of technical universities [9-13].

The research aims to know the impact of electronic collective scientific conversations in developing creative thinking and the ability to debate among students of technical universities in order to reach experimental results that can be used in developing the positive and active role of the university student in the learning process and developing the teaching methods that are used [14-17].

1.2 - the importance of the research:

The four technical universities that emerged from the Technical Education Authority represent the body directly responsible for everything related to technical education in Iraq in terms of its philosophy, goals, programs, curricula, and present and future plans. Therefore, these universities, their teachers and students gain their great importance from the importance of technical education and its active role in the process of construction and comprehensive development in all its aspects and fields in Iraqi society. In light of this, a serious and orderly endeavor should be made, in accordance with organized and purposeful educational plans, in order to develop the educational process in these universities and build the personality of the qualitative student and grant him a positive and active role in the learning process in order to be able to keep pace with the data of scientific and technological development and interact with it positively, whether that interaction is when he is a university student or after graduation and engage in the field of practical life. The technical university students represent the middle technical cadres of the workforce pyramid in society, and they are the pillar of technical construction in it, and they are the most dealing with modern technologies available in the labor and production sector in its various disciplines in various fields of engineering, medical, administrative, agricultural and applied arts [18-19].

1.3 - Research Objectives:

The research aims to know the effect of electronic collective scientific conversations in developing creative thinking and the ability to debate among technical university students.

1.4 - Research Limits:

1- Spatial: The Technical Institute in Nasiriyah at the Southern Technical University in the Republic of Iraq

2- Temporal: the academic year (2017-2018).

3- Humanity: first-year students in the Department of Electrical Techniques.

4- Cognitive: five topics from the subject of theoretical electrical installations**.**

1.5 - Research Hypotheses:

1 - There are no statistically significant differences at the level of significance (0.05) between the average scores of the experimental group students who used electronic collective scientific conversations and the average scores of the control group students who used the usual method in the creative thinking test.

2- There are no statistically significant differences at the level of significance (0.05) between the average scores of the experimental group students who used electronic collective scientific conversations and the average scores of the control group students who used the normal method in the discussion ability observation form.

1.6 - Defining the terms:

1 - Group Chatting: It is communication among many people and it allows them to learn with each other. For the conversation to be successful, the participants must strike a practical balance in contributions. A successful conversation includes the exchange of interesting ideas among the speakers by finding a specific topic of interest to them and they can exchange ideas about it. (Wikipedia, the free online encyclopedia [16])

Procedural definition: It is an electronic communication through the WhatsApp application via the Internet between a researcher and students of the experimental group, the research sample in the first stage in the Department of Electrical Technologies at the Technical Institute in Nasiriyah and among students themselves in order to establish electronic scientific group conversations to conduct discussions on the subject of Electrical Installations (theoretical lectures) in order to obtain additional information for the purpose of developing creative thinking and the ability to discuss.

2- (Reinforcement): it is defined by (Al-Sabaty 2004 [8]) as a planned activity that aims to bring about changes in the individual, the group, and the organization in terms of information and experiences, in terms of performance, working methods, and in terms of attitudes and behavior, which makes the individual and the group fit to occupy their jobs efficiently and with high productivity. (Al-Sabaty 2004 [8]).

Procedural definition: It is the magnitude of development and improvement in creative thinking and the ability to discuss among students the research sample in the two experimental groups that used the regular method in addition to the electronic scientific group conversations and the control group that used the normal method only after the completion of the experiment through their answers to the creative thinking test and a form of noticing the ability to discuss that is prepared by the researchers.

3 - Creative Thinking: it is defined by (Abdul-Hadi and others 2003 [11]): It is one of the advanced types of thinking where, through its practice, the individual can reach unique and distinctive solutions that no one has reached. (Abdul-Hadi and others 2003 [11]).

Procedural definition: It is the ability of the research sample students in the experimental and control groups to use creative thinking skills in an unusual way when solving problems presented to them related to the subjectز This is evident from their scores in the creative thinking test prepared by the researchers

4 – The Ability to Discuss: it is defined by (Mohammed 2006 [12]): It is a situation of verbal interaction that occurs in a planned and intentional manner based on the meeting of a number of people such as the teacher and students for the purpose of exchanging ideas and opinions under the supervision of a certain leadership in order to reach specific results that agreed upon by all participants in the discussion. (Mohammed, 2006 [12]).

Procedural definition: It is the ability of the research sample students in the experimental and control groups to discuss and dialogue in the lecture among themselves and the teacher and

this is measured by recording grades on the items of the discussion ability note form that was prepared by the researchers.

2. Theoretical background and previous studies

2.1 The theoretical background:

2.1.1 - Electronic Societies

Electronic societies are a natural result of scientific and technological progress occurred in modern technologies, including the network. It is a fictional simulation of a real society that is visualized and built through the capabilities provided by three-dimensional technology and graphics to produce life situations that attract those who interact with it and enter him/her in its world. (Mona, 2013, 483 [13]) and (Al-Shahrani [10]) shows that virtual education through it, is characterized by the multiplicity of services and applications it provides to educational institutions to ensure their quality, increase the efficiency of its teaching staff and students, provide multiple and renewable sources of information, increase the effectiveness of teaching and training methods, and develop the student's scientific, social and cultural personality due to the abundance of information existing in it and transcend the limits of time and space at a low cost and quickly.

(Al-Shahrani, 2008, 14 [10]) and (Kecmanovic) states that it is possible through the Internet to provide a new cooperative environment in which students can work together and share in understanding the subject matter, exchange ideas and trends and solve problems that face them cooperatively. (Kecmanovic,2000, p.73 [17])

(Al-Musa) indicates that one of the applications of these groups is the registration of teachers and students in them to benefit from the experiences of the specialists, each according to his/her specialization. As well as setting up an arena for group social conversations and joint forums for students and teachers for the purpose of exchanging points of views and ideas on various issues and discussing methods of cooperation among them. (Al-Musa, 2001, 173)

Among the important applications on the Internet, the social media application (WhatsApp), As its use and participation in it has spread to a large extent, because it contains many possibilities for exchanging information and ideas between different human cultures. It is a multi-platform instant messaging application for smartphones, and in addition to basic messages, the users can send photos, voice, video, and media messages. (Wikipedia, the free online encyclopedia [16]).

2.1.2- Creative thinking:

Thinking is a continuous daily process that accompanies the human being on a permanent basis and a natural performance that is carried out by the individual continuously (Al-Surour, 1996, 66 [9]). Thus, the development of thinking has taken the forefront in the goals of education In all stages of study and in all nations and populations, regardless of their degree of development. Each of (Jamal), (Jarwan) and (Al-Khalili [1,2]) indicate that there are several capabilities of creative thinking, represented by the following:

- **Fluency**: It represents the individual's ability to generate a large number of alternatives or ideas when responding to a particular stimulus, in addition to the ease of generating them and his ability to produce the largest possible number of ideas in a given time.
- **Flexibility**: it is divided into two types: spontaneous flexibility, which represents the ability to produce appropriate responses to a particular problem, and adaptive flexibility, which represents the ability to change the way of thinking about a particular problem and responding to it.

- **Originality**: It is the ability to quickly produce the largest possible number of serious indirect or unusual responses, and it expresses the uniqueness and excellence in the divergent production of the meanings transformations.
- **Verbosity**: It represents the ability to add new information, details, and components to the primary forms, such as expanding a certain idea or clarifying an ambiguous topic.
- Sensitivity to problems: It is the ability to perceive weaknesses in an exciting situation, as it means insufficiencies and shortcomings because his/her view of the problem is unusual.

(Jamel, 2005, 50), (Jarwan, 2002), (Jarwan, 2009), (Al-Khalili, 2005, 141) (Dalloul and Al-Assi) [1,2,6,7] confirmed that there are several elements for the success of creative thinking in educational institutions, including the following:

- Finding the appropriate educational environment that helps the student to think, and this is done by paying attention to the conditions of the educational environment, Focusing on the student's attention and training.
- The focused processing for the purpose of refreshing memory and emphasizing information and processing it accurately.
- Strengthening the thought and accepting students' positive attitudes and directing them in the desired direction and in proportion to their abilities and capabilities. Setting the goal, i.e. the desire to help the student to define his point of view and enhance his ability to self-learning. (Daloul and Al-Assi, 2008: 143 [7]).
- The discussion and dialogue: (Khawaldeh and Eid) shows that there is a difference between the dialogue and the discussion. Whereas, dialogue is an exchange of ideas and opinions between two parties in a regular and objective manner, while discussion is a discussion of ideas and opinions between two or more parties in depth and investigation. (Al-Khawaldeh and Eid, 2001, 313 [5])

2.2 - previous studies:

- Study of (Manal, 2006 [14]): This study was conducted at King Saud University in Saudi Arabia. The aim of the study was to know the effect of using metacognitive thinking strategies through the global information network on academic achievement and the development of higher-order thinking skills among students of the mathematical programming course. The research found the superiority of the experimental group students who used metacognitive thinking strategies through the global information network in academic achievement and the development of higher-order thinking skills over the control group students who did not use them. (Manal, 2006 [14])
- A study of (Stewart and others, 2007): conducted at the University of Houston, USA, and aimed at the effect of using a collaborative team consisting of a virtual course among students, developed by the researchers to increase the educational experience of students in a subject of study on the Internet in order to create a virtual environment for learning. The study reached a number of results that indicate the effectiveness of the virtual environment for learning in developing the educational experience of the students. (Stewart and others 2007 [18])

3. Research Procedures

1 - Experimental design: The design of the two equivalent experimental and control groups with (pre-) and (post-) test was chosen to be an appropriate experimental design, as shown in scheme No. (1):

Scheme No. (1): Experimental design of the research

group	The pre-application	the independent variable	the dependent variable	The post-application
Experimental + Control	Creative thinking test	Electronic collective scientific conversations	Creative thinking +ability to discuss	creative thinking test + Discussion Ability Form

3.1- Research community: The research community was determined by first-year students in the Department of Electrical Technology at the Technical Institute in Nasiriyah at the Southern Technical University in the Republic of Iraq for the academic year (2017-2018).

3.2 The research sample:

It is a random sample of (46) male and female students divided into two groups of equal numbers and equivalent in a number of influential variables, one of them is an experimental group and the other is a control.

3.3 Research requirements:

First - Determining the goal of using electronic collective scientific conversations: The two researchers identified the general goal of using electronic collective scientific conversations, which is (the development of creative thinking and the ability to discuss among students of technical universities).

Second - Preparing the necessary plans for the use of electronic collective scientific conversations: The two researchers prepared the necessary plans for students to use electronic collective scientific conversations via the Internet, and what are the procedures that are being taken to achieve the goal of the research. Some specialists were consulted to get their comments and points of views on this subject.

3.4 Research tools:

First - Creative Thinking Test: The researchers prepared a creative thinking test. It is a test consisting of a number of items of the multiple choice type and aims to measure the degree of creative thinking among students of technical universities, the research sample, by following the steps recognized in this field, where the goal of it has been determined, which is (measuring the degree of creative thinking among students of technical universities), which is a component in which the instructions were placed to answer it, and it was presented to a number of specialists, based on the (Cooper equation) to calculate the degree of agreement among them, with an agreement rate of (80%).

A - Extracting the validity of the test: a statistical analysis was achieved to test the creative thinking of students of technical universities by applying it to an exploratory sample other than the research sample consisting of (25) male and female students. The coefficients of discrimination, difficulty and effectiveness of the wrong alternatives were extracted using appropriate statistical methods. It was found that all the items are distinguished and their degree of difficulty is normal, and the wrong alternatives are effective, and thus the scale was considered valid (validity) for the purposes of this research.

B - Extracting the Reliability of the test: The method of re-application was used on the same exploratory sample two weeks after the first application of the test. The reliability coefficient was calculated using Pearson's correlation coefficient (0.85) and the reliability coefficient of the

Cronbach's alpha equation was (0.88) and the scale became in (Reliability) and valid for application to the research sample in its final form.

First - the form of noting the ability to discuss: The two researchers prepared a form for noting the ability to discuss among the students of technical universities. It consists of a number of items aimed at (measuring the ability to debate among technical university students). It was presented to a number of specialists and based on Cooper's equation to calculate the degree of agreement among them and with an agreement rate of (80%).

A - Extracting the validity of the form: the statistical analysis of the form for observing the ability to debate among students of technical universities was carried out by applying it to an exploratory sample other than the research sample (25) male and female students. The coefficients of discrimination and the degree of consistency of the items with the total degree of the form were extracted using the appropriate statistical methods. It was found that all the items are distinct and consistent with each other and with the items of the total form, and thus considered as valid (validity) for the purposes of this research.

B - Extracting the reliability of the form: The method of re-application was used on the same exploratory sample two weeks after the first application. The reliability coefficient was calculated using Pearson's correlation coefficient (0.84) and the reliability coefficient of the Cronbach's alpha equation was (0.86) and the form became in (Reliability) and valid for application to the research sample in its final form.

3.5 - Steps of applying the research:

First - Conducting the pre-application of the creative thinking test on the students of the two groups.

Second - Analyzing the results of students' answers in the pre-application of the creative thinking test.

Third - Creating a closed group in the WhatsApp application via the Internet between one of the researchers and the students of the experimental group to be a group to conduct electronic collective scientific conversations between them, during which additional information about the subject is exchanged, studied and discussed, which helps them in developing their creative thinking and ability to discuss.

Fourth - The participation of the experimental group students in the electronic collective scientific conversations for a period of five weeks through communication between the researcher and the students and among them.

Fifth - Adopting a form to note the ability to discuss in each lecture and record the results therein.

Sixth - Conducting the post application of the creative thinking test on the students of the two groups.

Seventh - Analyzing the results of students' answers in the post application of the creative thinking test.

Eighth- Comparing the results of the students' answers in the post application of the creative thinking test in each of the two groups and comparing the results of the students' answers on the form of observing the ability to discuss for the two groups.

4. Research Results

A - Creative thinking: From the observation of Table (1), we find that: There are statistically significant differences at the moral level (0.05) between the average grades of the experimental group students who used electronic group scientific conversations and the average grades of the control group students who used the usual method in the creative thinking test, in favor of the experimental group.

Table (1): Results of creative thinking

Group	Arithmetic mean	Standard deviation	Calculated t value
Experimental	59.91	10.433	3.476
Control	70.76	9.291	

B - The ability to discuss: From the observation of Table (2), we find that: There are statistically significant differences at the moral level (0.05) between the average grades of the experimental group students who used electronic group scientific conversations and the average grades of the control group students who used the usual method in the form to note the ability to discuss, in favor of the experimental group.

Table (2): Results of the ability of discussion

Group	Arithmetic mean	Standard deviation	Calculated t value
Experimental	62.348	12.120	6.919
Control	83.045	7.833	

C - Discussion of the results: Through the results of the research (in Tables No. 1 and 2), we find that the students of the experimental group who used the electronic collective scientific conversations have benefited from them in developing creative thinking and the ability of discussion to a greater degree than the students of the control group.

This indicates that it is possible to use collective electronic scientific conversations through the Internet. The electronic collective scientific conversations via the Internet were a new method that students were not accustomed to in communicating with others for scientific and cultural topics planned in advance. Thus, they saw in it an interesting method through which they can communicate with others and hold collective scientific conversations, enabling them to talk about it directly and freely and obtain information, topics, instructions, tips and educational guidelines for the purpose of developing creative thinking and the ability of discussion.

4. Conclusions and Recommendations

We can summarize the following as the main conclusions:

1 - The use of electronic collective scientific conversations via the Internet has helped in developing creative thinking among students and the ability of discussion among them.

2 - The possibility of developing and enhancing many of the positive aspects of the university student's personality and obtaining a variety of information through various social networking programs via the Internet.

3 - The possibility of using the Internet in social, scientific, cultural, individual and collective communication among teachers, students and various institutions.

Second - Recommendations:

1 - The use of electronic collective scientific conversations via the Internet in order to develop creative thinking and the ability of discussion among students of technical universities.

2- Interest in conducting applied research to identify the importance of using various social networking programs via the Internet for the purpose of meaningful scientific and cultural exchange between individuals and institutions.

3- Urging the teaching staff in technical universities about the importance of taking advantage of the numerous e-learning applications and using them in order to enhance the positive role of the student in the learning process.

References:

1. Jarwan Fathi Abdel Rahman (2009). Creativity, its concept, its standards and theories, its measurement and training, and the stages of the creative process, Dar Al-Fikr, Amman, Jordan.
2. Jarwan Abdel-Fattah (2002). Learning to think, concepts and applications, Dar Al-Fikr for printing, publishing and distribution, Amman, Jordan.
3. Jamal, Mohammed Jihad (2005): Developing creative thinking skills through school curricula, 1st Edition, University Book House, Al-Ain, United Arab Emirates.
4. Haris Abdel-Jaber Ammar (2010). The effectiveness of using self-learning based on computer expert systems in teaching in cognitive achievement, developing critical thinking and economic values among first-year secondary students, Faculty of Education, Sohaj University, Egypt (unpublished master's thesis).
5. Khaled Mohammed and Abdel Salam Mohammed (2011). The use of e-learning environments and its relationship to achievement motivation among students of Al-Quds Open University in the northern Gaza educational area. Palestinian Journal of Open Education.
6. Al-Khalili, Amal (2005). Developing children's creativity capabilities, Dar Safaa, Amman, Jordan
7. Dalloul Adnan and Al-Assi Wael (2008). Social subjects and their teaching methods, 2nd edition, Al-Aqsa University. Palestine.
8. Al-Sabti, Wassila (2004). Financing local development within the framework of the South Fund, a study of the reality of development projects in the Wilayat of Biskra, Mohamed Khidher University of Biskra (Unpublished Master's Thesis in Economics)

Al-Surour, Nadia Hael (1996). The effectiveness of the Master-Thinker program for teaching thinking and developing creative skills among a sample of students of the College of Educational Sciences at the University of Jordan, Journal of the Educational Research Center, Qatar University, Issue 10, Volume 5, Qatar

9. Al-Shahrani, Nasser bin Abdullah (2008), The demands of using e-learning in teaching natural sciences in higher education from the specialists point of view, Saudi Arabia, Umm Al-Qura University (unpublished doctoral thesis).
10. Abdel Hadi, Nabil and others (2003). Skills in Language and Thinking, Dar Al Masirah for Publishing and Distribution, Amman, Jordan.
11. Mohammed Mohammed Ali Shaalan (2006): The effectiveness of a program in language activities for the use of classical standerd language to develop some oral expression skills in the preparatory stage, an unpublished master's thesis, Faculty of Education, Ain Shams University.

12. Mona Hadi Saleh (2013). Studying the possibility of applying a virtual learning environment in educational institutions, Journal of Baghdad College of University Administrative Sciences, special issue, Baghdad College of Administrative Sciences, Baghdad.
13. Manal bint Abdul Rahman Youssef (2006). The effect of using metacognitive thinking strategies through the global information network on academic achievement and developing higher-order thinking skills among female students of the Mathematical Programming Course at King Saud University, College of Education, King Saud University, Saudi Arabia (unpublished master thesis).
14. Nahlawi, Abdul Rahman (2000) Education by Dialogue, House of Contemporary Thought, Beirut, Lebanon.

Wikipedia, the free online encyclopedia

15. Kecmanovic C. Dubravk and Carolyn Weeb. (2000). Toward Communicative Model of Callaborative Web- Mediated Learning, (in) Australian Journal of Education Technology, Vol.16, No.1.
16. Stewarts L. and others (2007). Virtual technology and education collaborative pilot case, The quarterly review of distance education, Vol.7, No.4.
17. Donnelly, A.E (1996). The effect of meta-cognitive skills training on hands - on learning from science objets museums, ERIC no. ED432528.

An International Comparison of Responses to the Covid-19 Pandemic by Universities and Schools

Fatima Al-Qaoud[1,2], Andrew Carruthers[2], Mumtaz Kamala[2], and Raed Abd-Alhameed[2,3]
{fnhalqao@bradford.ac.uk[1,2], A.Carruthers@bradford.ac.uk[2], m.a.kamala@bradford.ac.uk[2]}

Kuwait University, Block 4, Al-khaldiya, Kuwait[1]
Faculty of engineering and informatics, University of Bradford, Bradford, BD7 1DP, UK[2]
Information and Comms Eng. Dept., Basrah University College of Science and Technology, Basrah 24001, Iraq[3].

Abstract. This paper presents responses of several countries to the Covid-19 pandemic in educational institutions, and how universities and schools strove to complete the academic year during the pandemic. The pandemic forced institutions throughout the world to shift to fully online learning for students in schools, colleges, and universities. This paper also presents a comparison of different responses in universities and schools when implementing full online learning. Online platforms have been used by students and teachers, which requires gaining technical competencies and training courses to provide continuity of learning and teaching to complete the current academic year 2019/2020. Several countries such as the UK, Italy, Spain, Australia, and the USA have adopted various responses in their educational institutions during the Covid-19 pandemic to complete the academic year 2019/2020. Benefits of some implementations of fully online learning will also be presented, besides the concept of 'Smart City' as defined in academic research.

Keywords: Online learning, online environment, online system, ICT, IT, self-regulation, technology, education, Smart City, virtual environment, and Covid-19 pandemic.

1. Introduction

Since the Covid-19 pandemic first appeared in late 2019 in Wuhan, China, most countries have been forced to suspend schools, colleges, and universities for an unknown period to limit the spread of the virus. However, most of the developed countries such as the USA, the UK, Singapore, Japan, and developing countries such as Kuwait, Saudi Arabia, Qatar, and the United Arab of Emirates have resumed their school services in 2020 in different scenarios and at different times to complete the unfinished the academic year of 2019/2020 through online learning. To comply with the Covid-19 pandemic lockdown regulations, most educational institutions have been obliged to shift quickly to online learning to complete the current academic year 2019/2020. During the pandemic, countries which had already implemented a blended learning (BL) strategy, were generally better prepared to effectively make the transition to full online course delivery. Nevertheless, there were wide variations in how these countries had adopted BL and there is, as yet, no standardized approach to its implementation [1].

According to Lassoued [2], Covid-19 is a serious respiratory illness syndrome that can infect humans through being close to another person who is either infected or carrying the virus without exhibiting symptoms. Recovery following infection does not guarantee immunity

IMDC-IST 2021, September 07-09, Sakarya, Turkey
Copyright © 2022 EAI
DOI 10.4108/eai.7-9-2021.2315377

against being re-infected. The World Health Organization (WHO) [3] announced that this syndrome, caused by a coronavirus (SARS-COV-2), Covid-19 is an ongoing widespread disease that emerged in December 2019 in Wuhan, China, and then spread to all countries throughout the world. WHO declared that all countries would have to coexist with the Covid-19 pandemic until a vaccine could be found [3]. Fortunately, in 2021, certain countries have released several vaccines. The best-known vaccines are Pfizer, a product of Germany, and AstraZeneca, a product of the UK, in addition to vaccines from China and other countries. As a consequence, it is expected that all countries will resume normal life, including returning to schools, colleges, and universities within 2021.

Despite the advantages offered by full online learning to maintain the continuity of the educational process, other crucial advantages have been absent for students who were accustomed to having regular in-school activities [4]. The Organization for Economic Co-operation and Development (OECD) has reported that learning losses from school closure have affected students equating to a 3% drop in income over their lifetime [5]. Professional societies have strongly promoted regular in-school learning, considering Covid-19 rules and regulations in keeping the social distance among students and staff [6, 7].

It is important to shed light on how students regulate their time to accommodate a new form of learning such as fully online learning through systems and applications, taking all information and instructions from teachers to learn how to solve problems in mathematics, how to understand and comprehend information related to all other subjects remotely through an online system. Zimmerman and Schunk [8] defined self-regulation as a systematic exertion that students are making to control their learning process and effectively self-regulate to accomplish meaningful learning objectives. Self-regulation can take place between students and content, student and student, and student and instructor [9-12].

This work highlights different respondents of higher educational institutions to the Covid-19 Pandemic, as well as school respondents, besides, benefits gained of fully online learning and teaching during the Covid-19 Pandemic. Smart cities have been frequently used in educational researches and will be also presented in this work. Furthermore, this work will compare different respondents of universities and schools to Covid-19 among developed countries in Europe, Australia, and the USA.

2. Universities and Higher Education Respondent to Covid-19

Different strategies have been adopted by several countries throughout the world during the COVID-19 pandemic to keep the educational process. Universities have been affected by the pandemic just as other colleges, schools, and social activities in the community. Universities have adopted digital interfaces to deliver learning and teaching to their students [13]. In the future, global higher education will have to take account of the impact of Covid-19 on universities and educational institutions to meet the challenges and support benefits to satisfy successful online learning [14].

In this section, we will highlight different responses of educational institutions in some countries of Europe such as the UK and the Republic of Ireland (ROI), Italy, Germany, as well as Australia, and the USA.

2.1 The United Kingdom and Republic of Ireland (ROI)

The British government has closed schools with some exceptions for students with special circumstances [15]. Morgan [16] reported that students may face issues regarding admissions to the university, but Bothwell [17] asserted that universities must be more flexible to facilitate

admission procedures, recommending more support and opportunities related to international students. All social facilities, restaurants, and other institutions were closed on 20 March 2020 but with the government delivering support packages for staff and workers affected by the social distancing and quarantine requirements [18]. UK universities faced uncertain times for the number of international students as well as domestic students who faced difficulties in attending the university due to travel restrictions [19]. Later, [19] declared transforming to an online environment for teaching and working remotely, delaying graduation occasions, canceling open days, and rescheduling examination dates.

In the Republic of Ireland (ROI), Trinity College Dublin [20] closed its buildings and transferred to online learning as the first Irish university that took immediate action in response to the threat presented by Covid-19. On 12 March 2020, Andrew Deeks as a president professor at University College Dublin (UCD) announced to all staff and students that all buildings of the university would be closed from 13- 29 March 2020 except for the library and medical research facilities. According to Deeks et al. [21], on 16 March 2020, presidents of 21 higher education institutions with the collaboration of two student unions distributed emails to all registered students advising them how to remain safe during the Covid-19 pandemic and announcing their intention to make EdTech available as a new educational technology to be used for remote learning and assessment. A decision has been taken by many Irish higher educational institutions [20, 22-24], that all lectures and assignments must take place in a virtual and online environment until the end of the current academic year on 31st August 2020.

It is important to identify strategies for implementing anatomical education for medical students in a virtual environment. A total of 14 different universities have participated in a SWOT analysis (Strength, Weakness, Opportunity, Threat). According to [25], universities in the UK closed on 16 March, while in the ROI they closed on 12 March 2020. They shifted to online learning and communication provision through platforms supporting emails and webpages. Chatziralli [26] asserted that platforms such as Skype, Zoom, Cisco WebEx, Go to Meeting, Microsoft Teams, and other platforms have been used heavily during Covid-19. The highest percentage use was for Zoom that reached (55.8%) followed by Microsoft Teams (15%), meaning that Zoom was the most preferred platform for educational purposes. However, the curriculum of anatomy in the UK and the ROI depended on a system, problem, and traditional regional format; they used some platforms to deliver information for their students such as Panopto Platform (50%), Zoom (36%), Collaborate Ultra (36%), and Big Blue Button (36%). Human bodies have not been used for anatomy in Lancaster University Medical School, Peninsula College of Medicine and Dentistry, and the University of Limerick Medical School [27], while many resources have been used by UK and ROI to deliver teaching with different percentages. Based on Longhurst's study [28], the highest percentage was (42.9%) for universities that used both cadaveric and 3D virtual resources, followed by universities that used digitized cadaveric resources only (28.6%). The lowest percentage was (7.1%) for universities that used 3D virtual resources only.

2.2 Germany

Since 16 states follow governmental rules and regulations independently, different procedures have been applied to hinder the spread of the Covid-19 pandemic. Many of the 424 higher educational institutions in Germany have taken independent decision-making to sustain the educational process [29]. However, the government of Bavaria enforced lockdown on 21 March 2020. According to [30], a valuable case study was presented on the wise management of all challenges that faced the higher education sector during the Covid-19 pandemic. On 12 March 2020, the University of Passau (Bavaria) decided that face-to-face teaching would be temporally

suspended. The university adopted online working for staff, while extended time has been given for theses, dissertations, and all written assignments because the library was closed. Additionally, oral examinations have been suspended, while the number of written examinations was decreased to be at a minimum level as the university declared that buildings would be closed from 24 March to 19 April 2020 and virtual teaching was being established to continue the summer semester [30]. Also, Lower Saxony's University of Gottingen suspended teaching with immediate effect except for meetings and conferences were held through video conferencing technology [31].

Higher education did not prepare for managerial strategies, or expand efforts to train teachers; besides, no technical rules or regulations have been set to involve in the digital world, and coping with digitalization required concentrating on innovation and "modernization" [32] of learning and teaching in the context of higher education. German universities have been recommended to improve their digitalization strategies for teaching and learning [33]. To hasten the process towards a digital and online environment in German universities, the practice of Emergency Remote Teaching was highly recommended to build an IT infrastructure [33]. Moreover, on 22 March, Heidelberg University has closed all buildings and prepared for online learning [34].

2.3 Italy

On 4th March 2020, the Italian government compelled all schools and universities to close and terminate activities involving close physical contact. The universities of Milan, Turin, and Bologna have adopted online learning and teaching including examinations through the web [35]. Italy is one of the countries that have been highly infected by Covid-19 and the first case was recorded on 31st Jan 2020 [36]. According to [37], the Italian Minister of University and Research decided that universities would adopt online lessons starting from 2 March while graduate students would use Skype. However, a few universities kept their usual learning and teaching activities such as the university of Basilicata that set up thermal scanners to screen for infections [38].

Italian higher education has adopted the strategic model of distance learning to provide urgent remote education as a sustainable and dependable strategy [39]. According to [40, 41], sharing platforms enabled curriculum development through building new communities and authorized students for more accessible educational platforms. It is important to measure distance education in the context of advantages and disadvantages since it requires network collaboration, open access, and remote teaching. Nevertheless, they are susceptible to low completion rates, low-quality assurance, and limited measurable tools. Moreover, course content challenging, insufficient time, lack of a sense of community, and social impact were the most frequently reported reasons that caused dissatisfaction among learners [42-44].

Giovannella [45] conducted a study during Covid-19 to measure the fast and sudden transform from traditional physical learning to a fully online learning environment, including their perspectives and feelings regarding distance learning. A survey was distributed to bachelor students who studied the course "Educational Science of the University of Rome Tor Vergata, Italy. Because of the lockdown, the university shifted to online learning. Different devices have been used by students such as smartphones, tablets, desktop computers, and laptops before and after the Covid-19 pandemic. It was observed that utilization of the smart-phones has reduced to half (45%) during Covid-19 than the normal time (90%) as shown in Fig 1. [45].

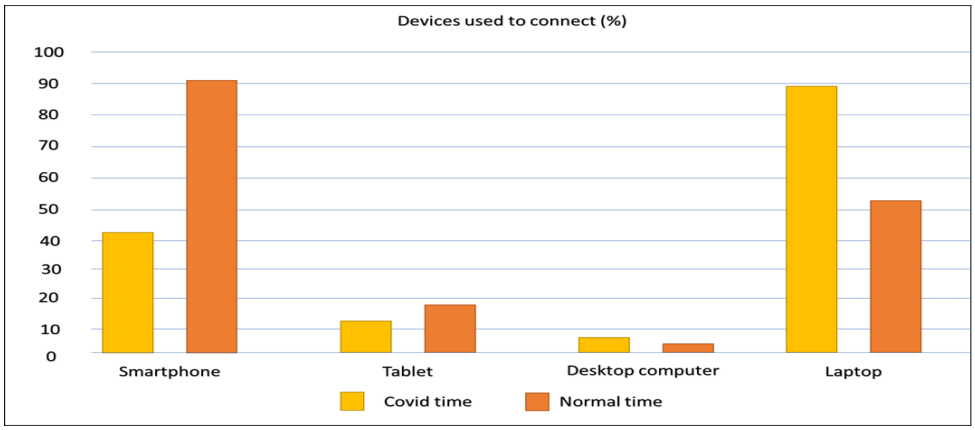

Fig. 1. Percentage of the devices used by the students to participate in virtual didactic activities (Adopted from [45]).

On the other hand, the utilization of laptops increased to reach about 90% from its previous level of 53%. This shows that students preferred using laptops during Covid-19 than their smartphones. Furthermore, students preferred to take lessons and exams face-to-face rather than in an online environment as shown in Fig 2. [45]. The study revealed that university students are prepared to use a new educational format.

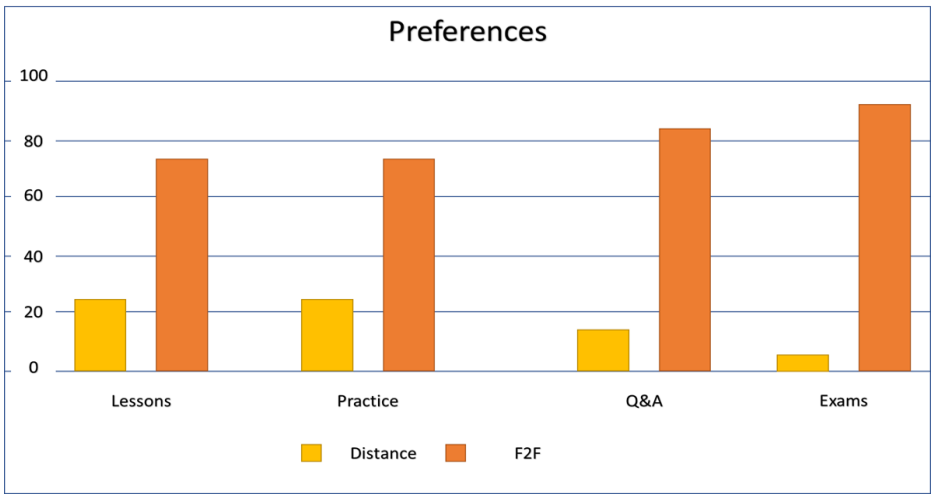

Fig. 2. Students' preferences in the percentage of distance vs. f2f (Adopted from [45]).

2.4 Australia

The universities in Australia did not shift to online learning immediately because the government prohibited public indoor gatherings to be less than 100 persons on 18th March [46]. Therefore, different procedures have been taken by different universities. Since there are international and domestic students, several regulations have been applied to each case. The University of Sydney began with fast cleaning activities after their first case of infection of a

student with Covid-19 [47]. At this stage, the universities began to adopt other options for learning. Some of the universities such as Macquarie University, Monash University, and Victoria University stopped learning activities for a period to design an online learning environment [48-50]; however, other universities such as the University of Queensland and the University of Technology, Sydney decided to continue learning by face-to-face communication but with social distancing protocols accompanied by online recordings [51, 52]. On the other hand, the Australian National University and the University of Tasmania made rapid improvements towards implementing online learning without any delay [53, 54].

2.5 United States of America

The United States of America, just like other Western Countries, responded to the Covid-19 pandemic in March 2020 despite earlier suspicions of the first infected Chinese student with Covid-19. With the dramatic rise of the infection rate [55], Harvard University [56] declared on 10 March that all delivery of learning would have to shift to a full online environment by 23 March 2020 just as Massachusetts Institute of Technology (MIT), Yale, Princeton, Stanford, and the University of California had done. However, Southern Oregon University [57] took speedy action to shift to online on 19 March. Other universities decided on different dates in March for online learning based on the analysis of higher education in Texas [58].

The level of self-regulation has a strong correlation with student motivation in the Application of Technology in Education at a university in the USA and represents a key predictor of the effectiveness of learning outcomes [59]. Since confidence or self-efficacy in learning is strongly related to self-regulation [8, 60], students with high confidence are inclined to become involved in more metacognitive and interaction regulation than students with less confidence in online learning. The self-efficacy of students who study online is positively increased with more exertion and cognitive management [61] and building the strategy of improvement in a self-paced online learning environment [62]. Therefore, motivation profiles are crucial for students' self-regulation and in their accomplishment of effective learning results [8, 60, 63-66]. Furthermore, students with higher motivation show a better level of self-regulation between students and content and self-regulation between students and instructor than those who have less motivation. Similarly, students with medium motivation are more highly self-regulated with content and instructor than those with lesser motivation levels. In conclusion, according to students' motivation profiles, the predictability of self-regulation ineffective learning results have different levels. Thus, the motivation profile in online courses is most significant since they are significantly correlated to self-regulation [59]. Based on theoretical background and related studies, Chauhan [67] has proposed a research model evaluating 18 hypotheses to analyze the continuous intention of full-time business school students and faculty who shifted to online learning during Covid-19 circumstances. The Expectation Confirmation Model (ECM) and the Task-Technology Fil (TTF) framework have been built and tested to verify the continuance intention of full-time students and faculty of business schools. The study revealed that all hypotheses were supported and provided evidence that of students' focused study as well as faculty focused study.

3. Schools Respondent to Covid-19

In the academic year, 2019/2020, countries around the world have swiftly transformed from traditional learning through attendance schools to online learning through remote access because of the Covid-19 pandemic which prevented attendance to schools. Online learning requires sharing information among students through an online environment in a collaborative manner. Zhang et al. [68] defined Collaborative Learning (CL) as "a sort of social activities,

including a network of students and educators, where individuals share and gain information". Therefore, culture could have fundamental impacts on the enhancement of CL among students and may influence their ability to communicate and interact with others [69].
According to [70], about 200 countries have closed schools with over 90% of learners being obliged to interrupt their education that used to take place regularly. It is estimated that about half a billion children [71] have been compelled to use a virtual learning environment at home, while families assumed a significant role as facilitators to assist their children to become involved in the new form of online learning. Most stakeholders such as parents, students, and teachers were unprepared to shift to a full online environment with variant levels of education [72]. Unfortunately, remote learning resources are not available for all families because they have lower income levels. However, even when online learning was available in the home, positive parental engagement was found to have an important impact on students to use online learning effectively and successfully.

3.1 Schools in the UK

It is important to highlight an exceptional experience of a school response in the UK during the Covid-19 pandemic since most schools had closed their doors and continued by offering online learning for the remainder of the semester [73]. According to Southall [73], some primary schools reopened schools on 1st June for students aged (4-5, 5-6, and 10-11), whereas students in secondary schools aged (14-15 and 16-17) resumed attendance on 15th June [74], and all other students received their learning at home through an online learning environment. A specific procedure has been taken by the government such that all students had to be back to school from 1st September in England with no medical support in the place [75]. Nevertheless, students were obliged to wear masks and to apply social distance for their safety, and parents were recommended to avoid gathering outside the school. In addition, students and teachers have been located in groups called 'bubbles' to avoid large-scale infection [76]. In case that a student or a teacher was infected, all other members of that bubble had to be quarantined for 14 days and required to take a test when symptoms appeared. Despite the indication of a positive relation between cases in society and cases in the schools, it cannot be assumed that schools contributed to any great extent to infection in the community.
Kristine Macartney and her colleagues developed a study in the UK to estimate the infection of coronavirus among school students and early childhood education and care facilities in New South Wales, Australia, during the beginning of the pandemic. When online learning was adopted, the attendance rate of all opened facilities in the UK declined precipitously in schools during March 2020. Since the number of cases was identified, most of the educational facilities were closed. Results showed that schools and educational institutions may continue to remain open on the condition that rules and measures such as keeping proper social distance among students and isolation were being observed [77].

3.2 Schools in Germany

A large number of schools were closed in March 2020 due to Covid-19 pandemic restrictions; nevertheless, schools began to reopen gradually in May 2020 having extensive restrictions still in place and estimating the suitable time for complete closure. Since the learning landscape has generally changed due to the fast shift towards technological innovation and digitalization, the majority of schools in Germany have closed [78, 79]. According to [80-82], Germany, as with many other European countries (e.g., France and Italy) remained slow to shift to proper Information and Communication Technology (ICT). Therefore, digitalization in schools has recently become an important issue. A serious arrangement has been prepared to fill the 'gap'

between students' conventional learning and improvements at school [83]. New teachers are capable of mastering challenges in this unprecedented situation and have successfully coped with the online learning environment during Covid-19 [84].
Germany's federal states decided to close all primary and secondary schools on 16 March 2020, then they reopened in April with protective procedures to prevent the spread of the disease. However, students of different ages were infected by Covid-19. During the reopening of schools, a proper evaluation of well-prepared protective procedures has been undertaken to estimate the effectiveness of measures to reduce the infection to make well-informed decisions. It is recommended that school reopening should be monitored in terms of their capability and the ability to fast test, track, and quarantine for any suspected Covid-19 cases and their contacts [85].

3.3 Schools in Spain

The Covid-19 pandemic also reached Spain and the government imposed lockdown there from 14 March to 10 May 2020, compelling all schools to shift to a virtual environment to continue learning in this new situation [86]. This unexpected situation has created a great challenge for educational institutions, teachers, and students in Spain to adopt an online environment strategy for learning and teaching [86]. Some countries have set up urgent plans to implement online learning; others such as China were not prepared for online learning and consequently, some constraints appeared because of the shortage of IT resources in schools and the lack of proper detailed plans to implement large-scale online education during unexpected circumstances [68]. In contrast, the Spanish Government obliged schools in Catalonia, as well as all regions in Spain, to adopt an online environment for learning and teaching [87]. In Catalonia, the law regulating the public schools' management takes place through a team that is arranged by the principal who is selected by a committee consisting of teachers, parents, and the administration. The principal is authorized to select the rest of the management staff such as teachers.
Cities are constantly changing, and with the spread of ICT, the concept of 'Smart City' is being mentioned more frequently in academic researches [88, 89]. Paskaleva [90] stated that "the term 'Smart City' focused on the relevance of ICTs for the achievement of more competitive status and a more sustainable development". Other researchers believed that the cultural and professional growth of individuals in a society is related to the smart city [91]. On the other hand, others related it with the effect of ICT and its evolution to the infrastructure [92]. However, [93] considered the smart city in terms of its relevance to ICT and its benefits to the users [94]. The European Parliament maintained that smart cities depended on the initiation and connection of human capital, social capital, and digital infrastructure to develop sustainable economic progress and a better lifestyle [95]. Covid-19 has marked a turning point in learning and teaching mechanisms [94]. Therefore, online psychoeducation should be considered by health authorities [96].
Olmos-Gomez [94] conducted a study in the city of Melilla, Spain to design and validate a Smart City tool to measure the effect of online learning on teaching during school closure, as well as to obtain descriptive results for the use of the Smart City tool for online learning and teaching purposes during Covid-19 pandemic, using Structural Equation Model (SEM). The participants were teachers from primary and secondary schools and university levels. The results indicated that the models used were highly reliable and validated; furthermore, the questionnaire used was very effective for teachers when using the Smart City concept.

3.4 Schools in Estonia

Estonia enforced emergency measures similar to those in other European countries during the Covid-19 pandemic. The government closed all schools on 16 March 2020 [97], and distance learning was recommended [98]. Lepp [97] states that distance learning is a sort of learning that includes controlled e-learning that is concentrated on knowledge and competencies using a virtual environment. The government of Estonia has obliged teachers as well as students to communicate through digital means to complete the school year by June 2020 [97]. According to the Ministry of Education and Research, Estonia [99], guidelines for teachers as well as school leaders were issued drawing on the fact that Estonia is considered as a highly digitized society that possessed the best IT- infrastructure implementing national e-services for its people. Therefore, shifting to online learning was quite straightforward and was sustained by the Estonian Lifelong Learning 2020 Strategic plan [100].

3.5 Schools in the United States of America

Schools in the USA also closed due to Covid-19 and used a new type of education which is virtual education [101, 102]. However, there were some concerns that some students would not cope with online learning because their skills and competencies in receiving information via an online environment were under-developed [103]. It is crucial to use Google search data which is a high frequent representative search engage to measure how students and parents navigate through online resources in real-time [104]. Some students needed additional support to overcome educational obstacles caused by Covid-19, However, school leaders and policymakers have given priority access to home computers and broadband internet. Enhanced access involving the online learning environment will importantly assist to equalize learning opportunities and avoiding any educational gaps [104].

Calhoun [105] asserted that students in K-12 schools in Washington State, USA have adopted learning online on 17 March 2020 to continue the unfinished academic year 2019/2020. The University of Washington, School of Medicine (UWSOM) is one of two medical schools in the state, which covers WWAMI region which includes (Wyoming, Alaska, Montana, and Idaho). The university school took a crucial decision for its medical students by shortening the 3rd year rotations and triage for the 4th year electives, as well as adopting virtual clerkship to keep up the learning process.

Bol [106] believed that families with high educational qualifications were taking more time to help their children to use online learning facilities and features than families with lower educational qualifications. According to [103], 38% of families with lower personal earnings stated that their children had massive online instructions, in comparison with higher-income families. Based on the three-parent survey items used to assess students' involvement in online learning, Domina [107] divided the survey into Enjoyed remote, complete assignments, and Log on each week. Fig 3. *[107]* illustrates how parents responded to all previous items taking relatively moderate disseminations. Therefore, Domina [107] suggested hard efforts to support students with strong and holistic learning opportunities that increased their academic and socio-emotional development. It is found that educational policymakers must consider the risk of social quarantine for students and their families.

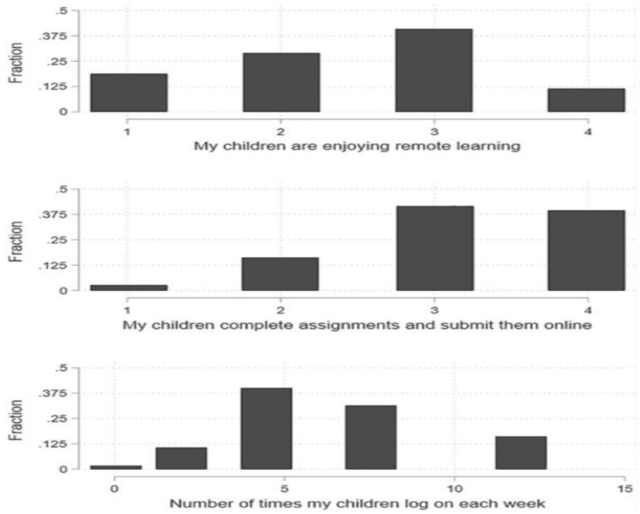

Fig. 3. Families' Reports about their Children Involvement in Online Environment (Adopted from [107]).

4. Benefits of online learning during Covid-19 pandemic

During Covid-19, all educational institutions were forced to shift to full online remote learning through a digital environment to complete the academic year 2019/2020. This required the availability of IT infrastructure and all related needs (e.g.: digital curriculum content, trained teachers, and students' technical skills) to implement online learning successfully. Despite the differences in availability across countries, many benefits have been gained during the Covid-19 pandemic.

Distance learning or online education enabled students to discover their technical competencies and capabilities. Such capabilities help them to use managerial functions perfectly such as downloading and uploading files and documents. Online courses are more beneficial than video courses and open education because students can interact with their instructors with immediate responses to their questions. Social communication applications such as WhatsApp, E-mail, Facebook, and Instagram played a significant role in delivering information from instructors to students [108]. Stacey [109] indicated that the application of online learning is not restricted to crises, but is an alternative option to face-to-face education. Likewise, the most obvious benefits of online learning are that students are not restricted to time or a place, so they can have their education at anytime and anywhere [110].

The utilization of ICT tools helps to develop students' comprehension of instructional materials [111]. Moreover, simulation of real processes can be implemented through ICT and enables students to engage with the virtual world [112]. Thus, the acceleration of the technology interaction rate is required as well as the optimization of educational online applications considering any future crisis [113]. For parents, they show positive impressions and attitudes regarding online learning; they encourage valuable technical competencies for their children. Practicing for managerial computerized functions of online applications is highly recommended [114]. However, parents are worried about potential perilous content that may negatively affect children's beliefs and morals.

5. Smart Cities

The term ‘Smart City’ has been repeated more frequently in researches, since some experiences indicate that some cities considered themselves to be smart; thus, it is important to shed light on the definition, concept, and principles of the ‘Smart City’ from the perspective of academic research [115]. It is difficult to create the features that form an ideal smart civilized city because such features are based on the size of the city, accessibility to other cities, and accessibility to service centers; thus, population size and suitable functions to implement a smart city should be considered [116]. Additionally, smart people, smart economy, smart governance, and smart environment are involved in smart city construction [117].

Drawing on previous in-depth studies, Caragliu [118] assumed that similar projects and solutions have been defined using several different words but with close similarities with one another. For instance, intelligent city, wired city, and digital city have a similar meaning, however, similarities and differences were not determined yet. On the other hand, Chen [119] states that technology is the main driver for the smart city and in particular ICT, which enables connections to be made to different agents in the civilized arena and to provide technical services. The most significant agents are universities, research institutions, and companies with high technology [120, 121]. Dameri [115] defines a smart city based on three characteristics which are: terminology; components; boundaries and scope. Similarly, ‘Smart Cities’ are considered as ecosystems that are defined as interacted organisms’ communities and their environment and described as a complicated formed network through interdependent resources [122]. Ecosystems consist of agents, organizations, material infrastructures, and symbolic resources that are independently gathered in a social system [123].

Lytras [124] conducted a study to discuss the smart city debate from citizens’ awareness perspectives and their ability to use services available in the smart city. Several (102) highly educated participants from 28 countries participated in this study. The survey covered 60% of Ph.D. holders, followed by 28% of Masters’ degree holders, the bachelor’s degree holders represented only 4%, while 2% represented undergraduates. Most of the respondents were from Europe and represented 44% of the sample, followed by Asia at 34%. The most notable countries which represented 70% of the sample were: China, Spain, Greece, Taiwan, Saudi Arabia, Pakistan, Brazil, and the Czech Republic. The results showed that many concerns hindered those educated individuals from using these services. Therefore, it is suggested that based on the utility, accessibility, and efficiency of services, users of the smart city can be divided into three groups as advocates, concerned users, and apathetic.

6. Results and Discussion

Based on all navigated researches that have been conducted throughout the Covid-19 pandemic, all educational institutions such as universities and schools have been obliged to shift to fully online learning, whether they have satisfied the technical needs and IT infrastructure or not. However, different levels of students’ comprehension and understanding will be recognized soon after they move to the second level in their education when the crisis has passed.

Table 1. Comparison of Different Universities' Respondents to Covid-19 of several countries.

Country	Institution	Respondent	Date of Action	Platform/Mean
UK	UK universities	- closed and shift to online - delaying graduation occasions - cancelling open days, and reschedule examination dates.	16 March	Online learning, Skype, Zoom (55.8%), Cisco WebEx, Go to Meeting, Microsoft Teams (15%)
Medical Schools in the UK	- Lancaster University Medical School - Peninsula College of Medicine and Dentistry - University of Limerick Medical School	- teleteaching and telemedicine modalities have been adopted - shift to online	16 March	- Panopto Platform (50%) - Zoom (36%) - Collaborate Ultra (36%) - Big Blue Button (36%) - cadaveric and 3D virtual resources (42.9%) - digitized cadaveric resource only (28.6%) - 3D virtual resource only (7.1%)
ROI	- Trinity College Dublin - University College Dublin - University College Cork - Queen's University	- closed and shift to online	12 March	- virtual, online learning - EdTech, virtual, online learning - virtual, online learning - virtual, online learning
Germany	Government of Bavaria	- enforced lockdown	21 March	- Not mentioned
	University of Passau (Bavaria)	- buildings closed - delayed face-to-face teaching - online working for staff - extended time for theses, dissertation, and assignments - library closed - oral examinations suspended - examinations decreased	24 March-19 April	-Virtual teaching
	University of Gottingen Heidelberg University	- suspended teaching - recommended to improve their digitalization strategies - building closed - prepare online learning	Not mentioned 22 March	- video conferencing technology - prepare online learning
Italy	Italian government	- enforced all schools and universities to close and terminate	4 March	- Not mentioned
	The universities of Milan, Turin, and Bologna	- adopted online lessons	2 March	- Skype - distance learning
	University of Rome Tor Vergata	- lockdown - shifted to online learning	4 March	- online environment
Australia	Australian universities	- shifted to online learning	18 March	- different procedures - online recording and offerings
	University of Sydney	- fast cleaning activities		- other options of learning
	National University University of Tasmania	- no delays - fast improvements towards online learning		- online environment
	Macquarie University Monash University Victoria University	- stopped learning for a while just to design an online learning environment		- online environment
	University of Technology Sydney University of Queensland	- continued face-to-face learning with social distance protocols		- online recording and offerings
USA	Harvard University Massachusetts Institute of Technology (MIT), Yale, Princeton, Stanford, and the University of California	- shift to full online environment	23 March	- online environment
	Oregon University	- shift to online	19 March	

The results indicated that all educational institutions in the UK, ROI, Germany, Italy, Australia, and the USA have been forced to transition to fully online learning to continue the remainder of the academic year, except for the University of Technology, Sydney, and the University of Queensland in Australia, which continued face-to-face learning but complying with social distance protocols as shown in Table 1. below. Additionally, Table.1 shows that Italy was the first European country that responded to Covid-19 and that was on 2 March 2020. Since the pandemic started there, Italy closed all schools and universities and adopted online learning. On the other end of the scale, the USA was the latest country that took action in response to the pandemic on 23 March 2020. USA universities have also shifted to fully online delivery to continue teaching and learning to complete the academic year. The most preferable platform used in the UK was the Online learning, Skype, Zoom (55.8%), followed by Cisco WebEx, Go to Meeting, Microsoft Teams (15%). However, medical schools used the Panopto platform which reached (50%), followed by Zoom, Collaborate Ultra, and Big Blue Button at 36%.

Table 2. School respondents to Covid-19 in different countries.

Country	School Respondent	Citation
The UK	- closed and continue online learning	[77]
	- some primary schools reopened schools on 1st June	[77]
	- students of secondary schools attended the school on 15th June	[78]
	- students implemented online environment.	[78]
	- on 1st September, students attend schools with no medical support in the place, but obliged to wear masks and apply social distance	[79]
	- students and teachers have been located in groups called 'bubbles'	[80]
Germany	- all primary and secondary schools closed in 16 March 2020	
	- reopened on April with protective procedures	
	- students were infected by covid-19 in different ages	[89]
	- During reopening schools, proper evaluation of well-prepared protective procedures has been taken.	
	- closed due to fast shift in technological innovation and digitalization	[82], [83]
Spain	- lockdown from 14 March to 10 May	[90]
	- all schools to shift to virtual environment	[90]
	- a study developed using Smart City concept	[99]
Estonia	- all schools closed in 16 March	[101]
	- distance learning has been approved	[102]
	- guidelines for teachers were assigned to implement online teaching	[103]
USA	- schools have been closed	[105], [106]
Schools in Washington State	- resumed learning for K-12 students through online on 17 March	[109]

Similarly, schools had to respond urgently to the Covid-19 lockdowns just like universities, however, some reopening scenarios have been applied in the UK and Germany as we can see in Table 2. below. For instance, in the UK, all schools closed and continued education through the online environment but later, on 1st June, the primary schools reopen for students [73], also students in secondary schools attended their classes on 15th June and all other students have received their learning remotely in an online environment [74]. However, the government obliged all students to return to schools on 1st September with no medical support in the place but obliged them to wear masks and comply with social distancing regulations [75]. Likewise,

in Germany, all primary and secondary schools closed on 16 March 2020 and reopened in April with protective procedures, despite well-prepared protective procedures that have been taken, students were infected by Covid-19 at different ages, proper evaluations have been taken to assess the effectiveness of decisions to reduce the infection and to make appropriate decisions for the future [85]. In contrast, Spain, Estonia, and the USA have implemented online learning to complete the academic year without physical buildings reopening. Spain has implemented a notable experience during Covid-19 to design and validate a 'Smart City' tool in the city 'Melilla' for learning purposes. According to Olmos-Gomez [94], the success of this experience has been achieved.

6. Conclusion

The covid-19 pandemic has spread throughout the world for almost two years. It expanded gradually from Asia to Europe and has reached America. Despite some vaccines having been released to prevent the infection of this disease, no one has yet confirmed the end of this pandemic. Educational institutions such as universities, colleges, and schools have been forced to shift to online learning during the pandemic. Developed and developing countries have different levels of IT infrastructure preparations; therefore, different levels of students' outcomes will be observed in the next few years. It is important to take advantage of this pandemic so that all countries can reconsider their preparations for IT infrastructure to avoid any constraints in the future.

Achieving a sustainable educational system should be considered by educational institutions through implementing the concept of the 'Smart City. This would assist them to achieve a sustainable online system to be used by all stakeholders such as students, teachers, educational staff, and parents. However, the ultimate decision-making must be taken to achieve proper education for all stakeholders who are engaged with online learning.

Reference

1. Al-Qaoud, F., et al., *An International Comparison of Blended Learning.* 2020.
2. Lassoued, Z., M. Alhendawi, and R. Bashitialshaaer, *An Exploratory Study of the Obstacles for Achieving Quality in Distance Learning during the COVID-19 Pandemic.* Education Sciences, 2020. **10**(9): p. 232.
3. *World Health Organization* [cited 2020 20 Sep 2020].
4. McGee, R.S., et al., *Model-driven mitigation measures for reopening schools during the COVID-19 pandemic.* medRxiv, 2021.
5. Hanushek, E.A. and L. Woessmann, *The economic impacts of learning losses.* 2020.
6. American Academy of, P., *COVID-19 planning considerations: guidance for school re-entry.* Critical Updates on COVID-19-Clinical Guidance, 2020. **2019**: p. 1-11.
7. Schweingruber H, D.K., Bond EC, *Reopening K-12 Schools During the COVID-19 Pandemic: Prioritizing Health, Equity, and Communities eds*, E. National Academies of Sciences, and Medicine, et al., Editors. 2020: Washington (DC).
8. Zimmerman, B.J. and D.H. Schunk, *Self-regulated learning and performance.* Handbook of self-regulation of learning and performance, 2011: p. 1-12.

9. Bernard, R.M., et al., *A meta-analysis of three types of interaction treatments in distance education.* Review of Educational research, 2009. **79**(3): p. 1243-1289.
10. Bol, L. and J.K. Garner, *Challenges in supporting self-regulation in distance education environments.* Journal of Computing in Higher Education, 2011. **23**(2): p. 104-123.
11. Cho, M.-H. and Y. Cho, *Self-regulation in three types of online interaction: a scale development.* Distance Education, 2017. **38**(1): p. 70-83.
12. Moore, M.G., *Three types of interaction*. 1989, Taylor & Francis.
13. Kernohan, D., *Which universities are moving to remote teaching.* WONKHE: https://wonkhe. com/blogs/which-universities-are-moving-to-remote-teaching, 2020.
14. Watermeyer, R., et al., *COVID-19 and digital disruption in UK universities: Afflictions and affordances of emergency online migration.* Higher Education, 2020: p. 1-19.
15. News, B. *COVID-19: What's happening with schools?*. 2020f, March 21 [cited 2021 12 March 2021].
16. Morgan, J., *Schools shutdown creates UK university admissions uncertainty.* Times Higher Education, 2020.
17. Bothwell, E., *Flexible admissions could mitigate COVID-19 impact.* Times Higher Education, 2020.
18. News, B. *UK PM Boris Johnson announces closure of pub, bars and restaurants* 2020b, March 20 [cited 2021 12, March 2021].
19. Gov.UK. *Travel advice: Coronavirus (COVID-19).* 2020 [cited 2021 12, March 2021].
20. Dublin, T.C. *COVID-19 (Coronavirus)*. 2020 [cited 2021 12, March 2021].
21. Deeks, A., *Message to Students from Presidents of Irish Universities and Institutes of Technology*. 2020, Email communication on.
22. Learning, U.T. *Teaching Continuity Measures*. 2020 [cited 2021 12, March 2021].
23. Cork, U.C. *University closure coronavirus (COVID-19) Safety Update* 2020 [cited 2021 12, March 2021].
24. Belfast, Q.s.U. *COVID-19 (Coronavirus): FAQs for students and staff.* . 2020 [cited 2021 12, March 2021].
25. RTE. *Coronavirus in Ireland – A timeline*. 2020a, March 20 [cited 2021 12, March 2021].
26. Chatziralli, I., et al., *Transforming ophthalmic education into virtual learning during COVID-19 pandemic: a global perspective.* Eye, 2020: p. 1-8.
27. Heylings, D.J.A., *Anatomy 1999–2000: The curriculum, who teaches it and how?* Medical education, 2002. **36**(8): p. 702-710.
28. Longhurst, G.J., et al., *Strength, weakness, opportunity, threat (SWOT) analysis of the adaptations to anatomical education in the United Kingdom and Republic of Ireland in response to the Covid-19 pandemic.* Anatomical sciences education, 2020. **13**(3): p. 301-311.
29. Bundesamt, S. *Hochschulen nach Hochschularten.* . 2020 [cited 2021 12, March 2021].
30. Passau, U.o. *Coronavirus (COVID-19) – important information.* . 2020 [cited 2021 12, March 2021].
31. Göttingen, U. *FAQ on the novel coronavirus*. 2020 [cited 2021 12, March 2021].
32. Getto, B. and M. Kerres, *Akteurinnen/Akteure der Digitalisierung im Hochschulsystem: Modernisierung oder Profilierung?* Zeitschrift für Hochschulentwicklung, 2017.

33. Zawacki-Richter, O., *The current state and impact of Covid-19 on digital higher education in Germany.* Human Behavior and Emerging Technologies, 2021. **3**(1): p. 218-226.
34. University, H. *COVID-19 Update: Remote classes, campus closed.* . 2020 [cited 2021 12, March 2021].
35. Crawford, J., et al., *COVID-19: 20 countries' higher education intra-period digital pedagogy responses.* Journal of Applied Learning & Teaching, 2020. **3**(1): p. 1-20.
36. Salute, M.d. *New coronavirus. Ministry of Health.* . 2020 [cited 2021 12, March 2021].
37. De Giorgio, T., *Coronavirus in Lombardy, at the Politecnico di Milano the degree thesis is discussed via Skype.* La Repubblica, 2020.
38. Associata)., A.A.N.S. *Coronavirus: Thermal scanner at Unibas [Italian]. Basilicata.* . 2020, February 26 [cited 2021 12, March 2021].
39. D'Adamo, I. and P. Rosa, *How do you see infrastructure? green energy to provide economic growth after COVID-19*. 2020, Multidisciplinary Digital Publishing Institute.
40. Tudorie, C.A.-M., et al., *Towards a Greener University: Perceptions of Landscape Services in Campus Open Space.* Sustainability, 2020. **12**(15): p. 6047.
41. Sonetti, G., P. Lombardi, and L. Chelleri, *True green and sustainable university campuses? Toward a clusters approach.* Sustainability, 2016. **8**(1): p. 83.
42. Hone, K.S. and G.R. El Said, *Exploring the factors affecting MOOC retention: A survey study.* Computers & Education, 2016. **98**: p. 157-168.
43. Zheng, S., et al. *Understanding student motivation, behaviors and perceptions in MOOCs*.
44. Singh, A.B., *Learning through massive open online courses (MOOCs): A case of the first international MOO offered by University of Oslo in 2015.* 2016.
45. Giovannella, C., *Effect induced by the Covid-19 pandemic on students' perception about technologies and distance learning*, in *Ludic, Co-design and Tools Supporting Smart Learning Ecosystems and Smart Education*. 2021, Springer. p. 105-116.
46. Bagshaw, E., *Travel warning raised, indoor mass gatherings over 100 people prohibited.* Sydney Morning Herald, 2020.
47. Sydney, U.o. *Confirmed case of COVID-19. University of Sydney.* . 2020 [cited 2021 12, March 2021].
48. University, M. *Coronavirus (COVID-19) infection: latest information.* . 2020 [cited 2021 12, March 2021].
49. University, M. *COVID-19 – fact sheet. Monash University.* . 2020 [cited 2021 12, March 2021].
50. University, V. *Coronavirus (COVID-19).* 2020 [cited 2021 12, March 2021].
51. Queensland, U.o. *UQ pauses teaching for one week [email to students].* . 2020 [cited 2021 12, March 2021].
52. Sydney, U.o.T. *Coronavirus advice and frequently asked questions.* . 2020 [cited 2021 12, March 2021].
53. University, A.N. *Information for students – 17 March 2020.* . 2020 [cited 2021 12, March 2021].
54. Tasmania, U.o. *COVID-19 updates*. 2020 [cited 2021 12, March 2021].
55. Organization, W.H. *Coronavirus disease (COVID-2019) situation reports. Situation report – 64 (29 March 2020).* . 2020a [cited 2021 12, March 2021].
56. Herpich, N., *Q&A on Harvard's move to online learning.* Harvard Gazette, 2020.

57. University, S.O. *Important details: for students, about spring break, spring term* 2020 [cited 2021 12, March 2021].
58. Bawab, N., *Here's what Texas universities and colleges are doing in response to COVID-19.* WFAA8 ABC, 2020.
59. Cho, M.-H., J. Cheon, and S. Lim, *Preservice teachers' motivation profiles, self-regulation, and affective outcomes in online learning.* Distance education, 2021. **42**(1): p. 37-54.
60. Pintrich, P.R., *A conceptual framework for assessing motivation and self-regulated learning in college students.* Educational psychology review, 2004. **16**(4): p. 385-407.
61. Shea, P. and T. Bidjerano, *Learning presence: Towards a theory of self-efficacy, self-regulation, and the development of a communities of inquiry in online and blended learning environments.* Computers & Education, 2010. **55**(4): p. 1721-1731.
62. Artino Jr, A.R. and K.D. Jones Ii, *Exploring the complex relations between achievement emotions and self-regulated learning behaviors in online learning.* The Internet and Higher Education, 2012. **15**(3): p. 170-175.
63. Dörrenbächer, L. and F. Perels, *Self-regulated learning profiles in college students: Their relationship to achievement, personality, and the effectiveness of an intervention to foster self-regulated learning.* Learning and Individual Differences, 2016. **51**: p. 229-241.
64. Mägi, K., M. Männamaa, and E. Kikas, *Profiles of self-regulation in elementary grades: Relations to math and reading skills.* Learning and Individual Differences, 2016. **51**: p. 37-48.
65. Vanslambrouck, S., et al., *A latent profile analysis of adult students' online self-regulation in blended learning environments.* Computers in Human Behavior, 2019. **99**: p. 126-136.
66. Zimmerman, B.J., *Investigating self-regulation and motivation: Historical background, methodological developments, and future prospects.* American educational research journal, 2008. **45**(1): p. 166-183.
67. Chauhan, S., et al., *Examining continuance intention in business schools with digital classroom methods during COVID-19: a comparative study of India and Italy.* Behaviour & Information Technology, 2021: p. 1-24.
68. Zhang, W., et al., *Suspending classes without stopping learning: China's education emergency management policy in the COVID-19 outbreak*. 2020, Multidisciplinary digital publishing institute.
69. Fatimah, F., S. Rajiani, and E. Abbas, *Cultural and individual characteristics in adopting computer-supported collaborative learning during covid-19 outbreak: Willingness or obligatory to accept technology?* Management Science Letters, 2021. **11**(2): p. 373-378.
70. UNESCO. *1.3 billion learners are still affected by school or university closures, as educational institutions start reopening around the world, says UNESCO*. 2020 [cited 2021 3/4/2021].
71. Cohen, J. and K. Kupferschmidt, *Countries test tactics in 'war'against COVID-19*. 2020, American Association for the Advancement of Science.
72. Garbe, A., et al., *Parents' experiences with remote education during COVID-19 school closures.* American Journal of Qualitative Research, 2020. **4**(3): p. 45-65.
73. Southall, E.R., et al., *An analysis of school absences in England during the Covid-19 pandemic.* MedRxiv, 2021.

74. Office, U.G.P.M.s. *Prime Minister's statement on coronavirus (COVID-19)* 2020 [cited 2020 25 March 2020].
75. Office, U.G.P.M.s. *Prime Minister's statement on re- turning children to school (2020).* . 2020 [cited 2021 4, April 2021].
76. Office, U.G.P.M.s. *Guidance for Schools, coronavirus: COVID-19 (2020)*. 2020 [cited 2021 4, April 2021].
77. Edmunds, W.J., *Finding a path to reopen schools during the COVID-19 pandemic.* The Lancet Child & Adolescent Health, 2020. **4**(11): p. 796-797.
78. Selwyn, N., *Education in a digital world: Global perspectives on technology and education*. 2012: Routledge.
79. McFarlane, A.E., *Devices and desires: Competing visions of a good education in the digital age.* British Journal of Educational Technology, 2019. **50**(3): p. 1125-1136.
80. Fraillon, J., et al., *Preparing for life in a digital world: IEA International computer and information literacy study 2018 international report*. 2020: Springer Nature.
81. Bildungsberichterstattung, A., *Bildung in Deutschland 2020.* Ein indikatorengestützter Bericht mit einer Analyse zu Bildung in einer digitalisierten Welt, 2020: p. 40-41.
82. Gew, G.E., *Wissenschaft (Hrsg.)(2017): Mehr Flexibilität auf Kosten der Erzieher* innen.* CDU und FDP liebäugeln mit anpassungsfähiger Kinderbetreuung. URL: https://www. gewnrw. de/meldungen/detail-meldungen/news/mehr-flexibilitaet-auf-kosten-der-erzieherinnen. html, letzter Zugriff, 2020. **5**.
83. Kozma, R.B., *ICT, education transformation, and economic development: An analysis of the US National Educational Technology Plan.* E-Learning and Digital Media, 2011. **8**(2): p. 106-120.
84. König, J., D.J. Jäger-Biela, and N. Glutsch, *Adapting to online teaching during COVID-19 school closure: teacher education and teacher competence effects among early career teachers in Germany.* European Journal of Teacher Education, 2020. **43**(4): p. 608-622.
85. Im Kampe, E.O., et al., *Surveillance of COVID-19 school outbreaks, Germany, March to August 2020.* Eurosurveillance, 2020. **25**(38): p. 2001645.
86. Palau, R., et al., *Analysis of the implementation of teaching and learning processes at Catalan schools during the Covid-19 lockdown.* Technology, Pedagogy and Education, 2021: p. 1-17.
87. Catalunya, G.d. *Coronavirus: Comunicats del Departament d'Educació. Departament d'Educació de la Generalitat de Catalunya.* . 2020 [cited 2021 12, March 2021].
88. AMETIC, *Smart Cities*. 2012, Spain. 92.
89. Güell, J.M.F., *Ciudades inteligentes: la mitificación de las nuevas tecnologías como respuesta a los retos de las ciudades contemporáneas.* Economía industrial, 2015(395): p. 17-28.
90. Paskaleva, K.A., *The smart city: A nexus for open innovation?* Intelligent Buildings International, 2011. **3**(3): p. 153-171.
91. Shapiro, J.M., *Smart cities: explaining the relationship between city growth and human capital.* Available at SSRN 480172, 2003.
92. Caragliu, A., C. Del Bo, and P. Nijkamp, *Smart cities in Europe.* Journal of urban technology, 2011. **18**(2): p. 65-82.
93. Klein, C. and G. Kaefer. *From smart homes to smart cities: Opportunities and challenges from an industrial perspective*. Springer.

94. Olmos-Gómez, M.d.C., et al., *Validation of the Smart City as a Sustainable Development Knowledge Tool: The Challenge of Using Technologies in Education during COVID-19.* Sustainability, 2020. **12**(20): p. 8384.
95. Europeo, P., *Mapping smart cities in the EU.* POLICY DEPARTMENT A: ECONOMIC AND SCIENTIFIC POLICY. Recuperado de la red mundial desde: http://www. smartcities. at/assets/Publikationen/Weitere-Publikationen-zum-Thema/mappingsmartcities. pdf, 2014.
96. De Pablos-Pons, J., et al., *Teacher well-being and innovation with information and communication technologies; proposal for a structural model.* Quality & quantity, 2013. **47**(5): p. 2755-2767.
97. Lepp, L., et al., *Teaching during COVID-19: The Decisions Made in Teaching.* Education Sciences, 2021. **11**(2): p. 47.
98. Haridussilm. *Külastatud Aadressil*. 2020 [cited 2021 3/4/2021].
99. Estonia, M.o.E.a.R. *Haridus-ja Teadusministeerium Soovitab Vähemalt Esimesel Kahel Nädalal Hoiduda Õpilaste Numbrilisest Hindamisest*. 2020 [cited 2020 18 March 2020].
100. Research, M.o.E.a., *The Estonian Lifelong Learning Strategy 2020*. 2020: Estonia. p. 15.
101. Hamilton, L.S., et al., *COVID-19 and the State of K-12 Schools: Results and Technical Documentation from the Spring 2020 American Educator Panels COVID-19 Surveys.* RAND Corporation, 2020.
102. Lake, R. and B. Dusseault, *Remote classes are in session for more school districts, but attendance plans are still absent.* Center on Reinventing Public Education, 2020.
103. Horowitz, J.M., *Lower-income parents most concerned about their children falling behind amid COVID-19 school closures.* Pew Research Center, 2020.
104. Bacher-Hicks, A., J. Goodman, and C. Mulhern, *Inequality in household adaptation to schooling shocks: Covid-induced online learning engagement in real time.* Journal of Public Economics, 2021. **193**: p. 104345.
105. Calhoun, K.E., et al., *The impact of COVID-19 on medical student surgical education: implementing extreme pandemic response measures in a widely distributed surgical clerkship experience.* The American Journal of Surgery, 2020. **220**(1): p. 44-47.
106. Bol, T., *Inequality in homeschooling during the Corona crisis in the Netherlands. First results from the LISS Panel.* 2020.
107. Domina, T., et al., *Remote or Removed: Predicting Successful Engagement with Online Learning during COVID-19.* Socius, 2021. **7**: p. 2378023120988200.
108. Doyumğaç, İ., A. Tanhan, and M.S. Kiymaz, *Understanding the most important facilitators and barriers for online education during COVID-19 through online photovoice methodology.* International Journal of Higher Education, 2020. **10**(1): p. 2021.
109. Stacey*, E., P.J. Smith, and K. Barty, *Adult learners in the workplace: Online learning and communities of practice.* Distance Education, 2004. **25**(1): p. 107-123.
110. Fatonia, N.A., et al., *University students online learning system during Covid-19 pandemic: Advantages, constraints and solutions.* Systematic Reviews in Pharmacy, 2020. **11**(7): p. 570-576.
111. Lee, Y.-H., C. Hsiao, and C.-H. Ho, *The effects of various multimedia instructional materials on students' learning responses and outcomes: A comparative experimental study.* Computers in Human Behavior, 2014. **40**: p. 119-132.

112. Hennessy, S., R. Deaney, and K. Ruthven, *Situated expertise in integrating use of multimedia simulation into secondary science teaching.* International Journal of Science Education, 2006. **28**(7): p. 701-732.
113. Ali, W., *Online and remote learning in higher education institutes: A necessity in light of COVID-19 pandemic.* Higher Education Studies, 2020. **10**(3): p. 16-25.
114. Hatzigianni, M. and I. Kalaitzidis, *Early childhood educators' attitudes and beliefs around the use of touchscreen technologies by children under three years of age.* British Journal of Educational Technology, 2018. **49**(5): p. 883-895.
115. Dameri, R.P., *Searching for smart city definition: a comprehensive proposal.* International Journal of computers & technology, 2013. **11**(5): p. 2544-2551.
116. Katoshevski-Cavari, R., T.A. Arentze, and H.J.P. Timmermans, *Sustainable city-plan based on planning algorithm, planners' heuristics and transportation aspects.* Procedia-Social and Behavioral Sciences, 2011. **20**: p. 131-139.
117. Kirimtat, A., et al., *Future trends and current state of smart city concepts: A survey.* IEEE Access, 2020. **8**: p. 86448-86467.
118. Caragliu, A., C.D. Bo, and P. Nijkamp, *Smart Cities in Europe «3rd Central European Conference in Regional Science–CERS.* A13 L, 2009. **90**: p. O18.
119. Chen, Y.-T., *Sketch industry promotion framework for smart living services by leveraging living lab harmonization cube.* International Journal of Electronic Business Management, 2012. **10**(2): p. 149.
120. Cosgrave, E. and T. Tryfonas. *Exploring the relationship between smart city policy and implementation*.
121. Dameri, R.P. *Defining an evaluation framework for digital cities implementation*. IEEE.
122. Gretzel, U., et al., *Conceptual foundations for understanding smart tourism ecosystems.* Computers in Human Behavior, 2015. **50**: p. 558-563.
123. Maheshwari, D. and M. Janssen, *Reconceptualizing measuring, benchmarking for improving interoperability in smart ecosystems: The effect of ubiquitous data and crowdsourcing.* Government Information Quarterly, 2014. **31**: p. S84-S92.
124. Lytras, M.D. and A. Visvizi, *Who uses smart city services and what to make of it: Toward interdisciplinary smart cities research.* Sustainability, 2018. **10**(6): p. 1998.

Legalization of Cannabis Cultivation a Comparative Study

Samer Hameed Safer[1]
Samer.alrikabi@stu.edu.iq[1]

Nassriyah Technical Institute, Southern Technical University, Iraq[1]

Abstract. Legalizing cannabis cultivation is one of the most important challenges that countries face considering the economic depression that these countries have been suffering from for a long time because of accelerated and unexamined economic policies and because of economic conditions in the Arab and global region, which led to the collapse of the economic systems adopted by countries. This caused a deficit in their budgets for this and that and considering the relentless pursuit of accepting the least loss, these countries began to search for legal solutions through which they could reduce the effects of the financial deficit, and at the same time try to limit negative phenomena by controlling them and trying to control them or lowering it or taming it by legal means.

Keywords: Cannabis, Countries, Cultivation, Drug

1 Introduction

Legalizing cannabis cultivation is among the most important challenges facing countries in the world considering the economic depression that these countries suffer from for a long period because of accelerated and unexamined economic policies and as a result of the economic conditions in the Arab and global region, which led to the collapse of the economic systems adopted by the countries. Which caused a deficit in their budgets for this and, and in light of the relentless pursuit of accepting the least loss, these countries began looking for legal solutions through which they could reduce the effects of the financial deficit and also at the same time try to limit negative phenomena by controlling them and trying to control, reduce or tame them by legal means, which reflects the prestige of the state. Discussions took place among many jurists in some Arab countries to try to legalize cannabis cultivation or not by confronting two trends. The first is that which supports this project or idea by opening the legislative door wide open to access legalized cannabis in a medical and humane method that aims to protect people instead of eliminating it. According to what is seen by the other side, which has tended to consider that such propositions do not fit with those societies, especially Muslim ones that follow the teachings of Islam, because this is contrary to Sharia and religion and because it undoubtedly leads to the collapse of the human being and society and the spread of corruption among the categories of individuals of those countries, provided that this And that from both directions did not prevent politicians and lawmakers in those countries from serious attempts at the level of adopting legal cannabis for its frequent use in medical fields and industrial purposes, although this would be following controls and procedures taken by those countries to legitimize such a measure and at the same time emphasize the international legal principles agreed upon between states.

IMDC-IST 2021, September 07-09, Sakarya, Turkey
Copyright © 2022 EAI
DOI 10.4108/eai.7-9-2021.2314921

To confront the phenomenon of drugs or to encourage them. The economic conditions that the world suffers from has led to some of those countries attempting to adopt the Western approach by legislating a law that recognizes cannabis and cultivates it in a way that secures a decent life for citizens and limits the increasing spread of the drug phenomenon, or reduces or limits it by legal means [1]. To achieve an economic recovery to adopt the cultivation of hemp and generate revenues from it, in addition to its use by roads According to the legal drivers used in those who used to legalize that material or cultivate it in a way that guarantees the higher values that prevail in it. The rejectionist trend and the trend in favour of legalizing cannabis with all its supporters or opponents formed a fertile ground for the jurists to address such a topic and try to explore its folds neutrally. Who tried to shed light on the legislation that regulated this aspect and to know the extent of the possibility of adopting such a legislative measure or not? It was necessary to adopt the historical approach to describe the previous historical events of countries that adopted such an idea in addition to the comparative approach by comparing the contexts followed in other countries and which implemented this legislative vision or not.

2 What is Cannabis?

In this proposal, we try to define cannabis by stating the most important countries in which it has spread and what definitions have dealt with it in medical, legal, and jurisprudential terms. The first requirement introducing cannabis (Cannabis Indica). Hemp is known as the Indian, marijuana, a plant that has a narcotic effect, and it also has effects on the body. One of the most used types of drugs in the world. Hemp products belong to the oldest known drugs, and hemp is, the name of the plant, while marijuana is the leaves, flowers, stems, and dried seeds of the hemp plant, while hashish is another product from the hemp plant that contains gum. (Abdel-Ghani, 2011, p. 10) Hemp and cannabinoids contain many substances, but the most important one is delta tetrahydrocannabinol, commonly known as THC. When a person smokes marijuana or hashish, THC passes quickly from the lungs into the bloodstream, which carries it to the brain and other organs throughout the body, according to the National Institute of Drug Abuse in the United States and the National Institutes of Health in the US Department of Health. THC acts on specific receptors in brain cells that normally interact with natural chemicals like THC. These natural chemicals play a role in normal brain development and function. Marijuana over-activity in the parts of the brain that contain the largest number of these receptors, and this causes a person to feel euphoric the use of cannabis and its products is addictive, and research indicates that between 9 and 30% of those who use marijuana may develop some degree of addiction. An Australian scientist warned in 2014 in his published research that cannabis damages the brain and leads to severe addiction, as one out of every six adolescents who use it become addicted, which carries the risk of harm to their brains and doubles their risk of developing schizophrenia, a mental illness. Wayne Hall, professor of addiction policy at London Kings College, a research university in the British capital, said that young people who abuse cannabis do less at school than their peers who do not [2]. They abuse this substance, and those who drive under the influence of cannabis have a double risk of colliding with others. Hall's research, published in Edition magazine, dispels the myth that smoking marijuana is not dangerous and is a safe alternative to cigarettes and hard drugs. Hall - who also heads the University of Queensland's Centre for Research on Young Substance Abuse and Drug Abuse - said it is likely that one in ten regular cannabis smokers will take a stronger drug. He added that the risk of taking stronger drugs rises to one in six young adults who start using cannabis in their teens. On the other hand, there are medical uses for cannabis, in Germany, hemp has been used since 2011 to prepare medical prescriptions based on special permits obtained by the German Institute of Medical Materials and Medicines. Medical

laboratories prepare medicines mixed with cannabis, which are taken in the form of drops that travel through the mouth and quickly into the patient's blood. Studies show the good effect of cannabis on some diseases. Although it does not completely cure the disease, it reduces the pain intensity and the degree of suffering of the patients [3].

3 Cannabis Cultivation

Hemp remains the most widely cultivated drug crop, which was reported by 129 countries over the period 2009-2014, far more than the 49 countries that reported the cultivation of opium poppy. Countries (mostly in Asia and the American continent), and the 7 countries that reported coca cultivation (7 countries) are [4]: (On the American continent). Regardless of the disparity in the number of countries that grow both opium poppies and coca, the cultivation of opium poppy decreased in the past year while the cultivation of coca increased. Cannabis also remains the most popular drug trafficked globally, and there has been a significant increase in seizures of synthetic drugs. Although there were 234 substances under international control in 2014 - 244 articles in January 2016), the bulk of trafficking (based on drug seizures that embody both law enforcement activities and the flow of drugs) is concentrated in a smaller number. Far from Materials. Cannabis in its various forms was intercepted in 95 percent of reporting countries in 2014 and accounted for more than half of the drug seizures reported to the United Nations Office on Drugs and Crime. The year, with several 2.2 million, is followed by ATS and opioids and substances related to coca. In all countries, more men (90 percent of the total, on average) who are formally represented before the criminal justice system for drug trafficking or possession of drugs for personal use exceed the number of women who are for the same reasons. However, the reporting of sex-disaggregated data has improved over the years, and it shows an increase in the number of women arrested for drug-related offenses in absolute numbers. Nevertheless, despite the fluctuation of the proportion of women in drug-related arrests, that percentage moved in a downward trend over the period 1998-2014, particularly related crimes [5]. Despite significant changes in some regions, global consumption of cannabis has remained largely stable in recent years with a noticeable increase in drug users.

4 The Legal Regulation of Cannabis Cultivation

The topic deals with the legal regulation of cannabis cultivation in European countries, then in Arab countries, as follows [6]. The issue of drugs and drug addiction is considered one of the living and fundamental issues of concern to the international community as a whole, and perhaps this international interest in this issue is not born today but extends back hundreds of years, and if you wish, then fewer thousands of years, as the ancient Egyptians used cannabis to help them work and produce, as they used Opium (poppy) helped calm hyperactive children, and after that, people used drugs With its different types, whether natural, such as cannabis (hashish) and poppy (opium), and the uses varied between those used in the absence of the mind, loss of balance, and the achievement of false and fleeting ecstasy There is no doubt that the increase in global addiction rates is due, in one way or another, to the weakness of the foundations necessary to curb the illicit trade in narcotic drugs and psychotropic substances, such as the international community or the internal societies of the world countries Hence, the drug problem has become one of the most important problems that the international community is dealing with, whether in the United Nations Organization or the League of Arab States. This is in addition to the efforts made by each country alone or through its bilateral cooperation with

another country, or multilateral cooperation between countries. The chapter on adherence to international agreements and to make joint efforts in the field of drug control and prevention, to achieve effective control over them, in addition to imposing tight control on cannabis to prevent its leakage for illicit use or the manufacture of narcotic drugs and psychotropic substances [7]. Therefore, we will divide this issue into the regional side in the fight against drugs (hashish) and the local side in this matter. The first requirement is regional organization: The Arab Convention for Combating Illicit Traffic in Narcotic Drugs and Psychotropic Substances was concluded for the year 1994 to strengthen Arab cooperation to address the drug problem in all its aspects. Arab efforts coordinated with international efforts in the field of combating narcotic drugs and psychotropic substances and controlling chemical precursors The Arab anti-drug agencies are as follows [8]:

1. The Council of Arab Interior Ministers: It works under the umbrella of the Arab League, and one of its most important achievements is a - Unified Arab model law for combating drugs that have not yet been implemented.
2. The Arab strategy to combat the illicit use of narcotic drugs and psychotropic substances.
3. The Guiding Model Arab Law for Combating Money Laundering
4. The Guiding Model Arab Law for Combating Drug Crimes Committed via the Internet

The Arab Office for Narcotics Affairs: Coordinates Arab efforts in the field of combating drugs within the framework of the 1994 Arab Agreement to Combat Illicit Traffic in Narcotic Drugs and Psychotropic Substances. The Arab Conference of Heads of Drug Control Agencies and its sub-groups. This conference is held annually and discusses the drug problem in Arab countries and ways to effectively address it. Three sub-working groups are divided into each group, which includes several neighbouring Arab countries with similar actors facing similar solutions to the drug problem. As for the control mechanisms that can be detected through the information and data that have been analysed, it is noted that all countries participating in this project have a department specialized in combating narcotic drugs and psychotropic substances and their trafficking. In most cases, it is a department within the security services of the Ministry of Interior. Where we can attribute the inclination of states to establish this specialized apparatus to the seriousness of the crime of illicit trafficking in narcotic drugs and psychotropic substances and the sheer volume of funds and networks that are used to commit them, which requires a cadre commensurate with this severity and size and specialization in the operations of prosecution, seizure, and evidence, and to provide these entities with the capabilities. The Arab countries had a position rejecting the cultivation and trade of cannabis according to the agreements concluded, and there is almost agreement to prevent this, but some of those countries, in light of the economic developments, began searching for a new source of revenue, including Morocco Where a law was put in place regulating the cultivation of cannabis, and in light of the economic needs, other countries began to demand, by their policies, the enactment of a law to regulate the cultivation of cannabis, including Lebanon, to meet the economic and health situation in the country, As for the Arab Gulf states, they refused that, including Iraq.

5 Local Organizations (Iraq)

Iraq, like other Arab countries, faced the drug problem before 2003, as a statistic of the Ibn Rushd Psychiatric Hospital in Baghdad showed that there were 3 drug addicts out of every 10 individuals in Iraq. Iraqi youth after 2003, according to its reports, and the statistics of the bureau did not record only two cases as drug trafficking only between 1970 and 1990, but after the entry of the American forces into the country, the security course changed dramatically, and imaginary numbers were recorded. This is because the United Nations report showed that out of every ten people between the ages of 18-30 years of age, three are addicted and that one out of every three members of the security forces takes a drug, and the reason for this is the lack of follow-up, awareness and treatment centres, as well as a low penalty rate. As for the present time, the penalty for drug traffickers is approximately 6 months, in addition to the fact that most of the dealers are supported by capable bodies in the state. It reveals that the statistics of outpatient clinics in government hospitals in 2009 indicated that 10% of the number of addicts to alcohol and psychotropic medicinal pills reached 2017, with about 320 people lying in hospitals [9].

According to the latest statistics of the Supreme National Commission for Drug Control, there are more than 7000 cases of addiction in Iraq, including cases of addiction to narcotic pills. Thus, Dr. Aqil Al-Sabbagh, Director of Mental Health in the Basra Health Department, says, “Narcotic pills were misused by some young people, so they used them as narcotic substances. Cheap and easy to get. " Concerning the Iraqi Narcotics Law issued on 2017, No. 50, we see that it emphasized the criminalization of drugs of all kinds, including hashish, as this law affirmed the establishment of a national body dealing with drugs, which is the Supreme National Authority for Narcotics and Psychotropic Substances in Article (3) of Law No. (50) For the year 2017, it shall be located in the Iraqi Ministry of Health and shall be specialized following the provisions of Article (5) with the following: Setting a general policy for importing any kind of drugs, including production and agriculture, and coordination and cooperation between ministries and competent authorities in this regard. A comprehensive national strategy to combat non-trafficking is also being developed. The drug project and preparing plans and programs for their implementation in the region and governorates that are not organized in a region through local committees that are formed in each governorate and region what is noticeable in the text of the previous article is that it depends on cooperation and coordination, uniting efforts and urging cooperation with civil society organizations to confront this phenomenon, even if that is in return for financial support, but that has not been achieved on the ground, especially about cooperation with civil society organizations, as for what is related to coordination And uniting efforts, this matter is related to the formation of committees that will result in sub-committees that try to achieve that cooperation for the success of this goal, which is the elimination of this phenomenon. The law also stipulated that a directorate shall be established in the Ministry of Interior called (the General Directorate of Narcotic Drugs and Psychotropic Substances) headed by an officer with experience and competence to undertake the following:

"Combating and controlling narcotic substances and cooperating with the Arab Office for Drug Affairs and with its counterparts in other countries and with international and regional bodies specialized in narcotic drugs and psychotropic substances, and with the International Criminal Police Organization (Interpol) about the prosecution of the perpetrators of the crimes of illicit drug trafficking and monitoring the offenders according to this law By importing, exporting, transporting, manufacturing, or possessing narcotic drugs or psychotropic substances to ensure their obligations within the limits of specified controls [10].

The law also stipulated that “a police directorate shall be established in each governorate at the level of a department headed by an experienced and competent officer specialized in the affairs of combating narcotic drugs and psychotropic substances. The keenness of the Iraqi legislator to restrict the spread of drugs in Iraq, but in light of the Iraqi legislative developments, which are among the most important of them Preventing the import, sale, circulation, and manufacture of alcoholic beverages, as this would encourage the spread of drugs that could be obtained from pharmacies in light of the chaos in some cities or the lack of control over the work of pharmacies despite the tightening of the Narcotic Law No. 50 of 2017 on how to sell narcotic substances by pharmacists, However, reality indicates the opposite of these measures, They are supposed to be available to achieve this cooperation between the government, pharmacists, doctors, stores and all the authorities working in nursing to prevent the spread of drugs of all kinds [11].
Through studying the law, it becomes clear to us that the Iraqi legislator has explicitly stated in the text of Article (23) thereof that it is not permissible to cultivate, import, export, possess, acquire, possess, purchase, sell, transfer, deliver, exchange, or assign plants that are produced. They contain narcotic drugs or psychotropic substances stipulated in the first schedule attached to this law in all stages of their growth, their seeds, exchange with them, or mediating anything of that except for medical or scientific purposes and in the circumstances the conditions stipulated in this law and the circumstances. Coca, khat, and plants that contain this are genetically modified, which have the same effect as the drug. As for the second chapter, the law dealt with penalties, including the text of Article (27) thereof (punishable by death or life imprisonment) whoever commits one of the following acts: Third: He planted a plant that produces narcotic substances or m) mental wealth, or imports or brings or export a plant of these plants at any stage of their growth to trade them or trade their seeds in other than the cases permitted by law)

6 Conclusion

Through the previous presentation, it becomes clear to us that the Arab countries have tried to cooperate to combat the phenomenon of the spread of hashish or cultivation, but the reality is now, and in light of the austerity that most Arab countries are experiencing, some of them have begun trying to find sources of public income by trying to ask the legislative authority to legalize A law permitting the trade in cannabis or cultivation, provided that the purpose of that is a medical purpose or personal possession, as is the case in Lebanon, which has begun trying to legalize this. Also, Egypt has raised voices while calling for the legalization of cannabis-based on the financial returns that result from cultivating or trading it that It was via the legitimate routes in the country; This case, which we presented in the last lines, is true, as it represents a major development in politics This would lead some to demand a law to allow prostitution or law to allow the arms trade.

The most important results we reached:

1. Many Arab countries considered the cultivation of hemp, especially medical hemp, among the most important financial resources that could be relied upon in the future to advance the economic reality of developing countries.
2. The Arab countries varied among themselves in this regard, some of them accepted the idea and accepted it, and some rejected it under the pretext of promoting drugs.

3. Some of the Arab countries have accepted this idea and accepted it as a fait accompli.
4. Others, and the other side of the world, rejected this idea but went so far as to criminalize such topics as they are contrary to what is stipulated in their constitution.

Through the previous results, we conclude the following:

1. There is no doubt that the acceptance of drug cultivation constitutes a precedent that is unknown in the countries of the Arab world, which means taking risks or accepting to proceed in contrast to the legislative policy of those countries.
2. The countries that accepted this idea and went to legalize it are considered countries that are more civilized and accepting of democracy, even if entering this field came as a matter of therapeutic purposes.
3. Acceptance of cannabis cultivation will lead to the spread of drugs in countries of the world or especially in the country that adopts agriculture in its laws, and this has both positive and negative aspects. The positive aspects are the elimination of the illegal trade of such acts and an attempt to legitimize those actions. The negative answer is that. This is represented by the spread of the drug phenomenon, which entails the spread of illegal trade in addition to the proliferation of weapons, which leads to crimes that devastate people.
4. We may find other countries join the list of countries that support the idea of growing or trading hemp in the future in light of the difficult economic conditions that are suffering, especially in light of the Corona epidemic.

References

[1] Weybright EH, Caldwell LL, Xie H, Wegner L, Smith EA. Predicting secondary school dropout among south african adolescents: A survival analysis approach. South African journal of education. 2017;37(2):1-11.

[2] Adinoff B, Reiman A. Implementing social justice in the transition from illicit to legal cannabis. The American journal of drug and alcohol abuse. 2019;45(6):673-88.

[3] Bodwitch H, Carah J, Daane K, Getz C, Grantham T, Hickey G, et al. Growers say cannabis legalization excludes small growers, supports illicit markets, undermines local economies. California Agriculture. 2019;73(3):177-84.

[4] Dei Cas M, Casagni E, Saccardo A, Arnoldi S, Young C, Scotti S, et al. The italian panorama of cannabis light preparation: Determination of cannabinoids by lc-uv. Forensic science international. 2020;307:110113.

[5] El-Khoury J, Bou Khalil R, Nemer A, Richa S. Legalizing medical cannabis in lebanon: The complex interface between medicine, law, ethics, and economics. Cannabis and Cannabinoid Research. 2020.

[6] Feinstein BA, Dyar C, London B. Are outness and community involvement risk or protective factors for alcohol and drug abuse among sexual minority women? Archives of Sexual Behavior. 2017;46(5):1411-23.

[7] Luo X, Reiter MA, d'Espaux L, Wong J, Denby CM, Lechner A, et al. Complete biosynthesis of cannabinoids and their unnatural analogues in yeast. Nature. 2019;567(7746):123-6.

[8] Muchiri BW, Dos Santos MM. Family management risk and protective factors for adolescent substance use in south africa. Substance abuse treatment, prevention, and policy. 2018;13(1):1-10.

[9] Nurzyńska A. International cooperation in combating organized crime. World Scientific News. 2018;106:105-16.
[10] Omelchuk O, Shekhovtsova L, Bodunova O, Lukasevych-Krutnyk I, Yanishevska K, Plutytska K. Criminal-legal and criminological research of illicit trafficking in narcotic drugs and their analogues with the use of computer technologies. International Journal of Management (IJM). 2020;11(6).
[11] Wang Z, Yang X, Zhang X. Relationships among boredom proneness, sensation seeking and smartphone addiction among chinese college students: Mediating roles of pastime, flow experience and self-regulation. Technology in Society. 2020;62:101319.

Visual Materials and their Impact on Students' Achievement during Virtual Learning

Baan Jafar Sadiq[1]
{ban@copew.uobaghdad.edu.iq[1] }

College of Education for Women/ Baghdad University[1]

Abstract. Visual materials are tools that could help the teachers in class to manufacture the necessary knowledge for effective and delightful teaching. The current research has used visual materials and investigated experimentally their impact on students' achievement in teaching English as a Foreign Language during the virtual learning of pandemic of Covid-19. The sample of the research is 64 students at the College of Physical Education and Science Sport for Women/Baghdad University which they are divided into two groups, the experimental is taught according to the visual materials (Sadiq, 2019) while the second one is taught by using the traditional textbook only (Abdul- Razzaq& Al-Mufti, 1987). After three months, the results of the pre and post-tests are analyzed statistically. And the results are revealed that there is a significant difference for the visual materials group. Therefore, it is indicated using visual materials in English foreign teaching is effective as a tool for presenting printing materials.

Keywords: Visual materials, Students' achievement, EFL, ESP, Virtual learning.

1 Introduction

1.1 The Problem and Its Significance

Visual materials are utilized in this research as a tool for teaching EFL which might help English lecturers to present knowledge with variegated, pleased and effective in school to create the teaching go easily and smoothly to all or any students furthermore teachers. This research has answered that visual materials have an impact on students' achievement. Because a variety of studies show that the utilization of visual materials is regarded as a useful means to motivate learners, arouse their interest, and expose them to life situations. Aisyah, Atmaja1, & Gina, Sonia [1] have used flashcards in teaching vocabulary while the present research is vocabulary and dictation. Students are tormented by many sports and their meaning in Arabic so this research is exposed to the scholars for another textbook.
Nowadays, English teachers are concerned about preparing students for world situations in the classes. Therefore, like other teachers around the world, teachers have to implement active teaching materials, to assist the students to learn English better [2].

IMDC-IST 2021, September 07-09, Sakarya, Turkey
Copyright © 2022 EAI
DOI 10.4108/eai.7-9-2021.2314784

1.2 Aim of the Research

Exploring experimentally the Visual Materials and their impact on student's achievement is the aim of the research.

1.3 Hypothesis of the Research

It is assumed that there are not any statistically significant differences between the experimental group who taught English by visual materials [3] and the control group who taught English by the textbook only [4].

1.4 Limits of the Research

The research is limited for the following:
Using the visual materials in English foreign language teaching.
Students at College of Physical Education and Sciences Sport for Women.
The educational year 2020-2021.

1.5 Definition of Basic Terms

Visual Materials:
Richards &Schmidt [5] define visual materials as “the use of materials that weren't originally developed for pedagogical purposes, like the utilization of magazines, newspapers, and advertisements. Such materials are often thought to contain more realistic and natural samples of language use than those found in textbooks other specially developed teaching materials”
According to Herod [6] states that visual materials and activities are designed to imitate important world situations.
Jacobson et al [7] see visual materials as printed materials, which are utilized in classrooms in the same way they might be employed in the world.

2 Method of the Research

2.1 The Experimental Design

An experiment design with two groups pre- post-tests design has been implemented to achieve the aim of the research as well as to identify whether visual materials are efficient in teaching English or not. Thus, The control group has taught according to the current textbook [4], while the experimental group has taught by using the visual materials using [3] as shown in Table 1.

Table 1. Experimental Design.

Experimental group	Pre-test	Independent variable Visual Materials (Sadiq, 2019)	Post-test

Control group	Pretest	Textbook (Abdul- Razzaq& Al-Mufti, 1987)	Post-test

2.2 Population and Sample Selection

The first-year stage at the College of education and Sciences Sport for Women at the educational year 2020-2021 is randomly chosen to represent the sample of the research. The full population of the research is 121 while the number of the sample is 64 divided into 31 as an experimental group, and 33 as the control group, thus it means the sample of the research is representative one as shown in Table 2.

Table 2. Number of Subjects before and after Excluding the Repeaters.

Group	Section	No. of Subject before excluding	No. of Subject After Excluding
Experimental group	C	34	31
Control group	A	35	33
Total		69	64

2.3 Equalization

Equalization of the sample in age and pre-test is made to ensure accuracy of the results of the research, as shown in Table 3 for statistics of equalization of the two groups in age and Table 4 for t-test statistics of equalization between the two groups in pre-test variables.

Table 3. The T-test Statistics of Equalization between the two Groups in Age.

Group		No. Students	X Mean	S.D	Degree of Freedom	T Value	
						Calculated Value	t-distribution
Pre-test	E.	31	20.36	1.410	62	0.425	1.98
	C	33	20.19	1.364			

Table 4. The T-test Statistics of Equalization between the Two Groups in Pre Test.

Group		No. Students	X Mean	S.D	Degree of Freedom	T Value	
						Calculated Value	t-distribution
Pre-test	E.	31	6.483	1.411	62	1.208	1.98
	C	33	6.969	1.793			

The mean score of the two groups in age is 20.36 for the experimental group while 20.19 for the score of the control group. The mean scores of the two groups in the pre-test are compared; the mean scores of the experimental group are 6.483, while the mean scores of the control group are 6.969 which indicates that there is no significant difference between the two groups in age and pretest.

2.4 Instructional Material

The teacher herself has taught both groups with two different textbooks [4] "A Course in English for Colleges of Physical Education" (see Appendix 4) for the control group, while [3] (See Appendix 3) for the experimental group.
The important thing in teaching education is introducing the scholars to sports and games in English. Therefore, the traditional textbook introduces games as a listing of words and their translation in Arabic, the scholars suffer from memorizing long lists of words and their spelling. Thus, they forget the spelling and also the game itself. So, to resolve this problem the scholars have handed printed pictures materials regarding the games. the coed has a good basis of data about the sports within the world, classify these sports as water games, strength games, target games, animals games, racket games, gymnastics games, cycling games, and so on). similarly, scholars have brought more pictures and charts to introduce games. The whole period of the experiment has lasted two months (first course) (1/12/2020- 1/2/2021).

2.5 The Written Test

The examiners are exposed to post-test including three questions as is shown in appendix (2) which it is tested the students' abilities in writing, spelling, and general information about games and sports also, it is contained recognizing the sport, complete the missing letters of the games and re-ordering the letters of the games and the test is scored out of twenty-five marks. The test is exposed to jury members for insurers its validity as well for reliability Person formula has been used to find out the correlation coefficient; the results show that the correlation coefficient of reliability is (+ .872) and this is considered a high stable correlation [8].

3 Results

To clarify whether there is a significant difference between pre and post-tests of students' achievement of a sample, the results have been analyzed. (Appendix 1)

3.1 Assessment of the Post-Tests

The mean score of the experimental group is 14.774, while the mean score of the control group is 8.393 which reveals that there is a statistically significant difference at the level of 0.05 and degree 62. Accordingly, the hypothesis is excluded. This could be explained by using the visual materials in teaching the experimental group. Thus, the visual materials are more efficient in teaching English than the current textbook as shown in Table 5.

Table 5. T-test of the two groups in post-test.

Group		No. Students	X Mean	S.D	Degree of Freedom	T Value	
						Calculated Value	t-distribution
Post-test	E	31	14.774	3.461	62	7.601	1.98

	C	33	8.393	3.239			

3.2 Discussion of the Results

The high scores of the experimental group could be explained to the following points:

- Visual materials are pleasant rather than a printed textbook.
- the students are motivated when they are used visual materials.
- The visual materials are accurate than the current textbook.
- The visual materials are recalled than the printed ones.

The research is going in parallel with [1] that flashcards are effective in teaching vocabulary.

4 Conclusion and Recommendation

The results which are revealed show the effectiveness of the proposed textbook therefore, Colleges of Physical Education and Sciences Sport are recommended to use visual materials in teaching English rather than printed textbooks, especially with virtual learning.

References

[1] Aisyah, Atmaja1, & Gina, Sonia . Using Flash Cards To Improve Students' Vocabulary: PROJECT (Professional Journal of English Education) Volume 3, No. 2, March 2020.
[2] Martinez, A.G. (2002). Visual materials. An overview. Free resources for teachers and students of English, Karen's Linguistics Issues, 1-7.
[3] Sadiq, Baan (2019) Sport: Write & Learn. Baghdad: Waghdy Publishing. ISBN: 978-9922-9260-0-1.
[4] Abdul- Razzaq& Al-Mufti (1987) A Course in English for Students in the Colleges of Physical Education. Baghdad: University of Baghdad Press.
[5] Richards, J. &Schmidt, R (2002) Dictionary of Language Teaching & Applied Linguistics. 3rd ED. London: Pearson Education.
[6] Herod, L. (2002). Adult learning from theory to practice. Heinle and Heinle Publishers. Heinemann.
[7] Jacobson, E., Degener, S., & Purcell-Gates, V., (2003). Creating visual materials and activities for the adult literacy classroom: A handbook for practitioners. USA: NCSALL.
[8] Valette, R.(1977) Modern Language Tests. 2nd Ed. New York: HarcoutBrance.

Proceedings of 2nd International Multi-Disciplinary Conference Theme: Integrated Sciences and Technologies

7-9 September 2021, Sakarya, Turkey

IMDC-IST 2021

Copyright © 2022 EAI, European Alliance for Innovation

www.eai.eu

https://www.imdc-sdsp.com/

ISBN: 978-1-63190-340-3

European Alliance for Innovation

EAI is a non-profit organization with free membership and the largest open professional society for advancing research careers through community collaboration and fair recognition. Members benefit from finding feedback and mentorship for their work and they are guaranteed to be evaluated fairly, transparently, and objectively through community.

ISBN: 978-1-63190-340-3

ISSN: 2593-7642

http://eudl.eu/series/CORE | www.eai.eu